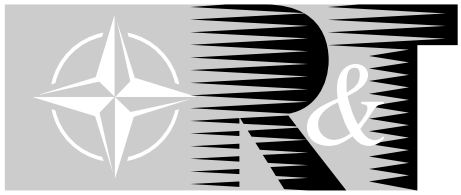
RTO-MP-051
AC/323(AVT-048)TP/35

RTO-MP-051

NORTH ATLANTIC TREATY ORGANIZATION

© RTO/NATO 2001
Single copies of this publication or of a part of it may be made for individual use only. The approval of the RTA Information Policy Executive is required for more than one copy to be made or an extract included in another publication. Requests to do so should be sent to the address below.



RESEARCH AND TECHNOLOGY ORGANIZATION

BP 25, 7 RUE ANCELLE, F-92201 NEUILLY-SUR-SEINE CEDEX, FRANCE

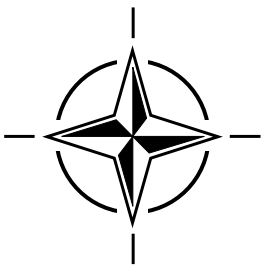
Note: There is an Addendum to this publication containing the PowerPoint presentations.

RTO MEETING PROCEEDINGS 51

Active Control Technology for Enhanced Performance Operational Capabilities of Military Aircraft, Land Vehicles and Sea Vehicles

(Technologies des systèmes à commandes actives pour l'amélioration des performances opérationnelles des aéronefs militaires, des véhicules terrestres et des véhicules maritimes)

Papers presented at the Symposium of the RTO Applied Vehicle Technology Panel (AVT) held in Braunschweig, Germany, 8-11 May 2000.



Published June 2001

Distribution and Availability on Back Cover

Form SF298 Citation Data

Report Date *("DD MON YYYY")* 00062001	**Report Type** N/A	**Dates Covered (from... to)** *("DD MON YYYY")*

Title and Subtitle Active Control Technology for Enhanced Performance Operational Capabilities of Military Aircraft, Land Vehicles and Sea Vehicles	**Contract or Grant Number**
	Program Element Number
Authors	**Project Number**
	Task Number
	Work Unit Number
Performing Organization Name(s) and Address(es) Research and Technology Organization North Atlantic Treaty Organization BP 25, 7 rue Ancelle, F-92201 Neuilly-sur-Seine Cedex, France	**Performing Organization Number(s)**
Sponsoring/Monitoring Agency Name(s) and Address(es)	**Monitoring Agency Acronym**
	Monitoring Agency Report Number(s)
Distribution/Availability Statement Approved for public release, distribution unlimited	
Supplementary Notes	
Abstract	
Subject Terms	
Document Classification unclassified	**Classification of SF298** unclassified
Classification of Abstract unclassified	**Limitation of Abstract** unlimited
Number of Pages 1032	

REPORT DOCUMENTATION PAGE

1. Recipient's Reference	2. Originator's References	3. Further Reference	4. Security Classification of Document
	RTO-MP-051 AC/323(AVT-048)TP/35	ISBN 92-837-0018-X	UNCLASSIFIED/ UNLIMITED

5. Originator Research and Technology Organization
North Atlantic Treaty Organization
BP 25, 7 rue Ancelle, F-92201 Neuilly-sur-Seine Cedex, France

6. Title

Active Control Technology for Enhanced Performance Operational Capabilities of Military Aircraft, Land Vehicles and Sea Vehicles

7. Presented at/sponsored by

the Symposium of the RTO Applied Vehicle Technology Panel (AVT) held in Braunschweig, Germany, 8-11 May 2000.

8. Author(s)/Editor(s)	9. Date
Multiple	June 2001
10. Author's/Editor's Address	**11. Pages**
Multiple	950 (text) 82 (slides)

12. Distribution Statement There are no restrictions on the distribution of this document. Information about the availability of this and other RTO unclassified publications is given on the back cover.

13. Keywords/Descriptors

Flight control	Fluid dynamics	Structural design
Control equipment	Hydraulic jets	Combustion control
Boundary layer control	Nozzles	Combustion stability
Flow control	Thrust vector control	Aerodynamic stability
Aerodynamic characteristics	Drag	Compressors
Military aircraft	Buffeting	Stalling
Gas turbines	Noise reduction	Surges
Helicopters	Vortices	Smart structures
Aircraft engines	Loads (forces)	Smart materials
Performance		

14. Abstract

The Symposium analysed the potential of active control technology for the performance demands of future vehicles and engines, in particular high manoeuvrability, lower specific fuel consumption, higher power-to-weight ratios and lower life-cycle cost. Performance, stability, control, fluid dynamics, structural and engine layout questions were dealt with in 5 keynotes and 77 papers. The following sessions were held:

– Boundary Layer Control
– Active Flow Control of Nozzle/Jet
– Drag and Buffet Control
– Noise Control
– Vortex Control
– Flight Vehicle Active Control
– Smart Structures Applications
– Active Control Technology For Load Alleviation
– Active Elements for Structural Design
– Active Materials and Applications
– Applications Overview
– Compressor Stall/Surge - Measurements
– Compressor Stall/Surge - Control
– Combustion Instabilities - Measurements and Predictions
– Combustion Instabilities - Control Fundamentals
– Combustion Instabilities - Control Applications

The Symposium was organised by the Applied Vehicle Technology Panel (AVT).

This page has been deliberately left blank

Page intentionnellement blanche

RTO-MP-051
AC/323(AVT-048)TP/35

NORTH ATLANTIC TREATY ORGANIZATION



RESEARCH AND TECHNOLOGY ORGANIZATION

BP 25, 7 RUE ANCELLE, F-92201 NEUILLY-SUR-SEINE CEDEX, FRANCE

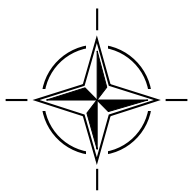
Note: There is an Addendum to this publication containing the PowerPoint presentations.

RTO MEETING PROCEEDINGS 51

Active Control Technology for Enhanced Performance Operational Capabilities of Military Aircraft, Land Vehicles and Sea Vehicles

(Technologies des systèmes à commandes actives pour l'amélioration des performances opérationnelles des aéronefs militaires, des véhicules terrestres et des véhicules maritimes)

Papers presented at the Symposium of the RTO Applied Vehicle Technology Panel (AVT) held in Braunschweig, Germany, 8-11 May 2000.



The Research and Technology Organization (RTO) of NATO

RTO is the single focus in NATO for Defence Research and Technology activities. Its mission is to conduct and promote cooperative research and information exchange. The objective is to support the development and effective use of national defence research and technology and to meet the military needs of the Alliance, to maintain a technological lead, and to provide advice to NATO and national decision makers. The RTO performs its mission with the support of an extensive network of national experts. It also ensures effective coordination with other NATO bodies involved in R&T activities.

RTO reports both to the Military Committee of NATO and to the Conference of National Armament Directors. It comprises a Research and Technology Board (RTB) as the highest level of national representation and the Research and Technology Agency (RTA), a dedicated staff with its headquarters in Neuilly, near Paris, France. In order to facilitate contacts with the military users and other NATO activities, a small part of the RTA staff is located in NATO Headquarters in Brussels. The Brussels staff also coordinates RTO's cooperation with nations in Middle and Eastern Europe, to which RTO attaches particular importance especially as working together in the field of research is one of the more promising areas of initial cooperation.

The total spectrum of R&T activities is covered by the following 7 bodies:

- AVT Applied Vehicle Technology Panel
- HFM Human Factors and Medicine Panel
- IST Information Systems Technology Panel
- NMSG NATO Modelling and Simulation Group
- SAS Studies, Analysis and Simulation Panel
- SCI Systems Concepts and Integration Panel
- SET Sensors and Electronics Technology Panel

These bodies are made up of national representatives as well as generally recognised 'world class' scientists. They also provide a communication link to military users and other NATO bodies. RTO's scientific and technological work is carried out by Technical Teams, created for specific activities and with a specific duration. Such Technical Teams can organise workshops, symposia, field trials, lecture series and training courses. An important function of these Technical Teams is to ensure the continuity of the expert networks.

RTO builds upon earlier cooperation in defence research and technology as set-up under the Advisory Group for Aerospace Research and Development (AGARD) and the Defence Research Group (DRG). AGARD and the DRG share common roots in that they were both established at the initiative of Dr Theodore von Kármán, a leading aerospace scientist, who early on recognised the importance of scientific support for the Allied Armed Forces. RTO is capitalising on these common roots in order to provide the Alliance and the NATO nations with a strong scientific and technological basis that will guarantee a solid base for the future.

The content of this publication has been reproduced
directly from material supplied by RTO or the authors.

Published June 2001

Copyright © RTO/NATO 2001
All Rights Reserved

ISBN 92-837-0018-X

Printed by St. Joseph Ottawa/Hull
(A St. Joseph Corporation Company)
45 Sacré-Cœur Blvd., Hull (Québec), Canada J8X 1C6

Active Control Technology for Enhanced Performance Operational Capabilities of Military Aircraft, Land Vehicles and Sea Vehicles

(RTO MP-051 / AVT-048)

Executive Summary

The performance demands of future vehicles and engines are becoming increasingly challenging with the trends to high manoeuvrability, lower specific fuel consumption, higher power-to-weight ratios and lower life-cycle cost. Conventional design including passive control has brought vehicle technology to its present high level and in many cases has reached the limits. Active control technology is aimed at enhancing system behaviour by controlling dynamics of processes such as: vibrations, structural deformation, combustion, flow instabilities, noise, etc. It is becoming one of the most important aspects of vehicle design and operation, having in some cases potential of retrofit as well. Tools of a new quality offer improvements in the behaviour of overall systems as well as in sub-domains. To be mentioned are computer technology, sensors and actuators, micro-mechanic technology (MEMS), smart materials, supported by innovative manufacturing technologies, and the improved insight into process laws. Smaller, more efficient, more powerful, and more integrated, solutions are becoming possible. The potential exceeds by far that which can be achieved nowadays by careful system design and the use of passive components, and while the application is possible and of advantage in all kinds of vehicles, land, air, and sea, civil as well as military, the most interesting overall advances have been made so far in air vehicles and in some specific areas in propulsion generally.

The engine including the inlet and exhaust, and the engine subsystems have their control systems in addition to the flight control system of the overall aircraft. The Symposium concentrated specifically on the compressor and the combustors of the gas turbine. Active control in these areas has been proven to be feasible in laboratory as well as in full scale engines, and there is a high potential of early application in particular in land vehicle engines aiming at lower emission levels of noise as well as toxicants. Active control stabilisation of flows permits for example higher pressure ratios which in the end can translate into smaller engines. Another consequence which in view of the better performance possible is often overlooked is the reduction on overall life cycle cost, savings in maintenance and damage due to better control and diagnostics offsetting the higher initial investment.

In fluid dynamics it is now possible to control boundary layer and vortex-flow over vehicles or inside engines. Control of flight attitude by influencing boundary layers and vortices has been proven as being possible, avoiding the use of - energy and weight consuming - control surfaces, and may find their first wide spread application in uninhabited and small or micro vehicles. Flutter and buffet can be avoided, as well as unnecessary high loads in manoeuvres. The application in active lift devices in particular for air vehicles such as STOVL fighters and the utilisation of active control in vectoring nozzles are other areas in which active control has proven its importance. Fluid dynamics application in the water vehicle environment were not treated and are usually strictly confidential. Missile application could as well only be mentioned once.

Last not least there is a high potential in structural applications. Two major roads are the introduction of flexible structures - a concept known from the beginning of aeronautics and now being again made possible by the availability of sufficiently fast and powerful actuators and computers, not to forget the control laws. This can be used for vehicle attitude control as well as for compensating unwanted vibrations in structures instead of making them rigid at a high weight penalty. Besides individual actuators for which the Micro Electro-Mechanical Systems offer an extremely interesting future the

so-called smart materials can be employed. Both areas are only at the beginning of their development, in mechanisms as well as in theory.

Some lessons drawn from this Symposium are: there is an urgent need for further development in fast and reliable actuators, and in sensors, both able to function reliably in adverse environments, in particular in high temperatures and under high vibration loads. Obviously the development of theory and control laws has to keep pace. The most important message for RTO and AVT is probably the observation that there is development being done for vehicles of all four environments, that there are similarities and analogies over all vehicle classes, and that the potential for mutual benefit needs to be probed by initiating Technical Activities aimed at this task.

Technologies des systèmes à commandes actives pour l'amélioration des performances opérationnelles des aéronefs militaires, des véhicules terrestres et des véhicules maritimes

(RTO MP-051 / AVT-048)

Synthèse

Les spécifications de performances des futurs moteurs et véhicules relèvent de plus en plus du défi permanent, l'accent étant mis sur la grande manoeuvrabilité, des consommations spécifiques réduites, de plus grand rapports poussée-poids et des coûts globaux de possession plus modestes. Les techniques de conception classiques, intégrant des commandes passives, qui ont porté la technologie des véhicules à son haut niveau actuel, commencent à atteindre leurs limites. La technologie des commandes actives a pour objectif d'améliorer la réponse du système en contrôlant les phénomènes dynamiques, tels que les instabilités de flux, les vibrations, les déformations structurales, la combustion, le bruit, etc. Elles sont en passe de devenir l'un des aspects les plus importants de la conception et l'exploitation des véhicules, offrant en plus, dans certains cas, des possibilités de remise à niveau. Des outils d'une qualité jamais atteinte permettent d'améliorer le comportement global des systèmes et des sous-systèmes. Il s'agit de matériaux intelligents, de technologies informatiques, de capteurs et de servocommandes, et de la micromécanique (MEMS), soutenus par des technologies de fabrication novatrices et par une meilleure compréhension des lois régissant les processus. Désormais, des solutions plus efficaces, plus étendues et plus intégrées sont envisageables. Les possibilités dépassent de loin ce qui est faisable aujourd'hui par le biais de la mise en oeuvre de composants passifs et de la conception soignée des systèmes, et bien que la mise en oeuvre de ces technologies soit réalisable et profitable pour tous véhicules civils et militaires terrestres, aériens et maritimes, c'est dans le domaine des véhicules aériens et dans certains domaines de la propulsion en général qu'ont été enregistrés les progrès les plus intéressants.

Le moteur, y compris les entrées d'air et l'échappement, ainsi que les sous-systèmes de propulsion ont leurs propres systèmes de commande en plus du système de commande global de l'aéronef. Le symposium était axé spécifiquement sur le compresseur et la chambre de combustion de la turbine à gaz. L'adéquation des commandes actives pour ces organes a été démontrée en laboratoire ainsi que sur des moteurs réels, et ce type de commande pourrait trouver des applications dans un avenir proche sur des moteurs de véhicules terrestres, où il permettrait de réduire les niveaux de bruit à l'émission ainsi que les substances toxiques. La stabilisation des flux par les commandes actives permet, par exemple, d'obtenir des taux de compression plus élevés, ce qui pourrait se traduire à terme par des moteurs plus petits. Une autre conséquence pour les performances, qui est souvent négligée, est la diminution des coûts globaux de possession, et les économies réalisables au niveau de la maintenance et des réparations grâce à un meilleur diagnostic, qui a pour effet de compenser l'investissement initial plus élevé.

En dynamique des fluides, il est désormais possible de contrôler la couche limite et les écoulements tourbillonnaires autour des véhicules ou à l'intérieur des moteurs. La possibilité du contrôle de l'assiette par la modification des couches limites et des tourbillons, évitant ainsi l'emploi, coûteux en énergie et en poids, de gouvernes, a été démontrée et cette technique pourrait être mise en oeuvre pour la première fois dans des petits véhicules, des micro-avions et des véhicules sans pilote. Cette démarche permettrait d'éviter le flottement et le tremblement, ainsi que l'application de fortes charges pendant les manoeuvres. La mise en oeuvre de telles techniques dans des appareils hypersustentateurs, en particulier dans des véhicules aériens tels que les avions VSTOL, et l'utilisation de commandes

actives pour les tuyères orientables sont d'autres exemples de leur importance. L'application de la dynamique des fluides aux véhicules maritimes n'a pas été traitée. Ce sujet est d'ailleurs normalement strictement confidentiel. Une seule communication a été présentée sur les applications missiles.

Enfin, le symposium a souligné les nombreuses possibilités existantes dans le domaine des applications structurales. Les deux principales voies sont, d'un côté, les structures souples - concept connu depuis le début de l'aéronautique, mais actuellement en cours de réexamen grâce aux possibilités offertes par les nouvelles servocommandes rapides, les progrès réalisés en informatique et enfin et surtout par les lois de commande. Ces structures peuvent être utilisées pour le contrôle de l'assiette du véhicule, ainsi que pour compenser d'éventuelles vibrations non désirées des structures, à la différence de la solution qui consiste à les rendre rigides et par conséquent, plus lourdes. En plus des servocommandes individuelles, pour lesquelles les systèmes micro-électro-mécaniques (MEM) offrent une solution très intéressante, les matériaux dits intelligents peuvent être employés. Les deux techniques sont au tout début de leur développement, tant du point de vue des mécanismes que de celui des théories.

Différents enseignements ont été tirés de ce symposium. Il est urgent de développer des servocommandes rapides et fiables, ainsi que des capteurs de fonctionnement fiable même dans des environnements défavorables, et en particulier à des températures ambiantes élevées et sous de fortes charges vibratoires. Il est évident que le développement des théories et des lois de commande doit suivre cette cadence. En conclusion, suite à ce symposium, la leçon la plus importante à retenir pour la RTO en général et pour AVT en particulier est que le développement est en cours pour des véhicules aériens, spatiaux, maritimes et terrestres, qu'il existe des similitudes et des analogies entre toutes ces catégories de véhicules, et que la possibilité d'en tirer des avantages mutuels doit être examinée en lançant les activités techniques appropriées.

Click inside the blue boxes or on the titles to view the corresponding section

Contents

	Page
Executive Summary	**iii**
Synthèse	**v**
Theme	**xiii**
Thème	**xiv**
Publications of the RTO Applied Vehicle Technology Panel	**xv**
Programme Committees	**xvi**

	Reference
Keynote Addresses	
Active Flow Control Applied to Military and Civil Aircraft by E. Stanewsky and H. Rosemann	**K1**
Active Control of Instabilities in Gas Turbines by A.P. Dowling	**K2**
Back to the Future - How Active Aeroelastic Wings Are a Return to Aviation's Beginnings and a Small Step to Future Bird-Like Wings by E. Pendleton	**K3**
Theory of Control Aspects by J-L. Gobert	**K4**
Keynote K5 withdrawn	
Programme Performance, Stability and Control, Fluid Physics (PSF)	
Technical Evaluation Report by D.J. Moorhouse	**T1**
Session I: Boundary Layer Control	
Hybrid Laminar Fin Investigations by V. Schmitt, J.P. Archambaud, K.H. Hortstmann and A. Quast	**1**
Transition Prediction and Design Philosophy for Hybrid Laminar Flow Control for Military Aircraft by M. Maina and P.W.C. Wong	**2**
Laminar Design for Supersonic Civil Transport by A. Traoré	**3**
Paper 4 withdrawn	
Characterization of Pulsed Vortex Generator Jets for Active Flow Control by C.P. Tilmann, K.J. Langan, J.G. Betterton and M.J. Wilson	**5**
Impulse Control of Anti-Tank Mortar Missile by R. Vogt and R. Głębocki	**6**

Session II: Active Flow Control of Nozzle/Jet

Paper 7 withdrawn

Active Control of Supersonic Impinging Jets **8**
by A. Krothapalli, R. Elavarasan, F. Alvi and C. Shih

Analysis of Jet Interaction for Supersonic Flow Control **9**
by E. Collin, S. Barre and J.P. Bonnet

Application of Active Core Exhaust Control to Eliminate the Core Thrust Reverser on Heavy Lift Aircraft **10**
by C.F. Chenault and J.D. Dorris

Thrust Vectoring Nozzle for Modern Military Aircraft **11**
by D. Ikaza

Integrated Thrust Vectored Engine Control **12**
by C. Rausch and K. Lietzau

Thrust Vectoring for Advanced Fighter Aircraft - High Angle of Attack Intake Investigations **13**
by N.C. Bissinger and M. Jost

Session III: Drag and Buffet Control

Active Flow Control Activities at ONERA **14**
by J-L. Gobert, D. Barberis, T. Mitchell, P. Molton, J-P. Archambaud, G. Pailhas and M. Corrège

Buffet Active Control - Experimental and Numerical Results **15**
by C. Despré, D. Caruana, A. Mignosi, O. Reberga, M. Corrège, H. Gassot, J.C. Le Balleur and P. Girodroux-Lavigne

Shock Control by Adaptive Elements for Transportation Aircraft Wings **16**
by H. Rosemann, J. Birkemeyer and A. Knauer

Active Dynamic Flow Control Studies on Rotor Blades **17**
by W. Geissler, M. Trenker and H. Sobieczky

Session IV: Noise Control

Active Control of the Directivity of Fan Tones Noise **18**
by J. Julliard, H. Antoine, Ch. Lozachmeur and A. Roure

A Modal Concept for Active Noise Control in Circular or Annular Ducts **19**
by U. Tapken, Y. Zhang, L. Enghardt, W. Neise

Paper 20 withdrawn

Session V: Vortex Control

Yaw Control at High Angles of Attack Through Vortex Manipulation Using Rotating Nose Strakes **21**
by P.R. Hakenesch

Active Control of Forebody Vortices on a Schematic Aircraft Model **22**
by R. Lee, R.J. Kind and E.S. Hanff

Contrôle actif de l'écoulement autour d'une pointe avant à grande incidence **23**
by C. François

Paper 24 withdrawn

Session VI: Flight Vehicle Active Control

Flight Control Design Best Practices Relative to Active Control Technology **25**
by D.J. Moorhouse

Thrust Vector Control and Visualisation for STOVL Aircraft **26**
by P.M. Lodge and C. Fielding

Use of ATTAS for ACT Research **27**
by J.-M. Bauschat, G. Duus, K-U. Hahn, W. Heine and D. Willemsen

Nonlinearities and PIO with Advanced Aircraft Control Systems **28**
by D.G. Mitchell and E.J. Field

Active/Adaptive Rotor Blade Control for Disturbance Rejection and Performance Enhancement **29**
by R. Kube, D. Schimke and P. Jänker

Helicopter Noise Reduction by Individual Blade Control (IBC) - Selected Flight Test and Simulation Results - **30**
by W.R. Splettstoesser, K.-J. Schultz, B. van der Wall, H. Buchholz, W. Gembler and G. Niesl

Practical Aspects of Implementing H-Infinity Controllers on a FBW Research Helicopter **31**
by D.J. Walker, M.C. Turner and A.W. Gubbels

Operational Lessons Learned from the F/A-18E/F Total Flight Control Systems Integration Process **32**
by R.J. Hanley, D.A. Dunaway and K.P. Lawson

Landing Approach Flying Qualities Criteria for Active Control Transport Aircraft **33**
by E.J. Field, K.F. Rossitto and D.G. Mitchell

Programme Mechanical Systems, Structures and Materials (MSSM)

Technical Evaluation Report **T2**
by O. Sensburg

Session I: Smart Structures Applications

Paper 1 withdrawn

Active Structural Acoustic Control as an Approach to Acoustic Optimization of Lightweight Structures **2**
by D. Mayer, B. Vogl and H. Hanselka

Paper 3 withdrawn

Adaptive Wing Model for Wind Channel Tests **4**
by L.F. Campanile, V. Carli and D. Sachau

Paper 5 withdrawn

A Concept of a Shapevariable Fowler Flap on Transport Aircraft **6**
by C. Anhalt, E. Breitbach and D. Sachau

Session II: Active Control Technology for Load Alleviation

Active Control Technology at NASA Langley Research Center **7**
by R.R. Antcliff and A-M.R. McGowan

Finite Element Approach for the Design of Control Algorithms for Vertical Fin Buffeting Using Strain Actuation **8**
by F. Nitzsche, D.G. Zimcik and S. Liberatore

Active Flutter Suppression Using ASTROS with Smart Structures and ASE Modules **9**
by C. Nam, P.C. Chen and D.D. Liu

Paper 10 withdrawn

Active Fin-Buffeting Alleviation for Fighter Aircraft **11**
by J.K. Dürr, U. Herold-Schmidt, H.W. Zaglauer and J. Becker

Development of Analysis Tools for Active Shape and Vibration Control **12**
by A. de Boer, R. Veul, P. Arendsen and M. Bakker

Session III: Active Elements for Structural Design

Offset Piezoceramic Stack Actuators and Acceleration Feedback Control for Tail Buffet Alleviation of a High Performance Twin Tail Aircraft: Robustness Issues **13**
by S. Hanagud, M. Bayon de Noyer and D. Henderson

Paper 14 withdrawn

Investigation on a Semi-Active Hydro Mount Using MR Fluid **15**
by R. Ay, M.F. Golnaraghi and A. Khajepour

Optimization of the Passive Shock Absorber of a Military Aircraft **16**
by B. Uhrmeister

Paper 17 withdrawn

Session IV: Active Materials and Applications

Design and Testing of a Mesoscale Actuator Device **18**
by J. Park, S. Keller, G.P. Carman and H.T. Hahn

Adaptive Rotor Blade Concepts - Direct Twist and Camber Variation **19**
by A. Büter, U.-C. Ehlert, D. Sachau and E. Breitbach

Programme Power Systems and Propulsion (PSP)

Technical Evaluation Report **T3**
by R.M. Murray

Session I: Applications Overview

Compressor Stability and Control: Review and Practical Implications **1**
by J.D. Paduano and A.H. Epstein

Active Control of Combustion and Its Applications **2**
by A.J. Moran, D. Steele and A.P. Dowling

Combination of Active Instability Control and Passive Measures to Prevent Combustion Instabilities in a 260MW Heavy Duty Gas Turbine **3**
by J. Hermann, A. Orthmann, S. Hoffmann and P. Berenbrink

Active Combustion Control for Military Gas Turbine Engines **4**
by M.H. Richman and M.S. Richman

Longitudinal Mode Aeroengine Combustion Instability: Model and Experiment **5**
by J.M. Cohen, J.R. Hibshman, W. Proscia, T.J. Rosfjord, B.E. Wake, J.B. McVey, J. Lovett, M. Ondas, J. DeLaat and K. Breisacher

Active Control of Combustor Processes **6**
by B.T. Zinn, M.G. Allen, A. Glezer, J.I. Jagoda, Y. Neumeier and J.M. Seitzman

Numerical Simulation of Adaptive Control Application to Unstable Solid Rocket Motors **7**
by M. Mettenleiter, F. Vuillot and S. Candel

Session II: Compressor Stall/Surge - Measurements

The Onset of Aerodynamic Instability in a 3-Stage Transonic Compressor **8**
by F.-O. Methling, R. Preute, H. Stoff and F. Grauer

Development of Flow Instability and Rotating Stall in a Multi-Stage Axial Compressor with Variable Guide-Vanes **9**
by W. Riess and M. Walbaum

Perspectives of Phase-Portraits in the Detection of Compressor Instabilities - Inception of Stall **10**
by M. D'Ischia and F.A.E. Breugelmans

Active Control of Compressor Surge Using a Real Time Observer **11**
by J.V.R. Prasad, Y. Neumeier and A. Krichene

Sensor Requirements for Active Gas Turbine Engine Control **12**
by A.D. Kurtz, J.W.H. Chivers, A.A. Ned and A.H. Epstein

Aeroengine Condition Monitoring System Based on Non-Interference Discrete-Phase Compressor Blade Vibration Measuring Method **13**
by R. Szczepanik and M. Witoś

Session III: Compressor Stall/Surge - Control

A Gas Turbine Compressor Simulation Model for Inclusion of Active Control Strategies **14**
by C. Cravero and A. Massardo

Active Control of Surge in Compressors Which Exhibit Abrupt Stall **15**
by P. Giannattasio, D. Micheli and P. Pinamonti

Active Stall Avoidance of an Axial Compressor Stage **16**
by S. Wagner and D.K. Hennecke

Optimization of Turbine Blade Performance by Active Control of Vortex Dynamics **17**
by N. Yurchenko and R. Rivir

Session IV: Combustion Instabilities - Measurements and Predictions

Combustion Oscillation in a Staged LPP Combustor **18**
by J.A. Austin, J.R. Tilston and I.R.I. McKenzie

Prediction of Combustion-Driven Dynamic Instability for High Performance Gas Turbine Combustors: Part I **19**
by B. Sekar, M.A. Mawid, T.W. Park and S. Menon

An Experimental Examination of the Relationship Between Chemiluminescent Light Emissions and Heat-Release Rate Under Non-Adiabatic Conditions **20**
by L.C. Haber, U. Vandsburger, W.R. Saunders and V.K. Khanna

Session V: Combustion Instabilities - Control Fundamentals - Part I

Control of Combustion Instabilities on a Rijke Tube by a Neural Network **21**
by R. Blonbou and A. Laverdant

Adaptive Algorithms for Control of Combustion **22**
by S. Evesque, A.P. Dowling and A.M. Annaswamy

Modeling and Control of Combustion Instability Using Fuel Injection **23**
by J.P. Hathout, A.M. Annaswamy and A.F. Ghoniem

An Investigation of Adaptive Signal Processing Approaches to Active Combustion Control **24**
by M.A. Vaudrey, W.R. Saunders and W.T. Baumann

Paper 25 withdrawn

Developments of Adaptive Methods for Active Instability Control **26**
by M. Mettenleiter and S. Candel

Active Feedback Control of Combustor Dynamics with Time Delay and Noise **27**
by C. Seywert, G. Isella and F.E.C. Culick

Wide-Range Robust Control of Combustion Instability **28**
by B-S. Hong, V. Yang and A. Ray

Session VI: Combustion Instabilities - Control Applications

Review on Activities in Active Combustion Control (ACC) at the Technische Universität München (TUM) **29**
by S. Gleis

Active Control of Combustion Instabilities in Gas Turbine Engines for Low Emissions. Part I: Physics-Based and Experimentally Identified Models of Combustion Instability **30**
by C.A. Jacobson, A.I. Khibnik, A. Banaszuk, J. Cohen and W. Proscia

Active Control of Combustion Instabilities in Gas Turbine Engines for Low Emissions. Part II: Adaptive Control Algorithm Development, Demonstration and Performance Limitations **31**
by A. Banaszuk, Y. Zhang and C.A. Jacobson

Performance Enhancement of Gas-Turbine Combustor by Active Control of Fuel Injection and Mixing Process—Theory and Practice **32**
by C.O. Paschereit, E. Gutmark and B. Schuermans

Active Optimisation of the Performance of a Gas Turbine Combustor **33**
by M.M. Miyasato, V.G. McDonell and G.S. Samuelsen

Active Control of Oscillations in Simulations of Gas-Turbine Combustors **34**
by S.R.N. De Zilwa, J.H. Uhm and J.H. Whitelaw

Optimization of Active Control Systems for Suppressing Combustion Dynamics **35**
by K. Kim, J. Lee, J. Stenzler and D.A. Santavicca

An Experimental Study on Actively Controlled Dump Combustors **36**
by K. Yu, K.J. Wilson, T.P. Parr and K.C. Schadow

Theme

The performance demands of future vehicles and engines are becoming increasingly challenging with the trends to high manoeuvrability, lower specific fuel consumption, higher thrust-to-weight ratios and lower life-cycle cost. This applies to both military and commercial vehicles and engines.

Active control technology is aimed at enhancing system behaviour by controlling dynamics processes such as flow instabilities, vibrations, structural deformation, combustion, noise, etc. Conventional design including passive control has brought vehicle technology to its present high level and in many cases has reached the limits. While active Flight/Ride Control is a technique already in use, a new quality of tools offer improvements in the behaviour of overall systems as well as in sub-domains. These tools are the development of smart materials, innovative manufacturing technologies, computer technology, sensors and actuators, micro-mechanic technology (MEMS) and the improved insight into process laws. Smaller, more efficient, more powerful and more integrated solutions are becoming possible. The potential exceeds by far that which can be achieved nowadays by careful system design and the use of passive components.

The Symposium will predominantly look at aircraft related technologies because in aircraft the need for active control technologies is very high. Other vehicles can greatly benefit from the transfer developed for air vehicles.

The Symposium will review the current status of active control and execute the short term and long term application potential. Three main streams are offered, namely flow flight control, structure control and engine control. In the field of flow control the symposium will focus on drag reduction techniques, vortex stabilisation, thrust vectoring, and noise control. The flight control session offers recent results of flight test experiences. In the structures and materials field adaptive structures, buffet-control, gust alleviation as well as new actuators are presented. The engine domain will focus on stall/surge and combustion instability control with presentations on laboratory and full-scale experiments for applications to gas turbines, ramjets and solid propellant motors. Different aspects of active control will be addressed, ranging from physical understanding to the control process, controller, sensors and activators and its integration into the whole system.

Thème

Les spécifications de performances des futurs moteurs et véhicules sont de plus en plus redoutables, l'accent étant mis sur une grande maniabilité, une consommation spécifique de carburant réduite, un plus grand rapport poussée-poids et des coûts globaux de possession plus modestes. Ces exigences concernent les moteurs et les véhicules tant civils que militaires.

La technologie des commandes actives a pour objectif d'améliorer la réponse du système en contrôlant les phénomènes dynamiques, tels que les écoulements instationnaires, les vibrations, les déformations structurales, la combustion, le bruit, etc. Les techniques de conception classiques, intégrant des commandes passives, qui ont porté la technologie des véhicules à son haut niveau actuel, commencent à atteindre leurs limites. En effet, la technique des commandes actives de vol/de confort est déjà employée, mais des solutions techniques d'une qualité novatrice promettent d'améliorer le comportement global des systèmes et des sous-systèmes. Il s'agit de matériaux intelligents, de technologies de fabrication novatrices, de technologies informatiques, de capteurs et de servocommandes, de la micromécanique (MEMS) et d'une meilleure compréhension des lois régissant les processus. Désormais, des composants et des systèmes plus petits, plus efficaces, plus puissants et plus intégrés sont envisageables. Les perspectives dépassent de loin ce qui est réalisé avec des composants passifs, et ce même avec une conception très soignée des systèmes.

Ce symposium examinera principalement les technologies aéronautiques puisque la demande de technologies de commandes actives pour aéronefs est très importante. Cela étant, d'autres véhicules pourraient profiter du transfert des technologies développées pour véhicules aériens.

Ce symposium fera le point des connaissances actuelles dans le domaine des commandes actives et évaluera les possibilités à court et à long terme. A la suite de la cérémonie d'ouverture plénière du lundi matin, trois grands axes seront proposés, à savoir les performances, la stabilité et le contrôle, la physique des fluides; les systèmes mécaniques, les structures et matériaux; les génératrices et les propulseurs. En ce qui concerne le contrôle des écoulements le symposium privilégiera les techniques de réduction de la traînée, la stabilisation des tourbillons, l'orientation de la poussée et le contrôle du bruit. La session sur les commandes de vol présente les résultats d'essais en vol récents. Dans le domaine des structures et matériaux, des structures adaptatives, le contrôle du tremblement, l'atténuation des rafales et les nouveaux actionneurs sont présentés. Les sessions sur les moteurs seront consacrées au calage/pompage et au contrôle des instabilités de combustion, avec des présentations sur des expériences conduites en laboratoire et sur le terrain pour applications aux turbomoteurs, aux statoréacteurs et aux moteurs à propergol solide. Différents aspects des commandes actives seront examinés, allant de la description du processus physique au processus de contrôle, au contrôleur, aux capteurs et aux actionneurs et à l'intégration des commandes actives dans le système global.

Publications of the RTO Applied Vehicle Technology Panel

MEETING PROCEEDINGS (MP)

Design for Low Cost Operation and Support
MP-37, September 2000

Gas Turbine Operation and Technology for Land, Sea and Air Propulsion and Power Systems (Unclassified)
MP-34, September 2000

Aerodynamic Design and Optimization of Flight Vehicles in a Concurrent Multi-Disciplinary Environment
MP-35, June 2000

Structural Aspects of Flexible Aircraft Control
MP-36, May 2000

New Metallic Materials for the Structure of Aging Aircraft
MP-25, April 2000

Small Rocket Motors and Gas Generators for Land, Sea and Air Launched Weapons Systems
MP-23, April 2000

Application of Damage Tolerance Principles for Improved Airworthiness of Rotorcraft
MP-24, January 2000

Gas Turbine Engine Combustion, Emissions and Alternative Fuels
MP-14, June 1999

Fatigue in the Presence of Corrosion
MP-18, March 1999

Qualification of Life Extension Schemes for Engine Components
MP-17, March 1999

Fluid Dynamics Problems of Vehicles Operation Near or in the Air-Sea Interface
MP-15, February 1999

Design Principles and Methods for Aircraft Gas Turbine Engines
MP-8, February 1999

Airframe Inspection Reliability under Field/Depot Conditions
MP-10, November 1998

Intelligent Processing of High Performance Materials
MP-9, November 1998

Exploitation of Structural Loads/Health Data for Reduced Cycle Costs
MP-7, November 1998

Missile Aerodynamics
MP-5, November 1998

EDUCATIONAL NOTES (EN)

Measurement Techniques for High Enthalpy and Plasma Flows
EN-8, April 2000

Development and Operation of UAVs for Military and Civil Applications
EN-9, April 2000

Planar Optical Measurements Methods for Gas Turbine Engine Life
EN-6, September 1999

High Order Methods for Computational Physics, Published jointly with Springer-Verlag, Germany
EN-5, March 1999

Fluid Dynamics Research on Supersonic Aircraft
EN-4, November 1998

Integrated Multidisciplinary Design of High Pressure Multistage Compressor Systems
EN-1, September 1998

TECHNICAL REPORTS (TR)

Verification and Validation Data for Computational Unsteady Aerodynamics
TR-26, October 2000

Recommended Practices for Monitoring Gas Turbine Engine Life Consumption
TR-28, April 2000

A Feasibility Study of Collaborative Multi-facility Windtunnel Testing for CFD Validation
TR-27, December 1999

Active Control, Technology for Enhanced Performance Operational Capabilities of Military Aircraft, Land Vehicles and Sea Vehicles

Programme Committee Chairman

Prof. Dr. H. Koerner
DLR, Institut fuer Entwurfsaerodynamik
P.O. Box 3267
D-38022 Braunschweig
em: horst.koerner@dlr.de

Programme Committee for Performance, Stability and Control, Fluid Physics (PSF)

Chairman
Dr. Y. Yu
National Rotorcraft Technology Center
Mail Stop 207-1
NASA Ames Research Center
Moffett Field, CA 94035-1000
em: yyu@mail.arc.nasa.gov

BELGIUM
Prof. Dr. R. Decuypere
Ecole Royale Militaire (MAPP)
avenue de la Renaissance, 30
1000 Brussels
em: decuypere@mapp.rma.ac.be

FRANCE
Jean-Claude COURTY
Head IAP/MCFD
Dassault Aviation
78, Quai Marcel Dassault
F-92552 Saint Cloud Cedex
Fax: 33 1 47 11 45 35

GERMANY
Prof. Dr. P. Hamel
DLR-Institut fuer Flugmechanik
Lilienthalplatz 7
D-38108 Braunschweig
em: Peter.Hamel@dlr.de

Prof. Dr. G. E.A. Meier
DLR-Institut für Stroemungsmechanik
Bunsenstrasse, 10
D-37073 Goettingen
em:g.e.a.meier@dlr.de

SPAIN
Dr. L. P. Ruiz-Calavera
INTA, Carretera Torrejon-Ajalvir,
Km.4.5,
E-28850 Torrejon de Ardoz
Madrid
em: ruizcl@inta.es

TURKEY
Prof. Dr. Cahit Ciray
Aeronautical Eng. Department
Middle East Technical University
Inonu Bulvari PK: 06531, Ankara
em: cciray@rorqual.cc.metu.edu.tr

UNITED KINGDOM
Prof. D.I.A.Poll
Cranfield University
Cranfield, Bedford, MK43 0AL
em: I. Poll@cranfield.ac.uk

UNITED STATES
Mr. D. Selegan
AFRL/XPA
1864, 4th Street, Suite 1
Wright Patterson AFB
OH 45433-7131
em: david.selegan@afrl.af.mil

Programme Committee for Mechanical Systems, Structures and Materials (MSSM)

Chairman
Ir. J. Meijer
National Aerospace Laboratory (NLR)
Dept. AE
Anthony Fokkerweg, 2, P.O. Box 90502
1006 BM Amsterdam, Netherlands
em: meijer@nlr.nl

BELGIUM
Prof. Dr. J. Vantomme
Royal Military Academy (RMA)
Department of Civil Engineering
avenue de la Renaissance, 30
B-1000 Brussels
em:jvt@cobo.rma.ac.be

CANADA
Mr. C. Perron
Bombardier Inc. Canadair
Military Aircraft Division
10,000 Cargo A-4 Street
Montreal, International Airport
Mirabel, Quebec 17N 1H3
em: claude.perron@dsd.canadair

Dr. D. G. Zimcik
Group Leader, Aeroacoustics +
Structural Dynamics - IAR
National Research Council Canada
Bldg. U-66A, Montreal Road
Ottawa, Ontario K1A 0R6
em: david.zimcik@nrc.ca

FRANCE
Mr. D. Chaumette
Dassault Aviation
78 quai Marcel Dassault
Cedex 300
92552 St Cloud Cedex
em: daniel.chaumette@dassault-aviation.fr

GERMANY
Dr. H. Hoenlinger
DLR, Institut fuer Aeroelastik
Bunsenstrasse 10
D-37073 Goettingen
em: heinz.hoenlinger@dlr.de

Mr. W. Luber
DaimlerChrysler Aerospace AG
Military Aircraft MT24
P.O. Box 80 11 60
81663 Munich
em: wolfgang.luber@m.dasa.de

UNITED STATES
Dr. D. Paul
Air Force Research Laboratory
2130 8th Street. Suite 1
Wright Patterson AFB
OH 45433-7562
em: donald.paul@va.wpafb.af.mil

Mr. J. Coyle
The Boeing Company
P.O. Box 516
Mail Stop 5064-2809
Saint Louis, Missouri 63166-0516
em: john.m.coyle@boeing.com

Mr. E. Pendleton
AFRL/VASD,
2130 Eighth Street, Suite 1
Wright Patterson AFB
Ohio 45433-7542
em: edmund.pendleton@afrl.af.mil

Programme Committee for Power Systems and Propulsion (PPS)

Chairman
Dr. K. C. Schadow
Consultant with Strategic Analysis, Inc.
2896 Calle Heraldo
San Clemente, CA 92673
em: schadowc@home.com

BELGIUM
Prof. F. Breugelmans
von Karman Institute
72, Chaussee de Waterloo
B-1640 Rhode St Genese
em: fb@vki.be

FRANCE
Mr. P. Donguy
SNECMA
2, bld du General Martial Valin
75724 Paris, Cedex 15
em: paul.donguy@snecma.fr

GERMANY
Prof. H. Weyer
Institut fuer Antriebstechnik
DLR, Postfach 90 60 58
51140 Koeln
em: heinrich.weyer@dlr.de

PORTUGAL
Prof. M. N. R. Nina
CTAMFUL
Instituto Superior Tecnico
avenida Rovisco Pais
1096 Lisboa Codex
em: nina@columbano.ist.utl.pt

SPAIN
Mr. M. Mulero Valenzuela
INTA
Crta. Torrejon a Ajalvir. km4
28850 Torrejon de Ardoz
Madrid
em: mulero@inta.es

UNITED KINGDOM
Mr. R.V. Cottington
Propulsion Department
Building 304
DTEO Pyestock
Hants, GU14 OLS
em: rvcottington@dera.gov.uk

UNITED STATES
Prof. F. Culick
California Institute of Technology
205 Guggenheim
Mail Stop 205-45
Pasedena, C 91125
em: culick@caltech.edu

Mr. T. Lewis
AFRL/PRTA, Bldg 18
1950 fifth Street
Wright Patterson AFB
OH 45433-7251
em: lewisti@wl.wpafb.af.mil

Dr. G. Roy
Office of Naval Research, Code 333
800 North Quincy Street
Arlington, VA 22217-5660
em: royg@onr.navy.mil

Mr. D. A. Santavicca
132 Research Building East
Penn State University
University Park, PA 16802
Fax: 1 814 865 3389

Active Flow Control Applied to Military and Civil Aircraft

E. Stanewsky and H. Rosemann

Deutsches Zentrum für Luft-und Raumfahrt, e.V., Institut für Strömungsmechanik,
Bunsenstr. 10, D-37073 Göttingen, Germany

Abstract

There are essentially two aspects to the application of active flow control: Firstly, the improvement of aircraft performance otherwise restricted by the development of the boundary layer and the interaction of the boundary layer with the outer "inviscid" flow field, exacerbated at high speed by the occurrence of shock waves which considerably increase aircraft drag; secondly, the direct control of the aircraft geometry to adjust to changing flight or freestream conditions for optimized performance at all points of the flight envelope. In the present paper both aspects are being considered and flow control and adaptive-wing concepts for military and civil air vehicle applications discussed. Examples for each control objective are provided and benefits associated with implementing adaptive-wing and flow-control technologies outlined. The discussion is based on results from the literature and results of two recent projects, namely, the German national adaptive-wing project ADIF and the EU-project EUROSHOCK II, the latter concerned with boundary layer and shock control. Main emphasis is being placed on aerodynamics.

Nomenclature

c, C	model chord length
C_L, c_l, / C_N	lift coefficient / normal force coefficient
C_D, c_d	drag coefficient (C_D = 0.0001 ≡ 1ct)
C_p	pressure coefficient (C_p^* ≡ C_p @ M = 1)
C_Q, CQ	mass flow coefficient (suction rate)
D	distance between VGs
h, h_{GF}, h_B	height of VGs, Gurney flaps and bump height
h_k	test section height
L/D	lift to drag ratio
l	body length
M∞, M	free stream Mach number
p	static pressure
p_0	total pressure
Re, Re_c	Reynolds Number generally based on chord length $(\rho Uc/\mu)\infty$ or one meter
U∞	freestream velocity
x, y, z	co-ordinates, generally from the leading edge of model
$(x/c)_{Suction}$	location of suction slot
$(x/c)_{tr}$	location of transition, upper/lower surface
x_b	vortex-breakdown location
α	angle of attack
δ^*/θ	displacement/momentum thickness
δ_{LE}, δ_{TE}	leading-edge, trailing-edge flap deflections
δ_{GF}	Gurney-flap deflection
Λ	leading-edge sweep
ρ	density
μ	dynamic viscosity
CG	Center of Gravity
HLF	Hybrid Laminar Flow (Wing)
HLFSC	HLF-wing with shock control
ISA	International Standard Atmosphere
MAW	Mission Adaptive Wing
NLF	Natural Laminar Flow
LFC	Laminar Flow Control
VG	Vortex Generator

1. Introduction

There are essentially two aspects to be considered when discussing flow control: Firstly, control to improve aircraft performance otherwise restricted by the development of the boundary layer and the interaction of the boundary layer with the outer 'inviscid' flow — exacerbated by the occurrence of shock waves at high speeds — and, secondly, the direct control of the aircraft geometry to adapt to changing flight or freestream conditions.

In the first category, flow control essentially involves passive and active devices to exert a beneficial change in the wall-bounded and/or free-shear flow with the objectives of ① delaying/advancing boundary layer transition, ② suppressing/enhancing turbulence and ③ preventing separation, Figure 1. The useful end results of these control actions mainly include drag reduction, lift enhancement, and flow-induced noise suppression [1]. In detail:

① Transition delaying mechanisms, mainly for skin-friction drag reduction, include favorable pressure gradients (NLF), suction in the nose region of an airfoil or wing (LFC), control of growing linear disturbances in the boundary layer and wall cooling. It is, of course, some times desirable to promote transition, e.g., when separation is imminent.

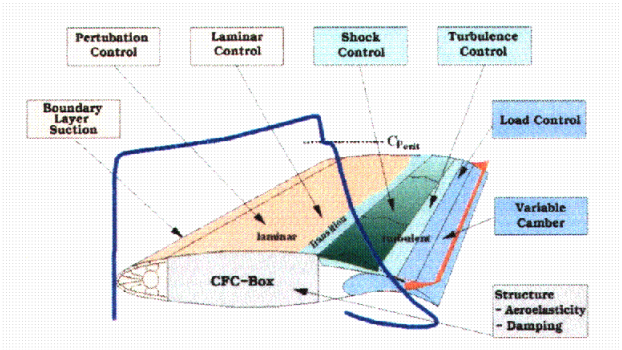
② Devices for turbulence manipulation, mainly for reducing skin-friction drag in turbulent wall-bounded flows, include, for instance, Large Eddy Breakup devices (LEBUs), riblets and other skin modifiers, the addition of polymers in the case of hydrodynamic flows [2], and, newly emerging, Micro-Electro-Mechanical-Systems (MEMS) to manipulate the high-shear-stress streaks in the boundary layer [3].

③ The most important control application in the present context is the control of the 'global' boundary layer development and the delay of separation in order to reduce form (viscous) drag, to enhance lift and to improve pressure recovery. Means of boundary layer control include, for instance, air-jet and sub-boundary layer vortex generators or zero-mass pulsing jets deployed to delay separation [4, 5, 6], discrete suction or blowing meant to reduce viscous drag [7, 8], passive and active cavity ventilation for shock control [9, 10], and (unconventional) deploying devices such as Gurney flaps and reversed-flow flaps to increase L/D and C_{Lmax} [11, 12]. MEMS, already mentioned, can also be utilized for vortex control on delta wings to enhance maneuver capability [13].

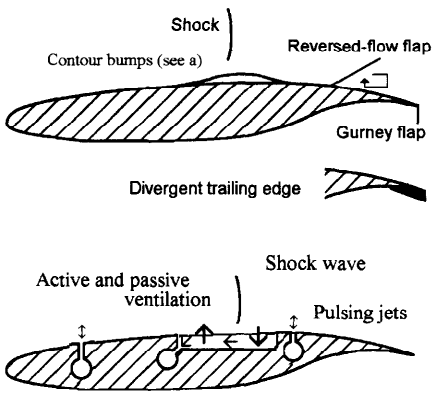
The second aspect of control concerns the *adaptation of the aircraft or flight vehicle geometry* in response to changing flight or freestream conditions. Generally, aircraft follow specific flight profiles consisting of take-off, climb, the mission (or missions) proper, descend and landing. The mission proper is again characterized by changing freestream conditions which are for a fighter aircraft, for instance, given by supersonic cruise to intercept, combat with extreme maneuvers, and optimum cruise during return, Figure 2 [14], while for a transport aircraft negative effects result, for instance, from fuel-burn and the corresponding weight reduction dur-

Paper presented at the RTO AVT Symposium on "Active Control Technology for Enhanced Performance Operational Capabilities of Military Aircraft, Land Vehicles and Sea Vehicles", held in Braunschweig, Germany, 8-11 May 2000, and published in RTO MP-051.

ing cruise, Figure 3 [15], but also due to off-design cruise conditions which cannot always be avoided [16].



a. Wing-adaptation and boundary layer control devices

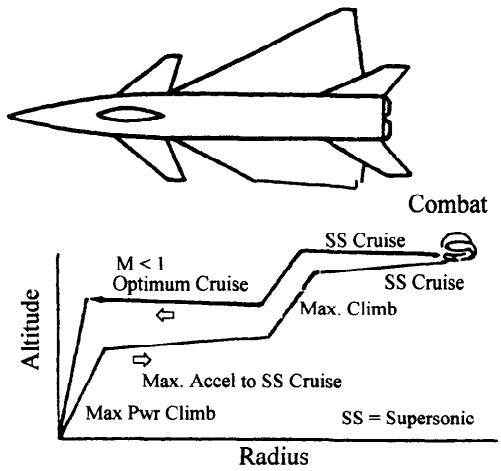


b. Bumps, trailing edge devices, ventilation and pulsing jets

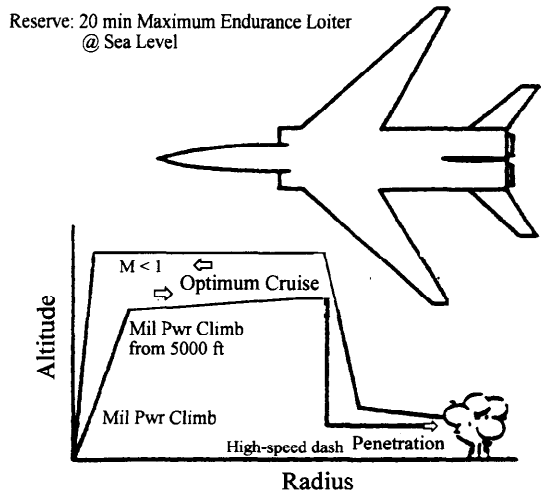
Figure 1. Examples of flow control and adaptation devices

The various requirements, Figures 2 and 3, are accounted for by multiple but fixed design points which compromise, however, the overall aircraft performance. Employing adaptive wing technology — and flow control in the above sense — where the effective wing geometry adjusts to the changing flow and load requirements, allows, on the other hand, to fully explore the aerodynamic flow potential at each point of the flight envelope resulting not only in aerodynamic performance gains during cruise and maneuver but also in an improved structural design [16, 17 to 21].

Means of realizing adaptive wing technology are predominantly geometrical adjustments including, besides conventional means such as variable sweep, the deformation of the complete wing to achieve the desired low-drag pressure distributions, the use of leading- and trailing-edge camber variation for the same reason, and local contour modifications, for instance, in the shock region to reduce shock strength with positive effects on the boundary layer development and drag, Figure 1.



a. Typical fighter mission (Supersonic Intercept)



b. Typical bomber mission

Figure 2. Flight missions for military-type aircraft [14]

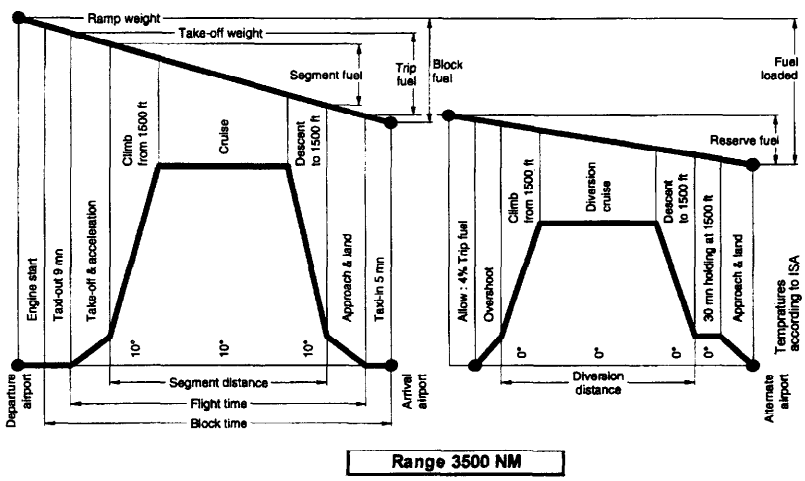


Figure 3. Flight mission profile for an A340-type HLF aircraft [15]

In the following chapters we will consider and discuss the effect of wing-geometry adaptation and active boundary layer and flow control on aircraft performance by employing characteristic results from the literature and from two recent programs, namely, the German adaptive-wing program ADIF [22, 23] and the EU-project EUROSHOCK II – Drag Reduction by Shock and Boundary Layer Control [24]. Emphasis will be placed on aerodynamics. In the presentation we will distinguish between military and civil applications dependent on whether results were obtained for a military or a civil air vehicle, which is, of course, generally somewhat artificial.

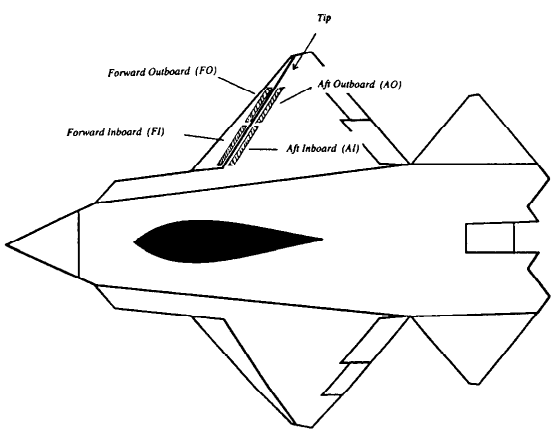
2. Application of control and adaptation to military-type aircraft

2.1 Low/medium aspect-ratio wings

2.1.1 Control for lift enhancement

Modern and advanced fighter aircraft require, to survive in the combat arena, the ability to aggressively maneuver in flight regimes that are characterized by highly separated flow fields and possibly strong vortical flows. These types of flows reduce the effectiveness of conventional aerodynamic controls and when combining these requirements with aircraft geometries designed for low observability, the problem is compounded. Such an aircraft, Figure 4, will be used here to demonstrate the effect of boundary layer and flow control on maneuver performance enhancement [27].

The aircraft (model) configuration considered corresponds to a near-term technology, low-observable multi-role fighter aircraft with a low-aspect-ratio diamond wing, a V-tail and a flow-through inlet on the lower side. Control surfaces include a full-span constant 10%-chord leading edge flap and two partial-span trailing edge flaps. Wind-tunnel tests were carried out at a Mach number of M_∞ = 0.19 and a Reynolds number of Re = 4×10^6/m. Control devices investigated included various types of vortex generators and Gurney flaps, Figures 5 and 6. The former are, of course, meant to energize the boundary layer thus avoiding or delaying separation, while the latter essentially increase effective camber thus lift and possibly L/D [27].



(Shaded area denotes insert plates for VG-attachment)

Figure 4. Advanced fighter/attack aircraft for lift control studies [27]

For the investigation of the effect of vortex generators baseline flap configurations of δ_{LE}/δ_{TE} = 15°/10° and 20°/0°, which gave the best L/D-improvement in comparison to the zero flap setting, were selected. Varied were the vortex-generator geometry, spacing, the orientation to the local flow direction and the location on the wing as indicated in Figure 4 by the insert-plate positions (shaded area).

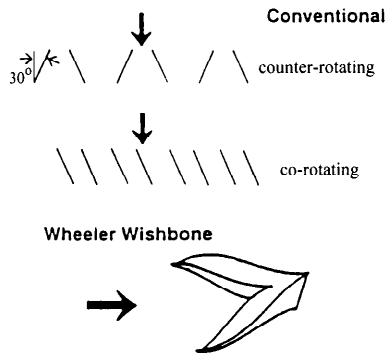
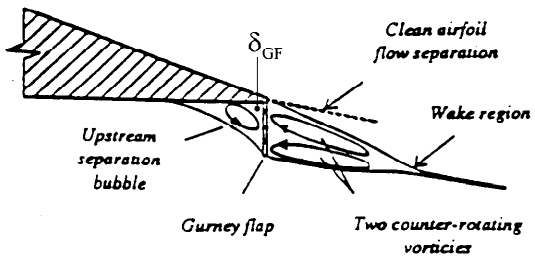


Figure 5. Vortex-generator concepts investigated [27]



(Gurney-flap angle $\delta_{GF} = 90°$)

Figure 6. Gurney flaps and envisaged local flow field [27]

Of the VG-configurations investigated, the co-rotating vortex generators gave, for the optimum flap setting selected here, i.e., δ_{LE}/δ_{TE} = 20°/0°, the best improvement in terms of $(L/D)_{max}$ with the maximum increase amounting to about 6%, Figure 7. The maximum improvement was obtained for the forward/inboard VG-location, a height of h = 0.1" — corresponding to the incoming boundary layer thickness — and a spacing of D/h = 9. The Wheeler-Wishbone vortex generators, which are rather insensitive to the local flow direction, showed about the same effectiveness, however, with only half the size of the co-rotating vanes required. The counter-rotating VGs were less effective in increasing L/D_{max} with best-case improvement being 3.5%.

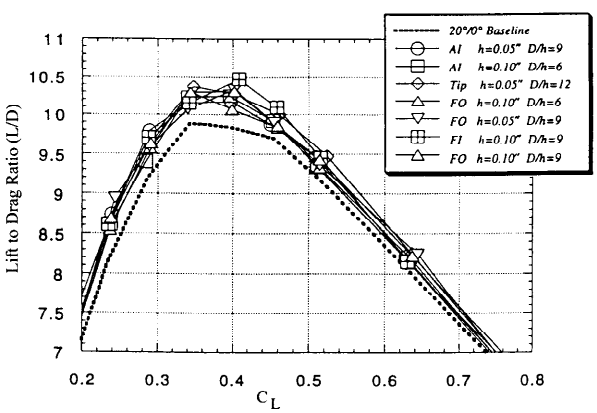
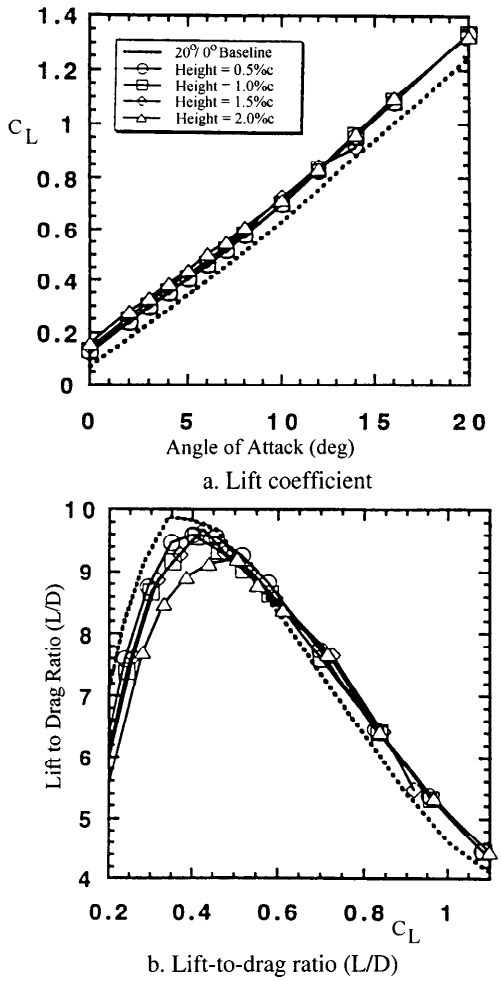


Figure 7. Effect of co-rotating VGs on L/D for a flap setting of δ_{LE}/δ_{TE} = 20°/0° [27]

As a second high-lift device, Gurney flaps, modifying the trailing edge as indicated in Figure 6, were investigated at the same reference conditions. Geometric variables of the Gurney flaps were the height of the flap and the deflection angle δ_{GF}. Figure 8 shows as an example of the flap effectiveness the influence of the 90°-Gurney-flap on L/D and lift. One observes that lift is increased due to the Gurney flap with the

largest increase occurring for a flap height of 2% chord, although the effect of the height is small for $h_{GF} > 1\%c$. The increase in drag associated with the Gurney flap causes a decrease in $(L/D)_{max}$ with increasing flap height; however, at lift coefficients greater than the one for $(L/D)_{max}$, all flap heights provide an increase in L/D — due to delaying the development of upper-surface separation — with the maximum gain being about 8%. (For further results see Chapter 3.1.)



a. Lift coefficient

b. Lift-to-drag ratio (L/D)

Figure 8. Effect of a Gurney flap on L/D and lift for a flap deflection angle of 90° [27]

2.1.2 *Mission-adaptive-wing aircraft investigations*

The F-111A Variable-sweep Fighter Aircraft was extensively used to investigate Transonic Aircraft Technology (TACT) by equipping this aircraft with a supercritical transonic wing [17] — similar to the German/French Alpha–jet experimental aircraft (TST) [28]. To explore the benefits of a Mission Adaptive Wing (MAW), which would allow the minimum-drag adaptation of the wing camber to the freestream conditions of the flight envelope, this aircraft was modified and equipped with a wing of variable camber leading- and trailing-edge flaps (Advanced Fighter Technology Integration aircraft AFTI), Figure 9 [18].

The flap system consisted of six independent trailing-edge flap segments (three per wing) and two leading edge flap segments (one per wing) providing smooth, continuously variable wing camber by using flexible fiberglass skins on the upper and sliding panels for the lower surface, Figure 9. Since we will here mainly consider aerodynamic performance improvements, the reader is referred to [17], [29] and [30] for systems and structural aspects and further MAW references.

Maneuver-camber control (MCC)

An extensive wind-tunnel and flight-test program has been performed with the MAW aircraft (AFTI) to predict the aerodynamic performance benefits of the smooth-skin variable camber wing [17]. For the former, test conditions covered a Mach number range of $M_\infty = 0.25$ to 2.50 at Reynolds numbers ranging from $Re = 6x10^6$ to $26x10^6$/m. Configuration variables included wing sweep, discrete variable-camber flap deflections and angle of attack.

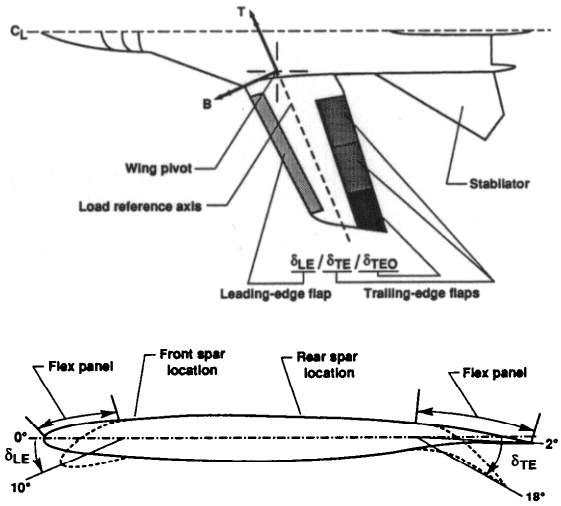


Figure 9. Flap configuration and smooth variable-camber airfoil, AFTI-111 aircraft [18]

At any given lift coefficient there is an optimum camber setting that produces minimum drag. The locus of combined variable-camber leading- and trailing-edge flap deflections providing minimum drag as function of lift constitutes the variable-camber drag polar as shown in Figure 10: in the present example ($M_\infty = 0.60$), there is obviously only little improvement due to variable camber at the lower lift coefficients of $C_L \leq 0.60$ but noticeable gains at higher lift. Also indicated in Figure 10 are lift levels corresponding to the aircraft flight envelope (compare Figure 2). Especially at maneuver conditions, i.e., conditions where the fixed-wing aircraft would be completely stalled, considerable improvements are possible due to variable camber.

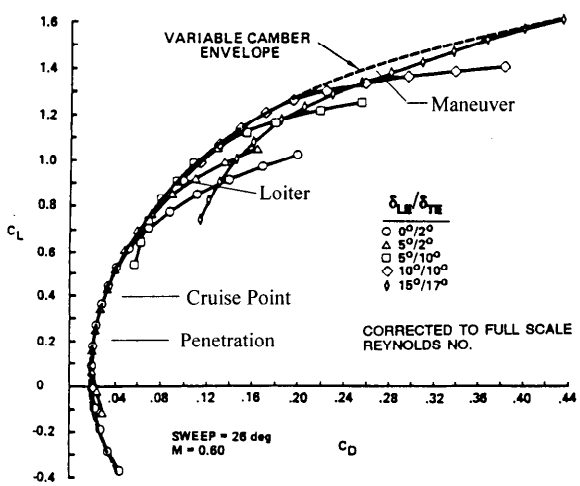


Figure 10. Variable camber envelope for the AFTI-aircraft model obtained in wind-tunnel tests [17]

The improvements are also demonstrated by flight-test results obtained for the variable-sweep (AFTI/F-111) and the fixed-wing (TACT) aircraft, respectively, at two Mach numbers, Figure 11: appreciable drag reductions are possible due to the MAW at the higher lift coefficients. It should be noted that the drag reduction in the cruise regime, i.e., C_L = 0.40, M_∞ = 0.85, is essentially due to the still more refined supercritical airfoil design of the AFTI wing, whereas the large drag reduction at the higher lift coefficients is entirely due to the application of the variable-camber concept.

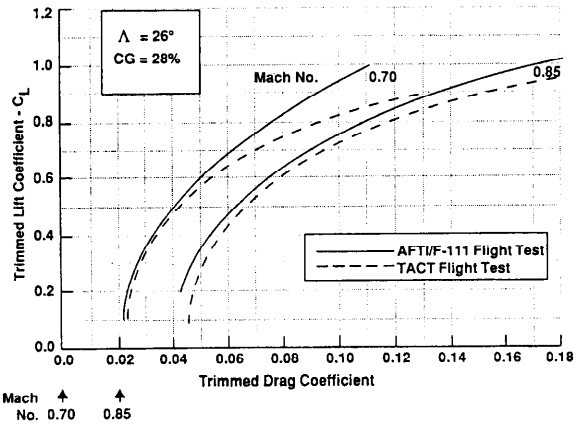
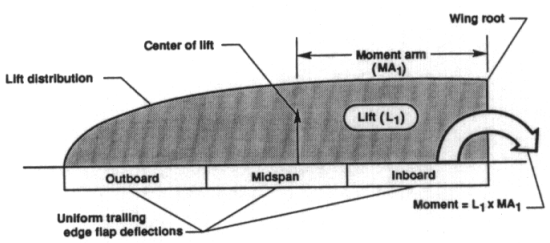


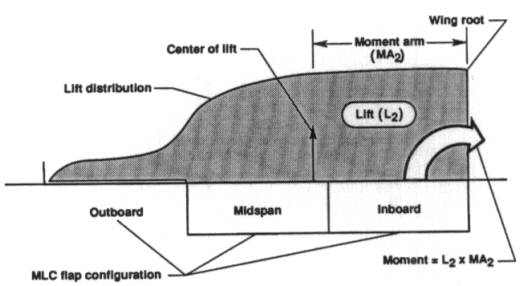
Figure 11. Comparison of the drag polars for the variable-camber and fixed-wing aircraft from flight tests [17]

Maneuver-load control (MLC)

Maneuver-load control is the technique of changing the spanwise lift distribution of the wing to move the center of lift inboard thus reducing the wing bending moments. This can be accomplished by changing the wing spanwise camber distribution, which the AFTI-aircraft is well able to do by corresponding deflections of the three independent trailing-edge maneuver flaps provided on each wing, Figure 12 [18].



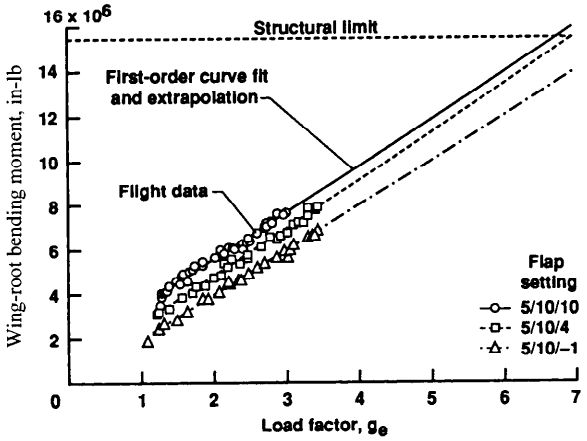
a. Without MLC



b. With MLC

Figure 12. Spanwise lift distribution for uniform and discrete flap deflections at equal total lift [18]

Corresponding results obtained in actual flight tests with the AFTI aircraft at M_∞ = 0.80 are presented in Figure 13 for three flap settings, namely, δ_{LE}/δ_{TE}(inboard and mid-span)/ δ_{TE}(outboard) = 5°/10°/10°, 5°/10°/4° and 5°/10°/-1°. Here, 5°/10°/10° corresponds to the base-line (elliptic) configuration. One observes that the wing-root bending moment, which is the most critical in limiting wing loads, is considerably reduced by the load redistribution, assuming the same equivalent load factor 'g_e', or, in other words, the load factor can be increased by Δg_e = 1 for the same wing-root bending moment noticeably improving maneuverability. Such control can, of course, also be applied to a transport aircraft to raise the buffet boundary or to eliminate gust loads [23].



g_e = (maneuver gross weight x load factor)/(design gross weight)

Figure 13. Wing-root bending moment for three flap configurations showing the effect of load redistribution [18]

2.2 Delta wings and bodies of revolution (vortex-dominated flows)

2.2.1 Delta-wing vortex management

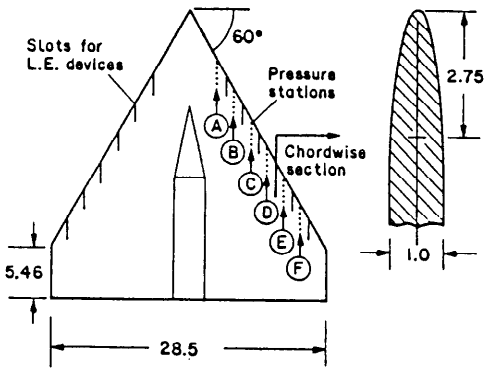
'Vortex management' refers to the purposeful manipulation and re-ordering of concentrated vortical structures resulting from flow separation from highly swept leading edges and slender (fore)bodies at moderate to high angles of attack. The aim is to enhance the aerodynamic performance and controllability of advanced, highly-maneuverable configurations. There have been innumerable devices proposed and investigated, ranging from geometrical swept-wing leading-edge extensions and forebody flaps and strakes to leading edge blowing and, recently, MEMS. For a survey of the more conventional devices, the reader is referred to [31]. Here, some examples of 'unconventional' control schemes will be given, starting, however, with a brief survey of characteristic geometrical devices taken from [31].

Conventional devices

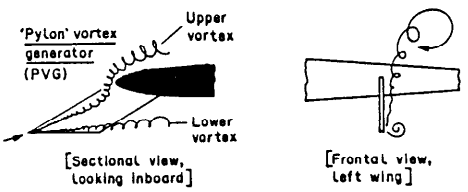
Leading-edge compartmentation: Blunt (delta-wing) leading edges generally encounter 'mixed' vortical conditions in spanwise direction, i.e., the coexistence of attached and separated flow in varying proportion as a function of angle of attack, resulting in pitch non-linearities and hence in severe trim and control problems. Compartmentation of the leading edge, Figure 14, by suitable leading-edge devices can improve controllability up to high lift. Effective leading-edge devices include chordwise fences, slot blowing and — most effective with little interference drag at cruise lift coefficients — pylon vortex generators extending forward of the leading edge, Figure 14b.

Upper- and lower-surface vortex flap: The upper-surface vortex flap, Figure 15, has some unique aerodynamic characteristics: at low angles of attack, a vortex forms inboard of the flap whose suction generates drag on the flap, but also

increases lift on the exposed wing area; at high angles of attack, a dominant vortex develops in front of the flap while the inboard vortex tends to weaken with the net effect being a thrust force or reduction in drag. This is reflected in the L/D dependence on lift indicating a considerable gain of up to 25% as lift (angle of attack) is increased, Figure 15. This figure also demonstrates the possible use of the flap as an adaptive-wing device, for instance, retracting the flap where the basic wing gives better performance. The lower-surface vortex flap, only sketched in Figure 15, is similarly effective has, however, the practical disadvantage to possibly interfere with the under-wing store carriage.



a. Wing model with compartmentation slots



b. Pylon vortex generator compartmentation device

Figure 14. 60-degree delta-wing compartmentation [31]

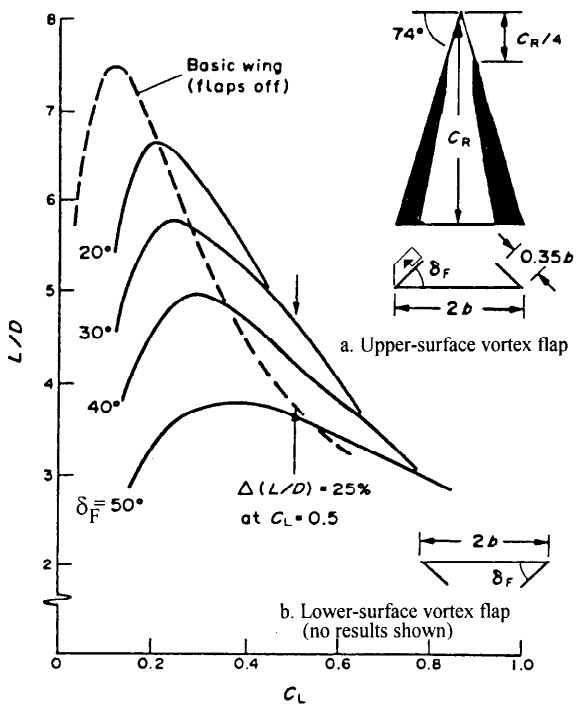
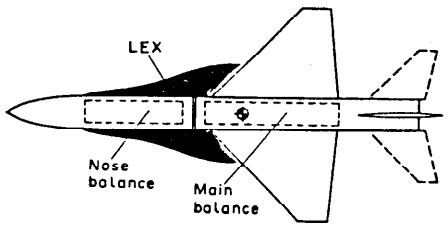
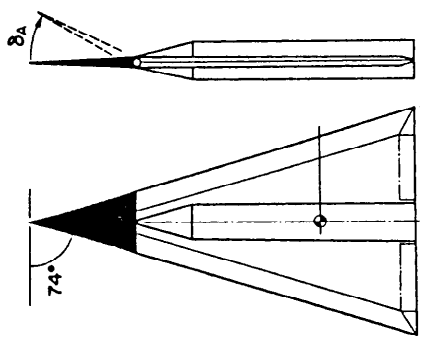


Figure 15. Upper-and lower-surface vortex flaps and effect of the former on L/D [31]

Leading-edge extensions (LEX) and apex flaps: Leading-edge extensions, Figure 16a, can be designed to minimize interference drag at high-speed cruise and to shed powerful vortices at moderate angles of attack, which interact with the wing flow field producing substantially higher maximum lift. The leading-edge extension shown can control the vortex development directly and maintain its stable state up to high incidences. Apex flaps, Figure 16b, are essentially a means of alternate pitch-control surfaces since they are located within an undisturbed flow environment allowing aerodynamic control to remain effective over a large angle-of-attack range otherwise limited by conventional trailing-edge control surfaces.



a. Example of a leading-edge extension (LEX) [31]



b. Concept of an apex flap

Figure 16. Example of a leading-edge extension and an apex flap [31]

Delay of vortex breakdown

One of the objectives of flow control in the case of delta wings is, of course, to avoid or delay vortex breakdown or, should it occur, keep it symmetrical to avoid strong uncontrollable forces and moments. Two schemes of vortex-breakdown control, quite different from the (more conventional) mechanisms discussed above, shall briefly be introduced here.

The first scheme employs trailing-edge jets to control the leading-edge vortices, Figure 17 [32]. The jets are arranged on either side of the wing close to the trailing edge and the direction of the jets can separately be adjusted from 45-deg downward to 30-deg upward with respect to the delta-wing surface. First experiments were carried out in a water towing tank using dye for flow visualization to locate vortex breakdown. Figure 17 shows the set-up of the nozzles and the general effect of blowing: for the case of the 30-deg downward jet (left side), vortex breakdown occurs considerably more downstream than for the 30-deg upward jet (right side).

The effect of the jet angle of symmetric jets on vortex breakdown as function of the angle of attack is depicted in Figure 18: for the uncontrolled case, the breakdown point moves very rapidly from 75% to 25% chord and, more gradually, to the apex when increasing the angle of incidence from 10° to 35°. All configurations of the vectored jet control, except the upward pointing jet, show a favorable effect on

vortex breakdown with the effectiveness increasing with the (absolute) jet angle. However, this favorable effect diminishes quickly as the jet angle exceeds 30° and as the angle of attack is increased. It seems that this phenomenon is closely related to the distance of the breakdown point from the trailing edge. Alternatives to trailing-edge jets are, therefore, blowing closer to the wing apex and along the vortex cores tangential to the leeward surface [33] or, although more complex as a control system, employing tangential leading-edge blowing [34]. Both methods have been found to delay vortex breakdown and ensure symmetrical vortices up to high angles of attack.

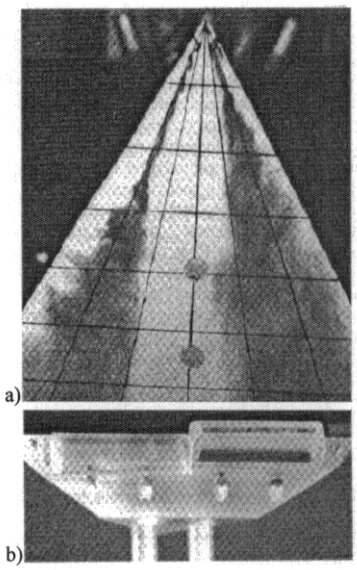


Figure 17. Nozzle set-up and effect of asymmetric jet control on vortex breakdown [32]

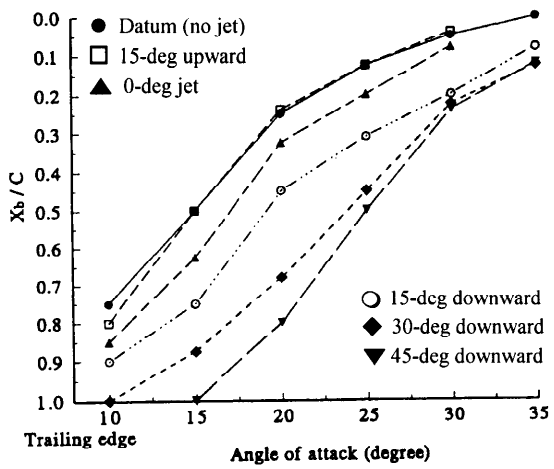
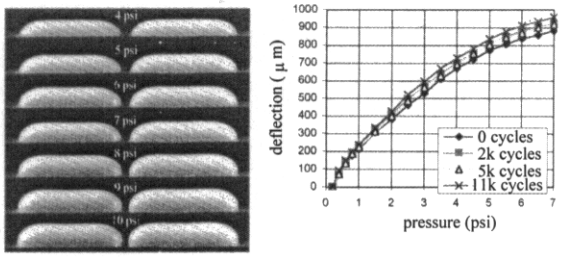
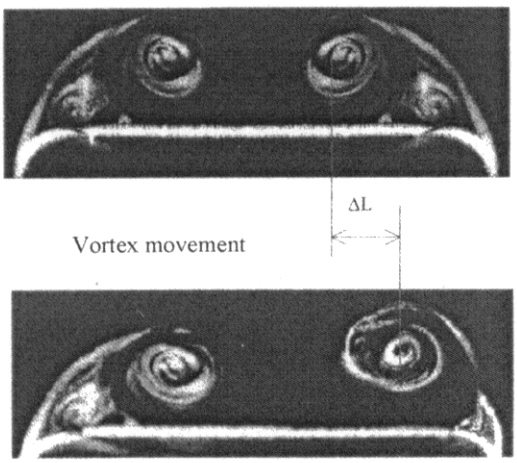


Figure 18. Effect of the symmetric trailing-edge-jet angle on vortex breakdown [32]

An at first unusual device to control vortical flow on delta wings is a Micro-Electro-Mechanical-System (MEMS), unusual since it is not directly apparent that a macro-scale flow system can be controlled by micro devices [13]. The link is, however, that the leading-edge vortex is very sensitive to perturbations at its origin. In order to use the leading-edge vortex pair for control — as envisaged in [13] — a detector must first be employed to locate the separation line where the vortices originate. Here, a flexible (MEMS) shear-stress skin of 80 micron thickness, containing 64 sensors, was wrapped around the leading edge of the delta wing. An array of MEMS actuators with a maximum deflection of 1 mm, Figure 19a, was then used to alter the separation line and break the vortex symmetry for control purposes. Figure 19b demonstrates, as an example, that the starboard primary vortex is shifted due to the deployment of the MEMS actuators. The resulting change in the pressure field will create a corresponding rolling moment.



a. Bubble actuation size and deflection



b. Shift of right primary vortex core due to control

Figure 19. Control of delta-wing vortex-core location by MEMS devices [13]

2.2.2 *Forebody vortex management*

When the leading edges of slender bodies are rounded, such as is the case on a body of revolution — missile or fighter forebody — the vortices become asymmetric due to an asymmetry in the flow separation and a large yawing moment may be introduced which cannot be compensated by a typical, fully deflected rudder [35]. For this reason, numerous means of alleviating the problem, such as blunting the forebody nose, small sidewise strakes, or blowing and suction, have been devised to control the asymmetry. Concerning the asymmetry and its existence, it seems, however, that perturbations at the apex of the (pointed) body play an important role and there is evidence that any asymmetric perturbation at the apex, even on the microscopic level, can dictate the form of flow asymmetry over the entire forebody. The amplification of this initial asymmetry, which leads to the serious control problem, is thought to be due to the interaction between the two vortices.

These considerations lead to the investigation of a possible control of the asymmetry by placing a small strake near the apex along the leeward axis of a tangent-ogive forebody so that the interaction between the two vortices in this region is reduced, Figure 20, inset [35]. First tests were conducted in a 24 inch x 36 inch flow visualization water tunnel. As an example of the results, a comparison of the approximate vortex positions at different angles of attack is given in Figure 20: without the strake, the forebody vortex flow becomes asymmetric at angles of attack above 30° with the asymmetry be-

coming stronger at higher incidences. With the strake, the vortex asymmetry is greatly reduced and the large yawing moment associated with the vortex geometry has most likely been attenuated. An application of the (single) strake is seen to be twofold: the strake can be deployed at the appropriate angle of attack to avoid the asymmetry and it can be employed, for instance, to control the missile attitude.

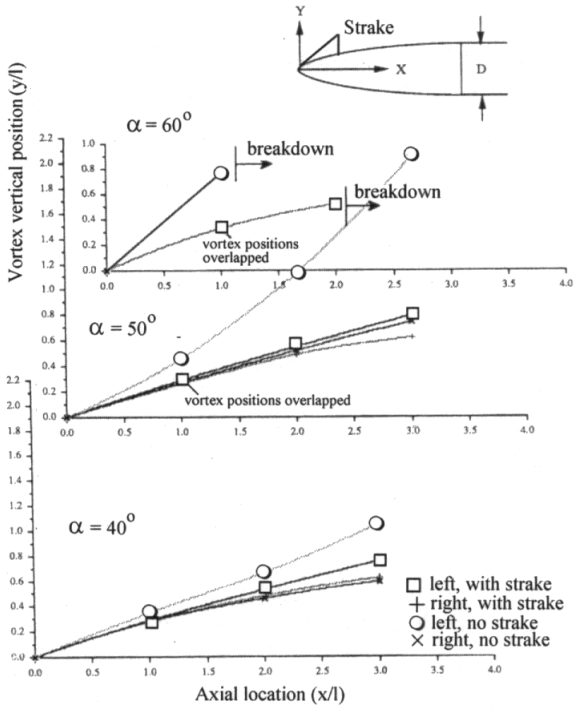


Figure 20. Approximate position of the vortices above the ogive-nosed body with and w/o strake [35]

3. Application of control and adaptation to long-range transport aircraft

Flow control is essentially concerned with the delay of boundary layer separation at low-speed high-lift conditions and with the control of shock waves to reduce drag and to delay drag rise and buffet onset at transonic conditions. Wing adaptation serves mainly to account for the change in aircraft weight due to fuel burn during long-range cruise, to account for off-design cruise conditions, which cannot be avoided, and to redistribute wing load when, for instance, approaching high-speed maximum lift with imminent outboard separation.

3.1 Lift enhancement and drag reduction

3.1.1 Low-speed applications

The high-lift-system design generally limits payload and greatly influences the cruise wing design for transport aircraft. Nevertheless, the best performance has traditionally been achieved with high-lift systems that use double or triple slotted flaps with the complexity of these designs, however, carrying significant weight penalties and requiring high maintenance [36]. Emphasis must, therefore, be placed on using flow control thereby allowing simpler high-lift systems. Candidate devices for applying lift-enhancing control are again vortex generators and Gurney–flap-type tabs.

These control devices have been experimentally investigated in [36] in conjunction with the single-slotted-flap airfoil depicted in Figure 21. The airfoil consists of a NACA 63_2 – 215 ModB main element and a 30%-chord slotted flap. The taps investigated were placed in the cove region and at the flap trailing edge; the vortex generators were of the Wheeler-wishbone type, Figure 5, placed on the upper surface of the flap at 10% flap chord. The data were taken at a freestream velocity of 68 m/sec ($M\infty \approx 0.20$). Various configurations, mainly differing in the flap deflection, ranging from 22° to 42°, and the corresponding overlaps and gaps, were investigated.

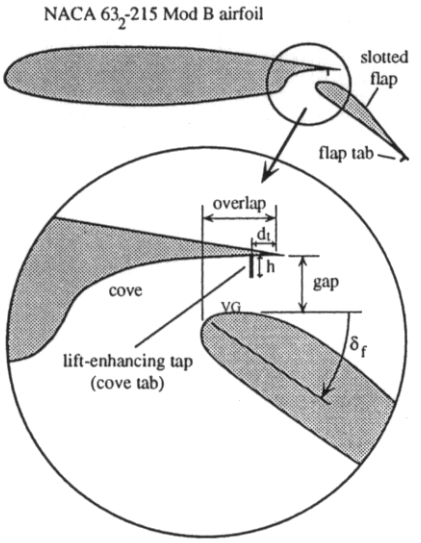


Figure 21. Lift-enhancing tabs and VGs on a two-element airfoil [36]

A summary of the improvement in lift due to control is depicted in Figure 22 for a flap deflection of 42°: the 1%c cove tab increases maximum lift by approximately 7% which is raised to 17% by adding vortex generators on the upper surface of the flap. Adding a tab at the trailing edge of the flap further increases maximum lift to 23% above the baseline maximum lift coefficient. The near parallel positive shift in the lift curves indicates the increase in effective camber due to control.

The application of the cove tab essentially shifts the location of separation from very near the leading edge of the flap to the 0.25%-chord position while, at the same time, increasing the load on the main airfoil element, Figure 23. With the addition of the vortex generators to the flap upper surface, the flow on the flap remains attached to the trailing edge and the main-element loading (negative upper-surface pressure) is further increased. Drag is generally reduced compared to the datum airfoil due to the delay in separation.

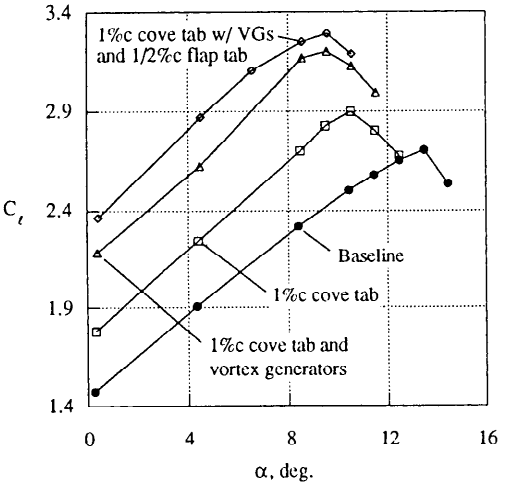


Figure 22. Effect of lift-enhancing tabs and vortex generators on lift, $M\infty \approx 0.2$, $Re_c = 3.7 \times 10^6$ [36]

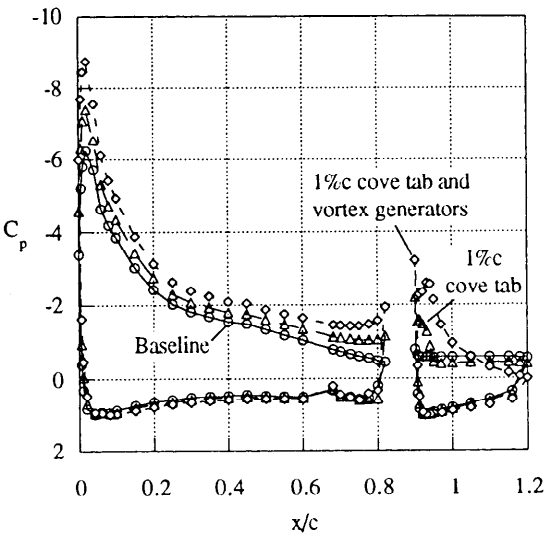


Figure 23. Effect of cove tab and vortex generators on the pressure distribution at $\alpha = 8°$, $M\infty \approx 0.2$ [36]

An alternative to the use of vortex generators to delay separation at high-lift conditions is the excitation of the flow by periodic blowing and suction (zero-mass air jets) through a narrow slot close to the leading edge of a deflected flap, Figure 24 [37]. For the wind-tunnel experiments cited here, the model, mounted on a three-component balance, consisted of an 180-mm-chord NACA 4412 main airfoil and an NACA 4415 flap of 72 mm chord. The flap was equipped with a 0.3 mm wide slot located at 3.5% flap chord. The periodic oscillating pressure pulses were generated externally by an electrodynamic shaker, driving a small piston which allowed the variation of jet frequency and intensity.

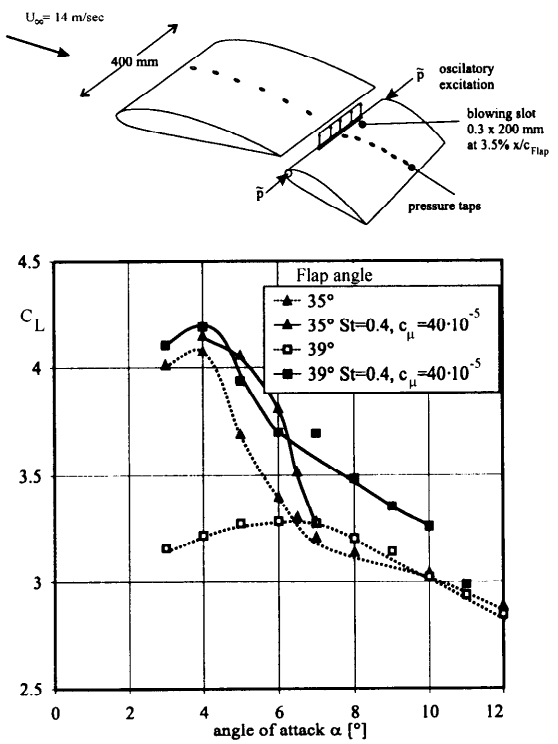


Figure 24. Effect of excitation by mass-less jets on lift of a single-flap airfoil for two flap deflections [37]

The effect of periodic excitations on lift is demonstrated in Figure 24 for two flap settings, viz., $\delta_{Fl} = 35°$ and 39°. Especially at the higher flap angle, the flow without control is totally separated over the flap; excitation causes here the flow over the flap to completely recover, yielding a strong increase in lift of about 30% up to a value higher than the maximum lift that could be achieved without excitation at the lower flap setting of 35°. The mass-less jet acts on the boundary layer by introducing turbulent structures into the flow which enhance the mixing process between the shear layer and the outer flow thus delaying total separation. Note that the results were obtained for a frequency of F = 80Hz (Strouhal number St = F c / $U\infty$ = 0.4) and a non-dimensional impulse coefficient of $c\mu = 2(H/c)(v'/U\infty)^2 = 40x10^{-5}$ where H is the slot width and v' the velocity fluctuation at the slot exit.

3.1.2 *High-speed applications*

Flow and boundary layer control at high speed (transonic) conditions has the objective to reduce shock strength in order to reduce wave drag, to keep the boundary layer growth as small as possible and to avoid or delay separation thus reducing viscous (pressure) drag, increasing L/D or C_{Lmax} and shifting the buffet boundary to higher Mach numbers and/or lift coefficients. Control methods to be considered here will include Gurney flaps, discrete slot suction, active control by a perforated plate / cavity arrangement and hybrid control combining the latter two.

Gurney flaps

The favorable effect of Gurney flaps or tabs on low-speed maximum lift lead to the investigation of such devices at transonic speeds by DLR/DASA-Airbus [39]. In this investigation, the Gurney flaps were used in conjunction with the transonic airfoil CAST10-2/DOA2 [38] characterized at near-cruise conditions by moderate to strong shock waves and relatively strong sustained rear adverse pressure gradients on the upper surface, Figure 25. Two flap sizes with a height of 0.5% chord and 1% chord, respectively, were investigated.

Experiments were carried out in the 1x1 Meter Transonic Wind Tunnel Göttingen [40] at Mach numbers of $M\infty$ = 0.73, 0.765, 0.78, and 0.80. The Reynolds number was $Re_c = 2.7x10^6$ with transition fixed at 30% chord on the upper surface. Measurements included surface pressure and wake-rake surveys and force and moment measurements by a side-wall balance.

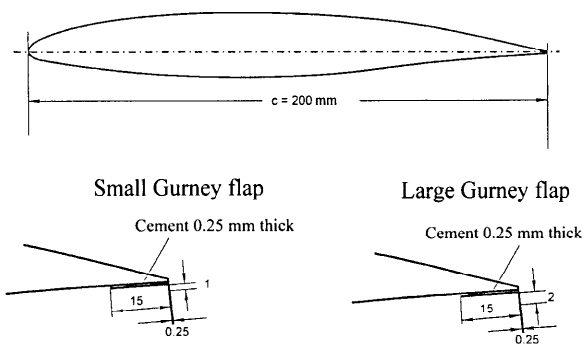


Figure 25. Airfoil CAST 10-2/DOA2 and arrangement of Gurney flaps [39]

Figure 26 shows the lift curves for the datum airfoil and the airfoil with the two different-size Gurney flaps at a freestream Mach number of $M\infty$ = 0.765: lift is considerably increased by the deployment of the flaps with the smaller flap exhibiting nearly the same effectiveness as the larger one. The parallel shift of the lift curves again indicates that the flap essentially increases effective camber.

The drag polars for the above conditions are shown in Figure 27: the Gurney flaps generate, as expected, higher

drag in areas where the flow is not separated. At higher lift coefficients the drag in the presence of the Gurney flaps is, however, considerably less than in the case of the datum airfoil resulting in an L/D that is higher than any attainable with the clean airfoil. The smaller Gurney flap is at these conditions the more effective device. The favorable effect of the Gurney flaps essentially results from shifting load from the forward part of the airfoil to the rear part (at constant C_L) thereby reducing shock strength hence wave drag. This shift causes, of course, a nose-down pitching moment which must, on the full aircraft, be compensated. Note that the Gurney flaps seem well suited to improve the buffet boundary, a feature needed when employing shock control to increase cruise speed.

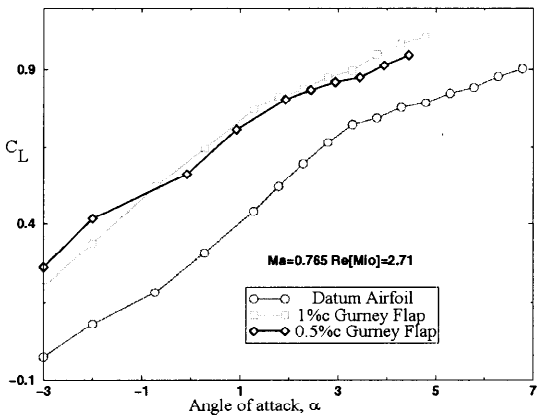


Figure 26. Effect of Gurney flaps on lift for the airfoil CAST 10-2/DOA2 at M∞ = 0.765 [39]

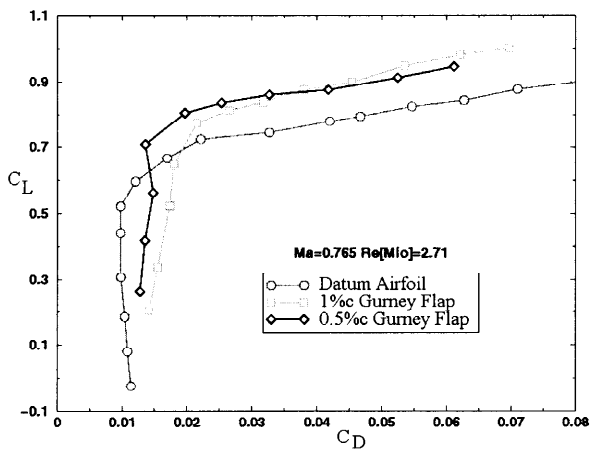


Figure 27. Effect of Gurney flaps on the drag polar for the airfoil CAST 10-2/DOA2 at M∞ = 0.765 [39]

Discrete suction and cavity ventilation

Active control by discrete suction and cavity ventilation, primarily designed to reduce airfoil or wing drag and to postpone buffet onset, was thoroughly investigated within the EU-project EUROSHOCK II - Drag Reduction by Shock and Boundary Layer Control [24]. Within this project, DERA carried out an extensive study of flow control by discrete suction, by active ventilation with part-suction through a perforated plate/cavity arrangement, and by hybrid control consisting of passive-cavity ventilation in the shock region combined with discrete suction downstream of the passive cavity, utilizing the DRA-2303 laminar airfoil [41]. Examples of results obtained for hybrid control and discrete suction, respectively, are presented in Figures 28 and 29.

The effect of **passive** control on drag — previously investigated within the EU-project EUROSHOCK I [10] — is essentially confirmed by the data shown in Figure 28 for the case CQ = 0: although wave drag is reduced, total drag is, as shown, considerably increased. Moreover, even if discrete suction is applied downstream of the passive cavity, drag, although generally reduced compared to passive control, is still higher than the one obtained for the datum airfoil. (Note that this also holds for active control by part-suction through a single cavity.)

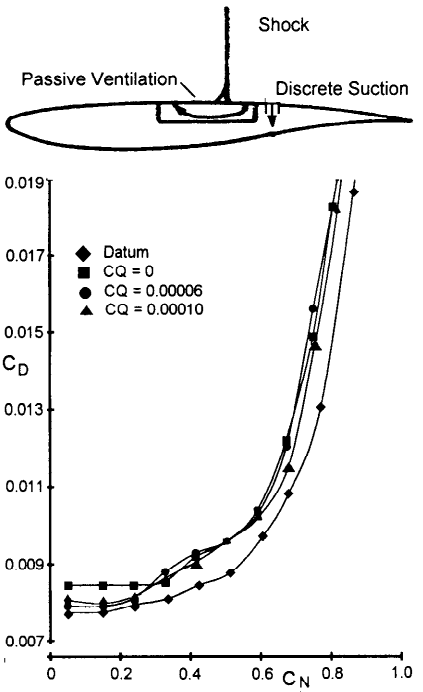


Figure 28. Effect of hybrid control on the drag polar for the airfoil DRA-2303, M∞ = 0.68, Re = 19x10^6 [41]

Figure 29 shows that when applying discrete suction upstream of the shock total drag is reduced, which is mainly due to a reduction in viscous drag, in spite of an increase in wave drag. This holds even when accounting for pump drag.

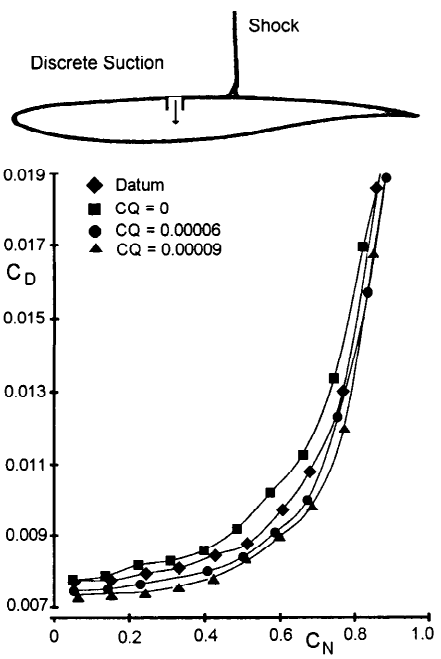


Figure 29. Effect of discrete suction on the drag polar for the airfoil DRA-2303, M∞ = 0.68, Re = 19x10^6 [41]

The above results lead to the conclusion that flow control involving ventilation via a perforated surface/cavity arrangement — either passive or active — is not a viable tool when drag reduction is the main objective, at least not for the laminar-type airfoils considered within EUROSHOCK II and suction rates considered feasible for aircraft installation [41]. However, for the purpose of stabilizing the shock wave and avoiding shock-induced separation, as is, e.g., required in engine intakes, this type of control seems well suited [42].

In order to determine the reason for the increase in total drag in the case of hybrid control, it is necessary to first consider the local flow and boundary layer development in the shock boundary layer interaction region, Figure 30 [43]: it is indicated that in the case of hybrid control, the displacement thickness — as well as the momentum thickness (not shown) — downstream of the interaction/control region is, in spite of the considerable amount of suction applied, higher than the one for the reference case without control due to the recirculating flow in the cavity region. Momentum-balance considerations for this case indicated that wave drag is reduced but friction drag increased, leaving, however, a net reduction in drag of about 4%. Why then is total drag increased in the case of airfoil flow?

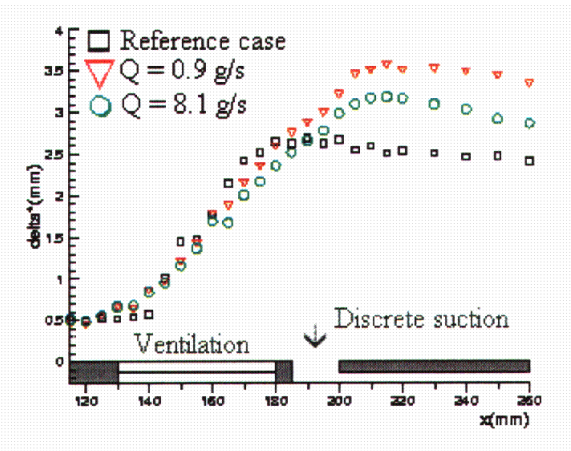
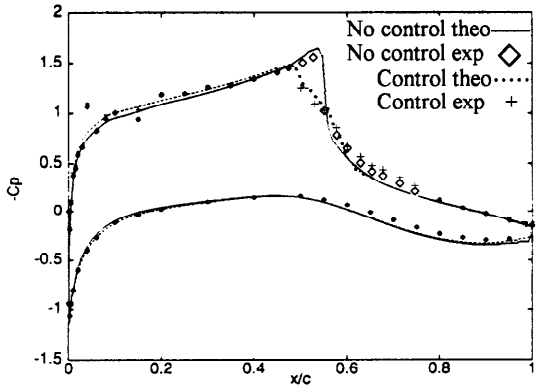


Figure 30. Effect of hybrid control on the boundary layer development, ONERA channel flow experiments [43]

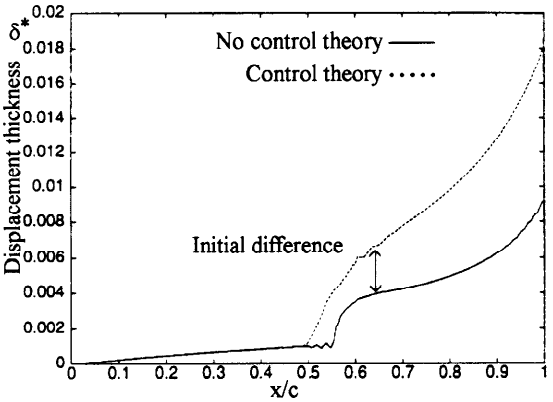
The explanation can be found in Figure 31 [44] by considering results for passive-cavity control: Figure 31a shows that the pressure rise associated with the shock is spread in chordwise direction due to control indicating a strong decrease in wave drag. The boundary layer displacement thickness in Figure 31b shows, similar to the results in Figure 30, the stronger initial increase in boundary layer thickness due to control; however, on the airfoil this initial increase is strongly amplified by the sustained rear adverse pressure gradients prevailing on the airfoil, resulting in a correspondingly stronger increase in viscous drag which overcompensates the decrease in wave drag thus resulting in higher total drag than in the case of the airfoil without control.

3.2 Wing-adaptation schemes

It has been pointed out in Chapter 2 that for the various points of a flight envelope wing camber can be adjusted to provide, for instance, minimum drag at a given lift coefficient. The variable camber was achieved by adjusting leading- and trailing-edge deflections [18, 20]. Also suggested, and actually realized, at least in model tests, were performance optimizations by changing the complete airfoil or wing contour [14, 45]. However, in all instances the effort in structural realization at full-scale conditions seems to be considerable, if not prohibitive.



a. Surface pressure distributions with and w/o control



b. Boundary layer development with and w/o control

Figure 31. Effect of passive control by ventilation for the airfoil DRA-2303, $M\infty = 0.68$, $Re = 19x10^6$, $C_L = 0.82$, DERA experiment [10], CIRA computations [44]

Within the EU-project EUROSHOCK II [24] and the German national project ADIF [22, 23] a somewhat different approach was, therefore, taken based on employing a local contour 'bump' (see Figures 1 and 32) in the shock region to reduce shock strength — the reduction of shock strength being a major concern of any high-speed adaptation — in combination with variable-camber flexible trailing-edge flaps.

3.2.1 Control by contour bump

Bumps for shock control have been investigated by DLR numerically and experimentally for two airfoils [47] and an infinitely-swept (sheared) wing [48]. Here, we will only consider as an example for bump effectiveness one of the airfoils, namely, the 'ADIF' airfoil, which is an A340-type transonic design [47]. For this airfoil, bumps of various heights were designed by numerical optimization studies. The modular ADIF airfoil model, tested in the Cryogenic Ludwieg Tube of DLR (KRG) [46], is shown in Figure 32 indicating the various bumps and a suction slot upstream of the shock region used for control.

The process of shock control is, of course, based on weakening the shock by spreading the pressure rise due to the shock over a certain chord-wise distance. This is demonstrated for the ADIF airfoil in Figure 33 for a Mach number and lift coefficient near the design condition: the pressure distributions exhibit an almost perfect isentropic recompression, at least near the surface, due to the bumps. Both bumps reduce the total drag as can be seen by examining the wake profiles in the right-hand diagram of the figure with the smaller bump, however, being somewhat more effective than the higher one. The reduced effectiveness of the latter is due to the not quite optimal position/height of the bump relative

to the not quite optimal position/height of the bump relative to the shock, also indicated by the weak expansion within the compression region.

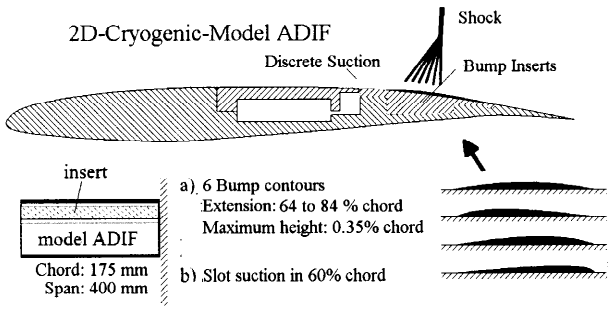


Figure 32. Sketch of the A340-type airfoil model with bumps and suction inserts [47]

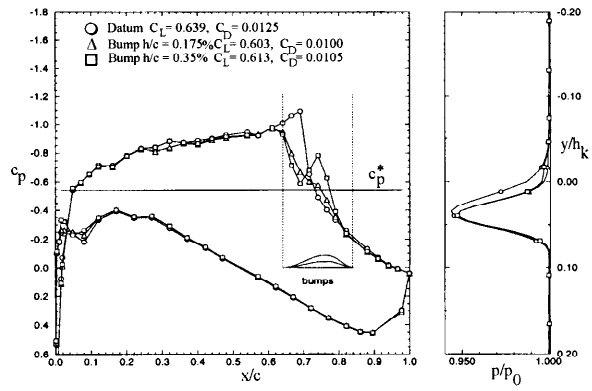


Figure 33. Pressure and wake profiles for the ADIF airfoil with and w/o bumps, M ∞ = 0.765, α = -0.5°, Re = 8x10^6, $(x/c)_{tr}$ = 0.3 / 0.7 [47]

The complete polar for the Mach number of M ∞ = 0.765 shows, Figure 34, that the higher bump is more effective at higher lift coefficients, i.e., in the presence of stronger shock waves, resulting in a drag reduction of ΔC_D = 0.0020 (20 cts) at a lift coefficient of $C_L \approx 0.62$ and reductions of up to ΔC_D = 0.0035 (35 cts) at higher lift, amounting to 17% and 23% drag reductions, respectively. The lower bump, although not as effective at higher lift, causes a noticeable drag reduction over a much larger range of lift coefficients so that, would one fly only at that Mach number, one would choose this bump as a fixed installation. However, it becomes quite clear from this figure that for optimum performance an adaptive bump arrangement should be selected.

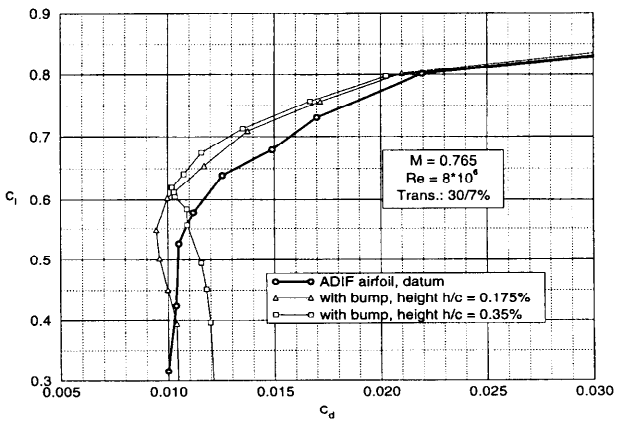


Figure 34. Effect of contour bumps on the drag polars at M ∞ = 0.765, Re = 8x10^6, $(x/c)_{tr}$ = 0.3 / 0.7 [47]

The sheared-wing tests [48] showed similar results as the 2D-tests with the drag reductions, however, being somewhat less. It was also shown in these tests that the buffet boundary can be noticeably improved by bump control with lift increases at buffet onset of up to 10% for a bump designed for that purpose. A bump designed for drag reduction was found to increase lift at buffet onset by 5% [49].

3.2.2 Contour-bump / flap optimization

Other means of wing adaptation to account for changing freestream conditions include, as discussed in conjunction with the MAW, conventional or advanced variable-camber trailing-edge flaps. Due to the potential of the latter and the contour bump — and as alternative to adapting the complete airfoil or wing — the optimization of a bump in conjunction with a variable-camber flap to achieve minimum drag was considered by DLR in cooperation with DASA-Airbus [50]. For the optimization process the coupled flow solver MSES [51] and the optimization procedure LINDOP were used [52]. The optimization was carried out for the airfoil 'VC-opt', designed by DASA-Airbus to be used with variable-camber (VC) trailing-edge flaps. The airfoil geometry, indicating bump locations and flap deflections, is sketched in Figure 35. The results of such an optimization are briefly outlined below.

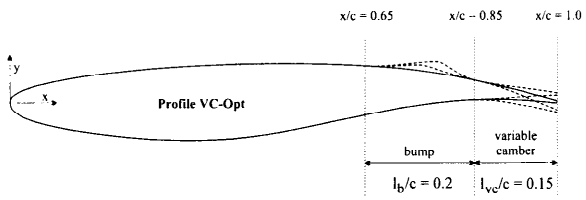


Figure 35. Airfoil 'VC-opt' with bump and variable camber contour modifications [50]

Drag-minimized polars for independent bump and flap optimizations, respectively, and for the combined flap/bump optimization are compared in Figure 36 with the datum drag polar: the bump — as already indicated above — results in a considerable drag reduction at higher lift coefficients where stronger shocks occur, but the gains deteriorate as lift decreases. Variable camber, on the other hand, results in noticeable drag reductions at low to medium lift coefficients while at higher lift drag with and w/o optimization is essentially the same. The latter is due to the flap not being able to achieve such high lift without the generation of strong shock waves. When combining contour bump and flap in the optimization process, considerable gains are attainable over the entire lift range investigated with maximum drag reductions of up to 24%.

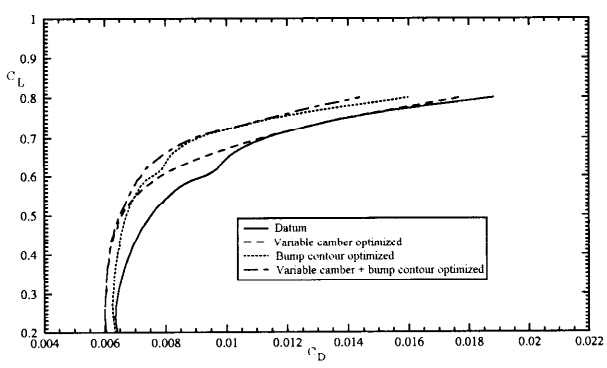


Figure 36. Effect of local contour optimizations on drag, airfoil 'VC-opt', M ∞ = 0.793, Re = 50x10^6 [50]

The optimization process is essentially as follows: in the lower lift range $C_L < 0.52$, minimum drag is achieved by flap adjustment only. At higher lift coefficients, drag is first minimized by flap adjustment which is then followed by adjusting bump height and bump crest position with respect to the shock for the final drag reduction.

Representative pressure distributions, corresponding to a lift coefficient of $C_L = 0.65$, are compared in Figure 37: variable camber produces – at equal lift – a higher absolute pressure level and a somewhat more forward, weaker shock with a (marginally) positive effect on drag. The bump reduces shock strength, thus considerably reducing wave and total drag, the latter in spite of an increase in viscous drag indicated by a somewhat reduced pressure recovery. By applying variable camber in addition to the bump, a higher absolute pressure level and a further reduction of shock strength, coupled with an improved pressure recovery, is achieved resulting in a further drag reduction.

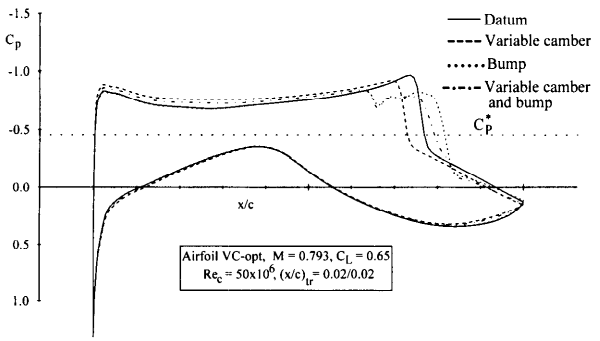


Figure 37. Effect of local contour optimizations on airfoil pressure distributions, airfoil 'VC-opt', $M\infty = 0.793$, $C_L = 0.65$, $Re_c = 50x10^6$ [50]

3.3 Benefits of control application

3.3.1 Long-range-mission benefits

When considering penalties and benefits of control application, certain criteria have to be established by which a design can easily be judged. One criterion was suggested by BAE SYSTEMS-Airbus [53], based on Cash Operating Costs (COC), given by the formula

$$\Delta \text{ COC/COC} = 0.49\ \Delta C_D/C_D + 1.9x10^{-3}\ \Delta W + \\ + 0.113\ \Delta \text{ mc/mc}.$$

Here, ΔC_D is the change in total aircraft drag due to control, ΔW is the weight increase due to control installation and Δ mc/mc is the increase in maintenance costs.

Of the control devices investigated within EUROSHOCK II [24], the most effective device was found to be the contour bump. A contour bump applied to a hybrid-laminar-flow wing of a long-range A340-type aircraft was, therefore, chosen for a benefit and penalty assessment study by DASA-Airbus [15]. For the study, a wing section with typical laminar-flow-sustaining pressure distributions was selected. These pressure distributions are depicted in Figure 38 for two Mach numbers, the chosen design Mach number $M_\infty = 0.82$ and the off-design Mach number of $M_\infty = 0.84$; they are characterized by highly accelerating flow with relatively strong shocks on the upper surface but limited shock movements with changing Mach number and lift coefficient.

The off-design Mach number of $M_\infty = 0.84$ and the local lift coefficient of $C_L = 0.48$ were selected to optimize the bump location with respect to the shock. The minimum-drag polar for that Mach number was then established by adjusting the bump height with changing lift coefficient — similar to the optimization procedure outlined above — and the estimated drag reductions transferred to the wing and the complete aircraft assuming that laminar flow covers 60% of the wing area, Figure 39. The corresponding flight polars and the drag balance for the complete aircraft at the two Mach numbers considered are shown in Figure 40. The highest drag reduction of about 4% is obtained for $C_L = 0.38$ at the off-design Mach number $M_\infty = 0.84$ and for $C_L = 0.58$ at the design Mach number $M_\infty = 0.82$.

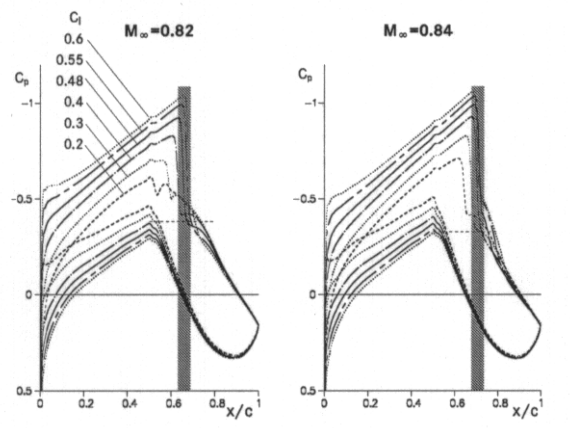


Figure 38. Pressure distributions for the HLF wing section at flight conditions, wing section PHLF1, $\phi = 26°$, $Re_c = 35x10^6$, $(x/c)_{trans} = 0.50$ [15]

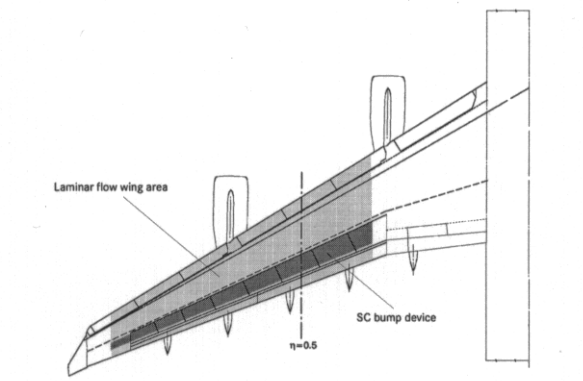


Figure 39. A340 HLF wing with integrated adaptive bump device [15]

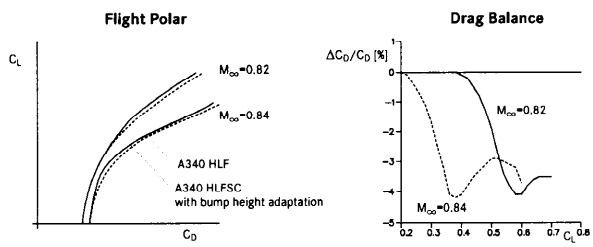


Figure 40 Predicted flight polar and drag balance for the A340 HLF-wing aircraft with bump control [15]

One more assessment aspect is the weight penalty associated with the bump installation: the optimized wing / bump design, as required here, interferes with the rear spar of the wing box, located at x/c = 0.64, and the spoiler, located between x/c = 0.74 and 0.86, of the original A340 wing so that wing modifications are needed. The wing box has to be shortened and, assuming the integration of the bump into the spoiler — an option considered here — the spoiler has to be

enlarged up to 23% chord, Figure 41. Furthermore, since strong shocks mainly appear at the outer wing, the spoiler has to be extended to the wing tip, Figure 39; for roll-control capability, a variable-camber flap is introduced over the whole span replacing the aileron. This flap can also be used to fine-tune the shock location relative to the bump. *The modification of the wing structure for shock control is estimated to carry a weight increase of 0.25 tons.*

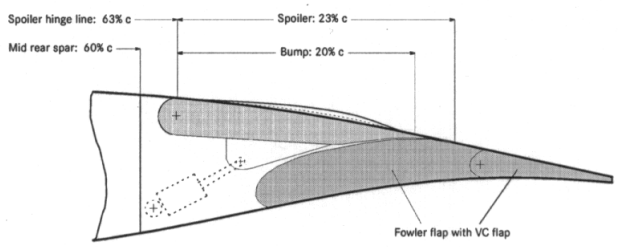


Figure 41. Integration of the adaptive variable-height bump control device into the modified A340-wing spoiler [15]

With the flight polars and the weight penalty given above, a standard North Atlantic flight mission with a range of 3500 nm was investigated assuming 600 trips per year at the cruise Mach number $M_\infty = 0.82$ and 620 trips per year at the off-design Mach number $M_\infty = 0.84$. The flight profile, Figure 1, has been predicted by the standard procedure with steps of 4000ft for optimal flight altitude as cruise proceeds. At these conditions, a reduction in fuel consumption per year due to shock control of about 353 tons (1.23%) at $M_\infty = 0.82$ and of about 792 tons (2.11%) at $M_\infty = 0.84$ is obtained from flight-mission computations, Table 1 [15]. Using the formula for Cash Operating Costs (COC) given above, **a decrease of 1.3% in COC** is achieved assuming an average aircraft drag reduction of $\Delta C_D/C_D = 3\%$, the weight penalty of $\Delta W = 0.25$ tons and an increase in maintenance costs of Δ mc/mc = 0.5. Note that for the combination bump/variable trailing-edge flap are further improvement is expected.

Table 1. Gains associated with bump-control implementation

	Trips/ year	Block -time	Block fuel	Fuel/ year	Fuel savings	Fuel savings
M=0.82		hr	Kg	to	to	%
HLF	600	7.9	47.998	28.799		
HLFSC	600	7.9	47.410	28.446	356	1.23
M=0.84						
HLF	620	7.6	55.797	34.594		
HLFSC	620	7.6	54.622	33.866	729	2.11

HLF = Hybrid-Laminar-Flow wing
HLFSC = HLF-wing with shock control

3.3.2 Possible structural bump realization

Concerning the structural realization of adaptive wings and/or their components, we will her only consider the possible realization of an adaptive contour bump as proposed within the German national project ADIF.

Considering the spoiler bump and the aerodynamic requirements derived at in the bump optimization process, viz., a bump length of 20% of the wing chord, a movement of the bump crest of 30% to 70% of the bump chord, and a bump height variation of up to 0.50% of the wing chord to adjust to changing shock strength and location, a three-layer structure of the spoiler has been envisaged, Figure 42 [54].

The structure consists of a load-carrying sub-structure into which a second layer of actuators is embedded. The upper layer, consisting of a flexible skin, forms the actual bump. The actuator itself consists of an CFRP (Carbon Fiber Reinforced Plastic) tube, acting as a spring, with two symmetrical rubber-lined compartments which can be pressurized. The free end of each compartment, linked to the skin-stringer via a flexible joint, allows an up and down movement of the actuator of two-thirds of the tube height. The flexible joint ensures that the actuator stroke is always perpendicular to the spoiler skin. Such an arrangement has been successfully dry-tested and a similar system is presently being integrated into an airfoil model for (adaptive) testing at variable freestream conditions. Note that it is anticipated to later actuate the 'spring-tube' by Shape Memory Alloys.

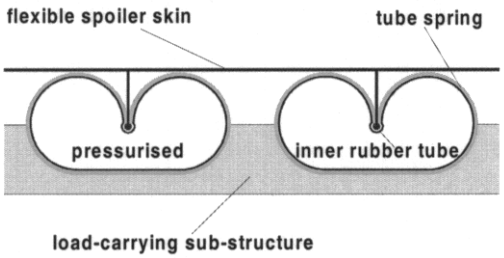


Figure 42. The spoiler-integrated adaptive bump concept [31]

4. Summary and conclusion

Essentially two aspects of the application of active flow control have been considered: firstly, the improvement of aircraft performance otherwise restricted by the development of the boundary layer and the interaction of the boundary layer with the outer "inviscid" flow field, secondly, the direct control of the aircraft geometry to adjust to changing flight or freestream conditions for optimized performance at all points of the flight envelope. In the present paper, flow control and adaptive-wing concepts for military and civil air-vehicle applications have been discussed. Examples for each control objective were provided and benefits associated with implementing adaptive-wing and flow-control technologies outlined. The discussions were based on results from the literature and on results from two recent projects, namely, the German national adaptive-wing project ADIF and the EU-project EUROSHOCK II. Main emphasis was placed on aerodynamics.

The following conclusions concerning control and adaptation effectiveness may be drawn:

- Vortex generators, be it counter-rotating or Wheeler-type, mini or air-jet VGs, and trailing-edge devices, such as Gurney flaps and taps, are very effective in improving low-speed high-lift capacity (L/D, C_{Lmax}) with gains of up to 27% over a clean single-flap configuration. These devices also considerably improve high-speed off-design conditions such as the drag-rise and buffet boundaries.
- Zero-mass pulsing jets seem at low speeds a viable alternative to VGs. Such devices should, therefore, also be investigated for separation control at transonic speeds where little information is available.
- Concerning vortex control and vortex breakdown, trailing-edge jets, tangential leading-edge blowing, chordwise blowing along the vortex core seem very effective, besides the more conventional means such as compartmentation of the leading edge, leading-edge extensions, apex flaps, strakes and others. MEMS are promising devices that must be further explored.
- Considering suction/ventilation arrangements, only discrete suction seems a viable tool if drag reduction is the main driver; however, for shock stabilization and the delay of separation active and passive ventilation via a perforated plate/cavity arrangement seem well suited.

- As a single device, an adaptive contour bump of variable height was found to be very effective in reducing total aircraft drag with a corresponding reduction in COC of up to 1.3% for an HLF-wing aircraft on a typical long-range mission. Especially in conjunction with a variable-camber flap, further improvements over a wider range of flight conditions can be expected.
- Control schemes may lead to simpler structural designs with corresponding reductions in weight and manufacturing costs despite a somewhat increased complexity due to control integration.

In future work it seems very vital for research and engineering to put greater effort into the realization and integration of control into real aircraft, foremost solving the structural problems also aiming at simpler designs.

5. Literature

[1] Gad-el-Hag, M., Pollard, A., Bonnet, J.-P. (Eds.), Flow Control, Fundamentals and Practices, Lecture Notes in Physics, N. s. M., Monographs, No. 53, Springer Verlag 1998

[2] Bushnell, D.M., Hefner, J.N. (Eds.) Viscous Drag Reduction in Boundary Layers, Progress in Astronautics and Aeronautics, Vol. 123, 1990

[3] Kimura, M., Tung, S., Ho, C.-M., Jiang, F., Tai, Y.-C., MEMS for Aerodynamic Control, AIAA 28th Fluid Dynamics Conference / AIAA 4th Shear Flow Control Conference, June 29 – July 2, 1997 / Snowmass Village, CO, Paper AIAA 97-2118, 1997

[4] Peake, D.J., Henry, F.S., Pearcey, H.H., Viscous Flow Control with Air-jet Vortex Generators, AIAA 17th Applied Aerodynamics Conference, June 28 – July 1, 1999 / Norfolk, VA, Paper AIAA 99-3175, 1999

[5] Lin, J.C., Application of Micro-Vortex Generators for Turbulent Flow Separation Control, in: IUTAM Symposium on Mechanics of Passive and Active Control, Göttingen, Sept. 7-11, 1998, Kluwer Academic Publishers, 1999

[6] Seifert, A., Pack, L.G., Oscillatory Control of Separation at High Reynolds Numbers, AIAA Journal, Vol.37, No.9, September 1999, pp. 1062 – 1071

[7] Stanewsky, E., Krogmann, P., Transonic Drag Rise and Drag Reduction by Active / Passive Boundary Layer Control, in: AGARD Report No. 723, Lecture Series Aircraft Drag Prediction and Reduction, 1985

[8] Hefner, J.N., Bushnell, D.M., Viscous Drag Reduction via Surface Mass Injection, in: Viscous Drag Reduction in Boundary Layers, Progress in Astronautics and Aeronautics, Volume 123, 1990

[9] Raghunathan, S., Mabey, D.G., Passive shock wave boundary layer control experiments on a circular arc model, Paper AIAA 86-0285, 1986

[10] Stanewsky, E., Délery, J., Fulker, J., Geissler, W. (Edit.), EUROSHOCK – Drag Reduction by Passive Shock Control, Notes on Numerical Fluid Mechanics, Volume 56, Friedr. Vieweg & Sohn Verlagsgesellschaft mbH, Braunschweig/Wiesbaden, 1997

[11] Jeffrey, D.R.M., Aerodynamics of the Gurney Flap, AIAA 14th Applied Aerodynamics Conference, June 17–20, 1996 / New Orleans, LA, Paper AIAA 96-2418, 1999

[12] Meyer, R., Bechert, D. W., Hage, W., Wind tunnel experiments with artificial bird feathers for passive separation control on airfoils, in: IUTAM Symposium on Mechanics of Passive and Active Control, Göttingen, Sept. 7-11, 1998, Kluwer Academic Publishers, 1999

[13] Ho, C.-M., Huang, P.-H., Yang, J.M., Lee, G.-B., Tai, Y.-C., Active Flow Control by Micro Systems, in: IUTAM Symposium on Mechanics of Passive and Active Control, Göttingen, Sept. 7-11, 1998, Kluwer Academic Publishers, 1999

[14] Siclari, M.J., van Nostrand, W., Austin, F., The Design of Transonic Airfoil Sections for an Adaptive Wing Concept Using a Stochastic Optimization Method, AIAA 34th Aerospace Sciences Meeting & Exhibit, January 15 – 18, 1996 / Reno, NV, Paper AIAA 96-0329, 1996

[15] Thiede, P., Dargel, G., Assessment of Shock and Boundary Layer Control Concepts for Hybrid Laminar Flow (HFL) Wing Design, in: EUROSHOCK II Final Technical Report, TR BRPR-95-76/1, 1999 and DASA-Airbus DA-Report No. EF-069/99, 1999

[16] DeCamp, R.W., Hardy, R., Gould, K., Mission Adaptive Wing, International Pacific Air and Space Technology Conference, Melbourne, Australia, SAE Paper 872419, 1988

[17] Smith, S.B., Nelson, D.W., Determination of the Aerodynamic Characteristics of the Mission Adaptive Wing, AIAA Journal of Aircraft, Vol. 27, No. 11, November 1990, pp. 950 - 958

[18] Thornton, S.V., Reduction of Structural Loads Using Maneuver Load Control on the Advanced Fighter Technology Integration (AFTI)/F-111 Mission Adaptive Wing, NASA TM 4526, September 1993

[19] Szodruch, J., The Influence of Camber Variation on the Aerodynamics of Civil Transport Aircraft, AIAA Aerospace Sciences Meeting, January 1985 / Reno, NV, Paper AIAA 85-0353, 1985

[20] Martins, A.L., Catalano, F.M., Viscous Drag Optimization for a Transport Aircraft Mission Adaptive Wing, Proceedings of the 21st ICAS Congress, 13 – 18 September, 1998, Melbourne, Australia, Paper A98-31499, 1998

[21] Ashill, P.R., Fulker, J.L., Simmons, M.J., Simulated Active Control of Shock Waves in Experiments on Aerofoil Models, Proceedings ICEFM, Turin, July 1994

[22] Anonym., Adaptive Wing ADIF – Work Package Descriptions for the Project, DASA-Airbus, DaimlerChrysler F&T, DLR, 1995

[23] Mertens, J., Aerodynamic objectives of the adaptive wing ADIF, in: DGLR-Yearbook 1998, 1998

[24] Stanewsky, E., de Matteis, P.P., Fulker, J., Doe, R., EUROSHOCK II – Drag Reduction by Shock and Boundary Layer Control, EUROSHOCK II Final Technical Report, TR BRPR-95-76/1, 1999, and Synthesis Report TR BRPR-95-76/2,1999 (to be published in Notes on Numerical Fluid Mechanics)

[25] McCormick, D.C., Shock/Boundary-Layer Interaction Control with Vortex Generators and Passive Cavity, AIAA Journal, Vol. 31, No. 1, January 1993, pp. 91 – 96

[26] Pearcey, H.H., Shock induced separation and its prevention by design and boundary-layer control, in: Boundary Layer and Flow Control, Vol. 2, Ed. Lachmann, G. V., Pergamon Press, 1961

[27] Langan, K.J., Samuels, J.J., Experimental Investigation of Maneuver Performance Enhancement on an Advanced Fighter/Attack Aircraft, AIAA 33rd Aerospace Sciences Meeting, 9-12 January 1995/ Reno, NV, Paper AIAA 95-0442

[28] Bryant, M.D., Gifford, R.M., Spurlin, C.J., Wind Tunnel Tests of a 1/10-scale Dornier Alpha-jet Model with a Transonic Technology (TST) Wing, Arnold Engineering Development Center, Report AEDC-TSP-94-P7, Nov. 1994

[29] Kudva, J.N., Lockyer, A.J., Appa, K., Adaptive Aircraft Wing, in: AGARD SMP Lecture Series on Smart Structures and Materials: Implications for Military Aircraft of the New Generation, AGARD LS-205, 1996

[30] Powers, S.G., Webb, L.D., Friend, E.L., Lokos, W.A., Flight Test Results from a Supercritical Mission Adaptive Wing with Smooth Variable Camber, NASA Technical Memorandum 4415, November 1992

[31] Rao, D.M., Campell, J.F., Vortical Flow Management Techniques, in: Progress in Aerospace Sciences, Vol. 24, pp. 173-224, 1987

[32] Shih, C., Ding, Z., Trailing-Edge Jet Control of Leading-Edge Vortices of a Delta Wing, AIAA Journal, Vol. 34, No. 7, pp 1447-1457, July 1996

[33] Mitchell, A., Molton, P., Barberis, D., Délery, J., Control of Vortex Breakdown Location by Symmetric and Asymmetric Blowing, 30th AIAA Fluid Dynamics Conference, 28 June-1 July, 1999/Norfolk, VA, Paper AIAA 99-3652, 1999

[34] Wood, N.J., Roberts, L., Celik, Z., Control of Asymmetric Vortical Flow over Delta Wings at High Angles of Attack, AIAA Journal of Aircraft, Vol. 27, No. 5, pp. 429 – 435, May 1990

[35] Ng, T.T., Effect of a Single Strake on the Forebody Vortex Asymmetry, AIAA Journal of Aircraft, Vol. 27, No. 9, pp. 844-846, September 1990

[36] Storms, B.L., Ross, J.C., Experimental Study of Lift-enhancing Tabs on a Two-element Airfoil, AIAA Journal of Aircraft, Vol. 32, pp. 1072-1078, Sept.-Oct. 1995

[37] Tinapp, F., Nitsche, W., On active control of high-lift flow, in: Engineering Turbulence Modeling and Experiments - 4, W. Rodi and D. Laurence (Editors), Elsevier Science Ltd., 1999

[38] Stanewsky, E., Interaction Between the Outer Inviscid Flow and the Boundary Layer on Transonic Airfoils, Journal of Flight Sciences and Space Research (ZfW), Vol. 7, No.4, pp. 242-252, July/August 1983

[39] Bechert, D.W., Stanewsky, E., Hage, W., Wind Tunnel Measurements on a Transonic Wing with Flow Control by Various Devices, DLR Internal Report DLR-IB 223-99C05 / IB 92517-99/b3-2, June 1999

[40] Binder, B., Riethmüller, L., Tusche, S., Wulf, R., Upgrading the Transonic Wind Tunnel Göttingen, in: Yearbook of the DGLR, Volume 1, 1992

[41] Fulker, J., Simmons, M. J., An investigation of active, suction, shock and boundary layer control, in: EUROSHOCK II Final Technical Report, TR BRPR-95-76/1, 1999, and DERA Report MSS4X/CR980817/1.0, 1999

[42] Lee, D.B., Leblanc, R., Interation onde de choc oblique-couche limite turbulente sur paroi poreuse avec aspiration, in: AGARD-CP-365 Improvement of Aerodynamic Performance Through Boundary Layer Control and High Lift Systems, August 1984

[43] Bur, R., Benay, R., Corbel, B., Soares-Margadinho, R., Soulevant, D., Study of control devices applied to a transonic shock wave/boundary layer interaction, in: EUROSHOCK II Final Technical Report, TR BRPR-95-76/1, 1999, and ONERA Technical Report RT 126/7078 DAFE/Y, 1999

[44] De Matteis, P., Dima, C., Numerical investigation of passive shock control on transonic airfoils through an Euler/boundary-layer coupling technique, in: EUROSHOCK-Drag Reduction by Passive Shock Control, Notes on Numerical Fluid Mechanics, Volume 56, Verlag Friedr. Vieweg&Sohn, 1997

[45] Rossi, M.J., Austin, F., VanNostrand, W., Active Rib Experiment for Shape Control of an Adaptive Wing, Paper AIAA 93-1700-CP, 1993

[46] Rosemann, H., The Cryogenic Ludwieg-tube Tunnel at Göttingen, in: AGARD-R-812, Special Course on Advances in Cryogenic Wind Tunnel Technology, 1997

[47] Knauer, A., Performance improvement of transonic airfoils through contour modifications in the shock region, DLR-Research Report 98-03, 1998 (also Ph.D.-Thesis University Hanover), and EUROSHOCK II Final Technical Report, TR BRPR-95-76/1, 1999

[48] Birkemeyer, J., Drag minimization on a transonic wing by ventilation and adaptive contour bumps, DLR-Research Report 1999-28, 1999 (also Ph.D.-Thesis University Hanover), and EUROSHOCK II Final Technical Report, TR BRPR-95-76/1, 1999

[49] Geissler, W., The effect of a contour bump on buffet onset determined by time-accurate Navier-Stokes computations, in: EUROSHOCK II Final Technical Report, TR BRPR-95-76/1, 1999

[50] Richter, K., Rosemann, H., Numerical investigation of transonic airfoil drag reduction by the combined application of a contour bump and variable rear camber, DLR Internal Report IB 223-1999 A 31, December 1999

[51] Drela, M., A User's Guide to MSES 2.95, MIT Computational Aerospace Sciences Laboratory, 1996

[52] Drela, M., A User's Guide to LINDOP 2.5, MIT Computational Aerospace Sciences Laboratory, 1996

[53] Doe, R., Application of Shock and Boundary Layer Control to Civil Transport Wings with Turbulent Boundary Layers, in: EUROSHOCK II Final Technical Report, TR BRPR-95-76/1, 1999

[54] Monner, H.P., Bein, Th., Hanselka, H., Breitbach, E., Design Aspects of the Adaptive Wing – The Elastic Trailing Edge and the Local Spoiler Bump, in: Multidisciplinary Design and Optimization, Conference Proceedings, Royal Aeronautical Society, London, 1998

Active Control of Instabilities in Gas Turbines

A P Dowling
Department of Engineering, University of Cambridge, Trumpington Street, Cambridge, CB2 1PZ, UK

Abstract

Active control of instabilities of compression and combustion systems is reviewed within a common framework. It is over ten years since the first full-scale demonstration of the feasibility of feedback control to delay the onset of instability in gas turbines. But challenges remain. In particular, practical implementation requires controllers that have guaranteed performance across a range of engine operating conditions and the development of robust sensors and actuators that continue to function over many tens of thousands of hours of running.

1. Introduction

For some operating conditions of gas turbines, an undesired unsteady flow develops, small amplitude disturbances grow in time, and if uncorrected eventually develop into a nonlinear limit cycle oscillation. This onset of instability can damage the engine and its avoidance can limit performance. Active control has been demonstrated to be a feasible way of preventing such large-scale oscillations and hence of extending the stable operating range.

Both compression and combustion systems are susceptible to instabilities. Two types of instabilities, 'surge' and 'rotating stall', are commonly observed in compressors. They occur at low mass flow rate, high pressure rise conditions. Surge is a very low-frequency one-dimensional pumping oscillation of the whole compression system, in which interaction between the inertia of an axisymmetric unsteady flow through the compressor and the compressibility of the air within the combustion chamber leads to self-excited oscillations. Rotating stall is of higher frequency and is characterised by a region of reduced air flow rate that rotates around the compressor annulus at a fraction of the rotor speed. Whether the compressor surges or stalls depends on the system configuration and in particular on the ratio of compressibility and inertial effects (Greitzer, 1981). In high-speed axial compressors, the onset of rotating stall in the compression system often triggers surge through a nonlinear interaction (Weigl *et al*, 1998). Both instabilities lead to a loss of compressor performance. Moreover, the resulting large unsteady forces may damage the engine. Recovery from rotating stall is not straightforward and, in practice, may involve shutting down the engine and restarting. Because of these far-reaching consequences, compressor design tends to be very cautious, leaving a good margin between the design mass flow rates and instability onset. This severe limitation on compressor pressure rise can be overcome by applying active control.

Many forms of combustion systems are susceptible to self-excited oscillations, with the resulting pressure waves and/or enhanced heat transfer being so intense that structural damage is done. Such flow instabilities occur because of interaction between unsteady combustion and acoustic waves. Essentially, unsteady combustion is an effective source of sound. However, most combustors are highly resonant systems, in which the acoustic waves are reflected from the boundaries to produce flow unsteadiness near the flame, leading to more unsteady combustion. If the phase relationship is suitable, acoustic waves gain energy from their interaction with the combustion (Rayleigh, 1896). Self-excited oscillations then occur: unsteady combustion generates sound, while the sound waves perturb the combustion.

In gas turbines there are various ways in which flow perturbations cause unsteady combustion, but usually the main coupling is through velocity fluctuations. These can, for example, change the fuel-spray atomisation, which is the main mechanism driving 'rumble' (Zhu *et al*, 2000), a low frequency instability of aeroengine combustors at idle and sub-idle. Alternatively in an afterburner, where the flame is stabilised in the wake of a bluff body, velocity fluctuations near the flame holder physically perturb the flame and thereby alter the instantaneous rate of combustion (Bloxsidge *et al*, 1988a). Lean premixed prevapourised combustion, introduced to reduce NO_x, is proving to be notoriously susceptible to instability. There, since the fuel and air supplies have different acoustic impedances, pressure fluctuations in the combustor cause unsteadiness in fuel-air ratio (Richard & Janus, 1998). When burning lean and premixed, the rate of combustion is very dependent on the instantaneous fuel-air ratio and fluctuates in response.

The feedback is usually through reflection from the combustor boundaries of the acoustic or entropy waves generated by the unsteady combustion, which at certain discrete frequencies reinforces the driving mechanism for unsteady combustion. Linear perturbations can then grow in amplitude. Active control is a way of interrupting the damaging interaction between linear waves and unsteady combustion.

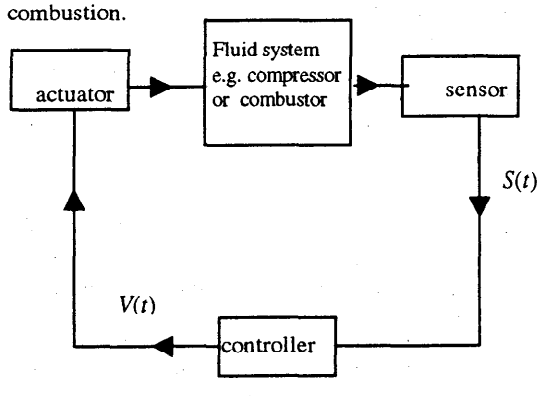


Figure 1 Generic system for active control of a gas turbine instability

The basic features of applying active control to these compressor and combustor instabilities are illustrated in Fig. 1. The characteristics of the fluid

Paper presented at the RTO AVT Symposium on "Active Control Technology for Enhanced Performance Operational Capabilities of Military Aircraft, Land Vehicles and Sea Vehicles", held in Braunschweig, Germany, 8-11 May 2000, and published in RTO MP-051.

system change with operating point and may display regimes of instability. This is illustrated in Fig. 2, which shows the changes in the power-spectral density of the pressure generated by a premixed ducted flame as the fuel-air ratio varies. When the fuel-air ratio is below a critical value, the combustion system has all the characteristics of a damped harmonic oscillator, the spectral level depending on external excitation which is preferentially amplified near the resonant frequency. An increase in fuel-air ratio reduces the damping, thereby increasing the resonant response. Beyond a critical fuel-air ratio, the system is unstable. Linear perturbations then grow rapidly with time until a non-linear limit cycle is established. New physics set the amplitude of the limit cycle and, in this particular example, it is controlled by saturation effects that occur in the heat-release fluctuation when the fluid velocity reverses. The pressure spectrum now has a different character and a narrow-bandwidth high-amplitude peak occurs. In many practical combustors the onset of instability may result in damaged hardware. The idea of active control is to extend the stable operating range.

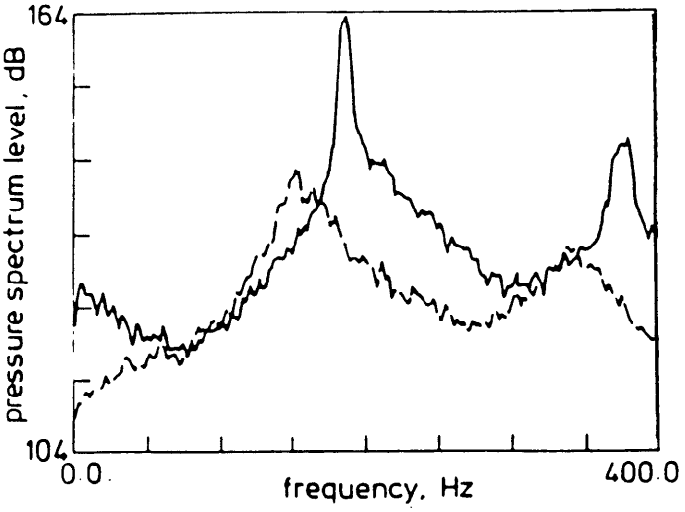


Figure 2 Pressure spectrum of a premixed ducted flame----- stable, below critical fuel-air ratio
——— unstable, above critical fuel-air ratio
(from Macquisten & Dowling, 1993)

A generic system is illustrated in Fig. 1: the sensor(s) monitors the fluid system, feeding the measured signal(s) $S(t)$ to a controller, which responds by producing an output signal $V(t)$ to drive the actuator(s). The aim is that the combined system fluid, detector, controller and actuator should be stable. Viewed in the form of Fig. 1, active instability control looks like a standard control problem. However, there are some features of the control of instabilities of gas turbines that make this application particularly challenging.

(i) the 'fluid system' is distributed, i.e. the variables satisfy partial differential equations,
(ii) it includes complicated fluid mechanics, e.g. wakes, combustion and turbulence, so that predictive models for the full system are not feasible. Although we may hope to develop sufficiently accurate models to provide help with the choice of location of the sensors and actuators and with the structure of the control design, we cannot expect to predict all the control parameters,
(iii) the system is open-loop unstable in part of its range. Moreover, the consequences of instability may be so traumatic that no open-loop data can be obtained in this regime,
(iv) the frequencies of oscillation are high (up to 600Hz) and time delays of many periods of this oscillation are inherent in the system.

If a strategy for the active control of instabilities in gas turbines is to be practical, it needs to address all these issues. Moreover, it must be effective across all regimes of engine operation. In addition, the designer must be able to give guarantees that the controller will not go unstable and cause harm. This requires the integration of ideas from fluid mechanics, turbomachinery, combustion, control and systems engineering. It is a genuinely multidisciplinary research area. In the next section, we review some of the background and then current issues are discussed in the following sections.

2. Background

The application of feedback control in both compression and combustion systems has followed similar development paths, starting with control of one-dimensional disturbances on small-scale laboratory systems, using loudspeakers as the actuator. In both cases this was followed by larger-scale control of one-dimensional oscillations. More recently control of circumferential modes in full-scale devices has been demonstrated.

Ffowcs Williams of the University of Cambridge was the first to see the potential of concepts developed in anti-noise research (Ffowcs Williams, 1984) for active instability control in gas turbines. The work of his students included both the earliest demonstrations of combustion control (Dines, 1983, Heckl, 1985) and, arising from collaborations with the Gas Turbine Laboratory MIT (Epstein, Ffowcs Williams & Greitzer, 1989), compressor control (Ffowcs Williams & Huang, 1989).

Dines (1983) controlled a ducted flame, whose open-loop behaviour exhibited a one-dimensional (longitudinal) oscillation. He used an optical filter and a photo-multiplier to detect the unsteady combustion. This signal was then phase-shifted and used to drive a loudspeaker near one end of the duct. The appropriate choice of phase found by trial-and-error and reduced the Sound Pressure Level by some 35dB. Since that pioneering work there have been many other demonstrations (Heckl, 1985, 1988, Lang *et al* 1987, Poinsot *et al*, 1987, 1988) of loudspeakers being used to modify the acoustic waves involved in the feedback processes, and hence to achieve stability in a combustor. However, it is not easy to use air-flow modulation as the control input at larger scale (Bloxsidge *et al*, 1987, 1988b). Then it is far more practical to modulate the supplied fuel. Langhorne, Dowling & Hooper (1990) showed that one-dimensional disturbances of a premixed ducted flame could be stabilised by the unsteady addition of 3% more fuel, reducing the pressure band level within 3dB

of the peak by 12dB, while the pressure band level below 400Hz was reduced by 7.5dB (see Fig. 3). With control on, it was possible to run at high fuel-air ratios not attainable without control. This increased the heat release within combustor and lead to a 10% increase in thrust.

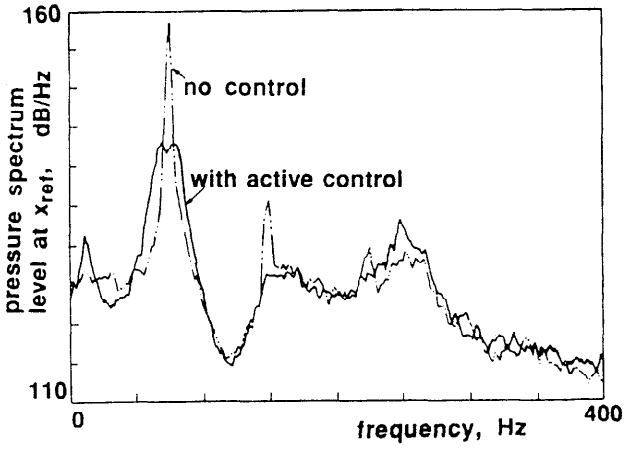


Figure 3 a) The Langhorne *et al* configuration
b) experimental results —— with control, --- no control

The work of Langhorne *et al* was supported by Rolls-Royce and we delayed publication to protect their commercial interests. Even before the results on the laboratory rig were published, Rolls-Royce and the Ministry of Defence had demonstrated the feasibility of combustion control on the afterburner of a full-scale RB199. That work was classified until recently, but will be presented at this meeting (Moran *et al*, 2000). Once again small levels of fuel modulation are found to be sufficient and the afterburner is able to achieve operating conditions impossible without control. It is therefore over ten years since the first full-scale demonstration of active control of combustion oscillations.

The emergence of combustion oscillations in land-based gas turbines has given new impetus to active control. Seume *et al* (1998) describe the application of control to a Siemens heavy-duty gas turbine. Control of the second and fourth azimuthal modes was obtained using a single input, multiple output system. Actuation was through modulation of the pilot fuel supply. Pressure amplitudes were reduced by 17dB during base-load operation. Hibshman *et al* (1999) have demonstrated control on a 67.5° sector of a liquid-fuelled lean premixed combustor, again at full-scale. Control reduced the amplitude of the dominant instability mode by 6.5dB. All these demonstrations have used very simple control algorithms. Typically a time-delay or phase-shift is applied for a single operating condition.

Compressor control has developed in a similar way, beginning by reducing surge in a small laboratory system. Figure 4 shows the configuration investigated by Ffowcs Williams & Huang (1989). A small centrifugal compressor supplies air to a plenum and surges as the throttle is closed. The control system uses a pressure transducer as the detector. This signal is phase-shifted and then used to drive a loudspeaker in the plenum, the optimal phase-shift being tuned by hand. Stable operation extends to lower mass flow rates with the controller on. The system controlled by Pinsley *et al* (1991) is similar, but there actuation was through an adjustable exit throttle. The active control of surge has also been demonstrated at full scale. Ffowcs Williams & Graham (1990) demonstrated that active control could enable recovery from a surge event in a centrifugal compressor.

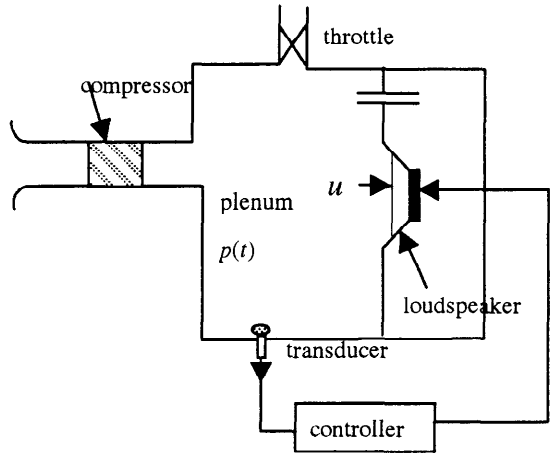


Figure 4 Active stabilisation of a centrifugal compressor (Ffowcs Williams & Huang, 1989)

Since rotating stall propagates around the compressor annulus, multiple inputs are required for its control. Paduano *et al* (1993) stabilised the small amplitude circumferential modes, which can be the precursor to rotating stall, in a single-stage low-speed compressor. Control of the first two circumferential modes extended the stable operating range by about 20%. Control has been demonstrated on an aeroengine gas turbine (Freeman *et al*, 1998) and on a transonic fan (Weigl *et al* 1997).

Excellent reviews of active instability control have been given by McManus *et al* (1993) and Yang & Schadow (1998) for combustors and by Greitzer (1998) for compressors. Our aim is not to give a complete historical survey, but rather to highlight the symbiosis between approaches to combustor and compressor control, and to discuss some of the current issues. We will concentrate, in particular, on feedback control where the ultimate aim is steady operation. Open-loop control, in which the system is continually driven by an external signal, has had some success in improving mixing and hence combustion stability, but is beyond the scope of the paper. See McManus *et al* (1993) for a summary of this work. With reference to the generic control system illustrated in Fig. 1, we will discuss in turn sensors, actuators and control strategies. Of these three components, the sensors are the least problematic.

3. Sensors

Pressure transducers are the most commonly-used sensor for active control. They are available with the required bandwidth and are reasonably robust. For the case of combustion control, the transducer(s) are

usually placed away from the flame zone to avoid the extremely high temperatures. The time taken for the sound to propagate from the region of actuation (usually modulation of the burning rate) to the transducer introduces an additional delay, which increases the demands on the controller. However, appropriately chosen control strategies continue to work effectively in the presence of such time delays (see Section 5). Since this detection time delay is, in general, much shorter than the actuation time delay, which typically involves convection and mixing, the benefits from reducing it by locating the transducers in the combustion zone are limited.

The light emitted by C_2- or OH-radicals in a flame provides a direct measurement of the instantaneous rate of combustion. From the earliest experiments on active control of combustion instabilities, (e.g. Dines, 1983) a bandpass optical filter and a photo-multiplier have been used as a detection system. This has been highly successful in laboratory demonstrations but there are difficulties in full-size implementation. The combustion instability couples to the integrated effects of heat release. While, in principle, optical fibres can be used to access this information in a large system (Hermann *et al*, 1999), there can be difficulty in getting a wide enough field of view. If only a limited portion of the combustion zone is seen, the signal can be very noisy, dominated by small-scale local events and not representative of the large scale coherent unsteadiness that is relevant for the instability. Pressure has the advantage that it is a global quantity giving a measure of the integrated effects of unsteady heat release.

In many instances, the driving mechanism for self-excited oscillations is velocity fluctuation and there are advantages for control system design if this is measured directly. Hot wires have been used in laboratory demonstrations of compressor control (Paduano *et al*, 1993) but are not, of course, sufficiently robust for installation in a practical system. A robust and reliable instantaneous measurement of velocity would be very valuable - perhaps something that MEMS can offer to active instability control? In LPP combustion systems, fuel-air ratio fluctuations are the main cause of unsteady combustion. The time response of Fast Ionisation Detectors, FIDs, is reducing and soon they will be candidates for the online detection of equivalence ratio. The advantage of measurements of velocity or fuel-air ratio is that they provide advance information about the unsteady combustion. Since practical actuators will aim to affect the unsteady combustion, this time-lead makes the control task simpler.

In summary then, current pressure transducers are suitable sensors for instability control in gas turbines, provided the control strategy is chosen appropriately. In the future, one might expect developments in sensor technology to provide more direct information, which will simplify the demands on the control algorithm.

4. Actuators

The first demonstrations of active instability control in both combustion and compression systems used a loudspeaker as the actuator (Dines, 1983, Ffowcs Williams and Huang, 1989). These have the advantage of having a good high frequency response, but are not sufficiently robust to apply in real systems. Early attempts at combustion control at larger scale tried to mimic the effects of a loudspeaker by providing a modulated air-mass flow rate (Bloxsidge *et al*, 1988b). This is feasible, but presents a number of mechanical challenges: moreover, it does not make best use of the chemical energy released in combustion.

Since unsteady combustion is one of the most effective ways of producing fluctuations in volume flow rate, more practical actuators operate on the fuel-flow rate, with the aim of influencing the rate of heat release. The first fuel modulation systems were based on car fuel injectors (Langhorne *et al*, 1990) and operated in a simple on-off mode. Similar fuel injectors have also been used in full-size applications. Solenoid valves have the potential of producing a linear form between input voltage and mass flow rate, enabling the advantages of linear control theory to be exploited. Solenoid valves (mostly manufactured by Moog) have been used in most full-scale demonstrations of combustion control (Hantschk *et al*, 1996, Seume *et al*, 1998, Moran *et al*, 2000), and can be effective up to about 450Hz (Hermann *et al*, 1999). Instability control places severe demands on actuators. To ensure recovery from a large transient perturbation, they ought to be able to produce an input of sufficient amplitude to affect the limit cycle oscillation. It is difficult to obtain such a large control authority and various systems have been devised to enhance the effect of a solenoid valve. These include exploiting the resonances of the fuel supply (Hantschk *et al*, 1996) and modulating the fuel supplied to a pilot flame rather than the main combustor (Seume *et al*, 1998). Once control has been achieved, an actuator needs only to be able to produce the appropriate small amplitude response to weak perturbations. Many actuators have difficulty in achieving a large turndown ratio, without either saturation at high amplitudes or hysteresis and 'sticking' at low. There are serious questions about the durability and integrity of a solenoid valve as an actuator. In application in an industrial gas turbine, they would need to work for over 20,000 hours without maintenance - some 10^{10} cycles of a typical instability frequency, if the combustor were to run continually at a condition not achievable without control.

Hermann *et al* (1996) developed a novel piezo actuator for use with liquid fuels. When the fuel supply line is tuned effectively, it is capable of operation over a broad frequency range (100Hz to several kHz are claimed).

Magneto-restrictive actuators have the advantages of combining a fast response time and a large actuation force, with longevity. However, the resulting displacements are small and mechanical means are needed to amplify their effect on the flow. Neumeier and Zinn (1996) exploit the variation in length of a magneto-restrictive rod in a varying strength magnetic field to move a needle valve in the fuel supply. This device provides a fuel modulation at frequencies up to 1kHz. Sattinger *et al* (1998) use it to drive an auxiliary fuel supply and hence control a scaled model of a LPP combustor. However, a disadvantage of magneto-restrictive actuators is that the material displays hysteresis and drift, and so needs its own feedback control system.

Actuators for compressor control present even greater difficulties. The amplifying effect of the unsteady combustion response to fuel modulation is not available and the air flow must be altered directly. A variable area throttle has been used for surge control (Pinsley *et al*, 1991). However, in high-speed axial compressors the dominant instabilities are non-axisymmetric and multiple actuators are required to affect these modes. Paduano *et al* (1993) actively vibrated inlet guide vanes to change their incidence angle, but modulated jet injection seems the most practical way of obtaining high bandwidth actuation. Once again, Moog solenoid valves have been used and are capable of injecting jets at up to 400Hz (Weigl *et al*, 1998). Freeman *et al* (1998) developed a novel system for the control of stall on an aeroengine gas turbine. Air was bled from compressor exit and re-injected into the compressor through six pipes positioned around the annulus, the recirculation through each pipe being independently controlled by an adjustable nozzle.

Actuation remains a major challenge which must be overcome before active instability control systems can be installed in the field.

5. Controller Design

The controller receives an input signal $S(t)$ measured by the sensors and outputs at voltage $V(t)$ to drive the actuator as shown in Fig. 1. (For multimodal control $S(t)$ and $V(t)$ may be vectors representing multiple inputs and outputs.) Controller design means determining an appropriate relationship between $V(t)$ and $S(t)$. Ideally, the controller will be effective across all regimes of plant operation. Moreover the designer must be able to give guarantees that the controller will not go unstable and cause harm.

5.1 Simple strategies

The first controllers for active instability control (e.g. Dines 1983, Heckl 1985, Bloxsidge *et al* 1988, Ffowcs Williams & Huang, 1989) just consisted of an analogue or digital feedback circuit designed to give a time delay or phase change. A variable component in the circuit was slowly adjusted manually to minimize the mean-square fluctuations. This showed the physical effectiveness of feedback control, and this trial-and-error approach has even been used in some full-scale demonstrations. However, since the amplitude of unstable oscillations is increased by a wrongly-phased 'control' effect, such tuning risks damaging the plant and a more systematic approach is needed.

Once the open-loop transfer function between the input voltage to the actuators $V(t)$ and the measured response signal $S(t)$ is known, standard techniques may be used to design a controller. Ideally this transfer function would be determined at the running condition of interest by applying a sinusoidal input voltage, $v_0 \sin \omega t$, for a range of frequencies ω and measuring the response. Unfortunately such a procedure is not possible for an open-loop unstable system undergoing a nonlinear limit-cycle oscillation, partly because this self-excited oscillation swamps any response to an imposed input voltage. But even if the response could be detected, the transfer function obtained would describe linear perturbations from the limit cycle, rather than from the quiescent state that is the objective of control.

Langhorne *et al* (1990) describe how the transfer function required for combustion control can be derived from measurements at a low fuel-air ratio at which the flame/duct arrangement is stable. The measured transfer function $T(\omega) = \hat{S}(\omega)/\hat{V}(\omega)$ can then be extended analytically to give a form for $T(\omega)$ at the higher fuel-air ratios at which the system is unstable. $T(\omega)$ was assumed to have the form

$$T(\omega) = F(\omega)\frac{1}{(\omega - \omega_R - i\delta)(\omega + \omega_R - i\delta)} \qquad (1)$$

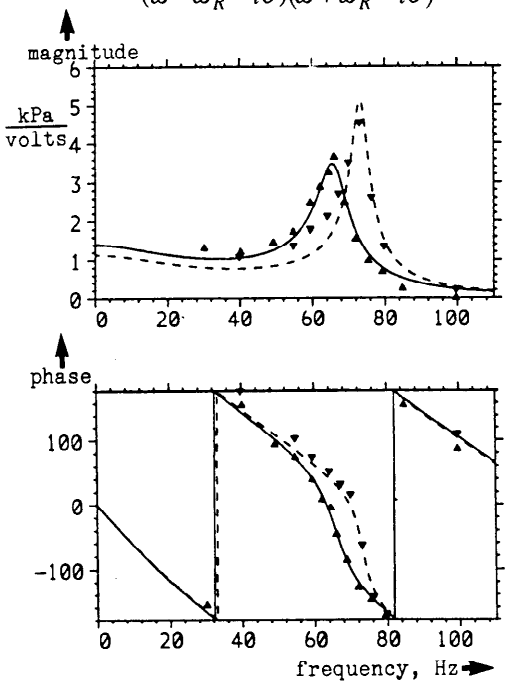


Figure 5 Comparison between theoretical and experimental transfer functions $T(\omega)$ for a stable ducted flame
$\phi = 0.63$ ▲ experiment, — model in equation (1)
$\phi = 0.65$ ▼ experiment, --- model in equation (1)
(from Dowling 1989)

where the resonant frequency ω_R and damping δ change with equivalence ratio ϕ, but the function $F(\omega)$ was treated as constant for small changes in ϕ near instability onset. Figure 5 shows the measured response to forcing at equivalence ratios $\phi = 0.63$ and $\phi = 0.65$, (equivalence ratio is fuel-air ratio normalized by the value for stoichiometric burning) compared with the model in equation (1), ω_R and δ were fitted to match the data. The agreement is encouraging. The transfer function $T(\omega)$ was then extrapolated to an unstable equivalence ratio $\phi = 0.68$, using the limit cycle frequency and, since linear disturbances grow, negative damping. Having obtained the open-loop response, many different techniques for control design may be used. Langhorne *et al* (1990) used a simple time delay, $\hat{V}(\omega)/\hat{S}(\omega) = e^{-i\omega\tau}$. Nyquist stability arguments and nonlinear simulations (Dowling, 1989) were used to predict the optimum time delay τ. Since the precise

value of the (negative) damping factor in the open-loop response was not known, it was reassuring that this optimum τ was found not to depend on it significantly. The theoretical optimum time delay was found to be close to that determined experimentally.

Perhaps the simplest physically-based control strategy is to use the feedback as a damping mechanism. In the compressor system illustrated in Fig. 4, this means driving the loudspeaker so that $\overline{pu}$ is positive; where $p(t)$ is the plenum pressure, $u(t)$ the velocity of the loudspeaker cone and the overbar denotes an average over one cycle of oscillation. Then flow perturbations lose energy by doing work on the loudspeaker, the maximum energy being extracted when $p(t)$ and $u(t)$ are in phase. This active damping changes the energetics of small perturbations and, in particular, delays the onset of instability. This principle was applied by Pinsley *et al* (1991) to control surge in a geometry similar to that in Fig. 4, but with actuation through an adjustable throttle rather than a loudspeaker. A simple proportional controller was used to increase the area of the throttle at plenum exit (and hence the mass flow rate) in phase with the plenum pressure. Figure 6 shows the resulting improvement in performance: the onset of surge is moved to lower mass flow rates.

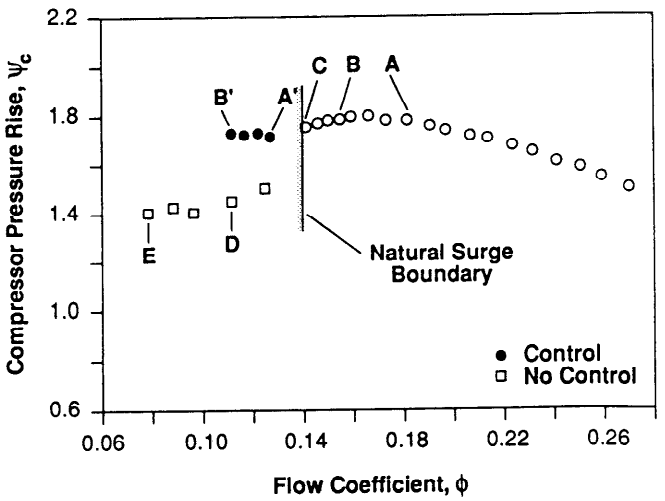


Figure 6 Effect of active control on compressor surge (From Pinsley *et al*, 1991)

Similar active dampers have been applied to combustion systems. Then the aim is to modulate the supplied fuel so that the fluctuations in fuel flow rates reduce the acoustic energy flux $E(t)$ out of the combustion zone, i.e. reduce

$$E = \int_{\Sigma} \overline{p\mathbf{u}} \cdot d\Sigma \qquad (2)$$

where $\mathbf{u}$ is the fluid velocity and Σ is a control surface enclosing the burning region (see Fig. 7). In a low Mach number flow, combustion occurs at almost uniform pressure and so equation (2) is equivalent to

$$E \approx \overline{p \int_{\Sigma} \mathbf{u} \cdot d\Sigma}. \qquad (3)$$

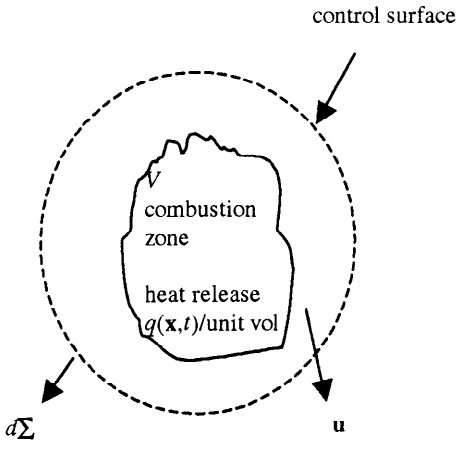


Figure 7 Control surface S enclosing combustion zone V

For a compact combustion zone, this volume efflux is directly related to the instantaneous rate of combustion. To see this, note that in a combusting gas,

$$\frac{D\rho}{Dt} = \frac{1}{c^2}\left(\frac{Dp}{Dt} - (\gamma - 1)q\right), \qquad (4)$$

where ρ is the density, c the speed of sound and γ the ratio of specific heats. $q(x,t)$ is the rate of heat release/unit volume. The first term on the right-hand side describes the change in density due to compressibility, while the second term accounts for the combustion effects. Equation (4) applies to a combusting gas provided that the reactants and products behave as perfect gases, and there is no molecular weight change during the chemical reaction (Williams, 1965). Substitution from (4) into the equation of mass conservation leads to

$$\nabla \cdot \mathbf{u} = -\frac{1}{\rho}\frac{D\rho}{Dt} = \frac{1}{\rho c^2}\left((\gamma - 1)q - \frac{Dp}{Dt}\right) \qquad (5)$$

and, after integration over V, a compact combustion zone, we obtain

$$\int_{\Sigma} \mathbf{u} \cdot d\Sigma = \frac{(\gamma - 1)}{\rho c^2} Q(t). \qquad (6)$$

where $Q(t) = \int_V q(\mathbf{x},t)dV$. It then follows from equation (3) that

$$E = \frac{\gamma - 1}{\rho c^2}\overline{pQ}. \qquad (7)$$

Maximum absorption occurs when p and Q are 180° out of phase (Rayleigh's criterion).

Active damping involves the unsteady addition of fuel so as to give heat release out of phase with $p(t)$.

That has been the strategy behind a number of demonstrations of active combustion control. Then the ideal detector is a pressure transducer in the combustion zone, i.e. $S(t) = p(t)$. Implementation of the appropriate feedback requires knowledge of the time delay τ_{ac} between $V(t)$, the input voltage to the actuator, and $Q(t)$. Since the feedback system involves some dynamics, τ_{ac} will inevitably be a function of the frequency of oscillation ω_{os}. The controller design essentially means setting

$$V(t) = -p(t-(NT_{os}-\tau_{ac})), \qquad (8)$$

where T_{os} is the period of oscillation, $2\pi/\omega_{os}$ and N is an integer just large enough to make NT - τ_{ac} positive. In principle, τ_{ac} can be obtained from open-loop forcing experiments and hence is available in a look-up table. One difficulty is that the application of control changes the frequency of oscillation. Neumeier & Zinn (1996) describe how it can be determined on-line from a short-time Fourier transform. The dominant frequency continually shifts during implementation of this form of feedback algorithm.

A second difficulty with a simple controller just involving a fixed time delay or phase is that it introduces a new mode of oscillation which becomes unstable as the gain is increased (Langhorne *et al* 1990, Fleifil *et al*, 1998, Hibshman *et al* 1999) and leads to a second peak in the pressure spectrum. Weigl *et al* (1998) noted the same effect when a constant gain feedback control was used for compressor stabilisation. A gain and phase that stabilised one circumferential mode, destabilised another. A dynamic controller, which can introduce the proper gain and phase at different frequencies, is needed, together with a strategy for choosing its form.

5.2 Model-based control

The fluid system within the 'black-box' of Fig. 1 is distributed, its parameters satisfying a set of PDEs. Before a model-based controller can be designed, this open-loop behaviour needs to be converted into a system of coupled ODEs. The usual procedure is through a Galerkin expansion, in which the unsteady flow parameters are expressed in terms of infinite sum, e.g.

$$p'(\mathbf{x},t) = \sum_{n=1}^{\infty} \eta_n(t)\psi_n(\mathbf{x}), \qquad (9)$$

Galerkin models of self-excited combustion instabilities are well-established. See Culick (1988) for a review. Typically, for a combustor, $\psi_n(\mathbf{x})$ $n = 1\ldots$ are the eigenfunctions for the case of no unsteady heat release $(Q'(t) \equiv 0)$. Substitution into the inhomogeneous acoustic wave equation leads to a coupled set of ODEs for the evolution of the modal amplitudes $\eta_n(t)$ when there is a specified relationship between $Q'(t)$ and the unsteady flow. There are some disadvantages with this approach: an infinite number of terms is needed to resolve all plane acoustic wave modes. Often the series in (9) is truncated with only a single term being detained. This can lead to significant errors (Dowling, 1995, Annaswamy *et al*, 1997). This is essentially because the expansion in (9) is in terms of modes for $Q'(t) \equiv 0$, not modes of the self-excited system with non-zero $Q'(t)$. All the $Q'(t) \equiv 0$ modes are coupled by concentrated unsteady heat release. Yang *et al* (1992) use a two-term Galerkin expansion to design a feedback control based on pole placement arguments.

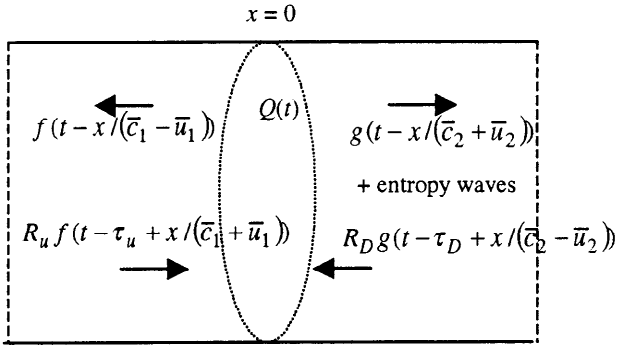


Figure 8 One dimensional waves within a combustion system

An alternative procedure is through a wave, rather than a mode, expansion. Then, as illustrated in Fig. 8, only two terms $f(t)$ and $g(t)$ are needed to resolve all plane acoustic wave modes. These describe respectively the wave strengths upstream and downstream of the combustion zone, the boundary conditions at the ends of the combustor relating the reflected waves $R_U f$ and $R_D g$ to the incident waves f and g. Perturbations to flow quantities at any location can be expressed in terms of the wave strengths f or g. A complete system of equations for the open-loop behaviour is derived from conservation of mass, momentum and energy across the combustion regime and a 'flame-model' which relates Q' to the flow perturbations and the actuator voltage V applied to inject additional fuel.

The real advantage of the wave approach is seen when the open-loop transfer function $T(\omega) = \hat{S}(\omega)/\hat{V}(\omega)$ is calculated. Possible sensor signals $S(t)$ are a pressure perturbation at a particular location or the total rate of heat release, $Q(t)$ (see Section 3). In the Galerkin approach this transfer function is rational i.e. both the numerator and denominator are polynomials of $(i\omega)$, but the order (the highest power of $i\omega$) increases rapidly when more terms in the Galerkin expansion retained. In contrast, the wave approach leads to an algebraically simple form for the transfer function. This is because in this formulation the time delays for acoustic propagation and reflection are displayed explicitly rather than as rational functions as in the Galerkin expansion.

Chu *et al* (1998) applied this wave approach to Dowling's (1999) nonlinear model of a premixed ducted flame. The control system consisted of a pressure transducer upstream of the flame zone and actuation was through a fuel injection system, with mass, stiffness and damping leading to additional unsteady combustion after a time delay τ_{ac}. This

model was used to demonstrate that advances in robust control can be used to methodically synthesize a controller and analyze the resulting closed-loop system. Figure 9 shows the open-loop transfer function of this model. The peaks of the fundamental, the third and the fifth harmonics are clearly observed. Chu *et al* (1998) designed a robust controller for this plant. This procedure involves using $\mathcal{H}_\infty$-loop shaping techniques (McFarlane & Glover, 1990, 1992) to design a controller for a linearised finite dimensional approximation to the plant. Since the controller is designed to be robustly stable, it should still be able to control the nonlinear time-delayed system. Chu *et al* (2000) were able to rigorously prove that to be the case, by using μ-analysis and Integral Quadratic Constraints. Figure 10 shows a nonlinear simulation of effects of applying this controller. The controller is switched on at $t = 0.15$s and rapidly dampens out the oscillations. The robust controller should continue to operate effectively under modest changes in operating conditions. For the case shown in Fig. 10, the inlet Mach number $\overline{M}_1$ is increased linearly from 0.080 at $t = 1.95$s to 0.095 at $t = 2.10$s. This shifts the frequency of the unstable mode by 9% and yet the robust controller maintains control. One of the most significant uncertainties is in τ_{ac}, the time delay between the control action of injecting fuel and the change it produces in the rate of heat release. Chu *et al* (2000) have shown that the system remains stable for an error of up to 2 ms in estimating this time delay, that is 12% of the fundamental period of oscillation.

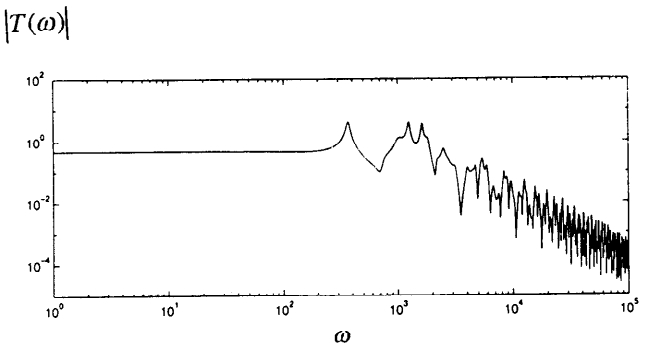


Figure 9 The frequency responses (magnitudes only) of the linearised plant (from Chu *et al*, 1999).

In a practical application, it may not be possible to derive an accurate theoretical model of the open-loop transfer function. One advantage of robust control is that closed-loop performance is relatively insensitive to the details of the open-loop model. Thus, we hope that sufficient information on the open-loop behaviour can be obtained by combining a measured flame-response with the wave approach. This is an area of current research.

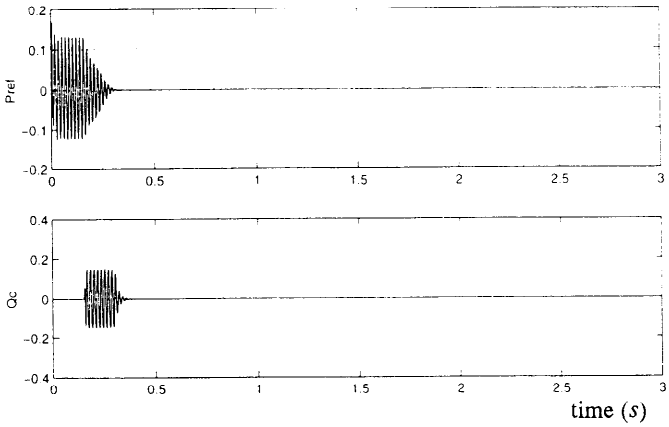


Figure 10 Robust controller applied to the model. Control is switched off at $t = 0.150$s, M_1 is varied linearly from 0.080 at $t = 1.95$s to 0.095 at $t = 2.10$s, ····· controller OFF, ——— controller ON after $t = 0.150$s (from Evesque *et al*, 1999)

An alternative approach is to measure a transfer function at a stable operating point and then extrapolate it into an unstable regime, as described in Section 5.1. That is the procedure adopted by Weigl *et al* (1998) to develop a model for rotating stall. Since this method of estimating the unstable dynamics introduces significant uncertainty in the model, they also use $\mathcal{H}_\infty$-techniques to design a robust controller, insensitive to these errors. The results of applying this controller to stabilise rotating stall and surge in a transonic single-stage axial compressor are shown in Fig. 11, and are very encouraging. However, not all compressors stall in the way suggested by this model, i.e. through the growth of low-order circumferential modes as the mass flow rate reduces. Stall inception in some compressors is due to a local short-length stall. Local action is required to postpone this 'spike-stall' (Day, 1993, Freeman *et al*, 1998).

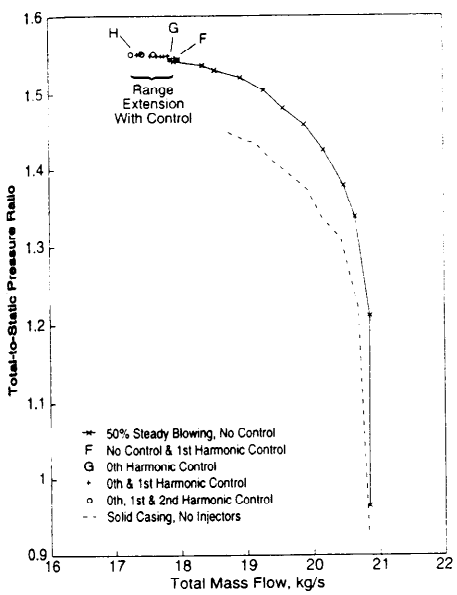


Figure 11 Stabilised compressor characteristic (from Weigl *et al* 1998)

Krstic *et al* (1998) have exploited the form of the nonlinearities in compressor performance to devise a simple control law that is based on a model, but needs little information about the system parameters. Moreover, the global stability of the controller is guaranteed by a Lyapunov function. In Section 5.4, we will discuss similar low-order controllers for combustion but there it is more convenient if some parameters are tuned adaptively.

5.3 LMS Controller for adaptive control

An adaptive controller, where the controller parameters are constantly updated, provides a way of eliminating gas turbine instabilities for a range of operating conditions. There have been a number of implementations of adaption based on the LMS algorithm (see for example, Billoud *et al* 1992, Kemal & Bowman, 1996). However, results are mixed. Sometimes it works well, but at other times the gradient research goes unstable or control introduces new frequencies of oscillation.

A LMS controller is based on the use of an IIR filter (Infinite Impulse Response) whose input is $S(t)$ and output $V(t)$ are related by

$$V(t) = \sum_{i=0}^{n-1} a_i(t) S(t - i\Delta t) + \sum_{j=1}^{m} b_j(t) V(t - j\Delta t) \quad (10)$$

where Δt is the sampling interval time delay. The controller coefficients a_i and b_j are updated at each time step in order to minimize the rms of an error signal measurement, $e(t)$. $e(t)$ could be a second sensor reading, or more simply $S(t)$. The aim is to drive $e(t)$ to zero.

The LMS algorithm updates the coefficients $a_i(t)$, $b_j(t)$ according to the procedure

$$a_i(t + \Delta t) = a_i(t) - \mu e(t)\alpha_i(t) \quad \text{for } 0 \le i \le n-1 \quad (11a)$$

$$b_j(t + \Delta t) = b_j(t) - \mu e(t)\beta_j(t) \quad \text{for } 1 \le j \le m \quad (11b)$$

where

$$\alpha_i(t) = r(t - i\Delta t) + \sum_{j=1}^{m} b_j(t)\alpha_i(t - j\Delta t) \quad (12a)$$

$$\beta_j(t) = w(t - j\Delta t) + \sum_{k=1}^{m} b_k(t)\beta_j(t - k\Delta t) \quad (12b)$$

$r = DS$ and $w = DV$, where the transfer function D describes the effect that V has on $e(t)$. One difficulty with a practical implementation of the LMS-algorithm is in determining D, because although the total signal $e(t)$ can be measured directly that contains contributions both from $V(t)$ and from the self-excited oscillation.

The LMS algorithm was developed for continuous signal identification, at a time when computers were slow and the speed of the algorithm was of vital importance. To make the calculations faster, but with no real mathematical justification, Feintuch (1976) neglected the series terms from the right hand sides of equation (12) and used the simplified forms

$$\alpha_i(t) = r(t - i\Delta t) \quad , \quad \beta_j(t) = w(t - j\Delta t) . \quad (13)$$

Applications of the LMS algorithm for combustion control have invariably used the truncated form of the algorithm in (13), rather than the mathematically correct form in (12). Evesque & Dowling (1998, 1999) applied the LMS algorithm to Dowling's (1999) nonlinear model of a ducted flame, for which the transfer function D was known exactly. They found that, when the coefficients were updated according to the algorithm in (13), the controller failed to converge to a stabilising set of coefficients. The terms neglected from (12) are of the same order as those retained in (13) and need to be taken into account to achieve control.

A major difficulty in applying the LMS algorithm is in identifying the transfer function D, i.e. of determining the effect that V has on $e(t)$. In practice, this means separating the contributions to $e(t)$ from V and from the self-excited oscillation. Several approaches have been used

(i) *to identify D at a nearby stable condition* (Billoud *et al*, 1992). Then there is no self-excited oscillation and so measuring $e(t)$ gives the direct effect of actuation. However this procedure has the disadvantage that it is not truly adaptive and cannot track changes in D with operating point.

(ii) *to identify D on condition with no control* The actuator is driven with a known signal $v_0(t)$ before applying closed-loop control. Under this procedure the combustor must run uncontrolled at an unstable condition, while System Identification is carried out. During that time, the oscillations grow (leading to a harder control challenge) and could break the plant.

(iii) *to identify D on condition with control* The difficulty in this case is that all the signals oscillate at the same frequency and the contribution to $e(t)$ from $V(t)$ cannot be separated easily from that due to the self-excited oscillation. Some authors have simply used Signal Identification techniques to determine the relationship between $e(t)$ and $V(t)$. Evesque and Dowling (1999) show that this does not give a good model of D. They propose a two parameter identification in which random noise is added to the signal driving the actuator, as shown in Fig. 12, $e(t)$ is then split into two parts by writing

$$e(t) = \varepsilon_1(t) + \varepsilon_2(t) \quad (14)$$

where $\varepsilon_1(t)$ is a random signal, $\varepsilon_1 = DV_{noise}$, while the residue $\varepsilon_2(t)$ is dominated by the resonant

frequencies of the self-excited oscillations. A '2-degrees LMS'-algorithm is used to obtain estimates of $\varepsilon_1(t)$ and $\varepsilon_2(t)$. Two IIR filters are used to relate $\varepsilon_1(t)$ to $V_{noise}(t)$ and $\varepsilon_2(t)$ to $V(t)$, the coefficients being determined by minimising the rms value of $e(t) - \varepsilon_1 t) - \varepsilon_2(t)$.

Evesque and Dowling (1999) show that this SI gives a good estimate of D, which, when used in the control algorithm described in equations (10) and (11), yields satisfactory control of a nonlinear simulation of a ducted flame. Results are shown in Fig. 13 for the same model and conditions as in Fig. 10. The control is switched on at $t = 0.15$s. The random noise required for SI is evident at all times, but the controller successfully eliminates the self-excited oscillations. The controller accommodates successfully for the change in inlet Mach number. With this '2-degrees' LMS-algorithm for on-line identification of the transfer function D, the LMS routine can be readily applied and in simulations has worked well. However, it will not work when there are significant time delays between $V(t)$ and its detected effect on $S(t)$. Another disadvantage of the LMS algorithm is that there are no theorems to guarantee its global stability. The same is true of neural network-based controllers, which again have to build a model (in this case nonlinear) for the control effect (Blonbou *et al*, 1999). In the next section we will discuss a 'self-tuning' controller which makes use of the structure of the transfer function $\hat{S}(\omega)/\hat{V}(\omega)$, but not its detailed form.

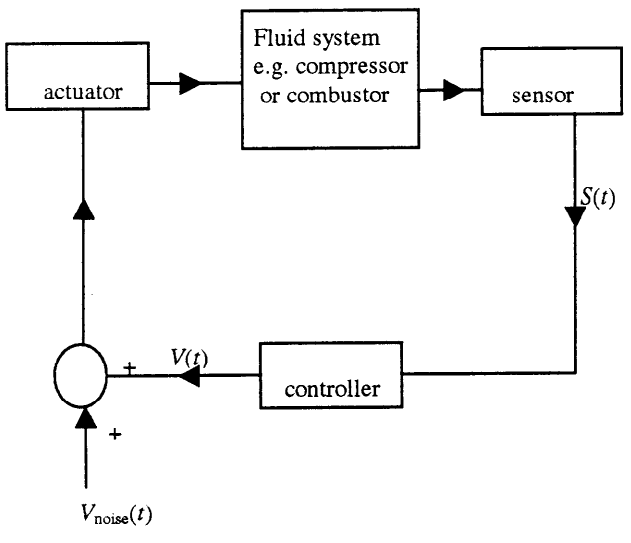


Figure 12 Introducing random noise for SI of the transfer function D needed in the LMS algorithm

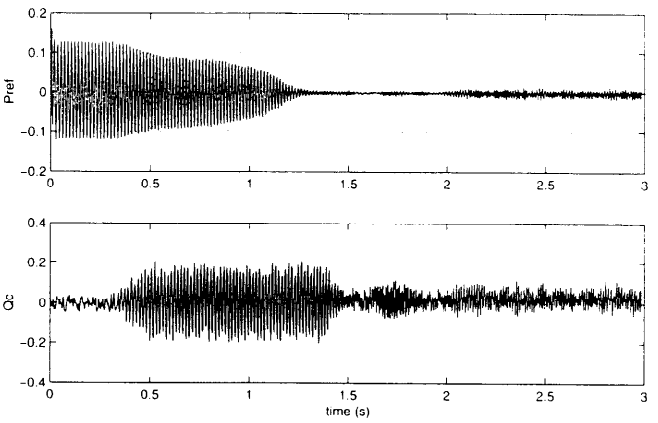


Figure 13 2-degrees LMS controller applied to a nonlinear model of a ducted flame. Control is switched on at $t = 0.150$s, $\overline{M}_1$ is varied linearly from 0.080 at $t = 1.95$s to 0.095 at $t = 2.10$s, ...controller OFF, ——— controller ON after $t = 0.150$s (from Evesque *et al*, 1999)

5.4 Self-tuning regulator

Self-tuning regulators have been developed for particular models of combustors. Krstic *et al* (1999) present a self-tuning scheme for adaption of the proportional integral control proposed by Fung and Yang (1992) for stabilization of two modes in a Galerkin expansion of a model combustor. The adaption scheme is Lyapunov-based to ensure convergence towards a stabilizing controller. The algorithm requires knowledge of the effect of the control input, which is obtained from System Identification in the nonlinear limit cycle.

Annaswamy *et al* (1998) develop a self-tuning regulator for a ducted laminar flame with control action provided by a loudspeaker. They show that provided the sensor and the loudspeaker are located in the flame zone, the transfer function $T(\omega) = \hat{S}(\omega)/\hat{V}(\omega)$ has no unstable zeros and is of relative degree 2. They use the general results derived by Narendra & Annaswamy (1989) to show that a particular adaption scheme for the coefficients of a phase-lead compensator guarantees convergence towards stabilising the controller.

It turns out that the wave approach discussed in Section 5.2 enables us to show that, provided the control action is chosen appropriately, a wide class of combustor oscillations meets conditions whereby they can be controlled by simple low-order controllers. Moreover a Lyapunov-based adaption scheme can be developed for the control coefficients, which guarantees convergence towards stabilising values. That work will be presented later in this meeting (Evesque *et al* 2000), and so it is not appropriate to give further details here.

6. Conclusions

Active control of gas turbine instabilities is feasible even at full-scale and has enormous potential. However, challenges remain still to be overcome before it can be used in practice. In particular, actuators require development to achieve the reliability and durability of other engine components. Progress has been made in the development of control strategies and algorithms, but so far these have been applied mostly to simulations or small-scale laboratory burners. Full-scale demonstrations have used relatively simple controllers, without guarantees of control being maintained over varying operating conditions.

References

Annaswamy, AM, Fleifil, M, Hathout, JP and Ghoniem, AF (1997). *Combust. Sci. Tech.*, **128**, 131-180.

Annaswamy, A M, Rifai, O M, Fleifil, M, Hathout, J P and Ghoniem, A F, (1998). *Combust. Sci. and Tech.*, **135**, 213-240

Billoud, G, Galland, MA, Huynh Huu, C and Candel, S, (1992). *Comb. Sci. and Tech.* **81**, 257-283.

Blonbou, R, Laverdant, A, Zaleski S, and Kuentzmann, P (1999) Active adaptive combustion control using neural networks. *To appear, Combust. Sci. and Tech.*

Bloxsidge, GJ, Dowling, AP, Hooper, N, and Langhorne, PJ, (1987). *J. Theoretical and Applied Maths.* **6**, 161-175.

Bloxsidge, GJ, Dowling, AP, and Langhorne, PJ, (1988a). *J. Fluid Mech.*, **193**, 445-473.

Bloxsidge, GJ, Dowling, AP, Hooper, N, and Langhorne, PJ, (1988b). *AIAA J*, **26**, 783-790.

Chu, YC, Dowling, AP and Glover, K, (1998). Robust Control of Combustion Oscillations, *Proc. IEEE, Int. Conf. on Control Applications*, Trieste, Italy, 1-4 September.

Chu, YC, Glover, K, and Dowling, AP (2000). Control of combustion oscillations via $\mathcal{H}_\infty$-loop shaping, μ-analysis and Integral Quadratic Constraints. Submitted to *Automatica*.

Culick, F E, (1988). *AGARD CP450.*

Day, IJ, (1993). *Trans. ASME, J. Turbomachinery*, **115**, 40-47

Dines, PJ (1983). Active Control of Flame Noise. *PhD Thesis, University of Cambridge.*

Dowling, AP (1989). *13th International Congress on Acoustics*, **1**, 91-106.

Dowling, AP (1995), *J. Sound Vib.*, **180**, 557-581

Dowling, AP (1999), *J. Fluid Mech.* **394**, 51-72.

Epstein, AH, Ffowcs Williams, JE, and Greitzer, EM (1989). *J. Prop. and Power*, **5**, 204-211.

Evesque, SMN and Dowling, AP, (1998). *AIAA-98-2351.*

Evesque, SMN and Dowling, AP, (1999). LMS Algorithm for Adaptive Control of Combustion Oscillations. *Submitted to Combust. Sci. Tech.*

Evesque, SMN, Chu, YC, Glover, K, and Dowling, AP (1999). Feedback control of a premixed ducted flame. In *Proceedings of the ISABE XIV International Symposium*, Florence, Italy, Paper IS-7187.

Evesque, SMN, Dowling, AP, and Annaswamy, A (2000). Adaptive algorithms for control of combustion. *NATO Symposium on Active Control Technology for Enhanced Performance Operational Capabilities of Military Aircraft. Land Vehicles and Sea Vehicles.*

Feintuch, PL, (1976). *Proc. IEEE*, **64**, 1622-1624.

Ffowcs Williams, JE (1984). *Proc. Roy. Soc. Lond.*, A**395**, 63-88.

Ffowcs Williams, JE and Huang, X (1989). *J. Fluid Mech.*, **204**, 245-262.

Ffowcs Williams, JE and Graham, WR (1990). *ASME 90-GT-224.*

Fleifil, M, Hathout, JP, Annaswamy, AM and Ghoniem, AF (1998). *Combust. Sci. and Tech.*, **133**, 227-265.

Freeman, C, Wilson, AG, Day, IJ and Swinbanks, MA (1998). *Trans. ASME J. Turbomachinery*, **120**, 637-661.

Fung, Y-T, and Yang, V, (1992). *J. Prop. and Power*, 1282-1289.

Greitzer, EM (1981) The stability of pumping systems - the 1980 Freeman Scholar Lecture. *ASME J Fluids Eng.* **103**, 193-243.

Greitzer, EM (1998). *JSME Int. J. Series B* **41**, 90-102.

Hantschk, C, Hermann, J and Vortmeyer, D (1996). *26th Symposium (International) on Combustion*, 2835-2841.

Heckl, MA, (1985). Heat Sources in Acoustic Resonators. *PhD Thesis, University of Cambridge.*

Heckl, MA (1988). *J. Sound Vib.* **124**, 117-33.

Hermann, J, Gleis, S and Vortmeyer, D (1996). *Combust. Sci. & Tech.*, **118**, 1-25.

Hermann, J, Orthmann, A & Hoffmann, S (1999). *6th Int. Cong. on Sound and Vib.*, 3341-3352.

Hibshman, JR, Cohen, JM, Banaszuk, A, Anderson, TJ, and Alholm, HA, (1999). *ASME*, 99-GT-215.

Kemal, A, and Bowman, CT (1996) *26th Symposium (International) on Combustion*, 2803-2809.

Krstic, M, Fontaine, D, Kokotovic, PV and Paduano, JD (1998). *IEEE Trans. Automatic Control*, **43**, 1739-1745.

Krstic, M, Krupadanam, A, and Jacobsen, C (1999). *IEEE Trans. on Control Systems Technology*, **7**, 424-436.

Lang, W, Poinsot, T and Candel, S (1987).*Combust. and Flame*, **70**, 281-289.

Langhorne, PJ, Dowling, AP, and Hooper, N, (1990) *J. Propulsion and Power*, **6**, 324-333.

Macquisten, MA, and Dowling, AP (1993). *Combust. Flame*, **94**, 253-264.

McFarlane, DC and Glover, K. Robust Controller Design Using Normalized Coprime Factor Plant Descriptions, **138**, *Lecture Notes in Control and Information Sciences*, Springer-Verlag 1990.

McFarlane, D C and Glover, K, *IEEE Trans. on Automatic Control*, **37**, 759-769, 1992.

McManus, K R, Poinsot, T, and Candel, SM (1993). A review of active control of combustion instabilities. *Prog. Energy Combust. Sci.*, **19**, 1-29

Moran, AJ, Steele, D and Dowling, AP (2000). Active control and its applications *NATO Symposium on Active Control Technology for Enhanced Performance Operational Capabilities*

of Military Aircraft, Land Vehicles and Sea Vehicles.

Narendra, KS and Annaswamy, AM (1989). Stable Adaptive Systems, *Prentice-Hall International*,

Neumeier, Y and Zinn, BT (1996). *26th Symposium (International) on Combustion.* The Combustion Institute, 2811-2818.

Paduano, JD, Epstein, AH, Valavani, L, Longley, JP, Greitzer, EM and Guenette, GR (1993). *ASME J. Turbomachinery,* **115**, 48-56.

Pinsley, JE, Guenette, GR, Epstein, AH, and Greitzer, EM (1991). *ASME J. Turbomachinery,* **113**, 723-732.

Poinsot, T, Bourienne, F, Candel, S, Esposito, E, and Lang, W (1987). *J. Propulsion and Power,* **5**, 14-20.

Poinsot, T, Veynante, D, Bourienne, F, Candel, S, Esposito, E, and Surget, J (1988). *Proc. 22nd Symposium (International) on Combustion,* 1363-1370.

Rayleigh, Lord, The Theory of Sound, London: Macmillan, 1896.

Richard, GA and Janus, MC (1998). *Trans. ASME, J. Engineering for Gas Turbine and Power,* **120**, 294-302.

Sattinger, SS, Neumeier, Y, Nabi, A, Zinn, BT, Amos, DJ, Darling, DD (1998). ASME 98-GT-258.

Seume, JR, Vortmeyer, N, Krause, W, Hermann, J, Hantschk, C-C, Zangl, P, Gleis, S, Vortmeyer, D, and Orthmann, A, (1998). *ASME J. Engineering for Gas Turbines and Power,* **120**, 721-726.

Weigl, HJ, Paduano, JD, Fréchette, LG, Epstein, AH, Greitzer, EM, Bright, MM and Strazisar, TJ (1998). *ASME J. for Turbomachinery,* **120**, 625-636.

Williams, FA (1965). Combustion Theory, Reading Massachusetts, Addison-Wesley.

Yang, V and Schadow, KC (1998). A*GARD Workshops on Active Combustion Control of Propulsion Systems, NATO-RTO Symposium on Gas Turbine Engine Combustions, Emissions and Alternative Fuels, Lisbon, Portugal.*

Yang, V, Sinha, A, and Fung, Y-T (1992). *J. Prop. Power,* **8**, 66-73.

Zhu, M, Dowling, AP and Bray, KNC (2000). ASME 2000-GT-108 to appear *ASME J. Engineering for Gas Turbines and Power.*

BACK TO THE FUTURE
HOW ACTIVE AEROELASTIC WINGS are a A RETURN TO AVIATION'S BEGINNINGS AND A SMALL STEP TO FUTURE BIRD-LIKE WINGS

Ed Pendleton
Air Vehicles Directorate
Air Force Research Laboratory
Wright-Patterson Air Force Base, Ohio 45433-7542, USA

We wished to employ some system whereby the operator could vary, at will, the inclination of different parts of the wings, and thus obtain from the wind forces the means to restore the balance the wind itself had disturbed. - Orville and Wilbur Wright

Introduction

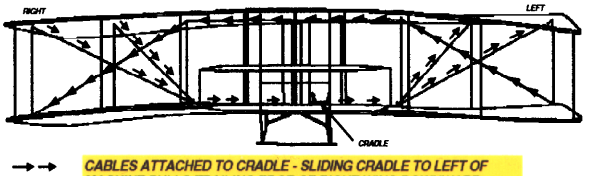
The evolution of birds has brought to the world a series of magnificent, optimized flyers. Flyers optimized by nature for weight and energy. Flyers that usc their feathers, bones, muscles, nerves, ligaments, ***and wing flexibility*** to soar through the air.

As we prepare for the centennial of powered flight in 2003, aviation historians are there to remind us that for man to first learn to fly, he had to abandon the quest to emulate these birds. Nevertheless, since we have learned to fly and have subsequently matured our current approach to flight, we must continue to consider the birds and the lessons they teach.

With nearly one hundred years of aviation development behind us, there are many that argue that aeronautics is a sunset technology. But consider this thought. Nature has always required that aerodynamic shapes must change to be optimum through various speed regimes. Until technologies similar to those used by the birds are developed, the ability to achieve true optimums in shape will never fully be achieved. Until technologies are developed that can optimally integrate aerodynamics, flight controls, with flexible lifting surfaces to maximize performance while minimizing energy and weight, aeronautics development is not at its sunset, it is not even noon

Wing flexibility – A key to control during the first manned powered flight

The Wright Brothers realized that the key to their successful first flight was the appropriate aircraft stability and control. When Orville Wright got airborne during the Wright Brothers' historic flight on Dec. 17, 1903, he didn't have ailerons or flaps to control his airplane. Instead, the brothers chose to twist or "warp" the wings of their craft as a means to control its rolling motion. Rather than using one of the craft's two control sticks to make the wingtips twist, they devised a "saddle'' in which the pilot lay.



CABLES ATTACHED TO CRADLE - SLIDING CRADLE TO LEFT OF MACHINE PULLS TRAILING EDGE OF RIGHT WING DOWNWARD

CABLE (NOT ATTACHED TO CRADLE) IS MOVED AUTOMATICALLY BY DOWNWARD MOVEMENT OF RIGHT WING

The accompanying picture of the Wrights' powered machine (with motor and propellers removed) shows the method of twisting the rear of the wings. A movement of only an inch or two, to the left or right, of the operators' hips resting on the little cradle was enough to give greater lift to whichever wing needed it, and to restore sidewise balance.

Figure 1. Wing warping technique used by the Wrights

Paper presented at the RTO AVT Symposium on "Active Control Technology for Enhanced Performance Operational Capabilities of Military Aircraft, Land Vehicles and Sea Vehicles", held in Braunschweig, Germany, 8-11 May 2000, and published in RTO MP-051.

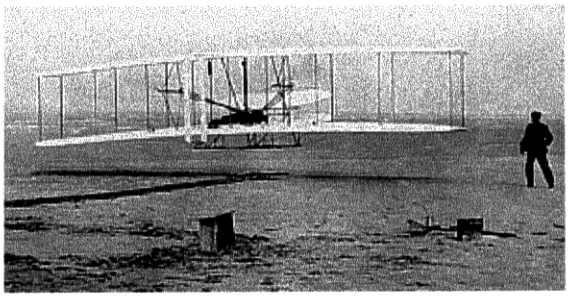


Figure 2. Wing flexibility was a key to control during the first manned flight

By moving his hips from side-to-side, the pilot tugged on a set of cables that warped either the left or right wingtip, providing the necessary flight control for the aircraft. So it was with man's earliest powered venture into the sky. The Wright brothers took advantage of wing flexibility to control their craft.

Wing flexibility - Used in the natural world for millions of years

Though the first successful manned aircraft used wing flexibility, mankind was not the first to employ wing flexibility. Eight separate fossil specimens tell us of the first living creature believed to have taken to the skies some 150 million years ago, the Archaeopteryx.

Archaeopteryx was part bird and part dinosaur. The creature had feathers and bones with air sacs like a bird, but also had many reptile features like free trunk vertebra and a long bony tail. Archaeopteryx, shown in Figure 2, weighed little more than a half-pound and had a wing span of more than 20 inches. The fossil evidence suggests Archaeopteryx needed to use wing flexibility to generate enough lift to fly. As Archaeopteryx took off from a running start, it went airborne by rotating its wings by 45 degrees at the shoulder, angled forward like two large oars beating the air. Archaeopteryx 's wings acted more like an airplane's engines than wings, providing more thrust than lift. Once in the air, Archaeopteryx had to rotate its wings back to horizontal, to maintain altitude.

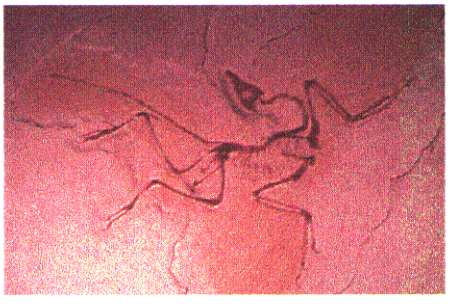


Figure 3. Archaeopteryx fossil

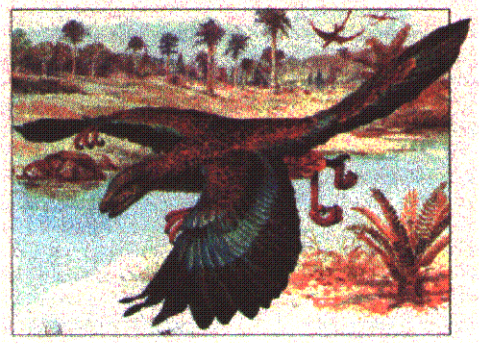


Figure 4. Artist's depiction of the proposed earliest bird - Archaeopteryx

In birds, wing flexibility is all in the wrist action

Since those days long ago, birds have evolved to the point where they can sustain powered flight over long distances. To do this, a modern bird needs feathers, muscle mass, a keeled sternum, and must employ anatomical wing flexibility.

In modern birds, the wing shoulder joint acts as a universal joint providing a high degree of mobility for downward wing movement, upward wing movement, extension, and retraction. It also allows significant rotation along the axis of the humerus. The elbow is a very restrictive joint that allows only planar extension and

flexure. The wrist joint is composed of two bony carpals that control the movement of the joint. Located beyond the wrist is a series of fused and incompletely fused carpal bones to which primary flight feathers are attached.

The wrist joint, articulating on two small, round carpals, allows an amazing range of movement and flexibility. This flexibility is vital to bird powered flight, since it allows the wrist to describe a lazy figure-of-eight during a complete flap. The elbow joint allows no rotation, but the wing must be able to present a solid open wing on the power stoke, but rotate during the recovery stroke to minimize resistance. The birds accomplish this by rotating the wrist and shoulder.

Wing flexibility – A negative in aircraft design for the 20th century

Though wing flexibility was a key to control during the first successful manned powered flight, wing flexibility affected other early designs adversely. Perhaps, the first designer to be affected was Dr. Langley. The unfortunate wing failure that wrecked his machine in 1903 was likely due to wing torsional divergence. The success of the Wright Brothers and the failure of the Langley monoplane provided one of the original reasons for early designer preference for biplanes.

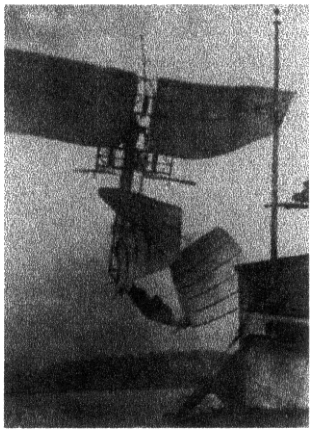


Figure 5. Dr. Langley's flying machine was subject to an early disaster caused by wing flexibility

By the mid-1930s, the quest for higher performance and speed led designers to promote monoplanes designs with semi-monocoque structures. As these designs were built and flown, aircraft encountered a wide variety of problems, which we now classify as aeroelastic problems. Wing flutter, wing divergence, buffeting, control effectiveness, and control reversal are examples of aeroelastic problems that have plagued aircraft designs ever since.

Today, aircraft lifting surfaces are designed to be strong enough to meet loading requirements and material is added to provide stiffness adequate to keep them free from flutter, divergence, and bucking. And as pilots and passengers on aircraft, we are glad this is so.

But this added stiffness usually means adding structural weight, so design trades are made between weight and aerodynamic performance for a given set of aerodynamic requirements. As speeds increase, designers often have opted to reduce wing span, increase wing thickness and live with the subsequent reduced aerodynamic performance in an attempt to save weight.

Wing flexibility used as a benefit... The first step towards a new era in aeronautics?

As we enter the second one hundred years of aeronautics development, we are poised to enter a potentially new era in aircraft design. To take full advantage of this, it will take vision and new aircraft materials and new ways of integrating wing design with adaptive control strategies to take advantage of it.

The AFRL Air vehicles Directorate and NASA have taken a first step by developing a novel technology that offers weight competitive wing designs and improved aerodynamic performance. It is called the Active Aeroelastic Wing or

AAW. AAW Technology is a synergistic technology that integrates air vehicle aerodynamics, active controls, and structures together to maximize air vehicle performance. The concept turns wing aeroelastic flexibility into a net benefit by using of multiple leading and trailing edge control surfaces activated by a digital flight control system.

AAW techniques employ the energy of the air stream to achieve this desirable wing twist with very little control surface motion. The wing then creates the needed control forces with outstanding effectiveness. At higher dynamic pressures, AAW control surfaces are used as "aerodynamic tabs" that promote wing twist for added control force capability instead of trying to overcome control surface losses due to wing elastic twist. At these high dynamic pressures, large amounts of control power can be generated using this approach. In the same design the AAW control can minimize drag at low wing strain conditions and/or minimize structural loads at high wing strain conditions. The AAW concept was successfully by a Air Force / NASA / Rockwell North American team tested in the transonic dynamics wind tunnel. Now, another joint Air Force /NASA/Boeing team is preparing to take it to flight in California at NASA Dryden.

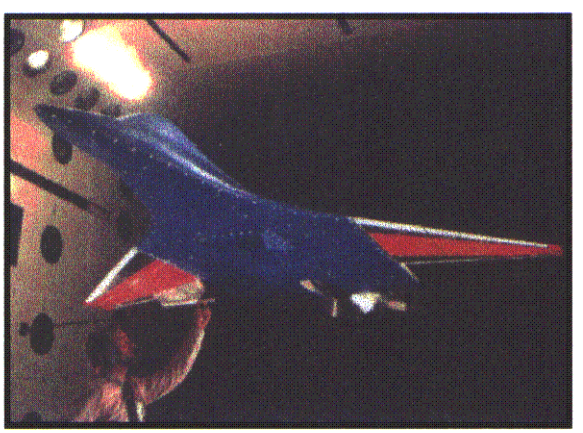


Figure 6. The Active Flexible Wing Transonic Dynamics Wind Tunnel Model proved the viability of the AAW concept

On the original F/A-18, wing flexibility was a negative. AAW will turn it into a positive.

Our joint Air Force, NASA, and Boeing team is modifying an F/A-18 fighter to demonstrate the feasibility of the AAW concept. To do this, we are taking advantage of some historical aspects of the F/A-18 wing development.

The early prototype F/A-18 wings were designed with stiffness adequate for strength, buckling, and flutter with no stiffness added for roll effectiveness. At high dynamic pressures where wing flexibility effects are most pronounced, the early F/A-18s prototypes were unable to roll sufficiently. Therefore, the aircraft's wing covers were stiffened and wing aft spars were beefed up to provide improve roll effectiveness.

The AAW modification returns the wings on one of the prototype aircraft to their original stiffness, which is representative of an Active Aeroelastic Wing. The existing wing panels along the trailing edge aft box of the wing have been replaced with original-type F/A-18 wing panels.

Other modifications include changes to the leading edge actuation system and a set of new flight control laws. A high rate leading edge control actuation system has been installed to drive the outboard leading edge flap as a control surface independent of the inboard flap. The inboard flap will also be used as a control surface.

New AAW control laws have been developed using an optimization algorithm called the "Integrated Structure-Maneuver Design (ISMD) Procedure". The AAW control laws actively command the control surfaces to optimal trim settings to control the aeroelastic twist of the wing and minimize loads at high speeds.

These basic AAW control laws are designed for the AAW F/A-18 flight test as "point designs" at 20 transonic and supersonic flight conditions. These control laws were designed using ISMD and

MATLAB using a linear flight test corrected aerodynamic database. The control laws provide large amounts of control power while minimizing a weighted percentage combination of induced drag and maneuver load. The control laws control the aircraft in all axes using control surfaces in an optimal manner by using combinations of leading and trailing edge control surfaces in their best direction, aeroelastically reversed or not. The control laws use basic roll, yaw, and pitch rate, Nz and lateral acceleration feedback and provide control surface output.

The control surface outputs are gearing functions that are linear with fixed gain constant coefficients. The gearing functions are scheduled with Mach and dynamic pressure. Current F/A-18, low Level I handling qualities are also a goal to be achieved using these control laws.

By using the trailing edge control surfaces and leading edge flaps to control the aeroelastic twist of the wing, the aerodynamic forces on the wing provide the roll forces desired. A lightweight flexible wing will now have a positive control benefit rather than a negative one.



Figure 7. F/A-18 Active Aeroelastic Wing Testbed will prove the AAW concept in full-scale

Wing flexibility used as a benefit is a shift in the aircraft wing design paradigm

Active Aeroelastic Wing (AAW) Technology is a novel way of providing powerful rolling control forces for high performance aircraft. AAW Technology is especially synergistic with thin, flexible wings and allows designers more freedom to exploit highly efficient, thin, higher aspect ratio aerodynamic wing planforms. The technology can be used not only to improve the capabilities of existing wing planforms, but to reduce the conflict in requirements for new wing design. The conflicting requirements between stiff versus flexible wings are removed for aircraft that must provide competitive performance for multiple design conditions.

Potential benefits to future air vehicles as a result of application of AAW technology include substantially increased control power from conventional control surfaces by maintaining their effectiveness, reduced aerodynamic drag through programmed optimum control surface deflections, and reduced aircraft structural weight due to relaxed stiffness and hinge moment requirements. Other benefits include reduced wing and control surface deflections by allowing the wing deflections to help in the control function and an overall increased design latitude in terms of wing span, sweep, and thickness due to relaxed stiffness requirements. These benefits come for little added hardware complexity.

The AAW Program - A first, small step toward the development of bird-like wings

The AAW Flight Research Program is a first, small step toward the development of bird-like wings. But there is much more to be considered and to be done. New adaptive control algorithms and optimization techniques must be developed that take advantage of wing flexibility.

With respect to the AAW design approach, maneuver load controllers need to be developed to help keep control surface

rates within bounds when load constraints are active in the optimal gearing function. Load constraints can cause significant changes to control surface output versus feedback input and can result in large actuator rates. More research needs to be conducted to determine the best way to design the gearing functions to maximize performance without exceeding rates, or to minimize rates within a performance goal.

Research needs to be conducted to determine how to appropriately "mix" load feedback with the AAW a-priori control approach. The mixing of feedback control could easily undo the a-priori controls objective, effectively resulting in a "fighting" of the a-priori and feedback controllers. Development of an adaptive controller that monitors load feedback signals and adjusts the a-priori gains accordingly could be one possible approach.

Adaptive controller research also needs to be conducted to determine both the controller architecture and the adaptive algorithms used to adjust the gains during flight. Research needs to be conducted to develop a robust processes to solve for and implement the gearing functions in a controller.

Toward the Future

In thinking toward a future where aircraft and their lifting surfaces are optimized for energy as well as performance and weight, lifting surfaces capable of emulating some aspects of flexible birds' wings will be highly desired. To achieve this idea, new materials that are strong, but flexible and provide new levels of flexibility will need to be developed. In addition, new ways of sensing wing deformation will need to be developed as "nerves" to feedback to the controller so that the adaptations can be made to the structure.

The propulsion "muscle" will probably always be provided by a jet-type or pulse type of propulsion system since they are so efficient.

But, the ability to change the aerodynamic shape to alleviate load, reduce drag, and improve lifting efficiency is still a worthy and needed capability.

Through the integration and optimization of new materials, structures, controls with aerodynamics, new highly efficient lifting surfaces can be devised that change aerodynamic shape as they traverse the low and high subsonic, transonic, supersonic, and hypersonic aerodynamic regimes. These active lifting surfaces will change shape through active twisting and morphing to provide optimal lift throughout the flight envelope while minimizing drag, and controlling loads such as a bird does.

Nature shows us the benefits of doing so. New air vehicles will require the performance and energy savings that can be achieved. They will be lighter and cost effective, while answering the performance challenges that inevitably lie ahead in the 21st century.

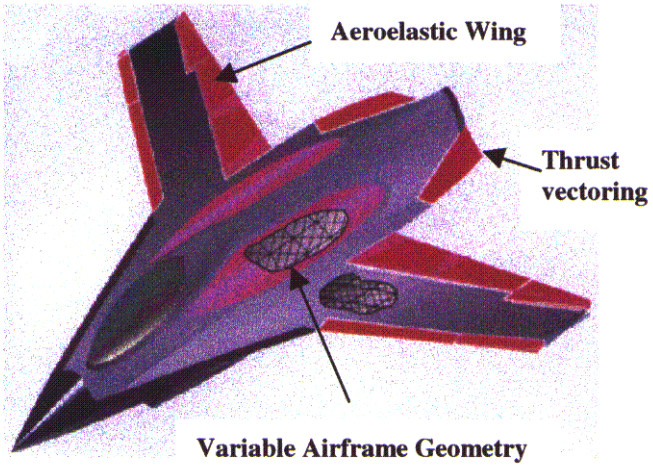


Figure 8. Active Aeroelastic Wing along with other innovative features will enable novel new air vehicle designs



Figure 9. A vision for the future --- Lightweight air vehicle with an active aeroelastic wing / multifunctional lifting surfaces

REFERENCES

1. Wright, O. and W., The Wright Brothers' Aeroplane, 1903.

2. Chris Nedin , "All about Archaeopteryx", Origins Archive, 1999.

3. Miller, G.D., "Active Flexible Wing (AFW) Technology," Air Force Wright Aeronautical Laboratories TR-87-3096, February, 1988.

4. Miller, G.D., "An Active Flexible Wing Multi-Disciplinary Design Optimization Method," AIAA Paper No. 94-4412-CP.

5. Perry III, B., Cole, S.R., and Miller, G.D., "A Summary of an AFW Program," Journal of Aircraft Vol. 32, No. 1.

6. Pendleton, Lee, and Wasserman, "Application of AFW Technology to the Agile Falcon", Journal of Aircraft Vol. 29, No. 3, May-June, 1992.

7. Yurkovich, R., and Miller, G.D., "An F/A-18 Wing Modification Study for Active Aeroelastic Wing", McDonnell/Rockwell/Air Force, TBP.

8. Yurkovich, R., "Optimum Wing Shape for an AFW", 36th AIAA Structures, Structural Dynamics and Materials Conference, New Orleans, La., April, 1995.

9. Pendleton, E., Griffin, K.E., Kehoe, M, and Perry, B. "A Flight Research Program for Active Aeroelastic Wing Technology," AIAA Paper No. 96-1574, 37th AIAA Structures, Structural Dynamics and Materials Conference, Salt Lake City, Utah, April, 1996.

10. Pendleton, E., Bessette, D., Field, P., Miller, G., and Griffin, K., "The Active Aeroelastic Wing Flight Research Program, Technical Program & Model Analytical Development", Journal of Aircraft, publish date pending.

This page has been deliberately left blank

Page intentionnellement blanche

THEORY OF CONTROL ASPECTS

Jean-Louis Gobert
ONERA
2, avenue Edouard Belin - F31055 Toulouse Cedex
gobert@cert.fr

Keynote presented at the AVT SYMPOSIUM on
Active Control Technology for Enhanced Performance Operation Capabilities of Military Aircraft, Land Vehicles and Sea Vehicles
Braunschweig, Germany, 8-11 May 2000

SUMMARY : The wide field of possible applications in various areas is one of the most fundamental aspects of control theory, the disciplines range from mechanics to finance through power plants, aeronautics, electronics, biotechnology, air traffic, control, etc….. As a consequence, any application involving control, requires the cohabitation of control engineers and engineers from other disciplines; generally the scientific background, education and culture of those categories of engineers are quite different. The contact between several cultures leads often to understanding and communication difficulties, which could jeopardise the normal development of a project. In extreme cases, control theory will be considered as an isoteric discipline dedicated to few specialists; a similar observation would surely exist in case cohabitation must be required between disciplines such as aerodynamics and psychology or finance. Control theory is well known for its ability to design devices in order to robustly control and/or stabilise a process in presence of perturbations, parameter variations and/or unmodeled dynamics. But, it shall not be forgotten that control is also the discipline of analysis, modelling, identification, simulation, evaluation, diagnosis and optimisation.

This short document seeks to show how the communication between participants from the different disciplines can be improved by taking into account the control discipline at an early stage of the project and by intensively using the capabilities of modelling. It is demonstrated that this approach enables to create a new synergy by taking the best of the complementary aspects of the different cultures.

An illustration, based on a traditional application, experience gained during the design and construction phases of the European Transonic Wind tunnel (ETW), erected in Cologne (Germany), is given at the end of the document.

RESUME : Un des aspects fondamentaux de la théorie du contrôle est qu'elle peut s'utiliser dans presque tous les domaines, de la mécanique à la finance en passant par la production d'énergie, l'aéronautique, l'électronique, la biotechnologie, le trafic aérien, etc.…. La théorie du contrôle se trouve donc toujours associée à une autre discipline avec pour conséquence la nécessité de faire cohabiter des ingénieurs d'éducation et de culture scientifiques très différentes, ce rapprochement de plusieurs cultures n'est pas sans créer des difficultés de compréhension et donc de communication qui, quelquefois, peuvent compromettre la progression d'un projet. Dans des cas extrêmes, le contrôle sera même perçu comme une discipline ésotérique réservée à quelques initiés, le même constat existerait sûrement si une discipline telle que l'aérodynamique devait cohabiter avec la psychologie ou la finance. Un des aspects le plus connu de la théorie du contrôle est sa capacité à concevoir des dispositifs fonctionnant en boucle fermée destinés à piloter et/ou à stabiliser avec robustesse un système en présence de perturbations, de variations de paramètres et/ou de modes dynamiques secondaires non identifiés ; mais, on oublie trop fréquemment que la théorie du contrôle est aussi la discipline de l'analyse, la modélisation, l'identification, la simulation, l'évaluation, le diagnostique et l'optimisation.

Ce court document essaie de montrer comment la prise en compte du contrôle très tôt dès l'origine d'un projet peut aider, principalement à travers la modélisation et la simulation, à établir des liens entre les participants des diverses disciplines en tirant profit de la complémentarité des cultures pour créer une nouvelle synergie.

Une illustration, issue d'une application de type traditionnelle, expérience acquise lors des phases de conception et de construction de la soufflerie transsonique européenne ETW érigée à Cologne (Allemagne) est donnée en fin du document.

1. Introduction

I would like first to thank Pr. Koerner who invited me for this lecture. I shall say that when he called me last year and asked me to speak about aspects of control theory, I was slightly embarrassed for two reasons, the first one is that I am not a control theorist, the second one is that, due to the breadth of the subject, it seemed to me impossible to find something general enough to be presented in a multidisciplinary session.

Paper presented at the RTO AVT Symposium on "Active Control Technology for Enhanced Performance Operational Capabilities of Military Aircraft, Land Vehicles and Sea Vehicles", held in Braunschweig, Germany, 8-11 May 2000, and published in RTO MP-051.

Finally, I realised that it is a good opportunity to be in front of a community of engineers and scientists from various disciplines such as fluid dynamics, energetics, structures, aircraft design, control, … to discuss about the aspects of the cohabitation of control theorists and other disciplines engineers.

Indeed, one particular aspect of automatic control is that it can be used in a wide range of applications such as mechanics, industrial plants automotive, aeronautics as well as biotechnology and even finance. Therefore, scientific knowledge and education of the control theorists are always different from those of the specialists who need to apply control theory in their process. These differences in culture and education might be a handicap in the communication leading sometimes to misunderstandings, which, in the worst cases, can jeopardise a project. It is not rare that the engineers from other disciplines consider control theory as an esoteric matter reserved to few insiders. As a consequence, it is frequent to find situations where control theorists are working alone using assumptions which are *sometimes far from the needs* of the possible users and situations where non control specialists are trying *to solve control problems on their own*.

Traditional control applications are usually dedicated to mechanical or electrical systems, power or chemical plants conscientiously designed and built by engineers in such a way that they can be controlled with existing and well known techniques. In many of these applications, the plant can be possibly redesigned and sensors or actuators can be added or modified to ease the control problem, if required. Many control engineers are used to deal with these types of applications and have a relatively good background and understanding of the process; usually classical solutions are used with possible relaxation of the required specifications when the original specifications cannot be satisfied.

During the last twenty years, non-traditional control applications such as noise control, combustion control, vibration control and aerothermodynamic flow control have appeared. Although these applications are quite different, similar control techniques are often implemented with a stronger need for new specific theoretical developments. One of the prime dissimilarities is that the degrees of freedom to redesign the system are usually much lower than in traditional applications, the only flexibility being in the possible modifications of the actuators and sensors, which often are one of the most critical points of non-traditional control applications.

During the same period, control theory has considerably developed by occurrence of new methods in the domains of classical control, adaptive control, optimal control, robust control, non linear control, neural networks … These new developments, usually dedicated to traditional control, are generally useable with some cares to both cases, traditional and non traditional control applications.

These new control theories are usually based on quite intricate mathematical developments with the result of building progressively a gap not only between the control theorists and the engineers from the other disciplines, but also inside the control discipline itself between the control theorists and the control designers and implementers.

All these considerations demonstrate that there is a strong requirement to build a bridge between control theorists and the other engineers to implement either new control techniques in traditional applications or simply control techniques (classical or new) in non traditional control applications [1, 2].

Good communication between the different communities is a prerequisite for the success of a multidisciplinary project in which control has a prime role.

One of the keys to overcome these difficulties is obviously in using the complementary knowledge and education of all the concerned persons, hence in generating a new and strong synergy.

The solution should not be in trying to get everybody understanding everything, ***but in providing the optimum interface between all the disciplines*** in order to improve the communication and to get each specialist giving the best of its own capabilities in the right direction. It shall never be forgotten that the key of the difficulties is at the level of the interactions between the participants.

Unfortunately, this part of the activity does not seem important to any of the participants; one of the main reasons is that it is half way of each discipline, therefore it looks without importance to everyone and nobody is giving enough emphasis to this task. Another important reason is that such a task requires to use every endeavour to reach a good level of co-operation and dialog; it is so much easier to work on his own!

One good method of approach shall include the following steps:

1- Some words are common to several disciplines, but sometimes with slightly different meanings. In order to avoid possible future misunderstandings, these words shall be listed and clarified, an agreement shall be found on a common definition.

2- A common mathematical tool shall be build in close co-operation, it will become the reference for any future technical discussions and will be used as the basis of the control theory.

3- The technical objectives shall be defined in terms of control: parameter to be controlled, performance requirement,….

This document presents some considerations on the two first points. It also shows how such an approach can considerably impact the overall system design procedure.

2. Terminology

One of the first obstacles, within a multidisciplinary project, is the difference of languages between disciplines, which is mainly the result of the

various education and of the use of dedicated technical jargons. As a consequence, some words have slightly different meanings from one specialist to another one, but the differences are sometimes so small that nobody thinks that clarification is required. Obviously, it is recommended to clarify all the words that are at the interface between disciplines as soon as possible.

As an example, the word "**Control**" itself can be used differently from one discipline to another one.

A specialist of fluid mechanics considers at least three types of flow control:

1- passive control
2- active control
3- reactive control

With his terminology, "Passive control" means control with **no energy expenditure** using static devices (e.g. riblets or LEBU's) or dynamic devices activated by the flow itself.

He considers "Active control" as a mean of control that requires the use of an **external energy** such as blowing or suction by simply setting it in a **predetermined way**.

"Reactive control" is a mean of control that requires the use of an external energy in which the control input is **depending on parameter measurements** through either feed forward control or feedback control loop.

For a control specialist, the notion of action is already implicit in the word "control" and he probably considers the words "active" and "control" as redundant. For him, "control" is equivalent to "reactive control". This means that he will not notice a difference between "active control" and "reactive control".

In the same way, "passive control" could probably be interpreted as a synonym of "monitoring".

Using the definitions given in fluid mechanics, he probably will consider passive and active controls more as "flow manipulation" than as control. As a conclusion for him, only reactive control is meaningful because it involves a continuous adjustment provided by an internal loop.

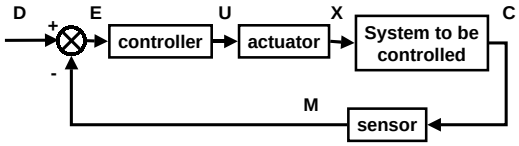
In the rest of the document, the word "control" is a synonym of "reactive control".

Another word could be the word "instabilities". For a control specialist instability is synonymous of parameter divergence and as an example, buffeting on an aircraft wing will not be considered as an unstable phenomenon whereas the aerodynamicists consider it as flow instabilities.

3. Reactive control

After the clarification on the word "Control", it seems to be interesting to introduce the most usual and simple reactive control diagrams.

The most important advantages of reactive control are to automatically adapt the controlled variable and to compensate for external perturbations, unmodeled dynamics and parameter variations . It makes possible the introduction of a cost function, thus enabling a control optimisation on either the quadratic error or the energy consumption or any other selected compromise.

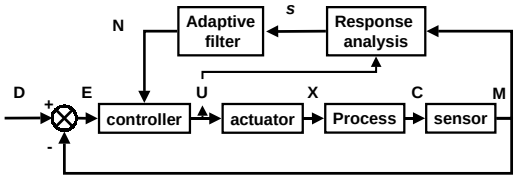


C = controlled variable
D = desired value of C
E = error signal
U = command to actuator
X = manipulated variable
M = feedback signal

Fig.1 : Typical feedback control loop

Control, as often as possible, operates in closed loop versus the parameter to be controlled. For that purpose, the variable is measured by the mean of a sensor and compared to the desired value, the error is introduced into a controller, which adapts the command in order to provide a zero error. Fig.1 gives a representation of a typical feedback mono-variable control loop.

Due to the presence of non-linearities and/or unmodeled dynamics, the controller parameters are usually not properly adapted. This can be compensated by the addition of a real time analysis of the system behaviour. The result is an improvement of the scheme by the use of an adaptive filter leading to an adaptive



C = controlled variable
D = desired value of C
E = error signal
U = command to actuator
X = manipulated variable
M = feedback signal
N = controller parameters
***s* = state analysis**

Fig.2 : typical closed loop adaptive control

control of the type described on fig.2.

In many applications, the perturbations can be measured in advance and introduced in the controller, this is the purpose of the feed forward control scheme illustrated on fig.3. This type of control enables to remove the problems due to the presence of pure time lags in the loop, this implies that the measurement of additional variable(s) can help in predicting the value of the parameter to be controlled. But it shall be noticed that this scheme corresponds to an open loop control versus the parameter to be controlled, the main drawback is that checking of the overall control performance is not available.

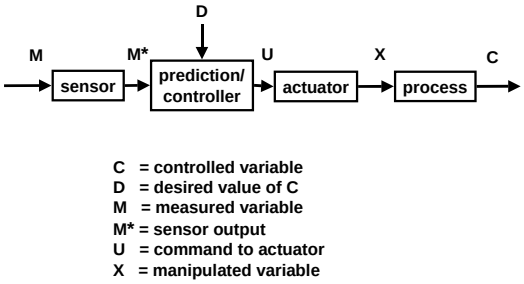


fig.3 : typical feed forward control

In order to partly cancel this drawback, an adaptive filter can be added, which corrects the controller coefficients by an analysis of the overall performance as described on fig.4. A first sensor or group of sensors (sensor 1 on fig.4) is/are used to detect the perturbations in advance, this is the first input to the control algorithm; a second sensor or group of sensors (sensor 2 on fig.4) is/are used to measure the controlled variable and correct

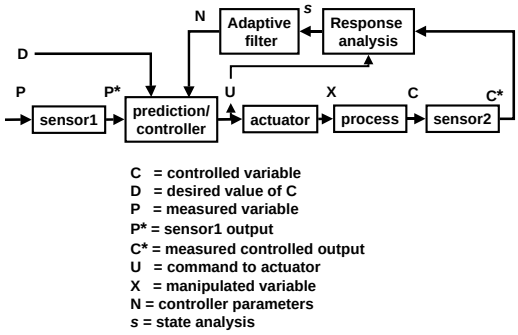


fig.4 : adaptive feed forward control

the controller parameters by the mean of the adaptive filter in order to progressively improve the control or to adapt it to external changes.

The control techniques described here are the basis of reactive control. Other schemes, usually derived from these basic techniques, can be established.

4. Examples

In this section, examples based on aerodynamic flow control are given to ease understanding.

They are taken from Tollmien-Schlichting (TS) waves control applications. TS waves are the first instabilities leading to the transition from a laminar to a turbulent boundary layer. Let's consider a flat plate surrounded by airflow. Under the effect of the outside flow fluctuations, instabilities appear in the laminar boundary layer, which grows from a critical abscissa downstream of the leading edge of the plate. The boundary layer acts as a selective amplifier, amplifying some frequencies and damping others, leading to the so-called Tollmien-Schlichting waves [3]. Above a given amplitude, the TS waves induce the transition to turbulent flow. It has been demonstrated [4,5,6] that the waves can be cancelled by using the wave superposition principle; an actuator generates a counter wave for cancellation.

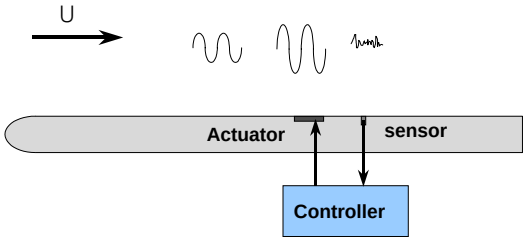


fig.5 : closed loop control for TS waves

Fig.5 gives the diagram of a TS waves closed loop control. It shall be noticed that the feedback signal is coming from a sensor located downstream of the actuator where the attenuation shall be performed. As the Tollmien-Schlichting waves are transported by the flow, a pure time lag, which cannot be compensated, appears in the transfer function of such a system.

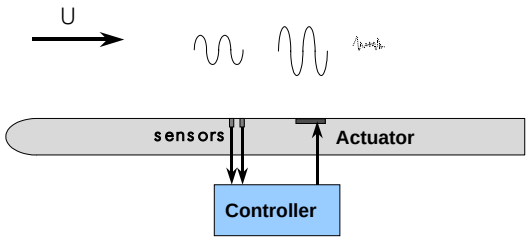


fig.6 : TS waves feed forword control

The use of a feed forward control scheme [fig.6] can compensate for this drawback, but in this case, the result of the control is not visible by the controller. However, better performances can be expected with such a scheme since incoming fluctuations are detected, thus enabling a prediction for "optimal" cancellation.

The addition of an adaptive filter [fig.7] improves this scheme; this configuration seems to be the most appropriate solution for TS waves cancellation. The phase and the amplification gain of the TS waves can be detected by the two upstream sensors enabling a good prediction of the signal at the actuator location while the downstream sensor is used to check efficiency and

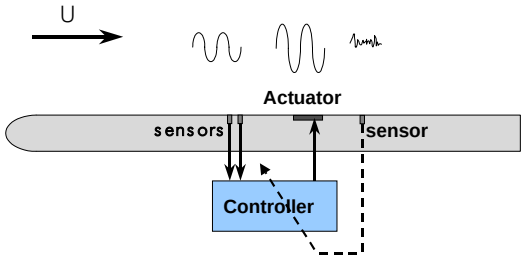


fig. 7: adaptive feed forward control for TS waves

correct the controller parameters to improve the control; such a solution should quickly converge to provide the best performances, even in presence of change of pressure gradient and external flow speed. A frequent mistake consists in assimilating pure time lags with time constant or phase shift; phase shift has a similar effect than pure time lag if only one frequency is implied.

5. Modelling

5.1. General aspects

Control theory is well known for its ability to design a feedback control law in order to robustly govern and stabilise a system in presence of perturbations, parameter fluctuations and/or unmodeled dynamics. But, it is often forgotten that control is also the discipline of analysis, modelling, identification, simulation, evaluation, diagnosis and optimisation.

In a multidisciplinary environment, modelling and simulation can have a very large importance by providing an efficient tool for system design analysis, evaluation and optimisation, ***but also for a practical support to make easier the communication between the different specialists.***

However here again, the meaning of "modelling" shall be clarified. Although its meaning is often the same between the various disciplines, several concepts are usually attached to this word according to the objectives of the model.

In fluid mechanics, at least two types of models can be found:

1- Knowledge-based models: heavy computer codes that solve accurately the physical equations that govern the process, for example the partial derivative equations of the flow such as the Navier-Stockes equations.
2- Simplified semi-empirical or experimental models: computer codes based on experimental data including some basic knowledge of the physical phenomenon.

For synthesising control laws, a control specialist will need to develop a so-called *synthesis model.*

The objectives of the synthesis model is to reproduce the behaviour of the phenomenon that shall be controlled, but with a structure that enables to apply a control theory. This means that its structure often depends on the control laws that are anticipated to be used or vice versa its structure dictates the type of the control laws.

The synthesis model requires a proper balance between simplicity and fidelity; it must be as simple as possible. The control specialists always try working with linear models when possible. The model shall represent the part of the dynamic (critical modes) of the process that can be controlled. True physical representation is not required; the implied equations have no relationships with the equations representing the physics of the process. A so-called "black boxes" representation or a state representation are among the most often used by control specialists. The synthesis model is usually analytical or based on ordinary differential equations (ODE).

The synthesis model is the tool of the control theorists and does not need to be fully understood by the other disciplines engineers.

Several solutions can be used to build a synthesis model such as:

- interpretation of heavy computer code results to build "black boxes" representation.
- interpretation of experimental data, when they are available.
- mathematical manipulation of either experimental data and/or the equations representing the phenomenon using data processing techniques such as Proper Orthogonal Decomposition (POD).
- Development of reduced order model directly from the equations that govern the phenomenon using state variable representation for example.
- …….

Some techniques, such as neural networks, enable to avoid in particular cases the use of structured synthesis model. All these techniques have advantages and drawbacks.

Often, the experience shows that there is a lack between the complete knowledge based models and the synthesis models and room is available for another type of model that can be called "simplified dynamic model".

The simplified dynamic model shall represent the behaviour of the process with a quite good fidelity, usually qualitative behaviour is more important than accuracy. It shall be much simpler than the complete knowledge-based model and capable to run quickly on normal computers, however real time performance is not required. This type of model can be used to evaluate and validate the performance of the synthesised control laws through computer simulations. Therefore, to perform a relevant evaluation, this model shall be different from the synthesis model and closer to the phenomenon behaviour; critical non-linearities shall be simulated. Of course, knowledge based models or a semi-empirical models can be used if dynamic behaviour is included, if time computation is acceptable, if actuator effects can be simulated and if sensor measurements can be made available. But often, these types of models will need to be adapted to perfectly suit the objective.

Frequently, not enough consideration is given in the development of a simplified dynamic model.

The main reasons leading to this situation are:

1- the control specialists usually do not get the required knowledge on the process to do it,

2- they usually have no strong inclination in looking in other disciplines, they prefer to deal with control theory,

3- the specialists of the other discipline either have at their disposal heavy computer codes and do not understand the need to build a simpler model or prefer to work on developing large computer codes.

4- they also are not in a good position to decide by themselves what can be discarded and what shall be kept to fulfil the control objectives.

5- Understanding of the phenomenon to be controlled is often not well known and development of a simplified dynamic model is not an easy task. As an example, we can list the cases of aerodynamic buffet or vortex breakdown.

6- and the last, but not the least, a strong multidisciplinary co-operation is required, which is not always an easy task. As already said, it seems often to everyone much more effective to work on his own.

The result is that a valid and well suitable "simplified dynamic model" is frequently missing in applications where control theory has to be applied.

In order to correct such a situation, a strong collaboration between the control theorists and the application engineers shall be established for developing the appropriate simplified dynamic model.

This type of model will not only become the basis of the control work, but ***it will also provide the perfect tool of communication between the different disciplines.*** In addition, this model can be used, as explained in the next section, for integrated system design.

5.2. Dynamic model characteristics

Therefore, it is very important not to minimise this task

The main characteristics of a suitable simplified dynamic model are:

1- As far as possible, *the model shall be based on physical considerations*. This enables to sense in advance all the potential difficulties and to minimise future unexpected behaviour. It often happens that non-expected control problems have their origin in behaviour of the process that was not anticipated. Considerations on the physics of the phenomenon should reduce this potential risk.

2- The process characteristics that shall be included and those that can be discarded must be carefully selected. The proper balance between simplicity and fidelity of the model mainly depends upon the result of this selection. A great attention shall be given to this task in which the dialog between the different specialists is very important. Keeping characteristics that are not relevant for control leads to useless complexity, forgetting important characteristics can be the source of future unacceptable control performance.

3- The process non-linearities shall be carefully analysed and included if it is anticipated that they are critical for control. Here again, the dialog between the specialists is very important.

4- All other critical non-linearities such as actuator output saturation, speed and/or acceleration saturation, hysteresis, … shall be carefully analysed.

5- The possible presence of time lags introduced in the control loop either by the actuators, the sensors, the computers or by the process itself shall be analysed with a special attention and included as far as possible. Pure time lags are always the source of control difficulties. One frequent mistake consists in assimilating pure time lags to first order time constants.

6- Actuator behaviour shall be included. In many non-traditional applications, actuators often are a difficult problem to solve. Many attention should be given in developing a simplified dynamic model in which realistic simulation of the actuators can be implemented. It shall include actuator behaviour as well as its effect on the phenomenon. In many applications, several types of actuator can be anticipated (i.e. control of vortices by use of mechanical devices, blowing or suction); a good simplified dynamic model structure should enable replacement of the actuator, thus allowing comparisons between several possible solutions. A recommended structure for an element of dynamic model is given on fig.8.

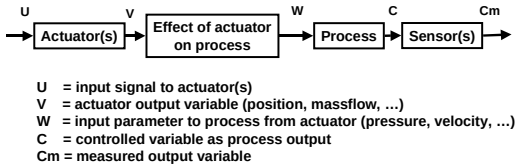


Fig.8: typical structured of simplified dynamic model element

7- Usually the sensors have quite good performances and can be forgotten; however an analysis of their performance can reveal some weakness which should be introduced, mainly when difficulties are anticipated at this level. Possible noise on actuators and sensors shall also be studied and introduced if required.

8- In some cases, the controlled variables cannot be directly measured and shall be estimated through other measurements. The impact of such a requirement shall be carefully analysed and introduced if potential problems are expected on this point.

9- The non-linearities introduced by a computer in the control loop (sampling period, input and output quantification levels, time lag…) shall in some cases be taken into account.

10- All details that can be anticipated to help in designing the synthesis model should be included.

11- It shall be checked that all the dynamic modes relevant for the commands are identified and included.

12- It shall be checked that all the dynamic modes that could be excited by the command are simulated.

13- Special considerations shall be given to design a dynamic model that enables to perform computer

simulations in an acceptable time; real time is usually not required at this level, but close to real time is recommended.

As the objectives of the synthesis model and those of the simplified dynamic model are totally different, it shall be noticed that the use of a simplified dynamic model is strongly recommended even if techniques, such as neural networks, which allow avoiding structured synthesis models, are foreseen to be used.

Obviously, if knowledge-based model and/or experimental data are available, a comparison with the simplified dynamic model can be performed.

Attention shall mainly be given to the qualitative behaviour; indeed the simplified model will mainly be used to elaborate and test a synthesis model that will enable to synthesise control laws, which will again be validated by use of the simplified dynamic model within computer simulations. Qualitative behaviour is a decisive element to select the type of control laws, quantitative errors will only affect the coefficients of the control which can later be readjusted or automatically adapted if adaptive control is used. In addition, it shall not be forgotten that a feedback control loop , if well selected, is very forgiving in front of model parameter inaccuracy.

6. System design procedure

The objective of this section is to demonstrate how the use of a simplified dynamic model can considerably impact and improve the overall design procedure applied in a project.

Starting from scratch, the procedure to design a system in which control theory is involved is usually conducted as represented on fig.9.

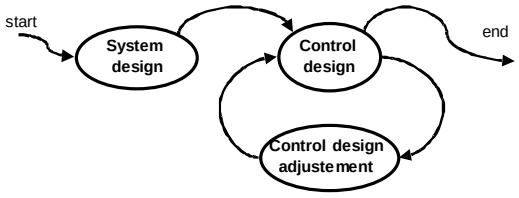


fig.9 : Classical system design procedure

Just after decision is made to proceed with the realisation of a project, the functional specifications and the performance requirements are established before entering the preliminary study phase, which is usually performed without involvement of the control engineers. Normally, the control engineers are contacted during or at the end of the detailed design phase. It is not rare to hear sentences such as “we must first proceed with the final design and when it will be done, we will see how to achieve the control …”. In the best cases, control designers are invited to discuss on actuators and sensors performance but with little mathematical consideration.

In general, the control theorists are involved at a later stage to perform the synthesis of control algorithms while the system design is already completely frozen by the engineers from the other disciplines including often hardware control system (sensors, actuators, computer system). At this stage, the control engineers shall implement the control to obtain the required performance from the system as already designed. The task of the control engineers consists in trying to adapt a control theory and adjust it by several iterations taking into account performance and robustness (fig.9). Their goal is simply to take the best of the existing design. In addition, it often happens that the control theorists adapt the theory they know the best instead to select the theory that fits the best to the problem. This approach, usually, requires a lot of controller design iterations, leading sometimes to unachievable goals and the need to relax the specifications or to proceed with expensive system changes.

Obviously, the results of such an approach are not always satisfying and are never "optimal". Control theory is considered as a mean to obtain the best with an existing system design, but not as a mean to design the optimum integrated system. This type of approach, made independently of the control engineers, can have a significant impact not only on the overall closed loop system performance, but also on the manufacturing cost as well as on the future operation and maintenance costs.

One alternative is an iterative approach involving control theory from the early stage of the project by first developing a simplified dynamic model, as described in the previous section. This model enables not only the development of a synthesis model, hence a control law synthesis, but it also enables the validation of the control laws and above all an overall system analysis and optimisation.

Mathematical iterations using intensive simulation during detailed design phase, as represented on fig.10, replace the expensive changes that are usually required during commissioning phase of the system to correct possible system design mistakes. Such an approach will considerably reduce the potential risks of unachievable performance.

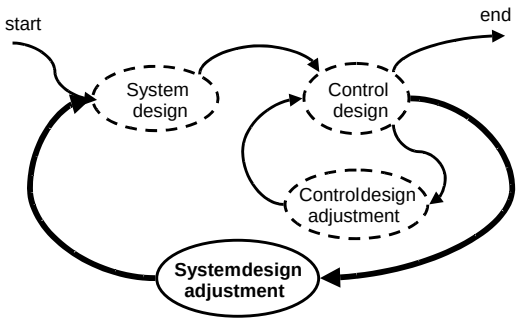


fig.10 Iterative design procedure involving control theory

This approach starts by a very first preliminary design enabling the establishment of a simplified dynamic model as explained in the previous section.

This model being made available, the control theorists have at their disposal a tool enabling the system analysis. Then, the model is integrated into a computer

simulation code that can simulate the overall behaviour, tests can be performed in open loop if needed. At that point, the control theorists can built a synthesis model in order to develop appropriate control laws. Once a system controller is synthesised, computer simulations can be performed to evaluate the system performances in closed loop. Changes, which may optimise the design can therefore be tested and evaluated. Several iterations between system design and controller design can be achieved until a satisfying solution is found. This procedure illustrated in details on fig.11 allows the integrated optimisation of the system and the controller.

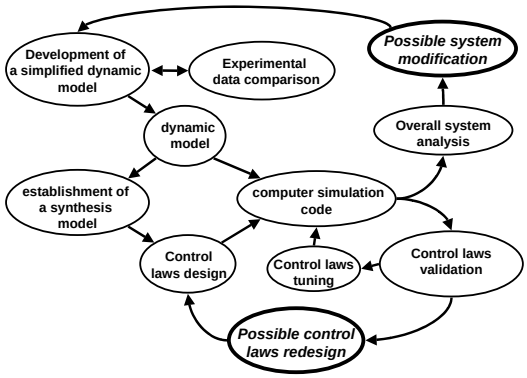


fig.11 : Details of iterative design procedure

In summary, the simplified dynamic model can be compared to a prototype of the system making possible any quick and cheap modifications.

During the integrated design procedure, the simplified dynamic model can be used to:

1- build a synthesis model
2- validate the control laws
3- define an overall control strategy
4- detect the critical points
5- select the parts where it is worthwhile to perform an optimisation
6- analyse the overall performance
7- check the robustness
8- optimise the design

Several tools from the control theory can be used for analysis, evaluation and optimisation as it is demonstrated in the next section.

7. Example of integrated system design procedure achievement

This section gives an example of the achievement of the previously described procedure.

It is an actual example based on a traditional control application. Several reasons lead to choose this application as example; among these reasons, we can list:

- the physics does not present difficulties and is quite easy to understand for everyone,
- a comparison between both the procedures (classical and integrated design) is possible,
- the impact of modelling and control theory on system design was very significant,
- the performance requirements were immediately satisfied,
- the acquired experience could be transposed to non-traditional control applications.

As already said in the previous sections, it is frequent that system design starts without early involvement of control theory and modelling.

It is what happens at the beginning of the 80's when the four European countries (France, Germany, The Netherlands and the United Kingdom) decided on the construction of a large transonic facility, the European Transonic Wind tunnel (ETW). More for political than for technical reasons, the preliminary design phase lasted 8 years before to enter in the detailed design phase in 1986.

During these 8 years, considerations were given to the aerodynamic circuit, the mechanical parts, the compressor design, the civil engineering and the control system. But, control system meant, at that time, computer hardware and sensors/actuators layout much more than control strategy and theory. But fortunately, in 1986 when entering in the detailed design phase, a large change in the insulation concept was decided whereas control engineers were just involved. This opportunity gave some additional time to enable performance of an integrated system design procedure.

ETW is a transonic, cryogenic and pressurised wind tunnel erected in Cologne (Germany) dedicated to high Reynolds numbers aerodynamic simulation.

ETW has a closed aerodynamic circuit [fig.12] contained inside an internally insulated stainless steel pressure shell. The compressor with a drive power of up to 50 MW circulates the nitrogen gas around the circuit. To achieve the desired low temperature of the test gas and to compensate for the compressor heat input, liquid nitrogen is continuously injected into the tunnel flow upstream of the compressor where it immediately vaporises and thus forms the cold gas flow. The corresponding gaseous nitrogen exhaust is upstream of the stilling chamber and is controlled by valves to maintain constant pressure inside the tunnel. The gas in the circuit then enters the wide angle diffuser where it passes through two filling screens into the stilling chamber and on through a honeycomb flow straightener and two anti-turbulence screens prior to entering the 12 to 1 contraction and the adjustable supersonic nozzle. It then passes through:

1- the test section, which houses the aircraft model,
2- the second throat area; the high speed diffuser;
3- A corner back to the liquid nitrogen injection station.

The overall layout of the circuit and especially the stilling chamber area, nozzle and test section are consistent with the high flow quality required for high Reynolds number testing.

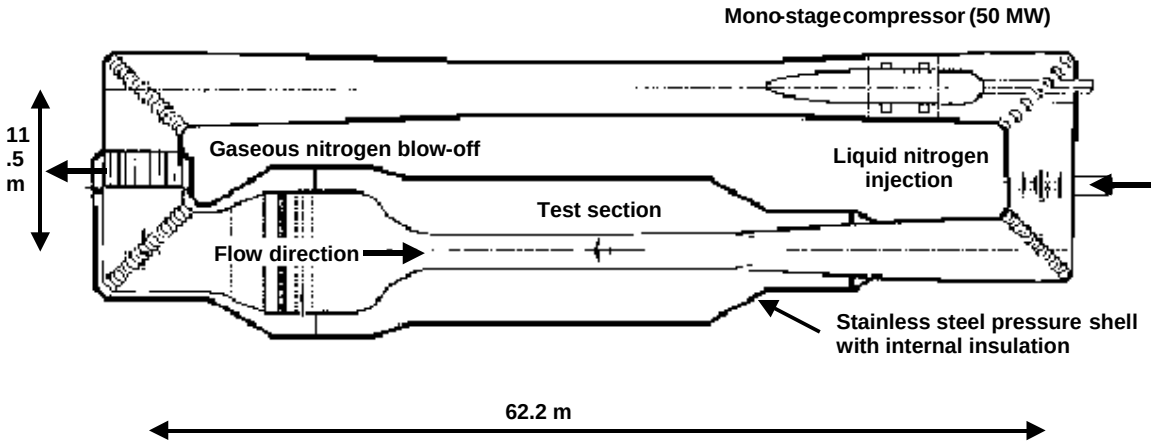


fig.12 : ETW aerodynamic circuit

The operating range is :
Mach number : 0.15 to 1.35
Temperature : 100 K to 313 K
Pressure : 1.25 bar to 4.5 bar

Accuracy requirements are :
Mach number = ± 0.001
Temperature = ± 0.25 K
Pressure : dP/P = ± 0.2%

During the preliminary studies, a so-called static pressure loss model has been established for aerodynamic circuit optimisation and sub-systems (compressor, LN2 injection system and blow-off system) specifications. It was also anticipated that LN_2 consumption would be one of the most critical point for future operating costs.

At that time, the control strategy seemed clear; the compressor provides the mean of achieving accurate Mach number in the test section, the LN2 injection enables the control of the temperature while the pressure is controlled by the use of the blow-off system. In addition, the strategy to control the second throat equipped with trim flaps in order to set the Mach number Mc and stabilise the shock location in the high speed

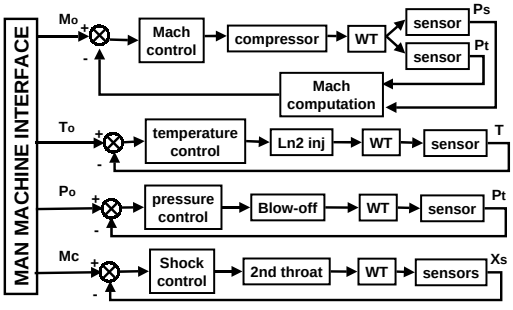


fig.13: initial ETW control system configuration

diffuser was not yet established. Although the coupling effects between the parameters were known, they were considered not important at this level of the design. Such technical considerations led to the control system configuration given on figure 13.

This configuration was designed by intensive use of distributed computers; one computer dedicated to each parameter. This decision was made more to follow a fashion than for real technical considerations.

The sub-systems specifications were defined in order to achieve the performance and productivity requirements and by using the static model results. The dynamic behaviour of the system was not considered at this level of the study. As a consequence, the results for the sub-systems specifications were as given on fig.14.

For the compressor, the maximum power is only limited by the highest requirement in stabilised conditions (maximum Mach number, maximum pressure, high temperature), but very hard requirements were put on accuracy and resolution to enable Mach number accuracy and resolution.

For the LN2 injection system, the maximum capacity was mainly to insure the set point changes at high power in acceptable times,. This led to a requirement of 600 $kg.s^{-1}$ that goes beyond the requirement for stabilised conditions, which is only 230 kg. s^{-1}.

For the blow-off, the same considerations were used than for the LN2 system. Here again the requirement for valve size of 200,000 in valve coefficient goes largely beyond the need during stabilised conditions, which is only a valve coefficient 32,000

In 1986, it was decided to proceed and to start the final detailed design; it was also decided to study the control strategy and to involve control theory. As already said, a quite large change in the insulation system was decided at the time and additional time was assigned. The control staff being involved, it has been decided to proceed with an integrated system design and to develop a so-called simplified dynamic model in a close collaboration with the aerodynamic staff.

	Before	After
Compressor :		
Maximum power	50 MW	50 MW
Resolution / accuracy :	0.01% of full speed	0.1 % of full speed
Maximum acceleration :	0 to full speed in 90 s	0 to full speed in 90 s
LN2 injection :		
Maximum capacity :	600 kg . s^{-1}	250 kg.s^{-1}
Resolution / accuracy :	0.05% of full range	0.1% of full range
Maximum acceleration	± 200 kg . s^{-1}	± 20 kg . s^{-1}
Blow-off :		
Maximum valve coefficient:	Cv = 200,000	Cv = 36,000
Resolution/accuracy (valve coef.):	Cv = 20	Cv = 20
Maximum acceleration :	0 to full opening in 4 s	0 to full opening in 4 s

Fig.14 Subsystems specifications before and after control involvement

A simple knowledge-based model was selected and elaborated in 6 months [ref.7]. This model is using simple fluids mechanics assumptions on circuit pressure losses and heat fluxes with the addition a compressor fan map as well as introduction of the effect of LN2 cooling capacity and blow-off mass flow. The pressure distribution along the circuit was considered as not important for control purpose, then the assumption that all pressure losses are concentrated in the test section was done. The integration step and the space grid was set in order to enable simulations at frequencies up to 20 Hz; it was assumed that no proper mode would be found beyond this value. Great care was given to properly simulate the temperature propagation from the LN_2 injection location to the test section. Indeed, the propagation of the temperature along the circuit was anticipated to create a pure time lag, which could compromise the overall performance.

Simulations were performed with this model enabling to define a synthesis model, as it would have been done on the actual process. A state representation was selected, of the following type:

$$X(k+1) = A\,X(k) + BU(k)$$
$$Y(k) = C\,X(k)$$

$X(k)$ is the state vector (Pt, Ps, T, Mc) at time k

$U(k)$ is the command vector (rpm, Ln2 flow, Cv, Sth) at time k.

$Y(k)$ is the output vector (Mach, Pt, T, Mc) at time k, which represents the controlled variables.

with :
Pt : total pressure
Ps : static pressure
T : total temperature
Mc : supersonic shock location in high speed diffuser
Rpm : compressor speed
Ln_2 flow : injected liquid nitrogen massflow
Cv : blow-off valve coefficient
Mach : test section Mach number
Sth : second throat area

Linearisations were performed around several set points and matrixes A, B *and* C were defined through computer simulation.

The next step consisted in solving two problems:

1- a trajectory problem to achieve the transients and to reach the desired set point.
2- A regulation problem to maintain properly the required set point.

The trajectory problem was studied by the use of dynamic programming to perform trajectory optimisation on a multivariable system. The dynamic programming is based on the Bellman's optimality principle which is :

"Any portion of an optimal trajectory, included between any intermediate point and the target, is also an optimal trajectory between the intermediate point and the target."

Then the problem is solved by recurrence going from the target to the origin. The main drawback of the method is to require considerable computational power and cannot be performed in real time. However it enabled through off line computation to determine some optimal trajectories which can be used afterwards to build sub-optimal trajectories.

As LN_2 consumption was expected to be the most critical energy cost, it was decided to perform the optimisation with a criterion on LN_2 mass flow:

$$J = \sum_{i=k+1}^{i=nT} \dot{m}_{LN2}(i)$$

The results of the study demonstrated that the coupling effects between the different parameters were much more important that it was previously anticipated. Solutions to perform the set point changes in a more efficient way than previously foreseen were found. It became clear that the best solution to achieve temperature cool-down at high power was not by temporarily increasing the LN_2 flow, but by temporarily reducing the compressor speed and therefore the dissipated power, thus increasing the cooling effect of LN_2 at constant massflow. Multiple simulations have demonstrated that undershoot of the compressor speed was much more beneficial than overshoot of the LN_2 injected mass flow leading to the conclusion that efficient control of set point changes can be achieved without oversize of the LN_2 injection system.

This trajectory optimisation also demonstrated that the cooling effect of depressurising compensates for a

large part the power dissipated by the compressor and that important reduction of the injected LN_2 massflow is required during such set point change, thus reducing the exhausted gaseous flow. This cooling effect was neglected during the preliminary studies leading to a useless oversize of the blow-off valves which was also exaggerated by traditional additional valve size margins taken by the process engineers.

Afterwards, the regulation was studied in simulation mode using classical PID controllers with gain schedulers to take into account the system non-linearities and with additional feed forward signals to reduce the coupling effects. It was demonstrated that the specified requirements for the set points accuracy's can be obtained with less performance in term of resolution and accuracy of the sub-systems (compressor, LN_2 injection system and blow-off valves). The obvious reason was that the initial rough assumption of no action required during 30 seconds (assumption made during the preliminary studies) is useless in presence of a closed loop control which permanently adapt the commands and compensate for the perturbations to maintain the desired conditions.

The systems specifications before and after control theory involvement are compared on fig.14. It shall be noticed that considerable reduction were allowed on maximum LN_2 flow and blow-off valve size leading to a considerable investment cost reduction. Accuracy requirement for the subsystems were also relaxed without change on overall specifications, this led also to considerable investment cost reduction. The estimation of the investment cost reduction is above US$ 5 Millions. But more important is the considerable reductions on operating cost by minimisation of the LN_2 consumption, on maintenance cost through the lower number of components (LN_2 pumps, valve number, …) as well on reduced control system specifications on actuators.

At the end of the detailed study, the new diagram of the control system was as described on fig.15. It corresponds to what is now running on the actual plant. This configuration, technical result of the study, is well adapted to take into account the coupling effects.

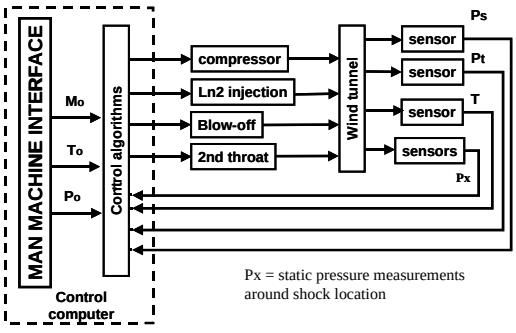


fig.15: ETW control system configuration after involvement of control theory

During the construction phase, the control laws structure was improved (fig.16) by addition of :

- a prediction model to enable removal of pure time lags effects.
- a real time identification to compensate for unknown inputs such as heat fluxes, which depend on past history of the process (time constant around one hour)
- an adaptive filter to adapt the control laws parameters to the changes in set points. In addition, the adaptive filter is using the memory of the past to speed up the adaptation.

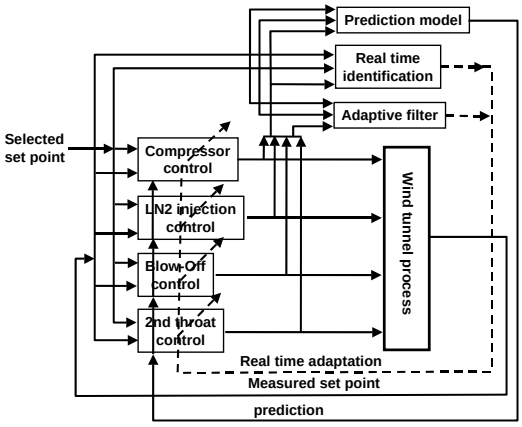


Fig.16 : ETW control laws structure

Such a structure has been intensively tested in simulation, using the simplified dynamic model, during the construction phase in order to check the sensitivity of the control laws in front of process uncertainties as well as the good functioning of the adaptive filter.

The dynamic model has been implemented in the actual control computer in order to provide a complete test tool of the overall control software and hardware.

Such a procedure enabled to start from the first day in fully automatic mode and to considerably reduce the time to tune the control system and to test the overall operating envelop. Performance in term of accuracy above ETW requirements were obtained from the very first days of operation.

8. Conclusion

Interaction between control theory and other disciplines can sometimes lead to communication difficulties; these problems shall be taken into account as soon as possible in the start-up phase of a project, early involvement of control specialists is of prime importance.

It has been shown that one good solution is to use as soon as possible the modelling and simulation capabilities of the control theory in developing a simplified dynamic model conjointly with the specialists of the other disciplines.

This type of model provides:

1- A communication tool between specialists from different disciplines; reference to this model can always be done.

2- A basic model to help the control theorists in building a synthesis model and therefore in synthesising control laws.

3- A simulation tool to perform integrated design optimisation.

4- A validation tool to perform factory tests, if needed.

5- A diagnosis tool. After validation and tuning on the actual process, the model can be used to detect possible abnormal behaviour of the process, thus providing an overall diagnosis tool.

Other usage of this type of model can also be intended, such as tool for diagnosis purposes, a full simulator for training if required.

But while developing such a dynamic model, the objectives shall never be forgotten. The natural tendency of the control specialists will be to build progressively a synthesis model whereas the natural tendency of the specialist from the concerned discipline will be to keep too many details that, at the end, will have no importance.

It has also been shown, through an example, that an approach using a so-called "simplified dynamic model" can considerably reduce the potential risk of design mistakes as well as the overall investment cost and can get a considerable impact on operation and future maintenance cost.

Such an approach is well demonstrated in traditional control applications, but logically the benefits should be similar for non-traditional control applications such as aerodynamic flow control, combustion control, vibration control…

One of the main difficulties in some non-traditional control applications is that the phenomena are frequently not enough understood, even by the specialists of the discipline themselves. This lack of knowledge makes difficult the development of a valid, well suitable and efficient dynamic model.

But, it also could be that not enough consideration is given in developing such an important tool and in improving the dialog between specialists to answer to the question:
"What shall be known and what is important to build a realistic dynamic model?"

In non traditional applications, permanent dialog between the control theorists and the specialists of the other disciplines will enable to progressively increase the knowledge of the phenomenon as well as the validity of the simplified dynamic model, mainly if laboratory tests can be performed in parallel to understand critical point and validate some assumptions. At the end, the return on investment for developing such a tool is worth for both disciplines by providing a good understanding of the dynamics of the phenomenon and an efficient tool for optimising the system design.

9. Acknowledgement

I would like to express my sincerest thanks to André Mignosi (ONERA Aerodynamics and Energetics Modelling Department) for his contribution in reading, reviewing and commenting this document.

10. References

1. A.J. FOSSARD : From Research to Industry, from Theory to Application.
Perspectives in Control – Theory and Applications
Springer 1998

2. I.D. LANDAU
Competition Interaction and Control
Colloquium « Perspectives in Control »
CNRS – Paris 29-30 June 1998

3. D. ARNAL
Transition prediction in transonic flow
IUTAM symposium
"Transonicum III" Göttingen
Ed. Zierep et Oertel, Springer-Verlag, 1988

4. V.V. KOSLOV, V.YA.LEVCHENKO
Laminar-turbulent transition control by excitation of disturbances
Institute of Theoretical and Applied Mechanics,
Novosibirsk - Russia

5. G. CASALIS, J.L. GOBERT, G. PAILHAS, S.PRUDHOMME
Active Control of Tollmien-Schlichting waves
Flow control - Fundamentals and Practices
Cargèse - Corsica 24 June-5 July 1996

6. J.L. GOBERT
ETW Control System - Design and first results
18th AIAA Aerospace Ground Testing Conference
Colorado Springs 20-23 June 1994

7. J.L. GOBERT
Control and Mathematical Model of Transonic Wind Tunnels.
79 Th AGARD Fluid Dynamics Panel Meeting and Symposium on "The Aerodynamics of Wind Tunnel Circuits and Their Components"
Moscow (Russia) 30 Sept.-3 Oct. 1996

Active Control Technology for Enhanced Performance Operational Capabilities of Military Aircraft, Land Vehicles and Sea Vehicles

Technical Evaluation Report

David J Moorhouse
Air Force Research Laboratory, VASD, 2210 Eighth Street, Suite 1
Wright-Patterson AFB, Ohio 45433, USA

Abstract

Control technology is becoming one of the most pervasive aspects of vehicle design and operation. The engine, subsystems, weapons, etc., etc. all have their individual control systems in addition to the flight control system of the aircraft overall. In addition, we can now control the boundary layer of the flow over the vehicle or inside the engines. As stated in the theme for the symposium: "The potential exceeds by far that which can be achieved nowadays by careful design using passive components". This report reviews the symposium relative to the stated objectives.

Overview of the Symposium

The last RTO symposium on Active Control Technology (ACT) was held in 1994 by the Flight Mechanics Panel of AGARD, Reference 1. The whole symposium was devoted to ACT of flight vehicles. Of the twenty-eight papers, four discussed specifications, six discussed design methodologies and the remainder were concerned with various aspects of flight test results. Relevant comments from the Technical Evaluation Report include: "Certain elements of the ACT system development process, such as specifications, design, implementation and verification, are not yet fully matured". Also, the author felt, "In five years time", that a symposium could be used as the starting point for a valuable exchange of information. A question to be asked is whether the current symposium papers will show significant maturation in ACT application in the intervening six years since the last symposium and provide that exchange of information.

The symposium under review here had a stated objective to review the current status of active control and evaluate the short term and long term potential. It consisted of thirty papers addressing Performance, Stability and Control, and Fluid Physics. Four of the scheduled papers were withdrawn, so that the numbers in this discussion are not continuous. In addition, however, it should be noted that there were two other parallel symposia addressing Mechanical Systems, Structures and Materials (19 papers) and Power Systems and Propulsion (36 papers).

For some of the technology areas presented, passive control has reached limitations and active control is showing the potential for significant performance improvements, just as it did with flight controls in the 1970s. Technology developments over the past decade, particularly in the areas of micro-electronics, and advanced materials and sensors, have made new applications of active control technology possible. The range of subjects covered in the symposium is an indication of the pervasive nature of Active Control Technology (ACT) application because it is now required in the efficient application of many other technology areas.

The Keynote Addresses

The keynote addresses covered a broad range of aspects to set the stage for the three symposia. The first address discussed a variety of active flow control concepts for applications to both military and civil aircraft. Various devices were shown to be capable of controlling the boundary layer, transition and shock location, resulting in improvements of lift/drag. The second address discussed control of compressor and

combustion instabilities in propulsion systems. Third, the Active Aeroelastic Wing concept was discussed, showing that Active Control Technology could now make use of an effect that was extremely adverse until now. Previously, if a wing was too flexible then aileron deflection would cause wing twist which resulted in control reversal. The solution was to add stiffness, i.e. weight. The new technology uses the wing twist as the control device and promises to reduce vehicle weight significantly. The fourth address covered a general theory of control applications. It was an excellent discussion of the control process and ended with six recommended best practices.

There was also a keynote presentation to lead off session 2, discussing Micro Electro-Mechanical Systems (MEMS) applications to Active Control Technology. This was a very interesting presentation, showing the possibilities of this new technology which included a flying demonstrator with leading edge vortex control on a delta wing configuration. One very important message in this presentation was that it is not possible to "just shrink traditional design".

Session 1 - Boundary Layer Control

This session consisted of five papers covering different aspects of control of separation and extension of laminar flow regions. First, suction was shown to reduce the drag of the vertical fin of a transport aircraft by 38%. In order to apply most of the concepts to an actual aircraft, it is necessary to have an accurate prediction or measurement of the transition location. The second paper discussed the state of the art in prediction methods, and a summary might be to take great care in the use of linear methods. Paper 3 showed that a wing designed to produce a favorable pressure gradient plus suction could reduce the drag for a supersonic civil transport by 6%. Paper 4 showed the results of periodic sucking and blowing to suppress Tollmien-Schlichting instability waves. In the fifth paper, pulsed vortex generator jets were the controlling mechanism. In this case there was an optimum blowing frequency and it was possible to blow too hard to have the desired effect. All of the papers showed a sensitivity to one or more of the controlling parameters, which would raise questions about applying the results to a full-scale aircraft.

There was to have been a sixth paper, which was withdrawn. It seemed to be in a different category from the others in the session. Numerical results were presented to show the performance of a missile controlled by jets producing transverse forces through the center of gravity. These forces produced a change in flight path and the static stability of the missile then aligned it with the flight direction. It was claimed that this approach produces higher flightpath bandwidth response than the conventional control approach of rotating first in order to generate forces. It was an interesting application of the "Control Configured Vehicle" technology of the 1970s.

Session 2 - Active Flow Control of Nozzle/Jet

This session was composed of two distinct parts, the first being different applications of jets as control devices (numbers 8 - 10). A STOVL aircraft in ground effect can experience very adverse forces caused by the flow of the lift jets impinging on the ground. First it was shown that a baffle under the aircraft close to the jet exhausts could suppress the acoustic feedback. Then, the baffle was replaced by micro-jets blowing parallel to the lift jet exhausts. This produced the same result and it was possible to modulate the jet blowing as a function of height above the ground. The next paper showed the results of jets blowing into a supersonic jet to enhance mixing. The results showed multiple effects of the geometric parameters. The last paper showed the beneficial use of jets to enhance the mixing of core flow and fan air flow in the engine exhausts of the C-17. Although test results showed the beneficial effects, the correlation with CFD predictions was only qualitative.

The second part of the session comprised three complementary European papers (numbers 11 - 13) addressing different parts of the latest development in pitch/yaw thrust vectoring exhaust nozzles. First was a very thorough discussion of the benefits of thrust vectoring nozzles for a military combat aircraft. A definition of the baseline design of a vectoring nozzle for the EJ200 engine was presented. The second paper presented the design aspects of the required integrated engine control system, including results from a ground test. The last paper was a complete documentation of the intake flow conditions and the issues that have to be addressed for flight at the angles of attack that are made possible by thrust vectoring. As a package, the three papers showed the maturity of the total design

effort so far, but also showed that there is still more work to be done.

Session 3 - Drag and Buffet Control

This session began with a paper summarizing activities at ONERA covering a number of experiments addressing Tollmien-Schlichting waves, 3-D separation and vortex breakdown. Good results were shown in all cases, and the author is to be commended for stating the need to "adapt results to cases closer to real flight". The second paper discussed both predictions and test results for active control of buffet caused by shock wave/boundary layer interaction and flow separation on the upper surface of a wing in transonic flow. The control device used was termed a "trailing edge deflector", i.e. a very small split flap under the wing trailing edge. The device was used both statically and driven by a closed-loop control system. The results showed very good results in a test on a 2-D wing, and also good correlation with CFD predictions. The author indicated the further work that was needed and planned to extend the research to 3-D effects. One interesting aspect of the third paper on shock control for drag reduction was the presentation of results from passive devices that were not very successful. Good results were obtained with a combination of devices plus active control. The last paper in the session started with a thorough overview of the problems of flow interactions on rotor blades. The proposed solution was a combination of airfoil shape design and active control of a nose-droop device. The paper presented numerical predictions of the beneficial effects, but concluded with a statement that experimental studies were now possible due to new actuator design. It was noted that all the authors in the session commented on what would need to be addressed by further research in order to consider full-scale application.

Session 4 - Noise Control

This session contained two papers (numbers 18 & 19) addressing the suppression or control of noise from turbine engines. The first showed the results of an active noise control system to reduce the tones of a fan, demonstrated in a scale model experiment. The system is comprised of a ring of sensors, a set of loudspeakers as the control device and control logic. The second paper discussed analytical results of an active noise control system with multiple sensor and actuation rings. Both papers presented positive results and problems encountered, with proposed future work.

Session 5 - Vortex Control

The papers in this session (numbers 21 - 23) all addressed aspects of controlling the position of forebody vortices in order to augment aircraft yaw control at moderate to high angles of attack. The first paper showed the yaw control obtained from a nose piece fitted with strakes rotating about the longitudinal axis. The model results were applied to a wind-tunnel model of the X-31 which loses rudder effectiveness completely at 50 degrees angle of attack. The rotating nose had effective yaw control between approximately 35 and 65 degrees, although very non-linear with alpha. The strakes also showed a significant yawing moment when at the vertical position rather than zero. Although this position would not normally be used in a control system, it shows a large effect from what must be a small model asymmetry. The author stated that a full-scale wind tunnel test is proposed, which should answer some questions of scale effect. The second paper discussed vortex manipulation using forward blowing jets. Results were presented that extended earlier work on an ogive cylinder to a circular fuselage/delta wing model. There was effective yaw control that was essentially linear with blowing duty cycle. The author pointed out the non-linearity and reversals of effectiveness with both angle of attack and momentum coefficient. The third paper showed similar results of blowing on a forebody, again with a reversal with blowing coefficient. An interesting result showed that 66% of the duty cycle was required to produce zero yawing moment at one angle of attack. A plan for future work was presented, covering an active control concept with vortex detection. All three papers showed interesting conceptual or model results that have extreme sensitivities to one or more parameters. This means that use of the results for design of a full-scale flight application could be very complex and great care would be needed during its flight testing. There is an extremely low probability that the full-scale flight condition characteristics would match the model predictions. There would be a very high risk of control law gain errors or even sign reversals in the sensitive areas of those parameters.

An example of potential problems that can be encountered when applying small-scale results to a full-scale application is given in Reference 2. Static

nose strakes that were stabilizing in wind tunnel tests were found to be de-stabilizing in flight.

Session 6 - Flight Vehicle Active Control

This last and largest session contained nine papers addressing a wide range of full-scale aircraft applications of ACT. The first paper discussed best practices for design of aircraft flight control systems, based on an RTO Technical Report in publication. The recommendation was that ACT aspects, or any control system, should be designed using a disciplined process. The second paper presented results from a program to develop control laws for the region of transition from wing-borne flight to hover for a STOVL aircraft. The integrated flight/propulsion control design problem is very complex, with regions of control saturation. The design that was presented formed a low pilot workload. A unique contribution of this presentation was a technique to visualize all the aspects of control activity. This was a very effective way to understand the operation of the control system, especially in the areas of saturation. The next paper discussed different ACT programs, with emphasis on the use of an in-flight simulator. Research results are obviously more credible when performed at full-scale flight conditions in an actual aircraft. The fourth paper presented results from analyses of Pilot Induced Oscillation (PIO) tendencies from control system non-linearities. This was a very thorough review of the causes and various problems with the specifications. It was shown that rate limiting, per se, is not the problem but rate limiters can be, and have been, placed in positions that do cause PIO tendencies. Effects of command sensitivity and hysteresis were also discussed. It was noted that there was consistency between this presentation, in quantifying the adverse effects of what were considered to be bad design practices in the first paper in this session.

Helicopters were the subject of the next three papers (numbers 29 - 31). Paper 29 presented results of active/adaptive rotor blade control to reduce noise and vibration of a helicopter. An initial result was a surprise showing that improved modelling was required. It was a very good documentation of the development of an adaptive controller that achieved good results. The control device was a trailing edge flap on the rotor. The work was a complementary effort with that reported in next paper. This showed flight test results of a project to reduce helicopter noise using individual blade control. First the ground noise levels from the helicopter fly-over and different descent angles were measured, and the parameters affecting the levels were identified. The noise reductions using this control technique were confirmed in the flight tests, and showed good correlation with predictions from wind tunnel tests. The seventh paper of the session presented results of the development and flight test of an H-infinity controller on a research helicopter. This was a good documentation of the practical problems encountered when trying to realize the claimed benefits of this theoretical design methodology. They presented five detailed lessons learned covering the design, implementation and the testing.

The last two papers applied to fixed-wing aircraft again. First, the development process of the F/A-18E/F control was discussed in detail. It showed a very rigorous and disciplined process from defining the requirements all the way through flight test. Nine specific lessons learned were presented in detail. This paper documented a real example of flight control design best practices and is considered complementary to paper number 25. The last paper discussed the development of flying qualities requirements for transport aircraft. The US military flying qualities specification is acknowledged to be more oriented towards high-performance combat aircraft. This paper presented an excellent discussion of available criteria and suggested improvements based on the latest data. It would form an excellent start in defining the control system design requirements for a new conventional transport.

The session showed the range of ACT applications for full-scale aircraft applications. Two papers addressed aspects of specifications, which represent the design criteria for a control system. One paper discussed a multi-variable control methodology, with flight test results. Three papers addressed good practices for the flight control design process, and another one discussed an excellent implementation of good design processes. Finally two papers showed the application of ACT to helicopter rotors.

Concluding Remarks

First, a negative comment: the title of the symposium included "Land Vehicles and Sea Vehicles", but every paper addressed aspects of flight vehicles. The theme

of the symposium did state that it would "predominantly look at aircraft related technologies because in aircraft the need for active control technologies is very high. Other vehicles can greatly benefit from the transfer of technologies developed for air vehicles". It is also suggested that an exchange of lessons learned could benefit all sides. Overall, the community still has a long way to go before the technologies of the different vehicle classes are integrated. It is recommended that RTO Task Groups address the question of what are the similarities and unique aspects of the different vehicle classes.

Within the realm of aircraft technology, this symposium was of very high quality. It provided an excellent forum for technical experts to be exposed to information from related fields. The researchers doing the initial explorations of new concepts could get an appreciation of the issues to be faced for a full-scale application. Any sensitivity to parameters is likely to be a problem because the real full-scale characteristics are likely to be different. Increased modelling effort will be needed in the future, in order to be able to accurately represent the physical observations. The models will need to be validated as increasing amounts of data and understanding are gained. The models should have estimates of parametric uncertainties, to allow system sensitivity studies to be performed - especially before any flight testing. The lessons learned from applying active control technology to flight controls over the last three decades, are equally relevant to any other active control application. The research community needs to be aware of the lessons learned in order to avoid implementation and testing difficulties that are not usually apparent when new concepts are in their infancy.

At the same time, everybody in the audience should benefit from gaining an appreciation for the wide range of activities underway in the NATO countries. It is unfortunate that there were so many parallel activities that attendees had to make difficult choices.

This author believes that the symposium did meet the objectives. Progress was also demonstrated relative to the comments of the Technical Evaluator of the previous symposium, noted in the introductory notes above. It is suggested that a symposium would be possible in another five years and show similar progress. At that time we should include the technologies of all vehicle classes.

References

1. "Active Control Technology: Applications and Lessons Learned", AGARD Conference Proceedings, AGARD-CP-560, January 1995.

2. Walchli, L. A., and D. J. Moorhouse, "Forebody Vortex Control", published in Advances in Flight Testing, AGARD Conference Proceedings, AGARD-CP-593, December 1997.

This page has been deliberately left blank

Page intentionnellement blanche

Hybrid Laminar Fin Investigations

V. SCHMITT
ONERA, BP 72, 92322 CHATILLON CEDEX, France

J.P. ARCHAMBAUD
ONERA, BP 4025, 31055 TOULOUSE CEDEX, France

K.H. HORTSTMANN, A. QUAST
DLR, INSTITUT FÜR ENTWURFSAERODYNAMIK, Lilienthalplatz 7, 38108 BRAUNSCHWEIG, GERMANY

ABSTRACT

In order to evaluate the HLFC concept which is seen as the most promising drag reduction technology for transport aircraft applications Airbus Industrie launched some years ago the laminar fin programme. The paper briefly describes the main phases of this programme, i.e. the theoretical evaluation, the experimental verification through adequate wind tunnel tests and the flight test demonstration with the Airbus A320 n° 1 as testbed.

It will be shown that the initial phase conducted by ONERA allowed the A320 fin to be chosen as the support for further HLF investigations. The next phase was devoted to wind tunnel tests of a ½ scale model in the S1MA wind tunnel. Carried out by ONERA and DLR, these tests enabled the flight test demonstration to be launched by Airbus Industrie and the partners. The flight tests have then been performed by the Airbus partners under the leadership of Daimler Chrysler Aerospace Airbus in the frame of the 3E/LATEC programme. Important topics like surface and suction imperfections have also been addressed during the flight tests as part of the EC-programme HYLDA. The main outcome at that stage of the analyses is an unambiguous proof of concept.

I – INTRODUCTION

The most efficient way to reduce skin friction drag is undoubtedly to maintain laminar boundary layer as far as possible by delaying the transition process. With the given Reynolds numbers and sweep angles on modern transport aircraft only the Hybrid Laminar Flow Control (HLFC) concept seems to offer, at least from aerodynamic point of view, a solution which presents the highest drag reduction potential with remarkable fuel burn savings of up to 15%. This concept basically combines suction in the leading edge region with favourable pressure gradients after the front spar of the wing or other aircraft components like horizontal tail, fin and nacelle.

The previous statements which are generally accepted are possible thanks to significant progress in transition research [1]. However, the availability of reliable transition prediction tools does not mean that the technology which does not only involve aerodynamics, but also systems, structures, etc., is ready for application. Nevertheless, Airbus Industrie soon demonstrated its interest in the development of this demanding technology [2] and defined a long term strategy plan which implied as first step the Laminar Fin Programme [3, 4].

The choice of the fin was essentially dictated by pratical considerations in view of a flight test demonstration. Without de-icing and high lift systems it offers significant advantages for the integration of the suction system in the leading edge. However, the high leading edge sweep constitutes an additional challenge from an aerodynamic point of view.

The purpose of the paper is to give an overview of the main phases of the Laminar Fin Programme, i.e. the theoretical evaluation, the experimental verification and the flight test demonstration.

II – THEORETICAL EVALUATION

The first phase of this programme was devoted to the theoretical evaluation of the laminarisation potential for the selected Airbus A320 fin. Carried out by ONERA this study led to rather encouraging results which may be summarized as follows :

- Due to its high leading edge sweep angle and cruise Reynolds number all relevant transition mechanisms may occur on the fin, i.e. Attachment Line Transition (ALT), transition due to Cross Flow Instabilities (CFI) in the leading edge region and transition due to Tollmien-Schlichting Instabilities (TSI) further downstream.

- An ALT-avoidance device is mandatory to prevent the fin from being turbulent at the attachment line.

- Suction ahead of the front spar would stabilize the laminar boundary layer and delay transition due to CFI.

- As a result of an adequate , but not optimised fin section extended laminar flow up to 50% of the chord could then be expected, the transition occurring through TSI.

In cruise conditions the situation is described by figure 1 in terms of the required suction power, the drag reduction of the fin and the corresponding fuel burn savings. As a matter of fact, assuming a suction power of 30 kW a drag reduction as high as 38% which corresponds to fuel burn savings up to 1.3% has been predicted.

Paper presented at the RTO AVT Symposium on "Active Control Technology for Enhanced Performance Operational Capabilities of Military Aircraft, Land Vehicles and Sea Vehicles", held in Braunschweig, Germany, 8-11 May 2000, and published in RTO MP-051.

III – EXPERIMENTAL VERIFICATION THROUGH WIND TUNNEL TESTS

At that point the experimental verification of these results appeared as the next obvious step. This was the aim of the second phase for which DLR joined ONERA and Airbus Industrie. The milestones were the design, the manufacture and the testing of a suitable wind tunnel model.

III.1 – Design aspects

In order to achieve in this wind tunnel test flight Reynolds numbers at cruise conditions a ½ scale model has been chosen to be tested in the ONERA S1MA wind tunnel. The major aerodynamic problems which had to be overcome during the design phase were the attachment line contamination and the transition by CFI through suction.

The solution for the first item consists of implementing a so-called Gaster-bump [5]. Its purpose is to create a stagnation point on the leading edge near the root which enables the disturbances coming from the fuselage to be deviated and a new laminar boundary layer to be generated. As a result of a careful design made by ONERA and based on advanced CFD-tools [3] the final shape which is schematically illustrated in figure 2 is supposed to fulfil all requirements in terms of Mach number and side slip angle range.

A critical issue for the second item and therefore a successful application of HLFC is the design of a suction system which constitutes a compromise between numerous aerodynamic and structural constraints. The layout of the final design for the A320 fin model which has been carried out by DLR is shown in figure 3. It is characterized by 45 compartments separated by stringers on which the laser drilled titanium panel manufactured by AS&T is glued. The compartments are connected in such a way that the suction mass flow can be controlled through 15 independent suction chambers and ducts. For this case figure 4 gives an impression of the theoretical pressure and velocity levels in a given section taking into account the static wall pressure and the mean suction velocity to be applied. This implies the choice of the characteristics of the perforated panel which is dictated by the following parameters :

- maximum and minimum mean suction velocity for each of the suction chambers ;

- uniformity of the local suction distributions.

It will be shown later that all these aspects were not completely mastered during this model design phase.

III.2 – S1MA wind tunnel tests

A first test campaign took place in 1993. The photo of figure 5 shows the test set-up in the ONERA S1MA wind tunnel. The 2.9 m span model which was built by Aero-construct under the responsibility of DLR is made of a glass-fibre reinforced expoxy shell connected to a steel spar by bolts. The model is equipped with an adjustable rudder. Due to its structural concept it allows the transition to be detected by infrared cameras. In order to avoid disturbances to be created its instrumentation is reduced to the strict minimum. The perforated panel of the suction nose can be clearly identified on the same photo.

Furthermore, in order to enable a HLF test to be performed in the S1MA wind tunnel an external suction device compatible with total force measurements by means of a half model wall balance has been developed. As depicted by the scheme of figure 6 the corresponding setting up including control and metering devices for up to 18 suction ducts is installed under the floor of the test section, the driving unit being an ejector.

The test campaign was a success, even if all the expected results were not observed. In particular, it demonstrated the effectiveness of the Gaster-bump in preventing ALT in the whole Mach number and the side slip angle range. As an example figure 7, exhibits RMS values delivered by a hot film which is located downstream of the Gaster-bump as a function of Mach number. The values correspond always to laminar flow which only becomes turbulent when a trip wire is placed on the bump as shown by the sketch of the same figure.

The achieved suction rates enabled laminar flow to be fully demonstrated up to a Mach number of 0.6. For higher Mach numbers a reduced laminar flow extent was observed in the root region of the fin model. This is clearly shown by figure 8 which reproduces infrared images of the fin model for different Mach numbers. As part of a detailed analysis of these experimental results compressible stability computations have been performed and the e^N method has been used following the envelope strategy to estimate the theoretical transition locations.

The input to these computations was first of all a streamwise velocity distribution deduced from the pressure measurements using a conical flow assumption. Then local suction velocity distributions derived from DLR measurements by means of a miniaturized probe constituted the necessary boundary conditions for 3D laminar boundary computations.

The sections in which pressure distributions and local suction velocity distributions have been measured are specified in figure 9. Two examples of such local suction velocity distributions are shown in figure 10. They correspond to data points at M = 0.6 and 0.78 in section 1 near the root. One has to notice the strong variation of the local suction velocity along the chord. In addition, the values obtained at the leading edge are rather small. The results of the corresponding stability computations are illustrated in figure 11. At M = 0.6 the experimental transition location at 50% of the chord corresponds to a N-factor of 10, a value which seems very acceptable. Furthermore, the N-factor does not exceed a value of 3.5 on the suction panel itself in this case. On the other hand, at M = 0.78 transition experimentally occurs on the suction panel itself. In that case, the N-factor reaches values as high as 8 in this area.

This means that the computational analysis was consistent with the experimental results. It showed that the local suction rates near the root were insufficient and smaller than the nominal values due to same deficiencies

of the actual model suction system especially on the leading edge at the root of the model.

In this situation, the interest to continue the wind tunnel investigations was recognized. As a consequence, after rework of the suction nose by DLR a second test campaign was prepared and performed in 1994. Due to an increased porosity of the suction panel higher suction rates were achieved. The results clearly showed an improved situation in the whole Mach number range, but even in these tests it was not possible to demonstrate at cruise conditions the full amount of laminar flow predicted [6]. At the time being a new suction nose is under preparation at DLR and subsequently a new test campaign.

IV – FLIGHT TEST DEMONSTRATION

Nevertheless, on the basis of the first wind tunnel results Airbus Industrie and partners already decided in 1993 the go-ahead for the flight test preparation of the A320 HLF fin.

In the framework of the Airbus 3E/LATEC programme this project was shared by Aerospatiale Matra Airbus, BAE Systems, CASA and Daimler Chrysler Aerospace Airbus as the responsible partner, in association with ONERA and DLR. The multidisciplinary work which involved, apart from aerodynamics, systems as well as structures and materials was seen as an exciting challenge [7] for the Airbus world in many aspects.

Of course, special attention has been paid to the design of the on-board suction system and the suction nose. In particular, a better knowledge of the suction panel characteristics was necessary [8]. The figure 12 schematically illustrates the main features of this suction nose which is constituted by 9 independent suction chambers covered by 2 perforated panels NT1 and NT2 with a total length of 5 m. Furthermore, the leading edge is equipped in the root region of the flight test article with a Gaster-bump as ALT-avoidance device. Its design is the same as in the previous S1MA wind tunnel tests which have demonstrated its efficiency.

Another key-point has been the flight test instrumentation of the HLF fin. As sketched in figure 13, it includes pressure taps in 3 sections, a wake rake with transverse mechanism, 2 infrared cameras installed on the horizontal tail plane (HTP) in order to visualize the transition locations on both sides of the fin, hot films along the attachment and on one side of the fin.

IV.1 – Turbulent reference flight tests

The Turbulent reference Flight Tests (TFT) were performed with the Airbus A320 n° 1 in Toulouse in 1995. The fin was not equipped with its suction nose, but the Gaster-bump was installed on the leading edge near the fin root. Among others one aim of these tests was to check the critical issues of the flight test instrumentation, i.e. the installation of the infrared cameras and the wake rake. On the photo of figure 14 which shows the A320 during TFT 3 pressure belts and the wake rake on the fin as well as the infrared camera housing on the HTP can be easily identified. All these items have been successfully checked.

As far as the Gaster-bump is concerned these tests also confirmed its efficiency as ALT-avoidance device.

IV.2 – Hybrid laminar flow flight tests

Finally, the Hybrid Laminar flow Flight Tests (HLFT) took place still in Toulouse in 1998. The Airbus A320 n° 1 as flying test bed was now equipped with the complete HLFC system of the fin. It is shown on the photo of figure 15 during these flight tests.

The main part of these tests has been performed in the frame of the nationally founded Airbus 3E/LATEC programme. In addition, specific tests devoted to surface and suction imperfections have been carried out in the frame of the european EC founded HYLDA programme [9].

The flight test conditions covered a wide range of various parameters : Mach number, altitude and side slip angle. Different suction rates from the necessary minimum to the achievable maximum have been applied. Of course, a huge amount of data was measured and recorded for basic and further analysis which is under way by the partners and will take still a long time.

In the following some relevant examples of basic results will illustrate the main features. First of all, figure 16 exhibits the measured pressure distributions on the fin at cruise conditions which are in rather good agreement with the predictions. This is an important issue for the boundary layer and stability analysis. Then, the Gaster-bump efficiency as ALT-avoidance device is demonstrated by figure 17 which represents power spectra of the hot films located along the attachment line. All these power spectra reveal laminar flow except that derived from the hot film situated upstream of the Gaster-bump which is indeed turbulent as expected. This holds for the whole Mach number and side slip angle range. One has to bear in mind that without this device the fin boundary layer would be turbulent from the attachment line.

Due to HLFC extended laminar which flow regions occur on the fin which have been detected by the infrared cameras. The figure 18 shows transition locations for different side slip angles gives an impression of the quality achieved. Each view of the fin is composed by 3 partial images taken from the HTP. A basic analysis of these transition visualizations enables the laminar flow extent on the fin to be determined at cruise conditions for different side slip angles. The resultats are illustrated by figure 19. An insight in further analysis through stability computations can be found in [10].

From pratical point of view future product applications of HLFC will also depend on the robustness of laminar flow. During the HYLDA flights, the effect of local disturbances has been investigated. Therefore, 2D and 3D surface and suction imperfections of various dimensions have been introduced in the laminar flow of the fin. Typical examples are given by figure 20 which illustrates the effect of cylinder type roughness elements with different heights on the transition location and figure 21 which shows the corresponding effect of circular regions without suction. Of course, all these results constitute a

valuable data base for the future development of the HLFC technology.

V – CONCLUSIONS

In order to evaluate the HLFC concept for transport aircraft applications in the framework of the Laminar Fin Programme defined by Airbus Industrie a complete cycle of investigations has been performed :

- the theoretical evaluation enabled the A320 fin to be chosen as the support ;

- the experimental verification through S1MA wind tunnel tests of a ½ scale HLF fin model led to the decision of Airbus Industrie and the partners to proceed with a flight test demonstration ;

- the flight tests performed with the Airbus A320 n° 1 under the responsibility of Daimler Chrysler Aerospace Airbus were a complete success. The results the analysis of which is in progress constitute a valuable data base.

With the HLF fin programme the proof of concept has been produced. Therefore, it represents an important milestone for the further development of this technology in Europe.

The ONERA-DLR co-operation proved to be fruitful and efficient in the initial phases of this programme. Both Research Establishments had also a significant contribution to the final phase.

REFERENCES

[1] ARNAL D.
Boundary Layer Transition Predictions based on Linear Theory.
AGARD Report 793, 1993.

[2] ROBERT J.P.
Hybrid Laminar Flow Control. A Challenge for a Manufacturer.
First European Forum on Laminar Flow Technology, Hamburg, 1992.

[3] THIBERT J.J., QUAST A., ROBERT J.P.
The A320 Laminar Fin Programme.
First European Forum on Laminar Flow Technology, Hamburg, 1992.

[4] HINSINGER R.
L'opération dérive laminaire sur l'A320.
32ème Colloque d'Aérodynamique Appliquée, Lyon, 1996.

[5] RENEAUX J., PREIST J., JUILLEN J.C., ARNAL D.
Control of Attachment Line Contamination.
Second European Forum on Laminar Flow Technology, Bordeaux, 1996.

[6] SCHMITT V., QUAST A., HINSINGER R.
Wind Tunnel Investigations of the A320 Laminar Fin.
Second European Forum on Laminar Flow Technology, Bordeaux, 1996.

|7] HENKE R., CAPBERN P., DAVIES A.J., HINSINGER R., SANTANA J.L.
The A320 HLF Fin Programme - Objectives and Challenges.
Second European Forum on Laminar Flow Technology, Bordeaux, 1996.

[8] PREIST J., PALUCH B.
Design Specifications and Inspection of Perforated Panels for HLF Suction Systems.
Second European Forum on Laminar Flow Technology, Bordeaux, 1996.

[9] HENKE R.
Airbus A320 HLF Fin Flight Tests.
European Drag Reduction Conference 2000, Potsdam, 2000 (to be published).

[10] SCHRAUF G.H.
Evaluation of the A320 Hybrid Laminar Fin Experiment.
ECCOMAS 2000, Barcelona, 2000 (to be published).

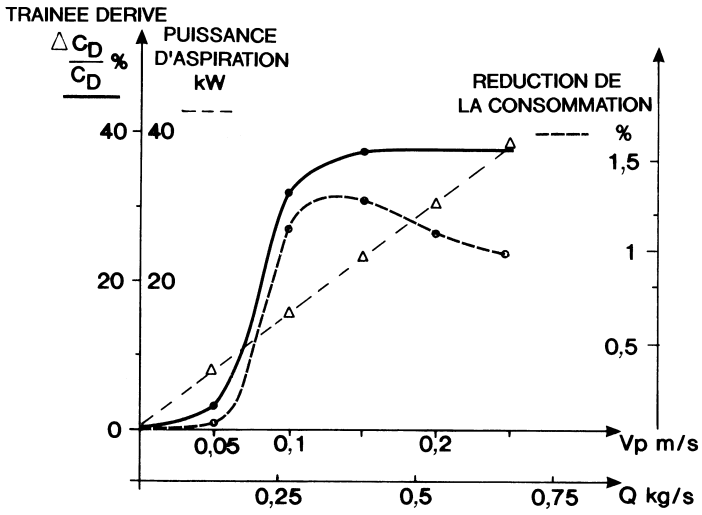


Fig. 1 - Estimated performance of the A320 laminar fin

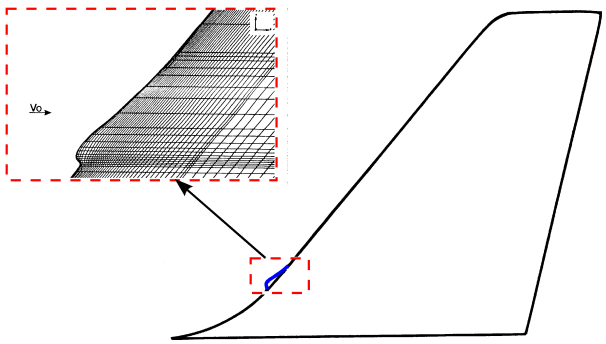


Fig. 2 – Implementation of a Gaster-bump on the leading edge

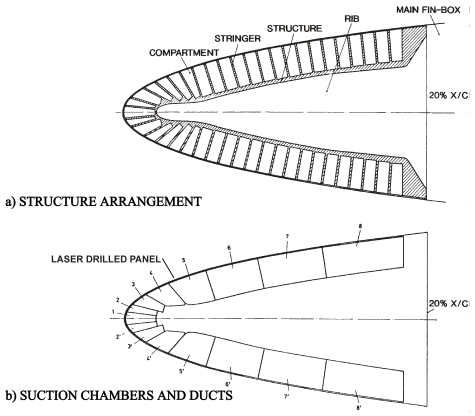


Fig. 3 - Details of the suction nose

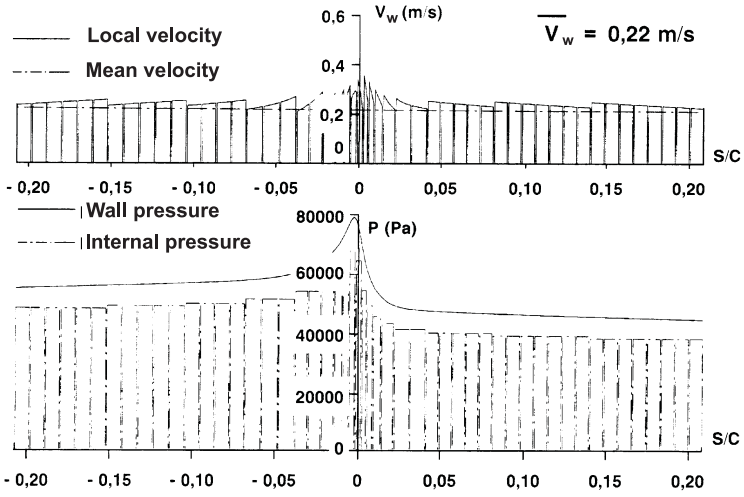


Fig. 4 - Suction velocities and pressures



Fig. 5 – Test set-up of the A320 fin model

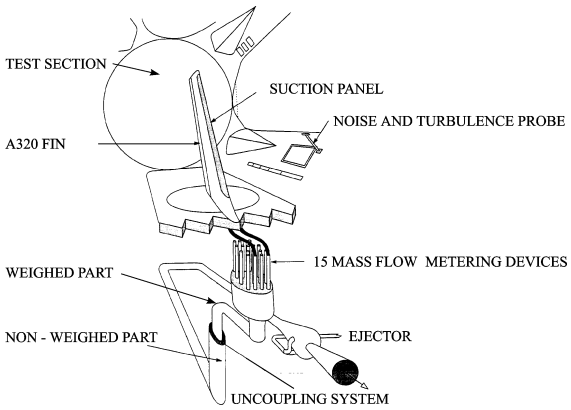


Fig. 6 – External suction device arrangement

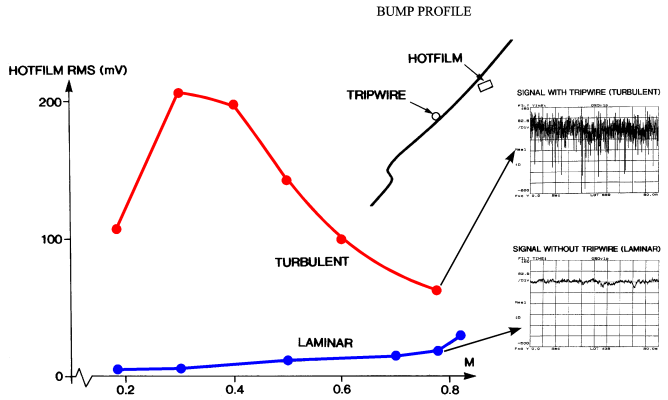


Fig. 7 – Gaster-bump efficiency as a function of the Mach number

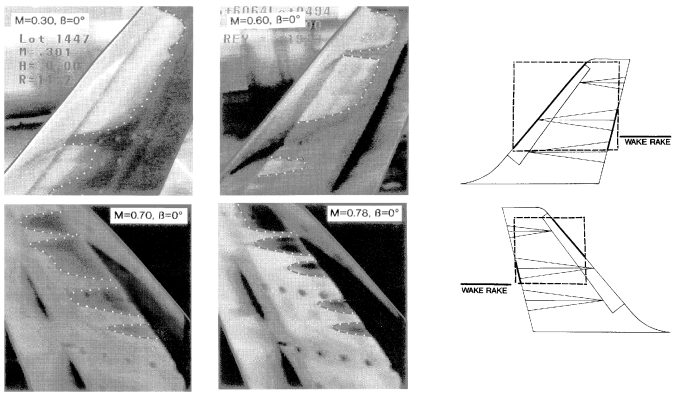


Fig. 8 – Laminar flow extent for different Mach numbers

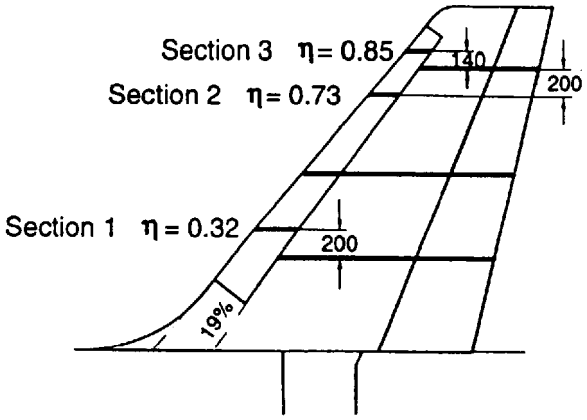


Fig. 9 – Sections with pressure and local suction velocity measurements

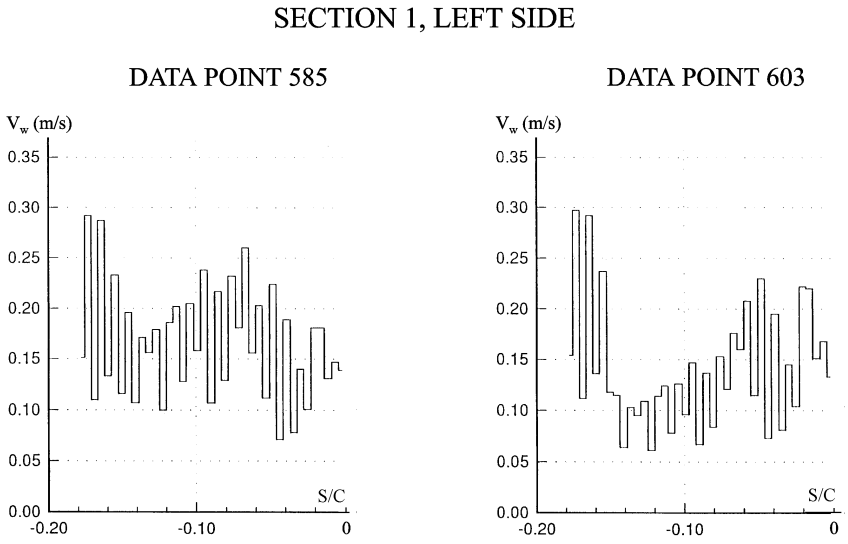


Fig. 10 – Measured suction distributions

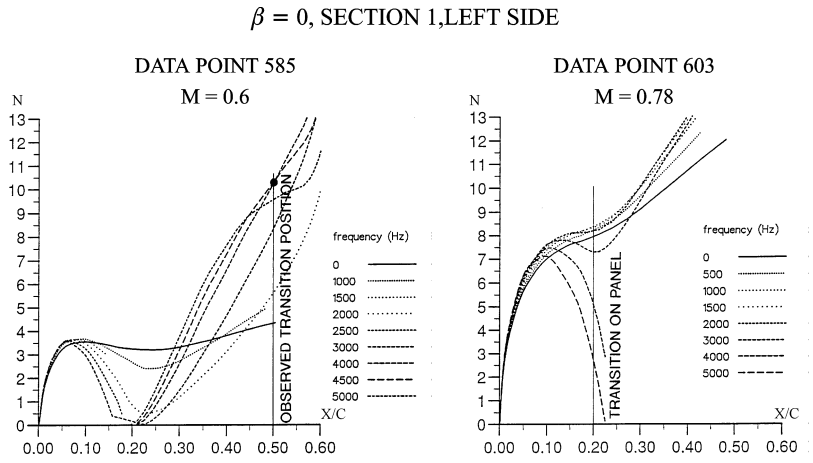


Fig. 11 – Stability analysis

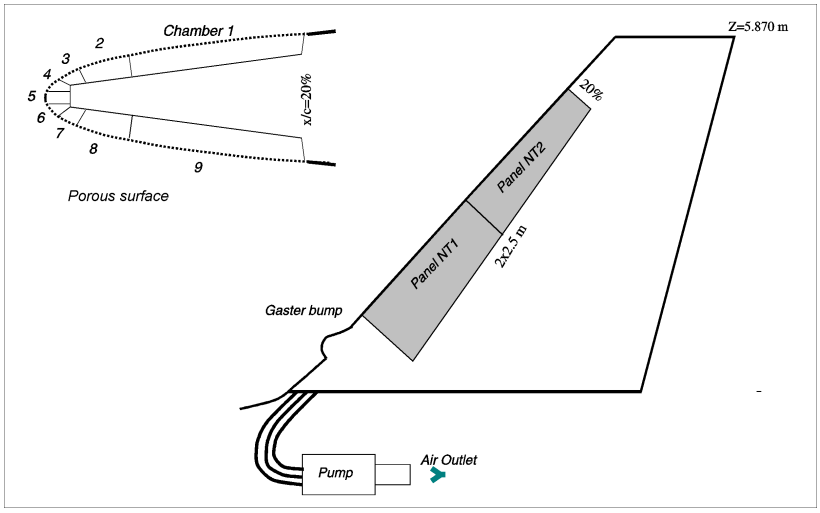


Fig.12 – Schematic suction nose layout

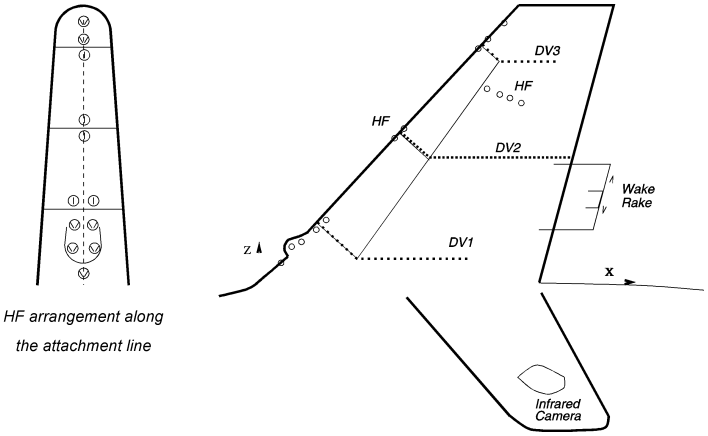


Fig. 13 – Flight test instrumentation



Fig. 14 - View of the A320 fin with flight intstrumentation



Fig. 15 – A320 HLFC fin flight tests

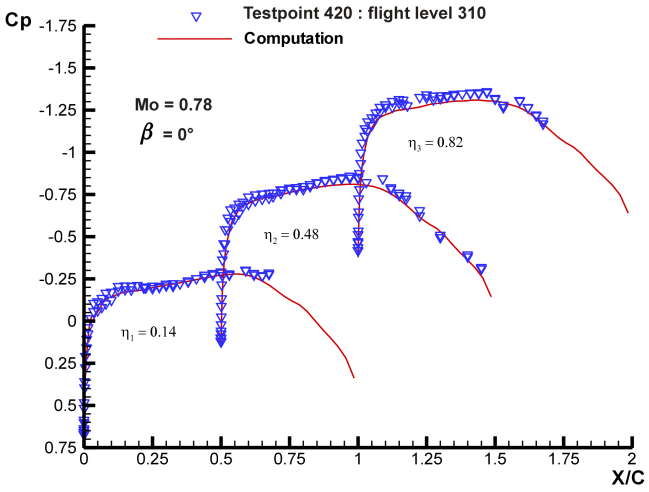


Fig. 16 – Pressure distributions at cruise

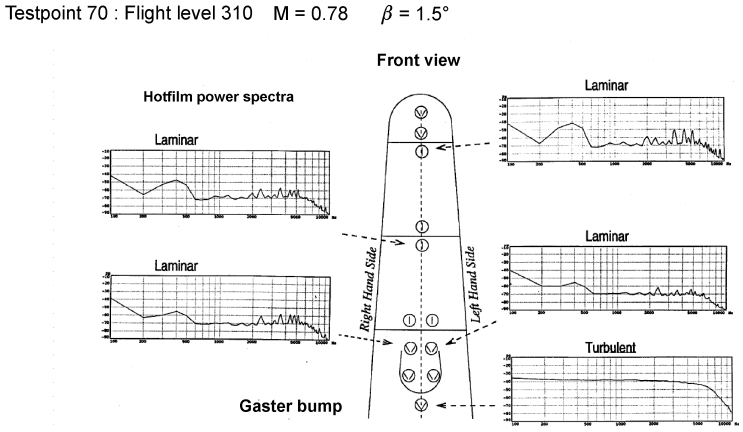


Fig. 17 – Gaster-bump efficiency at cruise

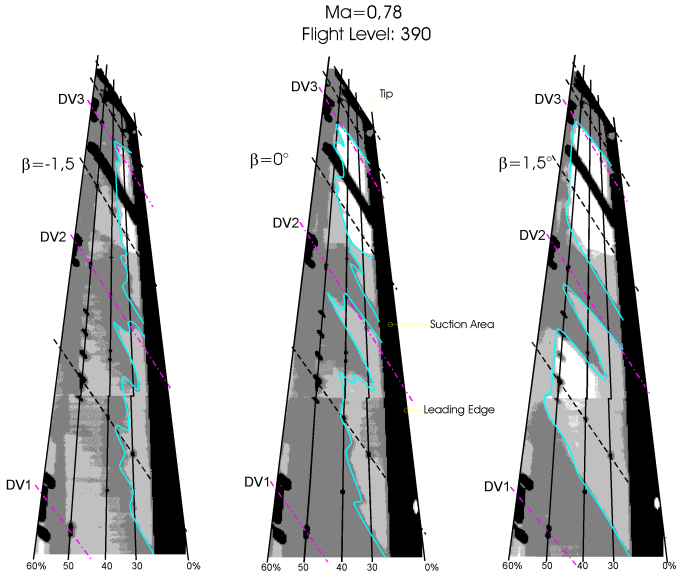


Fig. 18 – Transition locations for different side slip angles

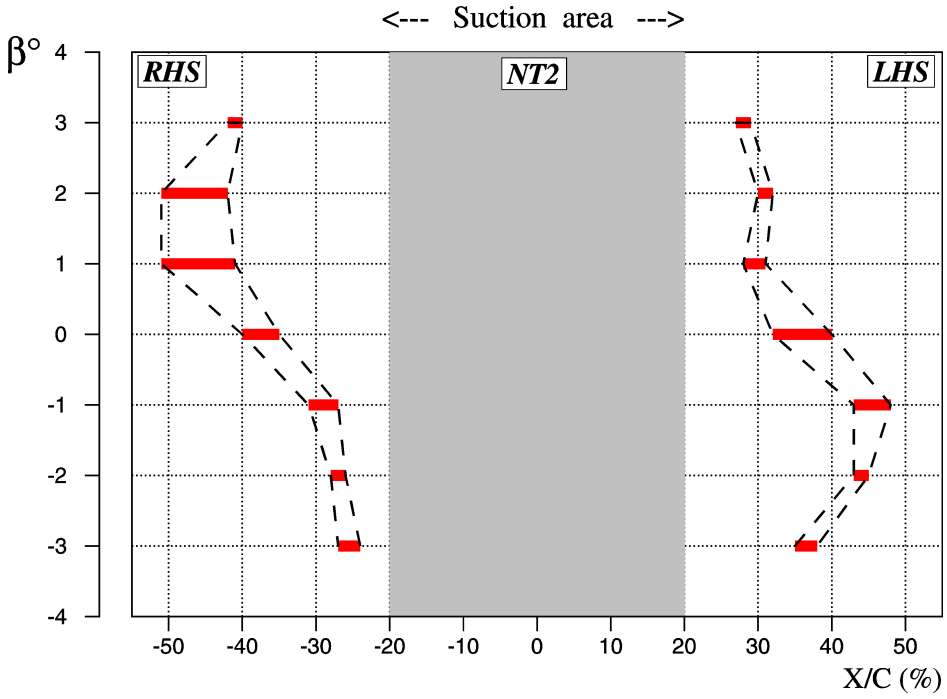


Fig. 19 – Laminar flow extent at cruise

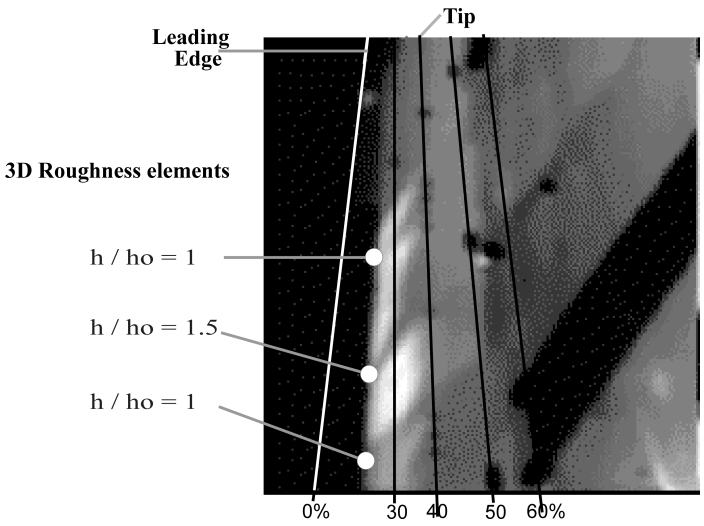


Fig. 20 – Roughness effects on transition locations

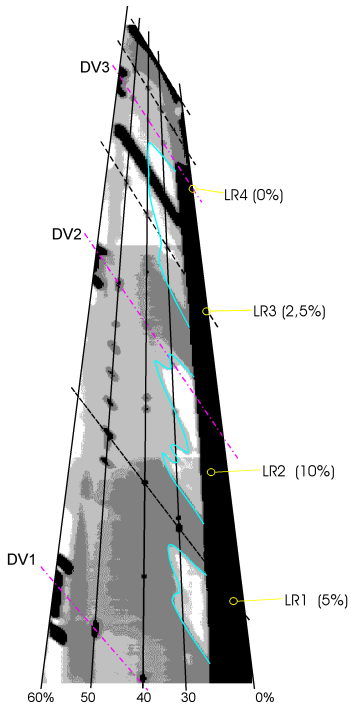


Fig. 21 – Suction imperfection effects on transition locations

Transition Prediction and Design Philosophy for Hybrid Laminar Flow Control for Military Aircraft

by
M. Maina and P. W. C. Wong
Aircraft Research Association,
Manton Lane, Bedford, MK41 7PF, UK

Abstract

An investigation into the application of transition prediction methods for hybrid laminar flow control for military aircraft has been carried out. Linear stability theory and the 'e^n' criterion are commonly used for predicting the onset of transition. Although a great deal of experience has been gained in their use over the years, there are still issues involved in the use of these methods which affect the accuracy of transition prediction. The investigation has shown the importance of the inclusion of negatively oriented oblique waves in the calculation of the N-factors. The effect of these waves on the predicted N-factor values and hence transition onset has been shown to be significant and cannot be ignored. These effects are more marked for the combination of adverse pressure gradients and high angles of sweep which are relevant to military aircraft.

A parametric study has been carried out to investigate the effect of surface suction or cooling on transition and to determine the appropriate suction quantities or cooling rates required to suppress the various instability modes in order to delay transition for military aircraft. Trends in the possible extents of laminar flow achievable for different pressure distributions and flow conditions with various suction and/or cooling distributions are shown and their implications for design are discussed.

Notation

c	Aerofoil or streamwise chord.
CF	Crossflow.
C_p	Pressure coefficient.
C_Q	Total suction quantity.
M_∞	Freestream Mach number.
n	N-factor in linear stability analysis.
R_c	Reynolds number based on chord normal to leading edge.
Re	Reynolds number based on streamwise velocity and chord.
$\bar{R}$	Attachment line momentum thickness Reynolds number.
T	Temperature, in Kelvin.
T_w	Wall temperature.
T_∞	Ambient temperature.
TS	Tollmien-Schlichting.
V_s	Suction velocity, non-dimensionalised by freestream velocity.
x	Ordinate in streamwise direction.
I	Angle of incidence.
β*, kz	Spanwise wavenumber. ($kz = \beta^* \times 10^{-3}$)
Λ	Sweep angle.
ψ, psi	Wave orientation.

Introduction

In recent years, there has been considerable interest in hybrid laminar flow control for aircraft applications, as this is seen as a promising technique for drag reduction and performance enhancement. This interest has been manifested in the initiation of a number of laminar flow research programmes which involve flight testing using various demonstration aircraft, for example, in Europe, the A320 laminar fin programme[1]. During the past few years, laminar flow research at the Aircraft Research Association (ARA) has been concerned with the evaluation of the suitability and accuracy of theoretical methods currently available to the UK aerospace industry for laminar flow aerofoil and wing design[2]. The methods have been applied in a parametric study which was carried out to investigate the effects of different pressure and suction distributions on transition location. This was initially aimed at the wing planform geometries and flow conditions typical of Airbus class civil transport aircraft[3,4].

Recently, the work has been extended to encompass pressure distributions and flow conditions more relevant to military aircraft. The wing planform geometries assumed in the analysis are typical of modern combat aircraft, with high leading edge sweep and thin wing sections. In addition to suction, the technique of surface cooling has been investigated as an

Paper presented at the RTO AVT Symposium on "Active Control Technology for Enhanced Performance Operational Capabilities of Military Aircraft, Land Vehicles and Sea Vehicles", held in Braunschweig, Germany, 8-11 May 2000, and published in RTO MP-051.

alternative means of control. This work has been carried out under contract to BAE SYSTEMS and forms the subject of this paper.

The successful design of hybrid laminar flow aerofoils and wings requires methods for predicting the position of transition onset with sufficient accuracy to enable consistent comparison and which lead to satisfactory accuracy in drag prediction. A commonly used method for doing this is linear stability analysis. The paper describes this method and addresses some of the issues arising from its use. Results illustrating various conclusions drawn from the parametric study are presented and their implications for design are discussed.

Transition Prediction

On swept wings, transition from laminar to turbulent flow may be caused by various mechanisms, which depend mainly on streamwise pressure gradient, Reynolds number and sweep angle. These mechanisms are, principally, attachment line contamination, crossflow (CF) instability and Tollmien-Schlichting (TS) instability.

Attachment line contamination is associated with a source of gross disturbance, such as the wing body junction, from which undamped turbulence is convected along the leading edge, thus causing the entire wing to be turbulent. This phenomenon is essentially a 'bypass' mechanism and its occurrence may be predicted by means of the empirical criterion due to Poll and Paisley[5]. This criterion utilises the concept of the critical attachment line Reynolds number, $\bar{R}$, where $\bar{R}$ is a function of the leading edge velocity gradient and sweep. If this parameter exceeds 245 then the attachment line is deemed to be susceptible to gross contamination; if greater than 580 then TS type instability may occur.

CF instability is predominant in the leading edge region and is associated with the initial flow acceleration; it is strongly sweep dependent. The TS mode dominates further aft on the wing, particularly in adverse pressure gradient flows.

Simple empirical criteria may be used to predict transition due to either CF or TS instability, see for example Refs 6 and 7, but they are restricted in their range of applicability. Most of these criteria are formulated for incompressible flows only and none allows for the effects of boundary layer suction or cooling. Hence, these criteria were not considered suitable for the exercise described here.

In the UK aerospace industry, linear stability analysis methods, coupled with the 'e^n' criterion, are widely used for transition prediction. The theory behind such methods has been well documented elsewhere, see for example Ref 8, and therefore will not be repeated here. The method employed for the work described here is the spatial method, CoDS, due to Atkin[9]. A prerequisite for the use of these methods is the accurate determination of the velocity and temperature boundary layer profiles and their derivatives. This is achieved using a differential laminar boundary layer method subject to the assumption of semi-infinite, swept-tapered flow conditions. The swept-tapered flow assumption is reasonable provided that the isobars follow the wing generators. Such an assumption has been shown to apply to the outer wing region of a civil transport aircraft, see Ref 4.

The flow on modern combat aircraft wings is highly three-dimensional. Strictly, this would imply that a fully three-dimensional laminar boundary layer method should be used. However, consideration of the flow pattern on typical military wings has shown that on the forward part of the wing the isobar sweep approximates to the leading edge sweep. Since this is the region of the wing of interest in terms of the stability characteristics of the boundary layer, it has been assumed that the flow can be approximated by infinite yawed wing conditions, with the leading edge sweep being applied.

Linear stability analysis methods require the definition of an N-factor value at transition onset which may be used for either wind tunnel or flight conditions. Generally, these N-factor values are arrived at through correlation with experimental data, which leads to different values for different facilities due to varying freestream environment. The calculation of the N-factor requires the use of one of several integration strategies, the principal ones being:- constant wave orientation (ψ); constant spanwise wavenumber (β^*); constant wavelength (λ) and the envelope method. For fully three-dimensional flow, it is unclear which, if any, of these strategies models the physics of the problem most accurately. However, from kinematic wave theory it can be argued that, assuming infinite swept wing conditions, the constant β^* strategy has the greatest physical relevance for crossflow dominated flows. This integration strategy has been extensively evaluated and has been shown to produce consistent results[10,11,12]. For the work described in this paper, this is the integration strategy which has been adopted.

The choice of N-factor for transition onset is open to question, as it is dependent on the freestream environment. Values arrived at based on correlation with wind tunnel and flight test data range from approximately 6 to 20. The lower value is consistent with the correlation derived using experimental data from the DERA 8ft wind tunnel and given in Ref 10. Higher values are typical of flight conditions, reflecting the lower freestream turbulence levels encountered.

The use of linear stability analysis presupposes that the CF and TS instability mechanisms may be treated independently. However, for some flow conditions, it is possible that there would be some degree of interaction between the two modes and such flows may need to be analysed using a non-linear, non-local method such as PSE (Parabolised Stability Equations), e.g. Ref 13. Although such advanced methods are now becoming available, they have not yet been evaluated sufficiently for use in routine design applications and so do not form part of the analysis discussed here.

Given the integration strategy to be used, the accurate determination of the N-factor for a specific condition is clearly of prime importance. Since CF instability occurs very close to the leading edge for most practical wing flows, it is necessary to ensure sufficient streamwise grid resolution in order to, firstly, identify the neutral stability point correctly and, subsequently, to predict the correct trend in N-factor. Figs 1 and 2 show the effect on the predicted N-factor of having insufficient detail in the leading edge region. Referring to Fig 1, the CF modes correspond to the spanwise wavenumbers (kz) producing N-factors which reach a peak in the initial 10% chord; the modes downstream are due to TS instability. It can be seen for this case, that coarsening the streamwise grid has resulted in a reduction in both the disturbance growth rate and the maximum N-factor. This would imply a degree of uncertainty in the prediction of the transition position and the suction levels required to stabilise the flow. This is clearly an important issue for pressure data which is experimental in origin and, therefore, relatively sparse. For theoretical data as used here, although it is more likely that the grid resolution will be sufficiently fine, it is still important to ensure this.

An important point to note for the TS instability mode is that the most amplified disturbance may not be in the streamwise direction but may be oriented at some oblique angle. This is particular true for compressible flow conditions. It is essential that these waves be taken into account when carrying out the N-factor integration. In the previous work aimed at civil aircraft applications[4], the most unstable oblique waves were oriented in a positive sense, i.e. towards the crossflow direction. For the sweep angles relevant to the military applications considered here, it was apparent that the most unstable modes were negatively oriented. Fig 3 illustrates this point by showing a typical result in terms of the N-factor variation for a range of β^* values, where the most amplified mode for this case is $\beta^* = -900$ ($kz = -0.9$). The associated wave orientations are shown in Fig 4, where the most amplified mode, corresponding to $\psi \approx -60°$, is marked on the figure for clarity. The important point arising from the existence of the negative waves is that TS transition is predicted further forward than would have been the case if positively oriented waves only were considered, typically this forward movement is of the order of 10% chord, as can be seen in Fig 3. While the results are numerically correct, it is unclear whether they are physically feasible and more fundamental research would be required to ascertain this. Such research is beyond the scope of this paper.

Parametric Studies

The military wing geometries under consideration in this research programme tend to have relatively high leading edge sweep. This feature implies that transition would be likely to be caused at or close to the leading edge by either attachment line contamination or CF instability. This would need to be controlled in such a way as to suppress the instability sufficiently to delay transition to aft of the minimum pressure point. In the region downstream of this point TS instability would be the mechanism most likely to cause transition. This implies that the control methodology may be considered in two separate parts: firstly, to suppress CF instability and, secondly, to delay TS induced transition.

In previous work carried out at ARA[4], structural constraints for large civil transport aircraft dictated that boundary layer control, in the form of surface suction, could only be applied to the wing upper surface forward of the front spar, typically located at around 20% chord. For the military applications considered here, these constraints were relaxed. Although still confining the flow control to the wing upper surface, the use of both suction and cooling was investigated. The technique of surface cooling was included as it was considered that there might be structural advantages in practice compared to a suction system. The design of practical suction and cooling systems requires considerable research and is beyond the scope of this paper.

The previous work involved a systematic investigation of the appropriate types of pressure distributions for hybrid laminar flow wings for large civil transport aircraft[4]. This has been extended to military applications with the aim of establishing trends with sweep and Reynolds number which could provide guidance for hybrid laminar flow wing design.

Pressure distributions

In the work described in Ref 4, a series of pressure distributions were constructed which were relevant to cruise conditions for the aircraft types of interest. These pressure distributions were defined in two parts: first the initial gradient just downstream of the attachment line and second the ‘rooftop’ gradient. A range of leading edge and ‘rooftop’ gradients was covered as indicated by the sketch in Fig 5. The initial gradient is related to the leading edge geometry of the wing section, with the steeper gradient associated with a smaller leading edge radius. Conventional civil aircraft wings would correspond to the less steep initial gradients. The smaller leading edge radii, and therefore steep initial gradients, are typical of combat aircraft wings or unconventional sections, such as the Pfenninger type. The smaller leading edge radii of the military aircraft wings are the result of the significantly thinner wing sections used compared to civil wing sections. In certain flow conditions, this type of section geometry may lead to the development of a pressure distribution that has a high suction peak in the leading edge region of the wing upper surface. For some military wings, this occurs at cruise conditions with the peak height varying across the span. The adverse pressure gradient downstream of the suction peak may lead to the occurrence of a laminar separation bubble, which in turn would cause forward transition.

Given the section geometry typical of military wings, for the purposes of the parametric study, the initial pressure gradient was restricted to the steepest case studied in Ref 4. This was followed by a mildly adverse ‘rooftop’ gradient, which may be an appropriate type of pressure distribution for cruise conditions. Previous work[3] has shown that such pressure distributions are beneficial for aircraft performance, in terms of lift to drag ratio. Additionally, a series of pressure distributions was constructed with a range of leading edge suction peaks of various heights, see for example Fig 6, which were considered to be relevant to military aircraft wings.

The parameters considered in the exercise were leading edge sweep, assumed to range between 40° and 60°, and Reynolds number. The Mach number range, 0.8 – 0.9, was assumed to be typical of subsonic cruise conditions for modern combat aircraft. Previous work has shown that transition location is relatively insensitive to Mach number in this range.

Attachment line contamination

As noted above, the likelihood of the occurrence of attachment line contamination may be assessed by applying the criterion due to Poll and Paisley[5]. Fig 7 shows the variation of $\bar{R}$ with Reynolds number based on chord normal to sweep for the range of sweep angles considered. Also shown is the critical value, $\bar{R}$ = 245, above which the attachment line is susceptible to gross contamination. This would imply that attachment line contamination needs to be controlled via a device, such as a Gaster 'bump', or suction, which would eliminate the propagation of disturbances emanating in, for example, the fuselage boundary layer. Ref 14 discusses the use of suction to relaminarise a turbulent attachment line and defines the quantities required. For the type of wing sections considered here which have small leading edge radii and, hence, steep initial pressure gradients, it can be seen that the values are well below the neutral stability value, $\bar{R}$ = 580, indicating that the attachment line is not susceptible to TS type instability.

Crossflow instability

To suppress CF instability sufficiently to delay transition it is necessary to apply boundary layer control so as to reduce the predicted N-factors below a specified value. As an example of this, Figs 1 and 3 show N-factors for the same flow condition, without and with suction, respectively. The exercise sought to establish the minimum amount of control necessary for the sweep and Reynolds number ranges of interest.

Given the uncertainty mentioned earlier regarding the N-factor for transition onset, an understanding of the sensitivity of the minimum suction requirement to assumed N-factor was gained by considering a number of different values. The chosen N-factors were 8, 10 and 15, which should cover the expected values found in wind tunnel facilities and flight conditions. To illustrate this sensitivity, Fig 8 shows the variation of the minimum required suction velocity, V_s, with Reynolds number based on chord normal to the leading edge, R_c, for Λ = 40°. Similar variation can be seen at other sweep angles. CF instability is strongly dependent on sweep as is shown in Fig 9. This figure also illustrates the point that the minimum suction requirement tends to an asymptote as Reynolds number increases. Here n = 10 has been assumed as an appropriate value for transition onset and will be used throughout the analysis presented here. This is lower than some results quoted for flight conditions but is considered a reasonably conservative value for use in design studies. The use of the normal chord Reynolds number instead of the freestream Reynolds number is considered more appropriate for identifying the effect of sweep, as it implies effectively the same wing chord for the different geometric conditions. From these results, interpolation or extrapolation to a particular condition would be possible.

The results discussed above are based on applying suction over a region of the wing surface covering the initial flow acceleration and including the minimum pressure point for the simple pressure distribution type shown in Fig 5, in this case 8% chord. However, it would also be possible to concentrate the suction over smaller chordwise extents. The use of shorter suction panels and, therefore, smaller plenum chambers may be beneficial for suction system design. This type of arrangement may be necessary when the effect of pressure gradient on suction velocity is taken into account. Fig 10 shows the minimum suction velocity required to constrain the CF N-factor to below 10 for a range of suction extents. The required suction velocity remains constant until the suction extent is less than 2.5% chord, when a sharp increase is observed. Although the suction velocity increases with reduction in panel length, the total suction quantity, C_Q, reduces, see Fig 11. The value of C_Q may be more relevant in terms of suction system design, as it is directly related to the pump drag. This implies that applying a higher suction velocity over a shorter suction panel may be beneficial when total drag is considered.

An alternative technique to suction for controlling instability is surface cooling. When this was investigated for the same cases described above, it was found that the required cooling rates were very high. As an example, Fig 12 shows the variation in maximum CF N-factor with wall temperature at two Reynolds numbers. It can be seen that to reduce the N-factor to below 10 as for suction, it is necessary to apply cooling rates, T_w/T_∞, < 0.5, which is probably impractical.

As commented earlier, military aircraft wings may have pressure distributions with a leading edge suction peak which may induce separation. The likelihood of a separation depends on the severity of the adverse pressure gradient downstream of the peak. The pressure distributions shown in Fig 6 were used to establish the suction quantity required to suppress both the separation and CF instability. Here suction was applied over the initial 5% chord covering the region of the suction peak. The results are shown in Fig 13 in terms of the minimum suction requirement for both separation control and suppression of CF instability, assuming n = 10. Clearly, for a given Reynolds number, there is a maximum peak height attainable before separation is predicted and below which suction is required for CF instability control only. Above this maximum, it appears that suction is a viable means of separation control, although it should be noted that, for the highest suction peak case, the suction velocities required are very high, and this may be unrealistic in practical terms.

Tollmien-Schlichting instability

Having delayed the onset of transition to aft of the minimum pressure point, TS instability becomes the dominant mode. Transition in this case depends on the 'rooftop' pressure gradient and Reynolds number. In previous work[3], it was shown

that, as Reynolds number increases, the predicted TS transition position becomes increasingly insensitive to pressure gradient. In contrast to CF instability, TS transition is independent of sweep. This is illustrated by Fig 14 which shows the transition location predicted assuming n = 10 for cases for which CF instability has been suppressed by the application of suction over the initial 8% chord.

For the types of pressure distribution considered here, in principle, boundary layer control may be used to delay TS transition to any specified position, provided this point is forward of a shock or recompression. Either suction or cooling may be used to achieve this, since both techniques are known to be effective for TS instability. Considering Fig 3 as a typical example of the N-factor variation for these types of pressure distribution, it can be seen that the suction applied to suppress CF instability is sufficient to move the TS neutral stability point to the end of the suction panel. It is therefore unnecessary to control TS instability with a suction or cooling panel immediately downstream; instead it is more efficient to place the panel further aft, allowing the instability to amplify until just below the value assumed for transition before control is applied.

As an illustration of the effectiveness of the two control techniques, Figs 15 and 16 show the variations in predicted transition onset position for suction and cooling respectively. For this case, which was chosen near the upper limit of TS sensitivity to the severity of the adverse pressure gradient, control is applied downstream of 15% chord. The results cover a range of suction velocities and cooling rates applied over different extents for two Reynolds numbers. As with CF instability control, there is a tendency for the variation in transition position to become independent of Reynolds number as the amount of control is increased. Clearly it is more effective to increase the extent of control than to increase the suction or cooling rate. It is worth noting that, in comparison with CF instability control, the suction velocities required are considerably reduced. The use of cooling may be a feasible technique for TS control as the cooling rates are not excessive; in this case, $T_w/T_\infty \approx 0.8$ has been shown to be sufficient for suppressing the instability and achieving a significant extent of laminar flow.

These results illustrate the use of a control methodology whereby discrete panels are used to suppress CF instability initially and subsequently to delay transition due to TS instability. For the example shown, suction can be applied over the initial 8% chord and then from 15% to 35% to delay transition to $x/c > 0.4$ for a streamwise Reynolds number of 40×10^6. For a less severe adverse pressure gradient, this methodology may be extended to encompass two or more discrete control panels for TS instability control, for instance 20 – 30% and 40 – 50%. Figs 17 and 18 illustrate this control strategy by showing the predicted N-factors for a mildly adverse pressure gradient case with $\Lambda = 40°$, $Re = 40 \times 10^6$. In these cases, suction has been applied over a single panel, placed at 20 – 30% chord (Fig 17), and over two separate panels, with the second placed at 40 – 50% chord (Fig18). The same suction velocity has been used in both cases.

Design Implications

The relatively high leading edge sweep typical of modern combat aircraft wings implies that the most likely cause of forward transition is CF instability. As a result of the parametric study, trends have been established for the minimum suction velocity required to suppress this instability sufficiently to delay transition. The asymptotic behaviour of this quantity with increasing Reynolds number implies that a maximum suction velocity can be defined for a given geometric configuration. This would allow the maintenance of laminar flow onto the inboard wing without incurring the penalty of excessively high suction rates.

The thin wing sections, with their correspondingly small leading edge radii, lead to pressure distributions with steep leading edge gradients. This has two important benefits. Firstly, the attachment line Reynolds number can be kept to a sufficiently low value that leading edge contamination may be avoided, either by using a Gaster 'bump' or applying suction. Secondly, the steep gradient helps to reduce CF instability and restrict it to a relatively short chordwise distance, thereby permitting the use of small suction panels in the leading edge region. On the other hand, this type of leading edge geometry may produce pressure distributions with a suction peak close to the leading edge at cruise conditions. If this suction peak is sufficiently high, the steep adverse pressure gradient downstream may precipitate laminar separation. It has been shown that suction can be used to prevent the occurrence of this separation. However, for low Reynolds numbers the required suction velocity increases rapidly with peak height thus implying a maximum peak height for practical applications. Therefore, careful design of the leading edge geometry is required to achieve the right balance in terms of the trade-off between the steep favourable initial gradient and the likelihood of causing laminar separation.

Transition due to TS instability has been shown to be independent of sweep. In addition, in previous work, it has been observed that TS instability becomes insensitive to the steepness of the adverse pressure gradient at higher Reynolds numbers. As a consequence, it is more effective to increase the chordwise extent over which boundary layer control acts than to increase the level of suction or cooling. This enables the application of a control technique whereby discrete suction or cooling panels are used. The suction velocities are small, typically an order of magnitude lower than that required for CF control. The exercise has established that cooling is a viable control technique, particularly for moderately adverse pressure gradients.

It has been shown that the required suction levels are sensitive to the value of the N-factor assumed for transition onset. This is particularly important for CF instability control, since an underestimate in the suction quantity required would lead to a total loss of laminar flow. For TS instability control, sensitivity to N-factor in terms of chordwise extent of laminar flow is generally less as the amplification rates for the disturbance waves tend to be high. However, it is important that all unstable modes are predicted as failure to do so may result in an over-prediction of transition position by more than 10% chord. This

sensitivity to N-factor must be borne in mind as inaccurate prediction of the transition onset position will result in misleading estimates of wing performance, as has been illustrated in Ref 3 for hybrid laminar flow aerofoils.

Concluding Remarks

a) It has been shown to be possible to use boundary layer control to delay transition onset for the types of pressure distributions relevant to modern combat aircraft wings. For these pressure distributions, transition would occur close to the leading edge due to either attachment line contamination or CF instability. For the leading edge geometries of interest, attachment line contamination may be readily avoided by means of suction or a device such as a Gaster 'bump'. The use of suction to suppress CF instability sufficiently to allow the onset of transition to move aft of the minimum pressure point, permits the use of either suction or cooling to control TS instability.

b) Clear trends with leading edge sweep angle and Reynolds number have been established in the variation of the minimum suction velocity required to suppress CF instability. It has been shown that the required suction quantity tends to become asymptotic at higher Reynolds number. It is beneficial in terms of total suction requirement to consider the use of short porous panels with a higher concentration of suction. The parametric study has provided sufficient information to enable the required suction quantity for a given leading edge pressure distribution to be established.

c) Suction has been shown to be a viable means of avoiding laminar separation resulting from the steep adverse pressure gradient downstream of a suction peak in the wing leading edge region. The results have shown that there may be a maximum peak height for which laminar separation can be prevented with the level of suction achievable in practice.

d) Transition due to TS instability has been shown to be independent of sweep. The concept of using separate suction panels or cooling strips for controlling TS instability has been shown to be feasible. The suction quantities required are significantly lower than those required to suppress CF instability. For a specified chordwise extent, the suction or cooling rates become asymptotic at higher Reynolds numbers. Consequently, it is more effective to increase the chordwise extent over which control is applied than to increase the suction or cooling rate. The effectiveness of using a succession of discrete control panels has been demonstrated.

Acknowledgement

The work described in this paper has been carried out as part of a research programme funded by BAE SYSTEMS.

References

1. Thibert, J. J., Quast, A. and Robert, J. P., 'The A320 Laminar Fin Programme'. 1st European Forum on Laminar Flow Technology, Hamburg, Germany, March 1992.

2. Wong, P. W. C. and Maina, M., 'Development and application of methods for laminar flow research at ARA'. ICAS 96-1.7.3, 20th ICAS Congress, Sorrento, Italy, September 1996.

3. Wong, P. W. C. and Maina, M., 'An investigation of hybrid laminar flow aerofoil pressure distributions and performance characteristics'. 2nd European Forum on Laminar Flow Technology, Bordeaux, France, June 1996.

4. Maina, M. and Wong, P. W. C., 'Study of methods and philosophies for designing laminar flow wings'. ARA CR M275/3, November 1996.

5. Poll, D. I. A. and Paisley, D. J., 'On the effect of wing taper and sweep direction on leading edge transition'. Aeronautical Journal, March 1985.

6. Poll, D. I. A., 'Some observations of the transition process on the windward face of a long yawed cylinder'. J Fluid Mechanics, Vol 150, pp329-356, 1985.

7. Granville, P. S., 'The calculation of the viscous drag of bodies of revolution'. David Taylor Model Basin Report 849, July 1953.

8. Mack, L. M., 'Boundary layer linear stability theory'. AGARD Special Course on Stability and Transition, March 1984.

9. Atkin, C. J. Unpublished work at BAe Regional Aircraft Ltd.

10. Ashill, P. R., Betts, C. J. and Gaudet, I. M., 'A wind tunnel study of transitional flows on a swept panel model at high subsonic speeds'. 2nd European Forum on Laminar Flow Technology, Bordeaux, France, June 1996.

11. Atkin, C. J. and Poll, D. I. A., ‘The correlation between linear stability analysis and crossflow transition near an attachment line’. Proc. of the Colloquium on Transitional Boundary Layers in Aeronautics, Amsterdam, December 1995.

12. Maina, M., ‘Evaluation of integration strategies for stability analysis’. ARA CR M368/1, May 1999.

13. Mughal, S. M. and Hall, P., ‘Parabolised stability equations and transition prediction for compressible swept-wing flows’. Imperial College Report, November 1996.

14. Poll, D. I. A. and Danks, M., ‘Relaminarisation of the swept wing attachment line by surface suction’. IUTAM Symposium on Laminar-Turbulent Transition, Sendai, Japan, September 1994.

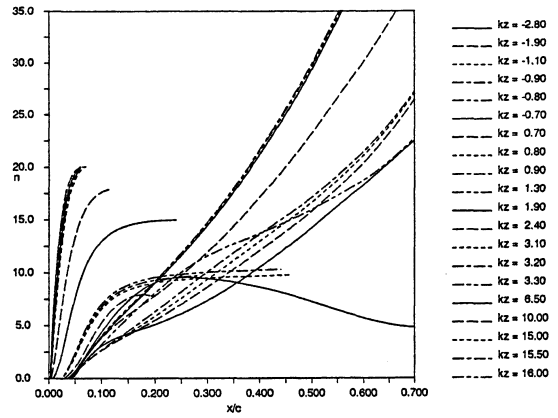


Fig 1 N–factors – Standard Point Distribution

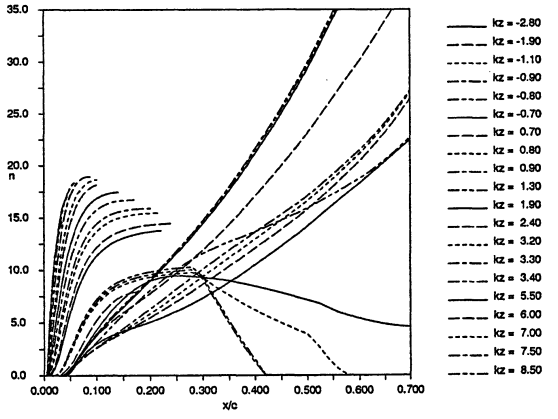


Fig 2 N–factors – Coarse Point Distribution

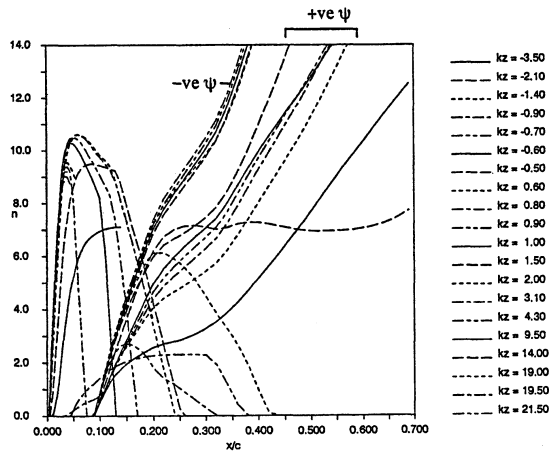


Fig 3 N–factor Variation

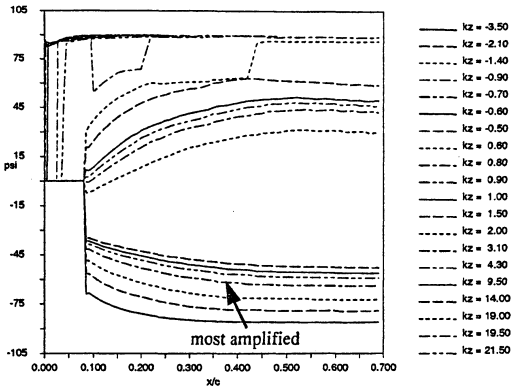


Fig 4 Wave Orientation – ψ

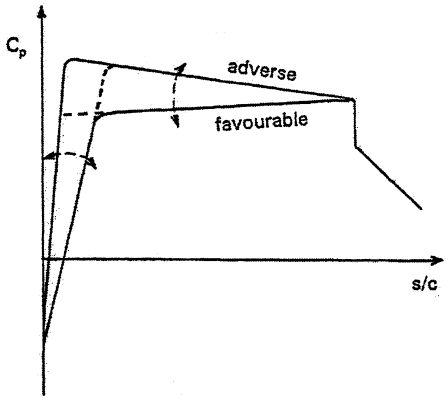


Fig 5 Sketch of Pressure Distributions

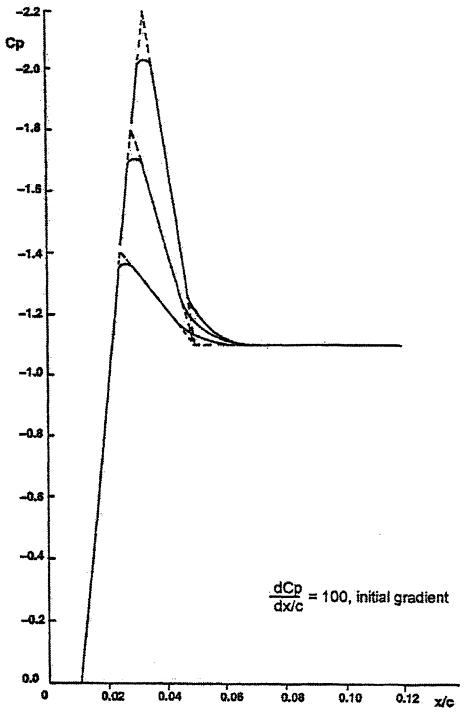


Fig 6 Pressure Distributions with a Range of Suction Peaks

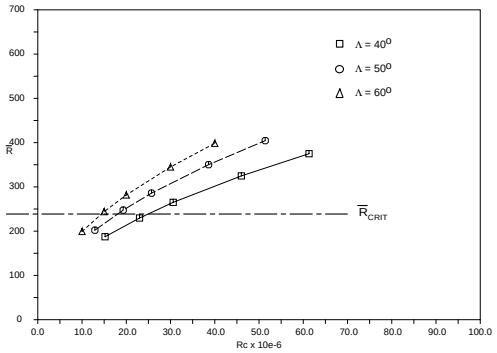


Fig 7 Variation of Attachment Line Reynolds Number

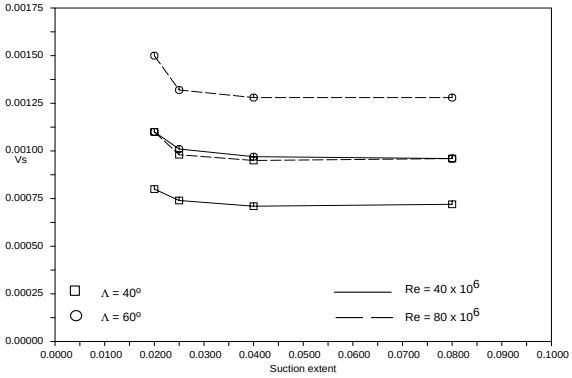


Fig 10 Leading Edge Suction Velocity

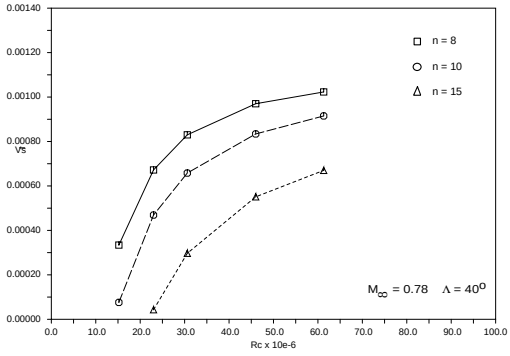


Fig 8 Effect of N−factor on Vs_{min} for CF Instability

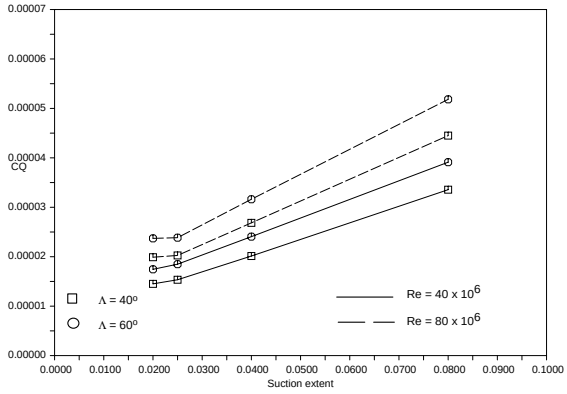


Fig 11 Leading Edge Suction Quantity, C_Q

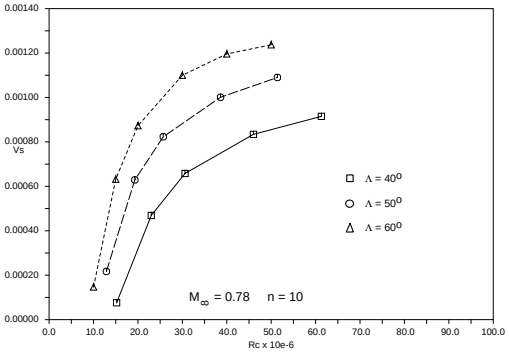


Fig 9 Effect of Sweep on Vs_{min} for CF Instability

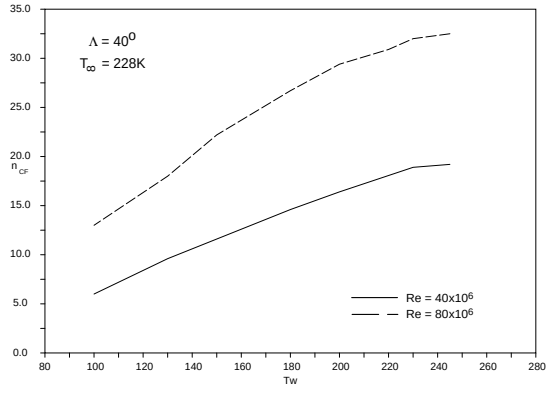


Fig 12 Effect of Cooling on CF N−factor

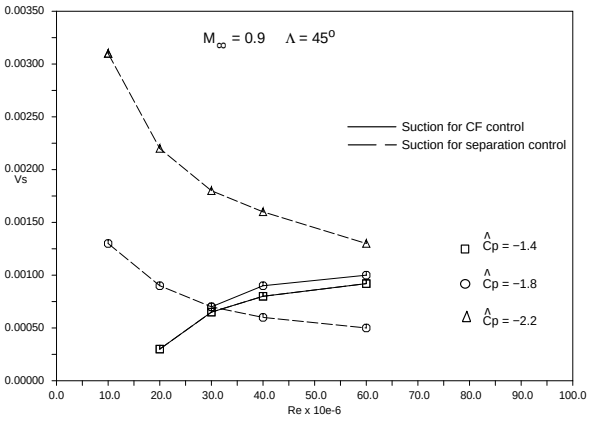


Fig 13 Suction Variation for CF and Separation Control

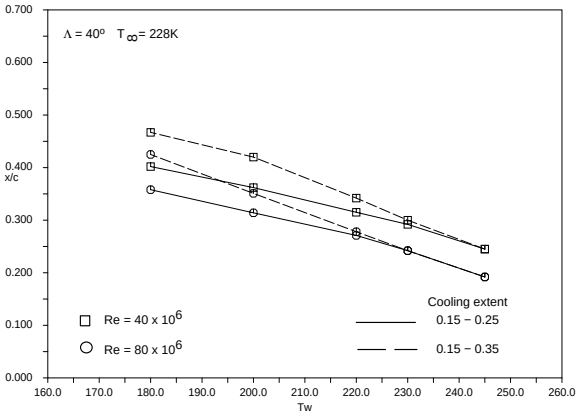


Fig 16 Effect of Cooling on TS Transition

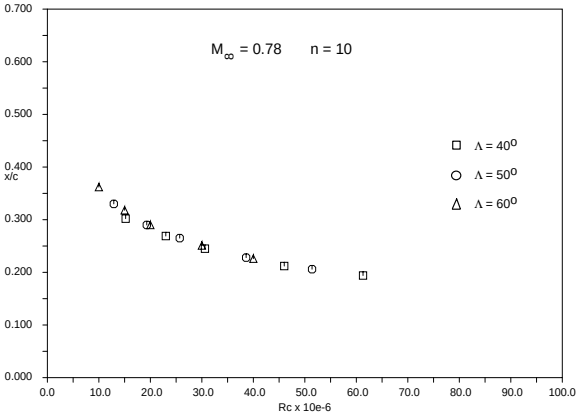


Fig 14 Effect of Sweep on TS Transition Location

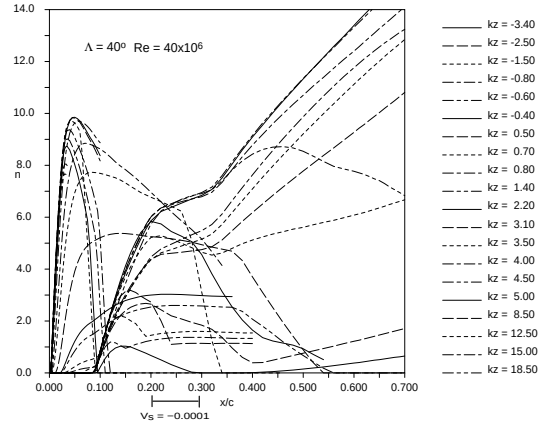


Fig 17 N−factor variation for TS Control
Suction Extent x/c = 0.2 − 0.3

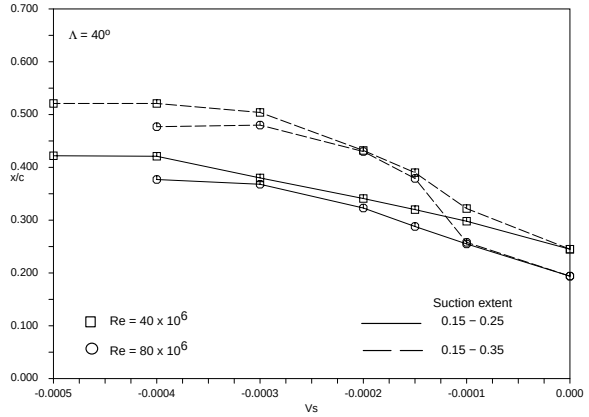


Fig 15 Effect of Suction on TS Transition

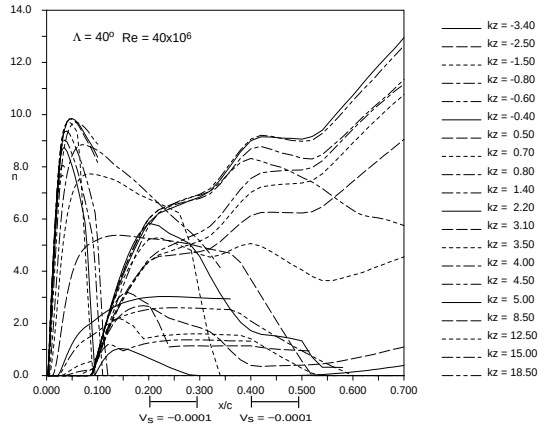


Fig 18 N−factor variation for TS Control
Suction Extent x/c = 0.2 − 0.3, 0.4 − 0.5

Laminar Design for Supersonic Civil Transport

Achmed Traoré
Institute of Design Aerodynamics
DLR, German Aerospace Center
D-38108, Lilienthalplatz 7, Braunschweig
Germany

ABSTRACT

The paper presents a design methodology for supersonic wing sections with hybrid laminar flow control. The approach is based on coupled Euler/boundary layer flow simulation and linear stability analysis for transition prediction. The investigations show that combinations of simple pressure distribution shapes can be used to optimize airfoils for maximum extent of laminar flow and hence minimum friction drag.

NOMENCLATURE

α	=	angle of attack
c_f	=	skin friction coefficient
c_l	=	lift coefficient
c_p	=	pressure coefficient
c_q	=	suction coefficient; $c_q=(V_s \rho)_w$
Ma	=	Mach number
Re	=	Reynolds number based on freestream condition
Φ_{LE}	=	Leading edge angle
N_{tr}	=	Transition N-factor (envelope method)

INTRODUCTION

Mission requirements of second generation supersonic civil transport (SCT) demand friction drag reduction which probably cannot be achieved with fully turbulent configurations. The technological potential of laminar control for SCT is up to now not entirely evaluated. Problems concerning suction rates or passive/active boundary layer control are at now subject of investigations. This is the context for the development of tools for, and the validation of, a laminar design methodology for SCT.

The aim of a laminar flow design is to move the region of the laminar/turbulent transition as far downstream as possible. In supersonic flow laminar control is only feasible using a combination of profile shaping and active laminar flow control. Appropriate measures could be air suction or wall cooling. High leading edge sweep angles in combination with blunt leading edges cause an enhancement of crossflow in the boundary layer in the leading edge region. Crossflow disturbances are amplified in this area and can provoke early transition. Particulary on the outer wing of supersonic aircrafts the leading edge is very thin. Hence it will be technically difficult to integrate suction panels in this area to control crossflow instability. To overcome this difficulties two possible solutions exists for the laminar design. First a sharp nose can be chosen as with the BCA-SST[1] concept. On such wedge shaped leading edges no crossflow disturbances are amplified in the nose region. But in high-lift conditions the flow separates at the leading edge. This generates additional vortex drag and may change the aircraft handling qualities. Another design option is to retain a blunt nose profile and to control the crossflow instabilities with an adequate leading edge shape. In both options Tollmien-Schlichting (TS) waves have to be damped with suction.

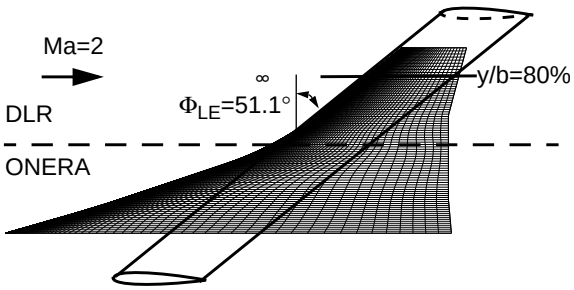


Fig. 1: Wing of the AS-1 configuration.

Since 1997 DLR and ONERA are cooperating in the supersonic laminar design with the goal to design and assess a three dimensional laminar wing. The investigations are carried out using the Aerospatiale AS-1 configuration for Ma=2 as a baseline wing shape. DLR investigates the outer wing with blunt supersonic leading edge. Similar investigations are performed by partner ONERA for the inner wing.

The investigation presented here is a qualitative and quantitative study of laminar airfoil design idealised as an infinite swept wing. As reference profile the wing section of the AS-1 configuration at 80% span is chosen (see **Fig. 1**).

Paper presented at the RTO AVT Symposium on "Active Control Technology for Enhanced Performance Operational Capabilities of Military Aircraft, Land Vehicles and Sea Vehicles", held in Braunschweig, Germany, 8-11 May 2000, and published in RTO MP-051.

1. DESIGN METHODOLOGY AND TOOLS

The laminar flow design methodology is based on a systematic study of different simple shaped pressure distributions with the goal to find the beneficial characteristics for laminarity. A combination of the most favorable distributions will yield the optimized laminar profile.

Starting from the reference airfoil new target pressure distributions are graphically defined and corresponding profile geometries are generated with an inverse design tool. After performing a laminar boundary layer computation and a stability computation the transition location can be determined with an assumed transition N-factor. Then a new boundary layer computation with known transition location provides the friction drag coefficient C_f.

1.1 Inverse design tool

According to **Fig. 2** the inverse design process starts with a graphic prescription of a target pressure distribution. Then an optimization loop starts. It consists of an optimizer EXTREM, the parametric profile generator PROFIX, the mesh generator MegaCads[7] , the flow solver FLOWer[6] and the tool CPDIFF which calculates the object function for the optimizer by a summation of local c_p-differences between actual and target distribution.

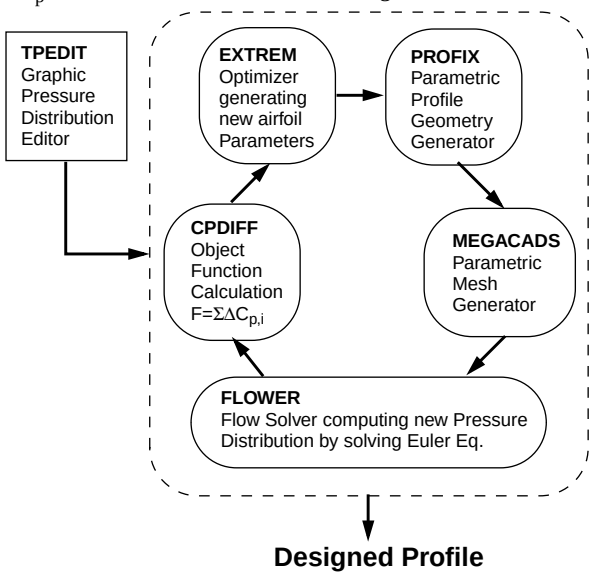


Fig. 2: Flowchart of the inverse design process.

The flow solver FLOWer

For the present application the FLOWer code solves the compressible three-dimensional Euler equations to provide the pressure distribution at each optimization step. This computation is performed on a grid of 122x20 cells. When the inverse design process stops a final Euler computation is achieved on a grid of 224x40 cells. This inviscid field solution is then used as the outer boundary condition for the boundary layer computation. As shown in **Fig. 3** an adequate residual convergence of the Euler computation is achieved after 54 iterations steps on the fine grid. The adopted convergence criterion for residual is 10^{-4}.

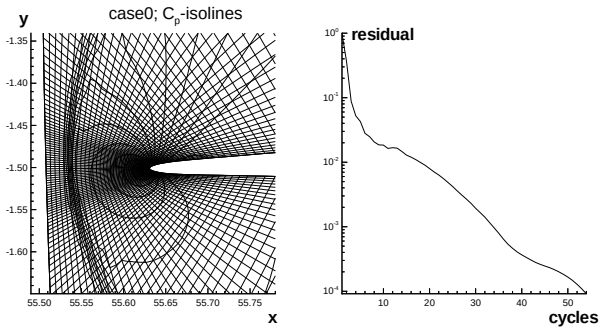


Fig. 3: Euler computation and convergence

The parametric profile generator PROFIX

This tool generates profiles by catenating geometric support points with Bezier curves. Each support point is defined by 3 parameters: the locations x, y and the local curve slope. To define a blunt nose a ramp function is used with a prescribed infinite slope at x/c=0. This tool uses the basic curve function routines introduced by H. Sobieczky[4] . **Fig. 4** sketches an example how the curve functions are used to define the airfoil.

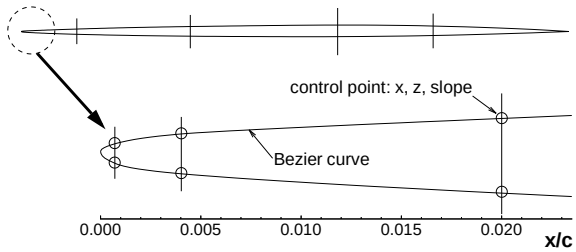


Fig. 4: Sketch of profile parametrization.

The number of support points can be changed by user input according to local profile shaping requirements. For the present application 14 support points are used which are controlled by 32 geometric parameters.

Performance of the inverse design tool

The location of the support points are chosen in a way to allow an accurate reproduction of the target pressure distribution. During the inverse design the angle of attack is a free parameter. **Fig. 5** shows the results of the design process after 12 optimization levels. The calculated profile has a pressure distribution in sufficient agreement to the graphically prescribed target pressure distribution.

For reason of structural constraints the profile thickness of the reference airfoil has to be retained. During the inverse design this is achieved by local adaption of the target pressure distribution.

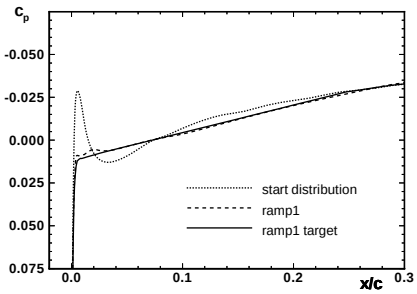


Fig. 5: Performance of the inverse design

Boundary-Layer Model

The code SOBOL[5] used here solves the second-order boundary-layer equations. Solution of this set of equations can be regarded as classical boundary-layer solutions corrected so that wall curvature, viscous interaction and wall-normal inviscid flow gradients are taken into account. The solution of the system of partial differential equation is performed with a space marching finite-difference method. The simulation of suction is implemented in the code. For the present design study a uniform suction panel with a suction power corresponding to a c_q=0.33 10^{-3} over a length of $\Delta x/c$=0.06 is selected. This suction power amount emerges from preliminary suction investigations.

Stability analysis

The code COAST[2] analyses the instability of compressible boundary layers with the semi-empirical e^N-method[3] . COAST solves the linear stability equations of compressible, parallel, three-dimensional flow along curved surfaces. The envelope N-factor integration method is implemented and used for the present application. Curvature effects are not considered. The transition N-factor for free flight conditions is assumed to be N_{tr}=6.

2. LAMINAR DESIGN

2.1 Investigated pressure distributions

Starting from the reference profile denoted by *case0*, three different series of generic pressure distributions were generated. The variation of the pressure distribution is restricted to the first 25% of chord. The first series denoted by *ramp* (**Fig. 6**) consists of a variation of the slopes of a linear pressure drop without suction peak. The second series denoted by *lev* shows a parallel pressure level shift of the linear pressure drop (**Fig. 7** top).

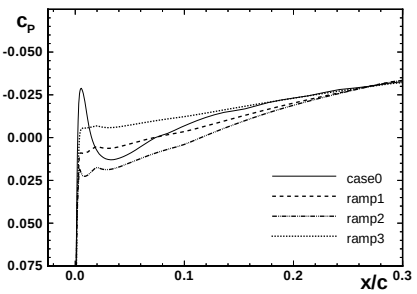


Fig. 6: Generic *ramp* pressure distributions.

The last series denoted by *top* combines three different suction peaks with a *ramp* distribution (**Fig. 7** bottom)

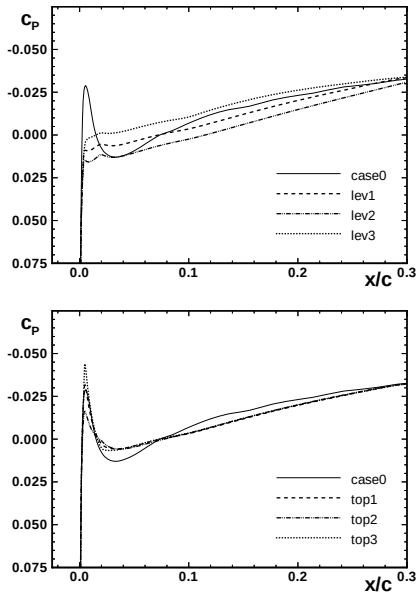


Fig. 7: Generic *lev* and *top* pressure distributions.

2.2 Investigation of suction models

Variation of suction panel position

The aim is to study the effect of the suction panel location on wave damping/amplification behavior. This is done by moving the suction panel with the same suction power up and downstream. This investigation is carried out on the *top1*-distribution. The stability situation without suction is shown in **Fig. 8**. Note that the stability relevant frequency are is 4kHz.

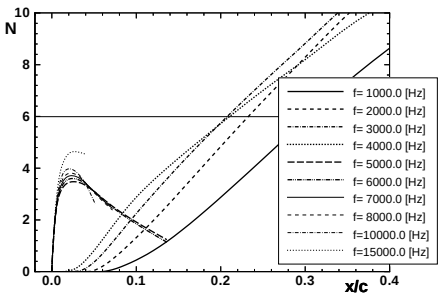


Fig. 8: Stability of case *top1* (no suction).

The first obvious suction approach is to begin suction at 19% chord in order to damp TS-waves around the estimated transition location. This trial fails as shown in **Fig. 9** (top). Here TS-waves are already too much amplified and this reduces the sensitivity of the waves to suction.

The following suction approach shifts the suction panel upstream. **Fig. 9** (bottom) shows an increase of the suction impact on

the TS-wave amplification by the chosen upstream shift. The optimized suction location is found at 8.4% chord. Here suction is performed where the waves just begin to grow. The transition is located now at 36% chord.

This investigation shows the necessity, for the suction fitness evaluation to perform an optimization of the suction panel location. This is particulary important for pressure distributions with a distinct streamwise separation of crossflow waves from TS-waves.

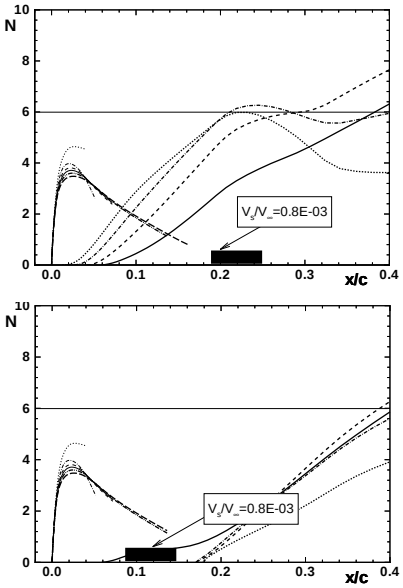


Fig. 9: Optimization of suction panel location.

Variation of suction panel extent

Here we vary the local suction coefficient by keeping the total suction power constant and the suction panel location unchanged at 5% chord. Three suction panel lengths are investigated on the *ramp1*-distribution whose natural stability is shown in **Fig. 10**. Note that the lack of the suction peak causes a distinct dominance of crossflow waves.

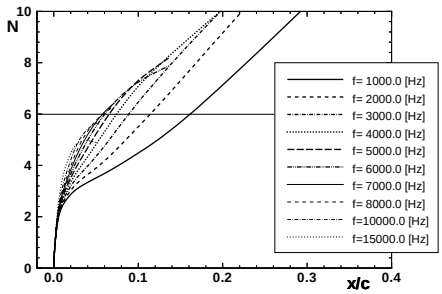


Fig. 10: Stability of the *ramp1*-distribution (no suction).

As given in **Fig. 11** increasing the suction length causes a dilution of the suction efficiency and so yields no better damping behavior on TS-waves. This instance meets the technical constraint which demand short suction panels.

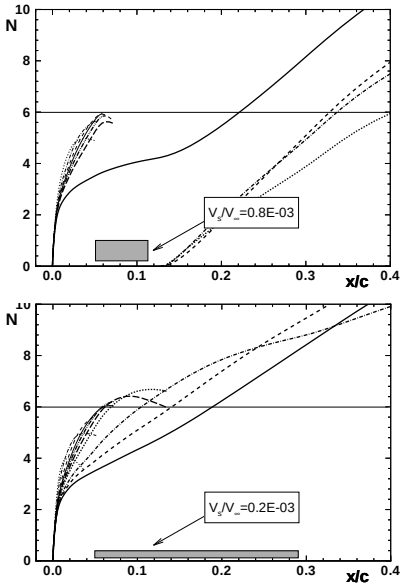


Fig. 11: Variation of the suction panel length

2.3 Design result

Laminarity with suction

All stability results shown here are optimized regarding the suction panel location according to 2.2. The most favorable *ramp* distribution is *ramp3* **Fig. 12** (top). Note that the lower slope of the pressure drop yields a longer laminar extent.

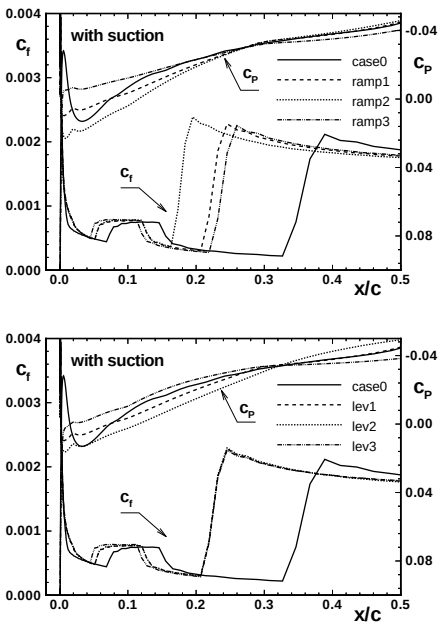


Fig. 12: Transition on *ramp* and *lev* distributions.

The transition location of the three *lev* distributions do not differ from each other (see **Fig. 12** bottom). This shows that the pressure level cannot be used as an effective design attribute. On this account the *lev* distributions are not considered for the further design.

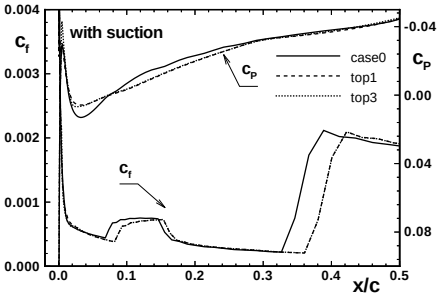


Fig. 13: Transition on the *top* distributions.

The *top1* and *top3* distribution have the same transition location at 36% chord (see **Fig. 13**) and so they represent the most favorable designs due to the property that suction peak damps crossflow disturbances.

Optimized design

Combining the characteristic shape of *top1* and *ramp3* a new pressure distribution is generated. With an optimized suction location the new designed profile has a laminar length of 46% chord, see **Fig. 14**.

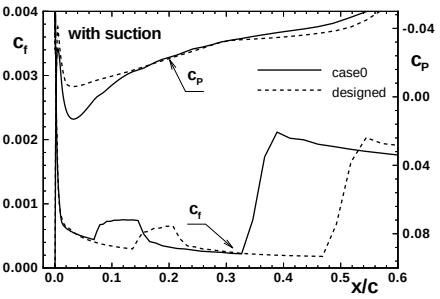


Fig. 14: Designed pressure distribution.

Fig. 15 illustrates the impact of the new pressure distribution on the stability. The higher suction peak has a damping effect on crossflow waves. The shorter pressure rise extent after the peak damps the TS-waves with a parallel shift of the N-curves downstream maintaining the effect of suction.

Table 1: Comparison of total drag

case	c_{dp}	c_{df}	$c_{dp}+2c_{df}$
case0 (no suction)	0.006828	0.001651	0.01013
case0 (suction)	0.006828	0.001280	0.009388
designed (suction)	0.006780	0.001039	0.008821

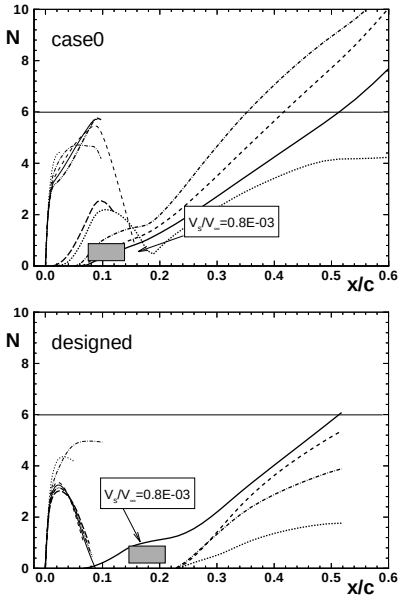


Fig. 15: Stability of the designed profile.

A comparison of both airfoil geometries in **Fig. 16** shows that the new designed profile has about the same curvature at the leading edge and the same thickness as the reference airfoil *case0.*

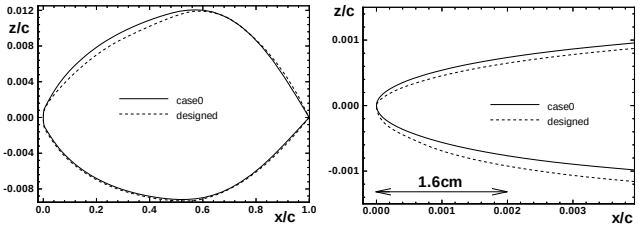


Fig. 16: Geometry of the designed profile.

Table 1 shows that with the new distribution the total drag can be reduced by about 5.9% compared with the reference distribution *case0*. In the third column the total airfoil drag of upper and lower surface was conservatively estimated by using twice the skin friction drag of the upper surface.

Reynolds number sensitivity

The aim is here to evaluate the spanwise range of the validity of laminar characteristics of the designed profile. This is done by increasing the Reynolds number about 1.5 times and decreasing 0.75 times with reference to the design Reynolds number of Re=4.8 10^6[m^{-1}]. This simulates a typical variation of the profile chord length.

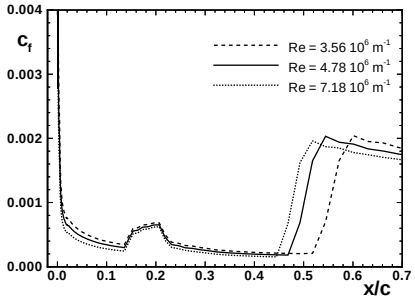


Fig. 17: Reynolds number sensitivity.

Fig. 17 shows the Reynolds number sensitivity of the designed profile. Transition location is not strongly affected by the given Reynolds number range. This indicates that the designed pressure distribution could be used over the whole outer wing of the AS-1.

Sensitivity to angle of attack

For the evaluation of the laminar pocket of the designed profile the angle of attack was changed in two directions by $\Delta\alpha$=0.3°. This causes an alteration of the lift coefficient of Δc_l=20%. The corresponding pressure distributions gives **Fig. 18**. The design angle of attack is α=2.02°

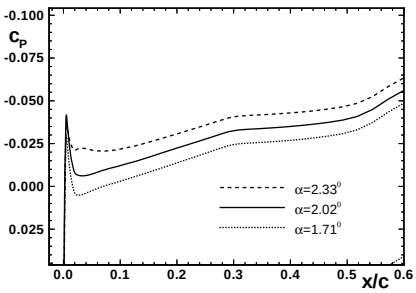


Fig. 18: Variation of the pressure distribution with the angle of attack.

The stability results in **Fig. 19** shows that the lower angle causes a negligible decrease of the laminar length of Δx/c=0.015. Increasing the angle of attack has a stronger impact. Here we have an amplification of crossflow waves due to the reduced suction peak and this causes a significant loss of laminar length shifting the transition location at about x/c=0.1.

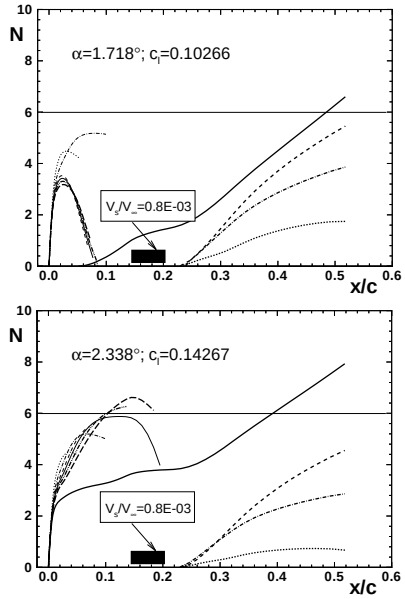


Fig. 19: Laminar pocket evaluation

3. CONCLUSION

The present work describes a successful design of laminar flow airfoils with a blunt supersonic leading edge. Simple shaped pressure distributions were generated and their stability analyzed. A combination of suction peak at leading edge to control crossflow and favorable pressure gradient after the peak to delay TS-instability were used to design an optimized pressure distribution for hybrid laminar flow control. The study shows that crossflow instability can be controlled only through profile shaping on a 51° swept wing with blunt leading edge at Ma=2. The location of a given suction panel was optimized to increase the efficiency of suction in order to enhance the extent of laminar flow. Compared to the turbulent reference design the new design has less wave drag and less skin friction drag, both for natural laminar flow and hybrid laminar flow control.

4. REFERENCES

[1] R.D. Wagner, m. C. Fischer, F.S. Collier, W. Pfenniger: “Supersonic Laminar Flow Control on Commercial Transports” ICAS-90-3.6.3

[2] Schrauf, G.: “COAST2 - A Compressible Stability Code, Users Guide and Tutorial”. Report No. EF1-1973, 1993

[3] Arnal, D., “Boundary-Layer Transition: Prediction based on Linear Theory”, *Special Course on Progress in Transition Modeling*, AGARD-R-793, Brussels, Belgium, 1993

[4] Sobieczky, H., Chourdhry, S., Eggers, T., “Parametrized supersonic transport configuration”, 7th European Aerospace Conference (1994)

[5] Monnoyer, F., “Second Order BOundary Layers SOBOL Mk 2.7 Handbook”, UVHC-LMF-001.

[6] Koll, N.; Rossow, C.C.; Becker, K.; Thiele, F., Megaflow A Numerical Flow Simulation System, Proceedings of the 21st ICAS Congress 1998, Melbourne.

[7] Brodersen, O.; Hepperle, M.; Ronzheimer, A.; Rossow, C.C.; Schöning, B., "The Parametric Grid Generation System MegaCads.",

Paper #3

Q by C. Ciray: What angle of attack was used in your calculations ? Did you try any value other than the design angle ?

A (A. Traore): The design angle of attack is 2.0 degrees. No, I investigated only the design angle.

This page has been deliberately left blank

Page intentionnellement blanche

Characterization of Pulsed Vortex Generator Jets for Active Flow Control

Carl P. Tilmann & Kevin J. Langan
Carl.Tilmann@afrl.af.mil — Kevin.Langan@afrl.af.mil
Air Force Research Laboratory, Air Vehicles Directorate, Aeronautical Sciences Division
2130 8th Street, Wright-Patterson AFB, Ohio 45433-7542, USA

John G. Betterton & Mark J. Wilson
JGBetterton@dera.gov.uk
Defense Evaluation and Research Agency, Aerodynamics and Hydrodynamics Centre
DERA Bedford, Clapham, Bedfordshire MK41 6AE, United Kingdom

SUMMARY

The flowfields produced by several active and passive flow control devices are being investigated experimentally and numerically as part of co-operative effort between the US Air Force Research Laboratory and the UK's Defense Evaluation & Research Agency (DERA). This manuscript reports the results of an experimental investigation of pulsed vortex generator jets (PVGJs) conducted at DERA's Boundary Layer Facility in Bedford. The focus of these tests was to investigate the influence of jet velocity, pulsing frequency, and duty cycle on the mean characteristics of the flowfield produced by a PVGJ in a turbulent boundary layer. The experiments were conducted in a zero-pressure-gradient flow at a freestream velocity of 32 m/s. The flowfield was explored using a three-component laser Doppler anemometry system, and the information is used to calculate local field properties such as velocity and vorticity as well as global parameters like total circulation. The data give insight into the effectiveness of the VGs in terms of location, strength, and persistence of the generated vortices and their influence on the boundary layer. While the planned computational simulation effort is in its infancy, preliminary steady-jet computational results are compared with the flow field data that has been acquired in the boundary layer facility.

LIST OF SYMBOLS

C_μ = blowing momentum coefficient, $\Delta\ VR^2\ (\pi d_{jet}^2/4S)$
d_{jet} = diameter of the jet (normal to jet velocity vector) = 1cm
ℓ = reference length
P = static pressure
q = dynamic pressure, $\frac{1}{2}\ \rho U^2$
Re = freestream unit Reynolds number, $\rho_\infty U_\infty \ell\ /\ \mu_\infty$
F^+ = dimensionless frequency, $f\ \ell\ /\ U_\infty$
S = reference area
T = temperature
U = mean velocity vector
u,v,w = mean Cartesian velocity components
VR = pulse velocity ratio, $V_{jet,max}/V_\infty$
x,y,z = Cartesian coordinates
y^+ = inner turbulent coordinate, yu_τ/ν; $u_\tau^2=\tau_w/\rho_w$
α = airfoil incidence or wing angle-of-attack
Γ = circulation (m^2/s)
Δ = pulse duty cycle, percentage of time that valve is open
δ = boundary layer thickness (where U=0.95U_∞)
δ_0 = reference boundary layer thickness, ~60mm
ν = molecular kinematic viscosity, μ/ρ
ρ = density
β_{VG} = skew angle, incidence of solid VG to freestream.

Subscripts
t = total condition
w = wall condition
∞ = free stream condition
0 = reference condition

1 INTRODUCTION

Separation control devices are used routinely on military, commercial, and general-aviation aircraft. The most common of these devices is the solid-vane vortex generator (VG), typically used on wings to improve flight characteristics during off-design operation. These surface-mounted VGs create vortices that travel over the upper surface bringing high-energy fluid from the free-stream into the boundary layer. This energizes the boundary layer making it much more resistant to flow separation. The separation point is forced further aft along the wing chord, or even eliminated. One operational benefit is that separation is delayed to higher angles of attack, increasing the maximum available lift for maneuver, or permitting flight at lower airspeeds with improved control authority.

While these devices are popular for the aerodynamic and handling improvements they provide, they are generally not an optimal solution. This is primarily due to their unalterable nature once they are installed, and their associated parasite drag. It would be advantageous to have a system that has the same benefits, but could be "deactivated" while not in use. Better yet would be a system that could be actively "tuned" to the specific operating condition to overcome whatever performance deficiency it is experiencing. One might also contemplate using separation to an advantage, if it could be reliably and predictably controlled in a closed-loop manner. These considerations have led to the development of numerous varieties of pneumatic VGs.

1.1 Pulsed Vortex Generator Jet Background

The pulsed vortex generator jet (PVGJ) concept for separation control was initially based on a previously developed method of producing streamwise vortices using transverse air jets, usually called vortex generator jets (VGJs). Since first conceived in the early 50's[1], steady-blowing techniques have been studied extensively[2,3,4,5,6] and are still being investigated today[7,8,9,10]. Most of the recent investigations have been aimed at optimizing the jet orientations and orifice shapes for specific applications. In this method, steady jets are pitched to the surface and skewed to the freestream to generate vortices somewhat similar to those produced by solid VGs. Early research showed that blowing through discrete jets located near the leading edge of an airfoil could impede separation. This is achieved by energizing the boundary layer through turbulent mixing of the high-speed external fluid into the low-speed boundary layer fluid, causing an increase in the boundary layer momentum flux. It has been shown that this interaction causes the formation of longitudinal vortices similar to those produced by solid VGs, which are largely responsible for the mixing and increased resistance to separation. Johnston[11] has recently published an excellent review paper of the progress made in this area.

Pulsing the jet was first considered as a means to reduce the mass-flow requirements of the steady jet, while possibly enhancing the mixing process. The PVGJ concept has been developed in various places for several specific applications. Its developmental history at the Air Force Research Laboratory (AFRL) has primarily been aimed at separation control over

Paper presented at the RTO AVT Symposium on "Active Control Technology for Enhanced Performance Operational Capabilities of Military Aircraft, Land Vehicles and Sea Vehicles", held in Braunschweig, Germany, 8-11 May 2000, and published in RTO MP-051.

wings and airfoils for enhanced maneuverability and off-design performance. Preliminary separation-control experiments were conducted under the Small Business Innovation Research program by McManus.[12] The primary objective of this program was to develop and test the PVGJ separation control system over a broad range of flight conditions on representative two- and three-dimensional aerodynamic surfaces. The aircraft application was control of the separation on a discontinuous leading edge flap.

Preliminary separation control experiments were conducted at low speeds on simple 'flat plate' airfoil with a 15° leading edge 'flap'[13,14]. The effects of jet diameter and spacing were examined for single and counter-rotating jet pairs located on the flap. The effects of pulsing amplitude and frequency, as well as the jet diameter spacing, were also evaluated. The time-dependent flow characteristics at the jet exit were characterized, but other diagnostics were limited to mean surface pressure measurements on the flat plate and pressure surveys of the wake.

More low speed experiments were conducted on a NACA-4412 airfoil with a flat leading edge flap to determine optimum pulsed jet operating conditions for airfoil stall suppression[15]. In these experiments, PVGJs effectively delayed stall on airfoil over large range of leading edge flap deflection angles. Compressible flow experiments were also performed at free stream Mach numbers from 0.3-0.6 on an SP215 airfoil that was modified to 'bend' at $0.25\,\bar{c}$ to form a leading edge flap. Results again indicated significant aerodynamic improvements at high angle-of-attack (α>12°) by reducing or eliminating separation. Lift was increased by up to 21% at M=0.4, and by as much as 14% at M=0.5. Lift-to-drag ratio (L/D) was increased by up to 35%.

Finally, low-speed tests were performed on a 7% scale 'lambda-wing-body configuration' fitted with embedded pneumatic jet actuators near the wing leading edge[16]. In these experiments, blowing coefficients (C_μ) of 0.007 were typical. Effectiveness was demonstrated for a range of flap settings for high-α. The system increased the maximum lift coefficient by as much as 7% and L/D by up to 17%. It was also demonstrated that asymmetric use of the pulsed jets could be used to produce substantial roll moment that increased monotonically with pulse intensity. Experiments have since been conducted[17] to study the use of PVGJs for *dynamic* stall.

All of these experiments, as well as the efforts of many others[18,19,20,21], have indicated that there is significant potential for pulsed jets and other oscillatory blowing techniques to suppress separation in a variety of environments. However, we have limited knowledge of how the time-dependent flowfield induced by the jet actually behaves, or how it interacts with the boundary layer to suppress separation more effectively than steady VGs, other than the flow visualizations of Johari & McManus[22]. In these experiments, effectiveness was quantified in terms of the degree of penetration of the jet fluid into the flow based on fluorescent dye and laser sheet visualizations.

Flow control device development and characterization are a significant part of the Aeronautical Sciences Division's technical activities in flow control.[23,24] An objective of these activities is to develop and demonstrate computational tools and analytical methods required to design active flow control systems. This will require the use of analytical models for flow control devices that are founded on a combination of theoretical, experimental, and numerical information. The experiments presented here were directed at establishing an experimental database to use in modeling and analysis efforts, and also to use as a baseline for extended computational fluid dynamics analyses. It is hoped that future CFD analysis of PVGJs will ultimately enhance our understanding of the physical mechanisms behind this form of separation control.

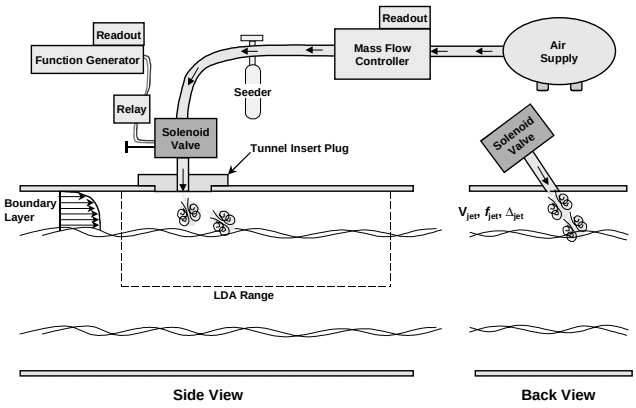


Figure 1: Schematic of experimental hardware setup.

1.2 Overview of Present Investigation

As part of a co-operative program between AFRL and the UK's Defense Evaluation & Research Agency (DERA), the flowfields around several active and passive flow control devices are being investigated. The goal of this collaboration has been to analytically and experimentally develop and validate sub-boundary layer flow control devices for future application on military aircraft wings. The AFRL share of this effort was conducted as part of a larger program aimed at improving the aerodynamic performance of military transport aircraft. This program is developing technologies necessary to develop transports to support the imminent 'Global Mobility' missions identified in the Air Force's *New World Vistas* (NWV) report.[25] The report advocates wing research which, it argues, could pay off in significantly higher aircraft efficiencies. It is our belief that emerging technologies in active flow control may provide significant improvements in aircraft performance that will extend beyond the NWV goals, enabling new classes of aircraft, and new mission capability.

Studies by DERA primarily have focused on micro-vane vortex generators and other passive sub-boundary layer flow control devices[26,27,28]. In these investigations, passive sub-boundary layer flow control devices have been tested, and limited CFD studies were conducted. In this partnership, the same experimental approaches are being used to quantify the aerodynamic effectiveness of the PVGJ active flow control concept, which has prior developmental history at AFRL.

This manuscript reports the results of the first effort in this collaboration. Specifically, recent experiments in the DERA Bedford Boundary Layer Facility directed at characterizing PVGJ flow control devices are discussed. The focus of these tests was to investigate the influence of jet velocity, pulsing frequency, and duty cycle on the mean characteristics of the flowfield produced by a PVGJ in a turbulent boundary layer. While the planned computational simulation effort is in its early stages, preliminary steady-jet solutions results are compared with the flow field data acquired in the boundary layer facility.

2 EXPERIMENTAL APPARATUS

2.1 Pulsed Jet Device

While several devices are being developed that are capable of producing pulsed jets for various applications, producing a PVGJ system suitable for controlled laboratory experiments can still be a challenge. Described below is a relatively simple apparatus that was developed and fabricated for the experiments.

The system used to generate the pulsed vortex generator jets in this experiment (Figure 1) was comprised of several off-the-shelf components. A large-volume tank supplied the pressurized air. The mean flow rate was regulated by a mass flow controller and monitored with digital readout. The pulsing was achieved with an industrial two-way solenoid valve (Figure 2). While these devices are not normally used for continuous operation, their rugged design and low response times of the smaller units

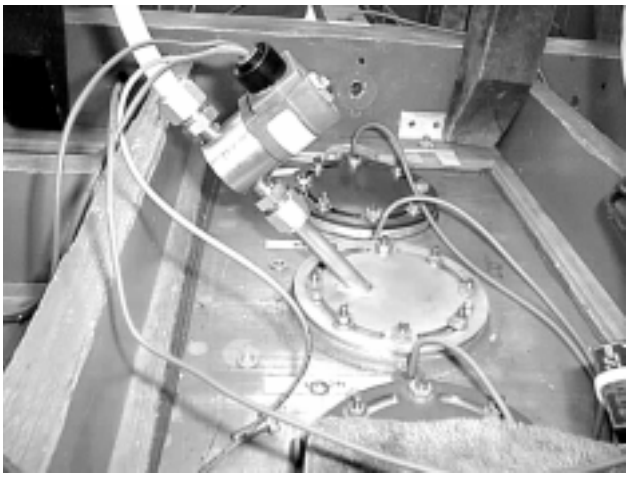


Figure 2: Photo of pulsed jet hardware used in experiment.

made them suitable for our purposes. The primary variables when selecting a valve are maximum flow rate, pressure capacity, and response time (maximum frequency). The tradeoff between size and momentum becomes significant. The larger the device is, the more sluggishly it will respond to the control signal, and sharp pulses have been found critical in previous experiments.[13] The solenoid valve chosen was a "normally closed" type that opened under AC voltage, and was pressure rated at 100psi.

The solenoid valve was controlled by a function generator that produces a square-wave voltage of appropriate magnitude and adjustable frequency and duty cycle. The usual US-UK power supply converters were also required. The valve was directly mounted to a short length of 1cm ID pipe that was run through a tunnel insert plug at 45° to the surface normal (Figure 2). The insert plug had been previously manufactured to fit into existing apertures in the ceiling of the DERA Boundary Layer Tunnel.

2.1.1 System Limitations

As mentioned above, the performance of the pulsing apparatus was primary limited by the solenoid's response time (which limited frequency and duty cycle) and the aperture size (which limited mass flow rate). The sustainable mass flow rate of the air supply was also a limitation. The maximum average mass flow that the system could maintain under any conditions was about 416slpm (0.0083 kg/sec). This yielded a maximum steady jet velocity of 88m/s. This translated to a maximum velocity ratio of 2.70 at the nominal tunnel conditions used.

It was found that if very long pulses (large duty cycles or low frequency) were attempted at high velocity ratios, the pressure in the feed line could not be maintained for the entire duration of a pulse. This caused flow to become very weak to non-existent toward the end of a pulse. Pulsing at very high frequency required the solenoid valve to respond at very short time intervals. The same limitation existed for very low duty cycles, since the response time required is proportional to Δ/f. Since the response-time of the valve was on the order of 4ms the shortest "on" cycle that we could expect the valve to achieve a relatively sharp square wave response to was about 15ms. This allowed a maximum operating frequency of 33Hz with a duty cycle of 50% (or 16Hz at 25%).

2.2 DERA Boundary Layer Facility

The experiments were conducted in DERA's Boundary Layer Facility in Bedford (Figure 3). This facility is an open-return tunnel with three 1.83m (6ft) long sections that are all 1.2m wide. The tunnel has a continuous flexible floor that permits a maximum height of 0.7m. While the adjustable floor allows the longitudinal pressure gradient to be manipulated, the present experiments have been conducted in a zero-pressure-gradient flow with a test section height of approximately 0.3m, and at a free-stream velocity of 32.6m/s. The third section is fitted with optical glass on one sidewall, and a large region of this section can be explored with a three-component laser Doppler anemometry (LDA) system to measure flowfield velocities. Flow control devices were mounted on the centerline of the tunnel roof, just downstream of the juncture between the second and third sections. In this configuration, the optical traverse could move the beams from about 10cm upstream to about 0.5m downstream of the devices.

A "jet catcher" is secured at the exit of the last section to diffuse the high velocity air to an acceptable level in the room. Physical access to the working-section is available through pairs of opening windows on either side of the tunnel. Due to the LDA seeding and tunnel noise, the manned data acquisition and control systems have been fitted outside the laboratory.

3 EXPERIMENTAL TECHNIQUES

This section will the outline the experimental techniques used to obtain raw flow data, as well as how the data was reduced to meaningful quantities representing the effectiveness of the control devices. The focus of these tests was to investigate the pulsed vortex generator jet (PVGJ) flow control device. Several pulsed and steady configurations were tested to investigate the effects of jet frequency, velocity, and duty cycle. Results from similar tests on conventional delta-vane VGs, which had been previously tested at several orientations to the flow, are used here as a baseline for comparison.

3.1 Laser Doppler Anemometer

Laser Doppler Anemometry (LDA) has been an established research technique for measuring flow velocity vectors for many years.[29] The technique uses pairs of similar intersecting laser beams defining a small measurement region in a flow. When correctly sized seeding particles are introduced into the flow stream and pass through the measurement region they reflect the probing laser beams as a short burst of light. The wavelength of this reflected light is slightly shifted proportionally to the particle velocity, due to the Doppler effect. If two similar laser beams with slightly different subtended angles to the flow illuminate the seeding particle, the Doppler shifted reflections can interfere and produce a fringe pattern within the reflected burst of light. With a known wavelength of the laser light and a known angle between the intersecting beams, a conversion factor between the Doppler frequency and the velocity can be calculated. The frequency of the fringe pattern is then measured, and the velocity component of the seeding particle perpendicular to the bisector of the two laser beams is determined. Using three correctly oriented pairs of interrogation laser beams of differing wavelength illuminating a single measurement region (and three photodetectors), it is possible to obtain three orthogonal velocity vectors at any given accessible position.

This technique has advantages over physical sensors like hot wires or pressure probes in that the only flow intrusion is that of the seeding particles used. It has been shown that for air-flow



Figure 3: DERA Bedford Boundary Layer Wind Tunnel

speeds up to Mach 2 spherical oil droplet seeding particles with diameters smaller than 2μm will follow the air flow direction without significant deviation. The method's particular advantages include: non-intrusive measurement, high spatial and temporal resolution, no need for calibration, insensitivity to temperature and pressure variations, and the ability to measure in reversing flows.[30] The advantages of this optical flow measurement technique over particle image velocimetry are the very high spatial and temporal resolution.

For each configuration tested, measurements were taken with the LDA at several planes downstream of the jet. This information was used as outlined below to calculate local field properties such as velocity and vorticity as well as global parameters like total circulation. The data give insight into the effectiveness of the VGs in terms of location, strength, and persistence of the generated vortices and their influence on the boundary layer.

3.2 Data Reduction

With the mean velocity information on planes behind the jet in hand, longitudinal vorticity can be calculated in the usual way

$$\omega_x = \frac{\partial w}{\partial y} - \frac{\partial v}{\partial z} \tag{1}$$

The total circulation over the x-plane can then be calculated by integrating the vorticity over the measurement plane.

$$\Gamma_x = \iint \omega_x \, dy \, dz = -\Gamma \tag{2}$$

Here, we have defined the circulation, Γ, as positive in the rotational direction of the primary vortex to avoid any confusion when comparing to data reduced with different choice of coordinate systems, and differing experimental device orientations. Several approaches to calculating these quantities were assessed; most of which used Amtec Engineering's *Tecplot*™ data visualization package[31] to some extent.

Since the region the flow that is influenced by the jet grows in the downstream direction, the data were generally obtained at varying spanwise locations and resolutions, and over dissimilarly sized and shaped regions. This caused the collected data to be somewhat "irregular". Throughout most of the data reduction, the irregular data at each plane were interpolated onto a "regular", or "structured" mesh. This associated each data point with its neighboring points, and consequently finite-difference methods could be applied in the normal way to calculate gradients (in Equation 1). These derivatives were calculated using built-in *Tecplot* functions (2^{nd}-order differencing). *Tecplot* integration functions were then used to calculate circulation (Equation 2). This entire process, including queries to the user regarding interpolation and plotting options, was incorporated in a single *Tecplot* macro.

Since this method was developed, Amtec Engineering's *CFD Analyzer* was available soon after, which automates the calculation of many flow variables, even on the unstructured data meshes. On a given grid, using the *CFD Analyzer* yielded the same results for vorticity and circulation that were calculated by the macro discussed above. The only differences were caused by the interpolation of the irregular data onto the regular grid. This interpolation process often helped to smoothly "fill in" spaced in the experimental data in a helpful way. However, at times it led to inconsistent estimates for field circulation, as will be discussed below.

In these experiments, the data were typically taken along vertical (*y*, normal to the wall) lines spaced 10mm apart in the lateral (*z*) direction. Each line of data had a resolution of 3.5-5.0mm, depending on the local flow gradients. In the results presented here, unless otherwise noted, the data were interpolated onto a regular mesh having resolutions of $\Delta z \times \Delta y$ =6.25×3.45mm, again depending on local flow gradients and the size of the interpolation region. At the highest jet velocity ratio (*VR*-4.60), the regular mesh had a resolution of 8.33×6.25mm.

4 NUMERICAL SIMULATION TECHNIQUE

The flowfield produced by steady and pulsed jets is also being numerically simulated using computational methods of varying complexity. All simulations completed to date under this effort have been for steady jets under tunnel conditions. The numerical results presented here were obtained by solving the Reynolds-averaged Navier-Stokes (RANS) equations, with the algebraic turbulence model of Baldwin and Lomax[32]. Solutions were obtained with a widely used commercial simulation package (*GASP*[33]), and the numerical results are compared to the experimental results. *GASP* is a fully conservative shock capturing code that has been widely used for the analysis of many types of flows.

4.1 Solution Strategy

The simulations were performed on relatively uncomplicated grids representing the jet issuing into a turbulent boundary layer. The entire computational mesh consisted of three computational zones, (the edges of which are shown in Figure 4) connected to each other by 2 zonal boundaries and was comprised of 575×10^3 cells. Flow information was passed through the zonal boundaries via five-point overlaps. To resolve the features of the flowfield near the jet and to provide the resolution required by the turbulence model, the grid was clustered near the jet and wall. At a location 0.2m ($20d_{jet}$) upstream of the jet, the wall grid spacing corresponded to a y^+ value of roughly 2.5, and 75% of the grid points were in the boundary layer. This dimensional wall spacing is maintained throughout the computational grid.

Adiabatic no-slip conditions and vanishing normal pressure gradient were enforced on the wall surface. The jet was modeled with a simple 'top hat' velocity profile, which has been shown to not to play a significant role in the developing vortex, provided the net momentum flux rate is maintained.[7] The jet flow was also assumed to be at ambient pressure and temperature. It was also assumed that tunnel was deep enough and wide enough to have minimal influence on the flowfield near the jet. Thus, flow variables were extrapolated from the interior at the downstream plane, and the Reimann invariants from characteristic theory are satisfied on the free-stream (top) boundary. Periodicity was imposed on the side planes to simulate a lateral row of distantly spaced co-rotating jets. Since the intent is to simulate the experiments, the data obtained from boundary layer surveys have been used for the numerical upstream boundary condition.

To allow for the specification of a two-dimensional upstream boundary condition obtained experimentally, the flow was simulated on a two-dimensional grid for a short distance (10cm) ahead of the three-dimensional simulation region. The LDA system allowed experimental data to be obtained very close to the wall, but not completely through the laminar sub-layer. The characteristics between y=0.32mm and the wall were obtained with a cubic interpolation to the no-slip wall. However, the two-dimensional region allowed the boundary layer to develop into a fully turbulent profile upstream of the three-dimensional region. Very little change in the boundary layer characteristics was

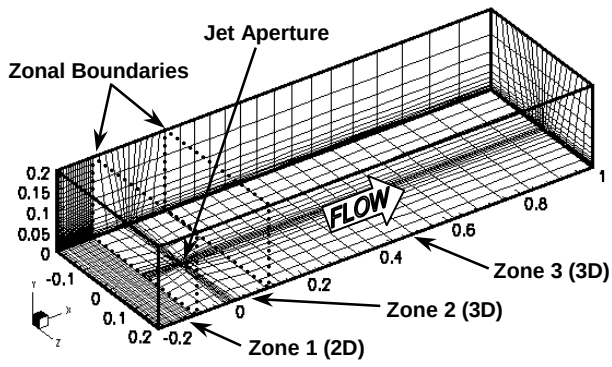


Figure 4: Grid features for numerical simulations.

observed through this region. A constant pressure was assumed through the upstream boundary layer. The two-dimensionality of the flow in the DERA Boundary Layer Facility has also been demonstrated (see Section 5.1).

Throughout the three-dimensional injection zone ($x \geq -10d$) the RANS equations were solved to 3rd-order spatial accuracy using Jacobi inner iterations[33]. The inviscid fluxes were split by the method of van Leer[34], and the min-mod limiter[35] was used. This region was comprised of two computational zones, containing a total of 574×10^3 cells.

4.2 Convergence Issues

A three-grid sequencing method was used where converged solutions were obtained on three grids of varying resolution. A converged solution is quickly obtained on the coarsest grid, then interpolated to a more refined grid. The solver is then restarted on this finer grid. In this case, groups of 8 cells (2×2×2) of the finest grid were combined to make the medium grid. This was done again to define the coarsest grid. This method not only accelerates solution convergence, but also affords an expedient means to evaluate grid consistency. Temporal convergence was demonstrated at each sequence by monitoring the progress of the solution as well as the residual vector and in time.

The computed vortical structures downstream of the jet increased in complexity and detail with each grid refinement. While the predicted flowfield was somewhat altered by the last grid refinement, the downstream flowfield and calculated forces the wall did not drastically change. Predicted integrated pressure forces over "Zone 3" normal to the surface for the two finest meshes were almost identical. However, there were 3.6% and 60% changes in the integrated lateral and longitudinal sheer stresses on the plate, respectively. This certainly indicates that grid convergence may not be achieved in the region of interest.

4.3 Computational Requirements

When using the mesh-sequencing scheme described above, the computational requirements for the calculations, both in terms of memory and computational effort, increase by approximately a factor of eight with each grid refinement. For the finest grid (574×10^3 cells), *GASP* required 7.3×10^6 Words of memory and 130 seconds/iteration on a Silicon Graphics R12000 processor.

5 RESULTS

While the floor of the tunnel is flexible to allow adjustable pressure gradients to be imposed, these experiments have been conducted with the tunnel floor tuned to maintain a flow with no longitudinal pressure gradient in the test section. While several pulsed and steady configurations were investigated to study the effects of jet pulsing frequency, velocity, and duty cycle, not every combination of parameters in Table 1 could be tested due to hardware limitations. Solid delta-vane vortex generators have previously been tested at several orientations to the flow, and are used here as a baseline for comparison.

Results obtained from the experiments and the preliminary CFD analysis are examined here with an eye toward quantifying the effectiveness of the devices based on the path, strength, and persistence of the generated vortices and their influence on the boundary layer.

5.1 Upstream Tunnel Conditions

The boundary layer was surveyed slightly upstream of the pulsed jet at several transverse locations to assess the two-dimensionality of the base flow, as well as to provide boundary conditions for numerical simulations. The measured boundary layer characteristics (Figure 5) are typical of a turbulent boundary layer under no streamwise pressure gradient.

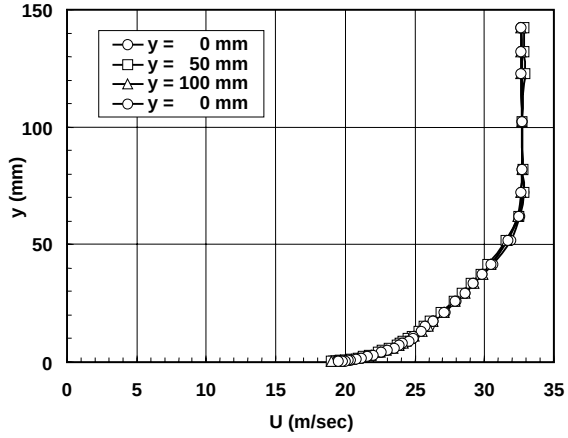
5.2 Conventional Delta Vortex Generator Vanes

To understand the desired behavior of traditional VGs, we first will examine the flowfield influenced by a solid delta-vane VG. A few of these traditional vane vortex generators, as well as many sub-boundary layer devices of varied shape and size, had been previously investigated at DERA. These experiments were conducted in the same facility, and under almost the same conditions (U_∞=32m/s, zero pressure gradient) as the pulsed jet studies. Vanes of varying shape, size, and orientation to the flow were assessed. The results discussed are for a delta-shaped vane with a 30mm height (h) and a 70mm length at the root (67° leading edge sweep). Data were taken with the LDA at several locations behind the vane. The data are examined here using the same methods used below to characterize the PVGJs. The solid-vane data are also used here to highlight the effects of different reduction methods on the calculated quantities.

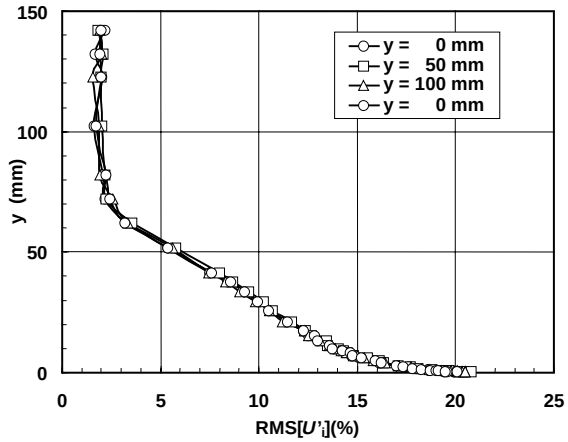
Table 1: Tunnel Conditions.

Parameter	Value
V	32.6 m/s
q	632 Pa
Re/ℓ	2.2×10^6 m^{-1}
T	294 K
f (Hz)	7.5, 15, 30
$F^+/\ell = f/U_\infty$ (m^{-1})	0.25,0.5,1.0
$VR = U_{jet}/U_\infty$	1.38, 1.84, 2.76, 4.60
Δ = Duty cycle	15, 25, 50,100%

From the field data obtained with the LDA system, we can compute the local longitudinal vorticity of the flow as discussed above. The longitudinal vorticity levels and secondary velocity vectors are shown in Figure 6 at four measurement planes downstream of the vane set at a skew angle of β_{VG}=20°. The longitudinal velocity contours are shown with secondary streamlines in Figure 7. The coordinate system origin is at the base of the fin trailing edge, with x in the longitudinal tunnel direction, and in the longitudinal tunnel direction, and y is in the direction normal to the wall. We observe that very near the vane, there are large positive and negative vorticity levels. In

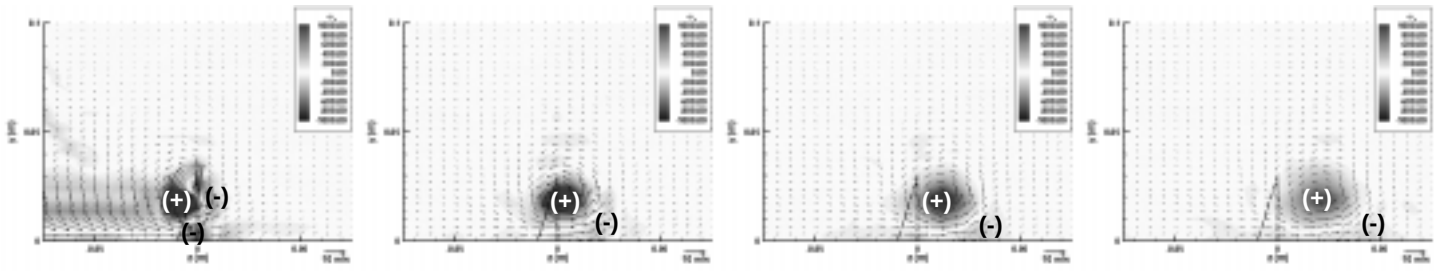


a) Mean longitudinal flow



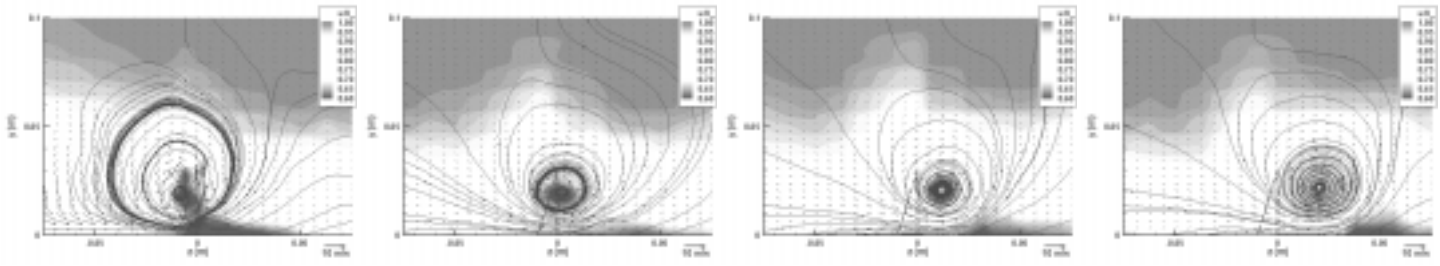
b) Turbulence intensity.

Figure 5: Measured upstream conditions (x = -10 d_j).



a) $x = 0.5h$ b) $x = 5h$ c) $x = 10h$ d) $x = 15h$

Figure 6: Longitudinal vorticity contours & secondary flow vectors. h=30mm; ℓ_{VG}=70mm; β_{VG}=20°.

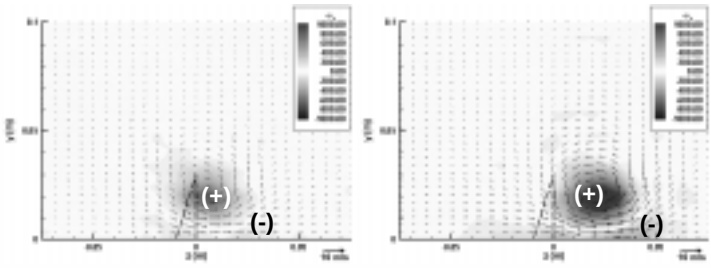


a) $x = 0.5h$ b) $x = 5h$ c) $x = 10h$ d) $x = 15h$

Figure 7: Longitudinal velocity contours, secondary streamlines. h=30mm; ℓ_{VG}=70mm; β_{VG}=20°.

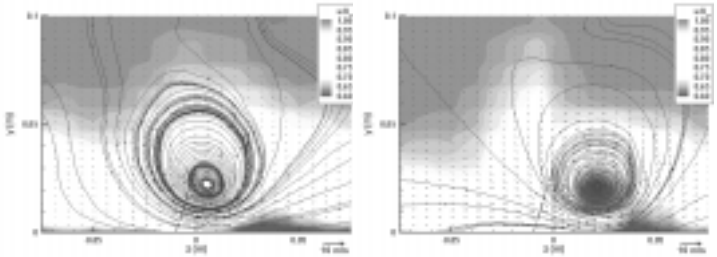
this region, the effects of the vane sweeping fluid positive z-direction very near the surface can still be seen. As the vortex travels downstream, it evolves into a single coherent structure of positive circulation (+), accompanied by a much smaller and weaker region of negative circulation (–). The primary vortex is established at about 0.7h from the surface, and maintains this elevation as it proceeds downstream. The vortex continues to move laterally in the direction of the vane skew. Note that the peak vorticity is monotonically decreasing downstream.

The velocity contours (Figure 7) indicate that the presence of the vane significantly distorts the outer boundary layer edge. The inner boundary layer is noticeably energized on the down-flow side of the vortex, as it pulls high-energy flow in from the freestream. As discussed earlier, this is the primary mechanism for stabilizing the boundary layer, and making it more resistant to separation. A significant region of low-energy fluid is also observed in the upwash region.



a) β_{VG}=10° b) β_{VG}=30°

Figure 8: Effect of skew angle for a solid vane VG at x= 10h. Longitudinal vorticity contours & secondary flow vectors.



a) β_{VG}=10° b) β_{VG}=30°

Figure 9: Effect of skew angle for a solid vane VG at x= 10h. Longitudinal velocity contours & secondary streamlines.

As the vane VG is skewed to higher incidence angles, the primary vortex is strengthened, and is swept further in the lateral direction (*cf* Figure 8 & Figure 6c). We also see more of an effect on the boundary layer at higher incidences (*cf* Figure 9 & Figure 7c). However, the primary vortex is maintains about the same elevation (0.7h) for all cases. Only at the highest skew angle are any regions of significant negative vorticity observed, and only very near the wall (Figure 8b).

Integrating the vorticity over these planes to estimate total longitudinal circulation for VGs set at varying skew angles yields the expected results. The total circulation of a vane VG generally increases monotonically with increased skew angle to the freestream. (Figure 10). Note also that the total circulation dissipates in the downstream direction, and very rapidly in the region very near VGs when they are highly skewed.

Other procedures were also used to extract vorticity and circulation from the experimental data. The simplest of these methods was to use a line integral from the wall, through the vortex core, and out of the boundary layer. Providing that you know the lateral (z) location of the vortex, this estimate could be calculated using a single line of LDA data. For the vane VGs, this simple method produced roughly the same trends in circulation. Exceptions occurred very near the fin in the β_{VG}=20° case, where extrapolation of the unusually limited data set (for x<2cm) resulted in an exaggerated estimate of total circulation (see Figure 6a). Also, at high skew angles, it is typical for line integration to yield higher circulation estimates that whole-field integration, since this method neglects the region of negative fringe that appears on the up-flow side of the

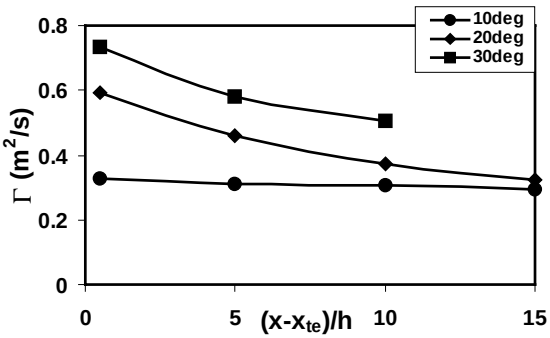
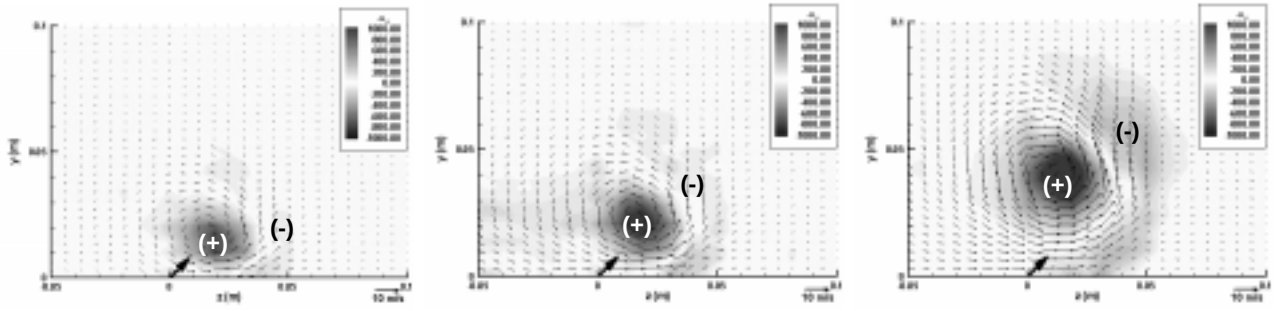
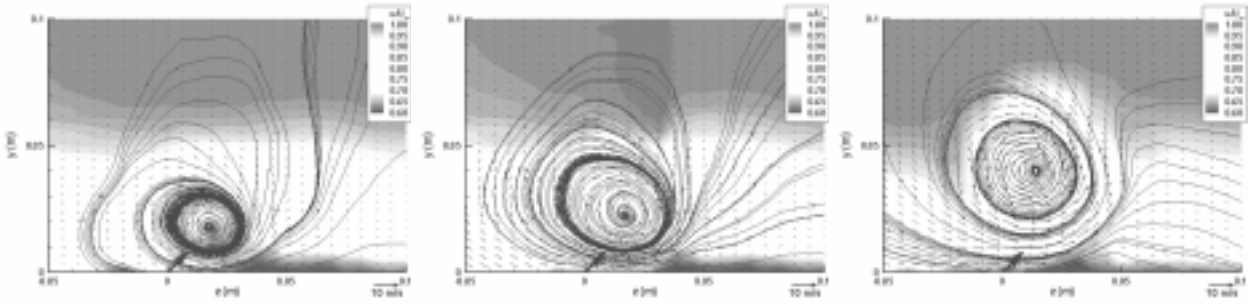


Figure 10: Trend in total longitudinal circulation for a 30mm×70mm delta-vane vortex generator.



a) *VR* = 1.38 b) *VR* = 1.84 c) *VR* = 2.70

Figure 12: Effect of blowing rate for steady jet. Longitudinal vorticity contours & secondary flow vectors, *x*= 20*d*.



a) *VR* = 1.38 b) *VR* = 1.84 c) *VR* = 2.70

Figure 13: Effect of blowing rate for steady jet. Longitudinal velocity contours & secondary streamlines, *x*= 20*d*.

vortex. For the highest skew angle shown, the line integration method resulted in higher circulation than field integration on either the raw data (*CFD Analyzer*) or the interpolated data (Figure 11). As will be shown below, this "fringe vorticity" is often a major feature of the pulsed jet flowfield.

In summary, for solid vane vortex generators, the VG height determines the primary vortex elevation. The skew determines the vortex strength and lateral path. The strength of the vortex decreases monotonically in the downstream direction.

5.3 Steady Jet

A steady jet was first studied to provide a baseline for the pulsed jet results to be judged against, as well as to assess the influence of blowing magnitude independently. The blowing rate was varied from very low (*VR*=1.38) to the maximum that the air supply and flow meter could sustain.

The longitudinal vorticity and velocity fields are shown in Figure 12 and Figure 13, respectively, for a plane at *x*=20*d* for three different steady jet velocities. We can see that blowing rate has a direct impact on the location and initial strength of the primary vortex. This vortex, in turn, directly impacts the boundary layer by bringing high-energy fluid toward the wall. We can see qualitatively that the overall effect on the flowfield is somewhat proportional to the blowing magnitude.

Integrating the vorticity over the entire plane, indicates that the total circulation does not necessarily increase monotonically with increased blowing intensity (Figure 14a). If we simply judge effectiveness based on the total circulation produced by a vortex generator, we could overlook important attributes of the flowfield. If we limit the field of circulation integration to only regions of positive vorticity, we can isolate the influence of the primary vortex that is responsible for energizing the boundary layer, calculating its strength independently of secondary vortices. Doing so for the steady-jet measurements indicates that the primary vortex circulation does indeed increase monotonically with increased blowing intensity (Figure 14b). Identifying the proper 'measure of merit' to evaluate the *effectiveness* of varying types of vortex generators, without actually applying them to a separating flow, has not been as straight forward as one might hope.

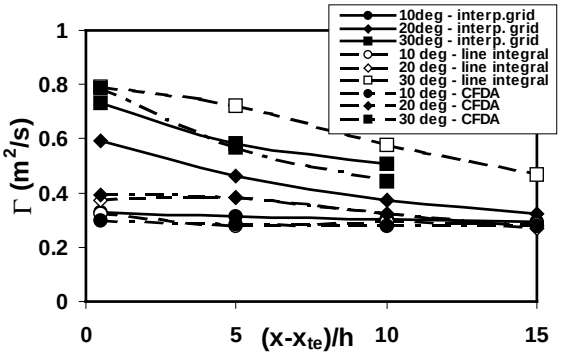
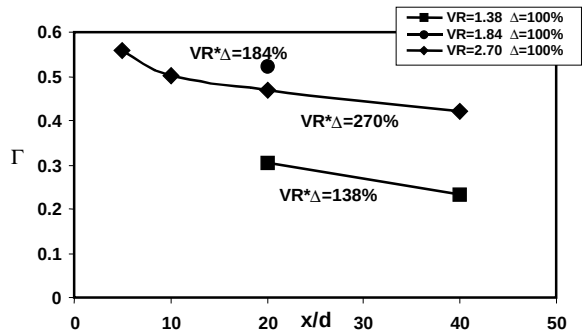
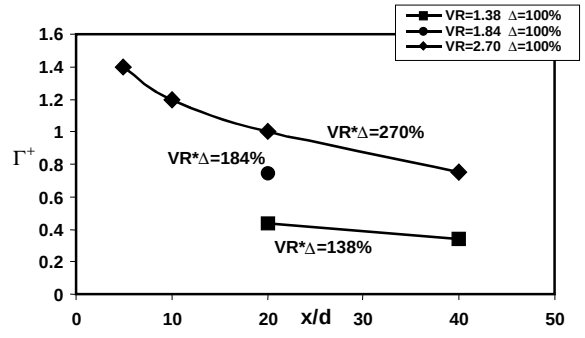


Figure 11: Effect of data reduction method on calculated circulation for 30×70mm vane vortex generator.

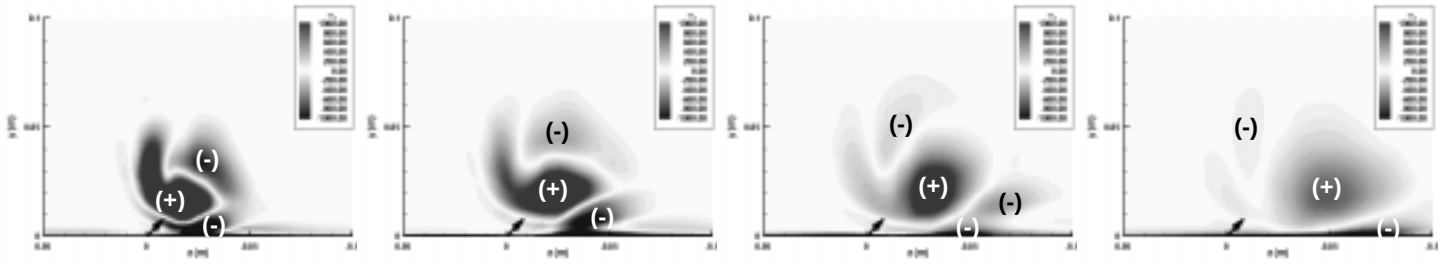


a) Total circulation, Γ_x



a) Positive part of circulation, Γ_x^+

Figure 14: Effect of blowing rate on longitudinal circulation.



a) $x = 5d$ b) $x = 10d$ c) $x = 20d$ d) $x = 40d$

Figure 15: Computed Longitudinal vorticity contours for steady jet at *VR*=2.7.

The computational results are thus far limited to steady-state solutions of the RANS equations for steady-jet simulations. While the computational domain extends beyond the measurable region of the flowfield in the tunnel, only the measurable region is examined here. Note that in these simulations, the jet was directed at a 45° inclination from the *negative z*-axis. This is unfortunately in the opposite *z* direction than in the experiments.

The basic character of the predicted flowfield is much as reasoned by early research based on surface flow visualizations and intrusive experimental methods (Figure 16). Two vortices are initially created, as by a jet issuing normal to the surface. However, the vortex on the obtuse side of the jet is strengthened by the enhanced entrainment, and remains closer to the surface (Figure 15 & Figure 17). This vortex remains close to the surface, as the other moves away and dissipates. Ultimately only the stronger vortex remains, trailing close to the surface.

The simple algebraic turbulence model used does not account for the turbulent mixing of the jet itself, and is not capable of predicting the increased mixing caused by the jet. The turbulence of the jet flow itself is also overlooked. The net effects can be seen in the predicted vorticity field (Figure 15), which has many dissimilarities to vorticity field deduced from the experimental data. Most noticeable difference is that the predicted path of the primary vortex is too close to the wall. The predicted vortex trajectory is also too highly swept with respect to the freestream. The periodic boundary condition, which actually simulated an infinite lateral row of co-rotating jets spaced at 40*d*, may be at least partially responsible for this.

Having said that, using this simple turbulence model did produce much more reasonable solutions than similar laminar predictions in which mixing was almost nonexistent. The primary expected features were predicted, and the overall effect on the boundary layer was rational.

The computed surface streamlines (Figure 18) are very similar to those computed by Zhang[7], who used a much more sophisticated turbulence model for the same jet geometry at a *VR*=2. They were calculated by seeding streamtrace particles in the first plane of data away from the wall, and constraining them to remain in that plane. It can be seen here that the primary vortex does not actually originate on the surface. The solutions reveal that most of the fluid in the primary vortex actually originates in the boundary layer ahead of the jet, passes very near the jet on the obtuse side, and is then entrained into the vortex.

Solutions have also been obtained at other jet velocities, and computations using two-equation turbulence models are underway. Based on the tentative success of these investigations, the next steps will include unsteady time-accurate simulations of the pulsed and steady jets. Since turbulence is a major contributor toward mixing, it is likely that successful time-accurate simulations of the PVGJ will require a better turbulence model. Two-equation (*k*-ε), algebraic Reynolds stress, and the Reynolds stress transport model have all been successfully used to simulate the steady jet flow field[7]. Of these, the latter was superior, provided that a good description of the upstream turbulent kinetic energy distribution was used.

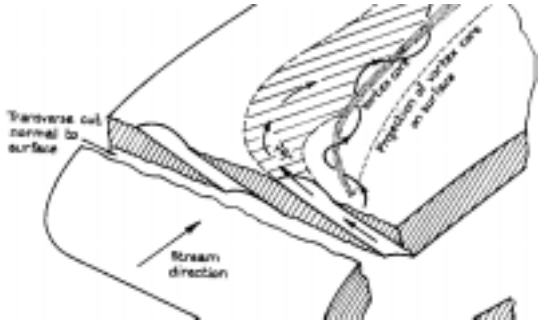
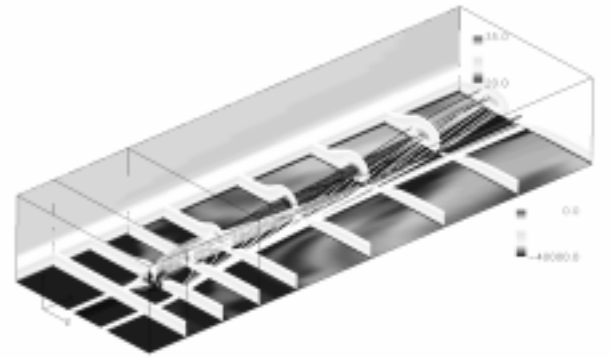


Figure 16: Sketch of steady VGJ flowfield (from reference 3).



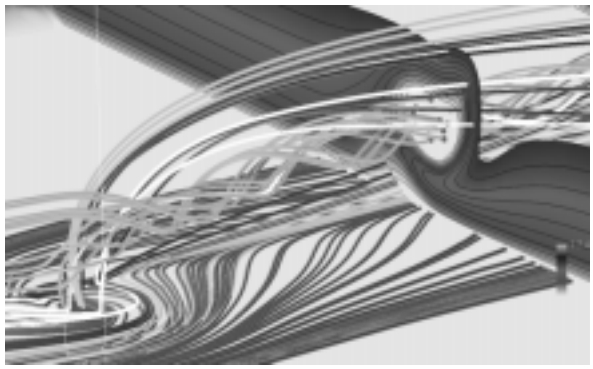


Figure 17: Computed flowfield for *VR*=2.7 steady jet.

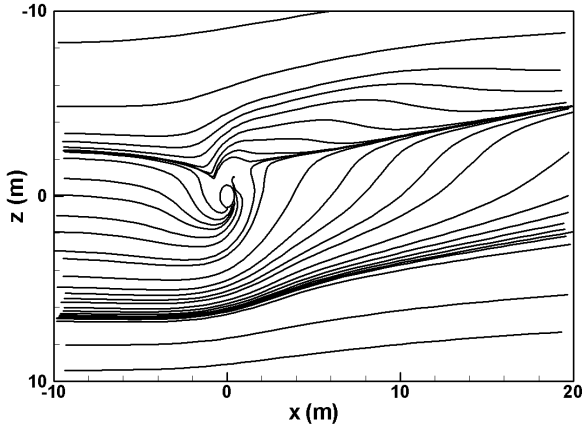
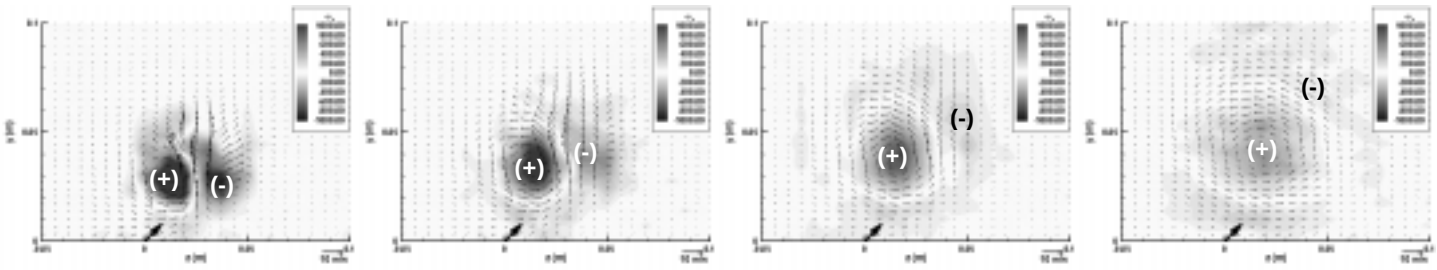
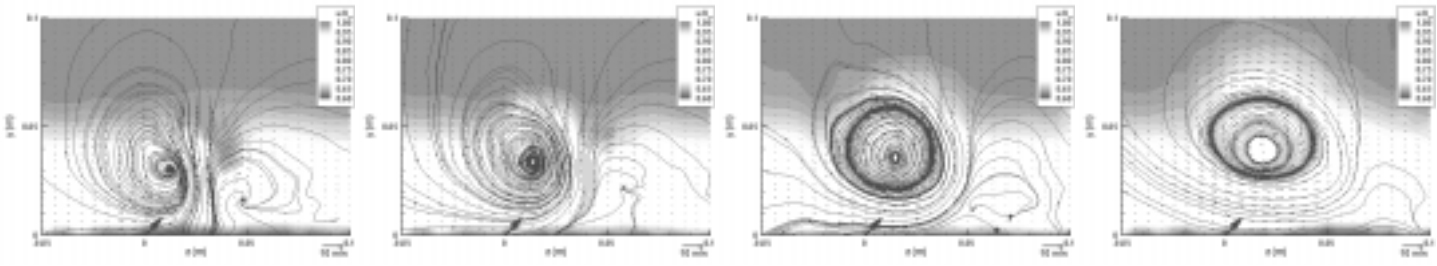


Figure 18: Computed surface limited streamlines (surface flow). *VR*=2.7 steady jet.



a) $x = 5d$ b) $x = 10d$ c) $x = 20d$ d) $x = 40d$

Figure 19: Longitudinal vorticity contours & secondary flow vectors. f =15Hz (F_x^+/ℓ = 0.5/m); VR=2.76; Δ=25%.



a) $x = 5d$ b) $x = 10d$ c) $x = 20d$ d) $x = 40d$

Figure 20: Longitudinal velocity contours, secondary streamlines. f =15Hz (F_x^+/ℓ = 0.5/m); VR=2.76; Δ=25%.

5.4 Pulsed Jet

If we want to increase the power of the steady jet, there are two obvious methods. We could simply blow harder (at higher velocity), or we could modulate (pulse) the flow. The latter alternative would enable a higher maximum jet velocity at the same average mass flow. Perhaps equivalent or superior performance could even be achieved at a reduced mass flow by pulsing at the same maximum velocity.

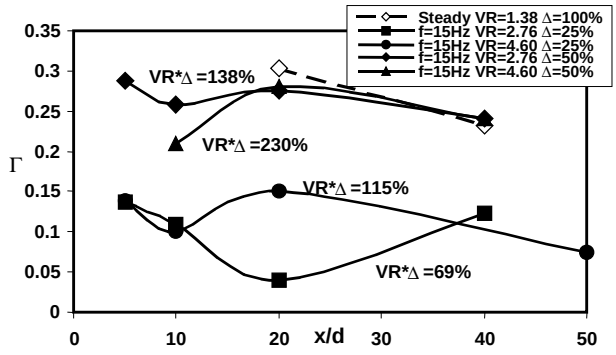
It is important to note that though this is a very dynamic time-varying flowfield, the results presented here are mean (time averaged) values. To extract unsteady phase-locked values or even dependable turbulence information at an equivalent number of locations would have required much more data to be taken. In the time since these experiments were conducted, the facility has been equipped with a much more powerful laser, putting turbulence quantities within reach in future experiments.

5.4.1 General Effects of Pulsed Blowing

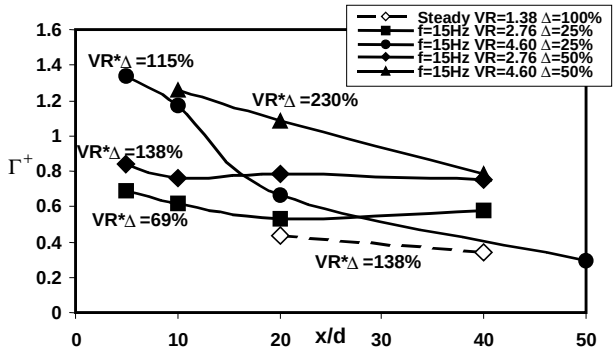
We will first examine a typical case of an acceptably effective pulse velocity, at a moderate frequency and representative duty cycle (f=15Hz, VR=2.76, Δ=25%). In Figure 19, the mean longitudinal vorticity levels and secondary velocity vectors are shown at four measurement planes downstream of the jet. The longitudinal velocity contours are shown with secondary streamlines in Figure 20. It is observed that very near the jet, there are large positive and negative vorticity levels, very similar to those observed near the solid VG shown above. However, in this case, the primary vortex is established slightly higher in the boundary layer, and it moves slowly away from the wall as it proceeds downstream. It is also seen that the peak vorticity level in the growing primary vortex (marked with (+)) is decreasing as it the observation plane is moved downstream. However, the negative vorticity "fringe" appears to vanish almost completely by the last measurement station. The sum effect is that the total longitudinal circulation is actually *increasing* at the end of the measurement region (Figure 21a). This phenomenon is not at all typical of steady vortex generation devices, including steady blowing. However, if we limit the field of integration to the region of positive vorticity, we observe the dissipative behavior similar to solid vanes (Figure 21b).

Examining the velocity contours at these planes (Figure 20) indicates that it is affecting the outer boundary layer in a similar manner as solid VGs, but seems to be affecting the inner boundary layer less. It is difficult to make definitive conclusions regarding inner boundary layer behavior and stability based solely on these data.

Comparing to steady blowing at twice the mean flow rate (VR=1.38), we have decreased the total longitudinal circulation proportionally to the reduction in mean mass flow rate (Figure 21a). However, we have actually *increased* the circulation in the primary vortex significantly (Figure 21b). This apparent contradiction is due to the negative vorticity in the pulsed jet case that is not significant under the influence of the steady jet at this velocity ratio (*cf* Figure 19c & Figure 12a). Also, the pulsing has moved the vortex core significantly farther away from the wall. It has been observed in these experiments that the primary influence on the position of this vortex is the maximum jet velocity, whether the jet is pulsed or not.

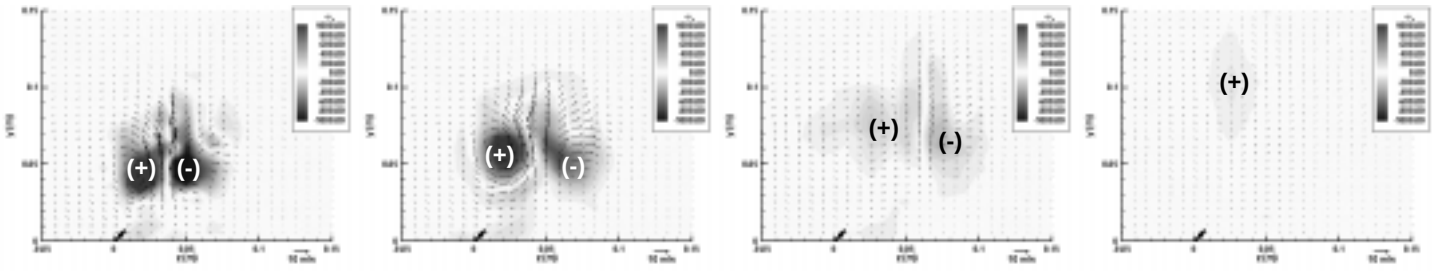


a) Total circulation, Γ



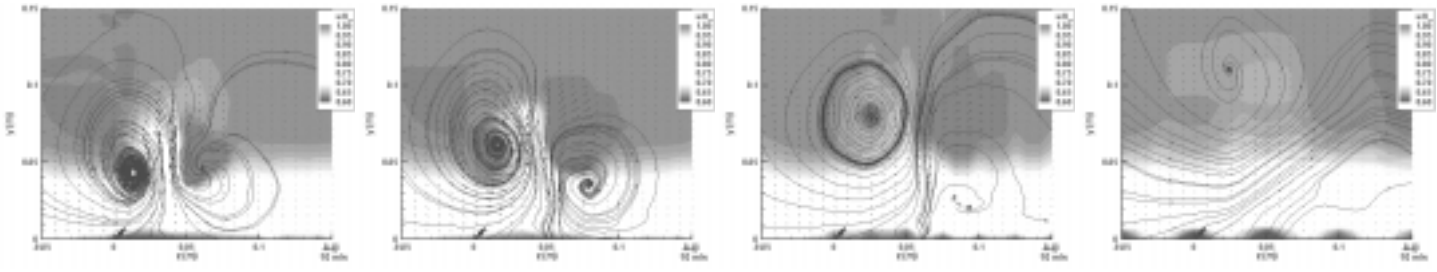
b) Positive part of circulation, Γ^+

Figure 21: Longitudinal trend in total longitudinal circulation. f =15Hz (F_x^+/ℓ = 0.5/m)



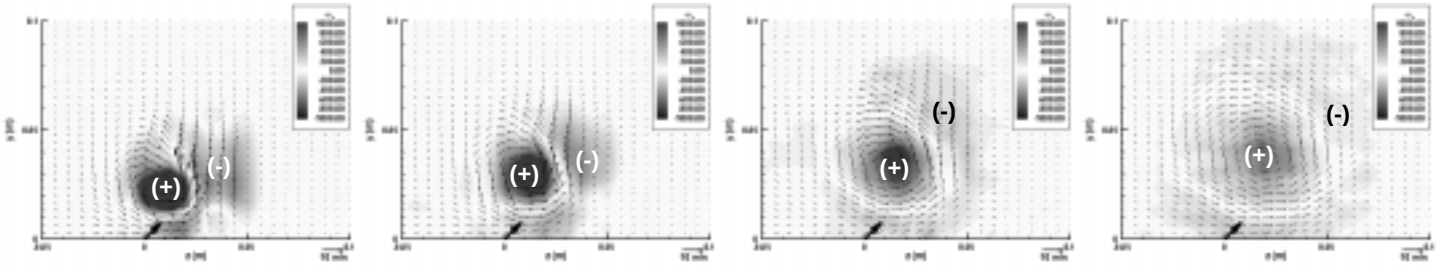
a) $x = 5d$ b) $x = 10d$ c) $x = 20d$ d) $x = 50d$

Figure 22: Longitudinal vorticity contours & secondary flow vectors. f=15Hz (F_x^+/ℓ = 0.5/m); VR=4.60; Δ=25%.



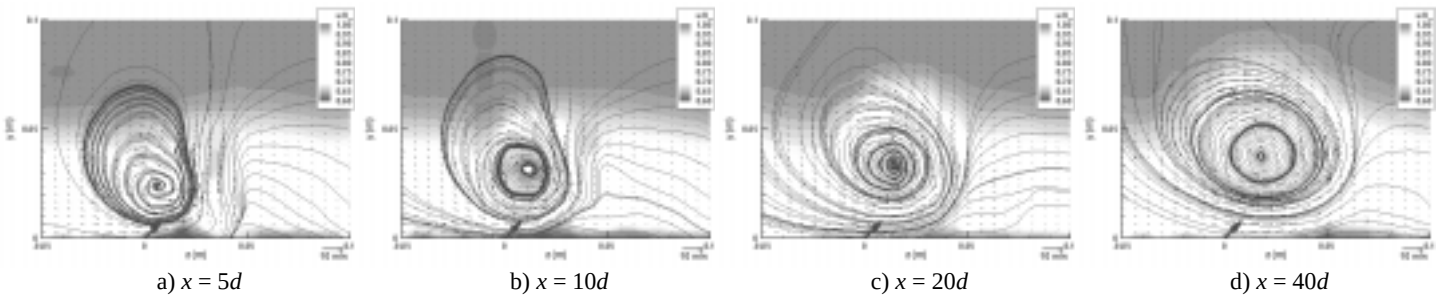
a) $x = 5d$ b) $x = 10d$ c) $x = 20d$ d) $x = 50d$

Figure 23: Longitudinal velocity contours & secondary streamlines. f=15Hz (F_x^+/ℓ = 0.5/m); VR=4.60; Δ=25%.



a) $x = 5d$ b) $x = 10d$ c) $x = 20d$ d) $x = 40d$

Figure 24: Longitudinal vorticity contours & secondary flow vectors. f=15Hz (F_x^+/ℓ = 0.5/m); VR=2.76; Δ=50%.



a) $x = 5d$ b) $x = 10d$ c) $x = 20d$ d) $x = 40d$

Figure 25: Longitudinal velocity contours & secondary streamlines. f=15Hz (F_x^+/ℓ = 0.5/m); VR=2.76; Δ=50%.

5.4.2 Stronger Pulses

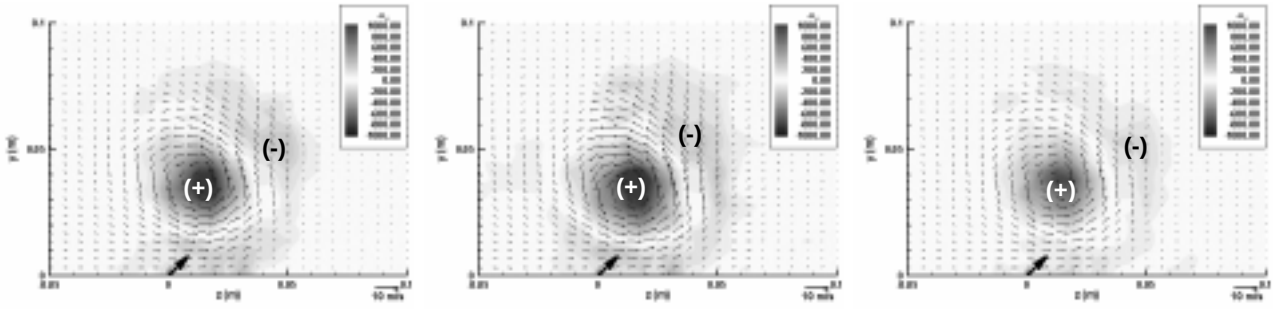
Using the unsteady case described above as a point of reference; there are a limited number of ways that we can attempt to increase the effectiveness of the PVGJ. Perhaps one's first thought is to simply blow harder. The destructive effects of increasing the blowing magnitude too much (VR=4.60) are apparent in Figure 22 & Figure 23. The calculated total circulation values (Figure 21a), imply that the vortex starts out about the same strength but quickly grows stronger than the VR=2.76 case. However, as seen in Figure 23, the vortex's trajectory soon takes it completely out of the boundary layer where it is overcome by the freestream momentum, then quickly dissipates (Figure 21).

5.4.3 Longer Pulses

We could instead attempt to increase effectiveness by increasing the duty cycle. Doubling the duty cycle (to Δ=50%) effectively doubles the total mass-flow rate from the jet. In doing so, we observe that the vortex is no longer ejected from the boundary layer, even though the overall mass flow rate is a bit higher than the previous case. (Figure 25). The vortex maintains essentially the same trajectory as it did at half the duty cycle (Δ=25%), though the overall circulation has approximately doubled (Figure 21). Note however, that the circulation is again *decreasing* by the time it gets 40d downstream of the jet. Also, there is only a 35-45% increase in primary vortex circulation at a cost of 100% more mass flow rate (Figure 21b)

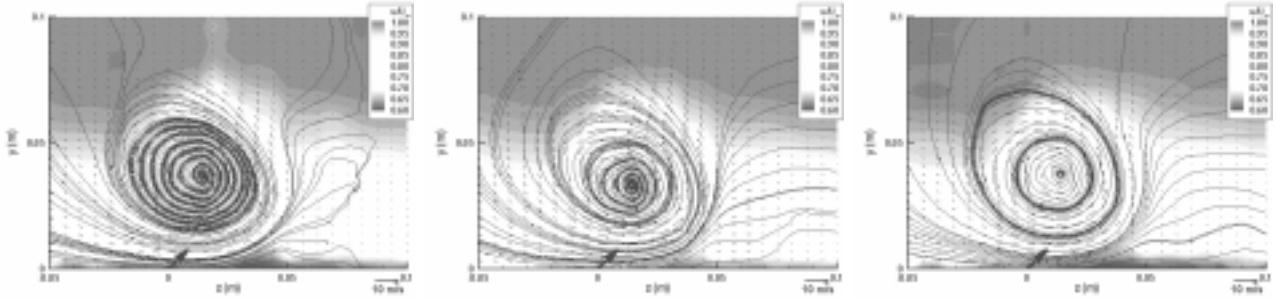
5.4.4 Stronger and Longer Pulses

The effects of increasing both the jet velocity and the duty cycle simultaneously were also examined at the same frequency (VR=4.6, Δ=50%). This produced nearly the same total circulation as only 60% the velocity (Section 5.4.1) and mass flow, at the same duty cycle (Figure 21a). The primary vortex circulation starts at about the same level as it did for the same velocity ratio at half the duty cycle (Figure 21b). This high circulation level was sustained for a slightly longer distance, but ultimately was dissipated at a similar rate. By the x=40d location, the primary vortex was no stronger than it was for the same duty cycle at 60% the jet velocity (Section 5.4.3), and dissipating much more rapidly.



a) f =7Hz (F_x^+/ℓ = 0.25/m) b) f =15Hz (F_x^+/ℓ = 0.5/m) c) f =30Hz (F_x^+/ℓ = 1.0/m)

Figure 26: Longitudinal vorticity contours & secondary flow vectors. x=20d; VR=2.76; Δ=50%.



a) f =7Hz (F_x^+/ℓ = 0.25/m) b) f =15Hz (F_x^+/ℓ = 0.5/m) c) f =30Hz (F_x^+/ℓ = 1.0/m)

Figure 27: Longitudinal velocity contours, secondary streamlines. x=20d; VR=2.76; Δ=50%.

5.4.5 Effects of Frequency

It is understood from past experience that frequency is a major factor when controlling separation in flows having dominant length scales. For example, in the case of trailing edge separation on an airfoil, the distance from the actuator to the trailing edge is the critical length scale that the frequency must be 'tuned' to. In this experiment there is no length scale, or even separation, to control. However, there did appear to be optimum frequencies for both generating circulation in the primary vortices, and maintaining it.

Using only the cases where VR*Δ=138% (constant mass flow rate) for comparison, the time-averaged primary vortex position and boundary layer edge profile remain relatively unchanged over the range of frequency tested (Figure 27). The pulsed vortex does have a substantially different path than for the steady jet though (*cf* Figure 12a). The total circulation is also relatively unaffected, and at no frequency was the total circulation greater that for the steady case (Figure 28a). However, pulsing always generated a stronger primary vortex than the steady jet (Figure 28b). There is significant variation due to frequency in the primary vortex circulation, with 15Hz clearly superior to the other frequencies investigated.

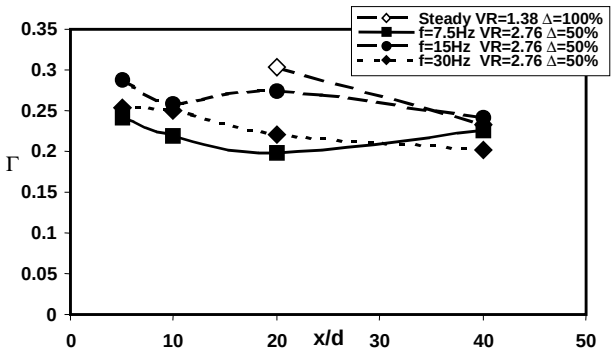
6 CONCLUDING REMARKS

Based on these experiments, we can make a few general observations about the effects of various jet parameters on the PVGJ flowfield, and its effect on an attached boundary layer.

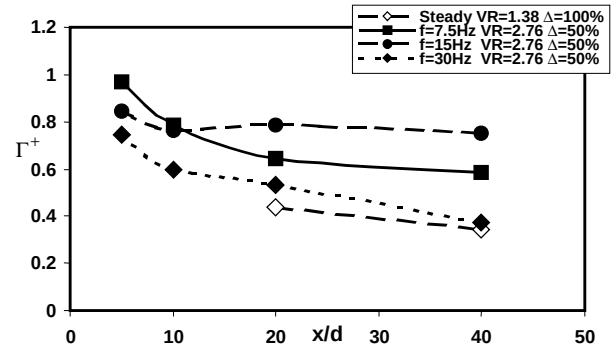
The path of the primary vortices appears to be primarily a function of the maximum pulse velocity, or the velocity ratio. On can certainly blow too little to have an appreciable effect. Conversely, to high of jet velocity can be applied, forcing the resultant vortices out of the boundary layer, resulting in great losses in effectiveness. Persistence of the circulation requires the vortex to remain in the boundary layer. If the vortex pulses leave the confines of the boundary layer, they are quickly overcome by the freestream momentum and dissipated.

The analysis has raised questions as to what might be the best 'measure-of-merit' for PVGJs in an un-separated flow. Basing judgments of effectiveness on the total circulation produced by a vortex generator can lead to different conclusions that looking at only the strength of the primary vortex, which is responsible for energizing the boundary layer.

Strength of the primary vortex is essentially a function of the time-average mass flow rate (i.e. the time-averaged energy that is being added to the flow). Pulsing is effective way to produce persistent vortices while greatly reducing mass flow. Pulsing significantly increases the strength of the primary vortex. For example, pulsing the jet at 50% duty resulted as much as twice the mean circulation in the primary vortex as steady blowing at the same average mass flow rate. When the duty cycle was reduced to 25% at the same pulse velocity, the primary vortex was still stronger that the steady jet, was more persistent, and required half the mass flow rate.



a) Total circulation, Γ



a) Positive part of circulation, Γ^+

Figure 28: Effect of frequency on longitudinal circulation.

7 FUTURE DIRECTION

The results from this boundary layer investigation have already been used to guide further validation work in a large-scale high-speed demonstration of separation control. Here, the PVGJ concept was integrated into an existing airfoil model (the DERA M2303) for a slightly different application for separation control. The primary emphasis was on reducing the loss of lift and drag rise due to shock-induced separation on transonic airfoils. These high Reynolds number transonic (M≈0.7) tests were conducted in the DERA Bedford 8ft×8ft High Speed Tunnel. Passive sub-boundary layer control devices developed at DERA were also investigated. These techniques offer a large potential for reducing boundary layer flow separation (and thus drag) behind the upper surface shock wave.

Future goals of the PVGJ analysis discussed in this paper include continuing the CFD effort to include unsteady time-accurate simulations of the pulsed and steady jets. Since turbulence is a major contributor toward mixing, it is likely that successful time-accurate simulations of the PVGJ will require a better turbulence model. Two-equation (k-ε), algebraic Reynolds stress, and the Reynolds stress transport model have all been successfully used to simulate the mean flow field[7]. Of these the latter was superior provided that a good description of the upstream turbulent kinetic energy distribution was used. A reduced order modeling effort is also being initiated, which will use the experimental and computational results to develop analytical models for PVGJs to be used in design studies.

REFERENCES

[1]Wallis. R.A., "The Use of Air Jets for Boundary Layer Control," Aero. Note 110, Aerodynamics Research Laboratories, Melbourne, Australia, Jan 1952.

[2]Wallis. R.A., "A Preliminary Note on a Modified Type of Air-Jet for Boundary Layer Control," Current Paper No. 513, Aeronautical Research Council, Australia, 1960.

[3]Pearcey, H.H., "Shock Induced Separation and its Prevention," in *Boundary Layer & Flow Control, Vol. 2*, Ed. G.V Lachmann, Pergamon Press, New York, pp. 1170-1344, 1961.

[4]Johnston, J.P., & Nishi, M., "Vortex Generator Jets – A Means for Flow Separation Control," *AIAA Journal*, 28:989, 1990.

[5]Compton, D.A., & Johnston, J.P., "Streamwise Vortex Production by Pitched and Skewed Jets in a Turbulent Boundary Layer," *AIAA Journal*, 30:640, 1992.

[6]Selby, G.V., Lin, J.C., & Howard, F.G., "Control of Low-Speed Turbulent Separated Flow Using Jet Vortex Generators," *Experiments in Fluids*, 12:394, 1992.

[7]Zhang, X., Zhang, H-L, & Collins, M.W., "Some Aspects of Streamwise Vortex Production Using Air Jets," *AIAA-96-0209*, January 1996.

[8]Peake, D.J., Henry, F.S., & Pearcey, H.H., "Viscous Flow Control with Air-Jet Vortex Generators," *AIAA-99-3175*, June 1999.

[9]Hasegawa, H., Matsuuchi, K., & Tanaka, J., "Development of an Active Separation Control System Using Vortex Generator Jets," 3rd ASME/JSME Joint Fluid Engineering Conference, *FEDSM99-6944*, San Francisco, California, July 18-23 1999.

[10]Khan, Z.U. & Johnston, J.P., "On Vortex Generating Jets," *1st International Symposium on Turbulence and Shear Flow Phenomena*, Santa Barbara, Sept. 12-15 1999.

[11]Johnston, J.P., "Pitched and Skewed Vortex Generator Jets for Control of Turbulent Boundary Layer Separation: a Review," 3rd ASME/JSME Joint Fluids Engineering Conference, *FEDSM99-6917*, San Francisco, CA, July 18-22 1999.

[12]McManus, K., et al., "Pulsed Vortex Generator Jets for Active Control of Flow Separation," AFRL Technical Report *AFRL-VA-WP-TR-1998-3082*, November 1997.

[13]McManus, K., Joshi, P.B., Legner, H.H., & Davis, S.J., "Active Control of Aerodynamic Stall Using Pulsed Jet Actuators," *AIAA-95-2187*, June 1995.

[14]McManus, K., Ducharme, A., Goldley, C., & Magill, J., "Pulsed Jet Actuators for Suppressing Flow Separation," *AIAA-96-0422*, January 1996.

[15]McManus, K. & Magill, J., "Separation Control in Incompressible and Compressible Flows using Pulsed Jets," *AIAA-96-1948*, June 1996.

[16]McManus, K. & Magill, J., "Airfoil Performance Enhancement Using Pulsed Jet Separation Control," *AIAA 97-1971*, June 1997.

[17]Magill, J. & McManus, K., "Control of Dynamic Stall using Pulsed Vortex Generator Jets," *AIAA 98-0675*, January 1998.

[18]Seifert, A., Bachar, T., Koss, D., Shepshelovich, M., & Wygnanski, I., "Oscillatory Blowing, a Tool to Delay Boundary Layer Separation," *AIAA Journal*, 31:11, pp.2052-2060, 1993.

[19]Seifert, A., Darabi, A., & Wygnanski, I., "On the Delay of Airfoil Stall by Periodic Excitation," *Journal of Aircraft*, 33:4, pp. 691-699, 1996.

[20]Seifert, A. & Pack, L.G., "Oscillatory Control of Separation at High Reynolds Numbers," AIAA Journal, 37:9, pp. 1062, Sep 1999.

[21]Seifert, A. & Pack, L.G., "Active Control of Separated Flows on Generic Configurations at High Reynolds Numbers," *AIAA 99-3403*, June 1999.

[22]Johari, H. & McManus, K., "Visualization of Pulsed Vortex Generator Jets for Active Control of Boundary Layer Separation," *AIAA 97-2021*, June 1997.

[23]Tilmann, C.P. & Osborn, R.F., "Active Flow Control for Drag Reduction at AFRL's Aerodynamic Configuration Branch," *Proceedings of the 17th Canadian Congress of Applied Mechanics*, Hamilton, Ontario, June 1999.

[24]Tilmann, C.P. & Osborn, R.F., "Active Control of Separation at AFRL's Aerodynamic Configuration Branch," *Proceedings of the 17th Canadian Congress of Applied Mechanics*, Hamilton, Ontario, June 1999.

[25]"*New World Vistas — Air and Space Power for the 21st Century*," USAF Scientific Advisory Board, 1995.

[26]Wheeler, G.O., "Means of maintaining attached flow of a flow medium," US patent No 4455045, 1984.

[27]Wheeler, G.O., "Low drag vortex generators," US Patent No 5058837, 1991.

[28]Lin J.C., "Control of turbulent boundary-layer separation using micro-generators," *AIAA-99-3404*, 30th AIAA Fluid dynamics conference. June 1999.

[29]Yanta, W.J., "A Three-Dimensional Laser Doppler Velocimeter (LDV) for Use in Wind Tunnels," *Proceedings of 8th International Congress of Instrumentation in Aerospace Simulation Facilities*, Monterey, California, pp. 294-301, 1979.

[30]Dantec Measurement Technology A/S, "Principles of LDA," [*http://www.dantecmt.dk*]

[31]Amtec Engineering Inc., ©1988-2000 [*http://www.amtec.com*]

[32]Baldwin, B.S. and Lomax, H., "Thin Layer Approximation and Algebraic Model for Separated Turbulent Flow," *AIAA-78-0257*, January 1978.

[33]"*The General Aerodynamic Simulation Program, Version 3 Users Manual*," Aerosoft Inc., Blacksburg, Virginia. 1996.

[34]van Leer, B., "Flux-Vector Splitting for the Euler Equations," *Lecture Notes In Physics*, Vol. 170, 1980.

[35]Hirsch, C., "*Numerical Computation of Internal and External Flows, Volumes 1 and 2*," John Wiley and Sons, 1992.

Paper #5
Q by N. Malmuth: Is DNS contemplated for this problem? Will laminar jets be considered?

A. (Tilmann) LES and DNS are contemplated for this problem, but significant computational resources will be required. Even when considering steady jets, it has been shown that using correct turbulence models accounting for Reynolds stress transport and including good turbulence profiles at the boundaries (at the jet and in the boundary layer) are crucial.
Laminar jets are not being considered at this time. The pulsed nature of the jet would also introduce many uncertainties for a laminar jet laboratory experiment.

Q (Mr. E. Collin): What about the reliability of the LDA mean flow results, since the seeding is done upstream of the pulsed VGJ's valve [in the freestream]?

A (Tilmann): In fact, we seeded the PVGJs themselves. The freestream was also eventually seeded due to the return design of the wind tunnel.

This page has been deliberately left blank

Page intentionnellement blanche

Impulse Control of Anti-Tank Mortar Missile

Ryszard Vogt,
Robert Głębocki
Warsaw University of Technology
Institute of Aeronautics and Applied Mechanics
Nowowiejska 24
Warszawa
robertg@dbi.piap.waw.pl

Introduction

Report explains problem of control dynamics of flying object with discontinuous impulse control inputs. Control is realised by the rocket correction motors locate around the centre of gravity of flying object. Start up the motor causes formation the force impulse direct perpendicular to main symmetry axis of object and direct along axis crossing object gravity centre. We tested possibilities of more effective influence on speed vector by impulse correction motors.

1. Problem description.

Goal of the paper is explain of guidance problem of anti-tank mortar missile. Missile is guiding from upper hemisphere. Flying trajectory is correcting by one time use, impulse, rocket correction motors. Projectile is firing from mortar and 80% of flight time is ballistic phase. To provide the missile aerodynamic stability and spin, the aft section is fitted with fins. The fins are immediately unfolded when the projectile left the barrel and their fixed cant angle impart slow spin to the projectile. Missile is guided at the last phase of flight. There is “fire and forget” projectile. Missile is launch over the targets activity area and at the last steep phase of the flight is automatically guided to the target. Missile mast be accurate launch over the targets activity area. We found that seeker has observation angel under 20^0 and find objects from distance under 1500m.

Paper presented at the RTO AVT Symposium on “Active Control Technology for Enhanced Performance Operational Capabilities of Military Aircraft, Land Vehicles and Sea Vehicles”, held in Braunschweig, Germany, 8-11 May 2000, and published in RTO MP-051.

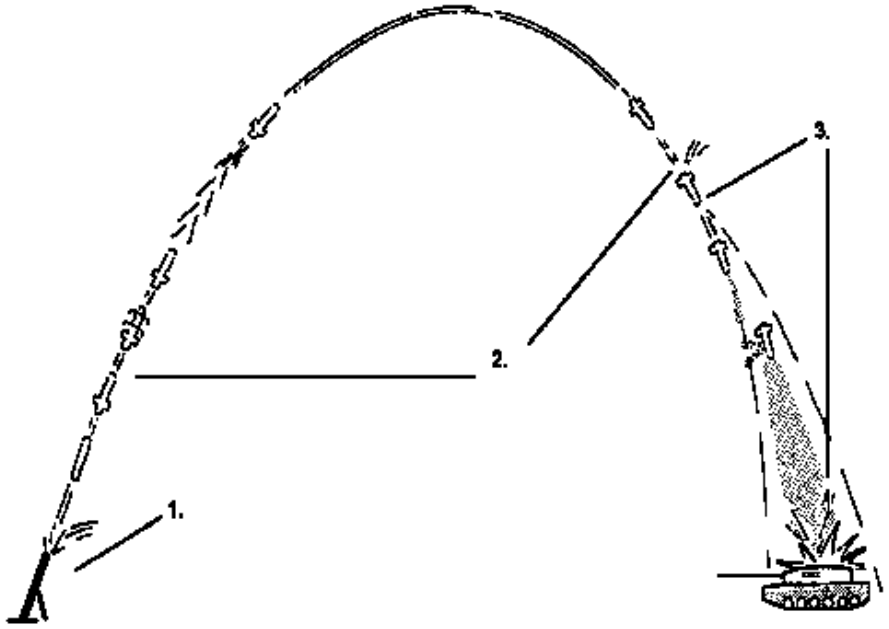


figure 1. Phases of flight:
1. launch
2. ballistic phase
3. guidance phase

These conditions give us an observation area with diameter around 300m. To launch projectile to that area is first and necessary condition of target intercept and successful missile attack. Phases of flight show the figure number 1.

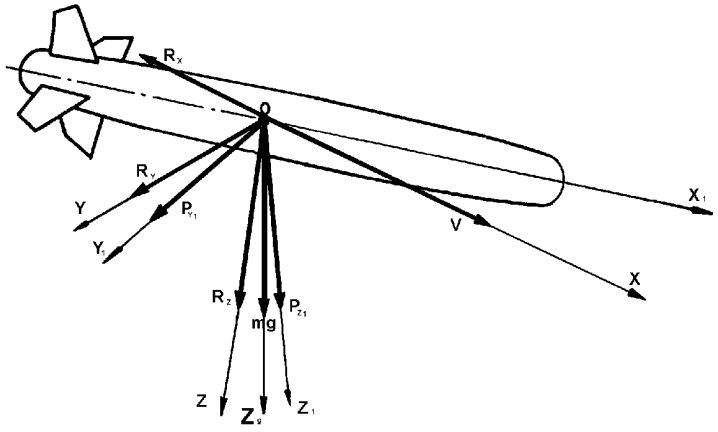


figure 2. Forces interacted to the missile at the control flight.

At this kind of projectile, where flight is controlling only at the last phase, we need not very big but quick influence on projectile's speed vector. This task we can do well by use control system made on the base rocket correction motors. Small rocket motors will have more successful influence on speed vector than classic aerodynamic control. This control conception will have to give better results of missile guidance.

2. Effect's dynamic.

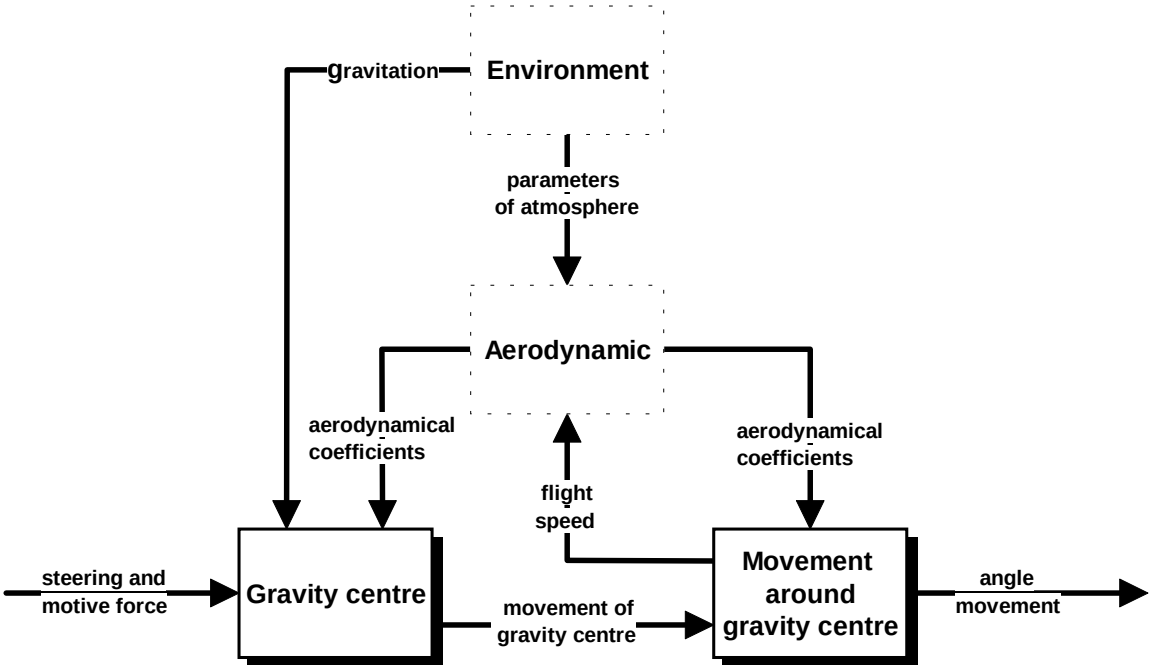


figure 3. Block scheme of object dynamic.

Classic methods of flying object control make assumption that the way of control system interaction on object is:

- steering forces first make change of force moment influence on object, it makes object rotation around gravity centre;
- supporting surfaces get necessary angels of attack and make steering forces.

At this way first we turn object around mass centre and the effect of this will be change of mass centre speed vector. This solution is characterised by big inercion between the control system's decisions and theirs commands execution. This effect makes inercion in control results. This is an important fault in situation when we need precision guidance of object to the goal in short time, or when control process

need very quick reactions on the informations coming to the missile seeker. This fault we can limited by the direct interaction to the gravity centre. In presented method servo control system's (correction rocket motors set) interacted to the gravity centre of object (figure 2).

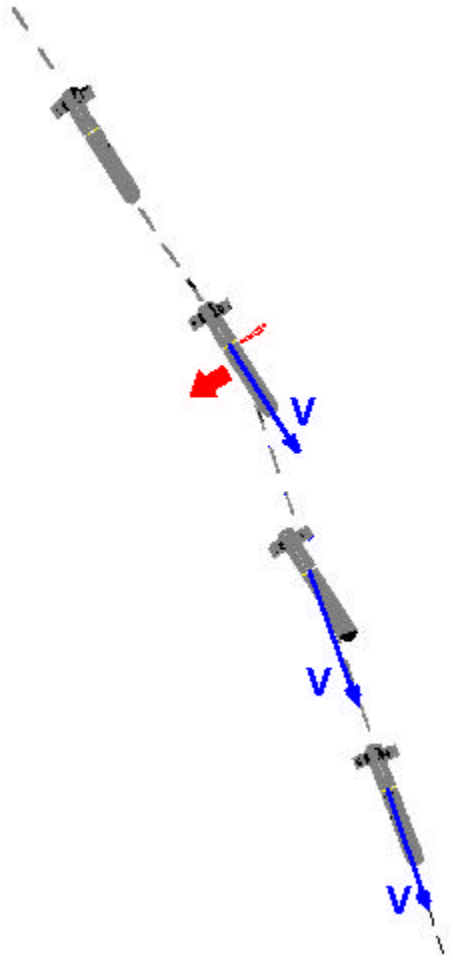


figure 4. Way to course change.

This method of flying object control make assumption that the way of control system interaction on object is:

- steering forces first make influence on object gravity;
- movement around gravity centre is an effect of gravity centre movement and aerodynamic interaction (figure 4).

Solution like this giving us more effectively interaction on speed vector. Block scheme of object dynamic show figure number 3.

At spinning object one channel is used to control in horizontal plane and vertical plane. These assumptions can be realised by gasodynamic impulse interaction to the object gravity centre. This solution give us not only quicker object reaction on seeker information and follow it possibility more precision object guiding to the attack target, but also make easier servo control system. We don't need complicated mechanics of aerodynamic servo.

3. Method of realising.

In that solution control is realised by one time used correction motors locate around the flying object centre of gravity. When the target has been selected, it is tracked during the rest of the flight of projectile. The error vector between the centre of the target and projected impact point of missile continuously monitored. As soon as

this error vector or error vector time derivative exceeds a pressed value, one or several rocket correction motors are fired in a direction to bring the value of the error close to zero. The impulse of the rocket correction motors passes through the centre of gravity of projectile, which gives instantaneous course correction when the rocket is fired.

By continuous calculation of the predicted impact point relative to predicted target position at impact, it is possible to use proportional navigation, which avoids any influence of target movement, wind effects etc. Missile can be used against both stationary and moving targets.

The tracking technique also makes it possible to make several course corrections in rapid succession. If necessary all rocket correction motors can be used with control in the last few seconds of flight.

The task of the rocket motors is to correct the course of the projectile in the last phase of the trajectory, making it home in on the target, achieving a direct hit. Correcting rocket motors are located in a cylindrical unit, arranged radial around the periphery. Each one of the correction rocket motors can be fired individually in a selected radial direction.

The correction motors set is placed close to the centre of gravity of the projectile. When the rocket motor is fired the course of the missile is changed instantaneously. Way to course change shows figure 4. By successive firing of several rocket motors, the projectile is steered with high precision on to the target. The chosen steering system gives a very fast response to the guidance signals.

4. Simulation researches.

Goal of researches was to find algorithms and dynamic properties of impulse control of flying object by ourselves methods. Researches were made on numerical model of dynamic of control missile. Model was a system of differential equations. Model was non-linear and discontinuous. It described space movement of projectile at all phases of flight. From launch till the hit to target or to ground. Description of movement is enough overall to research the control process with differential guided methods.

Two experiment results show figure 6. Error angle between seeker-target line and main symmetry axis of object oscillated in short range. Control system shows good results of control process. The huge errors at the last milliseconds of flight is the effect of assumption the target as a point.

5. Summary.

Numerical experiment shows large possibilities of control objects by interaction to their gravity centre. We can use impulse correction rockets to control falling objects. Like for example mortar control missiles and bombs. Attainable, at the phase of computer simulation, accuracy and control quality gives good prognostics to possibilities of practice use. This way of control more complicated control algorithms but make easier servo control. Servo has only correction rocket motors set and electrical system of initiation.

Researches show that for successful control missile must have proper charge of energy in correction rocket motors potential. Charge of energy depends from mass of missile. Their divide for the number of rocket motors and their time of work are constructor’s decision.

Results of numerical researches are used in program RAD. It is polish government military program currently at the field test.

Construction based on the similar effect was made in Sweden by SAAB Missiles and BOFORS Weapon Systems. Their product has named STRIX and is used by Swedish army.

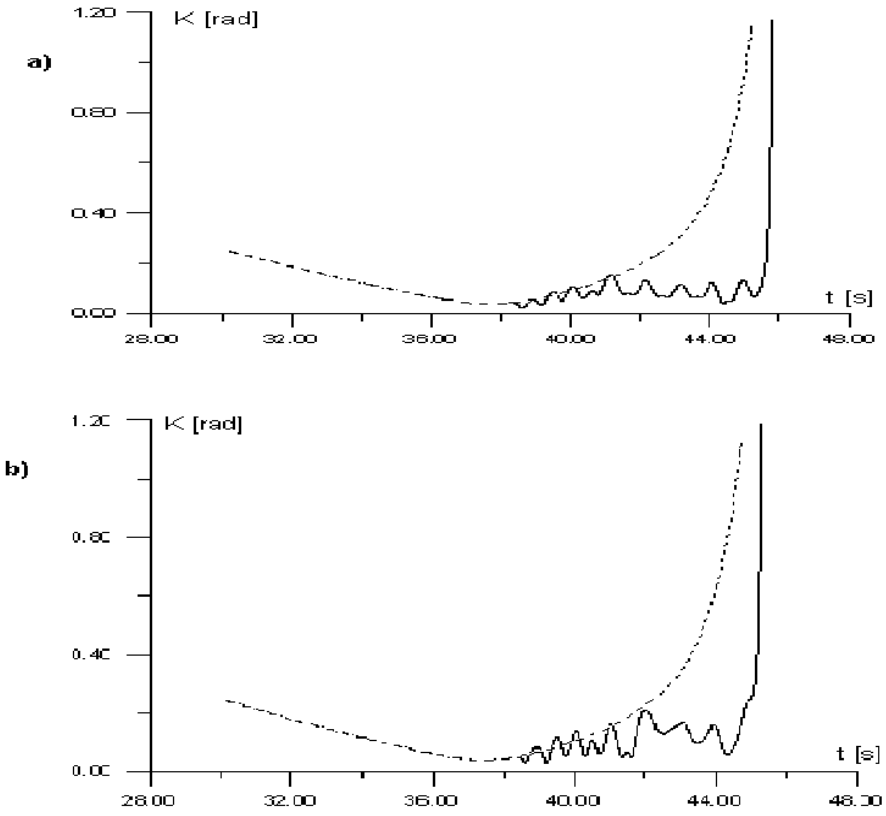


figure 5. Error angle between seeker-target line and main symmetry axis of object for two different numerical experiments. Solid line - controlling missile, dash line ballistic flight.

This page has been deliberately left blank

Page intentionnellement blanche

Active Control of Supersonic Impinging Jets

A. Krothapalli, R. Elavarasan, F. Alvi and C. Shih
Department of Mechanical Engineering
Florida A&M University and Florida State University
2525 Pottsdamer Street, Tallahassee, FL 32310, USA
kroth@fmrl.fsu.edu

Experimental studies of supersonic impinging jet flows suggest that they are greatly influenced by the flow-acoustic interactions through a feedback mechanism. The self-sustained oscillations of the jet column observed in these flows result in high velocities in the ambient medium induced by the large-scale coherent vortical structures in the jet shear layers. As a consequence, the suck down force on the surface from which the jet is issuing can reach as high as 60% of the primary jet thrust. In addition, the overall sound pressure levels (OASPL) increase significantly relative to a free jet. To alleviate these undesirable flow and acoustic characteristics, a novel control technique using supersonic microjets is demonstrated. Sixteen supersonic microjets are placed around the circumference of the main jet at the nozzle exit to disrupt the feedback mechanism. As a result, significant lift loss recovery (~ 50%) and reduced near field OASPL (~ 7dB) are observed.

1. INTRODUCTION

Short Take-off and Vertical Landing (STOVL) aircraft experience a number of performance-diminishing effects while hovering in close proximity to the ground. Some of the problems created by the impingement of high-speed hot lift jets on the landing surface are as follows. The lift loss associated with the jet entrainment results in low surface pressures on the airframe, creating a force opposite to lift. The loss in lift can be as much as 60% of the primary jet thrust and increases in magnitude as the aircraft approaches ground[1]. The impinging jet flow field generates significantly higher noise levels (8-10 dB) compared to that of a corresponding free jet. Increased Over All Sound Pressure Levels (OASPL) associated with high speed impinging jets affect the integrity of structural elements in the vicinity of the nozzle exhaust due to acoustic loading. In addition, the noise and the unsteady pressure spectra are dominated by high-amplitude discrete tones, which, in some cases, match the aircraft panel frequencies making the sonic fatigue problem more critical. Finally, the impingement of lifting jets results in areas on the landing surface with extremely high heat transfer rates and high wall shear. This produces significant erosion and spalling of the landing surface material in the jet impingement region and the outwash or 'wall jet' flow. Most of these problems have been observed in the Harrier/AV-8 family of aircraft. They are expected to become more severe when the jets operate at supersonic speeds and at higher temperatures, which is the case in the proposed Joint Strike Fighter aircraft.

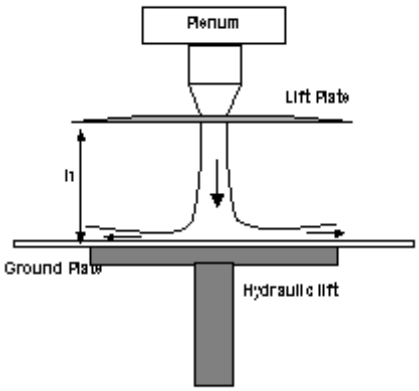
It is well known that the near field noise spectrum generated by the impingement of high speed jets on a surface is dominated by high amplitude, discrete tones, generally referred to as impingement tones[1]. Similar impinging tones have also been observed in the near field acoustic spectra of high temperature supersonic impinging jets. Krothapalli et al.[1] demonstrated that the impingement tones are governed by a feedback loop in the following manner. Instability waves of a particular wavelength (or frequency) are generated by the acoustic excitation of the shear layer very close to the nozzle exit; a region of high receptivity. As the waves travel downstream they evolve into large-scale, spatially coherent structures. Upon impinging the surface they give rise to high amplitude pressure fluctuations, which produce acoustic waves, these waves in turn excite the shear layer near the

Paper presented at the RTO AVT Symposium on "Active Control Technology for Enhanced Performance Operational Capabilities of Military Aircraft, Land Vehicles and Sea Vehicles", held in Braunschweig, Germany, 8-11 May 2000, and published in RTO MP-051.

nozzle exit, thus completing the loop. The presence of the discrete tones is generally accompanied by a globally oscillatory behavior of the primary jet column.

To address some of these issues, a number of basic studies examining the aeroacoustic properties of single and dual supersonic impinging jets of various geometries have recently been undertaken at the Fluid Mechanics Research Laboratory. One of the goals of this work was to obtain detailed velocity field measurements in the entire flow, including the impingement zone and wall jet region, using unique Particle Image Velocimetry (PIV) technique. The velocity field data, combined with conventional shadowgraphy, near-field acoustic measurements and mean and *unsteady* pressure distributions has allowed us to study and understand the global as well as the detailed behavior of this flow. The salient results of some these experiments, in the context of the present study, are described as follows.

Detailed results of single jet studies can be found in Krothapalli et al.[1, 2] and Alvi & Iyer[3] while the dual jet results appear in Elavarasan et al.[4] The schematic shown in Fig. 1 depicts the simple geometry used for single and multiple jets. The test model consists of an axisymmetric nozzle mounted perpendicular to the ground plane. The jet flow issues through a circular hole in an instrumented 'lift plate' where the lift plate represents a generic aircraft planform. The model used for dual impinging jets is essentially the same with the exception that two supersonic Mach 1.5 C-D nozzles are used for these tests.



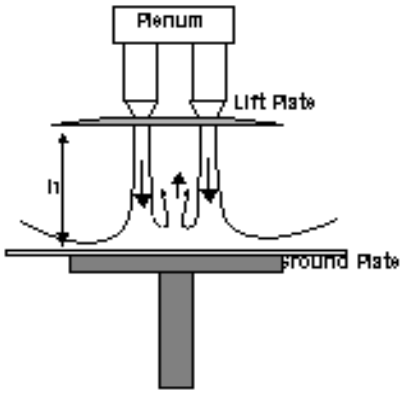


Figure 1. Schematic of single (a) and twin (b) impinging jet set up.

Two different nozzles, a converging (sonic) and a Mach 1.5 C-D nozzle, both with the same throat area, were used for the single jet studies. The combined areas of the two Mach 1.5 C-D nozzles used in the dual jet experiments are the same as the area of the nozzles used in the single jet studies.

The highly unsteady nature of the impinging jet flow-field and the presence of strong acoustic waves can be clearly seen in the instantaneous shadowgraph image of a single supersonic impinging jet shown in Fig. 2. The jet is issuing

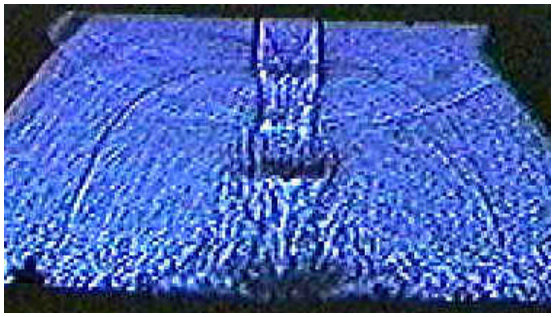


Figure 2. A schlieren picture of a supersonic axisymmetric impinging jet. NPR = 3.7, h/d = 4.

from the Mach 1.5 C-D nozzle operating under ideally expanded condition at a Nozzle Pressure Ratio (stagnation pressure/ambient pressure), NPR = 3.7 and impinging on the ground plane at a distance of h/d = 4 (h: the distance between the nozzle exit and the ground plane; d = the nozzle throat diameter). The strong acoustic waves, which appear as sharp lines in the image, are

readily visible. The incident waves, traveling towards the nozzle lip, appear to emanate from the ground plane near the center of the jet impingement region. As the acoustic waves reach the nozzle lip they excite the instability waves traveling downstream in the jet shear layer. These instability waves rapidly develop into large-scale spatially coherent shear layer structures while traveling downstream. Upon impingement on the ground plane, these structures generate coherent, high amplitude pressure perturbations, which in turn generate acoustic waves, thus completing the feedback loop.

The presence of such large-scale structures, not normally present in such high-speed jets, can be confirmed from the shadowgraph image in Fig. 2. However, more dramatic and direct evidence of these structures is provided in Fig. 3 which shows instantaneous PIV (Particle Image Velocimetry) images for the single and dual impinging jets issuing from C-D nozzles operating at a Nozzle Pressure Ratio, NPR= 3.7 at h/d = 4. The large-scale structures visibly grow as they travel downstream and then propagate outward along the wall jet, while maintaining their coherence. These observations show the dominant nature of the flow-acoustic interactions in the flow, which leads to the oscillatory behavior of the jet column.

To gain a better physical understanding of the global flow field, PIV images such as those shown in Fig. 3 were used to obtain detailed velocity and vorticity field data in the entire plane. Instantaneous PIV velocity fields corresponding to the images in Fig. 3 are shown in Fig. 4a and Fig. 4b for the single and dual impinging jets, respectively. The velocity field data shows that the presence of large-scale structures in the shear layers significantly enhance the entrainment velocities (measured velocities up to 100m/sec) in their vicinity. The high entrainment velocities result in suction pressures on the bottom surface of the lift plate and a downward force (lift loss). An additional feature observed for dual jet flows, which can further complicate the flow-field, is the fountain flow formed by the collision and coalescence of the radial wall jets in the region between the two jets. The results reveal that, for selected cases, the fountain flow can provide additional thrust, compensating some of the lift loss[4]. On the other hand, the impingement of the hot fountain fluid on the undersurfaces of the aircraft can lead to additional thermal loading and possible hot gas ingestion. Furthermore, coupling between the two jets can also add to the global unsteadiness of the flow field.

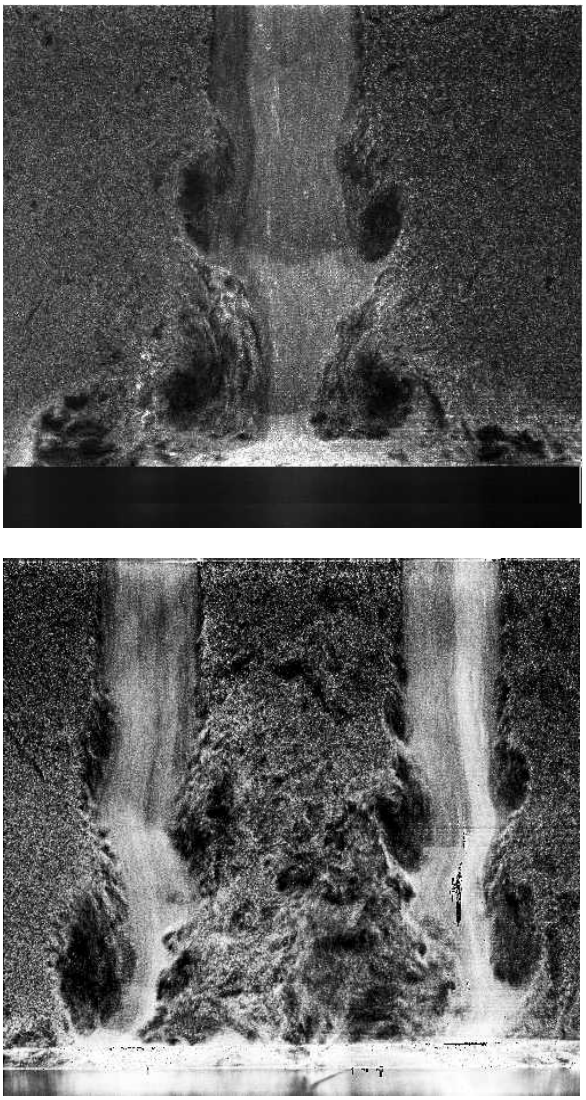


Figure 3. PIV Images of single and twin impinging jets. NPR = 3.7, h/d = 4.

It is evident from the previous discussion that the flow field for impinging jets is highly

unsteady. It is manifested as a highly fluctuating pressure field on the nearby surfaces, specifically on the lift plane and ground surfaces. Similarly, in the acoustic field, the unsteadiness results in high Over All Sound Pressure Levels (OASPL).

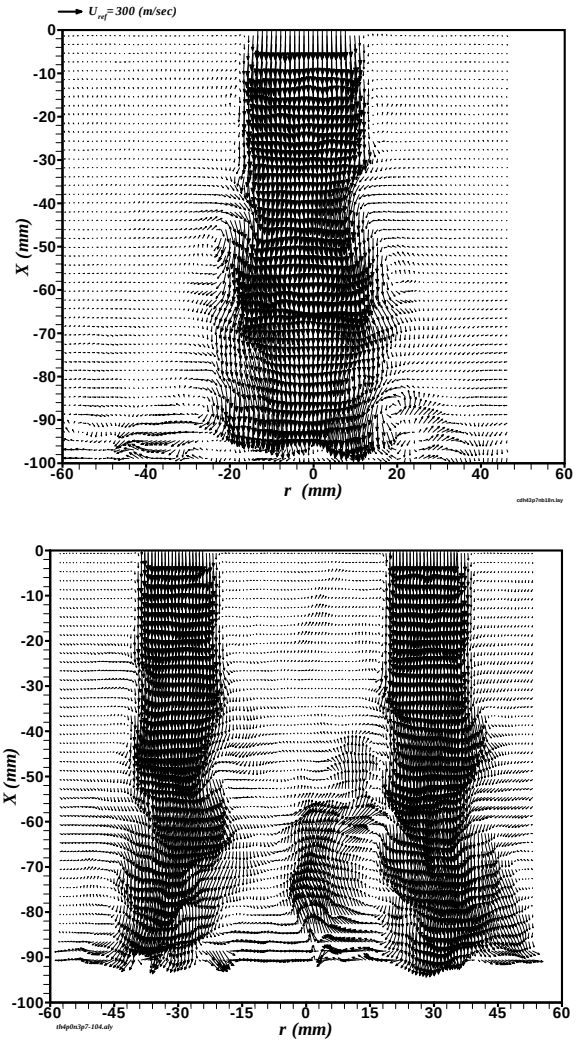


Figure 4. Instantaneous velocity fields corresponding to the images shown in figure 3.

Fig. 5 shows typical near field narrowband frequency spectra of ideally expanded free and impinging jets. The near-field microphone spectra clearly reveal the presence of tones for the impinging jet case. The results of an earlier investigation[1] show that a relatively small change in the h/d, can lead to a significant change in the magnitude and frequency of these tones. Representative acoustic spectra for dual supersonic impinging jets reveals a behavior very similar to that of single jets. As in single jets, the frequencies of these tones is a strong function of the jet NPR, h/d and geometry.

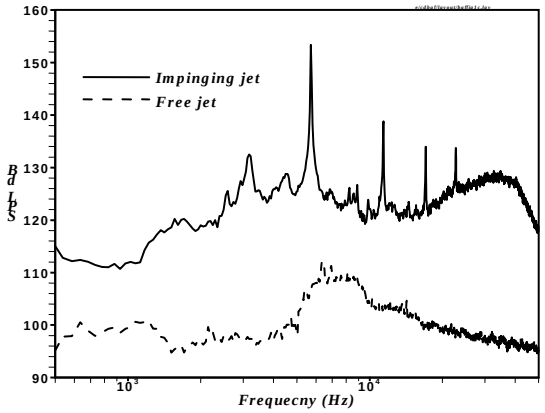


Figure 5. The near-field narrowband frequency spectra of an ideally expanded, single, free and impinging jet. NPR = 3.7, h/d =4.

Figure 6 shows a comparison of typical narrow band spectra of the lift plate unsteady surface pressure with that of the near field microphone signal. The unsteady surface pressures on the lift and ground planes were measured using high frequency response Kulite transducers. An inspection of these spectra provides further confirmation of the globally unsteady nature of the impinging jet flows. Whenever distinct impingement tones are present in the microphone measurements, spectral peaks also appear in the unsteady surface pressures, both on the lift and ground planes at nearly identical frequencies[3]. Furthermore, shifts in the spectral peaks in the noise measurements due to changes in the operating conditions, such as NPR or ground plane height, leads to a similar shift in the surface pressure spectral peaks, providing further evidence of the intimate relationship between acoustic and flow field properties. Fluctuating pressures as high as *170-180 dB were measured on the lift plane,* which can potentially compromise the structural integrity of nearby surfaces. Similarly, *unsteady pressures as high as 190 dB* were measured on *the ground plane* for some cases. Such an intensely fluctuating surface

pressure field together with the fact that the flow in the radial wall jet is usually transonic/supersonic with the peak velocities occurring very close to the surface (Alvi & Iyer[3]), will result in significant thermal (for hot jets) and shear loading of the ground surface leading to a significant ground erosion problem.

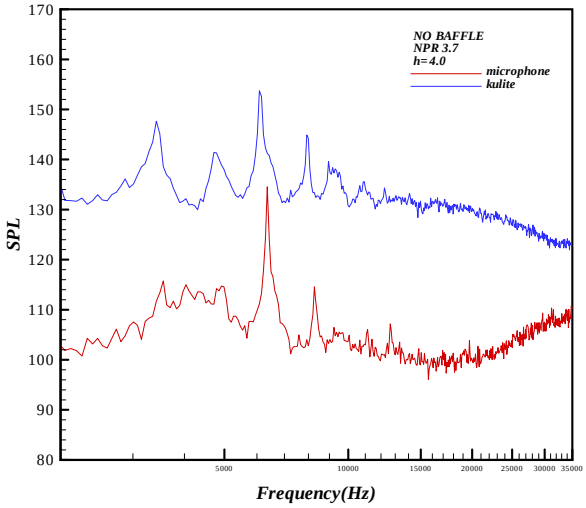


Figure 6. Narrowband frequency spectra for unsteady pressure on the *lift* plate and nearfiled micorphone measurements. Twin impinging jets, h/d = 4, NPR = 3.7.

Based on the above observations that a feed back loop is responsible for self-sustaining oscillations of the jet, an attempt was made to weaken it using a passive control technique by Elavarasan et al.[5]. The feedback loop was interrupted by preventing the acoustic waves from reaching the nozzle lip by placing a small plate near the nozzle lip. This technique was successful for some cases, wherein the disruption of the feed back loop led to a significant reduction in the appearance of large structures in the jet shear layers as shown in Fig. 7 (compare to Fig. 3). PIV results revealed that this led to a significant reduction in the entrainment velocities and a reduction in lift loss by as much as 20% for some cases. These results clearly suggest that the suppression of the feed back mechanism is the key to minimizing the thrust loss associated with the impinging jets. Although, the passive control technique has shown promising results in one particular configuration, its effect is strongly dependent upon operating parameters, such as NPR, temperature ratio and ground plate height and is therefore not well suited for implementation in an aircraft.

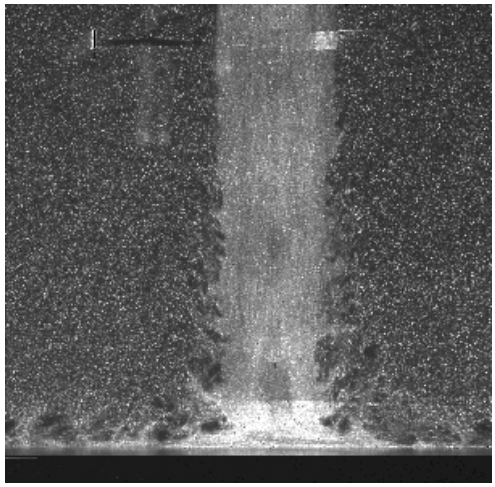


Figure 7. PIV image of an impinging jet with feedback loop suppression by passive control. NPR = 3.7, h/d = 4.

Although only selected results are presented here, all the undesirable features related to jet impingement discussed here, namely discrete tones, globally unsteady flow field, large scale structures, lift loss have been observed for single and dual nozzles of various geometries, including round (sonic and C-D nozzles) and elliptic. This behavior has been observed over a wide, JSF relevant, parametric space in terms of NPR and h/d for hot and cold jets. Given the many adverse effects of this flow, in this paper we propose an active flow control technique to suppress the feedback loop thereby enhancing the performance of STOVL aircraft in ground effect operating with lift jets.

The control strategy we aim to explore in this study is distinctive in that it takes advantage of the strong coupling between the fluid and acoustic fields near the jet exit to control the large-scale global unsteadiness of the flow. This is accomplished through the use of *actively controlled supersonic microjets*, which provide *on-demand-control* and disruption of the feedback loop. Initial results of this approach are presented in the following.

2. EXPERIMENTAL SET UP

Experiments were carried out in STOVL research facility of the Fluid Mechanics Research Laboratory at the Florida State University. The facility has been used to study jet-induced forces on STOVL configured aircraft models hovering in and out of ground. Positioning the ground plane at various heights relative to the model through a traversing mechanism simulated the hovering effect. An aluminum plate of size 1m x 1m x 25mm served as a ground plane. The height between the ground plane and nozzle exit (***h***) was varied from 0.04m to 1.5m. The schematic of the experimental setup is shown in Figure 1. A shock free nearly ideally expanded jet was obtained from a converging diverging (C-D) axisymmetric nozzle operating at design conditions. The throat (d) and exit diameters are 2.54cm and 2.75cm respectively. The nozzle was designed for an exit Mach number of 1.5. The divergent portion of the nozzle was a straight conic section with a 3-degree divergence angle. In order to simulate the airframe, a circular plate of diameter ***D*** (25.4 cm) was flush mounted with the nozzle. The circular lift plate contained 17 pressure taps arranged along a radial line and the pressure was measured with a Validyne strain gauge transducer mounted in a Scanivalve unit. At each port, several seconds of digitized data were taken. The lift force was calculated from the jet-induced mean pressures on the lift plate. The near field acoustic measurements were made using a 0.635cm diameter B&K microphone placed at 25 cm away from the nozzle exit and at 90^0 to the jet axis. The microphone signal and the lift plate surface pressures were acquired through a National Instruments data acquisition system with associated "Lab View" software. For the acoustic measurements, the nearby exposed metal surfaces were covered with 10 cm thick acoustic foam to minimize sound reflections.

All the experiments described here were conducted at a nozzle exit Mach number of 1.5 and at several **h/d**. The choice of the operating pressure and ground plane height was based on earlier experiments (Krothapalli et al.[1]) conducted in the same facility.

A top hat velocity profile with laminar boundary layers was maintained at the nozzle exit. The jet stagnation temperature was maintained with in $\pm 2^o$ of 20^oC. The nominal exit Reynolds number, based on the nozzle exit diameter and the exit velocity was $7x10^5$. A cylindrical coordinate system is used with its x – axis aligned with the centerline of the jet and r represents the radial direction. The corresponding velocity components are u and v respectively.

The jet control configuration used in the present study is shown in Fig. 8, where 16 axisymmetric convergent micro-nozzles (exit diameter = 400 μm) are placed around the circumference of the main nozzle. The microjet Nozzle Pressure Ratio was about 6. The total mass flow rate of these microjets is less than 0.3 % of the primary jet mass flow rate. The microjets are oriented about 20^o to the main jet axis. Injection of high-speed microjet streams into the primary jet can effectively thicken the shear layer and, consequently, reduce its receptivity to the external disturbances. In addition, the supersonic jet flow exhausting out from the micronozzles will locally prevent the upstream propagation of the acoustic disturbances back to the primary nozzle exit. It is hoped that a spatially

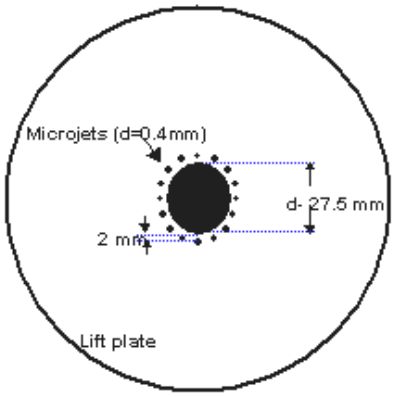


Figure 8. A schematic of the flow control arrangement using microjets.

incoherent microjet system could produce enough interference to disrupt the feedback

mechanism. A typical schlieren picture of the microjet operating at NPR = 6, issuing from a 400 μm diameter convergent axisymmetric nozzle is shown in Fig. 9. Clearly seen in the picture is the shock cell structure that is commonly observed in underexpanded jet. The first shock cell contains the Mach disc, and its distance from the nozzle exit is in agreement with the macro nozzle studies at the corresponding pressure ratio. The picture clearly depicts that shock cells extend over a distance of about 10 mm, indicating the extent of the supersonic flow.

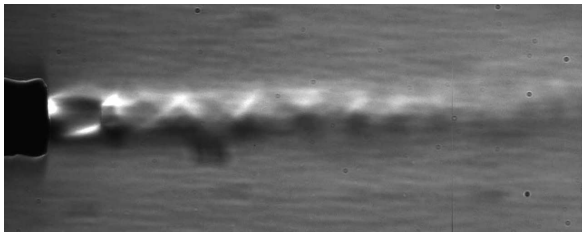


Figure 9. Schlieren picture of a supersonic microjet. NPR = 6, Exit diameter = 400 μm.

Much smaller microjets have also been fabricated on a 500-μm thick silicon wafer using the Deep Silicon Reactive Ion Etching (Deep Si RIE) processing. All nozzles and their corresponding settling chambers were patterned using photoresist as an etch mask and the unwanted

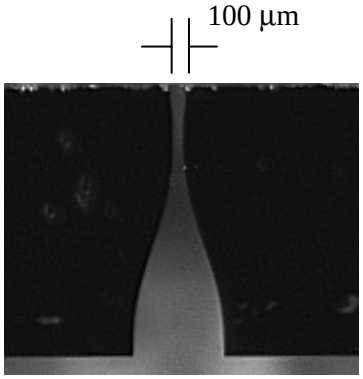


Figure 10. Converging-diverging micro supesonic nozzle.

parts were etched out using reactive ion beams with almost vertical (90°-95°) sidewalls. The C-D profiles of the microjet nozzles were computed based on a two-dimensional method of characteristics calculation without using boundary layer correction. A typical converging-diverging nozzle made with this technology is shown in Fig. 10. One of the most obvious advantages of using a micro-scale device for flow control is its small physical size, which produces minimal interference to the primary flow. Another advantage of the micro-devices is that they can be massively produced and patterned so that it is possible to fabricate an assembly of a very large number of microjets with desirable spatial distribution for multiple point control. Finally, micro fabricated sensors and actuators can be packaged with the control unit for multiple-point signal detection and control activation. This makes the in-situ active flow control possible. Such microjets/sensors will be used in future studies to achieve more precise, active control of the present flowfield.

4. RESULTS AND DISCUSSION

In this initial study, flow control was applied by simply activating the supersonic microjets placed at the nozzle exit. It was anticipated that

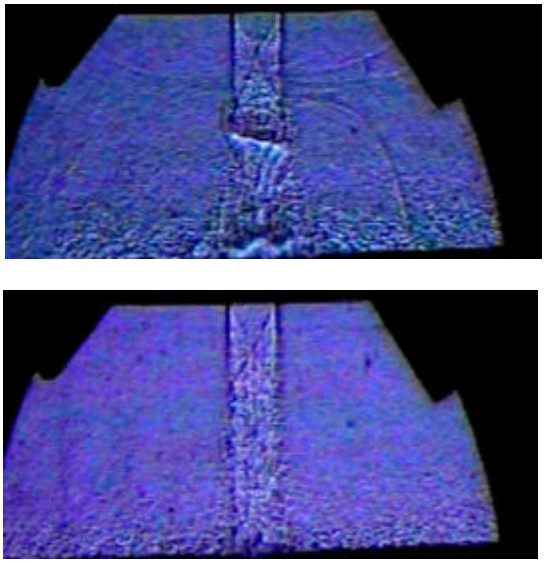


Figure 11. Instantaneous shadowgraph images of supersonic impinging jets without (top) and with (bottom) control at NPR = 3.7 and h/d = 4.5.

the penetration of the microjets into the primary lift jet shear layer at the nozzle exit will

sufficiently modify the shear layer stability characteristics to disrupt the feedback loop and alleviate the associated adverse effects. It must be noted that in these tests no attempt was made to actively modulate and control the microjets based on the local flow conditions. The results shown here only compare the relevant properties with and without the microjets operating. A comparison of the instantaneous shadowgraph shown in Fig. 11 visibly reveals that the strong acoustic waves, corresponding to impinging tones, have been eliminated when the microjets are activated. Furthermore, the large-scale shear-layer structures have also been significantly reduced. The near field narrow band frequency spectra corresponding to the conditions of Fig. 11 are shown in Fig. 12. The distinct tones corresponding to the uncontrolled impinging jet are almost entirely eliminated by the activation of microjets. In addition, a reduction in noise level is observed in the entire spectrum.

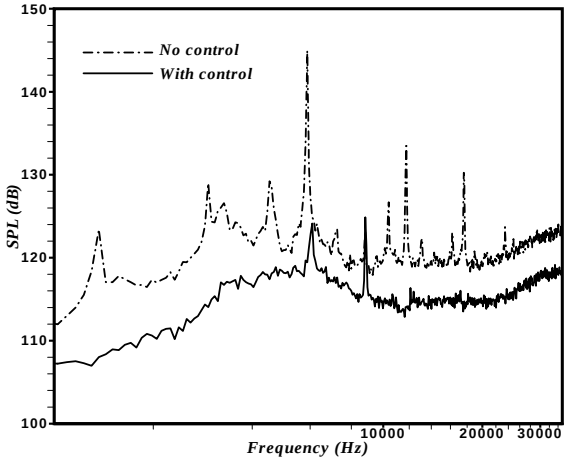


Figure 12. The effect of control on the nearfield noise spectra corresponding to the conditions of Fig. 11.

A comparison of the Overall Sound Pressure Level (OASPL) at different h/d, as shown in Fig.13, suggests the general trend of the overall noise reduction with the control. However, the noise reduction magnitude is dependent upon the h/d (e.g. a reduction of ~ 7 dB at ground plane h/d = 4.5 compared to 2-3 dB reduction at h/d = 3.5 and 4); an indication that the control technique does not track the flow changes brought about by the varying h/d.

The effect of microjet control on the lift plate surface pressure distribution is shown in-Fig. 14 at jet operating conditions corresponding to those in Fig.11. A significant increase in the surface pressure is observed with the activation of microjets. It is suggested that the surface pressure increase observed is due to the reduction in the magnitude of the entrainment velocities.

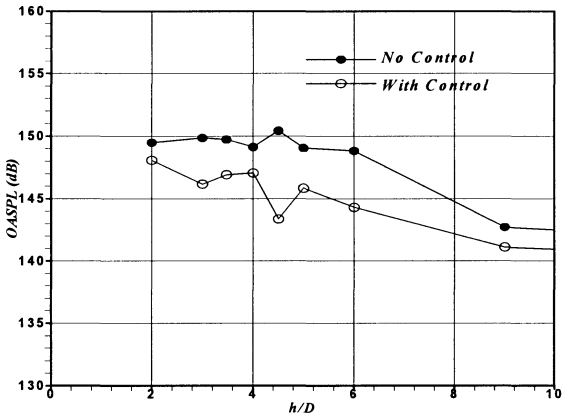


Figure 13. The variation of OASPL with h/d with and without control.

Typical variation of the negative lift force with h/d is shown in Fig. 15, where the lift force is normalized with the jet thrust calculated using one-dimensional isentropic equations. As the

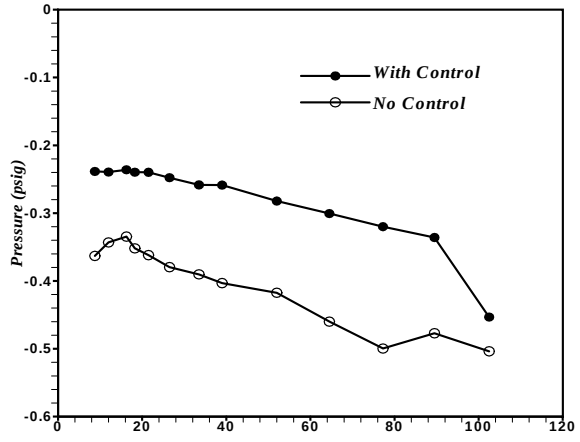


Figure 14. The distribution of the mean surface pressure on the lift plate with and without control. NPR = 3.7, h/d = 2.

ground plane approached the lift plate, a large downward force is generated. For example, at h/d = 2, the magnitude of the lift loss is greater

than 60% of the primary jet thrust. This force decreases rapidly in magnitude with increasing h/d and approaches an asymptotic value of the free jet. A significant lift loss recovery is observed with the control at h/d=2. With increasing h/d, the magnitude of the recovery is much less and shows a non-monotonic behavior. Figure 16 summarizes the lift loss recovery variation with h/d. It is observed that control effectiveness varies with h/d, suggesting that the active control strategies are necessary to achieve optimal performance at all operating conditions.

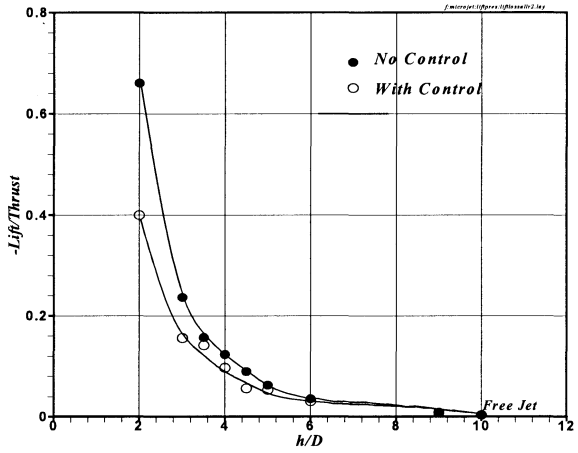


Figure 15. The effect of the control on the variation of lift loss with h/d.

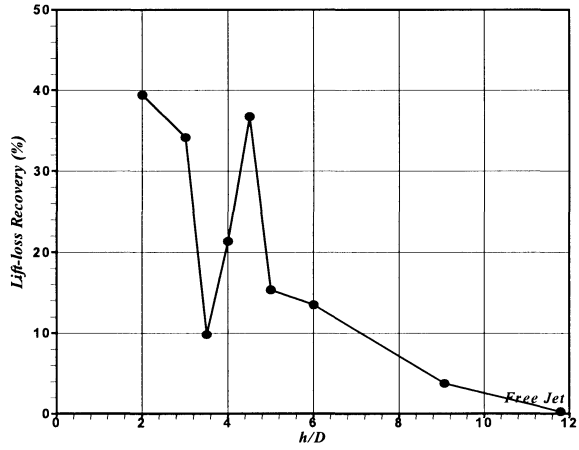


Figure 16. The variation of lift loss recovery with h/d.

4. CONCLUSIONS

The objective of this research program is to develop practical control strategies to enhance the STOVL aircraft performance under realistic operating conditions. In this paper we explored a novel control technique utilizing supersonic microjets to disrupt the feedback mechanism in supersonic impinging jet flows. The disruption of this feedback mechanism resulted in significant gains in lift and reductions in OASPL as well as elimination of discrete high amplitude tones in the noise spectra. However, the performance enhancements due to the control strategy are not uniform over the entire parametric space. We believe, that this is due to the fact that the microjets are used in a 'passive' mode. Due to the dynamic nature changes in the flow-acoustic interactions with operating conditions, an optimal control technique must be able to adapt to these changes.

Having demonstrated the efficacy and the potential for substantial gains in performance using this control technique in this initial, proof-of concept study, we are presently developing on-demand control methods using integrated sensor and supersonic microjet actuators. These control techniques will be implemented in more realistic planform geometries utilizing single and dual impinging jets.

5. ACKNOWLEDGEMENTS

Our research program on STOVL aircraft jet induced effects is supported by NASA Ames Research Center (Technical monitor: Mr. Doug Wardwell), Air Force Office of Scientific Research (Technical Monitor: Dr. Steven Walker) and The Boeing Corporation. The untiring efforts of Dr. William Bower of Boeing Corporation in support of our program are gratefully acknowledged. We also like to thank Dr Venkatakrishnan and Prof. Luiz Lourenco for their ongoing support and Mr. Gurav Garg for his help in conducting these tests.

6. REFERENCES

1. Krothapalli, A., Rajakuperan, E. Alvi, F. S. and Lourenco, L., "Flow field and Noise Characteristics of a Supersonic Impinging Jet," *Journal of Fluid Mechanics*, **392**, 1999, pp. 155-181.
2. Elavarasan, R., Venkatakrishnan, L., Krothapalli, A., and Lourenco, L., "A PIV Study of a Supersonic Impinging Jet", *Journal of Flow Visualization*, **2** (3/4), 2000, pp 213–221.
3. Alvi, F. S. and Iyer, K. G., "Mean and Unsteady Flow field Properties Of Supersonic Impinging Jets With Lift Plates", AIAA Paper 99-1829, presented at the 5th AIAA/CEAS Aeroacoustics Conference, May 1999.
4. Elavarasan, R., Venkatakrishnan, L., Krothapalli, A. and Lourenco, L, " Supersonic Twin Impinging Jets," AIAA Paper # 2000-0812, 38th AIAA Aerospace Sciences Meeting, January, 2000.
5. Elavarasan, R., Krothapalli, A., Venkatakrishnan, L. and Lourenco, L., "Suppression of Self-Sustained Oscillations in a Supersonic Impinging Jet", Submitted to the *AIAA Journal*.

Analysis of jet interaction for supersonic flow control

E. Collin, S. Barre and J.P. Bonnet
LEA/CEAT, Université de Poitiers
43, route de l'Aérodrome, 86036 POITIERS CEDEX (France)
Phone : 33 5 49 53 70 15
Fax : 33 5 49 53 70 01
E-Mail : erwan.collin@lea.univ-poitiers.fr

1. Introduction

In a lot of industrial applications, especially in ejectors and propulsive jets, most of the dynamical behaviour of the system is strongly influenced by the mixing efficiency in a supersonic jet. This is particularly the case when dilution of hot propulsive jets is required for example to reduce infrared signature of a military aircraft. Many mechanical devices have been used to increase mixing in free shear flows. Most of these devices stimulate the activity of longitudinal vortices naturally occurring in mixing layers[1]. For instance, the insertion of small tabs on the splitter plate of a plane mixing layer, or in the nozzle of a jet, produces large and small-scale vortical motions[2]. This results in a strong distortion of the mean flow and a strong mixing enhancement[3,4,5].

In order to prepare the development of an active hyper-mixing method, Davis[6] studied a pneumatic device. A schematic arrangement of this device is shown in figure 1. It is generally admitted that transverse jets generate longitudinal vorticity in a crossflow. Several control jets (CJ) can be used in order to improve the mixing in the initial part of a supersonic jet. This kind of device has been proved to be efficient in subsonic flows[6]. The question arises of the behaviour of such control jets in supersonic flows.

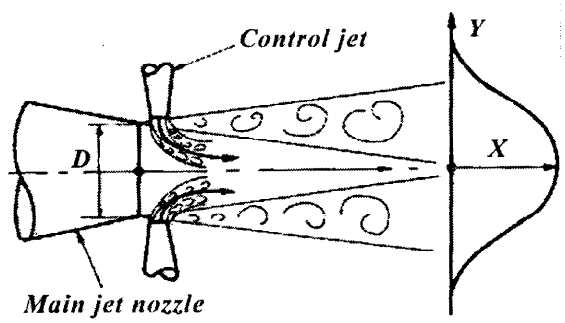


figure 1
General arrangement of the pneumatic device (from Davis[6])

A parametric study has been done by Collin et al[7] in order to evaluate the effects of one CJ dynamic pressure and geometry on the mixing enhancement in the case of a *M=1.37* cold jet. Pressure and temperature measurements in the far field region of the interaction between the CJ and the main jet revealed a strong distortion of the mixing layer. This distortion is shown on figure 2 and looks like the one obtained with tabs. The manipulated mixing layer has shown to be locally twice thicker under the action of the CJ (see figure 3). However, as shown on figure 4, no augmentation of the spreading rate has been noticed in the far field (e.g. one diameter or more downstream the main jet nozzle). Although the effects of the dynamic pressure ratio between the CJ and the main jet were almost understood, the effects of the CJ nozzle geometry were not clear at all. For all these reasons, we intended to realise some visualisations in the near field of the interaction between a main supersonic jet and only one control jet.

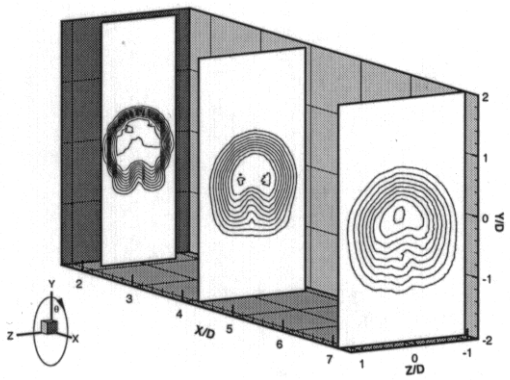


figure 2
Longitudinal evolution of the velocity distribution in cross-sections of the manipulated supersonic jet (from Collin et al[7])

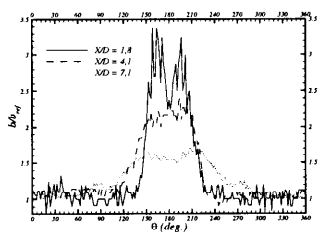


figure 3
Azimuthal distribution of the mixing layer thickness (from Collin et al[7])

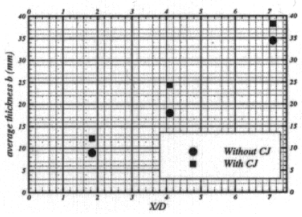


figure 4
Longitudinal evolution of the averaged mixing layer thickness (from Collin et al[7])

Paper presented at the RTO AVT Symposium on "Active Control Technology for Enhanced Performance Operational Capabilities of Military Aircraft, Land Vehicles and Sea Vehicles", held in Braunschweig, Germany, 8-11 May 2000, and published in RTO MP-051.

The visualisations obtained for fixed dynamic pressure ratio and CJ nozzle geometry are described in §3. These visualisations show a local augmentation of the spreading rate of the mixing layer. Whereas a strong intermittent behaviour is detected for the penetration of the CJ in the mixing layer, longitudinal vorticity has been put forward just downstream the CJ. In the §4, we present some visualisations obtained for 3 different CJ nozzles, in order to explain the effects of the CJ geometry.

2. Experimental set-up

2.1. Wind tunnel

The wind tunnel used in this study is the *S150* high-pressure facility of the *C.E.A.T.* of Poitiers, France. This is a *M=1,37* supersonic jet surrounded by a subsonic entrained coflow. Stagnation pressure and temperature for the main jet are respectively *3bar* and *260K*. The coflow velocity and stagnation temperature are $47ms^{-1}$ and *290K*. The convective Mach number is $M_c=0.49$. The supersonic jet has the same static pressure than the subsonic coflow. The nozzle diameter is *D=50mm*. The test section is $500 \times 500\ mm^2$. A 200bar dry air tank supplies the main jet.

2.2. Actuators

The CJ is supplied by the same *200bar* dry air tank as the main jet and is placed *5mm* downstream and *5mm* bellow the main jet nozzle. The CJ stagnation pressure is kept constant at *2.5bar*. The picture of figure 5 shows the test section, with the main jet and the CJ. Three different CJ nozzles (two rectangular and one circular) are used in order to understand the effects of the CJ geometry. Their description is given in table 1.

Type	*Shape*	Φ_{eq}	*L×l*	*L/l*	*position*
Rect1	*Rectangular*	*3.7*	*11 × 1*	*11*	➧ ▯
Rect2	*Rectangular*	*5*	*9.5×2*	*4.75*	➧ ▯
Circ	*Circular*	*5*			➧ ○

table 1
Descriptions of the control jet nozzles used in the study (dimensions are given in mm)

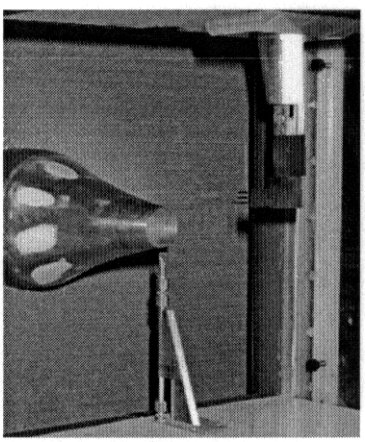


figure 5
Photography of the S150 test section

2.3. Visualisation technique

Visualisations of the flow are obtained with a PIV system. A laser sheet is realised with a Nd YAG pulsed laser beam. Pictures are acquired on computer by the use of a CCD camera. The time of exposure is about *6ns*, which is short enough to 'freeze' the flow.

Several kinds of visualisations are realised with different laser sheet and camera positions. Side views are easily performed thanks to large windows in the walls of the test section. The realisation of end views pictures (i.e. cross sections of the flow) is much more challenging. When we intend to have a global point of view of the cross sections, we install the camera in the diffuser. For more zoomed images, we have to realise 'pseudo-end' views from the side of the test section. That is to say that the camera is not strictly recording cross sections. Although, the angle between the laser sheet and the cross section of the tunnel never exceeds *14°*.

Three seeding techniques are used: natural seeding, ethanol droplets and SiO_2 particles. Natural seeding is obtained by condensation of the surrounding air mixed with the cold supersonic jet. This technique is used for cross-sectional views of the mixing layer itself in the far field region of the interaction. Ethanol droplets and SiO_2 particles are used in the very near field of the interaction. Side views of the mixing layer in this region are realised by seeding the boundary layer inside the main jet nozzle with ethanol droplets. Side and cross-sectional views of the CJ are done with a CJ seeded with SiO_2 particles.

2.4. Data analysis

We acquire 200 instantaneous pictures at *10Hz*. Each picture has 768×484 pixels, coded on 256 greyscale levels. Very simple homemade algorithms give well-converged average and *rms* picture for each run.

3. Results for one CJ geometry

This part of the study concerns the understanding of the mechanisms involved in the interaction between one CJ and the main jet. The CJ used here is type *rect1*, with a stagnation pressure of *2.5bar*.

3.1. Structures of the CJ

3.1.1. Cross–sectional views

The longitudinal aspect of the structures of the CJ is obtained with a laser sheet almost perpendicular to the main undisturbed jet. The CJ is seeded with SiO_2 particles. The figure 6 and figure 7 show respectively the average and the *rms* pictures obtained for three downstream positions. We can easily notice that the CJ is flattened when it reaches the mixing layer. Far downstream, the CJ is deformed.

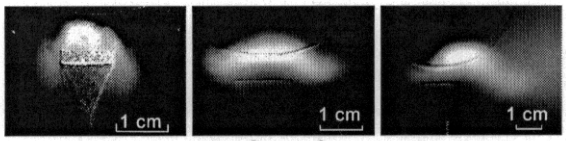


figure 6
Cross-sectional average views of the structures of the CJ (from left to right: X/D=0.14, 0.4 and 1.0)

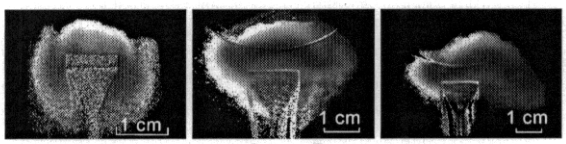


figure 7
Cross-sectional rms views of the structures of the CJ (from left to right: X/D=0.14, 0.4 and 1.0)

The figure 8 shows instantaneous pictures obtained in the cross-sections. These visualisations put forward the formation of small-scale longitudinal vorticity in the very first stage of the CJ. The small longitudinal vortices seem to reconnect themselves downstream. At the last cross-section, we can easily identify a pair of counter rotating vortices. However, it seems that an intermittent behaviour destabilise the longitudinal vortices. This behaviour is analysed thanks to side views visualisations.

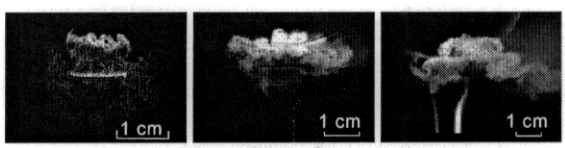


figure 8
Cross-sectional instantaneous views of the CJ (from left to right: X/D=0.14, 0.4 and 1.0)

3.1.2. Side views

Here, the laser sheet is positioned in the median plan of the main jet. The CJ is seeded with SiO_2. The figure 9 shows average and *rms* pictures. The main flow is from left to right. The trajectory of the CJ looks like the one obtained with jets in cross flows. However, the curvature seems to be much more important in the region where the CJ is impinging the main supersonic jet, and the CJ spreads downward. The average picture shows also that the CJ turns into the mixing layer.

The *rms* side view indicates that the boundaries of the CJ are turbulent. We can also notice that a part of the CJ turns upstream, very near the CJ nozzle. This behaviour is better understood in the analysis of the instantaneous pictures.

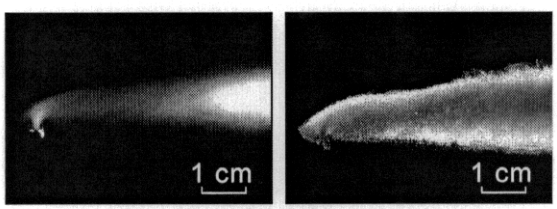


figure 9
Average (left) and rms (right) side views of the CJ

Close-up instantaneous views are represented in figure 10. We can see that we have two kinds of behaviour: either the CJ penetrates deeply in the mixing layer, or it is completely stopped when it reaches the mixing layer.

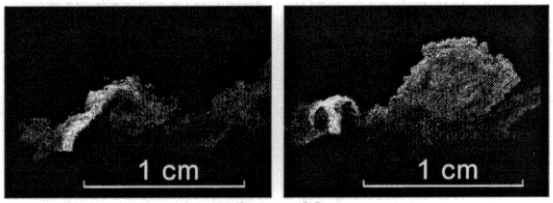


figure 10
Instantaneous side views of the structures of the CJ

Two kinds of phenomenon can explain this behaviour. First, as the CJ size is quite small, it is possible that the penetration depends on the presence of a Kelvin-Helmoltz structure in front of the CJ exit. Indeed, if the adverse pressure gradient were sufficiently strong just upstream a Kelvin-Helmoltz rollup, the penetration of the CJ would decay. On the other hand, when the CJ nozzle is facing the rear of a Kelvin-Helmoltz roll up, the penetration is furthered. However, this hypothesis implies that the Kelvin-Helmoltz rollups generate very strong pressure fluctuations.

The other hypothesis we can make in order to explain this intermittent behaviour is based on an intrinsic instability of the interaction between the CJ and the annular mixing layer. This instability may be due to the generation of a high-pressure region just upstream the CJ, caused by a local downward deviation of the main jet. When the pressure upstream the CJ is sufficiently strong (i.e. at least equal to the CJ stagnation pressure), the high-pressure zone is convected downstream, stopping the penetration of the CJ. Unfortunately, we would need further measurements and simulations in this way to confirm if the intermittent penetration behaviour is due to this kind of mechanism.

3.2. Structures of the manipulated mixing layer

3.2.1. Cross-sectional views

Cross-sectional views of the manipulated jet are realised from the wind tunnel diffuser. The seeding is obtained by condensation of the surrounding air when mixed with the cold main supersonic jet. The figure 11 shows three instantaneous pictures taken at *X/D=3, 4.1* and *7.1*. These pictures look like the mean flow measurements obtained previously (see figure 2). The visual aspect of these structures seems to be almost steady.

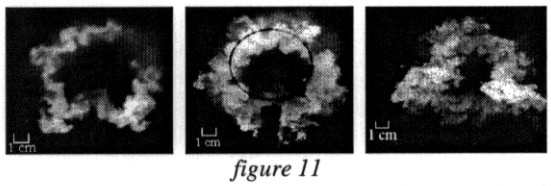


figure 11
Instantaneous cross-sectional views of the manipulated mixing layer (from left to right: X/D=3, 4.1 and 7.1)

3.2.2. Side views

Here, the seeding is realised by the addition of ethanol droplets inside the boundary layer in the settling chamber of the main supersonic jet.

The figure 12 shows the average and *rms* pictures obtained with a 200 pictures data set. The average picture puts forward the mixing enhancement very near the CJ exit. The spreading rate can be evaluated with the visual thickness. A comparison between the upper (unperturbed) and the lower (manipulated) mixing layer of the figure 12 leads to :

$$\left.\frac{\Delta\delta_{viz}}{\Delta x}\right|_{with\ CJ} \approx 1{,}2 \cdot \left.\frac{\Delta\delta_{viz}}{\Delta x}\right|_{without\ CJ}$$

The action of the CJ leads to a spreading rate 20% bigger very near the injection. The mixing layer thickness is increased just in front of the CJ.

The *rms* picture reveals a very intermittent phenomenon occurring just upstream the CJ.

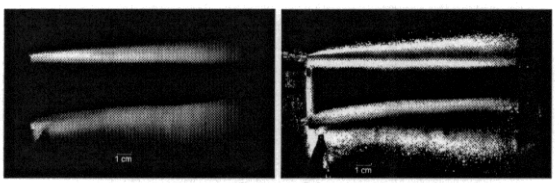


figure 12
average and rms side views
of the manipulated mixing layer

Two examples of instantaneous side views are given in figure 13. These pictures may indicate a strong acceleration of the Kelvin-Helmoltz rollups. Indeed, structures looking like Kelvin-Helmoltz's are more distinct under the action of the CJ. An approximation of the Strouhal number can be done with the definition:

$$St = \frac{F \cdot \delta_\omega}{Uc} \approx \frac{\delta_\omega}{l}$$

where l is the longitudinal structure spacing.

Taking the height of the structures for δ_ω , we obtain $St \approx 0.55$. As a comparison, the Strouhal number of the unperturbed mixing layer is approximately *0.3*. However, this must not mean that the CJ develops the second or the third sur-harmonic of the mixing layer instability: this just means that the aspect ratio of the structures of the mixing layer is completely changed under the action of the CJ. Indeed, by keeping constant the convective velocity and the Kelvin-Helmoltz instability frequency, we just have to increase the thickness to change the Strouhal number.

On the right hand of figure 13 we can see a different behaviour of the CJ penetration. A part of the flow issuing from the main jet nozzle turns down just upstream the CJ. This may be caused by the unsteady penetration of the CJ (see §3.1.2). The fact that a part of the mixing layer is turned down upstream the CJ may imply that the unsteady behaviour of the CJ penetration is due to an intrinsic instability of the interaction between a transverse jet and a free shear flow.

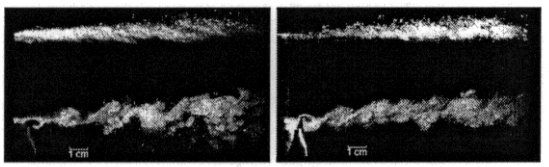


figure 13
Two examples of instantaneous side views
of the manipulated mixing layer

Finally, several remarks can be deduced from the visualisations obtained with a single CJ. First, side views of the manipulated mixing layer show an enhancement of the spreading rate near the injection. Secondly, instantaneous cross-sectional pictures revealed the presence of a pair of counter-rotating vortices generated by the CJ. However, these vortices are not steady at all. A very intermittent behaviour is detected concerning the penetration of the CJ inside the mixing layer.

The §4 deals with the effects of the CJ nozzle geometry in terms of penetration, structures of the manipulated mixing layer and longitudinal vorticity.

4. Influence of the CJ nozzle geometry

For a fixed CJ stagnation pressure (P_{CJ}=*2,5bar)*, we tested three kinds of CJ nozzle. The characteristics are shown in the table 1. We try here to separate the effects of the shape of the CJ nozzle (rectangular or circular), and the effects of the length scale (equivalent diameter). Note that the CJ type *rect2* and *circ* have the same equivalent diameter, and that the main difference between the CJ type *rect1* and *rect2* is the length of the small side of the nozzle.

4.1. CJ penetration

The CJ penetration information is obtained by the same technique as in §3.1.2. The figure 14 represent the average pictures obtained for each CJ nozzle. The global behaviour does not differ from one CJ type to the other: the CJ average trajectory does not seem to be affected by the shape or length scale of the nozzle. This may be due to the very sharp curvature of the CJ trajectory as it reaches the shear layer.

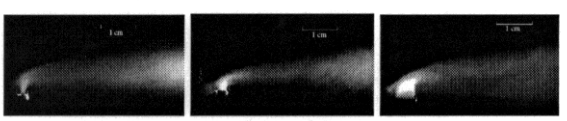


figure 14
Average side view for the CJ penetration
(from left to right: CJ type rect1, rect2 and circ)

The instantaneous pictures shown in figure 15 rise much interesting results. Although the rectangular CJ generate both the same kinds of structures, the behaviour is completely different for the circular CJ. Indeed, the CJ type *circ* never completely penetrates the shear layer. This may be caused by the fact that the longitudinal length scale of CJ type *circ* (e.g. the diameter) is far bigger than the rectangular ones, regarding the theoretical length of the Kelvin-Helmoltz structures. Taking $L_{KH}=15mm$ for the longitudinal structures spacing in front of the CJ nozzle exit, the longitudinal length scales of the CJ nozzles are:

$$\begin{cases} D_{circ} = L_{KH} / 3 \\ l_{rect1} = L_{KH} / 15 \\ l_{rect2} = L_{KH} / 7 \end{cases}$$

As a result, the transversal aspect of the structures of the CJ is not produced by the same mechanism.

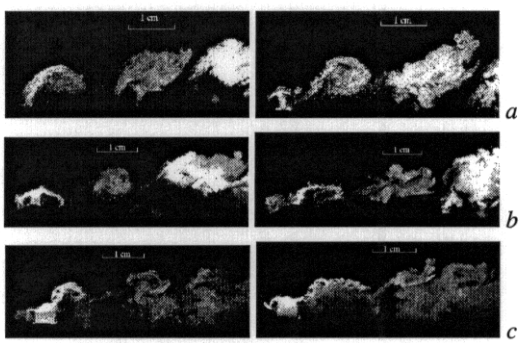


figure 15
Instantaneous side views for the three CJ nozzle types (a:rect1 – b:rect2 – c:circ)

4.2. Longitudinal vorticity

The effects of the CJ geometry are firstly observed very near the CJ exit. The figure 16 shows a fundamental difference between the rectangular and the circular CJ nozzles. The first structures look like those observed in a curved pipe (Dean's vortices). They seem to match the size of the CJ thickness or diameter.

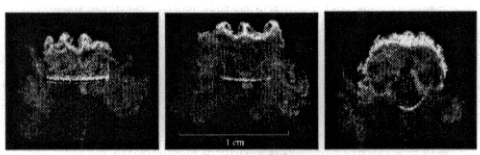


figure 16
Cross-sectional instantaneous views of the CJ at X/D=0.14 (from left to right: rect1, rect2 and circ)

However, looking far downstream (see figure 17), we can see that all these structures rearrange themselves to a pair of counter rotating vortices.



figure 17
Cross-sectional instantaneous views of the CJ at X/D=0.6 (from left to right: rect1, rect2 and circ)

Finally, the results obtained with the side and cross-sectional instantaneous pictures involve an important role of the CJ nozzle geometry on the structures generated in the very first stage of the interaction between the CJ and the free shear layer. The penetration behaviour is also strongly affected by the longitudinal length scale of the CJ nozzle. The next paragraph deals with the influence of the CJ geometry on the structures of the manipulated mixing layer.

4.3. Transversal aspect of the manipulated mixing layer

The figure 18 represents the average pictures obtained for the three CJ nozzles. The seeding is realised with ethanol droplets introduced in the boundary layer inside the main supersonic jet. The effects of the flow rate between the CJ and the main jet are obtained comparing the type *rect1* and *rect2*. It appears that a bigger CJ flow rate results in a more important mixing enhancement. The effects of the CJ nozzle shape is observed between CJ type *rect2* and *circ*, which have the same theoretical flow rate. No fundamental effect of the CJ nozzle shape issues from the average side views of the manipulated mixing layer.

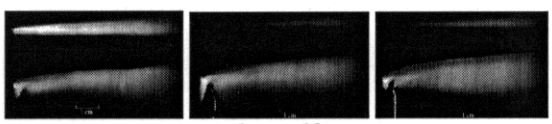


figure 18
Average side views of the manipulated mixing layer (from left to right: CJ type rect1, rect2 and circ)

The figure 19 represents instantaneous side views of the manipulated mixing layer. Both CJ type *rect1* and *rect2* produce well-organised roll-ups in the mixing layer of the main jet. The distance separating these structures is not changed between CJ type *rect1* and *rect2*. However, as the height of the roll-ups is more important for case *rect2*, the Strouhal number is different between CJ type *rect1* and *rect2*.

The picture of figure 19 relative to CJ type *circ* reveals a very complex transversal arrangement of the structures of the mixing layer. Here again, the CJ nozzle geometry is a very important parameter of the size and the kind of the structures of the manipulated mixing layer.

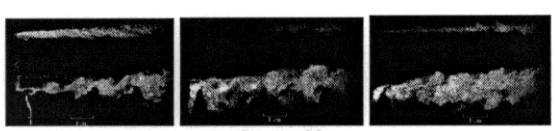


figure 19
Instantaneous side views of the manipulated mixing layer (from left to right: CJ type rect1, rect2 and circ)

5. Conclusion

The pneumatic device seems to be a good mixing enhancement technique for supersonic jets. The spreading rate of the manipulated case is shown to be approximately *20%* bigger than the natural spreading rate. An intermittent behaviour is detected for the CJ penetration in the mixing layer. The mechanism responsible of this behaviour is not well known. Two hypotheses can be done, involving the pressure fluctuations in the mixing layer, or an instability of the interaction between a transverse jet and a free shear layer. May be we could benefit by this intermittence to generated some kind of self pulsed CJ, although keeping a constant CJ stagnation pressure. One can imagine that a so called 'pseudo pulsed' CJ could produce an excitation of the natural Kelvin-Helmoltz modes of the mixing layer.

The study concerning the effects of the CJ nozzle geometry (size and shape) can be considered as a start point for future numerical developments. Since the visualisations presented in this paper put forward the very important part of the CJ geometry in the mechanisms of interaction with the mixing layer, a numerical simulation aiming at the optimisation of the CJ nozzle geometry must take into account the intermittent phenomena occurring in the near field of interaction between the main jet and the CJ.

The future developments of our investigations will concentrate on the intermittent behaviour detected for the penetration of the CJ into the free shear layer. We plan to determine the origins of this behaviour, mostly thanks to simple calculations. We also intend to evaluate the characteristics of the manipulated mixing layer: three-dimensional velocity field near injection, convective velocity of large eddies, and the structure organisation in the far field of the interaction.

References

[1] L.P. BERNAL & A. ROSHKO
"Streamwise vortex structure in a plane mixing layer"
J. Fluid Mech. (1986), vol.170, pp 499-525

[2] J.K. FOSS & K.B.M.Q ZAMAN
"Large and small-scale vortical motions in a shear layer perturbed by tabs"
J. Fluid Mech. (1999), vol.170, pp 499-525

[3] L.J.S. BRADBURY & A.H. KIIADEM
"The distortion of a jet by tabs"
J. Fluid Mech. (1975), vol. 70, part 4, pp. 801-813

[4] K.B.M.Q ZAMAN, M.F. REEDER & M. SAMIMY
"Supersonic jet mixing enhancement by 'delta-tabs'"
AIAA paper 92-3548, July 1992

[5] K.B.M.Q ZAMAN
"Axis switching and spreading of an asymmetric jet: the role of coherent structure dynamics"
J. Fluid Mech. (1996), col. 316, pp. 1-27

[6] M.R. DAVIS
"Variable control of jet decay"
AIAA Journal (1982), vol.20, n°5, pp 606-609

[7] E. COLLIN, S. BARRE, J.P. BONNET
"Supersonic mixing enhancement by radial fluid injection"
Euromech Colloquium 403, Poitiers 2-4 nov. 1999

Application of Active Core Exhaust Control to Eliminate the Core Thrust Reverser on Heavy Lift Aircraft

Clarence F. Chenault*
Air Vehicles Directorate, Air Force Research Laboratory
Wright-Patterson Air Force Base, OH 45433

John D. Dorris†
The Boeing Company
2401E Wardlow Road
Mail Code C078-0019
Long Beach, CA 90807-5309

ABSTRACT

Pulsed jet blowing for mixing enhancement in a hot jet is examined using numerical simulation. Numerical simulations have been completed for a sub-scale turbojet engine, a full scale ground demonstration case, and a High-Bypass Ratio Engine (HBRE). These simulations have shown that pulsed jet blowing can significantly reduce jet plume potential core lengths at static and forward flight conditions. The numerical scheme utilizes large timestep implicit integration for efficiency, and a second order physical space algorithm for robustness. The pulsed jet disturbance is calculated directly and a turbulence model is employed to represent the cascade to smaller length scales. Experimental data corresponding to the numerical simulations are also presented and indicate similar benefits from pulsed jet mixing.

INTRODUCTION

Active flow control technology is currently being evaluated for application in many areas of aircraft development. Performance of high-lift systems for transport and combat aircraft could be enhanced by modifying the effective aerodynamic shape of an airfoil or flap. Aircraft designed for minimum radar cross-section may benefit from thrust vectoring by fluidic injection since control surface deflections could be minimized or eliminated. Boundary layer separation in advanced compact inlets and diffusers may be minimized with the application of synthetic or pulsed jets at the appropriate locations. Control of cavity acoustics with pulsed jets has also been demonstrated by Shaw[1].

An application that has shown particular promise for active flow control technology is the enhanced mixing of a jet plume. For the case of large transport aircraft, three benefits may be realized from the active control of the jet plumes. One, the elimination of the need for a core thrust reverser for engine running offload and backing operations, since the core reverser is used primarily for the thermal protection of personnel loading and/or offloading cargo aft of the aircraft. Two, the reduction of flap temperatures while operating in the powered lift portion of the flight envelope. This benefit could lead to the flap surfaces being constructed of lower cost and lighter weight materials. Three, improved flap capture area for better, powered lift field length performance.

The benefits (and limitations) of active control of jet plumes has recently been investigated experimentally in research efforts conducted by the Boeing Company and the USAF. In one case, the centerline plume temperature reduction was measured for a sub-scale, single exhaust, turbojet engine, the J402-CA-700 (nozzle diameter of 6 inches), while under the influence of an opposing pair of pulsed jets near the external nozzle lip. In a second experiment, a full scale JT8D-15 mixed exhaust turbofan engine was modified to bleed air from the compressor to an array of pulsed jets located internally near the nozzle exit. The experimental setup for the JT8D is shown in Figure 1. Concurrent with the JT8D testing, an effort was undertaken to develop a computational methodology for the prediction of plume flowfields incorporating the unsteady pulsed jet technology demonstrated experimentally. This methodology, once validated, could be used to complement the experimental results and further the understanding of this technology. After validation is demonstrated with the results from the J402 and the JT8D simulations, this

* ACE Control Program Manager, AIAA Senior Member, email: clarence.chenault@va.afrl.af.mil
† Senior Manager, Advanced Airframe/Aircraft Systems, Boeing Transport and Tanker Technology
This material is declared work of the U.S. Government and is not subject to copyright protection in the United States

Paper presented at the RTO AVT Symposium on "Active Control Technology for Enhanced Performance Operational Capabilities of Military Aircraft, Land Vehicles and Sea Vehicles", held in Braunschweig, Germany, 8-11 May 2000, and published in RTO MP-051.

methodology is applied to an HBRE configuration with separate exhausts flow paths utilizing take-off mass flow rates.

To simulate flowfields of this nature, large timestep implicit integration is utilized for efficiency. There is no attempt to directly resolve all temporal and spatial scales. The grid resolution and timestep for the calculation is sufficient to resolve the large scale forced disturbance of the pulsed jet. A turbulence model is employed to represent the cascade to smaller scales. Since the turbulence model includes large scale turbulence effects, one should expect this approach to over predict mixing. For each of the nozzle flows, a steady state (unforced) calculation is completed, and then a forced calculation is initiated beginning from the steady state solution.

GOVERNING EQUATIONS

The Boeing (formerly McDonnell Douglas) compressible flow solver, NASTD, developed by Bush[2], is used. NASTD is the precursor to the WIND flow solver available through the NPARC Alliance. The NASTD flow solver incorporates an unsteady arbitrary inflow boundary condition to simulate the pulsed jet flow. In this case, the boundary condition is applied at the location of the pulsed jet nozzle exit, and thus, the flow within the pulsed jet system is not modeled. One, or more, of several fluid properties can be allowed to vary to simulate the pulsed jet. The unsteady fluid property varies in a sinusoidal fashion according to,

$$P(t) = Po + \Delta P \cos(\omega t + \varphi),$$

Where Po denotes the average of the fluid property, ΔP the amplitude of the perturbation, ω the angular frequency, and φ the phase angle.

Grid Generation

The grid generation software, MACGS, developed by Gatzke et al.[3], is used to construct the 3-D computational grids for the J402, JT8D and HBRE simulations. In order to simplify the grid generation process, the geometries of the J402, JT8D and HBRE were assumed to be axi-symmetric. For example, nozzle plug support structure was not included in any of the cases. Thus, all the computational zones are constructed by a simple rotation about the nozzle axis.

For the nozzle cases under consideration, the domain of interest is assumed to be downstream of the nozzle exit. As such, the downstream outflow boundary is placed at least 20 jet diameters downstream of the nozzle exit to prevent any influence of the downstream boundary in the domain of interest. Minimal grid stretching, e.g. 6% to 8%, in the axial direction is employed to properly resolve the primary forced disturbance. The maximum grid spacing is limited to 1/15 of the characteristic wavelength, λ, in the first 10 jet diameters downstream of the jet exit. The characteristic wavelength of the disturbance for the static round jet is given by,

$$\lambda = 0.6 \text{ ujet} / f$$

where ujet is the fluid velocity at the nozzle exit, and f is the pulse frequency in Hertz. The Strouhal number, a dimensionless scaling parameter for this type of calculation, is defined as

$$St = f*Djet/ujet$$

where Djet is the diameter of the nozzle exit.

Timestep

The solution timestep, Δt, is tied to the frequency, *f*, of the pulsed jets and the stability requirement of the flow solver. It is the stability requirement that sets the maximum allowable timestep for the particular spatial and temporal scheme. The timestep also must resolve the unsteady flow of the pulsed jet, however, with at least 100 timesteps per pulse. Thus,

$$\Delta t = \Delta ymin(CFL)/(ujet+ajet)$$
$$= 1/(\#timesteps/pulse)*f$$

The timestep is adjustable, to a certain extent, through the minimum grid spacing, $\Delta ymin$. The minimum grid spacing, however, is constrained to resolve the smallest features of the nozzle geometry, pulsed jet nozzle exit, and the forced disturbance in the plume.

Turbulence Model

For these calculations, the Menter[4] blended k-ε/k-ω shear stress transport (SST) turbulence model is used. For free shear layers, this model is virtually identical to the Jones-Launder[5] k-ε model for free shear layers.

RESULTS

An example of the computational grid for the J402 turbojet engine nozzle is shown in Figure 2a. The nozzle exit is at x=6.86 inches. The nozzle walls are embedded in the grid clustering in the lower and upper left of the figure. This clustering becomes the clustering for the nozzle shear layers downstream of the nozzle exit. The nozzle plug and the external annular ring that contains the pulsed jets occupy the space not filled with grid. Topologically, the grid is five zones and 1.144 million grid nodes. The minimum spacing of the grid is 0.0075 inches. Figure 2b shows more grid detail near the nozzle exit and pulsed jet. The minimum grid spacing is in this region near the nozzle exit. The pulsed jet is modeled with an arbitrary inflow boundary condition across four grid points at y=3.15 inches. The pulsed jet width is 0.063 inches located just external to the nozzle exit. Both the upper and lower pulsed jet occupies 90 degrees of circumferential arc.

The computational grid for the full scale JT8D-15 mixed flow turbofan engine nozzle is shown in Figure 3a. The nozzle exit is at x=0.0 inches. The split between the core and fan flow is evident at about y= $\pm$15.0 inches on the far left where the two streams enter the domain. The pulsed jets are located on the internal wall of the nozzle approximately two inches upstream of the nozzle exit. Topologically, the grid is eight zones and 1.48 million grid nodes. The minimum spacing for this grid is 0.025 inches. A close in view of the grid near the pulsed jet and nozzle

exit is shown in Figure 3b. Each of the pulsed jets (upper and lower) has a width of 0.925 inches and occupies 90 degrees of circumferential arc.

The computational grid for the full scale HBRE separate exhaust flow turbofan engine nozzle is shown in Figure 4a. The primary (core) nozzle exit is at x=0.0 inches, with a radius of about 15 inches. The secondary (fan) nozzle exit is upstream of the primary nozzle exit at about x=-80.0 inches, with an outer radius of approximately 40 inches. Topologically, the grid is 13 zones and just over one million grid nodes. The minimum spacing for this grid is 0.10 inches. Unlike the modeling done for the J402 and JT8D, a simplified model of the pulsed jet injector is included for the case of the HBRE. This is done to better simulate the flowfield in the region of the pulsed jet exit and the primary nozzle by removing the pulsed jet boundary condition from the nozzle wall. A close in view of the grid near the pulsed jet and nozzle exit is shown is Figure 4b. The pulsed jet exit is 1.5 inches upstream of the primary nozzle exit. Each of the pulsed jets (upper and lower) has a width of 0.80 inches and occupies 45 degrees of circumferential arc. An axial cut through the grid at x=-1.5 is shown in Figure 4c. The physical domain of the pulsed jet injector zones (upper and lower) indeed overlaps the primary nozzle external zone. This overlap, however, is visual only. Computationally, these zones are disconnected.

Pulsed Jet Model

There is more than one way to specify the pulsed jet flow for these calculations. NASTD/WIND allows for time varying Mach.number, pressure (total or static), temperature (total or static), angle of attack, angle of yaw, or velocity, at an arbitrary inflow boundary. The user may even specify a combination of any, or all, of these flow variables. From the experimental results, details of the pulsed jet flow, e.g. Mach number variation at the pulsed jet exit, were not available. The total mass flow of the pulsed jet system, however, was known. Assuming a constant static pressure at the pulsed jet exit, an average Mach number (and temperature) of the pulsed jet is deduced. The variation in Mach number, however, is subjective. For both the J402 and the JT8D configuration, the pulsed jets consisted of an opposing pair covering 90 degrees of circumferential arc for each jet, pulsed harmonically, 180 degrees out of phase.

For the case of the J402, the fluctuation of the pulsed jet exit Mach number from the average Mach number was $\pm$38% (Mach=0.66$\pm$0.25). A plot of the pulsed jet mass flow over one cycle is shown in Figure 5a. The total mass flow for the pulsed jet system is 0.21 lbm/sec, or approximately 3% of the primary nozzle flow.

For the JT8D, the fluctuation of the pulsed jet exit Mach number from the average Mach number was $\pm$72% (Mach=0.58$\pm$0.42). For this case, a plot of the pulsed jet mass flow over one cycle is shown in Figure 5b. The total mass flow for the pulsed jet system is 6.53 lbm/sec, again approximately 3% of the primary nozzle flow.

For the HBRE, the boundary condition for the pulsed jet is applied differently than the previous cases since the actual pulsed jet is being modeled. A harmonically varying total pressure is applied at the inflow of the pulsed jet model. Thus, the Mach number variation at the pulsed jet exit is dependent on the supply total pressure. For this case, the variation was on the order of 0.1 at minimum mass flow and 0.5 at maximum mass flow. A plot of the pulsed jet mass flow over one cycle is shown in Figure 5c. The total mass flow for the pulsed jet system is 2.84 lbm/sec, or approximately 1.5% of the primary nozzle flow.

J402 Simulation Results (Single Exhaust)

Qualitative comparisons of the effects of pulsed jet mixing for the J402 are shown in Figure 6. The contours are of static temperature. Figure 6a shows an unforced or steady state simulation of the plume. A snapshot in time of the forced simulation is shown in Figure 6b. In this view, the cut is through the plume centerline and the circumferential midpoint of the pulsed jets and depicts the flapping mode of the simulation. In this configuration, the amplitude of the flapping plume is well in excess of the nozzle exit diameter. Time averaged static temperature contours are shown in Figure 7. Figure 7a shows the flapping plane, which is essentially the time average of the flapping depicted in Figure 6b. Figure 7b is a view of the transverse plane, or the plane perpendicular to the flapping plane, and does not cut through either of the opposing pulsed jets.

Quantitative comparisons of the time averaged static and total temperature along the plume centerline for the computational and experimental results are shown in Figure 8. Beginning at two nozzle diameters downstream, the computational results predict a dramatic temperature reduction along the plume centerline. At five nozzle diameters downstream, a temperature reduction of 600 degrees is predicted. The experimental results show a similar trend. Discrepancies between the computational and experimental results are expected due to the simplification of the geometry and flow conditions of the computational model, particularly those of the pulsed jet.

JT8D Simulation Results (Mixed Exhaust)

Quantitative comparisons of the time averaged static and total temperature along the JT8D plume centerline for the computational and experimental results of are shown in Figure 9. As in the case of the J402, beginning at roughly two nozzle diameters downstream, the computational results predicted a dramatic temperature reduction along the plume centerline. At six nozzle diameters downstream, a reduction in total temperature of 550 degrees is predicted. The experimental results for this case are shown at 10 nozzle diameters downstream of the nozzle exit.

Notice for this case a marked increase in the static and total temperature of the primary nozzle flow at the nozzle exit. The increase in the total temperature is caused by bleeding the primary engine flow as a source for the pulsed jet flow. The bleeding of the engine also results in a 4% reduction in total pressure of the core flow. The combination of these two effects increases the static temperature on the plume centerline at the nozzle exit roughly 100 degrees F. This effect can be seen in the first two nozzle diameters downstream of the nozzle exit.

Similar qualitative comparisons for the JT8D are shown in Figure 10. As before, contours of static temperature are shown. Figure 10a shows the unforced or steady state simulation. Figure 10b depicts a snapshot of the forced simulation in the flapping plane, the plane that contains a cut through the pulsed jets. As was the case in the J402 simulation the amplitude of the flapping plume exceeds the nozzle exit diameter. Figure 10c is the time averaged static contour levels for the plume in the flapping plane.

HBRE Simulation Results (Separate Exhausts)

The HBRE simulation is the only one of the calculations done for a forward flight condition. Specifically, a takeoff condition at sea level with a freestream Mach number of 0.24. The primary flow NPR is 1.52 with a total temperature of 1014 F. The secondary flow NPR is 1.72 with a total temperature of 157 F. Once again, qualitative comparisons similar to the J402 and JT8D simulations are shown in Figure 11. As before, contours of static temperature are shown. Figure 11a shows the unforced or steady state simulation predictions. Figure 11b depicts a snapshot of the forced simulation in the flapping plane, the plane that contains a cut through the pulsed jets, and Figures 11c and 11d are the time averaged static contour levels for the plume in the flapping plane and transverse plane, respectively.

Quantitative comparisons of the time averaged static and total temperature along the HBRE configuration's centerline are shown in Figure 12. The diffusion of the core exhaust plume of the HBRE configuration is significantly slower than that observed for the cases of the J402 and JT8D. This is due to the influence of the secondary flow that envelops the core flow. One effect of the secondary flow is to increase the convection velocity of the disturbance responsible for mixing, thus increasing the distance downstream of the core nozzle exit where significant temperature reduction along the plume centerline is evident.

An additional effect of the secondary flow is depicted in Figure 11d. The mixing of the plume is naturally most effective in the geometric plane that contains the pulsed jets, the flapping plane. In the plane perpendicular to the flapping plane, the transverse plane, the plume has a natural tendency to bifurcate. For the J402 and JT8D, with no secondary flow, the bifurcation is minimal. For the HBRE, the secondary flow exasperates the bifurcation. Future work will focus on optimizing the pulsed jet configuration, particularly for the HBRE.

CONCLUSIONS

An efficient computational methodology has been developed for the analysis of unsteady pulsed jet mixing flowfields. The benefits of pulsed jet mixing at sea level static conditions are evident in the reduction of plume centerline temperatures aft of approximately two to three nozzle diameters downstream of the nozzle exit. Furthermore, significant differences in plume expansion characteristics are observed between single and mixed exhaust configurations and separate exhaust configurations.

ACKNOWLEDGEMENTS

The authors would like to thank Dr. Steven H. Walker for initiating this work and Dr. Yvette Weber of AFRL for their support as government program managers and comments on this effort. In addition, the efforts and support of Tim Smith, David Smith, and Doug Wiese, all of the Boeing Company, were essential to the success of this work. Funding for this investigation was provided by the Air Force Research Laboratory and the Joint Technical Coordination Group for Aircraft Survivability.

REFERENCES

1 Shaw, L., 1998, "Active Control of Cavity Acoustics," Proc 4th AIAA/CEAS Aeroacoustics Conference, June 2-4, Toulouse, France.

2 Bush, R.H., 1988, "A Three Dimensional Zonal Navier-Stokes Code for Subsonic Through Hypersonic Propulsion Flowfields," AIAA Paper 88-2830.

3 Gatzke, T.G., LaBozzetta, W.F., Finfrock, G.P., Johnson, J.A., and Romer, W.W., 1991, "MACGS: A Zonal Grid Generation System for Complex Aero-Propulsion Configurations," AIAA Paper 91-2156.

4 Menter, F.R., 1991, "Zonal Two Equation k-ε Turbulence Models for Aerodynamic Flows," AIAA 93-2906.

5 Jones, W.P., and Launder, B.E., 1973, "The Calculation of Low-Reynolds-Number Phenomena with a Two-Equation Model of Turbulence," International *Journal of Heat and Mass Transfer*, 16, pp.1119-1130.

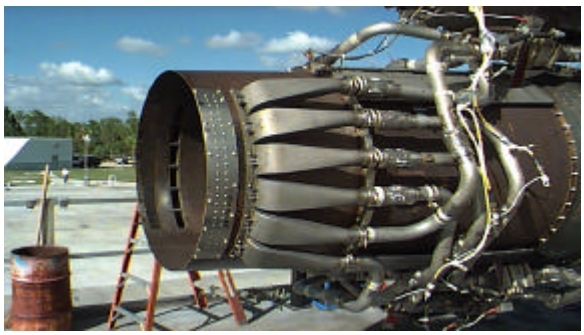


Figure 1. JT8D full scale engine pulsed jet experimental setup

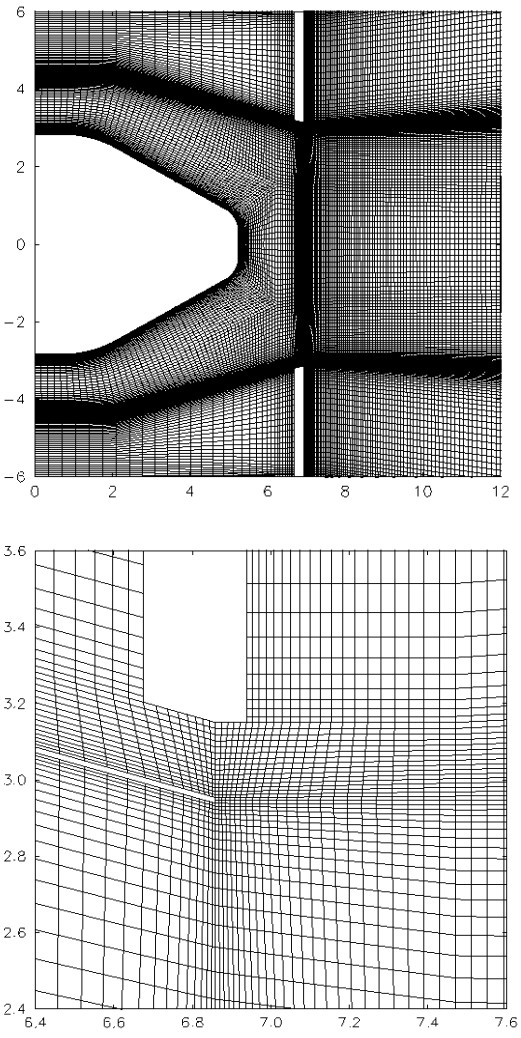


Figure 2. J402 computational grid in the region of the a) nozzle exit, b) nozzle lip and externally pulsed jet.

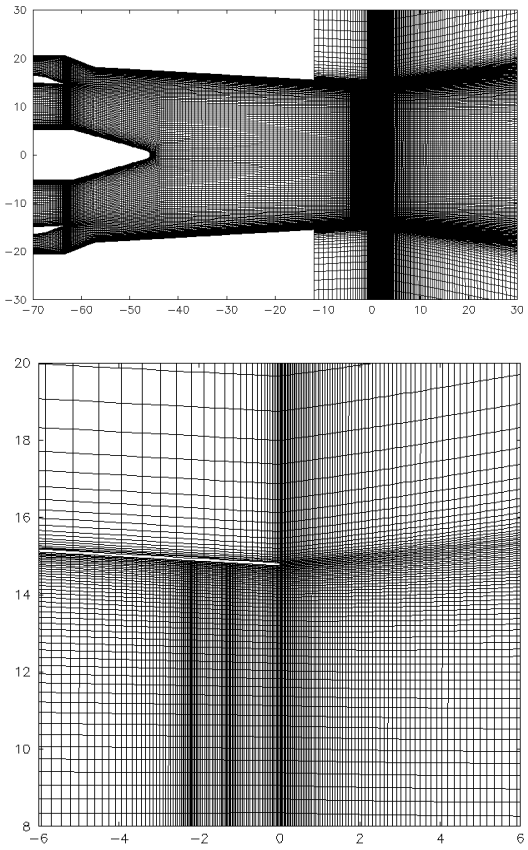


Figure 3. JT8D computational grid in the region of the a) nozzle exit, b) nozzle lip and externally pulsed jet.

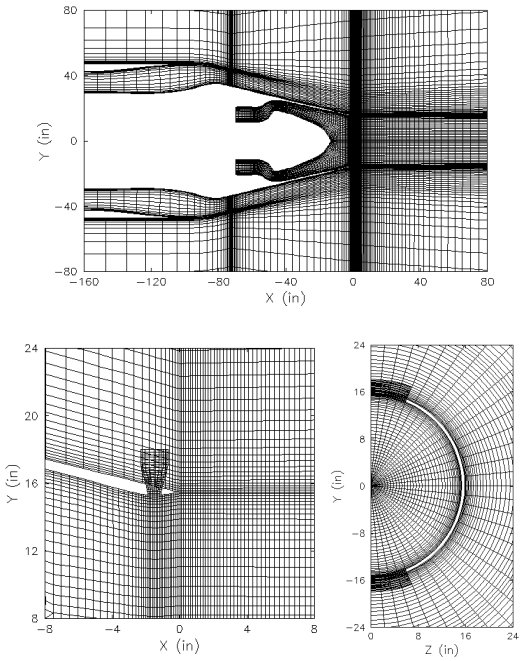


Figure 4. HBRE computational grid in the region of the a) nozzle exit, b) nozzle lip, c) external pulsed jet.

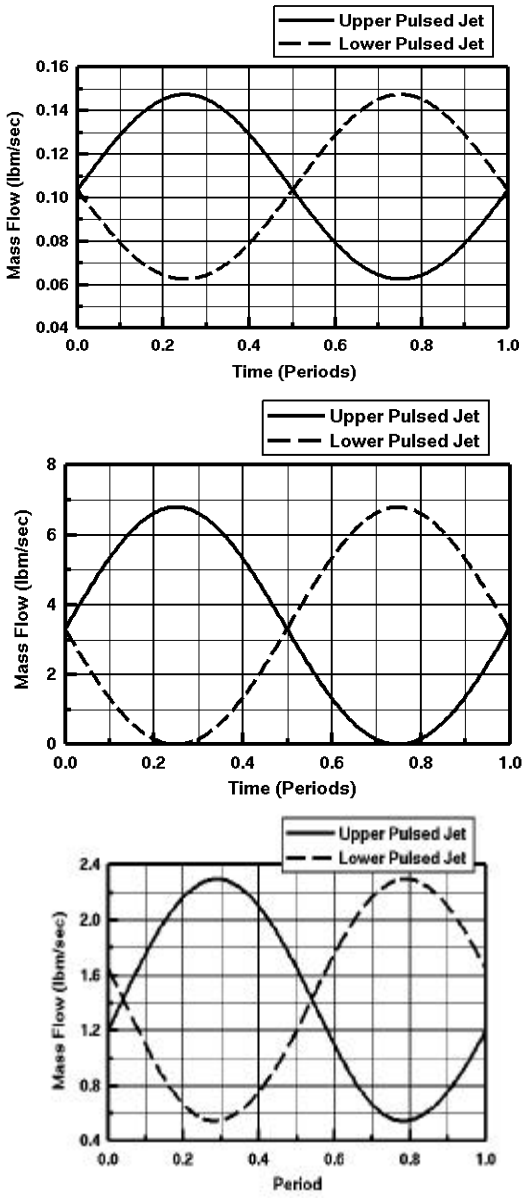


Figure 5. Mass flow for the pulsed jet systems over one cycle a) J402, b) JT8D, c) HBRE.

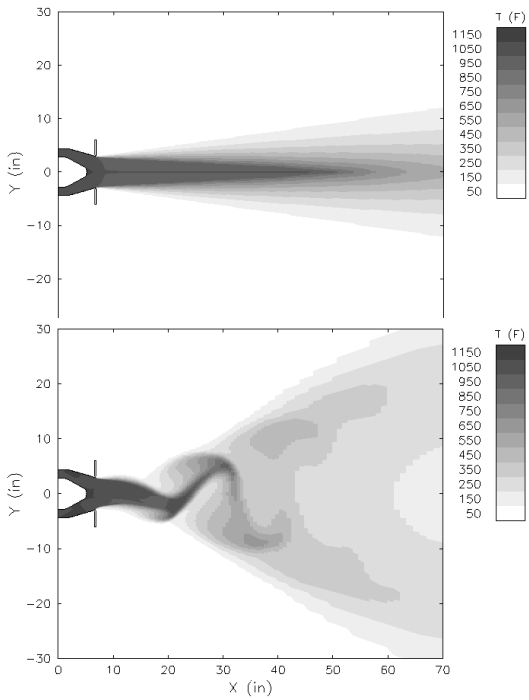


Figure 6. Static temperature (°F) contours from the J402 simulation a) unforced (steady state), b) snapshot of the flapping plane at maximum mass flow of the lower pulsed jet.

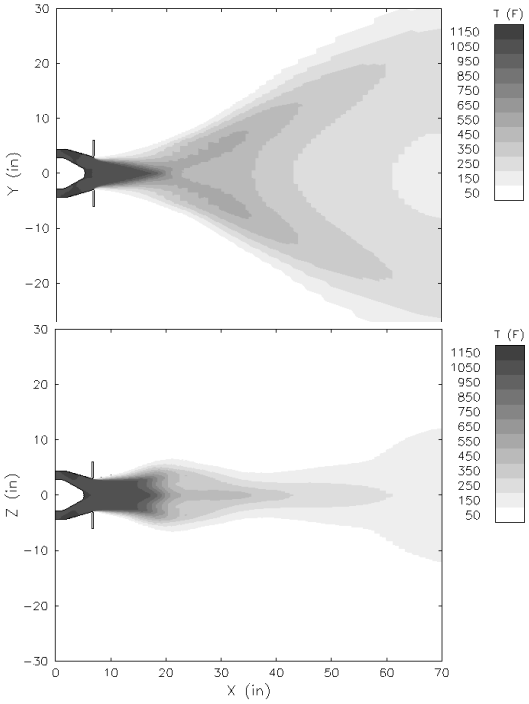


Figure 7. Time average static temperature contours from the J402 forced simulation a) flapping plane, b) transverse plane.

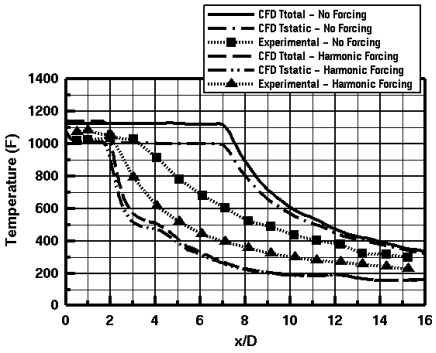


Figure 8. Time averaged plume centerline temperatures for the J402

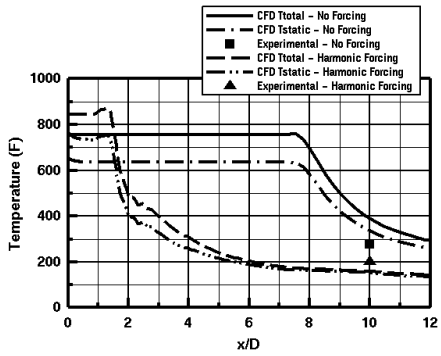


Figure 9. Time averaged plume centerline temperatures for the JT8D

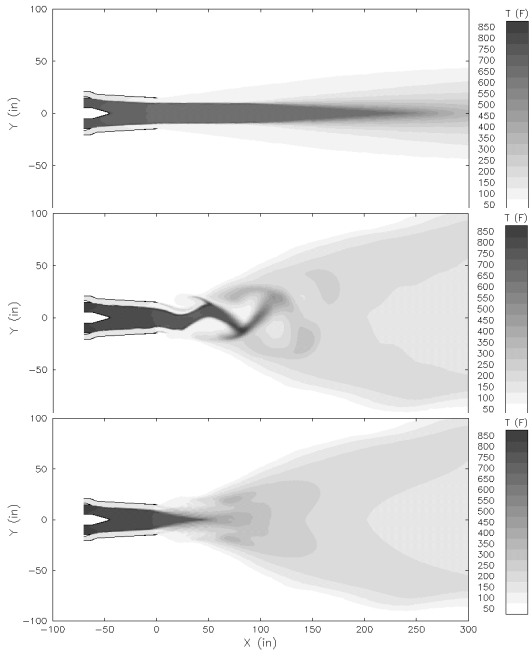


Figure 10. Static temperature (F) contours from the JT8D Simulations a) unforced (steady state), b) snapshot of the forced simulation in the flapping plane at maximum mass flow of the upper pulsed jet, c) time average of the forced simulation in the flapping plane

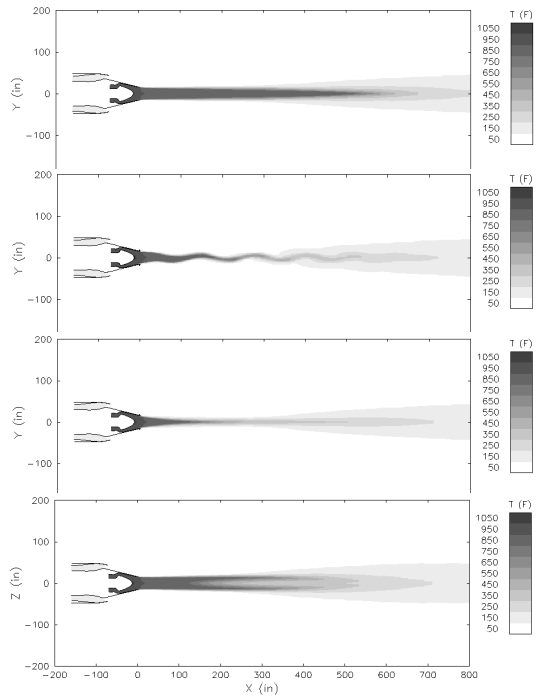


Figure 11. Static temperature (F) contours from the HBRE simulations a) unforced (steady state), b) snapshot of the forced simulation in the flapping plane, c) time average of the forced simulation in the flapping plane, d) time average of the forced simulation in the transverse plane

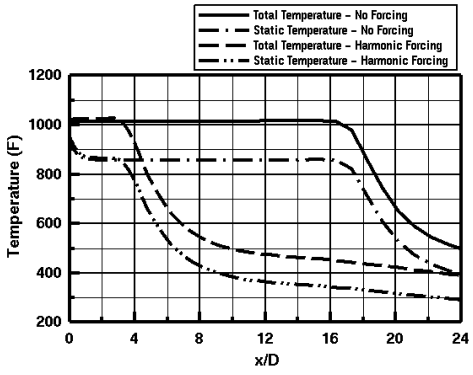


Figure 12. Time averaged plume centerline temperatures for the HBRE

Paper #10

Q by David J Moorhouse: Your first conclusion says an efficient computational methodology was developed, but it overpredicts the measured temperature reduction. You pointed out what was not modeled. It seems like an important result to show what improvements are needed for future CFD development. Please comment.

A. (C. F. Chenault): A comparison of the temperature predictions for the forced and unforced cases clearly implies that turbulence modeling in the root cause of the overprediction. Turbulence is introduced by many mechanisms in the acted turbine engine. Some of these are turbine swirl, steps and gapes in the nozzle surface and from the combustion process. None of the processes or surface imperfections are modeled. These items were ignored because we were only looking for gross flow characteristics and not exact quantities. The large error in the unforced solution was considered acceptable since we were not interested in the region with the large error.

If this is an area where one wishes to improve the prediction. I would recommend modeling the turbine swirl and introduce an initial level of turbulence. If this fails, then a turbulence model tailored for free jet shear flows should be used outside of the nozzle

Q by G.E.A. Meier: Did the periodic control for mixing increase also increase the noise level?

A. (C.F. Chenault): Yes, noise levels did increase on the JT8D Test by 5db $\rightarrow$20db depending on the power setting, pulse frequency and the mass flow rate.

Industria de Turbo Propulsores, S.A.

Thrust Vectoring Nozzle for Modern Military Aircraft

Daniel Ikaza

Industria de Turbo Propulsores S.A. (ITP)
Parque Tecnológico, edificio 300
48170 Zamudio, Spain
daniel.ikaza@itp.es

presented at
NATO R&T ORGANIZATION Symposium
on
ACTIVE CONTROL TECHNOLOGY FOR ENHANCED PERFORMANCE OPERATIONAL CAPABILITIES OF MILITARY AIRCRAFT, LAND VEHICLES AND SEA VEHICLES
Braunschweig, Germany
8th-11th May 2000

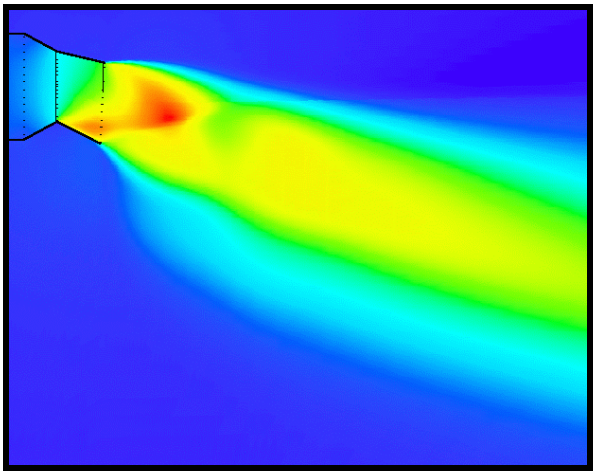


Fig. 1.- CFD Model of a TVN

ABSTRACT

This paper describes the technical features of the Thrust Vectoring Nozzle (TVN) developed by ITP and its advantages for modern military aircraft. It is presented in conjunction with two other papers by DASA (Thrust Vectoring for Advanced Fighter Aircraft High Angle of Attack Intake Investigations) and MTU-München (Integrated Thrust Vector Jet Engine Control) respectively.

Thrust Vectoring: advantages and technology

Thrust Vectoring is a relatively new technology which has been talked about for some time, and it can provide modern military aircraft with a number of advantages regarding performance (improved manoeuverability, shorter take-off and landing runs, extended flight envelope, etc...) and survivability (control possible in post-stall condition, faster reaction in combat, etc...).

Additionally, as a byproduct of Thrust Vectoring, there is also the capacity to independently control the exit area of the nozzle, which allows to have always an “adapted” nozzle to every flight condition and engine power setting. This means an improvement in thrust which in cases can be as high as 7%.

There are several types of Thrust Vectoring Nozzles. For example, there are 2-D (or single-axis; or Pitch-only) Thrust Vectoring Nozzles, and there are 3-D (or multi-axis; or Pitch and Yaw) Thrust Vectoring Nozzles. The ITP Nozzle is a full 3-D Vectoring Nozzle. Also, there are different ways to achieve the deflection of the gas jet: the most efficient one is by mechanically deflecting the divergent section only, hence minimizing the effect on the engine upstream of the throat (sonic) section.

The major aerodynamic aspects of the design of a Thrust Vectoring Nozzle include the correct dimensioning of the vectoring envelope, accounting for the difference between “geometrical” and “effective” vectoring; as well as the sealing pattern of the master and slave petals at and around the throat section.

Paper presented at the RTO AVT Symposium on “Active Control Technology for Enhanced Performance Operational Capabilities of Military Aircraft, Land Vehicles and Sea Vehicles”, held in Braunschweig, Germany, 8-11 May 2000, and published in RTO MP-051.

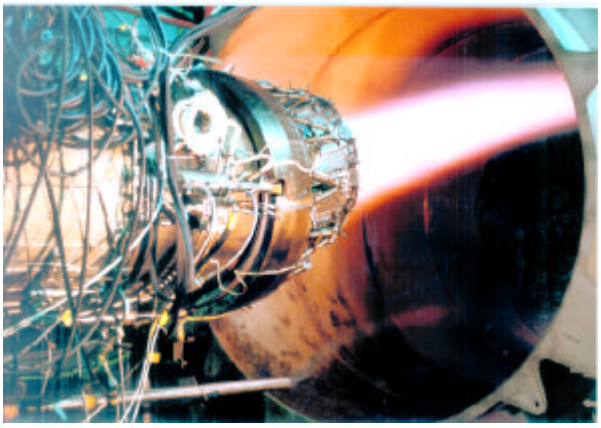


Fig. 2.- TVN ground tests at ITP

ITP Design

The ITP concept consists of a patented design featuring the so-called “Three-Ring-System”, which allows all nozzle functions (Throat Area, Exit Area, Pitch Vectoring and Yaw Vectoring) to be performed with a minimum number of actuators, which, in turn, leads to an optimized mass and overall engine efficiency.

The nozzle is controlled by four independent hydraulic actuators, each one with its own servovalve and position transducer. The level of redundancy will depend on the exact application.

There is also, only at design level, a simplified variant of the nozzle, with three actuators only, which has basically the same functions of the 4-actuator one, except the independent exit area control. This variant would be a little lighter, but it misses the thrust improvement capability.

The reaction bars of the ITP nozzle present an arrangement which allows for high deflection angles, without the risk of petal overlapping and/or disengagement. The present prototype has demonstrated deflections up to 23º, but studies have been performed of variants of the nozzle with deflection angles of up to 30-35º.

Finally, the ITP design makes use of a partial “Balance-Beam” effect, which takes advantage of the energy of the gas stream, on one hand to help close the nozzle under high pressures, hence reducing the maximum load required from the actuators; on the other hand to allow self-closing of the nozzle in case of hydraulic loss under low pressure conditions, specially interesting to retain thrust for take-off.

ITP TVN programme - Past, Present and Future

ITP has dedicated a research programme on Thrust Vectoring technology which started back in 1991, and which met an important milestone as is the ground testing of a prototype nozzle at the ITP facilities in Ajalvir, near Madrid, in 1998. Altitude testing is scheduled for 2000.

The next major goal will be the realisation of a flight programme, in order to validate the system in flight, and evaluate the capabilities and performance of the system as a means of flight control.

The design used for the ground prototype has been a simple one, for short life and limited safety. For the flight standard, a number of changes will be introduced, in order to comply with the very demanding aircraft requirements in terms of weight, life, safety, etc...

The experience acquired during the ground test phase has helped ITP learn a lot about the behaviour of the nozzle, showing areas in which the design has to be modified, providing data for the integration of nozzle and engine controls, etc... The main outcome of the tests has been the confirmation that the concept designed is valid and it works smoothly.

A decisive contribution is being done by ITP’s partner company MTU of Munich, Germany, by developing the electronic Control System.

This programme is making the Thrust Vectoring technology available in Europe for existing military aircraft such as Eurofighter, in which the introduction of Thrust Vectoring could be carried out with a relatively small number of changes to the aircraft and to the engine, and could provide it with an improved performance.

CONTENTS

1.- DEFINITIONS AND ABBREVIATIONS

2.- BACKGROUND

3.- BENEFITS OF THRUST VECTORING AND NOZZLE EXIT AREA CONTROL

4.- TYPES OF THRUST VECTORING

5.- ITP DESIGN: BASELINE AND OPTIONS

6.- ITP THRUST VECTOR PROGRAMME

7.- CONCLUSIONS

8.- ACKNOWLEDGEMENTS

1. - DEFINITIONS AND ABBREVIATIONS

A8	Nozzle throat area
A9	Nozzle exit area
ATF	Altitude Test Facility
CFD	Computational Fluid Dynamics
Con-Di	Convergent-Divergent
DECU	Digital Engine Control Unit
DOF	Degree of freedom
ESTOL	Extremely Short Take-Off and Landing
FCS	Flight Control System
R&D	Research and Development
RCS	Radar Cross Section
SFC	Specific Fuel Consumption
SLS	Sea Level Static
TVN	Thrust Vectoring Nozzle

2.- BACKGROUND

The Thrust Vectoring Nozzle developed by ITP was initially designed to fit and be compatible with an EJ200 engine, which powers the European Fighter Aircraft EF2000. This aircraft is developed by the European consortium Eurofighter, constituted by the companies British Aerospace (UK), DASA (Germany), Alenia (Italy) and CASA (Spain). Similarly, the above engine EJ200 is developed by the European consortium Eurojet, constituted by the companies Rolls-Royce (UK), MTU (Germany), Fiat Avio (Italy) and ITP (Spain).

The current EJ200 engine is equipped with a variable-geometry Convergent-Divergent (Con-Di) Nozzle, developed by ITP. This nozzle can modify the area to match the engine running point and afterburner setting, but it has no vectoring capability.

Through a dedicated R&D programme, ITP have now introduced a new Thrust Vectoring Nozzle which could be applied to EJ200 to significantly enhance the capabilities of EF2000 Aircraft.

Introduction to Military Aircraft Nozzles

In a military aircraft engine with reheat (also called afterburner or augmentor), the nozzle presents a convergent section, which has the task to accelerate the gas jet in order to generate thrust, yet with the characteristic that it must be capable of varying the throat area according to the requirement of the engine running point. These are called "variable geometry convergent" nozzles.

Some nozzles, additionally, comprise a divergent section downstream of the convergent section, which overexpands the jet between the throat area and the exit area in order to extract yet some extra thrust. These are called "Variable geometry convergent-divergent" (or Con-Di) nozzles.

Depending on the level of control upon this divergent section, variable geometry Con-Di nozzles can be of two types:

- One-parameter Nozzles: also called 1-DOF nozzles; the Convergent section (hence Throat Area) is fully controlled, and Divergent section (hence Exit Area) follows a pre-defined relationship to the convergent section behaviour (throat area). The current EJ200 nozzle is of this type.
- Two-parameter Nozzles: also called 2-DOF nozzles; the Convergent section (Throat Area) and Divergent section (Exit area) are fully controlled independently. This type can match the Divergent section to the exact flight condition in order to obtain an optimised thrust.

Also there are some intermediate solutions such as "floating" and some other "passive" means of exit area control, which are outside the scope of this paper.

One solution or the other is chosen according to the particular requirements of each case, in terms of weight, cost, reliability, thrust, priority missions, etc…

In the case of Thrust Vectoring Nozzles, they also have the task to direct the jet to generate side thrust to transmit it to the aircraft structure, so that the aircraft can make use of it as a means of flight and manoeuvre control.

3.- BENEFITS OF THRUST VECTORING AND NOZZLE EXIT AREA CONTROL

Although the description of benefits of Thrust Vectoring and nozzle exit area control for modern military aircraft is in fact the subject of a separate paper by DASA, a brief description of some of them is given here for reference.

They can be basically grouped in four categories:

- Enhanced performance in conventional flight
- Post-Stall flight
- Increased Safety
- Reduction of aero controls

Enhanced performance in conventional flight

The concept of Thrust Vectoring is often associated with spectacular loop-type manoeuvres performed by small aircraft in airshow demonstrations or combat simulations, and the operational use of these capabilities is often regarded with a lot of skepticism, due to the trends of modern air combat. However, there is a lot more to Thrust Vectoring than these funny manoeuvres, and in fact the greatest argument in favour of Thrust Vectoring is not found in combat characteristics but rather in conventional performance, as described in more detail below:

Stationary Flight Trimming

The use of the Nozzles as a complementary control surface allows the aircraft to better optimize its angle of attack in stationary level flight for a given flight point and load configuration, hence reducing the drag, which in turn leads to strong benefits in SFC, and therefore range.

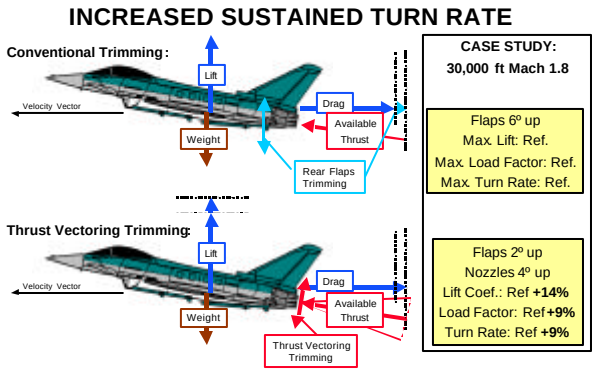


Fig. 3.- Increased Sustained Turn Rate with TVNs

Stationary and Transient Manoeuvres

Similarly to the above case, the nozzles can be used to increase the maximum load factor that is achievable under certain circumstances while maintaining the aircraft trimmed. This applies both for stationary manoeuvres (sustained turn rate) and for transient manoeuvres (rapid deceleration).

Nozzle Exit Area Control

As described in the Introduction to military aircraft nozzles, in one-parameter Con-Di nozzles the divergent section (hence A9) follows a pre-defined relationship to the

convergent section (hence A8). This relationship is optimised for an average of all missions, which normally means low A9/A8 Ratio for dry operations (without reheat) and high A9/A8 Ratio for operations with reheat.

In rough terms, this is reasonably optimised for low speed dry operations (cruise, climb, etc...) and for high speed reheat operations (high speed strike, etc...), but is not optimised for low speed reheat operations (take-off) and high speed dry operations (supersonic cruise).

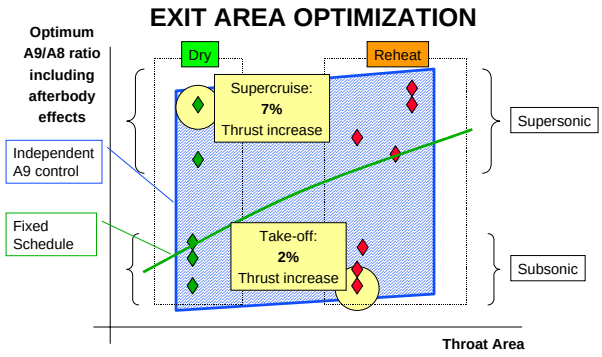


Fig. 4.- Optimization of Nozzle Exit Area

The use of an independently controlled divergent section allows A9 to be optimised for any engine running condition at any flight point, and has an improvement especially in those conditions where one-parameter A9/A8 Ratio is not optimized.

For example, for a supersonic cruise case (Mach 1.2, altitude 36,000 ft, engine at Max Dry condition) of EJ200 engine on Eurofighter, the use of independent A9 control could lead to an improvement of up to 7% in installed net thrust relative to the current performance. This is due to the combination of two effects: increase of nozzle internal thrust; and reduction of nozzle external drag.

In addition to thrust increase, independent A9 control also permits reduction in SFC for certain flight points.

Reduction of take-off and landing runs

The rotation of the aircraft for take-off and landing can be accelerated by using Thrust Vectoring. Also, Thrust Vectoring can be used to increase angle of attack, hence lift, while maintaining a trimmed aircraft. The combination of all these effects gives an important reduction in the take-off and landing runs for an aircraft such as Eurofighter.

Global mission performance

The combined effect of all the above items across a typical combat mission could add up to some 3% Fuel saving by using Thrust Vectoring.

Post-Stall Flight

The most spectacular benefit of Thrust Vectoring, although possibly not the most important, is the fact that it can exert an active control of an aircraft while the main aerodynamic surfaces are stalled, hence not suitable for control, and this opens a whole new domain of flight conditions where flight used to be unthinkable.

Extension of flight envelope

The use of Thrust Vectoring permits the aircraft to hold stationary flight in an area of the envelope where conventional controls are not sufficient.

In the Altitude/Mach-number envelope, Thrust Vectoring permits an extension of the envelope in the low speed-medium height region. In the Altitude/Mach-number/Angle-of-attack envelope, Thrust Vectoring permits operation at much higher values of Angle of attack.

Air superiority

A better control of the aircraft is achieved with Thrust Vectoring, especially at low speed conditions, where conventional aerodynamic controls are not effective, and where a good number of combat scenarios are to take place.

ESTOL

The ESTOL concept (Extremely Short Take-Off and Landing) is becoming more and more appealing to military aircraft operators, and it consists of performing the Take-off and Landing manoeuvres with the aircraft stalled. It reduces take-off and landing runs by a large amount.

This is only possible with Thrust Vectoring Nozzles, that operate when the aerodynamic controls are no longer useful.

Increased safety

This is probably one of the strongest arguments in favour of Thrust Vectoring. The existence of redundant means of aircraft control allows for a better survivability.

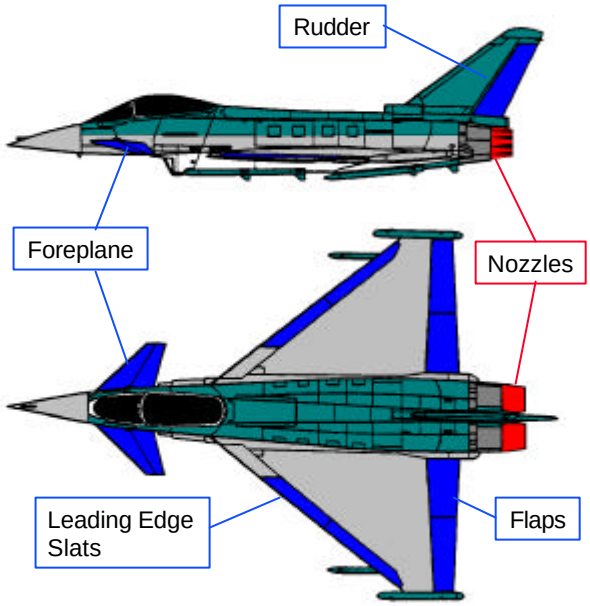


Fig. 5.- Redundant Flight Controls with TVNs

In peace time, an aircraft crash by loss of aerodynamic control could be avoided by the use of Thrust Vectoring.

In war time, damage to aerodynamic control surfaces can be compensated with Thrust Vectoring.

Next Step: reduction of aero controls

Once the Thrust Vectoring system has been sufficiently validated, it will be a primary control for the aircraft. This

means that it will allow a gradual reduction of existing conventional aerodynamic control surfaces such as horizontal and vertical stabilizers. This will have an impact, and there will be a reduction in:

- Mass
- Drag
- Radar Cross Section (RCS)

The extent of these impact could only be properly assessed in the future, and it will probably not be fully exploited until the next generation of combat aircraft, but mass reductions of 15%-20% of the total aircraft are conceivable.

4.- TYPES OF VECTORING NOZZLES

From the point of view of the type of actuation means, TVNs can be classified:

- Fluidic Actuation: The deflection of the gas flow is achieved by injection of secondary airflows. This type is specially suitable for fixed-area high expansion nozzles, such as those used in rockets and missiles.
- Mechanical Actuation: The deflection of the gas flow is achieved by mechanical movement of the nozzle, which is powered by hydraulic or pneumatic actuators. This type is specially suitable for variable geometry military aircraft nozzles.

* * *

From the point of view of the direction of vectoring, TVNs can be classified:

- Single-Axis TVNs: (also called 2-D or Pitch-only) The deflection of the gas flow is achieved in vertical direction only. They replace and/or complement horizontal control surfaces. This type is suitable for all types of variable geometry military aircraft nozzles.
- Multi-Axis TVNs: (also called 3-D or Pitch and Yaw) The deflection of the gas flow is achieved in any direction. They replace and/or complement horizontal and vertical control surfaces. This type is specially suitable for round nozzles.

* * *

If we focus on 3-D, Con-Di military aircraft TVNs with mechanical actuation, there are several ways to materialise the vectoring:

- Deflect whole nozzle. The disadvantages are: a large mass has to be moved; and there is a big impact on performance upstream of the nozzle.
- External Flaps. The disadvantages are: there is a need for additional mass; and the efficiency of vectoring is very low.
- Deflect Divergent section. This is the preferred solution. the size of the nozzle is optimised and the effect on performance is negligible. The ITP Nozzle is of this third type.

EXISTING 3-D THRUST VECTORING SYSTEMS

Mechanical Actuation, Con-Di Military Nozzles

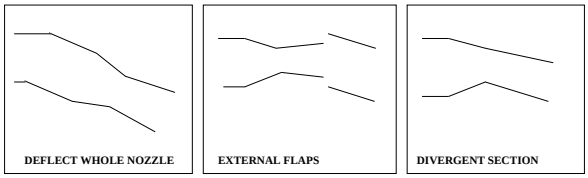


Fig. 6.- Existing types of 3-D TVNs

Regarding the nozzles of the third type, that is, those that deflect the flow by orienting the divergent section only, they generally need actuation means for:

- Controlling convergent section (hence A8)
- Controlling divergent section (hence vectoring and A9)

Where other designs make use of two separate actuation systems, the ITP design has a unified actuation system with a minimum total number of actuators.

5.- ITP DESIGN: BASELINE AND OPTIONS

One of the biggest problems encountered when designing a Thrust Vectoring Nozzle is how to find a mechanical configuration comprising casing, rings, etc…, which must be compatible with both functions of the nozzle: on one hand, open and close the convergent section to control throat area (optionally open and close the divergent section to control exit area); and on the other hand to direct the nozzle in directions different to axial, to obtain the jet deflection that provides vectored thrust.

The other big problem of a Thrust Vectoring Nozzle is how to find an actuation system (hydraulic, pneumatic, electro-mechanical, mixed, etc..) capable of generating the movements required in the nozzle, to accomplish all the above functions, and reasonably limited under criteria such as weight, size, etc…

Many different configurations have been studied at ITP for TVNs, the result being a “baseline” configuration, plus a series of options available for every particular application.

The main option is the A9 modulation capability, aimed at optimising the thrust as described above in the chapter “Benefits of Thrust Vectoring and nozzle area control”.

Baseline

The baseline ITP TVN design is a Convergent-divergent axisymmetric (round) nozzle with multi-axis Thrust Vectoring, mechanically actuated, and where the deflection of the gas flow is achieved by orienting the divergent section only. This way the moving mass is minimized, and the distortion to the engine turbomachinery upstream of the nozzle is negligible.

It has three degrees of freedom (DOFs), namely: Throat area (A8), Pitch vectoring and Yaw vectoring. Any oblique vectoring is made of a combination of pitch and yaw. Exit area (A9) follows a certain relationship to A8.

The actuation system consists of only three independent hydraulic actuators, a fact which is made possible by the basic feature of the design: the “Three-Ring-System”.

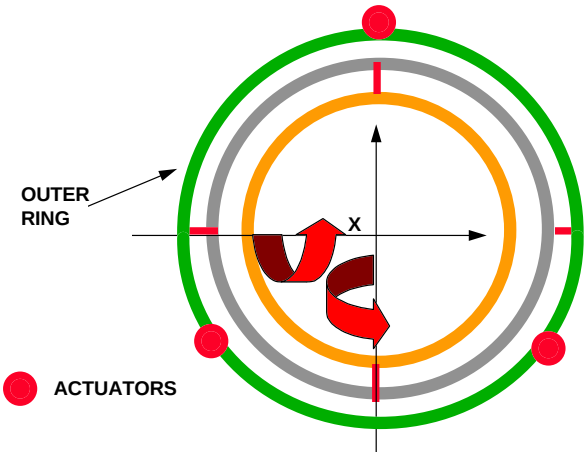


Fig. 7.- Three Ring System (3 actuators)

This system consists of three concentric rings which are linked by pins and form a universal (or "cardan") joint. The inner ring is linked to the convergent section of the nozzle, the outer ring is linked to the divergent section through the reaction bars, and the intermediate ring acts as the crossbar between the inner and outer rings. The actuators are linked to the outer ring only. The design of the rings and reaction bars is such that a small tilt angle on the ring is amplified to a large deflection angle on the divergent section.

The outer ring can be tilted in any direction while the inner ring can only keep a normal orientation to the engine centreline, but they both are forced to keep the same axial position along the engine. This is the key factor that permits a full control of the nozzle by acting on the outer ring only, hence minimizing the total number of actuators.

For pure throat area movements, all three actuators move in parallel, hence all three rings follow axially, and A8 is set to the appropriate value. A9 follows a pre-defined relationship to A8 according to the dimensions of the mechanism.

For Pitch and/or Yaw vectoring movements, the three actuators move differently, hence defining a tilt plane of the outer ring. The divergent section will deflect in the direction of that plane. Throat area (A8) is not affected unless this movement is combined with a throat area movement.

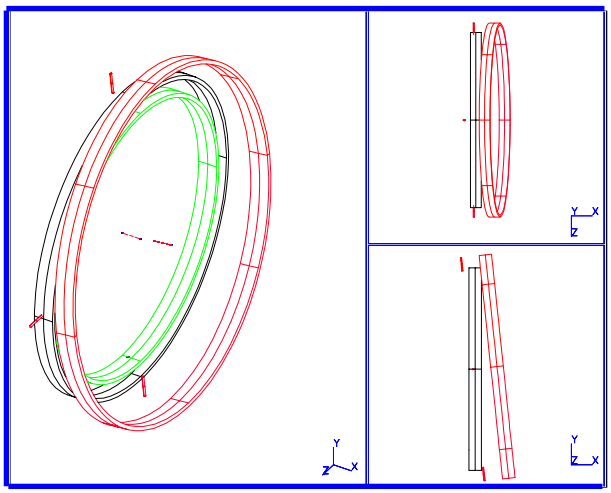


Fig. 8.- Ring Movement in vectoring

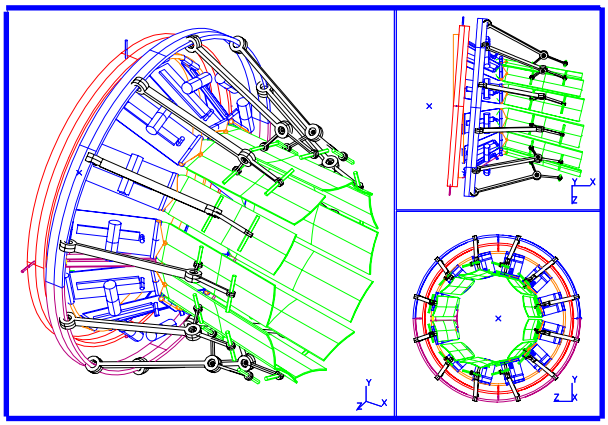


Fig. 9.- Nozzle Movement in vectoring

A9 Control option: optimised thrust

This option consists basically of the baseline design, except for the fact that the outer ring is split in two halves, forming a "hinged" outer ring.

It has four degrees of freedom (DOFs), namely Throat Area (A8), Exit Area (A9), Pitch vectoring and Yaw vectoring. Again, any oblique vectoring is achieved by combination of pitch and yaw.

The actuation system consists of four independent actuators, also linked to the outer ring only.

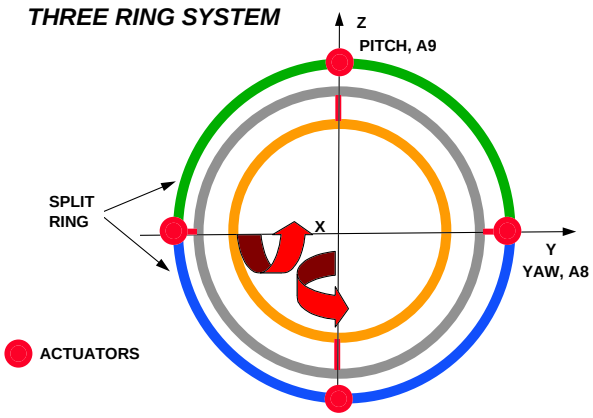


Fig. 10.- Three Ring System (4 actuators)

The same Three Ring principle is used as in the three actuator version, and A8 and vectoring movements are operated in a similar way, yet this time with four instead of three actuators.

Additionally, pure A9 control movements are performed by moving top and bottom actuators in parallel while the other two stay static, hence "hinging" the outer ring open or close. The divergent section opens or closes relative to the nominal position, acquiring an "oval" shape. Hence this movement is sometimes referred to as "ovalization". Of course, A9 movements can be combined with A8 movements and/or vectoring movements.

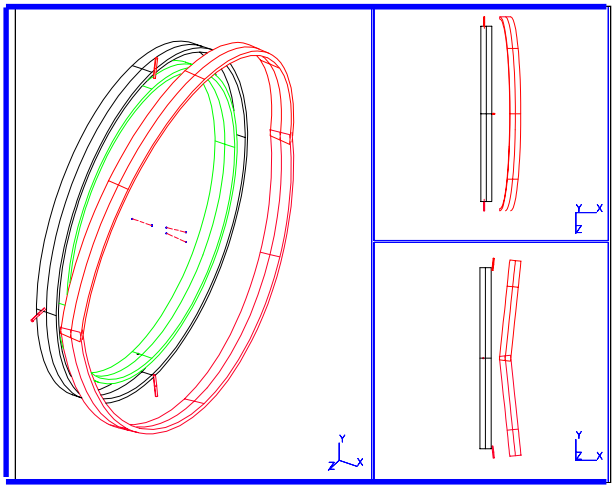


Fig. 11.- Ring Movement in A9 control

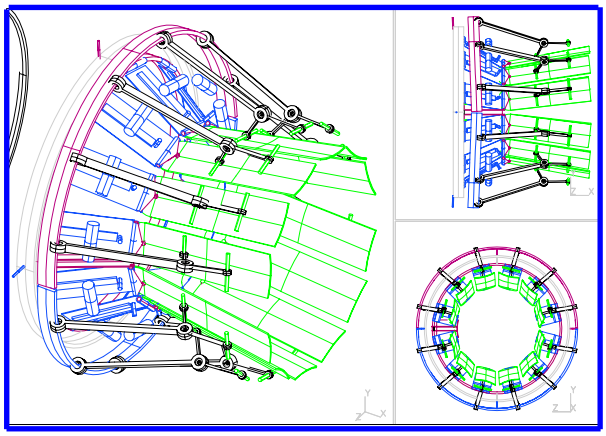


Fig. 12.- Nozzle Movement in A9 control

With this configuration there could be an improvement in installed net thrust of up to 7% in certain conditions.

In fact, this A9 option could well be considered as the baseline, leaving the non-A9 configuration as a “simplified option”.

Third Member of the Family: "Two-Ring" Pitch-only Nozzle

This is a simplified version of the ITP Nozzle where the intermediate Ring is deleted, hence reducing some weight and complexity. Outer Ring is split in two as in previous version.

It retains the four actuators and it has three DOFs (A8, A9, Pitch Vectoring).

It is suitable for application in aircraft with no Post-Stall capability, but where the benefits in conventional flight are important.

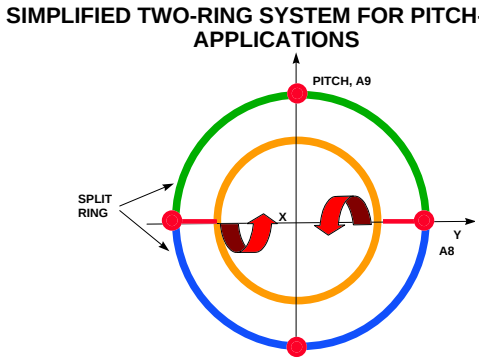


Fig. 13.- "Two-Ring" Pitch-only Nozzle

Other features: "hinged" Reaction Bars

The design of the reaction bars presents “hinged struts” which allow an optimised smooth movement of petals. Where other designs are limited to about 20º geometric deflection by the disengagement and/or interference between petals, the ITP design allows for growth if required, and studies have been carried out for deflections up to 30º-35º.

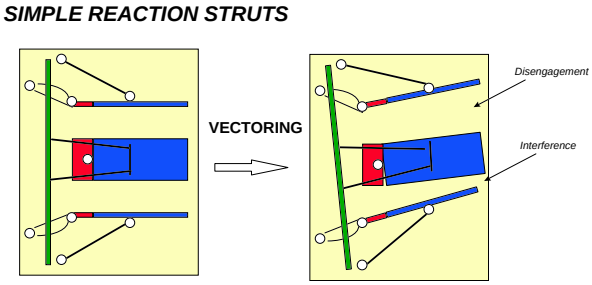


Fig. 14a.- Vectoring with simple reaction bars

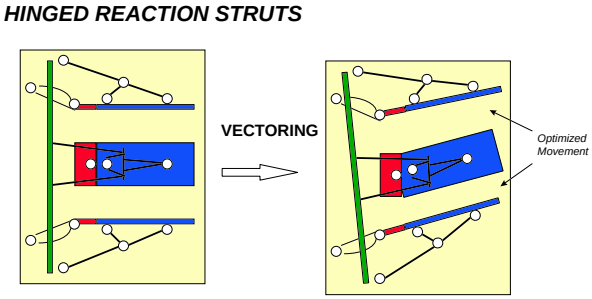


Fig. 14b.- Vectoring with hinged reaction bars

Balance-Beam

The ITP TVN makes use of a partial balance-beam effect, which consists of taking advantage of the energy of the gas stream to help close the nozzle in high pressure conditions.

The closing movement of the nozzle is accompanied by an axial displacement of the throat, so that the volume swept against the gas pressure is modified, in particular more volume is swept in the low pressure region of the nozzle, and less volume in the high pressure region.

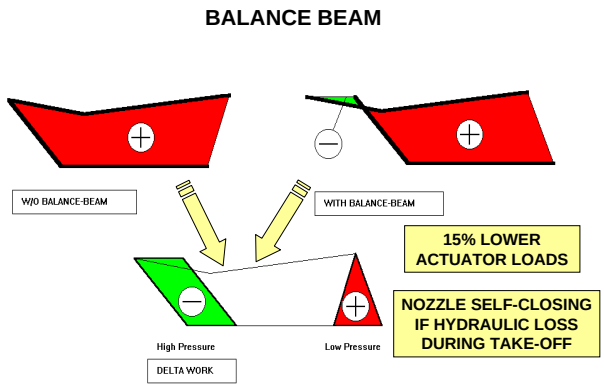


Fig. 15.- Balance Beam effect

This has two benefitial effects:

- On one hand, in high pressure conditions, the total work performed by the actuation system upon the gas stream is reduced by as much as 15%, which results in smaller actuator dimensions and better engine efficiency.
- On the other hand, in case of hydraulic loss in low pressure conditions, the nozzle self-closes, which is particularly interesting to retain thrust during take-off.

Actuation and Control System

The control system of the nozzle consists of three (baseline design) or four (A9 option) independent actuators, each with its own servovalve and position transducer. The servovalves are powered by the engine hydraulic pump; the electronic control loops and safety logic between servovalves and transducers are performed by the TVN Control Unit, which is built into the engine DECU, which, in turn, is connected to the aircraft Flight Control System (FCS).

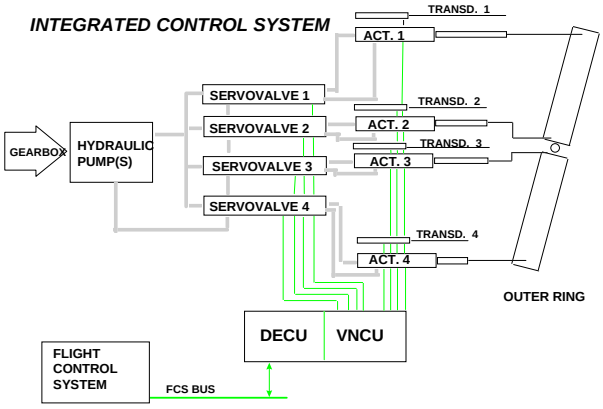


Fig. 16.- TVN Control System

For a twin-engine application such as Eurofighter, a simple hydraulic system and dual electrical system provide enough safety for a primary control.

On the other hand, for a single-engine application, there will probably be a need for duplex hydraulic system and triplex electrical system.

Changes to EJ200 engine

Relative to current EJ200 engine, the introduction of a TVN with "full capability" implies a number of changes:

- Nozzle
- Nozzle actuators, including Servovalves and transducers
- Bigger Hydraulic Pump
- DECU, including Thrust Vectoring functions
- Casing reinforcement
- Slight modification to engine mounts
- Reheat Liner, especially rear attachment
- Dressings (pipes and harnesses)

However, a reduced-capability TVN version of EJ200 is feasible with very minor changes.

In any case, these changes are small if compared with the advantages obtained by introducing Thrust Vectoring.

Advantages of ITP design

In summary, the ITP design presents a number of advantages relative to other designs, such as:

- **Minimum number of actuators**, which leads to lower weight and better overall engine efficiency.
- Unique reaction bar design for **high deflection angles**.
- Partial **Balance-Beam** effect for lower actuator loads.
- Nozzle **self-closing** in case of hydraulic loss during take-off allows thrust retention
- It is the only **proved example** of 3-D TVN for 20,000 lbf thrust engine class.

6.- ITP TVN PROGRAMME

ITP's R&D programme on Thrust Vectoring technology started in 1991, and within this programme a good number of general studies have been performed, including:

- CFD analyses
- Performance studies
- Concept design: Baseline plus options
- Trade-off studies with side loads, number of petals, etc...
- Patents
- Mechanical / Kinematic simulations
- Mock-ups
- etc...

* * *

Additionally, a feasibility study has been carried out together with DASA regarding the application of TVN for Eurofighter. The outcome of this study includes the definition of the requirements for the TVN on the

Eurofighter, and some of the operational benefits expected for Eurofighter.

An initial study was done in 1994-95, and an update study is being conducted now 1998-2000, this time with MTU also taking part.

* * *

ITP and MTU have a special co-operation agreement under which MTU has developed the electronic Control System that controls the ITP TVN and actuators.

Prototype Nozzle

In 1995 ITP launched what is called a "Technology Demonstration Phase" within the Thrust Vectoring technology R&D programme. This phase includes the design, construction and test of a prototype Thrust Vectoring Nozzle. The design of the prototype started in early 1996 and the first run took place in July 1998, becoming the key milestone in ITP Thrust Vectoring programme so far.

This prototype nozzle was aimed at demonstrating as much as possible, even if some things were not necessarily required from the aircraft point of view. Therefore it was designed for high vector loads (30 kN) even if the aircraft requirement will be not higher than 15 kN. Similarly, it incorporated the A9 option to optimise thrust. A deflection of 20º was specified for any engine running condition.

The prototype nozzle was constructed for an EJ200 engine vehicle, but maintaining a minimum impact on current EJ200, both regarding the hardware changes, as well as regarding the development programme.

In principle, only Sea Level Static (SLS) tests were scheduled, namely the ITP testbed in Ajalvir, near Madrid. However, the nozzle was specified to take the loads of the full flight envelope, and real flight standard materials were used in its construction, so that the mechanism could be validated as far as possible.

Most of the components were manufactured in ITP, hence keeping a high degree of flexibility to introduce quick changes in the design.

As part of the work associated to the tests of the prototype nozzle, a new detuner (exhaust duct) had to be installed in the ITP testbed (Cell No.2) at Ajalvir. The need for this new detuner was motivated both by the different flow pattern in the cell, and also by the need for cooling.

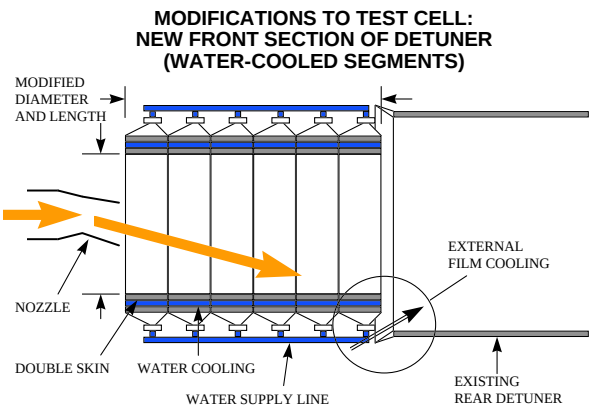


Fig. 17.- Modifications to Test Cell

* * *

The test results obtained during the running of the prototype include the following highlights:

- 80 running hours, including 15 with reheat
- Vectoring in all 360º directions, both dry and reheat
- 23,5º maximum vector angle
- 110º/sec maximum slew rate
- 20 kN maximum lateral force
- Programmed ramps and Joystick control
- Thermal case: sustained 20º vector in reheat for 5 minutes
- Rapid transients Idle-Dry-Reheat while vectoring
- 100+ performance points run
- Exit area control: 2% thrust improvement
- Endurance: 6700+ vectoring cycles
- Endurance: 600+ throttle cycles (with sustained 20º vector)

The nozzle performed smoothly and free of mechanical failures

* * *

The conclusion of the ground tests in Ajalvir represents the fulfilment of the Technology Demonstration Phase. From this point onwards, the next steps to be taken include a continuation of the general studies on Thrust Vectoring, as well as the continuation of the feasibility study with DASA and MTU.

Additionally, altitude tests with the prototype nozzle are scheduled for the second quarter of 2000 at the Altitude Test Facility (ATF) in Stuttgart.

The next big milestone in he Thrust Vectoring programme will necessarily be a flight programme, in order to validate the TVN in flight condition. Consequently, ITP as well as all ITP's partners are strongly pursuing this possibility.

ITP THRUST VECTORING NOZZLE PROGRAMME

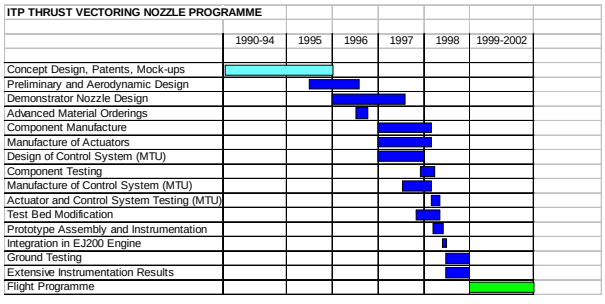


Fig. 18.- ITP Thrust Vectoring programme

7.- CONCLUSIONS

- Thrust Vectoring offers great advantages for modern military aircraft, in return for relatively small changes in the aircraft, and is clearly the way to go for the future.

- Thrust Vectoring technology has become available in Europe, helped by the R&D programme conducted by ITP, especially after the ground test of the prototype nozzle.
- The ITP design presents some advantages relative to other designs, which may prove vital on the long term.
- The aerospace community in Europe is actively in favour of this technology, and the institutions are willing to support this.
- With a very small number of changes to EF2000, a demonstration flight programme would be possible and produce a very important stepping stone for the introduction of this technology into service.

8.- ACKNOWLEDGEMENTS

The success of ITP's programme has only been possible with the contribution of partners and organizations, namely:

Spanish Ministries of Industry and Defence, with funding through an R&D programme

MTU, of Munich, Germany, developed the electronic control system under a dedicated agreement with ITP.

Eurojet and the Partner Companies (**Rolls-Royce**, **MTU** and **Fiat-Avio**), as ITP's partners in the EJ200 development programme for Eurofighter, gave support to ITP.

CESA, of Getafe, Spain, designed the hydraulic actuators for the TVN.

Sener, of Las Arenas, Spain, who started in the programme many years ago, also contributed to the engineering work of the programme.

DASA, of Munich, Germany, as partner in the Eurofighter feasibility study, provided the assessment of requirements and benefits for EF2000 with TVN.

Paper#A11

Q, by P. M. Lodge: What is the level of redundancy of the nozzle actuation?

A. (D. Ikaza) Simplex for the ground tests. Simplex will also be taken to flight for EF2000

This page has been deliberately left blank

Page intentionnellement blanche

Integrated Thrust Vectored Engine Control

Rausch Christian

Lietzau Klaus

Motoren- und Turbinen-Union München GmbH

Dachauer Straße 665

80995 Munich

Germany

Thrust vectoring has the potential to provide significant improvements in combat aircraft performance and flexibility. As Eurofighter Typhoon moves into the production phase, Industria de Turbo Propulsores (ITP) and Motoren- und Turbinen-Union München GmbH (MTU) are pursuing a research and technology acquisition project to investigate the design of a thrust vectoring nozzle system suitable for future applications of the EJ200 engine. This paper describes the work related to the engine control system carried out thus far by MTU within the ITP/MTU thrust vectoring technology programme.

Abstract

Thrust vectoring is a key technology for future combat aircraft. Together with an advanced thrust vectored engine control system, the ITP thrust vectoring nozzle concept with a common actuation system for all nozzle functions (throat area, exit area and all axis vectoring) is an appropriate solution to meet the stringent requirements concerning performance, reliability and safety resulting from the intended use of thrust vectoring for flight control. An enhanced link between the flight control system and the engine control system will be necessary and the combined engine and nozzle control will have to meet new functional requirements. These requirements are on one hand related to the nozzle itself and on the other hand to the interactions between the nozzle and the engine.

Compared to present jet engine control, e. g. the Eurofighter "Typhoon" engine EJ200, the main differences concerning the control system hardware arise due to the additional actuators for the vectoring nozzle and the corresponding drive and sensing equipment. This results in a higher number of external interfaces for the FADEC (**F**ull **A**uthority **D**igital **E**ngine **C**ontrol) and hence a further step of hardware miniaturization and increases in computing power are necessary to maintain / reduce the volume and mass of the engine control unit. The main task of the vectoring nozzle control is to drive the nozzle actuators according to demanded side forces and demanded effective throat and possibly exit areas. This involves both computation of nozzle kinematics and resultant gas flow, i. e. effective areas and thrust components. A key item of the nozzle control is to keep the nozzle during all steady-state and transient conditions within its allowed operating range, which is defined by geometrical limits and maximum allowable forces. Besides response time and accuracy requirements have to be met.

Interactions between nozzle and engine are numerous – not only because of the coupling of the different nozzle functions due to the unified actuation system. During vectoring resulting side forces are determined not only by the nozzle but also by the engine thrust. On the other hand vectoring may have an influence on the effective throat area and thus on engine operation – especially in reheat conditions. Additional dependencies are related to failures and abnormal operation of the nozzle and the engine itself. A common supervisory logic ensures optimum detectability and advanced reversionary modes include coordinated actions upon engine and nozzle control.

This paper describes the work related to the engine control system done at MTU within the ITP/MTU thrust vectoring technology program. Starting from the current Eurofighter "Typhoon" EJ200 FADEC, the modifications to operate the thrust vectored engine demonstrator (EJ200 + ITP 3D vectoring nozzle + MTU control system) are described. All control functionality needed for safe and flexible bench testing of the complete thrust vectored engine has been developed.

Finally a closer look to a production solution is given. The modern thrust vectored jet engine will be controlled by a single FADEC providing thrust and side forces as commanded by the flight control system. Also extensive monitoring functions will be included within the FADEC. A clear and simple interface will provide a suitable interaction between the flight control system and the engine control system, which becomes essential for future thrust vector application.

Paper presented at the RTO AVT Symposium on "Active Control Technology for Enhanced Performance Operational Capabilities of Military Aircraft, Land Vehicles and Sea Vehicles", held in Braunschweig, Germany, 8-11 May 2000, and published in RTO MP-051.

Nomenclature

AFCS	Air Flow Control System
ATF	Altitude Test Facility
A8	Convergent Nozzle Area
A9	Nozzle Exit Area
CFD	Computational Fluid Dynamics
DAS	Data Acquisition System
DEAR	DECU EMU Acceptance Rig
DECU	Digital Electronic Control Unit
DMSU	DECU Monitoring and Setting Up Unit
DPR	Dual Port RAM
EJ200	Jet Engine of Eurofighter Typhoon
EMU	Engine Monitoring Unit
FADEC	Full Authority Digital Engine Control
FCS	Flight Control System
FPGA	Field Programmable Gate Array
HPC	High Pressure Compressor
IO	Input / Output
LP	Low Pressure
MSU	Mil-bus 1553 Simulation Unit
PBAY	Pressure Engine Bay
PC	Personal Computer
PL	Power Lever
PLD	Power Lever Demand
PWM	Puls Width Modulation
RAM	Random Access Memory
TV	Thrust Vector
TVCU	Thrust Vector Control Unit
TVN	Thrust Vectoring Nozzle
TVDAU	Thrust Vector Data Acquisition Unit
T2	Engine Intake Temperature
VIGV	Variable Inlet Guide Vanes
VMSU	Vector Monitoring and Setting Up Unit
WDT	Watch Dog Timer

The current Eurofighter "Typhoon" EJ200 FADEC

A full authority digital engine control has been developed for the Eurofighter "Typhoon" EJ200 engine. The EJ200 control system plays an important role in the overall objectives of achieving both the high performance and the low life cycle cost objectives of the EJ200 programme.

The system comprises of

- Digital Electronic Control Unit (DECU)
- Ignition System
- Fuel Control System
- Air Flow Control System (AFCS)
- Sensors

It does not employ any hydro-mechanical computational elements or mechanical back-ups.

The main functions performed or supported by the Control System are:

- To control the engine dry and afterburner fuel flow, exhaust nozzle area and HPC Variable Inlet Guide Vanes (VIGV) position in response to thrust demands and to ensure that the engine functions throughout its operating range within the permissible flight envelope without exceeding any limitations
- To detect and compensate for control system defects and to automatically accommodate faults
- To provide the communication with aircraft and ground support systems
- To provide engine and monitoring data to the aircraft mounted Engine Monitoring Unit (EMU)

The DECU (Digital Electronic Control Unit) developed by MTU, shown in figure 1, is a key element of the EJ200 control system. It is fuel cooled and mounted via anti-vibration isolators on the underside of the LP casing. Although airframe mounted would provide a more benign environment for the DECU, engine mounted offers significant technical advantages in particular with respect to reduced harness length and consequently weight and reduced electrical interference.

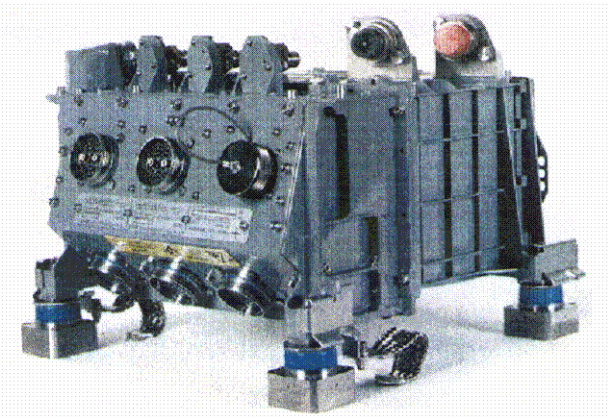


Figure 1: DECU (Digital Electronic Control Unit)

The DECU consists of two functionally identical lanes in a common chassis. Each of the DECU lanes incorporates two Motorola microprocessors communicating via intercomputer and interlane high speed serial links and having access independently to all sensors, actuators and data links.

There exist 7 actuator control loops (five fuel system, one VIGV and one nozzle) for controlling the engine.

Each of the two DECU lanes is fitted with two Mil-Bus 1553 interfaces. Two bus interfaces (one of each lane) are used to communicate with the flight control system computer, the remaining interface at lane 1 communicates with the Engine Monitoring Unit EMU. One Mil-Bus 1553 interface (lane 2) is a spare interface.

This configuration is basis to support the technology demonstration programme "Thrust Vectored Engine Control".

The Thrust Vector Demonstrator Control System

ITP is performing a R&D programme on thrust vectoring technology since 1991. In 1995 a "Technology Demonstration Phase" was launched with the aim to design, construct and test a prototype thrust vectoring nozzle for the EJ200 engine. The concept of the vectoring nozzle developed by ITP so far is very promising for future aircraft application e.g. in the Eurofighter as it provides a large 4 degree of freedom operating range combined with minimum extra weight and minimum changes to engine and aircraft.

MTU's participation in this programme began in 1995 being responsible for the engine and nozzle control system. The system presented in the following sections describes the first achievements on the way to an integrated thrust vectored engine control for future aircraft application. It addresses all requirements to support bench testing of the thrust vectored EJ200 engine.

New System Requirements for Vectoring Nozzle Control

The main functional requirements were to ensure safe operation both of the vectoring nozzle and the engine whilst providing the necessary flexibility to carry out all development tests. In addition to normal engine control the following vectoring nozzle functionality is required:

- Calculation of Nozzle Kinematics
- Geometrical Limitation of Nozzle Operation
- Vectoring Rate Limitation
- Nozzle Actuator Control
- Nozzle Actuator Supervisory
- Recovery Actions on Engine and Nozzle in Failure Cases
- Emergency Deactivation of Nozzle Actuation
- Extensive Test Features (related to the vectoring nozzle)

System Overview

In order to avoid hardware modifications to the DECU a separate control box, the **T**hrust **V**ector **C**ontrol **U**nit (TVCU), was designed and developed to control the thrust vectoring nozzle. This was necessary, since the vectoring nozzle is controlled by four independent actuators thus requiring four independent actuator control loops. The standard convergent-divergent EJ200 nozzle is controlled by a single electronic actuation control loop and four hydraulically synchronised actuators. The next figure shows the basic structure of the system used within the present technology demonstrator programme.

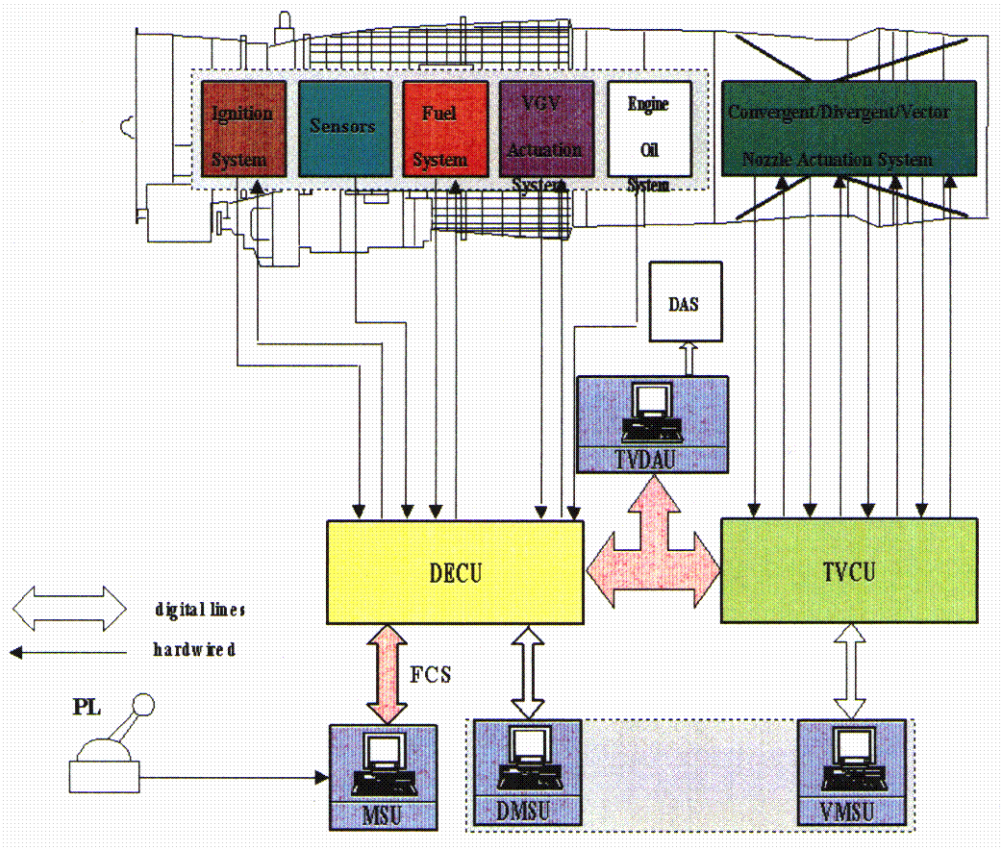


Figure 2: Thrust Vectored Engine Control System, Technology Demonstrator

The thrust vectored engine is controlled by two units,

- The DECU responsible for

  Fuel Metering System (dry and reheat), variable guide vanes, all valves and sensors except those fitted on the thrust vectoring nozzle

- The TVCU responsible for

  the complete convergent-divergent thrust vectoring nozzle including the nozzle control and area limitation, the actuator control, the safety and supervisory functions and the extensive test features for the system development.

These two units are connected by a Mil-Bus 1553. There is an additional unit in the digital bus connection between the DECU and the TVCU, the Thrust Vector Data Acquisition Unit (TVDAU) monitoring the bus transfers, which includes the TVCU control data and engine data. The DAS is a data acquisition system where the recorded data are stored on a mass media.

The Mil-Bus Simulation Unit (MSU) is a PC-based simulation of the FCS Mil-Bus 1553 Interface, providing the FCS demands (PL, nozzle vectoring), air data input and visual display of the DECU and TVCU control parameters. With this configuration bench testing of the thrust vectored engine is performed as follows:

- Throttle and geometrical vectoring demands are introduced via MSU
- Changing of engine control parameters and configuration is possible via DMSU
- Changing of nozzle control parameters and configuration including open loop modes is performed via VMSU (Vector Monitoring and Setting Up Unit)

The Thrust Vector Control Unit

The TVCU consists of two functionally identical lanes in a common chassis.

The following figure shows the hardware architecture:

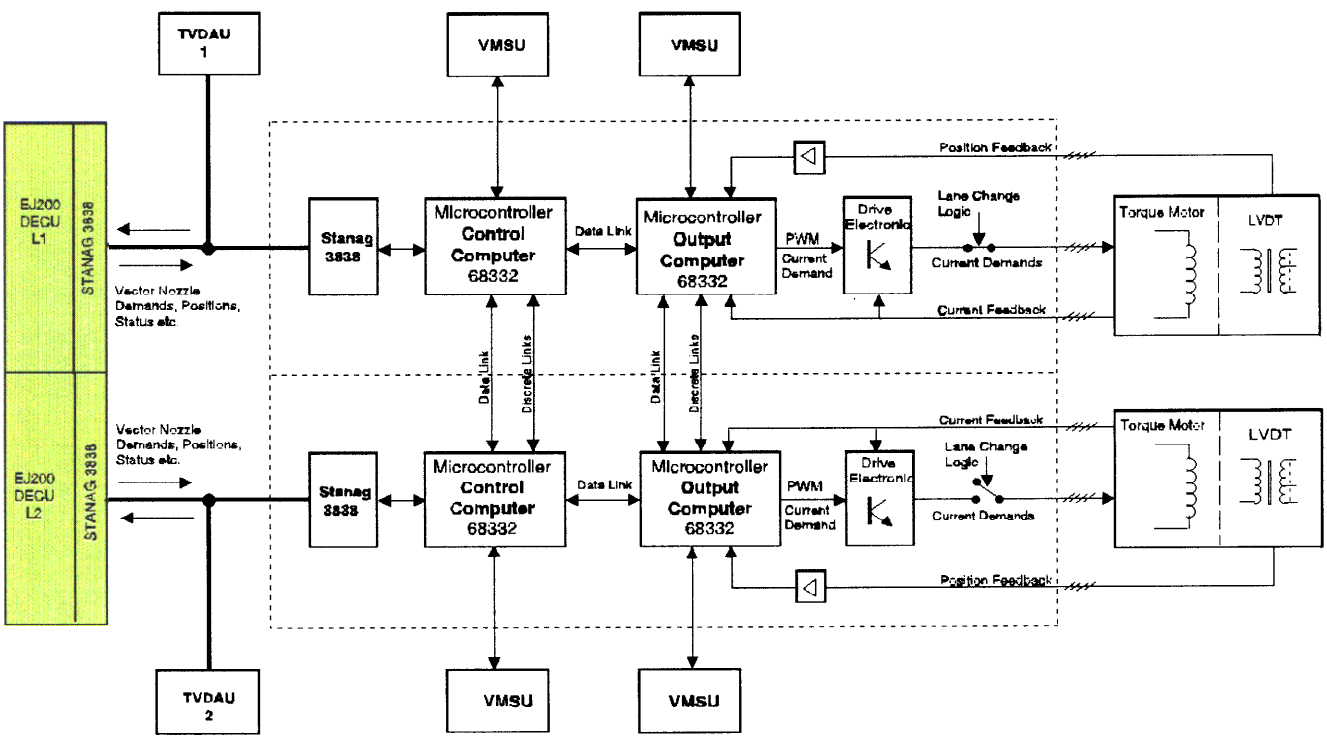


Figure 3: TVCU Hardware Architecture

Each of the two identical TVCU channels consists basically of a digital Mil-Bus 1553 interface to communicate with the DECU and the TVDAU, two microcontrollers Motorola MC68332 and the drive and sensing electronic necessary to operate the nozzle via four independent electro-hydraulic servovalves.

The two processors of one lane, i.e. the Control Computer and the Output Computer, are synchronised and communicate via a Dual Port RAM (DPR). In addition each of the processors of one lane communicates via a serial data link with the related processor of the neighbour lane. Also both TVCU channels are synchronised.

The tasks performed by each lane are distributed to the two microcontrollers which operate with different cycle times:

- Control Computer (10 ms cycle time)

  Mil-bus 1553 communication, nozzle kinematic calculation, nozzle operation geometrical limitation, vectoring rate limitation, nozzle actuator supervisory, emergency deactivation of nozzle actuation, extensive test features.

- Output Computer (2.5 ms cycle time)

  Nozzle actuator control, actuator drive current check, extensive test features (related to the actuator control only)

Functions such as the communication with the VMSU, the standard computer safety (memory check, address line checks, WDT supervisory, communication link checks) are performed on each of the processors.

This configuration enables a new approach with respect to EJ200 actuator control to be introduced, namely fully digital. A pulse-width modulated (PWM) signal with a basic frequency of 9.6 kHz is applied to the torque motors of the electro hydraulic nozzle actuators. The current / position control algorithms are implemented as microcontroller software. The following figure shows the basic architecture of the digital position controller.

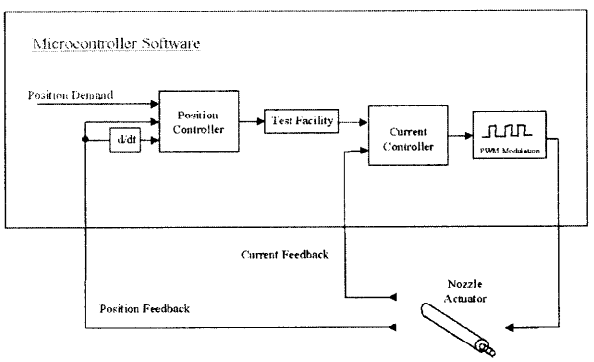


Figure 4: Digital Actuator Control, Overview

Basically the digital actuator control consists of:

1. A position controller calculating a current demand (outer control loop) as a function of the position error
2. A current controller (inner control loop) calculating a PWM ratio depending on the current demand and the current feedback signal
3. A module providing the PWM signal for the drive electronic
4. An open loop test facility which allows to apply defined currents to the nozzle actuators for test purposes

In addition to the digital actuator control the output computer performs also the supervisory of the drive currents. A model of the torque motor is introduced for this purpose and the "model current" is compared with the measured current taking into consideration state dependent limits. The reason to implement the drive current supervisory on the output computer is that the cycle time of 2.5 ms allows an appropriate modelling of the fast varying current.

The model of the actuator (piston position) and the supervisory of the sensing electronics are implemented on the control computer since the cycle time of 10 ms is sufficient to perform an accurate modelling.

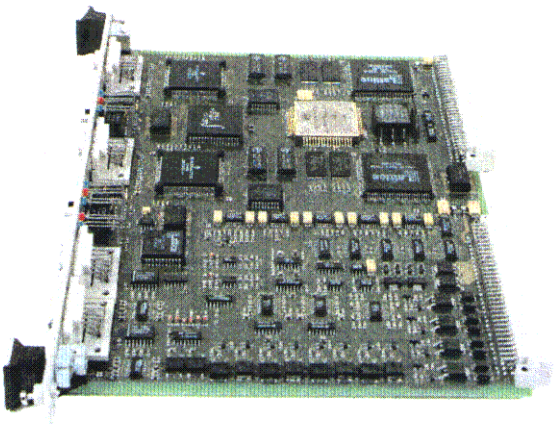


Figure 5: TVCU Board Containing One Lane

This figure shows one complete TVCU lane. The upper half of the board represents the computer part (control and output computers, memory, Mil-Bus 1553 interface), the lower half represents the drive current and the position sensing electronics.

Two boards are mounted, together with two off the shelf power supplies, in a standard rack system. The unit is designed to be operated at environmental temperatures from 0 deg Celsius to 40 deg Celsius, i.e. in laboratory type environment. The technological innovations of the TVCU are the introduction of fully digital actuator control loops implemented in the output computer and the implementation of new more accurate digital models for the actuator supervisory. The improved supervisory functions are essential when the thrust vectoring nozzle becomes an active aircraft control surface in future flight programmes.

The use of a Motorola MC68332 microcontroller for the purpose of digital actuator control allowed the introduction of four (4) control loops into one processor (taking into account the control cycle time of 2.5 ms). Further development work performed at MTU lead to the introduction of a special processor core optimised for the purpose together with the proven control algorithms into a FPGA of the XILINX XC4000XLA family (4085). This approach allows, together with the related sensing and drive electronics, the control of 15 actuators using one single chip. A big step in direction of highly miniaturised IO and improved actuator supervisory has been performed.

Development and Verification

Within the development of the control functions and the control system integration and verification simulation plays an important role, both in off-line and real-time environment. Simulation models are developed in off-line environment, adjusted and validated by analysis of real test data as far as available and can then be used for the different purposes in off-line and real-time simulation environments.

Simulation Models

For the purposes of the demonstrator programme the following models were developed:

1. Nozzle Kinematic Relations

   The thrust vectoring nozzle is characterised by its kinematic relations between the four actuator positions and the geometrical state of the nozzle, i.e. vectoring in two directions and throat and exit area.

2. Nozzle Actuator Loads

   The loads on the actuators vary strongly during vectoring. The data for the correlation between nozzle deflection and resulting actuator forces for various engine settings were obtained from CFD calculations performed at ITP.

3. Nozzle Actuators

   The actuation system consists of four identical hydraulic actuators. Dynamical models of the actuators were derived from the physical description of the actuator components.

Effects not modelled are related to the flow characteristics of the vectoring nozzle. Thrust deflection needed not to be modelled as there is no feedback to the control system. Vectoring influence on effective throat area was neglected and instead covered by the introduction of an increased A8-schedule within the engine control (increased surge margin).

Actuation System Tests on Hydraulic Rig

A hydraulic test facility was built which allowed to test and operate the real actuators under varying operating conditions, especially applying high tension and compression forces.

Extensive testing was performed with respect to the following purposes:

- Verification of actuators
- Validation of actuator models
- Determination of uncertain model parameters
- Test and validation of actuator control in closed loop mode

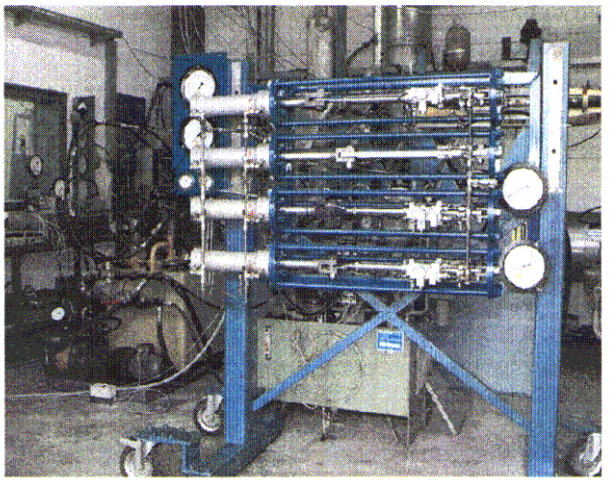


Figure 6: Nozzle Actuators on the All-Can-Do-Rig

Real-Time Testrig

For DECU development, testing and qualification MTU uses test facilities (DEAR = DECU EMU Acceptance Rig) incorporating real-time simulation of engine, actuators, sensors and aircraft signals. Thus the DECU can be operated in closed loop mode under realistic conditions enabling for example extensive testing of failure cases without the risk to damage real engine components. The standard test rig for the EJ200 DECU incorporates detailed dynamical models of the engine and the standard actuators as the DECU covers both engine control and control of subsidiary actuation systems.

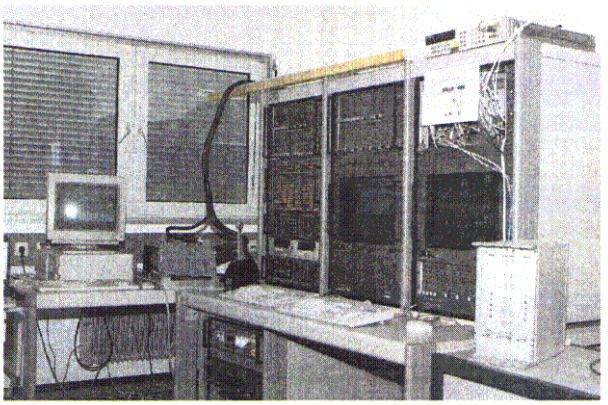


Figure 7: The thrust vectored engine DEAR

For vectoring nozzle control system integration and test a thrust vectored engine DEAR (TV-DEAR) was built. The TV-DEAR enables comprehensive simulation of the complete thrust vectored engine control system. The movements of the simulated nozzle actuators are controlled by the TVCU and are influenced by the varying loads, which in turn depend on nozzle vectoring and engine operating condition. The geometrical state of the simulated vectoring nozzle is determined by the four actuator positions. The computed exit area A8 influences in turn engine simulation and DECU control reaction.

The TV-DEAR was mainly used for the following purposes:

- Thrust vectored engine control system integration
- Robustness checks of actuator control (excessive variation of actuator forces due to vectoring and unknown friction forces)
- Failure simulations for development and testing of supervisory and recovery logic
- Acceptance testing of the complete control system

Results of Thrust Vectored Engine Bench Testing

The control and data acquisition system was integrated at the engine test bed at Ajalvir near Madrid in the week before the first West-European thrust vectored engine run on the 30. July 1998. The test results obtained during the running of the prototype include the following achievements:

- 80 running hours, including 15 with reheat
- Vectoring in all 360° directions, both dry and reheat
- 23,5° maximum vector angle
- 110°/sec maximum slew rate
- 20 kN maximum lateral force
- Thermal case: sustained 20° vector in reheat for 5 minutes
- Rapid transients Idle-Dry-Reheat while vectoring
- 100+ performance points run
- Exit area control: 2% thrust improvement
- Endurance: 6700+ vectoring cycles
- Endurance: 600+ throttle cycles

The fully digital control of the nozzle actuators was successfully tested. The control quality (transient and steady state) was excellent in all load conditions. The next figure shows an actuator movement at high load condition.

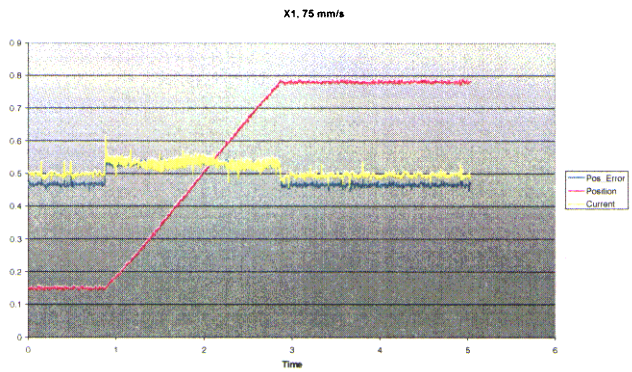


Figure 8: Actuator movement in max. Reheat

The blue line represents the position error (demanded position – measured position) which is 0.5 mm during the whole movement. There is no position overshoot at the end of the movement.

Also the new digital actuator modelling led to excellent results. Despite the fact that the nozzle actuators were supervised with significantly lower tolerances compared with the DECU, no false failure indication was noted during the tests. On the other hand, a loss of an external pump supplying the hydraulic power to the nozzle was immediately detected.

The conclusion of the ground tests in Ajalvir represents the successful conduction of the Technology Demonstration Phase 1. From this point onwards, the next steps taken include a continuation of the development work related to the FADEC, the control system integration taking into account safety aspects and the continuation of the feasibility study with DASA Military Aircraft and ITP.

Additionally, altitude tests with the prototype nozzle are scheduled for mid of 2000 at the Altitude Test Facility (ATF) in Stuttgart.

The next major milestone in the thrust vectoring programme will necessarily be a flight programme, in order to validate the TVN in actual flight.

The Future Modern Thrust Vectored Engine Control

The integration of the thrust vectored engine control with the flight control system is a major issue because the vectoring nozzle – as part of the engine – becomes an active control surface of the aircraft. A suitable interface between the flight control system and the engine control system becomes essential.

The redundant Mil-Bus 1553 between engine and aircraft control units is an excellent prerequisite for this integration.

The ITP thrust vectoring nozzle concept with a common actuation system for all nozzle functions (throat area, exit area and all axis vectoring) is an appropriate solution to meet the stringent requirements concerning performance, reliability and safety resulting from the intended use of thrust vectoring for flight control. The common actuation system means that for example the parameter nozzle area can NOT be controlled independently from the parameter vector deflection. This leads, together with other reasons as described below, to a system configuration as detailed within this section.

The baseline of the control system architecture is shown on the next figure. Principally the system is characterised by the following two major facts:

- The engine is controlled by a single FADEC providing all engine control (including thrust vectoring)
- The FADEC controls thrust and side forces as commanded by the flight control system

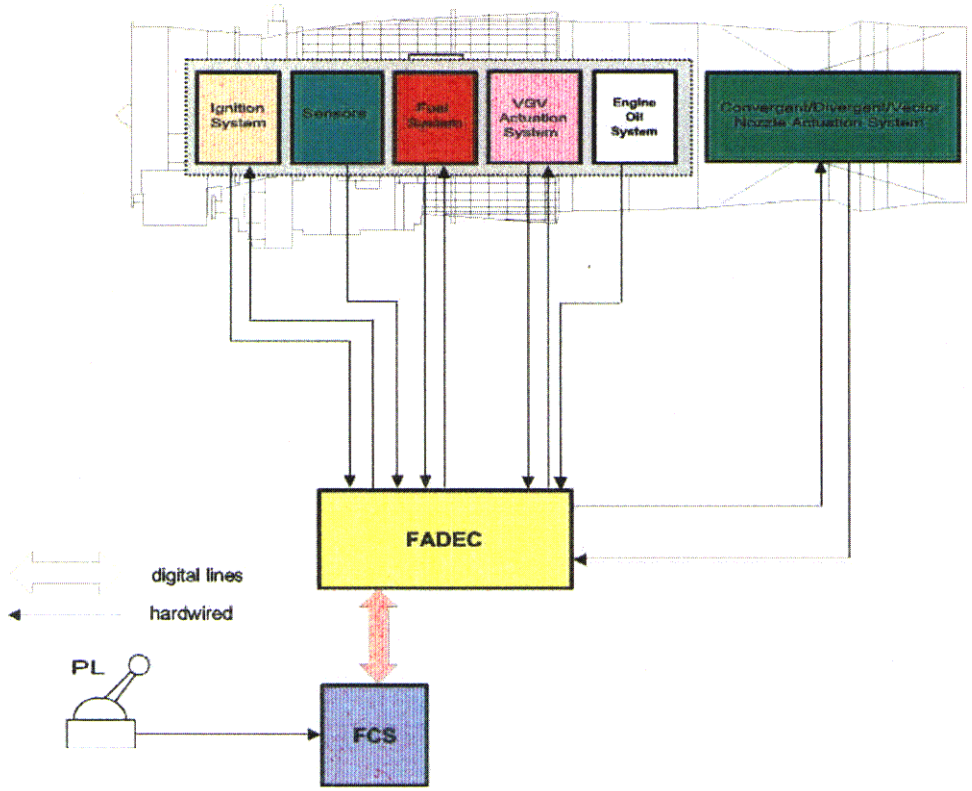


Figure 9: Thrust Vectored Engine Control System, Production System Configuration

The configuration as defined above has a number of advantages:

- Autonomous Engine Configuration
- Simple Interface
- Minimum Interaction FCS – FADEC
- Minimal Weight (minimised cabling, no additional control box)
- Optimum Architecture for Engine and Nozzle Supervisory
- Optimum Architecture for Reaction in Failure Cases (recovery actions)

Interface Flight Control System – Engine Control System

The basic intention is to keep the interface between the flight control system and the engine control system as clear and simple as possible (minimised system interdependency). Engine throttling will be determined by a power lever demand exclusively. Concerning thrust deflection the relevant variables for the aircraft and thus for the FCS are the lateral components (pitch and yaw) of the engine thrust, called side forces, together with their resultant point of attack. The most detailed information about engine and nozzle operating conditions which determine the side forces are available within the FADEC. This leads to the following basic concept for the interface:

FCS -> FADEC

- Power lever demand (PLD) to define engine throttling
- Side forces demand to define nozzle vectoring

FADEC -> FCS

- Current side forces, including point of attack, and thrust
- Maximum possible side forces, taking into account current engine power level, flight condition, nozzle limitations etc.
- Warnings in case of inability to provide required side forces, failure indications

The control loop of the vectoring nozzle system is required to have similar response characteristics as those of the aircraft control surfaces. A frequency response analysis has been performed and showed that the nozzle control system is inline with these aircraft requirements. Two major areas of influence have been identified with this analysis:

- The design of the nozzle control valves
- The synchronisation of the FCS and the FADEC

In case of independent cycle rates of the FCS and the FADEC an undeterministic time delay would be introduced into the thrust vectoring aircraft control with adverse effects on control performance and stability margins.

New Functional Requirements

For a flightworthy thrust vectored engine control additional and enhanced functionality is required compared to the basic functionality of the thrust vector demonstrator with respect to:

- Calculation of thrust and side-forces
- Operational limitations
- Recovery actions for failure cases

On-Board Calculation of side-forces and thrust

The requirement for the integrated thrust vectored engine control, to follow demanded side forces with an accuracy suited for flight control purposes (5% of possible maximum side forces are envisaged) makes the development of an on-board thrust and deflection model necessary.

For non-deflected nozzle the thrust can be calculated with sufficient accuracy from the performance model of the engine and nozzle which reflects the thermodynamic cycle of the engine. The deviation of the real convergent/divergent nozzle in comparison to an ideal nozzle is taken into account by introduction of correction factors for the discharge coefficient and the thrust coefficient.

For deflected nozzle flow phenomena are more complex and thus a simple physical description is not available. A model providing side forces and thrust has therefore to be derived from CFD calculations calibrated by test data. Extensive testing will be necessary to cover all non-linear effects occurring within the operating range of the engine and the multiple-degree-of-freedom vectoring nozzle.

Operational Limitations

Depending on engine operating condition, flight condition and available hydraulic power various limitations for vectoring ranges and rates of the nozzle have to be taken into account keeping forces and temperatures within safe limits. Transient control errors of the actuator control have to be avoided even during high deflection rate vectoring and during simultaneous performing of different nozzle operations.

Recovery Actions for Failure Cases

The most important task of the recovery logic is to avoid any unintended side forces due to failures of the control system. Furthermore limitations of the thrust modulation range should be kept to a minimum.

Accommodation of actuation system failures both involves changes to engine and nozzle control. For most of the flight conditions a centered nozzle is the appropriate reaction in order to maintain engine thrust as far as possible. Nozzle centering in failure cases will have to be initiated by the thrust vectored engine control possibly via some emergency actuation device but A8 control is also effected with significant influence on engine control, as e.g. loss of reheat and limited thrust range.

Further Impacts on the Control System

Thermal Management

Typically fuel cooling is the preferred method for optimum engine thermal management systems. The current EJ200 cooling concept has optimised to the extreme whereby only the fuel consumed by the engine is used, i.e. no recirculation is necessary. The introduction of thrust vectoring introduces additional heat rejection requirements into the system and consequently a different approach to the engine thermal management. This could be, for example, handled by the engine FADEC in controlling the fuel to be returned to the aircraft tank. The temperature of the fuel flow to the burner could be maintained to the maximum possible value to minimise the recirculation flow to the aircraft.

Hydraulic System

The introduction of thrust vectoring can double or triple the requirements for the hydraulic power. The maximum transient requirements, combined with the nozzle actuator loads, cause this significant increase for hydraulic power supply and electrohydraulic servovalve capability. Development work to define an appropriate system architecture (combination of gear and centrifugal pumps, FADEC controlled pressurizing valves) and advances in component technology are necessary to meet the requirements of the hydraulic system.

Conclusions

Successful ground runs with a thrust vectored EJ200 engine have been conducted. The engine control system was enhanced to support this ITP / MTU technology research and acquisition project. The proof of concept for the MTU control system is achieved.

Some of the challenges for a flightworthy solution are already addressed:

- Highly integrated actuator control
- Enhanced actuator supervisory

The ongoing activities are concentrated in

- Supporting engine tests on the altitude test facility in Stuttgart scheduled in mid 2000 and
- The continuation of the feasibility study with DASA Military Aircraft and ITP

The introduction of a thrust vectoring system in Eurofighter Typhoon is currently considered as part of future updates depending on Customer prioritisation of requirements and would take place in accordance with the Eurofighter and Eurojet Partner Companies.

This page has been deliberately left blank

Page intentionnellement blanche

Thrust Vectoring for Advanced Fighter Aircraft - High Angle of Attack Intake Investigations -

Dr. Norbert C. Bissinger
Michael Jost
DaimlerChrysler Aerospace AG
Military Aircraft Division
P.O. Box 80 11 60
81663 Munich, Germany

Abstract

In this paper the results of investigations will be presented which dealt with the determination of intake flows at high and very high angles of attack. The overall approach comprised of experimental and numerical (CFD) investigations will be detailed. Results and comparisons between flows at small and large angles of attack will be used to try to clarify the origin of possible disturbances in the intake flow. Intake bleed and the flow losses at the intake entrance are identified as major components contributing to the quality of the intake flow at the engine face

Nomenclature

A0/AC	area ratio of streamtube area A0 and intake capture area AC
AIP	aerodynamic interface plane (engine face)
Cp	pressure coefficient
DC60	steady state distortion parameter
DC60TA	instantaneous distortion parameter
$\dot{m}$	engine mass flow per unit time
Ma	Mach number
pt0	free stream total pressure
pt2	engine face total pressure
Rmax	engine face radius
Tt	total temperature
WAT	normalized engine mass flow $\dot{m} * \sqrt{Tt} / pt$
α	angle of attack
η	intake pressure recovery (pt2/pt0)
$\delta 1$	vari-cowl angle
$\theta 1$	foreplane angle

1. Introduction

Thrust vectoring has the potential to improve the performance of fighter aircraft throughout the flight envelope. Major performance improvements could be achieved when, e.g., using thrust vectoring for trimming the aircraft, especially in the supersonic flight regime, or when using thrust vectoring in case of failure or loss of a control surface and most importantly when using thrust vectoring for the enhancement of the manoeuverability/agility in the subsonic flight regime including poststall.

Higher agility and flight in the poststall regime in general is connected with angles of attack which are far out of the range for a conventional aircraft without thrust vectoring. The angle of attack range is definitely beyond that for which the intake usually is designed for. Therefore it must be ensured that at these high angles of attack the flow inside the intake will not be deteriorated so much that serious intake/engine compatibility problems would occur. These problems could lead not only to thrust losses at very critical flight situations but could also result in damages of the engine and/or aircraft due to the very high pressure loads connected with malfunctioning (surge) of the engine.

2. Aim of the investigations

When implementing a novel technology like thrust vectoring into an existing aircraft it is desirable to do this with as little changes to the aircraft design as possible. It would even be appreciated if no changes at all would become necessary. However this would only be possible if the existing intake design could be proven to deliver sufficient air mass flows with limited distortion and swirl to the engine not only within its design range but also at very high angles of attack. It was therefore decided to perform a windtunnel investigation with an existing windtunnel model without any modifications mainly in the extended angle of attack range. With this windtunnel investigation the performance of the intake in this extended range was to be demonstrated. With the data collected further work was to be identified and modifications to the intake were to be derived if considered necessary.

Numerical flow calculations (CFD) were to be performed to support the analysis of the windtunnel data.

3. Airplane/intake configuration considered

As an example for a modern fighter aircraft for which in Refs. [1 and 2] different aspects of the implementation of thrust vectoring have been investigated the Eurofighter (Typhoon) has been selected. This fighter is very powerful in the medium range and close-in air combat range. It also possesses an excellent secondary Air-to-Ground capability. In addition it has been designed for high superiority in the supersonic range. The configuration which is able to satisfy all these requirements is a Delta Wing configuration with all-moveable ‘long-coupled’ Canard foreplanes. The aircraft is powered by two EJ200 engines supplied with air by two side-by side chin intakes.

The shape of the intake entrance from a front-view is a rectangle which has been curved like the bottom of the fuselage (smiling intake). At supersonic flight Mach numbers a ramp which is separated from the fuselage by a diverter produces an oblique shock in order to decelerate the flow. The leading edge of the splitter plate separating the two intakes is located downstream of this oblique shock. For low Mach

Paper presented at the RTO AVT Symposium on “Active Control Technology for Enhanced Performance Operational Capabilities of Military Aircraft, Land Vehicles and Sea Vehicles”, held in Braunschweig, Germany, 8-11 May 2000, and published in RTO MP-051.

number and for high angle of attack operation a variable cowl lip (vari-cowl) has been implemented into the design. Because of the vari-cowl no auxiliary intake doors are necessary. Only in the side-view some S-shape curvature of the intake duct can be recognized in fig. 3.1. Viewed from the top the intake duct is more or less straight.

For the stabilization of the shock system at supersonic Mach numbers a bleed system (porous wall) has been incorporated on the intake ramp. For the improvement of the intake flow (reduced distortion) air is dumped via an intake bleed slot on the ramp side downstream of the intake throat.

4. Wind tunnel investigation

4.1 Intake model

The intake model that has been used during these investigations is shown in fig. 4.1.1 . Its scale is 1: 10.32. Only the forward part of the wing has been reproduced on this model. This can be justified by the fact that at the high angles of attack to be tested the intake on-set flow will be dominated by the shielding of the fuselage and the canard.

During all the testing the intake lip position has been held fixed at its most open position (which has been determined for the highest angles of attack considered sofar). Also the canard position has not been changed after pre-tests had proven that the canard position depicted a negligible influence on the intake performance (largest ‘nose-down’ position).

The intake mass flow has been varied between very low and very high values with the help of an ejector system at the exit of the two intake ducts.

4.2 Windtunnel

The model has been tested in the ONERA-S1MA windtunnel in Modane (France). This windtunnel is ideally suited for such testing because the large size of its test-section (about 40 m^2) allows testing at extreme angles of attack without undue windtunnel wall interferences. The only limitation existing may be the power of the windtunnel Pelton turbines.

4.3 Test program and test data

The test program is given in table 1. The angles of attack ranged from 20° to 110°, the Mach numbers from 0.3 to 0.8. For nearly all test points sideslip angle has been kept at zero with one exception at Ma = 0.3 where a sideslip angle of ±10° has been investigated.

For the determination of the steady state intake performance in the port intake AIP (aerodynamic interface plane ≅ engine face plane) a rake for the measurement of swirl and pressure recovery has been used. The five-hole probes and the pitot probes are arranged on different rake arms. Their position can be recognized in fig. 4.3.1. There exist 8 rake arms with 7 pitot probes and 8 rake arms with 2 five-hole probes. The flow angularity (swirl) is measured on two rings in the outer part of the intake AIP only. In the starboard intake AIP a fully dynamic rake for the measurement of dynamic distortion has been mounted (see fig. 4.3.2). Steady state total pressure with this rake is measured with the help of 16 rake arms with 5 pitot probes. For the dynamic total pressure on every second rake arm Kulites have been mounted on the side of the steady state pitots.

With these two rakes steady state pressure recovery can be calculated as the area weighted mean of the pitot pressures. The parameter swirl as used here is the arithmetic mean of the 8 circumferential flow angles on the outer most ring on which five-hole probes are located. Viewed from the front of the intake positive swirl is rotating clock-wise. Distortion DC60 is a measure for the “distortion” of the total pressure distribution in the AIP (and therefore for the flow losses within the intake duct flow). The areas where total pressures below the AIP mean occur are screened for the 60° sector with minimum mean total pressure. DC60 then is the difference between the (minimum) total pressure of this sector and the AIP mean total pressure scaled by the dynamic pressure in the AIP. For the determination of the dynamic distortion DC60TA the same calculation procedure is used with the time-dependent pitot pressure signals. (Details of the data reduction of these dynamic pressure signals are omitted here). Mass flows at the AIP, the ramp bleed and the intake slot bleed have been measured and are given in the form of an area ratio A0/AC or as WAT. At various stations on the fuselage and at intake walls steady state and dynamic wall pressures have been measured.

4.4 Data analysis

During the first test runs data points from former windtunnel entries were repeated in order to prove sufficient repeatability of the data [Ref 3]. The "old" data (marked TP1) have been measured with the same model but in a different windtunnel. This check showed an excellent agreement between the "old" and "new" data. To demonstrate this in fig. 4.4.1 a comparison of the intake pressure recoveries plotted versus the normalized intake mass flow WAT is given (SVS1 = "new" ONERA windtunnel data)

As must be expected the pressure recovery of the intake does reduce with angle of attack. This is due to the increasing losses inside the ineviteable flow separations at the intake entry. Because this intake has been designed for good supersonic performance too its sidewalls and lip shapes are not as blunted as would be necessary for the suppression or at least the delay of flow separations with high angles of attack. Therefore for angles of attack larger than 30 degrees the flow losses increase strongly up to angles of attack of about 90 degrees above which a slight drop up to 110 degrees can be observed. For a flight Machnumber of Ma = 0.7 in fig. 4.4.2 the pressure recovery at alpha = 110 degrees drops down to a value of about 0.5 at the highest intake mass flow tested. But even at alpha = 70 degrees the losses can be as high as 20%. This low total pressure recovery produces substantial thrust losses of the engine behind this intake. These thrust losses must be accounted for in the control of the thrust vectoring nozzle which for a demanded side-force must be deflected to a larger angle than without these losses.

Whereas the total pressure losses at high mass flows are larger than those at low mass flows the opposite is true for the two intake parameters mean swirl and dynamic distortion. In order to visualize these effects in fig. 4.4.3 these parameters are plotted for a low mass flow and in fig. 4.4.4 for a large mass flow.

In fig. 4.4.3 it can be recognized that at the low intake mass flow the pressure recovery up to an angle of attack of 40 degrees is nearly constant for all Mach numbers tested. The minimum pressure recovery is reached for Ma = 0.7 at an angle of attack of 110 degrees. Its value is about 0.60.

The mean swirl angles at an angle of attack of 20 degrees vary between zero and minus two degrees for all Machnumbers. With increasing angle of attack α and at a Mach number of Ma = 0.3 the negative swirl angles drop to minus four degrees at α = 50°, the magnitude of the flow rotation then reduces until at about α = 90° flow rotation is reversed and reaches swirl angles of 8° at an angle of attack of α= 110°. At higher flight Machnumbers the angles of attack at which the flow rotation changes its sign and at which the maximum positive swirl angles are reached take on lower and lower angles of attack. The magnitude of the maximum positive swirl angle is steadily increasing with Machnumber. For a flight Mach number of Ma = 0.7 the maximum positive swirl angle is larger than 10°. This magnitude of swirl is probably beyond the capabilities of most modern jet-engines. It is interesting to note that for Mach numbers Ma = 0.5 and 0.6 there exists a local minimum in the positive swirl angle between the point of rotation reversal and maximum swirl angle. In addition a strong drop in swirl angle with angle of attack can be observed beyond the angle of attack where the maximum of the positive swirl angle occurs.

The dynamic distortion DC60TA for all Machnumbers is increasing with angle of attack and depicts (except for Ma = 0.7) a maximum at about an angle of attack of α = 80°. For higher angles of attack dynamic distortion is dropping and then increasing again. In the same range of angles of attack a strengthening of negative rotation can be observed followed by a growing positive rotation. The reduction in dynamic distortion seems to be connected to the increasing negative rotation and its increase coincides with the increase in positive rotation.

It is rather obvious that the magnitudes of swirl and dynamic distortion at this low engine mass flow would pose a rather hazardeous problem for any jet engine.

At the higher engine mass flow the situation is much more promising (fig. 4.4.4). Between α = 20° and 40° the pressure recovery is slightly depending on the flight Machnumber because of the change of size of the intake air stream tube. Above α = 50° the dependency of the strong drop in pressure recovery on Mach number is depicted in this figure. A lowest value in total pressure recovery of pt2/pt0 = 0.50 is reached for a Mach number of Ma = 0.7 at an angle of attack of α = 110° .

The mean swirl angles stay nearly constant at about -2° for angles of attack of up to α = 60°. For Ma = 0.30 and increasing angles of attack the magnitude of the negative swirl angle is reduced until at an angle of attack of α = 90° a reversal of the flow rotation starts and is growing. Finally swirl angles of about +8° are reached at an angle of attack of α = 110° . For the other Mach numbers the magnitude of negative swirl angles reaches a maximum negative value at α = 80°. With further increasing angles of attack these negative swirl angles diminish with a steep gradient. Rotational flow reversal sets in at angles of attack between α = 87° and 92°. Whereas the positive swirl angles at Ma = 0.5 are very similar to those at Ma = 0.3 the positive swirl angles at Ma = 0.6 and 0.7 depict a maximum before they drop again to nearly zero at α = 110°. Beginning at an angle of attack of α = 50° negative rotation starts growing until at α = 80° positive rotation takes over. Negative rotation becomes predominant again at the highest angles of attack.

The values of the dynamic distortion parameter do not reach the high magnitudes as for the low intake mass flow. At least for a Mach number of Ma = 0.5 a similar dependency between dynamic distortion and swirl can be observed as for the low intake mass flow case where an increase in dynamic distortion occurs together with a strengthened negative rotation and a decrease in dynamic distortion is connected to an increase of a positive rotation. Whether or not this dependency is a physical one remains a question to be answered.

Both distortion and swirl depend on the flow into and inside the intake. At the large angles of attack as tested here flow separations can be expected to have a big influence on both parameters. In addition the flow through the bleed slot inside the intake will contribute in their production. So, some clarification of the flow situation inside the intake should be gained when considering in addition the steady state distortion and the throat bleed mass flow. Steady state distortion can be taken as a measure for losses possibly created by flow separations.

For the low intake mass flow these parameters are plotted in fig. 4.4.5 as a function of angle of attack. Comparing steady state and dynamic distortion (see fig. 4.4.3) first it can be recognized that up to an angle of attack of α = 50° both are increasing. Between α = 50° and α = 70° steady state distortion is reducing whereas the dynamic distortion is about constant. For larger angles of attack both show a similar behaviour with a maximum at α = 80° and a minimum at about α = 90°. There is a further increase in both parameters up to α = 110°. However there is a pronounced difference in the magnitude of the two parameters at this maximum angle of attack. Whereas the dynamic distortion values again reach the level of the maximum at about α = 80° the steady state distortion levels are even lower than those at an angle of attack of α = 20°.

Bleed mass flow (flow out of the intake) is nearly constant up to an angle of attack of α = 50°. The increase in distortion in this incidence range can therefore be interpreted as due to an increase in flow losses at the intake entrance. Bleed mass flow is dropping to zero at around α = 70°. Between α = 50° and α = 70° steady state distortion is decreasing. Because the flow losses at the intake entrance will definitely grow in this range it must be concluded that the reduction in bleed mass flow has a positive effect on the distortion. The distortion increase up to α = 80° is probably due to the increasing flow losses at the intake lip (flow separation). Here the bleed mass flow into the intake is small and cannot be expected to have a noticeable influence into the distortion. However, above α = 80° the bleed mass flow into the intake seems to be large enough to be responsible for the strong reduction in steady state distortion up to α = 90°. Above this angle of attack the flow losses inside the lip separation seem to dominate the production of distortion again.

At the high intake mass flow the increase in steady state and dynamic distortion with angle of attack is similar as for the low mass flow case (figs. 4.4.4 and 4.4.6). Depending on the flight Mach number the maximum of the dynamic distortion has been shifted to α = 60° or higher. Beyond this angle of attack the dynamic distortion seems to possess a sinus-like dependency on angle of attack. At α =110° the dynamic distortion values are higher or of the same order of magnitude as at the angle of attack of the maximum. The steady state distortion graph also depicts a sinus-like shape with values

which are somewhat lower at $\alpha = 110°$ than at the angle of attack of the maximum.

Although the general appearance of the throat bleed mass flow graphs is quite similar to that of the low intake mass flow case (compare fig. 4.4.5 with fig. 4.4.6) their level has been shifted towards smaller or more negative bleed mass flows. There is also a larger difference between the bleed mass flows at different Mach numbers.

Using the same reasoning as before it can be stated that up to $\alpha = 60°$ the increase in steady state and dynamic distortion is mainly due to the increasing flow losses at the intake entrance and not so much due to the bleed flow which is nearly constant in this area. Up to $\alpha = 90°/100°$ the bleed flow into the intake probably is responsible for the reduction in steady state and dynamic distortion. Beyond that angle of attack the increase in distortion can be explained by the most likely fully separated intake flow.

In order to analyze in more detail the distortion to be expected in the following the total pressure distribution at the AIP for a flight Mach number of Ma = 0.6 will be looked at. At the high intake mass flow the lines of constant steady total pressures in the AIP (figs. 4.4.7 to 4.4.10) depict a pronounced high and low on opposite sides of the intake duct. From $\alpha = 20°$ to $\alpha = 70°$ the positions of these extreme values rotate with angle of attack first in counterclock-wise direction by about 30 degrees. From $\alpha = 70°$ to $\alpha = 110°$ these positions rotate back in clock-wise direction by about the same angle. With angle of attack not only the level of the total pressures drops considerably but also the gradient between the high and low which reflects itself also in the low steady state distortion values at the highest angles of attack (see fig. 4.4.6). The lines of constant instantaneous total pressures in figs. 4.4.11 and 4.4.12 indicate some radial distortion at a 6 to 5 o'clock position the value of which still needs to be evaluated. Radial distortion can also be recognized in figs. 4.4.13 and 4.4.14 at the same or slightly different angles of attack but for the low intake mass flow.

How angle of attack affects the flow at the entrance of the intake can be deduced from the plots of static wall pressures at two different x-stations. The x-stations are given in fig.4.4.15 Static pressures at these x-stations all around the intake duct have been plotted for a high and a low intake mass-flow in fig. 4.4.16 and 4.4.17 respectively. On the ramp of the forward X-station (marked "TOP" in the figures) there is a pronounced pressure gradient from inboard to outboard with the maximum on the intake sidewall side. For small angles of attack the static pressure on the cowl lip (called "BOTTOM") at both x-stations is nearly constant. There is a larger pressure drop from the upwind to the downwind x-station for the higher mass-flow. This flow experiences a stronger acceleration with a reduced probability of flow separations. With increasing angles of attack up to about $\alpha \cong 80°$ the pressure on the cowl lip at the upwind x-station drops much stronger than the pressure at the ramp side. Its magnitude is also lower than at the downwind station. I.e., whereas at the cowl the flow is decelerated the flow on the sidewall, splitter plate and ramp is accelerated. For the low mass-flow and for angles of attack between 90° and 110° the pressures are nearly constant both around the circumference of the intake and between the two x-stations. For the cowl this could be interpreted as the result of a completely separated flow. For the high mass-flow the differences in pressure between the cowl lip and the ramp persist even for very high angles of attack although the differences in pressures become smaller with angle of attack. The low mass flow pressures at the aft-station between $\alpha = 80°$ and $\alpha = 100°$ are nearly constant indicating a fully separated flow.

5. CFD investigations

Numerical flow calculations can be used both for the understanding of windtunnel model results and their extrapolation to full-scale free-flight conditions. Understanding of the intake flow is of special importance if proposals would become necessary to improve the intake performance. Therefore parallel to the experimental work described above CFD work has been started on an isolated intake grid model. Due to limited computer power a more complex model comprised of the intake and the fuselage has been envisaged for the future. Because this is an on-going work only results of two Navier-Stokes calculations are presented here to demonstrate the progress accomplished sofar. Details of the numerical code used can be found in Ref. [4] and are not repeated here. The code is of a multi-block structured type. The turbulence model applied has been the Baldwin-Lomax model. Two Navier-Stokes grids have been constructed. One grid can be used for the calculation with the cowl lip in the zero position [Ref. 5], i.e. with no gaps between the lip and the sidewalls. In the second grid [Ref.6] the cowl is set at the most open position as it has been tested during the windtunnel investigations. A grid for such a configuration even today is quite a challenge.

The calculations have been performed for the flow conditions in the windtunnel at a Mach number of Ma = 0.6. The angle of attack in both calculations was set at $\alpha = 21.3°$. In figures 4.4.18 to 4.4.22 some calculation results of both configurations are depicted. The intake mass flow of the intake has been fixed by specifying the same static pressure at the engine face (AIP) for both configurations. As can be seen in figs. 4.4.18 and 4.4.20 the opening of the cowl changes the entrance flow of the intake. The pressure on the ramp is raised. There is much more expansion on the outside of the intake side wall (more side-spillage). The flow into the bleed slot is modified with the large area of local expansion drastically reduced. At the hinge line of the cowl a strong expansion over the whole width of the intake is created (fig.4.4.22). This expansion produces nearly sonic conditions. At the engine face with the cowl closed (fig. 4.4.19) there is an area of low energy flow (small Ma) at the bottom. The flow direction is from top to bottom. The Mach number distribution with the open cowl (fig. 4.4.21) is much more uniform with a nearly horizontal flow direction and some rotation at the top.

6. Interpretation of results and conclusions

The magnitude of the intake parameters swirl, steady state, dynamic radial and circumferential distortion characterize intake/engine compatibility. Any engine possesses limits for each of these parameters and combinations thereof. Exceeding of these limits can lead to power loss, engine surge and/or even loss of the engine. Because these limits are different for each modern jet-engine (and usually are restricted) the interpretation of the intake results in the following can be based only on the experience of the intake specialist.

It can be expected that the large swirl angles connected with the high distortion values (both steady state and dynamic) of the low intake mass flow will pose a problem to any jet engine. However it will be unlikely that at very high angles of attack a pilot will throttle down his engine. To prevent an

unintentional throttling back a limiter in the flight control system of the aircraft might be incorporated.

At the high intake mass flow intake/engine compatibility should be ensured up to angles of attack of about $\alpha \approx 60°$. Above this angle of attack detailed analysis by the engine manufacturer will be necessary in order to find out whether compatibility problems may arise not. In case of problems it would be possible to either modify the control laws of the engine, to incorporate modifications to the intake or to limit the maximum angle of attack of the aircraft. Modifications to the intake could be a modification of the throat slot bleed mass flow at the high angles of attack and/or a modification of the cowl lip shape that reduces flow separation. Both proposals would be relatively easy to implement. Both modifications could be checked by performing CFD calculations of the intake flow thus reducing necessary windtunnel investigations.

7. Acknowledgements

The work described in this paper has been performed as part of the company-funded Dasa technology program. Many colleagues both in the Dasa experimental and intake group have contributed. H. Malefakis was the technically responsible for the design of the experimental program and the analysis of the test data. The contribution of ONERA and their specialists is very much appreciated.

8. References.

[1] E. Grigat
Verbesserung der Flugleistungen von Kampfflugzeugen durch Einsatz von Schubvektorsteuerung
DGLR-JT99-137, DGLR Jahrestagung Berlin, 1999
DGLR Jahrbuch 1999

[2] G. Rauh, M. Jost
Thrust Vectoring – Growth Potential for Advanced Fighter Aircraft
7th European Propulsion Forum "Aspects of Engine/Airframe Integration", Pau/France, March 1999

[3] Malefakis
Analyse der Ergebnisse der FC10-Einlaufmessung bei hohen Anstellwinkeln im S1 Windkanal der Onera; Testphase SVS1
Dasa-S-TN-578, 27.3.2000

[4] R.K. Höld,
Development of the Navier-Stokes Code NSFLEX for Large Scale Numerical Calculation of Steady and Unsteady Flows.
ASME, International Symposium on Computational Technologies for Fluid/Thermal/Chemical Systems with Industrial Application, San Diego, 1998

[5] Th. Berens
Navier-Stokes-Raumnetz für den isolierten EF2000-Einlauf mit Throat Bleed
Dasa-S-TN-495, 1998

[6] Th. Berens
Navier-Stokes-Raumnetz für den isolierten EF2000-Einlauf mit 26° Lippenstellung für Strömungs-rechnungen im Hochanstellwinkelbereich
Dasa-S-TN-524, 1999

				Angle of Incidence									
Vari-cowl	M	β	Fore-plane	20°	30°	40°	50°	60°	70°	80°	90°	100°	110°
δ_1	0.3	0°	θ_1	X	X	X	X	X	X	X	X	X	X
		±10°	θ_1	X									
	0.50	0°	θ_1	X	X	X	X	X	X	X	X	X	X
	0.60	0°	θ_1	X	X	X	X	X	X	X	X	X	X
		0°	θ_2		X					X			
	0.7	0°	θ_1		X		X		X	X	X		X
	0.8	0°	θ_1	X	X	X	X						

Table 1: Test Program

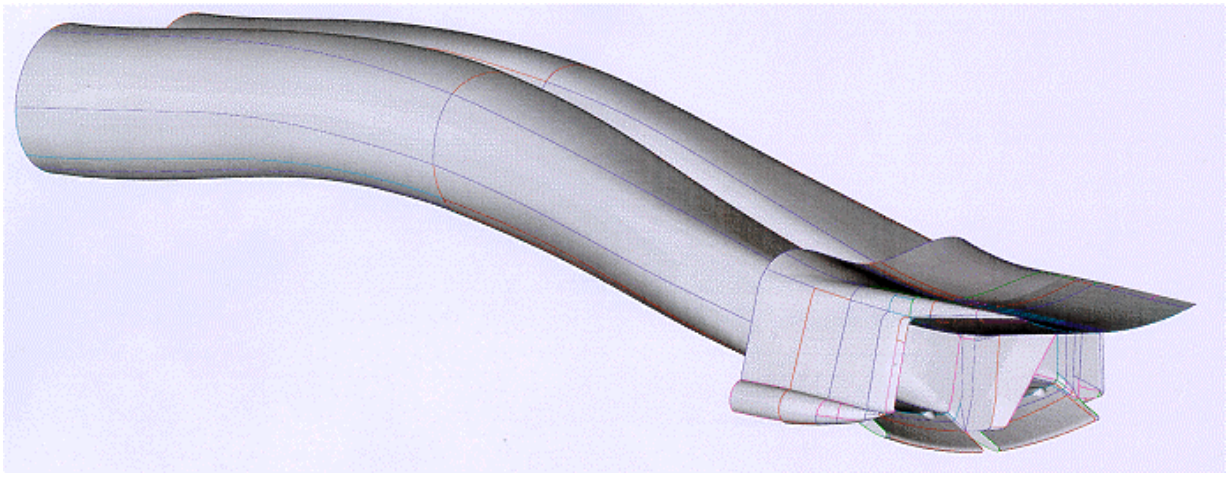


Fig. 3.1 : 3-D View of intakes

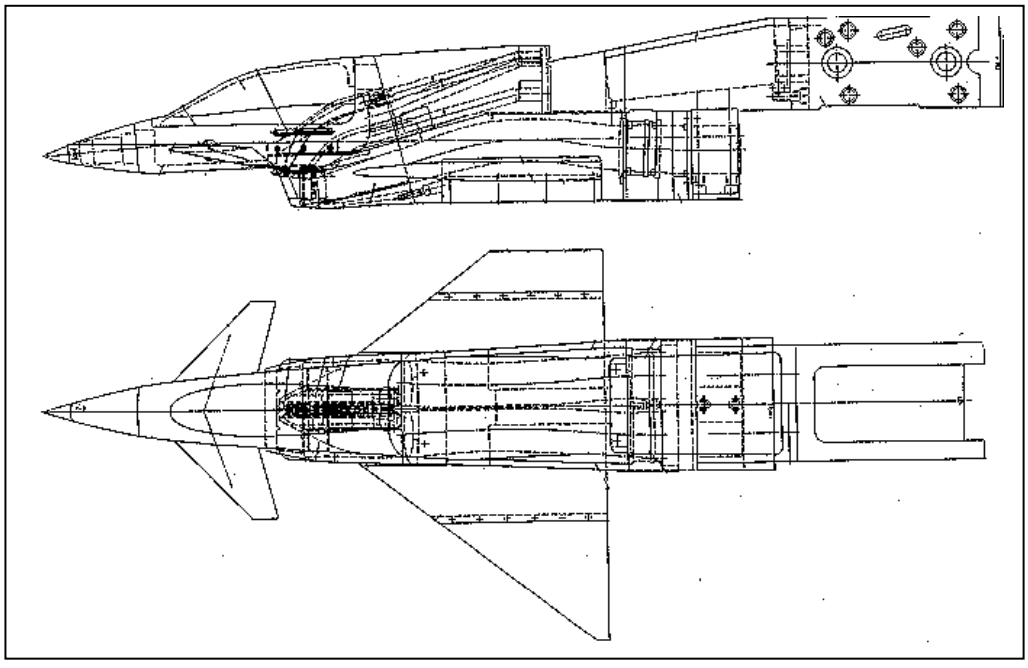


Fig. 4.1.1: Intake Model (1:10.32)

Port Intake

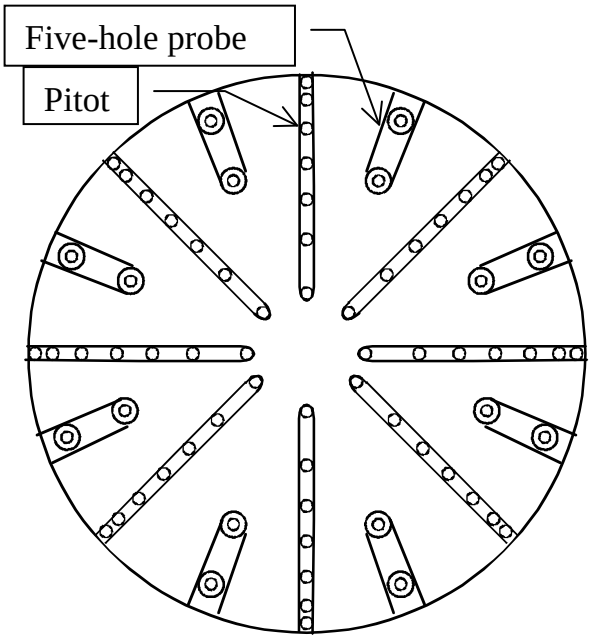


Fig.4.3.1: Port AIP Swirl Rake

Stbd Intake

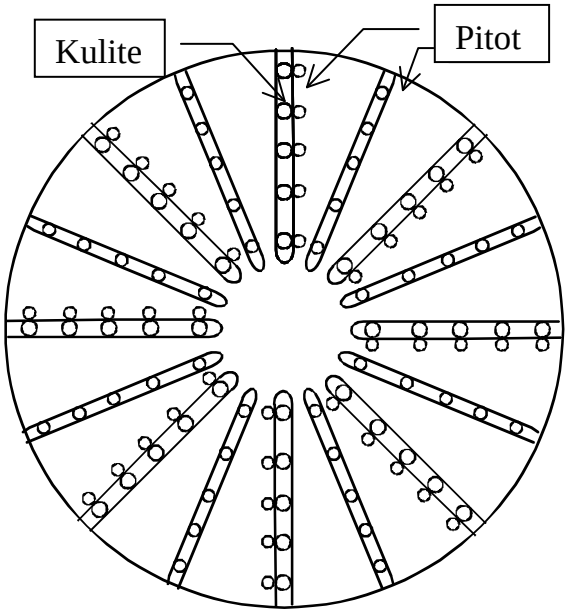


Fig.4.3.2: Starboard AIP Dynamic Rake

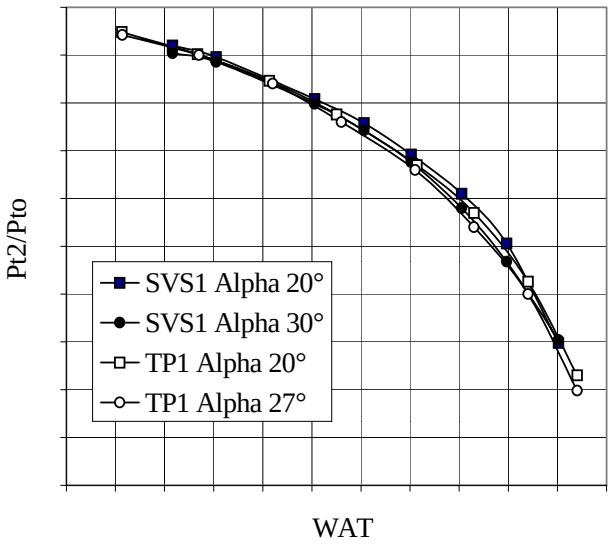


Fig.4.4.1: Repeatibility of Pressure Recovery

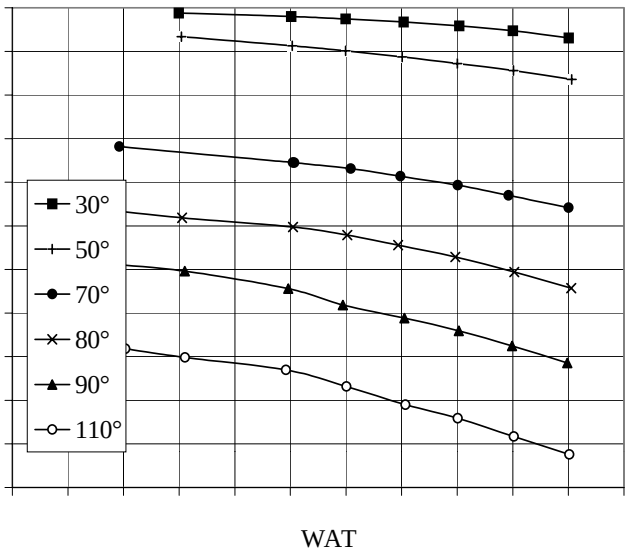


Fig.4.4.2: Pressure Recovery versus WAT at Ma=0,70

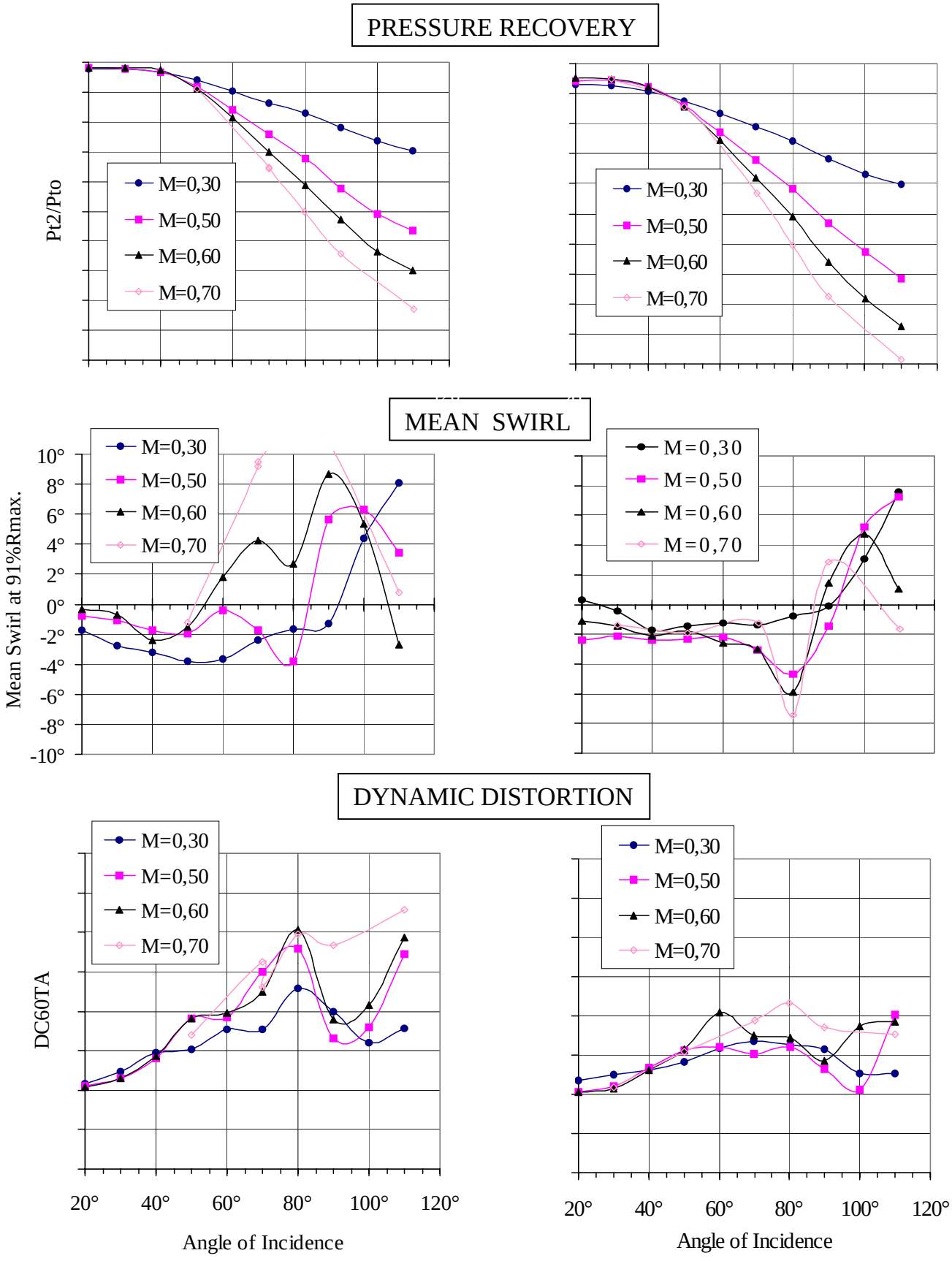


Fig.4.4.3: Pressure Recovery, Swirl and Dynamic Distortion at low WAT

Fig.4.4.4: Pressure Recovery, Swirl and Dynamic Distortion at high WAT

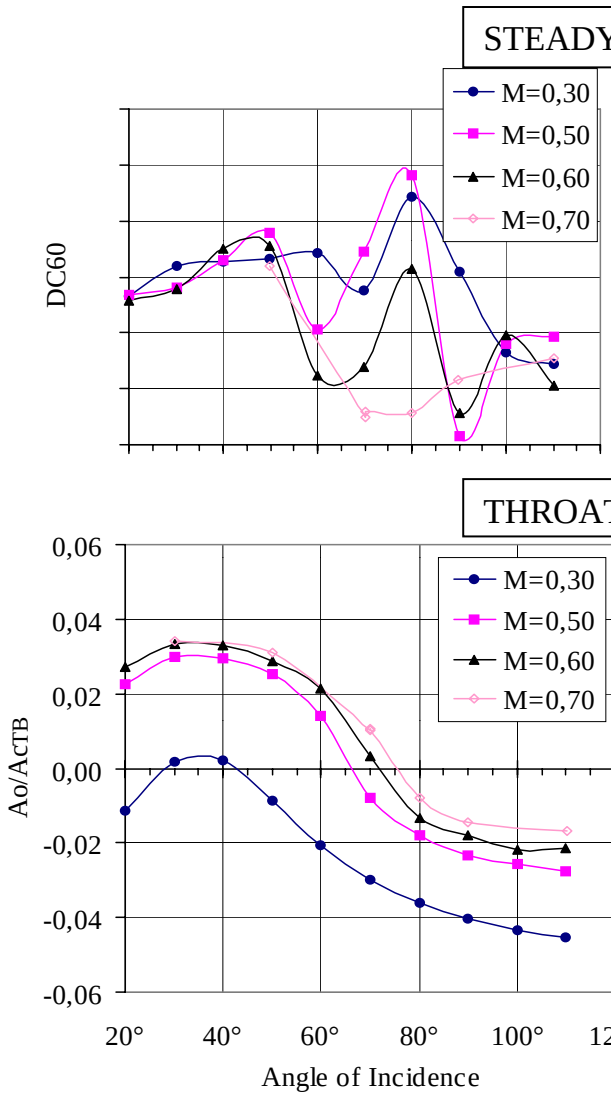


Fig.4.4.5 Steady State Distortion and Throat Bleed Mass Flow at low WAT

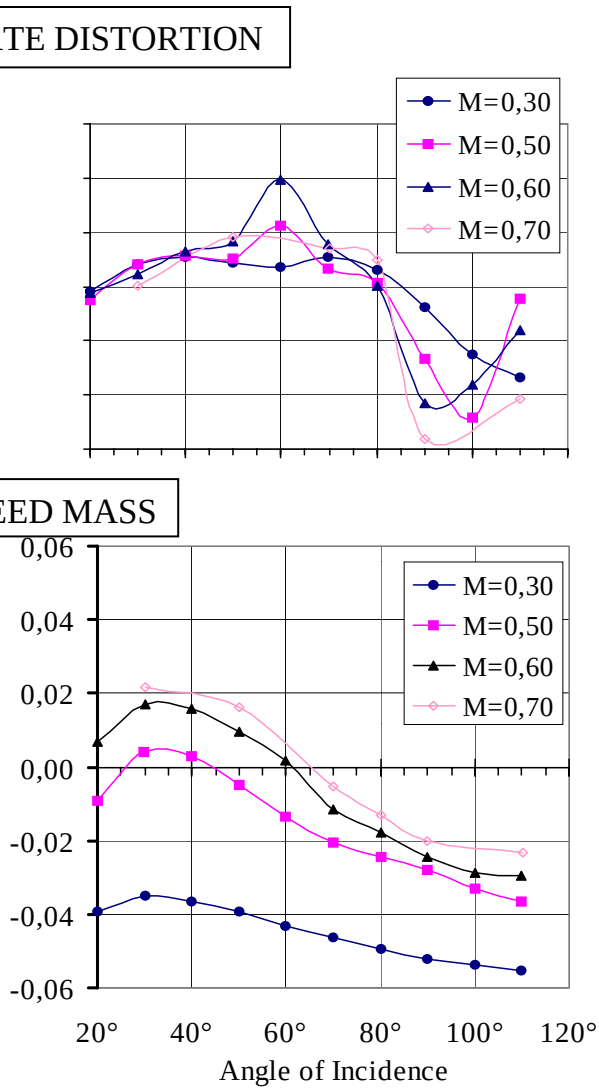


Fig.4.4.6 Steady State Distortion and Throat Bleed Mass Flow at high WAT

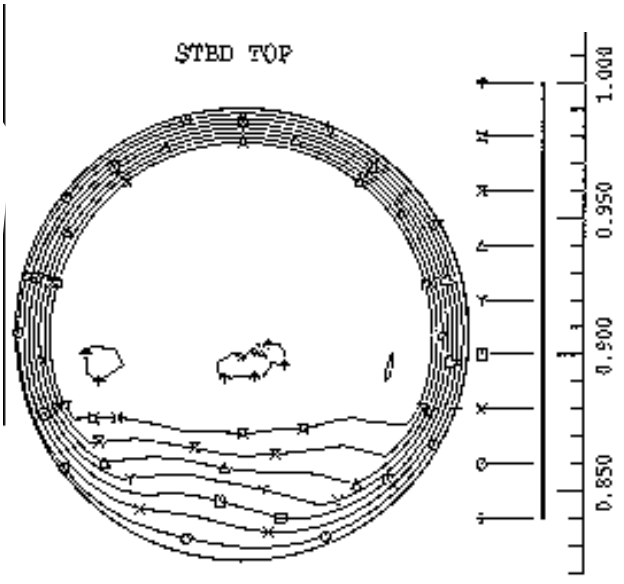


Fig. 4.4.7: Steady State Total Pressures in AIP (Ma = 0.6, α = 20°, high WAT)

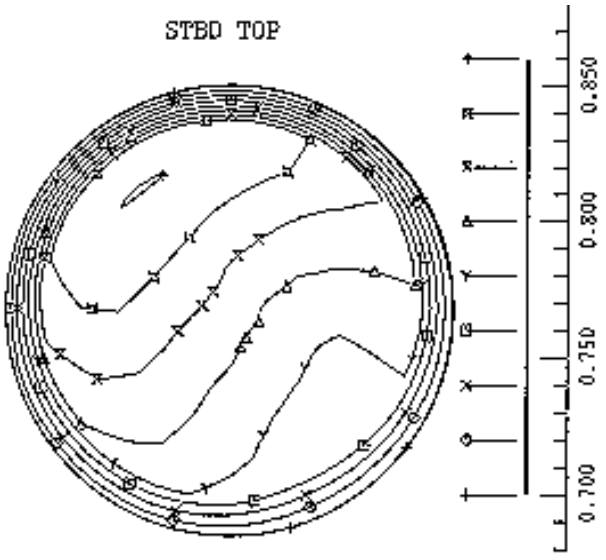


Fig. 4.4.8: Steady State Total Pressures in AIP (Ma = 0.6, α = 70°, high WAT)

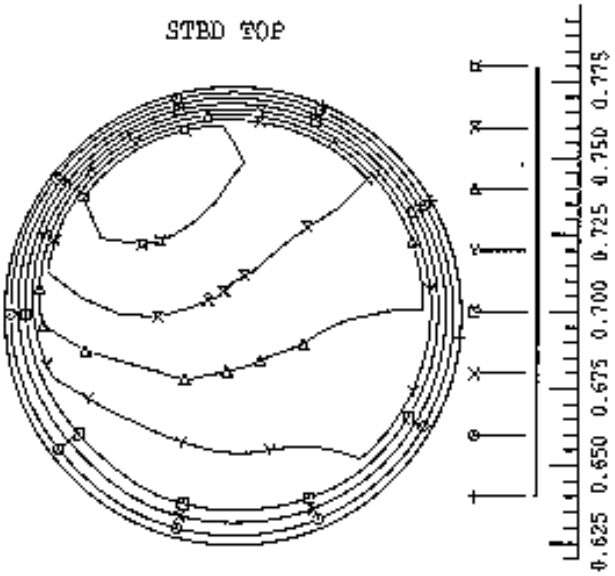


Fig. 4.4.9: Steady State Total Pressures in AIP
(Ma = 0.6, α = 80°, high WAT)

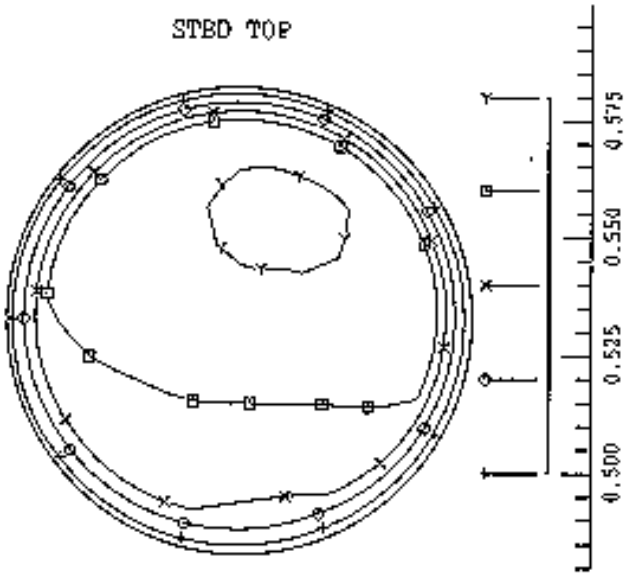


Fig. 4.4.10: Steady State Total Pressures in AIP
(Ma = 0.6, α = 110°, high WAT)

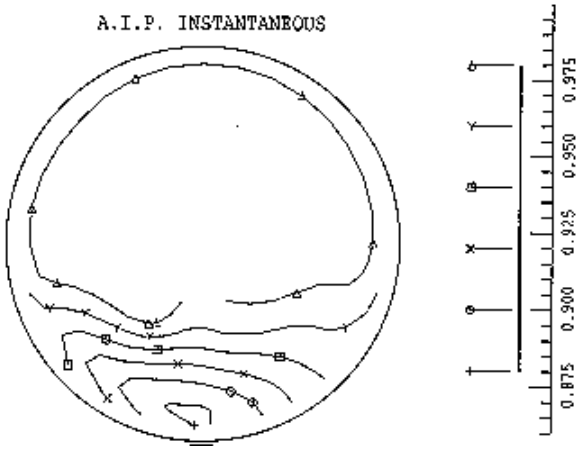


Fig. 4.4.11: Instantaneous Total Pressures in AIP
(Ma = 0.6, α = 30°, high WAT)

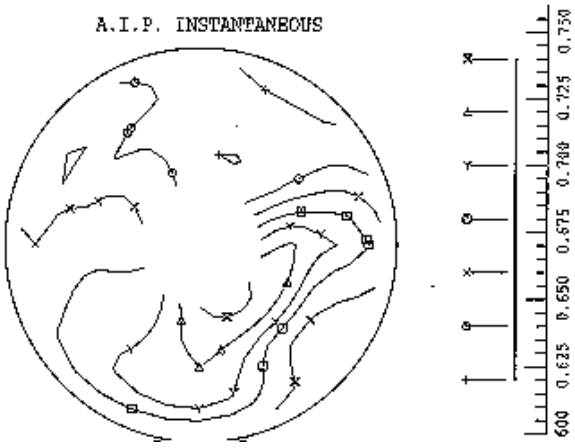


Fig. 4.4.12: Instantaneous Total Pressures in AIP
(Ma = 0.6, α = 90°, high WAT)

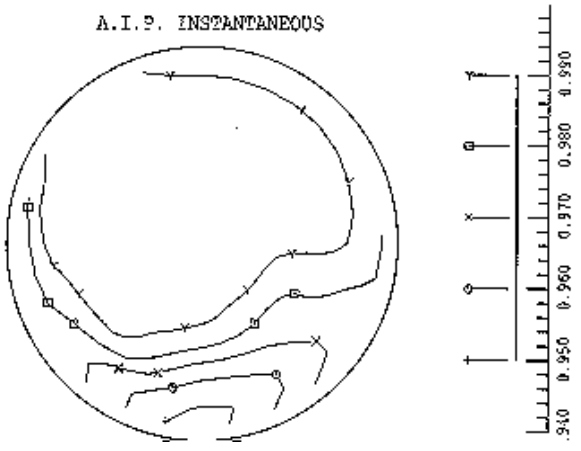


Fig. 4.4.13: Instantaneous Total Pressures in AIP
(Ma = 0.6, α = 30°, low WAT)

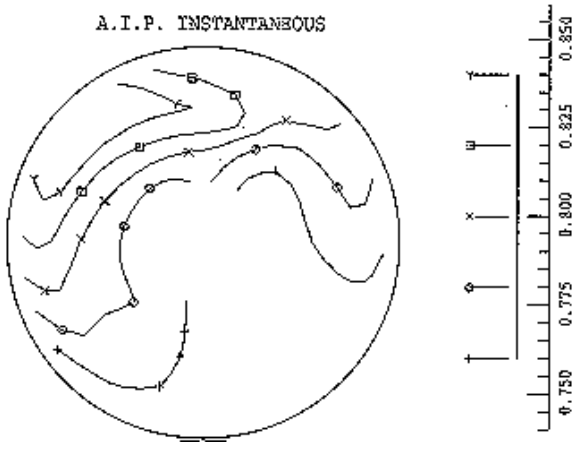


Fig. 4.4.14: Instantaneous Total Pressures in AIP
(Ma = 0.6, α = 80°, low WAT)

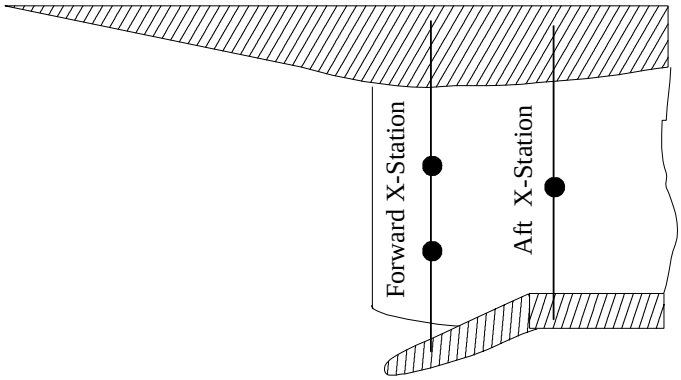
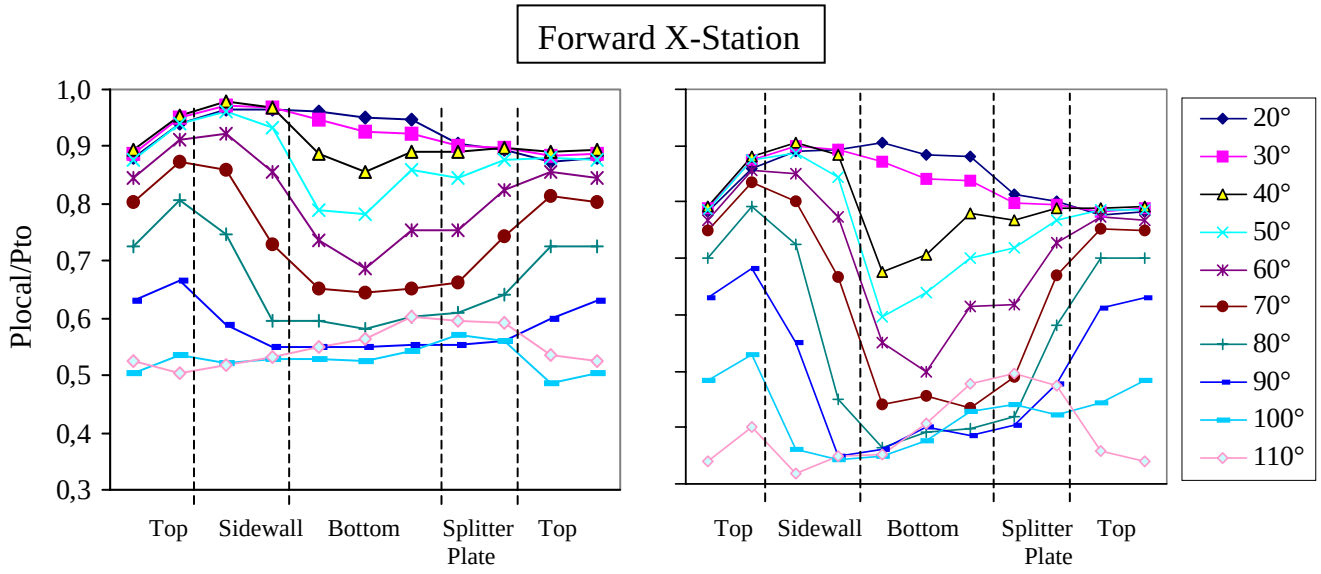


Fig.4.4.15 Position of Pressure Taps at Intake Entrace



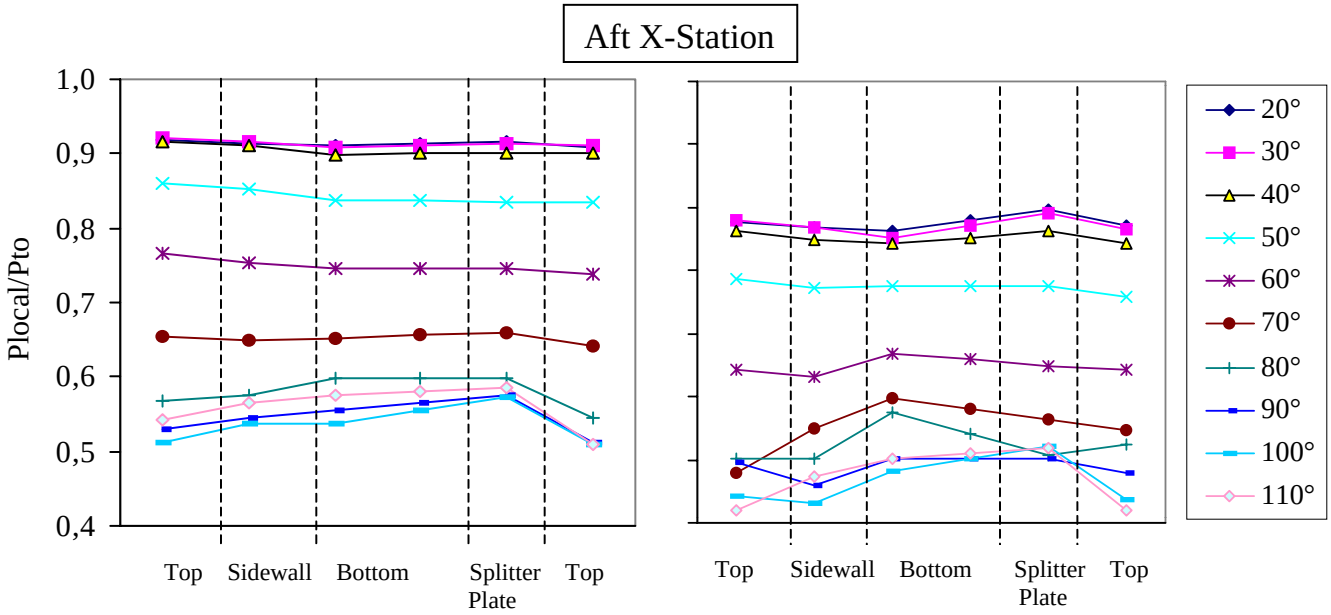


Fig.4.4.16 Static Wall Pressure at Forward and Aft X-Stations (Ma=0.6, low WAT)

Fig.4.4.17 Static Wall Pressure at Forward and Aft X-Stations (Ma=0.6, high WAT)

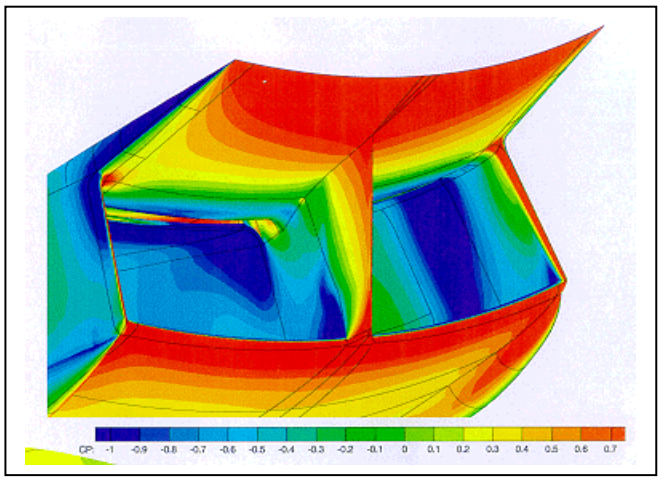


Fig. 4.4.18: Cp at entrance of intake (Ma = 0.6, α = 21.3°)
- intake lip closed -

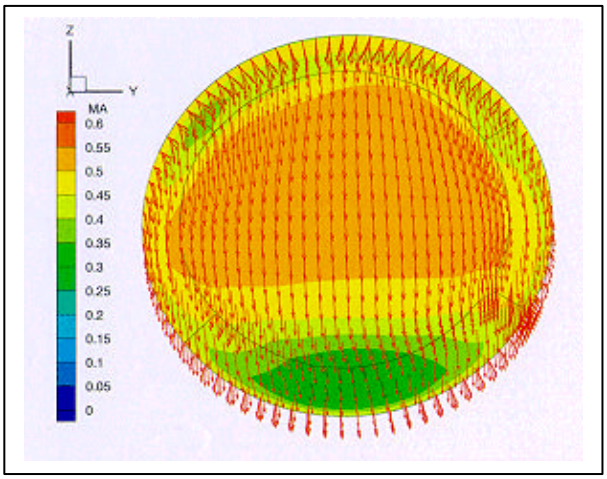


Fig. 4.4.19: Mach and velocity at engine face
(Ma = 0.6, α = 21.3°) – intake lip closed

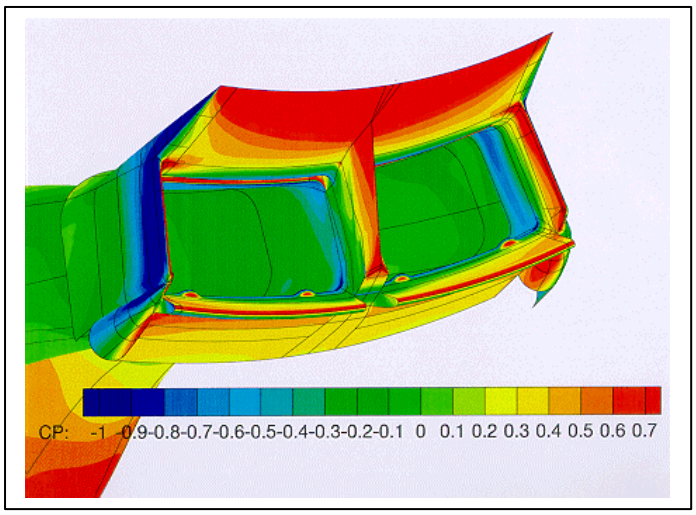


Fig. 4.4.20: Cp at intake entrance (Ma = 0.6, α = 21.3°)
- intake lip open -

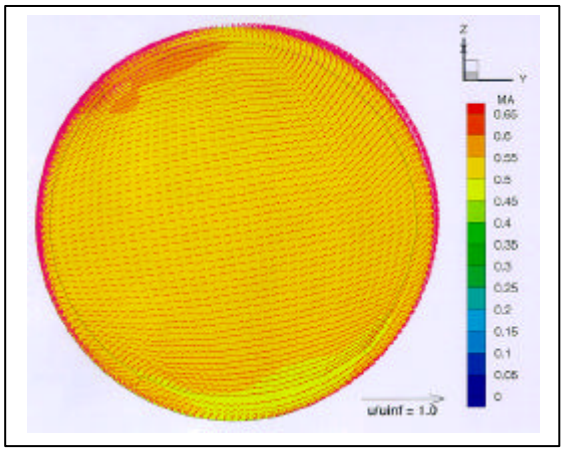


Fig. 4.4.21: Mach and velocity at engine face
(Ma = 0.6, α = 21.3°) – intake lip open

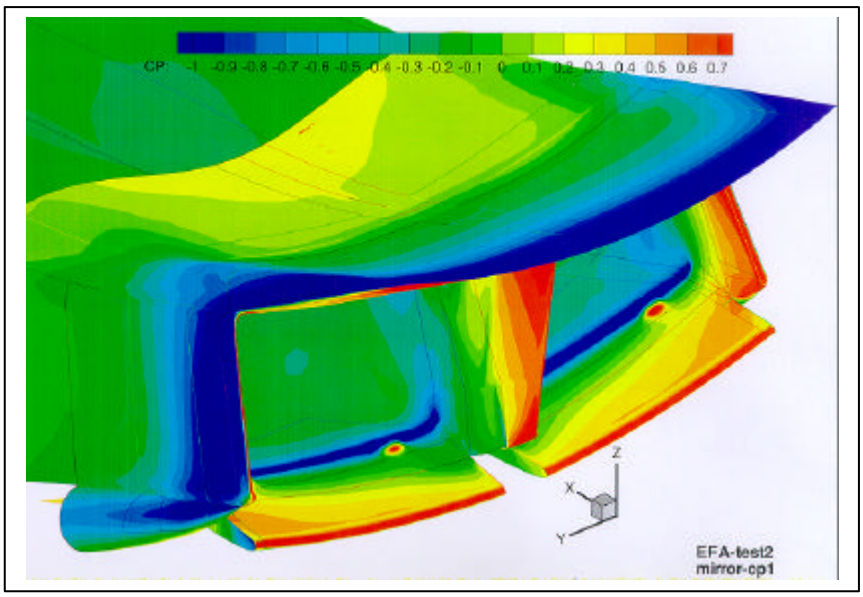


Fig. 4.4.22: Cp at intake entrance (Ma = 0.6, α = 21.3°) – intake lip open -

Paper#13

Q by Dr. R. Nangia: Relative to canard effects on intake performance - are they properly modeled?

A. (Bissinger): The position of the canard during testing has been at its most downward position as can be seen in the photograph of the model in the wind tunnel. Wind tunnel testing at high angles of attack has proven that the effect of the canard position on the intake performance is negligible.

This page has been deliberately left blank

Page intentionnellement blanche

Active Flow Control Activities at Onera

J-L Gobert, D.Barberis, T.Mitchell, P.Molton, J-P Archambaud, G.Pailhas, M.Corrège

ONERA
2, avenue Edouard Belin - F31055 Toulouse Cedex

Paper n°14 presented at the AVT SYMPOSIUM on
Active Control Technology for Enhanced Performance Operation Capabilities of Military Aircraft, Land Vehicles and Sea Vehicles
Braunschweig, Germany, 8-11 May 2000

SUMMARY : In 1997, O.N.E.R.A (French National Aerospace Research Establishment) created a multidisciplinary project on the subject of active flow control. Experimental work, computational fluid dynamic studies, modelling and synthesis of control laws constitute the main activities of this project. The investigations include laminarity control, buffet control in transonic conditions and control of separated flows and vortices.

This document presents the results obtained during some of these activities.

RESUME : En 1997, l'Office National d'Etudes et de Recherches Aérospatiales (O.N.E.R.A) a décidé de créer un projet interne réunissant des spécialistes de plusieurs disciplines sur le sujet du contrôle actif d'écoulements aérodynamiques. Ce projet inclut des travaux expérimentaux ainsi que des recherches en modélisation d'écoulements et synthèse de lois de contrôle. Les thèmes retenus sont ceux du contrôle de la laminarité, du contrôle de tremblement en conditions transsoniques et du contrôle des décollements et tourbillons.

Ce document présente quelques résultats obtenus dans certaines de ces activités.

1. INTRODUCTION

The natural instabilities of the flow which appear on aerospace vehicle surfaces are a source of energy dissipation increasing drag and producing noise and vibrations, therefore they have prejudicial consequences on the performances.

Competitive pressures are pushing civil aircraft designers towards low-cost solutions and some compromises have to be accepted leading to wing designs slightly different from the "optimum". Increased traffic around airports also leads to flight regimes outside of the design operating point.

Demands for more manoeuvrability and stealth are pushing military aircraft designers to develop new concepts for the control of separation and of vortices on the nose and wings at high angle of attack.

Active flow control might be a solution to these different problems.

In order to deal with these problems, ONERA has decided in 1997 to establish an internal project on this subject. The main goal is to build a staff including engineers from all of the required disciplines : experimental and theoretical aerodynamics, control theory, control design and implementation, actuator, sensor, ….

The basic idea is that a small and localised action (local deformation, suction, blowing, jet, …) can sufficiently modify global parameters of the flow (lift, drag, symmetry, …) with little energy consumption to considerably improve the situation.

In this document, the activities performed at ONERA are briefly presented :

1- Control of Tollmien-Schlichting waves in a laminar boundary layer
2- Control of the 3D separation caused by a wing-body junction,
3- Control of the 3D separation on an ellipsoid-cylinder model,
4- Control of Vortex breakdown on a Delta wing.

Other activities performed on active control of buffet and side force control on a generic forebody at high angle of attack are presented in other documents [1,2].

2. TOLLMIEN-SCHLICHTING WAVES CONTROL

The so-called Tollmien-Schlichting (TS) waves are the primary instabilities leading to the transition from laminar to turbulent flow. A study with the objective to control these waves started end of 1997 at ONERA. The main goal is to get a better understanding of the mechanism driving the TS waves and to try to develop a technique cancelling or at least reducing considerably them as soon as they start to grow.

TS wave cancellation is a quite complex problem. For that reason, it has been decided to study a simplified configuration. It consists in developing a system able to cancel one or a group of monochromatic waves on a flat plate with a zero pressure gradient. The control is based on the wave superposition principle: a counter disturbance is applied at a given point with the detected frequency and the appropriate phase and amplitude in such a way that the resulting signal will be zero.

The purpose of this paper is to describe the principle of the technique used and to present some examples of results [3,4].

2.1. EXPERIMENTAL SETUP

The experiments are carried out in a low speed wind tunnel equipped with a test section of 300mm high, 400mm wide and 1 100mm long. The freestream

velocity is equal to 12ms^{-1} with a turbulence level close to 0.5%.

An aluminium horizontal flat plate, 780mm

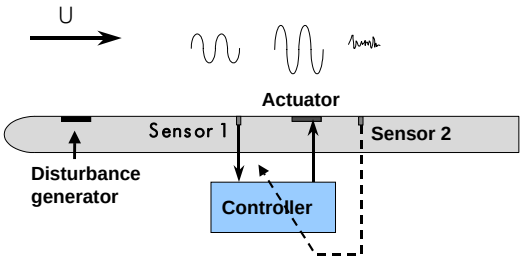


Fig.1: Flat plate instrumentation

long, is installed in the middle of the test section. The instrumentation mounted on the flat plate is shown on fig.1. A disturbance generator is installed under the surface of the flat plate, near the leading edge, producing a quasi-sine wave of adjustable frequency. This wave is an artificial TS which is convected by the fluid movement. Further the disturbance is measured on the flat plate surface by a sensor (hot film). This signal is

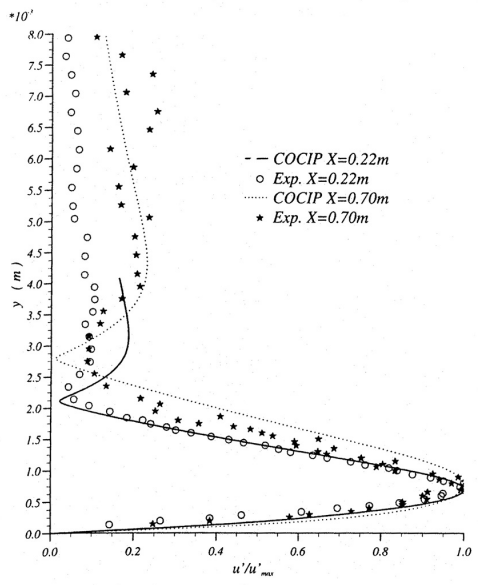


Fig.2: Comparison of experimental and theoretical stream-wise velocity fluctuation profiles

used by the controller to detect the wave frequency and to optimise the parameters sent to the actuator in order to cancel the initial disturbance. Downstream of the actuator, a second sensor measures the result of the TS manipulation ; this information can be used by the controller to compute a correction factor applied to the process.

In order to check the functioning of the disturbance generator and to characterise in detail the flow field around the flat plate, a hot wire probe can be moved in the x (longitudinal) and y (transversal) directions.

2.2. QUALIFICATION OF THE GENERATED DISTURBANCE

The natural boundary layer on the flat plate is laminar from the leading edge down to the trailing edge. In a first phase, a computation based on the boundary layer stability theory using a code developed at ONERA Toulouse (COCIP) [3] indicated that the frequencies of the most unstable waves range from 100Hz to 120Hz. So the generator will be excited within that range during the experiments in order to work in the most critical conditions.

As very first result, the stream-wise velocity recorded at several locations in the boundary layer shows that the instabilities appear on the form of sine waves as predicted by the theory. Moreover, fluctuation profiles measured with the hot wire probe at two stations (just behind the generator and close to the end of the flat plate) are compared to computed profiles (COCIP code) in the fig.2. The agreement between theory and experiment shall be highlighted.

In conclusion, the generated wave can be considered as a good representation of a TS wave.

2.3. CONTROL PROCEDURE

The control procedure is based on the relation:

$$U_a(t) = -K\,U_c(t-r)$$

where U_a = command signal to the actuator,
U_c = signal measured by the upstream sensor,
K = gain factor,
r = phase shift
K and r are the unknowns of the problem.

In a first step, the control system is operating in open loop. For a range of disturbance frequencies, the effect of the actuator is optimised in terms of best couple of values (gain factor, phase shift). All the final results are compiled in a data base.

During real tests, the control system operates in closed loop. The first sensor measures the incoming disturbance. A numeric filter analyses this input, detects the TS wave and extracts from the data base the relevant values of the parameters which are sent to the actuator. Then the residual instability is measured downstream of the actuator by the second sensor, allowing to qualify the actual action of the control.

2.4. EXAMPLES OF RESULTS

2.4.1. Monochromatic TS wave

The first tests have consisted in cancellation of monochromatic waves in the range of the most unstable frequencies. So TS waves of discrete frequency values (110, 120, 130, 140 and 150Hz) have been excited. The feedback control system has given a fairly good attenuation of the TS wave for all these frequencies except the highest value 150Hz. Fig.3 shows the result for 120Hz. On the left side, is drawn the incoming disturbance exhibiting a sharp peak of energy corresponding to the excited frequency. On the right side, are compared the open and closed loop modes are compared; the TS waves have been efficiently cancelled in both the cases.

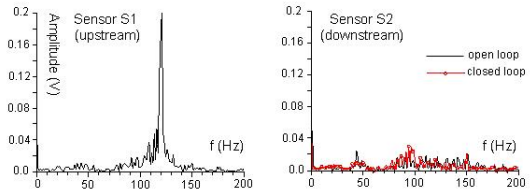


Fig.3: Cancellation of a TS wave (f = 120 Hz)

2.4.2. *Chromatic TS wave*

In the boundary layer, many fluctuations of different frequencies are superposed; they are amplified or damped independently in the linear amplification zone and finally they lead to the transition. Consequently some tests have been performed with a chromatic generated disturbance. Fig.4 presents the example of an excited frequency range within 100 and 150 Hz. On the left hand side are plotted the signal of the incoming disturbance (above) and the corresponding spectrum (below). On the right hand side are plotted the same variables measured downstream of the actuator by the second sensor. We can observe that the signal amplitude is strongly reduced and not well organised (above) and that remains only a small spot of energy between 140 and 150 Hz.

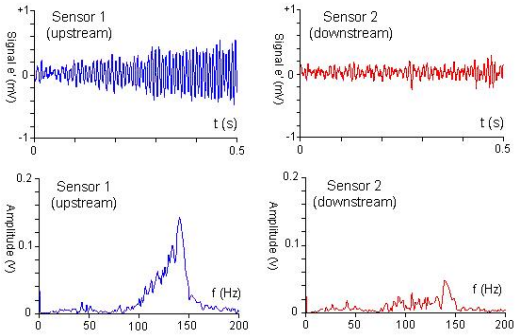


Fig.4: Cancellation of a TS wave (f = 120 Hz)

2.4.3. *Control influence on the amplitude of the flow fluctuations along the flat plate*

Then, investigations have been conducted to measure the influence of the control on the amplitude of the fluctuations contained into the boundary layer. For these investigations, the hot wire has been moved along the stream-wise axis, at 0.6 mm from the plate surface, which approximately corresponds to the location of the maximum velocity fluctuation. Fig.5 shows the fluctuation spectra measured at three stations and for two frequency values, with and without control. In the case of f=130 Hz it can be notice the strong reduction due to the control of the fluctuation amplitudes of all the frequencies. On the contrary, the control has practically no action for f=150 Hz. In the previous paragraph we have already noted that the attenuation just behind the actuator was not complete around this frequency. The reason is that the 150 Hz excited fluctuation causes a very unstable situation, some turbulent spots appearing just behind the actuator and being convected along the plate. In this case the actuator is no more efficient.

The effect of the actuator can also be seen through the modification of the total energy of the

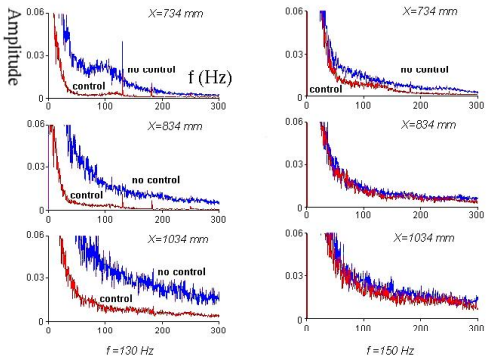


Fig.5: Spectra of the hot wire signal at three stations along the flat plate with/without control

fluctuation spectra previously considered. Fig.6 shows the evolution of this energy along the plate axis for different frequencies of TS waves. Obviously the energy is strongly reduced by the control on the entire plate length and for the different frequencies except for 150 Hz for which no reduction occurs. Nevertheless it can be remarked that the reduced level of energy (with control) seems to grow again but moderately behind X=800 mm. So we can imagine that a second actuator could be placed at this location in order to continue the action of the first one.

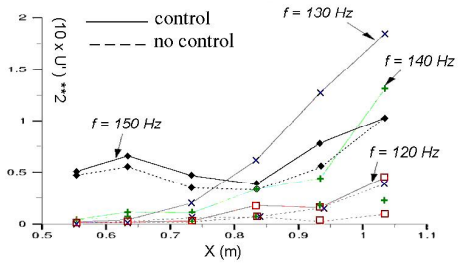


Fig.6: Energy levels along the flat plate with/without control

2.4.4. *Effect of the TS control on the position of the transition*

The final objective of the TS manipulation is to move the transition back. In our case the transition is not completely located on the flat plate which is too short. Nevertheless the tendency of the transition movement can be estimated by considering the local intermittency factor. This factor is roughly estimated as the ratio of turbulent spot duration over total duration of the signal sample measured by the hot wire probe (0.6 mm from the plate surface) at several stations. Fig.7 shows the evolution of the intermittency factor for 3 TS frequencies :130, 140 and 150 Hz. For 130 and 140 Hz, the level of the intermittency factor is reduced by the control and the shift of the first turbulent spot appearance can be estimated approximately to $\Delta X = +0.15$ m. For limit frequency of 150 Hz, the situation is globally unchanged with and without control.

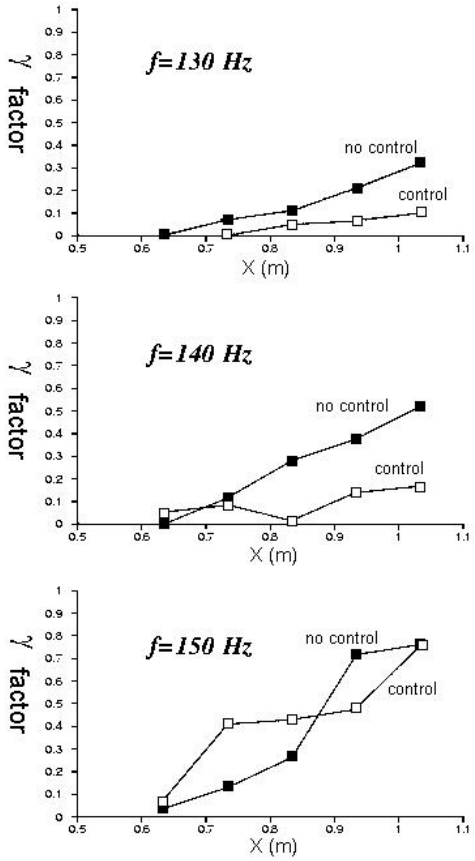


Fig.7: Energy levels along the flat plate with/without control

2.4.5. Use of a second actuator

A second actuator has been placed at x=800mm, 300mm behind the first one; it is equipped with its own sensors. Fig.8 presents the signals measured in front and behind the first actuator (above) and the analogous results for the second actuator (below). The incoming TS wave is generated at f=140 Hz. The fairly good efficiency of the first actuator is clearly pointed out by the reduction of the amplitude of the signal. The signal which is measured just upstream of the second actuator has a small amplitude and is not very periodic. In this conditions, the controller can not detect a predominant fluctuation and the second actuator has no favourable action. One possibility is that the second actuator has been placed too far from the first one. However, it can be noted that the second actuator provides a small benefit for f=120 Hz, which is less close to the limit of 150 Hz previously mentioned.

2.4.6. Conclusions

In first conclusion, the production of TS waves by the use of a generator has been demonstrated by comparison of experimental and computed results.

Secondly, a TS control system has been developed, including a reliable set-up and a simplified controller. It has been used in closed loop operation.

The control system has demonstrated a good efficiency in different configurations (monochromatic, chromatic waves). The action of the control on different parameters of the instability has been evaluated. However

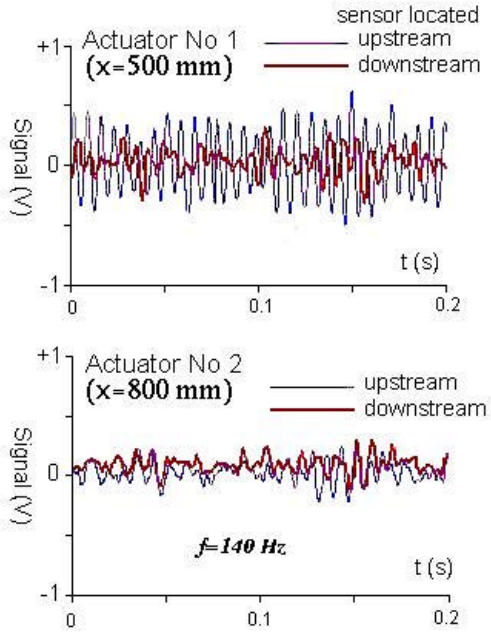


Fig.8: Introduction of a second actuator

a limit of the fluctuation frequency appeared, beyond which the control is invalid.

An attempt to extend the control with a second actuator located behind the first one does not success. Another investigation will be performed with a different configuration.

3. CONTROL OF 3D TURBULENT BOUNDARY LAYER SEPARATION AT A WING-BODY JUNCTION

3.1. MODEL DEFINITION

For this study, the experimental set-up is made up of a flat plate upon which an obstacle with a circular leading edge is normally mounted. A suction system can be placed in two locations, both consisting of a rectangular opening 100mm wide centred in the plane of symmetry of the flow. The first configuration, with the opening located between X=-184mm and X=-82mm from the obstacle's leading edge, was designed to locate the centre of the opening at the level of the primary separation line. In the second configuration, the suction is located further downstream (between X=-120mm and X=-37mm).

3.2. RESULTS

The surface flow properties have been characterised by using a viscous coating which allows the visualisation of the skin friction line patterns. The essential part of the study has been devoted to LDV and PIV measurements. The plane of symmetric flow ahead of the leading edge has been qualified by using 3-D laser

velocimetry in the forward scatter mode and PIV techniques.

3.2.1. Determination of the Aerodynamic Field Using Laser Doppler Velocimeter

The purpose of this work was to quantify the influence of a suction device on control of separation and vortex development using a simple experimental set-up [5]. In order to examine a large number of configurations in detail, we limited our investigations of the aerodynamic field to the plane of symmetry of the flow upstream of the obstacle's leading edge. The explorations were made for different longitudinal positions in a direction normal to the floor.

3.2.2. Influence of the Suction Rate

Fig.9 shows the mean velocity vector fields and streamlines obtained in the plane of symmetry of the flow with the suction device located further upstream of the obstacle leading edge. A gradual reduction in the vortex structure size is observed as the suction velocity is increased. Furthermore, as the suction rate increases, the vortex structure moves toward the obstacle leading edge. The turbulent kinetic energy follows the same trend as the vorticity. Its level inside the vortex decreases as the suction rate increases as shown on fig.10.

3.2.3. Influence of the suction device location

The results obtained with the second configuration at different suction rates are presented on fig.11, which shows the mean velocity fields and associated streamlines. Comparing this figure with the results obtained for the first suction configuration on fig.9 shows that the second arrangement is more efficient in decreasing and eliminating both the separation and the vortex structure observed in the plane of symmetry for the nominal configuration. Indeed, only at Vs = 5 m.s^{-1}, do the streamlines no longer show the presence of a vortex. Therefore, from the standpoint of reducing the extent of separation in the plane of symmetry, the objective can be achieved at the lowest suction rates, in opposite to what was observed for the first suction configuration. Fig.12 shows the constant turbulent kinetic energy levels for different suction rates. In the case Vs = 5 m/s, there is a region of high levels of turbulent kinetic energy near the suction opening. For this configuration, the suction rate is sufficient to decrease the size of the vortex, but does not allow complete absorption of the low velocity region originating in the separation point and producing high turbulent kinetic energy levels. At Vs = 10 m.s^{-1}, the suction rate is sufficient to absorb the boundary layer at the separation point and eliminate the low velocity region. Finally, above Vs = 10 m.s^{-1}, the region located at the junction between the floor and obstacle's leading edge, corresponding to high turbulent kinetic energy levels, gradually decreases and vanishes with the highest suction rate.

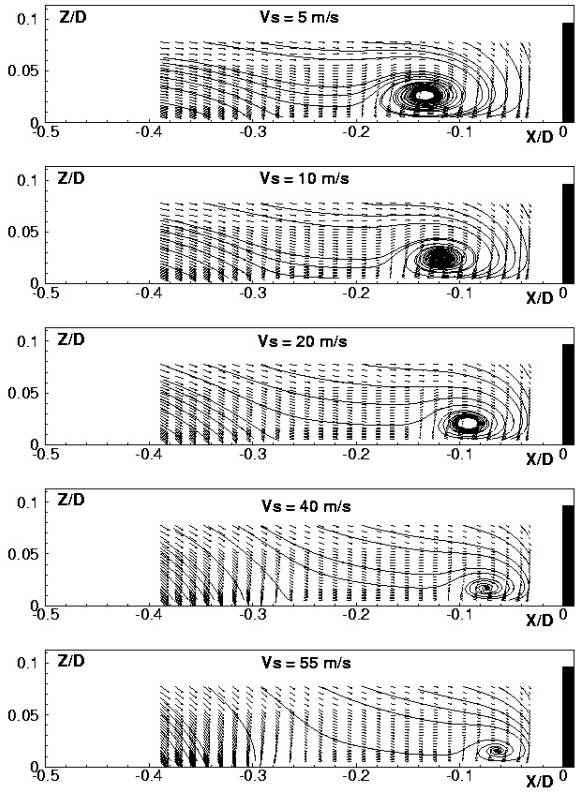


Fig.9 : Mean velocity vector and streamlines:

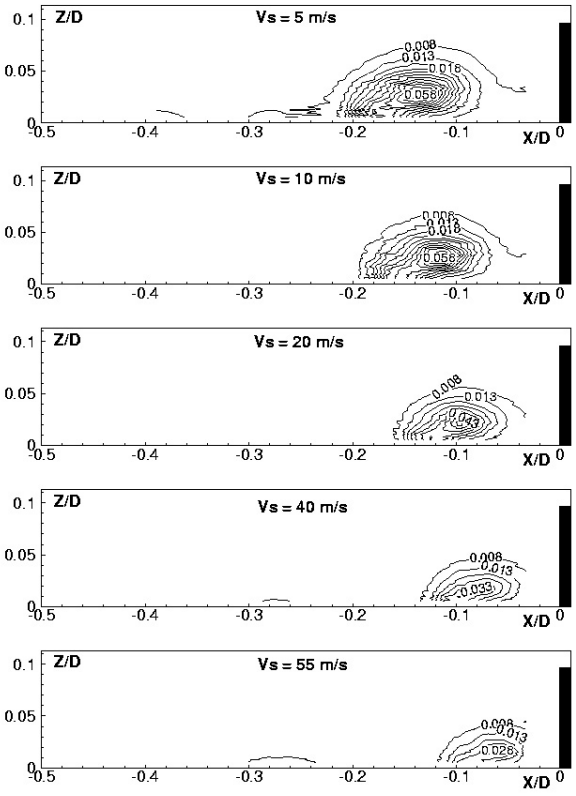


Fig.10: Turbulent kinetic energy:

Suction configuration n°1, plane of symmetry, V_0=50m.s^{-1}

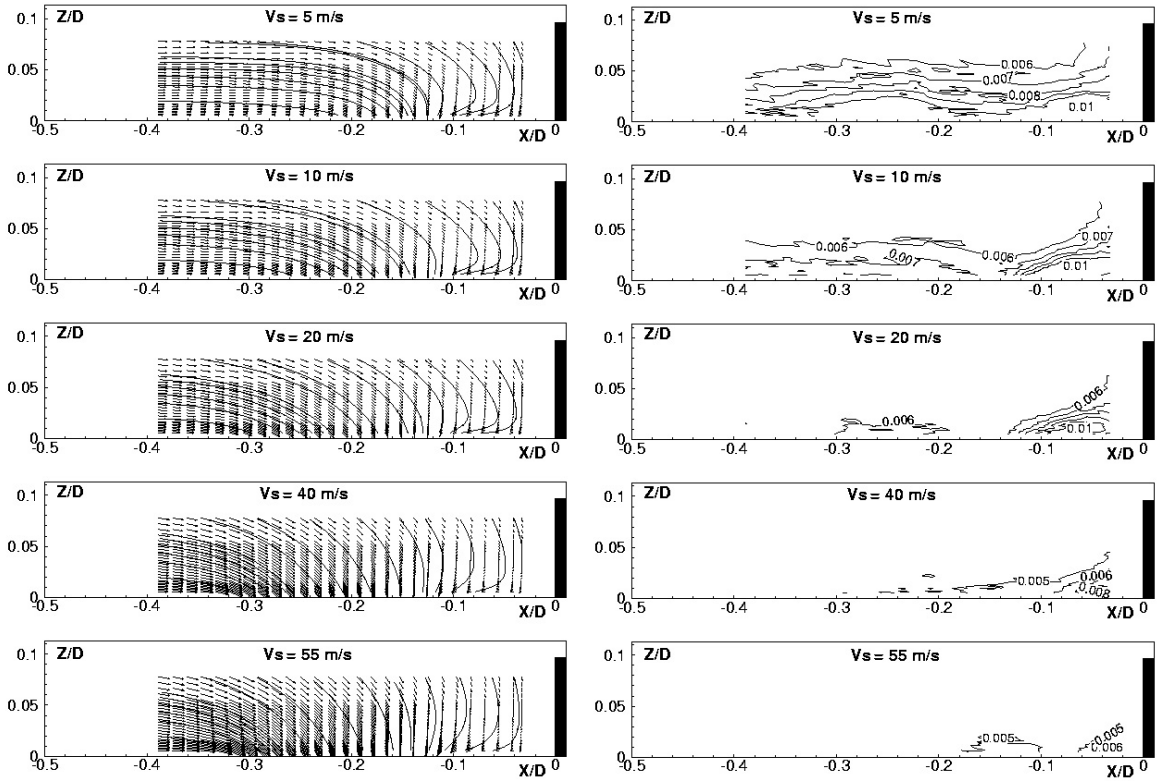


Fig.11: Mean velocity vector and streamlines

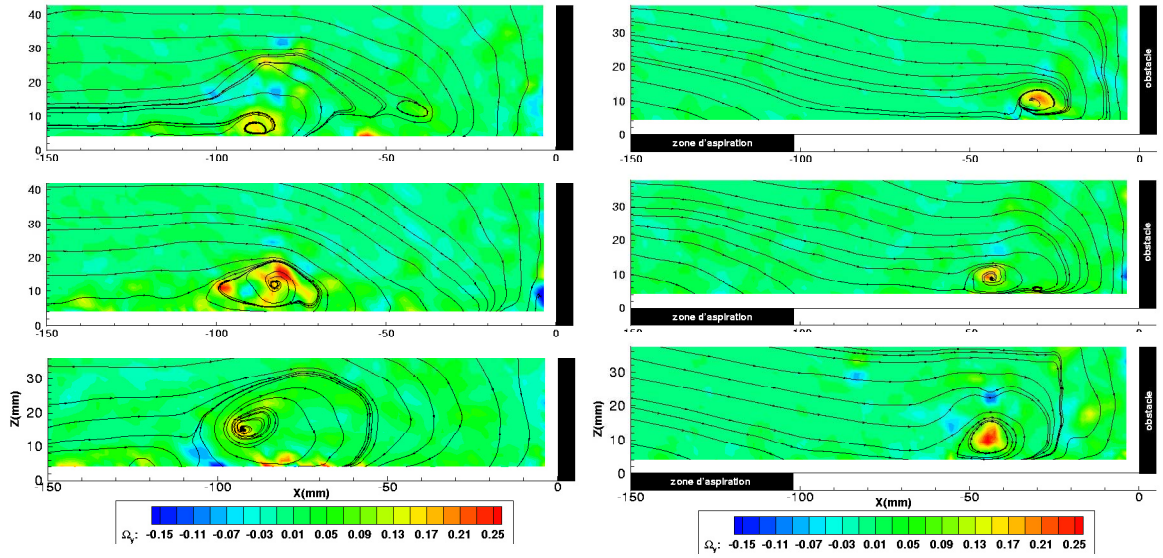
Fig.12: Turbulent kinetic energy

Suction configuration n°2, plane of symmetry, V_0=50m.s^{-1}

3.2.4. Determination of the Aerodynamic Field Using Particle Image Velocimetry

The instantaneous aerodynamic field was determined by PIV in the symmetry plane of the flow upstream of the obstacle in the nominal configuration, and then in two configurations for flow control.

Fig.13 shows the instantaneous fields obtained by analysis of PIV records, in the form of current line plots. Considerable variation can be observed in the topological structure of the flow in the symmetry plane. In the nominal configuration in particular, the main vortex can break up into more complex structures containing 1, 2 or 3 vortices. Introduction of wall suction



a-nominal configuration

b-configuration with control

Fig.13: Streamlines and iso-rotational values associated with the instantaneous velocity fields obtained by PIV

tends to cause the multiple-vortex topological structures to disappear. From this viewpoint, aspiration appears to stabilise the separation phenomenon.

Analysis of the results should enable construction of model of the vortex system which develops ahead of the leading edge of the obstacle.

4. EXPERIMENTAL STUDY OF 3-D SEPARATION CONTROL ON A ELLIPSOID-CYLINDER MODEL

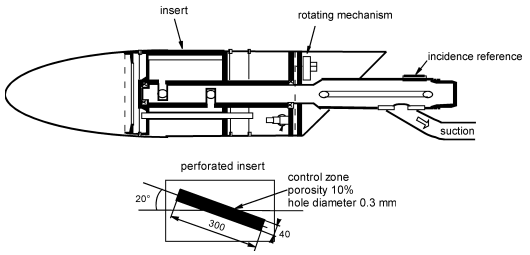


Fig.14: Schematic representation of the model and the suction device

The aim of this work was to study three-dimensional turbulent separation occurring on a regular surface whose radius of curvature was large compared to the thickness of the local boundary-layer.

This problem has already been investigated in detail by focusing on a prolate spheroid with a 1:6 semi-axis ratio. The experiments performed by Meier and Kreplin [6] were extensively exploited. These authors constituted several particularly well documented test cases including wall pressure and wall shear stress measurements as well as detailed flow probing with a multi-hole pressure probe. These experiments were conducted for two incidences : 10° and 30°. Results were obtained for both natural and forced transition; tests at high Reynolds numbers were made in a pressurised wind tunnel [7]

A detailed experimental investigation of vortex formation was performed [8] on a model consisting of a half-oblate ellipsoid followed by a cylinder terminated by a slanted flat base. Surface flow visualisations were made in conjunction with field measurements by five-hole pressure probes and LDV techniques.

The present results are obtained with an axisymmetric model tested in a subsonic wind tunnel. Attention was focused on the boundary-layer evolution in the separation region and the mechanism leading to formation of a clearly detached primary vortex [9]**.** The flow was investigated in detail using several experimental techniques: surface flow visualisations, surface pressure measurements, field explorations with an LDV system. The objectives of this investigation were to describe the boundary-layer behaviour during three-dimensional separation and to control separation by suction.

4.1. Model Definition

The shape of the investigated model has been defined from preliminary tests executed in a water tunnel. It consists of a half axisymmetric prolate ellipsoid with a cylindrical extension terminated by a flat base, inclined at 45° with respect to the model axis, in order to stabilise the separation on the rear part of the obstacle as shown on fig.14. The length, L, of the model between the nose and the middle of the base is equal to 1600 mm. The ellipsoid major axis (A1) is equal to 800 mm while its minor axis (A3) is 200 mm..

4.2. Results

Tests were carried out for an upstream velocity of 50m/s and an incidence of 30°. All the tests were conducted with a fixed transition. $XG^{1'}$ represents the distance along the model longitudinal axis measured from the nose. Circumferential angle φ has its origin at the windward plane of symmetry (φ=0°) and therefore the leeward plane of symmetry is at φ=180°. For the presents results, two locations of the suction device have been considered (M = 105° and M = 120°). The first value corresponds to a position of the control zone just upwind of the origin of the primary separation line and for the second value the suction device is located on the separation line.

4.2.1. Surface Visualisations

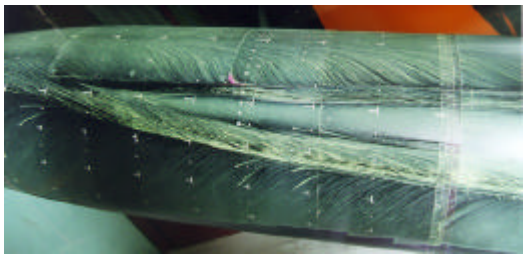
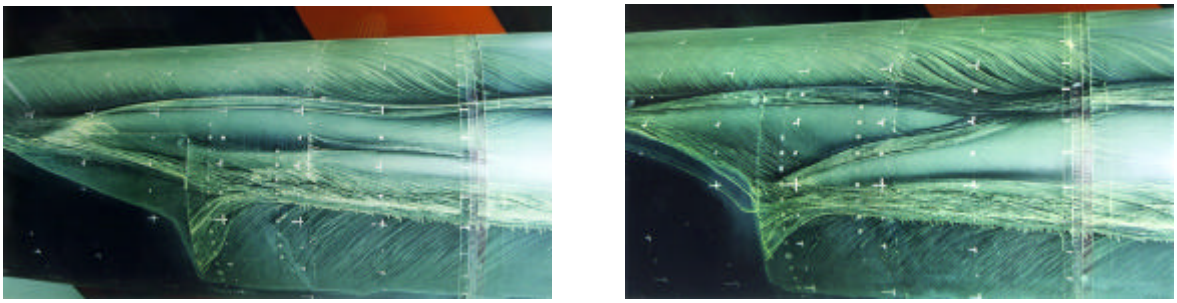


Fig.15: Oil flow visualisation, nominal configuration $\alpha=30°$, $V_0=50m.s^{-1}$, $R_e=5.6.10^6$

Fig.16 presents side views of the surface flow patterns obtained for both suction configurations. The suction flow rate was equal to 10 m^3/h. These photographs reveal several features common to the two configurations with suction and the side view obtained for the nominal configuration in Fig.15. On the rear part of the model, the skin friction lines coming from the windward plane of symmetry, converge towards a first separation line. Closer to the leeward plane of symmetry, a second separation line is present. The skin friction lines on one side of this separation line come from the leeward plane of symmetry. The picture should be completed by three attachment lines two in the windward and leeward planes of symmetry, one between the two previously mentioned separation lines. From this general description, we can observed some significant differences. The straight secondary separation line observed for the nominal configuration becomes curved on the rear part of



suction at Φ=105° suction at Φ = 120°

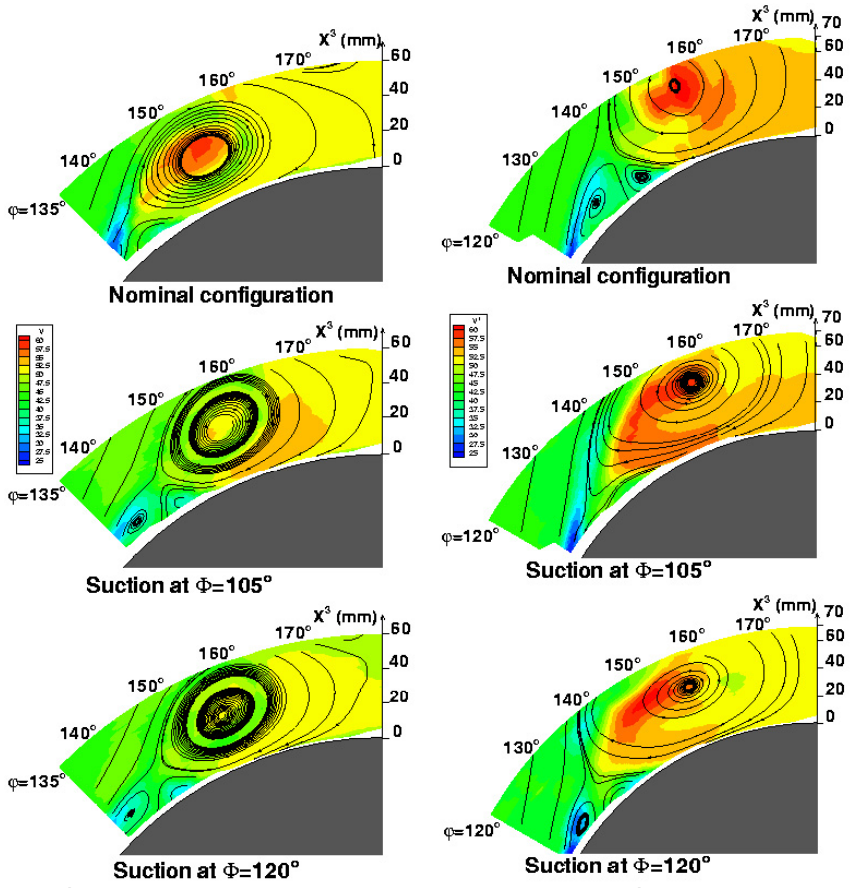
Fig.16: Oil flow visualisations - Suction device location effects
α=30° , V_0=50m.s^{-1} , Q=10m^3.h^{-1} , R_e=5.6.10^6

the model when suction is applied. This modification is associated with the development of a new separation line. For the configuration with suction at M = 105° this new separation line grows in the area between the primary and secondary separation lines and for the configuration with suction at M = 120°, this line realises a junction between these two lines. In both suction cases, the topological interpretation of the wall visualisations is different from the nominal configuration.

4.2.2. Determination of the Aerodynamic Field Using Laser Doppler Velocimeter

The first section considered is located at $XG^{l'}$ = 1060 mm, just downwind of the control region. The second section, at $XG^{l'}$ = 1300 mm, has been chosen further downstream to quantify the influence of the control at a large distance from the application region.

Fig.17 on the left hand side shows the contours of the longitudinal mean velocity component and streamlines obtained for the nominal configuration, the configuration with suction at M = 105°, and the configuration with suction at M = 120° in the section at $XG^{1'}$ = 1060 mm. For the nominal configuration, the development of a vortex structure is observed. The suction moves the vortex nearer the leeward plane of symmetry, but does not noticeably change its magnitude. In addition, it is observed that in the configurations with suction, a part of the boundary layer is absorbed and the



$XG^{l'}$=1060mm $XG^{l'}$=1300mm

Fig.17: Streamlines projection in the plane normal to the model longitudinal axis and longitudinal mean velocity component α=30° , V_0=50m.s^{-1} , Q=10m^3.h^{-1} , R_e=5.6.10^6

low velocity region near the wall is eliminated. Therefore the secondary vortex and counter-vortex are no longer confined in this part of the flow and we observed a vertical extension of these two vortices structures. Further downstream, results shows significant differences with the previous plane.

Fig.17 on the right hand side shows the contours of the longitudinal mean velocity component and streamlines obtained for the nominal configuration, the configuration with suction at M = 105°, and the configuration with suction at M = 120° in the section at $XG^{1'}$ = 1300 mm. Now, for the nominal configuration, the development of a complex vortex structure is described by the projected streamlines. The main vortex near the leeward plane of symmetry must be completed by a secondary vortex and a counter vortex near the model wall. Application of suction does not change the position and magnitude of the main vortex but does alter the secondary and counter vortices.

5. CONTROL OF VORTEX BREAKDOWN BY ALONG THE CORE BLOWING

The delta wing configuration is a popular design choice for current military aircraft and missile systems expected to perform at high speeds and angles of attack. The increased lift is generated by multiple three-dimensional vortical structures in the flow field around a delta wing configuration. The prominent vortical structures are called *leading-edge vortices* and as α increases, these leading-edge vortices experience a sudden disorganisation, known as *vortex breakdown*. In general, vortex breakdown can be described by a rapid deceleration of both the axial and swirl components of the mean velocity and, at the same time, a dramatic expansion of the vortex core. During the breakdown process, the mean axial velocity component rapidly decreases until it reaches a stagnation point and/or becomes negative on the vortex axis. This stagnation point, identified as the *breakdown location*, is unsteady and typically oscillates about some mean position along the axis of the vortex core [10].

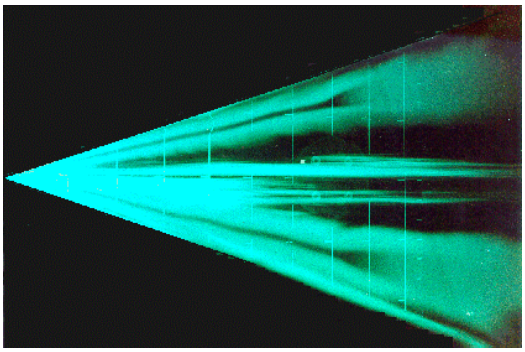
This research at ONERA by Mitchell *et. Al* [10,11,12] is examining along-the-core blowing as an effective method of controlling the vortex breakdown location over slender delta wings. In this study, open-loop, along the core blowing is used to manipulate the vortex breakdown location over the delta wing while the test configuration and freestream conditions remain constant. Results from laser sheet visualisation reveal the displacement of the vortex breakdown location under the influence of various blowing mass flow rates. The mean 3-D Laser Doppler Velocimetry (LDV) measurements within the vortical flow field and around the vortex breakdown are also discussed. The combined results demonstrate the influence of along-the-core blowing on the vortical flow field and the vortex breakdown locations.

A delta wing model with a 70° sweep angle (Λ) and root chord (c) of 950 mm has been configured to collect qualitative and quantitative surface and flow field data during these tests. The model has a wingspan of 691.5 mm at its trailing-edge, is 20 mm thick, and is bevelled on the windward side at an angle of 15° to form sharp leading-edge. The delta wing is equipped with a system of tubing which provides regulated compressed air to two nozzles located near the apex, which are symmetrically situated about the root chord. The nozzles are located 14% of the root chord downstream of the apex of the wing and are situated 30 mm from each leading-edge. Each nozzle consists of a circular jet which expands from an interior diameter of 2.07 mm into an open duct at an angle of 15.6º with respect to the leeward surface of the wing. The compressed air jet exits both nozzles slightly inward of the leading-edge vortex cores at supersonic exit velocities, based on isentropic relations and the measured total pressure of the compressed air, for all blowing mass flow rates considered in this study.

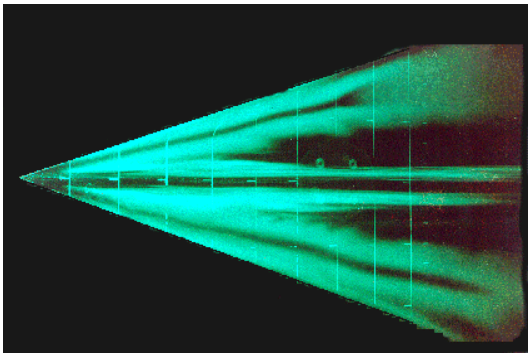
5.1. Results

All of the data presented in this paper was acquired at test conditions of α = 27° and U_∞ = 24 (Re_c = $1.56x10^6$). In the flow control study, along-the-core blowing mass flow rates were varied along each of the leading-edge vortices to compare their influence on the breakdown location of each vortex, controlled and uncontrolled. Blowing mass flow rates of 1.8, 2, 2.2, 3.3, and 3.7 g/s for each nozzle were studied during these tests. The influence of the flow control is determined by comparing the controlled flow results to the reference case, without blowing.

The vortex breakdown locations for the no-blowing and blowing configurations are determined from instantaneous video images from the laser sheet tests. (Fig.18) In these sample photographs, it is clear that the mean breakdown locations of both the portside and starboard vortices are not symmetrically situated over the wing. The results demonstrate the ability of the open-loop, along-the-core blowing to displace the vortex breakdown location toward the trailing edge of the wing. The effectiveness of the flow control to manipulate the controlled breakdown location is dependent on the blowing mass flow rate and the freestream velocity. As the blowing mass flow rates are increased, the effectiveness of the flow control improves and is more capable of displacing the vortex breakdown location further downstream. Due to the symmetry of the flow field over the leeward surface of the delta wing, with and without flow control, only the portside flow field of the delta wing is examined with LDV. Four planes perpendicular to the leeward surface of the wing and one longitudinal plane following the axis of the vortex core are explored. In the longitudinal plane, the portside leading-edge vortex is explored from X = 500 mm to X = 800 mm, with chordwise zones every 20 mm with meshes of 525 points. The location of the vortex core for the longitudinal plane was identified by the position of the maximum value of the axial velocity component (U) in the perpendicular plane measurements.

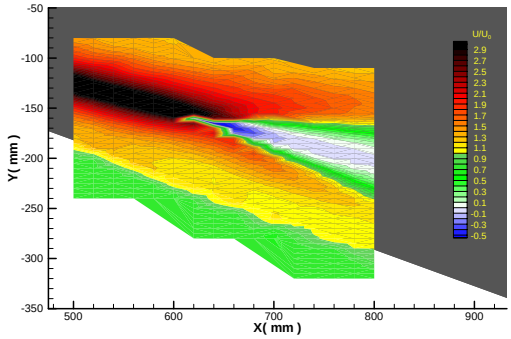


No flow control

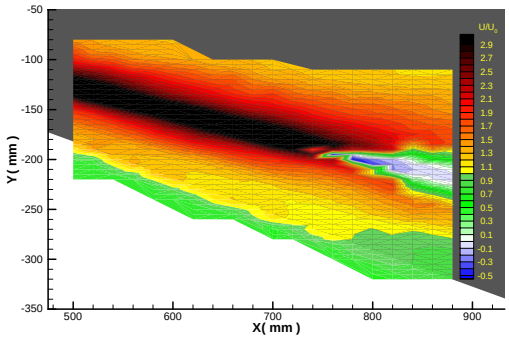


Flow control along lower vortex at Q_m = 1.8 g/s.

Fig.18: α = 27°, U_∞ = 24 m/s



no flow control



Along-the-core blowing with Q_m = 1,8 g/s.

Fig.19: 3-D LDV results of U/U_∞ in the longitudinal plane at α = 27° and U_∞ = 24 m.s^{-1}

Fig.19 presents the non-dimensional axial velocity component (U/U_∞) in the longitudinal plane intersecting the leading-edge vortex cores. A strong, jet-like, acceleration of the flow along the vortex core is observed upstream of vortex breakdown phenomena (X_b = 620 mm) with values of $U/U_\infty \geq 3.5$. There is an abrupt deceleration of the axial velocity component to a stagnation point (vortex breakdown location) which is followed by a zone of recirculation and a sizeable increase in the diameter of the vortex core. The post breakdown region has a wake-like axial velocity profile.

At locations upstream of the vortex breakdown, there are strong gradients of the vertical and horizontal components of the tangential velocity (V and W), indicating an intense rotation of the leading-edge vortex. Downstream of breakdown location these gradients diminish and the diameter of the vortex core expands. The results shown in Fig.19 indicate the effectiveness of along the core blowing in manipulating the vortex breakdown location downstream. The mean vortex breakdown location is displaced downstream at least 10% of the chord. These results compare well with those shown in Fig.18.

5.2. Conclusions

The ensemble of this data enabled the identification of the vortex breakdown location and provided characteristic details of the flow field and the vortex breakdown phenomena. Laser sheet visualisation enable identification of the vortex breakdown location and characterisation of its chordwise oscillation.

The 3-D LDV results verify the effectiveness of along the core blowing in manipulating the vortex breakdown location and reveal the physical changes that occur in the flow field and the vortical structures which cause the vortex breakdown location to be displaced aft. The LDV measurements provide a detailed description of the mean flow field in the vortex breakdown region.

Open-loop blowing along each of the leading-edge vortices on the leeward surface of the delta wing was examined. Both asymmetric and symmetric flow control configurations demonstrated the ability to displace the vortex breakdown location downstream toward the trailing edge of the delta wing. The ability of the various blowing configurations to manipulate the controlled breakdown location was dependent on the blowing mass flow rate and the freestream velocity. As the blowing mass flow rates increased, the effectiveness of the flow control improved and was more capable of delaying the vortex breakdown.

They confirm previous studies of the trends in the leading-edge vortices including the shift from a jet-like axial velocity profile upstream of the breakdown location to a wave-like profile. They are also used to identify the mechanism of the along core blowing which manipulates the vortex breakdown location. These results will allow for the development of more efficient flow control techniques and potentially a closed loop control system for vortex breakdown control.

6. CONCLUSION

In 1997, ONERA has decided to build a multidisciplinary project on aerodynamic active flow control. This project addresses several applications on which significant results have already be obtained.

On TS waves, it has been proven that active control is feasible, the next step, which has already started, consists in an extension to 3D including the control of the 3D steady waves that appear along the leading edge of a 3D wing.

On buffet control, 3D tests are on the way to be performed in the ONERA S2 Modane wind tunnel.

Closed loop control on vortex control will be performed before end the year 2000.

7. ACKNOWLEDGEMENT

The authors would like to express their sincerest thanks to the members of the F2 wind tunnel team for their help in accomplishing these tests.

8. REFERENCES

1- D.CARUANA, M.CORREGE, C.DESPRE, H.GASSOT,P.GIRODROUX-LAVIGNE, J.C.LE BALLEUR, A.MIGNOSI, O.REBERGA
Buffet Active Control - Experimental and Numerical Results
AVT SYMPOSIUM on Active Control Technology for Enhanced Performance Operation Capabilities of Military Aircraft, Land Vehicles and Sea Vehicles
Braunschweig, Germany, 8-11 May 2000

2- C.FRANÇOIS
Experimental Side Force Control on a Generic Forebody at High Angle of Attack
AVT SYMPOSIUM on Active Control Technology for Enhanced Performance Operation Capabilities of Military Aircraft, Land Vehicles and Sea Vehicles
Braunschweig, Germany, 8-11 May 2000

3- G.CASALIS
Instabilités primaire et secondaire dans la couche limite laminaire pour un fluide incompressible
Thèse de doctorat de l'Université de Paris 6 25 juin 1990

4- G.CASALIS, J.L.GOBERT, G.PAILHAS, S.PRUDHOMME
Active Control of TS Waves
Flow control - Fundamentals and Practices
Cargèse - Corsica 24 June-5 July 1996

5- D.BARBERIS, P.MOLTON, P.MALATERRE "
Control of 3D turbulent boundary layer separation caused by a wing-body junction " , Experimental Thermal and Fluid Sciences 16 (1998),pp.54-63.

6- KREPLIN H.P., MEIER H.U., and MAIER A.
"Wind Tunnel Model and Measuring Techniques for the Investigation of 3D Turbulent Boundary Layers," AIAA 10th Aerodynamic Testing Conference, San Diego, California, AIAA Paper 78-781, 1978.

7- RAYNAL J.C. and PELISSIER Ch.
"Essai dans la Soufflerie F1/CFM d'un Ellipsoïde de Révolution du DFVLR,"
ONERA Procés Verbal d'Essais 1/7252 ANG, 1983.

8- CHANETZ B.
"Contribution à l'Etude du Décollement 3D en Ecoulement Turbulent Incompressible,"
Thèse de Doctorat, ONERA NT - 1988-6, 1988.

9- BARBERIS D, MOLTON P.
" Experimental study of three-dimensional separation on a large-scale model"
AIAA Journal,Vol.33,No.11,
November 1995,pp.2107-2113.

10- MITCHELL A.M., BARBERIS D., DELERY J.
"Oscillation of Vortex Breakdown Location and Its Control by Tangential Blowing,"
AIAA-98-2914, AIAA 29th Fluid Dynamics Conference, Albuquerque, NM, June 1998.

11- MITCHELL A.M., MOLTON P., BARBERIS D., DELERY J.
" Control of Vortex Breakdown Location by Symmetric and Asymmetric Blowing"
AIAA-99-3652, 30th AIAA Fluid Dynamics Conference, Norfolk, VA, June 1999.

12- MITCHELL A.M., MOLTON P., BARBERIS D., DELERY J.
"Characterization of Vortex Breakdown by Flow Field and Surface Measurements"
AIAA-00-0788, 37th Aerospace Sciences Meeting and Exhibit, Reno, NV, Jan. 2000.

This page has been deliberately left blank

Page intentionnellement blanche

Buffet Active Control - Experimental and Numerical Results

C. Despré[1], D. Caruana[1], A. Mignosi[1], O. Reberga[1], M. Corrège[2], H. Gassot[3], J.C. Le Balleur[3], P. Girodroux-Lavigne[3]

[1,2] ONERA, 2 av. Edouard Belin, 31400 Toulouse, France
[3] ONERA, 29 avenue de la Division Leclerc, 92322 Chatillon, France

Abstract: The study aims are the active control of transonic buffet over airfoils and wings. A new moving device at the trailing-edge, a so-called "Trailing Edge Deflector" (TED) designed at ONERA, is used to decrease the buffet instabilities.
This study is limited to buffet phenomenon on upper surface of a stiff 2D airfoil in transonic flow.
Experimental and numerical results allow to better understand the phenomena and to validate the efficiency of the TED.
The TED can be moved sequentially to a static position, or better be driven by dynamic servo-motions. A selected static position increases aerodynamic performances for high lift coefficient and delays the buffet onset vs. lift. A preferable TED active control law, coupled with measured flow signals, allows to greatly reduce the aerodynamic instabilities.
The time-consistent strong viscous-inviscid interaction approach VIS15, developed previously for computing buffet or unsteady separated flows over airfoils, gives access to a direct time-accurate simulation of the active buffet control by TED servo-command, both in open-loop control, and in the closed-loop servo-command driven by the computed self-induced signals of buffet.

Key words: *Unsteady flow, buffet, buffet control, two-dimensional flow, shock-wave interaction, flow separation, numerical method, strong interaction, viscous-inviscid interaction, active control, control law, closed-loop control, open-loop control.*

List of Symbols

c	airfoil chord, $c = 200$ mm
x	longitudinal coordinate
z	vertical coordinate
M	Mach number
U	free-stream velocity
T	temperature
P	pressure
C_p	pressure coefficient
$Re_{c,o}$	Reynolds number
ρ	density
t	time
f, f_o	frequency, natural buffet frequency
ϕ	phase
Xsh	shock wave position
α	angle of attack (degrees)
δ	angle of deflector (degrees)
δ_{mean}	static position of the deflector
A	amplification of the control law
τ	time delay of the control law

Subscripts

$(.)_o$	free stream value
$(.)_t$	total value
$(.)_{def}$	deflector value
$(.)_{mean}$	mean value
$\|.\|$	amplitude function for fluctuations

1. Introduction

Buffeting is characterized by structure vibrations induced by aerodynamic excitations. The buffeting phenomenon can exist on different parts of the flows around vehicles. It can appear on aircraft, rockets, turbomachine stages... In this paper, the study is focused on the upper surface of a wing in a transonic flow.
The shock wave/turbulent boundary layer interaction and flow separations induce flow instabilities, named buffet. It results in pressure fluctuations on the wing, that create unsteady loads which can cause structure vibrations on its eigen modes. The buffet loads may cause fatigue problems. In addition, maneuverability and handling qualities are often degraded.
The buffet phenomenon appears when the Mach number or the angle of attack of the aircraft increases. The flight envelope is limited by this phenomenon.
Of course, any delay of the buffet onset by decreasing or canceling the aerodynamic instabilities would permit to increase flight performances of the aircraft. For example, the aircraft take-off weight, maneuverability, or the range, can be increased.
The aim of this study is to control the buffet phenomenon by a direct action device on the flow instability. As a new moving part at the trailing edge of the wing, a so-called "Trailing Edge Deflector" (TED), designed at ONERA, is used to decrease these instabilities.
This control system study, here limited to two-dimensional flows and to the aerodynamic aspect of the phenomenon, will be further studied in

[1]Dept. Models for Aerodynamics and Energetics (DMAE)

[2]Dept. System Control and Flight Dynamics (DCSD)

[3]Dept. Computational Fluid Dynamics and Aeroacoustics (DSNA)

Paper presented at the RTO AVT Symposium on "Active Control Technology for Enhanced Performance Operational Capabilities of Military Aircraft, Land Vehicles and Sea Vehicles", held in Braunschweig, Germany, 8-11 May 2000, and published in RTO MP-051.

three-dimensional flow [1, 2].
In order to analyze the effect of the new control system on the buffet instabilities and to help for better understanding of the manner in which the deflector can act on flow separations and shock wave oscillations over the airfoil, experimental investigations were performed on the stiff 2D airfoil (OAT15A) in the T2 wind tunnel.
Numerically in addition, the time-consistent strong viscous-inviscid interaction approach VIS15 [3, 4], developed previously for computing buffet or unsteady separated flows over airfoils, was used to give access to a direct time-accurate simulation of the active buffet control with TED servo-command, both in open-loop control, and in the closed-loop servo-command driven by the computed self-induced signals of buffet themselves [5].

2. Model and instrumentation

An experimental investigation on the effects of the deflector on buffet characteristics of an OAT15A airfoil was carried out in T2 wind tunnel of DMAE, a department at ONERA Toulouse (fig:1). T2 is a transonic, pressurized and cryogenic wind tunnel with closed circuit [6]. The test section, equipped with top and bottom flexible walls is $0,37m$ high by $0,39m$ wide and $1,4m$ long. The OAT15A airfoil is a supercritical airfoil designed by ONERA with a thickness-to-chord ratio of $12,6\%$, a chord of $200mm$ and a span of $0,39m$ extending the full width of the tunnel. The model has a design point of $M = 0,73$ and a lift coefficient of $C_l = 0,65$. It is equipped with 60 steady and 19 unsteady pressure transducers. Their locations on the airfoil are shown in figure 2. The signals were sampled at 15kHz with a filter at $5kHz$. All of the tests were performed at a Reynolds number of approximately $Re_c = 4,5.10^6$ with transition fixed at $\frac{x}{c} = 7\%$ on upper and lower sides of the model. The tests were performed at ambient temperature. The Mach number varied between $M_o = 0,72 - 0,78$ and the maximum value of the angle of incidence was $\alpha = 3,5^o$. For the design Mach number of $M_o = 0,73$, the shock wave position moves with a frequency of around $f = 75$ Hz in "buffet" conditions.

• Trailing-edge deflector description

The deflector is situated at the lower surface of the trailing edge (fig:3). It is maintained along the wingspan. Its chord-wise length is only 1 to 3 percent of the airfoil chord. It can be moved from -5^o up to 45^o, and have a maximum frequency of $200Hz$. For manufacturing problems, it is made of 3 parts. Each of them, simultaneously, are set to the same position or put in motion. It is driven by an electrical motor. Aerodynamic results of the deflector effects are presented in the next paragraphs.

3. Upper surface buffet description in two-dimensional transonic flow

Buffeting can appear in many flow conditions. In transonic flow, it is accentuated by the shock wave motion.
Natural instabilities on airfoil appear by an increase in the Mach number or the angle of attack. In transonic flow, the buffet is characterized by a complex interaction between shock wave and boundary layer [7, 8]. The shock wave oscillations are caused by flow separation, as shown by the numerical solution VIS15 (fig:4). The buffet onset starts when the separation bubble increases and joins the trailing edge. Then, instabilities develop on a large scale.
The shock-wave moves upstream, pushed by flow separation. Therefore, the flow separation decreases and the shock wave moves back downstream. Thus, the intensity of the shock wave increases and a new separation bubble is created. The flow separation spreads to the trailing edge and push the shock wave upstream again (fig:4).
One of the characteristics of the buffet in two-dimensional flow is that the harmonic spectrum of the shock wave motion exhibits a dominant frequency, plus lower harmonics. This fundamental frequency depends on the shape of the airfoil and on the aerodynamic flow conditions [9, 10].

4. Time-accurate numerical simulation of active buffet control : VIS15 code

The VIS15 numerical method is a "time-consistent strong" Viscous-Inviscid Interaction (VII) approach that was generated a few years ago [3, 4], and that was the first VII method giving the same capability of direct access to a time-accurate simulation of transonic buffet [3, 11, 12] or unsteady separated flows over airfoils [3, 4] as the RANS approaches. More recently, the VIS15 method was extended to the EUROSHOCK passive/active control of buffet through porous walls [13], and to the full time-accurate direct simulation of active buffet control in closed servo-command loop with the present TED device [5], or with the EREA deforming bump device.
The VIS15 code is basically issued from the common methodology of the Viscous-Inviscid Solvers "VIS" developed at ONERA from 1979 [14], using in unsteady equations the same turbulent models and viscous numerical schemes as first designed in steady 2D-3D viscous flows [14, 15, 16, 17], but restricting (in VIS15) the inviscid part of the VIS solver to the transonic small perturbation approximation, while extending the VII strong coupling to a time-consistent one (viscous and inviscid unsteady equa-

tions "discretized and coupled until convergence" at same time-step), so recovering the same domain of influence and same fully time-parabolic nature as the averaged Navier-Stokes RANS equations.
In VIS15, a thin-layer approximation of Le Balleur's "Defect-Formulation theory" [14, 15, 17, 16] for Navier-Stokes equations is used. This theory assumes at all points a splitting of the equations system (RANS Navier-Stokes) in two exactly equivalent strongly interacting equation systems : the viscous "Defect-Formulation" system and the pseudo-inviscid-flow, both of them being solved on the same physical domain. The advantages of this VII approach consist in a very low computational cost that doesn't grow with the Reynolds' number, a much lower undesiderable numerical viscosity, and a high flexibility in choosing at will the viscous approximations level, ranging from boundary-layer to full RANS. At any approximation level, the full overlay of viscous and inviscid computational domains ensures the respect of the full viscous upstream influence in supersonic areas [18], and of a normal pressure gradient inside viscous layers [14, 15, 17, 16].
The thin-layer viscous approximation in VIS15 is assumed in a "displacement-body reference frame" [17, 16], which extends the range of the thin-layer assumption and gives access to "massive separations" and "deep stall".
The viscous numerical method [14, 16, 17, 3] is a field/integral hybrid method, with y-discretization (but with y-rank lower than discretization), that involves a space-marching technique using non-linearly implicit schemes, implicit turbulence coupling, and a switch of direct/inverse modes of solution. It is usable both in steady or unsteady conditions. At each viscous station, "parametric" modeled turbulent velocity profiles [17, 16, 14, 15] — ranging from attached flow to massive separation — are discretized along the direction normal to the local inviscid interacting flow streamlines, on a normal grid that is self-adaptive to the boundary layer thickness and the maximal normal velocity gradient (fig.9).
The method includes first an algebraic turbulence model [14, 15, 17, 16], based on the discretized parametric velocity profiles and on a mixing-length, and secondly an out-of-equilibrium two equation model "$k - u'v'$ *forced* ", Le Balleur [14, 15, 17, 16], "forced" by the parametric velocity profiles modelling, and selected in all present computations.
For the resolution of the inviscid system, an unsteady transonic small perturbations (TSP) method, extension of [19] with revised schemes, is used in VIS15.
The strong coupling is numerically obtained using the original "Semi-Implicit" algorithm defined in 1984 [3, 4], which converges the VII coupling residuals both in direct and inverse viscous modes, after extracting a viscous influence operator, and with an iterative marching conditioning. The convergence is imposed at each time step in order to obtain a time-consistent strong-coupling method and thus to take into account at each time step the full downstream-upstream viscous influence (as in Navier-Stokes solutions). Doing this enables the proper treatment of strong viscous interaction phenomena in the unsteady case, such as unsteady separations and shock – boundary layer interactions.

5. Comparison of numerical solutions with experiments

5.1. Numerical conditions

Numerical flow conditions are identical to experiments (table 1).

R_{ec}	P_{to}	T_{to}	c	xtr/c
$4,3.10^6$	1.7 bar	300 K	0.2 m	7%

Table 1. Numerical conditions

The VIS15 inviscid grid-part used for calculations is (200 × 100), with a few streamwise refinements at leading-edge, trailing-edge, and in the region of oscillating shock-induced separation. Figure 8 shows a zoom of the inviscid grid. The extent of the computational domain is 10 chord lengths upstream/downstream, and 10 chord lengths upper/lower. The VIS15 overlaying viscous grid-part, figure 9, is made of 2 × (163 × 49) points, has wall nodes in coincidence with the 2 × (163) inviscid nodes along the upper/lower sides of the airfoil and wake-cut, and self-adapts its 49 nodes in normal direction to the local thickness and maximal gradient of the viscous velocity profiles. The VIS15 grid refinement at shock separation is designed, with local streamwise meshes smaller than the boundary layer thickness (ΔX about 0.5δ), in order to effectively discretize and resolve numerically the instantaneous physical extent of compressions at turbulent shock-induced separation.

To allow a good comparison between experiments and calculations, it is important to apply some corrections on the Mach number M_o and on the angle of attack.
T2 wind tunnel is equipped with top and bottom flexible walls. As a result, classical corrections for this two walls aren't necessary, at least at steady flow conditions. However boundary layers that appear on the lateral walls of the wind tunnel induce a flow deceleration. A negative correction of the Mach number is necessary. For T2 wind tunnel, this correction is estimated to $\delta M = -0.06$.
For a good comparison it is essential to compare the same level of buffet. So a correction of the angle of attack is done for the two particular studied

cases : one before the buffet onset and one another beyond buffet onset. Corrections applied to this two cases, which are still not fully optimized (in shock position), are indicated in table 2.

case	Mo_{expe}	Mo_{VIS15}	α_{expe}	α_{VIS15}
1	0.736	0.73	2.5^o	2.34^o
2	0.736	0.73	2.125^o	2.1^o

Table 2. Studied cases

5.2. Characteristics of OAT15A buffet

The transonic buffet is characterized by pressure fluctuations and oscillations of the shock wave. The figure 5 shows the pressure fluctuations on the airfoil. The unsteady pressure transducers on the oscillation band of the shock wave indicate a high level of fluctuations. Downstream of the shock wave, fluctuations are still important due to flow separation instabilities. Upstream of the shock wave, in the supersonic region, the fluctuations are low.
The numerical VIS15 solution reproduces well the fluctuations behaviour (fig:5), despite an optimal adjustment of the shock mean position is not here achieved, as shown by the zero-harmonic of the pressure (fig:6), which also displays the good prediction of the steep pressure evolution at trailing-edge on lower-side.
The instabilities are mainly-harmonic. Figure 7 illustrates the shock position vs time. The shock wave oscillation frequency is about $f = 75Hz$ in experiment, whereas a somewhat lower frequency (increasing with angle of attack from about $f = 53Hz$ for incipient buffet to $f = 60Hz$ for well established buffet) is computed by VIS15. It is not yet fully clear whether this numerical shift in fundamental frequency is due to the TSP inviscid truncation still used in the case of VIS15, or to the form of the TSP variant used [19], or to the free-air solution.
More informations on buffet measurements are given in references [20, 21, 22].

5.3. Effects of a static TED change

The trailing edge deflector can be moved to a particular position. Before buffet onset, increasing static TED defection acts on shock wave position and on flow separation levels. The supersonic level is increased and the shock wave moves downstream. Also, the trailing edge thickness is increased and the flow is modified in this region (fig:10). All these effects are well detected by VIS15 numerical calculations (fig:11).

The buffet onset can be detected by the pressure fluctuation levels. The lift coefficient can be determined by pressure integration. The figure 12 shows the buffet onset. The angle of attack of the buffet onset is well detected by the VIS15 solution, where however the buffet onset is somewhat more brutal than in the experimental results. The figures 12 and 13 indicate the effects of two positions of the deflector ($\delta = 0^o$ and $\delta = 15^o$) on the buffet onset. The incidence of buffet onset is decreased with a deflector angle increase, but the lift at buffet onset is increased. Both effects are well predicted numerically by VIS15.
The calculations overestimate slightly the lift coefficient because of their downstream shock-wave position. The figure 13 indicates the steady lift coefficient vs the angle of attack for the two positions of the deflector ($\delta = 0^o$ and $\delta = 15^o$). At iso-incidence, an increased deflector angle increases the lift coefficient for the airfoil.
The figure14 represents the buffet onset by means of the fluctuation amplitude of a local pressure coefficient ($x/c = 0.9$). Experimentally, the pressure fluctuations are calculated for two frequency bands $[5 - 4000Hz]$ and $[50 - 100Hz]$. This allows to know the difference between the separation flow noise and the buffet phenomenon. VIS15 calculations give a buffet onset that is very close to experimental buffet onset in the $[50 - 100Hz]$ frequency band. As a result, it seems that the buffet phenomenon is well modelized by VIS15. An important effect of the deflector is to delay the buffet onset at iso Mach-Cz. The figure 14 illustrates this benefit displayed by experiments, and well reproduced by VIS15 calculations.
The drag polar clearly shows the increase in aerodynamic performances for high lift coefficient (fig:15), but, for lower lift coefficient, there is no profit. VIS15 gives the same results (fig:15).

5.4. Open loop control - Effects of a dynamic TED motion

The deflector can be driven by dynamic movements around a static position. Different deflector motions were tested to try to understand the effects of the deflector motion on natural buffet (fig:16).

• Step motion of TED

Deflector step motions were tested. This kind of motion is very interesting because it allows to study and understand the crossing mechanisms from a flow state to another one. Different cases were studied. The figure 17 shows the buffet onset by variation of the deflector angle. This figure indicates the extremal upstream and downstream positions of the

shock-wave. The shock-wave oscillation starts more brutally by VIS15 calculations than by experiments. However, the comparison is very good.
An interesting case is the switch from a steady state to a buffet state. The figure 18 indicates the shock-wave oscillations for a step from $\delta = 5^o$ to $\delta = 25^o$. VIS15 can visualize the whole flow field. The figure 19 shows the propagation in time of the Mach number perturbation which is created by the step at the time $t = 0ms$. The perturbation takes about $1ms$ to go upstream in the subsonic region of the upper surface and to reach the shock wave. It seems to be an acoustic propagation. On the lower surface of the airfoil, the perturbation takes about $2ms$ to go to the upper surface. It's also an acoustic propagation. The perturbation goes round the leading edge and in the supersonic region. The required time to reach the shock wave is about $1ms$. It is not a simple acoustic propagation. Presently, we don't know how to explain it.

• Sine-shaped TED motions at steady flow conditions

Firstly, sine-shaped signals prescribed to the deflector motion were tested at steady flow conditions. Figure 20 shows the shock wave amplitude oscillations for different frequencies of the deflector (experimental results). The deflector motion creates shock wave oscillations. The amplitude of the shock wave oscillations and its frequency depend on the deflector motion. The deflector motion creates shock wave oscillations at the same frequency than the deflector. This hanging up of frequency is observed for all frequencies of the deflector. The higher the amplitude of the deflector is, the greater the amplitude of the shock wave oscillations will be. The amplitude of the shock wave oscillations varies with the frequency of the deflector. The highest amplitude of the shock wave oscillation is observed for a frequency of the deflector which is near the natural buffet frequency. All this remarks are well predicted by numerical VIS15 calculations in figure 21. Except for an amplitude deflector of $A = \pm 10^o$, the greater amplitude of the shock wave oscillation is observed for a frequency of the deflector which is lower than the computed natural buffet frequency.

• Sine-shaped TED motion at natural buffet flow conditions

At flow conditions with natural buffet, the motion of the deflector can, for certain amplitudes and frequencies, impose its frequency to shock wave and flow separations oscillations. The higher the amplitude of the deflector is, the greater the influence field will be. The figure 22 illustrates the domain of influence in frequency for 3 amplitudes ($A = \pm 2.5^o$; $A = \pm 5^o$; $A = \pm 10^o$) by calculations and experiments.
VIS15 calculation solutions give a slightly greater domain of influence than experiments, but behaviours are identical.
For deflector motion frequencies far from the natural buffet frequency, the shock wave keeps its natural frequency, but the amplitude of oscillations are modulated by the deflector motion.
Experimentally, the amplitude of the deflector $A = \pm 2.5^o$ have just few effects on the shock wave oscillations while calculation solutions give more effects. In experiments, the real position of the deflector was measured by a camera [20]. For little amplitudes ordered, the real deflector amplitude is lower than the commanded amplitude. For $A = \pm 2.5^o$, we find a real amplitude about $A = \pm 1.0^o$ [21]. For the amplitudes ordered of $A = \pm 5^o$ and $A = \pm 10^o$, the real deflector amplitude are near the commanded amplitudes. Experimental and numerical behaviours are comparable. For these amplitudes, the deflector motion causes an increase in shock wave oscillations.

5.5. Closed loop command - Active buffet control

Some phase shifts of sine-shaped open loop motions of the TED (deflector angle phase vs. shock position phase) have permitted a brief stabilization of the unsteady buffeting flow. But, it's impossible to control the buffet phenomenon only by this kind of motion. If an open loop command allows to understand the effects of a deflector motion, a closed loop of servo-command is required to stabilize the shock wave oscillations. It is based on the unsteady measurements of pressure fluctuations (fig:25). We saw in the previous sections that a decrease in the deflector angle involves an upstream motion of the shock-wave, and an increase in the deflector angle involves a downstream shock wave motion. So, the idea is to move the deflector in order that it is acting against the natural shock wave movement.
The control law for a measured signal P is described by:

$$\delta(t) = \delta_{mean} + \delta^{'}(t), \qquad (1)$$

with,

$$\delta^{'}(t) = A * (P(t - \tau) - P_{mean}), \qquad (2)$$

Different control laws were tested based on the same principle. Different measured signals can be used for control : pressure fluctuations taken on a transducer which is located on the shock wave oscillations region, or shock-wave position, or lift. The same signals were also enabled to drive the control law when this one was introduced in VIS15 [5]. The control law's parameters (A, τ) weren't determined a priori. Different gains A and time delays τ were looked for. We can find an optimal couple that depends on

the conditions and the chosen driving signal. Different couples (A and τ) were tested both by the experiments, and by the numerical VIS15 calculations in closed-loop self-command. Experiments as well VIS15 calculations showed [5] that a pressure signal coming from the rear part of the shock wave oscillating region is the most efficient choice with the present control law, due to it's persistent amplitude (i.e. the pressure jump through shock wave).
By using for the command signal the unsteady measurements of pressure fluctuations, the buffet and the shock wave oscillations were greatly reduced in experiment (fig. 26 and 27). By using the same control principle, the buffet can be completely reduced (fig:28) in the numerical VIS15 simulation. Calculations are less expensive than experiments. Then, different new laws will be tested by calculations in order to find new control laws for three-dimensional flow.

6. Conclusion

The experimental study has shown the efficiency of a trailing edge deflector on two-dimensional flow. The TED can be moved to a particular position or be driven by dynamic motions. A selected static position increases aerodynamic performances for high lift coefficient and delays the buffet onset. An active control law driven by unsteady measurements allows to greatly reduce the aerodynamic instabilities.
Numerical solutions obtained by the time-consistent viscous-inviscid strong interaction code VIS15 are in a whole accordance with experiments. The self-command within VIS15 computation of the deflector, driven in closed-loop by the computed buffet pressure signals themselves, provides very good results for time-accurate direct numerical simulation of the active buffet control. Numerical results allow to help to better understand the phenomena and to give a second validation of efficiency of the TED. Different new laws will be tested by calculations in order to find new control laws which could be used in three-dimensional buffet.
This new control system will soon be studied in transonic three-dimensional flow. A similar model extended to a transport aircraft was designed and manufactured with TED. Experimental tests are planned in 2000.

References

[1] D. Caruana, M. Corrège, O. Reberga, C. Despré, and A. Mignosi. Buffet and buffeting active control. *AIAA Fluids 2000 - Flow Control Symposium*, AIAA paper(2000-2609), 19-22 June 2000.

[2] C. Despré. Analyse de quelques résultats expérimentaux des essais DYVAS en vue de la préparation et de l'étude de la demi-voilure OAT15A-CA. Technical report ONERA n^o RT12/00866 DPRS/DMAE, ONERA, Mars 2000.

[3] J.C. Le Balleur and P. Girodroux-Lavigne. A semi-implicit and unsteady numerical method of viscous-inviscid interaction for transonic separated flows. *La Recherche Aérospatiale 1984-1, p.15-37, English and French editions*, Jan. 1984.

[4] J.C. Le Balleur and P. Girodroux-Lavigne. A viscous-inviscid interaction method for computing unsteady transonic separation. *Proceed. 3rd Symp. "Numerical and Physical Aspects of Aerodynamic flows", Long-Beach, USA, January 21-24, 1985), T. Cebeci ed., Springer-verlag 1987, or ONERA TP 1985-5.*

[5] H. Gassot, P. Girodroux-Lavigne, and J.C. Le Balleur. Simulation numérique instationnaire VIS15 du contrôle actif du tremblement transsonique bidimensionnel : actionneur de bord de fuite. *RT 4/6207 DPRS/N/DSNA, Mars 1999.*

[6] A. Séraudie J.P. Archambaud. The Cryogenic Induction Tunnel T2 at Toulouse. *AGARD FDP/VKI Special Course*, May 1996.

[7] N.C. Lambourne. Some instabilities arising from the interactions between shock waves and boundary layers. Technical Report, Advisory Group for Aeronautical Research and development. Report 182., April 1958.

[8] J.M. Délery. Shock wave/turbulent boundary layer interaction and its control. *Prog. Aerospace Sci.*, 22:209-280, 1985.

[9] B. Benoît. Etude du champ de pression instationnaire sur le profil RA16SC1 en régime de tremblement à S3MA. Technical Report, Rapport technique de synthèse ONERA, June 1986.

[10] B.H.K. Lee. Effects of trailing-edge flap on buffet characteristics of a supercritical airfoil. *Journal of Aircraft*, 29(1), January-February 1992.

[11] J.C. Le Balleur and P. Girodroux-Lavigne. Prediction of buffeting and calculation of unsteady boundary layer separation over airfoils. *Proceed. IUTAM Symp. "boundary layer separation", London, August 26-28, 1986, p. 19-35, editor F.T. Smith, S.N. Brown, Springer-Verlag 1987, or ONERA TP 1986-95.*

[12] J.C. Le Balleur and P. Girodroux-Lavigne. Viscous-Inviscid Strategy and Computation of transonic Buffet. *Proceed. Symp. IUTAM Transsonicum III, Gottingen, May 24-27, 1988, Springer-Verlag 1988, or ONERA TP 1988-111.*

[13] J.C. Le Balleur, P. Girodroux-Lavigne, and H. Gassot. Development of Viscous-Inviscid Interaction Codes for Prediction of Shock Boundary Layer Interaction Control (SBLIC) and Buffet over Airfoils. *Brite-Euram EUROSHOCK - Drag Reduction by Passive Shock Control. Notes on Numeri-*

cal Fluid Mechanics, Vol. 56, Chap. 15, pp. 221-244, Vieweg 1997.

[14] J.C. Le Balleur. Strong matching method for computing transonic viscous flows including wakes and separations. Lifting airfoils. *La Recherche Aérospatiale 1981-3, p.21-45, English and French editions*, May 1981.

[15] J.C. Le Balleur. Numerical viscous-inviscid interaction in steady and unsteady flows. *Proceed. 2nd Symp. "Numerical and Physical Aspects of Aerodynamic flows", Long-Beach, (1983), chap. 13, p. 259-284, T. Cebeci ed., Springer-verlag, (1984), (or ONERA TP 1983-8).*

[16] J.C. Le Balleur. New possibilities of viscous-inviscid numerical techniques for solving viscous flow equations, with massive separation. *Proceed. Fourth Symp. Numerical-Physical Aspects of Aero. flows, Long-Beach, USA, Jan. 16-19, 1989, Selected papers, chap. 4, p. 71-96, Cebeci ed., Springer-verlag, 1990. (or ONERA TP 1989-24).*

[17] J.C. Le Balleur. Viscous-inviscid calculation of high-lift separated compressible flows over airfoils and wings. *Proceedings AGARD-CP-515, paper 26, Symposium AGARD/FDP "High-lift aerodynamics", Banff, Canada, 5-8 octobre 1992, (or ONERA TP 1992-184).*

[18] J.C. Le Balleur. Viscous-inviscid flow matching : Analysis of the problem including separation and shock waves. *La Recherche Aérospatiale 1977-6, p.349-358, French, or English transl.ESA-TT-476*, Nov. 1977.

[19] M. Couston, J. J. Angelini, and P. Mulak. Application de l'équation de petites perturbations transsoniques aux calculs d'écoulements bidimentionnels instationnaires. *La Recherche Aérospatiale 1979-5, p. 325-341, (Sept 1979)*, Sept. 1979.

[20] D. Caruana, M. Corrège, O. Reberga, J.B. Dor, and C. Lempereur. Contrôle actif des instabilités aérodynamiques à l'origine du tremblement. Ecoulement transsonique bidimenssionnel. Phase 1. Technical Report, ONERA, Décembre 1998.

[21] D. Caruana, M. Corrège, O. Reberga, J.B. Dor, C. Despré, and J.F. Breil. Contrôle actif des instabilités aérodynamiques à l'origine du tremblement. Ecoulement transsonique bidimenssionnel. Phase 2. Technical Report, ONERA, Juin 1999.

[22] O. Reberga. *Etude expérimentale et numérique du phénomène de tremblement sur profil d'aile et son contrôle en écoulement transsonique avec onde de choc.* PhD thesis, ENSAE, June 2000.

7. Figures

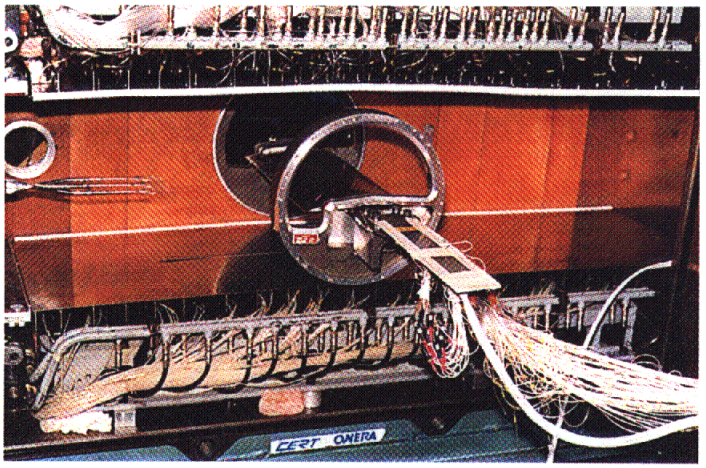


Figure 1. T2 transonic wind tunnel with OAT15A airfoil

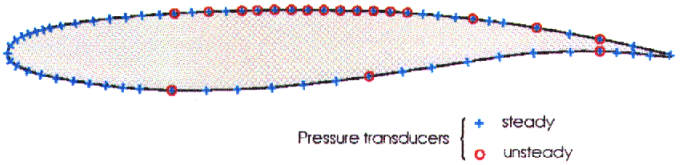


Figure 2. Model instrumentation

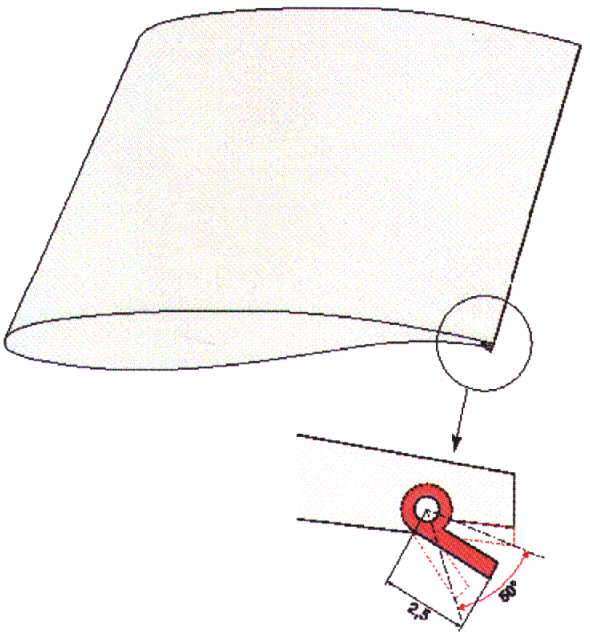


Figure 3. Trailing edge deflector

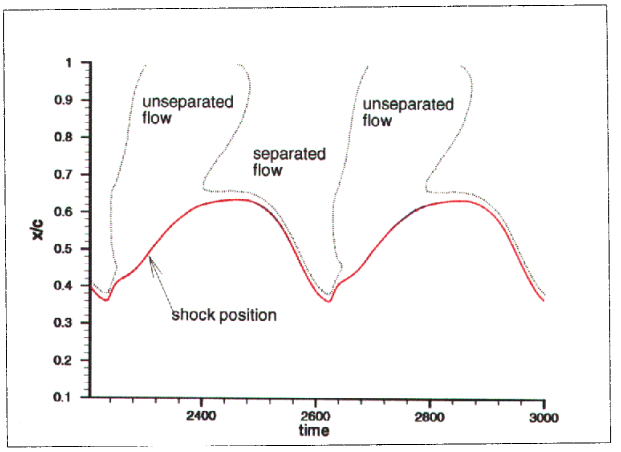


Figure 4. Flow separation areas with the shock position in buffet conditions (Numerical VIS15 solution)

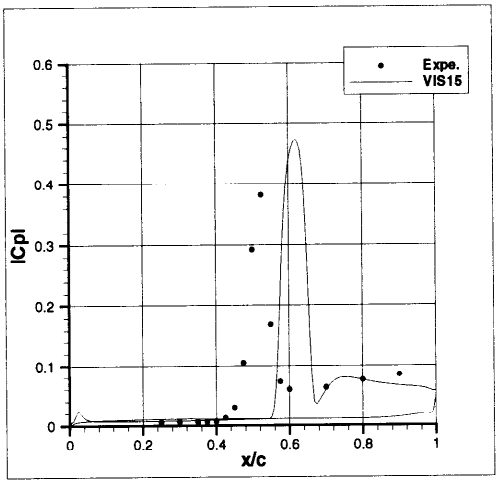


Figure 5. Pressure fluctuations on airfoil - Comparisons of numerical VIS15 solution (M=0.73; $\alpha = 2.34^o$; $\delta = 15^o$) with experiments (M=0.736; $\alpha = 2.5^o$; $\delta = 15^o$)

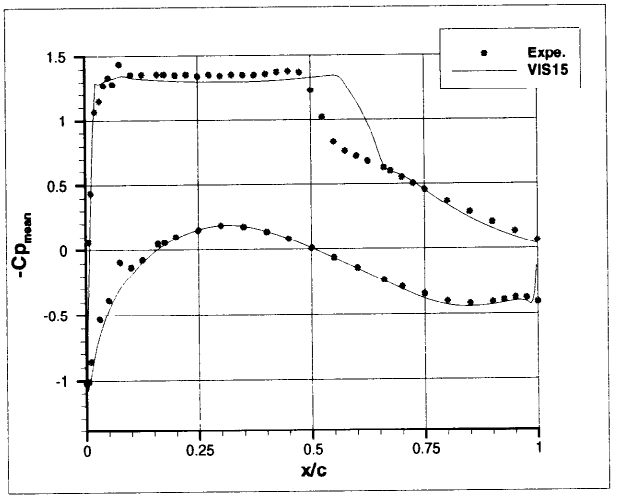


Figure 6. Zero-harmonic of the pressure coefficient - Comparisons of numerical VIS15 solution (M=0.73; $\alpha = 2.34^o$; $\delta = 15^o$) with experiments (M=0.736; $\alpha = 2.5^o$; $\delta = 15^o$)

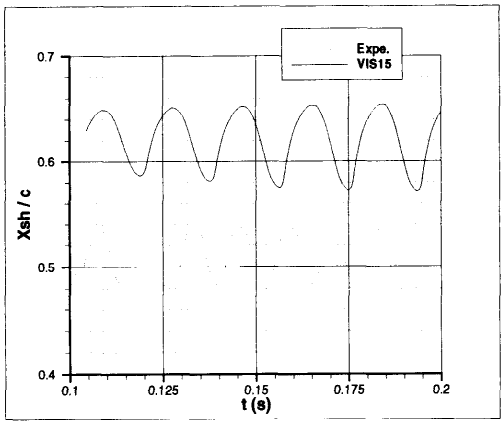


Figure 7. Shock wave position on the airfoil vs time - Comparisons of numerical VIS15 solution (M=0.73; $\alpha = 2.34^o$; $\delta = 15^o$) with experiments (M=0.736; $\alpha = 2.5^o$; $\delta = 15^o$)

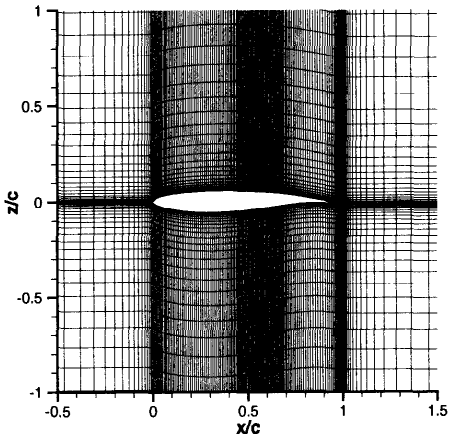


Figure 8. Inviscid part of VIS15 mesh - Zoom on partial view

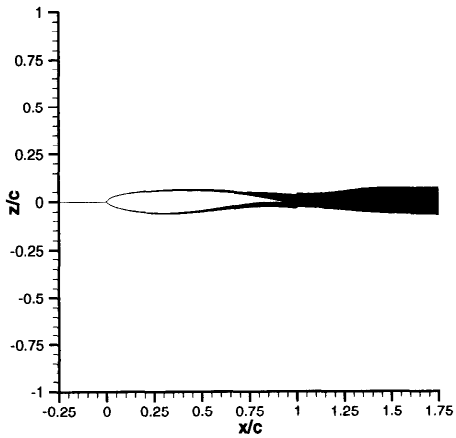


Figure 9. Viscous part of VIS15 mesh - Zoom on partial view

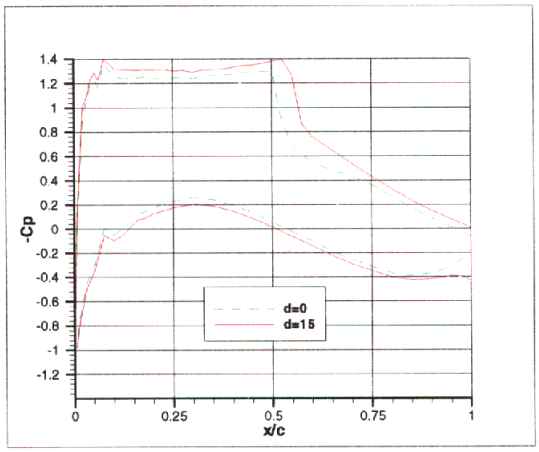


Figure 10. Effects of the static deflector position - Experimental Results (M=0.736; $\alpha = 2.0$; $\delta = 0^o$; $\delta = 15^o$)

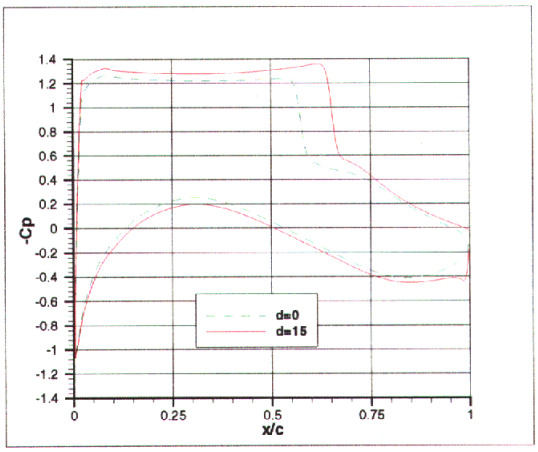


Figure 11. Effects of the static deflector position - Numerical VIS15 solutions (M=0.73; $\alpha = 2.0$; $\delta = 0^o$; $\delta = 15^o$)

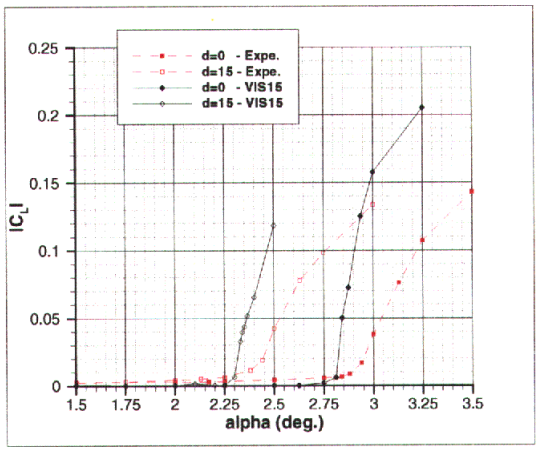


Figure 12. Variation of the fluctuations of lift coefficient with the angle of attack - Comparisons of numerical VIS15 solutions with experiments

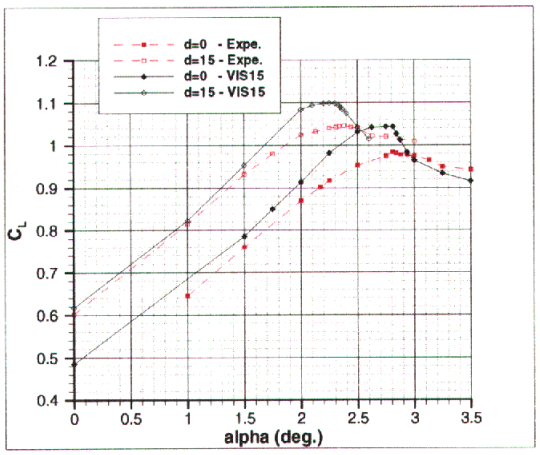


Figure 13. Variation of lift coefficient with the angle of attack - Comparisons of numerical VIS15 solutions with experiments

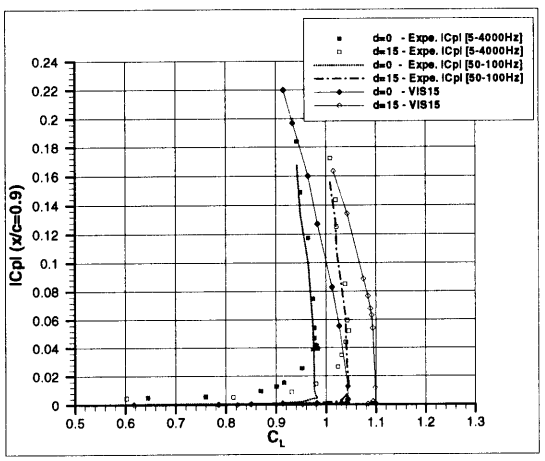


Figure 14. Buffet onset - Pressure fluctuations x/c=0.9 - Comparisons of numerical VIS15 solutions with experiments

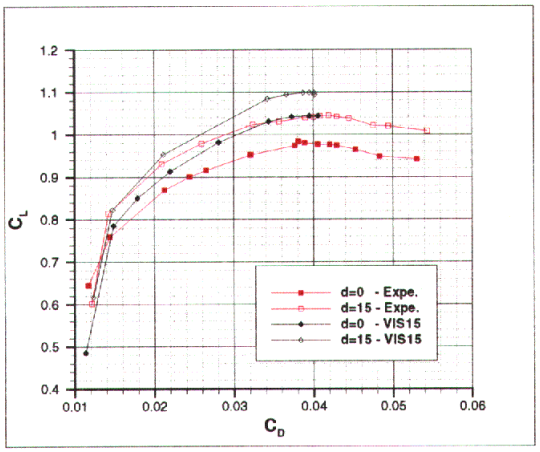


Figure 15. Drag polar - Comparisons of numerical VIS15 solutions with experiments

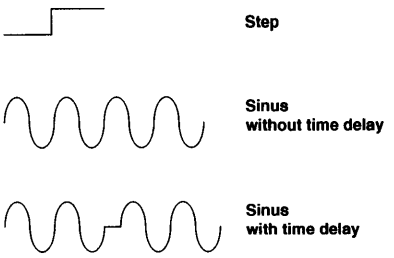


Figure 16. Different motions of the deflector

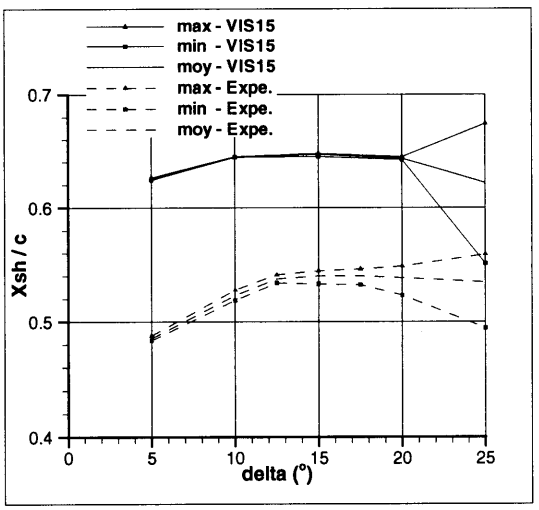


Figure 17. Variation of the extremal shock positions with the angle of the deflector - Comparisons of numerical VIS15 solutions (M=0.73; α = 2.1) with experiments (M=0.736; α = 2.13)

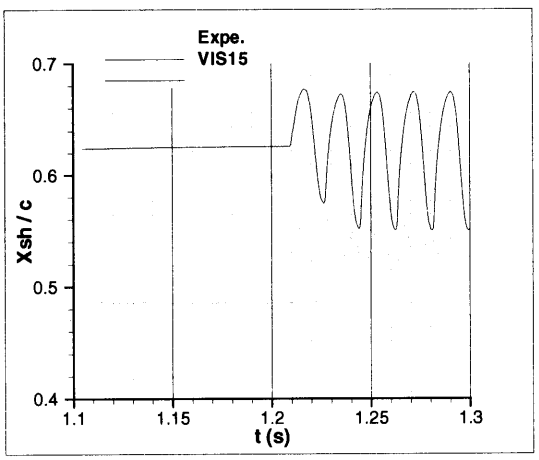


Figure 18. Variation of the shock position vs time after a step of deflector angle from $\delta = 5^o$ to $\delta = 25^o$ - Comparisons of numerical VIS15 solution (M=0.73; α = 2.1) with experiments (M=0.736; α = 2.13)

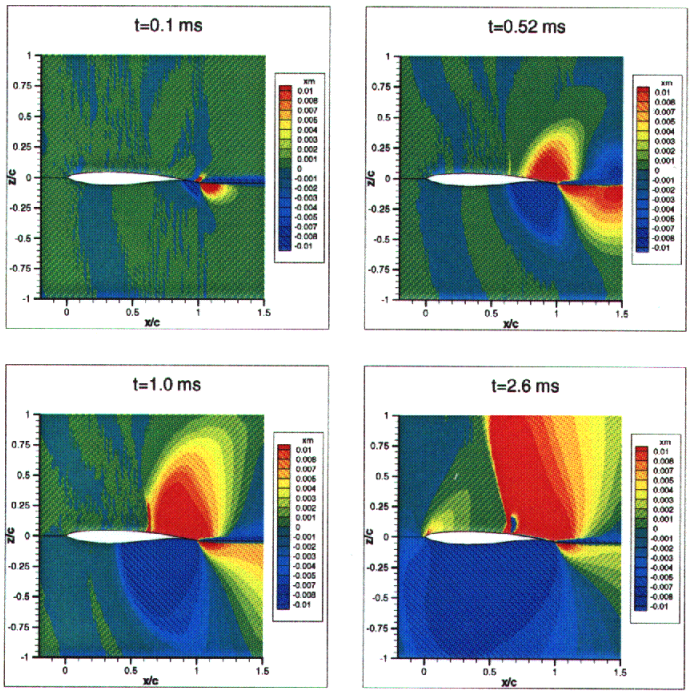


Figure 19. Propagation of the perturbation of Mach number generated after a step of deflector angle from $\delta = 5^o$ to $\delta = 25^o$ at a time $t = 0ms$ - Numerical VIS15 solution (M=0.73; $\alpha = 2.1$)

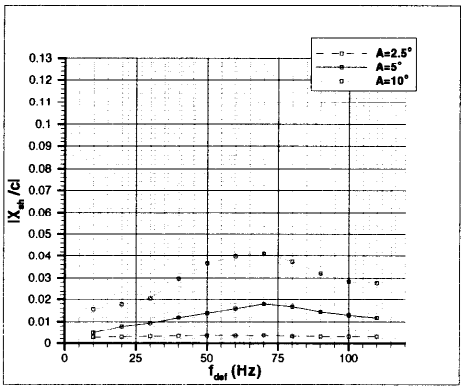


Figure 20. Effects of sine-shaped deflector motion before the buffet onset - Shock fluctuations vs deflector frequency at 3 amplitudes - Experimental results (M=0.736; $\alpha = 2.13$; $d_{mean} = 15^o$)

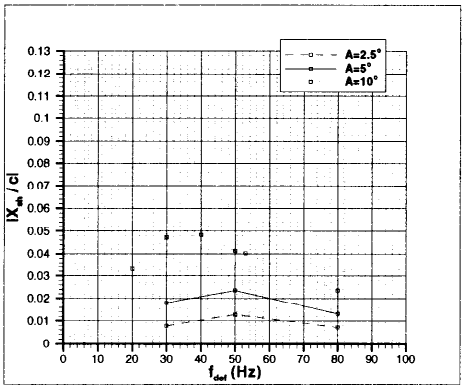


Figure 21. Effects of sine-shaped deflector motion before the buffet onset - Skock fluctuations vs deflector frequency at 3 amplitudes - Numerical VIS15 results (M=0.73; $\alpha = 2.1$; $d_{mean} = 15^o$)

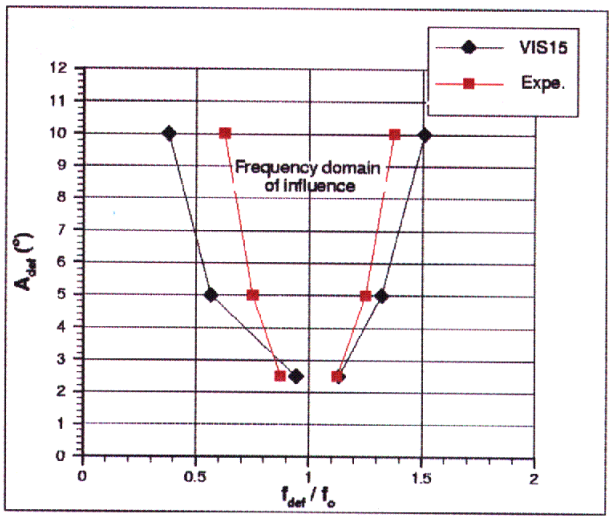


Figure 22. Frequency domain of influence on buffet of the deflector motion vs deflector amplitude - Comparisons of numerical VIS15 solutions (M=0.73; $\alpha = 2.34$; $d_{mean} = 15^o$) with experiments (M=0.736; $\alpha = 2.5$; $d_{mean} = 15^o$)

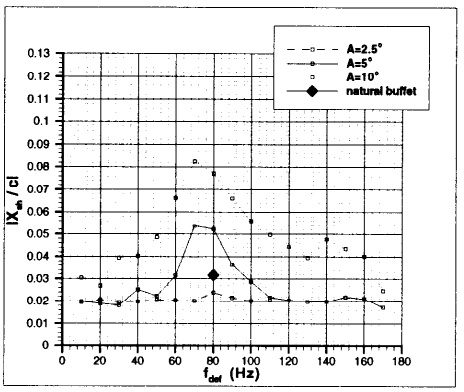


Figure 23. Effects of sine-shaped deflector motion at natural buffet conditions - Shock fluctuations vs frequency at 3 amplitudes - Experimental results (M=0.736; $\alpha = 2.5$; $d_{mean} = 15^o$)

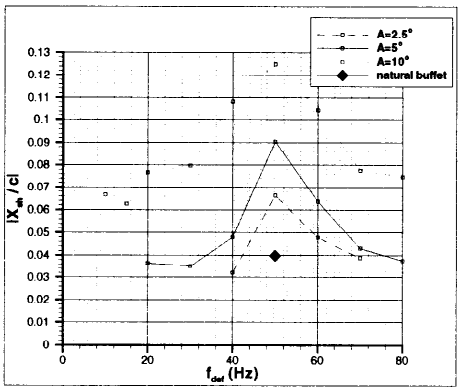


Figure 24. Effects of sine-shaped deflector motion at natural buffet conditions - Shock fluctuations vs frequency at 3 amplitudes - Numerical VIS15 results (M=0.73; $\alpha = 2.34$; $d_{mean} = 15^o$)

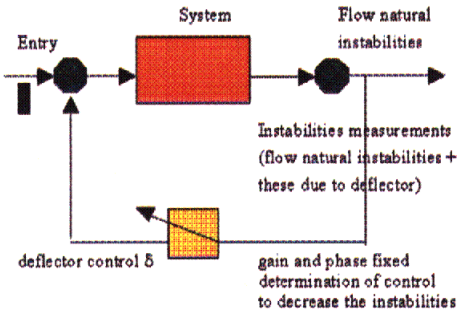


Figure 25. Principle of the active control law - Closed-loop active buffet control

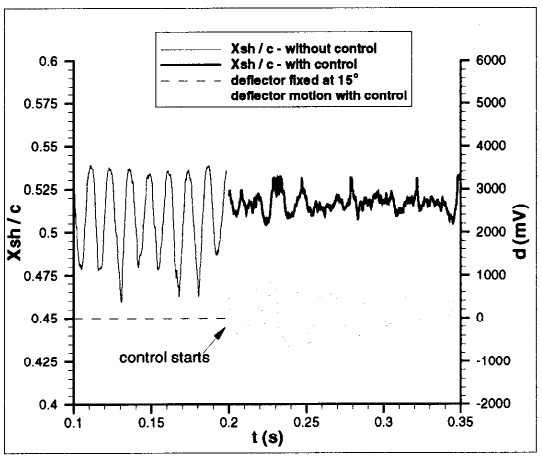


Figure 26. Effects of a closed-loop active buffet control on the shock position - Experimental results (M=0.736; $\alpha = 2.5^o$; $d_{mean} = 15^o$; Control law: $A = 5$; $\phi = 90^o$; $Cp(\frac{x}{c} = 0.525)$)

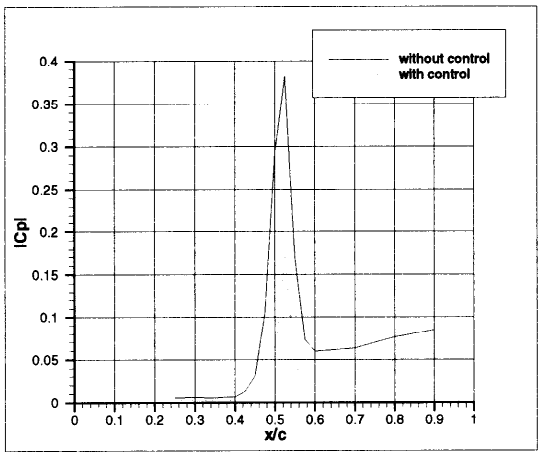


Figure 27. Effects of a closed-loop active buffet control on pressure fluctuations on the airfoil - Experimental results (M=0.736; $\alpha = 2.5^o$; $d_{mean} = 15^o$; Control law: $A = 5$; $\phi = 30^o$; $Cp(\frac{x}{c} = 0.525)$)

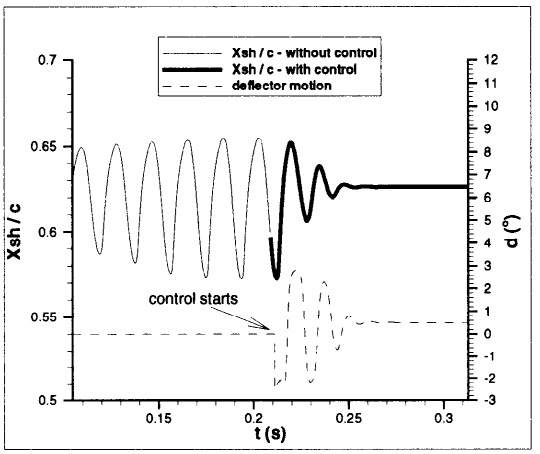


Figure 28. Effects of a closed-loop active buffet control on the shock position - Direct numerical VIS15 simulation (M=0.73; $\alpha = 2.34^o$; $d_{mean} = 15^o$; Control law: $A = 3$; $\phi = 45^o$; $Cp(\frac{x}{c} = 0.63)$)

Paper #15

Q by Dr. Bram Elsenaar: Is the preferred frequency of 75Hz related to a preferred structural mode of the model, like bending ? If yes, is this represented in the theoretical model; or can you explain the difference in frequency (50Hz in theory)

A. (Despre): No the model can be considered as stiff (2-D model spanning the walls). We don't have an explanation for this difference; it may be related to the difference in shock position, or maybe it is due to the TSP inviscid truncation still used in the case of VIS15, or to the form of TSP variant used.

This page has been deliberately left blank

Page intentionnellement blanche

SHOCK CONTROL BY ADAPTIVE ELEMENTS FOR TRANSPORTATION AIRCRAFT WINGS

H. Rosemann, J. Birkemeyer, and A. Knauer

Institut für Strömungsmechanik
Deutsches Zentrum für Luft- und Raumfahrt e. V.
Bunsenstraße 10, D-37073 Göttingen, Germany

ABSTRACT

Different devices for the application of shock and boundary layer control on transportation aircraft wings have been investigated on 2-d airfoils and on a swept wing model. A cavity in the surface underneath the foot of the shock covered with a perforated plate reduces shock strength and hence wave drag, but viscous drag increases such that a net drag reduction can not be achieved in most cases. The application of additional boundary layer suction reduces the additional viscous drag, but not enough to result in a significant gain in total drag.

On the contrary a contour bump underneath the shock, applied alone or in combination with suction, reduces very effectively wave drag without increasing viscous drag so that under off-design conditions up to 24% total drag reduction has been measured for a 2-d airfoil and somewhat lower values for the swept wing. This effect has been well predicted by numerical methods. Both devices, especially the perforation, have a positive influence on the buffet boundary.

Trailing edge devices such as conventional and Gurney-type flaps also effect wave drag by redistributing the pressure on the wing or airfoil. Combining them with a contour bump has been investigated numerically. The results show that by careful optimization of the flap deflection together with the corresponding bump location and height a better performance can be achieved compared to the application of either device alone.

NOMENCLATURE

Symbols

b	Span
c	Chord length
c_p	Pressure coefficient
c_D	Drag coefficient
c_{DV}	Viscous drag coefficient
c_{DW}	Wave drag coefficient
c_L	Lift coefficient
c_Q	Suction coefficient
h	Bump height
M	Mach number
p	Pressure
p_0	Total pressure
Re	Reynolds number
x	Streamwise coordinate
z	Normal coordinate

Greek Symbols

α	Model angle of attack

1 INTRODUCTION

The conventional design of a transportation aircraft wing is usually optimized for a given cruise flight operating point. Changing flight parameters, *e.g.* speed, altitude or weight, often implies a significant degradation of wing performance. Applying adaptive elements may increase the flexibility of a wing design by significantly reducing the cost of operating at off-design conditions.

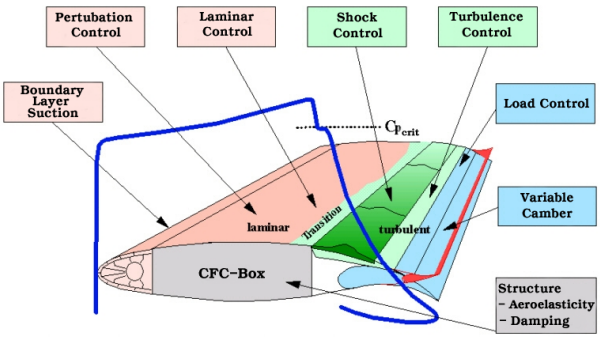


Figure 1: Flow control methods for application on the Adaptive Wing

Figure 1 shows a number of control devices attributed to the Adaptive Wing Technology. Besides the techniques directly acting on the boundary layer, the most effective methods are the global redistribution of the pressure by trailing edge devices (flaps, flexible trailing edge, Gurney flaps) and the local control of the shock to minimize wave drag (passive or active ventilation, contour bumps). These techniques can be utilized to extend the flight envelope to higher velocities, where it is usually limited by the increase of wave drag and shock induced separation caused by strong shocks.

The investigation of shock control by adaptive elements has been a major topic of the research activities in this field at the DLR Institute of Fluid Mechanics during the last years. First experiments started with the application of a perforated surface with a cavity underneath in the region where the shock impinges on the surface of the airfoil. This device was not very successful in reducing total drag; however, the results suggested that by replacing the ventilation by a solid contour bump a much better performance should be achievable.

Systematic experimental and numerical investigations were then undertaken in the framework of the EU-program EuroShock II and the German adaptive wing research program ADIF to study the underlying flow phenomena, optimize bump geometry and position and demonstrate the drag reductions achievable. To determine the additional effect of the 3-d boundary layer of a typical transonic wing on the shock/boundary layer interaction, the investigations included 2-d airfoils as well as a swept wing model.

The paper discusses some results obtained during these research programs for the application of the control devices alone and in combination with additional boundary layer suction. Recently,

Paper presented at the RTO AVT Symposium on "Active Control Technology for Enhanced Performance Operational Capabilities of Military Aircraft, Land Vehicles and Sea Vehicles", held in Braunschweig, Germany, 8-11 May 2000, and published in RTO MP-051.

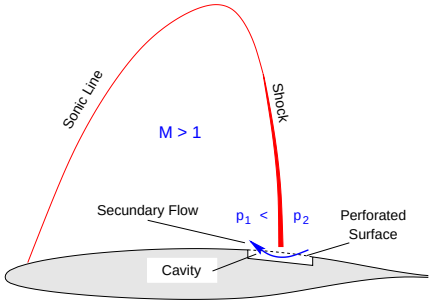


Figure 2: Passive ventilation for shock control

an optimization study on a combined application of a contour bump together with a flexible trailing edge has been performed and results will be shown together with first experiments on airfoils with Gurney flaps at transonic speed.

2 SHOCK CONTROL ON AIRFOILS BY A PERFORATED SURFACE

As outlined above, first attempts to reduce shock strenght and thus wave drag were made with a cavity in the surface of the airfoil under the shock position covered by a perforated plate. The basic set-up is sketched in Fig. 2

A secondary flow is established in the cavity driven by the pressure rise across the shock effectively creating a “pneumatic bump” by modulating the boundary layer displacement thickness when the flow exits the cavity in front of the shock and re-enters behind it. Compression waves emanating from the rising slope of the bump hit the shock, weaken it and thus reduce wave drag.

The details of the flow field in the region of the shock/boundary layer interaction above the cavity have been investigated in a channel flow by Bur *et al.*, Ref. 1, both experimentally and numerically. Their results show, that the single shock is indeed replaced by a lambda shock system, thus reducing wave drag. At the same time, however, the boundary layer thickness increases substantially due to the additional losses in the flow through the perforation such that viscous drag is increased.

These effects can be clearly identified also in Fig. 3, where passive ventilation was applied on the laminar-type airfoil LVA-1, tested in the $0.4\ \mathrm{m} \times 0.35\ \mathrm{m}$ DLR Cryogenic Ludwieg Tube (KRG) in Göttingen (Ref. 2, Ref. 5). As a result of the spreading of the shock the pressure gradient in the shock region is significantly reduced, when the perforation is open. The increase of the displacement thickness of the boundary layer shows up in the wake pressure distribution and in the lower trailing edge pressure. The additional viscous drag is higher than the reduction of wave drag such that total drag is increasing by 9% in this case.

A total drag increase has been found in all cases for laminar-type airfoils. Under certain conditions, slight gains in total drag were found for turbulent airfoils, but in general it had to be accepted that passive ventilation can not be applied successfully for drag reduction. An additional suction slot upstream of the interaction region reduces the drag increase, but not to the point were significant reductions are achieved.

Passive ventilation can, however, be applied successfully for reducing shock induced separation. The pressure distribution in Fig. 4 was obtained from an experiment on the VA-2 airfoil tested in the $1\ \mathrm{m} \times 1\ \mathrm{m}$ DLR Transonic Wind Tunnel Göttingen (TWG), Ref. 5.

The curves indicate for the closed surface a strong separation with an oscillating shock, as can be deduced from the spread of the pressure distribution in the shock region. When the cavity is opened, the shock strength is reduced, the flow stabilizes and the separation disappears. In this special case, drag is obviously also reduced by a large amount.

3 SHOCK CONTROL ON AIRFOILS BY CONTOUR BUMPS

The logical conclusion from the results reported above was to replace the cavity and the perforation by a solid bump in the surface of the airfoil or wing, thereby maintaining the positive effect on the shock without having to accept the increase of viscous drag. The following investigations were supported by the EU-program EuroShock II and represent the key aerodynamic element in the cooperation between DaimlerChrysler Aerospace Airbus, DaimlerCrysler Forschung and DLR cooperation on adaptive wing technologies, ADIF.

First, an extensive numerical study was carried out to determine the optimum values for the geometric parameters of the bump, as there are: shape, extension, position and height. It was found, that for best performance the length of the bump should be around 20% chord and the shape asymmetric with the maximum height at about 60% of the length of the bump without discontinuities in the contour, *cf.* Ref. 4. While these parameters are not very critical, the position of the crest of the bump and the height have to be very carefully adjusted to the position and strength of the shock.

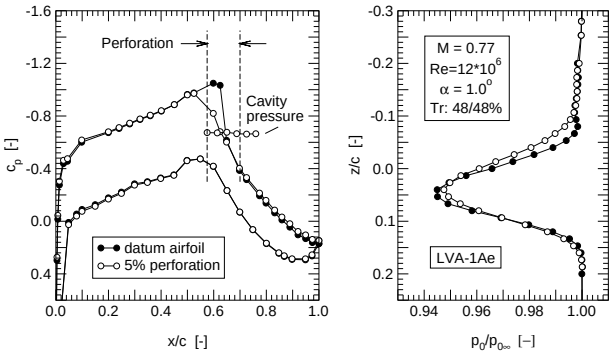


Figure 3: Surface and wake pressure distributions on the laminar-type airfoil LVA-1Ae with and without passive control

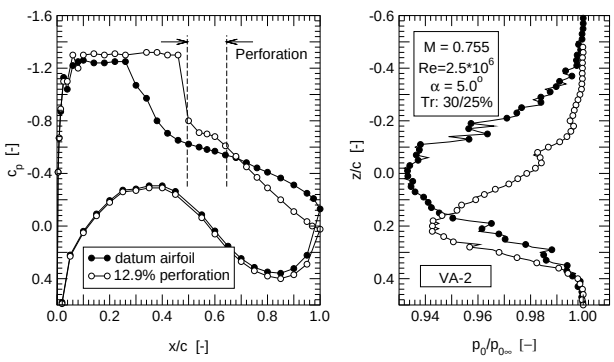


Figure 4: Surface and wake pressure distributions on the turbulent-type airfoil VA-2 with and without passive control

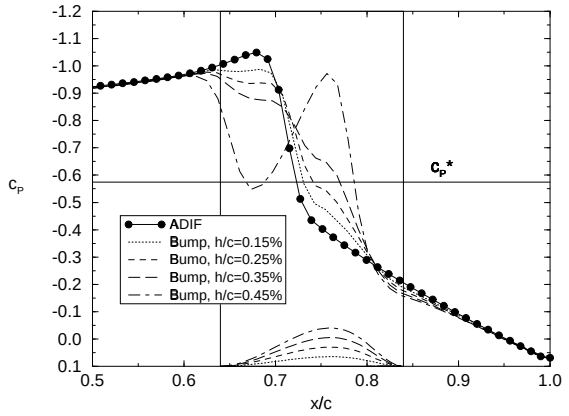


Figure 5: Calculated pressure distribution in the shock region of the ADIF airfoil for different bump heights for $M = 0.755$

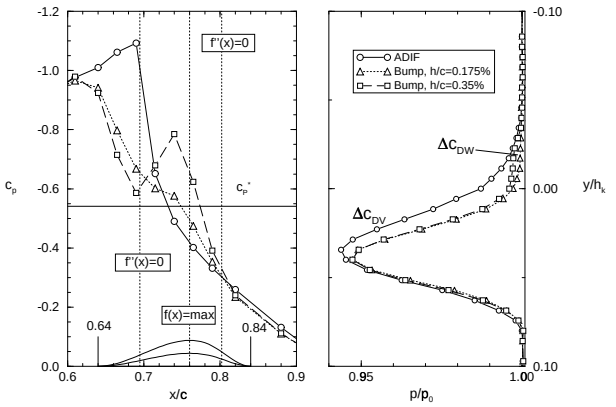


Figure 7: Measured pressure distribution in the shock region of the ADIF-airfoil for different bump heights for $M = 0.765$

Figure 5 shows a result of the pressure distribution in the shock region calculated for different bump heights on the ADIF airfoil. While initially the effect of a reduction of the pressure gradient of the shock increases with increasing bump height, the last curve for the highest bump exhibits a double shock configuration with a significant drag increase. Obviously the optimum bump height depends on the shock strength, while the position has to follow the shock such that the relative distance between bump maximum and shock position is maintained about constant.

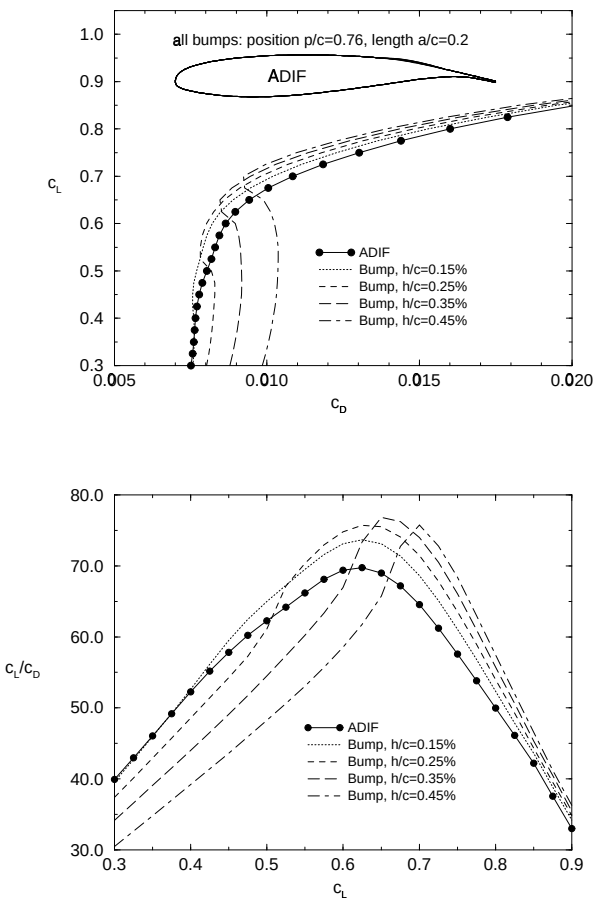


Figure 6: Calculated drag and lift-over-drag ratio for the ADIF airfoil for different bump heights at $M = 0.755$

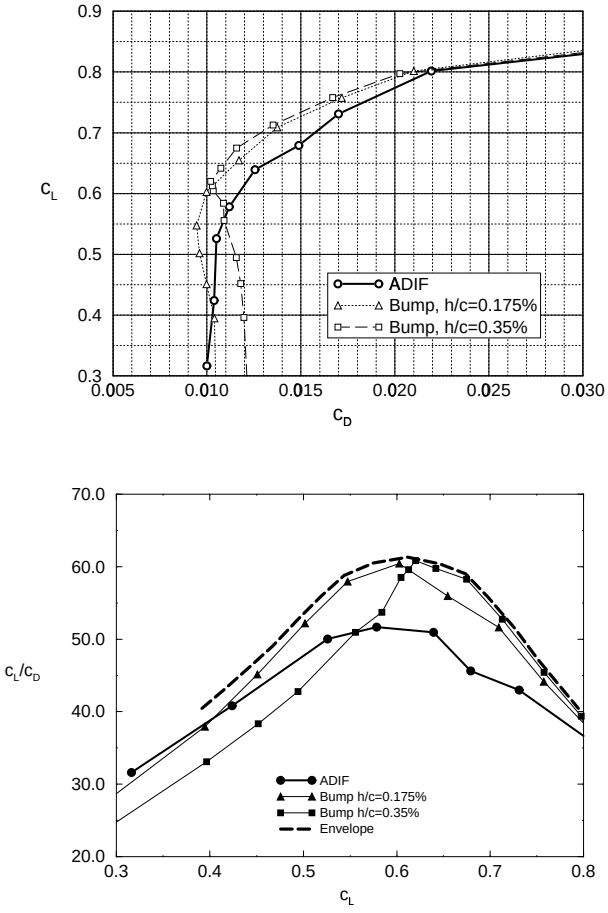


Figure 8: Measured drag and lift-over-drag ratio for the ADIF airfoil for different bump heights at $M = 0.765$

Figure 6 shows the computed lift polars and the L/D ratios for a Mach number slightly above the airfoil design Mach number and different bump heights. It can be seen clearly, that higher bumps reach their maximum performance at higher lift coefficients, whereas they produce additional drag at low lift coefficients due to unfavorable double shock configurations such as shown in Fig 5. To obtain the best results over the whole polar the bump therefore has to be adaptive, also adjusting its position which for the sake of simplicity was fixed for these examples. The benefits can be exploited in terms of a higher maximum of the L/D ratio for these off-design conditions as well as a wider usable range of lift coefficients with a given (minimum) L/D value.

The numerical results in Fig. 5 and Fig. 6 were confirmed by experimental data obtained in the Cryogenic Ludwieg Tube of DLR in Göttingen, given in Fig. 7 and Fig. 8. The model was equipped with two exchangeable inserts with bump heigths of 0.175% and 0.35% chord, respectively. The pressure distribution in the shock region in Fig. 7 as well as the polars and L/D ratios in Fig. 8 show the same trends as the numerical results. The maximum drag reduction for this Mach number was obtained with about 24% for the bump with a height of 0.35% chord.

4 SHOCK CONTROL ON A SWEPT WING BY CONTOUR BUMPS, PERFORATION AND SUCTION

To find out, whether the results of the 2-d airfoil investigations do also apply for a swept wing, where the boundary layer is three-dimensional and the shock/boundary layer interaction might respond differently to these control devices, a model of a swept wing was designed and built for the 1 m × 1 m TWG, Ref. 3. The swept wing design was chosen because a half model would not have been large enough in this wind tunnel to accomodate the different inserts. Contoured liners were necessary on the side walls of the test section to ensure infinite sweep conditions, see Fig. 9.

The test results showed that the effect of the flow control devices was in principle not very different from the 2-d case. Figure 10 shows an example of a pressure distribution in the shock region and Fig. 11 the polars for the swept wing equipped with a bump of 0.16% chord height with and without additional suction upstream of the shock.

There was basically no drag reduction achievable from the passive ventilation. The bumps showed a somewhat smaller drag

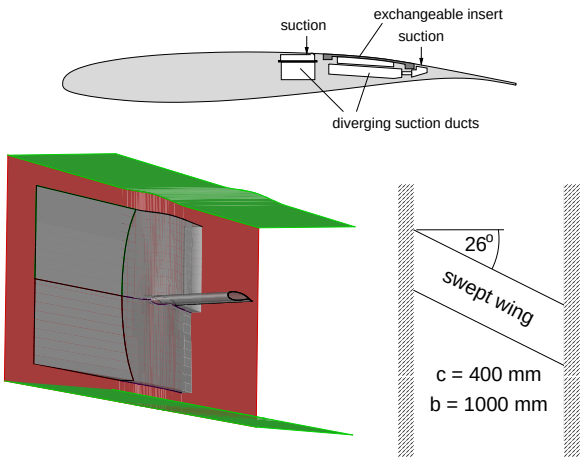


Figure 9: The ADIF swept wing model for shock control applications

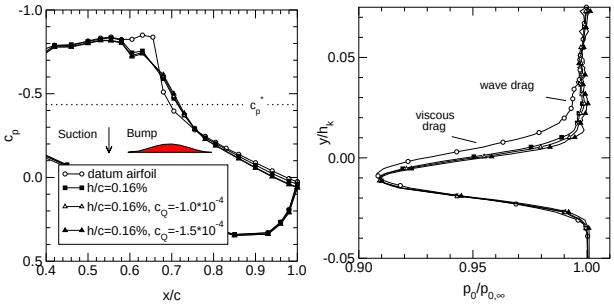


Figure 10: Pressure distribution in the shock region of the ADIF swept wing with and without bumps and boundary layer suction at $M = 0.852$

reduction as on the airfoil tests, *cf.* Fig. 11, this is however believed to be in part caused by a premature boundary layer transition leading to comparatively higher boundary layer thicknesses as in the 2-d experiment. The addition of boundary layer suction upstream of the shock reduces the boundary layer thickness again and leads to higher drag reductions and probably these values are to be compared with the 2-d results.

5 APPLICATION OF CONTOUR BUMPS IN COMBINATION WITH VARIABLE CAMBER

Modern wing designs will utilize variable camber to optimize aerodynamic performance for different flight conditions. For transonic speed one effect of variable camber is also to reduce wave drag by redistributing the pressure such that strong shocks are avoided. Therefore it was to be investigated, whether additional benefits may still be gained by a combination of variable camber and the contour bump for shock control.

A numerical optimization study was performed employing variable camber, here realized in form of a flexible trailing edge, together with a contour bump. For each lift coefficient, the optimum combination of trailing edge deflection, bump position and height for minimum drag was determined. An example of the results is given in Fig. 12.

For the Mach number chosen for this test case, the variable camber is most efficient for low values of the lift coefficient, whereas at high lift the bump achieves higher drag reductions. The combination of both devices gives a significantly better performance than either one alone. This balance changes with Mach number. In general, the contour bump is most effective at high Mach

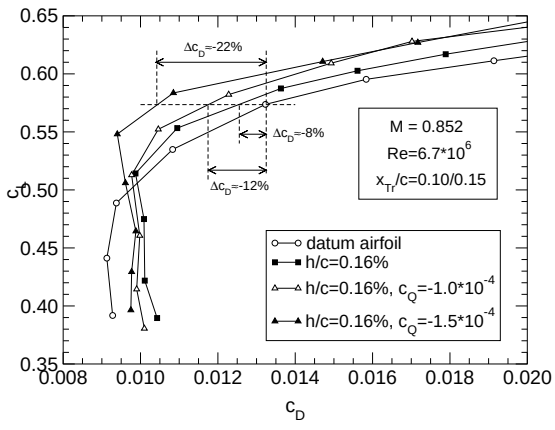


Figure 11: Drag polars for the ADIF swept wing with and without bumps and boundary layer suction

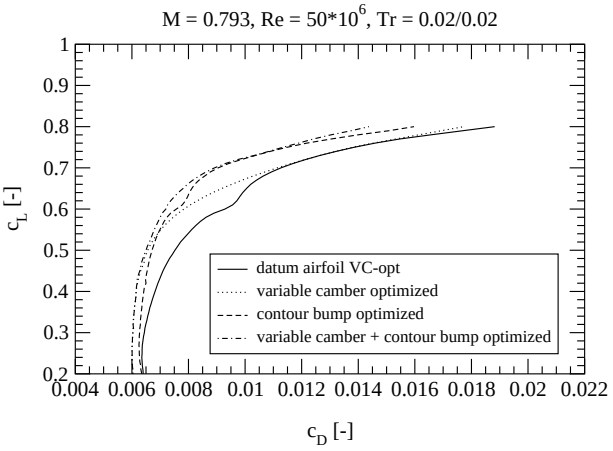


Figure 12: Drag polar for the VC-opt airfoil with optimized trailing edge deflection and bump

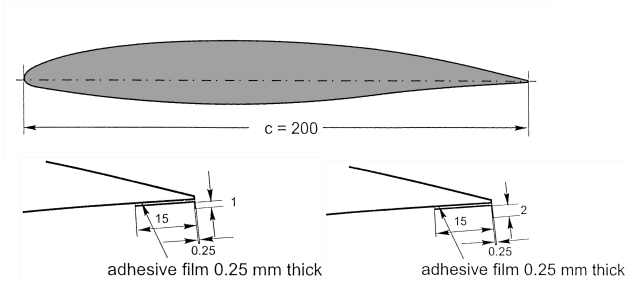


Figure 13: CAST-10 airfoil with 0.5% and 1% chord Gurney flaps

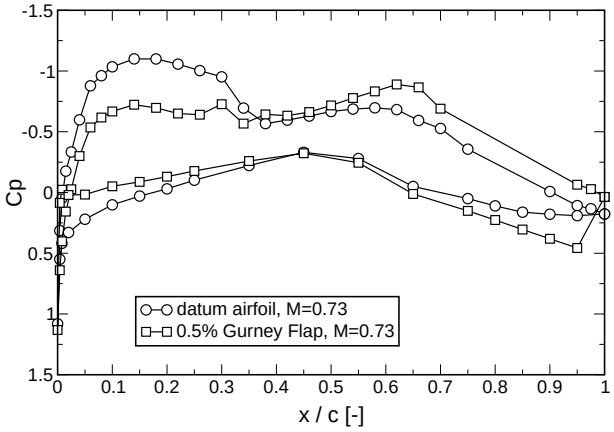


Figure 14: Pressure distribution for the CAST-10 airfoil with and without 0.5% chord Gurney flap

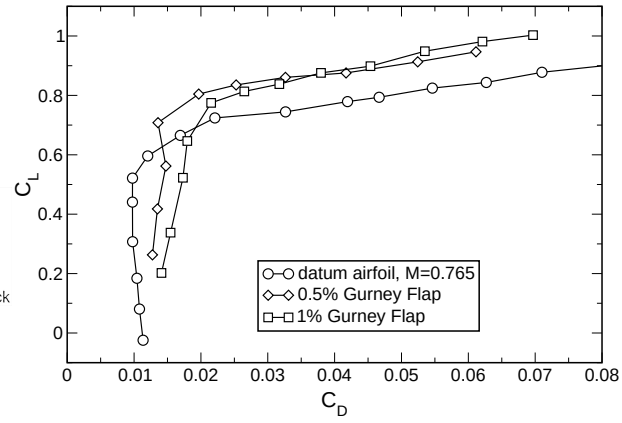


Figure 15: Drag polars for the CAST-10 airfoil with 0.5% and 1% chord Gurney flaps at $M = 0.765$

numbers/high lift coefficients, where the effect of the flap is not sufficient to eliminate wave drag.

A similar effect as with flexible trailing edges and flaps can be achieved with small trailing edge modifications like Gurney flaps. Two configurations on a CAST-10 airfoil were investigated experimentally in the 1 m × 1 m TWG, *cf.* Fig. 13.

The two pressure distributions in Fig. 14 at about the same lift coefficient explain, why in the drag polars in Fig. 15 the configurations with Gurney flaps develop a better performance at high lift coefficients. The re-distribution of the pressure reduces low pressures on the suction side of the airfoil, such that a shock is no longer formed and wave drag is avoided. Further investigations on trailing edge modifications to enhance aerodynamic performance at transonic speed with very small devices are planned.

6 SUMMARY AND CONCLUSION

Flow control by passive ventilation, contour bumps and trailing edge devices has been investigated both numerically and experimentally at transonic speed in the region of the drag rise. All these devices is in common, that they achieve most of their potential of drag reduction by minimizing wave drag, either by direct interaction with the shock, like the ventilation and the bump, or by changing the pressure distribution such that strong shocks are no longer necessary because the maximum velocities on the suction side of the airfoil are greatly reduced.

Total drag reductions can not be achieved by passive ventilation, since the reduction of wave drag is more than outweighted by an increase in viscous drag due to the losses in the flow through the perforation.

The contour bump is very effective in reducing wave drag at off-design conditions, especally at high Mach numbers and high lift coefficients. A maximum of 24% drag reduction could be achieved. Flexible trailing edges or flaps have similar benefits, but at lower Mach numbers and lift coefficients. By combining these two devices the drag polar for high Mach numbers can be enhanced over the whole range of lift coefficients.

Small trailing edge devices like Gurney flaps show promising results also in the transonic regime. Their potential for drag reduction will be subject to further studies.

REFERENCES

1. R. Bur, J. Délery, and B. Corbel. Basic study of passive control applied to a two-dimensional transonic interaction. In E. Stanewsky, J. Délery, J. Fulker, and W. Geißler, editors, *EUROSHOCK — Drag Reduction by Passive Shock Control*, pages 355 – 378. Vieweg, 1997.

2. H. Rosemann. The Cryogenic Ludwieg-Tube at Göttingen. In *Special Course on Advances in Cryogenic Wind Tunnel Technology*, AGARD-R-812, DLR, (Cologne, Germany), 20–24 May 1996.

3. J. Birkemeyer. Widerstandsminimierung für den transsonischen Flügel durch Ventilation und adaptive Konturbeule. DLR Forschungsbericht FB 99-28, DLR, 1999.

4. A. Knauer. Die Leistungsverbesserung transsonischer Profile durch Konturmodifikationen im Stoßbereich. DLR

Forschungsbericht FB 98-03, DLR, 1998.

5. H. Rosemann, A. Knauer, and E. Stanewsky. Experimental investigation of the transonic airfoils DA LVA-1A and VA-2 with shock control. In E. Stanewsky, J. Délery, J. Fulker, and W. Geißler, editors, *EUROSHOCK — Drag Reduction by Passive Shock Control*, pages 355 – 378. Vieweg, 1997.

Paper #16

Q by Chris Weir: The predicted benefit will be of great interest to the airframe companies and the airlines. When do you believe that the technology might enter service ?

A : The technology requires a new wing design. No prediction is given.

Active Dynamic Flow Control Studies on Rotor Blades

W.Geissler, M.Trenker, H.Sobieczky

Deutsches Zentrum für Luft- und Raumfahrt e.V., Institut für Strömungsmechanik,

Bunsenstr. 10, D-37073 Göttingen, Germany

Abstract:

Higher Harmonic Control (HHC) and Individual Blade Control (IBC) technologies have reduced noise and vibration levels of rotors considerably. Further improvements are expected with **on-blade** devices, i.e. the rotor blade is active only along a limited spanwise section of high aerodynamic efficiency.
On both advancing and retreating sides of the rotor disc local supersonic areas terminated by shock waves play a dominant role with respect to separation (dynamic stall) and buffet (moving shock) problems.
The present paper deals with new design methodologies to deform blade sections dynamically. The objective of airfoil deformation is to avoid strong shock waves which are responsible for shock induced separation (dynamic stall) on the retreating blade and which are the origin of high speed impulsive noise levels on the advancing blade.
A combination of different software components available at DLR Institute of Fluid Mechanics, i.e. Geometry Generation Tools and 2D-Time Accurate Navier-Stokes Codes have already shown their strong potential for the development of dynamic flow control devices. This system will be used intensively in the present study and systematically applied to separation and shock control problems.

1. Introduction

The design of helicopter rotor airfoils is a matter of compromise:

-Take care of transonic effects on the advancing side of the rotor disc

-Try to reduce or at least shift unsteady separation (dynamic stall) on the retreating side of the disc.

Fig. 1 shows the main flow problems on a helicopter in forward flight. With increasing flight speed the main rotor encounters transonic flow with shock waves on the outer part of the blade where strength as well as position of the shocks are dependent on time i.e. on the azimuth angle.
On the retreating side the incidence of the blade has to be increased to balance the overall lift of the rotor. Simultaneously with the transonic flow on the advancing side reversed flow and flow separation occurs on the retreating side a phenomenon called dynamic stall. The latter flow feature has frequently been described in the literature [1],[2].
A rigid airfoil design can not take care of all problems in an optimal way. Several investigators have therefore proposed passive as well as active control devices to favorably influence unsteady separation (dynamic stall):

- suction and blowing devices on the airfoil upper surface (both steady and dynamic), [3],
- leading edge flap, [4]
- trailing edge flap, [5], etc.

In recent years a different type of control device has been proposed: The dynamically deforming airfoil.
This type of device seems to have large potential with respect to dynamic stall control without the disadvantage of i.e. the static flap device which is not very useful on the advancing side of the cycle.
Different concepts have been tried with considerable benefit:
Fig. 2 shows two of recently applied devices which are the “nose-drooping” concept frequently investigated at DLR, [6] and the DDLE (Dynamically Deforming Leading Edge) concept, [7] investigated at NASA, [8].
Both concepts have the main feature to either shift (nose-droop) or reduce (DDLE) the local curvature at the airfoil leading edge and do this dynamically, that is time dependent. In the case of the DDLE-concept a wind tunnel model has been realized which has a flexible leading edge surface made from carbon fiber. The flexible structure is dynamically deformed by means of a pull/ push rod operating inside the model. By means of this device the curvature of the NACA 0012 airfoil model could be reduced considerably and leading edge separation was shifted to higher incidences or in optimal cases could be completely avoided.
Numerical investigations, [9] show at least qualitative comparison with the experimental data.
To realize the nose-droop concept on a wind tunnel model is a much more difficult task. The proposal given in Fig. 2 has frequently been calculated numerically. It has been shown, [10] that the dynamic stall vortex can be reduced considerably in strength (see Fig.3) resulting in improved force and moment hysteresis loops.
However the realization of this device which covers more than 25% of the airfoil surface with rather high deflection angles can not be realized nowadays on either a wind tun-

Paper presented at the RTO AVT Symposium on “Active Control Technology for Enhanced Performance Operational Capabilities of Military Aircraft, Land Vehicles and Sea Vehicles”, held in Braunschweig, Germany, 8-11 May 2000, and published in RTO MP-051.

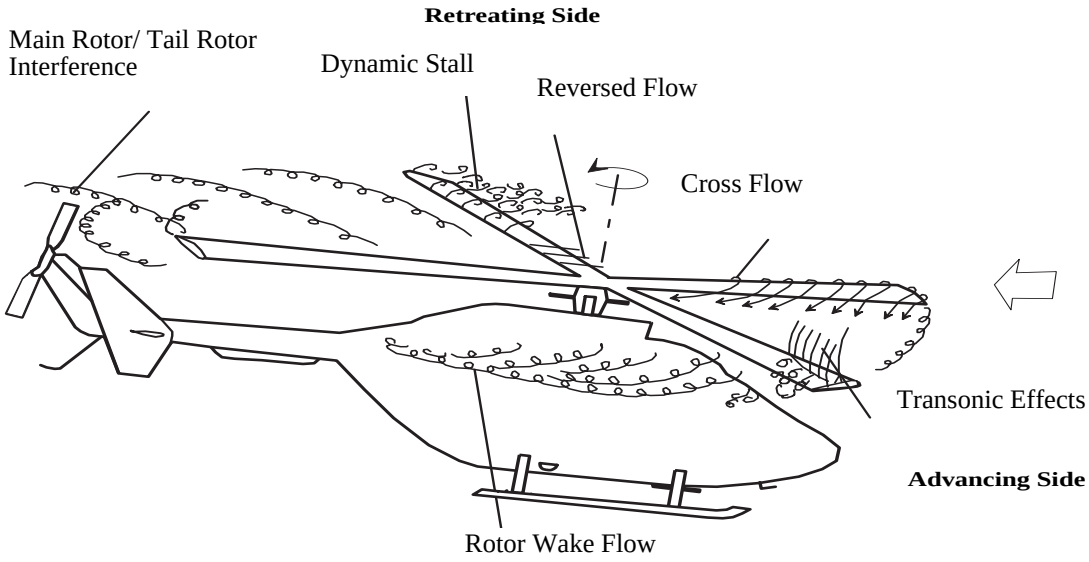
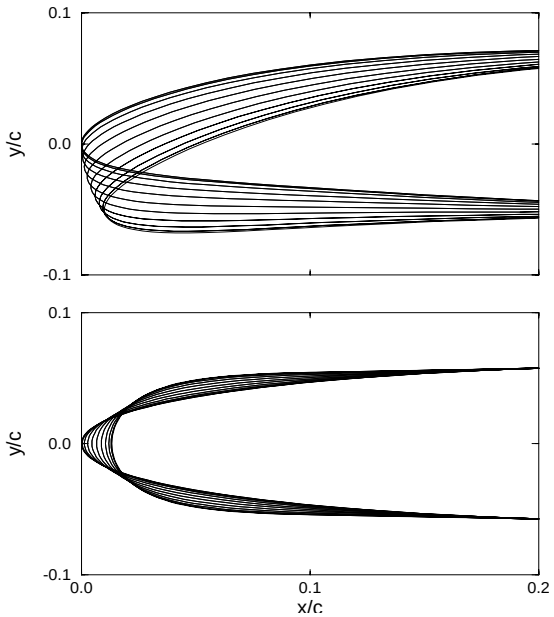


Fig. 1: Main Flow Problems on Helicopter in Forward Flight

nel model nor on the real rotor blade.

With the development of new actuator design based on pieco-electric devices it is now possible to move parts of the airfoil dynamically as rigid structures. In [11] it has been shown that corresponding actuators are able to oscillate a trailing edge flap with sufficient deflection angles and frequencies. The same actuator system will be used in future wind tunnel tests to operate a sealed leading edge flap under realistic aerodynamic loads (German project AROSYS, joint project between DLR, ECD, Daimler-Chrysler Research Lab).

In the present paper it will be shown first that this leading edge flap concept is already of considerable benefit with respect to dynamic stall control. However the advancing side of the blade has to be taken into account as well. New design methodologies are now available at DLR to take also care of the transonic flow conditions, [12]. By means



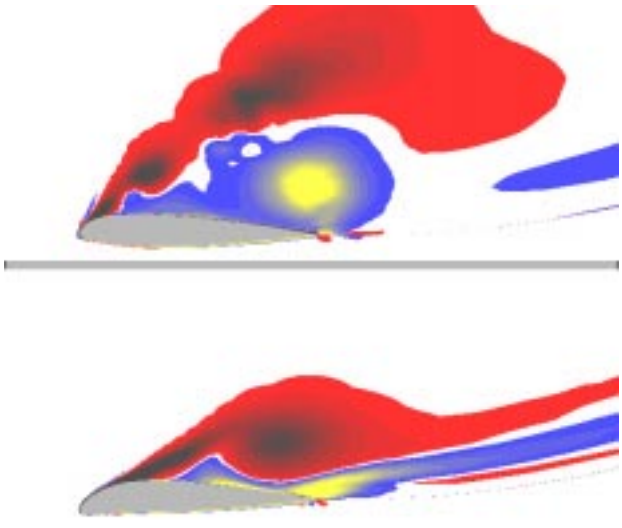


Fig. 2 ((Left): Nose-Droop (Upper), Dynamically Deforming Leading Edge (Lower), Fig. 3 (Right): Dynamic Stall Vortex reduction by a Nose-Drooping Device

of shock free design methods based on the “fictitious gas” concept, [13] a new airfoil will be developed which has optimal flow conditions at the transonic design point and which is in addition equipped with a nose-drooping device to favorably represent the retreating side of the rotor disc.

2. Realization of airfoil deformation on wind tunnel models.

Within the german RACT (Rotor Active Control) project, [11] it has been demonstrated that a system of pieco-electric actuators inside the wind tunnel model was able to operate a trailing edge flap under realistic aerodynamic loadings. Flap deflections of 3^o amplitude and frequencies of up to 5/ref of the fundamental model frequency of 7Hz was reached over the complete Mach number range $0.3 < M < 0.75$.

A similar model is under construction to operate on a leading edge flap with 10% chord and a maximum flap deflection of 10^o. Fig.4 shows the model arrangement with the oscillating part of the leading edge.

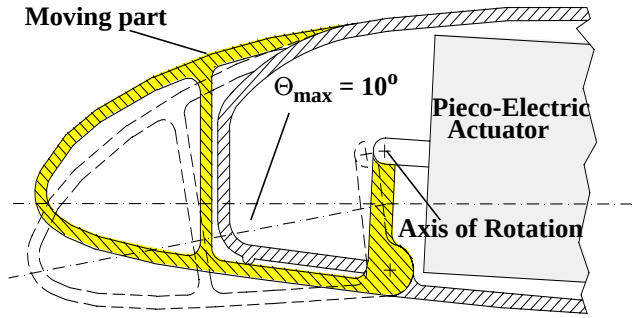


Fig.4: Structural Realization of Nose-Droop Design

The deforming leading edge surface is defined and discretized in space and time by means of the Geometry Generator Tools of DLR, [14]. With the pre-calculation of the deforming surface the calculation of the structured and deforming grid around the airfoil can start. The flow solver used for the flow calculations is a time-accurate Navier-Stokes code, [15] based on the Reynolds averaged Navier-Stokes equations (RANS). The grid around the sealed and deforming leading edge flap is allowed to deform with respect to time. This feature of the code is necessary to take into account dynamically deforming parts of the airfoil surface. Comparisons of numerical results show good correspondences with experimental data from the RACT-tests, [5] where a sealed trailing edge flap was oscillating. The present configuration is not an optimal device but it is a feasible construction for wind tunnel tests. In the following it will be shown that this device has already considerable benefits with respect to improvement of dynamic stall characteristics.

3. Selection of test case for aerodynamic design of airfoil with combined pitching and lead/lag-motions.

The numerical code, [15] has been extended to combine both pitching motion and lead/lag motion of the airfoil. The latter is simulating the Mach number variation. A characteristic set of parameters has been defined for numerical calculations:

a) Pitching motion about the quarter chord axis

$\alpha=10^o+10^o \sin(\omega^*T)$

b) Lead/Lag motion (Mach number variation)

$M=0.50-0.23 \sin(\omega^*T)$

c) Parameters:

$\omega^*=0.3$ (referred to chord)

$Re=2*10^6$

Maximum time-window for nose-drooping the airfoil: between 10^o upstroke and 10^o downstroke with the maximum deflection ($\Theta_{max} = 10^o$, Fig.4) at the maximum incidence of $\alpha=20^o$.

Numerical features of the Navier-Stoke code:

Structured grid with 361x71 grid points
Spalart-Allmaras turbulence model
20 000 time-steps/period
calculation of two to three periods.

The calculations have been carried out fully turbulent. In future investigations the transition options included in the code, [16] will also be taken into account to better match the experimental data.

4. Force, moment and pressures on helicopter airfoil with nose-droop.

Fig. 5 shows lift-, drag- and pitching moment hysteresis loops for the

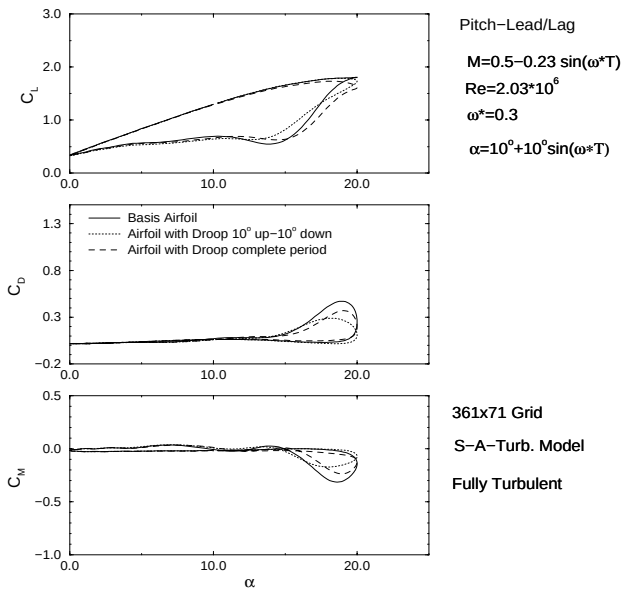


Fig.5: Force and Moment Distributions

- rigid airfoil
- drooping airfoil with droop between 10^o up and 10^o down
- drooping airfoil with droop over complete cycle

The main results of the plots are:
- the droop about the limited time window shows the same maximum lift compared to the rigid airfoil
- the maximum drag and minimum pitching moment are both reduced considerably in the drooping case compared to the rigid airfoil.

The benefit of dynamic stall i.e. the lift increase is retained in the drooping case, the drag and moment loops show strong improvements.

Figs. 6a (rigid airfoil) and 6b (drooping airfoil) show the corresponding pressure and skin friction distributions during the high incidence variation (retreating blade) of the airfoil. The pressure distributions in Fig.6a show a second maximum on the upper surface indicating the effect of the dynamic stall vortex moving along the airfoil upper surface into the wake. In the drooping case (Fig.6b) the effect of the dynamic stall vortex is not completely suppressed but its influence has been considerably reduced. Improvements can also be observed in the skin friction distributions (lower plots in Figs. 6a and 6b).

A more condensed presentation of the space and time dependent pressure distributions of both rigid and drooping airfoils are presented in the “mountain-plots” of Figs.7a (rigid) and 7b (drooping).

In Figs 7a and 7b the pressure is plotted versus the airfoil

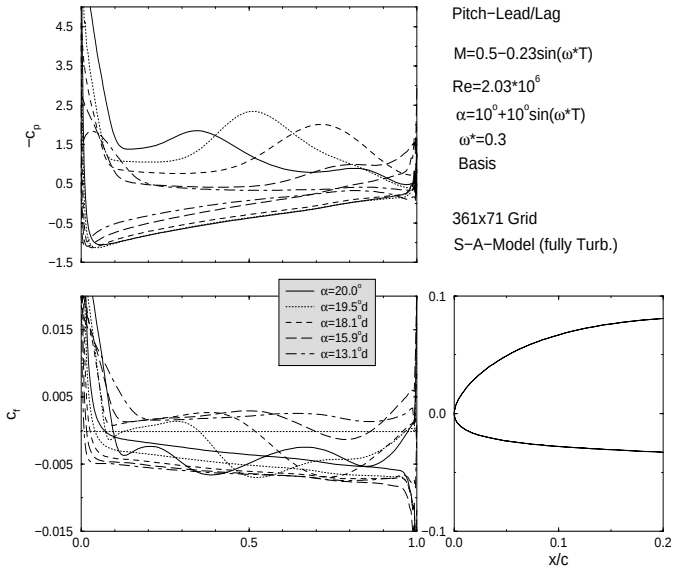


Fig. 6a: Pressure and skin friction on rigid airfoil

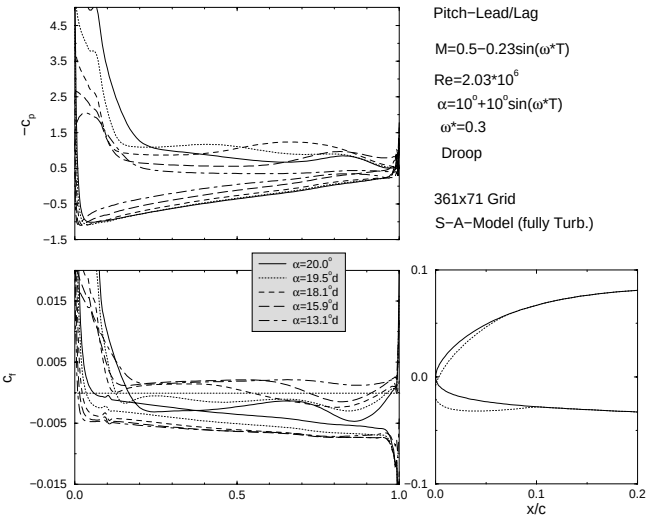


Fig. 6b: Pressure and skin friction on drooping airfoil

surface coordinate s/c from trailing edge lower to trailing edge upper side respectively and versus time with T as dimensionless time from start to end of one period of oscillation.

It can clearly be detected from Figs 7 that the strong pressure peak at the high incidence region

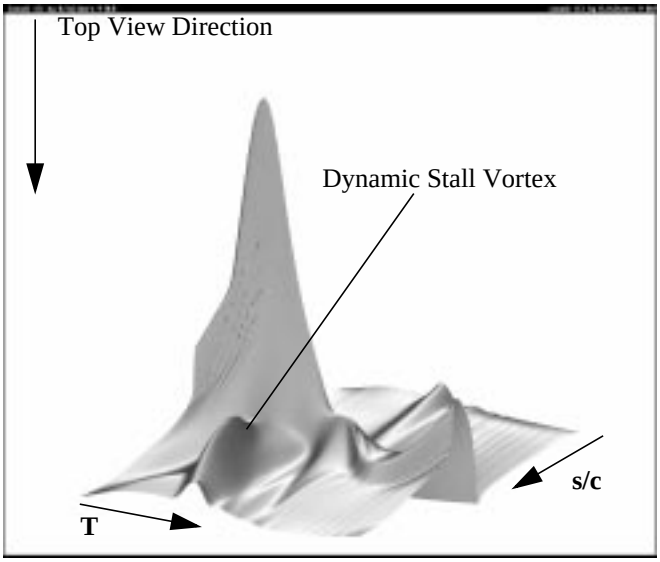


Fig.7a: Pressure Mountain versus Time and Space, rigid airfoil.

of the oscillation has been reduced remarkably by the airfoil drooping. The reason is that the adverse pressure gradient is smoothed, the dynamic stall vortex although still present has been reduced in strength as well. In both figures 7 a top view direction is indicated which is shown

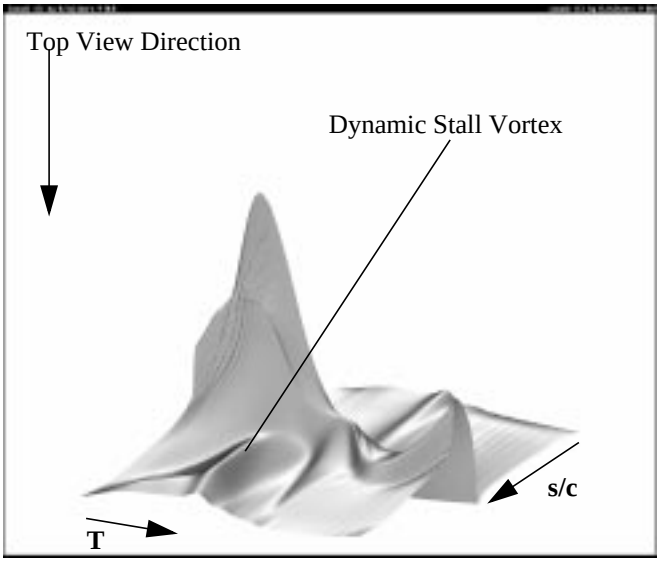


Fig.7b: Pressure Mountain versus Time and Space, drooping airfoil.

in Figs.8.
The effect of the dynamic stall vortex on the upper surface pressure distribution can again be detected in these plots. The strength of the vortex is reduced in the drooping case of Fig.8b. It can already be seen in Figs. 7 but it is more clearly indicated in Figs.8 that in the high Mach number regime of the oscillatory cycle a shock wave is developing both in space and time. It is obvious that this effect has not been influenced by the nose-drooping device. In the following the design methodology will be extended to improve also the aerodynamic behavior of the flow in the transonic region corresponding to the advancing side of the rotating blade.

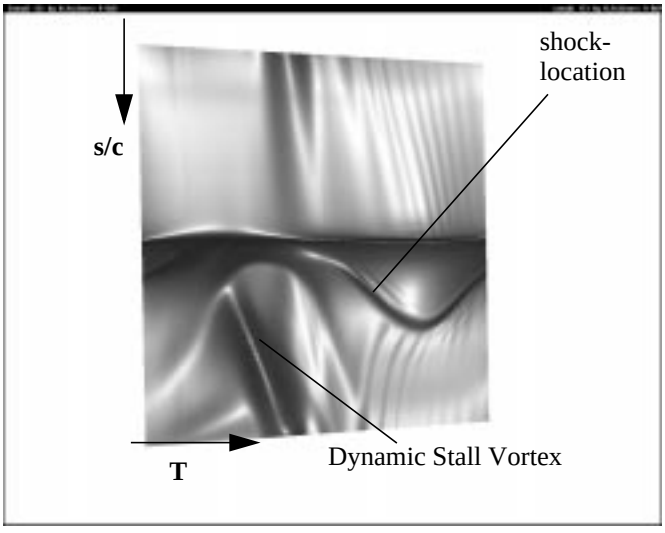


Fig. 8a: Top view of pressure distribution of Fig.7a

5. Design methodology for advancing part of rotor cycle (transonic area).

Up to now the helicopter airfoil has been modified at the leading edge for dynamically drooping the airfoil. It has been demonstrated that considerable benefit is achieved by the drooping device although the drooping has not been optimized with respect to stall control but has been designed in order to match the construction constraints for a planned wind tunnel model.
In the following it will be shown how the airfoil can be reshaped by means of the Geometry Generation Tool, [14] based on shock free design methodology. The drooping device as described above will also be kept with the new airfoil design. It will be shown that improvements are achieved on both advancing **and** retreating sides of the cycle.

6. Application of Fictitious Gas Concept for shock free design of airfoils.

The Fictitious Gas Concept (FGC) and its application to transonic design of shock free aerodynamic configurations was proposed and extensively investigated by Sobieczky and Seebass, [13]. The main objective of FGC is to develop shock free airfoils at the design conditions. FGC has recently been applied with numerical calculation procedures based on the Euler equations, [17].
For the following investigations the present time-accurate Navier-Stokes code has to be modified to account for FGC:

- the supersonic region filled with the fictitious gas of everywhere subsonic speed is different to inviscid flow now a **closed region** closing up inside the boundary layer

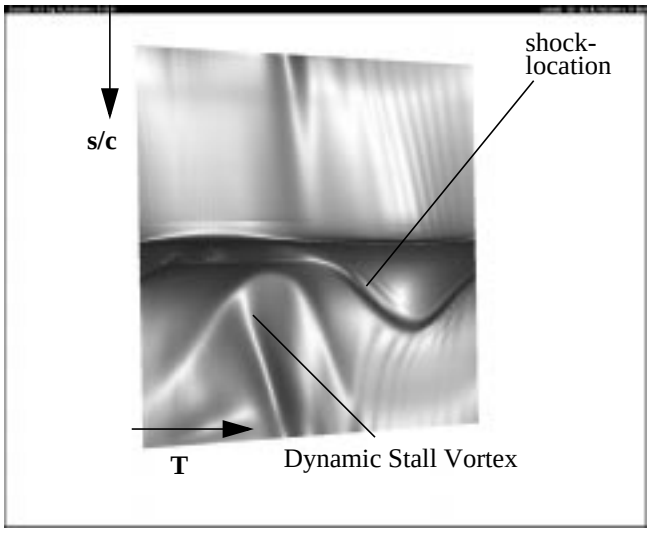


Fig. 8b: Top view of pressure distribution of Fig.7b

- the pressure and density along the sonic line limiting the FG-area is no longer constant inside the boundary layer. The dependency of p and ρ on turbulent viscosity is not known by analytical expressions but is dependent on the turbulence model chosen. Hence this dependency can only be determined numerically
-if the flow is time dependent, the development of the supersonic region with respect to time has also to be represented, if the NS-solver is running in the FG mode.

The main steps to be done to modify the NS-code are characterized as follows:
- switch between perfect gas and fictitious gas inside the supersonic region by changing the pressure density relation, [17],
- represent smooth transition from perfect gas in the outer flow field to subsonic FG-region inside the originally supersonic area, with M=1 along FG-boundary,
- calculate converged result including the FG-region.
Fig. 9 shows shematically a result of this calculation: The FG-region comes out to be smooth in the former shock wave region. But the result is fictitious. Additional steps have to be carried out to get a shock free solution:

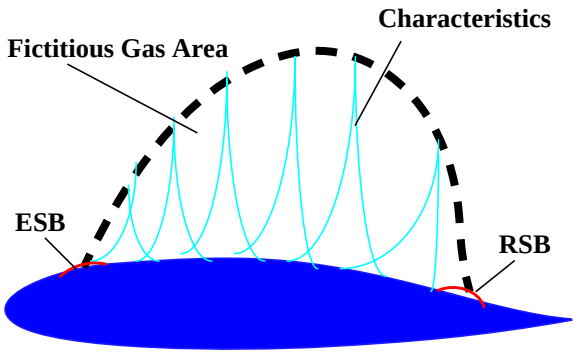


Fig.9: Fictitious Gas Concept (FGC)

a) The FG-region is filled again with perfect gas
b) inside the FG-area the method of characteristics is applied
c) the surface of the airfoil covered by FG is no longer a streamline
d) the airfoil upper surface is modified to be a streamline again
e) a numerical calculation in the perfect gas mode is done for the modified airfoil.

In order to keep the modification of the airfoil small a minor **local** modification of the airfoil surface using bumps at both upstream and downstream position of the intersection of the sonic line with the airfoil can be used.
Fig.9 shows these modifications as ESB (Expansion Shoulder Bump) and RSB (Recompression Shoulder Bump). This bump modification however will not be completely shock free.
Due to the fact that a viscous flow solver is used, the FG-region is not touching the airfoil surface but is sitting on top of the boundary layer (not indicated in Fig.9). To correctly modify the airfoil surface the boundary layer displacement surface is taken into account for the surface modification.

7. Results of approximately shock free airfoil (advancing side) and nose-drooping airfoil (retreating side).

For the selected incidence and Mach number variation selected in 3) the complete design procedure has been carried out step by step:
As start configuration a new airfoil section is developed by means of the Geometry Generation Tool.
This new airfoil which has the same thickness distribution as the original one is now modified to a shock free design using the different steps described in the previous section for the application of FGC. For the shock free design a design point with M=0.73 and $\alpha=1.1^{o}$ has been selected. The result is of course only shock free in the design point. It remains to be demonstrated how this airfoil behaves under unsteady conditions with varying α and M.
Fig.10 shows the results of the different design steps up to this point.
The upper left figure indicates the new airfoil design without pre-drooping and s-shape camber line. The NS-calculation in the selected design point determines a strong shock wave at about mid chord of the airfoil. The calculation in the FG-mode leads to Mach number contours
as shown in the lower left plot of Fig.10 with the FG-region indicated. Applying the method of characteristics inside the FG-region the airfoil upper surface has to be modified to be again stream surface as is shown on the lower right plot. The NS-calculation in the perfect gas mode about the modified airfoil finally gives an almost shock free pressure distribution as indicated in the upper right figure.
So far the design of the rigid airfoil section with shock free characteristics at the design point has been demonstrated. The next step is to modify the leading edge of this new airfoil by a dynamic nose-droop device as has been described in the previous sections and which is shown in Fig.4 to be suitable for realization on a real wind tunnel model with in situ actuator systems.
The design steps for the drooping device are identical as described before and have again been determined by means of the Geometry Generator Tools of DLR.
The final proof of the total system including dynamic nose-drooping has been calculated by the NS-code. In the following some typical results will show the benefit of the design procedures with respect to both transonic and separating flow domains.

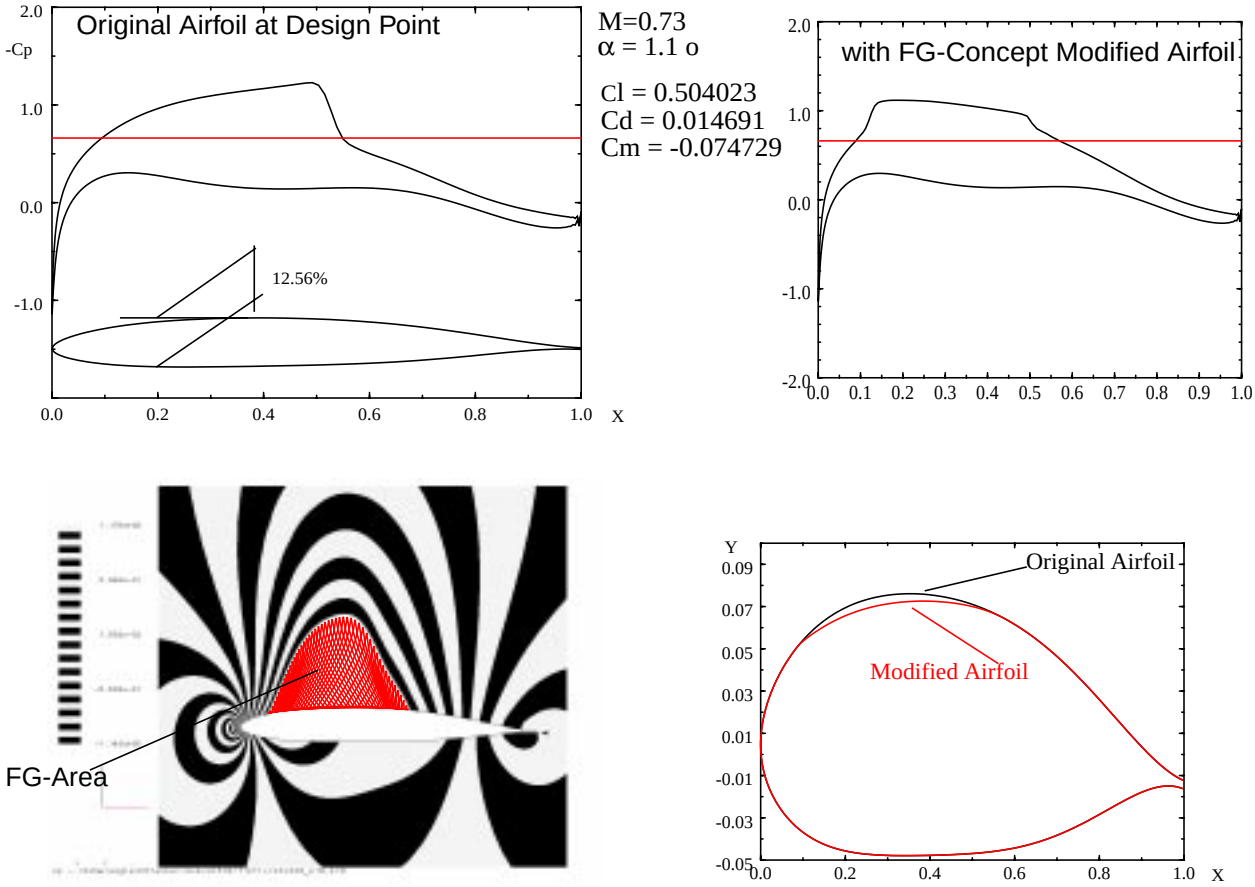


Fig10:Airfoil Shape Modification by Means of Fictitious Gas- (FG-) Concept

Fig.11 shows the final airfoil shape including the nose-drooping area at the leading edge with 10% chord flap area. With combined pitching and lead/lag motions as described in section 3) and with the additional nose-drooping now in the time-window between 12.1^o up and 12.1^o down (the incidence variation has slightly been increased to: $\alpha=12.1^o+11^o\sin(\omega*T)$) the Mach contours in Fig.12 and the following sequences of figures show improvements first of the shock free design compared to the basis airfoil: The airfoil is not only shock free at the design point but shows also improvements i.e. shock strength reductions within a larger time window during the oscillation cycle. This can be seen in Fig.12 at the second half of the cycle where the area of reduced shock strength is clearly visible. The first half of the cycle shows that the separation area has been shifted toward the trailing edge such that the leading edge part with the moving slat still produces aerodynamic loads.

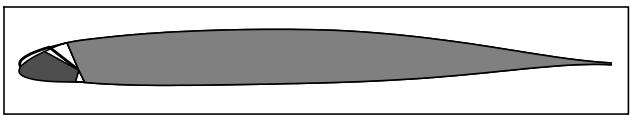


Fig.11 New airfoil design with nose-droop, A1510

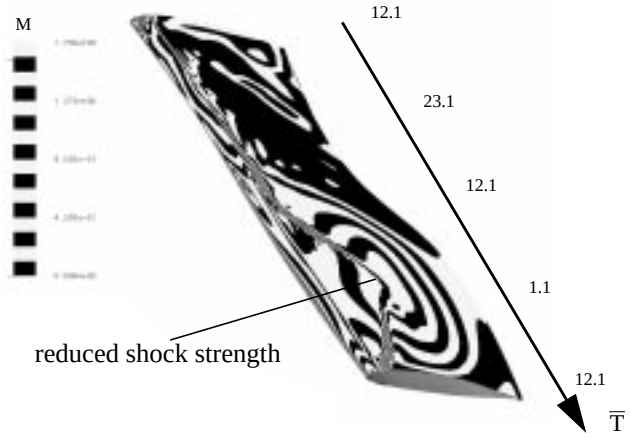


Fig.12 Mach-contours in time and space of final NS-calculation

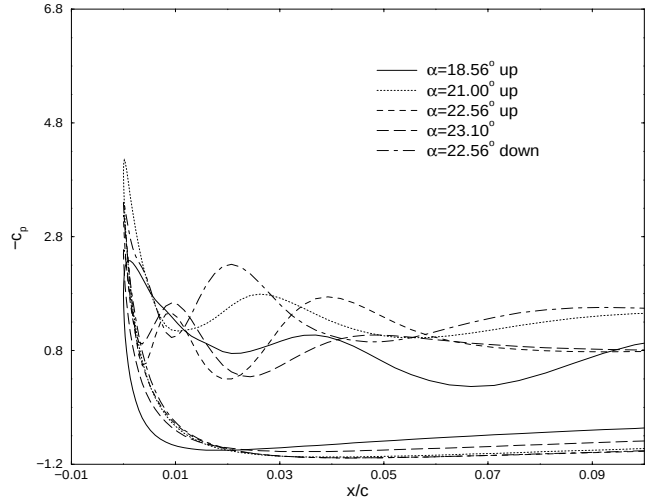


Fig. 13a: Pressure distributions in the leading edge region of the basis airfoil (separated flow)

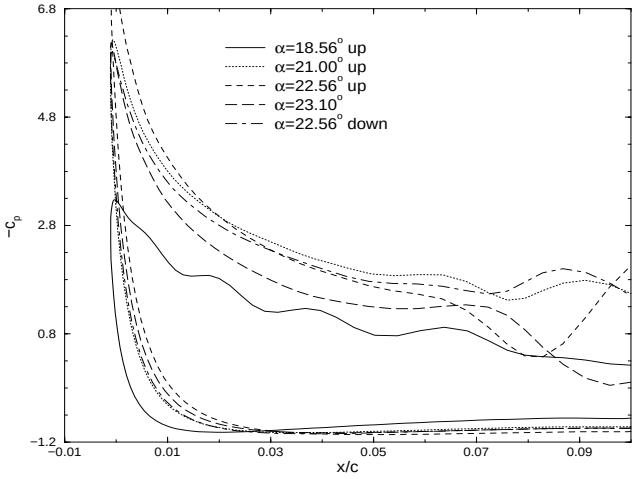


Fig.13b: Pressure distributions in the leading edge region of the modified airfoil with nose-droop (separated flow)

Figs. 13a and 13b show pressure distributions during the high incidence part of the oscillation loop where the formation of a dynamic stall vortex and its shedding takes place. Fig. 13a shows severe effects of the dynamic stall vortex indicated by a secondary pressure peak developing along the airfoil upper surface. Compared to the corresponding curves of Fig.13b the loading on the first 10% of the airfoil is considerably higher. The effect of a dynamic stall vortex is shifted further downstream. Similar improvements can also be detected from the skin friction distributions (not shown). In the basic airfoil case reversed flow occurs up to the very leading edge. The drooping airfoil has extended regions in time and space where the flow does not separate.

Figs.14 finally show the corresponding pressure distributions during the transonic flow regime (advancing side). Fig.14a includes again the pressure distributions of the basis airfoil. A rather strong shock wave can be detected which develops in time (α-variation). The modified airfoil (Fig.14b) shows shock free pressure distributions at the design point, i.e. at $\alpha=1.1^{o}$. But the pressure curves in the vicinity of the design point show also strong improvements with respect to shock strength development. Again the skin friction distributions (not shown) show improvements with respect to the fact that shock induced separation does not occur.

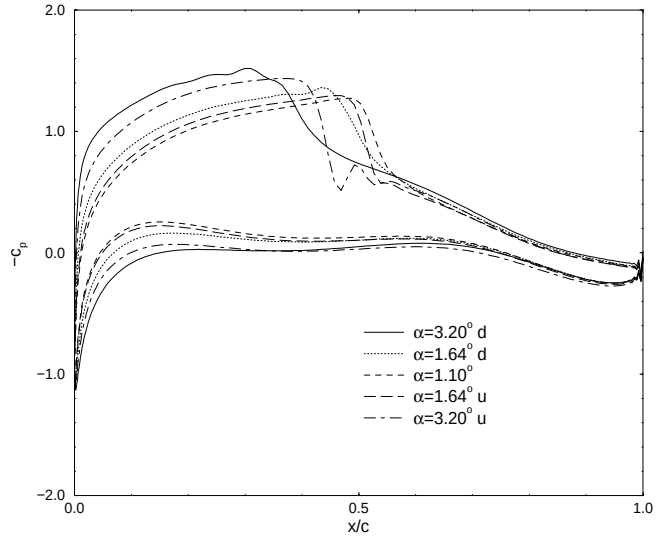


Fig.14a: Pressure distributions in the leading edge region of Basis airfoil (transonic Flow)

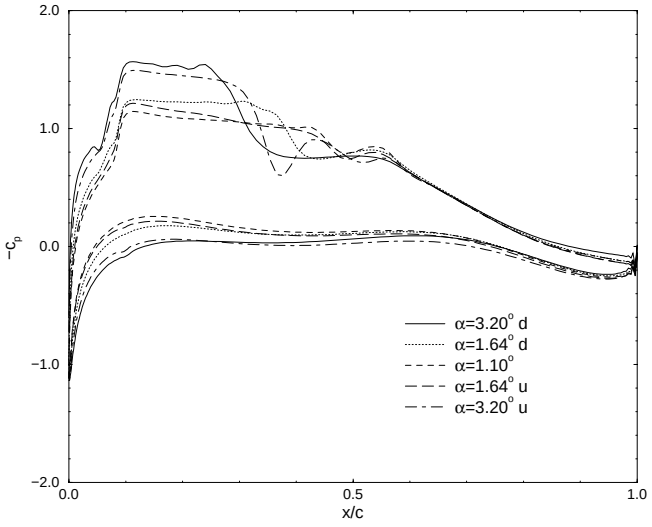


Fig.14b: Pressure distributions in the leading edge region of the modified airfoil (transonic flow)

8. Conclusions

New developments of design tools and their combination with suitable flow solvers based on the Reynolds averaged Navier-Stokes equations have demonstrated their capabilities to study new design concepts with dynamically deforming leading or trailing edge deformations. New actuator designs based on pieco-electric principles have shown their capabilities to 1) be small and light enough to be implemented inside a wind tunnel model or a rotor blade and 2) have shown to operate the flap with the necessary deflection angles and frequencies.

The present study goes one step further: A new airfoil shape is designed which is modified in such a way that it is shock free within a selected design point. This new airfoil is then equipped with a nose-drooping device similar to the one which will be realized on a wind tunnel model with embedded actuator system.

The results which have been found by numerical investigations show considerable benefits in the transonic area of the cycle (advancing side) as well as in the region of the development of dynamic stall (retreating side) of the cycle. The modified airfoil shows remarkable reductions of the shock strength not only at the design point but also within a time window adjacent to the design point. On the retreating side dynamic stall onset is shifted to later time (higher incidences) by means of the drooping device. The aerodynamic loading on the drooping area is kept over almost the complete cycle.

In the future the complete design procedure has to be improved and simplified towards an optimized design. It has to be investigated if a closed loop design procedure is feasible.

9. References

[1] McCroskey,W.J.," Some Current Research in Unsteady Fluid Dynamic - The 1976 Freeman Scholar Lecture", Journal of Fluid Engineering, Vol.99,March 1977, pp.8-38.

[2] Carr,L.W. "Progress in Analysis and Prediction of Dynamic Stall", Journal of Aircraft, Vol.25,No.1,January 1988, pp.6-17.

[3] Allrefai,M., Acharya,M. ,"Controlled Leading Edge Suction for the Management of Unsteady Separation over Pitching Airfoils", AIAA Paper 95-2188,June 1995.

[4] Carr,L.W., Chandrasekhara,M.S., Wilder,M.C., Noonan,K.W.,"The Effect of Compressibility on Suppression of Dynamic Stall Using a Slotted Airfoil", AIAA 36th Aerospace Sciences Meeting & Exhibit, January 12-15,1998,Reno, NV.

[5] Geissler,W.Sobieczky,H.Vollmers,H.,"Numerical Study of the Unsteady Flow on a Pitching Airfoil with Oscillating Flap" 24th European Rotorcraft Forum, 15-17th September,1998, Marseilles, France, Paper AE09

[6] Geißler,W., Sobieczky,H.,"Dynamic Stall Control by Variable Airfoil Camber", AGARD 75th Fluid Dynamics Panel Meeting and Symposium on Aerodynamics and Aeroacoustics of Rotorcraft.October,10-14,1994,Berlin,Germany,pp.6.1-6.10.

[7] Chandrasekhara,M.S., Wilder,M.C., Carr,L.W., "Unsteady Stall Control Using Dynamically Deforming Airfoils", AIAA-Paper 97-2236, June 23-25, 1997, Atlanta,GA.

[8] Chandrasekhara,M.S., Wilder,M.C., Carr,L.W., "Unsteady Stall Control Using Dynamically Deforming Airfoils", AIAA Journal,Vol.36,No.10,October 1998.

[9] Geissler,W., Carr,L.W., Chandrasekhara,M.S., Wilder,M.C., Sobieczky,H.,"Compressible Dynamic Stall Calculations Incorporating Transition Modeling For Variable Geometry Airfoils", 36th AIAA Aerospace Meeting and Exhibit, January, 12-15, 1998, Reno Hilton, Reno, NV.

[10] Geißler, W.,Sobieczky, H.,"Unsteady Flow Control on Rotor Airfoil", AIAA 13th Applied Aerodynamics Conference, 19.-22. June, 1995, San Diego, CA, USA, pp. 1-9.

[11] Schimke,D.,Jänker,P.,Wendt,V.,Junker,B.,"Wind Tunnel Evaluation of a Full Scale Pieco-Electric Flap Control Unit", 24th European Rotorcraft Forum,15-17 Sept.,1998,Marseilles,France.

[12] Sobieczky,H., Geissler,W.,"Active Flow Control Based on Transonic Design Concepts",17th AIAA Applied Aerodynamics Conference, June 28-July 1,1999, Norfolk, VA.

[13] Sobieczky,H., Seebass,A.R., "Supercritical Airfoil and Wing Design", Ann.Rev.Fluid Mech.16,pp.337-363 (1984).

[14] Sobieczky,H.,"Geometry Generator for Aerodynamic Design", CISM Course and Lectures No. 366, 'New Design Concepts for High Speed Air Transport', Springer, Wien,New York (1997), pp. 137-158.

[15] Geissler,W.,"Instationäres Navier-Stokes Verfahren für beschleunigt bewegte Profile mit Ablösung (Unsteady Navier-Stokes Code for Accelerated Moving Airfoils Including Separation)" in german, DLR-FB 92-03 (1992).

[16] Geissler,W., Chandrasekhara,M.S., Platzer,M., Carr,L.W.,"The Effect Of Transition Modeling On The Prediction Of Compressible Deep Dynamic Stall", 7th Asian Congress of Fluid Mechanics, Dec. 8-12, 1997, Chennai (Madras), India.

[17] Li,P., Sobieczky,H.,"Computations of Fictitious Gas Flow with Euler equations", Acta Mechanica (1994),[Suppl] 4:251-257,Spriger Verlag 1994.

This page has been deliberately left blank

Page intentionnellement blanche

Active Control of the Directivity of Fan Tones Noise

J. JULLIARD , H. ANTOINE & CH. LOZACHMEUR
SNECMA Villaroche
Département Acoustique
Rond Point René Ravaud
77550 MOISSY-CRAMAYEL
FRANCE

A. ROURE
CNRS
Laboratoire de Mécanique et d'Acoustique
31, chemein Joseph Aiguier
13402 MARSEILLE Cedex 20
FRANCE

ABSTRACT

Experiments on a fan model (diameter 47 cm, 48 blades, nominal rotation speed 12,600 rpm) installed in an anechoic test cell have recently been carried out to assess the technique of Active Noise Control (ANC) applied to reduce the tones noise at the blade passage frequency. This paper describes in details the test model with the selected test configurations, the test facility and the ANC system.

Having already demonstrate the feasibility and the interest to reduce engine tones by application of this technique, the objective of this study was to evaluate the acoustic benefits brought by this technology, to check the robustness of the controller especially with engine rpm variations and to identify the realistic and promising configuration in view of engine applications. Loudspeakers wall-mounted and located in a duct cross-section close to the fan source were used as secondary sources. Error sensors were successively located outside the inlet and wall-mounted in the duct according to different distributions.

A multichannel controller highly efficient in term of frequency (up to 2500 Hz) and channels number (up to 16 channels) was specifically developed for this application.

For a 3D visualization of the far field a moving acoustic antenna was used to measure the upstream directivity. As for downstream radiation it was measured by a moving microphone. In order to know the space structure of the sound field with and without ANC, measurements of acoustic spinning modes were achieved and some radial acoustic pressure profiles were measured. In a first step, an acoustic driver was used as primary source and experimental results have shown different ways to reduce the noise radiated from the air intake. The first one consists in rejecting the noise to the backward duct, the second consists in redirecting the noise in an unannoyant area, the third consists in reducing and canceling (particular case) the total energy. A combination of these phenomena is as well found.

With the fan running, tests have indicated that the controller was robust and stable even if the speed variations were important. At first, error sensors were located on the Inflow Control Device and in this case an important tone noise reduction was observed. According to the frequency and actuators/sensors configuration, it was found either a global reduction of the tone level or a large decrease in the controlled angular sector with reinforcement elsewhere.

The uncontrolled downstream radiation was as well affected with either a global decrease or increase of the tone noise according to the test configuration. An increase of error sensors number has allowed to extend the quiet area. Far field SPL reductions up to 15 dB were obtained in a large angular range. Experiments for controlling the broadband noise did not provide good results on the fan source due to the weak coherence between the reference microphone signal and error sensors signal. From some error sensors configurations within the duct (realistic configuration for engine application) a significant reduction of tones noise was achieved but the sensors locations are more difficult to define.

Further studies should on the one hand include a methodology leading to a better optimization of the in-duct sensors location and on the other hand take into account the

Paper presented at the RTO AVT Symposium on "Active Control Technology for Enhanced Performance Operational Capabilities of Military Aircraft, Land Vehicles and Sea Vehicles", held in Braunschweig, Germany, 8-11 May 2000, and published in RTO MP-051.

effects of combining conventional passive liner always essential (efficient to high order modes rather associated with medium & high frequencies) and active techniques (efficient to low order modes rather associated with low frequencies).

INTRODUCTION

The continuous increase of the air traffic linked to the operations around airports leads to increase the community noise problem. Face to this situation, a significant number of airports have implemented their own rules often drastically more stringent than the international standard (ICAO-Chapter 3 of the annex 16). So a new international noise regulation, leading to the adoption of more severe noise limits, is discussed to be applied in a near future and thus avoided to have a proliferation of specific rules for each airport.

With pressure continually building towards lower community and cabin noise environment, an important research effort to improve the noise control has to be undertaken. For current Turbofan engines (bypass ratio between 5 and 8), the fan noise (tones and broadband) is a major component at approach in spite of a quiet fan design and treated (passive liner) ducts. For the future turbo-machine concepts such as ultra high bypass ratio (UHBR) engines, the fan noise will be a component major at approach and as well at take-off. In addition, UHBR engines with shorter inlet and exhaust ducts, lower tip speed and lower blade numbers have a noise signature more extended to low frequencies and a nacelle treated area significantly reduced compared to current engines. So passive technology will not be likely sufficient to reduce the fan noise and especially low frequencies tones (Multiple Pures Tones for interior noise and Blades Passage Frequencies tones for community noise).

So novels means of further reducing engine noise have to be implemented and active techniques applied to the source (action on aerodynamic or acoustic mechanisms) and to the sound propagation are promising ways to improve the noise situation.

SNECMA in close collaboration with LMA/CNRS Marseille led a large number of tests on a fan model in order to investigate the application of the Acoustic Noise Control (ANC) to control the inlet noise radiation. They have experimentally demonstrated the potential of these techniques as efficient mean to reduce the fan tones noise. Others experiments mainly US performed on ducted fan showed as well a good potential for attenuating the tones radiation[1,2,3].

In this paper are described experiments performed by Snecma knowing that for developing controller and software SNECMA was associated with LMA Marseille. Hardware and measurements system relative to this experimental study are presented. Different tests configurations were assessed in positioning the control sensors at first outside the inlet in the spatial area where the noise is to be reduced and then for a realistic configuration wall-mounted in the inlet. Acoustic results are presented and discussed from far field measurements in a 3D visualization and in-duct measurements.

EXPERIMENTAL SETUP

A fan model driven by an electrical engine (1,2 MW) is installed in an anechoic test cell at the SNECMA Villaroche Center (figure 1).

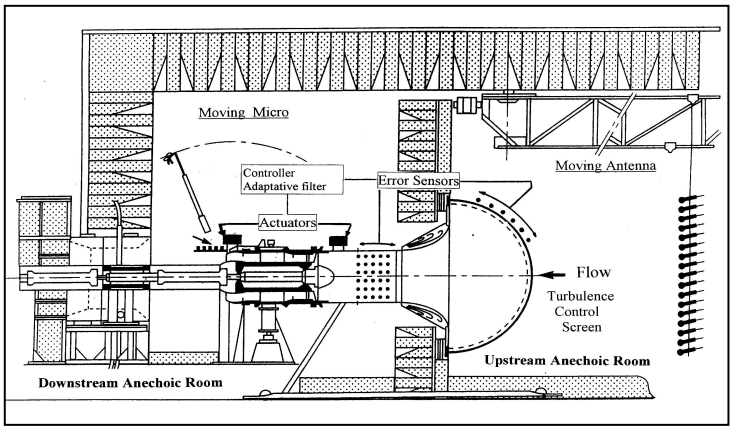


Figure 1 : Schematic diagram of the fan model in the anechoic test cell

The facility includes an upstream and downstream anechoic room separated by an acoustic barrier. A moving antenna equipped with 27 acoustic sensors enables the measurement of the radiated upstream sound field on a large angular range in two directions. In the downstream part, only a moving microphone gives information about the radiated noise.

The fan model used is a single stage axial fan with 48 blades and a stator with 98 blades. The design rotation speed is 12,600 rpm and the fan diameter is 47 cm. Nine and then twelve rods (figure 2), equally spaced circumferentialy, were located upstream of the fan stage in order to generate wakes interacting with the rotor blades. These interactions produce a relative high level of tones noise by exciting particular cut-on spinning modes function of rotor blades and rods number. The lower excited mode is a plane wave with 12 rods and a spinning mode 3 with 9 rods at the fan Blades Passage Frequency .

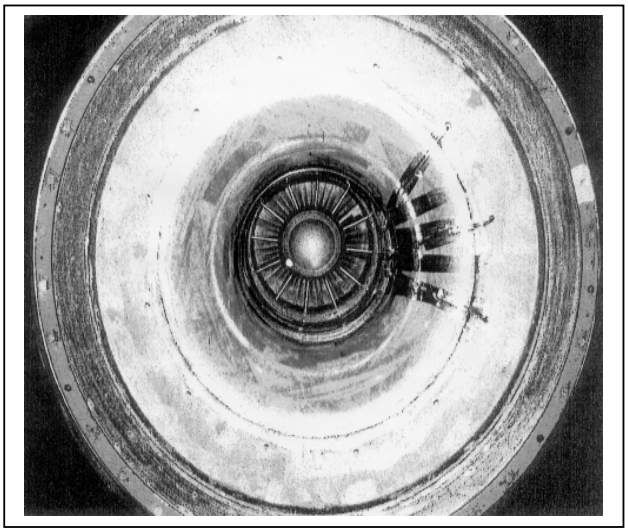


Fig. 2 : Face view of the inlet

THE ACTIVE NOISE CONTROL SYSTEM HARDWARE

As represented in figure 1, the ANC components are the followings :

- As secondary acoustic sources, an actuators ring constituted of eight loudspeakers flush mounted and equally spaced on 360° at the same axial location.
- As control transducers, eight electret sensors installed in a first stage out of the duct on the ICD to control the directivity and in the second stage inside the inlet to control the propagation.
- As controller, a multichannel designed and manufactured by LMA/CNRS Marseille has been used. It enables to manage signals coming from ten error transducers and to drive up to eight noise sources.
- Concerning the software relative to the control unit, several adaptive algorithms developed by LMA have been tested and the best selected one to control the fan noise is based on a least mean-square (LMS), a method which adapts continuously the coefficients of the adaptive filter to make the best of slightly rotation speed.
- The reference signal, required for the feedforward controller, is provided both from an optical sensor or an magnet sensor. It generates a sequence of pulses correlated with the RPM and therefore the fan BPF.

MINIMIZATION METHOD

The LMS algorithm requires a good evaluation of transfer function between all actuators and error sensors. So it is important than the degree of coherence between signals to be the closest of 1 to get an high level of attenuation.

The first step consists of identifying paths secondary sources to sensors from set of pulses injected successively on each actuators. The algorithm determines then in a real time the coefficients of filter (FIR) associated to each channel to drive actuators. It uses the filter reference coming from the convolution of the reference signal with the pulse response relative to the paths sensors/actuators. After determination of filters and in considering the reference signal, the controller is able to drive actuators through amplifiers in order to minimize (square mean method), the quadratic average of the function fast variation of phase with the frequencies. For instance at the same frequency a slight modification of the temperature leads to a fast variation of the transfer function phase. So it is important than the software to be enough robust in order to take into account these abrupt evolution.

STRATEGIES OF CONTROL

The approach selected is based on the well-known principe of destructive interference which consists of superposing at the fan noise an other sound field in order to reduce in all space or in a selected angular range the radiated tone noise. Two strategies have been investigated. The first one is the generation one or several antimodes. The second one is an approach based on the restructuration of the sound field to create a controlled quiet sector. The aim is to generate an acoustic field able to produce a modal structure which combined to the fan source modal structure rejects the acoustic energy in an annoyant area and create a quiet zone. This last strategy seems to be the way to privilege for engine application because of the BPF' tones modal structure is rich and complex and the interaction stator-rotor modes represent only a small part of tones energy. Nevertheless for buzz-saw noise the modal approach control appears more adequate with a known and specific spinning mode for each MPT's.

In order to examine the potential reduction of a perfect active noise control system implement on an relatively quiet recent engine (by-pass ratio between 5 and 7), calculation in EPNL by canceling discrete tones radiating from the engine fan inlet and fan exhaust was conducted. The conclusion is that the attenuation can reach 5 EPNL cumulated on the three

monitoring points with a consequent reduction at take-off and a smaller benefit at approach and sideline.

In our experimental work, it is the way the more difficult aiming the reduction of the far field noise which has mainly been investigated.

INTERNAL AND EXTERNAL ACOUSTIC INSTRUMENTATION

Besides the instrumentation relative to operate the ANC , in-duct measurements consists of :

- Wall-mounted microphones, one fixed and one moving (360° rotating ring) for spinning modal measurements
- A profiled acoustic probe allowing the measurement of the acoustic pressure radial profile

The upstream and downstream directivity pattern on engine is usually regarded as an axisymmetric radiation because of the modal richness and a weak coherence between modes. With the ANC working the combination between modes of secondary and primary sources which leads to create an area of silence is very often represented as an asymmetric field and thus a 3D visualization is recommended.

So in order to get a better characterization of the radiated noise in the upstream arc (controlled radiation) a vertical antenna (fig 3) equipped with 27 microphones has been developed to sweep an angular range from +60° up to -60°. In the downstream part a moving microphone allows to check if the system rejects or not additional tones noise to the aft duct .

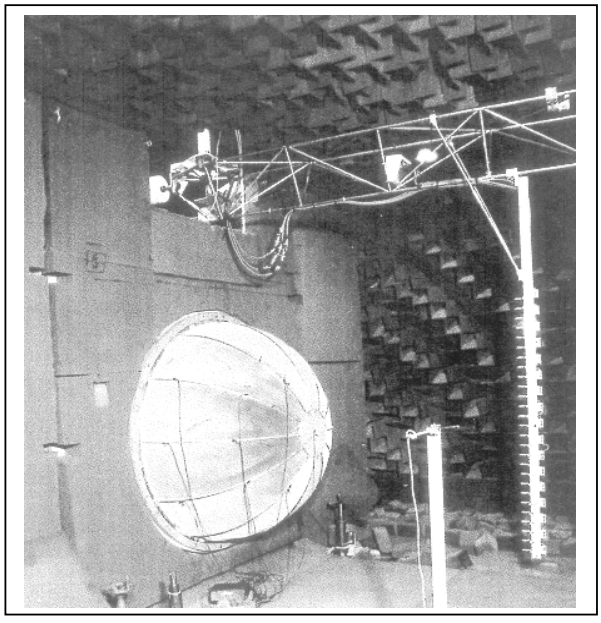


Fig. 3 : Upstream acoustic instrumentation

FIRST COMPAIGN OF TEST : RESULTS ANALYSIS

In a first step and especially for error sensors located in-duct, some configurations using a loudspeaker as primary source have been evaluated to study the influence of actuators and errors sensors number and location. Experimental results from fig 4 up to fig 11 are shown at 600 Hz and 1000 Hz for configurations using four error sensors and four actuators

At 600 Hz, a complete cancellation of the tone is observed as well in the aft arc as in the forward arc by using 4 errors sensors equi-distributed on the bell-mouth. Modal analysis confirms an attenuation of modes (1,0,-1) by 40 dB.

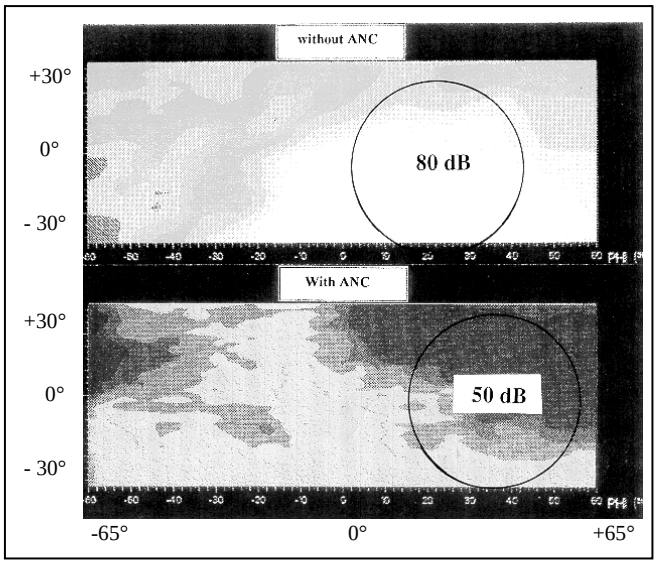


Fig. 4 : Upstream far field at 600 Hz

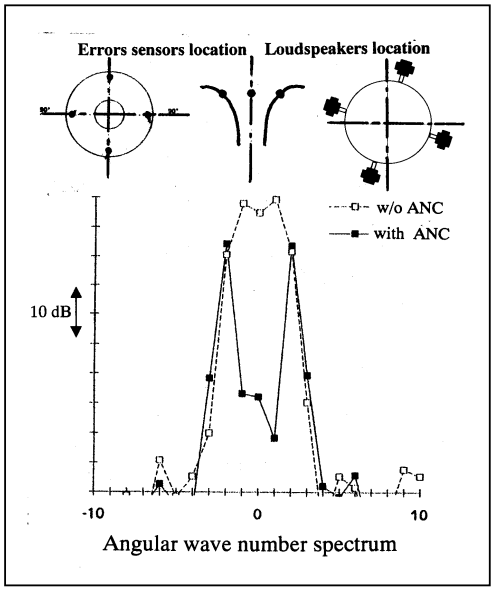


Fig. 5 : Angular wave number spectra at 600 Hz

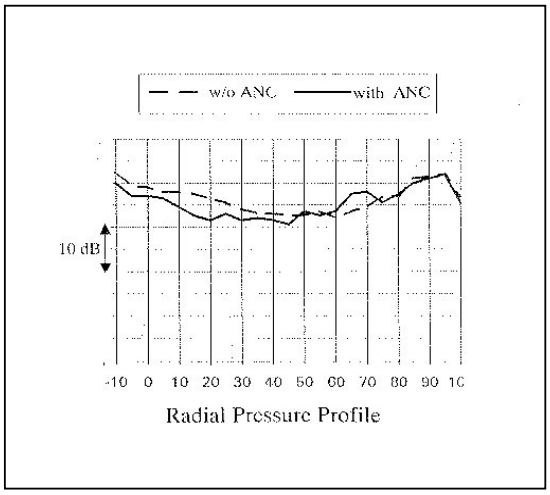


Fig 6 : Inlet Radial Pressure Profile at 600Hz

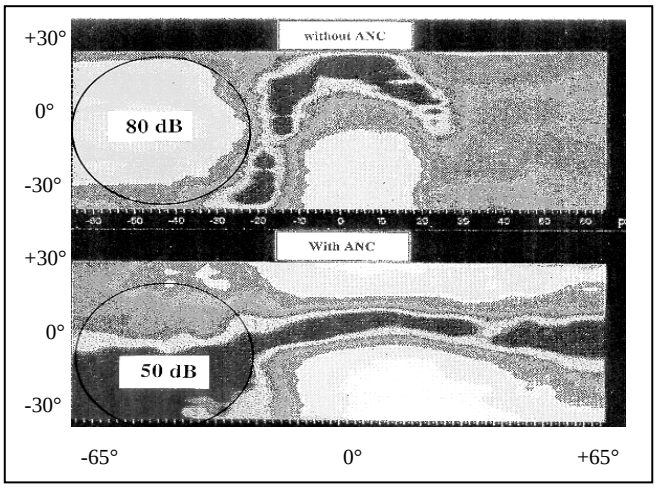


Fig. 8 : Upstream far field map at 1000 Hz

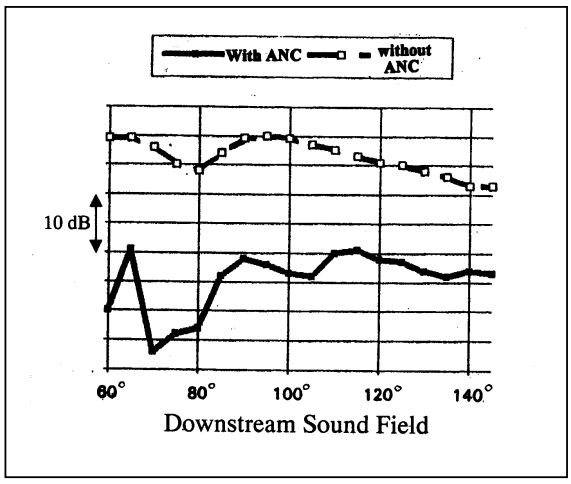


Fig 7 : Downstream far field at 600Hz

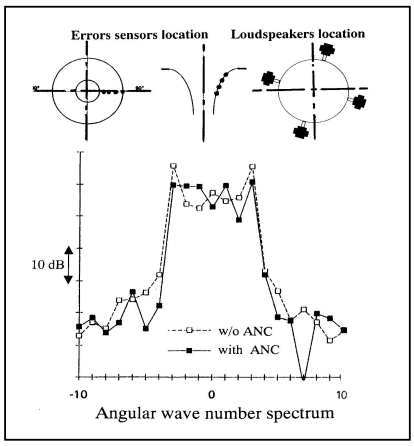


fig. 9 : Angular wave number at 1000 Hz

At 1000 Hz, with a more complex modal structure, acoustic results (fig 8 to 11) in the form of map of sound level, with active control on and off, are more difficult to analyze with in the forward arc a reduction in the opposite direction where the sensors are located (location on a axial line). However in the aft arc the tone level increases. With the ANC working the modal analysis shows that the inlet angular wave number spectra is enough similar whereas the radial pressure profile is different. In fact, the reduced number of error sensors does not allow an adequate modal control and it is rather aimed to have a control of the directivity.

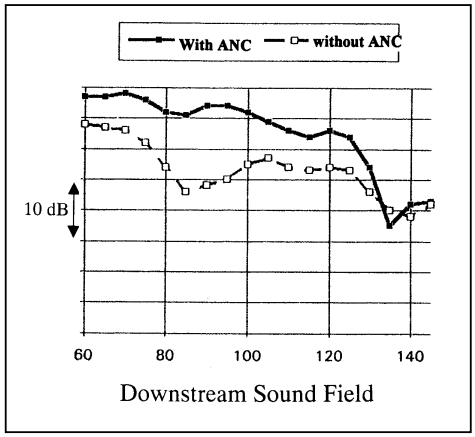


Fig. 10 : downstream far field at 1000 Hz

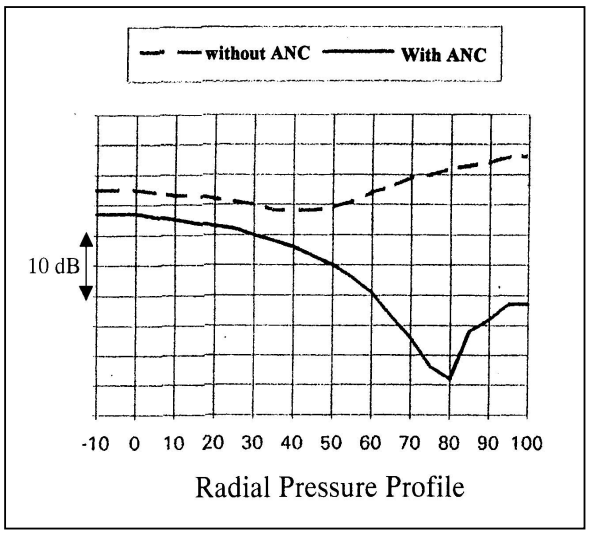


Fig. 11: Inlet radial pressure profile at 1000 Hz

Using a loudspeaker supplied from white noise and flush-mounted in the aft duct as primary source, it has been performed an active control by using 2 error sensors (out of the duct) and two actuators. Results in the far field show a significant reduction of noise on the frequency range 400-800 Hz in a large angular sector (fig 12).The good correlation between primary and secondary signal explains this good result, however no significant result was obtained from a fan broadband noise. The poor coherence between error sensors and reference signals explains this result.

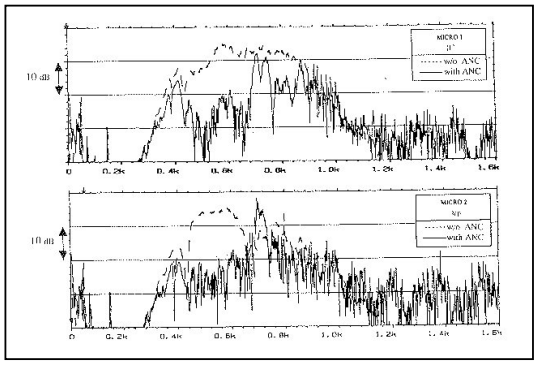


Fig 12 : Broadband far field spectra with and without control

In a second step, ANC was implemented on the fan fundamental tone (1 BPF). The fan model was running at low rpm because of the large number blades of the rotor and the low frequency range aimed for the ANC application. So the tones emergence was not always important compared to the broadband noise in spite of rods located in front of the fan for excited specific spinning modes.

In fact in term of frequency, it is representative of the aimed frequencies range on engine but not quite in term of ka (k : wave number & a : duct radius) and therefore of the modal richness.

Error sensors were at first located on the ICD. The first test[4] was achieved by using a microphone system to explore the forward radiation in a horizontal plane and the aft radiation in a vertical plane. Results presented in fig 13 and 14 show a good efficiency at 750 Hz (7 cut-on modes) with a global reduction anywhere of the BPF by 10 up to 20 dB and at 840 Hz a reduction by 10 dB on the controlled area with a reinforcement of level in the aft arc. The broadband noise is a floor noise which is a limitation to measure the true acoustic benefit at some angles.

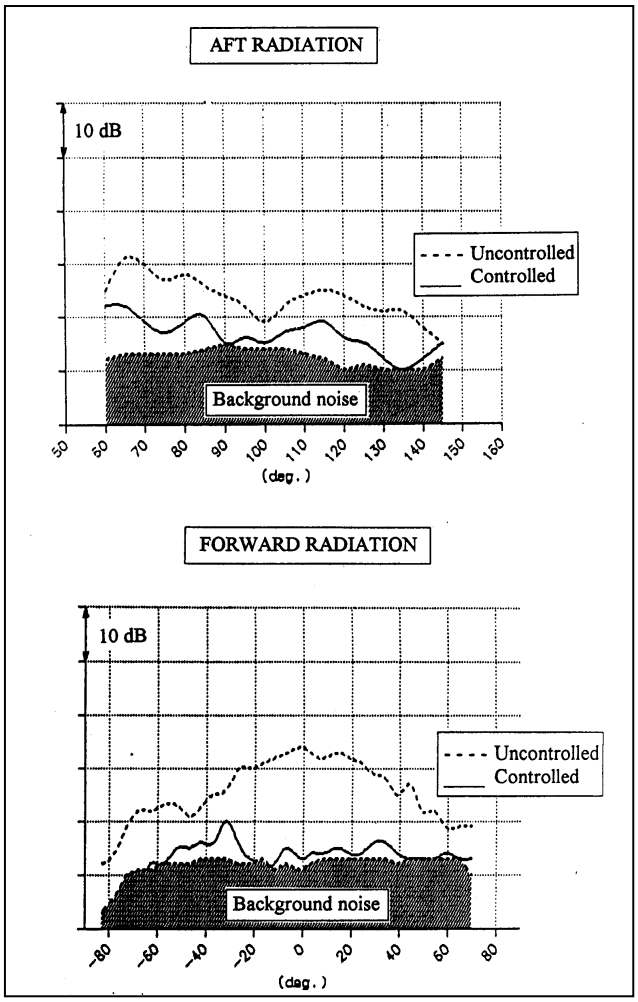


Fig. 13 : Upstream and downstream directivity (1 BPF / 750Hz) before and after control

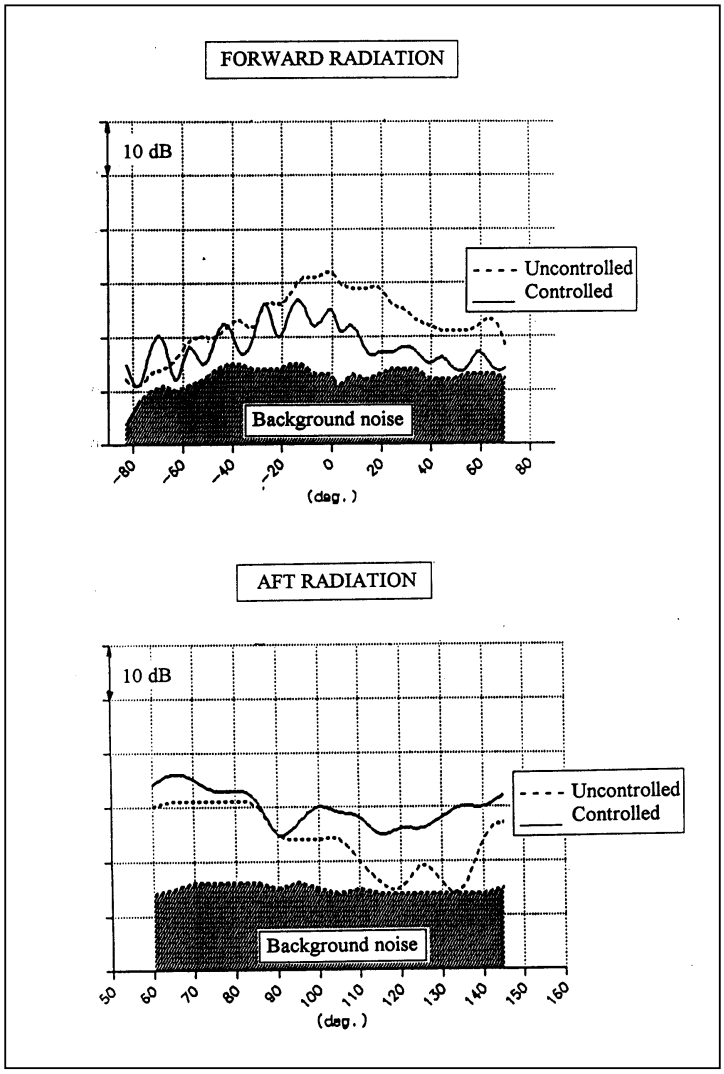


Fig 14 : Upstream and downstream directivity
(1 BPF / 840 Hz) before and after control

SECOND TEST CAMPAIGN : RESULTS ANALYSIS

An additional test was conducted by using several relevant error sensors & actuators configurations with the fan model running at different stabilized rpm. A new moving antenna measuring the radiated noise in a large area was installed.

All acoustic analysis was performed at the BPF by using a tracking system drove by the rpm.

Our strategy was to minimize the radiated energy over a sector rather to reduce the total radiated power.

The control, with error sensors located on the ICD (out-duct) shows a good efficiency and the quiet area is well in the extension of the controlled zone. In addition with an increase of the number of error sensors the quiet area is larger. In figure 15, it is shown a sound map representing the forward radiation of the BPF with and without control for a configuration of 3 sensors and 4 actuators at 2100 Hz. A reduction by at least 10 dB is noticed on a 60° angular range. Elsewhere, the trend is to increase the sound level and especially in the aft radiation. The acoustic pressure radial profile measured in the duct confirms this result.

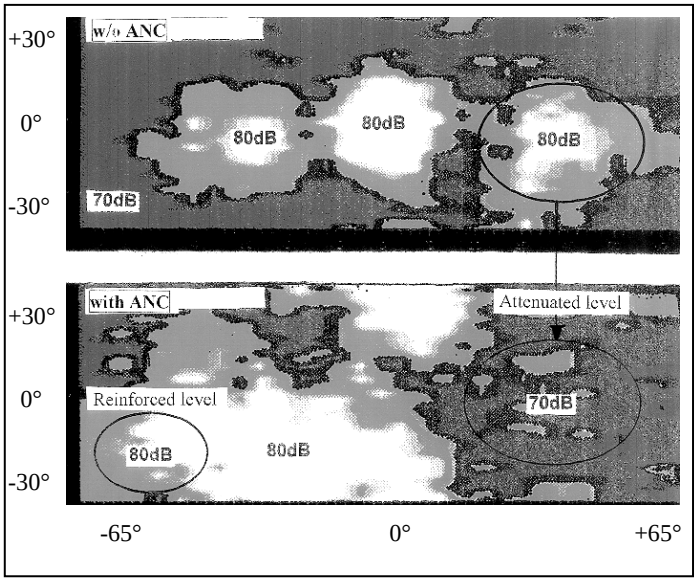


Fig. 15 : Upstream far field map (1 BPF / 2100 Hz)

The plots of the angular wave number spectrum in figure 16 are more complicated to analyze.

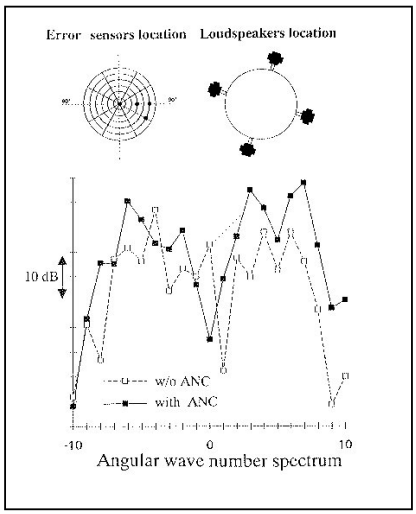


Fig 16. : Angular wave number spectrum
(1 BPF / 2100 Hz)

More interesting and realistic is the control from in-duct microphones. In figure 17 is shown, for a configuration of 7 in-duct error sensors distributed on 2 close axial arrays (figure 18) and 4 actuators, results obtained with the control working on the BPF at 1700 Hz. Relative to the forward radiation, it is found an increase of the tone level in the angular range towards sensors whereas a significant reduction

is measured in the opposite direction of the location sensors. In the aft, sound levels are reinforced on the overall measured angular range.

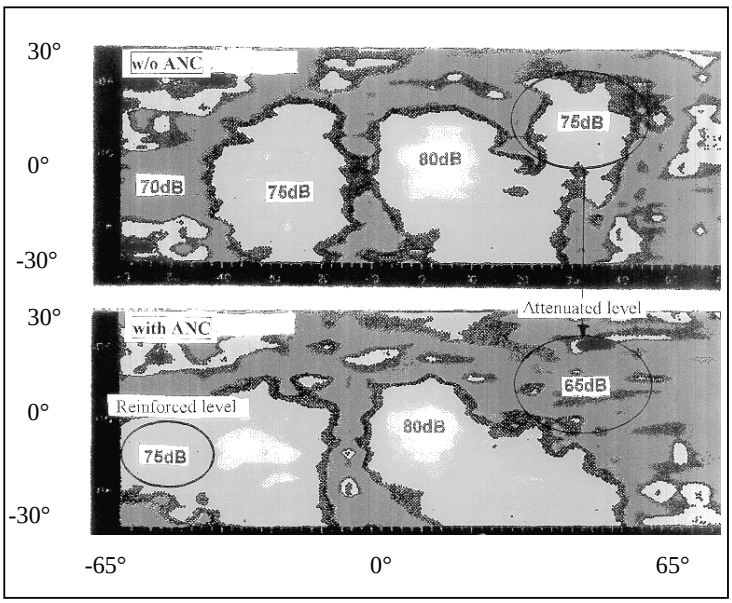


Fig 17 : Upstream far field map (1BPF/1700Hz)

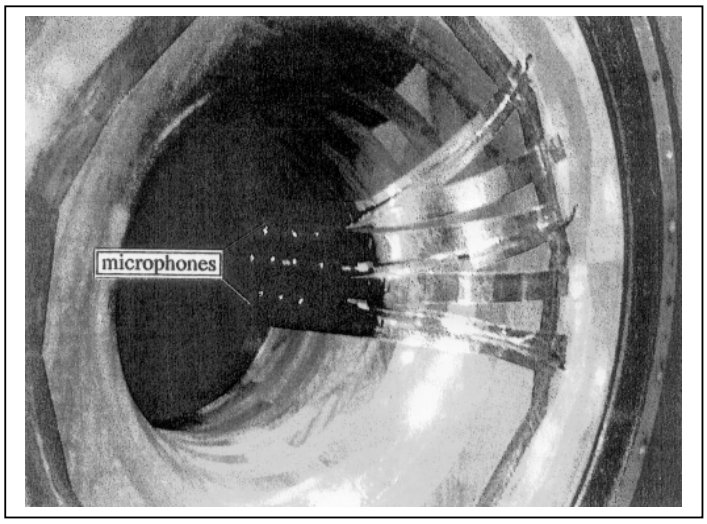


Fig. 18 : In-duct error sensors location

Others configurations were tested with results more or less good and it was observed that the number of channels was insufficient to investigate more. It was found that the reduction obtained in any particular case depended upon the frequency of tones and their shift with rpm and the amount of ANC suppression depended on as well the tone protrusion from the broadband noise.

DISCUSSION

The modal control strategy requires to use a large number of error sensors and actuators and its application gives relative good results for an acoustic source with some angular dominant mode. Nevertheless with a complex modal structure as met on engine results are probably less good. An other interest is a weak reinforcement in the uncontrolled area .

An other strategy consists in working on the duct axial wave-numbers which is connected to the radiation far field angle. Recent works [5,6] showed interesting results by minimizing a specific wave-number relative to the sideline radiation

With a limited number of transducers and a complex modal structure, a strategy aiming at redirection the radiation to obtain a low noise area in the far field by a mechanism of modal restructuring in combining for instance 2 different modal structure has been investigated. The difficulty consist of having the right information from the in-duct measurements to generate with actuators the required sound field .

FUTURE WORKS

Further experimental studies are going on in the European framework in order to assess and optimize different strategies based on the ANC technique applied to the control of the tones radiation. For instance, several rings of actuators should be used to have a better control of the secondary sources modal characteristic (especially the radial modal structure).

A combination passive and active technologies is to be investigated knowing that these techniques are complementary. Indeed the passive liner more dedicated for the broadband noise reduction has already shown it can contribute to improve the performance of the ANC to reduce tones. In fact the attenuation of the passive liner increases with the mode order and the frequency showing a good efficiency on higher modes which radiate on the side. Whereas the ANC is easier to work out on low modes and low frequencies. The benefit of combined effects are still to assess more accurately

An other way of work, in cooperation with European partners, is investigated to develop specific secondary compact acoustic sources to lead to flight-worthy actuators.

CONCLUSION

An active noise control system with out-duct & in-duct error sensors (inlet-mounted) and a ring of actuators has demonstrated a good performance to suppress the inlet tones noise from a fan model. Using a multichannel controller and an adaptive algorithm based on a Least-Mean-Square (LMS) method, the control system was robust enough to accommodate of rotation speed variations.

Control configurations of far field error sensors yields attenuation of up to 15 dB on the inlet fan tones noise on a large angular range in the radial extension of the sensors location. Elsewhere it is often obtained an increase of noise level. The aft duct radiation uncontrolled is slightly higher. In this case the mechanism of control involves a complex restructuring of the spinning modes leading to destructive interference in the control area. At low frequency with low order modes a sound power attenuation is observed everywhere and in this case the mechanism is rather a modal suppression.

The use of in-duct wall-mounted sensors evenly distributed according to either the azimuthal or axial direction allows to obtain in the far field a quiet angular range area with suppression up to 10 dB. Nevertheless, the quiet area is smaller and the benefit depends on test configuration and source characteristic. Criteria based on modal distribution and radial wave-number have been used as a guide.

The strategy of redirectioning in the space the tones radiation to provide a quiet area seems to be well adapted to the complex modal structure of the engine source. Nevertheless in function of specific source characteristic an other strategy can be required. So further works have to be undertaken in terms of criteria for designing optimal configurations, of development of hardware (controller, actuators,..), of combination passive and active technologies to provide a flight-worthy system.

REFERENCES

1 Smith, J.P., Burdisso R.A., and, Fuller C.R., " Experiments on the active control of inlet noise from a turbofan jet engine using multiple circumferential control arrays", AIAA/CEAS paper 96-1792.

2 Sutliff, D.L., Ziquiang, H., Pla, F.G., Heidelberg, L.J., " Active noise control of low speed fan rotor-stator modes" AIAA paper 97-1641.

3 Ikelheimer, B.J. and Nagel,R.T., " Active noise control of multiple acoustic modes in a circular duct ", AIAA paper 96-1781.

4 Julliard, J., Riou, G. and Lozachmeur, C.," Recent developments in turbomachinery noise control and reduction systems ", AIAA paper 93-4375.

5 Smith, J.P. & Burdisso R. A., "Active Control of Inlet noise from a Turbofan Using Inlet Wave-number Sensors", AIAA paper 99 - 1808

6 Joseph, P., Nelson, P.A., & Fisher, M.J.," Active Control of Turbofan radiation using an In-duct error Sensor Array " Proceedings of active 97, Budapest, Hungary, August 1997.

Paper#18

Q by G.E.A. Meier: A real engine generates sound of high power. Can one provide corresponding sound energy by a loud speaker?

A. (J. Julliard, H. Antoine): Some studies are on-going to design loud speakers which can generate high sound pressure levels. First results are very promising.

A Modal Concept for Active Noise Control in Circular or Annular Ducts

Ulf Tapken, Yanchang Zhang*, Lars Enghardt, Wolfgang Neise

DLR-Institut fuer Antriebstechnik, Abteilung Turbulenzforschung Berlin, Mueller-Breslau-Strasse 8, 10623 Berlin, Germany; *now with LUK GmbH & Co, Industriestrasse 3, 77815 Buehl, Germany

1. Introduction

Active control of sound propagation in ducts plays an important role in many technical applications, e.g. the attenuation of noise in ventilating systems or in the exhaust systems of combustion engines. Today many control strategies exist for the simplest case, which is the noise control in the low frequency range in ducts the lateral dimensions of which are small compared to the wavelength of sound. Up to the cut-on frequency of the first higher order mode a suppression of the propagating plane sound waves is possible in a broad frequency range.

The situation is more difficult when the lateral duct dimensions become large compared to the wavelength, as for example in the intake section of an aircraft engine. With increasing rotor speed an increasing number of acoustical modes becomes present. This means, the system comprises an increasing number of degrees of freedom. As a consequence, control of the sound field is practicable just in a narrow frequency band or even limited to discrete frequencies.

In figure 1 the frequency spectrum of the sound field in the duct section of a turbo-machine is depicted. Obviously the fan produces tones of high intensity compared to the broad band noise level. Attenuation of these tones by means of passive absorbers often is not sufficient. Therefore the active suppression of the tones represents a reasonable improvement.

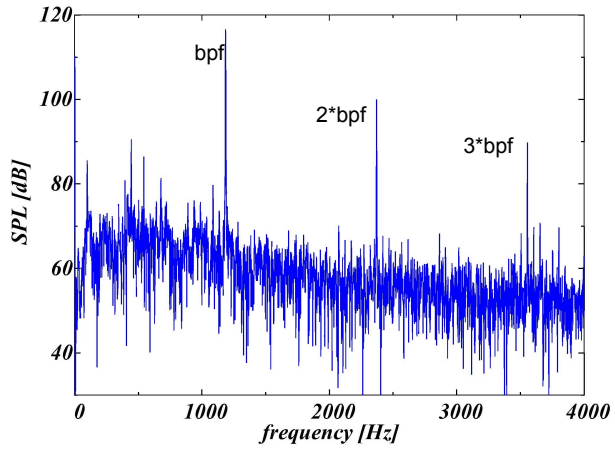


Figure 1: Sound pressure spectrum detected by a microphone in the duct section of a turbo-machine (bpf=blade passing frequency).

A common approach for active noise control consists in the use of the well known adaptive LMS-algorithm. This strategy ignores to a certain extent the properties of the physical system to be controlled. Furthermore, with increasing complexity of the modal sound field the numerical costs of the adaptive system increase fast and the problem of numerical instabilities occurs. Thus a physical approach is reasonable, which aims at minimisation of only the dominant modes of the undesired tone. This results in a reduction of the control effort. Furthermore the stability of the complete modal control process is improved due to its separation into a number of independent subprocesses for individual modes. Besides, as another control strategy, the directivity of the radiated tones in the far field outside the duct can be influenced through a specific control of the modal structure.

In this regard a azimuthal mode control strategy was developed and experimentally proved by NASA Lewis Research Centre in 1996 (Pla and Hu [1]). By use of a single ring with pressure sensors and one ring with actuators they were able to reduce one dominant azimuthal mode at the axial ring location of the sensors.

As the amplitude of the azimuthal mode is a function of the axial and the radial position in the duct, control at a single axial ring position does not ensure minimisation of that azimuthal mode at other duct positions, in particular if the sound wave has a high radial content.

A direct radial mode control strategy at present seems to be impossible in practice, because variations of temperature, frequency and flow velocity in the duct strongly influence the

Paper presented at the RTO AVT Symposium on "Active Control Technology for Enhanced Performance Operational Capabilities of Military Aircraft, Land Vehicles and Sea Vehicles", held in Braunschweig, Germany, 8-11 May 2000, and published in RTO MP-051.

accuracy of the online radial mode analysis. Besides, a large number of variables must be considered by the control system, leading to instabilities in the minimisation process.

Therefore, an improved control strategy has been proposed by Zhang et al: the indirect radial mode control (IRMC), which enables effective control of the modal sound field without directly determining the radial amplitudes. The method is based on the well-defined relationship between the azimuthal amplitudes at different axial positions, which is given implicitly by its composition of a fixed number of radial components. If one succeeds in reproducing the azimuthal amplitude and thus the correct linear superposition of radial components at different axial positions, suppression can be achieved not only at this distinct locations but also in the whole duct.

In the following chapters it will be shown, that the performance of the modal control strategy strongly depends on the proper choice of the number as well as the locations of the sensors and actuators.

2. The sound field description in circular and annular ducts

The propagation of sound pressure waves in cylindrical or annular ducts in the presence of uniform mean flow can be described by a linear acoustic wave equation, see e.g. [2]. A solution of the wave equation in cylindrical coordinates (x, r, φ) is given by a mathematical decomposition into azimuthal and radial components. In the frequency domain it can be written as (see [3]):

$$\tilde{p}(x, r, \varphi, \omega) = \sum_{m=-\infty}^{\infty} A_m(x, r, \omega) \cdot e^{im\varphi} \qquad \textbf{(1)}$$

$$A_m(x, r, \omega) = \sum_{n=0}^{\infty} f_{mn}(\sigma_{mn} \frac{r}{r_a}) \left[A_{mn}^{+}(\omega) e^{ik_{mn}^{+} x} + A_{mn}^{-}(\omega) e^{ik_{mn}^{-} x} \right] \qquad \textbf{(2)}$$

where $A_m(x, r, \omega)$ is the amplitude of the azimuthal mode of order m. $A_m(x, r, \omega)$ expands into a series of radial modes with amplitudes $A_{mn}^{+}(\omega)$ and $A_{mn}^{-}(\omega)$. "+" denotes wave propagation in flow direction, "-" against flow dirction. $k_{mn}^{+}(\omega)$ and $k_{mn}^{-}(\omega)$ are the respective axial wavenumbers, r_a is the outer duct radius, and f_{mn} denotes the cylinder functions which describe the radial distribution of the modal sound pressure field in the circular or the annular duct (a detailed description can be found in [3]).

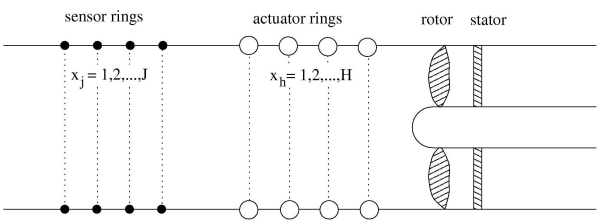


Figure 2: Longitudinal section of the duct.

3. The Indirect Radial Mode Control (IRMC)

In figure 2 the intake of a turbo machine is depicted with a sensor and an actuator array mounted flush with the inner duct wall. The sensors and actuators are arranged in several axial rings. In each ring the sensors resp. actuators are spaced evenly in the azimuthal direction φ. The number of sensors and actuators per ring must be chosen according to the Nyquist theorem. The arrangement of the sensors allows a azimuthal mode analysis for each ring as was demonstrated in [4]. It is a prerequisite for the IRMC-method processed in the azimuthal mode domain. Figure 3 gives an overview on the required signal processing.

With the azimuthal modal analysis realised as a real time application (see Böhning et al [5]) the modal amplitude $P_m(x_j, r_a, \omega)$ for each azimuthal mode order -m, ..., +m of the primary sound wave (produced by the rotor) can be determined for the set of sensor rings $\{x_j\}$. The objective of the IRMC is to cancel the azimuthal modes $P_m(x_j, r_a, \omega)$ by a secondary wave of adequate azimuthal mode amplitudes $S_m(x_j, r_a, \omega)$, which are generated by the actuators. Mathematically this is equivalent to minimisation of the sum of these mode amplitudes over all axial positions of the sensor rings, seperately for each azimuthal order m:

$$I_m(\omega) = \sum_{j=1}^{J} \left| P_m(x_{j,} r_a, \omega) + S_m(x_{j,} r_a, \omega) \right|^2 = Min. \qquad \textbf{(3)}$$

The secondary mode amplitude at the sensor locations $\{x_j\}$ generated by the actuators is given by

$$S_m(x_j, r_a, \omega) = \sum_{h=1}^{H} (t_m)_{hj}(\omega) \cdot \xi_m(x_h, r_a, \omega), \qquad \textbf{(4)}$$

where $\xi_m(x_h, r_a, \omega)$ represents the azimuthal mode amplitude of the actuator ring at the axial position x_h. $(t_m)_{hj}$ is the coefficient of the modal transfer matrix $\underline{\underline{T}}_m^{hj}$ which describes the modal transfer functions between the axial positions $\{x_h\}$ and $\{x_j\}$. The modal transfer matrix has to be determined in a separate step prior to application of ANC, see chapter 4.

From equation (2) it can be deduced, that in order to control an

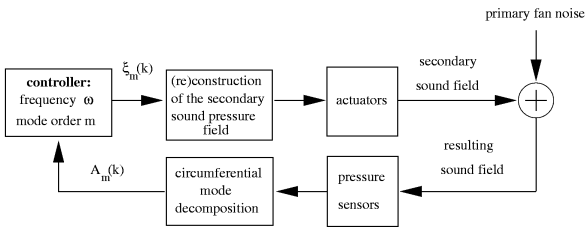


Figure 3: Schematic of the signal processing for IRMC.

azimuthal mode consisting of N radial modes, at least N sensor rings are necessary. If the azimuthal mode amplitude $P_m(x_j, r, \omega)$ at these N axial positions x_j is reproduced on the duct wall ($r = r_a$), the radial structure in the duct is also reproduced implicitly.

For simplicity a vector of azimuthal mode amplitudes of mode order m at the set of axial positions $\{x_j\}$ resp. $\{x_h\}$ is introduced:

$$\underline{P}_m := [P_m(x_1, r_a, \omega), P_m(x_2, r_a, \omega), ..., P_m(x_J, r_a, \omega)]^t ,$$

$$\underline{S}_m := [S_m(x_1, r_a, \omega), S_m(x_2, r_a, \omega), ..., S_m(x_J, r_a, \omega)]^t ,$$

$$\underline{\xi}_m := [\xi_m(x_1, r_a, \omega), \xi_m(x_2, r_a, \omega), ..., \xi_m(x_H, r_a, \omega)]^t . \qquad \textbf{(5)}$$

In equ.(5) single tones with constant frequencies ω are considered. Since only wall-flush mounted sensors and actuators are used, r_a can be dropped in the further analysis. Thus equation (4) can be rewritten as

$$\underline{S}_m = \underline{\underline{T}}_m^{hj} \cdot \underline{\xi}_m , \qquad \textbf{(6)}$$

and one obtains the solution of equation (3) as least square fit expression

$$\underline{\xi}_m = -((\underline{\underline{T}}_m^{hj})^{t*} \cdot \underline{\underline{T}}_m^{hj})^{-1} \cdot (\underline{\underline{T}}_m^{hj})^{t*} \cdot \underline{P}_m . \qquad \textbf{(7)}$$

Since the system is linear, the control process can be performed separately for each mode order m of a single tone.

The final actuator signals (in the frequency domain) can be computed according to equation (1) for each actuator at position (x_h, r_a, φ_l). In order to generate the secondary tone with the correct phase leading to the cancellation of the primary field, it is locked to a trigger signal, which is produced by the rotor.

Theoretically the system of linear equations (7) can be solved exactly. In practice the inversion of the included hermitian matrix may be critical numerically and lead to instabilities. The problems that appear in connection with a matrix inversion will be discussed in more detail in chapter 5.

4. Simulation of the IRMC

Before performing IRMC the modal transfer matrix $\underline{\underline{T}}_m^{hj}$ has to be determined by an azimuthal mode transfer function measurement for each azimuthal mode order -m ,..., +m. The transfer matrices include the acoustical transfer path as well as the electro-mechanical transfer characteristics of the actuators and the respective signal processing. For the numerical simulation and analysis of the IRMC here the modal transfer matrix $\underline{\underline{T}}_m^{hj}$ is determined theoretically.

In order to get a more realistic azimuthal modal spectrum as an input for the simulation, a modal noise amplitude appropriate to a measurement error of the sensors is added to the modal amplitudes in $\underline{P}_m(\omega)$. The magnitude of the noise amplitude is related to the maximum modal amplitude by considering a given 'signal-to-noise-ratio' σ.

In figure 4 the simulation of the IRMC in the azimuthal mode domain is divided into two parts. In the first step the modal vector $\underline{P}_m$ is used to calculate the actuator signal amplitudes $\underline{\xi}_m$ according to equation (7). For brevity the corresponding transformation is represented by the modal transfer matrix $\underline{\underline{T}}_m^{jh}$ in figure 4. Equation (6) gives the secondary modal amplitudes $\underline{S}_m$ generated at the sensor locations with help of the modal transfer matrix $\underline{\underline{T}}_m^{hj}$. The residual amplitudes $\underline{E}_m$ are the result of the superposition of the primary and the secondary tone.

The presence of noise leads to deviations between the "measured" and the actual modal amplitudes at each sensor location,

$$\begin{aligned} E_m(x_j) &= P_m(x_j) + S_m(x_j) \\ &= P_m(x_j) + \sum_{h=1}^{H} (t_m)_{hj} \cdot \xi_m(x_h) \geq 0. \end{aligned} \qquad \textbf{(8)}$$

For that reason an iterative algorithm is used in the following steps, which should optimise the actuator amplitudes step by step in order to minimise the residual mode amplitude.
The task is solved by a multiple-channel LMS-algorithm in the azimuthal mode domain. The iterative algorithm, originally

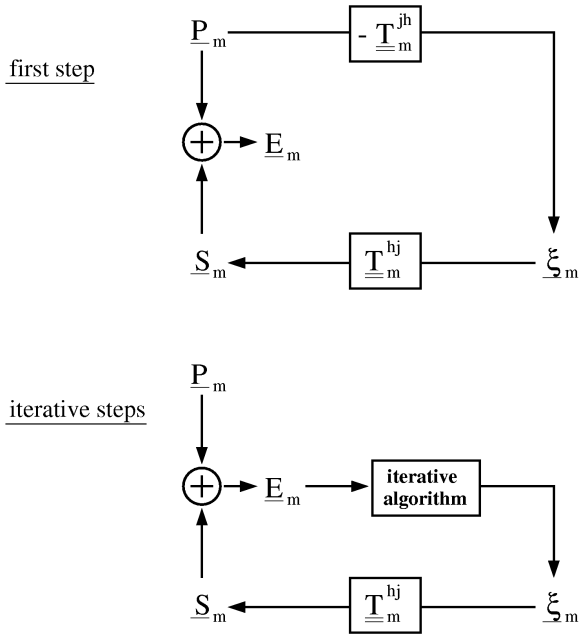


Figure 4: Initial and iterative steps implemented in the IRMC algorithm in the azimuthal mode domain.

designed for use in the frequency domain (see Kuo and Morgan [6]), minimises the residual mode amplitude according to equation (3) and gives the update prescription of the modal actuator vector for step n as

$$\underline{\xi}_m(n+1) = \underline{\xi}_m(n) + \mu \cdot (\underline{\underline{T}}_m^{hj})^{t^*} \underline{E}_m(n), \qquad \textbf{(9)}$$

where μ is the adaptive step size parameter.

If all parameters of the sound field, i.e. frequency, temperature and mean flow velocity, are constant in time, then the spatial structure of the sound waves in the duct repeats periodically. Thus, since the actuator amplitudes are set in relationship to the trigger of the rotor, there is no need to process the iterative algorithm in real time.

In fact, calculation of the initial modal actuator amplitudes $\underline{\xi}_m(0)$ in the first step of the iterative algorithm is not mandatory, however, it leads to a faster convergence of the iterative process.

5. Analysis of the modal transfer matrix

In theory, without additional noise, the modal actuator signal amplitudes given in equation (7) should produce a cancelling tone $\underline{S}_m$ that exactly eliminates the primary tone $\underline{P}_m$. However, this is true only for azimuthal modes with a low radial content, which is equivalent to a corresponding modal transfer matrix of low rank. In this chapter it will be shown, that with increasing radial mode order n numerical restrictions lead to limitations with regard to the solution, which is exact analytically.

All calculations presented in this paper have been carried out for the configuration depicted in figure 2. A uniform flow of M=0.3 and equally spaced rings in the axial direction of the duct are assumed for various parameters $k_0 r_a$ (k_0 denotes the wavenumber for free field propagation). The axial distance between two consecutive rings is denoted by δx.

Calculation of the modal transfer matrix $\underline{\underline{T}}_m^{hj}$ involves the inversion of a hermitian matrix, named $\underline{\underline{U}}_m$ in the following. The accuracy of the modal transformation process strongly depends on the condition of $\underline{\underline{U}}_m$, whereby a low condition corresponds to a transformation with good accuracy. In other words, the condition of $\underline{\underline{U}}_m$ is a measure for the quality of the detection of the modes at the specified positions. Thus by an analysis of $\underline{\underline{T}}_m^{hj}$ resp. $\underline{\underline{U}}_m$, the optimum positioning of the sensors and actuators for application of the IRMC-technique can be examined.

In figure 5 the variation of the condition of $\underline{\underline{U}}_m$ with ring distance δx is shown for all propagating azimuthal mode orders and for three different values $k_0 r_a$. Obviously, the lower the mode order m the smaller the intervals of δx with a low condition are. This can be explained by the fact, that the lowest mode order m=0 has the largest radial content; see for illustration figure 6, where the normalised axial wavelengths of all propagating modes (m,n) are depicted for $k_0 r_a$ =16.3. For a low mode order m the differences between the corresponding axial wavelengths $\lambda_{mn}^{\pm}$ (n=0,...,N) become smaller, which makes the implicit modelling of the radial modes by the mathematical mapping more difficult. Furthermore the complexity of this problem increases with increasing $k_0 r_a$. On the other hand, axial ring

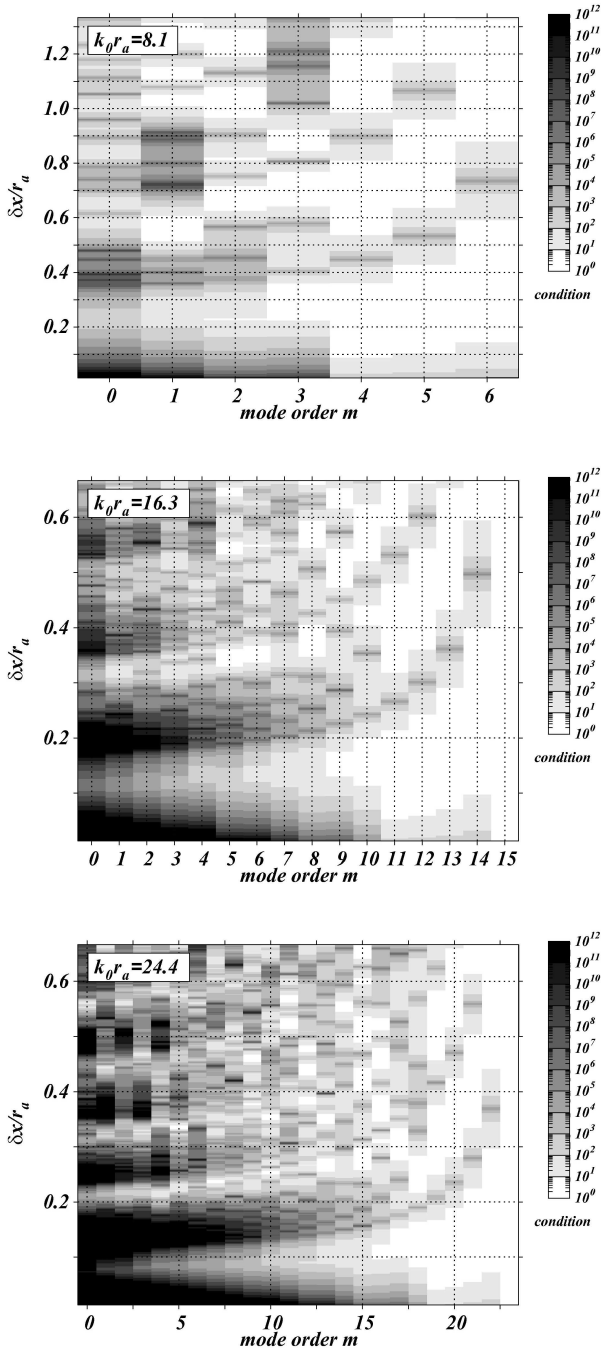


Figure 5: Condition of the hermitian matrix $\mathbf{U_m}$ as function of the axial ring spacing δx calculated for all propagating mode orders m and different values $k_0 r_a$.

spacing is almost arbitrary when the azimuthal mode order m is large and the radial mode content low.

In general, it is the lower mode order m that impose the essential restrictions with regard to the positioning of the rings. Comparison of the examples, shown in figure 5 leads to the conclusion, that for simultaneous control at several frequencies, the proper choice of the ring positions becomes a critical issue.

6. Analysis of the IRMC-Algorithm

The performance of the IRMC-algorithm in the presence of noise is examined in this chapter. The calculations have been carried out for the same parameters as in chapter 5 for $k_0 r_a = 16.3$. The magnitude of the amplitudes of the primary modes, that are radiated by the rotor and propagate upstream, are randomly distributed about $P^-_{mn} = 85$ dB. The reflected modes propagating in flow direction are assumed to be in the range of $P^+_{mn} = 70$ dB. The iterative control system is considered to be converged, if the mean residual amplitude over all sensors equals 50 dB.

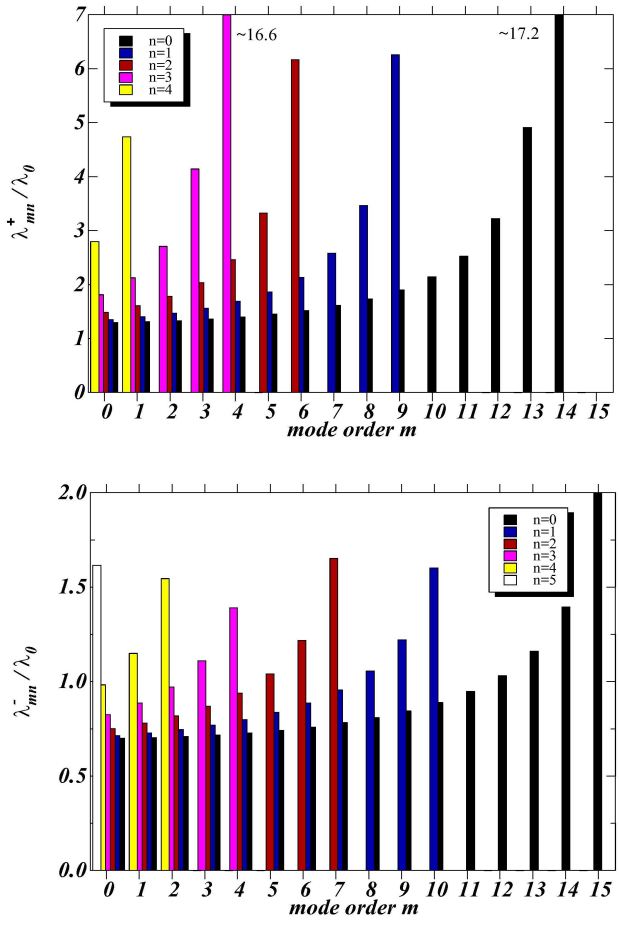


Figure 6: Normalized axial wavelengths λ^+_{mn} and λ^-_{mn} of the modes (m,n) propagating in resp. against flow direction for $k_0 r_a$ = 16.3.

As pointed out in chapter 5, a system with an ill-conditioned transfer matrix is very sensitive to small disturbances of the input vector. This is confirmed by figure 7, which shows the number of iterations until convergence of the iterative algorithm depending on the axial ring spacing δx. The calculations are performed for mode order m=8 and different noise levels, given by the modal signal to noise ratio σ. The larger the disturbances, the larger the deviations between the calculated output of the modal matrix transform and the optimal solution, as it is described by equation (8). In the absence of noise or with very low noise levels (σ >30dB), the IRMC cancels the primary tone completely after the first step for any δx. For σ <30dB and a ring distance δx corresponding to a quite good condition, the control is stable and after a few iterations the algorithm also converges. But with increasing noise level, and ring spacings corresponding to an ill-conditioned system, the system becomes unstable. In these cases lots of iterations are necessary until convergence is reached, or the control system even does not converge at all.

In Figure 8 a control attempt for the mode order m=8 and an optimal ring spacing δx is shown for σ =5dB in comparison with σ =30dB. In the coordinate system used here, the rotor is located at x=0 and the uniform flow goes in the positive axial direction. Depicted are the magnitudes of the complex azimuthal mode amplitudes over the duct axis after the iterative algorithm has converged. Obviously the actuators reproduce the primary mode well, resulting in the cancellation of $\underline{P}_m$. The residual mode amplitude $\underline{E}_m$ strongly depends on the uncertainty of the measured azimuthal mode amplitudes.

The contour plot in figure 9 shows the residual modal ampli-

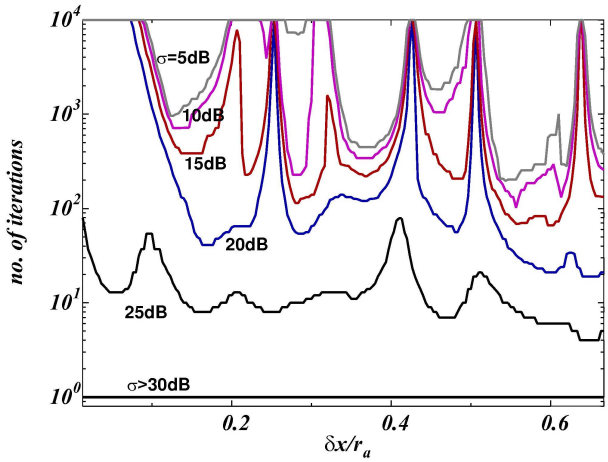


Figure 7: Number of iterations until convergence as a function of the sensor ring spacing for various modal signal to noise ratios σ (m=8, n=0,1, $k_0 r_a$ = 16.3).

tudes $E_m(x, r_a)$ along the duct axis for the mode order m=8 and σ =15 dB for different ring spacing δx. As examination of the matrix $\underline{\underline{U}}_m$ predicted, for a ring spacing δx connected with bad condition of $\underline{\underline{U}}_m$, the system does not cancel the primary mode or even diverges, which is indicated by residual modal amplitude E_m larger than the modal amplitude P_m of the primary tone.

Note, that control of the primary mode at the locations of the sensors is successful for arbitrary ring spacings δx: the reduction at the axial positions of the sensor rings are clearly visible in the contour plot as white lines (the arrows mark the moving positions of the rings with increasing δx). The important conclusion is, that a control observed at the sensors does not necessarily mean a reduction of the primary mode in the entire duct.

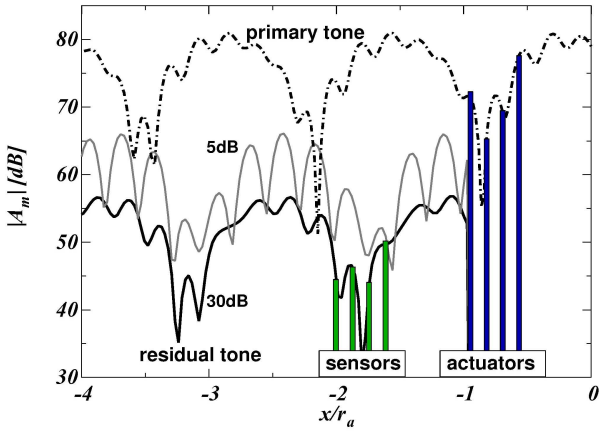


Figure 8: Azimuthal mode amplitude of the primary and the residual tone along the duct axis for modal signal to noise ratios of σ =5 and 30 dB after convergence of the IRMC (m=8, $n^{\pm}$=0,1, $k_0 r_a$ = 16.3, rotor at x=0).

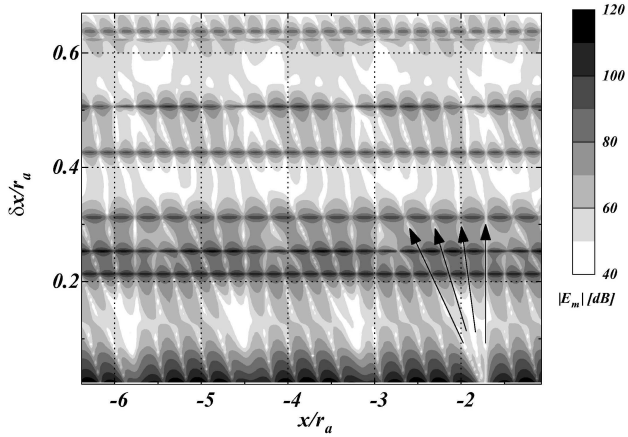


Figure 9: Residual azimuthal mode amplitude along the duct axis with a modal signal to noise ratio of σ =15 dB; the arrows mark the positions of the sensor rings depending on δx (m=8, $n^{\pm}$=0,1, $k_0 r_a$ = 16.3, rotor at x=0).

The upper graph of figure 10 shows a control attempt for mode order m=1 and σ =25dB. The azimuthal mode contains 10 radial modes (cp. figure 6) and should be detected by 10 sensor rings with an axial spacing $\delta x / r_a = 0.1$ corresponding to a matrix $\underline{\underline{U}}_m$ with minimum condition. Nevertheless the condition for this configuration is quite bad and convergence is not reached. This example again confirms, that control achieved at the sensor location does not imply control at all duct locations.
The situation is improved with additional sensor inputs, e.g. with 13 sensors, which is shown in the bottom graph of figure 10. The corresponding matrix $\underline{\underline{U}}_m$ still is bad conditioned. However, if the inverting process of the hermitian matrix is carried out via a singular value decomposition, columns corresponding to singular values close to zero can be rejected, which results in an improved condition and performance of the IRMC.

Since the IRMC-technique makes use of wall flushed sensors and actuators, one has to prove that not only the modal amplitudes at the duct wall are controlled but also the whole azi-

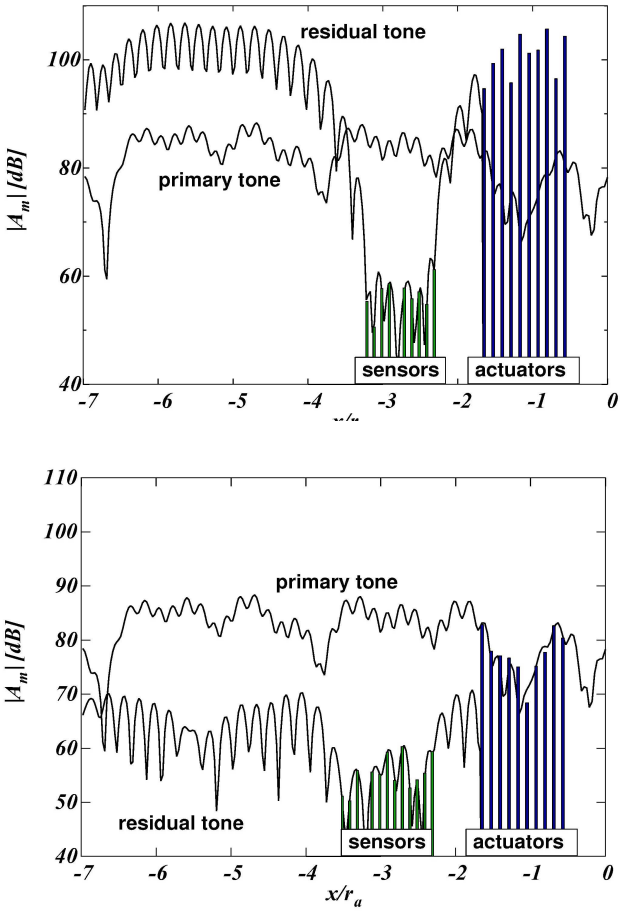


Figure 10: Azimuthal mode amplitude of the primary and the residual tone along the duct axis for a modal signal to noise ratio of 25 dB and 10 sensor rings (top) resp. 13 sensor rings (bottom) (axial ring spacing $\delta x / r_a$ = 0.1, m=1, $n^{\pm}$=0,...,4, $k_0 r_a$ = 16.3, rotor at x=0).

muthal and radial structure across the duct. Evidence to that regard is given in figure 11 and 12, which show the pattern of the primary and residual azimuthal mode, $\underline{P}_m$ and $\underline{E}_m$ resp., across the duct corresponding to the control attempt shown in figure 10.

7. Summary

The results of the analysis and simulation show, that the IRMC-concept enables an effective control of the azimuthal and radial structure of acoustical modes in circular and annular ducts without the need to determine the radial amplitudes directly. All azimuthal modes of a tone can be reduced by using the same ring spacing for the sensor rings and actuator rings. In this context, the lower azimuthal mode orders m impose the most stringent requirements for the axial spacing. For effective control of an azimuthal mode m with a high radial content (N radial modes), more than N sensor rings are necessary. Control attempts at several frequencies simultaneously require a detailed analysis with respect to the optimal ring spacing.

An important result with regard to the experimental analysis of active control concepts is, that noise control achieved at the positions of the sensors does not necessarily mean a complete control at all positions in the duct.

The simulation results show further, that it is not necessary to place the sensor rings in the axial direction according to a spatial Nyquist criterion. This can be explained by the fact, that in the adaptation process only the radial mode amplitudes belonging to certain discrete modal wavenumbers $k_{mn}^{\pm}$ have to be fitted implicitly.

Another result is, that complete control is possible in the duct although the sensor array covers less than half of the maximum modal wavelength.

In future investigations non equidistant axial spacing of the rings has to be examined with respect to matrices with improved conditions. Additionally improved methods for matrix inversions have to be tested. A perturbation method may give more information in this context.

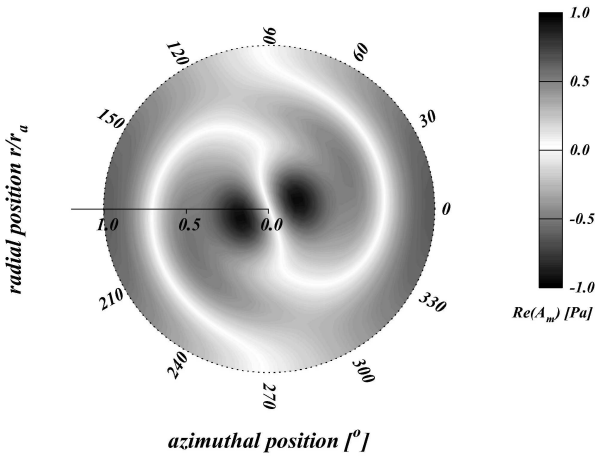


Figure 11: Pattern of the azimuthal mode amplitude (mode order m=1) of the primary tone in the cross section of the duct at x/r_a =-4.5 (parameters as in figure 10).

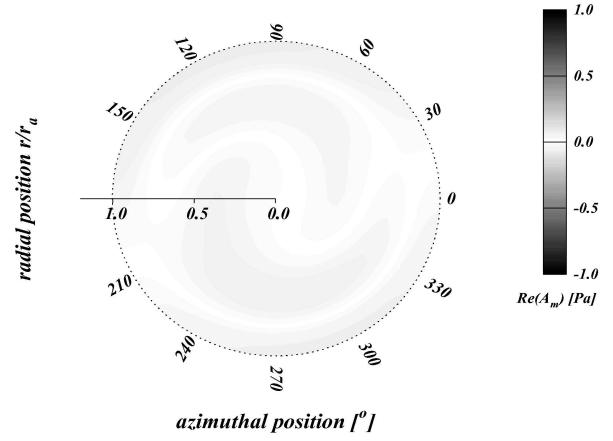


Figure 12: Pattern of the azimuthal mode amplitude (mode order m=1) of the residual tone in the cross section of the duct at x/r_a =-4.5 (parameters as in figure 10).

8. References

[1] Pla, F.G.; Hu, Z.: Active Control of Fan Noise: Feasibilty Study, Volume 3: Active Fan Noise Cancellation in the NASA Lewis Active Control Fan Facility, NASA Contractor Report NAS3-26617, September 1996

[2] Munjal, M.L.: Acoustics of ducts and mufflers; John Wiley & Sons, 1987

[3] Holste, F.; Neise, W.: Noise Source Identification in a Propfan Model by Means of Acoustical Near Field Measurements, Journal of Sound & Vibration, 203(4), pp. 641-665, 1997

[4] Enghardt, L.; Zhang, Y.; Neise, W.: Experimental verification of a radial mode analysis technique using wall-flush mounted sensors; Forum Acusticum – integrating the 25th German Acoustic DAGA Conference, Berlin March 1999, ISBN 3-9804568-5-4

[5] Böhning, P.; Enghardt, L; Neise, W; Költzsch, P.: Entwicklung einer Software zur Kurzzeit-Azimutalmodenanalyse; DAGA 2000, Oldenburg March 2000 - Fortschritte der Akustik (Proc. Annual Meeting of the German Acoustical Society, to be published)

[6] Kuo, S.M.; Morgan, D.R: Active Noise Control Systems, Wiley-Interscience Publ., 1996

This page has been deliberately left blank

Page intentionnellement blanche

Yaw Control at High Angles of Attack Through Vortex Manipulation Using Rotating Nose Strakes

Peter R. Hakenesch
DaimlerChrysler Aerospace - Military Aircraft
P.O. Box 801160, 81663 München, Germany
peter.hakenesch@m.dasa.de

Abstract
The effect of nose strakes on the flow field in the vicinity of the forward fuselage section of an aircraft was investigated. Emphasis was placed on the manipulation of the vortices in order to generate a significant side force and yawing moment with the purpose not only to stabilize the aircraft at high angles of incidence, but also to achieve yaw control. Aside from conventional control surfaces, an additional control device was realized by mounting a single strake on the nose section which could be rotated around its longitudinal axis. Experimental force and pressure data from low speed wind tunnel tests indicate the potential of this control device for aircraft flying at high angles of attack.

List of symbols

b	[m]	Wing span
C_l	[-]	Rolling moment coefficient
C_m	[-]	Pitching moment coefficient
C_n	[-]	Yawing moment coefficient
C_{lp}	[rad^{-1}]	Roll damping derivative
l_{ref}	[m]	Reference length
M_∞	[-]	Mach -number
p, q, r	[rad/s]	Rotation rates around x_f , y_f , z_f
S_{ref}	[m²]	Reference area
v	[m/s]	Velocity
α	[deg]	Angle of attack
β	[deg]	Sideslip angle
η	[deg]	Flap deflection
Λ	[-]	Aspect ratio b^2/ S_{ref}
φ	[deg]	Radial Strake position
x, y, z	[m]	Coordinates

Subscripts

a	Aerodynamic axis system
b	Body axis system
ref	Reference
∞	Free stream conditions

Abbreviations

BAR	Bihrle Applied Research
C	Canard
HARV	High Angle of Attack research Vehicle
LAMP	Large Amplitude Test Facility
LEF	Leading Edge Flap
MAC	Mean Aerodynamic Chord
MATV	Multi Axis Thrust Vectoring
R	Rudder
TEF	Trailing Edge Flap
W	Winglet

1. Introduction

Aircraft maneuvering at high angles of attack are faced with a dramatic loss of control power in yaw as the rudder almost loses completely its efficiency beyond 40 degrees angle of attack. So far, the only possibility to conduct controlled flights at angles of attack reaching into the post stall regime, is to take advantage of thrust vectoring, as demonstrated successfully by the experimental aircraft F-18 HARV, X-31 or F-16 MATV, Fig. 1. All three aircraft are flown in different programs and were developed independently. The NASA F-18 HARV is a testbed to produce aerodynamic data at high angles of attack to validate computer codes and wind tunnel research. The X-31 is being used to study thrust vectoring to enhance close-in air combat maneuvering, while the F-16 MATV is demonstrating how thrust vectoring can be applied to operational aircraft. Another promising possibility, aside from thrust vectoring, to control an aircraft in this angle of attack region, is to actively manipulate the vortices developing at the nose and fuselage through pneumatic devices such as different forms and directions of blowing or suction, or through mechanical devices such as strakes.



Fig. 1: Thrust vectoring aircraft

Paper presented at the RTO AVT Symposium on "Active Control Technology for Enhanced Performance Operational Capabilities of Military Aircraft, Land Vehicles and Sea Vehicles", held in Braunschweig, Germany, 8-11 May 2000, and published in RTO MP-051.

This paper deals with the possibilities to achieve vortex control and subsequently yaw control by introducing a controlled disturbance into the flow in the nose tip region of the aircraft through the use of a movable micro-strake.

The general structure of the vortex system around a slender body or an aircraft fuselage is indicated in Fig. 2. At low and moderate angles of attack (α_1), the flow still follows the contour and no vortices are formed. The resulting normal force increases linearly with angle of attack and no side force is generated. At more elevated angles of attack (α_2), the flow starts to separate from the fuselage and symmetric vortices are created. This leads to a non-linear increase of the normal force, similar to the non-linear lift curve of a delta wing. Due to the symmetric and basically stable vortex structure, side forces are virtually nonexistent. At even higher angles of attack (α_3), a quasi-stable but asymmetric vortex structure forms, which causes a considerable side force as well as a strong normal force. The side force may reach the same magnitude as the normal force but will again decrease and finally disappear again, as the angle of attack is further increased.

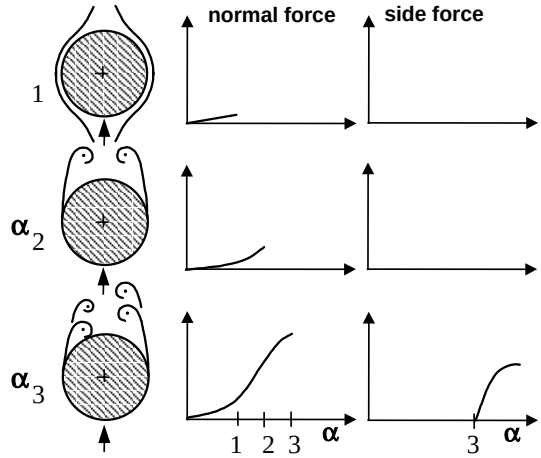


Fig. 2: Vortex structures and normal- and side forces vs. angle of attack [5]

Significant research concerning the use of forebody strakes for vortex control has been carried out so far. Two major fields of application can be distinguished: One consists of a pair of strakes positioned symmetrically in the nose region of the aircraft fuselage with the main purpose of forming and stabilizing a symmetric vortex structure in order to avoid the generation of asymmetric side forces or the switching from one quasi-stable state to another. The second group of application is not so much focussed on stabilizing but on actually controlling the aircraft. Control input is realized by two strakes which are located symmetrically in the nose area at fixed positions, and can be deployed and retracted. This concept was successfully flight tested in the F-18 HARV, Fig. 3. In order to use the nose strake as an operational control device with an efficiency similar to a conventional rudder, a control function must be established that describes the achievable forces and moments as a function of the flow conditions, aircraft attitude and strake position. The application under investigation in this study allows the positioning of the strake at any radial position on the nose depending on the control forces required for a specific maneuver.



Fig. 3: F-18 HARV Nose strake deployed

2. Experimental setup

Due to an extensive, and also flight test validated data base, all tests were carried out with a 1:7.5 scale model of the X-31 in the low speed wind tunnel LAMP of BAR Neuburg, Germany, Fig. 4. This test facility allows for static as well as dynamic testing in the low speed regime. Maximum free stream velocity in the 10ft vertical test section is 40 ft/s. The range of angle of attack is ±180° and the sideslip range is ±32°. For evaluation of dynamic characteristics, the model can be rotated around the wind-vector axis up to 150 rpm. A forced oscillation with maximum amplitudes of up to 40° around any of the body axis can be superimposed to the rotational movement.



Fig. 4: X-31 Force model in LAMP test section

The nominal test conditions as well as the model reference data are listed in Tab. 1.

Tab. 1: X-31 Reference data

Scale			1:7.5
Reference area	S_{ref}	[m²]	0.3738
Reference length	l_{ref} = MAC	[m]	0.502
Reference point	$c.g._{ref}$	[m]	0.908
Wing span	b	[m]	0.968
Free stream velocity	v_∞	[m/s]	10.83

As the size of the strake is of lesser importance than its position, a parametric study to specify the minimum strake size still suitable to have a noticeable effect on the vortex structure, was carried out, Fig. 5. As shown in the results, Fig. 7, even the smallest strake tested (no.1: 1/2"x1/8") and selected for subsequent determination of its efficiency function, showed little deviation from the larger sizes with respect to its effect on the achievable yawing moment and side force.



Fig. 5: Strakes tested, 2"x1/2" through 1/2"x1/2"

In order to determine the induced forces and moments as a function of angle of attack, sideslip and radial position of the strake, a modified nose section was designed for the X-31 force model which allowed the movement of the strake to any desired radial position by rotating the nose around its longitudinal axis, Fig. 6.

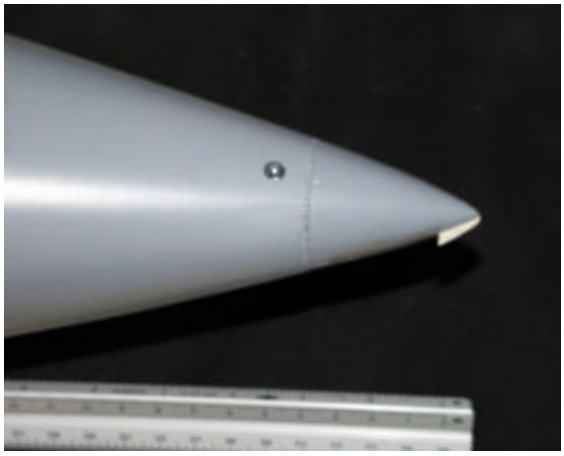


Fig. 6: Modified nose section - rotating around its longitudinal axis with strake

3. Results

During the investigation of strake position and strake efficiency, it became obvious that the actual size of the strake was of minor importance. The flow field around the forebody section seems to be fairly unstable and the vortex system formed at higher angles of attack tends to acquire one of the two possible quasi-stable and asymmetric states. The resulting flow turning direction can be influenced by even microscopic disturbances in the very beginning of the flow onset at the forebody. Therefore the size of the strakes plays a lesser role, as long as they are located at the tip of the nose. The yawing moments achievable by strakes of different sizes are shown in Fig. 7 for a strake positioned at the nose tip and rotated to a radial position of φ = -30°. Even though the efficiency of the strakes seems to depend stronger from the aspect ratio Λ than from the strake size, the results shown in Fig. 7 do not allow to establish an explicit function that relates strake efficiency, aspect ratio and strake size. The fact, that the strakes no.1 and no.2, with aspect ratios of Λ = 4 and 8 respectively, which are the smallest in size, show the maximum efficiency at an angle of attack of α = 50°, even above strakes of larger size, confirm the general trend that size is of lesser importance than aspect ratio.

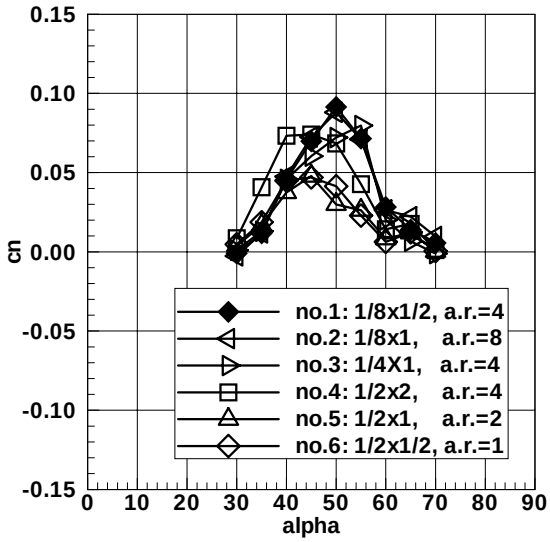


Fig. 7: Yawing moment as function of strake size

The pressure field induced at the foreward fuselage section by positioning one strake at an asymmetric position, i.e. φ = -45°, is shown in Fig. 8 for an angle of attack of α = 50°. The strong vortex on the right hand side induces a suction force on the foreward fuselage, which due to the large distance from the center of gravity, creates the considerable yawing moments.

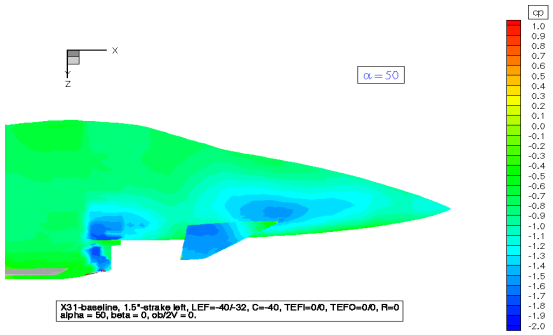


Fig. 8: Pressure distribution on nose section

The control power as a function of angle of attack and sideslip angle is shown in Fig. 9. The strake (no.1: 1/8"x1/2") is positioned at a radial position of φ = -45°. It becomes obvious, that full control power is available at angles of attack above α = 30° and can be maintained at positive and negative sideslip angles. For the sake of comparison, the rudder efficiency of the X-31 rudder, deflected to the maximum angle of η = 30°, is also depicted. Two aspects should be considered: First, the nose strakes allow yaw control of the aircraft at angles of attack where the conventional rudder has already lost its efficiency for good. So far, yaw control in this regime, i.e. 35° < α < 70° was reserved to aircraft featuring thrust vector control, but could now be expanded to more conventional aircraft as well by incorporating a rotating nose strake in the fuselage nose section. Second, this tremendous control power is achieved with micro-strakes, with a full scale size of only 0.002 m² (= 3.5 square inch). As shown in Fig. 7, the actual size of the strake is of minor importance, therefore a further miniaturization seems possible. This should be considered, as any disturbances of the radar integrated in the radom are to be avoided or at least they should be minimized.

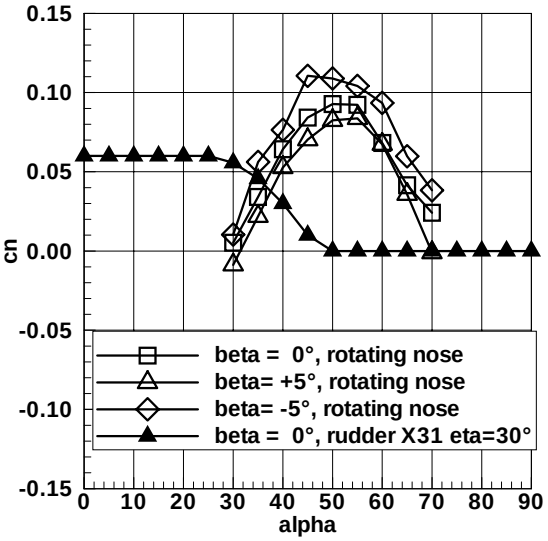


Fig. 9: Yawing moment vs. angle of attack

In order to use the rotating nose strake as a control surface, analogous to a rudder, a unique function must be established, that relates the achievable yawing moment C_n to the flow conditions α, β, M_∞, aircraft attitude and radial position φ of the nose strake. Fig. 10 shows the dependency of the yawing moment from the radial strake position φ for an angle of attack of α=45° and sideslip angles of β = 0°, ±5°. The experiments indicated that for large parts of the flight envelope, a linear dependency between radial strake position and yawing moment was established and therefore the usefulness of the rotating nose as a control device could be underlined.

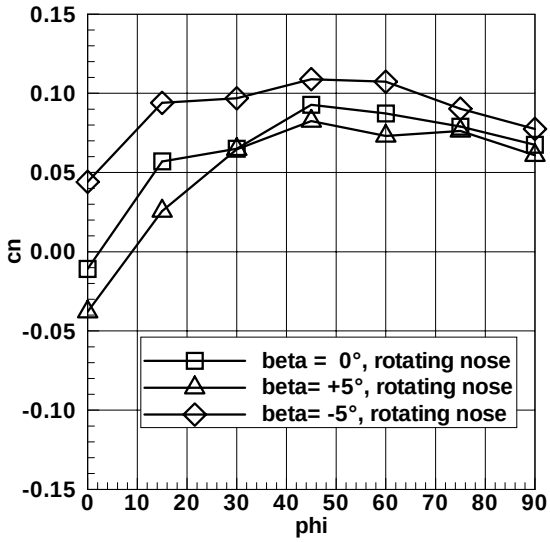


Fig. 10: Yawing moment vs. radial strake position

Another aspect to be considered are the coupled moments induced by the nose strake, i.e. the rolling moment C_l and the pitching moment C_m. As expected, the induced rolling moment due to an activated nose strake can more or less be neglected, Fig. 11. Even though the forces acting on the foreward fuselage section to generate a rolling moment are in the same order of magnitude as those responsible for the generation of the yawing moment, the resulting moment around the longitudinal axis is small, due to the very short hinge arm.

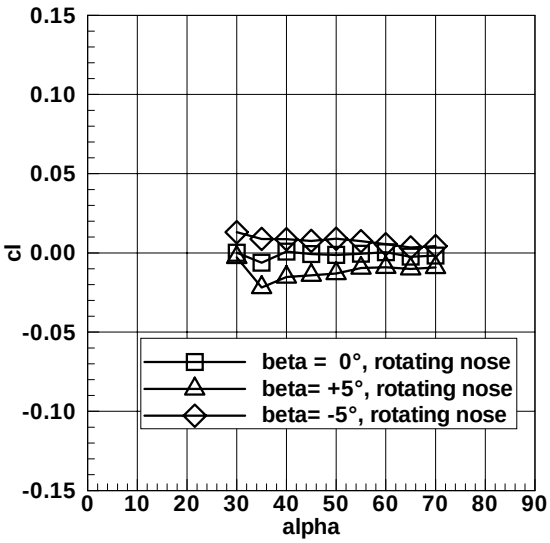


Fig. 11: Induced rolling moment due to a strake

The pitching moment due to an activated nose strake are considerably higher than the induced rolling moments Fig. 12, but are still within the margin that can be controlled by the elevator.

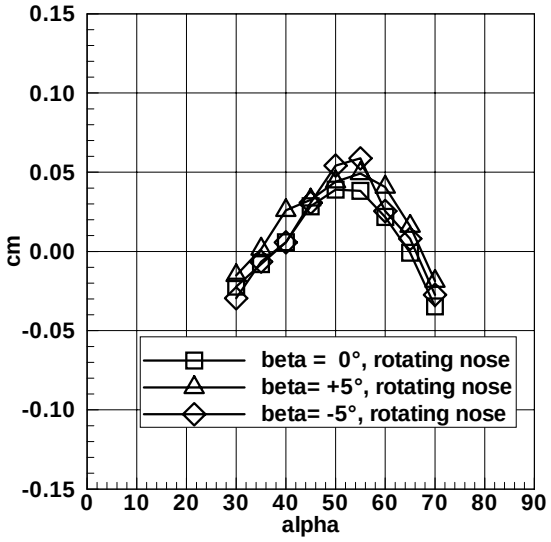


Fig. 12: Induced pitching moment due to a strake

Another possible application of nose strakes, besides yaw control in the high alpha range, is the potential for spin recovery, especially the recovery from a flat spin. Aerodynamic control devices like the rudder are of little use due to separated flow and in most cases a chute is required for spin recovery. However, the forward section of the fuselage encounters a very high relative flow angle at which the nose strakes can be used to produce adverse yawing moments to slow down and stop the rotating movement of the aircraft. As shown in Tab. 2, the yawing moment produced by the strake should be sufficient to recover an X-31-like aircraft.

Tab. 2: X-31 Mass and Inertia Data

Wing surface *S*	21.024	m²
Wing half span *b/2*	3.480	m
Mass *m*	6067.807	kg
Inertia moment x-axis I_{xx}	4465.346	kg· m²
Inertia moment y-axis I_{yy}	48137.355	kg· m²
Inertia moment z-axis I_{zz}	49049.676	kg· m²
Inertia moment fan	3.375	kg· m²
Thrust vector angle σ	0.	deg
Altitude *H*	MSL	m
Spin rate ω_z	80	deg/s
Radial velocity at nose tip v_r	10.22	m/s
Sink rate v_z	75 - 100	m/s
Dynamic pressure *q*	3509 - 6189	Pa
Local flow angle at nose tip α_r	80 - 82	deg
Yawing moment coefficient C_N	0.3 - 0.2	-

For the maximum load condition, the yawing moment due to a deployed nose strake which is rotated to its optimum position is

$$N = C_N \cdot q \cdot S \cdot \frac{b}{2} = 90561\ Nm \ .$$

Assuming that the moments are decoupled, the damping rate around the z-axis computes to

$$\dot{\omega}_z = \frac{N}{I_{zz}} = \frac{90561}{49049} = 1.85\ rad/s^2 \approx 106\ deg/s^2 \ .$$

A comparison with an assumed flat spin rate of ω_z = 80 deg/s shows, that complete spin recovery is achievable already after 0.75 s or less than one rotation around the z-axis.

4. Summary

A nose rotating around its longitudinal axis, with a fixed or deployable strake can be used as a precise steering device, similar to a rudder to achieve yaw control at angles of attack which have been previously reserved to aircraft featuring thrust vector control. During a series of static and dynamic force and pressure measurements, the optimum radial position of the strake was determined as a function of angle of attack and sideslip. The influence of the nose strake on coupled moments, i.e. rolling moment and pitching moment was measured. It became obvious that at higher angles of attack, not only the efficiency of the nose strakes was higher than that of a conventional rudder with respect to yaw control, but also for large parts of the flight envelope, a linear dependency of the achievable yawing moment as a function of the radial position of the strake was apparent. This is very remarkable, insofar as the tested micro-strakes are of very limited size, approximately 3.5 square inches or 0.002 m². In a subsequent step, it should be considered to integrate this concept as an additional steering device into a testbed, capable of controlled flight in the post-stall region, e.g. the X-31.

Acknowledgements

The results presented in this paper were achieved under a research contract granted by the BWB, Koblenz, Germany to DaimlerChrysler Aerospace AG, München.

References

[1] Bihrle W.: *Description of the LAMP facility Neuburg, FRG*, personal communications, 1996

[2] Ericsson L.E.: *Fluid/Motion Couplin in Conceptional Spermaneuvers*, AIAA 96-0787

[3] Klute S.M., Telionis D.P.: *The unsteady characteristics of the flow over an F/A-18 at high alpha*, AIAA 96-824

[4] Fisher D.F., Cobleigh B.R.: *Contolling Forebody Asymmetrics in Flight - Experience with Boundary Layer Transition Strips*, NASA-TM-4595, July 1994

[5] Malcolm G.N.: *Forebody Vortex Control*, AGARD-R-776-6

[6] Malcolm G.N., Ng T.T., Lewis L.C.: *Development of non-conventional control methods for high angle of attack using vortex manipulation*, AGARD-CP-465

[7] Malcolm G.N., Ng T.T.: *Aerodynamic Control of Fighter Aircraft by Manipulation of Forebody Vortices*, AGARD-CP-497-15

[8] Ng. T.T., Malcolm G.N: *Aerodynamic Control Using Forebody Strakes*, AIAA-91-0618

[9] Phillips E.H.: *F/A-18 HARV Exploits Forebody Controls*, Aviation Week & Space Technolgy, Nov. 20, 1995

Paper #21

Q by Dr. John E. Lamar: Has the author considered mounting nose strake on a nose boom? Nose strake parameters of size and aspect ratio were considered. What about strake Leading Edge shaping?

A. (Dr. P.R. Hakenesch): No, as it was intended for production in which the nose boom may not be present; also, radar across section could be a problem with a nose boom and strake. Due to limits of time and money constraints, only one shaping was considered; but it should/could be.

Active Control of Forebody Vortices on a Schematic Aircraft Model

R. Lee* and R. J. Kind†
Carleton University, 1125 Colonel-By-Drive Ottawa
Ontario, Canada K1S 5B6

E. S. Hanff‡
National Research Council, Ottawa, Ontario, Canada K1A 0R6

A wind-tunnel experiment has been performed to further investigate the potential of the dynamic manipulation of forebody vortices as a means of supplementing directional control of fighter aircraft at high angles of attack. Tests were conducted on a 65-deg delta-wing model fitted with a slender, pointed tangent-ogive forebody of circular cross-section. Forward-blowing nozzles located near the apex of the forebody served as the means of perturbing the forebody vortices. Results have shown that a linear relationship exists between the time-average yawing moment coefficient and a duty cycle parameter. These results, however, are accompanied by a peculiar reversal of yawing moment and side force that occurs when the blowing momentum exceeds a particular threshold value. Cross-coupling effects were also identified between the control method and time-average rolling moment, pitching moment, and normal force.

Nomenclature

b	wing span
c	mean geometric chord
$\overline{C}_\ell$	time-average rolling moment coefficient, $(1/n\sum_1^n \mathscr{L})/q_\infty S\, b$
$\overline{C}_m$	time-average pitching moment coefficient, $(1/n\sum_1^n M)/q_\infty S\, c$
$\overline{C}_n$	time-average yawing moment coefficient, $(1/n\sum_1^n N)/q_\infty S\, b$
$\overline{C}_Y$	time-average side force coefficient, $(1/n\sum_1^n Y)/q_\infty S$
$\overline{C}_Z$	time-average normal force coefficient, $(1/n\sum_1^n Z)/q_\infty S$
C_μ	coefficient of blowing momentum, $\dot{m}_j V_j/q_\infty S$ (positive for starboard blowing)
d	nozzle diameter
D	base diameter of forebody shell
L	total length of model
$\dot{m}_j$	nozzle mass flowrate, $\rho\pi d^2 V_j/4$
n	number of sample points within an ensemble-averaged record
q_∞	freestream dynamic pressure, $\rho {V_\infty}^2/2$
R	forebody cross-sectional radius at x
Re_D	Reynolds number, $V_\infty D/\nu$
S	wing reference area
T	period of an alternating blowing cycle
V_∞	freestream velocity
V_j	blowing velocity at nozzle exit
x_n	longitudinal location of nozzle exit relative to the nose apex
α	angle of attack
β	angle of sideslip
θ	azimuthal location of nozzle exit relative to the windward meridian
τ	duration a valve is open during the alternating blowing cycle
ω	angular frequency of alternating blowing
ω^*	reduced frequency of alternating blowing, $\omega D/V_\infty$

*Graduate Student, Dept. of Mechanical and Aerospace Engineering.
†Professor, Dept. of Mechanical and Aerospace Engineering.
‡Senior Research Officer, Aerodynamics Laboratory.

Introduction

The manipulation of forebody vortices has been recognized as a possible means for augmenting directional control of high-performance aircraft maneuvering in the post-stall flight regime. The approach is attractive for flight control at high angles of attack as it permits the generation of large side forces and yawing moments when the vertical tail(s) has lost its effectiveness.

Several techniques of manipulating the forebody vortices have been investigated.[1,2] Most methods are essentially steady schemes producing quasi-steady loads by forcing the forebody vortices into desired positions with respect to the forebody. To overcome the inherent bi-stability of the forebody vortices that prevails over a significant range of angles of attack, steady methods involve first forcing the vortices to adopt a symmetrical stance, typically by choosing an appropriate forebody geometry. Desired side forces and yawing moments are then generated by coercing the vortices into an asymmetric orientation by either pneumatic or mechanical means. The need to overcome the artifically induced symmetry may require considerable control power. Furthermore, it is difficult to implement suitable control laws due to the severely non-linear response of the vortices, and thus resulting loads, to the control variable.

Principle of Dynamic Vortex Manipulation

This paper outlines an active, oscillatory, vortex control scheme that has the potential to overcome the

Paper presented at the RTO AVT Symposium on "Active Control Technology for Enhanced Performance Operational Capabilities of Military Aircraft, Land Vehicles and Sea Vehicles", held in Braunschweig, Germany, 8-11 May 2000, and published in RTO MP-051.

problems associated with steady control methods. The principle is illustrated in Fig. 1. Unlike the steady methods, this scheme takes advantage of the bi-stable nature of the forebody vortices and makes use of the widely known fact that minute disturbances to the flow in the vicinity of the forebody tip can cause the forebody vortices to switch between their two stable states. Specifically, the scheme requires the forebody vortices to be deliberately switched, back and forth, between the two stable states at a sufficiently high frequency that the inertia of the aircraft prevents it from responding to the instantaneous loads. The aircraft would, however, respond to the time-average load which is controlled by varying the fraction (τ/T) of the switching-cycle period during which the vortices are in one state or the other. Load modulation is accomplished with intermittent perturbations of fixed intensity as opposed to variable intensity (of nozzle or slot flow rates, or strake deflection) which is required with steady schemes. Ideally the side force and yawing moment for steady port blowing (τ/T=100%) would be equal and opposite to that for steady starboard blowing (τ/T=0%). Then for oscillatory blowing the time-average side force and yawing moment would vary linearly with τ/T, being zero at τ/T=50%, as shown in Fig. 1(b).

The deliberate flow perturbation can be implemented by either pneumatic or mechanical means.

Previous Work

The investigation of this vortex control scheme began with water-tunnel experiments.[3] The model used in these early experiments was an ogive-cylinder with an included apex angle of 60 deg. A hydrodynamic means was used to perturb the vortices. The ogive forebody was fitted with two forward-facing, surface-flush nozzles symmetrically placed near the tip. 'Blowing' fluid could be supplied to either nozzle. By switching the blowing back and forth between the two nozzles it was found that a very low blowing coefficient ($C_\mu = 0.0013$) was sufficient to reliably switch the forebody vortices from one stable configuration to the other at a reasonably high reduced frequency ($\omega^* = 0.16$). Having established that the forebody vortices would respond to oscillatory forward-blowing, the next phase in the investigation was to determine the variation of the time-average side force and yawing moment as a function of blowing duty cycle parameter, τ/T. Scaled up tests were performed in a wind tunnel using a version of the water-tunnel model.[4] Forward-blowing nozzles were again used as the perturbation method. Figure 2 shows the key results from these experiments. Note the linear variation of time-average yawing moment and side force coefficients with duty cycle for any particular angle of attack, α. Only for $\alpha = 70$ deg is there some non-linearity. Note also, however, that the variation with α is highly non-linear reflecting the influence of α on the forebody vortex behaviour for steady or zero blowing (i.e., no vortices, symmetric vortices, asymmetric vortices for low, moderate and high α, respectively). The sign reversal of $\overline{C}_n$ in Fig. 2 indicates that the center of pressure moves aft of the moment reference point for $\alpha = 40$ deg.

The present paper focusses on work performed in subsequent wind-tunnel tests using a schematic aircraft model. The main objective of these tests was to ascertain whether the excellent results obtained on the simple ogive-cylinder models could be replicated on a more realistic aircraft-like configuration.

Experimental Setup

The investigation was conducted in the 2m × 3m low-speed, closed circuit wind tunnel at the National Research Council of Canada.

Model

The schematic aircraft model used in these experiments, Fig. 3, features a 65 deg delta-wing, a vertical tail, and a long slender forebody. This model was originally designed for dynamic wind-tunnel experiments at high roll and pitch rates. The forebody of the model has a circular cross-section and a tangent-ogive profile with an apex semi-angle of 12.8 deg. Once again forward blowing was used as the vortex perturbation method. The forebody was designed to accept interchangeable tips so that a series of nozzle locations could be readily tested. Emphasis was placed on locating the nozzle exits closer to the apex than in the previous tests in order to enhance blowing effectiveness. As shown in Fig. 4, the removable tip is 6.35cm long, containing symmetrically-placed nozzles oriented parallel to the forebody axis of revolution. The nozzles have a diameter of 1.52mm ($d/D = 0.0191$), which was found to be the smallest possible size that could be drilled without significant deviation of the drill path.

The redesign of the model's forebody also involved the installation of a blowing system within its cavity. The system comprised two miniature soleniod on/off pneumatic valves to control the flow to the nozzles, two flow metering orifices in series with the delivery ports of the valves, and the tubes that delivered the air to the nozzles in the tip. A differential pressure transducer was placed across each metering orifice to measure the flow on the basis of a calibration of the pressure drop as a function of volume flow rate, which was measured with a rotameter-type flow meter. The valves were fed with regulated shop air via a supply tube carried inside the support assembly and hollow balance. The valves were controlled by the data acquisition system.

Model Support

The model was sting-mounted on a vertical strut attached to turntables located in the floor and ceiling of the test section. The turntables were used to set the body inclination relative to the freestream, see

Fig. 5. The sting and model could be rolled such that combinations of turntable angle and roll angle could produce a range of angles-of-attack and sideslip. An internal five-component balance (no axial force) measured aerodynamic forces and moments in the body axes. A blockage correction was applied to the dynamic pressure using the simple 1/4-area ratio.[5]

Data Acquisition

Balance and pressure data (from the nozzle blowing system) were acquired by a computer featuring a real-time UNIX operating system and equipped with a high-performance digital signal processing (DSP) module. The DSP module included a 16-channel A/D converter board with a sampling rate of 150 kHz per channel. Ten channels were used to acquire balance data, pressure data and the solenoid-valve drive waveforms. The data acquisition process was synchronized with the valve drive waveforms and ensemble-averages over many blowing cycles were taken to minimize the effect of noise. The data acquisition system also generated the valve drive waveforms. Time-average results for moments and forces are the arithmetic mean of the respective ensemble-average waveform.

Validation of the complete system was achieved by comparing loads (without blowing) with those acquired for the same model and test conditions in a previous test in a different facility. The results agreed very well.

Limitations

A preliminary wind-tunnel entry revealed a serious vibration condition in which the model entered into a diverging lateral oscillation in its yaw plane at the resonance frequency of the model-support system. This was encountered frequently. A pattern in the combination of angle of attack and freestream velocity could not be detected, however, the tendency of the model to vibrate was reduced at lower freestream velocities. The source of excitation was suspected to be a positive feedback between the motion-induced sideslip, which may have switched the vortices, and the resulting change in side force. This appeared to be confirmed by the fact that blowing high-pressure air through one nozzle alleviated the vibration, presumably by preventing further switching of the vortex positions. It is important to note that the vibration problem is an artifact of these experiments as it results from the presence of a rather high frequency resonance due to the model-support stiffness. Such a resonance would be unlikely in free flight because the reduced frequency of normal modes, such as Dutch roll, of the aircraft would be much lower. Nevertheless designers should beware of possible coupling with modes of the flight control system. An emergency system was subsequently put in place that automatically applied the necessary steady blowing once the amplitude of the vibration, as sensed by suitably oriented accelerometers mounted on the platform of the above mentioned blowing system, exceeded a prescribed threshold. This emergency measure proved to be very successful in suppressing the oscillation in the vast majority of cases. It is interesting to note that the model displayed a lesser tendency to vibrate when the tips with nozzles located closest to the apex, were installed. This suggests that the nozzle cutouts in the vicinity of the apex tended to stabilize the forebody vortices by providing an edge that fixed flow separation. As a consequence of the vibration problem, the majority of the test cases were limited to a freestream velocity of 18.3 or 36.6 m/s. This prevented the study of behaviour at Reynolds number, Re_D, above 2.0×10^5.

Results and Discussion

Results are presented in non-dimensional form as coefficients of time-average yawing moment ($\overline{C}_n$), pitching moment ($\overline{C}_m$), rolling moment ($\overline{C}_\ell$), side force ($\overline{C}_Y$) and normal force ($\overline{C}_Z$). The uncertainties in these measurements are estimated to be ± 0.0015, ± 0.0065, ± 0.002, ± 0.035, and ± 0.025 respectively. The sign convention for the moments and forces, and all aerodynamic angles are shown in Fig. 3. Results for Tip 6-1 ($x_n/D = 0.095$, $\theta = 120$ deg) are presented for a freestream velocity of 36.6 m/s, except in Figs. 8 and 9.

The coefficient of blowing momentum is considered positive when air is applied through the starboard nozzle, and negative through the port nozzle. Nozzle blowing was always asymmetric, that is, blowing was applied to either the starboard or port nozzle, not to both simultaneously. The uncertainty in C_μ is about ± 0.0001.

Typical Result of Dynamic Blowing

Figure 6 shows a typical response of time-average moments and forces to duty cycle for $\alpha = 45$ deg. The symmetry and linearity in the variation of $\overline{C}_n$ is considered to be very good. The magnitudes of $\overline{C}_n$ under steady blowing conditions (τ/T=0 and 100%) compare very well with each other; for τ/T=50%, $\overline{C}_n$ is not precisely zero, but at only 3% of the largest value under steady blowing conditions, the result is considered to be reasonable. The results for $\overline{C}_n$ conform to expectations (Fig. 1) and to the previous results with the ogive-cylinder model (Fig. 2). The variation of $\overline{C}_Y$ is somewhat non-linear but note the low values, and thus degraded measurement accuracy, compared with the normal force, $\overline{C}_Z$. The principal difference from the previous results (Fig. 2) is the reversed slope of the linear variation. The cause of this will be discussed later.

Preliminary measurements were performed in order to obtain an estimate of the response time of the forebody vortices to the deliberate perturbations. Unfortunately results were insufficiently reliable to enable

an estimate to be made.

A cross-coupling effect between forebody vortex control and rolling moment is revealed by the linear variation of $\overline{C}_\ell$ with duty cycle, Fig. 6(e). This effect is thought to arise from the potential of a forebody vortex to strongly influence a wing leading-edge vortex.[6,7] The linearity of $\overline{C}_\ell$ is distorted somewhat at duty cycle values below 20% and above 80%. An examination of the instantaneous data indicates that the local non-linearity is due to a 'cutoff' of the instantaneous rolling moment as the vortices are switched, i.e., there is not enough time for the rolling moment to reach the magnitude arising from the other vortex orientation, before being forced to change back again. This non-linearity would disappear at lower reduced frequencies. Although $\overline{C}_\ell$ is not precisely zero at 50% duty cycle, it is much less than for no-blowing conditions (natural vortex asymmetry). This result confirms an earlier finding[6] that alternating blowing using a 50% duty cycle has the potential to eliminate asymmetric rolling moments due to forebody vortex asymmetry. Note that the rolling moment is positive when yawing moment is positive, and vice versa, a favourable juxtaposition for maneuvering.

The variation of τ/T was found to have a small effect on $\overline{C}_m$ and $\overline{C}_Z$. For $\alpha=45$ deg, as in Fig. 6(c) and (d), the nominal zero-blowing values of $\overline{C}_m$ and $\overline{C}_Z$ are 0.011 and 1.464 respectively, only a little lower than some values seen in Fig. 6 for dynamic blowing. The small magnitude of $\overline{C}_m$ indicates that the center of pressure for $\overline{C}_Z$ is close to the moment reference center. Furthermore, the variation in $\overline{C}_m$ is slight, signifying that the center of pressure has a very small range of movement. The small travel and close proximity of the center of pressure to the reference center are strong indicators that the increase in $\overline{C}_Z$, with dynamic blowing, is the result of an increased contribution by the wing rather than the forebody. As will be seen later, the switching of the forebody vortices causes a definitive increase in the normal force at lower angles of attack.

Effect of C_μ

The effect of C_μ on the time-average static yawing moment and side force is depicted in Fig. 7. The response of $\overline{C}_n$ and $\overline{C}_Y$ to C_μ are comparable although the side force results are thought to be affected by additional side forces unrelated to blowing, acting near the moment reference center. Examining the yawing moment response, it is seen that as negative (port) blowing momentum increases from zero, $\overline{C}_n$ remains reasonably constant at the baseline magnitude. Positive $\overline{C}_n$ signifies that the port vortex is situated farther above the forebody than the starboard vortex. However at $C_\mu \simeq -0.0013$, $\overline{C}_n$ begins to decrease rapidly until at $C_\mu \simeq -0.0025$, $\overline{C}_n$ has changed sign and stabilized at -0.075, nearly the same magnitude as before the change in sign. Clearly the arrangement of the vortices has switched from one stable state to the other. The 'reversal' of sign is also observed for positive C_μ, i.e., $\overline{C}_n$ changes from negative to positive at approximately the same magnitude of C_μ. It is noteworthy that very little blowing ($C_\mu \simeq 0.0004$) is required to switch the vortices away from their zero-blowing arrangement which happens to be that which gives positive $\overline{C}_n$ for the present model. Generally the magnitude of $\overline{C}_n$ is approximately the same before and after the reversal for either starboard or port blowing. Surface flow visualization conducted in the wind tunnel, supported by off-surface flow visualization using the forebody only in a water tunnel, verified the switching of the vortex arrangement as the magnitude of C_μ surpassed a threshold value. Also, in the water tunnel, it was observed that the reversal coincided with the blowing jet penetrating through the shear layer into the freestream flow. All dynamic blowing results presented in this paper are associated with a value of C_μ beyond the reversal threshold.

This reversal phenomenon could be undesirable from a flight control perspective. It is not perceived to be a serious problem with the present control scheme, however, as a C_μ magnitude significantly above the threshold, or below, could be used for dynamic blowing.

Effect of Angle of Attack

As seen in Fig. 8 the variation of $\overline{C}_n$ and $\overline{C}_\ell$ with duty cycle is reasonably linear as the angle-of-attack is changed. It is evident in Fig. 8 that for α below the onset value for forebody vortex asymmetry $\overline{C}_n$ is very small and essentially independent of the blowing duty cycle. This is obviously not a problem as at such low angles-of-attack the rudder has sufficient control authority. As α increases and vortex asymmetry develops, the slope of the linear variation of $\overline{C}_n$ also increases. For $\alpha>45$ deg the slope decreases from its maximum, reflecting the variation of $\overline{C}_n$ with α for steady blowing. The behaviour of $\overline{C}_\ell$ is similar. The slope of $\overline{C}_\ell$ versus τ/T becomes nearly zero by $\alpha=55$ deg. Time-average side force is very small and trends in the data are thus ambiguous due to poor signal-to-noise ratio. For C_μ within the reversal range, the results for $\overline{C}_n$ show less linearity and less symmetry between steady port and starboard blowing conditions.

The results for time-average normal force show an interesting gain in $\overline{C}_Z$ at some α values for alternating blowing as opposed to steady blowing. This is particularly evident for $\alpha=35$ deg and $\tau/T=50\%$, where the increase is about 15%. At that condition $\overline{C}_n$ and $\overline{C}_\ell$ are small or zero indicating that the increase in $\overline{C}_Z$ is not accompanied by ancillary effects in the other axes. It appears that this effect results from the influence of the forebody vortices on the leading-edge

vortex breakdown locations, which largely depends on the relative position of the corresponding vortices on each side. Under alternating blowing conditions, the varying interaction between the forebody and leading-edge vortices leads to a corresponding modulation of the latter's breakdown locations. It is known however, that the aft propagation speed of breakdown is considerably higher than its forward propagation speed,[8] thus, under dynamic conditions, the average location of breakdown is further aft than the corresponding static value, leading to the observed increase in normal force.

Effect of Reduced Frequency

The frequency of alternating blowing is an important parameter in the dynamic manipulation of forebody vortices. Forcing the vortices to switch at the highest frequency practicable will reduce the amplitude of oscillation of the aircraft. Conceivably, a reduced amplitude should ease pilot fatigue – a serious concern in view of the vibratory nature of the technique – and improve the pilot's ability to target weapons. Conversely, operation at a higher frequency would exacerbate possible structural fatiguing of the forebody.

Figure 9 presents results for three reduced frequencies ranging from $\omega^* = 0.16$ to 0.48. For $V_\infty = 18.3$ m/s, this change in ω^* translates into a frequency increase from 5.8 to 17.5 Hz. The linearity of the variation of $\overline{C}_n$ with duty cycle has remained intact with the increase of ω^*. This indicates that the vortices have no difficulty switching back and forth even at the highest ω^*, implying that the vortex response time is much less than the period, T, of the alternating blowing cycle, even at $\omega^* = 0.48$. Time-average pitching moment, normal force, and rolling moment all exhibit some response to changes in the reduced frequency. This is thought to be due to the phenomenon discussed in the preceding section. The behaviour is evidently rather complex as the trends seen in Fig. 9 are not monotonic with increasing ω^*. The time-average side force coefficient, $\overline{C}_Y$, remains small at all values of ω^*.

Effect of Sideslip

The effect of sideslip on the variation of time-average forces and moments with duty cycle is shown in Fig. 10 for $\alpha = 45$ deg.

It is apparent that nozzle blowing continues to be effective with non-zero sideslip. The results presented are for a tip configuration that has the nozzle exits, or cutouts, as close to the apex as practicable ($x_n/D = 0.095, \theta = 120$ deg). In fact the nozzle exit is even closer to the apex than for the tip shown in Fig. 4. It is thought that the large ratio of nozzle diameter to local cross-sectional radius of the forebody is primarily responsible for the continued effectiveness with sideslip. With a large ratio, the fraction of forebody surface area removed by the nozzle cutout is significant, allowing the nozzle flow to continuously influence the local shear layer separation process, in spite of the circumferential movement of the primary separation line caused by sideslipping.

The variation of $\overline{C}_n$ remains linear with duty cycle under sideslipping conditions. In Fig. 10(a) $\partial\overline{C}_n/\partial\beta$ is negative, indicating directional instability, as would be expected at high angles of attack due to blanketing of the vertical tail. Figure 10(c) reveals a cross-coupling effect between pitching moment, $\overline{C}_m$, and duty cycle, τ/T. Specifically, sideslip gives rise to a linear variation of $\overline{C}_m$ with duty cycle. For a given sideslip angle, a duty-cycle sweep is sufficient to change the sign or sense of $\overline{C}_m$. Since $\overline{C}_Z$ is always positive this implies movement of the centre of pressure. Shifting of the centre of pressure for $\overline{C}_Z$ is probably due to a more intense influence, or lack thereof, of the forebody vortices on the upper-surface (body axis) static pressure of the forebody. For example, with a positive sideslip angle of $\beta \simeq 15$ deg and starboard blowing stronger than the reversal threshold (i.e., $C_\mu > 0.0025$ and τ/T=0%), the starboard forebody vortex is attached and crosses over close to the upper surface of the forebody thus causing a positive increment in $\overline{C}_m$ relative to the zero-sideslip, τ/T=50% datum case. On the other hand, with port blowing, τ/T=100%, the starboard vortex will be detached and will pass relatively far above the forebody, having little effect on the static pressure on the upper surface of the forebody. The static pressure will consequently be higher than the datum case, giving rise to a negative increment in $\overline{C}_m$. The conjectured behaviour illustrated by this example is precisely what is seen in Fig. 10(c). In both of these duty-cycle cases the port forebody vortex will pass relatively far from the port side of the forebody, due to the sideslip velocity component, and will thus have little influence on the forebody pressure distribution.

The rolling-moment versus τ/T curves in Fig. 10(e) are approximately parallel to one another for all values of the sideslip angle. This indicates that sideslip affects rolling moment mainly by virtue of the conventional mechanism for delta-wings, namely higher effective incidence on the upwind wing panel and lower on the leeward panel.

Concluding Remarks

A scheme for actively controlling forebody vortices to obtain linear variation of yawing moment at post-stall angles of attack has been briefly reviewed. The concept involves oscillatory perturbation of the flow-field near the forebody apex and it has the potential to overcome the problems associated with steady vortex control methods. The results of wind tunnel tests using a schematic aircraft model are presented. Using forward blowing as the means of perturbing the vortices, these tests have shown that the proposed method of control is feasible on realistic aircraft configura-

tions. Significant differences, however, exist between the current results and those obtained with an earlier ogive-cylinder model. In the most recent experiments, the signs of the time-average yawing moment and side force were found to change when the nozzle blowing momentum exceeded a certain threshold value. Linearity of $\overline{C}_n$ with duty cycle is still observed.

With an aircraft configuration, cross-coupling effects on the roll and pitch axes are to be expected and were indeed observed. A range of angle of attack, sideslip angle and reduced frequency was investigated. An intriguing result was a gain in time-average normal force that occurs with 50% duty cycle and zero sideslip. Qualitative explanations of this and other results are offered in terms of the direct effects of the forebody vortices and the significant influence that forebody vortices can exert on delta-wing leading-edge vortices.

References

[1]Malcolm, G., "Forebody Vortex Control - A Progress Review," AIAA Paper 93-3540-CP, August 1993, pp. 1082-1116.

[2]Williams, D., "A Review of Forebody Vortex Control Scenarios," AIAA Paper 97-1967, June 1997.

[3]Alexan, K., Hanff, E., and Kind, R., "Water-Tunnel Investigation of Dynamic Manipulation of Forebody Vortices," AIAA Paper 94-0503, January 1994.

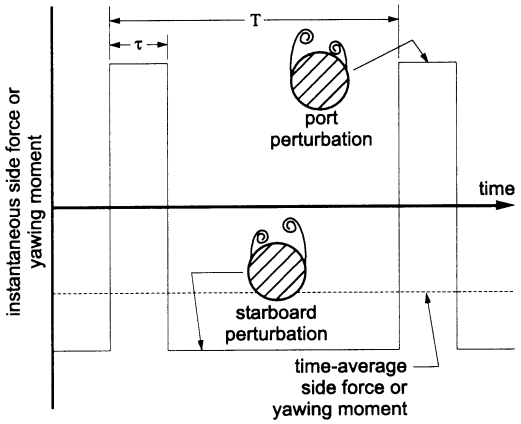
[4]Lee, R., Hanff, E., and Kind, R., "Wind-Tunnel Investigation of Dynamic Manipulation of Forebody Vortices," AIAA Paper 95-1794, June 1995.

[5]Pope, A. and Rae, W., *Low-Speed Wind Tunnel Testing*, Wiley, New York, 2nd ed., 1984.

[6]Ng, T., Suarez, C., Kramer, B., Ong, L., Ayers, B., and Malcolm, G., "Forebody Vortex Control for Wing Rock Suppression," *Journal of Aircraft*, Vol. 31, No. 2, March-April 1994, pp. 298–305.

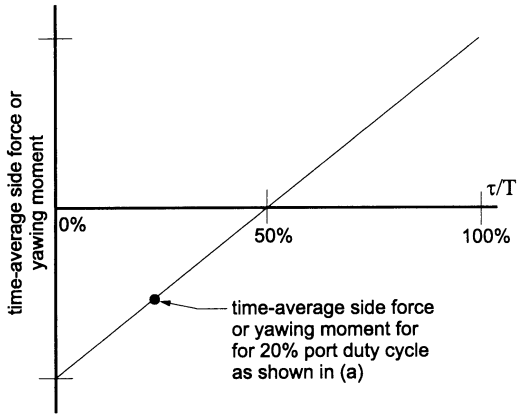
[7]Crowther, W., Hodgkin, F., and Wood, N., "Forebody Flow Control for Extended High Angle of Attack Manoeuvres," Royal Aeronautical Society Conference, High Lift and Separation Control, Paper 18, March 1995.

[8]Hanff, E. and Huang, X., "Roll-Induced Cross-Loads on a Delta Wing at High Incidence," AIAA Paper 91-3223, September 1991.



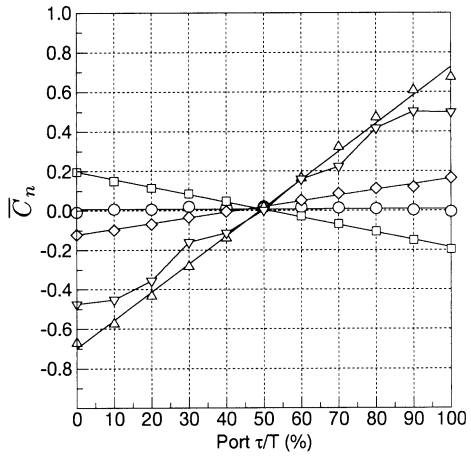
a) Idealized side force or yawing moment time-history.

Fig. 1 Principle of using dynamic manipulation of forebody vortices to control side force and yawing moment.

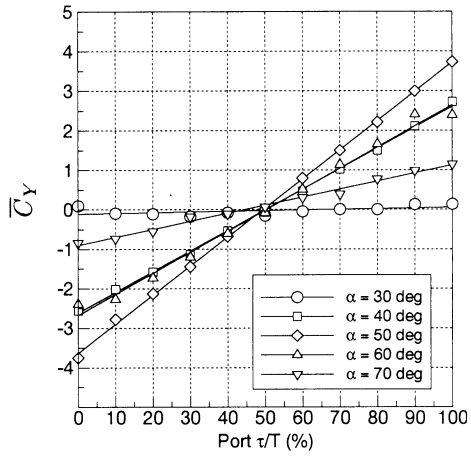


b) Expected variation of time-averge side force or yawing moment with duty cycle.

Fig. 1 (continued)



a) Yawing moment



b) Side force

Fig. 2 Variation of $\overline{C}_n$ and $\overline{C}_Y$ with duty cycle for an ogive-cylinder model. $C_\mu = 0.00066$, $Re_D = 1.76 \times 10^5$ (19.2 m/s), $\omega^* = 0.32$ (7.2 Hz), $\beta = 0$ deg. The moment reference center is $3.5D$ aft of the forebody apex. (Ref. 4)

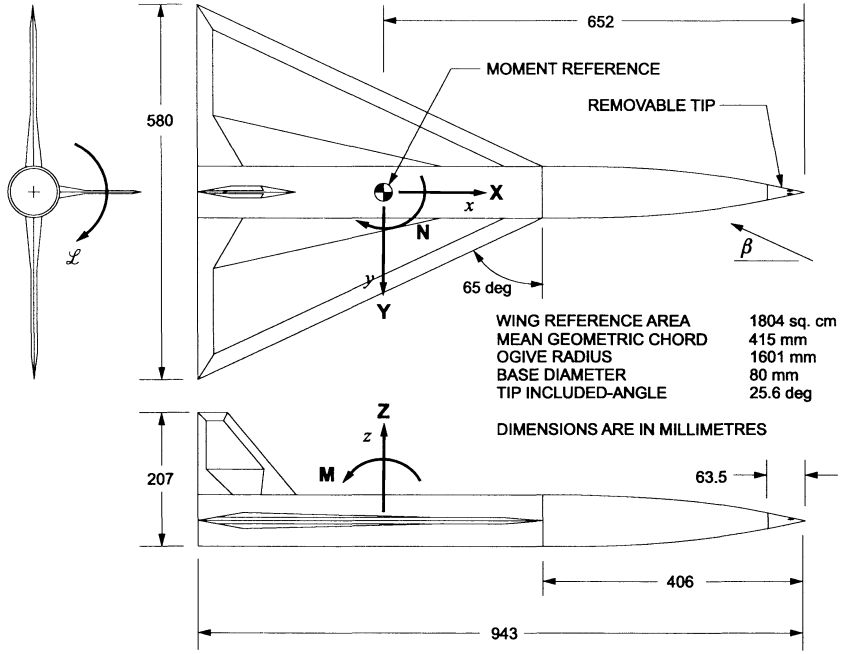


Fig. 3 65-deg delta-wing model with a long, slender forebody of circular cross-section, featuring a removable tip. Forces, moments, and angles are positive as shown.

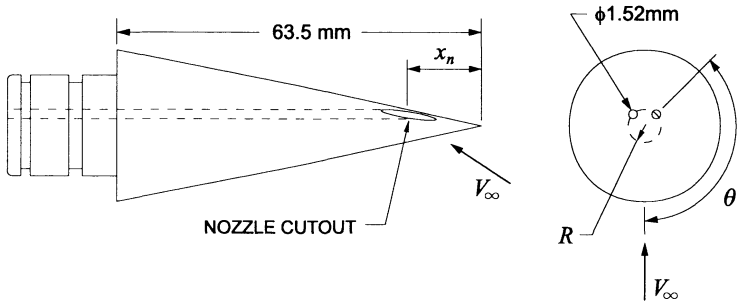


Fig. 4 Schematic of removable forebody tip.

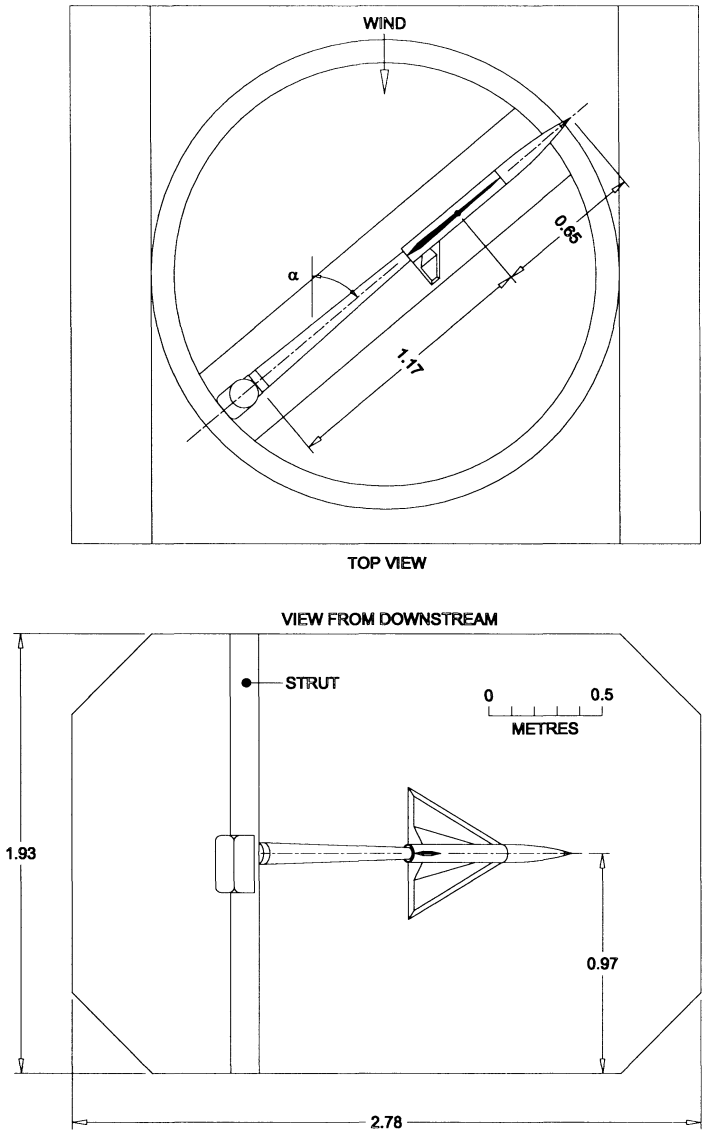
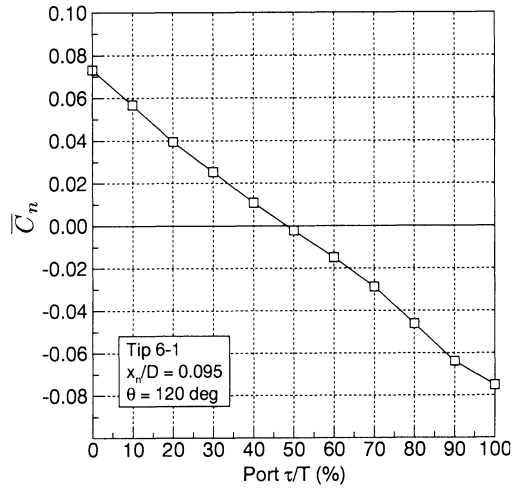
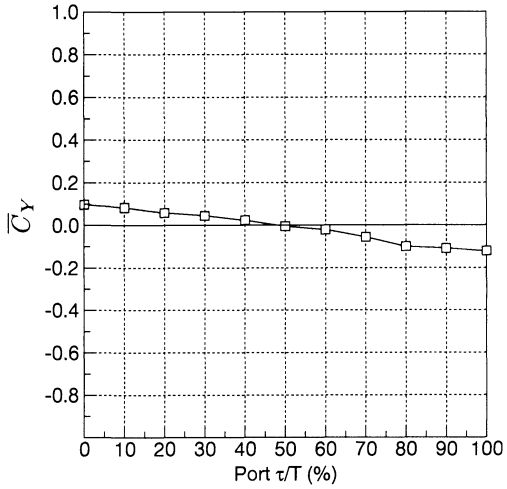


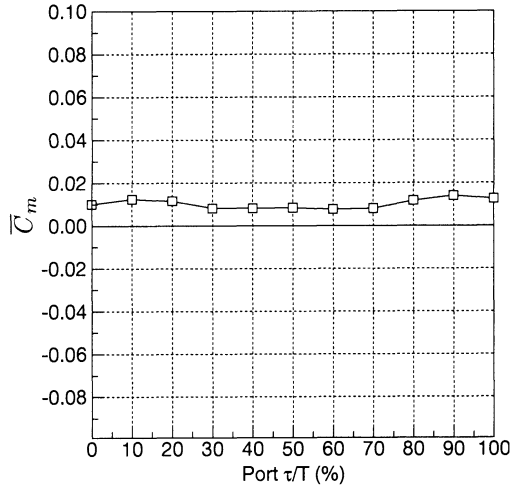
Fig. 5 Two views of the model installation in the working section of the 2m×3m wind tunnel.



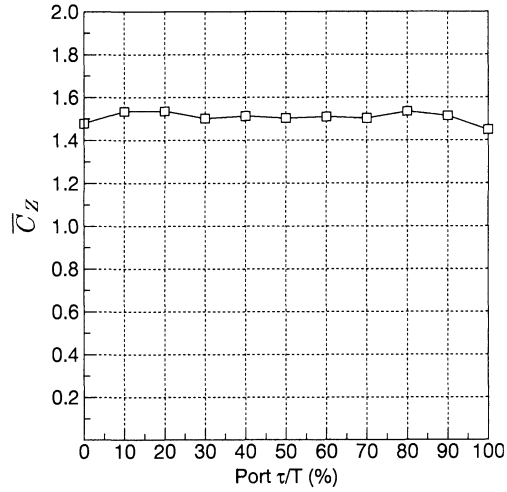
a) Yawing moment



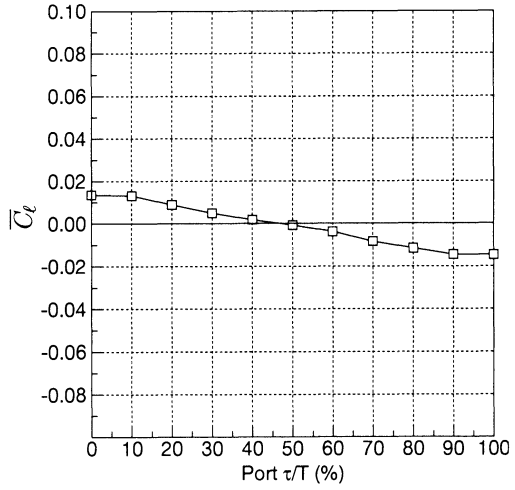
b) Side force



c) Pitching moment

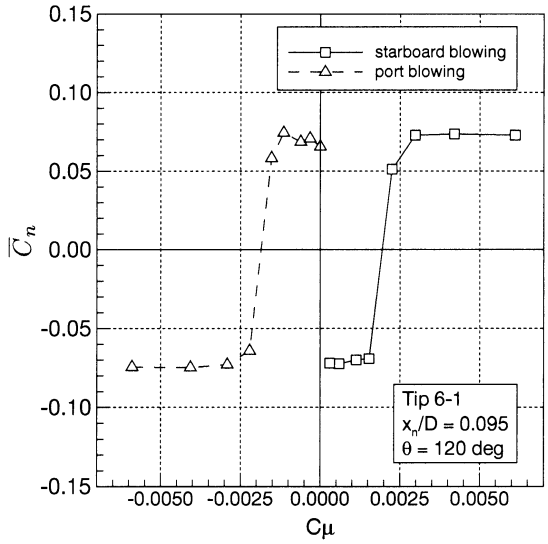


d) Normal force

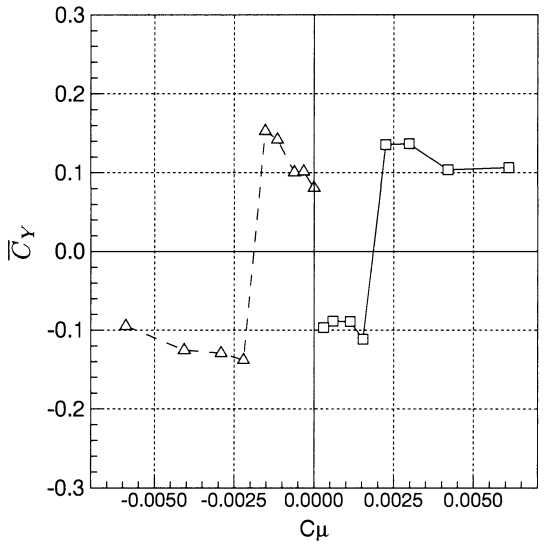


e) Rolling moment

Fig. 6 Typical variation of time-average forces and moments with duty cycle for the delta-wing model. $C_\mu = 0.00351$, $Re_D = 2.0 \times 10^5$ (36.6 m/s), $\alpha = 45$ deg, $\omega^* = 0.16$ (11.6 Hz), and $\beta = 0$ deg.

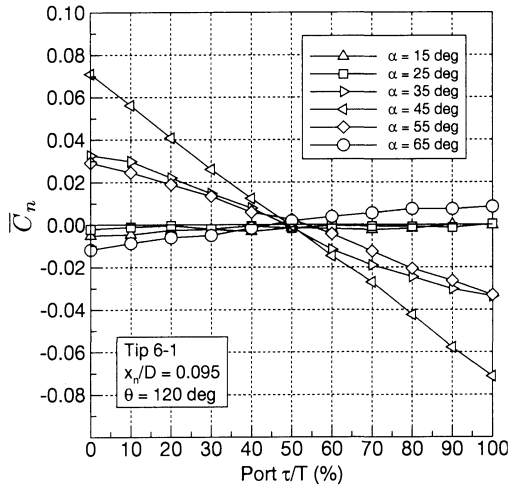


a) Yawing moment

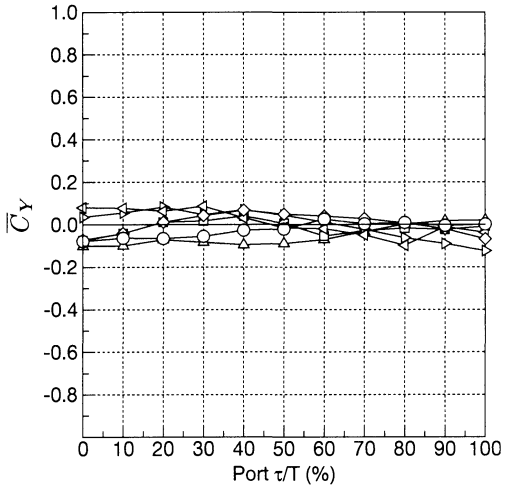


b) Side force

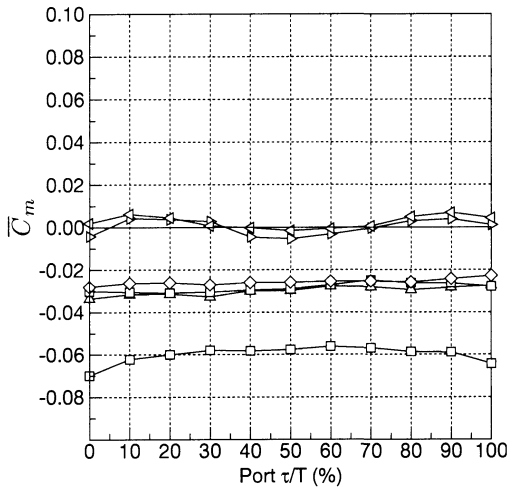
Fig. 7 Variation of time-average yawing moment and side force with blowing moment coefficient for the delta-wing model. $Re_D = 2.0 \times 10^5$ (36.6 m/s), $\alpha = 45$ deg, and $\beta = 0$ deg.



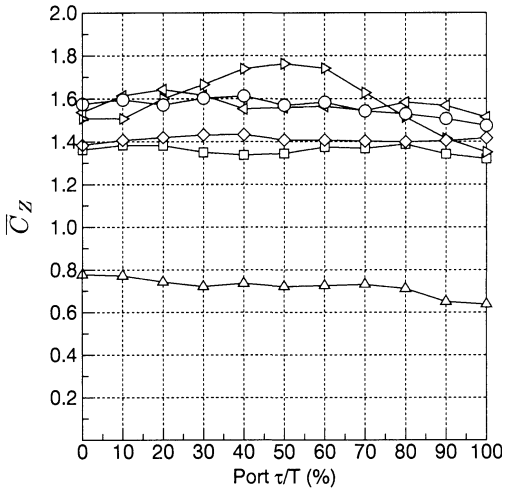
a) Yawing moment



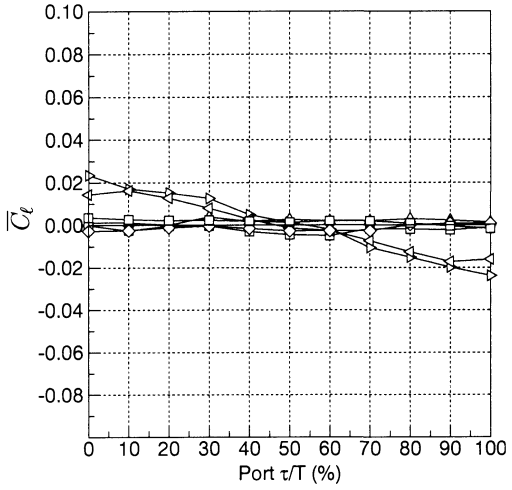
b) Side force



c) Pitching moment

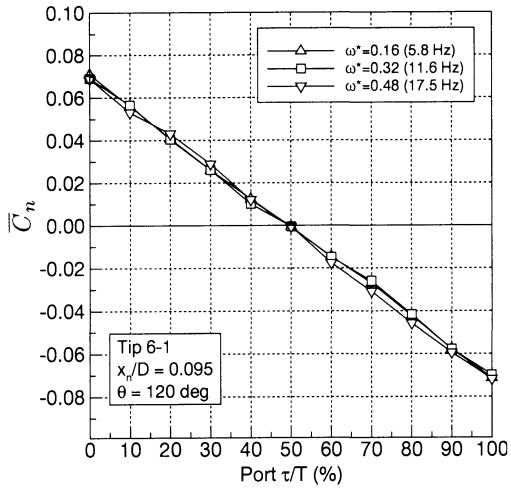


d) Normal force

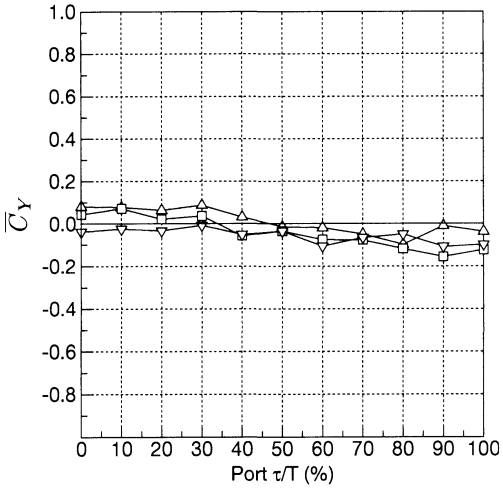


e) Rolling moment

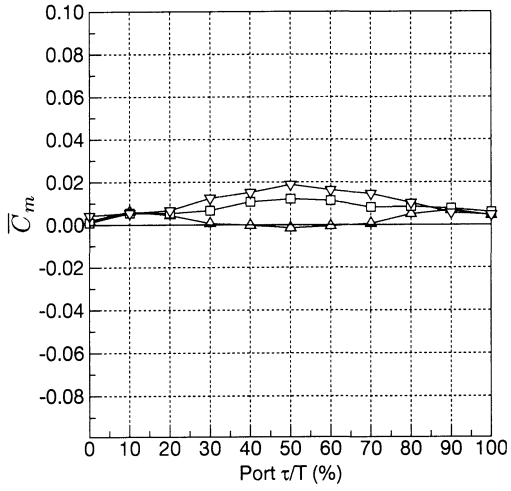
Fig. 8 Effect of angle of attack on the variation of time-average forces and moments with duty cycle for the delta-wing model. $C_\mu = 0.00686$, $Re_D = 9.8 \times 10^4$ (18.3 m/s), $\omega^* = 0.16$ (5.8 Hz), and $\beta = 0$ deg.



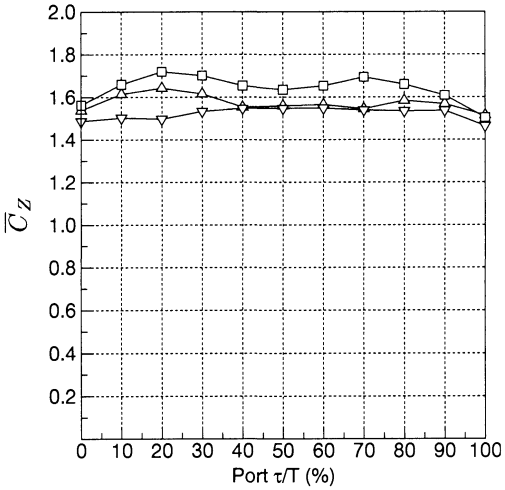
a) Yawing moment



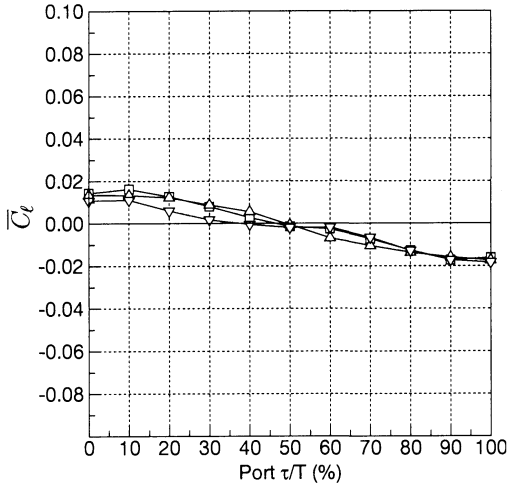
b) Side force



c) Pitching moment

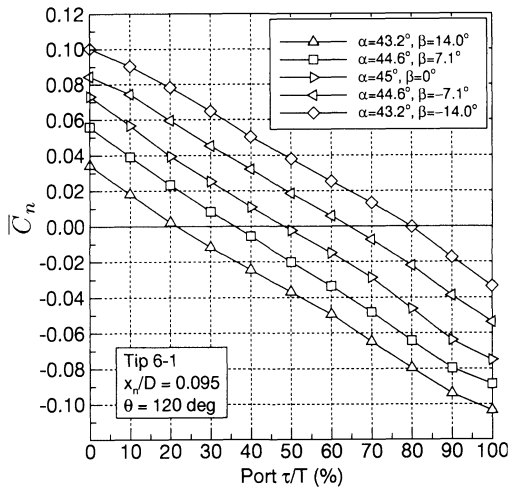


d) Normal force

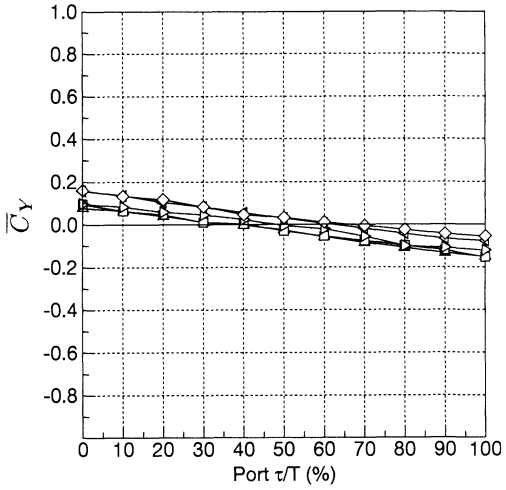


e) Rolling moment

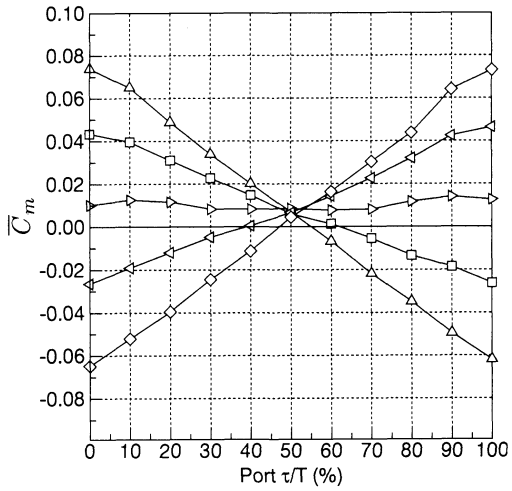
Fig. 9 Effect of reduced frequency on the variation of time-average forces and moments with duty cycle for the delta-wing model. $C_\mu = 0.00680$, $Re_D = 9.8 \times 10^4$ (18.3 m/s), $\alpha = 45$ deg, and $\beta = 0$ deg.



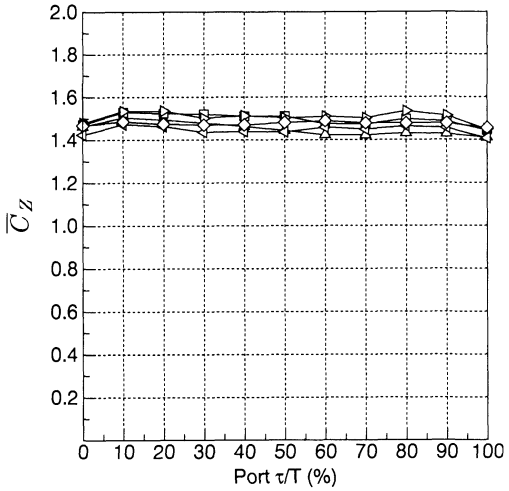
a) Yawing moment



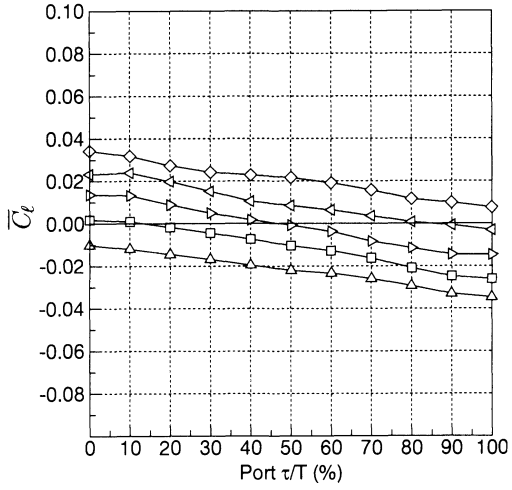
b) Side force



c) Pitching moment



d) Normal force



e) Rolling moment

Fig. 10 Effect of sideslip on the variation of time-average forces and moments with duty cycle for the delta-wing model. $C_\mu = 0.00351$, $Re_D = 2.0 \times 10^5$ (36.6 m/s), $\alpha \simeq 45$ deg, and $\omega^* = 0.16$ (11.6 Hz).

¶

Paper #22

Q, by David Moorhouse: Your results showed a linear relationship with blowing, but sensitivity and even reversal with angle of attack. This would be a problem using the results in a full-scale application, would you like to comment.

A (R. Kind): We believe that there is still much wind tunnel testing required before full scale testing would be appropriate. In particular, we need to develop a better understanding of the 'reversal' phenomenon and of the conditions under which it occurs and possibly how to avoid it or best deal with it. Also behaviour of the scheme needs to be explored at much higher Reynolds numbers than the maximum values reached to date. In addition, tests should be done at higher reduced frequencies because we have not yet reached the maximum reduced frequency at which the scheme still works.

Q, by F.R. Grosche: Can you tell us why you chose forward blowing to influence the vortex system?

A (R. Kind): This was an intuitive choice. I had worked on circulation control early in my career; consequently I appreciated that very modest amounts of blowing could be used to influence flow separation and thus cause quite dramatic changes in flow fields and the associated forces and moments. Also we felt that blowing would be easier to implement in practice than suction.

This page has been deliberately left blank

Page intentionnellement blanche

Contrôle actif de l'écoulement autour d'une pointe avant à grande incidence.

C. FRANCOIS
Office National d'Études et de Recherches Aérospatiales
29 Avenue de la Division Leclerc - 92322 Châtillon – FRANCE

RÉSUMÉ

Dans le cadre du projet de recherches fédérateur « Contrôle Actif des Ecoulements » mené à l'ONERA, une étude a été effectuée pour valider le principe du contrôle en latéral d'un avion à grande incidence au moyen d'un soufflage alterné sur la pointe avant.

Des essais en soufflerie d'une maquette générique d'avant-corps ont permis de déterminer les effets de différents paramètres sur les modifications de l'organisation des tourbillons d'ogive et de choisir un mode de fonctionnement de l'actionneur nécessitant un débit modéré.

Les visualisations réalisées à grande cadence ont mis en évidence les caractéristiques dynamiques de basculement des tourbillons et des détecteurs pariétaux capables de suivre leurs évolutions en temps réel ont été sélectionnés pour pouvoir contrôler la position des lignes de décollement sur la maquette.

NOTATIONS

C_y Coefficient de force latérale

C_n Coefficient de moment de lacet

C_μ Coefficient de quantité de mouvement

$C_\mu = m_{jet} V_{jet} / (1/2\ \rho_o V_o^2 S_{jet})$

F Fréquence d'alternance du soufflage

K_p Coefficient de pression $Kp = (p-p_o)/q_o$

m_{jet} Débit du jet

L_{ref} Longueur de référence (diamètre de la base du cône) $L_{ref} = 0{,}310$ m

p_o Pression statique de l'écoulement dans la veine

q_o Pression dynamique de l'écoulement dans la veine

R_d Taux d'ouverture du jet situé à droite sens pilote

$$R_d = \frac{t_d}{T}$$

S_{ref} Surface de référence (surface de la base du cône) $S_{ref} = 0{,}07548$ m²

T Période d'alternance du soufflage

t_b Temps de basculement de la structure tourbillonnaire d'un état stable vers son opposé

t_d Temps d'ouverture du jet situé à droite sens pilote (τ sur la figure 2)

V_{jet} Vitesse du jet

V_o Vitesse de l'écoulement dans la veine

X Distance longitudinale par rapport à la pointe du cône (mm) positif vers l'aval

ϕ Angle d'azimut mesuré à partir de la génératrice basse cône, positif à droite sens pilote

1. INTRODUCTION

Parmi les activités effectuées à l'ONERA dans le cadre du projet de recherches fédérateur « Contrôle Actif des Ecoulements », le contrôle de l'écoulement tourbillonnaire sur un avant-corps d'avion d'armes à grande incidence a fait l'objet d'une contribution importante du Département d'Aérodynamique Appliquée (DAAP).

La structure de l'écoulement qui se développe autour d'un avant-corps de révolution à grande incidence est marquée par une dissymétrie des tourbillons, à l'origine d'un moment de lacet important. Dans ce domaine de vol où la dérive et la gouverne de lacet perdent leur efficacité au-delà de 35° d'incidence, il convient d'avoir recours à d'autres modes de contrôle.

Pour des raisons d'utilisation opérationnelle, un système mécanique mettant en œuvre des surfaces mobiles présente un certain nombre d'inconvénients (proximité de l'antenne radar, temps de réponse, sécurité, …). On s'est donc orienté vers un actionneur fluidique s'inspirant des travaux de Lee, Hauff et King [1] pour le soufflage axial à contre-courant.

Le principe retenu dans l'étude présentée, consiste à utiliser le caractère bi-stable de l'écoulement dissymétrique provoqué par une micropertubation localisée à l'extrême pointe. L'effort latéral résultant de cette dissymétrie peut être contrôlé en créant une perturbation alternativement à droite et à gauche, la fréquence étant suffisamment élevée pour minimiser les régimes permanents. Dans ces conditions, l'effort latéral est quasiment une fonction linéaire du taux d'alternance.

Le présent document concerne trois campagnes d'essais réalisées dans la soufflerie horizontale L1 de l'ONERA-Lille, sur une maquette schématique cône-cylindre. Ces essais avaient pour objets de valider le concept tout en optimisant les actionneurs de type fluidique, puis d'évaluer un certain nombre de détecteurs placés à la paroi dans le but de réaliser une commande en boucle fermée.

Paper presented at the RTO AVT Symposium on "Active Control Technology for Enhanced Performance Operational Capabilities of Military Aircraft, Land Vehicles and Sea Vehicles", held in Braunschweig, Germany, 8-11 May 2000, and published in RTO MP-051.

2. DESCRIPTION DE LA MAQUETTE

La maquette générique de type cône-cylindre utilisée lors de ces trois campagnes d'essais simule schématiquement un avant-corps d'avion d'armes à l'échelle ≅ ¼ .
La configuration étudiée est constituée d'un cône de 15° de demi-angle au sommet, de 578,5 mm de hauteur et 310 mm de diamètre à la base (figure 1). Ce cône est équipé de deux injecteurs de diamètre intérieur 0,9 mm, orienté vers l'amont parallèlement à l'axe longitudinal de la maquette, positionnés à 5 mm de la pointe et ± 115° d'angle d'azimut. Ils sont alimentés indépendamment l'un de l'autre au moyen de deux électrovannes miniatures commandées par ordinateur, ce qui autorise une fréquence d'alternance F maximum de 300 Hz. Ce dispositif permet de faire varier de manière continue le taux d'ouverture R_d et d'intégrer éventuellement un déphasage entre l'ouverture et la fermeture des deux électrovannes.

En aval du cône, un carénage cylindrique assure une continuité de forme et protège la balance ainsi que quelques éléments d'instrumentation. Seule la partie conique de la maquette est pesée, le carénage cylindrique étant solidaire de la tête de mât du montage.

Cette maquette est aussi équipée d'une demi-couronne de huit capteurs de pression instationnaire équirépartis, située à l'extrados à 84 mm de la pointe. Ces derniers permettent de mesurer en temps réel le delta de pression droite-gauche caractéristique de la structure dissymétrique de l'écoulement autour d'un avant-corps à grande incidence.

La maquette comprend aussi 12 films chauds positionnés comme suit :
- 4 films chauds à droite sens pilote, orientés à 75° par rapport à l'axe longitudinal de la maquette, vers l'amont et l'intrados de cette dernière, à 32 et 72 mm de la pointe, 90° et 100° d'angle d'azimut ;
- 4 films chauds à gauche sens pilote, positionnés en vis-à-vis des précédents ;
- 4 films chauds à l'extrados dans le plan de symétrie vertical de la maquette, orientés suivant l'axe longitudinal et vers l'amont, à 88, 138, 188 et 238 mm de la pointe.

Les huit premiers films chauds sont destinés à détecter le déplacement des lignes de décollement primaires droite et gauche lors du basculement de la structure tourbillonnaire, alors que les quatre autres ont pour objectif de détecter le déplacement de la ligne de recollement primaire à l'extrados.

Ces 20 « détecteurs » instationnaires doivent permettre d'opérer un choix des capteurs les plus sensibles à utiliser pour réaliser la commande en boucle fermée des deux jets.

3. MOYENS D'ESSAIS

Les essais ont été réalisés dans la soufflerie L1 de l'ONERA-Lille. Cette soufflerie de type EIFFEL à hall de retour caréné, possède une veine guidée de section circulaire, dont le diamètre et la longueur sont de 2,40 m.

La maquette est installée sur un montage en mât autorisant un déplacement de 30° à 60° en incidence et 360° en dérapage.

Les mesures effectuées concernent des pesées, des pressions pariétales (stationnaires ou instationnaires) et des tensions aux bornes des films chauds au cours de variations de paramètres tels que l'incidence de la maquette, le coefficient de quantité de mouvement C_μ, la fréquence d'alternance F ou le taux d'ouverture Rd.

L'ensemble des essais est réalisé à V_o = 20 m/s ($Re = 0{,}45.10^6$), excepté quelques essais de la première campagne effectués à V_o = 40 m/s dans le but d'étudier l'effet du nombre de Reynolds.

Des visualisations des lignes de frottement sur la maquette (enduit pariétal) et des structures tourbillonnaires (tomoscopie laser dans des plans tranverses) sont réalisées pour les configurations les plus intéressantes. Un rail de tomoscopie fixé au plafond de la veine d'essai permet de déplacer le plan laser et de l'orienter perpendiculairement à la génératrice extrados du cône. La canne de l'émetteur de fumée est placée en amont du convergent au niveau du filtre pour éviter de perturber l'écoulement autour de la maquette. La caméra est fixée au montage en aval de la maquette afin de garder une position fixe par rapport à cette dernière. Pour les essais de jets alternés droite-gauche, une caméra à acquisition rapide (1000 images/s) équipée d'un intensificateur de lumière est utilisée.

4. ANALYSE DES RÉSULTATS OBTENUS

L'écoulement autour d'un avant-corps à grande incidence présente deux états dissymétriques stables, symétriques l'un de l'autre, générant des efforts latéraux d'amplitude similaire et de signes opposés (figure 2). Une microperturbation, localisée à l'extrême pointe, est suffisante pour faire basculer la structure de l'écoulement d'un état stable vers son symétrique. L'effort latéral moyen peut donc être contrôlé en créant une perturbation alternativement à droite et à gauche, à une fréquence suffisamment élevée pour réduire les régimes permanents. Dans ces conditions, l'effort latéral moyen est une fonction quasi-linéaire du taux d'alternance.

L'objet de cette étude est donc, dans un premier temps, d'optimiser un actionneur pneumatique permettant de provoquer le basculement des structures tourbillonnaires dans un domaine incidence-dérapage le plus vaste possible, puis dans un second temps de valider le principe de contrôle de l'effort latéral par alternance. Enfin, le dernier point abordé concerne l'évaluation de « détecteurs pariétaux » permettant de suivre en temps réel l'évolution de la structure tourbillonnaire.

4.1 Optimisation des actionneurs

Dans cette première phase, la qualification de l'actionneur est réalisée par un soufflage continu du côté droit.

La pesée de la maquette avec soufflage, effectuée sans vent dans la soufflerie, a permis de vérifier que la dynalpie du jet est négligeable vis-à-vis des efforts aérodynamiques mesurés.

4.1.1 Influence de la position azimutale du jet

L'ensemble de ces essais est réalisé à V_o = 20 m/s, le coefficient de quantité de mouvement rapporté à la base du cône Cμ étant réglé à la valeur de $1{,}8.10^{-3}$.
Le soufflage axial est effectué à 5 mm de la pointe, dans une zone de décollement laminaire qui se caractérise par une ligne de séparation primaire localisée autour de 90° d'angle d'azimut. Lorsque l'injecteur est positionné à ϕ = 95°, la seule présence du trou de diamètre ∅ = 0,9 mm, sans aucun soufflage, suffit à provoquer le basculement de la structure tourbillonnaire, ce qui n'est pas l'effet recherché. En faisant varier la position azimutale de la tuyère de 105° à 135°, les résultats obtenus avec soufflage continu au cours de polaires en incidence (figure 3) montrent que :
- l'efficacité du dispositif est maintenue pour une position azimutale de la tuyère allant de 105° à 125°, ce qui laisse présager une certaine robustesse de fonctionnement vis-à-vis de la mise en dérapage de la maquette ;
- cette efficacité chute considérablement vers 135° d'azimut.

Ces essais ont aussi permis de vérifier que la dissymétrie naturelle de la maquette peut être modifiée par la position azimutale de l'extrême pointe mais que l'efficacité du dispositif ne dépend pas du comportement naturel de la pointe avant.

Pour la suite de la campagne d'essais, le soufflage axial est maintenu à l'angle d'azimut ϕ = 115°.

4.1.2 Influence du débit de soufflage

Des variations du coefficient de quantité de mouvement C_μ de 0 à $2{,}5.10^{-3}$ sont réalisées à 30°, 40°, 50° et 60° d'incidence.

Les résultats de pesées mettent en évidence deux modes de fonctionnement opposés du dispositif de soufflage axial réalisé du côté droit (figure 4). A fort débit ($C_\mu > 1{,}4.10^{-3}$), le jet agit comme un obstacle fluide, provoquant le décollement prématuré du tourbillon primaire droit. Ce dernier se positionne au-dessus du tourbillon primaire gauche, lui-même recentré à l'extrados de la maquette. Il en résulte un moment de lacet négatif. Au contraire, à faible débit ($C_\mu < 1{,}2.10^{-3}$), le jet retarde le décollement du tourbillon primaire droit. On obtient dans ce cas une structure tourbillonnaire symétrique de celle obtenu à fort débit, qui se traduit par un moment de lacet positif. Ce mode de fonctionnement pourrait s'apparenter à un effet Coanda, mais la compréhension du mécanisme mis en jeu nécessiterait une étude spécifique.

Hormis dans la phase de transition entre ces deux régimes, l'efficacité du soufflage pour un même régime de fonctionnement ne dépend pas du débit injecté. On notera ainsi l'intérêt d'opérer à de très faibles valeurs du paramètre C_μ pour minimiser l'énergie à prélever sur le moteur.

Les visualisations par tomoscopie laser réalisées dans un plan situé à X = 400 mm de la pointe (figure 5) apportent quelques précisions quant à la structure de l'écoulement tourbillonnaire dans les deux régimes identifiés.

La différence essentielle entre les deux modes de fonctionnement concerne la structure globale de l'écoulement. Alors qu'à faible débit, elle est pratiquement identique à celle de l'écoulement naturel (à la symétrie près), les différences sont plus significatives à grand débit. Le tourbillon primaire droit se retrouve dans une position plus centrale, ce qui limite le recentrage du tourbillon primaire gauche à l'extrados de la maquette et permet le développement d'un second tourbillon sur le flanc droit.

Le premier mode de fonctionnement permet de piloter le sens de la dissymétrie sans altérer la structure naturelle de l'écoulement, au contraire du second mode beaucoup plus intrusif.

L'objectif étant aussi de minimiser l'énergie nécessaire pour agir sur l'écoulement, le deuxième mode de fonctionnement est abandonné dans la suite de l'étude, le coefficient de quantité de mouvement C_μ étant fixé à $0{,}5.10^{-3}$.

4.1.3 Effet du dérapage

Pour déterminer l'effet de la mise en dérapage de la maquette sur l'efficacité de l'actionneur « jet axial », des polaires en incidence ont été réalisées à $\beta = \pm 5°$. Les résultats obtenus (figure 6) montrent que ce dispositif conserve toute son efficacité dans le domaine $-5° < \beta < 5°$ et $30° < \alpha < 60°$, confirmant la robustesse du dispositif étudié.

4.1.4 Effet du nombre de Reynolds

Les mêmes essais ont été répétés à V_o = 40 m/s dans le but d'étudier l'influence du nombre de Reynolds sur le fonctionnement du jet axial.

Dans ces conditions, le jet axial reste fonctionnel, même s'il perd un peu de son efficacité au-delà de 45° d'incidence quand il est sous le vent (figure 7).

4.2 Validation du concept de commande alternée

Le réglage de la pression génératrice donnant un coefficient de quantité de mouvement C_μ de $0{,}5.10^{-3}$ en condition de soufflage continu est conservé pour la suite de l'étude. Ces essais sont réalisées à une fréquence d'alternance F fixée à 150 Hz pour diverses valeurs du taux d'alternance des soufflages à droite et à gauche.

La figure 8 rassemble les courbes de lacet correspondant aux configurations R_d = 50%, 66 %, 75 % et 100 %. Elles mettent en évidence que le dispositif de soufflage alterné permet bien de contrôler l'effort latéral dans tout le domaine d'incidence étudié. Néanmoins, on peut constater que le réglage R_d = 66 % est nécessaire pour annuler le moment de lacet à 60° d'incidence. Ce résultat est expliqué par la différence du comportement droit et gauche de la maquette, qui augmente avec l'incidence.

Les résultats relatifs aux polaires réalisées avec ± 5° de dérapage (figure 9) confirment un comportement sain de cette « gouverne de lacet » à grande incidence.

4.3 Optimisation du dispositif de soufflage alterné

Les différents modes propres de flexion verticale et latérale de l'ensemble maquette-balance-montage ont été déterminés avec précision pour éviter tout problème. Les fréquences propres associées sont :
- 14,5 Hz, 20 Hz, 27 Hz et 33 Hz en flexion verticale ;
- 17 Hz, 27 Hz, 39 Hz, 94 Hz et 104 Hz en flexion latérale.

L'ensemble mécanique et pneumatique associé aux deux électrovannes a été étalonné afin de déterminer les temps de réponse à l'ouverture et à la fermeture par rapport au signal de commande généré par l'ordinateur. Aucun déphasage n'a été introduit entre les commandes des deux électrovannes, ces dernières ayant un fonctionnement comparable donnant des temps de réponse à l'ouverture et à la fermeture de l'ordre de 1,5 ms. La pression génératrice en amont de la boîte à col est réglée afin de fournir un coefficient de quantité de mouvement $C\mu$ en soufflage continu de $0{,}5.10^{-3}$, la vitesse de veine V_o étant de 20 m/s.

Pour ces essais réalisés à 50° et 60° d'incidence, les valeurs de fréquence d'alternance retenues sont F = 150 Hz, 100 Hz, 60 Hz, 30 Hz et 11 Hz. Les tracés du moment de lacet en fonction du taux d'ouverture R_d (figure 10) montrent que le comportement du dispositif est d'autant plus linéaire que la fréquence d'alternance est basse, la linéarité étant obtenue à 50° d'incidence.

Ce phénomène s'explique aisément. Lorsque la fréquence d'alternance F augmente, le temps t_b nécessaire au basculement des structures tourbillonnaires d'un état stable vers son opposé (temps fixe de l'ordre de 1 à 2 ms) devient de moins en moins négligeable devant la période d'alternance T. Lorsque le taux d'ouverture R_d tend vers 0% ou vers 100%, les temps de soufflage à gauche ou à droite deviennent négligeables devant t_b et les tourbillons primaires droit et gauche ne peuvent atteindre leurs positions extrêmes. Le système tend alors à se comporter comme un dispositif de soufflage continu, et l'effet de saturation de la commande est de plus en plus prononcé lorsque la fréquence d'alternance F augmente.

Ce phénomène lié au temps de basculement de la structure tourbillonnaire t_b est illustré par les visualisations par tomoscopie laser rapide relatives aux conditions $\alpha = 50°$ et F = 60 Hz (figure 11). Alors que les clichés montrent parfaitement l'alternance des deux écoulements dissymétriques opposés pour $R_d = 50$ %, on constate que pour $R_d = 75$ %, le tourbillon primaire droit ne s'éloigne jamais de l'extrados de la maquette, et opère un déplacement latéral en fonction de la position du tourbillon primaire gauche.

La configuration F = 11 Hz a été retenue pour étudier l'effet du dérapage. La figure 12 montre le comportement quasi-linéaire du système de soufflage alterné dans tout le domaine incidence-dérapage étudié ($30° < \alpha < 60°$ et $-10° < \beta < 10°$).

4.4 Evaluation des « détecteurs » pariétaux

La dernière étape de cette étude concerne l'évaluation de « détecteurs pariétaux » indispensables à la réalisation d'une commande en boucle fermée.

L'écoulement développé autour d'un avant-corps à grande incidence se caractérise par une position dissymétrique des lignes de décollement primaires droite et gauche, par une ligne de recollement primaire décentrée à l'extrados, ainsi que par une différence de répartition de pression entre les flancs droit et gauche de la pointe, à l'origine de l'effort latéral que l'on cherche à contrôler.

Il est évident que les actionneurs ont pour effet de modifier de manière cyclique ces caractéristiques de l'écoulement pariétal et que les détecteurs doivent eux aussi être instationnaires pour pouvoir adapter et corriger la consigne des électrovannes.

La partie conique de la maquette est équipée :
- de 8 capteurs de pression instationnaires répartis à l'extrados;
- de 12 films chauds dont l'objectif est de mesurer les déviations des lignes de frottement pariétales provoquées par le déplacement des lignes de décollement et recollement primaires.

Afin de limiter au maximum le déphasage de leur réponse vis-à-vis de la commande des actionneurs, ces capteurs sont placés le plus près possible de la pointe et des injecteurs dans la zone de décollement laminaire, ce qui explique le positionnement azimutal de 90° et 100° des films chauds latéraux. Le rayon de courbure à la paroi étant relativement faible aussi près de la pointe, il n'a pas été possible d'étalonner les films chauds, et seules les variations des signaux doivent être prises en compte.

Les figures 13 à 16 regroupent, à titre d'exemple, les signaux des capteurs instationnaires à 50° d'incidence dans le cas d'un soufflage alterné à une fréquence volontairement basse F = 2 Hz et pour un taux d'ouverture R_d de 50 %.

Les capteurs de pression détectent parfaitement l'alternance des deux structures tourbillonnaires dissymétriques opposées (figure 13), les capteurs situés à ± 95° et ± 112,5° d'angle d'azimut étant les moins bruités.

Les variations des signaux relatifs aux 4 films chauds (figures 14 et 15) à 90° d'angle d'azimut sont relativement faibles, ce qui signifie qu'ils sont toujours positionnés en dessous des lignes de décollement primaires droite et gauche. Les signaux des 4 films chauds positionnés à 100° d'angle d'azimut suivent parfaitement l'alternance, les capteurs de gauche étant logiquement en opposition de phase avec les capteurs à droite.

En ce qui concerne les films chauds placés à l'extrados dans le plan vertical de symétrie (figure 16), ils détectent tous le déplacement de la ligne de recollement primaire.

Un choix de détecteurs peut ainsi être effectué à partir de cette base de données qui est en cours d'exploitation par le Département Commande des Systèmes et Dynamique du vol (DCSD) chargé de définir un modèle destiné à établir les lois de commande qui seront utilisées au cours des prochains essais en boucle fermée.

5. CONCLUSION

Les essais réalisés dans la soufflerie L1 ont permis de valider le principe de contrôle de l'effort latéral à grande incidence par soufflage alterné, tout en optimisant les différents paramètres (position, débit, fréquence d'alternance) des actionneurs de type fluidique.

Dans la plage de nombre de Reynolds explorée, le positionnement azimutal des deux jets axiaux à + et - 115° donne une grande efficacité de 30° à 60° d'incidence, et jusqu'à 10° de dérapage.

L'étude de l'influence du débit de soufflage met en évidence deux modes de fonctionnement des actionneurs :

- à grand débit, le jet agit comme un obstacle fluide, provoquant le décollement prématuré du tourbillon primaire du côté du soufflage ;
- à faible débit, au contraire, le jet retarde le décollement de ce même tourbillon, le mécanisme pouvant s'apparenter à un effet Coanda.

Les résultats concernant l'étude de la fréquence d'alternance montrent que le comportement de cette « gouverne de lacet » est d'autant plus linéaire que la fréquence est basse.

Les derniers essais ont permis de sélectionner un certain nombre de « détecteurs pariétaux » indispensables à la réalisation d'une commande en boucle fermée. Les capteurs retenus permettent de suivre en temps réel le déplacement des lignes de décollement et de recollement primaires ainsi que la différence de répartition de pression entre les flancs droit et gauche de la pointe, à l'origine de l'effort latéral que l'on cherche à contrôler. L'analyse en cours par le département DCSD de ces résultats permettra de réaliser les prochains essais en boucle fermée prévus en 2000.

6. BIBLIOGRAPHIE

[1] R. Lee, E.S. Hanff, R.J. King
Linear Control of Side Forces and Yawing Moments using the Dynamic Manipulation of Forebody Vortices.
ICAS-96-2.10.1

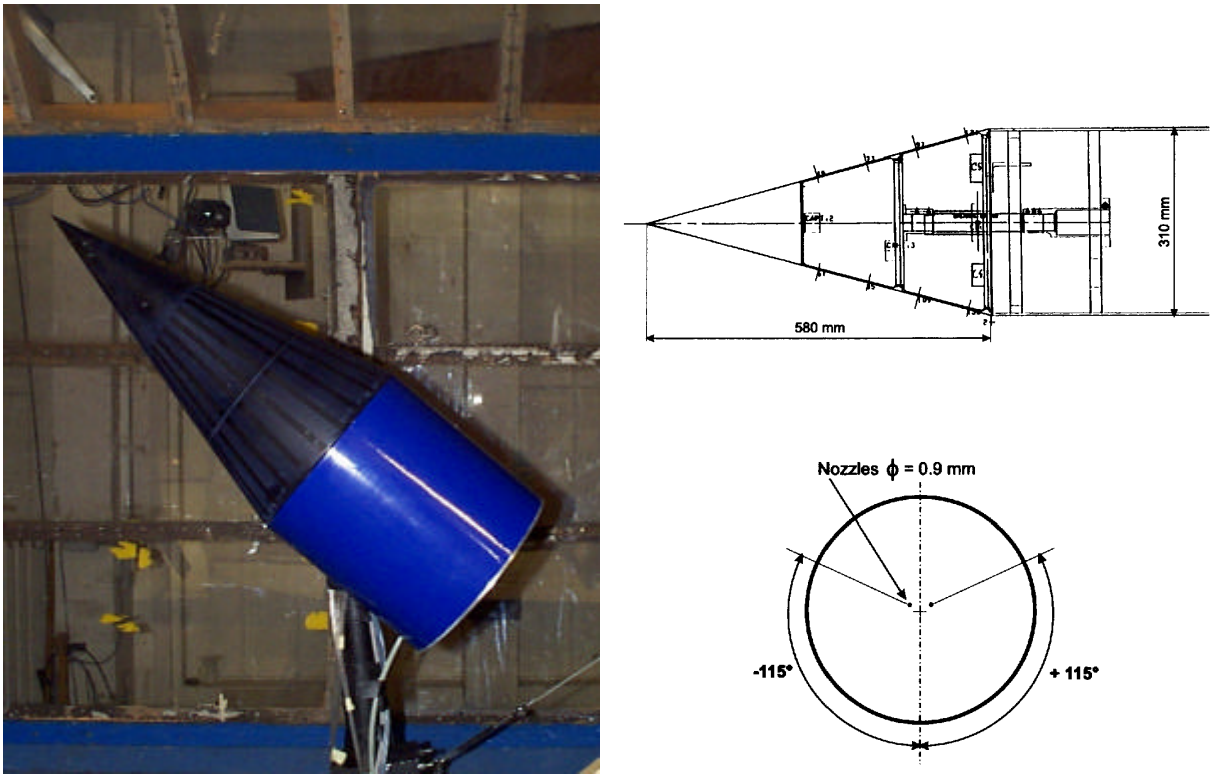
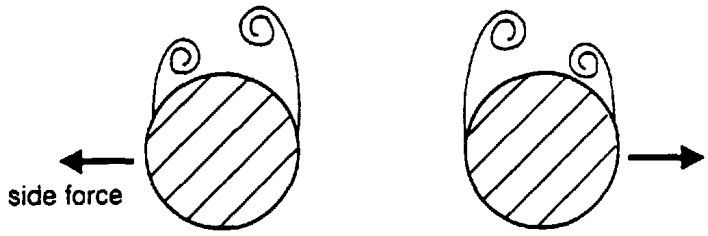


Figure 1 : Maquette et montage d'essai dans la soufflerie L1



– Two stable vortex patterns in a cross-flow plane on a forebody at a high angle of attack.

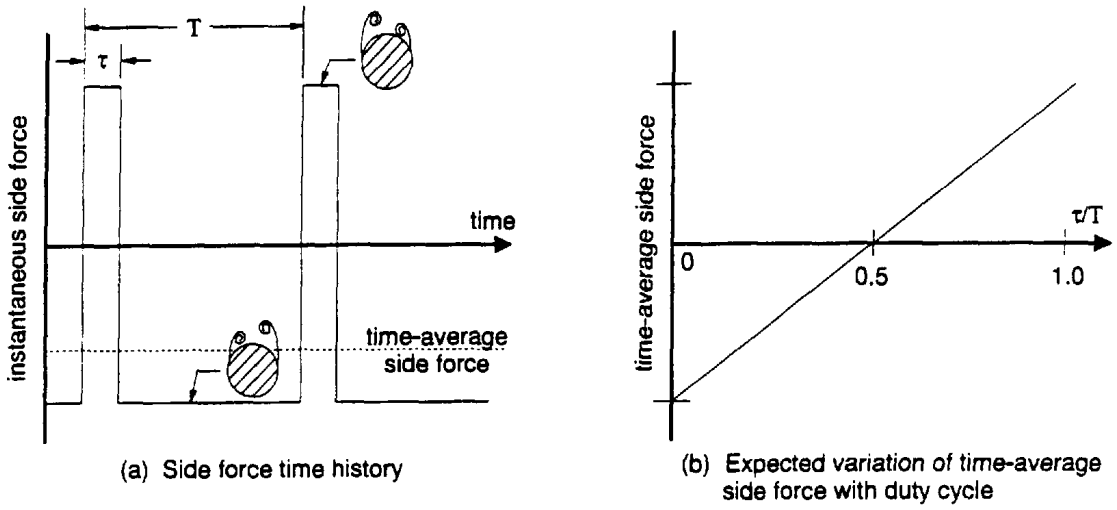


Figure 2 : Principe du contrôle des efforts latéraux (extrait de [1])

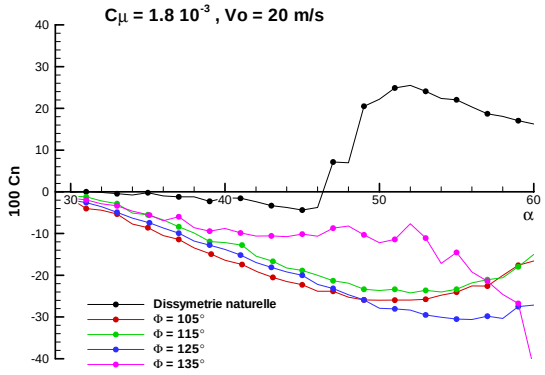


Figure 3 : Influence de la position azimutale du jet

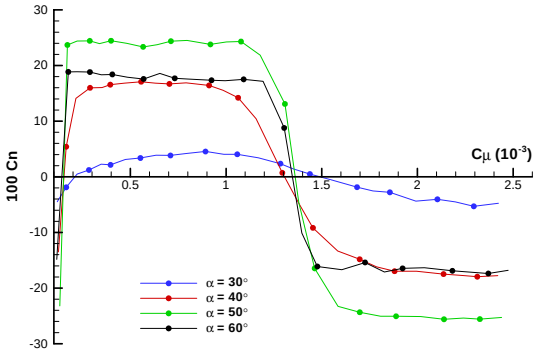
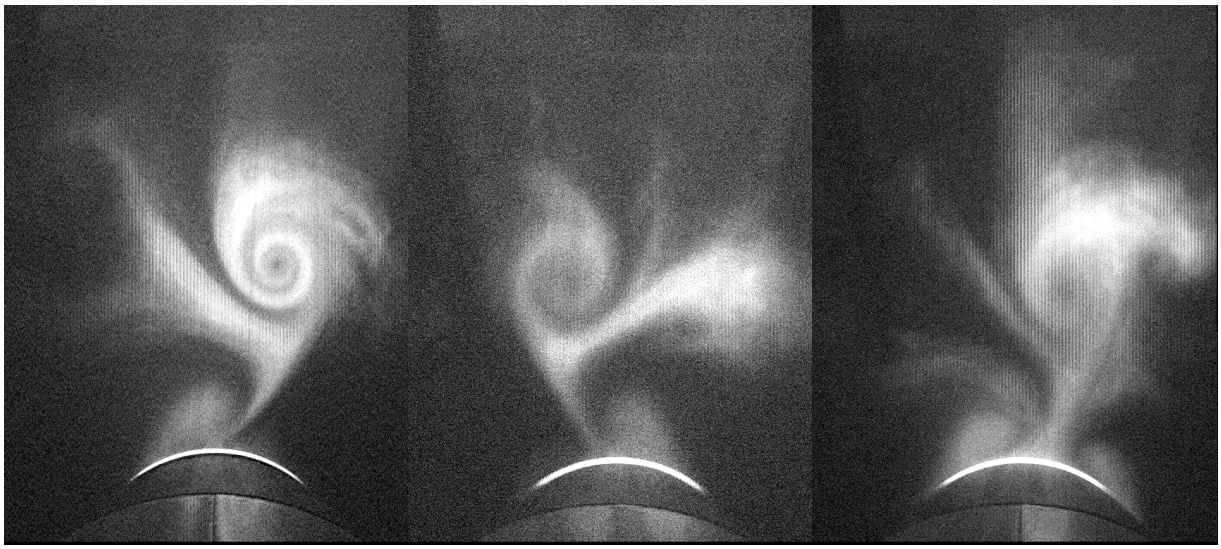


Figure 4 : Influence du débit de soufflage



Dissymétrie naturelle $C\mu = 0.3\ 10^{-3}$ $C\mu = 1.8\ 10^{-3}$

Figure 5 : Visualisations par tomoscopie laser (X = 400 mm, V_o = 20 m/s, α = 50°)

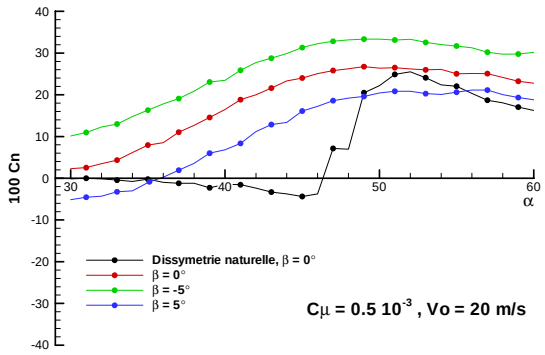


Figure 6 : Effet de dérapage

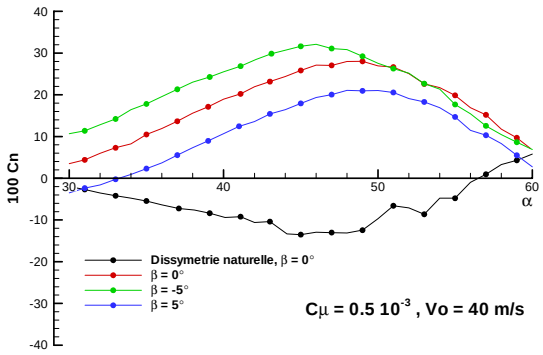


Figure 7 : Effet du nombre de Reynolds

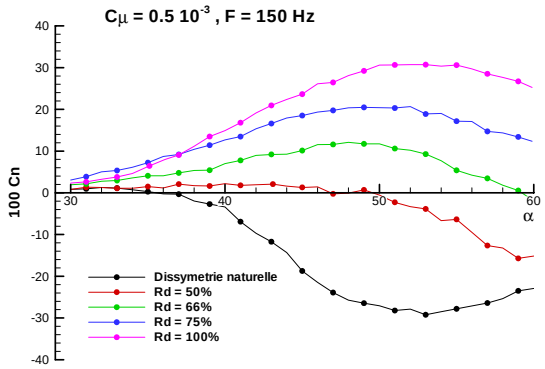


Figure 8 : Efficacité du dispositif de contrôle par soufflage alterné

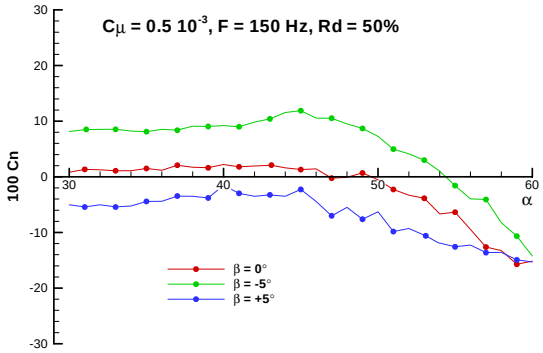


Figure 9 : Effet du dérapage sur le dispositif de soufflage alterné

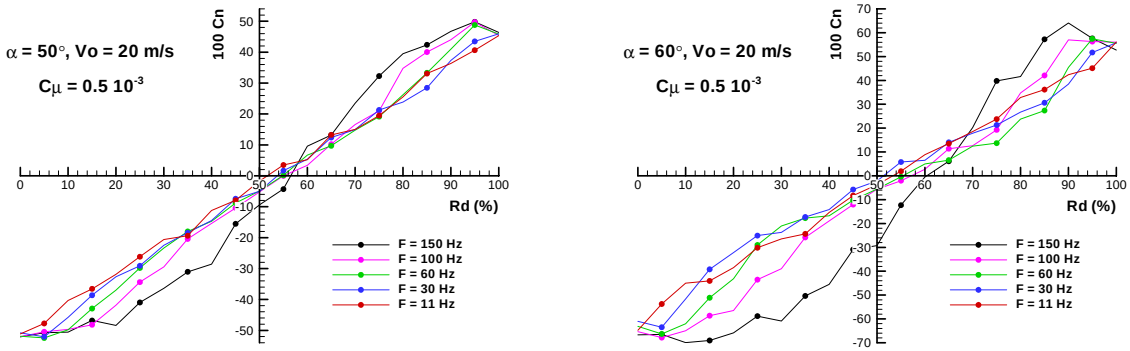


Figure 10 : Optimisation de la fréquence d'alternance

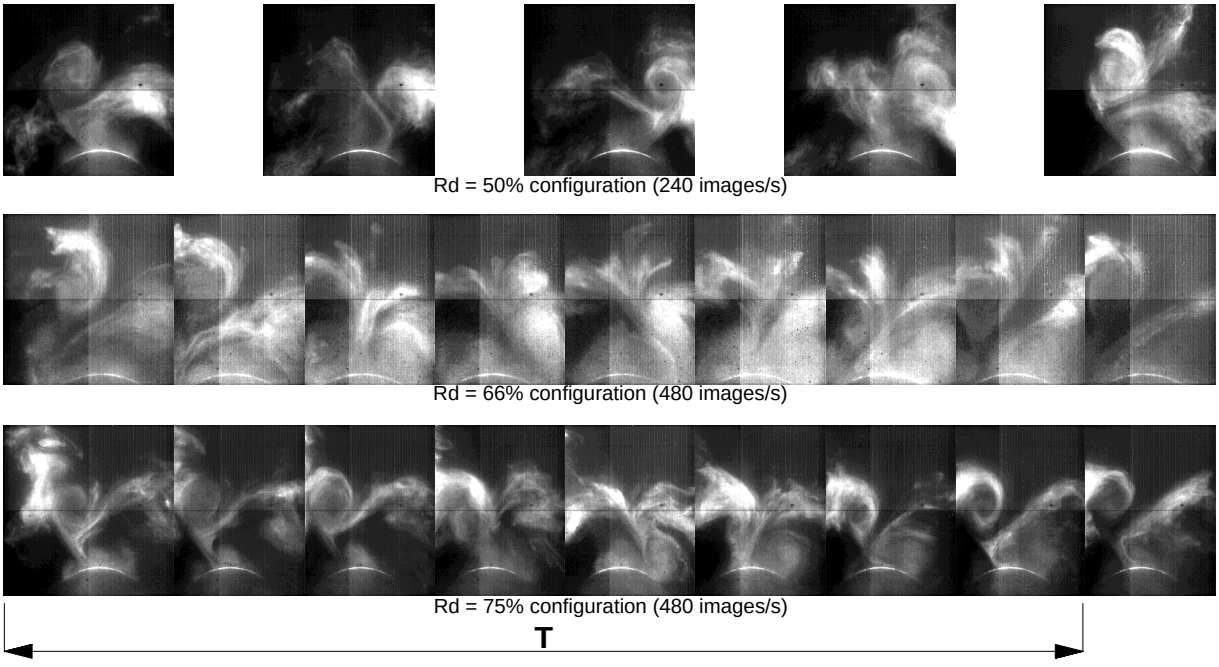


Figure 11 : Visualisations par tomoscopie laser rapide (X = 300 mm, α = 50°, F = 60 Hz)

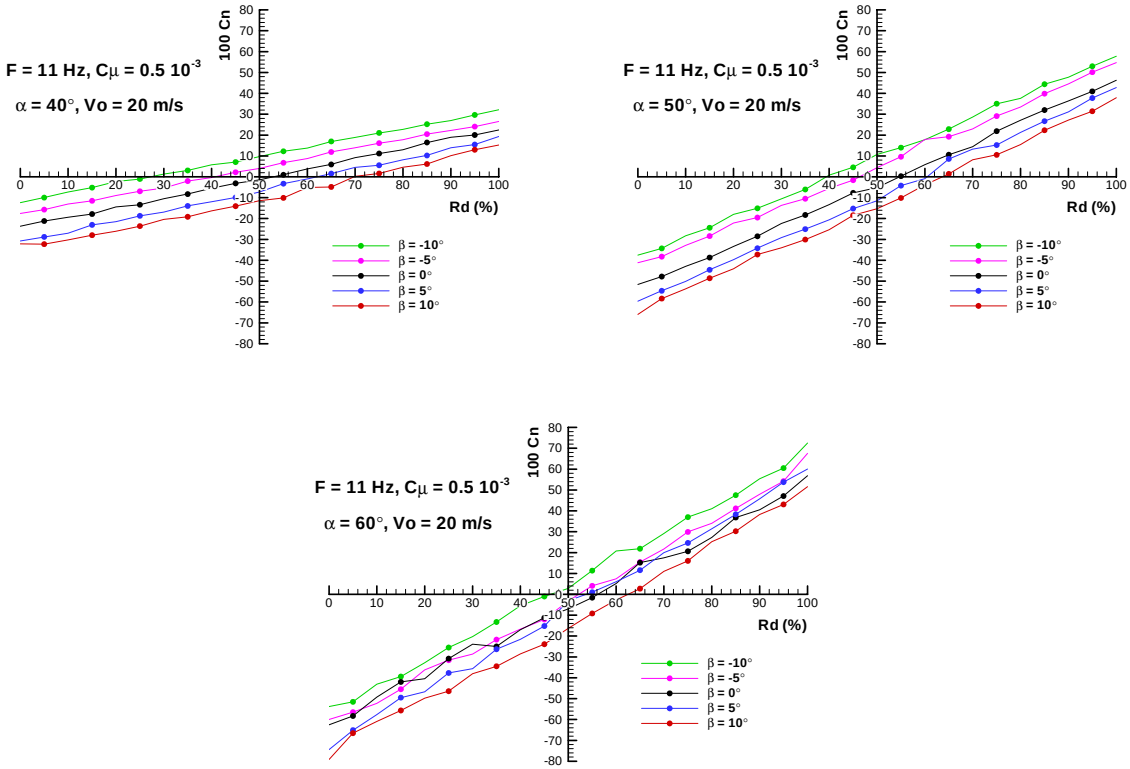


Figure 12 : Efficacité du dispositif de contrôle par soufflage alterné dans tout le domaine incidence-dérapage

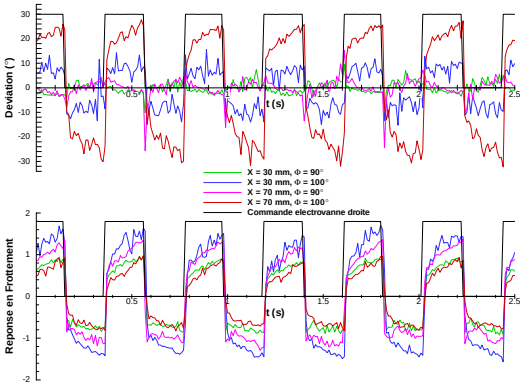


Figure 13 : Evaluation des films chauds gauches

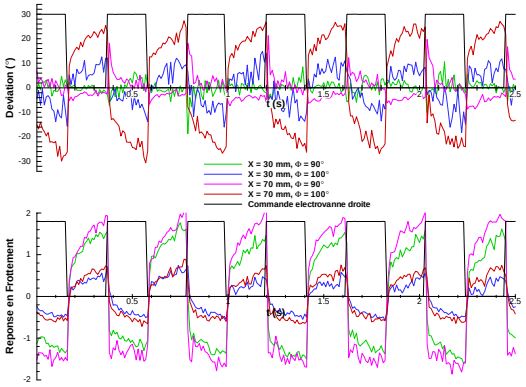


Figure 14 : Evaluation des films chauds droits

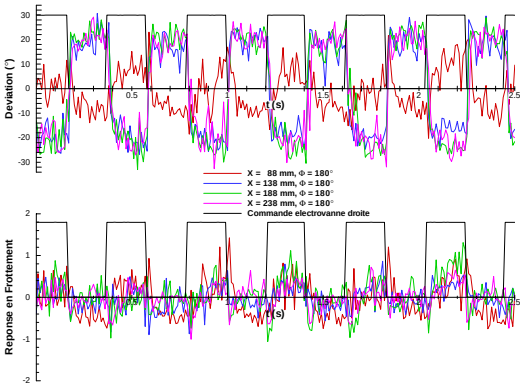


Figure 15 : Evaluation des films chauds d'extrados

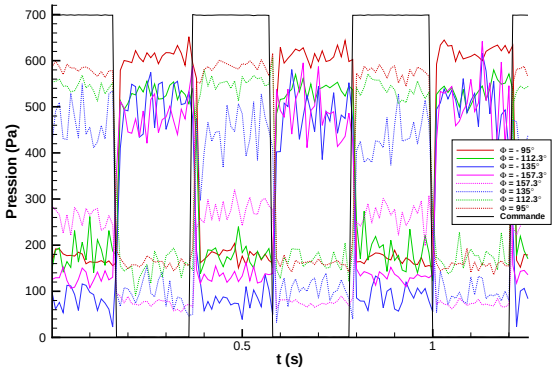


Figure 16 : Evaluation des capteurs de pression

Paper #23
Q by John Lamar: In which direction did the blowing occur ?

A (C. Francois): Forward blowing

Flight Control Design Best Practices Relative to Active Control Technology

Dr. David J. Moorhouse
Air Force Research Laboratory/VASD
2210 Eighth Street, Suite 1
Wright-Patterson AFB, Ohio 45433-7542, USA

Task Group SCI-26 was formally initiated in 1996, in response to well-publicized and highly visible accidents that had occurred in the latest technology aircraft both in the US and in Europe. These accidents were due to deficiencies in the flight control system designs. Other recent programs had less-well-publicized FCS development problems, with time and cost overruns more the rule than the exception. The Task Group has just published a report, which begins with a review of some examples of flight control problems. They span the history of flight from the time when the practice of flying was preceding theoretical developments up to more recent time when it might be thought that flight control designers "should know better". Then there is a chapter detailing lessons learned from various programs with positive results, which leads into a section detailing a series of recommended best practices. The second part of the report continues with some theoretical aspects. First, there is a discussion of flying qualities criteria, and the current state of the art of "carefree handling" which is related to this symposium. Next there is an extensive discussion of the latest results from research into PIOs, followed by a discussion of modelling and system identification. The Task Group members originally laid out this report to present an assessment of design methods, but no correlation was found between the method used and the problems of the past, or the successes.

The theme of the symposium, "Active Control Technology", is interpreted to mean the use of flight control technology to minimize the pilot's workload in accomplishing every mission task. Specifically, it covers a range of applications from tailoring the responses to prevent undesirable characteristics, such as departures or limit exceedances, all the way through to automatic recovery systems that take control away from the pilot. The objective of this paper is to summarize the Task Group results with particular emphasis on best design practices to achieve the optimum benefits from active control technology (ACT).

Introduction

Flight control design technology has evolved along with the development of the airplane itself. As flight envelopes expanded and mission tasks became more complex, flight control design became more sophisticated. Active control technology, by definition, means the tailoring of aircraft response to inputs beyond the basic pilot control and mancuvering. Even mechanical systems in recent aircraft were designed with scheduling to limit pilot inputs in certain conditions, e.g. to minimize susceptibility to departure. One example is to reduce the pilot roll command gain at higher angles of attack in order to prevent departure. The trend towards fly-by-wire technology has given designers even more flexibility in the application of ACT. Another example would be to prevent the pilot pitch commands from causing the aircraft to exceed a certain load factor. These effects can be achieved by tailoring the responses to the pilot commands so that they still appear natural, referred to as ACT1 for this discussion. At the extreme, however, is the application of systems such as Automatic Ground Collision Avoidance, where control is taken away from the pilot completely, ACT2 when there is any distinction to be made. In all cases we can consider that ACT is an extension of basic flight control design and should be integrated as much as possible.

The previous RTO symposium on ACT was in 1994, "Active Control Technology: Applications and Lessons Learned", AGARD-CP-560. The Technical Evaluator stated: "An AGARD Working Group might be the proper means to consolidate valuable insights gained during recent demonstrator and prototype projects ....". A Working Group was formed and has just completed a technical report which is in publication, Reference 1. As stated in the report, problems have occurred from the very beginning of flight up to the present time where it might be thought that "designers should know better". Also, FCS problems are not unique to digital systems, there have been problems with every form of FCS. There are, however, unique aspects of fly-by-wire (FBW) control systems. The most obvious, and frequently the most important, is that there is no direct connection between the pilot and the control surfaces. Since an extreme application of ACT is to take control away from the pilot, special attention is required to provide appropriate connectivity through the design of the FBW system. In

Paper presented at the RTO AVT Symposium on "Active Control Technology for Enhanced Performance Operational Capabilities of Military Aircraft, Land Vehicles and Sea Vehicles", held in Braunschweig, Germany, 8-11 May 2000, and published in RTO MP-051.

addition, the very flexibility of the digital technology has also given designers more flexibility for error in new ways. Reference 1 contains recommended Best Practices for FCS design. The object of this paper is to discuss each of the recommendations from that report in the context of applying ACT to a system design. It can also be admitted that some points are made repeatedly for additional emphasis.

Background

For the purposes of this discussion, we can assume that artificial stabilization is common. The focus of Active Control Technology is the extension of flight control design beyond stabilization and control. The term "carefree handling" is typically used to designate the design of the control laws to prevent pilot inputs that would cause departures, exceeding limit loads, etc. Then we can consider a progression to recovery directions for the pilot to follow, through to complete intervention of the control system.

The initial elements of ACT can be considered to be in systems like stick pushers as an indication of approach to stall. The later aircraft with mechanical control systems, such as the F-15, included ACT in the form of command gain reduction to minimize departure susceptibility. Fly-by-wire technology has given designers even more freedom to develop the technology. In Reference 1, the application of "carefree" handling to two aircraft with different technology status is discussed. An existing aircraft can be upgraded during its lifetime with the new technology development. There is also discussion of what is possible today for a combat aircraft of the newest generation. The principle is the same for both, a reliable control system with a good sensor system for measuring the flight condition enables the implementation of "carefree handling". The primary difference is whether the functions are added to an existing control system, or can be integrated into a new design from the start.

Also as discussed in Reference 1, a Pilot Activated Recovery System has been shown to be effective. This system was pilot selected and provided guidance which mimicked the recovery procedures that are taught to the pilots. It was very acceptable to the pilots, since it only provided guidance as an aid to manual control.

The above approaches are oriented towards helping the pilot to the maximum extent. There still exist possibilities where the pilot does not realize the situation or is temporarily incapacitated. In addition, there have been many accidents where warnings were not sufficient. A human pilot in a stressful situation will ignore everything except a primary focus which may not be the correct one. This leads to consideration of fully automatic systems to take over control. The flight test results from an Auto Ground Collision Avoidance System program show the benefits of an automated system (see References 2 - 4). It shows that nuisance warnings are almost zero and that interference with the pilot is basically non-existent. Pilot acceptance of automated systems has been a problem in the past. This reluctance was based on insufficient knowledge of automated system operation or experience with inadequate manual systems. Future aircraft will be more complex both in pilot workload and in display technology. These facts alone will make the need for more automation imperative. An automatic GCAS has the advantage over a manual GCAS in that it does not have to compensate for the pilot's reaction time. This fact alone should eliminate most nuisance activation. There are still database errors that can cause nuisance cases. As the database gets more accurate over time, these also will be eliminated.

All the design aspects of ACT and carefree handling are subject to the Best Practices discussed later. An early program decision is mandatory to define the extent of the technology. It does increase the design effort and therefore must be justified. Even in the simulation and especially in flight test a higher effort is needed to clear the aircraft for "carefree" maneuvering. Nevertheless the advantages are so big that it should be considered for every modern combat aircraft. In addition, many aspects could transition into commercial and military transport aircraft. The problem may be cost, unless it can be justified on the basis of improved safety.

The Design Process

The flight control system design process is expressed in graphical form in Figure 1.

This figure can be interpreted to apply to both an upgrade and a new design. It shows a logical process, starting with consideration of the various requirements, to establish a well-defined set of FCS design criteria. This is the time when the application and extent of ACT should be defined. The best results will be achieved if ACT is included in the design requirements and the design process as early as possible. It is essential that the whole team understands these requirements. These allow definition of the control law architecture and an initial design to be established. This is also the point at which consideration of non-linearities should start, such as those associated with actuation system specifications, aerodynamic characteristics, etc.

Some aspects of ACT can be included in the initial design requirements, such as load factor protection. Others may need to be considered as a response to problems that are encountered in flight test. It is quite common in the later stages of FCS verification and validation to perform sensitivity analyses accounting for uncertainties in the aerodynamic model used in the design process. These analyses are intended to ensure system stability for a certain

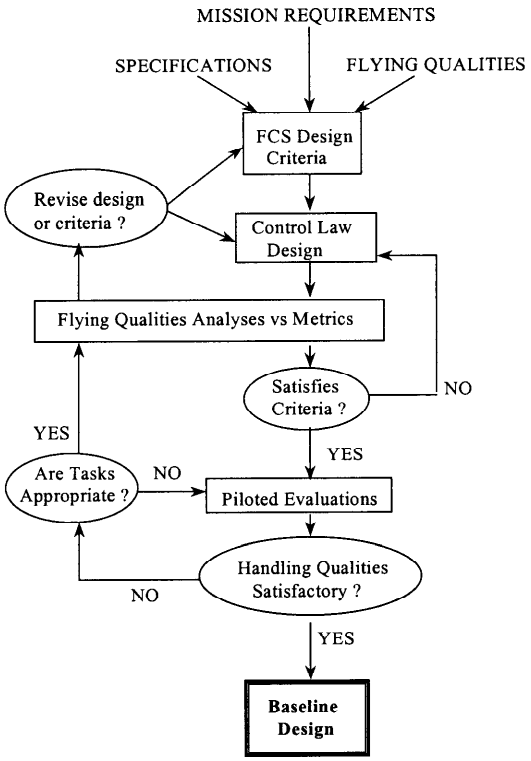


Figure 1. Flight Control System Design Process

percentage variation in aerodynamic derivatives. It may also be worth doing "what if" exercises to discuss potential approaches if there is some variation beyond these values. What if lateral/directional coupling is significantly different from predictions. Is there a feedback or command path that would be required that is not in the basic control laws? One may decide that it is prudent to include such a path with zero initial gain as cheap insurance.

After the design requirements are defined and agreed, there is then a loop of analyses to ensure that the control law design meets the criteria that were established. These analyses should be a package of methods that are complementary, documented and can initially be informal, but must be thorough. The recommended approach to achieving satisfactory flying qualities is to assess the predicted responses to cover all flight conditions, including all non-linearities and pilot input amplitudes. This becomes especially important if we are considering ACT as protection at the extremes of the flight envelope. One critical aspect of the process follows the assessment in piloted simulation, any deficiencies must be corrected by analysis.

Design Best Practices

The design process should not be considered as a rigid serial process, even though it is convenient to discuss it that way as in Figure 1. In fact, many parts are performed concurrently and/or in iterative loops but it is necessary to keep the total process in mind in order to maintain the appropriate connections between the various components. Similarly, the following Best Practices should be considered in total and not serially.

Establishing aerodynamic design and system performance requirements

Some of the difficulties associated with flight control laws design can be created very early in an aircraft's life-cycle by the design of the airframe and the related performance specifications used for its FCS hardware. It is important that the control law designer is involved in the definition of the aerodynamic characteristics and the associated FCS equipment performance, at an early stage. He or she should also be involved in aspects of the wind tunnel testing as the user of those characteristics. If these are not satisfactory, he may be tasked with compensating for undesirable physical behavior by including appropriate functionality within the flight control algorithms. Whilst it is accepted practice to provide artificial stabilization, there are bounds on what can be safely achieved, simply due to the laws of physics. Even before the physical limit is reached, the financial cost of providing artificial stability may be very high, owing to the required performance of the FCS hardware.

There are specific recommended best practices addressing sizing and placement of control surfaces, specification of data sensors and actuation system characteristics. These areas are particularly susceptible to being frozen early in the design process.

It is tempting to avoid analysis of non-linearities in the early stages, because they would mainly be engineering judgement. The real problem occurs if early decisions are made without any analysis and data. There is always resistance to changes, which only increases through the stages of the design process. For some aspects of ACT, differences from predicted characteristics are likely to occur in the later stages of flight testing because they are towards the flight envelope limits. At this point, it may be assumed that the characteristics are being identified with more certainty. It should be possible to accommodate differences up to some magnitude (within the range of sensitivity?) by gain changes. For larger differences, the really good design team would have it covered through the "what if" exercises discussed above !!

Modelling and analysis of the unaugmented vehicle

Before beginning any control law design, it is important to study and fully understand the dynamics and the non-linearities of the unaugmented vehicle, including those of the FCS hardware. This analysis will include the traditional aspects, such as actuators, the air data system, etc., but should include everything affecting the control system, such as the powerplant. It is also important to understand how these are likely to affect the aircraft's control characteristics as its operating condition varies. If this is not done then there are likely to be some surprises later in the design process, which will require re-work, i.e. overruns in time and money.

This is where considerations that were used in the aerodynamic design can be integrated into the modelling and analysis. An estimate of probable nonlinear aspects should be included. It is also wise to consider the probable accuracy of the predicted characteristics in order to define appropriate ranges for sensitivity analyses and "what if" exercises. Obviously, the decision on how ACT will be integrated into the FCS will have a large influence on the results.

Design criteria and flying qualities specifications

The two areas above are essential preparation for the FCS design, but the real critical point of the whole design process starts with definition of the design requirements. The biggest influence of ACT, and also the most critical, is in this definition of design criteria. The design team (which is discussed further as a management practice) needs to agree on the criteria. Many aspects of ACT are not covered explicitly in military specifications, therefore, a clear agreement on the intent and the extent needs to be documented at this point. The requirements will also vary significantly depending on the class of aircraft being considered and its mission.

The military flying qualities specifications may have been misused as often as they have been used correctly. A very common statement is that they apply only to the linear small-amplitude responses. The US military specifications have never stated this, they actually defined flight envelopes over which the required criteria were to apply. Because of the practical problem of the unavailability of non-linear theories, the non-linear effects have frequently been neglected, or even ignored, in the past.

The introduction of Equivalent Systems into MIL-F-8785C (Reference 5) provided a means to characterize the actual aircraft response, whether it was linear or non-linear. There was an explicit requirement stated in the specification that ALL non-linearities were to be included in the equivalent system. The characterization was in terms of a conventional linear response model, and was therefore, mathematically not exact. Such an approach would be a better start than nothing. Since the introduction of MIL-F-8785C, other methodologies have been developed which apply equally to non-linear responses as well as the linear, e.g. Reference 6. The problem will be how to produce credible models, especially the nonlinearities

Many aspects of ACT, especially protection against violating limits of the flight envelope, should be expected to require consideration of non-linearities. One example is the protection against departure as angle of attack increases into a range that may trigger uncontrollable yaw if the pilot commands too high a roll rate. The solution is typically a non-linear command gain as the aerodynamic characteristics are becoming more and more non-linear. This non-linearity is straightforward and relatively benign. At the other extreme may be the requirement to consider actuation deflection, rate and acceleration limits as part of the recovery control laws. The recommended approach is to include a spectrum of nonlinearities, even based on judgement until more refined models can be developed.

The recommended Best Practice to define the system flying qualities requirements would be to extend the military specification criteria rather than just discard them. The first question would be whether the mission required the system to limit responses to stay within a conventional envelope or provide satisfactory flying qualities in an extended envelope. As an example, the Permissible Flight Envelope can be defined to extend to any angle of attack. A first estimate of required characteristics throughout this envelope, including recovery into the conventional envelope, should be the starting point. They can then be augmented with automatic functions and a definition of the extent of intervention into the pilot control.

Control law design and development

In a classical design sense, having established the capability to produce linearized models of the aircraft, its powerplant and FCS hardware, a grid of design points are selected to cover the required flight envelope. A series of localized controllers are then designed and implemented using gain schedules to cover the flight envelope. At this stage, additional non-linear functionality is added, for example rate limiting functions and authority limits. There then follows a comprehensive assessment of the design, leading through to flight clearance.

Reference 1 then continues with twenty Best Practices, the last of which concerns the design methodology. In the report it is stated that no correlation was found between FCS problems of the past and the methods used. There is also the promise that future developments of modern control, such as robust control theory, will change the emphasis of

the given list of best practices. There should always, however, be the judgment and insight that comes from some application of a disciplined approach of designing to the agreed criteria. The physics of flight remain the same, irrespective of the design methodology.

When designing the control laws with ACT, at the lower levels, the pilot command inputs are reduced to avoid violation of all given stability and controllability margins and additional limitations (e.g. load factor). At the higher levels, the automatic system provides inputs that can change the pilot inputs dramatically. There is then always discussion as to whether the system is improving what the pilots think they can do. For the future, therefore, the "fuzzy logic" requirement for ACT is "to prevent all bad things from happening but the agility of the aircraft must not be reduced too much". This is a subjective evaluation when the pilots think that the control laws are preventing them from achieving some realizable performance objective. Part of the solution to this problem of acceptance is to design for minimum intervention, as discussed above in all three areas. Finally, it is mandatory that pilot selectable features should not be "dormant", i.e. it must be clear to every pilot exactly what the selected configuration is.

Control laws functional specification, implementation and verification

Whether the flight control laws are to be implemented in an analogue or, more usually these days, a digital flight control computer, some means of functional specification is needed to enable the laws to be implemented. For digital flight control, the functional specification will enable coding into the target machine's language and allow the implementation to be verified against the intentions of the designer. This, however, relates back to the previous Best Practice of thoroughly documenting "the intent of the designer". This does not change if the ACT aspects are an integral feature of the FCS, but 'add-on features' must follow the same rules.

Piloted simulation and handling qualities

It is common practice for the control laws to be thoroughly evaluated by piloted simulation. The initial task is to set up the control laws within the simulator's real-time environment and to establish the interface between the control laws and the pilot's controls and displays. The implementation must then be verified, prior to exposing the simulation to pilots. A series of piloted evaluations then takes place, during which the handling qualities and mission effectiveness of the augmented aircraft are assessed. This usually results in further developments of the control laws, as handling deficiencies are identified. It is critical, however, that this further development is done analytically.

A best practice is to plan for an integrated simulation program and ensure that all IPT members (especially pilots and managers) are clear that the various simulators are for evaluation purposes, to feed data back into the analytical design process. Also, deliberately search for handling problems, including the effects of design tolerances (parameter uncertainties) and failures. Identify the worst cases and any hidden weaknesses in the design, and fully explain any unexpected simulation results. A significant aspect of this recommendation is to use tasks which deliberately drive high pilot gain. This can be done through very stringent task performance requirements, or discrete gusts (not continuous turbulence that a pilot can ignore). It is critical that this part of the simulation should not be a check list of maneuvers that the pilot flies in a "relaxed" environment.

Relative to ACT2, evaluate the ability of the pilot to enter or re-enter the control loop, and obviously evaluate the pilot interface with the automatic functions. Show that there is no tendency for divergence between the automatic and manual control functions. Much of the preceding discussion has emphasized non-linearities. The simulation is where something like a non-linear stability problem may be found. In such a case, restricting the pilot's commands may help but is unlikely to provide a full solution. There still may be a stability problem provoked by an external disturbance, the effects of gusts should be examined.

Aeroservoelasticity and structural mode filter design

The primary function of the flight control laws is to provide the aircraft with good handling qualities by using feedback to the flying control surfaces. The airframe is not rigid and has many structural modes of vibration that may be excited by the control surface movements. The response of these lightly damped modes can be detected by the motion sensors and fed back to the control surfaces, with the potential for closed-loop instability at the structural mode frequencies. The application of modern high bandwidth flight control systems and advanced aerodynamic configurations has led to an increase in the levels of interaction between the airframe and its FCS. The aeroservoelasticity specialist has the task of defining a set of structural mode filters that provide sufficient attenuation of the structural mode content of motion feedback signals. The inclusion of ACT changes neither the requirement for these analyses nor the Best Practices in reference 1.

Design robustness and flight clearance

The certification or flight clearance process is essentially aimed at providing the evidence in order to certify that the aircraft is safe to fly. The qualification (validation) process is aimed at demonstrating that the design qualifies in meeting its design specification. If a satisfactory design has

been achieved in accordance with the design requirements and guidelines, and the functionality is clearly defined, then these tasks should be relatively straightforward. However, the task is usually large and detailed, since there are very many cases which need to be assessed, covering a wide range of aircraft configurations and states, including parameter uncertainties, which have to be evaluated against a range of criteria to assess different aspects associated with safety and performance.

For ACT aspects, the piloted simulator should be used to complement the off-line analyses and in particular, to carry out more detailed investigations for regions of low stability or unusual handling. A critical area to investigate is the sensitivity to variations in certain basic model parameters. Some FCS design methods provide an estimate of 'robustness'. This should also be augmented with a more deterministic approach based on an assessment of model accuracy. Transients due to gusts, failures and mode changes should also be considered. Assessment of carefree handling functions needs to be very thorough, in order to demonstrate that the system is fully effective. This effort, however, will clear the system to enter a flight test program where the system will be finally validated

Developments during flight testing

A safe and well-planned program for the flight testing of the aircraft and its flight control system is essential. Flight testing of a flight control system usually involves some risk due to the uncertainties in the models used to establish the design, although this can be minimized by some of the best practices already covered. Once the flight test program has commenced, parameter identification is usually carried out, in order to validate the aircraft model. This leads to further flight clearances and increased confidence, enabling flight envelope expansion to continue in a safe and progressive manner.

For the higher levels of ACT implementation, special flight test procedures may be used and an example is discussed in Reference 1. Before giving a clearance for "carefree" handling flight tests, there were numerical simulations to show that the violations of defined boundaries stayed inside the allowed safety margin even for the worst case configurations. One of the main problems is that it is a multi-dimensional problem, where some parameters can augment each other. Moreover we have to look at a wide range of center of gravity, and during the prototype tests there are big tolerances on the aerodynamic modelling and the sensor system. Additional emergency precautions were done for one prototype. There were spin tests in the wind tunnel, a spin chute was fitted to that prototype, automatic start of the APU if the main engines stop due to spin, an extended emergency limit for the actuator rate, an emergency recovery mode of the flight controller with increased pilot authority, etc. Only this one prototype was allowed to fly in certain flight regions that were restricted for all other vehicles in the flight program.

At some point, the aircraft behavior may become significantly different from that predicted. The difference must be analyzed carefully, especially any trend with flight condition. There are many cases where differences were observed but thought to be small enough to allow flight testing to continue – until an incident occurred. At some point the behavior is deemed to be unacceptable, then control law changes will need to be introduced during the flight test program. Clearly, this needs to be done efficiently and safely in order to meet overall program timescales. Any differences in predicted behavior should always be investigated and fully explained.

Design considerations for PIO prevention

Although the application of the best practices in reference 1 will help to avoid pilot involved oscillations, it is considered that this topic warrants further comment, due to the problems it has caused the flight controls community in general. Much research has been carried out on this subject in recent years and the many results available can be quite daunting for a budding flight control engineer. To continue the earlier theme, the overall fuzzy logic is for the aircraft 'a) to do what the pilot wants to do when he wants it, b) to prevent any unintended responses, and c) only take command if the pilot tries to do something really stupid'. In terms of PIO, however, the overriding two principles are extremely simple. First, minimize time delays and phase lag, and second ensure that the pilot's command gain is neither too high nor too low.

The first of these is actually very, very straightforward. The mil spec approach, through the use of equivalent systems, requires that the equivalent system time delay be less than 100msec for Level 1 flying qualities. The required definition is in the frequency range of pilot control and, with the previously discussed requirement to include all non-linearities, will satisfy the requirements. Couple that with the criteria by John Gibson in reference 6, which extends design guidance through the complete frequency range, and time delay and phase lag will not contribute to flying quality deficiencies. There is one overriding caveat on that assertion, the models used in the design process must be accurate to within a threshold defined and considered in the design process.

The second aspect has caused problems in the past through the design being driven by simulation rather than analytical criteria. In a simulator, it can be taken as a given that a pilot will ask for more command gain, more response, more, more, more. As stated above, it is critical to search for problem areas. The test plan must include tasks that are

more extreme than will be encountered in the expected mission use. It will not be sufficient to fly flight mission profiles or demonstration maneuvers in a straightforward, relaxed manner. A skilled pilot can often fly a deficient configuration until some event drives up his gain.

Management aspects

All good management practices are applicable to the development of the flight control system, and it is not intended here to write about what constitutes good management. However, there are some practices that are worth highlighting in order to emphasize their importance. The best overall management practice is to ensure that the detailed recommendations in Reference 1 are applied in any flight control system development.

First, a team must be formed to include representatives from each technical discipline and organization that have any contribution to the system.

A best practice is to plan carefully and don't underestimate the size of the job or the resources required. From collective experience of earlier projects, it must be assumed that there will be some surprises at some stage during the flight control system development, and some contingency planning might be necessary, including provision for software updates.

Lastly, the recommended management best practice relative to ACT is to ensure that it is integrated into the FCS design requirements as early as possible and follows the same disciplined design process.

Conclusions

Active Control Technology (ACT) can now be considered as part of the basic flight control requirements of a modern airplane. There is, however, a spectrum of detailed implementations from tailored flying qualities to automatic recovery functions. It is this author's prejudice that there are two absolutely critical points in any flight control design activity. First, define a complete set of design requirements, i.e. flying qualities criteria, up front. These should be based on the US Military Specifications augmented for the specific application with an understanding of the intent and expectations for each criterion. The design process is then to meet those criteria under all conditions, especially including predicted nonlinearities. Second, any deficiencies indicated by analysis, simulation or flight test must be supported analytically before any changes to the criteria are allowed. The control system must not be tuned in the simulator. If the specific requirements are defined early in the program, and then the design follows a disciplined process as indicated in Figure 1 and also expanded in Reference 1, then there is every reason to expect a successful system development.

Acknowledgement

The basic work that is reported in Reference 1 is the product of a working group comprised of:
Dr. David J. Moorhouse (Chairman), AFRL, USA
Mr. Wim de Boer, NLR, Netherlands
Mr. Chris Fielding, BAE, U.K.
Dr. Klaus-Uwe Hahn, DLR, Germany
Mr. Georg Hofinger, DASA, Germany
Dr. Leopoldo Verde, CIRA, Italy
Dr. Jean-Francois Magni, ONERA, France (part time).

In addition, there were contributions from many other people who are listed in the final report.

References

1. "Flight Control Design - Best Practices", Technical Report RTO-TR-29, in publication.

2. Huffman, R.E.; M.D. Cawood; M. Ferm and M.A. Skoog, "Determination of Nuisance Criteria for Ground Collision Avoidance Systems", presented at the 4th Saint Petersburg International Conference on Integrated Navigation Systems, May 26-28, 1997.

3. Huffman, R. E; M. A Skoog, L. Pinerio and M. Ferm, "Application of Ground Collision Avoidance System Nuisance Criteria", presented at the 21st Congress of the International Council of the Aeronautical Sciences, (ICAS 98), September 1998, Melbourne, Australia.

4. Swihart, D., and F. Barfield, "An Advanced Automatic Ground Collision Avoidance System for Fighter Aircraft", presented at the RTO Symposium, Flight in a Hostile Environment, October 1999, Maryland, USA.

5. Anon, Military Specification, "Flying Qualities of Piloted Airplanes", MIL-F-8785C, 1980.

6. Gibson, J.C., "Development of a Methodology for Excellence in Handling Qualities Design for Fly By Wire Aircraft", Delft University Press, Series 03: Control and Simulation 06, ISBN 90-407-1842-3, 1999.

Paper #25

Q by Bill Gubbels: Do you consider any other PIO criteria to be useful or is Gibson's criteria the only one you would say holds merit?

A. (D. Moorhouse): First, I would like to say that the best practice is to design for Level 1 flying qualities and not PIO avoidance. Gibson's is one criterion is a good way to do that. However, there are other valid PIO criteria. I have used Ralph Smith's criterion, although I do not agree that the feel system should be included in the formulation.

Q by Daniel Walker: What would it take to convince you that one design method for FCS was maybe better than another in a particular design problem? (vis-à-vis author's statement to the effect that the best design method is the one with which the designer was most comfortable) (sic.)

A. (D. Moorhouse): First, with the correct design criteria and good models, any method should arrive at the right answer but some more easily than others. I might also refer to a paper presented in 1994 that does discuss the best application of different methods for particular parts of the design problem. {Moorhouse and Citurs, "The Control System Design Methodology of the STOL and Maneuver Technology Demonstrator", AGARD Conference Proceedings, AGARD-CP-560}.

Thrust Vector Control and Visualisation for Stovl Aircraft

P.M. Lodge & C. Fielding
BAE SYSTEMS
Warton Aerodrome
Lancashire, PR4 1AX, UK

Summary

There are many areas where the design of control laws for short take-off and vertical landing (STOVL) aircraft are radically different from those of a conventional design. One the most challenging areas is related to control of the thrust vector, and in particular, how to design control laws that can deal with conflicting demands, control saturation and integrator wind-up. Unlike a conventional aircraft, where full primary control surface deflections are rarely used, the STOVL aircraft nozzle vector angle and engine thrust are often operated on their limits for significant periods of time. For example, to achieve maximum deceleration from wing-borne flight, the nozzles are vectored to their forward authority limits and remain there for several seconds.

The first part of this paper provides background on the UK's Integrated Flight and Propulsion System (IFPCS) programme, the BAE SYSTEMS P112C-6 aircraft configuration and the Rolls-Royce RB571 engine concept. A command strategy to control the aircraft during wing-borne flight and through the transition to the hover is introduced, which leads to the description of a suitable control law architecture to satisfy this command strategy.

With the approach chosen, 'thrust vector equations' are required to transform the pilot's commands into nozzle vector angle and engine thrust demands. The equations are derived for the Harrier and subsequently for the more complex P112C-6 configuration. These equations are then extended to cover the cases of saturated control conditions. Emphasis is placed on the visualisation and verification of the complex functions that result.

Discussion of the application of the thrust vector equations in a non-linear real-time simulation, including flight and engine control system integration aspects, is also covered and the paper concludes with lessons learned in this area.

Introduction

For over 30 years, BAE SYSTEMS has been involved in the design and development of control concepts for future STOVL aircraft. The majority of this research has been undertaken in support of the UK's VAAC Harrier [1,2] and IFPCS [3,4] programmes and has been aimed at improving the understanding of aircraft handling and flight control for transition and jet-borne flight.

One of the most interesting and challenging areas of this research has been in the design of control laws and in particular, development of thrust vector control strategies. This has resulted from the desire to reduce pilot workload in the launch and recovery of the aircraft [5], where direct open-loop control of throttle and nozzle angle can be replaced by closed-loop control. This allows the pilot to command the variables of primary interest and importantly, in the reference axes that are most appropriate to the flight regime and task.
Experience has shown that the algorithms required to implement the desired thrust vector control strategy can become complex and difficult to interpret and verify, without adequate visualisation tools. This paper will demonstrate a thrust vector control strategy appropriate to future STOVL aircraft, with the emphasis on the visualisation, verification and understanding of the functions required for implementation.

The UK's IFPCS Programme

The UK's Integrated Flight and Propulsion Control System (IFPCS) Technical Demonstration Programme is a joint UK MoD / Industry-funded research effort, which has mainly focused on investigating aircraft control and system architectures to meet the challenges associated with future STOVL aircraft.

The project has utilised the P112C-6 canard-delta aircraft configuration (shown below), which is largely based on BAE SYSTEMS' experience with the EAP aircraft. The main configuration differences are that the P112C-6 has side intakes and is a close-coupled canard-delta, as opposed to the chin intake and long-coupled canard-delta of the EAP aircraft.

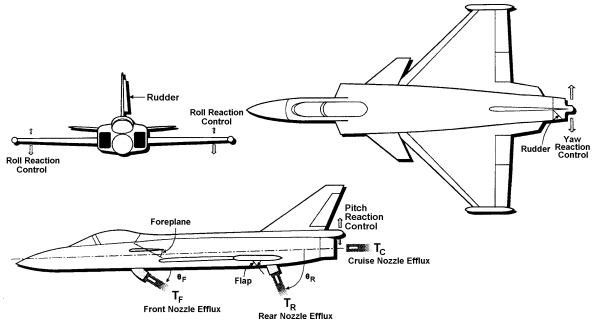


Figure 1. P112C-6 aircraft general arrangement

The project powerplant is the Rolls-Royce RB571-10 direct-lift engine concept, which has two distinct modes of operation:

- Flight mode – in which the lift system is disabled and the engine operates as a conventional turbo-fan as shown below.

Paper presented at the RTO AVT Symposium on "Active Control Technology for Enhanced Performance Operational Capabilities of Military Aircraft, Land Vehicles and Sea Vehicles", held in Braunschweig, Germany, 8-11 May 2000, and published in RTO MP-051.

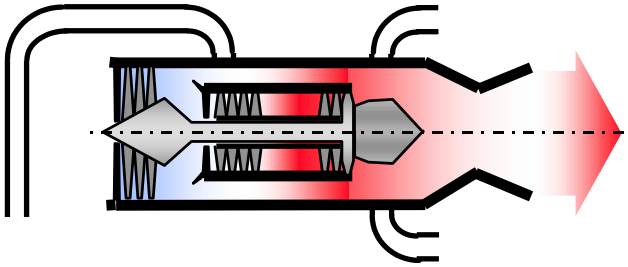


Figure 2a. RB571-10 engine configured in Flight mode

- Lift mode – in which the main core flow is directed through two rear-mounted vectoring nozzles and a proportion of the by-pass air is ducted through to a front lift nozzle. This provides a three-poster remotely unaugmented lift system.

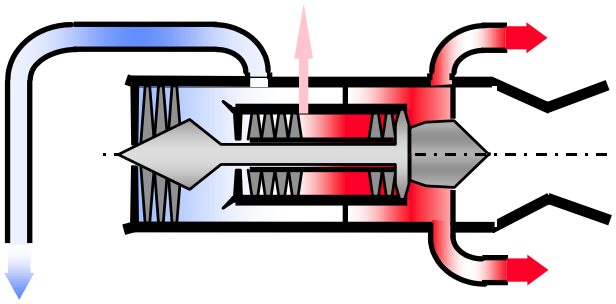


Figure 2b. RB571-10 engine configured in Lift mode

In Lift mode, the engine configuration allows the ratio between the front and rear thrust components to be varied, providing a source of pitching moment control in the hover. The front and rear nozzles are independently actuated, effectively providing four independent motivators:

- engine gross thrust, X_G
- engine differential thrust, X_S
- front nozzle angle, θ_F
- rear nozzle angle, θ_R .

A three-axis reaction control system, using engine bleed-air is also available.

In order to effect a transition between the Lift and Flight modes, the engine must undertake a mode change. This entails opening and closing the internal doors that enable (or disable) the lift system, and reconfiguring the engine control system.

Control strategy and architecture

In order to significantly reduce pilot workload whilst providing acceptable handling qualities in recovering the aircraft to a ship or dispersed site, the decision was made to adopt the 'two-inceptor' longitudinal control strategy shown below. This allows the pilot to control flight path using the right hand, and speed using the left hand, throughout the transition from wing-borne flight to the hover. Between 100 and 70 knots, there is a blending region, within which, the pilot's commands become referenced to earth-axes.

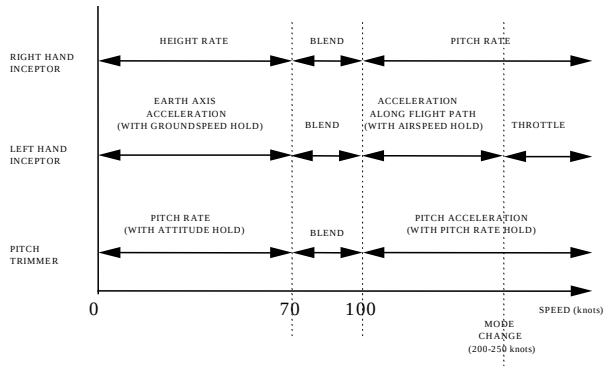


Figure 3a. Longitudinal control strategy

The lateral / directional control strategy adopted is shown below and is fairly conventional. However, the blend between bank angle and roll rate commands is worthy of note. This blend could be placed over a lower speed range, but has been chosen to allow the pilot to command a rate in each axis (height rate and turn rate), thereby providing control harmonisation.

Automatic turn co-ordination in pitch is also provided, throughout the Lift mode. This has been shown to be a significant contributor to workload reduction.

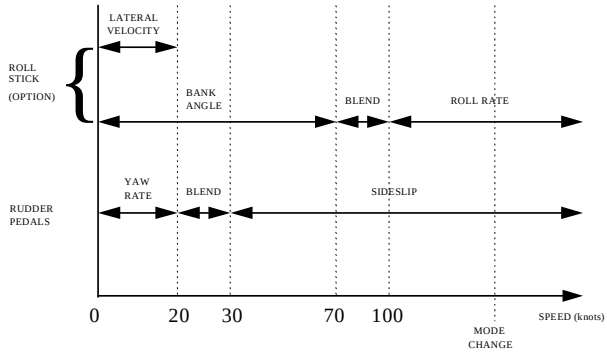


Figure 3b. Lateral / directional Control Strategy

In adopting this approach, high levels of closed-loop augmentation are required in each axis. This can only be realistically provided through a full authority digital flight control system. A typical high-level control law architecture is shown below.

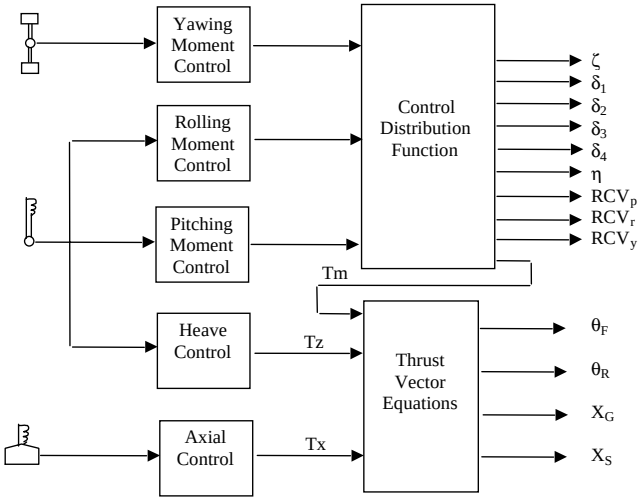


Figure 4. Typical control law architecture

The control distribution function routes the moment contoller outputs to the appropriate effector(s), taking into account control redundancy and the variation in control effectiveness across the flight envelope. It can route the pitching moment demand to either the flaps, foreplane, pitch RCS or the thrust vector equations.

Where the dynamic pressure is high enough, the aircraft is controlled conventionally via aerodynamic forces and moments. However, as dynamic pressure is reduced, the vectored thrust forces and moments (Tx, Tz and Tm) are phased in, eventually completely replacing the aerodynamic terms in the hover condition. The Thrust Vector Equations are used to transform the thrust vector force and moment demands (Tx, Tz and Tm), into front and rear nozzle angle and thrust component demands.

The Harrier Configuration

Prior to analysing the P112C-6 configuration in detail, it is worth considering the Harrier aircraft configuration. This is a relatively simple arrangement (shown below) based around a four-post lift system.

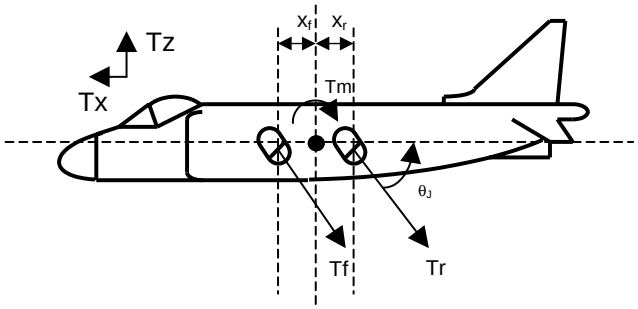


Figure 5. Harrier lift system

The front and rear lift-posts are provided by exhausting air from the engine fan and turbine stages, respectively, through two pairs of ducted nozzles, located fore and aft of the centre of gravity. Movement of the aircraft's centre of gravity is restricted such that thrust-induced pitching moments are minimised, but also that any pitching moment generated by the engine thrust is well within the trimming capability of the aircraft's reaction control system. This feature helps to make the aircraft flyable during the transition and hover, with a minimum of control augmentation.

Introducing automatic control to such a configuration by including the thrust vector within the feedback loops can introduce several new problems. For example, thrust vector saturation, in terms of dealing with conflicting demands and control law integrator conditioning. This aspect has been successfully addressed for the Harrier aircraft through the DERA's VAAC Harrier research programme [1], in which two-inceptor control laws were flight tested. However, the solutions to these problems are fairly straightforward, due to the relative simplicity of the Harrier's lift system.

The increased levels of augmentation needed to provide a two-inceptor control strategy result in functional complexity, in order to automate the management of the thrust vector. There are several ways that this might be done, such as the use of Trimmaps [6] or by using Non-linear Dynamic Inversion [7]. Here, the basic vectored thrust equations for the Harrier are represented by a simple static inversion of the equations used to transform the body-axis rectangular components of demanded thrust (Tx and Tz) into nozzle and throttle demands:

$$\text{Nozzle angle } (\theta_j) = \tan^{-1}(Tz / Tx)$$

$$\text{Throttle } (Tf + Tr) = K \sqrt{(Tx^2 + Tz^2)}$$

It should be noted that at low speed, where there is little or no aerodynamic control power, control of the aircraft's pitching moment is performed by the reaction control system alone.

The above equations are only valid if there is adequate nozzle angle and throttle quadrant ranges to satisfy the demands. When this is not the case, and either the throttle or nozzle angle demand reach an authority limit (i.e. become saturated), modified control action must be taken.

The diagram below shows a 2-D plot of a strategy for dealing with saturation of the thrust vector for the Harrier configuration.

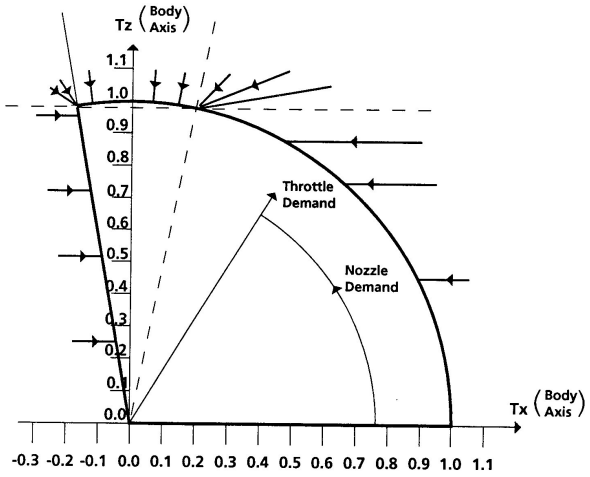


Figure 6. Saturation strategy for the Harrier

The diagram shows how demands that exceed the capability of the thrust vector are mapped back onto the available throttle and nozzle boundaries. It can be seen that generally, excessive Tx demands are mapped back onto the maximum throttle arc, by satisfying the Tz demand and reducing the Tx demand. This approach assigns priority to the vertical axis and ensures that heave transients are minimised.

Difficulty can be encountered in ensuring that the algorithms required to provide the above strategy are continuous and cover all possible combinations of pilot/FCS demands. In order to provide confidence that the algorithms perform their intended role, a pictorial representation of the operation of the algorithms is useful. Such a representation is shown in the figures below where advantage is taken of 3-D graphics. It should be noted that the Tx and Tz demands have been non-dimensionalised.

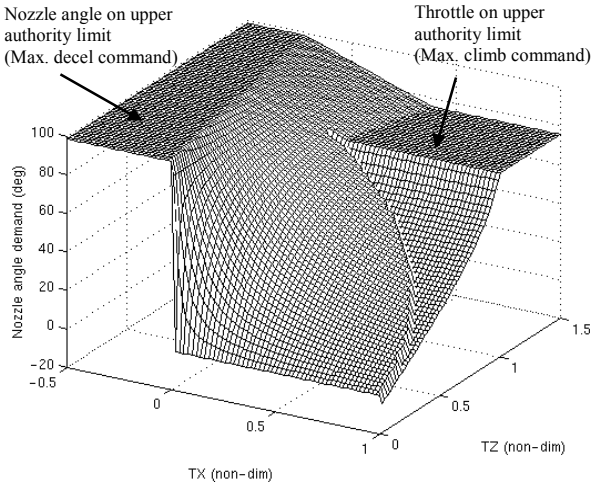


Figure 7a. Harrier nozzle angle visualisation

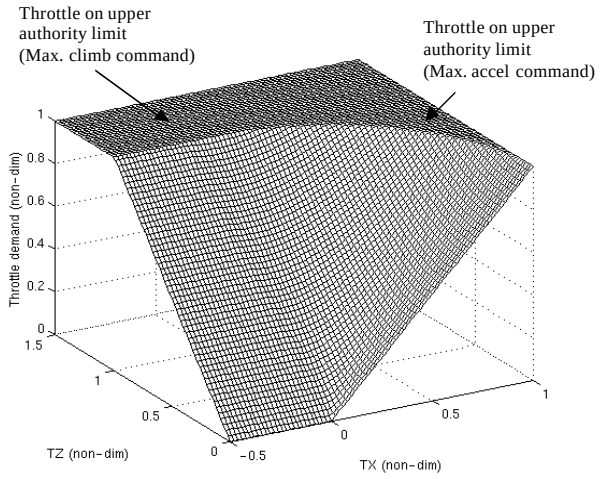


Figure 7b. Harrier throttle visualisation

Thrust vector equations for P112C-6

Having established the thrust vector equations for the simpler Harrier configuration, the more complex P112C-6 configuration can now be examined.

The figure below shows the P112C-6 aircraft, with its lift system geometry marked up with x- and z-axis distances between the centre of gravity and the points at which the front and rear thrust vector components act.

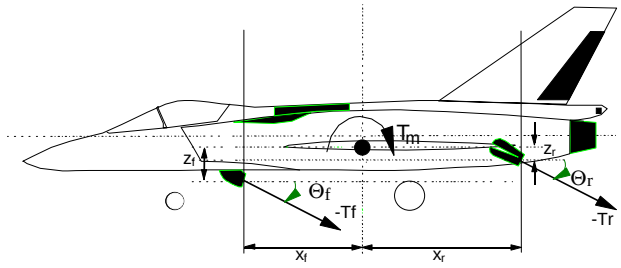


Figure 8. P112C-6 Lift System Geometry

By considering the above diagram, a static relationship can be derived between the front and rear thrust vector components and the body axis longitudinal forces and moment.

$$Tx = Tf \cos(\theta f) + Tr \cos(\theta r)$$

$$Tz = -Tf \sin(\theta f) - Tr \sin(\theta r)$$

$$Tm = Tf\,(Xf \sin(\theta f) + Zf \cos(\theta f)) + Tr\,(Zr \cos(\theta r) - Xr \sin(\theta r))$$

Since there are four control variables but only three longitudinal degrees of freedom, there exists a level of redundancy. By expressing the front lift nozzle vector angle as a function of Tz and Tx, as in the Harrier example above:

$$\theta f = \tan^{-1}(Tz / Tx)$$

the above equations can be re-arranged to give three thrust vector equations that satisfy the force and moment demands.

$$\tan(\theta r) = \frac{Tm + Tz \cot(\theta f)\,(Zf - Zr) + Tz.Xf - Tx.Zr}{\cot(\theta f)\,(Tm - Tx.Zf - Tz.Xr) - Tx(Xf + Xr)}$$

$$Tf = \frac{Tm - Tx.Zr - Tz.Xr}{(Xf + Xr)\sin(\theta f) + (Zf - Zr)\cos(\theta f)}$$

$$Tr = \frac{(Tm - Tx.Zf)\cos(\theta f) - Tx.Xf \sin(\theta f)}{(Zr - Zf)\cos(\theta r)\cos(\theta f) - Xr \sin(\theta r)\cos(\theta f) - Xf \sin(\theta f)\cos(\theta r)}$$

It should be noted that the above equations are unbounded, and are valid only where there exists adequate control authority to satisfy the force and moment demands. Upon saturation of one or more of the control effectors, in order to prevent any stability and control problems that would almost certainly ensue, the thrust vector equations must be modified to maintain control of the aircraft.

It is important to assign priority to each of the three degrees-of-freedom to determine in which order the control loops are to be 'opened' in the event of a first saturation.

Since the pilot is not directly commanding nozzle angle and throttle position, it is likely that when maximum commands are input, the resulting force demands will exceed the available performance capabilities of the aircraft. In this situation, at least one of the demands must be reduced to allow priority to be assigned to another.

Experience has shown that the highest priority should be allocated to the pitching moment demand in order to ensure that attitude control is maintained. The 'long-coupled' P112C-6 thrust vector geometry exhibits the ability to generate very large pitching moments when configured in its Lift mode, which can far exceed the pitch RCS authority. These moments must be controlled to within acceptable limits at all times. Allocating the highest priority to pitching moment control provides two benefits.

- It minimises uncommanded pitch interaction, improving the perceived handling.
- In extreme circumstances it helps provide a stable platform for ejection.

Medium priority should be allocated to the vertical thrust component to ensure that no significant uncommanded height change can occur.

Lowest priority should be allocated to the horizontal thrust component. This is most likely to result in acceleration/ deceleration performance limitations, but can in certain circumstances (for example in low speed tight turns) result in an uncommanded forward speed change.

By monitoring the front and rear nozzle angles and thrust components against their respective limits, thrust vector saturation can be detected and corrective action taken within the control laws.

These principles are best demonstrated by means of an example. For instance, if the pilot commands a straight-in maximum deceleration, it results in the front and rear nozzle angles moving to their forward authority limits. By setting the rear nozzle angle demand to the forward limit (to generate maximum negative Tx) and neglecting the Tx demand, equations can be obtained for Tf and Tr, in terms of Tm, Tz, θf and θr:

$$Tr = \frac{\sin(\theta f)\,(-Tz\ Xf - Tm) - Tz\ Zf \cos(\theta f)}{\sin(\theta f)\,(Xf \sin(\theta r) - Zr \cos(\theta r) + Xr \sin(\theta r)) + Zf \cos(\theta f)\sin(\theta r)}$$

$$Tf = -\frac{(Tr \sin(\theta r) + Tz)}{\sin(\theta f)}$$

By performing this process for each single saturation and then again for each double saturation, modified thrust vector equations result, which are switched in and out, depending upon the level of saturation and the combination of control devices involved.

As with the Harrier example, difficulty can be encountered in ensuring that the algorithms and switching logic that constitute

the vectored thrust equations, are continuous and cover all possible combinations of demands, without excessive transients. With the increased complexity of the P112C-6 geometry, it is important to gain confidence by verifying that the implementation is performing as intended. For example, for a maximum deceleration command, one would expect the rear nozzle angle to be demanded to its forward limit. For a maximum climb command, one would expect the front and rear nozzle thrusts to be demanded to their maximum values.

The complexities of the trigonometric functions and the switching logic provide plenty of scope for an incorrect functional implementation. It is extremely difficult to identify such errors from the coding, since detailed knowledge of how the compiler deals with trigonometric functions might be required. Tabulation of the solutions of the equations is helpful, but produces a mass of information that is difficult to check. It has been found to be beneficial to plot this tabulated data as a series of 3-D plots. The figures below depict the saturation effects, where a nose-up pitching moment of 15 kNm is required from the propulsion system. A series of plots can be produced by varying the pitching moment required.

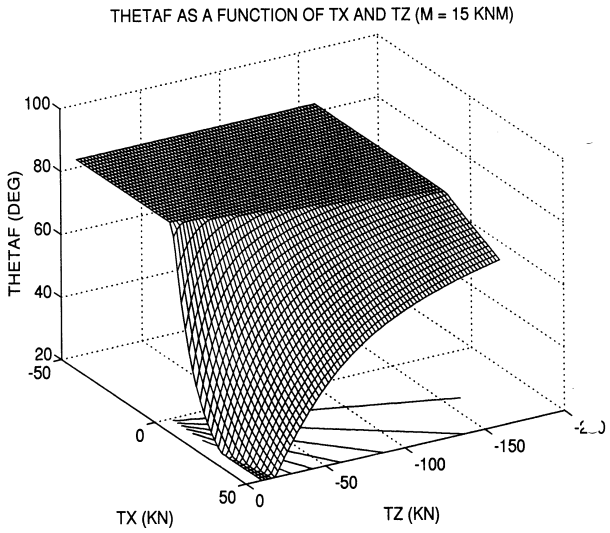


Figure 9a. P112C-6 front nozzle angle visualisation

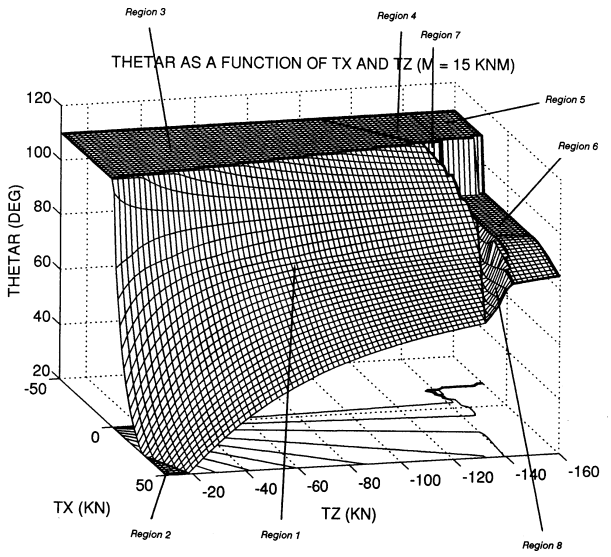


Figure 9b. P112C-6 rear nozzle angle visualisation

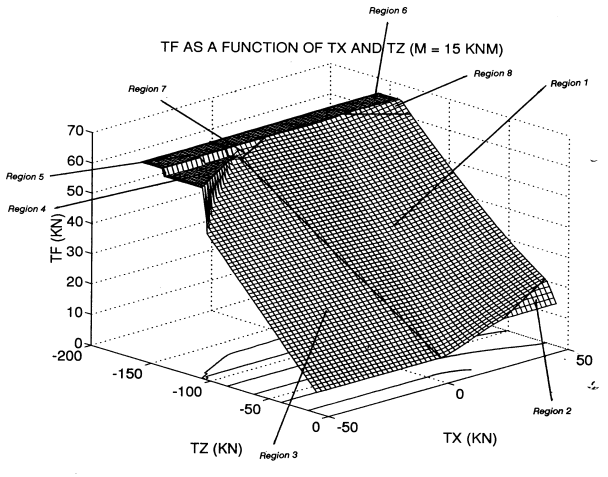


Figure 9c. P112C-6 front thrust visualisation

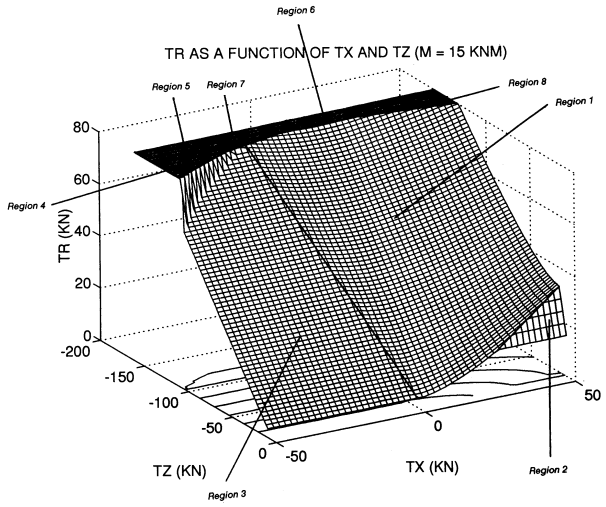


Figure 9d. P112C-6 rear thrust visualisation

Each of the marked up regions on the plots corresponds to a saturated condition:

- Region 1 – Unsaturated – not control limited.
- Region 2 – Single saturation - θ_R lower authority limit (maximum deceleration / maximum sink commanded).
- Region 3 – Single saturation - θ_R upper authority limit (maximum deceleration commanded).
- Region 4 – Double saturation – T_R & θ_R upper authority limits (maximum deceleration / maximum climb commanded).
- Region 5 – Triple saturation – T_R , T_F , θ_R upper authority limits (maximum deceleration / maximum climb commanded).
- Region 6 – Double saturation – T_R & T_F upper authority limits (maximum climb commanded).
- Region 7 – Single saturation – T_R upper authority limit (maximum climb commanded).
- Region 8 – Single saturation – T_F upper authority limit (maximum climb commanded).

This form of plot has proved to be invaluable in the development of the thrust vector equation algorithms and for verifying the implementation. It also aids the understanding of the control of the aircraft.

Development of the thrust vector equations

Ultimately, the thrust vector equations will form a major portion of the functional integration of the flight and propulsion control systems. In this role, the thrust vector equations will reside in the flight control computer where they will be required to take signals from the propulsion control system. These signals will indicate saturation of the engine controls, both in terms of gross thrust and thrust split.

In developing the thrust vector equations it is advisable to employ a staged development process:

- The first stage has been covered in the previous section, where the algorithms and switching logic that constitute the thrust vector equations have been fully tested, in an open-loop manner, over the full range of operating conditions.
- The equations need to be linearised and appropriate feedback loops designed to control the aircraft motions. The action of the controllers on the error signals will provide the Tx, Tz and Tm demands that need to be satisfied.
- In the next stage, the thrust vector equations need to be implemented in a closed-loop simulation of the aircraft, including a model of the engine and the full control laws. At this stage, the engine model should consist of a simple low order transfer function representation with notional, engine gross thrust and thrust split limits, as this will ensure rapid development and allow confidence to be gained in the closed-loop operation.
- Having established a satisfactory closed-loop arrangement, increased engine complexity can be introduced. At this stage, signals need to be synthesised from the engine control system variables, which can be fed into the thrust vector equations, to indicate when engine saturation has occurred.

Integrator anti-wind-up

Integral action is generally used in each of the control loops, to minimise drift in the commanded variable. In this case, specific action is required to prevent the integrators from 'winding-up' in the presence of saturation.

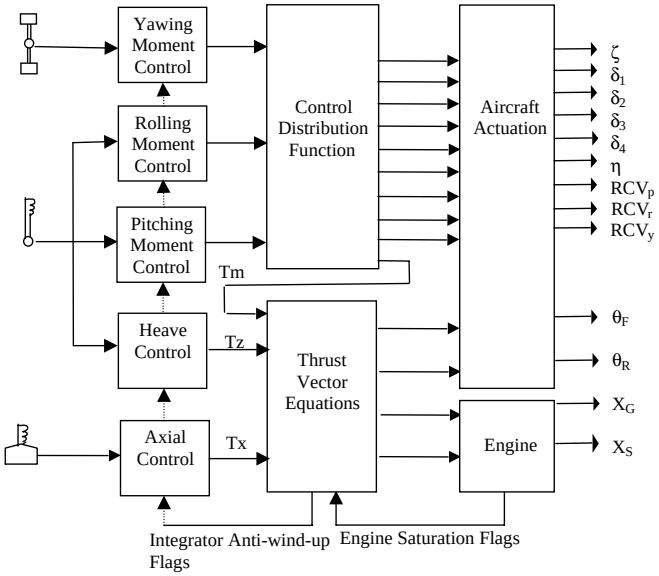


Figure 10. Functional arrangement of integrator anti-wind-up logic

A suitable control law structure is shown above, including the three separate control loops for the Tx, Tz and Tm demands, the thrust vector equations and the signals used to freeze the integrators. Also shown are the feedback signals from the propulsion control system (PCS) that are used to monitor engine saturation.

Simulation development and visualisation

At this stage, full development testing can start. Initially, off-line analysis using a full-envelope simulation model of the aircraft, engine and control system should be used to develop the control laws to an adequate standard for pilot-in-the-loop simulation. This model should include:

- A full aerodynamic representation of the aircraft including jet-induced effects. This should cover the extreme values of incidence and sideslip that can be achieved at low speed.
- A full non-linear representation of the flight control system, including control laws and hardware.
- A full non-linear representation of the engine and its control system.

During pilot-in-the-loop simulation, the operation of the engine and nozzles should be observed and recorded, as this will give an early warning, should a thrust vector-related problem occur. A typical engineering console display is shown below. Included on this display are all the aircraft and engine control devices.

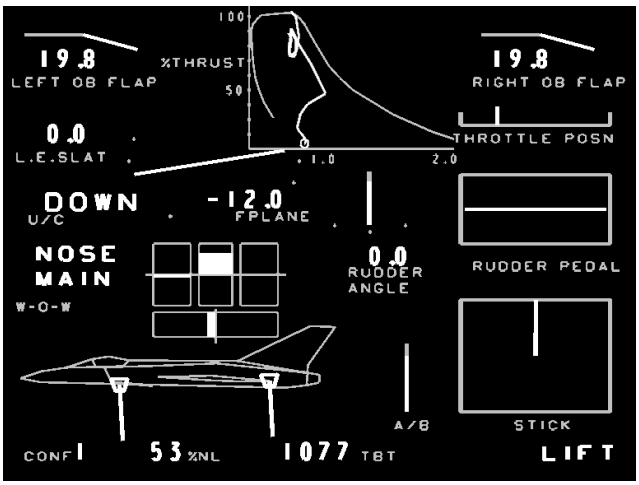


Figure 11. Simulator console engineering display

The engine response is represented by a 2-D plot of gross thrust versus thrust ratio (top middle). Experience has shown that a locus plot of the engine response is useful for observing the engine behaviour in relation to its control boundaries. Typically, the engine response locus should remain visible for between 2 and 5 seconds, to prevent excessive clutter. The front and rear nozzle vector angles are shown on the aircraft representation, which also moves with aircraft pitch angle, giving an earth-referenced view. Each of the aerodynamic surfaces is represented through a simple hinged surface and the RCS valve openings are represented by simple rectangles, representing the linear opening of each of the RCS valves.

Closed-loop response characteristics

The figure below shows the aircraft response to a full stick pull (+5 m/s height rate command) in the hover.

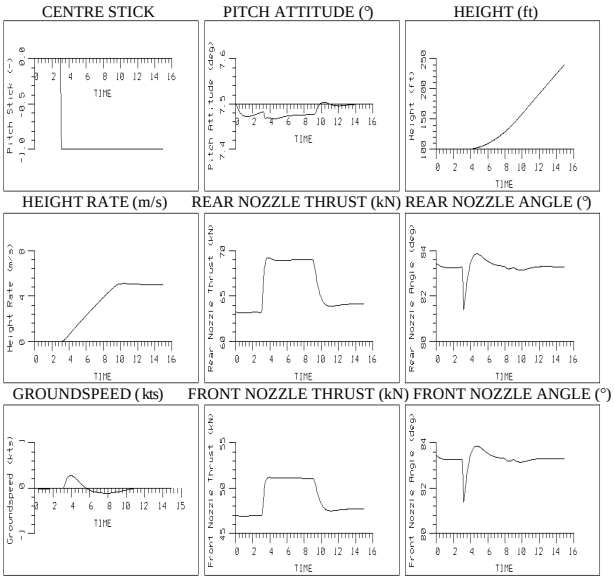


Figure 12a. Response to full back stick in the hover

It can be seen that the front and rear thrust limits are saturated for about 6 seconds, whilst the aircraft height rate builds up to the commanded value. The excellent level of decoupling can be seen in the minimal disturbances in pitch attitude (<±0.1°) and groundspeed (<±0.5 kts). The vectored thrust equations and anti-wind-up logic are working as intended.

The figure below shows the aircraft response to a maximum deceleration command (-0.4 g axial acceleration) at 80 knots.

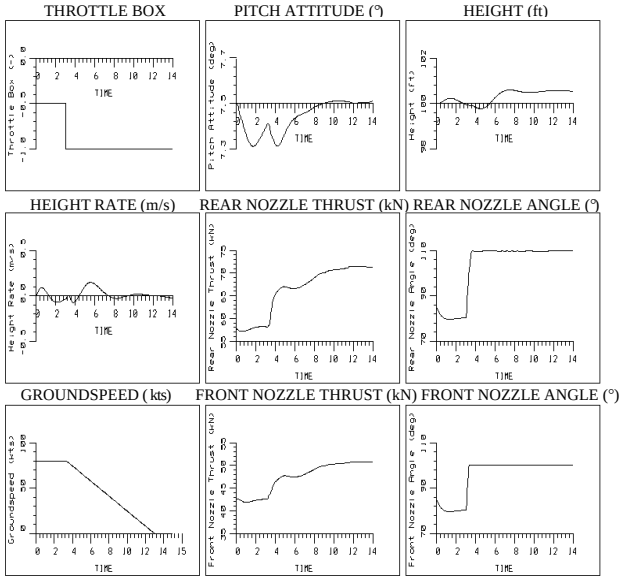


Figure 12b. Response to maximum deceleration at 80 knots.

It can be seen that the front and rear nozzle angles reach their respective forward limits in response to the command and remain there throughout the response. Again the excellent level of decoupling can be seen in the minimal disturbances in height (<±1 ft) and pitch attitude (<±0.2°) . Once again, the thrust vector equations are working as expected.

Whilst these responses show excellent decoupling characteristics, they are for the baseline model, where the thrust vector geometry is accurately measured. Studies have been performed to gain insight into how the decoupling degrades with centre-of-gravity movement. This showed that quite large movements could be tolerated (±0.2m), whilst maintaining satisfactory decoupling. The effect of varying aircraft mass is also a significant effect, as this changes the thrust margin. However, the integral action in each of the control loops helps to minimise decoupling and drift.

Lessons learned

In developing the thrust vector equations for the P112C-6 configuration, a number of lessons have been learned, which are listed below:

- It is considered essential to perform a staged development of the thrust vector equations, in order to gain confidence in their operation at each stage.

- The algorithms required to implement the thrust vector equations contain complex trigonometric functions and switching logic. Visualisation of these functions is vital in building confidence in their operation.

- An advantage of the analytical expressions used in the thrust vector equations, is that they can be easily differentiated to provide analytical expressions for the local gradients. These can then be used in the linear design of the feedback loops. This also eliminates the requirement to store a large amount of linearised data.

- Engine model complexity should be considered at each stage of the development. Generally, two or three engine representations will exist, each exhibiting various levels of complexity. These may range from a simple second-order transfer function representation, with rate and amplitude limiting, to a full thermodynamic representation of the engine with its control system. Experience has shown that much progress can be made early on in development with a very simple engine representation.

- The dynamic response characteristics of the engine / airframe combination are key to providing acceptable handling. Undesirable response characteristics in either can result in design difficulties. It is therefore important that the engine and airframe development teams work together effectively to enable a balanced design.

- Saturation of the thrust vector can be minimised by careful limiting of the pilot's commands and the Tx and Tz demands, upstream of the thrust vector equations. This effectively limits the accelerations required of the aircraft and should be achieved after considering the aircraft performance specification and the impact on aircraft handling. For example, minimising the Tx and Tz demands to improve decoupling at the expense of aircraft performance should be considered, but only if the performance penalty is marginal and acceptable.

Discussion

The concept of the vectored thrust equations, as presented in this paper, are a static inversion of the forces and moments associated with an aircraft's lift system. The equations form part of the flight control laws, in conjunction with other inverse terms such as those required to normalise aerodynamic control powers (to correct for changes in dynamic pressure). Dynamic conversion terms are excluded here, but could be added, to ensure common phasing of all the thrust vector components. This would help to minimise the coupling due to out-of-phase forces and moments.

The scheme described in this paper is just one of a number of options available for designing control laws for a complex STOVL aircraft. Other related approaches to control law design,

such as the use of Trimmaps [6] or Non-linear dynamic inversion [7], can be used to develop a satisfactory set of control laws.

All three approaches can potentially produce extremely good results for a datum aircraft configuration. There is a further major challenge in ensuring that the control system provides adequate handling over the full range of aircraft configurations and over the full flight envelope. For methods employing full non-linear dynamic inversion, there is the potential for an extremely complex inversion task, which may lead to adoption of on-board aircraft and engine models, with their associated complexity.

The complexity of the aircraft configuration and desired operating envelope will help to decide on the level of inversion that is necessary to generate the control system design. It is expected that all approaches will encounter similar challenges, since these will be mainly associated with the physical layout of the aircraft configuration and its propulsion system. For example, some of the major challenges include the determination of the following:

- The most appropriate pilot command strategy.
- The most effective use of the aerodynamic and propulsion controls.
- Satisfactory decoupling of aircraft responses.
- Correct conditioning of integrators and moding logic.
- Satisfactory handling qualities for transition and jet-borne flight. This is the subject of ongoing research [8].

This paper has outlined some of the aspects to be considered when designing flight control laws for a STOVL aircraft. The theme of the paper has been the visualisation of some of the control law functions, as this is believed to be an important aspect of any advanced design, which is complex and very non-linear. The use of advanced graphics should be used wherever possible to aid the understanding and to support the verification of complex systems. It is believed that this is an area of future research that may be beneficial for future systems, which will no doubt, further increase in complexity, in line with advances in computing capability.

Acknowledgements

The authors would like to acknowledge the support of the UK Ministry of Defence Procurement Agency and the Defence Research Agency for funding STOVL research programmes that provided the background to this paper.

References

1. C.Fielding & S.L.Gale, ‘Flight Demonstration of an Advanced Pitch Control law in the VAAC Harrier Aircraft’, AGARD-CP-560, 1995.

2. G.T.Shanks, S.L.Gale, C.Fielding & D.V.Griffith, ‘Flight Control and Handling Research with the VAAC Harrier Aircraft, in TISCHLER,M.B. (Ed.): ‘Advances in Aircraft Flight Control’, (Taylor and Francis, 1996).

3. D.A.Allen & R.J.Sleeman, ‘The Integrated Flight and Propulsion Control System Programme’, International Powered Lift Conference, London, 1994.

4. C.Fielding, ‘ Design of Integrated Flight and Propulsion Control Systems’, AGARD Conference Proceedings, CP-548, 1993.

5. J.D.B.Paines, ‘Optimising STOVL Flight Control Functionality for Flying Qualities’, International Powered Lift Conference, London, 1998.

6. B.W.Rawnsley, S.J.Andrews, G.W.D’Mello, L.D.Gillett ‘The Application of Trimmaps to the Design of STOVL Aircraft’, International Powered Lift Conference, London, 1998.

7. J.Franklin, ‘Revised Simulation Model of the Control System, Displays, and Propulsion System for an ASTOVL Lift Fan Aircraft’, NASA Tech. Memo 112208, 1997.

8. J.C.Gibson, P.M.Lodge & C.Fielding, ‘Development of handling qualities criteria for STOVL Aircraft', Powered Lift Conference, Arlington, 2000.

Paper #26

Q by Daniel Walker: Are the complex phenomena (e.g. engine behavior) modeled well enough that they (i.e. the models) provide useful information over-and-above the small perturbation model used in the control system design?
Are there any nasty dynamics that make this a potentially tricky contest problem?

A. (P. M. Lodge): Yes, the small perturbation model is derived directly from a full non-linear thermodynamic model of the engine and its control system. The interaction of the engine thrust flow field with the airframe is also fully modeled.
Yes, there is much potential for coupled response from the engine producing heave/pitching moment transients. The flight control laws can be used to minimize the coupling, but it is preferable for the FCS and PCS designers to work together, understand each other's problems and develop a balanced solution.

This page has been deliberately left blank

Page intentionnellement blanche

Use of ATTAS for ACT Research

J.-Michael Bauschat
Gunnar Duus
Klaus-Uwe Hahn
Wieland Heine
Dehlia Willemsen

Deutsches Zentrum für Luft- und Raumfahrt e.V.
Institut für Flugsystemtechnik
Lilienthalplatz 7, D-38108 Braunschweig, Germany
www.fm.bs.dlr.de/flugsystemtechnik

Summary

The application of active control technologies (ACT) has a potential to enhance the operational performance capabilities of aircraft. In particular the introduction of digital computers with today's processing power allows to think about more and more complex and/or unconventional control schemes for more efficient operation of aircraft. For the final validation and verification of new approaches the flight test is the ultimate test for concept demonstration under real world conditions. For this purpose DLR uses its flying testbed ATTAS (Advanced Technologies Testing Aircraft System) which is ideally suited due to its unique configuration. ATTAS is configured to meet the requirements of a variety of applications by freely programmable functions and interface capabilities to link customer soft- and hardware.

This paper summarises the recent and current projects and research activities relevant for ACT in which flight testing using ATTAS is an important factor.

Introduction

The use of modern flight control systems offers several improvements such as increased manoeuvrability, performance and flight safety as well as a reduced workload. The development, optimisation and investigation of advanced ideas requires precise system modelling of the augmented aircraft. This includes the application of non-linear simulation techniques for extensive system analyses.

In the future, a manipulation of the wing shape in order to optimise the aerodynamic characteristics will be used. This is often referred to as "smart wing". One rather basic example of this technique is the use of special flaps – the so-called direct lift control (DLC) – to simulate dynamic properties of other aircraft as it is done on ATTAS (see below). This also requires the use of sophisticated flight control systems.

In this paper the following programs are described. All of them deal with modern control laws and involve flight testing on ATTAS. The SAFIR project investigated control laws for a small transport aircraft and included aspects such as dissimilar software and mode transients. The European REAL project aims at establishing a more efficient approach for the design of autopilot systems of civil airliners. The proposed controllers will be flight tested on ATTAS. In order to validate a new criterion for the prediction of adverse aircraft-pilot coupling problems due to rate limitations in the flight control system the SCARLET3 program was conducted. In the ARCORE project unconventional control schemes (such as differential thrust for yaw control) and different reconfiguration strategies (in case of control surfaces failures) were examined and flight tested. To familiarise pilots with different control schemes in a safe but realistic environment the in-flight simulation capabilities of ATTAS can be used as was recently done for the French test pilot school E.P.N.E.R. ATTAS is also used for investigating the possible benefits of an active sidestick with force feedback that has been developed by DLR and TU Braunschweig.

Test aircraft ATTAS

DLR's flying testbed ATTAS (Advanced Technologies Testing Aircraft System, figure 1) is based on a VFW 614 civil transport aircraft (44 passengers, twin turbofan, short haul) that was modified to serve as an in-flight simulator and technology demonstrator. Modifications include the fly-by-wire/light flight control system, the in-flight simulation architecture (explicit model following system), complete flight test instrumentation, as well as data acquisition and recording. ATTAS is configured to meet the requirements of a variety of applications by freely programmable functions and interface capabilities to link customer soft- and hardware. The aircraft is primarily used for DLR's research in the fields of flight control, flight guidance, flying qualities, and man-machine interfacing.[1]

Paper presented at the RTO AVT Symposium on "Active Control Technology for Enhanced Performance Operational Capabilities of Military Aircraft, Land Vehicles and Sea Vehicles", held in Braunschweig, Germany, 8-11 May 2000, and published in RTO MP-051.



Fig. 1: DLR's flying testbed ATTAS

Programs

In this section the projects mentioned above are described more in detail.

SAFIR

With regard to the development of the Aerospace Technologies Demonstrator aircraft by DaimlerChrysler Aerospace (Dasa) Airbus new control laws for electrical flight control systems have been tested on ATTAS. In the SAFIR project (**S**mall **A**irliner **F**light Control Laws **I**nvestigation and **R**efinement), for the first time in Germany, this kind of manual flight control laws (FCLs) for small future civil transport type aircraft have been flight tested by a joint team from Dasa Airbus and DLR Institut für Flugsystemtechnik.[2,3]

The demand for modern electronic primary flight control systems in small transport aircraft (100 seater) formulates the need for new cost-effective concepts providing familiar standard control functions based on proven techniques that are accepted by the certification authorities. In the frame of a technology program for an electronic flight control system control laws have been developed by Dasa to cope with these challenges. The SAFIR project aimed at the validation, demonstration, and evaluation of the flight control laws by a flight test program. In April 1993 Dasa and DLR launched this project. Already half a year later the first flight test on ATTAS was carried out.[2]

Flight Control Laws

The investigated FCLs provide normal laws with different modes and various envelope protections (see figure 2). The protections prevent certain boundaries from being exceeded. For the operation of the normal laws numerous signals need to be measured, consolidated, processed, and fed back. In case of any system failure affecting adversely the correct operation of the normal laws a system degradation to the direct laws takes place. The direct laws link the inceptors directly to the control surfaces by fixed gains simply providing feed-forward control.

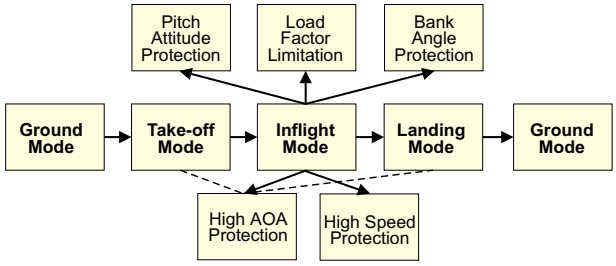


Fig. 2: Modes of the Normal Flight Control Laws[3]

Development Process

The FCLs were designed by Dasa using their Computer Aided Software Engineering (CASE) tool HOSTESS (High Order Structuring Tool for Embedded System Software) which provides a user interface on a graphical block diagram level.[4] This tool offers standardised software specification, automated coding process, automatic checks and testing, improved software documentation, and facilitated configuration management.

The optimisation of the FCLs was done in an iterative process over different loops illustrated by Figure 3. After the careful design of the FCLs using Dasa's Development Flight Simulator they were adapted to ATTAS in the ATTAS System Simulator. The latter provides the identical data processing environment as available on board the test aircraft. If any modification of the software was required from this checkout HOSTESS quickly produced the new code. After having successfully passed the final check in the ATTAS System Simulator the FCL software was qualified for test flight by a revision mark.

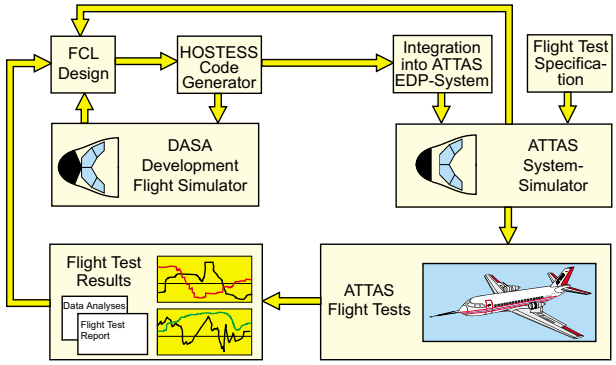


Fig. 3: Flight Control Law Development Process

The ATTAS system simulator was also used for the pilot's familiarisation with the current version of the FCL, for flight program optimisation, and training of the test procedures. This

includes the final design of test sequences and their arrangement for flight. Each flight sequence was precisely defined on a flight test card. The order of the test cards determined the course of the respective flight experiment.

Flight Tests

The SAFIR project was separated into two phases. In the first phase (SAFIR 1) the FCL software was organised in an independent subroutine which was completely transferred into ATTAS' Experiment and Control Computer (ERR, see figure 4). The data processing system supplied the required data to the FCL functions via an experiment-specific software interface. This included continuous stream data like sensor signals as well as artificially generated information only needed to satisfy the FCL inputs. The output of the FCLs were again transferred via the interface to fill the vector of control variables in the ATTAS data processing system directly stimulating the control surfaces. This first campaign, SAFIR 1, aimed at evaluating the functionality and the performance of the FCLs within the whole flight envelope. Mainly the correct function and the handling qualities of the normal laws (including flight envelope protections that prevent critical flight conditions) have been investigated.[2]

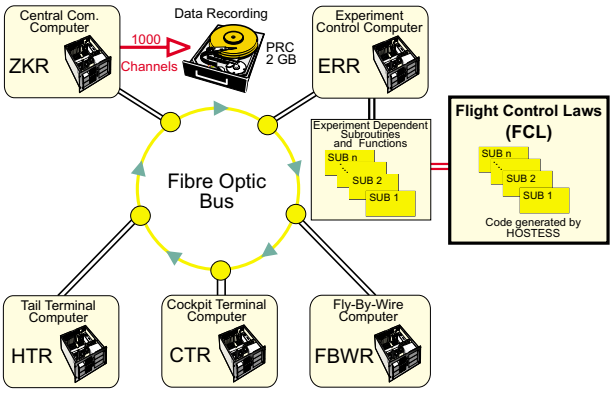


Fig. 4: Experiment Configuration of SAFIR 1

The second phase (SAFIR 2) focused on system relevant aspects.[3] Two dissimilar versions of the FCLs (in FORTRAN and ADA) were created to be implemented in a command and a monitor lane hosted by the high performance Flight Control Law Computer (FCLC). This FCLC had been installed on-board ATTAS for SAFIR 2 and was connected to the data processing system via the Central Communication Computer (ZKR) as illustrated in figure 5.

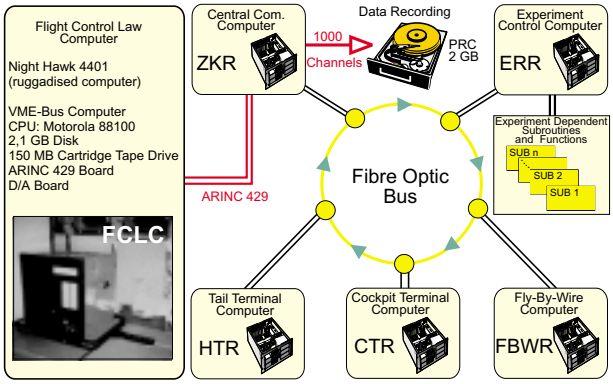


Fig. 5: Experiment Configuration of SAFIR 2

Special control inputs and flight tasks to validate the functionality of the FCLs throughout the entire flight envelope including the protections have been designed. The generic signals that have been used in this phase mainly consisted of precisely defined manually and artificially generated sidestick, pedal, and thrust lever inputs to stimulate the aircraft dynamics and to check the correct operation of the FCLs. For handling qualities investigations a specific manoeuvre was designed composed of combined movements in the horizontal and vertical plane (see figure 6). Pilot questionnaires have been developed asking for Cooper-Harper ratings for the different task sequences. The FCL performance in normal airline operation was investigated with typical manoeuvres like synthetic ILS approaches (ILS artificially generated by the ATTAS computer system on "push button" demand), turns and heading changes during (step) climb/decent manoeuvres.

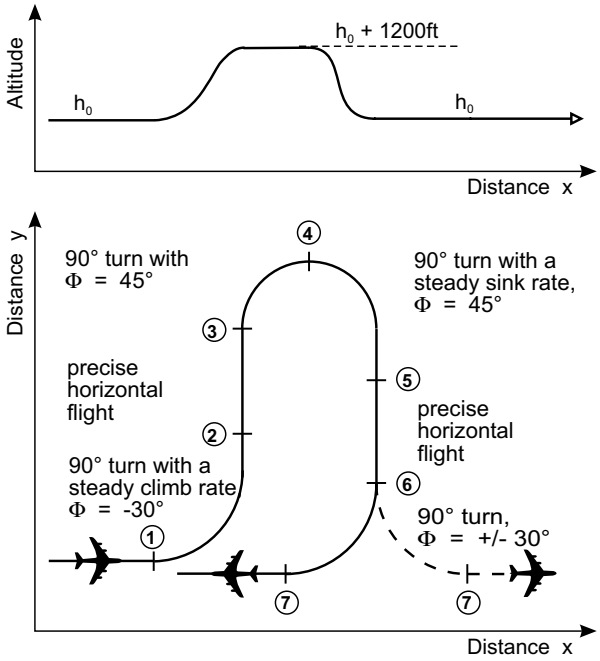


Fig. 6: SAFIR Manoeuvre

Conscientious briefings and debriefings completed the flight test approach.

Results

During the SAFIR project a very effective and well organised infrastructure has been built up between Dasa and DLR. The FCLs were thoroughly validated and successfully demonstrated by a comprehensive flight test program. Within the period from 1993 to 1996 more than 300 single test sequences were carried out with different test and airline pilots. The total flight time for the 12 test flights of the whole project was 32 hours. Altogether 9 different software versions with 110 modifications have been tested.

Due to the dedicated flight data processing system and the well trained flight test team a first analysis was possible a few hours after flight. The flight test results showed high precision of the FCL performance with respect to the requirements.

This is illustrated in figure 7. It shows the results of a dynamic pitch manoeuvre where the pilot applied full stick back. Although this step input to the pitch axis at V_{CAS} = 180 kts results in high pitch attitudes of more than 22° (and additional loads of 0.8g) the AOA protection is able to prevent the aircraft from exceeding the maximum angle of attack α_{lim}.

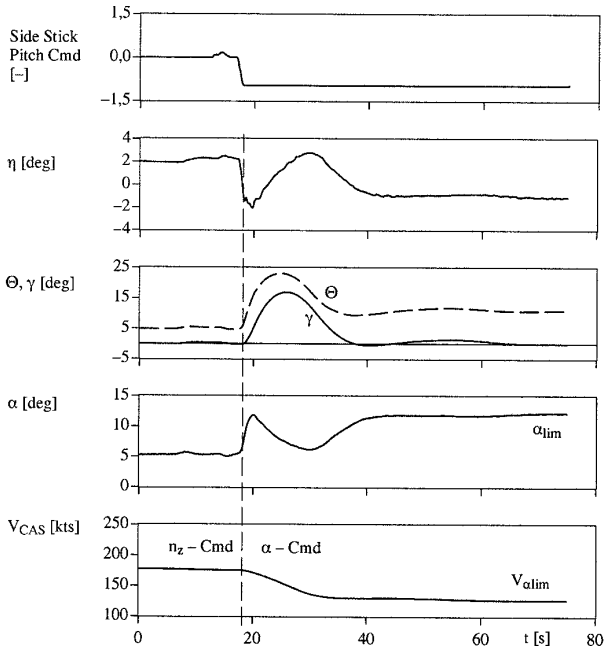


Fig. 7: High AOA Protection[3]

Equally good results have been achieved for the other protections. The handling qualities for airline typical operations were rated Level 1.

Due to careful preparation the flight tests were highly efficient. Because of the comprehensive on-board equipment and the safety pilot concept ATTAS is ideally suited to serve as an FBW (fly-by-wire) platform for flight testing of (uncertified) flight control soft- and/or hardware. Supported by a small but well trained team ATTAS provides the capability to perform experiments in a real world environment (weather effects, sensor characteristics and quality, operational conditions with pilot-in-the-loop etc.) with short term preparation and at low cost and low risk.

REAL

Today's development process for autopilot systems contains a time-consuming trial-and-error approach. This is especially true for automatic landing, which should be robust against a large number of parameters, like runway characteristics, weather and aircraft uncertainties. Modern robust design methods offer ways to handle such uncertainties and parameter variations in a structured manner, see e.g. contributions to Ref. 5. It is therefore interesting to know whether these methods offer the possibility to improve the design process of autopilot systems and to avoid trial-and-error practices. The central question to be answered in the REAL (**R**obust and **E**fficient **A**utopilot control **L**aws design) project thus is: "How can advanced design and synthesis methods contribute to a more efficient design process of robust controllers for CAT III autoland systems of civil airliners?". The REAL project is carried out under a contract awarded by the Commission of the European Communities as part of the 4th Brite/EURAM Frame Work Programme, and started in May 1998. The partners are from France (Aerospatiale Matra Airbus, ONERA), Germany (DaimlerChrysler Aerospace Airbus, DLR) and the Netherlands (Delft University of Technology, NLR).

Controller Design

Two design teams will propose a design process including a modern design method. One design team will use multi-model/multi-objective optimisation based synthesis[6] in combination with Dynamic Inversion[7] and the Total Energy Control System (TECS).[8] The other design team will apply multi-model eigenstructure assignment[6] to the design problem. Both design teams will develop two autoland control laws. First an autoland for a generic civil transport aircraft is designed. This phase results in a design process, which is further tested via a rapid design of an autoland for ATTAS. The project scheme is summarised in figure 8.

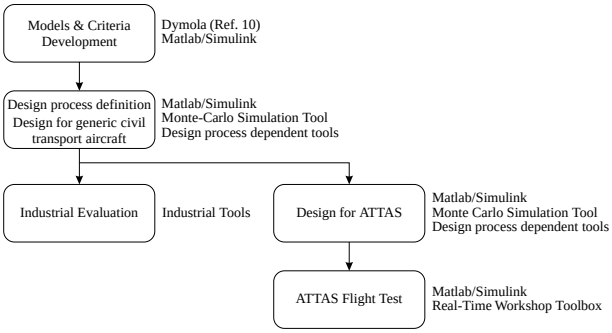


Fig. 8: Overview of the REAL project with the specified tools

For both designs, process criteria and design criteria have been defined. The main criterion for the design process is that it should cover the uncertainties and varying parameters from the beginning of the design. Another major criterion is that the process should offer a large potential for automation. The design requirements are basically the performance requirements of the Joint Aviation Requirements – All Weather Operations (JAR-AWO).[9] These requirements will be specifically tested for by the industrial partners of the project using Monte-Carlo simulation techniques. One product resulting from the project, apart from the design processes, is a Matlab-based Monte-Carlo simulation tool. With this tool each uncertain or varying parameter like terrain slope, runway elevation, wind conditions, etc., is varied according to a selectable probability distribution during a Monte-Carlo simulation run. The outcome of the simulations is statistically evaluated, resulting in histograms and cumulative probability distributions of e.g. the longitudinal touchdown point. Using this tool the design teams are able to test their designs before sending it to the industrial partners for evaluation.

Flight Test

The ATTAS autoland systems from both design teams will also be flight tested on ATTAS. Since the designs are made in the Matlab/Simulink environment, they can be quickly transferred into C-code using Matlab's Real-Time Workshop Toolbox. This code can be implemented on ATTAS' experiment computer.

Before performing a full automatic landing, the controllers will be tested, first in the simulator and then via landings on a virtual runway in about 200-300 ft radio altitude. After positive result of the tests, one or more landings on a real runway will be performed. Via the flight tests it is examined, whether the proposed design processes result in implementable autoland controllers with sufficient performance. The flight test phase of the project is planned for the summer of 2000.

SCARLET 3

Rate limiting in modern flight control systems is the main contributor to the triggering of Pilot-in-the-Loop Oscillations (PIO).[11,12] A new criterion capable of predicting non-linear PIO problems due to rate saturation had been developed at DLR. It is based on the location of the Open Loop Onset Point (OLOP) of the rate limiter in the Nichols chart. An OLOP location above the boundary indicates a danger of PIO problems due to rate limiting. The OLOP criterion has been validated on the basis of several PIO prone aircraft models, and recently new experiments utilising a three degree-of-freedom motion-base research flight simulator have been conducted and analysed.[13-17]

To continue the OLOP validation, especially to gain more experience in the pitch axis, to apply OLOP to a different aircraft type (all configurations flown in the ground-based simulator were fighters), and to examine a phase compensating rate limiter an in-flight experiment with ATTAS was conducted. A secondary goal was to test the automatic code generation tool Real-Time Workshop (RTW) for Matlab/ Simulink, which had recently been installed and configured for use with ATTAS. This section describes the design, conduction and results of that experiment. The project name stands for **S**aturated **C**ommand **A**nd **R**ate **L**imited **E**levator **T**ime delay, part 3, and has been chosen to show continuity with previous work in this field at the institute.

Controller Design

It was decided not to perform an in-flight simulation of another aircraft but to fly the ATTAS base aircraft. To obtain different configurations, simple controllers with multiple gain settings were defined. For the longitudinal axis a simple n_z law was implemented. This has been modified for the second flight in order to further increase the PIO potential. For the lateral axis, a very elementary structure was used, consisting only of roll and yaw rate feedbacks to increase the damping (figure 9). For both the longitudinal and the lateral control laws a rate limiter was integrated into the controller structure. Also in the second flight, a phase compensating rate limiter taken from Ref. 18 will be used. This element is supposed to diminish the negative effects of the rate limiting.

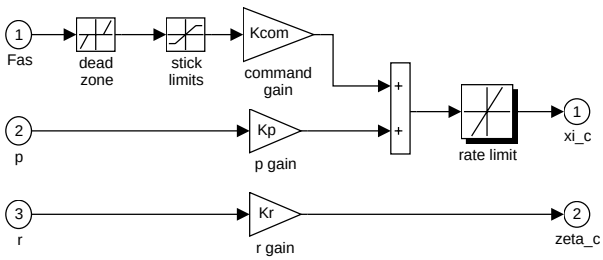


Fig. 9: Lateral controller structure

In each axis, two configurations were defined. Controller 1 used high feedback gains and was expected to exhibit good linear behavior (Level 1) but to have stronger problems after rate limit onset. Controller 2 had lower gains and was expected to have somewhat worse handling qualities in the linear case (Level 2 or 3) but to have a lower PIO potential in the non-linear rate limiting situation (known as Category II PIO).

The design of the controllers was assisted by evaluating the configurations with linear numerical handling qualities criteria such as Neal/Smith, phase rate and C* as well as the non-linear OLOP criterion.

For comparison, also the original ATTAS direct mode (direct link between stick and surface) was investigated in combination with the actuator rate limiter that had been integrated during ATTAS' flight envelope extension to landing capability in fly-by-wire mode.

For the application of the OLOP criterion a simple gain pilot model is needed. For the design of the controllers, gains corresponding to crossover phase angles of Φ_{cr} = -130 deg (longitudinal) and Φ_{cr} = -140 deg (lateral) were used, respectively. These values had been selected based on previous experience. As it turned out, the gains actually applied by the pilots were lower (see below). The OLOP locations for the selected configurations are shown in figure 10. The numbers indicate the rate limit in deg/s. The bold line represents the boundary, all points above that line are predicted to be PIO prone due to the rate limitation.

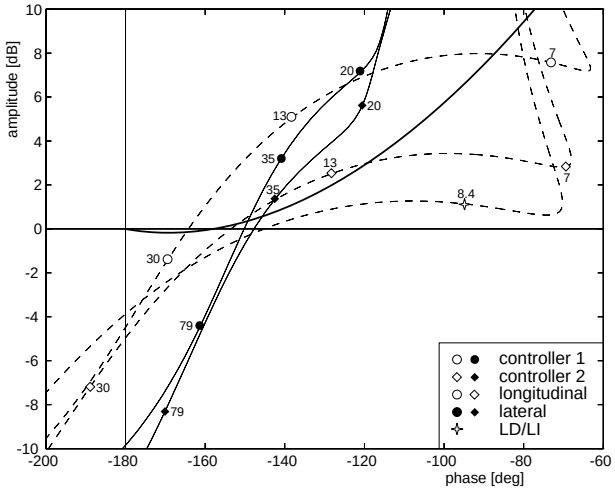


Fig. 10: OLOP locations as designed

As intended, controller 1 for both axes shows a greater Cat. II PIO potential than controller 2. The differences in the lateral axis are relatively small, though. The longitudinal direct mode configuration LD/LI is not Cat. II PIO prone, as is the lateral direct mode configuration whose OLOP lies outside the plotting range (bottom left corner).

Task

The pilot task was to follow a command attitude that was displayed on the primary flight display. A random selection of several predefined sequences was made via the switchboard on the experiment operating panel. A typical pitch sequence can be seen in figure 11. The roll command was similar but used larger amplitudes.

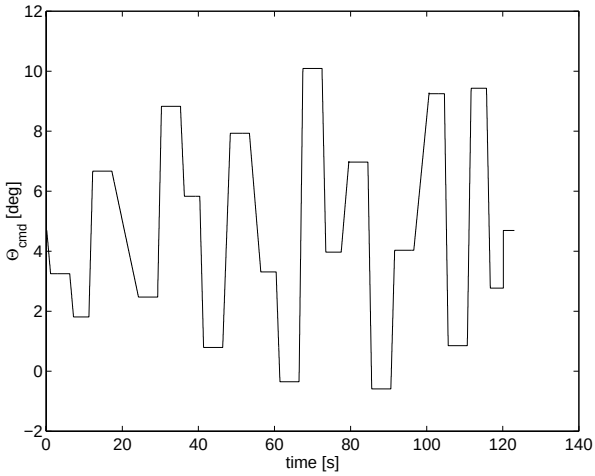


Fig. 11: Typical task sequence (pitch axis)

Conduction

All controllers were designed in Matlab/Simulink and transferred to ATTAS using Real-Time Workshop (RTW). Since in this experiment RTW was used for the first time to transfer Simulink-designed controllers to ATTAS some additional checks were performed to ensure that the automatic code generation worked as expected. As mandatory for ATTAS experiments, all configurations were tested prior to the flight in the ATTAS ground simulator. The data recorded during these tests was compared to Simulink results obtained by feeding the pilot stick input into the Simulink model (open loop) that had been used for the design of the control laws. All RTW related problems were corrected such that finally, the RTW code represented the intended Simulink model.

Results

A Cat. II PIO occurred only once, other cases with bad PIO ratings are due to linear issues. Although the task was designed for activation of the limiters this did only happen very rarely. It seems to be very difficult to get into Cat. II PIO with a stable aircraft. This was also observed in the HAVE LIMITS program,[19] where Cat. II PIO only occurred for extremely low rates.

Pilot model identification

As mentioned before, for the evaluation of the OLOP criterion a simple gain pilot model is required. The well defined tracking task allowed an identification of the pilot behaviour since the input and output signals of the human pilots were available. The same iterative method as described in Ref. 9 was used to obtain a suitable pilot model gain, which represents the real pilot behavior as closely as possible (see Refs. 15 or 17 for details). With these gains, each run can be located in the OLOP diagram.

The most important result is that the gains were lower than assumed. They corresponded to crossover phase angles of approx. -100 deg (longitudinal) and -120 deg (lateral). Therefore, only one of the cases that were designed to be Cat. II PIO prone actually exhibited PIO tendencies due to the rate limit. It has to be noted that not all cases could be flown and that, in the longitudinal axis, the sensitivity to changes of pilot gain is rather low, such that an inaccuracy in determining the gain does not significantly change the OLOP location.

OLOP evaluation

For the validation of the OLOP criterion the differences between the PIO ratings of non-linear (with rate limiting) and linear (w/o rate limiting) runs have to be considered because OLOP only predicts possible problems due to rate saturation. As in previous evaluations, the following parameter was used:

$$DPIOR = PIOR_{non\text{-}linear} - PIOR_{linear}$$

Since no really linear configurations were present in this experiment, the highest rate was used instead. This is justified by the fact that the limiters were not activated for the high-rate cases. For the direct mode cases such an evaluation is not possible since no linear configuration is available. This will be done in the second flight. Figure 12 shows the results, the numbers indicate the DPIOR value.

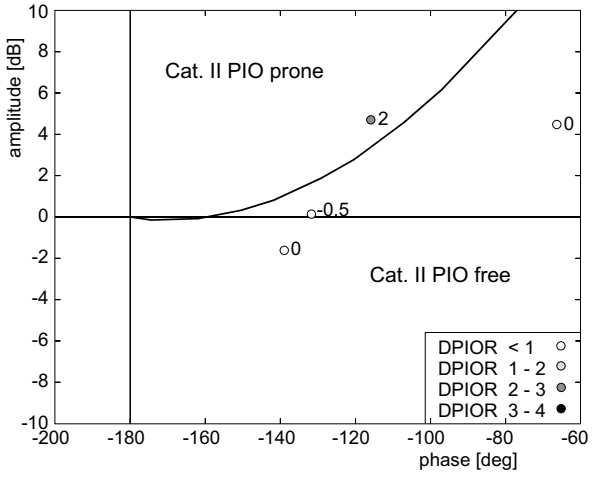


Fig. 12: OLOP evaluation

As can be seen from figure 12, only one configuration suffered from the limitation. Its OLOP is located in the critical area, whereas all other points are located in the non-critical area. This is also the only case where the limiter was significantly activated.

A second flight will be performed to add more configurations and to correct all shortcomings of the first flight. The results will be published in Ref. 20.

ARCORE

In the past numerous reconfiguration techniques have been published and discussed. Each of these techniques, like gain scheduling or online redesign, has advantages and disadvantages regarding speed, safety, accuracy, flexibility, complexity, etc. The ARCORE (**A**rtificial **R**edundancy **Co**ncept for **Re**configuration) project examined two reconfiguration strategies that enhance aircraft performance after severe actuator failures.

The first strategy, the so-called two-step approach, tries to reconfigure the control system facing time constraints and uncertain failure information. Due to the fact that most modern combat aircraft have little time to adjust themselves to a severe failure in the control system it makes sense to split reconfiguration tasks into those that are time-critical and those that are not.

The second strategy puts its emphasis on adding simple reconfiguration rules to existing control systems in order to reduce costs and complexity. This so-called modular approach focuses on specific failure cases like jammed actuators and specific manoeuvres like the landing approach.

Two-Step Approach

It is obvious that a combination of different techniques might be a successful strategy to improve the overall performance of a single reconfiguration technique.

The two-step approach tries to separate reconfiguration tasks that have to be done very quickly to maintain stability and controllability from tasks that try to improve handling qualities and performance of the aircraft in a slower but more sophisticated way (figure 13).

Fast knowledge based restructuring and additional online optimisation of the control parameters combines good reconfiguration speed and proper handling of failure information affected with uncertainties.

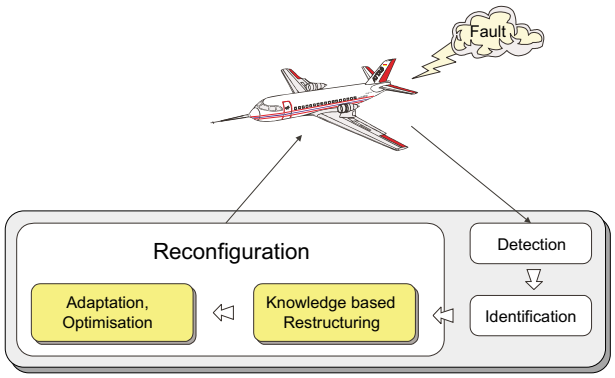


Fig. 13: Two-Step Approach

FAST

The first step of this two-step approach is the **F**ault **A**ccommodation by **S**tructure **T**uning (FAST). The restructuring of the controller depends on predefined control input structures and gains. The restructuring is based on the application of the control mixer concept using the pseudo-inverse to calculate the necessary inputs. As a prerequisite the control input matrix has to be known.

Two ATTAS experiments with elevators jammed in trim position have been conducted. In the first experiment the pilot was asked to use the stabiliser trim button instead of the side-stick to follow a given altitude profile with constant airspeed. While maintaining airspeed he encountered severe problems stabilising the phugoid mode with the slow stabiliser.

In the second experiment, the pilot used the side-stick and the old control law to command the aircraft after a control system reconfiguration. The reconfigured control system transforms his command, formerly sent to the elevator, into equivalent commands for the stabiliser trying to produce the same pitching moment. As a result, the reconfigured control system enables the pilot to fulfil his task much more accurately.

GRACE

Due to the large number of possible actuator failures and their numerous combinations an online adaptation period seems to be necessary as a second step to cover the often unknown impact on the control system. Especially in case of uncertain or missing failure information an optimisation technique can be applied to improve the overall performance of the damaged aircraft.

A **G**enetic **R**econfiguration **A**lgorithm for **C**ontrol system **E**nhancement (GRACE) has been developed to solve the adaptation problem. The reason for favouring evolutionary algorithms for optimisation is mainly that they produce near-optimal solutions very reliably in case of calculus-unfriendly cost functions or other difficult search regimes. Genetic algorithms (GA) successfully apply the principles of natural evolution, i.e. selection, recombination, and mutation, to mathematical and technical optimisation problems.[21,22]

GRACE was tested in simulation and flight experiments. Tracking tasks with an unpredicted elevator effectiveness reduction of fifty percent have been investigated. The feed-forward parameters of an explicit model following control system were continuously adjusted and the flight test results demonstrate a significant reduction in pitch tracking error (see figure 14). Elevator effectiveness degradation starts at zero seconds.

Only the feed-forward parameters of the control system were adjusted online by the adaptation algorithm to avoid stability problems. The adaptation period lasted nearly 25 seconds due to the significant computational effort and the relatively small available computer power (ROLM HAWK/32).

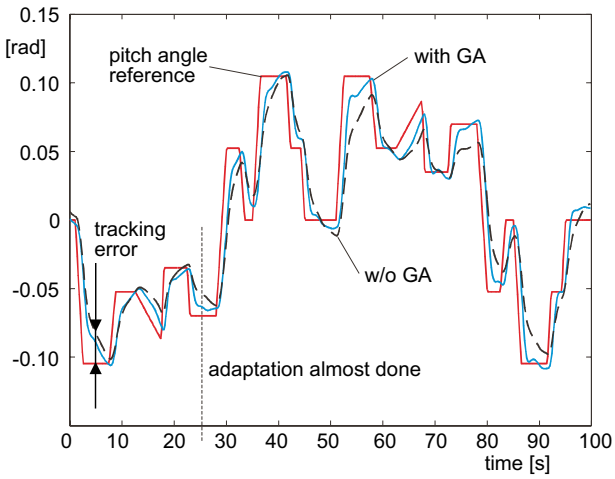


Fig. 14: GRACE Flight Test Result (tracking task with degraded elevator performance)

Since genetic algorithms are well suited for parallel processing a transputer network has been designed and connected to ATTAS' onboard FBW-system. The parallel processing almost halved the adaptation period while retaining the same accuracy.

However, the growing computational burden for covering additional failure cases and the necessary certification effort make it unlikely to combine genetic online optimisation with current control law design requirements – despite the fact that evolutionary algorithms usually provide near-optimum solutions very reliably. In addition, benefits of online optimisation might be small in cases where sufficient failure information is already available or maybe easier to procure.

Modular Approach

Important factors to influence the design process are costs, certification aspects, and the experience of the design team. With good reason modifying existing control systems instead of creating new structures and control laws is common practice in control system design. The objective of the modular approach is to use a given control system and to add a reconfiguration block, changing the existing control laws as little as possible. The development of an augmented thrust-only flight control system by NASA is a good example of that approach.[23]

In the following example a total loss of hydraulic pressure is assumed. All primary control surfaces, i.e. elevator, aileron, and rudder, are no longer available. The landing gear is lowered and the flaps remain locked. The only available controls are the two engines and the electrically driven stabiliser. This failure scenario represents a severe emergency situation with little controllability left. Pitch moments can only be controlled by very slow stabiliser deflections with a rate limitation of 0.25 deg/s. Yawing motion can be controlled by means of differential thrust and roll moments via the relatively small dihedral effect also involving differential thrust. Normal symmetric thrust is used for speed and flight path angle changes.

The original control system and the flight evaluation task used in this example were derived from the RCAM (Research Civil Aircraft Model) design challenge with modifications regarding the aircraft model and the failure conditions.[24]

To check the control system logic and to make the challenge more realistic, an evaluation trajectory was designed to reflect typical phases during approach and landing (figure 15).

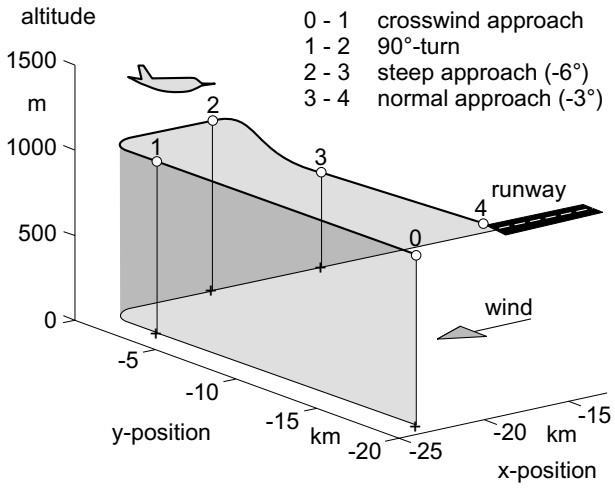


Fig. 15: RCAM Trajectory

The main controller architecture has not been changed in accordance with the main objective of the modular approach.

The modified RCAM problem uses the same disturbances like wind, gust, and wind shear as the original one. The choice of a trajectory as an evaluation criterion makes the evaluation independent of controller structure and design methodology and clearly illustrates the achieved accuracy. The most important modifications to the design challenge concern the failure conditions, the aircraft model used and the extension of the trajectory to the ground. Instead of the linear aerodynamics of RCAM a non-linear six degrees-of-freedom model of ATTAS was used. It features e.g. non-linear engine and actuator dynamics as well as the ground effect. The additional failure scenario includes a sudden loss of the control power of all primary control surfaces with normal engine behaviour left.

Reconfiguration Module

In order to overcome the severe control problem for this failure case a reconfiguration block is added to the normal control laws (figure 16). Only minor changes to the normal control laws were necessary.

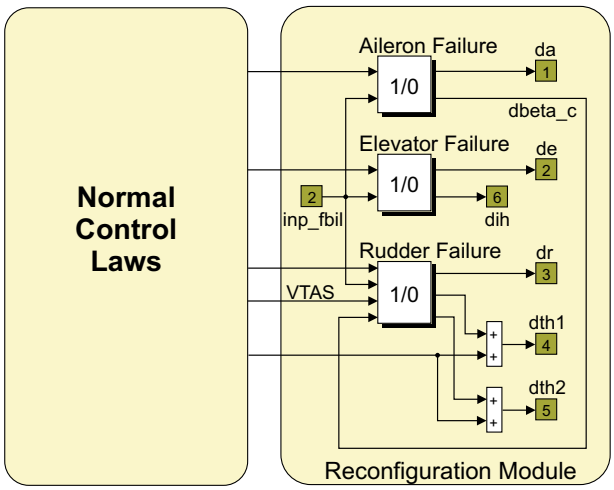


Fig. 16: **Reconfiguration Module**

The clear distinction between reconfiguration laws and normal control laws helps to investigate failure cases step by step and simplifies certification procedures. Furthermore, reconfiguration modes can be added automatically or by hand as an optional setting. Simulation runs for all segments of the mission were conducted in Matlab/Simulink for the normal landing as well as the landing with engines and stabiliser only. By and large, the aircraft stayed within the boundaries and landed safely even with substantial wind disturbances. Detailed results comparing the failure and the no-failure cases have been published in Ref. 25.

Considering the relatively simple reconfiguration module it can be concluded that the reconfiguration works well even under severe wind disturbances. However, it currently lacks the proof of suitability for additional envelope points or failures that had not been taken into account during the design. The reconfiguration approach depends on knowing in advance the attainable control forces and moments of the damaged aircraft and is not totally independent of the existing controller structure. The modularity still promises high applicability with low design risk. In order to prove the compatibility with other existing control systems the reconfiguration module has to be connected to a modern auto-pilot design capable of fulfilling normal design specifications and all certification requirements. Hence, the modular approach will be flight-tested on ATTAS in combination with the REAL autopilot design.

Education of test pilots

The education of high-level test pilots includes one important aspect: the flight-test. The students have to learn how to evaluate the dynamics of a given vehicle. Furthermore, they may have to pilot a large number of very different airplanes. The selection may include the whole bandwidth from glider to fighter, from amphibious fire-fighting aircraft to huge transport types. However, a flight-test school that has the high demand to provide all those aircraft types will have astronomical costs. Therefore, test-pilot schools have to find the most efficient and realistic way to meet this learning objective.

The in-flight simulation is a viable alternative and a good compromise to replicate different aircraft dynamics with a single airplane. The basic idea of in-flight simulation is to imprint the characteristics of a vehicle to be simulated on a fly-by-wire host aircraft. ATTAS' in-flight simulation capabilities were the reason for one of the most famous test-pilot schools, the French *Ecole du Personnel Navigant d'Essais et de Reception (E.P.N.E.R.)* to put DLR in charge of the non-linear in-flight simulation of a wide-body transport aircraft with a mass of about 130 tons. By this means the school was able to provide wide-body flight lessons to their students but had to pay only the operating costs of the small VFW 614.

The contract not only included the simulation of the wide-body but also the demonstration of effects caused by different flight control laws typically used on transport aircraft. Therefore, two more control laws were added to the existing rate command attitude hold (RCAH) system, an n_z law and an α law. Both laws were designed using Matlab/Simulink and transferred to ATTAS using Real-Time Workshop.

A pilot can only do a proper assessment if the task he has to perform adequately excites the aircraft dynamics. Two different tasks were offered to the test-pilot students:

- aggressive (high gain) tracking in the longitudinal and lateral-directional motion, similar to those described for the SCARLET 3 project
- approaches following an artificial (computer generated) Instrumental Landing System to a synthetic runway as well as visual approaches to a real runway combined with a simulated engine failure.

Some subtasks were also available. It was possible to deactivate the yaw damper or the turn compensation system, and a simulated turbulence model could be switched on in flight. After performing the task, the pilot had to make assessments in the form of general comments and Cooper/Harper Ratings.

As mentioned earlier, ground-based simulator sessions are part of the usual preparation phase for ATTAS experiments. The flight-tests for the test-pilot school E.P.N.E.R took place at Istres/France, where the ATTAS fixed-based simulator is not available. Therefore, a very sophisticated feature of ATTAS was used, namely the embedded ground-based simulation. The explicit model following system that is the basis of the ATTAS in-flight simulation[26] makes it possible to simulate the aircraft model in real-time. The ATTAS in-flight simulation software package includes the possibility to simulate the model while ATTAS is on the ground. Sitting in the cockpit like in flight, the evaluation pilot can control the model with the usual input devices (sidestick, pedals, throttles, etc.). The electronic flight instrument system (EFIS) indicates how the simulated model reacts. Using this ATTAS feature "familiarisation flights" were possible for the test-pilot students on the ground.

Figure 17 shows typical flight-test results using the n_z law. The bottom plot shows the commanded and the actual pitch attitude, the upper diagram depicts the pilot's sidestick pitch commands. It can be seen that a high activity is necessary to obtain an adequate result.

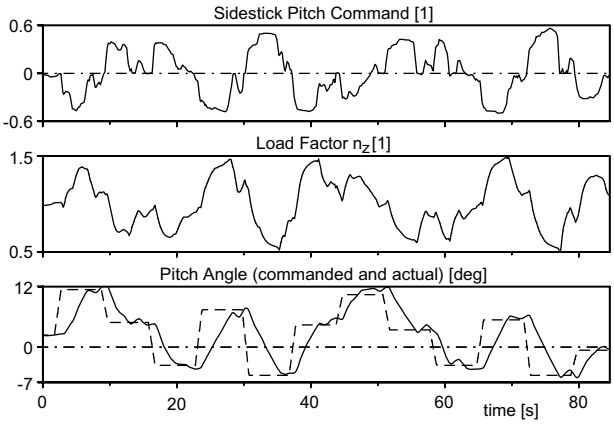


Fig. 17: Example from test-pilot training

Part of the education is an extended debriefing after the flight lesson. The test-pilot students, the ATTAS cockpit crew, flight-test engineer and the instructors of the school discussed results of the flight-test. DLR Institute of Flight Research aids those debriefings through a mobile data evaluation system. It consists of a high performance laptop computer (workstation class) and the DLR software package DIVA.[27]

EPIAS

Active tactile information provided by inceptors is not only important for a realistic in-flight simulation (force-deflection representation) but also for improving situational awareness of the pilot by force-feedback of aircraft/system information. A unique active sidestick concept based on an electro-magnetic force loading principle (MAGSI)[28,29] is under development at DLR's Institut für Flugsystemtechnik and the Department of Electrical Engineering of Technical University of Braunschweig (figure 18). This system is a key element in DLR's EPIAS research program (**E**nhanced **P**ilot **I**nformation by using **A**ctive **S**idestick).



Fig. 18: MAGSI sidestick with integrated electro-magnetic actuator

The EPIAS research program is scheduled to be flight tested on ATTAS in 2000. The program is directed towards the following subjects:

- investigate the benefits on situational awareness in the case of sidestick cross coupling for a two men crew (for training purposes the instructor pilot can feel what the student pilot is doing, both pilots will feel if there are conflicting commands),
- examine the effects of providing the pilot with suitable tactile event and warning information on situational awareness (e.g. in case of leaving the flight envelope, stall warning, gear locked, etc.),
- determine which form of tactile excitation is suitable for what type of warning or event indication and also what type of excitation can be perceived and distinguished by the pilot (regarding frequency and amplitude),
- clarify if control force characteristics that are adapted to individual flight conditions can improve handling qualities and overall system performance,
- establish the optimal force characteristics for different aircraft classes,
- find out how situational awareness can be improved by moving the stick in accordance to autopilot commands, and finally
- study the influence of loss of active sidestick functions (feel system degradation to passive behaviour) on the controllability of the aircraft.

Conclusions

In this paper, several recent and current programs that examine different aspects of the development, optimisation and investigation of modern flight control systems have been described. In all these programs, flight testing using DLR's flying testbed ATTAS has played (and still plays) an important role. These projects, therefore, illustrate the variety of ways in which ATTAS can be used for ACT research.

References

[1]Bauschat, J.-M., Lange, H.-H., "ATTAS and its contribution to System Design and In-Flight Simulation," Proceedings of the International Aircraft Flight Safety Conference, Zukovsky, 1993, pp. 3-44 to 3-56

[2]Buchholz, J.J., Bauschat, J.-M., Hahn, K.-U., and Pausder, H.-J., "ATTAS and ATTHeS In-Flight Simulators," AGARD CP-577, Paper No. 31, May 1996

[3]Heintsch, T., Luckner, R., Hahn, K.-U., "Flight Testing of Manual Flight Control Functions for a Small Transport Aircraft (Project ATTAS-SAFIR)," AGARD CP-593, Paper No. 26, Sep. 1997

[4]Kröger, A., "Data flow oriented control law design with graphical language HOSTESS," Conference Proceedings, International Conference and Exhibition, 8th international event on Civil and Military Avionics, Heathrow, 1994

[5]Magni, J.-F., Bennani, S., Terlouw, J. (eds), "Robust Flight Control, A Design Challenge," Lecture Notes in Control and Information Sciences 224, GARTEUR, Springer Verlag 1997

[6]Joos, H.-D., “A methodology for multi-objective design assessment and flight control synthesis tuning,” Aerospace Science and Technology Vol. 3, No. 3, pp. 161-176, Elsevier, Paris, April 1999

[7]Enns, D., Bugajski, D., Hendrick, R., Stein, G., “An Evolving Methodology for Flight Control Design,” AGARD Conference Proceedings 560: Active Control Technology: Applications and Lessons Learned, pp. 7-1 -- 7-12, Turin, Italy, May 1994

[8]Lambregts, A.A., “Vertical Flight Path and Speed Control Autopilot Design Using Total Energy Principles,” AIAA Paper 83-2239CP, August 1983

[9]Joint Aviation Authorities Committee, Joint Aviation Requirements – All Weather Operations, Printing and Publication Services Ltd, Cheltenham, England, 1996

[10]Moormann, D., Mosterman, P.J., Looye, G., “Object-oriented computational model building of aircraft flight dynamics and systems,”. Aerospace Science and Technology Vol. 3, No. 3, pp. 115-126, Elsevier, Paris, April 1999

[11]McRuer, D.T., et al, “Aviation Safety And Pilot Control. Understanding and Preventing Unfavorable Pilot-Vehicle Interactions,” National Research Council, National Academy Press, Washington, DC, 1997, p.15.

[12]McKay, K., “Summary of an AGARD Workshop on Pilot-Induced Oscillations,” AIAA Paper 94-3668, Scottsdale, AZ, Aug. 1994

[13]Duda, H., “Flying Qualities Criteria Considering Rate Limiting”, DLR-FB 97-15, Braunschweig, April 1997 (in German)

[14]Duda, H., “Prediction of Pilot-in-the-Loop Oscillations due to Rate Saturation,” Journal of Guidance, Control, and Dynamics, Vol. 20, No. 3, 1997, pp. 581-587

[15]Duda, H., Duus, G., Hovmark, G., Forssell, L., “New Flight Simulator Experiments on PIO due to Rate Saturation,” AIAA Paper 98-4336, Boston, MA, Aug. 1998

[16]Duda, H., Koehler, R., Fischenberg, D., “Analysis of Runway Steering PIO Incident of a modern Fighter Aircraft,” DLR-IB 111-98/27, Braunschweig, Sep. 1998

[17]Duda, H., Duus, G., “New Handling Qualities Database on PIO due to Rate Saturation,” DLR-FB 97/53, Braunschweig, Dec. 1997

[18]Rundqwist, L., Hillgren, R., “Phase Compensation of Rate Limiters in JAS39 Gripen,” AIAA Paper 96-3435, San Diego, CA, Aug. 1996

[19]Kish, B.A., et al, “A Limited Flight Test Investigation of Pilot-Induced Oscillation due to Rate Limiting”, AIAA Paper 97-3703, New Orleans, LA, Aug. 1997

[20]Duus, G., “SCARLET 3 – A Flight Experiment Considering Rate Saturation,” AIAA Paper 2000-3987, Denver, CO, Aug. 2000. (to be published)

[21]Buchholz, J.J., Heine, W., and Baumgarten, G., “Genetic Algorithms for Reconfiguration,” ZFW, Vol. 20. No. 3., June 1996

[22]Goldberg, D.E., “Genetic Algorithms in Search, Optimization, and Machine Learning,” Addison-Wesley, 1989

[23]Burcham Jr., F.W., Maine, T.A., and Burken, J.J., “Development and Flight Test of an Augmented Thrust-Only Flight Control System on an MD-11 Transport Airplane,” NASA Technical Memorandum 4745, 1996

[24]Lambrechts, P., Bennani, S., Looye, G., and Moormann, D., “The RCAM Design Challenge – Problem Description,” in “Robust Flight Control: A Design Challenge,” Lecture Notes in Control and Information Sciences 224, Editors: Magni, J.F., Bennani, S., and Terlouw, J., Springer-Verlag, London, 1997, pp. 149-179

[25]Heine, W., “Alternative Flight Control Strategies For Multiple Effector Failures,” RTO-SCI Symposium on “Flight in a Hostile Environment,” Solomons Island, MD, USA, 19-21 Oct. 1999

[26]Bauschat, J.-M., “On the Application of a Nonlinear In-Flight Simulation Technique,” Proceedings of the First European Control Conference (ECC 91), Grenoble (France), Volume 73, July 1991, pp. 2415-2422

[27]Wulf, G., Buchholz, J., “XDIVA - Anwendungshandbuch - 2. Auflage,” DLR IB111-97/26, 1997 (in German)

[28]Meins, J., Deeg, C., Hanke, D., Münscher, D., “Advanced Sidestick Controller with Electro-magnetic Loading System,” 'Making it Real' CEAS Symposium on Simulation Technology, Delft, The Netherlands, Oct. 30 - Nov. 1. 1995

[29]Hanke, D., Herbst, C., “Active sidestick technology - a means for improving situational awareness,” Aerospace Science and Technology, 3 (1999), pp. 525-532

Nonlinearities and PIO with Advanced Aircraft Control Systems

David G. Mitchell
Hoh Aeronautics, Inc.
2075 Palos Verdes Dr. North #217
Lomita CA 90717
USA

Edmund J. Field
The Boeing Company
2401 E. Wardlow Road, MC C078-0420
Long Beach CA 90807-5309
USA

ABSTRACT

Design methods for advanced aircraft control systems include feedbacks to stabilize relaxed-static-stability vehicles, command and feedback shaping, and gain scheduling. Extensive use of such designs increases the risk of adverse nonlinear response to pilot control inputs. A common form of this adverse response is pilot-induced oscillation (PIO). This paper examines the relationship between nonlinearities in advanced aircraft control systems and PIO. The results of recent research clearly demonstrate that actuator rate limiting, alone, does not always cause PIO. Other factors, such as the degree of instability of the unaugmented airplane and level of excess demand on the control surface, are greater determinants of PIO susceptibility. The paper evaluates two other, less thoroughly documented, contributors to PIO – command shaping (sensitivity) and hysteresis in the flight controls. Inferences about their impact on PIO may be made, but there is not enough data to draw specific conclusions.

INTRODUCTION

In the past, it has been assumed that the typical sources of nonlinear response to linear cockpit commands are negligible, at least as far as their overall impact on flying qualities. With minimal augmentation this may be a reasonable assumption, since even the most extreme of such nonlinearities should normally have a much smaller impact on effective-vehicle dynamics than, say, uncertainties in control power. (Some forms of nonlinearity may even be considered favorable, such as controller breakout forces and command shaping.) There are no real design criteria in the published literature to aid the flight control system designer in dealing with such nonlinearities.

Most flight research programs conducted by the agencies and contractors in the United States over the past 50 years or so have made great attempts to minimize the presence of nonlinear response elements. This has been sensible when, for example, we want to study the impact of short-period damping and natural frequency on handling qualities. We simply would not want to allow some nonlinear element to dominate the results of such a study.

The use of modern aircraft design methods, such as relaxed static stability, multiply-redundant control surfaces, and thrust vectoring, provides the flight control system (FCS) designer with immense capability for tailoring the response of the airplane to meet every possible challenge. Such advanced flight control systems come with a price, however, and one price seems to be the increased risk of pilot-induced oscillations (PIO) resulting from the unexpected interactions of the elements of the airframe and its FCS. Further, there is ample evidence that the major player in the occurrence of PIO in highly-augmented aircraft is the introduction of nonlinearities in the aircraft's response.[1]

Concern about nonlinearities and their impact on flying qualities in general is certainly not new. The US military flying qualities specification MIL-F-8785C,[2] released in 1980, referred to an "equivalent" airplane that includes, for example, "flight control system nonlinearities and higher-order characteristics or aerodynamic nonlinearities" to which the requirements must apply. It is sometimes forgotten that the military flying qualities requirements are intended to be applied to such an equivalent airplane, thus accounting for known nonlinearities.

There are, unfortunately, several shortcomings with the US military flying qualities specifications. First, little research has been done to verify that significant nonlinearities affect flying qualities and PIO in a manner similar to equivalent changes in linear characteristics. Second, the specifications do not contain explicit requirements for the prevention of PIO, and while meeting the criteria certainly will reduce the risk of PIO, there are times that degraded flying qualities may be tolerable, but not PIO. Third, the extreme levels of nonlinearity that have been encountered in recent PIOs are generally not even considered to be possible during initial design and verification.

Several recent analytical, ground simulation, and flight research projects have investigated the impact of certain nonlinearities on both the identification of the aircraft from familiar frequency-response techniques, and the occurrence of PIO.[3,4,5,6,7,8]

SOURCES OF NONLINEARITY

Some possible sources of nonlinearity are sketched in the representative flight control system block diagram in Figure 1. The most significant of these, in terms of PIO, are the rate limits that occur naturally on control actuators and those that are intentionally designed into the control system, in the form of command or software rate limits. These forms of limiting have received the most attention in recent years, and they will be the primary focus of this paper. Nonlinear elements in the cockpit effector, breakout and hysteresis, may contribute to PIO, and will be discussed. The final form of nonlinearity to be covered, command shaping, will be mentioned as well.

Paper presented at the RTO AVT Symposium on "Active Control Technology for Enhanced Performance Operational Capabilities of Military Aircraft, Land Vehicles and Sea Vehicles", held in Braunschweig, Germany, 8-11 May 2000, and published in RTO MP-051.

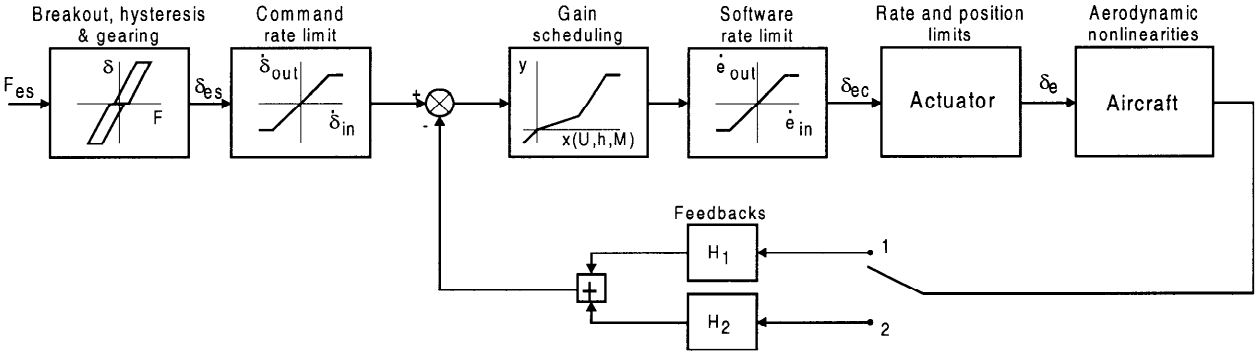


Figure 1. Some Sources of Nonlinearity in Modern Flight Control Systems

The effects of gain scheduling, mode switching, and aerodynamic nonlinearities on PIO have been reported but are not well-documented, and will not be discussed here.

All of the nonlinear elements described above can be represented for analytical purposes by simple describing functions.[9,10] Still, their interactions with the effective aircraft dynamics can be complex, requiring more sophisticated methods to measure their impact.

RATE LIMITING

As Figure 1 indicates, there are many possible sources of rate limiting in the typical modern flight control system. Rate limiters in the pilot's command path (command rate limit), or located just before the surface command (software rate limit) are inserted intentionally. Rate limiting of the surface actuators occurs as a consequence of actuator design.

The occurrence of rate limiting with hydraulic actuators is quite common, since it is difficult for most actuators to provide both the rates and amplitudes of deflection demanded of them for more than very small commands. Such limiting is typically momentary and is not usually noticed in normal flight. It is only when the demand becomes significantly greater than the maximum rate achievable, for an extended period of time, that actuator rate limiting becomes an issue.

In truth, many recent PIOs experienced on highly-augmented aircraft involve not the rate-limiting of the aerodynamic surface actuators themselves, but rather software rate limiters. Several PIOs experienced during full-scale development of the C-17A, for example, were attributed to a software rate limiter, installed to protect against excessive aerodynamic loads from the pitching surfaces.[11] One of the steps taken to alleviate the C-17A's PIOs was relocation of the limiter to the pilot's command path.

In most cases, as long as the limiting is within the command loop structure as sketched in Figure 1, the observed response of the airplane is the same whether it is the actuator or software that rate-limits. In the case of the actuator, there will be a reduction in bandwidth that does not occur in the infinite-bandwidth software limiter. For all practical purposes, however, the differences between these types of limiter are insignificant. The effect on the airplane will be a loss of all augmentation, resulting in the dynamics of the bare airplane, with the added detrimental effects of the rate limiter itself.

Effects of Rate Limiting on Aircraft Response

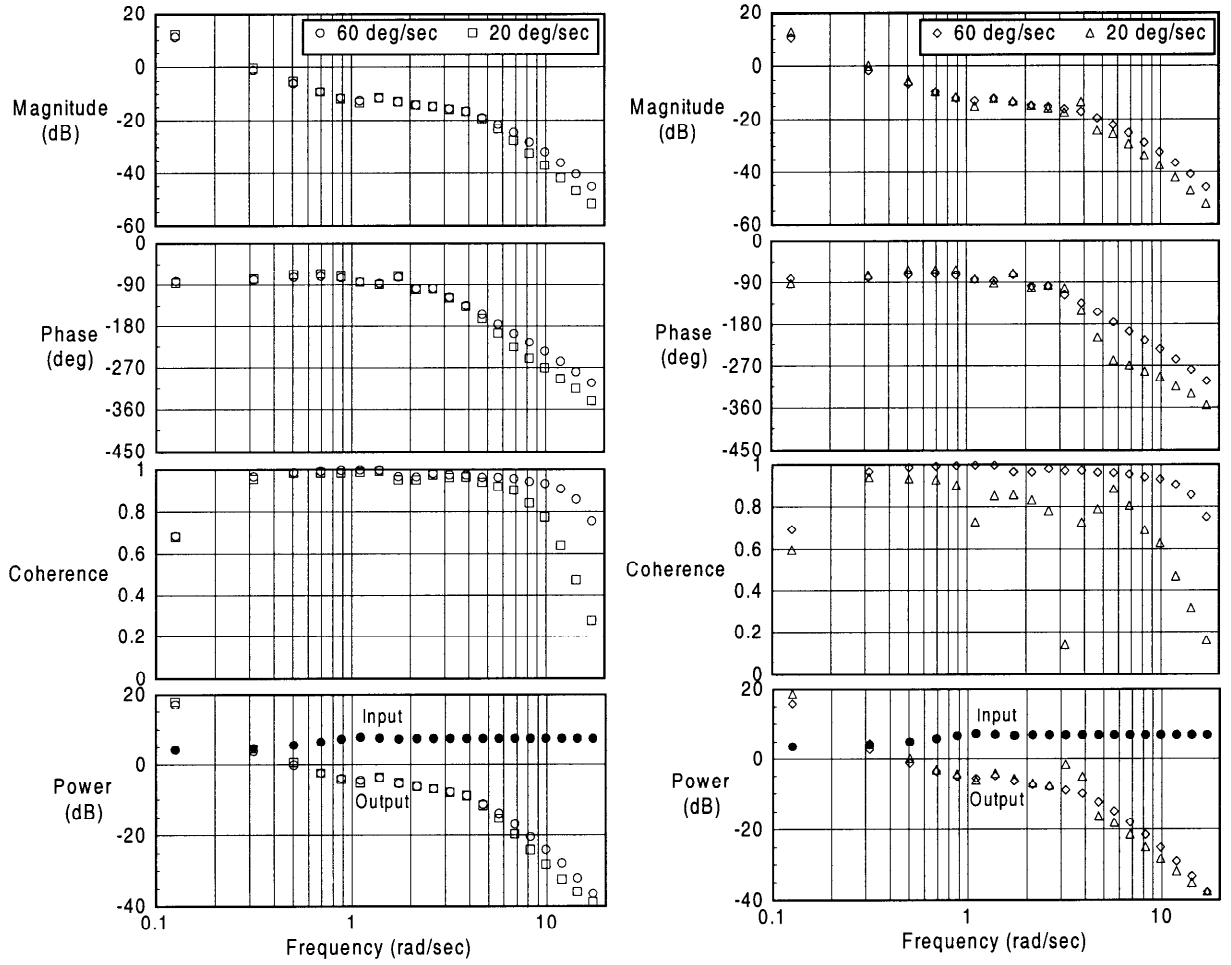
In the absence of feedbacks, there is no difference between the command path and software rate limiters (Figure 1), and little difference between these and the rate-limited surface actuator. Rate limiting with no feedbacks (or with the limiter outside the feedback paths) has a rather simple effect on the aircraft: the amplitude of response to control inputs is attenuated and phase is decreased.[10] As an example, the frequency responses in Figure 2a are for pitch-attitude-to-stick-force frequency sweeps of an airplane with rate limiting upstream of the feedback path. Reduction in rate limits from 60 deg/sec to 20 deg/sec produces the expected results, with a consistent drop in output/input coherence.

The more complex problem arises when feedback loops are wrapped around the rate limiter, such as the software limiter in Figure 1. In this case, nibbling at the limiter produces an airplane that looks like a combination of the augmented and unaugmented vehicles, plus the characteristics of the limiting itself. In this case the impact of the limiter will depend upon how highly the airplane is augmented – that is, the difference in dynamics between the unaugmented and augmented vehicles – and how low the rate limit is set.

The example frequency responses in Figure 2b are for an airplane that is unstable with a time to double amplitude of roughly 0.5 sec, augmented to have a short-period mode with a damping ratio of 0.7 and natural frequency of 4.9 rad/sec. The result is an airplane that performs well for tight tracking tasks until the rate limiter is reached – then it is almost impossible to control. At a rate limit of 60 deg/sec, a relatively smooth frequency response results that closely resembles that of the 60-deg/sec configuration in Figure 2a. When the limit is 20 deg/sec (triangles in Figure 2b), the frequency response shows the basic loss of amplitude and phase that result from rate limiting, but the coherence becomes ragged and very low over a wide frequency range – the range over which the rate limiter is encountered.

Effects of Rate Limiting on PIO

While there is no question that rate limiting and PIO are related, the details of their relationship have not been fully defined. For example, it has not been determined if rate limiting, alone, can *cause* PIO, or is merely a *result* of PIO. The relationship between rate limiting and PIO has been investigated in several recent research studies, including a US Air Force Test Pilot School flight experiment[3] on a variable-stability airplane, and numerous related ground-based simulations.[7] Examination of selected configurations from these experiments illustrates the possible relationships between rate limiting and PIO. Four configurations, identified in the experiments as 2D, 2P, 2DU, and 2DV, will be discussed in this paper. Transfer functions of pitch rate to elevator deflection (short-period approximation) for the configurations are listed in Table 1.



a) Configuration 2D

b) Configuration 2DU

Figure 2. Effect of Rate Limiting Upstream (Part a) and Downstream (Part b) of Feedbacks on Pitch-Attitude-to-Stick-Force Frequency Responses

Table 1. Selected Configurations from HAVE LIMITS[3] and PIO Simulation[7]

Config.	Fully augmented	Unaugmented
2D	$\frac{10(s+1.25)}{[s^2+(0.7)(4.6)s+4.6^2]}$	$\frac{10(s+1.25)}{[s^2+(0.7)(4.6)s+4.6^2]}$
2P	2D with added lag at 4/(s + 4)	
2DU	$\frac{10(s+1.25)}{[s^2+(0.7)(4.6)s+4.6^2]}$	$\frac{10(s+1.25)}{(s-1.33)(s+2.18)}$
2DV*	$\frac{10(s+1.25)}{[s^2+(0.7)(4.6)s+4.6^2]}$	$\frac{10(s+1.25)}{(s-0.52)(s+7.19)}$

*Evaluated in simulation only

The first set of values listed in Table 1 is for the non-rate-limited, fully-augmented case; the second set is with the augmentation loops opened, such as would occur with full rate saturation.

Configuration 2D (Table 1 and Figure 2a) did not exhibit PIOs for a HUD attitude tracking task with rate limits as low as 10 deg/sec. For this configuration the function of the limiter was that of a command path limit (Figure 1), making no changes to the dynamics of the effective aircraft (compare columns for "fully augmented" and "unaugmented" dynamics in Table 1).

Frequency-response characteristics for Configuration 2D, obtained from analytical frequency sweeps of a mathematical model of the airplane, show a reduction in pitch attitude Bandwidth and increase in Phase Delay as rate limits are reduced (Figure 3). For sweep amplitudes that produce load factor changes of ±2g or less, PIO is not predicted by criteria based on Bandwidth.[5]

A second configuration in the TPS experiment, Configuration 2DU (Table 1 and Figure 2b), exhibited rapidly divergent PIOs for rate limits as high as 60 deg/sec (the highest values evaluated were 60 and 157 deg/sec). In this case, augmentation was required to stabilize the airplane, and the slightest rate saturation resulted in almost immediate loss of control. As the analytically-derived frequency-response parameters show (Figure 4), rate limiting causes a sudden and dramatic increase in Phase Delay and loss of Bandwidth that corresponds to severe PIO.[5]

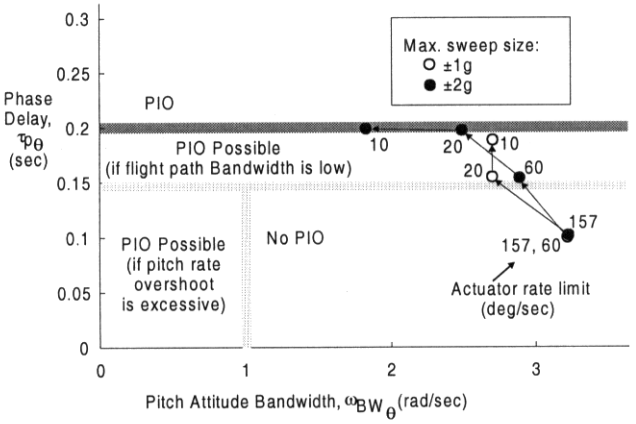


Figure 3. Effect of Rate Limit and Sweep Size on PIO Parameters for PIO-Resistant Airplane (Configuration 2D)

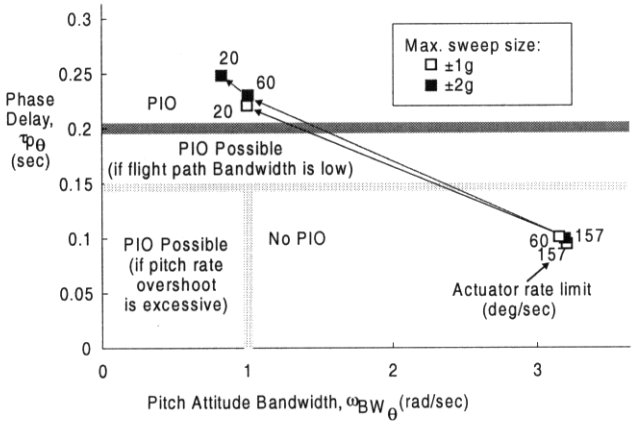


Figure 4. Effect of Rate Limit and Sweep Size on PIO Parameters for Highly PIO-Susceptible Airplane (Configuration 2DU)

The results of the HAVE LIMITS flight research project suggest that airplanes with sufficient Bandwidth are resistant to PIO. It is clear from the data generated in a moving-base simulation[7] that rate limiting, alone, is not the culprit in Category II PIOs. By its nature, the nonlinearity is highly sensitive to several factors, including pilot input bandwidth, the amount of rate limiting experienced, and the consequences of reaching the rate limit.

As a graphical example, consider the data plotted in Figure 5. Percent of time on the rate limit was computed for several selected configurations, all flown by one of the most aggressive pilots in the simulation (Pilot C), and the numbers are plotted against Pilot C's assigned PIO Tendency Classification Rating (usually abbreviated PIOR for "PIO Rating") for that configuration/rate limit combination. Cooper-Harper Handling Qualities Ratings (HQRs) are noted next to each data point.

Lines connect individual data points in Figure 5 and progress from higher to lower actuator rates in all cases. For example, the circles are Configuration 2D with rate limits of 20 deg/sec (PIOR = 1) and 10 deg/sec (PIOR = 3). At the lower limit, the actuator was rate-saturated for 25% of the run. Still, Pilot C did not consider this airplane to have tendencies to PIO, nor did any of the other pilots who evaluated it, consistent with the HAVE LIMITS flight results for this configuration.

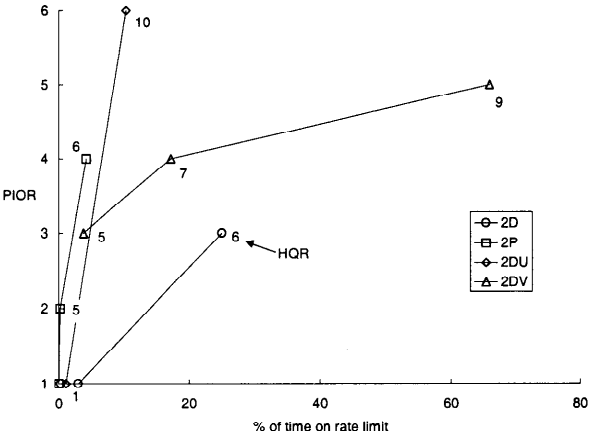


Figure 5. PIO Tendency Classification Rating (PIOR) as a Function of Percent of Time on Rate Limit for Selected Configurations (Data for Pilot C)

By contrast, for the sluggish Configuration 2P (2D with an added first-order lag filter at 4 rad/sec, squares on Figure 5), reductions in rate limit from 160 (PIOR = 1) to 10 deg/sec (PIOR = 4) resulted in an apparent tendency for PIO, even though the percent of time on the rate limiter increased to only 4% at the worst case. With augmentation and no rate saturation, Configuration 2DU (diamond symbols on Figure 5) flew like 2D and received a PIOR of 1. A reduction in rate limit to 30 deg/sec led to an occasional "nibble," resulting in saturation for only 1% of the run and no degradation in ratings. When the rate was decreased to 20 deg/sec, the overall percentage of time in saturation was only 10%, but it occurred all at once and resulted in a divergent PIO and a stoppage of the simulation. The PIOR of 6 and HQR of 10 reflect the extreme susceptibility to PIO for this configuration.

Because the bare-airframe dynamics for 2DV were not quite as unstable as those for 2DU, the trends are more gradual (triangles in Figure 5). With no saturation (fully augmented), 2DV looked like 2D (compare transfer functions in Table 1). The point with PIOR = 3 was for a 20-deg/sec rate limit, and it resulted in saturation for only 4% of the run, but that was enough to degrade the handling qualities. At a rate limit of 15 deg/sec, Pilot C was able to complete the task without crashing, with saturation 17% of the time and an assigned PIOR of 4. At the lowest rate limit of 10 deg/sec, Pilot C completed one run only with intense concentration, knowing that he was flying a highly PIO-susceptible configuration. He managed to maintain control of the airplane despite rate saturation for 66% of the run. His PIOR of 5 and HQR of 9 indicate the extremely poor characteristics of this configuration.

The data shown in Figure 5 simply serve to reinforce the observations that 1) hitting a rate limit, alone, and 2) spending considerable time on the rate limit, are not necessarily causes of PIO. The consequences of reaching the rate limiting, and the dynamics of the augmented airplane, are the key elements.

Rate Limiting and Pilot Technique

By their nature, the response dynamics of nonlinearities are dependent upon characteristics of the forcing function input – magnitude and form (frequency content). As a consequence, differences in piloting technique that may never show up in a linear system can become apparent in the presence of a nonlinearity.

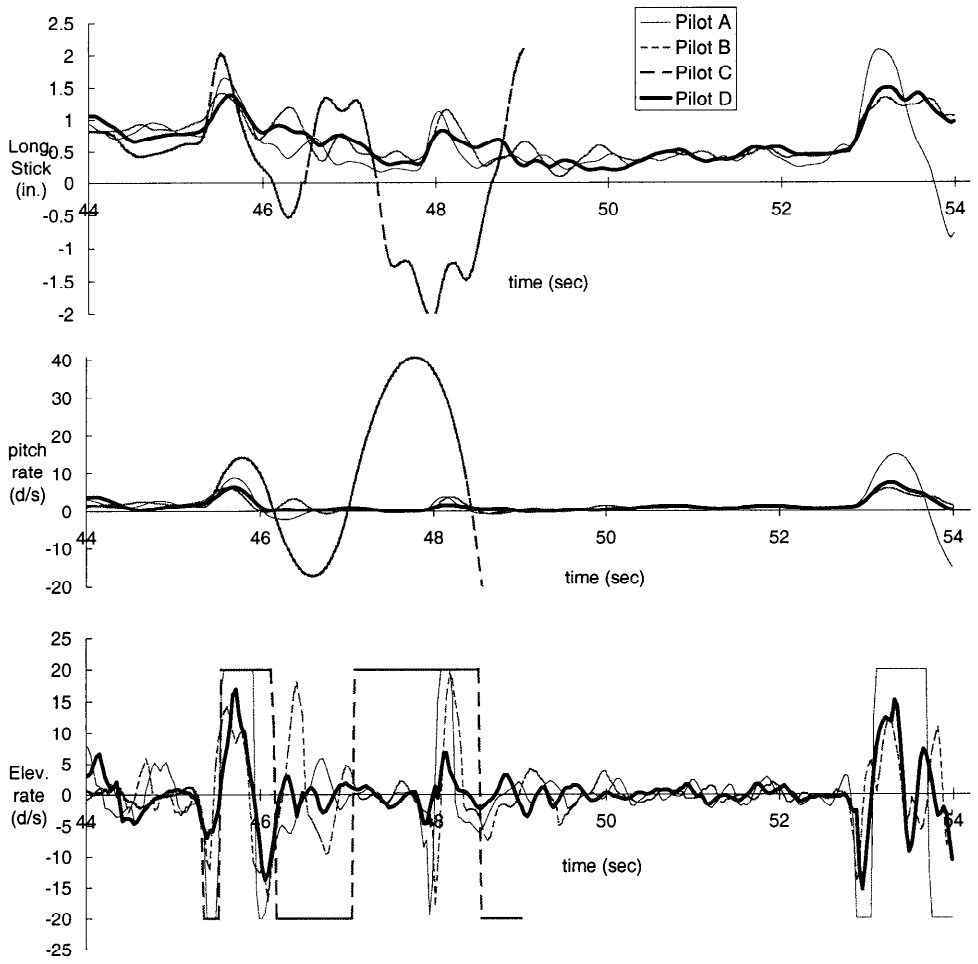


Figure 6. Sample Time History Comparison for Four Pilots Flying Configuration 2DU (20-deg/sec Rate Limit) in Moving-Base Simulation (HUD Tracking Task)

Strong evidence of this piloting difference was obtained in the recent moving-base simulation[7] for Configuration 2DU with a 20-deg/sec rate limit (Figure 2b). Of the seven pilots who evaluated it, six experienced divergent PIOs with this configuration and assigned PIORs of 5 or 6, and HQRs of 10. The seventh pilot, however, did not experience the PIOs, and assigned a PIOR of 1 and HQR of 2. The piloting technique of this one pilot was clearly different and received a considerable amount of attention.

A 10-sec segment of selected time traces for Configuration 2DU with a 20-deg/sec rate limit is shown in Figure 6. Traces are longitudinal stick deflection, pitch rate, and elevator rate. The data for four pilots are shown: Pilots A and C (two of the most aggressive) and B and D (two of the least aggressive).

In the time history segment in Figure 6, Pilot C encounters divergent PIO following the pull at about 45 sec; his run was stopped at 49 sec due to the rapidly diverging response. Pilot A has just reached the same condition at the end of the segment, and his evaluation is stopped at about 56 sec. Pilot B managed to almost complete the run, with his run ending at 129 sec, while Pilot D completed the task without encountering divergent PIO.

There are some noticeable differences in Figure 6. For example, on the pull at approximately 45 sec Pilot C applies the largest input, generating the highest pitch rate, and leading to rate saturation of the elevator. Pilot A is second in input size, resulting in a momentary saturation of the elevator, but he is able to recover by about 46 sec. Pilot B is third in aggressiveness, and his inputs at around 45 sec do not quite command the full 20 deg/sec of elevator rate. On several occasions during this segment Pilot B almost reaches rate saturation. Well below the other pilots is Pilot D, whose input magnitudes are almost always lowest, and his use of elevator rate is the lowest of all the pilots.

The time for peak input follows the same progression, with Pilot C generally applying the most rapid and D the least rapid (the pull at about 45 sec is the best example). These differences continue to show along the sequence for Pilots A, B, and D, even after Pilot C's run has ended.

COMMAND GEARING

Command gearing, or command/response sensitivity, describes the ratio of aircraft response (angular pitch acceleration or load factor) per unit command input (control deflection in inches or force in pounds). In flying-qualities research, we usually assume that the gearing is close to optimum for a particular airplane, either through pilot selection or *a priori* knowledge of pilot preferences. In addition, it is assumed that this gearing is constant with input amplitude. Both assumptions are generally incorrect in the real world, and gearing can have a direct impact on the occurrence of PIO.

Effects of Command Gearing on Aircraft Response

If the gearing is linear with amplitude, the only effect that changes in gearing will have on aircraft response is a shift in magnitude on frequency response plots. Nonlinear gearing can have a small effect on the overall quality of frequency response obtained from a pilot-generated frequency sweep.[5]

Three possible command shaping curves are sketched in Figure 7. (Only positive commands are represented in the figure; for this analysis, the commands were assumed to be symmetric.)

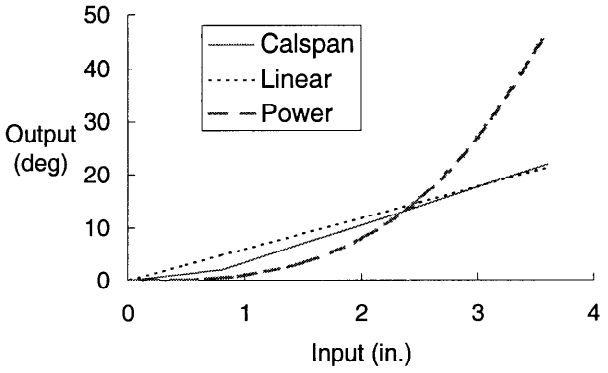


Figure 7. Command Shaping

The curve in Figure 7 labeled "Calspan" is the shaping used on the HAVE LIMITS flight experiment[4] and includes a 0.02-in. deadband around zero. The linear command was selected to give approximately the same overall response for full control input (3.6 in. of stick deflection). The power curve is simply a cubic gradient of the form $y = x^3$ and is meant to represent an extreme form of nonlinearity. The power gradient would probably not be acceptable in flight, since it has very low control command at low deflections, and extremely high command at higher deflections.

There was no mechanical breakout force on the control stick in HAVE LIMITS, and breakout was not included in this analysis.

The effect of command shaping was investigated analytically using the dynamics of Configuration 2DU with a 20 deg/sec rate limit, and input sizes selected to achieve peak load factors of ±1g from trim. As the response in Figure 2b (triangle symbols) shows, this configuration exhibits low coherence around 3 rad/sec, and again above about 10 rad/sec. Any additional complication from the change in input shaping should be apparent.

Frequency responses of pitch attitude to stick force for the three command gradients of Figure 7 are shown in Figure 8. The response labeled "Calspan" is identical to that in Figure 2b.

Changing the command shaping to purely linear (inverted open triangles in Figure 8) results in slightly higher magnitude overall. This translates to a slightly greater loss of phase at high frequencies, since the increased magnitude meant reaching the rate limiter at a slightly lower frequency. There is a slight improvement in coherence at almost all frequencies, especially above 10 rad/sec, possibly because of the more linear nature of the command in combination with the nonlinearity of the rate limiting. In general, however, the frequency response is not significantly changed from the Calspan shaping case.

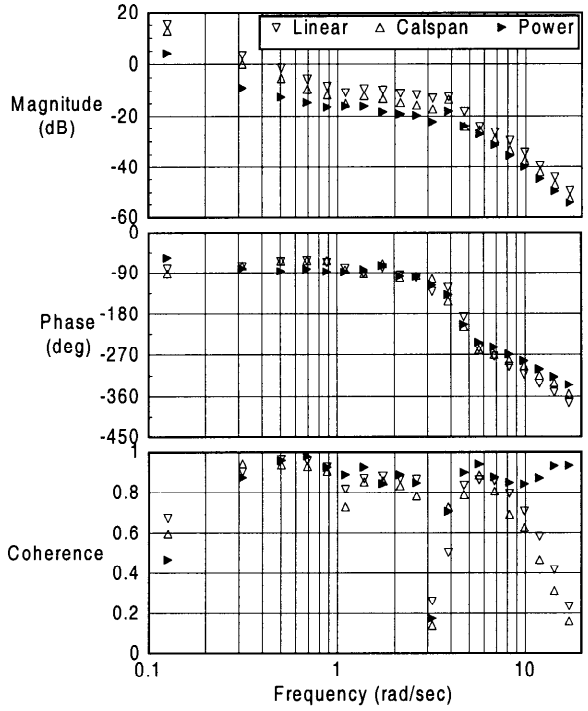


Figure 8. Effect of Command Shaping on Frequency Response (Configuration 2DU, 20 deg/sec Rate Limit, ±1g Load Factor Change)

Trends for the power curve are almost the opposite of those for linear in Figure 8: magnitude is slightly lower and phase loss is slightly less. As with the linear case, coherence is generally better at all frequencies, but in the ballpark of both other cases.

Effects of Command Gearing on PIO

In most research projects, command gearing has been either pilot-selectable or set by the experimenters at the outset. In either case it is possible that the inappropriate gearing has been selected.

Pitch Command Gearing

We have only a little evidence of the effect of pitch command sensitivity on PIO. A small example can be obtained from a 1986 flight research experiment on the Air Force's Total In-Flight Simulator, TIFS. In that study,[12] the majority of the pitch configurations had a "nominal" value of pitch command sensitivity, $\dot{q}/F_s = 0.42$ deg/sec^2/lb. A portion of the study investigated the effects of changes in sensitivity, repeating some configurations with a "high" value of 0.63 deg/sec^2/lb and others with a "low" value of 0.25 seg/sec^2/lb. The three sets of sensitivity were applied to two good configurations, to which time delay values of 0.1 and 0.2 sec were added.

Results for this experiment are shown in Figure 9. The plot shows added time delay versus pitch command sensitivity, with PIORs noted next to each data point. HQRs are in brackets below the PIORs. Slashes separate ratings from different pilots and commas separate repeats by the same pilot. The trends show that, with no added time delay, any value of sensitivity is acceptable as far as PIO tendency. There are Level 2 HQRs (4 and 5) for the high and low sensitivity values, suggesting the nominal value of 0.42 is best.

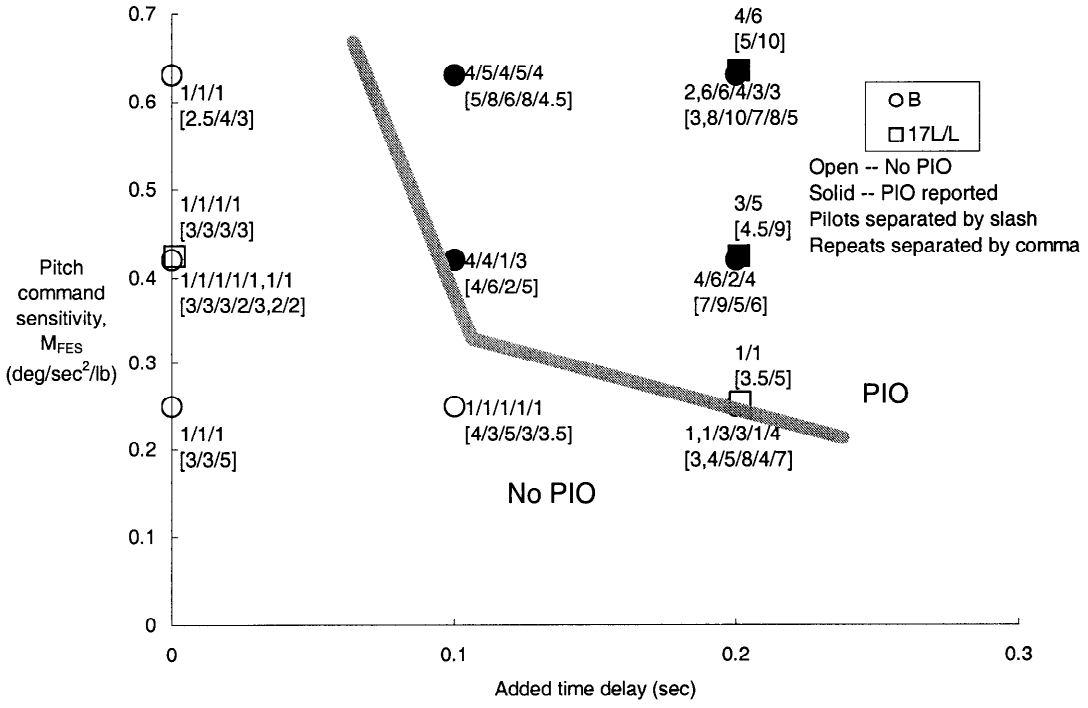


Figure 9. Effect of Pitch Command Sensitivity on PIO as a Function of Added Time Delay (Ratings are PIORs with HQRs in Brackets)

As time delay is added, however, the data in Figure 9 suggest a preference for lower values of pitch command sensitivity. When 0.1 sec of delay is added, there are reports of "moderate" PIO (HQRs better than 7) for the nominal sensitivity; with the high value, severe PIOs are reported; but for the low value, not only is there no indication of PIO, but the PIORs from five different pilots are all 1's, suggesting there was not even a hint of undesirable motions, either.

With 0.2 sec of added delay, only one pilot out of seven (counting both configurations) considered the low-sensitivity cases to exhibit PIO, while the nominal and high cases exhibited severe PIOs.

These data clearly suggest that 1) the "nominal" value of pitch sensitivity, $\dot{q}/F_s$ = 0.42 deg/sec²/lb, used in the study[12] was too high when time delay was added, and 2) it is possible to minimize the risk of PIO by adjusting pitch sensitivity to suit the dynamics of the airplane.

Support for the first observation can be gleaned from the pilot comments for the experiment; several pilots complained of excessive sensitivity and very light control forces, many of these associated with PIOs. These observations have also been confirmed by a series of flight experiments conducted by Boeing, Long Beach, in cooperation with the Air Force.[13]

The Boeing experiments, also performed on the TIFS, included two baseline Level 1 configurations to which were added time delays of 0.125 and 0.275 sec. Each of these configurations was evaluated at two pitch command sensitivities, a nominal value of 0.3 deg/sec²/lb, and an increased value of 0.45 deg/sec²/lb. These values approximately correlate with the "low" and "nominal" values of the Calspan experiment.[12] For the zero added time delay configurations the increased pitch command sensitivity did not cause PIO. For the configurations with added time delay, however, the increased pitch command sensitivity resulted in increased PIO tendencies.

Roll Command Gearing

Roll sensitivity is the initial acceleration per pound, written as either the lateral sensitivity derivative L_{FAS}, or simply as $\dot{p}/F_{AS}$, both in units of deg/sec²/lb. Results of two roll experiments[14,15] show trends similar to those for pitch. In both experiments the simulated airplane was a fighter performing air combat tracking tasks.

Figure 10 shows a plot of roll command sensitivity versus added time delay for a configuration from the LATHOS program[14] with roll damping T_R = 0.3 sec. Unfortunately, because PIO tendency ratings were not gathered in this experiment, we must rely on pilot comments and Handling Qualities Ratings to determine where PIO occurred. The ratings in Figure 10 are for the three pilots, separated by slashes; commas separate repeat evaluations by the same pilot. In several cases, at least one of the pilots reported a tendency for roll ratchet, rather than PIO, and this is noted by an "R" beside that symbol.

The data in Figure 10 clearly show a trend for reduced PIO tendency as roll sensitivity is reduced. Generally, pilot ratings degrade to Level 3 at about the same value of added time delay for all three values of sensitivity.

The importance of the linearity – or more correctly, the nonlinearity – of command shaping on flying qualities was demonstrated in the LATHOS flight research program[14] conducted by Calspan on the NT-33A. For roll maneuvering, configurations with high roll damping and essentially linear command shaping were susceptible to high-frequency roll oscillations identified as "roll ratchet"; addition of only a slight amount of shaping, around zero control input, improved the flying qualities drastically.[16] (Unfortunately, no explicit information on PIO was obtained for the experiment, so we cannot directly judge the impact of the changes in command shaping on PIO alone.)

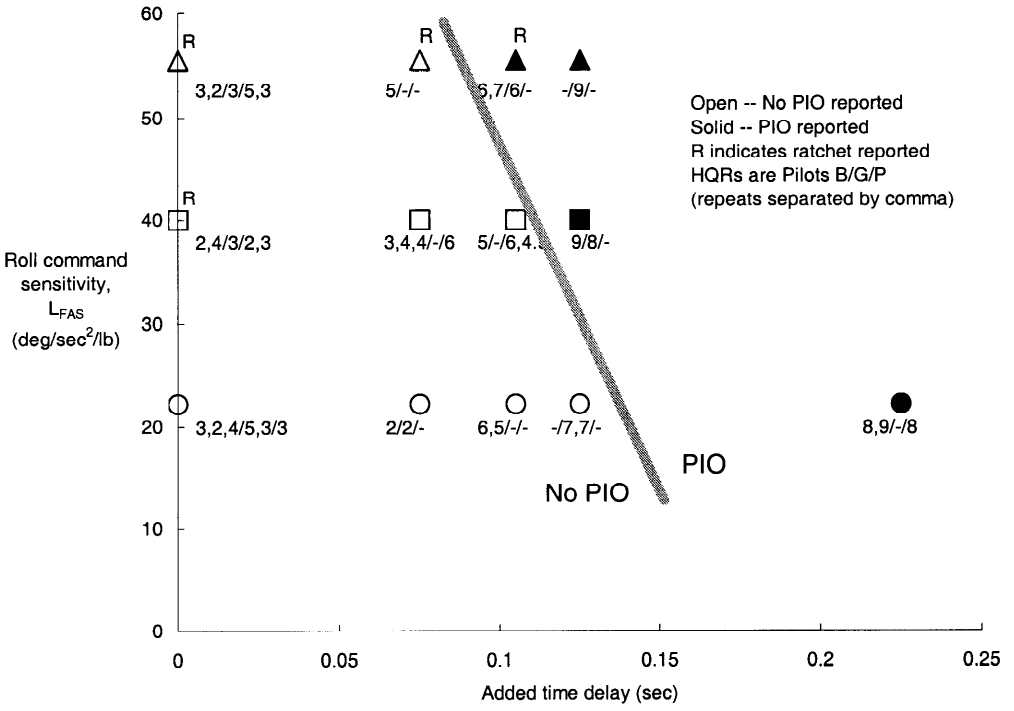


Figure 10. Effects of Roll Command Sensitivity on PIO Tendency as a Function of Added Time Delay (Configuration with Roll Damping T_R = 0.3 sec)

BREAKOUT AND HYSTERESIS

Breakout and hysteresis (freeplay) are unavoidable characteristics of mechanical control systems, and some degree of both is desirable. There is little in the way of quantitative information on the effects of such elements on PIO, so we can only discuss the issues involved.

Effects of Breakout on Aircraft Response

Breakout exhibits gain attenuation but has no effect on phase, so it can be represented by a simple describing function.[9] Its impact on aircraft response will be minimal, though measurements of effective control sensitivity or control power will be affected by the presence of a breakout.

Effects of Breakout on PIO

A small deadzone in a mechanical cockpit controller effectively desensitizes the controller for very small inputs. Too little breakout may make the airplane prone to high-frequency phenomena such as roll ratchet. Excessive breakout reduces precision, and may contribute to PIO by driving the pilot into overcontrol.

Effects of Hysteresis on Aircraft Response

Hysteresis introduces an attenuation in amplitude and loss of phase at all frequencies, the magnitude of which is dependent upon the ratio of depth of the hysteresis and input amplitude (Figure 11). The characteristics of hysteresis are described by the magnitudes of the nonlinearity 'a' and the input signal 'A'. The magnitude of the output is limited to 'A-a', and the output is lagged behind the input. The magnitude limiting causes the gain attenuation and the lag provides the phase loss.

The sinusoidal describing function for hysteresis is shown graphically in Figure 12. The magnitude of the gain attenuation and phase loss provided by the hysteresis is simply a function of the ratio of the magnitudes of the nonlinearity to the input, 'a/A' (see the sketches in Figure 11). When 'a/A' is zero (zero deadband), there is no gain attenuation or phase loss. As 'a/A' increases both gain and phase loss increase as the effect of part of the applied force is now lost in the deadband zone (-a to +a). As 'a/A' increases towards 1 (all applied force is in the deadband region) the gain attenuation approaches infinity: there is no output to the corresponding input.

Since hysteresis in the control system is a frequency independent nonlinearity, it will cause uniform gain and phase attenuation at all frequencies, as sketched in the aircraft frequency responses of Figure 13. Any parameters measured from the frequency responses will reflect the reduction in overall amplitude and bandwidth introduced by hysteresis.

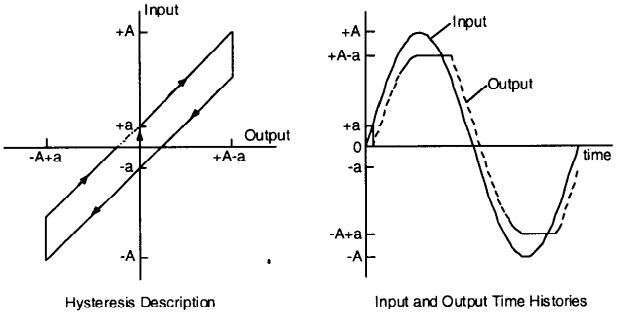


Figure 11. Hysteresis and Its Effect on Time Response

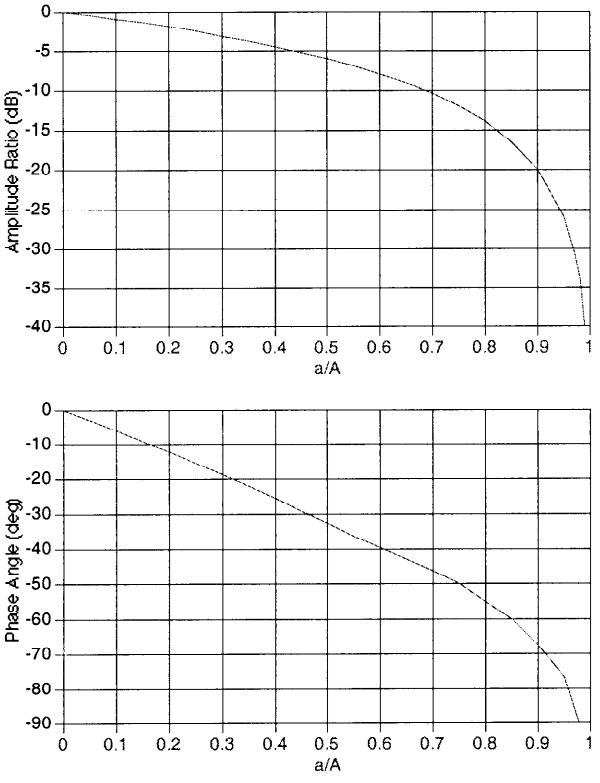


Figure 12. Sinusoidal Describing Function for Hysteresis[9]

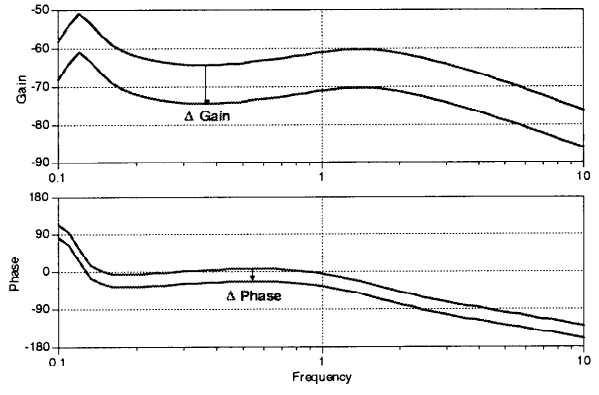


Figure 13. Effects of Hysteresis on Analytically Derived Frequency Response

Effects of Hysteresis on PIO

The phase loss and gain attenuation introduced to the frequency responses by the nonlinearities in the control system will have implications for flying qualities and PIO susceptibility of the aircraft. Linear analyses that exclude these nonlinearities are prone to error, and are likely to predict better flying qualities and lower PIO susceptibility than the real aircraft will exhibit. The choice of whether to use stick force or stick position as the input for such analyses will affect the results, since the feel system includes nonlinear effects such as hysteresis.

There is little information on the impact of hysteresis on PIO. As with breakout, it can be hypothesized that an excessive level of hysteresis will adversely impact flying qualities and increase the potential for PIO.

CRITERIA FOR THE REDUCTION OF PIO SUSCEPTIBILITY

PIO will never be eliminated from advanced aircraft. As long as there is a continuing push to reduce aerodynamic surface size, and increase the role of artificial augmentation, the potential for PIO will exist. Recent work has led to several proposed criteria for the reduction of PIO susceptibility. Based on a comparative assessment for Category I PIOs, criteria based on airplane Bandwidth were most effective at predicting the possibility for PIO.[17]

Parameters

Parameters for the airplane Bandwidth criteria are defined in Figure 14 and Figure 15.

For a purely linear airplane, a frequency response such as that in Figure 14 represents the dynamics of the augmented airplane for all input amplitudes. More typically, in the presence of nonlinearities the frequency response will be more like those shown in Figure 2: regions of low coherence and possibly non-trustworthy data, with large changes in both magnitude and phase angle of the frequency response.

Criteria

Limits for PIO and handling qualities Levels, for pitch response when the feel system is excluded from the dynamics of the aircraft, are shown in Figure 16. Experiences with these criteria – including the results shown in both Figure 3 and Figure 4 – strongly support their use as PIO prediction and prevention criteria.

The boundaries in Figure 16 are slightly different from those in Figure 3 and Figure 4: the latter include the dynamics of the cockpit force feel system, and hence the limits on the Phase Delay parameter are slightly higher.

Steps for Obtaining the Bandwidth Parameters in the Presence of Nonlinearities

Because it is difficult to obtain flight data for large control inputs, analytical models, in careful consonance with existing flight data, must be used to generate the frequency responses needed to test for PIO susceptibility. Some recommended steps for obtaining the required frequency-response data and parameters are given in Table 2.

With only slight modifications to the steps in Table 2, primarily in modifying the techniques and frequency ranges for the control-input frequency sweeps, the data generated can be used very effectively for parameter identification as well. The steps outlined in Table 2 are specifically oriented toward the Bandwidth criteria and their parameters and focus on the frequency ranges needed for the criteria.

CONCLUSIONS

Advanced flight control systems introduce the potential for significant nonlinearities in aircraft response. The occurrence of pilot-induced oscillations has been attributed to several of these nonlinearities.

This paper examined the results of recent simulation and flight research into the influence of actuator rate limiting (including limiting of software elements intended to prevent reaching the limits of the actuators) on PIO.

- The research data – as well as practical experience – indicate that rate limiting, alone, does not necessarily cause PIO.

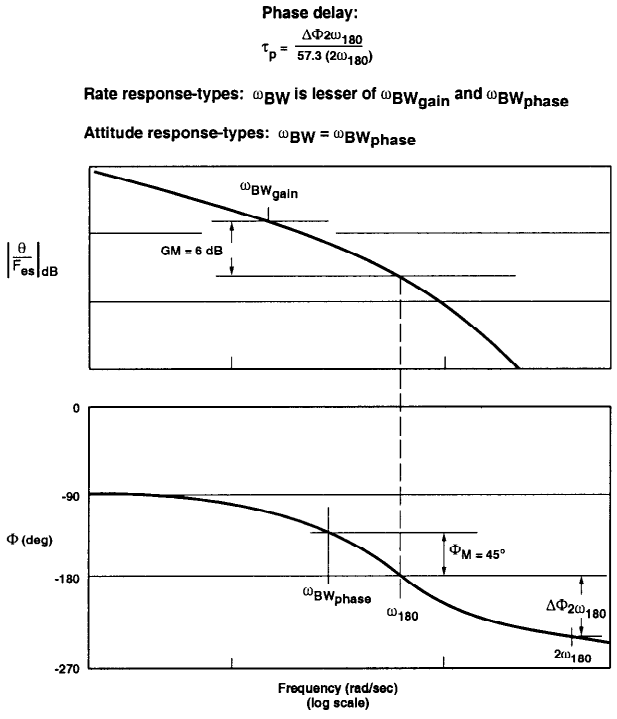


Figure 14. Pitch Attitude Bandwidth and Phase Delay (Flight Path Bandwidth ω_{BW_γ} is Measured from γ/F_{es} and is Defined as $\omega_{BW_{phase}}$)

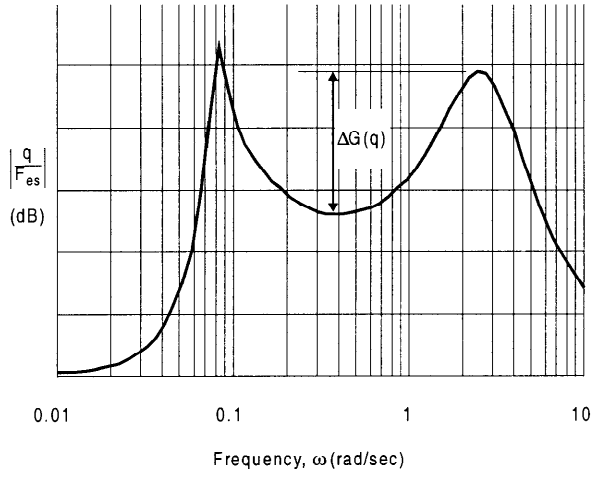


Figure 15. Definition of Pitch Rate Overshoot Parameter, ΔG(q)

- If an airplane has sufficient stability, the deleterious effects of rate limiting will not directly lead to PIO.
- There are three principal factors that determine the susceptibility to PIO for an augmented airplane: the location of the limiter, the degree of stability (or instability) of the airplane, and the demands made on the airplane.
- Rate limiting in the feedforward path (with feedback loops wrapped around it) is the most critical element of PIO susceptibility, since saturation will effectively open the feedback loops and introduce the gain attenuation and phase loss inherent to such limiting.

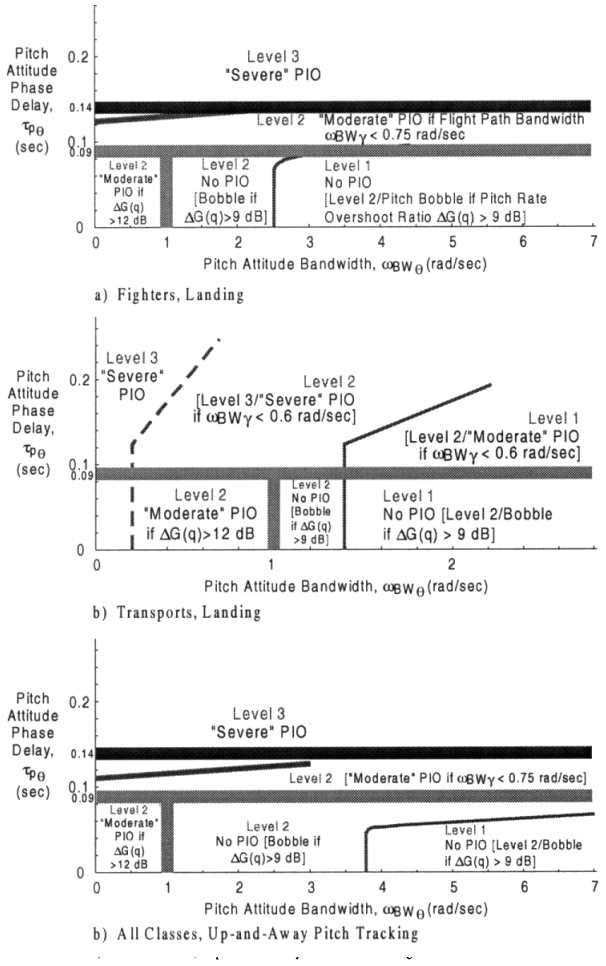


Figure 16. PIO Criteria for Pitch Response When the Dynamics of the Cockpit Control Feel System are Excluded

- Saturation of a limiter in the feedforward path is especially devastating if the augmentation is needed to stabilize a highly unstable airplane. With saturation, the change in dynamics may be more than the pilot can compensate for, again when the limiting itself further degrades the dynamics of the airplane.
- In combination with location of the limiter and the consequences of saturation, the demands placed on the flight control system are a factor. If only occasional "nibbling" at a rate limiter occurs on an airplane that is highly augmented but only slightly unstable, PIO is not likely to develop. But larger demands on that airplane lead to a further separation between demanded and achieved, and greatly increase the likelihood for PIO.

Overall, for aircraft that take full advantage of advanced flight control systems, the key to avoiding PIO is to avoid rate limiting. Since this is not always possible, it is less hazardous to encounter software limiting ahead of all feedback loops than within any such loops.

While not a true source of nonlinearity, the command sensitivity (commanded acceleration per unit cockpit control deflection or force) can have an effect on the susceptibility to PIO as well. Research suggests that as overall time delay increases, a reduction in command sensitivity can reduce the potential for PIO.

Table 2. Recommended Steps for Determining Bandwidth Parameters from Flight Test

Required Data: pitch rate (q), vertical velocity ($\dot{h}$), and cockpit control force (F_{es}) or position (δ_{es})	Define dynamics of prefilters and sensors for all signals
	Use instantaneous data (such as IVSI) as opposed to lagged data
	Verify correct sequence for data sampling and recording: all data from same time frame
Frequency Sweeps (General)	Frequency range can be narrow – Lowest frequency around 0.2 rad/sec or 0.03 Hz (30 seconds per cycle) – Highest frequency around 12-18 rad/sec or 2-3 Hz (3 cycles per second)
	Start from and end in trim conditions, sweeping from lowest to highest frequency
	Total time for the sweep should be no less than about 90 seconds
	Attempt to keep input amplitude relatively constant (smaller amplitude will be necessary for very low-frequency portion of sweep)
	Pilot-generated sweeps are preferred; pilot should be allowed to assist automated sweeps to remain near trim conditions
	Avoid dwelling at frequencies of aircraft natural response (linear and nonlinear modes)
	Repeat sweeps are useful
Frequency Sweeps in Simulation	Confirm that model includes expected nonlinearities – Control command shaping and control feel dynamics – Actuator rate and position limits – Surface effectiveness variations
	Run sweeps of varying input amplitude – Linear region of aerodynamics/control system: peak pitch rates of ±10 deg/sec – Near normal acceleration limits: between 0 and 2g for transports, larger for fighters – At or near full stick (will probably require automated inputs at higher frequencies)
Frequency Sweeps in Flight	Run sweeps of varying input amplitude – Linear region of aerodynamics/control system: peak pitch rates of ±10 deg/sec – Normal acceleration range of 0-2g (if peak pitch rates ±10 deg/sec do not cover this load factor range)
	Confirm that flight results are consistent with those from simulation
	Adjust simulation as necessary to improve correlation
Determination of PIO Susceptibility	Check both simulator and flight results with requirements – Generate required frequency responses using reliable software (e.g., CIFER) – If a "dip" occurs in coherence at any frequency where both input and output powers are high, use single sinewaves at the amplitude of the corresponding sweep and around the frequencies of the loss of coherence to verify results of the sweep – Convert pitch-rate-to-control-force response to effective pitch attitude (add 1/s) – Measure Bandwidth parameters
	Confirm that simulator and flight results are in good agreement for small-amplitude sweeps – If no PIO is predicted, no further testing is needed – If PIO is predicted from both simulation and flight, piloted closed-loop tracking should be performed in flight to test for susceptibility – If PIO is predicted from simulation for large-amplitude sweeps, further flight testing is necessary to confirm this
	Sensitivity to increases in input amplitude may be spot-checked in flight – Note frequency where pitch attitude is 180 degrees out of phase with stick, ω_{180_θ} (equivalently, where pitch rate is 90 degrees out of phase with stick, ω_{90_q}) – Apply several cycles of a sinewave at this frequency in flight, at highest control amplitude used for in-flight frequency sweeps – Repeat for progressively higher control input amplitudes, as flight safety allows – Analyze the single frequencies using time-series analysis (measure amplitude ratio and phase angle directly from time responses) – Compare the loss in phase with the full frequency sweep at the single frequency – This will provide a rough measure of the amplitude attenuation and phase rolloff with increasing amplitude without performing a full frequency sweep

Finally, characteristics of the mechanical cockpit controller, such as breakout and hysteresis, introduce gain attenuation and phase lag into the frequency response that may lead to an increased susceptibility to PIO.

Criteria for the reduction of PIO risk, and steps for obtaining the required frequency-response data and Bandwidth parameters, have been developed and were documented in this paper.

ACKNOWLEDGEMENTS

Most of the work presented here was supported by Contract No. F33615-95-C-3608 from the U.S. Air Force, Wright Laboratory, Wright-Patterson AFB, Ohio. Mr. Thomas J. Cord was the Air Force Contract Monitor. A portion of the work was performed through funding from The Boeing Company, Phantom Works, Long Beach, CA.

REFERENCES

[1] *Aviation Safety and Pilot Control: Understanding and Preventing Unfavorable Pilot-Vehicle Interactions*, National Academy Press, Washington D.C., 1997.

[2] *Military Specification, Flying Qualities of Piloted Airplanes*, MIL-F-8785C, Nov. 1980.

[3] Kish, B.A., *et al.*, *A Limited Flight Test Investigation of Pilot-Induced Oscillation due to Elevator Rate Limiting*, AFFTC-TR-97-12, June 1997.

[4] Mitchell, D.G., Kish, B.A., Seo, J.S., and Mosle III, W.B., "A Flight Investigation of Pilot-Induced Oscillation Due to Rate Limiting," *IEEE 1998 Aerospace Conference Proceedings*, Paper 270, Snowmass, CO, Mar. 1998.

[5] Mitchell, David G., Vineet Sahasrabudhe, and David H. Klyde, "Determining Bandwidth in the Presence of Nonlinearities," AIAA-99-0639, presented at the 37th AIAA Aerospace Sciences Meeting and Exhibit, Reno, NV, Jan. 1999.

[6] Mitchell, David G., "Flight and Ground Testing for Pilot-Induced Oscillations," *1999 IEEE Aerospace Conference Proceedings*, Paper 209, Snowmass, CO, Apr. 1999.

[7] Mitchell, David G., and Brian K. Stadler, "Simulation Investigation of Category I and II PIO," AIAA-99-4003, *AIAA Atmospheric Flight Mechanics Conference*, Portland, OR, August 1999, pp. 1-11.

[8] Markofski, Andrew R., and Randall E. Bailey, "Analysis of Pilot-Induced Oscillation Tendencies Due to Actuator Rate Limiting," AIAA-99-4005, *AIAA Atmospheric Flight Mechanics Conference*, Portland, OR, Aug. 1999, pp. 20-30.

[9] Graham, Dunstan, and Duane McRuer, *Analysis of Nonlinear Control Systems*, Dover Publications, NY, 1971.

[10] Klyde, D.H., McRuer, D.T., and Myers, T.T., *Unified Pilot-Induced Oscillation Theory, Volume I: PIO Analysis with Linear and Nonlinear Effective Vehicle Characteristics, Including Rate Limiting*, WL-TR-96-3028, Dec. 1995.

[11] Iloputaife, Obi, "Minimizing Pilot-Induced-Oscillation Susceptibility During C-17 Development," *AIAA Flight Mechanics Conference*, New Orleans, LA, Aug. 1997, pp. 155-169.

[12] Weingarten, Norman C., Charles J. Berthe, Jr., Edmund G. Rynaski, and Shahan K. Sarrafian, *Flared Landing Approach Flying Qualities, Vol. I - Experiment Design and Analysis*, NASA CR-178188, Dec. 1986.

[13] Field, Edmund J., and Ken F. Rossitto, "Approach and Landing Longitudinal Flying Qualities for Large Transports Based on In-Flight Results," AIAA-99-4095, *AIAA Atmospheric Flight Mechanics Conference*, Portland, OR, Aug. 1999, pp. 219-230.

[14] Monagan, Steven J., Rogers E. Smith, and Randall E. Bailey, "Lateral Flying Qualities of Highly Augmented Fighter Aircraft," AFWAL-TR-81-3171, June 1982.

[15] Bailey, R. E., and L. H. Knotts, *Interactions of Feel System and Flight Control System Dynamics on Lateral Flying Qualities*, NASA CR-179445, Dec. 1990.

[16] Mitchell, David G., and Roger H. Hoh, "Influence of Roll Command Augmentation Systems on Flying Qualities of Fighter Aircraft," *J. Guidance, Control, and Dynamics*, Vol. 7, No. 1, Jan.-Feb. 1984, pp. 99-105.

[17] Mitchell, David G., and David H. Klyde, "A Critical Examination of PIO Prediction Criteria," AIAA-98-4335, *AIAA Atmospheric Flight Mechanics Conference Proceedings*, Boston, MA, Aug. 1998, pp. 415-427.

Paper#A28

Q by David Moorhouse: Your paper illustrates the adverse effects of rate limits put in the wrong position in the control system. In that sense it is consistent with the best practices of paper #25. Would you please comment.

A. (Dave Mitchell & Edmund Field): That is true. More than that, however, we recognize that rate limiting is unavoidable, that any mechanical system can be driven to saturation. The question to be addressed is whether the aircraft flying qualities are affected. We tried to emphasize the importance of properly accounting for the adverse effects of rate limiting on handling qualities and PIO, and of avoiding rate limiting that is not compatible with the dynamics of the aircraft.

This page has been deliberately left blank

Page intentionnellement blanche

Active/Adaptive Rotor Blade Control for Disturbance Rejection and Performance Enhancement

R. Kube
Deutsches Zentrum für Luft- und Raumfahrt
Lillenthalplatz 7
D-38108 Braunschweig, Germany

D. Schimke
Eurocopter Deutschland
81663 München

P. Jänker
DaimlerChrysler
81663 München, Germany

Abstract

As part of a program for development of active/adaptive rotor systems, flight tests were performed with a helicopter featuring a powerful blade root actuation system and a comprehensive sensor instrumentation. The test results gave a deep insight in the mechanisms involved in the reduction of BVI noise emissions and fuselage vibrations through 2/rev blade root control inputs and allowed the derivation of an algorithm for online estimation of the BVI noise emissions experienced on ground. In combination with a closed loop control law it yields a system which allows an automatic reduction of the rotor disturbances on the basis of local blade surface pressure measurements. The closed loop system can also be applied to a trailing edge flap which has been realized and investigated in the Transonic Wind Tunnel Göttingen (TWG) in the second part of the active/adaptive rotor development program. The test results demonstrated the ability of a servo flap to twist the blade to a degree which is required for rejection of the rotor disturbances and enhancement of the rotor performance.

1. Introduction

Due to the azimuthal and radial variation of the flow velocity, the blades of a helicopter rotor experience within one revolution, the fuselage vibrations are comparatively high throughout the complete flight envelope. In descent flight the vibrations are accompanied by strong noise emissions originating from interactions of the rotor blades with the trailed vortices of the preceding blades. While the vibrations represent a considerable stress for the material and, in addition, lead to a reduced flight comfort for passengers and crew on board the aircraft, the **B**lade **V**ortex **I**nteraction (BVI) noise is very annoying for the population on ground.

Both disturbances can be reduced by means of active and adaptive rotor control respectively, techniques which are actually subjected to intensive investigations not only in the U.S. but also in Japan, for example. Although having no long tradition in helicopter development, the Japanese heavy industries started to realize trailing edge flap systems immediately after having initiated their rotor design activities [1]. In the U.S. a lot of experimental and numerical experience on the field of active and adaptive rotor control was gathered in the past 10 years [2, 3] which now forms the basis for the development of a piezo-electric driven trailing edge system [4] and its application to a full-scale helicopter rotor in free flight [5].

A comparable program consisting of wind tunnel, whirl tower and flight tests is jointly conducted by Eurocopter Deutschland (ECD), DaimlerChrysler (DC) and Deutsches Zentrum für Luft- und Raumfahrt (DLR) in Germany. Although its main objective is the realization of a trailing edge flap system, too, the program was accompanied in its first phase by flight tests with **A**ctive **R**otor **C**ontrol (ARC) in a form also known as **I**ndividual **B**lade **C**ontrol (IBC)**.** The IBC flight tests aimed on the generation of a data base which allows an identification of the mechanisms involved in active rejection of the rotor disturbances and the derivation of suited closed loop control laws.

2. Flight Tests with Active Blade Root Control

2.1 Open Loop Noise and Vibration Reduction

2.1.1 Experimental System

The IBC flight tests were conducted under participation of Zahnradfabrik Luftfahrttechnik (ZFL), the manufacturer of hydraulic actuators suited for substitution of the conventional pitch links in the rotating frame. As test bed served a BO105 helicopter (fig. 1) which featured a comprehensive sensor system and blade instrumentation. The latter one comprised pressure transducers, accelerometers as well as strain gauges in order to allow an investigation of the blade surface pressures, the tip displacement as well as the blade bending in flap and lead-lag direction.

The sensor signals were A/D converted in the rotating frame with a resolution of 512/rev before being transmitted via transputer link to the on board data acquisition system IBIS. IBIS merged the data stream of the rotating system with the signals originating from the basic instrumentation and stored them on an 80 MB silicon disc.

Paper presented at the RTO AVT Symposium on "Active Control Technology for Enhanced Performance Operational Capabilities of Military Aircraft, Land Vehicles and Sea Vehicles", held in Braunschweig, Germany, 8-11 May 2000, and published in RTO MP-051.



Fig. 1 BO105-S1 Test Helicopter

Simultaneously the noise experienced on ground was measured by means of a microphone array set up perpendicular to the flight path. The array consisted of 11 microphones and covered a range of ±300m. 15m apart from the center microphone a photo camera was erected in order to determine the overflight height and time. The flight trajectory was measured by means of a GPS receiver installed on board the aircraft [6].

The test matrix covered a wide range of BVI flight conditions with a systematic variation of IBC settings for numerous advance ratios and descent angles. The nominal test point was a 6°-descent flight with 65 knots. At this condition 2-, 3-, 4- and 5/rev blade pitch angles were superimposed individually and in a combined way to the conventional control inputs of the pilot. While the 3/rev amplitude was limited to 0.5°, the 2/rev blade pitch angle as the most interesting one was generated with an amplitude between 0.4° and 1°.

2.1.2 BVI Noise Reduction

The IBC flight test results demonstrated the strong IBC potential for avoiding blade vortex interactions. They obviously take place between 60° and 80° rotor azimuth and are reduced in number when a 2/rev blade pitch angle of 1.0° amplitude and 240° phase shift is applied (fig. 2). The few remaining blade vortex interaction occurring at approximately 90° rotor azimuth, however, yield pressure fluctuations of high intensity indicating that the rotor blade encounters with vortices of high strength at this position.

However, compared to baseline case, where the rotor blades perform a parallel interaction with the vortex filaments in the first quadrant of the rotor disc, non-parallel blade-vortex interactions take place for a 2/rev blade pitch angle of 1° amplitude and 240° phase shift (fig. 3). Since this modification of the interaction geometry yields a minimization of the interaction length, the rotor noise emissions are considerably reduced despite of a high vortex strength.

The mechanism leading to this modification of the interaction geometry can be derived from fig. 4 which shows the low pass filtered leading edge pressure distribution assumed to be proportional to the blade lift in a first step. From fig. 4 it can be seen that, compared to the baseline case, lift is obviously increased in the second quadrant of the rotor disc when a 2/rev blade pitch angle is adjusted with a phase shift of 240°. Although this increased blade lift is probably associated with a high vortex strength, it also yields a strong downwash which moves the BVI noise relevant vortices more downwards thus increasing the blade-vortex miss distance in the first quadrant of the rotor disc.

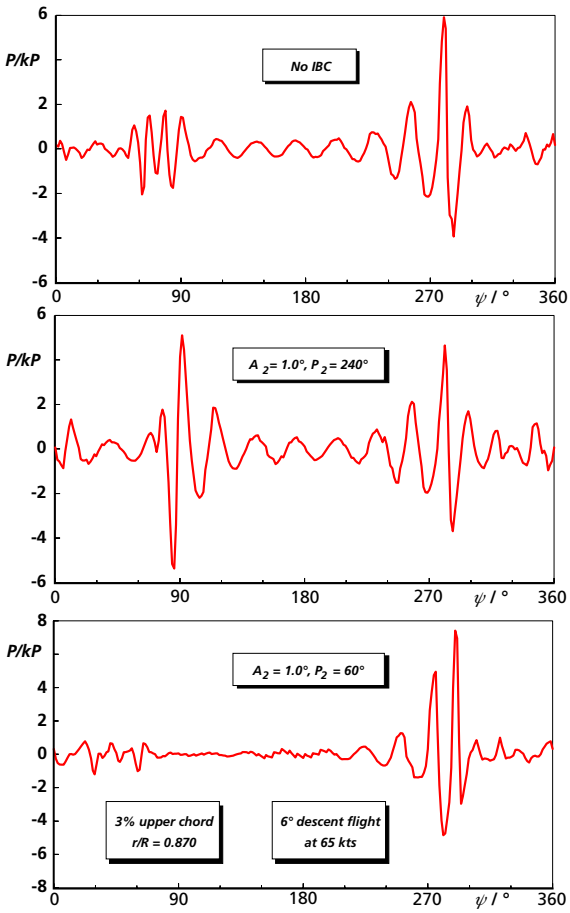


Fig. 2 Time History of High Pass Filtered Leading Edge Pressure

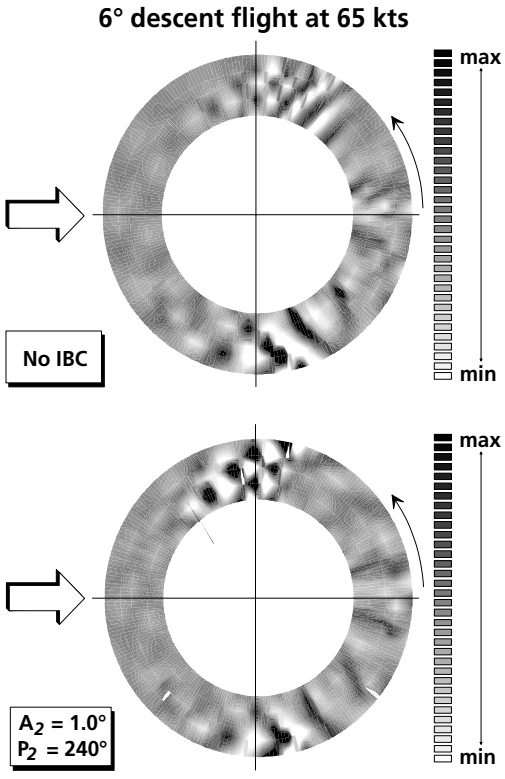


Fig. 3 Interaction Geometry Derived from High Pass Filtered Leading Edge Pressure

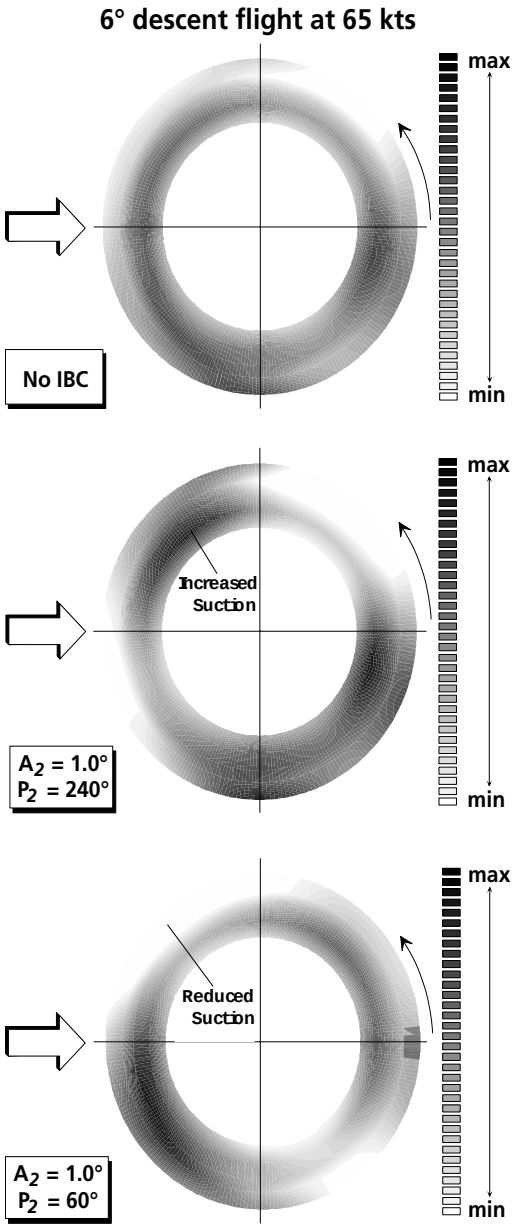


Fig. 4 Low Pass Filtered Leading Edge Pressure

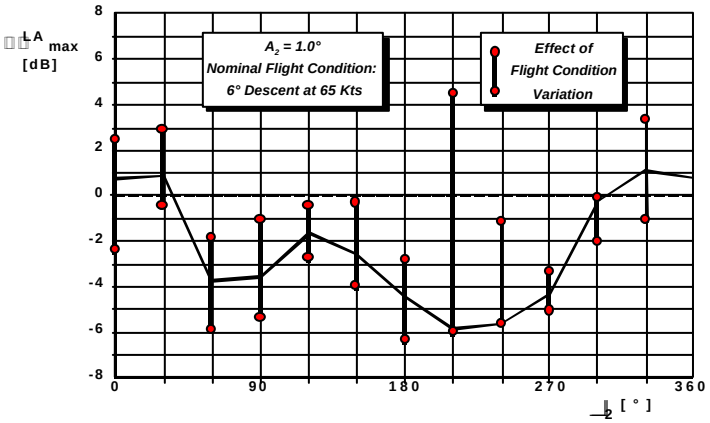


Fig. 5 BVI Noise Reduction due to 2/rev Blade Pitch

The opposite trend can be observed when the 2/rev phase shift is adjusted to 60°. In this case lift is obviously reduced in the second quadrant (fig. 4) thus yielding vortices of reduced strength. Since the lift becomes partially even negative, an induced upwash occurs within this area which can be assumed to increase the blade-vortex miss distance by moving the vortices above the rotor disc. As a result, blade vortex interactions are avoided and the pressure fluctuations between 60° and 80° rotor azimuth occurring in baseline case are dramatically reduced (fig. 2).

Due to the low vortex strength, the achieved BVI noise reduction is fairly insensitive to changes of the flight condition in this case. Therefore, the BVI noise level remains by at least 2dB below the baseline case for all flight conditions close to the nominal 6° landing approach even though amplitude and phase shift of the 2/rev blade pitch angel were fixed to 1° and 60° respectively (fig. 3).

In opposition to these findings, the noise reduction achieved with a 2/rev phase shift of 240° turned out to be very sensitive with respect to flight condition. Due to the high vortex strength occurring in this case, a reduction of the blade-vortex miss distance via a modification of the helicopter pitch or roll angle, for example, has a strong effect on the rotor noise emissions (fig. 5). Therefore a 2/rev phase shift of 240° may increase the BVI noise level by 5 dB while simultaneously having the potential for a reduction by up to 6 dB.

2.2 Vibration Reduction

According to [7], for example, a reduction of the vibrations generated by a 4-bladed rotor requires the superposition of a 3-, 4- and 5/rev blade pitch angle to the conventional one. While its 4/rev part theoretically affects the vertical fuselage vibrations only, the 3- and 5/rev part acts in lateral and longitudinal direction. However, this assumption is based on an infinite blade stiffness and therefore does not take into account the rotor dynamics.

They have turned out to play a major role in case of vibration reduction through active blade root control. For the hingeless BO105 rotor, for example, a strong 3/rev blade excitation was noticed and identified to correlate clearly with the 4/rev fuselage vibrations. The suppression of this 3/rev blade excitation by means of a 3/rev blade pitch angle, lead to a vibration reduction in all degrees of freedom [7].

The same could be achieved during the IBC flight tests which showed that the axial, lateral and vertical gearbox accelerations are affected simultaneously by a 3/rev blade pitch angle (fig. 6). Suprisingly, a 2/rev blade pitch angle turned out to have this potential, too. Although being not able to affect the 4/rev fuselage vibrations directly [8], the axial, lateral and vertical gearbox accelerations were diminished simultaneously within the S1 experiments (fig. 7). Since this vibration reduction in all degrees of freedom coincides, in addition, at least with a local BVI noise minimum (fig. 5), a 2/rev blade pitch angle is very attractive for applications aiming on a simultaneous BVI noise and vibration rejection with single-frequency control inputs.

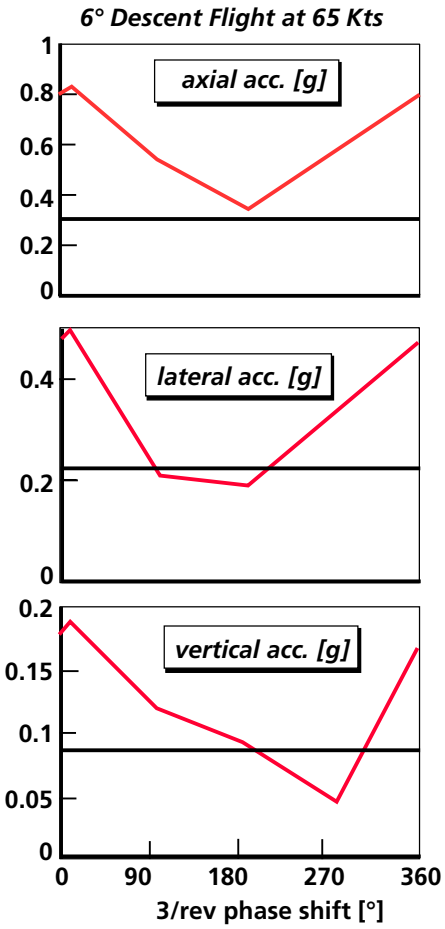


Fig. 6 Effect of 3/rev Blade Pitch Variation on Fuselage Vibrations

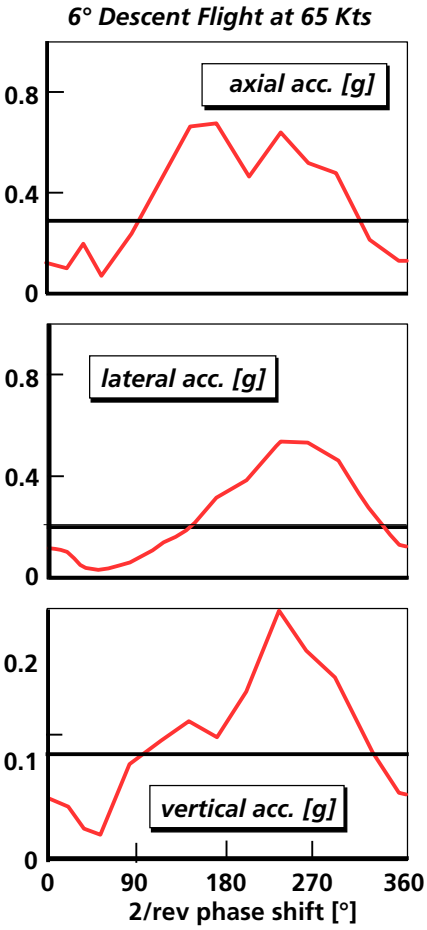


Fig. 7 Effect of 2/ref Blade Pitch Variation on Fuselage Vibrations

Multi-frequency inputs are obviously required for a reduced vibration level being associated with the absolute BVI noise minimum. Although this combination represents the optimum from both, the vibration and BVI noise point of view, it requires a closed loop control algorithm which is fast enough to keep the BVI noise emissions minimal even in case of their sensitivity to changes in flight condition.

3. High Order Control Law for Closed Loop BVI Noise and Vibration Reduction

3.1 Disturbance and Plant Characteristics

Considering a steady-state flight condition in a first step, the vibrations and noise emissions representing the disturbances to be suppressed are of periodic nature and mainly consist of so called rotor harmonics (fig. 8, 9). While the blade vortex interaction noise has a frequency content of 24/rev to 160/rev, the vibrations are of the 1st. 2nd, 4th and 8th rotor harmonic.

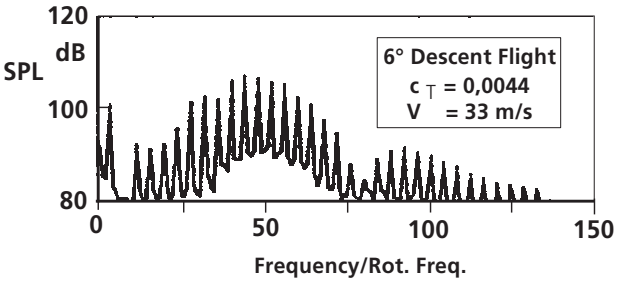


Fig. 8 Frequency Content of Rotor Noise

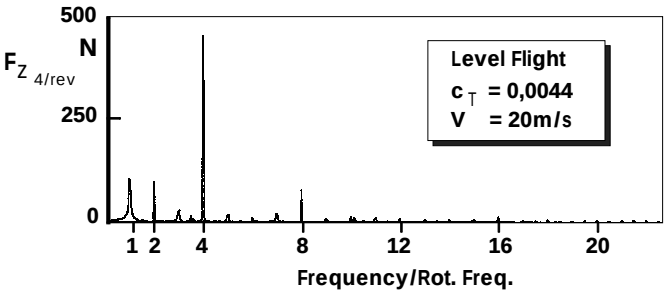


Fig. 9 Frequency Content of Vibrations

Due to their periodic nature the described disturbances can be represented by means of Fourier series which are characterized by their Fourier coefficients. The vibrations are dominated by integral multiples of the blade passage frequency for what reason the corresponding Fourier series becomes of the form

$$F_{FL} = \sum_{n=1}^{\infty} a_{nb} \sin(nb\psi) + b_{nb} \cos(nb\psi)$$

with

F_{FL}	vibratory force acting on fuselage,
ψ	rotor azimuth,
b	number of rotor blades,
a_{nb}, b_{nb}	Fourier coefficients

and

n	integral number.

For simplicity, the vibratory forces and moments acting on the rotor hub are usually combined to the vibration intrusion index

$$J_{Vib} = \sqrt{\frac{F_{x_4}^2}{N} + \frac{F_{y_4}^2}{N} + \frac{F_{z_4}^2}{N} + \frac{M_{x_4}^2}{Nm} + \frac{M_{y_4}^2}{Nm}}$$

with

F_{x_4}, F_{y_4}	4/rev inplane rotor forces,
F_{z_4}	4/rev out of plane rotor forces

and

M_{x_4}, M_{y_4}	4/rev pitching and rolling moment

As is shown exemplarily in fig. 10 this intrusion index keeps fairly constant from one rotor revolution to another and only varies slowly with flight condition.

For the noise emissions the Fourier series becomes of the form

$$J_{BVI} = \sum_{n=n_{min}}^{n_{max}} a_n \sin(n\psi) + b_n \cos(n\psi)$$

with

J_{BVI}	BVI noise intrusion index

and

n_{min}, n_{max}	integral numbers.

Although the noise intrusion index varies with flight condition, too, it also fluctuates strongly from one rotor revolution to another (fig. 11). These fluctuations can be assumed to be due to small changes of the local profile aerodynamics and the downwash geometry respectively which have a strong effect on the noise emissions when occurring at noise relevant rotor azimuth positions [9].

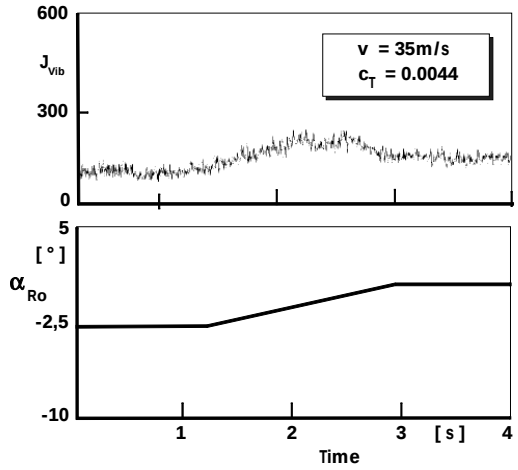


Fig. 10 Variation of Vibration Intrusion Index

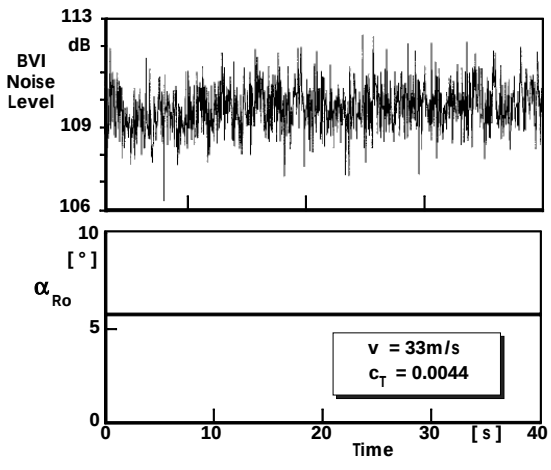


Fig. 11 Variation of BVI Noise Level

A closed loop controller for reduction of the rotor disturbances therefore needs to work with a high gain on the one hand in order to be fast enough for compensation of the strong BVI noise level changes occurring even in case of small flight condition variations. On the other hand low gain is required in order to avoid strong controller reactions to the feedback signal's fluctuations and possible amplification. In principle, this can best be achieved by means of robust control in the time domain where the disturbances are directly fed back to the closed lop controller. The feedback gains are of constant type and originate from an offline design procedure aiming on the realization of a minimum step response time, for example. Although this type of controller has the strongest potential to succeed in a reduction of the rotor disturbances despite of the strong fluctuating feedback signals, it runs the risk to become instable in case of rotor transfer function changes due to variations of the flight conditions. This disadvantage can be eliminated by using an adaptive controller algorithm for which a very satisfying controller performance throughout the complete flight envelope can be expected. Disadvantageous, however, is the high amount of mathematical operations to be performed online in addition to the control process itself. Since these operations have to be performed within a time interval which is inverse proportional to the feedback signal dynamics, an adaptive control algorithm working in time domain can hardly be realized for disturbances with high frequency content like rotor noise and vibrations, for example.

Realized, however, can be an adaptive closed loop controller for noise and vibration reduction which works in the frequency domain. It needs to take into account only a few of the feedback signal harmonics, for what reason the computational effort for the transformation from time to frequency domain by means of a recursive harmonic analysis and from frequency to time domain by means of a harmonic synthesis can be kept small. The resulting Fourier coefficients of the feedback signal harmonics vary comparatively slowly with the ones of the vibrations being mainly affected by changes of the flight condition.

The Fourier coefficients of the rotor noise harmonics, however, are in addition very sensitive to atmospheric disturbances, for what reason they fluctuate strongly from one rotor revolution to another. Since the dynamics of these fluctuations are much lower than the ones of the noise emissions themselves, a frequency domain controller represents a very promising solution for an active reduction of these disturbances. It can be operated at a low rate without running the risk to decrease the controller performance at least in steady state. In order to achieve, in addition, a satisfying transient behavior of the closed loop system, the control law has to be of high order with the feedback gains not being adjusted during the control process according to an online identification of the rotor transfer function. Since the result of this process only represents an estimate of the real value, it is affected at least by small errors which may mislead or even destabilize the controller temporarily. Therefore a minimum step response time can only be achieved by a frequency domain controller which is of high order and, in addition, works with constant gain settings.

4. Control Law Design Procedure

4.1 Classical Approach

Due to the periodic characteristic of the rotor noise emissions and vibrations and the quasi-steady behavior of their harmonics, the design of a frequency domain controller can in principle be based on the so called T-matrix model [10, 11]. It establishes a linear relationship between the vector of active rotor control inputs and the disturbance vector and can be formulated either in global form

$$\underline{y}(k) = \underline{y}_0(k) + \underline{T}(k) \cdot \underline{\theta}_{ARC}(k)$$

with

$\underline{y}_0(k)$ disturbance vector in baseline case

and

$\underline{y}(k)$ disturbance vector in ARC case

or in local form

$$\Delta\underline{y}(k) = \underline{T}(k) \cdot \Delta\underline{\theta}_{ARC}(k)$$

with

$\Delta\underline{y}(k)$ vector of disturbance change

and

$\Delta\underline{\theta}_{ARC}(k)$ vector of ARC input change.

While the global model assumes linearity within the complete range of active rotor control inputs, the local model represents a linearization around the actual point of controller operation (fig. 12) and therefore also allows an approximation of nonlinear effects. The transients of the noise and vibrations due to a change of active rotor control inputs, however, are not taken into account because both models describe the rotor transfer function in a quasi-steady way via the T-matrix. Therefore a closed loop controller which is based on the T-matrix approach can not operate with a high frequency but needs to let the disturbance transients decay after a change of the active rotor control inputs before the next control input is determined using the control law

$$\Delta\underline{\theta}_{ARC}(k+1) = \underline{K} \cdot \underline{y}(k)$$

with

$\underline{K}$ feedback gain

for example [12]. With that control law the closed loop system becomes of the form shown in fig. 13 and can be described by means of the equation

$$\underline{y}(k+1) = (\underline{I} - \underline{T} \cdot \underline{K}) \cdot \underline{y}(k) + \underline{T} \cdot \underline{w}(k)$$

with

$\underline{w} = \underline{0}$ the command vector.

From this closed loop system equation it can be derived that the disturbance vector vanishes within one step if the feedback gain is set identical to the inverse of the T-matrix. Thus the theoretical possible controller response time is one step, a value which seems to be very small. The real response time required for minimization of the rotor noise and vibrations, however, can become fairly large because on the one hand the T-matrix varies with flight condition and actual point of operation. Therefore the feedback gain can not be set identical to the inverse of the T-matrix in all cases and the number of steps required for vibration and noise minimization becomes higher than one.

On the other hand, one control step corresponds to approximately two rotor revolutions in case of vibration and 10-15 rotor revolutions in case of noise reduction. The reason for the high number of rotor revolutions per control step occurring in noise case are the strong fluctuations of the Fourier coefficients from one rotor revolution to another. They need to be averaged 10-15 times before being fed back to the closed loop controller in form of the quasi-steady mean value. Thus, the time required for minimization of the noise and vibration level becomes comparatively long, a characteristic which up to now was considered to be mandatory for a frequency domain controller.

The response time is extended further in case of an online feedback gain adjustment as it was considered to be mandatory up to now at least for closed loop control of the rotor noise emissions. This is due to the fact that strong nonlinearities obviously exist in case of BVI noise and vibration reduction through active rotor control with the gradients of the intrusion indices switching sign when passing either through the global or a local extremum (fig. 14, 15).

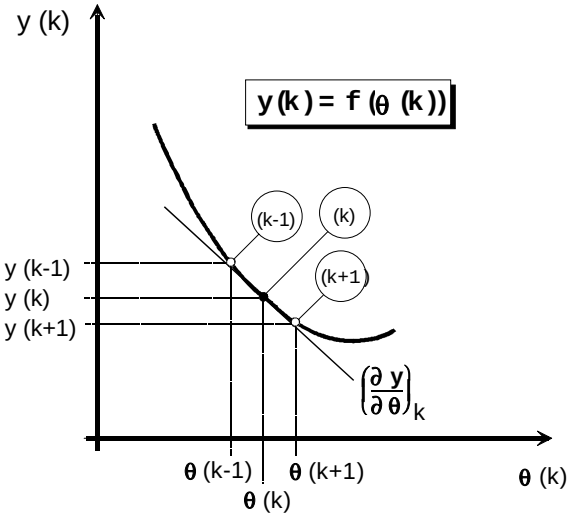


Fig. 12 Linearization Around Actual Point of Operation

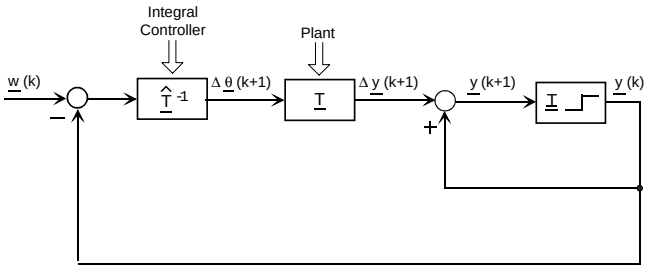


Fig. 13 Quasi-Steady Operating Closed Loop System

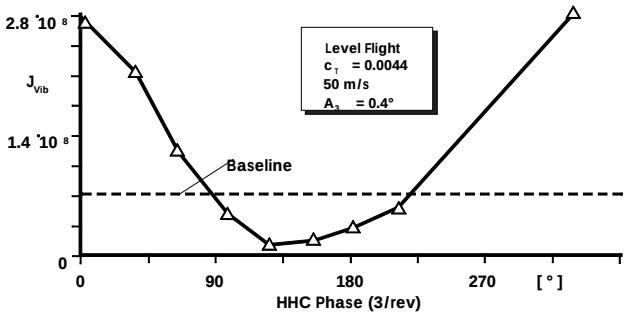


Fig. 14 Variation of Vibration Intrusion Index with 3/rev Phase Shift

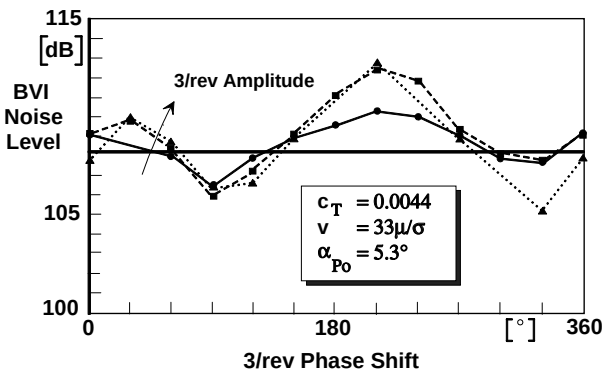


Fig. 15 Variation of BVI Noise Level with 3/rev Phase Shift

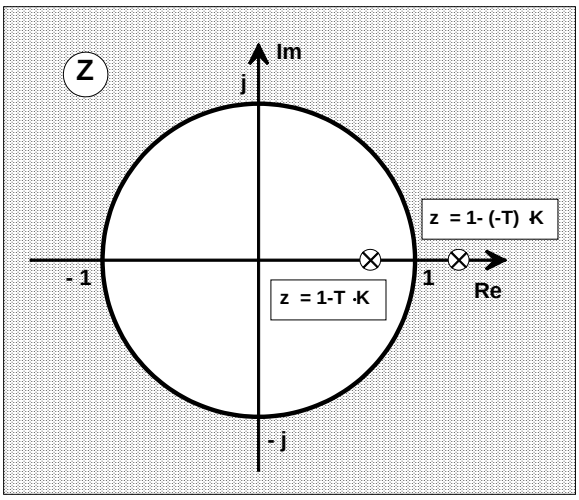


Fig. 16 Pole Placement for Conversion of Control Efficiency

Therefore a closed loop control algorithm which works with direct feedback of the intrusion indices is faced with a conversion of the control efficiency

$$T_{Vib} = \frac{\Delta J_{Vib}}{\Delta \theta_{ARC}}$$

and

$$T_{BVI} = \frac{\Delta J_{BVI}}{\Delta \theta_{ARC}}$$

respectively and thus needs to adjust at least the gain setting sign accordingly online. The necessity for this online adjustment of the gain settings when feeding back the vibration and/or BVI noise intrusion indices directly can be demonstrated easily for the single input/single output case where the characteristic system equation follows from the closed loop system equation as

$$z - 1 + T \cdot K = 0$$

and thus

$$z = 1 - T \cdot K$$

demonstrating that z becomes located outside the unit circle as soon as the sign of T and K differ from each other (fig. 16). Therefore the gain setting needs to be adapted online according to the actual value of T in order to avoid a controller instability.

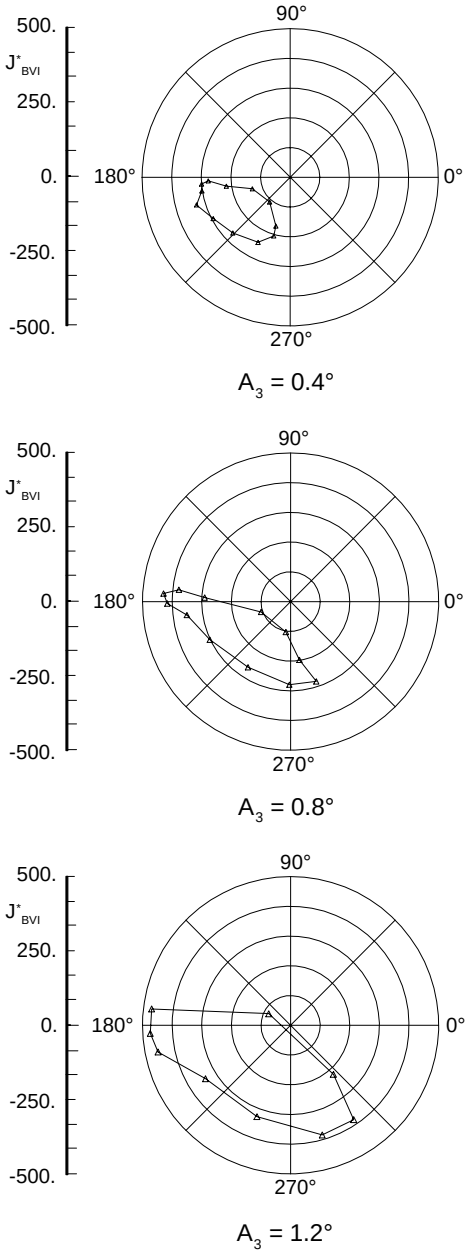


Fig. 17 ARC Effect on 38/rev Noise Emissions

The online adjustment of the gain settings, however, can be omitted when vibrations and noise are not fed back as scalar values but in form of a Fourier coefficient subset. If the real and imaginary parts of these Fourier coefficients are arranged within the vibration and BVI noise feedback vector according to

$$\underline{y}_{Vib}^{T} = \left(F_{x_{4R}}, F_{x_{4I}}, \cdots, M_{y_{4R}}, M_{y_{4I}}\right)$$

and

$$\underline{y}^{T} = \left(BVI_{38_R}, BVI_{38_I}, \cdots, BVI_{46_R}, BVI_{46_I}\right)$$

respectively, the effect of active rotor control inputs to noise and vibrations can be formulated in a linear way. In order to find out to what degree this linear formulation corresponds to reality, HHC wind tunnel data were used [13]. This time the real and imaginary part of the 38/rev noise emissions were plotted against each other. The resulting vector diagrams are shown in fig. 17 which demonstrates that the 38/rev BVI noise vector describes a closed line around a point corresponding to the baseline case. Since the surrounded area increases clearly with ARC amplitude and the vector surrounds the area exactly one time when the ARC phase shift is varied from 0° to 360°, the linear formulation of the ARC effects on the rotor noise can be assumed to be valid. Due to this fact, no sign conversion of the control efficiency needs to be feared for what reason a robust closed loop control system can be designed.

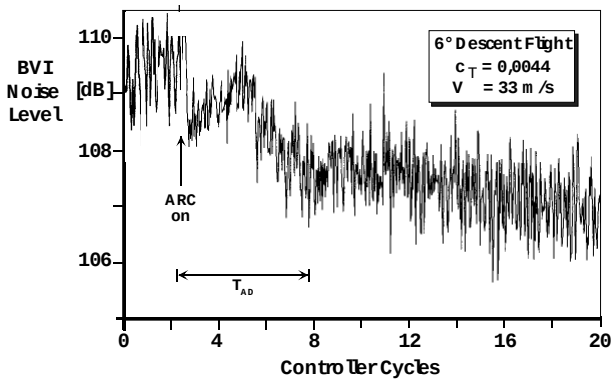


Fig. 18 Performance of Quasi-Steady Operating Controller with Online Gain Adaption

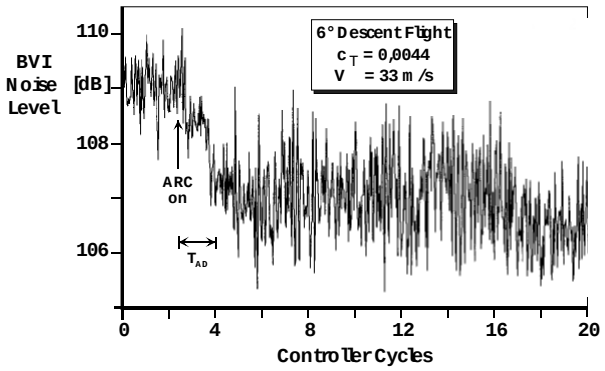


Fig. 19 Performance of Quasi-Steady Operating Controller with Fixed Gain

The advantage of that type of control system compared to an adaptive one could be determined by testing both type of controllers in combination with the DLR rotor test rig in the DNW [13]. The results are shown in fig. 18 and 19 which demonstrate that the number of steps required to reach the disturbance minimum is much lower in case of a robust controller. However, since one control step corresponds to 15 rotor revolutions, the controller response time is still too high and needs to be reduced further.

4.2 Derivation of High Order Control Laws

This required reduction of the system response time can be achieved when the design of the frequency domain controller is not based on the quasi-steady T-matrix approach but on a model which is able to describe the steady-state as well as the transients of noise and vibrations. A model of that type can be achieved by investigating the reaction of the noise and/or vibration Fourier coefficients to ARC step inputs being represented by a stepwise change of the ARC control amplitude. Fig. 20 shows for example the ARC signal of an actuator working with 4/rev and changing its amplitude of operation between revolution 6 and 7. The reaction of the 4/rev vibrations to that ARC step input is shown in fig. 21 which demonstrates that the rotor disturbances behave approximately like a system of 2nd order which is well damped and which reaches the steady state within 2 rotor revolutions. With this knowledge it is possible to design a closed loop control algorithm which allow a reduction of the rotor disturbances within very short time. In opposition to an algorithm which is based on the T-matrix model this control algorithm does not wait until the transients decay before the next cycle is initiated but which works with 64 steps per revolution.

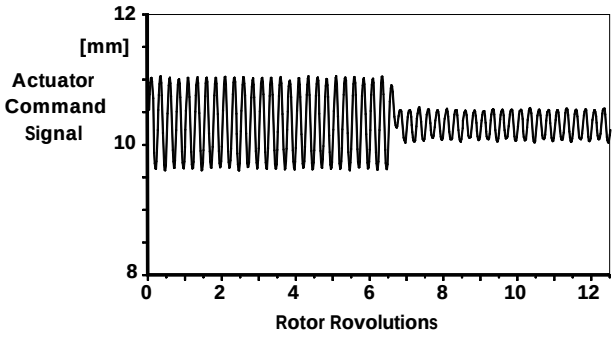


Fig. 20 ARC Step Input

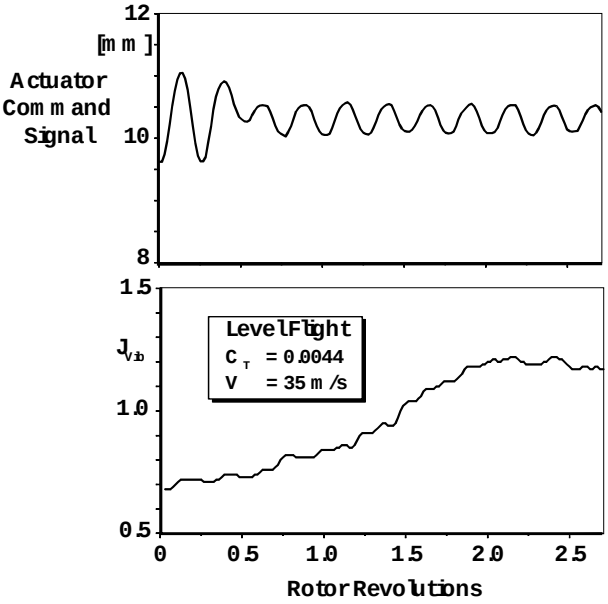


Fig. 21 Reaction of Rotor Disturbances to ARC Step Inputs

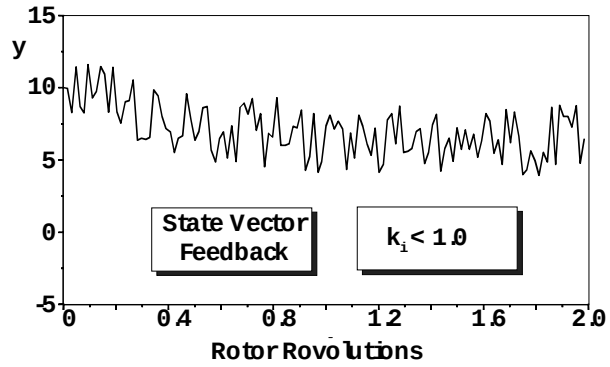


Fig. 22 Performance of High Order High Gain Controller

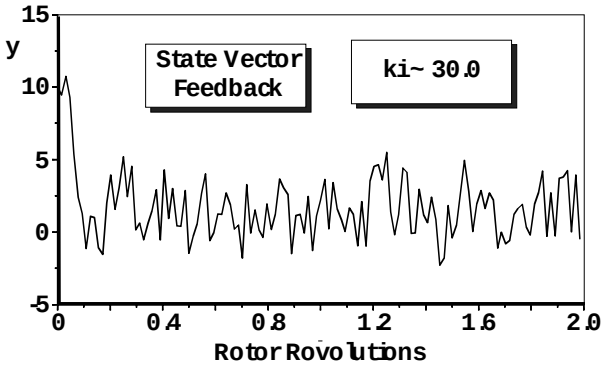


Fig. 23 Performance of High Order High Gain Controller

In fig. 22 and 23 the results of a controller are shown on which the system output vector is fed back. The results originate from numerical simulations of a 2nd order system consisting of a mass, damper and spring (fig. 24) and being excited with a force that leads to oscillations y_0 with 4/rev. The control objective is to eliminate the oscillations by determination of a suited control input amplitude at the spring. From fig. 22 it can be seen that the objective is already achieved when the feedback is selected to be comparatively low, i.e. smaller than 1. In this case the controller reaches steady state after approximately 0.8 rotor revolutions although the system output was heavily disturbed in order to account for the strong fluctuations of the noise intrusion index measured in wind tunnel. This result can be improved further when the feedback gains are increased (fig. 23) In this case steady state is already reached after 0.2 rotor revolutions and maintained although the heavily disturbed feedback signals are fed back via gain settings of approximately 30.

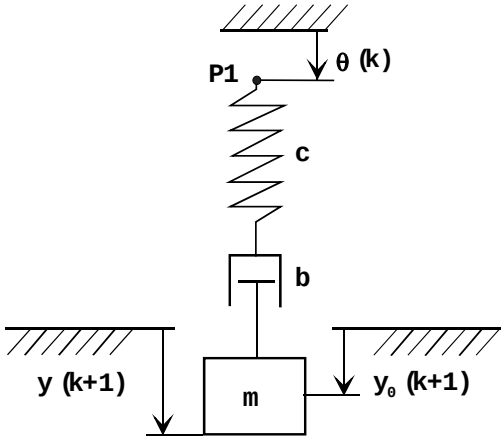


Fig. 24 System of 2nd Order for Numerical Simulations

5. Conclusions

Wind tunnel results with active rotor control demonstrated the necessity to work with high order control laws in order to reduce the rotor noise and vibrations within acceptable time. On the basis of results from step input tests a dynamic model for description of the disturbance reaction to ARC inputs was identified and two control algorithms working with output vector feedback were developed. Numerical simulations of the control algorithms in combination with the identified model showed that a stable behavior can be achieved despite of strong disturbances on the feedback signals. The controller response time is less than one rotor revolution even in case of low gain feedback.

6. References

[1] N. Kobiki, A. Murashige, A. Tsuchihashi, E. Yamakawa "Elementary Study for the Effect of HHC and Active Flap on Blade/Vortex Interaction" 23rd European Rotorcraft Forum, September 16th-18th, 1997, Dresden, Germany.

[2] S.A. Jacklin, A. Blaas, D. Teves, R. Kube "Reduction of Helicopter BVI Noise, Vibration and Power Consumption through Individual Blade Control" 51st Annual Forum of the American Helicopter Society, Fort Worth, Tx, 1995.

[3] T.F. Myrtle, P.P. Friedmann, M. de Terlizzi "New Developments in Vibration Reduction with Actively Controlled Trailing Edge Flaps" 24th European Rotorcraft Forum, September 15th-17th, 1998, Marseilles, France.

[4] N.A. Koratkar, I. Chopra "Design, Fabrication and Testing of a Mach-Scaled Rotor Model with Trailing Edge Flaps" 55th Annual Forum of the American Helicopter Society, Montreal, Canada, 1999.

[5] F.K. Straub, B.D. Charles "Comprehensive Modeling of Rotors with Trailing Edge Flaps" 55th Annual Forum of the American Helicopter Society, Montreal, Canada, 1999.

[6] W.R. Splettstoesser, K.J. Schultz, B. van der Wall, H. Buchholz, W. Gembler, G. Nies "The Effect of Individual Blade Pitch Control on BVI Noise – Comparison of Flight Test and Simulation Results" 24th European Rotorcraft Forum, September 15th-17th, 1998, Marseilles, France.

[7] R. Kube, K.-J. Schultz “Vibration and BVI Noise Reduction by Active Rotor Control: HHC Compared to IBC” 22nd European Rotorcraft Forum, September 17th-19th, 1996, Brighton, United Kingdom.

[8] R. Kube, B.G. van der Wall, K.-J. Schultz, W. Splettstoesser “IBC Effects on BVI Noise and Vibrations – A Combined Numerical and Experimental Investigation” 55th Annual Forum of the American Helicopter Society, Montreal, Canada, 1999.

[9] R. Kube “Derivation of High Order Control Laws for Active Rejection of Rotor Noise and Vibrations” 25th European Rotorcraft Forum, September 14th-16th, 1999, Rome, Italy.

[10] J. Shaw “Active Control of the Helicopter Rotor for Vibration Reduction” 36th Annual Forum of the American Helicopter Society, Washington, DC, 1980.

[11] J. Shaw “Higher Harmonic Control: Wind Tunnel Demonstration of Fully Effective Vibratory Hub Force Suppression” 41st Annual Forum of the American Helicopter Society, Fort Worth, Texas, 1985.

[12] R. Kube “Evaluation of a Constant Feedback Gain for Closed Loop Higher Harmonic Control” 16th European Rotorcraft Forum, Glasgow, Scotland, 1990.

[13] R. Kube, M. Achache, G. Niesl, W. Splettstoesser “A Closed Loop Controller for BVI Impulsive Noise Reduction by Higher Harmonic Control” Annual Forum of the American Helicopter Society, Washington , DC, 1992.

This page has been deliberately left blank

Page intentionnellement blanche

Helicopter Noise Reduction by Individual Blade Control (IBC) - Selected Flight Test and Simulation Results -

W. R. Splettstoesser, K.-J. Schultz, B. van der Wall, H. Buchholz
Deutsches Zentrum für Luft- und Raumfahrt (DLR), Lilienthalplatz 7, 38108 Braunschweig, Germany

W. Gembler, G. Niesl
Eurocopter Deutschland GmbH (ECD), 81663 München, Germany

A collaborative flight test programme was conducted to study among other objectives the potential of open-loop Individual Blade Pitch Control (IBC) to reduce the external noise of a helicopter in partial power descent, a flight regime known to generate the highly annoying Blade-Vortex Interaction (BVI) impulsive noise. The blade root control system employing actuators in the rotating frame, was installed on a BO 105 helicopter, which was flown over an extended linear microphone array. The acoustic measurements on the ground were synchronised to the flight track and rotor performance measurements supplemented by limited simultaneously acquired on-board acoustic and blade surface pressure data. Selected test results quantifying the noise reduction potential of the IBC technique, are presented and compared to numerical rotor simulation results calculated by the aeromechanic S4 code and the acoustic AKUROT code of the DLR. A significant noise reduction benefit (exceeding 5 dB) of the maximum A-weighted (BVI) noise level was obtained for the 2/rev IBC mode; further, over a wide range of IBC phase angles simultaneous noise and vibration reductions were observed. The complete data base acquired will contribute to the development and validation of a fast control algorithm for closed-loop IBC applications.

Introduction

Annoyance level and public acceptance of present days helicopters approaching heliports or landing pads in populated areas are strongly affected by blade-vortex interaction (BVI) impulsive noise dominating the external noise radiation during partial power descent and landing. BVI occurs when a rotor blade closely passes or directly encounters the blade-tip vortices shed by preceding blades, giving rise to impulsive noise radiation directed downwards from the rotor plane as well as to vibrations transmitted to the fuselage. The intensities strongly depend on flight velocity and rate of descent. Over the years, several attempts to reduce BVI noise and vibrations by modification of the blade-tip area have been performed with limited success [1]. But the research over the past decades has substantially improved the physical understanding of the BVI noise mechanisms and also of controlling techniques, particularly of active rotor control technology [2].

It has well been recognised that active blade root pitch control of a helicopter rotor represents an effective technique – either in form of higher harmonic control (HHC) or as individual blade control (IBC) – to reduce the impulsive BVI noise during partial power descent and landing approach.

Paper No.30, presented at the RTA – AVT Symposium, Braunschweig, Germany, 8 – 12 May 2000

HHC is based on a blade pitch control law depending on restricted multiples of the rotor rotational frequency (i.e. n/rev and (n ± 1)/rev of an n-bladed rotor) while IBC additionally allows for arbitrary pitch control inputs. Extensive model rotor wind tunnel tests employing higher harmonic blade pitch control (HHC actuators placed in the fixed frame acting on the fixed part of the swashplate) and some flight tests on a Gazelle SA 349 helicopter have demonstrated a significant noise reduction potential of about 6 dB for open-loop HHC, however, at elevated vibratory forces [3, 4, 5, 6]. It was found that, for optimum noise control at different operational flight conditions, different HHC schedules were necessary, thus requiring closed-loop HHC with optimised control algorithms. By application of this technique, noise reductions could be achieved without increase of vibrations [7].

A promising alternative to HHC offers IBC where the pitch actuators are placed in the rotating frame, thus allowing both unrestricted multi-harmonic blade pitch variations and arbitrary pitch motion for each individual blade. Initial flight tests on a BO 105 helicopter [8, 9] and comprehensive wind tunnel full-scale tests employing the BO 105 main rotor in the 40 by 80 foot wind tunnel of NASA Ames [10, 11], have shown a noise benefit exceeding 6 dB (in the wind tunnel test) at simultaneously reduced vibratory loads. For safety

Paper presented at the RTO AVT Symposium on "Active Control Technology for Enhanced Performance Operational Capabilities of Military Aircraft, Land Vehicles and Sea Vehicles", held in Braunschweig, Germany, 8-11 May 2000, and published in RTO MP-051.

reasons, in these early (1990/91) flight tests, the IBC input was restricted to 0.42° amplitude so that the full capability of the IBC system could not be completely explored; however, for the wind tunnel tests, an improved blade root control system was employed.

To fully explore the potential of the IBC technology concerning the reduction of external (BVI) noise, cabin vibration, and power required, the ongoing Rotor Active Control Technology (RACT) programme was launched being jointly conducted by Eurocopter Deutschland (ECD), the German Aerospace Center (DLR), the Daimler Benz Research Establishment (DB), the Technical University of Braunschweig, and ZF-Luftfahrt (ZFL). Alternatively to the blade root control concept, in a parallel activity, a smart actuation concept with trailing edge flaps is developed and investigated in a wind tunnel; more details of the RACT programme are given in [12, 13].

One major RACT milestone was the conduct of open-loop IBC flight tests with extended noise measurements on ground employing the upgraded BO 105 IBC demonstrator with the major objectives to generate a comprehensive data base for (1) the development of control laws for closed-loop IBC applications, (2) the verification of existing full-scale rotor wind tunnel results, and (3) the quantification of the noise reduction potential of IBC on a real helicopter and the validation of rotor aeroacoustic numerical simulations including IBC effects.

This paper is focussed on the third objective and addresses the experimental approach, rotor aeroacoustic simulations, and comparisons of flight test and simulation results. Further accomplishments of this open-loop IBC flight test concerning other objectives are provided in separate papers [14, 15, 16].

Experimental Approach

IBC Flight Tests

Open-loop IBC flight tests were conducted in March/April, 1998 to explore the potential of the IBC technology under real flight conditions. An upgraded IBC system (± 1.2° pitch control authority) developed by ZFL and extensive measurement and data acquisition equipment provided by ECD, DLR, and DB were installed on the experimental BO 105 S1 helicopter shown in flight in Figure 1. The key component of the IBC system is a servo-hydraulic actuator that replaced the conventional rotating pitch links of the main rotor. Additional components of the IBC system include hydraulic and electric sliprings, hydraulic components, and a digital controller. Safety of flight is guaranteed by an emergency shutdown feature that locks the actuators mechanically if hydraulic pressure drops. The IBC hydraulic system is separated from the helicopter hydraulics and can be shut down manually or automatically. A detailed description of the IBC system is given in [9].



Figure 1 IBC demonstrator BO 105 S1

Highly complex data acquisition systems on board of the IBC demonstrator rotorcraft and on the ground were employed for simultaneous measurements of operational parameters, vibrational forces, blade surface pressures, the helicopter positions, and the emitted noise on board and on the ground.

Objectives and Test Plan

The main objective of the open-loop IBC flight tests was the acquisition of a comprehensive acoustic, aeromechanic, and flight operational data base which were to be analysed under different aspects and is used:

(1) to develop a fast and stable control algorithm for a closed-loop IBC system capable of simultaneous noise and vibration reduction over the total flight envelope.

(2) to test and evaluate a closed-loop controller concept for vibration reduction. The analysis of the flight test data regarding this goal is communicated in [14].

(3) to study different BVI identification algorithms under real flight conditions. Results concerning this goal are presented in [15].

(4) to verify existing IBC wind tunnel results by careful analysis of the flight test results. The accomplishments regarding this objective are discussed in [16].

(5) to quantify the noise reduction potential of IBC on a real helicopter and to validate an aeroacoustic numerical simulation approach taking into account IBC effects. The analysis and comparison of the flight test and simulation results concerning this goal are provided and discussed in the present paper.

The test plan was designed to identify and cover flight conditions with intensive BVI noise generation. For a systematic variation of IBC parameters, a 6°-descent flight at nominal 65 kts IAS (ICAO approach) was chosen. Since there was little experience available for arbitrary IBC inputs (e.g. wavelets), harmonic IBC inputs of 2/rev, 3/rev, 4/rev, and 5/rev and some mixed-mode inputs were tested. A nominal IBC amplitude of ± 1° was used except for 3/rev for which a control amplitude of 0.5° was selected. Furthermore, for the 2/rev IBC mode, a variation of the control amplitude between 0.4° and 1.0° was examined.

On-board Test Equipment

Additionally to the IBC system, a sophisticated experimental system has been integrated in the helicopter, which is described in detail in [13] and summarised here.

The instrumentation in the rotating system comprises 19 pressure transducers embedded in one blade, 3 accelerometers each on the hub and at the blade tip, 2 strain gauges on each blade for flapping and lead lag moment and further sensors used in the actuation system. The data are conditionally sampled at a rate of 512/rev triggered by a rotor azimuth angle encoder. A fast interface computer collects and transmits the data via slipring to a control computer (called IBIS) located in the fixed system. IBIS also collects all data from the basic instrumentation and transmits via telemetry safety critical signals as well as data reflecting the control activity and the flight states to the ground station. For eventual use in the noise controller, three microphones are mounted on the starboard landing skids. To ensure accurate flight trajectory measurements, a GPS–receiver as part of a DGPS system is installed on-board, which communicates by its own telemetry with the GPS reference station on ground.

Acoustic Measurements on Ground

Flyover noise measurements were conducted by use of an extended linear microphone array arranged perpendicular to the flight track centreline covering a range of ± 300 m as shown in Figure 2.

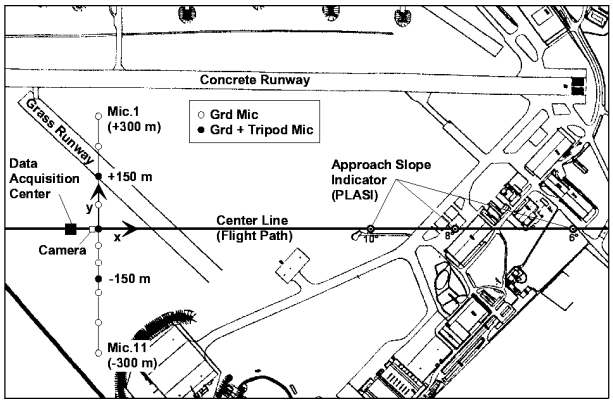


Figure 2 Test set-up on Dornier-Fairchild airfield showing microphone array and coordinate system

The microphone array consisted of 11 ground microphones and 3 microphones mounted on tripods 1.2 m above the ground at the ICAO noise certification positions 0 m and ± 150 m. The ground microphones were placed in an inverted position 7 mm above a circular metal plate (of 0.4 m diameter) out of the centre at 0.75 radius, to minimise reflection influences. For better resolution of the important advancing side BVI noise radiation, a smaller spacing of ground microphones was chosen on the starboard side of the helicopter in approach.

A photo camera was set up 15 m apart from the central microphone and used to determine the overflight height and the exact overflight time in terms of GPS time. Exact flight path co-ordinates, speed over ground, and flight path angles were acquired by a differential GPS system with the reference GPS receiver located at the acoustic data acquisition centre on ground (50 m away from the central microphone). Unfortunately, in a number of test runs, the DGPS system did not properly work. In these cases, the on-board recorded pressure altitude history and the photometric overflight height was used to evaluate the validity

of the test run concerning the flight path. All 14 signals of the ground based microphones were simultaneously acquired by the central acoustic data acquisition system (Figure 3).

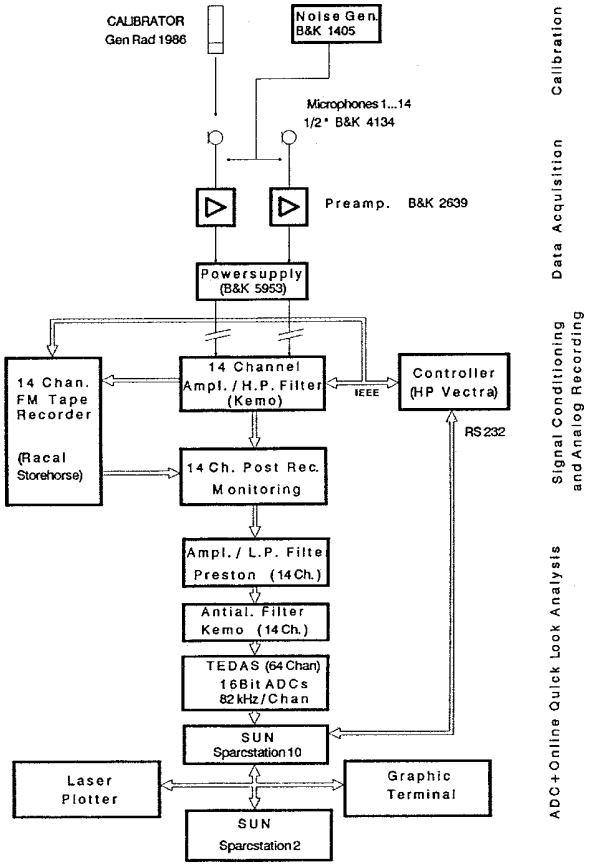


Figure 3 Acoustic data acquisition scheme

After PC-controlled signal conditioning, the data were recorded analogously on an FM tape recorder and, in parallel, were digitised at a rate of 14 336 Hz and 16 Bit resolution giving a useful frequency range of about 7 000 Hz, which is sufficient for meaningful full-scale helicopter noise analysis. A powerful workstation allowed to record and store the digitised data of all channels for complete overflights up to 90 seconds. In addition, the GPS data and the atmospheric data from the on-site weather station (2 m above ground) were recorded. On-line calculations provided "quick-look" graphic output of weighted sound pressure level histories and noise contours as well as flight trajectories that allowed evaluation of the validity of the test data.

Synchronisation of the acoustic, flight path and on-board data was established via the common GPS time and the recording of that instant in time when the camera took a picture of the helicopter in its overflight position.

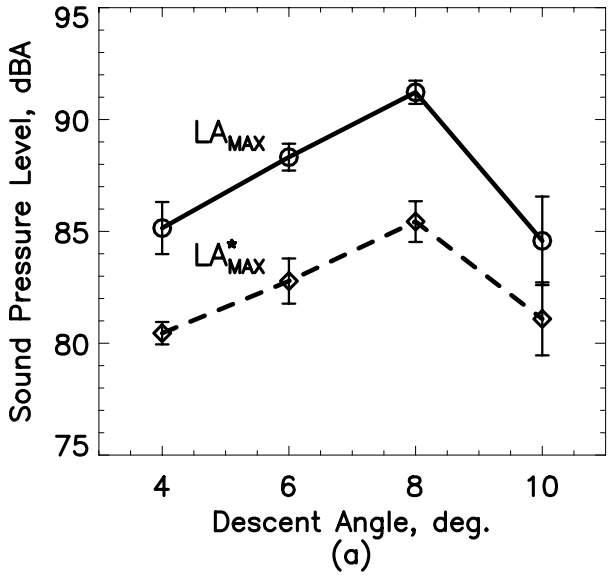
Test Conduct

The open-loop IBC flight tests were conducted in March/April, 1998 on the Dornier-Fairchild airfield in Oberpfaffenhofen near Munich. Each test series was started with the helicopter mass corresponding to the maximum take-off mass of 2 300 kg. Refuelling was mandatory after 10 per cent loss of mass. A very useful tool to guide the test pilot during the different approach flights was a powerful Pulse Light Approach Slope Indicator (PLASI) provided by Dornier Fairchild. The reference overflight height of 120 m was kept constant for all approach flights. For these landing approach flights, synchronous recording of the acoustic and flight path data started at least 1 200 m before the microphone array and ended about 500 m behind it to ensure recording of the noise maximum and the "10 dB-down" points particularly at the outer microphones. Synchronised on-board data were acquired over a period of 5 seconds when the helicopter was approaching and passing the microphone array.

Data Evaluation and Correction

After careful evaluation of the acoustic, the flight path and rotor operational data, in particular, of flight path angle, rotor tip path angle, collective and cyclic pitch in the important acoustic "10 dB-down" period, a number of test runs had to be excluded from further analysis. Since the flight test period was restricted, the number of valid flights per test condition is rather limited and the variance of the noise levels is rather high, probably a consequence of partly unfavourable wind conditions and different test pilots involved in the flight tests. Therefore, the noise levels are presented in terms of mean values with indication of the 90 per cent confidence intervals for each test condition.

The measured acoustic data shown in this paper have been corrected to reference flight path or, if not available, to the reference overflight height and to the International Standard Atmosphere (ISA + 10°C) sea level conditions.

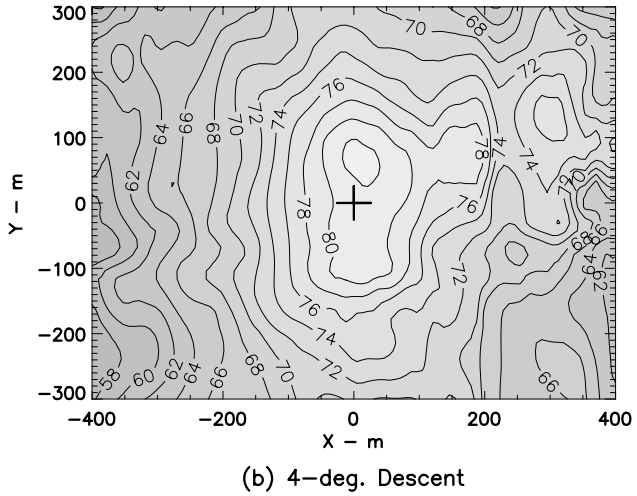


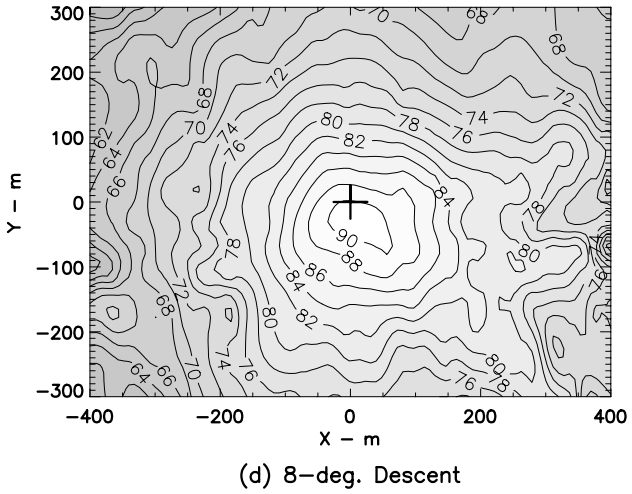
Acoustic Results and Analysis

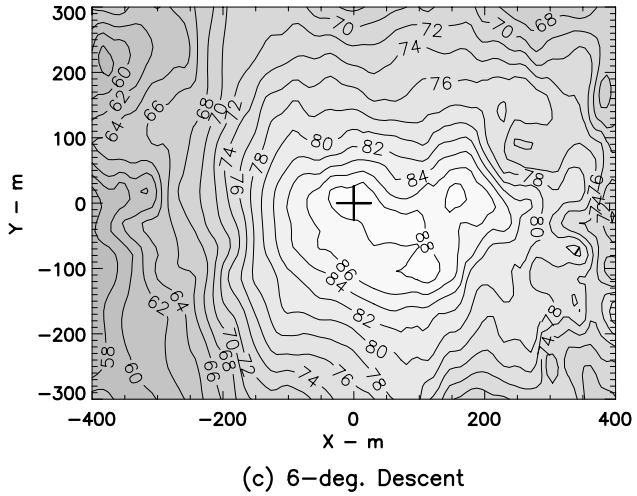
Variation of Descent Angle

A small part of the flight test was devoted to baseline (no IBC) descent flight conditions to determine the flight path angle range where BVI impulsive noise radiation is most intense for the BO 105 main rotor. The result, in terms of A-weighted noise levels (LA), of the descent angle sweep at constant speed of 65 kts IAS is shown in Figure 4.

In Fig. 4 (a), the maximum noise level LA_{MAX} of the ground microphones and the maximum noise level of the 11-ground microphone average (energetic average) LA^*_{MAX} are plotted versus descent angle, while in Figs. 4 ((b)-(e)), the A-weighted noise contours with the helicopter in the central position are presented marked by a







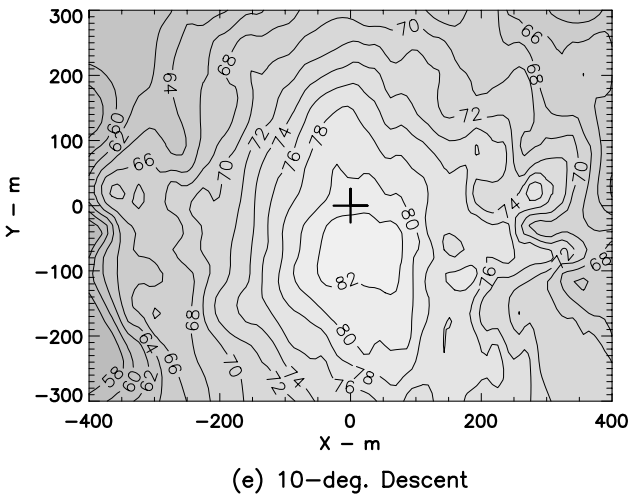


Figure 4 A-weighted noise levels (a) and noise contours (b-e) for different descent angles at nominal 65 kts IAS without IBC activated

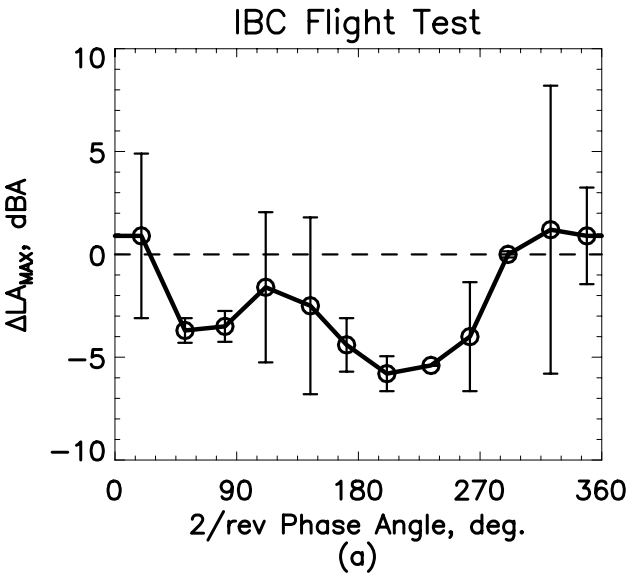
cross. Noise intensities and directivities correspond well with scaled model rotor wind tunnel results [17], where the maximum BVI noise radiation was identified for a descent angle between 6 and 7°. Maximum intensities are focussed below the helicopter on a pattern extended slightly forward and towards the advancing side of the main rotor. Increased descent angles mean increased backward tilt of the rotor tip-path plane and a change of the BVI encounters towards smaller azimuth angles; consequently, the radiation patterns for 8° and 10° show maximum intensities more downstream (at smaller X) and more extended on the advancing side (larger neg. Y) compared to the 6-degree case.

IBC Variations

For investigation of the IBC effects on noise and vibrations, the 6-degree descent ICAO approach at fixed 65 kts flight velocity was selected. As stated earlier, only higher harmonic pitch control laws have been tested.

2/rev Phase Variation: The results for 2/rev IBC phase variation at increments of 30° and 1° amplitude are presented in Figures 5 through 8. The noise reduction benefit in terms of ΔLA_{MAX} as well as of ΔLA^*_{MAX} and SEL* is shown in Fig. 5 (a) and Fig. 5 (b), respectively.

Like in the full-scale rotor wind tunnel test [10, 11], a significant BVI noise reduction is seen over a large range of phase angles. Minimum noise radiation (optimum reduction up to nearly 6 dBA for LA_{MAX}) is achieved in the phase angle range $170° \le \phi_2 \le 250°$, while a secondary minimum is found in the range between $45° \le \phi_2 \le 75°$. Increased levels have been measured for the phase angles ranging from $290° \le \phi_2 \le 30°$. The vertical bars indicate the 90 per cent confidence interval (u_{90}) within which, with 90 per cent probability, the "true" value for a specific test condition can be expected. Similar results are obtained for the Sound Exposure Level, SEL*, and LA^*_{MAX}, the noise measures based on 11-microphone averages (Fig. 5 (b)). Corresponding A-weighted noise contours for the baseline (no IBC) case and for two specific IBC phases ϕ_2 = 201° (minimum BVI noise) and ϕ_2 = 52° (secondary minimum) are compared in Figures 6 ((a)-(c)). A distinct reduction of high-intensity BVI noise radiated to the heliport neighbourhood can be achieved for both in flight direction and in lateral direction. In Figure 7 ((a) and (b)), the sound pressure histories for one rotor revolution, measured by the central



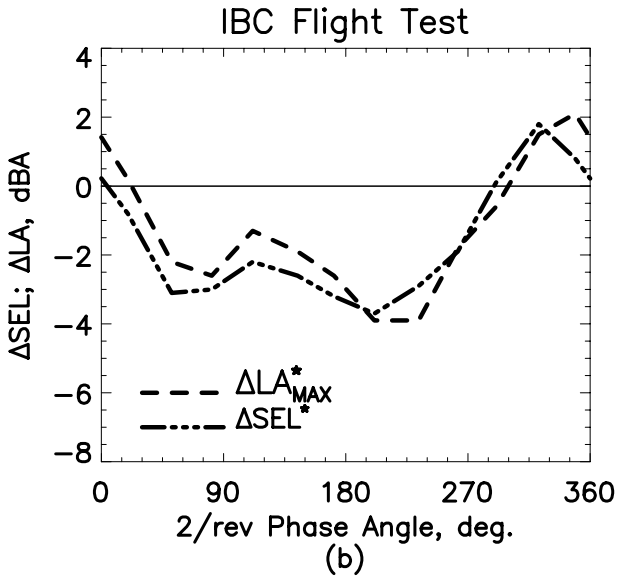


Figure 5 Effect of 2/rev IBC phase variation (θ_2 = 1°) on A-weighted noise levels for 6°-descent flight at 65 kts IAS referenced to the baseline case without IBC, (a) $\Delta LA_{MAX} \pm u_{90}$, (b) ΔLA^*_{MAX} and Δ SEL*

ground microphone, are illustrated for the baseline case (part (a)) and for minimum noise control (part (b)). A significant reduction of the impulsive content of the typical BVI noise signature is obvious, which is directly correlated with a smoothed blade surface pressure time history on the advancing side, as illustrated in Figure 8 for a leading edge (3 per cent chord) pressure sensor at r/R = 0.7. The comparison of the baseline case with the minimum noise case indicates that the blade-parallel BVI's on the advancing side in the azimuth range between 30° and 60° have been largely suppressed by IBC, which is the case on the retreating side between 300° and 330° as well.

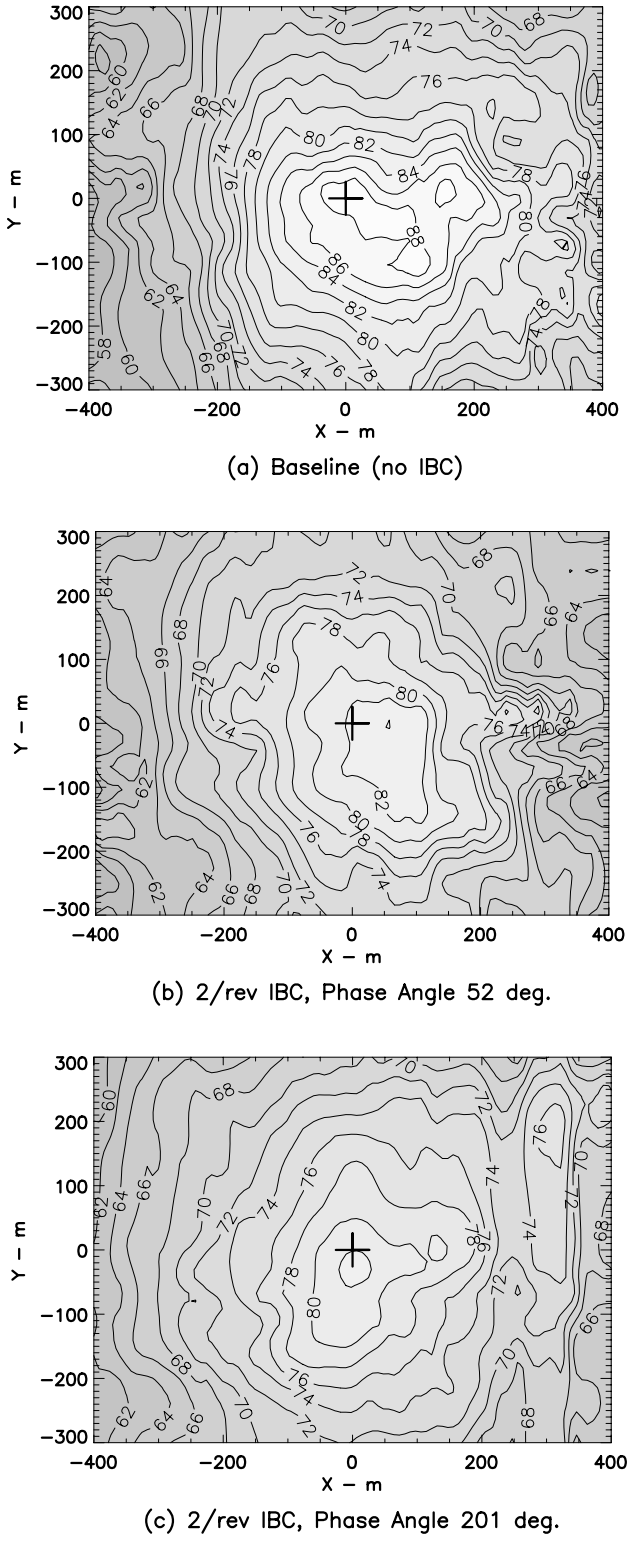


Figure 6 A-weighted noise contours for (a) baseline case (no IBC) and for selected 2/rev IBC-phase settings (θ_2 = 1°) of (b) ϕ_2 = 52° (secondary minimum noise) and (c) ϕ_2 = 201° (minimum noise). Flight condition as for Fig. 5

2/rev Amplitude Variation: Increasing the 2/rev amplitude from 0.4 to 1.0° in increments of 0.2° at a fixed phase angle of 60° resulted, as expected, in increasing acoustic benefit as shown and discussed in [16], however, in a non-linear way. Corresponding leading edge blade pressure histories showed indeed an increase in retreating side BVI for amplitudes 0.6° and 0.8°, which was not measured for 0.4° and 1.0°. This may have been caused by extraordinary rotor trim changes required due to unfavourable wind conditions prevailing during these test runs with retreating side cross and tail wind speeds partly exceeding the ICAO limits. Furthermore, due to the small number of test runs per condition, the confidence level is rather poor from a statistical point of view.

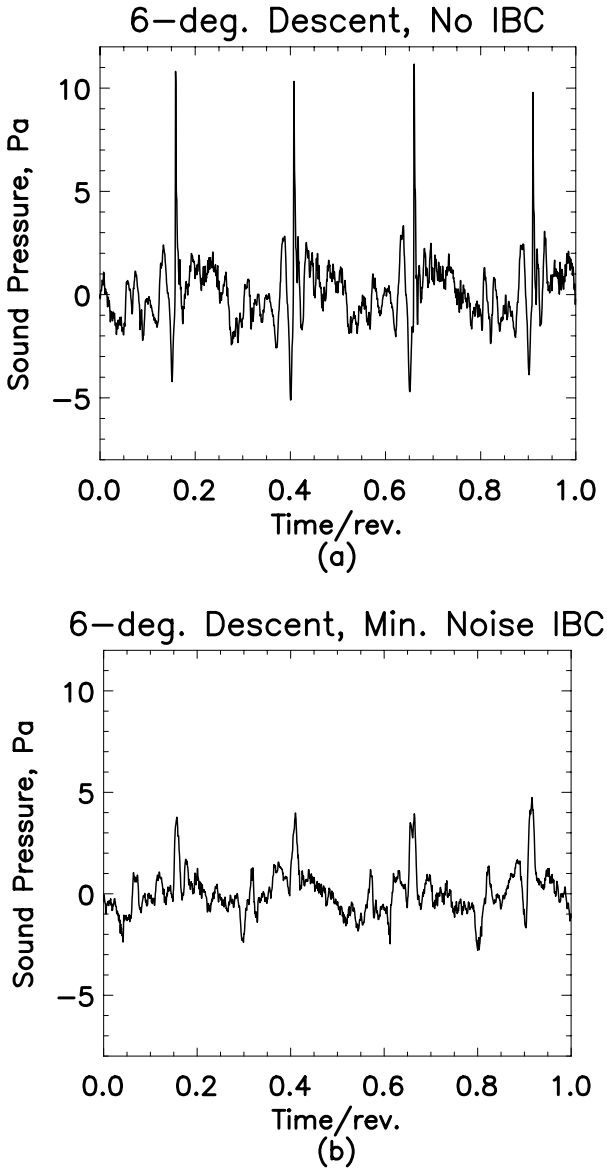


Figure 7 Sound pressure histories at maximum immission points for (a) baseline case (no IBC) and for (b) minimum noise IBC settings (2/rev, θ_2 = 1°, ϕ_2 = 201°. Flight conditions as for Fig. 5

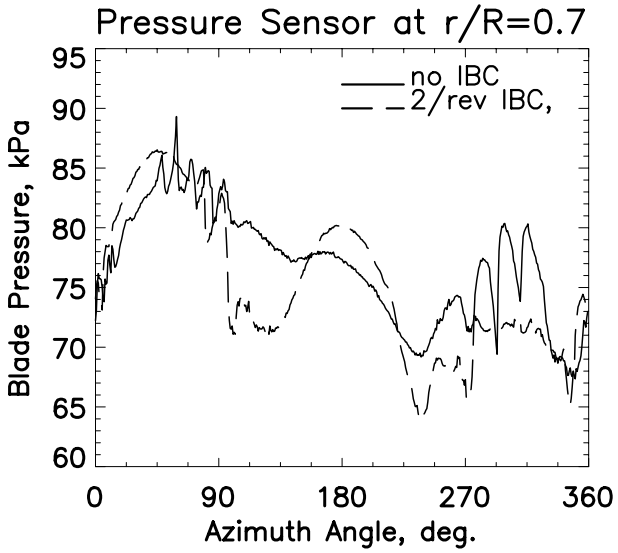


Figure 8 Leading edge (0.03 c) absolute blade surface pressure histories for the baseline case (no IBC) and for minimum noise IBC setting (2/rev, θ_2 = 1°, ϕ_2 = 201°). Flight conditions as for Fig. 5

3/rev and Mixed-Mode IBC Variations: Results of 3/rev and mixed mode IBC phase variations are shown in section "Comparison of Simulation and Flight Test Results".

Rotor Aeroacoustic Simulation

The DLR rotor code S4 here is used to compute the effects of active control (HHC, IBC) on the rotor dynamic forces and its acoustic emission via high-resolution blade air loads [18, 19]. It mainly consists of three modules: the aerodynamics, the structural dynamics and the induced velocities module, embedded in a trim algorithm [20]. The rotor is trimmed to prescribed values of thrust and hub moments from experiment by variation of the collective and cyclic controls. The acoustic postprocessing is done by using the high-resolution load distribution of the S4 program as an input for the Ffowcs-Williams and Hawkings equation. The program scheme is sketched in Figure 9.

For simulation of the IBC cases, the following combination is used: non-linear unsteady aerodynamics including yaw; hingeless blades with 3 flap modes, 2 lead-lag modes and 1 mode in torsion; prescribed wake geometry including HHC effects. For analysis of the IBC effects on the BO 105 main rotor noise emission, a typical rotor condition at 6°-descent flight is chosen from the experiments. This provides data for thrust, rotor roll and pitch moments, advance ratio, and shaft angle of attack. Then, the S4 code is run for this

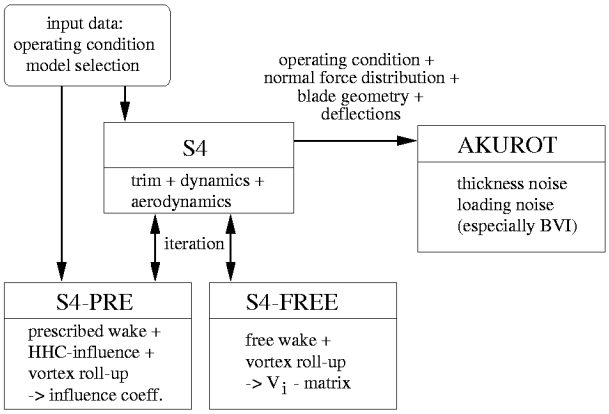


Figure 9 Computational scheme for rotor simulation and acoustic emission

baseline case (no IBC) first. The wake geometry and blade dynamics simulation is iteratively performed; typically 2 iterations are enough to obtain convergence. In this test campaign, the IBC input schedules followed the higher-harmonic blade pitch control law: $\theta = \theta_n \cdot \cos(n\psi - \phi_n)$, where θ_n denotes the amplitude, n the multiple of the rotational frequency, ψ the azimuth angle, and ϕ the phase angle. IBC variations are calculated in the similar way as the baseline case, namely prescribing the control angle (θ_2 = 1°) and its phase (ϕ_2 = 0°, 30°, ... 330°) and trimming again to thrust and moments of the baseline condition as the pilot did when flying the helicopter.

Comparison of Simulation and Flight Test Results

Baseline Case (no IBC) Comparisons

Since the aerodynamics of the S4 code essentially are based on lifting line theory, no pressure distribution is available from the code. On the other hand, due to scarce instrumentation of the BO 105 rotor blade, no local loading nor blade deflections are available for direct comparison. However, the blade's leading edge pressure distribution can be obtained from the transducers at 0.03c (c = blade chord length) of the upper surface between 0.6R and 0.97R. They are very sensitive to changes of oncoming flow conditions and thus are useful indicators for BVI events, provide information wether the vortices are flying above or below the rotor disk, and where they are closest to the blades. When applying a high-pass filter suppressing the lowest fluctuations (< 6/rev) that contain mainly dynamic pressure and blade motion components, the remaining pressure distribution is

originating mainly from BVI events, i.e. the upwash and downwash of individual vortices coming close to the blade's leading edge. This can be compared to the computed induced velocity distribution, filtered in the same way.

In Figure 10, the baseline case pressure distribution of one individual revolution from the flight test indicating the BVI geometry (Fig. 10 (a)) is compared to the BVI locations resulting from the simulation (Fig. 10 (b)).

The simulation predicts the vortices close to the rotor blades at the most critical locations for BVI noise emission, i.e. where the vortices are parallel to the rotor blade's leading edge (see [15]). The flight test, however, does not show this in that detail; here the vortices do pass the disk earlier, i.e. at azimuths of about 70° on the advancing and at 280° on the retreating side. Changing the flight path angle to 4°- descent, the simulation (Fig. 10 (c)) gives BVI locations that compare much better to the flight test, especially on the advancing side. Similar observations were made when wind tunnel and flight test results were compared [21]. One probable reason for this behaviour may be found in the wind conditions during the test, resulting in an instantaneous effective flight path that was slightly different from the geometrical flight path. Another reason for the differences in the BVI locations may be seen in the assumption of the basic wake geometry with rotor moments near zero, a trim condition that has been used in the HART [6] test in the DNW wind tunnel and for the code validation. In the flight test, a strong pitch moment in the range of 2000 Nm was measured, and the lift for that moment must have been created about 80° earlier in azimuth. Following the assumptions of momentum theory, this will cause extra downwash on the advancing side and some upwash on the retreating side relative to a condition with zero moments. Tip vortices thus will be convected more downwards on the advancing side and the BVI locations will shift to larger azimuth positions. Whatsoever, as a reference for the simulations, the 6°-descent condition was chosen and the changes of the wake structure relative to this baseline case resulting from IBC variations are the important features to represent.

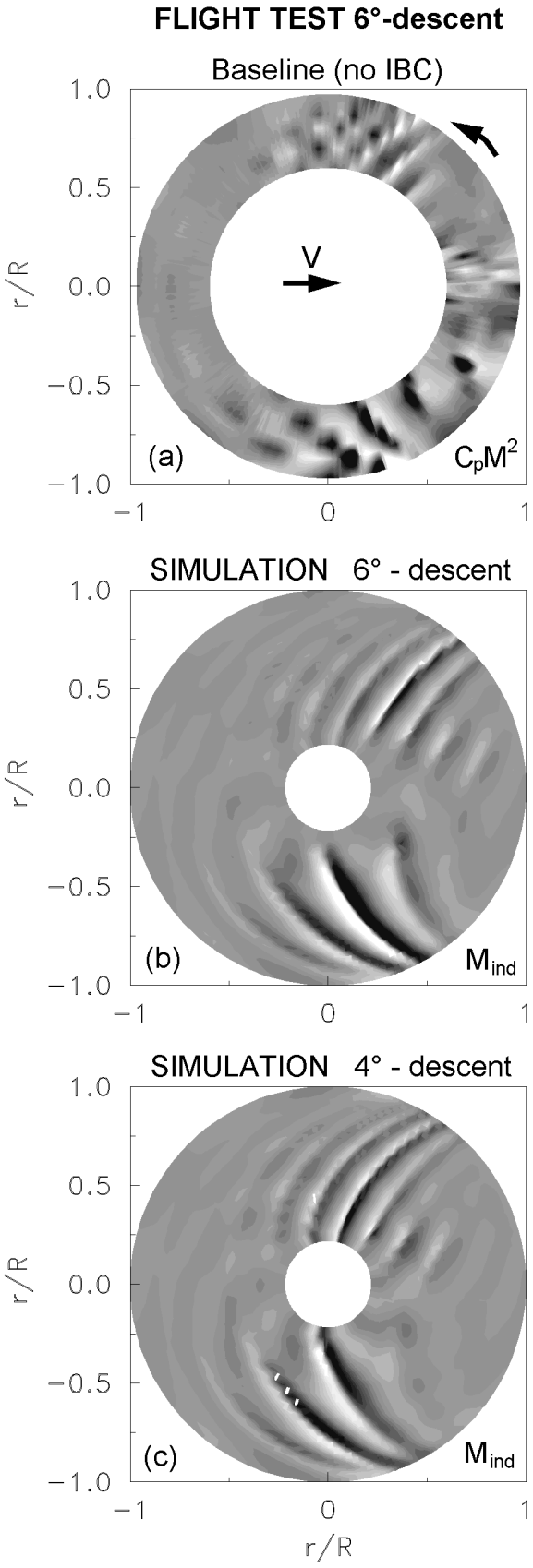


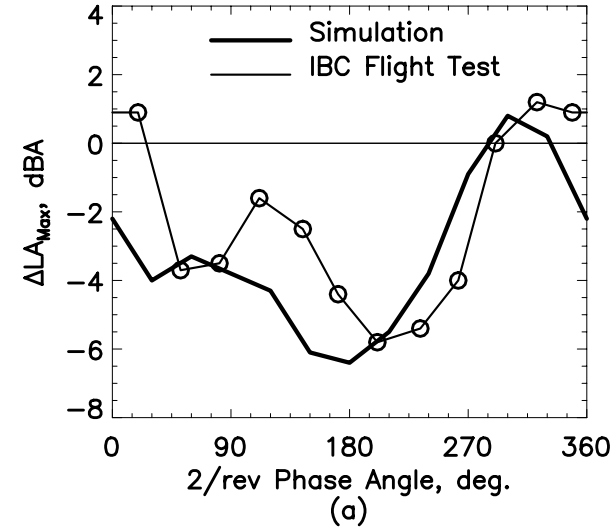
Figure 10 Comparison of (a) the measured leading edge blade pressure distribution C_pM^2 of the flight test at 6°-descent to computed induced velocity distributions M_{ind} for (b) 6°-descent and (c) 4°-descent flight at nominal 65 kts IAS; data h.p. filtered at 6/rev

Comparison of IBC effects

For analysis of 2/rev IBC effects on the rotor noise emission, the flight condition and steady rotor forces and moments from the baseline case are kept constant but, additionally, an IBC control

angle of θ_2 = 1° is applied with a phase varying from ϕ_2 = 0° to 360°. This does basically change the low-frequency content of the loading distribution but also affects the vortex flight paths through the rotor disc and, thus, the BVI locations via the prescribed wake. Therefore, the high-frequency content of the blade loading also is affected, and may result in different noise emission characteristics.

2/rev IBC comparisons: The A-weighted maximum noise levels measured on ground and those computed from the simulated loading distributions are compared to each other in Figure 11 (a). The computed noise levels appear to have a phase shift of about 20° relative to the experiment but the essential behaviour of noise emission or reduction with 2/rev IBC phase variation is well predicted.



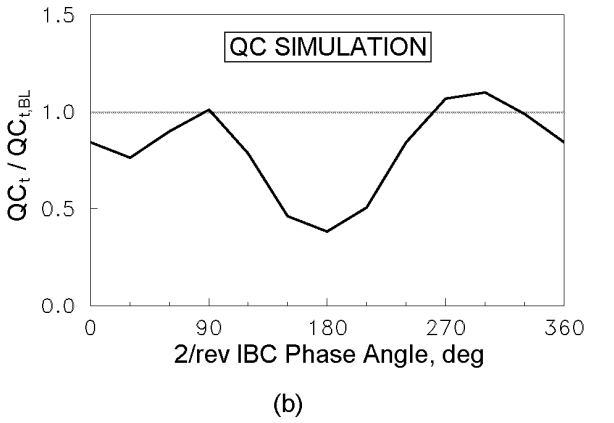


Figure 11 Comparison of (a) measured and computed A-weighted maximum noise levels with (b) calculated acoustic quality criterion for 2/rev IBC phase angle variation (θ_2 = 1°). Flight conditions as for Fig. 5

In the time domain, a BVI noise quality criterion based on the blade's leading edge pressure was developed as an indicator for the noise emission measured on ground [15]. This principle can also be applied to the unsteady simulated rotor blade loading, based on the non-dimensional normal force distribution $C_nM^2(r, \psi)$. Therein the azimuthal gradient of the loading is multiplied by weighting functions W_β and W_M, representing approximately the effect of the blade-vortex interaction angle and the local Mach number on noise intensity. The result of this quality criterion is given in Fig. 11 (b).

It is obvious that for most of the IBC control settings, a significant reduction of the predicted BVI noise level as well as of the acoustic quality criterion is achieved, with a minimum at ϕ_2 = 180° and a secondary minimum at 30°, while a slight increase is indicated at 90° and between 270° and 330° phase angle. Compared to the noise levels measured on ground, this curve appears to have the same shift of about 20° as the predicted noise curve (Fig. 11 (a)) but the essential features are represented. In terms of rotor azimuth, this shift reduces to half the value, and is within the uncertainty of the HHC wake deflection algorithm used for the prescribed wake approach. In Figure 12 ((a) and (b)), measured and predicted A-weighted noise contours are compared for the baseline (no IBC) 6°-descent case and for the minimum noise 2/rev IBC setting of Fig. 11.

Flight test and simulation results regarding noise directivity and level are in quite good agreement. It should be noted here that the simulation results have been corrected for the ground effect by adding 6 dB to the calculated values. The levels are underpredicted in lateral direction, probably an effect of the missing tail rotor noise contribution.

The behaviour of hub vibrations does exhibit a similar phase shift as was found for the noise predictions [15]. An important and promising result of the 2/rev IBC variations was identified in the phase range between 330° < ϕ_2 < 70°, where both noise and vibrations simultaneously are reduced. This is in favourable contrast to 3/rev HHC variations examined in the HART test [6], where vibrations were large when the noise was low and vice versa.

At the minimum of the calculated LA_{MAX} function corresponding to the minimum of the quality criterion (ϕ_2 = 180°), the measured pressure distribution is compared again to the induced velocity distribution from simulation. This is shown in Figure 13.

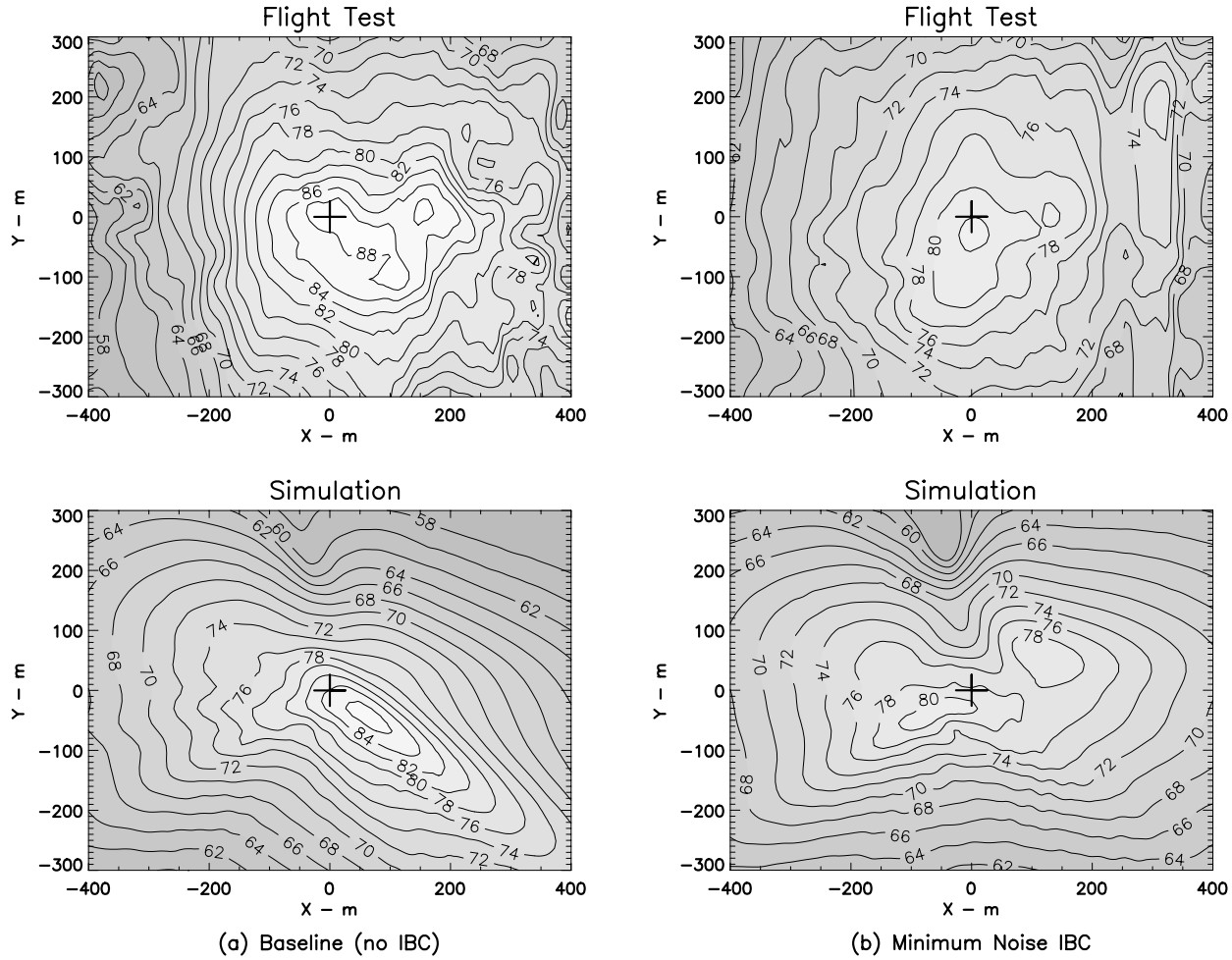


Figure 12 Measured and predicted A-weighted noise contours for (a) the baseline case (no IBC) and for (b) minimum noise 2/rev IBC settings of Fig. 11. Flight conditions as for Fig. 5

Compared to Fig. 10 (a), the tip vortices appear to penetrate the rotor disk at larger azimuth angles on the advancing side (at about ψ = 90° in the measurement and at 75° in the simulation) and at smaller azimuth angles (at ψ = 270° in the measurement) on the retreating side. The entire area downstream is mostly free from BVI traces because the vortices are below the rotor disk there and that is the reason why the noise emission is largely reduced. A similar behaviour was found for 3/rev HHC control in the wind tunnel [6]. Thus, the important parallel BVI occurring at about ψ = 50° in the baseline condition has no significant effect any more, since this vortex now is displaced below the rotor there. The essential behaviour of the tip vortex flight path, namely to penetrate the rotor disk at larger azimuth on the advancing side (where the blade-vortex interaction angle is large and BVI noise radiation low) is computed well.

3/rev and Mixed-Mode IBC Comparisons: Flight test and simulation results in terms of LA_{MAX} levels are illustrated and compared in Figures 14 (a) and 14 (b), respectively, for the variation of both a 3/rev IBC phase angle (at θ_3 = 0.6°) and a 5/rev phase angle (at θ_5 = 0.7°) for mixed mode 3/rev + 5/rev IBC inputs (at fixed 3/rev control settings θ_3 = 0.4° and ϕ_3 = 270°). Although the phase increments of 90° are rather large, BVI noise minima are measured at ϕ_3 = 278° (nominal value 270°) for the 3/rev input and at ϕ_5 = 79° (nominal value 90°) for the mixed-mode input for both flight test and simulation results. In the 3/rev IBC simulation, an optimum noise reduction benefit of nearly 5 dBA is predicted for ϕ_3 = 270°, which is in very good agreement with the HART wind tunnel results [6], but, compared to the flight test, the optimum noise reduction appears overestimated by approximately 3 dBA.

It is interesting to note here that, in the HART wind tunnel experiment, a 3/rev control amplitude of 0.85° and 3/rev phase variation increments of $\Delta\phi$ = 30° were used. In this way and in the controlled environment of the DNW, a second noise minimum was found for a phase angle corre-

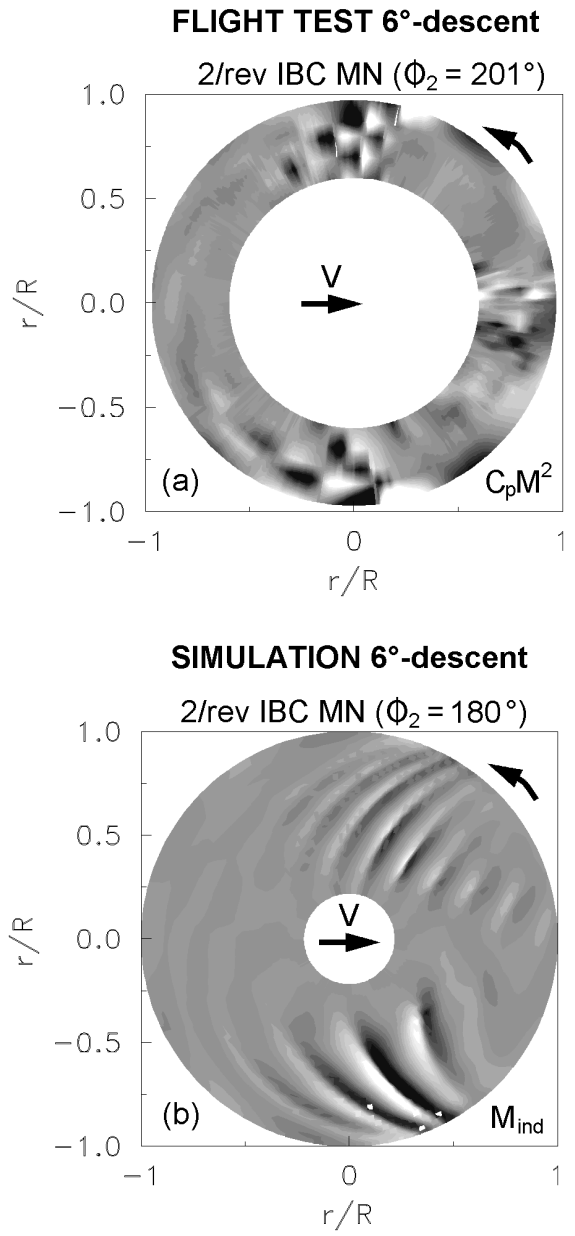


Figure 13 Comparison of (a) the leading edge blade pressure distribution C_pM^2 of the flight test to (b) the computed induced velocity distribution M_{ind} for the 2/rev IBC minimum noise case. Data h.p. filtered at 6/rev; rotor condition as for Fig. 5

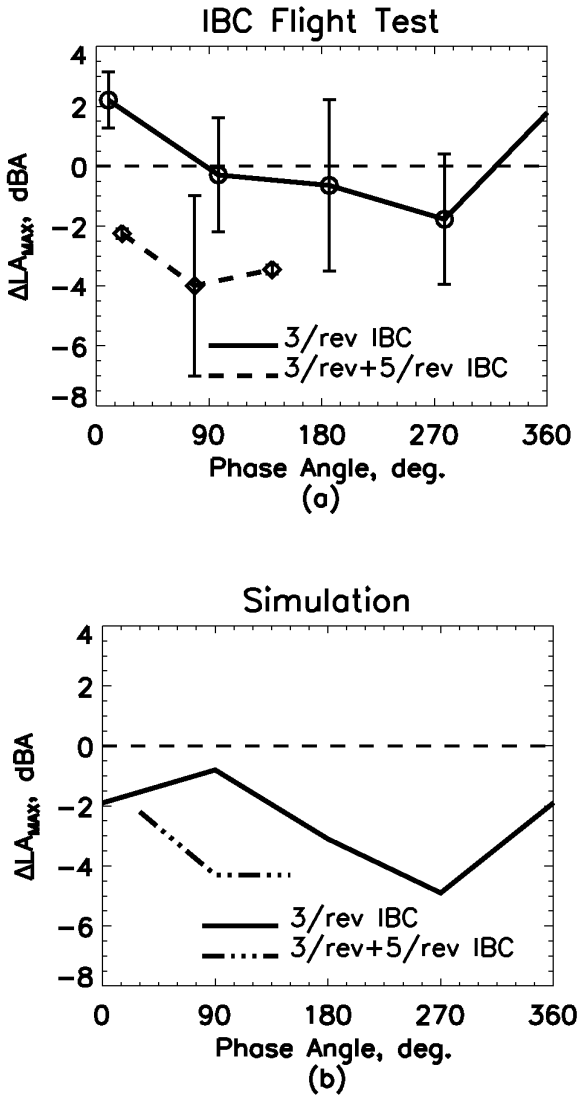


Figure 14 Comparison of (a) measured and (b) predicted A-weighted noise levels for a variation of 3/rev IBC phase angle and of 5/rev phase angle for mixed mode 3/rev + 5/rev IBC input. Flight conditions as for Fig. 5

sponding to ϕ_3 = 120° (of the phase angle definition used here), which could neither be found in the flight test nor in the simulation; it probably might have been missed because of the coarse phase increments employed here or it might have been reduced or eliminated due to the different rotor trim conditions between wind tunnel and flight test as discussed earlier.

The 3/rev + 5/rev mixed-mode case, however, shows excellent agreement of measured and predicted noise reduction benefit of about 4 dBA, a magnitude comparable to the 2/rev IBC results. The noise directivity from flight test and simulation also compares well, as is shown in Figure 15 for the mixed-mode minimum noise case (ϕ_5 = 79°) of Fig. 14.

Again, it appears that the lateral directivity on the retreating side is somewhat underestimated in the simulation due to the absence of the tail rotor noise contribution.

The partly very good and partly less satisfactory agreement between theory and experiment is mainly caused by the restricted testing time available and the resulting limited number of valid

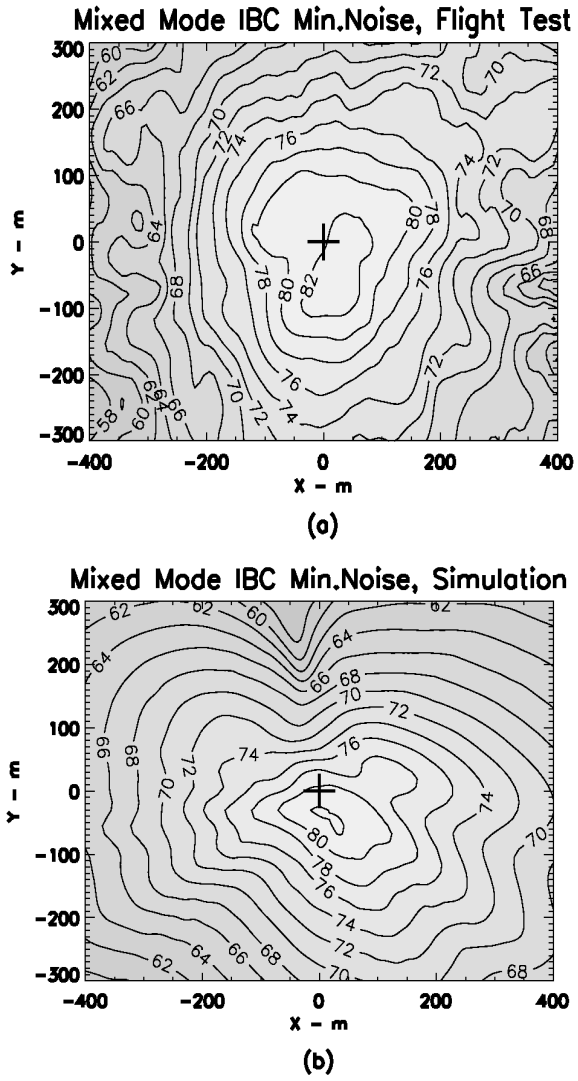


Figure 15 Comparison of (a) measured and (b) predicted A-weighted noise contours for the mixed mode minimum noise case of Fig. 14 (θ_3 = 0.4°, ϕ_3 = 270°; θ_5 = 0.7°, ϕ_5 = 79°). Flight condition as for Fig. 5 or Fig. 14, respectively

test flights per flight condition giving rise to partly large confidence intervals for the averaged experimental values; consequently, the quantitative test results have to be considered with some care. However, the general trends of the BVI noise emission and reduction potential with IBC variations indicate good agreement between flight test and simulation.

Conclusions

A joint open-loop IBC flight test programme was successfully conducted to study among other objectives the potential of individual blade root pitch control to reduce BVI impulsive noise and vibrations of a real helicopter. An upgraded IBC system with ± 1.2° control authority was installed together with extensive measurement equipment on the BO 105 S1 test aircraft, which was flown over an extended microphone array on the ground. The acoustic measurements were synchronised to the flight track and the on-board acquired data.

Precise flight path tracking to accurately define aircraft position, velocity, and flight path angle were found to be indispensable for acoustic data correction and interpretation. Selected test results quantifying the noise reduction potential of the IBC technique have been presented and compared to numerical simulation results allowing for the following conclusions:

(1) The effects of open-loop IBC variations employing harmonic 2/rev through 5/rev and multi-harmonic inputs on BVI impulsive noise, blade pressures, cabin vibrations, and on rotor trim and performance data have successfully been measured.

(2) A significant BVI noise reduction potential has been demonstrated confirming earlier full-scale and model-scale wind tunnel results.

(3) BVI noise predictions based on rotor aeroacoustic simulations correlate well with the measured noise levels and directivity patterns for most IBC variations.

(4) 2/rev IBC experimental and simulation results reveal the most promising potential for

- BVI noise reduction over a large range of IBC phase angles,
- optimum noise reduction benefit of more than 5 dBA,
- simultaneous noise and vibration reduction.

(5) 3/rev IBC experimental data base appears to be too small for substantiated conclusions concerning the noise reduction potential; simulation results compare better with model rotor wind tunnel results.

(6) 3/rev + 5/rev mixed-mode IBC results yield comparable noise and vibration reduction benefit like 2/rev IBC and are found in good agreement with simulation results.

(7) All test data, in particular the acoustic and blade pressure data, are highly useful for the development and validation of a robust controller for closed-loop IBC applications.

Acknowledgements

The RACT/IBC flight test programme was supported by the German "Bundesministerium für Bildung und Forschung" (BMBF). The authors want further to express their gratitude to the many unnamed specialists from the different partner organisations who combined their expertise to make this complex flight test campaign a success. Our special thanks go to Mr. Döring of Dornier Fairchild, who provided the PLASI indispensable for the approach flight tests.

References

[1] Brooks, T. F.: "Studies of Blade-Vortex Interaction Noise Reduction by Rotor Blade Modification", in: Proc. NOISE-CON 93, Noise Control in Aeroacoustics, Williamburg, VA, 1993

[2] Yu, Y. H.; Gmelin, B.; Splettstoesser, W. R.; Philippe, J. J.; Prieur, J.; Brooks, T. F.: "Reduction of Helicopter Blade-Vortex Interaction Noise by Active Rotor Control Technology", Progress in Aerospace Science, Vol. 33, pp. 647-687, 1997

[3] Brooks, T. F.; Booth, E. R.; Jolly, J. R.; Yeager, W. T. and Wilbur, M. L.: "Reduction of Blade-Vortex Interaction Noise Through Higher Harmonic Pitch Control", Journal of the American Helicopter Society, Vol. 35, No. 1, 1990

[4] Splettstoesser, W. R.; Schultz, K. J.; Kube, R.; Brooks, T. F.; Booth, E. R.; Niesl, G.; Streby, O.: "A Higher Harmonic Control Test in the DNW to Reduce Impulsive BVI Noise", Journal of the American Helicopter Society, Vol. 39, No. 4, 1994

[5] Polychroniadis, M.; Achache, M.: "Higher Harmonic Control: Flight Tests of an Experimental System on SA349 Research Gazelle", 42nd Annual Forum of the American Helicopter Society, Washington, DC, 1986

[6] Splettstoesser, W. R.; Kube, R.; Wagner, W.; Seelhorst, U.; Boutier, A.; Micheli, F.; Mercker, E. and Pengel, K.: "Key Results from a Higher Harmonic Control Aeroacoustic Rotor Test (HART) in the German-Dutch Wind Tunnel", Journal of the American Helicopter Society, Vol. 42, Nr. 1, 1997

[7] Kube, R.; Achache, M.; Niesl, G. and Splettstoesser, W. R.: "A Closed-Loop Controller for BVI Impulsive Noise Reduction by Higher Harmonic Control, in: 48th Annual Forum of the American Helicopter Society, Washington, D.C., 1992

[8] Niesl, G.; Swanson, S. M.; Jacklin, S. A.; Blaas, A.; Kube, R.: "Effect of Individual Blade Control on Noise Radiation", AGARD Aeroacoustics Conference, Berlin, Germany, 1994

[9] Richter, P.; Eisbrecher, H. D. and Kloeppel, V.: "Design and First Tests of Individual Blade Control Actuators", in: 16th European Rotorcraft Forum, Glasgow, U.K., 1990

[10] Swanson, S. M.; Jacklin, S. A.; Blaas, A.; Kube, R.; Niesl, G.: "Individual Blade Control Effects on Blade-Vortex Interaction Noise", 50th Annual Forum of the American Helicopter Society, 1994

[11] Jacklin, S. A.; Blaas, A.; Teves, D. and Kube, R.: "Reduction of Helicopter BVI Noise, Vibration and Power Consumption through Individual Blade Control", 51st Annual Forum of the American Helicopter Society, 1995

[12] Schimke, D.; Jänker, P.; Blaas, A.; Kube, R.; Schewe, G.; Kessler, C.: "Individual Blade Control by Servo-Flap and Blade Root Control – a Collaborative Research and Development Programme", 23rd European Rotorcraft Forum, Dresden, Germany, 1997

[13] Schimke, D.; Arnold, U.; Kube, R.: "Individual Blade Root Control Demonstration – Evaluation of Recent Flight Tests", 54th Annual Forum of the American Helicopter Society, Washington, D.C., 1998

[14] Dieterich, O.: "Application of Modern Control Technology for Advanced IBC System", 24th European Rotorcraft Forum, Marseille, France, 1998

[15] Honert, H.; van der Wall, B.; Fritzsche, M.; Niesl, G.: "Real Time BVI Noise Identification from Blade Pressure Data", Paper AC 08, 24th European Rotorcraft Forum, Marseilles, France, 1998

[16] Schöll, E.; Gembler, W.; Bebesel, M.; Splettstoesser, W.; Kube, R.; Pongratz, R.: "Noise Reduction by Blade Root Actuation – Analysis of Flight Test and Wind Tunnel Tests", Paper TE 06, 24th European Rotorcraft Forum, Marseilles, France, 1998

[17] Splettstoesser, W. R.; Niesl, G.; Cenedese, F.; Nitti, F.; Papanikas, D. G.: "Experimental Results of the European HELINOISE Aeroacoustic Rotor Test", Journal of the American Helicopter Society, Vol. 40, No. 2, 1995

[18] Van der Wall, B. G.: "Analytical Model of Unsteady Profile Aerodynamics and its Application to a Rotor Simulation Program", 15th European Rotorcraft Forum, Amsterdam, The Netherlands, 1989

[19] Beaumier, P.; Prieur, J.; Rahier, G.; Spiegel, P.; Demargne, A. (ONERA); Tung, C.; Gallmann, J. M.; Yu, Y. H. (AFDD), Kube, R.; van der Wall, B. G.; Schultz, K. J.; Splettstoesser, W. R. (DLR); Brooks, T. F.; Burley, C. L. (NASA); Boyd, D. D. (Lockheed): "Effect of Higher Harmonic Control on Helicopter Rotor Blade-Vortex Interaction Noise: Prediction and Initial Validation", AGARD-CP-552, 1995

[20] Petot, D.; Arnaud, G.; Harrison, R.; Stevens, J.; Teves, D.; van der Wall, B. G.; Young, C.; Szichinyi, E.: "Stall Effects and Blade Torsion – an Evaluation of Predictive Tools", 23rd European Rotorcraft Forum, Dresden, Germany, 1997

[21] Heller, H.; Buchholz, H.; Schultz, K. J.; Ahmed, S. R.; Splettstoesser, W.: "Helicopter Rotor Blade Aeroacoustics: A Comparison of Model-Scale Wind Tunnel and Full-Scale Flight Test Results", in: Proc. ICAS '96, Sorrent, Italy, 1996

Paper #30

Q by Chris Fielding: One of your figures showed a very good match between simulated and flight test results, but showed a fairly constant 20degree phase shift. Do you have an explanation for this phase offset ?

A (W. R. Splettstoesser): The simulation is based on a prescribed wake including effects of dynamically varying lift distribution as it is created by HHC or IBC. Due to locally increased or reduced lift, the appropriate downwash at that area is increased or reduced, leading to additional wake deflections which in reverse are important for BVI miss distance - the driving parameter for increase or reduction of BVI noise. Since the modelling is of low order, the principle effects are captured, but the accuracy with respect to control phase is as observed in the range of 20 degrees; in terms of rotor azimuth it is just 10 degrees. More cannot be expected in the current state of the model.

Practical Aspects of Implementing H-Infinity Controllers on a FBW Research Helicopter

D.J. WALKER
M.C. TURNER
Department of Engineering
University of Leicester
Leicester LE1 7RH, UK

A.W. GUBBELS
Flight Research Laboratory
National Research Council of Canada, Bldg U-61
Ottawa, Ontario K1A 0R6

ABSTRACT

This paper presents a summary of the design and testing of two H-infinity controllers, recently flight-tested on the NRC's Bell 205 experimental fly-by-wire helicopter. Lessons learned from the implementation and testing are described. Both designs were based on low-order mathematical models and H-infinity optimization. The first controller successfully engaged first time, and is believed to be the first H-infinity controller flight-tested on a rotorcraft. It was subsequently evaluated at hover and low/moderate speed by a test-pilot, and found to achieve level 2 Cooper Harper Handling Qualities on a number of tasks. The controller was re-designed using a different mathematical model and a different H-infinity cost-function. The result was a significant reduction in cross-couplings, better (though still Level 2) handling qualities ratings of 4-5, Level 1 pitch and roll bandwidths. This paper presents an analysis of data from these flights. The flight testing provided a number of important practical lessons that could be useful to anyone attempting to implement and test modern controllers in flight. The gap between robustness of the design method and accuracy of the flight mechanic model is one of the most critical issues in high bandwidth control. Improved aircraft models translate directly into better controller performance. Validation of the aircraft model against open loop helicopter flight test data has shown that both the models used were deficient in a variety of ways. Software implementation should be kept as simple as possible; a discussion of the methods used for this project is given. The use of an on-board aircraft model greatly assisted in trouble-shooting the code for errors before flying. Use of automated code generation greatly reduces transfer errors from the Matlab design environment. To assess new control laws fully, an experienced test pilot is essential.

INTRODUCTION

Helicopter flight dynamics are governed by many complex and still quite poorly understood phenomena. This makes accurate modelling hard, and designing new and better controllers challenging. There is, furthermore, a need for better helicopter control systems: for example, to meet new and demanding specifications like ADS-33 (1989) that will be applied in future procurements, civil as well as military.

Interest in H**.** control of helicopters dates back to the work of Postlethwaite and his co-workers Tombs and Yue in the mid-late 1980's: see Tombs (1987); Yue, Postlethwaite and Padfield (1989); Yue and Postlethwaite (1990). The Westland Lynx was also the focus of a more recent study: see Walker & Postlethwaite (1990), (1996). This all suggested that H**.** design methods offered considerable promise in helicopter control, but the limitations of ground-based simulation were recognized, and it was concluded by Walker & Postlethwaite (1996) that appropriately validated mathematical models containing higher order dynamics would be important if similar (Level 1) results were to be replicated in flight.

Recent collaboration between the University of Leicester and the National Research Council (NRC) of Canada has resulted in the opportunity to test H**.** controllers in flight using NRC's modified Bell 205 helicopter. This paper presents analysis of data from that work, and a comparison between two designs, which were tested in August 1997 and February 1999. More details of the respective flight tests are given by Postlethwaite *et al* (1998) and Walker *et al* (1999) respectively.



Figure 1: Bell 205 Airborne Simulator

BELL 205 AIRBORNE SIMULATOR

The Bell 205 is a multi-role utility and transport helicopter. NRC's Bell 205 airborne simulator (Figure 1) is an extensively modified version of the Bell 205A-1: see Sattler, (1984). Amongst the modifications, the standard Bell 205 stabilizer bar has been removed to enhance the control response of the teetering rotor. The aircraft serves as a fly-by-wire variable stability platform for in-flight simulation of other aircraft, and investigation of control systems and new cockpit technologies. It is configured to have a Safety Pilot (SP) flying from the left-hand seat and an Evaluation Pilot (EP) flying from the right-hand seat. The original actuators have been replaced with specially built dual-mode electro-hydraulic actuators that can be either electrically or mechanically controlled. During normal flight, these actuators are mechanically controlled and behave just as the original actuators. During FBW flight, they are electrically controlled by the EP, but can be mechanically overridden if the SP supplies a force that exceeds a pre-set control breakout force. During the H**.** controller tests, both EP and SP were test-pilots. The EP's role was to evaluate the experimental controller. The role of the SP is to monitor the aircraft actuator control activity fed back to the SP cyclic and commanded by the experimental controller. If this control activity is oscillatory, divergent or otherwise overly active, he will disengage the FBW system and take control of the aircraft. The aircraft has equipment for measuring and recording many variables, including: 3-axis attitudes, angular rates, accelerations, velocities, static and dynamic pressure, air temperature, angle-of-attack, side-slip, pilot control inputs and actuator positions.

Paper presented at the RTO AVT Symposium on "Active Control Technology for Enhanced Performance Operational Capabilities of Military Aircraft, Land Vehicles and Sea Vehicles", held in Braunschweig, Germany, 8-11 May 2000, and published in RTO MP-051.

AIRCRAFT MODELS

Two different mathematical models were used to design the controllers. These are now described.

NASA Model The linear model used to design the first controller (henceforth referred to as Controller I) was a 10 knot, six-state stability and control derivative model from a NASA contractor report by Heffley *et al* (1979). The six states are the three angular velocity components of the fuselage (p, q, r) and three translational velocity components of its mass centre (u_B, v_B, w_B). This model was augmented with pitch and roll attitudes (θ and ϕ) to enable an Attitude Command/Attitude Hold (ACAH) response to be designed. The dynamic response of a teetering rotor is sometimes represented by a transport delay, so the nominal model was cascaded with first-order Padé approximants in each of the three control channels. This doubled as a simple actuator model. The Padé approximation time constants were chosen to reflect the effective combined actuator and rotor time constants: i.e. about 0.156 sec in pitch and roll and 0.187 sec in yaw actuators. The first controller design was based on the resulting model.

Using a low-order rigid-body model for control law design has potential drawbacks. The NASA model captures the salient rigid body modes reasonably well, but the omission of rotor dynamics limits the achievable bandwidth. Furthermore, the stability derivatives given by Heffley *et al* relate to a standard model 205 with a stabilizer bar. The bar has been removed from the NRC Bell 205 on which the flight tests were conducted.

DERA Helisim Model (Padfield, 1981.) The Helisim generic helicopter non-linear model has been used for over ten years in its various Lynx configurations as the basis for the design and simulation of H**.** and other novel controllers. After Controller I had been tested, DERA re-configured the Helisim model to represent the NRC Bell 205; see Strange & Howitt, (1997). DERA also undertook a validation exercise on the Helisim 205 model, using flight test data from NRC's Airborne Simulator. Comparison was also made with the NASA linear model (case 126) from Heffley *et. al.* (1979). Although the control law design work was conducted at hover/low-speed, the model validation was performed at 60 knots because at the time of model development no high quality open-loop flight test data were available for the hover condition. The validation exercise indicated:

- Using a quasi-steady approximation to the rotor dynamics, the model captures the basic rigid body behaviour reasonable well, at least on-axis.
- Fidelity of the model can be further enhanced by incorporating coning and flapping dynamics, an inflow correction factor, and tail fin blockage and tail rotor blade root cut-out effects.
- Significant model uncertainty still exists and the model can only be considered to be of low/medium fidelity.
- The Helisim 205 model generally gives a better correlation than does the NASA model with flight data from NRC's Bell 205.

A nineteen-state 20-knot linearization from the Helisim model was the basis for the second design (Controller II) discussed here.

CONTROLLER DESIGN

Both controllers were designed to give an Attitude Command/Attitude Hold response type in pitch and roll, and a rate command in yaw. Both used five measurements: pitch and roll attitudes and rates and yaw rate, and had full authority over three control inputs: longitudinal and lateral cyclic and tail-rotor collective. Main rotor collective was left open loop, partly because the available instrumentation provided no suitable heave-axis velocity measurement with which to close that loop.

CONTROLLER I: MULTIVARIABLE LOOP SHAPING

The first design followed in precisely the same manner as the Lynx design of Walker and Postlethwaite (1996). It was based on the two degree-of-freedom H_∞ optimization proposed by Hoyle *et al* (1991). The main steps in the design process are: (i) selection of a low-order step response model (SRM) that encapsulates basic handling requirements; (ii) augmentation of the aircraft G(s) at input and output with filters W_1 and W_2; (iii) synthesis of a stabilizing controller K(s) minimizing the H_∞ norm of the transfer function from {v, w} to {u, y, z} (see Figure 2); (iv) incorporation of filters into K(s). Note that while only three outputs were actually controlled, measurements of a further two (the rates q and p) were also fed back into the controller, to enhance stability. H_∞ optimization produces a controller that forces the closed loop to approximate the SRM, by reducing the H_∞ norm of the difference between the two.

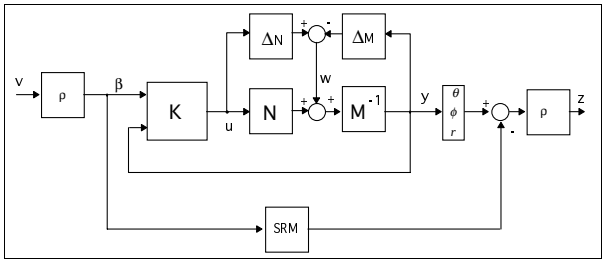


Figure 2: Two DoF Structure: Controller I

The design is based around a normalized coprime factor description of the augmented nominal aircraft model. [N M] denotes a left coprime factorization of the nominal augmented aircraft transfer function matrix G(s). This means that $G = M^{-1}N$, in which N and M are stable and there is no cancellation of any unstable dynamics between M^{-1} and N. The factorization is said to be *normalized* if, in addition, [N M] is all-pass. Further relevant information is given by McFarlane and Glover (1990).

Step Response Model A second order system with no zeros and with damping ratio ζ and undamped natural frequency ω_o was used in each of the three controlled axes. Damping ratios and natural frequencies are given in Table 1.

	Roll	Pitch	Yaw
Damping ratio (ζ)	0.9	0.9	0.7
Nat. Freq. (ω_o) (rad/s)	3.6	1.2	11.0

Table 1: Step Response Model Parameters

Loop Shaping The nominal aircraft model was pre- and post-multiplied by filters $W_1(s)$ and W_2 to produce a singular value loop-gain consistent broadly with frequency-domain performance and robustness requirements: high d.c. gain for steady-state disturbance rejection and tracking; low gain at high frequencies for robustness, noise attenuation etc.; slope

not less than minus 40 dB/decade at gain cross-over for stability. The filters chosen were:

$$W_1 = diag\left(\frac{s+2}{s},\ \frac{s+2}{s},\ \frac{s+2}{s}\right)$$

$$W_2 = diag(1,\ 1,\ 1,\ 0.5,\ 0.5)$$

To set the 0 dB crossover and to help decouple the aircraft in the mid frequency range, alignment was performed at $\omega = 4$ rad/s.

Design Optimization The controller K achieving the desired performance in the face of the assumed model error is obtained by minimizing the H**.** norm of the closed loop transfer function T from {v, w} to {u, y, z} subject to internal stability: see Figure 2. This has the effect of simultaneously reducing the energy in u, y, and z due to commands (v) and model error (w). The parameter ρ allows model-following to be balanced against robust stabilization; setting ρ=0 one reverts to the pure robust stabilization problem of McFarlane and Glover (1990). ρ = 1.9 gave a satisfactory compromise.

Stabilizing controllers minimizing the appropriate H_∞ norm can be found using standard algorithms for H_∞ optimization. Alternatively, as was the case here, an observer-based controller satisfying the above H_∞ optimization criterion can be found directly from formulae given by Walker (1996). This structure was exploited in the C-code implementation of the controller for real-time implementation. Euler numerical integration was used to integrate all the dynamic subsystems within the controller: i.e. the observer, ideal model and filter W_1. Also included in the command path were a dead-band and a low-pass filter.

CONTROLLER II: DECOUPLED MIXED-SENSITIVITY (S/KS) OPTIMIZATION

This design was based on the DERA Helisim model. The aim was to investigate whether robustness could be improved by eliminating from the control-law design terms representing cross-couplings. The resulting Controller II consisted of two independent sub-controllers for longitudinal and lateral dynamics respectively, each based on an appropriate decoupled model.

Longitudinal and Lateral Models The Helisim 205 model was linearized about a twenty knot flight condition to yield a nineteen-state linearization: nine rigid body, six rotor dynamic, and four actuator states. Based on the premise that Helisim's rotor representation was reliable at predicting steady-state rotor forces but less reliable in terms of its transient predictions, the six model states corresponding to rotor flap and coning were residualized: i.e. assumed to reach their steady-state values instantaneously. The resulting model was partitioned into longitudinal (θ, q, u_B, w_B, η_{1s}) and lateral (ϕ, p, r, v_B, w_B, η_{1c}, η_{0t}) states for design of the respective controllers (η's represent actuator states).

Figure 3 shows the structure used with Controller II, viz. separate longitudinal and lateral controllers. A full authority Attitude Command/Attitude Hold (ACAH) response type was again specified, in which pitch and roll attitudes and yaw rate (θ, ϕ, r) are demanded by the pilot. Pitch and roll rates (q and p) are again fed back in their respective loops. The longitudinal controller controls longitudinal cyclic (θ_{ls}) while the lateral controller controls lateral cyclic (θ_{lc}) and tail rotor collective (θ_{0t}). The main rotor collective was again left open loop. The longitudinal and lateral controllers were designed separately using continuous-time methods, then converted to discrete-time equivalents and implemented in state-space form at a fixed sample-rate of 64 Hz on the aircraft's flight-control computer. Dead-band and low-pass filters were again employed in the command path in order to clean up the signals from the pilot inceptors.

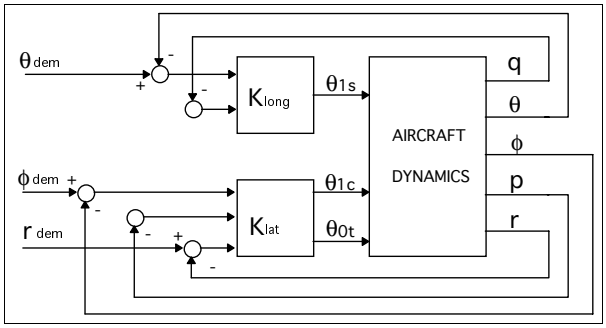


Figure 3: Decoupled Structure of Controller II

Design Optimization A weighted mixed-sensitivity, or S/KS, H_∞ optimization was used in both longitudinal and lateral designs. A stabilizing controller K(s) is sought such that:

$$K(s) = \arg\ \min \left\| \begin{bmatrix} W_1(I+GK)^{-1} \\ W_2K(I+GK)^{-1} \end{bmatrix} \right\|_\infty$$

The above cost function leads to a stabilizing controller that simultaneously attempts to reduce the energy in the weighted tracking-error and weighted control signal due to commands or disturbances at the aircraft output. The principal design parameters were a sensitivity weight W_1 and a robustness weight W_2. W_1 was a low-pass filter, used to shape the sensitivity function $(I + GK)^{-1}$; its 0 dB cross-over approximately defines the tracking bandwidth. W_2 is a high pass filter, used to shape $K(I + GK)^{-1}$, which in turn governs robustness to additive model error and control usage.

After some iteration, the filters chosen were:

Pitch Attitude: $W_1 = \dfrac{0.5}{s + 0.01}$

Roll Attitude: $W_1 = \dfrac{0.3s + 0.15}{s + 0.01}$

Yaw Rate: $W_1 = \dfrac{0.3s + 0.15}{s + 0.01}$

Pitch and Roll Rates: $W_1 = \dfrac{s}{s + 0.01}$

Control Weight: longitudinal cyclic: $W_2 = \dfrac{2s + 0.002}{s + 5}$

Control weight: lateral cyclic and tail rotor collective:

$$W_2 = \frac{2s + 0.002}{s + 4}$$

Solving two separate H_∞ optimizations using standard software algorithms led to longitudinal and lateral controllers of 8 and 12 states respectively. These were discretized using a zero-order hold for digital implementation.

MIXED ANGULAR RATES

Experience at NRC has been that feeding back measured rate signals p and q can lead to stability problems. This is believed to be due in part to the fact that the angular rate sensors detect structural modes as well as rigid body motion.

More important still, the teetering rotor interposes a characteristic dead time of between 120-180 mS in the control responses of the various axes: a dead-time that the models do not predict properly. Use of so-called mixed rate signals to alleviate this is described by Baillie *et al* (1994). The mixed rate signal is synthesized using a pair of complementary filters; the measured rate is fed to the low-pass filter, then summed with the output of the high-pass filter. The latter is driven by an open-loop predictor that consists simply a lag-free first-order model of the on-axis control response, driven in turn by the actuator command. As implemented on the NRC Bell 205, the mixed rate feedback is essentially an open-loop predictor-derived signal at frequencies above approximately 11.0 rad/s. Controllers I and II were both driven by mixed rate signals.

RESULTS

Controller I Figure 4 shows the primary response to a doublet demand on pitch attitude. The response lags by approximately 2 seconds. Pitch response was designed to be slower than roll (not shown), to allow for the aircraft's greater inertia about its pitch axis. The roll response (not shown) was damped oscillatory. Although the aircraft was quite flyable, undesirable cross-couplings were present, and the bandwidths achieved were quite low: considerably lower than predicted: see Table 2. (Bandwidths predicted using small-signal analysis are shown in parentheses).

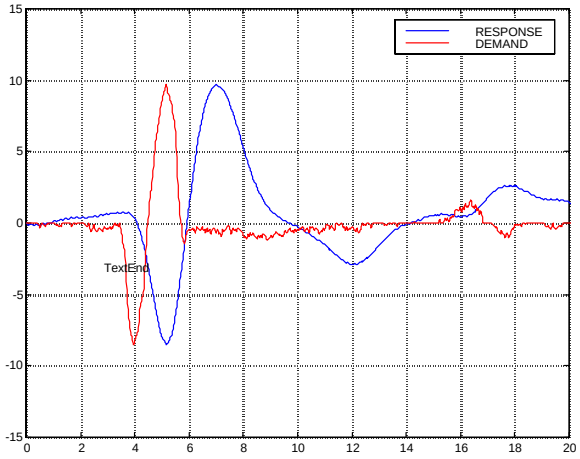


Figure 4: Controller I Pitch Attitude Response

Frequency sweeps were also conducted during the flight. Spectral analysis was used to extract frequency responses from the sweep data. Bode plots for the pitch axis are shown in Figure 5. Coherence of greater than about 0.7 is generally taken to indicate reasonable frequency response identification. Gain and phase information can be used to calculate the handling qualities bandwidth and phase delay parameters defined in ADS-33, and discussed by Padfield (1996). For an attitude command/attitude hold response type, the handling qualities bandwidth is defined as the frequency at which the phase of the closed loop system equals –135°. Phase delay is a measure of the rate-of-change of phase with frequency beyond the crossover frequency. It is defined as the ratio of the additional phase lag (in radians) beyond $-\pi$ rad at twice the bandwidth frequency to twice the bandwidth frequency (in rad/s).

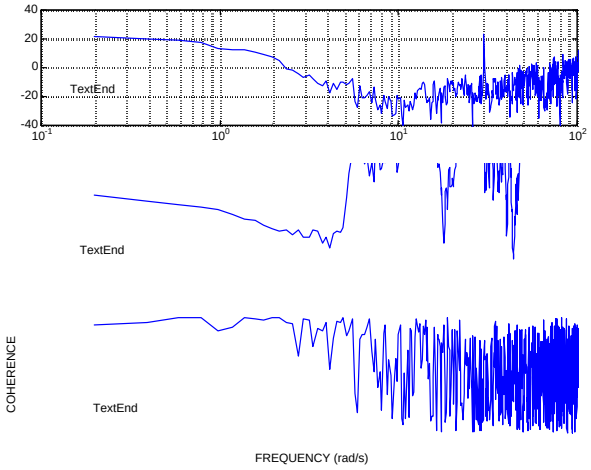


Figure 5: Controller I Pitch Axis Frequency Response

Bandwidth and phase delay for Controller I are represented by the '*' in Figures 8 and 9. In terms of short-term frequency response criteria, Controller I is Level 3 for combat/target tracking and Level 2 for all other mission task elements. The Cooper-Harper Levels and Pilot Ratings are explained in Figure 10.

Controller II The doublet response on pitch axis for controller II is shown in Figure 6. The EP reported that inter-axis coupling was not an issue at all with this controller. Frequency response (pitch axis) is shown in Figure 7. The bandwidth and phase delay parameters are represented by the '+' in Figures 8 and 9.

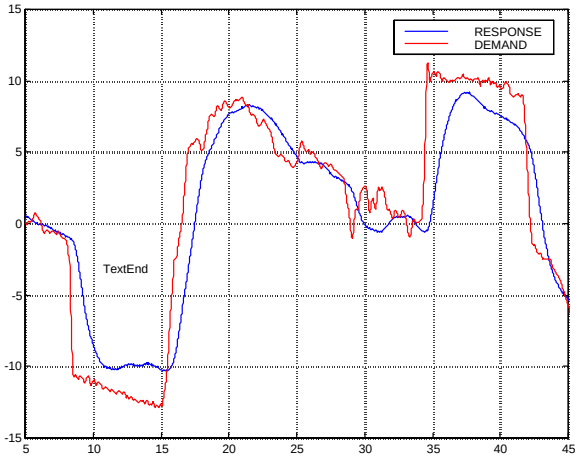


Figure 6: Controller II Pitch Attitude Response

This controller resulted in a Level 1 system in terms of its pitch and roll short term frequency response at hover/low speed. Overall it was rated Level 2 because of deficiencies, the principle being a yaw response that was too slow and unpredictable; pitch response was also deemed to be a bit too sluggish. Roll axis response was deemed to be about right.

Both controllers were subjected to rigorous testing in a set of ADS-33 manoeuvres. The procedures are described in more detail by Postlethwaite *et al* (1998) and Walker *et al* (1999). The test pilot ratings are summarized in Table 3.

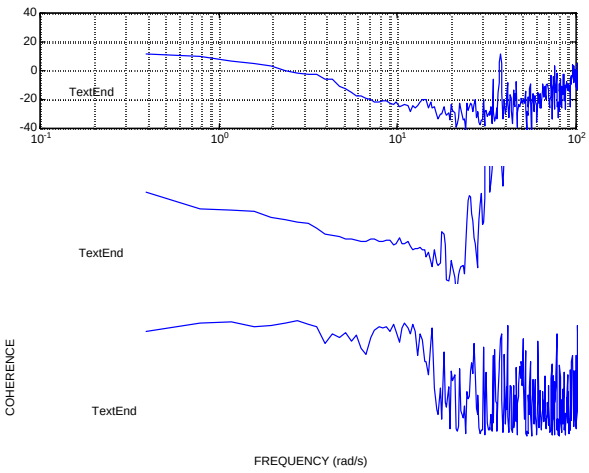


Figure 7: Controller II Pitch Axis Frequency Response

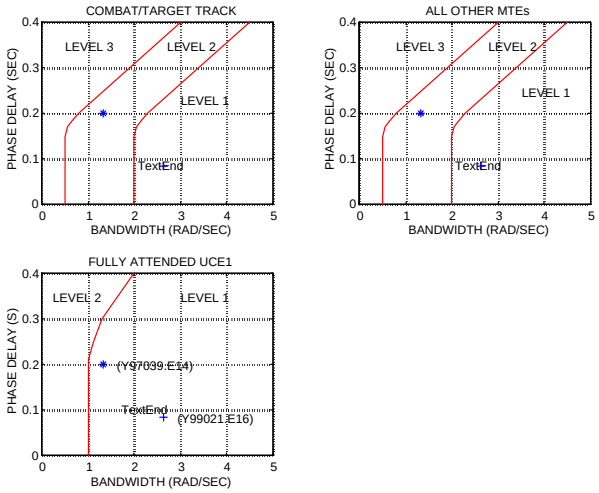


Figure 8: Bandwidth and Phase-Delay (Pitch)

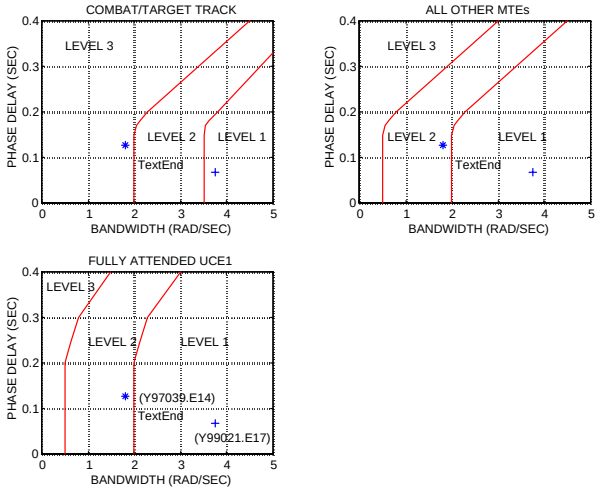


Figure 9: Bandwidth and Phase-Delay (Roll)

	Controller I		Controller II	
	Pitch	Roll	Pitch	Roll
B/W (rad/s)	1.32 (1.83)	1.81 (3.18)	2.64 (1.83)	3.75 (2.26)
Phase delay (s)	0.20	0.13	0.08	0.07

Table 2: Achieved (Predicted) bandwidths

Task	Controller I	Controller II
quick-hop	5	4
side-step	5	4
turn-to-target	4	5
precision hover	4	4
pirouette	5	4

Table 3: Handling Qualities Ratings from Flight-Tests

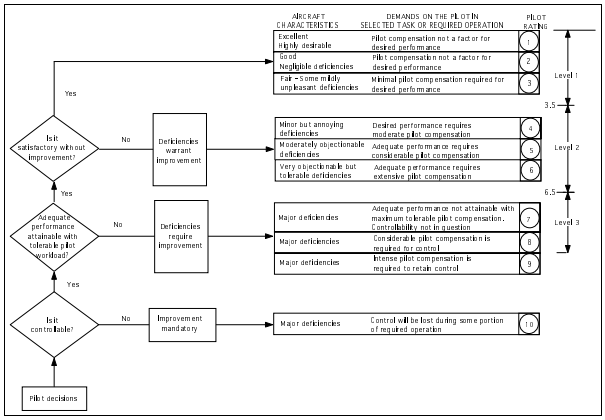


Figure 10: Cooper-Harper Rating Scheme

HQR 4: Minor but annoying deficiencies; Desired performance requires moderate pilot compensation;

HQR 5: Moderately objectionable deficiencies; Adequate performance requires considerable compensations;

LESSONS LEARNED

During the course of the H-infinity testing, many valuable lessons were learned that will help make future tests more efficient. These lessons would also be useful to any one attempting to implement and flight-test a modern controller on an aircraft.

Model Fidelity Two different aircraft models were used for controller designs in this experiment, as described above. Readily apparent deficiencies in the NASA model lead to the development of the DERA Helisim model. Validation of the response of both of these aircraft models against open loop helicopter flight test data has shown that both the models were deficient in a variety of ways. However, the DERA Helisim model was of higher fidelity than the NASA model. The result was that controllers designed with the Helisim model were more than twice as likely to function more-or-less as intended than were those designed with the NASA model. Another observation was that although the use of mixed rates was always required for controllers designed with the NASA model, not all of the controllers designed with the Helisim model required their use. One controller that was tested worked reasonably well, but only when a pre-filter was inserted into the yaw axis control input to smooth out the response. This type of remedy would not have been required had the aircraft model captured all the required dynamics adequately. It is for this reason that future control work is planned on the NRC Bell 412 Advanced Systems Research Aircraft, with this work being preceded by a model development program designed to create a full-envelope model of the aircraft that is of the highest possible fidelity.

Software Implementation The method of software implementation for the H-infinity program was not static from the first flight tests, and evolved a number of times. Since these controllers involved a large amount of matrix

manipulation and integration at each time cycle, processing time had to be carefully monitored to ensure that cycles were not overframing. Therefore, the code was kept as simple as possible, and was written in-line rather than in function calls to optimize for speed. Although initially the switch from ground-test mode to flight-test mode required a re-compile of the code, this was streamlined by adding a function switch to perform this change on-line. The switch was only active before a fly-by-wire engagement to prevent a change in mode while the evaluation pilot was flying the controller. For the first NASA-model based controllers, integrations were performed on-line in the code using a simple Euler method for faster computations. However, when the Helisim based controllers were implemented, the Euler method of integration was found to no longer be adequate, and was prone to instability. Several different methods of integration were attempted, but were either also prone to instability or required too much computational time, causing the flight control computer to skip cycles. The solution was found in using discretized controllers, which worked flawlessly and required much less computational time.

Automated Code Generation During the course of the first H-infinity experiment, it was quickly realized that the process of copying and implementing a large number of controllers, each consisting of 6 or more large matrices, from the Matlab environment to the Flight Control Computer was cumbersome. The solution was to write a Matlab routine that automatically generated C code from the output of the controller design process. It was then a simple matter to transfer the new controller file down to the helicopter and implement the new system. It is estimated that this automatic code generating routine required approximately 2 hours to write and saved over 8 man-hours of manual code manipulation per experiment. The other benefit of this system was that it was far less prone to coding errors than the manual method.

On-board Aircraft Model During the early stages of the work, when several controllers did not function as intended, it was unclear if this was as a result of implementation (e.g. coding) errors, or poor robustness of the design. Unlike with some standard controllers that will give meaningful output when tested open-loop, the H-infinity controllers, with a high integral component, cannot be tested open-loop on the helicopter prior to flight. A solution was devised to help eliminate implementation errors in the controller C-code; an aircraft linear model was implemented in the flight control computer and linked to the controller code. In this way the model was used to provide a closed-loop simulation of the aircraft/controller system in real-time using the same controller code. This greatly assisted in trouble-shooting the code for errors before flying, since this hardware-in-the-loop simulation proved that code was implemented correctly. If the controller did not work properly with the on-board model, then it was certain to fail in flight. (The converse is obviously not in general true, owing to the inevitable mismatch between the dynamics of the model and of the actual aircraft).

Experienced test pilot From past experience it was known that the use of operational evaluation pilots for handling qualities investigations is not desirable, and that the use of a qualified test pilot is essential to getting useful comments on the handling of the aircraft/controller system. Operational pilots are not generally capable of assigning appropriate Cooper-Harper ratings, because they have not been trained in the use of the scale: see Cooper & Harper (1969). Experience with the H-infinity flight tests have also shown that even trained, qualified test pilots often have difficulty defining deficiencies with the control system if they have had no prior experience in performing handling qualities evaluations of control systems. During the trials, the NRC test pilot (who has several years experience working in the area of handling qualities of fly-by-wire control systems with a variety of response types) was able to provide excellent handling information for directing new controller designs.

RECOMMENDATIONS FOR FUTURE WORK

Future work will concentrate on refinement of the H-infinity designs and on application of different synthesis methods, principally QFT.

Future rotorcraft models at NRC will include rotor states. This is almost certainly necessary for designing high-bandwidth control systems. Future work will include rotor-state-feedback controllers designed using these models.

CONCLUSIONS

Two helicopter controller designs have been compared. The first design clearly demonstrated the potential of H**.** optimization in the field of helicopter control. The controller led to a stable, flyable system. However, the first design caused us to ask whether, given current model fidelity, it would be better to decouple longitudinal and lateral controls, thereby reducing our reliance on a dubious part of the design model. Despite the yaw axis response of the second design being somewhat worse, the changes resulted overall in a number of significant improvements, particularly in reduced cross-coupling, so we would tentatively answer the above question in the affirmative.

The second design led to a stable and controllable system with desired performance, albeit with moderate work-load, in which coupling was not an issue. Predicted and achieved bandwidths showed fair agreement. Modifications to the controller design parameters had the desired effect on closed-loop responses. This leads us to believe that Level 1 handling qualities (satisfactory without improvement, desired performance requiring minimal pilot compensation) will be achievable with this type of controller.

Neither controller functioned without mixed rates, but we have demonstrated that it is possible to use a theoretically-derived flight mechanic model as the basis for multivariable controller design. This has important implications for the development of future generation flight control systems.

Practical lessons learned from this research include:

- Models of the highest fidelity are a requirement for the design of high bandwidth modern controllers.
- Software implementation issues are important, particularly for control of the flow of calculation and in deciding on how to perform integrations.
- Automatic code generation saves time and is less prone to errors than manual code manipulation.
- An on-board test facility to determine if code has been correctly implemented on the aircraft prior to flight is a great asset.
- The use of an experienced test pilot for handling qualities evaluations is essential.

ACKNOWLEDGEMENTS

The work was funded by the UK Engineering and Physical Sciences Research Council. The contributions of Alex Smerlas (now at Eurocopter Deutschland) and Michael Strange and Jeremy Howitt (DERA Bedford) to the design of Controller I and the model development, respectively, are gratefully acknowledged.

REFERENCES

Anonymous. 1989. *Handling quality requirements for military rotorcraft ADS-33C*. US Army Aviation Systems Command.

Baillie, S.W., Morgan, J.M. and Goheen, K.R., 1994. *Practical experiences in control system design using the NRC Bell 205 airborne simulator*. AGARD Flight Mechanics Panel Symposium on Active Control, Turin, Italy, May 1994.

Cooper G. E., and Harper, R.P., *The use of pilot rating in the evaluation of aircraft handling qualities*, National Aeronautics and Space Administration, Technical Note TN D-5153, Washington D.C., April 1969

Heffley, R.K., Jewell, W.F., Lehman, J.M., and Van Winkle, R.A. 1979 *A compilation and analysis of helicopter handling qualities data*. Contractor report 3144, NASA.

Hoyle, D., Hyde, R. and Limebeer, D., 1991. *An H· approach to two degree of freedom design* Proc IEEE 30th C.D.C. pp 1581-1585 Brighton U.K.

McFarlane, D. and Glover, K., 1990, *Robust controller design using normalized coprime factor plant descriptions*. Springer Verlag Lecture notes in control and information science series.

Padfield, G. D., 1981. *A theoretical model of helicopter flight mechanics for application to piloted simulation*. Technical Report RAE TR 81048, Royal Aircraft Establishment, Farnborough.

Padfield, G.D. 1996. *Helicopter flight dynamics*. AIAA Education Series.

Postlethwaite, I., Smerlas, A. Walker, D.J., Gubbels, A.W., Baillie, S.W., Strange, M.E., Howitt, J., Horton, R.I., 1998 *H_∞ control: From desk-top design to flight test with handling qualities evaluation*. Annual Forum Proceedings - American Helicopter Society, v 2, p 1313-1324

Sattler, D.E., 1984. *The National Aeronautical Establishment airborne simulator facility*. NRC, NAE Misc 58, May 1984.

Strange, M.E. and Howitt, J., 1997. *Configuration of the DERA HELISIM model to represent the flight dynamics of the NRC Bell 205 fly-by-wire research helicopter*. DERA Technical report AS/FMC/TR97459/1, March 1997.

Tombs, M.S. 1987. *Robust control system design with application to high performance helicopters*. D.Phil Thesis, University of Oxford.

Walker, D. J. and I. Postlethwaite. 1990. *Full authority active control system design for a high performance helicopter*. Proc. XVI European rotorcraft forum., III.3.2.1-III.3.2.14.

Walker, D.J. & Turner, M.C, Smerlas, A.J., Strange, M. and Gubbels, A.W. 1999. *Robust control of the longitudinal & lateral dynamics of the Bell 205*. Proc. 1999 American Control Conference pp 2742-2746.

Walker, D.J. and Postlethwaite, I., 1996. *Advanced helicopter flight control using two-degree-of-freedom H_∞ optimization*. Journal of Guid., Cont., and Dynamics, Vol. 19, No.2, pp.461-468.

Walker, D.J., 1996. *On the structure of a two-degree-of-freedom H_∞ loop shaping controller*. International Journal of Control 63, No. 6, 1105-1127

Yue, A. and I. Postlethwaite. 1990. *Improvement of helicopter handling qualities using H_∞ optimization*. IEE Proceedings Part D 137:115-129.

Yue, A., Postlethwaite, I., Padfield, G. 1989. *H_∞ design and the improvement of helicopter handling qualities*. Vertica, v 13, n 2, p 119-132.

Paper #31

Q, by David Moorhouse: In simple terms, you designed to desired responses. You should be able to get them with any methodology. Can you say why you did not achieve them and what you plan to do differently with your H-infinity refinements?

A: (Daniel Walker's): The performance was indeed not robust. Achieving robust performance when the dynamics are complex and the model poor is difficult. Trying to identify reasonable bounds on the various 'deltas' is something that needs more work. The available models are better in some respects than in others. For instance, they don't predict pitch-roll coupling well, so it makes sense not to make the controller design overly reliant on that part of the model. So, how best to use existing models is something I will concentrate on. Getting better models (and that probably means higher-order ones, with rotor and other modes) is also vital.

We are still (as a community) in the relatively early stages of devising ways to employ the degrees-of-freedom that H-infinity, mu-synthesis provide.

Q, by P.M Lodge: Do you have a feel for why the yaw controller bandwidth reduced in moving from controller I to controller II?

A: (Daniel Walker's): Controller I performed well in yaw. That perhaps led us to a false sense of security, assuming yaw to be the easy one. With hindsight, we didn't analyze the yaw behaviour carefully enough beforehand. We were expecting problems with pitch and roll, not yaw. (Subsequent analysis did reveal the low yaw bandwidth, but how much heed we would have paid to this, I'm not sure, because predictions based on simulations did not always prove reliable, to say the least!) An additional factor was that we simply had far less experience with the optimization used to synthesize controller II.

The Bell 205 apparently has a slightly nasty, second-orderish yaw mode, possible related to structural flexing. I'm fairly certain that none of the models we have captures that effect. All-in-all, the yaw axis control problem isn't trivial, and given the quite poor models we have, there was probably an element of hit-and-miss.

Operational Lessons Learned from the F/A-18E/F Total Flight Control Systems Integration Process

Mr. Robert J. Hanley[*]
Naval Air Systems Command
Bldg. 2187, Suite 3342
48110 Shaw Road
Patuxent River, Maryland 20670,

Commander David A. Dunaway[†]
United States Navy
Bldg. 2272, PMA-265
47123 Buse Road
Patuxent River, Maryland 20670 USA

Mr. Kenneth P. Lawson[‡]
Naval Air Systems Command
Bldg. 2187, Suite 1390A
48110 Shaw Road, Unit 5
Patuxent River, Maryland 20670 USA

ABSTRACT

The F/A-18E/F Super Hornet is a growth version of the F/A-18 A through D model "heritage" Hornet, first fielded in 1983. Some of the primary design goals for the Super Hornet included increasing the range, providing greater weapon loading flexibility, increasing carrier landing bring back weight, and improving survivability. Improving the survivability was addressed in various ways, including reductions in radar cross section, expanded self-protection systems, and enhanced maneuverability. The heritage Hornet was the first tactical aircraft in the world to fully exploit high Angle of Attack (AOA) maneuvering in the air combat environment. The heritage Hornet is widely known for its ability to attain and maintain high angles of attack, providing the pilot with a distinct advantage in the low airspeed, high AOA arena. Hornet pilots have achieved great success by simply "intimidating" threat aircrews. This intimidation can cause threat pilots to make grave tactical maneuvering errors in this flight regime. Despite these capabilities, the heritage Hornet has had a history of inadvertent departures from controlled flight, mostly in the low speed, high AOA flight regime. Heritage Hornet pilots must always maintain situational awareness of their aircraft state (aircraft store loading in combination with perceived yaw rate and sideslip, AOA and airspeed) to ensure they do not inadvertently cause one of these departures. One of the primary goals for improving the Super Hornet's maneuverability included addressing the total systems design and integration of the Flight Control System (FCS), Operational Flight Program (OFP), and Mission Computers (MC) in order to optimize the control effectors in all phases of flight, including failure modes and battle damage. This integration would be key to approaching, if not achieving, an inherent ability within the Super Hornet to be maneuvered without concern for inadvertent departures, even with heavy and/or asymmetric store loadings, and to remain a safe and potentially lethal weapon system even with flight control failures or battle damage to some control surfaces. This paper addresses this total integrated design with the FCS, OFP, and MCs in the Super Hornet, including discussion on how the control effectors were integrated with feedback sensors to reduce the likelihood of departures, how the flight envelope was expanded to provide greater maneuverability, some surprise lessons learned on the control of asymmetric flow characteristics over the wing, and the positive and negative lessons learned from this design concept by the fleet operators.

[*] Deputy Head, Airworthiness/Flight Clearance Office.
[†] Head, F/A-18E/F Operational Test and Evaluation Team.
[‡] Team Leader, F/A-18E/F Flight Dynamics Team.

Paper presented at the RTO AVT Symposium on "Active Control Technology for Enhanced Performance Operational Capabilities of Military Aircraft, Land Vehicles and Sea Vehicles", held in Braunschweig, Germany, 8-11 May 2000, and published in RTO MP-051.

BACKGROUND

The heritage Hornet first entered service in 1983 and quickly became one of the most successful and lethal weapon systems ever deployed. The intent of the original design, to provide a fighter capability even when configured for an attack mission, was proven during the Persian Gulf war when a F/A-18C carrying a heavy air to ground load, engaged and shot down an Iraqi fighter aircraft and then went on to successfully complete its primary air to ground mission. In the fighter arena, the heritage Hornet has always been able to attain and maintain high angles of attack. Unfortunately, the heritage aircraft is prone to inadvertent departures when a pilot loses track of the state of the aircraft. A significant number of heritage Hornet aircraft have been lost following these departures due to Out of Control (OOC) events, most commonly, the "falling leaf". This problem still persists today with three F/A-18C/D aircraft lost in the past nine months due to OOC and during the lifetime of the heritage Hornet, approximately 20% of all aircraft lost have been a direct result of OOC flight. In addition to the requirement for Hornet pilots to maintain close watch of the aircraft state, the heritage Hornet also has little to no tactical roll performance in the high AOA arena, inhibiting the pilot's ability to achieve a "quick kill" over threat aircraft. As a result, this area was a prime focal point during the preliminary design process for the Super Hornet. The heritage Hornet FCS design architecture possessed a limited capability for expanding the high AOA utility of the Super Hornet. A shift in thinking would be required in order to exploit new flight control integration concepts developed jointly by the Naval Air Systems Command, NASA, and Virginia Polytechnic Institute and State University (Virginia Tech) and independently by General Dynamics (now Lockheed) and McDonnell-Douglas (now Boeing). These new concepts deviated from the primarily "single focus flight control surface design" used by most aircraft up to and including the heritage Hornet, in favor of fully integrated "control effectors" design. Significant advancements were made in this area during the 1990's which matured rapidly when the US Navy and NASA married their joint program with similar projects being funded by the US Air Force under the "Innovative Control Effectors" (ICE) program. The Joint Strike Fighter program is now making extensive use of this concept. For the Super Hornet, a redesign of some of the basic flight control system architecture was required in order to allow full integration of the FCS, OFP, and MCs. Additional real-time aircraft state feedback were needed and new control surfaces were added that could be used in a multi-axis environment. The control system was being optimized to provide the maximum control about each axis after providing basic aircraft stability. The result was a dramatic improvement in departure resistance and near ability to maneuver with "reckless abandon". However, as will be discussed within this paper, it was realized that a significant increase in inherent FCS derived departure resistance could result in a loss of tactical utility by the fleet pilot if not implemented properly.

FLIGHT CONTROL SYSTEM DESIGN

The F/A-18E/F is a growth version of the F/A-18C/D but with additional control effectors (leading edge extension (LEX) spoilers) and increased multi-axis integration of the existing flight control surfaces as well as a fully integrated speedbrake function (making it possible to delete the heritage Hornet "dedicated" speedbrake control surface). The F/A-18E/F Super Hornet is shown in figure 1.



US NAVY PHOTO

Figure 1
F/A-18E/F Super Hornet

The Super Hornet FCS is a digital, quad redundant, fly by wire, full authority Control Augmentation System (CAS). Improved integration of the FCS has provided a significant increase in flight safety following FCS failures and/or battle damage to flight control surfaces. This has allowed for the elimination of the heavy and redundant mechanical backup system found in the heritage Hornet. All control law computations are performed by four digital computers that work in parallel. Redundancy in the control system allows multiple like failures to occur before the pilot notes any degradation in stability or controllability. Unlike the heritage Hornet which can revert to an alternate mechanical system without a CAS function, the Super Hornet CAS function always provides closed loop control with available control effectors even after failures and always attempts to provide acceptable flying qualities.

There are 12 primary flight control effectors on the F/A-18E/F. An example of the use of fully integrated controls in a multi-axis environment can be seen in the longitudinal axis where control is provided through a combination of stabilators, leading and trailing edge flaps, ailerons, LEX spoilers, and rudder toe-in. The FCS is a fully integrated system with cross dialogue/use of the hydraulic/electrical systems, cockpit controls and displays, MC, Stores Management Set (SMS), Air Data System (ADS), Inertial Navigation Set (INS), Data Link Receiver (DLR), landing gear control unit, Signal Data Computer (SDC), radar altimeter, AOA sensors, and pitot-static system. The aircraft is a "load factor (g)" command system above

corner speed and an AOA command system below corner speed. The SMS provides rate-limiting functionality when air-to-ground or external fuel stores are carried on wing stations. Sideslip and sideslip rates are fed back to the FCS to reduce sideslip buildup during dynamic maneuvers and to improve overall stability. To date, the Super Hornet FCS has met or exceeded all design expectations.

There are two flight phases configured in the control laws: Auto Flap UP (UA) for up and away flight and Power Approach (PA) for takeoff and landing. UA is activated if the cockpit FLAP switch is in the AUTO position or if the FLAP switch is in any position and the calibrated airspeed is greater than about 240 knots. The PA phase is activated if the cockpit FLAP switch is in the HALF or FULL position and the calibrated airspeed is less than about 240 knots. FULL flaps are used for ship based approach and for catapult takeoff. HALF flaps are used for field takeoffs.

There is one trailing edge flap, one aileron, and two leading edge flaps per wing, which can be deflected symmetrically or differentially. For longitudinal control the leading and trailing edge flaps, drooped ailerons, and toed-in rudders are scheduled to optimize lift, drag, pitching moment, and lateral-directional departure resistance. Laterally, roll damping is provided by the aileron, differential leading and trailing edge flaps, and differential stabilator.

There are two rudders, one per vertical tail, that can be toed-in or flared for additional control. In UA, the rudders are toed-in at high g's in the supersonic region to reduce hinge moments and are flared out at high AOA to improve nose-down pitch acceleration. In PA, the rudders are toed-in for takeoff and to smooth pitching moment variations with AOA. Rudders are only flared for nose-down pitch acceleration at higher AOAs. Above 25 degrees AOA the rudder signal is sent to the lateral axis and indirectly commands the rudder through the Rolling Surface to Rudder Interconnect (RSRI). The RSRI coordinates roll maneuvers by removing the yaw generated by the lateral surfaces using rudder commands. There is one LEX spoiler per side of the aircraft. In UA the LEX spoilers perform a speed brake function and augment nose down control power. The LEX spoilers are always retracted in PA.

The longitudinal stick commands load factor in UA and AOA in PA, through symmetric stabilator movement. In UA, AOA feedback is added to the control integrator above 22 degrees AOA. The primary feedbacks are load factor, pitch rate, and AOA. The AOA command system used in PA gives more precise airspeed control. The primary feedbacks for PA are AOA and pitch rate. Laterally, the stick position commands stability axis roll rate. Lateral-directional control uses deflection of differential stabilators, ailerons, differential leading and trailing edge flaps, and symmetric rudder deflection. Directional control is accomplished with a directional CAS that commands yaw rate via the rudders.

The control system contains an Automatic Spin Recovery Mode (ASRM) that provides the pilot with full control authority in order to recover from a spin. Spin mode will automatically engage when a spin is detected. All of the following conditions must be met to automatically engage the spin mode: lagged yaw rate greater than 15 deg/sec, the product of lagged yaw rate and actual yaw rate greater than 225 deg^2/sec^2, and the indicated dynamic pressure must be less than 50 pounds per square foot (approximately 120 knots). The spin mode logic will automatically disengage when the spin is arrested. Any of the following three conditions will disengage the spin mode: lagged yaw rate less than 15 deg/sec, the product of lagged yaw rate and actual yaw rate less than 225 deg^2/sec^2, or indicated dynamic pressure greater than 200 pounds per square foot (approximately 250 knots).

There are specific features of the F/A-18E/F control laws that are designed for high AOA flight with enhanced departure resistance and roll performance. Sideslip rate feedback to the ailerons and the differential tail provides additional roll coordination and increased roll rates. Above 22 degrees AOA, a stall warning is implemented by adding angle of attack feedback to the integrator error signal. A steady state AOA command system is created above 34 degrees by increasing the integral AOA gain. Nose-down pitch acceleration from high AOA is augmented by the use of LEX spoilers, rudders flare, and a "pitch bucking" modification. The LEX spoilers are deflected if the aircraft is above 22 degrees AOA and the pilot is making a large nose-down stick command. Symmetrically deflected rudder flare is also used during high AOA and large nose-down stick commands. Immediate pitch response is obtained by a modification to the forward loop integrator that is intended to eliminate "pitch bucking" at maximum trim AOA. This control law modification unloads excess (the difference between the unlimited stabilator command and the actual surface command) nose-up command from the pitch integrator. As such, the response to nose-down control inputs is immediate since the pitch integrator does not have to unwind from an over commanded state.

DESIGN PHILOSOPHY

The basic design philosophy for the F/A-18E/F can best be summarized as follows:

1. Reduce or eliminate all operational maneuverability issues that were inherent in the heritage Hornet, such as, falling leaf mode, low AOA (near zero degrees) departure susceptibility, maneuvering limitations with large lateral weight asymmetries, reduce/eliminate potential to enter OOC flight, increase high AOA roll performance, eliminate two seat high subsonic Mach maneuvering restrictions, eliminate center of gravity maneuvering limitations and decrease roll coupling departure tendencies with forward longitudinal control stick inputs.
2. Focus on the "Total Control Power" required to conduct the mission and implement a "Multi-Axis Control Effector" FCS design integration scheme vice a "Single Axis-Single Control Surface" control system design.

3. Actively solicit feedback from the end user, the fleet, on what the priorities should be for improving the Super Hornet.

The “how” for the implementation of this philosophy was drawn from on-going Joint Service/Agency efforts that were underway during the A-12 development. In the early planning days of the Advanced Tactical Aircraft (ATA), which became the A-12 (which was subsequently canceled), the US Navy, NASA, Virginia Tech (under a research grant) McDonnell-Douglas (now Boeing) and General Dynamics (now Lockheed/Fort Worth) worked closely to determine what the next generation fighter/attack aircraft should be. What is the principle design philosophy that should be the focus of these efforts? A quick look at the F-14A, F-16A and F/A-18A design progressions made it clear. It was no longer acceptable to hand an aircraft designer the Military Specification for Piloted Aircraft (MIL-F-8785C) and expect an aircraft that met the operational requirements would be delivered three years later. Rapid expansion in high AOA capability (due in part to advances in flight control system integration required for use with relaxed static or statically unstable longitudinal designs and in part to improved aerodynamic design) was first exploited by the F-14A Tomcat and exceeded the design areas covered by MIL-F-8785C. When this specification was first introduced, high AOA was considered to be about 16 degrees. The F-14 expanded that to over 50 degrees, although the Tomcat did not have the control power to exploit this region. The fact was that no clear design criteria were in place to govern this new generation of aircraft. In addition, the advances in flight control technology allowed the designer significant “wiggle” room in what design guidelines existed. In other words, the designer could “point design” the aircraft to meet vague design guidelines, sacrificing maneuvering about one axis that had no clear design goal in order to meet a requirement about another axis that did. This resulted in an aircraft with decidedly non-uniform maneuvering capability in the high AOA region. The F-14A can safely be maneuvered to 50 degrees AOA, but then requires the pilot to execute a “controlled departure” to maneuver tactically because it has very little excess roll/yaw control power above that needed for stability purposes in this area. The F-16A has an AOA limiter (incorporated because of an inherent deep stall problem in this design) which precludes maneuvering above approximately 27.5 degrees limiting its tactical maneuvering options when the pilot is flying on this limiter. The heritage Hornet has no AOA limiter, but does have aft center of gravity (cg) limitations to preclude AOA hang-up (defined by weak nose down control power with full forward control stick, which delays recovery to lower AOAs and results in severe altitude loss) and has very little roll capability in the high AOA region.

Clearly, design guidelines to preclude longitudinal problems (deep stall and AOA hang-up) and to define lateral-directional requirements for stability and control were needed for higher AOAs (AOAs not addressed in any existing specification). This need resulted in joint US Navy-NASA programs to address longitudinal (the “HANG,” High AOA Nosedown Guidelines program) and lateral-directional (the “HAIRRY,” High AOA Investigation of Requirements for Roll and Yaw program) problems in cooperation with the US Air Force and sharing of information from the ICE program. These efforts included extensive piloted simulation. The resulting guidelines were verified by flight experiments conducted on US Navy F/A-18C aircraft at Patuxent River and on the F-18 HARV at NASA Dryden Flight Research Center. Additional information and data were derived from the X-31, F-15 S/MTD and F-16 MATV projects, all flown at Edwards Air Force Base.

Initially, the longitudinal requirement seemed obvious, ensure the high AOA hang-up problem was eliminated. This would enhance safety of flight and eliminate center of gravity restrictions. What was not clear was how much additional nose down control was required/desired to enhance tactical utility. Likewise, a look at all current and projected roll performance capabilities of next generation aircraft would provide the baseline roll performance capability desired for the Super Hornet. Again, it was not clear how much roll/yaw capability was required just for safety versus an increase in tactical utility. Since no previously fielded aircraft has had these capabilities, the operational community has not reported on how these increased capabilities truly factor into the multi-aircraft threat engagement arena with off boresight, all aspect weapons employed. The typical response from the operators when asked these questions is “we’ll take as much as you can give us!” A viable concept, but one that can have significant impact on cost and aircraft weight (and require much soul searching to determine the need for additional control effectors such as thrust vectoring). Consequently, a Program Manager must consider the cost to benefit ratio of exploiting a portion of the flight envelope that may have an exposure time of only about two minutes during a two-hour tactical mission.

Data from the HAIRRY program was reviewed with the following question in mind, “what is the tactical utility of increasing roll performance with increasing AOA?” since a roll about the stability axis (the inherent design for rolling these generation of aircraft) really becomes more of a yaw maneuver rather than a roll. Combine this question with that of “how much nose down control power is required to be tactically useful versus providing safety of flight?” and you get a complex tradeoff in design that still has no clear answer. These questions were much easier to answer for 50/60’s generation aircraft that were very statically stable. In these cases, the horizontal tail was the longitudinal control and was typically sized by nose wheel lift-off requirements. The aileron was sized typically by low airspeed (landing) requirements and the vertical tail/rudder by stability and turn coordination requirements (and in the case of multi-engine aircraft, minimum control airspeeds). HANG, HAIRRY and ICE provided a more in-depth look at the “control effector” problem. Prior to these efforts, control allocation issues were discussed behind closed doors for very specific designs. The results of these designs

may have flown, but they were never reported publicly. The answers that eventually came forward were significant. The primary focus for all future designs would be on total mission control power requirements. The challenge is to identify early in the design process the control power requirement for each axis, regardless of flight phase. If the challenge is met, the resulting design will have sufficient control power to do all mission tasks. Boeing and Virginia Tech have been leaders in the development of methods for assessing control power requirements and have developed "Control Allocation" routines independently but with similar results. These methods help to ensure an optimum FCS, using the maximum amount of control power available about each axis for stability and controllability. Results from these efforts have now been coordinated and compiled in the Joint Service Specification Guide (JSSG) currently under development by the US Navy and US Air Force, with drafts already released to industry. The F/A-18E/F unique specification requirements were the forerunner for many of the new additions in the JSSG.

This new design guidance fit ideally with the initial development plan given by the Super Hornet's Program Manager. The program design goals for the F/A-18E/F was simple, provide significant improvement to the following critical areas over the heritage Hornet: range, weapon loading flexibility, carrier landing bring back weight, and survivability. All other areas should be equivalent or better than the baseline (F/A-18C/D). Improving the maneuvering aspect of survivability would require a clear understanding of what the user (the fleet pilot, hereafter referred to as "the fleet") wanted. What would really improve survivability from the maneuvering vantage point? The initial answer was clear: increase lateral, directional, and longitudinal control power at all AOAs.

As noted above, the design philosophy was not to ensure that you could fly the F/A-18E/F with reckless abandon or with "carefree" maneuvering as some would think. Since the Super Hornet was a growth version of an existing design, it was obvious that carefree maneuverability could only be a "goal" since a "derivative" aircraft has additional limitations in its design space over a totally new design. The primary goal was to improve the safety of flight issues first and then work on expanding operational utility to the maximum extent possible within the design constraints this aircraft derivative brought forward from the heritage design. The falling leaf was a significant safety of flight design concern, having claimed many heritage Hornet aircraft in OOC flight. This mode is a sustained in-phase roll and yaw event which produces a nose-up inertial coupling moment in excess of the generally weak (depending on cg location) nose down moment generating capability of the aircraft. The character of the motion is highly oscillatory in both AOA and sideslip and even though the AOA frequently oscillates down to low AOA (a typically "flyable" AOA) the accompanying sideslip (usually well beyond 10 degrees) helps to reinforce the falling leaf motion. Elimination of this problem was a primary design goal for the Super Hornet. The design goals were:

1. Enhanced departure resistance and post departure (should it still occur) elimination of "falling leaf" or unrecoverable spin modes.
2. Requiring the aircraft to meet all flying quality requirements with a centerline fuel tank since this is a common operational configuration in all services, foreign and domestic.
3. Elimination of high AOA hang up and the accompanying AOA/cg restrictions.
4. The aircraft must be able to land on an aircraft carrier following most flight control failures.
5. Improved roll performance at elevated AOAs in the gear up/flaps Auto configuration.
6. Expanded tactical utility with large lateral store weight asymmetries (since high value stores are frequently deployed one at a time and can result in significant lateral weight asymmetries and aircraft maneuvering limitations after release of one store).
7. Reduction of likelihood of encountering pilot induced oscillation/aircraft-pilot coupling tendencies.
8. Adequate control following a dynamic and/or static loss of one engine (which sized the F/A-18E/F vertical tail).
9. No reduction in flight envelope for the two seat F-model over the single seat E-model, since both aircraft would be mission capable aircraft.

ACHIEVEMENT OF DESIGN GOALS

How was it possible to achieve the design philosophy and associated goals? By changing the approach to integrating the systems on the aircraft. The goals could only be achieved if the team focused on the end result desired vice the "typical" method for achieving it in the past. Historically, ailerons were considered the primary, if not only, roll control surface. New generation aircraft, including the Super Hornet, have adopted the "control effector" philosophy. Adoption of this philosophy provides new freedoms to the designer. As noted earlier, the F/A-18E/F uses virtually all of its control surfaces, "effectors," to provide longitudinal control. This is the same for all three axes. In the roll axis, the team focused on what was needed to attain increased roll performance as a function of AOA as opposed to assuming that when you ran out of aileron control power you were basically finished. In fact, the F/A-18E/F does not even use ailerons for roll control in some portions of the flight envelope. Pitch, roll, and yaw generating capabilities were "book kept" for all control effectors and then blended as needed to achieve desired rate and/or angular change in the airplane. Certainly, this is not a new concept and definitely not invented here, but the Super Hornet has become the first operational aircraft in production to exploit this capability to an unlimited angle of attack range.

In order to achieve these goals, the team decided not to "photographically" enlarge the aircraft, as is often done in larger derivative aircraft. Instead, each part of the aircraft was looked at separately and enlarged, as needed, to meet the new design goals. In this way, better control of

unnecessary weight growth was maintained by not "over-designing" the aircraft. Figure 2 depicts the physical differences between the Super Hornet and the heritage Hornet.

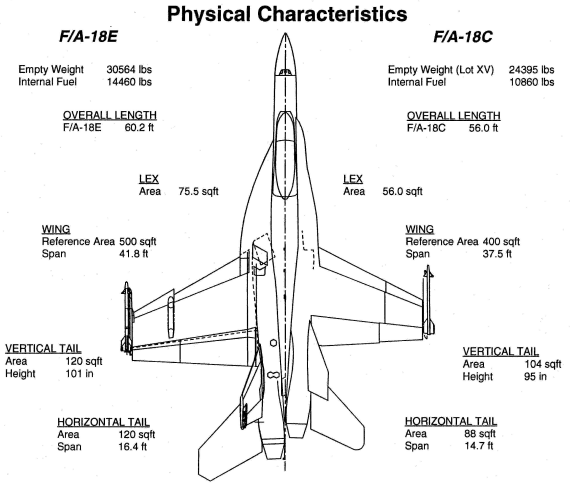


Figure 2
Planform Comparison - E/F to Earlier Models

As noted earlier, the vertical tail was sized by single engine minimum control airspeed in the approach/landing configuration. The vertical tail was grown 15% over the heritage aircraft, although initially, it was to remain the same size as the F/A-18C/D. The growth was added after stability and control assessments proved the baseline was inadequate. The wing was grown 25% to meet performance requirements. The horizontal tail was enlarged 36% to meet the demands of high AOA flight and eliminate AOA hang up and falling leaf. This nose down control is augmented by the addition of new LEX spoilers, which also function as part of a fully integrated speed brake. This was all part of the new systems approach to the aircraft design.

Nose down control power, a major deficiency in the heritage Hornet (resulting in complex cg/AOA restrictions as a function of store loading) was addressed by blending three control effectors, the horizontal stabilators, the new LEX spoilers and flared rudders.

The control effector allocation scheme was significantly improved at elevated AOAs over the heritage aircraft, which suffers from limited turn coordination and control blending flexibility as well as the lack of feedbacks for sideslip or sideslip rate. The heritage Hornet uses ailerons and differential stabilator working together to roll the aircraft, approximating a stability axis roll (since no sideslip feedback is available to help control sideslip buildup during the roll). Unfortunately, this differential stabilator produces significant adverse yaw which cannot be countered by the rudders, requiring reduced roll gains and hence, performance, in the heritage Hornet. The Super Hornet, in contrast, uses the ailerons and rudders to roll and coordinates the roll with differential stabilator (a very strong yaw generating effector). Sideslip and sideslip rate feedback were added to the ailerons and differential tails. These feedbacks are used to improve the Dutch Roll mode damping and essentially has eliminated the falling leaf. This would not have been possible without the targeted horizontal tail size increase noted earlier providing the necessary control power to accomplish the task.

The control stick and rudder pedal blending was also improved in the Super Hornet. Above 25 degrees AOA, a lateral stick and/or rudder pedal input should provide the same output to the control effectors in the heritage Hornet. No matter which combination (rudder pedal and lateral stick) or single input (rudder pedal or lateral stick) the pilot elected to use to roll the aircraft, theoretically, the same control effector deflection would occur. Unfortunately, this was not the case in reality for the heritage Hornet. It was discovered that this design could be defeated by clever pilots phasing rudder pedal and lateral stick in such a way as to induce a larger control effector deflection than the designers thought possible (because of the way the SAS and CAS interpret these inputs and act to provide stability and control). These larger inputs produced larger aircraft rates that were not accounted for in the SAS and could (and periodically do) result in unintentional departures from controlled flight. In the Super Hornet, cross-controlled inputs are canceled and combined inputs are limited to that which could be commanded by a full lateral stick. The desire here is for the pilot to always roll with lateral stick, letting the control blending functions within the FCS decide which control effectors to use to achieve the desired output. This significantly reduces pilot workload and improves safety compared to F-4 Phantom vintage aircraft which rolled with ailerons at low AOAs, but were only rolled with rudders at high AOA (unless you wanted to depart from controlled flight) because the ailerons generated significant adverse yaw with increasing AOA that would easily lead to OOC flight. An F/A-18E/F pilot can fly "feet on the floor." Lastly, roll/pitch limiting was added to the Super Hornet to preclude inertial coupling into the yaw axis when large roll and pitch commands are present. This feature significantly reduces departure susceptibility.

Departure resistance was a primary focal point throughout the design. Many aircraft since the F/A-18A/B was introduced in 1983 have attempted, with varying degrees of success, to implement Departure Resistance (DepRes) systems either implicitly (through Aileron-Rudder Interconnects and/or Rolling Surface to Rudder Interconnects) or explicitly (through the addition of a so-called DepRes system, Automatic Spin Recovery Mode or other FCS design concept) into their designs. No matter what they are called, they all attempt to do the same thing, control sideslip buildup and eliminate or reduce inertial and kinematic coupling. In order to be truly successful, DepRes type systems must have feedback paths for sideslip, sideslip rate, pitch rate, roll rate and yaw rate. These feedbacks are then integrated into a FCS to produce stability axis rolls (to eliminate kinematic coupling), to limit combined rate build-ups (to eliminate inertial coupling) and to control the Dutch

Roll mode and keep the aircraft in the stable region of directional stability. All of this is predicated on having sufficient control power and a control allocation scheme to make maximum use of the control power available about each axis after accounting for and maintaining stability. It also assumes that control effector actuator rates are fast enough to input the desired control effector command and achieve the desired deflection before the aircraft goes unstable. Figure 3 provides a summary of the control surface actuator rates and deflection limits for the F/A-18E/F.

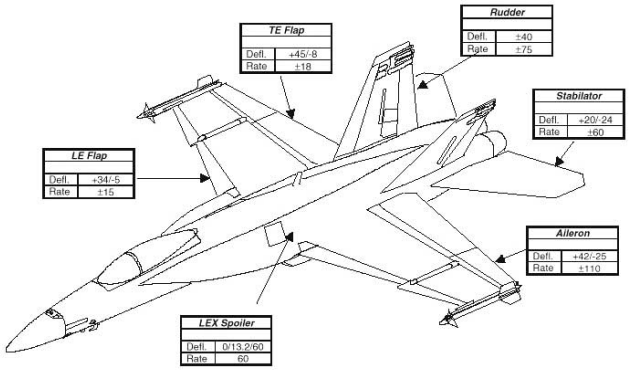


Figure 3
Actuator Rates & Surface Deflection Limits

As with all other DepRes systems, the F/A-18E/F relies on controlling the sideslip and rates to mitigate departure tendencies. Since this was an up-front requirement, adequate control power was ensured through design and redesign in the early phases of wind tunnel testing, validation in simulation and verification during both Developmental and Operational Testing. The Super Hornet generates direct control of sideslip and sideslip rate by feeding those signals to the ailerons and differential stabilator. The use of sideslip and sideslip rate feedback proved to be a significant improvement over the heritage Hornet DepRes system. Sideslip feedback is used to maintain directional stability and ensure stability axis rolls are achieved. The sideslip rate feedback works to dampen the Dutch roll mode, which in turn, helps eliminate the falling leaf mode (the falling leaf is considered an exaggerated Dutch roll). A roll/pitch (*pq*) product limiter and a *pq* "clamp" are included to reduce inertial coupling tendencies. The roll/pitch limiting was originally a feedback loop but the dynamic nature of some of the Super Hornet tactical maneuvers made it clear this was too slow to be effective at eliminating departures so it was subsequently supplemented by a feed forward path (*pq* "clamp"). By adding command limiting to the feed forward path, you risk losing some roll performance. After a closely examining this potential impact, it was found that departure tendencies were directly related to the rate of aft stick input. Using this information, a "clamp" was added to the feed forward path which made the *pq* limiting a function of aft stick input rate. This significantly reduced departure tendencies through continuous rolls of up to about 540 degrees of bank angle change, (well beyond the operational need of 360 degrees) but maintained the high level of roll performance.

The "DepRes" system on the Super Hornet works continuously to preclude inadvertent departures. The CAS does this by attempting to keep the aircraft from achieving certain thresholds (airspeed <121 knots, lagged yaw rate>15 deg/sec, and product of lagged yaw rate and yaw rate > 225 deg^2/sec^2) that could lead to departure. If these conditions are met, the ASRM will engage to provide additional control authority to the pilot to effect recovery.

The highly integrated FCS of the Super Hornet is the primary reason it has achieved great success. Success that is a direct result of priorities set in the wind tunnel to ensure the control power was inherent in the design to achieve the objectives. The F/A-18E/F has accumulated well over 14,000 tunnel occupancy hours of wind tunnel test to date. The hard lessons learned by many previous aircraft development programs; not ensuring adequate control power was provided up front, was not repeated here. While many people believe that a sophisticated FCS can solve all aerodynamic design flaws, it is has been proven time and time again that a FCS cannot *create* control power that does not exist. Once a control surface is fully deflected, the limit of that control effector's control power contribution is reached. If sufficient control power is inherent to the design, you can do great things, which the Super Hornet has done. The integrated process of the Super Hornet is best seen through the following summary of each control axis:

Longitudinal: Control is provided by symmetric stabilators, rudder toe-in and flare, symmetric leading and trailing edge flaps, symmetric ailerons and symmetric LEX spoilers.

Lateral: Control is provided by asymmetric use of aileron, differential stabilator, differential trailing edge flaps and differential leading edge flaps.

Directional: Control is provided by twin tail rudders deflected symmetrically and asymmetrically (toe in/out). The rudder is commanded by a combination of rudder pedal, RSRI, yaw rate feedback, lateral acceleration feedback, high AOA sideslip and sideslip rate crossfeed to the ailerons and differential stabilator, roll rate feedback, and directional coupling compensation.

The results from the Engineering and Manufacturing Development (EMD) flight test program demonstrated that the design goals had been achieved and the Super Hornet was ready for Operational Evaluation (OPEVAL). EMD flight testing in this high AOA regime was accomplished during approximately 221 flights, totaling some 378 flight

hours for both single and two-seat aircraft[1]. The flight test program was broken into five phases, with the first three phases covering simulation aerodynamic data base validation, verification of spin and spin recovery control power and recovery techniques and aggravated control input attempts to depart the aircraft from controlled flight. Phases 4 and 5 evaluated asymmetric store loadings. The improved departure resistance of the aircraft and integrated control effector blending enabled unrestricted clearances for both single and two-seat models in all external loadings with less than 8000 ft-lb asymmetry. Loadings between 8000 and 12,000 ft-lb permit unrestricted maneuvering at AOAs less than maximum lift, with less restrictive limits overall up to and including the maximum allowable asymmetry of 26,000 ft-lb. This provides the fleet user greater tactical utility and flexibility in weapon loadings and deployment.

THE UNKNOWN/UNKNOWNS

Every flight test program encounters some "unknown-unknown," things that were not planned, thought of, or considered possible to occur in flight-testing. The Super Hornet was no exception. Early in the flight test EMD program, the aircraft experienced uncommanded "wing drop" during wind up turns and straight and level accelerations. As the program matured and the envelope expanded, it became clear that this was a serious problem that would impact aircraft performance if not corrected. Over an eight-month period from August 1997 through March 1998, maximum resources were brought to bear to solve this problem. In all, over 10,000 wind up turns were executed on over 100 wing configurations before a solution was found. This effort required use of up to 4 of the 7 flight test aircraft to solve, causing significant rework to an already tight EMD schedule. The "wing drop" phenomenon was a rapid, uncommanded bank angle change of up to 180 degrees (if left unchecked by the pilot) that would cause a pilot to lose a guns-tracking solution on a threat aircraft. Wing drop occurred at all altitudes and from about 0.55 Mach to approximately 0.95 Mach. Extensive wind tunnel, simulation and CFD testing and analysis was conducted coincident with the flight-testing. In general, it was concluded that wing drop occurred due to a sudden, asymmetric wing stall event that was focused around the wing fold fairing (which is new and unique to the Super Hornet from the heritage Hornet). Some of the flight test "fixes" assessed included modified snag locations, vortex generators, grit, stall strips, modified flap scheduling, control surface biasing, fences and porous wing fold fairing covers. Eventually, the porous wing fold cover proved to be the most effective solution to the "wing drop" phenomenon, by dissipating adverse pressure gradients fore and aft of the shock forming on the wing and reducing the effect of the asymmetric stall. Throughout history, many aircraft have experienced "wing drop" or "roll off" tendencies, for various reasons, but none have proven to be as elusive to solve as the Super Hornet's. Expert panels were convened with some the best high-speed wing design engineers in the country participating from Academia, Industry, and Government. The conclusion was that this phenomenon was not well understood and required immediate attention for future aircraft program designs to ensure they too do not suffer the same set back the Super Hornet did. In 1998, a three-year National Abrupt Wing Stall (AWS) effort was funded by the Office of Naval Research in conjunction with NASA and Academia to investigate this phenomenon.

PREPARING FOR OPEVAL

Since OPEVAL pilots flew coincident with the Development Test (DT) pilots, they were able to monitor the progress of EMD testing and get a preview of what to expect during the formal OPEVAL period. The most notable concerns with the Super Hornet included the inability to perform a "pirouette" maneuver (a maneuver commonly employed by the heritage Hornet, described as a nose high to nose low 180 degree heading transition), sluggish roll performance at 20 to 25 degrees AOA, two seat aircraft directional instability at minus 20 degrees AOA, uncommanded roll reversal at full aft stick, "yaw-off" due to decreased directional stability with wing pylons and lateral stick plus full aft stick departures.

The pirouette maneuver was an interesting problem. The airplane was doing exactly what it was designed to do, preclude large yaw rate and sideslip buildup, thereby reducing departure tendencies. But, as expected, everything is a trade-off and this was no exception. By increasing departure resistance to the initial levels used on the Super Hornet, some "controlled" type tactical maneuvers/departures were no longer possible. In the heritage Hornet, you can execute a pirouette maneuver, but you are effectively executing a controlled departure by allowing yaw rate and sideslip to exceed that desired to maintain control of the aircraft. Since the aircraft ends up nose low, airspeed increases rapidly through the regions of directional instability and departures do not occur. Unfortunately, the Super Hornet FCS/CAS fights the pilot on this same maneuver and does not allow it to be executed in the same manner. To provide this capability to the Super Hornet pilot, fundamental stability and control techniques were employed which made use of proverse sideslip and dihedral effect to increase roll and yaw rates at high AOA. Since it was intended to provide basically a point design capability for executing a pirouette maneuver, it is only possible to command proverse sideslip when lateral stick and rudder pedal are combined at high AOA and low airspeed, exactly where and how the Super Hornet pilot wants to perform this maneuver. This was done since the generation of proverse sideslip does not produce linear or predictable responses with time, potentially allowing sideslip and yaw rate to build to unacceptable levels. The CAS was re-tuned to deviate from trying to produce a pure stability axis roll and allowing some proverse yaw to build. A control shaping filter was added to reduce this new sideslip command function with time so that the CAS function would return to normal at approximately the time it takes to complete the pirouette.

Sluggish and unpredictable/non-linear roll performance occurred in the 20 to 25 degree AOA region creating significant roll predictability issues during reversals, horizontal and rolling scissors maneuvers. Increasing aileron deflection and modifying the coordination with the rudders and differential tail solved this deficiency[2].

Two-seat directional instability at negative 20 degrees AOA resulted in a dramatic departure and entry into an inverted spin. This problem resulted from weak inherent directional stability, a fact that was known from early rotary balance wind tunnel testing, but thought to be insignificant in this region since the tactical need for maneuvering the airplane aggressively at negative angles of attack was not clear. However, when expanded capabilities are given to pilots, they will find a way to make it tactically useful, and this was no exception. This problem was solved by increasing sideslip and sideslip rate feedback which augmented the directional stability. Again, it was fortunate that the aircraft focused on control power early on in the wind tunnel design phase. This focus helped ensure that this control power was available to address issues just like this one[2].

Uncommanded roll reversals at full aft stick occurred around 45 to 50 degrees AOA and generated a fairly mild 5 to 10 deg/sec roll rate opposite to the commanded stick position. This was eliminated by decreasing aileron deflection for the same lateral stick deflection and increasing the rudder deflection in this region to decrease the adverse yaw, resulting in rolls in the expected direction[2].

Yaw-off with wing pylons mounted occurred in the 30 to 50 degrees AOA region at airspeeds near 300 knots. In this case, it was found that the aerodynamic simulation model predicted higher directional stability than was realized in flight. Consequently, the CAS provided too little augmentation. Increasing sideslip feedback to the ailerons and differential stabilator in this region solved this problem[2].

The lateral plus aft stick departures were eye-watering and resulted in a few events which exceeded the negative “g” limits of the aircraft and greatly exceeded the pilot “comfort” levels. These occurred at approximately 0.6 Mach and 1-g initial conditions. The result was a rapid sideslip and yaw rate build-up opposite the direction of the lateral stick followed abruptly by a nose tuck that, on the worst test point, hit negative 3.7 g’s. The solution to this problem was accomplished by iterating (tweaking) the inertial de-coupling *pq* limiter and adding the *pq* clamp discussed earlier[3].

With these problems fixed, the aircraft was now ready to be turned over to the end user for evaluation of the airplane performance in an operational environment - under real world scenarios.

OPERATIONAL EVALUATION (OPEVAL)

The US Navy announced on 15 February 2000 that the F/A-18E/F Super Hornet was awarded the best possible grade by the OPEVAL team calling the aircraft “operationally effective and operationally suitable.” In addition, the OPEVAL team recommended that the aircraft be introduced into the fleet. The Chief of Naval Operations stated that “The F/A-18E/F Super Hornet is the cornerstone of the future of Naval Aviation. The superb performance demonstrated throughout its comprehensive operational evaluation was just what we expected and confirms why we can’t wait to get it to the fleet.”

Air Test and Evaluation Squadron Nine (VX-9) at China Lake, California flew 1233 hours in over 850 sorties and expended more than 400,000 pounds of ordnance in the Super Hornet during nearly six months of evaluation. The 23 member team tested the aircraft in a wide range and complex variety of mission scenarios. The purpose of the OPEVAL was to test the aircraft in a realistic setting to determine its operational effectiveness as a weapon system and its suitability to be maintained and operated by the US Navy. The OPEVAL report specifically cited the aircraft’s key enhancing features, including, survivability, growth capability, bring-back weight, range and payload.

OPEVAL concluded that there are three fundamental maneuvering characteristics provided by the F/A-18E/F Super Hornet’s flight control law architecture that have proven to provide a significant advantage in the tactical employment environment. The three characteristics include aggressive and unconstrained pitch axis control to unlimited angles of attack (AOA) with all external loads up to 8000 ft-lb asymmetry, exceptional departure resistance, and the ability generate high yaw rates at high AOA. These three characteristics provide a combined, synergistic affect that allows even inexperienced F/A-18E/F aircrew to exploit the full capability of the aircraft and enjoy exceptional tactical maneuvering success. In spite of the fact that the Super Hornet did not incorporate expensive, high risk aeromechanical technologies associated with extreme agility such as a canard or vectored thrust, the three maneuvering characteristics achieved through ingenious flight control design provide an impressive agility and maneuverability. When the exceptional maneuverability is combined with the increased range, increased weapons capacity, improved survivability, mature weapons system and growth systems such as AIM-9X, Joint Helmet Mounted Cueing System (JHMCS) and Advanced Electronic Sensor Apparatus (AESA) the Super Hornet is and will continue to be a dominant force in any threat environment.

Unconstrained pitch pointing of the Super Hornet is exceptional. The peak instantaneous turn performance is similar to that of the heritage Hornet. However, the operational advantage provided by the Super Hornet is found in its ability to maintain that high instantaneous turn rate for a greater amount of time and to a higher AOA equating to increased total turn. For the fighter mission, the

increased total turn provides the Super Hornet the routine ability to achieve an angular advantage or a nose on position first. From an operational perspective, the pilot is able to commit to a full aft stick pull to maximum AOA before any other current fighter is able or willing to commit to the same maneuver. In many cases, the Super Hornet pilot is able to perform a maximum performance turn to a "nose on" position immediately if not within 180 degrees of turn from engagement initiation. At a minimum, this threatening maneuver forces the adversary to respond defensively. As a rule, the F/A-18E/F is able to employ the first weapon. In addition to impressive positive pitch pointing, the Super Hornet also has impressive negative pitch pointing. During initial operational test assessments, the negative pitch rates of the aircraft were deemed too slow for optimum operational employment. A simple flight control modification was incorporated to increase the pitch rates to a level just below the pilot's physical pain tolerance threshold. Although the pitch pointing is most useful in the fighter mission, it also has impressive applications in the air to ground mission. The unlimited angle of attack and high pitch rates allow the Super Hornet to perform highly effective evasive maneuvers and rapidly designate targets with full air to ground weapons loads. Pilots can maneuver as aggressively as they desire without regard for AOA limits and can achieve a valid designation and release solution very rapidly.

The incorporation of sideslip and sideslip rate feedback in DepRes system virtually eliminates departures. Throughout the course of OPEVAL, 15 pilots, utilizing seven airplanes and flying over 1200 flight hours had only one departure from controlled flight. The single departure occurred in the only known area of relaxed directional stability and was well outside the normal maneuvering envelope. Recovery was virtually immediate. More importantly is the fact that pilots with less than 10 hours in the Super Hornet are able maneuver using full stick and full rudder inputs at any airspeed and AOA without fear of departure. Instead of spending many hours learning the prohibited maneuvers, maneuvering limits or complicated control inputs, Super Hornet pilots are simply able to use logical inputs up to and including full stick and rudder to achieve their desired maneuver. One of the training missions provided to OPEVAL pilots was a high AOA demonstration. This demonstration included full aft stick stalls, full forward stick stalls, aggravated control inputs at all AOA and zero airspeed tail slides. Once the departure resistance of the airplane was demonstrated to aircrews, they were confidently able to maneuver to limits that were outside the frame of reference of adversary pilots. Comments from adversary pilots include amazement over the Super Hornet's ability to hold its nose up to a virtually zero airspeed with good nose pointing control, the rapid pitch pointing, and the ability of the airplane to continue rapid nose pointing at very high angles of attack.

In addition to the impressive pitch pointing and departure resistance of the Super Hornet, there are several performance characteristics at high AOA that will allow the Super Hornet to dominate the engaged maneuvering environment. During early operational tests, the inability to generate yaw rates at angles of attack above 25 degrees was identified as a major limitation to air to air combat. At that time, the use of sideslip and sideslip rate feedback to prevent departures had also limited the maneuverability of the airplane to an unacceptable level. Through an aggressive process of design and close interface with the operational community, the flight control logic was modified to allow proverse sideslip within a specific AOA and airspeed range. This change did not decrease departure resistance but significantly improved the ability of the Super Hornet to rapidly reposition the nose from a nose high to a nose low position. In addition to impressive pitch pointing, the Super Hornet has the combined roll/yaw axis to use in quickening the transition from nose high to nose low conditions. This maneuver is akin to the pirouette maneuver performed by the heritage Hornet with the notable exception of precise control. In the case of the heritage Hornet, the pirouette is essentially a controlled departure that quickly transitions the aircraft from nose high to nose low. Once the maneuver is initiated, the pilot is essentially along for the ride. By contrast, in the Super Hornet, the maneuver can be performed with good control throughout. In fact, the F/A-18E/F is easily transitioned from a pirouette to a precise guns tracking solution at virtually any point in the maneuver. A precipitous byproduct of the Super Hornet pirouette maneuver is an impressive horizontal plane maneuver that generates turn rates similar to maximum instantaneous turn rates but at airspeeds less than 150 knots. The maneuver is performed at full aft stick stall by invoking the pirouette maneuver for 2-3 seconds from a turn or level flight. Once initiated, the aircraft roll/yaws through 40-60 degrees of turn at which point the pirouette control inputs are removed and the aircraft is recovered back to level flight. This maneuver can be repeated in sequence to create an impressive "effective" instantaneous turn rate. This maneuver is frequently used as a secondary threatening maneuver after the pilot has used the impressive pitch pointing for a first shot advantage.

In summary, there is no single maneuvering characteristic that makes the F/A-18E/F an effective maneuvering platform. It is the synergy enjoyed by combining the effective pitch rate, pilot confidence that comes from departure resistance, high AOA maneuverability, pirouette, and deck transition. Although Air Combat Maneuvering (ACM) is usually avoided as much as possible and only used as a last resort, it is an excellent benchmark of maneuverability. The Super Hornet has proven to be an impressive ACM platform. Pilots have found that the Super Hornet is most effective when using an aggressive position fight. The pitch pointing provides the first shot capability, the departure resistance and high AOA maneuvering allows the Super Hornet to maintain the threatening position and lastly, the pirouette/deck transition allow the Super Hornet to achieve quick follow up shots. For a conventionally designed aircraft with relatively low thrust to weight ratio, the Super Hornet is one of the premier ACM aircraft available today.

END GAME

In contrast to the F/A-18A/B development in the early 1980's, the Super Hornet has delivered a fully capable weapon system to the users up front. The F/A-18A/B, an advertised strike-fighter, was delivered with virtually no air to ground capability in 1983. The Super Hornet has an extensive repertoire of weapons and is ready to go to war now.

LESSONS LEARNED

Some important lessons learned from the Super Hornet development include:

1. Make the end user a part of the development process, in this case, the Operational Community. Their inputs are critical to a successful program and delivering a weapon system that does its intended mission up front.
2. Unknown-Unknowns will occur. Fortunately, the F/A-18E/F Program Manager budgeted for these in management reserve, most of which was used solving "wing drop."
3. A fully integrated flight control system with control allocation algorithms making maximum use of all available control effectors is the present and the future of all piloted and unpiloted vehicles.
4. Ensure the preliminary design and subsequent engineering development has adequate wind tunnel testing included to determine if sufficient control power is inherent in the design. This should account for relaxed stability design concepts and completion of all critical mission tasks. It should also address what will be considered probable FCS failures for each individual design to make the FCS as robust as possible.
5. Wing design is still an art. Prediction of "wing drop" like phenomenon is still a "black art". Hopefully, the National AWS program will shed new light on this topic.
6. As more aircraft are able to exploit the high AOA region, new tactics will have to be developed. These tactics must be analyzed to determine exactly what kind of rates are necessary to be lethal in this environment without undue penalty to the airplane design in other areas (again, everything is a trade). To date, even with HANG and HAIRRY, it has been difficult to pin down critical design guidelines for high AOA tactical utility.
7. Regardless of how sophisticated, a FCS can do nothing without control power.
8. Designer engineers must realize that what they think is important is not always what a pilot thinks is important. Case in point, if the engineers think it is a great idea to design an airplane to be flown with "reckless" abandon by providing superior departure resistance in the flight control system automatically, they may actually (and probably will be) taking away some of the tactical utility of the aircraft. There was (and is) a lot of truth to the fighter pilots view of the world that you have to fly "to the edge of the envelope", the point just prior to a departure, in order to maximize the effectiveness of your aircraft in combat. As shown in the F/A-18E/F and the initial inability to perform a pirouette maneuver, too much artificial departure resistance inhibits the pilot from tapping into the maximum capability of the aircraft. There comes a point where you have to let the pilot judge where and how to use the edge of the envelope vice the engineer and the DepRes type system.
9. And lastly, the team wanted to eliminate the time consuming process of modifying flight control laws, which plagued the F/A-18A/B development. This was done by incorporating a "dial-a-gain" function in the test aircraft that would allow for limited changes to control laws in order to optimize the existing OFP more efficiently rather than having to produce a new OFP every time a small gain change had to be made. The F/A-18A/B had over 110 OFP changes, over 70 of which flew on the test aircraft. In contrast, the F/A-18E/F had less than 10 OFP changes.

---

[1] Heller, Niewoehner and Lawson, "High Angle of Attack Control Law Development and Testing for the F/A-18E/F Super Hornet." *AIAA-99-4051*, August 1999.

[2] Madenwald, Niewoehner and Hoy, "F/A-18 E/F High AOA Flight Test Development Program," *SETP 1998 Report to the Aerospace Profession: Proceedings*, September 1998, pg. 128-142.

[3] Hoffman and Heller, "Development of Improved High Angle of Attack Controllability in the F/A-18E/F." *SFTE European Chapter, 10th Annual Symposium Proceedings*, Linköping, Sweden, June 1998.

This page has been deliberately left blank

Page intentionnellement blanche

Landing Approach Flying Qualities Criteria For Active Control Transport Aircraft

Edmund J. Field and Kenneth F. Rossitto
The Boeing Company
2401 E. Wardlow Road, MC C078-0420
Long Beach, CA 90807-5309
USA

David G. Mitchell
Hoh Aeronautics, Inc.
2075 Palos Verdes Drive North # 217
Lomita, CA 90717
USA

ABSTRACT

Flying qualities databases and criteria have existed for fighter aircraft for several decades. However, there have been a lack of databases and criteria for active control transport aircraft. During the 1990's Boeing undertook a series of in-flight simulation experiments to generate a comprehensive longitudinal axis database for transport aircraft in the landing approach task. This database has subsequently been applied to the more established longitudinal flying qualities criteria that were developed for fighter aircraft. This paper summarizes the results of these analyses and appraises the performance of the various criteria for application to active control transport aircraft.

INTRODUCTION

Background

The earliest flying qualities requirements for an aircraft's dynamic responses were specified in terms of the frequency and damping characteristics of its rigid body modes of motion. In the longitudinal axis these concerned the short period and phugoid modes. As long as the frequencies of the short period and phugoid modes were well separated the requirements for each mode could be specified separately. Indeed, for fighters the two modes were well separated, about a decade apart, sometimes more. Additionally, the phugoid mode was usually stable, easily controlled by the pilot, and hence not a critical issue, leaving most attention to the short period mode.

The earliest requirements for the short period dynamics were task dependent graphical boundaries delineating acceptable combinations of short period frequency and damping ratio[1]. These boundaries were given the name "thumbprints", since that is how they appeared. Since they only included requirements for short period frequency and damping, they only addressed the aircraft's angle-of-attack response. The requirements did not capture the full pitch attitude response to elevator, or the flight path response to pitch attitude.

It soon became apparent that pilots' perceptions of an aircraft's flying qualities did not correlate directly with the thumbprint boundaries. Clearly, short period frequency and damping were not sufficient metrics to fully define an aircraft's apparent flying qualities. Resulting from an analysis of stick pumping characteristics, Birhle developed the Control Anticipation Parameter[2] (CAP), which is the ratio of the initial pitching acceleration to the steady state normal acceleration. Thus, CAP explicitly introduced requirements on the consonance between the pitch attitude and flight path responses, though only implicitly on the pitch attitude and flight path responses themselves. Correlation of CAP values and pilot ratings from flying qualities experiments led to the development of boundaries for acceptable flying qualities based upon CAP. These requirements were incorporated into the US military flying qualities specifications[3] and became the accepted means to characterize an aircraft's longitudinal flying qualities.

As the performance of aircraft increased, so did the complexity of their flight control systems. The elements of the flight control systems introduced their own dynamics in addition to those of the bare airframe, which is characterized by the short period and phugoid modes. When making control inputs the pilot no longer saw the bare airframe response, but now saw the "apparent" aircraft response, the combined dynamics of the bare airframe and flight control system. As a result a pilot's perception of an aircraft's flying qualities no longer correlated with the bare airframe parameters as specified by CAP. Alternative approaches were required that could correlate the total aircraft's dynamic response to the pilot's perception of the resulting flying qualities.

Since the 1960's several approaches have been developed to characterize an aircraft's flying qualities. By placing limits on these "characteristics", they have been developed into flying qualities criteria. The less successful have fallen by the wayside, but several have stood the test of time. After considerable development they have matured into established and accepted criteria for fighter aircraft. In line with the inherent dynamics of fighter aircraft, some of these criteria neglect the contribution of the phugoid response at short period frequencies. The criteria concern mainly two flight regimes, up-and-away tracking tasks and the approach and landing task. Additional elements or developments of the criteria also address the important issue of Pilot Induced Oscillations (PIO).

Paper presented at the RTO AVT Symposium on "Active Control Technology for Enhanced Performance Operational Capabilities of Military Aircraft, Land Vehicles and Sea Vehicles", held in Braunschweig, Germany, 8-11 May 2000, and published in RTO MP-051.

Transports

The evolution to augmented control and eventually fly-by-wire control in transport aircraft followed behind the developments in fighters. Fighters fully exploited the potential of fly-by-wire control by incorporating unstable airframes with their associated performance benefits. Initially, transports have remained statically stable, only incorporating slightly reduced static stability. Hence, many of the traditional design requirements emphasizing static stability have been retained, and have been essentially sufficient.

However, these static stability requirements do not account for the higher order dynamics of the fly-by-wire control system. Clearly, high order flying qualities requirements are required for active control transport aircraft, whether reduced static stability or not.

The main area of attention for transports is the terminal area, specifically the approach and landing task. Up-and-away flying qualities are less of a concern, although they should still be well behaved and predictable. An important consideration is high altitude flight, an area which is seldom flown manually on modern transports. If the flying qualities at high altitude are appreciably different from those at low altitude, with which the pilot is far more familiar, a pilot may adopt an improper control technique if he has to take manual control, such as after an autopilot disconnect.

The requirements for transports in up-and-away flight are very different from those for fighters, which are required to perform aggressive maneuvering. However, in the landing approach the task is similar to that for fighters, and so it is reasonable to consider the flying qualities criteria that were developed for fighters in this task.

However, there are distinct differences in the responses of the two classes of aircraft. Specifically, the separation between the short period and phugoid modes is not as great in transports as in fighters, the two modes often being in the same decade. As a result, the simplification that is employed in the analysis of many fighters, of neglecting the contribution of the phugoid response at short period frequencies, may not be successful in transports.

Databases

The results presented in this paper include only those configurations from the Boeing experiments. When developing the new criteria boundaries other databases were also considered. A review of available databases determined that the only applicable ones were those generated by Calspan during three experiments during the 1980's[4,5,6]. Additionally, only selected configurations from those databases were applicable, specifically, those that represented a conventionally configured aircraft (long aft tailed) and that exhibited a conventional response-type (angle-of-attack like). For clarity, only the Boeing configurations are presented in this paper.

THEORY

For pitch axis control tasks, pilots require precise and predictable control of pitch attitude and flight path, and their respective rates, pitch rate and normal acceleration. Therefore, most pitch axis flying qualities criteria address at least one of these responses, as do all the criteria appraised in this paper.

The frequency range of primary interest for piloted control is that between 0.1 and 10 rad/sec. Therefore, only the dynamics that affect the aircraft responses in this frequency range are of interest from a flying qualities, and hence flying qualities criteria, perspective. As discussed earlier, for most fighter aircraft the short period and phugoid modes are usually well separated. Hence, the phugoid can be neglected for flying qualities analyses concerning the short period maneuvering mode. The reduced order, constant speed approximation, transfer functions, commonly used in fighter flying qualities analyses, are:

$$\frac{\theta(s)}{\delta_{CC}(s)} = \frac{K_\theta\left(s + 1/\tau_{\theta_2}\right)}{s\left[s^2 + 2\zeta_{sp}\omega_{sp}s + \omega_{sp}^2\right]}$$

$$\frac{\gamma_{CG}(s)}{\delta_{CC}(s)} = \frac{K_{\gamma_{CG}}}{s\left[s^2 + 2\zeta_{sp}\omega_{sp}s + \omega_{sp}^2\right]}$$

$$\frac{q(s)}{\delta_{CC}(s)} = \frac{K_q\left(s + 1/\tau_{\theta_2}\right)}{\left[s^2 + 2\zeta_{sp}\omega_{sp}s + \omega_{sp}^2\right]}$$

$$\frac{n_{z_{ICR}}(s)}{\delta_{CC}(s)} = \frac{K_{n_z}}{\left[s^2 + 2\zeta_{sp}\omega_{sp}s + \omega_{sp}^2\right]}$$

As long as the short period and phugoid modes are well separated, the reduced order transfer functions above adequately represent the maneuvering response of the aircraft. Correlation of observed flying qualities with parameters obtained from analyses using these transfer functions is usually successful. For transport aircraft where the phugoid is usually above 0.1 rad/sec and not well separated from the short period, contributions from the phugoid dynamics may be appreciable at short period frequencies. In these cases it is necessary to consider the full order, three degree of freedom model, which for a conventional unaugmented aircraft has the following transfer functions:

$$\frac{\theta(s)}{\delta_{CC}(s)} = \frac{K_\theta\left(s + 1/\tau_{\theta_1}\right)\left(s + 1/\tau_{\theta_2}\right)}{\left[s^2 + 2\zeta_p\omega_p s + \omega_p^2\right]\left[s^2 + 2\zeta_{sp}\omega_{sp}s + \omega_{sp}^2\right]}$$

$$\frac{\gamma_{CG}(s)}{\delta_{CC}(s)} = \frac{K_{\gamma_{CG}}\left(s + 1/\tau_{\gamma_{CG_1}}\right)\left(s + 1/\tau_{\gamma_{CG_2}}\right)\left(s + 1/\tau_{\gamma_{CG_3}}\right)}{\left[s^2 + 2\zeta_p\omega_p s + \omega_p^2\right]\left[s^2 + 2\zeta_{sp}\omega_{sp}s + \omega_{sp}^2\right]}$$

$$\frac{q(s)}{\delta_{CC}(s)} = \frac{K_q s\left(s + 1/\tau_{\theta_1}\right)\left(s + 1/\tau_{\theta_2}\right)}{\left[s^2 + 2\zeta_p\omega_p s + \omega_p^2\right]\left[s^2 + 2\zeta_{sp}\omega_{sp}s + \omega_{sp}^2\right]}$$

$$\frac{n_{z_{ICR}}(s)}{\delta_{CC}(s)} = \frac{K_{n_z}\left(s+1/\tau_{n_{z1}}\right)\left(s+1/\tau_{n_{z2}}\right)\left(s+1/\tau_{n_{z3}}\right)\left(s+1/\tau_{n_{z4}}\right)}{\left[s^2+2\zeta_p\omega_p s+\omega_p^2\right]\left[s^2+2\zeta_{sp}\omega_{sp}s+\omega_{sp}^2\right]}$$

While the transfer functions for pitch attitude and pitch rate above may be familiar, those for flight path angle and normal acceleration at the pitch Instantaneous Center of Rotation (ICR) may need a little explanation.

For flying qualities analyses flight path angle is usually considered at two locations, the center of gravity and the pilot station. The center of gravity represents "where the aircraft is going", which is what the pilot is trying to control, while the pilot station represents "what the pilot sees". During maneuvering flight the two are not the same. Also of interest during landing tasks may be flight path at the main gear, but this is usually close to that at the center of gravity. The transfer function given above is for flight path at the center of gravity. The lowest frequency zero $1/\tau_{\gamma_1}$ is below phugoid frequencies and determines whether the aircraft is on the front or back side of the drag curve. The other two zeros are of similar frequency to one another, but in opposite halves of the 's' plane. Their frequencies are above that of the short period. Their 's' plane location determines the degree of non-minimum phase in the flight path response due to the pitch ICR. For a conventional aft tail configuration, at the pilot station these two zeros combine to form a complex pair that provide an initial lead in the flight path response at this location. Their frequency is slightly faster than the short period mode.

Normal acceleration is a scaled derivative of flight path, and so shares similar zero locations. As with flight path, normal acceleration can be measured at any location on the aircraft. One common location (especially for Low Order Equivalent Systems analyses) is the pitch ICR. The ICR is the point on the aircraft that exhibits no initial normal acceleration due to pitching. For a conventional aircraft, it is located between the center of gravity and the pilot station, closer to the former. Thus, normal acceleration measured at the ICR contains no contributions from pitching activity. For conventional transports, at the ICR the two lowest frequency zeros are below 0.1 rad/sec and the highest frequency zero is well above 10 rad/sec. Although outside the range of 0.1 to 10 rad/sec, the residuals from these three zeros can also influence the response within the frequency range of interest, and so cannot be entirely neglected. The remaining zero, $1/\tau_{n_{z3}}$, is usually between 0.1 and 10 rad/sec and so must be considered.

THE DATABASE

The database developed in the Boeing experiment totals 25 conventional response-type configurations, that were used for the criteria development reported here. The aircraft model used for the evaluations represented a large advanced technology active control transport aircraft in the one million pound category. The configurations were designed using a Low Order Equivalent Systems approach and included variations in pitch acceleration sensitivity (n/α), equivalent short period frequency (ω_{sp}') by the way of a selected CAP level, and equivalent time delay (T_θ). Additionally, two pitch sensitivities were evaluated. All seventeen dynamic variation configurations were evaluated with a pitch sensitivity of 0.3 deg/sec^2/lb. Additionally, eight of these were evaluated at an increased pitch sensitivity of 0.45 deg/sec^2/lb. Details of the configurations and experiment implementation can be found in Field and Rossitto[7]. This paper only includes the seventeen lower pitch sensitivity configurations, although reference is made to the higher sensitivity configurations.

The experiment used the Calspan operated USAF Total In-Flight Simulator (TIFS). Five experimental test pilots participated in the evaluations, which consisted of a lateral offset approach corrected at around 200 feet AGL and flown to a simulated eye-height landing. Pilot comments were recorded throughout the evaluations for subsequent analysis. Task performance metrics and pilot awarded Cooper-Harper and PIO ratings were recorded.

THE CRITERIA

Four established flying qualities criteria were applied to the Boeing database to appraise their performance as predictors of the flying qualities of transport aircraft in the approach and landing task. All these criteria were developed for fighter aircraft. Some of the criteria, or elements of the criteria, were developed for up-and-away tracking tasks and may not be applicable to the active control transport aircraft landing task.

Flying qualities criteria vary in the way that they consider the contributions of the feel system dynamics. Some criteria include the feel system in their analyses, others exclude the feel system, and others can be applied either way (although different criteria boundaries apply). The preferred approach followed here is to exclude the feel system, unless the criterion specifically calls for its inclusion, in which case that will be noted.

It is recognized that the feel system is an integral element of any aircraft's flight control system. However, there are many issues with feel systems that can introduce problems into an aircraft's flying qualities. The cause of these problems can be hidden when including the feel system in the flying qualities analysis, hence the decision to exclude the feel system from the analyses. Separate criteria should then be applied to the feel system, ensuring that it is tuned to the aircraft's dynamics and will introduce no deficiencies. Currently, there is a lack of such requirements.

Control Anticipation Parameter (CAP) through Low Order Equivalent Systems (LOES)

CAP is defined as the ratio of the initial pitch acceleration divided by the steady state normal acceleration. It is therefore a measure of the predictability of the long term response from the initial response that the pilot observes. Consistant with most criteria, it was based on the short period approximation, permitting the following approximations to be made:

$$\mathrm{CAP} \equiv \frac{\ddot{\theta}_0}{n_{z_{ss}}} \approx \frac{\omega_{sp}^2}{n/\alpha} \approx \frac{\omega_{sp}^2}{\frac{V}{g}1/\tau_{\theta_2}} \qquad \textbf{(Eq. 1)}$$

As discussed above, the CAP requirements formed the basis for specifying the short period frequency requirements of the US military flying qualities specifications[3] for unaugmented aircraft. While CAP does not explicitly define either the pitch attitude or flight path responses, it does so implicitly as a measure of the consonance between the pitch attitude and flight path responses. As aircraft flight control systems became more complex the bare airframe short period dynamics no longer described the total aircraft's dynamic response. As a result CAP, which was a measure of the bare airframe response, was no longer able to capture the flying qualities of the augmented aircraft that were apparent to the pilot.

However, the concept behind CAP remained valid. Regardless of how the aircraft response was produced, the precision and predictability of the aircraft's pitch attitude and flight path responses would still dictate the pilot's perception of the aircraft's flying qualities. CAP simply specified the desired characteristics of the pitch attitude and flight path responses, not how they are generated. It was therefore postulated that the requirements that previously were developed for an unaugmented aircraft should also apply to the "apparent" response of an augmented aircraft that the pilot observed. Thus, if a means could be derived to determine this "apparent" response, then the CAP criterion, and the military specification, could be retained.

The method that gained greatest acceptance was the frequency domain Low Order Equivalent Systems (LOES) approach. This method involves a frequency-domain matching of a Low Order Equivalent System to the aircraft model, that includes all the modes of the bare airframe plus all elements of the flight control system. Appropriate choice of the form of the LOES is important. The LOES must match the response-type of the augmented aircraft. Additionally, the LOES must properly represent all the dynamics in the frequency range over which the match is performed. For piloted control the frequency range of interest is from 0.1 to 10 rad/sec.

MIL-F-8785C[8] was the first specification to require the application of an "equivalent" model, although did not provide detailed guidance for the method. The replacement, MIL-STD-1797A[9], requires a simultaneous match to pitch rate and normal acceleration (at the ICR) responses for both control force and position inputs, over a frequency range of 0.1 to 10 rad/sec. The numerator for the normal acceleration response is specified to be only a single first-order lag, $1/\tau_{h_1}$. Although the full-order model is specified in MIL-STD-1797A, for fighters it is common neglect the short period mode and use the two-degree-of-freedom forms for these responses. While this is sufficient for fighters, for active control transport aircraft it is necessary to include the phugoid mode, and so the full order aircraft model is used. Additionally, as discussed above, for the transport aircraft angle-of-attack response-type configurations of this paper it has been found that the fourth order normal acceleration at ICR transfer function is most appropriate. While $1/\tau_{n_{z_1}}$ and $1/\tau_{n_{z_2}}$ are usually below the fit range (below 0.1 rad/sec) and $1/\tau_{n_{z_4}}$ is usually well above the fit range (above 10 rad/sec), $1/\tau_{n_{z_3}}$ is usually within the fit range.

Thus, for active control transport aircraft the following low order forms are used:

$$\frac{q(s)}{\delta_{CC}(s)} = \frac{K_q s\left(s+1/\tau_{\theta_1}\right)\left(s+1/\tau_{\theta_2}\right)e^{-T_\theta s}}{\left[s^2+2\zeta_p'\omega_p's+\omega_p'^2\right]\left[s^2+2\zeta_{sp}'\omega_{sp}'s+\omega_{sp}'^2\right]}$$

$$\frac{n_{z_{ICR}}(s)}{\delta_{CC}(s)} = \frac{K_{n_z}\left(s+1/\tau_{n_{z_1}}\right)\left(s+1/\tau_{n_{z_2}}\right)\left(s+1/\tau_{n_{z_3}}\right)\left(s+1/\tau_{n_{z_4}}\right)e^{-T_{n_z}s}}{\left[s^2+2\zeta_p'\omega_p's+\omega_p'^2\right]\left[s^2+2\zeta_{sp}'\omega_{sp}'s+\omega_{sp}'^2\right]}$$

In addition to the dynamics discussed earlier, these forms include a time delay. This time delay element is included in the matching algorithm to account for the combined phase lags in the high order aircraft that are not accounted for by the equivalent roots of the transfer functions. A simultaneous fit is performed between the pitch rate and normal acceleration responses to ensure correct definition of the high frequency zero in the pitch rate transfer function, $1/\tau_{\theta_2}$.

The equivalent parameters ω_{sp}' and $1/\tau_{\theta_2}$ obtained from this low-order matching are then applied to the CAP criterion. The equivalent time delay, T_θ, which approximates the phase loss due to high-frequency dynamics, is compared against the Level boundaries for acceptable time delay. Separate requirements also exist for equivalent short period damping, ζ_{sp}'.

Bandwidth Criteria

A measure of the pitch axis handling qualities of an aircraft is its stability margins when operated in a closed-loop compensatory tracking task. The maximum frequency at which such closed-loop tracking can take place without threatening stability is defined as the pitch attitude Bandwidth (ω_{BW_θ}). It follows that aircraft capable of operating at a large enough value of bandwidth will have superior performance when regulating against disturbances. No assumption of pilot dynamics is necessary in applying the requirement, since any such assumption would simply shift the boundaries. Additionally, the criterion is identically applicable to all response-types and to both the reduced and full order aircraft models. No assumption of the aircraft order is necessary because the criterion uses the actual frequency response. A detailed description of the calculation of the Bandwidth criterion parameters can be found in Mitchell et al[10].

The flight path Bandwidth (ω_{BW_γ}) criterion requirement is an auxiliary requirement intended to insure that the consonance between flight path and pitch attitude is consistent with the pilot's expectations. When pitch attitude is the primary short-term controller of flight path, excessive abrupt or sluggish flight path response to attitude changes will cause problems for precise control and possibly lead to pilot induced oscillations.

The phase delay parameter (τ_{p_θ}) is a measure of the shape of the phase response at frequencies above the 180° phase lag frequency. Phase delay is similar to the equivalent time delay

from the LOES fit, and is a correlating parameter with PIO tendencies.

The original limits of the Bandwidth criteria, developed for fighters, were considered overly stringent. A major reduction in the limits was made when the pitch rate overshoot / dropback portion of Gibson's criteria was incorporated as an auxiliary requirement. Experience proved the time domain overshoot / dropback criteria difficult to verify in flight, so a frequency domain version of pitch rate overshoot replaced the time domain requirement. The current criteria consist of limits on pitch attitude Bandwidth frequency and phase delay, flight path Bandwidth, and pitch rate overshoot. The flying qualities Levels for these criteria are now in close agreement with the limits on CAP and equivalent time delay given in this paper.

Gibson Criteria

Gibson developed a series of flying qualities design guidelines for fighter aircraft that have become labeled the "Gibson Criteria". Gibson, himself, states that they are "less a set of precise criteria to be followed in design than observations of a general connection between physical measures of response characteristics and pilot opinion"[11]. Further, he states that the purpose of his criteria is "to provide control law design guidance, on the assumption that the FCS is going to be used to optimise handling rather than just for some augmentation, and they were never intended for general purpose handling analysis".

Consistent with most criteria developed for fighter aircraft, Gibson considers only the reduced order aircraft model. As discussed above, this approach may not be appropriate for transport aircraft. Also, Gibson excludes the feel system dynamics from his analyses, considering that these can be designed to be well behaved and non-intrusive.

Gibson's early work involved a series of frequency response templates, that were drawn around the best rated configurations of the Neal-Smith[12] and LAHOS[13] experiments. These boundaries were plotted on the Nichols chart and provided insight into both the gain and phase characteristics of the pitch attitude response. The boundaries were intended to ensure a "desirable" response shape in the range of the crossover frequency, approximately that of an unaugmented aircraft's short period. The templates were aimed at ensuring desirable *flying qualities*, ending at a phase of around -160°, short of the "*PIO region*".

Due to the problems inherent in all criteria based on response templates, Gibson dropped the frequency response boundaries as a way of defining the short-term like dynamics, moving instead to the time domain.

In the time domain Gibson developed two criteria for the specification of the short-term dynamics. His requirements on pitch attitude dropback (to a boxcar control input) effectively determined the flight path responsiveness, for the given $1/\tau_{\theta_2}$. Initially Gibson published boundaries defining desirable areas of dropback as a function of pitch rate overshoot. More recently he has dropped the boundaries, relaxing the guideline to specify the ideal of zero dropback for tight pitch tracking tasks. However, zero pitch attitude dropback can result in a sluggish flight path response for tasks that require flight path changes. Gibson indicates that a wide range of dropback may be acceptable for such tasks depending on flight condition, for example the approach and landing in which dropback greater than 1.0 may appear excessively abrupt.

His second time domain criterion places limits on the flight path time delay, t_γ. This is a measure of the delay in the development of the response of the flight path to a control input. For the reduced order approximation of a conventional aircraft it is purely a function of short period frequency and damping, as given in Equation 2. Combining Equation 1 and Equation 2, t_γ can be written in terms of CAP, as given in Equation 3. Gibson suggests limits for acceptable values of flight path time delay of 1 second for up and away tasks, and 1.5 seconds for approach and landing tasks.

$$t_\gamma = \frac{2\zeta_{sp}}{\omega_{sp}} \qquad \textbf{(Eq. 2)}$$

$$t_\gamma = \frac{2\zeta_{sp}}{\sqrt{\mathrm{CAP}(n/\alpha)}} \qquad \textbf{(Eq. 3)}$$

Much of Gibson's work has been aimed at addressing the specific flying qualities phenomenon of PIO. Here, Gibson works in the frequency domain. Gibson considers the area around the phase of -180° in the pitch attitude to stick position frequency response. Phase rate is defined as the slope of the phase response in the frequency range between the phase at -180° and twice that frequency. Except for a scaling factor, Gibson's phase rate is identical to Phase Delay of the Bandwidth Criterion. However, Gibson plots phase rate against the frequency at -180° phase, compared to -135° for the Bandwidth criterion. Hence, Gibson's phase rate requirement is only concerned with the response at frequencies beyond the -180° frequency, the PIO region. In comparison, the Bandwidth Criterion also considers the shape of the response between -135° and -180°, the flying qualities region. As long as the frequency response between -135° and -180° is well behaved, both requirements should yield virtually identical results.

Smith-Geddes Criteria

Smith and Geddes have developed criteria for both flying qualities and PIO, all based in the frequency domain. Application of the criteria is referenced to force inputs, and so must include the feel system dynamics for position command systems. The results presented in this paper include the feel system dynamics. They define two requirements addressing flying qualities. The first is a requirement on the slope of the pitch attitude to stick force gain response in the crossover region, between 1.0 and 6.0 rad/sec. They define that for Level 1 flying qualities this slope must be less than -2 dB/Octave. While this is a requirement for Level 1 flying qualities, it does not guarantee Level 1 flying qualities. This requirement is designed to ensure a K/s like response in the crossover region, which is desirable for closed loop attitude

tracking tasks. However, it also allows for K/s^2 and greater slopes, which it is known can be undesirable.

The attitude phase criterion places limits on the pitch attitude phase angle at the criterion frequency, ω_c, which is calculated from the gain response slope in the crossover region:

$$\omega_c = 0.24s + 6 \quad \text{(rad/sec)} \qquad \textbf{(Eq. 4)}$$

where s is the slope in the crossover region. Level 1 and Level 2 limits are defined as -123° and -165°, respectively.

Addressing the phenomenon of PIO, Smith and Geddes define three types of PIO:

Type I Initiated by resonance of pilot-in-the-loop control of attitude and pilot switches from attitude control to acceleration control;

Type II Initiated by resonant open loop dynamics; and

Type III Initiated by resonance of the pilot-in-the-loop control of attitude, regardless of acceleration dynamics, and with no mode switching by the pilot.

Type III (attitude-dominant) PIO is predicted if the phase angle at the criterion frequency is more negative than -180°. Type II PIO is predicted whenever any open-loop mode has a damping ratio less than 0.2. To predict Type I (acceleration-dominant) PIO an additional parameter is defined, the Normal Acceleration Phase Parameter:

$$\Phi(j\omega_c) = \angle \frac{n_{z_{ps}}}{F_{cc}}(j\omega_c) - 14.3\omega_c \qquad \textbf{(Eq. 5)}$$

Type I PIO is predicted when the Normal Acceleration Phase Parameter is less than -180°, provided that the attitude phase is less than -165°.

RESULTS

For clarity, the results presented only include the Boeing configurations. However, in determining the new boundaries for the CAP and Bandwidth criteria the other Calspan configurations were included. For the Gibson and Smith-Geddes criteria only the Boeing configurations have yet been analyzed. Further analysis is required before changes to these criteria can be recommended.

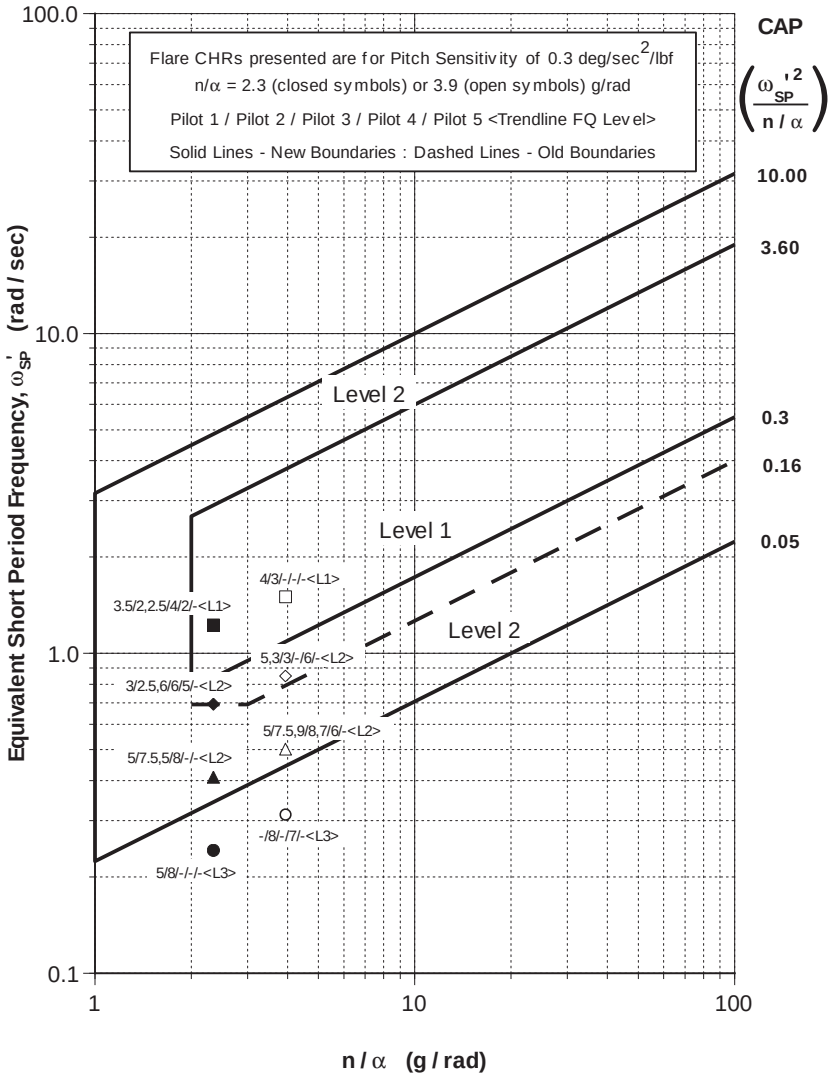


Figure 1. CAP Short Period Frequency Results

For each configuration of the Boeing TIFS experiment a "Trendline flying qualities level" was assigned[7]. This was determined from the individual Cooper-Harper ratings awarded, the median Cooper-Harper rating, the pilot comments and achieved performance. Additionally, model following and atmospheric condition issues were considered when weighting the relative contribution of the individual ratings. In the following sections only the trendline flying qualities level is annotated next to each configuration in the Figures, except in Figures 1 and 2 in which all the flare Cooper-Harper ratings are presented. Similarly, each configuration was assigned an overall PIO tendency and PIO severity classification. These classifications were based on pilot comments and, where available, PIO ratings.

In the criteria result Figures the configurations are identified by their LOES parameters. All configurations have an equivalent short period damping ratio of 0.7. Closed symbols represent configurations with an n/α of 2.3 g/rad, while open symbols represent an n/α of 3.9 g/rad. The shape of the symbol defines the value of CAP (see Figures 1 and 2). Equivalent time delay is annotated next to each configuration, except in Figures 1 and 2.

Control Anticipation Parameter (CAP) through Low Order Equivalent Systems (LOES)

In Figure 1 the configurations with no added time delay (minimum time delay of 0.125 seconds) are plotted against the CAP criterion requirements taken from MIL-STD-1797A, on the form of the requirement from MIL-F-8785C. Clearly, the existing Level 2 lower boundary is supported by these data. The published Level 1 lower boundary (dashed line) appears to be too relaxed. The modified lower Level 1 boundary, consistent with the data, has been established at a CAP of 0.3.

In addition to the requirements on CAP, MIL-STD-1797A also defines limits on acceptable levels of time delay. These separate requirements have been combined schematically in Figure 2 (dashed lines), together with the results of the Boeing experiment. Clearly the results reflect a multi-parametric correlation between CAP and time delay. This multi-parametric correlation is not reflected in the published requirements (dashed lines), but is reflected in the new boundaries developed from the database. The new boundaries stop as shown since there is no data to determine their extensions. The upper CAP limits of 3.6 for Level 1 and 10 for Level 2 are shown for equivalent time delays between 0 and 0.1 sec, taken directly from the limits of Figure 1.

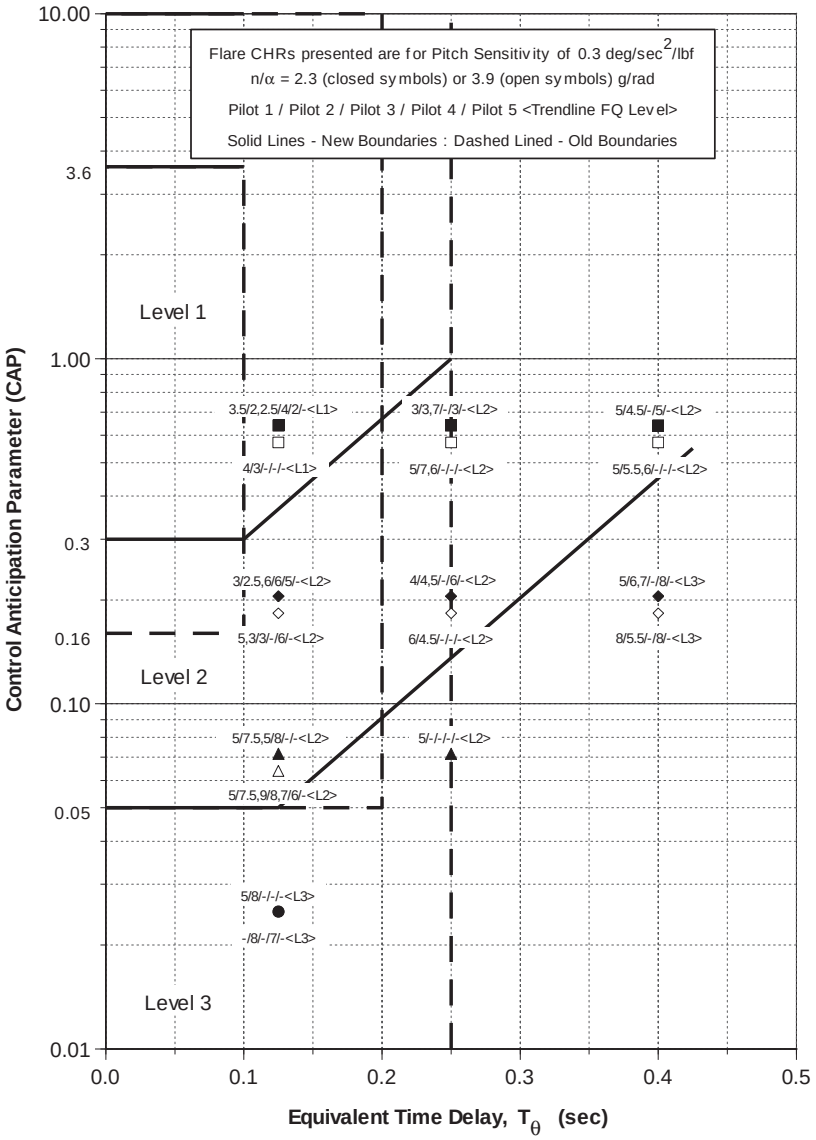


Figure 2. CAP / Time Delay Results

Bandwidth Criteria

The results from the Boeing experiment are applied to the pitch attitude Bandwidth / phase delay criterion in Figure 3. The old boundaries (solid line, Level 1 and dashed line, Level 2) are based on those proposed by Mitchell et al.[10], and have been adjusted to reflect the removal of the feel system in the application of the criterion. Clearly the data support the criterion, however, support relaxing the Level 2 boundary to the solid line shown. As discussed in Field and Rossitto[7], the reason for this dramatic relaxation of the Level 2 boundary is pitch control / response sensitivity.

The original boundaries were developed from the configurations of the Calspan experiments[5,6] which employed a pitch sensitivity of 0.42 deg/sec^2/lb. These boundaries correlated with the seven increased sensitivity configurations of the Boeing experiment, which employed a pitch sensitivity of 0.45 deg/sec^2/lb. Clearly the effects of control / response sensitivity on flying qualities must be considered, although sufficient requirements are currently lacking.

Consistent with the modifications to the boundaries for the pitch attitude Bandwidth / phase delay requirements, the data also support the relaxation of the Level 2 boundary for the pitch attitude / flight path Bandwidth requirements as shown in Figure 4. Insufficient data exist to determine whether changes to the slopes of these boundaries may be appropriate. It should be noted that two configurations rated Level 3 plot in the Level 2 region. This is because this requirement is auxiliary to that for pitch attitude Bandwidth / phase delay. These configurations correctly plot in the Level 3 region of the pitch attitude Bandwidth / phase delay requirement. Hence, the two requirements must be applied together.

The pitch attitude Bandwidth / phase delay requirements have been further developed as a PIO criterion[14]. The Boeing configurations are plotted in the somewhat busy Figure 5, annotated with their observed PIO severity. It should be noted that the pitch rate overshoot ($\Delta G(q)$) requirements were met for all configurations. A few configurations are noteworthy. Two configurations with low bandwidths plot in the Level 3 region with a prediction of "Severe" PIO, and yet were observed to only exhibit Moderate PIO. These mismatches are not of concern, since the configurations

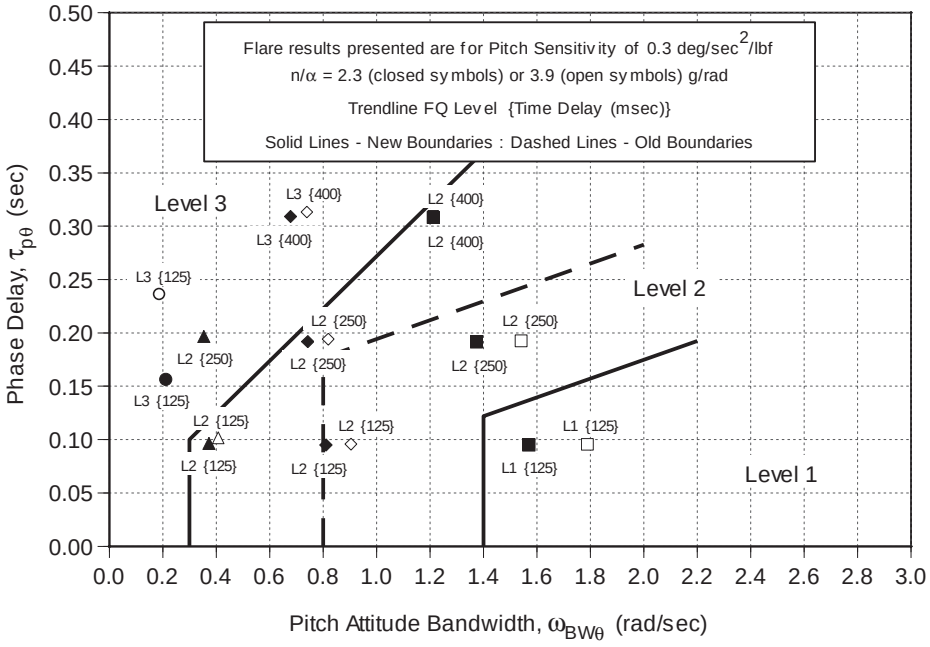


Figure 3. Pitch Attitude Bandwidth Results

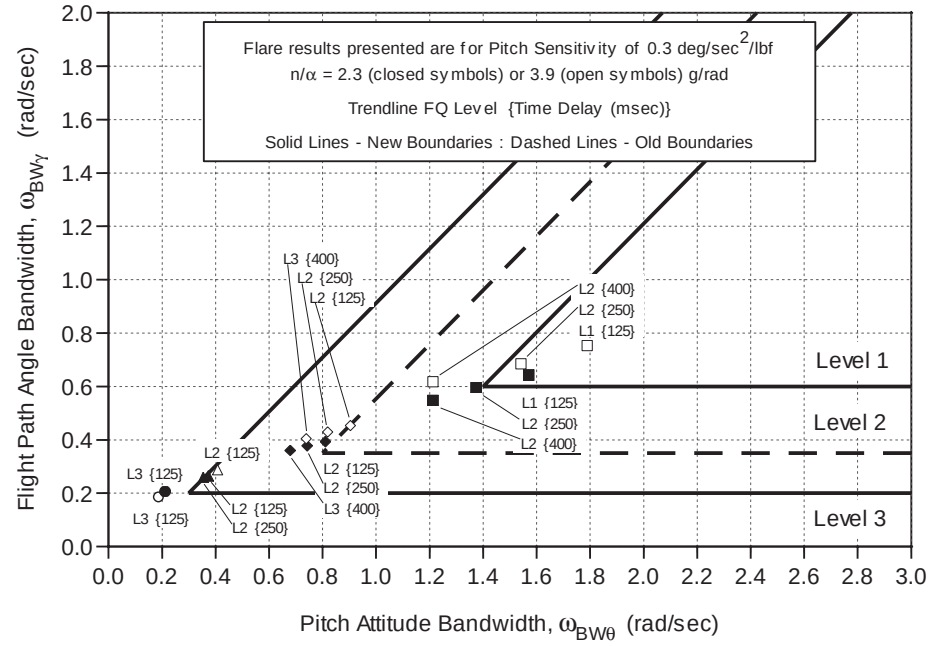


Figure 4. Flight Path Bandwidth Results

exhibited poor flying qualities and in time might well be expected to exhibit more severe PIO, if pilot gain were increased. Of more concern is the over-prediction of PIO severity in the Level 2 flying qualities region. For all these configurations the flight path Bandwidth was less than 0.6 rad/sec, resulting in a prediction of Level 3 flying qualities with "Severe" PIO. However, no worse than Moderate PIO was observed for any of these configurations. Once again, the classifications of the *criterion* were based on the results of the Calspan experiments[5,6] that used the increased pitch sensitivity of 0.42 deg/sec^2/lb. As discussed in Mitchell and Field[14], the combined effect of high pitch sensitivity with time delay (high phase delay) is increased PIO tendencies. Hence, for the lower pitch sensitivity configurations of this database it is recommended that this area be re-classified as predicting Moderate PIO. Otherwise, the Boeing database concurs with the Bandwidth PIO criterion.

Gibson Criteria

The results from Gibson's phase rate analyses are presented in Figure 6 and Figure 7. In the former, the configurations are annotated with their observed flying qualities, while in the latter they are annotated with their observed PIO severity. The distribution of the configurations in Figure 6 is almost identical to that for pitch attitude Bandwidth / phase delay in Figure 3. While phase rate and phase delay are identical (except for a scaling factor), differences in horizontal distribution between the criteria is possible if the responses between -135° and -180° are unconventional. The similarity between the two figures reflects the very conventional nature of the Boeing experiment configurations. Although Gibson's Level 1 boundary is close to correlating with the data, the Level 2 boundary is clearly too restrictive.

The phase rate criterion is not intended as a predictor of flying qualities, but of PIO severity. In Figure 7 observed PIO severity is annotated next to each configuration. Again, the distribution of the configurations is almost identical to that in Figure 5 for the Bandwidth PIO criterion. It is observed that the published boundaries are far too restrictive, although they do follow the form of the data. Further analysis, including the addition of the Calspan configurations, is required before new boundaries could be determined.

Due to the insufficient separation between the short period and phugoid modes of the configurations, determination of the time domain parameters from the full order aircraft model was not successful, especially for the slower configurations. As a result the reduced order model was used, developed from the parameters from the equivalent systems analyses.

The results of the dropback analyses are presented in Figure 8. Correlation of the results with the observed flying qualities is poor. Never the less, several interesting observations can be made. First, the addition of time delay moves the configuration to the left. In some cases this could be interpreted as an improvement in flying qualities. Second, the difference between the two values of n/α (open versus closed symbol) is far more evident than for the CAP or Bandwidth criteria (compare Figure 8 with Figures 2 and 3). As stated earlier, the ideal of zero dropback is specified for tight pitch tracking tasks. It is not clear what are the dropback requirements for the landing task, if applicable at all.

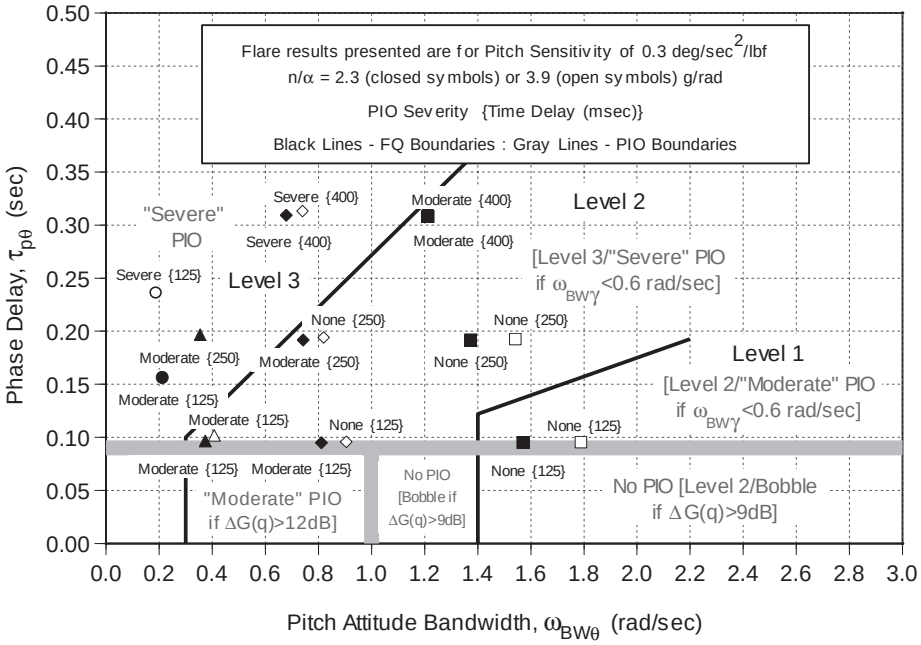


Figure 5. Bandwidth PIO Criterion Results

The results of the flight path time delay analyses are presented in Figure 9. The boundaries of Figure 9 are an exact transformation of those for CAP from Figure 1, transformed via Equation 3, for a short period damping ratio of 0.7. However, whereas the results for CAP in Figure 1 are only applicable to the short period dynamics without added time delay, all configurations are plotted on Figure 9, since the addition of time delay only increases the flight path time delay (moves the configuration up in Figure 9). And this produces an inconsistency in the results. Configurations with shorter flight path time delays are rated worse than those with longer flight path time delays, due to the added equivalent time delay. Clearly the equivalent short period dynamics are more dominant in determining t_γ than is the equivalent time delay.

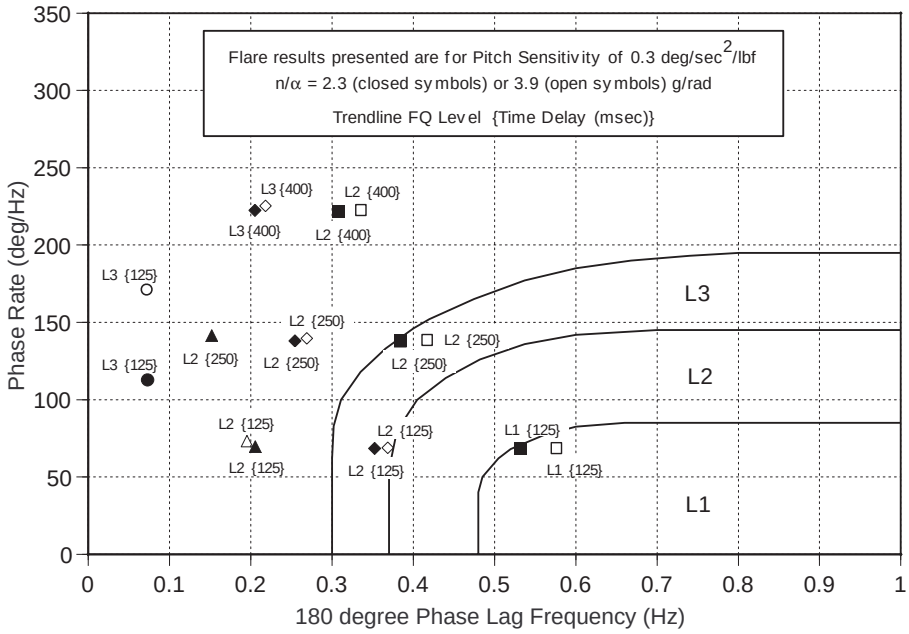


Figure 6. Phase Rate Results versus Flying Qualities

Gibson suggests upper limits for t_γ of 1.0 sec for up and away tasks and 1.5 sec for landing. A horizontal line has been drawn across Figure 9 at 1.5 sec, representing the upper limit for landing. Clearly, the two configurations rated Level 1 fall below this limit, correlating with Gibson's requirement. However, three configurations rated Level 2 also fall below the 1.5 sec limit line. It is interesting to note that the results appear to be dependent upon n/α, that is correlation of the results follow the diagonal boundaries converted from CAP. Since n/α generally increases with speed, it is fair to assume that for up and away tasks n/α will be greater than for landing. Thus Gibson's lower limit on t_γ for up and away tasks is reflected by the diagonal boundaries converted from CAP.

In summary, for the conventional configurations considered, the form of Gibson's phase rate requirements correlate with the Boeing results, although the boundaries appear over-restrictive. In the time domain, problems were encountered due to the insufficient separation between the short period and phugoid modes, a feature of transport aircraft. Application of the criteria to the reduced order approximations provides some insight, but correlation with the observed flying qualities appears poor. Some of the

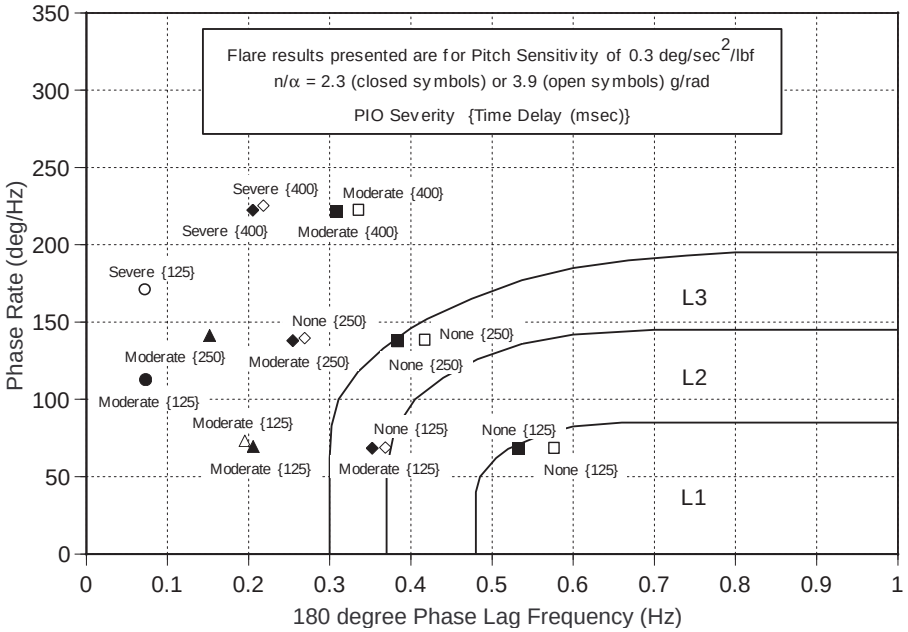


Figure 7. Phase Rate Results versus PIO Severity

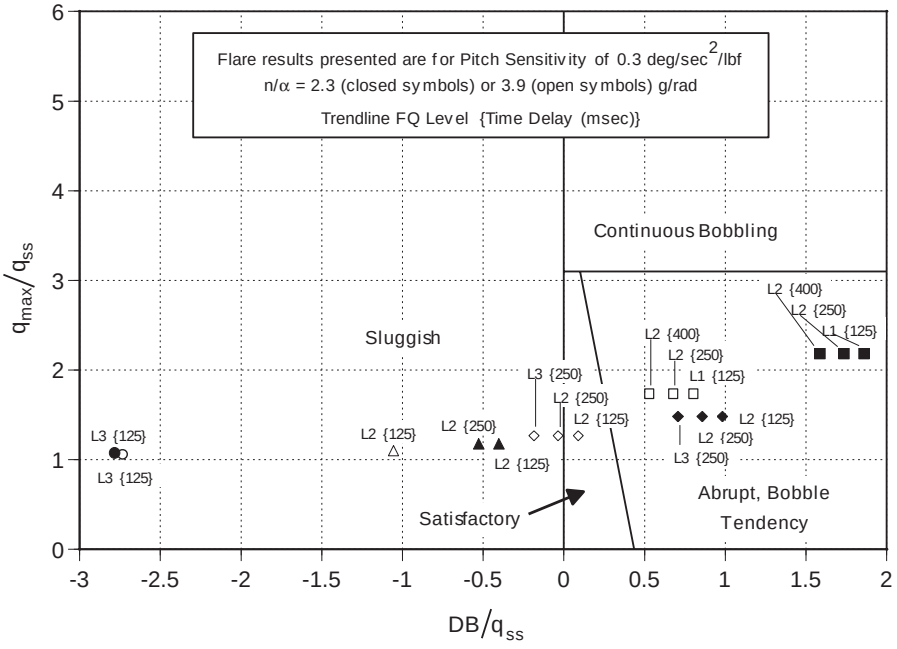


Figure 8. Dropback Results

problems encountered are due to the application to Level 2 and Level 3 configurations. As Gibson states, the purpose of his criteria are to optimise handling, they were never intended for general purpose handling analysis.

Smith-Geddes

The results of the Smith-Geddes slope criterion analyses determined all configurations to have a slope more negative than -2 dB/Octave. Thus, all configurations passed this requirement, which is necessary, but not sufficient for Level 1 flying qualities. These results properly correlate with the two Level 1 configurations. The attitude phase criterion analyses determined all configurations to have a pitch attitude phase angle at the criterion frequency of less than -165°, and so all were predicted Level 3. Clearly, this latter criterion does not correlate with the observed flying qualities.

The pitch attitude phase angle is plotted against the criterion frequency in Figure 10. Clearly, all configurations have a pitch attitude phase angle less than -180°, and so are predicted to exhibit Type III PIO. Due to these predictions, it is not necessary to calculate the normal acceleration phase parameter. It can be seen in Figure 10 that of the 17 configurations, PIO was observed with only eight, three exhibited a tendency to PIO while six exhibited no PIO tendencies. Clearly the predicted PIO tendencies do not correlate with those observed.

CORRELATION OF THE CRITERIA

While the various criteria appraised in this paper all address pitch axis flying qualities, they all define different parameters that they correlate with observed flying qualities. As has been shown in this paper several of these parameters are similar. Others are unique to a specific criterion. Low Order Equivalent Systems defines equivalent modal parameters from the high order aircraft frequency response, thus preserving classical modal criteria such as CAP. The other three criteria, in the frequency domain, all consider the overall aircraft frequency response, irrespective of order.

With the adoption of the multi-parametric boundaries for the CAP / time delay requirement, the form of this requirement and the pitch attitude Bandwidth requirement are now similar. However, the two requirements are not identical. The CAP / time delay requirement includes a measure of the consonance between the pitch attitude and flight path responses, and has a separate requirement for equivalent short period damping. In comparison, pitch attitude Bandwidth includes consideration of the short period damping, and has a separate requirement for the consonance between the pitch attitude and flight path responses. Therefore, results from these two criteria may differ for aircraft with damping ratios distant from 0.7. Additionally, two configurations with the same CAP but different values of $1/\tau_{\theta_2}$ can have appreciably different Bandwidths.

Gibson's phase rate requirement is of similar form to the pitch attitude Bandwidth requirement, both giving almost identical results, unless the phase response between -135° and -180° is unconventional. Indeed, phase rate and phase delay are identical to one another, except for a scaling factor. They are also similar to equivalent time delay.

Gibson's flight path time delay parameter maps well with the CAP criterion, for the minimum time delay configurations. With the addition of time delay to the configurations, correlation was less clear. The effect of changes in $1/\tau_{\theta_2}$ on t_γ were shown, exposing a correlation between n/α and observed trends in preferences for t_γ.

The Smith-Geddes criteria do not appear to correlate with any of the other criteria, nor with the experiment results.

Despite these various correlations, each criterion is a measure of a combination of different parameters. As a result, it is not possible to achieve an exact correlation of the criteria boundaries for all parameters.

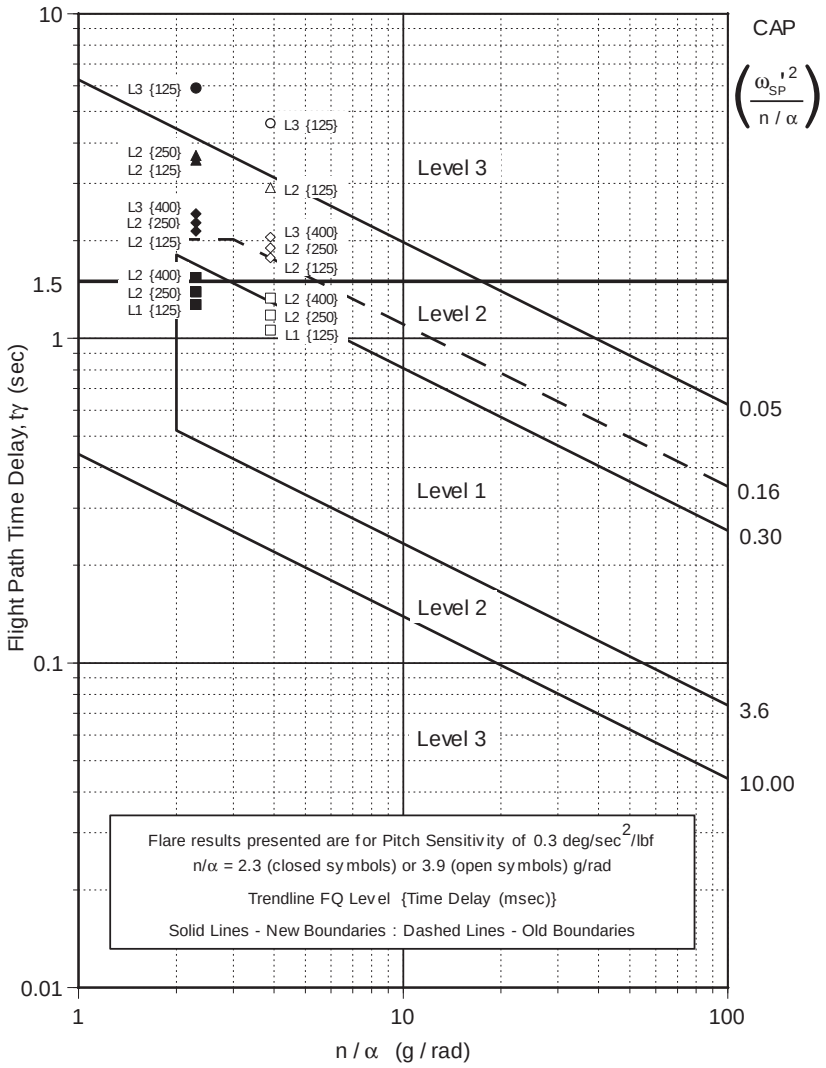


Figure 9. Flight Path Time Delay Results

SUMMARY

The criteria that have been appraised in this paper are of use at different stages of the design and development of an aircraft. Together with appropriate pole placement algorithms, LOES and CAP are applicable at all stages, from initial design through to analysis of flight test data. The Bandwidth criteria are less suited to the design phases, but are easily applicable to the pre-flight evaluation and flight test stages. Gibson's time domain criteria are most suited to the initial design stage, while his phase rate criterion is well suited to pre-flight evaluation. The Gibson criteria are less suited to the analysis of flight test data. Due to the poor correlation of observed flying qualities with the Smith-Geddes criteria, it is not recommended that these criteria be applied to transport aircraft in the landing task until these criteria have been further appraised. The applicability of the different criteria is summarized in Table 1.

Table 1. Applicability of Different Criteria

	Initial Design	Detail Design	Pre-Flight Evaluation	Flight Test
CAP	✓	✓	✓	✓
Bandwidth			✓	✓
Gibson	✓		✓	

CONCLUSIONS

Several flying qualities criteria were appraised against a validated flying qualities database for active control transport aircraft in the terminal flight phase.

The results support the raising of the lower Level 1 CAP criterion boundary to 0.3. A multi-parametric correlation between CAP and time delay was identified and reflected in a new criterion.

The Level 2 Bandwidth criterion boundaries were overly restrictive. New boundaries have been developed that fit the database. A modification to the Bandwidth PIO criterion classification was also recommended.

Gibson's phase rate analyses were found to produce almost identical results to Bandwidth. However, the criterion boundaries are overly restrictive, especially as a predictor of PIO severity. The Dropback criterion results did not correlate with the transport aircraft database. The results from the flight path time delay analyses were correlated with the CAP

criterion and exposed a correlation between desired values of t_γ and n/α.

None of the Smith-Geddes criteria for flying qualities or PIO correlated with the database. They appear to be not applicable to active control transport aircraft.

ACKNOWLEDGEMENTS

The Gibson and Smith-Geddes criteria analyses reported in this paper were performed by Dharminder Chahal, of Delft University of Technology, while working as an intern at the Boeing Company, Long Beach. John Gibson reviewed the paper and provided welcome feedback. The contributions of both of these individuals are gratefully acknowledged.

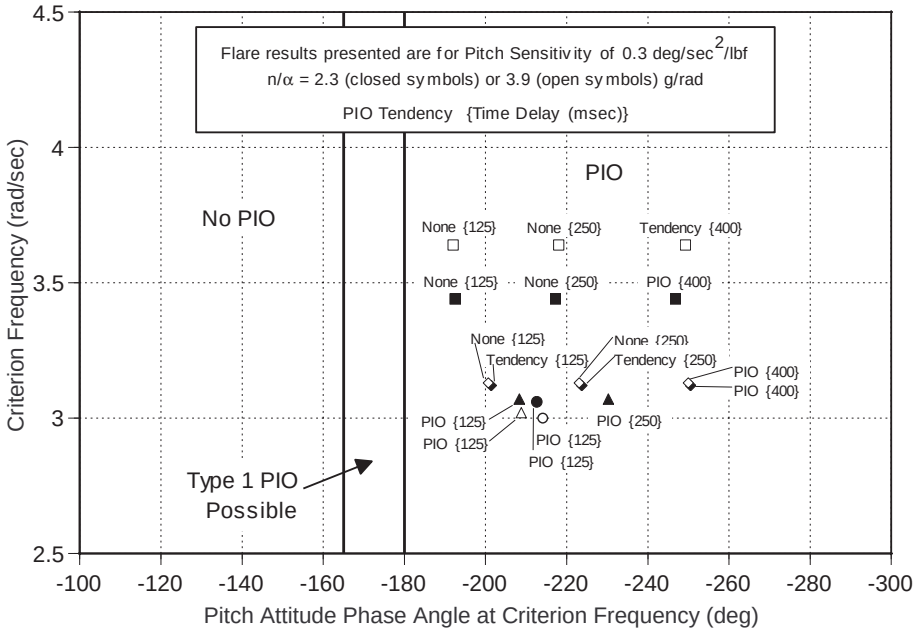


Figure 10. Smith-Geddes PIO Results

REFERENCES

1 Newell, F. and Campbell, G., "Flight Evaluation of Variable Short Period and Phugoid Characteristics in a B-26", WADC-TR-54-594, 1954.

2 Birhle, William, "A Handling Qualities Theory for Precise Flight Path Control," AFFDL-TR-65-198, June 1966.

3 Anonymous, "Military Specification – Flying Qualities of Piloted Airplanes," MIL-F-8785B(ASG), August 1969.

4 Weingarten, N.C. and Chalk, C.R., "In-Flight Investigation of Large Airplane Flying Qualities for Approach and Landing," AFWAL-TR-84-3118, September 1981.

5 Grantham, W.D., "Comparison of Flying Qualities Derived From In-Flight and Ground-Based Simulations for a Jet-Transport Airplane for the Approach and Landing Pilot Task," NASA TP-2962, December 1989.

6 Weingarten, N.C., et al., "Flared Landing Approach Flying Qualities," NASA CR-178188, December 1986.

7 Field, E.J. and Rossitto, K.F., "Approach and Landing Longitudinal Flying Qualities for Transports Based on In-Flight Results," AIAA 99-4095, presented at the AIAA Atmospheric Flight Mechanics Conference, Portland, OR, August 1999.

8 Anonymous, "Military Specification – Flying Qualities of Piloted Airplanes," MIL-F-8785C, November 1980.

9 Anonymous, "Department of Defense Interface Standard, Flying Qualities of Piloted Vehicles", MIL-STD-1797A, Change notice 1, June 1995.

10 Mitchell, D.G., Hoh, R.H., Aponso, B.L., and Klyde, D.H., "Proposed Incorporation of Mission-Oriented Flying Qualities Into MIL-STD-1797A", WL-TR-94-3162, October 1994.

11 Gibson, J.C., "Development of a Methodology for Excellence in Handling Qualities Design for Fly-by-Wire Aircraft", Ph.D. Thesis, Delft University, 1999.

12 Neal, P.T. and Smith, R.E., "An In-Flight Investigation to Develop Control System Design Criteria for Fighter Airplanes," AFFDL-TR-70-74, 1974.

13 Smith, R.E., "Efects of Control System Dynamics on Fighter Approach and Landing Longitudinal Flying Qualities," AFFDL-TR-74-9, 1974.

14 Mitchell, D.G. and Field, E.J., "Nonlinearities and PIO with Advanced Aircraft Control Systems," Research and Technology Organization, Applied Vehicle Technology Symposium, Braunschweig, Germany, May 2000.

Paper #33

Q by Chris Fielding: Where do you go from here, in terms of getting your results accepted by the large aircraft Flight Control Community?

A. (Edmund Field): We are already using the new boundaries in Long Beach, will publish them all in an Air Force report soon, and hope to have the Air Force accept them for future use.

Q by David Moorhouse: The landing requirements lower CAP boundary is affected by required touchdown precision. What touchdown precision was required for the task or was it a conventional landing?

A. (Edmund Field): The task was a 300 feet lateral offset approach corrected at around 200 feet AGL. The pilot was then required to perform a precise landing with the following performance standards:

Desired performance:	Landing box 20 feet wide by 500 feet long, touchdown sink rate less than 4 feet/sec.
Adequate performance:	Landing box 54 feet wide by 1500 feet long, touchdown sink rate less than 7 feet/sec.

This seems to be about the standard landing task that is now being used for transport aircraft, and is sufficiently tight to expose handling deficiencies.

You bring up an interesting point by stating that the lower CAP boundary is defined by landing precision. The upper CAP boundaries (certainly for transports) seem to be defined by issues of structural modes and pilots' tolerances for "jerky" type rides. We agree that the lower Level 1 CAP boundary is dictated by the task performance, however we feel that the lower Level 2 boundary is not. We feel that it is dictated by the ability to land the aircraft at all. By the time the pilot has given up on desired performance, the boundary between making adequate performance or not is determined by his ability to control the aircraft at all. At this point the idea of performance standards is probably "out the window". Thus, we don't think that the lower Level 2 boundary is dictated by the definition of adequate performance, but more by the pilot's ability to land the aircraft at all, with a tolerable pilot workload. Interestingly, in our experiment we expected the Lower Level 2 boundary to be relaxed, in fact it stayed in the same place. It was the Level 1 boundary that was raised, perhaps reflecting the tighter performance standards that we used in our experiment.

This page has been deliberately left blank

Page intentionnellement blanche

Mechanical Systems, Structures and Materials (MSSM)

Technical Evaluation Report

Otto Sensburg
DaimlerChrysler Aerospace AG
Military Aircraft MT2, Postfach 80 11 60
81663 Munich, Germany

Introduction:

Active **C**ontrol **T**echnology (ACT) was introduced in the seventies together with fly by wire and Control Configured Vehicle (CCV)-Technology [1].

Several technologies that are now available and widely used for aircraft are:

- Artificial longitudinal and lateral stability
- Manoeuver load control
- Vibration suppression (-leading to flutter suppression)
- Gust load Alleviation

The advent of smart adaptive structures, where distributed control with distributed actuators is applied even further increased the usage of ACT.

The RTO-meeting in Brunswick, Germany from May 8-11, 2000 gave an overview of existing and new technologies.

Hr. Luber, Daimler Chrysler acted as chairman for the Symposium on **M**echanical **S**ystems, **S**tructures and **M**aterials (MSSM).

The Symposium was structured into four sessions, namely:

Session 1: Smart Structures Applications

Session 2: Active Control Technology for Load Alleviation

Session 3: Active Elements for Structural Design

Session 4: Active Materials and Applications

These sessions were thoughtfully chaired by Messrs. P-M. Hutin, ONERA, France, H. Hoenlinger, DLR Germany, W. Luber, DaimlerChrysler, Germany, D.G. Zimcik, NRC, Canada respectively.

Two keynote speakers have given a very good approach to the way things should be done.

Ed Pendleton from the Air Force Research Laboratory (AFRL), Dayton, Ohio, US presented a concept where he uses the elastic deflections to his advantage similar to

the Wright Brothers in his paper: "How Aeroelastic Wings are a Return to the Past and a Gateway to the Future"

Though wing flexibility was a key to control during the first successful manned powered flight, wing flexibility affected other early designs adversely. Perhaps, the first designer to be affected was Dr. Langley. The unfortunate wing failure that wrecked his machine in 1903 was likely due to wing torsional divergence. The success of the Wright Brothers and the failure of the Langley monoplane provided one of the original reasons for early designer preference for biplanes.

By the mid-1930s, the quest for higher performance and speed led designers to promote monoplanes designs with semi-monocoque structures. As these designs were built and flown, aircraft encountered a wide variety of problems, which we now classify as aeroelastic problems. Wing flutter, wing divergence, buffeting, control effectiveness, and control reversal are examples of aeroelastic problems that have plagued aircraft designs ever since.

Today, aircraft lifting surfaces are designed to be strong enough to meet loading requirements and material is added to provide stiffness adequate to keep them free from flutter, divergence, and buckling. And as pilots and passengers on aircraft, we are glad this is so.

But this added stiffness usually means adding structural weight, so design trades are made between weight and aerodynamic performance for a given set of aerodynamic requirements. As speeds increase, designers often have opted to reduce wing span, increase wing thickness and live with the subsequent reduced aerodynamic performance in an attempt to save weight.

Wing flexibility used as a benefit... The first step towards a new era in aeronautics?

As we enter the second one hundred years of aeronautics development, we are poised to enter a potentially new era in aircraft design. To take full advantage of this, it will take vision and new aircraft materials and new ways of integrating wing design with adaptive control strategies to take advantage of it.

The AFRL Air Vehicles Directorate and NASA have taken a first step by developing a novel technology that offers weight competitive wing designs and improved aerodynamic performance. It is called the Active Aeroelastic Wing or AAW. AAW

Technology is a synergistic technology that integrates air vehicle aerodynamics, active controls, and structures together to maximize air vehicle performance. The concept turns wing aeroelastic flexibility into a net benefit by usage of multiple leading and trailing edge control surfaces activated by a digital flight control system. AAW techniques employ the energy of the air stream to achieve this desirable wing twist with very little control surface motion. The wing then creates the needed control forces with outstanding effectiveness. At higher dynamic pressures, AAW control surfaces are used as "aerodynamic tabs" that promote wing twist for added control force capability instead of trying to overcome control surface losses due to wing elastic twist. At these high dynamic pressures, large amounts of control power can be generated using this approach. In the same design the AAW control can minimize drag at low wing strain conditions and/or minimize structural loads at high wing strain conditions. The AAW concept was first successfully demonstrated by an Air Force / NASA / Rockwell North American team in a transonic dynamics wind tunnel. Now, another joint Air Force /NASA/Boeing team is preparing to take it to flight in California at NASA Dryden.

A similar concept was also presented by Vicky Tischler [2] at the 41st AIAA SDM meeting in Atlanta,GA, USA on 3-6.April 2000 using a fin which was made divergent by aeroelastic tailoring and therefore has higher efficiency than the rigid one. Weight, cost and signature savings can be realized in the order of 20 – 30%.
The MEMS approach of Chih-Ming Ho, US presented in his keynote paper: "MEMS Application to Active Control" is doing things differently by applying small actuators on delta wing tips to influence the vortices coming off that wing and that way controlling the aircraft motion. Again the controlling force comes from the surface not the control. It has to be checked whether such an approach is possible for a full size aircraft or if it just works for the small flying demonstration model shown.

Now the papers presented at the meeting will be reviewed separately:

The acoustic control with piezos of structural vibration (paper 2) is feasible but more research on control laws and applicability has to be done before it can be introduced in to practical designs, "Active Structural Acoustic Control as an Approach for

Acoustic Optimisation of Light Weight Structures" by D. Mayer, B. Vogl, H. Hanselka, Otto von Guericke University Magdeburg, Germany

The adaptive wind tunnel model proposed by L.F. Campanile, V. Carli, D. Sachau, DLR Brunswick, Germany (paper 4) and the smart wing model of Northrop, presented in paper 7 are similar in design and can do the job of otherwise very costly wind tunnel variants.

In paper 6, "Realization of a Shapevariable Fowler Flap on Transport Aircraft" by C. Anhalt, E. Breitbach, D. Sachau, DLR, Germany an intelligent concept for an Airbus A330/340 fowler flap is shown which improves the high lift behavior.

In paper 7, "Active Control Technology at NASA Langley Research Center" was presented by R.R. Antcliff and Anna-Maria McGowan NASA Langley, USA, giving an excellent overview of NASA activities in this field.

Paper 8, "Finite Element Approach for the Design of Control Algorithms for Vertical Fin Buffeting using Strain Actuation" by F. Nitzsche, S. Liberatore, D.G. Zimcik, National Research Council, Canada and paper 11, "Active Fin-Buffeting Alleviation for Fighter Aircraft" by J.K. Duerr, U. Herold-Schmidt, J. Becker, Daimler Chrysler Aerospace, Germany showed approaches for fin buffeting alleviation. Their tests have been performed on the ground. In order to assess useable amplitude or strain reductions from active controls the damping coming from unsteady aerodynamic forces in flight must be considered. It seems that a solution using the rudder for low frequencies and strain actuators for high frequencies would be viable.

Cost effectiveness has to be investigated as well as software integration cost, maintainability, reparability etc.

A very interesting study was presented in paper 9, "Active Flutter Suppression using ASTROS with Smart Structures and ASE models" by P.C. Chen, C. Nam, Zona Technology D.D. Liu Arizona State University, US. This is an approach for the future.

Paper 12, "Development of Analysis Tools for Active Shape and Vibration Control" by A. DeBoer, R. Veul, P.Arendsen, NLR, Netherlands gave an overview of analysis tools available at NLR.

Some interesting issues were investigated in paper 13, "Active Control of Buffet Induced Vibrations: Reliability, Maintainability and Robustness Issues" by S. Hanagud, M. Bayon de Noyer Georgia Institute of Technology, D. Henderson, Air Force Research Laboratory, WPAFB, Ohio, US.

An application of Magneto Rheologic Fluids was presented in paper 15, "Design and Fabrication of Semi-Active MR Fluid Based Engine Mount" by R. Ay, M.F. Golnaraghi, A. Khajepour, University of Waterloo, Canada for an engine mount which would allow to adjust the damping.

The problem of optimizing a passive shock absorber for a landing gear was addressed in paper 16, "Optimization of the Passive Shock Absorber of a Military Aircraft" by B. Uhrmeister, DLR, Germany.

A new actuator device was investigated in paper 18, " Active Materials Research at UCLA" by G.P. Carman, University of California, US. If it fulfills what it is promising it would enhance the application of smart structures tremendously.

The problem of applying adaptronics to Helicopter rotor blades was presented in paper 19, " Adaptive Rotor Blade Concepts Direct Twist and Camber Variation" by A. Blueter, U. C. Ehlert, D. Sachau, E. Breitbach, DLR, Germany

After all the papers were presented, W. Luber, DaimlerChrysler chaired a round table discussion with the following table participants:

W. Luber, GE

O. Sensburg, GE

D. D.Liu, US

E. Pendleton, Us

D. Zimcik, CA

P-M. Hutin, FR

H. Ottens, NE

After a lively discussion it was concluded that the lack of an actuator which fits all the requirements is impeding the progress. Also more analytical work must be done to bring together Multi Disciplinary Optimization, composite structures and smart materials.

References:

[1] O. Sensburg, H. Zimmermann
Impact of Active Control on Structures Design
AGARD Multi – Panel Symposium, Fighter Aircraft Design
Florence, Italy 3.-6- October 1977

[2] V.A. Tischler and V.B. Venkayya,
Airforce Research Laboratory,
Air Vehicles Directorate
Wright Patterson Airforce Base, OH
and Otto Sensburg
DaimlerChrysler Aerospace
Munich, Germany
Aeroelastic Tailerоring of Empennage Structures
41st AIAA/ASME/ASCE/AHS/ASC Structures, Structural Dynamics and Materials
Conference
Atlanta, GA USA, 3-6 April 2000

Active Structural Acoustic Control as an Approach to Acoustic Optimization of Lightweight Structures

Dirk Mayer, Bernd Vogl, Holger Hanselka
Otto-von-Guericke-University Magdeburg
Department of Adaptronics
Universitätsplatz 2
39106 Magdeburg, Germany
e-mail: dirk.mayer@mb.uni-magdeburg.de
e-mail: bernd.vogl@mb.uni-magdeburg.de
e-mail: holger.hanselka@mb.uni-magdeburg.de

Conventional approaches to optimizing the acoustic behavior of lightweight structures have mainly been restricted to the concept of *Active Noise Control* (ANC). This concept is aimed to attenuating primary noise sources with secondary controlled noise sources by taking advantage of destructive interference.
However, it is also possible to actively control the vibrating structure using piezoceramic actuators to alter very intensively sound-radiating operating deflection shapes. This approach is referred to as *Active Structural Acoustic Control* (ASAC). The applicability of this concept to real systems is demonstrated by means of a simple model with experimental measurement systems employed in the lower frequency range.
This study focuses on the utilization of a modern measurement technology, i.e. the *Spatial Transformation of Sound Fields* (STSF), which facilitates the determination of important parameters of the vibro-acoustic system at a time. The radiation efficiency is of major importance to the evaluation of the acoustic system behavior. As the lower frequency range is considered, the dynamic system behavior is determined by means of the *Experimental Modal Analysis* (EMA).
The results of this study show the radiation efficiency of the unregulated and of the actively controlled system.

1. INTRODUCTION

The adaptronic approach is aimed at combining mechanical systems by incorporating integrated actuators and sensors into the structure and by controlling the whole complex to obtain the desired adaptive response to physical effects which may be caused by external impacts. To this end, it is necessary to know the exact description of the mechanical system, choose appropriate actuator and sensor systems, and design the control algorithm on the basis of a predefined objective function.
For many applications in the industry approaches are employed which focus on the utilization of alternative materials to obtain a more economical and efficient design.
Often also aspects of convenience play a role.

The present study is not aimed at developing new optimization methods, but the authors want to demonstrate the potentials of adaptive systems by means of a simple experimental setup. Considering the intensified use of lightweight construction in future applications, a rectangular plate was investigated which was very thin compared to its dimensions. The material was steel, although composites with integrated piezoceramics as actuators are intended to be used for further investigations. In addition, this study was restricted to the lower frequency range where the low modal density makes efficient control less difficult. The merely passive approach of sound absorbing materials (sandwich panels) was not considered.
Future activities should concentrate on the efficiency of adaptive systems in the higher frequency range where deterministic model descriptions are not possible. An appropriate approach based on *Statistical Energy Analysis* (SEA) would facilitate investigations of the structural behavior at a high modal density.
On the way to improve the acoustic features of mechanical structures novel vibro-acoustic phenomena appear. Basically, it is possible to give a theoretical description of the sound field induced by known structure-borne sound within the lower frequency range (Finite Element Method, Boundary Element Method), but in reality deviation problems occur which require profound knowledge. In contrast to more conventional methods, such as *Active Noise Control* (ANC), which focuses on attenuating primary noise sources with secondary controlled noise sources (loudspeakers) by taking advantage of destructive interference, this study was aimed at altering structural properties. This method is referred to as *Active Structural Acoustic Control* (ASAC, [1]). It is applied to actively manipulate the vibrating structure by means of suitable actuators in order to obtain a specific repercussion onto the intensively sound-radiating structural behavior.
The present investigations were mainly based on experiments and demonstrate the chances offered by adaptive systems. An established measurement method is described facilitating important conclusions about the real vibro-acoustic behavior of a simple experimental setup.

2. EXPERIMENTAL SETUP

A wooden box with the overall dimensions of 930 x 635 x 620 mm was designed to investigate the efficiency of active sound-reducing measures. The wall material consisted of 20 mm thick glazed insulation pressboard. The box, which was open to the upper side, was covered by a steel frame holding the steel sheet in position. Hence, an efficient air cushion of 900 x 600 x 650 mm was built up below the plate. The plate dimensions in the fixing frame were 905 x 605 x 1 mm. A flexible rubber material was used between the two frame components.

Paper presented at the RTO AVT Symposium on "Active Control Technology for Enhanced Performance Operational Capabilities of Military Aircraft, Land Vehicles and Sea Vehicles", held in Braunschweig, Germany, 8-11 May 2000, and published in RTO MP-051.

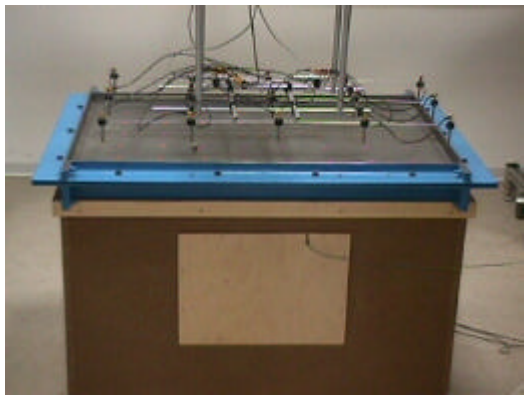


Fig. 2.1 Experimental Setup

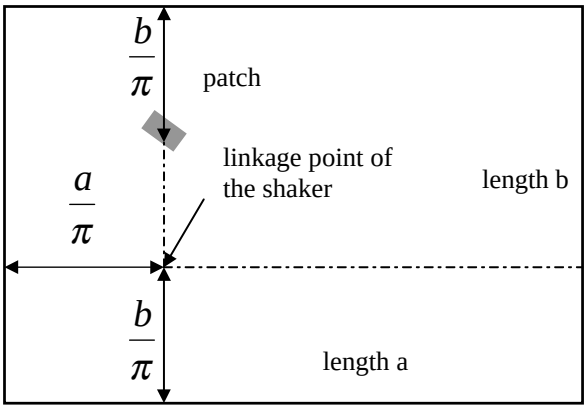


Fig. 2.2 Excitation Points

Primary excitation of the plate was caused by an electrodynamic shaker screwed to the bottom inside the wooden box. The π-th fraction of the surface dimensions was chosen as the exciter place in order to suggest as many eigenmodes as possible at a time. For superposition of a controlled secondary oscillation a piezoceramic patch (50 x 25 x 0.25 mm) was mounted to the bottom side of the plate opposite to the shaker position (see Fig. 2.2).
To measure the sound radiation of the plate above the wooden box, the *Spatial Transformation of Sound Fields* (STSF) measuring system of Brüel & Kjaer was used. The employed microphone array is presented in Fig. 2.1. Theoretical foundations and possible results of this measuring method are detailed in Chapter 4.

3. PRELIMINARY INVESTIGATIONS

To investigate in a first approximation the relationship between structural dynamics (structure-borne sound) and the resulting sound field (airborne sound) the steel sheet was subjected to a dynamic examination. By means of the CADA-X modal analysis software of LMS the deflection modes with their corresponding resonance frequencies were determined experimentally in the frequency range of 0 to 250 Hz. The following results were obtained:

No.	Eigenmode	Frequency [Hz]
1	(2,1)	28.2
2	(1,1)	29.1
3	(1,2)	37.9
4	(3,1)	48.0
5	(2,2)	49.7
6	(3,2)	66.6
7	(4,1)	68.6
8	(1,3)	78.3
9	(4,2)	87.9
10	(2,3)	90.5
11	(5,1)	96.9
12	(3,3)	105.5
13	(5,2)	114.9
14	(4,3)	-
15	(1,4)	126.8
16	(6,1)	132.8
17	(2,4)	141.2
18	(6,2)	152.3
19	(5,3)	156.8
20	(3,4)	158.5
21	(7,1)	173.3
22	(4,4)	180.4
23	(6,3)	-
24	(1,5)	192.6
25	(7,2)	194.4
26	(2,5)	205.9
27	(5,4)	208.6
28	(8,1)	220.6
29	(3,5)	223.3
30	(7,3)	-
31	(6,4)	-
32	(8,2)	241.6
33	(4,5)	246.5

Table 3.1 Results of the Modal Analysis

The frequency resolution of this measurement was 0.195 Hz. The plate was divided into 19 x 13 measuring points (247 frequency responses). Measurement was performed twice to obtain as many eigenmodes as possible. In the first test, the shaker was mounted to the exciter point described above, whereas in the second test it was arranged in th center of the plate.
As can be seen, a strong coupling occurred between the contained air cushion and the plate resulting in a displacement of the (1,1)-mode. The measured damping amounted to approx. 10% (attenuation of the (2,1)-mode was approx. 3.5 %).
The thickness of the steel sheet (d=1 mm) led to a high modal density even in the low frequency range and hence deterministic methods reached their limits very soon. For higher frequency investigations an approach based on the *Statistical Energy Analysis* (SEA) is recommended to describe the structural dynamic behavior.
Then the frequency response, i.e. the ratio of sound pressure with reference to the initiated force, was determined and compared with the mechanical frequency response of the plate (Fig. 3.1).
To measure the sound pressure, a microphone was arranged above the plate at the same distance (approx. 0.5 m) as that chosen for the control described in Chapter 5. Hence, the error signal of the non-controlled state measured later could be obtained in advance.
The "acoustic" frequency response (FRF between sound pressure and force), which was in qualitative agreement to the autopower spectrum of the sound pressure, revealed a marked increase in the effective sound pressure measured in the frequency ranges of 80 to 100 Hz and 170 to 210 Hz compared to the mean sound pressure level (Fig. 3.2).

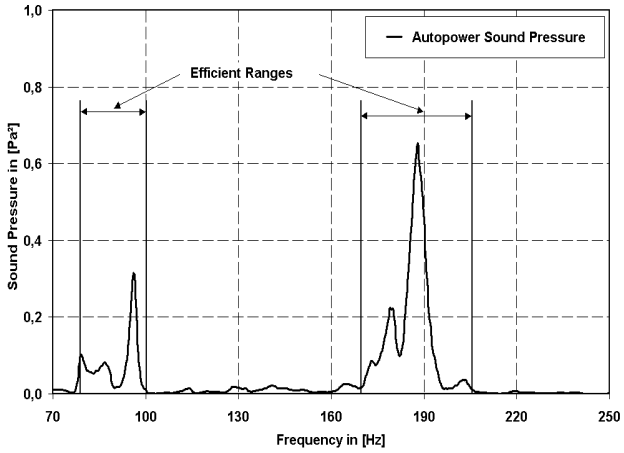


Fig. 3.1 Frequency Response Functions

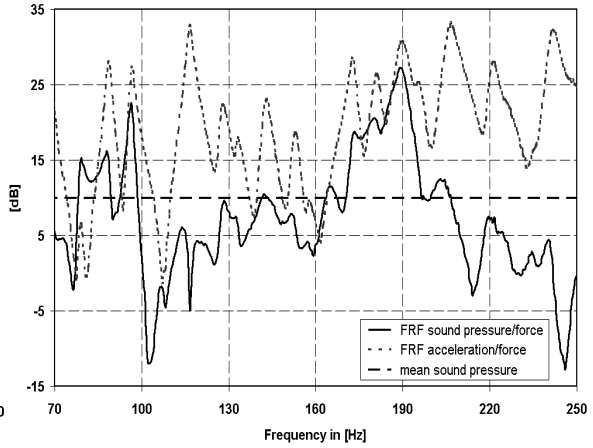


Fig. 3.2 Autopower Spectrum Sound Pressure (Linear)

The control approach which was used thereafter, was mainly aimed at minimizing the mean power of the error signal and yielding good results, in particular for these frequency ranges.
To facilitate a vibro-acoustic evaluation of the overall system, a characteristic parameter was introduced, i.e. the radiation efficiency ζ_{rad}.

Determination of the Radiation Efficiency ζ_{rad}

Radiation efficiency is defined as the ratio of the radiated power P_{rad} which is responsible for the audible airborne sound and the active power P_{in} applied to the plate by the primary vibration source [2]. The following equation leads to this characteristic:

$$\zeta_{rad} = \frac{P_{rad}}{P_{in}} \ . \tag{1}$$

The input power (active power) is calculated from the real part of the complex cross power spectrum of the oscillating velocity and the exciter force:

$$P_{in} = Re\left\{F \cdot v^{*}\right\}. \tag{2}$$

This variable was determined experimentally by using an impedance head at the shaker linkage point.
The radiated sound power results from the product of the active sound intensity and the crossed plate area:

$$P_{rad} = \iint_{A} \overrightarrow{I_A} d\vec{A} \, . \tag{3}$$

4. DETERMINATION OF THE RADIATED SOUND POWER

Determination of the radiated sound power of the plate requires the active intensity on its surface be established. To this end, the well-known method of *Nearfield Acoustic Holography* (NAH, [3]) was used. Major steps are described below to draw a complete picture of the calculations.
It is assumed that the sound pressure distribution in a level $z=z_1$ parallel to the radiating plate surface $z=z_0$ is known, for instance through measuring. Hence, a complex spectrum is obtained in the frequency domain:

$$p(x,y,\omega)\big|_{z=z_1} . \tag{4}$$

Using the spatial, two-dimensional Fourier transform, we obtain a corresponding spectrum in the complex variable domain:

$$p'(k_x,k_y,\omega)\big|_{z=z_1} , \tag{5}$$

where the variables k_x and k_y represent the components of the wave vector in the x- and the y- direction.

It is generally known that:

$$\left|\vec{k}\right|^2 = {k_x}^2 + {k_y}^2 + {k_z}^2 = \left(\frac{\omega}{c_0}\right)^2 . \tag{6}$$

As the velocity of sound in the air is defined to be approx. 343 m/s, the third component of the vector can be calculated. Then the sound pressure distribution within the complex variable domain on the plate surface is computed through:

$$p'(k_x,k_y,\omega)\big|_{z=z_0} = e^{-jk_z(z_1-z_0)}\, p'(k_x,k_y,\omega)\big|_{z=z_1} \tag{7}$$

The sound pressure spectrum on the plate surface can be calculated by means of re-transformation using the inverse spatial Fourier transform.
With this method the sound pressures in other levels are also available.
The normal velocity on the plate surface is computed through gradient formation, yielding again a complex spectrum:

$$\vec{v}_z(x,y,z,\omega) = -\frac{1}{j\omega\rho_0}\nabla p(x,y,z,\omega) . \tag{8}$$

Using the velocity and the pressure, the active sound intensity can be computed through the following expression that marks the active power flow:

$$\vec{I}_A = Re\left\{p^* \vec{v}\right\} \tag{9}$$

The radiated active sound power of the plate is obtained by integration over that plate area according to Equation (3). Then the radiation efficiency can be calculated following Equation (1) and Equation (2).

Regarding this *Nearfield Acoustic Holography*, measurements were based on the Brüel & Kjaer's *Spatial Transformation of Sound Fields* (STSF). With this approach the pressure spectrum was only recorded at discrete points in one level and only in a confined area. Hence, calculations require numerical methods (*Fast Fourier Transform*, FFT) and special windows filtering methods be applied to the data.
Upon evaluation of the readings also distant variables (e.g. radiation pattern) are available in addition to the near field variables.

5. IMPLEMENTATION OF ACTIVE MEASURES

The investigated lightweight construction structures of thin steel sheet are mainly used in aircraft construction and in the automotive industry. Hence, the disturbances in the overall structure are often caused by motors and other units. Consequently, the disturbance is deterministic and an adaptive counter-control (adaptive Feed-Forward Control) can be used. This principle has already been applied to practice, and was also used for this experiment.
The required reference signal for a narrow-band disturbance can be obtained either from the corresponding motor speed signals or from a component not affected by active measures, e.g. by means of acceleration sensors at an engine mount.
The system should work adaptively to be able to respond to changes in the characteristics of the disturbance or in the characteristics of the structural dynamic system. The performance is kept constant.

To this end, an error sensor, e.g. a measurable variable, is required to evaluate of the performance of the adaptive control system.
A microphone was used which was arranged at a distance of about half a meter above the center of the plate surface.
Adaptive signal processing was implemented as a digital filter system [4]. The actuator signals were obtained through filtering by means of an adaptive digital filter; the coefficients of the filter had been adapted using the so-called *Filtered-X-LMS* algorithm.
Figure 5.1 depicts the block diagram of the system. *W(z)* is the adaptive FIR digital filter (FIR: *Finite Impulse Response*) and *P(z)* represents the transfer function from the disturbance source to the microphone, *S(z)* is the transfer function from the actuator to the microphone and $\hat{S}(z)$ describes a model of this transfer function which had to be generated prior to test start. Again, an adaptive FIR filter is used to this end.
The model of the path *S(z)* is necessary to ensure the convergence of the filter coefficients *w* of the adaptive filter, following the known algorithm:

$$w(n+1) = w(n) + \mu \underline{x}'(n) e(n) \tag{10}$$

In contrast to most of the filter systems where the assembler language is used, the *MATLAB/Simulink* environment was employed here to ensure good readability as well as simple testing and changing. By applying the *dSpace* rapid prototyping system such models can be run on a signal processor. Figure 5.2 demonstrates the completed, simple Simulink model.
It still facilitates on-line adaptation of the so-called secondary path *S(z)*, where the signal is superposed low-power noise and the identification prior to the test start is updated.

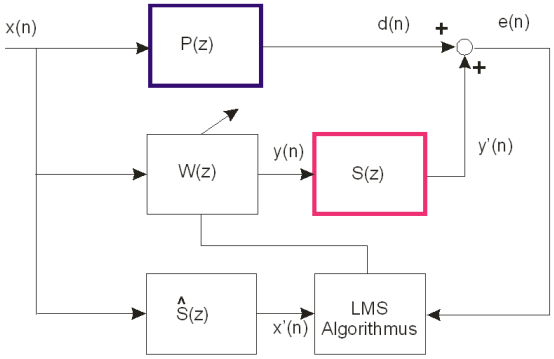


Abb. 5.1 Adaptive Feed-Forward Control System

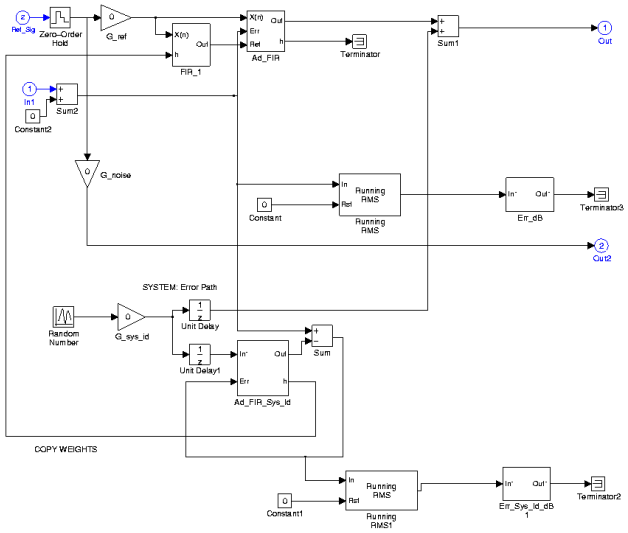


Fig. 5.2 *MATLAB/Simulink* Model

Hence, *W(z)* and the required model $\hat{S}(z)$ are adaptive which is an interesting property of control systems in structural dynamics. In particular in lightweight construction structures, this property may alter either the characteristics of the disturbance or the mechanical transfer functions between actuators and sensors, e.g. by loading of the structure or by changing of the boundary conditions, such as the temperature.
The adaptive feed-forward control system was first subjected to harmonic investigations under different sound radiating frequencies of the plate.
This paper presents two experiments which were carried out at a signal frequency of f=191 Hz. For this frequency a large signal was measured in the sound pressure spectrum at the microphone.
Figure 5.3 shows the progression of the error and the actuator signal when the adaptive feed-forward control is switched on, with all coefficients of the adaptive filter *W(z)* reset before.
To test the adaptability of the system to changed boundary conditions an additional magnetic weight with the mass m = 0.1 kg was arranged in the actuator position on the plate. Figure 5.4 shows how the adaptation algorithm follows the actuator signal when the weight has been placed. The overshoot of the error signal results from the noise occurring at the moment when the weight was placed onto the plate.
In the following experiments this controller was used for both harmonic and broadband excitation. In both cases it received reference signals from the generator.

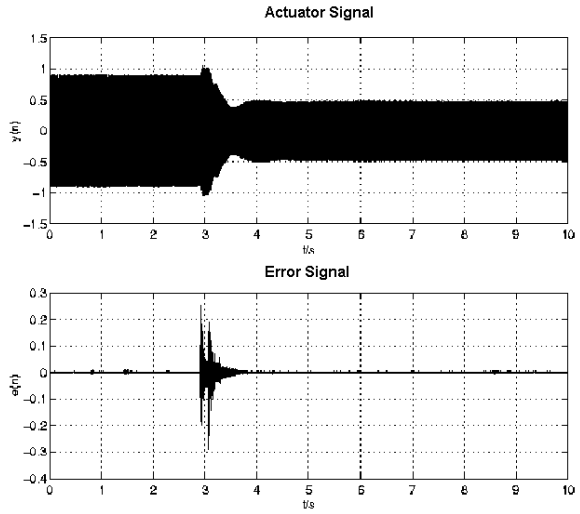


Fig. 5.3 Adaptation of the Feed-Forward Control

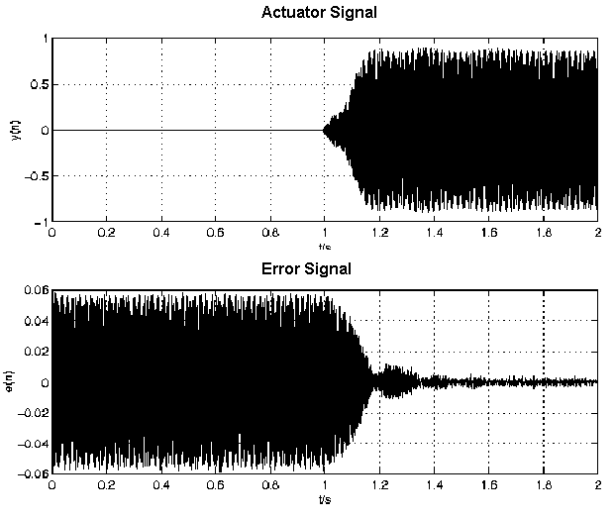


Fig. 5.4 Adaptation of the Actuator Signal to changing mechanical Conditions

6. RESULTS

This chapter is divided into sections to ensure precise analysis of the sound field and of the plate mechanics for harmonic and broadband excitation. The results of the STSF measurement are important to the understanding of the physical phenomena. The description of the vibro-acoustic parameter ζ_{rad} involves a comparison of the non-controlled actual state with the regulated state and provides an explanation of the changed radiation pattern. In addition, the properties of the actuators (PZT patches) used are detailed.
In an harmonic experiment the efficiency of the overall active system and the possibilities of measuring technologies were tested.
The results of this experiment served to evaluate the potential of the overall active system under the conditions of broadband excitation considering the parameters determined above.

Results of Harmonic Excitation

The plate was subjected to harmonic excitation at 96.9 Hz ((5,1)-eigenmode). The distribution of the normal surface velocity on the plate obtained by performing a STSF measurement is represented in Fig. 6.1. The minimum resolution of the STSF measurement is 1 Hz, and was limited to 2 Hz for reasons of the measuring period. A comparison of the plate movement with the results of the experimental modal analysis at resonance frequencies reveals similar vibrating forms. The result was the (5,1)-eigenmode of the plate causing high amplitudes in the sound pressure spectrum. In a simplified form this can be attributed to the oscillating mode of motion which assumes an odd-odd eigenmode where sources and depressions cannot be compensated for with regard to sound intensity (no acoustic short circuit).

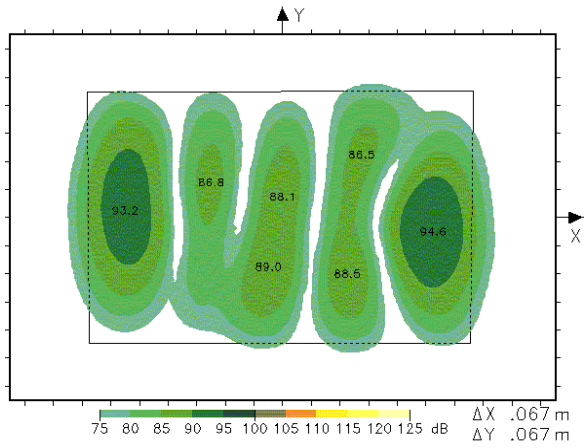


Fig. 6.1 Normal Velocity at 98 Hz; Non-Controlled

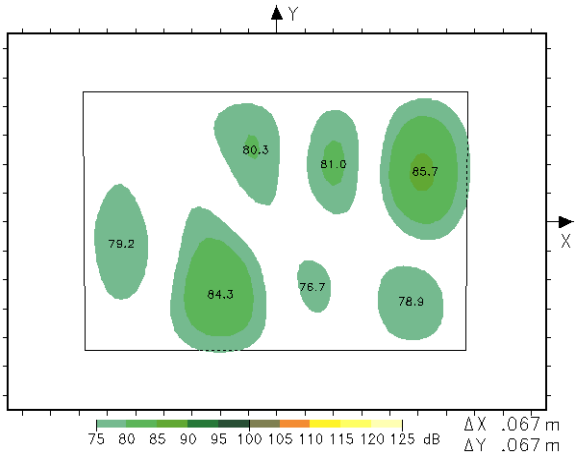


Fig. 6.2 Normal Velocity at 98 Hz; Controlled

To minimize sound radiation the adaptive controller described above was inserted. With the convergence of the filter coefficients a decrease in power of the microphone signal by approx. 20 decibel was obtained. A changed operating deflection shape occurred as shown in Fig. 6.2.
As clearly can be seen, the velocity amplitudes decreased. This size is correlated to the sound radiation in harmonic investigations. As the surface velocity could not be taken into consideration when calculating the sound pressure within the

far field basically (broadband), the active intensity for both the non-controlled and the controlled structure was measured (Fig. 6.3 and 6.4).

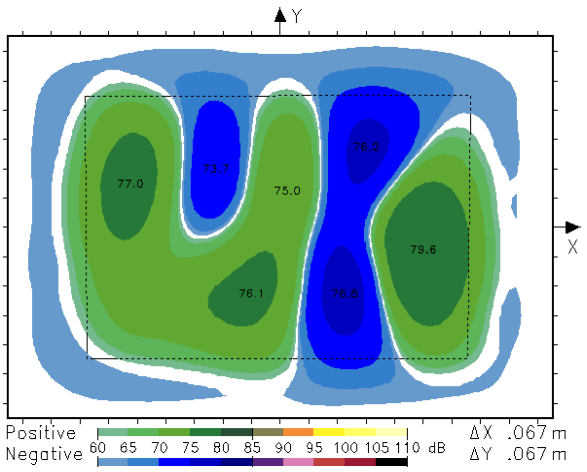


Fig. 6.3 Active Intensity at 98 Hz; Non-Controlled

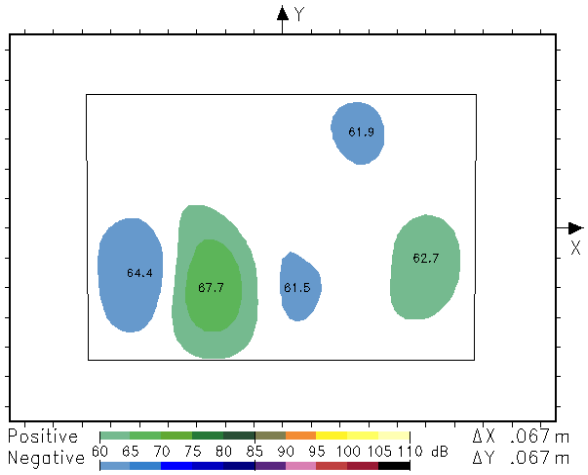


Fig. 6.4 Active Intensity at 98 Hz; Controlled

This variable is important to sound radiation into the far field and exhibits a dramatic drop caused by the adaptive controller. In addition, the figure shows that the decrease in intensity the force transmitting position of the shaker is rather small.

Results of Broadband Excitation

For this test the system was excited by white noise with a bandwidth of 70 to 250 Hz. The radiation efficiency ζ_{rad} described above was used to illustrate the radiation pattern of the investigated system already is used. By means of the measurement technology mentioned above, this parameter could be determined for broadband excitation.
First the performance of piezoceramic actuators (PZT patches) was analyzed with regard to an efficient broadband regulation. As can be clearly seen from the curve of the electrical active power incorporating a PZT patch with the dimensions of 50 x 25 x 0.25 mm (linkage factor neglected), the power increase follows the frequency and is very small in the frequency range considered here. As a result more energy and hence more or thicker PZT patches need be applied to obtain a better radiation compensation.
The incorporated electrical power of piezoceramics is determined by measuring the cross power spectrum of current and voltage.

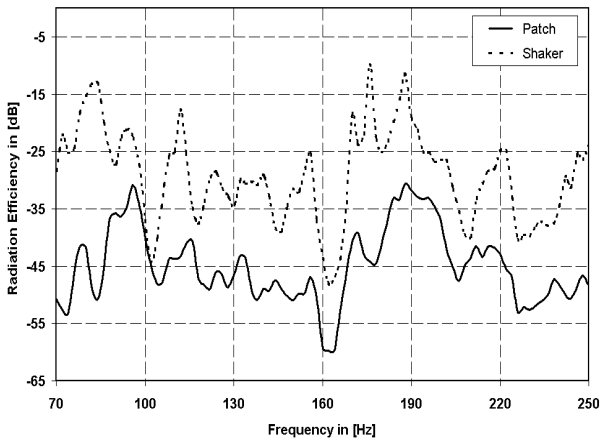


Fig. 6.5 Incorporated Active Power of a PZT Patch

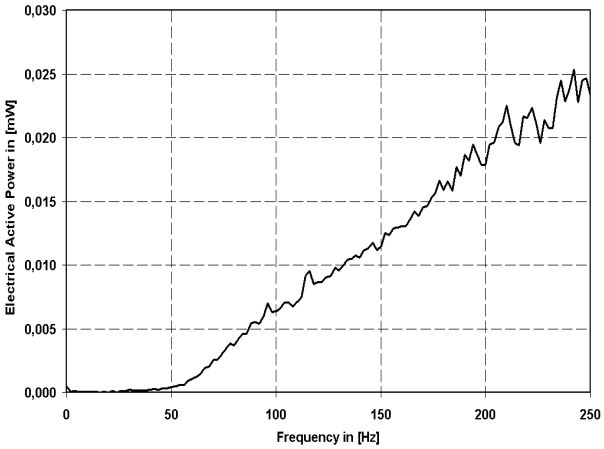


Fig. 6.6 Radiation Efficiency of Patch and Shaker; Non-Controlled

The radiation efficiency ζ_{rad} is obtained from the determined radiated power and the imported power of the exciters following Equation 1 (Fig. 6.6).
The distance between the two curves are caused by the different measuring methods of the input power for both the shaker and the patch. Only the electrical efficiency was taken into consideration when determining the input power of the patch. The result was a lower radiation efficiency caused by coupling losses of the mechanical structure which are still unknown. Hence, a vertically downward displacement occurred.

Considering the error signal for the measurement of the regulated system (Fig. 6.7), it turns out that the signal markedly decreased in various frequency ranges, whereas in other ranges it remained unaffected or was even extended. However, the total power decreased across all frequencies by 4.63 decibels because the adaptation algorithm caused a minimization of the total power of the microphone signal.

The limited efficiency and the restriction to a small range of the stimulated spectrum were mainly attributed to the following conditions:

- The microphone is not arranged in optimum position; several microphones might have been necessary.
- The PZT patch was not arranged in optimum position either, hence, its efficiency at low frequencies was extremely low and several piezoceramics in optimized positions might have been necessary.

Thereafter, the above method was used to determine the radiation efficiency for both adaptively controlled and non-controlled structures to analyze also the influence exerted by secondary excitation (by PZT patch) on the radiation behavior (Fig. 6.8).
As can be seen, the vibro-acoustic parameter improved in those ranges where the error signal of the adaptive controller was reduced and the radiation characteristics of the plate changed as desired.

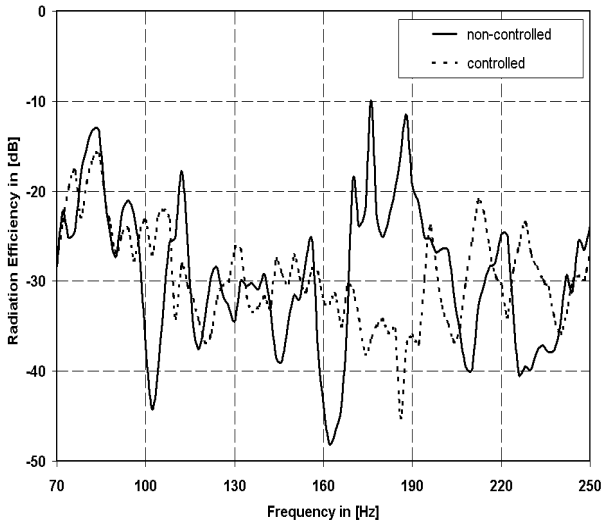


Fig. 6.7 Error Signal at the Microphone

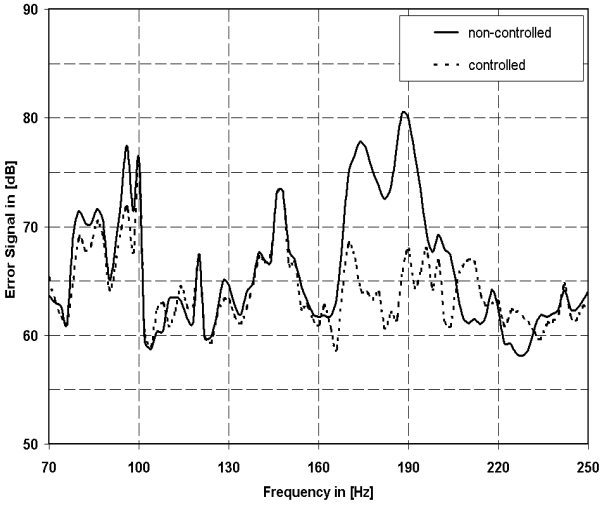


Fig. 6.8 Radiation Efficiency of Primary Excitation

7. CONCLUSION AND PROSPECTS

An active lightweight construction structure was examined by means of a basic experiment. It revealed that the vibro-acoustic behavior of the active system can be evaluated using the radiation efficiency. A method for calculating this parameter was presented and verified experimentally.
However, improvements were possible to an extent only when an adaptive feed-forward control was used which comprised only one piezoceramic patch as an actuator and one microphone as an error sensor.
Hence, future investigations must be aimed at optimizing the number and positions of actuators and sensors. In addition, such investigations should be conducted in the higher frequency range. The results would help to substitute damping materials as mentioned above. These studies will finally serve as a basis for analyzing real lightweight construction structures, e.g. in aviation and the automotive industry.

8. REFERENCES

[1] C.R. Fuller, S.J.Elliot, P.A. Nelson, *Active Control of Vibration*, Academic Press, London, 1996

[2] L. Cremer, M. Heckl, *Körperschall: Physikalische Grundlagen und technische Anwendungen*, 2. Völlig neubearbeitete Auflage, Springer, 1996

[3] J.D. Maynard, E.G. Williams, Y. Lee: "Nearfield acoustic holography. 1. Theory of generalized holography and the development of NAH" J. Acoust. Soc. Am. 78 (4), 1395-1412, (1985)

[4] S.E. Kuo, D.R. Morgan, *Active Noise Control Systems*, Wiley 1996

Adaptive Wing Model for Wind Channel Tests

L. F. Campanile, V. Carli, D. Sachau
German Aerospace Center (DLR) – Institute of Structural Mechanics
Lilienthalplatz 7, D 38108 Braunschweig (Germany)
Email: valerio.carli@dlr.de

ABSTRACT

The aim of this work is to realize an adaptive wind channel wing model by means of a "structronic" concept. The desired geometry changes are achieved through the use of the structural flexibility, and no moveable parts are required.

The wind channel model presents two active sections: the "bump" section, on the upper surface of the airfoil, and the adaptive trailing edge. The changes of the airfoil geometry by means of these parts of the model make possible to vary the distribution of the aerodynamic load on the wing. The activation of the bump and of the trailing edge is realized by means of solide state actuators. A sytem of ca. two hundred shape memory alloy actuators is used. The actuators give here also a contribution to the stiffness of the structure. Here the numerical results of the FEM investigations are presented, as well as the experimental results on the prototypes of the adaptive trailing edge and the bump actuators.

INTRODUCTION

The aerodynamic forces acting on a lifting surface depend directly on its geometry. The more control is exerted on the airfoil geometry, the more influence is gained on aerodynamics.
Aircraft designers are aware of this simple fact since the beginning of aviation history. And before them, zoologist had observed the flight of birds and insects over centuries, learning how nature chooses entire, continuous geometry control as the way of governing aerodynamics and maximize flight efficiency and safety.

Hence, why do airplanes fly with minimal geometry control? Why, even at the beginning of the 21st century, is the vision of an aircraft with full geometry adaptability, and therefore extreme efficiency and reliability, still far from reality?
During the 100 years of aviation history, a lot of changes and improvements occurred in aircraft design, in particular concerning avionics and materials. As far as geometry control is concerned, however, modern aircraft fly almost in the same way as the first ones: the relative motion of rigid surfaces (flight controls, high-lift devices, air brakes) controls very few geometric degrees of freedom. Of course, this constrains not only maneuverability but also efficiency: for most part of its service, the aircraft's geometrical configuration is far from the optimal one.

Since the beginnings of aviation's history scientists are looking for alternative or complementary forms of shape adaptability, with more degrees of freedom and continuous geometry changes. The first inventions concerning lifting surfaces with variable geometry date from the thirties (Hannah, 1930; Rocheville, 1932; Cone, 1939). Fifty years later the research activity in this field became very intensive, as documented by the large number of patents (Frost et al., 1981; Rowarth, 1981;

Paper presented at the RTO AVT Symposium on "Active Control Technology for Enhanced Performance Operational Capabilities of Military Aircraft, Land Vehicles and Sea Vehicles", held in Braunschweig, Germany, 8-11 May 2000, and published in RTO MP-051.

McKinney, 1982; Statkus, 1982), and papers (Hilbig and Wagner, 1984; Renken, 1985; Szodruch, 1985; Greff, 1990) on this topic.

As a rule, the proposed approaches were extensions of the classical solution – denoted “mechatronic” - used for flight controls and high-lift devices and based on mechanisms with moveable parts and discrete forces. The fact that none of the considered concepts is implemented in a practical case testifies that this design philosophy for geometry control is not appropriate for the strict requirements of aircraft design. If realized in such a way, each additional geometry degree of freedom must be paid for in terms of weight and maintenance. This price is evidently too high compared to the advantages of extensive geometry control. As a matter of fact, at the current state of the art, the use of geometry control devices is kept at the minimum indispensable to allow flight at all.

THE “STRUCTRONIC” APPROACH TO THE SHAPE CONTROL MATTER

A mechanical system with moveable parts does not constitute the only possible solution for the realization of structures with variable geometry.
Deliberate use of structural flexibility (the “structronic” way) represents the more complex task from the point of view of structural design; however, the potential of such solution, concerning structural optimization and realization of continuous, multi-degree-of-freedom geometry changes is definitely higher.

Unlike a mechatronic system, which alternates high-stiffness members and elements with infinite flexibility in one or more degrees of freedom (like hinges or linear bearings), a new constraint appears in the design process of a structronic system: an upper limit for stiffness. If stiffness exceed a certain level, it will not be possible to induce the desired shape changes without reaching a critical stress level and therefore endangering the structural integrity. Even if this critical level is not reached, high stiffness requires high actuator forces and, consequently, large and heavy actuator devices.

Due to the new constraint of upper stiffness limit, joining the classical constraints of lightweight design, i.e. maximum displacement under load - which implies a lower limit for stiffness – and an upper limit for the system’s weight, the structural design process becomes a real challenge. It can be expected that in most cases, if classical materials and actuators are used, no solution exists which fulfills all the requirements. Like nearly thirty years ago, when carbon-fiber reinforced composites opened new horizons in lightweight design, the solution of the complex requirement scenario of adaptive lightweight structures will be supplied by a new material class, the so-called active, smart or multifunctional materials.

The maximum-weight and the maximum-displacement-under-load requirements are only indirectly in contrast to another, and the use of a material with high stiffness-weight ratio – like carbon-fiber reinforced composites – can widen the range of possible solutions. However, the upper stiffness limit, imposed by the adaptation task, and the lower stiffness limit of the maximum-displacement-under-load condition are directly opposite requirements, which cannot be uncoupled if a classical, passive material is used.

Only the use of an active material, a solid-state, strain induced actuator provides stiffness for the structural, load-carrying task and, at the same time, comparatively large displacements under actuation.
The features of solid-state actuators make them very attractive even for the classical lightweight structural task: when used in connection with proper controller and sensor systems, such active materials can completely suppress the displacement under

load, and consequently realize a virtually infinite stiffness/weight ratio. That means theoretically zero weight for stiffness-designed structural parts.

A further aspect of solid-state actuators, which is relevant for the use in adaptive aircraft structures, is the very high specific energy compared to classic actuator principles. Due to this feature, the structronic-based geometry adaptation system is likely to be lighter than the mechatronic one not only due to structural weight saving but also due to reduced weight of the actuator device. Moreover, multifunctional materials allow the realization of distributed actuator devices, as requested by a structure with distributed flexibility.

Among available active materials, shape memory alloys (SMA), due to their high active strain and consequently extremely high specific energy are predestined to play an essential role in the field of adaptive aircraft structures.
Shape memory alloys are thermally activated. While activation can occur relatively fast (e. g. through electrical resistance heating), the deactivation process – ruled by cooling – limits the actuator's frequency response. This aspect, which usually constitutes one of the major drawbacks of shape memory alloys, is of secondary importance in the aeronautical environment, where low outside temperatures and high convection allow faster heat transfer.

THE GEOMETRY OF THE WING MODEL

The purpose of tests on the wind channel model is to investigate the possibility to weaken the transonic shock wave that occurs on the upper side of the wing and consequently to reduce the drag.
The model presents two active zones, the "bump" sector and the rear part of the model, usually occupied by the flap, close to the trailing edge. We will refer to this part as the adaptive trailing edge.
Below there are the geometric characteristics of the model and the position of the adaptive areas.

- Chord **c** = 400 mm
- Wingspan **b** = 1 m
- Bump region: between the 65% and the 85% of the chord.
- Adaptivetrailing edge: between the 85% and the 100%.

The wing model dimensions fit with the wind channel sizes, in order to have a two dimensional flow around the model and to reduce the three dimensional effects.

The use of the adaptive characteristics of the model allow to test a lot of different configurations of the wing, simply acting on the control system, avoiding the use of interchangeable rigid parts.
The air conditions during the wind channel tests are typical of a commercial aircraft during the cruise flight and in the high subsonic range.

- Mach number $\mathbf{M}_\infty$ = 0.9
- Total pressure $\mathbf{p_0}$ = 140 kPa
- Temperature **T** = 310 K

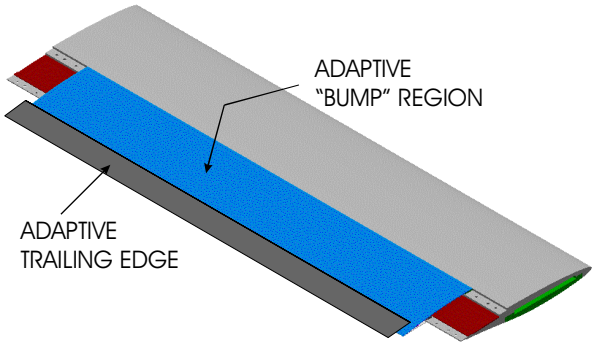


Fig. 1: The wing model and the active areas

THE ADAPTIVE "BUMP" REGION

The "bump" region extends for 80mm chordwise, and the depth of the available space for the actuators amounts to ca. 7 mm. Due to these extremely reduced space availability no practicable concept with classical actuators was found which could realize a reliable deformation independent of the spanwise position.

The maximum aerodynamic load is 47 kPa and it depends on the change of the airfoil camber.

THE ACTUATOR FOR THE "BUMP" REGION

The actuators for the "bump" region are driven by the force exerted by SMA wires. The passive component of the actuator is realized like a composite spring: Every spring is wrapped by a bundle of wires. The number of the wires of the bundle has been determined in order to perform the requested displacement.

The figures below show the design of the composite passive spring and the coupled spring with the wires.

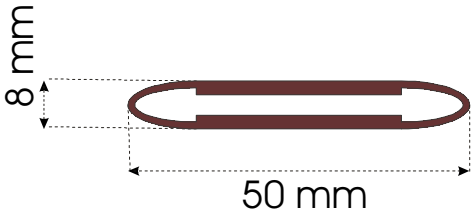


Fig. 2: The geometry of the passive spring actuator for the "bump" region.



Fig. 3: Picture of the "bump" actuator prototype

The longitudinal force exerted by the SMA wires deforms the composite spring, enabling the vertical displacement of the upper and lower straight part of the spring. The actuator element is equipped with a bundle of 20 SMA wires, in order to achieve a vertical displacement of 2 mm.

The figure below shows the spring actuators inserted in the “bump” region. The middle, straight part of the spring elements is bonded to the outer skin and provided with high stiffness in order to avoid local deformations. Both sides of the skin have a curved profile and bend when the wires are activated, producing the desired thickness increase.

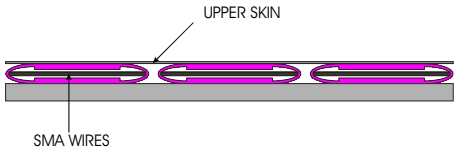


Fig. 4: Spanwise section of the “bump” region

THE RESULTS OF THE TEST ON THE “BUMP” ACTUATOR

Several tests have been conducted in order to determine the longitudinal and vertical displacement as a function of the force exerted by the actuators. The figure below shows the result curves of the test. The maximum transversal displacement was well above the required displacement of 2 mm. Some of this performance reserve will be used after mounting into the bump region, since the actuator elements have to balance the additional stiffness due to the skin. The wires were heated electrically. The minimum activation current was ca. 5A, and the corresponding voltage was 1 V.

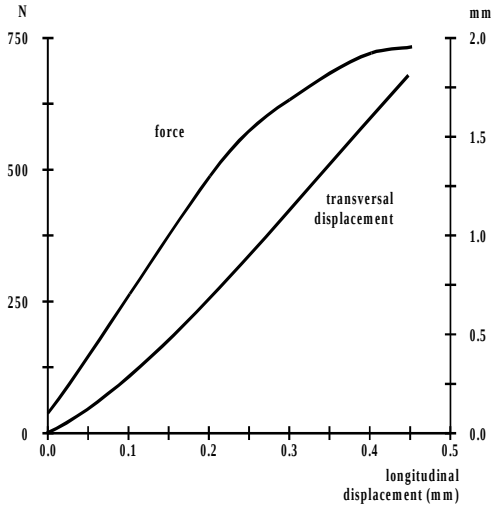


Fig. 5: Spring characteristics of the actuator prototype

GEOMETRY AND DISPLACEMENTS OF THE ADAPTIVE TRAILING EDGE

The trailing edge structure extends between the 85% and the 100% of the chord of the wing model, as already mentioned. That means a 60 mm chordwise extension of the adaptive trailing edge, and a maximum thickness at the root of 9.11 mm. The following figure shows the geometry of the adaptive structure.

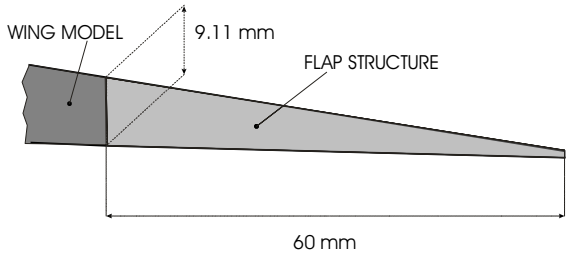


Fig. 6: The geometry of the adaptive trailing edge

The deflection of the adaptive trailing edge is directed either upward or downward, in order to achieve a cambering and a decambering of the wing model.
The minimum requested relative rotation of the trailing edge respect to the rest of the model is of 1° upward and of 3° downward.
The following figure shows the displacement of the tip of the trailing edge to achieve the requested rotations.

	ROTATION	TIP DISPLACEMENT
UPWARD	1 deg.	1.05 mm
DOWWARD	3 deg.	3.145 mm

Fig. 7: Displacements and rotations of the tip of the wing model

THE AERODYNAMIC LOAD

The aerodynamic load on the wing model depends on the deflection of the trailing edge. There are three different situations: the clean configuration, the three degrees cambered form and the one degree decambered form. The figure 8 shows the aerodynamic load on the upper and lower side of the trailing edge contour, as it has been computed in the numerical model of the structure, for the three degrees cambered configuration. With **P** we indicate the local value of the pressure respect to the adimensional coordinate **X/c** and with **p** the value of the freestream pressure.

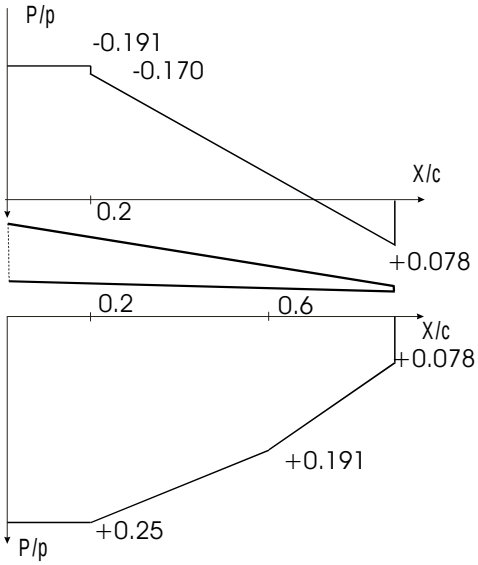


Fig. 8: The local pressure distribution on the trailing edge for the three degrees cambered configuration.

When the structure assumes the three degrees cambered configuration, the wing model experiences the highest aerodynamic load. The load on the wing model structure is 1300 N, that means an everage pressure of ca. 22 kPa. In the one degree decambered configuration the load is only 730 N, nearly half of the former situation.

THE MAXIMUM DISPLACEMENT DUE TO THE AERODYNAMIC LOAD

A very strict condition is assigned on the deformation of the adaptive structure induced by the aerodynamic load. For every load condition and every configuration assumed by the trailing edge the upper limit of the deformation is 0.1 mm.
A high stiffness structure is capable to control the deformation due to the aerodynamic load, while a low stiffness structure needs low forces exerted by the actuators to achieve the requested displacements.
Furthermore a very stiff structure could suffer high levels of strain and stress, those can bring the structure to fail.
Therefore the goal is to realize a trade off between the opposite characteristics of the adaptive structure, as will be clear in the next pages.

THE ACTUATORS ACTION AND THE WIRES-STRUCTURE COUPLING

The reduced dimensions of the wing model constitute one of the main problems to realize the adaptive structure. The use of solid state actuators, e.g. shape memory alloy wires, fits with the geometry of the trailing edge structure and with the purposes of the project.

The use of wireshaped actuators allows to insert them in the hollow shell structure of the model, achieving an internal actuator system. For our purposes we use Ni-Ti alloy based actuators with high transformation temperature, in order to have a quick response behavior. The diameter of the wires is 0.38 mm.

The following figure shows the coupling between the trailing edge passive structure and the SMA actuators.

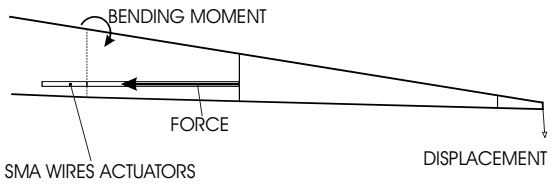


Fig. 9: The coupling between the trailing edge passive structure and the actuators.

The vertical stiffeners control the local deformations of the upper and lower skins. Furthermore the front stiffener connects the wires to the trailing edge structure and transfers the forces between the passive structure and the actuators. The action exerted by the wires determines a cambering bending moment that deforms downward the structure. The stored elastic energy of the deformed structure acts as “bias” effect to reactivate the memory of the material.

The use of “one way” shape memory effect actuators doesn‘ t allow to decamber the wing model as requested. In order to achieve also this feature of the trailing edge, a new reference configuration has been determinated, a one degree decambered configuration as new undeformed trailing edge structure. Partially heating the wires carries the structure to the clean form, the original shape of the airfoil. A further heating drives the structure through the cambered configurations up to the three degrees final feature.

As mentioned before the design of the adaptive structure should realize a trade off between a high stiffness value, in order to meet the upper bounded deformation task, and a reasonable flexibility, in order to realize the requested dispalcement.

Two possibilities have been investigated:

- A very high stiffness passive trailing edge structure, able to control the deformation under the maximum aerodynamic load , according to the request. As a consequence of this design, high actuation forces are necessary to displace the structure. Furthermore this implies high stress and high strain levels.

- A global stiffness of the adaptive trailing edge, i.e. the passive structure and the wireshaped actuators, able to match the minimum value to control the deformation due to the maximum aerodynamic load. This design allows to exert lower actuation forces and to bound the maximum values of stresses and strains.

FINITE ELEMENT ANALYSIS OF THE ADAPTIVE TRAILING EDGE

Through the finite element model of the trailing edge we want to analyze the 2D behavior of the structure. Exspecially we want to determine:

- The position of the vertical stiffeners inside the structure.
- The thickness of the skins.
- The number of the actuators.

Furthermore the new one degree decambered reference configuration needs to be investigated.
In the following we describe the design of the trailing edge, according to the second realization above mentioned. That design meets all the requirements of the project. At the end of this chapter can be found a comparison between the two designs of the adaptive structure.

In the actual design of the adaptive trailing edge the structural contribution of the SMA wires actuators play an essential role. This contribution allow us to determine a lighter structure and lower actuation forces as well.
An appropriate design of the cross section of the upper skin panel, together with the material selected for the analysis, determines the global and local stiffness of the airfoil in order to achieve:

- Together with the wires the required global stiffness able to bound the displacement under the maximum aerodynamic load.
- A smooth profile of the airfoil, under every aerodynamic load as well as under the actuators action.
- A “passive” stiffness, i. e. the contribution of the structure without actuators, able to stretch again the wires after activation and to reactivate the memory of the material.

The most important component of this design is the upper skin panel, between the root of the trailing edge and the inner vertical stiffener. This acts as a spring, carrying most of the aerodynamic load and provided of the right stiffness to deform under the actuators forces as required. The rest of the skin panels are designed in order to have a smooth contour of the airfoil.

The adaptive trailing edge is connected to the wing model through the extended upper skin panel. That solution avoids discontinuities in the wing profile and realizes a smooth shape. The lower skin panel is not connected with the wing model, enabling the deflection of the trailing edge structure. A double connection of the trailing edge even through the extended lower skin panel results too stiff for the purposes of the project. The position of the vertical stiffeners inside the hollow structure of the trailing edge is important to control the deformation of the panels due to the aerodynamic load. Expecially the inner stiffener performs several tasks:

- Transfers the loads between the coupled passive structure and the actuators. This should be done without appreciable derformation of the stiffener.
- The position inside the structure determines the width of the inner stiffener and the length of the wires.

The clockwise moment exerted by the actuators depends on the lever arm of the forces respect to the upper connection of the skin panel. The displacement of the application point of the forces, and as a consequence of the whole structure, depends on the length of the wires.

THE RESULTS OF THE FINITE ELEMENT ANALYSIS

The finite element analysis has been performed with the software ANSYS version 5.4. The figure below shows the section of the finite elemet model of the trailing edge and the wires actuators.

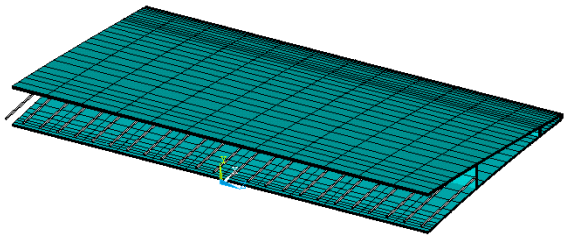


Fig. 10: The finite element model of the trailing edge.

The upper and lower skin panels as well as the two vertical stiffeners have been implemented with SHELL 99 elements, while the wires have been implemented with the LINK 8 elements. The design of the trailing edge structure, i.e. the optimization of the cross section of the panels, the position of the vertical stiffeners and the number of the wires, has been performed for the 0 degree cambered configuration under the maximum aerodynamic load condition experienced by the wing model. The front end of the upper skin panel is fixed in all 6 degrees of freedom: this assumption takes in count the high stiffness of the rest of the model, compared with the flexibility of the adaptive trailing edge.

The number of wires is a trade off between their contribution to the global stiffness of the adaptive structure and the force that they are able to exert to move the trailing edge. Each single wire contributes as a spring against the aerodynamic load acting on the wing model. The constant of the equivalent spring represented by the wire can be computed as:

$K_w = EA / L$

where E is the Young modulus of the alloy, A is the area of the section and L is the lenght of the wire. The Young modulus depends on the state of the alloy, i.e. on the temperature and on the applied load.

The upper and lower skin panels, as well as the vertical stiffeners, are carbon fiber reinforced laminates. The stacking sequence is optimizated according to the different properties of the panels.
In order to perform a linear analysis af the mechanical behavior of the wing model, and exspecially of the trailing edge structure, the new one degree decambered reference configuration has been determinated through the numerical application of opposite forces respect to the forces exerted by the actuators. For this pourpose the contribution to the global stiffness of the wires is neglected.



Fig. 11: The one degree decambered reference configuration

The finite element model has been updated according to the new reference shape. The following picture shows the new, one degree decambered, and the old reference configuration. The displacements of the following figures are not in scale.

The first step is to evaluate the deformation of the structure under the action of the aerodynamic load corresponding to the one degree decambered configuration. In this configuration the wires are in the cold state and they express the lowest Young modulus value. The following figure shows the deformation of the structure.

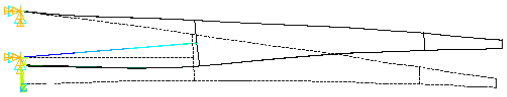


Fig.12: The displaced new configuration: Section

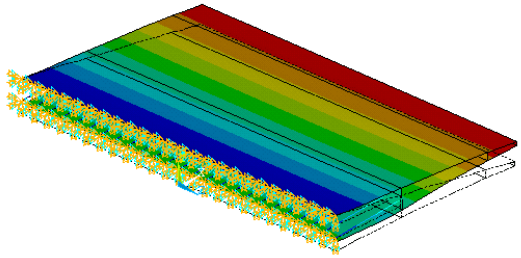


Fig. 13: Displacements due to the aerodynamic load of the new reference configuration

The activation of the wires in the numerical model is taken in count through forces acting in the nodes connecting the wires and the inner vertical stiffener. The next figures show the deformed section of the trailing edge and the distribution of the displacements in the structure.

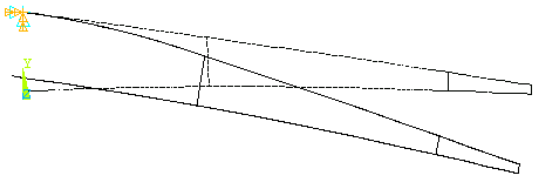


Fig: 14: Section of the displaced structure due to the action of the actuators

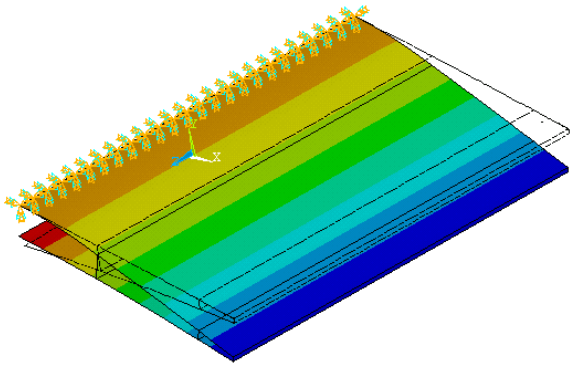


Fig. 15: The deformed structure under the action of the SMA wires

THE COMPARISON BETWEEN THE HIGH STIFFNESS STRUCTURE AND THE LOW STIFFNESS STRUCTURE

As mentioned before, two different approaches have been investigated to realize the adaptive structure: a very stiff passive structure, able to carry the aerodynamic load and to bound the consequently deformations, and low stiffness structure, able, with the structural help of the wires, to achieve the same task. The second solution showed better possibilities of success. We present now a brief comparison between the two structures, through the results of the ANSYS analysis. For this purpose the material is aluminium.

The comparison is made through the stiffness of the upper skin panel, i.e. the flexural rigidity D, and the forces exerted by the actuators.

Indicating with D the following quantity:

$$D = E h^3 / 12 (1 - \nu^2)$$

where h is the thickness of the panel, and with the index H and L the high and the low stiffness configuration, we have:

$D_H = 170$ Nm $\quad D_L = 31$ Nm

The forces exerted by the actuators, as a continuous distribution of wires along the wingspan, is:

$F_H = 1300$ N/ cm $\quad F_L = 250$ N/ cm

This short overview shows that the low stiffness structure is more suitable for the pourposes of this work. The reduced dimensions of the model make very difficult to insert a great number of actuators inside the structure and therefore the availability of high actuation forces.

EXPERIMENTAL RESULTS ON THE ADAPTIVE TRAILING EDGE PROTOTYPE

In order to test and verify the results of the numerical model and, expecially, to get some experience with this new technology, a prototype of the adaptive trailing edge with the internal actuators‘ set has been designed and built.
This prototype is slightly different from the numerical model: The main pourpose of the tests is to verify the connection between the wires and the passive structure and to verify the transfer of the forces between the actuators and the trailing edge structure. Both the upper and lower skin panels are carbon fiber reinforced laminates, according to the stacking sequences of the numerical model. The vertical inner stiffener is steelmade, instead of composite material fabrication and it is glued to the upper and lower skin panels. The prototype is lacking of the outer stiffener: During the experimental tests the adaptive structure doesn‘ t experience any aerodynamic load.
The prototype of the adaptive trailing edge extends 220 mm spanwise, and the lower skin panel extends 50 mm chordwise, in order to allow the clamping of the prototype for the tests. The figure 16 shows the prototype of the adaptive trailing edge.
For the purposes of the tests the heating of the SMA actuators has been achieved throug the Joule effect, as a consequence of the flow of an electric current in the wires.



Fig. 16: The prototype of the adaptive trailing edge

Therefore the actuators have been connected to a current-tension generetor, able to supply up to 580 Ampere. The cooling phase is effected through the surrounding air by convection.
The actuators‘ set consists of 192 wires, joined together in 12 bundles of 16 wires each one. The following pictures show the displacement of the upper left and right corner of the tip of the trailing edge and the average value, as a function of the current and the voltage.

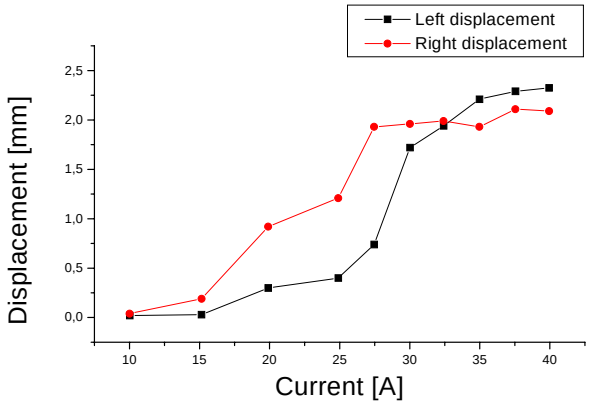


Fig. 17: The displacement as a function of the current

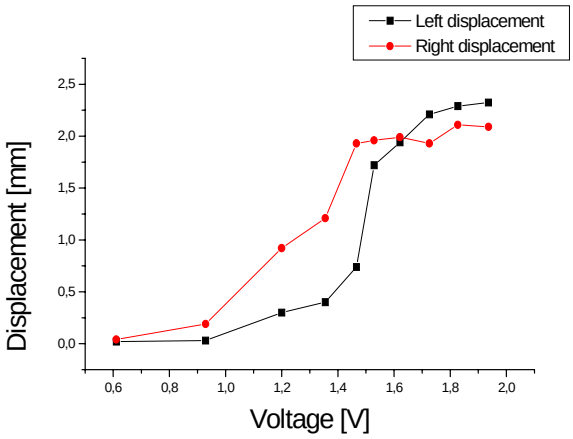


Fig. 18: The displacement as a function of the voltage

Unfortunately the failure of the glued connection of the metal stiffener with the upper skin panel carried the displacement of the tip of the trailing edge only up to ca. 2.5 mm. The high heat flux through the metal part, due to the heating of the wires, raised the temperature of the glued joint and reduces its strength.

CONCLUSIONS

The features of shape memory alloys make them very attractive as actuator materials for adaptive aerospace structures. In this work the use of such a material is extended to their structural contribution: this new approach allows to actively modify the stiffness of a structure, changing the internal structure of the material and using this property as an induced strain actuator. This new aspect of designing adaptive systems presents new problems and new fascinating opportunities.

The experimental tests show the feasibility of this concept, and new tests are performed at the present time.

A more fine analysis of the coupling between structures and SMA actuators and the integration of these materials in the composite materials must be carried on, to investigate all the possibilities that this new design can offer.

REFERENCES

" EXTENSIVE GEOMETRIC ADAPTABILITY IN AEROSPACE STRUCTURES BY MEANS OF SHAPE MEMORY ALLOYS"
L.F. Campanile, V. Carli, D. Sachau
38th conference of Metallurgist, Quebec 1999

" A NEW STRUCTURAL APPROACH TO VARIABLE CAMBER WING TECHNOLOGY OF TRANSPORT AIRCRAFT"
Claus Bauer, Willi Martin, Hans-Friedrich Siegling-
Dailmer- Benz A G
AIAA, 98 - 1756

"DEVELOPMENT AND DESIGN OF FLEXIBLE FOWLER FLAPS FOR AN ADAPTIVE WING"
Hans Peter Monner, Holger Hanselka, Elmar Breitbach
German Aerospace Center-Braunschweig.
SPIE's 5th Annual Int. Symposium on "Smart structures and Materials" San Diego, CA 1-5 March 1998.

"ADAPTIVE AIRCRAFT WING"
J.N.Kudva, A.J. Lockyer, K. Appa – Northrop Grumman Corporation
AGARD SMP Lectures Series,1996

"SHAPE MEMORY ALLOYS"
C.M. Wayman
MRS Bulletin, Aprile 1993

"ENGINEERING ASPECTS OF SHAPE MEMORY ALLOYS"
T.W. Duerig, K.N. Melton, D. Stockel, C.M. Wayman

This page has been deliberately left blank

Page intentionnellement blanche

A Concept of a Shapevariable Fowler Flap on Transport Aircraft

Christian Anhalt **Elmar Breitbach** **Delf Sachau** [1]

German Aerospace Center (DLR), Institute of Structural Mechanics, Lilienthalplatz 7, 38108 Braunschweig, Germany

Dipl.-Ing. C. Anhalt		Prof. Dr.-Ing. E. Breitbach		Dr.-Ing. D. Sachau	
Tel.	+49 (531) 295-2354	Tel.	+49 (531) 295-2300	Tel.	+49 (531) 295-2316
Fax	+49 (531) 295-2876	Fax	+49 (531) 295-2875	Fax	+49 (531) 295-2876
E-mail	christian.anhalt@dlr.de	E-mail	elmar.breitbach@dlr.de	E-mail	delf.sachau@dlr.de

ABSTRACT

This paper presents a part of the major project "Adaptive Wing (ADIF)" of the partners German Aerospace Center (DLR), DaimlerChrysler Research, and DaimlerChrysler Aerospace Airbus. Using the Airbus A330/340 fowlerflap as an example, the objective of this project is to show, how the high lift behavior of modern transport aircraft can be improved by intelligent structural concepts, without negative effects on cruise flight. Even an improvement in transonic flight is possible. For this, a combination of passive and active measures is necessary, as the following paper shows.

INTRODUCTION

Wings of modern transport aircraft are optimized for cruise flight. They have a transonic wing profile with the best lift/drag ratio at high speed. For flights at low speed this type of profile is inapplicable. Therefore, the required additional lift for take off and landing is achieved by using high lift devices, such as slats at the leading edge of the wing and flaps at the trailing edge [1]. In cruise configuration slats and flaps are retracted. A special type of a high lift device is the fowler flap, used in the Airbus A330/340. The lift increasing effect of this flap is based on enlarging the wing area, increasing the airfoil camber, and accelerating the airflow within the gap between wing and extended flap (**Fig. 1**).

The fowler flap used in the Airbus A340 has some disadvantages. Due to the elasticity of the carbon fiber, of which the flap skin is made, the trailing edge of the flap deforms when airload is applied. These deformations lead to higher drag during cruise flight, which means that the efficiency of the airplane is decreasing. Another disadvantage is the necessity of three flaptracks, which means higher weight, higher complexity, and higher costs, compared to a bedding on only two tracks. The middle track is used to force the elastic line of the flap into the same shape as the elastic line of the wing in this region. Matching elastic lines are necessary for the proper shape of the gap between wing and flap. The acceleration of the air inside the gap is based on the nozzle effect. If the gap is too wide, there will be no adequate acceleration. On the other hand, if the gap is too narrow, it will be plugged up with boundary layer which means, that no air from the lower side of the wing can go through the gap to the upper side. In both cases there is no adequate energy enrichment of the airflow on the upper side of the wing, which leads to flow separation. The lower lift due to separation can not be accepted in a part of the flight, when every percent of lift is needed. This means, that the size of the gap is crucial to the efficiency of the flap and finally to the whole high lift behavior of the aircraft.

Paper presented at the RTO AVT Symposium on "Active Control Technology for Enhanced Performance Operational Capabilities of Military Aircraft, Land Vehicles and Sea Vehicles", held in Braunschweig, Germany, 8-11 May 2000, and published in RTO MP-051.

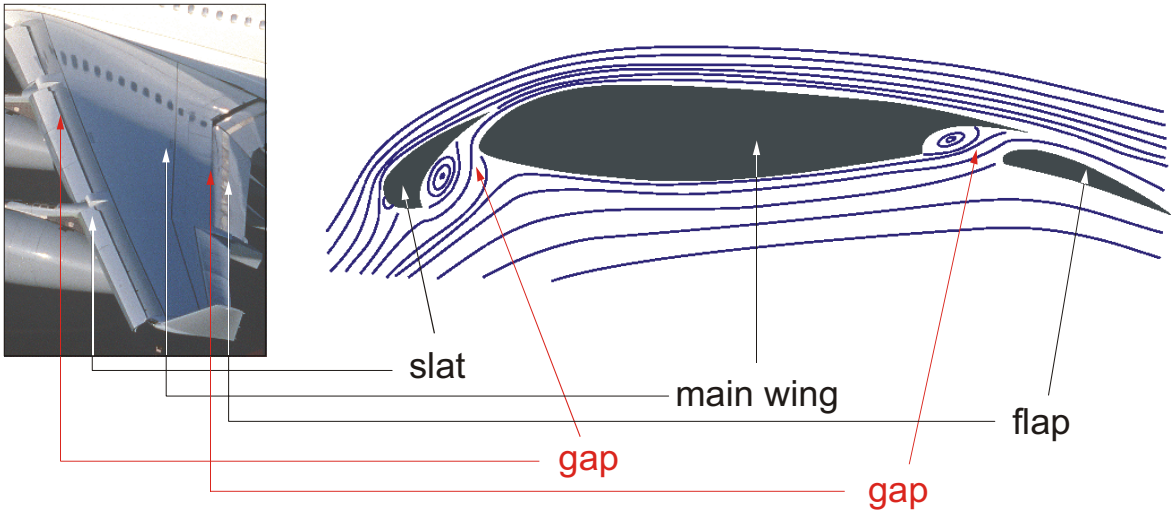


Figure 1: Airfoil with extended slat and flap

OBJECTIVES OF THE PROJECT

The topic “Shapevariable Fowler Flap”, part of the major project “Adaptive Wing (ADIF)” of the partners German Aerospace Center (DLR), Daimler-Chrysler Research, and DaimlerChrysler Aerospace Airbus has the objective to decrease drag, complexity, weight and costs. To realize this, the flap track number at the A340 will be reduced from three to two. Therefore, a totally new design of the flap due to the required higher stiffness in spanwise direction is unavoidable. In the course of this redesign it is possible to gain a better control of the gapshape, in order to improve the high lift behavior. To realize this, passive means, such as the optimization of the stiffness distribution and track positions, pre-deformation, and aeroelastic tailoring as well as active means like the integration of an actuator into the flap is necessary.

One positive effect of the higher flap stiffness is the decrease in deformations at the flaps trailing edge during cruise flight, leading to lower drag. With the structurally integrated actuator it is possible to reduce vibrations, induced by external loads. Furthermore, the additional loading of the wing due to the middle flap track disappears, the desired elastic line of the flap is accomplished with flap-internal constraints (e.g. actuators).

REDESIGN OF THE FOWLER FLAP

The redesign of the Airbus A340 fowler flap, bedded on two flaptracks is performed in the following steps:

1. Identification of the crucial load cases.
2. Determination of the wings elastic line as a reference for the elastic line of the flap.
3. Determination of the track position combination with minimal flap deformation using a simple beam model.

4. Calculation of the required stiffness distribution leading to the desired flap deformation with applied airload.
5. Design of a structurally integrated actuator allowing an adaptation of the elastic lines.
6. Transfer of the determined stiffness distribution from the beam model to the real flap using a parametric finite element model of the fowler flap including spars, ribs, stringers, and tailored skin. Pre-deformation, aeroelastic tailoring and the integrated actuator are considered.
7. Detailed design of critical parts, e.g. spar/actuator interface with an extremely high stiffness.
8. Examination of the dynamic behavior of the flap with integrated actuator.

To show, how the redesign actually is made, all the above mentioned steps are given in detail below.

There are some hundred loadcases at the design phase. For the preliminary design of the two-track-flap it is impossible and needless to consider all of them. Instead, the four dimensioning loadcases were chosen [2].

In loadcase RS1 the cruise load is applied and the flap is retracted. This loadcase is essential for the cruise flight stiffness design. The other loadcase with a retracted flap is R2. In this loadcase the recovery after an emergency dive is considered. With the highest possible airload this loadcase is used for the strength design of the flap. At the remaining two loadcases S26 and S32 the flap is extended with 26° and 32°. At these loadcases the stiffness design, crucial for the gapshape, is performed. With these four loadcases the main part of the flight envelope is considered, enough for a preliminary design.

The elastic line of the wing is the reference for the calculation of the flap stiffness. Both elastic lines have to match tightly, in order to guarantee a constant gap size. With a known reference line and known airloads it is possible to calculate the necessary flap stiffness for all four loadcases. The elastic line of the wing (reference line) is calculated with local deformations at the flaptracks and the spoiler hinge line. Due to the wing sweep there is a bending-torsion-coupling (**Fig. 2)**, that has to be considered. This coupling leads to the necessity of aligning the flap stiffness axis in a certain angle to the spanwise direction, known as aeroelastic tailoring[3,4,5]. With this measure it is possible to make sure, that there are no gaps between inner and outer flap and between flap and aileron.

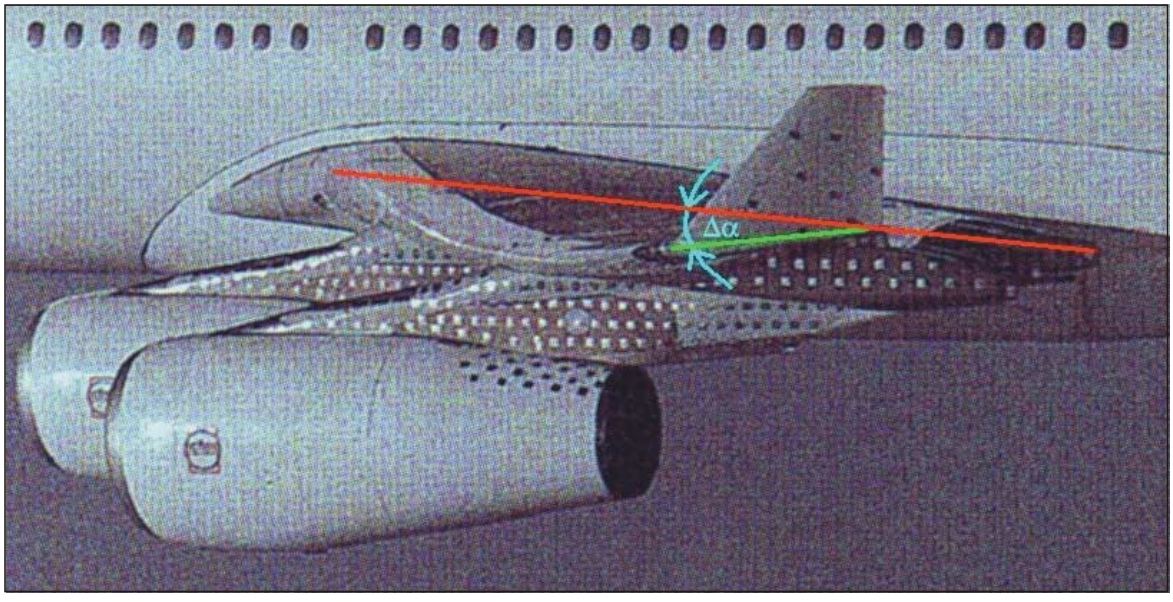


Figure 2: Elastic line of the wing

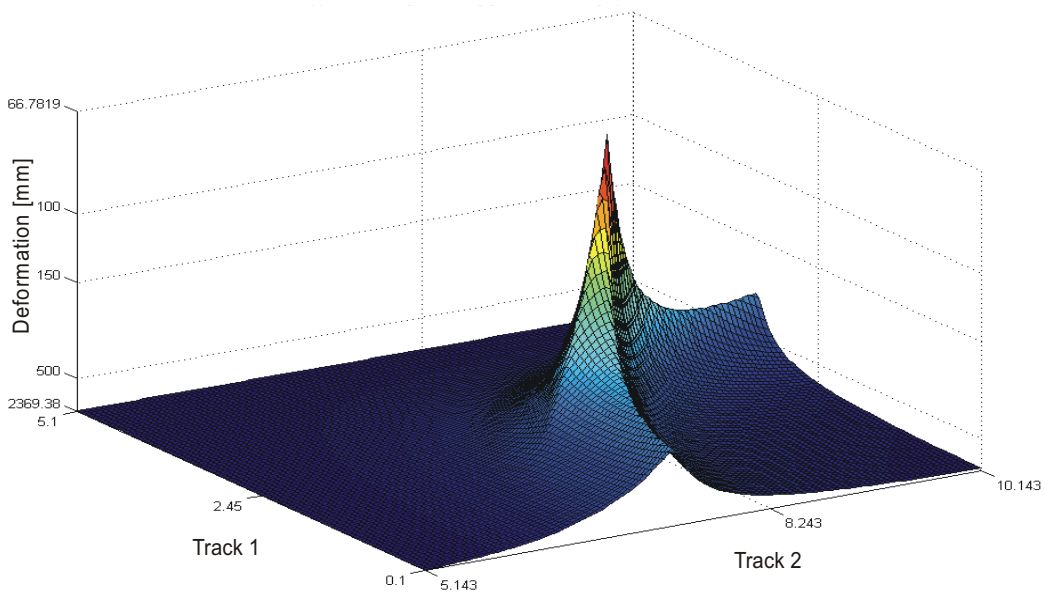


Figure 3: Optimization of the flaptrack positions

The determination of the best track positions is extremely important for the deformation of the flap. **Fig. 3** shows, that there is a difference of approximately 3500% in flap deformation between the best and worst track positions. For the track position calculations the stiffness distribution of the original flap was used.

The integration matrix method and a beam model of the flap was used for steps 3, 4, and 5 of the redesign. There are some advantages of this method, compared with a complex FE-model [6]. First of all, the calculation time is much lower, making parameter studies possible. Loop programming for a stiffness optimization is very simple. A big advantage of this method is the possibility to integrate an actuator into the model. It is possible to load the beam with a single actuator force or an active bending moment distribution. That makes it easy to see, how an actuator can influence the elastic line of the flap.

With the determined optimum track positions for all four loadcases it is possible to calculate the required stiffness distributions in order to achieve the desired elastic lines.

There is a difference in the four stiffness distributions, due to the different loads and reference lines. Therefore, the chosen passive flap stiffness can only be a compromise with special attention to the extended flap loadcases.

The adaptation between the elastic lines at different loadcases can only be achieved with an active adaptation of the stiffness distributions. Therefore, an actuator has to be integrated into the loadpath of the structure. Two different types of actuators are possible–a discrete actuator for a discrete active moment or a distributed actuator [7]. Both actuator types have advantages and disadvantages.

A distributed actuator can be integrated into the skin of the flap. The advantage is, that there is no necessity for a special load introduction due to the distributed load. This type of actuation is the most efficient one. Unfortunately there are some critical disadvantages. The most important problem is the capability of the present array-actuators (e.g. PVDF) to withstand the applied loads (forces, moments, and temperatures) and their amount of active deformations. Another problem is the integration into the skin without forcing delaminations.

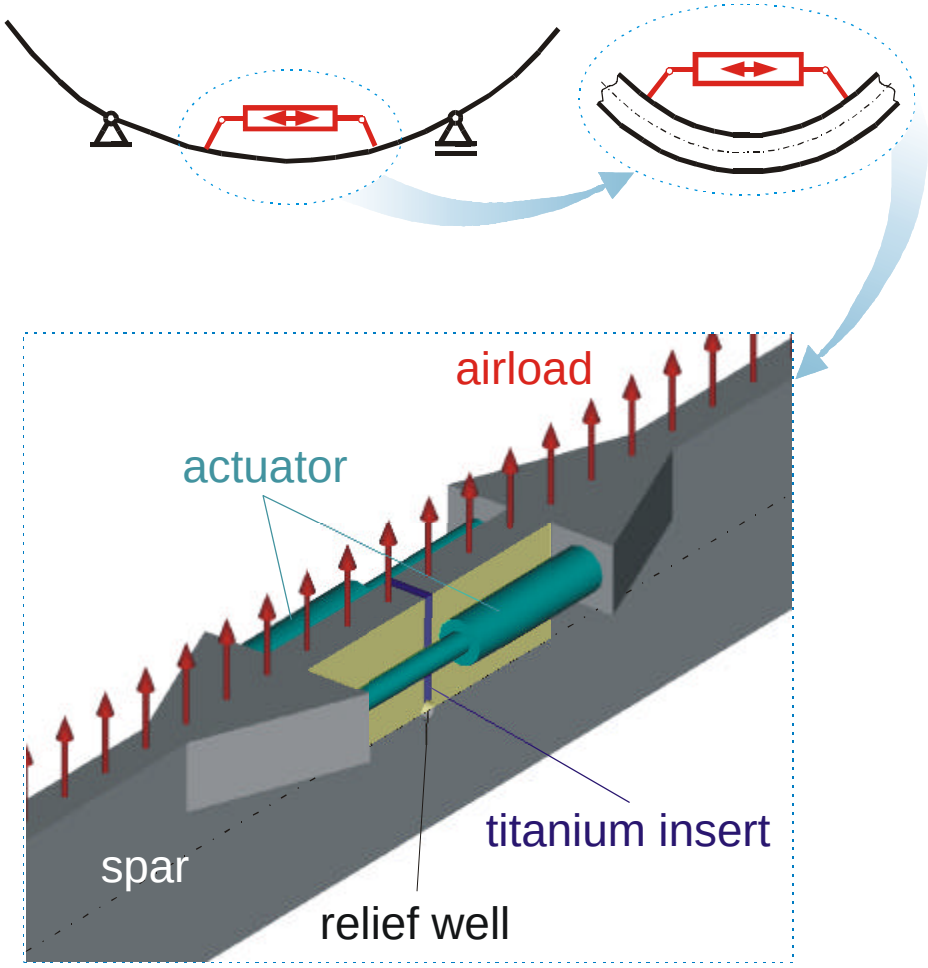


Figure 4: Integration of the actuator into the spar

The discrete actuation needs a special load spread and distribution into the structure. This interface has to be extremely stiff, otherwise the stroke of the actuator is lost due to the elasticity. There is a big variety of discrete actuators, for example piezo stacks, shape memory alloys or even hydraulic systems. For the best efficiency discrete actuators have to be integrated into the spar of the flap, because of the highest stiffness concentration. The other structural elements like ribs, stringers, and the skin remain as passive elements.

A concept for the integration of an actuator is shown in figure 4. The spar has an extremely narrow gap on the upper side (pressure side), reaching down to the relief well at or above the neutral axis. The gap is reinforced with a titanium insert for a smoother load distribution into the spar. When airload is applied, both sides of the gap are pressed together. In this case the spar acts like one without gap.

The remaining cross section of the spar must be able to withstand all occurring negative loads, e.g. landing shocks or gust loads. A stopper on the upper side of the spar guarantees, that there is no unacceptable large deformation in these cases. Due to the low negative loads, compared with the positive design loads, the stopper is only a safety device. Under normal circumstances it is not going to be used.

With the integration matrix method is it possible to calculate the deformation of the flap under the load of active forces and moments. Preliminary estimations with this method have shown, that the weight of a piezoceramic stack actuator is approximately 55 kg per flap, compared to 140 kg of the saved flaptrack.

All the above mentioned calculations were performed with a beam model and the integration matrix method. As a result, the required stiffness distributions are known. For the transfer into the real flap structure a parametric finite element model with spars, ribs, stringers, and tailored skin has to be designed (**Fig. 5**). The dimensions of the structural elements have to be varied, in order to find the solution with the lowest weight. A substitute-stiffness can be used to model the actuator. With the FE-model it is also possible to find the best fiber angle for the bending torsion coupling, in order to prevent gaps at the inner and outer side of the flap.

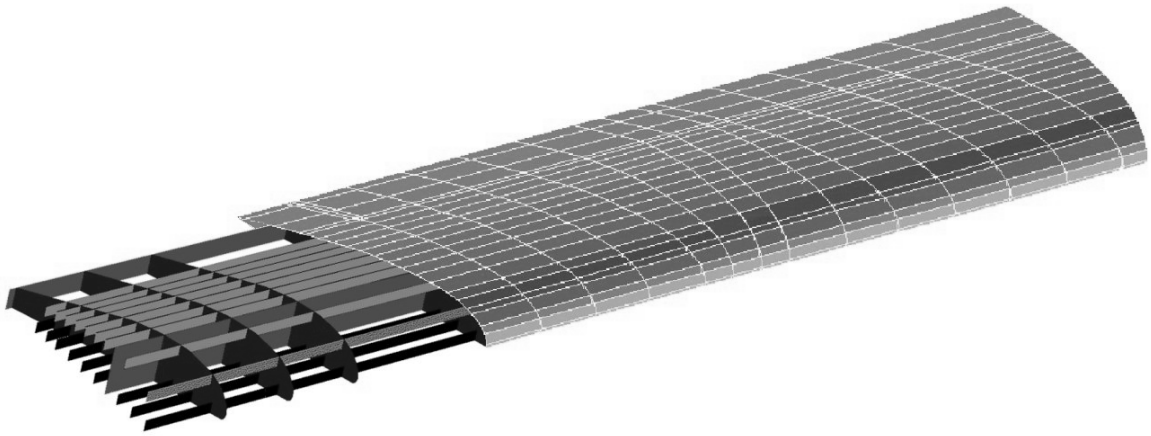


Figure 5: Finite element model of the fowler flap

When the global design of the flap is finished details have to be examined. One of the most difficult problems is the above mentioned interface between spar and discrete actuator. The spar has to be very stiff in order to provide an efficient integration, on the other hand the spar has to have a certain elasticity to be able to be deformed by the actuator [8].

Another difficult detail is the connection of the tracks and the flap itself. All forces between wing and flap are carried by the tracks. These forces are very high and have to be spread and distributed into the flap, without causing any damage.

If a piezoceramic stack actuator or a hydraulic system is used to deform the flap in the desired static way, it is possible and useful to check the dynamic properties of the flap. Although it was not a primary objective of the re-design, a vibration control will be necessary in future aircraft. At the moment there are no critical vibration problems, but with increasing size and elasticity of upcoming flaps (A3XX) this problem will become urgent in the near future. Even the influence of an actuator on the dynamic behavior of the flap can be determined. With a modal analysis is it possible to calculate the eigenvalues of the flap, using the existing finite element model. This eigenvalues are the basics for a following *Harmonic Response Analysis*. The result of this calculation is the reaction of the flap structure to the actuators stimulation.

PROBLEMS TO BE SOLVED

There are several problems that have to be solved during the redesign of the flap. The following list shows the most important ones, but does not claim to be complete.

- The optimization of the track positions and the stiffness distribution depends on a big variety of independent variables. Therefore, it is very difficult to find an absolute optimum.
- The transformation of the stiffness distribution from the beam model to the real flap offers a wide choice of structural opportunities. The solution with the minimum structural weight has to be found.
- There must be an input value of the gapsize, in order to know how the flap has to be deformed by the actuator. Two ways are possible to get this value, either with a sensor and a real time controller, or with previously measured values, depending on the angle of attack, the speed and the actual weight of the aircraft. If possible, the second way is to be favored, due to lower costs and fault liability.
- The interface spar/actuator must have an extremely high stiffness, in order to provide a good actuator performance.
- The *fail safe* concept has to be guaranteed, even if the actuator fails. Otherwise it is not possible to get the FAR- or JAR - approval for the aircraft.
- If piezoceramic stacks or shape memory alloys are used for actuation, the power supply can become problematic, due to the special energy demand of these actuators. The usage of a hydraulic actuator is no problem, due to the available hydraulic system in transport aircraft.
- The accessibility and maintainability of the active components must be possible, otherwise these elements have to be maintenance-free. The service life of the actuator or at least the TBO (time between overhaul) has to be as long as the normal maintenance interval of the flap mechanism.
- The biggest problem of all is the price of the active fowler flap. All efforts were made to increase the efficiency of the aircraft. If the achieved profit of this means is lower than their costs (initial and maintenance costs), it is not reasonable to change the flap design.

CONCLUSIONS

The presented paper describes an approach to save one flaptrack of a fowler flap, at the example of the Airbus A340. This requires a totally new design of the flap, in order to fulfill the aerodynamic demands. In the course of this redesign, a configuration can be found that improves high lift behavior as well as cruise flight efficiency. These improvements are the result of a smart combination of passive and active means. The passive design must be very accurate, in order to guarantee that the active parts of the flap are only necessary for finetuning. Therefore, a combination of optimal track positioning, reasonable stiffness distribution (including aeroelastic tailoring), pre-deformation of the flap, and integration of an actuator is necessary. First results show that the desired objectives are achievable.

ACKNOWLEDGEMENTS

The present investigation was carried out by the department Adaptronics of the DLR Institute of Structural Mechanics in collaboration with the partner DaimlerChrysler Aerospace Airbus as a part of the major project ADIF (Adaptiver Fluegel - Adaptive Wing).

REFERENCES

1. Roskam, J.; *"Airplane Design Part I-VIII"*; DAR Corporation, Lawrence, Kansas, USA; 1996
2. *"Report No. 27 F021 K7140 C02, Deflections of Wingbox for Movable Parts at Trailing Edge, Airbus A340-300"*; Deutsche Aerospace Airbus; 1994
3. Niu, M.; *"Composite Airframe Structures"*; Hong Kong Conmilit Press; Hong Kong; ISBN 962-7128-06-6; 1996
4. Niu, M.; *"Airframe Structural Design"*; Hong Kong Conmilit Press; Hong Kong; ISBN 962-7128-09-0; 1988
5. Moser, K.; *"Faser-Kunststoff-Verbund"*; VDI-Verlag GmbH; Düsseldorf; ISBN 3-18-401187-9; 1992
6. Büter, A.; *"Untersuchung adaptiver Konzepte zur Reduktion von Hubschraubervibrationen, zur Minderung des Hubschrauberlärms und zur Steigerung der aerodynamischen Effizienz"*; Dissertation RWTH Aachen; 1998
7. Barrett, R.; *"Introduction to Adaptive Aerostructures"*; Conference at the University of Stuttgart, Germany ; 1998
8. Breitbach, E.; *"Vorlesungsskript Adaptronik"*; Technische Universität Braunschweig; 1998

Active Control Technology at Nasa Langley Research Center

Richard R. Antcliff
NASA Langley Research Center, MS 113, Hampton, VA, U.S.A. 23681
Anna-Marie R. McGowan
NASA Langley Research Center, MS 254, Hampton, VA, U.S.A. 23681

NASA Langley has a long history of attacking important technical opportunities from a broad base of supporting disciplines. The research and development at Langley in this subject area range from the test tube to the test flight. The information covered here will range from the development of innovative new materials, sensors and actuators, to the incorporation of smart sensors and actuators in practical devices, to the optimization of the location of these devices, to, finally, a wide variety of applications of these devices utilizing Langley's facilities and expertise.

Advanced materials are being developed for sensors and actuators, as well as polymers for integrating smart devices into composite structures. Contributions reside in three key areas: computational materials; advanced piezoelectric materials; and integrated composite structures.

The computational materials effort is focused on developing predictive tools for the efficient design of new materials with the appropriate combination of properties for next generation smart airframe systems. Research in the area of advanced piezoelectrics includes optimizing the efficiency, force output, use temperature, and energy transfer between the structure and device for both ceramic and polymeric materials. For structural health monitoring, advanced non-destructive techniques including fiber optics are being developed for detection of delaminations, cracks and environmental deterioration in aircraft structures.

Innovative fabrication techniques for processing structural composites with sensor and actuator integration are being developed. A majority of this research will be completed for specific applications including the fabrication of a composite panel with embedded shape memory alloys (SMA) for reducing sonic fatigue in aircraft structures. The research in each of these key areas has been designed to meet application needs of the customers including aeroelastic tailoring, noise cancellation, and laminar flow control. Within this section, a portion of the ongoing research in each of the areas of materials research is highlighted.

The application of actuators, sensors, and controllers to alter the performance of structures has become a viable tool for designers. Controlled structures technology has matured and many new sensor and actuator types have been developed over the last two decades. Most examples of controlled structures involve surface mounting or bonding of the sensors and actuators. This approach often carries the least risk as the passive structural load paths are unaltered and failed components can be readily identified and corrected. Surface mounting is appropriate for inertial proof-mass actuators and for displacement/force actuators connecting the controlled structure to ground. However strain actuators, which create a relative displacement within the structure, are usually most effective when embedded into the structural elements. Structural integration of the actuators, sensors, power and data electrical buses, and perhaps the controller electronics should also lead to more robust and durable controlled structural systems.

Researchers at NASA Langley Research Center have extensive experience using active structural acoustic control (ASAC) for aircraft interior noise reduction. One aspect of ASAC involves the selection of optimum locations for microphone sensors and force actuators. We have investigated the importance of sensor/actuator selection, optimization techniques, and have produced some unique experimental and numerical results.

Optimized architectures are critical to the success of ASAC. For laboratory tests, with simplified acoustic sources and environments, the best locations possibly can be selected by inspection or modal methods. For small numbers of actuators and sensors, the evaluation of all possible combinations may even be practical. However, for complicated acoustic enclosures, such as an aircraft fuselage, and for reasonable numbers of candidate actuators and sensors, a combinatorial optimization method such as tabu search can improve the quality of the locations selected.

The application of smart sensors and actuators has only been limited by the human imagination. We will give a taste of some very important practical applications of these materials. All of these applications have been worked cooperatively with other organizations to take advantage of each organizations skills and resources.

NASA Langley has a long history of attacking important technical opportunities from a broad base of supporting disciplines. The research and development at Langley in this subject area range from the test tube to the test flight. The information covered here will range from the development of innovative new materials, sensors and actuators, to the incorporation of smart sensors and actuators in practical devices, to the optimization of the location of these devices, to, finally, a wide variety of applications of these devices utilizing Langley's facilities and expertise.

Paper presented at the RTO AVT Symposium on "Active Control Technology for Enhanced Performance Operational Capabilities of Military Aircraft, Land Vehicles and Sea Vehicles", held in Braunschweig, Germany, 8-11 May 2000, and published in RTO MP-051.

1. MATERIALS

Advanced materials are being developed for sensors and actuators, as well as polymers for integrating smart devices into composite structures[1]. Contributions reside in three key areas: computational materials; advanced piezoelectric materials; and integrated composite structures.

The computational materials effort is focused on developing predictive tools for the efficient design of new materials with the appropriate combination of properties for next generation smart airframe systems. Research in the area of advanced piezoelectrics includes optimizing the efficiency, force output, use temperature, and energy transfer between the structure and device for both ceramic and polymeric materials. For structural health monitoring, advanced non-destructive techniques including fiber optics are being developed for detection of delaminations, cracks and environmental deterioration in aircraft structures. The research in each of these key areas has been designed to meet application needs of the customers including aeroelastic tailoring, noise cancellation, and laminar flow control. Within this section, a portion of the ongoing research in each of the areas of materials research is highlighted.

1.1 COMPUTATIONAL MATERIALS

Developments in a number of areas of aeronautics are currently materials-limited. These areas include the creation of efficient, lightweight structures, some aspects of propulsion, noise and vibration abatement, and active controls. Recent, rapid increases in computer power and improvements in computational techniques open the way to the use of simulations in the development of new materials. At NASA-LaRC, computer-aided design of materials has concentrated on two classes of materials: high performance continuous-fiber reinforced polymer matrix composites and piezoelectric films from high temperature polyimides.

An integrated, predictive computer model is being developed to bridge the microscopic and macroscopic descriptions of polymer composites. This model will significantly reduce development costs by bringing physical and microstructural information into the realm of the design engineer. The range of length and time scales involved is huge, and different scientific and engineering disciplines are involved. Models at each level require experimental verification and must connect with models at adjacent levels.

1.2 ADVANCED PIEZOELECTRIC MATERIALS

Piezoelectric Polymers

A research problem that combines both computational and experimental studies is the development of high performance, piezoelectric polymeric materials. The piezoelectric response of a polymer is a function of its dipole concentration, the degree of dipole orientation, and the mechanical properties of the polymer. Currently, fluoropolymers such as polyvinylidene fluoride (PVDF) are the state of the art in piezoelectric polymers. The development of other classes of piezoelectric polymers could provide enabling materials technology for a variety of aerospace and commercial applications. Polyimides are of particular interest due to their high temperature stability and the ease with which various polar pendant groups may be incorporated[2]. Particularly interesting is the potential use of piezoelectric polyimides in MEMS devices as fluoropolymers do not possess the chemical resistance or thermal stability necessary to withstand conventional MEMS processing

In order to induce a piezoelectric response, the polymer is poled by applying an electric field (E_p = 100 MV/m) across the thickness of the polymer at an elevated temperature sufficient to allow mobility of the molecular dipoles. The dipoles are aligned with the applied field and will partially retain the induced polarization when the temperature is lowered below the glass transition temperature in the presence of the field. The resulting remnant polarization is proportional to the level of piezoelectricity.

To computationally simulate the experimental poling process, semi-empirical molecular orbital calculations on model segments of the polymers were used to obtain the electron distributions and potential energy surfaces of the segments. Calculated dipole moments of the model segments were compared with experimental data whenever possible. In addition, the torsional barriers were of interest because they dictate the flexibility of the polymer backbone and hence the ability of the dipoles to orient in response to an external field. A modified force field for use in molecular dynamics simulations was then created. A five unit long polymer was built and packed into a cell with three-dimensional periodic boundary conditions at the experimental density. The temperature and electric field were scaled to bring the poling response into the simulation time scale (200 picoseconds.) From this model, dielectric relaxation strengths were calculated which are in excellent agreement with experimental results, indicating that the computational model can be used as a reliable tool to guide the synthesis of new piezoelectric polymers[3].

Ongoing research, guided by computational models, should provide improved understanding of the requirements for heightened piezoelectric response and the ability to rapidly evaluate candidate structures in consultation with synthetic polymer chemists.

High-Displacement Piezoelectric Ceramic Actuators

Piezoelectric devices have been identified as a promising actuator technology for the implementation of active boundary layer control, high bandwidth noise suppression and aeroservoelastic tailoring. However, many potential aerospace applications require displacement performance larger than what is achievable in conventional piezoelectrics. Recently LaRC researchers have developed two high-

displacement piezoelectric actuator technologies, RAINBOW (Reduced And INternally-Biased Oxide Wafer) and THUNDER (THin layer composite UNimorph ferroelectric DrivER and sensor) to meet these requirements. These devices are unimorph-type actuators which consist of a piezoelectric ceramic layer bonded to one or more non-piezoelectric secondary layers. Because of the use of elevated temperatures during processing, internal stresses are created in the structures which significantly enhance displacement through the thickness of the devices. The reader is referred to the literature for more information on RAINBOW [4-6] and THUNDER [7-9] devices and their application.

Currently, the processing and characterization of these high-displacement actuators are under investigation. One recent characterization study involved the effects of electric field, load and frequency on the displacement properties of rectangular THUNDER devices. Results showed that individual actuators were capable of free displacements in excess of 3 mm when tested at ± 9 kV/cm. Increasing device stiffness through metal selection and thickness resulted in improved load-bearing performance at the expense of displacement, allowing devices to be designed with a range of performance capabilities.

1.3 ATTACH PROJECT

The Airfoil THUNDER Testing to Ascertain Characteristics (ATTACH) project[9,10] was a feasibility study that focused on identifying (1) the material characteristics, such as creep, hysteresis, and fatigue, and (2) the airfoil shaping effectiveness of the new THUNDER piezoelectric technology under aerodynamic loading. Characterization of the material behavior of THUNDER was the objective for Phase I, while Phase II examined its ability to reduce drag over an airfoil. The following sections present both the approach and preliminary findings of both phases of testing.

The concept behind drag reduction via airfoil shaping with a THUNDER wafer affixed to the upper surface of a symmetric airfoil and covered with a flexible membrane is shown in Figure 1. Figure 1a shows the typical flow field with the airfoil set at a small positive angle of attack and the THUNDER wafer unactuated. As identified in the figure, the flow remains attached to the upper surface of this nominal airfoil configuration only across a small region near the leading edge. The flow then separates because of the presence of a large adverse pressure gradient. Figure 1b shows the anticipated flow field over the same airfoil with the THUNDER wafer actuated up to meet the flow. With such an increase in camber of the upper surface, the onset of the large adverse pressure gradient would be delayed, allowing for a longer attachment region.

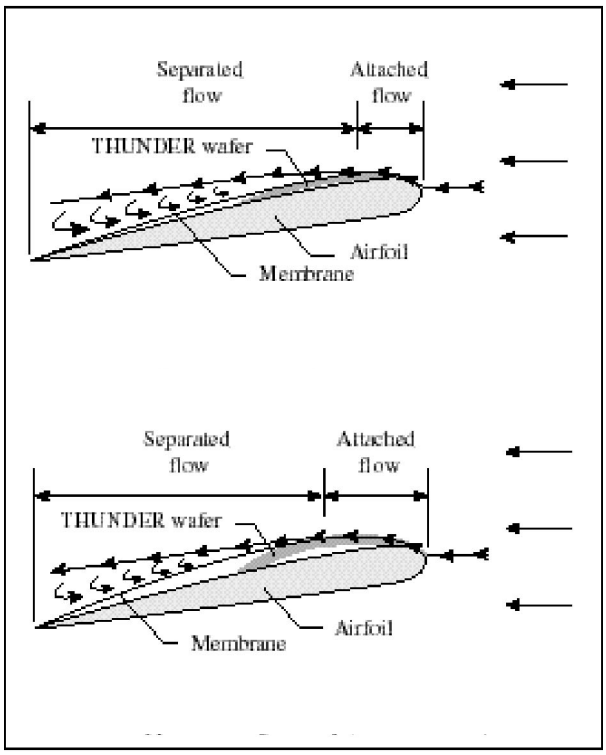


Figure 1. Concept for drag reduction via airfoil shaping with THUNDER.

The testbed used for both phases of testing in the ATTACH project was the 0.25-inch thick, 1.5-inch wide, 5-inch long, generic, roughly symmetric airfoil shown in Figure 2. This airfoil was supported by two 0.25-inch thick, 10-inch long sidewalls in the 6- by 6-inch test section of a tabletop wind tunnel. These sidewall inserts extended through 85% of the length of the test section, creating a nearly two-dimensional flow condition. A single 1.5-inch wide, 2.5-inch long rectangular wafer of THUNDER was placed near the leading edge of the airfoil to act as the first half of the upper surface. To smooth the airfoil/wafer interface, a sheet of thin fiberglass material was wrapped over the upper surface of the airfoil/wafer combination and held in place by a flexible latex membrane. A photograph of the installed model is shown in Figure 3.

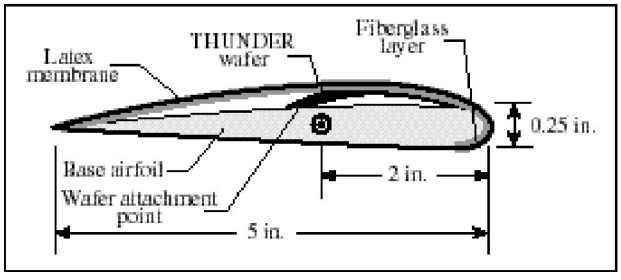


Figure 2. ATTACH testbed.

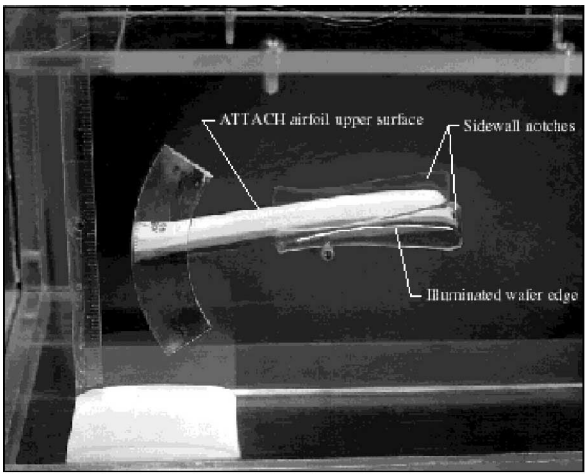


Figure 3. Photograph of the ATTACH model in the wind-tunnel test section.

ATTACH Phase I testing

The initial series of tests conducted during the ATTACH project were performed to identify the creep, hysteresis, and fatigue characteristics of a THUNDER wafer under aerodynamic loading. For this experiment, a total of 60 conditions were tested, consisting of combinations of the following parameters: five angles of attack (-2°, 0°, +2°, +4°, +6°), four steady-state input voltages (-102 V, +102 V, -170 V, +170 V), and three tunnel velocities (wind-off, 20 m/s, 35 m/s).

The data obtained during this experiment conclusively identified the presence of both creep and hysteresis of the wafer under wind-on (loaded) and wind-off (unloaded) conditions. After two weeks of testing, the performance of the wafer began to noticeably degrade. During subsequent examination, no visible flaws were found, but a 33% drop in capacitance was discovered, and repoling returned the wafer to its full capabilities. Thus, similar to other piezoelectric adaptive materials, the performance of THUNDER appears to be a function of capacitance.

ATTACH Phase II testing

To assess the ability of the THUNDER wafer to reduce drag over the airfoil, tests were conducted at the 40 wind-on conditions previously described for Phase I. For purposes of this feasibility study, it was assumed that variations in drag were directly proportional to velocity changes in the wake of the model. Comparisons of wake velocity for different test conditions, therefore, provided qualitative indications of the drag reducing potential of this piezoelectric actuator for this subscale model. Velocity measurements were taken by traversing a hot film anemometer velocity probe in 0.125-inch increments through the center of the test section sufficiently aft of the airfoil trailing edge to allow the wake to return to tunnel static pressure.

Results from this phase of testing were consistent with the results from Phase I. Positive applied voltages, which expanded the upper surface of the airfoil, had the effect of increasing the velocity in the wake, a result consistent with a decrease in drag. Increases in tunnel velocity and/or model angle of attack produced even greater expansions of the upper surface and, therefore, larger wake velocities at the positive voltages. Negative applied voltages produced the opposite effect. These results were obtained using only 32% of the maximum unloaded capability of the wafer. Thus, greater drag reductions would be expected if that percentage is increased.

The results of this research effort indicate that the new THUNDER actuator technology is a promising candidate for future airfoil shaping investigations. Despite decreases in the displacements of the wafer due to aerodynamic loading, noticeable drag reductions were obtained.

1.4 SHAPE MEMORY ALLOYS (SMAs)

Interior noise and sonic fatigue are important issues in the development and design of advanced subsonic and supersonic aircraft. Conventional aircraft typically employ passive treatments, such as constrained layer damping and acoustic absorption material, to reduce the structural response and resulting acoustic levels in the aircraft interior. These techniques require significant addition of mass and only attenuate relatively high frequency noise transmitted through the fuselage. Adaptive and/or active methods of controlling the structural acoustic response of panels to reduce the transmitted noise may be accomplished with the use of SMA hybrid composite panels. These panels have the potential to offer improved thermal buckling/post buckling behavior, dynamic response, fatigue life, and structural acoustic response.

Initial work in the fabrication of integrated composites has focused on the manufacture of E-glass/ Fiberite 934 epoxy panels with embedded shape memory alloys. Quasi-isotropic panels with unstrained SMAs embedded in the zero degree direction have been successfully fabricated. Since 1/2-inch wide Nitinol strips were not available, five 0.10 inch wide, 5 mil thick rectangular Nitinol ribbons were butted together side to side with a spacing of 1/2 inch between sets. The SMA strips were heated to 250°F for an hour after being cut and prior to being embedded to recover any initial strain that may have developed from being shipped wound on a spool. The SMA composite panels were processed using the standard 934-epoxy autoclave cure cycle (2hr @ 350°F, 100 psi). Test specimens machined from a cured hybrid panel are shown in Figure 4. Future panels will be fabricated with prestrained SMA strips. These panels require tooling which will restrain the SMA strips from contracting during the thermal cure. Panels with bi-directional (0°/90°) SMAs as well as hybrid built-up structure will also be fabricated.

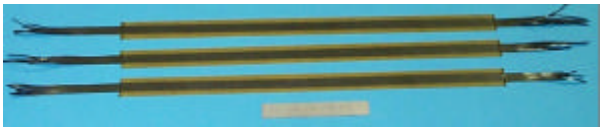


Figure 4. Test specimens machined from an E-glass/ 934 epoxy panel with embedded Nitinol shape memory alloy ribbons.

2. INTEGRATION ISSUES FOR HIGH-STRAIN

Strain actuators, used to induce a relative structural displacement, are most effective when integrally embedded into the host structure. The section summarizes progress and challenges in the field of embedding smart materials into structures[11]. The difficulties of embedding active elements within composite structures are described from a system design perspective. Issues associated with the application of strain actuators in primary aircraft structure are discussed. Development of new embedding technology to combat the difficulties associated with high strain applications is advocated.

The application of actuators, sensors, and controllers to alter the performance of structures has become a viable tool for designers. Controlled structures technology has matured and many new sensor and actuator types have been developed over the last two decades. Most examples of controlled structures involve surface mounting or bonding of the sensors and actuators. This approach often carries the least risk as the passive structural load paths are unaltered and failed components can be readily identified and corrected. Surface mounting is appropriate for inertial proof-mass actuators and for displacement/force actuators connecting the controlled structure to ground. However strain actuators, which create a relative displacement within the structure, are usually most effective when embedded into the structural elements.

Numerous advances have and continue to be made in developing “solid-state” strain actuators and sensors. In particular, shape memory alloys, piezoelectrics (including piezo fiber composites and single crystal materials), and magnetostrictive materials have been successfully demonstrated as strain actuators. Except for simple structural geometries such as beams and plates, surface mounting of strain actuators leads to less control authority than when they are embedded and impedance matched to the host structure. Structural integration of the actuators, sensors, power and data electrical buses, and perhaps the controller electronics should also lead to more robust and durable controlled structural systems.

Difficulties range from electronic circuit failures due to dielectric breakdown and arcing, breaking of the ceramic wafer and electronic leads, low performance due to internal heating and impedance mismatches, and compromised structural integrity due to microcracking and macrocracking in the composite structure. These complications were encountered in low to moderate strain level applications. Structural embedding is even more problematic when high strain, high stress applications are pursued. One such application, is the active load alleviation of aircraft. If an active wingbox structure could be designed, significant weight reduction could be achieved in the wingbox structure while simultaneously improving ride comfort and fatigue life.

3. OPTIMAL SENSOR/ACTUATOR LOCATIONS FOR ACTIVE STRUCTURAL ACOUSTIC CONTROL

Researchers at NASA Langley Research Center have extensive experience using active structural acoustic control (ASAC) for aircraft interior noise reduction. One aspect of ASAC involves the selection of optimum locations for microphone sensors and force actuators.

Active acoustic control, or the use of one acoustic source (or secondary source) to cancel another (or primary source), has a long history. In a recent survey paper, Fuller and Von Flotow[12] describe practical demonstrations of the technique as early as 1953 and a U.S. patent as early as 1936. In addition, these authors describe several commercially successful active noise and vibration control systems in use today. Their paper is highly recommended to any reader who desires a complete discussion of active acoustic control and its practical uses.

The scope of the present section is limited to active structural acoustic control (ASAC), with a focus on aircraft interior noise control research conducted at NASA Langley Research Center. The most obvious difference between the ASAC system and early acoustic control systems is that ASAC uses structural actuators like shakers or piezoelectric (PZT) patches attached to the aircraft fuselage rather than acoustic actuators like loudspeakers inside the fuselage. The ASAC concept is attractive because the structural actuators are more effective by weight and consume less interior volume than competing active or passive noise control options.[13]

One area of ASAC research is the determination of optimal locations for actuators and sensors. Early theoretical investigations[14-16] established the importance of actuator and sensor architecture and suggested optimization strategies and goals. In their survey paper, Fuller and Von Flotow[12] describe the actuator location problem from a practical standpoint. They note that researchers recommend a modal method, such that actuators are placed to excite a selected structural mode and sensors are placed to observe each important acoustic mode.

3.1 OPTIMIZATION OVERVIEW

Given a set of N_a actuator locations, the goal of an optimization run is to identify a subset of N_c locations that provides the best performance (e.g., reduces interior noise). Several combinatorial optimization methods, such as simulated annealing, genetic algorithms, and tabu search, are available. Tabu search was selected for use in the present study, based on previous experience.[16]

To apply a tabu search algorithm one must define a state space, a method for moving from state to state, a neighborhood for each state, and a cost function to minimize. For the actuator selection problem, the set of all possible subsets of size N_c chosen from N_a actuators is the state space. To bound the problem, the subset size N_c is constant for each search. An initial state can be prescribed by the user or can be generated randomly. At any given state, the subset N_c, of actuators that represent that state are flagged as "on;" the remaining actuators are flagged as "off." A move changes the state by turning one actuator off and one on. A neighborhood is the set of all states that are one move away from the current state. Finally, the cost function is based on the noise reduction estimate for the subset of actuators that are turned on.

Each iteration of the tabu search algorithm involves evaluating the cost function for each subset of actuators in the neighborhood of the current state. The move that improves the cost function the most is accepted. If no improving move is identified, then the move that degrades the cost function the least is accepted. The algorithm continues for a predetermined number of iterations. Cycling is avoided by maintaining a list (called the tabu list) of all accepted moves. The algorithm is prohibited from reversing any move on the tabu list. An exception can be made if the move is old or if the move produces a state that is clearly better than any previous state. The algorithm terminates after reporting the best state that was encountered during the entire optimization procedure.

3.2 SIMULATED ASAC

In this section, tabu search is applied to a simplified model of the ASAC problem. This simulation serves several purposes. First, the simulation illustrates the method and indicates the potential for reducing aircraft interior noise. Secondly, the relationship between the shell vibration level and the interior noise level is explored.

Problem Statement

Assume that an aircraft fuselage is represented as a cylinder with rigid end caps (fig. 5) and that a propeller is represented as a point monopole with a frequency equal to some multiple of the blade passage frequency. Piezoelectric actuators bonded to the fuselage skin are represented as line force distributions in the x and • directions. With this simplified model, the point monopole produces predictable pressure waves that are exterior to the cylinder. These periodic pressure changes cause predictable structural vibrations in the cylinder wall and predictable noise levels in the interior space. Using the PZT actuators to modify the vibration of the cylinder can dramatically reduce the interior noise level at any discrete microphone location. For a given set of microphones and a given set of actuator locations, the control forces that minimize the acoustic response are known.[14] However, methods for choosing good locations for the microphones and the actuators are needed.[17]

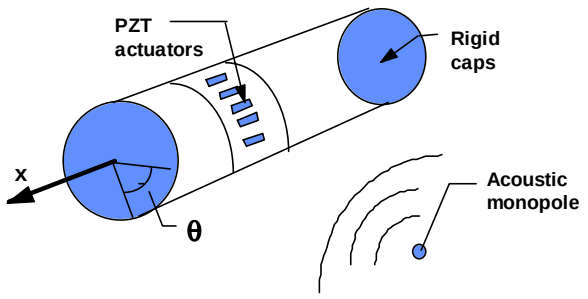


Figure 5. Schematic of simplified cylinder, point source, and actuator model.

Results

The results from the simulated studies are encouraging. For varying numbers of possible locations, subset sizes, source frequencies, and sets of interior microphones, the same trends are observed. Namely, the subset of actuators selected by tabu search to reduce interior noise tends to reduce cylinder vibration as well. The 16 best locations are chosen from a set of 102 possible locations. The initial set of 16 actuators reduces the noise by 13 dB but increases the cylinder vibration by 4 dB. However, after 15 iterations, both noise and vibration levels are reduced dramatically. Fifteen additional iterations produce no significant improvement. By adjusting the number of actuators up or down from 16, the noise-reduction goals can be satisfied without an increase in vibration and without exceeding the force capacity of the PZT actuators.

3.3 EXPERIMENTAL ASAC STUDIES

The simulation studies indicate the importance of actuator location in active structural acoustic control. Experimental tests are a necessary next step. In these tests, the transfer matrix is constructed by using measured data, and the effectiveness of selected locations can be verified experimentally. More complete descriptions and discussion of results are available in the references.

Langley Composite Cylinder

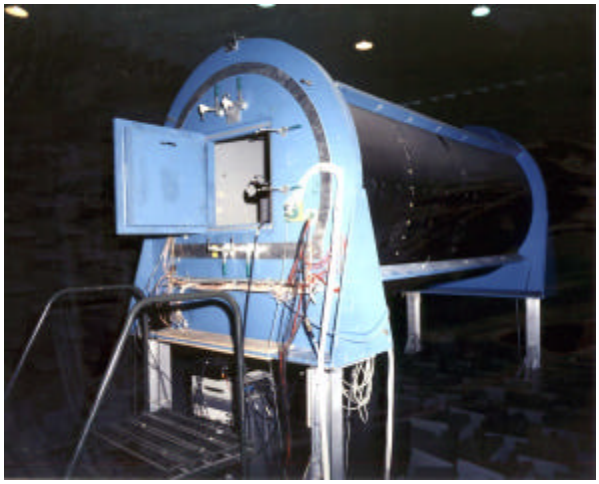


Figure 6. Composite cylinder at NASA Langley

The composite fuselage model is shown in figure 6. The cylinder is 3.6 m long and 1.68 m in diameter. The outer shell is graphite epoxy, which is stiffened by composite stringers and ring frames. The interior has a plywood floor and inner trim panels that are attached to the ring frame. The primary source is a 100-W electrodynamic loudspeaker that is mounted 0.3 m from the exterior sidewall. The secondary source is a subset of the eight piezoelectric actuators bonded to the interior trim panels. (See fig. 7)

Six boom-mounted microphones were used to collect data. The boom can translate and rotate to collect sound pressure levels at 462 data points within the cylinder volume. Two of the cross sections surveyed by the boom microphones are indicated in figure 7.

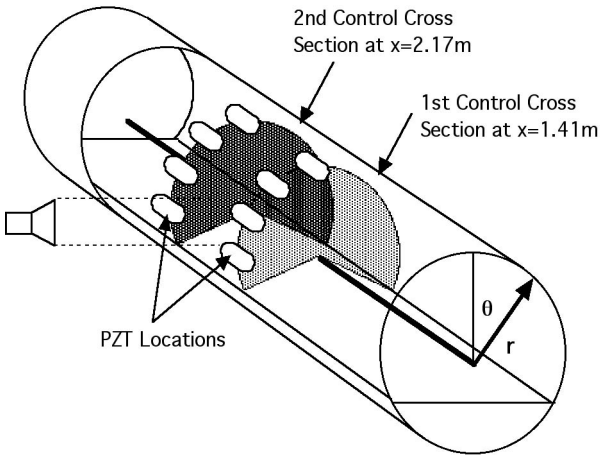


Figure 7. Schematic of composite cylinder

Six boom-mounted microphones were used to collect data. The boom can translate and rotate to collect sound pressure levels at 462 data points within the cylinder volume. Two of the cross sections surveyed by the boom microphones are indicated in figure 7.

The interior noise data are collected for three different frequencies: 210, 230, and 275 Hz. For each frequency, the data are collected for the primary source alone and then for the secondary source alone by using a single unit input separately at each of the eight actuators. The three frequencies are well chosen. The first (i.e., 210 Hz) represents a case in which a single dominant acoustic mode is easily controlled with a single structural mode. The other two frequencies represent cases in which no particular acoustic or structural mode is dominant or in which several modes are important.

Single Frequency Optimization Method

The goal of the optimization is to pick the four best actuators and the eight best sensors for use in active noise control. Tabu search may be used to select four out of eight actuators.

The goal of the composite cylinder laboratory tests is to reduce noise at all 462 microphone locations by using a linear control law with feedback from 8 of the 462 microphones.[18] Clearly, tabu search must identify microphones that are able to observe all important acoustic modes. Moreover, some linear combination of the selected actuator responses must approximately cancel out the primary response.

The initial tabu search results did not meet our expectations. The optimization procedure did identify architecture with greater noise reduction potential than any of those found by random trials. However, inspection of the contour maps of the interior noise indicates that many of the selected sensors are in low noise areas where the change in noise as a result of the control system is small.

To select better actuator/sensor combinations, the tabu search cost function was modified to include a variance measure in addition to a noise reduction measure. Both absolute value and sum of variances were tried with equal success.[19]

Composite Cylinder Results

The composite cylinder model was used to test the selected actuator and sensor locations. The four best and four worst actuators were tested. For each actuator set, the eight best sensors were determined by tabu search. These test results are compared with previous test results in which the actuators and sensors were selected by using modal methods.

Test results are reported in reference 18 and summarized here. As expected, the control forces predicted in the optimization procedure and the noise reduction predicted do not match the observed control forces or noise reduction. Possible explanations for the differences include premature

convergence of the optimal control algorithm and errors in the measured transfer functions. However, the trends are well predicted. For example, the noise reductions observed for the case in which the frequency was equal to 210 Hz are not sensitive to actuator set selection. This case has one dominant acoustic mode. On the other hand, the noise reduction observed for the cases with frequencies of 230 Hz and 275 Hz shows a strong dependence on actuator location.

The observed noise reduction is less than predicted. However, the four best actuators provide 3.5 dB more noise reduction than the four worst and, in addition, perform better than those selected by modal methods. This finding suggests that the tabu search procedure is particularly effective in those cases in which tradeoffs between several important acoustic modes must be considered.

3.4 OPTIMIZATION SUMMARY

Clearly, optimized architectures are critical to the success of ASAC. For laboratory tests, with simplified acoustic sources and environments, inspection or modal methods possibly can select the best locations. For small numbers of actuators and sensors, the evaluation of all possible combinations may even be practical. However, for complicated acoustic enclosures, such as an aircraft fuselage, and for reasonable numbers of candidate actuators and sensors, a combinatorial optimization method such as tabu search can improve the quality of the locations selected.

One weakness in the method is the need for accurate models of the closed loop performance of the control system. For now, the control system is modeled by using a linear transfer function. This transfer function is expensive to produce. The transfer function can be created experimentally, in which case the unit response must be measured for a large number of candidate actuator and sensor locations. On the other hand, the transfer function can be simulated, in which case a highly accurate model of the acoustic source and enclosure is required.

It is expected that this research on optimum sensor and actuator location for noise reduction will serve as a pathfinder for other applications like flow control or aeroelastic control.

4.0 APPLICATION OF SMART MATERIALS

The application of smart sensors and actuators has only been limited by the human imagination[20]. This section will give you a taste of some very important practical applications of these materials. All of these applications have been worked cooperatively with other organizations to take advantage of each organization's skills and resources. These applications include the Smart Wing program, and the Active Twist Rotor program.

4.1 DARPA/ AFRL/ NASA SMART WING PROGRAM

The overall objective of the DARPA/ Air Force Research Labs/ NASA Smart Wing program is to design, develop and demonstrate the use smart materials and structures to improve the aerodynamic performance of military aircraft including improvements in lift to drag ratio, maneuver capabilities and aeroelastic effects. The approach includes: 1) designing, fabricating and testing scaled semi-span and full-span wind-tunnel models; 2) addressing power, reliability, packaging and system integration issues; and 3) laying the ground work for technology transition in a potential follow-on program. An overview of the program is presented in reference 21. The Smart Wing program is led by the Northrop Grumman Corporation who was awarded DARPA contracts for Phase I, which began in March 1997, and Phase II, which began in August 1998. Phase I and Phase II contracts are being monitored by the Air Force Research Laboratory (AFRL) at Wright Patterson Air Force Base. Wind tunnel testing during the program is being performed at the NASA LaRC TDT via a Memorandum of Agreement between NASA LaRC and Northrop Grumman. In addition, the administrative responsibilities of the program are being coordinated through an Interagency Agreement between the AFRL and NASA LaRC. Other members of the large team of researchers on the program include: Lockheed Martin Astronautics and Control Systems; Naval Research Labs; Mission Research Corporation; Rockwell Science Center; Fiber & Sensor Technologies, Inc.; Etrema Products, Inc.; SRI International; University of California, Los Angeles; Georgia Institute of Technology, and the University of Texas at Arlington.

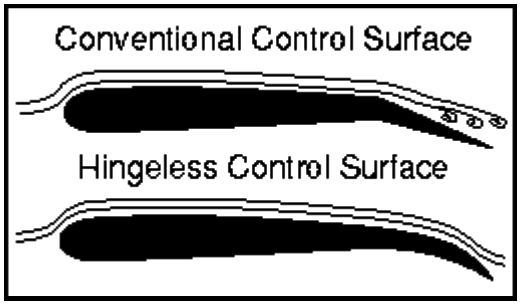


Figure 8: Hingeless control surface concept

During Phase I of the program, a 16% scaled semi-span model ("Smart Wing") of the F/A-18 aircraft was designed and fabricated incorporating three key features: 1) hingeless, smoothly contoured trailing edge control surfaces, 2) variable spanwise wing twist and 3) fiber optic pressure and strain transducers. Another identically scaled model of conventional construction (hinged control surfaces and no wing twist) was fabricated and used as a baseline for comparison. On the Smart Wing model, the hingeless aileron and flap are actuated using shape memory alloy (SMA)

tendons. As shown in Figure 8, the hingeless control surface concept reduces the separated flow region on the wing thereby increasing lift to drag ratio. On the Smart Wing model, wing twist is accomplished through the use of two shape memory alloy-actuated torque tubes. The schematic in Figure 9 depicts the wing twist concept.

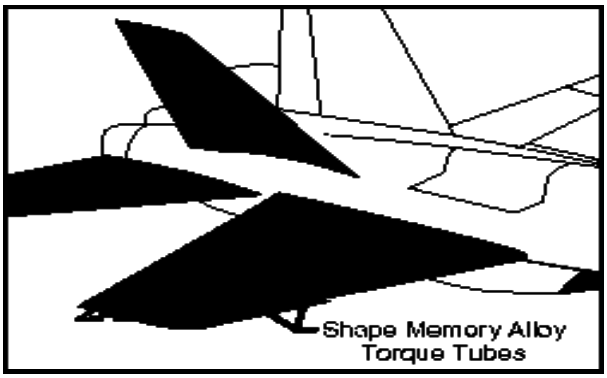


Figure 9: Wing twist concept

The first wind-tunnel test in Phase I took place at the LaRC TDT in May 1996. A photograph of the Smart Wing model in the TDT is shown in Figure 10. During the test, 1.25 degrees of twist was achieved using the SMA torque tubes resulting in approximately an 8% improvement in rolling moment. The hingeless control surfaces deployed up to 10 degrees, providing between an 8 and 18% increase in rolling moment and approximately an 8% increase in lift. A complete summary of wind-tunnel test results is presented in reference 22. The second wind-tunnel test of Phase I took place in June-July 1998 using a redesigned torque tube and hingeless control surfaces. During this test, 5 degrees of twist was achieved resulting in a 15% increase in rolling moment. In addition, 10 degrees of deflection on the hingeless control surfaces was obtained with improved controllability and repeatability. Phase II of the Smart Wing program includes plans to further mature the technologies developed in Phase I as well as investigate new actuation concepts. Two wind-tunnel tests in the LaRC TDT are currently planned for Phase II.

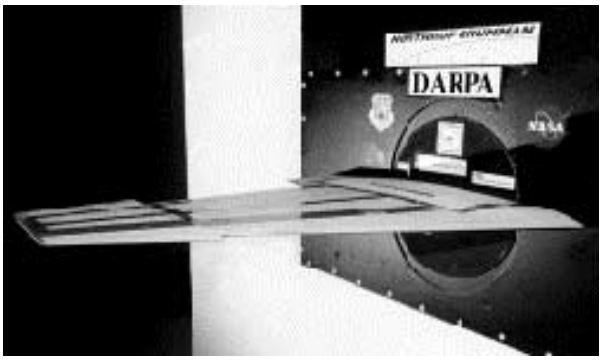


Figure 10: Smart Wing model in the LaRC TDT

4.2 ACTIVE TWIST ROTOR RESEARCH

Recent analytical and experimental investigations[23-28] indicate that helicopter rotor blades containing embedded interdigitated-electrode poled, piezoelectric fiber composite layers (*active fiber composites*) should be capable of meeting the performance requirements necessary for a practical individual blade control (IBC) system[29]. For this reason, twist-actuated helicopter rotor systems using active fiber composites (AFC) have become the focus of several advanced rotor blade control research activities at NASA Langley Research Center.

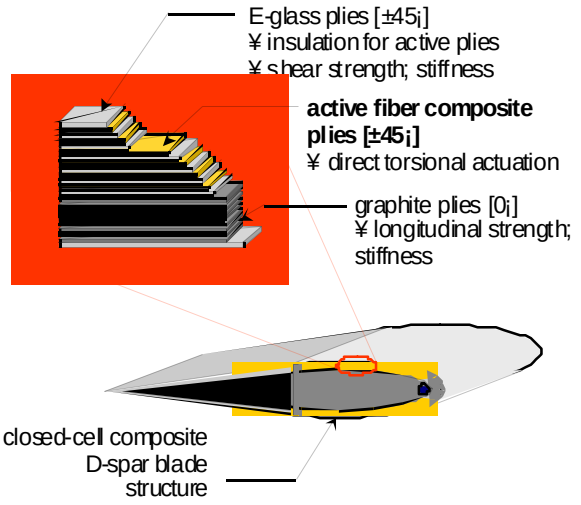


Figure 11: Full-scale active fiber composite rotor blade concept.

An example of the active fiber composite rotor blade concept is illustrated in Figure 11. Piezoelectric AFC plies are oriented at ±45 degrees within the primary structure of the blade in order to generate dynamic blade twisting. Mathematical models indicate that from 1 to 2 degrees of twist amplitude over a relatively wide frequency bandwidth are possible using the high strain actuation capabilities of the AFC plies. Systems studies also indicate that this magnitude of twist actuation authority should be possible at full-scale with only modest increases in blade weight and low levels of power consumption. AFC actuators utilize an interdigitated electrode poling method (IDE)[30] to generate large directional actuation strains in the actuator plane. Piezoelectric materials in fiber form are also used, and are protected by an epoxy matrix which improves the durability characteristics of the actuator.[31,32] Combining both of these technologies results in a high performance piezoelectric actuator lamina with induced stress, endurance, and conformability characteristics superior to typical monolithic piezoceramic actuators.

Aeroelastic Modeling of Active Fiber Composite Rotors

To investigate the potential of active fiber composite rotors, two active twist rotor mathematical modeling methods have been developed at NASA Langley. The first of these is a simple mathematical aeroelasticity model for composite helicopter rotor blades incorporating anisotropic embedded piezoceramic actuators. The computer implementation of this model, the Piezoelectric Twist Rotor Analysis (PETRA), has been created for use with the MATLAB[33] numerical analysis program and is ideally suited for conceptual active twist rotor design and optimization studies[25,26,28]. A procedure for using a commercially available comprehensive rotorcraft computer code (CAMRAD II[34]) for active twist rotor studies has also been developed. This allows active twist rotor numerical studies to be performed using a detailed state-of-the-art rotorcraft aerodynamics and structural dynamics model. Some examples of numerical results obtained using both active twist rotor blade analysis methods are described below.

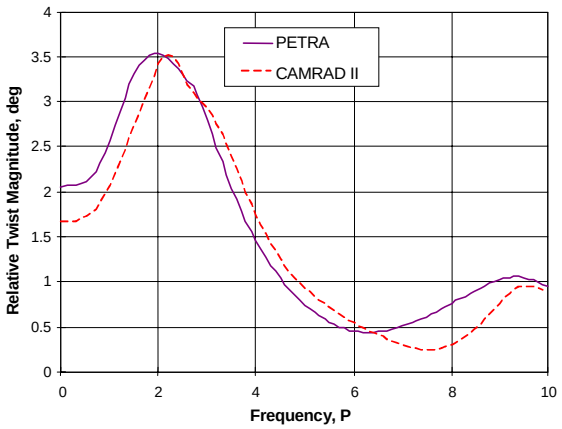


Figure 12: Hovering flight twist actuation frequency response for a full-scale active twist rotor blade concept. (Frequency scale is in multiples of the fundamental rotor frequency, P.)

Analytically determined hovering flight twist actuation frequency response curves for a full-scale active twist rotor blade concept similar to that depicted in Figure 11 are shown in Figure 12. These calculations were performed for a representative one-g hovering flight condition. Results using both PETRA and CAMRAD II are shown for comparison. Large amplitudes of blade twisting (greater than 2 degrees from center of rotation to the blade tip) are indicated with both modeling methods. The twist amplitude and bandwidth behavior shown here would be sufficient for many IBC applications, and vertical hub shear vibration reduction in particular. Agreement between the two analytical methods is also extremely good and shows that the fundamental active twist rotor dynamics are being modeled consistently.

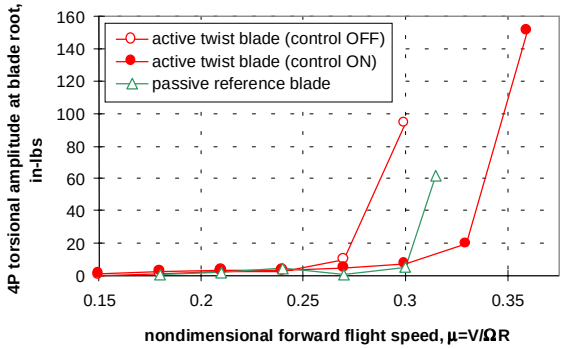


Figure 13: Suppression of dynamic stall induced torsional vibrations through active twist control. Constant rotor thrust condition shown.

An example of the predicted capability of active fiber composite rotor blades to alleviate stall on helicopter rotors is shown in Figure 13 [28]. Rapid buildup of torsional vibratory loads due to stall severely restricts the maximum lift and forward flight speed capabilities of conventional helicopters. Vibration trends with increasing flight speed are shown for a conceptual full-scale active twist rotor blade with and without twist actuation control. Trends for a conventional, passive-structure blade are also shown as a reference. The rapid rise in dynamic stall-induced torsional vibratory loads for the active twist rotor blade using twist control has been effectively delayed by approximately 10% in nondimensional flight speed with respect to the baseline blade and by as much as 22% with respect to the active fiber composite blade with no twist control. This delay in torsional vibration buildup represents a significant expansion of the dynamic stall limited operational flight envelope of the helicopter rotor.

Testing Active Fiber Composites Helicopter Rotor Blades

Based on these and other promising analytical findings, a cooperative effort between NASA, the Army Research Laboratory, and the Massachusetts Institute of Technology has been initiated to construct an aeroelastically-scaled active twist rotor research model suitable for testing in the heavy gas environment of the Langley Transonic Dynamics Tunnel (TDT). The heavy gas test medium employed in the TDT allows simultaneous matching of full-scale Mach and Froude numbers at approximately one-quarter model scale. The low speed of sound of the heavy gas used in the TDT also permits model rotors to be rotated more slowly than would be required for Mach number matching in air. This in turn reduces centrifugal blade stresses, which simplifies model design tasks considerably. The Aeroelastic Rotor Experimental System (ARES)[35], which will be used to operate the active twist rotor model, is shown in the test section of the TDT in Figure 14. These wind-tunnel tests will serve as an important demonstration of the active twist rotor concept, and will provide valuable experimental data for validation of active twist rotor analytical tools.

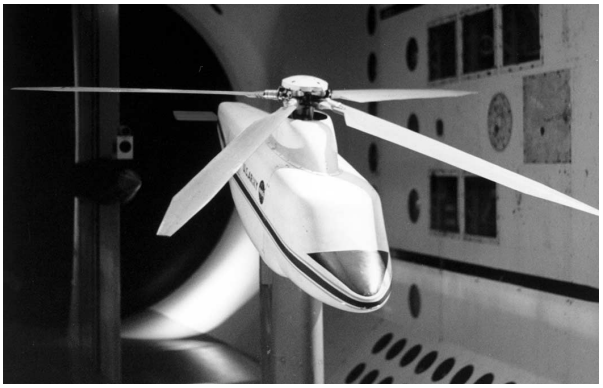


Figure 14: Aeroelastic Rotor Experimental System 9-foot diameter rotor testbed in the NASA LaRC Transonic Dynamics Tunnel.

The analytical and experimental activities described above are expected to form the foundation of a follow-on advanced active twist rotor research effort. This Future Technology Rotor (FTR) will incorporate advanced airfoils, planform geometry, and active twist capability in an optimized, integrated intelligent rotor blade structure. By considering active twist capabilities from the beginning of the rotor design process it should be possible to create an advanced rotor with aerodynamic performance, vibratory loads, and acoustic characteristics superior to that obtainable with purely passive-structure rotor blade designs.

4.3 APPLICATION COMMENTS

Several analytical and small- and large-scale experimental studies at the NASA Langley Research Center (LaRC) have demonstrated significant potential pay-offs by applying smart materials to practical problems. These pay-offs include reduced emissions and increased performance and safety using discrete piezoelectric patches and interdigitated electrode piezoelectric fiber composites (IDEPFC). While yielding notable results, these studies also highlight the need for critical advances in electrical, structural and aeroelastic modeling and testing to make these “smart applications” viable. In a new 6 year effort, NASA LaRC seeks to substantially advance the state of the art in smart materials technologies to fill the technology gaps, enabling a wide range of adaptive structural and aeroelastic applications of smart materials. This new effort will focus on developing the enabling technologies to apply discrete piezoelectric patches, THUNDER wafers, and IDEPFC to aircraft and rotorcraft. This research on the development of enabling technologies can be applied to a wide range of engineering applications.

ACKNOWLEDGEMENTS

The authors wish to acknowledge a few of the researchers at Langley whose work we are summarizing: Jean-Francois Barthelemy, Lucas G. Horta, Joycelyn S. Harrison , David L. Raney, Stephanie Wise, Richard Hellbaum, Rob Bryant, Jennifer Pinkerton, Keith Belvin, Garnett Horner, Rich Silcox, Ronald Joslin, Sharon Padula, Gary Fleming, Robert Rogowski, Roberto Cano, Karen Wood, Richard Silcox, Mercedes Reaves, Garnett Horner, Barmac Taleghani, and Keats Wilkie.

REFERENCES

1. Simpson, J. O., Wise, S. A., Bryant, R. G., Cano, R. J., Gates, T. S., Hinkley, J.A., Rogowski, R.S., and Whitley K. S., “Innovative Materials for Aircraft Morphing,“ Proceedings of the SPIE Smart Structures and Materials Symposium 1998, Industrial and Commercial Applications Conference, Vol. 3326, Paper 3326-20, March 1998.
2. J.O. Simpson, Z. Ounaies, and C. Fay, In Materials Research Society Proceediings: Materials for Smart Systems II, George, E., Gotthardt, R., Otsuka, K., Trolier-McKinstry, S., and Wun-Fogle, M., Ed., Materials Research Society: Pittsburgh, PA, Vol. 459, 1997.
3. Z. Ounaies, J. Young, J.O. Simpson, and B. Farmer, In Materials Research Society Proceediings: Materials for Smart Systems II, George, E., Gotthardt, R., Otsuka, K., Trolier-McKinstry, S., and Wun-Fogle, M., Ed., Materials Research Society: Pittsburgh, PA, Vol. 459, 1997.
4. G.H. Haertling, RAINBOW Ceramics – A New Type of Ultra-High-Displacement Actuator,” Am.Ceram.Soc.Bulletin, 73, pp. 93-6, 1994.
5. M.W. Hooker, Properties and Performance of RAINBOW Piezoelectric Actuator Stacks, in Smart Materials and Structures 1997: Industrial and Commercial Applications of Smart Structures Technologies, Proc. SPIE vol. 3044, J.M. Sater, ed., Bellingham, WA: SPIE, pp. 413-420.
6. S.A. Wise, R.C. Hardy, and D.E. Dausch, Design and Development of an Optical Path Difference Scan Mechanism for Fourier Transform Spectrometers using High Displacement RAINBOW Actuators, in Smart Materials and Structures 1997: Industrial and Commercial Applications of Smart Structures Technologies, Proc. SPIE vol. 3044, J.M. Sater, ed., Bellingham, WA: SPIE, pp. 342-9.
7. R.F. Hellbaum, R.G. Bryant, R.L. Fox, A.Jalink, W.W. Rohrbach, and J.O.Simpson, Thin Layer Composite Unimorph and Ferroelectric Driver and Sensor, U.S. Patent 5,632,840, May 27, 1997.

8. R.G. Bryant, “Thunder Actuators”, 5th Annual Workshop: Enabling Technologies for Smart Aircraft Systems, NASA Langley Research Center, May 14-16, 1996.
9. J.L. Pinkerton and R.W. Moses, “A Feasibility Study to Control Airfoil Shape Using THUNDER”, NASA TM-4767, November 1997.
10. Pinkerton, J. L., McGowan, A. R., Moses, R. W., Scott, R. C., Haeg, J., “Controlled Aeroelastic Response and Airfoil Shaping Using Adaptive Materials and Integrated Systems,” Proceedings of the SPIE Smart Structures and Materials Symposium 1998, Industrial and Commercial Applications Conference, Vol. 3326, Paper 3326-20, March 1998.
11. Belvin, K., Horner, G., Hardy, R., Armstrong, D. and Rosenbaum, D., “Integration issues for high-strain actuation applications”, Proceedings of the SPIE Smart Structures and Materials Symposium 1998, Industrial and Commercial Applications Conference, Vol. 3326, Paper 3326-20, March 1998.
12. Fuller, C. R., and Von Flotow, A. H., “Active Control of Sound and Vibration,” IEEE Control Systems, Dec. 1995, pp. 9•19.
13. Lyle, K. H., and Silcox, R. J., “A Study of Active Trim Panels for Noise Reduction in an Aircraft Fuselage,” Presented at the General, Corporate, and Regional Aviation Meeting and Exposition, Wichita, KS, May 3–5, 1995. See also SAE paper 95-1179.
14. Silcox, R. J., Lester, H. C., and Coats, T. J., “An Analytical Study of Intensity Flow for Active Structural Acoustic Control,” Presented at 1993 SAE Noise and Vibration Conference, Traverse City, MI, May 10–13, 1993.
15. Ruckman, C. E. and Fuller, C. R., “Optimizing Actuator Locations in Active Noise Control Systems Using Subset Selection,” Journal of Sound and Vibration, Vol. 186, No. 3, Sept. 1995, pp. 395•406.
16. Padula, S. L. and Kincaid, R. K., “Aerospace Applications of Integer and Combinatorial Optimization,” NASA TM-110210, October 1995.
17. Kincaid, R. K. and Padula, S. L., “Quelling Cabin Noise in Turboprop Aircraft via Active Control,” Journal of Combinatorial Optimization, Vol. 1, 1997, pp. 229–250.
18. Silcox, R. J., Fuller, C. R., and Lester, H. C., “Mechanisms of Active Control in Cylindrical Fuselage Structures,” AIAA Journal, Vol. 28, No. 8, Aug. 1990, pp. 1397•1404.
19. Palumbo, D. L., Padula, S. L., Lyle, K. H., Cline, J. H., and Cabell, R. H., “Performance of Optimized Actuator and Sensor Arrays in an Active Noise Control System,” NASA TM-110281, Sept. 1996.
20. McGowan, A. R., Wilkie, W.K., Moses, R.W., Lake, R.C., Pinkerton Florance, J., Wieseman, C.D., Reaves, M.C., Taleghani, B. K.,Mirick, P.H., and Wilbur, M. L., “Aeroservoelastic and structural dynamics research on smart structures conducted at NASA Langley Research Center”, Proceedings of the SPIE Smart Structures and Materials Symposium 1998, Industrial and Commercial Applications Conference, Vol. 3326, Paper 3326-20, March 1998.
21. Kudva, J., Appa, K., Martin, C., Jardine, P., Sendeckyj, G., Harris, T., McGowan, A., and Lake, R., “Design, Fabrication and Testing of the DARPA/WL Smart Wing Wind-Tunnel Model”, Proceedings of the 38th AIAA/ASME/ASCE/AHS/ASC Structures, Structural Dynamics, and Materials Conference and AIAA/ASME/AHS Adaptive Structures Forum, Paper 97-1198, April 1997.
22. Scherer, L. B., Martin, C. A., Appa, K., Kudva, J., and West, M. N., “Smart Wing Wind-Tunnel Test Results”, Proceedings of the SPIE’s 4th Annual Symposium on Smart Structures and Materials, Industrial and Commercial Applications Conference, Vol. 3044, Paper 3044-05, March 1997.
23. du Plessis, A., Hagood, N., “Performance Investigation of Twist Actuated Single Cell Composite Beams for Helicopter Blade Control”, Presented at the 6th International Conference on Adaptive Structures Technology, Key West, Florida, November 1995.
24. Derham, R., and Hagood, N., “Rotor Design Using Smart Materials to Actively Twist Blades”, Proceedings of the American Helicopter Society 52nd Annual Forum, Vol. 2, Washington, D.C., pp. 1242-1252, June 1996.
25. Wilkie, W. Keats, Belvin, W. Keith, Park, K. C., “Aeroelastic Analysis of Helicopter Rotor Blades Incorporating Anisotropic Piezoelectric Twist Actuation”, Proceedings of the ASME 1996 World Congress and Exposition, Adaptive Structures Symposium, Aerospace Division, November 1996.
26. Wilkie, W. Keats, “Anisotropic Piezoelectric Twist Actuation of Helicopter Rotor Blades: Aeroelastic Analysis and Design Optimization”, Ph. D. thesis, University of Colorado, Boulder, CO, 1997.
27. Rodgers, John P., Hagood Nesbitt W., and Weems, Douglas A., “Design and Manufacture of an Integral Twist-Actuated Rotor Blade”, Proceedings of the 38th AIAA/ASME/AHS Adaptive Structures Forum, Paper No. 97-1264, Kissimmee, FL, April 1997.
28. Wilkie, W. Keats, “Anisotropic Piezoelectric Twist Actuation of Helicopter Rotor Blades: Aeroelastic Analysis and Design Optimization”, Ph. D. thesis, University of Colorado, Boulder, CO, 1997.
29. Ham, N., “Helicopter Individual-Blade-Control Research at MIT 1977-1985”, Vertica, Vol. 11, pp. 109-122, 1987.
30. Hagood, N., Kindel, R., Ghandi, K., and Gaudenzi, P., “Improving Transverse Actuation of Piezoceramics Using Interdigitated Surface Electrodes”, Proceedings of the SPIE Smart Structures and Materials Symposium, Smart Structures and Intelligent Systems Conference, Vol. 1917, Part 1, pp. 341-352, February 1993.

31. Bent, A., Hagood, N., and Rodgers, J., “Anisotropic Actuation with Piezoelectric Fiber Composites”, Journal of Intelligent Material Systems and Structures, Vol. 6, pp. 338-349, May 1995.
32. Bent, A., Hagood, N., “Improved Performance in Piezoelectric Fiber Composites Using Interdigitated Electrodes”, Proceedings of the SPIE Smart Structures and Materials Conference, Smart Materials, Vol. 2441, pp. 196-212, February 1995.
33. MATLAB Reference Guide, The MathWorks, Inc., 1992.
34. Johnson, W., CAMRAD II, Comprehensive Analytical Model of Rotorcraft Aerodynamics and Dynamics, Johnson Aeronautics, Palo Alto, California, 1994.
35. Yeager, W., Mirick, P., Hamouda, M-N., Wilbur, M., Singleton, J., Wilkie, W., “Rotorcraft Aeroelastic Testing in the Langley Transonic Dynamics Tunnel”, Journal of the American Helicopter Society, Vol. 38, No. 3, pp. 73-82, July 1993.

This page has been deliberately left blank

Page intentionnellement blanche

Finite Element Approach for the Design of Control Algorithms for Vertical Fin Buffeting Using Strain Actuation

Fred Nitzsche*
Carleton University
Department of Mechanical and Aerospace Engineering
1125 Colonel By Drive
Ottawa, Ontario, Canada, K1S 5B6

David G. Zimcik‡ and Sauro Liberatore†
National Research Council Canada
Institute for Aerospace Research
Ottawa, Ontario, Canada, K1A 0R6

Abstract

It is difficult to predict buffet loads during the design stage of an aircraft. The present work describes the control design method used to address this problem for the F/A-18 aircraft which is often subjected to high-intensity buffet loads that produce high accelerations at the tip the vertical fin during maneuvers at high angles of attack. A NASTRAN finite-element model was constructed to represent the dynamics of the structure at the low frequencies of interest. The aeroelastic frequency response analysis and the thermal analogy available in NASTRAN were used together in a two-step procedure to simulate the strain actuation. This analysis was conducted for each group of actuators to obtain the transfer functions between the two control inputs (actuation groups), the disturbance (buffet load), and the two output variables (a choice among four accelerometers and five strain-gauge positions). Three independent white noise signals limited by the frequency band between 0 and 120 Hz were used in development of a 2×2 MIMO system. The result was a control system using strain actuation to attenuate the dynamic response caused by buffet loads. The predicted results were compared to full-scale test results in the IFOST Program test facility in Australia. The results demonstrated significant reductions in the root-mean-square (RMS) values of the fin dynamic response measured by the strain transducer at the critical point for fatigue at the root were achieved under the most severe buffet condition.

Nomenclature

$A,\ldots,F,\Gamma$	state-vector system matrices (Equation 1)
G	open-loop transfer function matrix
G_c	closed-loop transfer function matrix
G_u	controller transfer function matrix
H	feedback transfer function matrix
K	full-state feedback gain matrix
L	Kalman filter estimator gain matrix
u	vector of control variables
v	transducer noise
w	buffet disturbance
$x, \hat{x}$	state vector, estimated state vector
y, y_v	feedback vector, idem noise contaminated
z, z_c	vector of performance metrics

Introduction

It is difficult to predict buffet loads during the design stage of an aircraft. One such example is the F/A-18 known in Canada as the CF-118. This twin-tail aircraft is often subjected to high-intensity buffet loads that produce accelerations in excess of 450 g at the tip the vertical fin during maneuvers at high angles of attack. An initial approach to minimize the problem included the introduction of a leading edge extension (LEX) fence. This fence has been added to the aircraft wing root to reduce buffeting by generating additional vortices that interact with the vertical tail and assure airflow attachment to the surface. However, at very high angles of attack, the vortices generated by the LEX fence break down before reaching the tail, generating an even more turbulent wake. The loads produced substantially contribute to the fatigue of the

* Associate Professor
‡ Head, Aeroacoustics and Structural Dynamics Group
† Research Engineer, presently at University of California at Los Angeles

Copyright © by the National Research Council Canada.

Paper presented at the RTO AVT Symposium on "Active Control Technology for Enhanced Performance Operational Capabilities of Military Aircraft, Land Vehicles and Sea Vehicles", held in Braunschweig, Germany, 8-11 May 2000, and published in RTO MP-051.

tail structure, increasing the maintenance costs of the fighter.

This problem is of particular concern for those countries within The Technical Co-operation Program, (TTCP) that include the F/A-18 in their fleets. The TTCP is a program of technical collaboration and data exchange among five nations: Canada, the United States, Australia, United Kingdom and New Zealand. Of these participants, three countries, namely Canada, the United States, and Australia have initiated a collaborative research program aimed at solutions to the problem. The overall approach of the program is to develop an active control system that includes strain actuation using piezoelectric elements. However, the ability of the piezoelectric actuators to achieve control authority under the large aerodynamic buffet loads in a full-scaled aircraft needs to be demonstrated. Ground vibration tests were planned under the TTCP program with the objective of evaluating the performance of the "smart structures" solution. In this program, Australia contributed the test rig; Canada offered the input data information in the form of representative buffet time sequences measured in flight, and the United States provided the control system hardware. All TTCP partners contributed to the software design with unique control strategies.

The present work reports the control design strategy and the results obtained by the Canadian team in the closed-loop tests. The main objective was to investigate the most promising combination of sensors to achieve the required performance using the hardware installed on the airframe. This hardware was configured to accept a MIMO feedback control system with two inputs (consisting of a choice among several strain gauges and accelerometers distributed over the surface of the vertical fin to measure the performance of the system), and two outputs that drive two groups of piezoelectric actuators attached to both sides of the structure skin. Theoretical analyses with a NASTRAN model are presented in this paper to establish the control strategy. These analytical predictions re compared to full-scale tests carried out in the International Follow-on Structural Test (IFOST) rig in Melbourne, Australia. These tests represented an important milestone on the development of adaptive structures systems with application to aeroelastic problems because they were the first tests performed on a full-scale airframe to achieve aerodynamic buffet alleviation.

The objectives of the ground vibration test were: (1) to demonstrate active buffet suppression in a full-scale aircraft; (2) to measure vibration level reductions at different points on the tail, most significantly, at the critical points situated at the fin root where fatigue cracks have been spotted due to high bending stress; (3) to demonstrate piezoelectric control authority at full buffet loads; and (4) to measure vibration reduction at different flight conditions demonstrating the controller robustness under different excitation loads.

NASTRAN Model

Previous investigations were able to demonstrate that the first and the second natural modes of the structure contribute most significantly to the buffeting phenomenon.[1-4] Therefore, a NASTRAN finite-element model was built to represent as close as possible the dynamics of the structure at the low frequencies of interest. The finite element model of the vertical fin consisted of 1197 shell, 320 rod, 124 bar and 48 beam elements. In addition, 96 lumped mass elements located at selected grid points simulated the mass distribution. Also defined in the model were 8 scalar spring elements simulating both the structure boundary conditions and the stiffness of the rudder actuation system. The fin was restrained from moving in all degrees of freedom except for rotation with respect to the chordwise axis, where the springs emulated the stiffness of the bolts employed in fastening the fin to the fuselage. The shell elements were used to model both the skin and the internal stiffeners of the fin. The principal purpose of the rod elements was to simulate the piezoelectric patches working in unison in a push-pull configuration (out-of-phase extension-compression mode across the structure to generate bending). The latter elements were distributed along seven spanwise rows lying on the two skins of the fin, approximating the distribution of actuators suggested by the hardware designers to achieve authority over the first and second natural modes of the structure. The beam and bar elements had multiple functions, namely: (1) to connect the parts where the rod elements were interrupted to separate the actuators into two independent groups, (2) to perform a specific local structural reinforcement, and (3) to define the rudder structure. In the latter, only the rudder hinge was simulated because one is only interested in the rotational motion of the rudder. With this purpose, constraint cards were employed to average the displacement of the grids that represent the rudder hinge. Since the fin was a composite structure, several isotropic material properties were defined in the model.

Natural Frequencies and Mode Shapes

The NASTRAN Modified Givens Method was selected for searching the eigenvalues and eigenvectors associated with the free vibration of the structure. No structural or viscous damping was included as the motion-dependent aerodynamic loads were expected to

contribute most of damping observed by the system. The results of this analysis are shown in Table 1 for the natural modes of interest. The measured natural frequencies of the tested aircraft without the piezoelectric elements attached to its fin are also shown in the same table. When the mass of the piezoelectric elements was added to the model, the modal characteristics of the structure were slightly changed, and displayed in parentheses in Table 1.

Table 1: Natural Modes and Frequencies

mode shape description	model frequency (Hz)	actual frequency (Hz)
1st bending	15.8 (14.8)	15.7
1st torsion	42.6 (43.4)	43.3
rudder	47.6 (49.5)	49.6

In Figures 1 and 2, the mode shapes associated with the first two natural frequencies are plotted.

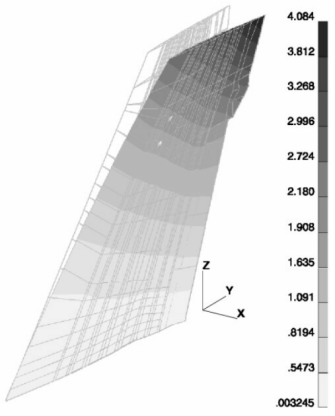


Figure 1: First Mode Shape (NASTRAN)

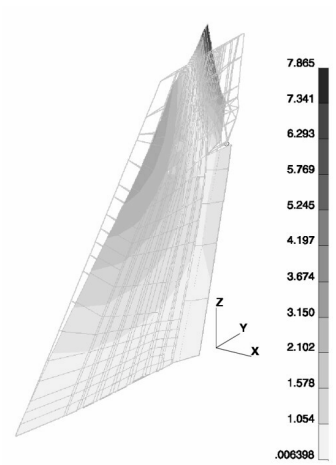


Figure 2: Second Mode Shape (NASTRAN)

Aeroelastic Model

According to the double lattice method,[5] steady horseshoe vortices and oscillatory doublets lying along bound vortex lines were used to model the lifting surfaces in subsonic flow. The vortices represent the steady flow effects, and the doublets represent the incremental effects due to the oscillatory motion. The lifting surface was divided into trapezoidal elements (boxes) arranged in strips parallel to the free stream. In the present model, two panels in the lower and upper parts of the vertical fin were defined. The lower panel was divided into 294 boxes: 21 in the chordwise and 14 in the spanwise direction including the rudder (84 boxes). The upper panel was divided into 168 boxes: 21 in the chordwise and 8 in the spanwise direction. The boxes were concentrated near the leading and trailing edges of the fin, and along the rudder hinge line. Using this refinement, the aspect ratio of the boxes was maintained at approximately one. To account for the forces arising from the body motion, slender body elements were provided in NASTRAN. Interference elements simulated the aerodynamic interference effects among the bodies and the lifting surfaces. In this model, nine slender bodies were used to represent the fuselage and the nacelle, and one interference element was defined to simulate the interference effects between the fuselage, nacelle and the vertical fin.

Strain Actuation

In order to simulate the strain actuation, the thermal analogy and the aeroelastic frequency response analysis available in NASTRAN were used together in a two-step procedure. First, a static and constant temperature field was applied only on the rod elements that represent the piezoelectric actuators. The temperature field had the same magnitude but opposite signs for elements lying on the opposite sides of the fin (no biasing considered). The reaction forces at the nodes of the rod elements that represent the piezoelectric actuators were obtained. The relative magnitude of these forces was used in a second step, where a forced frequency response analysis is performed. The forces obtained were applied in unison at the corresponding nodal points in order to simulate the external forces generated by the control system. This analysis was conducted for each group of actuators independently.

Open-loop Transfer Functions

Some earlier studies incorporating active control techniques to suppress aerodynamic buffeting focused on the classical aeroservoelastic approach, where the rudder was the actuation device.[6] However, adaptive structures provide an attractive solution to the

problem.[7-8] In principle, they allow for the development of sensor and actuator arrangements that are able to approximately perform independent modal state control, greatly improving the realization of a more efficient and robust closed-loop aeroelastic system.

The objective of the present work was to develop a control system using strain actuation to attenuate the dynamic response caused by buffet loads. Figure 3 shows the schematics of the closed-loop, output feedback control system analyzed. The buffeting pressure acting on the fin was treated as a disturbance of stochastic nature. The other input vector was due to the action of the two actuator groups which were patched to the structure to reproduce as closely as possible the strain distribution associated with each one of the first two modes referred in Table 1. Hence, each group had more control authority over one specific mode of the structure. Two vectors defined the system output: the first collected the signal produced by the sensor monitored for performance (normally the strain gauge located at the critical point for fatigue at the fin root), and the second the signal originated from the two sensors used for the feedback control.

The state-space representation of the referred system in the time domain is:

$$\begin{aligned} \dot{x} &= Ax + Bu + \Gamma w \\ y_v &= y + v = Cx + Du + v \\ z &= Ex + Fu \end{aligned} \tag{1}$$

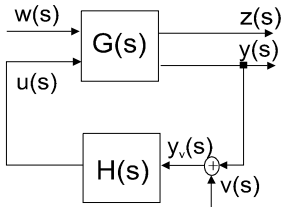


Figure 3: Output Feedback Active Control System (Disturbance Rejection).

In the present section, NASTRAN was employed to obtain the open loop transfer functions between the two control inputs (actuation groups G1 and G2), the disturbance (buffet load), and the two output variables (a choice among four accelerometers and five strain-gauge positions). For this, three independent white noise signals limited by the frequency band between 0 and 120 Hz were sent throughout the system between the chosen pair of input and output variables. The result was a 3×2 MIMO system where the third input variable was the disturbance load (Equation 2). In the present analysis, in order to reproduce the experimental setup better, the latter input was applied at a single point of the structure – the shaker position defined in the ground vibration tests.

$$\begin{Bmatrix} y_v(s) \\ z(s) \end{Bmatrix} = \begin{bmatrix} G_{11}(s) & G_{12}(s) \\ G_{21}(s) & G_{22}(s) \end{bmatrix} \begin{Bmatrix} u(s) \\ w(s) \end{Bmatrix} \tag{2}$$

The elements of the open-loop transfer function matrix were related to the original representation of the system shown in Equation 1 by:

$$\begin{aligned} G_{11}(s) &= C\left(sI - A\right)^{-1} B + D \\ G_{12}(s) &= C\left(sI - A\right)^{-1} \Gamma \\ G_{21}(s) &= E\left(sI - A\right)^{-1} B + F \\ G_{22}(s) &= E\left(sI - A\right)^{-1} \Gamma \end{aligned} \tag{3}$$

In order to calibrate the thermal loads used in the NASTRAN model to the actual piezoelectric loads, the magnitude of the white noise signal input to each actuation group was adjusted to reproduce the maximum values of strain obtained in the open-loop tests when each actuation group was operating alone and at full gain (saturation voltage).

System Identification using Numerical Data

Using the method explained in the previous section, the transfer functions listed in Equation 3 were numerically obtained. Polynomial fitting of the complex data was used to achieve an approximation for the transfer functions in the frequency interval of interest. Due to the fact that the state-space representation of a system was not unique, and those independent processes were used to obtain the individual transfer functions, the latter did not carry in general a common denominator. In order to proceed with the MIMO analysis, an optimization technique was employed to find the "best" fit in the least square sense of all transfer function elements bearing a common denominator.

In the present work, the buffet conditions presented in Table 2 were analyzed. Since flight conditions FC1 and FC3 were associated with the same flight speed and Mach number, the aeroelastic modes under the linear system assumption were identical, as were the related transfer functions. As representative examples of this analysis, the transfer functions between the strain gauge SG3 located at the critical point at the root and the three input signals (actuation groups G1 and G2, and the buffeting load) are depicted for FC1 in Figure 4.

Table 2: Buffet Conditions Analyzed

flight condition number	angle of attack (degrees)	dynamic pressure (psf)
FC1	12-16	225-300
FC3	20-24	225-300
FC5	28-32	300-350

Note: Sea-level conditions, Mach number 0.3.

Control Synthesis

The block diagram shown in Figure 5 provides a complete description of the active control system proposed in the present work. The regulator consists of a Kalman filter in-series with a Linear Quadratic Regulator (full-state feedback on estimated state values). A band-pass filter (not shown in the diagram) may be appended in-series to the controller output in some designs to cut either a DC signal (when strain is used for feedback) or an undesirable high-frequency response (to guarantee stability).

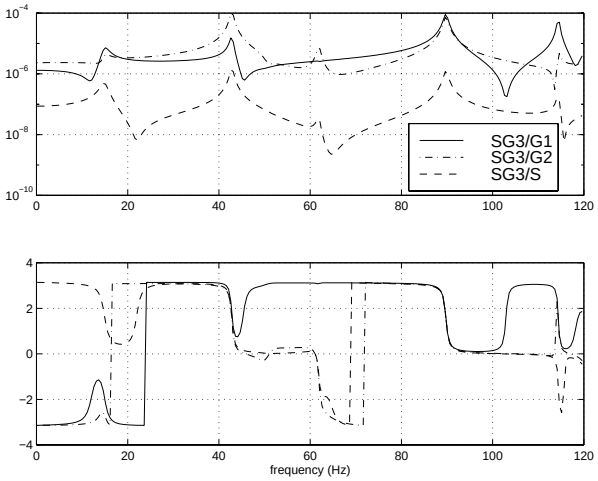


Figure 4: Complex Transfer Function between the Strain Gauge SG3 and Actuator Groups G1 & G2 and Shaker S. Upper Figure: Magnitude (1/lbf). Lower Figure: Phase (rad).

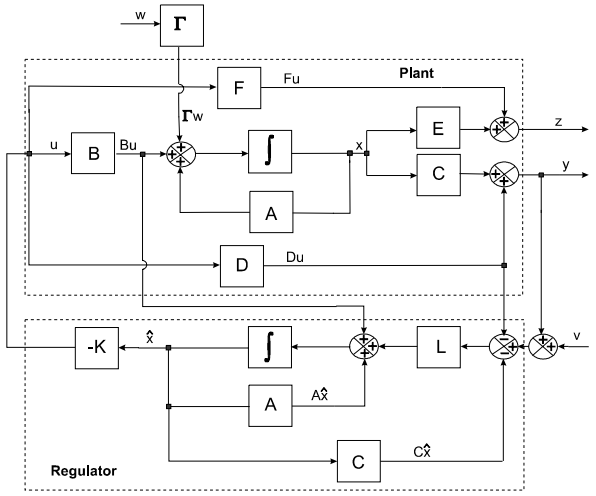


Figure 5: Block Diagram: Linear Quadratic Gaussian Regulator.

The preferred representation of the system for control design purpose was state-space, where the first and the second lines of Equation 1 were appended to the regulator dynamics,

$$\dot{\hat{x}} = A\hat{x} + Bu + L\left(y_v - C\hat{x} - Du\right) \qquad (4)$$
$$u = -K\hat{x}$$

yielding the following closed-loop equations,

$$\begin{Bmatrix} \dot{x} \\ \dot{\hat{x}} \end{Bmatrix} = \begin{bmatrix} A & -BK \\ LC & A - BK - LC \end{bmatrix} \begin{Bmatrix} x \\ \hat{x} \end{Bmatrix} + \begin{Bmatrix} \Gamma \\ 0 \end{Bmatrix} w \qquad (5)$$
$$\begin{Bmatrix} y \\ z \end{Bmatrix} = \begin{bmatrix} C & -DK \\ E & -FK \end{bmatrix} \begin{Bmatrix} x \\ \hat{x} \end{Bmatrix}$$

In the above equation, the single input variable is the buffet disturbance. Hence, the transfer function representation of the open-loop system obtained with NASTRAN needed to be converted into an equivalent state-space form. MATLAB routines based on methods described in Reference 9 were available to perform the task. In general, to avoid ill-conditioned matrices, MATLAB offered balancing transformations described in References 10 and 11.

The typical regulator was designed for performance in the bandwidth defined by 10 and 60 Hz, with roll-off at the lower and higher frequencies. The Separation Theorem of the classic LQE-LQR Optimal Control theory was used to obtain the Kalman filter and the full-state feedback gains. Emphasis in the control law synthesis was given to attenuate the dynamic response associated with both the first and second modes of the vertical fin (at 15 and 43 Hz).

Performance Calculations

The ultimate goal of the present investigation was to study control performance based on the ground vibration tests when the system transfer functions were directly measured. Therefore, in order to harmonize the present analyses, Equation 5 was not be used to evaluate the numerical results, but rather its transfer function equivalent.

For the open-loop case, Equation 2 gives:

$$z(s) = G_{22}(s)w(s) \tag{6}$$

Referring to Figure 3:

$$u(s) = H(s)y_v(s) \tag{7}$$

Substitution of Equation 7 into Equation 2 yields the closed-loop system transfer function:

$$G_c(s) = G_{21}(s)G_u(s) + G_{22}(s) \tag{8}$$

Hence,

$$z_c(s) = G_c(s)w(s) \tag{9}$$

In Equation 8, the transfer function relating the control signal to the disturbance is defined as:

$$G_u(s) = H(s)\left(I - G_{11}(s)H(s)\right)^{-1}G_{12}(s) \tag{10}$$

i. e.

$$u(s) = G_u(s)w(s) \tag{11}$$

The power spectral density (PSD) of the disturbance was a known input obtained from the flight tests. Due to hardware limitations, these PSD were band-limited. The frequency content lying outside of each one of the critical modes for buffeting was cut off (Figure 6). Furthermore, in the ground vibration tests, this PSD described the shaker input signal that excited the structure at a single point. Also, between the shaker and the structure there was a load cell (Figure 9). In this section, the PSD of the output of this load cell was assumed to correspond to the disturbance load applied to the NASTRAN model to simulate buffeting. The subsequent use of the product between Equations 6, 9 and 11 and their respective complex conjugates produced the PSD of the performance sensors in the open- and closed-loop cases, and the control signal, respectively:

$$PSD_{out} = \left|TransferFunction\right|^2 PSD_{in} \tag{12}$$

From these PSD, both the control effort RMS values of each actuator group (as a fraction of the maximum allowed by the hardware), and the ratio (closed- over open loop) of the RMS values of the performance sensors were obtained. These were the metrics used to access the performance. The other parameter to evaluate control system performance was the robustness to reject the disturbance under those different flight conditions.

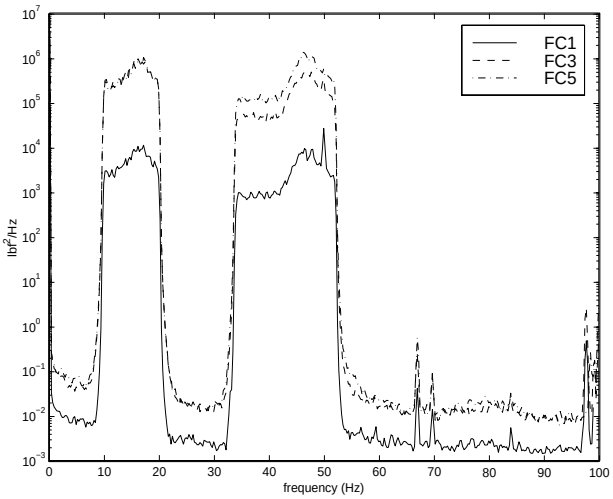


Figure 6: Power-Spectral-Density Functions for the Disturbance Input to the Shaker (Buffet Simulation for Flight Conditions FC1, FC3 and FC5).

Numerical Results

Control laws were synthesized based on NASTRAN numerical results using the method described in the previous sections. As a demonstration, a control law was designed using the feedback of the accelerometer A2 (situated at the trailing edge near the tip of the vertical fin) and strain gauge SG3 (located at the fin root near the rudder leading edge) – the critical location regarding fatigue effects. The results are summarized in Tables 3 to 5 for the buffet conditions listed in Table 2. The control law was synthesized based on data from FC1. Using the notation in Equation 1:

$$\begin{aligned} u &= \begin{bmatrix} G1 & G2 \end{bmatrix}^T \\ y &= \begin{bmatrix} A2 & SG3 \end{bmatrix}^T \\ z &= \begin{bmatrix} A2 & SG3 \end{bmatrix}^T \end{aligned} \tag{13}$$

Table 3: Control Law using Feedback of Accelerometer A2 and Strain Gauge SG3. Synthesis and Performance based on NASTRAN for FC1.

	Closed-/Open-loop RMS Values (%)		
	Mode 1	Mode 2	Modes 1 and 2
A2	68.5	48.3	65.2
SG3	67.4	30.3	40.3
	Control Effort 0-120 Hz (%)		
G1		90.2	
G2		100.0	

Table 4: Control Law using Feedback of Accelerometer A2 and Strain Gauge SG3. Synthesis and Performance based on NASTRAN for FC3.

	Closed-/Open-loop RMS Values (%)		
	Mode 1	Mode 2	Modes 1 and 2
A2	89.3	70.7	85.0
SG3	80.1	68.1	74.4
	Control Effort 0-120 Hz (%)		
G1		87.3	
G2		100.0	

Table 5: Control Law using Feedback of Accelerometer A2 and Strain Gauge SG3. Synthesis and Performance based on NASTRAN for FC5.

	Closed-/Open-loop RMS Values (%)		
	Mode 1	Mode 2	Modes 1 and 2
A2	93.2	81.1	89.9
SG3	89.7	82.7	87.6
	Control Effort 0-120 Hz (%)		
G1		89.2	
G2		100.0	

Experimental Setup

The IFOST rig in Australia was used for the ground vibration tests of the full-scale aircraft (Figure 7). The piezoelectric actuation devices were attached to both sides of the starboard vertical fin (Figure 8). A block diagram of the test setup is shown in Figure 9, from which one can observe the two banks of amplifies at each side of the fin driving the two groups of actuators acting in opposite phase to generate bending. The amplifiers fed the maximum voltage differential allowed across the piezoelectric devices (approximately 1500 V peak-to-peak). The third input signal was given by the 5000 lbf electromagnetic shaker attached to a single point at center of the starboard side of the fin through a load cell. Representative buffet time sequences associated with the different flight conditions analyzed were fed into the computer that controlled the shaker. A load cell was placed between the shaker and the structure to monitor the actual dynamic loads transmitted into the structure by the exciting mechanism.

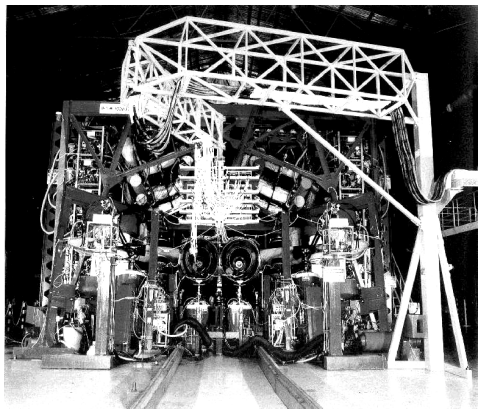


Figure 7: Full-Scaled Aircraft in the Australian IFOST Rig.

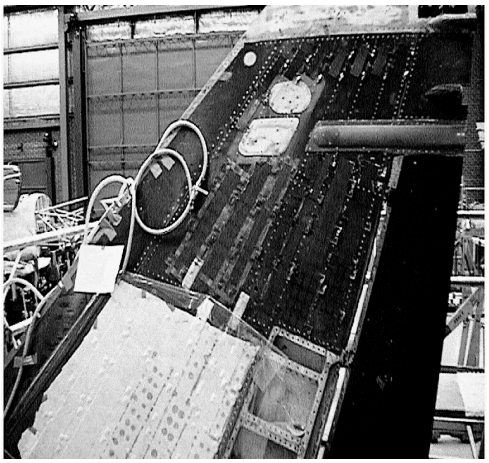


Figure 8: Instrumented Vertical Fin.

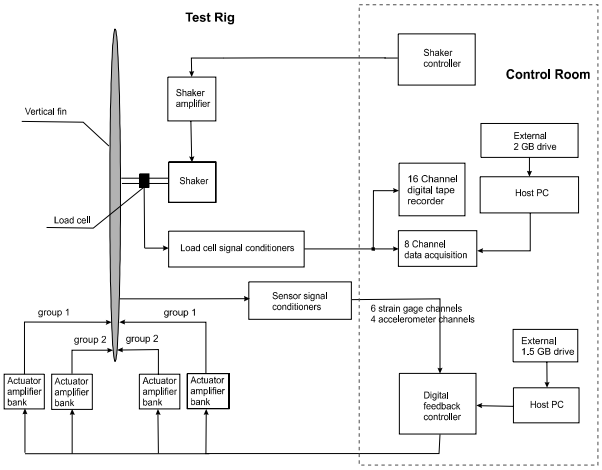


Figure 9: Block Diagram for the Test Set-Up.

Air bags partially inflated were used to simulate the aerodynamic damping provided by the motion-dependent airloads. Four accelerometers and six strain gauge rosettes situated at strategic points of the fin provided the output signals. In the control room, an 8-channel data acquisition system was used to acquire real-time frequency-domain data including transfer functions and auto-spectra. In addition, a 16-channel digital tape recorder was used to record data from all available signals for subsequent off-line analyses. The signal from two channels could be selected for feedback control through a computer driven DSP board.

System Identification

During the open-loop tests in September 1997, the standard technique of measuring system transfer functions by energizing each drive system (shaker and actuator groups) independently and measuring the sensor response provided unexpected results. These were ascribed to the internal damping of the large electrodynamic shaker changing the stiffness of the fin when not energized (a node was artificially forced at the shaker attachment point). Unfortunately, the magnitude of this damping was large compared to the singular effect of each actuator string thereby effectively masking the true transfer function. A solution to this problem was found by feeding all three input variables (actuator groups G1 and G2 and the buffet disturbance) using three simultaneous and independent random processes. However, this procedure slowed down the convergence of the transfer functions due to the increasing importance of the cross talk amongst drivers and transducers. Due to the fact that the shaker controller could only run relatively short time sequences, an unsatisfactory number of ensembles could be taken to determine the individual transfer functions. Therefore, optimization techniques were then required, obtaining the "best" estimate of the required transfer functions in a least square sense in terms of the cross- and power-spectral-densities measured between a given input and the correspondent output. In this case, the identification was performed in a 3×3 MIMO system where the third transducer was the load cell.

Experimental Results

Three control laws (CL1, CL2 and CL3) were designed based on open-loop test data using the feedback from different pairs of sensors. The identification of the sensors used and their respective participation in a determined control law is summarized in Table 6.

Table 6: Feedback Control Synthesis

sensor identification	approximate sensor position	control law identification
A1	fin tip, near leading edge	CL1
A2	fin tip, near trailing edge	CL1 & CL2
A3	1/3-span, near leading edge	none
A4	1/3-span, near rudder leading edge	none
SG3	fin root, near rudder leading edge (critical point)	CL2 & CL3
SG5	2/3-span, near rudder leading edge	CL3

Note: "A" defines accelerometer and "SG" strain gauge.

All control laws were designed based on open-loop test data for FC1. Tables 7 to 12 depict the control performance in the frequency intervals shown for control laws CL2 and CL3 that presented the best performance (the gain for control law CL1 was reduced during the tests due to indications of stability problems). The given intervals include modes 1, 2, and 1 and 2 together, respectively. The control effort as a fraction of the maximum allowed per group was calculated in the interval between 5 and 1000 Hz. In the same tables, both the estimated performance metric (using Equation 11) and the actually measured performance metric obtained in the closed-loop tests are listed. One can observe that the estimations in general show good agreement with the measured data. From this analysis, one can also observe that, in fact, actuator groups G1 and G2 had more authority over modes 1 and 2, respectively. The reduction in the vibration levels associated with mode 1 was in general less significant than those for mode 2, following the trend of lower control effort observed for group G1.

Table 7: CL2 (Feedback of Accelerometers A2 and Stain Gauge SG3). Performance based on Experimental Results for FC1.

	Closed-/Open-loop RMS Values (%)					
	5-25 Hz		25-100 Hz		5-100 Hz	
	Est.	Test	Est.	Test	Est.	Test
A1	72.4	68.3	71.2	72.7	71.5	71.8
A2	68.5	70.3	48.3	57.8	65.2	58.5
A3	73.4	68.3	57.7	59.8	58.2	60.1
A4	73.7	68.8	27.0	39.9	55.2	59.8
SG3	75.9	67.4	30.3	42.5	40.3	66.7
	Control Effort 5-1000 Hz (%)					
	Estimated			Test		
G1	90.2			81.3		
G2	100.0			97.1		

Table 8: CL2 (Feedback of Accelerometers A2 and Stain Gauge SG3). Performance based on Experimental Results for FC3.

	Closed-/Open-loop RMS Values (%)					
	5-25 Hz		25-100 Hz		5-100 Hz	
	Est.	Test	Est.	Test	Est.	Test
A1	91.0	92.5	92.7	94.2	92.0	95.5
A2	90.3	92.3	86.7	86.9	87.0	87.3
A3	92.2	92.2	83.3	88.1	85.9	88.4
A4	92.1	92.4	69.1	71.0	88.7	89.1
SG3	80.1	92.3	68.1	86.9	74.4	87.3
	Control Effort 5-1000 Hz (%)					
	Estimated			Test		
G1	83.7			81.4		
G2	100.0			107.5		

Table 9: CL2 (Feedback of Accelerometers A2 and Stain Gauge SG3). Performance based on Experimental Results for FC5.

	Closed-/Open-loop RMS Values (%)					
	5-25 Hz		25-100 Hz		5-100 Hz	
	Est.	Test	Est.	Test	Est.	Test
A1	92.4	94.4	92.0	92.3	92.3	92.6
A2	93.2	94.3	81.1	87.8	89.9	88.0
A3	92.9	93.9	86.3	88.7	87.9	88.8
A4	90.0	94.0	69.1	76.6	78.7	88.9
SG3	89.7	94.3	82.9	87.8	87.6	88.0
	Control Effort 5-1000 Hz (%)					
	Estimated			Test		
G1	89.2			99.3		
G2	100.0			97.1		

Table 10: CL3 (Feedback of Strain Gauges SG3 and SG6). Performance based on Experimental Results for FC1.

	Closed-/Open-loop RMS Values (%)					
	5-25 Hz		25-100 Hz		5-100 Hz	
	Est.	Test	Est.	Test	Est.	Test
A1	68.2	65.6	93.1	96.4	87.4	90.3
A2	68.2	64.8	86.2	84.9	85.5	84.9
A3	74.4	68.7	85.1	85.0	84.8	85.0
A4	70.5	67.3	69.1	66.7	69.8	66.7
SG3	74.5	70.0	72.8	67.2	74.2	69.6
	Control Effort 5-1000 Hz (%)					
	Estimated			Test		
G1	68.8			65.4		
G2	102.1			103.2		

Table 11: CL3 (Feedback of Strain Gauges SG3 and SG6). Performance based on Experimental Results for FC3.

	Closed-/Open-loop RMS Values (%)					
	5-25 Hz		25-100 Hz		5-100 Hz	
	Est.	Test	Est.	Test	Est.	Test
A1	92.5	92.5	99.8	98.6	97.2	96.6
A2	95.9	92.4	95.6	94.1	95.6	93.9
A3	94.7	93.2	94.1	94.3	94.1	94.3
A4	96.1	92.6	80.4	81.3	92.5	90.8
SG3	95.0	93.0	86.5	87.6	94.5	92.8
	Control Effort 5-1000 Hz (%)					
	Estimated			Test		
G1	61.4			53.4		
G2	102.4			98.1		

Table 12: CL3 (Feedback of Strain Gauges SG3 and SG6). Performance based on Experimental Results for FC5.

	Closed-/Open-loop RMS Values (%)					
	5-25 Hz		25-100 Hz		5-100 Hz	
	Est.	Test	Est.	Test	Est.	Test
A1	92.7	93.1	98.2	101.6	97.2	100.3
A2	92.5	93.0	95.1	98.2	95.0	98.0
A3	90.1	93.6	96.1	98.2	95.9	98.0
A4	94.7	93.1	79.6	84.4	88.9	90.5
SG3	96.2	92.6	88.5	92.4	95.4	92.6
	Control Effort 5-1000 Hz (%)					
	Estimated			Test		
G1	95.1			80.7		
G2	104.1			97.7		

Conclusions

An important step in the development of adaptive or "smart structures" system was given since for the first time a full-scale aircraft was tested aiming at buffet control using this new technology. Very promising results were obtained in the experimental work with a two-input, two-output controller using a standard linear time invariant LQG design. These results were based on a relatively simple method using NASTRAN to generate the aeroelastic transfer functions necessary for control law synthesis.

Vertical fin buffet attenuation approximately 60% for the nominal flight configuration FC1 and 30% for the most severe case FC5 was observed during the tests. Also, very significant vibration reduction measured by the most important performance metric – the strain gauge located at the critical point for fatigue (SG3) was verified for FC5: 17.1% (Mode 2) and 12.0% (Modes 1 and 2). In general, the control laws that included at least one strain gauge in the feedback loop revealed better performance. In fact, CL2 comprising feedback from one accelerometer situated at the tip of the fin and SG3 presented the best results. This is an indication that strain gauges can be better co-related to the control objective, which is to reduce the structural strain generated by buffeting. The method showed that the general trends of the system can be reproduced numerically, and it may be useful in preliminary analyses.

References

1. Zimmerman, N. H., Ferman, M. A., Yurkovich, R. N. and Gerstenkorn, G., "Prediction of Tail Buffet Loads for Design Application," *AIAA/ASME/ASCE/ AHS/ASC 30th Structures, Structural Dynamics and Materials Conference*, American Institute of Aeronautics and Astronautics, Washington, DC, pp. 1911-1919.
2. Ferman, M. A., Patel, S. R., Zimmerman, N. H. and Gerstenkorn, G., "A Unified Approach to Buffet Response of Fighter Aircraft Empennage," *Aircraft Dynamic Loads due to Flow Separation*, AGARD Report CP-483, North Atlantic Treaty Organization, Neuilly-Sur-Seine, France, September 1990, pp. 2.1-2.18.
3. Lee, B. H. K., Brown, D., Zgela, M. and Poirel, D., "Wind Tunnel and Flight Tests of Tail Buffet on the CF-18 Aircraft," *Aircraft Dynamic Loads due to Flow Separation*, AGARD Report CP-483, North Atlantic Treaty Organization, Neuilly-Sur-Seine, France, September 1990, pp. 1.1-1.26.
4. Edwards, J. W., "Unsteady Airloads Due to Separated Flow on Airfoils and Wings," *Aircraft Dynamic Loads due to Flow Separation*, AGARD Report CP-483, North Atlantic Treaty Organization, Neuilly-Sur-Seine, France, September 1990, pp. 16.1-16.18.
5. Albano, E., and Rodden, W. P., "A Doublet-Lattice Method for Calculating Lift Distributions on Oscillating Surfaces in Subsonic Flows," *AIAA Journal*, Vol. 7, pp. 279-285, 1969.
6. Rock, S. M., Ashley, H., Digumarthi, R. and Chaney, K., "Active Control for Fin Buffet Alleviation," in *Advances in Aerospace Sciences: A Tribute to Prof. Holt Ashley*, P. Hagela and S. C. McIntosh, Jr. Editors, Stanford University, 1993, pp. 413-421.
7. Nitzsche, F., Zimcik, D. G. and Langille, K. "Active Control of Vertical Fin Buffeting with Aerodynamic Control Surface and Strain Actuation," *AIAA/ASME/AHS Adaptive Structures Forum*, Kissimmee, FL, April 7-10, 1997, American Institute of Aeronautics and Astronautics, Washington DC, CP973, pp. 1467-1477.
8. Moses, R. W., "Vertical fin buffeting alleviation using piezoelectric actuators," in *Smart Structures and Materials 1997, Industrial and Commercial Applications of Smart Structures Technologies*, J. M. Sater, Ed., SPIE Vol. 3044.
9. Kailath, T., *Linear Systems*, Prentice-Hall, NJ, 1980, pp. 345-370.
10. Laub, A. J. *et al.* "Computation of System Balancing Transformations and Other Applications of Simultaneous Diagonalization Algorithms," *IEEE Transactions on Automatic Control*, AC-32, 1987, pp. 115-122.
11. Moore, J. B., "Principal Component Analysis in Linear Systems: Controllability, Observability and Model Reduction, "*IEEE Transactions on Automatic Control*, AC-26, 1981, pp. 17-31.

Active Flutter Suppression Using Astros With Smart Structures and Ase Modules

C. Nam* and P.C. Chen[†]
ZONA Technology, Inc.
7430 E. Stetson Drive, Suite 205
Scottsdale, AZ 85251-3540

D.D Liu[‡]
Department of Mechanical and Aerospace Engineering
Arizona State University, Tempe, AZ 85287-6106

Abstract

Recent development of a smart structures module and its successful integration with a multidisciplinary design optimization software ASTROS* and an Aeroservoelasticity (ASE) module is presented. Application examples have been worked out to demonstrate the integrated software capability. These include the neural net based active flutter suppression of a modeled F-16 wing using piezoelectric(PZT) actuators, the gust-load alleviation of a modeled F-18 aircraft using control surfaces, and trim drag reduction of TOMAHAWK with/without battle damage using PZT actuators.

Introduction

Requirements on future military aircraft structures are consistantly increasing with advancing technological progress. In recent years, considerable interest has directed toward application of smart (adaptive) structures to control the static and dynamic aeroelastic responses for rotary and fixed wing aircraft (Refs 1, 2). A number of different concepts have been proposed to actively suppress the aeroelastic instability or alleviate the vibration. Manser et al. conducted an experiment to investigate the concept for fin buffet vibration damping utilizing the distributed piezoelectric patch actuators (Ref. 3). Suleman et al. also conducted an experimental research to demonstarte the feasibility of using adaptive materials technology to suppress wing flutter and to alleviate buffeting (Ref. 4). Northrop Grumman Co. built a smart wing to invetigate the benefits of smart materials and structures adaptive wing technology. (Ref. 5,6,7)

For aeroelastic control, the selection of smart actuators requires a systematic parametric study of the best possible piezoelectric (PZT) and/or Shape Memory Alloy (SMA) combinations. Further, the total effort should amount to find their optimized size and location on a wing surface along with their integration with the wing structure. Such an effort would require tedious parametric study, which can only be conducted effectively through a multidisciplinary design and optimization (MDO) methodology. In this study, we adopt an MDO software system ASTROS*, previously developed by AFRL (Ref 8) and further integrated and maintained by ZONA Technology (ZONA) (Refs 9–11). ASTROS stands for Automated Structural Optimization System, which is a proven engineering design/analysis software including vast scope aerospace disciplines that impact a structural design. We will further elaborate on ASTROS* in the following section.

On the other hand, to formulate and make the smart-structure algorithm compatible with ASTROS* is not altogether a trivial task. The present paper present our recent development of a smart structure module and its integration with ASTROS* and the Aeroservoelasticity (ASE) module. To validate the developed software, we apply the smart structure module in conjunction with ASTROS* and ASE module for active flutter suppression of a modeled F-16 wing using PZT actuators. For demonstration of the capability of the ASE module, an example case was worked out showing the gust-load alleviation of a modeled F-18 aircraft using control surfaces. And TOMAHAWK cruise missile wing is designed to minimize the trim drag utilizing PZT actuators using smart structures and trim modules.

* Senior Engineering Specialist, changho@zonatech.com, (480)945-9988
† Vice President, pc@zonatech.com, (480) 945-9988
‡ Professor, danny.liu@asu.edu, (480) 965-4117

Copyright © 2000 by ZONA Technology, Inc.

Paper presented at the RTO AVT Symposium on "Active Control Technology for Enhanced Performance Operational Capabilities of Military Aircraft, Land Vehicles and Sea Vehicles", held in Braunschweig, Germany, 8-11 May 2000, and published in RTO MP-051.

ASTROS*, ASE and Trim Modules

ASTROS (Automated STRuctural Optimization System) is a finite element based procedure tailored for the preliminary design of aerospace structures (Ref 8). As such, it includes flexibility and generality in multiple discipline integration. For aircraft, spacecraft or missile design, the unique attributes of ASTROS lie in its savings in design effort and time, improvement in flight performance and reduction in structural weight. In principle, ASTROS was aimed at the effective multidisciplinary interactions between aerodynamics, aeroelastics, structures and other modules.

For structural analysis, ASTROS has both statics and normal modes capabilities, and is based on the NASTRAN style input format for its finite element methodology. For optimization, ASTROS adopts Vanderplatts method of feasible directions (Ref 12). Other analysis modules in ASTROS include the sensitivity analysis, aeroelastic analysis, control response and aerodynamic modules.

Under contracts with AFRL, ZONA has further developed ASTROS* through the integration of a unified steady/unsteady, wing-body aerodynamic module for all Mach numbers (the ZAERO module) and an aeroservoelastic module (ASE module) into the system (Refs 9-11). Thus, ASTROS* is named after the integration of ASTROS with the ZAERO module and ASTROS*/ASE is named after the integration of ASTROS* with the ASE module. Recently, a Smart Structures (SS) module and a Trim module have been developed for ASTROS* (see Fig. 1).

The ASE module facilitates the inclusion of multi-input, multi-output (MIMO) control system effects on the dynamic stability and response in multidisciplinary analysis in design/optimization (see Fig. 2). The ASE module is based on state-space formulations. The structure is represented by a set of baseline normal modes serving as generalized coordinates. The unsteady aerodynamic forces are represented by minimum-state rational approxi-mations (Ref 13) of the ZAERO module generated transcendental frequency domain generalized force coefficient matrices. The control system is represented by a state-space realization of a user-defined series of polynomial transfer functions. A gust filter is defined such that a white-noise input produces an approximation of either Dryden's or von Karman's power spectral density of atmospheric continuous gusts. The stability analysis and constraints are based on root-loci curves, Nyquist curves and transfer-function singular values in the frequency domain. The gust response analysis and sensitivities are based on the stochastic Lyapunov formulation. There are several options for the reduction of the order of the state-space equations. These options allow a combination of modal truncation, static residualization and dynamic residualization. The ASE module is applicable to open loop as well as closed loop systems.

The ASTROS* trim module performs the static aeroelastic analysis of flexible aircraft and determines the trim solution of a given maneuver conditions. Several special features are built in this module:

- As a default, the ASTROS*/Trim module uses the ZAERO aerodynamic module to generate the aerodynamic control forces of the trim variables. In addition, it can also adopt the aerodynamic forces from other aerodynamic methods such as the Navier-Stokes CFD codes.
- In addition to the conventional trim variables such as angle of attack, side slip angle, control surface deflections, etc., the deformations due to *smart actuators* (computed by the smart structures module) can also be defined as trim variable in which the ASTROS* trim module determines the required power to achieve the trim solution.
- The ASTROS*/Trim module is capable of solving the determined trim system as well as the over-determined trim system. The solution of the over-determined trim system is obtained by using an optimization technique which minimizes a user-defined objective function such as induced drag, component loads, etc.

Formulation of Smart Structures/ASE Modules

Smart Structures Module

Currently, the piezoelectric (PZT) materials are frequently used for dynamic control because of their rapid response to control a disturbance. The induced strain of PZT actuators is generated by applying control voltage. The Shape Memory Alloy (SMA) actuators, which work via a temperature-induced microstructural phase change in the material, exhibiting relatively large actuation force and high strain output compare to PZT materials. However, due to their slow response time, they are best suited for low frequency or static applications, such as shape control (Ref 1). Clearly, the SMA actuators would be a superior material for the static aeroelastic control because of its larger strain capability to achieve the desired camber and twist distribution for minimum drag reduction. On the other hand, the rapid response requirement of flutter control suggests that the PZT actuators could be the best candidate. The selection of the smart actuators requires a systematic parametric study of the best possible PZT/SMA combinations. Such a parametric study is

tedious and can only be conducted effectively by using the ASTROS*/Smart Structures module.

In order to use PZT actuators, it is assumed that wing has the segmented PZT actuators set which are attached at the top and bottom of the wing surface. It is also assumed that the opposite electric field is applied to the actuators set so as to create a pure bending moment for the aeroelastic control. When a voltage creates an electric field in the piezoelectric material, it will strain in three directions (Ref 14)

$$\varepsilon_{induced} = d_{ij} \frac{V_{Pi}}{t_P} \tag{1}$$

The constant measuring the strains per unit electric field are denoted as d_{ij} and measures the strain in the i direction due to a unit electric field applied in the j direction. V_{Pi} is the applied control voltage and t_P is thickness of piezoelectric materials. These induced strains are analogous to "thermal loads" that produce stress in the restrained structures.

$$\varepsilon_{TEMP} = \alpha_{ij} \ \Delta T \tag{2}$$

where α_{ij} is the thermal expansion coefficient and ΔT is the temperature change. The close similarity between the PZT induced strain and the thermal load induced strain suggests that the formulation of thermal load computation in the finite element method can be adopted to compute the PZT induced strain. In fact, the ASTROS* smart structures module for PZT actuators is developed by modifying an existing thermal loads module in the ASTROS*, where the thermal expansion coefficient α_{ij} and the temperature change ΔT is replaced by d_{ij} and V_{Pi}/t_P. Similarly, the induced smart actuator strain/stress of SMA can also be converted into the actuation forces in ASTROS* with smart structures module (Ref 15).

In order to include the effects of the induced strain due to PZT actuation, a smart structures module is developed by modifying the existing thermal loads module in ASTROS*. The thermal-PZT/SMA equivalence model enables the modifications of the thermal stress module to accommodate the smart structures module in ASTROS*. The control surface (CS)/ PZT/SMA equivalence model principle ensures the interchangeability between the CS force input and the PZT/SMA force input to the ASE modules in ASTROS*. Aerodynamic forces due to control surface modes can be expressed as

$$[F_c] = [AIC][\varphi_c] \tag{3}$$

where [*AIC*] is the aerodynamic forces coefficient matrix, $[\varphi_c]$ is the control surface mode defined at aerodynamic grid. Similarly, aerodynamic forces due to PZT/SMA modes are expressed as

$$[F_p] = [AIC][SPLINE][\varphi_p] \tag{4}$$

where $[\varphi_p]$ is the PZT/SMA mode defined at structural finite element grid. It is noted that the variables, [*AIC*], [*SPLINE*], $[\varphi_c]$, and $[\varphi_p]$ are all existing data entities in ASTROS*. Therefore, $[F_c]$ and $[F_p]$ are interchangeable inputs to ASE module, whereas ASE module requires no modification for PZT/SMA control application.

Aeroservoelasticity (ASE) Module

The equations of motion for aeroservoelastic analysis can be written as

$$\begin{aligned} &[M_s]\{\ddot{q}\} + [C_s]\{\dot{q}\} + [K_s]\{q\} + [M_c]\{\ddot{\delta}_c\} \\ &= q_d \left([A_a]\{q\} + [A_c]\{\delta_c\} + [A_P]\{V_P\} + [A_G]\frac{w_G}{V} \right) \end{aligned} \tag{5}$$

where $\{q\}$ are the generalized modal coordinates, q_d is the dynamic pressure. The matrices $[A_a]$, $[A_c]$, $[A_P]$ and $[A_G]$ are the generalized aerodynamic matrices due to flexible modes, control surfaces mode, PZT mode and gust, respectively.

The aerodynamic forces are approximated as the transfer functions of the Laplace variable by a least square procedure in order to define the aeroservoelastic equations of motion in a linear time invariant state-space form. In the ASE module, we adopt the minimum state method (Ref 13) that approximates the unsteady aerodynamic forces in the following form.

$$\begin{aligned} [A_{ap}] &= [A_q \, A_c \, A_P \, A_G] \\ &= [\overline{P}_0] + [\overline{P}_1]s' + [\overline{P}_2]s'^2 + [\overline{D}]([I]s' - [\overline{R}])^{-1}[\overline{E}]s' \end{aligned} \tag{6}$$

where $\overline{P}_i = \left[P_q \, P_c \, P_P \, P_G\right]_i$, $s' = ik = i\omega b / V = sb / V$ and s is the Laplace variable, k is the reduced frequency, b is the semi-chord and V is the airspeed. The subscripts q, c, p and G indicate elastic, control surface, PZT and gust modes, respectively.

The control surfaces/PZT actuator transfer functions can be expressed in a state space form as follows.

$$\begin{aligned} \{\dot{x}_c\} &= [A_c]\{x_c\} + \{B_c\}\delta_{command} \\ \{u_s\} &= [C_c]\{x_c\} \end{aligned} \tag{7}$$

The gust state space model is included for random gust response calculations. The vertical gust is modeled by a second order Dryden model;

$$\frac{w_g}{w} = \sigma_{wg} \frac{\sqrt{\frac{3V}{L}}\left(s + \frac{V}{L\sqrt{3}}\right)}{\left[s + \frac{V}{L}\right]^2} \tag{8}$$

where σ_{wg} is the root-mean square value of the gust velocity, L is the characteristic gust length and V is the airspeed. When the low pass filter is included, the state space equation of the gust is expressed as follows

$$\begin{aligned} \{\dot{x}_g\} &= [A_g]\{x_g\} + \{B_g\}w \\ \{w_G\} &= [C_g]\{x_g\} \end{aligned} \tag{9}$$

By including the gust dynamics system and the actuator system, the following state space aeroservoelastic model is obtained.

$$\begin{aligned} \{\dot{x}\} &= [A]\{x\} + [B]\{u\} + \{B_w\}w \\ \{y\} &= [C]\{x\} \end{aligned} \tag{10}$$

where $\{x\} = \left\lfloor q^T \dot{q}^T x_a{}^T x_c{}^T x_g{}^T \right\rfloor^T$, $\{y\}$ is the output vector.

Active Control System Design

In ASE module, currently two different control algorithms are available to design an active control system for aeroelatic control.

Optimal Output Feedback Control Scheme

For a given design airspeed, the linear quadratic regulator (LQR) theory can be used to design the controller for the aeroservoelastic control. The LQR theory determines the optimal control gains to minimize the performance index that is expressed as follows

$$J = \int_0^\infty [\{y\}^T[Q]\{y\} + \{u\}^T[R]\{u\}]dt \tag{11}$$

where $[Q]$ and $[R]$ are weighting matrices. The corresponding optimal control is given by

$$\{u\} = -[K_G]\{y\} \tag{12}$$

where $[K_G]$ is an output feedback gain matrix. By applying optimality conditions to this problem, the control gain matrix $[K_G]$ can be obtained by solving three coupled nonlinear algebraic matrix equations (Ref 16).

Another purpose of the active control system is to prevent performance degradation due to external disturbances such as gust. Thus, the root-mean square (RMS) values of gust response for the different modes are calculated. The square of the RMS of the system outputs is computed as follows,

$$\sigma_i^2 = [[C][X][C]^T]_{ii} \tag{13}$$

where $[X]$ is the state covariance matrix of the closed-loop system. The state covariance matrix is the solution of a Lyapunov equation in the form

$$[A_c][X] + [X][A_c]^T + \{B_w\}Q_w\{B_w\}^T = 0 \tag{14}$$

where $[A_c]$ is the closed loop system matrix and Q_w is the intensity of the white noise.

Neural Network Controller

In order to apply the neural net based control scheme, the continuous time model is first discretized using zero-order hold method with sampling frequency, f_s. The discrete time state space model can be written in the following form

$$\begin{aligned} \{x\}_{k+1} &= [A_i]\{x\}_k + [B_i]\{u\}_k + \{w\}_k \\ \{y\}_k &= [C_i]\{x\}_k + \{v\}_k, \quad i = 1,2,....,n_V \end{aligned} \tag{15}$$

where $\{x\}_k$, $\{u\}_k$ and $\{y\}_k$ represent the state, input and output vectors, respectively, and the matrices $[A_i]$, $[B_i]$ and $[C_i]$ are the system, input and measurement matrices for the air speed of V_i, respectively. n_V is the number of air speed set. The disturbance $\{w\}_k$ and sensor noise $\{v\}_k$ are both assumed to be stationary zero mean Gaussian white.

As a first step, a set of Linear Quadratic Gaussian (LQG) controller are designed at each specific air speed condition as follows

$$\begin{aligned} \{u\}_k &= -[K_i]\{\hat{x}\}_k \\ \{\hat{x}\}_{k+1} &= [A_i]\{\hat{x}\}_k + [B_i]\{u\}_k + [H_i]\{\{y\}_k - [C_i]\{\hat{x}\}_k\} \end{aligned} \tag{16}$$

where $\{\hat{x}\}$ denotes the estimated state and $[K_i]$, $[H_i]$ are the gain matrtix, Karman filter gain matrix, respectively. The control input can be determined subject to minimize the performance index which is expressed as follows;

$$J = E[\sum_{k=1}^{\infty} [\{x\}_k^T[Q]\{x\}_k + \{u\}_k^T[R]\{u\}_k] \tag{17}$$

where $[Q]$ is positive semi-definite and $[R]$ is positive definite matrices, respectively.

In ASE module, the input-output relations of the LQG controller are used to train the neural network system. The neural network that used for controller is a Multi-

Layer-Perceptron(MLP) trained with back-propagation. This type of neural network is a universal approximator, and able to learn any function to any degree of accuracy (Ref 18). Feedback from the sensor output is digitized and fed into the inputs of the neural network and passed through a digital tapped-delay-line for past time steps. A similar process is used for feeding the current and past controls into the network inputs. In order to account the air speed variant characteristics, air speed *V*, is also included as an additional input to the network.

In Fig. 3, a neural net based control system is depicted. The output from the network is compared to the output of the corresponding LQG controller when the mode selector is at the train mode, and any difference between them is backpropagated through the network to modify its learning parameters. The problem of finding a suitable set of neural net control parameters, that approximates the LQG controller, is solved using error back-propagation algorithm. The discrete time model of neural network as shown in Fig. 4 can be described by the following nonlinear difference equation

$$u_{NN}(k) = f[u(k-1), y(k), y(k-1), V] \tag{18}$$

The parameters of feedforward networks are trained so as to minimize the following cost function

$$E = \sum_{i=1}^{n_y} \sum_{j=1}^{k} \{[u_{LQG}(j) - u_{NN}(j)]^T [(u_{LQG}(j) - u_{NN}(j)]\}_i \tag{19}$$

where $u_{LQG}(j)$ and $u_{NN}(j)$ are the input vectors of LQG controller and neural network controller at sampling instant *j*, respectively. The Levenberg-Marquardt algorithm is used to minimize the defined cost function and obtain the next control input. After a neural network has been trained for varying the air speed, the mode selector is toggled to the control mode as shown in Fig. 3. Although the initial training time for a network may be long, it can be performed during off hours without much involvement of the designer.

Application Examples

Case I: Flutter Suppression System Design for a Modeled F-16 Smart Wing Using PZT Actuators

A modeled F-16 smart wing is used as an example model to design control system for flutter suppression. Fig. 5 (a) and (b) show the finite element and aerodynamic models of F-16 modeled wing (Ref 19). The FEM model contains 86 grid points. Total 62 membrane (CQDMEM/CTRMEM) element are used for modeling wing skin, 361 shear (CSHEAR) element for ribs and spars, and 111 rod (CROD) element for sparcaps and shear webs. The ZAERO module in ASTROS* is used to compute unsteady aerodynamic forces at Mach 0.9.

Total seven PZT actuator sets are used for the aeroservoelastic control (see Fig. 6). Fig. 7 indicates the typical control mode shapes due to PZT actuations. Aerodynamic forces due to seven PZT modes are calculated and transformed into time domain in ASTROS*. After vibration analysis, a modal reduction is performed using the first seven elastic modes (see Fig. 8). The resulting state space model is 45^{th} -order : These are seven displacement modes, seven rate modes, ten aerodynamic states due to minimum state approximation, and three actuator states for each PZT actuator due to minimum state approximation.

An open loop flutter analysis is conducted using ASTROS*. Fig. 9 shows the open loop flutter analysis results. The open loop flutter of this model occurs around 1043 ft/sec, at Mach 0.9 and flutter frequency is 19.9 Hz. As shown in the figure, second mode of the open-loop system becomes unstable. With this system model an active control system is designed for flutter suppression. The design airspeed is set to be V=1,166 ft/sec, Mach=0.9. Figs. 10 and 11 show the open loop and the closed loop eigenvalues of the system when LQG is used to design an active control system for flutter suppression at the design airspeed of 14000 in/sec. The design result shows that the closed loop system is stable up to 16000 in/sec.

A set of LQG controller are designed at each specific airspeed and the obtained data are used to train the neural network system. Fig. 12 shows the comparison of the trained neural net control input with the target control input. Figure indicates that the neural network's control input and the target control input match up very well.

Fig. 13 contains the control system design results. Figure show the responses of the closed loop system (Fig. a and b) and the control input (Fig c and d) which are the control voltage applied to the actuators. For the copmparison, LQG results are also plotted in the figure. The results show that the system designed by neural network gives a better settling time and requires a less control input compared with those obtained by using LQG controller.

Case II: Gust Response Reduction System Design for a Modeled F-18 Aircraft

Fig. 14 shows the finite element model of a modeled F-18 aircraft (Ref 20) that is used to design gust response reduction system. This model has four control surfaces; inboard/outnoard leading edge flaps, trailing edge flap

and aileron. The transfer function of each actuator is defined as

$$\frac{\delta_c}{\delta_{command}} = \frac{8.635E6}{s^3 + 274.04s^2 + 77891s + 8.635E6} \qquad (20)$$

The unsteady aerodynamic forces are calculated using ASTROS* at Mach 0.9, sea level. These forces are tranformed into time domain using minimum state method. The resulting state space aeroservo-elastic equation is 65th order. These are twenty vibration mode, ten aerodynamic states for rational function approximation, three states for each actuator, and three states for Dryden gust model including low pass filter.

Fig. 15 shows the open loop flutter analysis results. The open loop system results in flutter at an airspeed of 636 ft/sec. And the flutter is driven by the torsion mode as shown in Fig. 15 (b). The active control system for gust response reduction is designed at the design airspeed of 500 ft/sec, which is 78% of the open loop flutter speed. Fig. 16 shows the open loop and closed loop eigenvalues of the system at the design airspeed, 500 ft/sec. As shown in the figure, all the closed loop mode is shifted to the left, rendering a more subtle system.

Fig. 17 shows the RMS values of the second mode due to a gust over a range of airspeed. For comparison, the RMS values of both open loop and closed loop systems are shown in the figure. It is seen that, the RMS values of the closed loop system are substantially reduced throughout the airspeeds of interest.

Case III: Trim Capability of PZT Actuators for TOMAHAWK

PZT actuators are used to reduce the induced drag of the TOMAHAWK with/without battle damage. Fig. 18 shows aerodynamic model and a structural finite element model of the TOMAHAWK cruise missile. The wing consists of aluminum spars, ribs and composite skins whose thickness distributions are designed by ASTROS* optimization with strength constraints and minimum weight as objective function. PZT actuators are placed on the composite skins shown in Fig. 19. The flight condition is assumed to be a one g cruise at M = 0.7, sea level. For expediency ZAERO aerodynamic module (ZONA6, Ref 21) is employed to compute the aerodynamic control forces of all trim variables including the angle of attack, the horizontal tails and the 24 PZT actuators (total 26 trim variables). The ASTROS*/Trim module uses an optimization scheme to solve the 26 trim variables while minimizing an objective function; namely the induced drag. For comparison, the trim solution and the induced drag of the baseline configuration (involving only two trim variables; the angle of attack and the horizontal tail deflections) are also computed by the ASTROS*/Trim module.

The comparison between smart wing solution and baseline solution is shown in Table 1. Table shows a 40% induced drag reduction of the smart wing over the baseline wing. Since the induced drag is usually 1/3 of the total drag for the subsonic flight vehicle, the 40% induced drag reduction would amount to a 13% total drag reduction. This implies that if the baseline wing is replaced by the smart wing, the TOMAHAWK cruise missile would have a 10% increase in range.

The smart wing carries more lift than the baseline wing. Fig. 20 shows an exaggerated view of camber and twist distribution of the smart wing due to the PZT actuators. Since the total body lift plus the wing lift of these two configurations are the same at the one g cruise condition, the body of the smart wing configuration carries less lift than that of the baseline wing configuration. Because usually the body is not an efficient lift generator (in terms of induced drag), the less body lift of the smart wing configuration implies less induced drag. It is well-known that an elliptical spanwise lift distribution produces minimum induced drag. In Fig. 21, the desired elliptical distribution is also shown by the dash line. By comparing the spanwise lift distributions of the smart wing and the baseline wing with the desired elliptical distribution, it is seen that the smart wing yields closer elliptical-type of lift distribution than the baseline wing, rendering a considerable amount of induced drag reduction.

Fig. 22 shows an aerodynamic model of an impaired TOMAHAWK configuration due to battle damage where 4/5 of the outboard left wing is assumed to be destroyed by the anti-aircraft artillery. This gives an asymmetric configuration that requires a trim solution involving the pitch-yaw-roll coupling for one g cruise. In order to investigate the trim capability of the PZT actuators, the 24 PZT actuators, the 4 tails, as well as the angle of attack and side slip angle are included as the trim variables.

The ASTROS*/Trim solution is shown in Table 2 and the resulting camber and twist distribution of the right hand side wing is presented in Fig. 23. If only the two horizontal and two vertical tails are used to trim the damaged configuration, the ASTROS* trim module shows that a trim solution exists only if the deflection angle of the right hand side tail exceeds 47° and left hand side tail exceeds 40°. This is probably beyond the physical deflection limit of the horizontal tail. This trim solution shows that with the 24 PZT actuators, the required deflection angles of the horizontal tails are less than 15°. The camber and twist distributions of the right hand side wing suggests that the 24 PZT actuators

tend to suppress the unwanted rolling moment by providing a pitch down wing tip twist. The loss of lift due to the pitch down twist is compensated by increasing the angle of attack up to 7.58°.

Conclusion

Our recent development in a smart structure and trim modules and its integration with ASTROS* is presented. Successful integration is achieved as a result of the uncovered thermal versus PZT analogy and the control-surface versus PZT equivalence principle. The smart structure module is also integrated with the ASE module of ASTROS*/ASE, through a state-space aeroservo-elastic equation formulation.

For demonstration of the integrated software capability, application examples have been worked out. These include the neural net based active flutter suppression of modeled F–16 wing using PZT actuators, the gust-load alleviation of a modeled F-18 wing using active control, and the trim drag reduction of TOMAHAWK using PZT actuators.

- The PZT actuators enable to stabilize all unstable modes in a closed-loop system, whereas wing flutter occurs for an open-loop system. And the system designed by neural network gives a better settling time and requires a less control input compared with those obtained by using LQG controller.

- For gust-load alleviation, the RMS response values of the elastic modes were found to be substantially reduced in a closed-loop system as opposed to the open-loop system.

- Using smart actuators covered on the wing skin of the unimpared TOMAHAWK, 40% of induced drag reduction is achieved over the baseline wing.

References

1. Weisshaar, T.A., “Aeroservoelastic Control Concepts With Active Materials,” *1994 International Mechanical Engineering Congress and Exposition*, Chicago, IL, Nov. 1994.
2. Suleman, A., Venkayya, V.B., “Flutter Control of Adaptive Composite Panel,” AIAA Paper No. 94-1744, *Proceedings of the AIAA/ASME Adaptive Structures Forum*, SC, April 1994.
3. R. Manser, J. Simpson, J. Becker, J. Durr, E. Floth, U. Herold-Schmidt, H. Stark, H.W. Zaglauer, “Fin-buffet alleviation via distributed piezoelectric actuators – Full scale demonstrator tests,” *Proceedings of SPIE Conference on Industrial and Commercial Applications of Smart Structures Technologies*, Newport Beach, CA, March 1999.
4. A. Suleman, A.P. Costa, P.A. Moniz, “Experimental flutter and buffeting suppression using piezoelectric actuators and sensors,” *Proceedings of SPIE Conference on Industrial and Commercial Applications of Smart Structures Technologies*, Newport Beach, CA, March 1999.
5. A.P. Jardine J. Flanagan, L. Jasmin, B.F. Carpenter, “Smart Wing Shape Memory Alloy Actuator Design and Performance,” SPIE 3044-04, *SPIE Symposium on Smart Materials and Structures*, March 1997.
6. J.N. Kudva, B.P. Sanders, G.P. Sendeckyj and A.R. McGowan, “Overview of the DARPA/AFRL/ NASA Smart Wing Program, “ SPIE 3674-26, *SPIE Symposium on Smart Materials and Structures*, March 1999
7. L.B. Scherer, C.A. Martin, M.N. West, J. Florance, C. Wieseman, A. Burner and G. Fleming, “DARPA/AFRL/NASA Smart Wing Second Wind Tunnel Test Results,” SPIE 3674-28, *SPIE Symposium on Smart Materials and Structures*, March 1999
8. Johnson, E.H. and Venkayya, V.B., “Automated Structural Optimization System (ASTROS), Theoretical Manual,” AFWAL-TR-88-3028, Vol. 1, December 1988.
9. Chen, P.C., Sarhaddi, D., Liu, D.D. and Karpel, M., “A Unified AIC Approach for Aeroelastic/Aero-servoelastic and MDO Applications,” AIAA Paper No. 97-1181-CP, to appear in *Journal of Aircraft*.
10. Chen, P.C., Liu, D.D., Sarhaddi, D., Striz, A.G., Neill, D.J. and Karpel, M., “Enhancement of the Aeroservoelastic Capability in ASTROS,” STTR Phase I Final Report, WL-TR-96-3119, Sep. 1996.
11. Chen, P.C., Sarhaddi, D. and Liu, D.D., “A Unified Unsteady Aerodynamic module for Aeroelastic and MDO Application,” *AGARD Structured and Material Panel (SMP) – Workshop 2 “Numerical Unsteady Aerodynamics and Aeroelastic Simulation,*” Alborg, Denmark, Oct. 13-17, 1997.
12. Vanderplatts, G., “MICRO-DOT User’s Manual Version 1.0,” Engineering Design Optimization Inc., Santa Barbara, CA, 1985.
13. Karpel, A., “Extension to the Minimum-State Aeroelastic Modeling Method,” *AIAA Journal*, Vol.29, No.11, 1991, pp.2007-2009.
14. Crawley, E.F. and Anderson, E.H., "Detailed Models of Piezoceramic Actuation of Beams," *Proceedings of the AIAA/ASME Structures, Structural Dynamics and Materials Conference*, 1989, pp. 2000-2010.
15. Rogers, C.A., Liang, C., and Fuller, C.R., “Modeling of shape memory alloy hybrid

composites for structural acoustic control," *J. Acoustical Society of America*, Vol.89, No.1, 1991, pp.210-220.

16. Mueller, G.S., Adeniyi, V.O., "Optimal Output Feedback by Gradient Methods with Optimal Stepsize Adjustment," *Proceedings of IEE, Control & Science*, Vol.126, No.10, 1979, pp.1005-1007.
17. Moerder, D.D., Calise, A.J., "Convergence of a Numerical Algorithm for Calculating Optimal Output Feedback Gains," *IEEE Transactions on Automatic Control*, Vol.30, No.9, 1985, pp.900-903.
18. Sparks, D. W., Jr. and Maghmi, P. G., "Neural networks for rapid design and analysis," AIAA-98-1779, 1998.
19. Kolony, R.M., "Unsteady Aeroelastic Optimization in the Transonic Region," AIAA Paper No. 96-3983.
20. Chen, P.C., Sarhaddi, D., Liu, D.D., Jha, R., Liu, D.D., Griffin, K. and Yurkovich, R., "A Variable Stiffness Spar (VSS) Approach for Aircraft Maneuver Enhancement Using ASTROS," *AIAA/ASME/ASCE/AHS, 40th Structures, Structural Dynamics and Materials Conference*, St. Louis, MO, April, 1997.
21. Liu, D.D., Chen, P.C., Yao, Z.X. and Sarhaddi, D., "Recent Advances in Lifting Surface Methods," Paper No. 4, *Proceeding of International Forum on Aeroelasticity and Structural Dynamics*, Manchester, U.K., June 1995. Also in *The Royal Aeronautical Journal*, Vol.100, No.998, Oct. 1996, pp327-339.

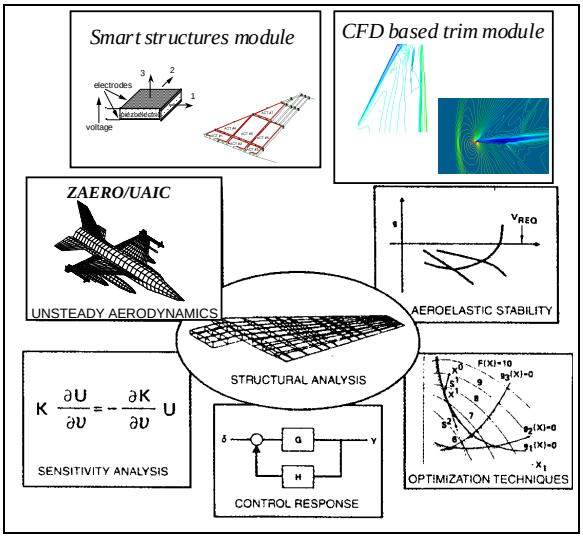


Figure 1. ASTROS*+smart structure/CFD based trim modules

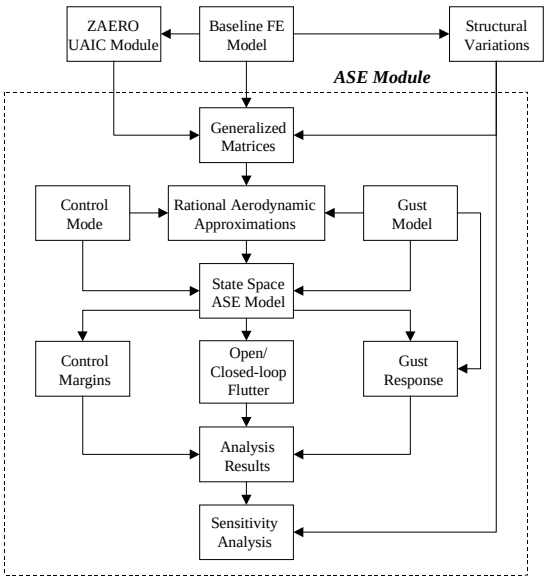


Figure 2. ASE module flow chart

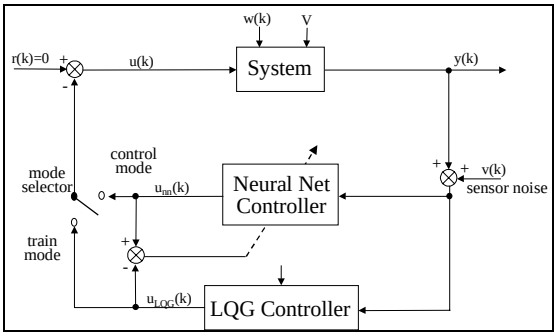


Figure 3. Block diagram of flutter suppression system

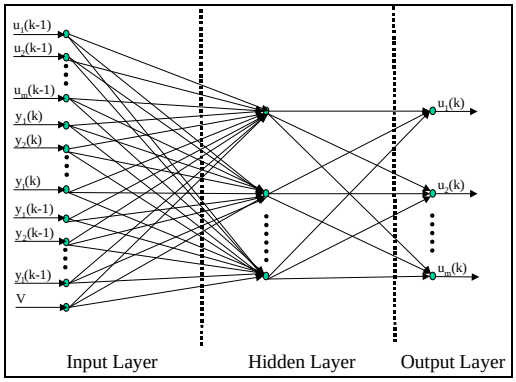


Figure 4. Neural network plant model

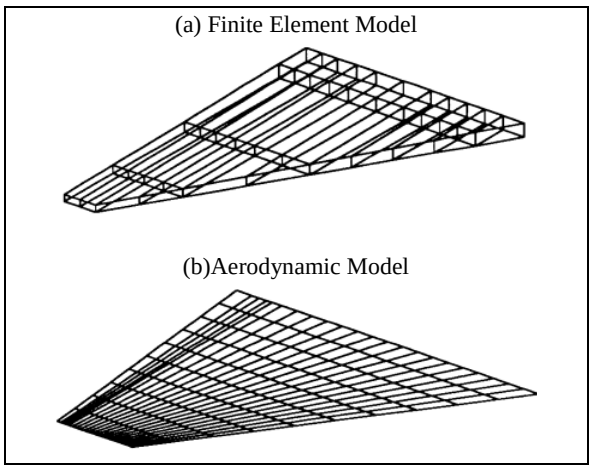


Figure 5. Finite element and aerodynamic models of a modeled F-16 wing

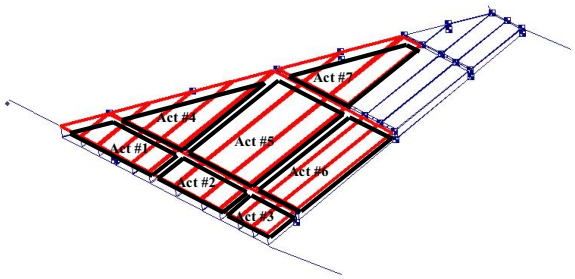


Figure 6. F-16 modeled wing with 7 Sets of PZT actuators

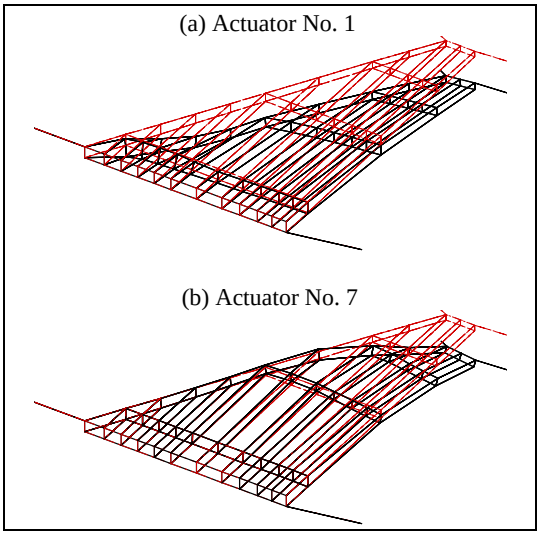


Figure 7. Control mode shapes due to PZT actuation (PZT actuator No. 1 and 7)

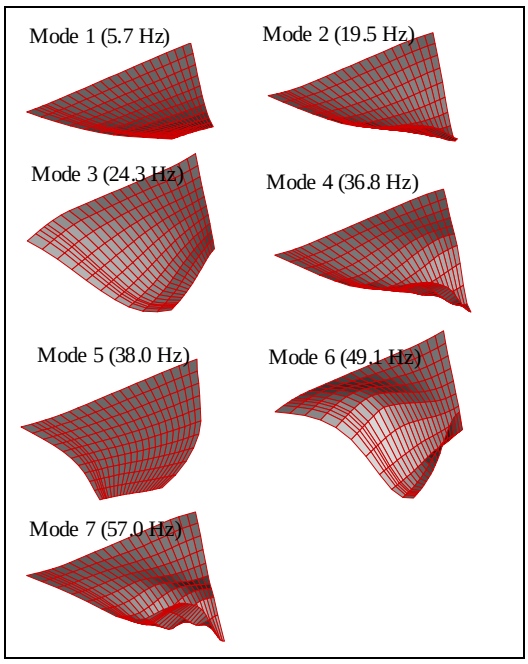


Figure 8. Natural frequencies and mode shapes of a F-16 modeled wing

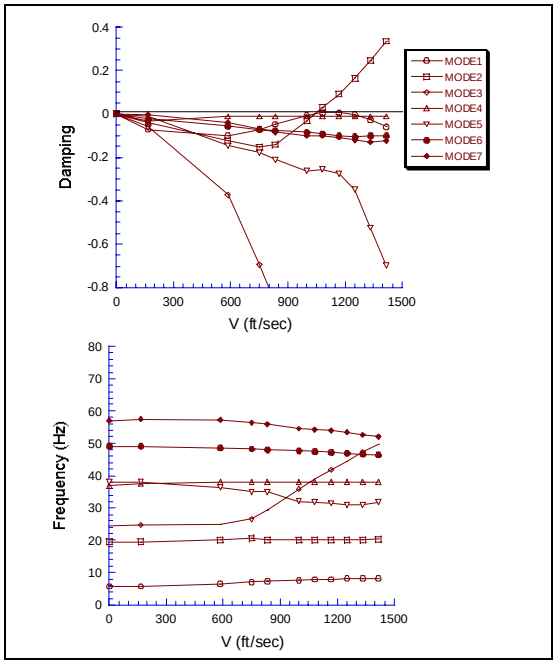


Figure 9. Open loop flutter analysis results of a F-16 modeled wing

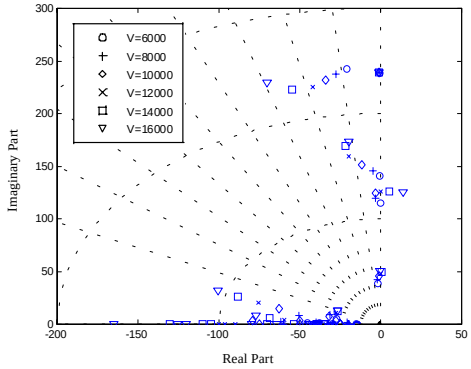


Figure 10. Open loop eigenvalues of the system at the various airspeed.

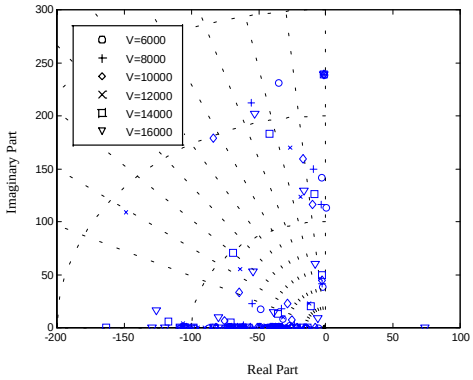


Figure 11. Closed loop eigenvalues of the system at the various airspeed.

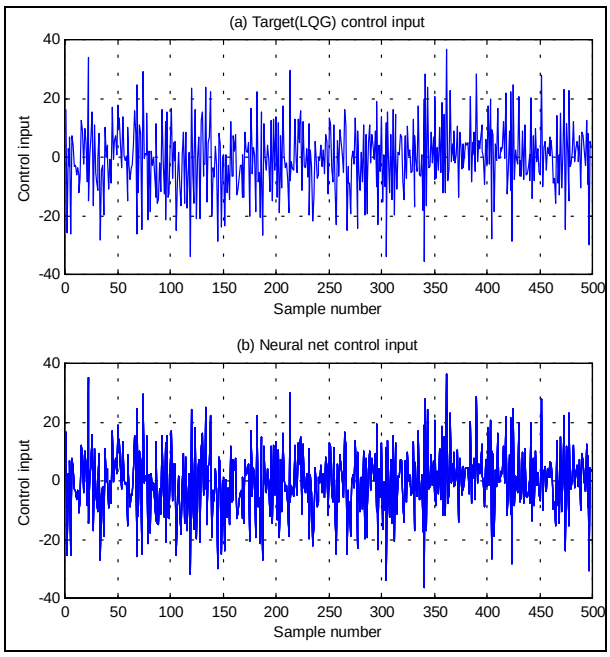


Figure 12. Comparison of the trained neural net control input with the LQG control input.

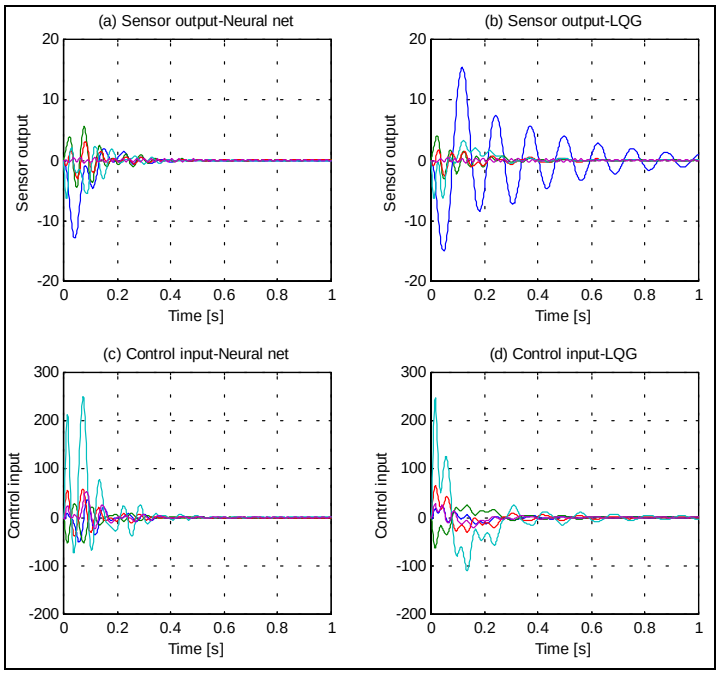


Figure 13. Comparison of the trained neural net control input with the LQG control input.

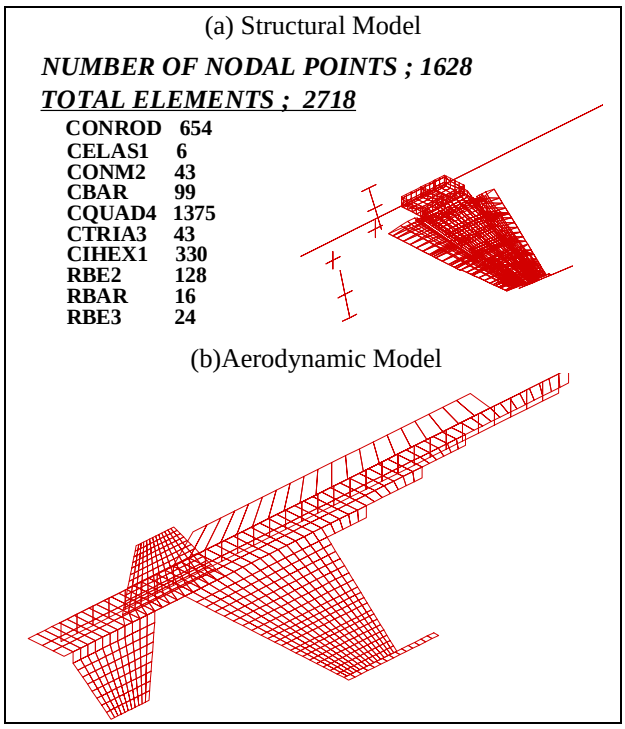


Figure 14. Modeled F-18 finite element and aerodynamic models

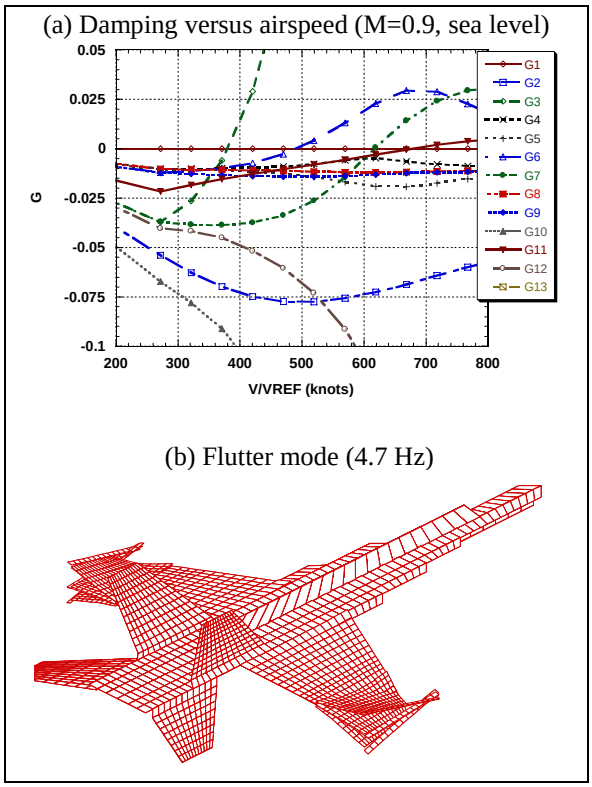


Figure 15. Open loop flutter analysis results: (a) damping, (b) flutter mode

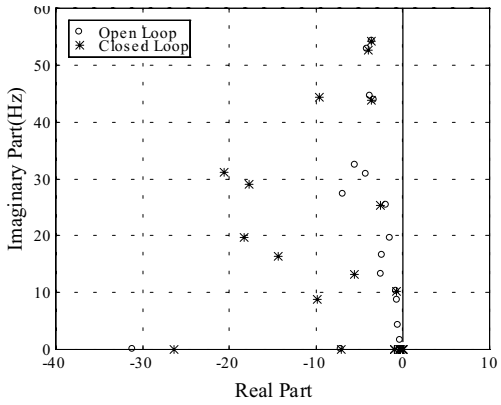


Figure 16. Open Loop and Closed Loop Eigenvalues of the Aeroservoelastic System at Airspeed of 500 ft/sec, Mach =0.9 Sea Level

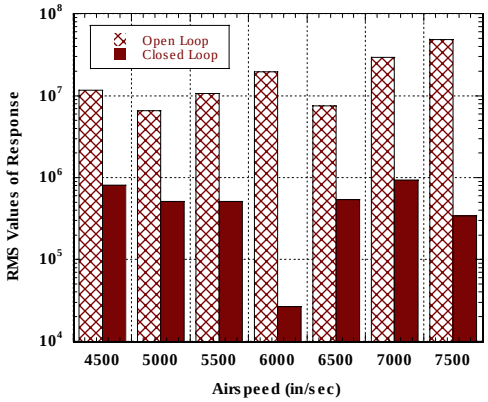


Figure 17. Root-mean square values of the response due to a gust versus airspeed

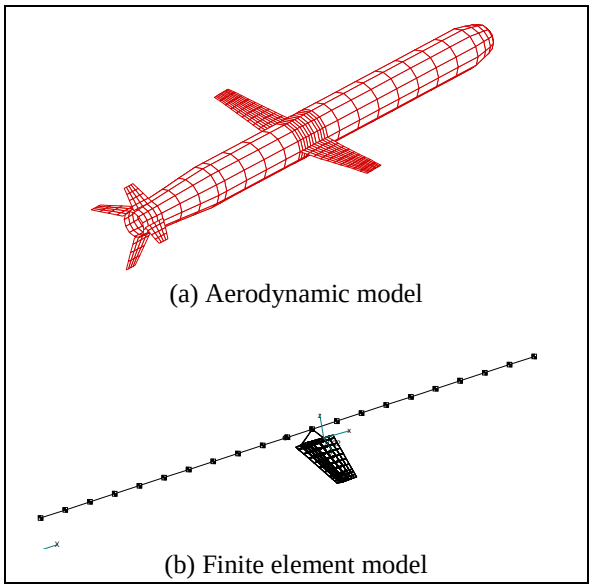


Figure 18. Aerodynamic and finite element models of the TOMAHAWK cruise missile

Table 1. Induced-drag improvement by ASTROS*/trim: *Smart vs. Baseline*

	Smart Wing	Baseline Wing
Angle of Attack	1.69 °	3.66 °
Horizontal Tail	- 0.343 °	- 0.747 °
Induced Drag Coeff.	0.01566	0.02610

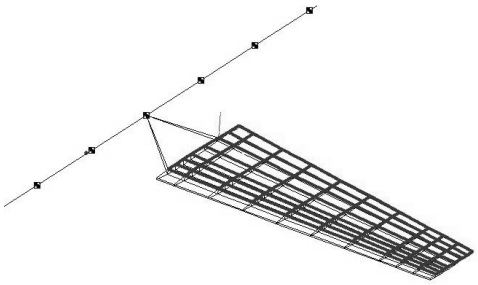


Figure 19. Locations of 24 sets of PZT actuators

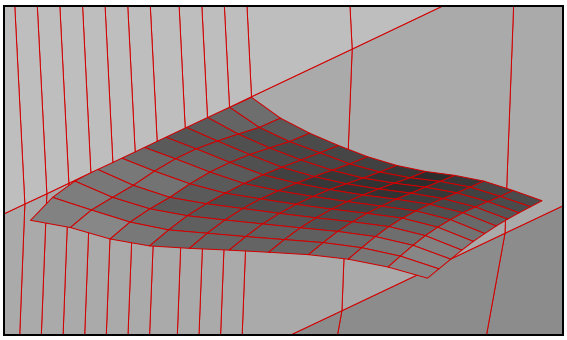


Figure 20. Exaggerated camber and twist distribution of smart wing

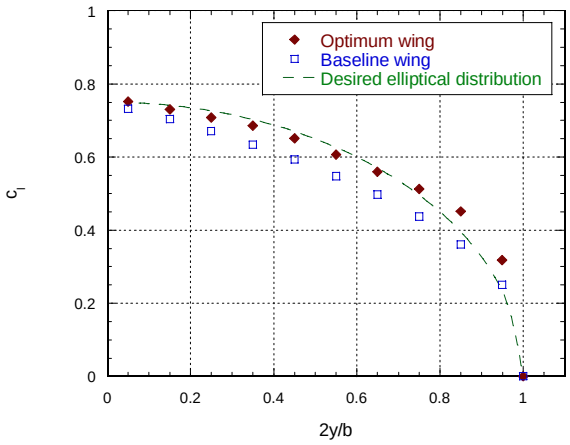


Figure 21. Spanwise lift distribution of the baseline and smart wings

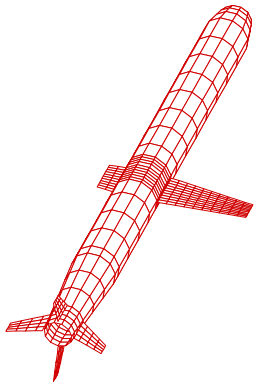


Figure 22. Aerodynamic model of a damaged TOMAHAWK cruise missile.

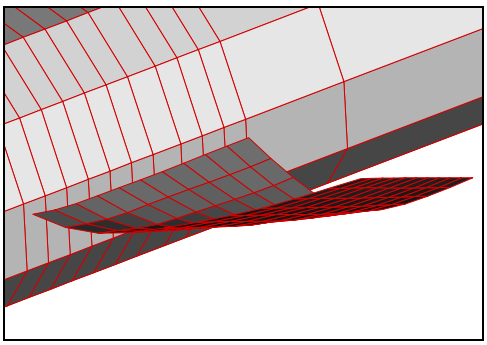


Figure 23. Exaggerated camber and twist distribution of right hand side wing for trim

Table 2. The ASTROS*/Trim Solution of an impaired TOMAHAWK (Smart vs. Baseline)

Trim Variables	Smart wing	Baseline wing
Angle of Attack	7.58°	6.14°
Side Slip Angle	-0.401°	-0.31°
Right Horizontal Tail	-13.08°	-47.17°
Left Horizontal Tail	-15.00°	-44.08°
Top Vertical Tail	-13.60°	6.34°
Bottom Vertical Tail	-14.99°	1.20°

Active Fin-Buffeting Alleviation for Fighter Aircraft

[1]Johannes K. Dürr [a], Ursula Herold-Schmidt [a], Helmut W. Zaglauer [a], and Jürgen Becker [b]

[a] DaimlerChrysler Aerospace Dornier, Research and Technology, An der Bundesstraße 31, D-88039 Friedrichshafen, Germany

[b] DaimlerChrysler Aerospace, Military Aircraft Division, P. O. Box 801160, D-81663 Munich, Germany

ABSTRACT

Severe structural vibrations can be induced in tails of high performance aircraft flying at high angles of attack by vortices originating from wing/fuselage leading edge extensions. The resulting loads may lead to increased material fatigue and require an augmented effort in aircraft maintenance. A number of different concepts have been proposed to either avoid the excitation of the tail fin by bursting vortices or to dampen the resulting structural vibrations. In the early 90s active system concepts were suggested as an efficient way for active buffet load alleviation.

In order to investigate the performance of such systems a collaborative research project was initiated between DaimlerChrysler Aerospace - Military Aircraft Division, the German Aerospace Center (DLR) and DaimlerChrysler Research and Technology within the framework of the Advanced Aircraft Structures Program. Four concepts were investigated in detail within this project:

- An active rudder,
- an active auxiliary rudder,
- a piezo-controlled interface and
- a system of surface-mounted or structurally integrated piezoelectric patch actuators.

The feasibility of all these concepts could be proven and their performance could be assessed in an extensive theoretical analysis that involved the complete aircraft system, as well as in wind tunnel tests on the rudder concepts and, for the piezo-controlled concepts, in tests on a laboratory demonstrator that was conceived, designed and manufactured to be dynamically equivalent to a typical fighter aircraft fin. In addition, a materials qualification program was initiated in order to demonstrate the compatibility of structures with integrated piezoceramic actuators with the requirements imposed through the application in a modern fighter aircraft tail. In this way the maturity of this emerging new technology could be shown and an eventual demonstrator phase was prepared.

1. INTRODUCTION

Fin-buffeting is an aeroelastic phenomenon occurring on various high performance fighter aircraft [1, 2]. Flying at high angles of attack vortices originate from the leading edges of wing and fuselage. These unsteady vortices burst drastically near the vertical tail of the aircraft exciting its natural modes. The resulting buffet fatigue loads can become an airframe fatigue and maintenance problem and might require either heavier structures, excessive inspection or active measures to reduce dynamic structural loads.

A number of concepts to reduce the adverse effects of these buffet loads have been discussed in the literature. They range from structural reinforcements of the aircraft tail to aerodynamic modifications along the leading edge of the wing in order to reduce the formation of vortices [3-6]. In the mid-90s active systems for fin buffeting alleviation were suggested and analyzed in the literature [7-9]. Here, damping of the unwanted fin vibrations is achieved by actively controlling the main or an additionally installed auxiliary rudder or by introducing counter-vibrations into the structure through suitable piezoelectric actuators.

Since these studies had shown that active control systems offer a promising solution to alleviate buffet induced strain and increase fatigue life of modern fighter aircraft tails a joint research program in the field of advanced aircraft structures was initiated between DaimlerChrysler Military Aircraft Division (DASA), DaimlerChrysler Research and Technology (DC-FT) and the German Aerospace Center (DLR). Within this research effort various different concepts for active vibration suppression on vertical fins were developed and investigated theoretically as well as experimentally. Two aerodynamic concepts for buffet alleviation, a rudder and an auxiliary rudder were investigated by DaimlerChrysler Military Aircraft Division [10-12], a piezo-interface concept was studied in collaboration with DLR [13] while a concept with structurally integrated piezoceramic actuators was realized in collaboration with DaimlerChrysler Research and Technology [14-16]. All active systems for vibration damping were designed as digital systems having either an interface to the flight control system (FCS) or being directly part of the FCS [17].

In parallel, a comparable research program was initiated in the United States – with participation from Canadian and Australian institutions – in which an active rudder concept and an integrated piezo concept were investigated for buffet alleviation on the F/A-18 fighter aircraft [18]. In addition to theoretical assessments, wind tunnel tests on a 1/6-scale model of an F/A-18 were conducted at NASA Langley. The project culminated in a full-scale ground test on an actual F/A-18 fin performed at the Aeronautical and Maritime Research Laboratory (AMRL) in Melbourne [19].

[1] Further author information:
J.K.D.: Email: Johannes.Duerr@DaimlerChrysler.com; Telephone: +49-7545-8-5501; Fax: +49-7545-8-14254
U.H.S.: Email: Ursula.Herold-Schmidt@DaimlerChrysler.com; Telephone: +49-7545-8-9844; Fax: +49-7545-8-2140
J.B.: Email: Juergen.Becker@m.dasa.de; Telephone: +49-89-607-24702; Fax: +49-89-60737200

Paper presented at the RTO AVT Symposium on "Active Control Technology for Enhanced Performance Operational Capabilities of Military Aircraft, Land Vehicles and Sea Vehicles", held in Braunschweig, Germany, 8-11 May 2000, and published in RTO MP-051.

The aim of this paper is mainly to demonstrate the benefits/deficits of each system investigated in the joint DASA, DLR, DC-FT research program by a detailed comparison of the different systems through total aircraft response calculations including the effects of the adaptive control systems. In addition the maturity of the qualification of the structure and of the subsystem fin with piezo-interface and the fin with integrated piezo-ceramic actuators will be demonstrated. In addition the maturity of system integration into the total aircraft system will be assessed.

Therefore for all concepts an investigation and comparison is performed using a total aircraft dynamic model which includes the flight mechanics, the structural dynamics as well as unsteady aerodynamics and a representation of the flight control system together with the active vibration control system for all systems [17]. The total aircraft structural dynamic model as well the unsteady aerodynamic modeling which is applied for the comparison study is updated based on ground test results as well as on flight test results and in one case on wind tunnel results [20]. The controller design considers stability requirements, aircraft dynamic load requirements and flutter requirements.

The rudder concept was investigated using a validated total aircraft model updated by flight test results including in-flight test results for high frequency rudder excitation. The auxiliary rudder concept was validated by wind tunnel tests on a 1/15-scale model of the total aircraft with fin/auxiliary rudder with respect to the unsteady aerodynamic forces of the auxiliary rudder [11-12].

For investigation and validation of the concepts involving either piezoelectric stack actuators attached to the bending bearing or piezoelectric patch actuators bonded to the structure's surface a Fin-Box-Demonstrator (FBD) representing the fighter aircraft fin with respect to structural design and structure dynamics was developed and tested in open and closed loop [14, 16].

Finally recommendations for a flight demonstrator are summarized.

2. QUALIFICATION PROCEDURE

A qualification program plan (QPP) was drafted to define the methodology for the qualification of the active buffet load alleviation system. It detailed the specific work packages and methods required for qualification and sets up a timetable for the procedure.

The development of the active vibration control (AVC) system proceeds in several phases with the objective of qualifying it for flight testing. Phase I comprised the technology qualification stage ending with a technology development qualification as a milestone that achieved:

- ➤ Definition of a framework of fundamental parameters for the AVC system.
- ➤ Experimental and/or analytical demonstration of AVC functionality.
- ➤ Experimental and/or analytical investigation of critical specifications and the abidance thereby of the AVC system within the framework of the QPP.

For the active fin buffet alleviation system the QPP identified the following activities that were performed in phase 1:

- ➤ Theoretical investigation of the performance of each of the four concepts using a whole aircraft dynamic model.
- ➤ Scale-model wind-tunnel tests to prove the aerodynamic authority of the rudder and auxiliary rudder concept.
- ➤ Laboratory demonstrator tests on a full scale fin box model to prove the actuating authority of the active interface and the structurally integrated piezoelectric actuator concept.
- ➤ A materials qualification program intended to demonstrate the compatibility of the AVC system based on distributed surface-bonded or integrated piezoelectric patches as well as discrete piezoelectric stacks with the requirements and specifications for aircraft applications.

The results of these efforts are compiled in section 4 for the four different systems under investigation.

With respect to the system qualification on the complete aircraft initial system level investigations on active buffet alleviation were performed for a limited flight envelope. For the ultimate flight control law development and flight system qualification with an active buffet vibration suppression system the following steps need to be taken:

- Description of aircraft configuration.
- Development of control laws for active buffet load alleviation system. A first definition has already been established within phase I in the context of the complete aircraft model, the definition for the demonstrator will follow in phase III.
- Definition of the complete flight envelope.
- Description of effects and treatment of possible failure modes.
- Development of controller and phase stabilization. In order to prepare design and implementation of the control laws a number of ground and flight tests are necessary. A ground resonance test for the complete aircraft with the modified fin has to be performed to update the computational aircraft model. A ground-based structural coupling test for the complete aircraft with a modified fin with the actuators installed has to be performed to establish the open loop transfer functions for validation of the open loop transfer functions on ground determined from computations. In addition, a flight-based structural coupling test is needed to validate the open loop transfer functions in flight determined through computations.
- Software Development – A first software development plan has been established in phase I. This plan lists all the activities starting with the controller development for the flight control system with an integrated active buffet alleviation system up to the installation of the software and the testing required.
- Demonstration of stability with the active buffet alleviation system.

- Demonstration of flutter stability with the active buffet alleviation control laws.

These activities will all be performed in phase III.

3. CONCEPTS FOR ACTIVE VIBRATION SUPPRESSION

A number of active systems for the alleviation of fin buffet vibrations have been suggested in recent years [3-9]. Four promising concepts were selected within the framework of the "Advanced Aircraft Structures" program for further investigation. An active mass damper concept was also considered in the early stages of the program, but was not pursued further due to budgetary constraints. This decision should, however, not be taken as a reason to rule this concept out from future considerations.

In the following, the concepts investigated in more detail shall be described briefly:

3.1 Distributed piezoelectric actuator concept

Wafer-like piezoelectric actuators can induce dynamic strains into structures that can be used to control the shape or reduce vibrations in the structure. Therefore, integrating or surface-bonding piezoelectric actuators across the fin of the aircraft has been suggested as an viable, innovative concept for fin buffet load alleviation (Figure 1). The distribution of the actuators across the most of the fin surface allows to dampen even higher modes. The concept requires provisions for the integration of the actuators in the skin, installation space for the power amplifiers and an added effort in cabling connecting the components.

3.2 Piezoelectric interface concept

The piezoelectric interface induces through a set of piezoelectric stack actuators forces and moments near the location where the fin and the rear fuselage of the aircraft are connected (Figure 2). The actuators will have to be pre-stressed in compression, as they will generally lie close to the static and dynamic load paths. Through its position they will, however, exhibit large actuation authority in particular for the first bending mode. The concept requires some structural modifications to the fin as well as to the rear fuselage section of the aircraft, in order to accommodate the interface as well as the power amplifiers that are necessary for its operation.

3.3 Rudder concept

The rudder concept requires no structural changes to the conventional fin structure except for an eventual modification of the actuator to allow for higher actuation speed. A set of control laws are added to the flight control system to steer the rudder in such a way that acrodynamic forces are excited to counter respectively reduce the buffet loads (Figure 3). This concept can effectively only be used to damp the first fin bending mode, as the inertia of the rudder would prohibit excitation of the rudder at frequencies of the order of the higher modes (above 50 Hz). The benefit of this concept is that it can in principle be implemented immediately with only minor changes to the rudder actuator being required.

3.4 Auxiliary rudder concept

The second active aerodynamic buffet alleviation concept tries to remedy the short-comings of the rudder concept by using a smaller auxiliary rudder that is steered by a second actuator (Figure 4). By using a small section of the original rudder as the auxiliary rudder with a separate actuator, modifications to the fin structure can be kept to a minimum. For flight control purposes this auxiliary rudder deflects in the same way as the main rudder, whereas in the case of buffeting at high angles of attack, it would generate appropriate aerodynamic forces to alleviate the induced vibrations. The control concept to be employed will basically be the same as for the rudder concept, however, with larger rudder deflections.

4. DEMONSTRATION OF COMPLIANCE

An extensive testing demonstration and analysis program was conducted in order to complete the technology qualification stage (phase I) and also a first preliminary qualification stage (phase II) demonstrating a principle compliance of the systems with the specifications that are required. A formal qualification (phase III) was not aspired and will only have to be conducted within the framework of an actual flight demonstration program. However, based on the status achieved in the preliminary qualification valuable conclusions can be drawn with respect to the tasks that still have to be completed for a formal qualification.

The achieved degree of qualification will be summarized in brief in the following sections:

4.1 Distributed piezoelectric actuator concept

As the use of piezoceramic actuators involved the introduction of a new composite material into the aircraft that has so far not been extensively qualified and certified for use in aircraft applications a detailed material qualification program was conceived in order to

- determine material properties of piezoceramic actuators from material samples,
- experimentally characterize actuators and smart composites to provide input data for model calculations,
- perform tests on composite test coupons to demonstrate the conformity of intelligent materials systems with specifications imposed upon them for their integration in aircraft,
- identify, define and perform non-classical tests on smart composite systems in order to test and assure the complete functionality of the intelligent material system,
- develop and demonstrate concepts to integrate smart materials and systems into aircraft design, manufacture and maintenance procedures and processes.

The standardized actuators used in the coupon tests as well as the customized actuator modules on the Fin-Box-Demonstrator were manufactured by Active Control eXperts (ACX) [21] using standard PZT-5A ceramic material. The Fin-Box-Demonstrator is shown in Figure 5. The technology and preliminary qualification extends to the principal design of the actuators, eventual future changes in design or material content may warrant to repeat certain qualification tests.

The following degree of qualification was achieved:

- Coupon tests on ACX QP20N QuickPack™ actuators showed that required **static** structural **strains** above 0.3 %

could be sustained by the actuators. The test was extended to the required temperature range of –50°C to +120°C with an insignificant decrease in the sustainable strains at the lower temperature limit. In addition, a structural **fatigue test with passive piezoelectric actuators** subject to dynamic maneuver loads was performed without failure to the actuators.

- An **engineering test** on a specimen equipped with actuator modules was performed to validate the bonding procedure and to identify the failure modes of the smart material system. For this purpose, the actuators were excited at the fundamental resonance frequency of the test specimen for an extended period of time (up to $30 \cdot 10^7$ cycles). While the bonding interface passed the test without failure, the copper leads within the actuator exhibited fatigue cracks that lead to sparking and short-circuiting.
- A specially devised structural **fatigue test with active piezoelectric actuator modules** subject to maneuver loads was performed showing again the same failure modes as identified in the engineering test. As a consequence, improvements in the design of the actuator modules that avoid these kinds of failures were conceived together with ACX.
- The **power requirements** of the piezoelectric actuators were determined from coupon tests as well as from the experiments on the fin box demonstrator. The **actuator performance** with respect to induced strain and force was determined for varying thickness, length and width ratios between actuator and structure, for plane and curved structures as well as under tensile and compressive loading at various temperatures and humidities.
- The **physical and electromechanical characterization** was completed through a compilation of data provided by the manufacturers and by the measurement of selected properties.
- **Inspection** and **non-destructive evaluation** procedures were investigated and tested in order to be able to assure the mechanical, electromechanical and electrical integrity of the smart structure continuously [22].
- Concept for planned **maintenance** procedures as well as indicators for non-plannable maintenance were developed.
- Concepts for mechanical and electromechanical **repair** respectively replacement of actuators were developed and shown on the fin box demonstrator.
- The requirements on **aircraft ground equipment** for inspection, maintenance and repair purposes were identified.
- An **installation and integration guideline** was established based on the integration procedure developed on the fin box demonstrator.
- Test coupons exposed to a variety of media and agents present in an aircraft environment showed no deterioration except for traces of **corrosion** of the external copper wires and pins leading to the actuator which can be avoided with standard corrosion protection techniques.
- Problems of **electrostatic discharge** (ESD) will only occur if the actuators with their dielectric surface are directly exposed to the airflow around the aircraft. In an actual active buffet alleviation system this will in all likelihood be avoided, otherwise standard protection measures against ESD have to be employed.
- The question of **electromagnetic compatibility** (EMC) was addressed in an analysis. EMC tests will be conducted in phase III.
- Passive **aging** tests were conducted on the actuators subject to different temperature and humidity conditions without showing a significant deterioration of electromechanical properties and performance.

The following analyses and system level tests were conducted for the distributed piezoelectric actuator concept [14, 20]:

- Establishment of a complete **finite element (FE) model** with piezoelectric actuators.
- **Fin-Box-Demonstrator test phase 1** – System identification of the fin box without piezoelectric actuators.
- **Update of fin box FE model based on test phase 1.** The original FE model showed good agreement with the experiment, an update had only to be conducted with respect to the local CFC panel thickness.
- **Fin-Box-Demonstrator test phase 2** – Excitation of structural vibrations through piezoelectric actuators. The predicted response levels could be shown.
- **Update of fin box FEM model based on test phase 2** turned out to be not necessary as the comparison between model predictions and experimental results showed excellent agreement.
- **Fin-Box-Demonstrator test phase 3/4** – Closed loop damping of the first bending and first torsion mode. The load alleviation due to a simulated buffet excitation compared well with the values predicted by the model.
- Based on the results of the Fin-Box-Demonstrator model predictions and experiments a **complete aircraft model** with integrated piezoelectric actuators distributed across the skin was established. Open loop transfer functions (IMU output to actuator input) were analyzed with the dynamic model of the aircraft. Control laws were determined based on the open loop transfer functions and power requirements for the buffet alleviation system were documented.

4.2 Piezoelectric interface concept

As the use of piezoceramic stack actuators in the piezo interface concept involved the introduction of a new material and actuator into the aircraft a detailed material qualification program had to be conceived just as in the case of the structurally integrated distributed piezoelectric actuator concept.

- **Static and dynamic qualification** tests were successfully performed on the stack actuators based on the expected operational loads at room temperature and at 120°C.
- An **engineering test** simulating buffet loads was performed were the actuators were excited in resonance for an extended period of time subject to various static pre-loads.

- Short-circuiting caused by an electrical breakdown between adjacent electrodes was identified as the major **failure mechanism** in the stack actuators.
- A qualification test was performed on the structure subject **maneuver loads** with active interface in open and closed loop operation. The results confirmed the findings of the engineering tests.
- The **power requirements** of the stack actuators were determined from the resonance test. The actuator performance with respect to induced strain and force was determined for various temperatures.
- The **depolarization pressure, as well as tensile, shear and bending strength** were quantified using manufacturer's data. Due to the large variations in the data some experimental checks should be performed for the demonstrator phase. The axial strength has been investigated for various stack actuators. In addition, experience from qualification tests according to ESA guidelines with respect to random vibration, vacuum temperature cycling and shock testing have also been considered.
- **Shear and angular compatibility** of the stack actuators do not pose a problem due to the configuration of the interface.
- The **physical and electromechanical characterization** was completed through a compilation of data provided by the manufacturers and by the measurement of selected properties.
- Concepts for **maintenance** were analyzed. In addition, the integration of the adaptive interface into an composite health monitoring system as it was developed in the different work packages of the "Advanced Aircraft Structures" program would provide a maintenance indicator that could point out failures not only in the interface but also on the aircraft fin itself [23]. This provides an effective **inspection** method for both the interface system and the fin.
- **Repair** - due to the modular design of the interface, defective stacks could quickly be replaced.
- Special **aircraft ground equipment** is not required.
- An **installation and integration guideline** was established based on the integration procedure developed on the fin box demonstrator. Alterations in the design of the rear fuselage of the aircraft have to be expected with the integration of the interface.
- Compatibility of the system with different agents and media present in the aircraft environment as well as with different levels of humidity will be investigated in phase III. The metallic parts of the interface have to be protected against **corrosion**. The electrical and electromechanical components are protected against corroding agents through their protective and electrically isolating coating.
- Problems with **electrostatic discharges** (ESD) has to be prevented in the aircraft through suitable standard protection procedures. In the qualification tests a suitable grounding strategy was pursued to carry away electrostatic charges that may build up.
- The question of **electromagnetic compatibility** (EMC) was addressed in an analysis. EMC tests will be conducted in phase III.
- Passive **aging** tests were conducted on the actuators subject to different temperature conditions without showing a significant deterioration of electromechanical properties and performance.
- In connection with space applications the behavior of piezoelectric actuator components in vacuum were tested on a material level. If suitable components are selected, no **toxic emissions** are to be expected during operation.

The following analyses and system level tests were conducted for the distributed piezoelectric actuator concept:

- Establishment of a complete **finite element model** with the adaptive interface.
- **Fin-Box-Demonstrator test phase 1** – System identification of the fin box without piezoelectric actuators and interface (see chapter 4.1)
- **Fin-Box-Demonstrator test phase 2** – Excitation of structural vibrations through piezoelectric stack actuators. The predicted response levels could be shown.
- **Update of fin box FEM model based on test phase 2.**
- **Fin-Box-Demonstrator test phase 3/4** – Closed loop damping of the first bending and first torsion mode. The load alleviation due to a simulated buffet excitation compared well with the values predicted by the model.
- Based on the results of the Fin-Box-Demonstrator model predictions and experiments a **complete aircraft model** with the adaptive interface was established. Control laws were determined based on the open loop transfer functions and power requirements for the buffet alleviation system were documented.

Based on the experiences and results of the interface concept that has been investigated within the framework of the "Advanced Aircraft Structures" program a more efficient interface concept was conceived, that promises significant improvements concerning weight, volume and installation location as compared to the original concept.

4.3 Rudder and auxiliary rudder concept

As the rudder and auxiliary rudder concept are based on materials, structures and concepts that are well established in aircraft, only analyses and system level tests based on the validated analytical aircraft model had to be performed. For the rudder itself results from ground and flight tests could be used for model update. For the auxiliary rudder concept the aerodynamic forces had to be determined from wind-tunnel measurements at the Technical University of Munich ([11-12]). The 1/15-scale wind-tunnel model is shown in Figure 6.

The following analyses and system level tests were conducted for the rudder concept:

- A **complete aircraft model** with the rudder was established. Control laws for the rudder concept were determined and power requirements for the buffet alleviation system were documented.

The following analyses and system level tests were conducted for the auxiliary rudder concept:

- Establishment of a **finite element model** for the wind-tunnel model with auxiliary rudder.
- **Wind-tunnel tests for the auxiliary rudder concept phase 1** – Excitation through the auxiliary rudder for angles of attack of up to 31 degrees. These experiments conclusively demonstrated the assumptions about the aerodynamic phenomena that had been used in the control law design as well as the effectiveness of the auxiliary rudder at least up to an angle of attack of 31 degrees.
- **Update of the fin FE model based on test phase 1.**
- **Wind-tunnel tests for the auxiliary rudder concept phase 2** – Excitation of the fin through buffeting, auxiliary rudder for vibration damping (closed loop testing). A reduction of the fin-tip acceleration caused by buffeting of 60 % could be shown for the closed loop control for all angles of attack up to 31 degrees.
- **Update of the fin FE model based on test phase 2.**
- A **complete aircraft model** with the rudder was established. Control laws for the rudder concept were determined and power requirements for the buffet alleviation system were documented.

5. EVALUATION OF THE CONCEPTS

The goal of designing and developing as well as demonstrating the principal feasibility and functionality of an active fin buffet alleviation system has been reached for all four concepts investigated in detail. The following degree of fulfillment of the qualification requirements has been achieved:

- The preliminary **structure qualification** for the distributed piezoelectric actuator and the piezo interface concept.
- The preliminary **system qualification** for the distributed piezoelectric actuator and the piezo interface concept based on the fin box demonstrator.
- The preliminary **system qualification** for the rudder concept based on ground and flight tests of a modern fighter aircraft for rudder excitation.
- The preliminary **system qualification** for the auxiliary rudder concept based on wind-tunnel tests on a scale model of a modern fighter aircraft with an experimental active vibration control system in closed loop.

Based on the results from the experimental tests and the computational results, the evaluation of the different concepts investigated was pursued using the complete dynamic aircraft model and assuming that the redundant IMU system is used to sense the state of the fin. In this analysis the following findings with respect to the **performance of the systems** were obtained:

- All four active buffet alleviation systems show very similar reductions of the fin acceleration up to an angle of attack of 30 degrees with the same power requirements.
- The distributed piezo actuator concept as well as the auxiliary rudder concept (but not the piezo interface and the rudder concept) show – with the same power requirements – the same reductions of the fin acceleration for angles of attack between 40 degrees and 50 degrees. This is presumably of interest for an extension of the flight envelope in connection with the use of trust vectoring. A further assessment with respect to the necessity of active vibration control for angles of attack that large has to be based on wind-tunnel tests. For angles of attack above 50 degrees the authority of the auxiliary rudder will be marginal, but in this case fin buffet vibrations are presumably also no longer of importance.
- For the computation of the performance of the different concepts a stiff fuselage structure was assumed. Taking into account the given flexibility of the rear fuselage can as a worst case lead to minor reductions in the buffet load alleviation.
- The piezoelectric interface constitutes a flexible connection of the fin to the fuselage that is governed by the stiffness of the interface. In the experiments on the fin box this led to slight reductions in the dynamic properties of the system – the frequency of the fundamental mode decreased for instance from 18.1 Hz to 16.45 Hz. Modifying the system by increasing the stiffness of the interface – for example, through an increase of the stack cross sections – or by reducing the weight of the fin itself could restore the dynamics of the conventional fin without adversely affecting the performance of the interface.
- The rudder concept is primarily useful for a reduction of low frequency elastic vibrations up to 15 Hz. For higher frequencies – for instance, for the alleviation of the fin torsion mode – the loads on the hydraulic rudder actuator will – due to the large rudder mass – become too high.

With respect to the **structural modifications of the aircraft** that become necessary with the installation of any of the buffet alleviation systems the following assessment has been obtained:

- The distributed piezoelectric actuator concept necessitates the design and construction of a modified fin.
- The piezoelectric interface requires in its original form a modification of the rear fuselage, which in a worst case scenario could alter the dynamic response of the aircraft as a whole. In this case, static and dynamic fatigue test and qualifications for the aircraft would need to be repeated. Based on the experiences and results of the original piezo interface concept a revised design has been conceived that promises significant improvements concerning weight, volume and installation location as compared to the original concept. For the new design, modifications would only be necessary for the fin structure itself.
- The rudder concept does not require any changes of the fin structure.
- The auxiliary rudder concept necessitates the installation of an adequate rudder actuator in the fin.

The following **additional installations in the aircraft** will be necessary in connection with the buffet alleviation system:

- The distributed piezoelectric actuator and the piezo interface concept require an increased effort in cable installation for the actuators as well as additional space onboard for the installation of the power amplifiers.
- The rudder concept does not mandate any additional installations.

- The auxiliary rudder concept affords additional cables running to and from the actuator.
- The distributed piezoelectric actuator concept will lead to a weight increase of about 20 kg at the fin.
- The piezoelectric interface concept also leads to an additional weight increase of about 20 kg at the root of the fin. The weight gain due to a modification of the rear fuselage could not be estimated. The modified interface may bring weight savings as compared to the original concept of up to 70 % and a modification of the rear fuselage would no longer be necessary.

An evaluation of all four concepts was also performed with respect to the **additional design and development effort necessary for integrating the system into the aircraft**:

- All four buffet load alleviation systems considered afford in principle the same effort for integrating their control system into the aircraft's flight control system (FCS). The development of the vibration control system and the qualification of the modified FCS will necessitate a rather large effort as it includes the complete system qualification for all aircraft configurations and flight conditions with the FCS, the qualification on the FCS rig, the flutter and structure coupling qualification through the required ground and flight tests.
- All four vibration control systems require the actuators to be excited with the correct phase for the respective modes (first fin bending mode, first fin torsion mode, first rear fuselage bending mode, first wing bending mode) in order for a controller to be designed according to stability criteria. The phases of the sensor signals due to actuator inputs are mainly governed by non-stationary aerodynamic forces due to the moving fin, rudder or auxiliary rudder. In flight, so far only the signal due to a rudder excitation up to 15 Hz have been validated. The phase response obtained purely from computations is, in particular for the higher vibration modes, not precise enough for a control system design. Therefore, a buffet load alleviation control system needs to be validated in flight tests before it can be certified.
- The distributed piezoelectric actuator and the piezoelectric interface concept require an additional development phase for a fail-safe actuator concept and eventually to integrate new more powerful piezoceramic materials as they become available. In addition, both concepts also require a further development phase for power amplifiers that are suitable for the use in aircraft.
- The aspect of repair and replacement of failed actuators is a specific problem for actuators that are integrated into the structure. If integration instead of surface-bonding is to be considered then suitable repair procedures have to be developed.
- For the vibration qualification test of the fin with distributed piezoelectric actuators specific requirements and test procedures have to be developed.
- Concerning higher angles of attack in connection with the introduction of thrust vectoring buffet loads for angles of attack above 30 degrees have to be determined from wind-tunnel measurements in order to assess the dynamic fin loads in the post stall regime.
- For the auxiliary rudder concept, it is necessary to perform wind-tunnel experiments for angles of attack above 30 degrees in order to evaluate the efficiency of the auxiliary rudder in this regime.

6. RECOMMENDATIONS

Based on the results of the research effort on active buffet alleviation systems for modern fighter aircraft the following recommendations are made:

- Advanced aircraft flight tests have indicated the presence of large vibration loads in the first fin bending mode when the airbrake is engaged. A demonstrator program to show the alleviation of the airbrake-induced fin vibrations could be implemented immediately for the **rudder concept** by including the lateral phase stability concept into the current flight control system without any modifications to the fin. (Short-term recommendation)
- The auxiliary rudder, piezo interface and distributed piezoelectric actuator concept have all exhibited considerable promise for the active suppression of fin buffet alleviation at large angles of attack up to 32 degrees. A demonstrator program employing one or more of these concepts should be implemented to show their viability for buffet-induced fin vibrations in flight tests. This would imply the completion of the remaining phase III tests to qualify the systems for the demonstrator flights. A decision on the system(s) to be implemented on an actual aircraft has then to be made based upon the complete test and analysis results. (Intermediate-term recommendation)
- If buffet-induced fin vibration loads become larger with angles of attack above 32 degrees, then one of the active buffet-load alleviation concepts could be implemented on thrust vector flight programs. (Intermediate-term recommendation)
- The technologies developed in the context of buffet load alleviation should be transferred into future military aircraft concepts – such as for instance UAVs – as well as to civilian aircraft and helicopters for active vibration suppression systems. (General recommendation)

For the concepts using piezoelectric actuators some additional development efforts could facilitate the introduction of these technologies into actual products significantly:

- Advances in actuator technologies to obtain more efficient and fault-tolerant actuators and in material development to have larger active strains available – for instance through the use of single-crystal ceramics or phase switching materials – need to be pursued vigorously to improve the actuator authority for vibration control applications.
- Concepts to integrate the actuators into the structure to allow for cost-effective manufacturing procedures need to be developed.
- Control electronics and in particular power amplifiers need to be improved with respect to their efficiency, their performance, their weight and their integrability for these systems to see more widespread use in aerospace applications.

7. SUMMARY AND CONCLUSIONS

Within the "Advanced Aircraft Structures" program four concepts for active buffet-load alleviation were investigated in detail. Benefits and drawbacks of the implementation of the individual concepts were assessed. A preliminary system qualification was performed for all these concepts, laying the foundation for an eventual flight demonstrator program that could show the viability and the benefits of such an active buffet-load alleviation system in the environment of the actual application.

8. ACKNOWLEDGEMENTS

The authors gratefully acknowledge major contributions in the field of fin-buffeting alleviation by Prof. Dr. B. Laschka and Dr. C. Breitsamter of the Technical University Munich's Institute for Fluid Mechanics with respect to wind-tunnel tests and development of prediction methods. The authors would also like to thank Dr. A. Büter and Mr. M. Stüwing of the German Aerospace Center's Institute for Structural Mechanics for fruitful contributions and good co-operation.

9. REFERENCES

[1] Zimmermann, N. H.; Ferman, M. A.; Yurkovich, R. N.: *"Prediction of Tail Buffet Loads for Design Application"*, AIAA 89-1378, August 1989.

[2] Ferman, N. A.; Patel, S. R.; Zimmermann, N. H.; Gerstenkorn, G.: *"A Unified Approach to Buffet Response of Fighter Aircraft Empennage"*, AGARD/NATO 70th Structures and Materials Meeting, Sorento, Italy, pp. 2-1 – 2-15, 1990.

[3] Bean, D. E.; Greenwell, D. I.; Wood, N. J.: *"Vortex Control Technique for the Attenuation of Fin Buffet"*, J. Aircraft, Vol. 30, No. 6, pp. 847-853, 1993.

[4] Hebbar, S. K.; Platzer, M. F.; Frink, William D.: *"Effect of Leading-Edge Extension Fences on the Vortex Wake of an F/A-18 Model"*, J. Aircraft, Vol. 32, No. 3, pp. 680-682, 1995.

[5] Bean, D. E.; Wood, N. J.: *"Experimental Investigation of Twin-Fin Buffeting and Suppression"*, J. Aircraft, Vol. 33, No. 4, pp. 761-767, 1996.

[6] Sheta, E. S.; Harrand, V. J.; Huttsell, L. J.: *"Active Vortical Flow Control for Alleviation of Twin-Tail Buffet of Generic Fighter Aircraft"*, AIAA Paper 2000-0906, AIAA 38th Aerospace Sciences Meeting Exhibit, Reno, NV, 10-13 January 2000.

[7] Ashley, H.; Rock, S. M.; Digumarthi, R.; Chaney, K.; Eggers, A. J.: *"Active Control for Fin Buffet Alleviation"*, Wright Laboratory Technical Report, WL-TR-93-3099, January 1994.

[8] Lazarus, K. B.; Saarmaa, E.; Agnes, G. S.: *"An Active Smart Material System for Buffet Load Alleviation"*, Proc. SPIE Vol. 2447, pp. 179-192, 1995.

[9] Hauch, R. M., Jacobs, J. H.; Dima, C.; Ravindra, K.: *"Reduction of Vertical Tail Buffet Response Using Active Control"*, J. Aircraft, Vol. 33, No. 3, pp. 617-622, 1996.

[10] Becker, J.; Luber, W. G.: *"Comparison of Piezoelectric Systems and Aerodynamic Systems for Aircraft Vibration Alleviation"*, Proc. SPIE Vol. 3326, pp. 13-27, 1998.

[11] Breitsamter, Ch.: *"Aerodynamic Active Vibration Control for Single-Fin Buffeting Alleviation"*, Deutscher Luft- und Raumfahrtkongress / DGLR Jahrestagung, Berlin, 27-30. Sept. 1999.

[12] Breitsamter, C.; Laschka, B.: *"Aerodynamic Active Control for EF-2000 Fin Buffet Load Alleviation"*, AIAA Paper 2000-0656, 38th Aerospace Sciences Meeting Exhibit, Reno, NV, 10-13 January 2000.

[13] Stüwing, M.; Sachau, D.; Breitbach, E. J.: *"Adaptive Vibration Damping of Fin Structures"*, Proc. SPIE Vol. 3674, pp. 31-39, 1999.

[14] Dürr, J. K. ; Floeth, E.; Herold-Schmidt, U.; Ihler, E.; Zaglauer, H. W.; Becker, J.; Dittrich, K.; Manser, R.; Simpson, J.: *„Fin-Buffet Alleviation via Distributed Piezoelectric Actuators: Materials Qualification Program* and Full-Scale Demonstrator Tests", Proc. Adaptronic Congress 1999, Potsdam March 3-4 1999, pp. 131-137.

[15] Dittrich, K.; Simpson, J.; Becker, J.; Dürr, J. K.; Floeth, E.; Ihler, E.; Herold-Schmidt, U.; Zaglauer, H. W.: *„Fin-Buffet Alleviation via Distributed Piezoelectric Actuators: Materials Qualification Program"*, Proc. SPIE Vol. 3674, pp. 22 –30, 1999.

[16] Manser, R.; Simpson, J.; Becker, J.; Dürr, J. K.; Floeth, E.; Herold-Schmidt, U.; Stark, H.; Zaglauer, H. W.: *„Fin-Buffet Alleviation via Distributed Piezoelectric Actuators: Full-Scale Demonstrator Tests"*, Proc. SPIE Vol. 3674, pp. 13-21, 1999.

[17] Becker, J.; Schröder, W.; Dittrich, K.; Bauer, E. J.; Zippold, H.: *"The Advanced Aircraft Structures Program - An Overview"*, Proc. SPIE Vol. 3674, pp. 2-13, 1999.

[18] Moses, R. W.: *"Vertical Tail Buffeting Alleviation Using Piezoelectric Actuators - Some Results of the Actively Controlled Response Of Buffet-Affected Tails (ACROBAT) Program"*, Proc. SPIE Vol. 3044, pp. 87-98, 1997.

[19] Hopkins, M. A.; Henderson, D. A., Moses, R. W.; Ryall, T.; Zimcik, D. G.; Spangler, R. L.: *"Active vibration-suppression systems applied to twin-tail buffeting"*, Proc. SPIE Vol. 3326, pp. 27-33, 1998.

[20] Simpson, J.; Schweiger, J.: *"Industrial Approach to Piezoelectric Damping of Large Fighter Aircraft Components"*, Proc. SPIE Vol. 3326, pp. 34-47, 1998.

[21] http://www.acx.com

[22] Dürr, J. K.; Krohn, N.; Nixdorf, K.; Lütze, S.; Herold-Schmidt, U.; Busse, G.: *„Non-Destructive Testing of Surface Bonded Piezoelectric Patch Actuators"*, Proc. SPIE Vol. 3674, pp. 39-50, 1999.

[23] Kaiser, S.; Melcher, J.; Breitbach, E. J.; Sachau, D.: *"Structural Dynamic Health Monitoring of Adaptive CFRP Structures"*, Proc. SPIE Vol. 3674, pp. 51-60, 1999.

10. FIGURES

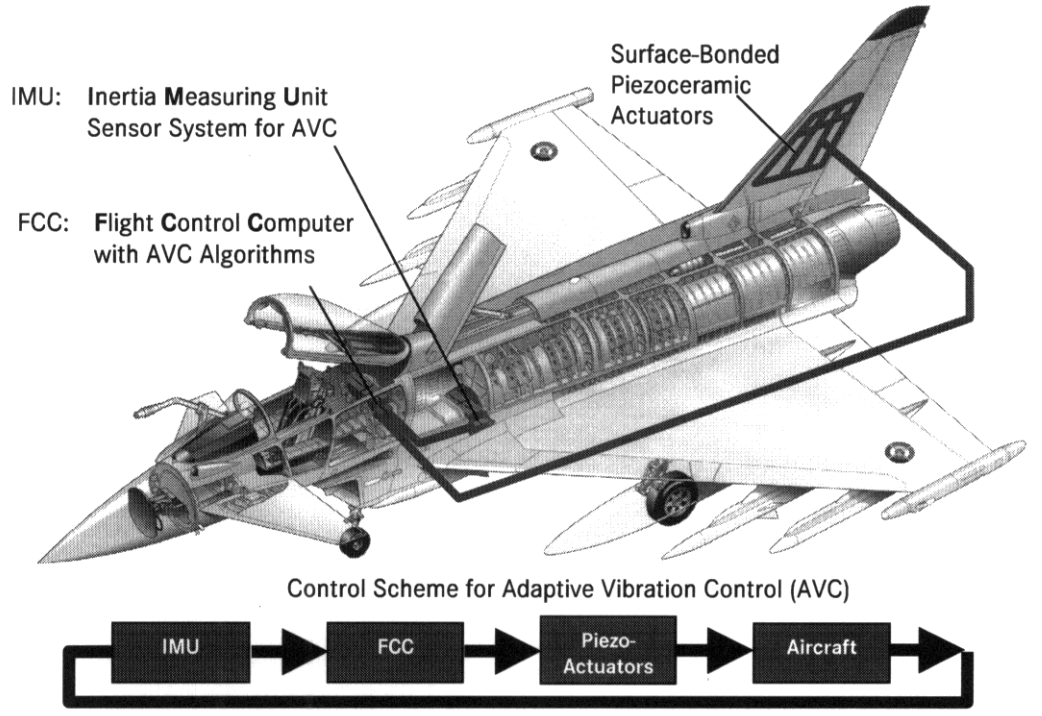


Figure 1: Adaptive fin vibration control using surface-bonded piezoceramic actuators.

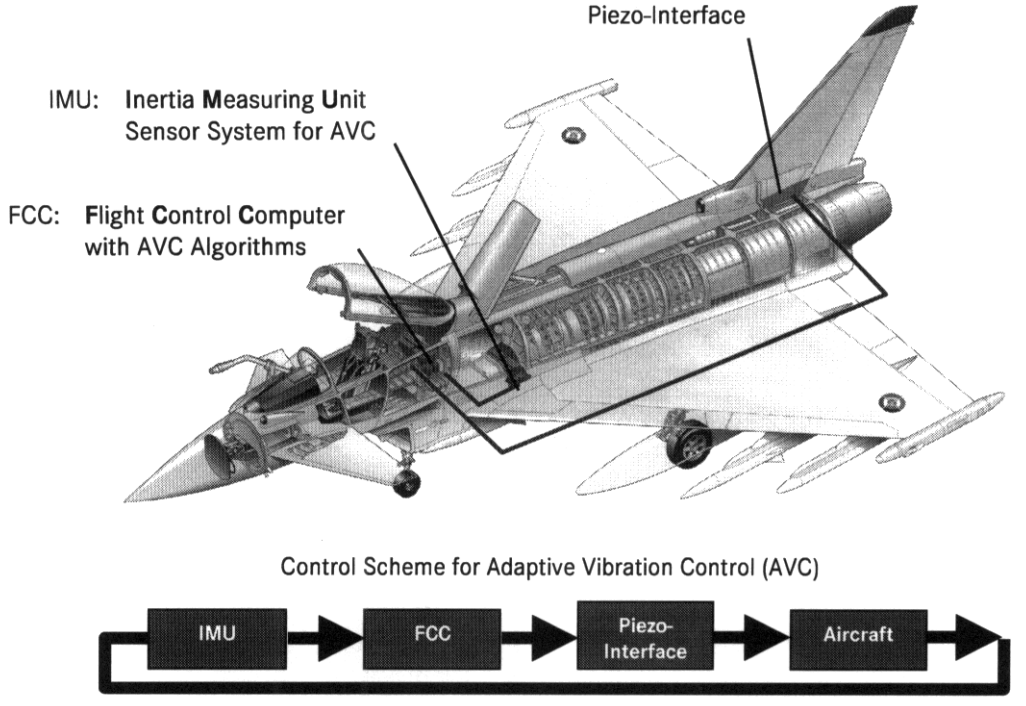


Figure 2: Adaptive fin vibration control using a piezoelectric interface.

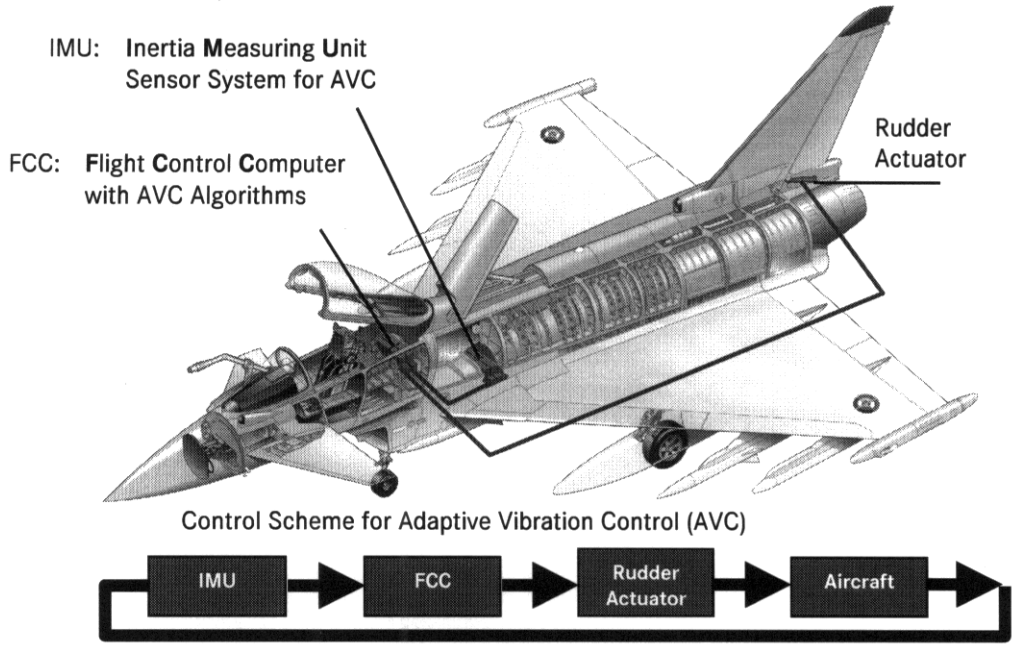


Figure 3: Adaptive fin vibration control using adaptive rudder steering.

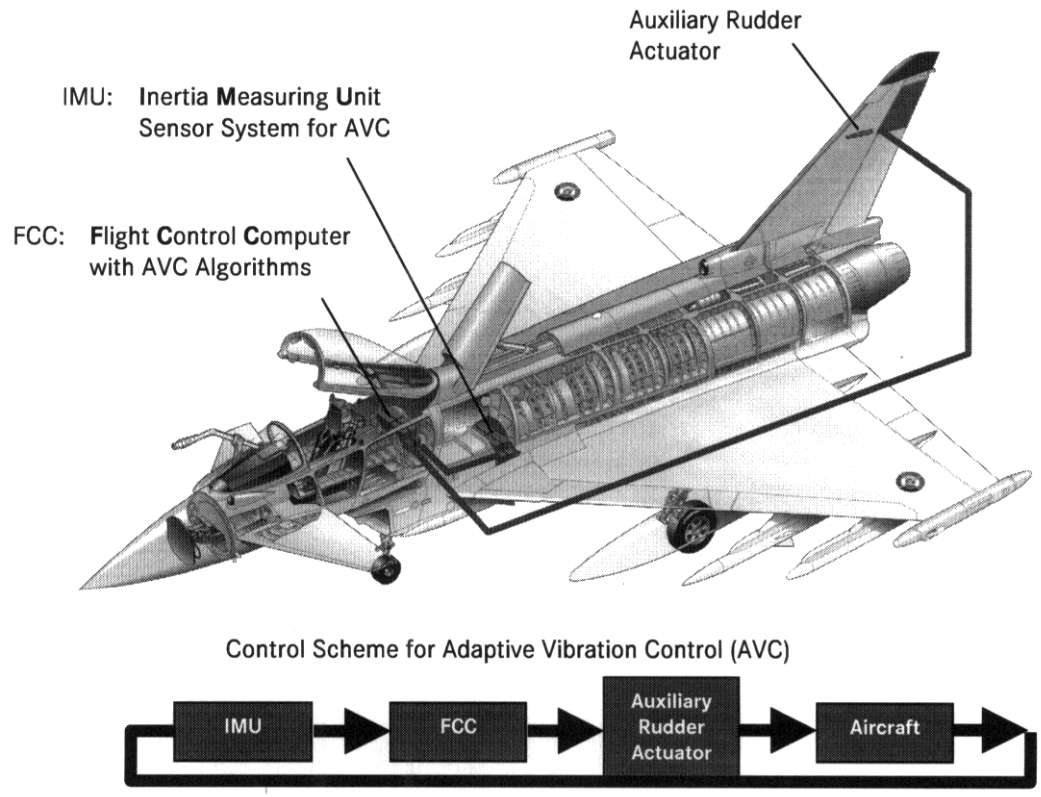


Figure 4: Adaptive fin vibration control using adaptive auxiliary rudder steering.

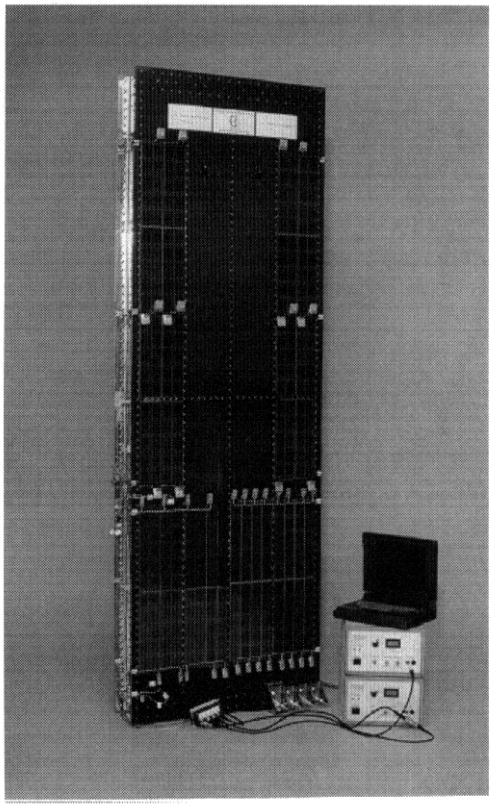


Figure 5: Fin-Box-Demonstrator [2000 x 700 x 156 mm³] to demonstrate the distributed piezoelectric actuator concept and the piezoelectric interface concept.

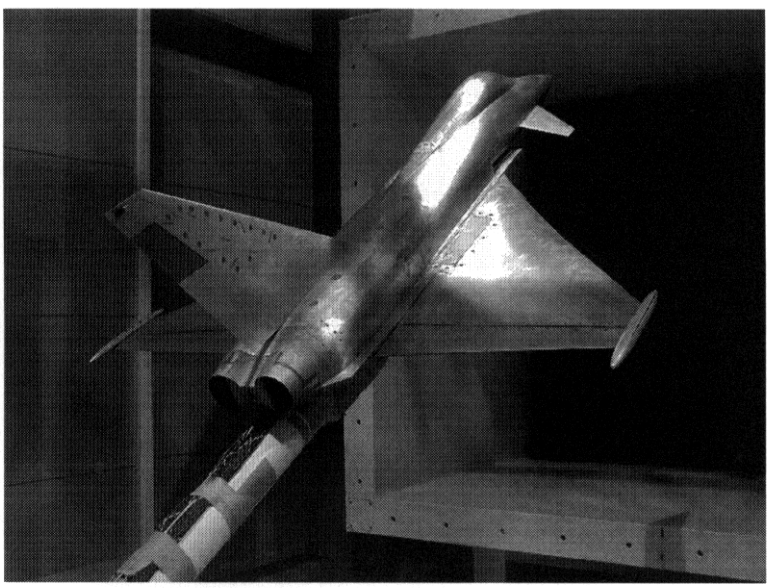


Figure 6: 1/15-scale wind-tunnel model to demonstrate the auxiliary rudder concept.

This page has been deliberately left blank

Page intentionnellement blanche

Development of Analysis Tools for Active Shape and Vibration Control

A. de Boer[¶], R. Veul[¶], P. Arendsen[¶], M. Bakker*
[¶]National Aerospace Laboratory, NLR
P.O. Box 153
8300 AD Emmeloord
The Netherlands
*Faculty of Mechanical Engineering, University of Twente
P.O.Box 217
7500 AE Enschede
The Netherlands

Abstract

Active shape and vibration control are means for obtaining optimal flow conditions around wings, ducts and channels under different conditions. This means that the structure can be adapted (deformed or damped) such that aerodynamic or vibro-acoustic behaviour is optimal for that particular situation. The fast developments in computer technology makes it possible that more complex analyses in which aerodynamic and vibro-acoustic is included can be applied in the design process. At NLR research is carried out on the integration of advanced analysis tools in design environments. In this paper the tools which are developed for the analysis of active shape and vibration control are presented.
The back bone of the design environment is an optimisation algorithm which helps the designer to come up with optimal designs of structures. In the case of active shape and vibration control the optimal design of controllers is a new aspect. This means that in addition to the optimisation of the locations of sensors and actuators the control parameters have to be optimised. In this paper a method is proposed to optimise locations and control parameters at once with the standard finite element representation of the equations of motion as a base.

1. Introduction

Active shape and vibration control are means for obtaining optimal flow conditions around wings, ducts and channels under different conditions. This means that the structure can be adapted (deformed or damped) such that aerodynamic or vibro-acoustic behaviour is optimal for that particular situation. It is no common practice to analyse the effect of active shape and vibration control in the design process due to the complexity of the algorithms and the high computation times. However, the fast developments in computer technology makes it possible that more complex analyses can be applied in the design process.
At NLR research is carried out on the integration of advanced analysis tools in design environments. This started at the end of the eighties with a multi-level optimisation tool for preliminary design of aircraft structures (Ref. 1). Currently this tool is extended to multi-disciplinary analyses and optimisation (MDO) like aero-elasticity and vibro-acoustics (Ref. 2, 3).
Recently a study has been started to incorporate the analyses and optimisation of ‘active structures’ in the MDO environment. The basis for this study is the knowledge and developed analysis tools obtained from NLR research on optimisation of damping treatments and piezoelectric materials. This will be presented in the first part of this paper. By implementing

Paper presented at the RTO AVT Symposium on “Active Control Technology for Enhanced Performance Operational Capabilities of Military Aircraft, Land Vehicles and Sea Vehicles”, held in Braunschweig, Germany, 8-11 May 2000, and published in RTO MP-051.

this knowledge in a MDO environment NLR wants to make it available for the engineer in the industry.
A new aspect which comes up with active shape adaptation and active vibration damping is control. In the second part of this paper attention is paid to the incorporation of control in the equation of motion and the optimisation analysis.

2. Finite element formulation of piezoelectric elements

To be able to simulate active damping, at NLR a finite element method has been developed with which piezoelectric material behaviour can be applied for all existing structural finite elements. This is realised by creating piezoelectric elements as so-called "overlay" elements. The finite element representation of the equations of motion for a piezoelectric element can be obtained by the assembly of the structural part and the electrical part of the element matrices as depicted in equation (1).

$$\begin{bmatrix} M_{uu} & 0 \\ 0 & 0 \end{bmatrix} \begin{Bmatrix} \ddot{u} \\ \ddot{\phi} \end{Bmatrix} + \begin{bmatrix} K_{uu} & K_{u\phi} \\ K_{\phi u} & K_{\phi\phi} \end{bmatrix} \begin{Bmatrix} u \\ \phi \end{Bmatrix} = \begin{Bmatrix} F \\ G \end{Bmatrix} \tag{1}$$

with:
- $[M_{uu}]$ the structural element mass matrix
- $[K_{uu}]$ the structural element stiffness matrix
- $[K_{\phi\phi}]$ the dielectric element matrix
- $[K_{u\phi}]$ the piezoelectric element couple matrix
- $\{u\}$ the mechanical nodal displacements
- $\{\phi\}$ the electrical nodal potentials
- $\{F\}$ the mechanical nodal load
- $\{G\}$ the electrical nodal charge

The finite element representation of the equations of motion for a structure consisting of piezoelectric material can be obtained by the assembly of all the element matrices as depicted in equation (1) to global system matrices. The solution of this global set of equations yields the mechanical displacements and electrical potentials in the structure with piezoelectric material.
The two sets of linear equations from equation (1) are coupled by the piezoelectric element matrix $[K_{u\phi}]$ and can be split into two separate matrix equations with diminishing piezoelectricity (piezoelectricity = 0 $\Rightarrow [K_{u\phi}] = 0$). These two separate (independent) sets of equations describe respectively pure structural mechanics problems (first row of Eq. (1) with $[K_{u\phi}]=0$) and electrostatic field problems (second row of Eq. (1) with $[K_{\phi u}]=0$).
The matrices $[M_{uu}]$ and $[K_{uu}]$ are the standard structural element mass and stiffness matrices for a beam, shell or volume element which are available in finite element programs. This means that the element stiffness matrix of the piezoelectric element can be assembled from an existing element stiffness matrix and the general dielectric element and piezoelectric element couple matrices of the overlay element. In this way piezoelectric material behaviour can be simulated in combination with all existing structural beam, shell and volume elements and a general piezoelectric overlay element.
The overlay element has been implemented in the modular finite element program B2000. This is a modular finite element package which is used by the NLR as ‘the computational mechanics laboratory’, a development and test environment for computational mechanics. The piezoelectric overlay element has been tested and verified with test cases from literature.

One of these test cases concerned the effect of piezoelectric material on the shape of a structure. It concerns a cantilevered laminated composite plate with on both the upper and lower surface a ceramic piezoelectric layer (see Fig. 1). Thirty six four node shell elements are used to model the plate. The composite plate is made of T200/976 graphite-epoxy composites with a stacking sequence of [-45/45-45/45]. Each layer has a thickness of 0.25 mm. The piezoelectric ceramic is PZT G1195N with a thickness of 0.1 mm.

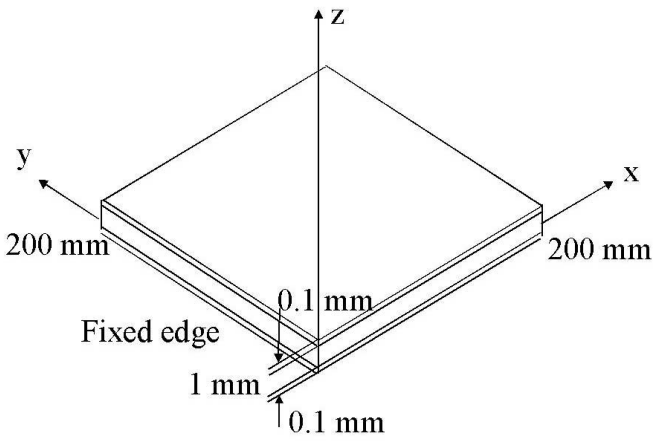


Figure 1 ***A laminated composite plate with piezoelectric layers.***

The plate is exposed to three different load cases namely a uniform distributed load of 100 N/m^2, a tip force of 0.1137 N and a tip moment of 0.01448 Nm. The deflections of the plate are calculated when a voltage of 0 V, 30 V and 50 V is applied over the upper piezoelectric layer and an opposite voltage over the lower piezoelectric layer. Figure 2 shows the calculated

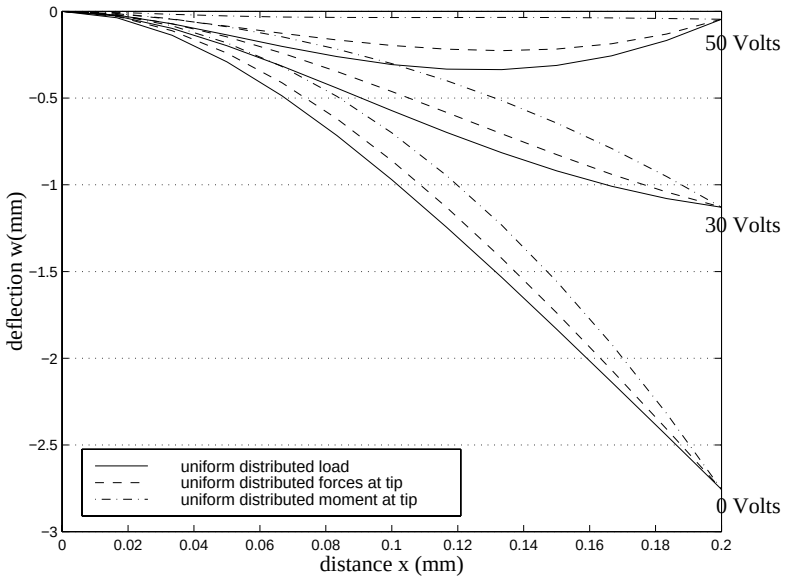


Figure 2 ***The centreline deflection under various loads and actuator input voltages***

centreline deflection of the composite plate under these different active input voltages. It is observed that for 50 V the tip deflection is almost zero. Further is shown that for 50 V combined with the tip moment the deflection of the whole centreline is almost zero. So, with a

piezoelectric layer which covers the whole plate the deformation due to a constant voltage corresponds with the deformation caused by a tip moment, as expected from the equations.

3. Optimisation

In the case piezoelectric material has to be added to a structure the mass of the structure will increase generally. Especially for light weight structures this is a disadvantage and therefore as less as possible piezoelectric material has to be added. This means that the actuator and/or sensor material to adapt the shape or vibration level has to be added at optimal locations.
At NLR research has been carried out in which the optimal locations of four tuned dampers on a vibrating rectangular plate have been calculated such that the response of the plate in a certain frequency range is minimal (Ref. 4). In principle this algorithm can be used for the determination of the optimal location of piezoelectric material, too. This has been evaluated in a pilot study on an on all sides clamped plate excited by a point force in the centre (see Fig. 3).

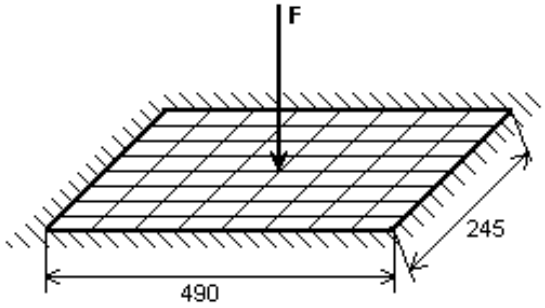


Figure 3 ***Finite element mesh of* an *on four sides clamped plate excited by a point force in the centre.***

Initially the whole plate is covered with a piezoelectric material layer of constant thickness. The objective of the optimisation is to calculate the optimal thickness distribution of the piezoelectric material layer such that the response in the centre of the plate at the first eigenfrequency is 50% of the initial response and the first eigenfrequency does not change. In figure 4 the final thickness distribution is depicted. As expected, this shows that the piezoelectric (actuator) material is concentrated around the location where the response has to be reduced. In the case the response at another location of the plate has to be reduced the piezoelectric material is concentrated on that location.

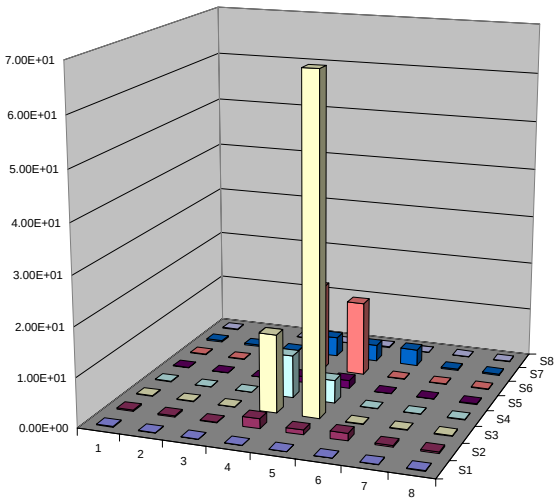


Figure 4 ***Optimal thickness distribution for 50% reduction of the response in the plate centre***

This preliminary study has proven that the optimisation algorithms developed for the optimal positioning of tuned dampers can be used for the optimal placement of piezoelectric material, too. At NLR research is going on to apply other optimisation objectives such as reduction of the response of the whole plate in a certain frequency range or reduction of the radiated sound intensity or to obtain a certain shape of the geometry.

4. Control

The basic ingredients for the analysis and design environment for active shape and vibration control are available in the analysis program B2000 namely static deformation, dynamic and vibro-acoustic analysis tools, optimisation algorithms, vibration reduction algorithms and piezoelectric overlay elements. The objective of this study is to combine these tools and to come up with a tool with which the effect of active shape and vibration control on the dynamic and acoustic behaviour of the structure can be predicted and optimised.
To perform a coupled structural dynamic and control optimisation in B2000 it should be possible to incorporate the control parameters in the equations of motion. For a structure with actuators and sensors the finite element representation of these equations is:

$$[M]\{\ddot{x}\} + [C]\{\dot{x}\} + [K]\{x\} = \{F\} - \{F_C\} \qquad (2)$$

with:
- $[M]$ the mass matrix
- $[C]$ the damping matrix
- $[K]$ the stiffness matrix
- $\{F\}$ the applied force
- $\{F_C\}$ the applied force by the actuators
- $\{x\}$ the vector with nodal displacements and voltages
- $\dot{}$ the derivative with respect to time

In the case of PID control of the velocity, the actuator force can be written as:

$$\{F_C\} = [R_I]\{x\} + [R_P]\{\dot{x}\} + [R_D]\{\ddot{x}\} \qquad (3)$$

with:
- $[R_I]$ the matrix with parameters of the I(ntegration) part of the control
- $[R_P]$ the matrix with parameters of the P(roportional) part of the control
- $[R_D]$ the matrix with parameters of the D(ifferential) part of the control

Substitution of eq. 3 into eq. 2 gives:

$$([M]+[R_D])\{\ddot{x}\}+([C]+[R_P])\{\dot{x}\}+([K]+[R_I])\{x\}=\{F\} \qquad (5)$$

The values for the control parameters in the matrices $[R_I]$, $[R_P]$ and $[R_D]$ can now be obtained with the same optimisation methods as used for the determination of the optimal locations of actuators and sensors.
In structural dynamics the dynamic behaviour of the structure is optimised by varying the structural properties such as thickness, mass density or damping ratio. This means that the components of the mass, damping and/or stiffness matrices are changed. With the same optimisation procedure the values for the control parameters in $[R_I]$, $[R_P]$ and $[R_D]$ can be determined.

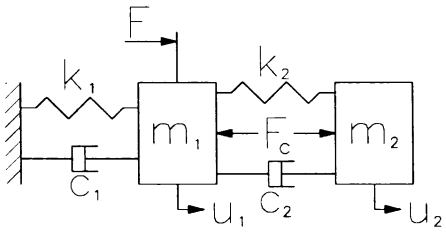


Figure 5 ***Two degrees of freedom mass, spring, dash pot system with control force.***

As an example the control parameters are determined for the two degrees of freedom (DOF) system as depicted in figure 5. The properties are summarised in table 1.
If full state feedback is applied with a PD controller, the control force F_c situated between mass 1 and mass 2 depends on the displacements and the velocities and can be written as:

$$F_c = \{r_1\ r_2\}\begin{Bmatrix} u_1 \\ u_2 \end{Bmatrix} + \{r_3\ r_4\}\begin{Bmatrix} \dot{u}_1 \\ \dot{u}_2 \end{Bmatrix}$$

The values of the control parameters can be determined with the standard pole placement routine in MATLAB. This is carried out for the case that the goal is to obtain a system with a certain value for the modal damping with the assumption that the undamped eigenfrequencies are equal to the damped ones. The results are depicted in the second row of table 2. The values of the control parameters obtained by optimisation of the standard equations of motion with the control parameters as unknowns in the stiffness and damping matrices are depicted in the third row of table 2. This table shows that for both methods approximately the same values for the control parameters are obtained.
At the moment research is going on to apply this method to determine values for the control parameters for more complex structures.

Table 1 ***Properties of the two degrees of freedom (DOF) system.***

m_1	= 2 kg	m_2	= 3 kg
k_1	= 10 N/m	k_2	= 15 N/m
c_1	= 0.5 Ns/m	c_2	= 0.1 Ns/m
$u_1(0)$	= 0 m	$u_2(0)$	= 0 m
$u'_1(0)$	= 0 m/s	$u'_2(0)$	= 0 m/s

Table 2 ***Calculated values for the control parameters obtained with pole placement method in MATLAB and optimisation of the equation of motions.***

Parameter	r_1	r_2	r_3	r_4
Values obtained with Pole placement	-0.66	0.00	0.10	5.44
Values obtained with optimisation	-0.62	-0.07	0.09	5.42

5. Conclusions

At NLR research is carried out on the integration of advanced analysis tools in design environments. The fast development in computer technology makes it possible to apply more complex analyses in such a design environment. Therefore a study has been started to incorporate in the design environment knowledge and analysis tools in the field of active shape and vibration control. In this way (theoretical) knowledge gathered by a research institute like the NLR comes available for the industry. The back bone of the design environment is an optimisation algorithm which helps the designer to come up with optimal designs of structures.
In the case of active shape and vibration control the optimal design of controllers is a new aspect. To incorporate this in the existing environment the control parameters have been included in the stiffness, damping and stiffness matrices of the finite element representation of the equations of motion.
Preliminary results show that this approach is promising.

6. Acknowledgements

Parts of the study described in this paper are carried out under a contract awarded by the Netherlands Agency for Aerospace Programmes (NIVR). Contract number 02805N.

7. References

1. Arendsen P., Dalen F. van, Bil C., Rothwell A., ADAS Structures modules evaluation report, NLR report TP 95442 U, September 1995.
2. Grooteman F.P., Schippers H., Boer A. de, A symmetrical boundary element formulation for sound transmission through fuselage walls-I; Theory, implementation and test cases, Proceedings of ISMA 21 in Leuven, September 18-20, 1996, pp. 681-696; Also NLR report NLR-TP 96504 L, August 1996.
3. Grooteman F.P., Boer A. de, Desmet W., Delmotte P., A symmetrical boundary element formulation for sound transmission through fuselage walls-II; Application, Proceedings of ISMA 21 in Leuven, September 18-20, 1996, pp. 697-718; Also NLR report NLR-TP 96507 L, August 1996.
4. Boer A. de, Derksen J.J., Reduction of noise using tuned dampers, In: Proceedings of ISMA19 in Leuven, September 12-14, 1994, Vol.3 pp. 1213-1224.

This page has been deliberately left blank

Page intentionnellement blanche

Offset Piezoceramic Stack Actuators and Acceleration Feedback Control for Tail Buffet Alleviation of a High Performance Twin Tail Aircraft: Robustness Issues

by

S. Hanagud, M. Bayon de Noyer,

Georgia Institute of Technology, School of Aerospace Engineering, Atlanta, Georgia 30332-0150

D. Henderson,

Air Force Research Laboratory

1950 Fifth Street

WPAFB, Ohio 45433 – 7251

Abstract

In high performance twin-tail aircraft, tail buffet occurs when unsteady pressures associated with separated flow excite the modes of the vertical fin structural assemblies. At high angles of attack, flow separates and is convected by the geometry of the wing-fuselage interface toward the vertical tails. This phenomenon, along with the aeroelastic coupling of the tail structural assembly, results in vibrations that can shorten the fatigue life of the empennage assembly and limit the flight envelope due to the large amplitude of the fin vibrations. The objective of this paper is to present a control system for buffet alleviation by the use of Offset Piezoceramic Stack Actuators (OPSA) in combination with acceleration feedback control. The emphasis of this paper is placed on the reliability and maintainability of the actuator and the robustness of the controller. The choice of actuator and controller is justified. Methods for the design and the placement of the OPSAs for tail buffet alleviation are elaborated. A method to design the acceleration feedback controller for tail buffet alleviation is presented. Finally, experimental validations of the effectiveness and the robustness of the controller are performed on a full-scale vertical tail sub-assembly and on a 1/16th-scale wind tunnel model.

Introduction

In a high performance twin-tail aircraft (HPTTA), buffet induced tail vibrations were first noticed through their destructive effects of induced fatigue cracks in the vertical tail structural assembly. In addition to the formation of fatigue cracks, buffet induced vibrations can restrict the flight maneuvering capability of the aircraft by restricting the angles of attack and speeds at which certain maneuvers can be executed. Because of these effects, a significant amount of maintenance efforts are spent on high performance twin-tail aircraft vertical tail assemblies in logistic centers. Buffet induced tail vibrations occur when unsteady pressures associated with separated flow, or when vortices, excite the vibration modes of the vertical fin structural assemblies. At high angles of attack, flow separates at the leading edge of the wings and vortices are generated at different locations such as the wing root or the leading edge extensions. These turbulent flows are convected by the geometry of the wing-fuselage interface toward the vertical tails. This phenomenon, along with the aeroelastic coupling of the tail structural assembly, results in vibrations that can shorten the fatigue life of the empennage assembly and limit the flight envelope due to large amplitudes of the fin vibrations.

Many different approaches to tail buffet alleviation have been investigated. These approaches can be divided into two sets, the aerodynamic methods[1-5] and structural dynamic methods. The structural dynamic approaches for buffet alleviation can also be divided into passive and active approaches. The passive structural method consists of reinforcing of the fin assembly with patches both to repair existing defects and to stiffen the assembly[6]. More recently, active structural dynamic approaches[7-18] have been developed. These methods use different types of actuators for buffet alleviation. The first type of actuator that was considered was an aerodynamic control surface[7,11,12], namely the rudder. Then, techniques based on smart structure concepts, which use active structural actuators, such as piezoceramic wafers[8-17] or stack assemblies[18] were investigated. Finally, a combination of the use of rudders for low frequencies and PZT wafers for higher frequencies has also been studied[16-17]. Simultaneously, controllers ranging from direct feedback[7] to neural predictive control have been studied[16].

The objective of this paper is to describe the results of our work in the area of buffet alleviation by the use of Offset Piezoceramic Stack Actuators (OPSA) in

Paper presented at the RTO AVT Symposium on "Active Control Technology for Enhanced Performance Operational Capabilities of Military Aircraft, Land Vehicles and Sea Vehicles", held in Braunschweig, Germany, 8-11 May 2000, and published in RTO MP-051.

combination with acceleration feedback control. The emphasis of this paper is placed on the reliability and maintainability of the actuator and the robustness of the controller. First, the choice of actuator and controller will be justified. Next, methods for the design and the placement of the OPSAs for tail buffet alleviation are elaborated. Third, methods to design the acceleration feedback controller for tail buffet alleviation are discussed. Finally, experimental validations of the effectiveness and the robustness of the controller are performed on a full-scale vertical tail sub-assembly and on a $1/16^{th}$-scale wind tunnel model.

Choice of Type of Actuator and Controller

Choice of Actuator

The selection criteria for the choice of vibration control actuator involve mechanical properties, electrical properties and cost. For tail buffet induced vibration suppression, the primary concern is the control authority that can be generated by the actuator. Comparisons between the use of the rudder or induced strain actuators for buffet alleviation by both Nitzsche et al.[11] and Moses[12] indicated that piezoceramic actuators are more efficient. Furthermore, as noted by Lazarus et al.[8], using induced strain actuators instead of the rudder enable the buffet alleviation system to run independently of the flight controls and hence does not restrict in any way the maneuverability of the aircraft.

For the purpose of buffet alleviation by induced strain actuation, every researcher[8-17], to date, has used Lead Zirconate Titanate (PZT) ceramic wafers as piezoelectric actuators. However, the control authority of PZT wafer actuators, unless used in large quantities, is usually not sufficient for this application. Stack actuators can increase the control authority through a more efficient use of the piezoceramic material properties. This increase is obtained by the use of the longitudinal d_{33} coefficient instead of the transverse d_{31} or d_{32} coefficient generally used with wafers. Furthermore, the increased stack strain results from the addition of the effective piezoelectric elongation of each PZT layer in series.

Piezoceramic stack actuators have been successfully used for vibration control. This type of actuator has been used, as active elements for vibration suppression, in truss structures[19]. These actuators have also been used to generate point loads to control vibrations in plates by placing them between the plate and a stiffener[20]. Furthermore, piezoceramic stack actuators have been implemented as moment inducing actuators by placing the stack within cutouts in stiff beams and plates[21] or mounting the stack in an external assembly for vibrations suppression in rapid fire guns[22].

These concepts have been the motivation for the choice of an actuator in this research program. Piezoceramic stack actuators can be used as “induced bending moment actuators”, which can generate much larger moments than PZT wafers. For this research program, an externally mounted actuator sub-assembly was designed, this actuator was called the “Offset Piezoceramic Stack Actuator” (OPSA). This OPSA was designed to have enhanced reliability and maintainability properties compared to previously designed piezoceramic stack based actuators. For active buffet alleviation, this piezoceramic stack actuator structural assembly would be bonded to the vertical tail skin and covered by aerodynamic shielding if necessary.

Choice of Controller

Previous investigations, in the field of buffet alleviation, have used different types of controllers ranging from direct feedback[7] to neural predictive control have been studied[16]. These different methods have some advantages and some drawbacks. For example, one of the problems associated with the use of an LQG controller is that it requires an accurate model for both the structure and the loads because the design of its observer depends on the external load influence matrix. Further, LQG controllers do not provide guaranteed robustness properties.

For the problem of buffet alleviation, the loads have not, to date, been accurately modeled. As a result, some of the control designs have used methods of identifying the load profile by using wind tunnel data[7], while others have used a “linearized” concept which models the aeroelastic buffeting behavior of the tail as a superposition of two independent mechanisms (unsteady airloads induced by structural oscillations and the driving airloads due to buffeting)[11].

Another significant problem associated with most controllers is their spillover effect. Spillover effects are the result of both sensing and actuating the unmodeled or uncontrolled modes or states of the controlled structure. These spillover effects will introduce changes between the modeled closed loop result and the actual behavior of the closed loop system. These changes may even result in instabilities. To decrease the spillover effects, it is important that the magnitude of the controller transfer function decrease rapidly as frequency increases which means that the controller has a fast roll-off at high frequencies that include unmodeled modes. Furthermore, for non-collocated accelerometers and actuators, the phase of the controller signal should be either 0 or 180 degrees, with respect to the sensor signal, at high frequencies such that the control forces do not drive the structure unstable by decreasing the closed loop damping.

Another problem is the order of the controller, which is significant for its implementation. The order of the controller, when implemented digitally, is directly related to the rate at which the controller can be implemented and the size of the code which must be stored in the memory on the controller system. This means that for large order controllers, their implementation cannot be executed rapidly and will require a large amount of memory.

In classical approaches to the control of flexible structures, system equations are usually rewritten in a state space domain. But these transformations to state space domain often lose insight into the physics of the problem from the point of view of a structural dynamicist. Since the work of Goh and Caughey[23] with the introduction of the Positive Position Feedback (PPF) controller, second order compensators enable designers to keep the system of equations of motion in their second order form. However, control schemes such as PPF and Strain Rate Feedback (SRF) are not unconditionally stable. Juang and Phan[24] proposed a second order compensator using acceleration feedback, that was unconditionally stable. The unconditional stability of the scheme, applied to flexible structure, was later proved for multiple pairs of collocated sensors and actuators with their actuator dynamics[25]. In 1996, Goh and Yan[26] developed a method of assigning the damping ratio and scalar gain to these pairs of collocated sensors and actuators which was based on the use of critically damped compensators. Then, Bayon de Noyer and Hanagud[27] have shown that the acceleration feedback control can also be applied to non-collocated actuators and sensors with stability restrictions. They further developed two methods[28] to obtain the parameters of the compensators for both single mode and multi-mode control using a single actuator or a single actuator array, one based on crossover point design and one based on the H_2 optimization of the closed loop transfer function.

As illustrated in the different designs[26-28] for Acceleration Feedback Control (AFC), the computation of the controller parameters does not require the external load influence matrix. As a result, the controller design does not require an accurate model of the loads. Further, AFC has a relative degree of two between the denominator and numerator of each of the controller transfer functions of two so that its roll-off at high frequencies is 40dB per decade and its phase at those frequencies is either 0 or 180 degrees, which is beneficial for non-collocated actuators and sensors. Furthermore, AFC enables the designer to control the vibration amplitude at selected frequencies within a given bandwidth without increasing the order of the controller for uncontrolled states. Finally, the equations of motion of the closed loop system and of the controller can be written in a similar second order equation form.

Offset Piezoceramic Stack Actuator

Actuator Design

The main challenge, associated with the use of stacked piezoceramic actuators in tail buffet alleviation, is that a piezoceramic stack produces only longitudinal motion or forces. Hence, an assembly was designed to transform the longitudinal motion of the stack into moments that will produce the control actuation. Such a transformation was achieved by placing the piezoceramic stack parallel to the controlled structure at a distance from its neutral axis and at a selected orientation. This distance creates a lever arm so that the longitudinal forces results in local moments on the structure.

This new high authority actuator assembly is made of two blocks bonded to the structure to provide an offset distance from the surface of the system to be controlled. A piezoceramic stack is placed between these two blocks and pre-compressed using a bolt. This pre-compression is necessary because the actuator can only provide control moments while extending from its rest position. By pre-compressing the active element, an offset stress is created that will enable the piezoceramic stack to provide control moments over almost the full control cycle. Furthermore, before any control signal is applied, the active element is also electrically pre-compressed by applying a DC bias. This design is illustrated in Figure 1.

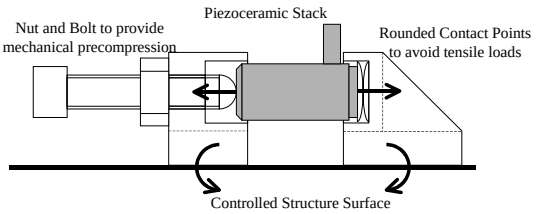


Figure 1. Offset Piezoceramic Stack Actuator

Reliability benefits associated with the offset piezoceramic stack actuator are as follows. Since the piezoceramic stack is only compressed between the two blocks of the assembly, tensile loads are not transmitted to the active element. This fact reduces the possibility of actuator failure. Furthermore, in this design, the rounded point contacts between the piezoceramic stack and the mounts insure that bending loads are not transmitted to the active element as well, which reduces even further the possibility of stack failure in local tension. It is to be noted that, for maintainability, the bolt is used to permit an easy removal of the piezoceramic stack while the actuator assembly is bonded to the system to be controlled. Hence, if failure were to occur, the active element could be replaced easily during regularly scheduled maintenance.

For large amplitude vibration suppression, the primary concern is the control authority that can be generated by the actuator. To obtain a maximum control authority, the resultant forces that the actuator develops should be as large as possible. However, the power requirement of the actuator increases with the maximum authority that the active element can deliver. To produce the needed control moments, the active element of the Offset Piezoceramic Stack Actuator can be chosen from different types of piezoceramic stacks. Low-voltage (100V) piezotranslators can generate blocked force in the range of 180N to 3kN while high-voltage (1000V) piezotranslators can generate blocked force in the range of 1.5kN to 30kN. Once the type of the piezoceramic

stack has been selected, the dimensions of the offset piezoceramic stack actuator assembly should be computed such that the chosen active element fits within the mount and optimal actuation energy transfer is obtained.

Actuator Offset and Placement Optimization

For controller design purposes, the modal influence matrix of the actuators is required to model the plant in the modal space. To obtain such a matrix for a complicated structure, a FEM model of the system should be developed. However, during this research work, to test the reliability of the finite element model of the OPSA and to gain insight into the physics of the actuator, an analytical solution for a simple structure was developed. The simple system studied was a steel cantilever beam, which was 24-in long, 0.5-in thick and 2-in wide. An offset piezoceramic stack actuator (OPSA) was bonded on the upper surface of the beam close to its clamped end. The OPSA was made of two steel blocks bonded to the cantilever beam with a piezoceramic low-voltage translator, Physik Instrumente PI-830.10, clamped between the blocks.

A modal expansion based model was developed to model the actuation of the OPSA on an Euler-Bernoulli beam with a torsional spring support on one end and free at the other end. Then, an optimization of the actuator placement and of the vertical offset distance was derived based on this model. Given the active element of the OPSA, namely the piezoceramic stack, the objective of this optimization was to maximize the control authority of the offset piezoceramic stack actuator for the control of vibrations of the cantilever beam. For acceleration feedback control, the control sensor optimal location on a cantilever beam is the free tip. In such a case all of the modal influence coefficients of the accelerometer are maximum. In order to maximize the control authority of the control system, we need to optimize the actuator authority of the OPSA. This means that we should maximize the modal influence coefficients of the OPSA for the modes that have been selected for control.

If the length of the actuator is small compared to the beam length, we can make the following two approximations. First, the natural frequencies of the actuated beam are independent of the vertical offset distance and actuator position. Second, the mode shapes of the actuated beam are also independent of the vertical offset distance and actuator position. These two approximations combined insure that an approximation of the optimal vertical offset distance would be the same for every mode and that the placement analysis can be performed on the structure without any actuator mounted. In this case, we take the derivative of any modal influence coefficient of the OPSA with respect to the vertical offset distance and set this derivative to zero. We obtain that the offset distance is optimal when the added bending stiffness due to the piezoceramic stack matches the bending stiffness of the beam alone. So that:

$$\delta_{opt} = \sqrt{\frac{E_b I_b}{A_s Y^E_s}} \qquad (1)$$

Where δ_{opt} is the optimal vertical offset, E_b and I_b are the Young's modulus and Moment of Inertia of the beam, and A_s and Y^E_s the cross sectional area and Young's modulus of the piezoceramic stack.

The placement of the actuator is based on reciprocity theory. The principal mode of actuation, which is induced by the offset piezoceramic stack actuator, is the input of a pair of bending moments in opposite directions located at the end mounts locations on the beam. The objective of the placement optimization is to obtain maximum transverse acceleration at the sensor location, the free tip of the cantilever beam, due to the pair of moments. By reciprocity theory, this optimization is equivalent to finding the locations with maximum curvature due to an input of transverse disturbance force located at the sensor position. As discussed before, if the length of the actuator is small compared to the beam length, the placement analysis can be performed on the structure without any actuator mount.

For a more complex structure, such as a vertical tail, the optimal offset distance can be obtained by matching the bending stiffness due to the piezoceramic stack with the local bending stiffness of the structure. Further, in order to obtain optimal placement of the actuator, an experimental method is developed. The optimization is performed such that local moments, which are induced by the offset piezoceramic stack actuators, produce maximum response from the control sensor. As discussed above and as illustrated in Figure 2, using reciprocity theory, the actuators are placed at the locations and in directions where the curvature responses due to a disturbance force at the sensor location, in the measured direction, are maximum.

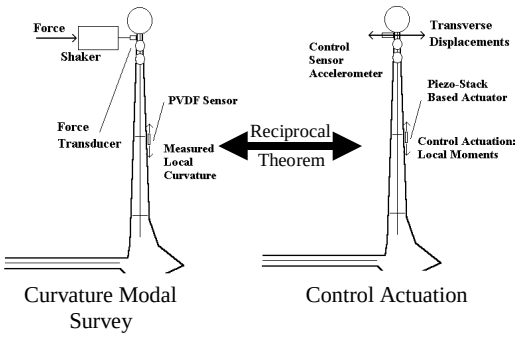


Figure 2. Principles of Actuator Placement

Since the actuators are bonded on the surface of the controlled structure, a local two-dimensional approximation of the system is assumed. This approximation means that, at each actuator location, the structure is supposed to behave like a two-dimensional

system. As a result, a curvature modal survey is performed in the neighborhood of candidate locations to obtain optimal placements of the actuators. The curvature modal survey is an experimental modal analysis, in which, instead of measuring acceleration, curvature is measured in three directions, due to the local two-dimensional approximation of the structure, at each point. This analysis is performed by disturbing the structure at the control sensor location and in the measurement direction. Then, the response from a curvature sensor, such as a PVDF film, is measured in the immediate area of each candidate actuator location in three different directions. From the three measured curvatures at a set of locations, the optimal location and optimal orientation of the actuator is obtained.

Acceleration Feedback Control

Acceleration feedback control (AFC) is based on measuring acceleration and applying a second order compensator to the sensor signal to obtain control forces. The equations of motion of the closed loop system and of the controller are in a second order equation form, as is illustrated in the following equation.

$$\begin{aligned} &[M]\{\ddot{x}\}+[C]\{\dot{x}\}+[K]\{x\}=-[\Gamma_{act}][G][\Omega_c]\{\eta\}+\{f\} \\ &\{\ddot{\eta}\}+[\Lambda_c]\{\dot{\eta}\}+[\Omega_c]\{\eta\}=\{1_p\}[\Gamma_{acc}]\{\ddot{x}\} \end{aligned} \quad (2)$$

In the above equations, $\{x\}$ is the vector of degrees of freedom of the system, $\{\eta\}$ is the vector of the p compensator coordinate, $[\Gamma_{act}]$ is influence matrix of the actuators, $[\Gamma_{acc}]$ is influence row vector of the accelerometer, $[\Lambda_c]$ is the compensator damping matrix and $[\Omega_c]$ is the compensator frequency matrix, $[G]$ is the feedback gain matrix and $\{1_p\}$ is a vector of length p, with one for each entry, to account for the fact that all compensators are placed in parallel.

Single Degree of Freedom AFC

The generalized equations describing the closed loop behavior of a single degree of freedom system under Acceleration Feedback Control (AFC) consist of a structural equation with a feedback force due to the actuator and a disturbance force, and a compensator equation with acceleration sensing. These equations are generalized by introducing influence parameters for the actuator and for the sensor. These equations, in the modal space, are:

$$\begin{cases} \ddot{\xi}+2\zeta_s\omega_s\dot{\xi}+\omega_s^2\xi=-a_1\gamma\omega_c^2\eta+f \\ \ddot{\eta}+2\zeta_c\omega_c\dot{\eta}+\omega_c^2\eta=a_2\ddot{\xi} \end{cases} \quad (3)$$

In these equations, ξ and η are the modal coordinates of the structure and of the compensator; respectively. Then, ω_s, ω_c, ζ_s and ζ_c are the natural frequencies and the damping ratios of the structure and the compensator, respectively. Further, γ is the controller gain applied to the feedback signal; and a_1 and a_2 are the influence parameters of the actuator and sensor, respectively. Finally, f is the external disturbance that drives the system.

Without loss of generality, by taking the Laplace Transforms of Equation (3), assuming zero initial conditions, and solving for η, the transfer functions of the closed loop system and of the controller, are obtained:

$$\begin{cases} G_s(s)=\dfrac{\bar{\xi}}{\bar{f}}=\dfrac{\left(s^2+2\zeta_c\omega_c s+\omega_c^2\right)}{\left(s^2+2\zeta_s\omega_s s+\omega_s^2\right)\left(s^2+2\zeta_c\omega_c s+\omega_c^2\right)+a_1a_2\gamma\omega_c^2s^2} \\ G_c(s)=\dfrac{\omega_c^2\gamma\bar{\eta}}{a_2s^2\bar{\xi}}=\dfrac{\omega_c^2\gamma}{\left(s^2+2\zeta_c\omega_c s+\omega_c^2\right)} \end{cases} \quad (4.a\text{-}b)$$

Equation (4.b) shows that the controller has a relative degree of two between its denominator and numerator. This results in a controller with 40 dB per decade roll-off and a phase of 0 or 180 degrees at high frequencies.

The stability of such a system can be studied by applying the Routh-Hurwitz criterion[48] to the closed loop characteristic equation:

$$\left(s^2+2\zeta_s\omega_s s+\omega_s^2\right)\left(s^2+2\zeta_c\omega_c s+\omega_c^2\right)+a_1a_2\gamma\omega_c^2s^2=0 \quad (5)$$

For the purpose of this analysis, the open loop system and the controller are assumed to be asymptotically stable. Then, if a_1 and a_2 have the same sign, meaning that the mode is observed in phase by the sensor with respect to the actuator input, a sufficient condition for stability is that γ is positive. On the other hand, if a_1 and a_2 have opposite signs, meaning that the mode is observed out of phase by the sensor with respect to the actuator input, a sufficient condition for stability is that γ is negative. Since the only term depending on γ always appears in the form $a_1a_2\gamma$ in Equations (5), a sufficient condition for stability is that $a_1a_2\gamma$ be positive.

Design of the AFC Parameters for a SDOF System based on the Optimization of the H_2 Norm of the Closed Loop Modal Receptance

In the case of vibration suppression in a given structure, an optimization of the controller design parameters can be performed to meet a selected objective or a performance criterion. One way to design the single degree of freedom AFC compensator for vibration suppression is to minimize the H_2 norm of the closed-loop receptance which is the system transfer function, $G(j\omega)$, between the modal displacement and the external disturbance force. The performance criterion is defined to be:

$$\begin{aligned} \|G\|_2 &= \left(\frac{1}{2\pi}\int_{-\infty}^{+\infty} \|G(j\omega)\|_F^{\,2}\, d\omega \right)^{1/2} \\ &= \left(\int_0^{+\infty} \|H(t)\|_F^{\,2}\, dt \right)^{1/2} = \|H\|_2 \end{aligned} \quad (6)$$

In this Equation, H is the impulse-response matrix of the system, which is the inverse Laplace transform of the transfer function matrix.

This design is equivalent to minimizing the L_2 norm of the impulse modal response of the closed loop system due to a unit impulse load. Or for a stochastic process, this design is equivalent to minimizing the covariance of the closed loop modal response due to a unit white noise disturbance. It is to be noted that none of the definitions depends on the control signal directly. Hence, on the basis of this criterion, the controller will be a high authority controller. For this design, it will be proved that there does not exist an optimal controller gain. Therefore, instead of defining the controller gain by weighting the control signal, it can be defined by iterations in such a way that the control signal is not saturated.

To optimize the acceleration feedback control compensator for the norms defined in Equation (6), we define a functional J, which depends on the controller parameters:

$$J(\omega_c, \zeta_c, \gamma) = \|G\|_2^{\,2} \tag{7}$$

The closed loop system can be rewritten in a state space based on the modal states of the controlled system and the controller states:

$$\begin{cases} \dot{x}(t) = \tilde{A}x(t) + \tilde{B}w(t) \\ y(t) = \tilde{C}x(t) \end{cases} \tag{8}$$

where:

$$x = \begin{bmatrix} \xi & \dot{\xi} & \eta & \dot{\eta} \end{bmatrix}^T$$

$$\tilde{A} = \begin{bmatrix} 0 & 1 & 0 & 0 \\ -\omega_s^{\,2} & -2\zeta_s\omega_s & -a_1\gamma\omega_c^{\,2} & 0 \\ 0 & 0 & 0 & 1 \\ -a_2\omega_s^{\,2} & -2a_2\zeta_s\omega_s & -(1+a_1a_2\gamma)\omega_c^{\,2} & -2\zeta_c\omega_c \end{bmatrix}$$

$$\tilde{B} = \begin{bmatrix} 0 & 1 & 0 & a_2 \end{bmatrix}^T \text{ and } \tilde{C} = \begin{bmatrix} 1 & 0 & 0 & 0 \end{bmatrix} \tag{9}$$

The functional defined in Equation (8) is then given by:

$$J(\omega_c, \zeta_c, \gamma) = \mathrm{tr}\left(\tilde{B}^T P \tilde{B}\right) = \mathrm{tr}\left(P\tilde{B}\tilde{B}^T\right) \tag{10}$$

Where, since the closed loop system is assumed to be stable, P is the observability Gramian of the closed loop system, which is the positive definite solution of the Lyapunov equation:

$$P\tilde{A} + \tilde{A}^T P + \tilde{C}^T\tilde{C} = 0 \tag{11}$$

Since P is symmetric, its 10 independent elements are obtained by solving the linear system of equations given by Equation (11). Then by computing the trace of the product of matrices defined by Equation (10), the H_2 norm of the transfer function between the modal response and the external disturbance is obtained. Then, the derivative of the norm with respect to ω_c, ζ_c and γ are set to zero. First, we obtain that the derivative with respect to γ that is strictly negative and increases uniformly toward zero as γ tends to infinity. Hence, there is no optimal solution for the controller gain as a design parameter.

However, for a particular controller gain, the following condition, to minimize the H_2 norm, is obtained:

$$\zeta_c\left(\frac{\omega_c^{\,2}}{\omega_s^{\,2}} - 1\right)\left(\frac{\omega_c^{\,2}}{\omega_s^{\,2}} + 2\frac{\zeta_c}{\zeta_s}\frac{\omega_c}{\omega_s} + 1\right) = 0 \tag{12}$$

In order to obtain a ratio between the natural frequency of the controller and the natural frequency of the open loop system that is real and positive, the only possible condition is:

$$\omega_c = \omega_s \tag{13}$$

With this condition, the second equation that should be satisfied to minimize the H_2 norm of the closed loop transfer function is as follows:

$$(\zeta_c + \zeta_s)^2\left(a_1a_2\gamma - 4\zeta_c^{\,2}\right) = 0 \tag{14}$$

For a stable controller, the compensator damping ratio should be positive. Hence, the only possible solution of Equation (14) is:

$$\zeta_c = \frac{1}{2}\sqrt{a_1a_2\gamma} \tag{15}$$

It is to be noted that for this design to meaningful, the controller damping ratio should be real. Hence, the product $a_1a_2\gamma$ must be positive and the closed loop system will be stable.

As a result, the design of an AFC controller that minimizes the H_2 norm of the closed loop transfer function between modal displacement and external load of an SDOF system begins with the choice of a controller gain such that the product $a_1a_2\gamma$ is positive. Then, Equation (15) is used to compute the optimal damping ratio for the controller. Finally, the natural frequency of the controller is set to be equal to the natural frequency of the open loop system. In order to insure that the control signal will not be saturated, closed loop simulations can be investigated and an iteration process on the controller gain can be performed.

Uncertainties and Robustness

The principal drawback associated with the use of optimal controllers arises from uncertainties in the model of the open loop system, which will create departure from optimality and may even lead to instabilities. As discussed previously, a sufficient condition for stability is that the product $a_1a_2\gamma$ is positive. Hence, the only uncertainties that may lead to instability are uncertainties in the sign of the product of the actuator and sensor influence coefficients, a_1a_2. However, such type of uncertainty are extremely unlikely since the phase of the modeled transfer function

is defined by this product and can be easily compared to the phase of the actual transfer function between the control sensor and the actuator input voltage. Hence, robust stability of the H_2 optimal design for a single degree of freedom system is insured.

To study the effect of uncertainty on the performance of the H_2 optimal design, the departure from optimality due to uncertainties in the open loop system parameters is studied. Since the open loop parameters are scalars, any type of linear uncertainty can be modeled as:

$$q_{s,true} = q_{s,identified}\left(1+\varepsilon_q\right) \tag{16}$$

The uncertainties are defined to be present in the natural frequency, ε_ω, the damping ratio, ε_ζ, and the product of the sensor and actuator influence coefficients, ε_a.

The departure from optimality due to uncertainties, D_{opt}, is defined as the difference between the H_2 norms of the closed loop system using controller parameters computed with the identified uncertain modal parameters and the H_2 norms of the closed loop system using controller parameters computed with the actual parameters normalized by the latest. Hence, the departure from optimality due to uncertainties is defined to be:

$$D_{opt} = \frac{\left\| G_{cl,\text{controller based on identified parameters}} \right\|_2 - \left\| G_{cl,\text{controller based on true parameters}} \right\|_2}{\left\| G_{cl,\text{controller based on true parameters}} \right\|_2} \tag{17}$$

By assuming small uncertainties, meaning all ε's small with respect to one ($\varepsilon<<1$), and then a small open loop damping ratio, since typical damping ratios are less than 0.05, a Taylor series approximation, of order two, of the departure from optimality is given by:

$$D_{opt} \approx \frac{1}{4}\left[\left(1-\frac{3}{2}\alpha\left(1+\varepsilon_\zeta\right)\right)\varepsilon_a + \left(1-\frac{5}{2}\alpha+\frac{\alpha^2}{\zeta_s{}^2}\left(1-\frac{7}{2}\alpha\right)\right)\varepsilon_\omega{}^2 + \frac{1}{4}\left(\frac{3}{2}\alpha-1\right)^2\varepsilon_a{}^2\right] + O\left(\varepsilon^3\right) \tag{18}$$

In this equation, the non-dimensional parameter α is the ratio between the open loop damping ratio and the controller damping ratio computed for the model. It is given by $\alpha = 2\zeta_s \big/ \sqrt{a_1 a_2 \gamma}$. For most applications, the parameter α is chosen to be larger than the open loop damping ratio, ζ_s, to obtain a less than critically damped compensator.

We can assess from Equation (18) that, for a large compensator gain (α << 1), the departure from optimality due to uncertainties in the model of the sensor and actuator influence parameters behaves like ε_a. This means that a controller with actual influence parameters larger than the one modeled will likely perform better than expected. Simultaneously, the departure from optimality associated with uncertainties in the damping ratio of the open loop system decreases when the value of the controller gain is large. This also applies to the case of the uncertainties in natural frequency. Furthermore, to keep the departure from optimality due to uncertainties in the natural frequency small, the coefficient multiplying $(\alpha/\zeta_s)^2$ in Equation (18) should be positive. Hence α should be kept below 2/7. This means that the minimum value of the gain that should be chosen for the controller is $\gamma_{min} = 49\zeta_s{}^2 \big/ a_1 a_2$.

AFC H_2 Norm Optimization of the Closed Loop Modal Response Design for Multi-Input, Single-Output Systems

The optimal controller design for multi-input, single-output systems is divided into three steps. The first step consists of choosing the output measurement vector and the controller gain matrix. The choice of the output measurement vector means the choice of modal weighting. When the output measurement vector is defined, a controller gain matrix should be defined in such a way that each entry of the 1 x n_c vector given by the product $\left[\tilde{\Gamma}_{acc}\right]\left[\tilde{\Gamma}_{act}\right][G]$ is positive. In the particular case where no mode is controlled by more than one actuator array, this condition is equivalent to insuring that the product $a_1 a_2 \gamma$ is positive for every controlled mode. Hence, as discussed previously, this restriction on the gain matrix is given to insure that under the assumption that the structural closed loop system is uncoupled, the system is stable.

The second step of the numerical optimization consists in the definition of some initial guess for the optimal controller natural frequencies and damping ratios. This definition is performed under the assumption that the closed loop system can be uncoupled in a set of uncoupled structural modes under acceleration feedback control and a set of uncoupled and uncontrolled structural modes. Under this assumption, the parameters of each of the controller second order compensator can be computed independently based on the formulas given in the single degree of freedom design section depending on the choice of weight matrices.

The final step of the optimization procedure computes the optimal natural frequencies and damping ratios for the controller. In this research work, the numerical minimization is performed using the fmins function of the Matlab software in which the minimization is performed using the Nelder-Mead simplex search which is a direct search method that does not require gradients or other derivative information. In order to complete the step, the H_2 norm criterion should be computed. This computation is completed in three steps. First, at each iteration of the optimization, the closed loop system state matrix, A_{cl}, and the closed loop input disturbance matrix, B_{cl}, are computed. The choice of the output measurement vector defines the output performance measurement matrix, C_{cl}. Then, the optimization criterion, J, given by the H_2 norm of the performance measurement for a unit white noise

disturbance, is defined to be, as a function of the observability Gramian, P, as follows:

$$\|z\|_2 = J(\{\omega_c\},\{\zeta_c\}) = \left[\mathrm{tr}\left(B_{cl}{}^T P B_{cl}\right)\right]^{1/2} \quad (19)$$

Since, the closed loop system is assumed to be stable, the observability Gramian of the closed loop system, P, is positive definite and is the solution of the Lyapunov equation:

$$PA_{cl} + A_{cl}{}^T P + C_{cl}{}^T C_{cl} = 0 \quad (20)$$

Hence, the second step of the computation of the optimization criterion consists in solving Equation (20) for the observability Gramian, P. Then, the last step of the computation consists of evaluating Equation (19) for the optimization criterion.

Wind Tunnel Tests

To validate the use of AFC in reducing the buffet-induced vibrations of the vertical tails of an HPTTA and the associated robustness, a 1/16th-scale wind tunnel model, shown on Figure 3, was designed and built. This model consisted of a rigid fuselage and wings with an aeroelastically scaled empennage.



Figure 3. Scaled model of the HPTTA

The wind tunnel tests were performed at the Georgia Tech Research Institute Model Test Facility (GTRI-MTF). The GTRI-MTF wind tunnel is a closed-return, atmospheric, low-speed wind tunnel that has a rectangular test section 30 inches high and 43 inches wide with a usable length of 90 inches. This facility is capable of empty tunnel speeds of up to 200 ft/sec and corrected maximum dynamic pressures of 50 psf. During the tests wall corrections were not considered for the following reasons. The vortices, which are responsible for the buffet, are formed near the junction of the fuselage, the engine inlets and wing leading edges. Furthermore, the tail sub-assembly, where the measurement of buffet loads are obtained, are near the center of the tunnel cross section. Because blockage correction factors for separated flow were not available, the free stream dynamic pressure was corrected by using approximate correction factors that were obtained from flows at low angles of attack.

Results from preliminary wind tunnel tests, MacAir experiments reported by Triplett[29] and earlier Georgia Institute of Technology tests reported by Komerath et al.[30] showed that there exists a characteristic frequency associated with the maximum buffet load and that its associated reduced frequency is almost the same for all experiments. Hence, we determined that it was very important for the active tail buffet alleviation tests to scale the model such that the reduced frequencies are conserved. To operate in the middle of the optimal range for the Georgia Tech Research Institute Model Test Facility (GTRI-MTF) wind tunnel, the scale model of the empennage was designed to have natural frequencies 2.25 time larger than the full-scale tail sub-assembly. This model would then operate at a free stream dynamic pressure of 9 psf to conserve the reduced frequencies of the flow and structure. This dynamic pressure was equivalent to a free stream velocity of 26.9 m/s that translates approximately (because of compressibility effects) to a free stream velocity of 191.5 m/s for the full-scale aircraft or about Mach 0.6 at 20,000 ft.

The main objective of the wind tunnel tests was to demonstrate our ability to suppress all the principal modes of the HPTTA vertical tails that participate in the buffet response at high angles of attack. In addition, to demonstrate the robustness of the control system, it should not only perform well at the angle of attack corresponding to the worst buffet conditions but also over a wide range of angles of attack and free stream dynamic pressure. Hence, to validate the controller, different experiments were conducted. First, a control experiment is run at the predetermined worse buffet condition of 20 degrees angle of attack and 9 psf of free stream dynamic pressure. Then four different angles of attack were selected and the free stream dynamic pressure was varied from 5 to 13 psf.

To locate the sensor for the control experiments, three conditions dictated the placement. First, the vertical tails of our model behaves like a cantilever tapered plate. Second, the sensor, which is generally used for acceleration feedback control, is an accelerometer. Third, to maintain the vortex cohesion, minimum flow disturbance due to the sensor should be obtained. As a result, the optimum location for the sensor was on the trailing edge tip of the vertical tail. The placement was validated experimentally to check that all modes in the control range were observable.

The next phase was to determine at which attitude the worse disturbances are encountered. Since we assume linearity of the structure, the dynamic response of the vertical tail was measured instead of the pressure. First, a fine survey was conducted for angles of attack ranging from 0 to 23 degrees, which showed that the angle of attack that displays the maximum tip response was approximately 20 degrees. This agrees with the results reported by Komerath et al.[30] during their tests. However, it does not agree exactly with the results of Triplett[29]. He reported a worse case at an angle of attack of 22 degrees.

At this point, the left vertical tail was instrumented with two pairs of offset piezoceramic stack actuators. The first pair of actuators was located to obtain large bending actuation authority and was bonded at the root

of the vertical tail along its mid-chord line. The second pair of OPSA actuators was placed for torsion control and was bonded at 35 degrees with respect to the mid-chord line above the first pair. This configuration is illustrated by Figure 4.

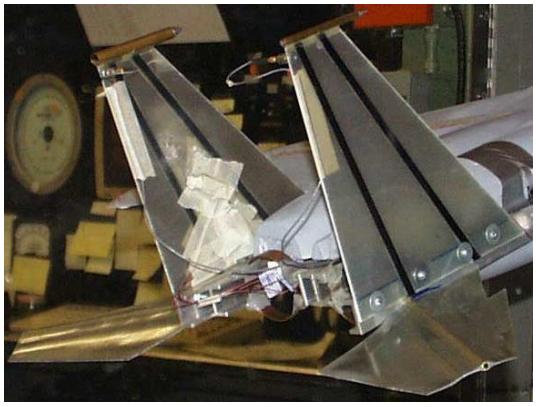


Figure 4. Active Buffet Alleviation Experiment Vertical Tails with OPSA Actuators.

Then, to assess the authority of the actuator arrays, the auto-power spectrum of the dynamic response of the control sensor excited by the buffet vortices was compared with the auto-power spectrums of the actuator arrays converted from the experimental transfer functions of the plant for a flat maximum input voltage. This operation showed that enough actuator authority was attained.

The next task associated with designing a controller was to obtain a mathematical representation of the system to be controlled. This representation is usually referred to as a "plant". To obtain the plant model, experimental transfer functions were obtained between the input voltage to each actuator array and the control sensor response voltage. Then, using a combination of system identification techniques such as single pole fitting and complex circle fitting around the poles, the parameters of each of the transfer functions were extracted.

Once the plant model had been developed and the actuator authority checked, the controllers were designed. For this experiment, the type of controller that was selected was acceleration feedback control (AFC). And the type of design for AFC that was used was the H_2 optimization of the closed loop transfer function design. Two different controllers were designed, one for the bending array and one for the torsion array. A single degree of freedom compensator was designed for each mode using the parameters extracted earlier. In order to avoid clipping of the control signal, the damping of each compensator was chosen to be seven times larger than the damping of the associated mode. Once the controllers were designed, their stability and effects on other modes were checked using root locus plots. Since root locus plots did not show any instability and each controller did not affect the parameters of the other controller, the controllers could be implemented simultaneously.

The controllers were implemented on a dSPACE system based on a digital signal processor (DSP). The coding of the overall control experiment was done using block programming with the Matlab extension called Simulink. The file was then converted to the DSP machine language and downloaded to the dSPACE system. Once the system started, the controllers were active.

To validate the controllers, three different experiments were carried out. First, a control experiment was run at the predetermined operating condition of 20 degrees angle of attack and 9 psf of free stream dynamic pressure. The auto-power spectrums of the uncontrolled and controlled trailing edge tip acceleration are illustrated in Figure 5. This figure shows that each of the controlled frequency has its auto-power spectrum reduced by a factor of at least 5. Furthermore, in the case of the first bending mode and second torsion mode, the responses are suppressed to a level equivalent to the one that would be obtained in the absence of these modes.

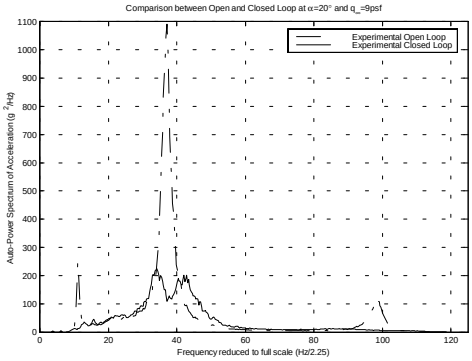


Figure 5. Comparison Between Open and Closed Loop Auto-Power Spectrum of Trailing Edge Tip Acceleration at θ=20° and q_∞=9psf.

Once the controller had been validated at its operating point, its effectiveness and robustness had to be checked at different conditions. For the second experiment, the operating free stream dynamic pressure of 9 psf was kept. However, the angle of attack was varied from 0 to 23 degrees. This control experiment showed that the root mean square of the trailing edge tip acceleration was reduced by up to 30% below 15 degrees and by about 20% at 20 degrees. This experiment also showed that the controllers were effective on the whole range of angles of attack.

Finally, four different angles of attack were selected. 14, 17, 20 and 23 degrees angles of attack cover the different regimes of buffet that the scaled model was encountering. For each angle of attack, the

free stream dynamic pressure was varied from 5 to 13 psf. As before, the results showed that as the disturbance increases the effectiveness of the controllers decreases. However, even at a free stream velocity 25% higher than the operating free stream velocity, the minimum RMS reduction was still 17%. These results, illustrated in Figure 6, prove that the controllers were stable and effective over the full buffet domain which means angles of attack ranging from 14 to 23 degrees and free stream velocity ranging from –25% to +25% of the full-scale equivalent of Mach 0.6 at 20,000 ft.

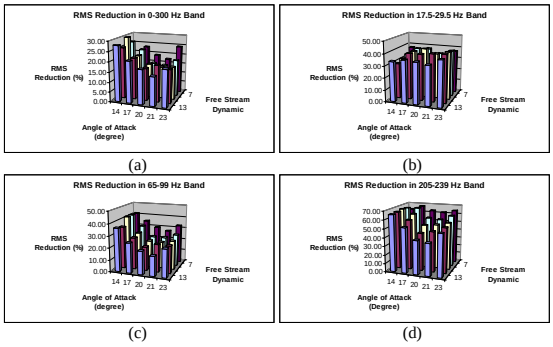


Figure 6. Percent RMS reduction in (a) the control bandwidth, (b) about the first bending mode, (c) about the first torsion mode, (d) about the second bending mode.

Conclusion

The objective of this paper was to present a robust control system for buffet alleviation by the use of Offset Piezoceramic Stack Actuators (OPSA) in combination with acceleration feedback control. The choice of actuator and controller was justified. Methods for the design and the placement of the OPSAs for tail buffet alleviation were elaborated. A method to design and study the robustness of the acceleration feedback controller for tail buffet alleviation was presented. Finally, experimental validations of the effectiveness and the robustness of the controller were presented on a full-scale vertical tail sub-assembly and on a 1/16th-scale wind tunnel model.

References

[1] Hebbar, S.K., Platzer, M.F., and Frink, W.D., "*Effect of Leading-Edge Extension Fences on the Vortex Wake of an F/A-18 Model*", J. of Aircraft, v. 32, n. 3, 1995, pp 680-682.

[2] Klein, M.A., and Komerath, N.M., "*Reduction of Narrow-Band Velocity Fluctuation Over an Aircraft Model*", 15th Applied Aerodynamic Conf., 1997, AIAA 97-2266.

[3] Bean, D.E., and Wood, N.J., "*Experimental investigation of twin-fin buffeting and suppression*", J. of Aircraft, v. 33, n. 4, 1996, pp. 761-767.

[4] Gee, K., Rizk, Y.M., and Schiff, L.B., "*Forebody Tangential Slot Blowing on an Aircraft Geometry*", Journal of Aircraft, Vol. 31, No. 4, 1994, pp. 922-928.

[5] Kandil, O A; Yang, Z; Sheta, E F, "*Flow control and modification for alleviating twin-tail buffet*", AIAA, Aerospace Sciences Meeting, 1998, AIAA-99-0138.

[6] Ferman, M.A., Liguore, S.L., Smith, C.M., and Colvin, B.J., "*Composite Exoskin Doubler Extends F-15 Vertical Tail Fatigue Life*", 34th Structures, Structural Dynamics, and Materials Conf., v. 1, 1993, pp. 398-407.

[7] Ashley, H., Rock, S.M., Digumarthi, R., Channey, K. and Eggers, A.J., "Active Control for Fin Buffet Alleviation", WL-TR-93-3099, 1994.

[8] Lazarus, K.B., Saarmaa, E., and Agnes, G.S., "Active smart material system for buffet load alleviation", Proc. SPIE, v. 2447, 1995, pp. 179-192.

[9] Moore, J.W., Spangler, R.L., Lazarus, K.B. and Henderson, D.A., "Buffet load alleviation using distributed piezoelectric actuators", Industrial and Commercial Applications of Smart Structures Technologies, ASME, AD v. 52, 1996, pp. 485-490.

[10] Hauch, R.M., Jacobs, J.H., Ravindra, K., and Dima, C., "Reduction of vertical tail buffet response using active control", J. of Aircraft, v. 33, n. 3, 1996, pp. 617-622.

[11] Nitzsche, F. ,Zimcik, D.G., and Langille, K., "Active control of vertical fin buffeting with aerodynamic control surface and strain actuation", 38th Structures, Structural Dynamics, and Materials Conf., v. 2, 1997, pp. 1467-1477.

[12] Moses, R.W., "Vertical-tail-buffeting alleviation using piezoelectric actuators: some results of the actively controlled response of buffet-affected tails (ACROBAT) program", Proc. SPIE, v. 3044, 1997, pp. 87-98.

[13] Hopkins, M; Henderson, D; Moses, R; Ryall, T; Zimcik, D; Spangler, R, "*Active vibration suppression systems applied to twin tail buffeting*", Smart structures and materials: Industrial and commercial applications of smart structures technologies, SPIE v. 3326, 1998, p. 27-33.

[14] Spangler, R.L., and Jacques, R.N., "*Testing of an active smart material system for buffet load alleviation*", 40th AIAA/ASME/ASCE/AHS/ASC Structures, Structural Dynamics, and Materials Conference, 1999, AIAA-99-1317.

[15] Nitzsche, F; Zimcik, DG; Ryall, TG; Moses, RW; Henderson, DA, "*Control law synthesis for vertical fin buffeting alleviation using strain actuation*", 40th AIAA/ASME/ASCE/AHS/ASC Structures, Structural Dynamics, and Materials Conference, 1999, AIAA-99-1317.

[16] Moses, R.W., "*Contributions to active buffeting alleviation programs by the NASA Langley Research Center*", 40th AIAA/ASME/ASCE/AHS/ASC Structures, Structural Dynamics, and Materials Conference, 1999, AIAA-99-1318.

[17] Pado, L. E., and Lichtenwalner, P. F., "*Neural predictive control for active buffet alleviation*", 40th

AIAA/ASME/ASCE/AHS/ASC Structures, Structural Dynamics, and Materials Conference, v. 2, 1999, pp. 1043-1053, (AIAA-99-1319).

[18] Hanagud, S; Bayon de Noyer, M; Luo, H; Henderson, D; Nagaraja, K.S., "*Tail buffet alleviation of high performance twin tail aircraft using piezo-stack actuators*", 40th AIAA/ASME/ASCE/AHS/ASC Structures, Structural Dynamics, and Materials Conference, v. 2, 1999, pp. 1054-1064, (AIAA-99-1320).

[19] Preumont, A., Dufour, J.P., and Malekian, C., "*Active Damping by a Local Force Feedback with Piezoelectric Actuators*", J. of Guidance, Control and Dynamics, Vol. 15, No. 2, 1992, pp. 390-395.

[20] Young, J.W., and Hansen, C.H., "*Control of Flexural Vibration in Stiffened Structures using Multiple Piezoceramic Actuators*", Applied Acoustic, Vol. 49, No. 1, 1996, pp. 17-48.

[21] Redmond, J., and Barney, P., "*Vibration Control of Stiff Beams and Plates Using Structurally Integrated PZT Stack Actuators*", J. of Intelligent Material Systems and Structures, Vol. 8, 1997, pp. 525-535.

[22] Mattice, M., La Vigna, C., "*Innovative Active Control of Gun Barrels Using Smart Materials*", Proc. SPIE, V 3039, 1997, pp. 630-641.

[23] Goh, C. J. and Caughey, T. K., "*On the stability problem caused by finite actuator dynamics in the collocated control of large space structures*", International Journal of Control, Vol. 41, No. 3,1985, pp. 787-802.

[24] Juang, J. N. and Phan, M., "*Robust Controller Designs for Second-Order Dynamic Systems: A Virtual Passive Approach*", Journal of Guidance, Control and Dynamics, Vol. 15, No. 5, 1992, pp. 1192-1198.

[25] Sim, E. and Lee, S. W., "*Active Vibration Control of Flexible Structures with Acceleration Feedback*", Journal of Guidance, Vol. 16, No. 2, 1993, pp. 413-415.

[26] Goh, C. J. and Yan, W. Y., "*Approximate Pole Placement for Acceleration Feedback Control of Flexible Structures*", Journal of Guidance, Vol. 19, No. 1, 1996, pp. 256-259.

[27] Bayon de Noyer, M., and Hanagud, S, "*Single Actuator and Multi-Mode Acceleration Feedback Control*", J. of Intelligent Material Systems and Structures, v 9, n 7, 1999, pp. 522-545.

[28] Bayon de Noyer, M., and Hanagud, S., "*Comparison of H_2 optimized design and cross-over point design for acceleration feedback control*". Collect Tech Pap, Struct. Struct. Dyn. Mater. Conf., v 4, 1998, pp. 3250-3258, AIAA-98-2091.

[29] Triplett, W.E., "*Pressure Measurements on Twin Vertical Tails in Buffeting Flow*", Journal of Aircraft, V. 20, N. 11, 1983, pp. 920-925.

[30] Komerath, N.M., Schwartz, R.J. and , Kim, J.M. "*Flow over a Twin-Tailed Aircraft at Angle of Attack, Part II: Temporal Characteristics*", Journal of Aircraft, V. 29, N. 4, 1992, pp. 553-558.

This page has been deliberately left blank

Page intentionnellement blanche

Investigation on a Semi-Active Hydro Mount Using Mr Fluid[#]

R. Ay [1], M. F. Golnaraghi [2], A. Khajepour [3]
1. Exchange Student, Fachbereich Maschinenbau, TU Braunschweig,
Schleinitzstr. 8, 38106 Braunschweig, Germany
2.Corresponding Author, Professor, Department of Mechanical Engineering, University of Waterloo, Canada
3.Assistant Professor, Department of Mechanical Engineering, University of Waterloo, Canada

Abstract
Hydraulic engine mounts (hydro mounts) are passive devices used to isolate automobile engine vibration from the chassis at different automobile operating conditions. In this paper we introduce a semi-active hydro mount, using Magneto Rheologic (MR) fluids. A semi-active hydro mount can be used to optimize the mount performance for a wider range of vehicle operating conditions. The MR fluid mount developed and mathematically modeled in this work can change its yield shear stress once under a magnetic field, and hence, it may be tuned by applying electromagnetic field. The tuning ability allows us to vary the natural frequency of the mount and to increase the damping of the mount. To verify the numerical results an experimental test bed has been developed. Preliminary results show that the experimental and numerical results correlate well.

Keywords: Hydraulic engine mounts; Semi-active hydro mounts, Magneto Rhelogic (MR) fluid

1. Introduction

With the clear thrust of the US Partnership for the New Generation Vehicle (PNGV) effort being mass reduction, the resulting vehicles will suffer from increased vibration levels due to higher engine to frame weight ratios, increased engine force density, and the use of lighter and more flexible vehicle frames. These increased vibration levels will reduce driver comfort and component longevity; the PNGV Sweet 16 does not address this aspect. The engine to frame weight ratio and the engine force densities is increasing in the quest to come-up with lighter and efficient automobiles. Furthermore, lighter and more flexible vehicle frames have led to the increased frame vibration levels. Consequently, recent research and development efforts have been focused on further improvement of engine mounting technology to achieve better vibration isolation, smooth vehicle ride and noise reduction.

Passive hydro-mechanical mounts have been designed to meet the requirements of such a system. A typical hydro mount is designed to have high stiffness and damped response for low frequency large amplitude vibrations (in most cars this is greater than 0.3 mm at 1-50 Hz). Conversely at high frequency small amplitude vibrations, a hydro mount is designed for low stiffness and damping characteristics (amplitudes less than 0.3 mm at 50-300 Hz).

These mounts allow passive adjustment by a variety of hydraulic design options (decoupler, inertia track, rubber shape and stiffness) based on the application and its optimal dynamic properties, engine performance requirements or operating conditions. All these design options allow tailoring the mount characteristics for the specific automotive application. The basic idea of the hydro mount is to add damping only at the resonant frequency and leave the damping almost unchanged at other frequencies [1-3].

Since a hydro mount can only be tuned for a specific frequency for an optimal performance, it is still a compromise. To further improve the performance of an engine mount to meet the requirements and overcome the limitations, an actively controlled system is required.

The need of an active system has long been recognized and different approaches have been taken to accomplish this [4,5,8]. Similar to the application of Electro-rheological (ER) fluids one can use magneto rheological (MR) fluids to achieve a controllable hydro mount.

In this work we have proposed a semi-active mount system based on MR fluids: non-colloidal suspensions of micron-sized, magnetisable particles in a fluid medium. These fluids have the ability to change from a free-flowing liquid to a semisolid in milliseconds when exposed to a magnetic field, and instantly back to a liquid when the field is removed. They provide simple, quiet, rapid-response, miniaturized, and continuously variable interfaces for electro-mechanical systems. By controlling the applied magnetic field, the fluid's yield stress can be precisely determined, enabling the design of active isolators with minimum weight and maximum control force to eliminate road- and engine-induced vibration.

The objective of this paper is to provide the basic ideas behind an active hydro mount using MR fluid and to design a tunable mount using experimental analysis. The experimental data are used to evaluate the effectiveness of MR fluids on semi-active mounts. This work is intended to provide a basis for future work

[#] Presented and appeared in the Proceedings of NATO, Symposium on Active Control Technology for Enhanced Performance Operational Capabilities of Military Aircraft, Land Vehicles and Sea Vehicles, Braunschweig, germany, 8-11 May, 2000.

in semi-active mounts using MR fluids. The experimental data can also be used to arrive at an empirical mathematical model.

2. Theoretical considerations

2.1 Hydro mounts

The ideas of conventional rubber mounts [1] are used in hydro mounts. As in the rubber mounts, the liquid filled mount or hydro mount, offers the possibility of vibration isolation in three orthogonal directions. However, in the primary direction (up down) the mount is very non-linear with frequency due to the fluid resistance and the decoupler action (Figure 1). The non-linearity arrives from the fact that the communicating orifice, connecting two liquid filled chambers, acts as a hydraulic damper, which influences the system due to its resistance to the motion of the fluid. In addition, the decoupler plate has very complicated characteristics, including impact of decoupler plate with the surrounding cage, possibility of turbulent flow, and flow leakage once the decoupler plate has bottomed out [3].

The cross section of a passive, liquid filled hydro mount with inertia track, decoupler, and bell in the upper chamber is shown in Figure 1. The primary rubber element has two functions. It has to carry the static and dynamic load on the mount and it has to act as a piston to pump the liquid through the orifice into the bottom chamber. The ability of the secondary rubber element to bulge will compensate the fluid increase in the lower chamber. Since the secondary rubber compliance acts as an accumulator for liquid passing back and forth through the orifice, it can take the form of a highly flexible diaphragm. When pumping the liquid through the orifice, the primary rubber element will also bulge slightly such that not all the liquid displaced by the piston action is forced through the orifice. The bulging effect of the top and bottom rubber elements is expressed as the change in the chamber volume, ΔV, over the pressure change, Δp, also referred to as the compliance of the top and bottom chambers. The unit of the compliance is [mm^3/Pa]=[mm^5/N].

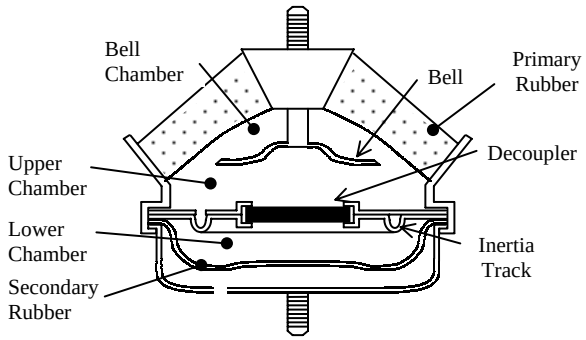


Figure 1. A Model of a Hydro mount

Different approaches have been taken to model a hydro mount [1-3]. Reference [2] describes a linear dynamic model with lumped mechanical and fluid elements. Another study with a non-linear model is by Golnaraghi and Nakhaie [3]. Such models are put up to achieve a dynamic stiffness spectra prediction. The desired characteristic of the hydro mount is the so-called cross point dynamic stiffness, defined as:

$$K^* = \frac{F_T}{x} \tag{1}$$

where F_T is the transmitted force to the base (chassis) and x is the excitation amplitude (engine). A typical frequency response curve and also the phase shift curve of a hydro mount with and without implementing a bell are shown in Figure 2 [9].

There are a few design options, which allow for passive tailoring of the mount characteristics for each specific application. These options include variation in the geometry and physical properties of the inertia track, the decoupler, and the mount rubber housing. A detailed description of the above-mentioned options is included in [9].

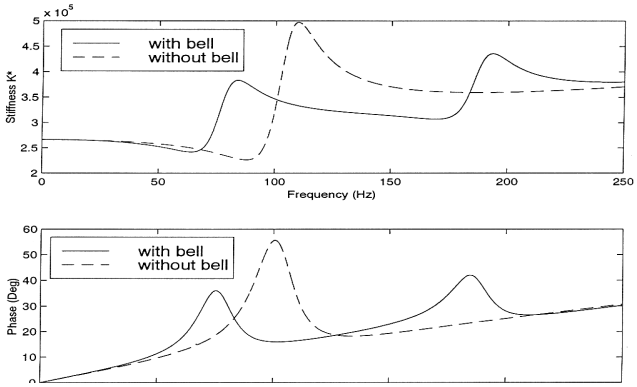


Figure 2. Dynamic Stiffness Curves

In this paper we introduce an idea to be able to actively shift the resonance peaks of the dynamic stiffness curve by external tuning of the mount. In addition to the basic components of a hydro mount MR fluid will be introduced to the system as the active component.

2.2 MR fluids

Magneto rheological fluids have been initially discovered by Jacop Rabinow in the 1940's. MR fluids belong to the controllable fluids and are the true magnetic analogues of electro rheological (ER) fluids. They are of interest because of their ability to provide simple, quiet, rapid-response (below 30 msec), miniaturised, and continuously variable interfaces between electronic controls and

mechanical systems. MR fluids are composed of non-colloidal suspensions of micron-sized, magnetisable iron or steel particles in a fluid medium. Water, oil, or silicon based MR fluids are available depending upon the application. In a MR fluid mount, the control action is due to the change in rheological behaviour to an applied external magnetic field. The key to these fluids is their ability to change from a free-flowing liquid to a semisolid in milliseconds when exposed to a magnetic field, and instantly back to a liquid when the field is removed. By applying an external magnetic field the fluid develops a precisely controllable yield stress. A yield stress versus magnetic induction curve for a commercial used fluid (MRF-240BS) is shown in Figure 3.

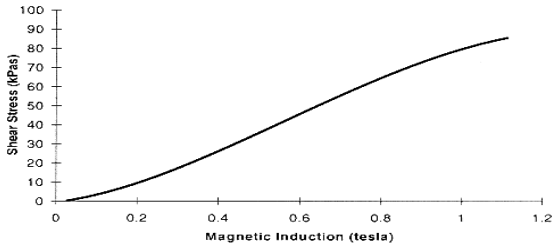


Figure 3. Magnetic Induction Curve (MRF-240BS) [7]

The formation of particle chains (microstructure) when applying a magnetic field restricts the movement of the fluid and thereby increases the viscosity of the suspension. The behaviour of such a controllable fluid is often represented as a Bingham plastic having variable yield strength [6].

MR fluids routinely exhibit dynamic yield strengths of 50–100 kPa for applied magnetic fields of 150 – 250 kA / m (for magnetic induction of 1.3–2.0 Tesla, for commercial used MR fluids). The strength of the fluid is limited by magnetic saturation (see Figure 3). The fluids can be used in a broad temperature range from about -40°C to 150°C and the yield strength varies only slightly over this range. MR fluid exhibits low thermal conductivity (between 0.20–3.80 W / m /°C) and have low coefficients of thermal expansion (between 0.2×10^{-3} and 0.7×10^{-3} in the temperature range from 0 to 150 °C). Temperature range, thermal conductivity, and thermal expansion generally depend upon the carrier fluid [7]. MR fluids have a high resistance to settling. At common flow conditions no separation between the particles and carrier fluid is observed.

Concentration and density of particles, particle size and shape distribution, properties of the carrier fluid, additional additives, applied field, and temperature are what the rheological properties of controllable fluids depend on. The interdependency of these factors is very complex and has not yet been completely discovered. Therefore, it is important to optimise the performance of the MR fluids for particular applications.

One of the three basic modes of operation is the fixed pole or pressure driven flow mode. The fixed pole mode is also referred to as the valve mode. Figure 4 illustrates how the valves can be accomplished with no moving parts.

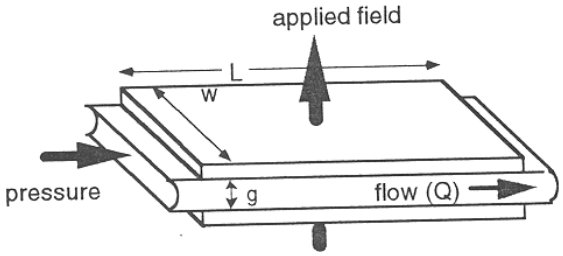


Figure 4. Fixed Pole Operating Mode [6]

The pressure drop developed across the device shown in Figure 4 is divided into a:

Viscous component: $$\Delta P_\eta = \frac{12\ \eta\ Q\ L}{g^3\ w} \qquad (2)$$

Field dependent component: $$\Delta P_\tau = \frac{c\ \tau_y L}{g} \qquad (3)$$

where η is the plastic viscosity, Q the volumetric flow rate, L the length, g the gab, w the width, τ_y the yield stress developed in response to an applied external magnetic field H, and c is a parameter which ranges from a minimum value of 2 (for $\Delta P_\tau / \Delta P_\eta$ less than 1) to a maximum value of 3 (for $\Delta P_\tau / \Delta P_\eta$ greater than 100) [6].

The total pressure drop in the device is approximately equal to the sum of ΔP_τ and ΔP_η. When algebraically manipulate Eq. (2) and Eq. (3) a different derived design equation can be provided

$$V = \frac{12}{c^2}\left(\frac{\eta}{\tau_y^2}\right)\left(\frac{\Delta P_\tau}{\Delta P_\eta}\right) Q \Delta P_\tau \qquad (4)$$

where η/τ_y^2 are fluid material properties, $\Delta P_\tau / \Delta P_\eta$ is the control ratio (or dynamic range), and $Q\Delta P_\tau$ is the mechanical power level, V is the minimum active fluid volume (V = Lwg). The minimum active fluid volume V is the volume which is necessary in order to achieve the desired control ratio at a given flow rate with a specified controlled pressure drop ΔP_τ.

The dynamic range $\lambda = \Delta P_\tau / \Delta P_\eta$ involves the viscous properties of the MR fluid (i.e., η and τ_y). In reality, the dynamic range of a device may also be significantly a function of other device properties such as seal and bearing friction.

3. Performance criteria

The fluid resistance due to the orifice and valve element influences the overall damping of the system (magnitude of the peak in the dynamic stiffness curve). Eq. (3) states that a change in pressure drop results in a change in shear stress of the fluid. The pressure drop across the valve is related to the fluid resistance (pressure drop-flow relation) as:

$$\left(P_1 - P_2\right)_{total} = R_f Q \tag{5}$$

where Q is the volumetric flow and R_f is the fluid flow resistance which is influenced by changing the shear stress. The emphasis of the experiments is to find whether the variable shear stress of the fluid within the valve element is also able to shift the resonance peaks.

As discussed earlier, the MR fluid behaves like a Bingham fluid, in which, before reaching the yield shear stress, the core flows like a solid (similar to toothpaste flow). The size of the solid core is increased or decreased according to the magnitude of shear stress. An increase in the size of solid core will increase the cross sectional area of the flowing fluid and also the mass of moving fluid. Since the area is proportional to the mass, the inertia of the fluid within the valve element will decrease as according to

$$I = \frac{\rho \cdot l}{A} = \frac{m}{A^2} \tag{6}$$

where ρ is the density of the fluid, *l* is the length of the valve, A is the cross-sectional area, and m is the mass of fluid in the valve. The controllable shear stress could be thought of as a controllable orifice size. Changing the orifice size will result in changing the system inertia, Eq. (6), or system natural frequency. Shifting the natural frequency was observed before in [3] using same concept.

When applying a magnetic field to the fluid in the valve element, the pressure in the upper chamber has to exceed a threshold pressure set by the yield shear stress of the fluid in order to allow for the fluid to pass through the mount valve into the lower chamber. This threshold pressure is set by the strength of the magnetic field. Unless the threshold pressure is reached, the valve would block the flow. In this case, the overall stiffness of the system would mainly be determined by the upper chamber compliance, the lower chamber compliance would not have any effect. Notice that in this case the mount will act similar to a regular rubber mount.

4. Designing the mount model

In this section the design of a proposed model of a semi-active hydro mount using MR fluid is discussed. For the mount model it is desirable to have the possibility to easily change the overall stiffness. The general approach is to design a model that has the flexibility to be used in different tests for various modifications of the hydro mount. These modifications are different number of chambers, different compliances, and different orifices. This flexibility is achieved through a modular design. The fundamental concepts of a lumped parameter fluid system model are used as a base for the design process. Since the emphasis of research is the dynamic effects of an active valve, the well-known linear Voigt model representing the primary rubber element (stiffness and damping) is not included in the design. This could later be implemented in a mathematical model to see the actual performance of the semi-active hydro mount. The model consists of an actuator, two chambers connected through a valve element, two devices representing the primary and secondary rubber element compliance, a magnetic circuit to activate the valve, and the incompressible MR fluid.

To model the pumping action of the primary rubber element a hydraulic cylinder is used as an ordinary piston pump. The piston pump accomplishes two main functions. Besides the pumping action, it also represents the upper chamber volume. The bore size of the cylinder is selected to be 3.81cm (1.5 inches).

The importance of the compliance elements arises from the fact that the overall stiffness of the system mainly depends upon them. To model the compliance, two basic ideas are investigated, the use of spring-loaded piston pumps or the use of accumulators. The advantage of using spring-loaded piston pumps is the flexibility of achieving different compliance values by using different springs or pistons. The compliance can be evaluated as

$$C = \frac{A^2}{k} \tag{7}$$

where A is the cross sectional area of the piston and k is the stiffness of the spring. Another advantage of this configuration is having a constant stiffness over the full operation of the piston. The disadvantages of this configuration are the seals of the piston and the piston rod. The seals experience Coulomb friction and would therefore negatively effect the dynamics of the overall system.

To avoid the negative effects, commercially available diaphragm accumulators have been selected for the actual model of the semi-active hydro mount. The accumulators work in the following manner. They have a reservoir, which is filled with a compressible gas such as nitrogen or air. If the pressure in the system outside the reservoir exceeds the pressure of the gas, the gas will be compressed; the pressure change will be compensated to a certain degree. The enclosed gas in the reservoir has a stiffness value depending on the volume and the pressure. Since the stiffness can be converted into a compliance value, an accumulator can be used to model a compliance element. To

determine the compliance of the accumulators, the simplified model shown in Figure 5 is used.

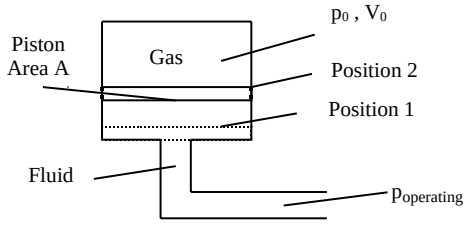


Figure 5. Simplified Model of an Accumulator

Position 1 is referred to as the pre-charged position and Position 2 represents the operating point. A few assumptions are made before stating the relationship for the compliance. The change of states of the ideal gas is assumed to be isothermal and the pressure in the accumulator and the one in the system is assumed to be in equilibrium.

The isothermal change of the states can be represented as follows:

$$p_1 \cdot V_1 = p_2 \cdot V_2 = \text{const.} \tag{8}$$

Therefore,

$$p \cdot V = (p + \Delta p) \cdot (V - \Delta V) \tag{9}$$

$$p \cdot V = p \cdot V + \Delta p \cdot V - p \cdot \Delta V - \Delta p \cdot \Delta V \tag{10}$$

The term $\Delta p \Delta V$ was neglected since only small changes are considered. Eq. (10) is arranged to

$$p \cdot \Delta V = \Delta p \cdot V \tag{11}$$

Knowing that

$$\Delta V = A \cdot \Delta x \tag{12}$$

where Δx is the displacement of the diaphragm and A is the cross sectional area which remains the same. For the steady state the stiffness of the gas can be represented as spring stiffness. The spring tension can be stated as:

$$\Delta F = k \cdot \Delta x \tag{13}$$

where the spring tension is in equilibrium with the force due to the pressure

$$\Delta F = \Delta p \cdot A \tag{14}$$

Substituting Eq. (12)-(14) into Eq. (11) gives a statement for the stiffness of the accumulator.

$$k = \frac{A^2 \cdot p}{V} \tag{15}$$

where p is the pre-charged pressure of the accumulator and V is the nominal volume of the gas in the reservoir.Using Eq. (7) gives an expression for the compliance:

$$C = \frac{V_0}{p_0} \tag{16}$$

where V_0 and p_0 are the volume and the pressure of the accumulator at the operating point, respectively. The stiffness of the gas is not constant, and therefore, a non-linear relationship between compliance and pressure is expected. When exciting the system at different operating pressures, different compliance values will be seen. Nevertheless, the compliance values of the accumulators are assumed to be constant once the pressure of the system is brought to the operating point. Only small pressure changes are expected when exciting the system.

Two different accumulators are used in this work. One has a 75ml reservoir handling operating pressures up to 250 bar and the other one has a 160ml reservoir handling the same pressure.

The size of the valve element determines the active fluid volume specified in (4). The volumetric flow rate and therefore, the required controllable mechanical power level are not known, and have to be found experimentally. Therefore, the equation for the minimum active fluid volume cannot be used for designing purposes in this particular case. The valve is designed to add as less inertia to the system as possible. Therefore the valve has a large cross sectional area and a short length (6). The Ampere-turns, generating the magnetic field, strongly depends upon the size of the valve, since the valve with the fluid inside will be part of the magnetic circuit. The valve has to be shaped in such a way that the magnetic core of the magnetic circuit can easily be interfaced. Quadratic shaped pole pieces are chosen with which a quadratic cross-section of 17 x 5 mm of the valve element is formed. Material considerations are very important since the flow channel is directly part of the magnetic circuit. If high permeable carbon sheet steel is used, the magnetic flux lines will go directly through the material without affecting the fluid (Figure 6b). For this reason very low permeable stainless steel sheet is used. In the magnetic circuit the core material, the stainless steel sheet of the valve element, and the fluid are in series as shown in Figure 6a.

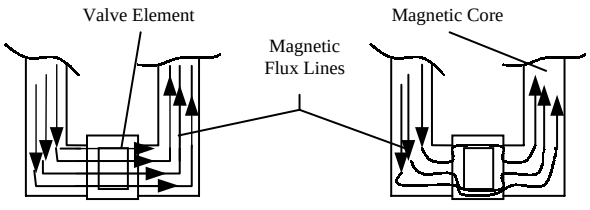


Figure 6. The Magnetic Circuit Including the Valve Element

In the last mentioned configuration, using stainless steel, which has a low permeability value of 1.3, the thickness of the sheet will almost act as an air gap and therefore high Ampere-turns are needed in order to achieve the required magnetic field within the fluid.

A more effective design was considered in this work. Figure 7 shows the cross section of the valve. As shown, carbon sheet metal was used at the long sides, which will be in direct contact with the magnetic core material, and stainless steel sheet metal was used on the short sides. Therefore, there will be no air gap effect and also no magnetic flux short. The magnetic flux can now be assumed to go straight through the fluid, of course with some leakage on the edges. Both sheet materials are 1.2 mm thick and were welded along their edges to form the quadratic shaped cross section. The length of the valve part was chosen to be 10 mm.

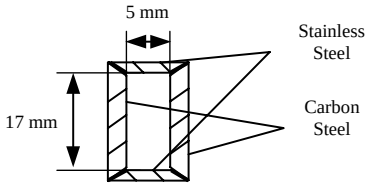


Figure 7. Valve Element-Cross-Section

Two main considerations can be pointed out when choosing the MR fluid. Firstly, the fluid had to be chemically compatible with all the other parts of the system, including seal materials as well as the diaphragm material of the accumulators. Secondly, the right carrier fluid had to be chosen accounting for lubrication aspects. The MRF-132LD fluid with a density of 3040 kg/m^3 was chosen because of its good dynamic viscosity and density values. The fluid can build up yield shear stresses up to 54 kPa at magnetic flux densities of 1.2 Tesla.

The magnetic circuit represents the variable interface between electronic control and mechanical system and provides the required magnetic field to the fluid needed to change its state. The field must be applied perpendicular to the direction of fluid flow. The parts of the magnetic circuit are: the iron core, the coil, which supplies the magnetomotiv force, the valve element, and the MR fluid. The magnetic circuit was capable to achieve the required magnetic field strength around the fluid. The circuit was designed in such way that the required field strength was reached at 2.6 A and 14.6 V. A variable power supply was used to tune the valve as needed.

A schematic of the overall model can be seen in Figure 8. A not so large reservoir was considered as the lower chamber of the system. The connector between valve, accumulator, and the pressure transducer was representing it. The system holds approximately 80 ml of the MR fluid. Since no feedback systems implemented into the system yet, the first model of the hydro mount using MR fluid is really considered to be an external tunable mount. A semi-active control unit is later on implemented, to actively tune the mount in response to the vibrations it is exposed to.

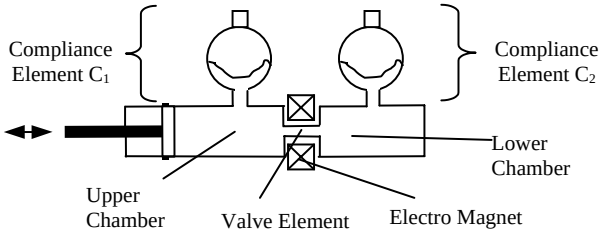


Figure 8. Overall Model of the Mount

5. Description of Experiments

A hydraulic operating dynamic testing machine was used in the experiments. Due to the frequency limitations of the test machine, the excitation amplitude dropped rapidly at higher frequencies. Hence, we could not test the mount performance in a more realistic frequency range of 200 to 250 Hz. However, the tests within the frequency range of 0 to 20 Hz, show great merit. Excitation amplitudes up to ±0.44 mm were achievable for the frequencies up to 20 Hz.

To monitor and select the pressures during the experiments, two pressure transducers were used. The pressure was measured in each chamber, on both sides of the valve element, in addition to the displacement of the actuator. The signal from the displacement sensor and the signal from the two pressure transducers were fed into a data conditioner card. The signal was low pass filtered at 70 Hz and then amplified in order to get an appropriate resolution when reading the data into the data acquisition card. The amplified and filtered data were fed into a 486 PC processing.

Tests were conducted initially to verify the mount model, and to confirm if it were designed properly to perform as intended, like a hydro mount. In addition experimental data were collected to achieve insight into the feasibility of this system for use as a semi-active mount in the future. Hence, the first experiments were made to form the basis of future experiments.

In the initial studies, different pre-charge pressures for the accumulators were tried out as well as different operating pressure points, which are directly dependent upon the zero point of the excitation piston. It could be seen that when pre-charging the accumulators to very low levels, it was hard to distinguish the peak to peak values of the pressures, since the accumulators were more capable to compensate for the pumped fluid. According to the tests made, it is recommended to keep the pre-charge pressure

in either of the accumulators above 0.8 bar (11.5 psi). The main experiments can be subdivided into three parts.

5.1 Fluid performance

Several tests were conducted to check the performance of the MR fluid. The accumulators were pre-charged to no particular values (P_{01}=19psi, P_{02}=45psi), and the system was excited with a harmonic input with a frequency of 10 Hz and displacement amplitude of 1.7 mm (peak to peak). The system was working around an operating pressure of approximately 48 psi. The current going through the coil, producing the magneto-motive force was stepped through 0 to 2.61 *A*, and different shear stresses of the fluid were observed. A typical data set printout is shown in Figure 9. In this case, the pressure P2 (lower chamber pressure) response has reached steady state above a current of around 1 A. It could be further recognized that the peak to peak value of the pressure P1 (upper chamber pressure) also did not change anymore in the same region of current.

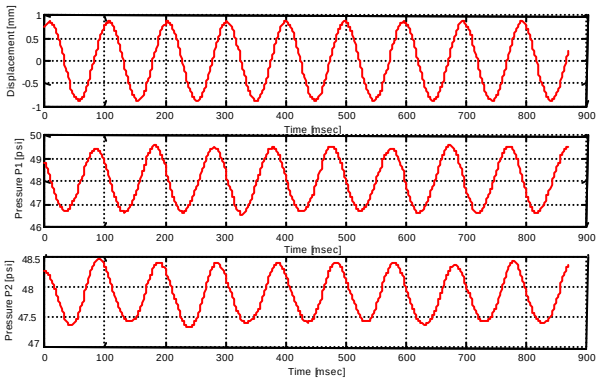


Figure 9. Typical Time Response Curves (0 A, C1=19psi, C2=45psi)

5.2 Frequency sweep

In this part of the tests, the excitation frequency was varied trough 0 to 20 Hz in 11 equally distributed steps. These tests were performed to see how the system behaves at a frequency sweep. There was no magnetic field applied to the valve part. The accumulators were set to 20 psi and 45 psi for P_{01} and P_{02}, respectively. The system was then brought to an operating pressure of approximately 48 psi. The excitation amplitude was kept the same throughout the frequency sweep. The value was the pre-determined maximum amplitude for 20 Hz, 0.88 mm. The test was then repeated. But before the next tests were performed, a rough magnitude calculation was done to predict the natural frequency of the system. The natural frequency was estimated as [1]

$$\omega_N = 2 \cdot \pi \cdot f_N = \sqrt{\frac{1}{I_i} \cdot \left(\frac{1}{C_1} + \frac{1}{C_2} \right)} \qquad (17)$$

where I_i is the inertia of the valve element and C_1 and C_2 are the compliance values. The pre-charged pressure of the accumulators (P_{01} and P_{02}) as well as the net volume of them, 75 ml and 160 ml, were used to determine the volume of the air within the accumulators (V_{OP1} and V_{OP2}) at the operating pressure point (8). The found volume and the operating pressure (P_{OP}) were plugged into (16) to achieve the compliance of the accumulators at operating pressure. The inertia of the valve is determined with (6). The compliance values and the inertia of the valve element could then be used to estimate the natural frequency of the system (17). Several iterations have been performed to get the natural frequency of the system within the 20 Hz. Another three tests have been performed. The values can be seen in Table 1.

Table 1. Values to Determine Resonance Frequency

P_{01} [psi]	20	37	20	12
P_{02} [psi]	45	35	19	9
P_{OP} [psi]	48	41	24	13
V_{OP1} [m^3]		6.768×10^{-5}	6.25×10^{-5}	6.923×10^{-5}
V_{OP2} [m^3]		1.366×10^{-4}	1.267×10^{-4}	1.108×10^{-4}
C1 [m^5/N]		2.39×10^{-10}	3.77×10^{-10}	7.72×10^{-10}
C2 [m^5/N]		4.83×10^{-10}	7.65×10^{-10}	1.23×10^{-9}
I_i [kg/m^4]	357647.06	357647.06	357647.06	357647.06
f_N [Hz]	29.8	21.04	16.74	12.21

5.3 Resonance frequency shift

The last part, which required the most number of tests, was intended to find out whether changing the magnetic field strength could shift the frequency response curves. In this part of the experiments, the accumulators were both pre-charged to 34 psi and the operating point was brought up to 41 psi. This almost matches the settings of a previous test, which was giving the most reasonable results. For various frequencies in between 0 and 20 Hz, data was collected for different applied magnetic fields. Therefore, the current was stepped through 0 to 0.5 A. The frequency was kept constant and the data was collected for each current step before switching to the next frequency. That could be done, since the MR fluid does not show considerable hysteresis loops. The values for the compliance of the upper and lower chamber were 2.264×10^{-10} m^5/N and 4.692×10^{-10} m^5/N, respectively.

6. Results and discussion

The following data was extracted from the time response curves to perform the evaluation of the results:

- the mean value of the piston road position
- the average of the maximum displacement of the piston road
- the frequency of the input signal
- the average of the peak to peak values of pressure P1
- the mean value for the pressure P1

- the average of the peak to peak values of pressure P2
- the mean value of pressure P2

In the presented graphs in this section, the peak to peak values of the pressures P1 and P2 have been used to plot over the frequency or the current. Usually the maximum pressures are used for evaluation purposes of hydro mounts. Since it could not be ensured that the piston road of the exciting machine moves exactly around the same point for each data collection, the peak to peak values have been used. The position of excitation varies only slightly. But already small variation in position would make it hard to evaluate the data. The input was a sinusoidal displacement, and therefore the peak to peak value of the pressure indicates the same behavior as the maximum values. Consider the excitation around a fixed point, when the maximum pressure increases, the peak to peak value increases as well, the increase would be twice as high as the increase of the maximum value.

6.1 Fluid performance

The results of two tests are shown in Figures 10a and b. The current was stepped through 0 to 1.2 A for the first one and through 0 to 0.5 A for the second one. All the other tests of this section indicated the same behavior and gave the same results. Delta P1 represents the pressure change in the upper chamber and delta P2 in the lower chamber. The pre-charge pressures and the operating pressure are sown in Table 1.

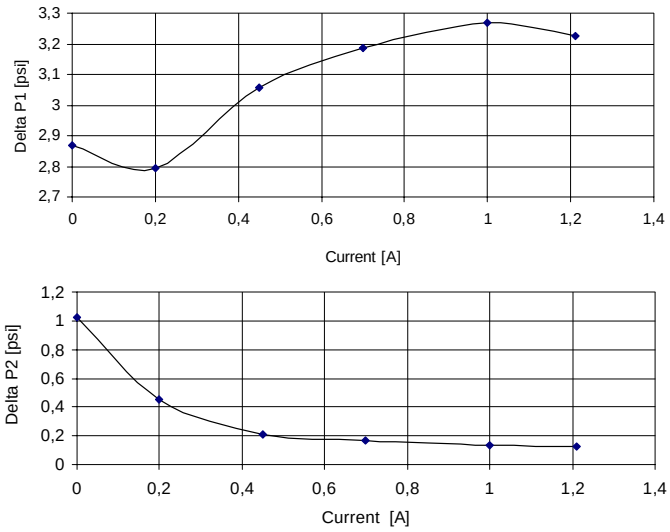


Figure 10a. Delta P vs. Current (0 – 1.2 A)

The exact frequency for these tests was found to be 10.42 Hz. Figure 10a clearly indicates that the pressure difference (delta P1) increases as the current increases. It can also be seen that the curve plateaus after a certain increase in current. The leveling was even better indicated for the test stepping up to 2.6 A with the current. That clearly indicates that the pressure built up in the upper chamber was not sufficient enough any more to work against the shear stress of the fluid and therefore can not pump the fluid through the orifice. As a reminder, the maximum achievable yield shear stress of the fluid

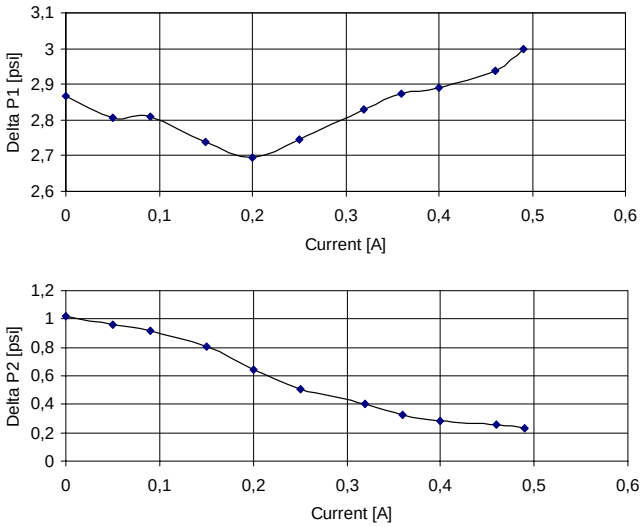


Figure 10b. Delta P vs. Current (0 – 0.5 A)

is theoretically reached around 2.6 *A*, but the leveling starts already way before that point. That confirms the just stated prediction. It can be assumed the valve is blocked. The applied current range of 0 to 0.5 A (Figure 10b) was not sufficient high enough to see the leveling. At both delta P1 curves a minimum could be observed around 0.2 A, which may not be explained yet at this stage.

The contrary change of delta P2 compared to the upper chamber can be recognized in both plots. That makes sense, since less fluid is pumped through the valve element, and therefore the pressure built up in the lower chamber will be less. The delta P2 curves seem to plateau before delta P1. This fact could not be explained yet, at this state of the experiments. Furthermore, the decrease in delta P2 was slightly higher than the increase of delta P1. This results in the different compliance values of the two chambers; the value of C2 was twenty times as large as the value of C1. Nothing could be seen in contrast to the minimum of the delta P1 curve around 0.2 Ampere.

To be complete, the pre-charge pressures of 19 psi, for the upper chamber representing compliance element, and 45 psi, for the lower chamber representing compliance element as well as the operating pressure of 48 psi results in compliance values of 8.97×10^{-11} m^5/N for the upper and 4.53×10^{-10} m^5/N for the lower compliance element.

6.2 Frequency sweep

In Figure 11 the results of the tests with the theoretical calculated resonance frequency at 21.04 Hz and 12.21 Hz are presented. The delta-P vs. Frequency curves indicate a non-linear relationship between those variables. It can be seen that the delta P1 values as well as the delta P2 values of both cases are heading towards a maximum point, which will occur at resonance frequency (natural frequency of the system). Even knowing that the theoretically determined resonance frequency of the second case (Figure 11b) suppose to be at 12.21 Hz, no peak in the curves could be observed for delta P1 neither for P2. However, it can be seen that the slope of the curves, for the second case, at higher frequencies decreased in comparison to the previous case (Figure 11a) and also that the maximum value of delta P1 and P2 at approximately 24 Hz increased slightly. This indicates that the maximum was shifted towards lower frequencies and therefore the natural frequency was shifted. It could also be observed for both delta P2 curves that there was a slight minimum between 5 and 10 Hz which then delays the increase of delta P2 in comparison to delta P1. This phenomena still needs to be explained.

Nevertheless, the typical behavior of a hydro mount with a simple orifice, since no magnetic field was applied, could beshown with this part of the tests. In the first set of experiments, it was not possible to get the natural frequency within the frequency range of 0 to 22 Hz. That indicates that the assumptions made to estimate the natural frequency of the system have to be thought over and than be implemented into an estimation formula for the natural frequency again. The assumptions include things such as neglecting the effects of the diaphragms of the accumulators.

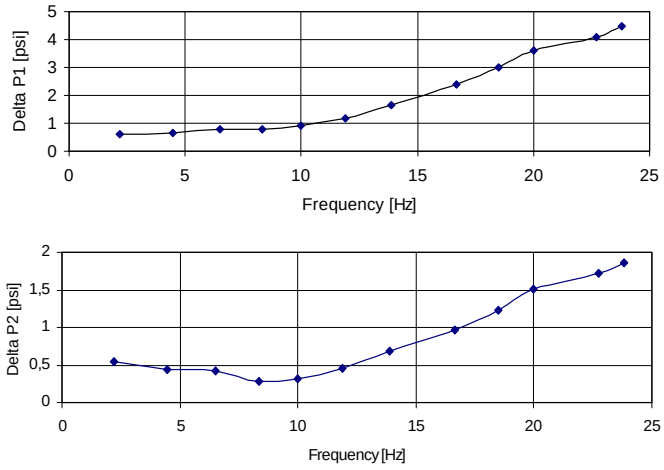


Figure 11a. Delta P vs. Frequency (P_{01}=37 psi, P_{02}=35 psi)

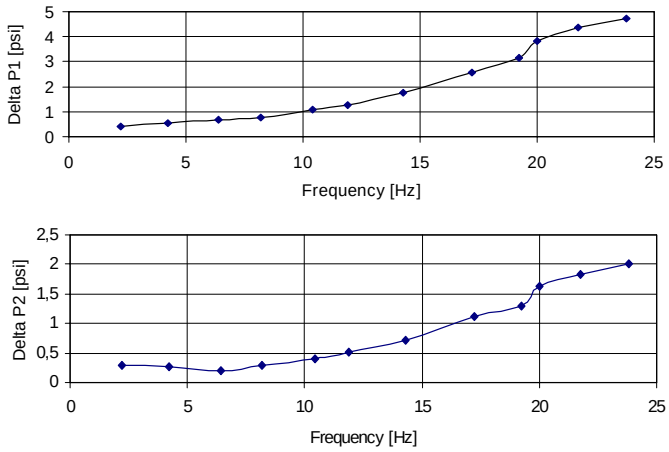


Figure 11b. Delta P vs. Frequency (P_{01}=12 psi, P_{02}=9 psi)

6.3 Resonance frequency shift

The peak to peak values of the pressure P1 and pressure P2 vs. Frequency curves are shown in Figure 12 for different currents producing the magnetic field. With this test the results of the previous tests could be confirmed, especially when looking at the curves for zero Ampere. The delta P2 increases with a slight delay and the minimum between 5 and 10 Hz could be seen again.

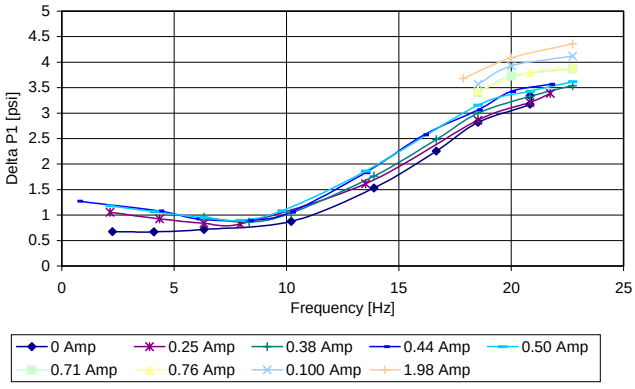


Figure 12a. Delta P1 vs. Frequency for different Currents

When looking at the delta P1 vs. frequency curve in Figure 12a, one basically recognizes that the curves are shifted towards higher values. Taking a closer look, one sees that the curves forming a minimum below 10 Hz. The minimum is getting more distinguishable as the current goes up. The minimum seems to be formed around 8 Hz. A shift of the curve, and hence, a shift of the resonance frequency, is hard to see since the resonance frequency was not reached within the 22 Hz. But one could assume a shift of the resonance peak, since the distance between the graphs change along the frequency, particularly for curves representing current

values of 0.71 A and higher. It was realized to late during the test, that the current could have been increase even further before seeing the blocking effect of the valve. Therefore only fractions of the curves from 0.71 to 1.98 A are shown.

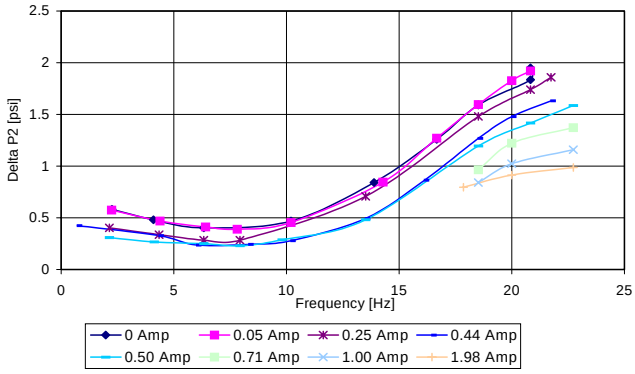


Figure 12b. Delta P2 vs. Frequency for different Currents

It can also be recognised that the delta P2 vs. Frequency curves are shifted to lower values when increasing the current. Taking a look at Figure 12b would lead to the conclusion that the minimum, recognised below 10 Hz, is straightened out when applying higher currents. That would be in contrary with the forming of a minimum for the delta P1 curves. Again it can be assumed that the resonance peak was shifted to a different frequency, since the distances between the curves changes with increase of the current, therefore the slope of the curves at a particular frequency is different.

7. Conclusion

A model of an external tunable hydro mount using the magneto rheological fluid MRF-132LD was designed, constructed, and tested. The important components of the system included a valve, magnetic circuit, and MR fluid, which represent the active components, and excitation piston and compliance elements. The results of the experimental investigations in general confirm the right choice of shapes and sizes. The typical behavior of a hydro mount was observed in preliminary tests.

Experiments have been performed within the limited frequency range of 0 to 22 Hz. Due to the test setup limitations, the accumulators were adjusted in such a way that the natural frequency of the system was brought close to the maximum achievable 22 Hz with the required displacement. The values of the pressures in both chambers predicted a heading towards a resonance peak with increasing frequencies. In further tests it was shown that the damping of the system could be adjusted by varying the applied magnetic field. This was indicated by an increasing or decreasing pressure in the upper chamber, caused by the changing of the yield sheer stress of the fluid within the valve part. The pressure data obtained from the tests suggested a shift of the pressure peak, in both chambers, when changing the applied magnetic field. This suggests the proposed system may be used as an active system.

In future studies, feedback will be added to study the performance of the system as an active mount.

Acknowledgements

The authors acknowledge and thank the Lord Corporation for providing a supply of MR Fluid and for its technical support. The authors would also like to thank the technical staff: Marius van Reenen, Ernst Huber , and Clarence Wallace for their assistance and advice in the manufacturing of the testing equipment. This project was supported in part by Natural Sciences and Engineering Council of Canada.

References

[1] R. Singh, G. Kim, P. V. Ravindra, “Linear Analysis of Automotive Hydro-Mechanical Mount with Emphasis on Decoupler Characteristics”, Department of Mechanical Engineering, The Ohio State University, Columbus, June 1991, Journal of Sound and Vibration (1992) 158(2), 219-243.

[2] W. C. Flower, “Understanding Hydro Mounts for Improved Vehicle Noise, Vibration and Ride Qualities”, Lord Corporation, Erie, PA, 1985.

[3] M. F. Golnaraghi and G.R. Nakhaie, "Development and Analysis of a Simplified Nonlinear Model of a Hydraulic Engine Mount", Presented in the 8th Conference on Nonlinear Vibrations, Stability and Dynamics of Structures, July 23-27, 2000 VPI/SU, Virginia. Also Submitted for publication in the Journal of Vibration and Control.

[4] T. G. Duclos, “An Externally Hydraulic Mount which uses Electro-Rheological Fluid”, SAE Paper #870963.

[5] A. Gennesseaux, “Research for New Vibration Isolation Techniques: From Hydro-Mounts to Active Mounts”, SAE Paper #931324, 1993.

[6] J. D. Carlson, D. M. Catanzarite, K. A. St. Clair, “Commercial Magneto-Rheological Fluid Devices”, Lord Corporation, July (1995), LL-8001.

[7] M. R. Jolly, J. W. Bender, J. D. Carlson, “Properties and Applications of Commercial Magnetorheological Fluids”, Lord Corporation, March (1998).

[8] P. L. Graf, F. Shourehi, “Modelling and Implementation of Semi-Active Hydraulic Engine Mounts”, ASME, Vol. 110, 422-429, Dec. 1988.

[9] A. A. Geissberger, A. Khajepour and M.F. Golnaraghi, "Nonlinear Modelling and Experimental Verification of a MDOF Hydraulic Engine Mount", To appear in the ASME, AMD Proceeding, symposium on Active noise and vibration control, November 5-10, 2000.

Optimization of the Passive Shock Absorber of a Military Aircraft

Bernd Uhrmeister

DLR – Deutsches Zentrum für Luft- und Raumfahrt
Institute of Aeroelasticity
Vehicle System Dynamics
P.O. Box 1116
D – 82234 Wessling, Germany

Summary:

For a large military transport the potential is assessed to improve its behavior during touch down and ground run by optimization landing gear parameters. Four oleo force parameters were chosen for the optimization: the damping coefficients at compression and expansion, the pre-load, and the length of the gas spring. With respect to feasibility the variation of the parameters is restricted to a band of 20% about the nominal value.
Aim of the optimization is the reduction of the vertical acceleration at touchdown. During ground roll the ride index has to be minimized. Touch down and ground run were first treated separately. Thus a basis is provided to assess whether switching the damping can satisfy the requirements of both phases. In addition the complete cycle from touch down to roll out was investigated.
Concerning the results: It is to be observed that the optimal performance is achieved with the parameters at their limits. The performance in terms of reduction of acceleration, respectively improvement of ride comfort is enhanced by an amount between 20% and 30%.

List of Symbols:

f_{damp}	oleo damping force
f_{gas}	oleo gas spring force
f_{g0}	pre-load force
d	damping coefficient
d_{com}	damping coefficient at compression
d_{exp}	damping coefficient at expansion
decel	deceleration of ac at touch down in vertical direction
$height_{jump}$	height of third wheel above ground
Ride-Index	ride comfort = weighted RMS of vertical acceleration
RMS	root mean square
s	oleo stroke
$\dot{s}$	oleo stroke rate
s_{gas}	length of gas chamber
k	polytropic exponent

Indices, Abbreviations:

ac	aircraft
mean	mean value
max	maximum
nose / n	nose of ac = pilot station/ nose landing gear
main / m	main landing gear

1.Introduction:

The designer of a landing gear is confronted with a host of often conflicting requirements. Its strengths must be sufficient to survive hard landings. When operating on a rough airfield the shocks encountered by the wheels should be absorbed to guarantee a high level of crew and passenger comfort and contribute to long service life of the gear itself and the airframe. All this should be achieved while ensuring reliability, avoiding complexity, and watching for good maintainability. The weight must be low and the dimension small so that the gear can be retracted into a narrow bay. Fulfillment of these and a multitude of additional requirements yields finally into a design which minimizes the direct operating costs. For the time being the airframe and gear manufacturers are still somewhat away from such an all embracing optimization. Up to now the various members of a design team strive to optimize their contribution – without inflicting too much on the requirements of the others. An iterative process between the various contributors issues into a more or less optimal design.
Coming back to the principal task of the landing gear, i.e. to provide the interface between the airframe and the ground: The investigation of the interaction is a complex task which can be attacked in different ways. One approach – probably the most expensive and time consuming – is to test a preliminary design on the aircraft, evaluate its performance, detect the deficiencies, modify some components, and embark on another test. Still rather laborious and prone to misjudgement is the attempt to reduce the problem by linearization and approximation and solve it by a small simulation program. The inaccuracies of such simplifications may lead to wrong answers which might disguise effects crucial for the performance.
In recent years computer simulations gained more and more importance and acceptance – especially for complex nonlinear systems. This method has been applied in the work presented here. The multibody system based simulation tool SIMPACK [1] permits to define the various bodies of a system and to connect them by joints and/or force elements. Excitation by runways is provided, where surfaces between "smooth" and "extremely rough" are available. Elasticity can be included. The optimization package MOPS [2] within SIMPACK facilitates to refine a design rapidly around a set of parameters - a task hardly to solve within reasonable time by manual variation, followed by single simulation runs.
The last remark leads to the approach chosen in this paper: First the variation of single parameters demonstrates their effect on the behavior of the system. Thus the basis for the physical interpretation of the systems reaction is given when the optimization brings all parameters to their optimal value.

Paper presented at the RTO AVT Symposium on "Active Control Technology for Enhanced Performance Operational Capabilities of Military Aircraft, Land Vehicles and Sea Vehicles", held in Braunschweig, Germany, 8-11 May 2000, and published in RTO MP-051.

2 Model description

Aircraft:

The aircraft is a large military transport in the 100 ton weight class. Span and length are roughly 40 meters. Four turbo-prop engines power the craft. The six legs of the main landing gear are of the swing type, while the nose gear is a cantilever one. Since here only symmetrical cases are treated the two legs of each main gear axle are put together as one "double leg". Correspondingly the values of the relevant data - as e.g. damping coefficients, pre-load, tire constants – have been doubled.

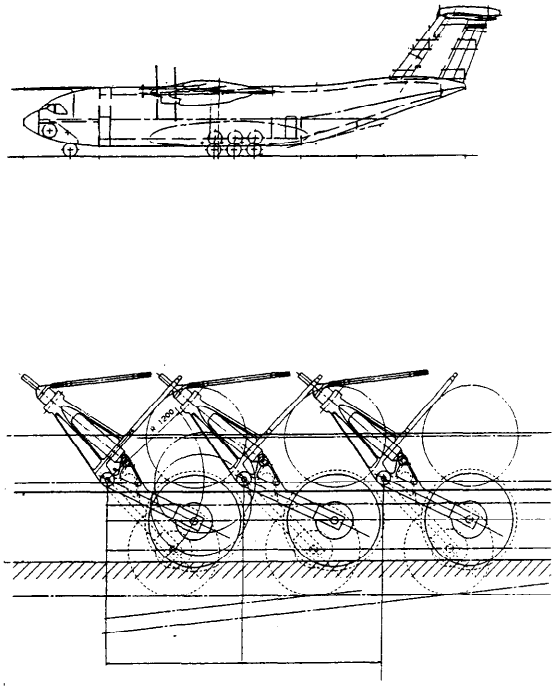


Figure 1: Side view of aircraft and main gear

Aerodynamics:

Though a subroutine with the complete aerodynamics and thrust is available, based on the manufacturers Aerodynamic Data Base, the investigations are made in compliance with the relevant specifications [3]: Before touch down lift is equal to weight, and during rolling lift has to be taken as zero. In this study it is assumed that immediately after touch down lift decays with the decrease of the angle of attack. Due to the hard landing the aircraft jumps. The final touch down occurs about 3.5 s after the initial ground contact. Half a second later the lift dumper and thrust reverse is activated. Within the next second lift and pitching moment are assumed to approach zero.

Oleo:

The gas spring force given by

$$f_{gas} = f_{g0} / (1.0 - s / s_{gas})^{\kappa}$$

shows an exponential climb towards the end of the stroke. Thus it is not surprising that all parameter changes of the optimization try to avoid that the gear approaches the steep end of the gas spring curve accompanied by force and acceleration spikes. A high value for the pre-load f_{g0} and for the length s_{gas} of the gas spring tend into the desired direction.

The damping force

$$f_{damp} = \text{sign}(\dot{s})\, d\, \dot{s}^2$$

is proportional to the square $\dot{s}^2$ of the stroke rate. By the closing of valves the damping coefficient at the expansion of the oleo is given a value d_{exp} which is usually by a factor of 10 higher than the d_{com} during compression. The high damping at expansion reduces the tendency that the aircraft is thrown off the ground. However, for comfortable rolling a low expansion damping would be beneficial.

Tire:

The tire force is modeled here as

$$f_{tire} = c_{tire}\, z_{tire} + d_{tire}\, \dot{z}_{tire}$$

The force is proportional to the compression and its rate as measured vertically below the wheel hub. Obviously this simplification would give inaccurate results when rolling over steps, since the model does not reflect the smoothing effect of a real tire which „flows around and over" the obstacle. Since the runways considered here do not have steps the simplification does not compromise the simulation results.

Elasticity:

The preprocessor BEAM [4] allows an easy inclusion of the calculation of elastic motions in SIMPACK. The component, the elasticity of which is to be modeled, e. g. the wing, is split into a number of sections – large enough the achieve a sufficient accuracy and small enough to keep the effort in tolerable limits. For such a section the relevant properties – like mass density, cross sectional area, area moment of inertia – are taken as constant. The number of elastic modes can be selected. The validity of the elastic model can be checked by comparison with the modes given by the airframe manufacturer.

Pilot procedure during landing:

The military specifications prescribe a touch down sink rate of 3.66 m/s. After some deliberations a flat landing with a pitch angle = 0, is selected as the worst case yielding into a higher impact acceleration (20 m/s^2) than with a pitch angle of e.g. 6^0 where the successive touch down of the three axles attenuates the acceleration (15 m/s^2). Touch down speed lies at 70 m/s.
After the hard landing the aircraft lifts off again. Especially the nose is thrown back off the ground. It is assumed that the pilot does not start a recovery action, but keeps the elevator fixed in the trimmed condition. Shortly after the second touch

down the lift dumper and the thrust reverser are activated. Half a second later braking of the wheels (of the main gear) commences.

Runway roughness:

Military transports operate frequently on airfields which are neither paved by nor covered by smooth grass, but they are un- or semi-prepared airstrips. In the first case flags mark a strip on a halfway suitable terrain. Given that the roughest unevennesses are eliminated the field is classified as semi-prepared. For a large variety of more or less rough fields MIL-SPEC defines the amplitudes of the unevenness as a function of their wave length [5]. After conversion of [5, fig.1] into metric units the amplitude a depends on the wavelength Λ as:

Semi-prepared field:

$$a_{semi} = 0.0254 + 2.0\ 10^{-3}\ \Lambda \quad ;$$
$$\text{for } \Lambda > 305 \text{ m is } a_{semi} = 0.63 \text{ m}$$

Unprepared field:

$$a_{unpre} = 0.05 + 8.9\ 10^{-3}\ \Lambda$$
$$\text{for } \Lambda < 46 \text{ m}$$

$$a_{unpre} = 0.406 + 7.5\ 10^{-4}\ \Lambda$$
$$\text{for } 46 < \Lambda < 305 \text{ m}$$

The term on the right hand side of the equations, which does not depend on the wave length, approximates single rocks lying on the runway.

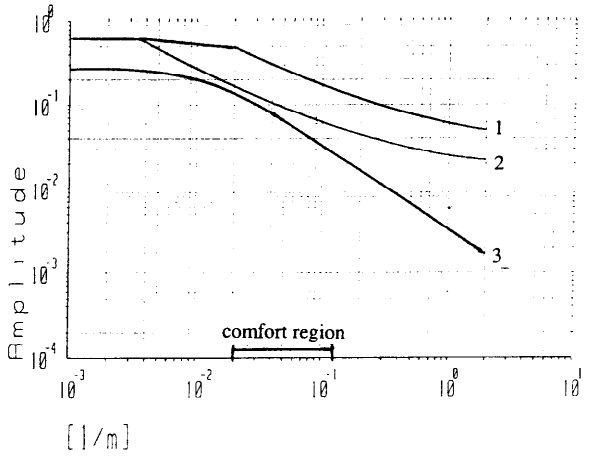


Figure. 2.1: Continuous amplitude spectra

1 : Unprepared airstrip (MIL-SPEC)
2 : Semi-prepared airstrip (MIL-SPEC)
3: „Very bad macadam", SIMPACK
Comfort relevant frequency range at 70 m/s:
$1/\Lambda = 0.03$ to 0.14 [1/m]

For our study a roughness was chosen close to that of a semi-prepared field in the frequency range from 2 to 10 Hertz. That interval defines the frequency band which is relevant for the ride comfort (fig. 2.1). SIMPACK offers a spectrum „Very bad macadam", which corresponds to this condition.

The dependence of the amplitude on the wavelength is given by

$$a = \left| F(j\Omega) \right| = \left| 0.705/\{2.66 + 34.2j\Omega + (j\Omega)^2\} \right|$$

with the spatial frequency

$$\Omega = 2\pi / \Lambda \quad [\text{rad/m}].$$

The roughness of the ground is developed as a series of sine-waves

$$z_{ground}(t) = \sum_i A_i \sin(2\pi f_i t + \Phi_i).$$

The frequencies f_i lies in the range from f_{min} to f_{max} which is divided by n equidistant steps. The amplitude A_i is determined by the formula above for the proper frequency f_i whereas a random number generator contributes the phase angle Φ_i between $-\pi$ and $+\pi$.

A number of 51 waves was chosen for the series. As smallest wave length a value close to the wheel diameter respectively wheel base should be selected to cater for a good representation of vibrations at the high end of ground excitation. The value of 4 meters taken here deviate from this recommendation regarding the nose wheel, but are agreeable for the main gear with its long wheel base. A smaller wave length turned out to be detrimental to computing time. The longest wave with Λ = 200 m yields in a frequency of 0.35 Hz at a speed of 70 m/s being sufficiently below the lowest aircraft mode. The height of the roughest bumps and depth of the holes measure 0.15 m. For the check of equilibrium each run begins on a flat stretch.

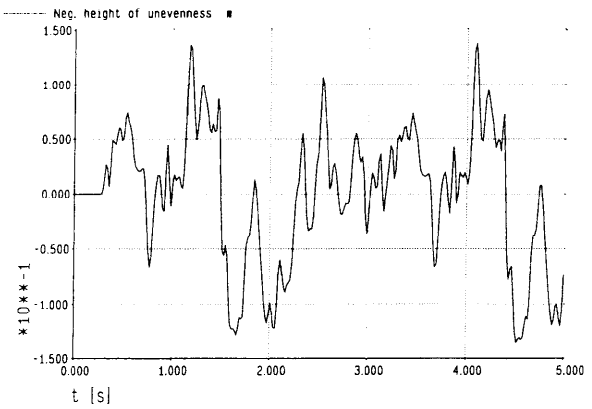


Figure 2.2 Unevenness of the airfield ("Very bad macadam")

3. Results

Before the optimization over all parameters - damping coefficient for compression and expansion, the pre-load, and the length of the gas spring – is started, they are varied one after the other to demonstrate the tendencies and explain their physical effects on the criterion.

3.1 Landing impact

3.1.1 Parameter variation

One of the major tasks of the gear is to reduce safely and comfortably the sink rate of the aircraft to zero. The deceleration in the vertical direction should be as small as possible. Jumping and violent heave and pitch should be avoided. During a rather short time span a large amount of energy has to be dissipated – being proportional to the high sink rate and a considerable aircraft mass.
For the analysis the whole process is here divided into two sections. The initial part, the compression of the gear, ends when the aircraft is closest to the ground the and compression rate reaches zero. During the compression energy is partially dissipated by damping, partially stored in the gas spring. The stored energy initiates the second phase – the expansion of the gear which lifts the aircraft. Whether the upward motion comes to an end before some or all wheels lift off, depends among other parameters on the touch down sink rate, the strength of the gas spring, and the damping. The higher the damping versus the gas spring force the smaller the tendency for the aircraft to jump off the ground after a hard landing (Hence the gears of most carrier based aircraft are dampers only. Jumping up and failing that the arrester hook engages could be fatal. Rolling on rough terrain does not occur, thus discarding the necessity for a spring). On land based aircraft a high value of the damping coefficient slows down the expansion of the gear and counteracts the jumping tendency. Generally the coefficient at expansion exceeds that at compression by a factor of ten. However, a expansion coefficient which is too high is detrimental to the comfort at rolling.
Though the investigation focuses on the acceleration at the pilot station a short deviation to the centre of the aircraft is taken here because the effects during touch down are more pronounced there in the vicinity of the main gear. When the damping (of the main gear oleos) is low, the gas spring has to absorb the bulk of the energy. The force climbs up the steep end of the gas spring curve and reaches high values (Line 1 in fig. 3.1a). The opposite holds for very high damping. The initial damping force exceeds the gas spring force (Line 3 in fig. 3.1a). The optimum with respect to the minimisation of the force and the deceleration would be attained when the two peaks generated by damping and gas spring show the same height (Line 2 in fig. 3.1a). Thus the ideal of a constant and low force during compression would be approached. However such a flat force curve is accompanied by a sudden onset of deceleration which is experienced as objectionable by most pilots. Hence a somewhat lower damping will be chosen as compromise.

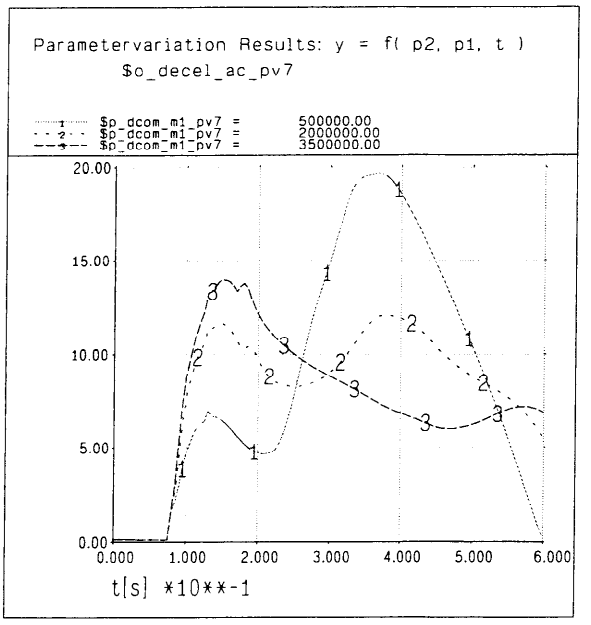


Figure 3.1a Effect of the damping at compression d_{com} on vertical deceleration of the centre of the aircraft

In figure 3.1a for demonstration's sake a large variation of damping coefficients has been chosen. Within the small boundaries of ± 20 % the improvement is naturally much smaller (Fig. 3.1b and fig. 3.2).

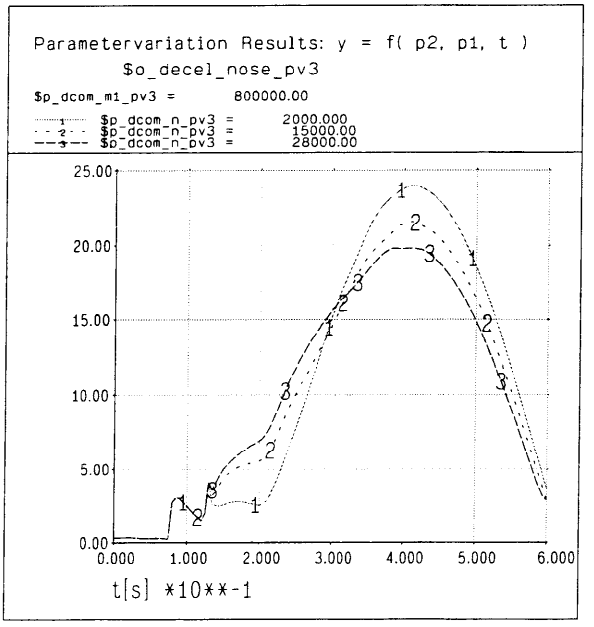


Figure 3.1b Effect of damping at compression d_{com} of nose gear on deceleration at cockpit
(Variation of d_{com} only ± 20 %)

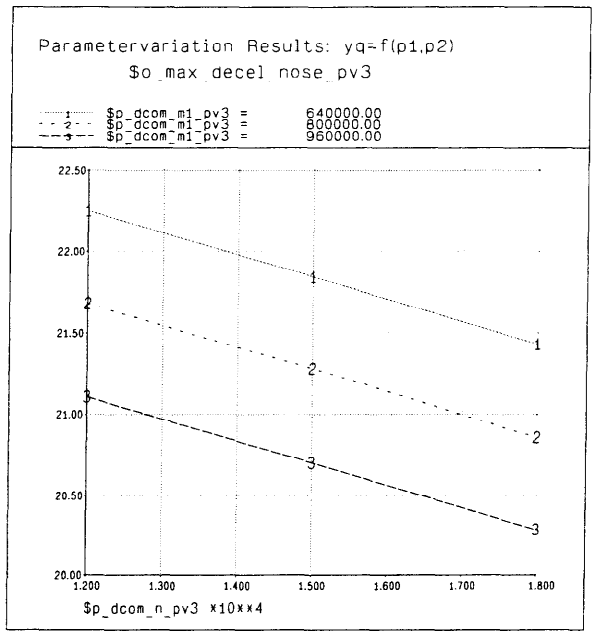


Figure 3.2 Maximal deceleration at cockpit as function of damping coefficient at compression of nose and main gear

The pre-load of the gas spring is another parameter to shape the deceleration at touch down. An increase raises the force at the begin of the touch down and reduces the tendency of the oleo to climb up the steep end.

The increase in gas spring length keeps the oleo away from the steep end of the force curve by permitting the damping to dissipate more energy over a longer stroke. A lengthening by 20% yields in a 13% improvement of the deceleration (Fig. 3.3)

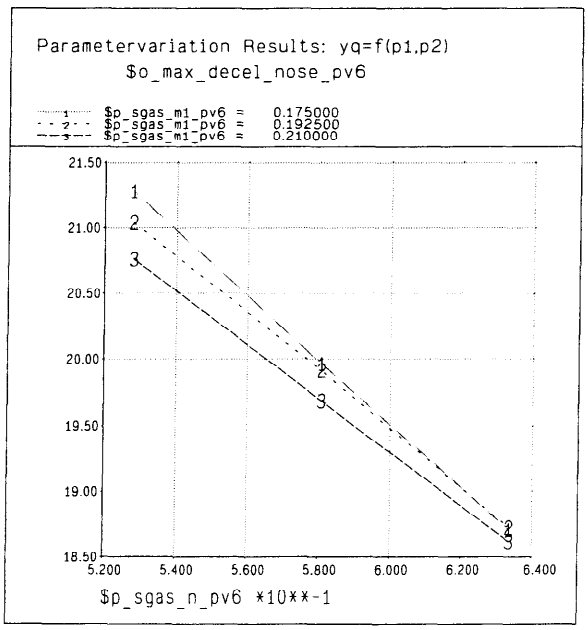


Figure 3.3: Effect of gas spring length s_{gas} on maximum deceleration at the cockpit

Jumping of the aircraft:

After a hard and flat touch down the aircraft is thrown back into the air. As a gauge for the jumping the root mean square RMS of the height of the third main wheel is taken. This wheel reaches a maximum height of 0.65 m (Fig. 3.4). Its time off the ground is about 3 seconds. Height and time off the ground decrease with increasing damping coefficient at expansion (Fig. 3.4 and 3.5).

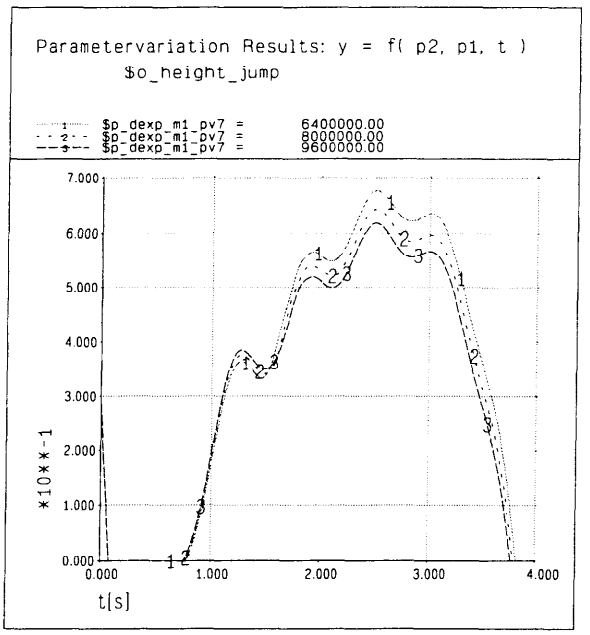


Figure 3.4: Height of third gear above ground as function of the damping coefficient at expansion for main gear

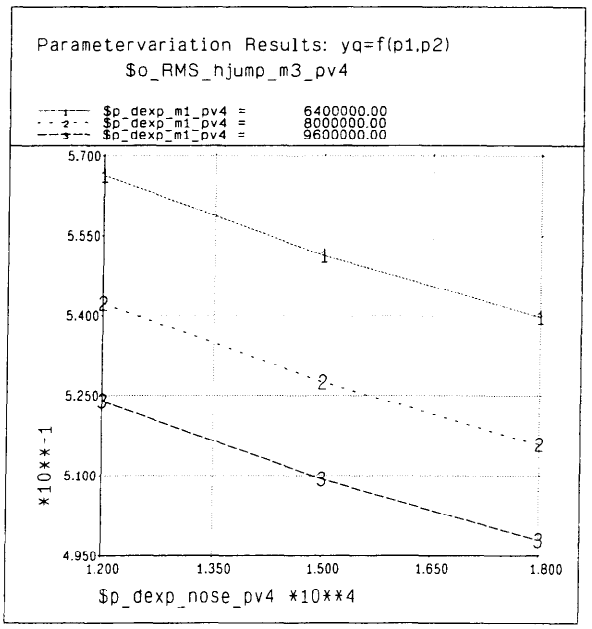


Figure 3.5: Height of third gear above ground as function of the damping coefficients at expansion for nose and main gear

3.1.2 Optimization of all oleo force parameters:

Returning to the compression phase of the landing, the optimization over all parameters – except the expansion coefficient – lowers the maximum of the deceleration at the cockpit from 21.3 m/s^2 to 16.8 m/s^2 or by 21% (Fig 3.6a and b).

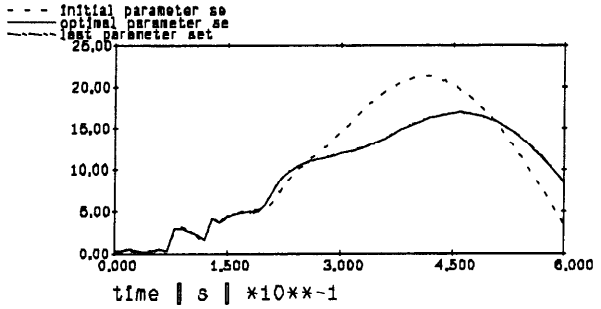


Figure 3.7a: Vertical deceleration at cockpit before and after optimization

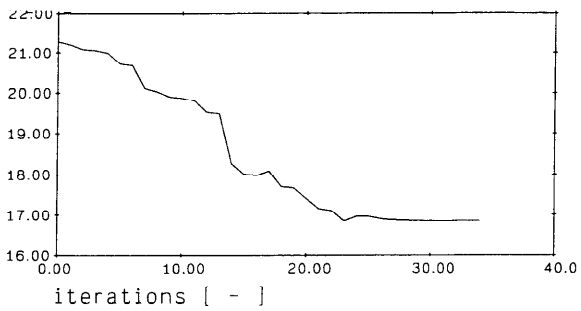


Figure 3.7b: Maximum of vertical deceleration at cockpit versus iterations

During the optimization all parameters move to their upper boundaries (Fig 3.8). The parameters are the damping coefficient at compression, the pre-load, and the length of the gas spring, both for the nose and the main gear. Since the first phase of the landing – considered here – ends before the expansion begins this coefficient stays unchanged.

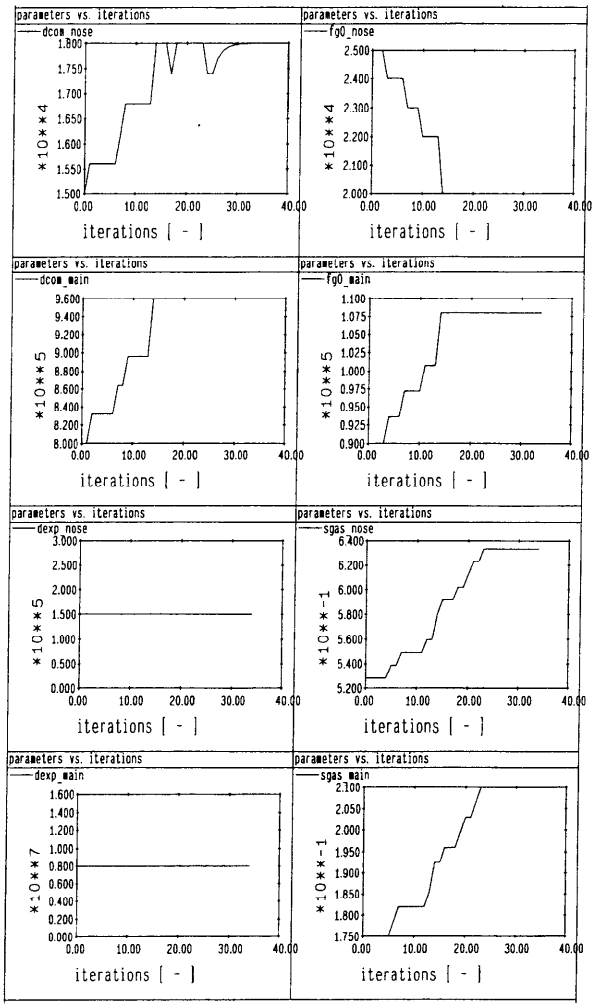


Figure 3.8: Development of parameters versus iterations of the optimization

As a rough guess: an increase of the parameters by 20% is accompanied by 20% reduction of the deceleration.

3.2 Ground roll

Rolling with touch down or take off speed over the rough runway subjects the aircraft to shocks up to 15 m/s^2 – accelerations in the same order of magnitude as those at landing impact, posing a lot of discomfort on passengers and pilot. As a measure for the discomfort – and as criterion for the optimization – the ride index at the cockpit is chosen. Basically it is the root mean square of the vertical acceleration weighted by human sensitivity to vibration. Due to bio mechanical factors man perceives certain frequencies to be more comfortable than others for a given amplitude. The International Organization for Standarization [6] specifies frequencies between 4 and 8 Hertz as most detrimental to comfort [6]. Hence the optimization of comfort has to concentrate on this frequency range.

3.2.1 Parameter variation

Damping coefficient for compression:

A change of the coefficients for both the nose and the main gear affects the comfort only slightly. An increase of 20% of the nose gear coefficient diminishes the ride index by 0.5% only. The low influence could be expected because the stroke rate of the oleo is rather small during ground roll - a remark which holds even more for the damping force which is proportional to the square of the low rate. In the investigated parameter range the highest values for nose and main gear give the best result. Similar to the tendency observed at the landing impact, an increase in damping flattens the force versus stroke diagram and keeps the oleo force curve away from the steep climb at the high end.

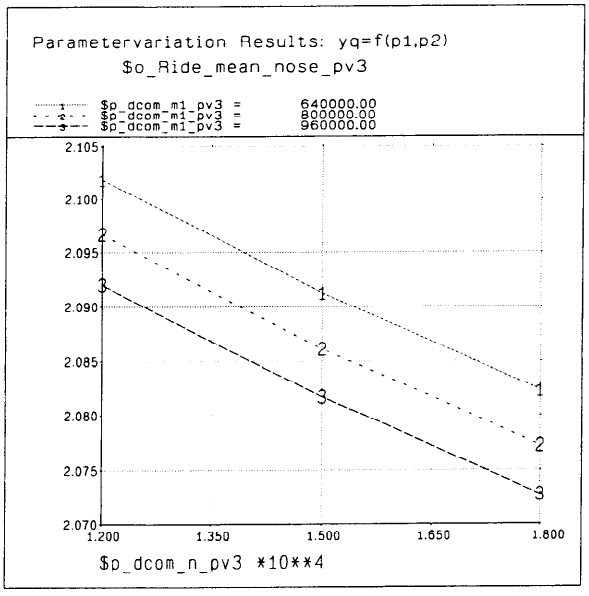


Figure 3.9: Ride comfort as function of damping coefficient at compression of nose and main gear

Damping coefficient for expansion:

A decrease of the damping during expansion allows the gear to follow rapidly declining slopes of the runway surface. Thus the wheels do not loose ground contact and can support the aircraft. Thus its downward motion is diminished and the shock reduced when the next ascending slope is encountered. The best comfort can be expected for the lowest values of the coefficient. For a 20% change of the nose gear coefficient 1.3% alteration in ride comfort are obtained.
Some warning is appropriate here: The criterion for comfortable ride during rolling is conflicting with another one concerning the jumping of the aircraft. Immediately after the touch down during a hard landing the gear is highly compressed. The ensuing expansion would throw the vehicle up off the ground. To counteract the tendency for jumping the coefficient for expansion is usually larger by a factor of 10 than that for compression. Switching of the damping coefficient between touch down and rolling could take care of the conflicting situations.

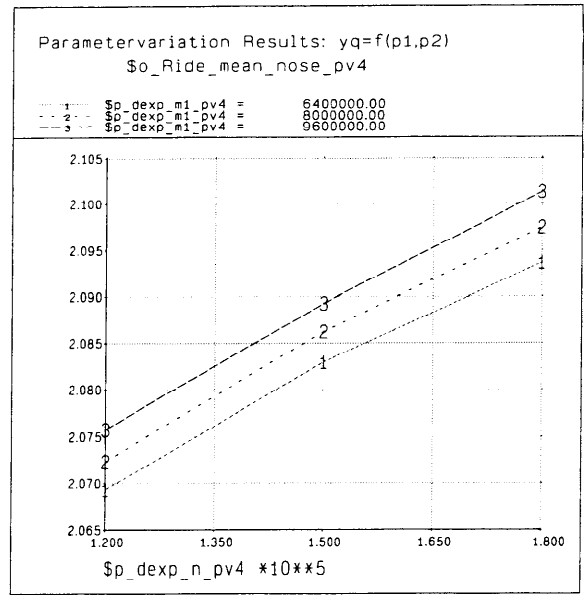


Figure 3.10 Ride comfort as function of damping coefficient at expansion of nose and main gear

Oleo pre-load:

A large pre-load proves to be favorable for comfort. It lifts the oleo force to a high level and refrains the oleo to climb up the steep end of the force curve at compression. During expansion it pushes the wheels down, supports thus the aircraft and prevents a sharp acceleration when hitting the next bump. A 2.5% improvement accompanies a 20% increase of the nose gear pre-load.

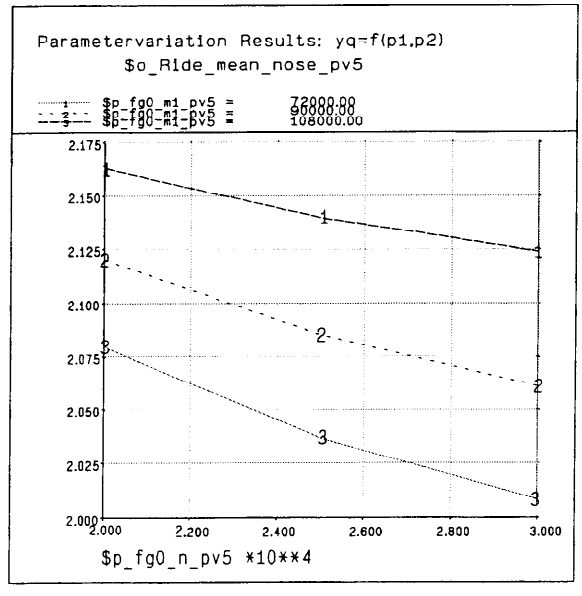


Figure 3.11 Ride comfort as function of oleo pre-load

Length of the gas spring:

The changes of the oleo, discussed so far, can be performed without a major effort. This is not true for the length of the gas spring. Its change has repercussion on the whole aircraft.

Obviously features like the height of the floor above ground, the size of the gear bay, or weight are involved. But also the dynamics e.g. heave and pitch motion of the aircraft are affected.
The results confirm the physically plausible expectation that an increase of the length of the gas spring enhances comfort. Increasing the nose oleo by 20% improves the ride by about 5%.

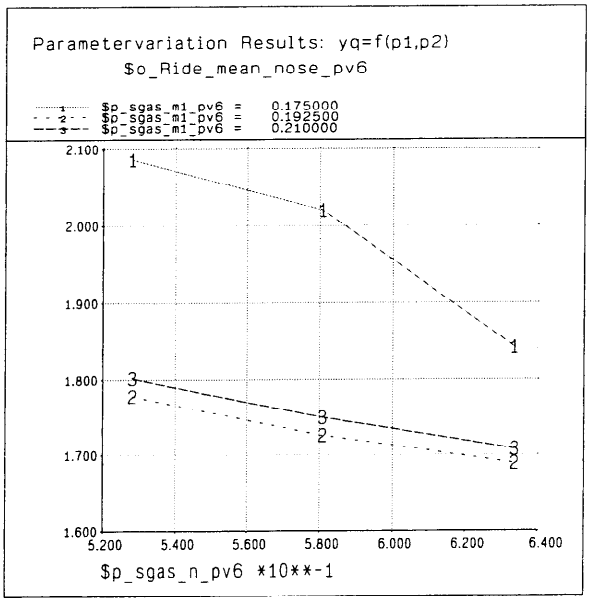


Figure 3.12 Ride comfort as function of gas spring length

3.2.2 Optimization of all parameters

All parameters move towards the boundaries, with the exception of the length of the main gear gas spring which stays slightly under the maximum possible (Fig. 3.13). They follow the tendencies shown by the variations of the single parameters.
While the improvements are quite small, when the parameters are varied one by one, the results for a simultaneous optimization of all parameters indicate that the effects are amplified and a significant improvement is achieved. The mean of the ride index decreases from 2.108 to 1.52 – or by 25% (Fig. 3.14). The peaks of the vertical acceleration at the cockpit are reduced by an amount between 10 and 20%, whereas the alleviation in the center of the aircraft is less pronounced (Fig. 3.15).
The optimization has reduced the damping coefficient during expansion. As mentioned above this enhances ground contact when rolling into holes, may however affect adversely the tendency of the aircraft to jump after a hard touch down. Considering only rolling on rough terrain the reduction of these coefficients decreases the time and height of the third gear being off the ground. The criterion, the RMS of the height of the third wheel above ground, decreases considerably (Fig. 3.16). It has to be admitted that rolling on very bad macadam does not cause a big problem of jumping. In the test case there has been only one instant where the wheel lifts off a few centimeters.

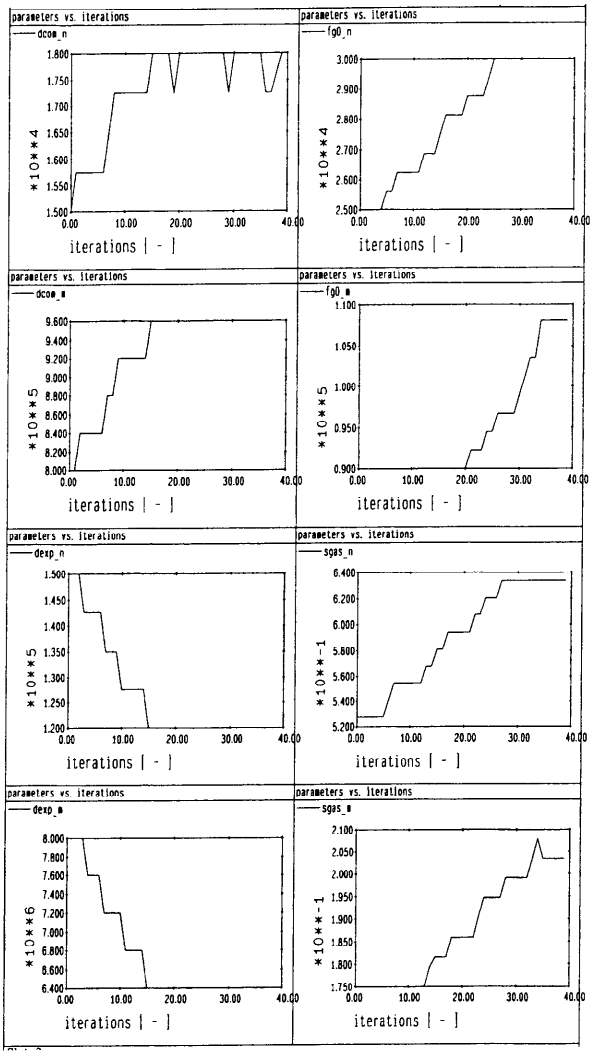


Figure 3.13 Development of parameters versus iterations of the optimization

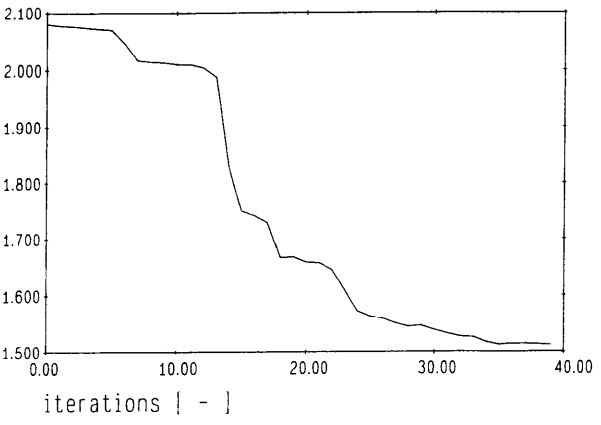


Figure 3.14: Development of ride comfort versus iterations of the optimization

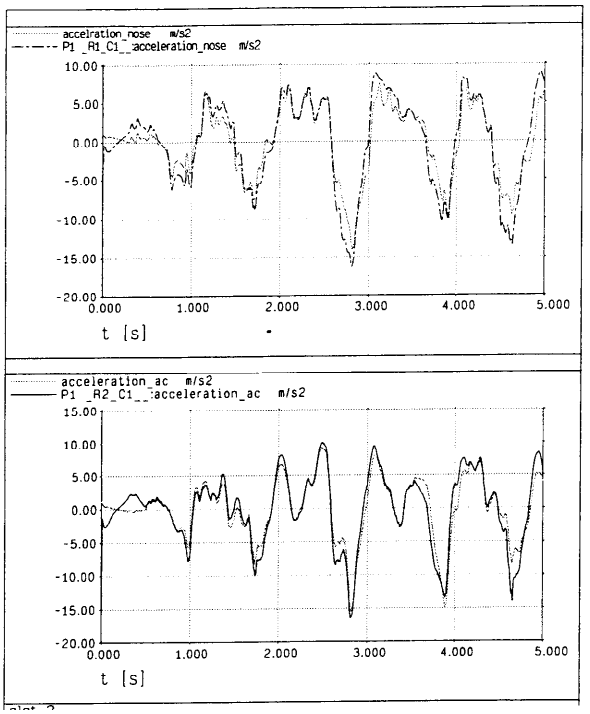


Figure 3.15 Vertical acceleration at the cockpit and at the center of the aircraft

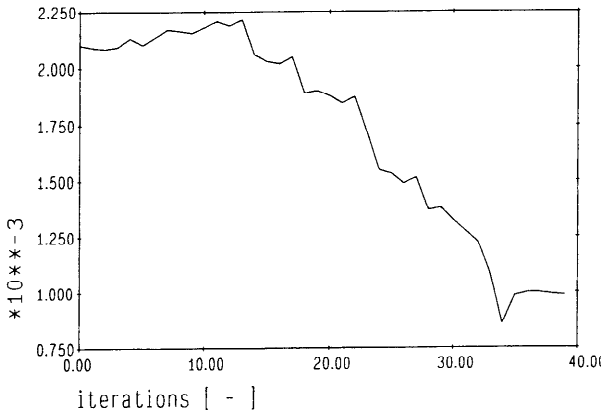


Figure 3.16 Criterion $RMS_{_jump}$ for jumping of the aircraft versus iterations of the optimization

3.3 The complete landing

By this expression the sequence of touchdown, jumping for several seconds, the final touch down and subsequent deployment of lift dumpers, thrust reverse and wheel braking is understood. The first ten seconds of this process are evaluated here. Speed decreases from 70 to about 30 m/s.
As criterion for the whole process the ride index is chosen. The parameters move to the same boundaries as in the two preceding optimizations (Fig. 3.17). Though the criterion for jumping is not activated, it benefits from the improvement of the initial touch down phase. Due to the higher damping more energy is dissipated during compression, leaving less to toss the aircraft up into a large jump. Both criteria improve by about 30% (Fig. 3.18, 3.19). Regarding the time histories: the sharp spikes of the acceleration are clipped off and the height of the jump is somewhat reduced (Fig 3.20, 3.21)

The parameters for the complete landing exhibit the same tendencies as for touch down or ground roll. The somewhat deviating behavior of the damping coefficient at expansion, when the importance of jumping is emphasized, is not appearing - mainly because the criterion for jumping has not been activated in this example. The choice of proper weights on jumping and rolling is an awkward task for the gear designer. To ensure comfortable rolling high weight should be put on this phase of the landing and vice versa, when jumping is of great concern a high weight is needed here. To complicate matters further the hardness of the touch down and the roughness of the runway as well as the duration of the ground run are influencing the importance of the various phases. Obviously, the longer and rougher the ground run, the higher the trend to low expansion damping. On the other hand: hard landings on smooth and short runways amplify the tendency towards a high expansion damping. To obtain a valid result the designer has to take into account the collective of all landings and runways the aircraft will encounter in its service life – not an easy task. All these deep deliberations are not performed here, but the potential of the optimization is demonstrated by the example specified above.

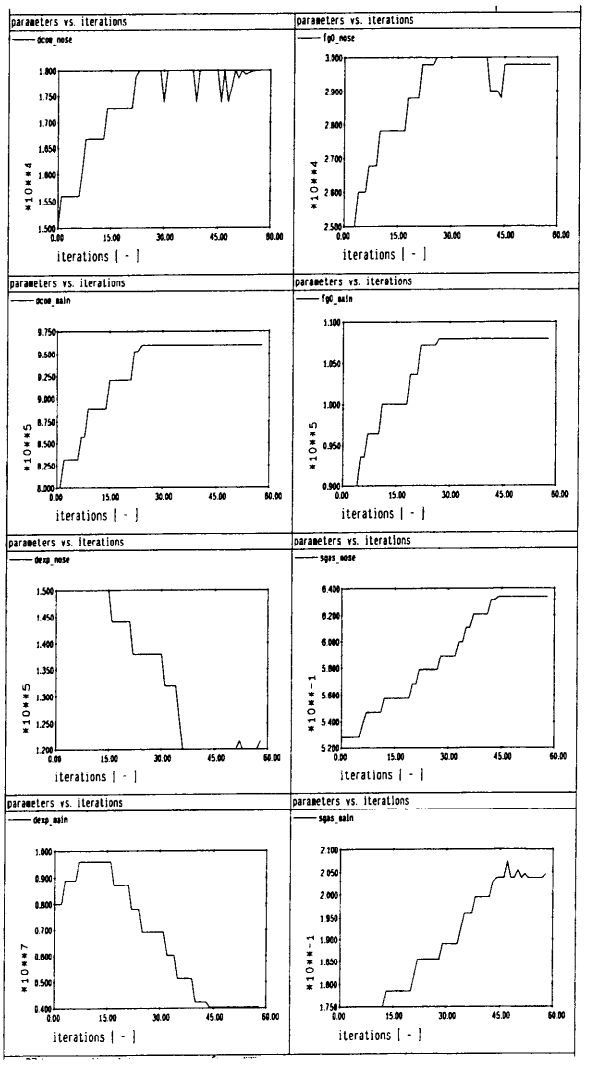


Figure 3.17: Development of parameters versus iterations of the optimization of the complete landing

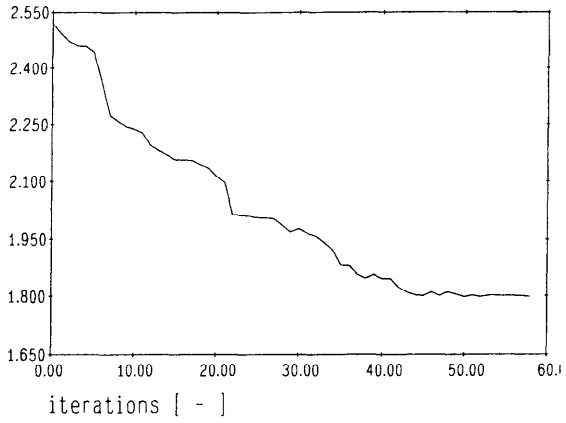


Figure 3.18: Ride index versus iterations of the optimization

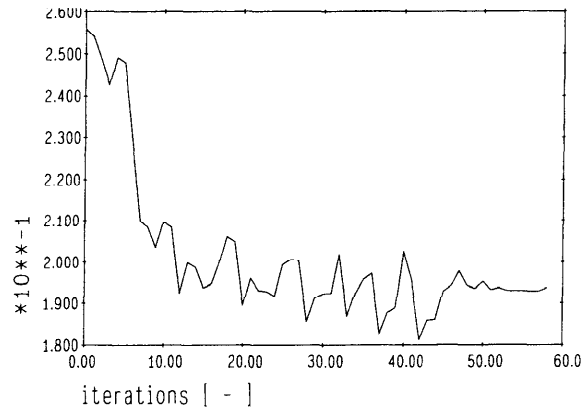


Figure 3.98: Criterion $RMS_{_jump}$ for jumping of the aircraft versus iterations of the optimization

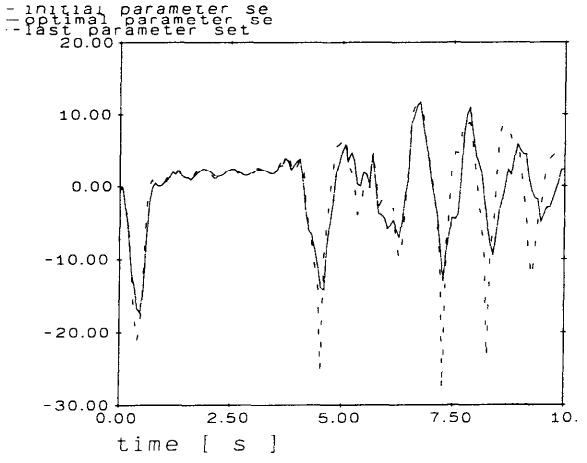


Figure 3.20 Decrease of vertical acceleration at cockpit

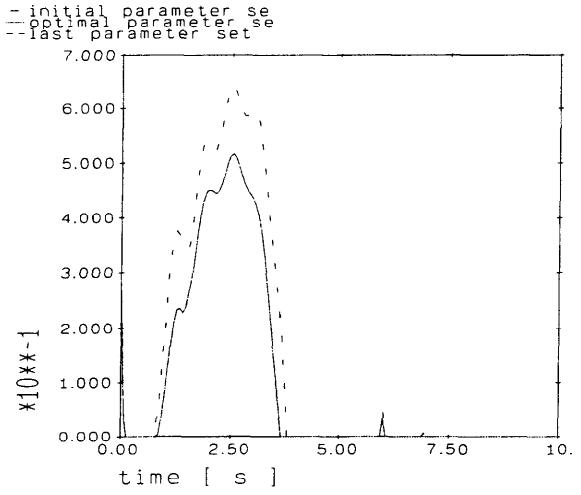


Figure 3.21 Decrease of jumping (Height of third wheel above ground)

Parameter:	original	optimal	Ride-index
d_{com_n}	0.15 e5	0.18 e5 **	
d_{com_m}	8.0 e5	9.6 e5 **	
d_{exp_n}	0.15 e6	0.12 e6 *	Original:
d_{exp_m}	8.0 e6	6.4 e6 *	2.5
f_{g0_n}	0.25 e5	0.30 e5 **	optimized:
f_{g0_m}	0.90 e5	1.08 e5 **	1.8
s_{gas_n}	0.528	0.6336 **	
s_{gas_m}	0.175	0.2035	
* lower boundary, ** upper boundary			

Table 1: Optimization within boundaries of 20% of the original parameter values

4. Summary:

The design of an optimal gear for a large multi-wheel flexible aircraft operating from a rough airfield is a demanding task, which necessitates the use of a powerful software tool (as e.g. SIMPACK). Thus the potential of the passive gear can be evaluated.

In the example presented here the various phases of a landing – touch down, jumping, ground roll – are analysed, first separately and then as a continuous sequence. As design aim the reduction of the vertical acceleration at the cockpit has been chosen. For the touch down the maximum of the deceleration is taken as the criterion. For the ground roll as well as for the complete landing the ride index measures the performance.

Putting aside for a moment the jumping of the aircraft, in all other phases of the landing the parameters move into the same direction for improved performance For both, the nose and the main gear, the damping coefficients at compression go to the upper boundary, while the damping at expansion settles down at the lower limit. The pre-load adopts the upper values. The gas spring length of the nose gear acquires the maximum value, whereas the main gear stays a few percent below the upper limit. Assessing the jumping after a hard landing as an isolated process, a high value of the damping coefficient at expansion would be optimal. However in the optimization of the complete landing the value of the expansion damping depends on the weight which is put on the criteria for jumping and for ground roll. In this example the jumping criterion has not been activated. Nevertheless, the improvement of the compression phase – high absorption of energy by an increased damping – alleviates the jumping.
To sum it up: The optimization moves the oleo force parameters to the boundaries of $\pm 20\%$ about their nominal values. The criteria "maximal deceleration" and "ride comfort" improve by 20% and 28%.

Literature:

1. Rulka,W: *Effiziente Simulation der Dynamik* mechatronischer System für industrielle Anwendungen, Ph. D Thesis, Universität Wien, 1998

2. H.-D. Joos: Informationstechnische Behandlung des mehrzieligen optimierungsgestützten regelungstechnischen Entwurfs, Dissertation, Universität Stuttgart, 1992

3. DEF-STAN 00 970, Appendix II, Chapt. 304

4. Schwertassek, R., Wallrapp, O: Dynamik flexibler Mehrkörpersysteme, Viehweg-Verlag, Braunschweig, 1999

5. MIL-A-8863 B (AS): Airplane Strength and Rigidity, Ground Loads for Navy Acquired Airplanes, 1987

6. International Organization for Standardization: Guide for the Evaluation of Human Exposure to Whole Body Vibration, ISO 2631-1974(E), July 1974

This page has been deliberately left blank

Page intentionnellement blanche

DESIGN AND TESTING OF A MESOSCALE ACTUATOR DEVICE

Joon Park, Scott Keller, Gregory P. Carman, and H. Thomas Hahn

Mechanical and Aerospace Engineering Department
University of California, Los Angeles
48-121 Eng. IV, Los Angeles, CA 90095-1597, USA

ABSTRACT

Design and testing of a mesoscale actuator device is presented in this paper. The device uses frequency rectification concepts to amplify the displacements while retaining comparable force outputs to current piezoelectric actuators. The design is based on an inchworm motor with the exception that microridges are used in the clamping system. A FEM model is used to design a device that produces a peak to peak amplitude of 900N at 11 mm/sec with a weight of 100 g (i.e. specific power of 99 W/kg). A prototype device is fabricated and tested with excellent agreement between analysis and testing results. Stress and modal analysis are used to demonstrate that the device has an infinite fatigue life and a first modal frequency at 1777 Hz.

Keywords: frequency rectification, inchworm motor, piezoelectric stack, microridges

INTRODUCTION

Active materials are being used in a wide range of applications including vibration reduction [1-6], noise suppression [7], adaptive optics [8-10], and solid-state motors [11-16]. For example, vibration in rotorcraft is a major problem resulting in fatigue, poor ride quality, high noise levels, deficiencies in handling qualities, and reduction of weapons system effectiveness [1-4]. One of the promising methods for reducing rotorcraft vibration is an Actively Controlled Flap (ACF) [3]. By articulating the flap ± 3° the vibration can theoretically be decreased by 90%. While AFC concepts are promising, developing an actuator system to produce sufficient flap deflection represents a major obstacle.

One approach to overcome the displacement limitation is to use frequency rectification concepts. Frequency rectification ideally increases displacements while retaining high force output. This is in sharp contract to displacement amplification techniques that increase displacements by reducing force output. Mender-line actuators [17-19] are an example of displacement amplification techniques while inchworm motors [11-12,14,16,20-22] and ultrasonic motors [13] are examples of frequency rectification concepts. Among these actuators, the inchworm motor is a popular device due to its large travel distance (mm) and precise positioning capability (submicron). While producing large displacements, current frequency rectification devices have limited force outputs.

Burleigh Instruments Inc. introduced the first inchworm linear motor mechanism in 1975. This inchworm provides nanometer resolution, a linear travel range of 200 mm, a speed of 2 mm/sec, and an output force of 1.5 kgf [20]. Recent research has focused on increasing the force and velocity output of these linear motors. For example, a hybrid transducer-type linear motor was developed for high speed [21]. The motor produced velocities of 50 cm/sec, but the force output was limited to 0.5 kgf. Miesner and Teter [22] designed a linear motor to produce large force output using piezoelectric stacks for clamping and a magnetostrictive material TERFENOL-D for stepping. The relatively large prototype (200 mm x 200 mm x 20 mm) is reported to provide a stall load of 10 kgf and a no-load speed of 2.54 cm/sec. Zhang and Zhu developed a linear motor using a monolithic flexure frame and a guideway to transfer large mechanical loads [12]. Although analysis showed that it could produce a 20 kgf force output, a large clamping region of 25 mm x 25 mm was required. Based on these reviews, the principal limitation of the linear motors are the force outputs and their relative size.

The clamping system in the linear motor determines the force output. Most linear motors use static friction as the clamping mechanism. This is limited by the coefficient of friction which is usually 0.2 ~ 0.3. Increasing the coefficient of friction by roughening the surfaces and applying a clamping preload improves load transfer, but causes other problems associated with positioning, disengaging, and wear [12, 22]. Electrostatic clamping [15] and electrorheological (ER) clamping [23] have also been attempted, but the clamping forces produced were less than 1 kgf. Recently mechanical locking MEMS ridges were used in a Mesoscale Actuator Device (similar to an inchworm motor) to replace the frictional clamp [24]. The feasibility of the MEMS ridges was tested and validated for interlocking efficiency, load transfer capability (36 MPa), and engagement frequency up to 500 Hz [25-27]. However, a detailed design of an operational frequency rectification device was not presented.

The main objective of this study is to design a device that integrates piezoelectric stacks and MEMS ridges in a linear motor design. FEM analysis is used to design a prototype device that is subsequently tested. The device is designed to push and pull 450N (i.e. peak to peak amplitude of 900N) at 11 mm/sec in a relative compact size (72 mm x 32 mm x 6.5 mm). The specific power for the device is calculated to be 99 W/kg neglecting the mass associated with power supplies.

DESIGN OF MESOSCALE ACTUATOR DEVICE

An illustration of the device is shown in Fig. 1. It contains four sets of MEMS ridges, three piezoelectric stacks, two guide rods, and a housing. The housing includes ridge blocks for

Paper presented at the RTO AVT Symposium on "Active Control Technology for Enhanced Performance Operational Capabilities of Military Aircraft, Land Vehicles and Sea Vehicles", held in Braunschweig, Germany, 8-11 May 2000, and published in RTO MP-051.

attachment of the MEMS ridges and load blocks to transfer mechanical loads from the housing to the piezoelectric stack. The housing is attached to a structure through bolts in the middle of the casing. The middle casing is also adhered to the structure to further enhance load transfer. The three critical features that determine power output of the device are the piezoelectric stacks, MEMS ridges, and housing.

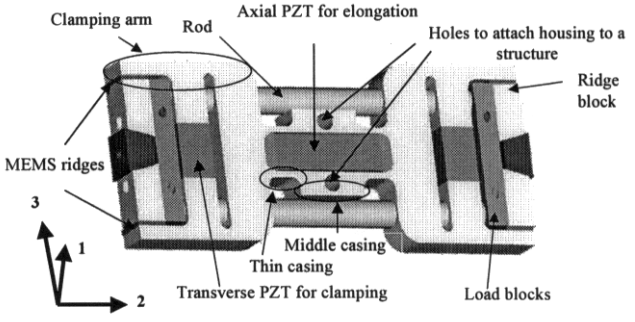
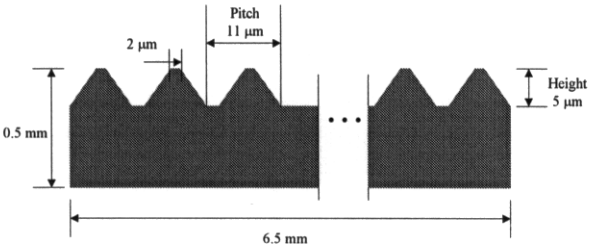


Fig. 1 A prototype device

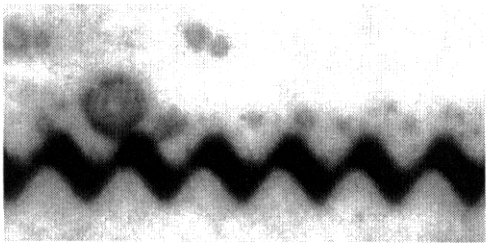
There are several beneficial features associated with the piezoelectric design in the device. First, without an applied voltage (i.e. fail safe), all four ridges are engaged and the device is locked into place. Another advantage associated with the design is that only positive electric field are applied to disengage and engage as well as to elongate or contract the inchworm motor. This reduces hysteresis, eliminates ferroelectric switching, and reduces fatigue degradation. In addition, the axial piezoelectric stack is preloaded with a 450N compression load. This mechanical bias allows the piezoelectric stack to externally pull 450N in addition to pushing 450N (stack takes up to 1000N). All of the piezoelectric stacks experience only compressive loads, i.e. absence of shear and tension loads.

Stack selection is based on electrical and mechanical properties including capacitance, resonant frequency, piezoelectric constants, and Young's modulus. In general, a low capacitance is preferred for high-speed operation since the required current is proportional to capacitance. The system is designed for a low voltage amplifier. For the characterization of piezoelectric stacks in the device, the reader is referred to reference [28].

A trapezoidal MEMS ridge is used in the clamping system of the device (see Fig. 2). The trapezoidal microridges offer substantial improvement over rectangular microridges by providing easy engagement and high shear strength [26]. These ridges are fabricated out of single crystal silicon and have a shear strength of 36 MPa. Two critical dimensions of the ridges are its height and pitch. The height (5 μm) of the ridges represents a minimum displacement that must be produced by the transverse (clamping) piezoelectric stack. One pitch (11 μm) of the ridge represents a minimum step that must be produced by elongation of the axial piezoelectric stack. For a detailed discussion on the MEMS ridge fabrication process, the reader is referred to references [25-27].



(a) Schematic diagram of trapezoidal microridges



(b) SEM picture of microridges

Fig. 2 Microridges used in the device

Another important consideration is the housing design. The housing design and material significantly influences the weight of the device and impacts the specific power. In addition to weight, the housing must be sufficiently stiff to prevent excessive deformation. Materials such as aluminum, titanium, and steel were considered, but steel was chosen because of its high stiffness. For a detailed discussion on the results obtained with other materials, the reader is referred to reference [27].

One complete cycle of operation consists of seven steps. These steps produce an axial displacement of 11 μm (one pitch of the ridge). Operating the device at 1 kHz produces a nominal speed of 11 mm/sec (11 μm x 1000 sec^{-1}). The operation sequence of the device is shown in Fig. 3.

(a) All ridges are engaged and locked at 0 volt.
(b) Right ridges are disengaged by elongation of the right transverse piezoelectric.
(c) Elongation of the axial piezoelectric moves the rods to the left relative to the housing.
(d) Right ridges are engaged again.
(e) Left ridges are disengaged by elongation of the left transverse piezoelectric.
(f) Contraction of the axial piezoelectric moves the rods to the left relative to the housing.
(g) Left ridges are engaged to complete the cycle.

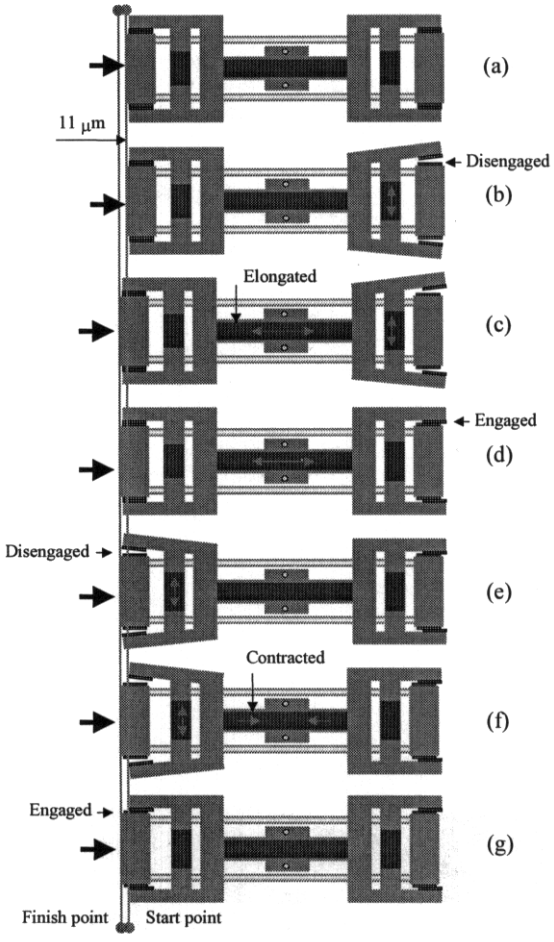


Fig. 3 Operation sequence of the device

A prcliminary analysis of the device using a simple 1-D piezoelectric model coupled with a uniform beam analysis was performed. Specifically, two areas of the housing, the thin casing and the clamping arm (see Fig. 1), were initially sized. The thin casing should permit an axial displacement of 11 μm (i.e. pitch of ridge) under mechanical loads (i.e. 450N external load plus a 450N internal mechanical bias load) while the clamping arm should permit a 5-μm (i.e. height of ridge) displacement at the ridges. In the preliminary analysis, a maximum electric field of 3 MV/m (~350 volts) was permitted but this large value was not required in the actual design. These requirements produced an initial design to begin a more detailed analysis.

A more detailed analysis using a coupled finite element model is required to adequately design the system. This model is based on the preliminary results obtained from the simple analysis. ANSYS version 5.5 was used because it provides a coupled-field analysis [29]. Several assumptions were made in developing the FEM analysis. First, it is assumed the problem is plane stress ($\sigma_{11} = \sigma_{12} = \sigma_{13} = 0$). This is reasonable because the device is load free and thin in the 1 direction. In the local coordinate system, the 1 direction is the thickness direction of the device while the 2 direction is the polarization direction of the axial piezoelectric stack (see Fig. 1). Second, the piezoelectric is assumed to be linear. Third, temperature is constant at room temperature. Fourth, steel and silicon are isotropic while the piezoelectric is transversely isotropic. Finally, the piezoelectric stacks can be modeled as a monolithic piezoelectric. The constitutive coupled equations for a piezoelectric are

$$\sigma_{ij} = c^{E}_{ijkl}\varepsilon_{kl} - g_{mij}E_m$$
$$D_m = g_{mij}\varepsilon_{ij} + e^{\varepsilon}_{mp}E_p \qquad (1)$$

where σ_{ij} is stress, c^{E}_{ijkl} is stiffness at constant electric field, ε_{ij} is strain, g_{mij} is piezoelectric coupling coefficients, E_m is electric field, D_m is electric displacement, and e^{ε}_{mp} is dielectric permittivity at constant strain. The piezoelectric coupling coefficients, g_{mij}, can be obtained by taking an inner product ($g_{mkl} = c^{E}_{ijkl}\, d_{mij}$). The general relationship between the displacement and the voltage are

$$\varepsilon_{ij} = \frac{1}{2}(u_{i,j} + u_{j,i})$$
$$E_i = -\phi_{,i} \qquad (2)$$

where u_i is displacement and ϕ is electric potential (voltage). ANSYS uses linear interpolation functions to approximate the displacements and voltages. These relations are used to satisfy the governing equations in the average sense. The governing equations are

$$\sigma_{ij,i} = \rho\ddot{u}_j$$
$$D_{i,i} = q \qquad (3)$$

where ρ is the density and q is charge. The dot above the displacement of u signifies partial time differentiation. By substituting Eq. (2) into (1) and subsequently into (3), a numerical method can be used to solve for the static and dynamic response of a structural analysis. Solution to these equations can be used to predict stresses, displacements, and mode shapes.

Two element types were used in the model. One element type is a 2-D plane stress solid structure for steel and silicon. The other element type is a 2-D element for piezoelectric materials that has structural field capability with limited coupling between the fields. The total number of elements used in the mesh is 3844. Those areas expected to have high stress concentration were meshed with a finer mesh compared to other areas. Mesh refinement techniques were used to verify that the stress values had converged. Static analysis was used to evaluate stresses and displacements while modal analysis was used to predict the resonance frequencies.

The housing is physically attached by bolt holes to a rigid structure (see Fig. 1). Therefore, the displacement boundary condition at/near the bolt holes is fixed and can be best represented by 0 displacement in the x and y direction. A reaction load defined by F_R is used to represent the load on the housing due to the mechanical preload (450N) on the stack. In addition to the reaction load, an external mechanical load is also applied to the device. The external load can vary from a maximum compressive load of 450N to a maximum tensional load of 450N. A wide range of external mechanical loads were studied [30] with the worst case scenarios presented in this paper. The worst loading case scenario is a maximum compressive load of 900N on the stack (i.e. external

compression mechanical load of 450N plus preload of 450N). The voltage on the piezoelectric stack is applied as a potential difference ($\Delta\phi$) between the two ends of the piezoelectric rather than each individual layer. This is acceptable if the global response of the piezoelectric stack is desired rather than internal stress/elastic field concentration in the stack.

Based on stresses obtained in the static results, a fatigue analysis was used to determine the life of the device. The endurance limit and tensile strength for the steel used in the housing (steel 4340) is 381 MPa and 774 MPa, respectively [31]. The modified endurance limit for fatigue was calculated using the equation by Marin [32]. The safety factor was found using the modified Goodman relation.

PROTOTYPE FABRICATION AND TESTING

A prototype device (see Fig. 4) was fabricated using a CNC milling machine. The prototype was used to evaluate translation and clamping mechanisms at low frequencies without an external load. Aluminum was used for the prototype device. Generally, aluminum is easier to machine than steel. The fabrication of a steel structure requires Electrical Discharge Machining (EDM) technique which was not available at the time when these tests were conducted.

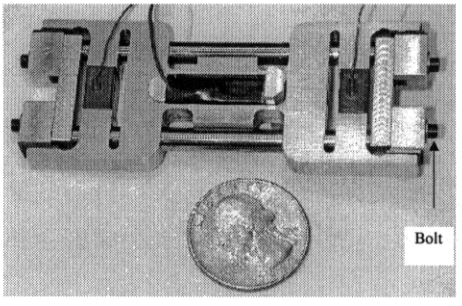


Fig. 4 Prototype device

Assembling the device is a critical process. There are several steps in assembling the device. Integrating the guide rods into the housing is a first step. This is done by honing the guide holes in the housing until an acceptable fit is obtained. If the fit is too loose, the microridges will become unaligned after a few stepping sequences. The second step is to integrate the axial piezoelectric stack in the housing. The position of the stack is adjusted and preloaded with a spacer until symmetrical displacements are produced. The spacer has a set screw that can be turned to preload the stacks up to 450N with an internal mechanical bias. Third, the transverse piezoelectric stacks are inserted. The mechanical slots are mechanically stretched until they are sufficiently wide to accommodate the stack. The return force from this distortion is sufficient to marginally preload the stacks and mechanically retain them during operation.

Mounting the ridges is the last step. The ridges are mounted in several stages. There are a total of eight ridges. Four ridges are first mounted to ridge blocks (one ridge for one ridge block) using TRA-BOND F113 epoxy adhesive. Each of four ridges is then engaged with one of the other four ridges. Each set (4 sets) of ridges is kept engaged until their introduction to the device. The assembled ridge blocks with the engaged ridges are mounted on the clamping arm using an epoxy adhesive. The assembled ridge blocks are then assembled to the load blocks with bolts (See Fig. 1 & Fig. 4). Assembly in this manner ensures proper spacing and engagement of the ridges on an assembled device.

Adhesives used to adhere the microridges to the device was evaluated. Two different epoxy adhesives were studied. One is fast cure epoxy adhesive, Araldite 2043 90-second multi-purpose epoxy adhesive, and the other is slow cure epoxy adhesive, TRA-BOND F113 high impact optically clear epoxy adhesive. These two epoxy adhesive are easy to handle, available, and low cost. Pot life and cure time are 90 seconds and 2 hours for the fast cure adhesive and 2 hours and 24 hours for the slow cure adhesive.

The bonding strength for steel-to-silicon was measured based on a single lap shear test (ASTM D1002) with some modifications. The modification was necessary since silicon cannot be gripped in a testing machine. Two steel pieces (air-hardened precision ground flat stock, AISI-SAE D-2) were adhered to a diced silicon wafer. The steel was prepared based on ASTM standard dimensions (101.6 mm x 25 mm and 1.62 mm). The silicon was prepared from one-side polished (100) wafers with thickness of 0.5 mm. The overlapped area was 12.7 mm x 25 mm based on the ASTM D1002. To minimize any bending and distortion caused by unaligned loading due to thickness of specimen, two extra steel plates were inserted into the grips. The specimens were loaded at a rate of 0.26 mm/min. Seven specimens for each adhesive were tested.

The prototype device was tested in a probe station. The piezoelectric stacks in the device were driven with a TREK model 50/750 High Voltage (HV) power supply. Dial gauge (see Fig. 5) was used to measure the travel distance of the device. Before operation, various voltages were manually applied to find the voltages required to produce an axial 11-μm displacement and a transverse 5-μm displacement. The required voltages were entered into the control software to operate the device 11, 110, 550, and 880 μm back and forth in the frequency range of 1 to 80 Hz. The testing was limited to 80 Hz due to limitations of the amplifier (100 mA) at 250 volts. The amplifier cannot supply the required current to operate the piezoelectric stack dynamically at frequencies larger than 80 Hz if the applied voltage is higher than 250 volts. A 1 kHz frequency is possible with a higher current amplifier.

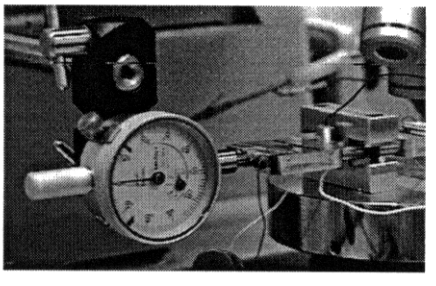


Fig. 5 Testing setup

RESULTS AND DISCUSSION

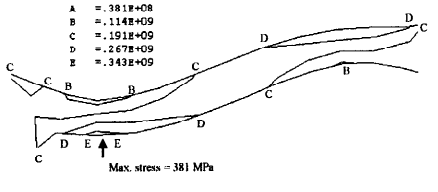
The FEM analysis was used to predict displacements and stresses in the device. The static analysis was first used to evaluate the axial displacements of the ridges due to elongation of the axial piezoelectric stack. An external mechanical load of

450N (compression) as well as an internal reaction load of 450N was applied in the model. Therefore, the maximum compression load on the piezoelectric is 900N load ($F_E + F_R$). This represents a worst case loading scenario. The axial displacement between the left and the right ridges is larger than 11 μm when a 330 volts is applied on the axial stack. This displacement is calculated by adding the displacement of 2.71 μm at left ridges and the displacement of 8.77 μm at the right ridges. This result indicates that the device can step the necessary 11 μm under a maximum compression load.

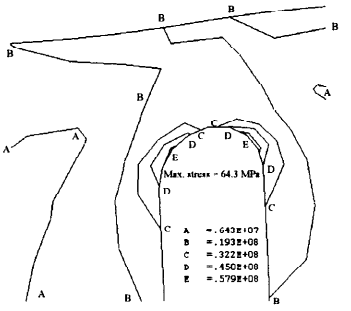
Similarly, a transverse displacement due to elongation of the transverse piezoelectric using static analysis is evaluated. Since the transverse piezoelectric stack is loaded only with a moderate compressive loading, a reaction load due to the small preload is not required. The displacement at ridges indicates that a 5.13-μm displacement is produced when 257 volts is applied to the transverse piezoelectric stack. This result verifies that the ridges can be engaged and disengaged in the device.

To evaluate the accuracy of the FEM model, the data was compared to experimental results. The required voltages for the transverse piezoelectric stack and the axial piezoelectric stack in the aluminum prototype without a external mechanical load were measured to be 225 volts and 235 volts, respectively. The displacements were measured using a microscope with a resolution of ± 0.25 μm. When the experimental results are compared to FEM results, the discrepancy is less than 6.7%. The result confirms that the finite element analysis is accurate and sufficient to predict actual static motion of the device.

The static analysis results were also used to assess the device durability. A fatigue analysis based on Von Mises stresses was used. The "worst" case scenario of maximum voltage and maximum mechanical load was used to evaluate fatigue life. These conditions are voltage (330 volts) and tension or compressive mechanical loads of 900N ($F_E + F_R$). As mentioned in the earlier section, two areas of the housing, the thin casing and the clamping arm, are potential fatigue failure regions during operation. The contour plot of Von Mises stress in the casing area of the housing (see Fig. 1) is shown Fig. 6(a). At the casing, the maximum and minimum Von Mises stress during operation is found to be 381 MPa and 0.8 MPa, respectively. Based on these stresses, the safety factor for fatigue is 1.17 using the modified Goodman relation. Safety factors higher than 1 indicate fatigue failure in this area does not likely occur during operation. Another possible fatigue failure region occurs at the end of the clamping arm, in Fig. 6(b), as shown in the contour plot of Von Mises stress. The maximum and minimum stress is 64.3 MPa and 0 MPa, respectively. The safety factor for the fatigue is calculated to be 5.76. Therefore, based on these results, the device can continuously operate for infinite life ($>10^8$) without fatigue failure.



(a) Contour plot of Von Mises stress at the casing in the device



(b) Contour plot of Von Mises stress at the end of clamping arm

Fig. 6 Contour plots of Von Mises stress created using FEM

Resonance frequencies of the unloaded device as well as mode shapes were found using modal analysis. The first mode shape of the device is a bending mode. The first resonance frequency is 1777 Hz which is higher than the operational frequency of the device at 1 kHz. The next two natural frequencies occur at 1817 Hz and 5487 Hz, respectively. When mechanical loaded or small amounts of damping is added, the frequencies should be further shifted upward. These results indicate that the device can be operated at 1 kHz.

The bonding strength of adhesives used to mount the ridges was measured. Based on the single lap shear test, the bonding strength of the fast cure epoxy was much lower than the bonding strength of slow cure epoxy. The average bonding strength of the fast cure and slow cure adhesive is 2.68 MPa and 7.22 MPa with a standard deviation of 0.47 MPa and 3.31 MPa, respectively. Most specimens had failures of the adhesive at the interface between silicon and adhesive suggesting poor surface preparation. In the strength test that yielded the highest value, it was observed that a uniform adhesive layer existed with few voids. Therefore, the bonding strength tests confirm that the adhesive can support more than 450N shear load with two engaged ridge sets of 6 mm x 6.5 mm glued area.

A prototype was tested for motion at different speeds. In Fig. 7, a plot of displacements versus time for three different frequencies is illustrated. For continuous stepping of the device, a voltage of 235 volts for both the transverse and axial piezoelectric stack was used in the control software to simplify the control program. Successful forward and backward linear motion was observed at all frequencies. This linear motion of the prototype using MEMS ridges validated that MEMS ridges successfully replaced the static friction as clamping system of the linear motors with potential higher load transfer.

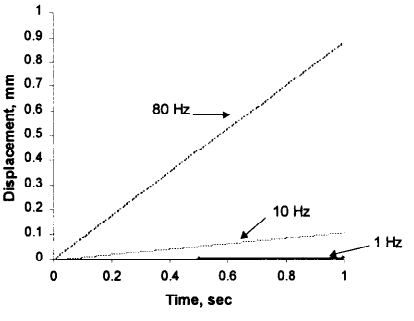


Fig. 7 Displacements measured under three different frequencies

CONCLUSIONS

A device producing large displacements and large force outputs was designed using FEM analysis. The analysis demonstrated that the device can step the necessary 11-μm displacement for the worst case loading scenario at 1 kHz. The bonding strength of the adhesives was also evaluated to ensure that failure does not occur in the bonded area of the ridges on the clamping arm. Results indicate that the adhesive supports more than 450N shear load required. An aluminum prototype device was fabricated and tested. Under open-loop control, continuous forward and backward stepping motion was observed at frequencies up to 80 Hz. Excellent agreement between the analysis and testing results was observed with a discrepancy less than 6.7 %.

ACKNOWLEDGEMENT

The authors gratefully acknowledge the support from John Prater, contract monitor, and the Army Research Office under the contract number DAAH04-95-1-0095.

REFERENCES

1. Walz, C. and I. Chopra. 1994. "Design and Testing of a Helicopter Rotor Model with Smart Trailing Edge Flaps," Presented at the 35th Structures, Structural Dynamics and Materials Conference, Adaptive Structures Forum, April 1994:309-319.
2. Narkiewicz, J. P. and G. T. S. Done. 1994. "Overview of Smart Structure Concepts for Helicopter Rotor Control," Presented at 2nd European Conf. on Smart Structures and Materials, Glasgow 1994:242-245.
3. Friedmann, P. P. and T. A. Millot. 1995. "Vibration Reduction in Rotorcraft Using Active Control: A Comparison of Various Approaches," Journal of Guidance, Control, and Dynamics, 18(4):664-673.
4. Spencer, B. T. and I. Chopra. 1996. "Design and Testing of a Helicopter Trailing Edge Flap with Piezoelectric Stack Actuator," Presented at SPIE's 1996 Symposium on Smart Structures and Materials, February 1996:120-131.
5. Tzou, H. S. 1991. "Design of a piezoelectric exciter/actuator for micro-displacement control: theory and experiment," J. J. Soc. For Prec. Eng., 13(2):104-110.
6. Tiersten, H. F. 1969. "Linear piezoelectric plate vibrations," Plenum Press, New York:55.
7. Koshigoe, S. and J. W. Murdock. 1993. "A Unified Analysis of Both Active and Passive Damping for a Plate with Piezoelectric Transducers," J. Acoust. Soc. Am. 93(1):346-355.
8. Jones, L. D., D. V. Newton, and E. Garcia. 1993. "Adaptive Devices for Precise Position Control," Proceedings of the SPIE, 1917:648-659.
9. Toshiyoshi, H., H. Fujita, T. Kawai, and T. Ueda. 1993. "Piezoelectrically operated actuators by quartz micromachining for optical application," Proceedings of IEEE Micro Electro Mechanical Systems:133-138.
10. Jones, L. and E. Garcia. 1994. "Self-sensing Control as Applied to a PZT Stack Actuator used as Micropositioner," Proceedings of the SPIE, 2190:228-237.
11. Bexell, M, A. L. Tiensuu, J. A. Schweitz, J. Soderkvist, and S. Johansson. 1994. "Characterization of an inchworm prototype motor," Sensors and Actuator A, 43: 322-329.
12. Zhang, B. and Z. Q. Zhu. 1994. "Design of an Inchworm-type Linear Piezomotor," Proceedings of the SPIE, 2190:528-539.
13. Morita, T., M. Kurosawa, and T. Higuchi. 1995. "An ultrasonic motor using bending cylindrical transducer based on PZT thin film," in Proc. of 1995 IEEE MEMS: 49-54.
14. Shimizu, N., T. Kimura, T. Nakamura, and I. Umebu. 1990. "An Ultrahigh Vacuum Scanning Tunneling Microscope with a New Inchworm Mechanism," Journal of Vac. Sci. Technol. A, 8:333-335.
15. Judy, J. W., D. L. Polla, and W. P. Robbins. 1990. "A Linear Piezoelectric Stepper Motor With Submicrometer Step Size and Centimeter Travel Range," IEEE Transactions on Ultrasonics, Ferroelectrics, and Frequency Control, 37(5):428-437.
16. Olin, H. 1994. "Design of a scanning probe microscope," J. of Measurement Science and Technology, 5: 976-984.
17. Robbins, W. P. 1995. "Ferroelectric-Based Microactuators," Integrated Ferroelectrics, 11:179-190.
18. Polla, D. L. 1997. "Application of PZT Thin Films in Microelectromechanical Systems," Proceedings of the SPIE, 3046:24-27.
19. Robbins, W. P., D. L. Polla, and D. E. Glumac. 1991. "High-displacement piezoelectric actuator utilizing a mender-line geometry-Part I: Experimental Characterization," IEEE Transactions on Ultrasonics, Ferroelectrics, and Frequency Control, 38(5):454-459.
20. Catalog of Burleigh Instrument, Inc. 1975. "Micro Positioning System," Fisher, NY.
21. Kurosawa, M., H. Yamada, S. Ueha. 1989. "Hybrid Transducer Type Ultrasonic Motor Using Flexural Vibrator," J. J. Appl. Phys., 30:209-211.
22. Miesner, J. E. and J. P. Teter. 1994. "Piezoelectric/Magnetostrictive resonant inchworm motor," Proceedings of the SPIE, 2190:520-527.
23. Dong, S., L. Li, Z. Gui, T. Zhou, and X. W. Zhang. 1995. "A New Type of Linear Piezoelectric Stepper Motor," IEEE Transactions on Components, Packaging and Manufacturing Technology, Part A, 18(2):257-260.
24. Zhu, J., D. Wang, C. J. Kim, and G. P. Carman. 1996. "Development of Mesoscale Actuator Device," Proceedings of ASME Aerospace Division, IMECE'96:649-654.
25. Chen, Q. D. J. Yao, C. J. Kim, and G. P. Carman. 1998. "Development of mesoscale actuator device with microinterlocking mechanism," Journal of Intelligent Material Systems and Structure, 9: 449-457.
26. Chen, Q., D. J. Yao, C. J. Kim, and G. P. Carman. 1998. "Influence of Fabrication and Crystal Orientation on the Strength of Silicon Microridges," Proceedings of MEMS, ASME Int. Mech. Eng. Congress and Exposition, DSC-66:413-420.
27. Chen, Q., L. H. Chu, D. J. Yao, G. P. Carman, and C. J. Kim. 1999. "Investigation of Large Force Mesoscale Actuator Device and Strength of Its Microridges," submitted to ASME conference.
28. Park, J., Mitrovich, M., Carman, G. P., and H. T. Hahn. 2000. "Design and Testing of a Mesoscale Actuator Device (MAD)," Proceedings of SPIE, 3985.
29. Manual of ANSYS, "Direct coupled-field analysis," Chapter 3.
30. Park, J. 1999. "Design and testing of Mesoscale Actuator Device," Prospectus of thesis dissertation, University of California, Los Angeles: 41.
31. Baumel, A and T Seegur. 1990. "Materials Data for Cyclic Loading," Elsevier Science Publishing Company, Inc., Supplement 1:A.154-A.156.
32. Marin, J. 1962. "Mechanical behavior of engineering materials" Prentice-Hall, Englewood Cliff, N. J.:224.

ADAPTIVE ROTOR BLADE CONCEPTS -DIRECT TWIST AND CAMBER VARIATION-

A. Büter , U.-C. Ehlert , D. Sachau , and E. Breitbach

German Aerospace Center (DLR), Institute of Structural Mechanics
Lilienthalplatz 7, 38108 Braunschweig, Germany

ABSTRACT

Applying adaptronics to helicopters has a high potential to significantly suppress noise, reduce vibration and increase the overall aerodynamic efficiency. Since the interaction of non-stationary helicopter aerodynamics and elastomechanical structural characteristics of the helicopter blades causes flight envelope limitations, vibration and noise, a good comprehension of the aerodynamics is essential for the development of structural solutions to effectively influence the local airflow conditions and finally develop a structural concept. With respect to these considerations, this paper presents recent investigations on two different structural concepts: the direct twist and the camber variation concept.

The direct twist concept allows to directly control the twist of the helicopter blades by smart adaptive elements and through this to positively influence the main rotor area which is the primary source for helicopter noise and vibration. The concept is based upon the actively controlled tension-torsion-coupling of the structure. For this, an actuator is integrated within a helicopter blade that is made of anisotropic fibre composite material. Driving the actuator results in a local twist of the blade tip, in such a way that the blade can be considered as a torsional actuator. Influencing the blade twist distribution finally results in a higher aerodynamic efficiency. The direct twist concept was analytically modelled using an expanded Vlassov Theory before a proof-of-principle demonstration structure was manufactured. Subsequently, a Mach-scaled Bo105 model rotor blade with an integrated piezoelectric actuator was designed and successfully tested. Next, small scale rotor tests and investigation of thermal loads are planned.

The camber variation concept uses the experiences gained in the design of the direct twist concept to create a rotor blade, that will be able to change the shape of its cross-section in operation. This shape control approach uses material anisotropy (e.g. tension-torsion-coupling) to create a smooth aerodynamic surface and to avoid the airflow disturbances created by the leading or trailing edge flaps, that have already been investigated. First, a structural model was numerically investigated to identify the most influential parameters of this concept. From this model, the two-dimensional surface quality of the deformed rotor blade was extracted as a basis for aerodynamic calculations that are necessary to derive the quantity of deformation needed to successfully delay aerodynamic stall onset. As a next step, a proof-of-principle structural demonstrator is presently being designed.

Both concepts were designed to be activated using a piezoelectric stack-actuator integrated at the blade tip. Since continiuously integrated piezo sheets promise a potential to increase the concepts' performance, thin actuator modules are currently under investigation.

1. INTRODUCTION

Present helicopter research mainly focuses on the improvement of the aerodynamic efficiency and on the reduction of vibrations and acoustic emissions. A direct approach is aiming at the physical sources of these problems. This can be reached by adaptive structural technology.

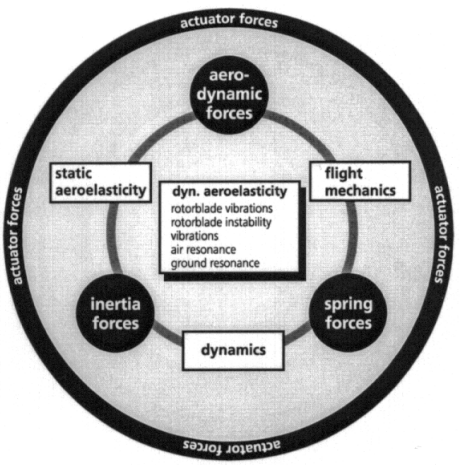


Figure 1: Adaptive aerolastic system

In general, helicopter vibrations and noise exist in all flight cases mainly due to the unsteady working conditions of the blade. This results

Paper presented at the RTO AVT Symposium on "Active Control Technology for Enhanced Performance Operational Capabilities of Military Aircraft, Land Vehicles and Sea Vehicles", held in Braunschweig, Germany, 8-11 May 2000, and published in RTO MP-051.

from interactions between the highly non-stationary aerodynamics induced by the rotating rotor blades and special aerodynamic phenomena like the stall effect at the retreating blade and the transonic effect at the advancing blade. All these vibrations are of a highly dynamic nature. The Blade Vortex Interaction (BVI) phenomenon in descent flight is extremely penalising as far as external noise is concerned.

The comprehension of this relationship between the aerodynamic sources and the resulting vibrations and noise is the basis for optimally designed control concepts. Special emphasis is placed on the optimisation of the standard blade control and active control of the blade deflection as the primary tools.

The different kinds of forces which are involved in adaptive rotor dynamics are shown in figure 1. The triangle of forces describes the passive aeroelastic system. In the adaptive aeroelastic system the aerodynamic, inertia and spring forces are influenced by actuator forces or by excited blade deflections.

All aerodynamic effects react highly sensitive to small variations of angle of attack and inflow velocity. Therefore, the main idea of the measures mentioned below, which aims at the reduction of vibrations and acoustic emission, is to dynamically change the blade pitch (twist) or the rotor blade characteristics. Different means are considered for this, e.g. adaptive blade twist, deformable airfoil sections or additional trailing edge flaps.

2. Overview of Conventional and Adaptive Concepts for Vibration and Noise Reductions

In general, control concepts can be divided into two categories (shown in figure 2) depending on where the control forces are introduced. Category I includes all control concepts that are based on blade actuations at the blade root. This can be done by the use of control rods or, alternatively, by designing an adaptive blade root.

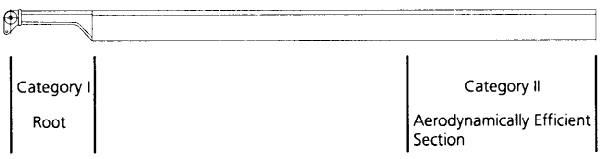


Figure 2: Locations for the use of adaptive material systems

Current research on rotor dynamics has resulted in the design and evaluation of two control concepts to counteract noise and/or vibration, which falls into category I. These concepts can be superimposed on the cyclic blade control deflections: higher harmonic control (HHC) and individual blade control (IBC). These additional mechanisms are two possible approaches to improve the aerodynamic efficiency and to reduce the vibration and noise levels, respectively. HHC is principally based on standard cyclic blade pitch changes using the first rotor harmonic (rotation frequency) to which higher harmonic control motions are added. The angle of attack, the inflow velocity, and the blade deformations can be influenced by these control motions.

IBC is similar to HHC, but the control forces are individually applied to each blade, thus forming a superposition to the global cyclic blade actuation.

By using the control concepts described above, the whole blade is actuated at the root. Aerodynamic reaction is induced after the control forces have travelled through the elastic structure of the blade. As the blade with its high aspect ratio is a highly elastic system, the aerodynamic forces are nonstationary and dependent on the spanwise coordinate and the blade motion. This requires control inputs of a dynamic nature and the evaluation of this system can be achieved only on the basis of global aspects. The real efficiency of this control approach is not clearly assessable.

Category II covers the aerodynamic efficient blade tip section. Here, the concepts aim at the control of the aerodynamic forces which interact with the blade motion.

One example which falls within category II is the *trailing edge flap* (15), which is able to influence lift and aerodynamic moments by flap deflections, is a second concept. However the efficiency of these flap concepts is questionable in respect to long blades with low torsional stiffness. Additionally, blade torsion due to the rudder moments and the additional vortices caused by changes in the lift distribution due to the flap may lead to problems. The trailing edge flap can be interesting for quite rigid blades to create a more adequate lift variation in oder to minimise the vibration and also the noise. It is the so called *Direct Lift Flap Concept* that has been studied especially by ONERA in the co-operation on *Active Blade Concepts* between France and German.

The second concept is the *adaptive twist control*. Investigations on this concept will be described in detail below.

The *adaptive camber variation* investigates active deformations of the cross-section on rotor dynamics. The principle of this actuator concept is presently being developed at the DLR and will be described in detail below.

3. Adaptive Blade Twist

In this concept, the rotor blade twist, especially at the outer part of the rotor, can be achieved by the following actuator principles:

- Torsion caused by a servo-flap (15)
- Torsion caused by 45° orientated tension forces (15),(9),(3),(13),(2)
- Torsion due to torsion-warping-coupling (5)
- Torsion due to torsion-tension-coupling (6),(9)

3.1 Torsion caused by a servo-flap

According to this actuator concept, the flap deflection should produce aerodynamic rudder moments leading to a torsional deflection of the blade. This concept called *servo-flap concept* is more adapted to blades with reduced torsional stiffness. The efficiency of this concept is questionable in respect to the change of the lifting force due to the flap deflection, which counteracts the lifting force caused by the blade twist (figure 4). Additionally, two new vortices caused by the change in the lift distribution due to the flap may lead to new BVI as well as the above mentioned *trailing edge flap*.

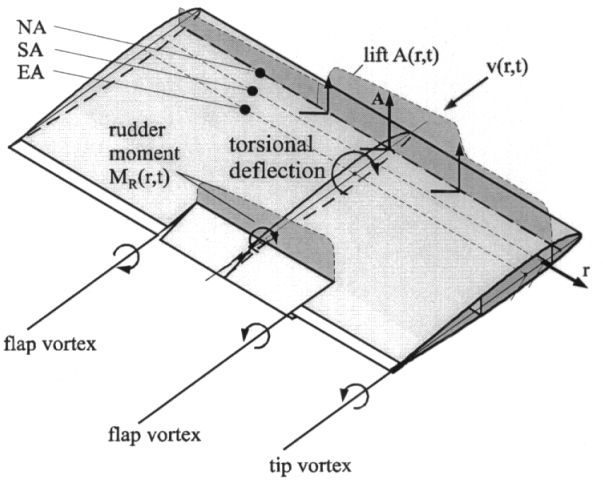


Figure 4: Different approaches by using flaps

A further disadvantage of this concept for using aerodynamic forces is the non-stationary character of the rotor aerodynamics. Constant flap deflections cause non-stationary rudder moments which lead to non-stationary torsional excitation of the rotor blade.

3.2 Torsion caused by tension forces oriented at 45°

In this concept, shown in figure 5, torsional moments caused by tension forces are utilised. Thin-walled actuator materials like piezoceramic plates or active fibers have to be implemented in the skin of the rotor blade to activate it.

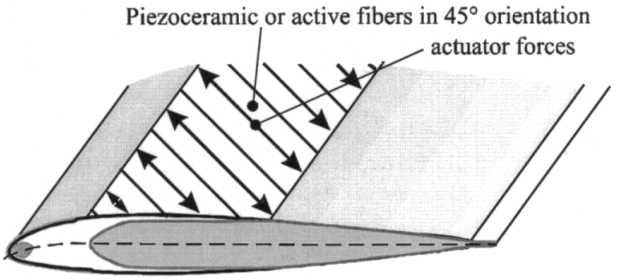


Figure 5: Torsion induced by tension forces

The advantage of this simple concept, that acts in the flux of work, is the good control characteristic. However, the effects of centrifugal forces and the blade flexions have to be taken into account to have access to an efficient design.
One disadvantage of this concept is the insufficient damage tolerance behaviour.

3.3 Torsion due to torsion-warping-coupling

As shown in figure 6, the torsional deformations of the rotor blade are caused by warping forces.

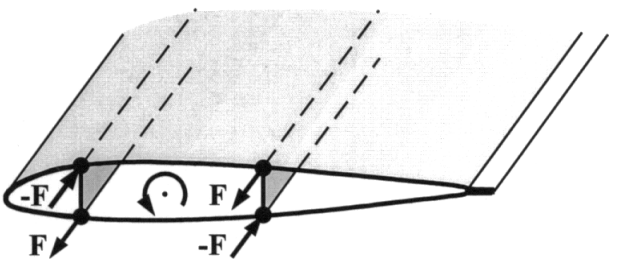


Figure 6: Torsion induced by warping forces

In comparison to the previously mentioned concept, cylindrical actuators, for example piezoelectric elongators (piezo-stacks) can be used to induce warping. It is however necessary to change the geometry of the rotor blade cross section to realise this warping-torsion-coupling. The locally restricted effect of the warping forces, the changes in the geome-

try, and the installation space of the actuators may cause problems for implementing this concept into a rotor blade.

3.4 Torsion due to torsion-tension-coupling

In general, torsion-tension-coupling is an anisotropic behaviour which appears in structural components. It can be realised by orientated stiffness. The anisotropic material behaviour clearly has to be separated from the anisotropic structure behaviour resulting from structure elements like ribs or stringers.

In this concept anisotropic material behaviour caused by helical winding is illustrated in figure 7.

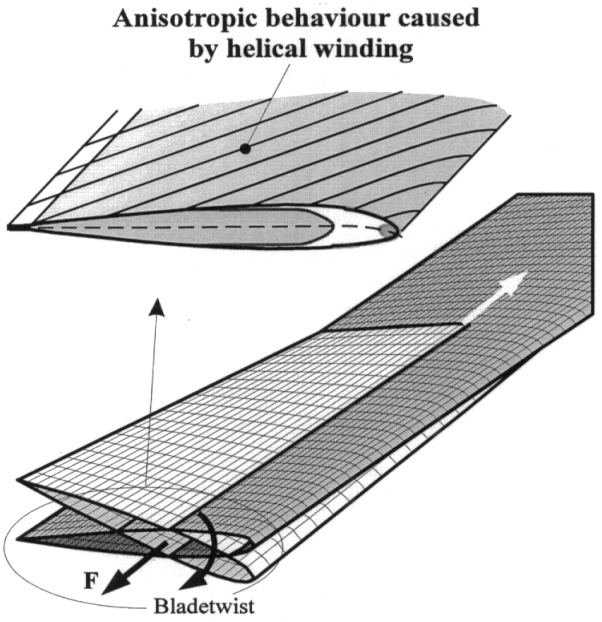


Figure 7: Adaptive blade twist

For practical realisation, cylindrical actuators like piezoelectric elongators (piezo-stacks) can also be used. A disadvantage of this concept is the high spanwise stiffness of the rotor blade spar. Thus, an uncoupling layer between the spar and the skin is needed. An actuator supported at the rotor blade spar generates the axial forces. The principle of this actuator concept is presently being developed at the DLR. (10)-(12)

Experimental Investigations

The experimental investigation comprises three steps.

First, structural investigations were performed based on a representative model in which the active part of the rotor blade is simplified by a thin-walled, tension-torsion-coupled, rectangular beam, that is structurally equivalent to a model rotor blade of the Bo105 with a scaling factor 2.54. The goals of these experiments were to validate the calculations and to gather first experiences with the tension-torsion-coupling and the resulting deformation behaviour. The results are valid for static and dynamic conditions. For the dynamic condition excessive deformations near the blade resonance frequency shall be utilised. Therefore, the actuated blade section has to be properly designed for these preconditions. This has been demonstrated and verified in experiments (7).

In the *second step* the development of a suitable manufacturing technique, the realisation of a simplified rotor blade with tension-torsion-coupling and measurement of the deformation behaviour were investigated.
The technical challenge of the adaptive blade twist concept is the high spanwise stiffness of the rotor blade spar. Thus, an uncoupling layer between the spar and the skin is required. For these experimental investigations the skin of the outer part of three model rotor blades was manufactured of fibre composite material using the above mentioned tension-torsion-coupling effect with different kinds of uncoupling layers between skin and spar.

Blade I: Uncoupling by rubber elements (type a).
Blade II: Uncoupling by rubber elements (type b).
Blade III: Uncoupling by friction.

The simplified cross-section is shown in figure 8.

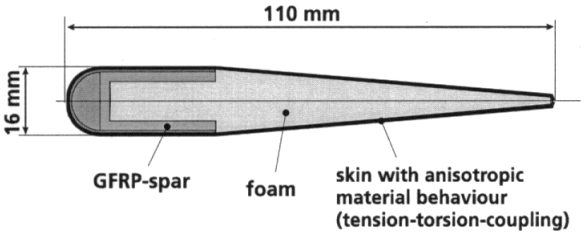


Figure 8: Simplified cross-section.

Equal to the investigation of the boxbeam a hydraulic tension proof machine was used to induce the actuator forces. The twist distribution and the torsional movements at the blade tip were measured for different harmonic tensional excitations between 1 Hz and 25 Hz. The experimental configuration and the results of the experiments are shown in Figure 9a and 9b.

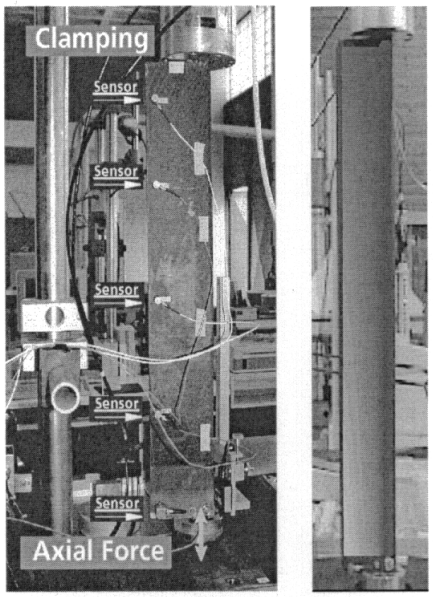


Figure 9a: Experimental configuration
(Blade Segment w. Tension-Torsion-Coupling).

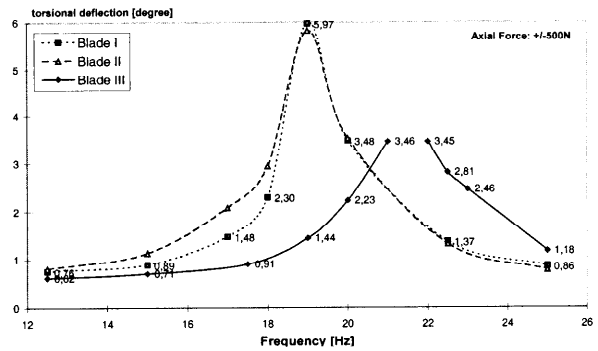


Figure 9b: Results from the dyn. tension test.

The right picture of figure 9a shows of *Blade I* the measured deflections out of plane at 19 Hz. It could be shown that for all uncoupled layers linear twist distributions are excited.

Figure 9b shows the torsional deflection at the blade tip for different excitation frequencies and actuator forces between ±550N. The differences in the torsional resonance frequencies of the three blades are caused by stiffness variations in the structures. Near the resonance frequencies at 19 Hz resp. 21.5 Hz dynamic forces of 550 ± 550 N are required for a deformation of ± 3 degrees at the blade tip.
In the dynamic tension tests the inertial mass of the hydraulic piston caused by the rotating clamping of the tensional testing machine reduced these frequencies. Nevertheless, it could be seen, that in case of harmonic excitations the necessary actuator forces to achieve a given angle of deflection are reduced in comparison to static loadings.

For the *third step* an active rotor blade with an integrated piezoelectric stack-actuator was build. The skin of this active model rotor blade was manufactured of fibre composite material using the tension-torsion-coupling effect with one of the above mentioned uncoupling layers between skin and spar. The actuator is supported at the rotor blade spar and generates axial forces at the blade tip. Figure 10 shows the active rotor blade segment with adaptive blade twist.

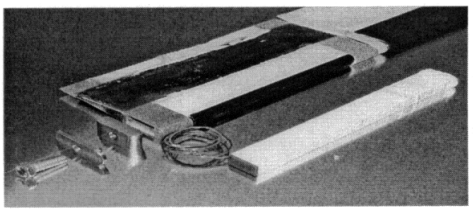


Figure 10: Active rotor blade segment.

In figures 11 the excited eigenmodes (1. Flap at 9 Hz, 2.Flap at 65 Hz and 1. Torsion at 113 Hz) are shown. Near to the torsional resonance frequencies at 113 Hz a deformation of ± 1.5 degrees is possible. For the first flapwise mode at 9 Hz deflections of ±1.2 mm were measured.

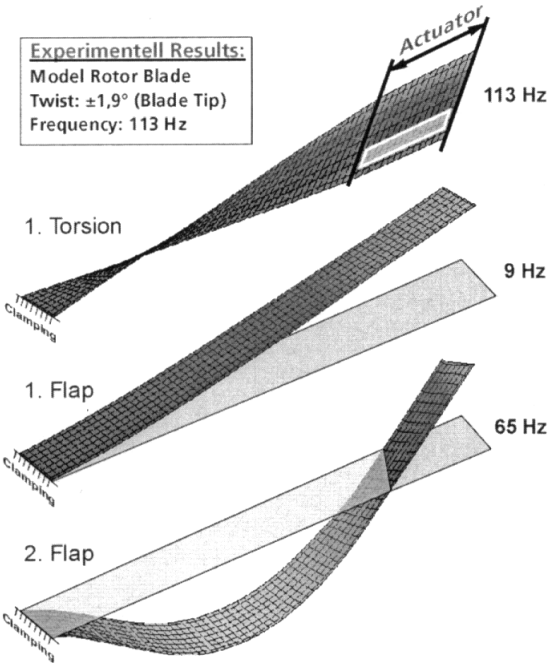


Figure 11: The first three mode shapes (3-dim).

To assess the influence of the aerodynamic, small scale wind tunnel tests were made.
Figure 12 shows for different inflow velocities the static deformations of the adaptive rotor blade segment in the wind tunnel.

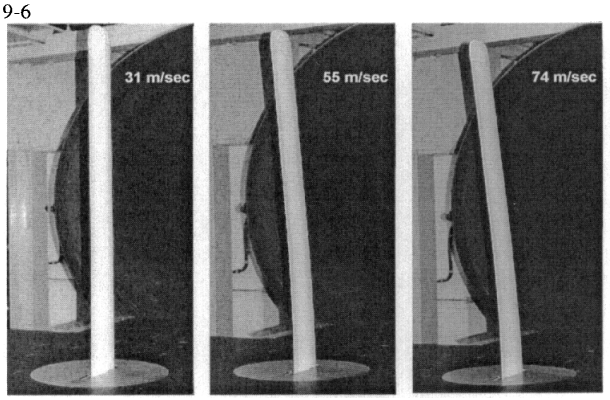


Figure 12: Static Blade Deformations.

The active rotor blade segment excited for different inflow velocities with mono-frequent excitations by 60% of the maximal actuator power. In figure 13 the measurement results are shown. Due to the positive aerodynamic stiffness (aerodynamic neutral axis behind elastic axis) the torsional deformation decreased by the inflow velocity.

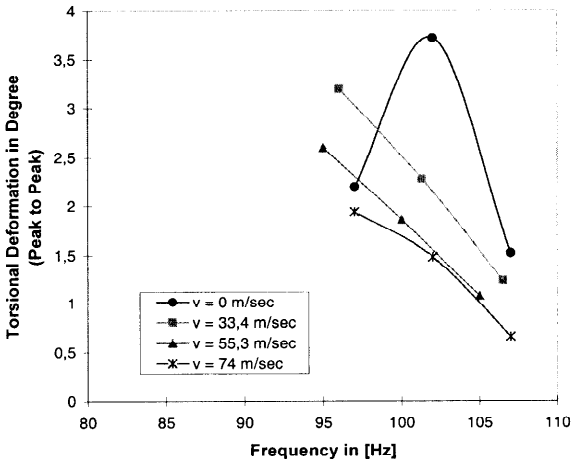


Figure 13: Active Rotor Blade
(60% of the Actuator Power)

It could be demonstrated that actuator systems based on smart materials are certainly able to excite the structure at the required frequencies and with suitable deformations. An adaptive helicopter rotor blade based on the adaptive blade twist concept could be realised. Furthermore these results show that for the rotating case the whole dynamic system has to be optimised for an efficient, dynamic working twist actuator.

With these experimental results it could be shown that:

- an adaptive fibre composite rotor blade based on tension-torsion-coupling can be manufactured.
- the uncoupling layer between skin and spar is suitable to be used for tension-torsion-coupling in rotor blades and
- a piezoelectric stack actuator is suitable to twist the blade. Near to the resonance frequency deformation of ± 1.5 degrees are possible. Therefore the actuated blade section must be specially designed for this.

It could be determined that an adaptive blade twist in the outer part of the rotor is realisable with a comparatively small effort and in its range of application, depending on the form of excitation, it shows to have a very great potential. The realisation of such a control concept, that can go from a static up to a controlled dynamic operation, is dependant on the choice of the actuator. In addition to the demands which the operation puts on this actuator, the installation space, the power specific mass, and the duration of life are further criteria which are decisive for the functionality and efficiency of this drive. Moreover the variety of applications, the small torsional stiffness and the small external forces (inertia force, propeller moment and aerodynamic force) are advantages, which make it attractive to integrate the actuator in the aerodynamically efficient outer part of the rotor. Beside these there are, based on the underlying physics, a lot of other advantages:

- It is possible to influence the aerodynamic forces at the outer part of the rotor. Disturbances induced by the flowfield can be compensated at the source.
- Its has been shown in (14) that for vibration reduction the damping of special blade modes is important. The adaptive blade twist allows active damping for important blade modes.
- Active influence of the blade deflections make it possible to reduce the dynamic stall at the retreating blade.
- Using controllers adaptive aeroelastic systems without instability can be realised.
- There is no increase of the aerodynamic drag. The actuator is completely integrated in the rotor blade and causes controlled changes of the blade twist.

4. Adaptive Camber Variation

The structural concept for an actively controllable camber variation is based upon a 3-cell blade design using tension-torsion-coupling together with piezoelectric stack-actuators to bend the cross-section about the blade axis. A

finite-element-model of an adaptive camber rotor blade is used to perform a parameter optimisation to maximise camber variation at the blade tip. Both, geometric as well as material and manufacturing parameters are evaluated.

In contrast to the active twist concepts the adaptive camber concept allows active *shape* control for rotor blades. Furthermore, no flaps or other moving parts are used so that the aerodynamic surface in the deformed state remains smooth without any gaps, edges, or dents.

Since this concept has not yet reached the same level of maturity as the adaptive twist, research efforts currently follow a different approach : prior to a detailed investigation of the aerodynamic effects of an adaptive camber variation first the exact shape of the deformed rotor blade is to be evaluated. The aim is to validate the expected surface quality of the deformed rotor blade and to collect the necessary data about the change of geometry that is required for the subsequent aerodynamic calculations.

4.1 Structural Concept

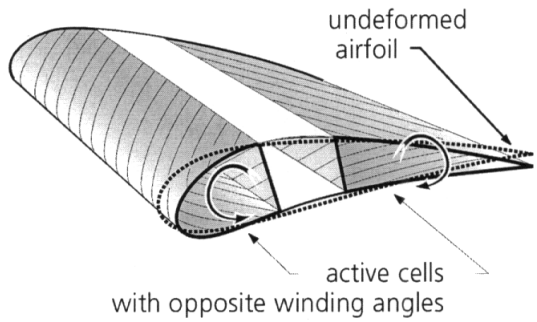


Figure 14: Principle of the Adaptive Camber Variation

The adaptive camber rotor blade has a three-cell cross-section that consists of carbon-glass-fibre composites supported by structural foam.

The desired change of camber is achieved using tension-torsion-coupling in the outer cells that are activated by piezo-electric stack-actuators integrated into the blade tip.

Manufacturing these active cells with helical windings at opposite fibre angles leads to simultaneous upward or downward movements of the blade's edges, as shown in Fig. 14. The resulting continuous change of the rotor blade's camber steadily increases from zero at the root to it's maximum at the tip.

4.2 Finite-Element-Model

The structural concept was investigated using a three-dimensional parametric model designed in a commercial finite-element code ANSYS® 5.3 (see Fig. 15). Aerodynamic as well as structural loads were not considered in the design of this model, since only the deformed airfoil's surface quality was of interest here. For the same reason, neither spars nor ribs were represented in the model rotor blade.

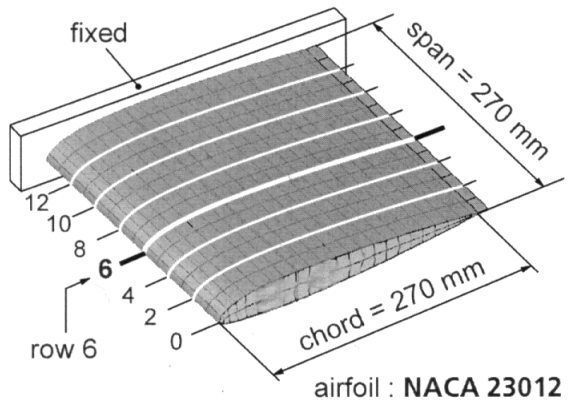


Figure 15: Finite Element Discretisation

Three different materials were used in the design of the ummerical model: Carbon-fibre-composite, glass-fibre-composite and structural foam.

The carbon-fibre-composite was used in the helical winding layers of both active cells to realise the desired tension-torsion-coupling. This composite consists of HM carbon fibre and epoxy resin with 60% fibre volume fraction.

The outer skin of the model consists of glass-fibre-composite made from glass fabric (100 g/m²) oriented at 45°. Resin material and fibre volume fraction were assumed to be the same as in the carbon-fibre composite.

Foam cores were used in each of the three cells to support the fibre layers and to guarantee the desired airfoil's shape.

The manufacturing process of a rotor blade equipped with active camber variation was supposed to begin with the active cells. First the helical carbon-fibre unidirectional (UD) layers were attached to the foam cores. Next the two outer cells were connected to the middle cell's foam core. Last the glass-fibre layers were attached as the outer skin in order to finish the rotor blade.

This process is not suitable for the design of a real rotor blade including structural and aerodynamic loads. Yet it was feasible for the proof-of-principle demonstration structure, that was required later to experimentally validate the expected deformation properties of this concept. The proposed manufacturing process determined the composite lay-up for the model, as it is shown in Fig. 16 for the model's cross-section.

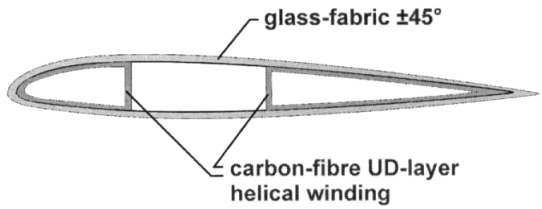


Figure 16: Composite Lay-up

Geometric as well as material parameters were considered in the evaluation of the adaptive camber concept.

Three groups of parameters were evaluated:

- the positions of the inner cell walls,
- the fibre angles of the carbon-layers, and
- the thickness of carbon- and glass-layers.

The inner cell walls' positions were given in percent chord, ranging from 15 % to 70 % for the front wall and from 35 % to 85 % for the rear wall. These parameter boundaries were arbitrarily chosen in order to allow for a wide range of possible cell wall position combinations. Furthermore, the rear wall was locally restricted, so that it was always positioned behind the front wall. This precaution was necessary for the subsequent automatic parameter optimisation. The increment was set to 5% c for both walls to keep the number of wall position combinations small.

The fibre orientation of the carbon-fibre layers ranged from 0° to 45° in the leading edge cell and from −45° to 0° in the trailing edge cell. An angular increment of 5° was chosen for both cells due to restrictions in manufacturing precision. The active cells' orientation angles were independend of each other.

The thickness of the carbon- and glass-fibre layers varied from 0.2 to 5 mm for each layer with a 0.2 mm increment according to manufacturing accuracy.

These seven parameters (2 cell wall positions, 2 fibre angles, 3 thicknesses) were investigated in the following calculations to gather information over the parameters' influence on the maximum camber variation.

4.3 Evaluation

In each of the subsequent calculations a different set of parameter values was evaluated concerning the maximum change of camber, the rearward position of this maximum, and the angle of attack at element row 6 (as illustrated in Fig. 15). These data were extracted from nodal positions and displacements within each program run and stored for later data processing.

The change of camber was calculated from the difference between the mean lines of the undeformed and the deformed rotor blade model. Therefore, the mean lines had to be extracted from the positions of FE nodes in each program run.

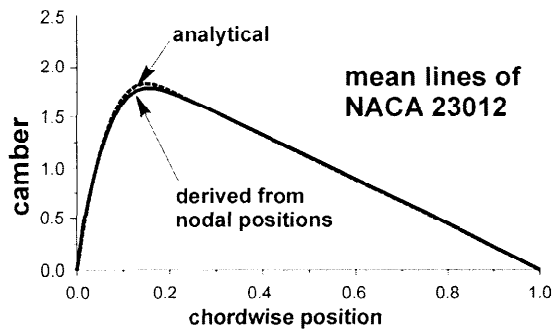


Figure 17: Comparison of Mean Lines

To prove the feasibility of this approach, the mean line of the NACA 23012 was derived from the nodal positions in the FE-model and compared to the mean line calculated from the analytical formula. The maximum difference was less than 0.1 % of the analytical mean line. This accuracy was sufficient for the subsequent parameter investigations.

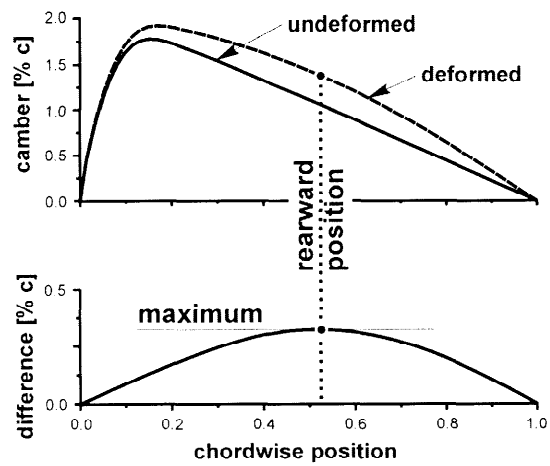


Figure 18: Change of Camber

The difference between undeformed and deformed airfoil camber gave the change of camber.

For the final evaluation of this change of camber only its maximum and the rearward position of this maximum were used, see Fig. 18.

Since both leading edge and trailing edge of the airfoil change their position when the camber variation is activated, an influence on the angle of attack was expected. For this reason, the angle of attack was derived from the displacements of the leading and trailing edge nodes prior to the evaluation of the change of camber. Afterwards, the coordinate system was rotated to compensate for the calculated blade twist before the change of camber was evaluated. In this way, the two degrees of freedom camber variation and blade twist could be investigated separately.

In general, the deformed airfoil's shape would be between two extremes. Case 1 has a rearward position of maximum change of camber between 45 %c and 50 %c and a positive angle of attack; case 2 has a rearward position of maximum change of camber beyond 65 %c and a negative angle of attack (Fig. 19).

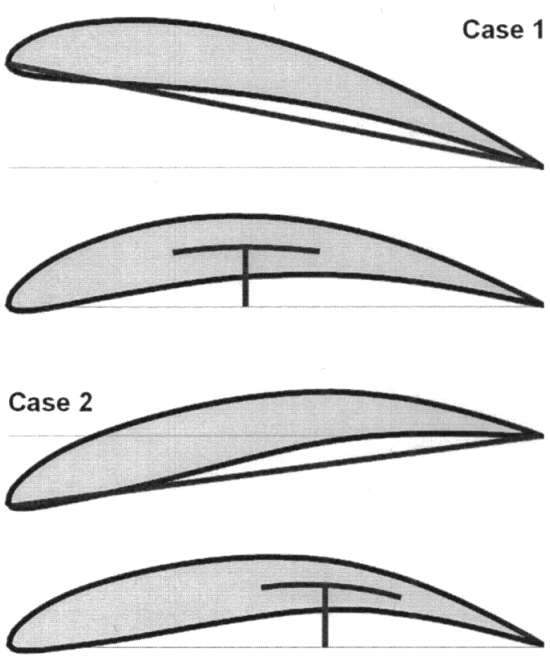


Figure 19: Two General Deformation Modes

All three parameter groups proved to have similarly great influence on the camber variation. Therefore, it was necessary to identify the combination of parameters, that yielded the largest change of camber.

4.4 Optimisation

Using the automatic optimisation capabilities of the FE-program, a parameter optimisation was performed. The thickness of the glass-fabric layer was set to 0.2 mm, all other parameters were free for variation within the given limits.

For the optimisation the resulting angles of attack were restricted to positive values, the rearward position of the maximum change of camber was constrained not to exceed 60% chord.

Under these conditions the maximum change of camber reached 0.547% chord. This was obtained from the following parameter combination :

front cell wall at 35% chord

rear cell wall at 55% chord

front carbon fibre orientation −20°

rear carbon fibre orientation 20°

carbon fibre thickness 2.0 mm

The maximum's rearward position was 52,5% chord, the angle of attack in this case was less than 0.01°.

To further increase the change of camber, it would be necessary to allow rearward positions beyond 60% chord and to accept negative angles of attack. This decision has to be taken carefully with respect to the aerodynamic effects of such an airfoil variation.

4.5 Aerodynamic Effects of Camber Variation

In order to assess the effects of the camber variation on an airfoil's aerodynamic performance, the stationary characteristics of the deformed airfoil were calculated in 2D. Therefore, the deformed airfoil shape calculated in the FE environment was transfered to a CFD enviroment to derive the desired polares.

Fig. 20 illustrates the changes in the lift coefficients c_L as a function of the angle of attack for the case 1 deformation of the NACA 23012.

Both, the effect of the camber plus the angle of attack and the effect of the camber only were investigated. The trends given in Fig. 20 were derived by scaling the deformation from the FE-calculations with a factor of 5, in order to illustrate the effect of the deformation quality.

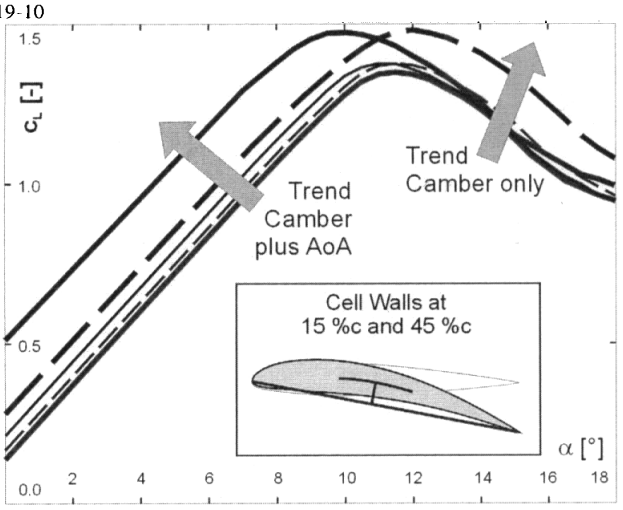


Figure 20: Aerodynamic Effects of Camber Variation

The camber variation concept proved to have the expected surface qualities in the deformed state. Steps to be taken include the consideration of thin airfoils (9% and less) to increase the maximum change of camber. Next a demonstration structure is to be designed and manufactured. The goal is to experimentally validate the deformation qualities and to investigate the dynamic properties and deformation quantities. As soon as the aerodynamic requirements are investigated another demonstration structure can be designed and manufactured taking into account the static and dynamic structural and aerodynamic loads.

5. Conclusions and Outlook

It could be demonstrated that actuator systems based on smart materials are certainly able to excite rotor blades at the required frequencies, so that a smart helicopter blade can be realised. At a lower level of maturity, a structural concept to actively change a rotor blade's aerodynamic shape in operation showed to have great potential to increase rotorcraft efficiency.

The solution of technical problems by means of adaptive structural technology must continue to be considered as a new field of research. Furthermore, the adaptive structural technology for helicopter applications is highly interdisciplinary and requires a considerable amount of research work. The comprehension of helicopter dynamics and aeroelastic interaction with the integrated adaptive structural technology is very important to reach an optimised helicopter design. A detailed evaluation of the effectiveness of this adaptive control approach can only be made on the basis of the understanding of the underlying physics. Therefore this work will be accompanied

- by investigations of alternative concepts of integrated actuators based on piezoceramic stacks, plates, films and fibres.
- by additional experimental investigations with aerodynamic loads of wind tunnel tests in nonrotating and rotating cases and
- by investigation of full-scale applications.

6. References

(1) Amerigo,M.P.; Baeder,J.D.: *Feasibility of Arbitrary Pitching Motion Controlled by Piezoceramic Actuators to Reduce Blade-Vortex Interaction Noise,* American Helicopter Society 51st Annual Forum, Fort Worth T.X., 1995

(2) Barrett,R.: *Intelligent Rotor Blade Actuation through Directionally Attached Piezoelectric Crystals,* M.S. Thesis, The University of Maryland, College Park, MD 1990

(3) Barrett,R. ; Brozoski,F. : *Adaptive Flight Control Surfaces, Wings, Rotors and Active Aerodynamics* ; SPIE Symposium on Smart Structures and Materials, San Diego, California, 1996

(4) Bielawa,R.L.: *Rotary Wing Structural Dynamics and Aeroelasticity,* AIAA Education Series 1992.

(5) Breitbach,E.; Büter,A.: *Adaptiver Schwenkan-trieb in Steckbauweise,* Deutsches Patent Aktenzeichen 195 39 201.9-32 (1995)

(6) Büter,A.; Ehlert,U.-C.; Breitbach,E.: *Profile,* Deutsches Patent Aktenzeichen 198 04 308.2

(7) Büter,A.; Piening,M.: *Verdrehbares Rotorblatt aus faserverstärktem Kunstharz,* Deutsches Patent Aktenzeichen 195 28 155.1 (1995)

(8) Büter,A.; Breitbach,E.; Hanselka,H.: *Calculations and Experimental Results of the Adaptive Twist Control Concept to Reduce Helicopter Vibrations and Noise Emissions,* Innovation in Rotorcraft Technology Conference, London, UK, June 1997

(9) Büter,A.: *Untersuchung adaptiver Konzepte zur Reduktion von Hubschraubervibrationen, zur Minderung des Hubschrauberlärms und zur Steigerung der aerodynamischen Effizienz,* Dissertation an der RWTH Aachen, DLR Forschungsbericht 98-12, Juni 1998

(10) Chopra,I.: *Development of a Smart Rotor,* 19. European Rotorcraft Forum, Cernobbio (Como), Italy, 1993

(11) Ehlert,U.-C.; Büter,A.; Melcher,J.; Sachau,D.: *Steigerung der Jahresenergieausbeute von Windkraftanlagen durch den Einsatz adaptiver Struktursysteme,* 4. Dt. Windenergiekonferenz DEWEK'98, Wilhelmshaven, Germany, Okt. 1998

(12) Ehlert,U.-C.; Günther,P.; Büter,A.; Sachau,D.; Breitbach,E: *Adaptive Chamber Variation Utilising Local Anisotropy,* 25. European Rotorcraft Forum, Rom, Italy, Sep. 1999

(13) Geißler,W.; Sobieczky,H.: *Unsteady Flow Control on Rotor Airfoils,* AAIA Applied Aerodynamics Conf., San Diego Ca., June 1991

(14) Geissler,W.; Sobieczky,H.: *DYNAMIC STALL CONTROL BY VARIABLE AIRFOIL CAMBER* ; AGARD 75th Fluid Dynamics Panel Meeting and Symposium on Aerodynamics and Aeroacoustics of Rotorcraft, Berlin, 1993

(15) Hagood,N.W.; Derham,R.C.: *Rotor Design Using Smart Materials to Actively Twist Blade,* American Helicopter Society 52nd Annual Forum, Washington D.C., 1996

(16) Kube,R.: *Aeroelastic Effects of Helicopter Vibration Reduction by Higher Harmonic Control,* International Forum on Aeroelasticity and Structural Dynamics, June 1991

(17) Strehlow,H.; Rapp,H.: *Smart Materials for Helicopter Rotor Active Control,* AGARD/SMP Specialist's Meeting on Smart Structures for Aircraft and Spacecraft, Oct. 1992

This page has been deliberately left blank

Page intentionnellement blanche

Active Control Symposium for Power Systems and Propulsion

Technical Evaluation Report

Richard M. Murray
Division of Engineering and Applied Science
Control and Dynamical Syst. 107-81
California Institute of Technology
Pasadena, CA 91125, USA

Executive Summary

The major themes in the symposium were compression system instabilities and combustion system instabilities, both important limiting factors of gas turbine performance. Results were presented in the area of active control of combustion instabilities demonstrating effectiveness across scales from laboratory rigs to full scale engines and a good understanding of the modeling and control issues. The status of compression systems is somewhat behind this, primarily lacking in successful demonstrations on a full-scale engine. The tradeoffs between cost and performance are also less clear in this case. Issues that have been identified for further study include actuation systems, especially the need for high frequency, high reliability actuators, sensing systems capable of operating in high temperature and high vibration environments, and control theory, specifically proving robustness and fundamental limits for controllers which are already working in application.

1 Introduction

Gas turbine engines face a variety of design constraints and operational requirements that limit the achievable performance. Fluid instabilities are a major constraint and determine many of the key features of a gas turbine engine (eg, number of compressor stages, emissions levels, noise levels). Active control presents an opportunity to radically change the behavior of a system and achieve better performance, reliability and affordability.

Feedback control of gas turbine engines has been an active area of research for over 20 years, since the full authority digital engine controller (FADEC) became a standard part of gas turbine engines. Combined with advances in sensor technology, the improvements in computational power have enabled the use of feedback control of increasingly complex phenomena. Feedback control is already an integral part of modern flight control systems ("fly by wire"), leading to a rich understanding of feedback principles in theory and practice of aerospace systems.

Early uses of feedback control in gas turbine engines were for low frequency phenomena such as scheduling of fuel flows and for component feedback loops such as servo control of rotational actuators and valves. In the last 10 years there has been increased interest in using control to alter the behavior of more complex instabilities, such as those associated with compression and combustion instabilities (the focus of this symposium).

The primary compression system instabilities which have been studied for possible application of feedback control are rotating stall and surge. Rotating stall is a non-axisymmetric flow condition in which a portion of a compressor experiences stalled flow near the peak pressure rise of the system. In multi-stage compressors, rotating stall can occur in some or all of the stages, full span or part span, and grow suddenly or relatively slowly. Surge is an axisymmetric instability mode in which the compression system drives a Helmholtz instability, with the combustion chamber acting as the resonant cavity. Rotating stall and surge can occur separately or together and the overall dynamics of the system near these instabilities is quite rich.

Active control of rotating stall and surge relies crit-

ically on the coupling of the actuation mechanism with the physics. A variety of actuation schemes have been developed, including high response inlet guide vanes, high response bleed valves and air injection. All of these techniques have been demonstrated to work in systems ranging from low-speed, single stage rigs to full-scale compression systems. The key difficulty is in obtaining actuators which have sufficient authority and frequency response at the same time as being low weight and highly reliable.

Combustion instabilities are a thermo-acoustic instability that arises from coupling between the combustion process and the acoustics of the combustion chamber. Combustion instabilities in rockets have been studied for several decades and great progress has been made in understanding some of the fundamental mechanisms responsible for these instabilities. In the context of gas turbines, combustion instabilities are a limiting factor in low-emissions combustion (for lean, pre-mixed industrial power) and operability in high-power applications (especially in afterburners).

Over the last five years, several organizations have demonstrated the use of active control to significantly enhance the operation of combustors by allowing them to operate beyond their natural operability limits. The primary actuation mechanism has been modulation of primary or secondary fuel systems. Alternative approaches to low emissions combustors include catalytic combustion and "wet" combustion (where the combustion temperature is reduced through injection of water).

There are many other instabilities in gas turbine engines to which active control techniques may be relevant. These include separation control in the engine inlet and internal diffusers, shear layer control for affecting jet noise, flutter suppression, enhanced mixing in combustors, tip clearance control and wake management for reducing fan and compressor noise. Most of these are under current study both in industry and academia and they face similar challenges to those described in this symposium.

2 Overview of the Symposium

The symposium was held in parallel with two other active control symposia, one on performance stability and control of fluid physics (PSF) and the other on mechanical systems, structures and materials (MSSM). All three meetings shared an opening session with four keynote addresses and there was a fifth shared keynote address on the second day.

The power systems and propulsion (PPS) symposium consisted of 33 papers (of 36 originally planned) split into six sessions:

- Applications Overview: 7 papers
- Compressor Stall/Surge—Measurements: 6 papers
- Compressor Stall/Surge—Control: 3 papers
- Combustion Instabilities—Measurements and Predictions: 3 papers
- Combustion Instabilities—Control Fundamentals: 7 papers
- Combustion Instabilities—Control Applications: 7 papers

In addition there was a keynote speech by Anne Dowling on "Active Control of Instabilities in Gas Turbines".

The 33 papers represented authors from 8 different countries, broken down as follows:

Belgium	1	Poland	1
France	3	Switzerland	1
Germany	5	UK	5
Italy	2	US	15

The breakdown in terms of type of organization was:

Government Institutions	5
Academic Institutions	21
Industry	7

As indicated by the session breakdown, the majority of papers were concerned with combustion instabilities, with approximately one third of the papers focusing on compression system instabilities.

3 Keynote Address

The keynote address was given by Professor Ann Dowling from the University of Cambridge and was entitled "Active Control of Instabilities in Gas Turbines". Professor Dowling described work related to both compression and combustion instabilities, with primary motivation from combustion dynamics and control. She listed a number of challenges in this general area, including the fact that the dynamics are spatially distributed, with relatively limited models available, that the systems are open loop unstable with high instabilities frequencies, and that the system contains time delays.

Despite the difficulties in active control of these systems, there have been a variety of demonstrations

of control working at full scale, including demonstration of 17 dB reduction in combustion noise by Siemens in 1998 and 25% increase in pressure rise on a Rolls-Royce Viper compressor in 1998. From these demonstrations, the main limitations appear to be actuators and intelligence (control design).

In the context of actuation, the needs include robust and durable operation, high frequency response, and wide amplitude range (combining small and large signals).

For control design, the current practice is to tune the control laws by hand or use relatively simple adaptation schemes. The next generation of control law will use more model-based control techniques, perhaps by measuring the system dynamics near the instability point and using this model to design the control law. A major challenge is developing controls that give guaranteed robust performance. Ongoing work in Professor Dowling's group includes the use of H_∞, μ-analysis, and integral quadratic constraint (IQC) methods for proving robust stability and the use of adaptive control to extend the operating range of the control law.

In summary, Professor Dowling felt that active control of gas turbines was feasible at full scale, with key technical challenges in the area of reliable actuation systems and provably robust control laws. These control laws have yet to be tested at full scale and this is needed in order to demonstrate the efficacy of these approaches in practical applications.

A second keynote address was given by Professor Chih-Ming Ho of the University of California on "MEMS Application to Active Control", which centered on air vehicle applications rather than their propulsion systems.

4 Technical Sessions

The technical presentations were broken into six main sessions, covering four broad themes:

- Applications overview from industry, government, academia
- Compression system instabilities: rotating stall and surge
- Combustion instabilities: LPP, afterburners (rumble)
- Sensing technology and control algorithms (linear + adaptive)

4.1 Applications overview

The first session of the workshop consisted of seven papers that gave high level descriptions of the current state of the art in applications of active control to gas turbine engines. The presenters were from academia (Paduano [1], Zinn [6], and Mettenleiter [7]), industry (Moran [2], Hermann [3], and Proscia [5]) and government (Richman [4]).[1]

The presentations from industry demonstrated that active control of combustion instabilities were successful in demonstration on full scale engines and rigs. Rolls-Royce [2] has demonstrated control of afterburner rumble as far back as the early 90s, although these results had not yet been made public until this meeting. Similarly, both Siemens [3] and UTRC [5] have shown active control of combustion stabilities in low-emissions, industrial gas turbines with premixed fuel and UTRC has recently built a rig for studying main combustor instabilities (without substantial premixing). The level of understanding of the underlying physical processes varies from strong physical insight of the underlying instabilities mechanisms to high fidelity modeling of the acoustics and flow field, combined with reduced order modeling of the flame dynamics.

The academic researchers focused more on fundamental aspects of dynamics and control of fluid instabilities and it is clear that there is a rich set of understanding of some of the main control techniques as well as modeling processes. However, it is clear that the current industrial demonstrations are moving more quickly than the theory for systematically designing and analyzing feedback controllers. This leaves a gap between what we are able to demonstrate in the field and what we are able to guarantee will work in the presence of uncertainty and noise.

Only Paduano described results in the area of compression systems. Although Dowling noted in her plenary talk that control of compression systems had been demonstrated by Rolls-Royce on a full-scale system, it seems clear that work in active control of combustion stabilities has been more successful in applications. This is despite convincing evidence by Paduano that the basic physics is understood and that control can be achieved. The evaluator's own experience in this area indicates that one of the key bottlenecks is effective actuation (high bandwidth, long life with low cost, low weight) and robust operation. In particular, for aeroengines (where rotating stall and surge are strong limiters of performance) the actuators required to achieve performance benefits do not

[1] Numbers in brackets refer to the paper number in the Symposium program.

trade well against the costs (price, weight, reliability) and the effects of failure in the control are potentially severe due to the nature of the instability.

4.2 Compression Systems

The next two sessions focused on active control of compression systems. Talks were presented from academic institutions [8, 9, 10, 11, 14, 15, 16], industry [12], and government labs [13]. The talks covered both control of rotating stall and surge, as well as sensors for compression systems.

In the context of modeling and control of compression instabilities, there were few new results presented in this collection of talks. This area is one which has been very active for the last 10 years and the physical phenomena of rotating stall and surge, as well as the measurement and control problems associated with this, appear to be well understood at this point.

One common thread through several of the talks was the distinction between stall avoidance and stall control. Roughly speaking, the idea of stall avoidance is to use pre-cursors to detect the onset of stall and then change the operating point before stall occurs. In this way, it is hoped that the stability margins might be reduced in some circumstances, allowing more efficient utilization of the compressor (through redesign). This is complicated by the fact that many compressors stall very rapidly, with no apparent precursor having slow growth characteristics. This area has been explored extensively in industry and academia over the past five years and the main bottleneck appears to be reliable detection of precursors in the presence of large amounts of noise and uncertainty. It did not appear that major new breakthroughs in this area are forthcoming.

Stall control consists of stabilizing the normally unsteady behavior associated with stall (or surge) and allowing the engine to operating beyond its normal operating limits. There is a large body of work in this area that has been developed in the last five years and most of the papers fell within the rough scope of the type of work that has been done in the past.

There were several talks on sensor technology for compressor systems, including one by Kulite [12], who is developing a new high temperature, leadless sensor, and one by the Polish Air Force Institute of Technology [13], who have used blade vibration sensors. These types of advances in sensing technology have the capability not only to enable stall avoidance and control, but also new diagnostic approaches that will allow self-tuning systems capable of higher performance. Given the difficulty in controlling stall behavior on practical systems, diagnostics systems for detecting wear and abnormal operating conditions may be the more important early application of control technology for compression systems.

4.3 Dynamics and Control of Combustion Instabilities

The largest portion of the workshop was devoted to combustion instabilities, which comprised the final three sessions of the workshop. Many of the leading research groups in the world were represented and the quality of the talks was very high. New results were presented, in addition to continued work that had been introduced at prior conferences and workshops. The talks spanned applications and theory.

Measurements and Predictions

The first section focused on measurements and predictions of combustion instabilities. The talk by Austin and Tilston (presented by R. Cottington) described the use of fuel staging between the main and pilot zones to reduce oscillations. The approach was mainly empirical, but is representative of the use of passive mechanisms to reduce combustion oscillations. The talk by Balu Sekar of the US Air Force Research Laboratory [19] gave a high level overview of the tools and limitations from an Air Force perspective and described the development of LES tools for modeling combustion instabilities. The final talk of this section, by Vandsburger [20], explored the relationship between chemiluminescence and heat release, which is a primary means of obtaining data about flame dynamics.

Control Fundamentals

The next session consisted of six talks in the area of modeling and control. The basic control algorithms being used for combustion instabilities are quite simple, usually consisting of a simple gain and phase delay between the sensor (typically combustor pressure) and the actuator (typically fuel modulation). A key feature in most combustion control approaches is the role of time delay between the actuation and the effect of that actuation. This is typically due to convection time constants associated with the mixing and combustion processes.

One common theme throughout these talks was the use of adaptive and learning algorithms for control. These techniques are required because of the sensitivity of the control to time delays, which can

vary based on operating condition. A variety of approaches were explored, ranging from the application of neural nets [21], to Smith predictors and related approaches [22, 23, 27], to LMS techniques [24, 26].

A common problem in adaptive techniques is the robustness of the closed loop system. This was addressed explicitly by Evesque [22], who proved stability of a Smith predictor method using fairly broad assumptions on the underlying dynamics, rather than a specific model. These assumptions included second order actuator dynamics, stable flame dynamics, no energy addition from the walls and no unstable zeros in the plant dynamics. While the validity of these assumptions is not clear in a full-scale combustor, the approach illustrated the use of theory to identify fundamental limits of performance. A clear next step is to extend this work to study disturbance rejection (as opposed to just stabilization), for which time delays present a particularly difficult problem.

Another common limitation in applications of control to fluid systems is the effect of actuator limits, including magnitude, rate, and bandwidth restrictions. This seems to be less of a problem in combustion systems than it is in compression systems, but is likely to be a major limitation as high frequency combustion oscillations are considered. The work of Hathout *et al.* [23] used an on/off actuator with both deadzone and hysteresis effects, which allows a more realistic evaluation of true performance.

Control Applications

Seven talks were given in this section, which focused on implementation of control algorithms in a variety of combustion rigs. All of the presentations demonstrated effective control of combustion instabilities, typically through the use of fuel modulation based on measured pressure oscillations.

A common theme through these talks was the use of fuel-air ratio modulation as a control mechanism and the focus on low emissions as a required output. The effect of control on emissions has not been modeled directly, but it appears that reducing pressure oscillations and allowing the system to run at lower fuel air ratios does give lower emissions [30]. Unlike most approaches, which feed back pressure oscillations and use fuel modulation to reduce these oscillations, McDonell [33] closed the loop on emissions explicitly and used fuel staging as the control mechanism. Although this does not stabilize the system explicitly, it did result in reduced emissions and appears to be a reasonable approach to improving system operability, if a sensor with sufficient reliability is made commercially available.

An issue raised by Santavicca [35] was the need to model spatial dependencies in combustion system models. This issue will become particularly important if distributed actuation is allowed, of the sort that would be required for better pattern factor control. Yu [36] also discussed the importance of large scale fluid structures, which can interact with liquid sprays during the active control process.

The success demonstrated by all of the talks in this session demonstrates the feasibility of active control of combustion instabilities in a variety of applications. The most likely early entry of active control appears to be in low-emissions, land-based applications, where stricter government requirements are pushing the limits of what can be achieved with other approaches. (However, it should be noted that catalytic combustion, which was not discussed in detail in this symposium, is one promising alternative.) If active control techniques are deployed in land-based applications, this will allow reliability and performance issues to be addressed under relatively favorable conditions and would presumably be a precursor to more broad application of active control to other gas turbine applications.

5 Summary and Conclusions

The symposium consisted of a broad cross-section of talks representing several fundamental areas in active control of propulsion and power systems. The work in compression systems continues to move forward but fundamental issues of high response, reliable actuation in an engine environment appear to be limiting the application of these results in full-scale engine hardware. Combustion concepts have been demonstrated in laboratory-scale rigs, full-scale rigs and engine hardware. Feasibility of the concept has been established and clear benefits are available for power generation (emissions and operability) and propulsion (operating envelope).

There are several areas where further research is warranted and should be encouraged by RTO:

Actuation Actuation continues to be a major bottleneck in the application of active control concepts to gas turbine engines, particularly aeroengines. The primary issues are low authority coupling to the physics and high reliability. These issues will be exacerbated as military engines move to higher fuel air ratios (requiring pattern factor control) and low emissions become a more important factor for land-, sea-, and air-based gas turbines. Novel approaches to ac-

tuation which involve low-weight, high-reliability actuation should be more vigorously explored.

Sensing Sensing requirements are likely to driven by diagnostic and prognostic applications, which will benefit active control as well. The main issues are reliable operation in high temperature and vibration environments. Control of pattern factor will require new sensing techniques in extremely harsh environments.

Control More work is required on developing systematic methods for control of fluid instabilities that result in provably robust control laws. Even if the assumptions required to prove robustness are not always valid, the insights from looking at representative problems will be valuable in understanding the fundamental limits of performance of compression and combustion systems. In developing these techniques, more attention should be paid to the role of actuator limits (spatial resolution, magnitude and rate constraints, bandwidth limits) and also to the possibility of passive solutions that exploit the dynamics of the system ("design of dynamics"). Additionally, there is a need to more effectively harness existing control techniques, such as adaptive and nonlinear control methods.

Modeling Although there has been significant progress in modeling of compression and combustion instabilities, there is a basic lack of system-oriented models that capture key interactions that are responsible for thermoacoustic instabilities and more work is required on development of procedures that link CFD models and control designs (along the lines of the work by Mettenleiter et al [7]). In addition, the methodology for incorporating actuators into fluid models is not well developed and the coupling between various engine components (inlet, compressor, combustor, afterburner/nozzle) has not been explored in detail. Finally, scaling laws that allow results from laboratory rigs to be evaluated against engine requirements are needed (this philosophy and an initial start was described by several presenters [5, 27, 30, 31].

Applications The use of control-enabled systems for diagnostics and life extension should be considered as an early benefit of active systems. Although this is done to some extent in almost all commercial gas turbines, rapid advances in sensing technology and computational capability will allow more sophisticated signal processing techniques that can provide high value information for improving life-cycle performance. Early insertion of diagnostic sensors into gas turbines will speed the development of active control techniques as experience is gained in incorporating higher levels of electronics and software into modern turbomachines.

An additional issue which is often ignored in early consideration of active control for gas turbines is cost benefit analysis. While active control can extend the operability of engines in a variety of situations, the overall life cycle costs, including maintenance and repair, must be considered as well. While initially it may appear that such analysis would preclude the use of more sophisticated systems, lessons from the automotive industry (where emissions restrictions forced the use of electronic controls in engines) show that it is possible to achieve low cost, high reliability, and consistent performance in long term, harsh environments. Careful analysis of these types of considerations should be a more vigorous part of the overall activity in research and development of active control technologies for gas turbine engines.

Compressor Stability and Control: Review and Practical Implications

James D. Paduano Alan H. Epstein
Gas Turbine Laboratory, Department of Aeronautics and Astronautics
Massachusetts Institute of Technology, Room 31-265
Cambridge, MA 02139 – 4307, USA

ABSTRACT

This paper discusses developments in axial compressor stability modeling over the last several years, and related work in active control of rotating stall and surge. Several major themes have emerged during this work. One theme is the interplay between hydrodynamic perturbations in axial compressors and instability inception. The former obey linearized dynamical equations, but their resonance and instability can trigger a variety of nonlinear events leading to violent oscillations in the compressor flow. An understanding of the key physical phenomena associated with stall inception, as opposed to those governing fully developed stall or surge, is critical to alleviating stall by design means or through active control. Another theme is the utility of actuators for understanding compressor stability. Active control work has prompted the installation of high-response forcing devices in compressors; even without feedback these have yielded much new information about compressor unsteady behavior. Finally, the paper reviews the methods and prospects for using active stabilization to extend the stable operating range of compressors, improving their surge margin and thus increasing overall reliability and performance. Experiments have progressed from laboratory scale demonstrations to full-scale rig and engine tests in about a decade. Competing theories about the physical mechanisms, the difficulties associated with stabilization, and the goals and control techniques for rotating stall have led to a rich research base on which compressor stability and control technology is being built.

1. INTRODUCTION

The concept of a 'smart engine', which utilizes augmented sensing, actuation, and computational power to increase the performance of its components, has captured the imagination of a variety of researchers since its introduction in the mid-1980's [1]. Fluid mechanicians, control specialists, experimentalists, nonlinear dynamicists, and mathematicians have all contributed ideas to the overall research mix. Concentration has been primarily on combustion control, and on stability and control of compressors and compression systems. The latter topic is the focus of this paper, where the phrase 'stability and control' is used in the same sense as in aircraft stability and control: understanding the equilibrium properties, the natural dynamics, and the influence of actuators is termed 'stability analysis', while augmentation of these properties through control mechanisms, usually applied through some sort of feedback loop, is called 'control'.

Compressor stability and control research parallels the early days of aircraft stability and control research in various ways. For instance, since certain regimes of operation are visited only infrequently (supersonic flight, hung stalls and spins are aircraft examples, very low flow rates and transient operation are compressor examples), various conjectures about the dynamics compete for precedence until enough information is amassed (and enough time has passed) that a workable consensus is reached. Also, in both cases instrumentation and in-operation (flight) test plays a critical role in verifying and refining conjectures. Finally, the lack of complete information often leads to the 'blind men and the elephant' syndrome, where either the perspective of the researcher or the limitations of the instrumentation in a particular experiment can bias the conclusions. Thus synthesis of all of the available research is required before a comprehensive picture can be constructed. This paper describes some of the competing views in compressor stability, and describes where some of the synthesis process has begun.

2. CHARACTERIZING THE DYNAMICS OF COMPRESSORS FOR CONTROL

The first challenge for creating the technology of stability and control of compressors is developing appropriate models. Here, as in any control problem, the fundamental requirement is to understand the key physical phenomena which drive the dynamic behavior. The focus of such characterization must be the stall inception process, as opposed to fully developed stall, for which many studies have been conducted (for a comprehensive review see [2]), but which exhibits different phenomena. Only after one develops at least a functional description of the processes at work during stall *inception* can effective control

Paper presented at the RTO AVT Symposium on "Active Control Technology for Enhanced Performance Operational Capabilities of Military Aircraft, Land Vehicles and Sea Vehicles", held in Braunschweig, Germany, 8-11 May 2000, and published in RTO MP-051.

architectures (sensors, actuators, control philosophy, and algorithms) be conceptualized, specified, and designed.

Fortunately a critical subset of the physics can be studied in low speed research compressors, and results in such compressors have carried over to full-scale devices. This approach creates a hierarchy of possible stall inception mechanisms, from those that appear in low speed compressors to those that appear in high speed and many-stage (*i.e.* more than three- or four-stage) machines.

A dialectic between two different points of view has dominated the discussion of physical mechanisms. For descriptive purposes, we take the thesis of this dialectic to be the following: long wavelength processes, or waves which span at least several blade pitches circumferentially, are the main physical entities that determine compressor stability properties. The antithesis is that short length scale events, which happen locally (within only 1 to 4 blade passages), are primarily responsible for stall inception. Although taken as the antithesis here, the associated physical explanation actually preceded the long length-scale hypothesis — here we wish to emphasize that it is antithetical to the concept of control (since control of short length scale events is difficult). Also, although this physical explanation dates back to the Emmons [3], it is a relatively new concept that rotating stall *inception* occurs in this way [4].

Waves as Precursors to Stall

The long length-scale description of rotating stall inception starts with a two-dimensional representation of the compression system as shown in Figure 1. Moore [5] developed a hydrodynamic stability analysis for this idealized system which was able to predict some of the basic characteristics of rotating stall. Moore and Greitzer [6] later developed this into a model which captured the interaction between rotating stall and surge.

The key physical processes which are represented in this model exist in low-speed as well as high speed rigs, and are the dominant factors in determining the rotation rate and stability properties of pre-stall waves [6-8]. The model incorporates the following assumptions (see Longley [9] for a review which contains the technical details):

1) Upstream and downstream flowfields impose linear impedance conditions upstream and downstream of the compressor.
2) The steady compressor characteristic is used as an empirical model of viscous processes in the compressor. The compressor's delivery of pressure rise in unsteady situations is modified by relatively simple models of unsteady loss, deviation, and blockage which retain two attributes:
    a) They remain empirical, tied directly to measured loss, deviation and blockage characteristics. These characteristics may be obtained from direct performance measurements in the compressor of interest, or be derived based on correlations or higher-order computational analyses [8, 10].
    b) Compressor blades are assumed to be infinitely closely spaced circumferentially (high solidity). Thus, only events whose circumferential profiles are smooth when compared to blade spacing are properly modeled.
3) The dynamics of the plenum, which acts as a mass storage device or 'spring', effects the mean flow through the system, coupling rotating stall and surge through changes in the compressor properties as a function of mean flow. Again, the nonlinear sensitivity of the compressor properties to mean flow is represented empirically.

The original manifestation of this model was derived by Moore and Greitzer [5, 6] assuming two dimensional (2D) incompressible flow in the ducts and compressor, and converted to a form suitable for control system analysis and design by Paduano *et al*. [11, 12] and Mansoux *et al*. [13]. If the flow in the ducts and blade rows is modeled as 2D, linearized, *compressible* flow, additional modes enter into the dynamic representation, although the basic features of the model are the same. Bonnaure [14] and Hendricks [15] developed a linearized compressible hydrodynamic stability model, which was converted to control theoretic form by Feulner [16]. This model has since been refined and validated against experimental data by Frechette [17] and Weigl [8, 18]. A three-dimensional, incompressible version of the model was developed by Gordon [19], and this has been extended to the compressible case by Sun [20].

In all of these models, the basic entity is a circumferentially sinusoidal wave of velocity perturbation, which rotates around the compressor annulus at a characteristic frequency, and either grows or decays as a function of time. The structure of this wave in the axial and radial direction depends on the assumptions of the model, but in every case one solves for the eigenmodes, which are sinusoidal circumferentially, and whose eigenvalues describe the rotation and growth rate of the modes. Presently we will give examples of velocity distributions near the compressor for various types of eigenmodes.

Several experimental investigations have focused on verifying that in fact compressors exhibit long length-scale perturbations which resonate and subsequently grow into rotating stall. The first of these were

conducted by McDougall [21], who showed that circumferentially rotating sinusoids of axial velocity perturbation preceded rotating stall inception in a low speed compressor. Garnier was able to measure these waves in low speed as well as high speed compressors [22]. A number of studies in high speed compressors followed [23-26], with varying conclusions depending on the instrumentation and data processing used.

In an attempt to come up with a more generally applicable description of stall inception, Tryfonidis *et al*. [7] applied identical processing to eight different high speed compressors, and showed two types of behavior, illustrated in Figure 2. Several compressors exhibited the resonance of sinusoidal waves prior to stall, with a resonance/rotation frequency of approximately half the rotor speed, as shown in a spectrogram in Figure 2a. This resonance corresponds to the eigenmode predicted by the Moore-Greitzer incompressible model. Where these waves were difficult to see in the raw traces or the spectral analyses, a different type of traveling wave was observed prior to stall. This is illustrated in Figure 2b, which is actually the same compressor at a higher rotation speed. In several compressors at 100% design speed, this wave traveled at exactly the rotor frequency, and grew in amplitude as the stall point was approached. It was postulated, and later verified in a single stage high speed compressor by Weigl, that the compressor can couple with the acoustic spinning modes [8] in the upstream and downstream ducts, and drive these modes to resonance or even instability. Operation near 100% design speed was found to be the critical speed in many compressors, due to an unfortunate (but not uncommon) coincidence of the acoustically coupled mode frequency and the rotor revolution frequency.

The compressor's ability to pump energy into acoustic waves is precisely the focus of the compressible stability model originally derived by Bonnaure and Hendricks [14, 15]. By accounting for compressibility in all of the ducts, the hydrodynamic analysis admits spinning acoustic modes in the upstream and downstream ducts. Figure 3 illustrates the difference between the incompressible flow solution in the upstream duct, which is the only solution coupled to the compressor in the Moore-Greitzer model, and a compressible flow solution which is coupled in by the compressible analysis. The ultimate mode shape of the system depends on the overall interaction between the upstream duct, the compressor, the downstream duct, and the boundary conditions. Figure 4a illustrates a typical compressible solution; Tryfonidis [7] and Weigl *et al*. [8] give further details on the characteristics of these modes.

Also shown in Figure 4 is the solution of an incompressible, three-dimensional hydrodynamic stability analysis [19]. Here although the mode shape is still sinusoidal circumferentially, radial variations in the mode shape are taken into account, as is the radial distribution of blade loading. Such modes may be important in low aspect-ratio compressors and fans.

Spike Stall Inception

In parallel to this research, a completely different model of stall inception was being developed. It was motivated by a picture originally drawn by Emmons *et al*. [3], and reproduced in Figure 5. The mechanism for stall inception was postulated by Day [4], who gave the following succinct explanation:

> "In a row of highly loaded blades, a minor physical irregularity, or flow nonuniformity, can result in momentary overloading and separation. This separation, or blockage, will restrict the flow through the blade passage and will therefore divert the incoming streamlines. On one side of the blockage the streamline diversion will cause increased incidence, and on the other side decreased incidence. The blade passage subjected to increased incidence... will therefore become stalled, while the one already stalled will unstall. The stall "cell" will thus propagate from blade to blade around the compressor... A cell like this would be called a disturbance of short length scale."

In this model it is postulated that while long length-scale, hydrodynamic modes exist in compressors, stall inception does not occur until the local mass flow through the blades is, at some spatial location, low enough that a small region of the annulus experiences catastrophic separation in the blade passage. This region then propagates via the mechanism described above, traveling and spreading rapidly into a fully developed stall or surge event. Features of this type of stall inception are:

1) Three-dimensionality. Separation tends to occur at the tip region of the blade, and the embryonic stall cell is initially concentrated in this region. The small circumferential and radial extent of the blockage causes a high rotation speed (approximately 70% of the rotor speed), which goes down as the size and extent of the stall cell increases (as rotating stall is initiated).
2) Nonlinearity. The 'spike' or 'pip' that develops is governed by separation and three dimensional flow redistribution phenomena [4, 25-28] both of which are nonlinear. Thus hydrodynamic stability analysis is not well suited to characterizing these flows.

3) Short time duration. The catastrophic nature of the separation event prevents any pre-stall signal ('precursor') from being detectable except immediately prior (on the order of a few rotor revolutions) to stall.

All of the features of short length-scale stall inception are detrimental to application of active control. Short, highly localized perturbations are difficult to detect unless sensors are placed very close to the location where they are occurring, and even then they appear on a given sensor only briefly. The lack of precursor information and the brief, nonlinear inception characteristics make linear controllers indefensible. In fact, Day's original control demonstration [29], which occurred just prior to the first long length-scale or 'modal' control demonstration, involved waiting for spikes to occur and then injecting air at the appropriate location to 'lead' the spike, thus canceling it in a nonlinear fashion and preventing it from developing into a stall cell. This approach would be impractical in a multi-stage environment, where one would have to determine the stage (or stages) at which spikes occur, and place actuators near those stages [30]. Changes in the operating point of the compressor invariably change the most highly loaded stage, so spike inception can move from one stage in the compressor to another.

Substantial experimental evidence for the importance of this form of stall inception has been amassed. The most detailed and convincing studies and reviews of data have been conducted by Day [25, 30], who has added considerable sophistication to the empirical description of these events. Figure 6 shows a typical stall inception example, which highlights the argument that spikes can sometimes lead into stall even when modes are present. Note that pre-stall traveling waves are evident in the data, but that the spike which ultimately develops into stall is not traveling at the same speed, nor is there any apparent relationship between the development of the stall cell and the pre-stall long length-scale waves. In some cases, waves are not evident at all, and stall inception consists only of the spike phenomenon. Silkowski [31] and Park [27] investigated the conditions under which spikes are initiated by rematching the downstream stages of a low speed compressor, and described some of the properties of the spikes.

Synthesis of Results

At this stage in axial compressor stall inception research, the question is not whether spikes exist or whether waves exist; both have been measured in many compressors and substantiated in great detail. The questions have to do instead with the importance of each to the stability and control of compressors. Under what conditions will a compressor exhibit spikes, and under what conditions waves? Which phenomenon sets the stability boundary of a compressor? How does compressor operating point effect these answers? Finally, what are the implications for control?

Recent developments have progressed toward answers about spikes versus modes. These developments are described by Camp and Day [28], who used experimental methods, and by Hoying [32], who gives a computational account and a postulates the fundamental mechanisms. Camp and Day showed that the first stage rotor in a four stage low-speed experimental compressor had an identifiable 'critical incidence' above which spikes occurred prior to stall inception. In this experiment, if the peak or zero-sloped portion of the overall compressor characteristic was reached before the first stage rotor reached its critical incidence, modal oscillations occurred, as predicted by long length-scale models. If, on the other hand, the critical rotor incidence was exceeded before resonance of the 'system' modes, then spikes appeared and transitioned the compressor into stall. Figure 7 shows the result of a number of experiments in which the first stage rotor incidence and compressor slope at stall inception were altered — either by restaggering the inlet guide vanes, or by rematching the compressor with incidence changes on the downstream stators. This plot clearly shows the connection between stall inception mechanism and rotor incidence.

Other developments also recognize the richness of the stall inception process. For instance, stall precursor identification is no longer based on searching for purely deterministic, linearized waves in time traces. Instead, nonlinear modeling and analysis of waves in compressors [13], as well as a realization of the highly stochastic nature of the environment, have led to the use of spectral methods to identify prestall disturbances [7]. Such methods are needed because stall inception, whether short or long length scale, involves nonlinear processes, so that the damping ratio of pre-stall eigenmodes may be small, but need not be zero at stall inception. Damping these eigenmodes can, however, significantly reduce the level of unsteadiness in a compressor, which may reduce the likelihood of spikes. Furthermore, nonlinear control techniques, discussed in Section 4, attempt to alter the global behavior of the system, so that the local (i.e. early inception) details may not be as important as the transition into large amplitude stall. During this transition, the larger size of the stall cell makes the dominant physical processes inertial; thus the nonlinear Moore-Greitzer model is sufficient to understand control of larger amplitude, developing stall cells. The

(perhaps prohibitive) penalty for such an approach appears to be larger requirements on the actuator strength.

Much of the understanding of rotating stall inception described in this section was gained or supported by experimental studies. These studies are distinguished from other rotating stall studies in two ways. First, as we mentioned above, they concentrate on the inception process, rather than fully developed stall. Second, many of these experiments have benefited from the existence of high speed actuators, which have provided a new look at compressor unsteady flows. Several actuated compressor experiments have been created, all with the primary goal of controlling rotating stall; each has also lent insight into the nature of stall inception. For instance, by stabilizing a mechanism that is postulated to lead to stall, and subsequently extending the operating range of a compressor, the postulated mechanism is proven to be the critical one. Details of the pre-stall dynamics are also best elucidated using high-response actuators.

3. ACTUATED COMPRESSORS FOR MODEL VALIDATION AND DEMONSTRATION OF CONTROL

This section reviews active control experiments that were conceptualized based on long wavelength concepts. These experiments have been focused on two objectives: verifying long wavelength models using system identification, and extending compressor operation through stabilization of hydrodynamic instabilities (see Figure 8). Approaches to rotating stall control which pursue different goals [33-35] often occurred in parallel to the research described in this section; this research will be presented in counterpoint in Section 4, rather than chronologically.

The original demonstrations of operating range extension via active stabilization of waves were by Paduano [36], followed soon after by Haynes [37] and Gysling [38]. All of these demonstrations were conducted in low speed compressors with clean inlet flow, using actuators with high bandwidth compared to the rotor frequency — on the order of 2.5 times the rotor frequency. In the work of Paduano and Haynes, 12 inlet guide vanes (IGVs) were modulated by servomotors mounted on the casing of the compressor. The actuators could independently set each IGV incidence at high bandwidth. This allowed a wave of actuation to be introduced in response to a wave of measured velocity perturbation - a feedback loop which stabilized the waves, allowing operation of the compressor below its normal stalling mass flow. The results of these demonstrations are reviewed by Greitzer *et al*. [39]. Gysling's approach [38] coupled an array of structural elements to the flow perturbations upstream. High-momentum air injection was modulated by flexible cantilevered plates ('reed valves') immediately upstream of the compressor face. The circumferentially distributed reed valves were deflected by the static pressure perturbations associated with prestall waves. This coupling created a new dynamical system with improved stability properties, without any sensing or computation (*i.e*. a dynamically tuned aero-structural system).

These demonstrations showed that in at least some low speed compressors, with clean inlet flow, small perturbation sinusoidal wave stability determines the stalling mass flow. The first sinusoidal circumferential harmonic goes unstable first, determining the stall point of the unmodified compressor. If this harmonic is stabilized, then the second harmonic goes unstable, at a reduced mass flow. By controlling the first and second Fourier harmonic, 8% to 20% increase in compressor operating range was achieved [36-37]. These demonstrations also showed the utility of system identification for model verification and refinement. See Haynes *et al*. [37], Longley [9], and Greitzer *et al*. [39] for a more complete review of this work and a discussion of the model refinements that resulted from forced response testing.

Once the possibility and utility of rotating stall stabilization were demonstrated, research began to focus on making active control more practical. Reducing the number of actuators and sensors required for control is one of the most compelling practical goals; this goal has motivated its own dialectic involving alternate control strategies (see Section 4). Two other critical practical issues are discussed here: inlet distortion and high speed implementation.

Implementing active control in the face of inlet distortion is of primary importance, since much of the current stall margin built into aircraft engines is there to maintain stability with inlet distortion. Van Schalkwyk [40] was the first to develop a control-theoretic model suitable for low-speed compressors with inlet distortion, and to implement controllers which stabilized the modes which arise when inlet distortion is present. Once again emphasis was placed not only on demonstrating control, but on demonstrating that the physical processes at work were well understood. The theoretical basis was the Hynes-Greitzer model [41], which relies on long length-scale assumptions, but which has very different behavior from the original Moore-Greitzer model, due to coupling of the spatial harmonics in the eigenmodes. This coupling of spatial harmonics renders the simple harmonic-by-harmonic control laws used in clean inlet flow much less effective — the eigenmodes of the system are no longer sinusoidal, and actuating a specific spatial sinusoid effects other modes of the coupled system.

Figures 9 and 10 illustrate the kind of steady and unsteady data which was obtained by van Schalkwyk in a low speed, 3-stage axial compressor with inlet distortion. Figure 9 shows the inlet distortion profile, comparing it to the prediction of the Hynes-Greitzer model. Clearly the physical processes are well accounted for in the modeling of the steady compressor response here. More importantly for control, the unsteady, input-output characteristics shown in Figure 10 are also well predicted by the theory, which relies only on steady-state compressor performance (total-to-static pressure rise and steady-state loss characteristics) and compressor geometry.

The current challenge for rotating stall modeling and control is high speed compressors. The challenges include modeling rotating stall inception when compressibility is important, effects which arise when many stages are present, distortion in the high speed environment, and development and implementation of suitable high speed actuators. Modeling high speed compressors was discussed in the previous section. The effects of many stages, and of distortion, are just beginning to be addressed — Day [30] and Freeman *et al*. [42] provide the most recent look at multistage compressors; this research will be discussed presently. Actuation development has been studied in the context of several projects, including [42-45]. We briefly review Berndt *et al*. [45] here to give a notion of the issues. The first high-speed demonstration of long wavelength mode stabilization was recently conducted by Weigl *et al*.[8, 18] using the actuators described below. This research will also be briefly described to illustrate the current state of the art.

The primary challenges in actuating high speed compressor rotating stall modes are the high bandwidth required, and the desire to have a large effect on the flowfield. Several researchers [29, 33, 34, 38, 42, 44, 45] have found that high speed valves which modulate airflow either into or out of the compressor are the most practical means to achieve high bandwidth and large effectiveness. Injection actuators were predicted to be the most effective based on low-speed analysis [43], so these have been developed for several applications. The valve's mass and internal volume as well as the placement and shape of the injector must be carefully designed to insure that high momentum air is introduced at the most beneficial location in a timely manner. Berndt [45] and Behnken [44] discuss design coupled with experiments to address these issues. Berndt discusses design of an actuator which was recently installed in a transonic single stage research compressor at NASA Lewis. These injectors have been shown to have a significant effect on both the pressure rise and stall flow coefficient, in part because the injected momentum is concentrated in the tip region of the compressor, which is known to have a strong influence on the overall compressor behavior. Similar results for steady injection were reported in [44]; for a detailed description of the use of this type of actuator for steady state performance improvement, see [62].

These actuators were used to perform thorough system identification and control tests in a NASA Lewis transonic single stage facility [45, 8]. While it was shown that the long wavelength approach is viable in this compressor, a more sophisticated implementation of the approach was required at 100% speed due to compressibility effects. Unlike the low-speed case in which each circumferential harmonic is a system eigenmode, each harmonic includes more than one lightly damped mode which can grow into rotating stall. Forced response testing identified several modes traveling at up to 150% of the rotor speed — these modes were found to be consistent with the 2D compressible hydrodynamic model discussed in Section 2. Robust dynamic control was required to stabilize the multiple modes which comprised the first three harmonic perturbations in the compressor — 0th (surge), 1st, and 2nd. Interestingly, surge and rotating stall occurred at almost the same mass flow in this compressor.

Figure 11 summarizes the results obtained, and demonstrates both the effectiveness of injection in steady state, and the additional improvement in stall margin that is obtained when active control is applied. As important as these results is the large amount of unsteady, forced-response data that was obtained, which provides a database against which the compressible model of rotating stall can be further developed and refined. This database represents a comprehensive look at high-speed compressor unsteady fluid mechanical characteristics. Such data can only be obtained using forced response measurements followed by application of system identification techniques.

Despite the success of these demonstrations, challenges still exist for implementation in a full-scale compressor with many stages. The most fundamental are those related to understanding the physical mechanisms; these have already been discussed. Day *et al*. [30], in a thorough examination of several compressors, concluded that in fact many stall inception mechanisms exist, and that they are so diverse, even in a single engine as it traverses its operational speed range, that an active control scheme which could handle them all is unlikely. D'Andrea, Behnken, and Murray [35] found that although the Moore-Greitzer model was sufficient to describe the behavior of their compressor, noise levels were too high to allow linear feedback concepts to be effective. Rolls-Royce, in a multi-year effort reported in Freeman *et al*. [42], also found that the stall inception details were not consistent with stabilization for range extension. Rather than

abandon active control of rotating stall, these researchers found alternate goals to pursue with active control. These goals, and how they relate to the goal of stabilization discussed in this section, are the subject of the next section.

4. ALTERNATIVE APPROACHES TO ROTATING STALL CONTROL

The debates concerning mechanisms for rotating stall inception, and the control demonstrations in ever more realistic environments, were described above under the following basic thesis: extension of the stable operating range of compressors is the goal of active control. Such extension allows compressor operation to be shifted closer to the no-control surge line (or beyond), allowing higher pressure ratios and rematching of the compressor design for higher compressor and/or overall cycle efficiency. Stall margin is maintained by active control's extension of the speed lines beyond their open-loop surge point.

The antithesis to the concept of range extension is this: maintenance of operating points near the peak of the compressor characteristic does not require range extension, and requires fewer actuators to implement. 'Maintenance' of an operating point means making it resist stall and surge in the face of disturbances, such as distortion, speed transients, and fuel spikes. If active control does this, then operability of the engine has been functionally enhanced at more desirable performance levels, regardless of the range extension which exists at mass flows below the operating point in question. Thus for instance the open-loop surge line could be transformed by active control into the operating line, not by range extension but by eliminating the tendency to surge along that line.

This subtle difference in goals was motivated by the desire to implement control with a single axisymmetric actuator - we will call this one-dimensional (1D) control. Liaw and Abed [46] conducted the seminal research in using 1D control for operability enhancement, although their interest was in how nonlinear control could be used to improve the 'bifurcation properties' of a simplified version of the Moore-Greitzer model first presented in [6]. The importance of this approach for operability enhancement was recognized by Badmus *et al*. [33], and subsequently demonstrated in a low speed compressor. Further enhancement and demonstration of the concept by Eveker *et al*. [34, 47] has been conducted in parallel to the 'range extension' research described in Section 3. It should also be mentioned that a form of 1D control was attempted by Ludwig and Nenni [48, 49] as early as 1976; these attempts suffered from lack of a theoretical basis as well as shortcomings in the testing equipment and procedures. These theoretical and technological shortcomings took another 20 years of research to overcome.

1D operability enhancement research has been conducted in the context of nonlinear control theory, introducing an entirely new set of researchers into the mix [50-55]. The centerpiece for this research is a three-state, nonlinear Galerkin approximation of the Moore-Greitzer incompressible model. This approximation was in fact introduced by Moore and Greitzer [6] for the purpose of elucidating the coupling between rotating stall and surge. McCaughan [50, 56] conducted a rigorous study of the model, in the context of bifurcation theory. This initial work showed that a very simple model exhibits the basic properties of surge and rotating stall inception, and their coupling, in a form which is simple enough to be analyzed by hand. Liaw and Abed [46] introduced control into the bifurcation analysis, postulating that by properly modulating a bleed valve in the compressor plenum, the peak of the compressor characteristic could be made resistant to disturbances.

The three states of the Galerkin Moore-Greitzer model are velocity in the compressor duct (Φ), pressure in the plenum (Ψ), and the amplitude of the 1st Fourier harmonic of velocity at the compressor face (A). The amplitude A is the Galerkin representation of the rotating stall cell amplitude. Note that in this model rotating stall is not an unsteady situation; in fact it is a *set of equilibria* along which A is non-zero[1]. Figure 12 shows the equilibria of MG3 and the open-loop stability properties. Note that there are four separate branches of equilibria, two of which are stable, and thus measurable in an open loop environment, and two which are unstable. The two unstable branches are the targets of the two approaches to control ('range extension' and 'operability enhancement'), as described below. The equilibrium to which the system settles is set by the intersection of the stable equilibrium branches with the throttle surface, $\Psi_T = (1/\gamma)\Phi^2$ (γ is proportional to the throttle area) which is independent of A and intersects either one or two of the stable solutions. The bottom inset in Figure 12 shows the migration of equilibria with γ, which is the most commonly used 'bifurcation parameter' for describing how the equilibria evolve.

In Figure 12, the two stable equilibrium branches are the points along the speed line, for which $A = 0$, and the rotating stall characteristic, along which A is large. As shown in the inset in Figure 12, as γ goes down in an uncontrolled compressor the system jumps from the no-stall branch to the in-stall branch in an abrupt way, which is undesirable. The hysteresis associated with recovery is also undesirable, as is the existence of two equilibria, one of which is rotating stall, at certain values of γ (in this case $1.4 < \gamma < 1.6$).

The first *unstable* equilibrium branch is the one along which $A = 0$. This is the extension of the compressor characteristic which has been discussed so far; stabilizing this set of equilibria is the goal of range extension. The second unstable equilibrium branch connects the peak of the compressor map and the rotating stall map; this is the focus of operability enhancement. If a control scheme can stabilize these equilibria, its existence may prevent the compressor from jumping directly between stable operation and fully developed rotating stall [34].

The inset in Figure 12 can also be interpreted as a bifurcation diagram with respect to a *disturbance* throttle area. The throttle characteristic is the same as described above, but here it represents effects which tend to undermine operability — changes in fuel flow, acceleration transients, etc. The fact that at a certain value of throttle area, the system jumps to a large amplitude rotating stall equilibrium, and that the area must be increase significantly before the system returns to normal operation, indicates that points near γ_{peak}, even if they are stable in the small-amplitude (linear) sense, tend to easily transition into rotating stall. Proof that these points do in fact have poor operability requires one to analyze the nonlinear stability properties of the equilibria; this has been done through simulation in [33], and in a more general context in [13] and [57].

Figure 13 shows the result of applying a feedback control of the following form:

$$\gamma_c = \gamma_o + K_A A^2$$

where γ_c is the area of a *controller* throttle valve, γ_o is its nominal area, and K_A is the controller gain. This control law does not stabilize the $A = 0$ branch of equilibria corresponding to range extension — such stabilization cannot be accomplished with a 1D controller. Instead, it stabilizes the $A \neq 0$ branch, along which A grows slowly and smoothly. The accompanying bifurcation diagram shows that with respect to the *disturbance* throttle, the system no longer exhibits a catastrophic jump into rotating stall. The compressor characteristic in Figure 13 indicates a subtlety associated with this change in the bifurcation characteristics: Although the disturbance throttle has closed down to a point well below the peak of the characteristic, the unsteady controller throttle opens partially, to maintain stability at a higher mass flow associated with the previously unreachable set of $A \neq 0$ equilibria.

The real utility of the controller is not measured by its ability to extend the mass flow range along this new branch of equilibria. Instead, it is measured by the resistance to instability of the peak of the compressor characteristic, which is the former surge line. Experiments by Eveker *et al*. [34, 47] have shown that transients on the disturbance throttle do not drive the system into rotating stall or surge when control is applied; without control the peak operating point has no resistance to disturbances at all. Thus control has effectively improved a surge margin-like operability measure, although it must now be quantified in a different way. Experimental demonstrations by Eveker *et al*. [47] showed that for systems which tend to surge (high B), the control law must be modified to balance rotating stall and surge requirements. Their controller adds feedback of mass flow acceleration in the compressor duct, taking the form:

$$\gamma_c = \gamma_o + K_A A^2 + K_{\dot{\Phi}} \dot{\Phi}$$

Research into 1D control, because of its reliance on nonlinear control theory, has followed a somewhat separate path than range extension, leading to a different culture and different concepts. For instance, research has almost exclusively been restricted to the three state Galerkin representation, and very little work on alternate actuators has been conducted, although it can be shown that 1D control will not work using plenum bleed in full-scale compression systems [58, 59], and in fact success of the approach in large-scale experiments was achieved by changing the placement of the actuators [47]. In addition, the effects of distortion, being difficult to model in the Galerkin framework, have been ignored.

Very recent publications in rotating stall control represent a research community which is more aware of all of the possible goals and methods to achieve them. Synthesis of the competing concepts of range extension through linear control and maintenance of operating points through nonlinear control is occurring in several ways, creating a knowledge base of the important concepts to incorporate, and methods to overcome experimental difficulties that often arise in practice. Two main synthesizing concepts have emerged: 1) maintenance of desired operating points with a small number of actuators can often be achieved more effectively with alternate actuators *(i.e.* other than plenum bleed); 2) nonlinear analysis and disturbance rejection can be incorporated into range extension control schemes.

All of the successful recent implementations of active control reported to date have occurred using either bleed valves immediately downstream of the compressor [47], injectors upstream of the compressor [8, 35], or both [42, 60]. In some of these cases nonlinear control concepts akin to those described above were used; bifurcation concepts have clearly been important. But the use of plenum bleed valves, which is very prevalent in the nonlinear control literature, is not realistic and therefore does not appear in the experimental demonstrations. Future research into nonlinear control should be restricted to systems with actuators that have demonstrated utility in real systems.

A study of alternative actuation mechanisms and their relationship to nonlinear control has been conducted by D'Andrea *et al*. [35], Behnken *et al*. [44], Wang and Murray [54], and Yeung and Murray [60]. High-momentum, low flow inlet injectors, as well as downstream bleed valves, have been implemented in a low-speed rig and used in various configurations and combinations. Two main points can be derived from this work. First, the use of 2D actuation to alter the bifurcation properties of compressors constitutes a useful combination of the concepts described above: using Moore-Greitzer type modeling, the nonlinear bifurcation properties are altered not through 1D actuation, but through triggered 2D injection similar to that originally used by Day [29]. In [35] and [44], only three very simple (on-off) actuators were used, so that reduction of complexity was achieved as in 1D control, while demonstrating good nonlinear disturbance properties. The second point stressed in this research is that the large-amplitude nonlinear stability properties promised by bifurcation control literature cannot be obtained in practice. A much more realistic picture of the limitations of bifurcation control, under the constraints of actuator rate limits, saturation of the actuators, and noise, was developed in [54]. This work has helped to create a more balanced picture of the trades between 1D and 2D control.

Weigl *et al*. [8] also demonstrated that 2D control can be used to achieve beneficial nonlinear properties. By turning off the stabilizing controller, allowing rotating stall and surge waves to grow, and then reinitiating the controller, the nonlinear domain of attraction of the linearly stabilized operating points was demonstrated. Setiawan [61] performed a trade study to demonstrate the nonlinear properties of various controllers, concluding that in compression systems prone to surge, plenum bleed has the worst nonlinear properties. This work also makes the point that at least two separate measures of nonlinear robustness are important: 1) the stabilized system must resist downstream disturbances such as backpressuring with a disturbance throttle, fuel spikes, or acceleration transients; 2) the system must also resist upstream disturbances, specifically inlet distortion, in order to be viable in an operational engine environment. Freeman *et al*. [42] incorporated these requirements into their testing, and Protz [57] did the first experimental measurements of a controller's 'distortion tolerance', that is the combined ability of the controlled system to resist both upstream and downstream disturbances.

In the Rolls-Royce study of Freeman *et al*. [42], the concepts of alternate actuation and distortion tolerance were incorporated. A Viper engine's eight-stage compressor was outfitted with a recirculation mechanism that allowed bleed air from either the exit of the fourth stage or the last stage to be injected either at the fourth stage or at the inlet of the compressor. Six circumferentially distributed pipes recirculated the flow, actuated by high-response (300 Hz) hydraulic Moog valves. High response pressure transducers were placed, in circumferential arrays of five or six, at various stages. The system was driven toward the surge line by various methods: bleeding air into the combustor, fuel spiking, or by hot gas ingestion (which introduces severe distortion). Control strategies similar to those reported by Paduano [36] and Day [29] were tested, as well as a technique which commanded all of the valves to open whenever any third stage unsteady pressure signal exceeded an experimentally determined threshold level. The last technique, a 1D 'nonlinear' approach implemented with flow recirculation instead of plenum bleed, was found to increase the stable operating range by up to 25% in pressure rise, and was able to extend the stable operating range at all speeds and with each method of inducing stall. The philosophy of the 1D strategy was to sense stall inception and subsequently clear the stall cell before it fully developed, by introducing a stabilizing uniform recirculation. The steady-state benefit of recirculation was thus introduced in an unsteady manner only when necessary, reducing the overall recirculation requirements over a scheduled method.

Freeman *et al*. [42] contains a number of interesting discussions. The paper compares their most successful control system to the one originally tested by Ludwig and Nenni [48, 49], finding the concepts very similar although the more recent application was more refined. It also describes how inlet distortion can be addressed directly, by concentrating recirculation in a region which is appropriately phase shifted from the measured distortion. A discussion of the efficiency trade-offs between scheduled bleed, active recirculation, and 'ideal stall control' is also provided. Here the upshot is that by recirculating air, and by doing so only when necessary, significant efficiency improvements over currently used bleed schedules is

likely. The importance of injection modulation, as a high-bandwidth way to introduce the stabilizing effect of inlet injection, is also discussed.

In this work, as well as in the work of Weigl *et al*. [8] and Yeung *et al*. [60], the importance of actuation which improves the flow properties in the compressor was clearly demonstrated. Freeman *et al*. take an overall efficiency standpoint, concluding that bleed valves alone are both less effective and less efficient. Weigl utilized injection in the tip region of the compressor, improving the flow properties (in the region demonstrated to be critical in Section 2) to achieve the highest actuation leverage. Finally, Yeung *et al*. found that by steadily injecting a small amount of air upstream of their compressor, the bandwidth requirements for downstream bleed stabilization were significantly reduced. All of these studies demonstrate that understanding and actuating the detailed flow properties of the compressor is key to successful active control.

Comparison of the control schemes used shows that the best performance is usually achieved by introducing a stabilizing flow influence in an unsteady manner. In most cases this stabilizing influence can be introduced in a steady manner, achieving (usually less extensive) stall margin improvements without the complexity associated with modulated actuation. A penalty is usually associated with this, however, as either bleed or inlet injection involves bleeding high-pressure air from downstream of the compressor. By bleeding or injecting only when necessary, active control provides an automatic way of introducing corrective action with a lower overall efficiency penalty. The trade between efficiency, surge margin, and complexity is a difficult one, which will fall in favor of implementing control only through very careful design and implementation.

5. POTENTIAL BENEFITS OF ACTIVE CONTROL

Active compressor control was a term originally intended to refer to the use of feedback control to extend the stable operating range of gas turbine compression systems Based on the discussions presented here, and on other ongoing work, it is clear that it now encompasses a wide range of technical approaches and goals. This includes feedback control to extend the operation range (active stabilization), feedback control to enhance robustness to disturbances (to permit operation closer to the no control surge line), change to the steady state operating point upon the detection of disturbances (opening bleed valves, restaggering stators, etc.), and even the use of high frequency response measurements within the compressor as a diagnostic and maintenance aid. The cost of these approaches vary considerably. By cost we refer to such things as the number, authority, and bandwidth of the actuators and sensors required, the computer power needed, engine performance penalties incurred, and overall weight. These costs are balanced against the benefits realized from the inclusion of active control in an engine design. It is the balance that is the topic of this section.

Compressor stability is really a singular state in the sense that a compressor is stable or it is not. The stability margin criteria commonly employed are used to account for stability “threats” encountered over the operating life of an engine. Some threats vary relatively rapidly with time because they are operating condition related, such as inlet distortion, engine transient, and altitude (Reynolds number) effects. Other threats have very long time constants such as those related to unit to unit manufacturing variations and long term engine aging. The threats are typically expressed in terms of a stall margin, a percentage pressure rise between the nominal surge line and the steady state engine operating line. Thus, the benefits of active control have often been expressed as a percentage increase in the surge margin. However, surge margin, as such, is a fairly crude measure of stability for a dynamical system as complex as a modern aircraft engine. Therefore, to regard active control mainly in terms of stall margin extension may mask some potential advantages.

Innovations such as active control can regarded in two ways. The first is how this new technology might allow us to do what we do now better. For most applications, better implies lower overall lifecycle cost for an airline or weapons systems. Alternatively, the new technology can be enabling, i.e. it can let us do something that either we could not do before, or let us do it in a new, significantly improved manner (stealth technology might be an example here). First, we will consider current stability practice. Modern engines ensure stability with steady geometry included flow variations imposed through a combination of passive design features and fuel control scheduled geometry changes. The primary passive design feature is multiple spool compressors. Scheduled steady state geometry changes include bleed valves, variable geometry stators, and exhaust nozzle are manipulation. Current approached are not without cost. In the case of multiple spools, the cost is mechanical complexity and increase weight an manufacturing cost. (Note that high bypass turbofans require either 2 spools or a gear to keep the fan drive turbine to reasonable size, but this is not true for low bypass ratio military engines.) Bleeds can be costly because loss of compressed air decreases compressor efficiency and so increases overall fuel consumption. (One informal

estimate is that the operator of a large commercial aircraft may spend $100,000 per year on stability bleed air fuel.) Variable stator mechanisms are relatively costly and heavy, adding about 50% to the weight of a stage. Also the stator settings required for stable operation are often not those for maximum efficiency.

Other penalties associated with current practice may be more subtle. Inlet distortion can fall into this category. For example, in a modern tactical aircraft application with a fixed geometry inlet, maximum inlet distortion is often encountered during rotation on takeoff. To reduce this distortion to a level no higher than that found during other portions of the flight envelope (such as maneuver), aircraft designers may oversize the inlet capture area relative to that required at cruise. This results in increased spillage drag at cruise. Thus this short time, single point stability requirement penalizes most of the aircraft flight regime with a concomitant increase in fuel consumption and decrease in range. One estimate place this drag penalty as equivalent to an 8% decrease in range. An additional benefit accrues if the increased stable operating range permits the engine to operate at lower mass flow at constant power during takeoff. In this case, the entire inlet can be downsized accordingly, to the benefit of inlet weight and drag.

Active compressor control can also be an enabling technology in that it can permit configurations that are not otherwise achievable with significantly downrated engines (which render the concept unattractive). One example might be top mounted inlets for tactical aircraft which require larger maneuver envelopes than the B-2 and a larger tolerance for inlet distortion. A somewhat different example is very high bypass ratio turbofan engines above about 12:1. The optimum fan pressure ratio falls with increasing bypass ratio. Once the pressure ratio is so low that the fan nozzle is no longer choked, the fan operating point shifts with flight condition and power setting so as to reduce the fan stall margin below requirement. Without some type of stability augmentation then variable geometry would be needed, either a variable area fan nozzle or a variable fan pitch.

6. REFERENCES

1. Epstein. A. H., Fowcs-Williams, J. E., and Greitzer, E. M., “Active Suppression of Aerodynamic Instabilities in Turbomachines,” *Trans. AIAA J. of Prop. and Power*, Vol. 5, No. 2 (1986) 204-211.
2. Pampreen, R. C., *Compressor Surge and Stall*, Concepts ETI, Norwich VT (1993).
3. Emmons, H. W., Pearson, C. F., and Grant, H. P., “Compressor Surge and Stall Propagation,” *Trans. of the ASME*, Vol. 79 (1955).
4. Day, I.J., “Stall Inception in Axial Flow Compressors,” *ASME J. of Turbomach.*, Vol. 115 (1993) 1-9.
5. Moore, F. K., “A Theory of Rotating Stall of Multistage Compressors, Parts I-III,” *ASME J. of Engineering for Power*, Vol. 106 (1984) 313-336.
6. Moore, F. K. and Greitzer, E. M., “A Theory of Post-Stall Transients in Axial Compression Systems, Part I - Development of Equations, and Part II - Application, “ *ASME J. of Engineering for Gas Turbines and Power*, Vol. 108 (1986) 68-97.
7. Tryfonidis, M., Etchevers, O., Paduano, J. ., Epstein, A. H., and Hendricks, G. J., “Pre-Stall Behavior of Several High-Speed Compressors,” *ASME J. of Turbomachinery*, Vol. 117, No. 1 (1995) 62-80.
8. Weigl, H. J., Paduano, J. D., Frechette, L. G., Epstein, A. H., Greitzer, E. M., Bright, M. M., and Strazisar, A. J., “Active Stabilization of Rotating Stall in a Transonic Single Stage Axial Compressor,” 97-GT-411, ASME Turbo Expo ‘97, Orlando. (1997).
9. Longley, J. P., “A Review of Non-Steady Flow Models for Compressor Stability,” ASME Paper 93-GT-17, 1993 ASME Turbo Expo, Cincinnati, (1993).
10. Spakovszky, Z. S., “Simulation of Engine Clearance Effects on Compressor Dynamic Behavior During Acceleration Transients,” Dipl. Masch. Ing. ETH Thesis (1997).
11. Paduano, J. D., Valavani, L., Epstein, A. H., Greitzer, E. M. and Guenette, G. R., “Modeling for Control of Rotating Stall,” *Automatica*, Vol. 30, No. 9 (1994) 1357-1373.
12. Paduano, J. D., Valavani, L., and Epstein, A. H., “Parameter Identification of Compressor Dynamics During Closed-Loop Operation,” American Control Conference, June, Boston (1991).
13. Mansoux, C. A., Gysling, D. L., Setiawan, J. D., and Paduano, J. D., “Distributed Nonlinear Modeling and Stability Analysis of Axial Compressor Stall and Surge,” American Control Conference, July, Baltimore (1994).
14. Bonnaure, L. P., “Modeling High Speed Multistage Compressor Stability,” M. S. Thesis, MIT Department of Aeronautics and Astronautics (1991).
15. Hendricks, G. J., Bonnaure, L. P., Longley, J. P., Greitzer E. M., Epstein A. H., “Analysis of Rotating Stall Onset In High-Speed Axial Flow Compressors,” AIAA paper 93-2233, 29th Joint Propulsion Conference, Monterey (1993).

16. Feulner, M. R., Hendricks, G. J., and Paduano, J. D., "Modeling for Control of Rotating Stall in High Speed Multi-Stage Axial Compressors," 94-GT-200, ASME Turbo Expo '94, June 13-16, The Hague, Netherlands (1994).
17. Frechette, L. G., "Implications of Stability Modeling for High-Speed Axial Compressor Design," Master's Thesis, MIT Department of Aeronautics and Astronautics (1997).
18. Weigl H. J., "Active Stabilization of Rotating Stall and Surge in a Transonic Single Stage Axial Compressor," Ph.D. Thesis, MIT Department of Aeronautics and Astronautics (1997).
19. Gordon, K., personal communication.
20. Sun, X. F., "Three-Dimensional Compressible Flow Stability Theory of Rotating Stall," BUAA Technical Report BH-B4765, Beijing University of Aeronautics and Astronautics, Department of Jet Propulsion (1996).
21. McDougall, N. M, Cumpsty, N. A., and Hynes, T. P., "Stall Inception in Axial Compressors," *ASME J. of Turbomachinery*, Vol. 112 (1990) 116-125.
22. Garnier, V. H., Epstein, A. H., and Greitzer, E. M., "Rotating Waves as a Stall Inception Indication in Axial Compressors," *ASME J. of Turbomachinery*, Vol. 113 (1991) 290-301.
23. Hoying, D. A., "Stall Inception in a Multistage High Speed Axial Compressor," 29th Joint Propulsion Conference, Monterey (1993).
24. Inoue, M., Kuroumaru, M., and Ando, Y., "Detection of a Rotating Stall Precursor in Isolated Axial Flow Compressor Rotors," *ASME J. of Turbomachinery*, Vol. 113 (1993) 281-287.
25. Day, I. J., and Freeman, C., "The Unstable Behaviour of Low and High Speed Compressors," *ASME J. of Turbomachinery*, Vol. 116, No. 2 (1994) 217-225.
26. Anderton, J. F., King, P. I., and Copenhaver, W. W., "Stall Analysis of High-Frequency Data for Three Swept-Blade Compressor Rotors," in *Proceedings of SPIE*, Volume 2494, Orlando (1995).
27. Park, H. G., "Unsteady Disturbance Structures in Axial Flow Compressor Stall Inception," Master's Thesis, MIT Department of Aeronautics and Astronautics (1994).
28. Camp, T. R., and Day, I. J., "A Study of Spike and Modal Stall Phenomena in a Low-Speed Axial Compressor," 97-GT-526, ASME Turbo Expo '97, Orlando (1997).
29. Day, I. J., "Active Suppression of Rotating Stall and Surge in Axial Compressors," *ASME J. of Turbomachinery*, Vol. 115 (1993) 40-47.
30. Day, I. J., Breuer, T., Escuret, J., Cherrett, M., Wilson, A., "Stall Inception and the Prospects for Active Control in Four High Speed Compressors," 97-GT-281, ASME Turbo Expo '97, Orlando.
31. Silkowski, P. D., "Measurements of Rotor Stalling in a Matched and Mismatched Multistage Compressor, GTL Report No. 221, Gas Turbine Laboratory, Mass. Inst. of Technology (1995).
32. Hoying, D. A., "Blade Passage Flow Structure Effects on Axial Compressor Rotating Stall Inception, Ph.D. Thesis, MIT Department of Aeronautics and Astronautics (1996).
33. Badmus, O. O., Chowdhury, S., Eveker, K. M., Nett, C. N., and Rivera, C. J., "A Simplified Approach for Control of Rotating Stall Part I: Theoretical Development and Part II: Experimental Results," AIAA 93-2229 and AIAA 93-2234, 29th Joint Propulsion Conference, Monterey (1993).
34. Eveker, K. M., Gysling, D. L., Nett, C. N., and Sharma, O. P., "Integrated Control of Rotating Stall and Surge in a Low speed Axial Compression System," in *Proceedings of SPIE*, Volume 2494, Orlando (1995) 17-18.
35. D'Andrea, R., Behnken, R. L., Murray, R. M., "Active Control of Rotating Stall via Pulsed Air Injection: A Parametric Study on a Low Speed, Axial Flow Compressor," in *Proceedings of SPIE*, Volume 2494, Orlando (1995) 152-165.
36. Paduano, J. D., Epstein, A. H., Valavani, L., Longley, J. P., Greitzer, E. M., and Guennette, G. R., "Active Control of Rotating Stall in a Low Speed Axial Compressor," *ASME J. of Turbomachinery*, Vol. 115, No. 1 (1993) 48-56.
37. Haynes, J. M., Hendricks, G. J., and Epstein, A. H., "Active Stabilization of Rotating Stall in a Three-Stage Axial Compressor," *ASME J. of Turbomachinery*, Vol. 116 (1994) 226-239.
38. Gysling, D. L., Dugundji, J., Greitzer, E. M., and Epstein, A. H., "Dynamic Control of Compressor Surge using Tailored Structures," *ASME J. of Turbomachinery*, Vol. 113 (1991) 710-722.
39. Greitzer, E.M., Epstein, A.H., Guenette, G., Gysling, D., Haynes, J., Hendricks, G.J., Paduano, J., Simon, J., and Valavani, L., "Dynamic Control of Aerodynamic Instabilities in Gas Turbine Engine," *Steady and Transient Performance Prediction of Gas Turbine Engines*, AGARD-LS-183 (1992).
40. van Schalkwyk, C. M., Paduano, J. D., Greitzer, E. M., and Epstein, A. H., "Active Stabilization of Axial Compressors with Circumferential Inlet Distortion," 97-GT-279, ASME Turbo Expo '97, Orlando (1997).

41. Hynes, T. P. and Greitzer, E. M. "A Method of Assessing Effects of Circumferential Flow Distortion on Compressor Stability," *ASME J. of Turbomachinery*, Vol. 109 (1987) 371-379.
42. Freeman, C., Wilson, A. G., Day, I. J., and Swinbanks, M. A., "Experiments in Active Control of Stall on an Aeroengine Gas Turbine," 97-GT-280, ASME Turbo Expo '97, Orlando (1997).
43. Hendricks, G. J., and Gysling, D. L., "A Theoretical Study of Sensor-Actuator Schemes for Rotating Stall Control," 28th Joint Propulsion Conference, Nashville, TN (1992).
44. Behnken, R. L., Leung, M., and Murray, R. M., "Characterizing the Effects of Air Injection on Compressor Performance for Use in Active Control of Rotating Stall," 97-GT-316, ASME Turbo Expo '97, Orlando (1997).
45. Berndt, R. G., Weigl, H. J., Paduano, J. D., and Epstein, A. H., "Experimental Techniques for Actuation, Sensing and Measurement of Rotating Stall Dynamics in High Speed Compressors," in *Proceedings of SPIE*, Volume 2494, Orlando (1995) 166-185.
46. Liaw, D. C., and Abed, E. H., "Active Stabilization of Rotating Stall: A Bifurcation-Theoretic Approach," Second IFAC Nonlinear Control Symposium, Bordeaux, France (1992).
47. Eveker, K.M., Gysling, D.L., Nett, C.N., and Sharma, O.P., "Integrated Control of Rotating Stall and Surge in High-Speed Multi-Stage Compression Systems," 97-GT-352, ASME Turbo Expo '97, Orlando (1997).
48. Ludwig, G. R., and Nenni, J. P., "A Rotating Stall Control System for Turbojet Engines," ASME Paper 76-GT-115 (1976).
49. Ludwig, G. R., and Nenni, J. P., "Tests of an Improved Rotating Stall Control System on a J-85 Turbojet Engine," ASME Paper 80-GT-17, Gas Turbine Conference and Products Show, New Orleans (1980).
50. McCaughan, F. E., "Application of Bifurcation Theory to Axial Flow Compressor Stability," *ASME J. Turbomachinery*, Vol. 3 (1989) 426-433.
51. Adomaitis, R. A., and Abed, E. H., "Local Nonlinear Control of Stall Inception in Axial Flow Compressors," AIAA Paper 93-2230, 29th Joint Propulsion Conference, Monterey (1993).
52. Ballieul, J., Dahlgren, S., and Lehman, B., "Nonlinear Control Designs for Systems with Bifurcations with Applications to Stabilization and Control of Compressors," Proc. 34th Conference on Decision and Control, New Orleans, LA (1995) 3062-3067.
53. Lin, F., "On the Practical Stability and Its Application to Nonlinear Control of Surge," ASME Paper 96-GT-512, 1996 ASME Turbo Expo (1996).
54. Wang, Y., and Murray, R. M., "Effects of Noise, Magnitude Saturation, and Rate Limits on Rotating Stall Control," 36th IEEE Conference on Decision and Control (1997).
55. Krstic, M., Protz, J. M., Paduano, J. D., and Kokotovic, P. V., "Backstepping Designs for Jet Engine Stall and Surge Control," Proceedings of the 34th Conference on Decision and Control, New Orleans, LA (1995) 3049-3055.
56. McCaughan, F. E., "An Analytical and Numerical Study of Axial Flow Compressor Instability," *ASME J. of Turbomachinery*, Vol. 3 (1989) 434-441.
57 Protz., J. M., Master's Thesis, MIT Department of Aeronautics and Astronautics (1997).
58. Simon, J. S., Valavani, L., Epstein, A. H., and Greitzer, E. M., "Evaluation of Approaches to Active Compressor Surge Stabilization," *ASME J. of Turbomachinery*, Vol. 115 (1993) 57-67.
59. Wang, H. H., Krstic, M., Larsen, M., "Control of Deep-Hysteresis Aeroengine Compressors, Part I and II," American Control Conference, Albuquerque (1997).
60. Yeung, S. and Murray, R. M., "Reduction of Bleed Valve Bandwidth Requirements for Control of Rotating Stall using Continuous Air Injection," Conference on Control Applications, East Hartford (1997).
61. Setiawan, J. D., "Distortion Tolerance of Stall/Surge Controllers in Axial Compression Systems," Master's Thesis, MIT Department of Aeronautics and Astronautics (1996).
62. Suder, K.L., Hathaway, M.D., Thorp, S.A., Strazisar, A.J., and Bright, M.B., "Compressor Stability Enhancement Using Discrete Tip Injection," ASME Turbo Expo, May 8-11, Munich (2000).

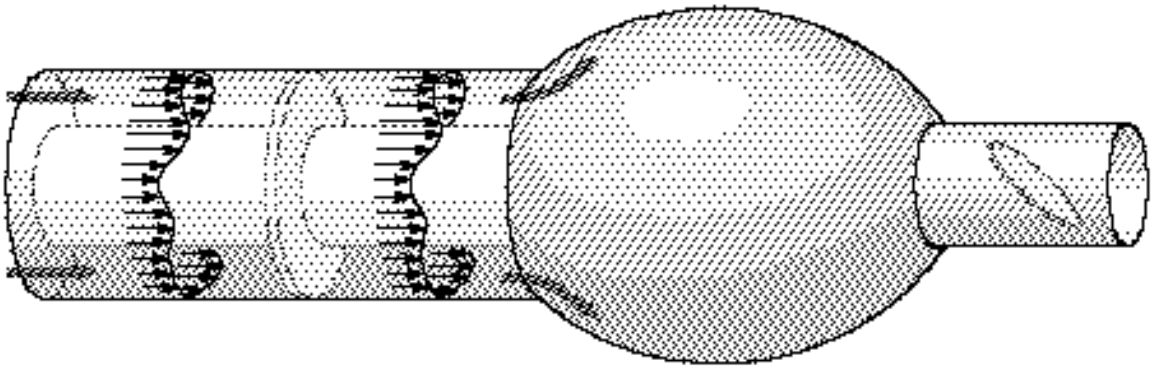
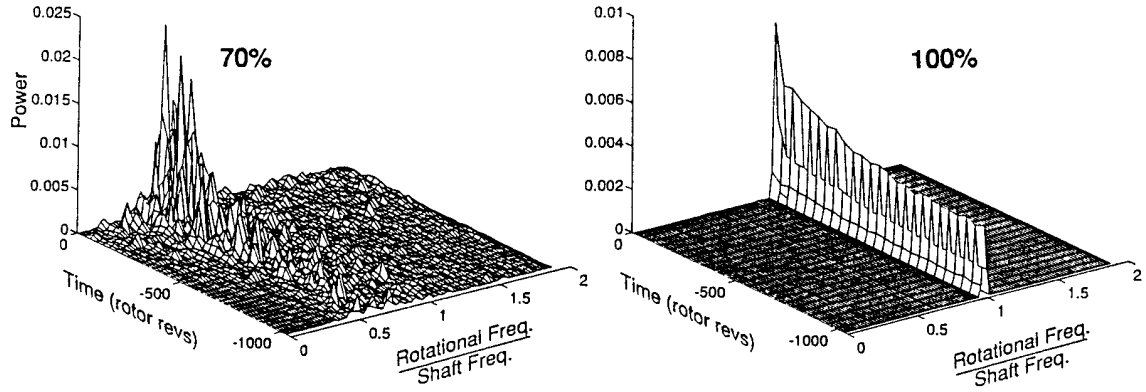


Figure 1 - Schematic of a compression system, including upstream and downstream ducts, compressor model, plenum, and throttle.



(a) (b)

Figure 2 - Spectrograms of two different precursor events, immediately prior to stall in a high-speed compressor. (a) 70% design speed; (b) 100% design speed. From Tryfonidis [6].

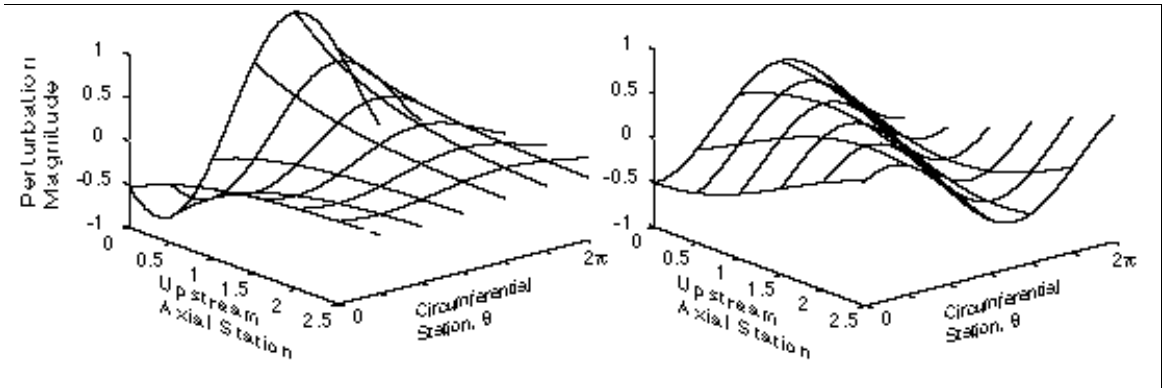
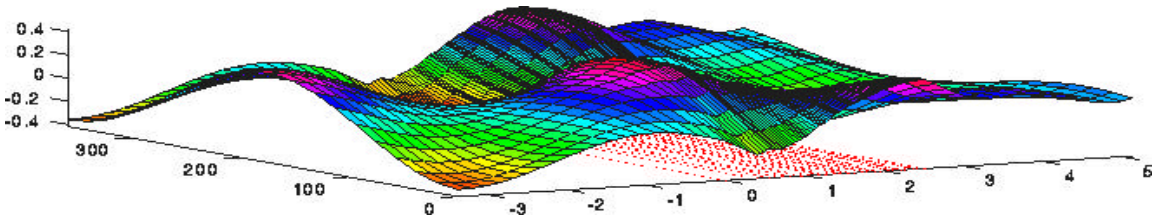
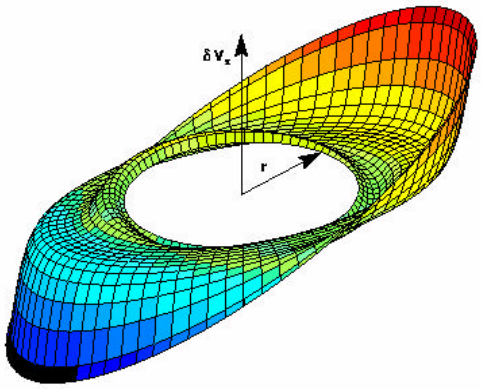


Figure 3 - Examples of upstream axial velocity distribution for incompressible (left) and compressible (right) 2D eigenmodes.



(a)



(b)

Figure 4 - Examples of eigenmode shapes in two hydrodynamic stability models.
(a) Compressible 2D model, (b) incompressible 3D model.

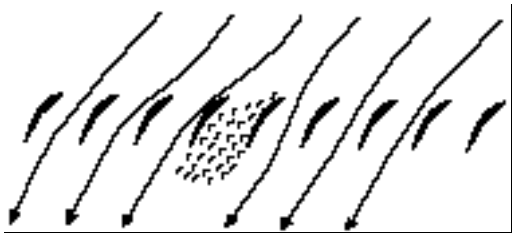


Figure 5 - Sketch of short-length scale rotating stall event. From Day [25].

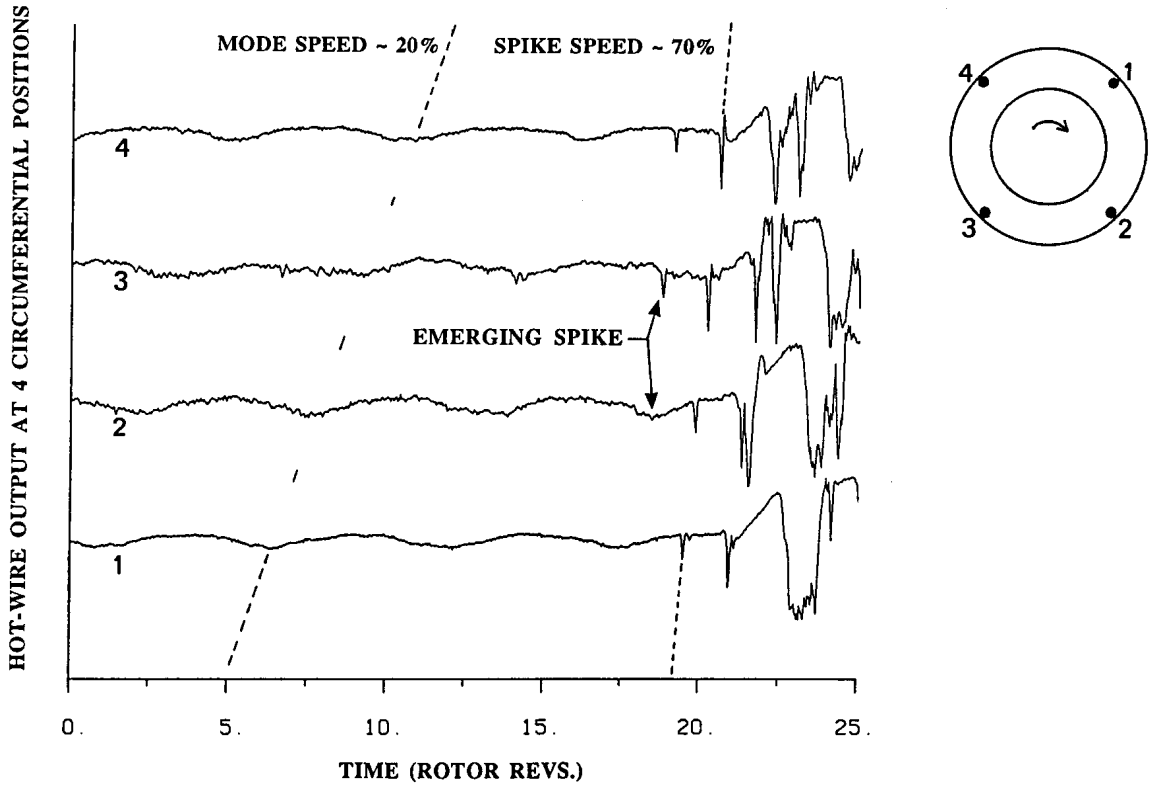


Figure 6 - Short length-scale event in a low speed compressor, from Day [25].

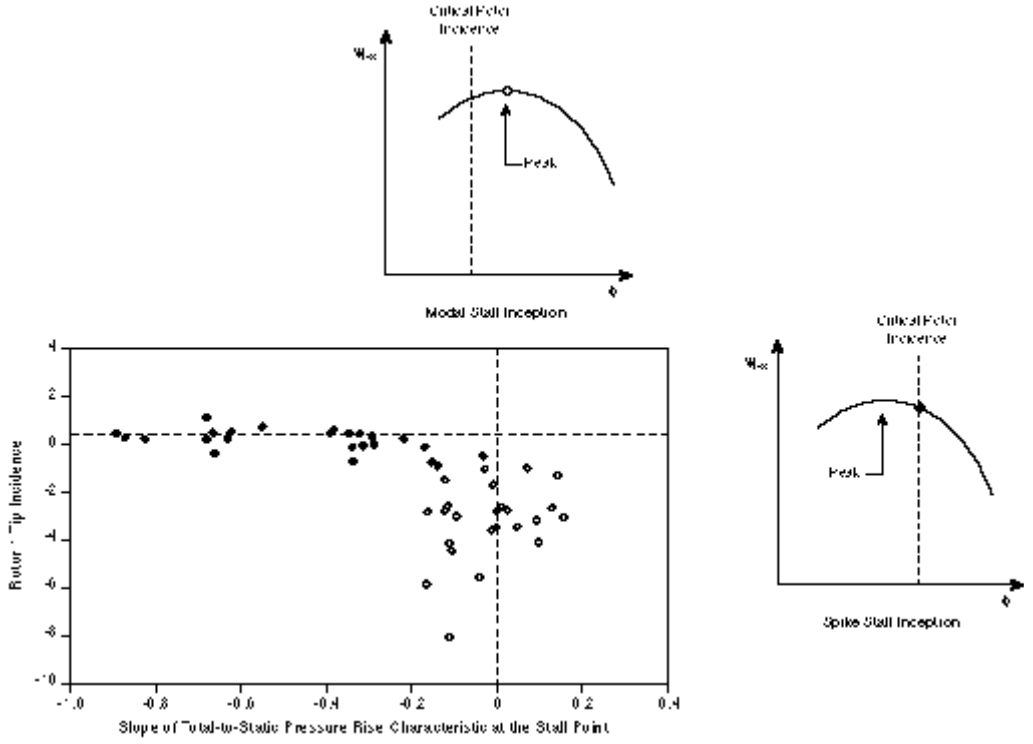


Figure 7 - Experimental Results from Camp and Day [31], showing the criticality of incidence in on the rotor of a four stage compressor.

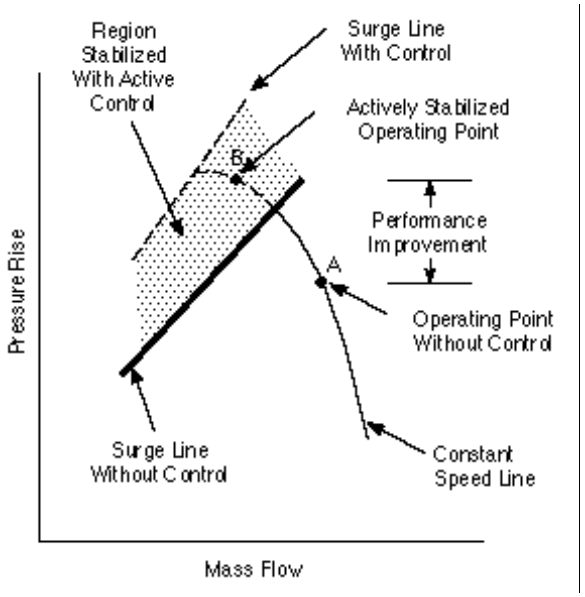


Figure 8 - Goal of active compressor operating range extension via stabilization.

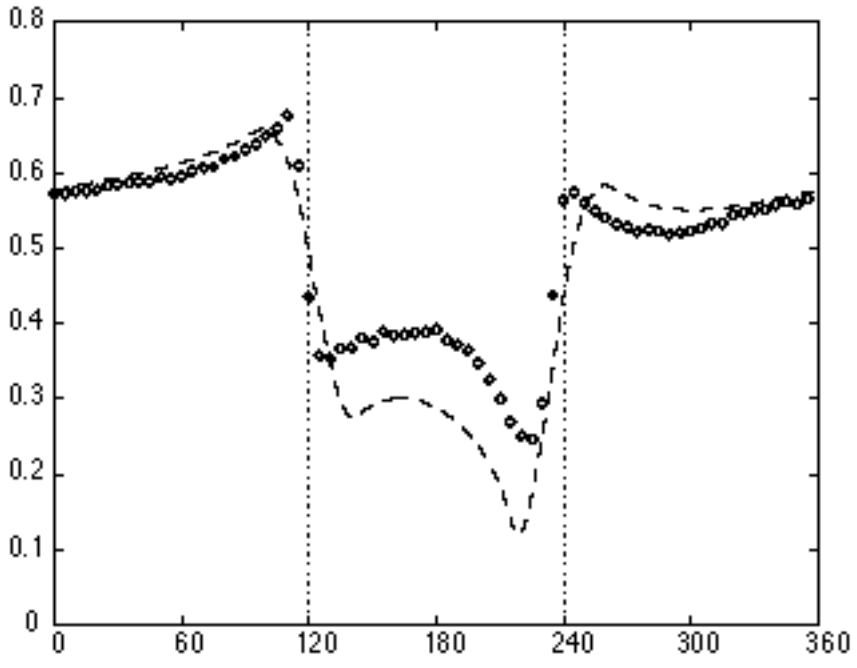


Figure 9 - Comparison of theoretical (dashed) and measured (circles) velocity profile due to an inlet distortion. From van Schalkwyk et al. [40].

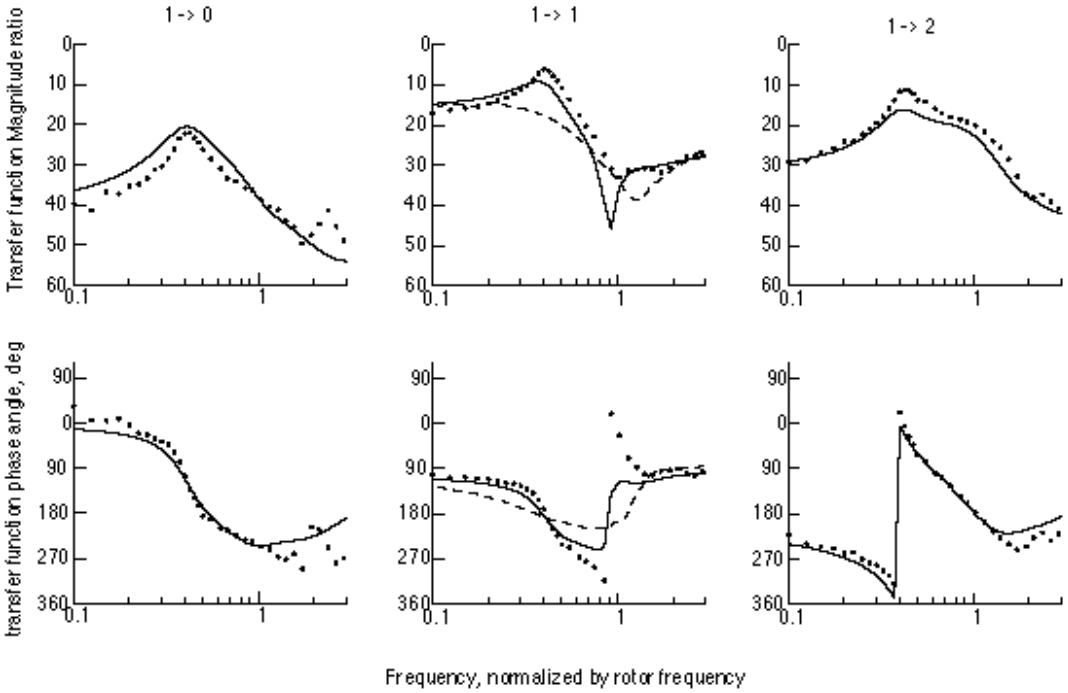


Figure 10 - Transfer function from first Fourier coefficient of inlet guide vane deflection to 0th, 1st, and 2nd Fourier coefficient of axial velocity. Data taken with 1.9 dynamic head inlet distortion (circles) and compared to theory (lines) dashed line represents undistorted flow prediction. From van Schalkwyk et al. [40].

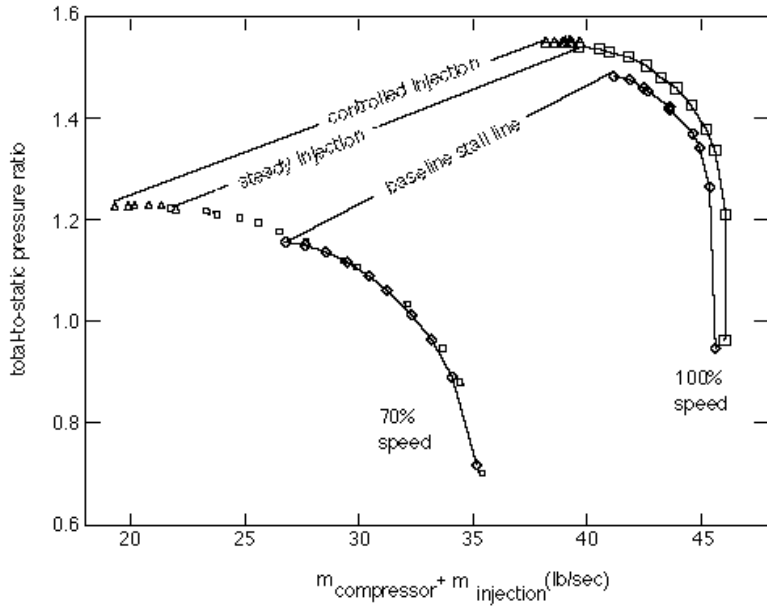


Figure 11 - NASA Stage 35 stability enhancement through steady, and through steady plus feedback-controlled unsteady inlet injection. Mean rate of mass injection was 1.57 lb/sec.

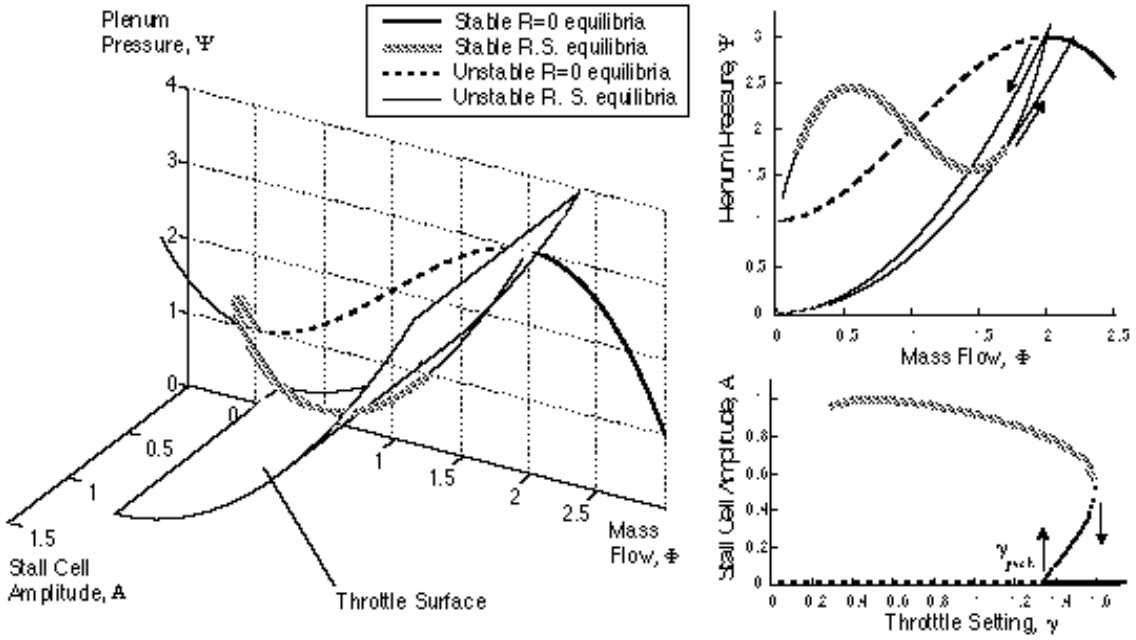


Figure 12 - Equilibria of the three-state Moore-Greitzer model.

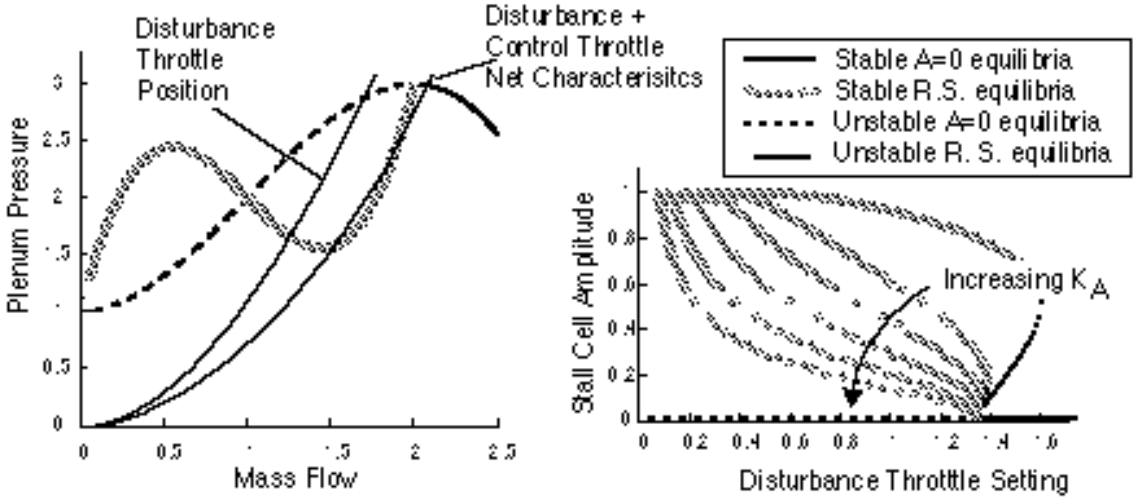


Figure 13 - Effect of plenum bleed feedback on equilibrium properites.

Paper 1, J. D. Paduano

Question (S. Candel, France)

Could you give more information on how you are using a single sensor to detect stall/surge?

Reply

Several methods exist in the literature to identify pre-stall signatures on a single sensor (usually wall static pressure) placed in an axial compressor (usually near the leading edge of the rotor, or over the rotor of the most critical blade row, which is often the first). These methods involve wavelet transformations, but methods based on the theory of time series analysis for nonlinear dynamical systems have also been employed. Often the methods are tailored for the specific data set of the compressor under consideration, and at this point there does not appear to be an approach that works universally.

In the application cited in my talk, the spectrogram (power spectral density computed over a moving window, so that it is time dependent) of the pressure transducer is computed, and the intensity of the peak signal at 1E is computed. Our modeling showed that there is an eigenvalue very near the 1E excitation, and that the stability of this eigenvalue is indicative of the instantaneous stall margin during transients. It was found that engine deterioration degrades transient stall margin, and that experimental results, model calculations and real-time 1E indicators all capture this effect. See the *J. Turbomachinery*, Vol 122 paper by Spakovsky *et al.*, July 2000, for more details.

Question (T. Lewis, USA)

Regarding the flow injection/recirculation for stabilization testing by NASA and MIT: was the internal air source the discharge of the compressor under test, or some external source? The concern would be the destabilizing effects of hot air injection and whether these effects would outweigh the measured stability improvements.

Reply

Tests to date have used cool ("shop") air injected from an external supply. Our understanding of the effect of hot air recirculation is that

a) as long as the injectors remain choked, no new instabilities will be introduced;
b) the effectiveness of the injector will be reduced, e.g., because the fluid density is reduced, affecting $\overline{V}_x / U_{tip}$;
c) the injectors must be rated for higher temperatures, a practical matter.

Question (M. Richman, USA)

Could you comment on the ability of the General Dynamics eddy current sensor to detect the precursor to stall versus a pressure sensor?

Reply

This depends on the blade stiffness. For core compressor stages (where the blades are stiff in twist), the eddy current sensor would not perform as well. For fan stages (lower stiffness), the eddy current sensor is more likely to be effective. The rotating stall cell will almost surely be detectable in either case, but the small amplitude stall precursors may be more difficult. This has yet to be demonstrated.

ACTIVE CONTROL OF COMBUSTION AND ITS APPLICATIONS

A.J.Moran
Rolls-Royce plc, Ansty, Coventy, England, CV7 9JR
D.Steele
Rolls-Royce plc, P.O Box 3,Filton, Bristol, England, BS34 7QE
A.P.Dowling
Engineering Department.University of Cambridge,Cambridge, England

ABSTRACT

The ducted flame in any of its forms can have the tendency to interact with its surroundings. When this interaction takes the form of thermo-acoustic instabilities the consequences can be grave. These instabilities have been recognised as a problem for many decades and have appeared in many forms of engine including rocket motors, ramjets, main engine gas turbine combustors and after burning systems.

It is true to say that the phenomena has not been truly understood and that many researchers have come up with several theories as to how these thermo-acoustic instabilities occur. In the field of engineering, the ability to fix the problem rather than fully understand the problem has been a principle that has been applied for many years. The approaches taken to fixing thermo-acoustic problems have been either radical re-design of the combustion system or the application of passive damping techniques. In the past decade, however, a further technique has been given to the combustion designer, that technique being the ability to use active control.

This paper outlines how the technique has been developed, from small scale pilot rig testing through to full engine demonstration, and how active control may be applied to land-based gas turbines in the future. With the introduction of ultra low emission lean pre-mixed combustion systems to land based gas turbines the propensity to exhibit thermo-acoustic instabilities has increased. Actively controlling the instability is a real option, the benefits of gaining extensive experience with the technology on land will help to promote the technology for future application to aircraft.

1.Introduction

The problem of combustion instability has existed since flames have been confined within ducts. They occur in many types of combustion system from domestic heating systems through to rocket motors and gas turbines. The instability can manifest itself in a number of different forms from relatively simple longitudinal waves to highly complex spinning structures. The way that the instability interacts with its surroundings may well be an annoyance to an operator of that system. Alternatively the instabilities could cause catastrophic mechanical failure of the combustion system or its surrounding. Neither of the above are acceptable the latter more so than the former and it has been the job of the combustion designer to lessen the effects of combustion instabilities. Within the designer's toolbox there are three methods of controlling the instability should it occur. The first two of these methods has been around for a considerable time, that is the use of so called passive dampers. As the name implies the device modifies the overall damping of the system either by means of an acoustic liner or helmholtz cavity, or by modification of burner aerodynamics which modifies the reaction zone/ sound field interaction. In practice the above techniques rely on knowledge of the transfer function across the flame and the properties either side. These are rarely known and hence there is always a degree of cut and try with this approach. The third method used to control instability is the use of active control and it is the main objective of this paper to describe how such a method has been developed through a laboratory scale experiment through to a full gas turbine demonstration of the principal.

2.Background

It is well known and often quoted that combustion instabilities occur due to the interaction between unsteady heat release from the combustion process and acoustic waves. Rayleigh[1] described the above in a clear and concise way.

According to Raylcigh[1] the amplitude of a sound wave will increase when there is heat addition in phase with its pressure. If on the other hand the heat is added out of phase with the pressure there will be a reduction in amplitude. In accordance with Dowling[2] for a simple combustor such as a Rijke tube where there is no mean flow equation (1) can be used as a generalised form of Rayleigh's criterion, ignoring viscous effects. The equation says that if the energy (left hand side) is greater than the surface loss term (right hand side) then the disturbance will grow.

$$\int_V \frac{(\gamma-1)}{\bar{\rho}\bar{c}^2}\overline{p'q'}dV > \int_S \overline{p'u}\cdot dS \qquad (1)$$

where ρ = density
c = speed of sound
p = pressure
u = particle velocity
γ = ratio of specific heats
q = heat release/unit volume
V= volume
S= bounding surface

The overbar denotes an average over one cycle and the prime denotes a perturbation.

It had been demonstrated that active control could be applied to relatively simple geometries such as a Rijke tube in the early to mid 80's, Dines[3]. Using the principal that equation (1) can be manipulated, for effective

Paper presented at the RTO AVT Symposium on "Active Control Technology for Enhanced Performance Operational Capabilities of Military Aircraft, Land Vehicles and Sea Vehicles", held in Braunschweig, Germany, 8-11 May 2000, and published in RTO MP-051.

control the inequality in the equation has to be reversed. This can be done by either increasing the losses at the boundary (right-hand side) or by decreasing the energy source term (left-hand side). Dines[3] eliminated the noise emanating from a Rijke tube, which had a laminar flame burning on a gauze. A loudspeaker near to one end of the tube was driven in such a way that it modified the acoustic energy lost on reflection. The phase of the oscillation was detected by measuring the light emitted by CH radicals in the flame. This signal was filtered through a narrow band filter, then phase-shifted and the signal amplified and used to drive the loudspeaker.

The experiment was repeated by Heckl[4] only in this case the light emission photo-multiplier was replaced by a microphone as the detector. What this work demonstrated was that stability could be achieved over a range of phases and that the imposed phase delay is not crucial to the performance of the controller.

3. Cambridge Buzz Rig

Having seen the success that had been gained in controlling the simple Rijke tube combustion system, a small combustion test facility was built that would anchor turbulent flames in a similar fashion to those in afterburners. This facility became known as the buzz rig. The rig consisted of a bluff body flame stabiliser mounted in a 70mm quartz tube, the dimension of the flame holder gave a similar blockage to that seen in the afterburner of a gas turbine. The facility ran on a blowdown air supply that would allow for adequate stable air supply for 20 minutes. The unit was supplied with ethylene as a fuel and the total thermal output of the rig being circa 0.25 MW.

Results were gained from this unit using two different modes of active control. The first mode of control was a device as shown in fig.1. This allowed for the inlet boundary to

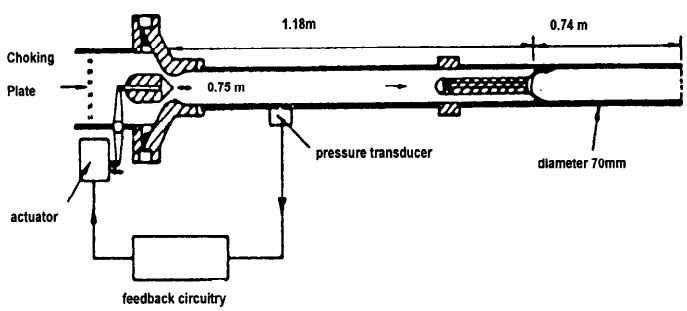


Fig. 1 Cambridge Buzz Rig – moving plug

the rig to be modified. Bloxsidge et al[5] reported this work, typical results from this rig are shown in fig. 2 and 3.

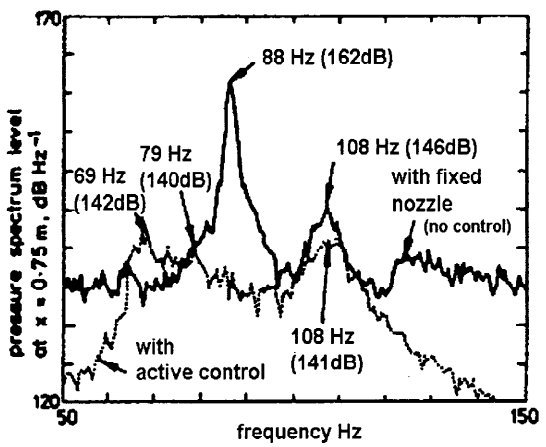
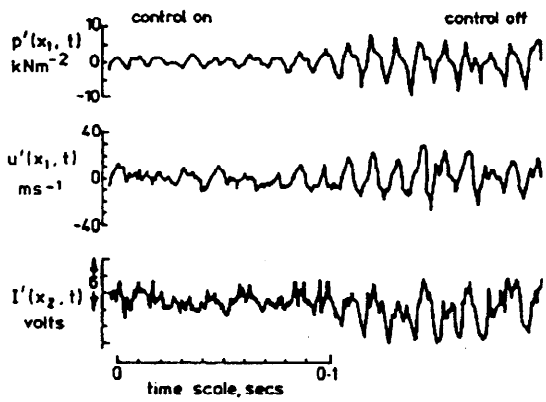


Fig. 2 Effect of control on pressure spectrum

Both figures show the effect on the pressure spectrum with and without control being applied.



p': unsteady component of pressure
u': unsteady component of axial velocity
I': unsteady component of light emission

Fig.3 Time history when control is cancelled

It can be clearly seen that there is a 21dB reduction in the peak and it was reported that in the frequency range 0-800 Hz a 90% reduction in acoustic energy was observed. In fig. 3 the pressure, axial velocity and light emission histories are plotted when the controller was turned off; the increases are clearly apparent.

The geometry as presented in fig.1 cannot be incorporated in any practical gas turbine afterburner design; an alternative technique of achieving control was explored. As shown in equation (1) modifying the energy balance at the boundary of the system is only one technique. The other method is to apply modification to the combustion and acoustic energy, this was done by the unsteady addition of fuel.

The rig shown in fig. 4 is the same as that shown in fig.1 but modified to fix the inlet boundary. The rig also has an

additional plane of fuel supply. This secondary fuel supply was located to give minimal delays.

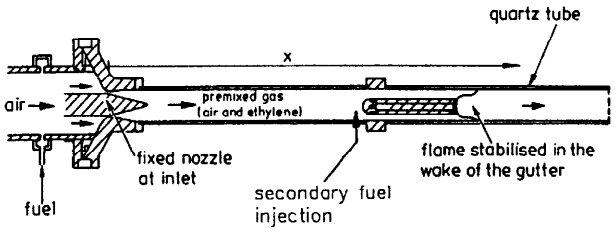


Fig.4 Cambridge Buzz Rig – modified unsteady fuel.

The secondary fuel was delivered to the unit via 4 off automotive fuel injectors, in order that the fuel did not appear as 4 rich streaks at the flame front secondary air was premixed with the fuel prior to delivery through 24 equi-spaced holes on the wall of the rig.

The result of this work is described by Langhorne et al [6,7]. The principal results from this rig are shown in Fig. 5 and 6.

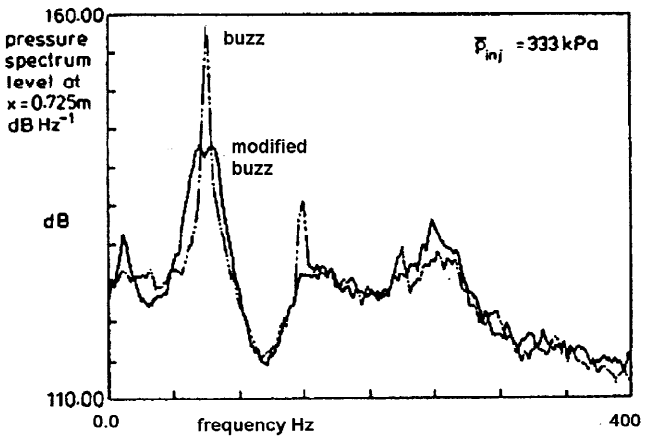


Fig. 5 Effect of control on pressure spectrum

Again it can be clearly seen that the control strategy applied to the rig has had a significant effect. The peak has been reduce by 15dB when the controller is in operation. The amount of fuel pulsed was an additional 3% of the total fuel supplied to the rig. The effect of switching the controller off on the combustion system is shown in Fig.6

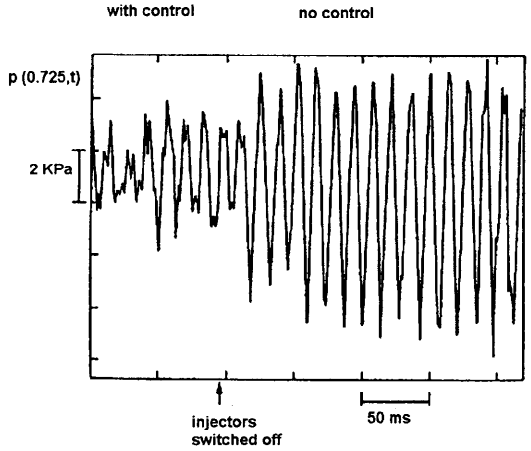


Fig. 6 Time History when the controller is cancelled.

4 Full Engine Demonstration

In 1988 having seen the very encouraging results that the Cambridge rig was delivering with regard to the ability to control combustion instabilities it was decided that a full engine demonstration should be carried out. The choice of test vehicle for the demonstration was the RB199 engine. This engine was chosen because its buzz characteristics were extremely well known and at that time the newer product such as the technology demonstrator engine XG40 and the EJ200 were less suitable because their characteristics were not as well developed. The older engine types such as the Spey and Adour did not have engine control systems that would lend themselves to this type of work.

The engine demonstration would bring more degrees of complexity than had been previously encountered on the Cambridge rig, the engine had multi-stream fuel in the afterburner, with 3 streams namely a core stream, a bypass stream and a primary stream. The proposed demonstration however would only look at the core and bypass streams, the primary fuel flow being a relatively small amount when compared with the other two. Also the function of the primary is to pilot the combustion process and therefore changing its characteristics may seriously diminish its operability.

It was proposed that fuel modulation be the preferred method of control as this was by far the easiest engineering solution. Unlike the Cambridge experiment fuel would be spilled from the engine as opposed to being added. There were two good reasons for doing this. The plot shown in Fig. 7 is a typical thrust boost characteristic for a high bypass ratio afterburning engine. The RB199 already uses passive control to get it into the high thrust boost regions, Henderson et al[7]. The addition of more energy in the form of fuel in the region where it is buzz prone would have little effect, because the curve of thrust boost is approaching a plateau, reflecting the change in energy. Therefore the removal of fuel from the system is more desirable as it takes the system into the steeper part of the thrust boost/fuel air ratio slope hence small changes in fuel flow have larger effects on heat release. The second reason for removing fuel was the ease of engineering. Addition of

fuel would require external fuel pumps and bleed in valves. This option may well have interfered with the engine control system due to changes to the volumetric flow rate / pressure/ flow number relationship.

The fuel modulation was achieved by the use of high response electro-hydraulic servo-valves. It was realised that the application was on the limit of where actuator technology lay at that time and to a greater or lesser extent where it is today. It was known that during operation the valves may have to be cycled up to 120 Hz and that they might be required to pass upto 15% of a streams flow rate. This was recognised as a challenge.

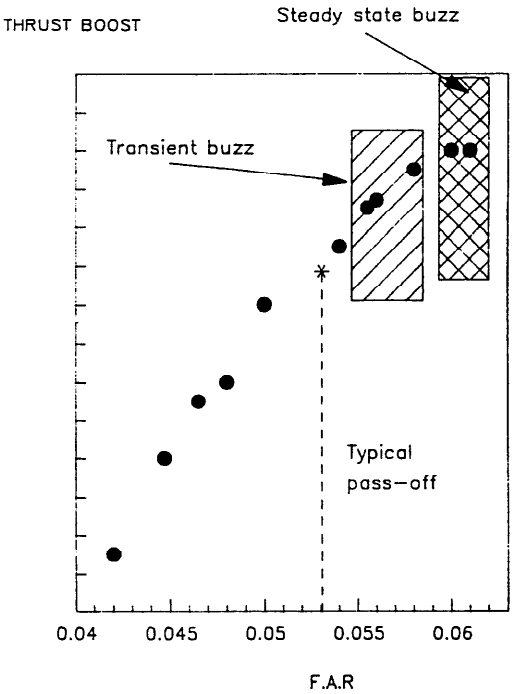


Fig. 7 Typical thrust boost vs. F.A.R

The programme was set up with 3 main phases to the work:-

- Fuel rig testing of the servo-valves.
- Establishment of jet-pipe response to pulsation over a range of spill flows and frequencies.
- The demonstration of active control, using the knowledge gained from the forcing experiments.

The valves used were Dowty high response servo-valves. These valves were subjected to a full range of dynamic and steady-state characterisation tests. As part of this test programme it was also desirable to know if there would be any unwanted side effects on the RHFCU (reheat fuel control unit) or on the fuel pumping system.

This phase of work was successfully completed and the valves were fully characterised. This confirmed that the valves would pass the flow and give frequencies to levels consistent with the programme requirements. One of the major side effects noted was that the engine fuel pump would produce 'noise' at undesirable levels and frequencies. In order that this would not feedback into the experiment the noise was damped by the installation of a pulsation damper in the fuel feed line between the fuel pump and the fuel distribution skid. The pulsation damper used was a commercially available bladder type accumulator. Whilst continually cycling the fuel spill valves it was also noted that large fluctuations in manifold pressure were observed similar in nature to water hammer. This was more than likely an artefact of the manifold/jet-pipe simulation used, however this was taken into account in the methodology applied to characterisation of the engine.

The engine test took place on an atmospheric engine test bed at DERA, Pyestock. The engine used was an RB199-04C, the engine was modified to accept the special fuel lines required for addition of the fuel spill valves. A schematic diagram of how the spill valves were implemented is shown in Fig.8.

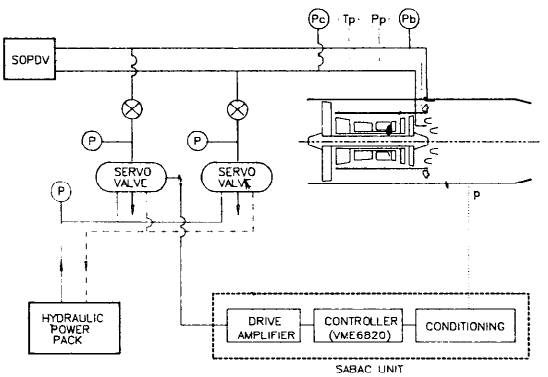


Fig. 8 Layout of spill system

The engine was also modified to include an off engine pallet mounted fuel and final nozzle control unit. This unit known as the Lucas 'fast-reheat' system obviated the need for the engine mounted main engine and afterburner Fuel Control Units (FCU's). A hydraulic power pack was required to provide power for the final nozzle actuation and for the driving of the servo spill valves. In Fig. 8 the configuration of the hardware for the active control can be seen. The feedback-input loop was from a Vibrometer CP102 type transducer, this type of transducer is standard on this engine and it measures the unsteady pressure in the jet-pipe. The output loop was to the Dowty 6-port servo valves as previously described. The unsteady pressure signal was taken into the SABAC unit via a conventional charge amplifier. The SABAC unit consisted of input signal conditioning, a processor unit and current drive outputs.

The active control logic was relatively simple and is shown diagramatically in Fig. 9. The filtered pressure transducer signal X is taken into the processor where it is compared with a preset value XT (threshold). When the signal exceeds the threshold level, the processor times the period of the transient, then outputs a drive signal of the same time period but with an appropriate time delay PHI and pre-defined amplitude DEL. The XT, PHI and DEL are all tuneable so that the user could input them in to the SABAC unit.

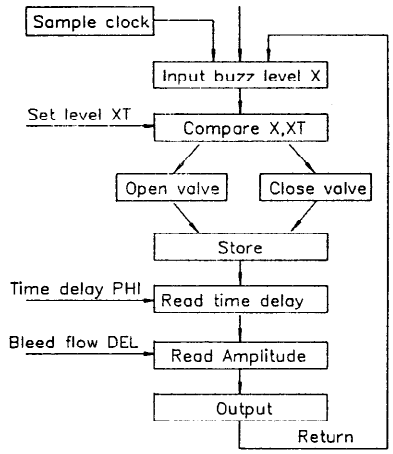


Fig. 9 Spill control programme Operation

The intended relationship between the input signals, threshold and the output signals are shown diagramatically in Fig. 10.

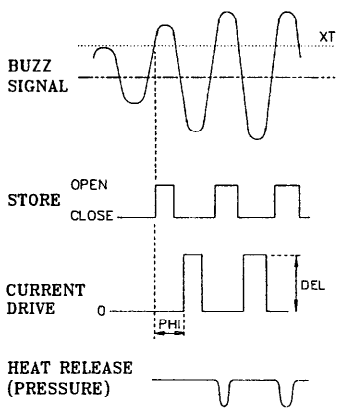


Fig. 10 Spill control function

It was important to understand how the combustion system would respond to being forced, that is no control on but stimulation of the system by pulsing fuel at different degrees of spill and at different frequencies. The transfer function of the system could then be determined from the forcing tests. Due to the experiences in the first phase of the programme where large fluctuations in manifold pressure were observed when the spill valves were subjected to continual sinusoidal motion, the response of the jet-pipe to stimulation was by a single dip in fuel flow of varying amplitudes.

The results of stimulating the combustion system are shown in Figs. 11 and 12. The response in the jet-pipe to a dip in bypass fuel flow is shown in Fig. 11. The demanded fuel flow reduction was circa 10% of the total flow for that stream the combustion delay time is of the order of 14 ms.

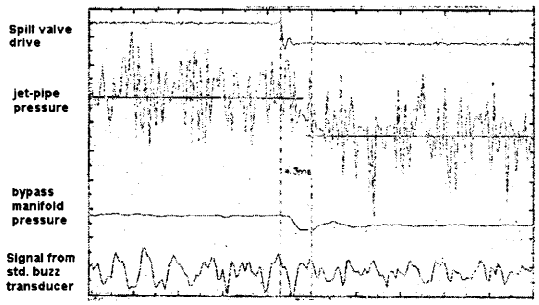


Fig.11 Fuel dip in bypass stream

When a similar magnitude fuel dip was applied to the core stream Fig.12. It again shows that the time delay was of a similar magnitude to that of the bypass stream 14 ms. From the data recorded from the engine it was apparent that the fuel spill from the bypass stream was more effective than that of the core stream at producing a larger effect on the jet-pipe pressure for an equivalent fuel dip.

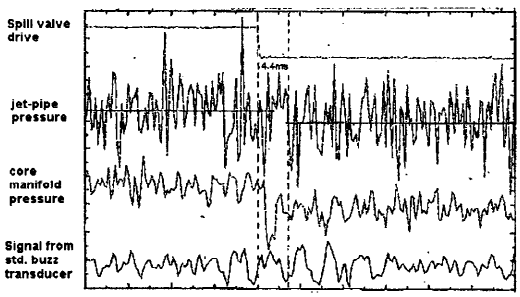


Fig. 12 Fuel dip in core stream

Because of time constraints the demonstration of active control was only given by the use of modulation of the bypass stream fuel.

Having determined that the system would react to a stimulus of dipping fuel the next part of the exercise was to now demonstrate active control. The demonstration took two different forms, running the engine up to a point where the engine protection system would chop the afterburner fuel due to excessive noise, then repeating the point to the same condition with the controller in use, this procedure was called "buzz-limiting". The second method was to have the controller on and then switch it off and monitor the system until the natural engine protection system shut the afterburner down.

An example of the former is shown in Fig. 13 and the latter in Fig. 14. It can be seen in Fig. 13 that the spill valve drive signal is operating only when it is required. When there are quiet periods i.e. the noise is below the set point no action is being taken by the device. The demonstration on the engine was carried out with spill flows between 5 and 10%

valve drive signal is operating only when it is required. When there are quiet periods i.e. the noise is below the set point no action is being taken by the device. The demonstration on the engine was carried out with spill flows between 5 and 10% and with time delays of 9.0 and 3.4 ms. The system showed adequate control over all of the conditions. The threshold at which the system was triggered was also changed within the range ± 1.0 kPa to ± 0.67kpa again adequate control was shown but there was not enough time allowed for an exhaustive look at the control parameters and to allow for a high degree of tuning to take place.

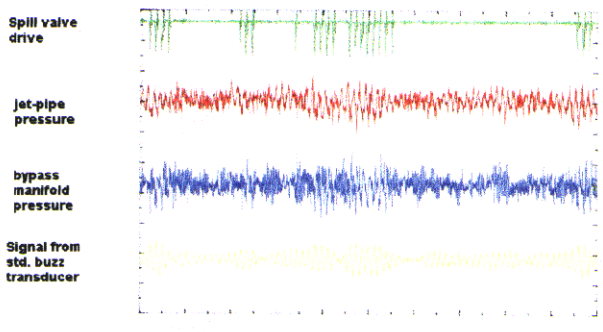


Fig.13 Steady state operation with active control

It can be clearly seen in Fig. 14 that when the controller is switched off, signified by no spill drive signal, that the unsteady pressure in the jet-pipe increases. The event is then terminated by the engine health monitoring system cutting the afterburner fuel this is signified by the reduction in bypass manifold pressure. In all of the events that were carried out like this the buzz amplitude grew to a maximum within 15 cycles of the chop event.

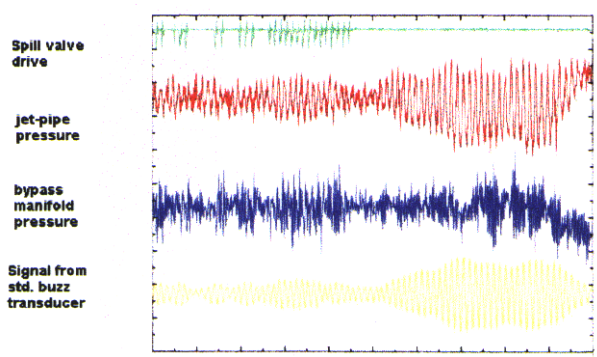


Fig 14 Cancellation of active control

In summary active control has been demonstrated satisfactorily on a full-scale military turbofan engine. The correlation between what happened on the small-scale rig and the engine was good. This is demonstrated in Fig 15, where it can be seen the reduction in the peak buzz frequency on the engine was 11.7 dB which is comparable with the 15.5 dB measured on the small-scale rig. If further time had been available maybe further reductions could have been made. It is true that with todays improved control logic that improvements would be gained over the extremely simple logic applied at the time of the demonstration.

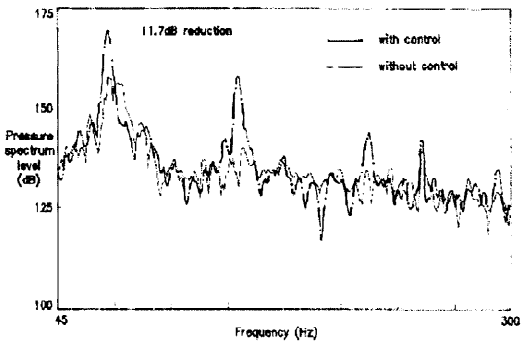


Fig. 15 Best result from the engine testing

5.0 The Future

The strive for ever lower emissions from industrial gas turbines and the control technology being applied by most engine manufacturers namely lean premix combustion is increasing the propensity to have instability problems. In some cases the lowest achievable emissions for the system cannot be achieved because of instability. The industrial RB211DLE system shown in Fig. 16 like all systems has seen some difficulties with combustion related noise. Unlike the afterburner the chances of seeing noise from one engine build to another varies i.e there are quiet engines and there are noisy engines.

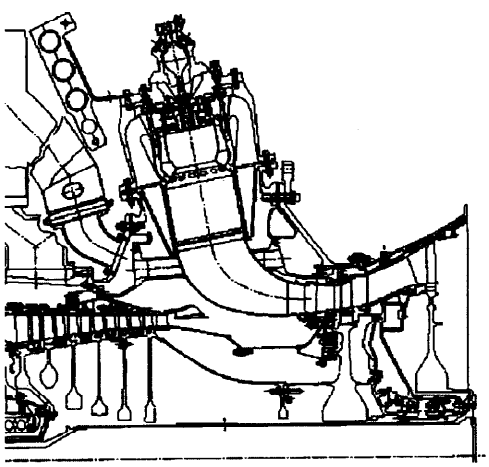


Fig. 16 Industrial RB211DLE

There are no features within manufacturing tolerances that can be picked up to tell which combustors will have a

applied to afterburners have also been used to good effect on the industrial systems Willis et al[8], however there are on occasions difficulties.

A typical noise map for an RB211-24G engine is shown in Fig. 17. The map shows the temperature in the primary and secondary combustion zones, the secondary temperatures can be read as power. The plot shows regions of noise islands and the amplitude. On a quiet engine there is a space between the 'D' and 'E' islands. It is conceivable that active control could deliver engines that will always be quiet.

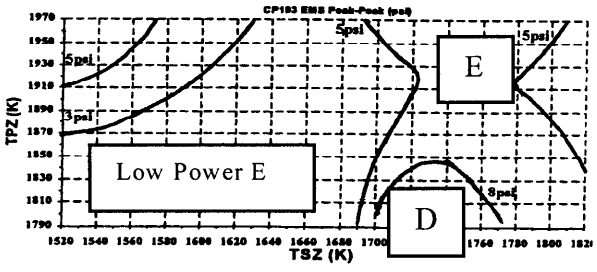


Fig. 17 Typical Noise Map for an RB211-24G.

The difference between the industrial unit and the military turbofan is the frequencies are very much higher 500 to 700 Hz. This poses problems in that current actuator technology can only operate at up to 250 Hz. Further work on actuators is essential for the technology to progress. The reliability of the servo-valves used in the afterburner case may be called into question if used for an industrial use. The normal life between overhauls on industrial engines is circa 24000 Hrs, if the valve is in use for only a fraction of that time it is not inconceivable that the valve could reach 10^{10} cycles which is outside the range of this type of device.

There are industrial units that are applying active control, Seume et al[9] ,Hoffmann et al[10], but these units exhibit lower primary frequency combustion instabilities <250Hz and therefore use current actuator technology.

6.0 References

1.Rayleigh, J.W.S, 1896, The Theory of Sound Macmillan.

2.Dowling, A.P, 1999, Active control of combustion oscillations. AIAA.

3.Dines, P.J., 1983, Active Control of Flame Noise,Ph.D Thesis . Cambridge.

4.Heckl, M.A., 1988, Active control of the noise from a Rijke tube, J. Sound Vib. 124, 117-133.

5.Bloxsidge, G.J., Dowling, A.P., Hooper, N. and Langhorne, P.J., 1988, Active control of reheat buzz, AIAA, J.. 26, 783-790.

6.Langhorne, P.J.,1988, Reheat Buzz an acoustically coupled combustion instability, J. Fluid Mech. 193, 417-443

7.Langhorne, P.J., et al, 1990, Practical active control system for combustion oscillation, AIAA J. Propulsion, 6, 324-333.

8.Willis, J.D., Moran, A.J., 2000, Industrial RB211 DLE Gas Turbine Combustion Update, ASME 2000-GT-109.

9.Seume, J.R., et al,1997,97-AA-118, Application of active combustion instability control to a heavy duty gas turbine.

10.Hoffmann, S., et al, 1998, Application of active control to Siemens heavy duty gas turbines. RTO MP-14

PAPER -2, A. J. Moran

Question (S. Candel, France)
In your experience, have you found a way to shape the signal of the fuel line to achieve optimal response?

Reply
There was a degree of shaping during the valve characterization. This was done to try to overcome a water hammer effect seen at that time. When the engine test was carried out, no shaping took place.

Question (A. Annaswamy, USA)
What is the role of more complex active control strategies?

Reply
Valve technology has to be improved to cope with high frequency instabilities and the control has to be appropriately designed.

Question (W. Proscia, USA)
Is most of the 14 ms delay that was measured attributable to fuel line transport delay from the valve to the injector?

Reply
Virtually all of the 14 ms is the transport time from the fuel injection point to gaining detectable heat release.

Combination of Active Instability Control and Passive Measures to Prevent Combustion Instabilities in a 260MW Heavy Duty Gas Turbine

J. Hermann, A. Orthmann

IfTA, Ingenieurbuero fuer Thermoakustik GmbH,
D-82194 Gröbenzell, Industriestr. 33

S. Hoffmann, P. Berenbrink

Siemens AG Power Generation,
D-45466 Muelheim, Wiesenstr. 35

Abstract

Reducing the output of NO_X pollutants and enhancing efficiency are the two major aims pursued by developers of modern gas turbines. In order to achieve them, lean premix combustion is preferred, turbine inlet temperatures and thus power densities within the combustion chamber system being continuously increased to augment efficiency. Due to this fact, the tendency of modern combustion systems to develop so-called self-excited combustion oscillations keeps increasing.

After briefly discussing the oscillation problems encountered with the annular combustion chamber of a Siemens type V94.3A stationary gas turbine, particular attention will be paid to suppressing these oscillations by passive and active means. The passive measures presented, i.e. extending the burner nozzle, were intended to detune the combustion system by prolonging the time lag required by the combustible mixture exiting the burner outlet to reach the combustion zone. Moreover, to suppress periodic vortex shedding, another possible cause for combustion instabilities, those extensions were inclined in a certain angle with respect to the main flow direction. To prevent the in-phase lock of all 24 burners promoting the excitation of any azimuthal mode, the burners were selected to have different time lags, and were arranged asymmetrically within the annular combustion chamber. In addition to these passive measures, a multi-channel Active Instability Control (AIC) system was implemented to achieve further damping. With the AIC system presented, any burner oscillations occurring are measured by p-ressure sensors; their signals are processed by means of a multi-channel controller, and then transmitted to actuators designed to damp down combustion oscillations. The points of intervention selected to do so were the gas supplies of the pilot flames. In order to achieve optimum response, every single one of the 24 burners was fitted with its own actuator.

In field demonstrations for various type V94.3A gas turbines, the presented measures were successfully tested and active suppression of combustion oscillations proved to be highly flexible in dealing with various oscillation problems.

1. Introduction

Self-excited combustion oscillations or instabilities are observed in various kinds of industry-type combustion or propulsion systems, reaching from domestic heating devices to gas turbines and rocket motors. The oscillations cause substantial pressure fluctuations at discrete frequencies which, particularly with systems characterised by high power densities, may reach levels leading to mechanical failure of the combustion chamber, or of upstream or downstream plant components.

Developments targeted at reducing NO_X pollution and increasing efficiency levels for modern stationary gas turbines involve lean burning and increased turbine inlet temperatures and thus power densities within the combustion chamber. Since these measures tend to bring about self-excited combustion instabilities, avoiding these instabilities constitutes one of the main tasks in developing modern combustion systems.

2. Rayleigh criterion and time lag

A fundamental element of the driving mechanism of self-excited combustion oscillations is the excitation of pressure oscillations by a fluctuating heat release rate of the flame. Generally speaking, for the heat release rate oscillations to result in amplification of pressure oscillations, heat addition must occur at or around times of high pressure. Lord Rayleigh [1] was the first to state this criterion, now bearing his name, which was developed further by various other authors, e.g. Putnam and Dennis [2].

To evaluate the Rayleigh criterion, the phase shift between pressure and heat release fluctuations can be used. Phase shifts occur because every heat release fluc-

Paper presented at the RTO AVT Symposium on "Active Control Technology for Enhanced Performance Operational Capabilities of Military Aircraft, Land Vehicles and Sea Vehicles", held in Braunschweig, Germany, 8-11 May 2000, and published in RTO MP-051.

tuation produces the corresponding pressure fluctuation only after a certain delay or "time lag" (and vice-versa). Time lags in combustion systems consist of various components τ_i , e.g. acoustic and convective time lags, as well as time lags attributable to the processes of mixing and reacting (see e.g. Hermann et al. [3] or, for a slightly different model, Lieuwen et al. [4]). These chronological components - and thus the system stability - are generally hard to predict. Accordingly, measures to suppress oscillations based on knowledge about time lags can usually only be taken when self-excited oscillations in a combustion system are already present.

3. Feedback mechanisms

For self-excitation of pressure oscillations to occur, it is not sufficient that the Rayleigh criterion be fulfilled. There must also be a suitable feedback mechanism between oscillations of pressure and heat release rate: pressure oscillations caused by fluctuations of the heat release rate must interact with other effects involved in the combustion process that in their turn - directly or indirectly - cause further oscillations of the heat release rate. This can for instance be due to sound pressure waves within the combustion chamber propagating against the flow direction. When these waves interact with the flow at fuel or air feed points or flame-stabilising components (bluff-bodies, wakes, etc), fluctuations of mass flow rate, equivalence ratio or periodic vortex shedding can occur. Subsequently, these disturbances will travel, at convective speeds, into the combustion zone where they cause corresponding fluctuations of the heat release rate. Other possible feedback mechanisms involve variations of the flame front area and periodic break-up, atomization and vaporization of liquid fuel (see e.g. Putnam [5]).

4. Possibilities of avoiding and/or suppressing self-excited combustion oscillations

During the design phase of a combustion system, predictions about its tendency to develop self-excited combustion oscillations are still only of limited validity. Thus, the development of methods allowing to avoid and/or suppress this type of oscillation during system testing is of crucial importance. The means available to do so can be subdivided, in principle, into two groups: passive and active measures.

4.1. Passive measures

The term passive measures refers to modifications of a combustion system that, during system operation, will not be changed any more and/or will require no external supply of energy. Typical passive measures are "detuning" a system by modifying its burners or the acoustics of its combustion chamber, by increasing acoustic damping via Helmholtz-type resonators, or by disturbing the propagation of sound waves via baffles (see e.g. Culick [6]). For passive measures to be successful, it is normally indispensable to do intensive research on system behaviour. Accordingly, any measures thus found are often valid and/or effective for a specific system only.

4.2. Active measures

Additionally, so-called active measures are an interesting alternative, the term active referring to any means of acting upon the current status of any combustion system in a targeted, controlled manner. Normally, an external power supply will be required.

One example of this kind of active system is "Active Instability Control" (AIC) of combustion oscillations. AIC uses an actuator to modulate some suitable parameter of a combustion system. Under ideal conditions, modulation is performed in a manner to have the corresponding system variable fluctuate precisely *in counter-phase* with the fluctuations constituting the combustion instabilities, thus damping them. To do so, some system parameter characterising the corresponding oscillation is measured, and processed via a controller, in order to generate the control signals for the actuators. For industry-type combustion systems, influencing heat release fluctuations by modulating fuel supplies has proved to be an efficient and practicable means of intervention. Because of the high volumes of air to be moved, another type of intervention - via system acoustics by imposing sound waves in counterphase to the sound field in the combustion chamber, e.g. by loudspeakers - is suitable only for low-power combustion systems.

5. Combustion instabilities in Siemens type Vx4.3A gas turbines and ways of avoiding them

5.1. Combustion instabilities and eigenmodes in annular combustion chambers

Siemens type Vx4.3A gas turbines (see Figure 1) feature annular combustion chambers comprising 24 hybrid burners distributed peripherally (see Figure 2). Hybrid burners make it possible to operate gas turbines on either gaseous or liquid fuels. The gas-burning mode offers, in addition to purely diffusion-based or premix operations, the possibility of combining both types of operation. Moreover, so as to stabilise the premixed flame, every burner features a small diffusion-based pilot-flame.

Using the standard hybrid burner within the annular combustion chamber of type Vx4.3A gas turbines resulted in unwanted self-excited combustion instabilities which limited, above all, the maximum achievable power output of the turbine. Moreover, it was found that certain part load operating modes were subject to oscillations. In addition to high sound pressure levels at discrete frequencies, standing sound waves - typical of combustion instabilities - were measured; these are characterised by localised amplitude minima and maxima, also called nodes and antinodes. Owing to their preferred orientation along the circumference of annular combustion chambers, these modes are designated azimuthal. Figure 6 shows a typical azimuthal mode, corresponding to the first harmonic, within the annular combustion chamber.

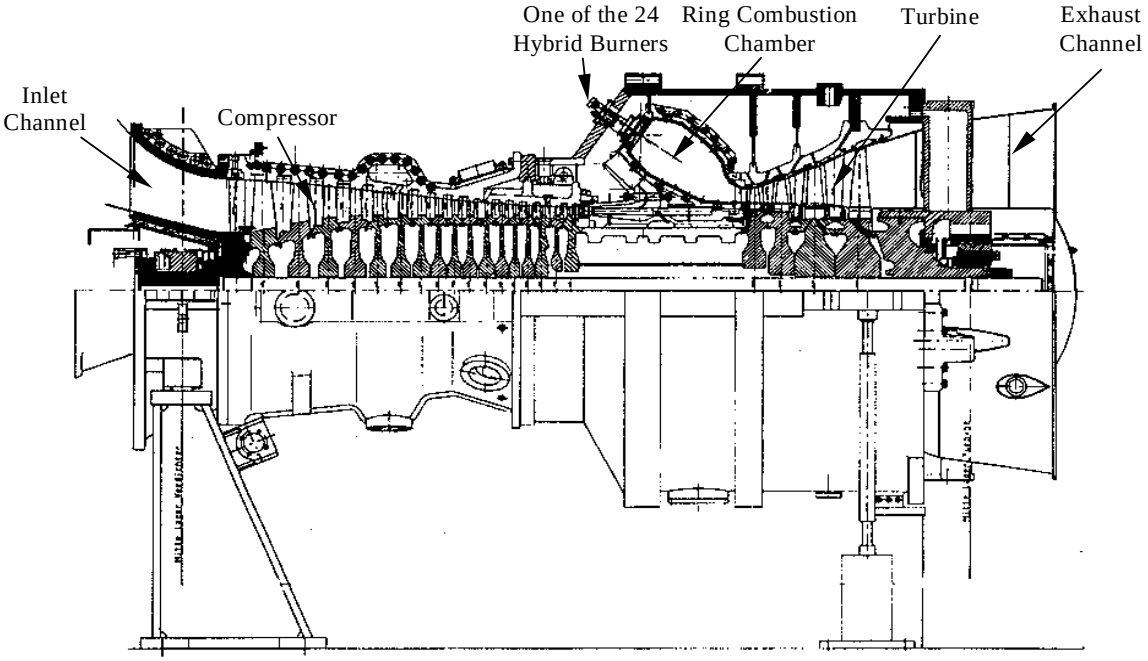


Figure 1: Half-section drawing of the Vx4.3A series gas turbine.

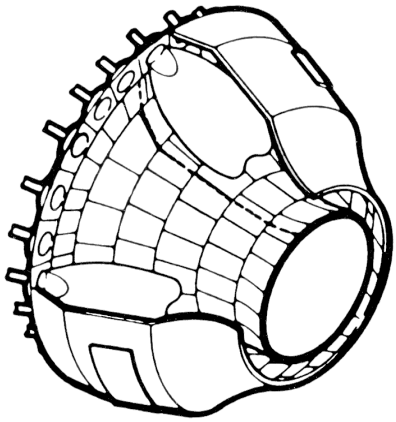


Figure 2: Vx4.3A Hybrid Burner Ring® (HBR) Combustor - One Annular Combustor with 24 Burners.

5.2. Measures used to suppress combustion instabilities

5.2.1 Passive measures

Considering the fact that the generation of self-excited combustion instabilities depends on certain time lags, selectively modifying those time lags is one possible means of suppressing combustion instabilities. The time lag most easily adapted is the convective time lag or the time required to convey the fuel/air mixture into the combustion zone. In order to make it possible to adjust this parameter in a precisely targeted manner, a cylindrical extension - called a cylindrical burner outlet (CBO) - was welded onto the burner nozzle (see Figure 3). The length of this extension was selected so as to prolong the convective time lag by slightly more than one quarter of the period of the self-excited oscillation.

As already mentioned in section 3, one possible cause for fluctuations of the heat release rate of the flame and thus for combustion instabilities are periodically generated

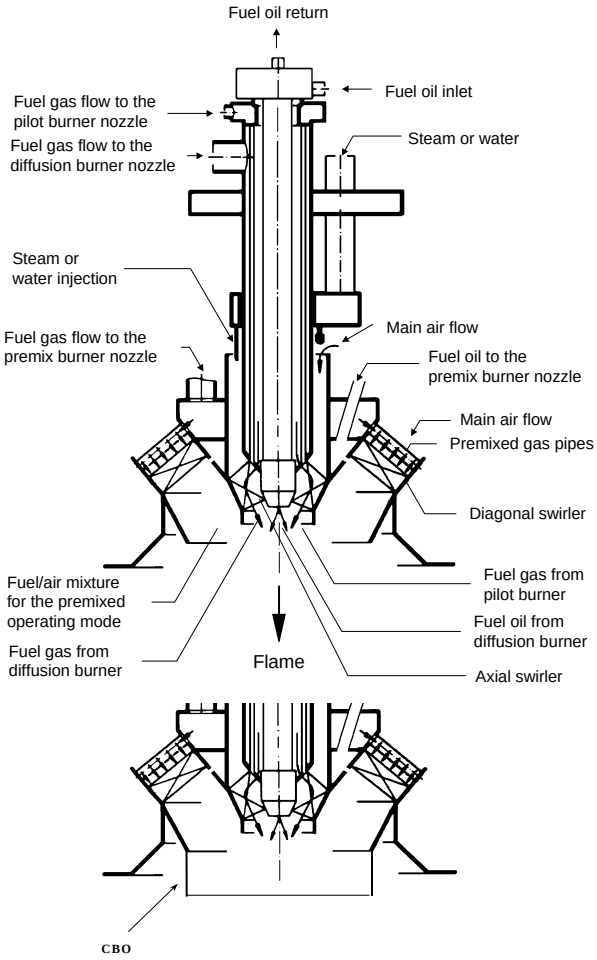


Figure 3: The standard Siemens Hybrid Burner (top) and with schematic CBO extension (bottom).

vortices, which can be provoked by flow disturbances in the shear layer. To prevent these flow instabilities, the cylindrical extensions attached to the burner nozzles were inclined by 10° in respect to the flow axis on two

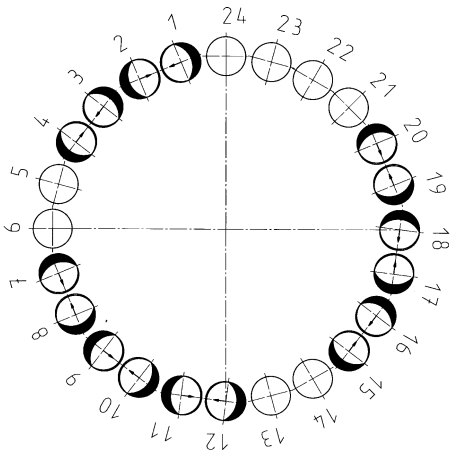


Figure 4: Asymmetric arrangement of 8 ABO pairs along the circumference of the annular combustion chamber.

neighbouring burners. Owing to the angle of inclination characterising these extensions, they are designated asymmetric burner outlets (ABOs). ABOs cause an uneven shear layer distribution around the burner nozzle, thus reducing the formation of coherent structures, and displace the combustion zone downstream of its former position, thus increasing the time lag.

Another passive measure taken is the use of several burner types characterised by differing flame frequency responses and installing burners belonging to the same type asymmetrically, with reference to potential azimuthal modes: if burners belonging to the same type are not precisely located, for example on the potential pressure antinodes of the azimuthal modes to be prevented, they will not be optimally excited to combustion oscillations by the prevailing acoustics. Figure 4 shows an example for an asymmetric burner arrangement using ABOs.

5.2.2 Active measures

The AIC system implemented for V94.3A turbines corresponds, in principle, to the active system developed for V84.3A prototype tests. However, major components, such as controller, actuators and certain methods to implement the system at the turbine, were redesigned comprehensively and developed into a system fully optimised for the power generation industry. Detailed descriptions are to be found in Seume et al. [7] for the first AIC implementation, and in Hoffmann et al. [8] and Hermann et al. [9] for the re-designed version. Figure 5 schematically shows the AIC-set-up for the gas turbine.

Active control was done by modulating the pilot gas supply for the various hybrid burners. The pilot gas was chosen because the pilot flames that stabilise the main premix flames, exert a very high degree of influence on the main flames. Owing to reduced mass flows, control via pilot gas flames is substantially easier than modulating the main gas flow. To obtain optimum control over the system, every burner was fitted with its own actuator, a Moog-made rapid direct drive valve (DDV). The amplitude loss of the used 3rd generation of the DDV valve is less than 3dB up to a frequency of 420 Hz and the valve can be used with a maximum allowed ambient temperature of about 120°C.

The success of AIC strongly depends on a sufficiently high modulation of the heat release rate of the pilot flame and thus, indirectly, on a high modulation of the mass flow rate in the pilot gas system by the actuator. Since the mass flow rate modulation on the other hand is strongly dependent on the acoustic field in the pilot gas system or rather its resonant behavior, the pilot gas system was tuned so as to allow for maximum mass flow rate modulation at the frequencies to be damped. Details about the tuning of a fuel system for AIC can be found in Hermann et al. [10] and Hantschk et al. [11].

Since any individual burner can excite combustion oscillations, each of the 24 burners has to be controlled. This requires, in addition to 24 actuators, a multi-channel AIC system providing the same number of control loops. However, the number of sensors and control units needed can be reduced by taking advantage of the

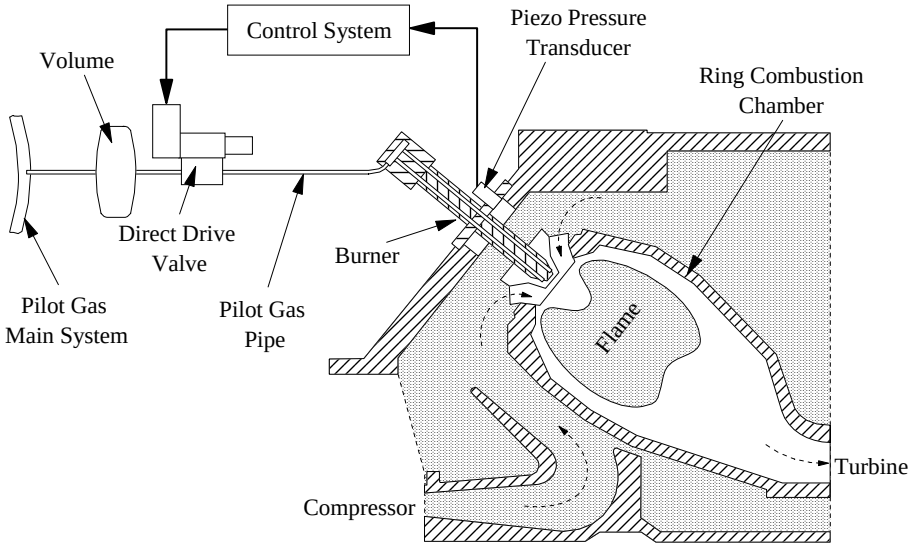


Figure 5: Schematical representation of the AIC setup for the Siemens Model Vx4.3A heavy duty gas turbine.

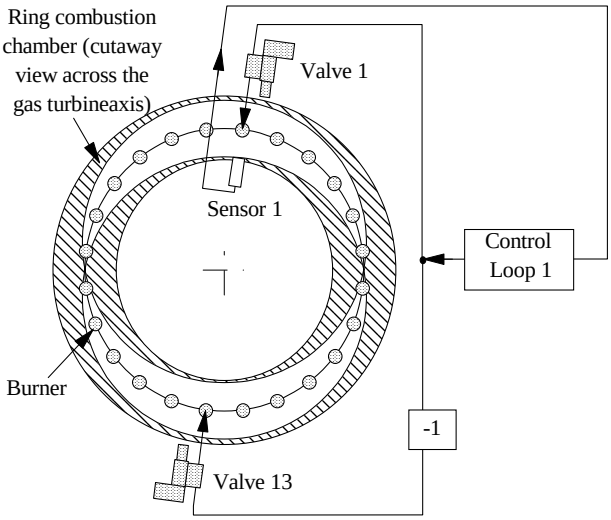


Figure 6: Use of the symmetry of azimuthal modes, e.g. for the first harmonic. One sensor and one controller provide the input signals for two DDVs.

symmetry of the excited azimuthal modes. As described by Seume et al. [7] it is possible to use a signal measured at a certain circumferential location of the azimuthal mode - or the annular combustor - to determine not only the actuator input signal for this particular location but also those for several other locations. Depending on the possible excitable azimuthal modes in the V94.3A, a total of 12 control loops were used, with each loop comprising a pressure sensor and 2 valves as actuators (see Figure 6).

The multi-channel controller is a self-contained modular industrial system and fully integrated into the gas turbine control system. In addition, the hard- and software set-up is optimised with respect to short commissioning and implementation time scales. The main control work is done by 6 digital signal processors, each of them handling two control loops. The control algorithm used works in the frequency domain and allows, in its latest version in combination with new expanded hardware outputs, simultaneous processing of any two oscillation frequencies.

As input signal for the control loops, the sound pressure value measured at the burner flange by high temperature piezoelectric transducers is used. As shown by Seume et al. [7], these signals are sufficiently correlated with sound pressure levels prevailing within the combustion chamber. For this purpose, a total of 12 transducers was installed along the circumference of the gas turbine.

5.2.3 Combining passive and active measures

Gas turbines are often operated over a wide range of power levels, ambient temperatures and in different modes of operation. This makes it a difficult task to protect all operating points against potential combustion instabilities by passive measures. Furthermore, implementing passive measures may bring about, beside any successful suppression of combustion oscillations at formerly unstable operating points, instabilities at points formerly quiet.

In contrast to that, the active control of combustion oscillations is a very flexible measure. At any operating point, AIC can easily be used to suppress unexpected new instabilities as well as those that cannot be overcome by passive measures.

The successful implementation of the passive and active measures described, as well as various combinations of these measures for different gas turbines with nominal power output levels between 233 MW and 267 MW at ISO conditions will be described in the following section.

6. Results

6.1. Application of passive measures

The first tests, using the passive measures developed, were designed to research several variants of installing asymmetrical burner extensions. 3, 5 and 8 pairs were used, the 8-pair arrangement being installed both symmetrically and asymmetrically (see Figure 4) along the circumference of the annular combustion chambers. The impacts of the various arrangements in terms of combustion oscillations were verified by running up the turbine to its new stability limits and/or a new level of maximum achievable turbine power. As the number of ABO pairs was increased, damping results improved; more particularly, asymmetrical arrangements given identical numbers of ABO pairs resulted in significant improvements (see Figure 7). With the best arrangement, it was possible to increase maximum turbine power by 7 percentage points. A further increase of ABO pairs to a total of 9 failed to produce any further improvement.

A further series of experiments was run to test various combinations of CBOs installed in a similar, i.e. asymmetric, manner as the ABO arrangements. Just as with ABO experiments, an increasing number of CBOs resulted in shifting stability limits towards higher levels of achievable maximum turbine power (see Figure 8). The best result achieved amounted to an increase of turbine power by 9 percentage points, with 20 CBOs.

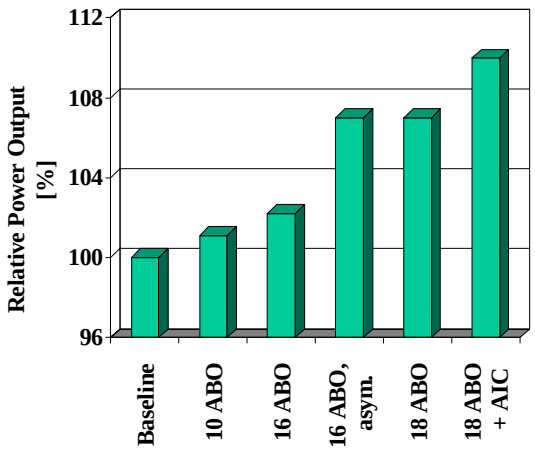


Figure 7: Stability limit at different ABO arrangements.

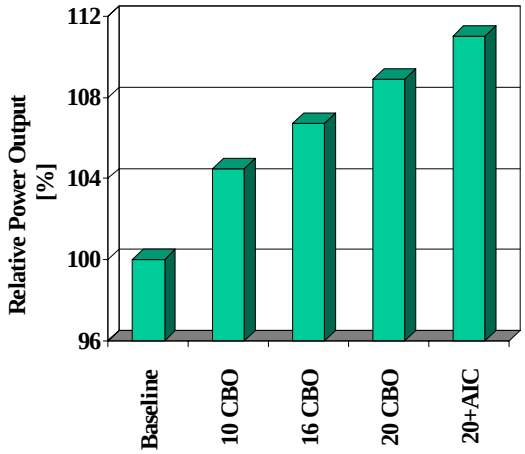


Figure 8: Stability limit at different CBO arrangements.

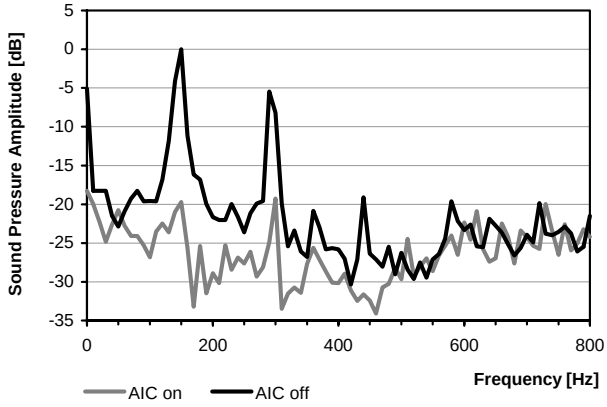


Figure 9: Suppression of two frequency peaks during part load operation by AIC.

6.2. Combination of passive and active measures

The good results achieved by passive measures were further improved by using an Active Instability Control system. Furthermore, in situations where implementing passive measures causes instabilities at points formerly stable – which can occur in some configurations – AIC was successfully applied to overcome these problems. More particularly, short-term stability problems at part load operations were dealt with successfully. In the process, AIC once again proved its high level of flexibility with regard to solving oscillation problems of various kinds.

6.2.1 AIC during start-up and part load operations

Using CBOs with a special burner configuration unexpectedly lead to increased oscillation tendencies during the start-up phase. During this phase, operation of the hybrid burners is ensured by means of diffusion-type flames since combustion chamber temperatures are still too low to stabilise a premix flame. Subsequent to start-up, and while loads increase up to the switch-over point towards mixed operation (combining diffusion and premix operations), the second and third harmonics of the annular combustion chamber were excited. Due to the strenuous commissioning schedule, there was no more time left for optimisation of the start-up sequences. Therefore it was decided to use the AIC system in order to resolve this issue. Even though, in view of its control via pilot flames, AIC was designed for premix operations, additional pilot gas was introduced during diffusion operation, while simultaneously the AIC was activated. This resulted in very good damping of the combustion oscillations, thus allowing the system to run up through the start-up and part load phases to mixed-mode operation without any problem. Figure 9 shows the sound pressure spectrum (the overlapped spectrum of the 12 AIC sensors) with and without AIC at a certain operating point. By activating AIC for both dominant frequencies, a damping by 20 dB (second harmonic) and 15 dB (third harmonic) was achieved. In order to allow the simultaneous damping of the second and third

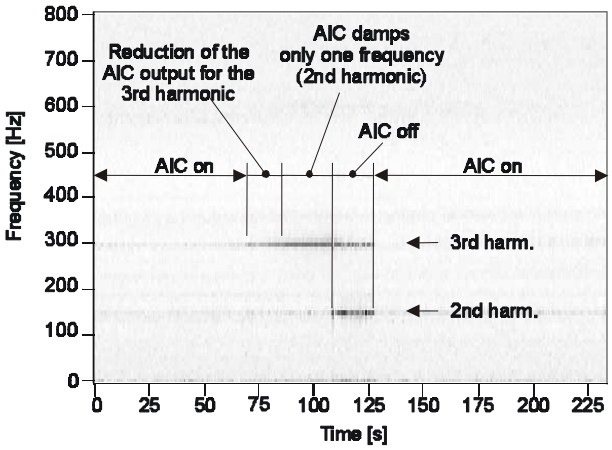


Figure 10: Separate damping of two dominant eigenmodes of a combustion instability by AIC.

harmonics within the annular combustion chamber, the AIC system was improved in terms of its independence in controlling valves located on opposite points of the combustion chamber. With this improvement the limitations on damping for certain frequencies described by Hermann et al. [9] were eliminated.

The individual damping of the two dominant eigenfrequencies of the combustion instability by the AIC system can be seen in Figure 10. It shows the frequency spectrum of the sound pressure versus time in a kind of contour plot: dark regions signify high pressure amplitudes. The two grey horizontal streaks at 145 Hz and 290 Hz belong to the two dominant frequencies of the prevailing combustion instability. It can be seen that by slowly reducing the AIC output signal used to suppress the 3rd harmonic this mode resurges step by step (line darkens for 70s < t < 85s). During the next 23 seconds only one of the self-excited frequencies - the 2nd harmonic at 145 Hz - is damped by AIC. After switching off the complete control loop at t = 108 s also the 2nd harmonic resurges to higher amplitudes: at that time a dark line appears at f = 145 Hz. After another 19 seconds, at t = 127 s, the AIC system is reactivated to damp both frequencies which leads again

to a complete suppression of the combustion instability. This example shows that in the prevailing case the two modes are excited independently of each other and therefore every mode must be suppressed separately by AIC to achieve a good damping of the combustion instability.

6.2.2 Increasing base load operating levels

In addition to part load operations, AIC demonstrated its high levels of flexibility in suppressing oscillations also for peak load operations. In combination with passive measures, it was thus possible to edge up stability limits for most applications by a few percentage points. For example, by using AIC in combination with the best arrangement of ABOs (9 pairs), it was possible to increase maximum turbine power by 3%, and in combination with the best CBO arrangement (20 CBOs) by 2%. In the latter case, further load increase was not possible because the maximum permissible turbine inlet temperature had already been reached. In addition to these improvements, with the AIC system active, the NO_x emissions could be reduced significantly by reducing the mean pilot gas mass flow rate: in premix mode, the pilot flames are the primary source of NO_x emissions.

6.2.3 Problems with frequency shifts

Near base-load operation, arising combustion oscillations did not only increase the pressure amplitude but simultaneously also led to a substantial shift of the oscillation frequency from 155 Hz to about 170 Hz (see Figure 11). During the tests it was observed that damping of these oscillations depends on synchronised modification of AIC set-up parameters. The determined set of parameters allowing optimum AIC performance indicates that, when this frequency shift occurs, the combustion zone will simultaneously be shifted towards the burner nozzle. To allow efficient compensation of the changes in boundary conditions thus produced, the AIC control algorithm was complemented by an appropriate frequency tracking feature. Taking this measure substantially improved long-term stability at base-load levels.

6.2.4 Failure tolerance and long-term AIC use

During the different tests, valve failures were simulated in order to test their impact on the overall AIC performance. A maximum of four valves was switched off during AIC runs resulting in no noticeable degradation of the system performance, regardless of the valve position. Switching off more than four valves were not tried out due to time constraints.

The Active Instability Control system presented here is currently being used for base load, with several V94.3A gas turbines featuring 20-CBO configurations. Two of the systems, in operation since January 1999, have demonstrated outstanding long-term stability. Up to now the AIC-Systems have operated for approximately 6,000 hours each. In co-operation with the gas turbine control system, the AIC system provides fully automated, stable gas turbine operations over the entire operating range. Moreover, inspection of some of the actuators used demonstrated that the wear and tear of the moving parts is negligible.

7. Summary

Self-excited combustion oscillations occurring within the annular combustion chamber of the Siemens type V94.3A stationary gas turbine featuring 24 hybrid burners limited, above all, the maximum achievable turbine power output. To avoid or suppress these oscillations, various passive and active measures were developed and successfully implemented. Stability improvements achieved by every single measure were demonstrated on various gas turbines.

In a first step, burner nozzles were equipped with cylindrical extensions whose length was adapted to extend the time lag between the flow entering the combustion chamber and the combustion zone. In order to avoid fluid-dynamic instabilities and change the time lag of the flames, the cylindrical extensions of neighbouring burners were inclined towards each other in an angle of 10° with reference to the main flow direction. By using an increasing number of burner pairs featuring these extensions, it was possible to increase turbine power in steps by suppressing the excessive flame oscillations. It was found to be highly effective to use an asymmetrical arrangement for 8 to 10 pairs. As compared to the standard configuration, these pairs allowed turbine power to be increased by 7%. Similar results have been achieved for the not inclined cylindrical extensions. These extensions were likewise installed asymmetrically within the combustion chamber. The best arrangement totalling 20 modified burner nozzles improved the stability limit by 9 percentage points, as compared to standard burners.

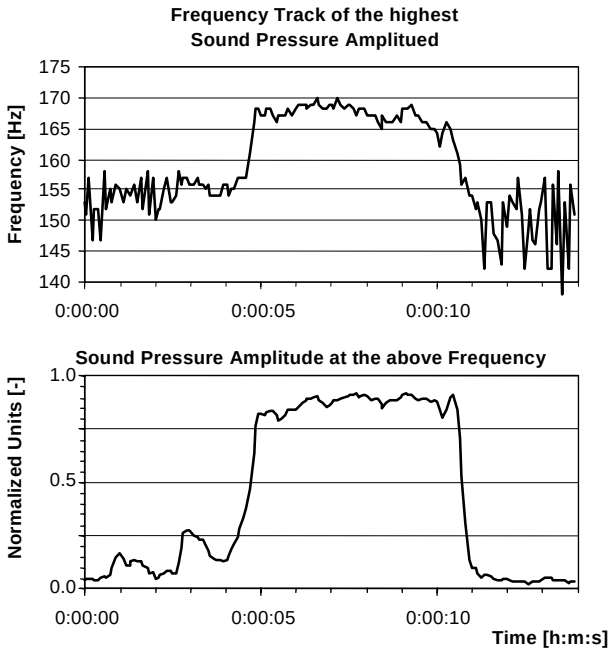


Figure 11: Frequency shift during arising sound pressure amplitude (without activated AIC-System).

The results achieved by means of passive measures were improved even more by employing an Active Instability Control (AIC) system. For the best burner configuration having ordinary, i.e. straight, extensions, AIC made it possible to increase the stability limit by 2%, as well as by 3% for the best configuration having inclined nozzle extensions. Moreover, at base load operations, AIC allows a reduction of NO_X emissions by more than 60% by lowering the pilot gas mass flows necessary for stable operation. Problems entailed by substantial frequency shifts whenever combustion instabilities occurred at maximum turbine power were rectified by rapidly and automatically adapting the appropriate control parameters. In addition to stabilising base load operations, the AIC system successfully dealt with stability problems occurring under part load conditions in diffusion operation of the gas turbine. At this point AIC reduced the two dominant frequency peaks by 20 dB (2^{nd} harmonic at 145 Hz) and 15 dB (3^{rd} harmonic at 290 Hz). To allow - in contrast to former AIC set-ups - the control of two modes with an even and an odd mode number, the AIC system was improved in terms of its independence in controlling any two modes.

The successful damping of combustion instabilities in various operating points of the gas turbine demonstrates the high flexibility of the employed active measures in dealing with this problem and allowing stable gas turbine operation over the entire range. The presented AIC system is currently being used with several V94.3A gas turbines. The field leading installation, implemented in January 1999 in a base loaded machine, has been operating for approximately 6,000 hours and continues to demonstrate its excellent long-term stability.

8. References

1. Rayleigh, Lord J.W.S.: The Explanation of Certain Acoustical Phenomena. Nature, pp. 319-321, 18. July 1878.
2. Putnam, A.A., Dennis, W.R.: Burner Oscillations of the Gauze-Tone Type. The Journal of the Acoustic Society of America, Vol. 26, No. 5, pp. 716-725, 1954.
3. Hermann, J.; Zangl, P.; Gleis, S.; Vortmeyer, D.: Untersuchung der Anregungsmechanismen selbsterregter Verbrennungsschwingungen an einem Verbrennungssystem für Flüssigkraftstoff. 17. Deutscher Flammentag, Hamburg-Harburg, VDI-Bericht Nr. 1193, S. 251-260, 1995.
4. Lieuwen, H.T.; Torres, H.; Clifford, J.; Zinn, B.T.: A Mechanism of Combustion Instability in Lean Premixed Gas Turbine Combustors. ASME paper 99-GT-3.
5. Putnam, A.A.: Combustion Driven Oscillation in Industry. Elsiever.
6. Culick, F.E.C.: Combustion Instabilities in Liquid-Fueled Propulsion Systems – An Overview, AGARD CP 450, pp. 1-1 – 1-73, 1988.
7. Seume, J.R.; Vortmeyer, N.; Krause, W., Hermann, J.; Hantschk, C.-C.; Zangl, P.; Gleis, S.; Vortmeyer, D.; Orthmann, A.: Application of Active Combustion Instability Control to a Heavy Duty Gas Turbine. ASME Paper No. 97-AA-119, 1997
8. Hoffmann, S., Hermann, J. and Orthmann, A.: Active Flame Instability Control for Heavy Duty Gas Turbines. PowerGen Europe 99, Frankfurt, Germany.
9. Hermann, J.; Orthmann, A.; Hoffmann, S.: Application of Active Combustion Control to a Heavy Duty Gas Turbines. 14th Int. Symposium on Airbreathing Engines, Florence, Italy, 5-10 Sep 1999.
10. Hermann, J., Gleis, S., and Vortmeyer, D.: Active Instability Control (AIC) of Spray Combustors by Modulation of the Liquid Fuel Flow Rate, Combust. Sci. and Tech., Vol. 118, pp. 1-25, 1996,.
11. Hantschk, C., Hermann, J., and Vortmeyer, D.: Active Instability Control with Direct Drive Servo Valves in Liquid-Fuelled Combustion Systems, 26. Int. Symp. on Combustion, Naples, 1996.

PAPER -3, J. Hermann

Question (B. T. Zinn, USA)

When you do active control, you basically change the manner in which the total fuel is supplied to the system. This, in turn, *may* affect the primary process that drives the instability. Thus, it is important to determine the relative damping of the instability provided by "redistribution" of the fuel injection and by the active instability control (AIC).

Reply

The mean gas mass flow is not changed by AIC. Because of this and the fact that we only modulate the pilot gas mass flow, which is about 5-10% of the total gas mass flow, around its mean value, we do not expect any damping of the instabilities by "redistribution" of the fuel injection. Furthermore, having been able to damp two different frequencies independently of each other is another proof that the damping is achieved purely by AIC.

Question (V. McDonell, USA)

What is the cost effectiveness of AIC? You are gaining an additional 1-2% in the total output, but at what relative cost of the AIC system. It is reasonable that costs will come down if more systems are installed/developed.

Reply

If you can produce some percent more electric power over some years, the cost of an AIC-system easily pays off.

Question (M. N. Nina, Portugal)

How much fuel was used in the pilot burner to control the oscillations?

Reply

About 5-10% of the total gas mass flow.

This page has been deliberately left blank

Page intentionnellement blanche

ACTIVE COMBUSTION CONTROL FOR MILITARY GAS TURBINE ENGINES

Marcus H. Richman and Michael S. Richman
Naval Air Systems Command
Propulsion and Power Engineering
22195 Elmer Road, Unit 4
Patuxent River, MD 20670-1534
USA

INTRODUCTION

The U.S. Navy, as a participant in the United States' Integrated High Performance Turbine Engine Technology (IHPTET) initiative, is dedicated to increasing aircraft engine performance to satisfy the propulsion requirements of future Navy aircraft. This is accomplished by identifying the propulsion requirements, in terms of performance and total cost, for specific Navy aircraft. The required engine technology advances are then broken down into specific engine component technology objectives. Advanced technology is then developed on the component level. Once an appropriate level of readiness is reached, the components are then assembled into an engine for overall advanced propulsion system demonstration. Technologies from this demonstrator engine are then made available to development engine programs, such as the Joint Strike Fighter (JSF), for further development and eventual transition to production engine programs.

The figure of merit used to measure performance is engine thrust/weight ratio. The role of the combustor in this endeavor is to provide the necessary temperature rise to increase core engine output. This drives the combustor to operate at higher fuel/air ratios which in turn drives a larger portion of the combustor volume to operate at or near stoichiometric conditions. Combustor operation at these levels must be achieved with an eye to numerous other parameters such as durability, weight, cost and emissions. Active Combustion Control is one of the key technologies required to meet these objectives simultaneously.

CONTROL SYSTEMS DESIGN

Propulsion controls technology programs have a two-fold focus. They funnel technologies into both legacy systems as well as the F414 and JSF programs (short term), and develop fundamental capabilities for future (2003 and beyond) propulsion systems. These programs revolve around two primary requirements; increased thrust-to-weight and reduced life cycle cost (LCC). Both have multiple primary technology development paths, which contain revolutionary control system (diagnostic and prognostic) components as enabling technology requirements.

Increasing thrust-to-weight can be accomplished in two primary ways. First, use exotic materials to reduce the weight of individual components: compression systems, fan, turbine, combustor/augmentor, controls and accessories (i.e. pumps, actuators, sensors, and electronics). Second, the system design must be weight optimized. The major components must lose weight via envelope reduction. Reduce core weight by reducing the number of stages required for fans, compressors, and turbines. Reduce length of combustor and augmentor. Putting the core on a diet, via the above methods, results in a much lighter system (good), but an extremely unstable (bad) one. As a result, the engine must be smarter. The major components must be actively controlled, avoiding stall, surge, and vibration (HCF) in the rotating components, as well as closed loop combustion to ensure efficient burning, and emission development within a shortened envelope. Cooperative with the use of exotic materials for the hot section, active

Paper presented at the RTO AVT Symposium on "Active Control Technology for Enhanced Performance Operational Capabilities of Military Aircraft, Land Vehicles and Sea Vehicles", held in Braunschweig, Germany, 8-11 May 2000, and published in RTO MP-051.

combustion control is the answer for improved performance, durability, and safety. Figure 1 illustrates this degradation of the hot section components (turbine inlet) as we push the limits of combustion performance.

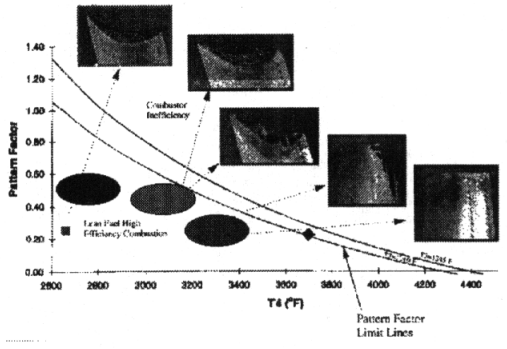


Figure 1

The technology involved in control system design for active combustion control relies primarily on actuation and sensing. The algorithms will be heavily laden with information fusion technology, combining a meriod of sensor inputs not only from the combustion system, but the entire engine. The true advantage of active combustion control will be as a component in a larger adaptive engine control algorithm providing the capability to optimize on performance, life, damage tolerance, and economy. Both systems will blur the lines between controls and diagnostics. Both systems will be model based, providing the necessary baseline and backup for each of the sensor suites. Active combustion control will not be based on a "point" type feedback which relies on "safe" operating limits around singular sensor information. Temperature, pressure, vibration levels, etc.. will all feed together providing a combustion system level feedback for use in actuating the combustion, aero, acoustic, and nox dynamics.

HIGH FUEL/AIR OPERATION

The most effective way of increasing engine output is to increase the energy added by the combustion of the fuel. In practice this means increasing the average combustor exit temperature (T4) by increasing the fuel air ratio (FAR). Traditionally, turbine materials and cooling technology have limited the exit temperature. As advances have been made in these areas, T4 has increased to take advantage of the increased capability [Figure 2]

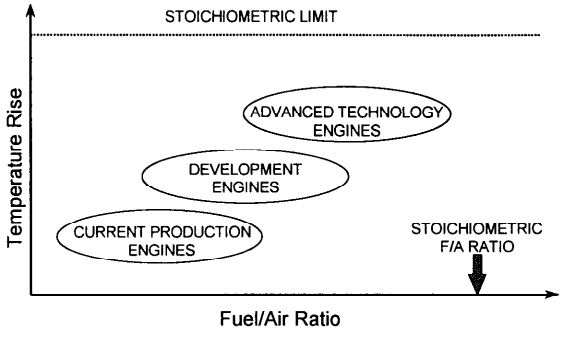


Figure 2

Combustor behavior is fairly well characterized at fuel/air ratios below 0.04. At these lower fuel/air ratios, the incidences of locally stoichiometric streaks exiting the combustor are infrequent. As the average FAR increases above 0.04, these locally stoichiometric streaks become more prevalent. As these stoichiometric steaks leave the combustor, and enter the turbine, they react with cooling air introduced in the turbine. This reaction produces enough energy to quickly destroy turbine hardware. Active Combustion Control offers a technology that may be able to address this problem.

COMBUSTOR EXIT FLOW CONTROL

Combustor exit temperature is usually quoted as an average temperature that is appropriate for performance calculations. Other aspects of combustor performance are equally, of not more important in turbine design. The temperature quality, or exit temperature profiles are important in designing durable turbine hardware. Historically, the temperature profiles have been reported in two ways. Profile Factor indicates the highest average temperature at a specific

spanwise location and the Pattern Factor indicates the maximum temperature at any location in the combustor exit plane. These values are expressed in equations 1 and 2.

$$\text{Profile Factor} = \frac{T_{\max,rad} - T_{ave}}{T_{ave} - T_{inlet}} \quad (1)$$

$$\text{Pattern Factor} = \frac{T_{\max} - T_{ave}}{T_{ave} - T_{inlet}} \quad (2)$$

Combustor concepts being pursued as part of the IHPTET program lend themselves to control of the exit temperature distribution. These concepts feature an array of fuel struts with multiple spanwise fuel injection points. This allows both spanwise and circumferential control of the fuel injection. Testing is planned to determine the effect of changes in the fuel injection profile on the exit temperature distribution. After this behavior is characterized, it is a simple matter to implement open loop control of the temperature profile.

While open loop control is relatively easy to achieve, closed loop control presents many more benefits. In theory, all that is required to implement closed loop control is a temperature sensor that can be mounted on the high pressure turbine vanes, and control logic to implement the system. The problem becomes the development of temperature sensors that can withstand combustor exit temperatures. Current temperature levels present a challenge for measurements in a laboratory rig environment and make direct measurement impossible in an engine environment.

The ability to actively control the temperature profiles in an engine allows for a higher performance and more durable engine. Manufacturing tolerances allow for combustor to combustor and fuel nozzle to fuel nozzle differences in temperature profiles. Temperature profiles can be influenced by small differences in combustor air distribution, fuel nozzle flow and compressor exit profile changes. Active control allows the engine to compensate for these differences and maintain the design temperature profile. In addition, as the engine degrades, the compressor exit profile changes and nozzle fuel flow may change. Active control allows the engine to compensate for these changes and prolong turbine life.

As fuel air ratios increase, simple temperature measurements may not be sufficient for useful control. Once a location in the combustor exit plane reaches stoichiometric, it has reached its maximum temperature. If this streak is richer than stoichiometric, the temperature may actually be lower. The average temperature rise across the combustor can continue to rise however. As shown by equation 2, this can artificially drive the pattern factor number down and conceal potential problems in the turbine. To address this problem, a new parameter is coming into favor by combustor and turbine designers. The Fuel/Air Factor (FAF) is defined as:

$$\text{FAF} = \frac{\text{FAR}_{\max} - \text{FAR}_{ave}}{\text{FAR}_{ave}} \quad (3)$$

This parameter is able to accommodate local fuel air ratios above stoichiometric without flattening out as pattern factor does, as shown in Figure 3.

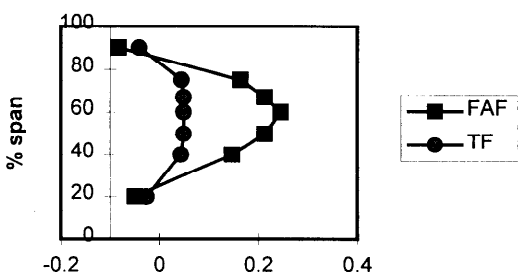


Figure 3

This phenomenon will also be present in the engine at very high fuel air ratios. Control of these rich streaks will require the development of instrumentation, which can

not only withstand the high temperature, but is capable of sensing products of combustion that may continue to react downstream.

ACOUSTIC CONTROL

Control of acoustic instabilities in gas turbine engines is a much more complex problem than the control of temperature profiles. Combustor rumble or augmentor screech can have a severe impact on the life of components. Acoustic instabilities can not only reduce the efficiency of the engine, but can cause serious damage to hardware, often causing component failures. Current passive control techniques include changing fueling schemes in areas of the envelope prone to instability, and hardware changes to the screech control section of the augmentor liner or combustion liner.

Active control of instabilities includes sensing both that the instability exists, as well as the frequency of the instability. Once the frequency is known, the fuel supply, or air supply can be pulsed in such a manner as to eliminate the instability. In a simpler form of control, the fuel distribution can be modified only when instability is present as opposed to any time the aircraft is operating at a certain point in the envelope, or performing a specified throttle maneuver. This latter method requires fuel injection patterns to be determined empirically for all conditions in order to determine solutions.

TECHNOLOGY NEEDS

Several key technologies are required in order to make active combustion control a reality. The most pressing need is for temperature sensors capable of withstanding temperatures seen at the combustor outlet that do not interfere with engine operation, and are flight quality. The sensors must be able to withstand high temperatures for 2000 hours of engine operation. In addition, they must be able to withstand the operational environment that Navy aircraft are subjected to.

In order to actively control combustion instabilities, sensors must be developed that can detect the presence of and determine the frequency of the instability. The control system must be able to differentiate between combustion instability and other vibrations that are common to military aircraft. Once instability is detected, actuators that are capable of pulsing the fuel at between 0 and 1 kHz and lasting 5.4 billion cycles are required. Again, these actuators need to be flight weight, and small enough to fit several in a single fuel nozzle.

MEASUREMENT & ACTUATION

State-of-the-art sensor technology allows only rudimentary insight into the real-time dynamics of combustion. The hurdle becomes living and working in 3500°+ Fahrenheit for long duration and providing useful information. What do we need to know, and what are we trying to control? The overarching goals of the Navy's controls and diagnostics S&T program focus on performance, safety and life cycle cost (LCC).

Any active control system derives value from its ability to accurately sense the current state of the plant and control the system dynamics within a minimal tolerance band. Understanding gas path parameters in the hot section is a tough problem to overcome. The solution lies in one of three options.

First, develop in-situ sensors capable of providing combustor gas path temperature, pressure, acoustic, emissions, or other critical parameters. These sensors or sensor sets must provide profile information in a non-intrusive manor. One value of active combustion control is to add life to the turbine. Placing rakes of sensors upstream of the turbine inlet is in direct violation of the concept. The technology hurdle becomes developing non-intrusive methods of measuring temperature and pressure profiles. Additionally, concepts to measure the acoustic state of the system need to be developed. This area overlaps with concepts

already mentioned concerning overall system health monitoring. Vibrations are closely monitored on existing engines in hopes that incipient failures can be identified. Improving on the fidelity of these measurements can help to provide combustion acoustic information. Concepts such as laser interferometry, and MEMS accelerometers should be explored.

The second option for providing combustor feedback poses a pure analytical solution. Adding sensors to an engine is generally not desirable. Therefore, if a real-time combustor model could be developed all gas path information would be known. However, real-time models of combustion systems are hard to come by, and provide a qualification nightmare. Many questions concerning model validation both initially and throughout the life of the engine would need to be address prior to fleet introduction. The Navy isn't ready to run a sensorless control system.

The third option is to develop a hybrid system relying on accurate real-time combustion system models to provide the "impossible" to measure parameters with advanced sensors providing tuning and feedback for the model. This type of system allows for much more than just a combustion controller. It provides valuable diagnostic information. As the model is "tuned" to match the existing state of the engine, these tuning parameters allow maintainers to track and predict the system health. In reality, this combustion model would simple be a portion of a greater engine system real-time model capable of optimizing the system performance based on any number of metrics such as; thrust, specific fuel consumption, component life, etc...

IMPLEMENTATION

Conceptually, we have designed the system and identified its correlation to existing initiatives within the Navy & DOD. From this baseline, the challenge focuses on developing components that will operate in a real-world environment. It's assumed that the control scheme will rely on modern multi-input multi-output algorithms optimizing a cost function with a variety of actuation points at hand. The actuation suite is fairly limited given the simplicity of a gas-turbine combustion system. Prime movers for affecting the combustion system dynamics will be the fuel delivery system. Pattern factor and acoustic characteristics will be affected by spatially and temporally actuating fuel delivery requiring that each fuel nozzle be controllable. As yet other methods have not been identified. Methods like direct flow modification via vortex generators, bleed or blowing devices are concepts that from a practical standpoint provide a reliability & safety liability. However, flow modification devices might address some of the overarching goals of active control, in which case the technology effort needs to focus not only on the physics but reliability & life issues as well.

SOFTWARE/ELECTRONIC HARDWARE

As with many intelligent engine concepts implementation requires a foundation capable of handling the necessary computing horsepower to run the real-time algorithms and engine system models. Most digital control systems contain components such as a 1553 data bus which can be used. However, few systems contain the necessary "extra" CPU & memory to run the model plus active control algorithms plus control schedules. Therefore, active model based combustion control will depend on the ability to attach or design in the necessary processing power. Future systems will have this as a built-in feature, legacy systems will require some degree of flexibility to accommodate additional control boxes.

ACC IN THE NAVY

The Intelligent Engine Initiative (AF/Navy) is focused at using advanced sensing, actuation, and information technology to maximize performance while minimizing operation and support cost. Areas focused on are: Nonlinear adaptive control;

Prognostics/diagnostics life-influencing factors; Active control for performance and durability; Advances in sensing and actuation. Within these areas are Navy "unique" requirements and technology development areas. Specifically, in the turboshaft area, requirements for a technology leap applied to missions such as search and rescue (SAR), sub hunter, and vertical replenishment (VERTREP) need to be addressed. The unique need for reliability and performance durability (i.e. prognostic and diagnostic improvements) while living in a severe corrosive environment drive technology planning to include detection/prevention algorithms for corrosion driven performance loss and system failures. Adaptive control to overcome this performance loss coupled with novel diagnostic algorithms providing on-wing system health and component level life management enable SAR, sub hunter, and VERTREP mission cost reduction as well as readiness improvement. Most engines operating in these missions are removed for performance loss rather than life issues. By improving health monitoring and integrating this with adaptive control we can improve engine durability, reliability, and reduce life cycle cost. Completing the Intelligent Navy Engine with active cold and hot section control allows real-time management of performance, engine and accessories health, and system efficiency while maintaining optimum life. Many of the turboprop/turboshaft needs for control technology overlap those required by turbofan/turbojet.

This Navy technology roadmap relies on advances in many areas of active control, primarily active compressor & combustion control. ACC seems to offer a solution that addresses many Navy requirements at once and should be a priority for technology development.

ACKNOWLEDGEMENTS

The authors would like to acknowledge the help and support of Mr. Barry Kiel and Mr. Tim Lewis of the Air Force Wright Laboratories' Turbine Engine Division.

PAPER -4, M. Richman

Question (F. E. C. Culick, USA)

You mentioned the possibility of new configurations for combustors, e.g., spray bars. Hasn't that sort of suggestion encountered resistance from the people designing combustors in industry?

Reply

The contractors (engine manufacturers) have been very willing to look at revolutionary designs. More resistance has come from the Department of Defense (DoD).

Question (D. A. Santavicca, USA)

What temperature resolution/accuracy are you looking for in your turbine inlet temperature sensor?

Reply

An accuracy of ±50° F at stoichiometric temperatures is required.

This page has been deliberately left blank

Page intentionnellement blanche

LONGITUDINAL MODE AEROENGINE COMBUSTION INSTABILITY: MODEL AND EXPERIMENT

J. M. Cohen, J. R. Hibshman, W. Proscia, T.J. Rosfjord, B.E. Wake
United Technologies Research Center, 411 Silver Lane, MS 129-15
East Hartford, CT 06108, USA

J. B. McVey
jbScienceS, Glastonbury, CT, USA

J. Lovett, M. Ondas
Pratt & Whitney, P.O. Box 109600-M/S 715-89
West Palm Beach, FL 33410, USA

J. DeLaat, K. Breisacher
NASA Glenn Research Center at Lewis Field, Cleveland, OH, USA

ABSTRACT

Combustion instabilities in gas turbine engines are most frequently encountered during the late phases of engine development, at which point they are difficult and expensive to fix. The ability to replicate an engine-traceable combustion instability in a laboratory-scale experiment offers the opportunity to economically diagnose the problem more completely (to determine the root cause), and to investigate solutions to the problem, such as active control. The development and validation of active combustion instability control requires that the causal dynamic processes be reproduced in experimental test facilities which can be used as a test bed for control system evaluation. This paper discusses the process through which a laboratory -scale experiment can be designed to replicate an instability observed in a developmental engine. The scaling process used physically-based analyses to preserve the relevant geometric, acoustic and thermo-fluid features, ensuring that results achieved in the single-nozzle experiment will be scaleable to the engine.

INTRODUCTION

Aggressive performance and emissions goals for aeroengine gas turbine combustors have led to the development of combustor concepts that may operate closer to static and dynamic stability boundaries. Lean, direct-injection combustors under development share many features with the lean, premixed combustors used in stationary gas turbines, in which combustion instabilities are widely observed.

In order to minimize development costs and time, it is critical to posses the ability to evaluate the dynamic behavior of a combustor design during the component-development phase, thereby mitigating the need for expensive full-scale engine testing late in the development cycle. Solutions to combustion instability problems, such as active and passive controls, can be evaluated and developed more quickly in a laboratory-scale experiment, enabling a faster transition of technology into production engines.

Laboratory- or component-scale testing of developmental combustor concepts is standard practice in the aircraft gas-turbine industry, using single-nozzle flame tubes, single- and multi-nozzle sectors and full-annular combustor rigs. The gas turbine community has developed an experience base regarding the fidelity with which such test rigs must replicate engine design details in order to characterize the emissions and operability characteristics of engine combustors. At this time there is no proven methodology for replicating engine-scale combustor dynamics in laboratory-scale rigs. The

Paper presented at the RTO AVT Symposium on "Active Control Technology for Enhanced Performance Operational Capabilities of Military Aircraft, Land Vehicles and Sea Vehicles", held in Braunschweig, Germany, 8-11 May 2000, and published in RTO MP-051.

challenge in designing laboratory-scalc combustion dynamics experiments is to replicate the engine dynamic environment in as simple (low-cost) an apparatus as possible. Recent published work suggests that bulk mode and longitudinal mode instabilities can be replicated in single-nozzle rigs. Cohen et al (1998) and Hibshman, et al (1999) performed active instability control experiments in single-nozzle and sector combustors that reproduced a bulk-mode instability observed in a lean, premixed industrial combustor. Paschereit et al (1998) have developed a sub-scale combustor in which the boundary conditions at the inlet and exit ends can be varied to impose a desired acoustic mode. No relevant work has been published on replication of tangential modes in multi-nozzle sector or configurations other than full annula rcombustors.

While the aforementioned investigators have shown that it is possible to create a realistic, laboratory-scale combustion dynamics experiment, the scaling processes through which these experiments can be designed have not been described with sufficient specificity to allow the methodology to be adopted by the technical community at large. In order for the results of sub-scale experiments to be useful to engine designers, there must be a system in place to translate those results to engine-scale. This paper discusses such a process and presents an example problem, beginning with the analysis of an engine-traceable instability and culminating in the comparison of the lab-scale results to those from the engine. The process involves the following steps:

1. Analysis of dynamic data from the subject engine to determine characteristics of instability: frequency, amplitude, and sensitivity to changes in hardware configuration and operating conditions.

2. Acoustic analysis of the engine in order to determine acoustic modes associated with instability.

3. Conceptual design of single-nozzle experiment, reproducing thc engine's acoustic environment and replicating the relevant dynamic processes, as determined in steps 1 and 2.

4. Acoustic analysis of sub-scale experiment to determine its fundamental acoustic modes in order to confirm similarity with those observed in the engine.

5. Test of the finalized laboratory-scale experiment and comparison of data to analyses and engine data.

ENGINE PROBLEM ANALYSIS

The sample problem that was selected for this effort was a combustion instability that was observed during the development phase of a high-performance aero-engine that employed a full-annular combustor employing 24 fuel nozzles. The frequency of the instability varied from about 420 Hz at low-power conditions to about 580 Hz at high-power conditions, as shown in Fig. 1. At a mid-power operating point, corresponding to that used for the analytical phase of this study, the frequency of the instability was 525 Hz. The magnitudc of the pressure oscillations resulting from the instability were sufficient to cause unacceptable vibratory stresses in the turbine component of the engine

Passive means of reducing the magnitude of the pressure oscillations were developed during engine testing. This series of tests was able to detect a notable difference in the pressure oscillation magnitude when the fuel nozzle /air swirler design was changed.

A limited series of non-reacting experiments were conducted (Anderson, et al, 1998) to dctcrmine thc acoustic and fluid mechanic response characteristics of the air swirlers that were used in the engine tests. The aim of these experiments was to measure differences in the responses of the air swirler / fuel injector designs that might explain their behavior in engine tests. It was found that the air swirlers associated with the largest pressure oscillations exhibited a preferential response to air flow perturbations in the frequency range between 300 Hz and 500 Hz. Air swirlers that performed better in the engine did not exhibit this phenomenon in the non-reacting tests.

While fast-response combustor pressure data were acquired during the engine tests, they were acquired at a limited number of locations. For this reason, it was difficult to draw any significant conclusions about the nature of the instability purely from the engine data. The analyses describcd in the next section of this paper were used to augment and interpret the engine data. The combination of the engine data, the acoustic analyses and the non-reacting swirler/injector characterization provided the basis for replicating the problem in a single-nozzle combustor rig.

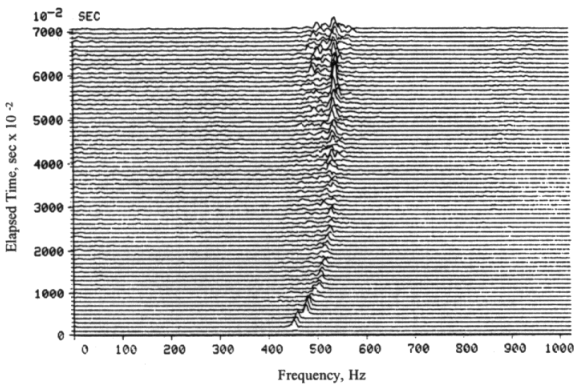


Figure 1. "Waterfall" plot of combustor pressure spectra from an engine test, showing evolution of the instability during an acceleration event.

Analysis of Engine Acoustics

A quasi-1D unsteady Euler analysis (Wake et al., 1996) was used to predict the bulk and longitudinal modes of the engine combustor. The one-dimensional Euler equations were solved with area variation and modeled source terms to account for mass addition, heat addition and pressure losses. The resonant acoustic frequencies of the combustor were determined by solving for the unsteady time-accurate response of the system and monitoring the fluctuating pressure at a specified location. The analysis can be used to examine the sensitivity of the frequency and pressure amplitude to system parameters such as physical dimensions, temperature distribution, Mach number, flow rate and pressure drop. The solver was first used to compute the steady-state results, and then unsteady results were obtained by forcing the system. Forcing was accomplished by adding an unsteady component to the heat release. Two types of forcing signals were used: 1) broadband white-noise distributed forcing, and 2) swept sine forcing at a fixed frequency. The resulting pressure response indicated the frequency dependence of the combustion system.

It should be recognized that this analysis is useful for its intended role of the determination of acoustic modes. The analysis does not attempt to incorporate the physics of the interaction of the fluid mechanics/acoustics with the heat release (effects of flame shape variation, local fuel/air variations, etc.) and therefore is not capable of predicting the *absolute magnitude* of the pressure response. The approach demonstrated in this paper will show that it is, however, a satisfactory tool for evaluating test rig acoustic characteristics for combustion dynamics experiments.

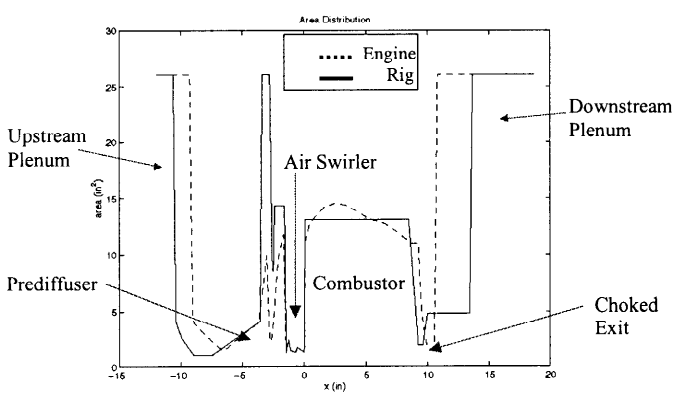


Figure 2. Cross-sectional area vs. axial position for quasi-1D Euler model.
---------- Engine configuration _____ Rig configuration

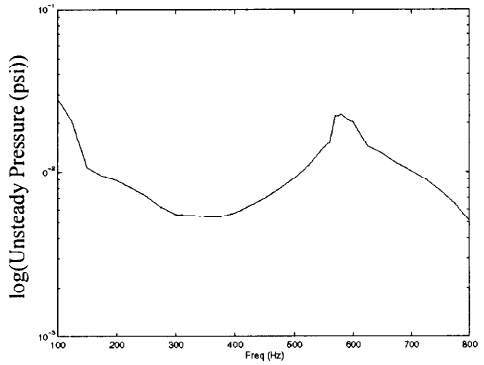


Figure 3.Computed power spectrum of combustor pressure for engine configuration with sine-sweep forcing.

Quasi-1D Euler calculations were conducted for the engine configuration at an intermediate operating condition: 771 F (684K) and 200 psia (1.2 MPa). The engine geometry was converted into a one-dimensional description of area vs. axial position as shown by the dashed line in Fig. 2, which shows the distributions for both the engine and the rig (to be discussed later). The geometry used included an inlet plenum, the engine prediffuser, diffuser plenum, the cowl or hood, the swirler, the combustor liner and turbine vanes. The combustor lies between x = 0 and 9.25 in. Beyond the turbine vane exit the area was expanded rapidly to create a plenum dump. The boundary conditions used were constant total pressure at the inlet plenum and constant static pressure at the exit plenum.

The acoustic response of the system was obtained by swept-sine forcing of the entire heat release distribution. The fluctuation levels imposed on the heat release were 10% of the mean. The unsteady pressure amplitude at the x = 3 in. location in the combustor (3 in. downstream of the combustor dump plane) was used to determine the pressure response. The swept-sine response is shown in Fig. 3 and indicates a resonance at approximately 575 Hz. The width of the amplitude response peak indicates a large amount of damping. However, the width of the response also indicates a broad range of frequencies over which the system may be susceptible to combustion instability.

These results indicated a longitudinal mode in the combustor near 575 Hz, near the observed frequency of about 525 Hz. The pressure mode shape for the 550 Hz mode is shown in Fig. 4. The mode represents a full-wave solution to the system equations with zero unsteady pressure specified at each end. Given the high impedance at each end due to the high Mach number boundaries, the mode shape can also be interpreted as a half-wave across the diffuser-combustor domain with closed ends. Note there is a pressure node apparent at the air swirler/fuel injector (x=0). The calculated fluctuating pressure in the diffuser was 180 deg. out of phase

from the pressure in the combustor. It is believed that this was the basic acoustic mode that occurred in the engine configuration instability. Although tangential acoustic modes exist in the full-annular engine combustor, analysis of the engine data and two-dimensional Euler results have indicated that they are not associated with the observed instability.

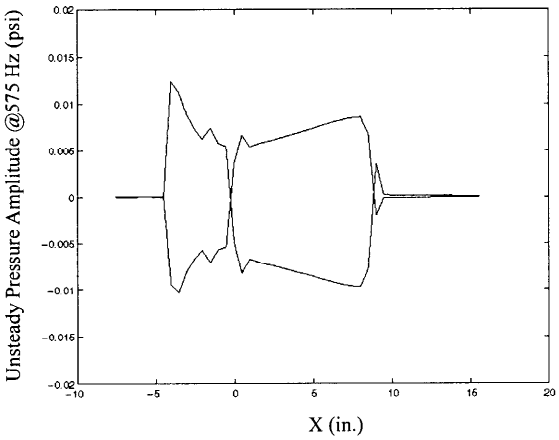


Figure 4. Computed pressure mode shape for 575 Hz mode for the engine configuration at evaluation point conditions.

SUB-SCALE EXPERIMENT DESIGN

Test Apparatus Features

Based on prior experience (Peracchio et al, 1998) the test rig design approach incorporated the following guidelines:

A. Use of full-scale fuel preparation sub-components (fuel nozzles, air swirlers)

Prior evaluations (Anderson et al, 1998) indicated that the prototype injector/swirler exhibited an enhanced response near the 500 Hz frequency observed in the engine data so it was important to utilize that precise design. While reduced-size hardware may be of interest in order to minimize facility requirements, this approach was not taken, due to the introduction of uncertainties associated with reduced-scale flows.

B. Reproduction of the longitudinal acoustic behavior

The critical elements in this regard were the combustor, the diffuser, the pre-diffuser, and the cowl (hood) which guided the diffuser air to the fuel nozzle. Table 1 shows a comparison of the geometric features of the annular engine burner with those of the rig. Cross-sectional areas were chosen to replicate associated volumes and expansion/contraction ratios.

Feature	Engine	Rig
Combustor Volume per Injector (in^3/cc)	113 / 1851	108 / 1770
Combustor Length (in./cm)	8.5 / 21.3	8.5 / 21.3
Shroud Volume per Injector (in^3 /cc)	129.3 / 2119	103.4 / 1695
Nominal Shroud Height (in./cm)	1.2 / 3.0	0.80 / 2.0
Diffuser length	2.7 / 6.9	2.7 / 6.9
Pre-diffuser Length (in./cm)	3.9 / 9.9	3.9 / 9.9

Table 1. Comparison Engine and rig acoustic features.

C. Acoustic isolation of the combustor from facility air piping

A venturi was used to choke and meter the inlet air flow. Since the isolation provided by the sonic throat condition was desired over a range of conditions, the venturi was designed to be underexpanded, resulting in a normal shock at a distance of 1.38 in. (3.5 cm) downstream of the venturi throat. The upstream boundary was largely established by the normal shock and the sudden expansion of the flow at the pre-diffuser dump. The downstream boundary was defined by using a choked exhaust nozzle at the station occupied by the first turbine inlet vane.

D. Reproduction of the air flow distribution, pressure drops and flow damping characteristics

The pressure drops and airflow splits used in the engine were duplicated. That is, the fractions of air used for liner cooling and for primary and dilution air were reproduced. Designing for equivalent damping is important to achieving similar instability amplitudes between the test rig and the engine. The resistive damping of the system was maintained by replicating the system's pressure drops. Reproducing the airflow splits between the different air flows replicates the distribution of stoichiometry and heat release rate within the combustor.

E. Design for testing at engine operating conditions

The instability observed in the engine occurred over a range of test conditions. A single "Evaluation Point" was chosen at 200-psia (1.2 MPa) combustor pressure, an entrance temperature of 771 deg F (684K), and combustor fuel-air ratio of approximately 0.03. All analyses were conducted at these conditions. Operating at reduced conditions with full-scale hardware can change the operating characteristics of the components (pressure drops, atomization, etc.).

The final consideration was whether to utilize an apparatus with a simple cylindrical cross-section burner or an apparatus having a cross-section representative of 1/24 of the 24-nozzle engine burner – i.e., a 'single sector' burner. A circular cross-section was employed, as this represented the lower-cost, higher-strength approach. The number and size of the combustion and dilution air holes was adjusted to provide proper penetration of these air jets.

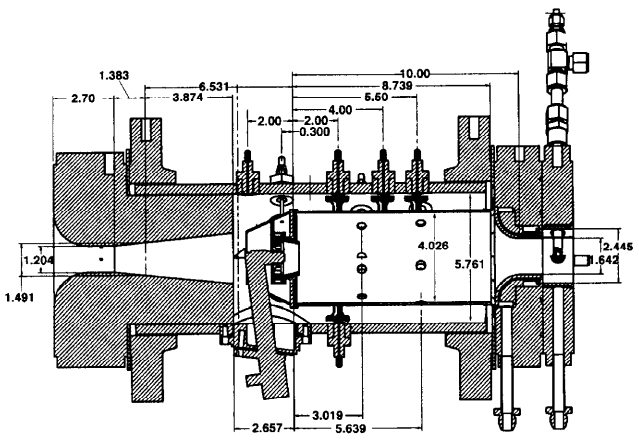


Figure 5. The combustor test section assembly. Dimensions are in inches.

The configuration of the test section is illustrated in Fig. 5. Provisions for high-response pressure transducers and for gas sampling (not reported herein) were incorporated.

Three transducer bosses, equally spaced around the circumference, were located in the primary combustion zone. One was located in the secondary zone, and one in the dilution zone. Floating seals on the liner captured extension tubes attached to the pressure-vessel-mounted transducers such that the pressures at the inside liner surface could be recorded.

Bosses for shroud flow pressure measurements were provided at the location of the liner primary and dilution holes. Bosses for diffuser pressure measurements, upstream of the combustor, were also provided

PCB piezo-electric pressure transducers (P/N 124A21) were selected for this application based on demonstrated ability to withstand the severe environment encountered in the combustor and pre-diffuser (high temperature and pressure). Originally developed for measuring combustion instability in liquid rockets, they are capable of measuring $\pm$250 psi. pressure fluctuations at frequencies between 0.5 Hz and 10 kHz. Satisfactory durability was achieved by use of an integral water-cooled mounting fixture that maintained an acceptable temperature around the sensor. The liner pressure sensors communicated with the combustor through a 0.062 in. (1.6 mm)-diameter, 0.83 in.(2.1 cm) -long sensing tube. A 1000 psia nitrogen supply was used to purge the tube – the amount of purge flow rate was negligible. The ¼-wave resonant frequency of the cavity within this tube was far above the frequency range of interest in this experiment. Analog data were low-pass filtered at 2 kHz and digitally sampled at 5 kHz using a simultaneous sample-hold data acquisition system.

Analysis of Single-Nozzle Rig Acoustics

The single-nozzle combustor rig design was established to preserve the axial lengths and cross-sectional areas of the engine configuration relative to a single nozzle. The area vs. axial position distribution was maintained approximately the same (ref. Fig. 2), but some variation existed due to differences in engine hardware and the axisymmetric hardware to be used in the single-nozzle combustor. Airflow splits and pressure losses – swirler, bulkhead, liner, primary and dilution jets were also preserved by design. The inlet and exit of the rig were choked to acoustically isolate the system. The Euler models included inlet and exit plenums upstream and downstream of the choke points to allow constant total pressure and constant static pressure to be specified, respectively, as boundary conditions to be applied to the Euler code domain.

Quasi-1D Euler calculations were conducted for the baseline rig configuration at the evaluation point operating condition: 771 F (684 K), 200 psia (1.2 MPa). Swept-sine forcing over the frequency range from 100 to 800 Hz was applied to the heat release. The resulting power spectrum of the pressure response is shown in Fig. 6, indicating the presence of resonances at 115 Hz and 550 Hz. The level of forcing employed in the analysis is arbitrary, and within the linear response range, so that no significance should be attached to the absolute levels of the ordinates in Figs. 4 and 6.

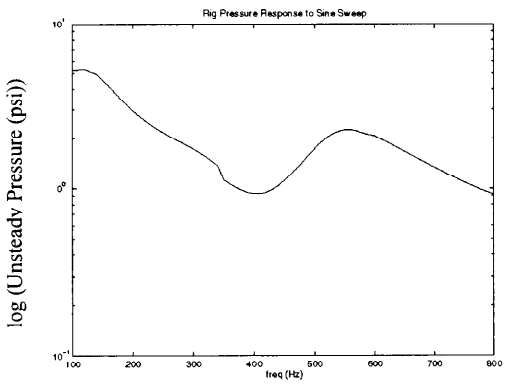


Figure 6. Computed power spectrum of combustor pressure at x = 3.0 in. for the rig configuration. Quasi-1D Euler code results for 100-800 Hz swept-sine forcing of heat release.

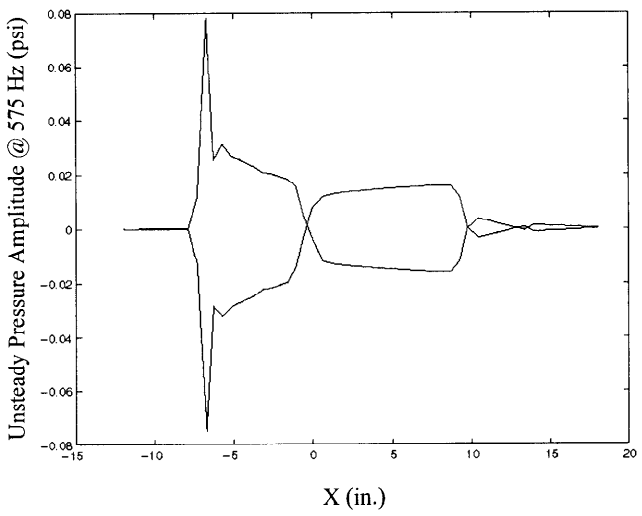


Figure 7. Computed pressure mode shape for the 550 Hz mode. Rig configuration at evaluation point conditions.

Further analysis of the mode shapes associated with these resonances revealed that the low frequency 115 Hz mode was a first-order longitudinal mode where the diffuser and combustor were in phase. The primary mode of interest was the 550 Hz mode since the observed instability frequency in the engine was 525 Hz. The pressure mode shape is shown in Fig. 7. The 550 Hz mode was essentially a half-wave longitudinal mode considering closed/closed acoustic boundary conditions from diffuser inlet to combustor exit. A pressure node appeared to occur at the air swirler/ fuel injector location. The pressure in the diffuser was 180 deg. out of phase from the pressure in the combustor. Note there was some activity downstream of the combustor exit, but calculations performed with varying exit plenum length did not indicate significant changes in the resonant frequency.

The main conclusion drawn from the acoustic analyses is that the single-nozzle combustor rig configuration will have a longitudinal acoustic resonance at about 550 Hz that is very similar to the mode observed in engine data and predicted by Euler analysis of the engine configuration.

EXPERIMENTAL RESULTS

The operating conditions of the combustor could be completely described by the following parameters: diffuser air pressure (P3), diffuser air temperature (T3) and combustor fuel/air ratio (f/a). Values for each of these parameters were chosen to correspond to three different engine operating conditions. These are shown in Table 2. The fuel/air ratio referred to is that estimated at the exit of the combustor and accounted for all of the air flowing into the combustor through the air swirler, primary and dilution holes and liner/bulkhead cooling passages. It was not possible to vary the test parameters independently because of the choked, fixed-area combustor exit.

Inlet Air Pressure, P3 (psia/MPa)	Inlet Air Temperature, T3 (F / K)	Fuel/Air Ratio
70 / 0.48	500 / 533	0.016
110 / 0.76	600 / 589	0.024
175 / 1.21	*771 / 684*	*0.030*

Table 2. Test conditions corresponding to engine operating points. Evaluation-point conditions are in italics.

For the evaluation point operating conditions, an instability was observed at a frequency of 566 Hz (see Fig. 8). The amplitude of this mode at these conditions was +/- 0.39 psi (2.7 kPa). The unsteady pressure results presented here are from the transducer located at 1.9 in. (4.7 cm.) downstream of the combustor bulkhead. The amplitude of the instability increased with increasing fuel/air ratio for fixed P3 and T3. At higher fuel/air ratios, the overall RMS pressure fluctuations were dominated by this single tone. There was significant noise generated in the 100-300 Hz range, although none of it was particularly coherent.

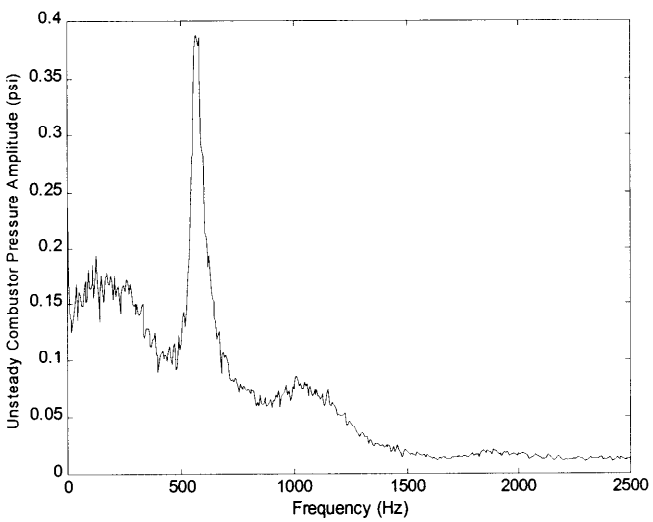


Figure 8. Measured power spectrum of unsteady combustor pressure at x = 1.9 in. for Evaluation Point operating conditions, showing resonance at 566 Hz, with an amplitude of 0.39 pi (0.78 psi p-p).

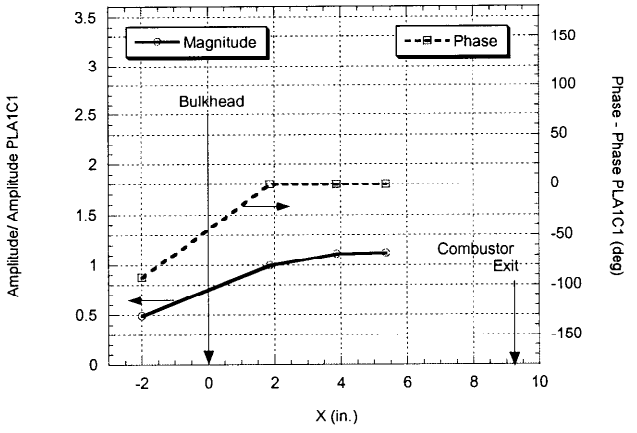


Figure 9. Measured distribution of 566 Hz mode, showing magnitude and phase referenced to pressure measurement PLA1C1 at x = 1.9 inches downstream of the combustor bulkhead.

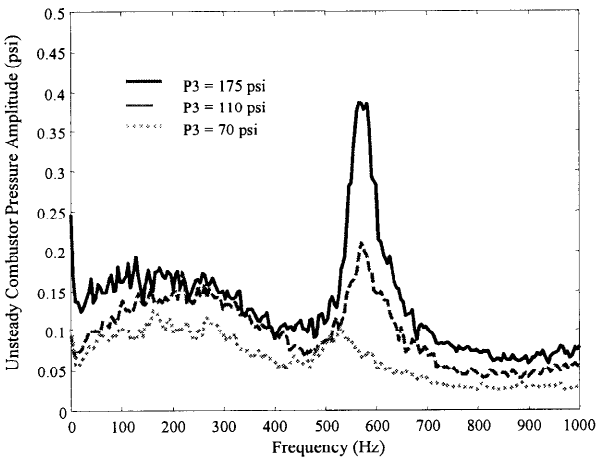


Figure 10. Power spectra of unsteady combustor pressure at three operating conditions corresponding to those in Table 2 showing decreasing amplitude of 566 Hz mode with decreasing power level.

Figure 9 shows the spatial distribution of the unsteady pressure at three locations within the combustor and one location in the diffuser region upstream. Within the combustor, there was no phase difference between measurements at different axial stations, and only small differences in amplitude. Significant 566 Hz signal was also apparent upstream of the combustor, which lagged the combustor pressure by 92 degrees in phase and was smaller in amplitude by a factor of 2. There were no phase or magnitude differences (at 566 Hz) between pressure measurements at equivalent axial, but differing circumferential stations, consistent with a longitudinal acoustic mode. The unsteady pressure in the shroud, just outside the dilution holes was a factor of 2 smaller than that in the combustor and lagged the combustor pressure by approximately 40 degrees

This mode was also observed at the other two, lower-power, operating conditions, although at a smaller amplitudes and lower frequencies, as shown in Fig. 10.

ANALYSIS OF RESULTS

Comparison with Analytical Results

The experimental results can be compared to the analytical results by referencing Fig. 6, which shows the predicted pressure spectrum, and Fig. 8, which shows the measured pressure spectrum. Recall the Euler code model predicted broad acoustic resonances at about 575 Hz and 115 Hz. In the experiment, a broad instability centered near 570 Hz was observed, and there was some incoherent activity indicated near 100-200 Hz. Thus, the agreement appears to be good. The mode shape measured in the experiment was of limited spatial resolution and showed little spatial variation of unsteady pressure amplitude or phase within the combustor chamber itself for the 566 Hz mode (ref. Fig. 9). This was consistent with the mode shape of the 575 Hz mode predicted by the Euler code (ref. Fig. 7). Note both results did indicate a slight decrease in amplitude towards the upstream end of the combustion chamber. The Euler code prediction indicated the unsteady pressure in the diffuser upstream of the combustor would be 180° out-of-phase with the combustor pressure. The experimental results indicated a significant phase shift in the diffuser section, lagging the combustor pressure by about 90 degrees at 566 Hz. This discrepancy is likely associated with the 1-D limitations of the model. For example, it is expected that some level of coupling to the outer shroud passage would occur which is also coupled to the combustor via the air mixing holes. Therefore, some transition of the phase from in-phase with the combustor outside the mixing holes to out-of-phase in the diffuser section is expected in the 3-D problem. The result could be a phase relation in the diffuser section between 0 and 180 degrees.

Note that, because the Euler code is essentially an acoustic calculation, it is fundamentally limited in its ability to calculate the amplitude of the pressure oscillations without the addition of a combustion / acoustic coupling model. In calculations for the engine using a constant relative forcing level, the Euler code indicated that both the frequency and amplitude of the instability should increase with increasing engine power level. This trend was validated with engine data and was also reproduced in the single-nozzle experiment (ref. Fig. 1 and Fig. 10). It is also encouraging that the damping mechanisms present in the calculations produced a broad peak at 575 Hz, much like that seen in the experiment (see Fig. 10).

Comparison with Engine Data

Figure 11 shows a comparison between the fluctuating pressure spectrum in the engine and the single-nozzle combustor at comparable operating conditions. Both data sets were acquired over 10 seconds, and were processed using the same techniques. The frequency of the "target" mode was reproduced within 12%. The amplitude of this mode was matched within 3%. The spectral peak was significantly narrower in the engine data, indicating a more coherent instability. The single-nozzle combustor also exhibited a higher overall level of noise in the signal, especially at frequencies below 350 Hz.

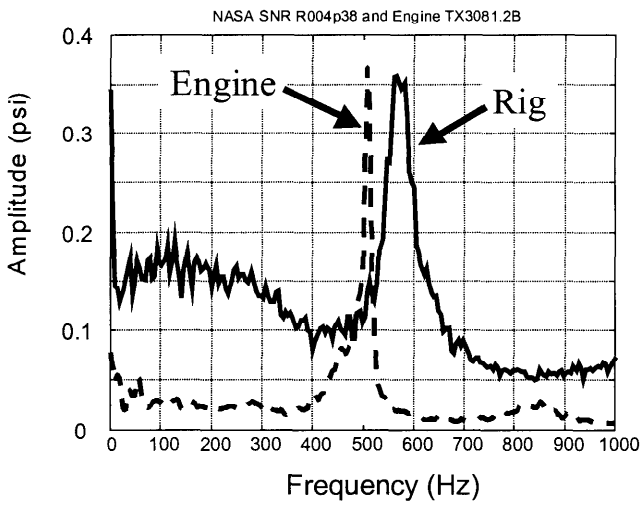


Figure 11. Comparison of engine and combustor rig pressure spectra for Evaluation-Point operation.

CONCLUSIONS AND RECOMMENDATIONS

A methodology for replicating longitudinal combustion instabilities observed in an aircraft engine in a single-nozzle test rig was successfully demonstrated. The experiment reproduced the frequency of the engine instability within 12% and its amplitude within 3%.

Necessarily, the replication procedure must use both predictions from analytical tools and engineering judgements based on prior combustion dynamics studies. A relatively simple, quasi-one-dimensional Euler analysis is satisfactory for the prediction of the dynamics of longitudinal instabilities in geometrically complex burners.

The one-dimensional analytical acoustic tools applied in this program predicted the basic acoustic frequencies of both the engine and the rig within about 10%, and supported a methodology to define a test rig with specific acoustic frequency characteristics. However, because the tool is a one-dimensional analysis, it cannot capture all the dynamic features of this combustor. For example, as reported, it did not quantitatively predict the phase relationship between the combustor and diffuser. The development of an analytical tool would include multi-dimensional capability to either identify other modes or include the influence of parallel acoustic paths (e.g., shroud) is recommended.

An extension of these tools to design sub-scale experiments in which instabilities associated with tangential acoustic modes would also be useful. Inclusion of acoustic-heat release coupling would also increase the tool's utility. Acoustic-heat release coupling models could provide a capability for further reductions in the scale of the experiment, in such parameters as geometric size, flow rates and operating pressure.

In summary, a methodology for design of laboratory combustors, which reproduce combustion instabilities observed in aircraft engine combustors, has been demonstrated. A realistic platform for the development and validation of active combustion instability control systems was constructed, and will be utilized in subsequent programs.

ACKNOWLEDGEMENTS

This study was funded by the NASA-Glenn Research Center. The authors would like to thank the following for their contributions to this effort: Mr. Saumil Shah of Pratt & Whitney, Mr. Paul Hamel, Dr. Donald Hautman, Ms. Andrea Karalus and Mr. James Tracy of United Technologies Research Center, and Mr. Kestutis Civinskas of NASA-Glenn.

BIBLIOGRAPHY

Anderson, T.J., D.W. Kendrick and J.M. Cohen, "Measurement of Spray / Acoustic Coupling in Gas Turbine Fuel Injectors," AIAA Paper 98-0718, Presented at the 36th AIAA Aerospace Sciences Meeting & Exhibit, January 1998, Reno, NV.

Cohen, J.M., N.M. Rey, C.A. Jacobson and T.J. Anderson, "Active Control of Combustion Instability in a Liquid-Fueled Low-NO_x Combustor," ASME Journal of Engineering for Gas Turbines and Power, Vol. 121, No. 2, pp. 281-284, April 1999.

Hibshman, J.R., J.M. Cohen, A. Banaszuk, T.J. Anderson and H.A. Alholm, "Active Control of Combustion Instability in a Liquid-Fueled Sector Combustor," ASME Paper 99-GT-215, Presented at the International Gas Turbine and Aeroengine Congress & Exposition, Indianapolis, IN, June 1999

Paschereit, C.O., E. Gutmark and W. Weisenstein, "Control of Combustion Driven Oscillations by Equivalence Ratio Modulations," ASME Paper 99-GT-118, Presented at the International Gas Turbine and Aeroengine Congress & Exposition, Indianapolis, IN, June 1999

Peracchio, A. A., T. Rosfjord, J. McVey, T. Anderson, A. Banaszuk, J. Cohen, J. Hibshman, C. Jacobson, A. Khibnik, W. Proscia and N. Rey, "Active Control for Marine and Land-Based Aeroderivative Gas Turbine Engines" Volume 1, DARPA Final Contractor Report, UTRC Report 98-16, December 1998.

Wake, B.E., D. Choi, G.J. Hendricks, "Numerical Investigation of Pre-Mixed Step-Combustor Instabilities," AIAA Paper 96-0816, Presented at the 34th AIAA Aerospace Sciences Meeting & Exhibit, January 1996, Reno, NV.

PAPER -5, W. Proscia

Question (A. Annaswamy, USA)

Is peak-splitting due to active control (in general) or phase-shift control (in particular)?

Reply

The plant delay in the sector combustor is much longer than would be necessary on an engine, due to long fuel valve to injector length. This large delay made *broad band* attenuation of pressure oscillations difficult. Because of the long delay between the valve command signal and pressure pulsations, the plant phase changed rapidly over a relatively wide range of frequencies near the resonant frequency, where the plant had considerable gain. The quickly changing phase resulted in positive feedback control on both sides of the attenuation band centered at the resonant frequency, yielding an apparent splitting of the dominant instability mode.

More information is available in ASME Paper 99-GT-215 by Hibshman *et al.*, presented at the ASME Turbo Expo in Indianapolis, Indiana, June 1999.

Question (F. E. C. Culick, USA)

What damping do you have in the Euler code and why do you seem to have more noise predicted by the Euler code than measured in tests?

Reply

The Euler code includes lumped losses to represent pressure losses in the air swirler and at the dump plane. Air flow through linear cooling holes, primary holes, and secondary holes is modeled as a plenum fed with appropriate pressure losses across the linear.

Regarding the differences between the prediction and the tests, the swept-sine spectra are obtained by forcing the heat release in the Euler code (Figures 3 and 6 in the paper) and not by an unstable feedback system. The experimental amplitudes are likely due to the nonlineaityr of the heat release response leading to limit cycle behavior. Also, the Euler code spectra are plotted on a log scale, the experimental results on a linear scale.

This page has been deliberately left blank

Page intentionnellement blanche

ACTIVE CONTROL OF COMBUSTOR PROCESSES

B. T. Zinn*, M. G. Allen, A. Glezer, J. I. Jagoda, Y. Neumeier and J. M. Seitzman
Schools of Aerospace, Mechanical and Electrical and Computer Engineering
270 Ferst Drive
Georgia Institute of Technology
Atlanta, GA 30332-0150, USA

Abstract

This paper describes results of several studies of sensors, actuators and control systems for active control of combustor processes. First, the paper discusses the performance of an adaptive active control system (ACS) for controlling detrimental combustion instabilities. This ACS consists of an observer that determines the time dependent characteristics of the instability in real time, a adaptive controller and a fuel injector actuator. During control, the controller sends a time varying signal to the actuator and the corresponding system's response is determined by the observer in practically real time. These data are then used to determine the optimum control parameters. Results obtained in several studies demonstrate that this ACS can rapidly and effectively damp combustion instabilities without apriori knowledge of the characteristics of the instability.

The second part of the paper discusses two open loop applications of synthetic jets (SJ) aimed to improve combustor mixing processes. Specifically, the paper describes studies whose objective was to improve the mixing between fuel and air and the combustor pattern factor. The results of these studies show that both improvements are possible. These studies also show that SJ can be used to enhance both small and large scale mixing processes and that they significantly improve the pattern factor.

The third part describes a study of the possibility of using an internally mixed fuel atomizer to control the spray characteristics; i.e., independently control the spray's flow rate and mean droplet diameter. Results of experimental and theoretical studies show that by controlling the supply pressures of the air and fuel streams it is possible to independently vary the spray's mean diameter while keeping the fuel flow rate constant and vice versa.

The last part of the paper discusses the development of a wireless, MEMS scale, pressure transducer for high temperature applications; e.g., gas turbines compressors and combustors. The developed pressure transducer is constructed of high temperature ceramic liners that are used in electronic packaging. Using appropriate construction, a cavity is formed between two external liners, resulting in a device that behaves as a capacitor. The capacitor is connected to an inductor that is "deposited" on one of its external liners to form an LC circuit with a specific resonant frequency. When a change in pressure deforms one (or both) of the external liners, the system's capacitance and, thus, resonant frequency change. This frequency change is sensed by an "external" antenna and is "related" to the pressure change, thus providing means for determining the pressure and its wireless transmission.

Introduction

This paper presents the findings of several studies on active control of combustion processes that are being performed at Georgia Tech under several government-sponsored programs. Specifically, this paper discusses: 1) active control of combustion instabilities in rocket motor and gas turbine combustors, 2) application of SJ in active control of mixing processes and the pattern factor in gas turbine combustors, 3) a "smart" fuel injector for controlling combustion processes, and 4) a MEMS, wireless, pressure sensor for gas turbines and related applications. These active control studies were stimulated by 1) the realization that active control systems (ACS) may offer the only or the most rational approach for attaining certain propulsion systems performance goals and 2) recent improvements in computer hardware and software, microelectronics, actuators, sensors and control approaches that provide the capabilities needed for developing advanced ACS for the next generation of propulsion systems. Examples of combustor phenomena that may be controllable using with ACS include combustion instabilities, flame holding, emissions, combustion efficiency and combustor pattern factor. Additionally, ACS could potentially improve engine reliability by, e.g., improved health monitoring and prognostication, and compensating for problems caused by design shortcomings, component failure and aging.

ACS for propulsion systems and gas turbines generally operate in a closed loop and consist of one or more sensors, a controller and one or more actuators. The sensors measure data, e.g., pressures, temperatures, or concentrations. These data are used by the controller to determine the state of the system and generate control signals for the actuators, whose role is to modify the system's operation in a desired way. To meet the expected demands of future ACS, ongoing studies aim to develop advanced sensors, actuators, control approaches and computer hardware and software that will provide capabilities for operation with a wide bandwidth and control of complex phenomena that are not controllable with state of the art technologies. To be practical, the developed ACS will have to be lightweight, integratable with the engine's hardware and control system, and exhibit robustness that will allow them to survive in the harsh engine environment over a long period of time. The remainder of this paper presents results of studies that were undertaken to meet these goals.

*Corresponding author; David S. Lewis Jr. Chair and Regents' Professor, Schools of Aerospace and Mechanical Engineering

Paper presented at the RTO AVT Symposium on "Active Control Technology for Enhanced Performance Operational Capabilities of Military Aircraft, Land Vehicles and Sea Vehicles", held in Braunschweig, Germany, 8-11 May 2000, and published in RTO MP-051.

Active Control of Combustion Instabilities

Combustion instability occurs when a periodic combustion process excites large amplitude oscillations of one or more natural acoustic modes of the combustor[1,2]. Such an instability may be driven by one or more feedback mechanisms that involve interactions between, e.g., acoustic oscillations in the combustor and flow rate oscillations in the air and/or fuel supply, and combustion in vortices and/or shear layers. These feedback mechanisms drive acoustic oscillations when the magnitude of the phase difference between the heat release and pressure oscillations is smaller than ninety degrees[1]. Combustion instability occurs when the driving by the oscillating combustion process is larger than the acoustic damping by, e.g., viscous processes, acoustic liners and acoustic energy radiation out of the combustor. An instability generally starts as a small amplitude oscillation whose amplitude grows exponentially in time until it stabilizes at some constant amplitude, limit cycle, oscillation. Combustion instabilities are undesirable because they generally increase the mechanical loads on the combustor wall and engine components, excite vibrations in various components and significantly increase convective heat transfer rates to the combustor wall and adjacent components. Alone or in combination, these phenomena shorten component life and can cause catastrophic engine failure.

Until recently, passive approaches were used to control combustion instabilities[2]. These often consisted of changing the combustor design and/or operating conditions in an effort to decrease the combustion process driving and/or increase the damping of the excited acoustic modes, and prevent amplification of unstable acoustic modes. These changes included, e.g., modifications of the reactants injection systems to make them less responsive to combustor disturbances, elimination of sharp corners and "sudden" area changes to minimize shear layer formation and, thus, periodic combustion in vortices, changing fuel properties, and the addition of damping devices, e.g., acoustic liners, to increase the system's acoustic damping. Unfortunately, due to inadequate understanding of the damping and driving processes, development of passive control approaches often required lengthy and costly research and development programs that did not produce satisfactory results. Furthermore, passive control approaches that worked well in one system have, on occasion, reduced combustor stability when applied to another system, thus clearly demonstrating the lack of understanding and shortcomings of passive control approaches.

The persistent appearance of combustion instabilities in a wide variety of combustors and the inability to "design" them out of the system or rapidly damp them after their unexpected excitation stimulated efforts to develop ACS for unstable combustors in the early 1980s. Since most of these efforts are discussed in several review articles[1,3,4], the discussion of this subject matter in this paper will focus on the ACS developed at Georgia Tech[1,5]. These efforts started with the development of an ACS for unstable liquid rockets and subsequently demonstrated that the developed ACS can also control combustion instabilities in gas turbine combustors. The goal of the Ga. Tech studies was to develop a practical ACS that could rapidly damp large amplitude, nonlinear, high frequency combustor oscillations whose characteristics are not known a priori. To meet this goal, the developed ACS needed capabilities for 1) determining the unknown, (possibly) time varying, characteristics of the instability; i.e., the amplitudes, frequencies and phases of several combustor modes, in real time, 2) determining the control signals needed to damp one or more unstable combustor modes, 3) providing large actuation, and 4) damping high frequency oscillations.

The original ACS developed to meet these goals is shown in Fig. 1. It consists of a pressure sensor, an observer, a controller and a fuel injector actuator. The sensor measures the combustor pressure and sends its output to the observer, which analyzes the measured pressure to determine the amplitudes, frequencies and phases of the unstable combustor modes in practically real-time. The observer's output is then sent to the controller where the required control signal for the modes of interest are either determined adaptively[6] or with the aid of data measured in open loop combustor controllability tests[1,5]. The generated control signals (for different modes) are then synthesized into a time dependent control signal that is sent to the fuel injector actuator. The latter modulates the injection rate of a secondary fuel stream to generate heat release oscillations within the combustor that are out of phase with the unstable pressure oscillations and, thus, rapidly damp the combustion instability.

The development of this ACS was guided by the knowledge, based upon Rayleigh's criterion[1], that heat addition oscillations damp acoustic pressure oscillations when the two are out of phase. Thus, it was assumed that the instability consists of a number of independent modes whose amplitudes, frequencies and phases are not known a priori, and may change with time. To damp such an instability, it was necessary for the ACS to track the characteristics of each unstable mode in real time, generate a control signal for damping each mode separately, and modulate the injection rate of the secondary fuel stream at the frequency of each unstable mode with the appropriate amplitude and a phase delay.

Initially, an attempt was made to use FFT to analyze the measured pressure signal. When the FFT failed to accomplish this in real time, an observer "algorithm" was developed[7]. This algorithm assumes that the measured combustor pressure $P_m(t)$ can be expressed in the following Fourier-like series:

$$P_m(t) = \sum_{n=1}^{N} \left[a_n(t) \sin(\varpi_n(t)t) + b_n(t) \cos(\omega_n(t)t) \right] \quad (1)$$

whose frequencies $\omega_n(t)$ and amplitudes $a_n(t)$ and $b_n(t)$ are unknown, and may be time dependent. These unknowns are determined in an iterative procedure that starts with an assumed value of the unknown frequency $\omega_n(t)$ and rapidly converges to the correct values of the unknown coefficients $\hat{a}$ and $\hat{b}$ and the frequency $\hat{\omega}$[7]. This procedure first determines the characteristics of the mode with the largest amplitude. Once this mode has been identified, it is "subtracted" from the measured signal P_m, see Eq. 1, and the above described procedure is applied to the resulting signal to determine the amplitude, phase and frequency of

the largest amplitude mode in the "remaining" signal. This procedure is repeated until the characteristics of a desired number of modes are determined. An alternate procedure for simultaneous determination of the characteristics of a number of modes is described in Ref. 7. Fortunately, results obtained to date strongly suggest that successful damping of an instability may only require identification and active damping of one or two unstable modes, which can be accomplished by this observer in practically real-time.

Another important contribution of this program was the development of a unique fuel injector actuator that can modulate the flow rate of the "control" fuel stream over a large frequency range. It uses a magneto-strictive actuator, i.e., Terfenol D, which changes its length in response to changes in the intensity of an imposed magnetic field. The latter is controlled by the electric current in a coil that is wound around the actuator. As the length of the actuator varies, it changes the cross sectional area in the flow path of the "controlled" fuel stream into the combustor, thus changing the flow rate of this fuel stream in a desired manner by effectively opening and closing a fuel valve. To date, fuel injector actuators were developed and operated that are capable of modulating the flow of gaseous fuels over a 0-2000 Hz frequency range[5] and liquid fuels over a 0-3000 Hz range[8]. Since the upper limits of these frequency ranges are considerably higher than those of any other known fuel injector, these fuel injector actuators provide the propulsion community with capabilities for controlling high frequency combustion instabilities.

Typical performance of this ACS while actively (and adaptively) controlling a large amplitude, 100 Hz instability is shown in Fig. 2. For the first two seconds of this test, the pressure oscillations in the combustor are uncontrolled, oscillating with a limit cycle amplitude of over 2psi. After two seconds, an algorithm to automatically identify the proper control phase is invoked. This identification process permits control without costly open loop testing that is typically required for closed-loop active control. In this case, the identification process spans two seconds, and then control is applied. When the control is activated, the unstable pressure oscillations are reduced by approximately 15dB within ten cycles, or 100 milliseconds[6]. Similar performance was demonstrated on small and large-scale low NOx gas turbine combustors, at atmospheric and high pressure test conditions.

In summary, the above-discussed research has clearly demonstrated that ACS potentially offers a very promising approach for controlling combustion instabilities in propulsion systems and gas turbines.

Synthetic Jet Actuators for Combustor Mixing and Pattern Factor Control

This section describes the application of synthetic jets (SJ) to improve combustor mixing processes and, thus, combustor performance. For example, poor mixing in gas turbine combustors can produce a non-uniform distribution of equivalence ratio, which, in turn, may increase emissions and specific fuel consumption. Mixing problems can likewise lead to "hot" spots at the turbine inlet and increase the likelihood of combustion instabilities. Inefficient mixing may also extend the combustion process into the turbine, resulting in an unacceptable operating condition.

SJ[9] may offer an attractive approach for controlling combustor mixing processes through open or closed loop excitation of large and/or small-scale structures in the combustor flow. A schematic of a SJ actuator is shown in Fig. 3. It consists of a cavity whose lower wall is a membrane that is oscillated at a desired frequency by, e.g., a piezoelectric transducer. The cavity is connected to the flow above by a small orifice. As the membrane moves downward during the first half of the cycle, the cavity's pressure decreases and gases from all directions flow into the cavity (in a "sink-like" manner). As the membrane moves upward during the second half of the cycle, the gases that entered the cavity earlier are ejected as vortex rings (in axisymmetric SJ). The membrane is often driven at a resonant frequency of the actuator to maximize the strength of the generated vortices. Continuous operation of the actuator forms a train of vortical structures that coalesce into a SJ. The vortical structures that synthesize each SJ scale with the oscillation frequency of the cavity's membrane and can be adjusted to match, and directly interact with, small-scale eddies within the equilibrium range of the embedding shear flow. Large-scale flow structures and global entrainment away from the cavity are affected by amplitude modulation of the membrane's excitation waveform.

This section describes studies that are concerned with two potential applications of SJ in the control of combustor mixing processes. The first involves installation of SJ in the fuel injector to improve the mixing of fuel and air, especially under extreme conditions where passive mixing techniques fail. An example would be high altitude relight conditions, when there is little airflow, and devices such as swirlers do not produce rapid fuel-air mixing. A second goal is to gain control authority over the spatial distribution of fuel in the combustor, which may be needed to compensate, for example, for fuel injector problems.

The second study involves the use of SJ to control the temperature profile at the combustor exit. Detailed tailoring of pattern factors in the flow entering turbines in future turbine engines is gaining importance because of the higher temperatures of the combustion products leaving the combustor. At the same time, as permissible turbine entrance conditions approach stoichiometric flame temperatures, less dilution air is available to enhance mixing. Therefore, alternative techniques have to be found to replace the mixing effects of cross flow jets of cold, high pressure air from the compressor, which are currently used to enhance mixing downstream of the combustor.

Fuel-Air Mixing:

The present work focuses on mixing enhancement between coaxial round jets. The traditional approach to small-scale mixing enhancement in such free shear flows has been *indirect* and has relied primarily on the manipulation of large-scale, global instability modes of the base flow upstream of mixing transition. More efficient control of mixing in fully turbulent shear flows might be achieved by direct (rather than hierarchical) control of both the large-scale entrainment *and* the small-scale mixing processes. The present work focuses on mixing enhancement based on concurrent manipulation of *both* the small- and large-scale dynamical processes and the coupling between the large- and

small-scale motions in the shear and mixing layers of the coaxial round jets.

Two similar experimental systems, one focusing on velocity measurements and the other on scalar mixing, have been developed to ascertain the efficacy of the SJ. In both experiments, the outer boundary of the annular jet is 2.54 cm in diameter, while the inner air jet is produced with a 1.4 cm diameter central tube having 1 mm wall thickness. This yields an inner/outer flow area ratio of 0.5. In the velocity facility, a nozzle having a contraction ratio of 36:1 forms the outer boundary of the annular flow. In the mixing facility, the outer boundary of the annular jet is formed by a simple 2.54 cm diameter tube, and the annular gas stream is acetone seeded into air (~23% acetone by volume). Three inner/outer velocity ratios (nominally 0.35, 0.65, and 1.4) have been investigated, with some results for $U_I / U_o = 0.65$ presented here. The total volume flow rate of the combined jets is nominally constant, and is equivalent to a uniform jet issuing out of the combined flow area $A_o + A_i$ at 11 m/s (Re_{DH} = 7700 based on the hydraulic diameter). Nine individually controlled actuators, equally spaced around the outer circumference of the main flow, produce SJ. Each SJ issues from a rectangular, arc-shaped orifice having a width and length of 0.5 and 9 mm, respectively. The carrier waveform of the actuators is nominally 1.2 kHz (near their resonant frequency), and the amplitude, duty cycle, and relative phase of each of the modulating waveforms of the individual actuators are computer controlled. The flow mechanisms induced by the excitation are inferred from detailed phase-locked measurements of the velocity field using two-component hot wire anemometry, and the resultant mixing of a passive scalar is studied using planar laser-induced fluorescence (PLIF) of the acetone seeded into the annular jet.

The power spectra of the streamwise velocity at the radial location where $U(x,r)/U_{max}(x) = 0.5$ for $U_I / U_o = 0.65$ are shown in Figs. 4a and b for high frequency forcing only and pulse-modulated forcing, respectively. The corresponding spectral distributions of the unforced flow are also shown for reference in each figure. The flow scales that are introduced by the forcing are apparent in the figure. High frequency forcing results in spectral peaks at the forcing frequency (1180 Hz) and some of its higher harmonics. The amplitude of the spectral peak at the forcing frequency decreases with downstream distance, but is still discernible compared to the background flow, even at $x / D_o = 5$. Amplitude modulation of the excitation waveform, with a modified square wave, results in spectral peaks at the carrier and modulation frequencies as well as at several harmonics in the near field. At $x / D_o = 2$, the high-frequency spectral peaks correspond to the carrier forcing frequency and its sidebands. The peaks at the carrier and modulation frequencies are still discernible at $x / D_o = 5$. The regions of the spectra with slope m = -5/3 indicate that the forcing frequency is within the equilibrium range of the flow.

Cross-stream distributions of the streamwise and radial velocity components are measured in a plane that intersects the jet centerline and passes through the azimuthal center of an actuator at the edge of the jet on one side and between two actuators on the other side. The measurement domain is $x / D_o \leq 5$ with increments of $\Delta x / D_o = 0.25$ and $\Delta r / D_o = 0.025$. For the amplitude-modulated cases, data are acquired phase locked to the modulation waveform at 72 equal phase increments. Figure 5 shows raster plots of the mean streamwise velocity for $U_i / U_o = 0.65$ and $x / D \leq 3$ with all three forcing conditions. The increase in jet spreading and decrease in annular jet velocity are apparent. While the mean effect is not as dramatic with amplitude modulated forcing, the raster plot of phase-averaged streamwise velocity shows formation of well-defined large-scale structures. The effect of unmodulated excitation input on radial distributions of U, u', and V for $U_i / U_o = 0.65$ at several streamwise stations is shown in Figs. 6a,b, and c. The corresponding distributions for the unforced flow are shown for comparison using open symbols. Since the jet actuators are placed near the radial edges of the outer jet, their effect on the mean streamwise velocity is most apparent through a radial expansion of the jet flow field (more than $0.1D_o$ at $x / D_o = 0.04$). As mentioned above, the actuation is asymmetric left to right in the distributions in Fig. 6. This asymmetry is apparent at $x / D_o = 0.25$ and 1 where the jet spreads radially towards the active actuator on the right. Davis and Glezer[10] obtained similar spreading by azimuthal non-uniform forcing having a three-fold symmetry of a single jet. The forcing leads to an increase in u' throughout the entire width of the annular flow for $x / D_o < 1$ but does not increase the turbulence in the core flow. By $x / D_o = 1$, the differences between distributions of U and u' in the forced and unforced flows are reduced and by $x / D_o = 3$ the unforced and forced flows are quite similar with less turbulent intensity in the forced flow. The reduction in u' downstream with forcing is ostensibly due to increased dissipation in the near field. The radial velocity is especially significant to the mixing of the two streams because it leads to entrainment of the jets. In Fig. 6c the radial velocity away from the jet centerline is taken to be positive to the right of the centerline and vice versa on the left. The strongest effect of the forcing occurs near the jet exit plane ($x / D_o = 0.04$). In the unforced flow, the radial velocities in the core and annular flows are of opposite sign and are directed towards the wake region of the pipe wall. In the presence of forcing, the mean radial velocity in both the core and annular flows is directed outward except within the wake and near the jet actuators. This mean outward radial velocity results from the time-periodic entrainment by the SJ. Time series of the radial velocity (not shown), indicate that in the wake region of the center tube, while the mean radial velocity is nearly zero, the instantaneous velocity oscillates at the forcing frequency resulting in the formation of vortical structures in the mixing region.

The effect of actuation on mixing is seen in the images of Fig. 7, which compares, instantaneous, side view images up to $x/D_o = 3$, for the three forcing cases with $U_i/U_o = 0.62$. The intensity of each pixel is converted to a local mixture fraction (f), which is defined as the ratio of the mass of fluid that originated in the annulus at the jet exit to the total mass in a measurement volume (pixel). The unforced case (Fig. 7a) has large amounts of pure annular fluid persisting downstream. The annular fluid just begins to mix into the center of the flow at $x/D_o = 5$ (not shown). The high frequency forcing (Fig. 7b) produces an enhancement of the jet growth and a broadening of both mixing layers (between the ambient and the annular jet, and between the annular and inner jets). The annular fluid is mixed into the center of the flow more rapidly, and the regular structures visible at the

outer edge correspond to the individual pulses of the high frequency forcing. The amplitude modulation result (Fig. 7c) shows what appear to be large, coherent structures that correspond to the modulation frequency. These periodic scalar fields are convected at a velocity of the order of the mean flow.[11] The large-scale structures significantly increase the entrainment between the central jet and the annular flow, and are able to penetrate to the jet centerline within a few jet diameters.

One measure of mixing effectiveness of the SJ is the rate at which pure annular fluid becomes mixed. The axial variation of the unmixed fuel (defined as $f \geq 0.95$) for unforced and forced cases was determined from radial and azimuthal integration of data similar to that shown in Fig. 7. This comparison shows that high frequency, forcing, relative to the unforced case, greatly increases the rate at which pure fluid becomes at least partially mixed, and that amplitude modulation further increases the rate of fuel mixing. In the latter case, virtually all the pure fluid is gone as early as $x/D_o = 0.5$, while the high frequency forcing and unforced flows do not achieve this until farther downstream. The improved effectiveness of amplitude modulated forcing results from the increased entrainment produced by the large-scale structures in this case. The evolution of these structures is clearly seen in Fig. 8, which compares the velocity and mixing measurements at selected phases of the amplitude modulation.

Pattern Factor Control:

Next, the results of a study of the application of SJ in the control of pattern factor (combustor-exhaust/turbine- inlet temperature profiles) are described. It was conducted in the facility shown in Fig. 9a. It consists of a rectangular chamber (450mm x 92mm x 75 mm) with provisions for optical and probe access. Separate streams of room temperature air and combustion products from a premixed methane-air flame are introduced in parallel streams into the chamber. SJ enter through an orifice plate in the chamber floor, 145 mm downstream of the its entrance. These jets are generated by a piston in a cylinder below the orifice plate. Temperature distributions at the exit to the chamber are measured with a K-type thermocouple rake that can be translated laterally across the flow. Hot film anemometry is used to measure the SJ velocities.

The temperature stratification in the flow without actuation is clearly seen in the profile shown in Fig. 9b, where different temperature ranges are represented by gray scales. As the mixing between the layers of flow at different temperatures increases, the temperature profile becomes more uniform. This mixing is quantified using an entropy method, which utilized the fact that entropy increases with mixing. Each temperature distribution, therefore, is associated with a given level of entropy, or more precisely, an entropy difference (Δs) between the measured system and a (hypothetical) uniformly mixed system of the same average temperature. A fractional improvement in mixing (ζ) is then defined as the difference between Δs without actuation and that with actuation, as a fraction of the non-actuated Δs. Thus, ζ varies between 0 and 1, and increases as the mixing enhancement by the SJ improves.

Tests to date have shown that mixing can be very significantly enhanced with the SJ[12]. This enhancement increases with the degree of actuation, measured as the ratio between the *peak* velocity from the SJ and the mean velocity of the main flow, see Fig. 10. Mixing improves once the jet velocity exceeds twice the main flow speed and the effect levels off (at a nearly uniform composition) when that ratio reaches ten. So far, changes in frequency (from 2 to 30 Hz) appear to have no effect on mixing. Furthermore, test with plates having different orifices, such as rows of circular orifices and long narrow slots of same total aperture areas have shown that mixing is only weakly dependent on actuator orifice shapes or orientation (crosswise vs. streamwise relative to the flow).

The mechanism by which these relatively small SJ can so significantly affect the temperature distribution in the much larger main flow is currently being investigated. High speed shadowgraphy is being utilized to visualize the interaction between the SJ and the main flow. Mie scattering techniques are planned to quantify the local degree of mixing between hot and cold flow in the region where SJ and main flow interact, and planar laser-induced fluorescence of acetone injected into the actuators will be used to measure the degree of dissipation of the synthetic jet flow into the main stream.

Internally Mixed Liquid Atomizer for Active Control of Spray Characteristics

The quality of combustion processes, e.g. ignition, flame stability, efficiency and emissions, in liquid fueled engines, strongly depends on the atomization quality[13]. There is evidence that the characteristics of the combustion process for a given operating condition may be optimized by burning a spray that is characterized by a specific droplet size, which may not be the droplet size generated by the injector. For example, Rink and Lefebvre[14] report that fine atomization causes a decrease in the production of unburned hydrocarbon because of the reduction in evaporation time. This, in turn, increases the time available for NO reactions in the post flame region to proceed towards equilibrium, thus increasing NO_x emissions. These and related studies strongly suggest that a combustor's performance could be optimized by using fuel atomizers that could be controlled to produce sprays with desired properties.

The objective of the research described in this section is to develop a fuel atomizer that could be actively controlled to provide a fuel spray with desired properties over a wide range of operating conditions of airborne gas turbines. Such an injector would overcome the shortcomings of the state-of-the-art pressure and air-blast atomizers that produce poor sprays during some operating conditions; e.g., startup and idling. Furthermore, active control of fuel droplet size at any desired fuel flow rate during a flight can be used to control UHC, NOx and CO emissions.

A schematic of the investigated internally mixed atomizer is shown in Fig. 11. Liquid fuel is axially supplied to the atomizer at its upstream end and air is injected through series of holes symmetrically distributed around the injector's periphery downstream of the liquid entry point. As the air expands within the injector and occupies an increased fraction of the available cross sectional area, the cross

sectional area available to the liquid is reduced. This is accompanied by acceleration of the liquid phase and, thus, an increase in its kinetic energy, which leads to liquid atomization. Also, the relative motion between the phases produces shear forces at their interfaces that "strip" liquid droplets from liquid ligaments, resulting in further liquid atomization. Together, these processes produce a mixture of liquid ligaments and droplets and air inside the injector[15].

The performance of the developed injector has been investigated in an experimental setup specifically developed for this purpose. It consists of a vessel, with windows, that can be operated over a wide range of pressures. The injector is installed at the top of the vessel and the injected liquid is collected at the bottom. The windows provide optical access for determining the properties of the spray. To date, series of tests were conducted to determine the dependence of the spray properties upon the amount of atomizing air, the liquid supply pressure and the test chamber pressure[15]. This study also sought to determine the mode of operation that would permit control of the characteristics of the generated spray.

A performance map of the investigated injector is shown in Fig. 12. It shows the dependence of the Sauter Mean Diameter (SMD) of the generated spray upon the liquid flow rate and supply pressure. It should be noted that in these experiments the liquid flow rate was controlled by varying the flow rate of atomizing air. The data in Fig. 12 show that by varying the liquid supply pressure while keeping the liquid flow rate constant, i.e., moving along the vertical line in Fig. 12, which requires variation of the air flow rate, one can vary the droplet sizes while keeping the liquid flow rate constant. Figure 12 also shows that simultaneously changing the liquid supply pressure and flow rate (again, by varying airflow rate) while moving along the horizontal line in Fig. 12 permits operation with a constant droplet size over a range of liquid flow rates. Thus, for a given combustor pressure, the injector's performance can be controlled by changing the airflow rate and the liquid supply pressure simultaneously[15].

In parallel efforts, a model for predicting the performance of the above-described injector is being developed. The objective of this study is to develop an analytical tool that could be applied in the design of improved internally mixed injectors and to predict the injector's flow and spray characteristics, e.g., the liquid flow rate and mean droplet size, under different operating conditions. The developed two phase flow model assumes that the flow is one-dimensional, wall friction is negligible, the liquid flow is isothermal incompressible, the flows are uniform and steady and the air behaves as a perfect gas. Also, the airflow injection ports are approximated by an annular slit of a finite width at the injector's wall. Finally, it has been also assumed that as the two phase flow evolves the liquid break ups into droplets in a manner that maintains the local Weber number ($We = \rho_a V_r^2 D/\sigma$; i.e., the ratio of the inertial and surface forces) at a value of 10 and that the droplets do not coalesce to form larger droplets[16].

The system of equations governing the two-phase flow in the injector's passage are the air mass conservation, liquid mass conservation, combined air and liquid momentum conservation, combined air and liquid energy conservation and liquid energy conservation. The interaction between the phases, which appears only in the liquid energy equation, is modeled as a drag force acting on the liquid. These equations are solved numerically to determine various flow and spray properties inside the injector[16].

Figure 13 compares the predictions of the model with measured data. Figure 13a shows that the measured and predicted liquid flow rates are in good agreement, while Fig. 13b shows that measured and predicted mean droplet diameters are in good qualitative agreement[16].

In summary, the results obtained to date strongly suggest that the developed, internally mixed, atomizer can be used to control fuel spray properties. Such control can be attained by simultaneously varying the liquid supply pressure and air flow rate. It has also been shown that a developed theoretical model reasonably predicts the injector's performance.

High Temperature Ceramic Pressure Sensors

Micromachined silicon pressure sensors are widely utilized in industry. In general, the pressure sensor design is based on a flexible silicon membrane as the sensing element, coupled with silicon piezoresistors or a capacitive structure and silicon circuitry for data retrieval. These sensors are well developed and have been documented extensively in the literature[19]. However, micromachined silicon sensors are typically subject to operating temperature limitations due to a variety of factors, including piezoresistive temperature sensitivity and the poor mechanical properties of silicon at higher temperatures. Thus, applications such as sensing pressure in turbine engine compressors require development of other types of sensors that offer high temperature stability.

In the literature, potential high-temperature materials have been investigated as an alternative to silicon processing. Silicon carbide, polycrystalline diamond and ceramic materials have been reported as high-temperature materials for sensor fabrication[20,21]. Silicon carbide pressure sensors employ the flexible membrane design and use piezoresistors to measure pressure changes. Silicon carbide circuitry is also possible to retrieve the pressure data. Polycrystalline diamond pressure sensors also employ a flexible membrane and piezoresistors. These technologies show great promise for integrated high temperature pressure sensors, but their manufacturing infrastructure is not nearly as well developed as that for silicon and electronic packages for silicon.

The microelectronics packaging industry offers a well-developed ceramic packaging procedure using ceramic co-fireable tape. The ceramic tape consists of alumina particles and glass particles suspended in an organic binder, which is subsequently fired to form a ceramic structure. In general, this type of tape is referred to as low temperature co-fireable ceramic (LTCC) because the curing (firing) temperature is only 900°C[22]. Ceramic tapes made solely from alumina particles are also available and have curing temperatures above 1600°C. Besides high temperature stability, the co-fired ceramic tape has good mechanical properties that allow membrane designs similar to those of the silicon pressure sensors. From our investigations, the ceramic tape is an excellent choice for the fabrication of pressure sensors for high temperatures. By incorporating a passive wireless readout technology with the sensors[23], it is possible to also circumvent the issues associated with contacts and wired connections in a high temperature environment. The focus of this study has been to develop such a sensor for turbine compressor pressure sensing.

A schematic of the wireless pressure sensor concept is shown in Fig. 14. The sensor consists of a sealed cavity, ideally containing vacuum, on which two capacitor plates are formed. If either the top or the bottom (or both) bounding sides of the cavity are made of a flexible ceramic diaphragm, the value of this capacitor will change with pressure. In order to measure this capacitance change, a resonant technique is employed, in which a planar spiral inductor coil fabricated using ceramic-based integral passives techniques is electrically connected to the capacitor. These components form a passive resonant LC circuit, where the resonant frequency is given by[24]:

$$f_o = \frac{1}{2\pi\sqrt{L \bullet C(P)}} \qquad (2)$$

Thus, as the external pressure increases, the capacitance increases and the resonant frequency of the LC circuit will decrease.

To achieve passive wireless telemetry, the circuit is placed in proximity to an external loop antenna coil and the impedance and phase response of the antenna coil are monitored as a function of frequency by an impedance meter. At frequencies far from the sensor frequency (and below the self-resonant frequency of the antenna itself), the antenna appears as an inductance, with a rising impedance response with frequency and a phase shift of +90 degrees. At the sensor resonant frequency, the antenna impedance decreases and the phase response of the antenna drops from +90 degrees.

Although the magnitude of the phase peak depends upon the details of the specific sensor-to-antenna coupling, there are configurations in which the peak position (i.e., frequency) dependencies are negligible. Thus, this wireless data retrieval scheme could also work for a sensor in motion within the antenna (e.g., mounted on a moving part). In addition, it is possible to have an array of such sensors, with each sensor designed to have a distinct 'center' frequency (i.e., frequency given by equation (1) under zero applied pressure), with the number of such sensors limited by the available frequency bandwidth.

Pressure Sensor Design and Fabrication:

The design of the sensor involves the creation of the flexible membrane, the sealed cavity and the integration of the LC resonant circuit. To create the flexible membrane, sealed cavity, and ultimately the capacitor, a multilayer structure is required, see Fig. 15a. A typical sensor is fabricated using 4 sheets of Dupont 951AT ceramic tape[22]. The tape consists of alumina and glass particles suspended in an organic binder. Each sheet is cut to a size of 2.5 inch square with a thickness of ~100μm each. Of the four sheets, two are punched to create the via for the sealed cavity. The diameter of the via is 7.6mm. The four layers are aligned in a press mold that consists of two aluminum plates that are 2.5 inches square and 0.25 inches thick. The ceramic sheets are laminated together in a hot vacuum press for 10 minutes at a press temperature of 70°C and a press force of 9.38 tons under ambient vacuum. After lamination, the sample is cut down to a 1.5 inch square before firing. The sample is fired in a box furnace in air for 30 minutes at 500°C to bake off the organics and then for 20 minutes at 850°C to melt the glass particles and harden the sample.

To create the LC circuit, the top side of the sensor is DC sputtered with an electroplating seed layer of 500Å of titanium followed by 3600Å of copper. Shipley 5740 photoresist is used to create a plating mold that will define the inductor coil and one electrode of the parallel plate capacitor. Using a copper electroplating bath, copper is electroplated onto the seed layer to a thickness of ~28μm and the plating mold and seed layer are removed using wet etching. On the back side of the sensor, the other electrode of the capacitor is patterned using a DC sputtered titanium/copper layer sputtered through a shadow mask. Contact from the outer arm of the inductor coil on the top side of the sensor to the capacitor electrode on the back side is made using Dupont 6160 silver-filled external conductor paste for co-fireable tapes. A diagram of the fabrication process is given in Fig. 15 and a photo-micrograph of a fabricated sensor is given in Fig. 15e.

Sensor Operation:

An antenna coil is placed in the chamber in proximity the sensor and connected to an impedance meter via feedthroughs from a pressure/temperature chamber. The impedance meter reads the phase value of the antenna coil over the frequency range. At atmospheric pressure, the phase of the antenna is +90° except at the resonant frequency of the sensor. At the resonant frequency, the capacitor of the sensor couples to the antenna coil and causes a dip in the phase from +90°. As the chamber pressure increases, the ceramic membrane will deflect causing an increase in the sensor capacitance and a decrease in the resonant frequency and thus, the dip in the phase will shift down in the frequency range.

Wireless pressure and temperature tests were performed using an HP4194A impedance analyzer, a Parr 4570 pressure vessel for high pressure tests, and a VWR vacuum oven for low pressure and temperature tests. Figure 16 shows the raw data obtained, phase versus frequency, for zero and full-scale (1 bar) applied pressure for a single sensor. Figure 18 presents the raw data of Fig. 16 at a variety of pressures between 0 and 1 bar, at 25°C and 200°C. For the results in Figs. 16-17, the pressure sensor was designed to have an electrode radius of 5mm, a membrane thickness of 96μm, and an effective electrode gap of 217μm. The sensitivity of the sensor was calculated from the measured data to be 2.6MHz/bar. The same sensor was tested at 25°C and 200°C and except at low pressures, little difference is seen in sensor performance between the two temperatures. Higher temperatures may have a more significant effect. The highest temperature at which sensors have been successfully tested is currently 400 °C.

Figure 18 illustrates the array concept. Three sensors were tested simultaneously using the same antenna coil. Each sensor was designed for a different center frequency. The variation in peak height for the three sensors reflects different degrees of sensor/antenna coupling (i.e. proximity of the sensor to the antenna coil). However, to determine pressure, only the frequency of the peak is required. Since each sensor has a different carrier frequency and thus a different frequency shift due to pressure, each sensor can be monitored simultaneously by tuning into a particular sensors frequency band.

Acknowledgments

The research described in this paper was supported by AFOSR Contract No. F49620-99-1-0142 (monitored by Dr. Mitat Birkan), DOE/AGTSR Contract No. DE-FC21-92MC29061 (monitored by Dr. Lawrence Golan) and Army MURI Contract No. DAAH04-96-1-0008 (monitored by Dr. David Mann). Special thanks to Dr. Larry Matta who significantly contributed to assembling and editing of the paper. Finally, the authors would like to acknowledge the contributions of graduate students Staci Davis, Jennifer English, Clifford Johnson, Michael Fonseca, Brian Ritchie, Brian Scully, Dilip Mujumdar and Abhijit Kushari to the reported studies.

References

1. Zinn, B. T. and Neumeier, Y., "An Overview of Active Control of Combustion Instabilities," AIAA-97-0461, 35th Aerospace Sciences Meeting and Exhibit, Reno, NV, January 6-9, 1997.
2. Harrje, D. T. and Reardon, F. H., "Liquid Propellant Rocket Combustion Instability," NASA SP-194, 1972.
3. McManus, R. K., Poinsot, T. and Candel, S. M., "A Review of Active Control of Combustion Instabilities," Progress in Energy and Combustion Sciences, Vol. 19, pp. 1-29, 1993.
4. Candel, S. M., "Combustion Instabilities Coupled by Pressure Waves and Their Active Control," 24th Symposium (International) on Combustion, Sydney, Australia, July 1992.
5. Neumier, Y. and Zinn, B. T., "Experimental Demonstration of Active Control of Combustion Instabilities Using Real Time Modes Observation and Secondary Fuel Injections," Proceedings of the 26th International Symposium on Combustion, Naples, Italy, July 28, 1996
6. Johnson, C.E., Neumeier, Y., Lee, J.Y., Neumaier, M. and Zinn, B.T., "Suppression of Combustion Instabilities in a Liquid Fuel Combustor Using a Fast Adaptive Control Algorithm," AIAA-2000-0476, 38th Aerospace Sciences Meeting & Exhibit, Reno, NV, January 10-13, 2000.
7. Zinn, B. T. and Neumeier, Y., United States Patent No. 5,719,791, "Methods, Apparatus and Systems for Real Time Identification and Control of Modes of Oscillations," Feb. 17, 1998
8. Neumeier, Y., Lubarski, E., Heising, R., Israeli, O., Neumaier, M., and Zinn, B. T., "Liquid Injector Actuator for Control of Combustion Instabilities and Processes," 34th AIAA/ASME/SAE/ASEE Joint Propulstion Conf. And Exhibit, Cleveland, OH, July 13-15, 1998..
9. Smith, B. L. and Glezer, A., "Vectoring and Small-Scale Motions Effected in Free Shear Flows using Synthetic Jet Actuators, " AIAA Paper 97-0213.
10. Davis, S. and Glezer, A., "Mixing Control of Fuel Jets Using Synthetic Jet Technology Velocity Field Measurements" AIAA-99-0447, 37th AIAA Aerospace Meeting, Reno, NV, January 1999.
11. Ritchie, B. and Seitzman, J., "Mixing Control of Fuel Jets Using Synthetic Jet Technology Scalar Field Measurements", AIAA-99-0448, 37th AIAA Aerospace Meeting, Reno, NV, January 1999.
12. Chen, Y., Scarborough, D., Liang, S., Aung, K., and Jagoda, J., "Manipulating the Pattern Factor Using Synthetic Jet Actuators," AIAA-2000-1023, 38th Aerospace Sciences Meeting, Reno, NV, January 2000.
13. A. H. Lefebvre, "Fuel Effects on Gas Turbine Combustion – Ignition, Stability and Combustion Efficiency", *ASME J. Eng. Gas Turbines and Power,* vol. 107, pp. 24-37, 1985.
14. K. K. Rink and A. H. Lefebvre, "Pollutant Formation in Heterogeneous Mixtures of Fuel drops and Air", *AIAA J. Propulsion,* vol. 3, No. 1, pp. 5-10, Jan-Feb, 1987.
15. A. Kushari, Y. Neumeier, O. Israeli, A. Peled and B. T. Zinn, "An internally mixed injector for active control of atomization process in liquid fueled engines", AIAA 99-0329, *37th AIAA Aerospace Sciences Meeting and Exhibit*, Jan. 11-14, 1999, Reno, NV.
16. A. Kushari, Y. Neumeier and B. T. Zinn, " A Theoretical Investigation of the Performance of an Internally Mixed Liquid Atomizer", AIAA 2000-1021, *38th AIAA Aerospace Sciences Meeting and Exhibit*, Jan. 2000, Reno, NV.
17. G. Blasquez, P.Pons, and A. Boukabache, "Capabilities and limits of silicon pressure sensors", *Sensors and Actuators*, vol. 17, pp. 387-403.
18. R. Okojie, A. Ned, D. Kurtz, and W. Carr, "6H-SiC pressure sensors for high temperature applications", Proc. MEMS 1996, pp. 146-149.
19. E. Obermermeier, "High Temperature microsensors based on polycrystalline diamond thin films", Proc. International Conf. Transducers '95, pp. 178-181, 1995.
20. Dupont Applied Technologies Group, "Green Tape Material System, Design and Layout Guidelines", pp. 1-17.
21. J. English and M.G. Allen, "Micromachined Wireless Ceramic Pressure Sensors," Proc. IEEE Microelectromechanical Systems Conference, January, 1999.
22. A. Sedra and K. Smith, Microelectronic Circuits, Saunders College Publishing, 1991, pp. 786-788.

Figures

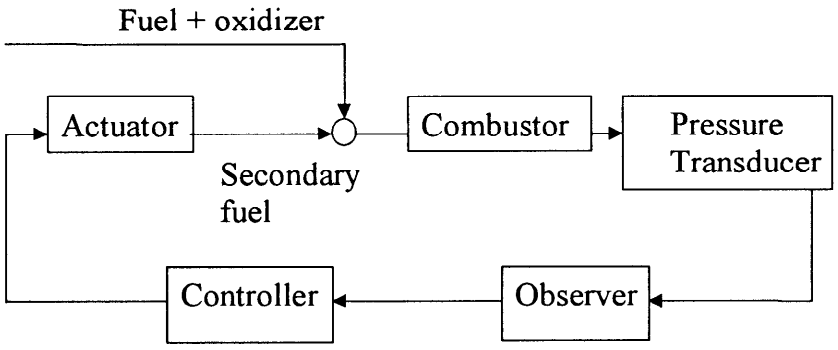


Figure 1. A schematic of the active control system developed at Georgia Tech.

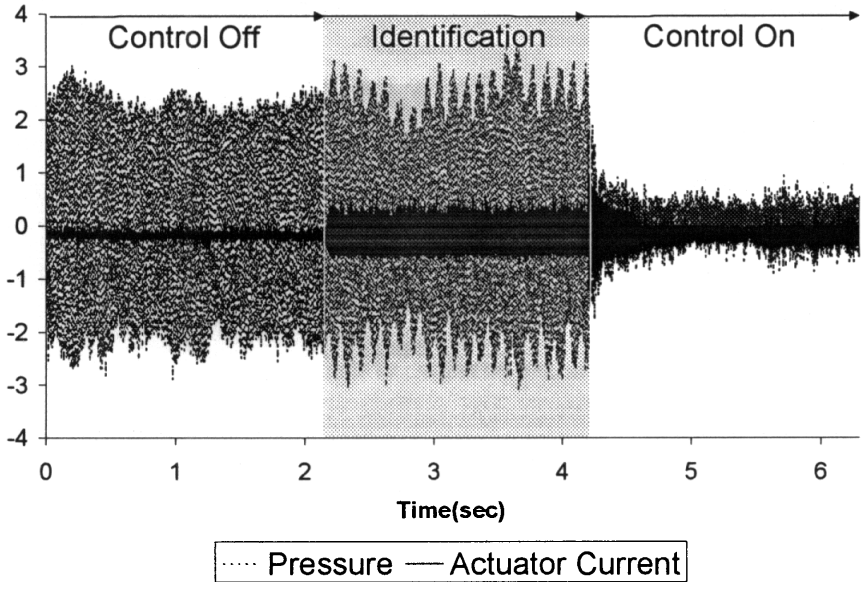


Figure 2. Active adaptive identification and control of combustion instability in the Ga. Tech. combustor (taken from Ref. 6).

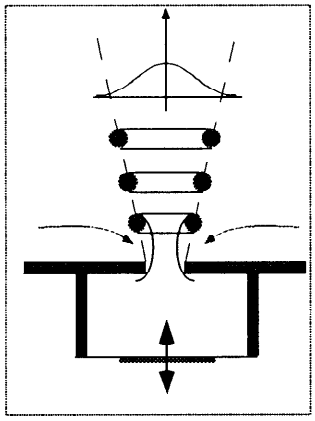


Figure 3. Schematic of a generic synthetic jet actuator.

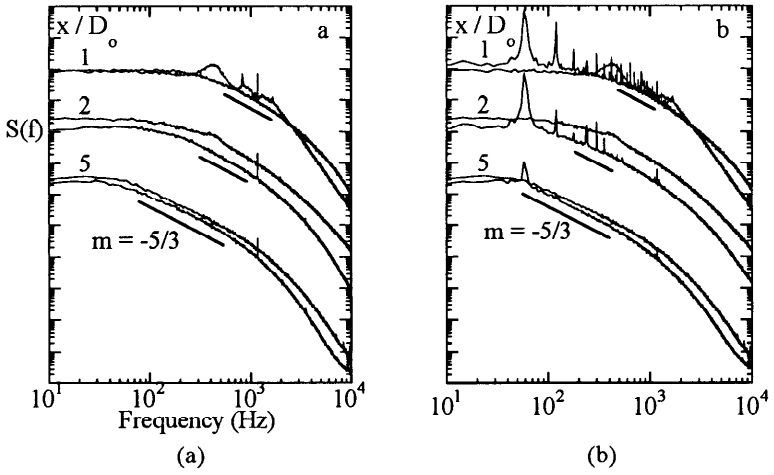


Figure 4. Power spectra of the streamwise velocity at the radial location where $U(x,r) / U_{max}(x) = 0.5$ with $U_i / U_o = 0.65$ for (a) carrier only and (b) amplitude modulated excitation at 60 Hz. Corresponding power spectra of the unforced flow are plotted using gray curves.

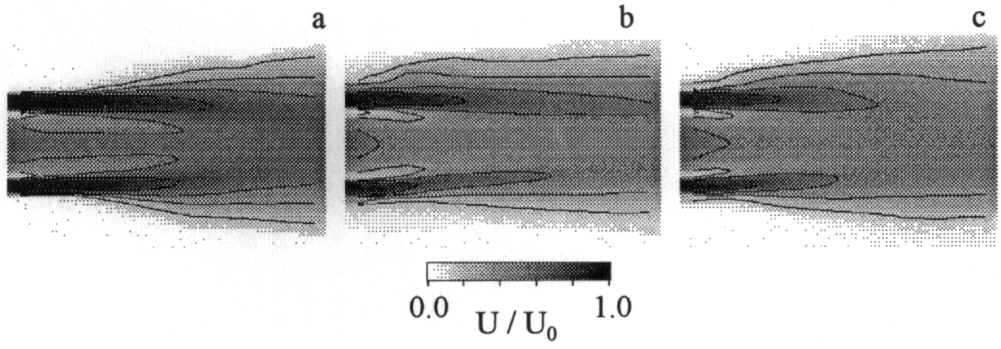


Figure 5. Raster plots of normalized mean streamwise velocity for $U_i / U_o = 0.65$, $x / D_o \leq 3$: (a) unforced, (b) carrier only, and (c) amplitude modulated at 60 Hz. Contours are plotted from 0.2 m/s to 0.8 at intervals of 0.2.

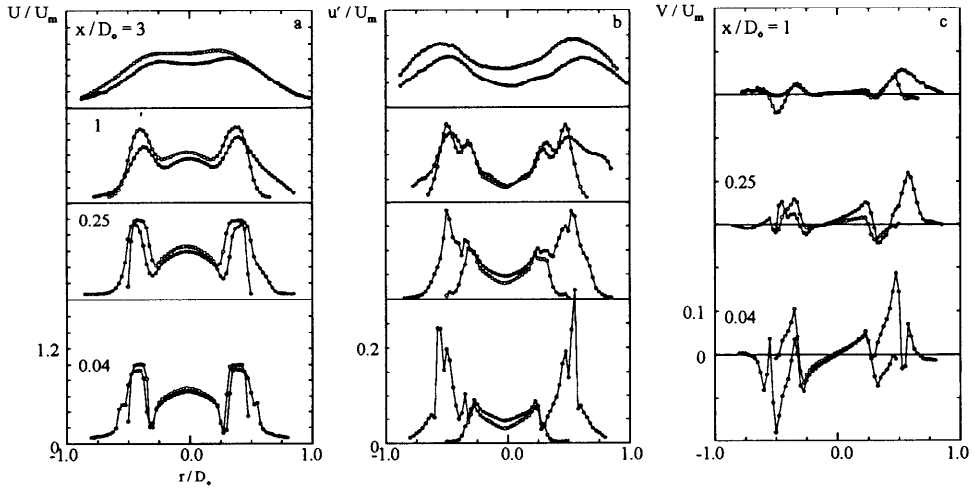


Figure 6. Radial distributions of (a) U, (b) u' , and (c) V for $U_i / U_o = 0.65$: unforced (○), unmodulated forcing.

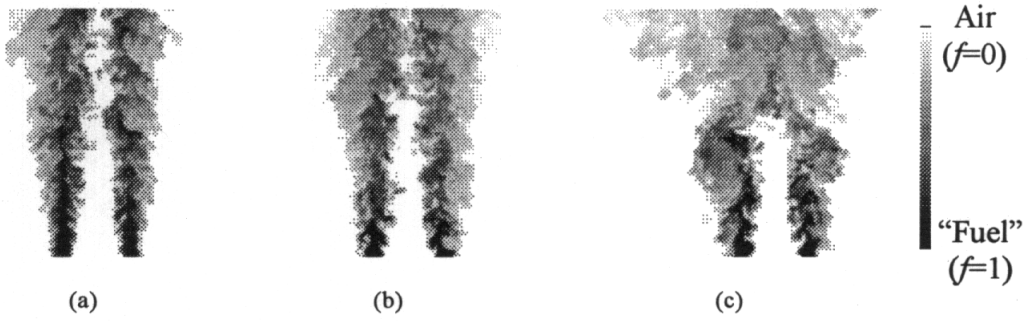


Figure 7. Acetone concentration for $U_i / U_o = 0.65$, $x / D_o \leq 3$: (a) unforced, (b) carrier only, and (c) amplitude modulated at 60Hz.

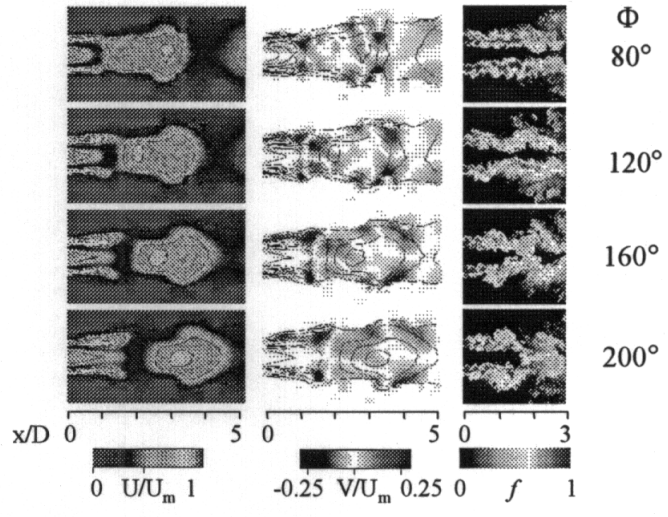


Figure 8. Comparison of velocity (U/U_m = normalized axial velocity, V/U_m = normalized radial velocity) and mixture fraction (f) results for four phases of pulsed forcing and 3 (mixing) or 5 (velocity) diameters downstream.

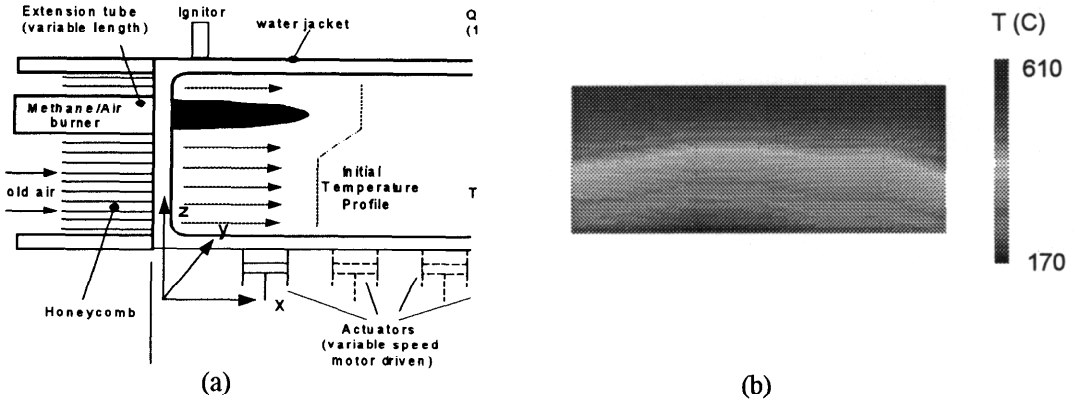


Figure 9. Facility to investigate pattern factor control using SJ – (a) schematic of the setup and (b) typical thermal profile with SJ not activated.

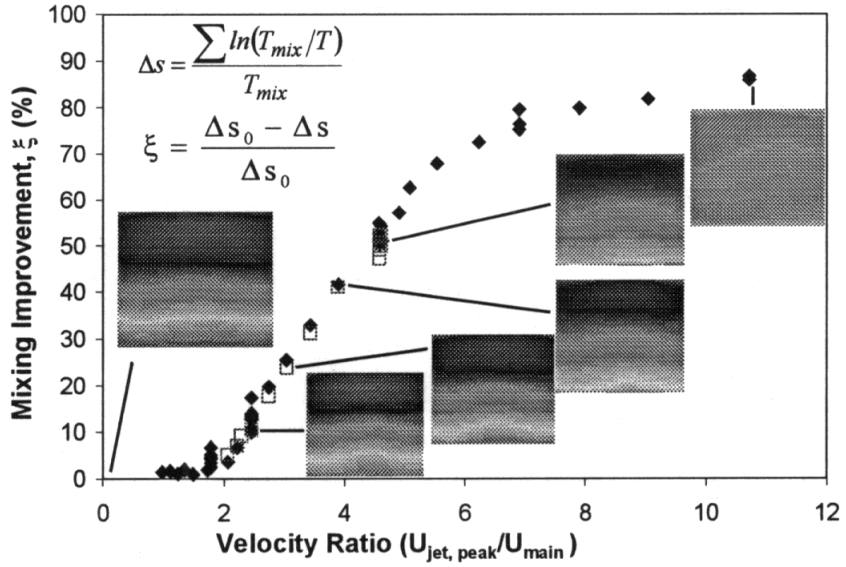


Figure 10. Mixing enhancement due to SJ actuation. Selected temperature profiles are shown to illustrate the mixing improvement.

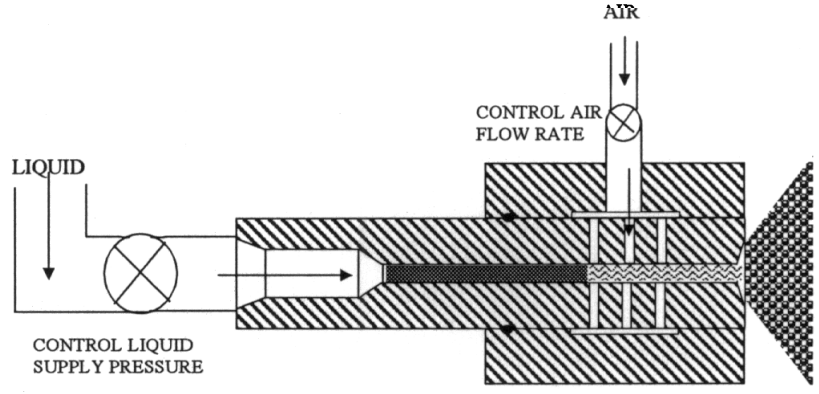


Figure 11: Schematic of the investigated internally mixed atomizer.

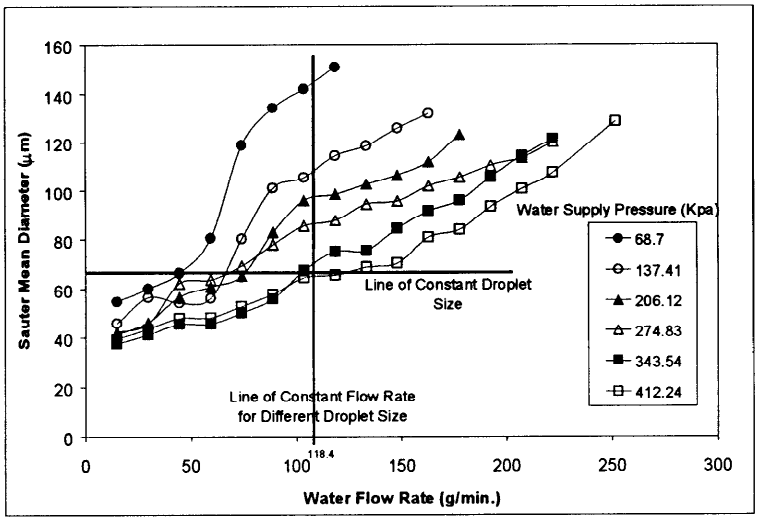


Figure 12: Performance map of the tested atomizer.

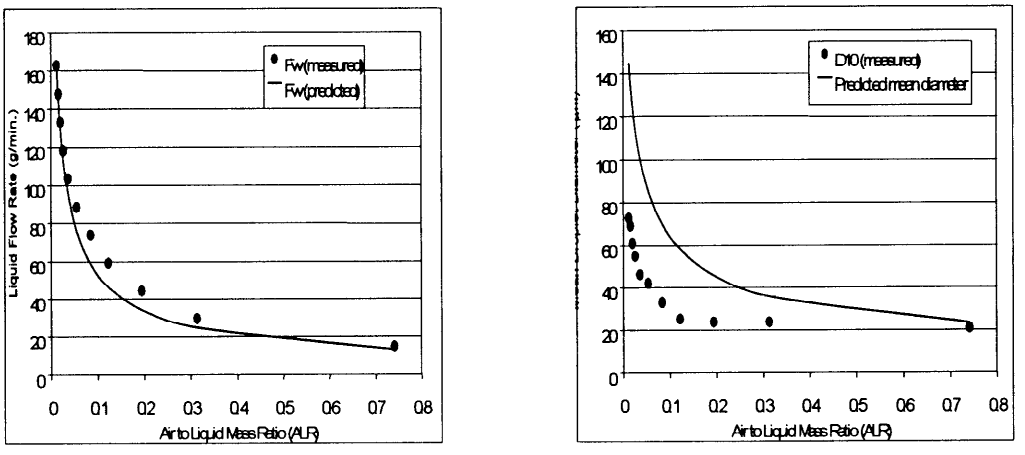


Figure 13. Comparison of thcorctical and experimental values of (a) liquid flow rate and (b) drop size.

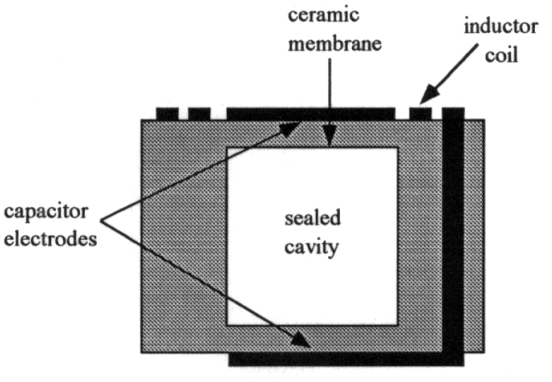


Figure 14. Pressure sensor concept.

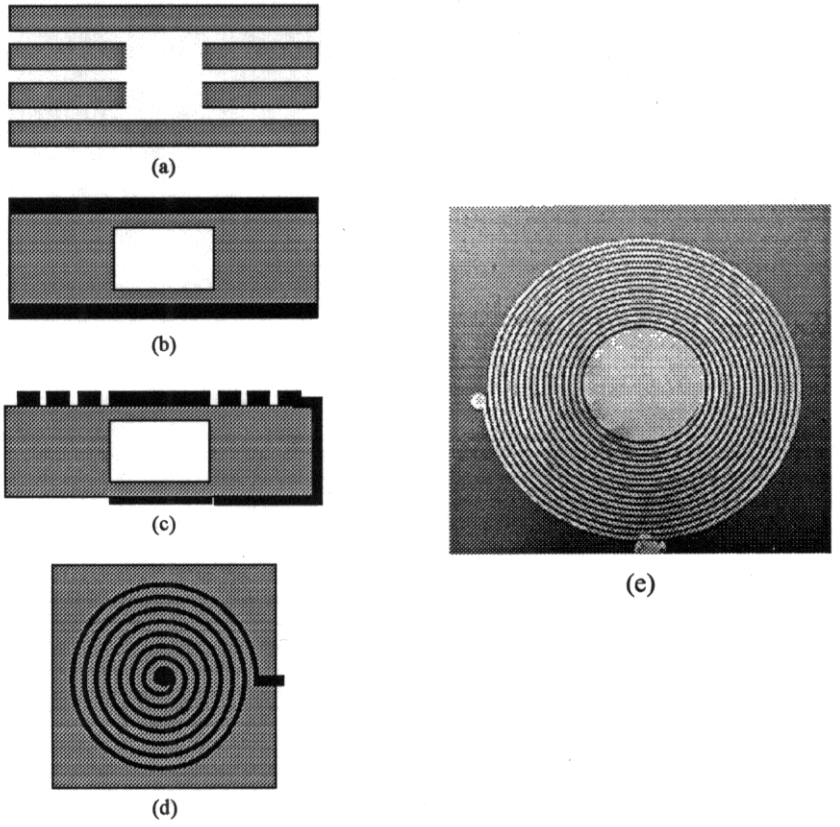


Figure 15. Ceramic micromachined pressure sensor fabrication. (a) ceramic tape layers punched and aligned. (b) after lamination, firing and metallization. (c) after electroplating coil and electrodes. (d) top view of wireless ceramic pressure sensor (e) fabricated sensor.

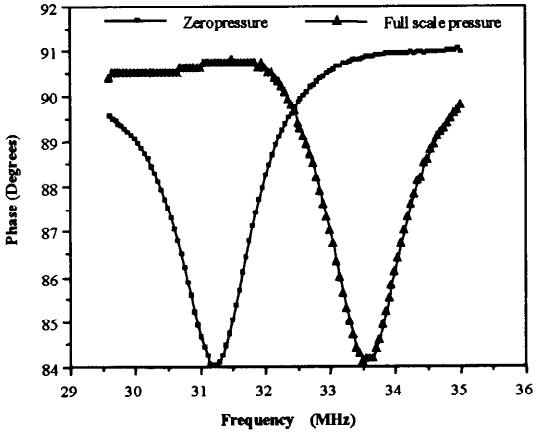


Figure 16. Phase versus frequency for zero and full scale applied pressure (0-1bar).

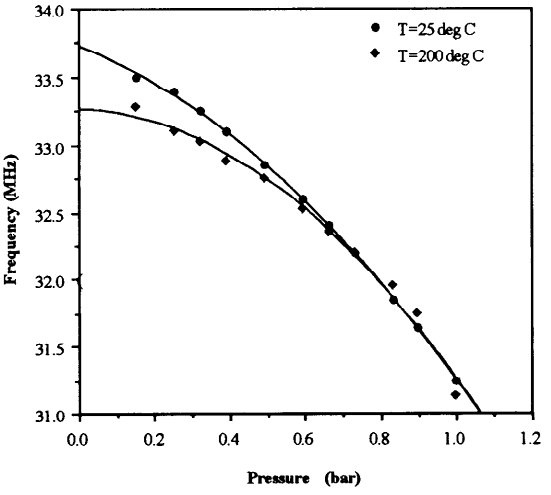


Figure 17. Frequency versus pressure for 25°C (upper curve) and 200°C (0-1bar)

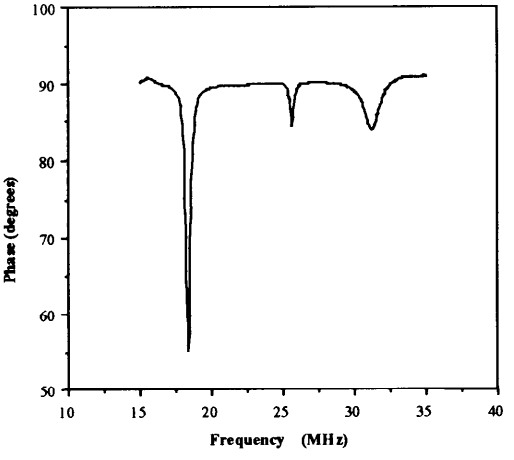


Figure 18. Simultaneous data logged from three sensors within a single loop antenna. Each sensor is designed to have a distinct center frequency, thereby allowing simultaneous readout.

PAPER -6, B. Zinn

Question (A. Annaswamy, USA)

Can you increase the temperature limit to 400-500° C?

Reply

We believe that the higher temperature operation of these sensors could be attained by use of ceramic tapes of different composition. The reported sensors were fabricated from tapes consisting of organic binders, ceramics, and glass. Higher temperature performance could be attained by using available tapes consisting of organic binder and glass only.

Question (D. A. Santavica, USA)

Do you think the synthetic jets will be as effective as your preliminary results show for pattern factor control at typical combustor main flow velocities?

Reply

Synthetic jets have the potential to improve mixing rates within the combustor. Also, they could potentially be used to improve the combustor pattern factor by controlling air/fuel mixing downstream of the burner and the mixing of "hot" and "cold" air pockets downstream of the combustion process. A significant amount of R&D work will be required to achieve these goals.

Question (F. E. C. Culick, USA)

Concerning the missing 2 seconds from the pressure record in your slide (the gap labeled "proprietary"). This is presumably a pressure record faithfully recording what is going on in the chamber. So does the censoring of the tape here mean that the process of system identification in fact interferes with the processes in the chamber?

Reply

The "blacked out" record included descriptions of the measured combustor pressure behavior and control signal to the actuator during the "adaptation" period. These data were omitted on purpose because they are proprietary.

Numerical Simulation of Adaptive Control Application to Unstable Solid Rocket Motors

M. Mettenleiter†, F. Vuillot‡ and S. Candel†

† *Laboratoire E.M2.C,*
CNRS, Ecole Centrale Paris,
F-92295 Châtenay-Malabry Cedex

‡ *ONERA Châtillon*
F-92322 Châtillon Cedex

Abstract

This article describes current developments in the numerical simulation of active control. The objective of this investigation is to devise software tools for the development of active control. The present approach uses a numerical simulation of the system based on the Navier-Stokes equations. It differs from the more standard simulations relying on lower order dynamical models.

The main difficulties associated with the present strategy are related to the representation of the actuator in the flow simulation module and with the interfacing of this module with the adaptive control routine. These issues require careful treatment to obtain a suitable numerical model of flow control. It is first shown that the actuator may be described by a distribution of sources in the field.

The time stepping needed by the flow simulation module and by the control unit differ widely (the ratio between the time steps is of the order of 100 or more). This constitutes a source of perturbation and it may introduce unwanted high frequency components in the flow simulation. It is shown that this problem is alleviated by placing numerical filters at the controller input and output.

A set of calculations are carried out to simulate vortex shedding instabilities of a simplified solid propellant rocket. These instabilities are then adaptively controlled. This example serves to illustrate the simulation methodology and provides insights into the operation of the flow controller.

1 Introduction

Active control strategies have been mainly developed from experiments. More recent efforts have been directed at the computer simulation of control with the objective of testing and improving control algorithms. Numerical simulation complements experimentation and it has had considerable impact on the development of active flow control. The present investigation aims at devising reliable tools for the numerical simulation of active control. It adresses problems arising when one wishes to couple a flow simulation module and an adaptive control algorithm. The study is motivated by research directed at the control of vortex driven instabilities found in solid segmented rocket motors. Calculations are based on the solution of the Navier-Stokes equations using the Sierra software originating from ONERA. The flow simulation module has been used extensively to analyze vortex instabilities in configurations of interest in solid propellant propulsion. It is here used as a platform for active control. Numerical simulation is now more and more used to predict the behaviour of unstable subscale solid rocket motors. A recent example is given by Le Breton et al. [1], which already shows the interest of industry in this kind of simulation.

After a short review of the literature dealing with simulation of flow control (section 2), the flow simulation module is briefly described (section 3). One important aspect of the problem is to devise a suitable representation of an actuator or of a set of actuators. It is shown in the same section that this is best accomplished by distributing sources in the field. Modifications of the Sierra code are described and a series of open loop tests are carried out to show that the sources operate as expected. Problems related to the coupling of the flow simulation module with the control algorithm are considered in section 4. Specific issues arise because flow simulation and control require very different time sampling rates. The time step of the flow solver is much smaller than the sampling period of the controller. It is then necessary to take some precautions when dealing with the input and output of the control routine. The last section provides numerical simulations of vortex instabilities in a small rocket motor and control of these instabilities using an adaptive algorithm. Two situations

Paper presented at the RTO AVT Symposium on "Active Control Technology for Enhanced Performance Operational Capabilities of Military Aircraft, Land Vehicles and Sea Vehicles", held in Braunschweig, Germany, 8-11 May 2000, and published in RTO MP-051.

are considered. In the first the controller input is a pressure signal provided by a sensor located near the nozzle while the actuator is located near the motor head. In the second, the sensor is assumed to be sensitive to vorticity and the actuator is located near the point where the vortices are being shed. These two examples serve to show that the active control simulator is flexible and may be used to study the control strategy and examine the modification of the flow under control.

2 Previous studies dealing with simulation of active control

The simulation of active control of instabilities and noise may be divided in two main groups. One finds in the first group studies based on simplified dynamical models coupled to simple or more complex control schemes. A typical example from the field of sound and vibration control is due to Koshigoe. This author considers adaptive algorithms to reduce the noise from a confined cavity. Vibrations originating from outside the cavity walls may induce large pressure fluctuations in the cavity. The problem arises during space launchers take-off, the noise induced under the fairings may harm the payload and have detrimental effects on the future operation of the spacecraft. Koshigoe et al. [2] formulate a dynamical model of the system which is then used to test the filtered X-LMS algorithm with off-line identification of the secondary path [3]. On line identification is explored with the same model in a more recent study [4] and the LMS algorithm is compared to other control schemes [5] with regard to the convergence rate.

In the field of combustion instability Annaswamy et al. [6] develop a dynamical first order model of thermoacoustic interactions in a small laminar burner. This model is then used to design a controller and simulate its operation. The control algorithm is then used in the experiment. To account for changes in the system dynamics an adaptive controller is devised and compared with simulations carried out with an LMS algorithm [7].

Culick et al. [8] take into account linear and nonlinear coupling in their comprehensive dynamical model of instability. It is thus possible to describe some of the effects which lead to limit cycle oscillations found in practical systems. Fung et Yang [9] use this general formalism to design a PI controller of pressure oscillations in a combustion chamber. Annaswamy et al.[10] study the influence of mode coupling on controller design using the same general formulation. Koshigoe et al. [11] propose an adaptive algorithm with on-line identification to control a dynamical model of combustion instability.

In the second group of studies dealing with active control simulation, the flow is calculated by solving the Navier-Stokes equations. This provides a more realistic description of the flow dynamics and of the complex couplings taking place in practical devices. This approach uses the recent advances made in computational fluid dynamics. Menon [12] is perhaps the first to investigate active control in a large eddy simulation (LES) of a dump combustor typifying the geometry of a 2D ramjet. His controller uses a simple gain and phase applied to a pressure sensor signal and reinjected through a loudspeaker located at the backward facing step. Neumeier and Zinn [13] devise a special observer which identifies the unstable modes of a system. The modes are then amplified and phase delayed by a controller and reinjected into the computational domain. The balance equations are solved in one dimension.

Kestens [14] considers the adaptive (LMS) multiple channel control of aeroacoustic instabilities of cavities driven by an adjacent flow. The Navier-Stokes equations are solved in two dimensions. An actuator of the loudspeaker type or a pulsed jet is used to reduce the pressure level observed by different sensors.

Analysis of work belonging to this second group shows that some success has been reached but that the methodology needs further consolidation. It is our aim to devise a complete simulation of active control by coupling a non-steady Navier-Stokes solver with an adaptive controller. To reach this goal it is necessary to :

- Define a numerical representation of the actuator
- Study the actuator effect in open loop simulation tests
- Examine problems of controller interfacing

These different aspects are considered in the following sections.

3 The flow simulation module Sierra and the C1-geometry

The Sierra code is used to simulate the large scales of flow in order to analyze aeroacoustic instabilities generated in internal geometries found in solid rocket motors. The code operates in the planar or axisymmetric modes. It was designed by Vuillot [15] (see this reference for details on this platform). The Navier-Stokes equations are solved with a second order finite volume centered scheme. Time marching is explicit and uses the MacCormack predictor/corrector

method. Artificial viscosity is calculated with the Jameson method (see [16]). Simulations carried out in the present study do not use a subgrid model but the laminar viscosity has been augmented by a factor of 4 to dissipate the smaller scales of turbulence.

The code is used in what follows to simulate the flow in a specific geometry designated as C1. Parameters adopted in the simulations are gathered in table 1. Indices i et j specify locations of actuators and sensors with respect to the mesh. Figure 1 shows some positions in terms of their i-index.

The actuators will be defined as distribution of sources on the computational mesh. Their location is specified by the first and last values (i_d et i_f) of index i corresponding to the source and by the transverse size of the source specified in terms of elementary cells by index h. In the first case considered, the actuator sources are located on the first and second columns of cells composing the mesh and they occupy $h = 30$ cells in the transverse direction.

The computational domain is represented in Figure 1. The lower boundary 1 delivers a uniform stream of gases and represents the solid propellant surface. The mass flow rate per unit surface is imposed at this boundary, the gas temperature is prescribed and the tangential velocity component is zero at this limit. The boundary 2 represents the motor front head, the velocity vanishes on this boundary and the temperature is imposed. The line 3 is a symmetry plane. The outflow in section 4 is supersonic and numerical boundary conditions in this section are treated by simple extrapolation from the computational domain. At the wall 5 the flow velocity vanishes and the temperature is imposed.

This computational case was defined by ONERA to study the strong aeroacoustic oscillations resulting from vortex shedding from the propellant edge coupled with one of the modes of the system (see Lupoglazoff et Vuillot [17]). This constitutes a generic case, it is well documented and requires a limited amount of grid nodes (less than 10000) allowing long computational sequences.

In a first attempt at controlling the instabilities observed in the C1 case the actuator was simulated by a modified front end boundary condition. Perturbations were imposed on the incoming characteristic lines while outgoing waves were allowed to propagate out of the domain without reflection. Systematic tests carried-out in this situation indicated that the flow simulation did not respond adequately to the imposed fluctuations. For a given modulation frequency differing from that of the instability and for a small level of perturbation, one expects to find a superposition of acoustic waves in the system and a beating between these two waves if the frequencies are close. If that were the case it would have been possible to act on the signal delivered by the pressure sensor to control the vortex shedding. Calculations however indicated that beating was only produced at the beginning of the simulation and that vortices were very rapidly synchronized by the excitation signal introduced by the actuator. Closed loop control could not be achieved under these circumstances. This behavior was due to the modified boundary condition used to represent the actuator. Because the boundary did not reflect the incident waves the resonant properties of the system were changed and the vortex shedding phenomenon was altered.

It was then decided to use an alternative method to model the actuator. The boundary conditions were left untouched but source terms were distributed in the field. A somewhat similar approach was devised independently by Mohanraj et al. [18] who use sources in a one dimensional version of Euler's equations.

Without describing the details of the Sierra code, we only summarize the steps required to incorporate source terms in the balance equations.

- In the first step one has to define the number, location and type of source. This is done in a "driver" module which is read at the simulation beginning. This driver also contains information on the sensors used in the control scheme.
- During the calculation and at each time step the sources and sensors are updated.
- After each step the sources are added to the right hand side of the discretized balance equations.

If $\dot{\omega}_s$ designates the source of rate of mass addition per unit volume, the sources appear in the balance of mass, momentum and energy as follows :

$$\begin{aligned}
\rho^{n+1} &= \rho^{n+1} + \delta t \dot{\omega}_s \\
(\rho u)^{n+1} &= (\rho u)^{n+1} + (\delta t \dot{\omega}_s) u_s \\
(\rho v)^{n+1} &= (\rho v)^{n+1} + (\delta t \dot{\omega}_s) v_s \\
(\rho E)^{n+1} &= (\rho E)^{n+1} + (\delta t \dot{\omega}_s)(e_s + k_s)
\end{aligned}$$

Velocity components u_s, v_s and the internal energy of the injected stream e_s may be freely specified. The kinetic energy k_s is a function of u_s and v_s. In the present calculations a normalized value is adopted for the internal energy $e_s = 1$, and the velocities and kinetic energy u_s, v_s and k_s are set equal to zero.

The rate of mass addition $\dot{\omega}_s$ may be defined in various ways. In open loop tests this term takes the form

$$\dot{\omega}_s = a + b\sin(2\pi f t + \phi) + c\mathrm{sir}(f_1, f_2, dt).$$

This expression features a continuous component ($a \neq 0$), a sinusoidal modulation ($b \neq 0$) and/or a linear frequency modulation with a frequency sweep from f_1 to f_2 ($c \neq 0$). The source term $\dot{\omega}_s$ may also follow the active control output designated in what follows as "rac" :

$$\dot{\omega}_s = \text{rac}.$$

Tests of the source terms were carried out systematically to verify the proper operation of the concept. A constant section duct with closed/open left and right sections is filled with fluid. The mass flowing out of the tube exactly equals that injected by the sources.

In a second test a source was placed at various sections of the duct to excite the acoustic modes of the system. The mesh comprises in this case 61×20 nodes and the excitation frequency is that of the 3/4 wave mode.

The source was distributed over the height of the duct and occupied two cells in the axial direction. In the case shown in Figure 2 the source is located in the first and second cell which correspond to a pressure antinode. The acoustic mode develops uniformly in the transverse direction, the pressure and velocity distributions are exactly identical to those expected theoretically.

Other test cases show that the source terms incorporated in the Sierra code allow simulations of acoustic modulation without modification of the boundary conditions.

A second test series is now aimed at analyzing the response of the vortex driven flow in the C1 configuration under an external excitation. Parameters are those gathered in Table 1, case 1. The calculation begins with an established oscillation in the flow. Effects of different levels of source excitation are displayed in Figure 3.

The signal detected by the pressure sensor pfar2 is shown on the left. This signal will serve later as error signal in the control scheme for the first simulation. The signal detected by the differential pressure signal diff32 is shown on the right. Both signals feature the instability frequency. When the excitation amplitude is augmented two frequencies are detected, a further increase in amplitude leads to a decrease of the instability frequency level. Analysis of other sensor signals confirm this behaviour (for more detailed information, see [19]).

These calculations indicate that the C1 configuration responds to the new source terms placed in the field. The following points are noticeable :

- The instability phenomenon coexists with the frequency delivered by the actuator when the level of excitation is low.
- The frequency shifts towards the excitation frequency when the level of modulation is larger.
- The vortex shedding process is reorganized when the excitation frequency is very large.

Before describing closed loop calculations we now consider the control algorithm and examine issues related to interfacing.

4 Interfacing the control algorithm with the flow simulation module

The interface between the flow simulation module Sierra and the subroutine RAC which corresponds to the adaptive controller is designed to come as close as possible to a typical experimental configuration. The Sierra code is then used as a black box providing signals detected by different sensors and receiving the signal driving the actuator.

The integration step in the simulations is of $2.44\ 10^{-7}$ s, which corresponds to a sampling frequency $f_{\text{sierra}} = 4.096\ 10^6$ Hz. Results are recorded periodically every $d_w = 25$ Sierra time steps. The writing frequency is $f_{\text{write}} = 1.64\ 10^5$ Hz. It is not necessary and not recommendable to use the adaptive filter at these very high rates. Such frequencies would require extremely long filters in order to represent the system with sufficient precision. The filter renewal should be effected at a much lower rate, typically at a frequency $f_{\text{rac}} = 20480$ Hz. This value corresponds to the Sierra frequency divided by a factor $d_s = 200$.

To link a typical flow experiment featuring an analog sensor to the discrete control algorithm one uses an anti-aliasing filter. The same precaution seems necessary in connecting the flow simulation module Sierra to the control routine RAC. The sampling rate reduction by a large factor $d_s = 200$ induces a loss of information and may lead to problems of spectral overlap as those found when analog signals are sampled into discrete sequences. This justifies filtering of the controller input as shown in Figure 4.

The flow simulation module Sierra yields an input to the controller RAC at each integration step. One may then choose to keep each d_s value provided by Sierra or one may first low pass filter the values generated by Sierra and then keep the result every d_s sample.

A similar situation prevails at the controller output. One possibility is to use a "sample and hold" which keeps a constant value of the RAC output during the following d_s integration steps of SIERRA. Or

one may low pass filter the values in order to eliminate the high frequencies introduced by the successive jumps in the sampled and blocked values returned by the controller (see Figure 4).

The effects of filtering may be examined with the following tests. In a first trivial case (which is not shown here) $d_w = d_s = 25$. This means that the sensor values are written at the same frequency by SIERRA as they are updated and written by RAC. Hence, the sensor and actuator signals measured by RAC and SIERRA are identical.

In the second test case the sampling rates differ : $d_w = 25$ and $d_s = 200$. These values are later on adopted in the simulations with control. The corresponding results are now displayed on the left plot of Figure 5 (upper figure: actuator signal generated by RAC; second figure: pressure sensor measured by RAC; third figure: actuator signal measured by SIERRA; bottom figure: pressure sensor measured by SIERRA). The actuator signal measured by SIERRA clearly shows the discretisation effect. Sierra receives a discretized sinusoid (third curve from the top). The signal detected by the pressure sensor features high frequency oscillations which were not observed in the previous test. The high frequencies introduced by the sampled signal feeding the actuator interfere with the calculation. The controller input is formed by the samples without filtering (second plot from the top). High frequency components appear which perturb the signal and the initial frequency is less visible.

Using the same downsampling as in the previous test ($d_w = 25$ and $d_s = 200$) but including a low pass filter at the controller input and output one obtains the results shown on the right plot of Figure 5. The actuator signal seen by the Sierra sensor is smooth. The high frequency components in the pressure sensor signal are essentially suppressed. The controller input is noise free but a phase is introduced by the filter.

5 Active control simulation results

To control the C1 flow it is first necessary to identify the system seen by the controller. With this information the controller filter may be brought to convergence to a steady solution

5.1 Secondary path identification

Off-line identification is used in the context of this simulation to describe the secondary path. As in experiments it is possible to get this information in two regimes of operation :

- Identification may be carried out in the presence of the vortex instability phenomenon.
- Identification may be carried out in the absence of vortex shedding. This is achieved by multiplying the viscosity by a factor which is typically of the order of 20

During identification, the controller RAC delivers a frequency which varies linearly in time (a siren signal). The signal detected by the pressure sensor (pfar2) is recorded by RAC and Matlab is used to calculate an IIR filter comprising 21 coefficients in the numerator and denominator.

Figure 6 displays the results obtained in the two cases. On the left the secondary path is estimated in the presence of vortex shedding. On the right, the vortices are suppressed. In this second case the peak in amplitude corresponding to the instability amplitude is reduced to a great extent and this is also true for a second peak around 1800 Hz. The phase also changes notably as the viscosity coefficient is augmented. The filters reproduce the real behavior quite well.

On physical grounds it seems more appropriate to use the identification result obtained in the presence of the vortex shedding process. The corresponding secondary path transfer function is used in what follows.

5.2 Adaptive control

The NSC (Noise Source Control) algorithm described in [20] or [19] is used in the simulations presented in this section. The control loop is closed when the flow simulation has reached a limit cycle with a well established vortex shedding instability. Figure 7 shows the time evolution using different sensors after the controller is switched on. This event is represented by a vertical line. The error signal (pressure sensor pfar2) is shown on the top left. A considerable reduction is observed in the beginning but the algorithm does not converge to a steady state. A stationary solution is reached after a transient phase featuring short modulations. The actuator signal shown at the bottom left also features pulsations before converging to a steady state. One also notices that a large amplitude is initially generated to act on the process. This amplitude diminishes later and converges to a lower level when the signal becomes stationnary. This behaviour is also observed in experiments (see [20]) suggesting that the controller acts on the vortex shedding process which drives the oscillation in the system.

This interpretation is confirmed by the velocity signal u2far2 shown at the right and at the bottom of

Figure 7. After an initial phase with modulations the amplitude is stabilized at a lower level. The frequency also changes and the shift during the transition may be at the source of modulations detected by all the sensors.

Finally, the pressure sensor pfav placed on the motor front end (displayed on the right and at the top of Figure 7) features a notable reduction of amplitude when the controller is on but it is worth recalling that this signal is not used in the control process.

The power spectral densities calculated during steady state operation confirm the controller influence on the instability phenomenon. Figure 8 shows on the left the spectral density of the pressure signal pfar2 without and with control.The component at the instability frequency vanishes completely (> 40 dB) but a new peak appears at a different frequency at a much reduced level (factor of 10).

The spectral density of the velocity signal u2far2 can be seen on the right of the same Figure. It clearly shows that the oscillation is shifted to a higher frequency. The initial peak has disappeared. The new component reaches a significantly reduced level (factor 3). This peak at 3900 Hz is close to the 3L mode of the C1 configuration and it may excite an acoustic oscillation at that frequency (this explains the small peak appearing in the left in Figure 8).

A similar behaviour can be observed for the pressure signal pfav. The peak at the initial frequency vanishes and the phenomenon is shifted to the higher mode. The overall level is reduced by a factor of 3. These results are not shown here.

The controller does not suppress the vortex shedding but it shifts the phenomenon to another eigenmode. The intensities at this new frequency are nevertheless significantly reduced.

The vorticity field before and after control is shown in Figure 9. The lower image corresponding to the controlled operation shows that coherent vortices are still present but their size and shedding frequency are modified in agreement with observations of the velocity spectral density.

It appears that in the numerical simulation the vortex shedding is more persistent than in the experimental case. This could be explained by the difference in the broad band content of the signals detected in the two situations. Without coupling the acoustic signal is submerged in the broad band noise existing in the experimental facility and it cannot trigger the vortices in a coherent fashion. The shedding takes place more randomly (this is demonstrated in experiments described in [19]) or it may even be completely suppressed as described by Huang and Weaver [21]. In the numerical simulation, the flow conditions are much "cleaner". There is no broad band noise which could prevent the synchronization between acoustics and vortex dynamics. The vortices find in all circumstances a phase reference even when the acoustic signal level is strongly reduced.

In the case examined the controller acts on the acoustics and then indirectly through coupling on the vortex shedding. A more efficient reduction of velocity fluctuations could be obtained by acting directly on the shear layer. It is interesting to see if an additional decrease in the signal amplitude could be obtained with a new arrangement in which the actuator is set at the edge of the propellant surface (case 2 in Table 1) and the sensor provides a vorticity signal.

After identification of the secondary path corresponding to this new set-up (with vortex shedding) a new simulation is carried out. Figure 10 shows the pressure signal pfar2 (top left) and pfav (top right). The actuator signal is at the bottom left of figure 10. The velocity sensor u2far2 appears at the bottom right. Reduction of this last signal is effectively more direct than in the previous calculation (compare Figures 7 and 10). The pressure sensors also behave in a different manner. The pressure levels are first slightly augmented, reduction taking place in a second stage (Figure 10). The same increase is observed in the velocity fluctuation for the first simulation (Figure 7).

The reduction in amplitude obtained in the steady state may be compared to that obtained previously. In general, the same frequency shift can be observed as in case 1. The initial peaks disappear and the phenomenon is shifted to the 3L mode, where it reappears with largely reduced levels. The spectral densities of the different signals are shown in Figure 11. The pressure signal pfar2 is slightly lower in case 1 than in case 2. This is not surprising since this signal is to be minimized in the first arrangement. In case 2, the pressure level at the front end is lower and the velocity fluctuations u2far2 are diminished by a factor of 4.5. The overall reduction in the error sensor (a vorticity signal) is also considerable. As for the other sensors, the initial frequency has disappeared and the 3L peak appears with a level reduced by a factor 6.3 (this result is not shown here). It is also worth noting that convergence in the second case is smoother perhaps because the controller acts more directly on the instability process.

It is interesting to note that between $t = 0.12$ et $t = 0.14$s all signals are reduced significantly (see Figure 10). This reduction is unfortunately not maintained and the signals reach a steady state at a greater level. There are some possible reasons for this behavior. The frequency shift drives the controller towards a new solution. As the sensor level is greatly reduced,

the rate of convergence for this new situation is diminished (a factor of 10 reduction in amplitude reduces the convergence rate by a factor of 100). One may also invoke the fact that the sensor signal is too "clean". In the numerical calculation the error signal e detected by the sensor cannot be driven to zero because this would not lead to a steady state of the controller (see [20] or [19] for more details). The controller action would tend to zero but with a vanishing output the instability mechanism will not be controllable. This scenario requires further testing.

Figure 12 shows the vorticity distribution at a point in time ($t = 0.1264s$) where the level of fluctuations is quite small. Coherent vortices have essentially disappeared from the flow-field and the shear layer develops without roll-up.

6 Conclusions

The simulation of active control is investigated in this article. A Navier-Stokes solver is coupled to an adaptive control algorithm. It is shown that the actuator may be defined by distributing sources in the computational domain. This method is first used in open loop tests. The coupling of the flow simulation module with the control algorithm is then considered. Because the rates of operation of the flow solver and active control are widely different the signals at the controller input and output must be filtered. It is shown that this eliminates high frequency components which would otherwise perturb the calculation. The simulation of active control is then developed in a solid rocket motor geometry in which vortex shedding takes place which leades to acoustic resonance of the system. Results obtained demonstrate that control is feasible and that the method may be used to examine the changes in the flow field induced by the controller.

Acknowledgment

This work was supported in part by the CNES. It is part of the ASSM research programme coordinated by CNES and ONERA.

References

[1] P. Le Breton, J.-F. Guéry, F. Vuillot, and M. Prévost. Recent advances in the prediction of SRM thrust oscillations. In *Premier Colloque Européen sur la Technologie des Lanceurs "Vibration des Lanceurs, Toulouse"*, 1999.

[2] S. Koshigoe, J. T. Gillis, and E. T. Falangas. A new approach for active control of sound transmission through an elastic plate backed by a rectangular cavity. *J. of the Acoustical Society of America*, 94(2):900–907, 1993.

[3] S. Koshigoe, A. Teagle, and A. Gordon. A time domain study of active control of sound transmission due to acoustic pulse excitation. *J. of the Acoustical Society of America*, 97(1):313–323, 1995.

[4] S. Koshigoe, A. Teagle, C.-H. Tsay, S. Morishita, and S. Une. Numerical simulation of active control with on–line system identification on sound transmission through an elastic plate. *J. of the Acoustical Society of America*, 99(5):2947–2954, 1996.

[5] S. Koshigoe, A. Teagle, and C.-H. Tsay. A rapidly convergent adaptive controller applied to suppresion of random noise transmission. *Journal of Vibration and Acoustics*, 120:449–454, 1998.

[6] A. M. Annaswamy, M. Fleifil, J. W. Rumsey, J. P. Hathout, and A. F. Ghoniem. An input-output model of thermoacoustic instability and active control design. Technical Report No. 9705, MIT, 1997.

[7] A. M. Annaswamy, O. M El Rifai, M. Fleifil, J. P. Hathout, and A. F. Ghoniem. A model–based self–tuning controller for thermoacoustic instability. *Combust. Sci. and Tech.*, 135:213–240, 1998.

[8] F. E. C. Culick, W. H. Lin, C. C. Jahnke, and J. D. Sterling. Modeling for active control of combustion and thermally driven oscillations. In *Proceedings of the American Control Conference, Boston MA*, 1991.

[9] V. Yang Y.-T. Fung. Active control of nonlinear pressure oscillations in combustion chambers. *J. Prop. and Power*, 8(6):1282 1289, 1992.

[10] A. M. Annaswamy, M. Fleifil, J. P. Hathout, and A. F. Ghoniem. Impact of linear coupling on the design of active controllers for the thermoacoustic instability. *Combust. Sci. and Tech.*, 128:131–180, 1997.

[11] S. Koshigoe, T. Komatsuzaki, and V. Yang. Active control of combustion instabilities with on–line system identification. In *34th. Aerospace Sciences Meeting & Exhibit, Reno, Jan. 15–18.* AIAA Paper 96-0759, 1996.

[12] S. Menon. Active combustion control in a ramjet using large-eddy simulations. *Combust. Sci. and Tech.*, 84:51–79, 1992.

[13] Y. Neumeier and B. Zinn. Active control of combustion instabilities using real time identification of unstable combustor modes. In *Proceedings of the IEEE Conference on Control Applications*, pages 691–698, 1995.

[14] T. Kestens. *Etude numérique du contrôle adaptatif multivoies des instabilités aéroacoustiques des cavités.* PhD thesis, Institut National Polytechnique de Toulouse, 1999.

[15] N. Lupoglazoff and F. Vuillot. Two-dimensional numerical simulation of the stability of a solid propellant rocket motor. In 29^{th} *Aerospace Science Meeting, Reno, USA.* AIAA Paper 91-0205, January 7–10 1991.

[16] A. Jameson and W. Schmidt. Some recent developments in numerical methods for transonic flows. *Computer Methods in Applied Mechanics and Engineering*, 51:467–493, 1985.

[17] N. Lupoglazoff and F. Vuillot. Numerical simulations of vortex shedding phenomenon in 2D test case solid rocket motors. In 30^{th} *Aerospace Sciences Meeting.* AIAA Paper 92-0776, 1992.

[18] R. Mohanraj, Y. Neumeier, and B. T. Zinn. Characteristic-based treatement of source terms in euler equations for roe scheme. *AIAA J.*, 37(4):417–424, 1999.

[19] M. Mettenleiter. *Contrôle adaptatif des instabilités aéroacoustiques. Application aux systèmes de propulsion.* PhD thesis, Ecole Centrale Paris, 2000.

[20] M. Mettenleiter, E. Haile, and S. Candel. Adaptive control of aeroacoustic instabilities. *J. Sound Vib.* (in press), 2000.

[21] X. Y. Huang and D. S. Weaver. On the active control of shear layer oscillations across a cavity in the presence of pipeline acoustic resonance. *J. Fluids and Structures.*, 5:207–219, 1991.

Number of grid points	318×31
Pressure sensor pfar1 (i, j)	210,1
Pressure sensor (error measure, case 1) pfar2 (i, j)	245,1
Pressure difference sensor diff32	pfar2-pfar1
Forward plane pressure sensor pfav (i, j)	1,30
x-velocity sensor u2far2 (i, j)	245,24
Vorticity sensor (error measure, case 2; i, j)	245,24
Actuator position, case 1 i_d, i_f, h	1,2,30
Actuator position, case 2 i_d, i_f, h	64,74,5
Reference length	0.47m
Reference velocity	1075.37 m/s
Integration time step	1/4.069e+6 = 2.4414e-7 s
Excited acoustic mode frequency (close to 2L)	2540 Hz

Table 1: Parameters of the C1 computations .

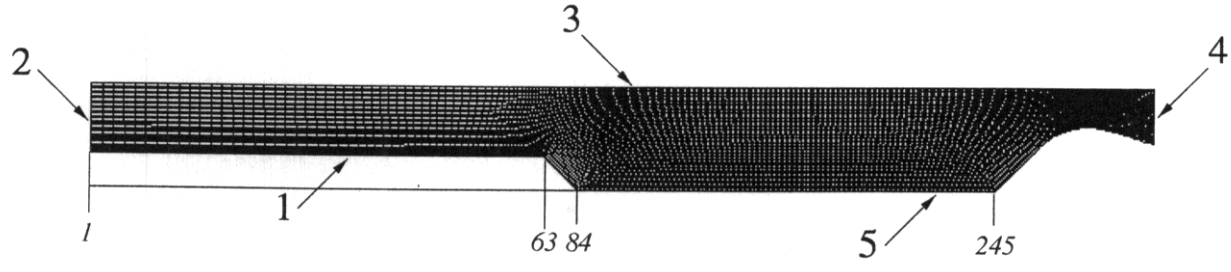


Figure 1: The C1 computational domain.

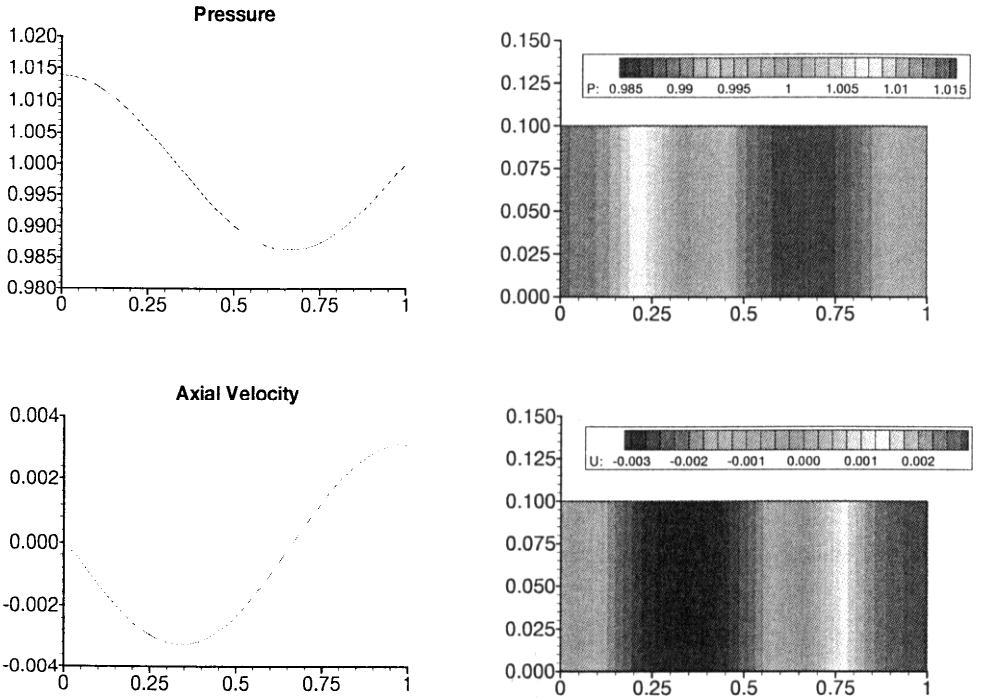


Figure 2: Excitation at a pressure antinode. At the top : pressure signal. At the bottom : acoustic velocity signal.

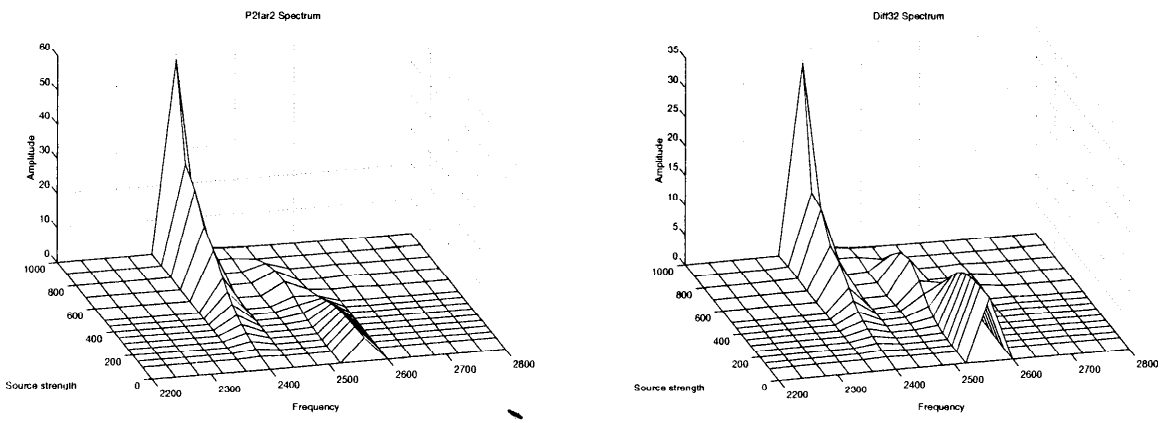


Figure 3: Influence of a single acoustic source on the pressure signal detected by the pfar2 error sensor (left) and by the differential sensor diff32 (right). The level of excitation varies from low to high.

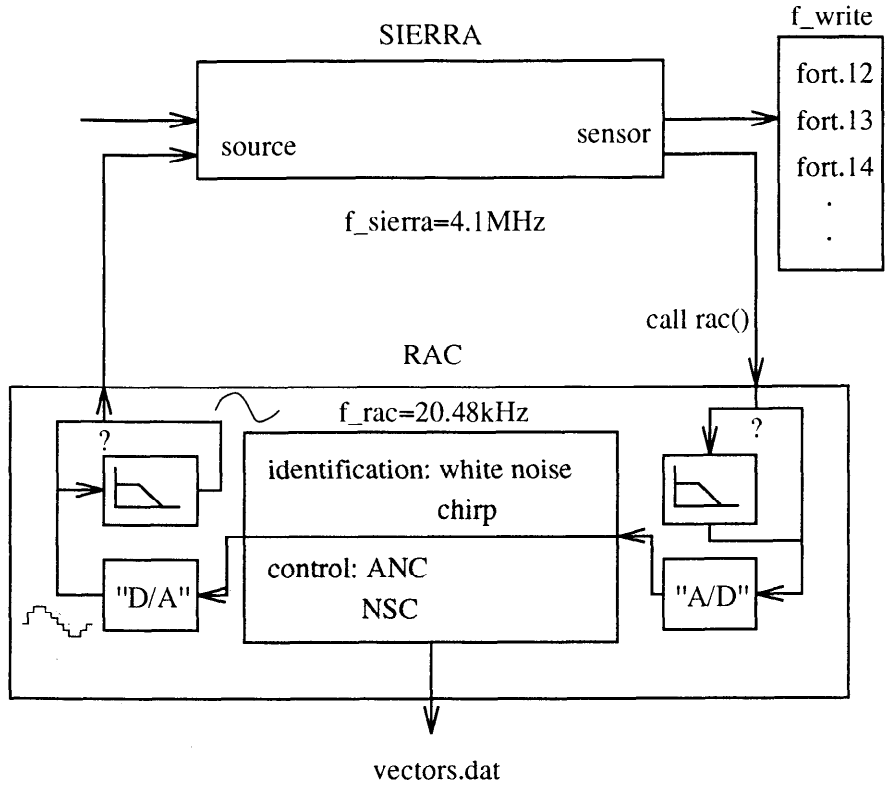


Figure 4: Diagram of the Sierra interface with the adaptive controller RAC

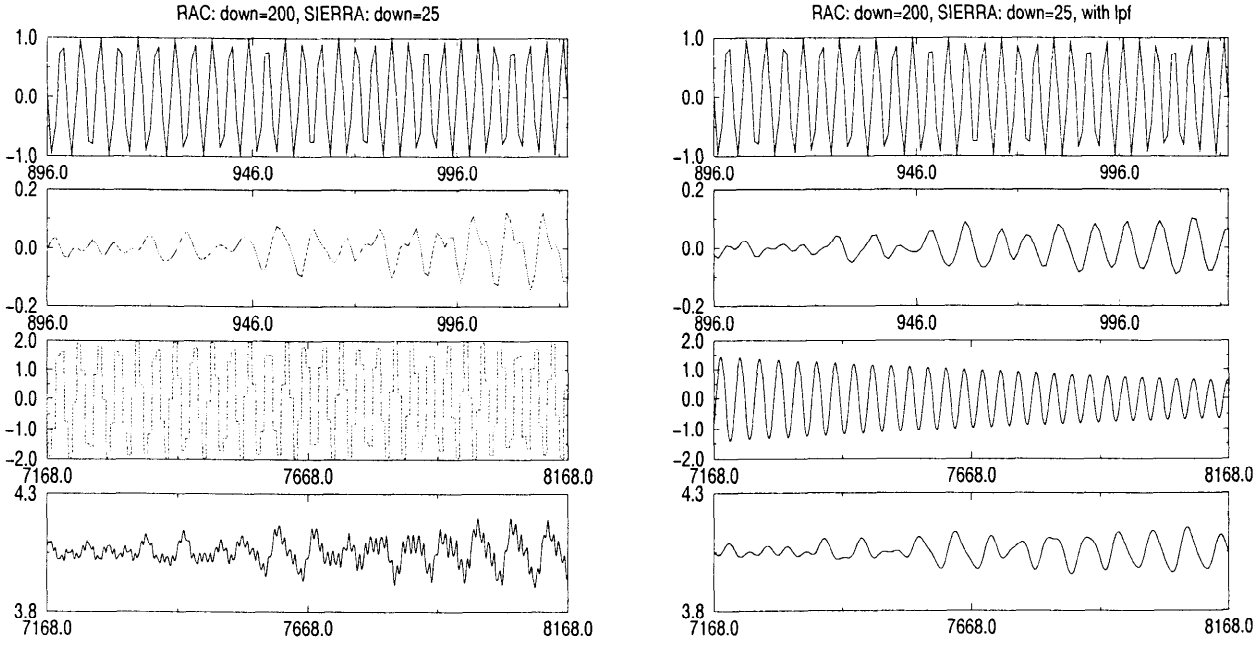


Figure 5: Comparison between actuator/sensor in RAC (top) and SIERRA sensors (bottom), $d_w = 25$, $d_s = 200$. Left: no filtering. Right: with filtering.

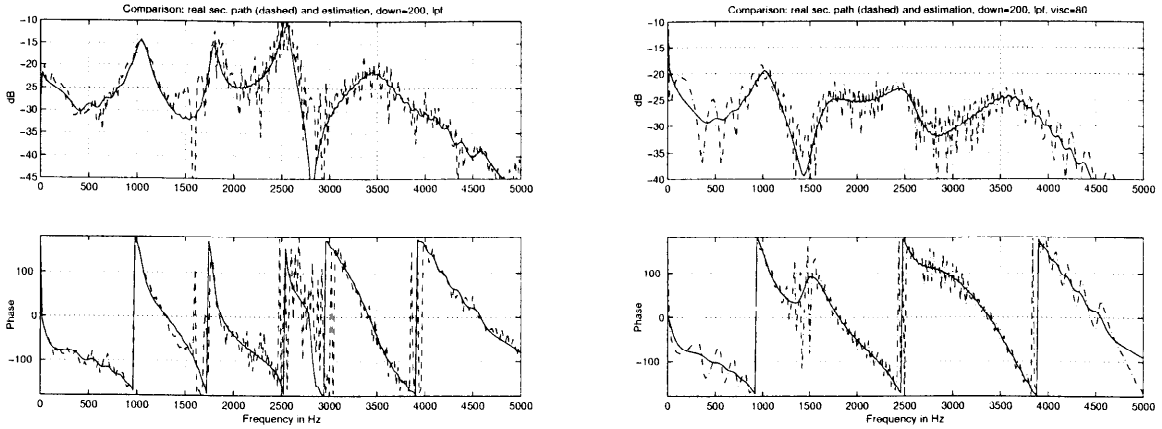


Figure 6: Real (—·—) and estimated (——) secondary path IIR filter (21/21). On the left, identification is carried out in presence of vortex shedding. On the right identification is carried out with an augmented viscosity coefficient.

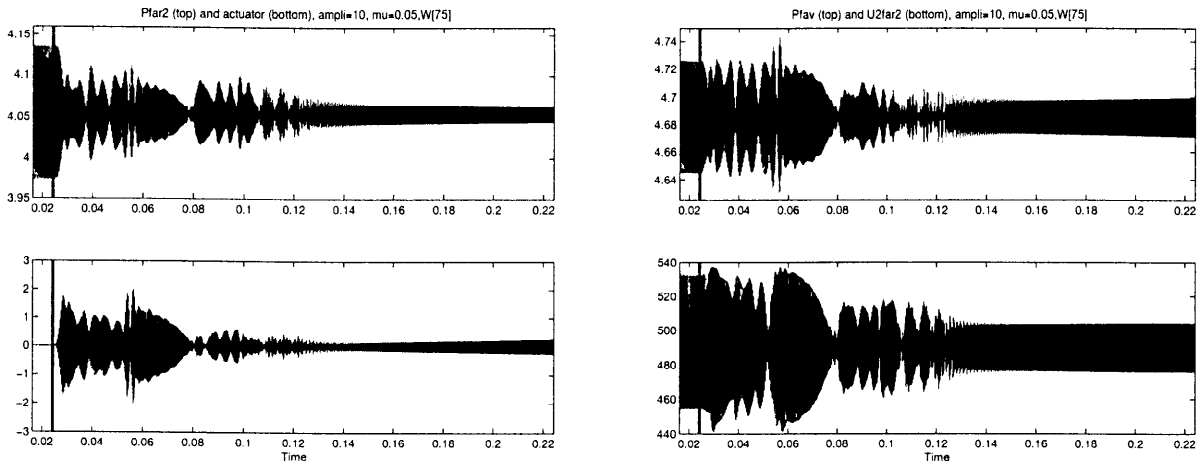


Figure 7: Control results. On the left and top : error sensor pfar2, left and bottom : actuator signal. On the right and top : pressure sensor pfav, on theright and bottom : velocity signal u2far2. The vertical line indicates that the controller is switched on.

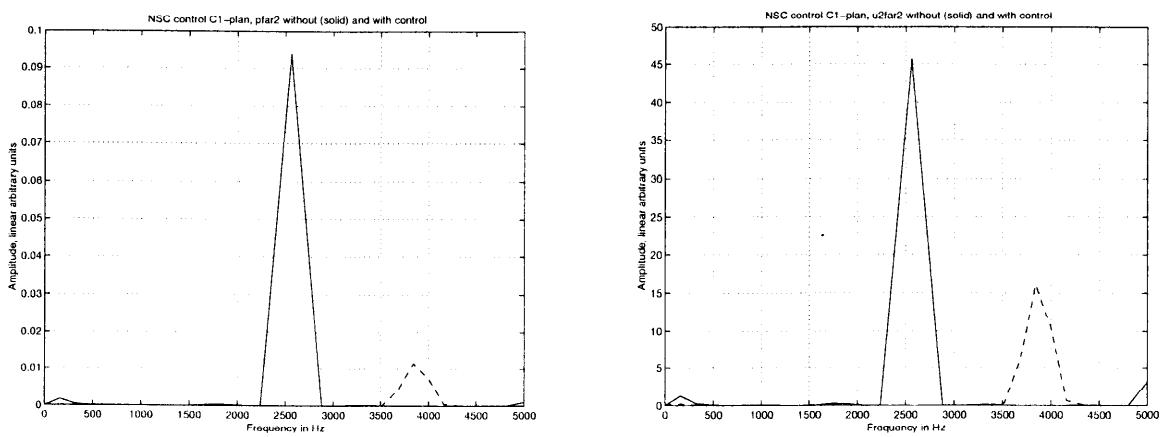


Figure 8: Control results. On the left:power spectral density of pfar2, on the right power spectral density of u2far2. Without control (——) and with control (----).

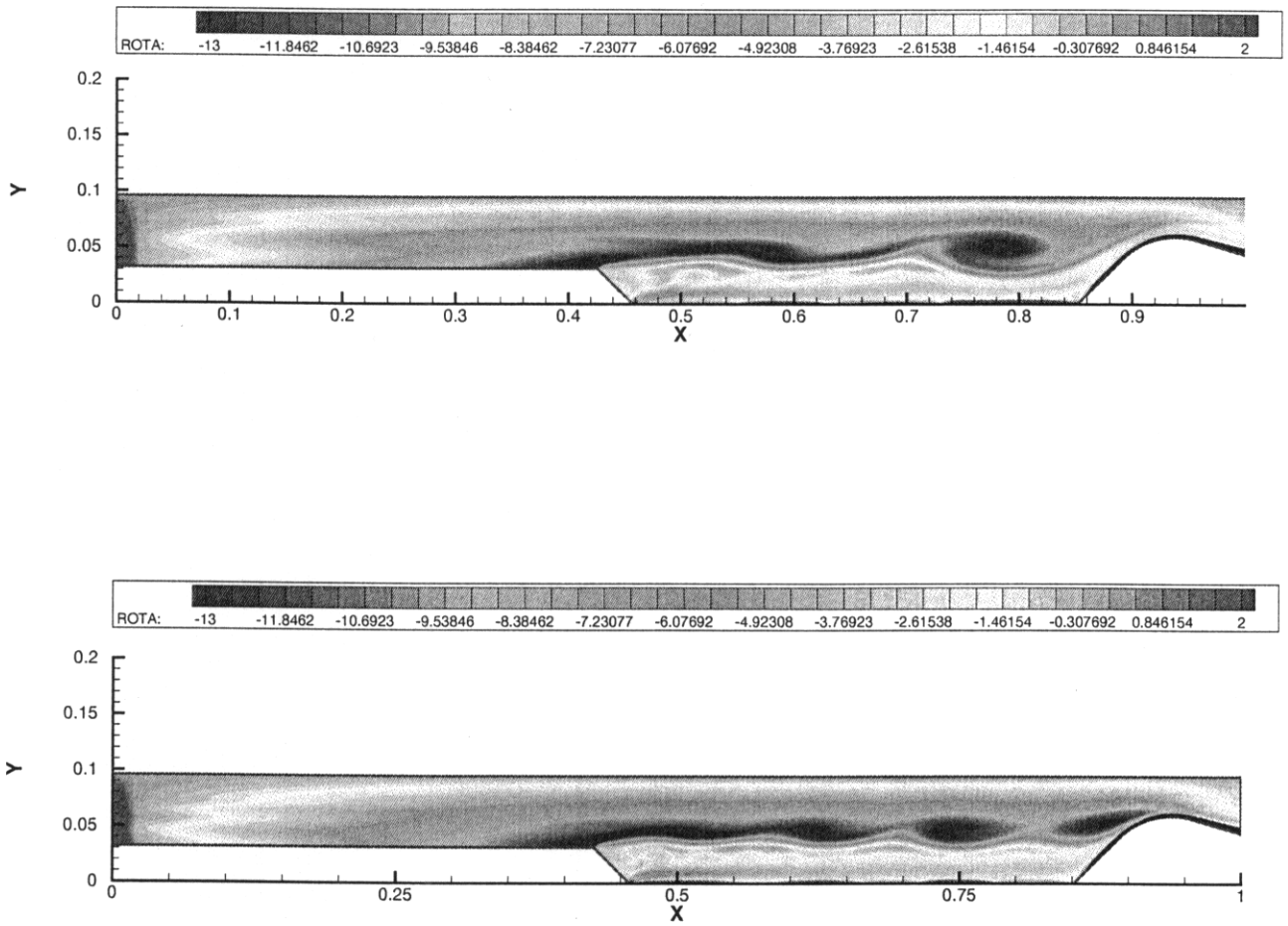


Figure 9: Vorticity field before (top) and after (bottom) control The controller input is the pressure signal pfar2 (case 1).

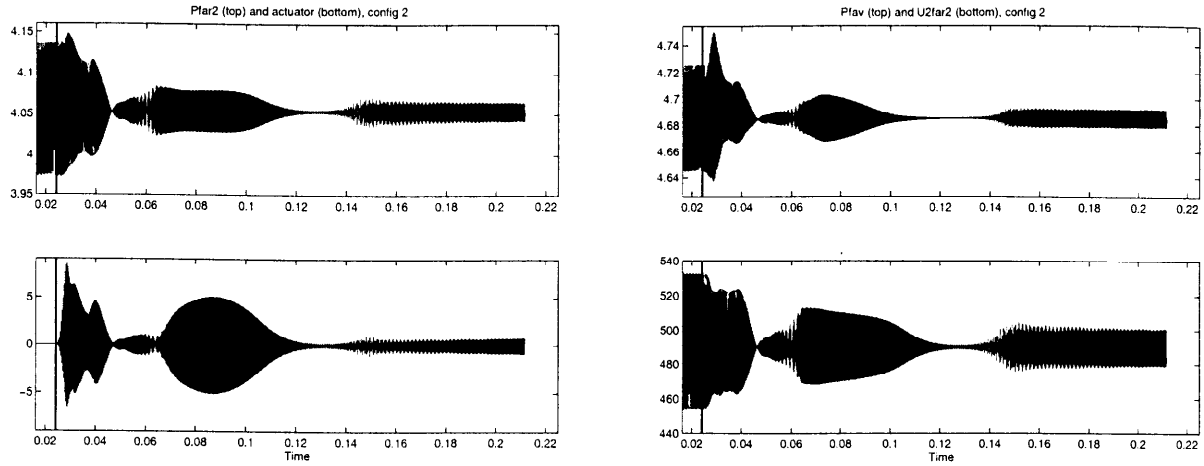


Figure 10: Control results obtained in case 2. A vorticity sensor provides the input to the controller. Top left : pressure sensor pfar2. Bottom left : actuator signal. Top right : pressure sensor pfav. Bottom right : velocity signal u2far2. The vertical line indicates control switch on.

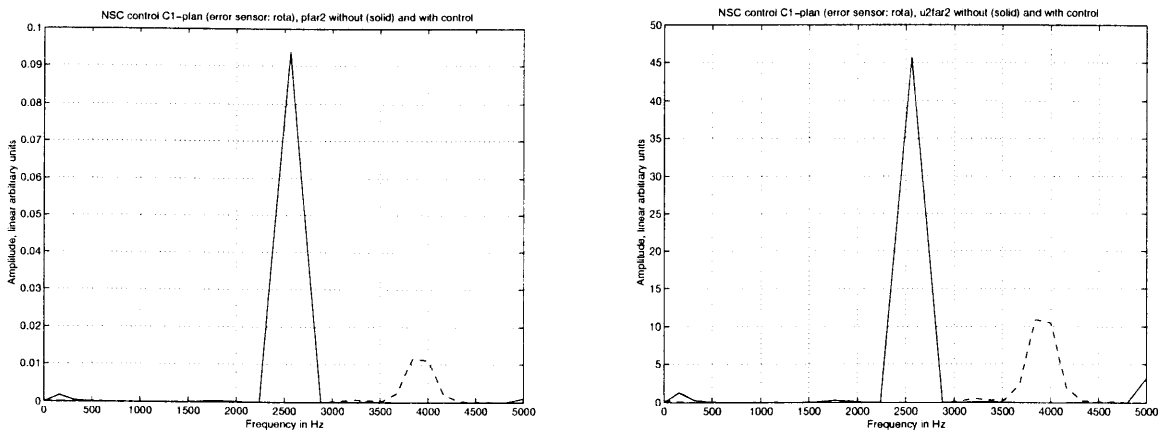


Figure 11: Control results obtained in case 2. A vorticity sensor provides the input to the controller. Left : pfar2 spectral density right : u2far2 spectral density. With (———) and without (----) control.

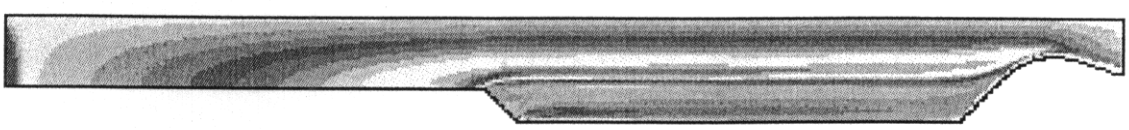


Figure 12: Vorticity field at $t = 0.1264s$. Control is achieved with a vorticity sensor and an actuator located at the propellant surface edge (case 2)

PAPER -7, M. Mettenleiter

Question (M. Huth, Germany)

Which kind of practical system can represent the modeled actuator and which parameters of the actuator driver were optimized by the adaptive controller?

Reply

The modeled actuator represents a mass injector in the numerical simulation. The corresponding velocities and the internal energy of the added mass were specified. In practical systems, this corresponds to a propellant injector.

The adaptive controller phase shifts and amplifies the sensor signal before it is re-injected by the actuator. The appropriate phase shift and amplification (which changes for different instability frequencies) is determined by the adaptive scheme.

The Onset of Aerodynamic Instability in a 3-Stage Transonic Compressor

F.-O. Methling, R. Preute, H. Stoff
Fluid Energy Machines, IB 4-152
Ruhr-University, D-44801 Bochum (Germany)

F. Grauer
MTU (TPKE), POB 500 640
D-80976 Muenchen (Germany)

ABSTRACT

The actual research activities concerning the aerodynamic instability of compressors aim at an improvement of the usable range of the compressor performance map. Usually there must be a safety margin between operating point and stability limit to avoid stall and surge. In this paper we give a survey of the pre- and the post-instability behaviour of a 3-stage transonic axial aero-engine compressor. The measurement results of fluctuations of static and total pressure, temperature and velocity under the influence of stall and surge are presented. For that were used piezo-resistive transducers, cold wires and triple-split-film sensors. The pressure signals show, that the investigated compressor flow goes into instability by a spike-type stall.

The rotating stall frequency corresponds to nearly half of the shaft speed. The stall cell spreads at once over all three stages of the compressor and, after an oscillation at the beginning, extends approximately over a range of 1/3 to 1/2 of the circumference. Depending on the shaft speed different forms of instability occur like rotating stall, classic surge (local backflow) and deep surge (complete flow reversal).

In the second part of this paper we analyse results using fast fourier transform and artificial neural networks. It is shown, that by using the fast fourier transform peripheral disturbances can be identified, but that an artificial neural network is the most useful tool to indicate an approaching instability in case of spike-type stalling.

INTRODUCTION

In a compressor performance map the surge line is the aerodynamic stability limit towards low massflow. The different forms of those aerodynamic instabilities are rotating stall and surge. Rotating stall defines a compressor instability where regions of reduced or reversed flow occur locally whereas surge is characterized by a system instability with violent oscillations in the annulus flow throughout the compression system. Surge can be devided into two different forms, the so called *classic surge*, that means, the mass flow decreases intermittently and *deep surge* in which the mass flow becomes negative. The different forms are described in detail by e.g. Day, 1996a or Rippl, 1995.

Figure 1 shows the schematic view of a performance map of a compressor for the purpose of discussing forms of instability.

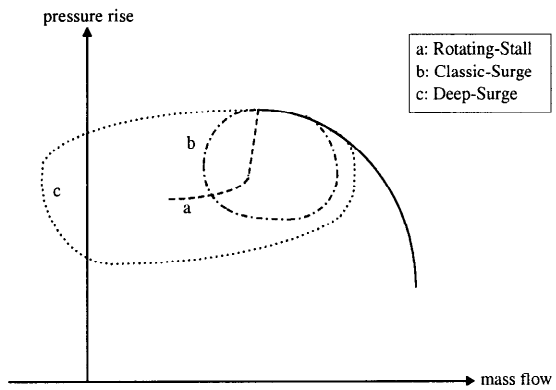


Figure 1: Compressor performance during stall and surge

All of those forms of instability are stressing the engine heavily, sometimes even leads to destruction. Strain gauge measurements in the literature report of bending stress in vanes exceeding stable operation by a factor of 2 during surge and by 5 under conditions of rotating stall (Baumann, 1970; Rippl, 1995). For this reason numerous investigations are under way to find reliable means for monitoring an eventual approach to the stability limit while running the machine (Nenni & Ludwig, 1974; Ludwig & Nenni, 1978; Day et al., 1999; Höss et al., 1998; Walbaum & Rieß, 1998). Ways for alerts have been identified for individual test beds but a reliable warning of general validity also for foreign compressor designs is still unattained (Ludwig & Nenni, 1980; Schulze u.a., 1998; Regnery, 1998; Grauer, 1998), but there is still a quest for proof of reliability fostering more research projects. Two different concepts have been devised to avoid compressor instability, known as *passive control* and *active control*.

The concept of *passive control* is related to activities to extend the usable range of operating, e.g. casing treatment. The second concept, known as *active stall control*, means to prevent the compressor from entering

Paper presented at the RTO AVT Symposium on "Active Control Technology for Enhanced Performance Operational Capabilities of Military Aircraft, Land Vehicles and Sea Vehicles", held in Braunschweig, Germany, 8-11 May 2000, and published in RTO MP-051.

unstable operation by increasing the distance to the surge line as soon as a critical approach is detected. This may be done by blow-off valves, guide vane adjustment (Day, 1991) or fuel reduction. Another concept attempts to move the surge line actively towards lower throughflow and higher pressures by the influence of actuators. Doing this enables to maintain the speed line and shifting the surge line to provide for increased operating range (Day, 1991, 1996b). For the concept of active stall control it is at first necessary to detect the approach to unstable conditions reliably.

The following sections present investigations of the onset of stall and surge in a high-speed compressor of 3 stages by using high resolution measurement techniques and in the second part results of data analysis are presented that aim to deliver a reliable technique to detect the approach to the unstable range.

EXPERIMENTAL SETUP

Compressor test rig

The 3-stage test compressor at the lab in the University of Bochum (Figure 2) is equipped with double circular arc aerofoils (DCA) in blades and NACA-65 in vanes. Its specifications are listed in table 1.

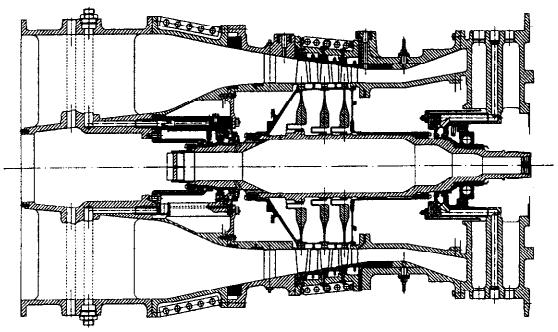


Figure 2: 3-stage compressor

As the test rig simulates the flow in the intermediate compressor of the RB 199 jet engine, the Bochum test rig is equipped with a hub spoiler (wire screen) to achieve an inlet velocity distribution similar to the discharge of the low-pressure compressor. The spoiler influences the amount of throughflow but does not change the instability phenomena in their character. For this reason the hub spoiler configuration is not varied here and all results include this influence. For closed-loop operations, the compressor is connected by rather extensive piping of more than 15 m in length equalling to a volume of 3,5 m^3 towards the inlet throttle and 5,5 m^3 towards the back-pressure throttle. The influence of the length of the piping must be the reason of a waviness of about 10 Hz superposed by disturbances from travelling waves in the piping. For conveniently isolating the different types of unstable flow regimes (during stall and surge), all tests are taken with the "large" volume (5.5 m^3), as indicated above and demonstrated on this installation by Rippl, 1995.

Compressor geometry

Rotor diameter (inlet)	494 mm
Rotor diameter (outlet)	453 mm
Hub diameter (const.)	384 mm
Hub / Tip ratio (inlet)	0.78
Hub / Tip ratio (outlet)	0.85
Aspect ratio	1.6 – 2.3
Solidity	1.2 – 0.92

Design performance data

Pressure ratio	2.67
Maximum mass flow, 100 % speed	15.1 kg/s
Relative Mach number	1.12 – 0.92
Number of revolutions	- confidential -

Compressor blading

Position	Blade type	Number of blades
IGV	NACA 65	52
Rotor 1	DCA	59
Stator 1	NACA 65	127
Rotor 2	DCA	67
Stator 2	NACA 65	159
Rotor 3	DCA	89
Stator 3	NACA 65	157

Table 1: Compressor data

Instrumentation

Data about the unsteady movement of the flow are acquired from wall-mounted pick-ups for static pressure and from traversing individually a piezo-resistive transducer for fluctuations in total pressure, a triple-split-film probe for velocity-density and flow angle as well as a cold-wire sensor for temperature. Figure 3 shows a scheme of the instrumentation.

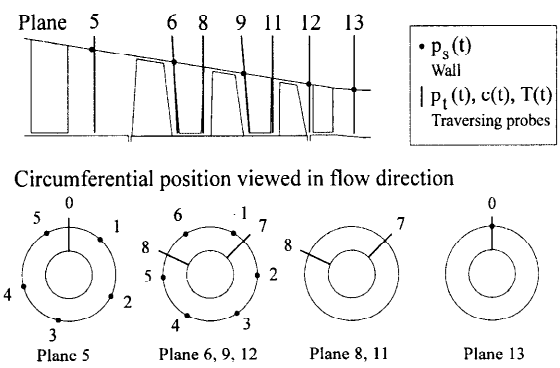


Figure 3: Instrumentation and measurement sections

As shown in figure 3 there are 5 pressure transducers in front of rotor 1 and 6 pressure transducers in front of the stators. Further it is possible to traverse sensors over the blade height in one circumferential position in front of stage 1 and behind stage 3 as well as in two different circumferential positions within the three stages.

As the bladed duct converges from a height of about 54 mm down to 34 mm, flow data are acquired only at 10 %, 50 % and 90 % of the blade span in the axial gaps

upstream of rotor 1, downstream of rotor 2 as well as of stators 2 and 3 during the occurrence of rotating stall at 50 % speed and classic surge at 60 % speed with local backflow. Speeds of 70 % and more destroy the highly sensitive wire probe due to an increased stress because of growing velocity-density. Test data have been taken with individual traversing probes in order not to obstruct the flow unduely because the pitch is going down to only 8 mm locally. The axial gaps of sizes of 5 to 6 mm restricted the probe sizes. They were of the order of 2 mm in diameter.

All transducers and probes involved in measurements of unsteady quantities enable to resolve frequencies of 1 kHz or higher (semi-conductor pressure probes 70 kHz, split-film for velocity-density 1 kHz and cold wire for total temperature 2 kHz). A low-pass filter of 10 kHz has been applied to cut off blade-passing frequencies. The instability of the compressor flow is governed by frequencies lower than the revving speed. With the exception of the total-pressure traversing probe, which is a development by Lohmberg, 1995, all other sensors (split film, cold wire) are commercially available tools. Preute, 1997, describes the calibration of the cold-wire temperature probe. The components of the measurement chain are standard equipment likewise.

With some of the signals displayed as phase averages of 4 to 5 traces, the compound effort in instability events amounts to 147 for the compressor (Preute, 2000) preceded by at least the same number of events during earlier investigations (Rippl, 1995).

RESULTS OF UNSTEADY MEASUREMENTS

Flow field results

A problem associated with measurements of the unsteady movement of the flow field is that several pick-ups for physical quantities have to be distributed throughout the flow field to capture instantaneous information in a synchronous way to reproduce a correct impression of the situation, as required e.g. for turbulence, which is considered to be a random phenomenon and cannot be reproduced in a certain moment. Unsteady movements in the flow of turbomachinery such as interacting wakes, pressure waves or stall cells can be traced in phase space with their deterministic features if it is possible to detect them. In the case discussed here an arrangement of many probes for simultaneous data acquisition throughout the flow field risks to influence the result due to blockage by the shafts of several probes. Therefore the present experiments are extracted from sequences of repeated tests with only a single traversing probe immersed in the flow field. As the phenomena of unstable flow occur rapidly, there is no time for traversing the probe over the channel height.

Separate test runs have to be performed for each measurement location. Synchronisation of the events is achieved by triggering on ramps of stall or surge events over the elapsed time or the position of the shaft. In this way characteristic pattern in the signals may be enhanced by phase-averaging several events if a single signal is blurred by random motion. 6 flush-mounted wall-pressure probes, which do not obstruct the cross section of the flow, measure simultaneously in distributed positions in the wall of the casing. Wall pressure signals measured in section 5 upstream of rotor 1, shown in figures 4 and 5, reproduce the distinctly different forms of instabilities as they have been found by Rippl (1995) for the setting of velocity and backpressure throttle: Rotating stall occurs at 50 % rated speed where flow reversals take place only locally near blades and vanes (top of figure 4).

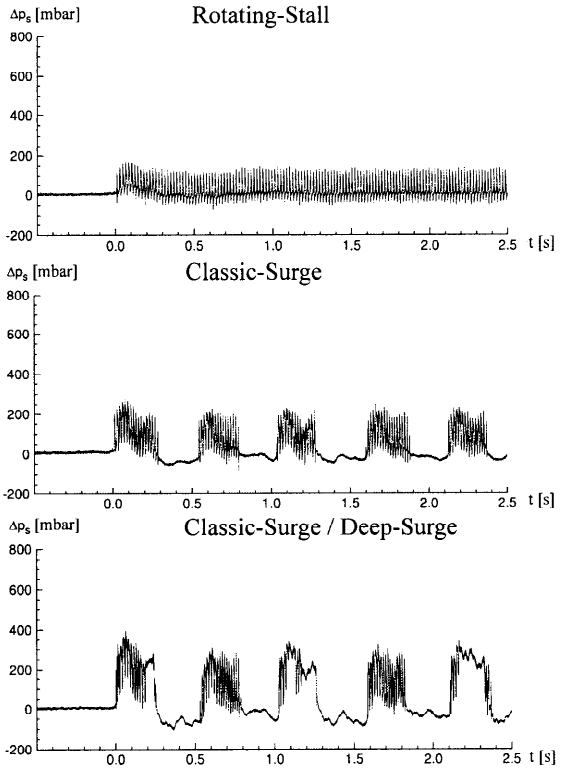


Figure 4: Static pressure in front of rotor 1 (section 5) during transition from stable to unstable flow for rated speeds of 50 % (rotating stall, top), 60 % (classic surge, middle) and 70 % (intermittent classic surge and deep surge, bottom).

The so-called "classic surge" with momentary flow reversal in single rows appears on the operating line of 60 % rated speed in the compressor map when throttling brings the operating point over the limit of stability. The integral mass flow is still through the outlet (Figure 4, centre).

At 70 % rated speed (Figure 4, bottom) a transitional form of instability takes place, changing alternately between classic surge and deep surge, occasionally reversing the flow.

At 80 %, 90 % and 100 % rated speed excessive throttling produces flow reversal alternately emptying the back-pressure piping and consecutively recovering the back-pressure in the outlet. The latter flow regimes may be reached only with inlet throttling because of power limits in the transmission gear. The results in figure 5

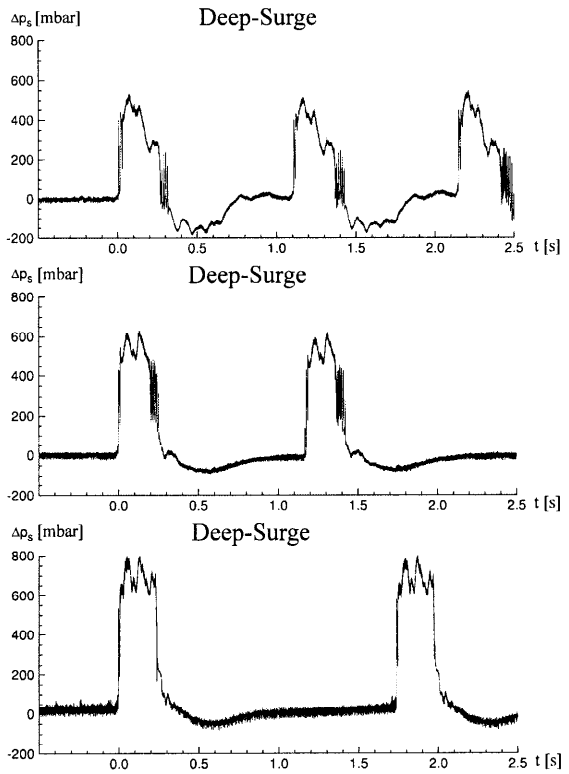


Figure 5: Static pressure in front of rotor 1 (section 5)during transition from stable to unstable flow for rated speeds of 80 %, 90 % and 100 % showing deep-surge with flow reversal during static pressure rise.

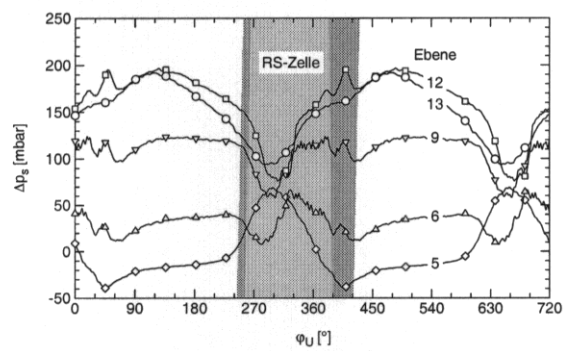


Figure 6: Measurements of wall pressure in the sections 5, 6, 9, 12 and 13 extending peripherally along the circumference. Within the domain of the stall cell the pressure drops in the rear stages and overshoots ahead of rotor 1.

verify the reproduceability of the situations encountered by Rippl (1995) during preceding tests. The flow regimes of rotating stall at 50 % and of classic surge at 60 % rated speed proved to be accessible to the equipment of measuring distributions of velocity-density and total temperature. Flow conditions at 70 % rated speed and above wiped out the high sensitivity temperature transducer (cold wire of 2.5 µm) and requires other dispositions for the velocity-density measurement due to high temperature levels.

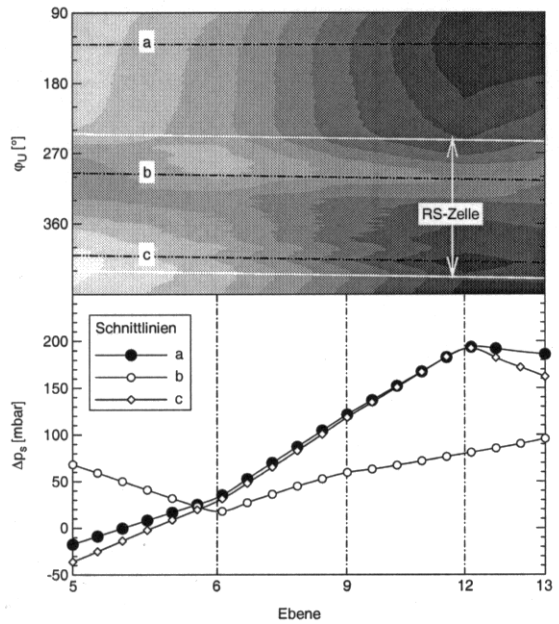


Figure 7: Static pressure Δp_s along 3 circumferential positions φ_u on the casing wall showing the axial distribution under the influence of a stall cell. A S2 computation by ZORBA2 (Novak, 1966) matches with distribution a (- ● -)

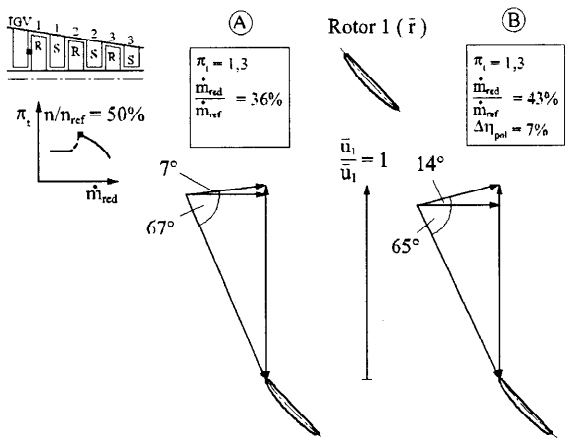


Figure 8: Velocity triangles in the aerodynamically stable range near the stall limit at 50 % rated speed and mid-height in front of rotor 1: - A) computed from measurements; - B) taken from a S2 computation (Novak, 1966)

Figure 6 displays the peripherally distributed pressure pattern for the sections at 50 % speed collectively. The development of pressure over the stages is displayed in figure 7 at one instant showing the rise and fall of pressure for 3 selected peripheral positions of which one is affected by the travelling stall cell. Comparison with a time-independent off-design S2 computation with the

axisymmetric streamline-curvature method ZORBA2 (Novak, 1966) show the flow to compare well with quasi-steady conditions in moments where flow recovery returns. It should be mentioned here that Rippl (1995) found out that the mean swirl angle of the flow leaving the inlet guide vane varies between 4° and 10° with the chord Reynolds number and the computation used the vane angle of 14°. The Carter turbine rule (Hawthorne, 1964) yields 6° of deviation, i.e. 8° for the flow angle.

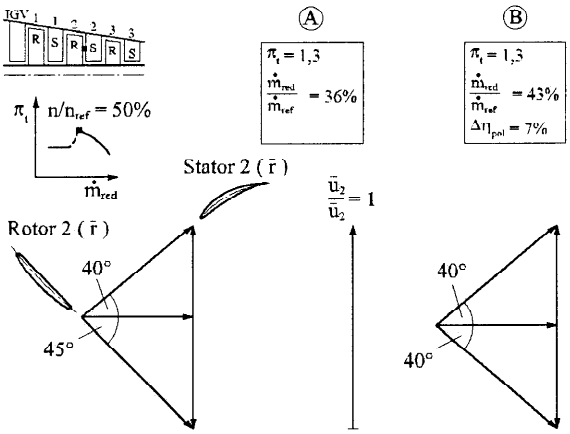


Figure 9: Velocity triangles in the aerodynamically stable range near the stall limit at 50 % rated speed and mid-height in front of stator 2:
- A) computed from measurements;
- B) taken from a S2 computation (Novak, 1966)

But as the S2 computation does not rely on the measurement, a discrepancy remains here. The results at 50 % rated speed presented hitherto (figures 8, 9) originate from an operating point on the 50 % speed line which, when crossing the limit of stability, drops in total pressure ratio from π_t = 1,3 to π_t = 1.2 with a mass flow decrease from 36 % to 27 % due to local flow reversal (figure 10).

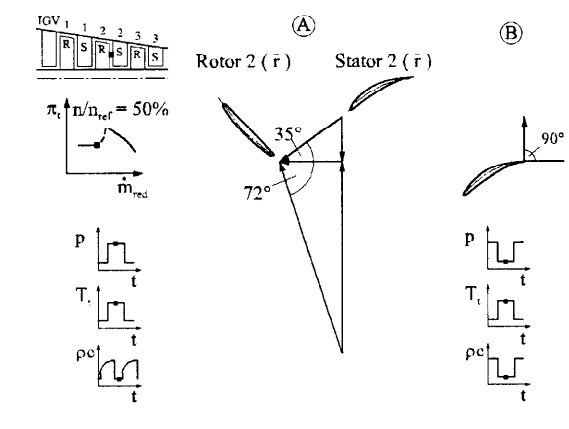


Figure 10: Velocity in the aerodynamically unstable range at 50 % rated speed and mid-height:
- A) The moment of local backflow in front of stator 2 computed from measurements;
- B) The moment of cirumferential flow at the trailing edge of stator 2 from figures 11, 12

The velocity triangle (figure 10) is computed from measured data, see figures 11 and 12.

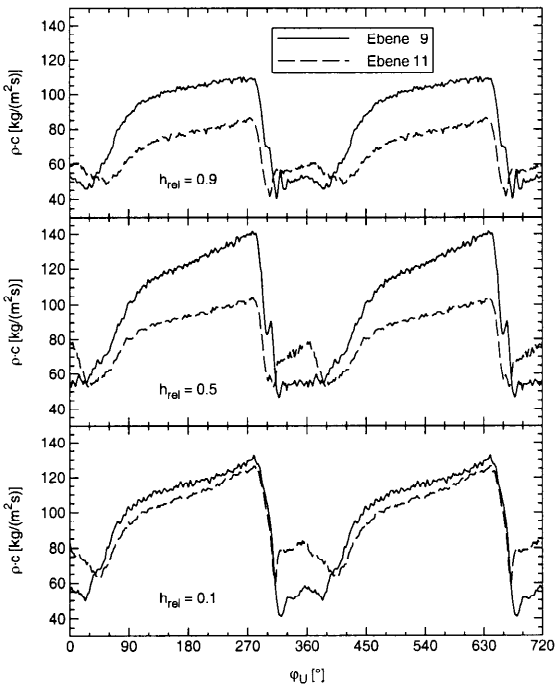


Figure 11: Distribution of the modulus of the velocity-density over the peripheral direction at 10 %, 50 % and 90 % height of the channel in front of stator 2 (section 9: —) and behind stator 2 (section 11: - - -) at 50 % rated speed

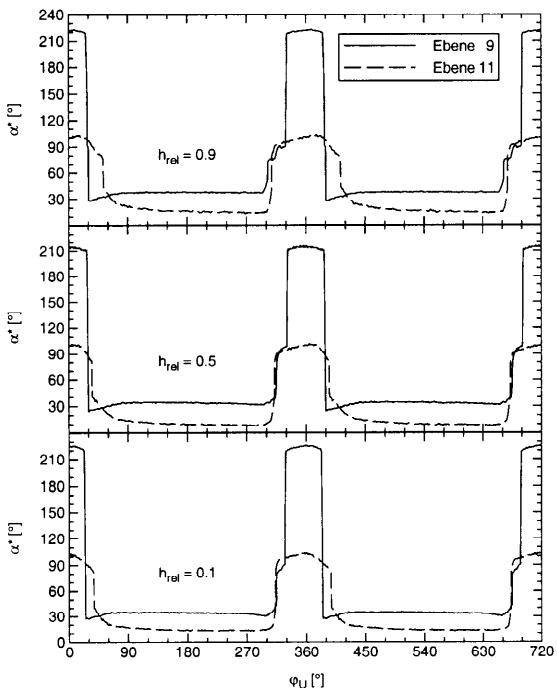


Figure 12: Distribution of flow angle over the peripheral direction at 10 %, 50 % and 90 % height of the channel in front of stator 2 (section 9: —) and behind stator 2 (section 11: - - -) at 50 % rated speed

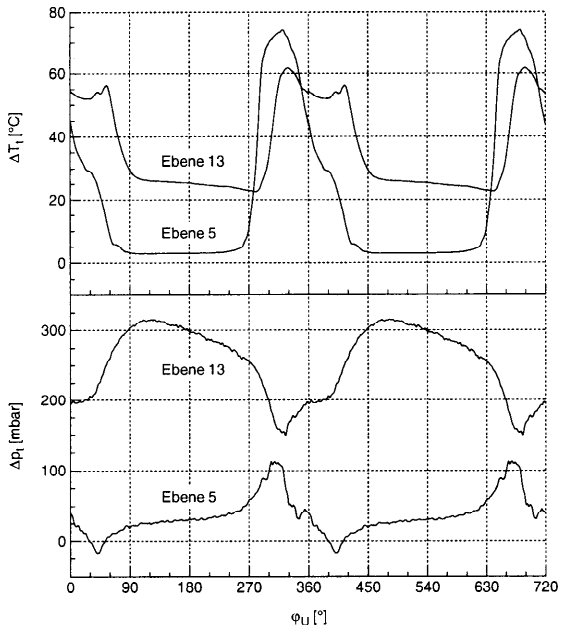


Figure13: Distributions of wall pressure and total temperature over a sector of the blading before the first (section 5) and after the last stage (section 13) during rotating stall at 50 % shaft speed and mid-height

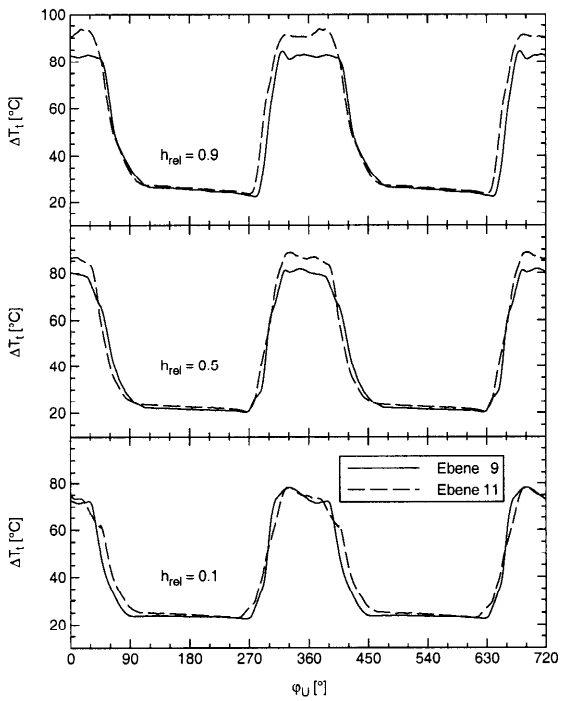


Figure 14: Distribution of total temperature over the peripheral direction at 10 % (bottom), 50 % (middle) and 90 % (top) height of the channel in front of stator 2 (section 9: —) and behind stator 2 (section 11: - - -) at 50 % rated speed

In this situation it is interesting to see how, during moments of stall, the wall pressure drops over a sector of about 120° in a row at the rear end of the blading. During that time the pressure rises in front of the blading as the local recirculation jams the flow through this peripheral sector (figure 13). A rise of the total temperature to 2 to 3 times the stable level goes along with the drop in the backpressure and the burst in front of the blading. By estimating the continuous energy input from the shaft at constant speed, it can be estimated that the amount of energy supplied, reduced by the energy requirement for the remaining through flow, is high enough to bring the air enclosed in the volume of the stall cell to such a temperature as measured here (figure 14).

The volume of the stall cell spreads over 1/3 (Rippl, 1995) to 1/2 (Preute, 2000) of the blading (figure 15). The strong increase in temperature observed here is confirmed by other observations in which blade failures during stall can be clearly attributed to overheating as their colour turned to blue (Strub & Suter, 1965) or the blading melted away (Hoffeins et al., 1980).

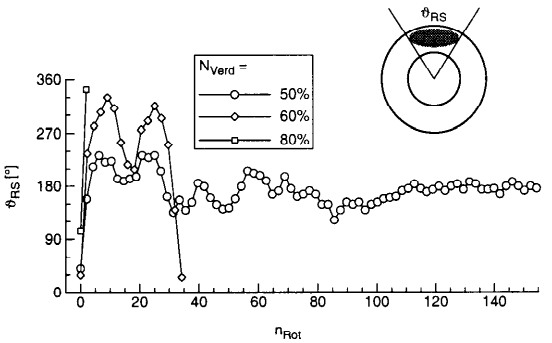


Figure15:Peripheral extension of the stall cell over the number of revolutions of the shaft for rated speeds of 50 % (- o -), 60 % (-◇-) and 80 % (-□-)

The measured unsteady results appear to be plausible when compared in a quasi-steady manner to S2 data from a streamline-curvature method which had been adjusted for the target pressure ratio by input of a corresponding mass flow, without tuning deviation and loss to fit efficiency and through flow to the experiment. The pressure rise in figure 7 as well as the velocity triangles in figures 8, 9, 16 and 17 support the measured results.

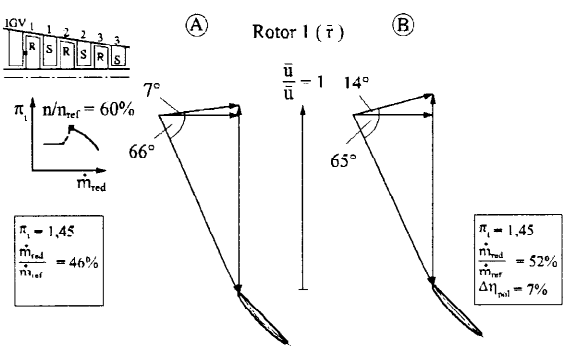


Figure 16: Velocity triangles in the aerodynamically stable range near the stall limit at 60 % speed and mid-height in front of rotor 1:
- A) computed from measurements
- B) taken from a S2 computation (Novak, 1966; ZORBA2)

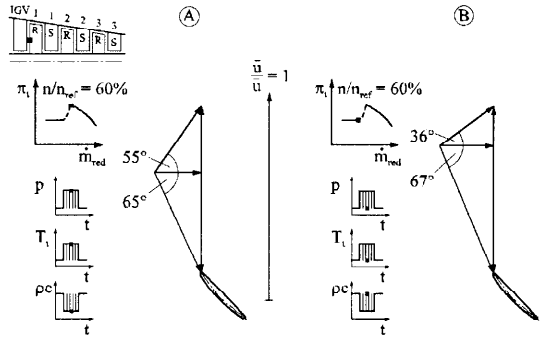


Figure 17: Velocity triangles for intermittent flow of classic surge at 60 % rated speed and mid-height in front of rotor 1:
- A) moment of minimum through flow:
- B) moment of maximum through flow

Keeping in mind that the electric power drops by up to 10 % when entering stall at 50 % speed from the primary characteristic (π_t = 1,3; $\dot{m}$ = 5,5 kg/s) to the secondary characteristic (π_t = 1,2; $\dot{m} \approx$ 4,2 kg/s), then the power requirement would drop to half its value.

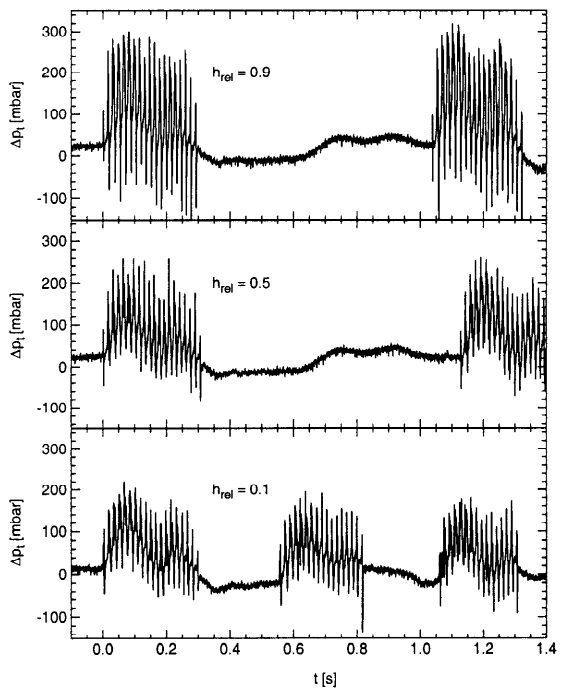


Figure 18: Distribution of total pressure over the time for 10 %, 50 % and 90 % height of the channel at 60 % rated speed in front of rotor 1 (section 5)

If the same efficiency applies, then about 40 % of the shaft power enters the air and heats up 5,5 kg/s – 4,2 kg/s = 1,3 kg/s of mass flow recirculating in the cell, which brings the temperature inside the stall cell up to approximately 50 °C whereas 20 °C to 30 °C would be the temperatures associated with an adiabatic compression for pressure ratios of π_t = 1,2 to 1,3. Similarly to 50 % speed, at 60 % speed the total temperature rises to more than 100 °C whenever local detachment of flow occurs with the flow angle snapping from 7° to about 50°, the speed falling to less than half the stable level and the pressure shooting up in front of the blading (figures 18, 19, 20).

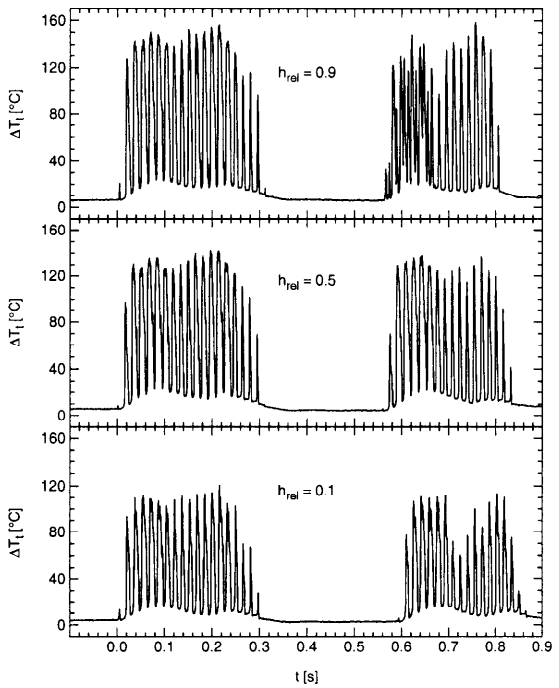


Figure 19: Distribution of total temperature over the time for 10 %, 50 % and 90 % height of the channel at 60 % rated speed in front of rotor 1 (sec. 5)

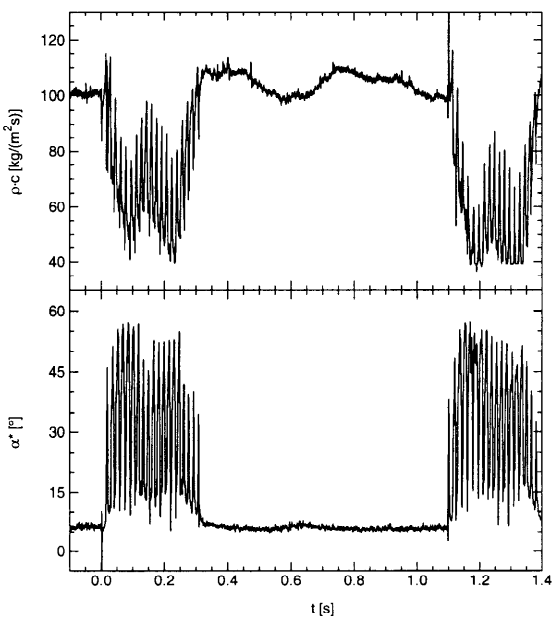


Figure 20: Distributions of the modulus of the velocity-density and the flow angle over the time at 60 % rated speed and mid-channel in front of rotor 1 (section 5)

When approaching the situation of stall, it is not easily possible to recognize the appearance of precursor wave patterns at a time sufficiently large to allow for

preventive action. Figure 21 shows the signals as acquired from the measurement beginning about 4,5 revolutions ahead of the stall event. First disturbances show only ½ revolution before stall. A precursor wave information serving as a stall detector cannot be discerned sufficiently early without special analysis of the signal, as will be shown below.

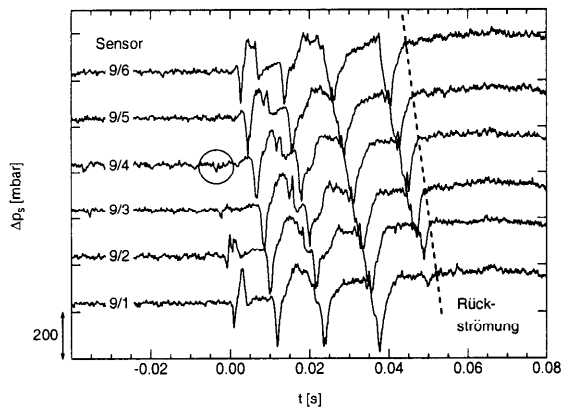


Figure 21: Distribution of wall pressure over the time for 6 transducers mounted peripherally in the casing in front of stator 2 (section 9) at 50 % rated speed. The trace of the signal starts about 40 ms, i.e. 4.5 revs., ahead of the first visible indication of stall.

RESULTS OF DATA ANALYSIS

As mentioned above, first it is necessary to detect the approach of the compressor operating point to unstable conditions before developing a control system to avoid this. Therefore different analysis techniques were developed and tested at the University of Bochum which aim at a reliable detection of reaching unstable regions of the compressor performance map. An extensive database was taken to compare data of the stable region to data nearby the surge-line at different speeds. The database for the analysis is given in figure 22.

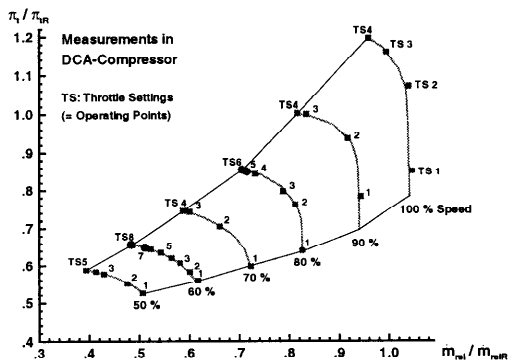


Figure 22: Database

The static pressure was recorded at 5 different circumferential positions in front of rotor 1, see fig. 3. The results of the analysis are given in the following sections.

Circumferential Fourier-Transform

This method takes advantage of the circumferentially distributed pressure transducers. The spatial Fourier-transform provides information about the amplitude and the phase of a peripheral pressure fluctuation. By calculating the change in phase between each time step, information about the rotational speed of the disturbance can be extracted. Another way to uncover rotating perturbations from the data has been described by Tryfonidis et al. (1994). Further explanations about these techniques are given by Grauer (1998). The time-dependent behaviour of these rotating perturbations can be observed by introducing a time window, which is shifted along the complex result of the first Fourier-transform.

The results of this analysis show, that there exist frequency ranges, where the amplitudes grow when the working line approaches the stability limit. One criterion for a stall warning can be figured out by integrating the amplitudes within a frequency band between 20 % and 50 % of the rotor frequency (Grauer, 1998).

Figure 23 displays the results for the 60 %, 80 % and 100 % speed of the compressor by comparing the sum of amplitudes which means the intensity of rotating disturbances.

Figure 23, at left, shows the results for a working point in the stable region and, at right, for a working point approaching the surge line. It can be seen, that there is a clear increase of the amplitudes.

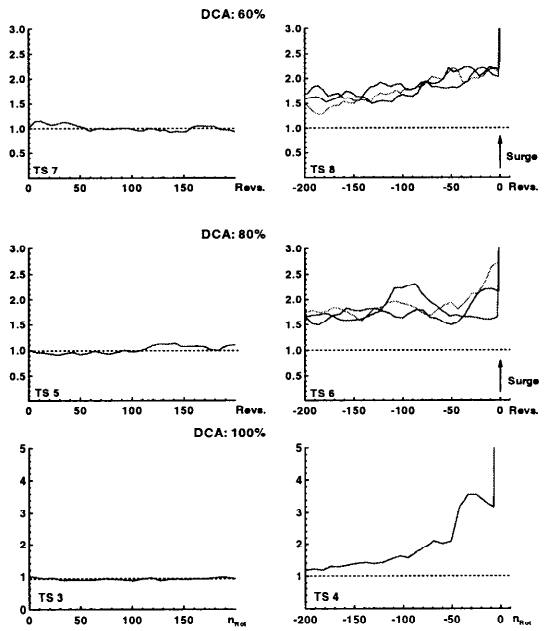


Figure 23: Intensity of rotating disturbances

For the application of this analysis technique, the signals of at least 3 pressure transducers are necessary, because the presented results were calculated from the first harmonic of the spatial Fourier-transform. The data of the

measurement section in front of rotor 1 were taken because earlier investigations have shown, that the best results were obtained from the signals of the transducers installed in front of the first stage (Grauer, 1998). Stage matching and hence the axial location of the onset of stall did not play an important role for this investigation. This may be due to the comparatively small length of this compressor.

Grauer (1998) has found out by investigating data of different compressors, that this behaviour is typical and can be used in a compressor control system to detect the approach to unstable conditions. A great disadvantage of this technique is, that it needs a minimum of three transducers over the compressor circumference, to calculate the Fourier-transform.
The described calculations not only deliver a criterion easy to obtain for a stall warning, they furthermore give a deeper insight into the characteristics of the signal during the stall inception process, which is helpful for the development of other analysis techniques to reduce data processing and instrumentational effort. One of these techniques, which centres on the observation of the rotor-speed periodic disturbances, is based on artificial neural networks and will be described below.

Classification using Artificial Neural Networks
Artificial neural networks attempt to imitate the biological brain in technical applications in the fields of pattern recognition and control. They can be adapted to a variety of problems and are able to extract information from data submerged in noise. Their capability goes beyond a simple analysis of the data as they can also serve for purposes of control

Figure 24 shows the basic elements of a neural network. It consists of many non-linear computational elements called nodes (represented by rectangles in figure 24) which are connected by links of variable weights. Data that have to be processed by the network reach the net via an input layer and are transmitted to the following layers by the weighted links. Basics about neural networks can be found in the literature (for example: Ritter et al., 1991; Zell, 1994).

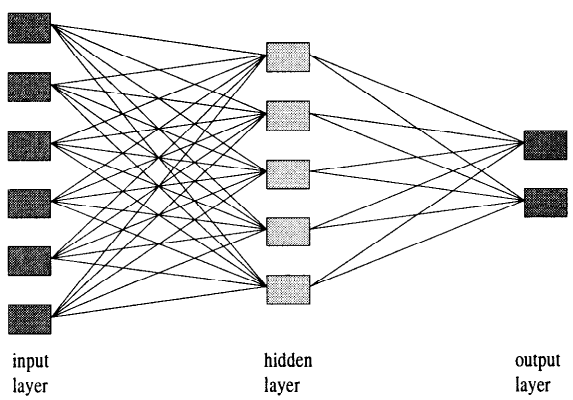


Figure 24: Basic elements of neural networks

Working with a neural network first requires adapting the net to the special problem. This is done during a separate process called the learning or training phase. One of the methods most frequently used is called *supervised learning*, which means that representative data, which describe the problem as detailed as possible, are presented to the net together with the respective output. The learning process is finished, if the calculated error between the network output and the teaching output reaches a given tolerance margin.

The presented results were obtained by the *Stuttgart Neural Network Simulator* (SNNS) which is developed at the *Institute for Parallel and Distributed High Performance Systems* (IPVR) of the University of Stuttgart, Germany. The simulator consists of various network types and other variable parameters. For the following investigations a feedforward net and the *cascade correlation learning algorithm* was used (Zell, 1994), as this combination yielded the best results.

Every neural network will work as well as the data, which were presented during the learning period, describe the problem to be handled. Therefore, apart from a good choice of network models, connection types and learning rules, which all have a significant influence on the network's performance, the most important step is to extract clear sets of data (called *input pattern*). Measured data can be improved by appropriate preprocessing, which can be achieved by different analysis techniques. As described in the former section, rotor-speed periodic disturbances were found in the pressure signal, that changed during stall inception.

Different analysis techniques gave a detailed insight into the structure of the pressure fluctuations. Referring to figure 23 a difference between the throttle settings 1-7 (60%), 1-5 (80%) or 1-3 (100 %) to those settings representing the stall inception [TS 8 (60%), TS 6 (80%) and TS 4 (100%)] was clearly indicated for example by the circumferential Fourier-transform described in the former section. As these differences should also be visible in the untreated pressure signals, they were observed in detail to find out comparable structures.

To remove noise, the signal was ensemble averaged over 10 rotor revolutions and then observed over a time of about one rotor revolution. The signals were normalised in an interval of [0,1] for each throttle setting, so differences due to the absolute pressure value were avoided. The length of the generated pattern covers an interval of 50 samples which means nearly one rotor revolution. The way of input pattern generation from the pressure signal is given in figure 25.

This generating of input pattern for the neural network has been done for all different speeds of the compressor. The network was trained and tested with the data of sensor 4. The validation has been done by using data

from different sets of measurements. The network generated with those data is given in figure 26. The output-layer design of the network belongs to the different compressor speeds.

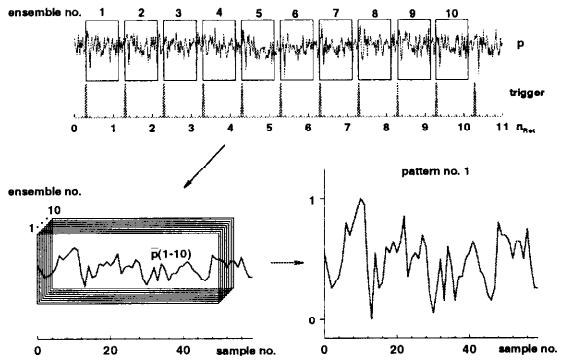


Figure 25: Generation of input pattern

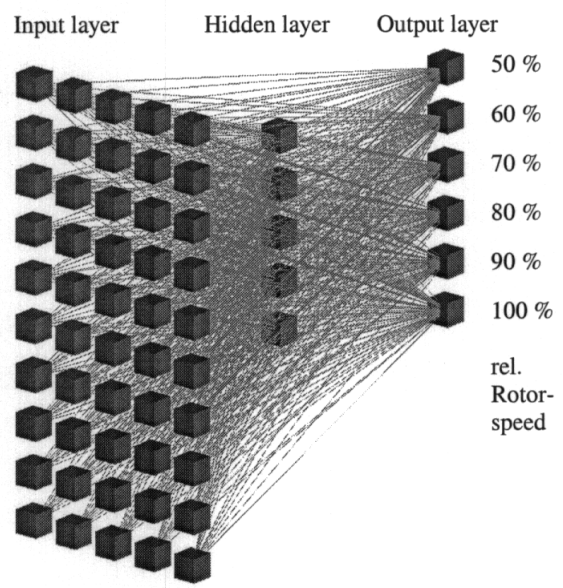


Figure 26: Neural Network after training

The teaching output of the network was 0.3 for regions of stable operation and 1.0 for operating points that are approaching the surge line. Fig. 27 displays the results of data classification using the network shown above (figure 26) with the "unknown" testdata put into the network.

Figure 27 displays an example of the network output for each compressor speed. One or two datasets are from a stable operating range (S#) and the other output (TR) comes from a dataset approaching the surge line. As it can be seen, the network output does not exactly correspond to the teaching output (defined before as 0.3 or 1.0) but it can clearly be decided between stable and unstable compressor operation by using such an artificial neural network.
Due to the high-speed data acquisition of transient data, this behaviour of the network output is expected.

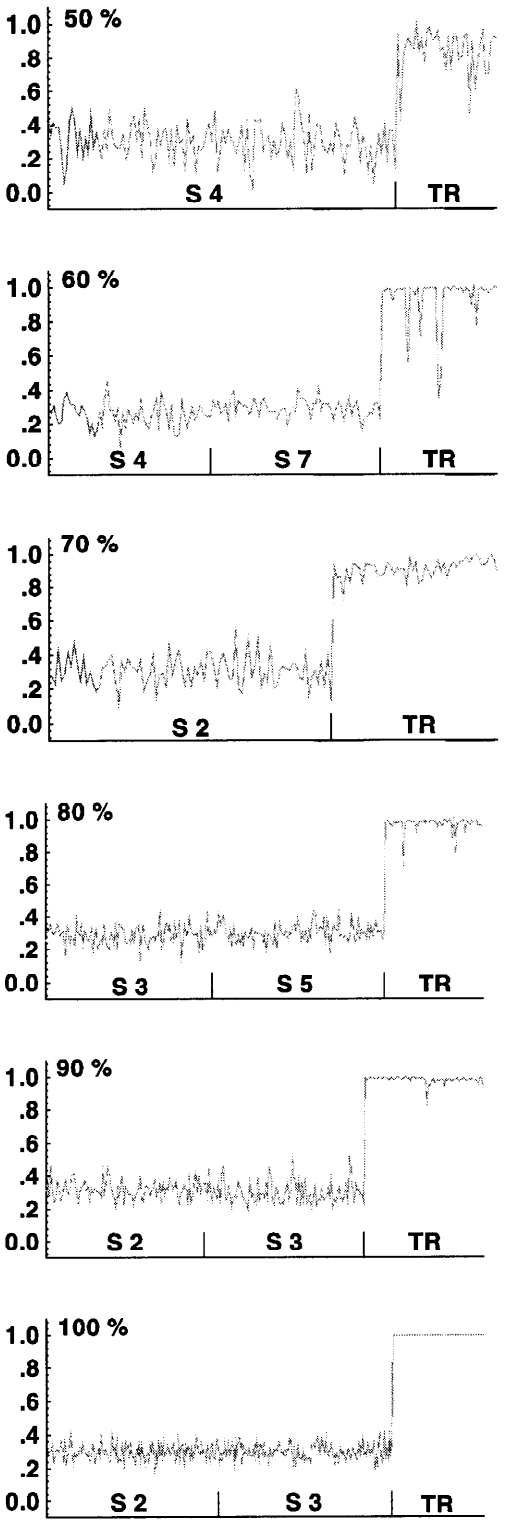


Figure 27: Network output of the different output nodes belonging to the individual rotor speeds

It is impossible to eliminate all noise of the signal by ensemble averaging. Nevertheless the network output is unambiguous if it is interpreted e.g. by a decision as "less than 0.5" or "greater than 0.7".
By analysing the network output in this way it can be stated that with the exception of 2 input patterns at rated speed of 50 % and 3 input patterns at rated speed of 60 % all input pattern are classified correctly. If the decision

between stable and unstable compressor operation is then based on taking e.g. 3 following networkoutputs, the system is absolutely reliable.

This result shows that a stall warning based on this network produces a warning in time. Nevertheless it is possible to improve the performance by treating more data during the learning process, which can easily be obtained by further measurements. Such measurements are planned in the future to investigate the performance of the described method over the whole speed range and with repeated stall events.

The described method centres on the observation of the disturbances being periodic with the rotor speed. Those disturbances can be found in compressors with a spike-type stall and in those with modal waves (Day et al., 1997). It should be possible to apply this method to both types of onset of instability. This will be a subject for investigations in the future.

CONCLUSIONS

Single-probe measurements of total temperature and velocity-density vector in front of rotor 1, behind rotor 2, stator 2 and stator 3 have been acquired at 10 %, 50 % and 90 % height of the channel at revving speeds of 50 % and 60 % of the operating range. Through the use of split-film and cold-wire probe, flow-field data with a resolution of 1 kHz in time are available to validate computer codes for unsteady simulation of unstable compressor flow situations of rotating stall and classic surge.

Steady-state streamline-curvature S2 computations have been compared to quasi-steady situations of the time-dependent flow measurements confirming the validity of velocity triangles. In this way, future measurements of high resolution in time with a direction-dependent total pressure miniature probe (2.2 mm axial extension) are enabled in axial gaps inside the stages during selected instants of time.

Unsteady measurements of wall pressures in the casing in front of the stages and at the exit as well as behind each rotor complement the temperature measurements to determine the density.

Peaks in the temperature measurement during moments of stalled flow grow to levels of 2 to 3 times the corresponding values at the same speed in the aerodynamically stable range. An energy balance estimation with the input of shaft power into locally enclosed volumes of recirculating stall cells support the temperature levels measured here.

The unsteady distributions of pressure signals over time allow to recognise precursor waves not more than about 1 revolution (approx. 5 to 10 milliseconds) prior to stall. The signal analysis using Fourier-Transforms has shown to extend the available warning time to the order of a second (i.e. 300 revs) and artificial neural networks to more than 3 seconds (800 revs) prior to stall.

ACKNOWLEDGEMENTS

The stall and surge measurements on the compressor rig at the University of Bochum were supported by the German Ministry of Education and Research (BMBF) together with MTU during the project "AG TURBO – Turbotech" under grant no. 0327041C. The signal treatment was funded by MTU during project "Engine 3E". R. Stromberg and the workshop members of the Energy Institute contributed to operation and maintenance of the test rig, D. Becker to the electronic chain of instrumentation, Mrs. M. Regulski, O. Narin and J. Schäfer to the lay-out of text and graphics. The S2 computations were put at our disposal by P. Mertes and by M. Schwarz from DEMAG. We gratefully acknowledge all these contributions.

REFERENCES

Baumann, H., 1970: "Messungen der Schaufel-beanspruchung von Axialgebläsebeschaufelungen bei rotierender Ablösung", Schweiz. Bauzeitg. 88 (11. Juni 1970)24, 541-543

Breuer, T., Servaty, S., 1995: "Stall Inception and Surge in High Speed Axial Flow Compressors", AGARD CP-571 pp. 26/1-17

Breuer, T., 1996: "Compressor Flow Instabilities: Part I: Multistage Environment, Modelling Approaches; Part II: Analysis Techniques", see VKI

Day, I.J., 1991: "Active Suppression of Rotating Stall and Surge in Axial Compressors", ASME 91-GT-87

Day, I.J., 1996a: "The Fundamentals of Stall and Surge in Axial Compressors", see VKI

Day, I.J., 1996b: "Stall and Surge in High Speed Compressors and the Prospect for Active Control", see VKI

Day, I.J. et al., 1997: "Stall Inception and the Prospects for Active Control in four High Speed Compressors", ASME 97-GT-281, Journal of Turbomachinery 121 (Jan. 1999)1, 18-27

Grauer, F. et al., 1998a: "Detection of Precursor Waves announcing Stall in two 3-Stage Axial Compressors", ASME 98-GT-520

Hawthorne,W.R., 1964: "Aerodynamics of Turbines and Compressors", Princeton Univ.Press

Hoffeins, H. et al., 1980: "Die Inbetriebnahme der ersten Luftspeicher-Gasturbinengruppe", Brown Boveri Mitt. Vol. 67 (August 1980)8, 465-473

Höss, B. et al., 1998: "Stall Inception in the Compressor System of a Turbofan Engine", ASME 98-GT-475, Journal of Turbomachinery 122 (Jan. 2000)1, 32-44

Lohmberg, A., 1995: "Entwicklung einer Sonde zur Messung flukturierender Druckspannungen im Axialverdichter", Interner Bericht, Ruhr-Universität

Bochum, Lehrstuhl für Fluidenergiemaschinen (AN99-008)
Ludwig,G.R.; Nenni,J.P., 1978: "A Rotating Stall Control System for Turbojet Engines", ASME 78-GT-115; Journal of Engineering for Power 102(Jul1979)3, 305-314
Ludwig,G.R.; Nenni,J.P., 1980: "Tests of an improved rotating stall control system on a J-85 turbojet engine", ASME 80-GT-17; Journal of Engineering for Power 102(Oct.1980)4, 903-911
Nenni, J.P., Ludwig, G.R., 1974: "A Theory to predict the Inception of Rotating Stall in Axial Flow Compressors", AIAA-74-528, AIAA 7th Fluid Plasma Dynamics Conf.
Novak, R.A., 1966: "Streamline Curvature Computing Procedures for Fluid-Flow Problems", ASME 66-WT/GT-3, Journal of Engineering for Gas Turbines Power 89 (October 1967)4, 478-490
Preute, R. et al., 1997: "Sensoren für Strömungsinstabilitäten am Beispiel eines Axialverdichters", tm – Technisches Messen 64 (Juni 1997), 238-246
Preute, R., 2000: "Experimentelle Untersuchung der aerodynamischen Instabilität in einem mehrstufigen transsonischen Axialverdichter", Dissertation, Ruhr-Universität Bochum (expected 2000)
Regnery, D., 1998: "Development of a System for the Observation of the Stable Operation in Multistage Axial Compressors", VDI-Ber. Nr.1425, 199-210.
Rippl, A., 1995: "Experimentelle Untersuchungen zum instationären Betriebsverhalten an der Stabilitärsgrenze eines mehrstufigen transsonischen Verdichters", Dissertation, Ruhr-Universität Bochum
Ritter, H. et al., 1991: "Neuronale Netze", Addison Wesley Publishing Company
Schulze,R. et al., 1998: "Experimental Examination of an Axial Compressor as a Basis for an Active Stall Avoidance System", ISROMAC-7 Paper, 22-26 Feb.1998, Honolulu, ev.IJRM Intern.Journal of Rotating Machinery
Schwarz,M., 1990: "Berechnung der Strömung und der Seitenwandgrenzschichten in mehrstufigen Axialverdichtern unter besonderer Berücksichtigung der Randzonenkorrektur", Dissertation, Ruhr-Universität Bochum
Strub, R.A., Suter, P., 1965: "Compressor Surge in Gas Turbines and Blast Furnace Compressor Installations", ASME 64-GTP-5, Journal of Engineering for Power 87(April 1965)2, 193-196.
Tryfonidis, M. et al., 1994: "Pre-Stall Behaviour of Several High-Speed Compressors", ASME 94-GT-387
Walbaum,M., Rieß,W., 1998: "Einfluß der Leitschaufelverstellung auf die Entwicklungsformen des Rotating Stall in mehrstufigen Verdichtern", VDI-Ber. Nr.1425 (1998) 177-188.
VKI LS 1996-05 "Unsteady Flows in Turbomachines"
Zell, A., 1994: "Simulation Neuronaler Netze", Addison Wesley Publishing Company

PAPER -8, F. O. Methling

Question (W. Reiss, Germany)
Do you think that this early warning method is a general solution to the problem?

Reply
The neural net method has to be trained for each machine, but seems to be quite capable.

Question (H. Weyer, Germany)
Please comment on the reasons for the sawtooth type of total pressure distribution of the first rotor.

Reply
The total pressure probe that was used, similar to a Pitot probe, is only in one particular direction which is sensitive to the total pressure. Due to the flow angle within the stall cell (see figure 12 of the paper), such a total pressure distribution can be explained.

Development of Flow Instability and Rotating Stall in a Multi-Stage Axial Compressor with Variable Guide-Vanes

W. Riess, M. Walbaum

Institute for Turbomachinery

University Hannover, Appelstr. 9

30167 Hannover, Germany

Introduction

Many well-known investigations on flow instabilities of axial compressors have been conducted in low-speed research machines, often in a single stage configuration. It is at least not assured, that the results can be transferred directly to multi-stage compressors with compressible flow, therefore measurements in machines of this type are of considerable practical interest.

These machines, however, pose a lot more problems in realisation, operation and measuring techniques. They have to be of robust and elaborate design and manufacture to withstand high rotational speed and to avoid problems with blade vibrations and critical rotor speed. They need - even as model machines with reduced size - driving power of several hundred kW up to the MW range, preferably with variable speed.

Equipment

At the Institute for Turbomachinery at University Hannover in an open-loop compressor test stand a six -stage model axial compressor with variable guide vanes is available. Fig. 1 shows a cross section, the relevant data are:

Mass flow	10 kg/s
Speed	14175 rpm
Pressure ratio	2
Outer Diameter	340 mm
DC Motor	1300 kW

Paper presented at the RTO AVT Symposium on "Active Control Technology for Enhanced Performance Operational Capabilities of Military Aircraft, Land Vehicles and Sea Vehicles", held in Braunschweig, Germany, 8-11 May 2000, and published in RTO MP-051.

The six rows of guide vanes can be adjusted individually and independently. The flow is regulated by a throttle ring directly behind the diffusor, so that the pressure side volume of the system is minimized. The compressor therefore falls into a stable rotating stall upon crossing the stability limit, surge will not occur. It has been proven experimentally, that the stability limit is identical for operation with large and small pressure side system volume.

For investigation of the transition into rotating stall simultaneous measurement and data acquisition for several quantities has been applied. In stable rotating stall operation also consecutive measurements (p.e. probe measurements at different blade heights) can be made and put together correctly, if a trigger signal is used, which is locked definitely and exactly to the stall cell.

Measurements of unsteady casing wall pressure is not problematic and might in fact be easier than in low-speed machines because of the larger amplitudes. The necessary temporal resolution of several dozens of kHz can be achieved with available transducers.

Application of a single transducers per plane indicates p.e. increasing pressure fluctuation during approad of the stability limit. Three or more transducers distributed along the circumference of the casing will show with a suitable evaluation disturbance waves and their movement.

Much more problems poses the measurement of - necessarily unsteady - flow quantities inside the machine. The familiar hot-wires have often a limited life-time under these conditions. Their signal is influenced by variable fluid temperature, especially under rotating stall and surge conditions and they give, in a single wire configuration, values for the flow velocity only.

Their small dimensions are an advantage in practical use. In connection with a multichannel signal processing equipment they permit the installation of several probes throughout the compressor for simultaneous measurement. This is valuable for monitoring the transition process in a multi-stage machine and we have applied this principle for these cases.

Laser-Doppler-Anemometry might be a good alternative, but optical access for a 2D-configuration through the necessary window considering the small dimensions of model machines and the provision of sufficient particles at the measuring points without undue deposits on blades and windows is still a problem.

At the Institute for Turbomachinery a probe especially for unsteady flow measurements in stall and surge conditions was developed.

The necessary requirements were:

- Large measuring range for flow velocity (50 - 200 m/s)
- Large measuring range for flow angle in S1-plane (± 180° if possible)
- High temporal resolution (limit frequency > 50 kHz)
- Measurement of static pressure simultaneously with flow velocity
- Low sensitivity to fluid temperature variations
- Small geometrie dimensions (diameter > 10 mm)

These requirements were satisfied rather well by a cylinder probe with six unsteady pressure sensors at 60° circumferential spacing (fig. 2).

By suitable calibration

- flow velocity
- flow angle in S1-plane in a 360°-range
- total pressure
- static pressure

can be measured. Dynamics calibration showed a limit frequency of about 200 kHz. The central thermocouple measures the operating temperature, by (static) calibration of the pressure transducers at variable temperature this influence can be taken care of, too. The diameter of 6 mm is not really subminiature, but the interference with flow seems to be acceptable.

Measurements

The test compressor has been operated during the extensive investigations at different speeds - from nominal to 50 % nominal speed - with design position of all guide vane rows, indicated by I Le(0), and at different guide vane settings. These are shown in fig. 3, an identical movement of all guide vane rows by 22° in closing direction is marked by II Le(3), a degressive closing from 30° to 10° by I Le(4) and a progressive closing from 8° to 22° by III Le(3). The resulting characteristics at nominal speed are shown, too, in fig. 43

Not all of these operating regimes might be very close to technical reality, they have been chosen to cover a very broad field of possible aerodynamic conditions.

9-4 The influence of speed and guide vane setting on aerodynamic loading is shown exemplary in fig. 4. The relative loading factor $\varepsilon^* = \varepsilon / \varepsilon_{nom}$, where $\varepsilon = \varphi / \varphi^2$, is shown for different speeds and the guide vane settings I Le(0) and I Le(4). The dependency on speed is much more pronounced for the nominal setting I Le (0), while setting I Le(4) shows a definite increase of loading for stage 1.

The different types of measuring systems described above were utilized to investigate the transition to instability under varying operating conditions and some examples of stable rotating stall cells in detail.

The installation of several - at least three - unsteady wall pressure transducers in an axial plane between blade rows, the simultaneous recording of their signals and a suitable evaluation shows the development of disturbance waves during the formation of a rotating stall cell travelling at about 50 % of the blade speed.

Fig. 5 shows this for rotor 1 at nominal speed and guide vane setting. Small disturbance waves form about 20 to 30 ms before transition and grow finally within 10 ms to one fully developed rotating stall cell.

The propagation of the onset of rotating stall through the complete compressor at these operating conditions is shown in fig. 6 and 7 with the same measuring technique. Under these conditions the progress of instability is very rapid, as is the resulting break-in of pressure ratio.

It can be clearly seen, that the destabilisation is initiated by the growth of a local pressure disturbance in stage 1. Almost simultaneously with the formation of the stall cell in stage 1 the pressure in stage 6 begins to fall, the propagation of the rotating stall through the machine takes a few revolutions. In the front-stages the stall cell is characterized by positive excursions of the static pressure - it blocks the fluid flow -, while in the rear stage it creates rather a pressure depression - it obstructs the fluid flow.

The vector probe permits a more detailed insight into the flow. Fig. 8 shows static pressure p_{st}, axial flow component c_a, relative flow velocity w and relative flow angle β at 75 % blade height behind rotor 1 during transition to rotating stall. The local static pressure exhibits periods with larger and smaller fluctuations similar as the axial flow component. The relative velocity shows in the early phase sudden high amplitude excursions, the relative flow angle, too. The developed stall cell, then, has typically low resp. back flow areas combined with increased static pressure.

The presentation in fig. 9 of the relative flow vector at the position of the vector probe behind rotor 1 during transition to rotating stall makes evident, that in the early phase stochastic flow disturbances as local excursions of flow velocity and/or flow angle occur (no modal wave was found during the complete investigations), which grow in number and intensity until finally one disturbance becomes permanent and grows massively. Fig. 10 shows the same event as absolute velocity, completed by the curves of total and static pressure. It is interesting to note that many of the flow disturbances are connected with increasing total pressure, which might indicate an other possibility to deduct an early instability signal.

The vector probe measurements at different blade heights and in different axial planes revealed, that at nominal speed and guide vane setting the stall cell does not extend over the complete blade height, as shown in fig. 11 for rotor 1, although the stall exhibited the character of a "full span stall", i.e. a distinct decrease of pressure ratio in the characteristic field after crossing the stability limit. Fig. 12 shows the origin and the development of the stall in a cross section of the compressor at nominal speed and guide vane setting.

The effect of operating speed on the mode of transition into instability and the configuration of the resulting rotating stall is obvious in the comparison of figs. 13 and 14. At full speed the transition is rapid, beginning with small pressure fluctuations and changing abruptly into a single-cell stall. At 50% speed the process takes much longer and develops first a two-cell stall, which finally changes into a single-cell stall.

Setting of the guide vanes acc. to II Le(3) reveals (at 80% nominal speed) a very different pattern of transition to rotating stall. Simulanteous hot-wire measurements in different stages near the tip and near the root behind the rotors, shown in fig. 15 and fig. 16, show that already before crossing the stability limit (time = 0, drop of static pressure at exit) velocity fluctuations occur near the tip of rotor 1. Somewhat later instability begins at the root, mainly in stage 3 and extends rapidly over stages 3 to 6. Only after 300 ms rotating stall is marked in the tip region, too, throughout the machine.

Fig. 17 indicates the positions of the onset of instability, fig. 18 illustrates further the beginning and extension of tip stall in the characteristic field and the pattern of wall pressure fluctuations in stage 1 before the stability limit is reached. It is obvious that this tip stall is not completely stable as in other cases. Sometimes two cells emerge ,

which reunite again. The ratio of rotating frequency of stall cell and rotor, indicated in fig. 15 displays these variations, too.

A drop of overall pressure ratio, however, has not yet taken place (see Fig. 16), i.e. the existence of local stall - perhaps acting as excitation of blade vibrations - is externally not manifest. This phenomenon does not exist at nominal guide-vane setting.

A degressive guide vane setting acc. to I Le(4), which is comparable to practically applied setting laws, shows a different type of transition to rotating stall. The wall pressure measurements behind the six rotors in fig. 19 show increasing fluctuation mainly in stage 1 already before the drop in pressure ratio at 240 ms. The rear stages are rather quiet. The velocity measurements at 75 % blade height by hot wire in fig. 20 exhibit the same behaviour more pronounced. At time = 0 (resp. 240 ms) the fluctuation type changes rapidly, seemingly more abrupt in the velocity traces than in the pressure lines, and ends up in a stable single cell rotating stall, evidently emerging from stage 1. The presentation of the circumferential unsteady pressure distributions for the first three stages in fig. 21 makes clear, that rotor 1 still has some kind of multi-cell tip stall before time zero while mainly in stage 3 a typical single cell stall has already begun to develop, which finally dominates the whole machine. A close look into fig. 20 corroborates this observation. Fig. 22 shows the origins of instabilities in the machine cross section.

Conclusions

The comparison of the different measuring systems applied and their results suggests some conclusions

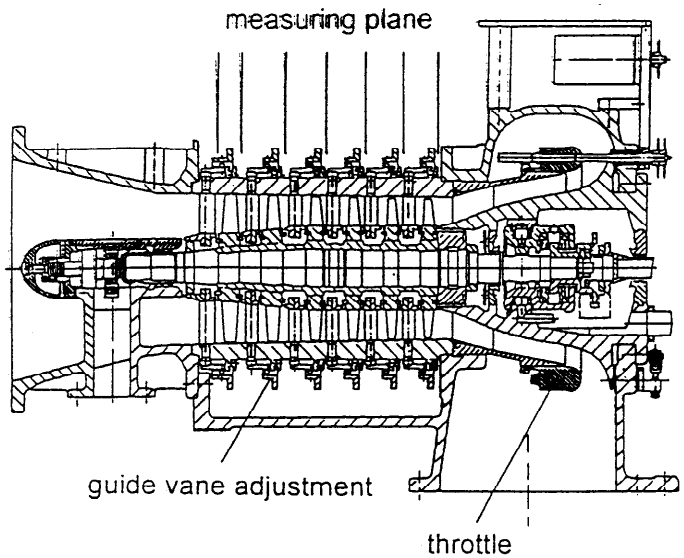
- Unsteady casing wall pressure measurements can indicate imminent instability
- For exact localisation of the origin of instability suitable unsteady measurements in the flow field seem indispensable
- Measurements of this type, combined with measurements to determine the local aerodynamic working conditions of the blading, could promote the development of reliable aerodynamic instability criteria

- For the definition and investigation of efficient methods for active stabilisation unsteady flow measurements within the machine are probably inevitable

The analysis of the different modes of transition into instability and the resulting stall configurations observed shows for multi-stage axial compressors with compressible flow

- High operating speed evokes a rapid transition into instability with strong interaction of the stages
- Lower operating speed retards the transition, two-cell stalls with less stage interaction are formed intermediately. Permanent multi-cell stall configuration are stable at very low speed only
- Variations of guide vane setting angle can result in very low interaction of stages with localised instabilities. Partial stalls without influence on the overall stability can arise.

It seems evident, that more research efforts on the process of destabilisation, preferably in multi-stage compressors with compressible flow, are necessary. Only if we understand these phenomena efficient means for active stabilisation can be developed.



design data :

mass flow rate	10.2	kg/s
pressure ratio	2.0	
rotational speed	14575	rpm
degree of reaction	0.84	
tip diameter of blading	340	mm
hub/tip ratio	0.44	

Fig.: 1 Six Stage Axial Compressor

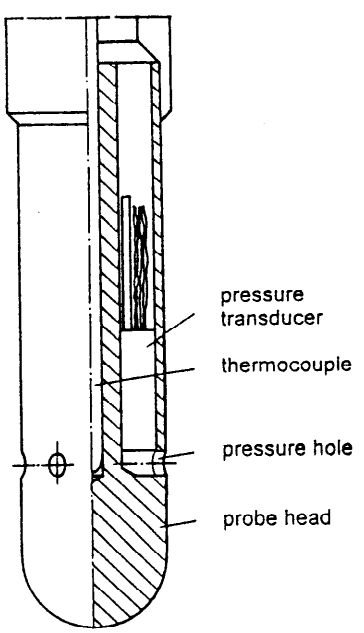
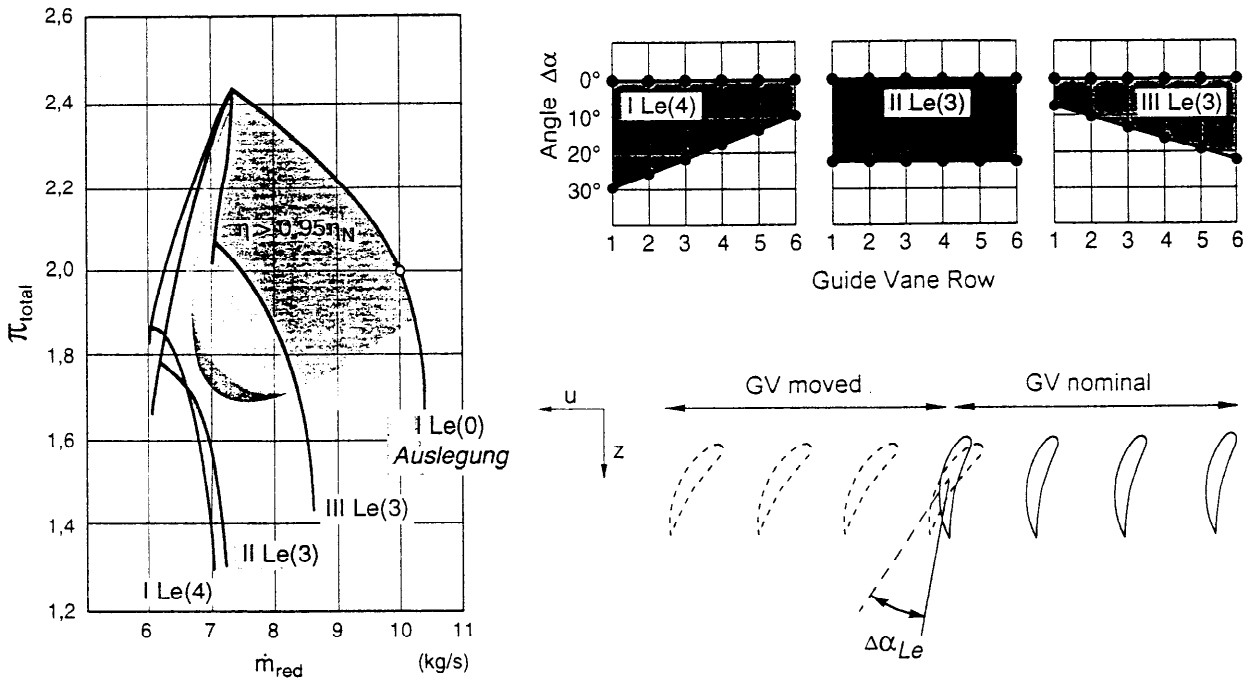


Fig.: 2 Flow-Vector Probe

Fig. 3 Guide Vane Setting Laws



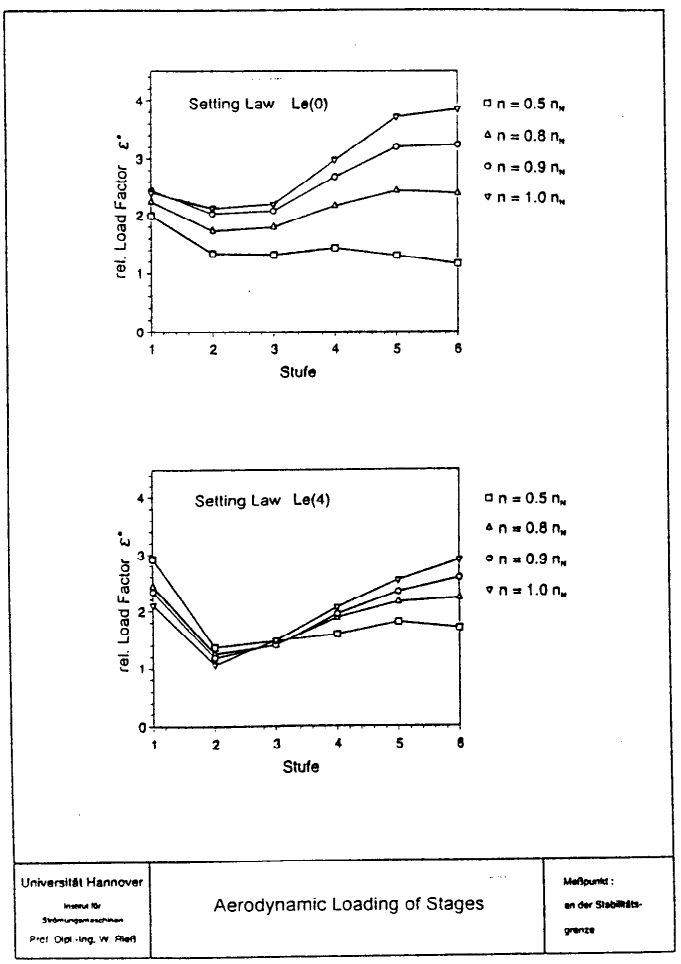
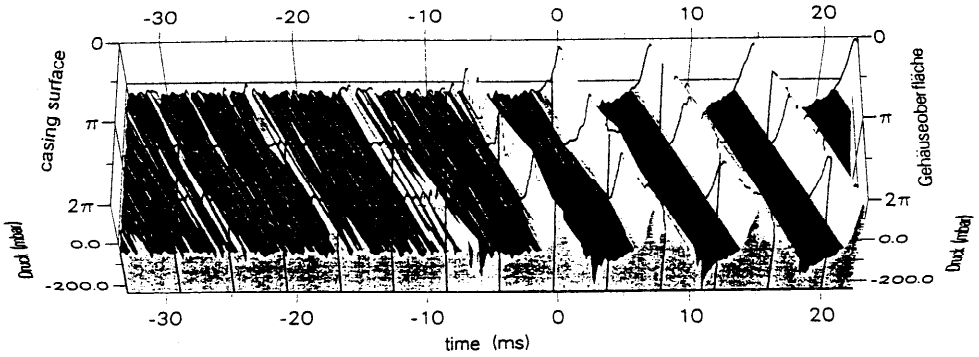


Fig. 4
Distribution of aerodynamic stage loadind in function of speed and guide vane setting

Fig. 5 Development of Rotating Stall at High Load



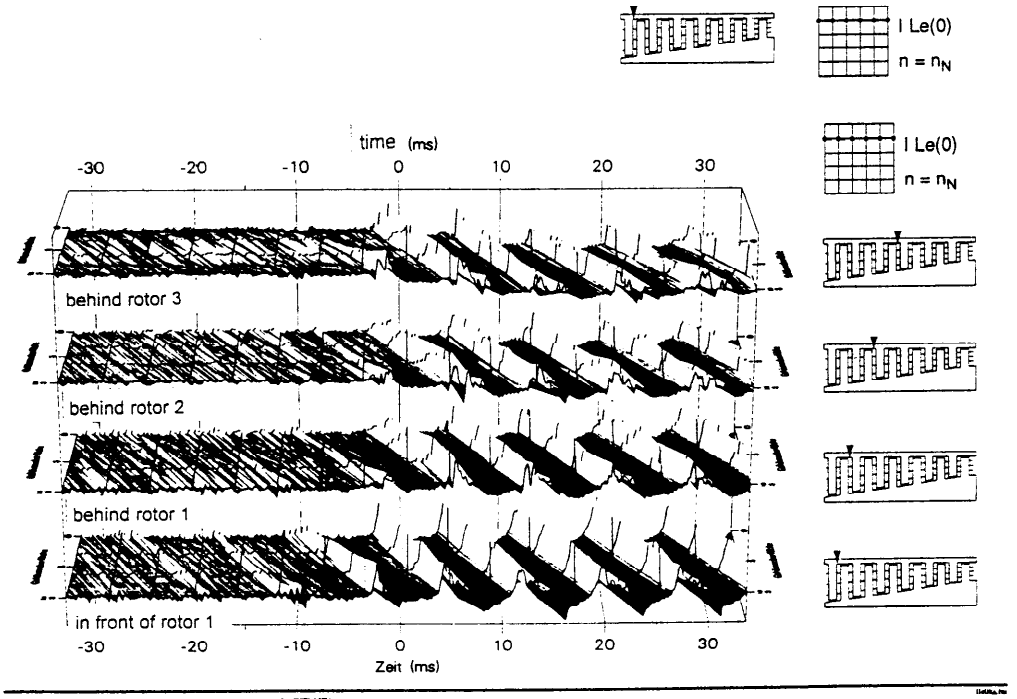


Fig. 6 Development of Rotating Stall at High Load

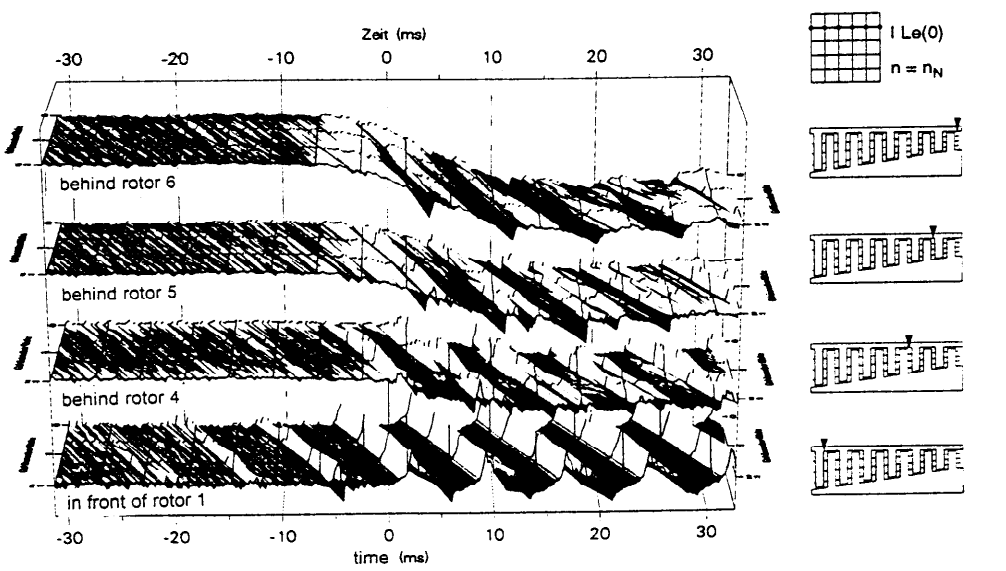


Fig. 7 Development of Rotating Stall at High Load

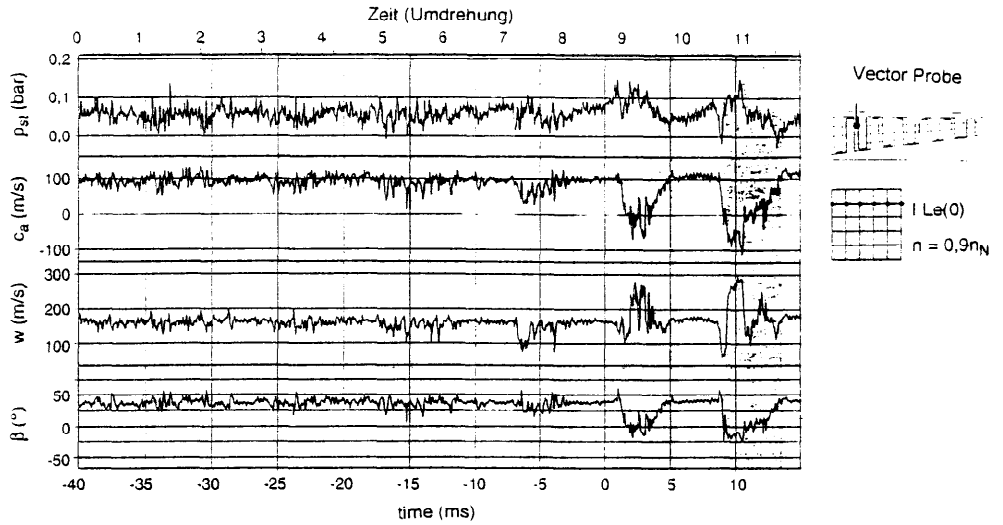


Fig. 8
Transition into Rotating Stall in Rotor 1 at nominal conditions

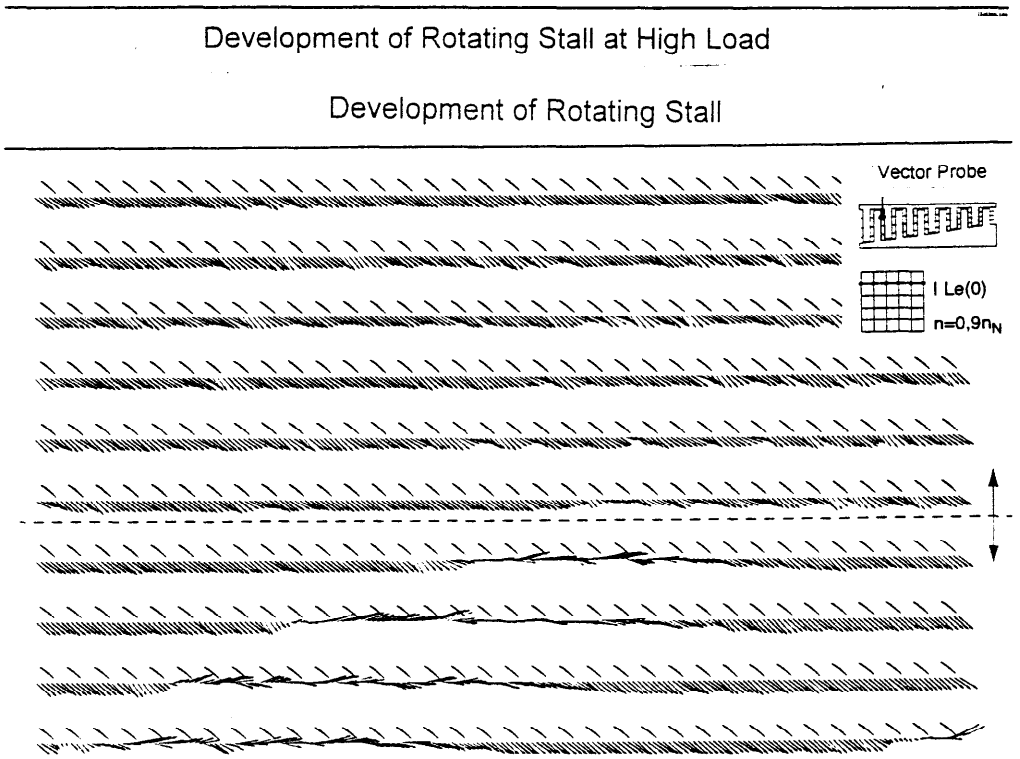


Fig.9
Development of relative velocity behind rotor 1 during transition into rotating stall

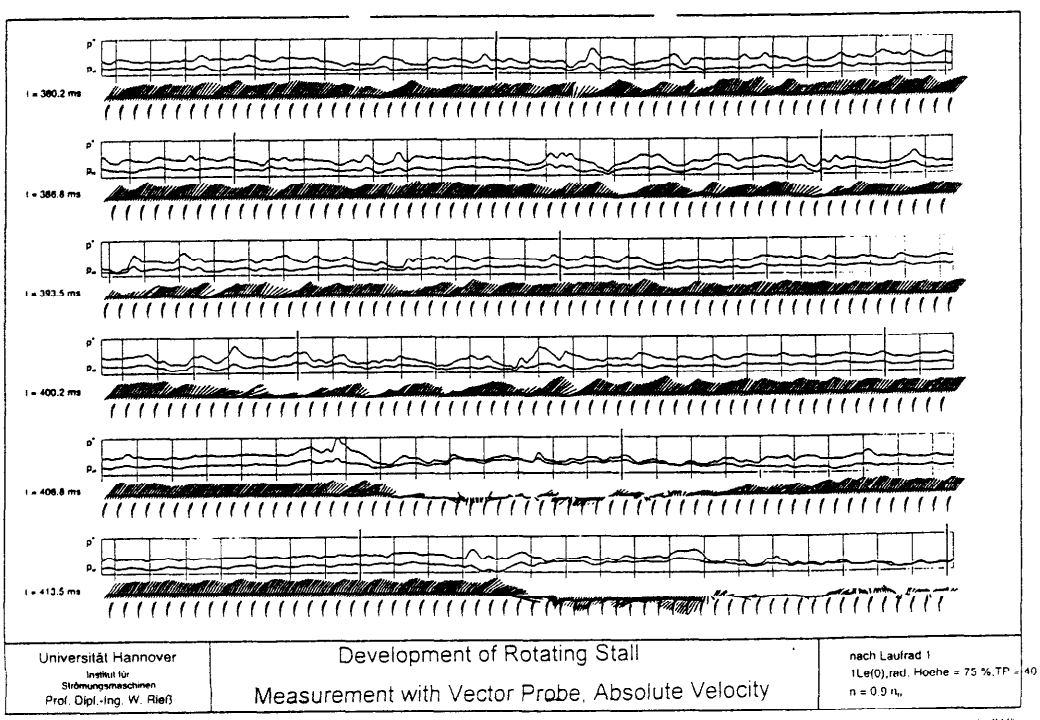
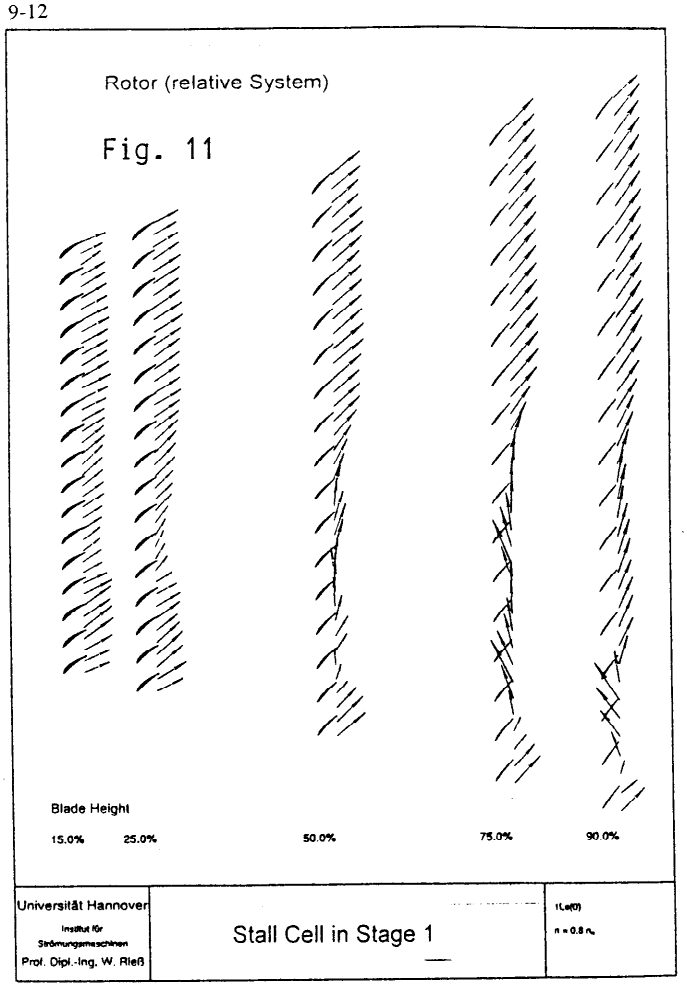
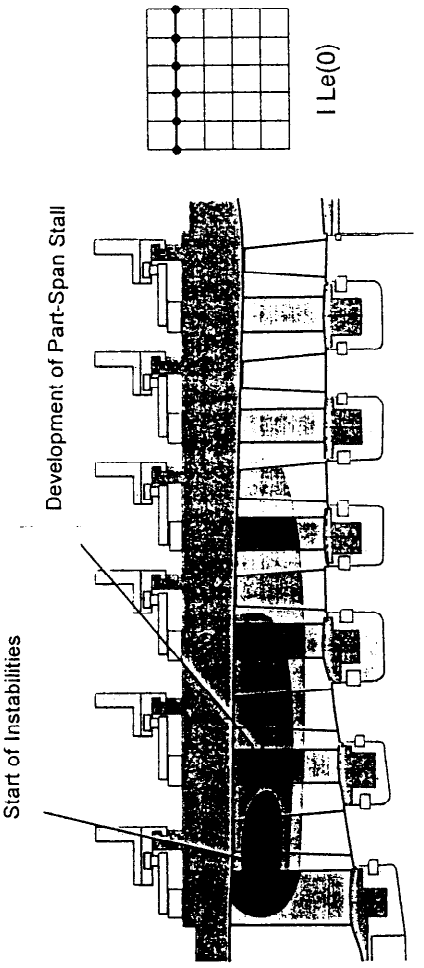


Fig. 10
Development of absolute velocity behind rotor 1 during transition into rotating stall





Origin of Instabilities

Fig. 12

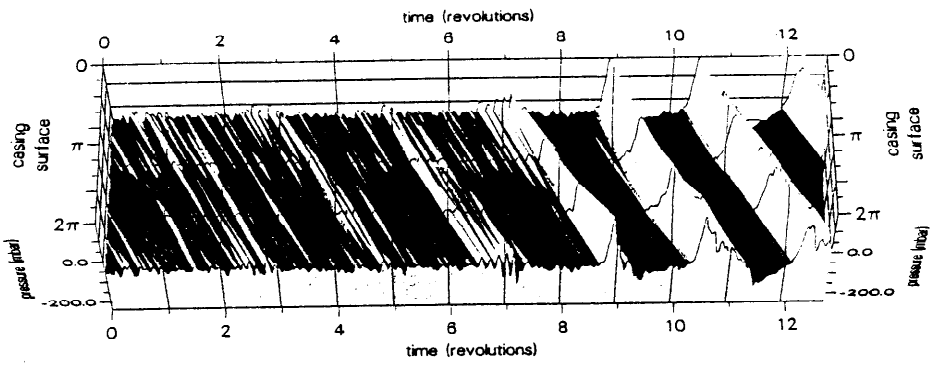


Fig. 13
Casing wall pressure during transition to rotating stall at full speed

Pressure at the casing in front of rotor 1, $n = n_N$

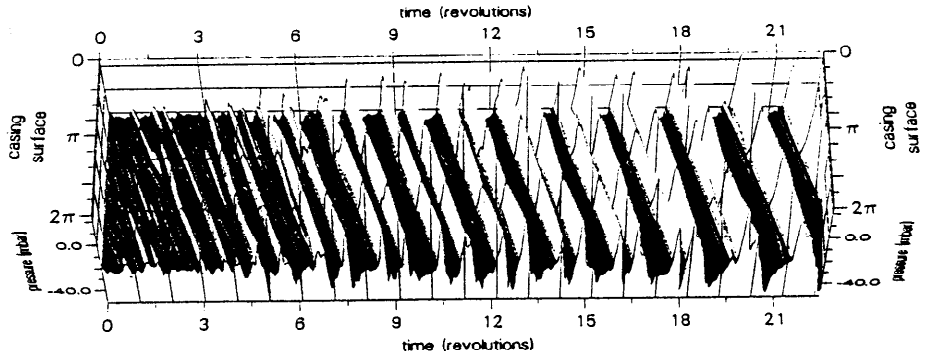


Fig. 14
Casing wall pressure during transition to rotating stall at 50 % speed

Pressure at the casing in front of rotor 1, $n = 0.5\ n_N$

Development of Rotating Stall near Tip

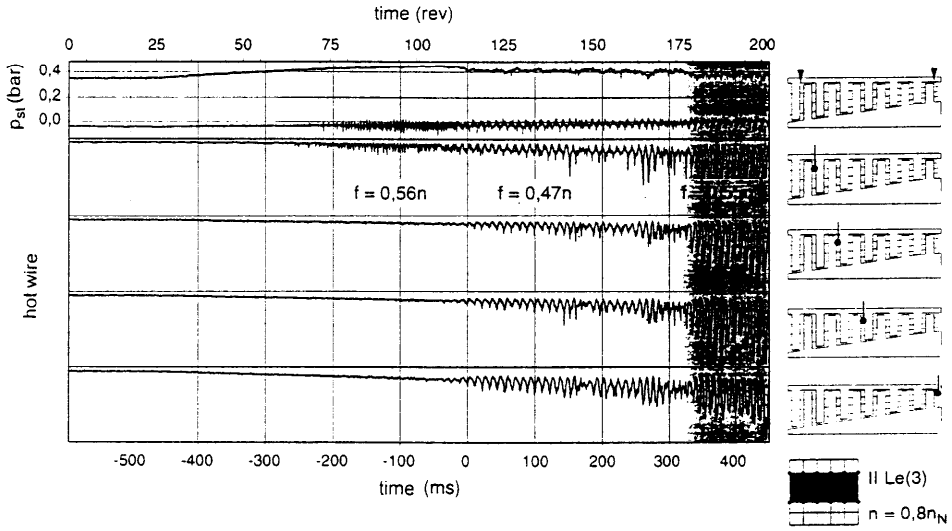


Fig. 15
Hot wire measurements near tip during transition to rotating stall at guide vane setting II Le(3)

Development of Rotating Stall at Hub

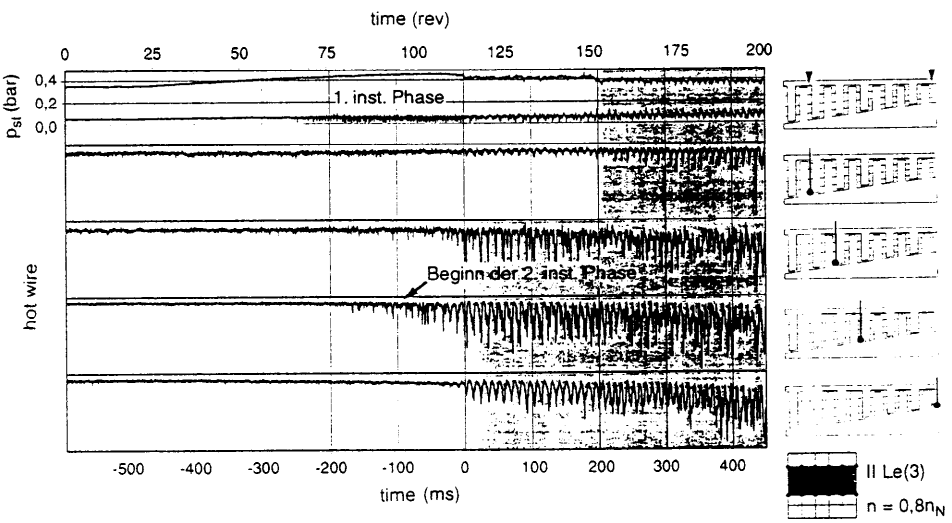


Fig. 16
Hot wire measurements near hub during transition to rotating stall at guide vane setting II Le(3)

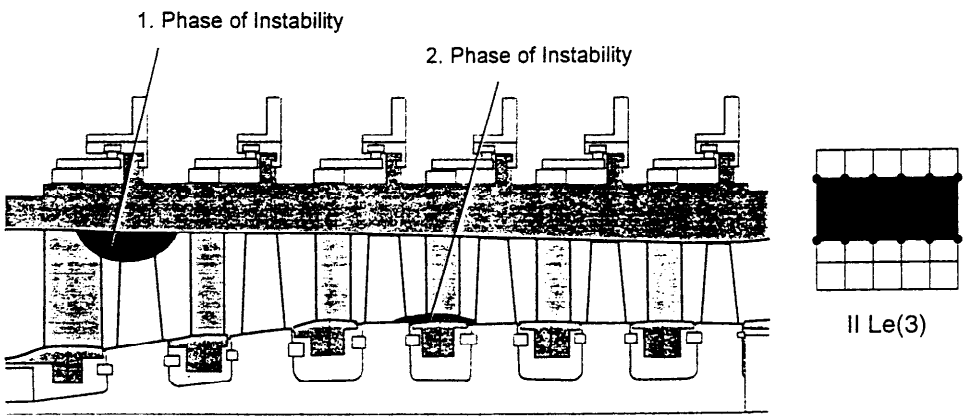
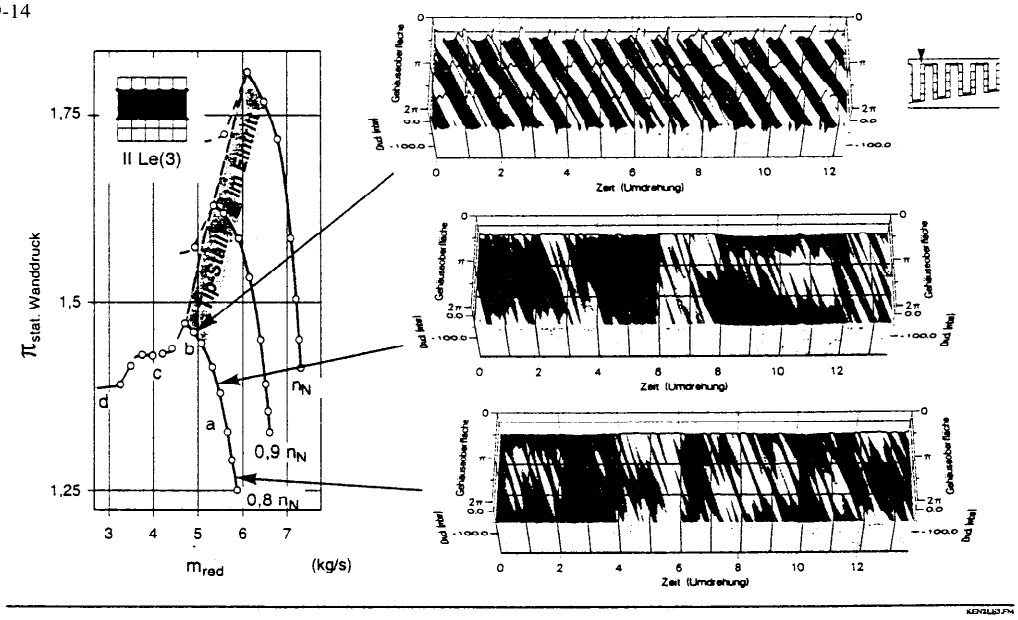


Fig. 18



Phases of Instability in Characteristic Field

Fig. 18
Form and extension of tip stall at guide vane setting II Le(3)

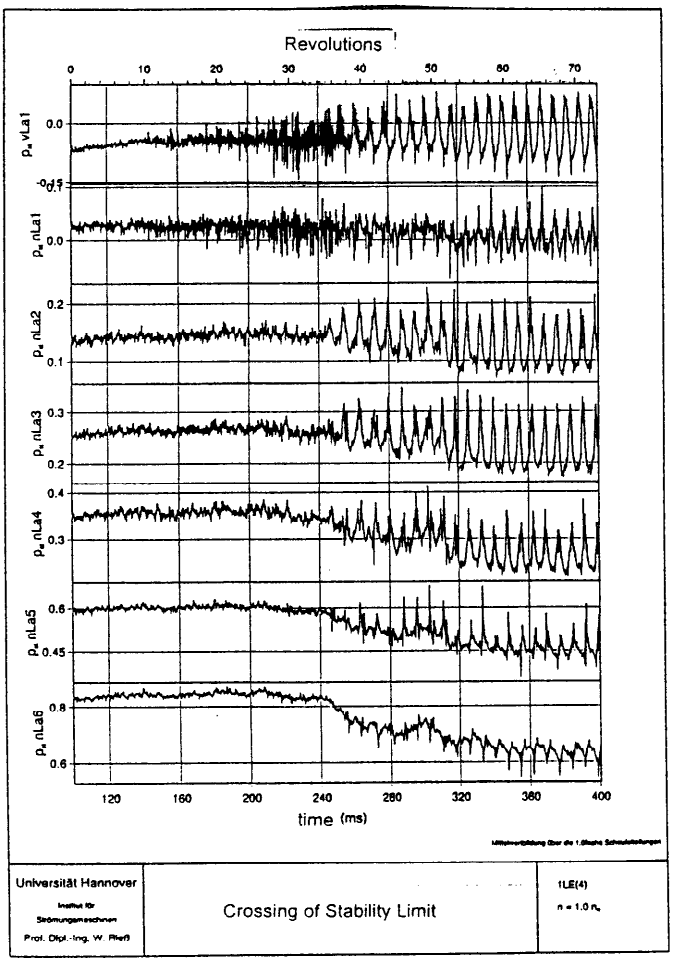


Fig. 19 Casing wall pressures during transition to rotating stall at guide vane setting I Le(4) in stage 1 - 6

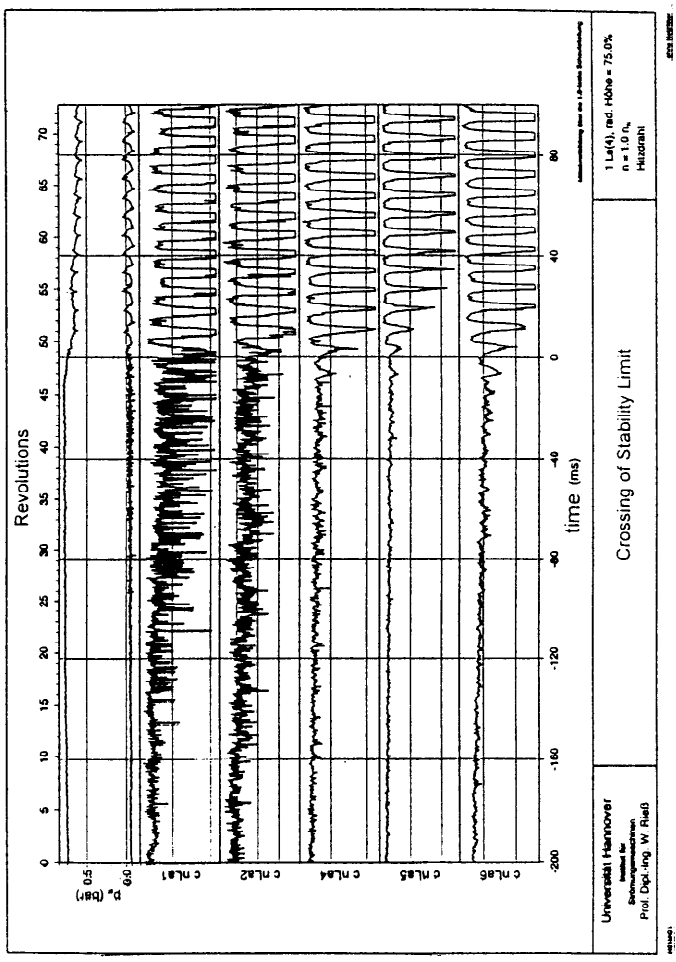
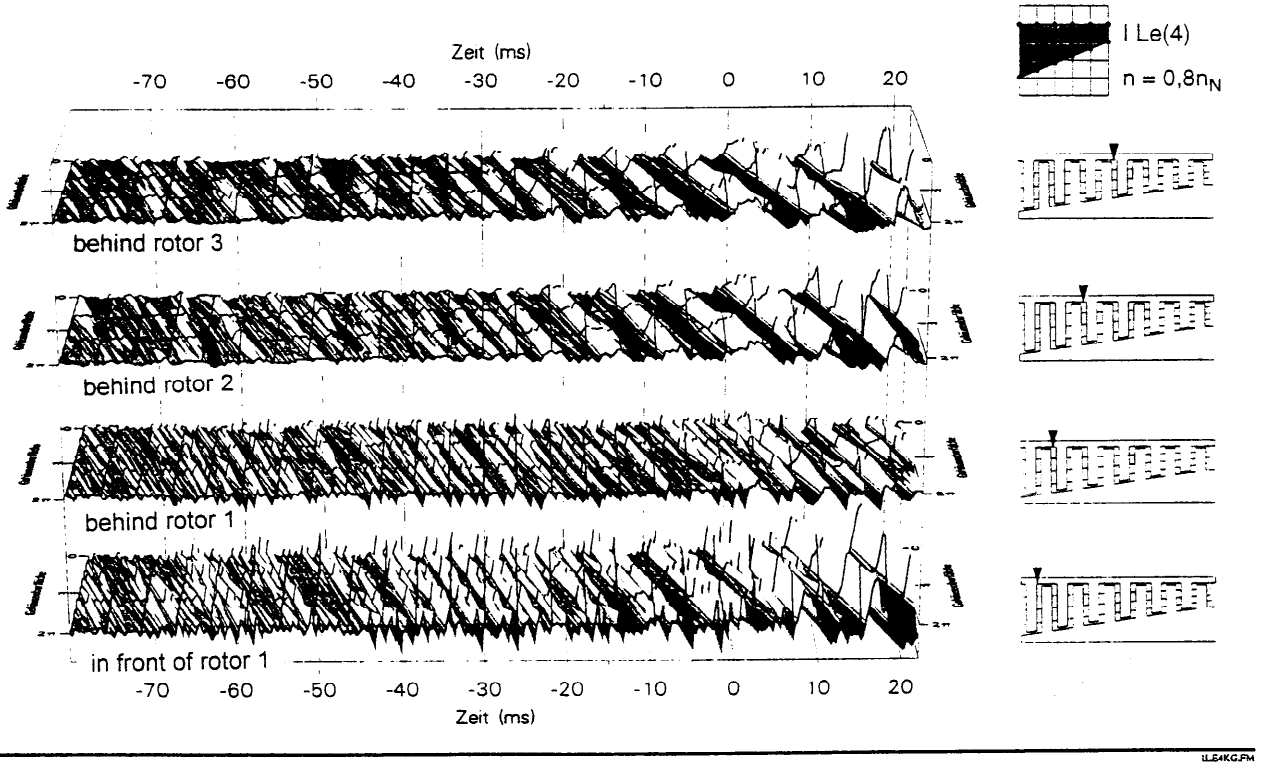
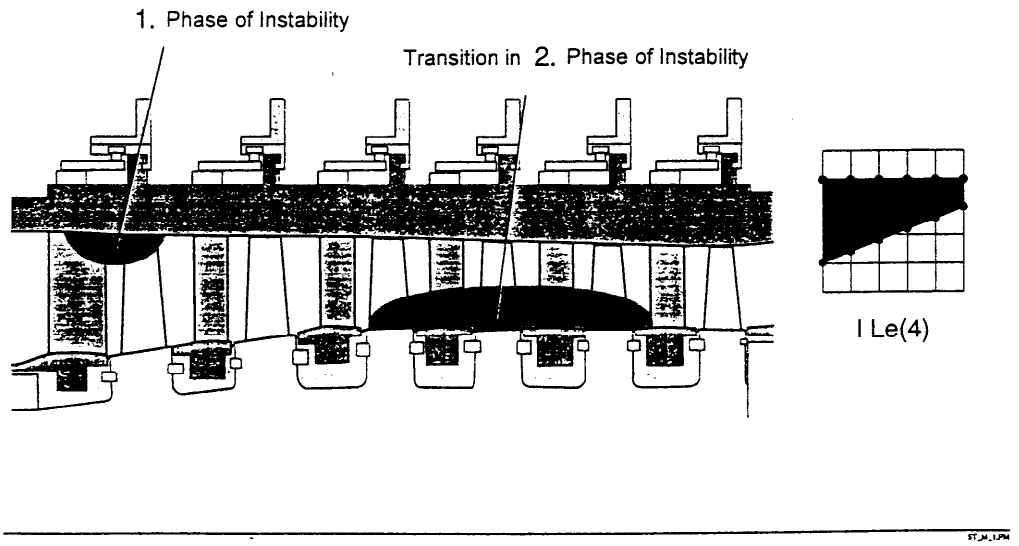


Fig. 20 Hot wire signals during transition to rotating stall at guide vane setting I Le(4) in stage 1 - 6



Interaction of Instabilities in Different Stages

Fig. 21 Casing wall pressures behind rotor 1 - 3 during transition at I Le(4)



Origin of Instabilities

Fig. 22 Development of instabilities at guide vane setting I Le(4)

PAPER -9, W. Riess

Question (H. Weyer, Germany)
What is the Reynolds number of the vector probe and might vortex shedding and unsteady separation affect the reading and accuracy of the flow parameters?

Reply
The cylinder diameter is 6 mm, giving a resulting Reynolds number according to flow conditions of $50\text{-}100\,x10^3$. We supposed that periodic vortex shedding will not develop under unsteady flow conditions in the compressor. According to Gyarmathy (ETH), e.g., probe bodies with sharp edges, etc will develop hysteresis of separation under unsteady conditions and result in large errors. This should not occur on a cylindrical probe.

PERSPECTIVES of PHASE-PORTRAITS in the DETECTION of COMPRESSOR INSTABILITIES – INCEPTION of STALL.

M. D'ISCHIA*; F.A.E. BREUGELMANS
VON KARMAN INSTITUTE
72, Ch. de Waterloo
B-1640 Rhode St. Genese
Belgium
* Presently Universita di Napoli "Federico II".

ABSTRACT

The operative range of axial-flow compressors is limited by the onset of instabilities, namely rotating stall and surge that arise when the mass flow is reduced at constant rotational speed. The difficulties in correctly predicting the point of stall onset have made it necessary to establish a limit line on the performance map that cuts out operative points of high efficiencies. The particular behavior of this non-linear complex-but-structured phenomenon has suggested a scientific approach with the tools of Chaos theory. The result given by the Phase-Space reconstruction from experimental time series has suggested the possibility of applying this technique, not only to characterize the system's dynamics, but also for monitoring purposes. The experiments have been planned to capture the transition from clean flow to stalled conditions. The Phase-Portrait of the different types of stall is presented. The results from the different sensors are compared and an indicator for stall inception detection presented.

INTRODUCTION

Rotating stall has been widely investigated, both theoretically and experimentally. Recent experiments on the inception and development of stall cells are reported in [2,9,11,12,17,18,19,20,37]. Generally, stall inception can be experimentally detected as a small cell whose wave shape is obtained from a low pass filtering of a high frequency response sensor. It is, however, difficult to avoid stall upon recognition of the small cells because it takes only a few rotor revolutions for the full cell to develop: the hysteresis in the pressure rise characteristics makes it longer to recover under any active action. Garnier et al.[11,12] have investigated this phenomenon on two low speed and one high speed compressor with spatially and temporally resolved measurements. They found that rotating stall was preceded by a period in which small amplitude waves were observed travelling around the circumference at a speed slightly less that the fully developed cell's speed. The evolution into full cell was smooth and without sharp variations. The waves were clearer, for the multistage compressor, in the stage that stalled first. According to their results these waves were detectable 10 to 200 rotor revolutions before the onset and can be used for active control purposes. The data fitted the model by Moore and Greitzer [27] both qualitatively and quantitatively. This technique requires as many probes as the number of spatial harmonics to be examined. In the cited work 8 hot wire were necessary.
Rotating stall is a phenomenon that has also widely investigated theoretically during the last 40 years [10,16,25,26,27]. Recent numerical studies, McCaughan [25], on the Moore and Greitzer [27] model, have shown the importance of both spatial and temporal non-linearities already at the early stage of rotating stall inception. McCaughan [26] presents a parametric study of a simplified version of the same model. For a given set of parameters the final state, reached by a compressor when it goes unstable, strongly depends on the initial conditions. In the same study, strange attractors are thought to be possible for rotating stall. All these aspects suggest the possibility of an underlying chaotic dynamics in rotating stall in axial-flow compressors. From this point of view a compressor may be regarded as a non-linear, open, externally driven, dissipative dynamical system that experiences transitions to different dynamics as an external parameter, in this case the mass flow, is varied.
The applicability of the Phase-Portrait representation and the properties has been studied in [3,4,17,29,30,31,32]. A few concepts have to be mentioned shortly such as: Deterministic Chaos, Dimensions, Attractor, and Phase-Portrait reconstruction, which are used in the paper.

DETERMINISTIC CHAOS.

Chaos stands for states of irregularity and disorder. The appellation deterministic for a dynamic system implies the existence of a prescription, either in terms of difference or differential equation, that allows to predict the future behavior of the system starting from a given initial condition. The two terms seem to be in contradiction as one would normally think that only regular motions belong to the class of deterministic systems The idea is that the different structures possible for rotating stall for different values of the mass flow,

Paper presented at the RTO AVT Symposium on "Active Control Technology for Enhanced Performance Operational Capabilities of Military Aircraft, Land Vehicles and Sea Vehicles", held in Braunschweig, Germany, 8-11 May 2000, and published in RTO MP-051.

are chaotic states for the physical system. Examples of classic observations of rotating stall can be found in [2,11,22,23,24].

DISSIPATIVE DYNAMIC SYSTEMS

Consider a dynamic system for which each value of the variable represents one of the degrees of freedom of the system. The state of the system can be seen as represented, at a given instant in time, by a point or a vector in the Phase-Space that is the space in which all possible states for the system are represented. The property of dissipative systems dictates that they will settle from some transient to a simpler steady state response. Their trajectories in the Phase-Space reduce in volume, so that the flow contracts onto a set of lower dimension called attractor. A qualitative description of the system's dynamic is obtained through a geometrical description of the trajectories on the attractor. As an example, one could refer to the condition of a damped pendulum after a transient: the trajectory evolves in time starting from a given initial condition and is attracted to a fixed point coinciding with rest condition for the pendulum (**Fig.1**). The trajectory can be presented in a velocity – position graph. Systems undergoing periodic states will show a limit cycle or n-dimensional tori as attractors. Strange attractors are typical of chaotic motions while random motions tend to equally fill the available Phase-Space [5,6,8,34].

CHAOTIC SYSTEMS, FRACTALS AND DIMENSIONS

Chaotic attractors [13,14,15,33] have the property of exponentially separating initially close trajectories in a bounded region of the Phase-Space in a time evolution of the system. A measure of this divergence is represented by the Lyapunov exponent. They quantify the sensibility to initial conditions, and for a system to be chaotic it must have at least one positive Lyapunov exponent. From this point of view the Chaotic attractor can be thought of as a noise amplifier: it brings to a macroscopic level the microscopic fluctuations. Strange attractors have another difference with respect to Attractors belonging to regular motions: they have a fractal dimension. The reader is referred to [34] for further mathematical definition of a Strange attractor. In order for the attractor to be strange, the trajectory must show sensitive dependence on initial conditions and its dimension must be a fractal greater than two.

The definition of the dimension [36] of a geometrical object is based upon the concept of measure in space and the dimension of the space in which one observes a geometric object is fundamental for the recognition of its topological properties. Whitney [38] has proven that an m-dimensional object may be embedded in a space of dimension n. The minimum space dimension for a curve (dimension 1) is 3. In fact, if a 3-dimensional curve is projected into a plane, intersections and closed areas may appear and the image does not represent a 1-dimensional object any more (**Fig. 2a**). The dimension of the space will be called the embedding dimension to distinguish it from the dimension of the object itself.

There are several definitions of dimension but only few of them are topologic in nature, in the sense that they attribute the same dimension to topologic equivalent objects.

The **Covering Dimension** is the first definition presented and it is topologic in nature. The idea is to take a geometric object and try to cover it with disks of small radius (**Fig.2b,c**). There are other definitions for the dimension of an object that are able to capture the differences in the internal structure of topological equivalent. These definitions can be divided into two groups: those which only depend on metric properties (the **Capacity dC** and the **Hausdorff Dimension dH**) and those depending on metric and probabilistic properties thus taking into account the frequency with which each region is visited by the trajectory (**Correlation Dimension**). [8,13,14,29,36].

RECONSTRUCTING PHASE-PORTRAIT FROM EXPERIMENTAL TIME SERIES. TAKENS THEOREM.

The construction of the multi-dimensional object in the Phase-Space, to characterize the state of the system is difficult. This paragraph illustrates how the time evolution of a system in the Phase-Space can be reconstructed using experimental data. Takens [35] gave full mathematical proof of the theorem whose practical implementation constitutes the so-called 'method of delays'. It states that, in order to reconstruct the Phase-Space Portrait of a system that has m degrees of freedom, one only needs to measure one of them and substitute the others with time delayed values of the measured quantity. This mapping constitutes an embedding, from the m-manifold to the Euclidean space provided that one uses at least n = 2m+1 delayed values. The dynamic of a single parameter contains the information about the other parameters that influence the phenomenon and therefore of all the important degrees of freedom.

If n is the embedding dimension, δ is the delay time and τ is the sampling time, then from the signal x(t) one can extract the vector x(t1), that represents a point in the in Phase-Space, whose components are n values delayed one from the other of the delay time starting from x(t1), the first data point of the time series. The following vector will correspond to the time instant t2+δ and so on to build the so-called trajectory matrix. The value N depends on the length of the time series and on the choice of the embedding parameters: if one has M data points then N = M - n .

However very powerful, Takens' theorem gives no hints for a practical implementation. Most of the time the experimenter is faced with a finite number of sampled data that contain noise and have a finite precision. There are no indications regarding the choice of the time scales like time delay or sampling time, any value is good in infinite algebra. The dimension of the attractor of the dynamic system is not known a priori making it difficult to satisfy the embedding requirement. Theoretically these problems are still open, especially with respect to the proper choice of the time scales and of their influences on the attractor reconstruction. Some of these problems have been discussed in [3,4] and only a few concepts will be qualitatively presented here. The necessary mathematical support can be found in the literature.

As for the choice of the sampling time, the suggestion is that of over-sampling with respect to the cut-off frequency of the anti-aliasing filter in order to smooth out trajectories, Darbyshire and Price [8]. The amount of information that is possible to extract from a sampled time series is finite. The scope of the time delay method is that of reconstructing the dynamics of the system. Therefore, all the relevant dynamics must be present in the chosen variable and the delay time should be chosen so that even the fastest modes are reconstructed.

APPLICATION TO ROTATING STALL.

The complicated phenomenon of stall, inception and stabilized unsteady conditions expresses itself by fluctuations in pressure, velocity vector, noise changes, stress variation and vibrations of the compressor. The condition of the turbomachine can be represented in a multi-dimensional space with these parameters as dimensions. The transition from one point to the next is controlled by the time step of the data acquisition. The Takens theorem, applied to a compressor, means that it is sufficient to measure one parameter and still be able to reconstruct the Phase-Space. All the information about the phenomenon is contained in each signal. An attractor can be build and the properties investigated. A few issues remain open: Does each parameter contain the full information? Otherwise one is not sure about the representative aspect of the attractor. The choice of the sensor is also dependent on these conclusions. The multi-dimensional aspect is recreated by the time delay method. How large must the time delay be? Does the resulting attractor have fractal properties? How can we preserve a maximum of information from the multi-dimensional Phase-Portrait in a simplified three-dimensional map? Which of the multi-dimensional axis should be selected for the three-dimensional representation? What about an idealized attractor, a "cleaned-up" one, which can be used as model for predictive purposes? How good can it be applied to the specific case of stall in a compressor? Do we observe pre-stall indicators by using a single sensor and does the Phase-Portrait analysis show it? If this can be demonstrated in a difficult case (rotating stall), it provides an indication of validity of the principle and maybe can be used in real time control and monitoring by using the predictive capability of the attractor.

DESCRIPTION OF EXPERIMENTS

One of the aims of this study is that of verifying the possibility of tracing the same physical phenomenon i.e. rotating stall, by measuring different physical quantities influenced by it. These are for example: flow vector fluctuations in the rotor annulus, the pressure fluctuations at the casing wall, vibrations of the casing structure, blade stresses and acoustic noise. As the technique of the Phase-Portrait construction does not require the knowledge of the absolute values of the measured quantity, no calibration of the instruments is required [4]. The data acquisition was performed on PC equipped with a Metra Byte DAS20 card. It is a multifunction high speed A/D, I/O expansion board that allows precision data acquisition and signal analysis directly on the PC. The capability of the card is of 100 kHz with 16 single or 8 differential ended input channels. The acquired data are stored in two 8 bit bytes. Between the card and the transducers an anti-aliasing low-pass filter was used.

The static pressure signal at the casing is recorded with two different sensors. The first one is a flush mounted Kulite pressure transducer. The second one is an inductive type of pressure transducer i.e. a Valydine connected to the casing pressure taps by a short tube. The displacement volume together with the dimensions of the connecting tube characterizes the unsteady response capability of this transducer. No low-pass filtering has been used in this case since the high frequencies are naturally damped. The frequency content of the signals from the microphone and the accelerometers was measured sending the non-filtered signals to a HP 35660A Dynamic Signal Analyzer. This analyzer digitally samples the B&K Signal analyzer output signal and displays, in real time, the frequency content of the analogue signal.

Preliminary experiments have been organized to determine :

1. The influence of the sensor type, hot wires, pressure transducers, vibration pick-up, microphone in the time series and the Phase-Portrait construction.
2. The determination of the fractal properties of the Phase-Portrait during stall.
3. The determination of the required delay time to apply to the time series.
4. The determination of the dimensions of the object and the embedding space.
5. The application of smoothing of the object.

6. An attempt to find the representative equations for the three axis so that an equivalent attractor is generated in a synthetic way.
7. The use of the predictive capability of a Phase-Portrait of a stall event and application to a time series.
All these aspects have been treated in the references 3,4,22,23,24,29,30,31 and 32.
The investigation of rotating stall inception is treated in this paper. The experiments have been organized to cover a transient from the clean operating point to the occurrence of rotating stall by a continuous throttling of the compressor.

ROTOR FACILITIES.

The R1 low-speed axial-flow compressor test facility at the VKI is the first presented. It is an open loop, constant annular section facility with inner conical diffuser and throttle valve. The rotor is driven by 55 KW DC motor with a continuous speed control from 0 to 1500 rpm. The tip radius is 0.704 and the hub to tip ratio is 0.78. The facility is equipped with 39 IGV, 25 rotor and 25 stator blades. Tip radius is 0.704m and hub-tip ratio 0.78. The IGV and rotor blades are of NACA 65-A10 type, while the outlet guide vanes have constant thickness, non twisted thin metal airfoils of 35 deg. camber and constant chord of 80 mm. As the mass flow is reduced, a multi-cell small stall pattern is first encountered, followed by a 1-cell and then 2-cell large stall pattern. Reopening of the throttle valve produces a 1-cell large stall pattern in the hysteresis branch of the characteristic curve [2].
Instrumentation: Hot-wire (axial and tangential position) 17mm.: upstream rotor leading edge, 7mm. from casing. Validyne and Kulite pressure transducer : 17mm. Upstream rotor LE and flush mounted.
The second facility is the R2 axial-flow compressor (**Fig. 3**). A DC motor of 180 KW power drives the rotor. The inlet is bell shaped and followed by the test chamber with the rotor and the stator. The tip diameter is 400 mm with a hub to tip ratio of 0.5. There are 24 subsonic blades of the NACA 65 family. This facility presents immediately large stall with an abrupt drop in pressure rise. The rotor starts in rotating stall for speeds from 0 to 3000 rpm . Above 3000 rpm, unstalled flow is observed at open throttle. The low compression ratio of the tested rotor and the testloop internal losses are the reason for this behavior.
Instrumentation : Hot-wire (axial and tangential position): 15mm. upstream of rotor LE; 10mm. from casing, midheight and 10mm from inner casing. Validyne and Kulite pressure transducer : 70mm. upstream of rotor LE and flush mounted.

THE STALL INCEPTION.

The stall inception can be defined as the process by which the flow trough the compressor changes from an axi-symmetric distribution to an asymmetric one; as indicated by Day [9] and by Höss et al. [18]. There are three different kinds of inceptions that can be observed for various conditions in a low pressure compressor:
1. Stall rising from a spike-type precursor,
2. Long wavy pressure fluctuations corresponding to modal waves,
3. Dominant action of the shaft unbalancing as an external forcing action.
In case of distorted inlet flow the whole velocity range is dominated by the spike-type stall inception behavior.

These very short length scale disturbances are localized only in few rotor revolutions and travel around the annulus increasing in amplitude until fully developed stall occurs.
The spike-type precursor occurs when the disturbance is small and localized to just few blade passages, in term of the circumferential length its dimensions are very small and they increase quickly until full stall conditions are established.
The long length scale disturbances, a model proposed by Emmons et al. [10] and extended to multi-stage machines by Moore and Greitzer [27], involve perturbations that are of the same scale of the circumferential length and are referred to as modal waves or "modes". According to this model of stall inception these pre-stall waves start as weak disturbances and grow in intensity without abrupt variation in amplitude or frequency until a fully developed stall cell is formed.

In order to see the stall inception, various techniques have been used. Tryfonidis et al. [37] analyzed the behavior of nine different machines (fan, core and engine compressors) using the method of the spatial Fourier analysis. They were able to identify low amplitude traveling waves prior to stall. The structure of these waves is different for different speeds and, for the same speed, depends on the position on the characteristic curve.
Höss[18], on the other side, analyzed the behavior of a two-spool turbofan engine using the wavelet analysis. The presence of the three kind of stall precursors and the importance of external influences (e. g. the shaft unbalancing) are verified.
In the present report the attention is focused on the analysis of stall inception using the Phase- Space Portraits method, without trying to identify a certain kind of stall precursor but trying to identify a possible stall warning that can be clearly seen with this technique. The different aspects will be demonstrated using one of the compressor experiments.

THE RECORDED TIME-SERIES.

Given that the purpose of this work was to carry on a qualitative analysis of the stall inception there is no need to know very accurate values for velocity and

pressure and the experimental accuracy in this case is not relevant. For that reason no calibration was done on the different sensors and the results presented here are only the digits as they were recorded by the acquisition system. This means that the data obtained with the hot-wire are not proportional to the speed values but depend on them according to King law.

a. The low speed compressor R1

The experiments are carried out at 1000 rpm. The characteristic curve **(Fig. 4a)** shows a stable part to maximum loading (point A), 7 to 10 small perturbed regions (point B). All the small stall cells grow in size and collect themselves to give origin to a single big cell (point C), the single big cell splits in two (point D). An increase of the mass flow starts the hysteresis loop and the flow becomes clean again (point A).

The axial hot-wire

The hot-wire is parallel to the axis of the machine and is sensitive to the variations of the tangential component of the velocity. After 21 rotor revolutions in the acquisition sequence, the peak-to-peak amplitude of the signal grows **(Fig. 5)**. The small cells collect together into a single big cell ; this process can be seen when, after about 88 rotor revolutions, the amplitude and the relative frequency of the large peaks increase. The single big cell starts growing and is fully established at 105 revolutions. (1 horizontal.unit = 10 revs.)

The tangential hot-wire

The hot-wire is orthogonal to the axis of the machine and is sensitive to the variations of the axial component of the velocity, showing the massflow variations **(Fig. 6)**. During the first 11 rotor revolutions the flow is quite clean while the mean value of the signal decreases for increasing throttling. In small stall conditions the negative peaks of the signal grow in amplitude and in relative frequency (11 to 100 rotor revolutions) while the largest oscillations are visible in deep stall conditions (from about 100 rotor revolutions on).

The Validyne pressure transducer

When the main velocity component decreases because of throttling, the wall static pressure grows as shown by the output of the transducer. The passage of a stall cell through the sensor location causes a sudden increase of the pressure (the axial speed decreases suddenly).

This can be observed in the time traces recorded with this transducer **(Fig. 7)**: during the first 11 rotor revolutions the flow is clean. Between 11 and 34 rotor revolutions the throttling is causing an increase of the mean value of the pressure, but the small peaks due to the passage of the small perturbation cells are not yet evident. Between 34 and 87 rotor revolutions one picks up the small perturbations. After about 87 rotor revolutions, the small cells are collecting together and a single big cell is growing. This process takes about 20 rotor revolutions until deep stall conditions establish after 109 rotor revolutions.

The Kulite pressure transducer

A period of almost clean flow (about 10 rotor revolutions) is followed by about 30 revolutions during which there is a smooth passage from clean flow to small stall conditions. The deep stall condition starts its development around 80 revolutions and is completed at 100 revolutions in the acquisition **(Fig. 8)**. A cut-off filtering is set at f_f=500 Hz.

b. The R2 compressor

The experiments are carried out at 4000 rpm. The characteristic curve is shown **(Fig. 4b)**. The lack of suitable IGV's causes the rotor hub section to operate at positive and the tip one at negative incidence angle. The hub is expected to be the most critical in the stall triggering and a sudden occurrence of deep stall is observed. Experiments at three radial positions (hub, mean and tip) are carried out.

The axial hot-wire

From the results obtained it can be deduced that the behavior of R2 is quite different from the one seen with the R1 compressor. No small perturbations of increasing amplitude up to stall are observed and deep stall occurs quite suddenly. The axial hot-wire is sensitive to the variations of the tangential component of the velocity. No perturbations are detected until stall conditions are established at the three radial positions.

The tangential hot-wire

The sensor is sensitive to the axial component of the velocity and shows the reduction of the mass flow for increasing throttling. The mean value of the output of the wire decreases until stall conditions cause the wide fluctuations of the signal for hub and tip radius**(Fig. 9a,b)**. (1 horizontal.unit = 40 revs.for all R2 figs.)

The Validyne pressure transducer

The wall pressure increases **(Fig. 10)**; again there is no sudden variation in flow condition up to full stall, where the passages of the stall cells are clearly visible.

The Kulite pressure transducer

The higher frequency response of this provides the time trace of **Fig. 11**. The evolution of the stall transient is quite similar to the one recorded with the Validyne.

THE PHASE-SPACE PORTRAITS.

The in-house developed routines for the evaluation of the average mutual information (as function of the time delay) and of the false nearest neighbors' percentage (as a function of the dimensions) respectively are used. The value of τ_d (time delay) and ED (embedding dimension) are used for the application of the Takens principle and the construction of the Phase-Space. In this kind of analysis a steady state condition is represented by a single point in the Phase-Space, while small oscillation of the data around a constant mean value will be represented by a cluster of points contained in a relatively small region. If the mean value changes the center of this cluster moves. Finally big oscillations are

represented by a set of points contained in a larger region. These Phase-Space portraits are derived from the time series discussed in the previous paragraph.

a. The low speed compressor R1

The axial hot-wire

The analysis of these data gave the following parameters: $\tau_d = 50\tau_s$ and ED = 5

(τ_d : time delay , τ_s : sampling time , ED = embedding dimension.)

The 3-D reconstructed portrait is shown in **Fig. 12**. Given that the mean value of the time trace doesn't change too much during the first part of the transient, what can be expected is a gradual growth in size of the region that contains the portrait.

In a 2-D projection there is an increase of the size of the region that represents the operation before deep stall. The small perturbations cause an increase of the peak-to-peak amplitude of the sensor output without changing too much the mean value.

From this analysis, it can be inferred that a possible application for a monitoring system consists in looking at a bounded sub-domain of the Phase-Space that contains the portrait of the system in clean flow. In this way the stall warning should be activated when the portrait goes out of this control volume.

The tangential hot-wire

The reconstruction of the Phase-Portrait is done using: $\tau_d = 44\tau_s$ and ED = 5

A 3-D projection of the portrait is shown in **Fig. 13**; the situation here is quite different from the previous one because now the main variation can be seen in the mean value of the time trace.

From the analysis of this Phase-Portrait it could be inferred that a possible monitoring system that uses this sensor could check the motion of the center of the portrait and give a stall warning when it goes over a certain distance from its original position.

The Validyne pressure transducer

The reconstruction of the Phase-Portrait used: $\tau_d = 49\tau_s$ and ED = 5. The 3-D projection of the portrait is shown if **Fig. 14** and there is a wide displacement of the geometrical center during the transition to stall and compared with the operating conditions A,B,C, and D.

During the first 20 rotor revolutions the mean value of the signal doesn't change much and the displacement of the center of the portrait is relatively small as well as the size graph (clean flow means small peak-to-peak amplitude of the signal). During the period between 20 and 35 rotor revolutions there is a displacement of the center due to the decrease of the mass flow, proportional to the mean value of the signal. The next step (from 35 to 88 rotor revolutions) shows a large displacement of the graph center while there is an increase of its size because of the increased fluctuations of the time trace (small perturbations). Finally, the large size of the portrait is caused by the large fluctuations of the time trace during deep stall.

As it can be seen comparing the portraits, the large displacement of the graph center is such that the common areas between the preceding step and the following one are very small.

The Kulite pressure transducer

The reconstruction is carried out using: $\tau_d = 49\tau_s$ and ED = 5. The 3-D projection of the Phase-Portrait is shown in **Fig. 15**; this object is very similar to the one obtained in the case of the Validyne. These transducers are measuring the same variable, wall static pressure, and the main characteristic of the reconstructed portrait should be the same as well as the required time delay. The similarity of the portraits indicates that all information about the chaotic evolution is contained in low frequency. The faster response of the Kulite provides more details on the unsteady motion.

A second small cluster appears in deep stall condition, at a position close to the portrait obtained in clean flow. The "steady" reverse flow in the core of the stall cell is treated in this representation as a "clean" condition. It is also an illustration for the need of the correct embedding. The two "stable" conditions are not clearly separated in a 2-D projection, while the 3-D view reveals that they are different structures.

b. The R2 compressor

The axial hot-wire

The experiments are carried out at three different radial positions and three phase portraits can be built, after the calculation of the average mutual information and the false nearest neighbors. The time delay is between 45 and 49, while the embedding dimension is 5. The clean flow condition is represented by a cluster of points, around a mean value. When stalled flow conditions occur, the portrait suddenly explodes (**Fig. 16**). The main difference between the hub and tip portraits is in the size of the initial cluster because of the higher fluctuations of the time trace recorded near the tip.

The tangential hot-wire

From the analysis of the 3D projections of the portraits taken near the hub and near the tip (**Figs. 17**) it is clear that the main characteristic of the motion is the variation of the mass flow. The displacement of the center is very large, the size of the graph doesn't increase too much for increasing peak-to-peak amplitude of the time trace.

The Validyne and Kulite pressure transducer

The behaviour of both pressure transducers is similar and is similar to what already shown with the tangential hot-wire. , In both cases the main phenomenon that can be seen in the time series is the variation of the mean value of the signal, while the peak-to-peak amplitude changes only when stall occurs. The 3D projections of the portraits are shown in **Figs. 18, 19**. Like in the case of the R1 compressor, the similarities between the two portraits are a indication that interesting information on chaotic motion is also present in the low frequency.

CONCLUSIONS.

A clear advantage of this method is the fact that there is no need for a calibrated instrument, what has been analyzed is the raw output of sensor.
The embedding dimension has been evaluated between 5 and 6 for all the sensors and for the compressors investigated. The percentage of false nearest neighbors is very low in the fifth dimension, probably this "degree of freedom" is more affected by measurement noise then by the physical information.
The data acquisition has to be performed in real time and the reconstruction of the portrait done, giving in advance the values of the time delay and of the embedding dimension.
The speed by which the point moves on the stable part of the portrait is an indication for the proximity to stall during a transient.
From the analysis of the signals recorded on the R2 facility what comes out is that a monitoring system based on the displacement of the center of the portrait should have better performances then the one based on the check of the size because the sudden instability leaves almost no time for a control.
This concept has to be verified on transonic fan type and multistage compressors.

BIBLIOGRAPHY.

1. **Abarbanel, H., et al.**; "The analysis of observed chaotic data in physical systems." Reviews of Modern Physics, 65(4), October 1993.
2. **Breuer, T.;** "Compressor Flow Instabilities Part II: Analysis Techniques", VKI-LS 1996-05 "Unsteady Flows in Turbomachines" , Brussels, March 11-15 1996.
3. **Breugelmans, F.A.E., Palomba, C.;** 1998, "Recherche récente en décrochage tournant : Chaos, Fractales et Attracteurs." Revue Française de Mécanique, N° 1998-4. 31 Décembre 1998.
4. **Breugelmans, F.A.E., Palomba, C. and Funk, T.;** 1994, "Application of strange attractors to the problem of rotating stall rotating stall", 7th ISUAAT, September 25-29, Fukuoka, Japan (Elsevier)
5. **Broomhead, D.S., and King, G.P.;** 1992, "Extracting qualitative dynamics from experimental data", Physica 20D, pages 217-236.
6. **Broomhead,D.S., and King, G.P.;** "Singular system analysis with application to dynamical systems" Physica D, 20:217, 1986.
7. **Cawley, R., and G. H. Hsu, G.H.;** "Local-geometric-projection method for noise reduction in chaotic maps and flows". Physical review A, 46(6):3057, September 1992.
8. **Darbyshire, A.G., Price, T.J.;** 1991, "Phase-Portraits from chaotic time series", Fractals and Chaos, ed. Crilly, Springer, pages 247-257.
9. **Day, I.J.;** "The fundamentals of stall and surge in axial compressors." VKI-LS 1996-05 "Unsteady Flows in Turbomachines" , Brussels, March 11-15 1996.
10. **Emmons, H.W., Pearson, C.F., Grant.H.P.;** "Compressor surge and stall propagation." Transactions of the ASME, vol.77, pages 455-469, 1955.
11. **Garnier, V. H ., Epstein, A. H., Greitzer, E. M.;** "Rotating Waves as a Stall Inception Indication in Axial Compressors", Journal of Turbomachinery, vol. 113, April 1991, pages 290-302.
12. **Garnier, V., Escuret, J.F., Previtali, R. e Duvaut, P.;** "Stall Inception Measurements in the High-Speed Multi-Stage H4 Compressor." VKI LS "Unsteady Flows in Turbomachines" 1996-05, Brussels, March 11-15 1996.
13. **Grassberger, P., Procaccia, L.; "**Measuring the Strangeness of Strange Attractors" , Physica 9D, 1983, pages 189-208.
14. **Grebogi, C., Ott, E., Yorke, J.A.;** 1987, "Chaos, strange attractors and fractal basin boundaries in nonlinear dynamics", Science, vol. 238, October, pages 632-638.
15. **Grebogi, C., Ott, E., Pelikan, S., Yorke, J.A.;** 1984, Physica 13D, page 261.
16. **Greitzer, E.M. and Moore, F.K.,** 1986, "A theory of post stall transients in axial compression systems: Part 11-Application", ASME Journal of Engineering for Gas Turbines and Power, vol. 108, pages 231-239.
17. **Gu, C., Yamaguchi, K., Nagashima, T., Higashimori, H.;** 1999, "Observation of Centrifugal Compressor Stall and surge in Phase-Portraits of Pressure Time Traces at Impeller and Diffuser Wall." The International Gas Turbine Congress 1999 Kobe, pages 555-560.
18. **Höss, B., Leinhos, D., Fottner, L.;** "Stall inception in the compressor system of a turbofan engine." Proceedings of the Gas Turbine & Aeroengine Congress & Exhibition, Stockholm, June 1998.
19. **Inoue, M., Kuroumaru, M., Iwamoto, T., Ando, Y.;** 1991, "Detection of Rotating Stall Precursor in Isolated Axial Flow Compressor Rotors", ASME Journal of Turbomachinery, vol. 111, pages 281-289.
20. **Jakson, A. D.;** 1987, "Stall Cell Development in Axial Compressor", ASME Journal of Turbomachinery, vol. 109, No 4 pages 492-498.
21. **Mandelbrot, B.;**"The fractal geometry of nature", W.H. Freeman and company, page 15.
22. **Mathioudakis, C.**; "Rotating stall in axial flow compressors", PhD Thesis K.U.Leuven, 1985
23. **Mathioudakis, K., Breugelmans, F.A.E.;** 1985, "Development of Small Rotating Stall in a Single Stage Axial Compressor", ASME paper, 85-GT-227.
24. **Mathioudakis, K., Breugelmans, F.A.E.;** "Three dimensional flow in deep rotating stall cells of an axial compressor." Journal of Propulsion and Power, vol. 4,n0 3, pagcs 263-269, June 1988.

25. McCaughan, F.E.; 1994, "When are nonlinearities important at stall inception?", ASME 94-GT-338.
26. McCaughan, F.E.; 1989, "Application of bifurcation theory to axial flow compressor instability", Transaction of the ASME, vol. I I 1, October, pages 426-433.
27. Moore, F. K., and Greitzer, E. M.; 1986, "A Theory of Post-Stall transients in Axial compressors: Part I - Developments of the Equations", ASME Journal of Engineering and Power, vol. 108, pages 68-76.
28. N. H. Packard, N.H., et al.; "Geometry from a time series." Physics Review Letters, 45:712, 1980.
29. Palomba, C.; "L'Analisi sperimentale dello stallo rotante secondo le techniche della teoria del caos deterministo." PhD Thesis, Universita Degli Studi Di Cagliari, July 1997.
30. Palomba, C., Breugelmans F.A.E.; "Phase-Portraits from Rotating Stall Time Series." XII ISABE Conference, Melbourne Australia Sept. 1995.
31. Palomba, C., Puddu, P., Breugelmans, F.A.E., Nurzia, F.;. "Caratterizzazione delle Condizioni di Funzionamento di un Compressore Assiale in Prossimita' dello stallo rotante secondo le tecniche della Teoria del Caos." Proceedings of the Conference Turbomachine 96' Genova 11-12 July 1996, pages 761-772.
32. Palomba, C., van der Horst, L., Breugelmans, F.A.E.; " Strange Attractor Characte-risation of Rotating Stall in an axial flow Compressor." JSME Centennial, July 1997 Tokyo.
33. Peitgen, H.O., Jiirgens, H., Saupe, D.; 1992 "Chaos and Fractals, new frontiers of science", Springer Verlag New-York, Inc. pages 106-119.
34. Schuster, H.G.; 1984, "Deterministic Chaos", Physic Verlag – Weinheim.
35. Takens, F.; 1981, " Detecting strange attractors in turbulence", Lecture Notes in Mathematics, Rand and Young eds. Springer, Berlin 1981, page 366.
36. Theiler J.; "Estimating Fractal Dimension." Journal Optical Society, vol.7, No. 6, June 1990, pages 1055-1073.
37. Tryfonidis, M., Etchevers, O., Paduano, J.D., Epstein A.H., Hendricks, G.J.; "Prestall Behaviour of Several High Speed Compressors", Journal of Turbomachinery, vol. 117, January 1995, pages 62-80.
38. Whitney, H.; 1936, "Differentiable Manifolds", Ann. Math. 37, page 645.

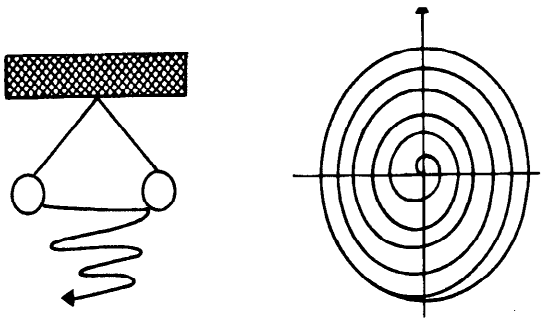


Fig. 1 Pendulum and Phase-Space Portrait

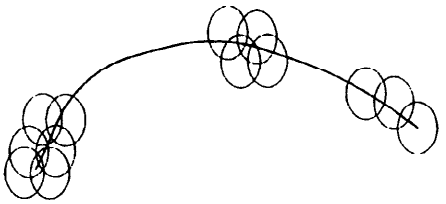


Fig. 2b. Covering Dimension – Line

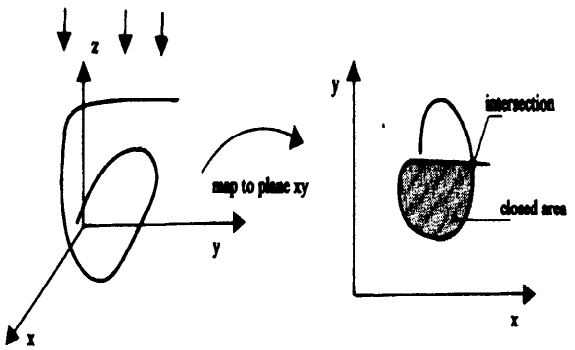


Fig. 2a. Presentation Dimension

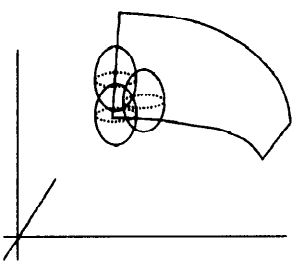


Fig. 2c. Covering Dimension – Surface

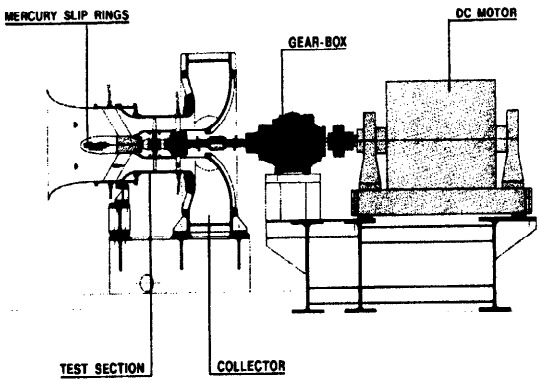


Fig. 3. R2 Compressor test facility

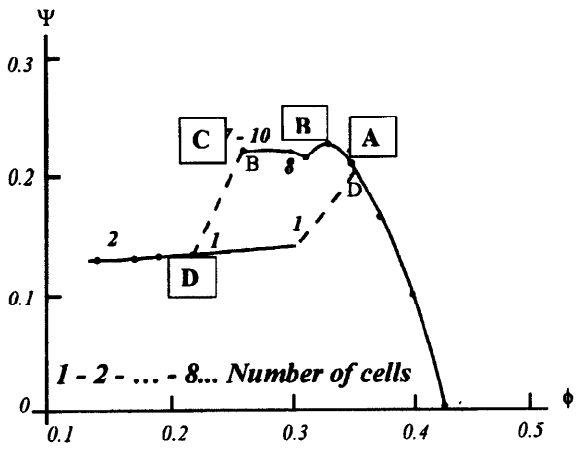


Fig. 4a. R1 Characteristic curve

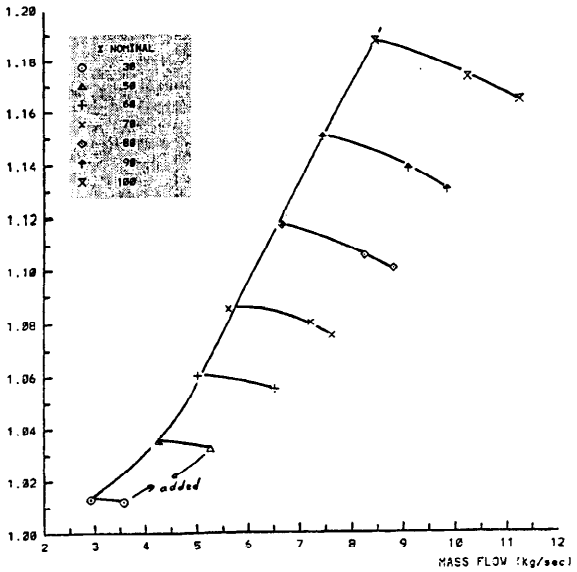


Fig. 4b. R2 Performance map.

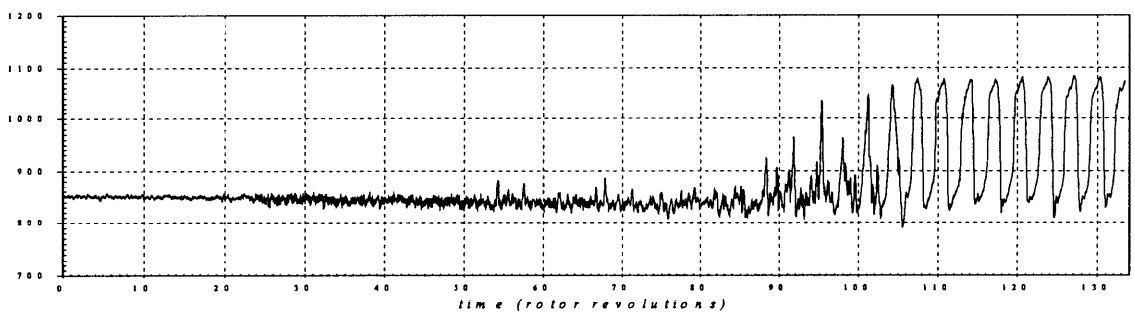


Fig. 5. R1-Time trace – Hot-wire axial position

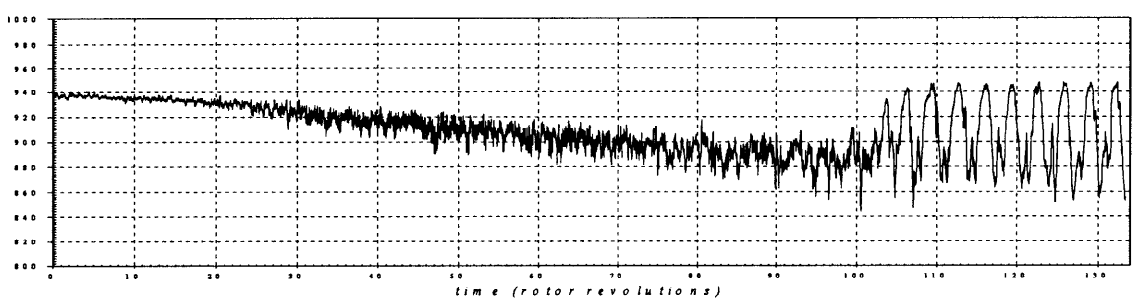


Fig. 6. R1-Time trace – Hot-wire tangential position

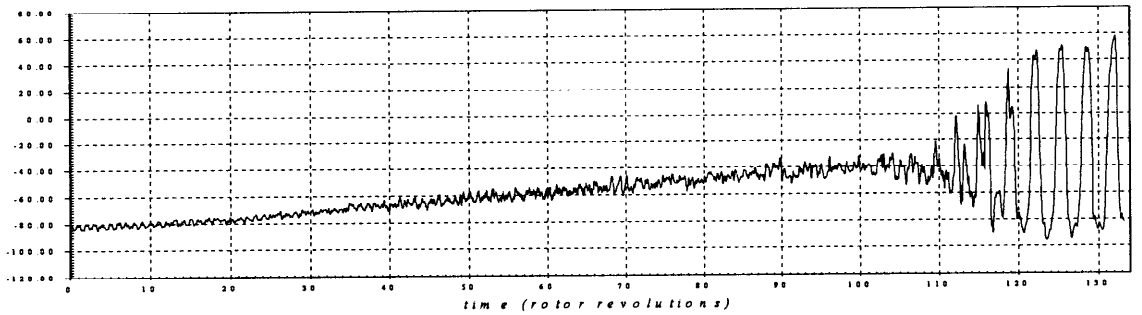


Fig. 7. R1-Time trace – Validyne pressure transducer

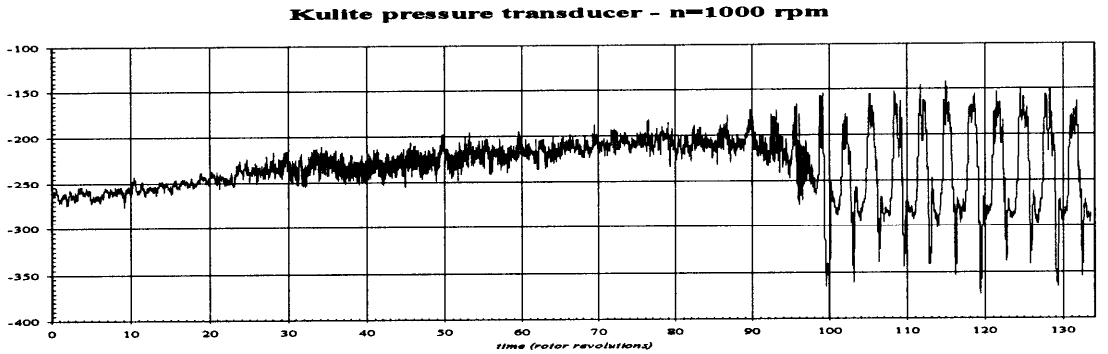


Fig. 8. R1-Time trace – Kulite pressure transducer

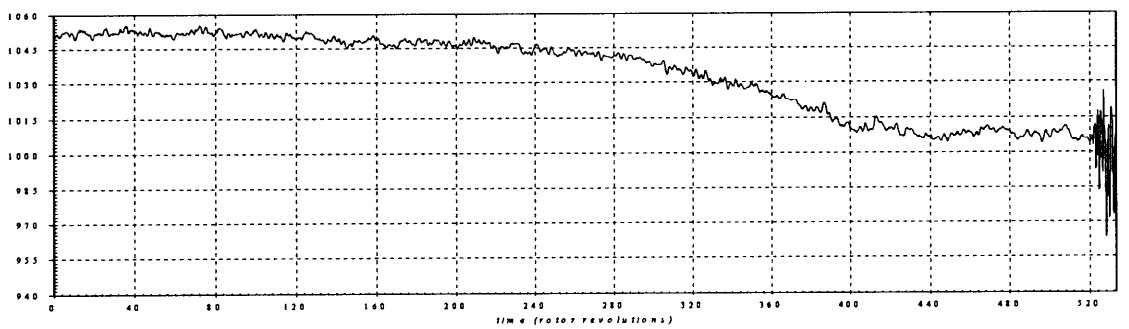


Fig. 9a. R2-Time trace – Hot-wire tangential position-Hub

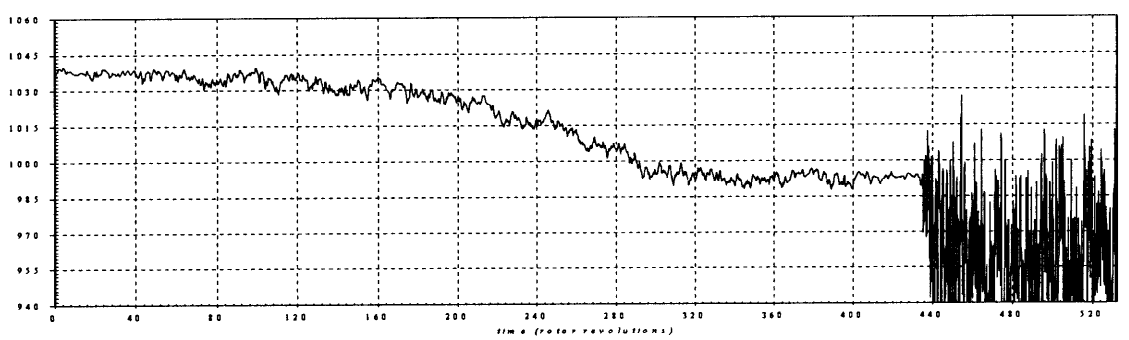


Fig. 9b. R2-Time trace – Hot-wire tangential position-Tip

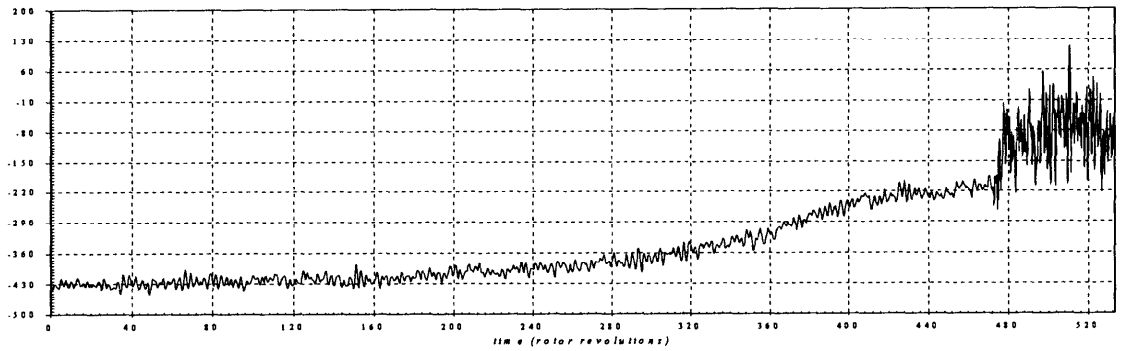


Fig. 10. R2-Time trace – Validyne pressure transducer

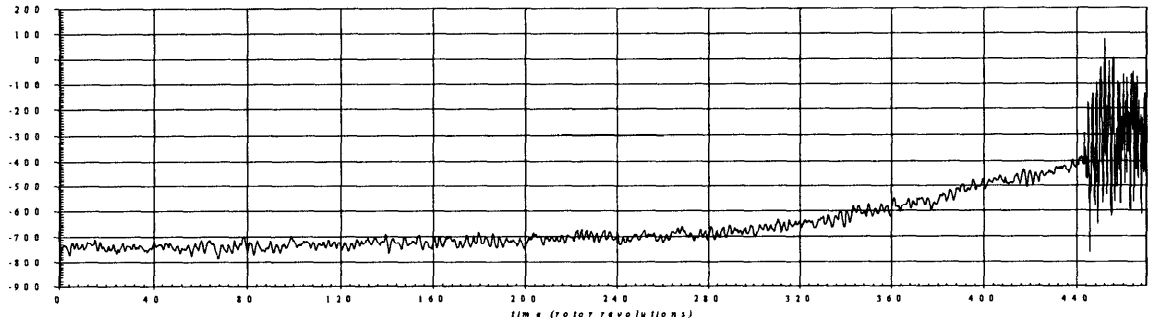


Fig. 11. R2-Time trace – Kulite pressure transducer

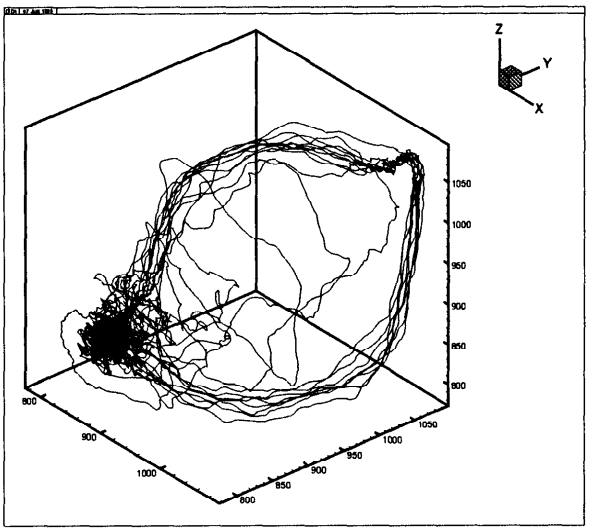


Fig. 12. R1-3-D Projection of Phase-Space portrait - Hot-wire axial position.

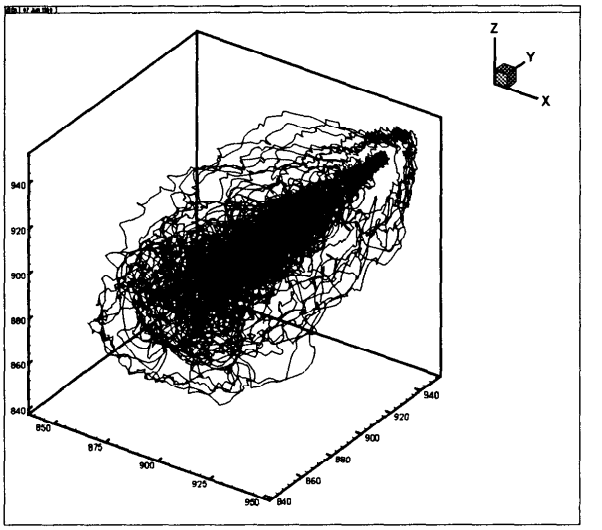


Fig. 13. R1-3-D Projection of Phase-Space portrait - hot-wire tangential position.

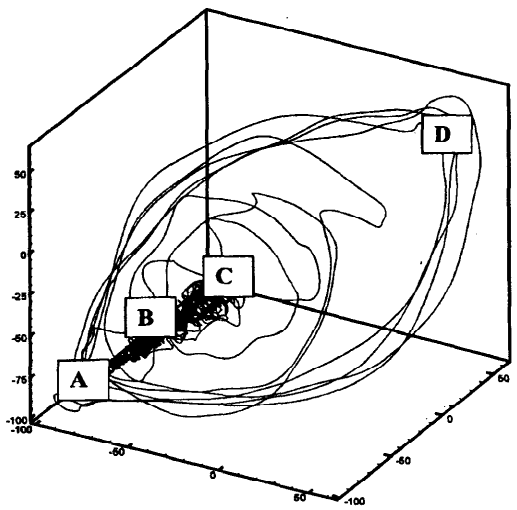


Fig. 14. R1-3-D Projection of Phase-Space portrait -Validyne pressure transducer.

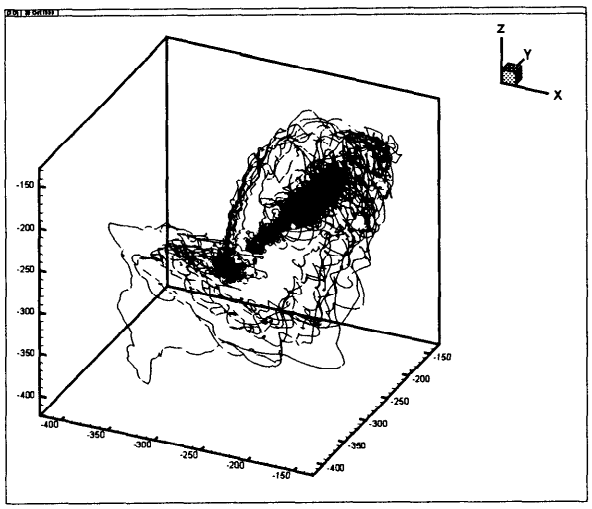


Fig. 15. R1-3-D Projection of Phase-Space portrait from Kulite pressure transducer.

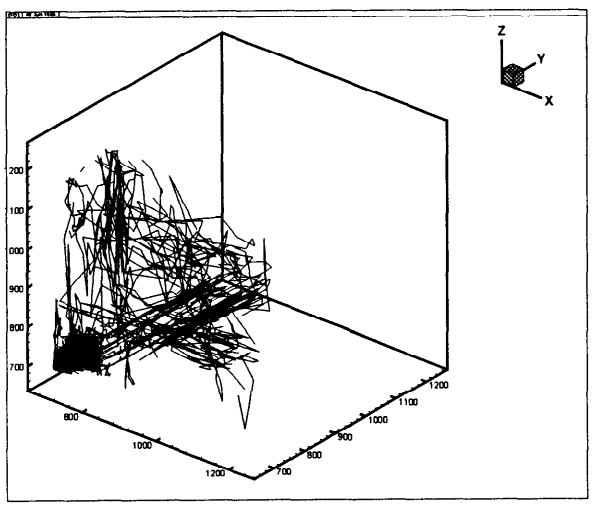


Fig. 16. R2-3-D Projection of Phase-Space portrait - Hot-wire axial position.

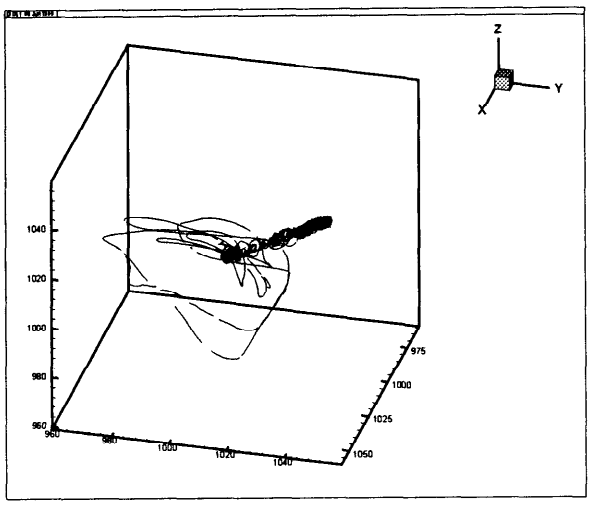


Fig. 17. R2-3-D Projection of Phase-Space portrait-hot-wire tangential position - hub.

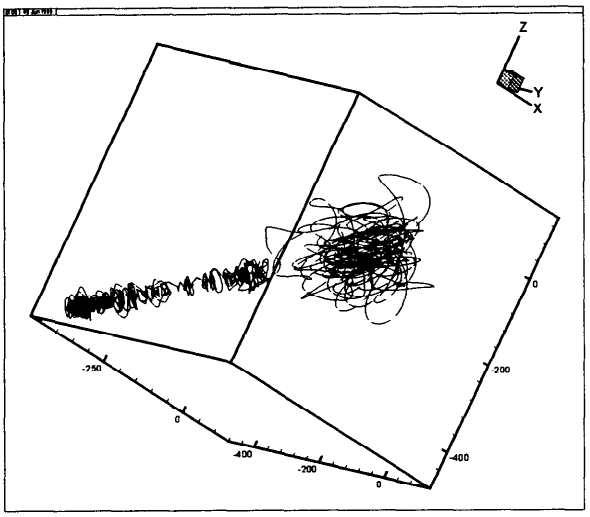


Fig. 18. R2-3-D Projection of Phase-Space portrait -Validyne pressure transducer.

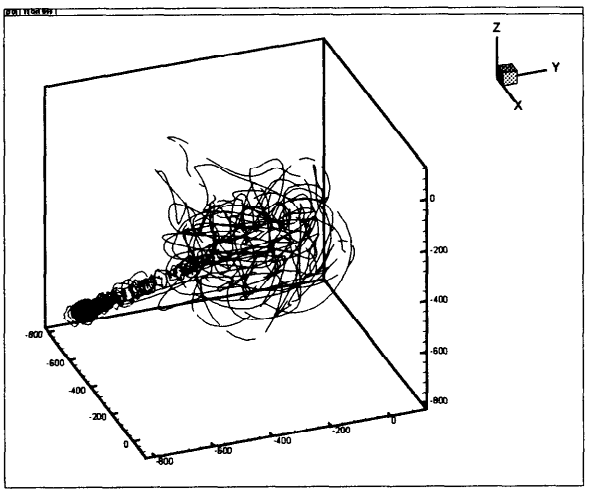


Fig. 19. R2-3-D Projection of Phase-Space portrait from Kulite pressure transducer.

Active Control of Compressor Surge Using a Real Time Observer

J.V.R. Prasad[1], **Yedidia Neumeier**[2], **Assaad Krichene**[3]
School of Aerospace Engineering
Georgia Institute of Technology, 270 Ferst Drive
Atlanta, GA 30332-0150, USA

Abstract

Approaches for active control of surge in axial and centrifugal compressors are based, for their majority, on sensing them after they occur and then taking appropriate action. On the other hand, some studies in the past have showed that precursors to surge exist in some cases. But very few studies have actually made use of precursors for active control. In this paper we show experimentally that surge precursors exist in centrifugal compressors. Further, we formulate a novel control scheme in which a real time observer is used for on-line identification of magnitude and frequency of dominant precursor waves. The observer outputs feed into a fuzzy logic control scheme, and the identified frequency and amplitude of the precursors are used to actuate a bleed valve and/or a fuel valve for active control of compressor surge. Experimental results demonstrating the viability of the overall scheme are presented.

Introduction

The design and operation of jet engines are faced with many challenges that limit the operating range of those engines. Among those challenges are aerodynamic phenomena that occur in the compression system such as rotating stall and surge. Rotating stall manifests itself as a region of severely reduced flow that rotates at a fraction of the compressor rotational speed and causes a drop in performance. Surge is a pumping oscillation that can cause flameout and engine damage.

Due to the importance of these phenomena, considerable effort in compression system studies has been focused primarily on the design and implementation of active control schemes to ensure stable operation of the compression system over a wide range of operating conditions[1-9]. However, those schemes, in their majority, are based on sensing after those phenomena have occurred and then taking appropriate control action. But the severity of those phenomena and their impact on the engine performance make it highly desirable to have a controller that is able to avoid the operation of the compressor in a region where the compressor is susceptible to those phenomena.

Some studies focused on the identification of precursors for surge and were able to show that such precursors exist for axial compressors and may or may not exist for centrifugal compressors depending on the compressor under consideration[10-17]. However, very little use of precursors was made in the design and implementation of controllers, primarily because of the difficulty associated with on-line identification of such precursors.

In this paper, a previously developed real time observer[18] scheme is used for on-line identification of surge precursors. Then, using the outputs from the real time observer, a fuzzy logic control scheme is synthesized for control of compressor bleed and/or fuel flow to the combustor so as to recover or prevent surge occurrence while maintaining the maximum attainable pressure ratio. The new control scheme is implemented and evaluated on the centrifugal compressor facility in the School of Aerospace Engineering at the Georgia Institute of Technology.

This paper is organized as follows: First, the centrifugal compressor facility is described followed by a brief description of the real time observer scheme used in this study. This is followed by a description of the fuzzy logic control scheme developed in this study. Next, experimental results from the centrifugal compressor facility are presented to illustrate the validity of the overall approach, followed by conclusions and current focus of our research.

Centrifugal Compressor Facility

The primary purpose of the centrifugal compressor rig in the School of Aerospace Engineering at the Georgia Institute of Technology is to provide a laboratory facility for control-oriented studies on surge and rotating stall in centrifugal compressors. Therefore, it is imperative that the rig exhibits these phenomena at reasonable time-scales and yet be compact enough to be housed in one of the bays available in the experimental facility.

---

* Paper presented at the NATO Symposium on Active Control Technology, Braunschweig, Germany, May 8 – 11, 2000.
[1] Professor
[2] Senior Research Engineer
[3] Graduate Research Assistant

Paper presented at the RTO AVT Symposium on "Active Control Technology for Enhanced Performance Operational Capabilities of Military Aircraft, Land Vehicles and Sea Vehicles", held in Braunschweig, Germany, 8-11 May 2000, and published in RTO MP-051.

The centrifugal compressor rig includes an inlet duct, a single-stage centrifugal compressor, a compressor discharge duct, a special plenum, a burner, an exhaust duct and a throttle. Air enters the system from a conical opening at the tip of the compressor inlet duct for smooth transition of flow from the room inlet duct into the compressor. The inlet duct has a constant diameter of 4 inches (101.6 mm). It is angled and extended from the air inlet duct to the compressor inlet. At the compressor inlet, the duct diameter is slightly reduced to fit the diameter of the compressor impeller. The impeller directs the flow radially outward into the compressor discharge duct that leads directly into the plenum. Heat is generated in the plenum by means of a propane burner. The flow leaves the plenum through the plenum exhaust duct where it has to pass through the throttle (butterfly valve) before it finally reaches the room exhaust duct. The parameters of the compressor are given in Table 1.

The single-spool V-5 supercharger compressor is belt-driven by a 40 HP, 3-phase inverter heavy-duty electric motor. It can be operated at variable speeds from approximately 15,000 rpm to 60,000 rpm without the need to stop and make changes or adjustments. At the maximum speed of 60,000 rpm, the compressor is capable of achieving a pressure ratio of approximately 2.25:1.

Parameter	Value
Compressor Inlet Area	0.003888 m^2
Compressor Exit Area	0.002150 m^2
Compressor Inlet Duct Area	0.008107 m^2
Plenum Inlet Duct Area	0.002027 m^2
Plenum Volume	1 m^3
Plenum Exhaust Duct Area	0.008107 m^2
Compressor Inlet Duct Length (L-shaped)	0.889 m
Plenum Inlet Duct Length	0.3048 m
Plenum Diameter	1.016 m
Plenum Exhaust Duct Length	0.3048 m
Compressor Maximum Speed	60,000 rpm
Compressor Nominal Speed	50,000 rpm

Table 1. Centrifugal compressor paprameters.

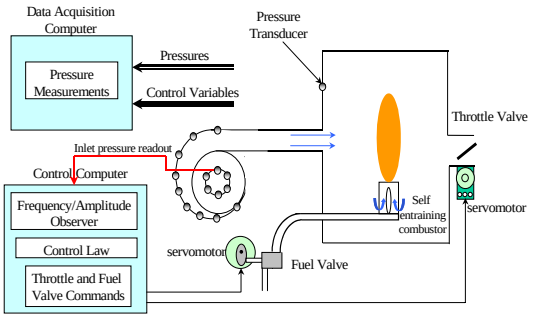


Figure 1. Schematic of the centrifugal compressor facility.

The plenum is a large metal chamber of 1 m^3 in volume. It is made of aluminum that is 3 inches (76.2 mm) thick, and is designed to withstand pressures of up to 400 Psi (27.6 bar). A self-entraining burner is coupled to the plenum at the bottom. The fuel to the burner is controlled by a servo valve. With maximum fuel rate, the burner provides about 15 KW of heat addition. A commercial safety circuit which overrides the operator is used for safe operation of the burner. A quartz window provides visual access to the flame.

The rig is equipped with a throttle actuator and a fuel flow actuator, which are controlled by a computer. Both actuators have a bandwidth of roughly around 10 Hz. The fuel flow actuator consists of a special flow control valve driven by another servomotor. A schematic of the facility together with the control computer and the data acquisition computer is given in Figure 1.

Real Time Observer Scheme

The observer used in this study was previously developed at the Georgia Institute of Technology for identification of combustion instabilities[18]. The observer is capable of real time identification of amplitude, frequency and phase of one or several dominant waves present in a signal. A brief description of the observer and its implementation for the case of identification of one dominant wave is presented here. For a more detailed description, the reader is referred to Ref. 18.

The developed observer assumes that the measured compressor pressure can be expressed in the following Fourier-like series[19]:

$$P_m(t) = \sum_{n=1}^{N} [a_n(t)\sin(\omega_n(t)t) + b_n(t)\cos(\omega_n(t)t)] \quad (1)$$

whose time dependent amplitudes, i.e., $a_n(t)$ and $b_n(t)$, and frequencies $\omega_n(t)$ are as yet unknown and need to be determined by analyzing the measured pressure signal $P_m(t)$. Qualitatively, the determination of these unknowns consists of an iterative solution process that is schematically described in Figure 2[19]. At the start of the calculations, the frequency of the unknown oscillation $\hat{\omega}$ is assumed and substituted into the integrals in Figure 2 and their lower limit of integration. The resulting integrals are then solved for the unknown coefficients $\hat{a}$ and $\hat{b}$. The calculated values of $\hat{a}$, $\hat{b}$ and $\hat{\omega}$ are then substituted into another relationship (not shown in Figure 2) that determines an improved value of the unknown frequency $\hat{\omega}$. The latter is then substituted again into the integrals in Figure 2 to obtain improved values of $\hat{a}$ and $\hat{b}$. This

calculation procedure is repeated until the calculated values of $\hat{a}$, $\hat{b}$ and $\hat{\omega}$ converge to final values. These values of $\hat{a}$, $\hat{b}$ and $\hat{\omega}$ are then used to determine the unknown amplitude, frequency and phase. This solution procedure determines the characteristics of the mode with the largest amplitude first.

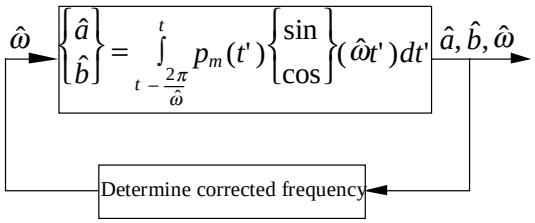


Figure 2. Observer block diagram.

Open Loop Results

The observer described in the previous section was implemented on the control computer of the centrifugal compressor facility. The measured signal and observed frequency and amplitude of the dominant wave for different operating conditions of the compressor are shown in Figures 3, 4 and 5. Figure 3 shows results for the case of low compressor loading, i.e., for the case of nearly full throttle opening. The identified frequency varies randomly in the range of 1 to 2 KHz, indicating a signal dominated by noise. As the loading on the compressor is increased by closing the throttle (see Figure 4), the identified frequency drops to around 100 Hz indicating the presence of dominant waves in the pressure measurements.

As the loading on the compressor is further increased, the compressor surges (see Figure 5), which is evident from large oscillations in pressure. It is also important to note the presence of cursor waves during part of each surge cycle as evidenced by the observed frequency and amplitude.

In order to verify the performance of the observer, an off-line Fast Fourier Transform (FFT) analysis was performed on part of the input signal indicated by two vertical lines in Figure 5. The results are presented in Figure 6. The first plot in Figure 6 shows the inlet pressure variation during the time frame used for performing the FFT analysis. The second plot in Figure 6 is the time dependent identified frequency output from the observer and the third one is a plot of frequency spectrum obtained from FFT analysis over the selected interval. A comparison of the identified frequency output and the FFT results indicates good agreement. Note the peak around 90 HZ in FFT results and the observer identifies the frequency of the dominant wave to be around 90 HZ as well.

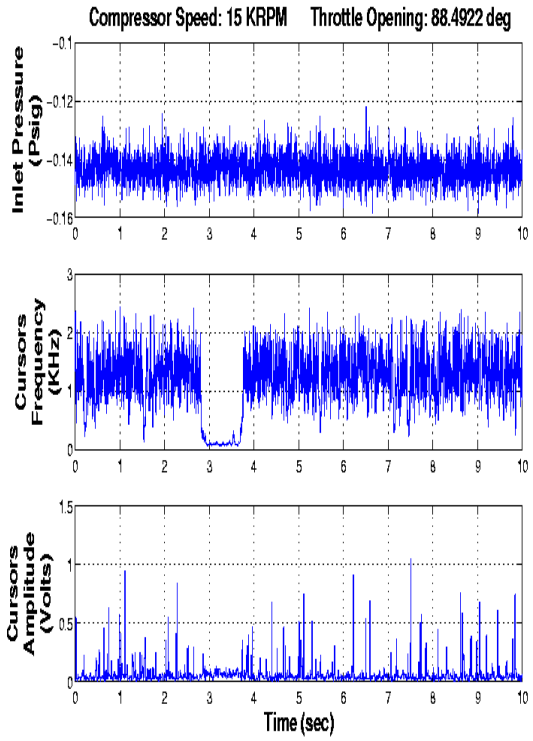


Figure 3. Observer performance for the low back pressure case (15,000 rpm)

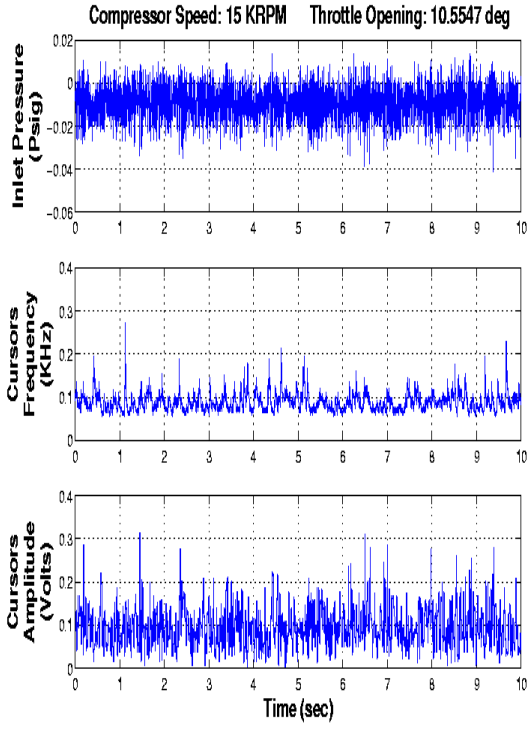


Figure 4. Observer performance for the high back-pressure case (15,000 rpm)

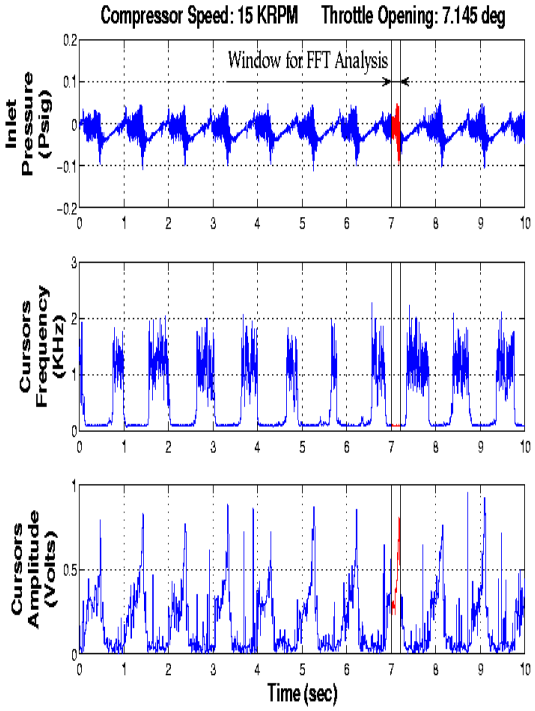


Figure 5. Observer performance during uncontrolled surge (15,000 rpm).

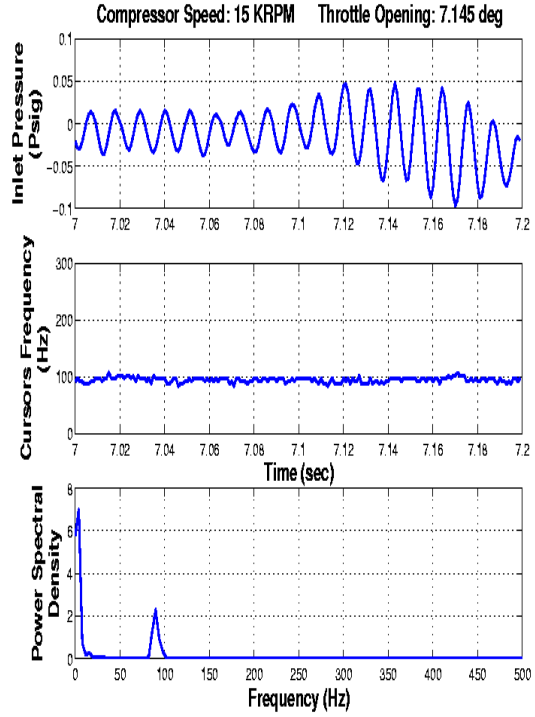


Figure 6. Comparison of observer frequency output and FFT results (15,000 RPM)

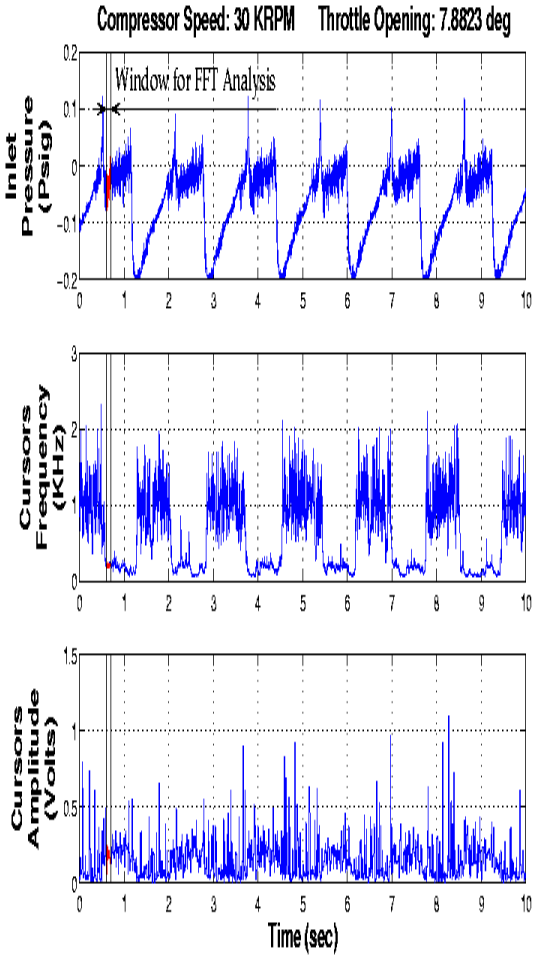


Figure 7. Observer performance during uncontrolled surge (30,000 rpm).

The influence of compressor rpm on the frequency of cursor waves was investigated by repeating the open loop experiments with the compressor rpm set at 20,000, 25,000 and 30,000. Figure 7 shows observer performance during uncontrolled surge with the compressor rpm set at 30,000. Figure 8 is a comparison of the observer frequency output and the results from off-line FFT analysis performed using data over a small time interval (as indicated by the vertical lines in Figure 7). There is a good agreement between the identified frequency from the observer and the FFT results. Note the small peak around 200 Hz in the FFT, which compares well with the average value of observer frequency output of around 200 Hz. Though not shown, similar results were also obtained from experiments conducted at 20,000 rpm and 25,000 rpm. From those results, it was concluded that the precursor frequency varied almost in proportion to the compressor speed and this fact was latter used in closed loop experiments.

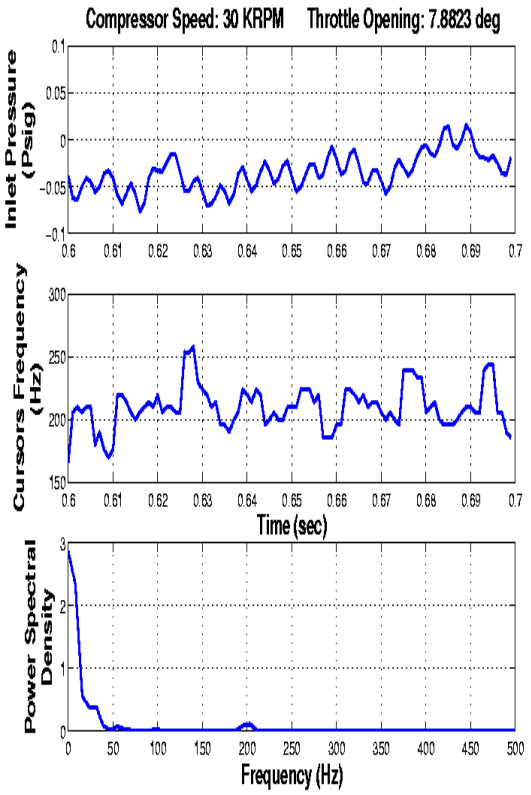


Figure 8. Comparison of observer frequency output and FFT results (30,000 rpm).

Fuzzy Logic Control Scheme

The control scheme uses a pressure transducer located at the inlet face of the compressor. The observer is continuously identifying the frequency and amplitude of dominant waves in the pressure signal. A fuzzy logic scheme is synthesized to make use of the identified frequency and amplitude outputs from the observer and apply appropriate commands to the actuators of a bleed valve or a fuel valve. The objective of the controller is to achieve maximum attainable pressure from the compressor while avoiding surge. It is very important to note that this is achieved with very little knowledge of the compressor characteristic map.

The fuzzy logic scheme consists of a fuzzifier, an inference engine and a defuzzifier. The inputs to the fuzzifier are the frequency distance $|\Delta f|$, and the amplitude difference, ΔA. The frequency distance, $|\Delta f|$, is the absolute value of the difference between the identified frequency and the expected frequency of precursors which depends on compressor rpm; i.e., $|\Delta f|$ = |Identified Frequency – Expected Frequency|). Likewise, ΔA is the difference between the identified amplitude and a threshold amplitude. These inputs are fuzzified using triangular membership functions with two fuzzy sets ("Small" and "Big") for each input (see Figures 9 and 10).

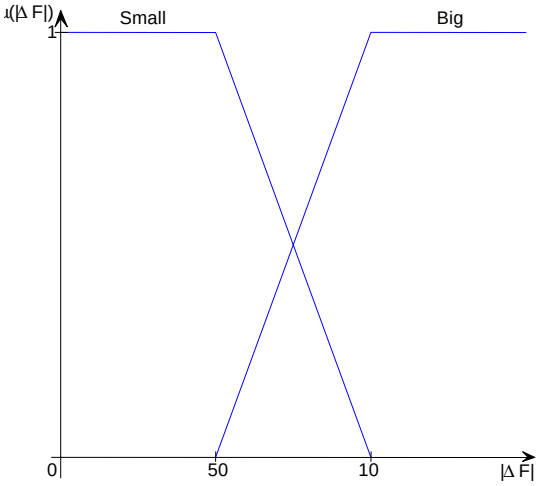


Figure 9. Membership functions for identified $|\Delta f|$.

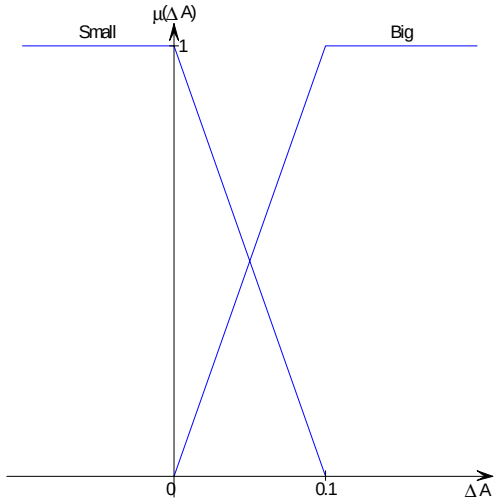


Figure 10. Membership functions for the identified precursor amplitude (ΔA).

ΔA \ $\lvert\Delta f\rvert$	S	B
S	N	N
B	P	AZ

Table 2. Rule base used for the Fuzzy logic Controller.

The fuzzified values of the frequency distance and amplitude difference are then passed through the inference engine consisting of user specified rule-base. The output consists of three fuzzy sets, viz., "Negative (N)", "Approximately Zero (AZ)" and "Positive (P)", (see Table 2).

The fuzzy membership of the output is calculated using Sugeno's product inferencing procedure[20] as follows:

$$x_N = \min(\mu_S(\Delta A), \mu_S(|\Delta f|)) + \min(\mu_S(\Delta A), \mu_B(|\Delta f|))$$

$$x_{AZ} = \min(\mu_B(\Delta A), \mu_B(|\Delta f|)) \quad (2)$$

$$x_P = \min(\mu_B(\Delta A), \mu_S(|\Delta f|))$$

The crisp value of control is obtained using the weighted average of the fuzzy output values.

$$control = w_N x_N + w_{AZ} x_{AZ} + w_P x_P \quad (3)$$

where w_N, w_{AZ} and w_P are pre-selected output weights.

Closed Loop Results

Closed loop experiments were used to evaluate the performance of the surge controller described in the previous section. Two types of control actuation were considered in this study; viz., bleed valve actuation and fuel valve actuation. In the case of bleed valve actuation, the exit throttle itself was used to emulate a bleed valve. We feel that the fuel control scheme offers inherent advantages such as greater control authority and overheating protection of the turbine.

For each control actuation scheme, two sets of experiments were conducted. In the first set, the performance of the controller for recovery from surge was evaluated. In the second set of experiments, the performance of the controller in avoiding surge was evaluated.

Throttle Control

Figure 11 shows the time dependence of the inlet pressure (which is used as input to the observer), relative plenum pressure rise and throttle position in surge recovery tests. The upper trace in Figure 11 indicates that at large throttle openings, i.e., for low compressor loading, the gage pressure at the inlet is negative indicating that air is flowing into the compressor. Then, as the throttle is closed, this pressure starts to increase which is synonymous to a reduction in the mass flow through the compressor, and this trend continues until the system gets into surge. Note that during parts of surge cycles, the inlet gage pressure is positive indicating flow reversal.

The middle plot in Figure 11 shows that as the throttle is closed, the plenum pressure increases until the system gets into surge at which point the plenum pressure starts oscillating. Note the large decrease in the plenum pressure during surge. Eventually, when the controller is turned on, the surge oscillations diminish and the plenum pressure is recovered to its maximum value.

The lower trace in Figure 11 shows the throttle position commanded by the user and the actual throttle position versus time. When the controller is turned on, although the user commands a more closed position for the throttle, the controller modulates the throttle position just enough to get out of surge and recover the maximum plenum pressure. The throttle modulation would be synonymous to bleed valve modulation in a real engine.

The plots in Figure 12 are similar to those of Figure 11 with the only difference being that in this case, the controller is turned on all the time to demonstrate the surge avoidance capabilities of the controller. In this case, we see that although the commanded position of the throttle goes from a fully open position to a fully closed position, the controller does not allow the actual position of the throttle to go lower than what is necessary to keep the system from surging while maintaining the maximum plenum pressure.

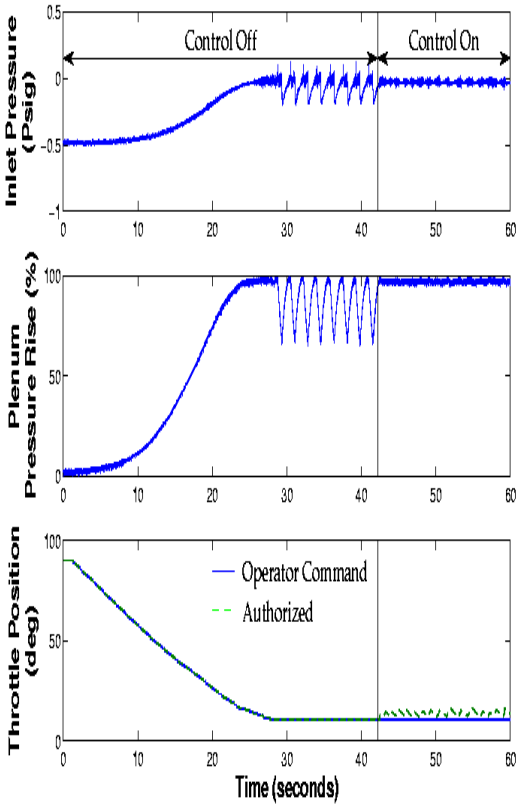


Figure 11. Surge recovery using throttle control.

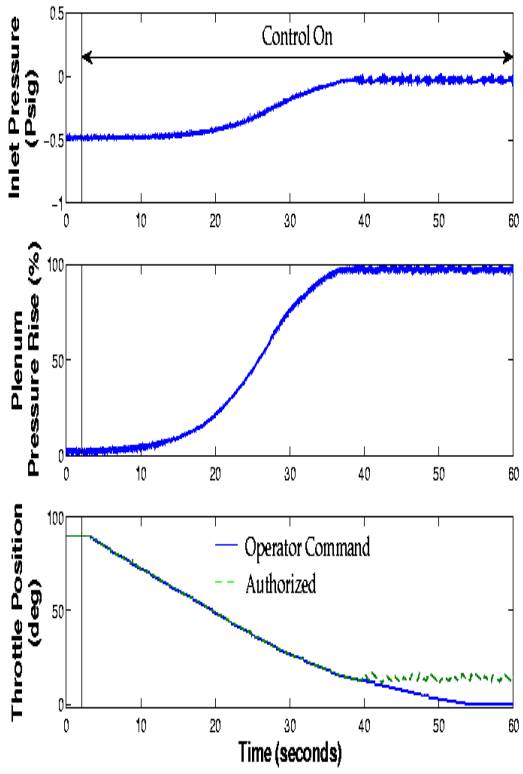


Figure 12. Surge avoidance using throttle control.

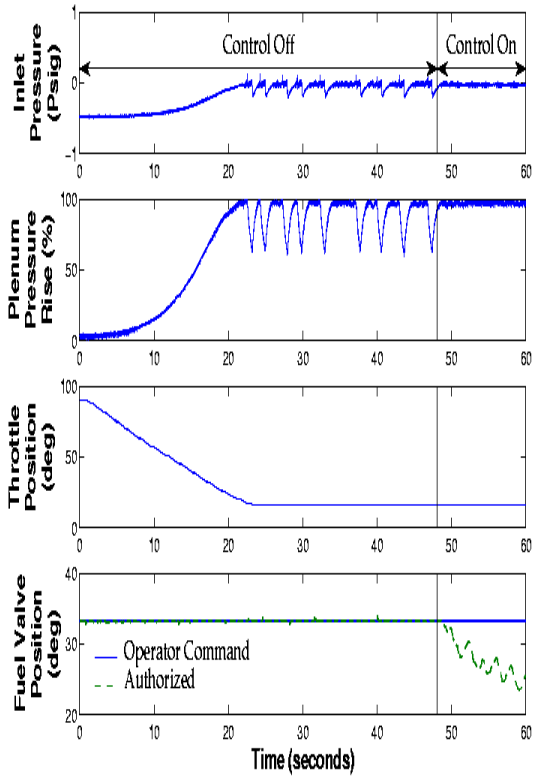


Figure 13. Surge recovery using fuel control.

Surge Control Using Fuel Valve

The same controller as before was used with a fuel valve actuation with the only change being that the output of the controller was multiplied by a constant gain to account for differences between control sensitivities associated with the throttle valve actuation and fuel valve actuation.

Figure 13 shows the process of surge recovery using the fuel flow control. The first three traces are similar to those in Figure 11. The additional trace in Figure 13 shows the position of the fuel valve, which is indicative of the fuel flow rate.

Initially, the throttle is open, the fuel valve is fully open and the controller is off. Then, the throttle is closed gradually until the system gets into surge. Once the fuel flow control is turned on, it starts to reduce the fuel flow to recover from surge while maintaining the maximum plenum pressure.

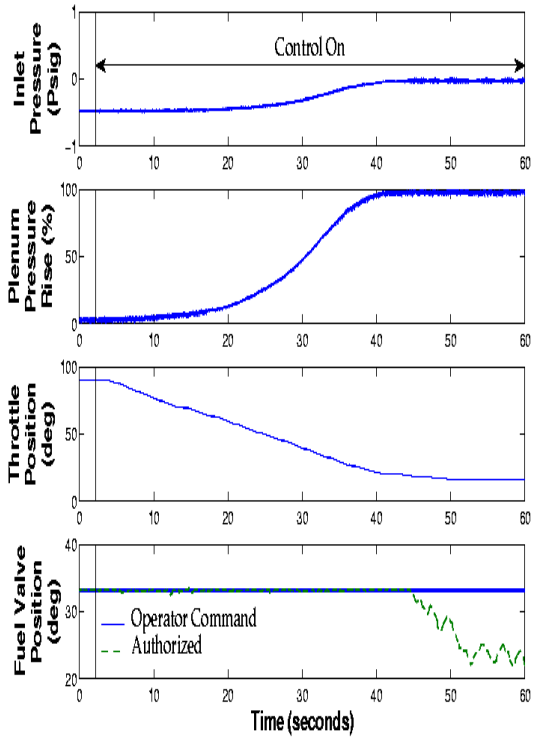


Figure 14. Surge avoidance using fuel Control.

Figure 14 shows similar plots for the surge avoidance case using the fuel valve actuation. In this case, the controller is turned on all the time. The throttle is closed gradually until the system is brought to operate in the surge region while the fuel valve is set at a constant value. Initially, when the system is away from surge, there is no reason for the controller to adjust the fuel flow. As the system gets closer to surge, the fuel flow controller starts reducing the fuel in order to prevent the appearance of surge while maintaining the maximum plenum pressure. In a real

engine, reducing the fuel flow when the compressor gets closer to surge is very desirable since this reduces the temperature, thus protecting the engine components from damage.

Conclusions

An observer previously developed at the Georgia Institute of Technology is used to identify the amplitude and frequency of the dynamic cursors that appear in compressors before and during surge. The amplitude and frequency identified by the observer are used as inputs to a fuzzy logic scheme for active surge control. The surge control scheme has been implemented on the centrifugal compressor facility in the School of Aerospace Engineering at the Georgia Institute of Technology using both throttle valve (that emulates a bleed valve) and fuel valve actuation schemes. Experimental results demonstrate the effectiveness of the surge control scheme developed in this study for both surge recovery and surge avoidance.

Currently work is in progress in providing a detailed understanding of the dynamic cursors and in exploring the potential of the active control schemes developed in this study for full scale compressors.

Acknowledgments

This study was performed under the MURI (Multidisciplinary University Research Initiative) on Intelligent Gas Turbine Engines at the Georgia Institute of Technology sponsored by the U.S. Army Research Office under project DAAH04-96-1-0008.

References

1. Day, I. J., "Active Suppression of Stall and Surge in Axial Compressors," *ASME International Gas Turbine and Aeroengine Congress and Exposition, Paper No. 91-GT-403,* June 1991.

2. Epstein, A. H., Ffowcs-Williams, J. E. and Greitzer, E. M., "Active Suppression of Aerodynamic Instabilities in Turbomachines.," *Journal of Propulsion and Power, Volume 5, pages 204 - 211,* March-April 1989.

3. Simon, J. S. and Valavani, L., "A Lyapunov Based Nonlinear Control Scheme for Stabilizing a Basic Compression System Using a Close-Coupled Control Valve," *Proceedings of the 1991 American Control Conference, Volume 3, pages 2398 - 2406,* 1991.

4. Haddad, W. M., Chellaboina, V. S., FauSz, J. L. and Leonessa, A., "Optimal Nonlinear Robust Control for Nonlinear Uncertain Cascade Systems," *Proceedings of the American Control Conference, Volume 1, pages 403 - 407,* 1997.

5. Markopoulos, N., Neumeier, Y., Prasad, J. V. R. and Zinn, B. T., "Active Control of Compressor Rotating Stall Using Linear Amplitude Feedback," *36th Aerospace Sciences Meeting and Exhibit, Reno, NV,* January 12-15, 1998, Paper No. 98-0971.

6. KrstiC, M., "Lyapunov Feedback Design for Stabilization of Stall and Surge in Axial Compressors.," *Nonlinear Dynamics and Controls, ASME Design Engineering Division Publication, Volume 91, pages 73 - 78,* 1996.

7. KrstiC , M., Protz, J. M., Paduano, J. D. and KokotoviC, P. V., "Backstepping Designs for Jet Engine Stall and Surge Control," *Proceedings of the IEEE Conference on Decision and Control,* volume 3, *pages 3049 - 3055,* 1995.

8. Swaminathan, R., Prasad, J.V.R., Neumeier, Y. and Lal, M., "Combined Model and Rule Based Control of Compression System Rotating Stall," *33rd AIAA/ASME/SAE/ASEE Joint Propulsion Conference, Seattle, WA.* July 1997.

9. Krichene, A. and Prasad, J.V.R., "Synthesis of Adaptive Neural Network Based Rotating Stall Controllers for Axial Compressors," *AIAA Guidance, Navigation, and Control Conference and Exhibit, Portland, OR, pages 365 – 373,* Aug. 9-11, 1999.

10. Bright, M. M., Qammar, H. K., Weigl, H. J. and Paduano, J. D., "Stall Precursor Identification In High-Speed Compressor Stages Using Chaotic Time Series Analysis Methods," *Journal of Turbomachinery, Volume 119, No. 3, pages 491 – 499,* July 1997.

11. HÖss, B., Leinhos, D. and Fottner, L., "Stall Inception in the Compressor System of a Turbofan Engine," *Proceedings of the 1998 International Gas Turbine & Aeroengine Congress & Exhibition, Paper No. 98-GT-475,* 1998.

12. Grauer, F., Volgmann, W., Stoff, H. and Breuer, T., "Detection of Precursor Waves Announcing Stall in Two 3-Stage Axial Compressors," *Proceedings of the 1998 International Gas Turbine & Aeroengine Congress & Exhibition, Paper No. 98-GT-520,* 1998.

13. Lawless, P. B., Kim, K. H. and Fleeter, S., "Characterization of Abrupt Rotating Stall Initiation in an Axial Flow Compressor," *Journal of Propulsion and Power, Volume 10, No. 5, pages 709 – 715,* September-October, 1994.

14. Chen, J., Shi, L., Hasemann, H. and Rautenberg, M., "Stall Inception Behavior in a Centrifugal Compressor," *Proceedings of the 1994 International Gas Turbine & Aeroengine Congress & Exhibition, Paper No. 94-GT-159,* 1994.

15. Lawless, P. B. and Fleeter, S., "Rotating Stall Acoustic Signature in a Low Speed Centrifugal Compressor: Part 1 - Vaneless Diffuser," *Proceedings of the 1993 International Gas Turbine & Aeroengine Congress & Exhibition, Paper No. 93-GT-297,* 1993.

16. Lawless, P. B. and Fleeter, S., "Rotating Stall Acoustic Signature in a Low Speed Centrifugal Compressor: Part 2 - Vaned Diffuser," *Proceedings of the 1993 International Gas Turbine & Aeroengine Congress & Exhibition, Paper No. 93-GT-254,* 1993.

17. Inoue, M., Kuroumaru, M., Iwamoto, T. and Ando, Y., "Detection of a Rotating Stall Precursor in Isolated Axial Flow Compressor Rotors," *Journal of Turbomachinery, Volume 113, No. 2, pages 281 - 289,* April 1991.

18. Neumeier, Y., Markopoulos, N. and Zinn, B. T., “A Procedure for Real-Time Decomposition, Observation and Prediction for Active Control of Combustion Instabilities,” *Presented at the IEEE Conference on Control Applications, Hartford CT*, October 5-7, 1997, Paper No. 97-318.
19. Neumeier, Y. and Znn, B. T., "Active Control of Combustion Instabilities using Real Time Identification of Unstable Combustor Modes," Proceedings of the 4th IEEE Conference on Control Applications, Albany, NY, September 28-29, 1995.
20. Driankov, D., Hellendoorn, H. and Reinfrank, M.: An Introduction to Fuzzy Logic Control, Springer-Verlag, 1991.

PAPER -11, J. Prasad

Question (F. Grauer, Germany)
Was the detector influenced by the blade passing frequencies?

Reply
No, the observer could be selected to operate over a range of frequencies, thus eliminating other frequencies.

Question (F. Grauer, Germany)
Do you expect your fuel controller to be slow, as was found from another study?

Reply
The bandwidth of the fuel actuator we have used is 10 Hz. We believe similar results could be expected from full scale experiments.

SENSOR REQUIREMENTS FOR ACTIVE GAS TURBINE ENGINE CONTROL

Dr. A. D. Kurtz, Dr. J. W. H. Chivers, A. A. Ned
Kulite Semiconductor Products Inc.,
One Willow Tree Road,
Leonia, NJ 07605 USA

Professor A. H. Epstein
Massachusetts Institute of Technology
Massachusetts,
Cambridge, MA 01239 USA

1. ABSTRACT

This paper considers the potential benefits of active gas turbine engine control and briefly reviews a selection of the published material in the fields of detection and control of stall in axial flow turbomachines from the perspective of an instrumentation engineer. The use of a variety of sensors and mechanical installations is discussed and a specification for a pressure sensor which can be used to detect gas path instabilities in axial flow compressors is developed.
Recent developments of Silicon-On-Insulator (SOI) piezoresistive pressure sensors for gas turbine research and development and basic aerodynamic research are described in this paper. Problems which can arise from use of these sensors in ultra harsh environments are discussed. The design of a new miniature dynamic pressure transducer capable of operating reliably under extreme environmental conditions - temperatures in excess of 480°C (900°F) and accelerations greater than 200g - is described in detail. The performance of such "leadless" pressure transducers is presented and indicates that ruggedised, high frequency, piezoresistive transducers are now feasible for use in the dynamic control of turbomachines.

2. INTRODUCTION

The modern aero gas turbine engine is generally considered to be a relatively mature device, having been the subject of intense development throughout the world for over half a century for both military and civil applications. Consequently the cost and difficulty of achieving further improvements to the gas turbine in terms of specific fuel consumption, weight and price have risen steeply. However the explosive growth in computing and microelectronics gives rise to optimism in achieving dramatic improvements in the performance of gas turbines in the future when this technology is applied to engine control systems. Significant improvements have already been made in the performance, economy and handling of modern gas turbine engines by the use of Full Authority Digital Engine Control systems (FADEC). Many modern turbomachines, in particular multistage axial flow compressors, now rely on complex scheduling of stator vanes and bleed valves and monitoring of pressures, temperatures and flows to achieve stable operation. The ability of a FADEC to process the many sensor inputs from an engine, to apply sophisticated control laws and control a range of actuators simultaneously, enables many modern gas turbines to function economically and reliably. A return to the previously used hydro-mechanical control systems would, in many cases, be impossible without significant mechanical and aerodynamic redesign of the turbomachine.
The modern FADEC controls the starting, steady operation and transient conditions of a gas turbine and incorporates fault tolerant designs appropriate to a flight critical system. The next step which is predicted will generate a significant improvement in efficiency of operation of a gas turbine has been identified as the improvement in stability of compressors through the anticipation and suppression of surge and rotating stall. The natural aerodynamic instabilities of turbomachines often limit their performance, but increased stability potentially leads to lighter more efficient compressors with fewer stages and shorter airfoil chords, reduced fan noise from lower tip speeds, faster engine acceleration as the surge constraints have been removed and greater operating flexibility.
The subject of the control of stall and surge in turbomachines has been investigated widely with Ludwig's work in 1980 being the earliest identified reference [1]. However the phenomenon of stall and surge in the compression systems of gas turbine engines has been the subject of investigation since the 1950s. Twelve teams have been identified through a non rigorous review of the published technical data in this field [2] and in addition, there

Paper presented at the RTO AVT Symposium on "Active Control Technology for Enhanced Performance Operational Capabilities of Military Aircraft, Land Vehicles and Sea Vehicles", held in Braunschweig, Germany, 8-11 May 2000, and published in RTO MP-051.

are other currently active teams who eschew publicity.

3. SENSOR SELECTION

The selection of the sensor type and location(s) are critical factors in determining the effectiveness and practicality of an engine surge and stall control system, as is the selection of the actuator type and the algorithms used to process the data from the sensors. This paper will confine itself to the issues relating to the choice and design of the sensors, although similar importance needs to be attached to the selection of the actuators and signal processing software and hardware in order to create an engine control system which is both effective and safe.

A review of the most recently published material in the field of active control of surge and stall in axial flow compressors concludes that the most widely used physical parameter to monitor the stability of a compressor is pressure, although the measurement of gas flow using hot wire anemometers and the measurement of gas temperature using high response thermocouple probes have been used successfully.

The paper by Day, Breuer, Escuret, Cherrett and Wilson [3] assessed the generic features of stall inception using four high speed compressors. In the experiments on all four compressors, large numbers of miniature Kulite pressure transducers were used (MTU – 24, DRA – 24, SNECMA – 40, Rolls-Royce – 27). Similarly in the reported work by Freeman, Wilson, Day and Swinbanks [4] on the applied stall control of a Rolls-Royce Viper engine, 30 miniature Kulites were employed. In addition, the work by Eveker, Nett and Sharma on the demonstration of a non-linear control strategy on a high speed 3 stage axial flow compressor used 15 miniature Kulites. The paper by van Schalkwyk, Paduano, Greizer and Epstein [5] describes the first experimental validation of transfer function modelling and active stabilisation on a 3 stage low speed axial flow compressor and is the exception in the use of 8 hot-wire anemometers, which measured the gas flow, as the sensors for the control system. DiPietro and O'Brien [6]and [7] report on the effects of transient inlet temperature fluctuations on the stability of a 2 stage subsonic axial flow compressor using medium response thermocouples and static and pressure tappings connected to Datametrics and Omega pressure transducers.

4. SENSOR INSTALLATIONS

In the experimental work referred to in the previous section, the pressure transducers have been physically installed in a compressor in two configurations to sense the stability of operation of the machine by the measurement of high response pressure fluctuations. First the transducer can be attached to a total pressure pitot probe and can be either embedded within the probe or mounted remotely using a non-resonant pipe system, or semi-infinite line, as shown in Figure 1.

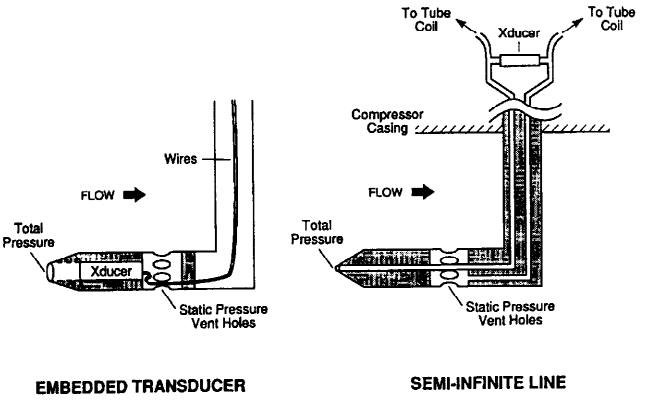


Figure 1

The second configuration is referred to as a wall static installation with the pressure transducer either directly mounted in the wall of the compressor casing with a flush sensing diaphragm or remote from the static tappings using a non-resonant pipe system similar to that referred to in the pitot probe configuration and is shown in Figure 2.

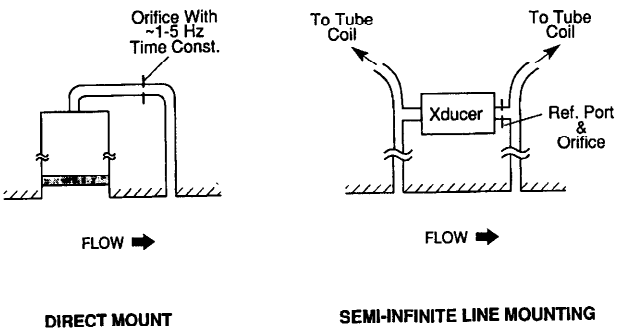


Figure 2

Both configurations have strengths and limitations; the measurement of dynamic total pressures using the pitot probe potentially generates the largest unsteady pressure signals under stall and surge conditions but is intrusive which may affect compressor efficiency and weight, especially if multiple probes are required. Additionally, a long experience of working closely with compressor designers suggests that they are likely to be unhappy with a significant increase in the quantity of intrusive gas path instrumentation from the perspectives of reliability and efficiency.

The wall static installation typically generates dynamic pressures which are approximately half the amplitude of the signals produced from a total pressure pitot installation under similar conditions. However the wall static installation is mechanically superior in that it is non-intrusive and hence is unlikely to affect aerodynamic efficiency or weight and will be more reliable.

On the basis of the above considerations, the authors are of the opinion that the wall static configuration is the one which is most likely to be selected for application to production gas turbine engines. A flush diaphragm arrangement is also likely to be more acceptable thus avoiding the additional cost, weight and complexity of semi-infinite line systems.

5. PRESSURE SENSOR SPECIFICATION

The high response pressure data which is generated by the dynamic pressure transducers is processed using one of many proprietary algorithms in order to predict or detect the onset of stall and surge. Although the operation and logic of the algorithms described in the technical publications vary considerably, the data requirements from the pressure sensors appear to be remarkably similar. The required characteristics for a stall and surge pressure sensor have been derived from both published technical papers and informal discussions with leading researchers in the field.

The pertinent characteristics which are required of a compressor mounted stall and surge pressure sensor are high sensitivity (ability to detect 70Pa (0.01psi) peak to peak fluctuations), stability of sensitivity with temperature and time (±5% to 10% FS) and the ability to survive in an extremely hostile environment (operating ambient temperatures and transients between -54°C and 400°C (-65°F and 750°F) and acceleration levels of up to 200g peak between 1kHz and 18kHz). The pressure transducer installation should also have sufficient bandwidth to measure frequencies between 100Hz and 1kHz for large gas turbines and between 500Hz and 8kHz for small gas turbines with negligible phase shift. During surge conditions, the pressure transducer must survive gas path pressure and temperature transients of up to 3.4MPa (500psi) and 1000°C (1830°F) for several seconds. Finally, if active surge and stall control systems are to be applied to production civil and military gas turbine engines in the future, the reliability and cost of the dynamic pressure transducers must be competitive with the pressure transducers currently used to measure oil, fuel, air and hydraulic pressures on airframes and engines.

6. THE SILICON-ON-INSULATOR (SOI) SENSOR

For the last 40 years, Kulite has supplied high performance pressure transducers to the aerospace industries for both research and development and for production applications. These transducers are based upon the piezoresistive silicon technology which Kulite pioneered and developed to its current high levels of performance and reliability. In order to describe the research and development which has led to the creation of the leadless pressure transducer, it is relevant to consider the original silicon-on-insulator pressure capsule design.

The heart of the piezoresistive SOI pressure sensor is a silicon diaphragm which is supported upon a Pyrex glass pedestal in such a manner as to enable a pressure differential to be applied across the diaphragm without introducing a mounting strain in the diaphragm. An "anodic" molecular bond is used to attach the silicon diaphragm to the glass pedestal which ensures a very stable, permanent assembly without the use of glues or adhesives. Piezoresistive silicon strain gauges are integrated within the silicon diaphragm structure but are electrically isolated from the silicon diaphragm as shown schematically in Figure 3. The piezoresistors measure the stress in the silicon diaphragm which is a direct function of the pressure of the media.

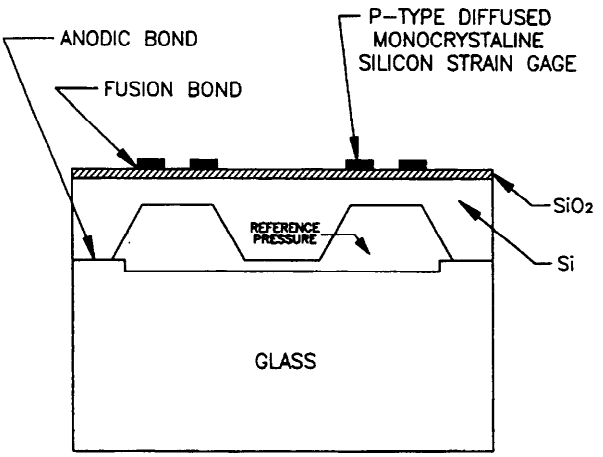


Figure 3.

The silicon diaphragm is usually thinned in selected areas underneath the piezoresistors by anisotropic chemical etching in order to increase the pressure sensitivity of the diaphragm. A photograph of the top of a silicon diaphragm is shown in Figure 4.

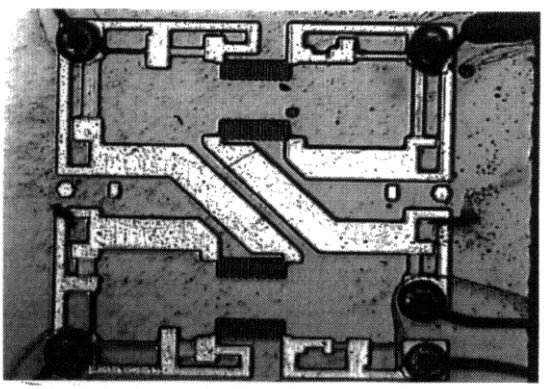


Figure 4.

The photograph clearly shows the four darker piezoresistors which are connected electrically via the lighter coloured metallic interconnections to form a fully active Wheatstone bridge. Also clearly

visible at the corners of the diaphragm are five 0.024mm (0.001 inch) diameter gold bond wires which are ultrasonically ball bonded to the diaphragm metallisation and are used to connect electrically to the bridge.
Under extreme conditions of temperature and vibration, the ultrasonic agitation used to form the ball bonds causes abrasion to take place during the welding process and allows microscopic holes to develop in the platinum metallisation through which, at high temperatures, the gold can migrate and form a gold-silicon eutectic which causes the leads to fail. In addition, the pressure media is in direct contact with the stress-sensing network, leadouts and interconnects which at high temperatures and in the presence of aggressive chemical can fail. The key elements in the design of a ruggedised pressure sensor is the elimination of the gold bond wires and the protection of the sensing elements from corrosive environments at high temperatures, hence the reference to the new sensor capsule as the "leadless" design.

7. LEADLESS SENSOR DESIGN

The leadless sensor capsule is comprised of two main components, the sensor chip and the cover wafer which are eventually assembled to form the pressure capsule.
The sensor chip is manufactured from two separate wafers. First a carrier wafer is fabricated which forms the mechanical structure, the diaphragm. The second wafer is referred to as the sacrificial wafer on which is defined the areas which the high conductivity P^+ piezoresistive strain gauges occupy. After oxidising the carrier wafer to form an electrically insulating layer over its surface, the two wafers are bonded together using a Diffusion Enhanced Fusion bonding (DEF) process [8], [9]. The bond is a direct chemical molecular bond between the P^+ regions and the silicon oxide and uses no adhesive or additional components. Once the bond is formed, the non-doped areas of the carrier wafer are selectively removed chemically. The piezoresistive P^+ are now permanently bonded to the dielectrically isolated carrier wafer in which the diaphragm is now micromachined. In order to optimise the mechanical performance of the force collector, the diaphragm is formed in the shape of a picture frame [10].
Figure 5 shows a view of the sensor chip with the four piezoresistive gauges strategically positioned inside the "picture frame" and connected in a Wheatstone bridge. The entire sensing network is P^+ and there are separations between the contact regions of the bridge, Metal is deposited to form ohmic contacts to the P^+ regions located inside the large contact regions. There is also a rim of P^+ material around the periphery of the sensor chip. When the cover wafer is assembled to the sensor chip, an hermetic seal is formed between the cover and this area of P^+ material thus protecting the stress sensing network and all the electrical interconnections from the harsh environmental conditions.

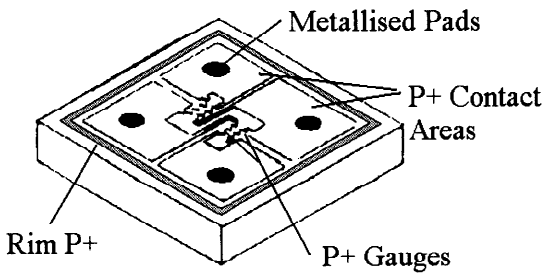


Figure 5.

The cover wafer is manufactured from either silicon or a Pyrex glass to the same dimensions as the silicon wafer. Four holes are drilled in the cover, one in each corner, which align with the metallised contact pad areas. A recess is also created in the centre of the cover wafer to allow the diaphragm to deflect freely when assembled.
The sensor chip and the cover wafer are then assembled using an electrostatic bond. Figure 6 shows a top isometric view of the components just prior to sealing. Once the two wafers have been bonded, only the metallised leadout pads are exposed whilst all the gauges and electrical interconnections on the sensing side of the silicon chip are sealed by the cover. Thus the active portion of the pressure sensor is hermetically isolated.

8. THE LEADLESS CONNECTION

To avoid the use of gold ball bonds and fine gold wires, a high temperature metal frit is used to provide the electrical connection between the sensing chip and a specially designed header. The frit is a mixture of high conductivity metal powders in appropriate physical form and glass and is used to fill the holes in the cover wafer after it is bonded to the sensor chip.
The specially designed header contains a group of four hermetically sealed pins protruding from its surface which are spaced so as to fit the holes drilled in the cover wafer. Figure 7 shows a section of the assembled pressure capsule and also a section of the pressure capsule mounted in the header. The pressure capsule is bonded to the header at a high temperature using a non conductive glass frit, during which process the metal frit in the cover wafer holes melts and creates low resistance electrical connections between the header pins and the metal contact pads on the sensor chip.

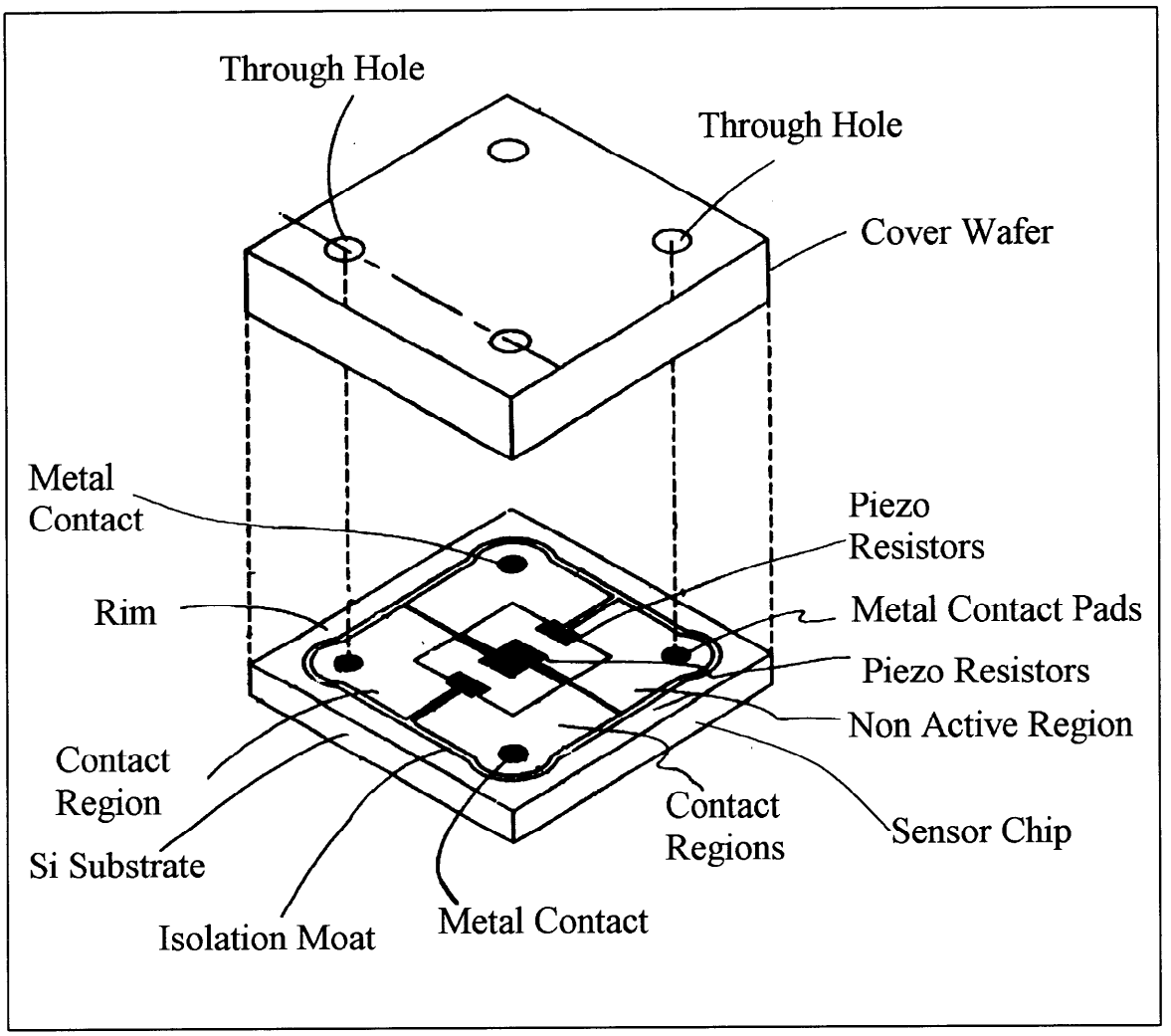


Figure 6

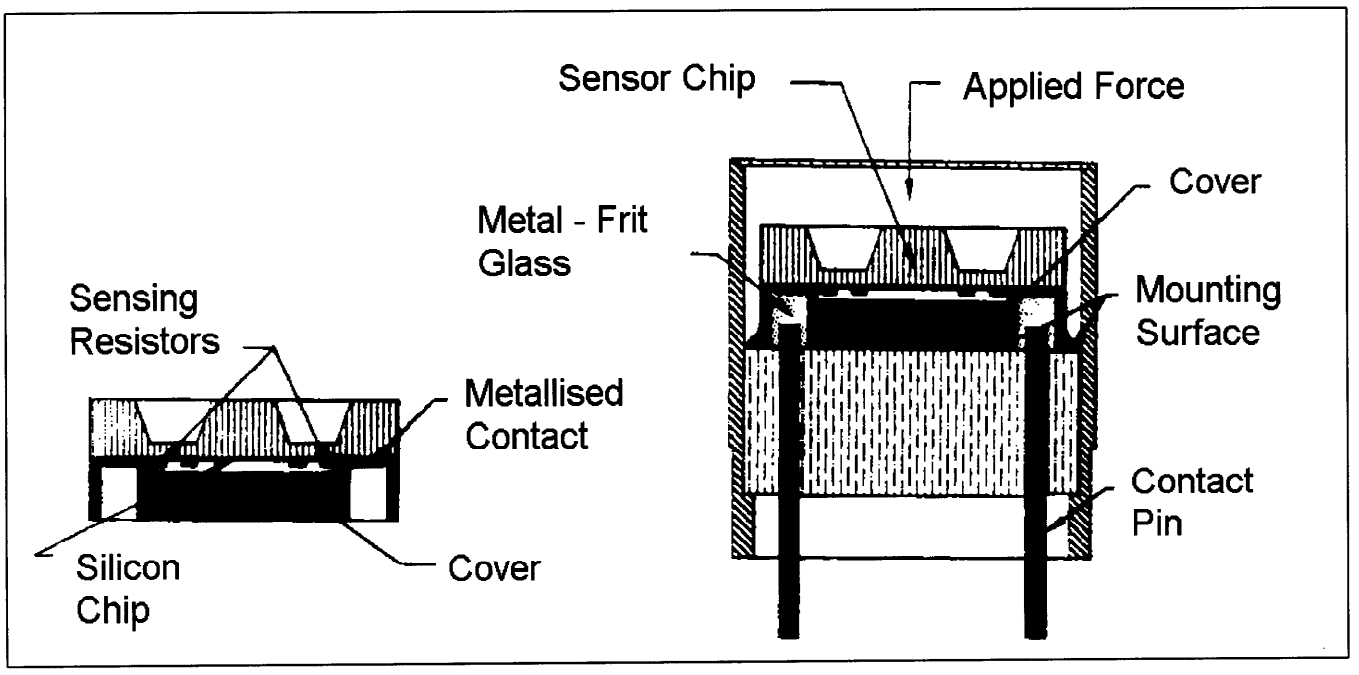


Figure 7

After this firing process, only the non-active side of the diaphragm is exposed to the pressure medium. The small ball bonded gold leads have been eliminated and the entire sensor network and contact areas are hermetically sealed from the environment and the pressure media.

9. TRANSDUCER ASSEMBLY

The hermetically sealed pressure sensing capsule bonded to the header is the starting point for the assembly into a pressure transducer. Typically most transducers must be attached to a mounting surface which is exposed to the pressure media, frequently by means of a threaded port. In addition, the header pins must be electrically connected to a high temperature cable assembly without the use of solder joints which may fail at high temperatures. The high temperature cable assembly must also contain material which will provide electrical insulation between individual leads, whilst the interconnects between the header and the cable as well as the cable itself must be strong enough to withstand the mechanical stresses of handling. The package is completed using a building block approach and Figure 8 shows the assembly of a typical ultra high temperature leadless pressure transducer.

A sleeve (1) is welded between the first header and a second header. A minerally insulated (MI) cable containing nickel wires is used to interconnect to the pins from the first header and the exposed leads from the first header are welded to the second header to ensure low resistance electrical connections between the leads of the MI cable and the header leads.

The header/ MI cable assembly is then inserted into a port (2) and welded to the port. At the end of the port is a tubulation (4) which is crimped to retain the MI cable.

A cover sleeve is then assembled over the MI cable to give additional support and is welded to the rear of the cover (5) which in turn is welded to the port (2).

This design of assembly results in the transducer being totally hermetically sealed from any atmospheric contamination or oxidation. Every single internal metallised surface such as metal to silicon and metal to glass frit, header pins to header tubes, header pins to MI cable wires and even the mineral insulation itself is hermetically sealed from the atmosphere. In addition the welding of the sleeve to the port together with the addition of the third header greatly increases the structural integrity of the entire electrical interconnect system and reduces the chances of any damage in severe environments.

10. STATIC PERFORMANCE

The first generation of leadless transducers (five units) have been tested in the laboratory with the following results. Figure 9 shows the change in zero output during repeated temperature cycling between room temperature and 455°C (850°F). This demonstrates that exposure to high temperatures has negligible effect on the internal electrical connections and contacts. A few ohms change in a contact resistance would result in changes in the output of many millivolts. All observed changes in output were less than 2 mV. Figure 10 plots the full scale output at 455°C (850°F) for two sensors over repeated cycles. Stable and repeatable outputs were observed throughout this study.

Figure 11 shows the pressure v output voltage performance measured at room temperature, 177°C (350°F), 343°C (650°F) and 455°C (850°F) for one of the sensors. There is a small element of zero shift but the unit is very linear and exhibits a repeatable span shift of approximately 2-3%/100°C (1-2%/100°F). Figure 12 shows sensor performance up

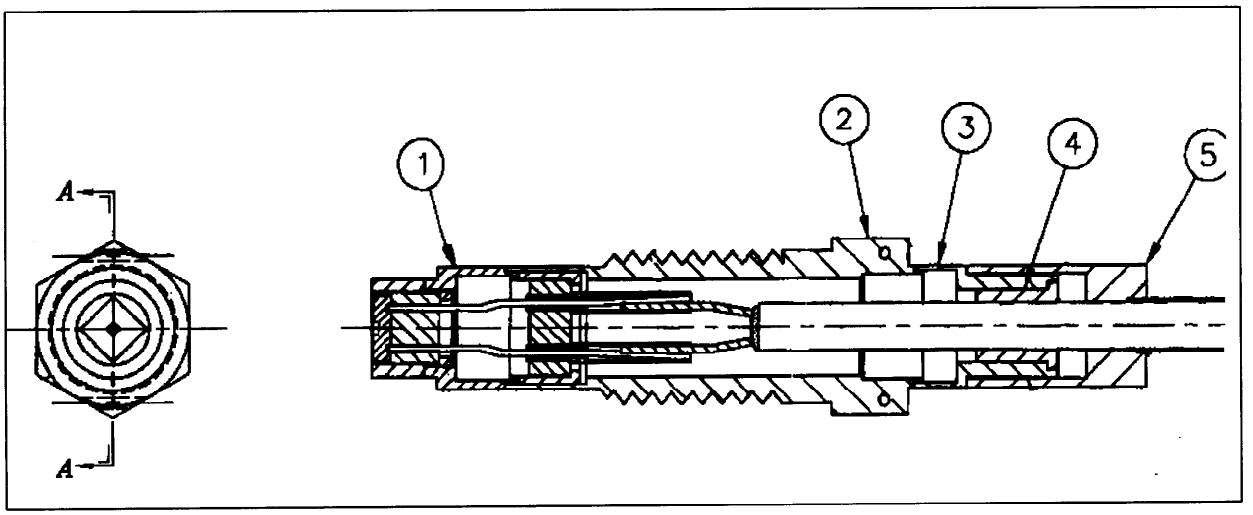


Figure 8

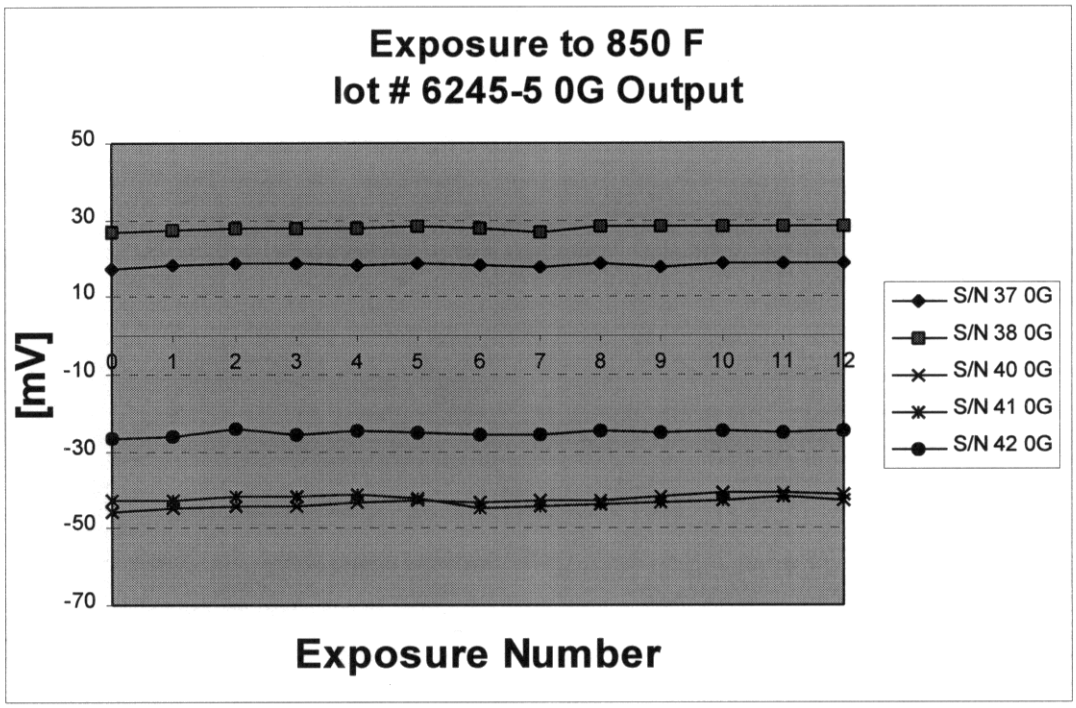


Figure 9

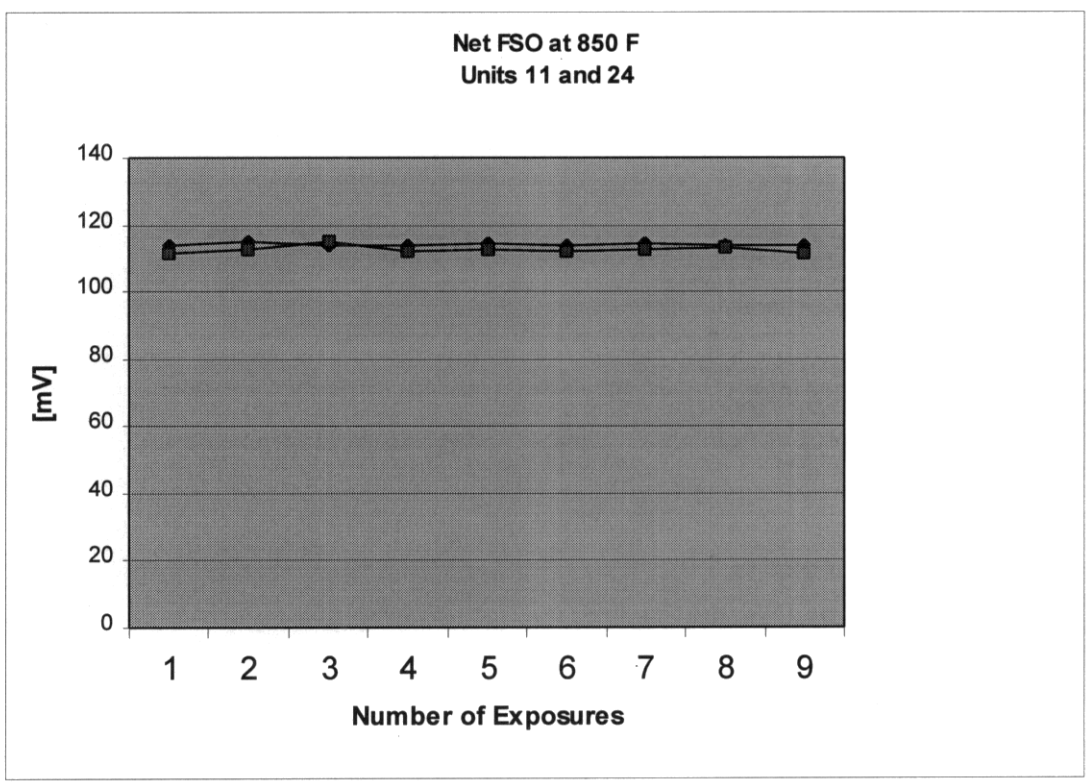


Figure 10

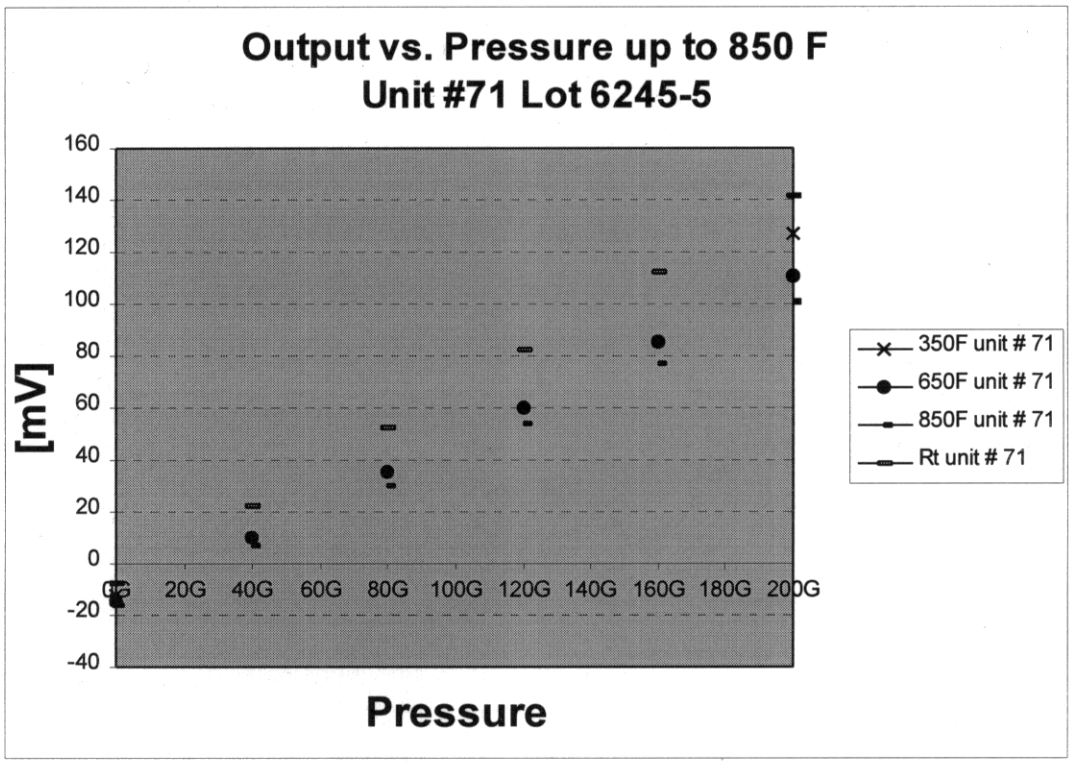


Figure 11

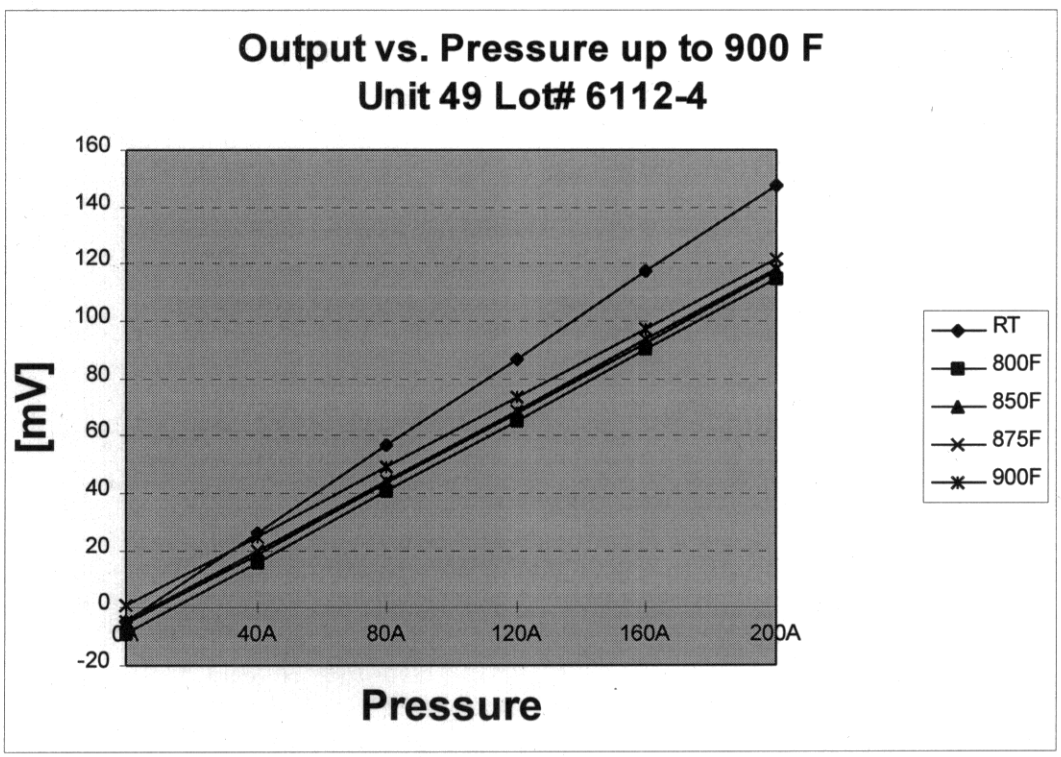


Figure 12

to 482°C (900°F) for another one of the tested sensors. Linearity and span shift remain virtually identical.

Test data from the latest generation of leadless transducers manufactured have confirmed the original results.

To summarise the test results, the devices appear to have less than 0.02%F.S. non-linearity and no measurable hysteresis up to temperatures of 482°C (900°F). At temperatures of 454°C (850°F) the non-linearity increases to around 0.1%F.S. but a static error band of better than 0.15%F.S. can be expected. All units tested exhibited only minor changes in performance characteristics after repeated exposure to high temperatures. When the latest units were compensated, span and zero shifts of less than 1%F.S. over the temperature range from room temperature to 480°C (900°F) were achieved.

11. DYNAMIC PERFORMANCE

The design of the high temperature sensor is such that it should have high frequency response characteristics similar to those of more familiar, low temperature capability Kulite sensors. To verify this experimentally, a pulsed air apparatus was set up in an oven. The frequency response test configuration is shown in Figure 13.

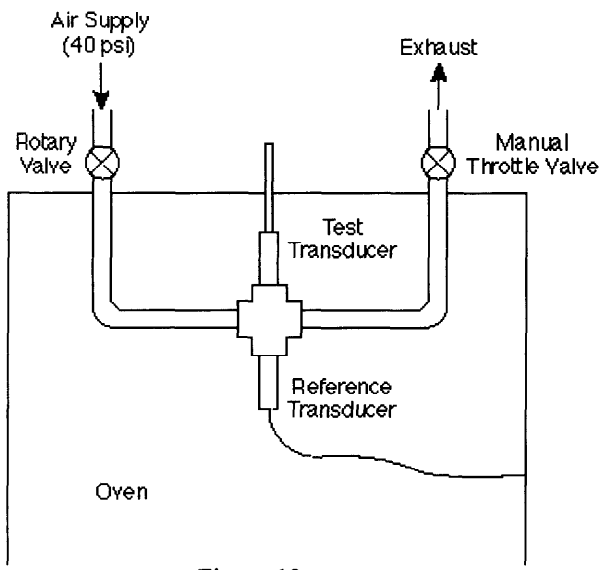


Figure 13

Large scale pressure primary pulsations at frequencies up to 400-500Hz were generated by a water cooled, motor driven rotary valve with an 1/4" port. The valve was close mounted externally to an oven containing the test transducer. About 15 cm of 1/4" stainless steel line connected the valve to the transducer, which was mounted on one leg of a T-piece inserted in the line. A second, standard, lower temperature capability transducer (model XTC-190) was mounted in the opposite leg of the T. The air flow, after passing by the transducers, exited the oven through 15 cm of line to a manual throttle valve.

The response of both transducers was first established at room temperature. The high temperature unit and low temperature reference unit had essentially identical waveform shapes and frequency responses. This verified that the transducers and test arrangement were responding as expected. The reference unit was then removed and the test repeated at elevated temperatures, after an appropriate soak time.

An example of the transducer response at 650 F when subjected to a nominally 250 Hz sinewave excitation is shown in Figures 14 and 15.

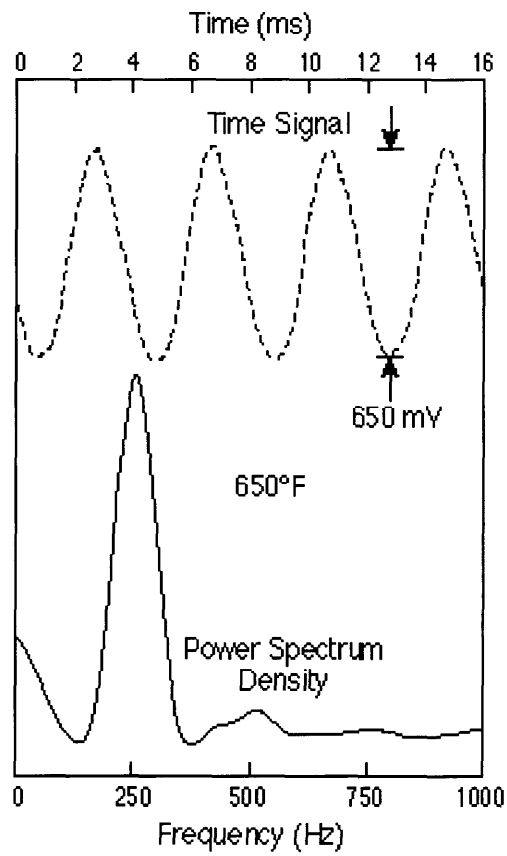


Figure 14

The amplifier gain used was 200. At the higher frequency of 400Hz, the wave form is less sinusoidal due to resonance in the flow system. The second harmonic response is clearly visible at 800Hz. These tests are greatly constrained by the limitations of the excitation mechanism and so do not fairly illustrate the frequency response capabilities of the sensor, which is in excess of many tens of kilohertz. The data do however, demonstrate nearly ideal ac response through the range of interest for many gas turbine active control applications.

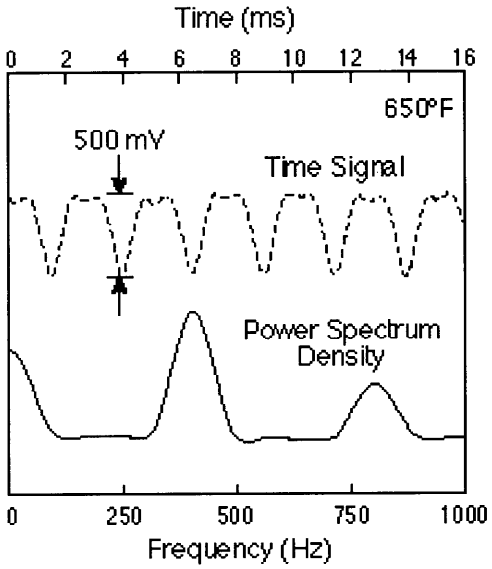


Figure 15

11. CONCLUSIONS

The latest generation of leadless sensors have been designed, fabricated and evaluated within Kulite with very encouraging results. The key features of the leadless design, which are protected by U.S. Patent Number 5,955,771, are the elimination of the gold ball bonding and gold lead wires and the hermetic sealing of the pressure capsule and the transducer assembly which will enable these transducers to operate reliably in the most hostile environments.

Currently these second generation leadless dynamic pressure transducers are being evaluated both in laboratories and on gas turbines by the majority of the US and European aero engine manufacturers and many aerospace industry test organisations. The results of these test program will be the subject of further technical papers.

12. REFERENCES

[1] Ludwig, G.R., Nenni, J.P., 1980, "Tests of an Improved Rotating Stall Control System on a J-85 Turbojet Engine", ASME Paper 80-GT-17.

[2] Active Control of Compressor Stall – Research Groups:-
California Institute of Technology, Pasadena, CA
DRA, Farnborough
Massachusetts Institute of Technology, MA
MTU, Munich
NASA Lewis, Cleveland, OH
Pratt & Whitney, East Hartford, CT
Rolls-Royce, Derby, UK
Scientific Systems Co. Inc., Woburn, MA
SNECMA, Paris
United Technologies Research Centre, East Hartford
Virginia Polytechnic Institute and State University, Blacksberg, VA
Whittle Laboratory, Cambridge University, UK

[3] Day (Whittle Lab., Cambridge), Breuer (MTU), Escuret (SNECMA), Cherrett (DRA), Wilson (RR), "Stall Inception and the Prospects for Active Control in Four High Speed Compressors", ASME Paper 97-GT-281, Orlando, Fl.

[4] Freeman & Wilson (RR), Day (Cambridge University), Swinbanks (MAS Research, "Experiments in Active Control of Stall on an Aeroengine Gas Turbine" ASME Paper 97-GT-280, Orlando, Fl.

[5] Schalkwyk (Scientific Systems), Paduano, Greitzer & Epstein (MIT), "Active Stabilization of Axial Compressors with Circumferential Inlet Distortion" ASME Paper 97-GT-279, Orlando, Fl..

[6] A.L. DiPietro Jr. and W.F. O'Brien, (Virginia Polytechnic and State University), "Stall and Recovery Aerodynamics of a Low Speed Multi-Stage Compressor With Inlet Temperature Transients", AIAA Paper 97-0163, Reno, NV.

[7] A.L. DiPietro Jr. and W.F. O'Brien, (Virginia Polytechnic and State University), "A New Technique for Active Recovery from Rotating Stall", AIAA

[8] A.D. Kurtz, A.A. Ned, US Patent #5,286,671 issued to Kulite Semiconductor Products, Inc., Leonia NJ 1994

[9] A.A. Ned, A.D. Kurtz, "High Temperature Silicon on Insulated Silicon Pressure Sensors with Improved Performance Through Diffusion Enhanced Fusion (DEF) Bonding", International Instrumentation Symposium, Reno, NV, June 1998.

[10] A.D. Kurtz, J.R. Mallon, T.A. Nunn, US Patent #4,236,137 issued to Kulite Semiconductor Products, Inc., Leonia NJ 1994

PAPER -12, J. W. H. Chivers

Question (W. Riess, Germany)
What is the price level of the sensor?

Reply
After commercial introduction, a price range similar to that charged for other aerospace pressure transducers used for the measurement of oil, fuel, hydraulic oil, etc is possible. I.e., US$ 1000-1200 per unit in quantity.

Question (S. Candel, France)
Are these sensors sensitive to acceleration and were you able to test them in high amplitude vibrational environments?

Reply
The leadless sensor has an acceleration sensitivity, but it is extremely small. It is similar to the sensitivity of other miniature Kulite pressure transducers, i.e., 0.00005% full scale output per g.

This page has been deliberately left blank

Page intentionnellement blanche

AEROENGINE CONDITION MONITORING SYSTEM BASED ON NON-INTERFERENCE DISCRETE-PHASE COMPRESSOR BLADE VIBRATION MEASURING METHOD

Ryszard SZCZEPANIK, Mirosław WITOŚ
Air Force Institute of Technology
Ul. Księcia Janusza, 00-961 Warszawa 42, po box 60
POLAND
e-mail; ryszard@afit.polbox.pl, fax 8364471, tel. 6852194

1. INTRODUCTION

There are many different technical engine failures we can face in turbine engine life and exploitation process. The rotor blade fatigue cracks propagation and as a consequence the blade breakaway, the excessive main engine fuel supply and bearing system getting out of order always as a rule cause a formidable danger for flight safety, engine life and reliability.

A detailed analysis each of engine fault occurred during last years in Polish Air force units showed that:

- there were some cases of fatigue blade breakaway in spite of an earlier, check using blade ultrasonic and eddy current defectoscopy and technology,
- there were some cases of bearing system damages in spite of complying with engine maintenance technical requirements,
- the engine fuel system getting out of order was observed as a result of fuel aggregates dynamic characteristics failure of their components as well as exploitation adjustment activities faults caused by deficient adjustment technology or methodology.

Base on above there is of utmost interest the need of looking for new method to recognise stochastic loads during engine operation, their influence on structural engine reliability and running engine technical condition. These methods should comply with present aviation trends i.e. should reduce the number and minimise the weight of control devices as well as reduce the quantity of measured parameters.

The paper presents non-interference technique of turbomachine blade vibration phase method, one of the most interesting such complex jet engine diagnostic method as well as the tool for dynamic phenomena investigation of a running engine. The method is based on discrete blade vibration amplitude measurement and its numerical response analysis referred to the jet engine technical condition analysis [2, 4, 5, 6, 7]. The described method is used in some units of Polish Air Force as SNDŁ-1b/SPŁ-2b SO-3 jet engine diagnostic system. This engine powers polish TS-11 “Iskra” training aircraft.

2. ANALYSIS OF A TURBINE ENGINE MAINTE NANCE PROBLEMS IN POLISH AIR FORCE.

About 70% of all faults observed during turbine engine maintenance in Polish Air Force appeared to be located with fuel systems faults or strictly maintenance faults. Turbine engines maintenance monitoring process resulted with conclusion that some of them were caused by external reasons like poor condition of fuel and power supply airfield devices. Some of engine faults originated in pilots engine operating faults relying on not obeying engine warming up and conditioning procedures. Such deficiencies cause as a rule mechanical or thermal low cycle fatigue (LCF). In spite of measurement equipment dynamic development as well as aircrafts providing with flight parameters recorders the expert diagnostic system were not properly elaborated so far in Poland. The reasons of that are many. First there is a little knowledge about the engine construction data specially with Soviet Union origin. Second: there is a lot of discrepancies between the maintenance technical conditions and characteristics and overhall technical conditions.

So far the most popular diagnostic systems are based on MIN – MAX formulae used in stationer machines which states;

If all observed values of all observed parameters are in $<MIN_i, MAX_i>$ range complying with technical maintenance condition requirement it means that engine is fit to fly;

Assumption to this formulae is all observed parameters have no any links and interference between them and controlled object is in constant state of operation. For turbine engine this assumption has to be changed to the following shape;

If all observed values of all observed parameters are in $<MIN_i, MAX_i>$ range complying with technical maintenance condition requirement it means the engine is with high probability is fit to fly.

Paper presented at the RTO AVT Symposium on “Active Control Technology for Enhanced Performance Operational Capabilities of Military Aircraft, Land Vehicles and Sea Vehicles”, held in Braunschweig, Germany, 8-11 May 2000, and published in RTO MP-051.

3. DIAGNOSTIC SYSTEM SNDŁ-1b/SPŁ-2b

3.1. Theoretical assumptions of the system.

The consciousness of low plausibility of existing diagnostic systems based on multi engine parameters MIN-MAX control formulae as well as repeated first stage compressor blades fatigue breakaway causes (damages) created the urgent need to elaborate more effective, sensitive system based on minimum quantity of measured and analysed parameters. To solve this complicated problem a qualitative evaluation of applicability of non-contact blades vibration measuring method was done. A particular attention was drawn to the possibility of estimating the condition of a blade (crack initiation and propagation) on a running engine [2] [3]. The measured blades vibration spectrum is analysed using the phase plane. It is worth noticed that such solution enables measurement of rotational speed of the engine rotor by frequency method and the basic difference rely on using the vibrating and rotating blades as a phase marks. This enables to consider measured signal as a composition of two different signals:

- one is a periodic signal of rotational speed (configured by average time value of consecutive rotation of engine rotor),
- second describes oscillation of distance between two adjacent vibrating blades which is stroboscoped by rotational speed.

Basing on narrow band filtering of measured signal we are getting some signal components very useful to expert analysis of engine technical condition following assemblies and structure:

- I compressor stage blades,
- engine fuel system,
- bearing system.

The major concept of expert analysis of engine technical condition is projection of momentary working object characteristics point (i.e. blade, fuel system or bearing system) on phase plane which equals an 3 m – vector of technical state (m – the number of analysed signals).

(1)

$$\forall i \in (1,2,...,m)\ \ WS = \left(par\ , \frac{d\,\mathrm{Pr}_i}{dt}, \frac{d^2 Par_1}{dt^2} \right) \in WT$$

⇨ *ENGINE OPERATIONAL*

In simplest case, having only one analysed signal, for example, engine rotational speed, the working engine range is described in 3 three dimensional space.

The momentary point of engine performance is monitored not only on the transient value of rotational speed but basing on first and second derivative of rotational speed which project some trends of parameters changes (and assisting them excitations).

It can happen that signal Par_i can comply with technical requirement of the engine but first or second derivative will not comply with new widen technical requirement installed during object dynamic characteristics identification process by inverse operation. This case usually projects (the most frequently) the hidden faults of the engine or disadjustment of the particular systems.

The link between engine thermodynamics, fuel system and kinematics describes equation (2). It should be noticed that engine dynamic characteristics identification is based on simply measured signal.

(2)

$$\frac{d^2 n}{dt^2} + a(n)\frac{dn}{dt} + b(n)n = f(m_{pal}, m_{pow}) \approx f(Q_{pal})$$

$$\frac{dn}{dt} = const\,\frac{M_T - M_S - M_F}{I}$$

Where: n – engine rotational speed,
m_{pal} – mass fuel consumption,
m_{pow} – mass air consumption,
Q_{pal} – volumetric fuel consumption,
M_T – turbine rotational moment,
M_S – compressor rotational moment,
M_F – others assemblies rotational moment

During identification process we were looking for transient function which was describing the linle between technical condition of an engine (characterised by multi-dimensional technical condition vector WS) and measured rotational speed. During engine technical state analysis we employ finite set of phase characteristics points:

TECHNICAL CONDITION =

(3)
$$\left(WS\ , \frac{dWS}{dt}, \frac{d^2 WS}{dt^2} \right) \approx \left(n, \frac{dn}{dt}, \frac{d^2 n}{dt^2} \right)_m$$

3.2. Structure of SNDŁ-1b/SPŁ-2b diagnostic system

The system SNDŁ-1b/SPŁ-2b consist of:

- blade excessive vibration signalling device SNDŁ-1b – (fig.1)

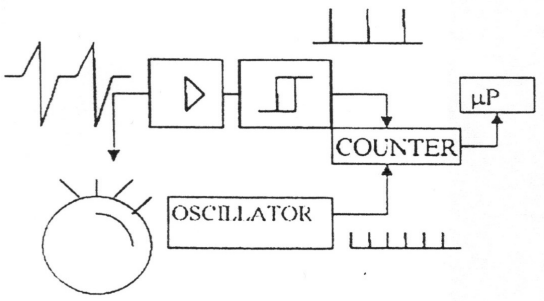


Fig 1. Measurement method

The board device for crew or ground staff warning about dangerous level of blade vibration above 12000 rpm.

- blade crack signalling device SPŁ-2b – (fig.2)

Ground control device for periodic:

a) recording and computer analysis of first compressor stage blade vibration spectrum,
b) SNDŁ-1b technical condition control performance without its disassembly,
c) The engine rotational speed in I and II cabin indicator faults control without their disassembly,

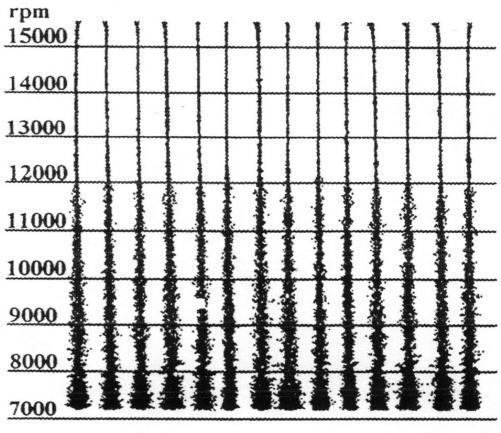


Fig. 2. First stage amplitude – phase compressor blade vibration model spectra of SO-3 engine,

- SPŁ-2b software

Set of specialised procedures for SPŁ-2b numerical maintenance and numerical data analysis, particularly: blade vibration spectra; fuel and bearing system technical condition analysis.

3.3. The functional potentialities of the system
3.3.1 Numeral analysis of blades vibration

The effect of blade upon its numerically analysed by considering the blades as appropriately shaped, beam fixed to the rotor disc (self – likeness condition) in centrifugal force field. An actual flow disturbances level running engine is evaluated by employing the linear dependence of disturbances with vibration amplitude (in elastic deformation range). Numerical procedures employ sectional statistical analysis to get average values of blade vibration amplitudes and standard deviation. The analysis results are compared with the engine type model see fig. 2 and 3.

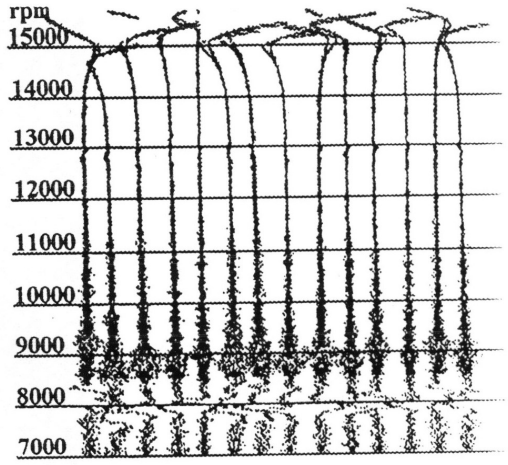


Fig.3. Influence of foreign object dwelling in compressor first stage stator blades on first stage amplitude – phase compressor blade vibration of SO-3 engine

Fig. 2. Introduces projection of first compressor stage amplitude vibration spectrum model of SO-3 engine, fig. 3 – amplitude vibration spectrum during foreign object dwelling on the first stage compressor stator blades. (Y – axis – amplitude of vibration, x-axis rotational speed of the engine). Effect of blade phase resonance characteristic project by low fluctuation of vibration amplitude (in dynamic pitch) was used in numerical procedure. Narrow band filtering of measured signal was implemented with use if aliasing effect in numerical procedure. The core blades technical condition analysis is based on comparing of the engine dynamic pitch projection to the model projection of an engine.

To get explicit identification of crack suspect or suspect blade an numerical procedure was used to estimate blade free vibration frequencies. Narrow band filtering of measured signal was implemented by low square (LS) method.

After blades free vibration frequencies estimation an identification process with factory or overhall basic blades frequencies is following. During test bench investigations the lowering of blades vibration amplitude was observed particularly in blade resonance excitations range. This phenomena is lowering of Q –-factor the mechanical narrow band filter which the blade creatures. During cracks propagation process the correction of the blade is decreasing which causes decrease of free vibration frequency "f_s" and blade dynamic frequency factor "B". During engine run these changes project in decreasing of blades forced vibration frequencies "'"$_d$" –Fig fig. 4 (y-axis – dynamic pitch phase, x-axis rotational speed). For first compressor stage blades of SO-3 engine the dynamic changes were the most distinct near maximum of rotational speed of the engine in which the second synchronous excitation of resonance vibration occurs – fig. 5 (y-axis rotational speed, x-axis synchronous component of vibration amplitude phase change).

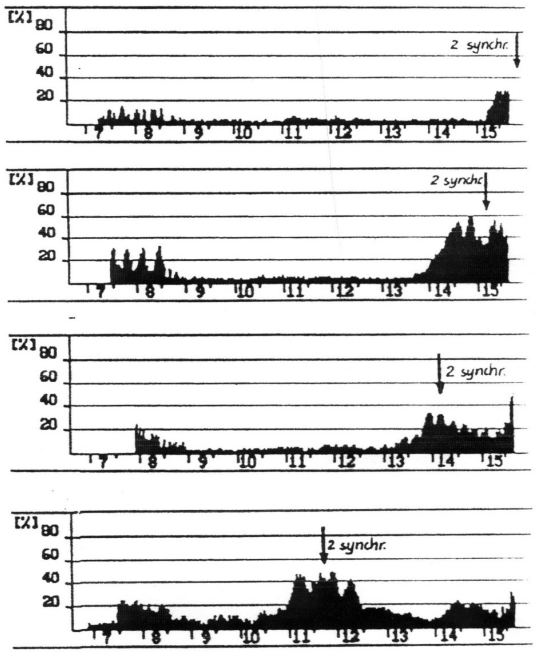


Fig. 4 Projection of blade crack propagation process in blade phase vibration spectra.

3.3.2. Numeral analysis of dynamic load of engine rotor bearings

Blades amplitude and vibration frequency data having got during numerical analysis of all rotor blades were used for identification of some disadvantageous dynamic phenomena time to time occurred during engine exploitation process. For this numerical procedure gives relation between:

- bearing system technical state and blade load effect,
- blade characteristic vibration and bearings dynamic load level.

Procedure has sufficient sensitivity for revealing such phenomena like synchronous and asynchronous rotor blades resonance vibration – fig. 5.

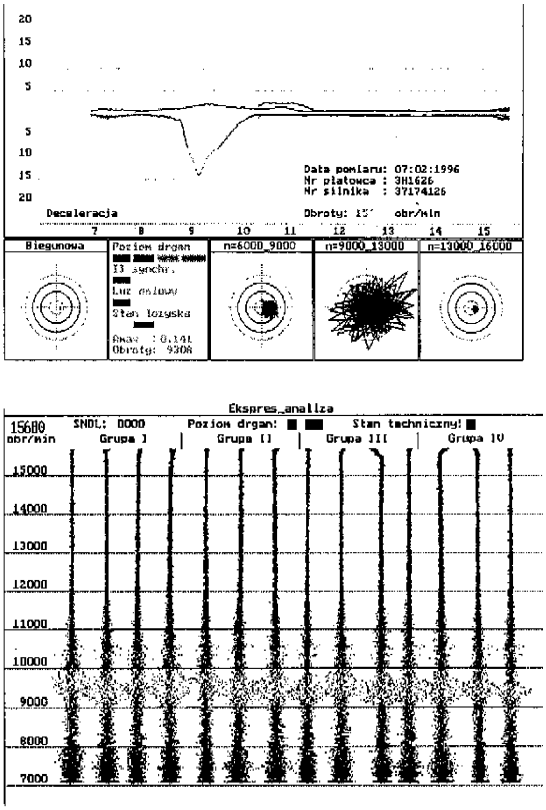


Fig. 5 Influence of blades vibration on the rotor dynamic conventional disbalance level

The results of the analysis are projected conventionally in the shape of normalised radius and dynamic rotor unbalance phase (y-axis-engine rotational speed, x-axis – conventional, normalised dynamic unbalance radius).

3.3.3. Technical estimation of fuel system condition

Big frequency of sampling of the rotational speed of the engine (once for each rotor turn allows in very simple way to possess information concerning transient value of rotational speed. Having in view relations-between engine fuel consumption and rotational speed (related to real atmospheric weather conditions) an numerical procedure for fuel system technical conditioned estimation was elaborated. Procedure compares real dynamic characteristic taken during non stabilised range of engine operation (acceleration and deceleration) with

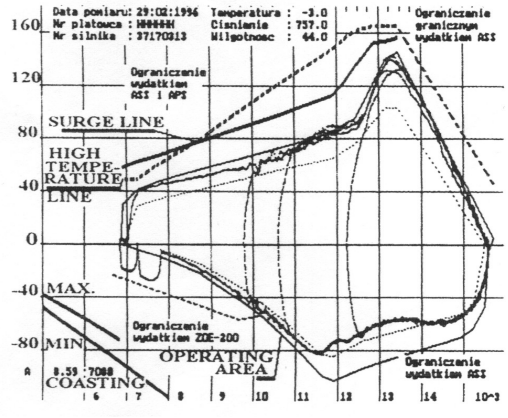


Fig. 6. Model characteristic of engine fuel system during transient condition of SO-3

model dynamic characteristics – fig. 6 (Y-axis – engine rotational increase of rotational speed). Having in view structure and principles of the engine fuel system work, procedure allows:

- all fuel system aggregates and the whole fuel system adjustment and control – fig. 7;
- early revealing of engine fuel system and fuel aggregates failures – fig. 8.

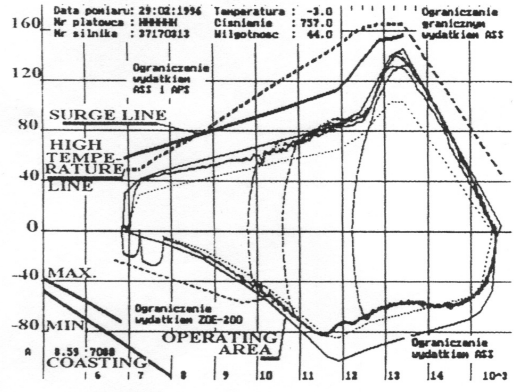


Fig. 7. The presentation of improper engine acceleration time adjustment – reduction of the margins of compressor stability (surge threat)

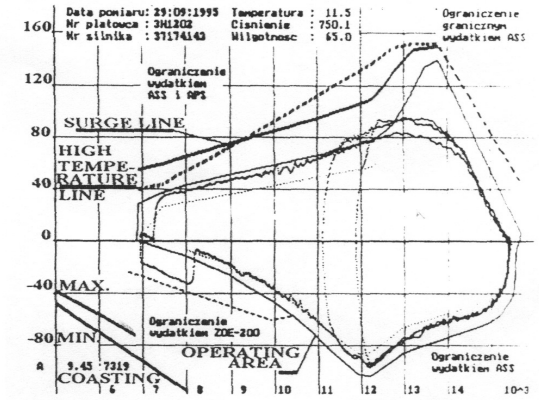


Fig. 8. Typical presentation of engine acceleration aggregate fault.

4. CONCLUSIONS

1. Described method is of great importance for flight safety and may be recommended as a completion of the existing systems of diagnostic of turbine engines.
2. By using the discrete, non-contact method of measuring blades vibration and numerical analysis of blade vibration spectrum it is possible to conduct complex, monitoring of technical state of major engine components like:

- compressor blades
- fuel system
- bearing system.

REFERENCES

1. Kudelski R., Szczepanik R. *Urządzenie do bezdotykowego wyznaczania amplitudy drgań w łopatkach sprężarki silników lotniczych*, V KNT "Metody pomiarowe w technice lotniczej", ITWL Warszawa 1987.

2. Szczepanik R. *Analiza i badanie przyczyn urywania się łopatek I stopnia sprężarki silników SO-3/SO-3W*. Sprawozdanie ITWL Warszawa 1987 (nie publikowana).

3. Szczepanik R. Badanie stanu drgań i naprężeń w łopatkach I stopnia sprężarki silników typu SO-3 w eksploatacji. Sprawozdanie ITWL Warszawa 1988 (nie publikowana).

4. Szczepanik R., Witoś M. *Quality Assessment of Diagnostic Non-Interference Discrete-Phase Method of Measuring Compressor Blades Vibration*, XIX Konferencja ICAS Anheim 1994.

5. Szczepanik R., Witoś M. *Wpływ procesu eksploatacji turbinowego silnika odrzutowego na żywotność łopatek wirnikowych*, VII KNT Przepływowe Maszyny Wirnikowe, Rzeszów 1993.

6. Szczepanik R., Witoś M. *Computer Aided Engine Condition System based on non-interference discrete phase blade vibration measuring method, SAE/SAS*, Symposium/Workshop Stockholm 1995.

7. Szczepankowski A., Witoś M. *Obiektywna kontrola stanu technicznego układu paliwowego turbinowego silnika odrzutowego typu SO-3 (SO-3, SO-3W, SO-3W22)*, Konferencja DIAG 95 Szczyrk 1995.

8. Szczepankowski A., Witoś. *Wpływ stanu technicznego układu paliwowego turbinowego silnika odrzutowego na drgania łopatek wirnikowych sprężarki*, Konferencja DIAG 95 Szczyrk 1995.

9. Witoś M. *Bezdotykowa metoda kontroli stanu technicznego łopatek wirnikowych sprężarki osiowej*, Konferencja DIAG 95 Szczyrk 1995.

10. H.Dąbrowski,R.Kudelski, J.Spychała, R.Szczepanik, A.Szczepankowski, M.Witoś.Turbojet Engine Diagnostic System Based on Compressor Blade Vibration and Vibroacoustic Analysis. XX Konferencja ICAS, Sorento, 1996.

11. R.Szczepanik, M.Witoś. Komputerowy system diagnostyczny silników odrzutowych bazujacy na dyskretno-fazowej metodzie pomiaru drgań łopatek. Zeszyty Naukowe Instytutu Lotnictwa Nr 152/1/1998.

PAPER -13, R. Szczepanik

Question (H. Weyer, Germany)

Blade vibration is often flow-triggered. Have you tried to actively control the vibration by flow management using the monitoring system?

Reply

Yes, but not directly by the adjustment of the fuel system. We noticed in an early stage of our work that there is a strong link between the adjustment quality of the fuel system and the level of blade vibration. So with time we significantly reduced the level of blade vibration by proper adjustment of the fuel system of individual engines. The nine year period of exploration of our diagnostic system without engine damage provides strong evidence of the success of this approach.

A Gas Turbine Compressor Simulation Model for Inclusion of Active Control Strategies

Carlo Cravero, Aristide Massardo
DIMSET - Università di Genova
via Montallegro n.1 - 16145 Genova
ITALIA

ABSTRACT

A one dimensional time-marching model to solve the dynamic behavior of a compression system is presented. The computational method is described in some details and it is applied to a three-stage axial compressor with different plenum configurations. This computational model for the simulation of a multistage axial compressor is used to investigate the insertion of an active control system.

NOMENCLATURE

A, a	duct section, sound speed
e	internal energy
F	mass, momentum and energy flux vector
F_{blade},$F_{friction}$	blade force, external force due to friction
h, h_{bleed}	enthalpy, enthalpy of m_{bleed}
k	specific heat ratio c_p/c_v
L,l_c	duct length, compressor length
NX	number of computational sections
m_{bleed}	mass flow bleed
p	static pressure
Q	conservative flow variables vector
R	gas constant
t, T	time, static temperature
u, U	velocity, peripheral speed
x, y	Cartesian co-ordinates
Vp	plenum volume
W	work exchange
Greek	
Δ_+,Δ_-	forward and backward finite differences
Φ,Φ_{ext}	flow coefficient, external heat flux
Ψ	pressure coefficient
μ	valve coefficient
ρ	density
Subscript	
t	total quantity
1,2	inlet, outlet sections

INTRODUCTION

The need for a wider operability range of modern compressors for gas turbine applications is the "prime mover" for a large research effort that is nowadays undertaken in many international laboratories, organisations, companies and universities. This effort is both experimental and computational. The overall behaviour of a gas turbine compressor outside its stability range has been understood and can be modelled using a simplified lumped parameters approach (Greitzer, 1976, Baghdadi et al., 1982). Many detailed experimental analysis are nowadays focused on stall inception (Day et al, 1999, Camp-Day 1998, Spakovsky et al., 1999) to understand the fluid-dynamic mechanism of formation and to be able to improve its computational modelling. On the other hand the computational models for the analysis of a multistage compressor in steady flow (through-flow or 3D Navier-Stokes) are not directly applicable to unsteady (transient or dynamic) flows because they are either inappropriate (standard through-flow) or they require an excessive computational effort (3D Navier-Stokes). The most simplified approach is the zero dimensional lumped parameter technique that considers each component of the compression system as a node and by writing the balance for mass flow, momentum and energy it results in a set of differential equations to be solved with respect to time (Greitzer, 1976, Massardo et al. 1989, Botros, 1994).

The one dimensional model for the analysis of the unsteady flow in a compression system can be a good compromise between the accuracy in capturing the main system performances and the computational effort. This approach introduces the conservation equations (continuity, momentum and energy) for a continuum and, after a domain discretization, are integrated using a time-marching technique; the effect of blades, mass bleeds, friction etc…. are introduced as external body forces. This technique has been considered and a time-marching technique, previously developed for 2D/3D turbomachinery flows (Cravero, 1995), has been converted in 1D form with the insertion of the appropriate external forces to model the dynamic of the compression system. The 1D time-marching approach is preferred over the lumped parameter technique, because it allows the analysis

Paper presented at the RTO AVT Symposium on "Active Control Technology for Enhanced Performance Operational Capabilities of Military Aircraft, Land Vehicles and Sea Vehicles", held in Braunschweig, Germany, 8-11 May 2000, and published in RTO MP-051.

inside the compressor (interstage analysis) and this is an important feature when an active control strategy must be defined. In fact the control devices and the transducers should be placed in the most efficient way (Escuret-Elder, 1993, Gysling-Greitzer, 1994, Montazeri et al., 1996, Sun-Elder, 1998) and this can be done if a reliable technique for the compression system analysis is implemented Active control of compressor instabilities (surge) has received attention recently (Epstein et al., 1989); it aims to allow the compressor to operate beyond the surge line suppressing the flow instabilities by means of a feedback control system. The design of active control systems for multistage axial compressors is still a challenging topic; it requires a good representation of the compression system under unsteady flows in order to detect the instability and to help the optimisation of the control system (transducer and actuator positioning).

COMPUTATIONAL MODEL

The geometrical domain is divided into a number of sections where the thermal-fluid-dynamic variables (pressure, velocity, Mach number, temperature etc....) are computed according to the 1D flow hypothesis. In Fig. 1 a sketch of a reference domain divided into 1D sections is presented.

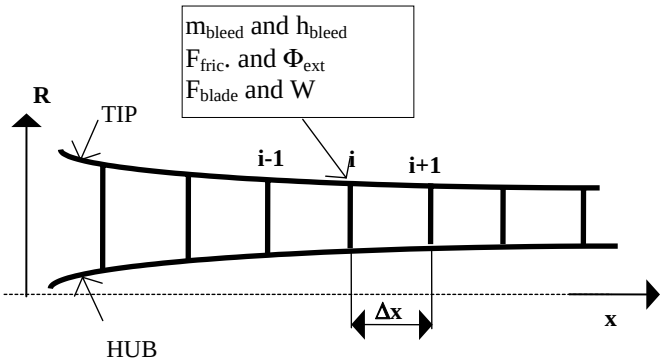


Fig.1: Computational model

Governing equations

The system of mass, momentum and energy 1D equations, for each control volume (sections i-1, i, i+1 in Fig.1), are written in the following conservative form:

$$\frac{\partial Q}{\partial t}+\frac{\partial F}{\partial x}=B \tag{1}$$

with

$$e_t = c_v T + 0.5u^2 \qquad B=\left(m_{bleed}, p\frac{\partial A}{\partial x}+F_{blade}+F_{friction}, W+\Phi_{ext}+h_{bleed}\right)^T$$

$$B=\left(m_{bleed}, p\frac{\partial A}{\partial x}+F_{blade}+F_{friction}, W+\Phi_{ext}+h_{bleed}\right)^T \tag{2}$$

the total energy e_t is defined as $e_t = c_v T + 0.5u^2$. Using the perfect gas equation of state:

$$e_t = \frac{R}{k-1}T+0.5u^2 \qquad p=(k-1)\left[\rho e_t - 0.5\rho u^2\right] \tag{3}$$

Time-marching technique

In order to integrate the nonlinear hyperbolic differential system of eq.1, a time marching technique, previously developed for 2D and 3D steady/unsteady-inviscid/viscous turbomachinery flows (Cravero 1995, Cravero-Satta 1995, Cravero-Satta 2000), has been set up for the 1D case. After the integration in space the system of eq.1 can be written as:

$$\frac{d Q_i}{dt}+\left(C_i+D_i-B_i\right)=0 \tag{4}$$

where the suffix i refers to the actual grid node. The term in parenthesis is defined as the residual R_i and will be driven to zero in steady flow calculations. The convective fluxes are integrated with central differences:

$$C_i=\frac{F_{i+1}-F_{i-1}}{2\Delta x_i} \tag{5}$$

In order to prevent odd-even points decoupling and, in general, to solve transonic flows with shock waves, an artificial dissipative term is added: this is a blend of second and fourth order dissipative terms:

$$D_i=\frac{1}{\Delta t_i}\left[\delta_i \Delta_+\Delta_- - \varepsilon_i\left(\Delta_+\Delta_-\right)^2\right]Q_i \tag{6}$$

where

$$\delta_i = \vartheta_2 \max\left(\nu_{i+1}, \nu_i, \nu_{i-1}\right) \tag{7}$$

$$\varepsilon_i = \max\left(0, \vartheta_4 - \delta_i\right) \tag{8}$$

$$\upsilon_i=\frac{\left|p_{i-1}-2p_i+p_{i+1}\right|}{\left|p_{i-1}+2p_i+p_{i+1}\right|} \tag{9}$$

The coefficient θ_2 (eq.7) and θ_4 (eq.8) are fixed and their typical values are1/4 and 1/32. The integration in time of eq.4 is performed with the following explicit multistep Runge-Kutta scheme with N steps:

$$\begin{aligned} Q_i^0 &= Q_i(t) \\ Q_i^1 &= Q_i^0 - \alpha_1 \Delta t_i R(Q_i^0) \\ Q_i^m &= Q_i^0 - \alpha_m \Delta t_i R(Q_i^{m-1}) \\ Q_i(t+\Delta t) &= Q_i^N \end{aligned} \tag{10}$$

The dissipation term in the residual R is computed only at the first step. A four step scheme with standard coefficients (1/4, 1/3, 1/2, 1) has been used. For steady flow analysis the local time step is computed according to:

$$\Delta t_i = CFL\frac{\Delta x_i}{(u+a)_i} \tag{11}$$

where the Courant-Friedricks-Levy has its limit of 2.8 with a four steps scheme. When unsteady flows are computed the minimum time step over the domain is considered.

Source term evaluation

The source term B in eq.1 contains the effects of a mass flow bleed (m_{bleed} and h_{bleed}) or injection, of heat addition/removal (Φ_{ext}), of

channel section variation ($p\partial A/\partial x$), of friction at the walls due to viscous effects ($F_{friction}$) and of a turbomachinery stage (F_{blade} and W). Introducing this last contribution allows the unsteady flow in a multistage turbomachinery (compressor or turbine) to be computed with many information of the flow inside the machine compared to a lumped parameter approach. In the following the attention will be focused on the stage force and work exchange evaluation. Each computational station is identified with a label that defines its kind (i.e. 0-duct, 1-stator, 2-rotor). At present a computational model for axial compressor stages is implemented. When a compressor stage is detected, the axial blade force and the work exchange are computed either by the stage characteristics (read from an external data file) or by a routine implemented into the code that returns the stage performances in the actual working point. The blade force is equally distributed for each station defining a blade (rotor+stator) in the stage while the work exchange is "spread over" the stations in the rotor. If the internal routine is called to compute the compressor stage characteristics, the pre-stall part of the stage characteristics is computed with a standard 1D approach with correlations while the post-stall and reverse flow parts are evaluated using the model proposed by Moses et al. (1986) and by O'Brian (1992). A time-lag equation for the blade force is introduced to compute the actual blade force in unsteady calculations, following:

$$\tau \frac{dF_{blade}}{dt} + F_{blade} = F_{blade_steady} \qquad (12)$$

Inlet and Outlet boundary conditions

At the inlet section, in the most frequent case of subsonic flow, total pressure and temperature are fixed as boundary conditions. The conservative variables (vector Q of eq.1) are updated extrapolating the Riemann invariant (Cravero, 1995) from the interior points. At the outlet section static pressure is fixed as boundary condition; when a steady state solution is required the conservative variables are obtained from the interior points by extrapolating the Riemann invariant together with the assumption of isentropic flow in the last two sections. When a time dependent boundary condition is required, a model of an isoentropic expansion through a variable section control valve is modeled. The "reduced mass flow" trough the valve is used to compute the Mach number, and therefore all the required quantities:

$$\overline{m}_{valve} = \frac{p_t A_{NX}}{\sqrt{T_t}} \mu = (\rho u A)_{NX} \qquad (13)$$

The total quantities T_t and p_t are extrapolated from the station NX-1. The valve characteristic coefficient μ is computed with a steady flow run and it is, in general, function of time during the unsteady flow calculation.

APPLICATIONS

To test the model previously described, the available geometrical and experimental data of the compressor of Gamache (1985) have been utilized. The three-stage, low-speed compressor consists of three non-repeating stages with a constant cross-sectional annulus area (hub to tip ratio 0.88). From the cited work and from the work of Eastland (1982), a complete set of steady stage pressure characteristics and corresponding overall steady system performances are available.

For each stage, the energy input to the overall system is given in terms of torque coefficient. Here the stage temperature rise characteristics are obtained based upon the overall torque data and two isolated flow points in rotating stall (all the stage temperature characteristics were considered to be identical).

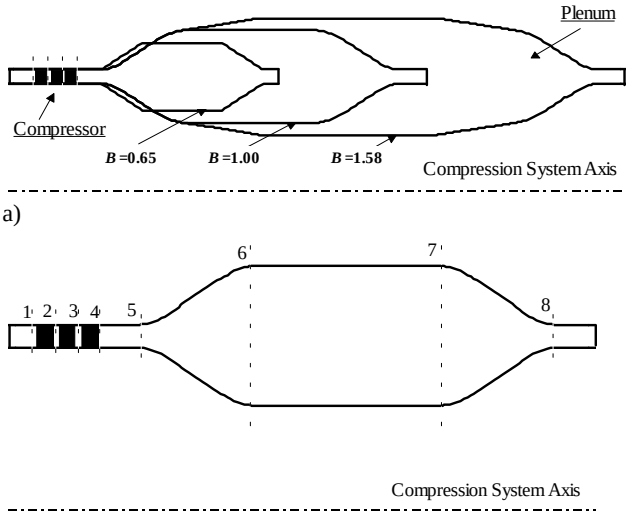


Fig.2: Compression system geometry - a) Different plenum geometry; b) section numbering

As already observed by O'Brien (1992), the referenced three-stage compression system provides excellent stage characteristic data, but, unfortunately, overall system behavior during surge and rotating stall was not available. However, the rig was similar to one used in a previous experimental investigation of surge and rotating stall by Greitzer (1976). Taking into account this aspect, the compression system here analyzed has been configured to the geometry specified for the plenum rig of Greitzer's tests, but using the computed stage characteristics for the Gamache's compressor. The theoretical stage performance curves have been used for the following calculations.

For the analysis of compression systems Greitzer's B parameter was used as a reference variable for the experimental compressor. The parameter B is defined as:

$$B = \frac{U}{2a} \cdot \sqrt{\frac{V_P}{l_C \cdot A_{in}}} \qquad (14)$$

The B value can be modified by changing the plenum volume Vp, as shown in Fig.2; three cases were computed: rotating stall (B=0.65); classical surge (B=1.00); deep surge (B=1.58).

In Fig.3 the dynamic responses of the compression system with B=0.65-1.0-1.58 are shown. The compressor rig throttle was slowly closed to the point of instability and then held constant. In case of B=0.65 the system became unstable at the uniform flow stall point, and then traversed to rotating stall. A second calculation has been done with the compressor rig reconfigured to operate at B=1.00 (see Fig.2a). In this condition the system exhibited surge cycles. In Fig.3 the time-dependent distributions of static pressure in different stations along the machine clearly show the different wave amplitude and the need for a distributed model to simulate the system. Another test has been considered with the compressor rig reconfigured to operate at

B=1.58 (see Fig.2a). In this configuration the system exhibited deep surge cycles.

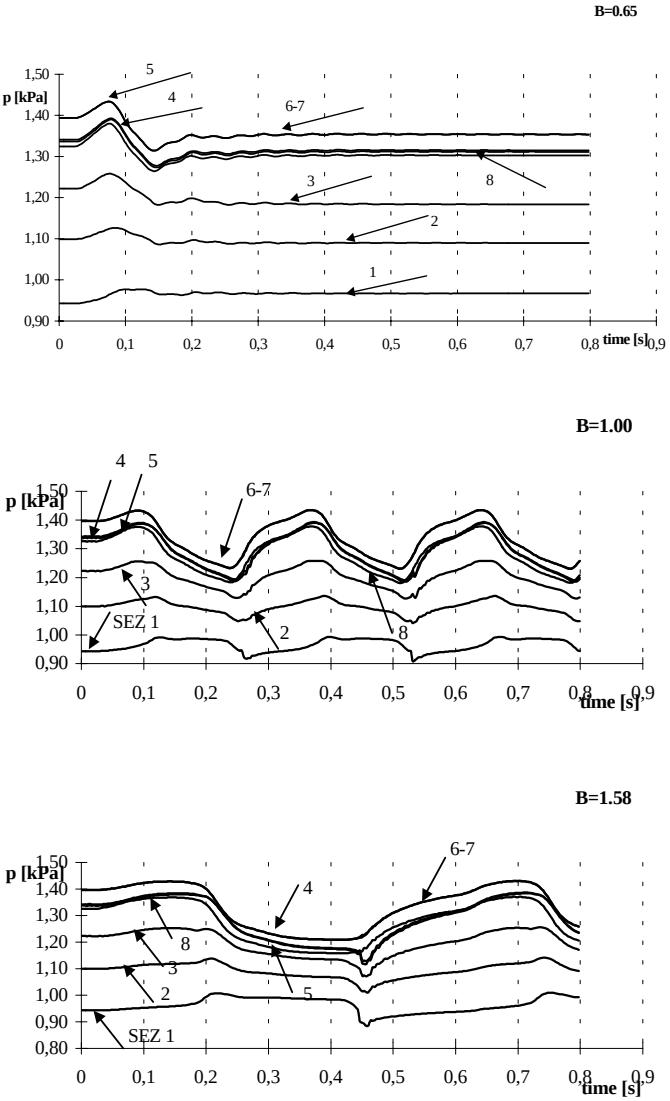


Fig.3: Pressure and velocity variations in different sections in case of B=0.65 - B=1.0 - B=1.58

The large amplitude variations of static pressure inside the compressor can be detected by the 1D code as shown in Fig.3. It is clear from the examples that the present 1D model, compared to a lumped model approach, can give detailed information about the flow behavior inside the compressor (i.e. interstage fluid dynamic data) and inside the plenum. This is an important feature of the model that allows the influence of different active control strategies (interstage bleed, cooling mass flow rate, valves ….) to be analyzed and discussed. In Fig.4 the time dependent velocity distributions within the system, obtained with different configurations (B=0.65-1.0-1.58), are shown in a 3D plot to highlight the strong variations inside the compression system. This kind of inspections can be used to understand the optimum placing of transducers and active control devices.

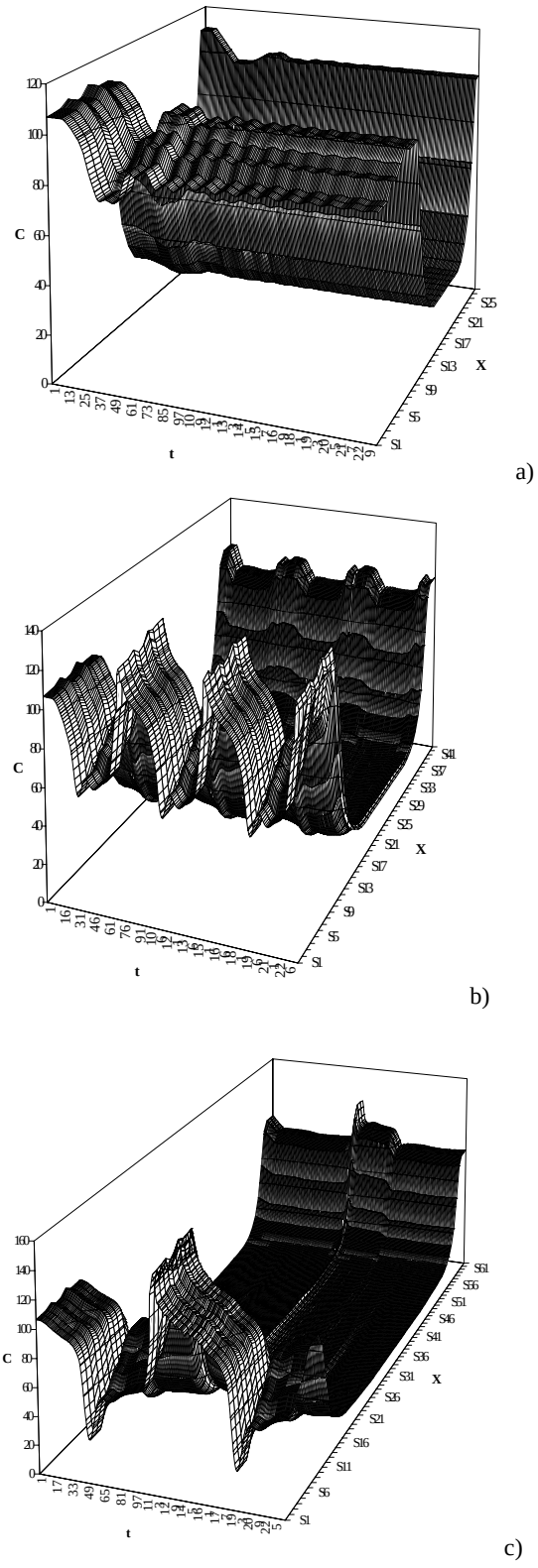


Fig.4: 3D views of velocity distributions with respect to time and space- a) B=0.65 - b) B=1.0 - c) B=1.58

ACTIVE CONTROL STRATEGY

Compression systems have their operating range limited at high flow rate by choking and at low flow rates by occurrence of aerodynamic instabilities, namely rotating stall and/or surge. If we concentrate our attention on a cascade: as flow rate decreases, the incidence angle grows up until flow separates so that the cascade pressure rise and efficiency fall out. Depending on the compressor and plant characteristics there will be stall or surge. The former is a non-axisymmetric perturbations with one or more cells with lower meridional velocity and "clean" flow zones, but stationary circumferentially averaged flow rate; virtually it might be not dangerous. On the contrary, the latter involves strong perturbations in flow rate, sometimes exhibiting reverse flow periods, and it can seriously damage both compressor and plant. Compressor map and expander line (if it is a throttle valve) or map (if it is a turbine), but also volumes (tubes, burner and plenum) between them play a role to lead to stall or surge. Greitzer (1976) pointed out that it is not only a "local" matter, so that surge instability can arise even if the slopes of the characteristics seem "good". Despite of this, most researchers utilize linear models (Ffowcs Williams and Huang, 1989; Gysling et al., 1991; Pinsley et al., 1991; Simon et al., 1993; Jungowsky et al., 1994). However, to avoid surge, traditional devices keep the compression systems away to work close to low incidence angles, i.e., low flow rates. By the way, such zones would exhibit very good pressure rise and efficiency.

In the last decade new techniques have been searched, which are more effective than purely inhibiting dangerous zones. Formerly Greitzer found that instability was related to a rate of energy, so that many researchers thought that, if this energy could be dissipated, instability had to disappear.

Two families of techniques were suggested: passive and active control. The former is based on the aeroelastic coupling of the compression system with a mass-spring-damper device (Gysling et al., 1991) or a hydraulic oscillator (Arnulfi et al., 2000), able to catch and dissipate the instability energy. Unfortunately, this approach involves serious practical problems and actually no industrial plant has been equipped with such a device. The latter family is based on a classic feedback control system, i.e., a sensor/actuator pair and a suitable control law. Ffowcs Williams and Huang (1989) stabilized the unstable flow in a small compression system by using a pressure sensor located in the plenum and a movable wall as an actuator (a sort of loudspeaker diaphragm). One hardly can think of an industrial size compression unit with a device like this. Pinsley et al. (1991) suggested a more promising control system, where the plenum pressure signal modulates the compressor exit area by a throttle valve, located downstream of the plenum. Although they experimentally validated their idea with a small centrifugal compressor for automotive turbo-charging, it seems to be suitable to large industrial units too. Many other researchers concentrate their study on active stabilization of surge in small units (for example, Jungowsky et al., 1994, Komatsubara and Mizuki, 1995).

As far as axial compressors, and particularly aero-engine units, there is a lack of experimental work. Cargill and Freeman (1991) describe an active control scheme. The control effectiveness needs two requirements: very fast response to frequency and a large number of sensors and actuators. The former conflicts with the use of analogic or digital filters: they have to be utilized in order to remove both noise and DC component of the experimental signals, but cause some phase shift. The latter makes the plant complex and hardly manageable. However Montazeri et al. (1996) wrote a theoretical paper on an active control device using one actuator only. It deals with an air bleeding strategy and the location of the bleeder was optimized.

Several control strategies can be considered for the active stabilization of a compressor system under transient operations that can cause the compressor instability. With the computational model described above the effect of different interventions (distributed mass flow bleed, variable geometry devices, control valves etc…) made to stabilize the compressor system can be evaluated and the most efficient active control strategy can be outlined.

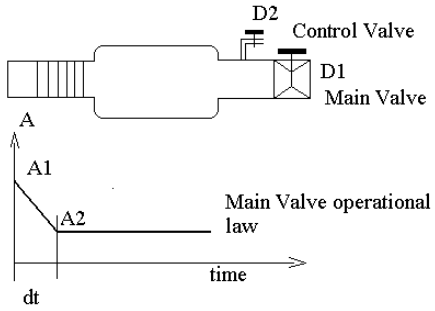


Fig.5: Compression system with control valve and main valve with its operational law

In this paper a preliminary application of a simple active control strategy has been considered in order to verify the stability properties of the iterative solution method and to estimate the potential application of the code to more complex control devices. The compression system operation point is set by the main valve (device D1 of Fig.5) whose operational law is defined by the initial (A1) and final (A2) values of the channel section (related to the coefficient μ of eq.13) and by the time step dt of the operation.

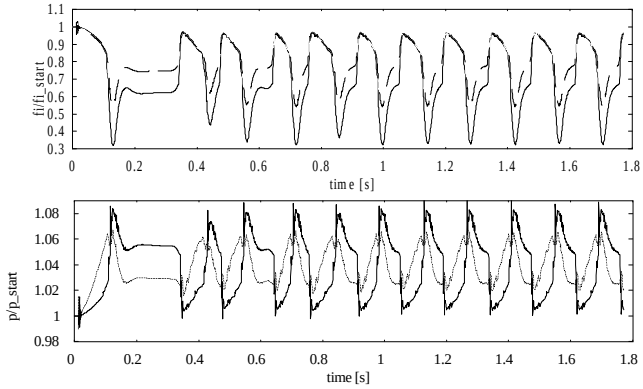


Fig.6: Compression system instability. a) flow coefficient, b) static pressure

A control valve (device D2 in Fig.5) is introduced in the exit duct in order to stabilize, with a defined control law, the system. The following simple control law for the valve B has been introduced:

$$\Delta A = K dp/dt \qquad (14)$$

where ΔA is the section variation and the pressure gradient is taken at the compressor exit.

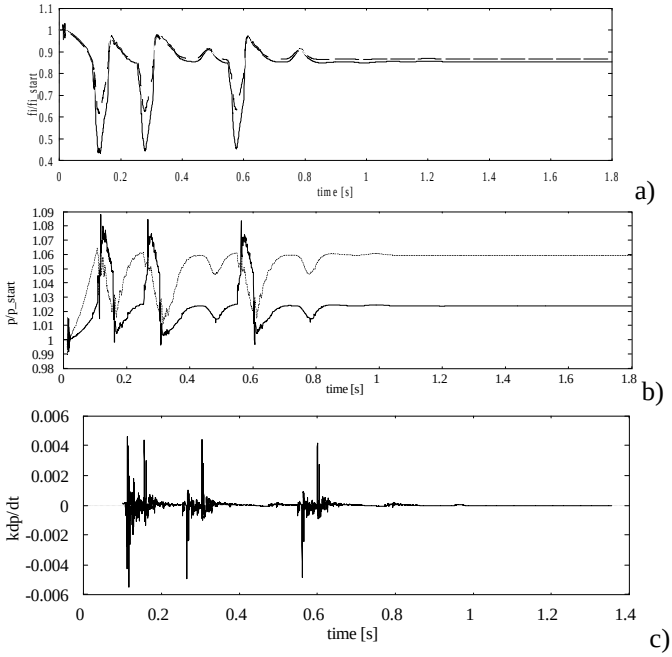


Fig.7: Compressor system stabilization. a) flow coefficient, b) static pressure, c) control valve operation

If, starting from the nominal operating condition, a reduction of about 25% in the exit duct section is operated in 0.1 s by the main valve D1, the compression system goes into a surge behavior. This is shown in Fig.6 where the flow coefficient and the static pressure (referred to the starting values) transient behavior are plotted for the inlet (solid line) and outlet (dashed line) compressor stations. With the same transient operation set by the main valve D1 the compression system is stabilized by acting on the control valve D2 with the law set by eq.14. In Fig.7a-7b the flow coefficient and the static pressure are plotted against the time for the inlet (solid line) and outlet (dashed line) compressor stations. The initial instability is damped after a short time by the active intervention of the control valve D2. The control valve is activated after the transient operation as shown in Fig.7c where the unsteady section variation is plotted. As predicted by the model very small variations are required, but with very high gradients.

This is a preliminary simulation for an active control strategy using the distributed computational model and the calculation has been performed mainly to verify the stability of the explicit scheme when introducing variable sections. Actually no attention has been devoted to the practical aspects for the implementation of the above control strategy in a real system. In future work the effect of different control strategies on the active stabilization of the compression system will be assessed with respect to their practical implementation.

CONCLUSIONS

A time-marching one dimensional simulation model has been set up for the unsteady aerodynamic analysis of a gas turbine compressor. The model considers the system with its real geometrical configuration and it is therefore suitable to the computational analysis of the effect of different active control devices on the compressor performances. After the verification of the ability of the code to give reliable solutions for a multistage axial compressor, even with an unstable operating mode, a preliminary active control strategy has been implemented in order to check for the stability of the numerical scheme. The code has demonstrated good stability properties and it will be therefore used in future works to understand the effectiveness of different active control strategies. The fluid-dynamic solver has been written as a general solution tool for one dimensional problems in order to be able to extend the analysis to a complete gas turbine engine with minor modifications to the code. This approach will be used to simulate the effect of different fluid-dynamic instabilities (compressor surge, burner humming etc…) on the whole system with allowance of active control strategies.

AKNOWLEDGMENTS

The present work is part of a research activity funded by the Italian National Research Council (CNR) - grant 99.02048.

The authors wish to thank Ing. G.L.Arnulfi, from the University of Udine, for his help and for the interesting discussions concerning the active control strategy.

REFERENCES

Arnulfi, G.L., Giannattasio, P., Micheli, D., Pinamonti, 2000, “An Innovative Device for Passive Control of Surge in Industrial Compression Systems”, ASME paper 2000-GT-0352.

Baghdadi S., Lueke J.E., 1982, “Compressor stability analysis”, ASME J. of Fluids Eng., vol.104, pp.242-249;

Botros K.K:, 1994, “Transient phenomena in compressor stations during surge”, ASME J. for Gas Turbine and Power, vol. 116;

Camp, T.R., Day, I.J., 1998, "A study of spike and modal stall phenomena in a low-speed axial compressor", ASME, Journal of Turbomachinery, vol.120 n.3, pp. 393-401;

Cargill A.M., Freeman, C., 1991, “High Speed Compressor Surge With Application to Active Control”, ASME Journal of Turbomachinery, Vol. 113, pp. 303-311.

Cravero C, 1995, “Three-dimensional compressible flow calculation in a turbomachinery stage by means of a finite volume solver” (in italian), Ph.D Thesis, Università di Genova, Genova, Italy;

Cravero C., Satta A., 1995, "Three-dimensional numerical solutions of turbomachinery annular cascade flow", ASME Cogen Turbo Power, Vienna, Austria, August;

Cravero C., Satta A., 2000, "A CFD model for real gas flows", ASME paper 2000-GT-0518, Turbo Expo, Munich (Germany), 8-11 May;

Day I.J., Breuer T., Escuret J., Cherrett M., Wilson A., 1999, “Stall inception and the prospects for active control in four high-speed compressors”, ASME J. for Turbomachinery, vol.121, pp.18-27;

Eastland, A. H. J., 1982, “Investigation of Compressor Performance in Rotating Stall: I - Facility Design and Construction and Initial Steady State Measurements”, Massachusetts Institute of Technology, *Gas Turbine and Plasma Dynamics Laboratory Report N° 164*;

Escuret J.F., Elder R.L., 1993, “Active control of surge in multi-stage axial-flow compressors”, ASME Paper 93-GT-39, Cincinnati (OH);

Epstein A.H., Ffowcs Wiliams J.E., Greitzer E.M., 1989, "Active suppression of compressor instabilities", AIAA J. Of Propulsion and Power, vol.5, pp.204-211;

Feulner M.R., Hendricks G.J., Paduano J.D., 1994, “Modeling for control of rotating stall in high-speed multi-stage axial compressors”, ASME Paper 94-GT-200, The Hague (NL);

Ffowcs Williams, J.E., Huang, X.Y., 1989, “Active Stabilization of Compressor Surge”, Journal of Fluid Mechanics, Vol. 204, pp. 245-262.

Gamache, R. M., 1985, “Axial Compressor Reversed Flow Performance”, *Ph. D. Dissertation*, Massachusetts Institute of Technology

Garrard D., Davis M., Wehofer S., Cole G., 1997, “A one dimensional, time dependent inlet/engine numerical simulation for aircraft propulsion systems”, ASME Paper 97-GT-333, Orlando (FL);

Giannattasio, P., 1999, “Analisi di stabilità di un sistema di compressione industriale con controllo attivo del pompaggio”, LIV Congresso Nazionale Associazione Termotecnica Italiana, L’Aquila, Italy, p. 1437.

Gysling, D.L., Dugundji, J., Greitzer, E.M., Epstein, A.H., 1991, “Dynamic Control of Centrifugal Compressor Surge Using Tailored Structures”, ASME Journal of Turbomachinery, Vol. 113, pp. 710-722.

Gysling D.L., Greitzer E.M., 1994, “Dynamic control of rotating stall in axial flow compressors using aeromechanical feedback”, ASME Paper 94-GT-292, The Hague (NL);

Greitzer, E. M., 1976, “Surge and Rotating Stall in Axial Flow Compressors”, ASME Transactions, *Journal of Engineering for Power*, vol. 98, N° 2, pp. 190-217.

Ishii H, Kashiwabara Y, 1996, “Study on surge and rotating stall in axial compressors (A numerical model and paqrametric study for multiblade-row compressors)”, JSME Int. Journal, series B, vol.39 n.3;

Jungowsky, W.M., Weiss, M.H., Price, G.R., 1994, “Pressure Oscillations Occurring in a Centrifugal Compressor System With and Without Passive and Active Surge Control” ASME paper 94-GT-133.

Komatsubara, Y., Mizuki, S., 1995, “Active Control of a Centrifugal Compressor”, II International Conference on Pumps and Fans, Beijing, China, pp. 387-398.

Massardo, A. F., Cinquetti, P., Satta, A., 1989, “Modelli non Lineari nello Studio del Comportamento Dinamico degli Impianti Motori e dei loro Componenti”, *Convegno dinamica e regolazione delle centrali termoelettriche*, Genova;

Montazeri-Gh M., Allerton D.J., Elder R.L., 1996, “Actuator placement for active surge control in a multi-stage axial compressor”, ASME Paper 96-GT-241, Birmingham (UK);

Moses H.L., Thomason S.B., 1986, “An approximation for fully stalled cascades”, AIAA J. of Propulsion, pp.188-189;

O'Brian W.F., 1992, "Dynamic simulation of compressor and gas turbine performance", AGARD LS183, 27-28 May, Cambridge (MA);

Pinsley, J.E., Guenette, G.R., Epstein, A.H., Greitzer, E.M., 1991, “Active Stabilization of Centrifugal Compressor Surge”, ASME Journal of Turbomachinery, Vol. 113, pp. 723-732.

Simon, J.S., Valavani, L., Epstein, A.H., Greitzer, E.M., 1993, “Evaluation of Approaches to Active Compressor Surge Stabilization”, ASME Journal of Turbomachinery, Vol. 115, pp. 57-67.

Spakovsky Z.S., Weigl H.J., Paduano J.D., C.M: Van Schalkwyk, Suder K.L., Bright M.M., 1999, “Rotating stall control in a high-speed stage with inlet distortion: Part I - Radial distortion”, ASME J. of Turbomachinery, vol.121, pp.510-516;

Spakovsky Z.S., Weigl H.J., Paduano J.D., C.M: Van Schalkwyk, Suder K.L., Bright M.M., 1999, “Rotating stall control in a high-speed stage with inlet distortion: Part II - Circumferential distortion”, ASME J. of Turbomachinery, vol.121, pp.517-524;

Sun J., Elder R.L., 1998, “Numerical optimization of a stator vane setting in multistage axial-flow compressors”, IMechE J. of Power and Energy, vol.212 part A;

This page has been deliberately left blank

Page intentionnellement blanche

Active Control Of Surge In Compressors Which Exhibit Abrupt Stall

P. Giannattasio[*], D. Micheli[**], P. Pinamonti[*]

[*]*Dipartimento di Energetica e Macchine, University of Udine, Via delle Scienze 208, 33100 Udine, Italy.*
[**]*Dipartimento di Energetica, University of Trieste, Via A. Valerio 10, 34100 Trieste, Italy.*

ABSTRACT

The present paper reports a study on the dynamic behaviour of a compression system based on a multi-stage centrifugal blower and provided with a device for the active suppression of surge instability. The control device includes a sensor of total pressure at the compressor inlet, a proportional-derivative controller and an actuation valve at the plenum exit. A non-linear lumped-parameter model of the controlled compression system is presented, which considers also the time-lags in the compressor and actuator unsteady responses. The numerical simulation shows that: *i)* the predictions of control effectiveness provided by the non-linear model are rather different from the estimates of a linear approach, mainly due to the abrupt stall which affects the compressor characteristics; *ii)* the present control device is capable of suppressing surge within almost the whole unstable operating range of the compressor, with values of the proportional gain small enough to avoid actuator saturation (stroke-end occurrence); *iii)* the derivative component of the control law exerts a poor influence on the system stabilization and can be thus removed; *iv)* the proposed control strategy is effective over a wide range of stability parameter *B*, which implies the possibility of suppressing surge also at the highest compressor speeds and when using large plenum volumes. On the basis of the numerical results, a practical control device has been designed, which consists of a transducer of differential pressure between plenum and compressor exit (equivalent to a sensor of compressor face total pressure), a butterfly throttle/actuation valve driven by a stepper motor and a computer, provided with proper interfaces, for signal acquisition, data processing and motor control. The device has been installed in an industrial-size compression system and an exhaustive set of measurements has been planned in order to verify the effectiveness of the proposed control strategy and to validate the theoretical model.

INTRODUCTION

In the last decade much work has been devoted to the study of active suppression of compressor surge. Epstein et al. (1989) firstly proposed that surge can be prevented by actively damping the small disturbances which originate the instability while their amplitude is low. The active stabilization technique is based on the use of suitable sensor/actuator pairs in closed loop control devices. The output signal from the sensor (of pressure, flow rate, etc.) is fed to a controller which applies a proper control law to drive the actuator (valve, moving plenum wall, etc.). The control is effective if the actuation is capable of absorbing and damping the unsteady energy surplus introduced in the system by the compressor when it operates in the stalled region. An experimental demonstration of active stabilization of surge has been given for centrifugal compressors by several investigators, for example, Ffowcs Williams and Huang (1989) and Pinsley et al. (1991). Furthermore, an extensive study has been carried out by Simon et al. (1993), who analyzed the influence of sensor and actuator selection on the maximum stabilized compressor characteristic slope by solving the linearized equations of the controlled system dynamics. According to this study, most of the literature on surge modelling and suppression employs a linear stability analysis to predict the effectiveness of active control devices. Such an approach provides reliable results as long as it can be assumed that surge instability originates from small amplitude perturbations, which is not the case of compressors which exhibit abrupt stall. This point has been examined closely by Giannattasio and Giusto (1998), with reference to a compression system provided with a device for the passive control of surge. They pointed out that the finite disturbance introduced by the sudden pressure drop associated with the abrupt stall causes non-linear effects to be responsible for system instability in conditions where the linear analysis predicts stable operation.

The present paper considers the active suppression of surge in a compression system based on a multi-stage centrifugal compressor which exhibits abrupt stall. This system has been employed for various experimental investigations in both stable and unstable operating conditions (Arnulfi et al., 1995, 1996). To study surge dynamics, a plenum of sufficiently large volume was connected to the compressor delivery pipe and detailed experimental data were collected on deep surge limit cycles and compressor internal flows (Arnulfi et al., 1999a). A non-linear lumped-parameter model of the compression system was also worked out, which proved to be capable of correctly predicting the system dynamics at different compressor speeds and throttle valve settings (Arnulfi et al., 1999b).

The active control device considered here includes a sensor of total pressure at the compressor inlet (or, equivalently, of differential pressure between plenum and compressor exit), a proportional-

Paper presented at the RTO AVT Symposium on "Active Control Technology for Enhanced Performance Operational Capabilities of Military Aircraft, Land Vehicles and Sea Vehicles", held in Braunschweig, Germany, 8-11 May 2000, and published in RTO MP-051.

derivative (PD) controller and an actuation valve at the plenum exit. The sensor/actuator pair has been selected on the basis of a theoretical analysis performed by Giannattasio (1999), who critically revised the work of Simon et al. (1993).

In the present study, a non-linear model and a preliminary experimental analysis of the actively controlled compression system are performed. The model is derived from the lumped-parameter approach used by Arnulfi et al. (1999b); the non-linear differential equations which describe the system dynamics are coupled to the control equations and are solved in the time domain by using an implicit second-order accurate numerical procedure. The dynamics of the controlled system has been simulated at various operating conditions of the compressor (flow rates and rotational speeds) and for different values of the control parameters (proportional and derivative gains). On the basis of the numerical results, a proper control device has been designed and installed in the experimental compression plant. At present, unsteady measurements of compressor and plenum pressure, mass flow rate and actuator position are being carried out in order to verify the control effectiveness in compressors which exhibit abrupt stall and to validate the proposed model of the system dynamics.

NOMENCLATURE

A	area
a	speed of sound
B	Greitzer parameter
E	surge unsteady energy
G	valve parameter
K_p	proportional gain
K_d	derivative gain
L	equivalent length
$\dot{m}$	mass flow rate
p	absolute pressure
t	time
T	period
T_H	Helmoltz period
U	impeller tip speed
u	system input = $(A_t - A_{ts})/A_{ts} = \Delta A_t / A_{ts}$
V	volume

Greek symbols

α_t	valve fraction open = $A_t / A_{t,max}$
φ	flow coefficient = $\dot{m}/\rho_0 U A_c$
ρ	density
τ	dimensionless time
τ_a	actuator time constant
τ_c	compressor time constant
ω_H	Helmoltz angular frequency
ψ	pressure coefficient = $2(p - p_0)/\rho_0 U^2$

Subscripts

0	ambient
1	compressor inlet
c	compressor
p	plenum
r	required
s	steady-state
t	throttle valve

SENSOR-ACTUATOR SELECTION

Figure 1 shows a sketch of a compression system fitted with the present device for the active suppression of surge. A signal of total pressure at the compressor inlet is fed to a PD controller, the output of which is employed to drive the throttle valve at the plenum exit. In unsteady conditions, the compressor face total pressure is directly related to the flow acceleration inside the compressor duct and can be thus considered as a representative output of the system during unstable operation. In the present case, the plenum valve performs both functions of throttling device and actuator. These functions can be kept apart by simply introducing a bleed valve, as the actuator, in parallel with the throttle valve (Simon et al., 1993). The two options are quite equivalent from a conceptual point of view, the best choice depending only on technical considerations. For example, it can be argued that the use of a bleed valve implies a gas leakage from the plenum also during steady operation. In fact, the actuator is required to move in both directions around the equilibrium position to make the control effective, so that the bleed valve cannot be completely closed in any operating condition.

The present sensor/actuator pair has been selected from the twelve different options suggested by Simon et al. (1993), who considered all the combinations of four sensors (compressor flow rate, plenum pressure, compressor face total and static pressure) and three actuators (close-coupled valve in the compressor delivery pipe, plenum bleed valve, movable plenum wall). On the basis of a linear stability analysis, Simon et al. attained to the conclusion that the combination of a sensor of compressor mass flow rate with a close-coupled valve is far the best choice for a control device of maximum effectiveness. However, such a result was obtained for fixed values of some operating parameters (steady equilibrium positions of throttle valve and close-coupled valve) which, moreover, were not reported in the paper. On the contrary, the variation of the steady operating point of an actual compression system was duly considered by Giannattasio (1999), who revised the comparative analysis of Simon et al. by using the same linear approach. The results of this study show that pair "compressor mass flow sensor/close-coupled valve" is clearly superior to the other ones only for small values of the close-coupled valve fraction open, which imply large pressure losses in the

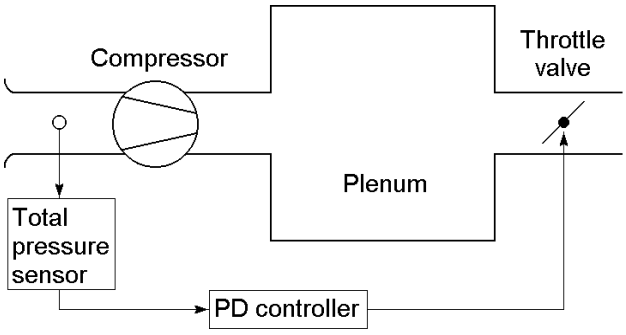


Fig. 1 - Controlled compression system.

compressor delivery pipe. Moreover, it turns out that five of the twelve sensor/actuator pairs have to be discarded because of severe gain-independent stability constraints, which cannot be removed by the control. Finally, some other combinations require extremely large values of the proportional gain for an effective system stabilization (compressor face total or static pressure/close-coupled valve) or involve technical complications (control of both speed and position of the movable plenum wall). In conclusion, the best compromise between control performance and technical requirements appears to be attained by the use of a sensor of total or static pressure at the compressor inlet and of an actuation valve at the plenum exit. The linear stability analysis shows that, when applied to the present compression system, the two pressure sensors produce equally effective controls. However, it can be shown that the compressor face total pressure is equal to the differential pressure between plenum and compressor exit, which is easier to be measured in unsteady conditions with the required accuracy. This explains the present sensor choice.

MODEL OF THE COMPRESSION SYSTEM

The dynamics of the controlled compression system is described by means of a non-linear lumped-parameter model derived from Greitzer (1976). This approach has been successfully adopted by the authors for modelling an uncontrolled compression system (Arnulfi et al., 1999b) as well as a compression plant provided with a novel device for the passive suppression of surge (Arnulfi et al., 2000).

The model is based on the following assumptions: *i*) one-dimensional incompressible flow in the compressor and valve ducts, which are replaced by constant area pipes of equivalent length L_c and L_t, respectively; *ii*) compressor regarded as an actuator disk; *iii*) uniform pressure and negligible flow velocity in the plenum; *iv*) quasi-steady flow through the valve. The further assumption, frequently retained, that the unsteady response of the compressor follows its steady-state characteristic is here replaced by the more realistic assumption of a time-lag which obeys to a first-order dynamics. The same approach is used to model the actuator dynamics, since the inherent bandwidth limitation of this component can introduce a non-negligible time lag between the controller output and the response of the flow train element.

The foregoing assumptions allow the following nondimensional equations of the system dynamics to be written (see, for details, Greitzer, 1976, Arnulfi et al., 1999b):

$$\frac{d\varphi_c}{d\tau} = B\left(\psi_c - \psi_p\right), \tag{1}$$

$$\frac{d\varphi_t}{d\tau} = \frac{B}{G}\left(\psi_p - \psi_t\right), \tag{2}$$

$$\frac{d\psi_p}{d\tau} = \frac{1}{B}\left(\varphi_c - \varphi_t\right), \tag{3}$$

$$\frac{d\psi_c}{d\tau} = \frac{1}{\tau_c}\left[\psi_{cs}\left(\varphi_c\right) - \psi_c\right], \tag{4}$$

$$\frac{du}{d\tau} = \frac{1}{\tau_a}\left(u_r - u\right), \tag{5}$$

$$\psi_t = \left(A_c/A_t\right)^2 \varphi_t^2 = \left(A_c/A_{ts}\right)^2 \left(\frac{\varphi_t}{1+u}\right)^2, \tag{6}$$

$$u_r = \left(\frac{\Delta A_t}{A_{ts}}\right)_r = -K_p \psi_{01} - K_d \frac{d\psi_{01}}{d\tau}, \tag{7}$$

$$\psi_{01} = \psi_p - \psi_c. \tag{8}$$

Equations (1) and (2) are the momentum conservation equations in the compressor and valve pipes, respectively; Eq. (3) expresses mass conservation in the plenum; Eqs. (4) and (5) are first-order models of the compressor and actuator dynamics, respectively; Eq. (6) represents the steady-state characteristic of the throttle/actuation valve; Eq. (7) expresses the system input (nondimensional valve area) required by the PD control law; finally, Eq. (8) represents the system output (nondimensional total pressure at the compressor inlet) as a function of the system state variables (Simon et al., 1993).

Greitzer parameter *B*, which appears in Eqs (1)-(3), is defined as $B = U/2\omega_H L_c = \left(U/2a_p\right)\sqrt{V_p/A_c L_c}$ and can be interpreted as the ratio of pressure and inertial forces acting in the compressor pipe (Greitzer, 1976). The value of this parameter strongly affects the system stability and the control effectiveness. Valve parameter *G* in Eq. (2) is defined as $G = L_t A_c / L_c A_t$ and exerts a minor influence on the system dynamics (Greitzer, 1976). Term $\psi_{cs}(\varphi_c)$ in Eq. (4) refers to the steady-state compressor characteristic, while the time constant of the compressor dynamics, τ_c, can be related to the time needed for the complete development of a stall cell (Giannattasio and Giusto, 1998). Equation (5), which models the actuator dynamics, can be regarded as a first-order low-pass filter, its cut-off frequency being equal to the reciprocal of time constant τ_a (in the present work it is assumed $\omega_{cut} = 10\omega_H$ and hence $\tau_a = 0.1$). Finally, parameters K_p e K_d in control law (7) are real constants and represent the proportional and the derivative gains, respectively.

If ψ_t is eliminated from Eq. (2) by using Eq. (6) and Eqs (7)-(8) are introduced in Eq. (5), a non-linear system of five ordinary differential equations is obtained in the unknowns φ_c, φ_t, ψ_p, ψ_c and *u*. It can be solved numerically for given values of parameters *B*, *G*, τ_c, τ_a, K_p and K_d, if the steady-state characteristics of the compressor, $\psi_{cs}(\varphi_c)$, and of the throttle valve, A_{ts}, are known.

The present model is used to simulate the dynamic behaviour of an industrial compression system, which consists of a four stages centrifugal blower with vaned diffusers and a plenum of large capacity (detailed technical data on the present compression system are provided in paragraph “Experimental Procedure”). The steady-state characteristics of the compressor at the rotational speeds of 2000, 3000 e 4000 *rpm* are shown in Fig. 2. These curves show the presence of abrupt stall at all the considered rotational speeds. As observed by Giannattasio and Giusto (1998), such an occurrence strongly affects the dynamic behaviour of the system with and without control devices. The values assumed by stability parameter *B* at the three rotational speeds (0.304, 0.457 and 0.608) turn out to be far higher than the critical value of the present compressor, $B_{crit} = 0.06$ (Greitzer, 1976, Giannattasio and Giusto, 1998), which results in a great system tendency to instability and accounts for the deep surge conditions observed by Arnulfi et al. (1999a) also at the lowest compressor speeds.

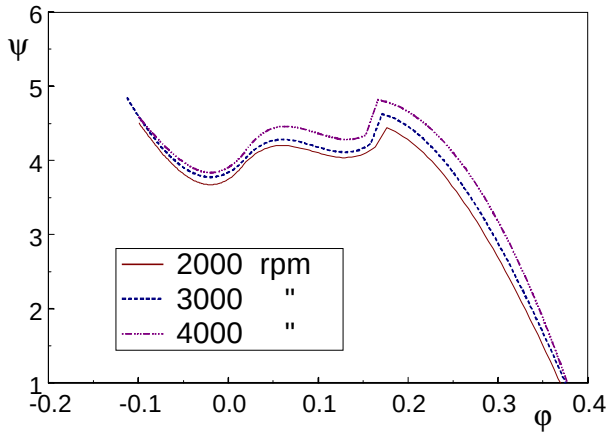


Fig. 2 - Compressor characteristic curves.

NUMERICAL RESULTS

The equations of the controlled system dynamics have been solved numerically by using an implicit second-order accurate time discretization and a Newton-Raphson procedure for the iterative solution of the resulting non-linear algebraic equations. The use of an implicit scheme is due to the stiffness of the present differential equation system, which can cause a severe numerical instability if an explicit discretization is employed.

The initial conditions are assigned by simulating a valve throttling process, with constant closing rate, from a steady operating point on the stable branch of the compressor characteristic. Differently from the assignment of an arbitrary perturbation of the steady equilibrium point, this procedure allows the effects of realistic initial conditions on the non-linear system dynamics to be taken into account.

At the end of each Newton-Raphson iteration, the possible occurrence of actuator stroke-ends is checked by verifying that the system input required by the controller (u_r in Eq. (7)) is within its limit values, corresponding to fully open or closed valve. If this is not the case, the control law is inhibited and the subsequent iterations are performed by fixing u_r at its limit value, until Eq. (7) yields again an achievable value of the system input. Furthermore, in the case of complete valve closure, Eq. (6) is no longer valid and it is replaced by equation $\varphi_t = 0$.

Early numerical results were obtained by simulating single operating conditions of the compression system at different values of the proportional and derivative gains. As representative examples, Figs 3 through 5 show some results, obtained at the compressor speed of 3000 *rpm*, in terms of system trajectories in plane $\varphi_c - \psi_p$ and time traces of variables φ_c , ψ_p and valve fraction open α_t. Part *a)* of each figure also shows, for reference, the steady-state characteristics of compressor (dashed line) and throttle valve (dot-dashed line).

Figure 3 refers to a steady operating point ($\varphi_s = 0.15$) near the stall limit and to the case of purely proportional control ($K_d = 0$). This operating condition turns out to be normally unstable, since a deep surge limit cycle is observed when $K_p = 0$. However, it is noticed that a gain value of -10 is sufficient to stabilize the system, while higher absolute values of K_p result in an increasingly damped system response. As far as the actuator response is concerned, Fig. 3*b* shows moderate oscillations of the valve fraction open around the steady equilibrium value, the actuator stroke-ends being never reached. In particular, the peaks of α_t represent the actuator response to the strong system perturbation caused by the crossing of the abrupt stall region.

Figures 4 and 5 refer to a steady operating point at a lower flow rate, namely, $\varphi_s = 0.075$. Contrary to the prediction of the linear stability analysis (Giannattasio, 1999), this operating condition turns out to be unstable in the case of uncontrolled compression system, as shown in Fig. 4 by the deep surge cycle obtained at $K_p = 0$. Nevertheless, the inherent local stability of this point, promoted by the negative slope of the compressor characteristic, allows stability to be attained already at $K_p = -5$. Also in this case the oscillations of α_t have limited amplitude at all gain values and an overdamped actuator response is observed at the highest value of K_p. Figure 5, which represents the effects of the derivative gain on the system dynamics, shows that, as long as K_d assumes negative values, system stability is not affected. The main consequence of an increase in the derivative gain appears to be a smaller overshoot and an increased delay in the actuator response. On the contrary, a positive value of K_d can cause unstable operation, as in case *c* of Fig. 5*a*. This case shows a progressive departure of the system state from the steady equilibrium point, which finally results in small amplitude oscillations around a flow rate value much larger than the desired one.

In order to attain a global evaluation of the control device effectiveness, the unstable branch of the compressor characteristic ($0 < \varphi_s < \varphi_{stall}$) has been discretized in a sufficiently high number of equally spaced points, where stability has been tested at fixed values of K_p and K_d. By repeating this procedure for different values of the gains, contour-plots of the stabilized fraction of operating points in the gain plane have been obtained. The diagrams corresponding to the compressor speeds of 2000, 3000 and 4000 *rpm* are shown in Figs 6*a*, *b* and *c*, respectively, while Fig. 7 reports, for comparison, the analogous results obtained by the linear stability analysis (Giannattasio, 1999). Both linear and non-linear results show that negative values of K_p and K_d are required for system stabilization and that the derivative gain does not exert any significant influence on stability (the maximum extensions of the stable flow range can be obtained also with $K_d = 0$). Furthermore, it is observed that an increase in the compressor speed, and hence in parameter *B*, produces a rapid reduction in the control effectiveness, much larger absolute values of K_p being required to stabilize the same fraction of operating points. From a quantitative point of view, the predictions of the linear and non-linear models appear to be rather different. In fact, under uncontrolled conditions ($K_p = 0$), the contour-plots in Fig. 7 show that more than 40% of the considered flow range is stable, while the non-linear model predicts unstable operation everywhere. Nevertheless, as soon as the proportional control is introduced, the predictions of the non-linear model turn more optimistic than the linear ones. In fact, already at a comparatively small value of K_p ($K_p \cong -20$) both approaches provide the same estimate of the control effectiveness, while at higher absolute values of K_p the stable flow range fraction predicted by the non-linear model turns out to be the larger. In any case, the proposed control strategy appears to be suitable to the stabilization of the present compression system, since 80-90% of the unstable branch of the compressor characteristic can be stabilized with reasonable values of the proportional gain.

The evaluation of the control effectiveness on the basis of the stabilized flow range fraction allows an immediate comparison between linear and non-linear approaches to be established, but it can

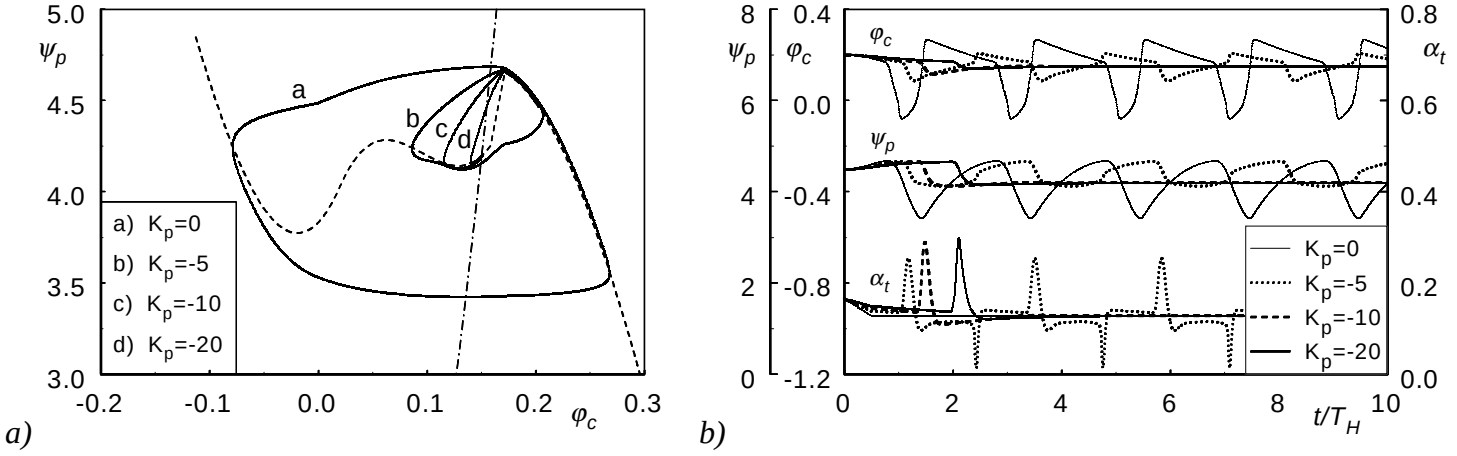


Fig. 3 - Simulated dynamics of the compression system at $n = 3000$ *rpm*, $\varphi_s = 0.15$ and $K_d = 0$ for different values of the proportional gain.
a) System trajectories in φ_c - ψ_p plane. *b)* Time traces of compressor mass flow rate (φ_c), plenum pressure (ψ_p) and valve fraction open (α_t).

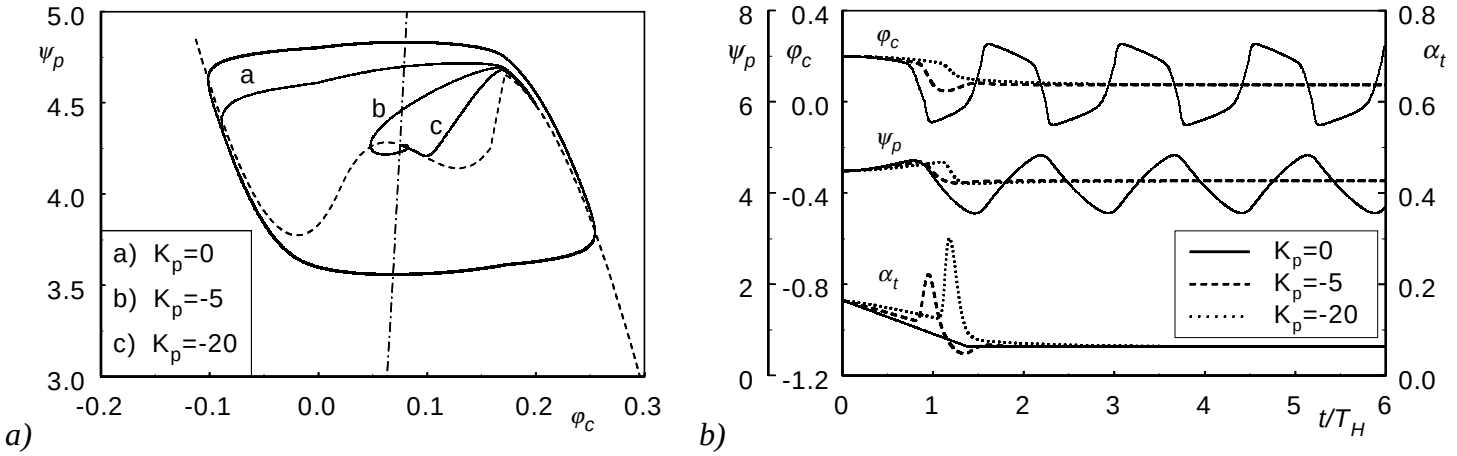


Fig. 4 - Simulated dynamics of the compression system at $n = 3000$ *rpm*, $\varphi_s = 0.075$ and $K_d = 0$ for different values of the proportional gain.
a) System trajectories in φ_c - ψ_p plane. *b)* Time traces of compressor mass flow rate (φ_c), plenum pressure (ψ_p) and valve fraction open (α_t).

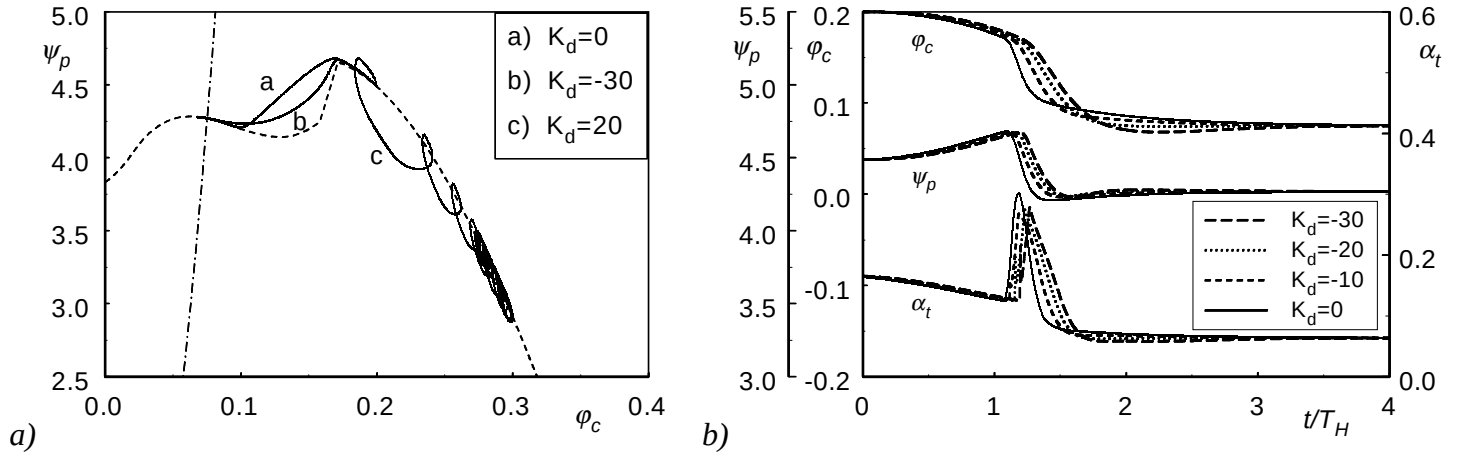


Fig. 5 - Simulated dynamics of the compression system at $n = 3000$ *rpm*, $\varphi_s = 0.075$ and $K_p = -20$ for different values of the derivative gain.
a) System trajectories in φ_c - ψ_p plane. *b)* Time traces of compressor mass flow rate (φ_c), plenum pressure (ψ_p) and valve fraction open (α_t).

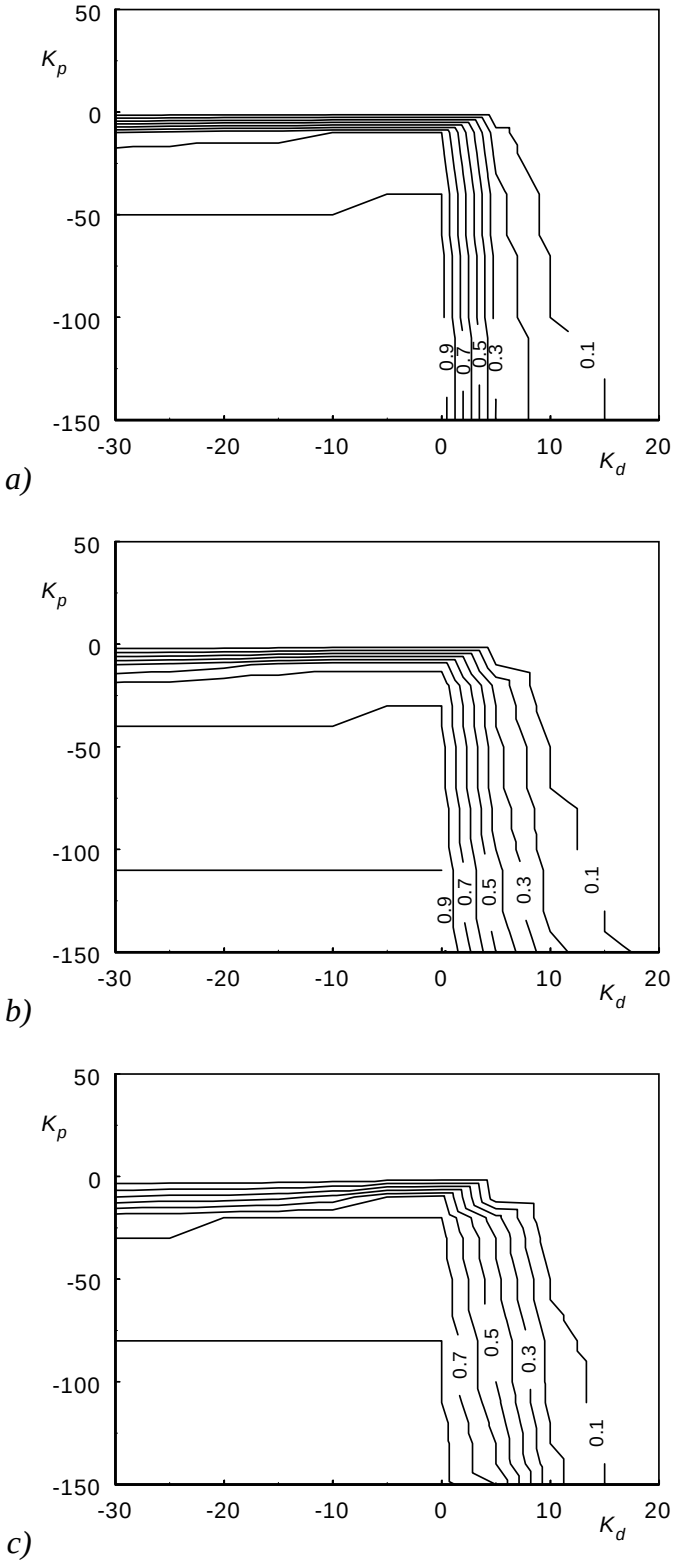


Fig. 6 - Contour-plots of the stabilized flow range fraction in the gain plane at the compressor speeds of *a)* 2000, *b)* 3000 and *c)* 4000 *rpm*. Results of the non-linear model.

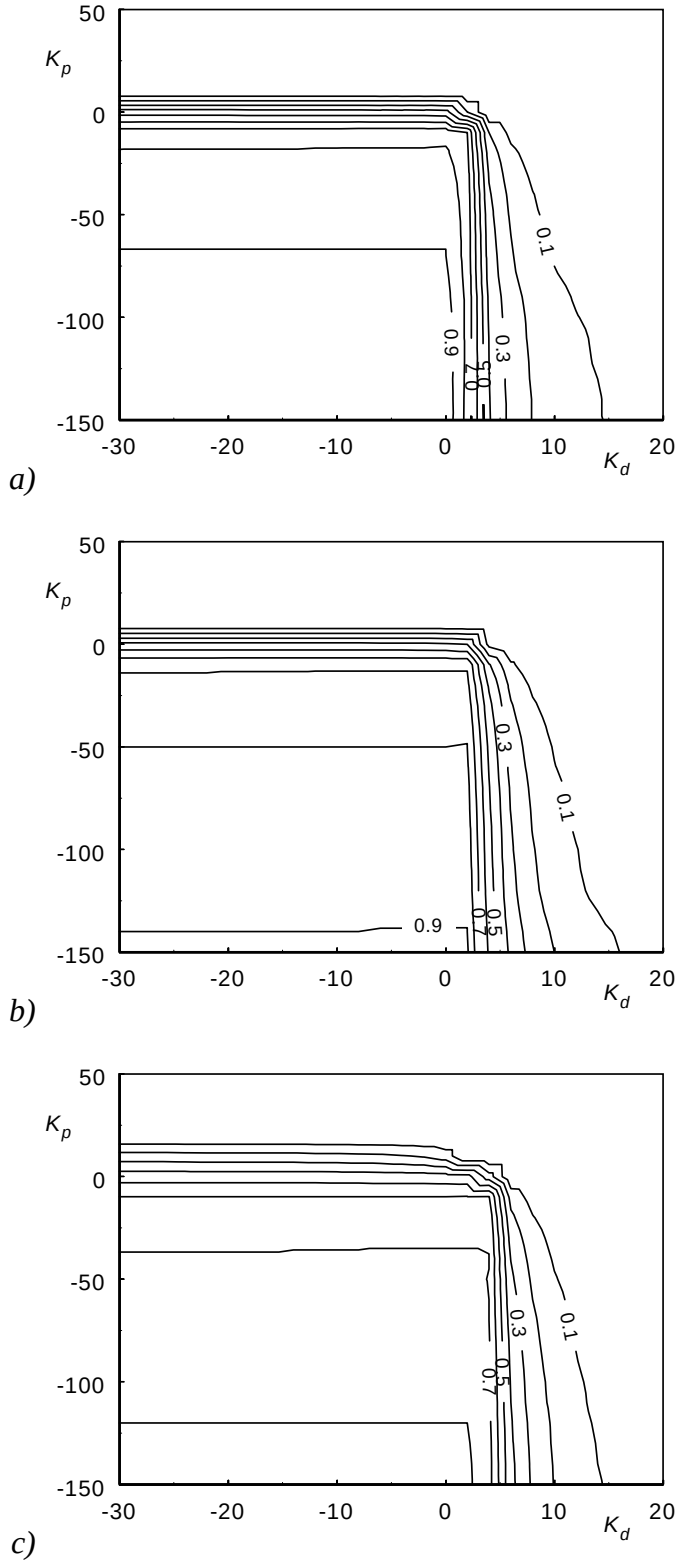


Fig. 7 - Contour-plots of the stabilized flow range fraction in the gain plane at the compressor speeds of *a)* 2000, *b)* 3000 and *c)* 4000 *rpm*. Results of the linear stability analysis (Giannattasio, 1999).

be inadequate to fully understanding the impact of the active control on the compression system dynamics. For example, the results in Fig. 6 provide no information about the changes in the amplitude of the surge cycles in the operating points which remain unstable after the active control has been introduced. In order to attain to a truly quantitative estimate of the control effectiveness, a proper stability index has been introduced by Giannattasio (1999), which is defined as:

$$E = \int_{\bar{\tau}}^{\bar{\tau}+T} \left(\psi_c - \psi_p\right) \frac{d\varphi_c}{d\tau} d\tau = B \int_{\bar{\tau}}^{\bar{\tau}+T} \left(\psi_c - \psi_p\right)^2 d\tau = \frac{1}{B} \int_{\bar{\tau}}^{\bar{\tau}+T} \left(\frac{d\varphi_c}{d\tau}\right)^2 d\tau \tag{9}$$

where the integrals are computed over period T of a surge oscillation and the second and third equalities descend from Eq. (1). Parameter E can be interpreted as the unsteady energy associated with the surge cycle, being defined as the integral over the cycle period of perturbing "force" $(\psi_c - \psi_p)$ multiplied by "displacement" $d\varphi_c$ (Greitzer, 1976). Furthermore, it can be immediately shown that, in the case of instantaneous compressor response ($\tau_c = 0 \Rightarrow \psi_c = \psi_{cs}$), E is equal to the area of the limit cycle in plane (φ_c, ψ_p). It is clear that $E = 0$ in a stable operating point, while high values of this parameter indicate an ineffective stabilization.

A useful representation of the control effectiveness can be obtained by plotting the values of E in all the operating points on the unstable branch of the compressor characteristic curve. This is done in Fig. 8, which refers to the compressor speed of 3000 *rpm* and shows E plots for different values of the proportional gain and $K_d = 0$. According to the results in Fig. 6*b*, the uncontrolled system ($K_p = 0$) turns out to be unstable all over the flow coefficient interval, E being different from zero everywhere. However, very small gain values are sufficient to stabilize a large part of the operating range, even if for $K_p > -20$ narrow unstable regions remain near the stall limit ($\varphi_{stall} \cong 0.16$). At $K_p = -50$ the stabilized interval amounts to about 70% of the whole range, while further small increases require much larger absolute values of the gain. Finally, Fig. 8 shows that the active control produces a general reduction in the unsteady energy of the system, also in the operating points which remain unstable. As far as the actuator dynamics is concerned, it turned out that the valve does not reach its stroke-ends in any of the operating points considered. Consequently, the gain values in Fig. 8 can be assumed to be acceptable for a practical control device.

The present analysis has been generalized further on, by investigating the combined influences of parameters K_p and B on system stability. On the basis of the numerical results in Figs 5 and 6, the derivative gain was excluded from this parametric study as well as from the control law of the experimental device. In order to obtain a concise representation of the control effectiveness over the whole unstable flow range of the compressor, an average value of stability index E is here introduced, namely,

$$< E >= \frac{1}{\varphi_{stall}} \int_0^{\varphi_{stall}} E \, d\varphi \, . \tag{10}$$

Figure 9 shows a 3D diagram (*a*) and a contour-plot (*b*) of parameter $log_{10}(1 + < E >)$ as a function of K_p and B (the logarithmic representation was preferred for a better graphic resolution at the

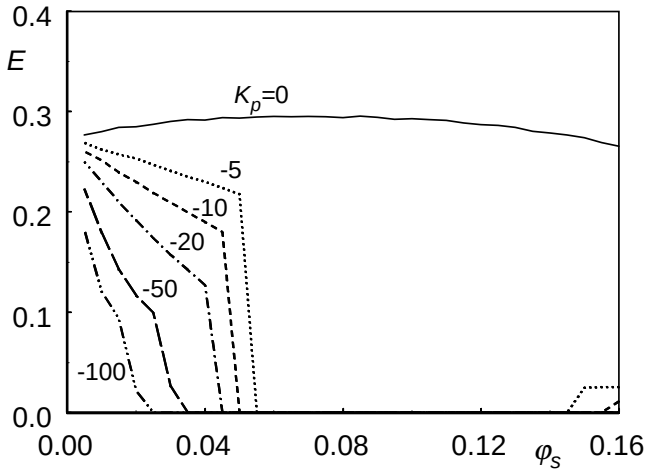


Fig. 8 - Unsteady energy E throughout the unstable flow range of the compressor characteristic at different values of the proportional gain ($K_d = 0$, $n = 3000$ *rpm*).

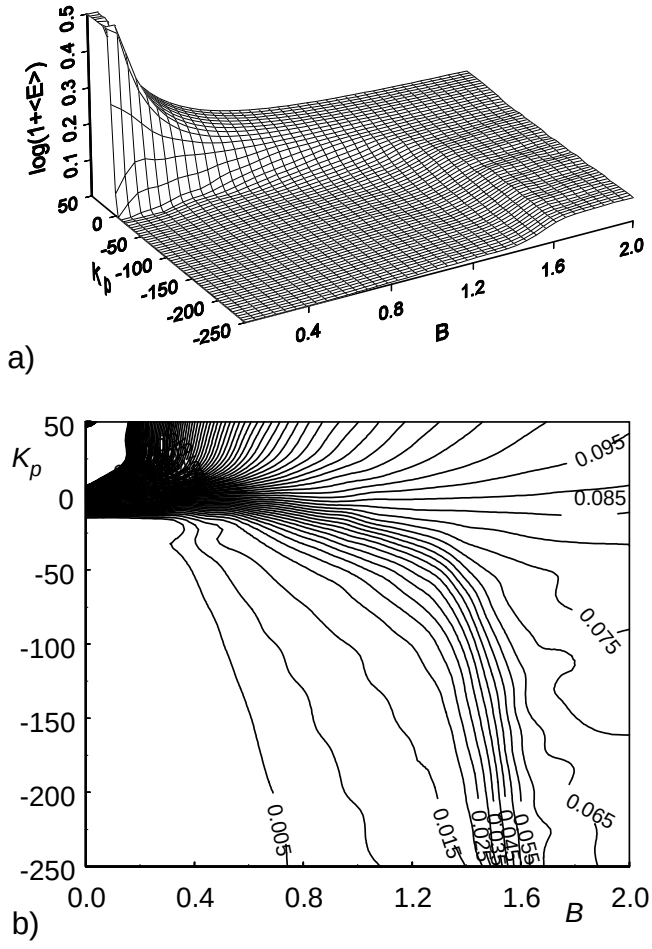


Fig. 9 - 3D plot (*a*) and contour-plot (*b*) of the average unsteady energy as a function of Greitzer parameter and proportional gain.

smallest values of $<E>$). Both plots show that the region of low unsteady energy (high control effectiveness) lies in the range of negative gains and B values less than about 1.2. Inside this region stability index $<E>$ increases very slowly with parameter B, which demonstrates the robustness of the proposed control strategy when applied to the present compression system. In fact, the maximum compressor speed is close to 4000 *rpm*, which corresponds to a B value of 0.608 for the present system geometry. This means that the stable operating range of the compressor can be enlarged considerably also under the heaviest conditions by using acceptable values of the proportional gain ($0 > K_p > -100$).

EXPERIMENTAL PROCEDURE

In order to verify the effectiveness of the proposed control strategy and to validate the theoretical model, an industrial compression plant has been coupled to a properly designed control device. A comprehensive set of measurements has been planned and preliminary tests are in progress.

The compression system, shown in Fig. 10, is installed at the Laboratory of the *Dipartimento di Energetica*, University of Trieste. It is based on a low pressure multi-stage centrifugal compressor driven by a DC motor through a speed increasing gear. The blower includes four impellers, with 16 backswept blades and 465 *mm* outer diameter, and vaned diffusers. The compressor inlet consists of a radial bellmouth duct with a 125 *mm* inner diameter ($A_c = 122.7$ cm^2), while the delivery pipe is connected to a cylindrical plenum of large volume ($V_p = 3.132$ m^3). The equivalent length of the compressor ducting turns out to be $L_c = 13.5$ *m*. A butterfly valve at the plenum exit performs both functions of throttling device and actuator. The valve is 101 *mm* inner diameter and it is driven by a stepper motor with a resolution of 200 *steps/rev*. The motor is capable of delivering a torque higher than 11 *Nm* in the speed range of 100-500 *steps/s*.

The present compression system, without the control device, has been employed in a previous experimental work to perform detailed measurements of pressure, flow rate and flow velocity in deep surge conditions (Arnulfi et al., 1999a). Furthermore, the plant has been used to test the effectiveness of an innovative device for the passive control of surge (Arnulfi et al., 2000). This control device consisted of a hydraulic oscillator coupled to the plenum, the volume of which was reduced to 0.78 m^3 in order to obtain B values consistent with the stability limits of the device.

The instrumentation system is shown in Fig. 11, where the capital letters refer to the transducer locations in Fig. 10. Pressures and temperatures are measured by means of inductive transducers and K-thermocouples, respectively, while a magnetic pick-up is used for the compressor rotational speed. The mass flow rate is measured by means of an orifice flow meter mounted in the compressor delivery pipe. Although this instrument is normally used for steady flow measurements, it was considered acceptable in the present case because of the slow dynamics of surge (a few cycles per second).

The temperature signals are acquired by using a GPIB board as an interface to the HP3497A device. The pressure signals are first amplified and then conveyed to the NI SC-2040 board, which allows the simultaneous sampling of eight channels to be performed. This unit is an accessory of the multifunction I/O NI PCI-MIO-E1 board, which includes the A/D converter and is plugged in the PC (Pentium MMX 233MHz processor). The stepper motor is driven by a Power Driver Unit which allows a half-step resolution to be selected. The throttle angular position is measured by means of a precision potentiometer with a linearity error of ±0.25%. The software for data acquisition and motor control has been developed in LabView 5.0 environment.

The signal of differential pressure between plenum and compressor outlet is acquired at a sampling rate of 20 *Hz*, which was considered high enough to represent surge dynamics. The signal is first processed by means of a digital low-pass 2nd-order Bessel filter with a cut-off frequency of 8 *Hz*. A proportional control law is then applied to the filtered data by using selected values of K_p, so obtaining the valve flow area required by the control. This area value is used to compute the angular displacement of the actuator and hence the number of square-wave pulses to be sent to the stepper motor. The pulse frequency, which determines the motor speed, is set equal to 500 *Hz*, so allowing the required angular displacement of the actuator to be completed within a sampling period while enabling the motor to operate at high torque values. The signal from the potentiometer is used to provide an absolute reference for the angular position of the valve and to check the actual motor displacement.

The developed software allows the throttle valve to be moved to the desired position and the control device to be enabled or disabled when required, while recording the corresponding time evolution of the system parameters.

Preliminary experimental tests have been carried out in order to verify the operating features of the present control equipment. As a representative result, Fig. 12 shows the time traces of flow coefficient, plenum pressure coefficient, system output and valve angular position corresponding to a steady equilibrium point on the unstable branch of the compressor characteristic. The large amplitude oscillations at low frequency which are observed in the initial part of each diagram are due to surge. As soon as the control device is started, a significant reduction in the amplitude of the oscillations is obtained, but they are not completely suppressed. Perturbations of comparatively high frequency continue to affect the compression system, which cannot be considered as effectually stabilized. Further tests show that the amplitude of such oscillations becomes larger and larger as the absolute value of the gain is increased. Since higher gains are required to suppress surge at larger B values, the effects of the amplification of the high frequency disturbances rendered the system stabilization more and more ineffective as the compressor speed was increased beyond 2000 *rpm.*

The main reason for the lack of system stabilization appears to be the excessive time-lag (about 0.2 seconds) between the system output signal and the actuator response. Such a delay turns out to be comparable with the period of the high frequency perturbations observed under controlled conditions. Its main effect is an increased sensitivity of the system to measurement disturbances, which are amplified, rather than rejected, by high values of the gain.

The slow dynamics of the present control equipment is due both to the phase shift introduced by the Bessel filter and to software-hardware limitations which determine a low sampling frequency and a slow actuator response. Therefore, an effort has been undertaken aimed at improving the technical features of the present control system, by using more appropriate hardware and software tools and low phase-shift filtering techniques.

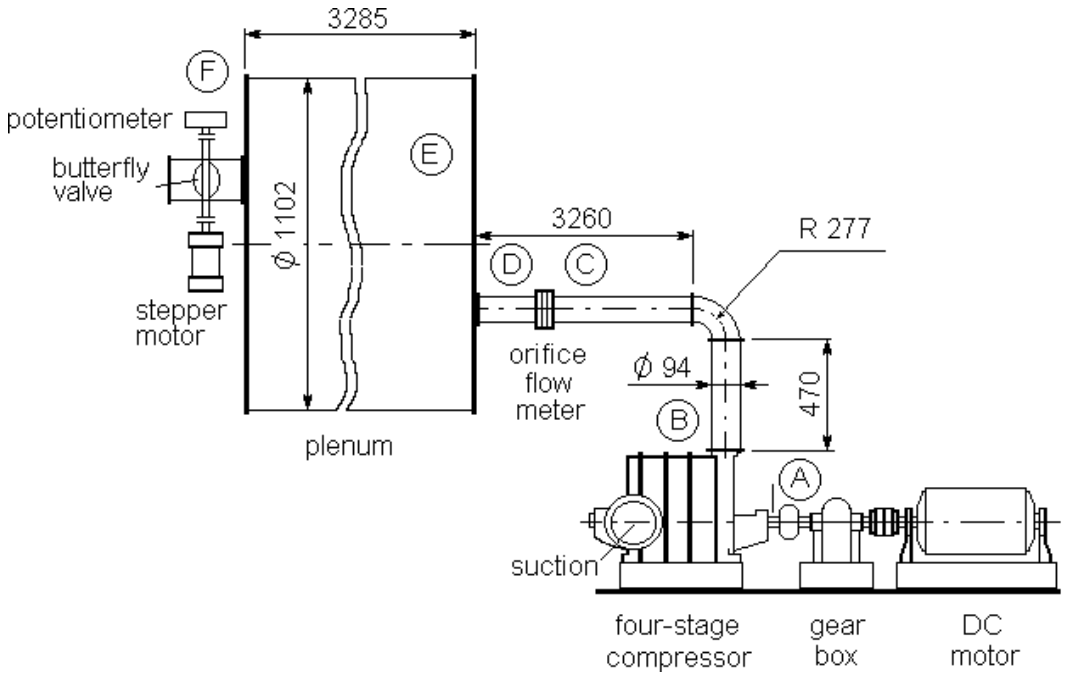


Fig. 10 - Experimental compression plant.

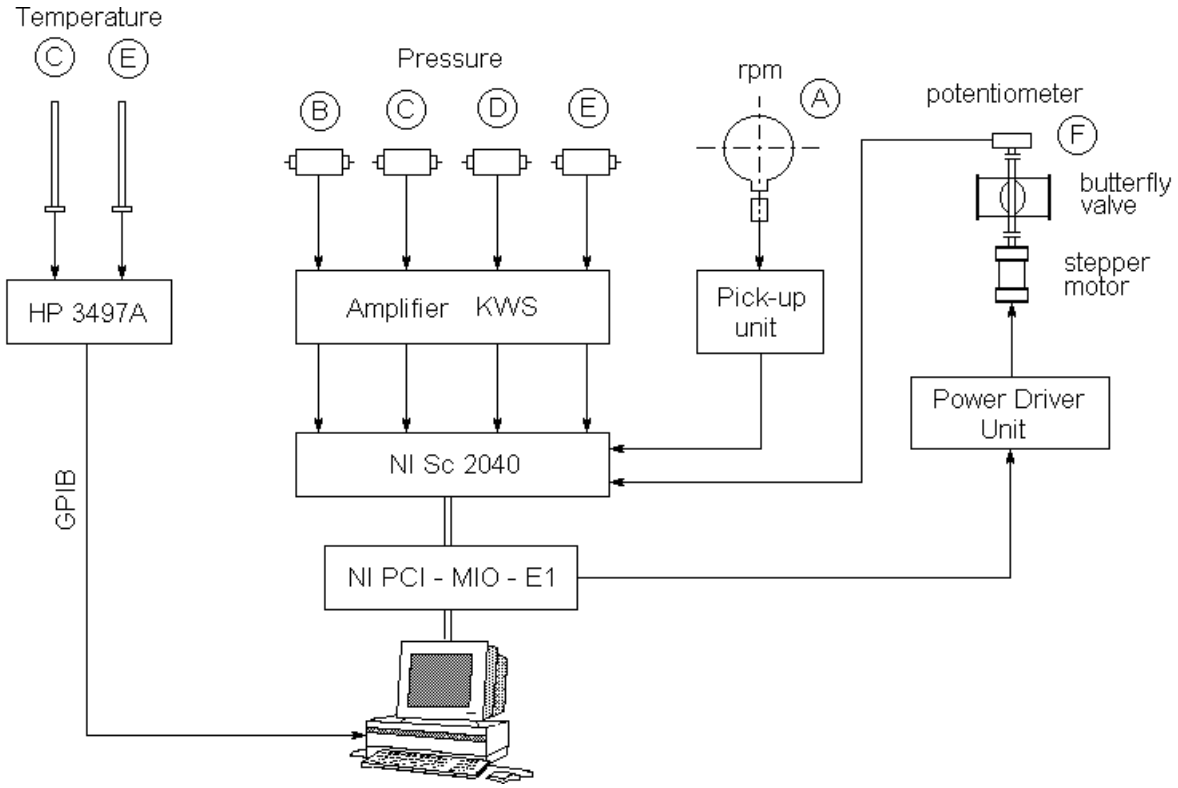


Fig. 11 - Schematic of the instrumentation system.

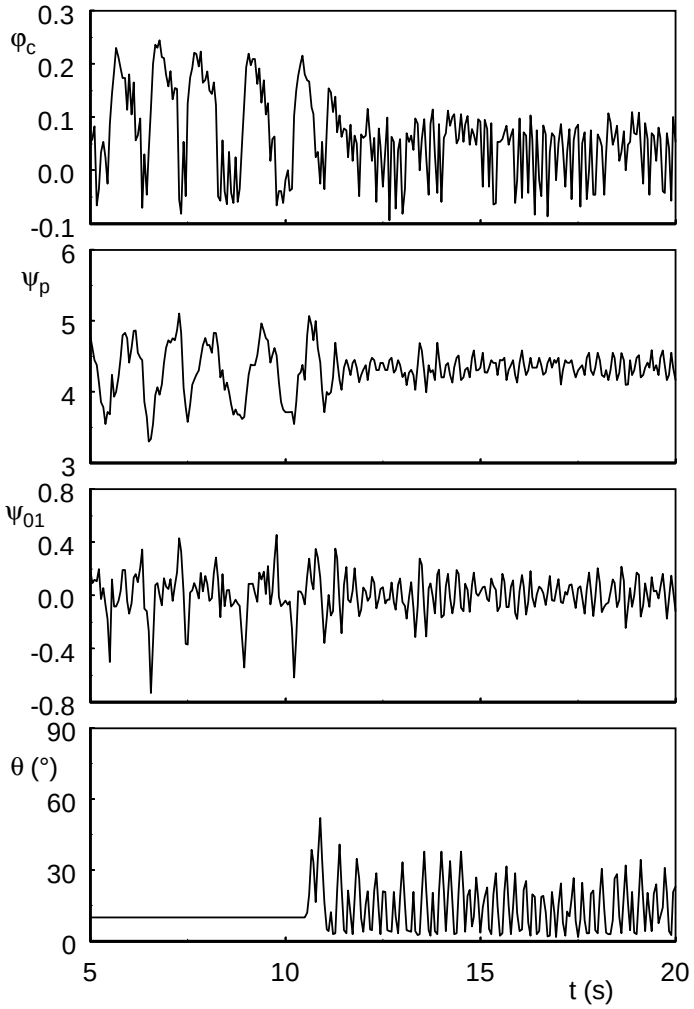


Fig. 12 - Preliminary experimental results at n=2000 *rpm*, φ_s=0.03 (θ_s=10°) and K_p=-50

CONCLUSIONS

The dynamic behaviour of an industrial compression system, provided with a proper control device for the active suppression of surge, has been investigated. The sensor/actuator pair has been selected on the basis of a linear stability analysis and technical considerations from previous works (Simon et al., 1993, Giannattasio, 1999) and results in a sensor of differential pressure between plenum and compressor outlet and a throttle/actuation valve at the plenum exit. A non-linear model of the controlled system has been developed which considers the general case of a proportional-derivative control law. The results of the numerical simulation allow the following conclusions to be drawn:

- A non-linear model must be used for a correct prediction of system dynamics and control effectiveness, at least in the case of compressors which exhibit abrupt stall. In fact, the finite amplitude perturbations introduced into the system when the stall limit is crossed strongly affect the system stability and cannot be predicted by a linear approach.
- The selected control device is capable of suppressing surge within almost the whole unstable operating range of the compressor, with values of the proportional gain small enough to avoid the actuator reaches its stroke-ends.
- The derivative component of the control law exerts a negligible influence on the system stabilization, while it produces only slight modifications in the transient evolution towards stability.
- The proposed control strategy is effective over a wide range of stability parameter *B*, which implies the possibility of suppressing surge also at the highest compressor speeds and when using plenum volumes also much larger than the present one.

On the basis of the numerical results, a proper control device has been designed and coupled to an industrial-size compression system. An appropriate instrumentation and data acquisition system has been set up and a comprehensive set of measurements has been planned.

Preliminary experimental results seem to confirm the effectiveness of the present control system, as the low-frequency surge oscillations are really suppressed by the device, at least at low compressor speeds and when using moderate gain values. However, an excessive delay in the actuator response is responsible for residual high frequency oscillations which are probably due to the amplification of measurement disturbances. The amplitude of such perturbations increases as the gain is raised, so preventing the compressor system from being stabilized at high compressor speeds. Therefore, further work is required to achieve an effective system stabilization within a wide operating range of the compressor, by improving the software efficiency and the technical features of the instrumentation system.

ACKNOWLEDGMENTS

The present research has been supported by the National Council of Research (*CNR*).

The authors are very grateful to F. Zampis for her contribution to the development of the software for data acquisition and control.

REFERENCES

Arnulfi G.L., Micheli D., Pinamonti P. (1995), "Velocity measurements downstream of the impellers in a multistage centrifugal blower", *ASME Journal of Turbomachinery*, Vol. 117, 4, p. 593.

Arnulfi G.L., Micheli D., Pinamonti P. (1996), "Experimental Investigation on Rotating Stall in a Two-Four Stages Centrifugal Blower with Vaneless Diffusers", ASME paper 96-GT-171.

Arnulfi G.L., Giannattasio P., Giusto C., Massardo A.F., Micheli D., Pinamonti P. (1999a), "Multistage Centrifugal Compressor Surge Analysis; Part I.: Experimental Investigation", *ASME Journal of Turbomachinery*, Vol. 121, 2, p. 305.

Arnulfi G.L., Giannattasio P., Giusto C., Massardo A.F., Micheli D., Pinamonti P. (1999b), "Multistage Centrifugal Compressor Surge Analysis; Part II: Numerical Simulation and Dynamic Control Parameter Evaluation", *ASME Journal of Turbomachinery*, Vol. 121, 2, p. 312.

Arnulfi G.L., Giannattasio P., Micheli D., Pinamonti P. (2000), "An Innovative Device for Passive Control of Surge in Industrial Compression Systems", ASME paper 2000-GT-0352, ASME

TurboExpo 2000, May 8-11, Munich, Germany (proposed for publication in *ASME Transactions*).

Epstein A.H., Ffowcs Williams J.E., Greitzer E.M. (1989), “Active Suppression of Compressor Instabilities”, *Journal of Propulsion and Power*, Vol. 5, p.204.

Ffowcs Williams J.E., Huang X. (1989), “Active Stabilization of Compressor Surge”, *Journal of Fluid Mechanics*, Vol. 204, p. 245.

Giannattasio P., Giusto C. (1998), “Modellizzazione e analisi parametrica di un sistema di controllo passivo del pompaggio” [in Italian], Proc. 53° Congresso Nazionale ATI, Florence, Italy, p. 1179.

Giannattasio P. (1999), ”Analisi di stabilità di un sistema di compressione industriale con controllo attivo del pompaggio” [in Italian], Proc. 54° Congresso Nazionale ATI, L’Aquila, Italy, p. 1437.

Greitzer E.M. (1976), “Surge and Rotating Stall in Axial Flow Compressors - Part I: Theoretical Compression System Model”, *ASME Journal of Engineering for Power*, Vol. 98, p. 190.

Pinsley L.E., Guenette G.R., Epstein A.H., Greitzer E.M. (1991), “Active Stabilization of Centrifugal Compressor Surge”, *ASME Journal of Turbomachinery*, Vol. 113, p. 723.

Simon J.S., Valavani L., Epstein A.H., Greitzer E.M. (1993), “Evaluation of Approaches to Active Compressor Surge Stabilization”, *ASME Journal of Turbomachinery*, Vol. 115, p. 57.

This page has been deliberately left blank

Page intentionnellement blanche

Active Stall Avoidance of an Axial Compressor Stage

S. Wagner
D. K. Hennecke
Gas Turbines and Flight Propulsion
Darmstadt University of Technology
Petersenstr. 30, D-64289 Darmstadt
email: wagner@gfa.tu-darmstadt.de
Germany



Figure 1: View of the compressor rotor (in flow direction)

Summary

An active stall avoidance system was designed comprising a stall recovery controller, a nonlinear compressor operating point controller and a scheme for switching between these two.

Different control schemes with respect to stall removal and switching have been developed and implemented on a real-time computer.

The system's capability of successful stabilization of a stalled compressor with respect to performance loss was demonstrated by several experiments conducted on a low-speed axial compressor stage.

The experiments were analyzed in detail and governing parameters of stall recovery and performance are identified.

Finally, improvements for the control scheme are suggested.

1 Introduction

Compressor design is currently restricted by keeping a certain distance to the aerodynamic stability line, the so called surge margin. To benefit future gas turbine developments in terms of safe compressor operation and improvement of the global efficiency systems for active control of compressor stability are recognized to be essential.

Two basic strategies have been proposed for improvement of the compressor stability behaviour [9]. Active control of rotating stall and surge relies on the detection and damping of unstable flow phenomena prior to the onset of rotating stall and surge. 2-d non-axisymmetric actuation is utilized to enhance the compressor operating range [1, 6, 7].

Avoidance control on the other hand prevents crossing of the surge line and thus the onset of rotating stall by operating the compressor with a certain distance from the surge line. Bleed and recycle valves are used to fix the compressor operating point to a predefined control line.

However, until now there is no reliable stall related disturbance prior to the onset of stall present for all compressor applications and speeds. It is the objective of the approach presented in this paper to combine the means of active stall control (stall detection) with the goal of stall avoidance (operating point control) as active stall avoidance.

The control system setup shall be as simple and robust as possible, using inexpensive sensors and 1-d actuation. The ultimate goal of this system is to maintain stable compressor operation with a reduced surge margin while keeping variation of the operating point and thus compressor performance as small as possible in case of upcoming stall.

2 Experimental Setup

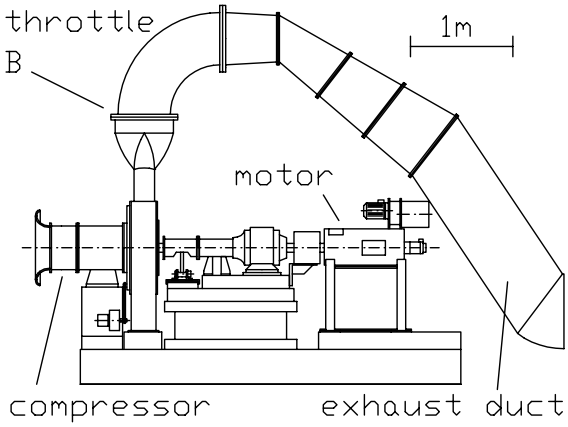


Figure 2: Overview of the test stand

2.1 Compression System

Fig. 2 shows the test stand configuration. The configura-

Paper presented at the RTO AVT Symposium on "Active Control Technology for Enhanced Performance Operational Capabilities of Military Aircraft, Land Vehicles and Sea Vehicles", held in Braunschweig, Germany, 8-11 May 2000, and published in RTO MP-051.

tion is similar to that described in [3]. A cross section of the inlet duct with the test compressor and a downstream throttle can be seen in Fig. 3. Tab. 1 gives an overview of the compressor data. The compressor intakes air from the environment. A diffuser (see Fig. 3) connects the inlet duct with a downstream plenum. The plenum discharges through an exit duct into the environment (see Fig. 2). Fig. 1 gives an impression of the compressor rotor. A dynamic throttle between the plenum and the exit duct is used for adjusting the mass flow in the system identification experiments and as actuator in the control system (see Fig. 2, Pos. B).

Configuration:	axial: Rotor, Stator
No. of Blades:	24, 27
Blade Sections:	NACA 65, DCA
Hub-to-Tip Ratio:	0.5
Tip Diameter:	0.4 *m*
Speed:	3700 *rpm*

Table 1: Compressor data

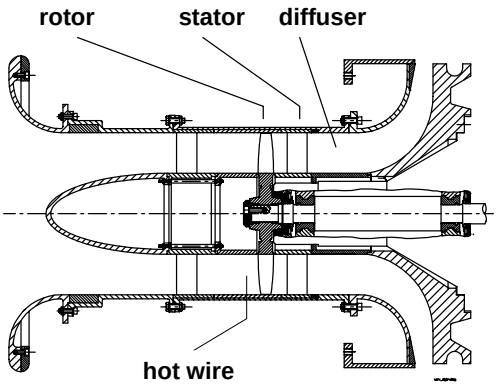


Figure 3: Cross section of the inlet duct with the compressor and the downstream ring-type throttle

2.2 Instrumentation

Fig. 4 gives an overview of the instrumentation applied for the experiments. Wall static pressure measurements were carried out by the means of piezo-resistive sensors. Due to their configuration their maximum response frequency is about 1 *kHz*. Compared to commonly used high-bandwidth pressure sensors they are very robust at a significantly lower price. The capability of these sensors for serving in the control system was compared in [4] to that of high-bandwidth surface mounted sensors.

Fig. 5 gives an overview of the circumferential (1...8) and axial (A...D) probe locations as well as an impression of the blade sections at mid-span.

For the control experiments 7 out of the 8 sensors were used as the mass flow was additionaly measured for reference reasons.

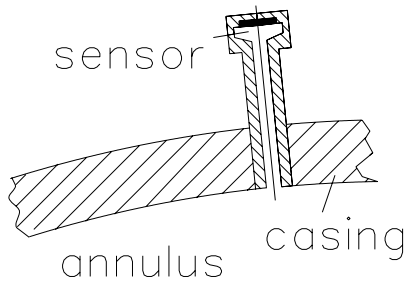


Figure 4: Dynamic pressure probes

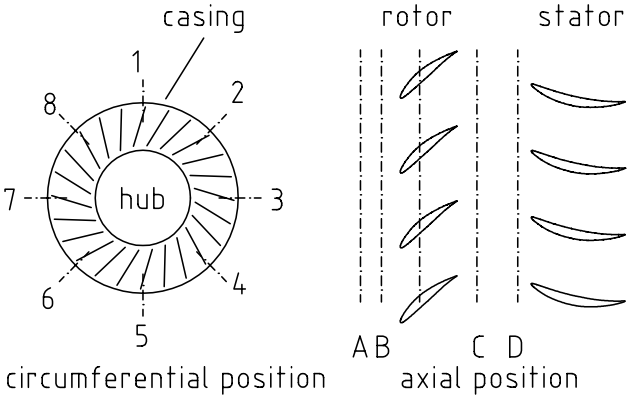


Figure 5: Probe locations and blade sections at mid-span

The mass flow measurements were carried out using hot wire anemometry in front of the rotor (see Fig.3). For details of the mass flow measurement technique see [4].



Figure 6: The dynamic throttle

2.3 Actuator

A dynamic throttle (see Fig. 6) comprising two arrays of lamellas as described in [3] was used as actuator for the control system. For the control experiments the two throttle areas were adjusted separately, i.e. each by its own step motor and control algorithm. The ratio of the throttle areas is 0.3, the maximum angular acceleration is $1.0 \cdot 10^4 \, \mathrm{deg}/sec^2$. The bandwith of the step motors is

3000Hz. The fully open fully closed bandwith of the throttle is 5Hz.

2.4 Real-Time Computer

A standard Digital Signal Processor (DSP) was applied as Real-Time Computer. The algorithms for the data acquisition, the stall detection, the observer, the controller, and for controlling the step motors of the dynamic throttle were implemented on the DSP.

High-level programming tools have proven to generate unefficient computer code that could not be run on the DSP in real-time. Consequently, the algorithms were implemented in the programming language *C* on the hardware level (register programming). This method proved to be simple and efficient in terms of both programming and computation time.

3 Experimental System Identification

The dynamic behaviour of the compression system at stall inception and in the unstable operating regime was extensively examined [4, 3]. Here the main results will be summarized.

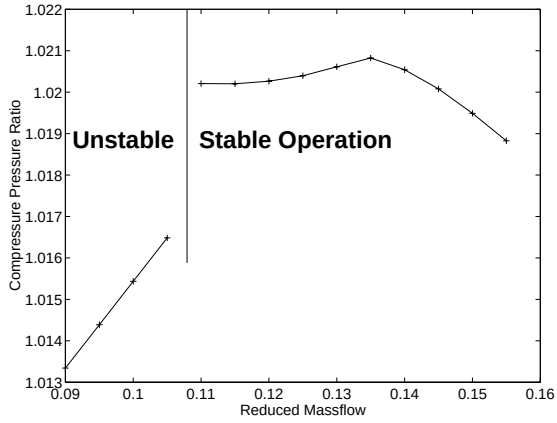


Figure 7: Compressor characteristics

3.1 Stable and Unstable Operating Regime

Fig.7 shows the stationary compressor characteristics for stable and unstable points of operation. Due to the small value for the B-parameter of 0.35 the ultimate mode of unstable operation is rotating stall [4].

3.2 Stall Inception

Stall inception experiments clearly indicated that stall develops at blade tip thus allowing the application of wall static pressure sensors for the stall detection. Furthermore the examined compressor does not exhibit any stall precursors [4].

3.3 Model of the Test Stand

On the basis of the lumped parameter model [2] a mathmatical model of the transient system behaviour in the stable operating regime was developed. Details about the

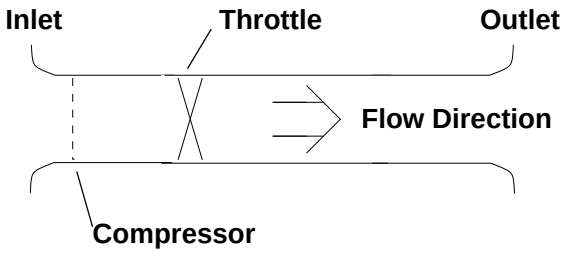


Figure 8: Schematic of the compression model

modelling will become avaiable with the release of [8]. Fig.8 depicts the fluid model used for controller and observer design. The fluid is assumed to be incompressible thus allowing to introduce the mass flow as control variable. The compressor is modelled by its stationary compressor map, neglecting the time lags associated with dynamic compressor response time. It was found that the 1-d mass flow dynamics are governed by the moment of inertia of the gas in the system and the load dynamics rather than the compressor dynamics.

The parameters of the lumped parameter model as well as the load characteristic have been determined by experimental system identification.

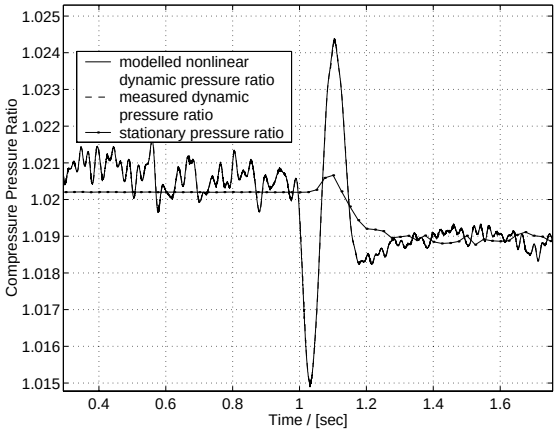


Figure 9: Transient compressor model

In [8] a nonlinear model of the compressor dynamics in the stable operating regime is developed. Although the influence of the compressor dynamics on the mass flow transients can be neglected the dynamic amplitudes of the compressor pressure ratio are of conciderable amount (see Fig.9). This will become important when optimizing the stall controller as discussed later.

4 Control Law Design

Fig. 10 depicts the principle of the designed stall avoidance system. The controller comprises two parts, namely the operating point controller and the stall recovery controller. The operating point controller is in charge of tracking a desired mass flow and thus a desired operating point for stable compressor operation. The stall recovery controller

on the other side has to damp out stall in order to evacuate the compressor from unstable operation. The switching scheme between the two controllers is triggered by compressor stability.

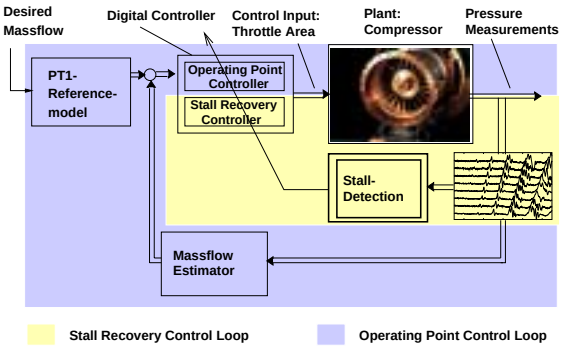


Figure 10: Principle of active stall avoidance system

4.1 Operating Point Controller

The operating point controller is essentially a mass flow controller that uses the current compressor mass flow and the stationary compressor pressure ratio as control variables rather than the dynamic compressor ratio. In order to avoid expensive and non-robust mass flow measurements a nonlinear observer was designed to estimate current compressor mass flow from annulus averaged wall static pressure measurements.

The mass flow estimator utilizes the simple 1-d fluid model of the system to calculate the current mass flow. Details of the observer and controller design will become avaiable with the release of [8].

To simplify the controller design the position of the big throttle was kept fixed during operating point control. Thus Single-Input-Single-Ouput (SISO) control strategies can be applied.

The control problem in the stable operating regime is a tracking problem rather than a stabilizing problem which led to a nonlinear controller design based on autopilots [8, 5]. The so called sliding mode controller is a model-based nonlinear controller, which is robust with respect to model and parameter uncertainties. As compressor performance and plant parameters are subject to change with respect to time this was considered to be an essential feature of the controller.

4.2 Stall Recovery Controller

The stall recovery controller simply opens the dynamic throttle when stall arises. To determine fundamental mechanisms of stall recovery two strategies where examined:

I. : open both throttles

II. : open small throttle

The fundamental difference between the two control strategies is that the impact of throttle position changes and thus the pressure drop versus flow characteristic of the load is much higher when applying strategy I.

4.3 Synthesis of Active Stall Avoidance Controller

Crucial to the success of the active stall avoidance and performance optimization control is the switching scheme between the controllers. Therefore the current stability of the compressor is estimated and utilized as the switching criteria. To obtain this information the amplitudes of the pressure fluctuations caused by stall (further on called stall amplitudes) are determined using digital filter techniques.

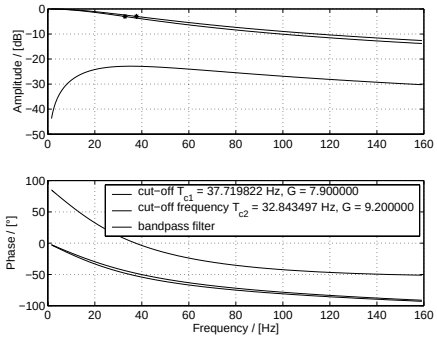


Figure 11: Filter characteristic of stall detection

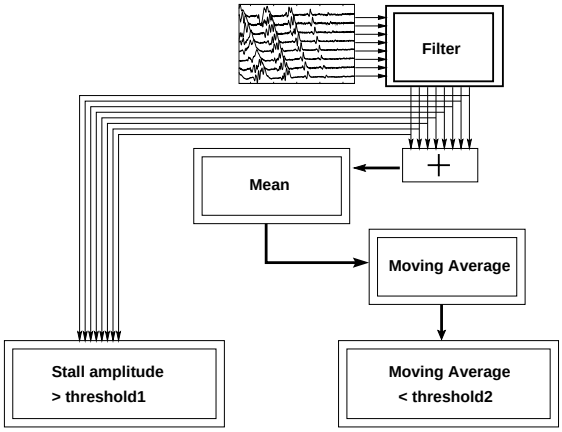


Figure 12: Processing of data for switching algorithmn

The filters are obtained by utilizing a statistical method (stall detection algorithm, see [3]). It comprises two low-pass filters which are combined to amplify stall typical frequencies. The resulting characteristic of the two filters is depicted in Fig. 11. For determination of stability two signals are generated out of the filtered pressure signals. Fig. 12 depicts the preprocessing of the pressure signals to obtain the two necessary stability criteria.

First the stall filter provides the stall amplitude for each sensor individually. Second the moving average of the mean value of all stall amplitudes is calculated. The compressor is assumed to be unstable if the stall amplitude of one sensor exceeds a certain limit (threshold1). Stable compressor operation is assumed to be reestablished for

phase	stall amplitude $>$ threshold1	moving average $<$ threshold2	stable-flag
1	no	yes	yes
2	yes	yes	no
3	yes/no	no	no
1	no	yes	yes

Table 2: Switching logic

decreasing stall amplitudes and for the moving average of the mean stall amplitude of all sensors lower than another limit (threshold2).

An overview of the stability criterium is given in Tab.2. The phases in Tab.2 denote the signal conditions present in different stability stadiums, moving from stable to unstable and back to stable operation again.

4.4 Improvement of Stall Avoidance Controller

One problem involved with the utilization of the stall detection filter for stability determination is the fact that stall typical frequencies are very close to the frequencies generated by control action of the operating point controller (see Fig.15, Sec. 5.1). In order to improve robustness of the stability criterium the signal-to-noise ratio of the stall amplitudes was improved by careful design of the stall filter and by calculating the moving average from the maximum of the current stall amplitudes rather than the mean stall amplitudes.

One disadvantage encountered with the previous switching logic is that the criterium for stable compressor operation is not independent from the stall detection threshold. This leads to performance loss as the throttles are completely opened by the stall recovery controller. To circumvent this the gradient of the moving average was introduced as additional stability criterium. This results in the following control logic:

- unstable operation: stall amplitude $>$ threshold1a, gradient moving average $>$ threshold1b
- stable operation: moving average $<$ threshold2a, gradient moving average $<$ threshold2b

Due to this modification it was possible to examine control schemes were the switching to the operating point controller was carried out in an early state of flow stabilization and thus optimization of the control scheme with respect to performance becomes feasible.

5 Closed-Loop Experiments

To evaluate the concept of active stall avoidance closed loop experiments were carried out on a low-speed axial compressor stage. To force the compressor into stall the dynamic throttles were closed until stall occured. In this phase both controllers were switched offline. The time axis in the subsequent plots was rearranged with respect to the first detection of rotating stall.

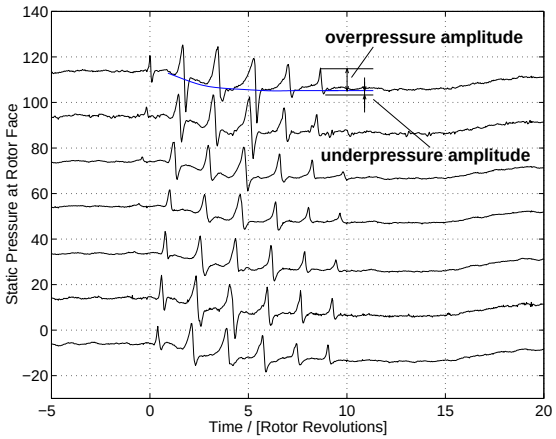


Figure 13: Strategy I: static pressures at rotor face

5.1 Stall Recovery: Strategy I

Fig. 13 depicts the static pressures at rotor face when using both throttles to recover stable compressor operation. It can be seen that stable compressor operation establishes within 10 rotor revolutions. The mass flow transient is shown in Fig. 14. As a reference the mass flow was measured using a hot wire in front of the rotor. The estimated and the measured mass flow are in good agreement for stable compressor operation. During stall the velocity field in front of the rotor is influenced by the passing stall cells. So the mean value of the hot wire measurements represents the compressor mass flow.

The same is true for the estimated mass flow as the fluid model is not valid for the stall inception period. The stall amplitudes of all the sensors and the stability criterium is depicted in Fig. 15. Due to robust design of the stall filter the increase in stall amplitude after 15 rotor revolutions is because of controller action rather than stall (compare Fig. 13).

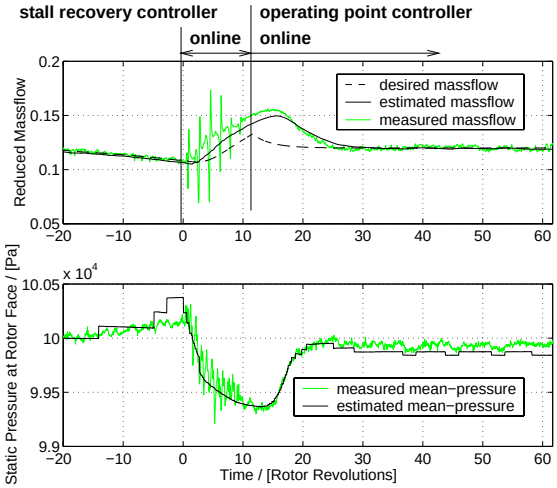


Figure 14: Strategy I: mass flow and mean static pressure

5.2 Stall Recovery: Strategy II

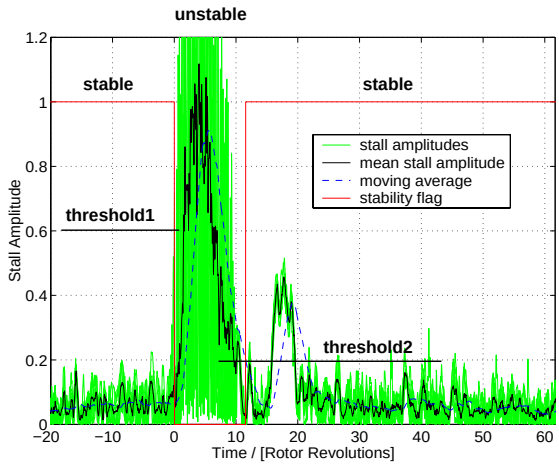


Figure 15: Strategy I: stall amplitudes and stability flag

When applying strategy II the pressure fluctuations caused by the onset of stall reside over a much longer period of 24 rotor revolutions (Fig. 16, 18). The increase in mass flow during stall recovery is smaller when using strategy II (Fig. 17).

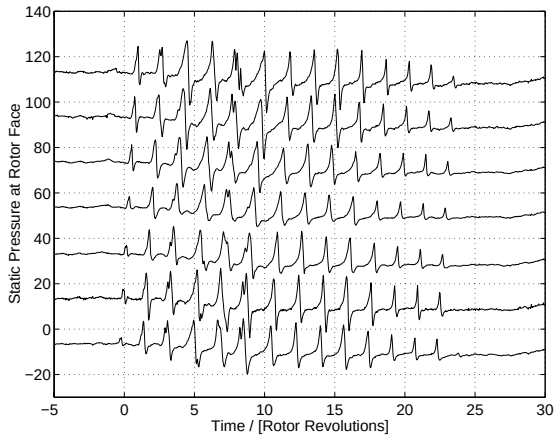


Figure 16: Strategy II: static pressures at rotor face

5.3 Stall Recovery: Improved Controller

Fig. 19 depicts the principle of the stability criterium when using the improved scheme. For comparison of the strategies experiments with different values for threshold2b were carried out. There exists a limit for threshold2a were strategy II does not stabilize the compressor. The system exhibts limit cycles and stable flow can not be reestablished. (see Fig. 22, 24, 23). For strategy I the compressor can be unstalled even if threshold2a is increased to the top of the moving average amplitude (see Fig. 19, 21, 20).

6 Analysis

To analyse the experiments the estimated mass flow transients and pressure fluctuations are studied in detail. During the onset of stall the overpressure amplitudes are significantly higher than the underpressure amplitudes (see

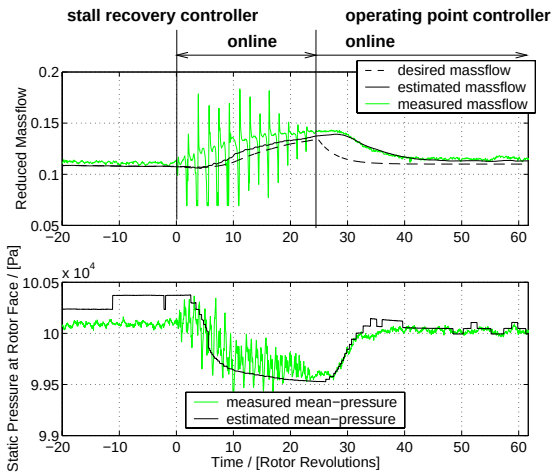


Figure 17: Strategy II: mass flow and mean static pressure

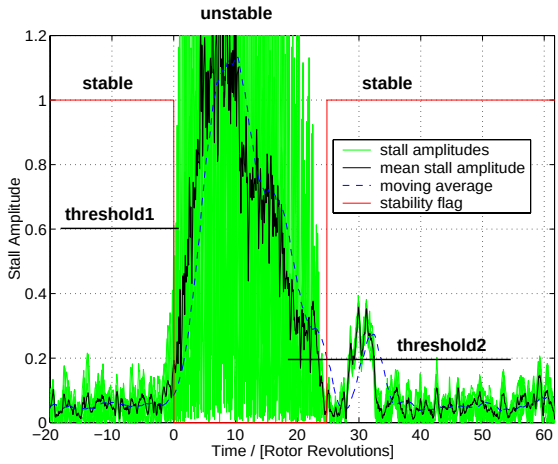


Figure 18: Strategy II: stall amplitudes and stability flag

Fig. 13). Consequently, the annulus averaged static wall pressure calculated from these signals is higher than the real value. This in turn leads to an underestimation of compressor mass flow as the mass flow is estimated from the mean static pressure of all sensors. However, comparison of the estimated and measured mass flow transient during the onset of stall show that they are in a good qualitative agreement (Fig. 14,17). Consequently, the estimated mass flow and mean static pressure are used to analyse and compare the different strategies.

When applying strategy I the compressor is unstalled in half the time compared to strategy II (Fig. 14,17) at the cost of greater variation of the operating point. This is mostly evident from the fact that a hysteresis in mass flow exists between the onset of stall and restabilization of the flow [3],[2]. When using strategy I the compressor load is decreased much quicker compared to strategy II and thus recovery mass flow is reached sooner. These observations are confirmed by the experiments with the improved controller.

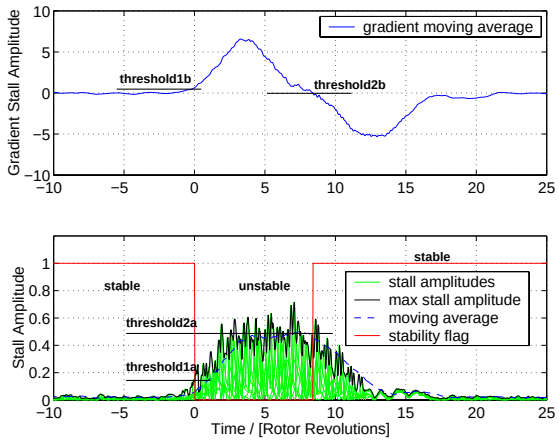


Figure 19: Improved strategy I: stall amplitudes and stability flag

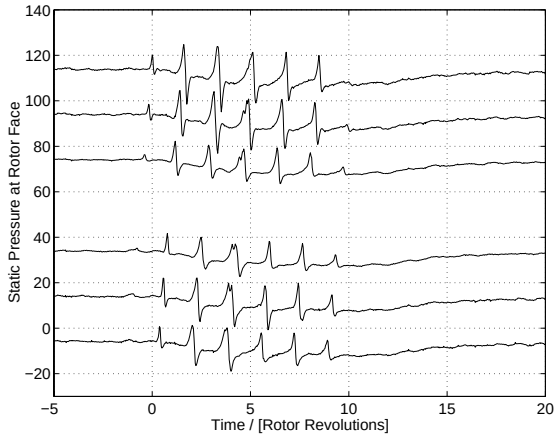


Figure 20: Improved strategy I: static pressures at rotor face

Although stall amplitudes are decaying the compressor can not be unstalled by the strategy II / threshold2a=0.3- configuration (see Fig. 25, 26). Apparently, the stall recovery mass flow is not reached for this configuration while for the others stable compressor operation can be maintained. As a result stable compressor operation can only be regained if the swichting to the operating point controller and thus the increase of compressor load is done after exceeding the recovery mass flow.

Futher analysis of the controller schemes for different values of threshold2a (Fig. 25, 26) yield, that operating point variation is less when using strategy I at the cost of a longer and stronger ”stalling” period. By increasing the threshold2a the variation of mass flow can be slightly decreased (Fig. 25). Also the mean amplitudes of the pressure fluctuations are lower if the stall recovery controller is interrupted in an earlier state (see Fig. 26).

7 Summary and Conclusions

The successful combination of stall recovery and operating

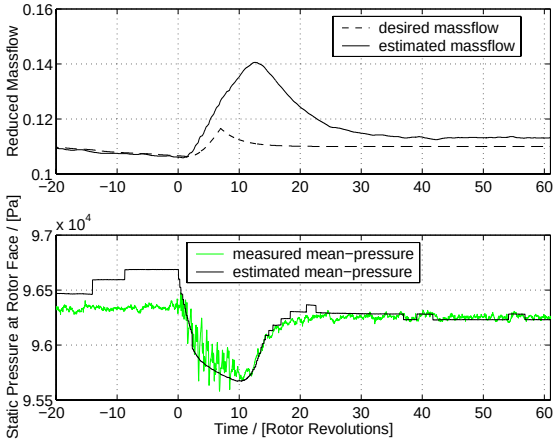


Figure 21: Improved strategy I: mass flow and mean static pressure

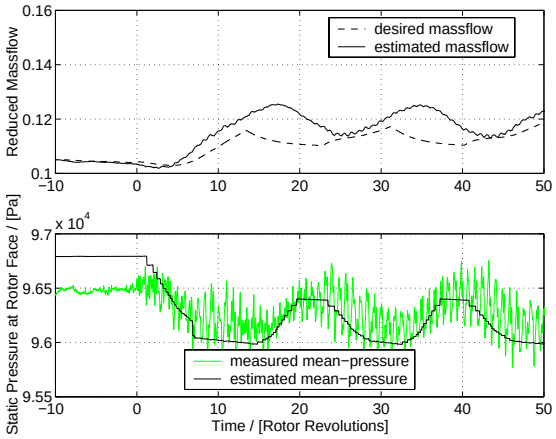


Figure 22: Improved strategy II: mass flow and mean static pressure

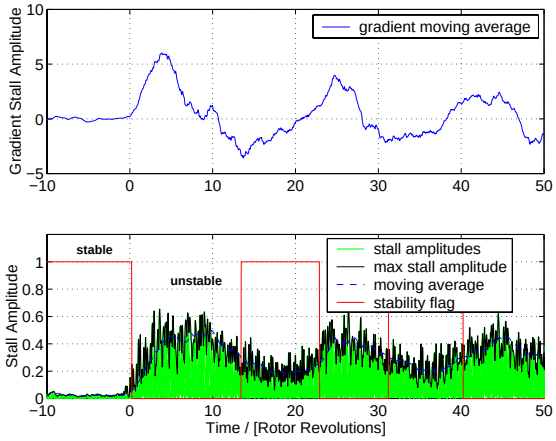


Figure 23: Improved strategy II: stall amplitudes and stability flag

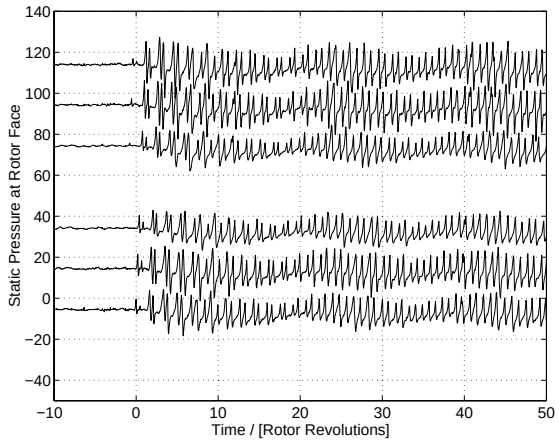


Figure 24: Improved strategy II: static pressures at rotor face

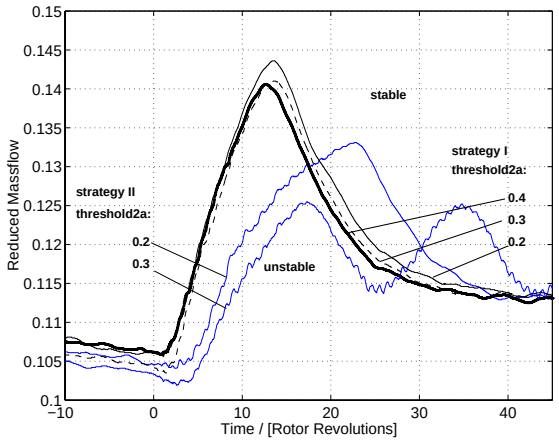


Figure 25: Comparison of mass flow transients for different strategies

point control to stabilize a low-speed axial compressor has been demonstrated. Experiments with two different stall recovery strategies yield that a tradeoff has to be made between fast stall recovery (short stalling period) and loss of current operating point.

A robust stability criterium has been introduced allowing optimization of the controller scheme with respect to performance and robustness. Analysis of the experiments with the improved control scheme indicate, that the hysteresis in mass flow is the governing value for regaining compressor stability after the onset of stall.

Furthermore the estimation scheme designed for stable compressor operation yields reasonable results for the compressor mass flow transient during the onset of stall.

Based on these results the estimated stall recovery massflow should be introduced as additional stability parameter.

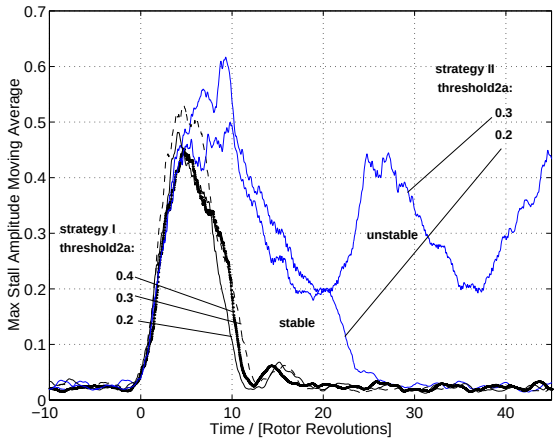


Figure 26: Comparison of stall amplitudes transients for different strategies

8 Outlook

The dynamic compression system model will be extended for compressor operation during stall inception to allow better estimation of current compressor performance. This will become important when optimizing the control scheme with respect to performance.

The influence of the stall detection scheme and the controller strategy on stall recovery mass flow and thus performance loss of the compressor during stall recovery will be examined further.

Experiments with inlet distortion will be carried out to assess the control systems robustness.

Another promising approach will be control systems based on estimation of the surge line where information of stall precursors will be used whenever available. In this context a dynamic compressor model for the stable operating regime will be of great value. The development of such a control system will be addressed in future work.

References

[1] K. M. Eveker, D. L. Gysling, C. N. Nett, and O. P. Sharma. Integrated Control of Rotating Stall and Surge in High-Speed Multistage Compression Systems. *ASME Journal of Turbomachinery*, 120:440–445, 1998.

[2] E.M. Greitzer. Surge and Rotating Stall in Axial Flow Compressors, Part I: Theoretical Compression System Model. *Journal of Engineering for Power*, 98:190–198, 1976.

[3] R. Schulze and D.K. Hennecke. Design of an Active Stall Avoidance System for a Subsonic Compressor. In *Proceedings of the RTO/AVT Symposium on Design Principles and Methods for Aircraft Gas Turbine Engines, Toulouse*, 1998, RTO-MP-8.

[4] R. Schulze, D.K. Hennecke, Th. Le, and M. Glesner. Experimental Examination of an Axial Compressor as a Basis for an Active Stall Avoidance System. In *Proceedings of the 1998 ISROMAC-7 Symposium, Vol. C, page 1265*, 1998, and *Int. J. Rotating Machinery*, 4:1-11, 1998.

[5] J. E. Slotine and W. Li. *Applied Nonlinear Control*. Prentice Hall, Englewood Cliffs, New Jersey, USA, 1991.

[6] Z. S. Spakovszky, H. J. Weigl, J. D. Paduano, C. M. van Schalkwyk, K. L. Suder, and M. M. Bright. Rotating Stall Control in a High-Speed Stage With Inlet Distortion: Part I - Radial Distortion. *Journal of Turbomachinery*, 121:510–516, 1999.

[7] Z. S. Spakovszky, H. J. Weigl, J. D. Paduano, C. M. van Schalkwyk, K. L. Suder, and M. M. Bright. Rotating Stall Control in a High-Speed Stage With Inlet Distortion: Part II - Circumferential Distortion. *Journal of Turbomachinery*, 121:517–524, 1999.

[8] S. Wagner and D.K. Hennecke. Observer Based Nonlinear Control of Compressor Operation. In *ASME 7th Mechatronics Forum International Conference, Atlanta*, 2000.

[9] F. Willems and B. de Jager. Modeling and Control of Compressor Flow Instabilities. *IEEE Control Systems Magazine*, 1999.

This page has been deliberately left blank

Page intentionnellement blanche

Optimization of a Turbine Blade Performance Due to Active Control of the Vortex Dynamics

N.Yurchenko[1], R. Rivir[2]

[1] Institute of Hydromechanics, National Academy of Sciences, Kiev, Ukraine
[2] Propulsion Directorate, AFRL/PRTT, Wright-Patterson AFB, Dayton, OH, USA

Abstract

Geometry and thermal stratification of the flow around a turbine blade specify this flow as one affected by buoyancy and centrifugal forces. An approach is proposed and tested of a boundary-layer control under body forces using generation of counter-rotating streamwise vortices that are an inherent vortical structure of such flows. The active mode of vortex generation is realized due to an imposed surface temperature gradient periodic in the spanwise direction, which must be correlated with basic flow parameters. Values of two independent variables, temperature gradient and spanwise scale of induced vortices, can be adjusted to current flow conditions thus changing the vortex dynamics in a favorable way.
Velocity fields and spectrum redistribution in boundary layers with embedded streamwise vortices show efficiency and prospects of the proposed method to control flow characteristics.

1. Introduction

Flows of practical interest for engineering applications are the flows under body forces which can account for a complex geometry of a body, flow-body temperature difference, gravitational or electromagnetic fields for some types of fluids. It means that to be efficient, the boundary-layer control techniques must be

- correlated with specific features of the vortex dynamics of such flows;
- flexible or active i.e. allowing to adjust control parameters to changing flow conditions or to any other requirements of a unit operation;
- simple and reliable in design, operation and long-term exploitation;
- based on the advanced fundamental science involved to solve formulated problems and to use practical experience including successful results obtained due to numerous trial-and-error methods.

Recognized common features of vortex dynamics distinguish a group of flows, which can be studied under rigorous formulation of the problem [1, 2, 3]. These are flows of viscous fluid affected by body forces (e.g. centrifugal forces or buoyancy). Balanced interaction between body forces (because of the surface curvature or its temperature different from one of the fluid) and viscous forces (because of the wall presence) gives rise to the development of streamwise vortices in boundary layers. Being an essential item for fundamental analysis of boundary-layer problems related to the laminar-turbulent transition and turbulence production, this flow structure is of interest for applied studies related to the fluid transport control.
One of such typical and important applications deals with the improvement of low-pressure turbine blade performance, which is strongly influenced by unsteady flow separation and transition. It is connected with the specific conditions of a gas turbine engine operation from take-off to high altitude cruise causing significant variations of Reynolds number. Since the flow around a turbine blade is a turbulent flow affected by centrifugal forces and buoyancy, it can be investigated and controlled in the frame of known general formulations.

In this connection, extensive studies of a boundary-layer flow over a concave surface were carried out on a basis of the classical Goertler stability theory [4, 5] and receptivity approach [6, 7]. They provided an insight into

Paper presented at the RTO AVT Symposium on "Active Control Technology for Enhanced Performance Operational Capabilities of Military Aircraft, Land Vehicles and Sea Vehicles", held in Braunschweig, Germany, 8-11 May 2000, and published in RTO MP-051.

mechanisms of the vortical structure evolution and behavior on condition of natural (unforced) emergence and development of streamwise vortices as well as of their generation with a given scale. Matched experimental and numerical investigations [8, 9] showed vortex scale transformation occurring downstream and across boundary layer that should be taken into account in applications of the obtained fundamental results.

The objective of the present work is to show that regular streamwise vortices are an effective control structure to maintain preferable scales and amplitudes of fluid motion in a boundary layer under body forces what can be applied for optimization of turbine blade performance.

From a viewpoint of basic studies, it means special organization of the surface-flow interaction aimed, e.g. to delay early flow separation. From a viewpoint of technological applicability, it means the development of a reliable, convenient and flexible way of flow management with minimum energy outlay. Practically, the work consists of the following interconnected parts,
(1) analysis of a flow around a turbine blade;
(2) establishment of typical features and scales of vortical motion for a set of basic flow parameters of interest;
(3) controllable stimulation of the vortical motion of a similar type but of different scale and intensity depending on parameters and objectives of a formulated task.

2. Analysis of a flow around a low-pressure turbine blade

A key point of the present investigations is generation of streamwise vortices with given parameters in a flow where this type of motion is inherent, i.e. in boundary layers affected by body forces. The present formulation of the problem originated from a practical need to improve flow conditions around a low-pressure turbine blade. First of all, it deals with the development of a simple and reliable method to control flow separation on a suction side of the blade. Figure 1 illustrates the configuration of the flow field around a low-pressure turbine blade showing a position of a separation bubble on its surface [10].

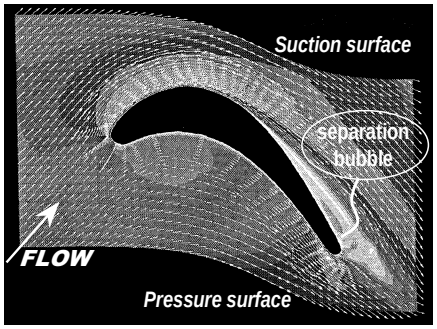


Figure 1. Velocity field pattern around a low-pressure turbine blade; 1/2 cascade passage

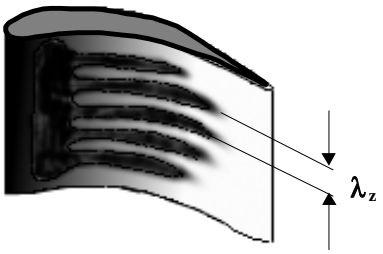


Figure 2. Visualized streamwise vortical structure on a pressure side of a low-pressure turbine blade

To estimate space-scales of a vortical motion in a boundary layer over the turbine blade that can be taken as a reference value for the flow control purposes, one can assume it to be of the order of regular vortices found due to liquid crystal visualization on its pressure side. Figure 2 gives an idea about this naturally self-organized streamwise vortical structure arising at Re_C =67,500 with a scale λ_z=8 mm (Re_C is a cord-based Reynolds number). Analysis of the boundary-layer vortex dynamics in the frame of Goertler stability theory explained physical mechanisms of the vortical structure formation [7] and enabled the formulation of present studies.
In particular, non-dimensional wavelengths of the experimentally observed 8-mm scale vortices were estimated according to the well-known centrifugal stability diagram. They were found to be $\Lambda=\lambda_z^{3/2}Re_C/cR^{1/2}$=24-36, for typical values of Re_C=67,500 and 100,000. The Λ values appeared to be close to "neutral", $\Lambda\approx$39, scales, i.e. those having zero amplification rates for a wide range of Goertler numbers, $G=U_0\delta_2^{3/2}\nu^{-1}R^{-1/2}$. It means that the streamwise vortical structure naturally arising in the boundary layer of a low-pressure turbine blade trends neither to grow, nor to decay in a downstream direction. However turbulent environment (or in general, not ideal flow conditions like considered in the stability theory) does not help to maintain this structure far downstream and thus to provide a necessary thermodynamic balance in a boundary layer preventing its separation.

Therefore efficient flow control techniques in such situations are those bringing minimal amount of energy to save the natural deterministic flow structure as long as possible. This mechanism of the flow control can be understood and applied in the frame of the receptivity problem. In the case under

consideration, it means the investigation of a boundary layer response to generated streamwise vortices, which are an inherent element of the flow affected by centrifugal forces. In general case, vortex dynamics of the flow around a turbine blade can be considered as a prototype problem to study the vortical structure evolution in boundary layers under centrifugal forces and possibilities to effectively manipulate this structure.

3. Investigation approach and methods

To reveal physical mechanisms of the studied phenomena, the Goertler stability theory [4, 9] was assumed as a basis. The stability diagram was used as a reference for the scale choice of induced vortices, which covered a range from neutral ones to those most amplified according to the theory.

Experiments were carried out over a bottom of a water channel (10 x 25 x 300 cm test section) containing a changeable concave part with a curvature radius, R = 1.0, 4.0 or 12 m [6]. Values of a length-based Reynolds number and of a Goertler number based on a momentum thickness were maintained correspondingly in a range of Re_x=(0.6-1.0)x10^5 and G_θ≈0.3-10.0.
A flow field was visualized using electro-chemical Tellurium method similar to the well-known smoke-wire visualization technique in air. It gave very informative for these studies wavy $U(z)$ velocity distributions [9] similar to those shown in Figure 3. In addition, hot-wire measurements were carried out (using one-component probes of a DISA system) at U_0=0.1, 0.2 and 0.6 m/s that enabled to get spectral characteristics of the boundary layer. These flow conditions corresponded to subsequent stages of the natural laminar-turbulent transition manifested in a form of propagating Tollmien-Schlichting waves, formation of streamwise vortices and their breakdown to turbulence. Hot-wire probes were placed at y=4mm from a test surface and at Δx=5 cm downstream of the vortex-generator array, i.e. in a region of the most intense interaction of natural and generated disturbances. Both normal velocity profiles and spectral characteristics were measured at three spanwise positions along λ_g (as shown in Figure 3) corresponding to downwash (z= 0) and upwash (z=λ_g/2) interfaces between neighboring vortices and between these two positions (z=λ_g/4).

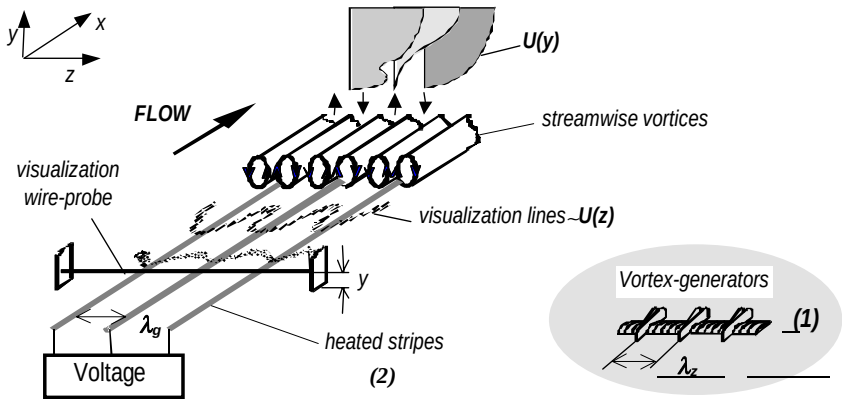


Figure 3. Sketch of the experiment

Streamwise vortices were induced using mechanical vortex-generators (1) having been mounted on the surface regularly in z-direction at a λ_g distance from each other. Besides, electrically heated flush-mounted stripes oriented downstream and separated from each other by thermally insulated stripes were proposed as an engineering solution to initiate and maintain necessary flow structure. It meant a boundary condition given in a form of a changeable z-periodic temperature gradient, ΔT (z). Compared to known techniques to influence the near-wall region (e.g. like riblets), such a solution enables to keep the surface smooth that is undoubtedly beneficial from operational and technological viewpoints. In addition, an active regime of the vortex dynamics control can be realized imposing different configurations of surface temperature fields strictly correlated with the basic flow parameters. Primarily, it relates to the spanwise scale of induced vortices, λ_z, (temperature pattern over the surface) and to control ΔT values (local T temperature of the heated stripes), both characteristics depending on operation requirements.

4. Spectral response of boundary layers to generated vortical structures

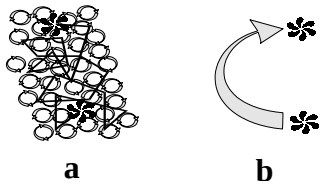


Figure 4. Patterns of fluid transport in (a) homogeneous vortical fields and (b) those containing large-scale vortices

Specific features of flow fields with available large-scale vortices are caused by their longer lifetimes compared to the smaller scale motion as illustrated in Figure 4 [11]. It shows that once trapped by a large-scale vortex, a fluid particle is transported to significant distances without a noticeable change of direction. Such prevailing mode of motion defines specific mechanisms of momentum, heat and mass transfer as well as specific ways of their description.

In spectral terms, a role of large-scale vortices in fluid transport near a wall is recognized due to their basic contribution to the long-wave "energy-carrying" part of the turbulent kinetic energy spectrum. Deterministic investigations of a streamwise vortical system supplemented with the general studies of energy redistribution between a long-wave and inertial intervals of turbulent fluctuations can bring deeper insight into the phenomena mechanisms and formulation of basic principles of flow control.

Figure 5 shows a typical spectrum of turbulent fluctuations.
Short-wave part of the spectrum corresponds to dissipation scales of fluid motion characterized by comparatively low kinetic energy, which transforms into heat due to available viscosity. The long-wave part of the spectrum contains a main part of turbulent energy and dominates in the course and type of transport processes. Therefore large and medium-scale vortices contributing to the energetic and inertial intervals of the spectrum are most important for fundamental studies dealt with practical applications.

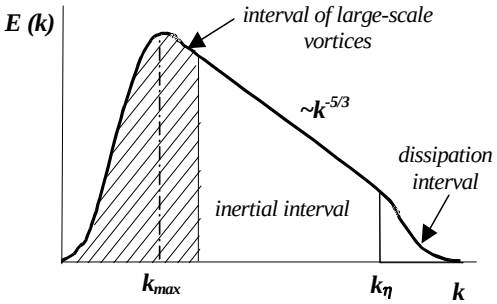


Figure 5. Spectrum of turbulent fluctuations
(η - Kolmogoroff's lengthscale)

Thus, the analysis of spectral properties of a near-wall flow with embedded large-scale vortices both in laminar and turbulent environment can show important aspects of the vortical structure evolution under natural and controlled conditions. In its turn, better understanding of the vortex dynamics must bring to optimal ways/techniques to interfere the process so that to sustain a favorable structure for a formulated flow control problem.

Large-scale streamwise vortices were generated in transitional and turbulent boundary layer using a vortex-generator array mounted on a surface normally to the free-stream velocity vector (see Figure 3).

First, fluctuating streamwise velocities were measured in naturally developing transitional and turbulent boundary layers, i.e. without vortex generation. Standard procedure using fast Fourier transform was applied to recorded hot-wire signals to get the results depicted in Figure 6. Reference spectral curves are shown here both for transitional and turbulent boundary layers. The turbulent reference curve 4 obtained closer to the wall displays more uniform, smoothed spectral pattern than the curve 3 due to statistically dominating smaller scale vortices. Analysis of the transitional case (curve 2) brings to a conclusion that streamwise vortices naturally developing during laminar-turbulent transition result in a specific energy distribution along the spectrum characterized by a strongly pronounced long-wave interval with an amplitude peak around $k \approx 0.5$.

Table 1: Vortex-generation and flow parameters (curve 1)

λ_z, cm	U_0, m/s	y_{vg}/δ_1	y/δ_1	y/δ
1.2	56.0	1.22	0.615	0.091

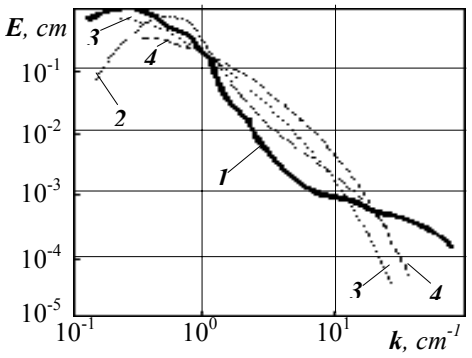


Figure 6. Power density spectra of u'-velocity fluctuations in boundary layers:
1 – in case of generated streamwise vortices;
2 – reference curve for natural laminar-turbulent transition, Re~10^5, y/δ_1=1.08;
3-4 – reference curves for turbulent boundary layers, Re~10^6, y/δ=0.21 (3), y/δ=0.063 (4)

At the same time, the large-scale motion significantly suppresses intensity of fluctuations in the inertial interval ($0.5<k<20$) but increases dissipation (spectral components of $k>10$).

A legend for experimental conditions of vortex generation is given in Table 1. Here y is a distance of a hot-wire probe over a surface, y_{vg} is a normal size of vortex-generators, δ_1 is a boundary-layer displacement thickness, δ is a boundary-layer thickness.
The obtained results (curve 1) explicitly show that even in case of fully developed turbulent flow, generated streamwise vortices change the boundary-layer characteristics redistributing spectrum in favor of its long-wave part, i.e. approaching the transitional spectral pattern. To some extent, it can be considered as flow relaminarization with appeared deterministic vortical elements. Practically, it shows a way to change transport properties near a wall both in transitional, and in turbulent boundary layers.

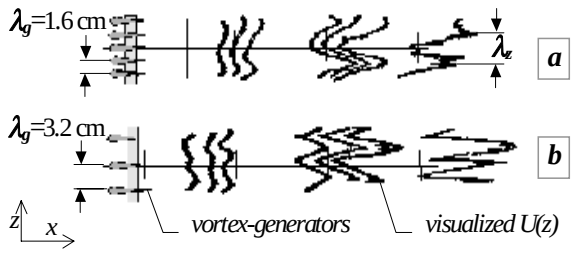


Figure 7. Boundary-layer flow response to twice differing scales of generated streamwise vortices

Spanwise velocity profiles (as a sensitive indicator of embedded streamwise vortices [3, 9]) were registered for the same flow and control (vortex-generation) conditions. They clearly demonstrated different receptivity of boundary layers to the scale of generated vortices. For instance, if a process of natural transition to turbulence was at the stage of self-formation of streamwise vortices, controlled excitation of smaller scale vortices could be seen as superposition of two $U(z)$ waves (Figure 7,a): generated small-scale λ_g and naturally developing large-scale λ_z vortices. In spectral terms, it meant energy redistribution into a more uniform spectrum (without a sag in the inertial interval). It can be interpreted as an effect of turbulization since the spectrum shows a good agreement with the turbulent reference curve 4 obtained in the vicinity of the wall. The lower pattern of Figure 7 demonstrates adequate reaction of the boundary layer to introduced vortices. It corresponded to a spectrum similar to one shown in Figure 6, case 1, i.e. it evidenced available streamwise vortices.

Thus, depending on a match of generated vortex scale and basic flow parameters, one can expect to obtain either large-scale deterministic vortical structure typical for laminar-turbulent transition (here, flow "relaminarization") or dissipative small-scale vortices (flow "turbulization").

5. Thermal excitation of streamwise vortices

Flow fields taking place in practice around operating units like turbine blades are far from the idealized numerical or laboratory conditions where types and values of disturbances introduced in a boundary layer are strictly defined and dozed. To approach the applicability of the analyzed flow control method based on excitation of the organized vortical structure, it was tested using another way of vortex-generation (Figure 3 (2). Besides, to model effects of random uncontrolled factors, heated longitudinal stripes were flush-mounted in a thermally insulated plate that provided, on the one hand, necessary temperature gradient $\Delta T(z)$, and on the other hand, influenced the boundary layer through the surface compliance.
Such surface properties are known to damp any near-wall disturbances. Therefore it must be very demonstrative to see a combined effect of a generally mild $\Delta T(z)$ influence and that of the compliant surface. Three values of temperature T were used in the experiments corresponding to electric power applied, P_1=0 (no influence), P_2 =7.8 W and P_3=12.2 W. The $\Delta T(z)$ control effect was registered at two distances from the wall, y=2 and 3 mm. shown accordingly in left and right pattern sets of Figure 8. As it was mentioned above, flow-field visualization in xz-plane yielded sensitive and convenient $U(z)$ characteristics to estimate a boundary layer response to certain excitation and, subsequently, to choose the control parameters.
(**a**) The first $U(z)$ patterns of both sets, reference velocity profiles, show varying in time $U(z)$ shape that is an evidence of a started meandering motion of a streamwise vortex system or their strongly unsteady behavior.
(**b**) The available z-periodic mechanical properties of the surface (due to rigid longitudinal stripes implanted in the compliant basement) stabilize $U(z)$ velocity distributions at different distances from the surface hampering the naturally developing meandering motion in the boundary layer; however the $U(z)$ amplitude stays large enough characterizing a significant rate of transition to turbulence. Besides, the spanwise periodicity of visco-elastic properties of the wall appears to be not a strong boundary condition to introduce a given smaller-scale, λ_g=1.2 cm, vortical structure in a boundary layer.

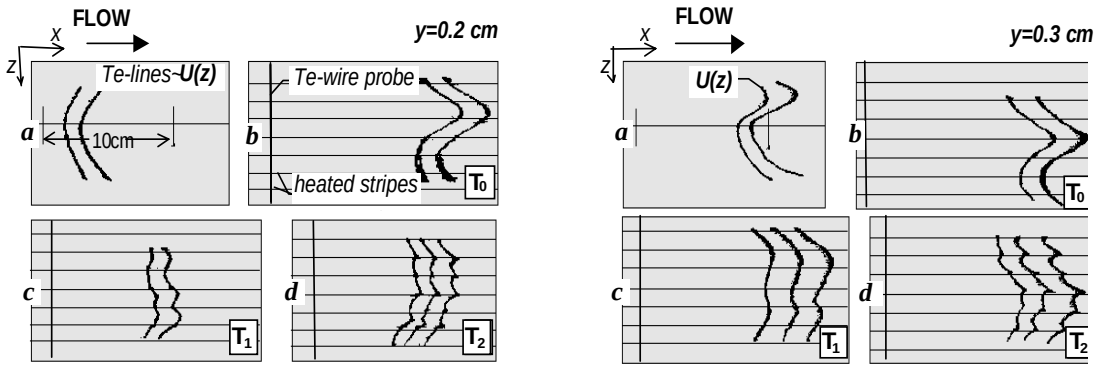


Figure 8. Visualization of a boundary layer over a concave surface controlled by the heated stripes, Re~10^5, G_ϑ=2 (U_0 =5 cm/s, x=2.18 m; R=12 m); y=2 mm (left set); y=3 mm (right set); ***a***: natural development of transition; **b**-**d**: excitation of longitudinal vortices, λ_g=1.2cm: ***b*** – unheated stripes, $T = T_0$ =20°C; ***c***, ***d*** - heated stripes: $T_2 > T_1 > T_0$

(**c**) Moderate heating (corresponding to the value of electric power P_1=7.8 W) straightens $U(z)$ velocity profiles; it can be interpreted so that the transition rate decreases here compared to the undisturbed case. However visualized flow patterns show yet almost twice larger spanwise scale of the developing vortical structure than one induced by the heated stripes, i.e. λ_z=2.4 cm=2λ_g.

(**d**) A higher ΔT value (P_2=12.2 W) keeps the averaged $U(z)$ profile straightened along a whole length of the control section and downstream; in addition, it induces the smaller-scale vortical structure corresponding to the scale given by the stripe disposition. It should be noted, that while being noticeable in the vicinity of the wall (y=2 mm), it transforms into a larger scale structure in the outer part of the boundary layer (for comparison, see patterns of Figure 8, **c**, left and right sets).

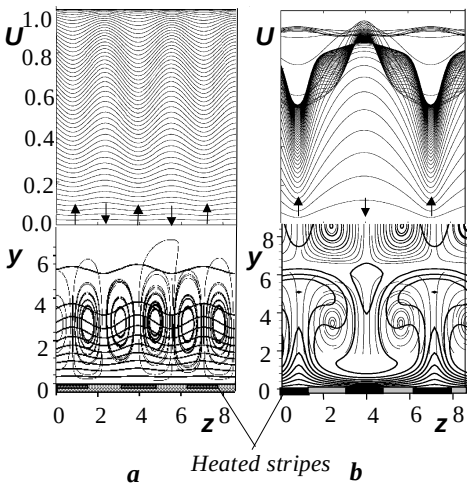


Figure 9. Calculated consecutive stages of the velocity field and flow topology (iso- velocity contour lines) development over a surface generating streamwise vortices

A tendency of the forced small-scale structure to grow was observed both experimentally and numerically for all considered modes generated in a boundary layer, i.e. for nondimensional vortex scales Λ<240 according to the Goertler stability diagram. However the life-time of incoming (or generated by any means) small-scale vortices, or their self-sustaining ability, depends very much on the spanwise scale of the forcing factor correlated with the basic flow parameters. It is well seen from comparison of the two numerically considered cases [9]:

(***1***) excitation of the pure second mode, Λ_2=84, and

(***2***) slightly "incorrect" excitation of Λ_2 that assumed a spectrum, rather than a single mode induced, including the most amplified first mode. It means a little irregularity in the arrangement of the heated stripes what is very probable in practice; numerically, it was introduced through a shifted first stripe as well.

In both cases, the constant boundary condition imposing the permanent preference to a given vortex scale could not prevent from developing and final dominance of a larger scale vortical structure. However in case (***1***) shown in Figure 9, the flow structure transformation took a longer time, while in case (***2***), the initially strongly prevailing second mode gave up almost immediately to the first one. Experiments showed even more slow vortical structure evolution to its breakdown if vortices were generated with a scale close to the neutral one. It proved a possibility to control the vortex dynamics and, through chosen dominating scales of motion, to influence momentum transfer in a boundary layer.

Practical benefit of embedded streamwise vortices is demonstrated in Figure 11 in a form of the boundary layer separation control over a surface of complex configuration. The top view of a visualized flow field shows

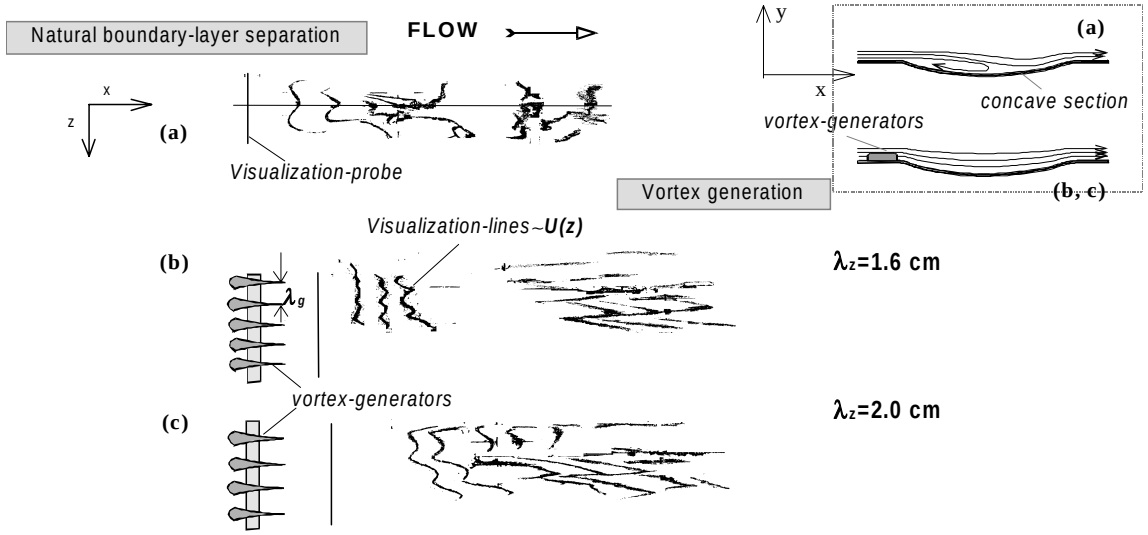


Figure 10. Boundary-layer separation control using generated streamwise vortices, U_0=7 cm/s, R=4 m

immediate flow separation (a) downstream of the rounded backward surface step, while vortices generated upstream of the critical point make the flow pattern orderly with the space-scale of the vortical structure corresponding to the one induced. Preliminary tests (using liquid-crystal visualization) of a turbine blade with flush-mounted electrically heated stripes showed similar encouraging results, i.e. a separation line shifted downstream under voltage applied to the stripes.

Conclusions

An approach to performance optimization of a turbine blade was formulated and realized with a primary assumption about a boundary layer as a viscous flow affected by centrifugal forces. In this connection, Goertler stability theory and receptivity methods were attracted to get an insight into the vortex dynamics and possibilities of its control in a required way. The basic idea was the utilization of the inherent structure (streamwise vortices) of the flow under body forces.

A method was proposed and developed of non-intrusive generation of streamwise vortices with a given scale. It is based on heating of a flush-mounted array of longitudinal elements (stripes) regularly spaced in the spanwise direction. Depending on boundary conditions given by a distance between the adjacent heated stripes λ_g, and their temperature gradient with an ambient flow ΔT, properties of the induced vortex system (space scale, intensity and growth rate) could work in a desirable way. Choosing the values of the control parameters, one can get either prolonged, low-rate vortex field development with stabilized smoothed velocity profiles or direct generation of streamwise vortices with a given scale, moderate long-term or well-pronounced short-term effects.

Obtained experimental and numerical results are in a good agreement having revealed typical characteristics and response of a boundary layer to generated streamwise vortices:

- growing scales of the dominating vortical motion both downstream and normally to the surface;
- mode competition in favor of definitive prevalence of a large-scale fundamental even under condition of a constant different-scale forcing from the wall;
- non-zero receptivity of both transitional and turbulent boundary layers under centrifugal forces to induced streamwise vortices;
- power spectra redistribution in favor of a long-wave interval in transitional and turbulent boundary layers with embedded streamwise vortices that directly influenced transport properties of a near-wall flow.

The latter was shown can be manipulated as required and be applied, e.g. for the flow separation delay.

Governing ideas and methods of the flow control tested for laminar/transitional boundary layers proved to be efficient in case of a developed turbulent boundary layer that is more congruous to practical applications, in particular, related to the improvement of the turbine blade operation.

Acknowledgements

This material is based upon work supported by the European Office of Aerospace Research and Development, AFOSR, AFRL under the Contract F61775-99-WE075. The authors acknowledge the stimulating interest to the work of Dr. C. Raffoul, EOARD, and Dr. M. Maurice, AFOSR, as well as the numerical results placed at the authors' disposal by Dr. J. Delfs, DLR, Braunschweig, that helped to analyze the problem exhaustively.

References

1. Yurchenko, N. F. Essential features of boundary layers developed under body forces, 1994. *Proc. 2nd European Fluid Mech. Conference*, Warsaw, Poland.
2. Nikiforovich, E. I., Yurchenko, N. F. Boundary-layer flows with centrifugal forces, 1997. *ERCOFTAC Bulletin*, March, **32**, 61-65.
3. Delfs, J.W., Yurchenko, N.F., Rivir, R.B., Vortex dynamics of boundary layers under body forces: dominating mechanisms and control, 1999. *Proc. Workshop "Cooperation between Eur. and Sib. Scientists in a Field of Physical Hydromechanics"*, Novosibirsk, Russia.
4. Saric, W. S. Goertler vortices, 1994. *Annual Review of Fluid Mechanics*, **26**, 379-409.
5. Floryan, J. M., 1989. Goertler instability of boundary layers over concave and convex walls, *Phys. Fluids*, **29** (8), 2380-2387
6. Yurchenko, N.F. Experimental technique to study longitudinal vortices in a boundary layer, 1981, *Engineering-Physical J.*, **41**, 6, 996-1002.
7. Yurchenko, N.F., Rivir, R.B. Flow management using inherent transition and receptivity features, 1998. *Proc. International Symposium on Seawater Drag Reduction*, Newport, USA.
8. Yurchenko, N.F., Delfs, J.W., Boundary layer control over an active ribleted surface, 1999. *Proc. IUTAM Symp. on Mechanics of Passive and Active Flow Control*, Goettingen, Germany, eds. G.E.A.Meier and P.R.Viswanath, Fluid Mechanics and its Applications, Vol.53, 217-222, Kluwer Acad. Publishers.
9. Yurchenko, N., Delfs J. Optimal control of boundary layers under body forces, 1999. *Proc. IUTAM Symposium on Laminar-Turbulent Transition*, Sedona, U.S.A.
10. Rivir, R. B., Transition on Turbine Blades and Cascades at Low Reynolds Numbers, 1996. 14th AIAA Fluid Dynamics Conference, New Orleans, *AIAA 96-2079*, June 1996.
11. Ilyushin, B., Institute of Thermophysics, Russian Academy of Sciences, Siberian Branch *(Private communication)*

Combustion Oscillation in a Staged LPP Combustor

J. A. Austin, J. R. Tilston and I. R. I. McKenzie
Propulsion and Performance Department, DERA Pyestock, Farnborough, Hants, GU14 0LS, United Kingdom

1 Summary

The presence of combustion oscillation, caused by self amplification of the pressure and heat release fields, is very common within Lean Premixed Prevaporised (LPP) combustors. After suffering significant structural damage from oscillations of this type, an axially staged combustor was subjected to a programme of diagnostic testing to establish a series of safe running conditions. Using fuel staging to vary the local air to fuel ratios (AFR), a series of conditions exhibiting much reduced levels of oscillation were identified.

2 Introduction

Combustion oscillation occurs when the heat release of the flame within a combustor couples with the dynamic pressure field. Generally, if the heat release and pressure fluctuations are in phase, then a positive feedback loop is created and self-amplification will occur. The corresponding pressure oscillations increase rapidly to a finite limit. The amplitude of these oscillations can result in increased noise and damage to, or destruction of, the combustor.

The move towards advanced low emissions combustors has made this phenomenon more common. Techniques such as LPP combustion rely upon burning a weak flame to minimise the production of nitrogen oxides (NO_X) by maintaining low combustion temperatures.

To provide the required combustion most of the air enters the combustor with the fuel, consequently it is normal for there to be no primary, secondary or dilution holes. This arrangement essentially provides a resonant geometry that is highly susceptible to combustion oscillation.

A programme of research, named LOWNOX, was established to investigate methods for reducing NOx emissions from gas turbine aircraft engines. The European Union sponsored programme involved a consortium of 23 organisations from around Europe including industrial companies, research establishments and universities.

It is commonly acknowledged that, subject to limitations, NOx production and combustion efficiency increase with combustor length. Thus a programme of high pressure testing, Part 1, was proposed to determine the optimum length and volume for an LPP combustor of a specific architecture. During these tests, combustion oscillations were encountered of such intensity that the test combustor was damaged preventing the completion of the programme.

© Crown copyright 2000 Defence Evaluation and Research Agency

To allow the programme to proceed, a series of diagnostic tests, Part 2, was identified to provide a set of safe running conditions. The combustor was repaired and strengthened and re-tested to establish a safe operating envelope.

3 Overview

The unit tested was an axially staged LPP three-sector combustor; a diagrammatical representation is shown in Figure 1. The combustor was required to operate within the constraints of Engine E, the operating conditions of which are listed in Table 1 for the full size 24-sector combustor. Engine E[1] was a theoretical prediction, produced in the early 1990s during the first LOWNOX phase, of an engine cycle for a large subsonic civil turbofan engine with a service entry date of around 2000. The test combustor was supported at its exit in a high pressure test rig[2] that had initially been selected for its novel capability for internal mapping of the hot gas species. The installation provided the combustor with air, conditioned to the required temperature and pressure, from an entry plenum. The exhaust gasses then vented into a large exhaust drum on to which was mounted the internal traversing gas sampling probe. The arrangement is illustrated in Figure 2.

The combustor was designed to pass approximately half of the total air flow through the main ducts, proportionately less through the pilot ducts and the remaining one third was used for cooling. These proportions were determined by the need to maintain the stoichiometry of the main and pilot zones within certain limits to control the flame temperature and NO_X levels.

The combustor is shown assembled, complete with the LPP ducts, in Figure 3. Each of the three sectors had one main and one pilot LPP duct. Nickel alloy cooling tiles, inset in Figure 3, were fitted to the upper and lower faces of the casing to facilitate the efficient use of cooling air. The casing incorporated removable windows in the main zone for observation of the flame. If required, the windows could be replaced with metal panels to provide greater structural integrity.

The main LPP ducts were mounted outboard of the pilot zone and angled towards the engine axis. Each duct consisted of two co-axial air passages incorporating axial swirlers. The fuel was injected radially into the inner passage through a number of small holes.

The pilot LPP ducts were mounted parallel to the engine axis and some distance forward of the main ducts. Radial fuel injection into a swirling airflow was again employed. A fraction of the fuel was injected close to the duct exit via a centrally positioned pressure jet atomiser to provide combustion stability.

Previous single sector test experience had shown that both the pilot and main LPP ducts were prone to oscillatory

Paper presented at the RTO AVT Symposium on "Active Control Technology for Enhanced Performance Operational Capabilities of Military Aircraft, Land Vehicles and Sea Vehicles", held in Braunschweig, Germany, 8-11 May 2000, and published in RTO MP-051.

combustion instability. Therefore, additional instrumentation was incorporated into the design to obtain as much dynamic pressure information as possible. This consisted of pressure tappings connected to pressure transducers located close to the rig. Certain processing treatments were applied to the measurements during testing to provide the necessary information to progress the trial, whereas, more thorough analysis treatments were applied following the tests.

During the Part 1 tests, conducted at DERA, pressure oscillations were encountered. At the Engine E Approach condition, one of the two sidewall mounted quartz windows failed. Both windows were replaced with the alternative metal panels prior to the next test run. However, pressure oscillations were again observed at the same test condition but, on this occasion, they were at increased amplitude and further damage resulted. The damage to one of the sidewall panels is illustrated in Figure 4. The panel has been bent inwards following failure along three sides of the mounting. Both combustor sidewalls were distorted and localised cracking was observed on a number of combustor components.

The combustor was repaired and reinforced, Figure 5, prior to the start of the second phase of tests.

4 Test Conditions

The combustor was required to operate within the constraints of Engine E conditions, Table 1, up to pressures and temperatures of 47bar and 917K. Some scaling of the combustor was required for it to match the test facility combustor entry capability and this is reflected in the test conditions listed in Table 2.

At the lower power conditions the fuel had to be staged to obtain suitable flame temperatures for low NOx and high efficiency. At the Idle and Descent conditions the combustor was operated using only the pilot injectors. At the Approach condition a full engine combustor would operate with all pilots and 1 in 4 main injectors fuelled to optimise the zone temperatures. With the three-sector test combustor, one of the main injectors (the central one to minimise wall effects) was fuelled with the appropriate flow to simulate 1 in 4 staging. To identify the safe areas of operation, further staging and fuel management was employed to alter the local AFRs that have a direct effect on the magnitude of oscillation.

5 Analysis

The levels of oscillation encountered at various AFRs and engine conditions were assessed to determine the safest conditions for operation. The combustor pressure instrumentation was used to determine the fuelling arrangement that gave the greatest reduction in acoustic power.

A total of eleven tappings was installed on the combustor, ten on the headplates, Figure 6, and one at the exit plane of the combustor. Three other tappings, external to the combustor, were used for reference. These monitored dynamic pressures in the entry plenum, in the central main LPP duct and the transducer reference pressure. The pressure lines from tapping to transducer were each 2m long and 1.08mm in bore. The system was calibrated at frequencies up to 2kHz. Good agreement with theoretical prediction was achieved providing confidence that the application of any corrections would be valid[3]. Good resolution of the dynamic pressure component was achieved by using low range transducers in a differential mode. The entry plenum pressure was used for the reference with line damping to avoid the transmission of any pressure perturbations. The amplified transducer signals were recorded on a personal computer based data acquisition system capable of operation in the following two modes:
Multichannel : up to 14 channels, each sampled at 4kHz with a 1.35kHz low pass elliptical filter.
7-channel : 7 channels, each sampled at 8kHz with a 2.5kHz low pass elliptical filter.

During testing, the data were presented graphically to provide early warning of the onset of significant oscillations. Post-test data processing, to determine the power spectra and the levels of acoustic power, was used to characterise the compound waveforms and, or, identify low amplitude resonances.

At the Approach condition during Part 1 testing, a resonance, at 1230Hz was detected when the pilot ducts were fuelled showing peak-to-peak values of 5kPa and 15kPa respectively for the two test runs. When the central main duct was also fuelled the peak-to-peak measurements increased to 37kPa and the frequency dropped to 680Hz. The power spectra is shown in Figure 7 (this, and the subsequent illustrations of oscillation characteristics are presented as power spectra using data acquired from pressure tapping No 1; arbitrary units have been used for the vertical, power, scale). This 680Hz frequency is consistent with a longitudinal quarter wave resonance of the combustor based on the assumption that it approximates to a pipe open at one end. This mode could only propagate if reflections were to have occurred from a sudden expansion at the combustor exit. The standard method of mounting combustors in the test facility provides such an opportunity, Figure 2. The inclusion of a flared exit channel to the combustor, an acoustic horn, may be appropriate to suppress any longitudinal standing waves. The observation of the second harmonic at 1360Hz may be due to a non-linear propagation within the combustor or the pressure tapping tubing, or a combination of both.

On both occasions when damage occurred during the early tests the oscillation characteristics changed. The failure of the glass window resulted in the oscillations ceasing due to the permanent disruption of the feedback loop. The partial failure of the replacement panel resulted in the oscillation frequency changing intermittently from 680Hz to 510Hz as the feedback loop varied due to panel flutter.

During the Part 2 tests, very low level oscillations of 0.4kPa peak-to-peak were present at a frequency of 1160Hz whilst at the Idle condition. These were only revealed following post-test data processing as they were masked by the system noise. The magnitude of these oscillations remained almost constant over a range of AFRs from 18.4 to 29.5.

The pilot flame was then enriched as the combustor was advanced to the Descent condition. Once again, low amplitude oscillation was present. This time the frequency was 1170Hz, Figure 8; the peak-to-peak amplitude of 0.7kPa was again hidden by noise. This mode persisted over a range of AFRs from 18.3 to 27.5, but rose significantly outside this range.

At the Approach condition, the response was similar to that observed during the earlier tests. Initially, only the pilot ducts were fuelled, operating within the safe limits determined at

Decent. Fuelling the central main duct, at 22.5 AFR, again generated a significant oscillation, this time at a frequency of 630Hz. The change in frequency is directly attributable to a reduction in flame temperature of approximately 300K due to changes in running conditions. The second harmonic, at 1260Hz, was also present, Figure 9. The respective peak-to-peak measurements were 13kPa and 7kPa representing ±0.7 and ±0.38% of the combustor inlet pressure. These amplitudes were lower than those measured during the earlier tests. The amplitudes increased dramatically when the main duct AFR dropped below 21.1 or rose above 25.9 whilst maintaining the overall combustor AFR constant.

Two resonant frequencies, namely 470, and 700Hz, were detected at the Cruise condition where the main and pilot AFRs were 31.8 and 31.2 respectively. The predominant 700Hz signal measured 15.1kPa peak-to-peak. As the main was enriched the oscillations at 700Hz increased significantly in magnitude. Operation over a range of main AFRs from 23.8 to 36.1 revealed a significant increase in magnitude, ranging between 20 and 32kPa peak-to-peak at AFRs below 28.3.

Frequencies of 675Hz and 2075Hz were observed at the Climb-out condition whilst varying the main AFR between 33.3 and 25.8 but maintaining the overall AFR constant. At a main AFR of 28.9 the magnitude of the signal at 675Hz was an acceptable 10.1kPa peak-to-peak but rose significantly when the AFR was set at richer levels. The effect of circumferential staging on both pilot and main ducts was investigated. Neither was successful in reducing oscillation in that the former had a minimal effect, whereas, the latter resulted in a sharp increase in magnitude to 19.0kPa peak-to-peak, due possibly to the creation of large thermal gradients. The detrimental effect of thermal gradients may explain why, at similar AFR settings, the operation of all three main ducts resulted in the level of acoustic power being 70% less than when two ducts were fuelled.

At the Take-off condition, oscillations were identified at frequencies of 464, 720 and 1424Hz, Figure 10. The more dominant resonance at 720Hz measured 10.9kPa peak-to-peak. The main fuel flows were again varied whilst maintaining the overall AFR. This level of oscillation only existed between AFRs of 28.1 and 29.6, with peak-to-peak levels rising to 20kPa outside this range. All the frequencies observed differed from those measured when the pilot and main ducts were tested separately on a single sector combustor. Pilot oscillations were observed at 1450Hz with frequencies of 300Hz and 1550Hz measured for the main duct, the latter being attributed to the first longitudinal mode of that combustor.

The oscillation measurements referred to above are average values and were subjected to considerable short-term fluctuation. Two mechanisms of oscillation appeared to co-exist, a constant lower amplitude oscillation periodically overlaid by short bursts of higher amplitude activity. The influence of these short bursts of activity is not fully understood at present.

The phase relationships between the pressure signals were determined at each operating condition for the dominant frequency. Pressure tapping 1, Figure 6, was used as the reference position.

The phase relationships proved to be different for each operating condition and also suggested that a complex series of modal patterns existed within the combustor, featuring both transverse and longitudinal components. These varied considerably with changes in operating condition. The limited data available made it impossible to determine what modes were present. An additional complication in understanding the modal patterns is the acoustic waveguide effect[4] due to temperature gradients between the main and pilot zones and the burning zones associated with each LPP duct.

6 Conclusions

Tests have been carried out on an axially staged LPP combustor to identify the limits for the onset of combustion oscillation. Combustion oscillation was encountered at all the conditions tested but, by varying the local AFR and mapping the intensity of oscillation, a series of safe operating conditions was established. In general, the magnitude of oscillation could be reduced by increasing the main duct AFR whilst maintaining the overall combustor AFR constant by reducing the fuel to the pilot ducts. Operating at the design values of AFR should be possible with adequate safety margins at all the operating conditions with the exception of Take-off. At this condition there is little, or no, safety margin.

At all conditions, where the main ducts were fuelled, the dominant oscillation frequency lay in a band between 675 Hz and 720Hz depending upon the prevailing temperature profiles within the combustor. This is consistent with a longitudinal standing quarter wave within the combustor.

The phase relationships determined from the pressure measurement positions suggested that a complex series of modal patterns existed and that these patterns were different for each operating condition. The limited data available made it impossible to determine what modes were present.

Much empirical work is still required to understand the phenomenon of combustion oscillation.

The present work was supported by the European Commission as part of the Brite-Euram Research Programme ‘Low Emission Technology Programme Phase III / LOWNOXIII - part 1’ under contract number BRPR-CT95-0122, which is gratefully acknowledged. DERA’s participation in this programme was co-funded by the UK DTI (CARAD), whose sponsorship is also gratefully acknowledged.

7 References

1. The design and evaluation of a piloted, lean burn, premixed, prevaporised combustor, M I Wedlock, J R Tilston & R E Seoud, NATO RTO Meeting Proceedings 14, AC/323(AVT)TP/10, June 1999
2. Design considerations for NGTE Combustor Test Rig, J B Bullard, DERA, 1982
3. Measurements of sound propagation in narrow bore tubes, R W Copplestone, DERA, to be published
4. Fundamentals of Acoustics, 3rd ed., L E Kinsler A R Frey A B Coppens J V Sanders, John Wiley & Sons, 1982

Condition	Thrust	Combustor inlet conditions			AFR	Exit Temp
	%	Temp (K)	Pressure (kPa)	Mass flow (kg/s)		(K)
Idle	7	551	701	33.3	115.11	886
Descent	15	617	1090	47.0	98.90	1110
Approach	30	709	1817	73.1	68.57	1232
Cruise	44	846	1758	60.3	39.91	1672
Climb-out	85	878	4109	140.3	40.83	1683
Take-off	100	917	4760	157.2	36.88	1792

Table 1 Engine E Conditions

Condition	Inlet P	Combustor P	Inlet T	Air Flow	Total Fuel Flow	Main Fuel Flow	Pilot Fuel Flow
	Bar	Bar	K	kg/s	g/s	g/s	g/s
Idle	7.01	6.73	551	3.89	31.7	-	31.7
Descent	9.20	8.83	617	4.33	40.9	-	40.9
Approach	9.20	8.83	709	4.33	66.8	31.4	35.4
Cruise	9.60	9.22	846	3.85	90.0	63.0	27.0
Climb-out	9.60	9.22	850	3.90	89.2	62.4	26.8
Take-off	9.60	9.22	850	3.85	97.8	68.4	29.4

Table 2 Combustor operating conditions

Condition	LPP Duct	AFR Range	Design AFR
Idle	Pilot	29.5 – **18.4**	26
Descent	Pilot	27.5 – **18.3**	22.6
Approach	Pilot	30.5 – 25.2	26.1
	Main	25.9 – **21.1**	23.9
Cruise	Pilot	39.9 – **24.5**	30.4
	Main	36.1 – **28.3**	31.8
Climb-out	Pilot	39.9 – 30.3	31
	Main	33.3 – **28.9**	32.5
Take-off	Pilot	31.9 - **28.1**	28.1
	Main	29.6 - **28.1**	29.4
Note: Values in **bold** indicate the operational limit of the combustor.			

Table 3 Table of AFRs for reduced oscillations

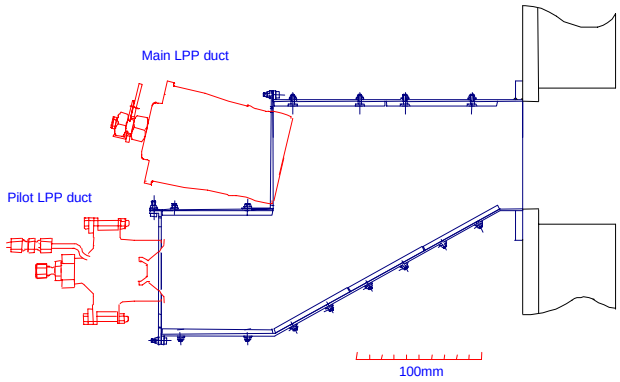


Figure 1 Axially Staged LPP Combustor

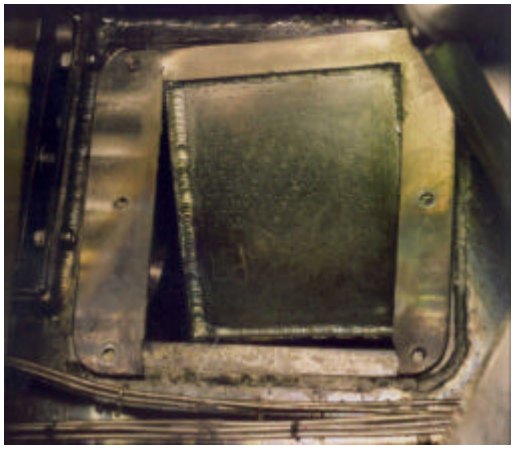


Figure 4 Damage to one of the sidewall panels

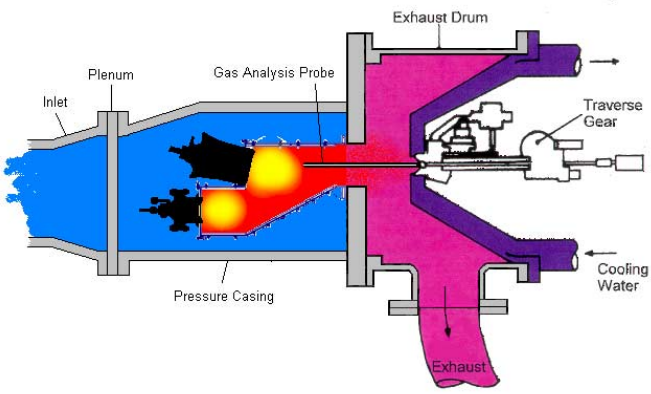


Figure 2 Schematic of Combustor Installation

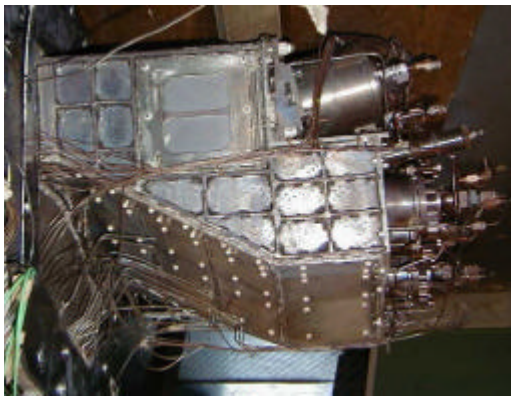


Figure 5 Reinforced Combustor

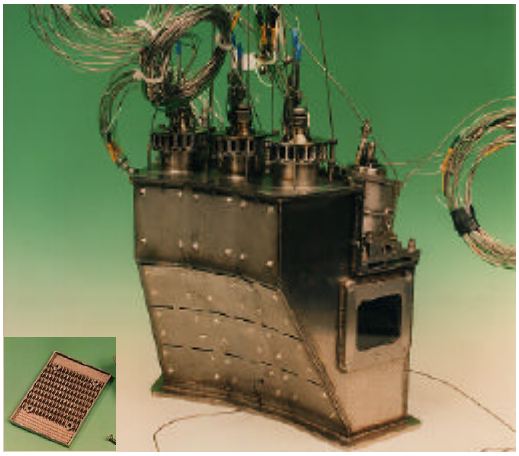


Figure 3 Test Combustor, cooling tile shown in inset

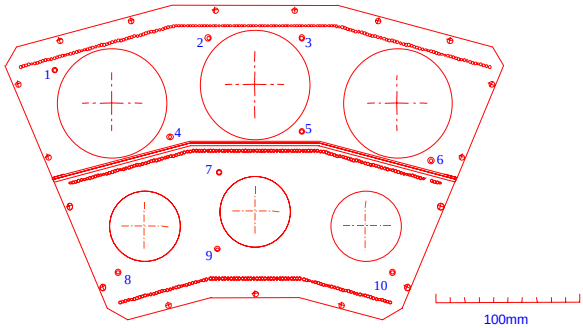


Figure 6 Pressure tapping locations on the combustor headplates

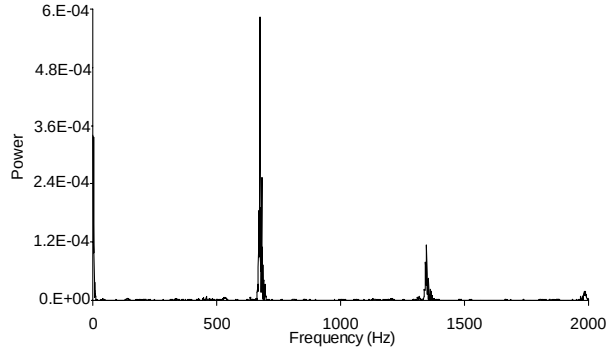


Figure 7 Power Spectra from Approach Condition, Part 1 Tests

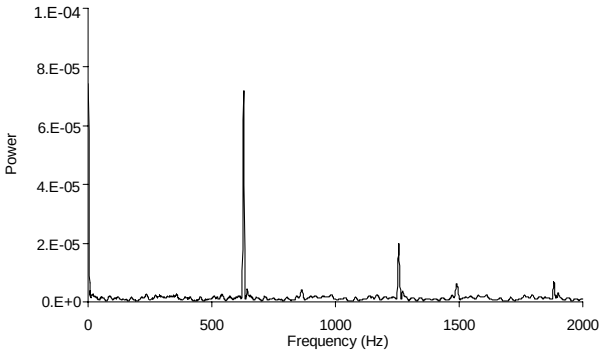


Figure 9 Power Spectra from Approach Condition, Part 2 Tests

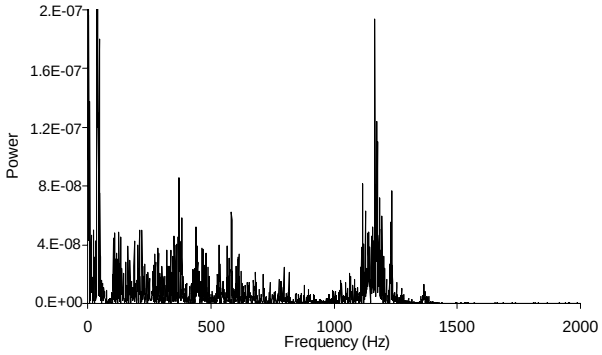


Figure 8 Power Spectra from Descent Condition, Part 2 Tests

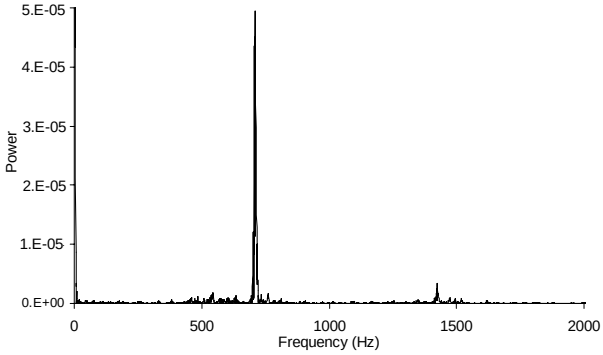


Figure 10 Power Spectra from Take-off Condition, Part 2 Tests

PAPER -18, J. Tilston

Question (U. Vandsburger, USA)

Comment: modeling of acoustics of test rigs like this has proven rather complex, even in cold flows. You get many features which are of the whole rig and not the combustor along. E.g., the effects of a perforated plate instead of a closed boundary.

Why use linear scales on the p' graphs? Nonlinear scaling will show all, rich, features. Some of these will be related to the analysis above.

Reply

The primary purpose of the test program was to establish an envelope of safe combustor operation by identifying the fueling conditions at which damaging levels of oscillation existed. The work was not intended to be a detailed combustion oscillations research exercise. Therefore, it was only necessary to identify the dominant frequencies where the power was greatest. For this purpose, the use of linear power scales is adequate.

Question (S. Candel, France)

What was the mean pressure in the combustor? Where did you place the pressure sensor (or sensors)? If there was more than one sensor, did you measure the phase differences?

Reply

The mean combustor pressure for each test condition is shown in Table 2 of the paper. Eleven pressure sensing points were measured, ten in the combustor head plates and one at the combustor exit (see Section 5 of the paper). The phase relationships were determined and proved to be different for each operating condition, suggesting that complex modal patterns existed. See Section 5 of the paper for additional information.

This page has been deliberately left blank

Page intentionnellement blanche

Click here to view PowerPoint presentation; Press Esc to exit

Prediction of Combustion-Driven Dynamic Instability For High Performance Gas Turbine Combustors: Part I

B. Sekar
Turbine Engine Division
Air Force Research Laboratory
Room D 138, Building 18
1950 5th Street
Wright-Patterson AFB, OH 45433

M. A. Mawid & T. W. Park
Engineering Research and Analysis Company
Wright-Patterson AFB, OH 45433, USA

S. Menon
Department of Aerospace Engineering
Georgia Institute of Technology
Atlanta, GA 30332, USA

ABSTRACT

This paper describes the development and application of a combined detailed three-dimensional large eddy simulation (LES) and one-dimensional analysis tool to predict and actively control combustion-driven dynamic instabilities in gas turbine combustors. The integration of detailed finite-rate kinetics into LES and use of In-situ Adaptive Tabulation (ISAT) to efficiently calculate multi-species finite-rate kinetics in LES along with the use of global kinetics in the one-dimensional analysis tool was demonstrated. The results showed that LES can be effectively used to simulate complex reacting flows in gas turbine combustors and to identify regions of combustion instabilities. The results also showed that the one-dimensional combustor analysis with global kinetics can then be used both to capture the combustor unstable modes of the predicted regions of instabilities and to actively control these instabilities. In particular, the results demonstrated that by modulating the primary fuel injection rates and the time-lag between the instant of fuel-air mixture injection and heat release, damping out the instabilities may be achieved.

NOMENCLATURE

a^* = Reference speed of sound
D = Diffusion coefficient
K_0 = Reaction rate constant
k = Bulk modulus of the fluid
L = Combustor length
$\dot{m}$ = Fuel-air mixture injection rate
Pr_t = Turbulent Prandtl number, $\mu_t c_p / k_t$
p = Non-dimensional pressure, $\bar{p}/p^*$
p^* = Reference pressure
p' = Combustor pressure fluctuations
Q_{fh} = Heat transferred from/to the flameholder
q_0 = Heat of reaction
R = Non-dimensional reaction rate
Re^* = Reference Reynolds number, $\rho^* a^* L/\mu$
Sc_t = Turbulent Schmidt number, ν/D
T = Non-dimensional temperature, $\bar{T}/T^*$
T^* = Reference temperature
T_i = Non-dimensional temperature in the i^{th} numerical cell
T_i^{fh} = Non-dimensional temperature at the flameholder location
T_{ign} = Non-dimensional ignition temperature
t = Non-dimensional time, $\bar{t}/t^*$
t^* = Reference time, L/a^*
u = Non-dimensional axial velocity, $\bar{u}/a^*$
V = Volume of the fuel feed system
x = Non-dimensional distance, $\bar{x}/L$
y_i = Mass fraction of i^{th} species

Greek Letters

α = User specified constant in Eq. (7)
ε_t = Turbulent to laminar viscosity ratio, μ_t/μ
ϕ = Equivalence ratio

Paper presented at the RTO AVT Symposium on "Active Control Technology for Enhanced Performance Operational Capabilities of Military Aircraft, Land Vehicles and Sea Vehicles", held in Braunschweig, Germany, 8-11 May 2000, and published in RTO MP-051.

γ = Specific heat ratio, c_p/c_v
μ = Molecular viscosity
μ_t = Turbulent viscosity
ρ = Non-dimensional density, $\bar{\rho}/\rho^*$
ρ^* = Reference density
ω = Non-dimensional fuel pulsation frequency

Superscripts

$*$ = Reference quantities
– = Dimensional quantities

Subscripts

o = Total quantities

1 INTRODUCTION

The Air Force Integrated High Performance Turbine Engine Technology (IHPTET) combustors must operate free of combustion-driven dynamic instabilities that could compromise the structural integrity of high performance engines. To double the thrust to weight ratio, as required for future high performance military engines, the combustor will be required to operate at much higher overall design equivalence ratios, P3 and T3 than the existing military aircraft engines combustors. In addition, weight reductions in the combustor, diffuser and fuel injectors can be only achieved through innovative integration and packaging of these components. Therefore, combustor, diffuser and fuel injectors must be designed in a manner that will lead to instability-free (or substantially damped instabilities) operation. Active combustion control techniques may also be implemented to damp instabilities. While the active control technology attempts to introduce an out of phase disturbance with the combustor pressure acoustics, the passive control technology requires a profound understanding of the various driving mechanisms such as air and fuel flows variations, unsteady heat release and their interaction that cause combustion instabilities.

Most existing combustors design databases lack a provision for predicting combustion-driven instabilities during the predesign and design phases. Currently, a need exists to predict and quantify combustion instabilities in high performance military combustors. Axial, tangential and radial instability modes may all develop in the combustors that could severely impact the engine performance and its structural integrity. Various approaches are presently used to predict combustion instabilities. These approaches range from one-dimensional linear stability-based [1-3], to one, two and three-dimensional non-linear-CFD-based [4-8]. Mohanraj et. al. [5] developed a one-dimensional combustor model using a heuristic mixing model along with a semi empirical open loop active controller. Quinn and Paxson [9] used a one-dimensional model to study thermo-acoustic instabilities in combustion systems. Other analytical models [10-11] based upon the unsteady-pressure wave equation in three-dimensions were also developed and calibrated/anchored to experimental results under controlled conditions such that extrapolation to other conditions can be performed.

In LES modeling of the momentum transport scales larger than the grid size are computed using a time- and space-accurate scheme, while the effect of the unresolved smaller scales (assumed to be mostly isotropic) on the resolved motion is modeled using an eddy viscosity based subgrid model. This approach is acceptable for momentum transport since all the energy containing scales are resolved and all the unresolved scales (that primarily provide for dissipation of the energy transferred from the large scales) can be modeled by using an eddy dissipation subgrid model. However, these arguments cannot be extended to reacting flows since , for combustion to occur, fuel and oxidizer species must mix at the molecular level. Since, this process is dominated by the mixing process in the small-scales, ad hoc eddy diffusivity concepts cannot be used except under very specialized conditions. To deal with these distinctly different modeling requirements, a new subgrid mixing and combustion model has been developed that allows for proper resolution of the small scale scalar mixing and combustion effects within the framework of a conventional LES approach.

The earlier studies [12, 13] have established the ability of the LES model in premixed combustion and in fuel-air mixing. To reduce the computational cost, the past calculations employed flamelet models (for premixed combustion) or simulated fuel-air mixing without detailed chemical kinetics. However, for realistic simulations for the reacting flow, detailed finite-rate kinetics must be used, especially if pollutant formation is to be studied. As is well known, the computational effort involved when using detailed kinetics is so large as to make LES of even a simple configuration computationally infeasible. Typically, global kinetics are employed to reduce the computational cost. However, such kinetics are not able to deal with ignition and extinction processes and are also unable to accurately predict pollutant (No_x, CO and UHC) formation.

Due to the limited data available on combustion-driven instability for gas turbine combustors, no consensus as to what approach should be used to predict instabilities during the diffuser/fuel injectors/combustor predesign and development stages yet exists. The primary objective of this study is to demonstrate the application of a combined large eddy simulation and an unsteady one-dimensional combustor model approach for predicting the combustor's unstable modes and for

investigating the effectiveness of the fuel flow modulation methodology to actively control and suppress the combustor's instabilities. The present study is considered work-in-progress towards using LES along with a simpler analysis tool to predict instabilities at the pre-design and design stages of gas turbine combustors. The paper is organized as follows. The LES model formulation along with its numerical implementation is presented in the next section, followed by sections on the governing equations and combustion model for the one-dimensional combustor analysis tool and results. The final section is the conclusion.

2 LES MODEL

The compressible LES equations are obtained by Favre-filtering Navier-Stokes equations using a top-hat filter (appropriate for finite-volume schemes). The filtering process results in terms in the resolved LES equations that require modeling. The final LES equations are avoided here for brevity since they are described elsewhere [14]. In general, the subgrid terms representing the subgrid stress tensor, the subgrid heat flux, the subgrid viscous work, the subgrid species mass flux, and the subgrid enthalpy flux all require modeling.

The subgrid stresses in the LES momentum equations are modeled using an eddy viscosity, which in turn, is modeled in terms of the LES filter width Δ and the subgrid kinetic energy K^{sgs}. A transport model equation for the subgrid kinetic energy is solved along with the other LES equations. The effects of subgrid turbulence on flame structure (and propagation) in premixed combustion can be quantified in terms of the subgrid kinetic energy and thus, it is advantageous to use this type of LES model for reacting flows. Another distinct advantage of this approach is that this model does not assume equilibrium between subgrid kinetic energy production and dissipation (implicit in algebraic models) and thus, helps to attribute a relaxation time associated with the nonequilibrium in the subgrid scales.

To handle the distinctly different physics of scalar mixing and chemical reactions a new subgrid model has been developed. Details of this model have been reported elsewhere [12, 13] and therefore, only summarized here. This model is called Linear Eddy Model (LEM) [15].

2.1 LEM MODEL FORMULATION

The details of the LEM model have been given elsewhere [15] and therefore, are only briefly summarized here. LEM is a stochastic model, which treats reaction-diffusion and turbulent convection separately but concurrently. Reaction-diffusion processes evolve on a one-dimensional (1D) domain in which all the characteristic length scales in the turbulent field (from L to η) are fully resolved (6 cells are used to resolve η). The orientation of the 1D domain is in the direction of the scalar gradient and within this domain, the equations governing constant pressure, adiabatic laminar flame propagation are solved. The deterministic simulation of the reaction-diffusion processes can be viewed as a local direct numerical simulation. As a result, the reaction rate terms do not require any closure.

Turbulent stirring of the scalar field is implemented as distinctly independent process that interrupts the deterministic evolution of the reaction-diffusion processes on the 1D domain. Stirring is implemented as stochastic re-arrangement events called triplet maps, each of which represents the action of a turbulent eddy on the scalar fields. It has been shown that this mapping can capture correctly the physical increase in scalar gradient (without affecting the mean scalar concentration) due to eddy motion. Three parameters are needed to implement these turbulent stirring events: the typical eddy size, the eddy location within the 1D domain and the stirring frequency (event rate). The method to obtain these parameters is given elsewhere [12].

2.2 NUMERICAL IMPLEMENTATION OF LES MODEL

LES studies have been applied to methane-air flame studies [16-18] and to a generic combustor concept. Methane-air flames similar to those in the experiments [16-18] are studied here. In order to obtain a realistic chemical state over a wide range of operating conditions, a 15-step, 19-species skeletal mechanism is employed. This mechanism (which included No_x kinetics) has been shown to be quite accurate over a wide range of equivalence ratios. It is also capable of predicting extinction and re-ignition, which is particularly relevant here since F1 flame, is considered close to extinction limit. Table 1 summarizes the chemical species and reactions in this skeletal mechanism.

The numerical method is the same as in the earlier study [12] and therefore, only briefly summarized. To simulate a stationary flame, a moving observation window is used that translates with the flame brush to maintain approximately the same relative position between flame center and observation window (even though the flame propagates freely into the reactants). All statistics are obtained relative to the flame center. The computational domain is chosen large enough to fully capture this flame brush (typically 6L). Earlier studies and the present study show that statistically, stationary flames can be simulated using this approach.

A fractional operator splitting method is used to first evolve (via molecular diffusion and turbulent stirring) the scalar equations (without the reaction terms) for a small time step δt to obtain the thermo-chemical state after mixing. Then the reaction

system is integrated over δt to get the final scales and hence, the computational cost for the time integration can be very high. Here, the ISAT approach is used to efficiently handle the finite rate kinetics.

In ISAT, only the accessed region of the composition space, which is a subset of the whole realizable region (the set of all possible combinations of compositions for a given number of species), is tabulated. This tabulation is done as a part of the simulation and when the same composition re-occurs, the table is searched and the stored information is retrieved using fast binary tree search algorithm. Since only the accessible region is stored, the overall time required to build, retrieve and store information reduces significantly. Further details of the ISAT algorithm is given elsewhere [13] and therefore, avoided here for brevity.

To further reduce computational cost, the present model was parallelized with message passing (needed for the solution of the reaction-diffusion equations) handled by MPI directives. For the chemistry point problem no communication is needed. Each processor builds a table for the composition that occurs inside its domain during the computation. This localizes the ISAT table to each processor and reduces the overall load (including search and retrieve time) for each processor (as opposed to building a single table for all the composition that occurs over the whole of the domain). All simulations were done on a 32 processor CRAY-T3E system.

Computational efficiency of ISAT is significant as reported earlier. The size of the table and cost depend upon the error tolerance (which determined the allowable error in each of the scalar for a given initial state). For higher accuracy, this parameter should be low, leading to an increase in the total simulations time and storage. For a value of ε_{tol} = 0.0008 a speed-up of around 30 in the chemical update is achieved by using ISAT. This is consistent with the speedup reported earlier. Table 2 summarizes the present results.

3. GOVERNING EQUATIONS FOR ONE-DIMENSIONAL COMBUSTION INSTABILITY MODEL

The combustor model numerically integrates the following governing differential equations for a calorically perfect gas. The governing equations are given below in non-dimensional form [9] as

$$\frac{\partial w}{\partial t}+\frac{\partial F(w)}{\partial x}=S \tag{1}$$

where the dependent vector w is given as

$$w=\begin{bmatrix} \rho \\ \rho u \\ \dfrac{p}{\gamma-1}+\dfrac{\rho u^2}{2} \\ \rho\ y_i \end{bmatrix} \tag{2}$$

and the flux vector is given by

$$F=\begin{bmatrix} \rho u \\ \dfrac{p}{\gamma}+\rho u^2 \\ u\left(\dfrac{p}{\gamma-1}+\dfrac{\rho u^2}{2}\right) \\ \rho\ u\ y_i \end{bmatrix} \tag{3}$$

The non-dimensionalization of pressure, p, temperature, T, density, ρ, and velocity, u has been obtained by using the reference quantities p^*, T^*, ρ^*, and a^*. The coordinate x has been scaled by the combustor length L. The time has been scaled using the sound wave transit time $t^* = L/a^*$. The heat of combustion q_0 is assumed to be a constant. The ratio of specific heats is denoted by γ.

The non-dimensional form of the equation of state is given as

$$p=\rho T \tag{4}$$

The source vector in Eq. (1) is given as

$$S=\begin{bmatrix} 0 \\ \dfrac{\partial}{\partial x}\left(\dfrac{\varepsilon_t}{\mathrm{Re}^*}\left(\dfrac{\partial u}{\partial x}\right)\right)+\sigma_2 u\left|\rho u\right|^{0.75} \\ \dfrac{\partial}{\partial x}\left(\dfrac{\varepsilon_t}{\mathrm{Re}^*}\dfrac{\partial}{\partial x}\left(\dfrac{u^2}{2}+\dfrac{p}{(\gamma-1)\,\mathrm{Pr}_t}\right)\right)+q_0 R+Q_{fh} \\ \dfrac{\partial}{\partial x}\left(\dfrac{\varepsilon_t}{\mathrm{Re}^*\,Sc_t}\left(\dfrac{\partial y_i}{\partial x}\right)\right)-R \end{bmatrix} \tag{5}$$

Equation (5) contains contributions from the reaction, turbulent eddy diffusion, wall viscous forces, and flameholder heat transfer. The Reynolds number, Re^* is defined as $\rho^* a^* L/\mu$. The

turbulent viscosity ratio, ε_t is defined as the ratio of turbulent to molecular viscosity, μ_t/μ. R is the reaction rate, defined below. Pr_t and Sc_t are the turbulent Prandtl and Schmidt numbers respectively.

3.1 COMBUSTION MODEL FOR ONE-DIMENSIONAL COMBUSTION INSTABILITY MODEL

The combustion model employed in this study was based upon a single-step chemistry reaction scheme. The non-dimensional reaction rate has the form:

$$R = K_0 \rho\ y_f\ y_{o_2} \begin{Bmatrix} 1-\left(T_{ign}/T_i\right) & ;T_i > T_{ign} \\ 0 & ;T_i < T_{ign} \end{Bmatrix} \qquad (6)$$

where K_0 is the reaction rate constant, T_{ign} is the ignition temperature and T_i is the temperature in the i^{th} numerical cell. Due to the one-dimensionality of the combustor model, flame holding is accomplished by a 10% change of the ε_t over the combustor length from zero to a specified value.

3.2 FLAMEHOLDER HEAT TRANSFER FOR ONE-DIMENSIONAL COMBUSTION INSTABILITY MODEL

The term Q_{fh} in Eq. (5) is represented by a simple algebraic expression

$$Q_{fh} = \alpha(0.9T_{ign} - T_i^{fh}) \qquad (7)$$

where α is a user specified constant, $0.9T_{ign}$ represent the assumed temperature of the flameholder to or from which heat may be transferred, and T_i^{fh} is the (computed) gas temperature at the flameholder location. Note that when this model is used, energy is not strictly conserved in the system. That is, energy may be brought into or taken from the system by this term. T_{ign} is assumed to be constant, since the flame response time scale is much smaller than that of the flameholder wall temperature.

3.3 NUMERICAL METHODOLOGY FOR ONE-DIMENSIONAL COMBUSTION INSTABILITY MODEL

The combustor model numerically integrates the above equations of motion using a very simple, second-order MacCormack scheme. Artificial viscosity has been added in order to damp non-physical oscillations in the vicinity of strong gradients such as those brought about by the combustion process [19-22]. A number of grid independent studies were conducted to ensure that physical instability would not be damped [22]. In the current study, the grid size was Δx = 0.005 mm for which the results were very much grid-independent, as will be shown in the results.

3.4 BOUNDARY CONDITIONS FOR ONE-DIMENSIONAL COMBUSTION INSTABILITY MODEL

Boundary conditions may be imposed as either partially opened, fully open, or choked inflow (e.g. constant mass flux) ends. In either case the model anticipates the flow direction and applies appropriate (e.g. well posed) states. If the flow is outward from the computing domain, only the static pressure is imposed. The remaining information, density, velocity, and mass fraction are obtained from the interior of the computational domain. If the flow is inward, total pressure and temperature, and mass fraction are imposed. The remaining unknown quantities (velocity, static temperature and pressure) are obtained through an iteration procedure by using isentropic relations for static and total temperature and pressure. In other words, the velocity is first obtained by using $\partial u/\partial x = 0$ at the exit. Then, the static temperature is obtained iteratively through the relation $T_o/T = 1 + 0.5(\gamma - 1)u^2/(\gamma RT)$. Finally, the static pressure is obtained through p_o/p_t relation.

4 RESULTS

In this part of the study, efforts were mainly focused on demonstrating the uncombined performance of the one-dimensional combustor model and the LES methodology in suitable combustor configurations. The objective here is to provide confidence that the two models are capable of predicting the reaction flow field. In sequent study Part II, the information obtained from LES will be used to guide the application of the one-dimensional model in a combined manner. Results obtained from the one-dimensional combustor model will be first presented, followed by the results obtained from LES respectively.

4.1 ONE-DIMENSIONAL RESULTS

Numerical results have been obtained to demonstrate the applicability of the unsteady one-dimensional combustor model to predict combustion-driven instability in a generic gas turbine combustor. Figure 1 shows the schematic of the combustor geometry investigated in this study. Fully premixed fuel-air mixture was assumed at the inlet of the combustor. The fuel

type used was JP-8. Combustor model constants used in this study are given in Table 3. As indicated earlier, two different types of exit boundary conditions were implemented in the combustor model, namely, full open and choked. In this preliminary study, only the open exit boundary condition was used. The boundary condition imposed at the exit corresponds to a non-dimensional pressure value of unity. In fact, the reference pressure in this study was assumed to be equal to the back pressure. Due to the one-dimensionality of the combustor model, the effects of the swirl velocity component was accounted for by using a 1.1 % reduction in the static pressure at the combustor inlet.

The combustor model assumes that a constant fuel-air flux can be specified at the inlet in the absence of combustor pressure acoustics. This condition is essentially a choked boundary in which the effect of the downstream pressure acoustics are not sensed upstream of the inlet. However, a choked inlet condition would lead to stable combustion as the computations showed. The dependence of the inlet fuel-air mixture flux upon the combustor pressure should, therefore, be determined through a fuel injection system model. Since the current study assumes the computational domain to start at the backward facing step, a lumped-element parameter model for the fuel injectors/swirlers was considered.

$$\dot{m}_2 = \dot{m}_1 - \frac{\rho V}{k}\frac{dp'}{dt} \tag{8}$$

Equation (8) expresses the dependence of the fuel-air flow rate at the inlet of the combustor, $\dot{m}_2$, on the combustor pressure oscillations p'. The fuel-air mixture mass flow rate $\dot{m}_1$ is a constant. Equation (8) also implies that as the combustor pressure oscillation $p' \to 0$, $\dot{m}_2 = \dot{m}_1$ and a constant fuel-air mixture flow rate is then imposed at the combustor inlet.

The location of the fuel injection and the time required for the fuel-air mixture to react are very critical parameters for either driving or damping the instabilities [6,7]. The time delay between the instant of fuel injection and the instant of heat release is primarily governed by the mixing and chemical kinetic times. To account for this time delay, various estimations of this time delay were made based on the location of the fuel injector and chemical times for different equivalence ratios (i.e., ϕ = 0.5 - 0.8), initial temperatures (i.e., T_{inlet} = 700 - 900 K) and Damkohler numbers (Da = 1.0 - 100). The time delay was then used in the combustor model to determine the instant at which the fuel-air mixture, $\dot{m}_1$, is injected. The resultant mixture injection was therefore shifted in time by an amount equal to the time delay (i.e., injection time = $t \pm \delta t$) and $\dot{m}_1(t \pm \delta t)$ is injected.

Figures 2 and 3 show the combustor limit cycle pressure oscillations and the corresponding heat release in non-dimensional form and for a time delay of 1.97×10^{-3} s and at a non-dimensional location x = 0.8. This value of the time delay was found to produce the largest amplitude of the pressure oscillations. The cycle limit pressure oscillations have a non-dimensional period of approximately 0.9 (or 3.6×10^{-3} s) and a corresponding non-dimensional frequency of 1.11 (or 278 Hz). It can also be seen that these strong oscillations have shock waves characteristics, which indicate that these are a strong longitudinal instability of the fundamental mode 278 Hz. In addition, a close examination of the limit cycle pressure oscillations and that of the heat release fluctuations clearly exhibits the phase relationship between the heat release and the pressure oscillations. Pressure and heat release oscillations were predicted to be in phase and thus satisfy Rayleigh's criterion for driving instability.

Figure 4 shows the pressure field oscillations for a time delay of 3.8×10^{-3} s which is equal to 1.97×10^{-3} + half the limit cycle period shown in Fig. 2. It is clearly seen that the strong limit cycle oscillations of Fig. 2 have been substantially damped, consistent with the time lag theory of Crocco [23]. This demonstrates the capability of the combustor model to simulate non-linear behavior. Additional simulations were carried out to substantiate the time delay effect and the results were all consistent. It should be mentioned that when calculations were made for constant fuel-air mixture mass flow rate (time delay and p' are set equal to zero), a steady-state combustion was predicted.

To further demonstrate the ability of the combustor model to carry out active control calculations, the combustor response to fuel flow modulation as a means to actively control instability was predicted. The fuel injection was pulsed sinusoidally at different frequencies and amounts. The predictions represent the open loop response of the controlled combustor as shown in Fig.1. Note here that no phase shift and controller gain were used in the current study. The inlet condition for the open loop calculations was set to be a constant fuel-air mixture flux with various time delays (i.e., non-choked inlet) and the exit condition was also open with a specified non-dimensional pressure of unity. The combustor length was also kept the same to ensure that the combustor resonant frequencies are considerably higher than the fuel pulsation frequencies. The amplitude of the amount of fuel pulsed was varied between 2% to 10% of the total primary fuel injection rate and the combustor response was studied.

Figures 5-8 show the predicted combustor response in terms of the non-dimensional pressure, temperature, velocity

and primary fuel mass fraction for a time delay of 1.97×10^{-3} s and at the non-dimensional location x = 0.8. The non-dimensional fuel pulsation frequency ω was 0.6 (i.e., ω = 150 Hz) and the non-dimensional magnitude A was 2% of the primary fuel rate. The sinusoidal fuel pulsation was turned on at the start of the computations (i.e., after one computational time step for convergence and code stability). The results clearly show that significant damping of the pressure, temperature and velocity oscillations occurred. In particular, it can be seen that the pressure initially increases due to the rapid rise in the temperature and then it is followed by a period over which the pressure oscillates and finally the oscillations damp out. This behavior is also reflected in temperature and velocity fields.

Figures 9 and 10 show the non-dimensional pressure and temperature in the combustor for A = 10% of the primary fuel rate and for the same conditions as in Figs. 5 through 8. It can be seen that increasing the amount of pulsed fuel does not always result in more damping. In fact, the amplitude of the final oscillations appear to be somewhat greater than that of the previous case, for A = 2%. However, the increase in the oscillation magnitude is not significant.

To further study the effect of fuel pulsation on the combustor response, the fuel pulsation was turned on after the limit cycle pressure oscillations were reached for the case presented in Figs. 2 and 3. The combustor response predictions are shown in Figs. 11-13. It is clearly demonstrated that if the fuel is pulsed after the system has reached a limit cycle, the decrease in the amplitude of the pressure oscillations appears to be limited and never goes to zero as the computations revealed. The reason for this behavior may be attributed to the inability of pulsed fuel to produce a secondary heat release oscillation of sufficient amplitude and be completely out of phase with the strong limit cycle pressure oscillations. This can further be seen in Fig. 11 where the heat release fluctuations are not entirely out of phase with the pressure oscillations. It should also be indicated that a similar behavior was seen [5], when an active control was turned on after the system has reached the limit cycle behavior. This is indicative of the unsatisfactory performance of fuel pulsation to control instability in the limit cycle regime. Multiple fuel pulsation frequencies based on multiple pressure modes sensed in the combustor will be required to damp non-linear instabilities, which will be investigated in the near future.

4.2 LES OF TRAPPED VORTEX COMBUSTOR

The TVC is a combustor design under investigation for IHPTET applications. In this concept, the combustion occurs in a vortex trapped within a cavity and past results suggests that this can increase flame stability. Figure 14 shows schematically, the combustor simulated in the present study.

Various studies into the application of cavity-flow interaction have been conducted in the past. Earlier [24] it was noted that a cavity-locked vortex entrains very little main-flow air and would result in a low exchange of mass and heat between the cavity and the main flow, Since combustion requires a continuous supply of reactants, fuel and air must be directly injected in the cavity to sustain the burning processes. However, direct injection (mass addition) can disrupt the flow dynamics, possibly resulting in cavity instability. Previous attempts at numerical modeling of TVC [25, 26], noted the possibility of mixing-limited reactions in the TVC. For this reason, fuel/air mixing and its effect on combustion in the TVC is investigated in this study.

The model formulation and the various closure models are summarized in a recent paper [27] and therefore, not repeated here. In the following, we briefly highlight some of the salient features observed in this study.

To investigate the fluid dynamic mixing properties of the TVC, two cases (I & II) were conducted under identical conditions except that the air velocity at the inlet was changed from 20 m/s (case I) to 40 m/s (case II). Non-reacting mixing was studied with fuel is injected into the cavity with an equivalence ratio far above stoichiometric (ϕ = 4.4). Thus, entrainment and mixing with the ambient air is critical in order to achieve efficient combustion.

To increase mixing rates, higher turbulence levels are also desired. Regions of high mean and, perhaps more importantly, high RMS velocities will tend to enhance mixing rates. Therefore, we investigated the effect of increasing in the primary airflow rate.

For visualization, the time averaged and instantaneous velocity vectors for cases I & II are shown in Figs. 15(a) & 15(b), respectively. The higher annular flow rate (Fig. 15(b)) enhances the trapped-vortex strength, allowing for increased annular/cavity flow interaction. In the time averaged results, it is seen that two vortices are present for case I. In addition to a vortex rotating in the direction of the annular flow, the second vortex rotates in the reverse direction. However, these vortices are not observed in case II. Rather, only a single, large vortex rotates with the flow. The instantaneous images on the other hand do show transient vortices in the shear layer and in the cavity indicating a process of unsteady entrainment of the primary air from the inlet. As discussed elsewhere [27] and noted below, this turbulent mixing appears to be beneficial for fuel-air mixing.

Two reacting-flow cases (IV & V) were also used to investigate the impact of fuel/air mixing rates under reacting conditions. The primary equivalence ratio of the cavity jets in both cases was again 4.4 and the injection temperature was a slightly elevated value of 500 K. As observed by Sturgess et al.

[28], the cavity flow entrains relatively little annulus air and will tend to be fuel-rich under reacting flow conditions. This was confirmed by looking at the mean fuel and oxygen mass fractions [27] (not shown here). For the low speed case, near the injection ports, the RMS values are much higher due to fluctuations in velocity and species composition. Far from the injectors, however (near the fore-body wall), the oxygen is almost entirely consumed leaving a fuel-rich cavity region. The remaining fuel is finally consumed outside the cavity in either the dump shear layer or downstream of the after-body, depending on the inlet flow velocity. For the higher flow velocity, on the other hand, more fuel is consumed in the cavity. This indicates that the primary air stream is entrained more with increase in flow velocity and the increase turbulence enhances fine-scale mixing.

The rate at which the fuel is mixed can be viewed by examining the species mixture fraction, Z, as a function of inflow velocity. Shown in Figs. 16(a) and 16(b) are the instantaneous and time averaged stoichiometric mixture fraction surfaces, $Z = Z_{st}$, for both reacting flow cases (The stoichiometric surface, Z_{st}, has been highlighted by a single black line, where Z_{st} for methane air is approximately 0.055). As can be seen in Fig. 16(b) (U_o = 40 m/s), Z_{st} is almost entirely contained inside the cavity region for both the instantaneous and the time averaged results. For the lower inflow velocity, the surface extends far downstream of the cavity zone.

Also shown in Figs. 16(a) and 16(b) are the instantaneous and time-averaged temperature color contours for cases IV & V. Following the same trends as Z, the peak temperature regions are seen to shift from outside the cavity region for a lower annular velocity to inside the cavity in case V. In both mean and instantaneous views, the cavity temperature increases with increases flow velocity.

Comparisons with experimental data is possible for case V. The mean and RMS temperature profiles reported by Hsu et al. [24] (obtained with CARS technique) are super-imposed in Fig. 17. The combustor conditions were nearly identical to those simulated in case V, U_o = 42 m/s, ϕ = 4.4, H/d = 0.59: however, propane instead of methane was used as the primary fuel. Despite this difference, the mean temperature trends should still be comparable. A maximum instantaneous temperature of 2025 K was obtained inside the cavity in case II which is slightly lower then the 2150 K reported by Hsu et al [24].

For both inflow velocities, the mean temperature near the injection ports has not been greatly effected. However, away from the injectors, the higher inflow velocity resulted in higher cavity temperatures for both mean and instantaneous profiles. The peak temperature region for the case IV is not inside the cavity but downstream in the after-body wake resulting in longer thermal residence times. The longer residence times may increase thermal No_x production. As would be expected with the higher inflow velocity, the downstream temperature is lower despite higher cavity temperatures. This is mainly due to the higher volume flow rate and lower overall equivalence ratio. The combination of a higher fuel consumption rate and higher velocity results in a lower thermal residence time. This is beneficial to lower combustion pollutant formation.

5 CONCLUSION

Large eddy simulation and one-dimensional analysis were carried out to predict combustion-driven dynamic instabilities. The one-dimensional combustor model was first used to study active control of combustion-driven instabilities in a generic gas turbine combustor. The numerical predictions clearly demonstrated the effect of the time delay between the instant of fuel injection and heat release. By varying this time delay, damping or driving of the instability may occur. The predictions showed that there existed a single time delay value for the combustor geometry considered here and for which strong instability can set out and is manifested by a limit cycle behavior. The analysis also showed that these strong pressure oscillations can be damped out by changing the delay time by some factor multiplied by the oscillation period.

The one-dimensional combustor model was also used to investigate the combustor response to fuel flow pulsation to control instability. The results clearly demonstrated that for fuel pulsation to be effective in controlling instability, the fuel modulation must be turned on at the start of the engine. Moreover, the results indicated that multiple frequency-based fuel pulsation might be required to damp out strong shock wave type instability oscillations.

The use of In-situ Adaptive Tabulation (ISAT) to efficiently calculate multi-species finite-rate kinetics is demonstrated in this study. It is also demonstrated that the LEM model can be used to simulate premixed combustion regardless of the nature of the flame structure (i.e., flamelet or thin-reaction-zones) without requiring any ad hoc fixes. This study when combined with the earlier studies clearly suggest that subgrid combustion modeling for LES is a viable option even when finite-rate kinetics is to be simulated.

Finally, it should be mentioned that the combustor model developed here is a very useful predictive tool that can be used during the predesign and design stages to predict the dynamic instability characteristics of new combustor designs in a very efficient manner. However, detailed description of the unsteady flow field must be predicted in order to use the one-dimensional model to suppress combustion-driven dynamic instabilities.

ACKNOWLEDGMENTS

The authors would like to thank Dr. Paxson from NASA Glenn Research Center for the technical discussion and providing us with the original baseline code for one-dimensional combustor model. The LES work was supported by the Army Research Office under the Multidisciplinary University Initiative.

REFERENCES

1. Darling, D., Radhakrishnan, K., Oyediran, A., and Cowan, E., "Combustion-Acoustic Stability Analysis for Premixed Gas Turbine Combustors," NASA TM 107024.
2. Bloxsidge, G. J., Dowling, A. P., and Langhorne, P. J., "Reheat Buzz: an Acoustically Coupled Combustion Instability. Part 2. Theory," *J. Fluid Mech.*, Vol. 193, pp. 445-473, 1988.
3. Bloxsidge, G. J., Dowling, A. P., and Langhorne, P. J., "Active Control of Reheat Buzz," *AIAA Journal*, Vol. 26, No. 7, pp. 783-790, 1988.
4. Shyy, W. and Udaykumar, "Numerical Simulation of Thermo-Acoustic Effect on Longitudinal Combustion Instabilities," 26th JPC, *AIAA 90-2065*, 1990.
5. Mohanraj, R. and Zinn, B. T., "Numerical Study of the Performance of Active Control Systems for Combustion Instabilities," 36th JPC, *AIAA 98-0356*, 1998.
6. Smith, C.E., and Leonard, A., D. "CFD Modeling of Combustion Instability in Premixed Axisymmetric Combustors," *ASME Paper 97-GT-305*, 1997.
7. Habiballah, M. and Dubois, I., "Numerical Analysis of Engine Instability," 31st JPC, *AIAA 95-37213*, 1995.
8. Kim, Y. M., Chen, C. P., Ziebarth, J. P., and Chen, Y. S., "Prediction of High Frequency Combustion Instability In Liquid Propellant Engines," 28th JPC, *AIAA 92-3763*, 1992.
9. Quinn, D., D and Paxson, D. E., "A Simplified Model for the Investigation of Acoustically Driven Combustion Instability," 34th JPC, *AIAA 98-3764*, 1998.
10. Hsiao, G., Pandalai, R., Hura, H., and Mongia, H. C., "Combustion Dynamic Modeling for Gas Turbine Engines," 34th JPC, *AIAA 98-3380*, 1998.
11. Yang, V., and Anderson, W., "Liquid Rocket Engine Combustion instability," *Progress in Astronauts and Aeronautics*, Vol. 169, 1995.
12. Menon, S., Kim, W.-W., Stone, C., and Sekar, B., "Large-Eddy Simulation of Fuel-Air Mixing and Chemical Reactions in Swirling Flow Combustor," *AIAA 99-3440*, 30th Plasma Dynamics and Lasers Conference, Norfolk, VA, June 1999.
13. Menon, S., Stone, C., Sankaran, V., and Sekar, B., "Large-Eddy Simulations of Combustion in Gas Turbine Combustors," *AIAA 00-0960*, Jan. 2000.
14. Kim, W.-W. and Menon, S., "A New Incompressible Solver for Large-Eddy Simulations," *International Journal of Numerical Fluid Mechanics*, Vol. 31, pp. 983-1017, 1999.
15. Kerstein, A. R., "Linear-Eddy Model of Turbulent Transport II," *Combustion and Flame*, Vol. 75, pp. 397-413, 1989.
16. Chen, Y., Peters, N., Schneemann, G., Wruck, N., Renz, U., and Mansour, M., "The Detailed Structure of Highly Stretched Turbulent Premixed Methane-Air Flames," *Combustion and Flame*, Vol. 107, pp. 223-244, 1996.
17. Mansour, M., Peters, N., and Chen, Y., "Investigation of Scalar Mixing in the Thin Reaction Zones Regime Using a Simultaneous CH-LIF/Rayleigh Laser Technique," *Twenty-Seventh Symposium (International) on Combustion*, pp. 767-773, 1998.
18. Bedat, B. and Cheng, R. K., "Experimental Study of Premixed Turbulent Flames in Intense Isotropic Turbulence," *Combustion and Flame*, Vol. 100, pp. 486-494, 1995.
19. Paxson, D. E., "A General Numerical Model for Wave Rotor Analysis," NASA TM 105740, July 1992.
20. Paxson, D. E., "An Improved Numerical Model for Wave Rotor Design and Analysis," *AIAA 93-0482*, Jan. 1993, also NASA TM 105915.
21. Paxson, D. E., "A Comparison Between Numerically Modeled and Experimentally Measured Loss Mechanisms in Wave Rotors," *AIAA Journal of Propulsion and Power*, Vol. 11, No. 5, 1995, pp. 908-914, also NASA TM 106279.
22. Nalim, R. M. and Paxson, D. E., "A Numerical Investigation of Premixed Combustion in Wave Rotors," *ASME Journal of Engineering for Gas Turbines and Power*, Vol. 119, No. 3, 1997, pp. 668-675, also ASME Paper 96-GT-116, June, 1996, also, NASA TM 107242.
23. Crocco, L. and Cheng, S.-I., "Theory of Combustion Process Instability in Liquid Rocket Engines," IL, Moscow, 1958, pp. 59-69.
24. Hsu, K.-Y., Goss, L. P., and Roquemore, W. M., "Characteristics of a Trapped-Vortex Combustor," *Journal of Propulsion and Power*, Vol. 14, No. 1, pp. 1-12, 1998.
25. Katta, V. and Roquemore, W., "Numerical Studies on Trapped-Vortex Combustor," *AIAA 96-2660*, 1996.
26. Katta, V. and Roquemore, W., "Study of Trapped-Vortex Combustor – Effect of Injection on dynamics of Non-Reacting and Reacting Flows in a Cavity," *AIAA 97-3256*, 1997.
27. Stone, C. and Menon, S., "Simulation of Fuel-Air Mixing and Combustion in a Trapped Vortex Combustor," *AIAA 00-0478*, 2000.
28. Sturgess, G. and Hsu, K.-Y., "Entrainment of Mainstream Flow in a Trapped-Vortex Combustor," *AIAA 97-0261*, 1997.

Table 1 15 Step, 19 Species Mechanism

$H + 0.5O_2 = OH$
$H_2 + 0.5O_2 = H + OH$
$HO_2 = 0.5O_2 + OH$
$0.5O_2 + H_2O_2 = OH + HO_2$
$0.5O_2 + 0.5C_2H_2 = H + CO$
$CH_3 + CO + C_2H_4 = 0.5O_2 + CH_4 + 1.5C_2H_2$
$0.5O_2 + 2CH_3 = H_2 + CH_4 + CO$
$0.5O_2 + CH_3 = H + CH_2O$
$0.5O_2 + CH_4 = OH + CH_3$
$0.5O_2 + CO = CO_2$
$0.5O_2 + C_2H_6 = CH_4 + CH_2O$
$H + OH = H_2O$
$H + CH_4 + NO + HCN = 0.5O_2 + 2CH_3 + N_2$
$H + 0.5O_2 + CH_4 + HCN = 2CH_3 + NO$
$0.5O_2 + CH_4 + NH_3 + HCN = H_2O + 2CH_3 + N_2$

Table 2 ISAT Performance

	ϵ_{tol} = 5E-3	ϵ_{tol} = 8E-3	*DI*
Total CPU time	16.66 h	9.46 h	31.11 h
Chemistry time	0.0108 s	7.3e-3 s	0.2278 s
Speed up in Chemistry	21	31	-
Speed up in simulation	2	3	-
No. of Records	40500	16500	-

Table 3

Model Constants	
γ	1.37
ε_t	0.002
Sc_t	1.0
Pr_t	1.0
T_{ign}	1.25

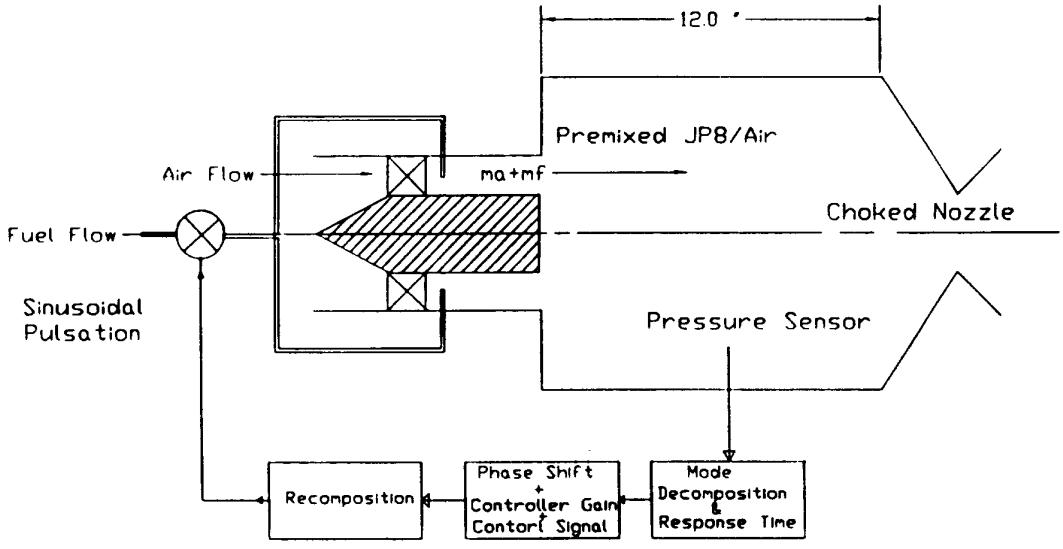


Fig. 1 A Schematic of the Combustor and Control System.

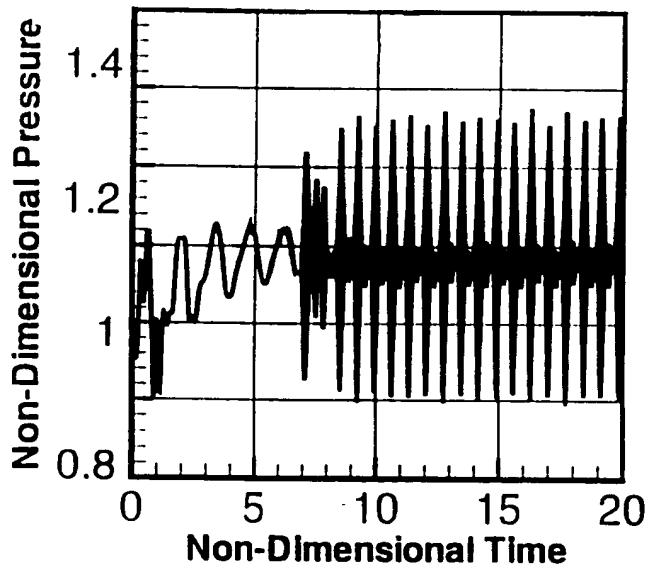


Fig. 2 Limit Cycle Pressure Oscillations for a Time Delay $\delta t = 1.97 \times 10^{-3}$ s.

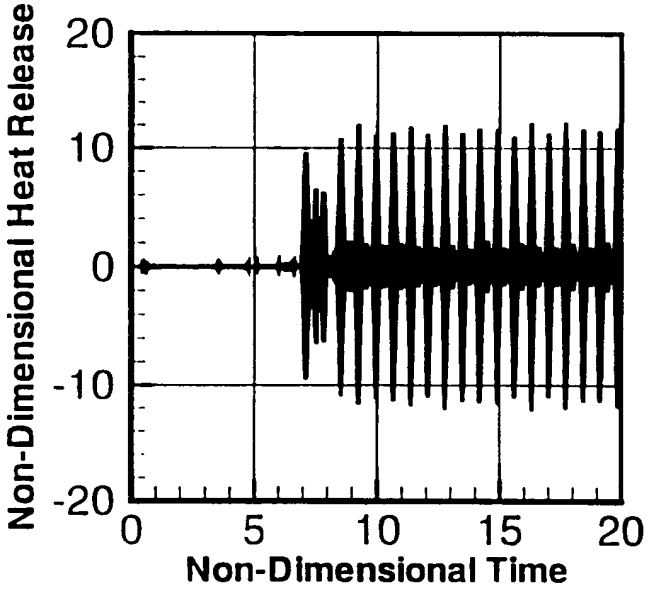


Fig. 3 Non-Dimensional Limit Cycle Heat Release Oscillations Corresponding to $\delta t = 1.97 \times 10^{-3}$ s.

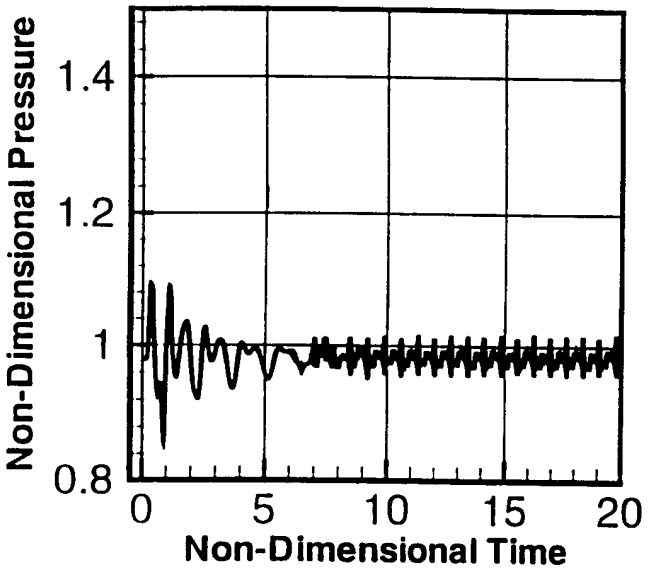


Fig. 4 Effect of Time delay on the Limit Cycle Pressure Oscillations for a Time Delay $\delta t = 1.97 \times 10^{-3} + 1.8 \times 10^{-3}$ s.

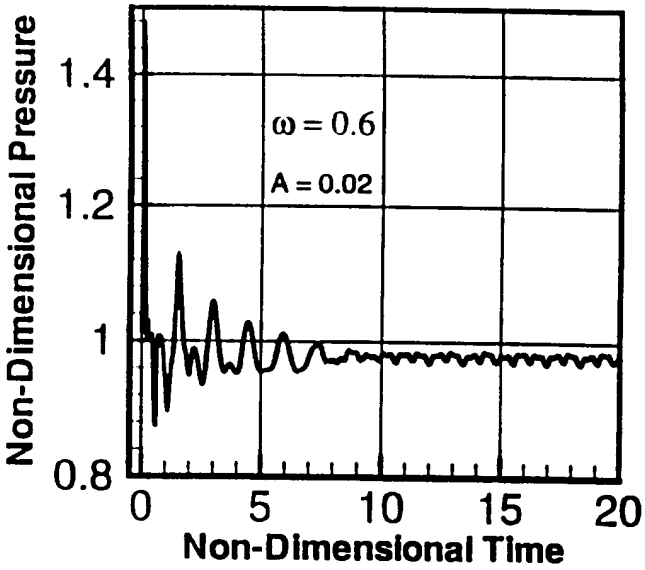


Fig. 5 Effect of Fuel Modulation on the Pressure Oscillations for Concurrent Primary and Pulsed Fuel Injection.

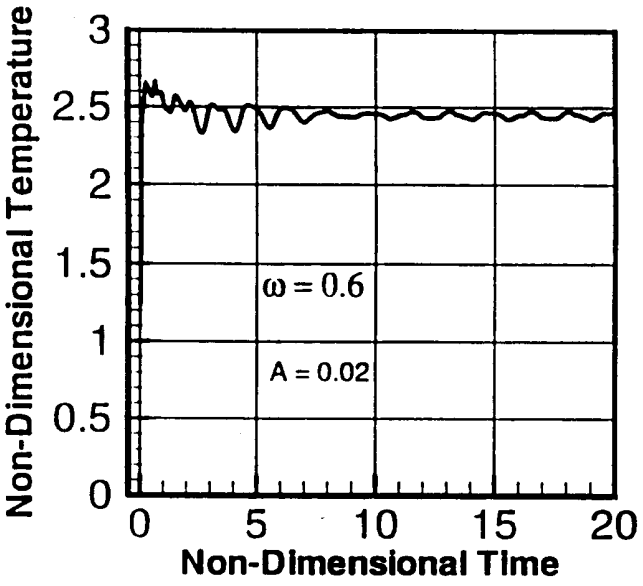


Fig. 6 Effect of Fuel Modulation on the Temperature Oscillations for Concurrent Primary and Pulsed Fuel Injection.

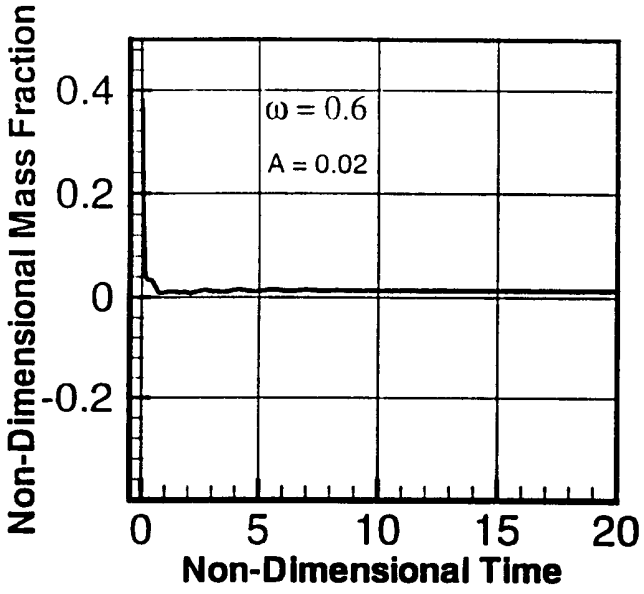


Fig. 8 Effect of Fuel Modulation on the Fuel Concentration Oscillations for Concurrent Primary and Pulsed Fuel Injection.

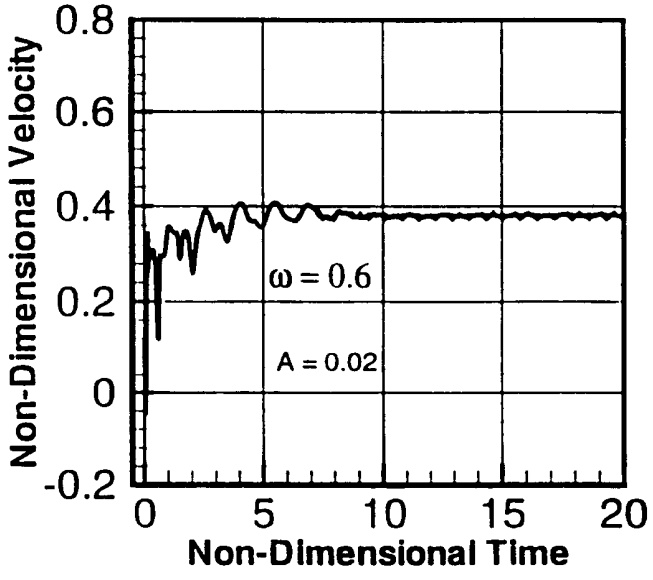


Fig. 7 Effect of Fuel Modulation on the Velocity Oscillations for Concurrent Primary and Pulsed Fuel Injection.

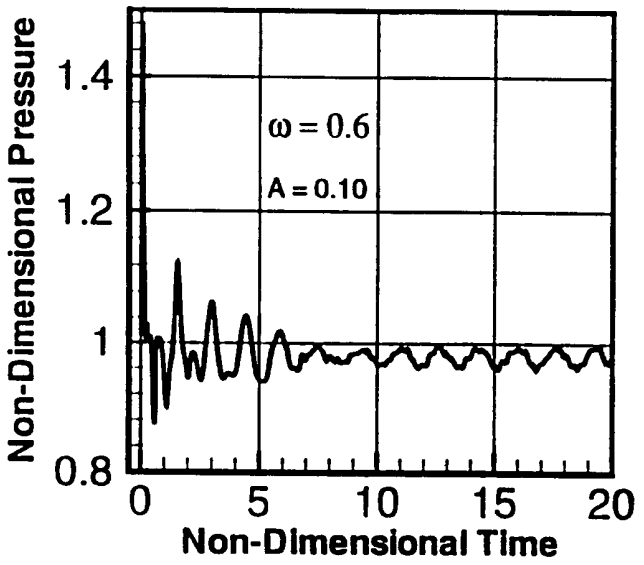


Fig. 9 Effect of the Amount of Fuel Modulation on the Pressure Oscillations for Concurrent Primary and Pulsed Fuel Injection.

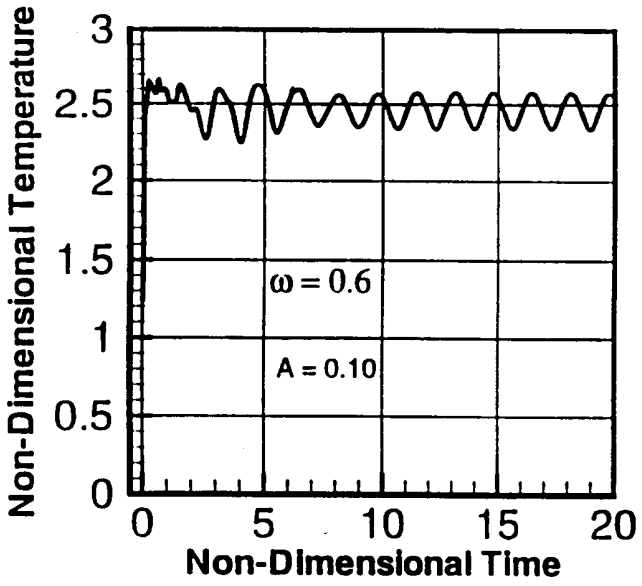


Fig. 10 Effect of the Amount of Fuel Modulation on the Temperature Oscillations for Concurrent Primary and Pulsed Fuel Injection.

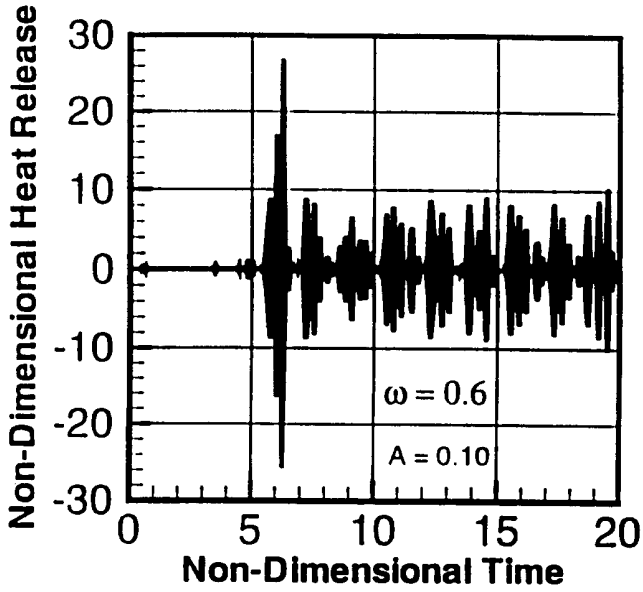


Fig. 12 Effect of Fuel Modulation on the Limit Cycle Heat Release Oscillations for Non-Concurrent Primary and Pulsed Fuel Injection.

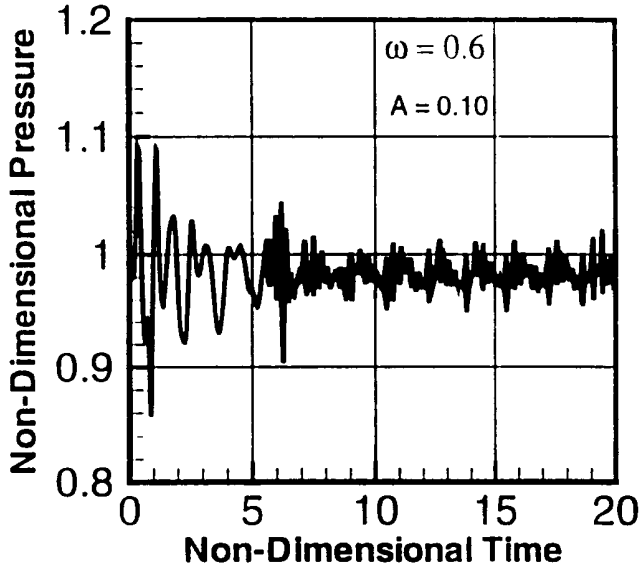


Fig. 11 Effect of Fuel Modulation on the Limit Cycle Pressure Oscillations for Non-Concurrent Primary and Pulsed Fuel Injection.

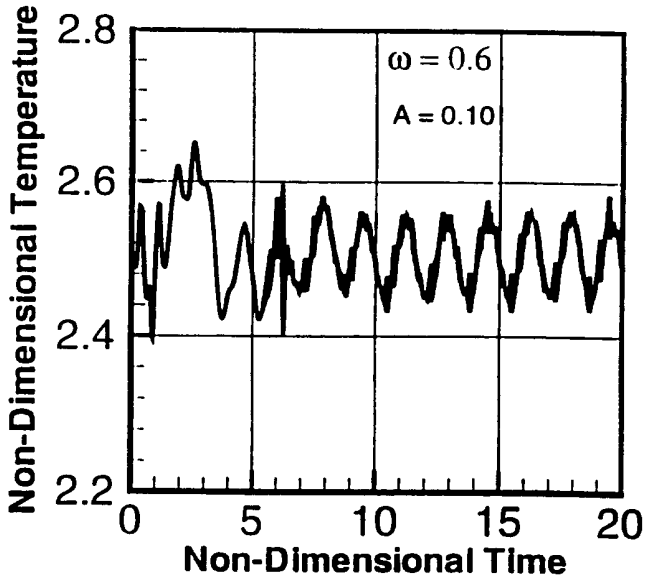


Fig. 13 Effect of Fuel Modulation on the Limit Cycle Temperature Oscillations for Non-Concurrent Primary and Pulsed Fuel Injection

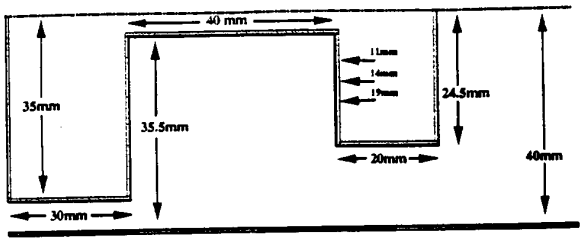
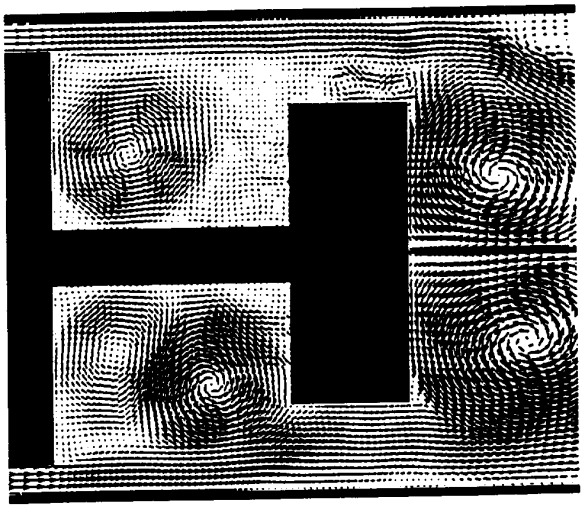
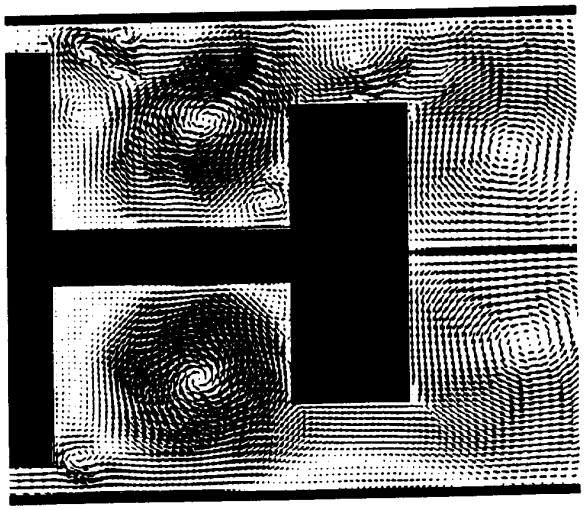


Fig. 14 Trapped-Vortex Geometry Used in This Numerical Study. Total Length (x) = 285 mm.

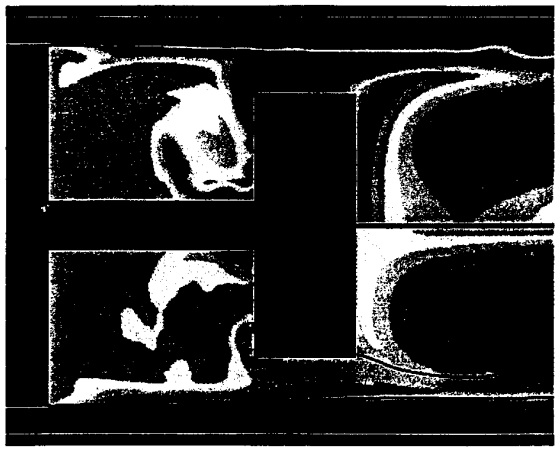


a) U_o = 20 m/s

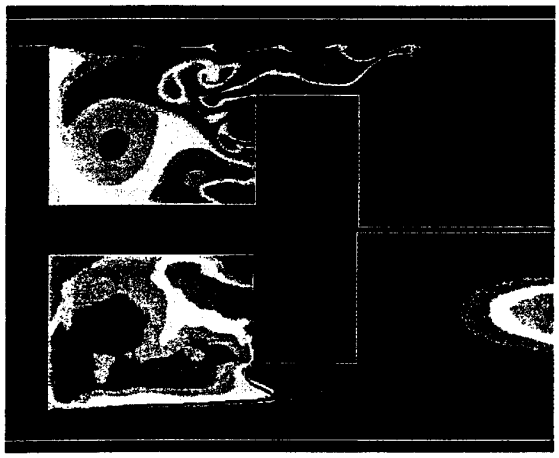


b) U_o = 40 m/s

Fig. 15 Non-Reacting Velocity Vectors for U_0 = (a) 20 m/s, (b) 40 m/s (cases I & II). Upper Halves are Instantaneous, Lower Halves Are Time Averaged.



a) U_o = 20 m/s



b) U_o = 40 m/s

Fig. 16 Reacting Flow Temperature Field and Stoichiometric Surface for U_0 = (a) 20 m/s, (b) 40 m/s. Upper Halves are Instantaneous, Lower Halves Are Time Averaged. Temperature Color Contour Ranges Are 300 K (Blue) and 2000 K (Red). Stoichiometric Mixture Fraction, $Z = Z_{st} \cong 0.055$, Shown with Black Line.

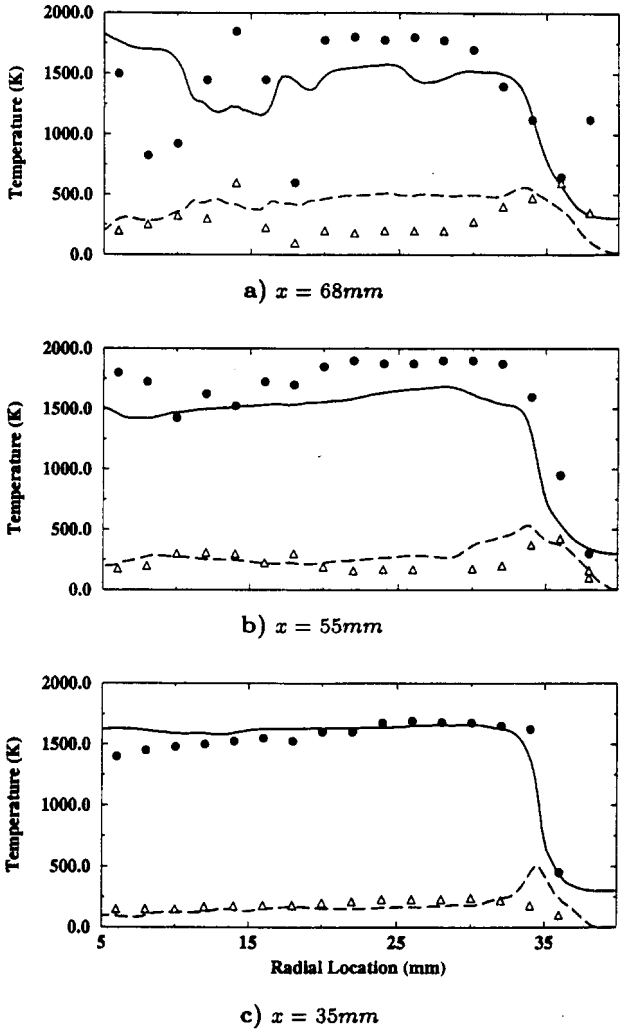


Fig. 17 Mean and RMS Temperature Profiles at x = (a) 68, (b) 55, (c) 35 mm for U_o = 40 m/s (Case V).
$< \widetilde{T} >$ (—), $\widetilde{T}^{RMS}$ (– –), T_{exp} (•), T_{exp}^{RMS} (Δ).
Experimental results ($_{exp}$) from Hsu *et al.*

PAPER -19, B. Sekar

Question (J.-P. Hathout, USA)

According to the authors, pulsing in open loop causes the "unstable" system to become "stable". Can the author clarify the physics behind this behavior? Can it be inferred from the dynamics of the model what type of nonlinearities are responsible for stability?

Reply

The idea is, when the system is unstable, it could be damped by giving a frequency and modulating a portion of the fuel to different amplitude magnitude. But totally this cannot be made to be stable. There will still be oscillations, but either reduced or amplified depending on the frequency or amplitude. Thus, you could change the oscillating pattern and magnitude by different input of either the time delay or frequency or amplitude. The nonlinearities to predict the limit cycle behavior comes from time dependent boundary conditions, time dependent formulation of the basic equations, and the coupling of unsteady pressure fluctuations and the fuel-air oscillations.

An Experimental Examination of the Relationship between Chemiluminescent Light Emissions and Heat-release Rate Under Non-Adiabatic Conditions

L. C. Haber, U. Vandsburger, W.R. Saunders and V. K. Khanna
Reacting Flows Laboratory, Department of Mechanical Engineering
Virginia Tech, Blacksburg VA 24061-0328, USA

ABSTRACT

Combustion instability research has matured over the last decade and with it the need for more detailed diagnostics has increased. One main gap in the diagnostics is the ability to obtain a reliable quantitative measure of unsteady heat–release rate. In an effort to move in this direction using chemiluminescence as the measured quantity, this paper examines the formation of chemiluminescent light in premixed flames under non-adiabatic conditions. The main chemiluminescent emitters considered in the study are OH^* and CH^*. Experimental results for two types of burners are reported, a laminar Bunsen burner with co–flow and a ceramic honeycomb flat flame burner. The study shows that although the chemiluminescence observed in the two burners behaves very differently with respect to changes in experimental variables, the variation can be fully understood. OH^* chemiluminescence is found to be a good indicator of heat–release in both burners, whereas CH^* chemiluminescence is shown to be insensitive to some changes in heat–release rate. Based on the experimental results, the notion that chemiluminescence yield behaves linearly with flow–rate cannot be universally supported. The non–linear variation observed is shown to correspond to an equally non–linear variation of heat–release with flow–rate. The results of the study thus have important ramifications for the interpretation of chemiluminescence measurements in dynamic combustion environments.

1 INTRODUCTION

To truly understand the nature of combustion instabilities the ability to measure the influence of acoustic velocity and pressure perturbations on the flame heat–release rate is indispensable. The heat–release measurement capability is also important in the development of models that predict combustion instabilities. Chemiluminescence measurements have often been made to obtain some qualitative indication of the nature of the above described interaction (Samaniego et al., 1993). Quantitative heat–release rate deductions from chemiluminescence measurements have also been made but on a purely empirical basis, assuming a relationship between heat–release rate and chemiluminescence without direct verification (Langhorne, 1988).

To develop confidence in chemiluminescence as a reliable measure of heat–release rate, the relationship between the two quantities must be fully understood. Previous studies (Price et al., 1968) have not analyzed the connection between chemiluminescence and heat-release in great detail because knowledge of the reaction mechanism was very limited. The work presented here uses a detail analysis of experimental results on two very different burners to help develop the desired level of understanding of the relationship between chemiluminescence and heat–release. The study also has included a large modeling effort (Haber et al., 2000) to help provide a foundation for the analysis results presented below.

The understanding of the relationship between chemiluminescence and heat–release relies heavily on a final complete knowledge of the formation paths of chemiluminescent species. The formation chemistry of chemiluminescent species has received some recent attention (Devriendt and Peeters, 1997) but is still not fully understood. In the case of OH^* the currently accepted mechanism was proposed by Krishnamahari and Broida (1961) and has only been verified indirectly by Porter et al. (1967), by Becker et al. (1977) and by Dandy and Vosen (1992) .

The present study considers OH^* and CH^* as the main chemiluminescent species of interest. CO_2^* has been studied as another possible indicator of heat–release rate (Samaniego et al., 1995) but will not be discussed in this paper. OH^* and CH^* are the major chemiluminescence emitters in lean hydrocarbon flames, apart from the CO_2^* emission continuum.

Paper presented at the RTO AVT Symposium on "Active Control Technology for Enhanced Performance Operational Capabilities of Military Aircraft, Land Vehicles and Sea Vehicles", held in Braunschweig, Germany, 8-11 May 2000, and published in RTO MP-051.

The fuel used in both present burner studies is methane. Methane was chosen not only for its relatively well known reaction mechanism but also because methane forms a large percentage of natural gas, which is used in most modern lean premixed gas turbine combustors. The use of methane gas allows conclusions drawn from the present study with respect to heat–release relationships to be more easily applied to the gas turbine combustor environment. The present report, however, does not include the study of a turbulent type flame. Since however, the chemical kinetic path of methane reaction remains the same in any combustion system, it is expected that at least qualitatively correct deductions about chemiluminescence measurement in gas turbine combustors can be made.

The experimental setup used to perform measurements in each of the burners is discussed in Section 2. Experimental results obtained from these burners are shown in Section 3. Analysis of the results with respect to heat–release rate and chemiluminescence formation paths is presented in Section 4. Conclusions and ongoing research are given in Section 5.

2 EXPERIMENTAL SETUP

Bunsen burner

The Bunsen burner used in the present study consists of a 12 mm stainless steel tube that is mounted concentrically into a long quartz chimney. The shroud around the stainless steel burner is required to protect the Bunsen burner flame from drafts. To keep the flame from extinguishing inside the quartz chimney, an annular co–flow of air is added. The co–flow is kept constant for all experiments. To assure flows of relatively low turbulence fine screens are mounted upstream in the main combustion flow as well as in the annular co–flow.

The Bunsen burner flame is such that very lean equivalence ratios could not be tested. The experiments cover a range of equivalence ratios from 0.75 to 1.1. The rich stoichiometrics tested serve the purpose of elucidating chemiluminescence formation paths. Flow–rates studied cover the range of air–flow from 55 cc/sec to 75 cc/sec.

Honeycomb burner

The ceramic honeycomb burner consists of a ceramic matrix of small, 1.12 mm, square channels, that is mounted to the top of a 4 inch to 3 inch carbon steel bell–reducer. The bell reducer is used to thin the boundary layer and generate a flatter velocity profile on input to the honeycomb. The flame obtained by lighting mixture flowing through the ceramic honeycomb is essentially flat. A quartz chimney again protects the flame from drafts. Co–flow is not needed in the honeycomb burner to aid in flame stabilization.

The honeycomb burner in contrast to the Bunsen burner allows the study of very lean mixtures. The experimental study reported in the present paper varies the equivalence ratio between 0.6 and 1.1. The flow–rates studied for the honeycomb burner also have a wider range than that studied for the Bunsen burner. The flow–rates varied from an air–flow of 130 cc/sec to an air–flow of 270 cc/sec.

Optical system

To collect the chemiluminescence, a two–lens optical system coupled to a fiber–optic cable is used. Each of the lenses has a focal length of 1 inch and is made of fused silica for good ultraviolet light transmission. The fiber–optic cable as well is made of fused silica. The fiber–optic cable used for the Bunsen burner measurements has a diameter of 200μm while the fiber–optic cable used for the honeycomb burner measurements has a diameter of 1000μm. The lens system in each case was set up to collect chemiluminescence evenly across the entire area of the burner, i.e. the intensity measurement is truly a measure of the total chemiluminescence emitted by the flame.

The fiber–optic cable transmits the collected light to a 0.5 m Ebert monochrometer, where the light is filtered by wavelength. OH^* measurements were performed at 308 nm and CH^* measurements were performed at 431 nm. In order to allow relative comparisons between OH^* and CH^*, each of the voltage measurements was corrected not only for the wavelength dependent losses in the optical train but also for the spectral shapes of the radiation emitted by OH^* and CH^*. Several complete spectra at various experimental conditions on both burners were measured to calculate an integrating scale factor to be used in correcting the single wavelength voltage measurement for the fact that the voltage only represents a certain part of the total energy radiation by the transitions of a certain type of molecule. Upon correction of the voltage in this manner, a measure of the true chemiluminescence yield from the entire flame is obtained. Units for the corrected chemiluminescence are given as (cV-A), which stands for corrected volt - Angstroms.

3 EXPERIMENTAL RESULTS

Bunsen burner

The results for the OH^* chemiluminescence yield variation with equivalence ratio for all flow–rates studied are shown in Figure 1. The maximum for the chemiluminescence is located near stoichiometric mixture conditions. The decrease in chemiluminescence on the rich side is somewhat less steep than on the lean side. The dependence of OH^* on equivalence ratio resembles that of laminar flame–speed on equivalence ratio. The shape of the curve does not appear to change significantly between flow–rates. Furthermore, each of the curves seems to be equally spaced at each equivalence ratio, suggesting a linear dependence of chemiluminescence on air–flow rate. Scaling relationships for Bunsen burner chemiluminescence are examined further in Section 4.

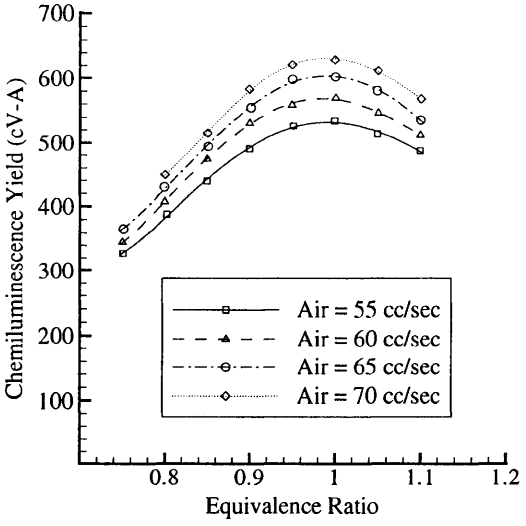


FIGURE 1: OH* chemiluminescence yield as a function of equivalence ratio for the Bunsen burner flame

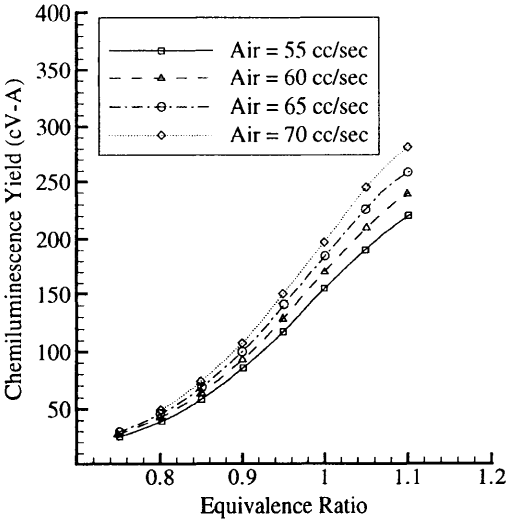


FIGURE 2: CH* chemiluminescence yield as a function of equivalence ratio for the Bunsen burner flame

The CH* chemiluminescence variation with equivalence ratio for all flow–rates studied is shown in Figure 2. CH* behaves very differently from OH*. The peak for CH* chemiluminescence lies on the rich side, beyond the range of the experimental conditions studied. As stoichiometric conditions are approached from the lean side, a near exponential dependence on equivalence ratio is found. CH* chemiluminescence increases six–fold over the equivalence ratio range studied. OH* chemiluminescence in contrast only exhibits an increase of 85%. The scaling relationship with flow–rate is not immediately clear upon examining Figure 2. If the dependence on flow–rate is linear for each equivalence ratio, the proportionality factor changes drastically in the equivalence ratio range studied.

Honeycomb burner

The honeycomb burner results are shown in Figure 3 and Figure 4. At an air flow–rate of 270 cc/sec, the experiment was limited to equivalence ratios below 0.925 due to the onset of a combustion instability. The variation of OH* chemiluminescence yield with equivalence ratio for several air flow–rates is shown in Figure 3. Peak OH* chemiluminescence for the honeycomb burner is observed near an equivalence ratio of 0.90. As the air flow–rate is increased chemiluminescent emission increases and the shape of the curve stays approximately the same. The honeycomb burner results differ significantly from those found for the Bunsen burner. The Bunsen burner OH* chemiluminescence exhibited the peak yield near an equivalence ratio of 1.0. Full analysis of the results is presented in Section 4, but the fact that flame area for the honeycomb burner remains constant for all experimental conditions is bound to contribute significantly to the differences observed between the two burners.

The variation of CH* chemiluminescence yield with equivalence ratio for several air flow–rates is shown in Figure 4. Peak CH* chemiluminescence for the honeycomb burner is observed near an equivalence ratio of 1.00. The decline of CH* emission for leaner mixtures is much steeper than the decline of emission for richer mixtures. The emission of CH* chemiluminescence almost appears to be leveling off for equivalence ratios above 1.0. As the air flow–rate is increased chemiluminescent emission increases and the shape of the curve stays approximately the same with the possible exception of the data for the high air flow–rate of 270 cc/sec. The large increase in chemiluminescence may be due to the relatively large increase in flow–rate. The dependence on flow–rate, as was seen for the Bunsen burner is very equivalence ratio dependent. Whereas in the honeycomb burner the CH* chemiluminescence yield for all flow–rates appears almost equal at low equivalence ratios, a drastic dependence on flow–rate is seen at higher equivalence ratios.

4 ANALYSIS AND DISCUSSION

The experimental results presented in Section 3 demonstrate how chemiluminescence measurements are particular to a specific burner and chemiluminescence type. The aim of the present paper is to elucidate the observed chemiluminescence trends with experimental variables in terms of associ-

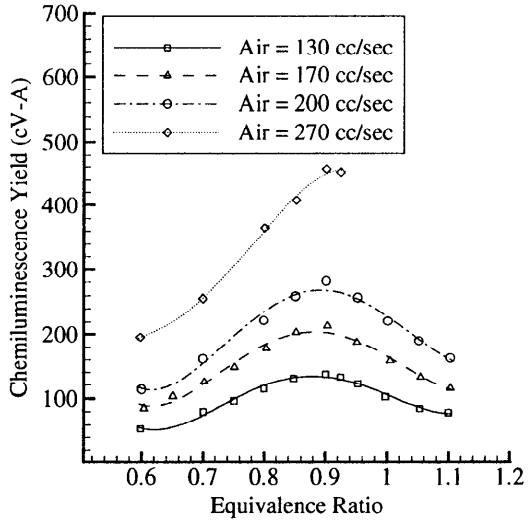


FIGURE 3: OH* chemiluminescence yield as a function of equivalence ratio for the flat flame honeycomb burner

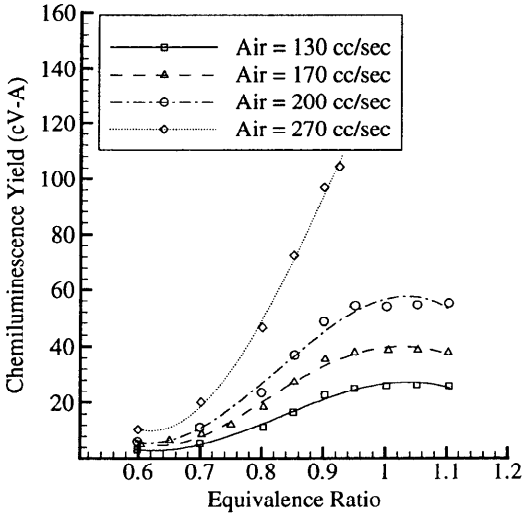


FIGURE 4: CH* chemiluminescence yield as a function of equivalence ratio for the flat flame honeycomb burner

ated variations in heat-release. To accomplish the analysis goal, the chemical kinetics of the chemiluminescent species and the combustion as well as other physical processes occurring in each of the burners are studied in detail. In the course of the analysis, each of the chemiluminescent species will be evaluated as a potential indicator of heat-release.

The discussion of the analysis results will benefit greatly from an introduction to the formation paths of the two types of chemiluminescence considered. The introduction focuses on chemiluminescence formation in methane combustion, although some of the conclusions are applicable for higher hydrocarbon combustion as well. A lot of the information pertaining to reactions involving precursors of chemiluminescence species was obtained by examining GRIMECH 3.0 (1999) .

Chemiluminescence formation paths

In combustion environments CH* is predominately formed from C_2H and atomic oxygen. The reaction was studied in detail by Devriendt and Peeters (1997) who found the reaction to have a low activation energy. The concentration of the precursor C_2H depends greatly on the concentration of C_2H_2. C_2H forming reactions have both comparatively high and low activation energies, depending on the other species participating in the reaction. The formation paths of C_2H and CH* are illustrated in Figure 5. C_2H_2 forming reactions are not high activation energy reactions but are clearly very sensitive to the concentration of carbon radicals. The large variation of CH* with equivalence ratio is a good indicator of this fact.

OH*has long been thought to be the product of a reaction between CH and molecular oxygen, but recently Haber et al.(2000) have suggested that OH* is formed by a reaction between the formyl radical (HCO) and atomic oxygen. The reaction rate constant used, similar to CH*, has a low activation energy. The formyl radical (HCO), precursor of OH*, is an important intermediate species in methane combustion because HCO-consuming reactions are generally very exothermic and contribute significantly to flame heat-release. HCO is formed primarily from CH_2O. HCO-forming reactions generally have no or very low activation energies as illustrated in the reaction diagram shown in Figure 5. HCO consumption reactions however exhibit a variety of activation energies.

Analysis of experimental results

Researchers starting with Clark (1958) have found that all types of chemiluminescence commonly measured including OH*, CH* and C_2^* vary linearly with Reynolds number, i.e. flow-rate. The slope of the lines varied with equivalence ratio for each of the chemiluminescence types. If one assumes that the heat of reaction per unit mass of fuel is constant with flow-rate, then the linear relationship found indicates that chemiluminescence is a good indicator of heat-release rate. Indeed, normalizing the CH* chemi-

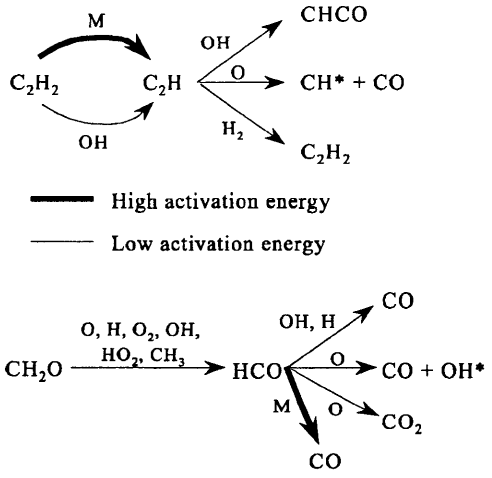


FIGURE 5: Reaction diagram for the production of CH* and OH* chemiluminescence

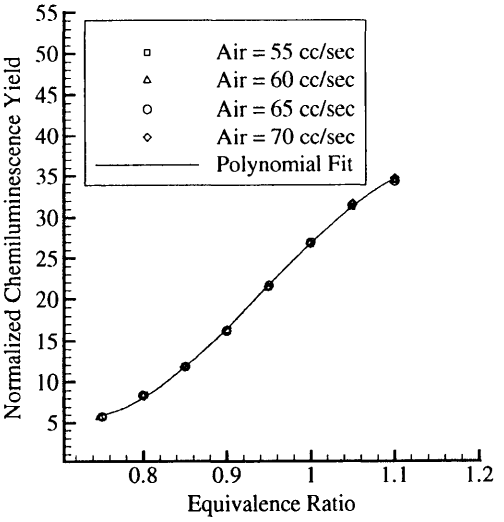


FIGURE 6: Normalized CH* chemiluminescence yield as a function of equivalence ratio for the Bunsen burner

luminescence results for the Bunsen burner by dividing by the fuel flow–rate yields a single curve, that is a function of equivalence ratio only as shown in Figure 6. As a result one may want to write a functional relationship of the form $I_{CH^*} = F(\phi\ ,\ \dot{m}_{fuel}\ \Delta\text{HR})$. However, the heat–release rate calculated by multiplying the the heat of reaction by the fuel flow rate does not account for the fact that not all heat liberated by chemical reaction contributes to the enthalpy change in the gas. Some heat is lost to the surroundings by radiation and conduction.

The sensible enthalpy change, which is related to the total temperature increase across the flame is however the quantity of interest in combustion dynamics research. A time rate of change of the temperature increase of the gases through the flame causes a time rate of change of the gases' acceleration through the flame. The time variation of the acceleration causes the flame to act like an acoustic source and drives the combustion instability. An appropriate indicator of heat–release must be sensitive to changes in the temperature increase of the gases through the flame.

It is thus important to check the sensitivity of the given indicator to changes in the temperature rise through the flame, independent of changes in the total heat liberated and changes in equivalence ratio. The examination of the OH* experimental results for the Bunsen burner is an excellent example of a case where chemiluminescence is not merely a function of the total heat liberated and the equivalence ratio.

As was done for CH* chemiluminescence, OH* Bunsen burner results were normalized with fuel flow–rate. In contrast to CH*, OH* chemiluminescence does not collapse onto a single curve. The OH* chemiluminescence results need to be further normalized by multiplying by the square root of Reynolds number. The resulting curve of normalized OH* chemiluminescence as a function of equivalence ratio is shown in Figure 7. The results mean that the amount of OH* chemiluminescence obtained per unit mass of fuel burned is consistently lower at all equivalence ratios tested when the flow–rate is increased, because the normalization required a multiplication by the square root of Reynolds number.

Several clues help in the interpretation of these results. First, as mentioned, the yield of OH* per unit mass of fuel burned is lower for all equivalence ratios including rich equivalence ratios when the flow–rate is increased. Second, a developing boundary layer scales with the square root of Reynolds number. The first clue shows that mixing phenomena are not responsible for the observed scaling because the admixture of air for rich mixtures would increase the yield of OH* chemiluminescence per unit mass of fuel burned by an effective decrease in the equivalence ratio.

The second clue points to another boundary layer dependent phenomenon, that of heat transfer. Indeed, the fine wire mesh screens are mounted less than 5 inches upstream of the burner lip. The boundary layer does not have time to develop fully by the time the flow reaches the burner lip. The result is that heat transfer from the heated stainless steel tube is enhanced for higher flow–rates. The temperature increase in the incoming mixture in turn produces an increase in the flame temperature. The flame temperature increase is not equal to the increase in the incoming mix-

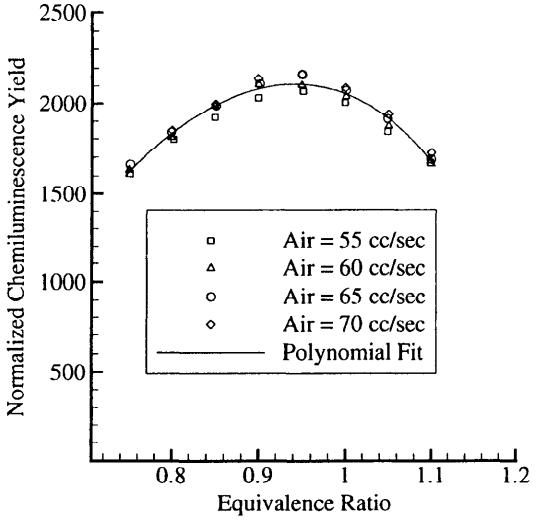


FIGURE 7: Normalized OH* chemiluminescence yield as a function of equivalence ratio for the Bunsen burner

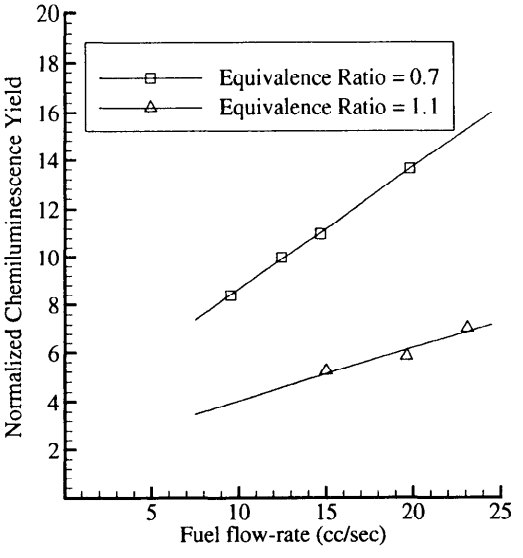


FIGURE 8: Normalized OH* chemiluminescence yield as a function of fuel flow–rate for the honeycomb burner

ture temperature due to higher heat–losses by radiation, conduction as well as product dissociation. The increase in temperature within the flame affects OH* formation detrimentally by favoring higher activation energy formyl radical (HCO) consumption reactions (see Figure 5).

Based on the above reasoning, CH* chemiluminescence should have exhibited some sensitivity to the flame temperature change. However, CH* chemiluminescence formation, as discussed above, combines high and low activation energy processes. As a consequence the flame temperature increase enhances some CH* precursor formation reactions and discourages others. The small flame temperature increase therefore is not seen to affect CH* chemiluminescence. Note that the above explanation shows that the decrease in OH* chemiluminescence per unit mass of fuel burned is related to a net decrease in temperature rise across the flame. CH* fails to show the same sensitivity to heat release.

Najm et al. (1998) also found that CH* chemiluminescence was not a good indicator of heat–release rate in methane flame environments of very high curvature, near extinction. The recommended indicator of heat–release rate based on their study is the formyl radical (HCO). As discussed above, the formyl radical is a precursor of OH* which makes OH* an indicator of formyl radical concentration and by inference a good indicator of heat–release rate, even in high flame curvature environments, near extinction.

The quality of OH* chemiluminescence as an indicator of heat–release rate can be verified further by examining the results reported for OH* chemiluminescence on the honeycomb burner. The normalization of the chemiluminescence data by the fuel flow–rate leaves a residual trend with flow–rate. A plot of normalized OH* chemiluminescence versus fuel flow–rate is shown in Figure 8 for equivalence ratios of 0.7 and 1.1. It is seen that for both equivalence ratios the amount of chemiluminescence obtained per unit mass of fuel burned is an increasing function of flow–rate. To validate OH* as an indicator of heat–release rate, as defined above, the dependence of normalized OH* chemiluminescence on flow–rate must be shown to correspond to a relative decrease in heat–losses from the flame.

An analysis of the burning process in the honeycomb burner will help elucidate the chemiluminescence formation process. The flow–rate per unit area of the honeycomb burner is very low when compared to the maximum laminar burning rate. The highest flow–rate studied corresponds to a flow–rate one third of the maximum laminar burning rate. In the honeycomb burner, the flame area is always constant and the reaction rate increases to accommodate increases in flow–rate. Closely tied to increases in reaction rate are increases in the flame temperature.

Reaction rate is an exponential function of temperature. Radiation heat–loss from the flame is a function of the flame temperature raised to the fourth power. For an overall activation temperature of 16000 K°, a base temperature of 1800 K°and a required increase in the reaction rate of 30%, the increase in flame temperature only has to be about 3%. A 3% increase in the flame temperature results only in a 13% increase in radiation heat–loss. The radiation heat–loss is thus relatively lower at a higher burner

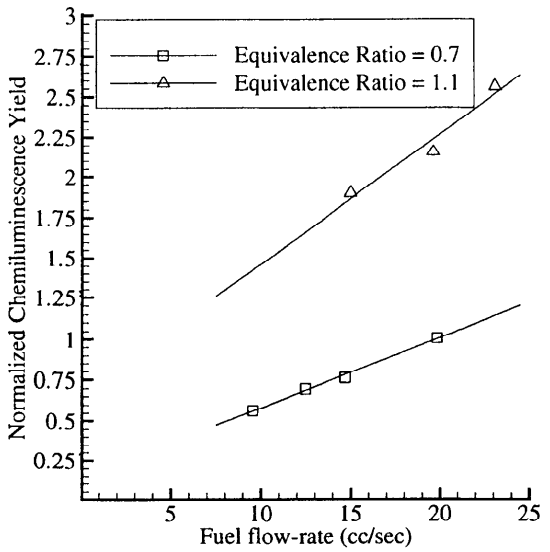


FIGURE 9: Normalized CH^* chemiluminescence yield as a function of fuel flow–rate for the honeycomb burner

flow–rates. Note also that since the flame temperature is higher, the temperature rise through the flame is higher. The increase in OH^* chemiluminescence obtained per unit mass of fuel burned thus corresponds to an increase in the heat–release per unit mass of fuel burned.

As was done for OH^* chemiluminescence, CH^* chemiluminescence was normalized by dividing by the fuel flow–rate. Figure 9 shows a plot of normalized CH^* chemiluminescence as a function of fuel flow–rate for equivalence ratios of 0.7 and 1.1. Again, a residual trend with flow–rate can be detected for both equivalence ratios. The reaction rate increase and associated flame temperature increase appears to affect CH^* and OH^* chemiluminescence in similar ways. Note that in contrast to the Bunsen burner, the flame temperature increase in the honeycomb burner is not caused by an increase in the temperature of the incoming gas and thus does not exhibit a similar shift towards higher activation energy reactions. The temperature increase in the honeycomb burner is tied to the reaction rate increase necessary to support the higher flow-rate, resulting in an overall increase of the throughput of all reaction paths.

All of the identified scaling relationships and trends have important consequences for the use of chemiluminescence as a dynamic heat–release rate indicator. Assuming the variation in the flow–rate occurs on a much slower time–scale than the reaction rate, the flame will adjust itself to changes in the flow–rate very quickly. Oscillations in flow–rate can then be viewed from a quasi–steady standpoint in terms of the fluctuations in chemiluminescence these oscillations produce. The non–linear scaling relationships and trends reveal that for large oscillations in flow–rate, the oscillations in heat–release rate will show significant non–linear effects. For the honeycomb burner for example, the non–linearity appears to be quadratic in flow rate because normalization by fuel flow–rate leaves an approximately linear residual trend in the same variable.

5 CONCLUSIONS

Experimental studies of chemiluminescence were performed for two different types of non–adiabatic burners, measuring OH^* and CH^* chemiluminescence yield. The experiments covered a wide range of equivalence ratios and flow–rates. The results underlined the fundamental differences between the two chemiluminescent species, especially in terms their variation with equivalence ratio.

An attempt was made to identify all major processes that affect the scaling of chemiluminescence yield with flow–rate. The traditionally accepted view that chemiluminescence yield behaves linearly with fuel flow–rate must be rejected based on the OH^* chemiluminescence results in both burners. CH^* chemiluminescence on the Bunsen burner was linear with flow–rate but CH^* chemiluminescence on the honeycomb burner was found to exhibit similar behaviour to OH^* chemiluminescence. The linear relationship with fuel–flow observed on the Bunsen burner confirms the results of the study by Najm et al. (1998) that CH^* is not a good indicator of heat–release rate in all flame environments. CH^* chemiluminescence fails to capture a decrease in the sensible enthalpy change of the gases through the flame. OH^* chemiluminescence does capture the decrease and again further confirms the results of Najm et al. (1998) that the formyl radical and by inference OH^* chemiluminescence is a good indicator of heat–release rate.

The results of the analysis, even though strictly valid only in steady combustion environments, have interesting implications for chemiluminescence measurement in dynamic combustion environments. The non–linear scaling of chemiluminescence with flow–rate for a burner may point out important non–linear processes influencing such important combustion instability characteristics as limit cycle amplitude and frequency content.

The present study represents only a small step in the direction of obtaining a quantitative measure of heat–release rate. The conclusions drawn from the experimental results above are currently being verified through a detail combustor modeling effort. The methods used in the experimental study are also going to be applied to more complex flame environments in an effort to achieve the same level of understanding for turbulent flames as for laminar flames. Finally, it is important to mention that experimental studies are currently being conducted on laminar flames in dynamic flow environments.

ACKNOWLEDGMENTS

The authors would like to acknowledge the support of Mr. Ludwig Haber by a NSF Graduate Fellowship.

REFERENCES

Becker, K., Kley, D., and Norstrom, R. (1977). OH^* chemiluminescence in hydrocarbon atom flames. *Fourteenth Symposium (International) on Combustion*, pages 405–411.

Clark, T. (1958). Studies of OH, CO, CH and C_2 radiation from laminar and turbulent propane-air and ethylene-air flames. *NACA Technical Note 4266.*

Dandy, D. and Vosen, S. (1992). Numerical and experimental studies of hydroxyl radical chemiluminescence in methane-air flames. *Combustion Science and Technology*, 82:131–150.

Devriendt, K. and Peeters, J. (1997). Direct identification of the CH^* chemiluminescence in C_2H_2 / O / H atomic flames. *Journal of Physical Chemistry A*, 101:2546–2551.

Haber, L., Vandsburger, U., Saunders, W., and Khanna, V. (2000). An examination of the relationship between chemiluminescent light emissions and heat release rate under non-adiabatic conditions. *Proceedings of the IGTI*, (2000-GT-0121).

Krishnamhari, S.L.N.G. and Broida, H.P. (1961). Effect of molecular oxygen on the emission spectra of atomic oxygen-acetylene flames. *Journal of Chemical Physics*, 34(5):1709–11.

Langhorne, P. (1988). Reheat buzz: An acoustically coupled combustion instability. part 1. experiment. *Journal of Fluid Mechanics*, 193:417–443.

Najm, H., Paul, P., Mueller, C., and Wyckoff, P. (1998). On the adequacy of certain experimental observables as measurements of flame burning rate. *Combustion and Flame*, 113:312–332.

Porter, R., Clark, A., Kaskan, W., and Browne, W. (1967). A study of hydrocarbon flames. *Eleventh Symposium (International) on Combustion*, pages 907–917.

Price, R., Hurle, I., and Sugden, T. (1968). Optical studies of the generation of noise in turbulent flames. *Twelfth Symposium (International) on Combustion*, pages 1093–1102.

Samaniego, J., Egolfopoulos, F., and Bowman, C. (1995). CO_2^* chemiluminescence in premixed flames. *Combustion Science and Technology*, 109:183–203.

Samaniego, J., Yip, B., Poinsot, T., and Candel, S. (1993). Low-frequency combustion instability mechanisms in a side dump combustor. *Combustion and Flame*, 94:363–380.

Smith, P., Golden, D., Frenklach, M., Moriarty, N., Eiteneer, B., Goldenberg, M., Bowman, C., Hanson, R., Song, S., Gardiner, W., Lissianski, V., and Qin, Z. (1999). *http:// www.me.berkeley.edu/gri_mech/.*

Control of Combustion Instabilities on a Rijke Tube by a Neural Network

R. Blonbou*¶, A. Laverdant *
* Office National d'Études et de Recherches Aérospatiales,
29, avenue de la Division Leclerc,
BP n° 72, 92322 Châtillon Cedex, France.
mail : laverdan@onera.fr
¶ present address : Engineering Department, Cambridge University, Trumpington Street
CB2 1PZ CAMBRIDGE, CAMBRIDGESHIRE, UK.
mail : rhb26@eng.cam.ac.uk

Abstract

Combustion instabilities still constitute a major problem for powerplant development. In this paper, a Rijke tube which presents, for some operating conditions, instabilities with pressure level up to 145 dB/Hz, is considered. In order to control instabilities, an Internal Model Control System for nonlinear plants, that uses two neural networks, has been developed. The first one is an Internal Model which approximates the plant forward dynamic (the learning process). The second one gives the adaptive control input. The capacity of approximating the noisy signals of instabilities (microphone or photomultiplier for OH emission proportional to heat release), with a good precision, is demonstrated. Attenuation of instabilities, for fixed or variable operating conditions, with pressure level attenuation up to 60 dB/Hz, has been obtained.

Introduction

Combustion instabilities represent an important difficulty encountered during the conception of aeronautical or aerospace powerplant [1-4]. These oscillatory mechanisms have disastrous consequences like structure vibrations, increased heat transfer versus stable regime, undesired roll torque and, sometimes, destruction of the powerplant. According to Williams [2], several types of oscillations are observed (system -, intrinsic - or chamber instability). In this paper, only the last case is considered. As an example, in a ramjet, one or several acoustic modes of an air intake and / or chamber, are coupled with unsteady combustion heat release. Here, the burner involved is a Rijke tube with propane-air mixture burning above a porous plate. Similar setups have been considered in previous studies at Cambridge University [5,6] or Ecole Centrale de Paris [7].

The control of instabilities (passive or active) is a natural way to overcome these unwanted oscillations. The first way - the passive control [4,8] - consists in modifying the chamber geometry by the introduction of baffles or Helmholtz resonators which change eigenfrequencies and introduce additional damping of instabilities. Unfortunately, this approach increases mass and dimensions of the powerplant. Moreover, its damping efficiency is limited. The second way - the active control - (see [9] for a good review), consists in the introduction of a secondary acoustic signal with a correct phase shift to obtain a stable regime. The original aspect of the present work is the use of a nonlinear filtering technique : the neural network.

The active control has been used with success to suppress instabilities in laboratory combustors [5-7, 9]. The control loop consists of one or more sensors (microphone or photomultiplier which detects light emission proportional to heat release) [5], a phase shift device and an actuator (generally an electro-pneumatic driver) [9, 10]. The control schemes control unstable modes at sufficiently distant frequencies. Despite of some success, this techniques presents limitations. First, the parameters of the controller are set manually. Secondly, when several modes are present with the same level, the control fails.

In order to overcome this limitation, Huynh *et al.* [10], Billoud *et al.* [11], have used an adaptive control algorithm based upon energy minimization of the global response sensor signal, through optimization of the controller parameters (Widrow [12]). The filter is linear (Infinite Impulse Response -IIR). Different unstable modes are controlled in a 250 kW turbulent burner.

Neumeier and Zinn [13] uses an observer which identifies the unstable modes and determines their phases and amplitudes. These informations are inputs for a controller which stabilizes each unstable mode. This approach has obtained some success for the reconstruction of an unstable pressure signal with transition from low to high frequency. However, the control scheme is limited by the linear modeling of flame response to acoustic perturbations.

More recently, Yu , Wilson and Schadow [14] have used liquid injection (ethanol, heptane and JP 10) to damp combustion instabilities of a dump combustor. Droplets entrainment and flame/large scale vortex interaction limit the damping to 15 dB/Hz. It seems that the injection pass band is limited to several hundred of Hertz. However, this research has given a better understanding of physico - chemical processes involved in an unstable dump combustor.

Paper presented at the RTO AVT Symposium on "Active Control Technology for Enhanced Performance Operational Capabilities of Military Aircraft, Land Vehicles and Sea Vehicles", held in Braunschweig, Germany, 8-11 May 2000, and published in RTO MP-051.

In order to improve the different techniques, we use an artificial neural *network with a non linear algorithm*. This device is a powerful tool and a universal parsimonious approximer for any nonlinear function (Bishop [15]). Neural networks are able to model and control nonlinear plant (Hunt *et al.* [16]). In the present work, an adaptive control strategy, based on Internal Model Control Systems (I.M.C.S.), is presented.

The experiments are made on a Rijke tube [17-20].

The experimental setup is described in paragraph 2. Results without control are presented in paragraph 3. Then, a short description of Artificial Neural Networks (A.N.N.) is proposed in paragraph 4. Results with control are described in paragraph 5 before conclusion in paragraph 6.

2 - Experimental setup [19,20]

Description

Air and propane are injected into the premixed chamber below the flame holder. The ignition is obtained with a high energy spark plug disposed above the porous plate. Four glass windows are set up at right angle at the bottom of the chamber for flame visualization and radical emission measurements.

The experimental setup is shown in Fig. 1. The burner consists in two square section tubes of 50 mm x 50 mm separated by a porous wall made of Poral ®. This porous plate, which acts as a flame holder, is located at 25 cm of the bottom of the tube. Chambers of 75 cm and 1 m lengths have been tested. The tube is closed at the bottom and open at the opposite. This geometry allows only longitudinal acoustic waves to propagate at frequencies below 5 kHz.

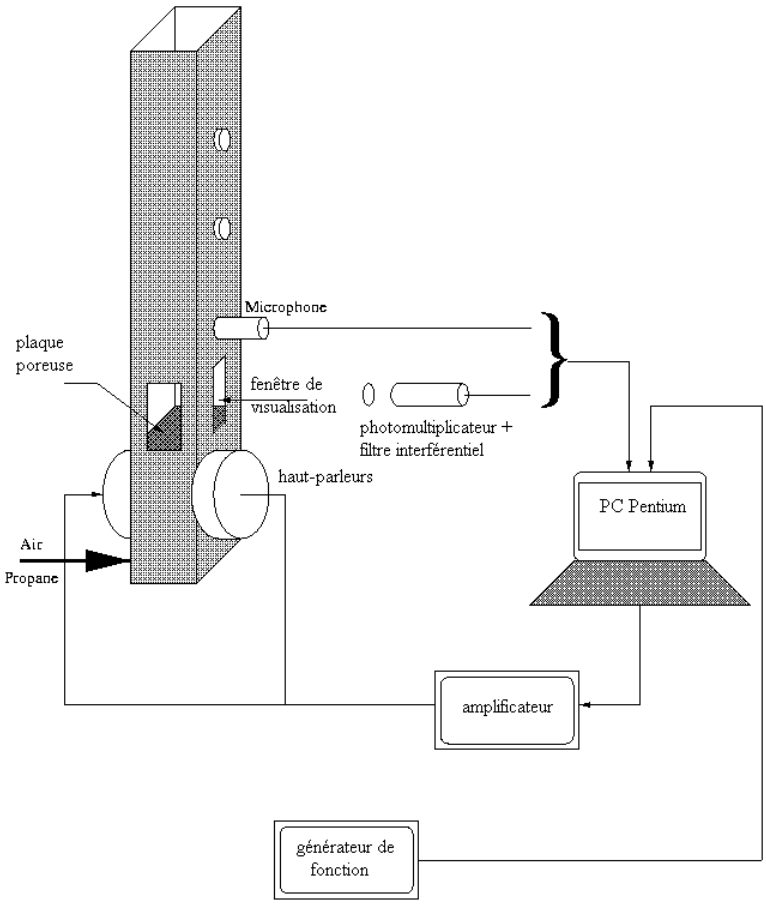


Fig. 1 - Experimental configuration

Measurements

A Chromel-Alumel thermocouple is fitted in the porous plate. Experiments, where temporal temperature variation in the flame holder were above 300 °C/min, have been limited in time in order to avoid porous wall destruction.

Brüel and Kjaer microphones of type 4136 (1/8 ") have been installed along the Rijke tube (maximum pass band starts of 10 kHz).

Diederichsen and Gould [22] have verified that for premixed flames, the intensity of CH, OH or C_2 radical emissions are proportional to the flame heat release. Following Dines [5], OH emission is measured with a photomultiplier tube after rejection of spurious light with an interference filter centered at 310 nm.

Pressure and OH chemiluminescence signals are recorded on a PC computer with a KETLEY data acquisition card.

The actuation system is composed of two electro-pneumatic drivers JBL 2490H (pass band from 100 Hz to 1 kHZ). These drivers are disposed on two opposite walls, below or above the porous plate. The acoustic signals are issued of a Hewlett-Packard function generator. Theses signal are amplified by a JBL MPX 300 amplifier.

3 - Experimental results without control [19]

Configuration and regime tested

Experiments are conducted with flow velocities below 20 cm/s; thus the flame is a laminar one. The equivalence ratio Φ lies between 0.6 and 1.4 and the flame is plane in the majority of cases. In this situation, laminar flame speed is close to 40 cm/s for stoechiometric conditions. So the flame zone is closed to the porous plate. For equivalence ratios between 0.8 and 1.3, large sustained acoustic oscillations are observed. The maximum air mass flow rate is of 0.4 g/s.

The operating conditions are summarized in Table 1. In the following developments, each operating case is referenced as "regime I", *etc.*

regimes	L (mm)	$\dot{m}\acute{Y}_{air}$ (mg/s)	$\dot{m}\acute{Y}_{C3H8}$ (mg/s)	Φ
I	750	250	15.5	1
II	750	300	20	1
III	750	225	15.5	1.1
IV	750	300	15.5	0.8
V	1000	200	13	1
VI	1000	300	25	1.3

Table 1 - Characteristics of operating conditions used in test of active control.

Description of instabilities

Temporal variations of pressure and OH emission signals, in presence of instabilities, are plotted in Figures 2 and 3. The instability presents a limit cycle (Fig. 2). The relative phase between the two signals is close to zero (Fig. 3), in agreement with the Rayleigh's criterion [23].

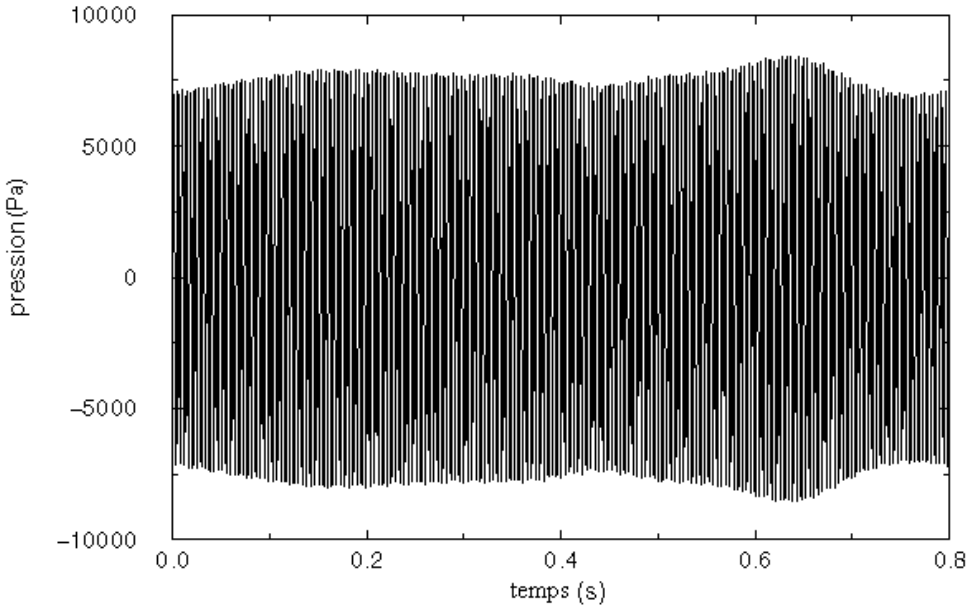


Fig. 2 - Temporal variation of pressure signal in an unstable regime [19].

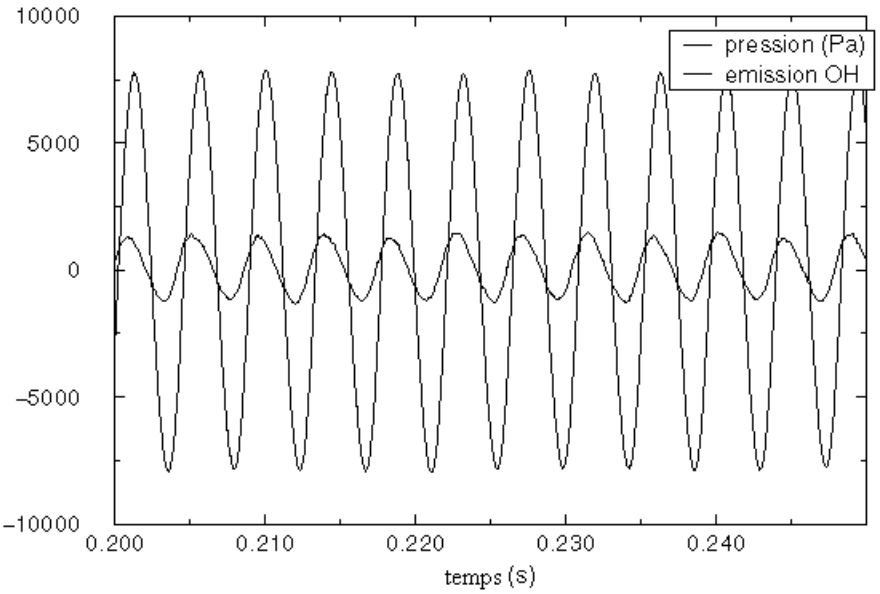


Fig. 3 - Temporal variations of pressure and OH emission for an unstable regime
(pressure is in Pa and OH signal in arbitrary units) [19].

The diagrams of the instability zones, for tube lengths of 75 cm and 1m, are shown in Fig. 4 and 5 respectively. The characteristic of the instabilities depends of several factors :

• the operating point : frequency and amplitude of oscillations vary as a function of this parameter. For a 1m tube length and rich conditions, the oscillations are intermittent.

• porous wall temperature : some instabilities are observed only when $T_{wall} > 100$ °C. When this parameter is greater than 300 ° C, the instabilities observed for high values of Φ are attenuated. This parameter gives only indications on combustion. It is

possible to suppose that increase of porous wall temperature implies growing of fresh mixture temperature also. This variation is quasi-steady and the critical value of 300 °C is reached after a long time of operation.

• operating duration : frequency and amplitude of oscillations can present weak variations with time.

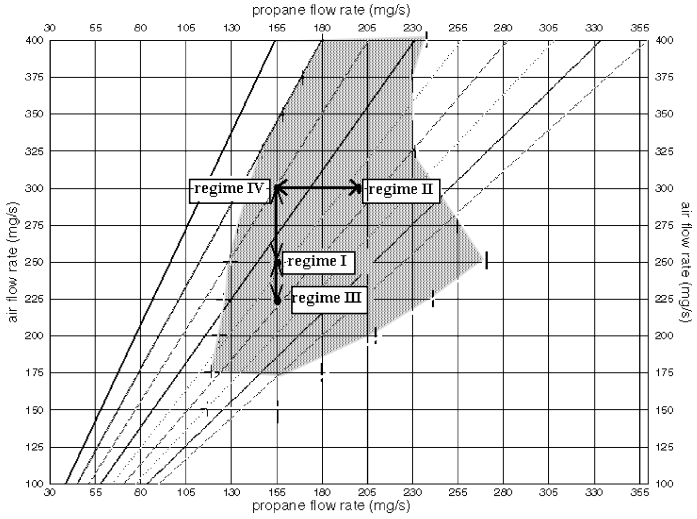


Fig. 4. Instability boundaries for a tube length of 750 mm. The unstable regime corresponds to the shaded zone. The command of instabilities in variable regimes (I, II, III, IV) is also shown [19].

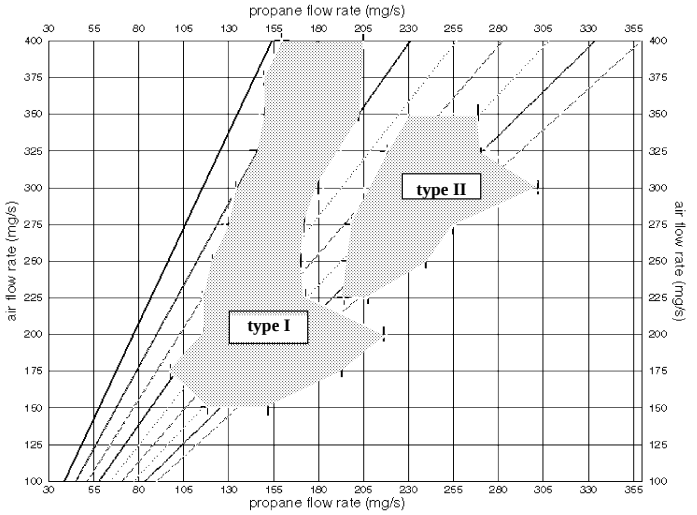


Fig. 5 - Instability boundaries for a tube length of 1m. Two unstable zones are shaded. The type I, which corresponds to weak values of propane mass flow rates, is similar to instabilities observed in Fig. 3 [19].

For a chamber length of 75 cm, power spectral densities of acoustic pressure or OH emission present a dominant peak of 145 dB/Hz at a frequency of 230 Hz. Other peaks of lower level are also observed.

For a tube length of 1m, two types of instabilities exist. The first one, which is observed for weak values of air mass flow rates, is similar to the instabilities encountered on a 75 cm chamber length. The dominant peak of 145 dB/Hz is also still present. This corresponds to the regime V. The second type of instability is encountered for air mass flow rates > 225 mg/sec and $\Phi > 1$ (regime VI). It is characterized by the presence of two peaks at 235 Hz and 460 Hz with 135 dB/hZ and 145 dB/Hz level respectively .

4 - Description of the Artificial Neural Networks (A.N.N.)

The ANN are sets of interconnected cells arranged in such a way that each cell receives its inputs from one or more cells and its output is sent, through weighted connections, to one or more cells. Hence, the ANN are multi-input-output (MIMO) signal processing, which operate nonlinear mapping between their inputs and outputs.The nature of the mapping depends on the ANN set of parameters, also called synaptic weights. These parameters are set up through a learning process. This consists in presenting to the ANN a sample set of input/output, called the training set, where the training algorithm iteratively adjusts the synaptic weights in order to obtain the desired output.

The multilayer feed-forward neural networks

Among different types of ANN, a multi-layer feed-forward networks (also called Multi-Layer Perceptron (MLP) is retained for this research. It is given in Fig. 6. It consists of an input layer, one or more hidden layer, and an output layer. In this study, we use one hidden layer feed-forward neural networks with one output.

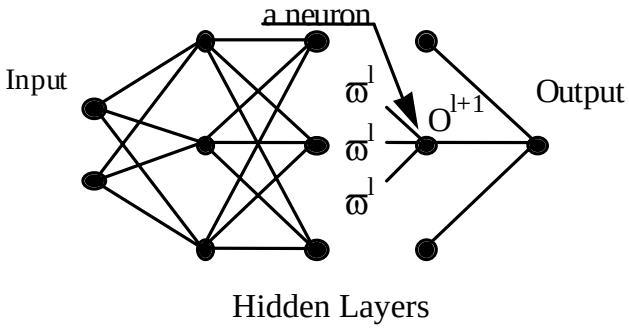


Fig. 6 -Scheme of a multi-layer Perceptron.

The cells in the hidden layer are called neurons. This element simply sums all the inputs multiplied by their respective synaptic weights. Then a nonlinear transfer function is applied to this sum. A bias term I_i^{hid} is also added to the input of each neuron. Let O_i^{hid} be the output of the i^{th} neuron of the hidden layer. We have :

$$O_i^{hid} = f\left(S_i^{hid}\right) = f\left(\sum_{j=1}^{Ninp} \varpi_{ij}^{hid} O_j^{inp} + I_i^{hid}\right)_{i=1,\ldots,N_{hid}}, \quad (1)$$

where f is the cell transfer function; S_i^{hid} is the input of the i^{th} neuron of the hidden layer; ϖ_ι^{th} is the value of the weight of the connection between the j^{th} network input and the i^{th} neuron of the hidden layer; N_{hid} is the number of cells in the hidden layer. The choice of the transfer function is essential. It is often a non decreasing function of the total input of the cell. Here f is *tanh* (*x*) function. Its first derivative is strictly positive.

The output of the network is obtained by a linear combination of the outputs of the hidden neurons. Let O^{out} be the network's output, we have :

$$O^{out} = \sum_{i=1}^{Ninp} \varpi_i^{out} O_i^{hid} + I^{out}, \quad (2)$$

where ϖ_ι^{th} is the value of the weight of the i^{th} hidden neuron and the output; I^{out} is also a bias.

The weight optimization problem

The training of an ANN consists in a search of the optimal weights that minimize the error between the desired and actual output of the training set.

The error function is defined as the sum of the square error :

$$J = \sum_{n=1}^{K} e^2(n) = \sum_{n=1}^{K} \left(d^n - O^{out,n}\right)^2, \quad (3)$$

where K is the number of examples of input/output in the training set. The desired and the network outputs at time n are d^n and $I^{out,n}$ respectively. The error J is a differentiable function of the weights. We use a back-propagation algorithm [24] which gives an estimate of the error function derivatives and that is less computationally expensive than feed-forward (Pineda [25]). Using the chain rule, the required partial derivatives in the backward direction (from outputs to inputs), are computed.

Let introduce the new variables :

$$\delta_i^{hid} = -\partial J / \partial S_i^{hid} ; \delta^{out} = -\partial J / \partial O^{out} . \qquad (4)$$

Using the chain rule :

$$\delta_i^{hid} = f'(S_i^{hid}) \sum_{k=1}^{K} \delta^{out} \varpi_i^{out} ; \delta^{out} = 2e(n). \qquad (5)$$

The partial derivative of the cost function takes the form :

$$\frac{\partial J}{\partial \varpi_{ij}^{hid,n}} = \left(\frac{\partial J}{\partial S_i^{hid}} \right) \left(\frac{\partial S_i^{hid}}{\partial \varpi_{ij}^{hid,n}} \right) = -\delta_i^{hid} O_j^{inp} . \qquad (6)$$

The weights and the bias are updated using the momentum technique [24]. This method tries to avoid oscillations found in gradient descent algorithm. The weights are computed with the relation :

$$\varpi_{ij}^{l,n+1} = \varpi_{ij}^{l,n} + \eta \delta_i^{l+1,n} O_j^{l,n} + \alpha \left(\varpi_{ij}^{l,n} - \varpi_{ij}^{l,n-1} \right) \qquad (7)$$

with $\alpha \in [0,1]$. This algorithm accelerates the convergence of gradient method during “steady downhill” descent. Moreover, it presents a stabilizing effect in regions where the gradient oscillates. However, the choice of α and η is difficult. They are adjusted by a process of trial and error.

The neural control scheme

We present here the Internal Model Control System (ICMS). We are interested to a single input output process. The methods relies on the assumption that the process can be described as follows :

$$y_p(n) = h\left[y_{p,n-1}, \ldots, y_{p,n-N_y}, u_{n-1}, \ldots, u_{n-N_u} \right] + w(n), \qquad (8)$$

where y_p is the output of the process; u, the control input; h, an unknown nonlinear function which represents the plant dynamic; w, the noise measurement. The controller objective is to provide the correct control input to drive a nonlinear plant from an unstable to a stable regime. Adjustment of parameters is described in details in [19,20]. Tests have first been made on a numerical signal generated by solving a simplified nonlinear model of combustion instabilities [1,25,26].

The I.C.M.S. is described in Fig. 7. On one hand, the Internal Model (IM) is trained before the control sequence to approximate the unknown function h. On the other hand, the controller continuously adjusts the weights in order to minimize the distance between the IM and the desired output. This forces the controller to represent the inverse of the IM. Therefore, if the IM is good, the process will tend to make the plant output to follow the desired regime.

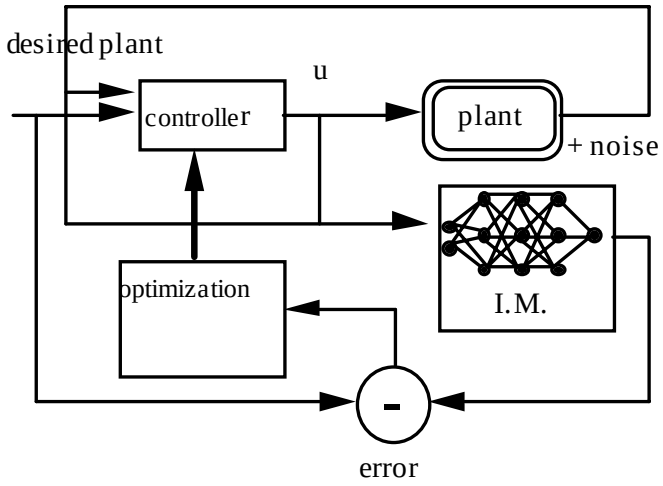


Fig. 7 - Internal Model Control System (I.M.C.S.).

The objective of this study is to minimize the rms value of pressure oscillation. The desired output is obviously $y_d = 0$. Let e_n be the difference between the desired and IM outputs at time *n*. We have :

$$\varepsilon_{n+1}^2 = \left(y_{IM}(n+1) - y_d(n+1)\right)^2 = y_{IM}^2(n+1). \qquad (9)$$

Let Ω_C, the set of weights of the controller, which defines the value of the control input. During control, the weights are adjusted in order to minimize the instantaneous square error given by eq. (10). The weight correction $\Delta\Omega_C$ is computed using the gradient descent technique. For real time control purposes, the correction is computed through the following relation:

$$\Delta\Omega_c = -\mu_c \left(\frac{\partial \varepsilon_{n+1}^2}{\partial y_{md}(n+2)}\right)\left(\frac{\partial y_{md}(n+2)}{\partial u(n+1)}\right)\left(\frac{\partial u(n+1)}{\partial \Omega_n}\right) , \qquad (10)$$

where $\varepsilon_{n+1}^2 = y_{md}^2(n+2)$.

Identification of the internal model

The burner is excited by sending acoustic sine waves to the loudspeakers at frequencies close to those of the instabilities. This response of the system is delivered by a microphone mounted downstream from the porous plate. The excitation signal and the response of the burner provide the training set for the identification process. The selection technique of the model is described in details in [19]. The number of parameters to adjust is less than 20.

5 - Results with control [19]

In all these experiments, the constant in eq. (10) is $\mu_C = 0.05$. In this test, the OH signal is used to detect instabilities.

Figures 8, 9 and 10 give examples of spectra obtained with control. Compared to the situation without control, considerable attenuation is observed for regime I (Fig. 8); V (Fig. 9); VI (fig. 10). Similar results are obtained with microphone and photomultiplier.

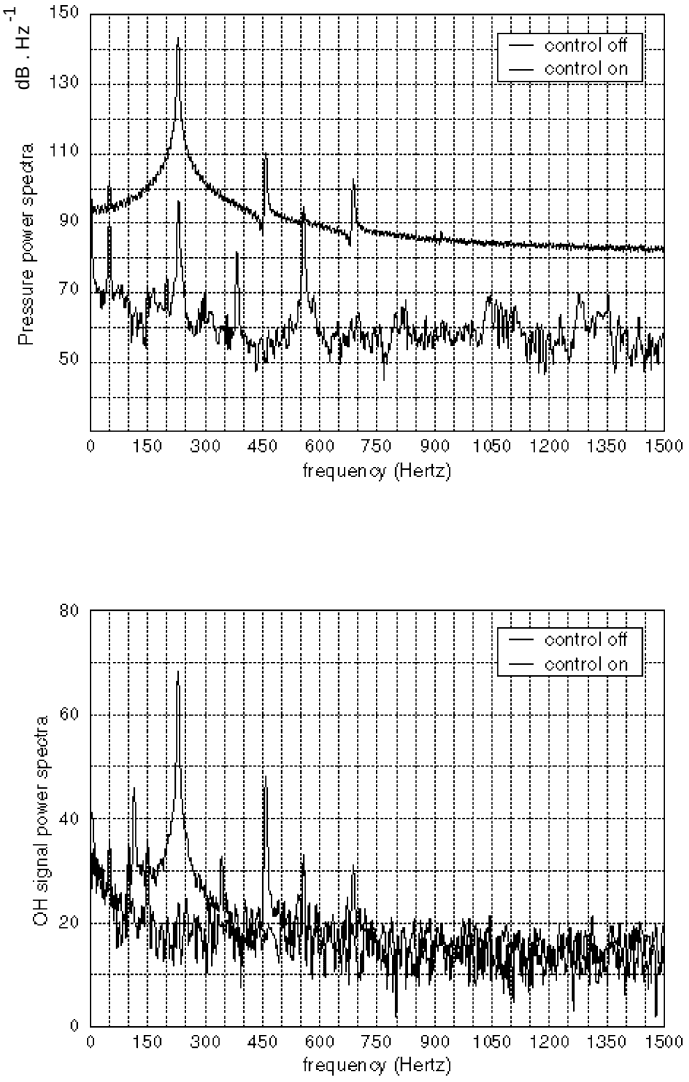


Fig. 8 - Power spectral densities of pressure and OH emission signals for regime I, with and without control [19].

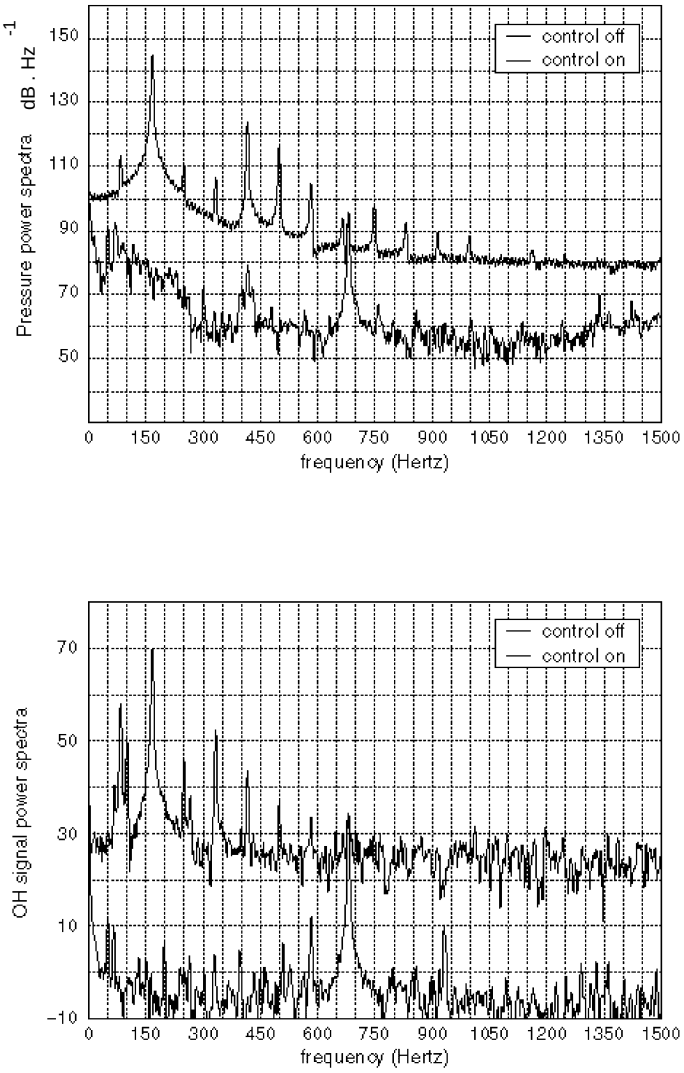


Fig.9 - Power spectral densities of pressure and OH emission signals for regime V, with and without control [19].

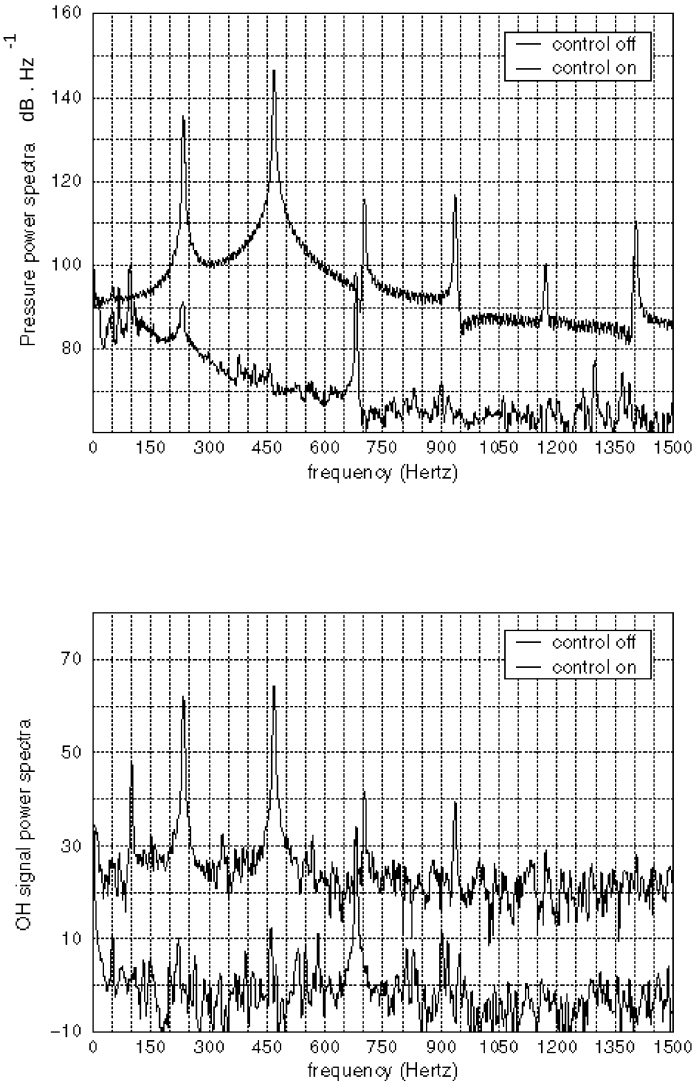


Fig. 10 - Power spectral densities of pressure and OH emission signals for regime VI, with and without control [19].

Figure 11 shows the temporal signals during a control sequence. The controller is turned on at $t \approx 1.65$ s. A subsequent damping of the instabilities is obtained in a short time ($t \approx 1.9$ s). Before control, the actuator signal amplitude is weak. After the control is on, the actuation signal increases fastly then it decreases to a low level. When the controller is off, the instabilities starts again, proving its efficiency (Fig. 12).

The possibilities of this control system have also been tested when changing operating conditions during a control sequence. The changes performed follow the path shown in Fig. 4. The IM identification has been performed only for conditions corresponding to regime I. Fig. 13 shows successive power spectral densities of the pressure signal with and without control. Global attenuation is observed. Moreover, reductions of instabilities up to 60 dB/Hz have been obtained. This again proves the efficiency of the active control of the IMCS.

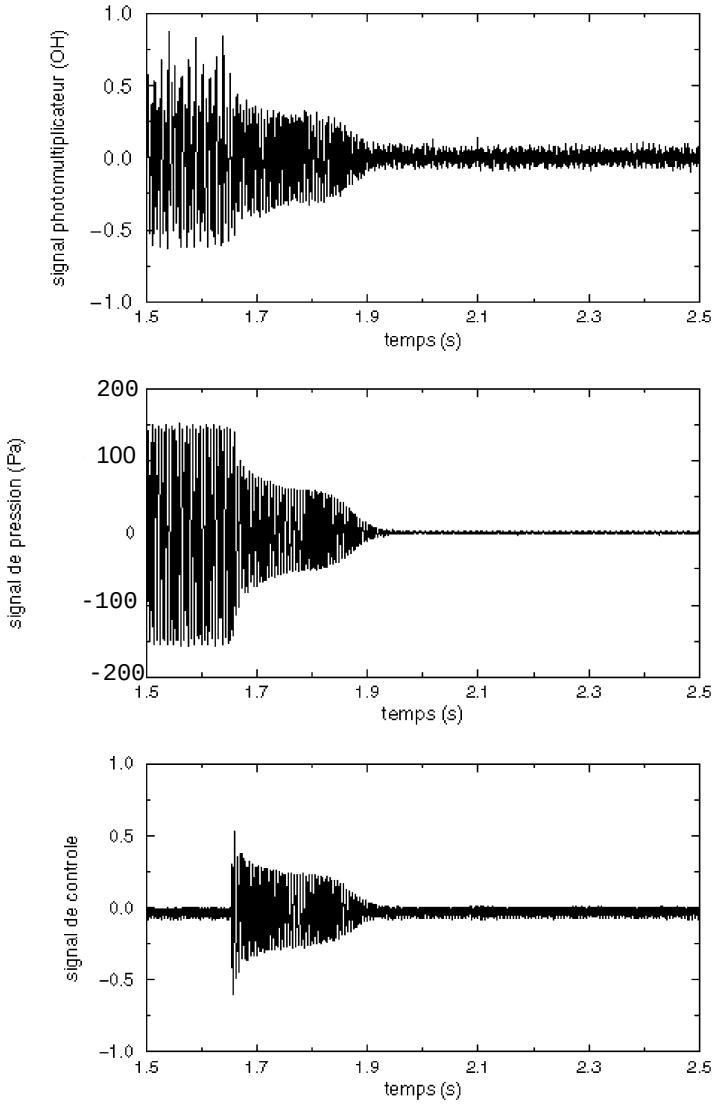


Fig. 11 - Temporal signal of pressure, OH emission and control obtained during a sequence of control of instabilities for regime VI. During this experiment, photomultiplier signal is used at the loop entry [19].

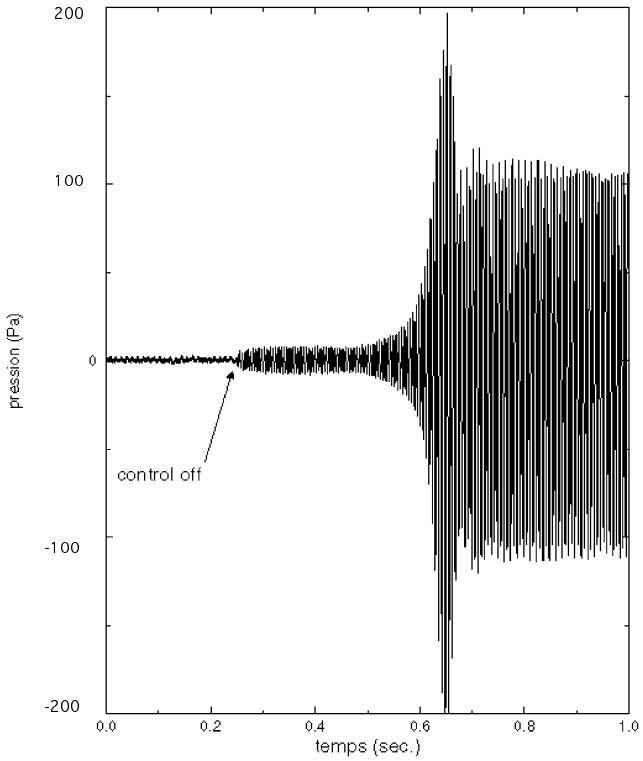


Fig. 12 - Temporal signal of pressure obtained when the control sequence is stopped. The instabillity starts again, proving the control algorithm efficiency [19].

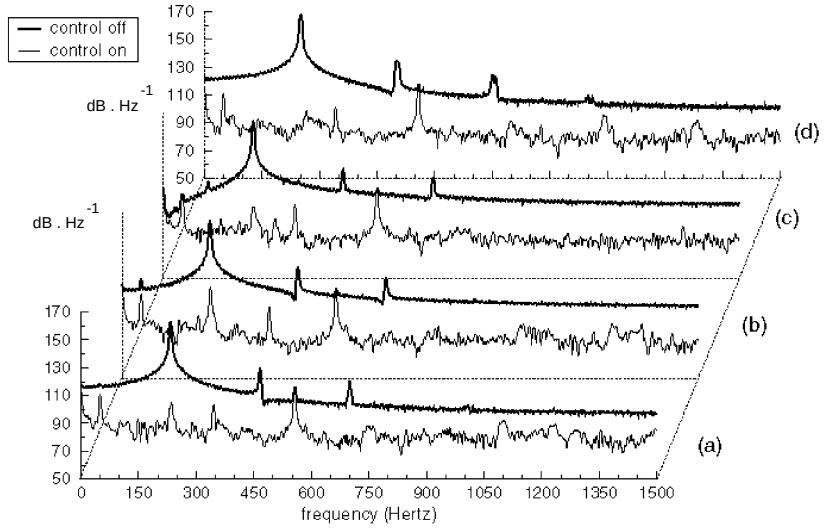


Figure 13 - Microphone signal power spectral density without and with control. Different changing operating conditions, indicated in Fig. 4, which corresponds to regimes I to IV, are considered. a) regime III; b) regime I; c) regime IV; d) regime II [19].

Conclusion

In this paper, we have described a Rijke tube and an active control of combustion instability based on neural networks technique. This burner, tested for two lengths and different operating conditions, shows combustion instabilities of level up to 145 dB/Hz. The pressure signals produced by a microphone or the OH emission signals of a photomultiplier are correctly predicted by the Internal Model of the neural network. A control algorithm is also proposed. It is an efficient device which is able to control the burner for fixed or varying operating conditions. Pressure level attenuation up to 60 dB/Hz have been obtained. This result proves the ability of Artificial Neural Networks to approximate noisy instability signals and to control it. The following investigation would consist, on one hand, in testing this ANN techniques on aeronautical powerplant; on the other hand, in defining a new actuator for this type of motor.

Acknowledgments :

This work has received financial support from ONERA. Real time learning and control algorithms, in assembly langage on PC computer, have been written by Kurtosis society.

References

[1] Culick, F.E.C. AGARD conference Proceedings, n°450, 1988.

[2] Williams, F.A., *Combustion Theory*, 2nd ed., Benjamin Cummings, Menlo Park, CA, 1985.

[3] Poinsot, T. “Analyse des Instabilités de Combustion de Foyers Turbulents Prémélangés”, Thèse d’Etat , University of Paris - Sud, Orsay, France, Feb. 2 nd 1987.

[4] Laverdant, A.M. “Contribution À l’Étude des Instabilités de Combustion des Foyers Aérobies”, Thèse d’Etat , University of Rouen, France, 1991.

[5] Dines, P.J., “Active Control of Flame Noise”, Ph. D. Thesis, Cambridge University, 1983.

[6] Heckl, M.A. “Heat Sources in Acoustic Resonator”, Ph. D. Thesis, Cambridge University, 1985.

[7] Lang, W., Poinsot, T. and Candel, S.M., Comb. & Flame, 70, 281-289, 1987.

[8] Crocco, L. Tenth Symposium (International) on Combustion, The Combustion Institute, Pittsburgh, PA, 1965, 1101-1128.

[9] MC Manus, K.R., Poinsot, T. and Candel, S.M., Prog. Energy & Combust. Sci., 19, 1-29, 1993.

[10] Huynh-Huu, C., Le Helley, P., Poinsot, T. Esposito, E. and Candel, S.M., “Contrôle Actif Adaptatif des Instabilités de Combustion”, Final Rept. DRET 89-262, june 30 th 1993 and E.M2.C. lab. Rept. C.N.R.S., Ecole Centrale de Paris.

[11] Billoud, G., Galland, M.A., Huynh-Huu, C. and Candel, S.M., Combust. Sci. & Tech., 81, 257-283, 1992.

[12] Widrow, B., *Adaptive Filters*, Aspects of Network & System Theory, Holt Rinehart, New-York, 1971.

[13] Neumeier, Y. and Zinn, B.T., AIAA Paper n°96-0758, 34 *th* Aerospace Sci. Meeting, Jan. 1996.

[14] Yu, K.H., Wilson, K.J. et Schadow, K.C., "On liquid-fueled active combustion control: instability suppression in dump combustors", ISABE paper n° 99-71184 et AIAA paper n° 99-34185, 1999.

[15] Bishop, C.M., *Neural Networks for Pattern Recognition*, Clarendon Press, Oxford, 1995.

[16] Hunt, K.J., Sbarbaro, D., Zbikowski, R., and Gawthrop, P.J., Automatica, 28, 359-366, 1989.

[17] Rijke, P.L. Phil. Mag. ,17, p. 419, 1859.

[18] Raun, R.L., Beckstead, M.W., Finlinson, J.C. and Brooks, K.P. Prog. in Energy & Comb. Sci., 19, 313-364, 1993.

[19] Blonbou, R. “Commande des Instabilités de Combustion par Réseaux de Neurones”, Ph. D Thesis, Paris Sud University, France, 1999.

[20] Blonbou, R., Laverdant, A., Zaleski, S. and Kuentzmann, P. to be published in Comb. Sci & Tech.

[22] Diederichsen, J. and Gould, R.D., Comb. & Flame, 9, 25-31, 1965.

[23] lord Rayleigh, J.W.S., Roy. Inst. Proc., VIII, 536-542,1878.

[24] Rumelhart, D.E., Hinton, G.E. and Williams, R.J., *Learning Internal Representations by Error Propagation*, in Parallel Distributed Processing : Exploration in the Microstructure of Cognition, Rumelhart, J.L. Mc Clelland and the PDP research group (eds.), Vol. I : Foundations, MIT Press, Cambridge, Mass, 1986.

[25] Pineda, F.J. Neural Comp., 1, 161-172, 1989.

PAPER -21, A. Laverdant

Question (B. Zinn, USA)

Has the neural net ever amplified the instability during the transient process during which the neural net is determining the optimal control parameters?

Reply

Generally, the neural net has given a precise prediction of the instability signal during the transient process. When the identification process is correctly done, the controller damps the instabilities. However, on real-time applications, algorithmic instabilities can occur during the transient process.

Question (A. Annaswamy, USA)

Can you provide a comparison between neural net control and other linear control?

Reply

Classical active control damps one peak and amplifies another one. The neural network predicts instability from noisy signals with a low global error. Therefore, the adaptive control is efficient in real-time for stabilizing all modes.

Question (F. E. C. Culick, USA)

Why are the fundamental frequencies for the two tubes approximately the same even though the lengths are in the ratio 1:0.75? Also, it seems that the your data show consistently that the noise level is higher when the tube is controlled. Is this a correct inference? (If so, why?)

Reply

The fundamental frequencies are different: 160 Hz for a 75 cm tube and 230 Hz for a 1m tube. The noise level is reduced at least 20 dB when the control is on.

Question (M. Mettenleiter, France)

Did you try to analyze the mapping function of your neural network?

Reply

No classical analysis of the mapping of the neural net has been done yet (eg, gain and phase plots). However, the neural net model has a nonlinear transfer function and its accuracy has been evaluated in the time domain by comparing the combustor response to open loop excitation with the neural net response to the same excitation.

Adaptive Algorithms for Control of Combustion

S. Evesque
Engineering Department
Cambridge University
Trumpington Street
Cambridge CB2 1PZ, UK

A.P. Dowling
Engineering Department
Cambridge University
Trumpington Street
Cambridge CB2 1PZ, UK

A.M. Annaswamy
Dept of Mechanical Engineering
Massachusetts Institute of Technology
Room 3-461B – 77 Massachusetts Avenue
Cambridge MA 02139-4307, USA

Abstract

Rather than investigate a particular combustor, a whole class of combustion systems, susceptible to damage from combustion instabilities, is considered. Under some simple and realistic assumptions (pressure waves reflected from the combustor boundaries smaller than incoming waves, flame stable in itself, limited bandwith flame response), it is demonstrated that a finite dimensional approximation to the open-loop transfer function of such a combustion system satisfies some general properties (stable zeros, small relative degree) that are exploited to design adaptive active controllers guaranteed to stabilise the self-excited combustion oscillations. In particular, for the practical case of a combustion system with time delay, a completely new and simple adaptive control design is presented and a formal proof for stability is given. The performance of such stable adaptive controllers is illustrated in a simulation.

1. Introduction

In order to meet stringent emission requirements, combustors are increasingly being designed to operate in a lean premixed mode. Although this reduces the *NOx* emissions, it has the disadvantage that premixed flames are particularly susceptible to self-excited oscillations, and the associated large-scale pressure waves can cause structural damage. *Active* control provides a way of extending the stable operating range of a combustion system, by interrupting the damaging interaction between acoustic waves and unsteady combustion. However, to be useful in practice, an active controller needs to be effective across a range of operating conditions. An efficient approach is to use an *adaptive* controller in which the controller transfer function is continually altered as the engine condition changes.

They are already some algorithms that describe how to update the controller parameters. The most popular adaptive schemes used for active control of combustion instability is the Least Mean Squares (LMS) algorithm applied to an IIR (Infinite Impulse Response) filter [5],[17],[12],[11]. The LMS is very attractive because it does not require any theoretical model: the combustion process is considered as a 'black box' and is learnt during a system identification procedure, performed off-line [5] or on-line [17],[12],[11] thanks to measurements. However, the major drawback is that an LMS controller might lead to a divergence of the control scheme if, for some operating conditions, the poles of the IIR become unstable. The features of a LMS controller have been extensively studied by Evesque & Dowling [12],[11], and here it was necessary to introduce a parallel algorithm (based on the Laguerre's method [28]) to prevent a starting divergence due to the controller. Other adaptive schemes already developed include neural networks [6] which is a nonlinear version of the LMS-controller, and a minimisation scheme based on the downhill simplex algorithm [25]. All these schemes provide no guarantee that the controller can stabilise the self-excited combustion process.

An efficient way to prevent any divergence of the adaptive control scheme is to use systematic methods for designing stable adaptive systems. The adaptive controller, called STR (Self-Tuning Regulator) by Annaswamy et al [2], is designed based on a Lyapunov stability analysis and is therefore guaranteed to be stable for any operating conditions. Furthermore, the STR has the advantage of avoiding a system identification procedure (which is one of the main difficulties in implementing a LMS controller [12]), since it uses little information about the physical process. However, so far, only a specific simple combustor has been shown to have the structure required for the design of a STR [2]. Moreover, the STR cannot accommodate a time delay between control action and its detection.

Our purpose in this paper is to:
(i) determine the general features of a self-excited combustion system, rather than investigate a particular combustor in detail.
(ii) exploit these features to design a novel adaptive controller that is guaranteed to stabilise the combustion system, the major challenge being to guarantee stabilisation in the presence of time delay in the combustion system.
Step (ii) involves first the choice of a low order fixed controller structure that can stabilise the system, and second the determination of adaptive laws for the controller parameters guaranteed to converge to stabilising values.

Hence, the paper is divided as follows: in section 2, a whole class of self-excited combustion systems is described, and its features used to build a controller are given. Section 3 describes low order fixed regulator structures that can control a combustion system with or without time delay, while section 4 deals with the design of a Self Tuning Regulator (STR) guaranteed to stabilise a self-excited combustion process, containing or not some time delays. In section 5, the performance of the STR is illustrated on a simulation based on a nonlinear model of a premixed ducted flame developed by Dowling [10].

2. General features of self-excited combustion systems

Most premixed combustors are highly resonant systems and may develop combustion instabilities for some operating conditions. These self-excited oscillations result from an interaction between unsteady combustion and acoustic waves: unsteady combustion generates sound, while acoustic waves reflected from the boundaries perturb the combustion still further. Rather than investigate a particular combustor in detail, we determine the general structure of this interaction, which will then be exploited to design fixed and adaptive controllers in sections 3 and 4 respectively.

2.1 Open-loop characteristics

A wide class of combustion systems, including lean premixed prevapourised (LPP) combustors and aeroengine afterburners, can be modelled as a combustion section embedded within a network of pipes, as shown in figure 1. We will investigate linear low frequency perturbations to the flow in such a pipework system. The flow at inlet to the combustor is assumed to be isentropic, and the frequencies of interest are low. This ensures that the combustion zone is short compared with the wavelength. Moreover, since only plane waves transport acoustic energy, it is sufficient to consider one-dimensional disturbances. The pressure and velocity upstream the flame can therefore be written as a linear combination of the waves g and f, and downstream the

Paper presented at the RTO AVT Symposium on "Active Control Technology for Enhanced Performance Operational Capabilities of Military Aircraft, Land Vehicles and Sea Vehicles", held in Braunschweig, Germany, 8-11 May 2000, and published in RTO MP-051.

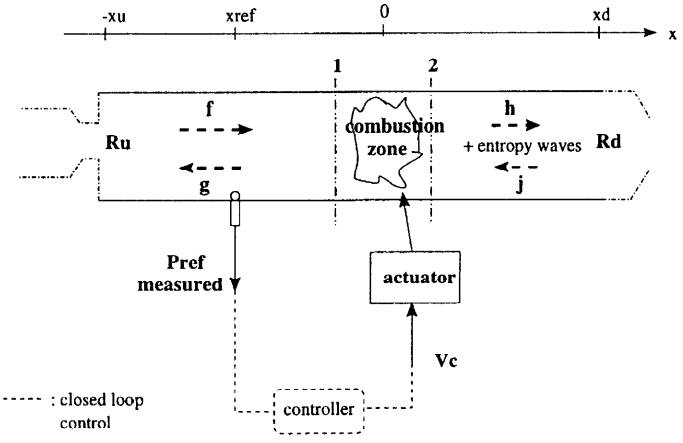


Figure 1: Open-loop self-excited combustion process with actuation

flame as a linear combination of the waves h and j:
in $-x_u < x < 0$,

$$\begin{aligned} p(x,t) &= \bar{p}_1 + f\left(t - \frac{x}{\bar{c}_1 + \bar{u}_1}\right) + g\left(t + \frac{x}{\bar{c}_1 - \bar{u}_1}\right) \\ u(x,t) &= \bar{u}_1 + \frac{1}{\bar{\rho}_1 \bar{c}_1}\left[f\left(t - \frac{x}{\bar{c}_1 + \bar{u}_1}\right) - g\left(t + \frac{x}{\bar{c}_1 - \bar{u}_1}\right)\right] \end{aligned} \quad (1)$$

in $0 < x < x_d$,

$$\begin{aligned} p(x,t) &= \bar{p}_2 + h\left(t - \frac{x}{\bar{c}_2 + \bar{u}_2}\right) + j\left(t + \frac{x}{\bar{c}_2 - \bar{u}_2}\right) \\ u(x,t) &= \bar{u}_2 + \frac{1}{\bar{\rho}_2 \bar{c}_2}\left[h\left(t - \frac{x}{\bar{c}_2 + \bar{u}_2}\right) - j\left(t + \frac{x}{\bar{c}_2 - \bar{u}_2}\right)\right] \end{aligned} \quad (2)$$

p,u,ρ and c are respectively the pressure, velocity, density and speed of sound. The suffices 1 and 2 denote flow quantities just upstream and downstream of the combustion zone, and the overbar indicates a mean value. The distances x_u and x_d are the lengths upstream and downstream of the combustion zone.

The boundary conditions of the combustor are characterized by upstream and downstream pressure reflection coefficients R_u and R_d respectively. Since this boundary condition neglects the conversion of combustion-generated entropy waves into sound at any downstream nozzle, we expect it to be a good approximation when the time taken for entropy waves to convect through the straight duct, $\bar{u_2}/x_d$, exceeds their diffusion time. We consider linear disturbances with time dependence e^{st}, and assume that in the half plane $Real(s) \geq 0$:

$$\begin{aligned} |R_u(s)| &< 1, \\ |R_d(s)| &< 1. \end{aligned} \quad (3)$$

Physically, this means that the amplitude of the reflected wave is less than the incoming wave and may include some time delay. Simple duct terminations like open and choked ends trivially satisfy this condition, provided appropriate energy loss mechanisms are included. In appendix A, we show that condition (3) is also satisfied by reflection from general pipework configurations with negligible mean flow. The reflected waves f and j are easily obtained from g and h using the combustor boundary conditions*:

$$\begin{aligned} f(t) &= R_u(s)[g(t - \tau_u)] \quad at \quad x = -x_u \\ j(t) &= R_d(s)[h(t - \tau_d)] \quad at \quad x = x_d, \end{aligned} \quad (4)$$

where $\tau_u = 2x_u/\bar{c_1}(1 - \bar{M_1}^2)$ and $\tau_d = 2x_d/\bar{c_2}(1 - \bar{M_2}^2)$ are respectively the upstream and downstream propagation time delays, and $\bar{M}$ is the mean flow Mach number.

*$F(s)[\ ]$ is an operator of the variable $s = \frac{d}{dt}$. For instance, $x(t) = \frac{1}{s+1}[y(t)]$ means that $\frac{dx}{dt}(t) + x(t) = y(t)$.

The equations of conservation of mass, momentum and energy across the short flame zone at $x = 0$ can be written in a form that is independent of downstream density and temperature [9]:

$$\begin{aligned} p_2 - p_1 + \rho_1 u_1 (u_2 - u_1) &= 0 \\ \frac{\gamma}{\gamma - 1}(p_2 u_2 - p_1 u_1) + \frac{1}{2}\rho_1 u_1 (u_2^2 - u_1^2) &= \frac{Q}{A}. \end{aligned} \quad (5)$$

Q is the instantaneous rate of heat release, A is the combustor cross-sectional area and γ is the ratio of specific heat capacities. Substitution from (1), (2) and (4) into (5), making use of the isentropic condition p_1/ρ_1^γ, and linearising in the flow perturbations give the time evolution of the outgoing waves g and h generated by the unsteady heat release $Q(t)$:

$$\begin{pmatrix} X_{11} & X_{12} \\ X_{21} & X_{22} \end{pmatrix} \begin{pmatrix} g(t) \\ h(t) \end{pmatrix} = \begin{pmatrix} Y_{11}R_u & Y_{12}R_d \\ Y_{21}R_u & Y_{22}R_d \end{pmatrix} \begin{pmatrix} [g(t-\tau_u)] \\ [h(t-\tau_d)] \end{pmatrix} + \begin{pmatrix} 0 \\ \frac{Q(t)-\bar{Q}}{A\bar{c}_1} \end{pmatrix} \quad (6)$$

where X_{ij} and Y_{ij} are constant coefficients depending on the mean flow only, and given in appendix B.

After taking the Laplace transform† of the system (6) and using (1) and the boundary condition (4), one obtains the transfer function

$$G(s) = \frac{u_1(s)}{Q(s)} = \frac{(R_d Y_{12} e^{-s\tau_d} - X_{12})(R_u e^{-s\tau_u} - 1)}{\det(N)} \quad (7)$$

where

$$N = \begin{pmatrix} X_{11} - R_u Y_{11} e^{-s\tau_u} & X_{12} - R_d Y_{12} e^{-s\tau_d} \\ X_{21} - R_u Y_{21} e^{-s\tau_u} & X_{22} - R_d Y_{22} e^{-s\tau_d} \end{pmatrix}.$$

$G(s)$ describes the generation of unsteady velocity $u_1(t)$ at the flame, due to the unsteady heat release $Q(t)$.

Since the self-excited oscillation results from a coupling between unsteady heat release and acoustic waves, the forcing of unsteady heat release due to incoming flow disturbances at the flame must be also described. In many applications, the combustion responds most strongly to velocity fluctuations. This is because in acoustic waves the fractional change in flow velocity is order $\bar{M}^{-1}$ larger than the fractional change in pressure, ie a large factor at the low Mach numbers at which combustion can be sustained. This dependence on flow velocity can either be seen directly through its influence on flame kinematics and shape [10],[13], or indirectly through its influence on fuel-air ratio and hence on the rate of combustion in LPP systems [29]. A transfer function

$$H(s) = \frac{Q(s)}{u_1(s)} \quad (8)$$

is introduced to describe this combustion response. In many circumstances, $H(s)$ will include substantial time delays. Models for the flame transfer function $H(s)$ have been published in the literature for different combustors. However, we do not want to restrict our controller design to any particular combustion system or model. Instead we will make general, non-restrictive observations about the structure of the transfer function $H(s)$:

- (I) The flame is stable when there is no driving velocity u, which means that the poles of $H(s)$ are 'stable' (ie, are in the half plane $Real(s) < 0$ and so lead to eigenmodes with negative growth rate).
- (II) The flame response has a limited bandwith, therefore $H \to 0$ when $s \to \infty$.

These assumptions about $H(s)$ fit many flame models given in the literature, including premixed flames [10] and LPP systems [14]. The eigenfrequencies can be determined by combining equations (7) and (8). They satisfy

†The same notation is used for a temporal signal and its Laplace transform, for instance $u(t)$ and $u(s)$.

$$1 - G(s)H(s) = 0. \tag{9}$$

When a combustor is unstable, there are roots of equation (9) with $Real(s) > 0$: linear perturbations grow exponentially in time. We will design a feedback controller to stabilise such a system.

2.2 Actuated combustion system

In order to apply active control to our self-excited combustion system, an actuator is used to inject a perturbation and hence break the damaging coupling between unsteady combustion and acoustic waves. The two most commonly used active control inputs are loudspeaker forcing and fuel-forcing ([18] [26][4]). We will concentrate on fuel forcing which is the most relevant for practical applications. An actuator is driven to provide extra fuel (and sometimes air) which in turn produces additional heat release. In order to describe the impact of this input on the combustion system characteristics, we study the relationship between V_c, a voltage sent to the actuator, and P_{ref}, the fluctuating pressure measured at a location x_{ref} (see figure 1). That is, our goal is to characterize the transfer function

$$W(s) = \frac{P_{ref}(s)}{V_c(s)}, \tag{10}$$

which represents the actuated open-loop combustion process. We derive this transfer function in the following.

We assume that the fuel injection is arranged so that the external voltage V_c results in the additional heat release Q_c through the following transfer function

$$\frac{Q_c(s)}{V_c(s)} = W_a(s)e^{-s\tau_a}, \tag{11}$$

where $W_a(s)$ represents the actuator dynamics. Typically the actuator will be a valve with the characteristics of a mass-spring-damper system, whose dynamics are described by the transfer function $W_a(s)$. If the fuel-air mixture is injected directly into the combustion zone, the combustion response will be instantaneous ($\tau_a = 0$). However, if only fuel is added, there will be a small mixing time delay before it is burnt ($\tau_a > 0$). Often it is hazardous to inject fuel directly into the flame. If the additional fuel is introduced some distance upstream of the combustion zone, there will be a convection time delay τ_a between injection and combustion. In a LPP system, it is convenient to modulate the main fuel supplied in the premix ducts, in which case τ_a may be a significant proportion of the period of the self-excited oscillations. Notice that τ_a is independent of the flame radial position, which means that we assume the same time delay between all fuel injection and its combustion. When the combustion zone is short this is trivially satisfied. If the combustion zone is extensive, it may be necessary just to inject fuel in a localised region to meet this constraint.

There will be additional unsteady heat release driven by the flow fluctuations. We will denote this naturally occuring rate of heat release by Q_n. It is related to the velocity fluctuations by the flame model in (8):

$$H(s) = \frac{Q_n(s)}{u_1(s)}. \tag{12}$$

For linear fluctuations, we can superimpose the fluctuating heat release due to external actuation Q_c and the naturally occuring heat release Q_n to give the total fluctuating rate of heat release:

$$Q(s) = Q_c(s) + Q_n(s). \tag{13}$$

The acoustic waves generated by $Q(s)$ are described by (7), ie

$$G(s) = \frac{u_1(s)}{Q(s)}. \tag{14}$$

From equations (11)-(13), one obtains that:

$$\frac{u_1(s)}{V_c(s)} = \frac{G(s)W_a(s)e^{-s\tau_a}}{1 - G(s)H(s)}. \tag{15}$$

If the unsteady pressure P_{ref} is measured upstream the flame ($x_{ref} < 0$), then P_{ref} is a linear combination of the upstream waves f and g. Using (1) and the boundary condition (4) at $x = -x_u$, one easily obtains:

$$\frac{P_{ref}(s)}{u_1(s)} = \bar{\rho}_1\bar{c}_1\frac{1 + R_u e^{\frac{-2s(x_u + x_{ref})}{\bar{c}_1(1-\bar{M}_1^2)}}}{R_u e^{-s\tau_u} - 1} \cdot e^{\frac{sx_{ref}}{\bar{c}_1 - \bar{u}_1}} \tag{16}$$

Therefore, it follows from (15) and (16) that the open-loop transfer function of the actuated system given in (10) can be written in the form:

$$W(s) = \frac{P_{ref}(s)}{V_c(s)} = W_0(s)e^{-s\tau_{tot}}, \tag{17}$$

where

$$\tau_{tot} = \tau_{det} + \tau_a \tag{18}$$

is the total time delay in the actuated system, τ_a is the time delay due to the actuation, $\tau_{det} = -x_{ref}/(\bar{c}_1 - \bar{u}_1)$ is the detection time delay due to the pressure measurement location, and

$$W_0(s) = \bar{\rho}_1\bar{c}_1 \cdot \frac{G(s)W_a(s)}{1 - G(s)H(s)} \cdot \frac{1 + R_u e^{\frac{-2s(x_u + x_{ref})}{\bar{c}_1(1-\bar{M}_1^2)}}}{R_u e^{-s\tau_u} - 1}, \tag{19}$$

with $G(s)$ and $H(s)$ given in equations (7) and (8).

If P_{ref} is measured downstream the flame ($x_{ref} > 0$), then P_{ref} is a linear combination of the downstream waves h and j. A simple calculation, using the wave structure in equations (1) and (2) and the continuity condition across the combustion zone in equation (5)a, shows that the transfer function $P_{ref}(s)/V_c(s)$ again has the form given in (17), provided that the right-hand side of equation (19) is multiplied by

$$P_{du}(s) = \frac{-X_{11} + R_u Y_{11} e^{-s\tau_u}}{X_{12} - R_d Y_{12} e^{-s\tau_D}} \frac{1 + R_d e^{-2s\frac{x_d - x_{ref}}{c_2(1-\bar{M}_2^2)}}}{1 + R_u e^{-2s\frac{x_u + x_{ref}}{\bar{c}_1(1-\bar{M}_1^2)}}} e^{-s\left(\frac{x_{ref}}{\bar{c}_2 + \bar{u}_2} + \frac{x_{ref}}{\bar{c}_1 - \bar{u}_1}\right)} \tag{20}$$

2.3 General structural properties of the open-loop system useful for control design

For the sake of clarity, only the case of an upstream pressure measurement is considered here, but similar results can be derived for a downstream pressure measurement, using the expression of $P_{du}(s)$ given in (20). The wave description of linear perturbations in sections 2.1 and 2.2 gives the open-loop transfer function $W(s)$ in a particularly convenient form:

$$W(s) = e^{-s\tau_{tot}}W_0(s), \tag{21}$$

ie the product of a pure time delay and the transfer function $W_0(s)$ defined in (19). We will now show that $W_0(s)$ has some general structural properties that are useful for the control design. First $W_0(s)$ given in equation (19) is expanded into a rational form. This is achieved by applying the Padé approximation technique [3] for each exponential term of $W_0(s)$. This technique has been widely used in handling systems with time delays. We will use the notation $\left[\frac{L}{M}\right]_{f(s)}$ to denote the $(L, M)^{th}$ order Padé approximant of a function $f(s)$, which is a rational function $P(s)$ whose numerator has order L and denominator order M. The rational function $P(s)$ is chosen such that the first $L + M + 1$ terms in the power series of $P(s)$ will match those of $f(s)$, ie

$$f(s) = \left[\frac{L}{M}\right]_{f(s)} + O(s^{L+M+1}). \tag{22}$$

Lemma 1: *The zeros of W_0 are stable (ie are in $Real(s) < 0$): $W_0(s)$ is said to be 'minimum phase'*

Note that a rational approximation of the multiplying time delay $e^{-s\tau_{tot}}$ in equation (21) introduces unstable zeros into the open-loop transfer function $W(s) = W_0(s)e^{-s\tau_{tot}}$: it is $W_0(s)$ that is minimum phase, and not the overall transfer function $W(s)$. The time delays in the expression of $W_0(s)$ given in (19) are approximated by Padé expansions to give a rational approximation to the transfer function $W_0(s)$, and the stability of the zeros of $W_0(s)$ is discussed. First, it is evident from equation (19) that the poles of the flame transfer function $H(s)$ become zeros of $W_0(s)$. As noted in assumption (I), the condition that the flame is stable when there is no driving velocity u_1 ensures that these zeros are all in $Real(s) < 0$. Therefore $H(s)$ does not introduce unstable zeros for W_0. Secondly, $G(s)$ appears at the numerator and the denominator of $W_0(s)$, therefore its poles do not influence the zeros of $W_0(s)$. Thirdly, we assume that $W_a(s)$ has no unstable zeros. Fourthly, the numerator of W_0 includes $G(s)$ defined in (7) and is the product of terms of the form $K_1(s) + K_2(s)e^{-s\tau}$, where τ is a time delay, and $|K_1(s)/K_2(s)| > 1$ for $Real(s) \geq 0$ (because the reflection coefficients $R_u(s)$ and $R_d(s)$ have modulus strictly smaller than 1 for $Real(s) \geq 0$, and also because $X_{12} > |Y_{12}|$). These factors have no zeros in $Real(s) \geq 0$, because at a zero

$$e^{-s\tau} = -\frac{K_1(s)}{K_2(s)}. \tag{23}$$

Equation (23) cannot be satisfied in the half-plane $Real(s) \geq 0$, because there $|e^{-s\tau}| \leq 1$, while $|K_1(s)/K_2(s)| > 1$. We need to check that this remains true after a suitable Padé expansion of $e^{-s\tau}$. After the Padé approximation is made, one has to solve equations of the type

$$\left[\frac{L}{M}\right]_{e^{-s\tau}} = \frac{-K_1(s)}{K_2(s)}, \tag{24}$$

in order to find the remaining zeros of W_0. Baker & Graves-Morris [3] introduce the concept of A-acceptability for rational functions: a rational function $R(z)$ is A-acceptable if $|R(z)| < 1$ for $Real(z) < 0$. They go on to prove that the Padé approximant of the exponential function $[L/M]_{e^z}$ is A-acceptable provided that $M = L$, $L+1$ or $L+2$. Therefore, with such a choice of L and M, we obtain that

$$|[L/M]_{e^{-s\tau}}| < 1 \qquad for \qquad Real(-s\tau) < 0. \tag{25}$$

However, $|K_1(s)/K_2(s)| > 1$ for $Real(s) \geq 0$, so equation (24) has no roots in $Real(s) > 0$. On $Real(s) = 0$, the numerator and denominator of the Padé approximant $[L/M]_{e^{-s\tau}}$ are complex conjugate when $L = M$, which means that $|[M/M]_{e^{-s\tau}}| = 1$ in $Real(s) = 0$. Hence, since $|K_1(s)/K_2(s)| > 1$ for $Real(s) = 0$, equation (24) has no roots on $Real(s) = 0$, when $L = M$.

Therefore, it has been proved that all the zeros of W_0 are stable, provided that the $(L, M)^{th}$ order of each Padé approximant is chosen so that $M = L$, for any M.

Lemma 2: *The relative degree of W_0 is equal to the relative degree of the actuator transfer function*

An essential feature required for the control design is the relative degree n^* of W_0, denoted $n^*(W_0)$, which is the degree of the denominator of W_0 minus the degree of its numerator. $n^*(W_0)$ is the sum of the relative degrees of its various factors. Again working from the definition from the definition of W_0 in (19):

- $n^*(G(s)) = 0$ when the $(L, M)^{th}$ order Padé approximant for each exponential term $e^{-s\tau_u}$ and $e^{-s\tau_d}$ satisfies $L \leq M$ (we assume that $R_u(s)$ and $R_d(s)$ have a relative degree equal to zero, as it is described in Appendix A).
- similarly, $n^*(\frac{1+R_u e^{\frac{-2s(x_u+x_{ref})}{\bar{c}_1(1-M_1^2)}}}{R_u e^{-s\tau_u}-1}) = 0$ when the $(L, M)^{th}$ order Padé approximants for each exponential term $e^{-s\tau_u}$ and $e^{\frac{-2s(x_u+x_{ref})}{\bar{c}_1(1-M_1^2)}}$ satisfies $L \leq M$.
- $n^*(H) \geq 0$ since the flame has a limited bandwidth response (assumption (II)). Therefore, $H(s)$ does not affect the relative degree of W_0.

Finally, it appears that the relative degree of W_0 is equal to the relative degree of the actuator transfer function W_a, when each Padé approximant $[L/M]$ satisfies $L \leq M$.

Lemma 3: *The high frequency gain of W_0 is positive*

The controller design requires information on the sign of the high frequency gain k_0 of W_0 [21], defined as follows:

$$W_0(s) = k_0 \frac{Z_0(s)}{R_0(s)}, \tag{26}$$

where k_0 is a constant, and $Z_0(s)$ and $R_0(s)$ are two monic[‡] polynomials. To find $sign(k_0)$, we simply need to find equivalent expressions at large s for each factor of W_0. As noted in assumption (II), $H \to 0$ for $s \to \infty$. Furthermore, $n^*(G) = 0$, so that

$$1 - G(s)H(s) \sim 1 \qquad for \qquad s \to \infty. \tag{27}$$

The other factors of W_0 are terms of the form $1 + R(s)e^{-s\tau}$, where τ is a time delay. Make a Padé approximation: $e^{-s\tau} = [L/M]$, with $L = M$. Hence the high frequency gain of $[L/M]$ is $(-1)^M$. In appendix A is shown that the high frequency gain h of $R(s)$ satisfies $|h| < 1$. Therefore, the high frequency gain $1 + h(-1)^M$ of the term $1 + R(s)e^{-s\tau}$ has the same sign as 1. Finally, at high frequencies, the gain of W_0 is easily found to be positive when each Padé approximant $[L/M]$ satisfies $L = M$.

There is a straightforward reason why $W_0(s)$, in the open-loop transfer function $P_{ref}/V_c = W_0(s)e^{-s\tau_{tot}}$, has the simple properties outlined in lemmas 1 and 2. For $Real(s) \geq 0$, the amplitudes of the oscillations do not decrease with time and the boundary conditions $|R_u|, |R_d| < 1$ ensure that the largest contribution to P_{ref} is from the acoustic wave leaving the combustion zone, rather than the waves subsequently reflected from the boundaries. Under these circumstances, the main structure of $W_0(s)$ in equations (19) and (20) is dominated by the properties of $W_a(s)$, the other multiplying factors do not introduce unstable zeros nor affect the relative degree.

It is interesting to note that this argument remains true if the form of actuation is a loudspeaker, provided the loudspeaker is located within the combustion zone. However, this situation is more complicated when the loudspeaker is at a general axial position in the combustor. Then, since the combustion zone is an active component, it can reflect a wave of greater amplitude than the incident wave: if R_f denotes the reflection coefficient at the flame, $|R_f| > 1$ is possible even in $Real(s) \geq 0$ [27]. Under these circumstances, P_{ref}/V_c can have unstable zeros for some positions x_{ref}. Lemma 1 therefore is not true for general loudspeaker positions. This is consistent with the observations of Annaswamy et al [1] who calculated P_{ref}/V_c for a particular idealised combustor with loudspeaker actuation. They found that no simple relationship could be derived between the locations of the sensor, actuator and flame, and the zeros stability. For instance, for the particular case of sensor and actuator collocated at the flame, their open-loop plant P_{ref}/V_c had no unstable zeros. However, for the particular case of fuel forcing, the open-loop transfer function satisfies lemmas 1 and 2, properties that greatly help in the control design.

3. Fixed regulator design

We have shown that for fuel actuation the open-loop transfer function has a simple form: it can be written as the product of a pure time delay and a transfer function $W_0(s)$ which is rational after a Padé expansion is made: $P_{ref}(s)/V_c(s) = e^{-s\tau_{tot}}W_0(s)$. We will begin by designing a controller for the particular case

[‡]a monic polynomial denotes a polynomial whose leading coefficient is unity

$\tau_{tot} = 0$ and will then extend these ideas to the general and more practically relevant case $\tau_{tot} \neq 0$.

3.1 System without time delay ($\tau_{tot} = 0$)

It is clear from equation (18) that $\tau_{tot} = 0$ requires that the control fuel is injected and burnt with no time delay ($\tau_a = 0$), and that the reference pressure is measured in the combustion zone ($x_{ref} = 0$). Our open-loop combustion process is then described by

$$W_0(s) = \frac{P_{ref}(s)}{V_c(s)} = k_0 \frac{Z_0(s)}{R_0(s)} \tag{28}$$

where k_0 is a positive constant, and Z_0 and R_0 are two monic polynomials. Furthermore, Z_0 and R_0 are 'coprime' polynomials, which means that they have no common factors. From lemma 1, we also know that Z_0 is a stable polynomial (ie it has only zeros in $Real(s) < 0$), whereas $R_0(s)$ has unstable zeros since our system exhibits self-excited oscillations. Finally, if R_0 has degree n, Z_0 has degree $n - n^*$, where

$$1 \leq n^* = n^*(W_a) \leq 2. \tag{29}$$

($n^* = n^*(W_a)$ comes from lemma 2, and most practical actuators have a relative degree of 1 or 2).

To this open-loop system, we will apply an active feedback

$$\frac{V_c}{P_{ref}} = -K(s). \tag{30}$$

The aim of the regulator is to stabilize the system, ie to make all the closed-loop poles stable. Combining (28) and (30) shows that these poles are the zeros of

$$R_{cl}(s) = R_0(s) + K(s) k_0 Z_0(s), \tag{31}$$

The regulator transfer function $K(s)$ is to be determined using roots locus arguments [8]:

If $n^*(W_0) = 1$, consider the transfer function

$$K_1(s) = k_c, \tag{32}$$

where k_c is a constant. Then the closed-loop poles are the zeros of the

$$R_{cl}(s) = R_0(s) + k_0 k_c Z_0(s). \tag{33}$$

For $|k_c|$ 'large', $n - 1$ zeros of $R_{cl}(s)$ will be moved towards the $n-1$ stable zeros of $k_0 Z_0(s)$. Investigation of the large $|s|$ asymptotic form shows that the n^{th} zero of $R_{cl}(s)$ is also stabilised if $sign(k_c) = sign(k_0)$. Therefore, a finite value $k_{c_{min}} > 0$ exists such that

$$|k_c| > k_{c_{min}}, \quad sign(k_c) = sign(k_0) \tag{34}$$

is a necessary and sufficient condition to stabilize our minimum phase plant of relative degree 1.

If $n^*(W_0) = 2$, and the regulator $K_1(s)$ is used, then a large $|k_c|$ will guarantee that $n-2$ zeros of $R_{cl}(s)$ will be moved towards the stable zeros of $k_0 Z_0(s)$. The two remaining complex conjugate roots of $R_{cl}(s) = 0$ will be moved towards the stable half plane $Real(s) < 0$ only if

$$\begin{aligned} sign(k_c) &= sign(k_0) \\ \sum(zeros\ of\ R_0) - \sum(zeros\ of\ Z_0) &< 0. \end{aligned} \tag{35}$$

As explained by Dorf & Bishop [8], equation (35)b guarantees that the asymptote centroid of the root locus is situated in the left half plane $Real(s) < 0$. However, since (35) is not true in general, a better strategy is to use the following regulator:

$$K_2(s) = k_c \frac{s + z_c}{s + p_c}, \tag{36}$$

where p_c and z_c are some positive constants, $p_c > z_c$. $K_2(s)$ corresponds to a phase-lead compensator, which adds phase, ie damping, in a frequency range $[z_c, p_c]$. Then the closed-loop poles are the zeros of

$$R_{cl}(s) = (s + p_c) R_0(s) + k_0 k_c (s + z_c) Z_0(s). \tag{37}$$

For a 'large k_c' and an adequate choice of z_c and p_c, the n zeros of $R_{cl}(s)$ can be moved towards the left half plane. More precisely, a finite value $k_{c_{min}} > 0$ and some positive constants p_c and z_c exist such that

$$\begin{aligned} |k_c| &> k_{c_{min}} \\ sign(k_c) &= sign(k_0) \\ \sum(zeros\ of\ R_0) - \sum(zeros\ of\ Z_0) &< p_c - z_c \end{aligned} \tag{38}$$

is a necessary and sufficient condition to stabilize a minimum phase plant of relative degree 2 with the regulator $K_2(s)$. Notice that $K_2(s)$ is also guaranteed to stabilize a minimum phase plant of relative degree 1.

In the following, the compensator $K_2(s)$ given in equation (36) will be implemented as shown in figure 2. The feedback transfer function for this system is given by

$$V_c = -\frac{k_2 V_c}{s + z_c} - k_1 P_{ref} \tag{39}$$

ie

$$\frac{V_c}{P_{ref}} = -\frac{k_1 (s + z_c)}{s + z_c + k_2}. \tag{40}$$

It is clear from equations (40) and (36) that k_1 represents the gain k_c and k_2 determines the phase lag p_c in $K_2(s)$.

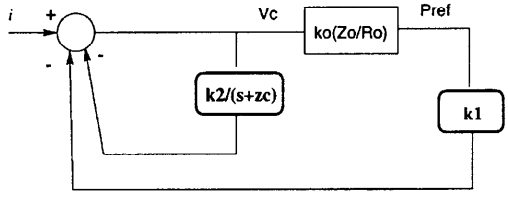


Figure 2: Fixed low-order controller structure for $\tau_{tot} = 0$, $n^* \leq 2$

However, the major drawback of such a fixed regulator $K_2(s)$ is that a cautious choice of p_c is necessary if the inequality (38)c is to be guaranteed without detailed knowledge of the plant. This in turn can mean that the gain k_c required to achieve control is large, especially to ensure stabilization under varying operating conditions, ie under uncertainties in the unstable frequencies ω_u. A large k_c means a large control effort, which is to be avoided. Therefore, to improve the response of our regulator $K_2(s)$ under varying operating conditions, one can choose a fixed $z_c > 0$, and make the other control parameters k_c and p_c adaptive. This is the topic of section 4 .

3.2 Combustion system with known time delay ($\tau_{tot} \neq 0$)

Here the combustion process is described by

$$W(s) = \frac{P_{ref}(s)}{V_c(s)} = k_0 \frac{Z_0(s)}{R_0(s)} e^{-s\tau_{tot}} = W_0(s) e^{-s\tau_{tot}}, \tag{41}$$

with k_0 a constant, Z_0 and R_0 two coprime and monic polynomials, and τ_{tot} is a known time delay. R_0 has degree n, and Z_0

has degree $n - n^*$, with $n^* = 1$ or 2 (lemma 2). It was shown in section 2 that Z_0 is a stable polynomial (lemma 1) and that k_0 is positive (lemma 3).

In section 3.1, low order controllers of the form (32) and (36) were used to control the combustion process. Here, the presence of the time delay τ_{tot} makes such controllers inadequate, especially when τ_{tot} is of the order of the period of the unstable mode. Control of systems in the presence of time delays has been extensively studied [30][19][15]. A popular approach to accommodate large delays is due to O.J.M. Smith [30]. The Smith Controller (SC) attempts to estimate future outputs P_{ref} of the system using a known model, and provides an appropriate stabilization action. In Manitius & Olbrot [19], the SC was modified to control systems that are open-loop unstable by using finite-time integrals of inputs V_c to estimate future outputs (the goal of this modification was to avoid unstable pole-zero cancellations). In Ichikawa [15], a SC controller with finite-time integrals was derived to serve as a pole-placement controller. In [24] and [16], adaptive versions of the pole-placement controller have been developed and proved to be stable.

Since our plant is open-loop unstable, we want to implement a SC using the finite-time integral suggested by Manitius & Olbrot [19] and used in Ichikawa [15], and which is given by

$$V_{SC}(t) = \int_{-\tau_{tot}}^{0} \lambda(\sigma) V_c(t+\sigma)\, d\sigma, \tag{42}$$

where $\lambda(\sigma)$ is a weighting function (it is shown in section 4.2 how discrete values of $\lambda(.)$ can be found by adaptation).

Briefly, the controller used in [15] and shown in figure 3 has the following form:

$$V_c(t) = -\frac{C(s)}{E(s)}[V_c(t-\tau_{tot})] - \frac{D(s)}{E(s)}[P_{ref}(t)] + \int_{-\tau_{tot}}^{0} \lambda(\sigma) V_c(t+\sigma)\, d\sigma \tag{43}$$

where the operators $C(s)$, $D(s)$ and $E(s)$ are chosen such that the denominator of the closed-loop transfer function matches a chosen stable polynomial. This can be achieved only if $degree(E) = n$, $degree(C) = n-2$ and $degree(D) = n-1$. This means that even for a plant of low relative degree ($n^* = 1$ or 2), if the order n is large, then the controller dynamics C/E and D/E will be of high order. This differs from the delay-free case described in section 3.1, for which a first order compensator could stabilize the plant of relative degree 2 or 1.

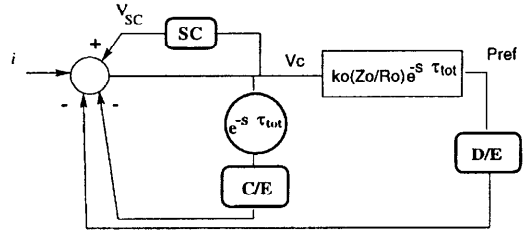


Figure 3: A n^{th} order controller structure for $\tau_{tot} \neq 0$, given in Ichikawa's paper [15]

However, our aim is to keep a low order compensator to control the plant as it was done in section 3.1. Therefore, we suggest the controller structure given in figure 4. We begin as in [15] by choosing $\lambda(\sigma)$, the weighting function in the Smith Controller, to have the form

$$\lambda(\sigma) = \sum_{i=1}^{n} \alpha_i e^{-\beta_i \sigma}, \tag{44}$$

where β_i are chosen to be the n zeros of the polynomial $R_0(s)$, whereas (at this stage) the α_i are arbitrary coefficients. Then, after substitution into (42) and evaluation of the integral, we obtain

$$V_{SC}(t) = \left(\frac{n_1(s)}{R_0(s)} - \frac{n_2(s)}{R_0(s)} e^{-s\tau_{tot}}\right)[V_c(t)], \tag{45}$$

where

$$\begin{aligned} \frac{n_1(s)}{R_0(s)} &= \sum_{i=1}^{n} \frac{\alpha_i}{s-\beta_i} \\ \frac{n_2(s)}{R_0(s)} &= \sum_{i=1}^{n} \frac{\alpha_i}{s-\beta_i} e^{\beta_i \tau_{tot}} \end{aligned} \tag{46}$$

We prove in the following that the low order controller associated with the SC (see figure 4) will stabilize our minimum phase plant of relative degree 1 or 2 for a small τ_{tot}. With the controller structure described in figure 4, the closed-loop transfer function is given by

$$W_{cl}(s) = \frac{k_0(s+z_c)Z_0(s)e^{-s\tau_{tot}}}{R_{cl}(s)} = W_{cl_0}(s)e^{-s\tau_{tot}}, \tag{47}$$

where the closed-loop poles are the zeros of

$$R_{cl}(s) = A(s) + B(s)e^{-s\tau_{tot}}, \tag{48}$$

with

$$A(s) = (s+z_c)(R_0(s) - n_1(s)) + k_2 R_0(s) \tag{49}$$

$$B(s) = (s+z_c)\,(n_2(s) + k_1 k_0 Z_0(s))\,. \tag{50}$$

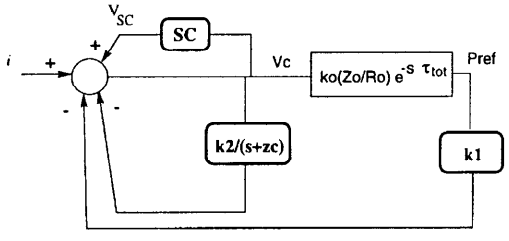


Figure 4: A fixed low-order controller structure for $\tau_{tot} \neq 0$, $n^* \leq 2$

If $\tau_{tot} = 0$, then equation (46) gives that $n_1(s) = n_2(s)$. Therefore,

$$\begin{aligned} R_{cl}(s) &= (s + z_c + k_2)R_0(s) + k_1 k_0 (s+z_c)Z_0(s) \\ &= A_0(s) \quad say. \end{aligned} \tag{51}$$

That is, the closed-loop polynomial coincides with that in equation (37), which was for the delay-free case. As shown in section 3.1, $A_0(s)$ is stable for certain choices of k_1 and k_2.

If $\tau_{tot} \neq 0$, we show that the controller structure given in figure 4 still guarantees stability. Since the polynomial $n_2(s)$ is of degree $n-1$, its coefficients can be chosen such that

$$n_2(s) = -k_1 k_0 Z_0(s), \tag{52}$$

which implies, from equation (50), that $B(s) = 0$ and therefore $R_{cl}(s) = A(s)$.

Furthermore, it is clear from equation (46) that the polynomials n_1 and n_2 of the SC are linked. More precisely, the choice of n_2 in (52) imposes restrictions on n_1: it means that the coefficients α_i, and hence n_1, are proportional to $k_0 k_1$. When $\tau_{tot} = 0$, $n_2 = n_1$, we will emphasise this scaling by writing:

$$n_2(s) = n_1(s) + \tau_{tot} k_0 k_1 n_3(s), \tag{53}$$

where n_3 is a polynomial of degree $n-1$, with finite coefficients. Therefore, using (52) and (53) in (48), the closed loop poles are the roots of

$$R_{cl}(s) = (s+z_c+k_2)R_0(s) + k_1 k_0 (s+z_c)\,[Z_0(s) - \tau_{tot} n_3(s)] \tag{54}$$

For 'small' τ_{tot}, ie for $\tau_{tot}\omega_a$ <O(1) where ω_a is the highest frequency among the zeros of Z_0, the zeros of $T(s) = Z_0(s) - \tau_{tot}n_3(s)$ are close to the zeros of $Z_0(s)$, and hence are stable. Therefore, for $|k_1|$ large, $n-1$ zeros of $R_{cl}(s)$ are stabilised. The 2 remaining zeros of $R_{cl}(s)$ are obtained at large s, $(k_1^{-1}(s+z_c+k_2)R_0(s)$ is not negligible compared to $(s+z_c)(Z_0(s)-\tau_{tot}n_3(s))$ when $s \geq O(k_1^{-1})$, and this is where we find the 2 remaining zeros of $R_{cl}(s)$). After division by s^{n-1} of the 3 highest coefficients of $R_{cl}(s)$, we obtain

$$s^2 + (k_2 - k_1k_0\tau_{tot}C)s + (k_1k_0 - k_1k_0\tau_{tot}Cz_c) \qquad (55)$$

where C is the highest coefficient in $n_3(s)$. The 2 remaining roots of $R_{cl(s)}$ are stable if the polynomial (55) is stable, ie if

$$\begin{aligned} k_2 - k_1k_0\tau_{tot}C &> 0 \\ k_1k_0(1 - \tau_{tot}Cz_c) &> 0. \end{aligned} \qquad (56)$$

In the range of values of τ_{tot} considered (ie $\tau_{tot}\omega_a$ <O(1)), one easily checks that $C \sim +1$ and that (56) is satisfied for some $k_1 > 0$ and $k_2 > 0$. Therefore, we proved that for 'small τ_{tot}', all the closed-loop poles, ie the roots of $R_{cl}(s)$, are stabilised for some $k_1 > 0$ and $k_2 > 0$. In other words, a plant of relative degree $n^* \leq 2$ with a time delay τ_{tot} not too large is stabilized by the controller structure given in figure 4, and the controller equation is given by:

$$V_c(t) = -k_1P_{ref}(t) - \frac{k_2}{s+z_c}[V_c(t)] + \int_{-\tau_{tot}}^{0} \lambda(\sigma)V_c(t+\sigma)\,d\sigma. \qquad (57)$$

In practice, the constraint on the size of τ_{tot} is not so strong: simulation results for a nonlinear model of an infinite order plant descibed in section 5, show that control is obtained with $k_1 > 0$ and $k_2 > 0$ for $\tau_{tot} \leq \frac{1}{\omega_u}$ where ω_u is the main unstable mode. Furthermore, for higher values of τ_{tot}, up to $\tau_{tot} \sim 3$ cycles of oscillations, we observe some periodic stability bands according to the values of $\omega_u\tau_{tot}$ (figure 5b): a 'stability band' corresponds to values of $\omega_u\tau_{tot}$ for which control is obtained after a finite time called settling time. Between two consecutive 'stability bands', there are a few values of $\omega_u\tau_{tot}$ for which control is not obtained (the settling time is then infinite). It was also observed that the sign of the first order compensator gain k_1 achieving control changes between two consecutive stability bands (see figure 5a). These observations on $sign(k_1)$ and on the stability bands pattern can be interpreted as follows: for frequencies smaller or equal to ω_u, the open-loop transfer function can be approximated by a second order system

$$k_0' \frac{1}{(s-\sigma_u)^2 + \omega_u^2} \qquad (58)$$

where $k_0' = k_0(\sigma_u^2 + \omega_u^2)\frac{constant\ coefficient\ of\ Z_0}{constant\ coefficient\ of\ R_0}$ is a positive gain[§]. It is shown in appendix C that a plant of order 2, whose transfer function is given by (58), is stable for any delay τ_{tot} which satisfies

$$\begin{aligned} k_1 \sin(\omega_u\tau_{tot}) &< 0 \\ 1/\tan(\omega_u\tau_{tot}) - \frac{z_c}{\omega_u} &< 0. \end{aligned} \qquad (59)$$

Hence, such a plant is characterized by a pattern of periodic stability bands according to the values of $\omega_u\tau_{tot}$, as shown in figure 5a. We see also from (59) that the sign of k_1 required for control satisfies

$$sign(k_1) = -sign(\sin(\omega_u\tau_{tot})), \qquad (60)$$

which corresponds to observations from the simulation (see figure 5a). In a practical combustor, the time delay τ_{tot} would usually not exceed 3 cycles of oscillations, therefore our controller appears very adequate for control of combustion oscillations.

[§]the zeros of R_0 are complex conjugates, hence the constant coefficient of R_0 is positive. Z_0 is monic and stable, therefore its constant coefficient is also positive.

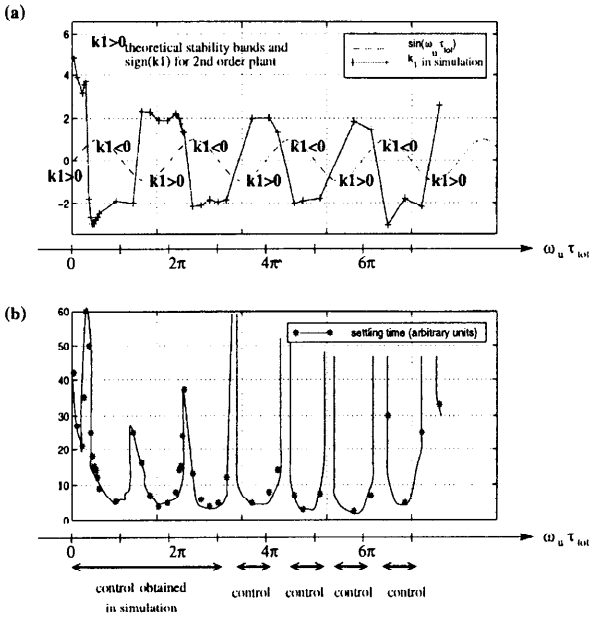


Figure 5: Comparison of simulation results for an infinite order plant (model described in section 5, $\omega_u = 370$ rad/s) with theoretical results for a second order plant (appendix C). (a) k_1 obtained in simulation and $sign(k_1)$ required for stability for a second order plant. (b) simulation: control obtained periodically up to $\omega_u\tau_{tot} \sim 3$ cycles of oscillations.

4. Adaptive regulator design

4.1 System without time delay ($\tau_{tot} = 0$)

It was shown in section 3.1 that a first order regulator $K_2(s) = k_c(s+z_c)/(s+p_c)$ will stabilize our combustion process which is minimum phase and of relative degree less or equal to 2. The adaptive version of this regulator, called Self-Tuning Regulator (STR), is given in figure 6.

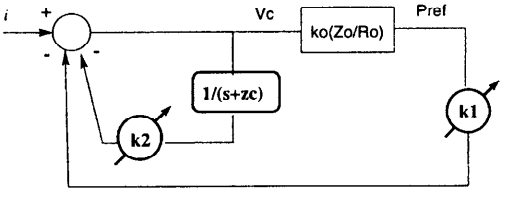


Figure 6: Low order adaptive controller for $\tau_{tot} = 0$, $n^* \leq 2$

With this controller structure, the closed-loop transfer function between some input noise i and P_{ref} is

$$\frac{P_{ref}(s)}{i(s)} = W_{cl}(s) = \frac{k_0(s+z_c)Z_0(s)}{R_{cl}(s)}, \qquad (61)$$

and the closed-loop poles are the roots of

$$R_{cl}(s) = (s+z_c+k_2)R_0(s) + k_1k_0(s+z_c)Z_0(s), \qquad (62)$$

where $z_c > 0$ is fixed, and two controller parameters, $k_1(t)$ and $k_2(t)$, are tuned. It is clear from equations (62) and (37) that k_1 represents the gain k_c of the fixed regulator $K_2(s)$, while k_2 is used to tune p_c. In the following, vectors are denoted in bold characters and ^{T} denotes the transpose of a vector. We introduce:

- the unknown controller parameter vector $\underline{\mathbf{k}}(t)^T = [-k_1(t), -k_2(t)]$, and the error parameter vector $\tilde{\mathbf{k}} = \mathbf{k} - \mathbf{k}^*$, where * denotes a value for which closed-loop stability is achieved.

- the data vector $\mathbf{d}(t)^T = [P_{ref}(t), V(t)]$, where $V(t) = \frac{1}{s+z_c}[V_c(t)]$ and z_c is a positive constant. In an experiment, $\mathbf{d}$ can be determined at each t from the measurement P_{ref} and known V_c.

We now need to find an updating rule for $\mathbf{k}$, so that stabilisation can be accomplished fo any parameters in $W_0(s)$.

Case (i) : $n^*(W_0) = 1$. This corresponds to a case for which Narendra & Annaswamy [21] have developed a STR. However, we will repeat the main points of their argument because they provide the background to our novel STR for the case with time delay in section 4.2. When $n^*(W_0) = 1$, the closed-loop transfer function W_{cl} given in (61) has then a relative degree equal to 1 and is 'Strictly Positive Real' (SPR), which is the essential property required to develop a global stability analysis based on Lyapunov's direct method [21]. Such a method aims at finding adaptive laws for $\mathbf{k}$ which are guaranteed to stabilize the self-excited combustion process. Essentially, the strictly positive realness of W_{cl} means that it is possible to find a quadratic positive function V_l, that decays in time when $\mathbf{k}$ is updated correctly. Such a function V_l is referred to as a 'Lyapunov function', and can be viewed as an energy function: if this function decreases, it implies that the system is stabilised. To summarize Narendra & Annaswamy's results [21], when W_0 has a relative degree equal to 1, the STR which guarantees the stability of the system is described by:

$$\begin{aligned} V_c(t) &= \mathbf{k}^T(t).\mathbf{d}(t) \\ \dot{\mathbf{k}}(t) &= -sign(k_0)P_{ref}(t)\mathbf{d}(t), \end{aligned} \tag{63}$$

where $sign(k_0) = +1$ from Lemma 3. For reference, equation (63) comes from the application of lemma 5.1 in Narendra & Annaswamy [21], noting that

$$P_{ref}(t) = W_{cl}(s)[\tilde{\mathbf{k}}^T(t).\mathbf{d}(t)]. \tag{64}$$

Case (ii) : $n^*(W_0) = 2$. In this case W_{cl} is not SPR, but the approach of Annaswamy et al [2] shows that modifying the control signal V_c as indicated in figure 7 effectively makes the closed-loop transfer function W_{cl} have relative degree 1. Following their approach, we write

$$V_c(t) = (s+a)[\mathbf{k}^T(t).\mathbf{d_a}(t)] \tag{65}$$

where $\mathbf{d_a}(t) = \frac{1}{s+a}[\mathbf{d}(t)]$. After some simple algebra, V_c can be written as

$$V_c(t) = \mathbf{k}^T(t).\mathbf{d}(t) + \dot{\mathbf{k}}^T(t).\mathbf{d_a}(t). \tag{66}$$

Now, we have

$$\begin{aligned} P_{ref}(t) &= W_{cl}(s)(s+a)[\tilde{\mathbf{k}}^T(t).\mathbf{d_a}(t)] \\ &= W_m(s)[\tilde{\mathbf{k}}^T(t).\mathbf{d_a}(t)], \end{aligned} \tag{67}$$

where $W_m(s) = (s+a)W_{cl}(s)$ is the new closed-loop transfer function of our system, which has relative degree 2 and is SPR. Noting that equation (67) looks similar to equation (64), lemma 5.1 [21] can be applied: the STR which will guarantee the stability of the system of relative degree 2 is given by:

$$\begin{aligned} V_c(t) &= \mathbf{k}^T(t).\mathbf{d}(t) + \dot{\mathbf{k}}(t)^T.\mathbf{d_a}(t) \\ \dot{\mathbf{k}}(t) &= -sign(k_0)P_{ref}(t)\mathbf{d_a}(t), \end{aligned} \tag{68}$$

where $sign(k_0) = +1$ from Lemma 3.

An important remark is that the STR described for the case $n^*(W_0) = 2$ will also work if $n^*(W_0) = 1$, which means that even if the actuator dynamics are not very well known in practice, the STR design given in equation (68) will always give satisfactory results.

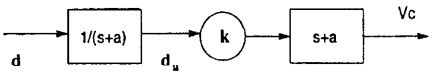


Figure 7: Modification of the control input V_c

4.2 Combustion system with known time delay ($\tau_{tot} \neq 0$)

The controller structure given in figure 4 includes fixed controller parameters k_1, k_2, α_i and β_i which need to be chosen based on the system parameters. Under uncertainties and variations in the operating conditions, it is more appropriate to adapt those control parameters. Hence, we choose an adaptive controller structure as shown in figure 8.

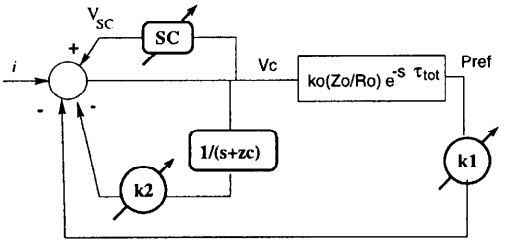


Figure 8: A low-order adaptive controller for $\tau_{tot} \neq 0$, $n^* \leq 2$

In the control law given in equation (57), the finite-time integral due to Smith Controller and given in equation (42) is approximated as follows:

$$V_{SC}(t) = \sum_{i=1}^{N} \lambda_i(t) V_c(t - i\mathrm{dt}). \tag{69}$$

Similar to the delay-free case, we define the controller parameters and data vectors $\mathbf{k}$ and $\mathbf{d}$ respectively:

- $\mathbf{k}(t)^T = [-k_1(t), -k_2(t), \lambda_N(t), ..., \lambda_1(t)]$, and its error vector $\tilde{\mathbf{k}} = \mathbf{k} - \mathbf{k}^*$.
- $\mathbf{d}(t)^T = [P_{ref}(t), V(t), V_c(t - N\mathrm{dt}), ..., V_c(t - \mathrm{dt})]$, where $V(t) = \frac{1}{s+z_c}[V_c(t)]$.

Therefore, as the time delay τ_{tot} is increased, N must be increased and more controller parameters are required. We are looking for an updating rule for $\mathbf{k}$.

General case : $n^*(W_0) \leq 2$. As in section 4.1, the closed loop transfer function W_{cl_0} given in (47) is made to effectively have relative degree 1 by using a modified control signal V_c (see figure 7). Then we obtain:

$$P_{ref}(s) = W_{cl_0}(s)(s+a)e^{-s\tau_{tot}}[\tilde{\mathbf{k}}^T(t).\mathbf{d_a}(t)], \tag{70}$$

where $\mathbf{d_a}(t) = \frac{1}{s+a}[\mathbf{d}(t)]$. Due to the presence of the time delay $e^{-s\tau_{tot}}$, the Lyapunov function V_l used in the delay-free case will not decay in time. So we need to add an extra positive term in V_l, in the form of a double integral $\int_{-\tau_{tot}}^{0} \int_{t+\nu}^{t} \|\dot{\tilde{\mathbf{k}}}(\xi)\|^2 d\xi d\nu$, to account for the time delay τ_{tot}. Then we have $\dot{V}_l \leq 0$, and hence a system whose energy is decaying in time (see details of proof in Appendix D). Therefore, with the Lyapunov function given in equation (98), the stability of the system is guaranteed when one uses the following STR:

$$\begin{aligned} V_c(t) &= \mathbf{k}^T(t).\mathbf{d}(t) + \dot{\mathbf{k}}(t)^T.\mathbf{d_a}(t) \\ \dot{\mathbf{k}}(t) &= -sign(k_0)P_{ref}(t)\mathbf{d_a}(t - \tau_{tot}), \end{aligned} \tag{71}$$

where $sign(k_0) = +1$.

Particular case : $n^*(W_0) = 1$. Then the manipulation on V_c shown in figure 7 is not required, and therefore the following simpler algorithm can be implemented:

$$\begin{aligned} V_c(t) &= \mathbf{k}^T(t).\mathbf{d}(t) \\ \dot{\mathbf{k}}(t) &= -sign(k_0)P_{ref}(t)\mathbf{d}(t-\tau_{tot}), \end{aligned} \tag{72}$$

where $sign(k_0) = +1$.

5. Application to a premixed ducted flame (simulation)

5.1 Nonlinear flame model used in the simulation

A model for nonlinear oscillations of a ducted flame developed by Dowling [10] will be used to verify the controller performance. The theory involves extension of the flame model of Fleifil et al[13] to include a flame holder at the centre of the duct and nonlinear effects. Due to page limitations, the reader is asked to refer to [10] for details.

5.2 Adaptive regulator design

The flame model described in [10] fits in the class of combustion systems given in section 2, since:

- the upstream reflection coefficient has a modulus strictly smaller than 1 (choked end: $R_u = (1-\bar{M}_1)/(1+\bar{M}_1)$) , in agreement with equation 3. Notice that the downstream reflection coefficient has modulus just equal to 1 (ideal open end: $R_d = -1$). However, with care the condition $|R_d(s)| < 1$ in equation 3 can be relaxed to $|R_d(s)| \leq 1$ provided an upstream pressure measurement is made. This is because in the transfer function $G(s)$ given in (7), $|X_{12}| > |Y_{12}|$ and $|X_{22}| > |Y_{22}|$.
- after linearisation for small perturbations, the flame transfer function is given by (see [10]):

$$H(s) = \frac{Q_n(s)}{u_G(s)} = \frac{2\eta\Delta H e^{-s\tau_2}}{s\tau_f \bar{c}_1^2(b+a)}\left[a - be^{-s\tau_f} + \frac{b-a}{s\tau_f}(1-e^{-s\tau_f})\right] \tag{73}$$

  Therefore, $H \to 0$ as $s \to \infty$, and $H(s)$ has no poles: hence assumptions (I) and (II) are satisfied.

Hence, section 2 proves that, once the system is approximated as finite dimensional, the relative degree of the open-loop transfer function W_0 is equal to the relative degree of the actuator transfer function. As in Evesque et al [11], the actuator chosen is a fuel injection system modelled as follows:

$$\frac{Q_c(s)}{V_c(s)} = \frac{e^{-s\tau_a}}{s^2/\omega_c^2 + 2cs/\omega_c + 1} \tag{74}$$

where ω_c and c are respectively the resonance frequency and damping of the fuel injector. From equation (74), we deduce that the relative degree of W_0 is 2. Section 2 shows also that the 'high frequency gain' k_0 is positive and that the zeros of W_0 are stable.

Two cases are studied in the simulation:

- a system without time delay ($\tau_{tot} = 0$). This is achieved by making the pressure measurement at the flame (ie $x_{ref} = 0$) and by setting the time delay τ_a to zero in equation (74). Then the STR is implemented as indicated in equation (68), with $sign(k_0) = +1$.
- a system with time delay ($\tau_{tot} \neq 0$). The pressure measurement is chosen for instance at $x_{ref} = -x_u/2$ and the delay τ_a can be varied. Then the adequate STR to control the self-excited oscillations is given in equation (71), with $sign(k_0) = +1$.

For both cases, a convergence coefficient μ is added in the adaptive law for each controller parameter. The controller parameter vector $\mathbf{k}$ is initialized to zero. Simulations results are given in the next section.

5.3 Simulation results

System without time delay ($\tau_{tot} = 0$). Figure 9 shows the time evolution of the pressure measurement P_{ref} and the corresponding control signal V_c for varying operating conditions. The control is switched on at $t = 0.15$ s, when the limit cycles are already established (operating conditions: $\phi = 0.7$, $\bar{M}_1 = 0.08$). The oscillations tend to zero within 1 s; note that the settling time depends on the convergence coefficient μ used. Then from $t = 1.95$ s to $t = 2.1$ s, $\bar{M}_1$ is increased to 0.095: in the open-loop system such a change shifts the frequency of the unstable mode from 58 to 63 Hz. Nevertheless, the STR is able to maintain control. Changes in the fuel air ratio ϕ have also been successfully tested. It has been observed that the STR works fine even if x_{ref} is chosen anywhere upstream the flame, which is interesting for practical applications where a pressure measurement directly at the flame may be difficult to perform.

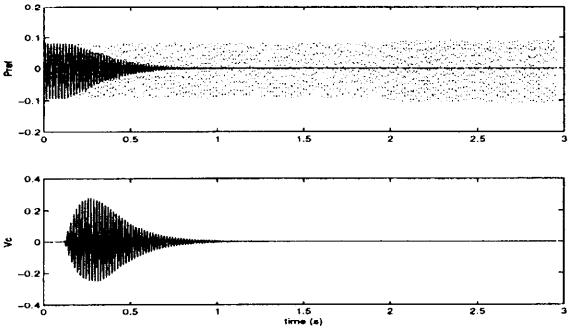


Figure 9: STR for $\tau_{tot} = 0$, $\bar{M}_1$ is varied linearly from 0.08 at $t = 1.95$ s to 0.095 at $t = 2.1$ s. ...: controller OFF, —: controller ON after $t = 0.15$ s.

System with time delay ($\tau_{tot} \neq 0$). This is the most interesting case for practical applications. As already illustrated in section 3 (see figure 5), control is obtained for values of τ_{tot} much larger than those predicted by the theory: control is achieved periodically up to $\tau_{tot} \sim 3$ cycles of oscillations (ie up to $\omega_u \tau_{tot} \sim 6\pi$ where ω_u is the unstable mode). The settling time varies periodically: control is easier in the middle of a stability band, and becomes more difficult on the boundaries of a stability bands. As in the delay free case ($\tau_{tot} = 0$), the actual value of the settling time depends on the convergence coefficient μ chosen. A typical time evolution of the pressure oscillations while control is applied is shown in figure 10. There, in order to test the adaptability of our STR under varying operating conditions, the mean upstream Mach number $\bar{M}_1$ is increased from 0.08 to 0.095 between $t = 1.95$ s and $t = 2.1$ s: the STR successfully maintains P_{ref} at zero.

6. Conclusions

A general combustion system, susceptible to combustion instabilities, and satisfying the following assumptions, was considered:

1. the pressure reflection coefficients at the boundaries of the combustor have a modulus strictly smaller than 1 in $Real(s) \geq 0$.
2. the flame response has a limited bandwidth: at high frequencies, the flame does not follow incoming velocity fluctuations.
3. the flame is stable in itself, it becomes unstable only due to the interaction with the acoustic waves in the combustor.

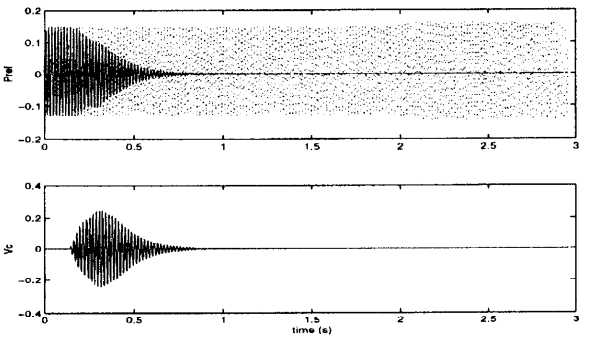


Figure 10: STR for $\tau_{tot} = 23$ ms, $x_{ref} = -x_u/2$, $\overline{M}_1$ is varied linearly from 0.08 at $t = 1.95$ s to 0.095 at $t = 2.1$ s. ... : controller OFF, — : controller ON after $t = 0.15$ s.

4. the actuator used for control is a fuel injector which produces a heat release rate Q_c related to the voltage V_c driving the actuator simply by a time delay and a first or second order differential equation.

We demonstrated that such a combustion system is essentially represented by an open-loop transfer function

$$W(s) = \frac{P_{ref}(s)}{V_c(s)} = k_0 \frac{Z_0(s)}{R_0(s)} e^{-s\tau_{tot}}$$

where P_{ref} is a pressure measurement in the combustor and V_c is the voltage driving the fuel injector used as control actuation. Some general properties have been derived:
(i) the zeros of $Z_0(s)$ are all stable (ie are in $Real(s) < 0$)
(ii) Once Z_0/R_0 has been made rational using a Padé expansion, the relative degree of $Z_0(s)/R_0(s)$ is equal to the relative degree of the actuator transfer function, ie 2 for a fuel injector.
(iii) k_0 is a positive gain.
These properties have been exploited to design an adaptive controller guaranteed to stabilise the self-excited combustion system. In particular, for the case of a combustion system with time delay ($\tau_{tot} \neq 0$), which is the most realistic case, the design is completely novel: it involves a first order compensator combined with a Smith Controller. The adaptive laws for the controller parameters are derived based on a Lyapunov stability analysis. The adaptive controller has been tested successfully on a simulation of a premixed ducted flame. An experimental verification is planned over the next months.

ACKNOWLEDGMENTS

Part of the work described in section 3 was carried out while APD was the Jerome C Hunsaker Visiting Professor and SE a Visiting Engineer at the Massachusetts Institute of Technology. The support of MIT in making this collaboration possible is gratefully acknowledged. AMA is sponsored by the Office of Naval Research, under grant N00014-99-1-0448.

APPENDIX

Appendix A. Consider linear disturbances with time dependence e^{st} in the pipework system upstream the combustion zone, as shown in figure 11. The Mach number considered is so low that we assume there is no mean flow in the pipework system. The pressure reflection coefficient at an axial position x_i is $R_{u_i}(s)$. The cross-sectional area of the duct i between $x = x_i$ and $x = x_{i+1}$ is A_i. The mean speed of sound is $\bar{c}$ and the mean density is $\bar{\rho}$. At x_0, we assume that the pressure reflection coefficient $R_{u_0}(s)$ satisfies

$$\begin{aligned} |R_{u_0}(s)| &< 1 \quad in \quad Real(s) \geq 0 \\ n^*(R_{u_0}(s)) &= 0. \end{aligned} \tag{75}$$

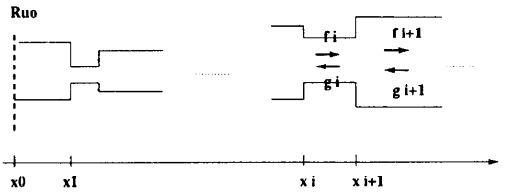


Figure 11: upstream pipework system

These assumptions are true for a choked end at $x = x_0$ for instance. In the following, we show by induction that for all i, $|R_{u_i}(s)| < 1$ in $Real(s) \geq 0$, and $n^*(R_{u_i}(s)) = 0$.

At $x = x_i$, the reflected wave f_i is related to the incoming wave g_i:

$$f_i(t) = e^{-2s\frac{x_{i+1}-x_i}{\bar{c}}} R_{u_i}(s)\,[g_i(t)]\,. \tag{76}$$

Writing the continuity of pressure and mass flux across $x = x_{i+1}$, and using the boundary condition (76) leads to the following relationship between the reflected wave f_{i+1} and the incoming wave g_{i+1} in the duct $i+1$:

$$f_{i+1}(t) = e^{-2s\frac{x_{i+2}-x_{i+1}}{\bar{c}}} R_{u_{i+1}}(s)\,[g_{i+1}(t)]\,, \tag{77}$$

where

$$R_{u_{i+1}}(s) = \frac{K_i + R_{u_i}(s)e^{-s\tau_i}}{1 + K_i R_{u_i}(s) e^{-s\tau_i}} \tag{78}$$

$$K_i = \frac{A_{i+1} - A_i}{A_{i+1} + A_i} \tag{79}$$

$$\tau_i = \frac{-2(x_{i+1} - x_i)}{\bar{c}}. \tag{80}$$

By inspection $|K_i| < 1$. Furthermore, from (78), one deduces that $n^*(R_{u_i}(s)) = 0$ implies that $n^*(R_{u_{i+1}}(s)) = 0$ after a Padé expansion $[M/M]$ for $e^{-s\tau_i}$ is made. Let us write R_{u_i} in the form $R_{u_i}(s) = |R_{u_i}(s)|e^{-s\alpha_i}$ in equation (78). Then one easily obtains

$$|R_{u_{i+1}}(s)|^2 = \frac{K_i^2 + |R_{u_i}|^2 e^{-2\delta_i} + 2K_i|R_{u_i}(s)|e^{-\delta_i}\cos(\theta_i)}{1 + K_i^2|R_{u_i}|^2 e^{-2\delta_i} + 2K_i|R_{u_i}(s)|e^{-\delta_i}\cos(\theta_i)} \tag{81}$$

where $\theta_i = Imag(s)\tau_i + \alpha_i$ and $\delta_i = Real(s)\tau_i$.

The difference P between the numerator and the denominator of $|R_{u_{i+1}}(s)|^2$ is equal to

$$P = (1 - K_i^2)(|R_{u_i}|^2 e^{-2Real(s)\tau_i} - 1) \tag{82}$$

Therefore, in $Real(s) \geq 0$, $|R_{u_i}(s)| < 1$ implies that $P < 0$ and hence $|R_{u_{i+1}}| < 0$.

Now we assume that at $x = x_0$, the high frequency gain h_0 of $R_{u_0}(s)$ satisfies

$$|h_0| < 1. \tag{83}$$

(this is true for a choked end). We show by induction that for all i, the high frequency gain h_i of $R_{u_i}(s)$ satisfies $|h_i| < 1$.

From (78), after a Padé expansion $[M/M]$ for $e^{-s\tau_i}$ is made, one deduces that

$$h_{i+1} = \frac{K_i + h_i(-1)^M}{1 + K_i h_i (-1)^M}. \tag{84}$$

and hence

$$|h_{i+1}^2| = \frac{K_i^2 + h_i^2 - 2(-1)^M K_i h_i}{1 + 2K_i h_i (-1)^M + K_i^2 h_i^2}. \tag{85}$$

The difference Q between the numerator and the denominator of h_{i+1} is

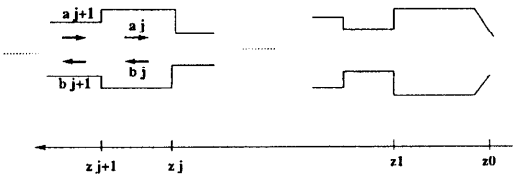


Figure 12: downstream pipework system

$$Q = (1 - K_i^2)(h_i^2 - 1). \tag{86}$$

Hence, $|h_i| < 1$ implies that $Q < 0$ and therefore $|h_{i+1}| < 1$.

Similarly, for a pipework system downstream the flame, ended by a nozzle (see figure 12), we assume that at $z = z_0$, the pressure reflection coefficient R_{d_0} satisfies the assumptions (75) and (83), which is true if the nozzle is compact [20]. By induction, it can be shown that at any position $z = z_j$, the downstream pressure coefficient R_{d_j} and its high frequency gain h_j satisfy

$$\begin{aligned} n^*(R_{d_j}) &= 0 \\ |R_{d_j}(s)| &< 1 \quad in \quad Real(s) \geq 0 \\ |h_j| &< 1. \end{aligned} \tag{87}$$

Appendix B. The full form of the coefficients in equation (7) is:

$$\mathbf{X} = \begin{pmatrix} -1+\bar{M}_1\left(2-\frac{\bar{u}_2}{\bar{u}_1}\right)-\bar{M}_1^2\left(1-\frac{\bar{u}_2}{\bar{u}_1}\right) & 1+\bar{M}_1\frac{\bar{\rho}_1\bar{c}_1}{\bar{\rho}_2\bar{c}_2} \\ \frac{1-\gamma\bar{M}_1}{\gamma-1}+\bar{M}_1^2-\bar{M}_1^2(1-\bar{M}_1)\frac{1}{2}\left(\frac{\bar{u}_2^2}{\bar{u}_1^2}-1\right) & \frac{\bar{c}_2}{\bar{c}_1}\frac{1+\gamma\bar{M}_2}{\gamma-1}+\bar{M}_1\bar{M}_2\frac{\bar{\rho}_1}{\bar{\rho}_2} \end{pmatrix} \tag{88}$$

$$\mathbf{Y} = \begin{pmatrix} 1+\bar{M}_1\left(2-\frac{\bar{u}_2}{\bar{u}_1}\right)+\bar{M}_1^2\left(1-\frac{\bar{u}_2}{\bar{u}_1}\right) & \bar{M}_1\frac{\bar{\rho}_1\bar{c}_1}{\bar{\rho}_2\bar{c}_2}-1 \\ \frac{1+\gamma\bar{M}_1}{\gamma-1}+\bar{M}_1^2-\bar{M}_1^2(1+\bar{M}_1)\frac{1}{2}\left(\frac{\bar{u}_2^2}{\bar{u}_1^2}-1\right) & \frac{\bar{c}_2}{\bar{c}_1}\frac{1-\gamma\bar{M}_2}{\gamma-1}+\bar{M}_1\bar{M}_2\frac{\bar{\rho}_1}{\bar{\rho}_2} \end{pmatrix} \tag{89}$$

Appendix C. Consider an unstable plant of order 2, defined by $Z_0(s) = 1$ and $R_0(s) = (s - \sigma_u)^2 + \omega_u^2$ ($\sigma_u < 0$ for an unstable mode), and whose total time delay is τ_{tot}. Using the controller defined in figure 4, the denominator of the closed-loop transfer function is easily calculated analytically and is found to be:

$$R_{cl}(s) = s^3 + as^2 + bs + c \tag{90}$$

where

$$\begin{aligned} a &= -2\sigma_u + z_c + k_2 - k_0 k_1 \frac{\sin(\omega_u \tau_{tot})}{\omega_u} \\ b &= \sigma_u^2 + \omega_u^2 - 2\sigma_u(z_c + k_2) + k_0 k_1 e^{-\sigma_u \tau_{tot}}\left[\frac{\sigma_u - z_c}{\omega_u}\sin(\omega_u\tau_{tot}) + \cos(\omega_u\tau_{tot})\right] \\ c &= (\sigma_u^2 + \omega_u^2)(z_c + k_2) + k_0 k_1 e^{-\sigma_u\tau_{tot}} z_c\left[\frac{\sigma_1}{\omega_u}\sin(\omega_u\tau_{tot}) + \cos(\omega_u\tau_{tot})\right] \end{aligned} \tag{91}$$

Assuming that $|\sigma_u| << \omega_u$ (realistic assumption: the growth rate is much smaller than the frequency of the unstable mode), the Routh criteria applied to $R_{cl}(s)$ shows that $R_{cl}(s)$ is stable for some $k_2 > 0$ if

$$\begin{aligned} k_1 \sin(\omega_u \tau_{tot}) &< 0 \\ 1/\tan(\omega_u\tau_{tot}) - \frac{z_c}{\omega_u} &< 0. \end{aligned} \tag{92}$$

Consider the angle θ defined by $\frac{1}{\tan(\theta)} = \frac{z_c}{\omega_u}$ and $\sin(\theta) > 0$. Then, as illustrated in figure 13:

- for $\theta < \omega_u\tau_{tot} < \pi/2$ and $k_1 < 0$, $R_{cl}(s)$ is stable.
- for $\theta + \pi < \omega_u\tau_{tot} < 2\pi$ and $k_1 > 0$, $R_{cl}(s)$ is stable.

Hence the periodic stability bands shown in figure 5a. Also note the result that k_1 required for control satisfies $sign(k_1) = -sign(\sin(\omega_u\tau_{tot}))$.

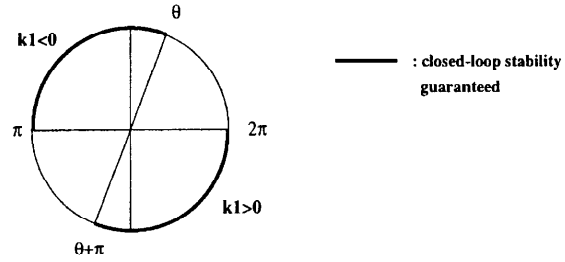


Figure 13: $sign(k_1)$ and values of $\omega_u\tau_{tot}$ for which a plant of order 2 is guaranteed to be stabilised by the fixed controller described in figure 4

Appendix D. We start from equation (70):

$$P_{ref}(t) = W_m(s)e^{-s\tau_{tot}}[\tilde{\mathbf{k}}^T(t).\mathbf{d_a}(t)], \tag{93}$$

where $W_m(s) = W_{cl_0}(s)(s + a)$ is SPR and $\mathbf{d_a}(t) = \frac{1}{s+a}[\mathbf{d}(t)]$.

The adaptive law is chosen as

$$\dot{\tilde{\mathbf{k}}}(t) = -P_{ref}(t)\mathbf{d_a}(t - \tau_{tot}) \tag{94}$$

(a positive sign for k_0 is assumed).

Equation (93) can be expressed in a state-variable representation as

$$\begin{aligned} \dot{\mathbf{x}} &= A\mathbf{x}(t) + (s+a)\left[\mathbf{b}(\tilde{\mathbf{k}}^T(t - \tau_{tot}).\mathbf{d_a}(t - \tau_{tot}))\right] \\ P_{ref}(t) &= \mathbf{h}^T.\mathbf{x}(t). \end{aligned} \tag{95}$$

$\mathbf{x}$ is the 'state vector' of the system and A is a matrix. $(A, \mathbf{b}, \mathbf{h})$ is the 'state representation' of W_0.

We note that equation (95) can be rewritten as

$$\begin{aligned} \dot{\mathbf{x}}(t) = A\mathbf{x} + (s+a)\left[\mathbf{b}\left(\tilde{\mathbf{k}}^T(t).\mathbf{d_a}(t - \tau_{tot})\right)\right] \\ -(s+a)\left[\mathbf{b}\mathbf{d_a}^T(t - \tau_{tot})\left(\int_{-\tau_{tot}}^{0} \dot{\tilde{\mathbf{k}}}(t+\nu)d\nu\right)\right]. \end{aligned} \tag{96}$$

Using equation (94), this leads to

$$\begin{aligned} \dot{\mathbf{x}}(t) = A\mathbf{x} + (s+a)\left[\mathbf{b}\left(\tilde{\mathbf{k}}^T(t).\mathbf{d_a}(t - \tau_{tot})\right)\right] \\ +(s+a)\left[\mathbf{b}\mathbf{d_a}^T(t - \tau_{tot})\left(\int_{-\tau_{tot}}^{0} P_{ref}(t+\nu)\mathbf{d_a}(t+\nu-\tau_{tot})d\nu\right)\right]. \end{aligned} \tag{97}$$

As in Burton [7] and Niculescu [23] [22], the Lyapunov function candidate is chosen as

$$V_l = \mathbf{x}^T(t)P\mathbf{x}(t) + \tilde{\mathbf{k}}^T(t)\tilde{\mathbf{k}}(t) + \int_{-\tau_{tot}}^{0}\int_{t+\nu}^{t} \|\dot{\tilde{\mathbf{k}}}(\xi)\|^2 d\xi d\nu. \tag{98}$$

Using equations (94) and (97), equation (98) leads to the time-derivative

$$\begin{aligned} \dot{V}_l = \mathbf{x}^T(A^TP + P^TA)\mathbf{x} + 2\mathbf{x}^T(t)P(s+a)\left[\mathbf{b}\left(\tilde{\mathbf{k}}^T(t).\mathbf{d_a}(t - \tau_{tot})\right)\right] \\ +2\mathbf{x}^T(t)P(s+a)\left[\mathbf{b}\mathbf{d_a}(t - \tau_{tot})\left(\int_{-\tau_{tot}}^{0} P_{ref}(t+\nu)\mathbf{d_a}(t+\nu-\tau_{tot})d\nu\right)\right] \\ -2P_{ref}(t)\tilde{\mathbf{k}}^T(t).\mathbf{d_a}(t - \tau_{tot}) + \frac{d}{dt}\left[\int_{-\tau_{tot}}^{0}\int_{t+\nu}^{t} (P_{ref}(\xi))^2 \|\mathbf{d_a}(\xi - \tau_{tot})\|^2 d\xi d\nu\right] \end{aligned} \tag{99}$$

Since $W_m(s)$ is SPR, lemma 2.4 [21] can be used: given a matrix Q symmetric strictly positive, there exists a matrix P symmetric strictly positive, such that

$$A^T P + P^T A = -Q, \qquad P(s+a)\mathbf{b} = \mathbf{h}, \tag{100}$$

which leads to

$$\dot{V}_l = -\mathbf{x}^T Q\mathbf{x} + 2P_{ref}(t)\mathbf{d_a}(t-\tau_{tot})\left(\int_{-\tau_{tot}}^{0} P_{ref}(t+\nu)\mathbf{d_a}(t+\nu-\tau_{tot})d\nu\right)$$

$$+ \int_{-\tau_{tot}}^{0} \left[\|P_{ref}(t)\mathbf{d_a}(t-\tau_{tot})\|^2 - \|P_{ref}(t+\nu)\mathbf{d_a}(t+\nu-\tau_{tot})\|^2\right] d\nu. \tag{101}$$

Denoting

$$\mathbf{y} = P_{ref}(t)\mathbf{d_a}(t-\tau_{tot}), \qquad \mathbf{z} = P_{ref}(t+\nu)\mathbf{d_a}(t+\nu-\tau_{tot}), \tag{102}$$

equation (101) can be rewritten as

$$\begin{aligned}
\dot{V}_l &= -\mathbf{x}^T Q\mathbf{x} + \int_{-\tau_{tot}}^{0} \left(2\mathbf{y}^T\mathbf{z} + \mathbf{y}^T\mathbf{y} - \mathbf{z}^T\mathbf{z}\right) d\nu \\
&= -\mathbf{x}^T Q\mathbf{x} - \int_{-\tau_{tot}}^{0} \left(\|\mathbf{z}-\mathbf{y}\|^2 - 2\mathbf{y}^T\mathbf{y}\right) d\nu \\
&\leq -\mathbf{x}^T Q\mathbf{x} + 2\tau_{tot}\|P_{ref}(t)\mathbf{d_a}(t-\tau_{tot})\|^2 \\
&\leq -P_{ref}^2(t)\left(k - 2\tau_{tot}\|\mathbf{d_a}(t-\tau_{tot})\|\right) \\
&\leq 0 \qquad for \quad \|\mathbf{d_a}\| \leq k/2\tau_{tot}.
\end{aligned} \tag{103}$$

Therefore, the stability of the delayed plant under control is guaranteed for all τ_{tot}. A domain of attraction results, given by $\|P_{ref}\mathbf{d_a}\| \leq k/2\tau_{tot}$; this domain reaches $\mathbb{R}^n$ as $\tau_{tot} \to 0$.

[1] AM Annaswamy, M Fleifil, JW Rumsey, JP Hathout, and AF Ghoniem. An input-output model of thermoacoustic instability and active control design. Technical report, MIT, 1997.

[2] A.M. Annaswamy, O.M. El Rifai, M. Fleifil, and A.F. Ghoniem J.P. Hathout. A model-based self-tuning controller for thermoacoustic instability. *Combust. Sci. and Tech.*, 135:213–240, 1998.

[3] G.A. Baker, Jr and P. Graves-Morris. *Pade approximants, 2nd edition.* Cambridge University Press, 1996.

[4] A Banaszuk, CA Jacobson, AI Khibnik, and PG Mehta. Linear and nonlinear analysis of controlled combustion processes. In *Proceedings of the 1999 IEEE Internation Conference on Control Applications*, Hawai'i, USA, August 1999.

[5] G Billoud, MA Galland, C Huynh Huu, and S Candel. Adaptive control of combustion instabilities. *Combust Sci Tech*, 81:257–283, 1992.

[6] R Blonbou, S Zaleski, A Laverdant, and P Kuentzmann. Active adaptive combustion control using neural networks. To be published in *Combust Sci Tech* in 2000.

[7] T.A. Burton. *Stability and periodic solutions of ordinary and functional differential equations.* Academic Press, Orlando, 1985.

[8] R Dorf and R Bishop. *Modern control systems (7th edition).* Addison Wesley, 1995.

[9] AP Dowling. Nonlinear self-excited oscillations of a ducted flame. *J Fluid Mech*, 346:271–290, 1997.

[10] AP Dowling. A kinematic model of a ducted flame. *J. Fluid Mech.*, 394:51–72, 1999.

[11] S. Evesque, Y.C. Chu, A.P. Dowling, and K. Glover. Feedback control of a premixed ducted flame. In *Proceedings of the ISABE XIV International Symposium*, Florence, Italy, September 1999. Paper IS-7187.

[12] S Evesque and AP Dowling. Lms algorithm for adaptive control of combustion oscillations. Submitted to *Combust Sci Tech* in 1999.

[13] M Fleifil. Response of a laminar premixed flame to flow oscillations : a kinematic model and thermoacoustic instabilities results. *Combust Flame*, 106:487–510, 1996.

[14] S Hubbard and AP Dowling. Acoustic instabilities in premix burners. 4th AIAA/CEAS Aeroacoustics Conference, Toulouse, June 1998, 1998.

[15] K. Ichikawa. Frequency-domain pole assignment and exact model-matching for delay systems. *Int J Control*, 41(4):1015–1024, 1985.

[16] K. Ichikawa. Adaptive control of delay system. *Int. J. Control*, 43(6):1653–1659, 1986.

[17] A Kemal and CT Bowman. Real time adaptive feedback control of combustion instability. In *Twenty-Sixth Symposium (International) on Combustion*, pages 2803–2809, 1996.

[18] PJ Langhorne, AP Dowling, and N Hooper. Practical active control system for combustion oscillations. *J Prop Power*, 6:324–330, 1990.

[19] AZ Manitius and AW Olbrot. Finite spectrum assignment problem for systems with delays. *IEEE transactions on automatic control*, AC-24:541–553, 1979.

[20] F.E. Marble and S.M. Candel. Acoustic disturbance from gas non-uniformities convected through a nozzle. *Journal of Sound and Vibration*, 55(2):225–243, 1977.

[21] K.S. Narendra and A.M. Annaswamy. *Stable Adaptive Systems.* Prentice-Hall International, 1989.

[22] S.I. Niculescu. *Qualitative aspects on the stability and stabilization.* (in French), Diderot, Paris, Nouveaux Essais, 1997.

[23] S.I. Niculescu, E.I. Verriest, L.Dugard, and J.M.Dion. *Stability and control of time-delay systems*, chapter "Stability and robust stability of time-delay systems: A guided tour". (Ed: Dugard and Verriest), LNCIS, Springer-Verlag, London, 1997.

[24] R Ortega and R Lozano. Globally stable adaptive controller for system with delay. *Int J Contr*, 47:17–23, 1988.

[25] KT Padmanabhan, CT Bowman, and J David Powell. On-line adaptive optimal combustor control. *IEEE transactions on control systems technology*, 4(3), May 1996.

[26] CO Paschereit, E Gutmark, and W Weisenstein. Control of thermoacoustic instabilities in a premixed combustor by fuel modulation. In *37th AIAA Aerospace Science Meeting and Exhibit*, Reno, Nevada, January 1999.

[27] T Poinsot, C Le Chatelier, SM Candel, and E Esposito. Experimental determination of the reflection coefficient of a premixed flame in a duct. *Journal of Sound and Vibration*, 107(2):265–278, 1986.

[28] W.H. Press, S.A. Teukolsky, W.T. Vetterling, and B.P. Flannery. *Numerical Recipes, 2nd ed.* Cambridge University Press, New York, 1992.

[29] GA Richard and MC Janus. Characterization of oscillations during premix gas turbine combustion. *ASME J. Eng. for Gas Turbines and Power*, 120:294–302, 1998.

[30] OJM Smith. A controller to overcome dead time. *ISA*, 6(2):28–33, 1959.

PAPER -22, S. Evesque

Question (M. Mettenleiter)

In order to guarantee the correct update of the algorithm you use a Lyapunov function. How does this function depend on the model of your combustion system?

Reply

The Lyapunov function is not model-based at all. Its existence relies only on the four assumptions made on our system (see paper), but no other information on the system is required in the Lyapunov stability analysis.

This page has been deliberately left blank

Page intentionnellement blanche

Click here to view PowerPoint presentation; Press Esc to exit

Modeling and Control of Combustion Instability Using Fuel Injection [1]

J.P. Hathout, A.M. Annaswamy and A.F. Ghoniem
Department of Mechanical Engineering
Massachusetts Institute of Technology
Cambridge, MA 02139, USA

Abstract

Active control using periodic fuel injection has the potential of suppressing combustion instability without radically changing the engine design or sacrificing performance. In this paper, we carry out a study of optimal model-based control of combustion instability using fuel injection. The model developed is physically based and includes the acoustics, the heat-release dynamics, their coupling, and the injection dynamics. A heat-release model with fluctuations in the flame surface area as well as in the equivalence ratio is derived. We show that area fluctuations coupled with the velocity fluctuations drive longitudinal modes to resonance caused by phase-lag dynamics, while equivalence ratio fluctuations can destabilize both longitudinal and bulk modes caused by time-delay dynamics, similar to experimental observations. The dynamics of proportional and two-position (on-off) fuel injectors are included in the model. Using the overall model, two different control designs are proposed. The first is an LQG/LTR controller where the time-delay effect is ignored, and the second is a Posi-Cast controller which explicitly accounts for the delay. Injection at (i) the burning zone and (ii) further upstream is considered. The characteristics of fuel injectors including bandwidth, authority (pulsed-fuel flow rate), and whether it applies a proportional or a two-position (on-off) injection are discussed. We show that increasing authority and bandwidth result in improved performance. Injection at (ii) compared to (i) results in a trade-off between improved mixing and increased time-delay. We also note that proportional injection is more successful than on-off injection since the former can modulate both amplitude and phase of the control fuel.

[1] This work is sponsored in part by the National Science Foundation, contract no. ECS 9713415, and in part by the Office of Naval Research, contract no. N00014-99-1-0448.

1 Introduction

Active control using periodic fuel injection has been recognized as a promising technology to abate combustion instability in practical systems [1]-[6]. Most current designs are based on phase-shift algorithms which, despite their success, are not optimal in terms of fuel consumption, settling time, and robustness. Phase-shift controllers, due to their limited dynamics, are known to succeed only within a limited frequency band (around the unstable frequency), and over a small range of operating conditions. In this paper, we present alternative control designs using LQG/LTR and Posi-Cast control methods which are based on a physical model, and demonstrate their advantages.

Control algorithms must be based on an accurate description of the system dynamics to achieve optimal performance. Much effort has gone into modeling acoustics [1],[7]-[10]. Modeling of heat-release dynamics and its coupling with acoustics, mixing dynamics, and actuator dynamics, despite their crucial role in the instability mechanism, have not been dealt with to the same extent. Recognizing that heat-release oscillations can be caused by fluctuations of the flame surface area due to velocity perturbation or the equivalence ratio due to pressure perturbation, we derive a model that incorporates both for the case of a weakly turbulent premixed flame. We show how certain acoustic modes can couple with either or both forms of heat oscillations.

The feasibility of control design is tightly correlated with the performance of sensors and actuators. While high-bandwidth devices of the first are available, e.g., pressure transducers and heat-release sensors, actuation by means of fuel injection is hindered by low bandwidth, limited authority, and nonlinearities (in the form of dead-zone, saturation and on-off effects) [11]. The impact of ideal actuators was studied extensively in [12]. The ability of the actuator to convey the control signal faithfully to the combustor, thus introducing the correct forcing, is key to stable performance. This however is often not the case due to (i) non-ideal injection

Paper presented at the RTO AVT Symposium on "Active Control Technology for Enhanced Performance Operational Capabilities of Military Aircraft, Land Vehicles and Sea Vehicles", held in Braunschweig, Germany, 8-11 May 2000, and published in RTO MP-051.

dynamics, and (ii) injection locations which may impose a delay in the control input. To capture the contribution of these effects in the control design, we develop a model of the injector dynamics and incorporate it in the overall analysis of the system.

In Sec. 2, we model the heat release dynamics forced by velocity and equivalence ratio fluctuations, the acoustic dynamics, the coupling and mixing dynamics, their effect on stability, and a generic model of typical solenoid injectors which captures its relevant features. In Sec. 3, control is developed for a multi-mode combustor and injection at as well as upstream of the burning zone is implemented. For the former, an optimal Linear-Quadratic Gaussian with Loop-Transfer Recovery (LQG/LTR) controller is used, and for the latter, a novel technique known as Posi-Cast control that accommodates combustion systems with delays is developed and implemented.

2 Combustor Model

Physically-based modeling has been shown to be indispensable for optimal control design for suppression of combustion instability [13]. The dynamics leading to combustion instability is known to occur due to the resonant coupling between acoustics and heat release. This coupling may occur through flame-area fluctuations, as shown experimentally in [1], and by modeling in [14]. It can also occur through mixture inhomogeneity (reactants' equivalence-ratio fluctuations), observed experimentally in [15]-[17], and modeled in [18, 19]. While both mechanisms can destabilize longitudinal modes [4, 7, 16, 20], bulk modes are more strongly affected by the latter [3, 18]. A rigorous model for the response of heat-release dynamics to these oscillations is shown next. This is followed by a description of acoustics, coupling mechanisms, and fuel-injector dynamics.

2.1 Heat-Release Dynamics

The response of the heat-release rate to perturbations in the flow velocity, u, as well the equivalence ratio, ϕ are modeled in this section. The flame kinematics equation is used to derive this model. The following assumptions are made: (i) The flame is a thin interface separating reactants and products and is insensitive to pressure perturbations [1]. The flame can model turbulent premixed combustion if conditions of high Damkohler number and weak to moderate turbulence intensity prevail [21]-[23]. (ii) The flame is weakly convoluted, i.e., it can be described by a single-valued function, $\xi(r,t)$, describing the instantaneous location of its surface.

Under the above assumptions, the heat-release model is of the form [1]

$$\frac{\partial \xi}{\partial t} = u - v\frac{\partial \xi}{\partial r} - S_u(\phi)\sqrt{\left(\frac{\partial \xi}{\partial r}\right)^2 + 1}, \quad (1)$$

$$Q = \kappa(\phi)\int_0^R \sqrt{1+\left(\frac{\partial \xi}{\partial r}\right)^2}\,dr\,, \quad (2)$$

where Q is the heat-release, S_u is the burning velocity, $\kappa(\phi) = 2\pi\rho_u S_u(\phi)\Delta h_r(\phi)$, ρ_u is the density of the unburnt mixture, and Δh_r is the heat of reaction.

Assuming negligible velocity component in the radial direction, and linearizing around nominal values $\overline{u}$, $\overline{S}_u$, and $\overline{\xi}(r)$, denoting $\overline{(.)}$ and $(.)'$ as steady and perturbation, respectively, we get

$$\frac{\partial \xi'}{\partial t} = u' + \overline{S}_u\frac{\partial \xi'}{\partial r} + \frac{\partial \overline{\xi}}{\partial r}\left.\frac{dS_u}{d\phi}\right|_{\overline{\phi}}\phi', \quad (3)$$

with boundary conditions [2]

$$\xi'(R,t) = 0 \;\forall\, t, \qquad \xi'(r,0) = 0 \;\forall\, r,$$

while

$$Q'(t) = \overline{\kappa}\int_0^R \xi'(r,t)dr + d_1\phi', \quad (4)$$

where [3]

$$\overline{\kappa} = 2\pi\rho_u S_u \Delta\overline{h}_r,$$

$$d_1 = 2\pi\rho_u\left(\overline{S}_u\left.\frac{d\Delta h_r}{d\phi}\right|_{\overline{\phi}} + \Delta\overline{h}_r\left.\frac{dS_u}{d\phi}\right|_{\overline{\phi}}\right)\left(\int_0^R \overline{\xi}dr\right).$$

It is worth noting that the flame area fluctuation, A_f', is given by $A_f'(t) = 2\pi\int_0^R \xi'(r,t)dr$. This with Eq. (3) shows that the flame area is affected by both u' and ϕ', and the area in turn impacts Q' as shown in Eq. (4). This also shows that ϕ' affects Q' directly, and indirectly through the area fluctuations.

Equation (3) can be manipulated further and solved for ξ' in the Laplace domain as:

$$\xi'(r,s) = \left(\frac{u'(s)}{s} + \frac{\partial \overline{\xi}}{\partial r}\left.\frac{dS_u}{d\phi}\right|_{\overline{\phi}}\frac{\phi'(s)}{s}\right)\left(1 - e^{-(R-r)\frac{s}{\overline{S}_u}}\right), \quad (5)$$

where s is the Laplace operator. Differentiating Eq. (4) with respect to time, using Eq. (3), and integrating over $[0,R]$, we obtain that

$$\dot{Q}' = \overline{\kappa}\left(Ru' - \overline{S}_u\xi'(0,t) + \int_0^R \frac{\partial \overline{\xi}}{\partial r}\left.\frac{dS_u}{d\phi}\right|_{\overline{\phi}}\phi' dr\right) + d_1\dot{\phi}'. \quad (6)$$

[1] We consider here a flame stabilized over a perforated plate, R is the radius of the perforation.

[2] It should be noted that with the appropriate change in coordinates and boundary conditions, Eq. (3) can also represent flames stabilized behind a gutter [24], or a dump [22].

[3] The factor $\left.\frac{d\Delta h_r}{d\phi}\right|_{\overline{\phi}}$ is positive and $\left.\frac{dS_u}{d\phi}\right|_{\overline{\phi}}$ is also positive when $\phi \leq 1$.

Taking the inverse Laplace of Eq. (5) at $r = 0$, and substituting in Eq.(6), after some manipulations, we get

$$\dot{Q}' = \overline{\kappa}\left(Ru' - \overline{S}_u \int_{t-\tau_f}^{t} u'(\tau)d\tau - \overline{S}_u d_2 \int_{t-\tau_f}^{t} \phi'(\tau)d\tau + d_3\phi'\right) + d_1\dot{\phi}', \quad (7)$$

where

$$d_2 = \left.\frac{d\overline{\xi}}{dr}\right|_0 \left.\frac{dS_u}{d\phi}\right|_{\overline{\phi}}, \qquad d_3 = -\overline{\xi}(0)\left.\frac{dS_u}{d\phi}\right|_{\overline{\phi}},$$

and $\tau_f = R/S_u$ is the characteristic propagation delay of the flame surface into the reactants flow. Note that for the class of flames considered in the paper, the slope at the flame tip, which is typically conical, is zero, therefore the third term in the RHS of Eq. (7) can be omitted.

The effect of u' on Q' was previously considered in [14] where the time-delay effects were assumed to be small. The effect of ϕ' on Q' was addressed in [18] where a lumped parameter approach was used where once again, the time-delay effects were neglected. In contrast, we have analyzed the effect of both perturbations on the flame dynamics where the impact of a time-delay, τ_f, is taken into account.

2.2 Acoustics

Acoustic resonance of a combustor can be captured by analyzing the wave equation and linearizing the conservation equations [20]

$$\frac{\partial^2 p'}{\partial t^2} - \overline{c}^2\frac{\partial^2 p'}{\partial x^2} = (\gamma - 1)\dot{q}'(x,t), \quad (8)$$

where p is the pressure, and $\overline{c}$ is the mean speed of sound. We consider flames localized close to the anchoring plane, $q'(x,t) = q'(t)\delta(x - x_f)$.

Using an expansion in basis functions

$$p'(x,t) = \overline{p}\sum_{i=1}^{n}\psi_i(x)\,\eta_i(t), \quad (9)$$

where in most cases, $\psi_i(x) = \sin(k_i x + \phi_{i0})$, k_i and ϕ_{i0} determined from the boundary conditions, and performing a weighted spatial averaging, the modal amplitudes can be shown to follow [20]:

$$\ddot{\eta}_i + 2\zeta\omega_i\,\dot{\eta}_i + \omega_i^2\eta_i = \sum_{i=1}^{n}\widetilde{b}_i\,\dot{q}'_f, \quad (10)$$

where $\widetilde{b}_i = \gamma a_o\psi_i(x_f)/E$, $E = \int_0^L \psi_i^2(x)\,dx$, γ is the specific ratio, $a_o = \frac{\gamma-1}{\gamma\overline{p}}$, ζ represents the passive damping ratio in the combustor[4], L is its length, and $\omega_i = k_i\overline{c}$.

[4] Dissipation in a combustor can be caused by heat losses in the flame zone and friction due to viscous effects.

2.3 Coupling Dynamics

Perturbations in the flame area and the equivalence ratio which couple in a resonant way with the acoustic field are caused by velocity or pressure oscillations. Perturbations in the velocity and pressure are related to the perturbation in acoustic field via the energy equation [20]

$$\frac{\partial p'}{\partial t} + \gamma\overline{p}\frac{\partial u'}{\partial x} = (\gamma - 1)q', \quad (11)$$

which can be integrated over the combustor length to obtain (using Eq. (9))

$$u' = \sum_{i=1}^{n}\widetilde{c}_i\,\dot{\eta}_i + \theta a_o q', \quad (12)$$

where $\widetilde{c}_i = \frac{1}{\gamma k_i^2}\frac{d\psi_i}{dx}(x_f)$, $a_o = (\gamma - 1)/\gamma\overline{p}$, and θ represents the effect of the velocity ahead and behind the flame on q'. This equation can be used with Eq. (7) to couple the heat release to the velocity perturbations.

Perturbations in the equivalence ratio at the fuel source due to coupling with the acoustics can be modeled starting from the mass conservation at the mixing section which results in

$$\frac{\phi_s}{\overline{\phi}} \cong 1 \mp \frac{u'}{\overline{u}}, \quad (13)$$

for fluctuations in the air flow only (fuel inlet is choked) or in the fuel flow only (air inlet is choked). Now using the momentum equation:

$$\overline{\rho}\frac{\partial u'}{\partial t} + \frac{\partial p'}{\partial x} = 0, \quad (14)$$

and p' as in Eq. (9), after some manipulations, we get

$$\dot{\phi}_s' \cong \pm\overline{\phi}\frac{\overline{p}}{\overline{\rho u}}\sum_{i=1}^{n}\frac{d\psi_i(x)}{dx}\eta_i, \quad (15)$$

according to fluctuations in the air flow only or in the fuel flow only. The equivalence ratio at the burning zone is related to that at the fuel source by a convective delay, $\tau_s = L_s/\overline{u}$, as

$$\phi' = \phi'_s(t - \tau_n), \quad (16)$$

where $\tau_n = \tau_s + \tau_{comb}$, and the latter is the combustion time delay. In most cases $\tau_s >> \tau_{comb}$, and hence $\tau_n \sim \tau_s$ is an acceptable approximation. We should also mention that in this analysis the radial distribution of the local equivalence ratio is assumed to be constant.

It is worth noting also that instability can arise in combustors where flue-gas recirculation is used to reduce NO_x formation, e.g. [25]. The recirculated products may couple with the acoustics and cause perturbations

in the equivalence ratio which can be described in a similar manner as in Eqs. (15) and (16). Also, when injection is used as actuation, it introduces an additional term to appear in the RHS of Eq. (16) and is discussed in Sec. 3.1.

2.4 The Overall Model

Combining the acoustics, heat-release dynamics, and convective-lag effects in Eqs. (10), (7) and (16), respectively, we obtain the following equations:

$$\ddot{\eta}_i + 2\zeta_i\omega_i\,\dot{\eta}_i + \omega_i^2\eta_i = \frac{\widetilde{b}_i}{A_c}\overline{\kappa}\{Ru' - \overline{S}_u\int_{t-\tau_f}^{t} u'(\tau)d\tau + d_3\phi_s'(t-\tau_s)\} + d_1\,\dot{\phi}_s'\,(t-\tau_s), \quad (17)$$

where A_c is the cross-sectional area of the combustor. Equation (17) shows that two different time delays, τ_f and τ_s, can lead to instability, one arising from flame propagation effects, and the other from fuel convection. The RHS of Eq. (17) can be simplified further noting that for a certain class of flames τ_f is small when $\overline{S}_u$ is large (e.g., in a turbulent flow), and when the characteristic size of the flame, R, is small. Also, around the unstable acoustic frequency, $\dot{\phi}$ scales as $\omega|\phi|$, and $O(\overline{\kappa}d_3) \sim O(d_1)$, thus the second and third terms in the RHS can be neglected:

$$\ddot{\eta}_i + 2\zeta\omega_i\,\dot{\eta}_i + \omega_i^2\eta = \frac{\widetilde{b}_i}{A_c}\left[\overline{\kappa}Ru' + d_1\dot{\phi}_s'(t-\tau_s)\right]. \quad (18)$$

The overall model of the combustor is represented by Eqs. (18), (12), and (15) when multiple modes are present. For ease of exposition, we restrict our discussion to the case when only one mode is present, a similar approach can be extended to the multi-mode case. Substituting for the coupling dynamics in Eqs. (12), (15) and (16), and assuming $\theta = 0$, we get

$$\ddot{\eta} + 2\zeta\omega\dot{\eta} + \omega^2\eta = \Gamma_1\dot{\eta} + \Gamma_2\eta'(t-\tau_s), \quad (19)$$

where $\Gamma_1 = \frac{\widetilde{bc}}{A_c}\overline{\kappa}R$ and $\Gamma_2 = \pm\frac{\widetilde{b}}{A_c}d_1\overline{\phi}\frac{\overline{p}}{\overline{\rho u}}\frac{d\psi(x)}{dx}$.

Defining the equivalent damping ζ_0 as

$$\zeta_o = \frac{2\zeta\omega - \Gamma_1}{2\omega}$$

when perturbations in the flame area change the equivalent damping in the combustor, such that $\zeta_o < 0$, the oscillator is always unstable. In this case, Γ_1 represents a "negative" damping added by the flame area fluctuations[5], and is suspected to cause the instability in [4, 26] where the reactants inlet were choked implying no ϕ' fluctuations. This condition arises when the flame is located in a position where the modal amplitude of the pressure and the velocity (represented by $\widetilde{b}$ and $\widetilde{c}$) are of the same sign. For example, in a closed-open combustor with fixed equivalence ratio, a quarter-wave mode is always stable whereas a three-quarter-wave mode gets destabilized when the flame is located between the node and the anti-node of the pressure mode [20].

If on the other hand, $\zeta_o > 0$, even though this implies that the damping is positive, perturbations in the equivalence ratio can destabilize the combustor due to the convective time-delay τ_s. When $\tau_s = 0$, the system is stable. As τ_s increases, the system becomes unstable if τ_s lies between τ_s^- and τ_s^+, where

$$\tau_s^{\mp} = \frac{1/\omega}{\sqrt{1-2\zeta_o^2 \pm \sqrt{\Gamma_2^2/\omega^4 - 4\zeta_o^2(1-\zeta_o^2)}}} \times cos^{-1}\left(\pm\frac{\sqrt{\Gamma_2^2/\omega^4 - 4\zeta_o^2(1-\zeta_o^2)} - 2\zeta_o^2}{\Gamma_2/\omega^2}\right),$$

if

$$2\zeta_o\sqrt{1-\zeta_o^2} < \frac{|\Gamma_2|}{\omega^2} < 1.$$

If $|\Gamma_2| > \omega^2$, there exists only one switch to instability at τ_s^-, though in most practical cases, we have $|\Gamma_2| < \omega^2$ [18].

When $\zeta_o \sim 0$, the above instability conditions simplify to [18, 19]: Defining the acoustic time constant $\tau_a = 2\pi/\omega$, the system is unstable if

$$\frac{n+1}{2} < \frac{\tau_s}{\tau_a} < \frac{n+2}{2} \quad (20)$$

$n = 0, 2, 4...$, if $\Gamma_2 < \omega^2$, and unstable if $\frac{\tau_s}{\tau_a} > \frac{1}{2}$, if $\Gamma_2 > \omega^2$.

The above discussion indicates that the instability pattern depends on the distance between the source of ϕ_s', the convective velocity, and the acoustic frequency if perturbations in the equivalence ratio instigate the instability which appears to the instability mechanism in the rigs in [3, 16, 17]. The dependence of the stability bands on τ_s/τ_a can be judiciously exploited for optimizing the active-control designs [19].

2.5 Fuel Injector Dynamics

2.5.1 A Proportional Injector: The pulsating fuel injector delivers oscillations in the mass-flow rate in response to a voltage input. The injector system consists of an electro-mechanical part and a fluidic part, where in the former, the input voltage generates an

[5] The notion of "negative" and "positive" damping is used here to indicate heat-release perturbation which is out-of-phase and in-phase with the pressure oscillation, respectively. We have shown in previous work [12] that the effect of flame-area perturbation can be modeled as a negative damping term. Heat release can be modulated using active forcing to produce a positive damping term, as shown in [19].

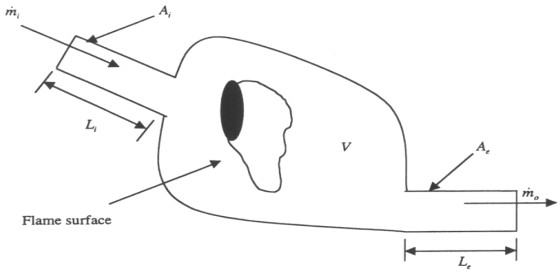


Figure 1: A schematic of a typical injector.

electro-magnetic field that causes a poppet to move against a spring (as seen in Fig. 1). The motion of the poppet controls the aperture of the injector allowing fluid to flow.

The electro-mechanical part relates the voltage E to the poppet position x through the electrical, electromagnetic, and mechanical components, which can be modeled as

$$E = iR_e + L_e\frac{di}{dt} + V, \quad (21)$$

$$V = B_e l\frac{dx}{dt}, \quad (22)$$

$$F_m = B_e l i, \quad (23)$$

$$m\frac{d^2x}{dt^2} + b\frac{dx}{dt} + kx = F_m, \quad (24)$$

where i is the current, F_m is the magnetic force, x denotes the motion of the armature in the direction of the magnetic force, R_e, L_e, B_e, and l denote, the resistance of the solenoid coil, the inductance of the coil, the magnetic flux density, and the length of the armature which moves orthogonal to the magnetic field, respectively. m, b, and k represent the effective mass, damping, and the stiffness of the armature/poppet system.

The fluidic part can be modeled using the unsteady Bernoulli equation, and the conservation of mass across the injector assuming incompressible flow. The unsteady velocity, v, can be obtained from the former applied between the inlet to the valve which is connected to a pressurized tank (where the flow velocity is ≈ 0, and $p = p_o$), and the outlet to the combustor where $p = p_c$, and $\Delta p = p_o - p_c$, as

$$\rho L_i\frac{dv}{dt} + \frac{1}{2}\rho v^2 = \Delta p, \quad (25)$$

In case small perturbations in p_c affect the velocity out of the injector, the unsteady velocity out of the valve, v, is linearized as

$$\tau_{fluid}\frac{dv'}{dt} + v' \cong \frac{-p_c'}{\sqrt{2\Delta\overline{p}\rho}}, \quad (26)$$

where $\tau_{fluid} = L_i/\sqrt{2\Delta\overline{p}/\rho}$ is the fluidic time constant, and L_i is the distance between the tank and the valve's outlet. τ_{fluid} is negligible for conditions where $L_i << 1m$, $\Delta\overline{p}$ is large (which is expected), and ρ is small ($O(1kg/m^3)$ for most gaseous fuels)[6].

The mass flow rate, defined as $\dot{m}_f = \rho v A$, is perturbed, assuming oscillations in v (caused by the dynamics in Eq. (26)) and A (caused by the motion of the poppet x), as

$$\dot{m}_f' = \rho\overline{A}v' + \rho\overline{v}A', \quad (27)$$

where we assume $A' = k_o x$, and $k_o > 0$. Equations (26) and (27) describe the fluid dynamics due to perturbations in p_c' and/or x. In most practical cases, $\Delta\overline{p}$ is large to guarantee choked conditions in the injector's discharge, thus, the first term in the RHS of Eq. (27) can be neglected. Using $\overline{v} = \sqrt{\frac{2\Delta\overline{p}}{\rho}}$ from Eq. (25), we simplify Eq. (27) as

$$\dot{m}_f' \cong k_o\rho\sqrt{\frac{2\Delta p}{\rho}}x. \quad (28)$$

Equations (21)-(24) and (28) determine the input-output relation between the fuel-injector input E and the output $\dot{m}_f'$ which is expressed in the Laplace domain as:

$$\frac{\dot{m}_f'(s)}{E(s)} = \frac{k_v}{(\tau_e s+1)(ms^2+bs+k) + B_e^2 l^2/R_e s}, \quad (29)$$

where $k_v = B_e l k_o \rho\sqrt{\frac{2\Delta\overline{p}}{\rho}}/R_e$.

In most solenoid systems, the armature electric time constant, $\tau_e = L_e/R_e$, is negligible compared to the acoustics time constant [27]. In these valves, the stiffness of the spring, k, is large, for a fast closing of the valve, when the voltage is turned *off*. Also, the mass, m, of the armature is very small in many of the typical injectors to minimize inertia forces [27]. The damping term, b, contains the overall damping including stiction and friction, and typically is large. Thus, the mechanical system can be simplified as a first-order system; a damper-spring system [28]. The mechanical time constant usually limits the bandwidth of typical injectors to approximately 100 Hz. (Note that other effects, such as impact dynamics are not included here, since we expect them to be of higher frequencies than the combustor dynamics). Thus, Eq. (29) is simplified as

$$\frac{\dot{m}_f'(s)}{E(s)} = \frac{k_v\tau_m}{\tau_m s+1}, \quad (30)$$

where $\tau_m = (b + B_e^2 l^2/R_e)/k$.[7]

[6] In the case of liquid fuels, the time constant can be comparable to the acoustics time constant due to large ρ, $O(1000kg/m^3)$.

[7] For more advanced proportional injectors, internal feedback loops exist (using for example a position transducer for the armature) to guarantee accurate metering, and increase its bandwidth, e.g., a Moog DDV proportional valve has a bandwidth of 450 Hz [29].

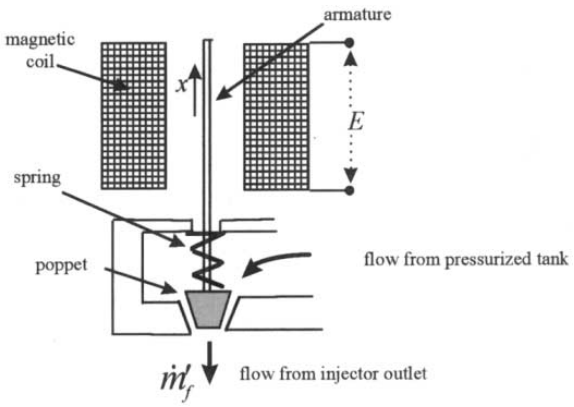


Figure 2: Block diagram of a typical two-position injector.

2.5.2 A Two-Position (on-off) Fuel injector: Some fuel injectors currently used for combustion control [6, 11, 30] operate only between two positions, *on* and *off*. Unlike the proportional injectors discussed above, the physical stops play a more prominent role in the dynamics. However, one can still model two-position injectors in the same manner as above by including the effect of the physical stops as a saturation block together with Eq. (30) as shown in Fig. 2. A two position injector is set *on*, after the voltage input overcomes a certain threshold, thus creating a dead-zone in the control input (see figure) which will be discussed further when control is implemented in Sec. 3.

An additional point to note is the distinction between the injector dynamics during transition from closing and opening. Typically, the injector is over-driven by a high voltage in the opening mode to ensure fast opening. The opening time constant is different than the closing one. This effect can also be included in the injector model, as seen in Fig. 2, by assuming that τ_m varies between two values τ_{m_1} and τ_{m_2} depending on whether the injector is transitioning from *off* to *on* or *on* to *off*. Note that $\tau_{m_1} = \tau_m$ (as defined before) and $\tau_{m_2} = b/k$. We refer the reader to [31] for more details regarding this model when validated against two different Parker-Hannafin Series-9 injectors *9-130-905* and *9-633-900*.[8]

3 Control

In this section, we investigate model-based control strategies for abating combustion instability using secondary fuel injection. We assume that the pressure signal is the measured output, using a pressure transducer. The transducer dynamics is neglected since it typically has a much higher bandwidth than the combustion dynamics. We examine the control with an injector located at (i) the burning zone or (ii) further upstream. We assume in particular that the combustion dynamics is determined by several coupled acoustic modes [20]. We also assume that instability is primarily induced by fluctuations in the flame area coupled with the acoustics. We refer the reader to [18, 19] for investigations of instability caused by equivalence ratio fluctuations and its control.

3.1 Actuated Combustor

Denoting the contribution of the fuel injector to the equivalence ratio as ϕ'_c, we have that $\phi'_c = \frac{\dot{m}'_f}{\overline{\dot{m}}_a}/\alpha_o$, where $\overline{m}_a$ and α_o are the mean air mass flow rate, and the stoichiometric fuel to air ratio, respectively. We assume that ϕ'_c is uniform radially, and that perturbations are carried intact by the mean flow to the burning zone, after a time delay τ_c, where $\tau_c = L_c/\overline{u}$, L_c is the distance between the injector discharge and the burning zone, and $\overline{u}$ is the mean velocity of the reactants in the combustor.

From Eq. (18), the impact of ϕ'_c on the combustion dynamics can be taken into account as

$$\ddot{\eta}_i + 2\zeta\omega_i\,\dot{\eta}_i + \omega_i^2\eta = \frac{\widetilde{b}_i}{A_c}\left[\overline{\kappa}Ru' + d_1\dot{\phi}_c(t-\tau_c)\right], \quad (31)$$

for $i = 1, 2, .., n$, where i denotes the mode number.

3.2 Injection at the Burning Zone

Injection at the flame has shown success in several experimental facilities [6, 11, 30], and in a practical full-scale 170 MW gas-turbine combustor [5]. We carry out active control design assuming that the injection is at the flame, using the model in Eq. (31) while $\tau_c \approx 0$, together with the injection dynamics described by Eq. (30). The input-output model relation between the injector input voltage, E, and the pressure, p', is given by

$$p'(s) = W_p(s)E(s), \qquad W_p(s) = \frac{k_p Z_p(s)}{R_p(s)}, \quad (32)$$

where $W_p(s)$ is the transfer function of a finite-dimensional model of the combustor, k_p, $Z_p(s)$ and $R_p(s)$ are the corresponding gain, numerator and denominator, respectively.

An optimal control for the finite-dimensional system as in Eq. (32) is LQG/LTR [32]. This method has been successful in suppressing combustion instability

[8] It should be noted that when inertia forces in the armature are important, a second-order fuel-injector model, with high damping, is more appropriate. The experimental measurements in [30] for a General Valve injector show similar dynamics.

[13]. Its success lies in its ability to generate satisfactory performance over a wide range of frequencies, unlike phase-shift controllers which can destabilize stable dynamics [33]. Experimental validation of the LQG/LTR for combustion control has been demonstrated in [31, 34, 35]. In [34], a similar physically-based model was used with a loudspeaker as an actuator. In [31, 35], a system-ID approach based on subspace and ARMAX methods [36] was used to suppress pressure oscillations in a dump and a swirl-stabilized combustors, respectively, using pulsed injection. In this paper, we show through simulation studies that, as in [13], LQG/LTR can also be used successfully based on a physical model, using fuel injector as an actuator. For details of the LQG/LTR control design, we refer the reader to [13, 34].

3.2.1 Simulations of the LQG/LTR Controller: A fifth order combustor dynamics model including the first two modes, the flame dynamics, and the injector dynamics is considered. The combustor parameters and conditions are taken as in [13], these cause a three-quarter-mode instability which resonates at 500 Hz approximately, and has unsteady pressure amplitudes of $O(100Pa)$.

We choose first a proportional injector, as in [5], with a bandwidth of 300 Hz which is in the range of available high-speed injectors [29]. Figure 3 shows the time response of the pressure and the control input, $\phi_c'/\overline{\phi}$ ($\overline{\phi} = 0.7$). Control is applied at $t = 50ms$. We note that although the bandwidth is lower than the system dynamics, the control with proportional injector is still capable of stabilizing the system, since the dynamics of the injector are taken into consideration in the design of the LQG/LTR. As seen in Eq. (30), the injector dynamics are first order, and the gain and phase introduced by the injector depend on its bandwidth. For smaller bandwidths cases, the phase increases while the control authority, i.e., the gain, is dramatically decreased around acoustic frequencies. The controller, however, has enough degrees of freedom to adjust the phase, and increase the voltage amplitude into the injector to produce the required control authority, $\phi_c'/\overline{\phi}$, around the acoustics frequencies thus guaranteeing stability.

While a low bandwidth proportional injector is capable of maintaining the system at vanishingly small pressure perturbations, a two-position injector may not be as effective [11, 30, 35]. Using a 300 Hz bandwidth injector, the LQG/LTR is still capable of stabilizing the system, but the pressure is suppressed to a small but finite amplitude limit cycle as seen in Fig. 4. The reason is that the injector has a threshold input voltage value at which it is activated. Thus, following the suppression of the instability, the injector stops pulsing at from

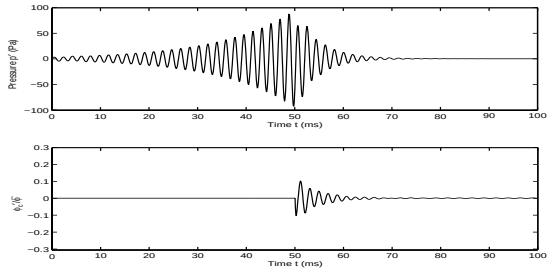


Figure 3: Response of the controlled combustor with a proportional injector with a bandwidth of ≈ 300 Hz.

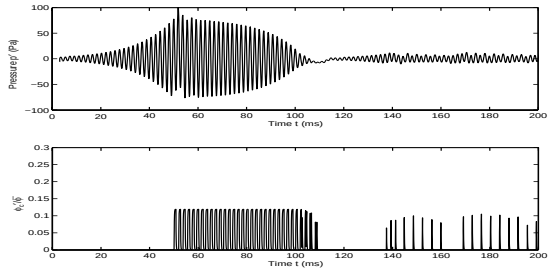


Figure 4: Response of the controlled combustor with an on-off injector set to deliver $\frac{\phi_c|_{max}}{\overline{\phi}} \approx 0.125$ and with a bandwidth $\approx$ 300 Hz.

$t \approx$105-138ms, as seen in the figure. Disturbances in the combustor force the pressure to grow, until the measured voltage by the microphone reaches the threshold at which the injector starts to fire again. In the case simulated, this occurs at $t > 138ms$. This sequence is repeated indefinitely.

Increasing the control fuel-flow rate, and thus $\phi_c|_{max}$, the combustor is stabilized in a smaller settling time. As seen in Fig. 5, when $\phi_c'|_{max}/\overline{\phi}$ is doubled, the settling time diminishes by $\sim 80\%$. Moreover, the rms of the steady-state pressure is smaller. A similar effect has been observed in [11].

We also investigate the effect of bandwidth for a two-position injector. Limiting it to 50 Hz, as seen in Fig. 6, the pressure settles to a higher-amplitude limit cycle, and the injector is incapable of tracking the command

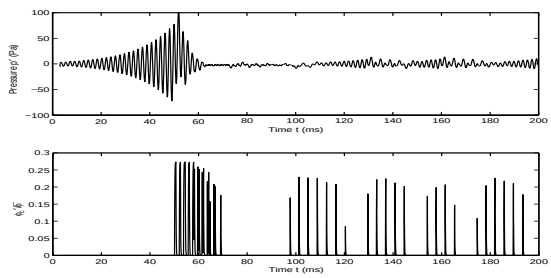


Figure 5: Response of the controlled combustor with on-off injector set to deliver $\frac{\phi_c|_{max}}{\overline{\phi}} \approx 0.27$, and with a bandwidth of 300 Hz.

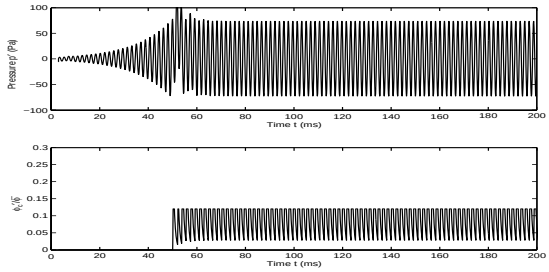


Figure 6: Response of the controlled combustor with on-off injector with lower bandwidth $\approx$ 50 Hz (the acoustics unstable frequency is 500 Hz, approximately).

from the controller; the injector stays open all the time. This shows that injector bandwidth is a serious problem [11, 35]. Different solutions have been proposed that include: (i) Developing faster injectors [29]. (ii) Use of multiple injectors which are fired alternatively to increase the apparent frequency of actuation [11]. A different approach that has shown promise regardless of high-bandwidth injectors is through fuel pulsing at low frequencies (much lower than the acoustics). This is demonstrated experimentally in [4, 37], and analytically in [38].

3.3 Injection Upstream the Burning Zone: Delay in the Control Input

While injecting fuel directly on the flame [5, 6, 11, 30] can avoid actuation delays, it introduces hot spots at the flame surface thus increasing emissions. In addition, if mixing is weak at the injection port, we run the danger of creating a secondary diffusion flame which can be completely decoupled from the main premixed flame, and hence become ineffective in suppressing the instability [9].

In this section, we study the effects of pulsed-fuel injection upstream the burning zone. This has been utilized in [3] where secondary injection was done at the primary fuel source. In [19], we presented a Posi-Cast control capable of working with an injector located at an arbitrary distance upstream the flame. In that case, a bulk mode was unstable. Here, we extend the analysis of the Posi-Cast control, and show that it is capable of stabilizing longitudinal modes as well.

3.3.1 Posi-Cast Control: A powerful approach for controlling systems with known time-delay was originated by Smith [40], known also as Posi-Cast for "positive forecasting" of future states. The idea is to compensate for the delayed output using input values stored over a time window equal to the delay time, i.e. $[t-\tau_c, t]$, and estimate the future output using a model of the combustor. Only stable systems were considered. An extension to include unstable systems was proposed in [41] using finite-time integrals of the delayed input values thereby avoiding unstable pole-zero cancellations which may occur. A frequency-domain pole-placement technique for unstable systems was first proposed in [42] and a similar technique will be presented here.

The model in Eq. (32), in the presence of a time delay, τ_c, can be re-written as

$$p'(t) = W_p(s)[E(t-\tau_c)], \qquad W_p(s) = \frac{k_p Z_p(s)}{R_p(s)} \tag{33}$$

Due to the nature of the combustion system, not all states are accessible, only the system input, i.e. the voltage to the injector $E(t)$, and the output, p' in our case are measured. A standard pole-placement controller is required (for more information, see [42, 43]). The presence of the time-delay, τ_c, in the control input, motivates the use of an additional signal in the control input, $E(t)$, denoted as $E_1(t)$ which anticipates the future output using a model of the system [19]. The resulting controller structure is described as

$$\begin{aligned} E(t) &= \frac{c(s)}{\Lambda(s)}E(t-\tau_c) + \frac{d(s)}{\Lambda(s)}p'(t) + E_1(t), \\ E_1(t) &= \frac{n_1(s)}{R_p(s)}E(t) - \frac{n_2(s)}{R_p(s)}E(t-\tau_c), \end{aligned} \tag{34}$$

where $\Lambda(s)$ is a chosen stable polynomial of degree $n-1$, $d(s), n_1(s)$ and $n_2(s)$, are polynomials of degree $n-1$ at most, and $c(s)$ is of degree $n-2$ at most. For stability, these must satisfy the relations

$$c(s)R_p(s) + k_p d(s) Z_p(s) = \Lambda(s) n_2(s), \tag{35}$$

$$n_1(s) = R_p(s) - R_m(s), \tag{36}$$

where $R_m(s)$ is the desired characteristic equation, which is a stable monic polynomial of the same order of $R_p(s)$.

Using the controller structure in Eq. (34) with the conditions in Eqs. (35) and (36), the closed-loop transfer function can be computed as

$$W_{cl}(s) = \frac{k_p e^{-s\tau_c}}{R_m(s)}. \tag{37}$$

The control input law, in Eq. (34), introduces additional dynamics including non-minimum phase zeros having the same eigen-values of $R_p(s)$. Obviously, these lead to unstable pole-zero cancellations since the combustor model is open-loop unstable (i.e., $R_p(s)$ has unstable eigen values). Unstable pole-zero cancellations are

[9] This has been noticed in experiments at MIT and at UTRC [39].

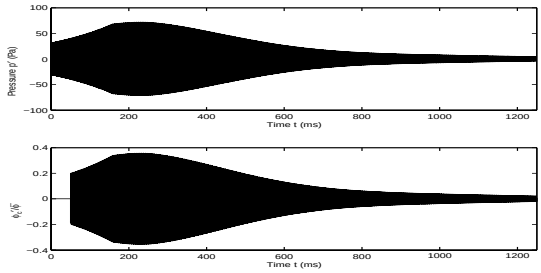


Figure 7: Response of the controlled combustor with a time-delay of $100ms$ in the input signal, proportional injector. Note: only the envelope of the response is shown for clarity, since the scale of the plot does not permit seeing individual cycles.

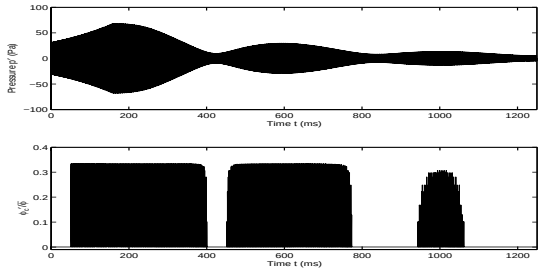


Figure 8: Response of the controlled combustor with a time-delay of $100\,ms$ in the input signal, on-off injector. Note: only the envelope of the response is shown for clarity, since the scale of the plot does not permit seeing individual cycles.

known to cause problems concerning observability and controllability of the plant (see [27] for more details). As a result, a modification in the synthesis of $E_1(t)$ in Eq. (34) was suggested by [41]. To avoid unstable pole-zero cancellations, $E_1(t)$ must be generated as a finite integral of the form

$$E_1(t) \quad = \quad \sum_{i=1}^{n} \left(\int_{-\tau_c}^{0} e^{-\lambda_i \sigma} E(t+\sigma) d\sigma \right), \quad (38)$$

where λ_i's are the eigen values of the combustor system, i.e. $R_p(s) = \Pi_{i=1}^{n}(s - \lambda_i)$. Taking the Laplace transform of Eq. (38), one can show that

$$\frac{n_1(s)}{R_p(s)} = \sum_{i=1}^{n} \frac{\alpha_i}{s - \lambda_i}, \frac{n_2(s)}{R_p(s)} = \sum_{i=1}^{n} \frac{\beta_i}{s - \lambda_i}, \quad (39)$$

where $\beta_i = \alpha_i e^{\lambda_i \tau_c}$. Another condition for the successful use of the finite integral in Eq. (38) is that $R_p(s)$ has no repeated roots [42].

The controller described in Eqs. (34) and (38) is sufficient to stabilize the combustor provided that an accurate description of the plant and the time delay are available. This controller has been shown to provide robustness to uncertainties in the plant including the time delay [41]. Adaptive versions of the same controller have been investigated [44, 45], and have shown to extend the robustness of the controller to parameter uncertainties.

3.3.2 Simulations of the Posi-Cast Controller: The controller in Eqs. (34) and (38) is implemented for injection at a distance of $\sim 3cm$ upstream the burning zone. τ_c is estimated to be $100ms$, which is about 50 times the time constant of the unstable frequency.

The closed-loop simulation is illustrated in Fig. 7. Although control is switched *on* at $t = 50ms$, the pressure keeps increasing for an additional $t = \tau_c = 100ms$ (from $t = 50 - 150ms$), then stalls for another 100 ms (from $t = 150 - 250ms$) before decaying. The reason for the former delay is physical and is due to the time taken for the pulsed-fuel to reach the burning zone. The latter is due to a computational delay in the controller. Specifically, the finite integral in Eq. (38) outputs incorrect values for a period of τ_c. This is because the computation of the finite integral relies on a stored window of the past values of the control input of the size of τ_c. When control is switched *on*, the window consists of control inputs proportional to p' which has not yet "felt" the effect of control due to the physical delay τ_c (the values of p' are still those of the open-loop combustor). It requires therefore $t = 2\tau_c$ to start forming a window of integration with control input corresponding to closed-loop values. This confirms observations in [41].

In Fig. 8, a two-position injector is used. The control design is based on the linear model, and its parameters are fine-tuned to handle the nonlinearities. As discussed earlier, the control is switched *on* at $50ms$, and stabilizes the system. The injector stays *on* as long as the voltage signal into the injector is greater than a threshold, as discussed before in Sec. 2.5.2.

It should be noted that when combustion instability is caused by ϕ_s' fluctuations, as discussed in Sec. 2, the characteristic equation will look different than in Eqs. (32) and (33). $R_p(s)$ will have terms which are delayed, due to the convective delay, τ_s, carried by ϕ_s'. Hence, $R_p(s)$ becomes infinite dimensional. To circumvent this, a Padé approximation [46] is used to get a finite dimensional description of $R_p(s)$, and thus the LQG/LTR and Posi-Cast controllers as described in Secs. 3.2 and 3.3, respectively, can similarly be used for this case.

4 Summary

In this paper, a complete model of the combustion dynamics leading to instability is developed. A model encompassing the acoustics, the heat release, the cou-

pling, mixing and injector dynamics is presented. The heat release is derived using flame kinematics for flames with high Damkohler numbers and moderate turbulence, and the effect of forcing in the velocity and the equivalence ratio is illustrated. Different stability criteria are discussed for the different dynamics resulting from the coupling of these with the acoustics. While velocity perturbations cause instability of a phase-lag nature, equivalence-ratio oscillations introduce a time-delay instability. Injection both at and upstream of the burning zone is studied. An LQG/LTR control is used for the former while a Posi-Cast control is developed and used for the latter. Both proportional and two-position (on-off) pulsed injection is examined. Proportional injectors show superior performance to two-position ones. Performance is shown to be plagued by limited injector authority and bandwidth. Some of the short-term fixes proposed for this problem include the use of multiple injectors [11] and low frequency pulsing [4, 37, 38]. A long-term solution is clearly the design of a high-speed, high-authority injector.

References

[1] G. J. Bloxsidge, A. P. Dowling, N. Hooper, and P. J. Langhorne. Active control of an acoustically driven combustion instability. *Journal of Theoretical and Applied Mechanics*, supplement to vol. 6, 1987.

[2] K.R. McManus, T. Poinsot, and S.M. Candel. A review of active control of combustion instabilities. *Progress in energy and combustion science*, 19(1):1–30, 1993.

[3] J. M. Cohen, N. M. Rey, C. A. Jacobson, and T. J. Anderson. "Active control of combustion instability in a liquid-fueled low-NO_x combustor". *ASME 98-GT-267, ASME/IGTI, Sweden*, 1998.

[4] G. A. Richards, M. C. Yip, and E. H. Rawlins. Control of flame oscillations with equivalence ratio modulation. *Journal of Propulsion and Power*, 15:232–240, 1999.

[5] J.R. Seume, N. Vortmeyer, W. Krause, J. Hermann, C.-C Hantschk, P. Zangl, S. Gleis, and D. Vortmeyer. "Application od active combustion instability control to a heavy duty gas turbine". In *Proceedings of the ASME-ASIA*, Singapore, 1997.

[6] S. Murugappan, S. Acharya, E. Gutmark, and T. Messine. "Active control of combustion instabilities in spray combustion with swirl". *AIAA-2000-1026, 38th AIAA Aerospace Sciences Meeting, Reno, NV*, 2000.

[7] W. Lang, T. Poinsot, and S. Candel. Active control of combustion instability. *Combustion and Flame*, 70:281–289, 1987.

[8] F. E. C. Culick. Nonlinear behavior of acoustic waves in combustion chambers. *Acta Astronautica*, 3:715–756, 1976.

[9] B.T. Zinn. *Pulsating combustion. Advanced Combustion Methods*. Academic Press Inc. (London) LTD., London, 1986.

[10] V. Yang, A. Sinha, and Y.-T. Fung. State feedback control of longitudinal combustion instabilities. *Journal of Propulsion and Power*, 8, 1992.

[11] K. Yu, K.J. Wilson, and K.C. Schadow. Scale-up experiments on liquid-fueled active combustion control. In *34th AIAA/ASME/SAE/ASEE Joint Propulsion Conference*, pages AIAA 98–3211, Cleveland, OH, 1998.

[12] J. P. Hathout, M. Fleifil, A. M. Annaswamy, and A. F. Ghoniem. Role of actuation in combustion control. In *1999 IEEE CCA/CACSD*, Hawai'i, August 22-27 1999.

[13] J. P. Hathout, A. M. Annaswamy, M. Fleifil, and A. F. Ghoniem. Model-based active control design for thermoacoustic instability. In *Combustion Science and Technology*, volume 132, pages 99–138, 1998.

[14] M. Fleifil, A. M. Annaswamy, Z. Ghoniem, and A. F. Ghoniem. Response of a laminar premixed flame to flow oscillations: A kinematic model and thermoacoustic instability result. *Combust. Flame*, 106:487–510, 1996.

[15] A.A. Putnam. *Combustion Driven Oscillations in Industry*. American Elsevier Pub. Co., NY, 1971.

[16] G.A. Richards and M.J. Yip. Oscillating combustion from a premix fuel nozzle. *The Combustion Institute/American Flame Research Committee Meeting, San Antonio TX*, 1995.

[17] T. Lieuwen and B.T. Zinn. "The role of equivalence ratio oscillations in driving combustion instabilities in low NO_x gas turbines". *The Twenty Seventh International Symposium on Combustion*, pages 1809–1816, 1998.

[18] M. Fleifil, J.P. Hathout, A.M. Annaswamy, and A.F. Ghoniem. "Reduced order modeling of heat release dynamics and active control of time-delay instability". *AIAA 2000-0708, 38th AIAA Aerospace Sciences Meeting, Reno, NV, 10-13 January*, 2000.

[19] J. P. Hathout, M. Fleifil, A. M. Annaswamy, and A. F. Ghoniem. Heat-release actuation for control of mixture-inhomogeneity-driven combustion instability. In *28^{th} International Symposium on Combustion*, University of Edinburgh, Scotland, July 30-August 4 2000.

[20] A. M. Annaswamy, M. Fleifil, J. P. Hathout, and A. F. Ghoniem. Impact of linear coupling on the design of active controllers for thermoacoustic instability. *Combust. Sci. Tech.*, 128:131–180, 1997.

[21] H.M. Najm and A.F. Ghoniem. "Modeling pulsating combustion in vortex stabilized pre-mixed flames". *Combustion Sci. Tech.*, 94:259–278, 1993.

[22] A. A. Peracchio and W. Proscia. Nonlinear heat release/acoustic model for thermoacoustic instability in lean premixed combustors. In *ASME Gas Turbine and Aerospace Congress*, Sweden, 1998.

[23] A.P. Dowling. "A kinematic model of of a ducted flame". *Journal of Fluid Mechanics*, 394:51–72, 1999.

[24] A. P. Dowling. Nonlinear acoustically-coupled combustion oscillations. *2nd AIAA/CEAS Aeroacoustics Conference*, May 6-8 1996.

[25] J.D.. Anderson. *Fundamentals of Aerodynamics*. McGraw-Hill, Inc., New York, 1991.

[26] K.K. Venkataraman, L.H. Preston, D.W. Simons, B.J. Lee, J.G. Lee, and D.A. Santavicca. "A study of the mechanism of combustion instability in a lean premixed dumb combustor". *Submitted to the Journal of Power and Propulsion*, 1998.

[27] K. Ogata. *Modern Control Engineering*. Third Edition, Prentice Hall, Inc., NJ, 1997.

[28] L. Meirovitch. *Elements of Vibration Analysis (Second Edition)*. McGraw-Hill, Inc., NY, 1986.

[29] C. Hantschk, J. Hermann, and D. Vortmeyer. "Active instability control with direct drive servo valves in liquid-fuelled combustion systems". In *Proceedings of the International Symposium on Combustion*, Naples, Italy, 1996.

[30] J.C. Magill, M. Bachmann, and K.R. McManus. Combustion instabilitydynamics and control in liquid-fueled direct injection systems suppression in liquid-fueled combustors. *38th Aerospace Sciences Meeting and Exhibit*, AIAA-2000-1022, 2000.

[31] B. J. Brunell. "A system identification approach to active control of thermoacoustic instabilities". In *S.M. Thesis*, MIT, Cambridge, MA, 2000.

[32] G. Stein and M. Athans. The LQG/LTR procedure for multivariable feedback control design. *IEEE Transactions on Automatic Control*, 32:105–114, 1987.

[33] M. Fleifil, J. P. Hathout, A. M. Annaswamy, and A. F. Ghoniem. The origin of secondary peaks with active control of thermoacoustic instability. *Combustion, Science, and Technology*, 133:227–265, 1998.

[34] A. M. Annaswamy, M. Fleifil, J. Rumsey, R. Prasanth, J. P. Hathout, and A. F. Ghoniem. Thermoacoustic instability: Model-based optimal control and experimental validation. *IEEE Control Systems Technology*, vol. 8, pp. 905-918, November 2000.

[35] S. Murugappan, S. Park, S. Acharya, A.M. Annaswamy, E. Gutmark, and A.F. Ghoniem. "Optimal control design for a swirl-stabilized combustor using system identification methods". *38th Aerospace Sciences Meeting and Exhibit*, AIAA-2001-0779, Reno, NV, January 2001.

[36] L. Ljung. *System Identification: Theory for the User*. Prentice-Hall, Englewood Cliffs, NJ, 1987.

[37] S. Sivasegaram and J. H. Whitelaw. Active control of oscillations in combustors with several frequency modes. In *Proceedings of the ASME Winter Annual Meeting*, Anaheim, CA, 1992.

[38] R. Prasanth, A.M. Annaswamy, J.P. Hathout, and A.F. Ghoniem. "When do open-loop strategies for combustion control work?". *36^{th} AIAA/ASME/SAE/ASEE Joint Propulsion Conference, paper no. 2000-3350*, 2000.

[39] J. M. Cohen. *Private Communication*, 2000.

[40] O.J. Smith. "A controller to overcome dead time". *ISA Journal*, 6, 1959.

[41] A.Z. Manitius and A.W. Olbrot. Finite spectrum assignement problem for systems with delays. *IEEE Transactions on Automatic Control*, AC-24 no. 4, 1979.

[42] K. Ichikawa. Frequency-domain pole assignement and exact model-matching for delay systems. *Int. J. Control*, 41:1015–1024, 1985.

[43] W.A. Wolovich. *Linear Multivariable Systems*. Springer Verlag, Berlin, 1974.

[44] R. Ortega and R. Lozano. Globally stable adaptive controller for systems with delay. *International Journal of Control, Vol. 47, No. 1, pp 17-23*, 1988.

[45] S. I. Niculescu and A. M. Annaswamy. A simple adaptive controller for positive-real systems with time-delay. In *The American Control Conference in Chicago, IL., (to appear)*, February 2000.

[46] G.A. Baker and P Graves-Morris. *Padé Approximants*. 2nd edition, Cambridge University Press, 1996.

PAPER -23, J. P. Hathout

Question (A. Banaszuk, USA)

How effective is the Smith predictor-type controller if there is a large unmeasurable disturbance, such as turbulent velocity components driving the system? Don't you use the assumption that you know all the inputs during the delay block?

Reply

Robustness of Posi-Cast controllers has been analyzed in several publications. See, for example, references [41] and [45] in the paper.

Question (J. Hermann, Germany)

As you have shown, in a system with long time delay, there must be a long delay from activating the active control to achieving suppression of the oscillations. Applied to a realistic system, this may be too long. Can this problem be reduced?

Reply

The large delay τ_c is due to the fact that the secondary injection is at a certain distance upstream of the burning zone. This is a physical constraint that affects closed-loop control performance in general, regardless of the control algorithm. The implication of this constraint is that the effect of the control on the pressure will not take place for a minimum period of τ_c. After this period, the more sophisticated the controller, the smaller the settling time. The Posi-Cast control indeed results in the latter, as described in the presentation.

The time-delay effect may be reduced by introducing other actuating inputs closer to the burning zone. For example, it may be possible to introduce acoustic drivers or auxiliary fuel-injectors closer to the flame, which will not have the same time-delay constraint. The disadvantage of injection close to the flame may lie in the increase of emissions; an acoustic driver obviously avoids this problem, but may have limited authority. In either case, by designing a multi-input control strategy, where inputs closer to the flame act only over the time interval $[0, \tau_c]$, it may be possible to cope with the large delay.

An Investigation of Adaptive Signal Processing Approaches to Active Combustion Control

Michael A. Vaudrey, William R. Saunders, and William T. Baumann
Virginia Polytechnic Institute and State University
Blacksburg, VA 24061-0328, USA

Introduction

There has been significant progress made in understanding dynamic models and control system designs for active control of thermoacoustic instabilities. During the past several years, there has been an increasing trend away from mostly empirical or experimentally-based *active combustion control* (ACC) methods in exchange for control systems that rely on more accurate understanding of the dynamic processes involved in the thermoacoustic limit cycling response. Early demonstrations of phase-shifting ACC designs (Gutmark et al., 1993; McManus et al., 1990) relied simply on a measurement of the acoustic pressure and actuation of the unsteady heat release after appropriate delay (i.e. phase shift) relative to the measured pressure signal. The phase-shifting controllers proved to be effective in many situations but were plagued by inadequate knowledge of how to predict the required phase, and gain, of the controller for varying operating conditions of the combustor. These problems naturally led to investigations of adaptive control methods.

A number of ACC researchers recognized that adaptive signal processing methods offered a possible alternative to the manually-tuned, phase-shifting controller. These adaptive filtering methods, such as the LMS algorithm proposed by Widrow and Stearns (1985), had been highly successful in the active noise and vibration control community for narrowband disturbance rejection. The most relevant application of LMS control for noise or vibration control was the so-called Filtered-U algorithm (Kuo and Morgan, 1995) which required feedback compensation for the reference sensor. The ACC implementation is similar in its need for compensation because the reference sensor is identical to the error sensor. A limited number of combustion researchers investigated the usefulness of these LMS algorithms for ACC (Billoud et al., 1992; Kemal and Bowman, 1995; Mohanraj, 1998, Annaswamy et al., 1998, and Koshigoe, 1999). However, most of the results from those experiments and numerical simulations indicated an unacceptable degree of uncertainty about the stability of the LMS-based adaptive controllers. The literature shows that the LMS controllers often seemed to promote the occurrence of peaks of unknown origin, or apparent divergence of the controllers, sometimes occurring minutes after the combustors' pressure signatures seemed to have been reduced to acceptable levels. Explanations for such behaviors have been attempted, in part, but it was recently stated that more research would be required before this class of adaptive controllers might be used reliably (Mohanraj, 1998).

This paper extends the existing research into the design of LMS adaptive filters for suppression of thermoacoustic instabilities. Through detailed numerical simulations, supported by relevant experiments on a simple tube combustor, we provide one possible method for achieving stabilizing control using an adaptive feedback architecture. As discussed by Annaswamy et al. (1998), previous researchers have not been able to avoid divergence of the LMS adaptive schemes in most cases where it has been tested. The reasons for the divergent behavior have not been made clear, but most often there have been remarks made about the stability of the gradient search algorithm or stability of the IIR filter structures that have been used for some implementations. In this paper, we carefully distinguish between two fundamental modes of instability that may be responsible for the aberrant behaviors reported by previous researchers. The first mode is related to the generation of feedback instabilities that can arise as the adaptive filter converges to the optimal solution. The second mode is related to convergence of the gradient search algorithm, analogous to the convergence issues that have been presented by Elliott et. al. (1987) for Filtered-X or Wang and Ren (1999) for Filtered-U. The primary focus of this paper is on the feedback-related instability mode as it appears to be most dominant and may be directly related to the selection of system identification method used for the adaptive filter implementation. Previous researchers have struggled with how to conduct the system identification task that is required for the LMS algorithm for this ACC application.

The key result of this paper is a description of an ACC experiment on a tube combustor that demonstrates a repeatable, stable implementation of a LMS adaptive filter controller for suppression of a limit cycling oscillation. A system identification method is proposed that results in identification of a stable plant model suitable for control of the unstable combustion oscillation. A nonlinear analysis of the system identification technique indicates that this approach, first reported by Saunders et al. (1999-2), offers advantages for adaptive filtering controllers also. Nonlinear simulations of the ACC experiment are used to

Paper presented at the RTO AVT Symposium on "Active Control Technology for Enhanced Performance Operational Capabilities of Military Aircraft, Land Vehicles and Sea Vehicles", held in Braunschweig, Germany, 8-11 May 2000, and published in RTO MP-051.

explain the detailed behavior of the plant for those cases where control is achieved. Additionally, we propose plausible explanations for the source of unstable applications of the LMS controller (observed mostly for higher equivalence ratios in this research) although the detailed proof for those explanations is left for future work.

The paper is organized as follows. The following section introduces several different adaptive filter architectures that must be understood to appreciate LMS control of combustion oscillations. A stable system, subject to an exogenous disturbance, is used to illustrate the key issues that arise when the error signal must also serve as the reference signal input to the adaptive filter and LMS weight update equation. Then, a self-excited system is investigated to show the differences between controlling the effects of a disturbance on a stable plant and suppressing the unstable, limit cycling system response of the self-excited system. The system ID method used for the adaptive filter is introduced and supported using describing function arguments. In Section 3, simulations and experiments for a tube combustor (Saunders et al., 1999-1) are presented and compared. It is shown that there appears to be a range of operating conditions that the adaptive filter can predictably control based on the system identification method chosen for the work. A comparison between simulations and experiments reveals identical behaviors and will form the basis for more detailed future studies. Section 4 provides the concluding remarks.

Adaptive Feedback Control

Classical Disturbance Suppression

The adaptive feedback control considered in this paper can be viewed as a special case of Filtered-U control where the control-to-reference path and the control-to-error path are identical because the error sensor also serves as the reference sensor (Kuo and Morgan, 1996). Figure 1 shows the adaptive feedback control block diagram for the case of an external disturbance (completely unrelated to a self-excited limit cycle). It is instructive to briefly examine this system as a precursor to controlling the self-excited system.

In a purely feedforward control system, a separate reference signal that is correlated with the disturbance is used as the input to the adaptive filter and it is well-known that correct estimation of the dynamic phase, within ninety degrees, is sufficient to prevent divergence of the LMS gradient search (Elliott et al., 1987). In adaptive feedback control, the reference signal is derived directly from the error sensor by removing the component of the error signal that is due to the control signal, leaving only a measure of the disturbance. If we let the control signal be the output of the FIR adaptive filter (W), we note that it must go through the plant dynamics (G_p) before acting on the external disturbance (n). The dynamics represented by the plant will include everything present in the control signal-to-error signal path, including the A/D and D/A. Therefore, removing the component of control from the error requires subtracting the output of the adaptive filter, filtered by the plant estimate, from the measured error signal. Therefore, if the plant estimate is not perfect, a non-zero feedback path is introduced. The closed loop transfer function between the error and the disturbance can then be written as:

$$\frac{e}{n} = \frac{1 + \hat{G}_p W}{1 + \hat{G}_p W - G_p W} \qquad [1]$$

Unlike the self-excited system (discussed shortly), if the plant estimate is exact (i.e. $G_p = \hat{G}_p$), there is no feedback loop (the denominator of the above transfer function vanishes) and the system behaves as a strictly feedforward system where $\hat{G}_p$ and W are both stable systems. For the case where $G_p \neq \hat{G}_p$, it is clear that the poles of Equation 1 will change with the adaptation of the filter W and no guarantees are made concerning system stability. This is the first mode of instability that may exist in the adaptive feedback design, and is easily analyzed using Bode or Nyquist gain and phase relationships for the loop gain:

$$\frac{G_p W}{1 + \hat{G}_p W} \qquad [2]$$

In adaptive feedforward systems such as Filtered-X control, algorithm divergence can result when the step size of the update equation is too large, or when there is a phase error in the plant estimate greater than 90°. A similar analysis is much more difficult for the adaptive feedback case but has been discussed by (Wang and Ren, 1999). Their convergence result requires a strictly positive real assumption on a transfer function that depends on the unknown plant. Thus, it is of limited applicability for many real world

problems. The adaptive feedback weight update shown in Equation 3 clearly illustrates nonlinear characteristics, indicating that the 90° rule for the Filtered-X algorithm is not necessarily applicable to this problem.

$$w(k+1) = w(k) + \mu(\hat{G}_p n + \hat{G}_p G_p c - \hat{G}_p \hat{G}_p c)(-n - G_p c) \quad [3]$$

Our ongoing research in adaptive filtering methods for ACC has shown that the dominant instability mode is not related to algorithm divergence. The following simulation results for an adaptive feedback system illustrate an occurrence of a feedback loop instability; however, the ID error does not result in a divergence of the algorithm. The plant shown in Figure 1 was chosen to have unity magnitude and linear delay while the plant estimate was chosen as the same system with a different linear delay. The difference in phase between the plant and estimate increased almost linearly, reaching an excess of 1000° of phase error by 1000 Hz, thus ensuring the possibility for divergence of the weights due to an inaccurate system identification. Figure 2 illustrates the uncontrolled and controlled power spectra of the disturbance at 40 Hz. Initially, the tone is suppressed with only two adaptive filter weights but the 'out-of-band' gain that accompanies the optimal adaptive filter causes a loop instability at 810 Hz to occur as evidenced by the frequency response magnitude in excess of 0 dB at the 810 Hz phase crossover frequency. Stated otherwise, this LMS control diverges because of the feedback loop instability, NOT divergence of the algorithm. Simply increasing the number of adaptive filter weights reduces the gain of the adaptive filter at frequencies away from the disturbance, so that the filter provides sufficient gain at 40 Hz to suppress the disturbance without generating feedback loop instabilities. For this stabilizing situation, the phase error between the plant and estimate is still in excess of 90° at many frequencies but the algorithm *never* diverges. It is interesting to observe that some previous researchers have attempted to achieve control with only two-weight adaptive filters, hereby shown to destabilize the system unnecessarily. This problem is minimized for real experiments where narrow bandpass filters shape the error signal but is noteworthy, nonetheless.

If the gradient search algorithm itself is diverging due to an inaccurate identification, the increasing magnitude of the adaptive filter may also be sufficient to cause a loop instability. Likewise, the algorithm may be converging (with a certain plant error) to a solution that results in a feedback loop instability. It is impossible to completely separate the gradient search divergence from the potential loop instabilities described in the example above. Analysis of algorithm divergence is a focus of future research.

Self-Excited Systems

The existence of a feedback path, related to using the error sensor to generate the reference signal, is responsible for transforming the LMS control approach into an adaptive feedback system. As illustrated in the previous section, the feedback loop for the external disturbance adaptive feedback system (Figure 1) disappears for cases where the plant and plant estimate are identical. This is certainly desirable because one advantage of an adaptive feedforward control is its inherent stability. Unfortunately, it is not possible to eliminate the corresponding feedback path when this same adaptive control is applied to a self-excited system, as discussed next. This is one of the first important distinctions associated with applications of LMS adaptive filtering for ACC.

Figure 3 illustrates a simplified block diagram of an adaptive feedback controller applied to a self-excited system, such as the VPI tube combustor. The output of the adaptive filter is filtered by the plant estimate and is used to generate the reference signal from the error signal as before; although the plant estimate is quite different now as a result of the inclusion of the self-excited system. The control signal is altered by the plant and actuator dynamics (G_{ACT}) before generating a pressure that interacts with the pressure from the self-excited system (G_A and G_F) containing acoustic and flame dynamics. The role of the nonlinearity in the self-excited feedback loop is critical in establishing the ability to achieve a stable estimate of the plant – an important comment referring to system identification of a limit cycling system that will be discussed in detail in the following section. For now, it is possible to examine the feedback structure of the system without incorporating the nonlinearity, and assuming the self-excited system is marginally stable. The total pressure (P_T) serves as the error signal to be reduced and is used by the adaptive feedback structure to update the weights and create the reference signal. If the feedback system of Figure 3 is analyzed, the expression for the autonomous response P_T results in the following system characteristic equation:

$$1 - \frac{G_{ACT} W}{1 + \hat{G}_p W - G_A G_F - G_A G_F \hat{G}_p W} \quad [4]$$

where for a marginally stable linear system model, Equation 5 can be substituted in Equation 4 as the plant estimate.

$$\frac{P_T}{p} = \hat{G}_p = \frac{G_{ACT}}{1 - G_A G_F} \quad [5]$$

Equation 4 shows that even if the control-to-error path of Equation 5 (i.e. the probe input p to the total pressure P_T) is identified perfectly in a linear system sense, it does not guarantee that the roots of Equation 4 (poles of adaptive feedback system) will be stable. Recall that it did for the external disturbance feedback problem of Figure 1. It is also clear that the characteristic equation for LMS control of the self-excited plant has roots that depend on the self-excited system, the actuator path, and the adaptive filter.

The previous result shows that it is not possible to break the feedback loop created by the reference signal estimation when dealing with a self-excited plant. Before addressing the stabilizability of the self-excited system with the adaptive filter W, we will limit the selection of the plant estimate to only stable $\hat{G}_P$. The question still arises as to how one makes $\hat{G}_P$ a stable representation of Equation 5 when the roots of $(1-G_AG_F)$ are in the right half plane. The following section explains how the limit cycling plant *can* be accurately represented by a stable system due to the nonlinearity in the self-excited system. Previous researchers have indicated problems using a 'stable' representation of the self-excited system for the required plant estimate. However, the approach documented below has not been previously discussed as a means for acquiring a stable plant estimate $\hat{G}_P$ that accurately represents the dynamics of the limit cycling system and can ultimately be used for stabilizing control.

System Identification

The approach to identifying the open-loop plant for inclusion in the adaptive algorithm relies on a probe signal consisting of low-amplitude sinusoids at frequencies near the limit-cycle frequency and within the passband of the bandpass filter used to filter the pressure signal before control. Using a Fourier transform of the output signal, the frequency response of the plant at a small number of frequencies can be determined. Using a least-squares approach, a low-order, discrete-time model can be fit to this data and is used as the model of the plant.

Since the open-loop plant is in a steady limit cycle, it is not immediately clear whether such an identification approach will produce a reasonable linear model or whether such a model will be stable or unstable. Our experimental results have shown that very low-order linear models can account accurately for the frequency response data and that these models are always stable.

To understand this, consider the block diagram in Figure 4. From a describing function analysis, the gain of the limit cycle through the static nonlinearity is such that the total gain around the loop is unity. When a probe signal is injected into the system, we expect that the frequency response at the probe frequency will be that of the linear system made up of the linear blocks in the diagram and with the nonlinear block replaced by a suitable linear gain.

To determine the value of this gain, consider an input to the nonlinearity of the form

$$x = A_1 \sin \omega_1 t + A_2 \sin(\omega_2 t + \theta) \quad [6]$$

where ω_1 is the frequency of the limit cycle, ω_2 is the frequency of the probe and $A_1 >> A_2$. A first order approximation of the output of the nonlinearity, $f(x)$, is given by Equation 7.

$$f(A_1 \sin \omega_1 t + A_2 \sin(\omega_2 t + \theta)) = f(A_1 \sin \omega_1 t) + f'(A_1 \sin \omega_1 t) A_2 \sin(\omega_2 t + \theta) \quad [7]$$

and will be valid for A_2 sufficiently small. The gain of the nonlinearity at the limit cycle frequency is given by Equation 8.

$$\frac{2}{A_1 T} \int_0^T \left[f(A_1 \sin \omega_1 t) + f'(A_1 \sin \omega_1 t) A_2 \sin(\omega_2 t + \theta) \right] \sin \omega_1 t dt \quad [8]$$

where T is the length of a period of the overall waveform. If no period exists, then the limit as $T \to \infty$ can be taken. By arguing that the integral of incommensurate frequencies will vanish, the second term in the integral disappears and the linear gain associated with the limit cycle frequency, which is equal to the describing function of the nonlinearity, is

$$g_{LC} = \frac{2}{A_1 T} \int_0^T f(A_1 \sin \omega_1 t) \sin \omega_1 t dt \quad [9]$$

The gain of the nonlinearity at the probe frequency is given by Equation 10.

$$\frac{2}{A_2 T}\int_0^T \left[f(A_1 \sin\omega_1 t) + f'(A_1 \sin\omega_1 t)A_2 \sin(\omega_2 t+\theta)\right]\sin(\omega_2 t+\theta)dt \qquad [10]$$

Arguing as before, the first term in the integral will go to zero. In addition, the only part of the second term which will contribute to the integral is the constant component of $f'(A_1 \sin\omega_1 t)$ times the constant component of $A_2 \sin^2(\omega_2 t+\theta)$. Thus, the gain at the probe frequency is given by Equation 11.

$$g_{\Pr} = \frac{1}{T}\int_0^T f'(A_1 \sin\omega_1 t)dt \qquad [11]$$

Note that the gain of the probe signal is independent of the amplitude and frequency of the probe signal, subject to the restriction that the amplitude of the probe be small.

For the tanh nonlinearity considered in this paper, the limit-cycle and probe gains can be computed numerically and are shown in Figure 5. The gain of the probe signal is less than the gain of the limit cycle signal through the nonlinearity. Since the gain of the limit cycle frequency is just that value needed to make the closed-loop system marginally stable, the lower probe gain will cause the closed-loop system to appear stable. Since the probe gain is not a function of the probe frequency, the system identified by considering the frequency response at the probe frequency will appear linear and stable.

Analysis of Adaptive Feedback Applied to Self-Excited Systems

It is clear from the above discussion, how a linear representation of a nonlinear self-excited system can represent the measured control-to-error path if Equation 5 is re-written as

$$\frac{P_T}{p} = \hat{G}_p = \frac{G_{ACT}}{1 - G_A G_F g_{\Pr}} \qquad [12]$$

This plant estimate is stable at all probe frequencies, thereby avoiding the issue of attempting to use an unstable system identification, or a time-delay plant, as other investigations have discussed. On a related note, we point out that this system ID method also makes it possible to design a feedback controller that will apply the correct phase to the system while avoiding secondary peaks induced from the controller feedback loop (Vaudrey et al., 2000). The required gain for stabilization can be predicted only if the system gains of G_A and G_F are known, thus defining the location of the linear system poles in the right-half Laplace plane.

To summarize the issues to this point, we reiterate that Equation 12 solves only the problem of performing the system identification task for an unstable dynamic plant. There remain the issues of whether the optimal adaptive filter weights can be shown to stabilize the self-excited system, how to determine whether feedback-related instabilities (related to the plant estimate or transient adaptive filter weights) will destabilize the adaptive wideband application, and further analyses that will shed insight on the selection of a stable plant estimate $\hat{G}_P$ for use in the controller. The following discussion attempts to clarify some of these issues.

First, we examine the form of the optimal adaptive filter weights. (The reader is cautioned that the definition of the optimal adaptive filter used here is not based on the classic definition of the Wiener weights.) The self-excited adaptive feedback control system, illustrated by Figure 6, can be used to determine the optimal adaptive filter that sets the total pressure P_T of the controlled plant equal to zero. Equating the top loop to the bottom loop (with a minus sign) and solving for the optimal adaptive filter (W_{OPT}), Equation 13 results.

$$W_{opt} = \frac{-G_A G_F}{G_{ACT} + G_A G_F \hat{G}_p} \qquad [13]$$

By substituting Equation 13 into the block diagram of Figure 6 as the adaptive filter W, it is obvious that the lower loop (feedback controller) exactly cancels the upper loop $G_A G_F$ resulting in a completely stabilized closed loop system. Equation 14 illustrates this result for the probe input shown in Figure 6

$$\frac{P_T}{p} = \left.\frac{G_{ACT}(1+\hat{G}_p W)}{(1-G_A G_F)(1+\hat{G}_p W) - G_{ACT} W}\right|_{W=W_{opt}} = G_{ACT} \qquad [14]$$

Discussion of the optimal adaptive filter weights is more interesting for this self-excited plant application because of the quiescent state that the combustor will reach as soon as the poles have crossed back into the left-half Laplace plane (under the action of the controller). Because the open loop self-excited system of Equation 14 does not contain dynamics that are on the imaginary axis (i.e. marginally stable), there is a set of gains (between the imaginary axis and the optimal solution) that will stabilize the system without requiring the adaptive filter to reach the optimal solution. This system will be more lightly damped than the open loop system but still stabilized. If the adaptation causes the system to stabilize, the error signal will go to zero and the adaptation will stop, never reaching the optimal gain. **This is easily understood by recognizing that the adaptive filter solution that will ensure that the real parts of the roots of Equation 4 are all negative, is a different solution than the optimal solution of Equation 13.** The former will occur before the latter and cease adaptation as long as Equation 14 represents stable dynamics.

As mentioned earlier, there are two methods in which the adaptive wideband feedback system may not achieve stabilizing control. The first is easily identifiable as a feedback loop instability (see Equation 4), whereas the second is less well-defined as a gradient search error. The gradient search error may arise as a result of the step size parameter being too large or because the phase error of the Filtered-X control results in the LMS searching in the wrong direction on the mean-squared error performance surface. The plant estimation error analysis will be left for future work but cannot be completely separated from the feedback loop instabilities, as discussed next.

The roots of Equation 4 represent the closed loop poles of the controlled self-excited system. While it is possible to analyze each component of the system for stability in terms of gain and phase margins, it is more straightforward to insert the adaptive filter in Equation 4 to determine the closed loop root locations. It should be noted however, that because the characteristic equation is a function of the adaptive filter, an algorithm divergence will eventually result in a loop instability due to the increasing gain of the adaptive filter. It is important to distinguish between the two cases of instability by examining the convergence or divergence of the weights toward the optimal solution prior to inducing a loop instability.

It is now possible to see how the adaptive filter imparts the needed gain and phase to control the limit cycling system through the feedback loop. The significance of the control-to-error path in the controller transfer function is evident from Figure 6, which is a rearrangement of Figure 3. $\hat{G}_P$ clearly contributes to the gain and phase of the controller. However, there is another even more important issue that needs to be appreciated about the use of $\hat{G}_P$ identified by Equation 12. After inspection, it is clear that the version of $\hat{G}_P$ used during control is the correct identification of the control-to-error path *only* when the control loop is open. This important distinction is made apparent by examining the same (actual) control-to-error path *after* the control loop has been closed as shown in Figure 3. Performing the block diagram algebra, Equation 15 illustrates the new control-to-error transfer function in terms of the error signal (P_T) and the probe signal "p".

$$\frac{P_T}{p} = G_p = \frac{G_{ACT}(1+\hat{G}_p W)}{(1-G_A G_F g_{LC})(1+\hat{G}_p W) - G_{ACT} W} \qquad [15]$$

It is now obvious that after the control loop is closed and the adaptive filter grows in magnitude, its influence over the control-to-error path becomes more significant. (Note that setting W=0 in Equation 15 yields Equation 12). The fixed control-to-error path estimate $\hat{G}_P$ used in this control scheme (Equation 12) also influences the actual control-to-error path as the adaptive filter grows. Therefore, for adaptive filters requiring large magnitudes to stabilize the self-excited system, it is more likely that the actual control-to-error path will differ significantly from the fixed control-to-error path estimate obtained prior to closing the control loop.

Simulation and Experimental Results

Simulation Description

A simulation has been designed to permit rapid and easy investigation of the performance of the adaptive feedback controller in conjunction with the self-excited, limit cycling system. As will be seen, initial results from the simulation agree closely with the behavior of the actual experiment.

Figure 3 represents the general form of the adaptively controlled self-excited system that was simulated. The self-excited loop consists of a low pass filter to represent a model of the flame dynamics (G_F), a static nonlinearity represented by a hyperbolic tangent function, and a single mode lightly damped (2%) acoustical model (G_A) at approximately 175 Hz. The loop gain and nonlinearity gain were adjusted to yield a

steady limit cycle after approximately 2 seconds at a sampling rate of 1600 Hz. The actuator path consists of the acoustical model plus some amount of phase delay. For the experiment this delay represents all components in the control-to-error path.

The simulation runs in two separate modes, as does the experimental setup. After the limit cycle is established, a multi-tone probe signal is applied to the open loop plant as shown in Figure 4. The input to output relationship at the probe frequencies establishes the magnitude and phase of the linear plant as described in the system identification section above. This discrete frequency response data is then used to generate a least squares infinite impulse response (IIR) transfer function fit in the z-domain, typically of order less than 6, and always stable with a pole very near the unit circle (representing the limit cycle frequency). This fit is then used as the plant estimate during the second mode of the simulation. After the limit cycle has reached a steady state, and the probe frequencies have been turned off, the plant model mentioned above is used in the adaptive feedback control loop shown in Figure 3, both as the filtered-X part of the LMS and the plant estimate used to derive the reference signal.

The first simulation illustrated here is a case having a relatively low heat release, corresponding to a low gain in the self-excited feedback loop. Since broadband control is not the goal, only two adaptive filter weights were used to control the single tone instability. In the experimental setup, a steep (8-zero, 16-pole) bandpass filter was used to eliminate frequency content other than the limit cycle tonal. In the simulation, the only significant content in the error signal is the limit cycle sinusoid so a filter was not necessary. Using the stable plant model generated from the fit of the FRF obtained from the process shown in Figure 4, and a relatively fast convergence parameter for the LMS weight update equation, it is seen that the two adaptive weights shown in Figure 7 quickly reach a steady state condition that completely stabilizes the limit cycle as shown by the controlled and uncontrolled (dotted) power spectra in Figure 8.

As discussed in the Analysis section above, it is not required that the adaptive filter achieve the optimal gain in order to drive the error signal to zero. Figure 9 clearly illustrates this by showing the path of the magnitude and phase of the actual adaptive filter during adaptation, as compared to the optimal magnitude and phase as computed from Equation 13.

Also addressed in the analysis section was the possibility of feedback loop instabilities for the adaptive feedback system. An inaccurate plant model may contribute to causing a feedback loop instability by raising the gain near a phase crossover frequency. In order to analyze this more carefully, the frequency of the limit cycle instability (governed primarily by the frequency of the acoustic resonance) was deliberately altered while leaving the plant *model* unchanged. The frequency of the acoustic mode can shift at least 6 degrees in the negative direction while still stabilizing the system with the 175 Hz based plant model while it could only shift 4 Hz in the positive direction (to 179 Hz) before it was unable to control the system. (This would seem to imply that a plant model shifted higher in frequency would provide more robustness to changes in the plant under the action of the controller. More investigation is required in order to substantiate this theory). As shown by the power spectra in Figure 10, the instability occurred at the same frequency as the limit cycle and was predicted by the open loop Bode diagram of Figure 11 for the system of Figure 6.

While intentional creation of plant model error is instructive for tracking the source of divergence, it is not exactly true to the experiment itself. The plant changes under the action of the controller for higher heat releases, more drastically than it changes for lower heat releases. When the self-excited system is amplified to simulate higher heat release (moving the unstable pole further into the right half plane), the simulation has the same difficulties as the experiment in stabilizing the system. Figure 12 shows an upward shift in frequency of the limit cycle under the action of the control (solid trace). The time domain behavior searches between amplitudes higher and lower than the original limit cycle, unable to achieve stabilizing control because the plant model is too inaccurate when the limit cycle begins moving higher in frequency, a behavior that is amplified by the increased heat release.

Experimental Results

The experimental process was identical to that described in the simulation section above. A multi-tone FRF was performed on the entire plant and a least squares fit was applied to the data to generate an infinite impulse response filter model that represented the limit cycling plant. This model was then used in the experimental structure shown in Figure 13.

With the heat release at a relatively low gain (controlled by adjusting the equivalence ratio to a value of 0.51 and a total flow rate of 120 cc/sec), the Rijke tube combustor instability at 175 Hz was stabilized indefinitely with a two weight adaptive filter and the stable plant model obtained prior to control. Figure 14

shows (in asterisks) the actual magnitude and phase data collected from the tube with the 6th order model frequency response shown as the solid line.

Figure 15 shows the uncontrolled (dotted) and controlled power spectra of the total pressure in the tube (converted from voltage units). The second harmonic at 350 Hz disappears under control, revealing the shape of the third acoustic mode of the tube. The natural damping of the second acoustic mode is greater than that which is shown in Figure 15, but as discussed earlier, the system can be stabilized by having a pole in the left half plane that is more lightly damped than the natural acoustic mode.

A manually adjustable gain and phase shift controller was also applied to the same limit cycling system. Referring to Figure 6, it is apparent that the fixed gain controller replaces the transfer function:

$$\frac{W}{1+\hat{G}_p W} \qquad [16]$$

Examining the magnitude and phase of the converged Equation 16 at 175 Hz as compared to the magnitude and phase of the phase shifting feedback controller, it is seen in Figure 16 that the phase of both controllers is nearly the same at 175 Hz. The magnitude however is significantly lower for the adaptive system because the error signal has been driven below the 1-bit noise floor of the A/D. In addition, excessive gain was applied to the manual control system, that might have induced feedback instabilities (Vaudrey et. al. 2000, Saunders et. al. 1999-2). The adaptive controller can prevent controller induced instabilities by changing its shape and adjusting its magnitude to minimize the mean squared error.

Although no data was collected, the adaptive controller was used to control a higher equivalence ratio of 0.57 at the same total flow rate. This corresponded to the increase in gain for the simulation shown in Figure 12. The searching time domain behavior and the upward shift in frequency apparent in the simulation were both witnessed in the experimental application of the same system. While the adaptive controller was unable to completely stabilize the higher equivalence ratio system, it was able to exercise significant authority over the instability by cycling its amplitude over time, as seen in the simulation.

Conclusions

An adaptive control strategy based on the LMS algorithm was used to stabilize a limit cycling Rijke tube combustor. It was shown that a stable linear model of the nonlinear limit cycling control-to-error path can be used in an adaptive feedback arrangement to achieve the stabilizing control. It was also shown that ill-behaved controller performance is often due to unstable feedback loops caused by inaccurate plant models and large adaptive filter amplitudes required by high heat release situations. Finally, it was shown that a numerical simulation has been developed that accurately predicts the experimental performance, and can be used as a tool for designing control strategies that are effective over a broad range of operating conditions.

Previous research (Annaswamy et. al., Billoud et. al., Kemal et. al., Koshigoe et. al.) in the area of adaptive LMS control for combustion instabilities has met with limited success. Structures incorporating fixed system models of stable and unstable plants have exhibited numerical instabilities over time. This paper provides analytical, simulation, and experimental proof-of-concept for using a stable plant model for adaptive feedback control of limit cycling oscillations. In addition, a method for tracking loop instabilities that can result in spurious behavior of the adaptive feedback system has been presented.

References

Annaswamy, A.M., O.M. El Rifai, M. Fleifil, J.P. Hathout, and A.F. Ghoniem, "A Model-based Self-tuning Controller for Thermoacoustic Instability," *Combustion Science and Technology,* **135**, 1998, pp. 213-239.

Billoud, G., M.A. Galland, C.H. Huu, and S. Candel, 'Adaptive Active Control of Combustion Instabilities,' *Combust. Sci. and Tech.*, **81**, 1992, pp.257-283.

Elliott S.J., I.M. Stothers, and P.A. Nelson, 'A Multiple Error LMS Algorithm and Its Application to the Active Control of Sound and Vibration, ' *IEEE Transactions on Acoust., Speech, and Sig.Proc.*, Vol.ASSP-35, No.10, Oct., 1987.

Gutmark, E., T.P. Parr, K.J. Wilson, D.M. Hanson-Parr, and K.C. Schadow, 'Closed-loop Control in a Flame and a Dump Combustor,' *IEEE Control Systems*, **13**, 1993, pp.73-78.

Kemal, A. and C. Bowman, 'Active Adaptive Control of Combustion,' *Proceedings of the IEEE Conference on Control Applications*, 1995, pp.667-672.

Koshigoe, S., T. Komatsuzaki, and V. Yang, 'Adaptive Control of Combustion Instability with On-Line System Identification,' *Journal of Propulsion and Power*, **15**, 1999, pp.383-389.

Kuo, S.M. and D.R. Morgan, 'Active Noise Control Systems, Algorithms and DSP Implementations,' John Wiley and Sons, Inc., New York, NY, 1996.

McManus, K.R., U. Vandsburger, and C.T. Bowman, 'Combustor Performance Enhancement Using Direct Shear Layer Excitation,' *Combustion and Flame,* **82**, 1990, pp. 75-92.

Mohanraj, R. and B.T. Zinn, "Numerical Study of the Performance of Active Control Systems for Combustion Instabilities, " AIAA 98-0356, 36th Aerospace Sciences Meeting & Exhibit, Reno, NV, Jan., 1998.

Saunders, W.R., L. Nord, C.A. Fannin, X. Huang, W.T. Baumann, V. Khanna , U. Vandsburger, L. Haber, B. Eisenhower, S. Liljenberg, 'Diagnostics and Modeling of Acoustic Signatures in a Tube Combustor, *' Proceedings of the 6th Int. Congress on Sound and Vib.*, Copenhagen, Denmark, 1999-1.

Saunders, W.R., M.A. Vaudrey, and B. A. Eisenhower, U. Vandsburger, and C.A. Fannin, 'Perspectives on Linear Compensator Designs for Active Combustion Control,' AIAA 99-0717, 37th AIAA Aerospace Sciences Meeting and Exhibit, Reno, NV, Jan. 1999-2.

Vaudrey, M.A., W.R. Saunders, and B. A. Eisenhower, 'A Test-Based Methodology for Apriori Selection of Gain/Phase relationships in Proportional, Phase-Shifting Control of Combustion Instabilities,' Proceedings of ASME Turbo Expo 2000, Munich, Germany, May 2000.

Wang, A.K. and W. Ren, 'Convergence Analysis of the Filtered-U Algorithm for Active Noise Control,' *Signal Processing Journal* 73 (1999), pp.255-266.

Widrow, B. and S.D. Stearns, 'Adaptive Signal Processing,' Prentice-Hall, Inc., Englewood, N.J., 1985.

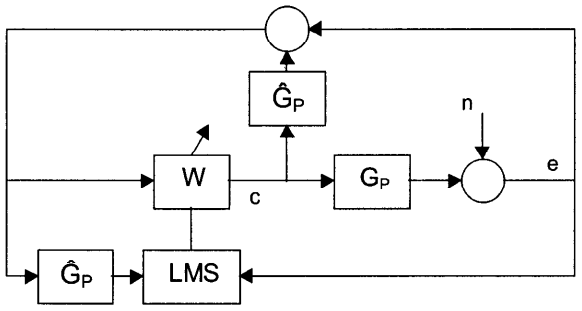


FIGURE 1: ADAPTIVE FEEDBACK EXTERNAL DISTURBANCE

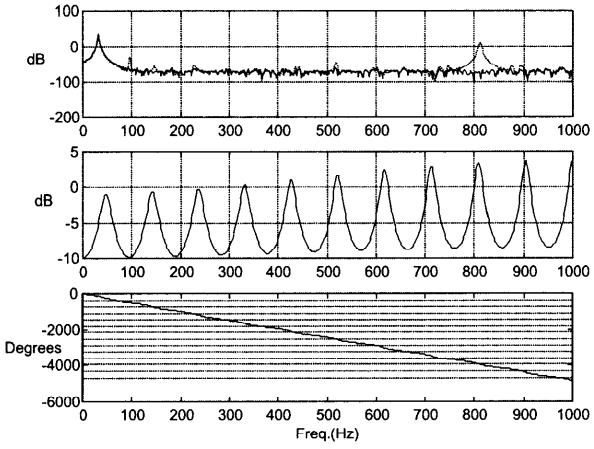


FIGURE 2: POWER SPECTRA AND OPEN LOOP FRF

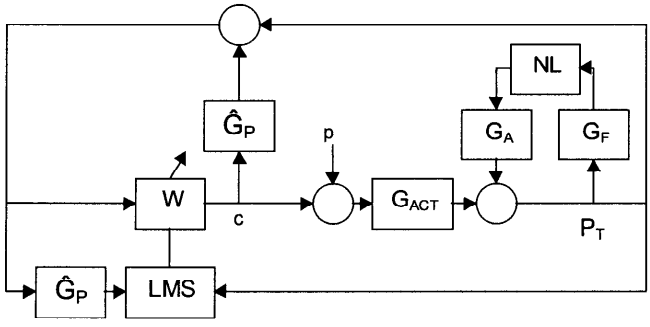


FIGURE 3: ADAPTIVE FEEDBACK SELF EXCITED

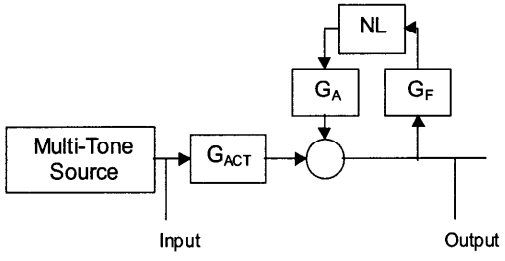


FIGURE 4: SYSTEM ID– OPEN LOOP

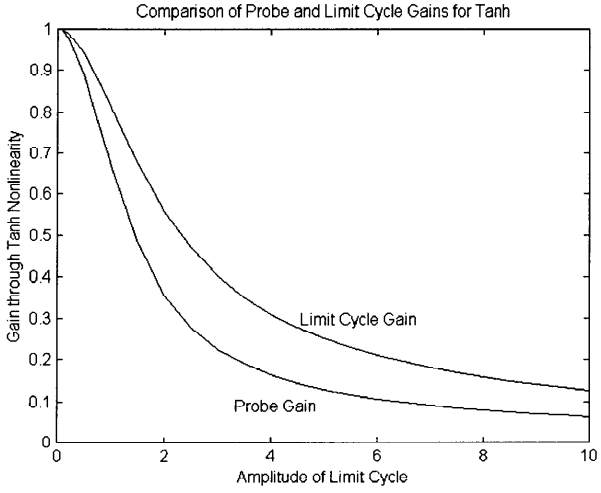


FIGURE 5: PROBE GAIN AND LIMIT CYCLE GAIN

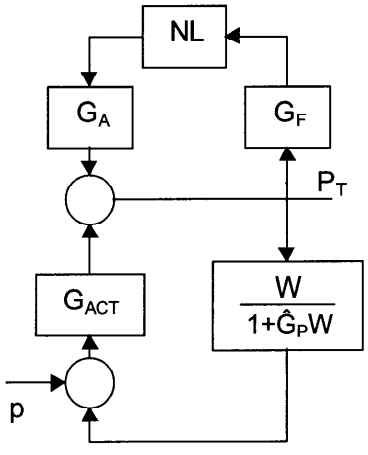


FIGURE 6: ADAPTIVE FEEDBACK SELF EXCITED

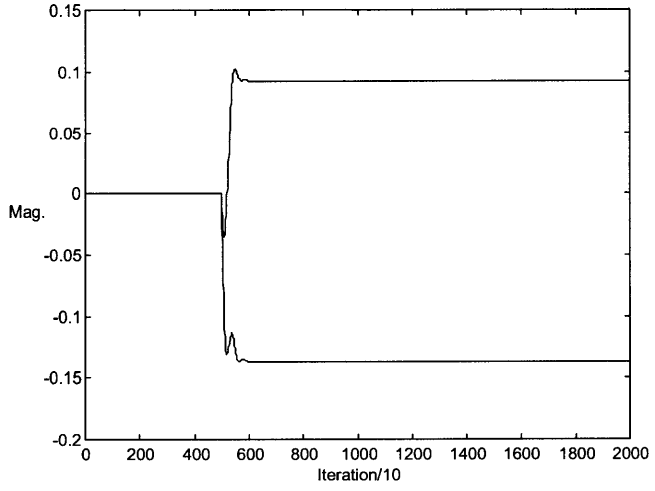


FIGURE 7: WEIGHTS IN TIME

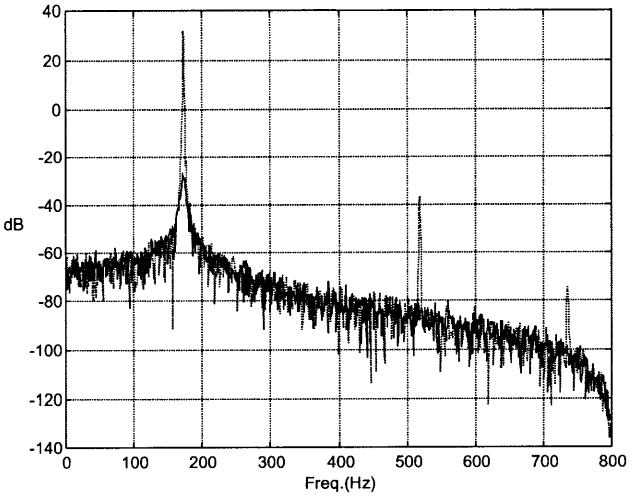


FIGURE 8: POWER SPECTRA CONTROLLED (SOLID)

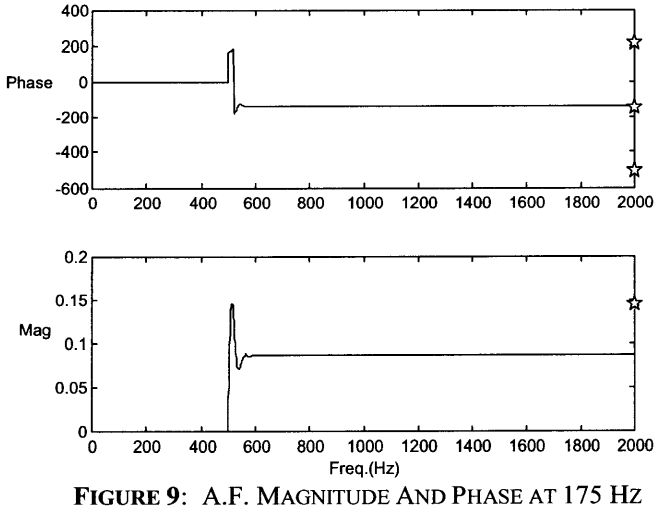


FIGURE 9: A.F. MAGNITUDE AND PHASE AT 175 HZ

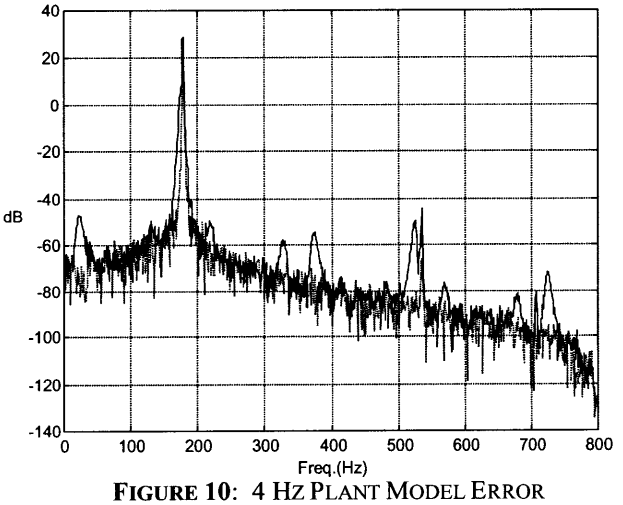


FIGURE 10: 4 HZ PLANT MODEL ERROR CONTROLLED SOLID

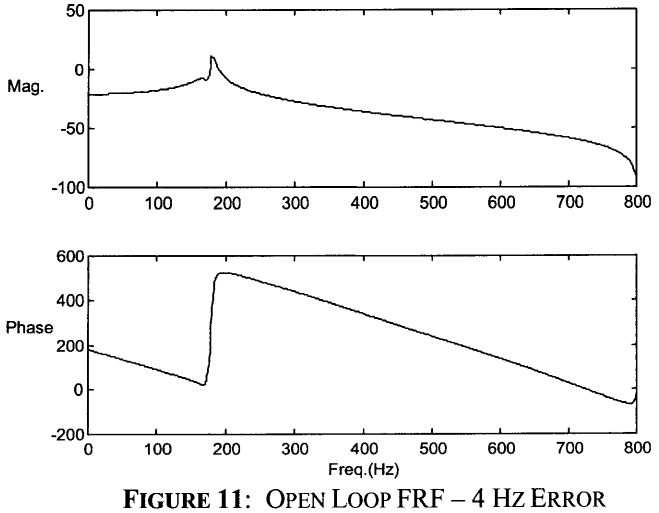


FIGURE 11: OPEN LOOP FRF – 4 HZ ERROR

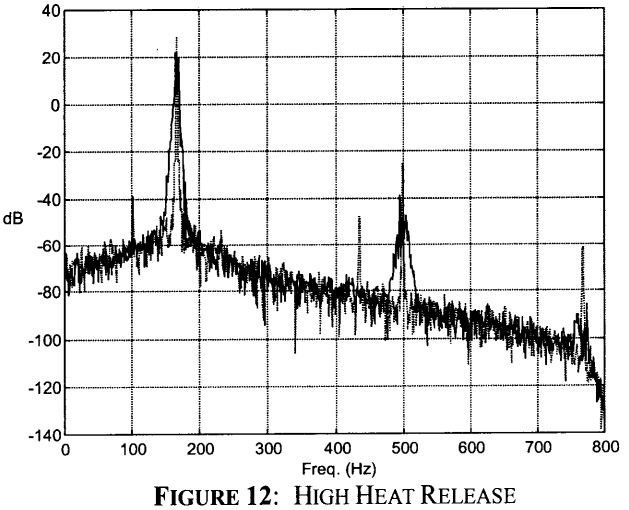


FIGURE 12: HIGH HEAT RELEASE CONTROLLED-SOLID

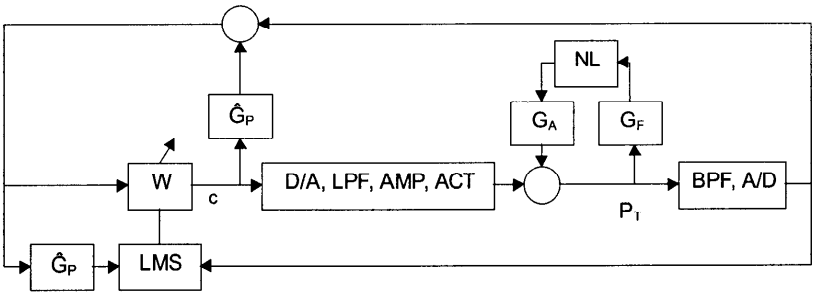


FIGURE 13: ADAPTIVE FEEDBACK EXPERIMENTAL SETUP

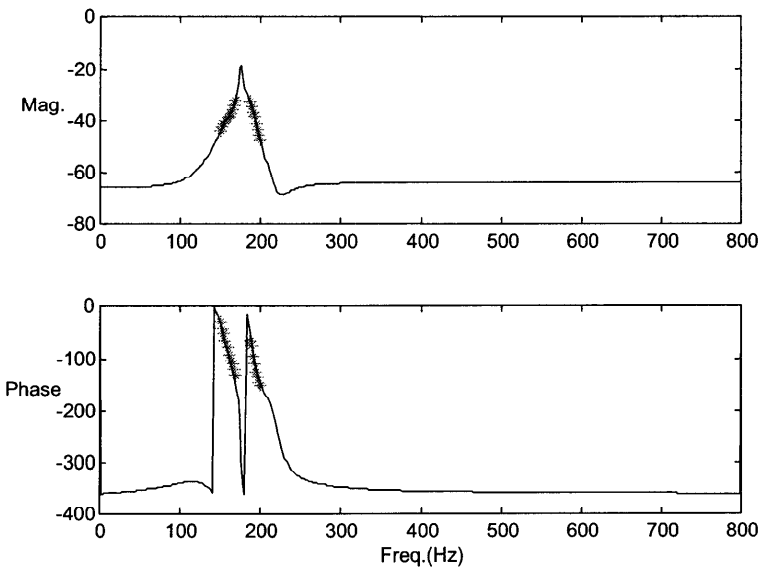


FIGURE 14: EXPERIMENTAL PLANT MODEL FIT

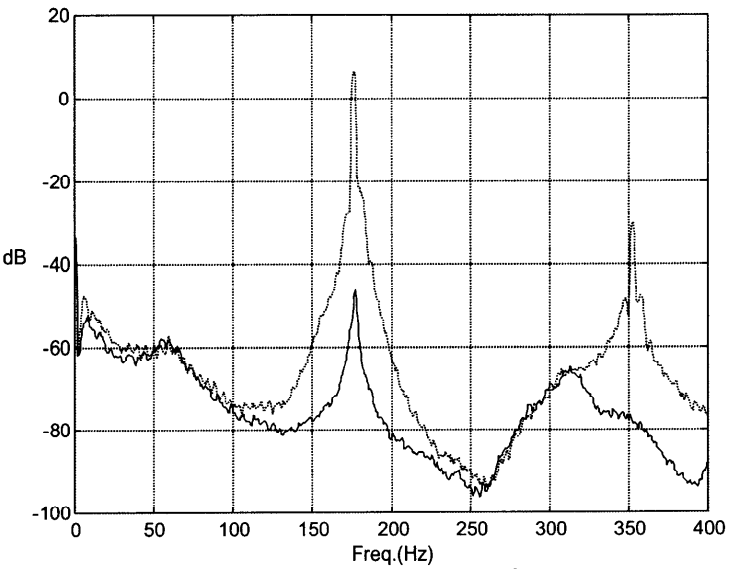


FIGURE 15: EXPERIMENTAL CONTROL

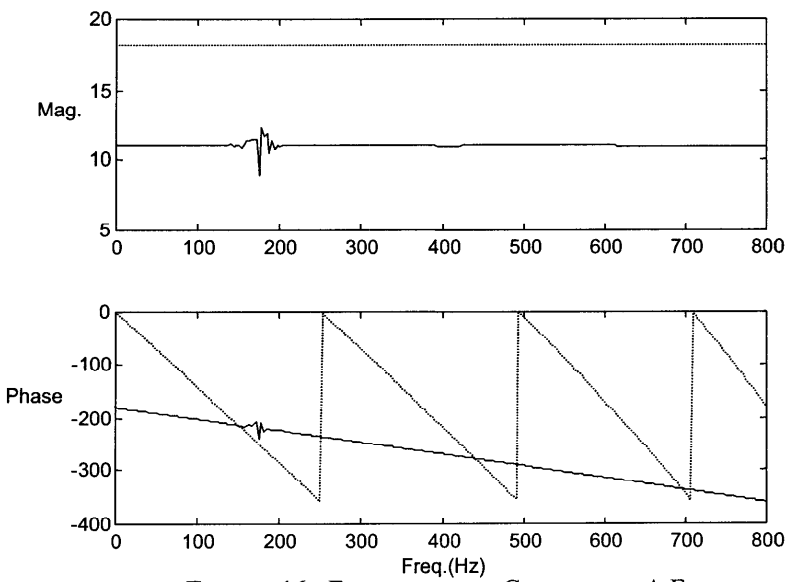


FIGURE 16: FEEDBACK AND CONVERGED A.F.

Developments of Adaptive Methods for Active Instability Control

M. Mettenleiter and S. Candel

Laboratoire E.M2.C, CNRS, Ecole Centrale Paris, F-92295 Châtenay-Malabry Cedex

Abstract

Adaptive algorithms are considered in many applications of active flow control. Independent on the controller type, it is always necessary to provide information on the system to be controlled. A standard method is to identify the system in a first step and then provide the result to the controller. The secondary path information obtained is necessary for the proper convergence of the adaptive filter. This two–step procedure is applicable in many cases but it is not sufficient when the system changes significantly during operation.

This study focuses on self adaptive controllers operating with an on–line identification procedure. These systems are devised in this article to control acroacoustic instabilities of the type found in segmented solid rocket motors. Instabilities are driven by vortex shedding which are coupled by a resonant mode of the system. Two laboratory scale experiments are used as testbeds for the control schemes. Self adaptive control is compared with a standard adaptive method using an off–line identification procedure.

1 Introduction

Research on active control has taken considerable momentum with a rapid expansion of domains of application. Many developments have concerned control of flow instabilities. External and internal aerodynamics have been considered, the special case of combustion has received much attention (see McManus et al. [1] for a review of the control of combustion instabilities). These instabilities are observed in many practical systems (jet engines, rocket motors, gas turbines, ...) and they have many undesirable effects.

Active means of their reduction or suppression have been devised in recent years. Control methods in this area are mainly based on feedback principles in which the signal detected by a sensor is returned through the controller unit to an actuator which injects perturbations into the combustor. Initial developments were based on simple control concepts, the sensor signal was just amplified and phase delayed and then returned to the actuator. Instabilities were reduced quite successfully but it was soon found that the method was only applicable in a limited range of operation of the combustor. An important progress was made by replacing the gain and phase control by adaptive algorithms (Billoud et al. [2]). It was shown that control could be achieved over an extended domain around the nominal point of operation. The adaptive controller was able to follow the changes in the mode of combustion and different types of instabilities were reduced leading to a significant augmentation of the stability domain of the combustor. Adaptive techniques have been applied in many other areas with notable developments in anti–sound and active vibration control (see the books of Nelson and Elliott [3], Kuo and Morgan [4] and articles by Eriksson [5], [5], [6], [7] and Kuo and Morgan [8]). Methods of adaptive filtering and adaptive control are well described by Widrow and Stearns [9], Haykin [10], Goodwin and Sin [11] or by Åström and Wittenmark [12] amongst others. Glentis et al. [13] give a general introduction to LMS (least mean square methods) which have been extensively used in recent years.

Whatever the structure of the control algorithm is, it is always necessary to have some information on the system to be controlled. The adaptive methods explored up to now in experimental combustion and flow control applications have relied on information obtained from an off-line identification process. The so called "secondary path" which corresponds to the system as it is seen by the controller is described by a transfer function $\hat{\boldsymbol{S}}$ (filter) which is identified in a first step. When the secondary path is essentially acoustic (ie featuring a microphone as sensor and a driver unit as actuator) the transfer function does not change too much with the operating conditions and the result of identification may be used over a certain range of

Paper presented at the RTO AVT Symposium on "Active Control Technology for Enhanced Performance Operational Capabilities of Military Aircraft, Land Vehicles and Sea Vehicles", held in Braunschweig, Germany, 8-11 May 2000, and published in RTO MP-051.

operating conditions. If however the secondary path involves a convective process, the identification will be valid in a very limited range of flow parameters.

If the secondary path $\boldsymbol{S}$ differs markedly from its representation in the control algorithm $\hat{\boldsymbol{S}}$, the adaptive filter $\boldsymbol{W}$, which amplifies and dephases the sensor signal to produce the controller output, will not converge. One may show that the problem arises when the error in phase of $\hat{\boldsymbol{S}}$ with respect to that of $\boldsymbol{S}$ exceeds $\pm 90°$. When the difference between the real and identified systems is too important it is necessary to update the model in order to maintain control. This could be accomplished by incorporating the identification procedure in the controller. The combination of identification and control is now seen as a key issue in the development of practical controllers.

In the active control of aeroacoustic vortex instabilities of solid rocket motors, which motivates the present study, on–line identification is the only possible strategy for practical implementation. It is presumed that a model for the secondary path with fixed parameters will not be able to render the changes taking place during operation of the motor. Even if some information is available on the system, it may only be used as a starting description with the on-line identification progressively taking-over during the control process.

Self adaptive control (SAC) or equivalently adaptive control with on-line identification are explored in the domain of anti-sound and vibration control and some experimental investigations are available. Theoretical studies of the application of SAC to combustion instabilities are also reported (see for example Koshigoe et al. [14]). The system is described by a reduced order dynamical model which provides a simplified representation of the real behavior. The practical implementation of SAC in flow instability experiments is not found in the technical literature.

The objective of this article is to describe some of our results on self adaptive control. This topic has been systematically investigated in order to control aeroacoustic instabilities. A comparison between the different possible structures of controllers incorporating on-line identification was carried out using an experimental testbed "CAPS". Performance of SAC was measured with respect to that of adaptive control with off-line identification. Self adaptive control was also achieved in a model scale experiment representing the geometry of a segmented solid rocket motor (detailed results are reported in [15]).

We begin with a description of self adaptive control concepts (section 2). The self adaptive controller structure is discussed in section 3. Selected test results are given in section 4 and 5 for two different experiments.

2 Self adaptive control concepts

Most of the self adaptive algorithms used in the area of instability control are inspired by schemes developed in the anti–noise domain. These algorithms normally operate with at least two sensors. The primary sensor signal x is used as input of the controller and the secondary or error sensor signal e provides a measure for quantifying the success of control (refer to Figures 1 or 2). Using x (which is generally stationary or slowly varying) as signal which is correlated to the primary noise d, the objective is to generate an anti–noise signal y_r to counteract d. If the error sensor signal e is reduced, the control is successful. As can be seen in the two figures, an estimate $\hat{\boldsymbol{S}}$ of the secondary path is necessary in order to properly adapt the filter coefficients of $\boldsymbol{W}$.

In configurations using off–line identification, this transfer function can be determined by using for example a white noise signal to excite $\boldsymbol{S}$. The filter $\hat{\boldsymbol{S}}$ is then determined as to match as close as possible the output of $\boldsymbol{S}$.

In schemes using on–line identification of the secondary path, two basic structures can be distinguished. The first uses an additional signal (white noise for example) for identifying the secondary path (an example from Kuo and Morgan [4] is shown in Figure 1). The second structure is using the filter output of $\boldsymbol{W}$, the signal y, as input of the secondary path estimation $\hat{\boldsymbol{S}}$ (see an example from Kuo and Morgan [4] in Figure 2). Note that in this example the signal y corresponds to the shifted primary sensor signal during a first "identification phase".

The objective of the two structures is to get an estimate of the error signal e by using a system modeling procedure (shown in the lower half of the two figures). As the signal e comprises two components (d and y_r), it is sufficient to use two filters to reproduce an estimate of these signals to form an estimate $\hat{e}$. One of the filters ($\hat{\boldsymbol{S}}$) represents an estimate of the real secondary path. Therefore it can be used to calculate the signal x' for the control algorithm. Control and system modeling (that is identification) is performed at the same time for the scheme in Figure 1. Figure 2 proposes first an identification procedure carried out off–line (in the presence of the instability phenomenon) before switching to the real control with continued identification on–line.

Kuo and Morgan [4] note two important conditions which should be fulfilled by self–adaptive algorithms.

First, the estimation of $\hat{\boldsymbol{S}}$ should be independent of the filter $\boldsymbol{W}$. This guarantees robustness of the algorithm. The structure proposed in Figure 1 fulfills this requirement: the white noise signal helps getting an estimate $\hat{\boldsymbol{S}}$ which is independent of the filter $\boldsymbol{W}$. The second requirement demands that the estimation of $\hat{\boldsymbol{S}}$ should not interfere with control. This is not the case for the scheme proposed in Figure 1 (the white noise signal interferes with y and perturbs the control). The algorithm in Figure 2 does fulfill the second requirement, but not the first. As y is generally narrow band, $\hat{\boldsymbol{S}}$ will not be correctly identified on the whole frequency band of interest. One can see that the two conditions cannot be fulfilled at the same time and hence a compromise has to be found between interference and robustness.

3 Self adaptive structure for control at the noise source

In anti–noise situations it is generally easy to use several sensors. The primary sensor may measure a signal which is correlated with the primary noise generated later on (this signal could for example be the angular rotation of a motor) and the error sensor measures the pressure fluctuations in the passenger cabin for example. If only one sensor is employed, the error signal is used to reconstruct an estimate of the primary noise which replaces x in the Figures shown in the last section. Note, that for this estimate $\hat{d}$ the same assumption holds as for the signal x: it does not change rapidly during operation.

Control schemes for combustion or aeroacoustic instabilities differ from the usual concepts adopted in the area of pure noise control based on anti–noise principles. It has been pointed out that generally the primary sensor signal x (or $\hat{d}$) does not change rapidly in noise control. But this is the case for combustion or aeroacoustic problems. The control acts on the noise source (the unsteady heat release in combustion problems or the regular vortex shedding in aeroacoustic instabilities). Therefore, a different control scheme should be employed in these situations (see Mettenleiter et al. [16] for more details). If only one sensor is used, the controller input x (or $\hat{d}$) is now replaced by the error signal e. This difference can be seen in the upper part of Figure 3. Examining the behaviour during control, one can write :

$$\begin{aligned} e &= d - y_r \\ e &= d - \boldsymbol{S}\boldsymbol{W}e \\ (I + \boldsymbol{S}\boldsymbol{W})e &= d \end{aligned}$$

$$e = \frac{d}{I + \boldsymbol{S}\boldsymbol{W}}.$$

It can be seen that this controller only converges towards a stable state $e \to 0$ if the primary noise d itself is modified and driven to zero. This is contrary to a classical anti–noise situation with $y_r \to d$ for $e \to 0$ (and $d = cnst.$).

The lower part of Figure 3 represents the system modeling. As in the schemes shown in the previous section, the aim of this modeling part is to reproduce the error signal e. This estimate is called $\hat{e}$ and it is composed of two components: $\hat{y}_r$ which reproduces the output of the secondary path and $\hat{d}$, which is an estimate of the primary noise d.

The identification process adopted in this scheme does not interfere with the adaptive control. As indicated above, the method is not without problems:

- The input signal of $\hat{\boldsymbol{S}}$ is not normally wide band and as a consequence identification is only carried out in a narrow band an not in the full range of frequencies
- The filter coefficients may diverge because the solution is not unique (adaption of different filters at the same time causes problems if their input signal is not decorrelated, see for example [9]). Divergence of the coefficients can also be observed in real time applications if the input signal is not persistently exciting the filter (see for example [4]).

The first point is not too critical. It is in fact sufficient to get an secondary path estimation which is sufficiently precise for the frequency range of the instability. If this range changes during operation, the algorithm may adapt itself to the new frequencies.

The second point is more problematic. For successful control long term divergence problems have to be resolved. This can be done in different ways. It is possible to observe the coefficient adaptation history and adjust a leak coefficient. Starting from a solution which satisfies a certain criterion one may augment or reduce the leak coefficient in order to stay close to this criterion. If the estimated filter coefficients do not allow a proper operation of the controller (because the operating point has changed) one defines a new criterion for the filter coefficients.

A second strategy consists in freezing the coefficient adaptation of $\boldsymbol{F^{11}}$ and $\hat{\boldsymbol{S}}$ if the model represented by these two filters features a response which comes close to that of the real system. If the model does not reflect reality, the learning process should be resumed. The adaptation of $\boldsymbol{F^{11}}$ and $\hat{\boldsymbol{S}}$ proceeds until the model represents again the real system with

a sufficient precision. One may thus avoid problems of model divergence over a long period of operation.

It is interesting to analyze the system in the steady state. The three error functions in Figure 3 are given by :

$$\begin{aligned} e &= d - \boldsymbol{SW}e \\ e_2 &= (d - \boldsymbol{SW}e) - (\boldsymbol{F^{11}} - \hat{\boldsymbol{S}}\boldsymbol{W})e \\ \hat{e} &= (\boldsymbol{F^{11}} - \hat{\boldsymbol{S}}\boldsymbol{W})e. \end{aligned}$$

The first expression has the same solution as shown above. The third equation gives the estimate of the error sensor simulation. In the second equation, this estimate is compared with the sensor signal in order to adjust the filters $\boldsymbol{F^{11}}$ and $\hat{\boldsymbol{S}}$. One possible solution for minimizing e_2 is given by :

$$\hat{\boldsymbol{S}}^0 = \boldsymbol{S}.$$

In this case, the filter $\boldsymbol{F^{11}}$ becomes :

$$\boldsymbol{F^{11^o}} = \frac{d}{e}$$

and it follows that $\hat{d} = d$. It might be disturbing to represent the primary noise as a function of the error signal $\hat{d} = \boldsymbol{F}^{11}e$. This follows the assumption that the primary noise is proportional to the error signal itself and it holds only if control acts at the source of the noise.

4 Flow instability control in a laboratory testbed

Different SAC algorithms (with and without additional white noise) have been developed and tested on a simple laboratory scale experiment (see Figure 4) designed to reproduce some features of aeroacoustic coupling of the kind observed in solid rocket motors. Air is injected in the lower part of the device. The small cavity acts as a "vortex generator". The number of vortices and their frequency are determined by the eigenmodes of the setup, the position of the cavity with respect to the eigenmodes and the flow speed (see [17] or [16] for more details about the phenomena). Certain volume flows lead to a strong acoustic resonance. The pressure fluctuations can be measured by different microphones. Velocity fluctuations in the cavity are detected by a hot film probe.

We will present in this paper a comparison between one of the SAC algorithms (introduced in Figure 3) and the equivalent scheme with off-line identification of the secondary path (denoted as "reference"). Both controllers work with the same sampling frequency (3 kHz) and contain FIR filters with 64 coefficients for $\boldsymbol{W}$ and 90 tabs for $\hat{\boldsymbol{S}}$. In addition to that, the filter $\boldsymbol{F}^{11}$ for the SAC scheme contains 32 elements. During the tests, the reference algorithm is started with the knowledge of $\hat{\boldsymbol{S}}$, the filter $\boldsymbol{W}$ is initialized with zero and adapts during control. The SAC scheme starts with no knowledge and all three filters adapt at the same time during the first period of control.

The merits of the algorithms may be rated at different levels:

- Comparison of the steady state after convergence
- Rapidity of the transient response
- Comparison of the transfer functions of $\hat{\boldsymbol{S}}$ and $\boldsymbol{W}$ after convergence

In what follows, we compare the two algorithms with respect to the three points noted above. Although only one volume flow rate is shown here, these results are representative for the whole domain of application of the setup.

4.1 Comparison of the steady state after convergence

A volume flow rate of 16 m^3/h is injected into the experimental device. The instability develops and the resulting pressure fluctuations are measured and the spectrum is calculated. Then, the controller is switched on and after convergence a second spectrum is obtained. These spectra are shown in Figure 5 on the left for the reference algorithm and on the right for the SAC scheme. Dashdotted lines represent the spectra without control, the solid lines are obtained with control. A comparison between the two algorithm shows a slightly better performance for the reference controller. The reduction in the main peak is about 40 dB (compared to 35 dB for the SAC). The first harmonic at 1100 Hz is also reduced. An intermediate peak at 800 Hz is slightly increased by both schemes, whereas the increase for the SAC algorithm is more important. Nevertheless, the main frequency is largely reduced and the self-adaptive controller performs equally well.

4.2 Rapidity of the transient response

The speed of convergence is compared for the same volume flow rate as above. The reference algorithm is shown on the left of Figure 6 while the SAC scheme is displayed on the right. The top image shows the error sensor signal, the bottom image visualizes the controller output. The vertical line indicates the switch on of the algorithm.

The reference algorithm shows a quick reduction of the pressure signal. The controller output reaches large amplitudes at the beginning of control. Later on a relatively small component is sufficient to maintain control. This behaviour is typical for algorithms acting at the source of noise: once, the feedback mechanism which leads to instability is broken, only a small amount of energy is necessary to prevent the growth of the phenomenon. The SAC scheme needs more time to react. After a first period where the pressure signal is not noticeably reduced (the controller output as well is small), the reduction takes place and a comparable steady state behaviour is reached (note the different scalings between the figures). This additional delay is attributed to the learning phase of $\hat{\boldsymbol{S}}$ and $\boldsymbol{F}^{[1]}$ during which the controller does not (and can not) act properly.

4.3 Comparison of $\hat{\boldsymbol{S}}$ and $\boldsymbol{W}$ after convergence

It is particularly interesting to compare the secondary path estimation and the filter $\boldsymbol{W}$ for the two control algorithms. This may show if the SAC scheme converges towards the reference solution or not.

Using the same operating conditions as above, the filter coefficients have been acquired and their transfer functions are calculated. The left of Figure 7 shows the secondary path estimation $\hat{\boldsymbol{S}}$, the right displays the behaviour of the $\boldsymbol{W}$ filter (the amplitude is on the top, the corresponding phase on the bottom of the figures). The reference filters are printed with dashed lines, the SAC filters are shown with solid lines.

The amplitude of the SAC estimation $\hat{\boldsymbol{S}}$ does not correspond well to the path identified off–line. More important than the amplitude is the phase behaviour of $\hat{\boldsymbol{S}}$. Close to the frequency of the instability (550 Hz) the SAC phase is indeed close to the reference phase. Other frequencies (particularly the lower ones) are not contained in the error signal and hence the identification does not work for these components. Using an additional white noise signal for the identification procedure, all frequencies could be excited and a valid estimate could be obtained for the whole range of interest.

The comparison of the $\boldsymbol{W}$ coefficients shows a similar behaviour for the two algorithms. The amplitudes are comparable for the 550 Hz component (although it seems as if the reference algorithm shifts its action closer to 500 Hz). The 820 Hz component, the second frequency appearing in the spectra of Figure 5, is equally amplified by $\boldsymbol{W}$ for the two algorithms. The phases of the two schemes correspond well, particularly for the frequencies of interest. This indicates that the SAC scheme converges toward a solution comparable to the reference algorithm.

5 Control of a model of a segmented solid rocket motor

The experimental setup PLEXI used at the Von Kármán Institute in Belgium for studies concerning aeroacoustic noise generation in segmented solid propellant boosters is a down-scale cold flow facility of the P230 accelerator of the Ariane–5 rocket. The setup is based on a 1/15–scale similarity with the full scale motor obtained by conserving the Mach number when 50 % of the propellant is burnt (see Figure 8). The length of the test section is 1.26 m, the internal diameter is given by 11.3 cm. The inhibitor height is 17.4 mm and the inhibitor–nozzle distance of 14 cm corresponds to an optimized flow acoustic coupling (for more details about the setup, refer to [18] and [19]). Adaptive control was used in order to study the influence of the acoustics on the vortex driven instabilities (the results are shown in Ref. [20]).

The SAC algorithm described before has been tested in this facility and results are again compared to the reference scheme using off–line identification. The performance after convergence of the algorithms is shown in Figure 9. The results for the reference algorithm appear on the left, on the right the SAC scheme is shown. Dashed lines indicate pressure spectra without and solid lines with control. As in the previous example, the reference scheme shows a slightly better behaviour. Note that for this experiment the reference scheme uses a higher sampling frequency and longer filters.

The transient behaviour can be examined in Figure 10. The reference case is on the left, the SAC algorithm is shown on the right. The top plots represent the error signal (pressure sensor), the bottom plots specify the controller output. The vertical line indicates the switch on of the controller. Again, the reference scheme shows a better transient behaviour. The controller output grows faster than for the SAC algorithm. Nevertheless, the steady state is comparable for the two controllers.

Again, the results shown here for the SAC scheme are representative for the behaviour on a larger domain of application. These results are documented in Ref. [15].

6 Conclusion

Self adaptive control schemes are investigated in this article for active control applications. The control of aeroacoustic instabilities driven by large scale vortices is specifically considered. Two experimental facilities serve as testbeds for control. The self adaptive controller is compared with more standard adaptive methods relying on off-line identification procedures. It is shown that the self adaptive controller is able to achieve control. Convergence is slowed down by the additional task of identification. The steady state behaviour is nearly as good as with the reference algorithm and the different filters show similar behaviour for the different algorithms. Long term divergence problems, often encountered in real time implementations, are resolved by monitoring the development of the different filter coefficients.

Acknowledgments: This research was supported in part by CNES and ONERA in the framework of the ASSM project. The authors are also grateful to J. Anthoine from VKI Bruxelles for providing the PLEXI facilities.

References

[1] K. R. McManus, T. Poinsot, and S. Candel. A rieview of active control of combustion instabilities. *Prog. Energy Combust. Sci.*, 19:1–29, 1993.

[2] G. Billoud, M. A. Galland, C. Huynh Huu, and S. Candel. Adaptive active control of combustion instabilities. *Combust. Sci. and Tech.*, 81:257–283, 1992.

[3] P. A. Nelson and S. J. Elliot. *Active Control of Sound.* Academic Press, 1992.

[4] Sen M. Kuo and Dennis R. Morgan. *Active Noise Control Systems.* John Wiley & Sons, 1996.

[5] L.J. Eriksson and M.C. Allie. Use of random noise for on–line transducer modeling in an adaptive active attenuation system. *J. Acoust. Soc. Am.*, 85(2):797–802, 1989.

[6] L. J. Eriksson. Development of the filtered–u algorithm for active noise control. *J. Acoust. Soc. Am.*, 89(1):257–265, 1991.

[7] L.J. Eriksson. Active sound and vibration control: A technology in transition. *Noise Control Eng. J.*, 44(1):1–9, 1996.

[8] S.M. Kuo and D.R. Morgan. Active noise control: A tutorial review. *Proceedings of the IEEE*, 87(6):943–973, 1999.

[9] B. Widrow and S. D. Stearns. *Adaptive Signal Processing.* Prentice Hall, 1985.

[10] S. Haykin. *Adaptive Filter Theory.* Prentice Hall, 1991.

[11] G. C. Goodwin and K.S. Sin. *Adaptive Filtering, Prediction and Control.* Prentice Hall, 1984.

[12] Karl J. Åström and Björn Wittenmark. *Adaptive Control.* Addison-Wesley, 1995.

[13] K. Berberidis G.O. Glentis and S. Theodoridis. Efficient least squares adaptive algorithms for fir transversal filtering. *IEEE Signal Processing Magazine*, July:13–41, 1999.

[14] S. Koshigoe, T. Komatsuzaki, and V. Yang. Active control of combustion instabilities with on–line system identification. In *34th. Aerospace Sciences Meeting & Exhibit, Reno, Jan. 15–18.* AIAA Paper 96-0759, 1996.

[15] M. Mettenleiter. *Contrôle adaptatif des instabilités aéroacoustiques. Application aux systèmes de propulsion.* PhD thesis, Ecole Centrale Paris, 2000.

[16] M. Mettenleiter, E. Haile, and S. Candel. Adaptive control of aeroacoustic instabilities. *J. Sound Vib.* (in press), 2000.

[17] M. Mettenleiter, E. Haile, and S. Candel. Adaptive control of aeroacoustic instabilities with application to propulsion systems. In *RTO Symposium on "Gas Turbine Engine Combustion, Emission and Alternative Fuels", Lisbon, Portugal, 12–16 october*, 1998. RTO–MP–14 AC/323(AVT)TP/10.

[18] P. Planquart J. Anthoine and D. Olivari. Cold flow investigation of the flow acoustic coupling in solid propellant boosters. In 36^{th} *Aerospace Sciences Meeting.* AIAA, 1998. Paper 98-0475.

[19] J. Anthoine and D. Olivari. Cold flow simulation of vortex induced oscillations in a model of solid propellant boosters. AIAA Paper 99–1826, 1999.

[20] J. Anthoine, M. Mettenleiter, O. Repellin, J.-M. Buchlin, and S. Candel. Influence of adaptive control on vortex driven instabilities in a scaled model of solid propellant motors. *J. Fluid Mechanics* (submitted), 2000.

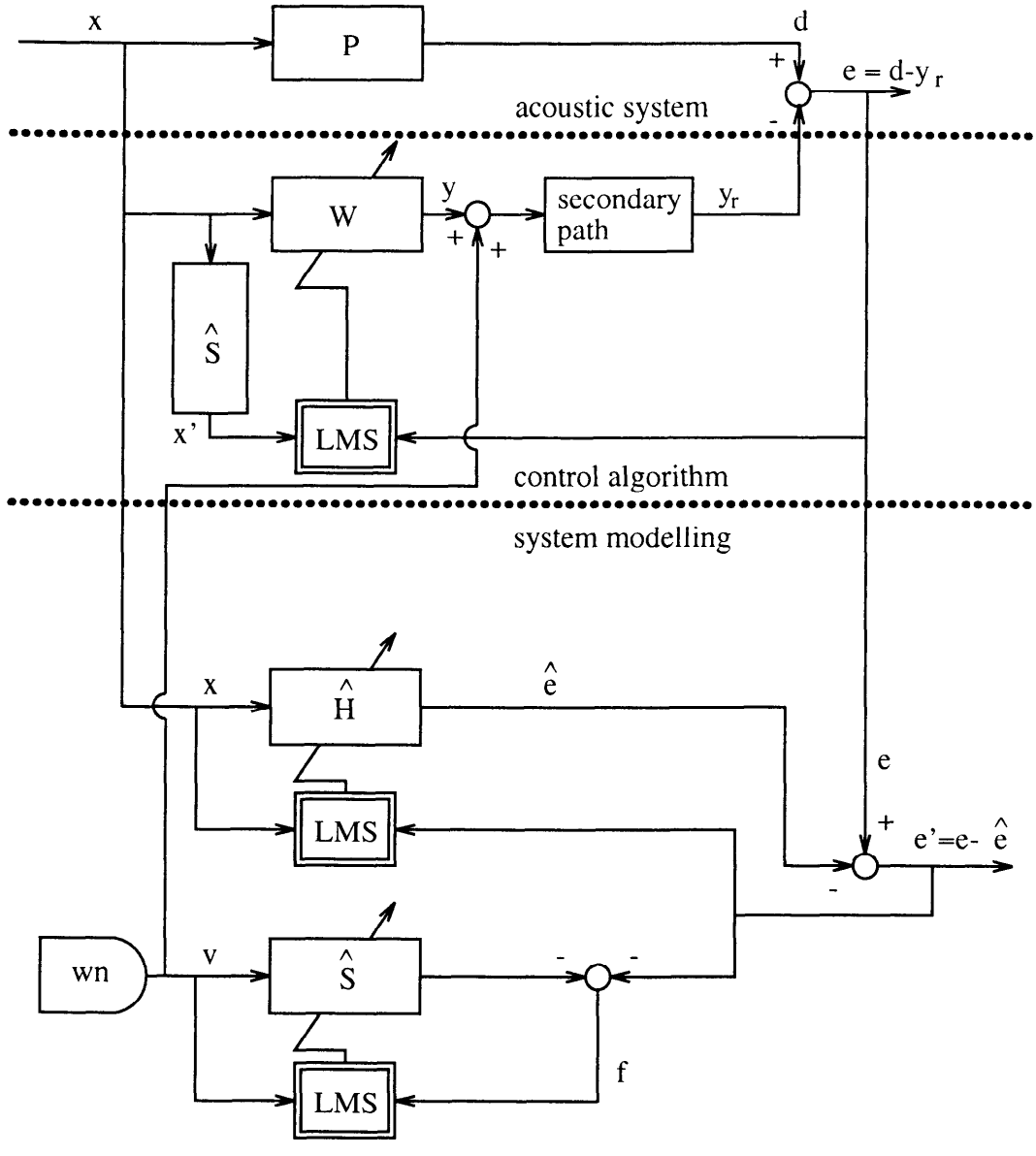


Figure 1: Self–adaptive anti–noise algorithm using a white noise signal for the identification procedure and two sensors.

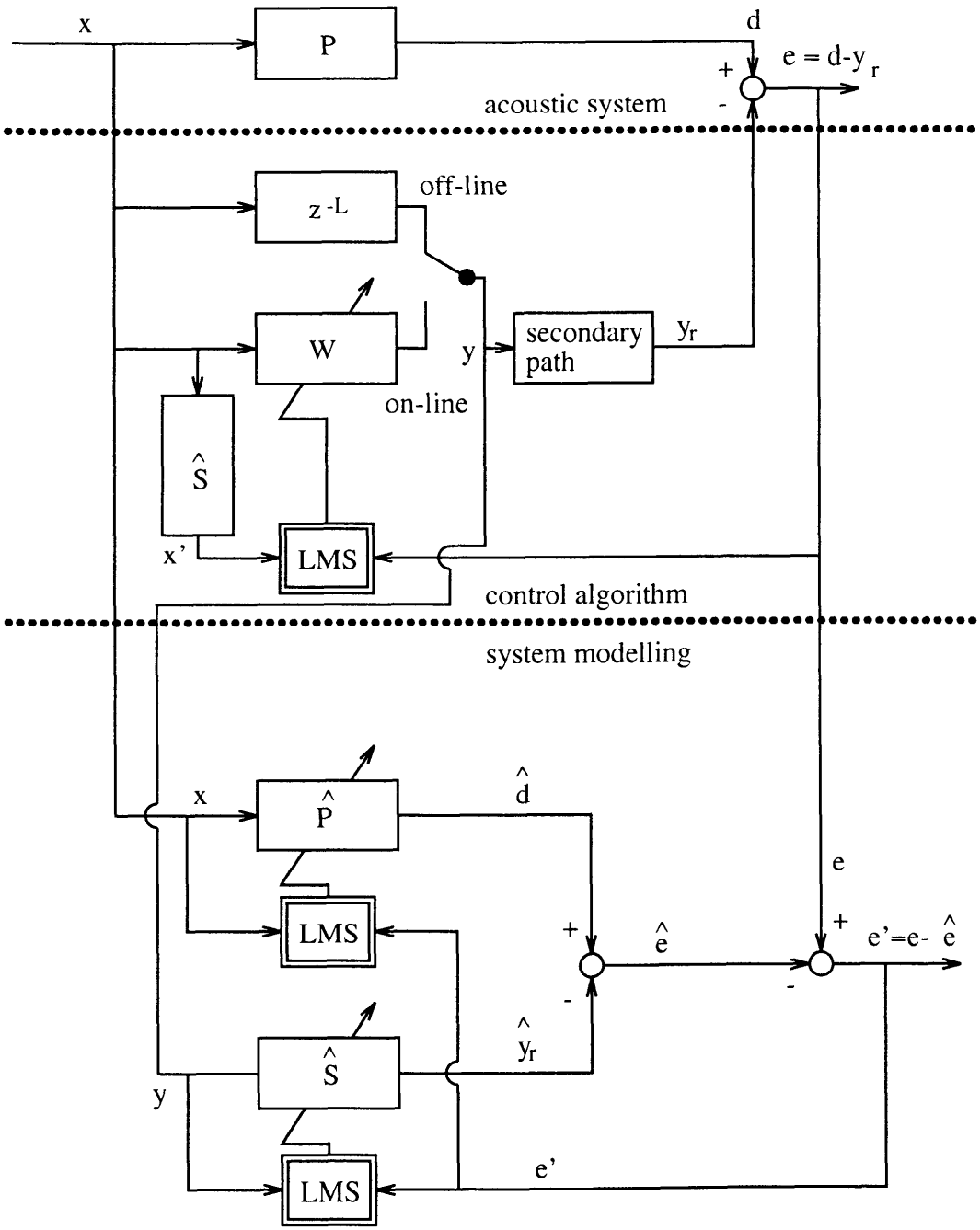


Figure 2: Self–adaptive overal modelling anti–noise algorithm using two sensors.

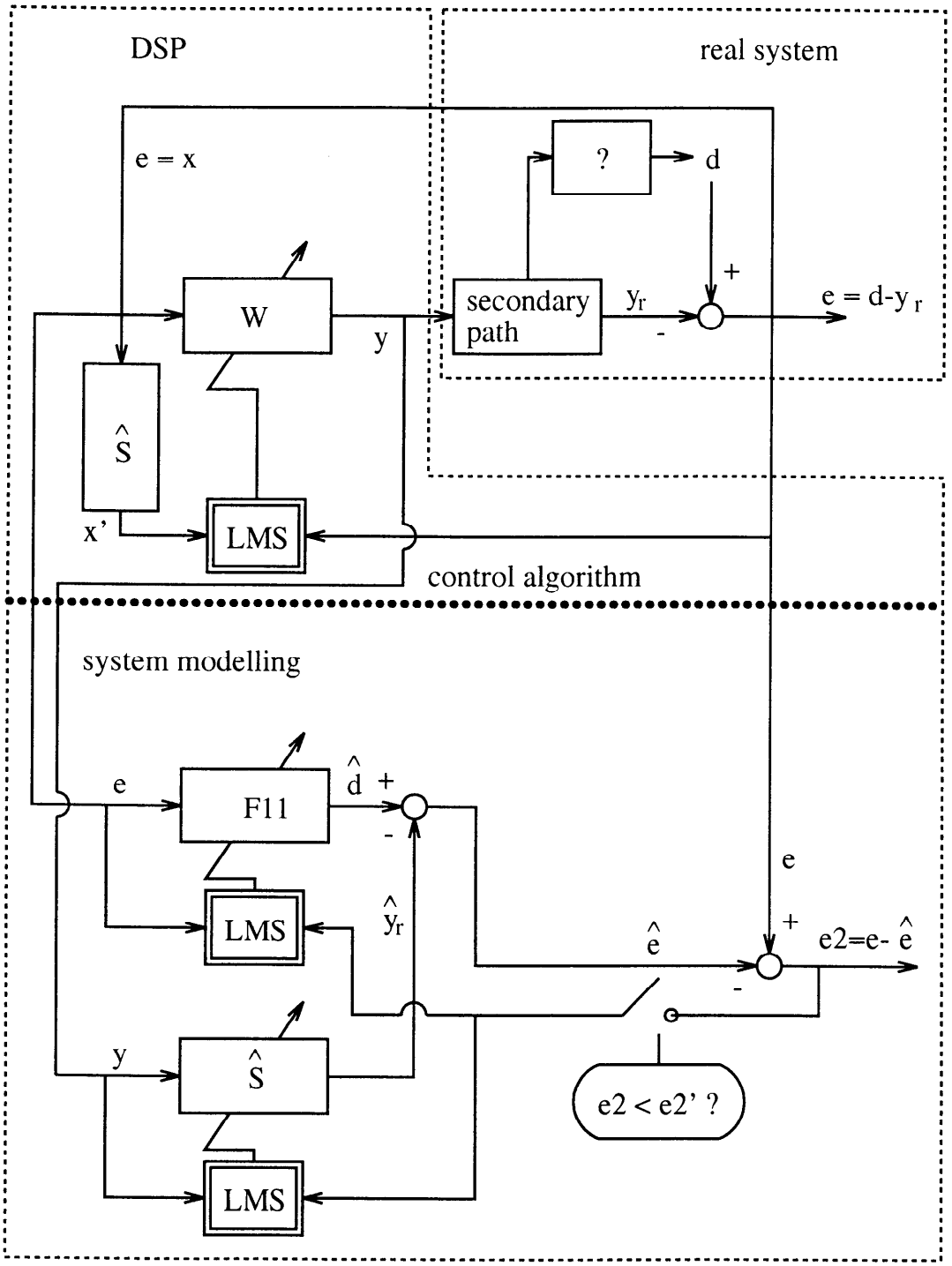


Figure 3: Self-adaptive overall modelling noise source control algorithm using one sensor.

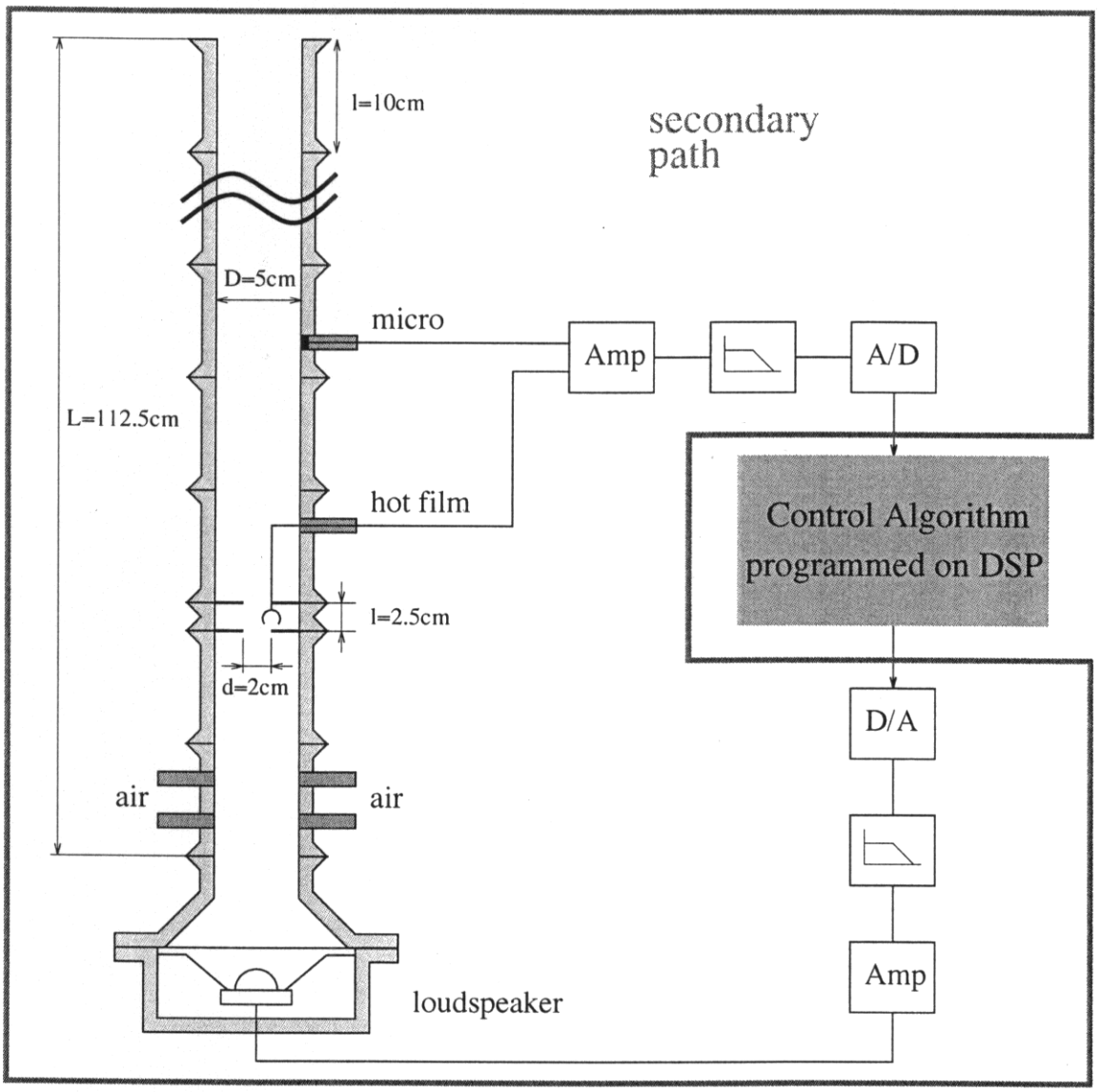


Figure 4: Experimental setup CAPS. The pressure signal is measured by a microphone, the flow velocity by a hot wire. The loudspeaker serves as actuator during control. The secondary path is given by the transfer function between the output of the control algorithm and its own input (inside the thick line).

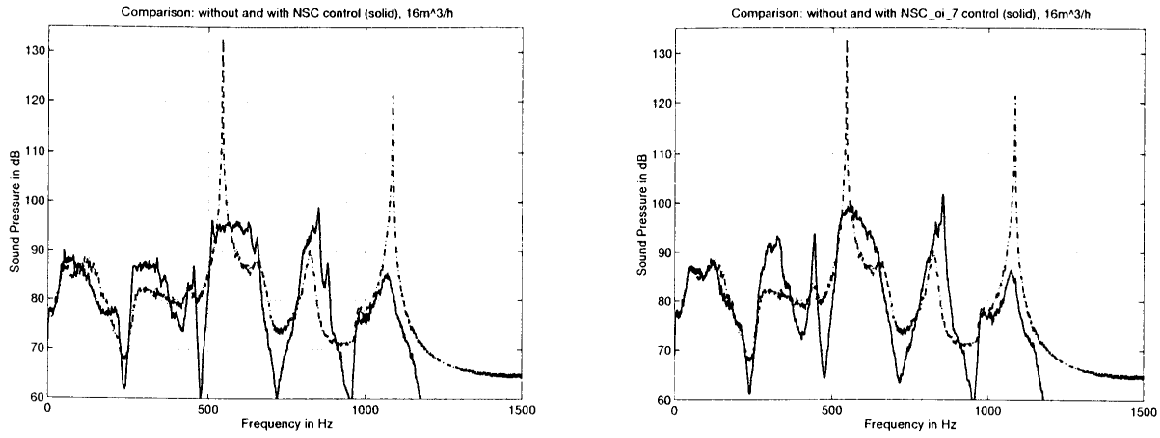


Figure 5: Pressure spectra (----) without and (——) with control. Volume flow rate of 16 m^3/h. On the left: reference algorithm, on the right: SAC scheme.

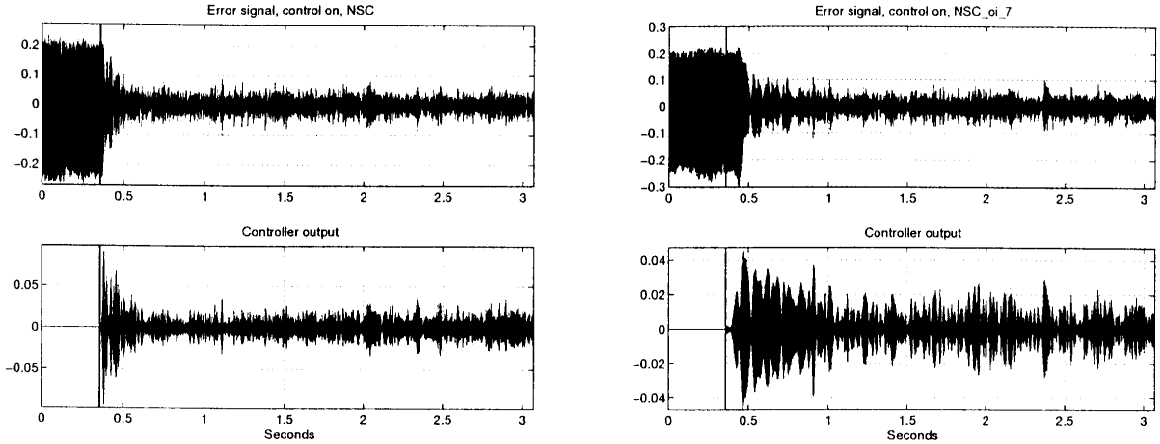


Figure 6: Error sensor (top) and control output (bottom) for a volume flow rate of 16 m^3/h. On the left: reference algorithm, on the right: SAC scheme. Switch on of the control (vertical line).

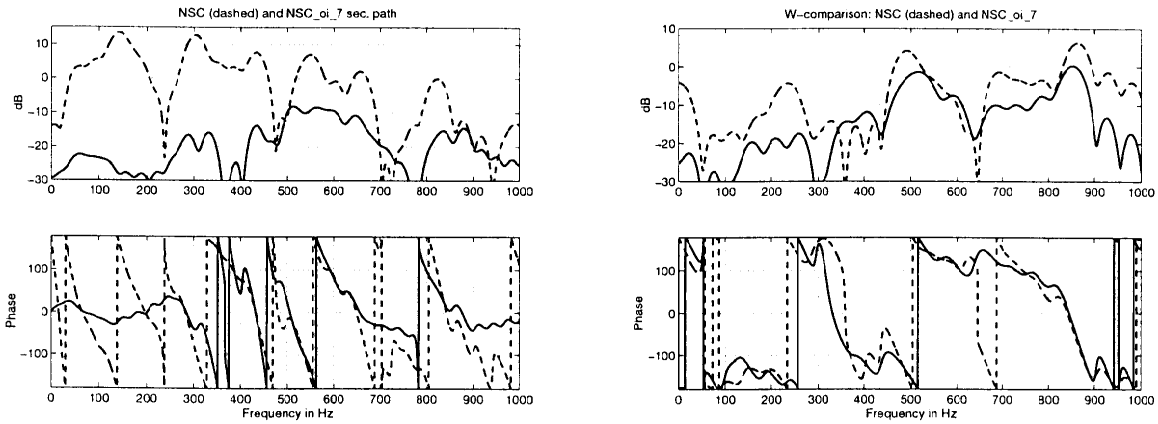


Figure 7: Comparison of the filter tranfer functions. On the left: $\hat{\boldsymbol{S}}$, on the right: $\boldsymbol{W}$ for the reference algorithm (----) and the SAC scheme (——). The amplitudes are on the top figures, the phases on the bottom.

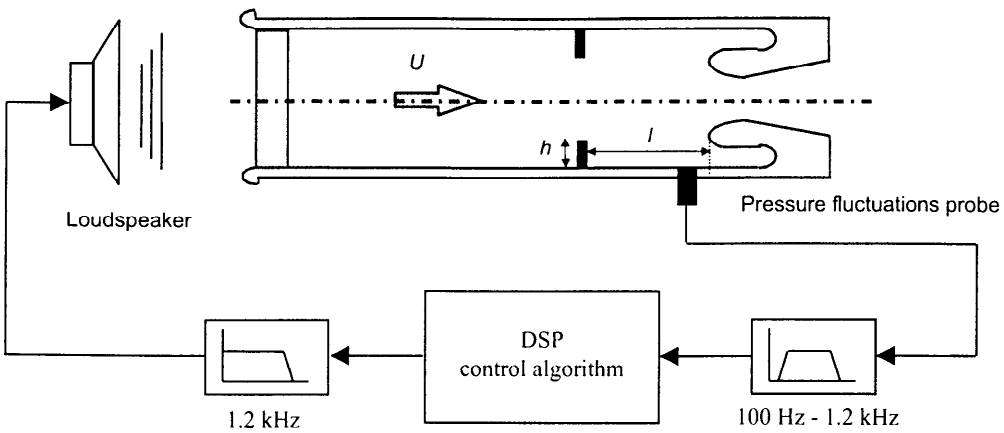


Figure 8: Sketch of the PLEXI facility and the control system.

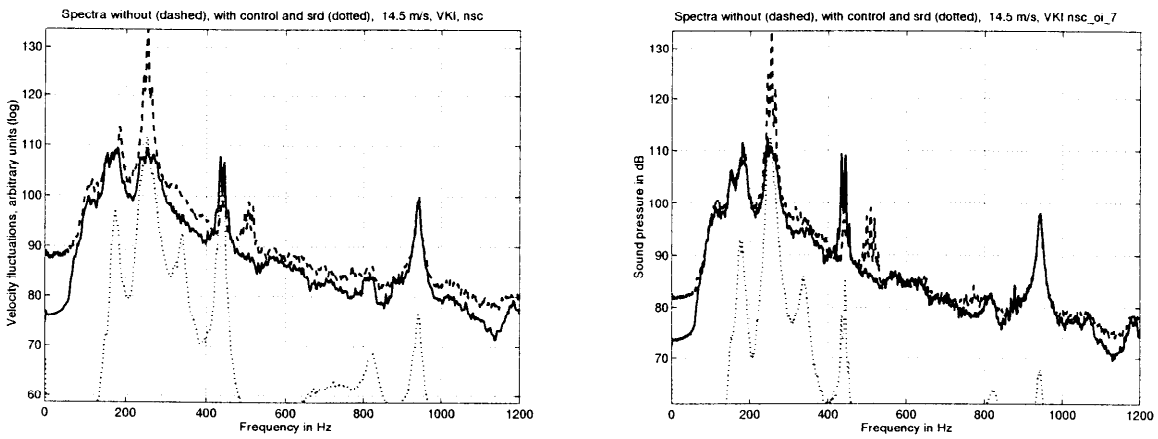


Figure 9: Pressure spectra without (----) and with (——) control. The flow speed is 14.5 m/s. On the left: the reference algorithm, on the right: the SAC scheme.

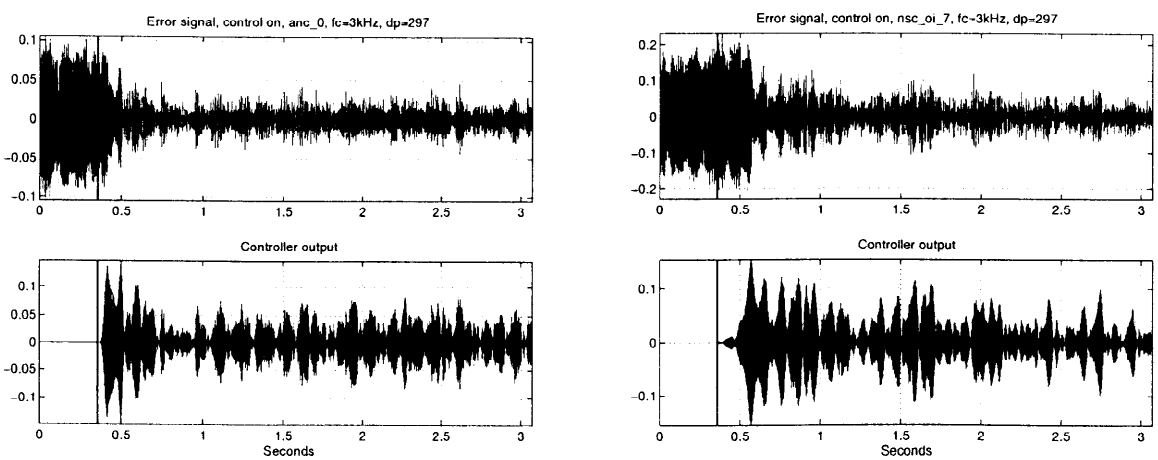


Figure 10: Error signal (top) and controller output (bottom) for a flow speed of 14.5 m/s. On the left: the reference algorithm, on the right: the SAC scheme. Vertical line: switch on of the controller.

PAPER -26, M. Mettenleiter

Question (A. Annaswamy, USA)

Regarding divergence of the coefficients of S: is adding a "leak" term sufficient? Do you understand enough about the "leak" so that you know when to add the "leak" terms?

Reply

The leak is a standard technique in adaptive controllers. We have devised a special technique to tune this procedure (see the paper for more information)

Question (S. Evesque, UK)

Did you try to vary the self-excited mode in the experiment while active control with in-line system identification was applied and, if yes, how well did the controller perform? Same question with off-line system identification. Also, how do you compare performance of FIR and IIR filters in your experiments?

Reply

Varying the self-excited mode was already tested in our initial work on adaptive control of the instability (Billard *et al.*, 1992). It has been tested with the present controller for off-line identification and it works because in this case the secondary path does not change too much. It also works well with the online system. If the secondary path changes, the online algorithm performs better.

Regarding FIR versus IIR filters, it was possible to represent the necessary impulse responses with an FIR filter without too many coefficients. There is no improvement with an IIR system.

Question (F. E. C. Culick, USA)

Do you have any results for flow visualization to show what's happening? What do you think is the origin (mechanisms) of the transfer of energy from vortices to the acoustic pressure field?

Reply

We have carried out experiments at the VKI in which adaptive control was used to suppress oscillations in a configuration simulating the back end of a rocket motor. In these experiments, the flow field was characterized with PIV and the vortices were detected. A statistical analysis of these structures (with and without oscillation) was carried out and this is reported in an article submitted to JFM.

The origin of the transfer of energy is probably (based on experiments at VKI), the periodic impingement of the vortices on the downstream obstacle or nozzle lips.

This page has been deliberately left blank

Page intentionnellement blanche

Active Feedback Control of Combustor Dynamics with Time Delay and Noise

C. Seywert **G. Isella** **F.E.C. Culick**

California Institute of Technology
1200 East California Boulevard, MS 205-45
Pasadena, CA 91125, USA

Abstract

Longitudinal pressure oscillations in a combustion chamber are studied theoretically by means of a low order model obtained by systematic reduction from a complete representation. The formulation is based on the derivation of a generalized wave equation that accommodates the effects of mean flow, combustion, noise and control action. By using spatial averaging, the equations describing the dynamics of the chamber are reduced to a set of coupled ordinary differential equations. The form of the resulting equations is particularly convenient for model reduction and for introducing feedback control terms, while retaining all physical processes.

Active feedback control of longitudinal instabilities is then introduced by using the same formulation, rewritten in state-space form. The broad objective of control simulations covered here is to investigate in a unified fashion various aspects of the problem. These include the influences of noise, parameter uncertainties, unmodeled modes and time-delay.

A criterion is derived that guarantees the stability of the controlled closed-loop system in the presence of those quantities. The particular controller used here is based on a standard LQR design, but any design technique can be used as long as the stability criterion is fulfilled.

1 Introduction

The need to extend the operating range of combustion systems due to more stringent performance demands (lower emission levels, reduced vibration tolerances,...) has led to increased research activity on control of combustion instabilities. Traditionally these pressure oscillations have been dealt with through passive control techniques. However since these techniques are inadequate under varying operating conditions, active control methods have become more widespread. McManus, Poinsot and Candel (1993) gives a review of the different approaches taken nearly a decade ago. Considerable progress has been made since that time, particularly with investigations of the suitability of known control strategies applied to combustor dynamics.

Combustion systems are highly complex and are naturally represented by infinite-dimensional models. So as to reduce the order of the controllers several researchers have made use of an approximate finite-dimensional representation of the flowfield (Culick 1989) as the basis for their controller design (Hathout, Annaswamy, Fleifil and Ghoniem 1998, Dowling 1997, Haddad, Leonessa, Corrado and Kapila 1997, Koshigoe, Komatsuzaki and Yang 1999, Hong, Yang and Ray 2000). Since any model is prone to uncertainties in the parameters, the controller needs to be robust to changes in those parameters. Haddad et al. (1997) achieves this

Paper presented at the RTO AVT Symposium on "Active Control Technology for Enhanced Performance Operational Capabilities of Military Aircraft, Land Vehicles and Sea Vehicles", held in Braunschweig, Germany, 8-11 May 2000, and published in RTO MP-051.

robustness using a Lyapunov function framework while Koshigoe et al. (1999) achieves robust performance by using adaptive control. Other authors (Hong et al. 2000) use an H_∞ technique to reach the same goal.

The typical characteristics of combustors make designing a controller a challenging task. The model used in the design is normally a considerably reduced representation of the real system; this causes large uncertainties in the parameters. In addition to that, there are very intense internal noise sources due to gasdynamics and combustion and significant time delays that reduce the stability margin. Scaling is also an issue: most of the experiments are conducted in laboratory-scale combustors. Nonlinear processes, especially in the flame models, are not completely understood, and the models normally include a limited representation of those processes. In the case of laboratory combustors, it is possible to ignore the nonlinearities and design a controller on the system linearized around the 'unstable' equilibrium point that the control aims to reach. In the case of classical controllers, they scale linearly with dimensions, but, at this point, it is not clear how the nonlinear processes in the combustor scale: they could become a major issue in large combustors. Moreover, a clearer understanding of nonlinearities is required for the design of nonlinear controllers, that have the potential of being much more efficient in terms of the ratio of the energy going into the control effort versus the total energy released into the system. Instabilities in combustion chambers typically manifest themselves as pressure oscillations growing to limit cycles. Experiments (Isella, Seywert, Culick and Zukoski 1997) show that in some combustors there is a subcritical bifurcation leading to the instability: in this case nonlinear control might be more appropriate, and results from linear simulations could be misleading, especially in the vicinity of the bifurcation point. For the case of heat release depending on velocity fluctuation, Wang (2000), through linear analysis, finds conditions on the heat release function that determine if the bifurcation is subcritical or supercritical. In particular, he has shown that, if the heat release function presents a saturation level, the amplitude of the resulting limit cycle, away from the bifurcation point, is independent of the actual shape of the heat release function. This result plays an important role in simplifying the combustion models for control simulations. If the conditions for supercriticality are satisfied, using the appropriate value for the saturation of the heat release function is enough to capture the correct dynamical behavior of the combustor.

While several of the studies cited include sensor noise and/or parameter variations as part of the system, none of them makes a clear distinction between those uncertainties, the intrinsic noise sources of the system (additive and multiplicative), and the unmodeled dynamics. In the following we will describe how each one of these effects can be included in the control design process. Time-delay, often overlooked in the consideration of combustion systems, can be introduced in the control design as a further uncertainty by using the same framework. A different method, based on an external compensation network, is also presented.

The controller is designed and tested on the model of a small cylindrical combustor with an instability in the first longitudinal mode. This particular model has been widely used in literature as a test case for the analysis (Culick and Yang 1992, Yang, Sinha and Fung 1992, Haddad et al. 1997); even if this might not be realistic in the specific value of the parameters, the model presents a dynamical behavior representative of a combustion chamber, and serves well as a test case. The methods described are obviously not limited to this specific case, and can be applied in general.

As shown below the noise sources arise from nonlinear fluid mechanics and as such form an integral part of the system; previous studies have only taken into account external noise sources (such as noisy sensors/actuators). Recently we have shown how these intrinsic noise sources affect the system response and how they can be used to identify the linear parameters of a stable system (Seywert and Culick 2000).

2 Combustion Instability Model

The fluid dynamical equations (continuity, momentum and energy) governing the flow in the combustion chamber can be combined to yield a nonlinear wave equation for the pressure which in turn, after applying 'spatial averaging' leads to a system of coupled oscillator equations. This system can be truncated to a finite number of modes to get a low order representation of the combustion chamber. This procedure has been described elsewhere in full detail (Culick 1976, Culick and Yang 1992); thus only a brief summary is given here.

We begin with the inhomogeneous wave equation and its boundary condition for the pressure fluctuation:

$$\begin{aligned} \nabla^2 p' - \frac{1}{\bar{a}^2}\frac{\partial^2 p'}{\partial t^2} &= h \\ \hat{n}\cdot\nabla p' &= -f \end{aligned} \tag{1}$$

The functions h and f contain *all* relevant physical processes including motion of the boundary, but whereas the contributions from gasdynamics are known explicitly every other process included requires modeling, a separate matter. Explicit forms for h and f are given in (Culick and Yang 1992) and need not be repeated here.

Next 'spatial averaging' is applied, the idea being that any unsteady disturbance in a combustion chamber can be synthesized of an infinite set of basis functions, chosen normally to be acoustic modes. For a rocket motor having a chocked exhaust nozzle, the modes are those for a volume enclosed by a rigid boundary having the same shape as the internal surface of the motor, but with no combustion and flow.

Hence we write the familiar series representation of the pressure field,

$$p'(\vec{x};t) = \bar{p}\sum_{j=1}^{\infty}\eta_j(t)\psi_j(\vec{x}) \tag{2}$$

where $\eta_j(t)$ is the time-dependent amplitude of the j^{th} mode. The spatial distribution or mode shape $\psi_j(\vec{x})$ is calculated as the solution to

$$\begin{aligned} \nabla^2\psi_j + k_j^2\psi_j &= 0 \\ \hat{n}\cdot\nabla\psi_j &= 0 \end{aligned} \tag{3}$$

and $k_j = \omega_j/\bar{a}$ is the wavenumber, $\bar{a}$ is the mean speed of sound and ω_j is the natural frequency of the mode.

Substitution of (2) in the left-hand side of (1a), multiplication of the equation by ψ_n and integration over the volume (i.e. spatial averaging with the weighting function ψ_n) leads eventually to the system of oscillator equations,

$$\frac{d^2\eta_n}{dt^2} + \omega_n^2\eta_n = F_n \tag{4}$$

$$\text{where} \qquad F_n = -\frac{\bar{a}^2}{\bar{p}E_n^2}\left\{\int\psi_n h dV + \oint\psi_n f dS\right\} \qquad \text{and} \qquad E_n^2 = \int\psi_n^2 dV \tag{5}$$

The central idea motivating the structure of the analysis is that combustion instabilities are dominated by acoustic waves. Hence the pressure field has been represented by the expansion (2) with p' identified as the acoustic pressure. However, following a principle discussed by Chu and Kovasznay (1956), small disturbances are in general made up of three kinds of waves: acoustic, entropy and vorticity waves. Unlike previous analyses in which only the organized oscillatory acoustic field was accounted for all three wave kinds

were retained in the analysis given by Burnley (1996) and Burnley and Culick (1999). The extra waves give rise to stochastic terms in the equation which we choose to retain here.

In lowest approximation (small amplitude, uniform mean flow) the three types of waves propagate independently and hence we can write:

$$\begin{aligned} p' &= p'_a \\ \vec{\Omega}' &= \vec{\Omega}'_\Omega \\ s' &= s'_s \\ \vec{u}' &= \vec{u}'_a + \vec{u}'_\Omega + \vec{u}'_s \end{aligned} \tag{6}$$

The 'forcing function' F_n in equation (5) is a nonlinear function of p' and $\vec{u}'$. In previous applications of spatial averaging (Culick and Yang (1992), Culick (1994) and references cited there) the velocity fluctuation $\vec{u}'$ is related to p' through the classical linear acoustics equation:

$$\vec{u}'_a = \sum_{j=1}^{\infty} \frac{\dot{\eta}_j(t)}{\bar{\gamma} k_j^2} \nabla \psi_j(\vec{r}) \tag{7}$$

With entropy and vorticity waves present, the terms $\vec{u}'_\Omega$ and $\vec{u}'_s$ make new contributions to F_n. Those contributions can be written explicitly as functions of $\vec{u}'_\Omega$ and $\vec{u}'_s$ (Burnley and Culick 1999) but since no model for $\vec{u}'_\Omega$ or $\vec{u}'_s$ exists, we lump them together as stochastic sources. The result of this reasoning is the following system of acoustic equations that are the system used in previous work (Culick 1995, Culick and Yang 1992, Culick 1994) with the additional source terms representing stochastic or noise sources:

$$\ddot{\eta}_n + \omega_n^2 \eta_n = -\sum_{l=1}^{\infty} [D_{nl}\dot{\eta}_l + E_{nl}\eta_l] + \sum_{i=1}^{\infty} [\xi^\nu_{ni}(t)\dot{\eta}_i + \xi_{ni}(t)\eta_i] + \Xi_n(t) \tag{8}$$

Here we have retained only the linear terms in the acoustic amplitudes. Since we are going to design a controller to eliminate the pressure oscillations (i.e. drive all acoustic amplitudes to zero) this is equivalent to linearizing the nonlinear system around the unstable equilibrium point. Note that the linear terms include all linear processes, including linear combustion dynamics. The linear combustion part has in this formulation been lumped together with the linear gasdynamics into the coefficients E_{nl} and D_{nl}; in fact it is the linear combustion that makes the system unstable to begin with. As noted by (Wang 2000), this is a valid approximation as long as the system presents a subcritical bifurcation at the point of instability. Note also that while the higher order acoustic terms have been neglected the nonlinear dynamics due to the vorticity and entropy waves are included in the noise terms ξ^ν, ξ, and Ξ. The combustor is linearly stable if and only if all modes are linearly stable.

For control applications it is advantageous to reformulate this set of equations in state-space form with state $x = [\eta_1 \dots \eta_N \dot{\eta}_1 \dots \dot{\eta}_N]^T$, control input u, and output $y = p'/\bar{p}$. The following definitions are needed:

$$A = \begin{bmatrix} 0 & 1 \\ -\Omega^2 - E_{nl} & -D_{nl} \end{bmatrix} \qquad B = \frac{\bar{a}^2}{\bar{p}} \begin{bmatrix} 0 \\ \psi_n(x_{actuator})/E_n^2 \end{bmatrix} \qquad C = [\psi_1(x_{sensor}) \dots \psi_N(x_{sensor})] \tag{9}$$

With this notation, equation (8) – without the noise terms – becomes equivalent to

$$\begin{aligned} \dot{x} &= Ax + Bu \\ y &= Cx \end{aligned} \tag{10}$$

3 Control Theory

General Considerations

Even before the development of models including combustor dynamics and feedback control, experimental application of feedback control of combustion instabilities was successfully tested on small systems (mainly using loudspeakers as actuators). Those laboratory demonstrations report examples in which the amplitudes of limit cycles in linearly unstable combustors have been significantly reduced, sometimes even to vanishingly small values (for example: Poinsot, Bourienne, Candel and Esposito (1987), Gulati and Mani (1992)). In most cases, the 'practical' controller was a simple proportional feedback or a variation of a *PID* controller. One might wonder why that simple approach works or, conversely, ask why we need more sophisticated control methods. From a general viewpoint, experiments show that an unstable combustion chamber is a system exhibiting a linear instability (rapidly) growing to a limit cycle (defined by the non-linearities) that typically shows a marked predominant frequency. In terms of dynamical systems, the combustor is characterized by two unstable complex-conjugate poles and then a series of stable poles with relatively large damping. Provided that the combustor is observable and controllable, for this kind of system, a proportional feedback or a *PID* controller can be successfully tuned to obtain a stable feedback loop (Franklin, Powell and Emami-Naeini (1995)). Regarding the issue of controllability (and observability) of the system, for the purpose of this argument, we will say that controllability has been proved in practice by the success of the experiments cited. A detailed analysis of this point would allow optimization of the position of actuators and sensors, but that is out of the scope of the present discussion. The need for more sophisticated control methods derives mainly from two aspects: first one might want to impose performance specifications on the controller, for example on the maximum control action, or on the noise or disturbance rejection. Second, combustion systems show a high degree of uncertainty and variability (Lieuwen and Zinn 2000), and a controller 'tuned' on a particular operating point does not guarantee a reliable performance. Modern control design methods allow for the introduction of this kind of consideration during the synthesis of the controller.

All the considerations above and the design method presented in the following section are based on a linear model of the combustor. On the other hand, the real system is manifestly nonlinear: the main indication of that is the fact that the pressure oscillations in the combustion chamber rapidly reach a limit cycle. A complete understanding of the dynamics of the combustor would allow tracing the source of the nonlinear behavior observed in the experiments (limit cycles, hysteresis, as in, for example, Isella et al. (1997) and Lieuwen and Zinn (2000)) to its origin: nonlinear gasdynamics or nonlinear combustion. In that case nonlinearities in the system could be exploited by an 'ad hoc' form of (nonlinear) control to overcome the main limitations of linear control: requirement of a relatively high control effort and actuation frequency at the same frequency of the instability. Since such a complete model is not available, we decided to limit the analysis to the linear case. Note that the linear model of the combustion chamber presented in the previous section is actually a linearization of the full model around the operating point. Since the main purpose here is to keep the system 'stable', i.e. as close as possible to the linearized equilibrium point, the linear model and simulation is a valid and realistic approximation to the real case, provided that the nonlinearities do not give rise to a subcritical bifurcation (Wang 2000). Note that nonlinearities have the effect of limiting the amplitude of the oscillations: hence the linear model is in this sense a 'conservative' approach to the problem (for example, in terms of required control action, we will find an upper limit). In short, within the present approach, nonlinearities can actually be neglected, except as a formal vehicle for rigorously introducing noise sources. As a consequence, we will not be able to capture the effects of any instability mechanism different from the linear growth and phase shifting included in the model presented above. On the other hand, the present approach allows for a clear distinction of the effects of uncertainties, intrinsic noise sources, external noise sources, unmodeled dynamics and time-delay.

Robustness

The controller strategy proposed in this section is based on results described in Chou, Chen and Chao (1998) and Biswas (1998). It allows to treat parameter uncertainty (due to uncertainties in the modeling or system identification process), multiplicative noise (in this case intrinsic to the system, arising from vorticity and entropy waves) and residual dynamics (neglected in the control design in order to achieve a low order controller) in a unified way.

Including parameter uncertainty in the controller design

Chou et al. (1998) considers the following system:

$$\begin{aligned} \dot{x}_c(t) &= [A_c + \Delta A_c(t)]x_c(t) + A_{cr}x_r(t) + [B_c + \Delta B_c(t)]u(t) \\ \dot{x}_r(t) &= A_{rc}x_c(t) + A_r x_r(t) + B_r u(t) \\ y &= [C_c + \Delta C_c(t)]x_c + C_r x_r \end{aligned} \tag{11}$$

In this description the system has been split into two parts: the controlled dynamics (state x_c) which will be used in the design of the controller and the residual dynamics (state x_r) which are neglected in that design. The reasoning behind this splitting is that we want to achieve a controller that is as simple as possible. This desire leads to a need for a low order model of the system; the controlled dynamics describe that low order system (which at the minimum needs to include all unstable modes) whereas the residual modes describe those parts of the original system that the designer chooses to disregard (the higher acoustic modes which are strongly attenuated in the combustion chamber).

The uncertain parameters of the controlled system are assumed to be bounded ($|\ |$ denotes the modulus matrix):

$$|\Delta A_c(t)| \le Q^{(A)}, \qquad |\Delta B_c(t)| \le Q^{(B)}, \qquad \text{and} \qquad |\Delta C_c(t)| \le Q^{(C)} \tag{12}$$

$Q^{(A)}$, $Q^{(B)}$ and $Q^{(C)}$ are nonnegative constant matrices that describe the highly structured uncertainty of the parameters.

Now consider a controller based on a Kalman filter (used to reconstruct the state from the measured output, i.e. the pressure signal from the sensor) with estimator gain L and feedback gain K:

$$\begin{aligned} \dot{\hat{x}}_c(t) &= A_c\hat{x}_c(t) + B_c u(t) + L[y(t) - C_c\hat{x}_x(t)] \\ u(t) &= -K\hat{x}_c(t) \end{aligned} \tag{13}$$

Then the controlled closed-loop system is described by H_c and its interaction with the residual system is governed by H_{cr} and H_{rc} (note that H_{cr} and H_{rc} have been changed to allow for the presence of A_{cr} and A_{rc} when compared to Chou et al. (1998)).

$$H_c = \begin{bmatrix} A_c - B_cK & -B_cK \\ 0 & A_c - LC_c \end{bmatrix} \qquad H_{cr} = \begin{bmatrix} A_{cr} \\ LC_r - A_{cr} \end{bmatrix} \qquad H_{rc} = [A_{rc} - B_rK \quad -B_rK] \tag{14}$$

Define the matrices G_c and G_r as follows:

$$G_r \ge [\ \sup |g_{ik}^{(r)}(j\omega)|\ ] \qquad \text{and} \qquad G_c = [\ \sup |g_{ik}^{(c)}(j\omega)|\ ] \tag{15}$$

Where $\omega > 0$ and $g_{ik}^{(r)}$ and $g_{ik}^{(c)}$ are the ikth elements of $(j\omega I - A_r)^{-1}$, respectively $(j\omega I - H_c)^{-1}$. Also define the uncertainty matrix U as

$$U = \begin{bmatrix} Q^{(A)} + Q^{(B)}|K| & Q^{(B)}|K| \\ Q^{(A)} + Q^{(A)}|K| + |L|Q^{(C)} & Q^{(B)}|K| \end{bmatrix} \tag{16}$$

According to results given in Chou et al. (1998) (with the trivial extension to include A_{cr} and A_{rc}), the closed-loop system will be stable if the matrices H_c and A_r are stable matrices and the following inequality

$$\rho[\, G_c U \,+\, G_c\, |H_{cr}|\, G_r\, |H_{rc}|\,] < 1 \tag{17}$$

is satisfied (here $\rho[\,]$ denotes the spectral radius).

Including multiplicative noise in the controller design

Now consider the system below, as in (Biswas 1998):

$$\begin{aligned} \dot{x}(t) &= [A + \xi^{(A)}(t)]x(t) + [B + \xi^{(B)}(t)]u(t) \\ y &= [C_c + \xi^{(C)}(t)]x \end{aligned} \tag{18}$$

Here $\xi^{(A)}$, $\xi^{(B)}$,and $\xi^{(C)}$ are random time functions. Lacking precise information about their nature (as in many practical applications) they are assumed to be described by Gaussian white noise processes with zero mean and can be characterized through the quantities $\Xi^{(AA)}$, $\Xi^{(BB)}$, $\Xi^{(AB)}$, and $\Xi^{(CC)}$ where ($E[\,]$ denotes the expected value)

$$\begin{aligned} \Xi_{ij}^{(AA)} &= \sum_{k=1}^{N} E[\xi_{ki}^{(A)}(t)\xi_{kj}^{(A)}(t)] \qquad 1 \le i,j, \le n \\ \Xi_{ij}^{(BB)} &= \sum_{k=1}^{N} E[\xi_{ki}^{(B)}(t)\xi_{kj}^{(B)}(t)] \qquad 1 \le i,j, \le N_u \\ \Xi_{ij}^{(AB)} &= \sum_{k=1}^{N} E[\xi_{ki}^{(A)}(t)\xi_{kj}^{(B)}(t)] \qquad 1 \le i \le N, 1 \le j \le N_u \\ \Xi_{ij}^{(CC)} &= \sum_{k=1}^{N} E[\xi_{ki}^{(C)}(t)\xi_{kj}^{(C)}(t)] \qquad 1 \le i,j, \le N_y \end{aligned} \tag{19}$$

As before a controller with estimator gain L and feedback gain K is considered.

Following the approach of Biswas (1998) (expanded to include $\Xi^{(CC)}$ and modified by considering the process $V(t) = \frac{1}{2}||x(t)|| + \frac{1}{2}||\hat{x}(t) - x(t)||$) we conclude that the closed-loop system is exponentially mean square stable if there exist K and L such that the expected closed-loop matrix given by

$$H = \begin{bmatrix} A+BK+\Xi^{(AA)}+\Xi^{(AB)}K+(\Xi^{(AB)}K)^T+K^T\Xi^{(BB)}K+L^T\Xi^{(CC)}L & BK+\Xi^{(AB)}K+K^T\Xi^{(BB)}K \\ (\Xi^{(AB)}K)^T+K^T\Xi^{(BB)}K & A-LC+K^T\Xi^{(BB)}K \end{bmatrix} \tag{20}$$

is negative definite.

Combining both approaches and designing a controller

We can combine both approaches (i.e account for bounded parameter uncertainty and random Gaussian noise perturbations) by including the Ξ-terms in equation (20) in the uncertainty of the closed-loop matrix H_c in equation (3). Thus by redefining the uncertainty matrix U,

$$U=\begin{bmatrix} Q^{(A)}+Q^{(B)}|K|+\Xi^{(AA)}+\Xi^{(AB)}|K|+(\Xi^{(AB)}|K|)^T+|K|^T\Xi^{(BB)}|K|+|L|^T\Xi^{(CC)}|L| & Q^{(B)}|K|+\Xi^{(AB)}|K|+|K|^T\Xi^{(BB)}|K| \\ Q^{(A)}+Q^{(A)}|K|+|L|Q^{(C)}+(\Xi^{(AB)}|K|)^T+|K|^T\Xi^{(BB)}|K| & Q^{(B)}|K|+|K|^T\Xi^{(BB)}|K| \end{bmatrix}$$

and fulfilling equation (17), robust stability can still be guaranteed.

Up to this point we have derived conditions that L and K need to fulfill without specifying how to design them. Note that the controller is to be designed for the nominal, undisturbed plant; we can then check equation (17) to make sure it is also effective on the perturbed system - or we can use that equation to see how much noise or parameter variation our controller can handle.

The design of the controller depends of course on the performance we wish to achieve. Any method can be used: Biswas (1998) uses a pole-placement technique, here we follow Chou et al. (1998) in using a standard LQG method.

LQG is advantageous because it allows for the inclusion of additive system noise ($\xi^{(x)}$) as well as sensor noise ($\xi^{(y)}$). Thus the complete system we try to control is given by:

$$\begin{aligned} \dot{x}_c(t) &= [A_c + \Delta A_c(t) + \xi^{(A)}(t)]x_c(t) + A_{cr}x_r(t) + [B_c + \Delta B_c(t) + \xi^{(B)}(t)]u(t) \\ \dot{x}_r(t) &= A_{rc}x_c(t) + A_r x_r(t) + B_r u(t) + \xi^{(x)} \\ y &= [C_c + \Delta C_c(t) + \xi^{(C)}(t)]x_c + C_r x_r + \xi^{(y)} \end{aligned} \tag{21}$$

In using this method we minimize the performance index J given by

$$J = \int_0^\infty \left[x_c^T(t)Qx_c(t) + \rho_c u^T(t)Ru(t)\right] dt \tag{22}$$

In this case ρ_c is the design parameter that will be changed to fulfill condition (17). Since we want to reduce the pressure oscillations at a specific location x_p, it is natural to choose Q such that $x_c^T Q x_c$ represents our best estimate of p' at this point

$$Q = \bar{p}^2 \cdot \begin{bmatrix} \psi_1^2(x_p) & 0 & 0 \\ 0 & \ddots & 0 \\ 0 & 0 & \psi_N^2(x_p) \end{bmatrix} \qquad \text{and} \qquad R = 1 \tag{23}$$

Time Delay

Time delays often arise in combustion systems: for example, even when no control is present, there is delay between injection of the fuel mixture and fully developed combustion for the case of liquid or gas combustors. When feedback control is present, there are delays intrinsic to the controller due to finite rates of actuators and sensors, time spent for signal acquisition and processing, and clock time in case a digital computer is used. Even for the typical laboratory-scale combustor, when a loudspeaker is used as an actuator, time delays might play an important role: suppose the first unstable acoustic mode has a frequency of $1kHz$, then a typical reaction time for the controller (if we consider linear approach, the bandwidth of the controller should at least match the typical frequencies of the instability in the plant) is of the order of $1ms$. Modern electronic equipment can certainly process the required computation for determining the control input much faster than that; the bottleneck for this case is the time it takes for the pressure input (from the loudspeaker) to influence the chamber acoustic response. This time, for a $50cm$ chamber, is of the order of 1-$2ms$, just the same order of the instability. In the case of industrial scale combustors, or when using secondary fuel injection as control actuation, the necessity of considering time delays becomes even more compelling, since in these cases the time delay can easily be larger than the characteristic timescale of the instability.

Time delays always reduce the stability of a system (Franklin et al. 1995), hence it is very important to take them into consideration when simulating a realistic combustor and when designing a suitable controller. Regarding the controller design phase, three general approaches are possible.

- *Classical Control.* If we look at the transfer function of the system, and indicate with τ the time delay, the problem with time delay is reduced to a conventional one by expressing the non rational function $e^{\tau s}$ in terms of a rational function. Note that the function $e^{\tau s}$ is analytic (for finite values of s), so approximation with a rational function is allowed. A typical approach is to use a Padé approximant, based on a McLauren series expansion of the exponential function. The value of the method is limited by two factors. First, the rational approximation of the delay rapidly increases the effective order of the plant, making the control design problematic. Second, large values of time delay will decrease the available phase margin to the point where it is no longer possible to design a stabilizing controller. Also, (Wang 2000) shows that a low order polynomial approximation of the time delay is not enough to have a satisfactory model in terms of dynamical behavior of the original system. In the present paper we do not take this method into consideration, since we focus our attention on control design methods capable of incorporating robustness requirements.

- *Modern Control.* In this case, time delay can be viewed as an uncertainty in the system and incorporated in the design as a perturbation to the original plant. More details are given in the following section.

- *Delay Compensation.* This category includes all the other methods used to compensate for time delay. An important group includes compensation networks that bring the delay 'out of the loop', and hence allow to design the controller using conventional methods applied to the plant without time delay. A typical example is the Smith Regulator. A caveat here is constituted by the fact that most networks based on linear elements generally do not modify the eigenvalues of the original plant, so they only apply to stable (or marginally stable) plants. On the other hand, by using these methods, arbitrarily large time delays can be accounted for without loss of stability margin.

Modern Control Approach

Time delay can be incorporated in the design of a controller by considering the time delay as a multiplicative perturbation to the plant. Let $\tilde{P}(s) = P(s)e^{-\tau s}$ be the perturbed plant. The perturbed plant can be included in the set

$$\{(1 + \Delta_{plant} W_{unc})P : \| \Delta_{plant} \|_\infty \leq 1\} \tag{24}$$

with the choice of an appropriate weight function W_{unc}

$$|e^{-\tau j\omega} - 1| \leq |W_{unc}(j\omega)| \qquad \forall \omega, \tau \tag{25}$$

The design of the controller then proceeds in the same way as before. Note that, if the time delay is 'large', condition (25) typically imposes a significant limitation on the controller; in general performance is degraded and, if τ is large enough, it might be impossible to design a stabilizing controller for the delayed system. On the other hand, when a solution exists, stability and performance are guaranteed according to the design. Uncertainty in the numerical value of the time delay, as it is typical in combustion systems, is automatically taken into consideration by the design method. Application of this approach is included in the example presented later.

Delay Compensation Approach

In this section we will examine a method based on *predictive control*: the time delay is compensated by a predictor that acts on the measured or estimated state and feeds the controller with the appropriate signal to perform the feedback action at the compensated time. The control system consists of a predictor and a

controller; the closed loop equations can be written as

$$\begin{cases} \dot{x}(t) = Ax(t) - Bu(t-h) \\ y(t) = Cx(t) \end{cases} \tag{26}$$

$$p(t) = e^{A\tau}x(t) + \int_{-\tau}^{0} e^{-A\tau}Bu(t+\tilde{t})d\tilde{t} \tag{27}$$

$$u(t) = Kp(t) + i(t) \tag{28}$$

where $i(t)$ is the external input to the system and might not be present. The predictor written as in (27) is simply derived by integrating (26) from the current time t to the time $t+\tau$. A change of variables produces the form (27), which contains information only up to the current time and consequently it can be physically implemented.

Furukawa and Shimemura (1983) prove (based on direct computation of the closed-loop characteristic equation) that if the pair (A, B) is controllable, then the predictor (27) and the controller (28) yield a finite spectrum of the closed-loop system, located at arbitrarily preassigned points in the complex plane.

Note that the predictor (27) contains an integral term up to the current time. It is impossible to integrate up to current time without solving an integral equation, or iterating on the solution, but it can be shown (Manitius and Olbrot 1979) that the limits in the integral term appearing in (27) can be substituted by $-\tau - \epsilon$ and $-\epsilon$ if ϵ is sufficiently small. Let us now consider the following scheme:

$$\dot{x}(t) = Ax(t) - Bu(t-h) \tag{29}$$

$$\begin{cases} \dot{\tilde{z}}(t) = A\tilde{z}(t) - Bu(t) \\ z(t) = \tilde{z}(t) - e^{A\tau}\tilde{z}(t-\tau) \\ p(t) = e^{A\tau}x(t) + z(t) \end{cases} \tag{30}$$

$$u(t) = Kp(t) \tag{31}$$

A simple substitution shows that computing $z(t)$ from the equations above results in the evaluation of the correct predictor term (27). The scheme (29)-(30) can be physically implemented in Simulink by using the network connection presented in figure 1, where symbols refer to the letters used in (29)-(31) and p is the signal sent to the controller. Since the time delay is compensated in this secondary predictor-loop, application of this scheme to the plant presented above allows to include significant time delays in the system without compromising performance in the design of the controller. On the other hand, the use of a second loop reduces the robustness of the system to uncertainties in the value of the parameters.

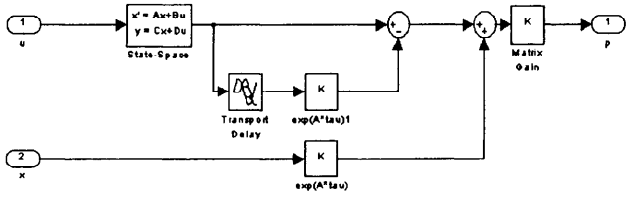


Figure 1: SIMULINK realization of the predictor block, equations (30)

D_{nl}	$n=1$	$n=2$	$n=3$	$n=4$	E_{nl}	$n=1$	$n=2$	$n=3$	$n=4$
$l=1$	-.01	.007	-.001	.007	$l=1$	-.005	-.005	.0025	.0016
$l=2$	.01	.1	.007	-.001	$l=2$	-.0025	-.015	.01	.01
$l=3$	-.01	.01	.75	.008	$l=3$	-.005	.0	-.02	.02
$l=4$	.02	-.005	.01	1.5	$l=4$	.01	.02	.02	-.025

Table 1: Combustion chamber parameters

4 Example

In the following we will briefly demonstrate the described design procedures on a particular example. The example has been chosen solely because it has been used previously in the literature. The methods used are obviously much more general and can be applied to any linearized (combustion) system – as mentioned previously, *all* processes, including combustion, have been linearized and are embedded in the model parameters.

The numerical example used is the same one as given in Haddad et al. (1997) and used previously by Culick and Yang (1992) and Yang et al. (1992). The combustion chamber is assumed to be cylindrical of length L and only longitudinal modes are considered. The chamber is closed on the upstream end and has a nozzle at the downstream end which acts as an acoustically closed boundary. The sensor detecting the instability is a microphone located at x_s whereas the actuator used to control the pressure oscillations is a loudspeaker located at x_a. The internal dynamics of the loudspeaker are modeled as a second order system and included in the state-space formulation, i.e. they form an integral part of A_c in equation (21) through augmentation of the state x_c. In this way the actuator dynamics are accounted for in the design of the controller. In this example the actuator (and sensor) are treated as perfectly known systems; within the framework described here it is straightforward to include uncertainties or noise in those systems too. Note that the model of the actuator as a 'loudspeaker', a second order system with a high gain, is actually more general than it seems. If we wanted to represent an injector, the same model would still apply, with a longer time delay, and some difference in the numerical value of the parameters, but substantially the same structure, i.e. second order dynamics and very high gain; see Neumeier, Nabi, Arbel, Vertzberger and Zinn (1997) for an example.

The linearized model of the combustion chamber is characterized through the parameters E_{nl} and D_{nl} which are given (after non-dimensionalization of time by $\frac{\pi L}{\bar{a}}$) in table 1 for the first 4 longitudinal modes – the parameters are originally taken from Yang et al. (1992) and are typical for solid propellant rockets.

In this design study we only consider uncertainty in the parameters E_{nl} and D_{nl} and noise in those terms given in equation (8). In other words there is no noise or uncertainty in the sensing or actuation process and the stochastic sources act (as described by the model) as random perturbations of E_{nl} and D_{nl}. Thus we put (keeping the notation of the previous section)

$$Q^{(B)} = 0 \qquad Q^{(C)} = 0 \qquad \Xi^{(AB)} = 0 \qquad \Xi^{(BB)} = 0 \qquad \Xi^{(CC)} = 0 \tag{32}$$

Furthermore we assume that all stochastic sources (due to the vorticity and entropy modes in the chamber) are uncorrelated and have the same variance σ^2. Finally we assume that the parameter uncertainties can all be described by a single variable ϵ. These assumptions are only made to simplify the expressions as we can now write:

$$Q^{(A)} = \epsilon \cdot \begin{bmatrix} 0 & 0 \\ |E_{nl}| & |D_{nl}| \end{bmatrix} \qquad \text{and} \qquad \Xi^{(AA)} = N \cdot \sigma^2 \cdot 1 \tag{33}$$

A controller was designed using an LQG technique by taking only 1 mode (the unstable first mode) into consideration. It is assumed that the complete system is given by 4 modes and thus the remaining 3 modes

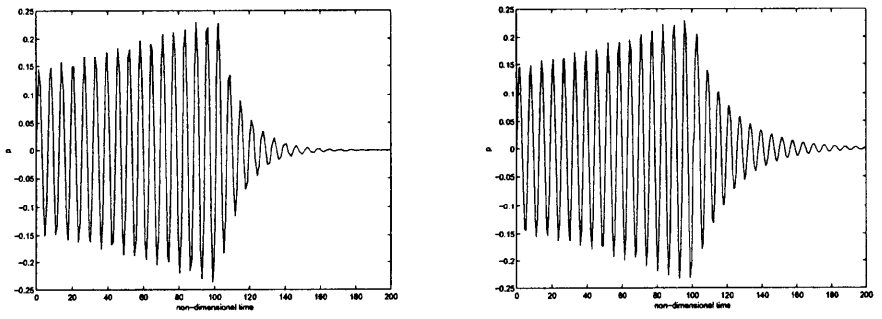


Figure 2: Left: Nominal system (only 1 mode) response to control. Right: Response of complete system (all 4 modes) to the same controller

are considered to give the residual dynamics. Basing the controller on a minimal set of modes is desired as it reduces reduces the order of the controller and thus allows for easier implementation. Figure 2 shows the response of the reduced and complete system to the controller (turned on at $\tilde{t} = 100$). As expected the presence of the extra modes (not considered in the design) in the full system reduces the performance of the controller (slower decay).

Figure 3 shows the guaranteed stability limits (in terms of ϵ and σ) of the controller. The solid line is the limit predicted by equation (17) for the truncated system where only 1 mode is used in the simulation. The other lines describe the stability region as more modes are added in the simulation, i.e. as the system approaches the 'complete' system. The region shrinks as additional modes are introduced into the simulation while the same controller (based on 1 mode) is retained. In this extreme case (where we considered only one mode to base the controller on) the changes are drastic, but as the neglected modes become more heavily damped their influence grows smaller (as can be seen by the lines moving closer together).

Figure 4 illustrates the effect the (stable) residual system can have in the presence of noise. The same controller (based only on the unstable first mode) is used in all three cases. In case A (low noise) the controller is able to stabilize the full system (all 4 modes included in the simulation); however at a higher noise level (case B) the pressure oscillations do not decay to zero. Note that this noise level is well within the stability limits as predicted with the truncated (1 mode) system and thus underlines the importance of the neglected dynamics. If the simulation is performed with the reduced system, the instability does indeed decay as anticipated (case C).

Example with Time Delay Compensation

The delay compensation approach allows separating the control problem from compensation of the time delay. Figure 5 presents the results of the application of the method to our model combustor. The non-dimensional time delay is chosen to be $\tau = 10$, which corresponds to a delay of about $10ms$, i.e. 5 periods of an oscillation at $500Hz$ and constitutes a reasonable upper limit to the delay that can be expected in a real combustor controlled by modulating the injection of a secondary fuel. Note how the predictor works: the controller (control action is plotted in the bottom half of figure 5) starts sending commands immediately when it is activated. The control is computed on a prediction of the future state of the system, i.e. the state of the system when the control signal will effectively reach the plant. The system response, plotted in the

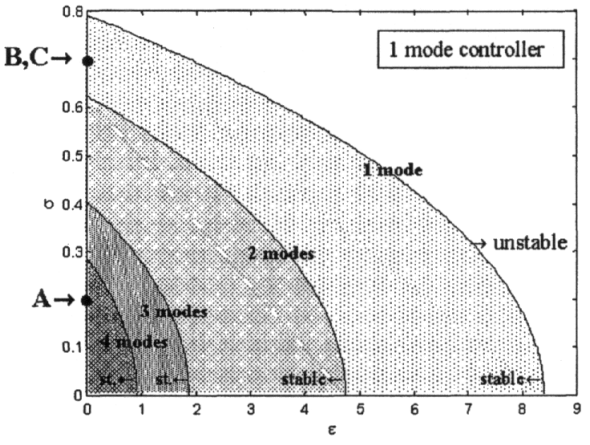


Figure 3: Guaranteed stability limits for closed-loop system in $\sigma - \epsilon$ plane (noise variance and uncertainty) depending on number of residual modes considered

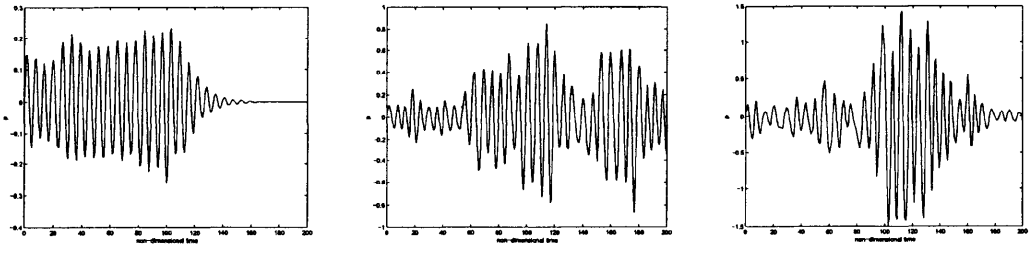


Figure 4: From left to right: time simulations of cases A,B (complete system), and C (reduced system) as defined in figure 3.

top half of 5, shows that the system effectively starts reacting to the control at a non-dimensional time of 40 when the controller is put online at a non-dimensional time of 30.

5 Concluding Remarks

In this paper we have shown how uncertainties, noise, unmodeled dynamics and time-delay can be included in the controller design for combustion instabilities.

A clear distinction has been made between the uncertainty and the noise. This is necessary as the parameter uncertainty can be bounded; e.g. in practical applications we might know that in the operating range of interest the various parameters are located within certain numerical bands. In contrast, true noise sources can in general not be bounded, and thus do not fit in the common control frameworks; they are characterized by their mean values, which we include in the system parameters and by their variation.

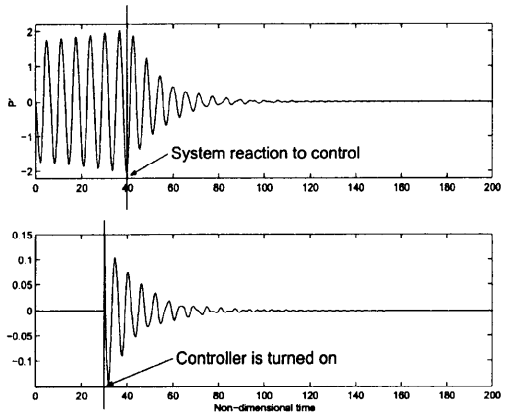


Figure 5: Control with time-delay, ($\tau = 10$). Top half: system response. Bottom half: control action.

Explicit consideration of the neglected modes allows studying their influence on the controller robustness. This is especially important since in most experimental implementations to date the controller has been designed by taking only the unstable mode(s) into account. In the example given here only the first mode is unstable and it is in fact possible to stabilize the system by solely controlling this one mode. Note that the controller is designed to accommodate large uncertainties (or noise) since we anticipate that the residual modes will affect the dominant first mode. This is the way unmodeled dynamics are traditionally handled: by including them in the uncertainties of the system. The framework presented here shows how much of that uncertainty can be attributed to the neglected modes. In the example given, the damping of the ignored modes (notably the second one) is rather small and thus we see that the actual parameter uncertainty ϵ (or noise intensity σ) that the controller can tolerate declines dramatically as additional modes are considered. Therefore we conclude that the residual dynamics dominate the uncertainty unless the neglected modes are highly damped.

Inclusion of a time-delay in the modern-design framework as an uncertainty is adequate when the time-delay is of the same order of the characteristic time of the instability, defined as the inverse of the frequency of the unstable mode. Cases with longer time delays, as it might be the case in full-scale combustors, can be treated by adding a second loop to compensate for the delay: simulation shows very good performance, but issues about robustness to uncertainty and perturbations need to be addressed carefully. An adaptive observer might be needed for application to real systems. Future work in this area should include testing of the concepts on an experimental combustor; and system identification to define better models of real actuators, in particular injectors and fuel flow modulators. More analysis is also needed to characterize (and eventually take advantage of) nonlinearities naturally present in combustion chambers.

References

Biswas, S. (1998). Robust stabilization of linear systems in the presence of gaussian perturbation of parameters, *Optimal Control Applications and Methods* **19**: 271–286.

Burnley, V. (1996). *Nonlinear Combustion Instabilities and Stochastic Sources*, PhD thesis, California Institute of Technology.

Burnley, V. and Culick, F. (1999). The influence of combustion noise on acoustic instabilities, *to be published.*

Chou, J., Chen, S. and Chao, C. (1998). Robust stabilization of flexible mechanical systems under noise uncertainties and time-varying parameter perturbations, *Journal of Vibration and Control* **4**: 167–185.

Chu, B.-T. and Kovasznay, L. (1956). Nonlinear interactions in a viscous heat-conducting compressible gas, *Journal of Fluid Mechanics* **3**(5): 494–514.

Culick, F. (1976). Nonlinear behavior of acoustic waves in combustion chambers, parts i and ii, *Astronautica Acta* **3**: 714–757.

Culick, F. (1989). Combustion instabilities in liquid-fueled propulsion systems - an overview, *AGARD CP-450* pp. 1–73.

Culick, F. (1994). Some recent results for nonlinear acoustics in combustion chambers, *AIAA Journal* **32**(1): 146–169.

Culick, F. (1995). Nonlinear acoustics in combustion chambers with stochastic sources, *Documents on Active Control of Combustion Instabilities.* Guggenheim Jet Propulsion Center, California Institute of Technology.

Culick, F. and Yang, V. (1992). Prediction of the stability of unsteady motions in solid propellant rocket motors, nonsteady burning and combustion stability of solid propellants, *Progress in Astronautics and Aeronautics* **143**: 719–779.

Dowling, A. (1997). Nonlinear self-excited oscillations of a ducted flame, *Journal of fluid mechanics* **346**: 271–290.

Franklin, G., Powell, J. and Emami-Naeini, A. (1995). *Feedback Control of Dynamic Systems*, Addison Wesley.

Furukawa, T. and Shimemura, E. (1983). Predictive control for systems with time delay, *Int. Journal of Control* **37**: 399–412.

Gulati, A. and Mani, R. (1992). Active control of unsteady combustion-induced oscillations, *Journal of Propulsion and Power* **8**(5): 1109–1115.

Haddad, W., Leonessa, A., Corrado, J. and Kapila, V. (1997). Robust reduced-order control of combustion instabilities, *Proceedings of the 1997 IEEE International Conference on Control Applications.* Hartford, CT.

Hathout, J., Annaswamy, A., Fleifil, M. and Ghoniem, A. (1998). A model-based active control design for thermoacoustic instability, *Combustion science and technology* **132**(1-6): 99–138.

Hong, B., Yang, V. and Ray, A. (2000). Robust feedback control of combustion instability with modeling uncertainty, *Combustion and Flame* **120**(1-2): 91–106.

Isella, G., Seywert, C., Culick, F. and Zukoski, E. (1997). A further note on active control of combustion instabilities based on hysteresis, *Combustion Science And Technology.*

Koshigoe, S., Komatsuzaki, T. and Yang, V. (1999). Adaptive control of combustion instability with on-line system identification, *Journal of propulsion and power* **15**(3): 383–389.

Lieuwen, T. and Zinn, B. (2000). Experimental investigation of limit cycle oscillations in an unstable gas turbine combustor, *38th Aerospace Sciences Meeting and Exhibit.* AIAA paper No. 2000-0707.

Manitius, A. and Olbrot, A. (1979). *IEEE Transactions Automatic Control* **24**: 541.

McManus, K., Poinsot, T. and Candel, S. (1993). A review of active control of combustion instabilities, *Progress in energy and combustion science* **19**(1): 1–29.

Neumeier, Y., Nabi, A., Arbel, A., Vertzberger, M. and Zinn, B. (1997). Open-loop performance of a fast-response, actively controlled fuel injector actuator, *Journal of Propulsion and Power.*

Poinsot, T., Bourienne, F., Candel, S. and Esposito, E. (1987). Suppression of combustion instabilities by active control, *Journal of Propulsion* **5**: 14–20.

Seywert, C. and Culick, F. (2000). Some influences of noise on combustion instabilities and combustor dynamics, *to be published.*

Wang, Y. (2000). *Effects of Actuator Limits in Bifurcation Control with Applications to Active Control of Fluid Instabilities in Turbomachinery,* PhD thesis, California Institute of Technology.

Yang, V., Sinha, A. and Fung, Y. (1992). State-feedback control of longitudinal combustion instabilities, *Journal of Propulsion and Power* **8**(1): 66–73.

PAPER -27, F. Culick

Question (F. Vuillot, France)

To analyze numerical simulation results in terms of control efficiency, it would be useful to apply the flow decomposition (into acoustic-vorticity-entropy fields) to the energy. Do you know of work in that direction?

Reply

Not specifically for the situation I discussed here. However, I believe that the basis exists for doing so. The equations exist, of course, and I suggest that work by Morfey many years ago in acoustic energy in moving media would be a good place to start. Flancho (?) later used Morfey's ideas in his work on nonlinear acoustics; his approach and results may well be helpful.

This page has been deliberately left blank

Page intentionnellement blanche

Wide-Range Robust Control of Combustion Instability

Boe-Shong Hong, Vigor Yang and Asok Ray

Mechanical Engineering Department
The Pennsylvania State University
University Park, Pennsylvania 16802, USA

Abstract

This paper presents the concept and design of a two-layer robust control system for suppression of combustion instabilities over a wide range of operation. The control law synthesis based on a multiple-time-scale model of combustion dynamics. Control actions on the fast-time scale are provided by secondary fuel injection, realized as modulation of the primary fuel flow, and are gain-scheduled according to the variations of mean-flow temperature and velocity on the slow-time scale. A linear parameter varying (LPV) L_2-gain control law is formulated in the setting of differential game theory. Simulation experiments have been conducted to evaluate the control law under wide-range operation of a generic combustor in terms of the trade-off among: (i) fuel injection rate and pressure oscillation; (ii) transient and steady responses; and (iii) stability robustness and performance.

1. Introduction

Unsteady motions in confined combustion chambers often result from mean-flow dependent interactions between heat release and acoustic oscillations. The underlying physical mechanisms involve a wide range of time scales that can be broadly classified into two categories: one representing mean-flow motions on a slow time-scale and the other representing acoustic oscillations on a fast time-scale. The disparity of time scales allows for the development of a hierarchically structured control law for regulating the various processes involved. The overall combustor system may consist of two interacting modules: slow-time supervisory controller and fast-time flame controller, as illustrated in Fig.1 [1]. The slow-time supervisory controller in the outer loop attempts to optimize the overall combustor performance and pollutant emissions based on the measurements of quasi-steady variables, and to identify the flame control parameters that determine the operating points of the fast dynamic phenomena such as pressure oscillations. The flame controller in the inner loop is responsible for suppression of combustion instability and for prevention of lean blowout of the flame. When coupled with a global engine control system, such a two-layer strategy will lead to an energy-efficient and clean system for propulsion and power-generation applications.

As part of their research on feedback control of combustion instabilities in various propulsion systems, Yang and co-workers established a series of control designs with distributed actuation [2-6]. The recent work by Hong et al. [6] was based on the H_∞-optimization, which guaranteed robust stability and performance within specified bounds of model and parameter uncertainties as well as sensor noise and plant disturbance. The nominal system parameters, however, were treated as time-invariant constants, thereby rendering the control laws valid only for narrow range of operating conditions. The present paper attempts to remedy this deficiency by taking into account the temporal variations of mean-flow dynamics in such a unified manner that the resultant control laws function effectively over a wide-range of operations. The work incorporates an H_∞-based linear-parameter-varying (LPV) control [7,8] for modulating combustion dynamics. Its major contributions beyond the previous studies on narrow-range control [6] are

- establishment of a two-time-scale model of combustion dynamics for robust control systems analysis and synthesis, and
- development of an observer-embedded robust LPV control law within the aforementioned two-layer architecture.

The paper is organized in six sections including the introduction. Section 2 develops a two-time-scale model of combustion dynamics in a liquid-fueled propulsion system. The wide-range robust control law is formulated and analyzed in Sections 3 and 4, respectively, based on the concept of differential game theory. Section 5 presents the results of simulation experiments for evaluating the system performance under different control laws. The paper is summarized and concluded in Section 6 with recommendations for future research.

2. A Two-Time-Scale Model of Combustion Dynamics

The disparate time scales involved in the various combustion and flow processes allows for the decomposition of the conservation laws into two settings governing slow-time mean-flow dynamics and fast-time acoustic dynamics, respectively. The fast-time dynamics is parametrically dependent on the slow-time mean-flow variables. Using a spatial-averaging procedure equivalent to modal analysis, a family of linear finite-dimensional parameterized models is derived for parameter-dependent robust feedback control design.

The equations governing the dynamics of a liquid-fueled combustion device with feedback control actuators can be succinctly expressed as [2]:

$$\frac{\partial \rho}{\partial t} + \mathbf{v}_g \cdot \nabla \rho + \rho \nabla \cdot \mathbf{v}_g = W + W_c \tag{1}$$

$$\rho \frac{\partial \mathbf{v}_g}{\partial t} + \rho \mathbf{v}_g \cdot \nabla \mathbf{v}_g + \nabla p = F + F_c \tag{2}$$

$$\frac{\partial p}{\partial t} + \bar{\gamma} p \nabla \cdot \mathbf{v}_g + \mathbf{v}_g \cdot \nabla p = P + P_c \tag{3}$$

where the source terms W, F, and P represent the two-phase interactions and combustion influence, and W_c, F_c and P_c the total mass, momentum and energy control inputs, respectively.

It is apparent from experimental or computational observation that motions in the fluid field take place in two time-

Paper presented at the RTO AVT Symposium on "Active Control Technology for Enhanced Performance Operational Capabilities of Military Aircraft, Land Vehicles and Sea Vehicles", held in Braunschweig, Germany, 8-11 May 2000, and published in RTO MP-051.

scales: one representing the mean-flow motion with a slower time-scale and larger amplitude-order, and the other representing acoustic motion with fast time-scale and smaller amplitude-order. Now, the purpose is to decompose each single conservation law, described in Eqs. (1), (2) and (3), into two time scales describing the slow behavior of mean-flow motions and primary combustion inputs, and fast behavior of acoustic oscillations and secondary-fuel injection into the combustion chamber. The components of the fluid-variable vector $x \equiv [\rho \quad \mathbf{v}_g \quad p]^T$ in the following table have their own time-scales and amplitude-orders where the subscripts s and f represent the slow and fast time scales, respectively.

Table I Two Time-scaled Motions

	Time scales	Amplitude Orders
Mean-flow motion $\tilde{x}(t_s)$	$t_s = \varepsilon_s t$	$A_s \approx \varepsilon_s A_t$
Acoustic motion $x'(t_f)$	$t_f = \varepsilon_f t$	$A_f \approx \varepsilon_f A_t$

In the table, the referenced time-scale and amplitude-order are denoted as t and A_t, respectively, and the referenced time t here is taken as the regular time used in the physical laws. The time-scale and amplitude order are described by the pair $(\varepsilon_s, \varepsilon_f)$, with $\varepsilon_f \sim o^1(\varepsilon_s)$ where $\left|\frac{o^1(\theta)}{\theta}\right| \to 0 \; as \; \theta \to 0$.

Remark 1: When observing events in the fast-time scale, $t_f \sim t$ implying that $\varepsilon_f \sim 1$ and $\varepsilon_s >> 1$. Similarly, when observing events in the slow-time scale, $t_s \sim t$ implying that $\varepsilon_s \sim 1$ and $\varepsilon_f << 1$.

The combustion control inputs (W_c, F_c, P_c) are also decomposed as two components: one is the primary component with the same (i.e., slow) time-scale and amplitude-order as those of the mean-flow motions, and the other is secondary component with the same (i.e., fast) time-scale and amplitude-order as those of acoustic oscillations. The former primarily affects the mean-flow field, while the latter is a modulated component influencing the acoustic field. Similar treatments are applied to the two-phase interaction variables (W, F, P) of the uncontrolled combustion process.

The universally independent variable in time-domain is the regular time t. However, for separation of the local and global behavior, the fluid, combustion, and two-phase interaction variables are treated in the form:

$$x(t) \equiv x[t_f(t), t_s(t)] \tag{4}$$

It follows from the above equation that there are two components in $x(t_f, t_s)$: $x'(t_f)$ is only a function of the fast time t_f, governed by the acoustic motion and the other $\tilde{x}(t_s)$ is only a function of the slow time t_s following the mean-flow motion. The two-time scale model is generated as follows:

When observing an event in two different time-scales, we may separate the time-derivative terms $\frac{\partial \rho}{\partial t}$, $\frac{\partial \mathbf{v}_g}{\partial t}$ and $\frac{\partial p}{\partial t}$ in Eqs. (1), (2) and (3) in corresponding two time-scales in the following format, say:

$$\frac{\partial \mathbf{v}_g[\mathbf{r}, t_f(t), t_s(t)]}{dt} = \frac{\partial \mathbf{v}_g}{\partial t_s}\frac{dt_s}{dt} + \frac{\partial \mathbf{v}_g}{\partial t_f}\frac{dt_f}{dt} \equiv \frac{\partial \tilde{\mathbf{v}}_g}{dt_s}\varepsilon_s + \frac{\partial \mathbf{v}'_g}{dt_f}\varepsilon_f \tag{5}$$

Equation (5) implies the fluid variables ρ, $\mathbf{v}_g$ and p can be linearly expanded as, say:

$$\rho(\mathbf{r}, t) = \tilde{\rho}(\mathbf{r}, t_s) + \rho'(\mathbf{r}, t_f) \tag{6}$$

As the slow-time variables are related to system performance, the fast-time variables become related to the internal stability. If proper slow-time dynamics is pursued in operation of the system, based on Eq. (6) and the magnitude orders indicated in the above table, those terms $\mathbf{v}_g \cdot \nabla\rho + \rho\nabla \cdot \mathbf{v}_g$; $\rho \mathbf{v}_g \cdot \nabla \mathbf{v}_g + \nabla p$; $\bar{\gamma} p \nabla \cdot \mathbf{v}_g + \mathbf{v}_g \cdot \nabla p$; (W, F, P); and (W_c, F_c, P_c) in Eqs. (1), (2) and (3) are decomposed into two equations by Taylor series expansion, say, as:

$$\begin{aligned} \rho\nabla \cdot \mathbf{v}_g(\mathbf{r}, t_s, t_f) &= \tilde{\rho}\nabla \cdot \tilde{\mathbf{v}}_g(\mathbf{r}, t_s) + \rho'(\mathbf{r}, t_f)\nabla \cdot \tilde{\mathbf{v}}_g(\mathbf{r}, t_s) \\ &+ \tilde{\rho}(\mathbf{r}, t_s)\nabla \cdot \mathbf{v}'_g(\mathbf{r}, t_f) + \text{higherorder terms} \end{aligned} \tag{7}$$

which follows the following general form

$$\begin{aligned} f[x(t_f, t_s)] = f[\tilde{x}(t_s)] + \frac{\partial f}{\partial x}\Big|_{\tilde{x}(t_s)} x'(t_f) \\ + \text{higher order terms} \cdots\cdots \end{aligned} \tag{8}$$

Finally, the term $\rho \frac{\partial \mathbf{v}_g}{\partial t}$ in Eq. (2) is separated based on Eqs. (5) and (6) as:

$$\rho \frac{\partial \mathbf{v}_g}{\partial t} = (\tilde{\rho} + \rho')\left(\frac{\partial \tilde{\mathbf{v}}}{\partial t_s}\varepsilon_s + \frac{\partial \mathbf{v}'_g}{\partial t_f}\varepsilon_f\right) \tag{9}$$

which is approximated to the first-order accuracy as:

$$\rho \frac{\partial \mathbf{v}_g}{\partial t} \approx \varepsilon_s \tilde{\rho} \frac{\partial \tilde{\mathbf{v}}}{\partial t_s} + \varepsilon_s \rho' \frac{\partial \tilde{\mathbf{v}}_g}{\partial t_s} + \varepsilon_f \tilde{\rho} \frac{\partial \mathbf{v}'_g}{\partial t_f} \tag{10}$$

By using the above first-order approximations (5), (7) and (10), the conservation equations, (1), (2) and (3), are decomposed in two time scales. Collection of those slow-time variables yields

Slow-time Conservation Law:

Mass

$$\begin{aligned} \varepsilon_s \frac{\partial \tilde{\rho}}{\partial t_s} + \tilde{\mathbf{v}}_g(t_s) \cdot \nabla\tilde{\rho}(t_s) + \tilde{\rho}(t_s)\nabla \cdot \tilde{\mathbf{v}}_g(t_s) \\ = \tilde{W}(t_s) + \tilde{W}_c(t_s) \end{aligned} \tag{11}$$

Momentum

$$\begin{aligned} \varepsilon_s \tilde{\rho}(t_s) \frac{\partial \mathbf{v}_g(t_s)}{\partial t_s} + \tilde{\rho}(t_s)\tilde{\mathbf{v}}_g(t_s) \cdot \nabla\tilde{\mathbf{v}}_g(t_s) + \nabla\tilde{p}(t_s) \\ = \tilde{F}(t_s) + \tilde{F}_c(t_s) \end{aligned} \tag{12}$$

Energy

$$\begin{aligned} \varepsilon_s \frac{\partial \tilde{p}}{\partial t_s} + \bar{\gamma}\tilde{p}(t_s)\nabla \cdot \tilde{\mathbf{v}}_g(t_s) + \tilde{\mathbf{v}}_g(t_s) \cdot \nabla\tilde{p}(t_s) \\ = \tilde{P}(t_s) + \tilde{P}_c(t_s) \end{aligned} \tag{13}$$

And collections of fast-time variables yields

Fast-time Conservation Law:

Mass

$$\begin{aligned} \varepsilon_f \frac{\partial \rho'(t_f)}{\partial t_f} + \tilde{\mathbf{v}}_g(t_s) \cdot \nabla\rho'(t_f) + \mathbf{v}'_g(t_f) \cdot \nabla\tilde{\rho}(t_s) \\ + \tilde{\rho}(t_s)\nabla \cdot \mathbf{v}'_g(t_f) + \rho'(t_f)\nabla \cdot \tilde{\mathbf{v}}_g(t_s) \\ = W'(t_f) + W'_c(t_f) \end{aligned} \tag{14}$$

Momentum

$$\varepsilon_f \tilde{\bar{\rho}}(t_s)\frac{\partial \mathbf{v}_g'(t_f)}{\partial t_f} + \nabla p'(t_f) = -\tilde{\bar{\rho}}(t_s)(\tilde{\mathbf{v}}_g(t_s)\cdot\nabla\mathbf{v}_g'(t_f) + \mathbf{v}_g'(t_f)\cdot\nabla\tilde{\mathbf{v}}_g(t_s)) - \rho'(t_f)(\varepsilon_s\frac{\partial \tilde{\mathbf{v}}_g(t_s)}{\partial t_s} + \tilde{\mathbf{v}}_g(t_s)\cdot\nabla\tilde{\mathbf{v}}_g(t_s)) + F'(t_f) + F_c'(t_f) \quad (15)$$

Energy

$$\varepsilon_f \frac{\partial p'(t_f)}{\partial t_f} + \tilde{\bar{\gamma}}\tilde{\bar{p}}(t_s)\nabla\cdot\mathbf{v}_g'(t_f) = -\bar{\gamma}p'(t_f)\nabla\cdot\tilde{\mathbf{v}}_g(t_s) - \tilde{\mathbf{v}}_g(t_s)\cdot\nabla p'(t_f) - \mathbf{v}_g'(t_f)\cdot\nabla\tilde{p}(t_s) + P'(t_f) + P_c'(t_f) \quad (16)$$

The set of conservation equations (11) to (13) in the slow-time scale governs the mean-flow dynamics, and the set of conservation equations (14) to (16) describes the mean-flow-dependent acoustic dynamics in the fast-time scale.

Subtracting the fast-time derivative of the energy equation (16) from the spatial derivative of the momentum equation (15) yields:

$$\nabla^2 p' - \frac{1}{\bar{a}^2(t_s)}\frac{\partial^2 p'}{\partial {t_f}^2}\varepsilon_f = h + h_c \quad (17)$$

$$h_c = \nabla F_c' - \frac{1}{\bar{a}^2(t_s)}\frac{\partial P_c'}{\partial t_f} \quad (18)$$

where the speed of sound $\bar{a}$ is a local thermodynamic property given by $\bar{a} \equiv \sqrt{\left.\frac{\partial \tilde{\bar{p}}}{\partial \tilde{\bar{\rho}}}\right|_s} = \sqrt{\bar{\gamma}\bar{R}\tilde{\bar{T}}}$ slowly varying in an ideal gas mixture. The function h_c represents the high-frequency control inputs, and h contains the driving and dissipation terms that depend on the spatial and temporal properties of mean-flow temperature and velocity.

The acoustic dynamics is mainly dependent on the mean properties $\tilde{\mathbf{v}}_g$ and $\tilde{T}$ that determines the temporally and spatially compressible properties of the fluid medium in the combustion chamber. Locally and temporally, low $\tilde{T}$ implies reduced speed of sound and consequently the dominant natural frequencies in the combustion medium, and vice versa. The mean-flow velocity $\tilde{\mathbf{v}}_g$ represents the instantaneous and spatial speed of the coordinate frame in which an acoustic mass element travels, providing a driving/dissipated force due to an accelerated/decelerated coordinate frame. Therefore, $\tilde{T}(\mathbf{r}, t_s)$ and $\tilde{\mathbf{v}}_g(\mathbf{r}, t_s)$ are used as gain-scheduling parameters for control of mean-flow dependent acoustic dynamics.

Since $\tilde{T}(\mathbf{r}, t_s)$ and $\tilde{\mathbf{v}}_g(\mathbf{r}, t_s)$ are continuously varying with respect to both temporal and spatial variables, measurements with finitely many point sensors may cause loss of relevant information. Furthermore, even if distributed sensors are used to measure the spatial distribution of $\tilde{T}(\mathbf{r}, t_s)$ and $\tilde{\mathbf{v}}_g(\mathbf{r}, t_s)$, the gain-scheduling control law is likely to be excessively time-consuming and hence unsuitable for on-line computation. To synthesize a control law that is executable in real time on an inexpensive platform, the following approximation is made for spatial representation of the gain-scheduling variables $\tilde{T}(\mathbf{r}, t_s)$ and $\tilde{\mathbf{v}}_g(\mathbf{r}, t_s)$:

Space-time separation of mean-flow motions

The mean gas velocity $\tilde{\mathbf{v}}_g$ is first separated as the product of the temporal variable t_s and the spatial (vector) variable $\mathbf{r}$ as:

$$\tilde{\mathbf{v}}_g(t_s, \mathbf{r}) \approx \mathbf{v}_t(t_s)\phi_v(\mathbf{r})$$
$$\tilde{T}(t_s, \mathbf{r}) \approx T_t(t_s)\phi_T(\mathbf{r}) \quad (19)$$

where the scalar-valued functions $\phi_v(\mathbf{r})$ and $\phi_T(\mathbf{r})$ are non-negative at each spatial point $\mathbf{r}$. The mass flow rate of gas through a combustor of cross section $A(\mathbf{r})$ is given by:

$$\dot{m}(t) \approx A(\mathbf{r})\tilde{\mathbf{v}}_g(t_s, \mathbf{r})\tilde{\bar{\rho}}(t_s, \mathbf{r})$$

implying that the mean gas density $\tilde{\bar{\rho}}$ is inversely proportional to $A(\mathbf{r})\tilde{\mathbf{v}}_g$. Here, the spatial variable $\mathbf{r}$ only includes the longitudinal direction after spatial averaging over the cross-section.

Since the mean pressure $\tilde{\bar{p}}$ has been assumed to be independent of the spatial variable $\mathbf{r}$ in high-pressure combustors, the ideal gas law dictates that $\tilde{T}$ is inversely proportional to $\tilde{\bar{\rho}}$. This, in turn, implies that $\tilde{T}$ is directly proportional to $A(\mathbf{r})\tilde{\mathbf{v}}_g$ as:

$$\tilde{T}(t_s, \mathbf{r}) = \frac{\tilde{\bar{p}}(t)}{\bar{R}\dot{m}(t)}A(\mathbf{r})\mathbf{v}_g(t_s, \mathbf{r}) \quad (20)$$

Using Eq. (19) in Eq. (20) yields:

$$T_t(t_s) \equiv \frac{\tilde{\bar{p}}(t)}{\bar{R}\dot{m}(t)}\mathbf{v}_t(t_s)$$
$$\phi_t(\mathbf{r}) \equiv A(\mathbf{r})\phi_v(\mathbf{r}) \quad (21)$$

For a combustor of uniform cross-section (i.e., $A(\mathbf{r}) = A$ for all $\mathbf{r}$), the constant term A can be absorbed in the temporal part $T_t(t)$ so that Eq. (21) is modified as:

$$T_t(t_s) = \frac{A\,\tilde{\bar{p}}(t_s)}{\bar{R}\dot{m}(t_s)}\mathbf{v}_t(t_s)$$
$$\phi_t(\mathbf{r}) \approx \phi_v(\mathbf{r}) \quad (22)$$

Therefore, for uniform cross-section of the combustor, Eq. (19) can be rewritten as:

$$\tilde{\mathbf{v}}_g(t_s, \mathbf{r}) \approx \mathbf{v}_t(t_s)\phi(\mathbf{r})$$
$$\tilde{T}(t_s, \mathbf{r}) \approx T_t(t_s)\phi(\mathbf{r}) \quad (23)$$

where the function $\phi(\mathbf{r})$ is normalized over the total volume V_{comb} of the combustor, i.e.,

$$\frac{1}{V_{comb}}\iiint_V \phi(\mathbf{r})dV = 1 \quad (24)$$

In the sequel, Eq. (23) will be used for modeling combustion dynamics and control systems analysis based on the gain-scheduling variables $\mathbf{v}_t(t_s)$ and $T_t(t_s)$ that are available from the slow-time scale dynamics of the combustion control system. The scheduling variables $\mathbf{v}_t$ and T_t together are referred to as the scheduling vector:

$$\bar{\mathrm{v}} = \begin{bmatrix}\mathbf{v}_t \\ T_t\end{bmatrix}$$

The speed of sound $\bar{a}$ is expressed as

$$\bar{a} = a_t(t_s)\sqrt{\phi(\mathbf{r})} \quad (25)$$

The pressure perturbation can be modally decomposed as:

$$p'(\mathbf{r}, t_f) = \sum_{n=1}^{\infty}\eta_n(t_f)\psi_n(\mathbf{r}) \quad (26)$$

subject to specified boundary conditions along the surface of the chamber. In this coordinate frame, p' has a time-dependent component η_k along the direction of the k^{th} unit vector of an orthonormal basis $\{\psi_n\}_{n=1,2,\cdots}$, which completely spans the space of pressure functions. That is, the set $\{\psi_n\}_{n=1,2,\cdots}$ satisfies the following conditions

- Orthonormality: $\langle \psi_n, \psi_m \rangle \equiv \iiint \psi_n \psi_m dV = \delta_{mn}$ for all integers m and n;
- Completeness: $\langle \varphi, \psi_n \rangle \equiv \iiint \varphi \psi_n dV = 0 \quad \forall n$, then $\varphi = 0$.
- Admissibility: $\psi_n(\mathbf{r})$ satisfies specified boundary conditions $\forall n$

where $\langle \bullet, \bullet \rangle$ defines the inner product.

Modal analysis of acoustic pressure, Eq. (26), is performed as follows.

$$\begin{aligned}
\eta_n &= \iiint \sum_{m=1}^{\infty} \eta_m \psi_m \psi_n dV = \iiint p' \psi_n dV \\
\frac{\partial^2 \eta_n}{\partial t_f^2} &= \iiint \frac{\partial^2 p'}{\partial t_f^2} \psi_n dV \\
&= \iiint \bar{a}^2 \nabla^2 p' dV - \iiint \bar{a}^2 h dV - \iiint \bar{a}^2 h_c dV \\
&= \sum_{m=1}^{\infty} \eta_m \iiint \bar{a}^2(\mathbf{r}, t_s) \nabla^2 \psi_m \psi_n dV + F_n + U_n
\end{aligned} \tag{27}$$

where

$$\begin{aligned}
F_n &= -\iiint \bar{a}^2 h \, dV \\
U_n &= -\iiint \bar{a}^2 h_c \, dV
\end{aligned} \tag{28}$$

In view of Eq. (27) we introduce the following integral relationship:

$$\iiint \bar{a}^2(\mathbf{r}, t_s) \nabla^2 \psi_m \psi_n dV = -\omega_n^2 \delta_{mn} \quad \forall m, n \tag{29}$$

to approximate the mode shapes $\{\psi_n\}_{n=1,2,\cdots}$ and natural frequencies $\{\omega_n\}_{n=1,2,\cdots}$ corresponding to specified boundary conditions. By completeness property of the orthonormal set $\{\psi_n\}_{n=1,2,\cdots}$, Eq. (29) is equivalent to the following algebraic relationship:

$$\bar{a}^2(\mathbf{r}, t_s) \nabla^2 \psi_n(\mathbf{r}) + \omega_n^2(t_s) \psi_n(\mathbf{r}) = 0 \tag{30}$$

A set of ordinary differential equations is derived as an approximation of Eqs. (27) and (28) based on the space-time separation of mean-flow conditions in Eq. (23):

$$\frac{d^2 \eta_n}{dt_f^2} + \omega_n^2(T_t(t_s)) \eta_n = F_n(t_s, t_f) + U_n(t_s, t_f) \tag{31}$$

where

$$F_n \approx -a_t^2 \iiint \phi(\mathbf{r}) h \psi_n(\mathbf{r}) dV \tag{32}$$

$$U_n \approx -a_t^2 \iiint \phi(\mathbf{r}) h_c \psi_n(\mathbf{r}) dV \tag{33}$$

and $\omega_n(t_s) = a_t(t_s) k_n$ (34)

where ω_n is the slowly varying frequency of the n^{th} mode shape, and k_n is the corresponding wave number. Based on the Eqs. (25) and (30), approximated mode shapes are derived as:

$$\phi(\mathbf{r}) \nabla^2 \psi_n + k_n^2 \psi_n = 0 \tag{35}$$

subject to the boundary conditions, where the spatially dependent weighting function $\phi(\mathbf{r})$ puts a smaller weight on the mode shapes of pressure perturbation in the low-temperature region and a larger weight in the high-temperature region.

The fast-time scale control command for secondary fuel injection is superimposed on the slow-time scale primary fuel flow. Control actions arising from the distributed combustion of secondary fuel are modeled by an ensemble of point actuators; the output of each actuator is determined by its position, the local burning characteristics of the fuel, and the time delay from the instant of fuel injection. A detailed derivation of the actuator command U_n in Eq. (33) is presented below [2]:

$$U_n = \frac{-\bar{R} \Delta H_c}{\bar{C}_v} \sum \psi_n(\mathbf{r}_i) u_i(t_f; \bar{\mathrm{v}}) \tag{36}$$

$$u_i = b_i(\bar{\mathrm{v}}) \frac{\partial \dot{m}_{in}[t_f - \tau_i(\bar{\mathrm{v}})]}{\partial t_f} \tag{37}$$

where ΔH_c is the heat of combustion per unit fuel mass and the injection rate of secondary fuel is represented by $\dot{m}_{in}$ with spatial distribution density b_i, the time delay τ_i associated with the ith point actuator.

Finally, the open-loop plant model of the mean-flow dependent acoustic dynamics (in the fast-time scale) becomes

$$\begin{aligned}
&\frac{d^2 \eta_n}{dt_f^2} + \omega_n^2(\tilde{T}(t_s)) \eta_n \\
&+ \sum_{i=1}^{\infty} D_{ni}(\tilde{T}(t_s), \tilde{\mathbf{v}}_g(t_s)) \frac{d\eta_i}{dt_f} + E_{ni}(\tilde{T}(t_s), \tilde{\mathbf{v}}_g(t_s)) \eta_i(t_f) = \\
&- \frac{\bar{R} \Delta H_c}{\bar{C}_v} \sum_k b_k(\tilde{T}(t_s), \tilde{\mathbf{v}}_g(t_s)) \psi_n(\mathbf{r}_k) \frac{\partial \dot{m}_{in}[t_f - \tau_k(\tilde{\mathbf{v}}_g(t_s))]}{\partial t_f}
\end{aligned} \tag{38}$$

The formulation described above is considered as a wide-range model of combustion dynamics and provides a framework for accommodating both the global and local behavior in the two time-scale control systems. For both control and estimation, a state-space realization of the combustion dynamics represents a family of $\bar{\mathrm{v}}$-parameterized models. The models that include uncertainties and effects of mean-flow dependence are presented below:

$$\begin{aligned}
\dot{x}_p &= (A_p(\bar{\mathrm{v}}) + \Delta_p(\bar{\mathrm{v}})) x_p + G_1(\bar{\mathrm{v}}) v + G_2(\bar{\mathrm{v}}) d \\
y &= C x_p + \theta
\end{aligned} \tag{39}$$

where $\bar{\mathrm{v}}$ is the scheduling vector consisting of mean-flow temperature and velocity, d is the plant disturbance and θ is the sensor noise. The state vector is chosen as $x_p = (\varsigma \quad \dot{\varsigma})^T$ with $\dot{\varsigma} = \eta$, and $\eta \equiv [\eta_1, \eta_2, \cdots, \eta_N]^T$. Unsteady heat release Q' and acoustic pressure p' provides *effort* and *flow* information in mechanical systems, where their phase difference determines the dissipated or liberated energy. For the nominal linear model, the system matrix is given as:

$$A_p \equiv \begin{bmatrix} 0 & I \\ -\Omega(T_t) - E(\bar{\nu}) & -D(\bar{\nu}) \end{bmatrix}$$

with $\Omega \equiv diag(\omega_1^2, \omega_2^2, \cdots, \omega_N^2)$ (40)

The input vector $v(t)$ associated with a set of point actuators is related to the mass injection rate of the secondary fuel, $\dot{m}_{in}$, as:

$$v(t) = \begin{bmatrix} b_1(\bar{\nu})\dot{m}_{in}(t-\tau_1(\bar{\nu})-\delta\tau_1(\bar{\nu})) \\ b_2(\bar{\nu})\dot{m}_{in}(t-\tau_2(\bar{\nu})-\delta\tau_2(\bar{\nu})) \\ \vdots \\ b_M(\bar{\nu})\dot{m}_{in}(t-\tau_M(\bar{\nu})-\delta\tau_M(\bar{\nu})) \end{bmatrix} \quad (41)$$

where $\delta\tau_i$ is the modeling error associated with the time delay of the control input. Equation (41) represents the actuator dynamics from the excitation of the point actuator(s) to the actual energy release of control fuel. Since the mean flow is slowly varying compared to the motion of the secondary-fuel injector, the mean-flow-dependent transfer function of actuator dynamics can be approximated as:

$$\boldsymbol{A}(s;\bar{\nu}) = \left[b_1(\bar{\nu})e^{-\tau_1(\bar{\nu})s} \quad b_2(\bar{\nu})e^{-\tau_2(\bar{\nu})s} \quad \cdots \quad b_M(\bar{\nu})e^{-\tau_M(\bar{\nu})s} \right]^T \quad (42)$$

An additive operator $\Delta_p(\bar{\nu})$, that is dependent on the mean-flow conditions, represents the effects of model and parametric uncertainties of the plant. It can be treated as a disturbance to the plant, $w_s = \Delta_p(x_p)$, to realize the energy amplification from input to output through this operator. The global behavior of the operator Δ_p is characterized by the L_2-gain as follows:

$$\left\| \Delta_p(\bar{\nu}) \right\|_\infty < \delta p(\bar{\nu}) \quad (43)$$

A physical interpretation of Eq. (43) is that individual dynamics of the uncertainty operator $\Delta_p(\bar{\nu})$ yields to the following energy amplified relationship from its input x_p to its output w_s as:

$$\int_0^T \left\| w_s \right\|^2 dt < \int_0^T \delta p^2(\bar{\nu}) \left\| x_p \right\|^2 dt \quad \forall T \in [0, \infty) \quad (44)$$

for zero initial conditions.

3. Formulation and Analysis of the Wide-Range Robust Control Law

This section focuses on robust performance issues of the inner-layer within the two-layer wide-range combustion control system as an extension of the narrow-range control concept presented in the previous publication [9]. The acoustic dynamics at the inner layer is parametrically dependent on mean-flow dynamics at the outer-layer. For *robustness*, the inner-layer controller is synthesized such that stability is guaranteed over a wide operating range of persistently varying mean-flow variables and the associated modeling uncertainties. For *performance*, the controller should have the capability for disturbance rejection and meeting the requirements of acoustic energy and control energy under both steady-state and transient conditions. The role of the controller design in this section is to simultaneously satisfy these two objectives for persistently varying mean-flow conditions over a wide range.

3.1 Two-layer Control Structure

In Section 2, the fluid-combustion dynamics have been decomposed into acoustic dynamics in the fast-time scale and mean-flow dynamics in the slow-time scale, in which the parameters of acoustic dynamics are dependent on mean-flow temperature and velocity. In the integrated control strategy, the fluid-combustion dynamics are transformed into a combination of slowly varying trajectory of quasi-steady equilibrium points, defined by mean-flow dynamics, and the associated linear perturbations are defined by the mean-flow-dependent acoustic dynamics in the fast-time scale. While the temporal trajectory of mean-flow variables is tracked for global performance by the slow-time controller, the fast-time controller locally suppresses the acoustic motions with its slowly varying parameters being gain-scheduled by the mean-flow temperature and velocity. The control system of fluid-combustion dynamics is therefore designed to have a two-layer hierarchical structure. The aforementioned mean-flow dynamics represents the open-loop plant in the outer-layer whereas the acoustic dynamics, parametrically dependent on the mean-flow variables, represent the open-loop plant in the inner-layer. The temporal trajectory of mean flow variables is tracked by manipulating the primary-fuel flow in the slow-time scale, while, in the inner-layer, the acoustic dynamics is feedback-controlled by secondary-fuel flow, that is realized as fast modulation of the primary-fuel flow.

Figure 1 and figure 2 show a schematic view of the hierarchical structure of the two-layer control strategy. The inner-layer controller continuously receives gain-scheduled signals from the outer layer to update its parameters that are related to the temporal equilibrium points defined by the mean-flow temperature and velocity, in response to the change of perturbation dynamics at quasi-steady equilibrium points. A slow-time scale mean-flow controller at the outer layer is responsible for global-performance of the combustion chamber. Its design is well known in industry and is not reported in this paper. The inner-layer controller processes the fast-time-scale signals of pressure oscillations and slow-time-scale signals of gain-scheduled variables to modulate the primary-fuel flow. The modulated signal then manipulates the actuator(s) of the combustion chamber to locally suppress perturbations along the temporal trajectory of the mean-flow variables for wide-range control of the combustion dynamics.

3.2 Analysis of the Robust Control Law

To design the robust controller at the inner layer, a family of $\bar{\nu}$-parameterized generalized plants $\boldsymbol{P}(s;\bar{\nu})$ is first constructed following the block diagram in Figure 3. It includes the $\bar{\nu}$-parameterized nominal plant, actuator dynamics, modeling uncertainties and performance requirements for synthesis of a wide-range robust control law. The feedback controller $\boldsymbol{K}(s;\bar{\nu})$ is derived as a function of the gain-scheduling vector $\bar{\nu}$ for controller adaptation under slowly varying operating conditions. Figure 3 shows the internal structure of the $\bar{\nu}$-parameterized generalized plants. The metric of L_2-gain facilitates transformation of the coupled performance-stability robustness analysis problem into a stability robustness problem (Zhou et al., 1996). To incorporate the disturbance rejection capabilities for robust performance, the control objective is related to the metric of L_2 gain, indicating energy amplification from the generic disturbance w to the objective variable z. The generic disturbance w consists of disturbances induced by plant uncertainties w_s, disturbances induced by $\bar{\nu}$-parameterized modeling errors of the time delay function w_τ, weighted plant disturbances w_d, and weighted sensor noise w_θ. The objective variable z consists of stability variables associated with plant uncertainty z_s and time-delay errors z_τ, and performance

variables associated with the acoustic pressure response z_p and the secondary-fuel injection z_u.

The subsystems in the generalized plant family are the nominal plant dynamics specified in the $\bar{\nu}$-parameterized state-space realization, (A_p, G_1, G_2, C), shaping filters associated with the plant disturbances W_d, sensor noise W_θ, performance weighting functions, W_p and W_u, associated with pressure response and secondary-fuel injection, respectively, and the stability weighting function W_τ associated with time-delay errors. Note that the plant uncertainty Δ_p and phase uncertainty Δ_τ induced by time-delay errors are not included because modeling uncertainties are represented as uncertainty-induced disturbances, w_s and w_τ. Two shaping filters W_d and W_θ are incorporated to characterize the main frequency components of the plant disturbances and sensor noise. The performance weighting functions W_p and W_u are specified for the desired frequency responses of acoustic motions and secondary-fuel injection, respectively, providing the trade-off between (high-frequency) transient and (low-frequency) steady-state responses. Those subsystems are derived as analytic functions of the gain-scheduling variable $\bar{\nu}$ to serve as the database of the LPV controller synthesis.

Fast-time modulation of the primary fuel is realized as a secondary-fuel injection. In modeling the secondary-fuel distribution, the possible parametric error of time delay $\delta\tau(\bar{\nu})$ causes $\bar{\nu}$-parameterized phase uncertainty of the closed-loop. The $\bar{\nu}$-parameterized transfer function $e^{-\delta\tau(\bar{\nu})s}$ is represented as one member of the following set:

$$\left\{(1+\Delta_\tau(j\omega;\bar{\nu})W_\tau(j\omega;\bar{\nu})\ \forall\omega\ \forall\bar{\nu} : \left\|\Delta_\tau(j\omega;\bar{\nu})\right\| \le 1\right\} \tag{45}$$

where $\Delta_\tau(j\omega;\bar{\nu})$ accounts for the $\bar{\nu}$-parameterized phase uncertainty and acts as the magnitude scaling for each component of $\bar{\nu}$. The $\bar{\nu}$-parameterized stability weighting function $W_\tau(j\omega;\bar{\nu})$ specifies allowable joint phase-magnitude margins in the closed-loop system and serves as a metric of robustness. Equation (45) is equivalent to:

$$\left|e^{-\delta\tau(\bar{\nu})j\omega} - 1\right| \le \left|W_\tau(j\omega;\bar{\nu})\right|\ \forall\omega\ \ \forall\bar{\nu} \tag{46}$$

where $\delta\tau(\bar{\nu}) \equiv \max_k \left|\tau_k(\bar{\nu})\right|\ \ \forall\bar{\nu}$. For the second source of modeling uncertainty, the $\bar{\nu}$-parameterized plant uncertainty $\Delta_p(s;\bar{\nu})$ acts as an internal feedback to the nominal dynamics. It accounts for modeling inaccuracies of intrinsic coupling between flow dynamics and combustion responses. The bound of $\Delta_p(s;\bar{\nu})$ is specified by its L_2 gain as $\left\|\Delta_p(s,\bar{\nu})\right\|_\infty < \delta_p(\bar{\nu})$. Based on the small gain theorem (Zhou et al., 1996), a sufficient condition of robust stability of the closed-loop system is:

$$\int_0^T \left(\left\|z_s\right\|^2 + \left\|z_\tau\right\|^2\right)dt \le \int_0^T \left(\left\|w_s\right\|^2 + \left\|w_\tau\right\|^2\right)dt\ \ \forall T\in[0,\infty) \tag{47}$$

for the zero-state initial conditions and z_s being equal to $\delta p(\bar{\nu})x_p$.

The inequality in Eq. (47) implies that the robust controller can stabilize all perturbed plants within the $\bar{\nu}$-parameterized uncertainty bounds characterized by $\delta p(\bar{\nu})$ and $\delta\tau(\bar{\nu})$ without specifying any performance requirements that provide trade-off between the control energy and the acoustic energy; transient response and steady-state response; and stability robustness and performance. The performance weights within the system bandwidth are included in the $\bar{\nu}$-parameterized generalized plants for regulation of the secondary-fuel injection and pressure dynamics. Shaping filters are used to penalize the dominant frequency components of plant disturbances and sensor noise for effective rejection. The ability to suppress flow oscillations is quantified by a positive quadratic energy-like function:

$$H = \frac{1}{V}\iiint_V p'(\mathbf{r},t)^2\,dV \tag{48}$$

Orthonormality of the acoustic mode shapes simplifies Eq. (48) as:

$$H = \frac{1}{V}\left\langle \sum \varphi_n\eta_n, \sum \varphi_m\eta_m \right\rangle = \sum \eta_n^2 = \|\eta\|^2 \tag{49}$$

The combustion chamber tends to become free of pressure oscillations if H in Eq. (49) approaches zero.

To achieve small steady-state amplitude and short settling time of pressure oscillations, a new performance variable z_p is introduced as:

$$\hat{z}_p(s) = W_p(s;\bar{\nu})\hat{\eta}(s) \tag{50}$$

where the Laplace Transform of a time-dependent quantity is denoted by "^"; and the weighting function $W_p(s,\bar{\nu})$ is defined as:

$$W_p = \begin{bmatrix} W_{p1} & 0 & \cdots & 0 \\ 0 & W_{p2} & \ddots & \vdots \\ \vdots & \ddots & \ddots & 0 \\ 0 & \cdots & 0 & W_{pN} \end{bmatrix} \tag{51}$$

A procedure for selecting the performance-weighting matrix $W_p(s,\bar{\nu})$ of pressure oscillations is outlined below:

The Bode plot of $W_{pi}(s), i = 1,2,\cdots,N$ resembles that of an integration operator within the bandwidth around each natural frequency $\omega_i(\bar{\nu})$ over the range of the gain-scheduling variable $\bar{\nu}$. The shape of each $W_{pi}(s)$ outside the respective bandwidth is assigned to be flat. The amplitude of each $W_{pi}(s)$ represents the extent of overshoot of the amplitude of its mode shape for trade-off between transient and steady state responses in the sense that a high overshoot usually leads to a short settling time. Thus, the resulting performance variable z_p yields small steady-state amplitude and short settling time of pressure fluctuations. Note that the bandwidth of $W_{pi}(s)$ could be altered by mean-flow-dependent modeling uncertainties. The nominal bandwidth corresponds to the natural frequency of acoustic oscillations. To determine the possible bandwidth range for all perturbed plants, natural frequencies within the uncertainty bound of $\bar{\nu}$ need to be calculated.

The other performance requirement involves secondary-fuel injection. The frequency response of mass flow rate of secondary fuel has limited bandwidth and overshoot amplitude due to the inertial effects of the fuel flow. To this end, a performance weight $W_u(s,\bar{\nu})$ is incorporated into the generalized plant model, and a new performance variable z_u is defined as:

$$\hat{z}_u(s) = W_u(s;\bar{\nu})\hat{u}(s) \tag{52}$$

where $\hat{u}(s)$ and $\hat{z}_u(s)$ are the Laplace transforms of $\dot{m}_{in}(t)$ and $z_u(t)$, respectively. The $\bar{\nu}$-parameterized performance weighting $W_u(s,\bar{\nu})$ is chosen via the following procedure:

The Bode plot of $W_u(s)$ resembles that of a derivative operator within the frequency range of interest. A small z_u implies that the high-frequency component of secondary fuel flow rate $\dot{m}_{in}$ has been filtered out. At each $\overline{\nu}$, the shape of W_u outside the bandwidth is assigned to be flat. The bandwidth range is altered by uncertainties in the (mean-flow-dependent) scheduling vector $\overline{\nu}$.

The nominal performance is specified by the relationship between exogenous inputs, plant disturbance d and sensor noise θ, and performance variables, z_p and z_u. A shaping filer W_d is included in the generalized plant such that the resulting robust controller focuses on rejecting the dominated frequency components of plant disturbance. Therefore, the weighted plant disturbance w_d is used for performance specifications, instead of the disturbance d itself, where

$$\hat{w}_d(s) = W_d(s)\,\hat{d}(s) \tag{53}$$

Similar conditions are introduced in the sensor noise θ as:

$$\hat{w}_\theta(s) = W_\theta(s)\,\hat{\theta}(s) \tag{54}$$

where $\hat{w}_\theta$ is the weighted sensor noise and W_θ is shaping the sensor noise θ.

A linear parameter varying (LPV) robust controller is designed such that the plant disturbance d and sensor noise θ have minimum effects on the acoustic motions and control actions from the energy perspectives. The nominal performance is specified by:

$$\int_0^T \left\|q(\overline{\nu})z_p(t)\right\|^2 + \left\|z_u(t)\right\|^2 dt \le \int_0^T \left(\left\|w_d(t)\right\|^2 + \left\|w_\theta(t)\right\|^2\right)dt \quad \forall T \in [0,\infty) \tag{55}$$

where q is a $\overline{\nu}$-parameterized positive scalar, representing the weighting factor of acoustic motion at each $\overline{\nu}$. As q is set larger, then the response of acoustic motions is more emphasized than that of control actions, and vice versa. Furthermore, increasing q implies a better rejection ability of exogenous inputs.

Based on Eq. (47) and Eq. (55), a sufficient condition for robust performance (i.e., a combination of robust stability and nominal performance) of the control system is:

$$\int_0^T \|z\|^2\, dt \le \int_0^T \|w\|^2\, dt \quad \forall T \in [0,\infty) \quad \forall w \in L_2[0,T];$$

$$\text{with } z = \begin{bmatrix} z_s \\ q z_p \\ z_u \\ z_\tau \end{bmatrix}; w = \begin{bmatrix} w_s \\ w_d \\ w_\theta \\ w_\tau \end{bmatrix} \tag{56}$$

If Eq. (56) holds, then the controller internally stabilizes the closed-loop for all perturbed plants with desired performance, subject to an uncertainty bound.

Following the internal structure in Fig. 3, the generalized plant family $\boldsymbol{P}(s;\overline{\nu})$ can be expressed, similar to that narrow-range control in the previous publication [9] by state-space realization as:

$$\begin{aligned} \dot{x} &= A(\overline{\nu})x + B_1(\overline{\nu})w + B_2(\overline{\nu})u \\ z &= C_1(\overline{\nu})x + D_{12}(\overline{\nu})u \\ y &= C_2(\overline{\nu})x + D_{21}(\overline{\nu})w \end{aligned} \tag{57}$$

Note that Eq. (56) is conservative because it ignores the structure of the uncertainly robust performance operator $\Delta(s;\overline{\nu})$, which consists of model uncertainties and performance-induced uncertainties. The generalized plant family $\boldsymbol{P}(s;\overline{\nu})$ in Eq. (57) can be compensated to make the requirements of robust performance specified in Eq. (56) less conservative. Figure 4 shows that the generalized plant family is compensated by two $\overline{\nu}$-parameterized compensators, $D^{-1}(s,\overline{\nu})$ and $D(s,\overline{\nu})$. The resulting compensated generalized plant represents the structure Δ without altering the uncertainty size and performance requirements. This is achieved by choosing the D-compensator as:

$$D(s,\overline{\nu})\Delta(s,\overline{\nu}) = \Delta(s,\overline{\nu})D(s,\overline{\nu}) \quad \forall \overline{\nu} \tag{58}$$

This compensation approach, known as the D-K iteration (Packard and Doyle, 1993), can be iterated many times.

4. Synthesis of the Wide-Range Robust Control Law

The inner-layer control law is synthesized using the concept of Linear Parameter Varying (LPV)-L_2-gain methodology that is presented in this section. The objective of the LPV-L_2-gain control law is to reject the effects of chamber disturbances and mean-flow dependent model uncertainties while optimizing the specified performance. The LPV-L_2-gain controller has a H_∞-structure and is derived as a gain-scheduling process accommodating continuous variations of the mean-flow conditions. The major challenge is to synthesize a family of $\overline{\nu}$-parameterized control laws that guarantee robust performance under the continuously varying mean-flow conditions over a wide operating range.

The LPV L_2-gain controller consists of two main components. The first component is a $\overline{\nu}$-parameterized observer that dynamically estimates the states of the $\overline{\nu}$-parameterized generalized plants described by Eq. (57). The estimator structure is not formulated as an exact plant state observer due to the presence of a calibration term $w_{cal}(\overline{\nu})$ that protects the control system from being excessively sensitive to exogenous inputs and modeling uncertainties, entering the observer state equation. The second component is a state-feedback control gain matrix, which determines the control action based on the estimated state $\hat{x}$ as seen in the controller configuration of Figure 5.

The remaining task lies in the determination of the $\overline{\nu}$-parameterized observer matrix $L(\overline{\nu})$, controller matrix $K(\overline{\nu})$, and the calibrated term $w_{cal}(\overline{\nu})$ such that the sufficient condition for robust performance in Eq. (56) holds. Usage of parameter-dependent Lyapunov functions in the controller synthesis leads to differential matrix inequalities as reported by Hong [9]. The results are derived based on the following assumptions,

Assumption#1: The parameter-dependent matrices D_{12} and D_{21} are normalized as:

$$D_{12}(\overline{\nu}) = \begin{bmatrix} 0 \\ I \end{bmatrix};\; D_{21}(\overline{\nu})\,D_{21}^T(\overline{\nu}) = I; \tag{59}$$

Assumption #2: D_{11} is reduced to zero by loop shifting [10];

Assumption #3: D_{22} is set to zero without loss of generality [10];

Assumption #4: The parameter vector $\bar{\mathbf{v}}(t)$ is a continuous function belonging to a compact subset of $\Re^s$ and the parameter variation rate $\dot{\bar{\mathbf{v}}}(t)$ is bounded as $\left|\dot{\bar{\mathbf{v}}}_i(t)\right| \le \beta_i \quad \forall i \in \{1,2,\cdots,s\}$

Assumption #5: The system matrices of the generalized plant family, $(A, B_1, B_2, C_1, C_2, D_{12}, D_{21})$, are continuous functions of $\bar{\mathrm{v}}$;

Assumption #6: The control matrix $K(\bar{\mathbf{v}})$ and the observer matrix $L(\bar{\mathbf{v}})$ are continuously differentiable functions of $\bar{\mathrm{v}}$;

The main results are summarized below as Theorem 1 below and the detailed proof has been presented by Hong [9].

Theorem 1: All candidate LPV L_2-gain controllers for γ-performance and β-variation are synthesized by solving the following two linearly coupled matrix inequalities for $X(\bar{\mathrm{v}})$ and $Z(\bar{\mathrm{v}})$:

$$\begin{bmatrix} X^{-1}A_X^T + A_X X^{-1} - \sum \pm\beta_i \frac{\partial X^{-1}}{\partial \bar{v}_i} - B_2 B_2^T & X^{-1}C_1^T(I - D_{12}D_{12}^T) & B_1 \\ (I - D_{12}D_{12}^T)C_1 X^{-1} & -I & 0 \\ B_1^T & 0 & -\gamma^2 I \end{bmatrix} < 0 \quad (60)$$

where $A_X = A - B_2 D_{12}^T C_1$

and

$$\begin{bmatrix} Z^{-1}A_Z + A_Z^T Z^{-1} + \sum \pm\beta_i \frac{\partial Z^{-1}}{\partial \bar{v}_i} - C_2^T C_2 - C_2^T D_{21} F_1 - F_1^T D_{21}^T C_2 & Z^{-1}B_1 & F_2^T \\ B_1^T Z^{-1} & -I & 0 \\ F_2 & 0 & -\gamma^2 I \end{bmatrix} < 0 \quad (61)$$

where $A_Z = A + B_1 F_1 - B_1 D_{21}^T C_2$

$$F_1 = \frac{1}{\gamma^2} B_1^T X$$

$$F_2 = -(B_2^T X + D_{12}^T C_1)$$

The LPV L_2-gain control law in Figure 5 is derived in terms of the control matrix

$$K(\bar{\mathrm{v}}) = -(B_2^T(\bar{\mathrm{v}})X(\bar{\mathrm{v}}) + D_{12}^T(\bar{\mathrm{v}})C_1(\bar{\mathrm{v}})), \quad (62)$$

the estimation matrix is

$$L(\bar{\mathrm{v}}) = Z(\bar{\mathrm{v}})C_2^T(\bar{\mathrm{v}}), \quad (63)$$

and the calibration term is:

$$w_{\max}(\hat{x}, \bar{\mathrm{v}}) = (B_1(\bar{\mathrm{v}}) - Z(\bar{\mathrm{v}})C_2^T(\bar{\mathrm{v}})D_{21}(\bar{\mathrm{v}}))F_1(\bar{\mathrm{v}})\hat{x} \quad (64)$$

The resulting dynamics of the LPV robust controller becomes

$$\dot{\hat{x}} = [A + B_1F_1 + B_2F_2 - ZC_2^T(C_2 + D_{21}F_1)]\hat{x} + ZC_2^T y$$

$$u = -(B_2^T X + D_{12}^T C_1)\hat{x}$$

where $\hat{x}$ is the estimated state.

The differential matrix inequalities in Theorem 1 are discretized by a finite-element approach as a series of solvable linear matrix inequalities [9]. The commercially available package of Matlab-LMI toolbox that numerically solves these inequalities via a convex optimization procedure has been used for controller synthesis in this paper.

Remark3: Theorem 1 enhances the theory of linear parameter varying (LPV) control in the following two areas:

- The features of the LPV L_2-gain control law in Theorem 1 are similar to those of the existing LTI H_∞ control (Doyle *et al.*, 1989).
- Unlike the LPV control law of Wu et al. (1996), the proposed LPV control is not explicitly dependent on the temporal rates of the scheduling variables. This feature is attractive from the perspectives of real-time implementation because measurements of time derivatives of the scheduling variables may not usually be available.

5. Simulation Results and Discussion

This section presents a series of parametric studies and transient simulations of a generic combustor model to validate the wide-range robust control methodology. The objective is to investigate the relationships among system performance, stability robustness, and plant operation based on the transient response and frequency spectrum of pressure oscillations under different operation scenarios. The relationships among the uncertainty bounds of system dynamics, the response of flow oscillations and control actions, and the allowable variation rates of mean-flow parameters are investigated and quantified.

Table II lists the parameters of the generic combustor that represents typical scenarios encountered in practical combustion chambers. Table III lists the dimensionless quantities that are needed to investigate the four dominant modes of longitudinal acoustic oscillations under H_∞ Control, Gain-scheduled Control, and the LPV-L_2-gain Control. Table IV lists the parameters needed for modeling and simulation.

Two bandwidth-limited performances weighting functions W_p and W_u have been fitted as continuous functions of the scheduling variables: mean-flow temperature $\tilde{T}$ and velocity $\tilde{\mathbf{v}}_g$ at each of the selected modal frequencies $\omega_1, \cdots, \omega_N$. The shaping filters W_d and W_θ are taken as unity as the chamber disturbances and sensor noise are assumed to be white. The system robustness is represented by the bound $\delta p(\bar{\mathrm{v}})$ of plant modeling uncertainties. The system performance is represented by the weighting factor of pressure response $q(\bar{\mathrm{v}})$. The plant operation is characterized by the bounds of absolute values of the normalized rates, $\left|\dot{\rho}_T\right|$ and $\left|\dot{\rho}_v\right|$, respectively, of the scheduling variables $\tilde{T}$ and $\tilde{\mathbf{v}}_g$. Increasing $\left|\dot{\rho}_T\right|$ and $\left|\dot{\rho}_v\right|$ implies that the scheduling variables can be varied faster with guaranteed robust performance. On the other hand, increasing the performance parameters q implies a more stringent requirement of system performance in terms of the transient oscillations of each acoustic mode and the ability to reject chamber acoustic and thermal noise. Extensive simulation experiments have been conducted to realize the trade-off relationship among system robustness, performance and operation of the control system.

The dimensionless bounds of the variation rates $\left|\dot{\rho}_T\right|$ and $\left|\dot{\rho}_v\right|$ jointly define the allowable varying rate of plant operation from the perspectives of performance. Figure 6 shows the trade-off between system performance and plant operation. For the plant uncertainty bound set at $\delta p = 0.03$, the family of curves in Figure 6 serve as a constraint under which the LPV robust controller guarantees system stability and performance in the operating range of dimensionless scheduling variables $\rho_T \in [0.6, 1.4]$ and $\rho_v \in [0.5, 1.5]$. The triple $(\left|\dot{\rho}_T\right|, \left|\dot{\rho}_v\right|, q)$ defines the design point which is evaluated in the modeling

process prior to the controller design. For example, with the maximum variation of the mean-temperature rate $|\dot{\rho}_T|$ being 0.1 and the maximum variation of the mean-velocity variation rate $|\dot{\rho}_v|$ being 0.016, the weighting factor of system performance q should be less than or equal to 0.09 to guarantee robust performance. This is a conservative design and, in the simulation stage, much larger q may be allowed. A larger q leads to a larger risk, since it implies a larger probability that the combustion system may enter into a (potentially) unstable region beyond what is specified by the plant uncertainty model. The insufficient information of uncertainty dynamics, except its size specified by the induced L_2-norm, prevents precise quantification of the region of risk. Figure 6 qualitatively reveals the sensitivity of each design point. Robust performance of the closed-loop system is sensitive to the mean-velocity variation rate $\dot{\rho}_v$ because the L_2-gain control tends to maximize the entropy of the closed-loop system. The effects of mean-velocity rate $\dot{\rho}_v$ on the dissipation or driving force of acoustic dynamics represent the varying condition of the irreversible process in the acoustic field. Since the entropy-oriented scheme is sensitive to the controlled irreversible process, the L_2-gain control system of acoustic dynamics is sensitive to mean-velocity variations. Figure 6 also suggests that the robust performance of the closed-loop is relatively insensitive to the mean-temperature variation rate $\dot{\rho}_T$ because the mean temperature determines the natural frequencies of the acoustic vibration. This phenomenon also leads to the fact that the bandwidth of the open-loop system is almost the same as that of the closed-loop system. In other words, the feedback control does not change the natural frequencies of the system. Therefore, model reduction originally performed in the open-loop plant remains valid after the feedback control is formed. Consequently, for large natural frequencies, the control actions would require fast actuators.

Figure 7 shows that the robust performance of the closed-loop system is not very sensitive to mean temperature variation rate with $|\dot{\rho}_v|$ being set to 0.01. The results indicate that robustness of the closed-loop system becomes sensitive to mean-velocity variation rate only in the region of high performance. Figure 7 can be used to realize a trade-off between robustness δp and performance q. In the low-performance region, the trade-off between robustness and performance is almost linear, i.e., the increment of δp is approximately proportional to the decrement of q.

Two plates in Figure 8 show the temporal trajectories of mean velocity and mean temperature generated from CFD calculation. In the simulation of the closed-loop system for the wide range of mean-flow conditions, the plant uncertainty bound is set to be $\delta p = 0.03$, time delay uncertainty bound $\delta\tau = 3/\omega_0$, plant disturbance intensity $10^{-1}\,\frac{\omega_0^2 \overline{C}_v p_0}{\overline{R}\Delta H_c}$, and sensor noise intensity $10^{-1}\,\frac{\omega_0^2 \overline{C}_v p_0}{\overline{R}\Delta H_c}$. Simulation experiments are conducted under three different controllers:

- Controller #1: Single H_∞ control;
- Controller #2: Gain-scheduled H_∞ control;
- Controller #3: LPV L_2-gain control.

Figure 9 shows the system response using a single H_∞ controller for the entire range of $\rho_T \in [0.6, 1.4]$ and $\rho_v \in [0.5, 1.4]$ where the system response exhibits instability and hence the performance is obviously unacceptable. Note that H_∞ control may be suitable for narrow-range operation as discussed in the previous work (Hong *et. al.*, 1999), but not for wide-range operation here. Figure 10 shows the system performance under the gain-scheduled controller, which is synthesized without considering the variations in the mean-flow variables $\tilde{\bar{T}}$ and $\tilde{\bar{\mathbf{v}}}_g$. The results show that the control system is unstable. This establishes the necessity for LPV robust control.

Figures 11, 12, 13 and 14 show the responses of four modes of acoustic oscillations in the combustion chamber under the LPV robust control. The total acoustic oscillations are significantly improved since the controller exhibits the ability to reject exogenous inputs on the first two modes without degrading the responses of high-frequency modes. This suggests that model reduction has not caused any significant loss of robustness under the LPV control for wide-range operation. Therefore, usage of LPV robust control may not require a meticulous consideration of the high-frequency excitation provided that the scheduling variables are appropriately rate-bounded. It is also shown that the closed-loop system is asymptotically stable in the absence of exogenous inputs.

The embedded observer located in the LPV robust controller is capable of estimating the internal states of acoustic dynamics under a wide range of continuously varying mean-flow condition as seen in Figures 11, 12, 13 and 14. The embedded observer provides an estimation of acoustic vibration of each mode. The transient and steady-state errors, due to modeling uncertainties and exogenous inputs, are shown to be small. This implies that the calibration terms in the embedded observer are able to keep the system away from the high-risk region, and yet they are small enough not to significantly change the estimated states. In the absence of modeling uncertainties, the performance of the observer embedded in L_2-gain controller approaches that of the minimum variance state estimator.

Figure 15 shows the secondary-fuel injection in the LPV robust control system. The fast-time modulation does not cross 4 % of primary fuel flow rate, while the amplitude of acoustic pressure oscillations exceeds 10% of the mean pressure. Figure 16 shows the frequency spectrum of the normalized pressure perturbations before and after the controller is brought in. The responses exhibit two frequency-scaled components corresponding to two time-scaled motions.

6. Summary and Conclusions

To synthesize a robust control law for wide-range operations, a two-time-scale model of combustion dynamics has been formulated by decomposition of the conservation laws and thermodynamic state relations based on the slowly varying mean-flow and fast perturbed conditions of the process variables. The fast-time scale acoustic-flame dynamics are parametrically dependent on the mean-flow temperature and velocity. Control actions on the fast-time scale are provided by secondary fuel injection that is realized as fast modulation of the primary fuel flow. The structure of control system follows a two-layered hierarchy. In the outer-layer, mean-flow dynamics of the combustion process is controlled in the slow-time scale by manipulating the primary-fuel flow, while the fast-time acoustic controller in the inner-layer is parametrically gain-scheduled by the mean-flow temperature and velocity from the outer-layer.

In the fast-time scale inner-layer, a robust control law is formulated based on the concept of linear parameter varying (LPV) L_2-gain in the setting of differential game theory. The LPV L_2-gain control law has an embedded observer that dynamically estimates the plant states. Time derivatives of the gain-scheduling variables need not be computed or estimated to realize the interactions between inner-layer and outer-layer segments of the control system.

For both narrow-range and wide-range conditions of the mean-flow variables, the robust control law is designed in terms of robustness, performance and parameter variation rate. Procedures for selection of mean-low-dependent and frequency-dependent weighting functions have been proposed in this paper. Physics of the thermo-acoustic phenomena have a significant bearing upon the selection of these performance weights and very little iterations are needed to arrive at the final design of the robust control law. In addition, a numerical tool for synthesis of the LPV robust control law is formulated based on the concept of finite-element analysis. Parametric studies and simulation experiments have been performed to evaluate the robust control system in terms of trade-off between: (i) fuel injection and pressure oscillations; (ii) transient response and steady response; and (iii) stability robustness and performance.

The results generated in this paper potentially lead to a design methodology for wide-range robust control of pressure oscillations in a generic combustor. The findings of this paper could be applied to a multitude of other combustion processes. Although the simulated results clearly indicate efficacy of the robust controller design methodology, several issues concerning implementation of robust control laws need to be addressed before applications to operating combustors.

Acknowledgements

The research work reported in this paper has been supported in part by the Office of Naval Research under Grant No. N00014-96-1-0405.

References

1. Yang, V., Santavicca, D. A., and Ray, A., *Proceedings of Twelfth ONR Propulsion Meeting*, 1999, p. 61-66.
2. Fung, Y. T., Yang, V., and Sinha, A., *Comb. Sci. Technol.*, 78:217-245 (1991).
3. Yang, V., Sinha, A., and Fung, Y. T., *J. Propulsion and Power*, 8:66-73 (1992).
4. Fung, Y. T., and Yang, V., *J. Propulsion and Power*, 8:66-73.
5. Koshigoe, S., Komatsuzaki, T., and Yang, V., *J. Propulsion and Power*, 15:383-389 (1999).
6. Hong, B. S., Yang, V., and Ray A., C*omb. Flame*, 120:91-106 (2000).
7. Packard, A., *Systems and Control Letters*, 22:79-92 (1994).
8. Wu, F., Yang, X. H., Packard A., and Becker, G., *International Journal of Robust and Nonlinear Control*, 6:983-998 (1996).
9. Hong, B. S. *Robust Control of Combustion Instabilities* Ph.D. Dissertation, The Pennsylvania State University, 1999.
10. Zhou, K., Doyle, J. C., and Glover, K., *Robust and Optimal Control*, Prentice-Hall, New Jersey, 1996

Table II. Parameters of the Generic Combustion Chamber

Time average sound speed a_0	795.8 m/s
Time average mean temperature T_0	1415 K
Time average mean pressure p_0	0.5 Mpa
Combustor length L	1.0 m
Combustor diameter d_c	0.6 m
Specific heat ratio $\bar{\gamma}$	1.2
Gas constant $\bar{R}$	373 J/(kg.K)
Constant volume specific heat $\bar{C}_v$	1500 J/(kg.K)
(MMH) heat of combustion (ΔH_c)	5×10^6 J/kg
Average fundamental frequency $\omega_0 \equiv \pi a_0 / L$	1000 rad/s
Average mean velocity $\mathbf{v}_0$	300 m/s
Average mixed density $\bar{\rho}$	0.9473 kg/m^3

Table III Dimensionless Quantities

Dimensionless time t'	$\omega_0 t$
Dimensionless frequency ω'	ω / ω_0
Dimensionless injected rate of control-fuel u'	$\dfrac{-\bar{R}\Delta H_c}{\omega_0^2 \bar{C}_v p_0} u$
Dimensionless damping ratio D'_{ni}	D_{ni} / ω_0
Dimensionless frequency shifting E'_{ni}	E_{ni} / ω_0^2
Dimensionless gain-scheduling mean velocity ρ_v	$\mathbf{v}_t / \mathbf{v}_0$
Dimensionless gain-scheduling mean temperature ρ_T	T_t / T_0
Dimensionless ρ_v variation rate $\dot{\rho}_v$	$d\rho_v / dt'$
Dimensionless ρ_T variation rate $\dot{\rho}_T$	$d\rho_T / dt'$

Table IV Parameters Used in Simulation and Modeling

Maximum time delay error	$\delta\tau = 3/\omega_0$
Plant uncertainty bound	$\delta p = 0.03$
Weighting factor	$q = 0.1$
White plant disturbance intensity	$10^{-1}\ \dfrac{\omega_0^2 \bar{C}_v p_0}{\bar{R}\Delta H_c}$
White sensor noise intensity	$10^{-1}\ \dfrac{\omega_0^2 \bar{C}_v p_0}{\bar{R}\Delta H_c}$
Initial conditions	an impulse $0.01\ p_0$ /sec.

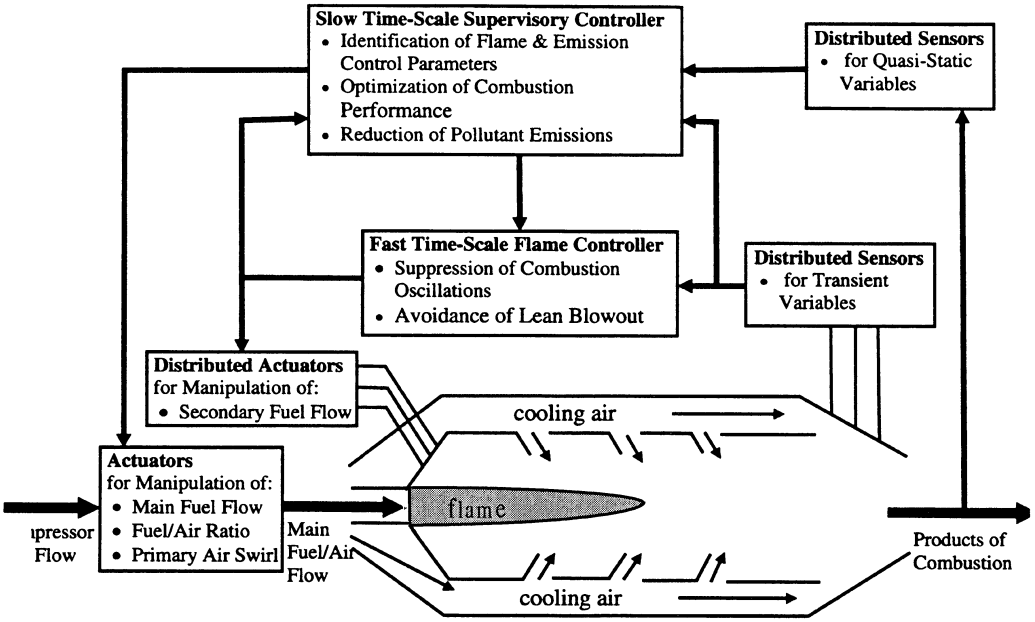


Figure 1 Two-layer Control System for Modulating Combustion Dynamics

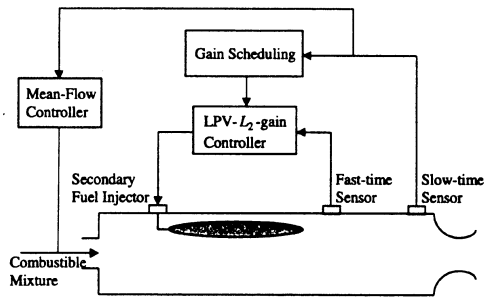


Figure 2 Two-Layer Robust Control System for Combustion Dynamics

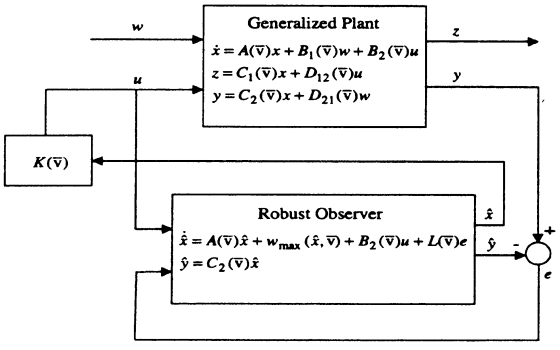


Figure 5 Synthesis of LPV Robust Control System

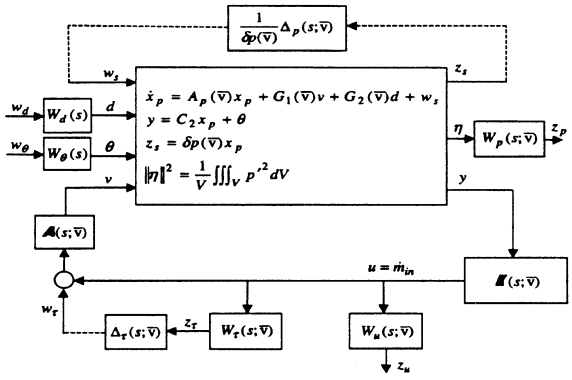


Figure 3 Mean-flow Parameterized, Generalized Plant of Combustion Dynamics

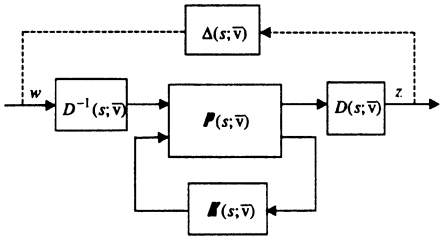


Figure 4 Compensated Generalized Plant of Combustion Dynamics

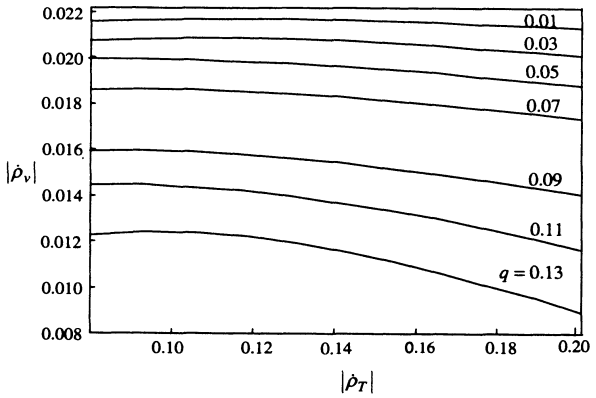


Figure 6 Trade-off between Performance and Plant Operation

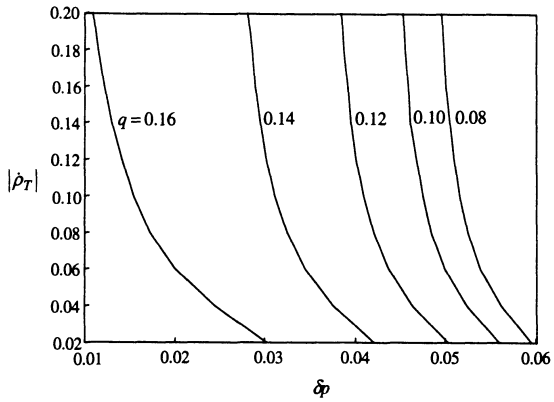


Figure 7 Trade-off between Robustness and Performance

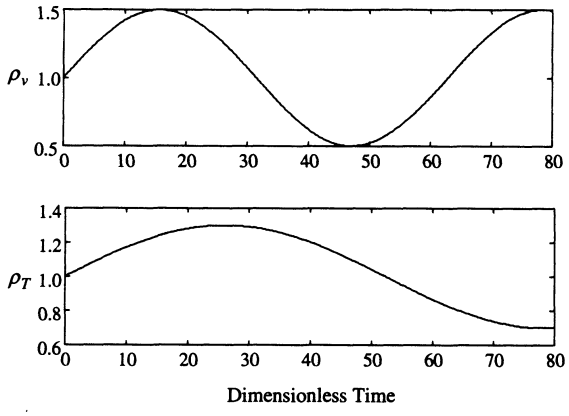


Figure 8 Time History of Mean Velocity and Temperature

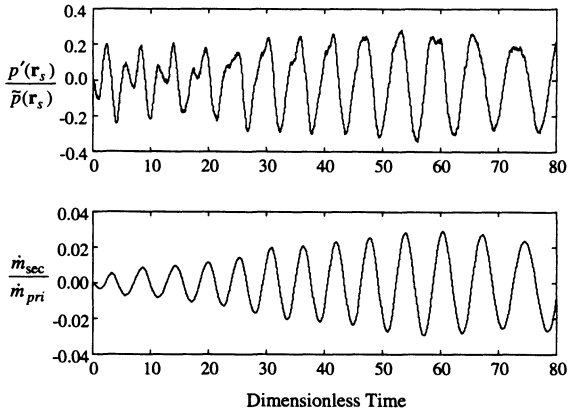


Figure 9 System Response under H_∞ Control

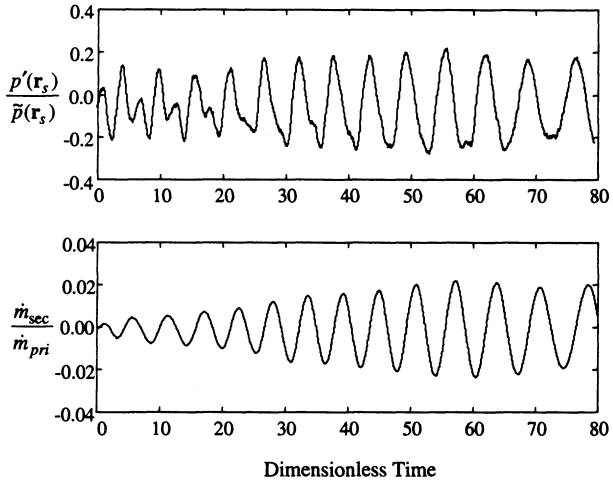


Figure 10 System Response under Gain-Scheduled Control

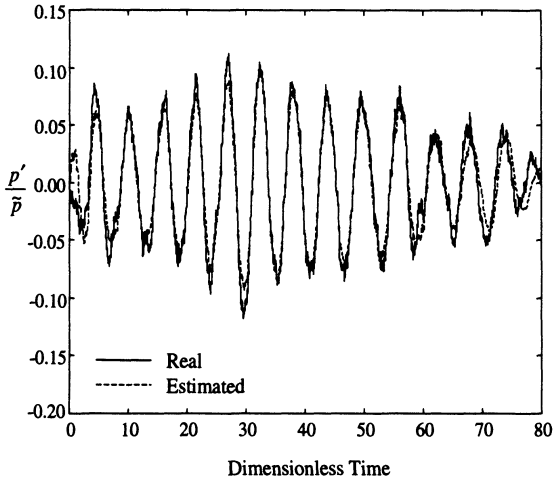


Figure 11 Time History of First-Mode of Pressure Oscillation under LPV-L_2- Gain Control

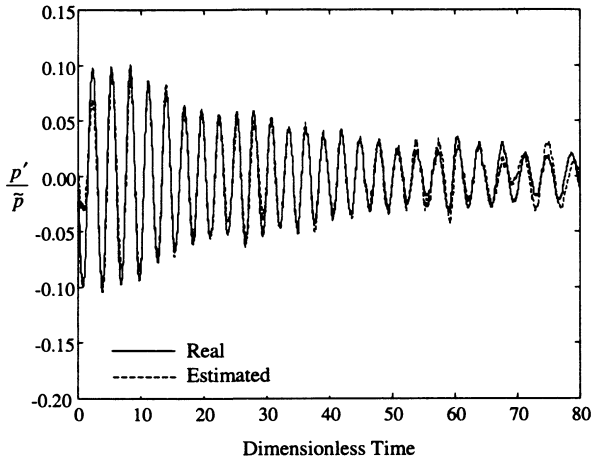


Figure 12 Time History of Second-Mode of Pressure Oscillation under LPV-L_2 - Gain Control

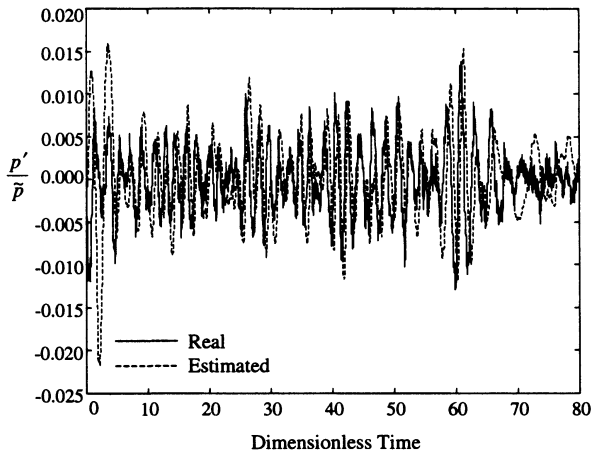


Figure 13 Time History of Third-Mode of Pressure Oscillation under LPV-L_2 - Gain Control

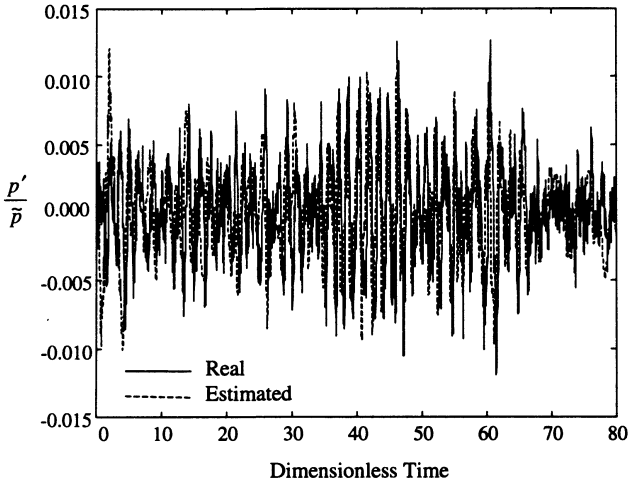


Figure 14 Time History of Fourth-Mode of Pressure Oscillation under LPV-L_2 - Gain Control

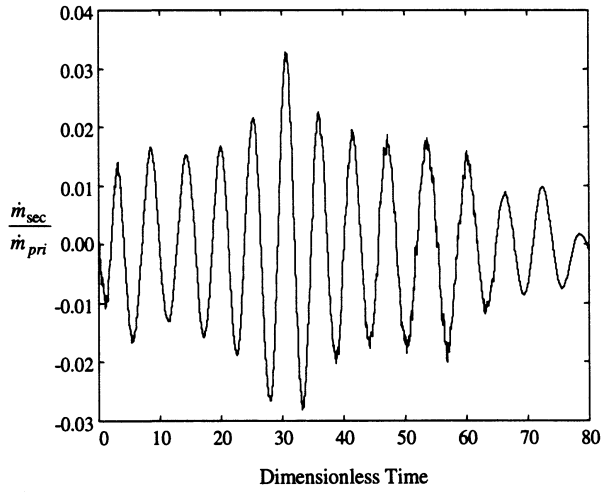


Figure 15 Secondary Fuel Injection Rate under LPV L_2-Gain Control

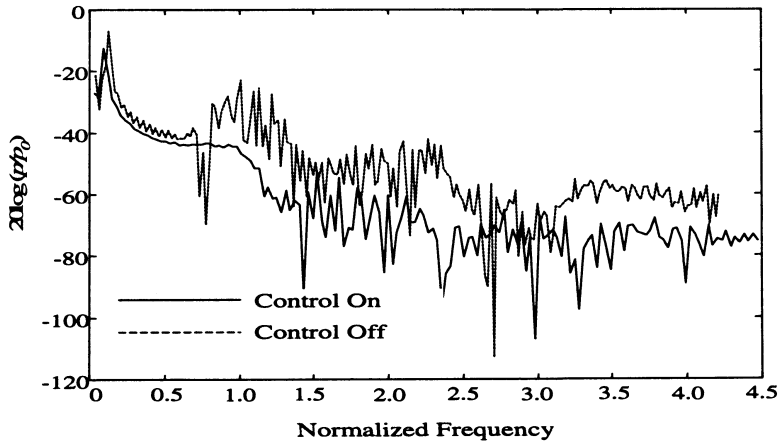


Figure 16 Frequency Spectrum of Pressure with and without LPV L_2-gain Control

Review on Activities in Active Combustion Control (ACC) at the Technische Universität München (TUM)

Stephan Gleis
Thermodynamik B, Technische Universität München
Boltz mannstrasse 15
85747 Garching, Germany

Abstract

About 30 years ago Professor Dieter Vortmeyer, who has been retired in March 1999, started his research in the field of acoustic instabilities in combustion systems and began the research in active combustion control in 1986. To the honour of Prof. Vortmeyer herewith a review on his work in the field of ACC is given.

Introduction

In the most technical combustion systems the flame is enclosed by combustion chambers and under certain operating conditions the excitation of combustion instabilities occur. These instabilities are characterised by intense pressure oscillations inside the combustion chamber at discrete frequencies. The dimensions of the combustion system, mainly the combustion chamber, determine the acoustic resonant frequencies. Longitudinal as well as radial and tangential acoustic modes may be excited. The occurrence of these oscillations increase with the specific thermal load. So there exist only a few publications reporting about problems with combustion oscillations on small combustion units as gas- or fuel oil fired boilers for heating facilities in residential buildings or transportation systems /1, 2 /. In these cases the oscillations with frequencies of several 100 Hz and pressure amplitudes up to 160 dB mainly are an unacceptable noise.
On industrial combustion systems the combustion instabilities cause much more severe problems. A lot of references can be named reporting the occurrence of combustion instabilities and measures for their elimination on boilers of power plants /3/, blast heaters in steel production /4, 5/, process gas heaters in the chemical industry /6/ as well as on gas turbine combusts /7-9/ and rocket motors /10-12/. Hereby the amplitudes of the pressure oscillations in these practical combustion chambers reach extremely high values, e.g. 0.5 bar in combustors operating under atmospheric conditions /6/ and 5 bar in rocket motors /13/. The consequences of these high pressure amplitudes are damages to the combustion chambers /4-7/, failures in the control units as well as negative effects on subsequent parts of the installation.
These combustion instabilities can be avoided or damped by passive or active means The passive means consist of e.g. geometrical modifications of the combustion chamber or the addition of sound-absorbing devices such as Helmholtz resonators. But at lower frequencies these measure often don't lead to sufficient low amplitudes.
The active methods to control the combustion instabilities use an input signal of the oscillation, e.g. the sound pressure or the fluctuating heat release of the flame, being phase shifted and amplified in an adequate manner and then transmitted to an actuator which obliterates the oscillation in the combustion system. An overview of some approaches in active control of combustion instabilities is given by Candel /14/.

Historic background on the research in ACC at the TUM

In 1968 Professor Vortmeyer became holder of the chair for Thermodynamik B at the TUM. During his preceding research activities he was research assistant at the Imperial College London and worked there together with D.B. Spalding in the field of combustion /15, 16/. Very early after having the chair at the TUM Vortmeyer started the research activities in the field of combustion oscillations /17, 18/ and continued this work perseveringly for about 30 years. At the begin the main goal of this work was the application and refinement of the Rayleigh Criterion /19/ for the prediction and stabilization of combustion oscillations in practical systems /6, 18, 20-24/. During the 21st International Symposium on Combustion in 1986 at the TUM Professor

Paper presented at the RTO AVT Symposium on "Active Control Technology for Enhanced Performance Operational Capabilities of Military Aircraft, Land Vehicles and Sea Vehicles", held in Braunschweig, Germany, 8-11 May 2000, and published in RTO MP-051.

Candel and some co-workers visited the lab of Thermodynamik B which has been the trigger off in the research of ACC at the TUM. Outgoing from an experimental set-up for the open loop excitation of a premixed propane-air flame the idea was borne to use this set-up in a closed loop configuration in order to stabilize a self excited flame oscillation similar to the anti noise methods and the experiments of Heckl on a Rijke tube /25/.

Basic Experimental Investigations in Active Control of Combustion Instabilities

The first investigations were performed on a very small laboratory combustor of about 1 kW thermal power with a laminar premixed flame. A very high level of attenuation (66 dB) has been achieved and the results of a theoretical analysis of the stable domains of the phase shift and gain of the closed loop controller show a good agreement with the experimental data /26/. These investigation has been extended to a combustor with a turbulent diffusion flame with a thermal power of about 30 kW /27/. An attenuation of the main unstable mode of about 24 dB in the sound pressure leads also to a elimination of the harmonics. Just in this article it is remarked that the active control of combustion instabilities can be applied in the future for damping of instabilities in full scale combustors as well as a new technique for the investigation of the initiation of a combustion instability, when the controller is switched off after the successful stabilization. That this technique can give very interesting insights in the transient behaviour of a combustion system has been shown in a further investigation.

The initiation of the combustion instability in a laboratory gas combustor burning a near stoichiometric premixed air/propane/hydrogen mixture has been investigated. The experimental set-up is shown in figure 1 and more details are given in /28/. Without active control a combustion oscillation with a frequency of 405 Hz and a pressure amplitude of 130 Pa inside the combustion chamber is present. By the active control system shown in figure 1 the combustion process can be stabilized within a few milliseconds with only 50 dB of noise left. The development of the combustion oscillation is shown in figure 2. After switching off the ACC within about 25 msec at first a transition from the controlled quiet operation to an oscillation with a frequency of 405 Hz and a pressure amplitude of 65 Pa is observed. In figure 2 this state of oscillation is described as "region 1". This oscillation remains for about 100 msec. Only then a transition to the final state of oscillation with the same frequency but a pressure amplitude of 130 Pa takes place. being described in figure 2 as "region 2".

The analysis of the oscillations of the heat release and the sound pressure gives a probably explanation for the stepwise rise in amplitude up to the limit cycle. While the phase shift between the heat release and the sound pressure oscillation is about 20° in "region 1", it becomes 0° in "region 2". Due to the better fulfilment of the Rayleigh-criterion the driving force has become much stronger leading to increased oscillation amplitudes. A view into the behaviour of the flame during the transition from stabilized combustion to the oscillatory state in "region 2" is given in figure 3 by Schlieren photos of the flame having been recorded by means of a high speed camera. The sequence a) of images in figure 3 shows the flame being stabilized by ACC. The sequence b) represents one cycle of oscillation from "region 1" in figure 2 and the frames from sequence c) come from "region 2". While the sequence a) shows a flame of more or less the same shape, the flame in sequence b) performs mainly a change in the flame length during one cycle of oscillation. Only in the images of sequence c) a clear vortex roll up at the flame tip can be observed. By this simple experiment it has been shown, that even if vortices are present during a combustion oscillation they must not be the original cause of the instability.

Even research in the field of combustion enhancement by an active periodic excitation of the flame has been done. This study verifies the possibility to reduce pollutant emissions from a residential hot water boiler heated with fuel oil. Although the investigated combustion system used state of the art technology for a clean combustion a further reduction of the NO emissions of 21 % and of the CO emissions of 46 % could be achieved /29/. But all possible implementations to industrial combustion systems seemed not to be practicable in terms of costs, durability and noise.

Investigations for the Practical Applicability of Active Combustion Instability control (AIC) on Industrial Combustion Systems

The first stimulation for the practical application of the active combustion instability control was given during a project for the calming of combustion oscillations in an industrial process gas heater in 1988 /6/. This process gas heater is a part of a natural gas plant cleaning the crude gas of hydrogen sulphide by a Claus process /30/. The Claus tail gas still contains a residue of sulphur compounds being removed in a subsequent process for which the tail gas has to be heated up in the process gas heater with a thermal power of 28 MW. The frequencies of the observed combustion instabilities were between 30 and 50 Hz at amplitudes up to 0.5 bar. These very strong pulsations led to the destruction of the combustion chambers liner shown in figure 3 and a grinding of catalyst pellets in a subsequent reactor due to the mechanical vibrations caused by the acoustic pressure oscillations.
During the activities in this project also the application of AIC has been discussed, but the lack on suitable actuators led to a passive solution and the decision to develop actuators for the AIC in forthcoming research projects.

Development of actuators for the modulation of liquid fuel

Until 1995 the existing papers on AIC mainly dealt with combustion systems for gaseous fuel where loudspeakers had been used as actuators. Consequently an actuator for liquid fuel has been developed, which is applicable in a broad frequency range /31/. This actuator, shown in figure 4 uses piezo stacks driving pistons which impose pressure fluctuation on the liquid fuel. The performance of the piezo actuator has been demonstrated on a diesel oil burning turbulent laboratory combustor exhibiting strong self excited combustion oscillations at operating conditions of about 50 kW thermal power and a nearly stoichiometric equivalence ratio. The result is shown in figure 5 and it can be seen that the sound pressure, as well as the heat release oscillation, are both attenuated remarkably if the AIC is switched on. The frequency plots in figure 5c present an attenuation of about 40 dB at the controlled oscillation frequency of 360 Hz, while a second oscillation mode at 295 Hz is slightly amplified.
An alternative actuator for liquid fuel has been presented at the International Symposium on Combustion in Naples in 1996 /32/. Here a direct-drive valve for hydraulics was modified to our specifications by Moog Germany to a cut off frequency of 450 Hz. It is shown that an acoustic decoupling and a tuning of the fuel line length is helpful to get a maximum efficiency for the actuator. Even this actuator has been implemented successfully to calm an combustion oscillation in a turbulent diesel oil fired combustor with a thermal power of about 137 kW at a air equivalence ratio Φ=1.2.

Application of Active Combustion Instability Control to a Heavy Duty Gas Turbine

All the tools having been developed as well as the experiences having been obtained in the research activities described above were necessary for the successful application of the AIC to an industrial combustion system. The demonstration of the AIC could be performed on a gas turbine at the Siemens testfield in Berlin /33/. A scheme of the AIC installation on the gas turbine annular combustor is shown in figure 6. Only the fuel of the pilot diffusion flame burning about 10 % of the whole fuel is modulated by a Moog direct drive valve. The sound pressure in the air plenum serves as input to the AIC controller. Each of the 24 burners of the annular combustor has been equipped with an actuator, while the number of pressure transducers and controllers could be reduced to six due to the symmetry of the excited azimuthal acoustic mode. With this installation the combustion oscillation in the 170 MW_{el} gas turbine has been reduced up to 17 db at the controlled frequency of 433 Hz. Professor Vortmeyer decided that this demonstration should be the final point in the development of complete AIC installations for his university institute and returned to other interesting questions in combustion instabilities of more basic nature. The AIC activities led to a spin off by two co-workers founding the firm IFTA.

So Vortmeyer's last activities are concerned with the numerical simulation of self excited combustion instabilities. Even the research in this field is successful and the CFD calculations /34, 35/ are in good agreement with experimental results of former publications /36, 37/.

Summary

Although the main field of Professor Vortmeyer's activities is on the research of the thermal and fluid mechanic phenomena in catalytic packed bed reactors, he did some remarkable achievements in the field of combustion instabilities by his continuous and farsighted research. At least partly due to his excellent job the AIC is now recognized as a promising technology for the practical application in future combustion systems which is on the other hand very important to get the necessary fundings for the basic research topics in the field of AIC. We will be glad if Professor Vortmeyer will be at our disposal in the future even if not actively but with his advices. The research in the field of combustion instabilities at the TUM nevertheless will go on in the future, because these activities have been taken over by Professor Thomas Sattelmayer at his chair "Lehrstuhl A für Thermodynamik" (LAT).

References

1. Schimmer, H.: Selbsterregte akustische Schwingungen in Brennräumen mit flacher Flamme. Dissertation, TU München, 1974.
2. Fritsch, W. H.: VDI-Bericht Nr. 423, 1981.
3. Benelli, G.; Cossalter, V.; De Michele, G.: AGARD CP 450, pp.17-1 - 17-11, 1988.
4. Sucker, D.; Glas, P.; Boenecke, H.: Stahl und Eisen 100, Nr. 22, pp. 1310-1317, 1980.
5. Günther, R.; Lenz, W.: VDI-Bericht Nr. 346, pp. 163-171, 1979.
6. Gleis, S.; W. Rau; Vortmeyer, D.: Proceedings of the 4th European Conference, 1. - 4. April 1997, ISBN 972-8034-03-2; Volume 1; pp 63-74
7. Henderson, B. E.; Lewis, J. S.: AGARD CP 450, pp. 3-1 - 3-8, 1988.
8. Kenworthy, M. J.; Bahr, D. W.; Mungur, P.; Burns, D. L.; Mehta, J. M.: AGARD CP 450, pp. 4-1 - 4-13, 1988
9. J. R. Seume, N. Vortmeyer, W. Krause, J. Hermann, C.-C. Hantschk, P. Zangl, S. Gleis, D. Vortmeyer und A. Orthmann: Transactions of the ASME, J. Engineering for Gas Turbines and Power 120(4), pp. 721-726 (Oktober 1998)
10. Crocco, L.; Harrje, D. T.; Condomines, A.: 29th Quarterly Progress Report, Princeton University Aeronautical Engineering Report No. 216-cc, Sept. 15. , 1959.
11. Crocco, L. ; Grey, J.; Harrje, D. T.: ARS Journal, Feb. 1960.
12 Ross, C. C.: Datner, P. P.: Combustion Instability in Liquid-Propellant Rocket Motors - A survey. Selected Combustion Problems, p. 352, Butterworth Scientific Publications, London, 1954.
13. Preclik, D.; Spagna, P.: AGARD CP 450, pp. 6-1 - 6-18, 1988.
14. Candel, S. M.: Combustion Instability Coupled by Pressure Waves and Their Active Control. Invited general lecture, 24th Symposium (International) on Combustion, Sydney, July 1992.
15. Vortmeyer, D.: Proc. of the 9th Symposium (international) on Combustion 1963; pp. 936-948; Academic Press; New York; 1963
16. D.B. Spalding; Vortmeyer, D.: Combustion and Flame, Vol. 6, 1; pp. 35-41; 1962.
17. Schimmer, H.: ISL/AGARD Workshop on Laser-Doppler-Anemometry, Report R117/76, pp. 375f, 1976.

18. Schimmer, H.; Vortmeyer, D.: Combustion and Flame, Vol. 28, pp. 17-24, 1977.

19. Rayleigh, Lord J. W. S.: Nature, July 18, pp. 319-321, 1878.

20. Schimmer, H.; Vortmeyer, D.: Gas Wärme International, Band 25, Heft 1/2, pp. 25-29, 1976.

21. Vortmeyer, D.; Kunz, W.: VDI-Bericht Nr. 423, pp. 119-123, 1981.

22. Kunz, W.; Vortmeyer, D.: Acustica, Vol. 50, No. 4, 1982.

23. Joos, F.; Vortmeyer, D.: Combustion and Flame, Vol. 65, pp. 253-262, 1986.

24. Lang, W.; Vortmeyer, D.: Combustion Science and Technology, Vol. 54, pp. 399-406,1987.

25. Heckl. M. A.: Proc. of the IUTAM Symposium 1985, Lyon (Springer-Verlag).

26. Lang, W.; Poinsot, T.; Candel, S.: Combustion and Flame, Vol. 70, pp. 281-289, 1987.

27. Lang, W; Poinsot, T.; Bourienne, F.; Candel, S; Espositio, E: AIAA, SAE, ASME, and ASEE, 23rd Joint Propulsion Conference, San Diego, CA, Paper No. AIAA-87-1876, 1987.

28. Gleis, S.; Vortmeyer, D.: Rau, W.: AGARD CP 479, pp. 22-1 - 22-7, 1990.

29. Casentini, F., Hermann, J..; Vortmeyer, D..; Gleis, S.: Proc. of the Fourth International Conference on Technologies and Combustion for a Clean Environment, Lisbon 7-10 July 1997, Vol. II, Session 23.3, pp. 17-25.

30. Ullmanns Encyklopädie der technischen Chemie, 4th edition, vol. 21, chapter 4.2.2.4, Verlag Chemie, 1982.

31. Hermann, J.; Gleis, S.; Vortmeyer, D.: Combustion Science and Technology 1996, vol. 118, pp.1-25.

32. C.-C. Hantschk, J. Hermann und D. Vortmeyer.: 26th Symp. (Int.) on Combustion", pp. 2835-2841. The Combustion Institute (1996).

33. J. R. Seume, N. Vortmeyer, W. Krause, J. Hermann, C.-C. Hantschk, P. Zangl, S. Gleis, D. Vortmeyer und A. Orthmann. Transactions of the ASME, J. Engineering for Gas Turbines and Power 120(4), 721-726 (Oktober 1998).

34. Hantschk, C.-C.; Vortmeyer, D.: Numerical simulation of self excited combustion oscillations in a 50 kW burner. accepted for publication in: Conference Proceedings Eurotherm Seminar No. 67, Acoustics of Combustion, Enschede. The Netherlands, University of Twente, July 2000.

35. Hantschk, C.-C.; Vortmeyer, D.: Journal of Sound and Vibration 227 (1999), Nr. 3, pp. 511-522.

36. Kunz, W.: Untersuchungen zum Anregungsmechanismus thermoakustischer Schwingungen am Beispiel des Rijke-Phänomens. Dissertation, TU München, 1981.

37. Hermann, J.: Anregungsmechanismen und aktive Dämpfung (AIC) selbsterregter Verbrennungsschwingungen in Flüssigkraftstoffsystemen, Dissertation, TU München, VDI-Fortschrittsbericht Nr. 364, 1996.

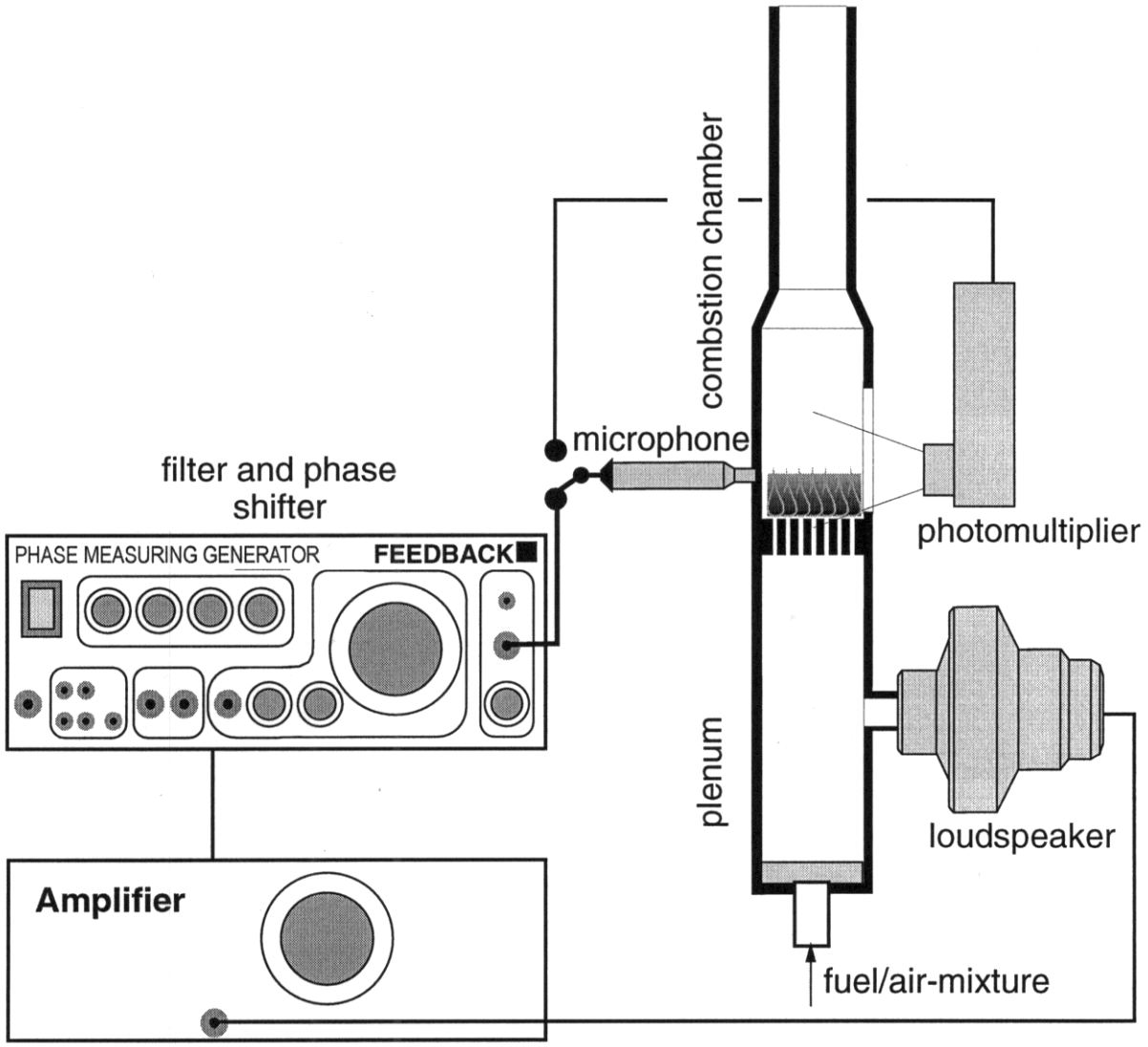


Figure 1: Experimental setup for basic AIC experiments

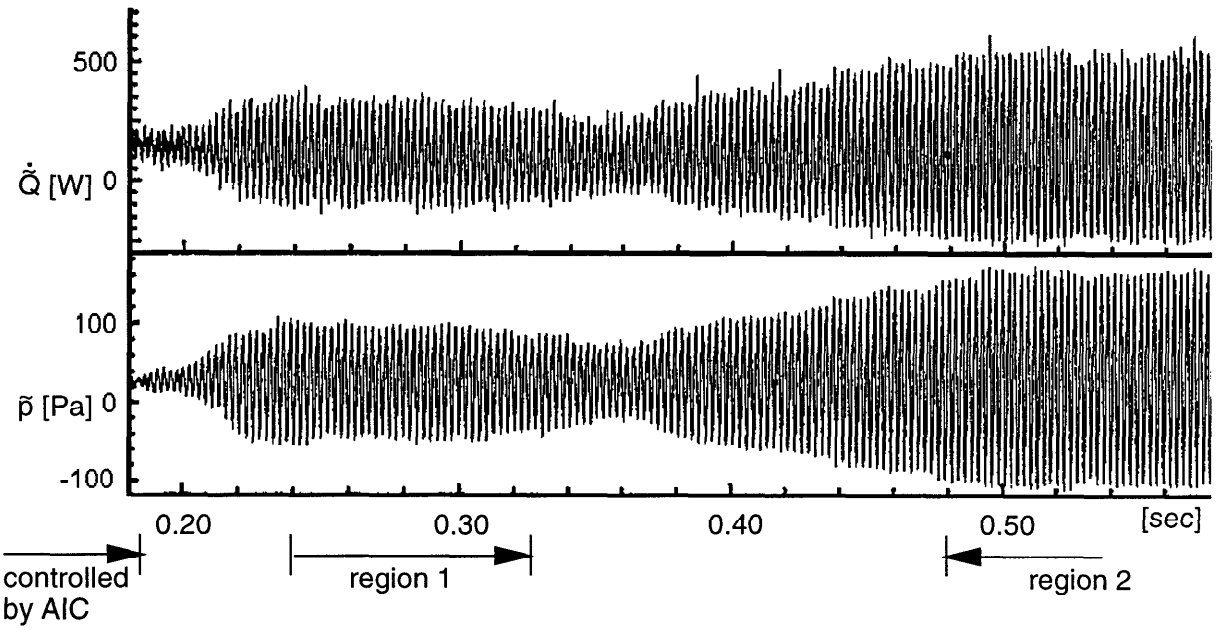


Figure 2: Transition from stable to unstable combustion

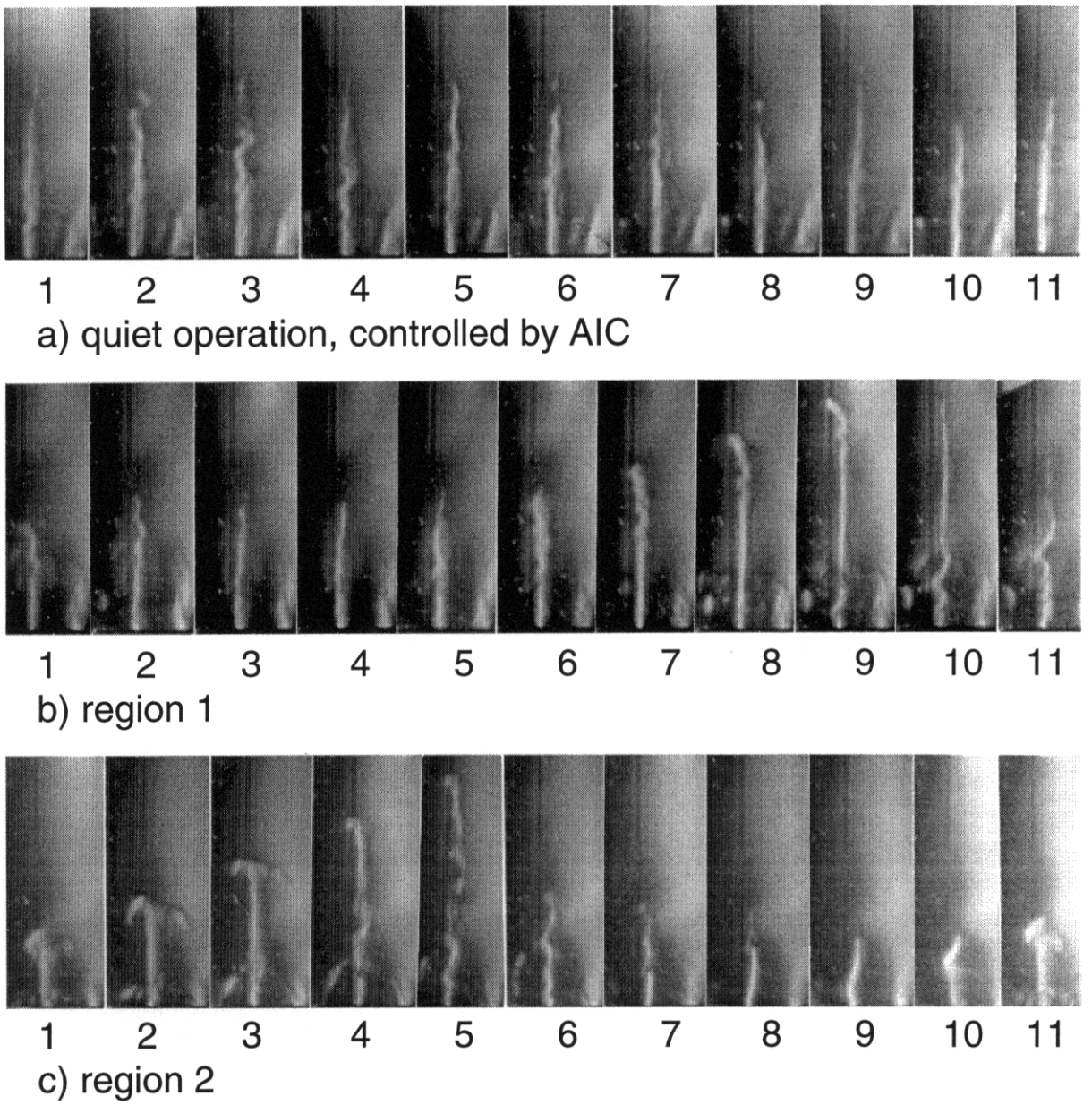


Figure 3: Schlierenphotos from a high speed movie showing the initation of the combustion oscillation from figure 2 (frame rate 5000 frames/sec)



Figure 4: Combustion chamber of the process gas heater with 14 MW thermal power and a diameter of about 1 m, the brick lining is destroyed due to combustion oscillations

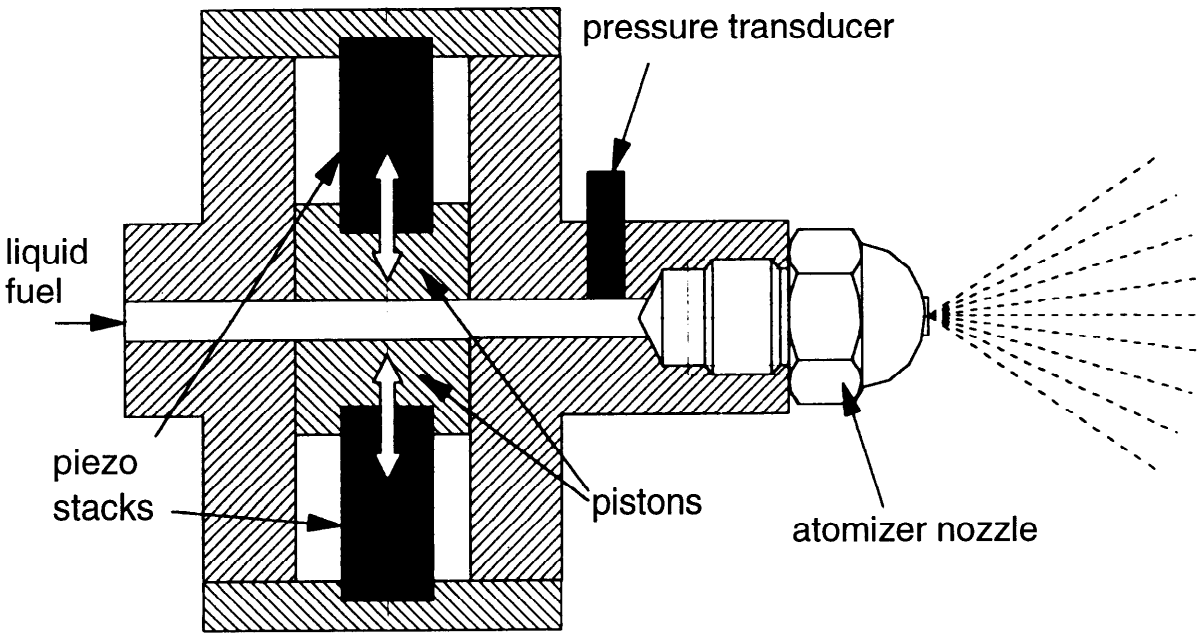


Figure 5: Piezo actuator with injection nozzle /37/

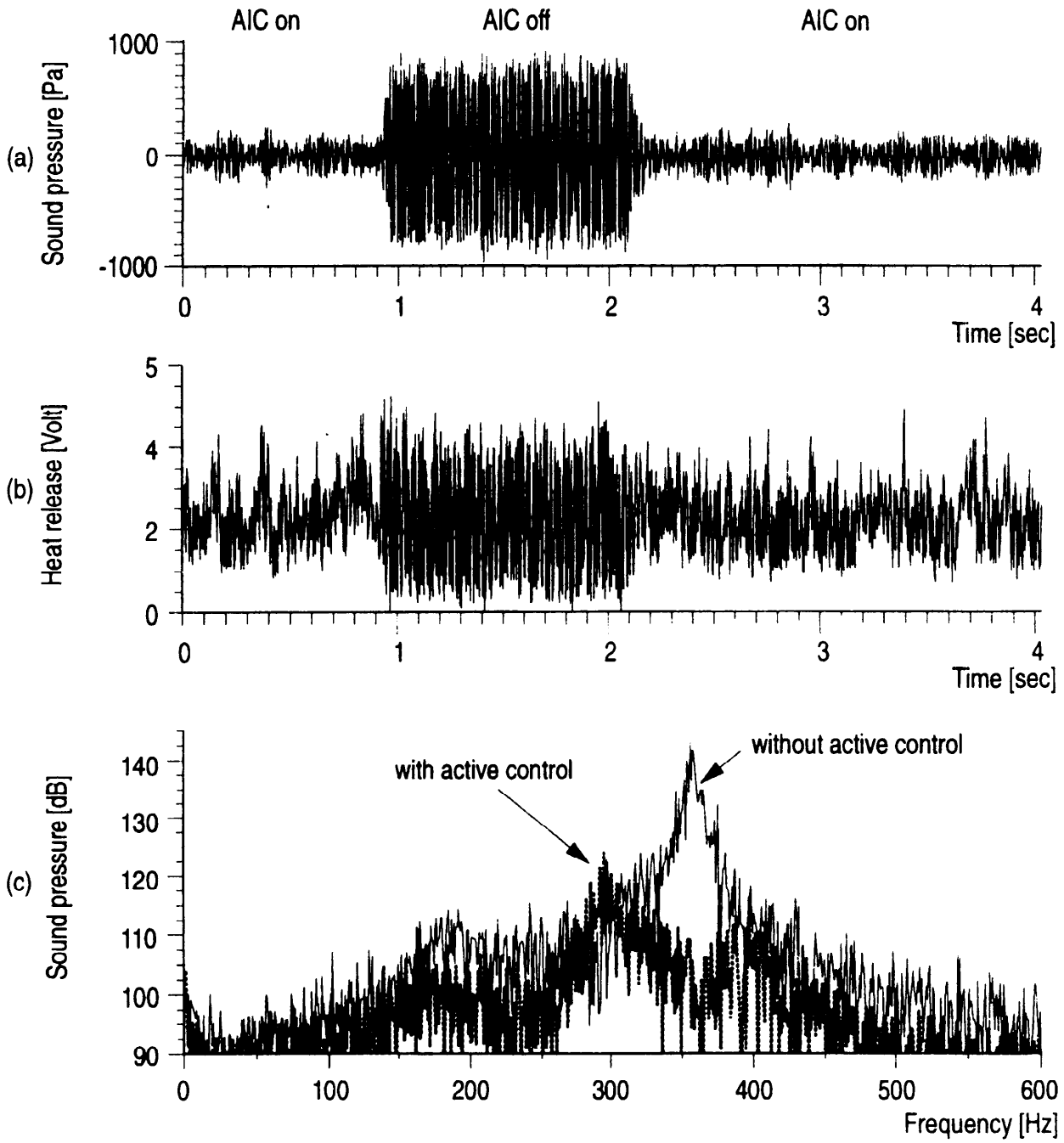


Figure 6: Sound pressure (a) and heat release oscillation (b) with AIC system switched off and on. Frequency spectrum of the sound pressure with an without active control (c) /31/.

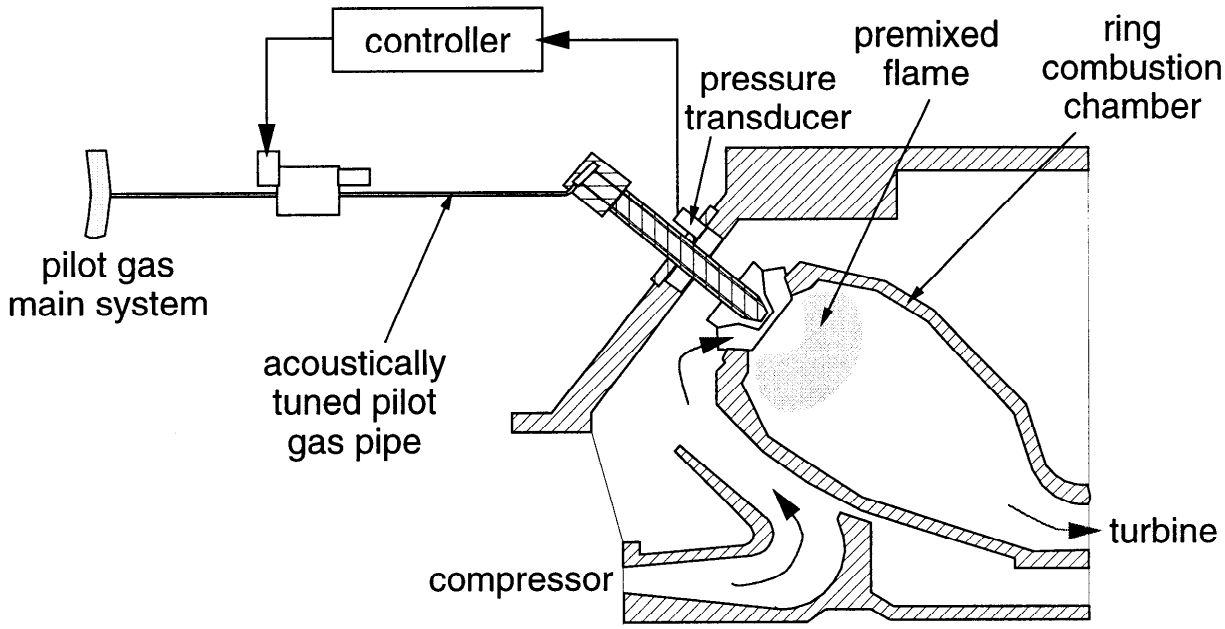


Figure 7: Schematic of the AIC applied to the Siemens Model V84.3A gas turbine /33/

Active Control of Combustion Instabilities in Gas Turbine Engines for Low Emissions. Part I: Physics-Based and Experimentally Identified Models of Combustion Instability

C.A. Jacobson
United Technologies Research Center,
MS129-15, 411 Silver Lane, East Hartford, CT 06108, USA
tel. 860 610 7652, **jacobsca@utrc.utc.com**

A.I. Khibnik
United Technologies Research Center,
MS129-15, 411 Silver Lane, East Hartford, CT 06108, USA
tel. 860 610 7403, **khibniai@utrc.utc.com**

A. Banaszuk
United Technologies Research Center,
MS129-15, 411 Silver Lane, East Hartford, CT 06108, USA
tel. 860 610 7381, **banasza@utrc.utc.com**

J. Cohen
United Technologies Research Center,
MS129-16, 411 Silver Lane, East Hartford, CT 06108, USA
tel. 860 610 7973, **cohenjm@utrc.utc.com**

W. Proscia
United Technologies Research Center,
MS129-16, 411 Silver Lane, East Hartford, CT 06108, USA
tel. 860 610 7679, **prosciw@utrc.utc.com**

May 2000

Abstract

This paper details the development of a thermoacoustic model and associated dynamic analysis. The model describes the results obtained in a gas fueled experimental combustion program carried out at UTRC.

The contents of the paper are (a) the development of a thermoacoustic model composed of acoustic and heat release components, (b) the dynamic analysis of the resulting nonlinear model using harmonic balance methods to compute linear stability boundaries and the amplitudes of oscillations and (c) the calibration of the model to experimental data.

1 Introduction

This paper presents a thermoacoustic model structure for describing the dynamics associated with lean premixed combustion instabilities. The model developed is used to describe the dynamics of a single nozzle rig (SNR) experimental program carried out at UTRC. This paper also contains analysis of this model for both linear stability boundaries as well as amplitudes of oscillations subsequent to the loss of linear stability. The calibration of model parameters using experimentally measured data is also included. The purpose of the modeling effort is to obtain a calibrated model of the single-nozzle combustor that can be used to analyze the effects of closed loop control, and most importantly, to ultimately predict the control authority needed to reduce the amplitude of the pressure oscillations to an acceptable level. This paper represents a contribution from a continuing program at UTRC that develops combustion dynamics and control from a set of scaled experiments where the scaled experiments are carefully constructed to capture the behavior of full scale engine dynamics and, importantly, the scaled experiments may be reflected back to gain insight into the governing phenomena under investigation.

The results presented in the current work both complement as well as extend related research efforts in obtain-

Paper presented at the RTO AVT Symposium on "Active Control Technology for Enhanced Performance Operational Capabilities of Military Aircraft, Land Vehicles and Sea Vehicles", held in Braunschweig, Germany, 8-11 May 2000, and published in RTO MP-051.

ing reduced order models of combustion instabilities. The works of [5, 7, 8, 11] are of particular interest. The papers [5, 7] concern the development of coupled acoustic-heat release models where the heat release models are focused on unsteady flame dynamics. The work of [11] is more closely related to the current paper where the heat release model is focused on unsteady equivalence ratio variations. This is also true of the work of [6] which models afterburner instabilities that are driven by fluctuating equivalence ratio, however, the coupling to the acoustics is different in that work from the current paper.

The contribution of this paper is to develop a thermoacoustic model that describes the single-nozzle combustor experimental results. The methodology developed here consists of describing the physics based model components and then performing analysis and calibration using this framework. The model framework consists of a feedback interconnection of an acoustic component driven by a heat release component. The nature of the feedback is as follows. The fluctuating heat release component is dependent on the fluctuating equivalence ratio at a flame sheet a distance away from the nozzle exit, and, as it is assumed that the fuel flow rate is constant the fluctuating equivalence ratio is thus dependent on the fluctuating velocity at the nozzle exit which closes the feedback loop. The spatial distance of the flame sheet from the nozzle exit can be viewed as a temporal time delay (convective lag) of the nozzle velocity to create a variation in equivalence ratio and hence the structure of the resulting model is a nonlinear delay differential equation.

The resulting model of the combustion instability is then analyzed using harmonic balance methods to compute linear stability boundaries and amplitudes of oscillation. The model contains an empirical gain factor and the paper develops a methodology to calibrate the model to experimental data using dynamic and stochastic analysis tools. The metrics for this calibration are (a) to match the trend in amplitude as a function of mean equivalence ratio, (b) to match the frequencies of oscillation and (c) to match the power spectral densities and probability function distributions of the measured pressure time traces.

The organization of this paper is as follows. Section 2 presents the modeling framework. This includes both the modeling of the acoustics as well as the heat release in the combustor. Section 3 presents analysis of the model that gives some qualitative insight into the structure of the dynamic behavior with special attention to the self-excited oscillatory behavior. Section 4 presents the calibration procedure that has been used to date. Section 5 summarizes the structure of the models, the methodology that has been developed, the results from this investigation and finally the enumeration of major remaining items of investigation.

2 Thermoacoustic Model Structure

This section presents the basic structure of the thermoacoustic model for single nozzle rig (SNR). The model is composed as a feedback interconnection of acoustic and heat release submodels. The physical single nozzle rig is shown in Figure 1. The subsections below divide the modeling into acoustic considerations and heat release considerations.

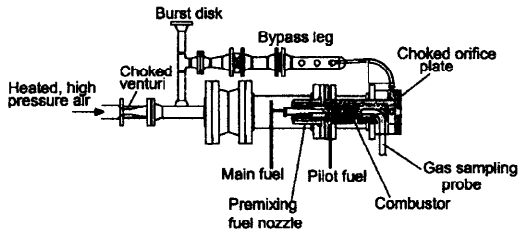


Figure 1: Single Nozzle Rig Used in Experimental Study

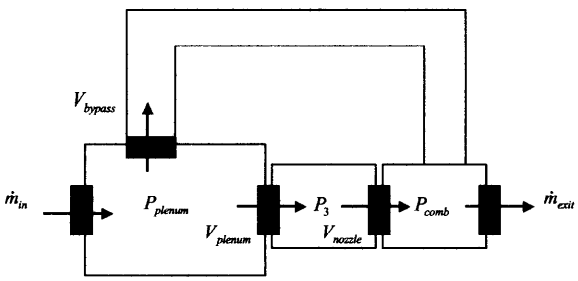


Figure 2: Schematic for Acoustic Modeling

2.1 Acoustic Component

The schematic representation used for modeling the single nozzle rig is depicted in Figure 2. The modeling of this schematic by a set of coupled ordinary differential equations can be done using momentum and mass conservation equations for flow through the orifices and volumes. Choking of the exit orifice is clearly applicable as the combustor pressure is roughly 220 psia and the pressure in the exhaust is roughly 20 psia. The boundary condition at the choked inlet venturi is taken to be a fixed mass flow rate. The equations for this description are as follows. Details may be found in [15] for the orifice relation and [4] for the volume and choked orifice conditions.

$$
\begin{aligned}
\dot{m}_{exit} &= \frac{\kappa C_d A_e P_{comb}}{\sqrt{T_4}} \\
C_{comb}\frac{dP_{comb}}{dt} &= \dot{m}_{nozzle} + \dot{m}_{bypass} \\
&\quad -\dot{m}_{exit} + F \\
\dot{m}_{nozzle} &= \rho_3 A_{nozzle} V_{nozzle} \\
\dot{m}_{bypass} &= \rho_3 A_{bypass} V_{bypass} \\
\rho_3 L_{nozzle}\frac{dV_{nozzle}}{dt} &= -\frac{\rho_3}{2} k_{nozzle} V_{nozzle}^2 \\
&\quad +P_{pre} - P_{comb} \\
C_{pre}\frac{dP_{pre}}{dt} &= \dot{m}_{perf} - \dot{m}_{nozzle} \\
\dot{m}_{perf} &= \rho_3 A_{perf} V_{perf} \\
\rho_3 L_{perf}\frac{dV_{perf}}{dt} &= -\frac{\rho_3}{2} k_{perf} V_{perf}^2 \\
&\quad +P_{plenum} - P_{pre} \\
C_{plenum}\frac{dP_{plenum}}{dt} &= \dot{m}_{in} - \dot{m}_{bypass} - \dot{m}_{perf} \\
\rho_3 L_{bypass}\frac{dV_{bypass}}{dt} &= -\frac{\rho_3}{2} k_{bypass} V_{bypass}^2 \\
&\quad +P_{plenum} - P_{comb}
\end{aligned} \tag{1}
$$

The parameters are described in Table 1.

The resulting model is a nonlinear differential equation where the nonlinearity occurs in the unsteady momentum equation.

The calibration of the model from the mean values of the pressure drops and the air velocity, using mean flow rates and cold flow (nonreacting) experimental data, is as follows. The issue is to choose the effective flow areas ($C_d A$) of the orifices, particularly, the nozzle and the bypass leg. We can use analytical formulas for steady states to guide this choice. Steady state values for pressures and velocities across the system can be computed using the equations alone:

$$
\begin{aligned}
V^s_{nozzle} &= \frac{\dot{m}_{in}}{\rho_3(A_{bypass}\delta + A_{nozzle})} \\
V^s_{bypass} &= \delta V^s_{nozzle} \\
V^s_{perf} &= \frac{A_{nozzle}}{A_{perf}} V^s_{nozzle} \\
P^s_{comb} &= \frac{\sqrt{T_4}}{\kappa C_d A_e}(\dot{m}_{in} V^s_{nozzle}) \\
P^s_{pre} &= P_{comb} + \frac{\rho_3 k_{perf}}{2}(V^s_{nozzle})^2 \\
P^s_{plenum} &= P^s_{pre} + \frac{\rho_3 k_{perf}}{2}(V^s_{perf})^2
\end{aligned} \tag{2}
$$

where

$$
\delta = \left(\frac{k_{nozzle} + k_{perf}\left(\frac{A_{nozzle}}{A_{perf}}\right)^2}{k_{bypass}} \right)^{1/2}
$$

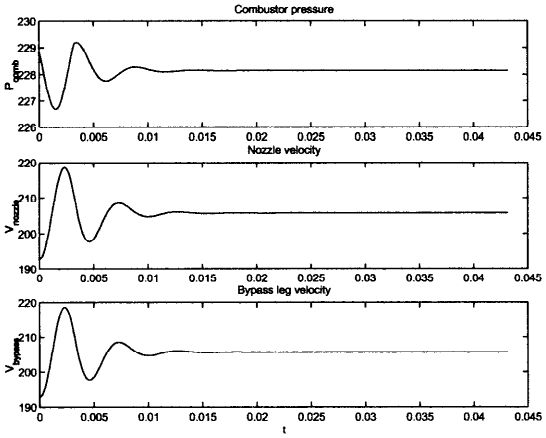


Figure 3: Combustor pressure, nozzle velocity and bypass leg velocity with no combustion

The physical area, A_{nozzle}, and the effective flow area, $C_d A$, for the nozzle have been measured. The length coefficients (L_{nozzle}, etc) are taken as physical parameters for the physical length (but also could be fit to experimentally measured admittance data for the nozzle used in single nozzle rig tests). The bypass leg parameters are set similarly. The discharge coefficient (C_d) for the bypass leg is taken as 0.7, a typical value for a sharp edge orifice. The physical area A_{bypass} is adjusted so that 21% of the flow is through the bypass leg. Again, the physical length of the orifice is taken for L_{bypass}. This sets all parameters for the acoustics. The final choice of parameters for the model is given in Table 2. The steady state values for these parameters using (2) are $P_{comb} = 228.15, P_{pre} = 233.56, P_{plenum} = 242.07, V_{nozzle} = 205.69, V_{perf} = 283.86, V_{bypass} = 282.86$.

Calibration procedure can also include mean flow rates and cold flow (nonreacting) experimental data. Specifically the mass flow rates (in lbm/sec) predicted by the model can be compared to design values for the combustor. The design value of mass flow rate is 6.2 lbm/sec for the single nozzle rig which compares with the mass flow rate (through the nozzle) as 5.15 in the model after calibration. The pressure drop across the nozzle was calculated as 2.4%.

A simulation of the equations of motion with parameter values in table 2 produces the velocity and pressure plots shown in Figure 3. The initial conditions were chosen to be off steady state to reveal a heavily damped system.

2.2 Heat Release Component

This section outlines the modeling of the heat release subsystem as a velocity sensitive mechanism.

The addition of a heat release component to the acoustic component considered above can proceed from the equation for mass conservation as in [10]. The equation is

$$
\frac{\partial \rho}{\partial t} + \nabla \cdot (\rho U) = 0
$$

where U is the air velocity and ρ the density. The density is represented as a function of pressure P and entropy S, $\rho = \rho(P, S)$. Then

$$\frac{\partial \rho}{\partial t} = \left(\frac{\partial \rho}{\partial P}\right)_S \frac{\partial P}{\partial t} + \left(\frac{\partial \rho}{\partial S}\right)_P \frac{\partial S}{\partial t}$$

Then [10] the first term can be expressed in terms of the local sound speed and noting that

$$\left(\frac{\partial \rho}{\partial S}\right)_S = -\frac{\rho}{c_P}$$

with c_P the specific heat per unit mass at constant pressure. In addition if there is a continuous volume distribution of heat release at a rate of q per unit mass then the second term is actually the source term, that is,

$$\left(\frac{\partial \rho}{\partial S}\right)_P = -\frac{\rho}{c_P T} q$$

The equation for conservation of mass then becomes

$$\frac{1}{c^2}\frac{dP}{dt} = -\nabla \cdot (\rho U) + \frac{\rho}{c_P T} q$$

and the conversion to a volume average proceeds by integrating over the surface of the control volume as done in [10]. The main point in the above discussion is that the heat release rate term enters into the equation representing the conservation of mass.

The assumption that is made in this paper is that the heat release rate q is a function of the velocity in the fuel nozzle $q = q(u)$. This modeling assumption has been discussed in detail in [16, 17]. The basis of the assumption is that the unsteady heat release is a function of the equivalence ratio at a flame surface a distance l from the nozzle exit, moreover, the equivalence ratio is only a function of the nozzle exit airflow velocity if the fuel flow is held fixed. The result is that the unsteady heat release $q(t) = f(u(t - l/\bar{u}))$ where $\bar{u}$ is the mean velocity in the nozzle. The main point to be made here is that when a stability boundary is to be computed for the coupled combustion system — the coupling of the acoustics and the unsteady heat release — a feedback loop should exist between the nozzle velocity and the equation for pressure fluctuations in the combustor nozzle.

The form of the feedback can be given more explicitly. The source term F given in equation (1) that represents the effects of combustion is as follows:

$$F(t) = \frac{\rho}{c_p T} q \tag{3}$$

with q being the heat release rate per unit mass. The development in [17] can be used to give a functional form that depends on the nozzle velocity. A modification to the development in [17] is now made. The modeling assumption is that the heat release is split into the mean and fluctuating portions and that the fluctuating component depends only on the fluctuating velocity in the nozzle. Furthermore the heat release model explicitly splits the heat release rate into constant and fluctuating part. This split accounts for the fact that in the thermoacoustic model the coupling of heat release to acoustics in feedback loop occurs through the fluctuating heat release; the corresponding gain parameter for the heat release is then naturally introduced as multiplying the fluctuating portion of the heat release rate. The split between constant and fluctuating heat release rate is given as follows:

$$F(t) = \frac{1}{c_p T}\rho_c A_{nozzle} \bar{u} \overline{\Delta H_s} \left(\bar{\phi} + N \frac{\hat{H}(\phi) - \hat{H}(\bar{\phi})}{\hat{H}(\bar{\phi})}\right) \tag{4}$$

where $\phi = \frac{\bar{\phi}}{1 + u'/\bar{u}}$ is the instantaneous equivalence ratio which depends on fluctuating nozzle velocity $u' = u - \bar{u}$ at time $t - \tau$, τ is the convective lag.

In this equation the heat release function $\hat{H}$ is taken from [17] and N is the gain parameter to be used in computing stability characteristics of the model. It is assumed that the mean velocity $\bar{u}$ is equal to the nozzle velocity at steady state conditions, V^s_{nozzle} (see equation (2)) [1]. The steady state conditions refer to the situation when the rate of change of all variables is zero. Figure 4 presents typical time traces for the thermoacoustic model in the instability region. The time traces show the limit cycle behavior captured by the model as the system starts from initial conditions and goes to steady state. Parameter values in (4) are set as $c_p = .24$ $(BTU/\,^\circ\mathrm{R} - lbm)$, $T = T_4 = 3285$ $(^\circ\mathrm{R})$, $\rho_c = .5807(lbm/ft^3)$, $\overline{\Delta H_s} = 1222$ $(BTU/lbm - mix)$, $\bar{u} = 205.69$ (ft/sec), $A_{nozzle} = 0.0431$ (ft^2).

3 Thermoacoustic Model Analysis: Consequences of Nonlinearities

In this section we analyze the dynamics of the thermoacoustic model. We compute the stability boundary and a few cases showing the dependence of the amplitude of oscillations on parameters of the model. The three varying parameters in the model are N (gain), τ (convective delay) and $\bar{\phi}$ (mean equivalence ratio).

The harmonic balance method combined with parameter continuation (see Appendix) is used to compute the stability diagram and the dependence of amplitude of the limit cycle on model parameters. The $N - \tau$ stability diagram is shown in Figure 5 and it consists of several branches. Only one of them (with lowest frequency) is actually computed; the others are obtained from it by $2\pi k$ (k positive integer) shifts of

[1] Varying $\bar{\phi}$ doesn't change steady state values for any of velocity components but do change all the pressures. Note that when the system is destabilized the unsteady combustion can create mean flow rates that are different from the steady ones because the combusting term F does not generally have zero mean. The nonlinearity takes as input an unsteady fluctuating nozzle velocity with zero mean but will produce as output a fluctuating equivalence ratio with nonzero mean. These effects might be essential when the instability is significant; in this paper, however, the instability is relatively weak and the drift of the dc value with gain can be safely ignored.

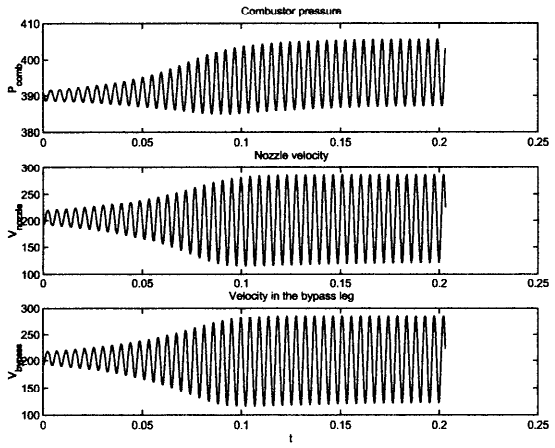


Figure 4: Combustion oscillations in thermoacoustic model at $(N, \tau, \bar{\phi}) = (.25, 3.23, .58)$.

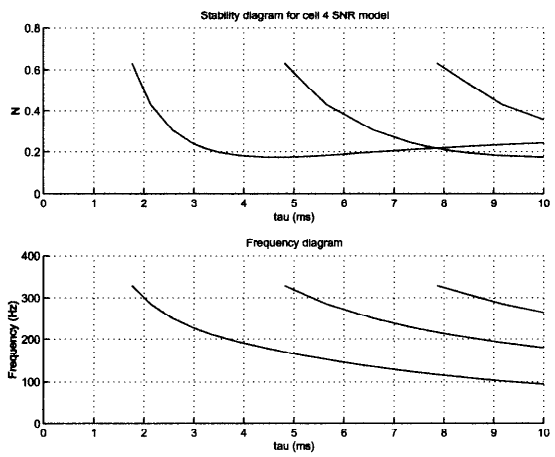


Figure 5: $N - \tau$ stability diagram for thermoacoustic model.

the phase $\omega\tau$ where ω is the frequency. Note that as τ increases ω decreases, which is consistent with a linear stability analysis conducted from a Nyquist diagram of the linearized system. The structure of bifurcation diagram as shown on top panel Figure 5 has certain implications particularly there will be several instabilities encountered as the gain increases. This corresponds to multiple crossings of eigenvalues of the system into the right half of the complex plane which is a consequence of the infinite dimensional nature of the model (delay differential equation). In this paper the focus is on the initial loss of linear stabilty — the first pair of complex conjugate eigenvalues to cross into the right half plane — and the ensuing limit cycle behavior after this loss of linear stability. The dynamic behavior is known as a Hopf bifurcation.

Figures 6, 7 and 8 present parametric studies of limit cycle regime with varying only one parameter, N, τ and $\bar{\phi}$ respectively. The amplitude diagram is typical for supercritical Hopf bifurcation where the amplitude of oscillation grows smoothly (no jump behavior) after the loss of linear stability.

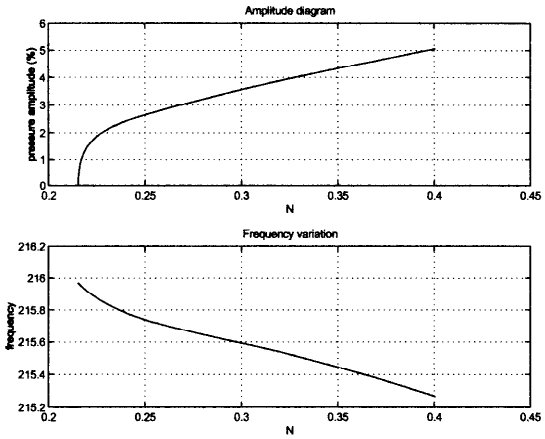


Figure 6: Amplitude diagram with varying gain ($\tau = 3.23, \bar{\phi} = .57$).

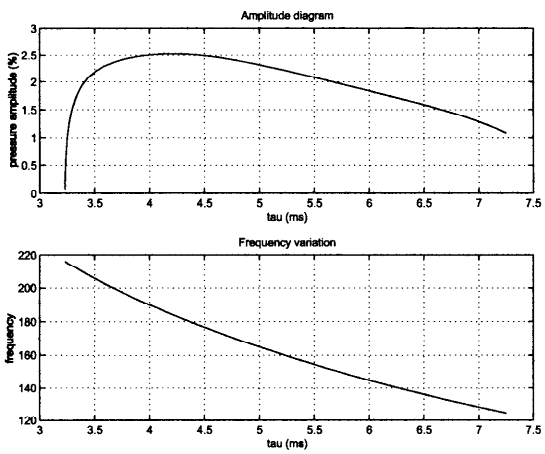


Figure 7: Amplitude diagram with varying delay ($N = .2153, \bar{\phi} = .57$).

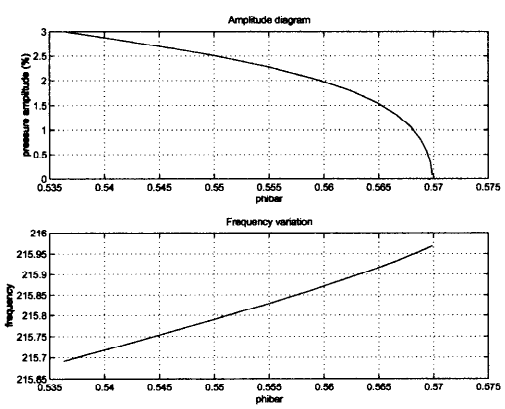


Figure 8: Amplitude diagram with varying mean equivalence ratio ($N = .24, \tau = 3.23$).

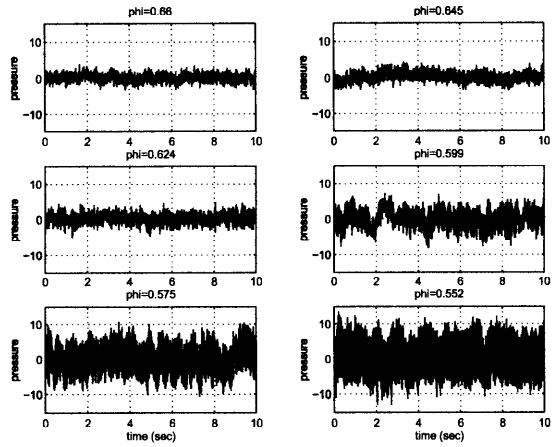


Figure 9: Time traces for the data used for calibration.

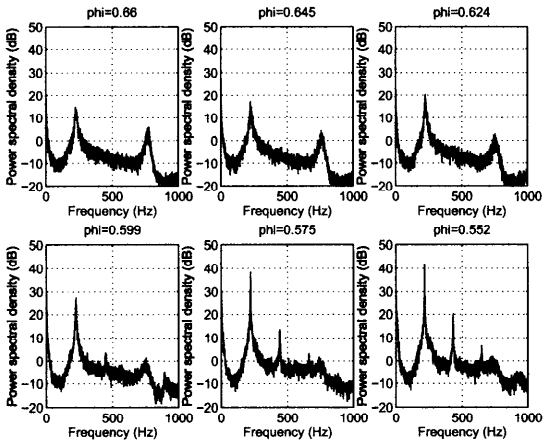


Figure 10: Power Spectral Density for the data used for calibration.

4 Thermoacoustic Model Calibration to Experimental Data

This section describes an approach for model calibration using data obtained in the experimental program. The data used in this section includes five data points with the mean equivalence ratio $\bar{\phi}$ varying between .55 and .66. The magnitude of oscillations reaches 3% at the lowest $\bar{\phi}$, and the frequency varies near 220 Hz. Note that the data are quite noisy so we should make some assumptions in order to interpret the observed behavior as a limit cycle contaminated by noise. The main such assumption is that oscillations in the system are due to the nonlinear mechanism of a feedback coupling of acoustics and heat release (thermoacoustic instability) which leads to the emergence of a limit cycle via a Hopf bifurcation as the equivalence ratio becomes smaller. The equivalence ratio decreases from the top left to the right bottom in the figure. The most important features of Hopf bifurcation, for the purposes of this study, are that the amplitude grows as a square root of the criticality parameter and the frequency varies linearly with the perturbation parameter.

Time traces and power spectral density of pressure signal for chosen data points are shown in Figure 9 and Figure 10. The identified values of the magnitude and (basic) frequency are shown in Figure 11. These qualitatively agree with the Hopf bifurcation scenario, but we notice that the identification procedure we have used produces less reliable results, especially in terms of frequency, for small amplitude oscillations. This may be explained by the low signal to noise ratio. We will consider two approaches to model calibration: one for the original thermoacoustic model where no noise is present and another where noise is included (into the heat release portion) to simulate the effects of turbulence.

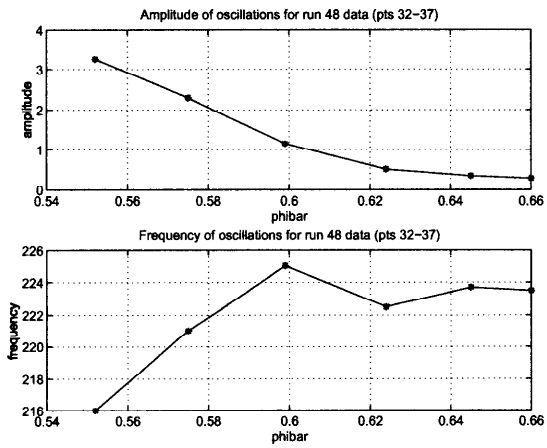


Figure 11: Identified magnitude and frequency of pressure oscillations.

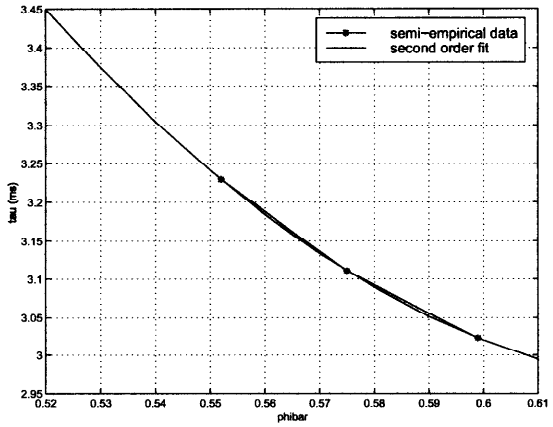


Figure 12: Identified convective delay as a function of equivalence ratio (run 48 data, points 32-34).

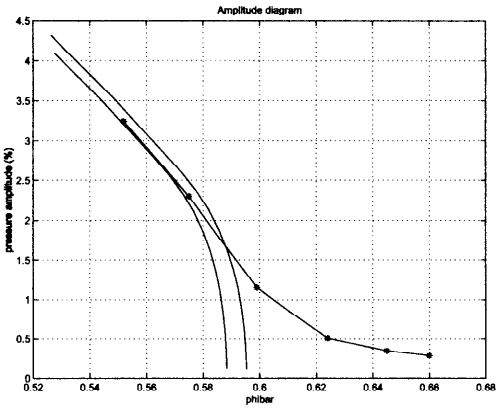


Figure 13: Amplitude dependence on $\bar{\phi}$ for the calibrated model plotted against the experimental data (marked by stars). Three computed curves correspond (from left to right) to $N = .27, .28, .29$.

4.1 Model calibration without noise

The calibration procedure without noise proceeds as follows. We first find a value of the time delay as a function of mean equivalence ratio. The dependence of frequency on the time delay is used to solve the inverse problem: that is knowing the frequency of the limit cycle find the corresponding time delay. The inverse problem can be easily solved graphically or by interpolating data for the stability boundary. It is important to note that the results of this step do not depend on the particular choice of equivalence ratio for which the stability boundary was computed. Using the fact that the frequency of oscillation for available data points is known the corresponding values of time delay can be found. This gives the delay as a function of mean equivalence ratio and a parameterization of this function is found by fitting a second order polynomial. This allows the computation of the dependence of the amplitude of oscillations on $\bar{\phi}$.

The result of applying the outlined procedure to model (1) and experimental data is given in the set of figures described below. Table 3 contains identified values of convective delay. A connection between $\bar{\phi}$ and τ is described by quadratic dependence as illustrated in Figure 12. Using this dependence, amplitude curves have been computed for several values of N; the results and their comparison to the data are shown in Figure 13. The comparison to data indicates that the data fits best with N in the range $.25 - .26$.

4.2 Calibration with noise using statistics of data

It is seen that the pressure data has a large stochastic component that we will refer to as the noise. Especially for the low amplitude oscillations, which occurs the higher mean equivalence ratios, the histogram of the time traces shows a distinctly Gaussian distribution. Therefore, we assume that the system is driven by noise. Note that in [12] effect of addition of noise to a combustion model was studied showing good agreement between the model and data. The noise addition to the model was also supported by results in ([2, 3, 9]). In this work empirical models of single nozzle rig and sector rig operating at high equivalence ratio conditions from forced frequency response experiment were obtained. A stable second order lightly damped system was identified from this experiment. The model was augmented by addition of a white noise input to match the open-loop PSD of the combustor pressure signal. Excellent matches of pressure PSD from the model simulation and from experiment for controlled and uncontrolled system were obtained. A general theory for comparison of models of systems with complex non-equilibrium attractors and stochastically driven systems with applications to model validation and parameter identification is laid out in [14]. This paper also contains an example of parameter identification (delay and noise standard deviation) of a semi-empirical combustion model of the controlled single-nozzle rig operating at high mean equivalence ratio using statistics of data.

In order to deal with this stochastic input explicitly, a random fluctuation is added to the velocity in the nozzle. This random component models turbulence.

If no noise were present, as mentioned earlier in the paper, the equivalence ratio would be $\phi(t) = \bar{\phi}\bar{u}/u(t-\tau)$. The noise is introduced into it in the following manner

$$\phi(t) = \bar{\phi}\bar{u}/\left(u(t-\tau) + N_n\bar{u}r(t)\right) \tag{5}$$

where r is a normally distributed random number with variance 1. The parameter N_n determines the level of input noise entering the system (as a percentage of the mean nozzle velocity).

By comparing statistics of the data with the simulated output of the model, a fit can be done on the model parameters. With noise addition, the parameters of the model are gain N, time delay τ and noise level N_n. Statistics compared are the Power Spectral Density (PSD) and the Probability Density Function (PDF). Since the model can only describe the

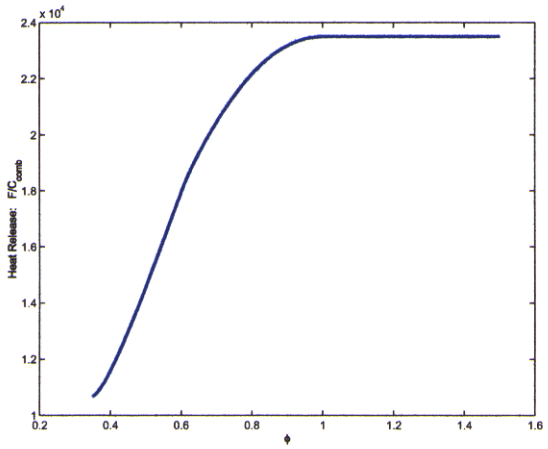


Figure 14: The combined heat release function.

bulk acoustic mode, and the data shows strong component around 750Hz corresponding to a longitudinal mode, the data is filtered around the bulk mode frequency before comparison. Six data sets are available for six different mean equivalence ratios, and for each of these data points, values of these parameters are determined which make the model reproduce the characteristics of the data closely (PSD and PDF). In particular, six values of N and τ, and one N_n are determined. These are shown in Table 4.

Since the heat release rate given by $F(t)$ in equation 4 has N and $\bar{\phi}$ as parameters, this would mean a different function is required to fit the data for every data point. For this reason, a single heat release function was constructed with the help of these six identified functions so that when the model was simulated with it, the model output again matched the data statistics as well as it did with the individual N-dependent functions. Figure 14 shows the heat release function. Figure 15 shows the comparison of PSD and PDF estimates between the data and the model output with this heat release function (N_n and τ values used were the ones given in Table 4). These plots show that the model with the identified heat release function can reproduce the chosen statistics of the data reasonably well. Figure 16 additionally confirms this by showing the comparison of rms as a function of $\bar{\phi}$ from data and the model.

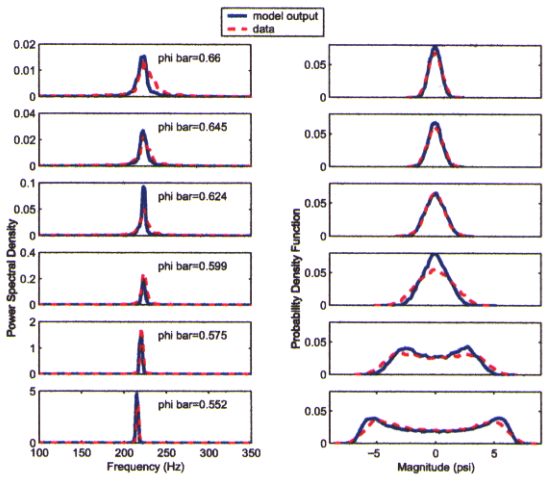


Figure 15: Comparison of data characteristics with that of model output with best-fit heat release function (10% noise). Left column: PSD's; right column: PDF's.

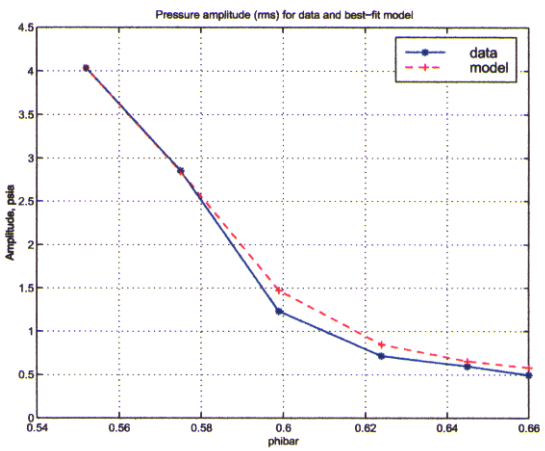


Figure 16: Pressure amplitude (rms) for run 48 data and best-fit model with noise (noise level is the same at all points.)

5 Conclusions

This paper has presented a thermoacoustic modeling framework that describes the results obtained in an experimental program conducted at UTRC.

The paper details the overall modeling approach including the development of physics based acoustics and heat release components. The feedback interconnection of acoustics and heat release — the thermoacoustic model — has been analyzed using a harmonic balance method. This analysis is used to calibrate the model to experimental data, especially, to match amplitudes and frequencies of oscillations seen in

experiments. The matching is accomplished by selection of the empirical portions of the model — the time delay and the heat release gain. The confirmation or match of the model to trends in the amplitude of oscillation as a function of mean equivalence ratio forms the validation of the model.

This paper has developed a methodology for both modeling and analysis that captures experimental data. This methodology consists of the following steps:

1. The development of an acoustic model based on conservation laws. The acoustic model captures the bulk motion in the combustion chamber. The model uses realistic boundary conditions for the premixing nozzle and the exit orifice. The calibration of the acoustic model is done using steady state rig measurements of pressures and mass flow rates and the model predicts the dynamic behavior including acoustic resonance frequencies and damping.

2. The development of a heat release model based mainly on first principles. The heat release model captures the mean heat release as well as the fluctuating component. The fluctuating component is a function of a convective time delay and an empirical gain that both need to be identified from experimental data. The mean heat release is a function of the fuel mass flow rate and equivalence ratio and can be calculated separately.

3. The calibration of the empirical portions of the model to match experimental data. The paper presents two methods for calibration of the model. In the first method the time delay is estimated from experimental data to match the frequency of oscillation and is expressed as a function of mean equivalence ratio. The heat release gain is chosen so that the amplitudes of oscillation of the model matches the experimental data at one value of equivalence ratio. The model is then used to predict the trend of amplitudes with respect to equivalence ratio and this validates the model against experimental data. The validation shows good agreement. In the second method a stochastic fluctuation in the fuel nozzle velocity is introduced and the PSD and PDF properties of the data are matched through adjustment of the noise and gain values. The validation shows better agreement with the data than the first method particularly in the low amplitude portion of the pressure data where the system is expressed as a noise driven stable linear system.

The paper enables a number of subsequent investigations. Some of the immediate ones are as follows:

1. Use of closed loop data for model calibration and validation.

2. Prediction of control authority to match experimental data in a quantitative manner.

3. Use of forced response data to validate the model against experimental data.

4. The calibrated model allows the use of control theory to understand the fundamental limits of controlled performance. This is a standard use of control theory as developed in [18] and applied to combustion processes in [2, 3]. This study of the limits of controlled behavior allows the central parameters to be understood and controllers to be evaluated against absolute metrics and not relative advantages of control design methods.

All of these investigations are expected to increase the fidelity of the model by examining possible deficiencies and through the incorporation of alternate parameter selection or physical mechanisms more accurately describe a wider range of experimental conditions than the open loop matching that is contained in this paper.

Acknowledgments.

The authors wish to acknowledge the overall guidance and program management provided by Drs. Thomas Rosfjord, John McVey, Alan Eckbreth and Richard Murray. The authors also thank Dr. Aldo Peracchio for insightful conversations related to this work. The authors would like to acknowledge significant contribution of Prabir Barooah to calibration of the model with noise. The staff of the Jet Burner Test Stand at UTRC is to be commended for their dedication and professionalism in assisting the authors in obtaining the data that has been used in this paper.

Appendix: Harmonic balance method

The purpose of this appendix is to provide a computational framework, using harmonic balance method, for tracing stability boundaries and tracking periodic orbits as parameters in the model vary. We assume the model to be in the form of differential-delay equation:

$$\dot{x} = F\left(x(t), x(t-\tau), \alpha\right) \tag{6}$$

Here $x \in R^n$ denotes the state vector, τ is the system delay, and α is a scalar parameter.

Let $x = X(t)$ be a periodic solution of the system (6), $X(t+T) = X(t)$, where T is an unknown period. Assuming that $x(t)$ can be approximated by the truncated Fourier series with M harmonics then

$$X_M(t) = x_0 + \sum_{k=1}^{M} \left(p_k \sin(2\pi k\omega t) + q_k \cos(2\pi k\omega t)\right) \tag{7}$$

where $\omega = 1/T$, $x_0, p_k, q_k \in \mathbb{R}^n$. Substituting (7) into (6) and requiring the truncated Fourier series of both sides of (6) be equal yields the following set of M-*th* order harmonic

balance equations:

$$\begin{aligned} F_0 &= 0, \\ FS_k - 2\pi k\omega q_k &= 0, (k = 1, ...M), \\ FC_k + 2\pi k\omega p_k &= 0, (k = 1, ...M), \\ (p_1, q_1) &= 0. \end{aligned} \tag{8}$$

where

$$\begin{aligned} F_0 &= \omega \int_0^{1/\omega} F(X_M(t), X_M(t-\tau), \alpha)dt, \\ FS_k &= 2\omega \int_0^{1/\omega} F(X_M(t), X_M(t-\tau), \alpha)\sin(2\pi k\omega t)dt, \\ FC_k &= 2\omega \int_0^{1/\omega} F(X_M(t), X_M(t-\tau), \alpha)\cos(2\pi k\omega t)dt, \end{aligned} \tag{9}$$

Note that the last equation in (8) fixes the phase thus removing the singularity due to translation invariance of the periodic solution. The algebraic system (8) contains $(2M+1)n+1$ equations and the same number of unknowns (vectors x_0, p_k, q_k, $(k = 1, ...M)$ and frequency ω). Taking τ as another unknown yields a standard continuation problem [1] since the solution set of (8) will generally be a curve. It determines the evolution of a periodic solution as τ varies. Note that instead of τ we may choose α as an active parameter and analyze the dependence of the periodic solution, particularly, its amplitude and frequency, on α.

For the purposes of linear stability analysis linearize equation (6) at the equilibrium point (which is to be determined) and find critical value of delay τ and α such that linearized equation has periodic solutions. Since these solutions are pure harmonics, we use (8) with $M = 1$. We also have to fix the amplitude of oscillations (which because the system is a linear system can be arbitrary, moreover is set by the initial conditions of the defining system of equations) which we do by adding the constraint $(p_1, p_1)(q_1, q_1) - (p_1, q_1)^2 = 1$. In more detail, the defining system for stability calculations is given as follows.

The linearized system (6) at the equilibrium x_0 $(F(x_0, x_0, \alpha) = 0)$ has the form

$$\frac{du(t)}{dt} = Z(x_0, \alpha)u(t) + W(x_0, \alpha)u(t-\tau) \tag{10}$$

where Z and W are $n \times n$ matrices. The defining system now reads:

$$\begin{aligned} F(x_0) &= 0, \\ Zp_1 + NW(p_1\cos(2\pi\omega\tau) + q_1\sin(2\pi\omega\tau)) + 2\pi q_1 &= 0, \\ Zq_1 + NW(-p_1\sin(2\pi\omega\tau) + q_1\cos(2\pi\omega\tau)) - 2\pi p_1 &= 0, \\ (p_1, q_1) &= 0, \\ (p_1, p_1)(q_1, q_1) &= 1 \end{aligned} \tag{11}$$

This system contains $3n+2$ equations and the total number of unknowns (x_0, p_1, q_1, ω) is $3n+1$. Adding τ and α as another unknowns yields a continuation problem for computing the onset of (linear) instability. The projection of the solution curve onto (α, τ) plane defines the α-τ stability diagram. The evolution of frequency along the stability boundary can be seen from projections of the same curve onto (τ, ω) or (α, ω) plane.

We now turn to the problem of computing limit cycles of small amplitude near the stability boundary. Limit cycles near Hopf bifurcation [13] can be approximated with two harmonics $(M = 2)$. The corresponding algebraic system of harmonic balance equations contains $5n + 1$ equations and unknowns. Adding τ (or α) to the set of unknowns yields a continuation problem. The solution of these equations determines the dependence of the amplitude and frequency of oscillations on τ. As we move away from the onset of instability into the unstable region, adding more harmonics might be necessary to represent the limit cycle (particularly when saturation effects of nonlinearity become important) with sufficient accuracy.

References

[1] E.L. Allgower and K. Georg. *Numerical Continuation Methods.* Springer-Verlag, New York, 1990.

[2] A. Banaszuk, C.A. Jacobson, A.I. Khibnik, and P.G. Mehta. Linear and nonlinear analysis of controlled combustion processes. Part I: Linear analysis. In *1999 Conference on Control Applications*, 1999.

[3] A. Banaszuk, C.A. Jacobson, A.I. Khibnik, and P.G. Mehta. Linear and nonlinear analysis of controlled combustion processes. Part II: Nonlinear analysis. In *1999 Conference on Control Applications*, 1999.

[4] J.F. Blackburn, G. Reethof, and J.L. Shearer. *Fluid Power Control.* MIT, Cambridge, MA, 1960.

[5] G.J. Bloxsidge, A.P. Dowling, and P.J. Langhorne. Reheat buzz: an acoustically coupled combustion instability. part 2. theory. *J. Fluid Mechanics*, 193:445–473, 1988.

[6] R. Ernst. Augmentor stability management program. Technical Report AFWAL-TR-2001, Pratt & Whitney, February 1982.

[7] M. Fleifil, A. M. Annaswamy, Z. A. Ghoniem, and A. F. Ghoniem. Response of a laminar premixed flame to flow oscillations: A kinematic model and thermoacoustic instability results. *Combustion and Flame*, 106:487–510, 1996.

[8] J.P. Hathout, A.M. Annaswamy, M. Fleifil, and A.F. Ghoniem. A model-based active control design for thermoacoustic instability. Technical Report 9703, MIT, 1997.

[9] J.R. Hibshman, J.M. Cohen, A. Banaszuk, T.J. Anderson, and H.A. Alholm. Active control of combustion instability in a liquid-fueled combustor. In *1999 ASME Turbo Expo*, 1999.

[10] K.U. Ingard. Analysis of combustor instability. Technical report, UTRC, December 1997.

[11] T. Lieuwen and Ben T. Zinn. The role of unmixedness in driving combustion instabilities in low NOx gas turbines. Technical report, Georgia Institute of Technology, 1999.

[12] T.C. Lieuwen and B.T. Zinn. Investigation of limit cycle oscillations in an unstable gas turbine combustor. In *AIAA Paper 2000-0707, 38th AIAA Aerospace Sciences Meeting*, 2000.

[13] A.I. Mees and L.O. Chua. The Hopf bifurcation theorem and its applications to nonlinear oscillations in circuits and systems. *IEEE Transactions on Circuits and Systems*, CAS-26(4):235–254, April 1979.

[14] I. Mezić and A. Banaszuk. Comparison of complex systems. Submitted to Physica D, 2000.

[15] P.M. Morse and K.U. Ingard. *Theoretical Acoustics*. Princeton University, Princeton, NJ, 1986.

[16] R.M. Murray, C.A. Jacobson, R. Casas, A.I. Khibnik, C.R. Johnson Jr., R. Bitmead, A.A. Peracchio, and W.M. Proscia. System identification for limit cycling systems: A case study for combustion instabilities. In *Proceedings of 1998 American Control Conference*, 1997.

[17] A.A. Peracchio and W. Proscia. Nonlinear heat release/acoustic model for thermoacoustic instability in lean premixed combustors. In *1998 ASME Gas Turbine and Aerospace Congress*. ASME, 1998.

[18] M.M. Seron, J.H. Braslavsky, and G.C. Goodwin. *Fundamental Limitations in Filtering and Control*. Springer, New York, 1997.

Parameter	Description
ρ_3	density at the nozzle exit, (lbm/ft^3)
$L_{nozzle}, L_{perf}, L_{bypass}$	effective nozzle (perforated plate, bypass leg) length, (ft)
$k_{nozzle}, k_{perf}, k_{bypass}$	$1/C_d^2$ for nozzle (perforated plate, bypass leg) flow, (dimensionless)
$V_{nozzle}, V_{perf}, V_{bypass}$	velocity at nozzle (perforated plate, bypass leg) exit, (ft/sec)
$P_{comb}, P_{plenum}, P_{pre}$	pressure in the combustor (plenum, prediffuser), (psia)
$C_{comb}, C_{plenum}, C_{pre}$	capacitance of combustor (plenum, prediffuser) volume, $(ft - sec^2)$
A_e	physical area of exit cross section, (ft^2)
κ	constant in choked flow equation, $(\sqrt{^\circ\text{R}}/\text{sec})$
C_d	discharge coefficient, (dimensionless)
T_4	exit temperature in combustor, (°R)
$\dot{m}_{in}$	upstream mass flow, (lbm/sec)
F	mass flow addition due to heat release(lbm/sec)

Table 1: Description of Model Parameters

Parameter	Value	Comments
ρ_3	.5807	lbm/ft^3
L_{nozzle}	.65	ft
L_{bypass}	.95	ft
L_{perf}	.042	ft
k_{nozzle}	2.0408	dimensionless
k_{bypass}	2.7778	dimensionless
k_{perf}	1.6866	dimensionless
A_{nozzle}	.0431	ft^2
A_{bypass}	.0083	ft^2
A_{perf}	.0313	ft^2
C_{comb}	2.7455×10^{-4}	$\text{ft} - \text{sec}^2$
C_{pre}	1.8122×10^{-3}	$\text{ft} - \text{sec}^2$
C_{plenum}	4.1853×10^{-3}	$\text{ft} - \text{sec}^2$
$\dot{m}_{in}$	6.52	lbm/sec
κ	.532	R/sec
C_d	.98	dimensionless
A_e	.0218	ft^2
T_4	2825+460	° R

Table 2: Parameter Values for Acoustic Portion of Model (1).

Mean equivalence ratio	Amplitude (percent to the mean)	Frequency (Hz)	Identified delay (ms)
0.5520	3.25	216	3.23
0.5750	2.3	221	3.11
0.5990	1.149	225	3.02
0.6240	0.5075	222	N/A
0.6450	0.3410	223.7	N/A
0.6600	0.2795	223.5	N/A

Table 3: Data from run 48 and identified value of delay

Mean equivalence ratio	Best-fit N	Best-fit τ (ms)	N_n (noise level)
0.66	0.278	3.0	0.1
0.645	0.272	3.0	0.1
0.624	0.259	3.0	0.1
0.599	0.244	3.0	0.1
0.575	0.22	3.08	0.1
0.552	0.19	3.20	0.1

Table 4: Best fit values of N, τ and N_n to data from run 48.

PAPER -30, C. Jacobson

Question (M. Huth, Germany)

How can models developed for a single burner test rig be used in an annular combustion arrangement? How are the circumferential modes described?

Reply

The UTRC approach has been to develop combustion dynamics models by reducing the number of fuel injectors, but keeping the environment (pressure, temperature) realistic relative to the engine operating conditions. Hence the heat release models are realistic and the acoustic model may be changed to model different situations (longitudinal, tangential modes).

Question (S. Candel, France)

Can you explain the meaning of the gain parameter and is this gain parameter a function of frequency? Also, in many cases the response of a confined flame is strongest in regions where the gain of the transfer function is not very large but where the phase is large.

Reply

The dynamic model developed uses physics-based models. However, these models were very simplified. In the procedure described in the paper, a free parameter ("gain") is interested to capture some neglected heat release characteristics. This gain parameter is expected to be O(1) if the model is accurate (which it was found to be when N $\approx$ 0.2 in the calibration procedure).

The heat release model was derived based on the work of Proscia and Peracchio. In this model, both equivalence ratio and flame sheet dynamics are considered and, in this full model, there will be a frequency dependence (because of the flame sheet dynamics). This dependence was not found to be significant for the behavior being captured by the model and hence was deleted to have the simplest model available.

Active Control of Combustion Instabilities in Gas Turbine Engines for Low Emissions. Part II: Adaptive Control Algorithm Development, Demonstration and Performance Limitations

Andrzej Banaszuk
United Technologies Research Center,
MS129-15, 411 Silver Lane, East Hartford, CT 06108, USA
tel. 860 610 7381, **banasza@utrc.utc.com**

Youping Zhang
Numerical Technologies, Inc.
70 West Plumeria Drive San Jose, CA 95134-2134, USA
tel. 408 919 1910 ext 343 **yzhang@numeritech.com**

Clas A. Jacobson
United Technologies Research Center,
MS129-15, 411 Silver Lane, East Hartford, CT 06108, USA
tel. 860 610 7652, **jacobsca@utrc.utc.com**

Abstract

We present results of experiment with two distinct extremum-seeking adaptive algorithms for control of combustion instability suitable for reduction of acoustic pressure oscillations in gas turbine over large range of operating conditions. The algorithms consists of a frequency tracking Extended Kalman Filter to determine the in-phase component, the quadrature component, and the magnitude of the acoustic mode of interest, and a phase shifting controller with the controller phase tuned using an extremum-seeking algorithms. The algorithms are also applicable for control of oscillations of systems whose oscillation frequency and optimal control phase shift depends on operating conditions, and which are driven by strong broad-band disturbance. The algorithms have been tested in combustion experiments involving full-scale engine hardware and during simulated fast engine transients.

1 Introduction

Emphasis on reducing the levels of pollutants created by industrial gas turbine combustors has led to the development of lean, premixed combustor designs, as premixing large amounts of air with the fuel prior to its injection into the combustor greatly reduces peak temperatures within the combustor and leads to lower NOx emissions. However, premixed combustors are often susceptible to thermoacoustic combustion instabilities, which can lead to large pressure oscillations in the combustor. These pressure oscillations result in increased noise and decreased durability. The goal of using active combustion instability control on a gas turbine engine is to keep pressure oscillations at an acceptable level over a large range of operating conditions.

Experiments and model-based analysis determined that pressure measurement and a simple phase-shifting algorithm with an appropriately chosen control phase is sufficient for suppression of oscillations, given enough control authority ([11, 7, 14, 6, 8, 3, 4]). Model based analysis determined that minimum information needed to calculate the best control phase requires estimation of parameters, including transport delay (or at least the corresponding phase shift), that are hard to obtain from pressure measurements alone [8, 3, 4]. Even if this difficulty could be circumvented, the sensitivity to modeling errors was likely to be high.

Need for developing an algorithm that would allow finding the best phase with minimum amount of a priori information that would work over large range of operating conditions and with minimum model assumptions seemed apparent. The operating conditions include fast engine acceleration and deceleration transients.

An experiment with active control of pressure oscillations in an industrial combustor has been conducted on 179MW and 230MW gas turbines by Siemens [16]. The pilot fuel has been modulated using a phase-shifting mechanism. The best control algorithm parameters were found manually at each operating condition. However, problems developed when the conditions were changing suddenly. Here is a quote from the paper by Siemens engineers and they coworkers describing experiments with Active Instability Control on 170MW engine:

"Further investigations of the effects of AIC showed de-

Paper presented at the RTO AVT Symposium on "Active Control Technology for Enhanced Performance Operational Capabilities of Military Aircraft, Land Vehicles and Sea Vehicles", held in Braunschweig, Germany, 8-11 May 2000, and published in RTO MP-051.

pendence of the required control parameters (gain and phase shift) on the operating conditions of the gas turbine (e.g., power level, pilot gas fraction). AIC operating parameters wich result in a clear reduction of oscillations for certain gas turbine operating conditions can cause a significant loss in performance of the control system during other gas turbine operating conditions. In the worst case, the heat release rate modulation induced by the controller can be in phase with the one resulting from the self-excitation, which results in a positive feedback and further amplification of the undesired oscillations. Therefore, the control parameters must be adjusted to the operating conditions quickly. Since the control parameters were set manually, difficulties arose when the operating conditions were subject to sudden changes. Therefore, an adaptive control algorithm is being developed, which seeks the optimum settings for gain and phase shift." [16].

The lack of a control algorithm that would allow for the search of control parameters automatically and would not magnify the pressure oscillations in the process of tuning was perceived by Siemens engineers to be the major obstacle in implementing Active Instability Control to suppress pressure oscillation on an industrial gas turbine.

The algorithm presented in this paper allows fast automatic tuning of control parameters and (under reasonable assumptions) can be guaranteed not to amplify the oscillations. Two extremum-seeking algorithms [17] were selected for tuning of the control phase. There was a technical challenge in finding a phase shifting mechanism that works for pressure oscillations varying over large frequency range and reliable pressure magnitude detection mechanism. This challenge has been overcome with a frequency tracking observer algorithm (based on Extended Kalman Filter described in [12]) that allows for fast and reliable estimation of the in-phase and quadrature components of the bulk pressure mode over large range of frequencies.

Performance specifications for extremum-seeking algorithms have been defined for algorithm initialization transients and engine acceleration transients. When initialized with a phase corresponding to amplification of oscillations, the algorithms should quickly produce and maintain phases corresponding to suppression of the oscillations. In the engine acceleration transients the algorithms should be able to suppress oscillations relative to uncontrolled levels.

The algorithms were tested on a single nozzle combustion rig at United Technologies Reserach Center in August 1998. More details on frequency tracking and classical extremum-seeking algortithm are included in [5]. The paper [18] provides more details on the triangular search extremum-seeking algorithm.

2 Adaptive algorithm description

2.1 Control architecture

The model analysis indicates that the combustion process can be modeled by a feedback interconnection of a second order lightly damped system representing an acoustic mode, and a large delay followed by a saturated nonlinear function representing the heat release process [15] [13]. If the phase shift due to the heat release delay provides a positive feedback, then the damping of the system will be reduced and possibly achieve a negative value. In the latter case the system dynamics can settle on a limit cycle. One can easily show that phase-shifting control is an effective way of reducing the magnitude of the limit cycle. The phase shift can be implemented in many ways, including introducing a delay in control, using phase lead or lag, using LQG control, and self-tuned LMS algorithms. For our purpose phase-shifting using an observer was selected. The observer-based phase shifting control has several advantages: it is conceptually simple and its digital implementation requires less CPU time and offers better phase resolution that the delay algorithm. However, the most important feature of the observer based phase-shifting controller is its suitability for tuning. Firstly, the controller phase-shift is directly available for tuning. Secondly, an estimate of the magnitude of the pressure oscillations is readily available from the observer states. Hence, an extremum-seeking algorithm to tune the controller phase to reduce pressure magnitude can be implemented.

There was a technical challenge in finding an adaptive observer that works for pressure oscillations varying over large frequency range and reliable pressure magnitude detection mechanism. This challenge has been overcome with a frequency tracking observer algorithm based on Extended Kalman Filter described in [12] that allows for fast and reliable estimation of the in-phase and quadrature components of the bulk pressure mode over large range of frequencies. An extremum-seeking algorithm has been selected for tuning of the control phase. One of the reasons for choosing extremum-seeking for tuning the phase is that it is possible to guarantee convergence of the control parameters to the optimal value and stability of the overall system [9, 10].

Figure 1 shows the structure of the control algorithm. The control gain was fixed and only the control phase has been updated. Two distinct extremum-seeking algorithms were used. The first one described in more details in this paper relied on estimation of derivative of the pressure magnitude with respect to control phase by introducing a small sinusoidal variation in the control phase and measuring the response of the pressure magnitude at the corresponding frequency. The mean control phase was incremented by amount proportional to the estimated derivative. This algorithm will be referred to as a classical extremum-seeking algorithm. The other algorithm, described in [18], called the triangular search algorithm, used three past sampled average magnitude values to determine the new control phase. The idea behind this algorithm was to first find an interval that contains the extremum of a function and reduce the size of this interval at an exponential rate.

2.2 Frequency Tracking Observer Design

Observer based phase-shifting control algorithm that can work during engine acceleration and deceleration transients

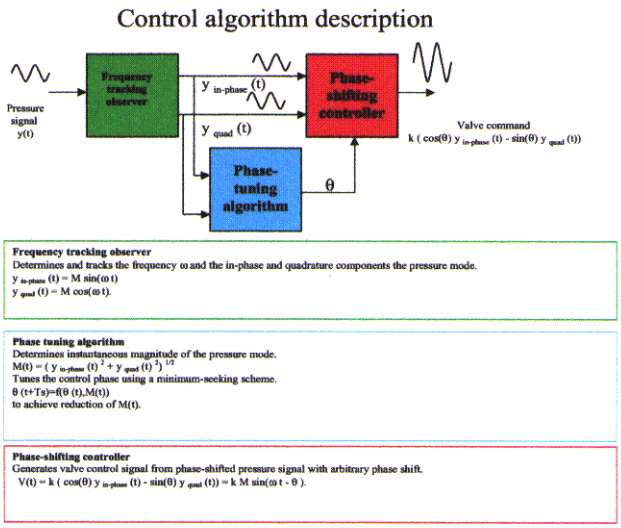


Figure 1: Adaptive algorithm for control of harmonic oscillations

requires a frequency tracking algorithm. A generalized version of a frequency tracking algorithm based on an Extended Kalman Filter studied in [12] has been implemented. Below we describe a digital version of the algorithm.

Consider a problem of estimation of in-phase and quadrature components of a sinusoidal signal $y(t) = M\sin(2\pi ft)$ with unknown frequency f, sampled at sample time T_s from a noisy measurement. Th idea used in [12] was to represent the measurements $y(k) = M\sin(2\pi fkT_s)$ as the output of a nonlinear discrete-time system with the unknown constant frequency being one of the states.

$$x_c(k+1) = \cos(w(k))x_c(k) - \sin(w(k))x_s(k) \quad (1)$$
$$x_s(k+1) = \sin(w(k))x_c(k) + \cos(w(k))x_s(k) \quad (2)$$
$$w(k+1) = w(k). \quad (3)$$

The corresponding output equation is

$$y(k) = x_s(k). \quad (4)$$

Given measurements $y(k) = M\sin(2\pi fkT_s)$, under certain conditions one can estimate the unknown frequency f (from the formula $f = \frac{w(k)}{2\pi T_s}$), and the in-phase and quadrature components of the signal $x_s(k)$, $x_c(k)$ using an observer.

We constructed an estimator for the nonlinear model (1)-(3) using an Extended Kalman Filter, i.e., a Kalman Filter designed for the linearization of the model about the current estimate (see [1]). In general, an Extended Kalman Filter algorithm estimates state x(k) of the nonlinear discrete-time system

$$x(k+1) = f(x(k)) + v_1(k) \quad (5)$$

from the measurement

$$y(k) = h(x(k)) + v_2(k). \quad (6)$$

$v_1(k)$, $v_2(k)$ are assumed to be Gaussian, independent, white noise signals, with zero means, and covariance matrices Q, R, respectively.

The Extended Kalman Filter (to be sometimes abbreviated to EKF) uses the measurement $y(k)$ to update the estimate of the state. The filter state is denoted $\hat{x}(k)$ and the state estimate error covariance matrix is denoted $P_s(k)$. The filter states are initialized at zero except for the frequency estimate.

Extended Kalman Filter update equations are:

given: previous filter state $\hat{x}(k-1)$, state estimate error covariance matrix $P_s(k-1)$, measured signal $y(k)$.

1. $K(k) = P_s(k-1)H(k-1)' * (H(k-1)P_s(k-1)H(k-1)' + R)^{-1}$ calculate update gain

2. $y_d(k) = y(k) - h(\hat{x}(k-1))$ filter output prediction error

3. $x_m(k) = \hat{x}(k-1) + K(k)y_d(k)$ state estimate using prediction error

4. $H(k) = \frac{\partial h}{\partial x}$, at $x = \hat{x}(k-1)$ linearization of output function

5. $F(k) = \frac{\partial f}{\partial x}$,, at $x = x_m(k)$ linearization of vector field f

6. $P_m(k) = (I - K(k)H(k))P_s(k-1)$ state estimate error covariance update

7. $\hat{x}(k) = f(x_m(k))$ state prediction

8. $P_s(k) = F(k)P_m(k)F(k)' + Q$ state estimate error covariance prediction

We assume $R = 1$ and $Q = diag(q_1, \ldots, q_n)$. The choice of weights q_i is the main tuning mechanism for the EKF. While they were introduced in the formulation of the filtering problem was as the variances to the state noise terms they can be thought of as tuning knobs for the filter.

A modified and extended version of the algorithm from [12] has been implemented in a digital control system on a D-SP board to provide a frequency tracking and phase-shifting mechanism for control of combustion instability. Several extensions of model (1-2) were implemented. The most complex one has 8 states and involves modeling of first two harmonics of the bulk pressure mode, its unknown frequency, DC (low frequency) component, and longitudinal acoustic (750Hz) mode component.

Figures 2 and 3 illustrate performance of the frequency tracking Extended Kalman Filter. An 8-second long data record has been constructed off-line by concatenating four 2-

second long time traces of a pressure signal obtained during control experiment on United Technologies Research Center test rig. The four data points correspond to four different control phases. Figure 2 shows that the frequency estimate from the EKF algorithm agrees well the one obtained with a short-time PSD analysis. From Figure 3 we see that the EKF output traces the pressure signal very well.

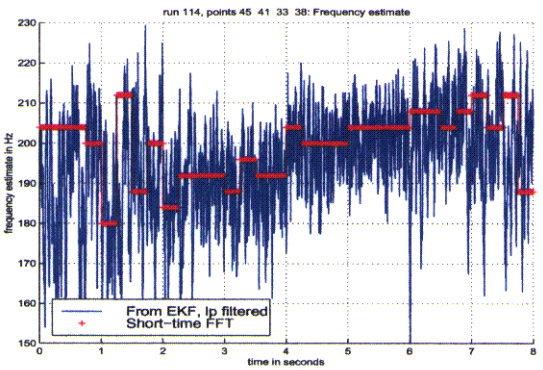


Figure 2: Frequency estimate from EKF and short-time PSD

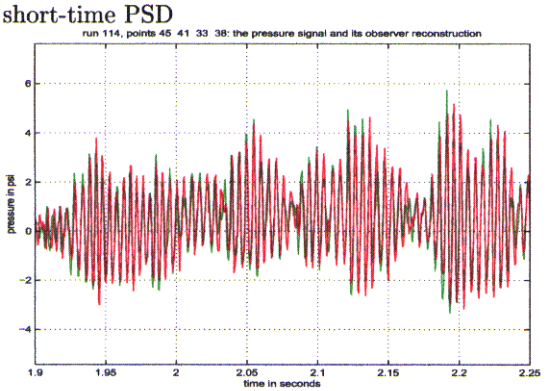


Figure 3: Pressure signal and its reconstruction with EKF

Figures 4 to 9 show frequency tracking with Extended Kalman Filter when the combustor in the sector rig was warming up. Figures 4 to 6 show the on-line frequency estimate from EKF and short-time PSD. The frequency of the bulk acoustic mode increases because the speed of sound increases with temperature. Note that the frequency tracking algorithm was tracking the maximum frequency of the bulk pressure mode. The frequency estimate from EKF algorithm was smoother than the one shown in the previous section because the estimate from EKF was smoothen with an additional low-pass filter. Figures 7 to 9 show pressure signal and on-line estimates of the in-phase component of the pressure signal reconstructed with EKF. From comparison of FFTs one can see the band-pass filtering properties of the EKF. The in-phase and quadrature components of the bulk pressure mode have spectral content around 200Hz and thus the phase-shifted control signal would not be contaminated with other frequencies.

Figures 4 to 9 illustrate how fast the pressure oscillations frequency and magnitude can increase when the combustor operating conditions change. Figure 4 alone shows increase of frequency of pressure oscillation by $30Hz$ in 9 seconds. Overall, in less than 2 minutes the frequency of oscillations changed from about 150Hz to around 230Hz and its magnitude increased by a factor of 3. Changes in the frequency and magnitude of acoustic oscillations during an engine acceleration or deceleration could be even faster and more dramatic. It is very unlikely that a robust controller could cope with such conditions. The need for controller phase and gain scheduling with operating conditions is clear. Since for the lack of models the model-based scheduling of controller parameters is impossible, scheduling of controller parameters using an adaptive algorithm remains the only option.

2.3 Controller phase tuning using classical extremum-seeking algorithm

The classic algorithm for finding control phase θ such that the pressure magnitude achieves a local minimum at θ^* relies on introducing a sinusoidal variation into the control parameter θ. Namely, at time t the control parameter is given by

$$\theta(t) = \theta_m(t) + \theta_1 \sin(\omega t). \tag{7}$$

$\theta_m(t)$ is the mean value of the control parameter that is adjusted using an update equation that is described later. θ_1 is the control parameter variation magnitude, usually chosen to be small. If the frequency ω is small enough, the magnitude $x_0(t)$ approximately follows the value of x_0 corresponding to the magnitude of the limit cycle corresponding to the control phase, so that the measured magnitude is

$$A(t) \approx g(\theta_m(t) + \theta_1 \sin(\omega t)) + \nu(t), \tag{8}$$

where $\nu(t)$ is a random component of the pressure magnitude that models disturbances driving the combustion process, and $g(.)$ is the function representing the dependence of the magnitude of the limit cycle corresponding on the control phase. Assuming that θ_1 is small, one can approximate $A(t)$ as

$$A(t) \approx g(\theta_m(t)) + \frac{dg}{d\theta}(\theta_m(t))\theta_1 \sin(\omega t) + \nu(t). \tag{9}$$

An observer has been used to extract the components of the magnitude estimate of $A(t)$ at the frequency ω. The observer has been constructed assuming that $A(t)$ is composed of a constant component and a harmonic component at the frequency ω, i.e., the magnitude estimate $A(t)$ is an output of a linear system with three states, one modeling the constant component, and two modeling in-phase and quadrature component of a harmonic oscillator with the frequency ω. The observer equations were

$$\dot{x}_1(t) = -\omega x_2(t) + l_1(A(t) - A_o(t)) \tag{10}$$
$$\dot{x}_2(t) = \omega x_1(t) + l_2(A(t) - A_o(t)) \tag{11}$$
$$\dot{x}_3(t) = l_3(A(t) - A_o(t)) \tag{12}$$
$$A_o(t) = x_2(t) + x_3(t). \tag{13}$$

with the gains l_1, l_2 , l_3 chosen so that the observer error dynamics is stable. (In fact, a discrete-time version of this observer was implemented). Now, assuming that the observer gains are properly chosen, one can assume that after some transient the observer states are approximately

$$x_1(t) \approx \frac{dg}{d\theta}(\theta_m(t))\theta_1 \cos(\omega t) \quad (14)$$

$$x_2(t) \approx \frac{dg}{d\theta}(\theta_m(t))\theta_1 \sin(\omega t) \quad (15)$$

$$x_3(t) \approx g(\theta_m(t)). \quad (16)$$

Now, an estimate of $\frac{dg}{d\theta}(\theta_m(t))$ can be obtained by the following demodulation of observer states:

$$z(t) := x_2(t)\sin(\omega t) + x_1(t)\cos(\omega t) \approx \frac{dg}{d\theta}(\theta_m(t))\theta_1. \quad (17)$$

The control parameter equation will take form

$$\dot{\theta}_m(t) = -\sigma z(t), \quad (18)$$

The parameters to choose are: the control parameter variation frequency ω, the observer gains l_1, l_2 , l_3 , and the update gain $-\sigma$.

2.4 Controller phase tuning using triangular search algorithm

The triangular search algorithm is a self-exciting scheme. No external probing is required to find the direction of search. The purpose of the contraction coefficient is to gradually decrease the level of excitation when the control phase θ is close to the optimizing point. In a noise free and time invariant environment, this is to guarantee convergence with no residual error such as the case of a region of attraction. However, when noise is present and the plant is time varying, the excitation level must be kept at a sufficiently large level for all time in order to extract the correct information about the direction along which to move the control input. More details on the algorithm are presented in [18].

3 Experimental Results

In this section we present results of experiments in United Technologies Research Center conducted on 4 MW Single Nozzle Rig in August 1998 using full-scale engine fuel nozzle at realistic operating conditions. About 10% of the net fuel was modulated for control purposes using linear proportional valve. (For more details on the UTRC experiments see [6] and [8].)

Performance specifications for the adaptive algorithm have been defined for algorithm initialization transients and engine acceleration transients. When initialized with a phase corresponding to amplification of oscillations, the algorithms should quickly produce and maintain phases corresponding to suppression of the oscillations. During the engine acceleration transients the algorithms should be able to suppress oscillations relative to uncontrolled levels.

To test the transient performance of the adaptive algorithm initialization transients have been introduced. The initial control phase varied significantly from the optimal one. The algorithms behaved very well at higher power condition (small pressure oscillations and medium level of broad-band disturbance) and reasonably well at lower power conditions (large pressure oscillations and large level of broad-band disturbance). Once reaching a neighborhood of the optimal value, the control phase usually stayed in a reasonably small neighborhood of that value, rarely produced control phases corresponding to level higher than uncontrolled levels, and always provided better average pressure oscillations levels than uncontrolled levels.

The triangular search algorithm tracked the minimum value well in a transient from higher power to lower power condition. This was a slow transient but the frequency changed by about 40Hz and the pressure magnitude and noise levels were changing dramatically. Classical algorithm with a fixed gain did not work during the transients, as the controller gain that was optimal at the higher power level was destabilizing the system at the lower power level. Gain adaptation would be needed for the classical algorithm to work at both power levels. The frequency and magnitude tracking mechanism worked very well during the transients.

The dependence of the mean pressure magnitude and frequency of the corresponding mode on the control phase has been determined experimentally at two power conditions, so that the optimal control phase was known a priori. This information allowed to check performance of the extremum-seeking algorithms. Initialization transients have been introduced, where the initial control phase varied significantly from the optimal one. Figures 10 to 31 show typical time historics of control phase and pressure magnitude (instantaneous and mean) estimate at two power conditions. The open-loop and optimal levels of the pressure as well as the optimal control phase are indicated by horizontal lines in the corresponding plots. oscillations

The experimental results are presented in Appendix.

For more details on experiments we refer to [5]. In general both phase tuning algorithms behaved very well at higher power condition (medium noise and small pressure oscillatios) and reasonably well at lower power conditions (large noise and pressure oscillations). Once reaching a neighborhood of the optimal value, the control phase usually stayed in a reasonably small neighborhood of that value, rarely produced control phases corresponding to level higher than uncontrolled levels, and always provided better average pressure oscillations levels than uncontrolled levels.

It has been concluded that the major factor affecting the performance of the extremum-seeking schemes is the "noise" present in the pressure magnitude. More precisely, the main trouble with implementation of extremum-seeking algorithm is that the pressure oscillations do not have a consistent instantaneous magnitude. In fact, the magnitude varies wildly. However, changing the control phase affects the mean value of the pressure and after some averaging time it is possible to determine the mean pressure magnitude as a function of

control phase with one minimum and one maximum (modulo 360 degrees). The fluctuating component of the pressure magnitude for a fixed phase is what we call noise. The noise can be attributed to an efect of turbulent flow in the combustor on the acoustic mode either directly, or via chemical reaction.

Since magnitude of the noise is a crucial factor that determines performance of the tuning mechanism, it is necessary to include a representative noise model in the engine dynamics model, if the latter is used to study performance of the tuning algorithms.

3.1 Simulated engine acceleration transient

A nominal gas turbine engine transient from 50% to 100% power conditions lasts a fraction of a minute. The changes in operating conditions appearing during engine acceleration and deceleration are likely to resemble the transients between different power levels on the single nozzle rig. Engine transient lasting fraction of a minute could not be simulated in experiments on the single nozzle rig. Instead, we tested the extremum-seeking algorithms in a simulated engine 30-second transient, where the measured magnitude versus control phase functions and lower and higher power were interpolated.

To simulate the transients the form of the averaged pressure magnitude model was assumed in accordance with the predictions of analysis of the physics-based reduced order model and the unknown parameters of the averaged model were determined from experiments (experiments are described in [5]). The identified model was

$$\dot{x}_0(t) = -\alpha(\theta(t))\,(x_0(t) - g(\theta(t))) \quad (19)$$

$$A(t) = x_0(t) + \nu(t), \quad (20)$$

where $\theta(t)$ is the controller phase, $x_0(t)$ is the mean pressure magnitude, $A(t)$ is the instantaneous pressure magnitude, and $\nu(t)$ is a random noise. The functions $g(.)$, $\alpha(.)$, and the statistics of (colored) noise $\nu(t)$ were identified from experiment. To simplify analysis we do not include the frequency tracking algorithm in the model. This is justified under the assumption that the frequency changes faster than the magnitude and that the frequency tracking algorithm is fast and stable. In other words, we assume that the frequency dynamics and the tracking algorithm contribute to the fast stable dynamics whose time scale is separated from the slow magnitude dynamics.

The triangular search algorithm performed well in the simulated transient (see Figure 11). It was determined that in order to work in a simulated transient from lower to higher power conditions, the classical algorithm would have to be modified to allow for adaptive gain change (by a factor of five). One fixed gain would not work at both power conditions.

Ability of an extremum-seeking algorithm to track the fast changing optimal control phase shift during the engine acceleration and deceleration transient conditions in the present of disturbance driving the system has been demonstrated in a simulation. However, there is need to study stability, robustness, and performance of the algorithms using analytical tools. Traditional methods based on time-scale separation are not sufficient as the time scale of of change of operating conditions is not well separated from the time scale of the transients in the dynamics. Preliminary analysis of performance limiations of extremum-seeking algorithms that does not expoits time-scale separation has been presented in [10].

Conclusions

We presented results of experiments with two distinct extremum-seeking adaptive algorithms for control of combustion instability suitable for reduction of acoustic pressure oscillations in gas turbine over large range of operating conditions. The algorithms consists of a frequency tracking Extended Kalman Filter to determine the in-phase component, the quadrature component, and the magnitude of the acoustic mode of interest, and a phase shifting controller with the controller phase tuned using an extremum-seeking algorithms. The algorithms have been tested in combustion experiments involving full-scale engine hardware and during simulated fast engine transients.

Acknowledgements

We would also like to thank the whole UTRC combustion dynamics and control team for making this work possible. In particular, we would like to acknowledge help and support from J. M. Cohen, J. R. Hibshman, W. M. Proscia, T. J. Anderson, A. Khibnik, T. Rosfjord, and R.M. Murray. We also acknowledge contribution from M. Krstic and Kartik Ariyur from UCSD. In particular, the identification of the average pressure magnitude model used in simulations of fast transients was performed by Kartik Ariyur. This work was performed under AFOSR contract F49620-98-C-0006.

References

[1] B.D.O. Anderson and J.B. Moore, *Optimal Filtering*, Prentice-Hall, Englewood Cliffs, New Jersey, 1979.

[2] A. Banaszuk, "A note on combustion instabilities," *UTRC Technical Report*, September 1997.

[3] A. Banaszuk, C. A. Jacobson, A. I. Khibnik, P. G. Mehta, "Linear and nonlinear analysis of controlled combustion processes. Part I: Linear analysis," *Proc. of the IEEE Conf. on Control Applications*, Kohala-Coast, Hawai, pp. 199–205, Aug. 1999.

[4] A. Banaszuk, C. A. Jacobson, A. I. Khibnik, P. G. Mehta, "Linear and nonlinear analysis of controlled combustion processes. Part II: Nonlinear analysis," *Proc. of the IEEE Conf. on Control Applications*, Kohala-Coast, Hawai, pp. 206–212, Aug. 1999.

[5] A. Banaszuk, K. Aryiur, M. Krstic, C. A. Jacobson, "An Adaptive Algorithm for Control of Combustion Instability," *submitted to Automatica*, 2000.

[6] J. M. Cohen, N. M. Rey, C. A. Jacobson, T. J. Anderson, "Active control of combustion instability in a liquid-fueled low-NO_x combustor," *ASME/IGTI Gas turbine Expo and Congress*, Stockholm, Sweden, June 1998.

[7] J. P. Hathout, A. M. Annaswamy, M. Fleifil, A. F. Ghoniem, "A model-based active control design for thermoacoustic instability", *Combustion Sci. and Tech.*, vol. 132, pp. 99–105, 1998.

[8] J. R. Hibshman, J. M. Cohen, A. Banaszuk, T. J. Anderson, and H. A. Alholm, "Active control of combustion instability in a liquid-fueled combustor," *Proceedings of 1999 ASME Turbo Expo,* Indianapolis, 1999.

[9] M. Krstić and H. H. Wang, "Stability of extremum seeking feedback for general nonlinear dynamic systems," accepted for *Automatica*, 1998.

[10] M. Krstic, "Performance improvement and limitations in extremum seeking control," *System and Control Letters*, to appear.

[11] P. J. Langhorne, A. P. Dowling, N, Hooper, "Practical active control system for combustion oscillations," *Journal of Propulsion*, vol. 6, pp. 324–333, 1990.

[12] B. La Scala, "Approaches to Frequency Tracking and Vibration Control," *Ph.D. Thesis*, Dept. of Systems Engineering, The Australian National University, December 1994.

[13] R.M. Murray, C.A. Jacobson, R. Casas, A.I. Khibnik, C.R. Johnson Jr., R. Bitmead, A.A. Peracchio, and W.M. Proscia, "System Identification for Limit Cycling Systems: A Case Study for Combustion Instabilities," *Proceedings of 1998 American Control Conference*, Philadelphia, June 1997.

[14] Y. Neumeier, B. T. Zinn, "Active control of combustion instabilities using real-time identification of combustor modes", *Proc. of the IEEE Conf. on Control Applications*, Albany, NY, pp. 691–698, Sept. 1995.

[15] A. A. Peracchio and W. M. Proscia, "Nonlinear heat-release/acoustic model for thermoacoustic instability in lean premixed combustors," *ASME/IGTI Turbo Expo '98*, Stockholm, Sweden, June 1998.

[16] J.R. Seume, N. Vortmeyer, W. Krause, J. Hermann, C.-C. Hantschk, P. Zangl, S. Gleis, D. Vortmeyer, and A. Orthmann, "Application of Active Combustion Instability Control to a Heavy Duty Gas Turbine, ", *Proc. of ASME Asia '97 Congress and Exhibition*, Singapore, October 1997, ASME Paper 97-AA-119.

[17] J. Sternby, "Extremum control systems: An area for adaptive control?" Preprints of the *Joint American Control Conference*, San Francisco, CA, 1980, WA2-A.

[18] Y. Zhang, "Stability and Performance Tradeoff with Discrete Time Triangular Search Minimum Seeking", *Proc. of American Control Conference*, Chicago, June 2000.

Appendix: experimental results with controller phase tuning using classical extremum-seeking algorithm

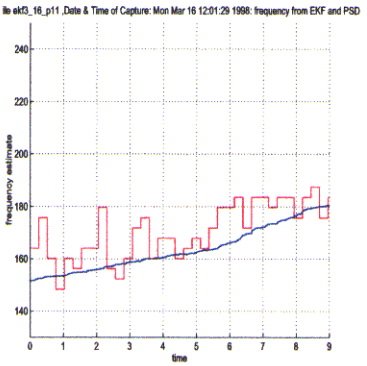


Figure 4: Frequency estimate from EKF and short-time PSD

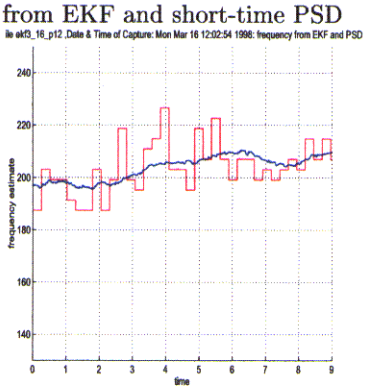


Figure 5: Frequency estimate from EKF and short-time PSD

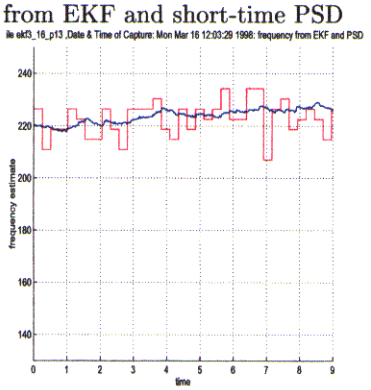


Figure 6: Frequency estimate from EKF and short-time PSD

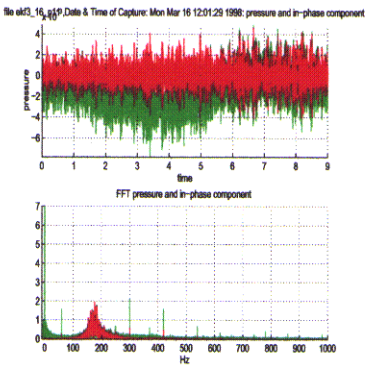


Figure 7: Pressure signal and its in-phase component recontracted with EKF: time traces and FFT

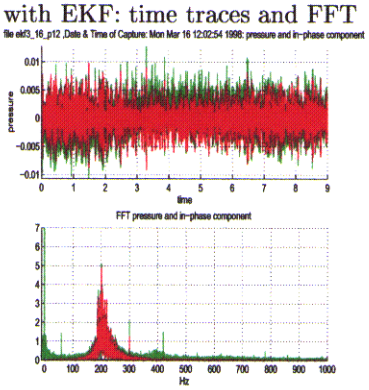


Figure 8: Pressure signal and its in-phase component recontracted with EKF: time traces and FFT

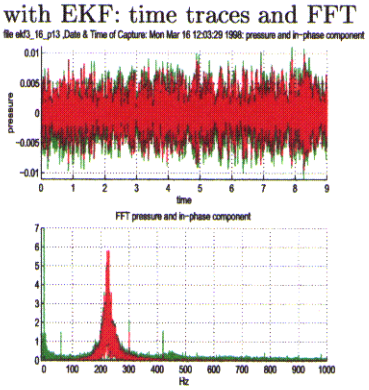


Figure 9: Pressure signal and its in-phase component recontracted with EKF: time traces and FFT

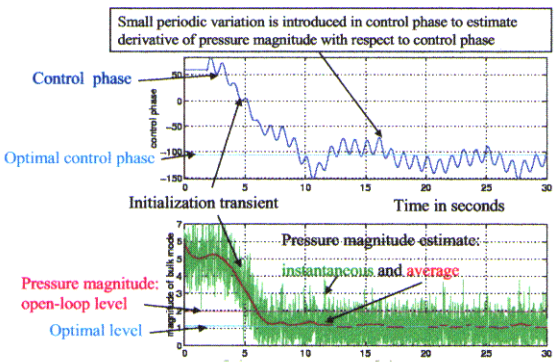


Figure 10: Classical extremum-seeking algorithm. Typical initialization transient for higher power. Control phase and pressure magnitude as functions of time. Horizontal lines show optimal and close loop levels of mean pressure magnitude.

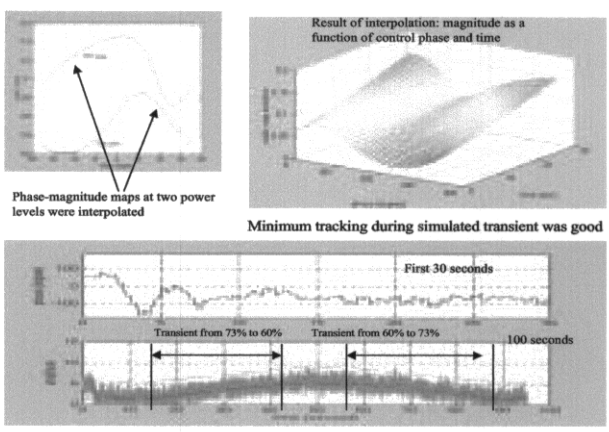


Figure 11: Perfomance of triangular extremum-seeking algorithm during a simulated engine transients

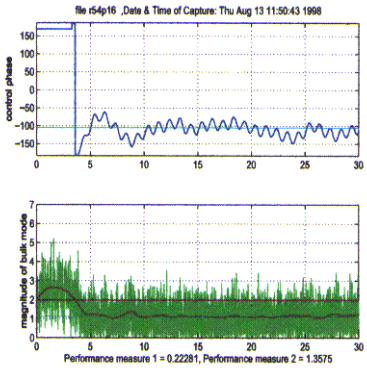


Figure 12: Controller phase tuning using classical algorithm. Initialization transient for higher power. $f = 1Hz$, $\theta_1 = 15$, $k = 1000$, $\theta_m(0) = 170$. Control phase and pressure magnitude as functions of time.

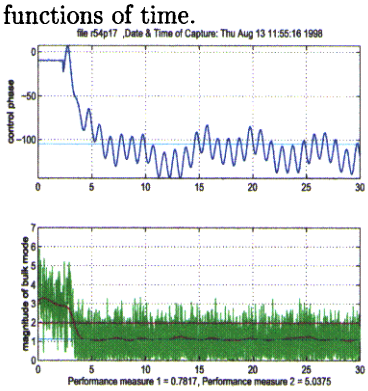


Figure 13: Controller phase tuning using classical algorithm. Initialization transient for higher power. $f = 1Hz$, $\theta_1 = 15$, $k = 1000$, $\theta_m(0) = -10$. Control phase and pressure magnitude as functions of time.

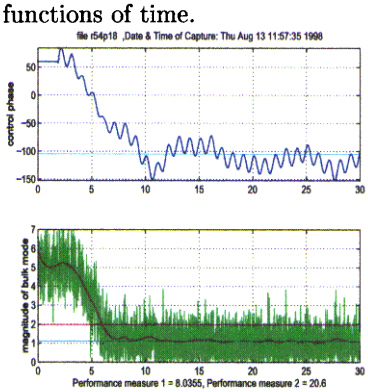


Figure 14: Controller phase tuning using classical algorithm. Initialization transient for higher power. $f = 1Hz$, $\theta_1 = 15$, $k = 1000$, $\theta_m(0) = 60$. Control phase and pressure magnitude as functions of time.

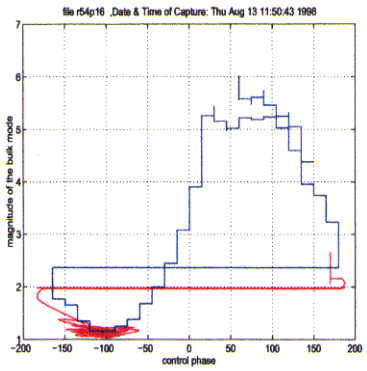


Figure 15: Controller phase tuning using classical algorithm. Initialization transient for higher power. $f = 1Hz$, $\theta_1 = 15$, $k = 1000$, $\theta_m(0) = 170$. Pressure magnitude as function of control phase.

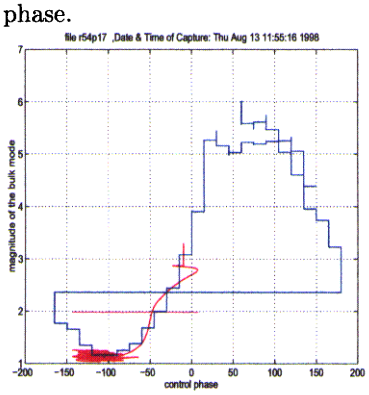


Figure 16: Controller phase tuning using classical algorithm. Initialization transient for higher power. $f = 1Hz$, $\theta_1 = 15$, $k = 1000$, $\theta_m(0) = -10$. Pressure magnitude as function of control phase.

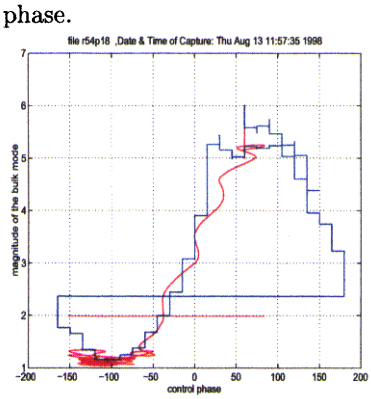


Figure 17: Controller phase tuning using classical algorithm. Initialization transient for higher power. $f = 1Hz$, $\theta_1 = 15$, $k = 1000$, $\theta_m(0) = 60$. Pressure magnitude as function of control phase.

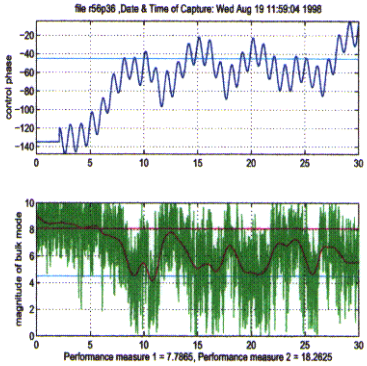


Figure 18: Controller phase tuning using classical algorithm. Initialization transient for lower power. $f = 1Hz$, $\theta_1 = 15$, $k = 150$, $\theta_m(0) = -135$. Control phase and pressure magnitude as functions of time.

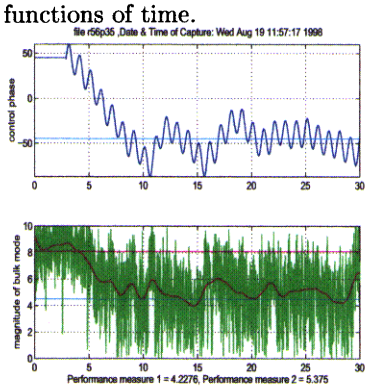


Figure 19: Controller phase tuning using classical algorithm. Initialization transient for lower power. $f = 1Hz$, $\theta_1 = 15$, $k = 150$, $\theta_m(0) = 45$. Control phase and pressure magnitude as functions of time.

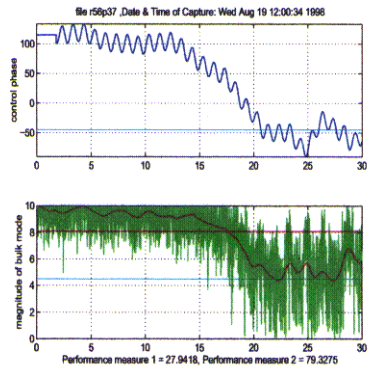


Figure 20: Controller phase tuning using classical algorithm. Initialization transient for lower power. $f = 1Hz$, $\theta_1 = 15$, $k = 150$, $\theta_m(0) = 115$. Control phase and pressure magnitude as functions of time.

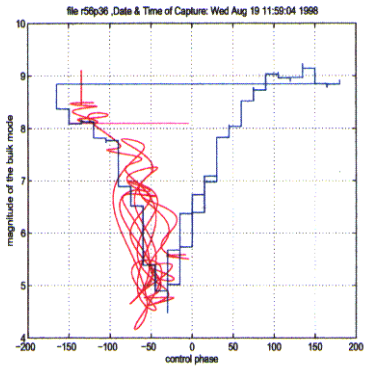


Figure 21: Controller phase tuning using classical algorithm. Initialization transient for lower power. $f = 1Hz$, $\theta_1 = 15$, $k = 150$, $\theta_m(0) = -135$. Pressure magnitude as function of control phase.

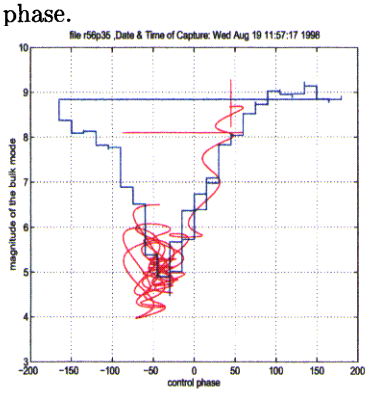


Figure 22: Controller phase tuning using classical algorithm. Initialization transient for lower power. $f = 1Hz$, $\theta_1 = 15$, $k = 150$, $\theta_m(0) = 45$. Pressure magnitude as function of control phase.

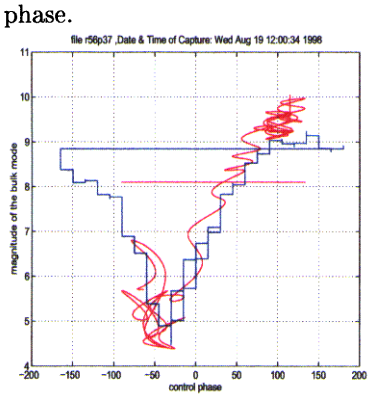


Figure 23: Controller phase tuning using classical algorithm. Initialization transient for lower power. $f = 1Hz$, $\theta_1 = 15$, $k = 150$, $\theta_m(0) = 115$. Pressure magnitude as function of control phase.

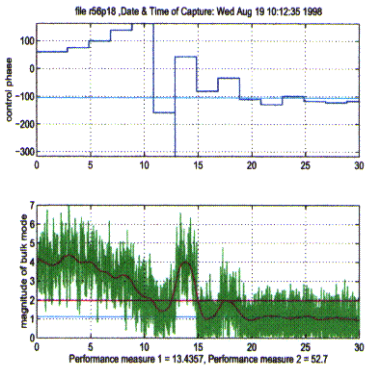


Figure 24: Controller phase tuning using triangular search algorithm. Initialization transient for higher power. $\theta_m(0) = 170$. Control phase and pressure magnitude as functions of time.

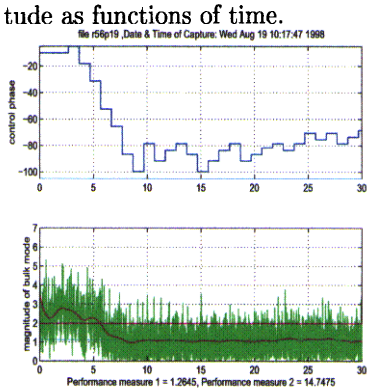


Figure 25: Controller phase tuning using triangular search algorithm. Initialization transient for higher power. $\theta_m(0) = -10$. Control phase and pressure magnitude as functions of time.

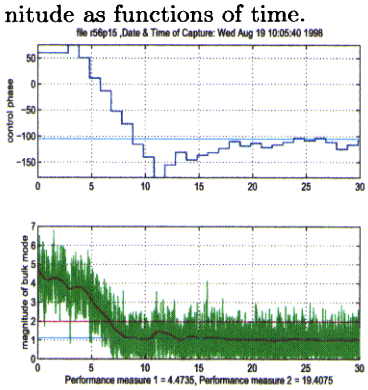


Figure 26: Controller phase tuning using triangular search algorithm. Initialization transient for higher power. $\theta_m(0) = 60$. Control phase and pressure magnitude as functions of time.

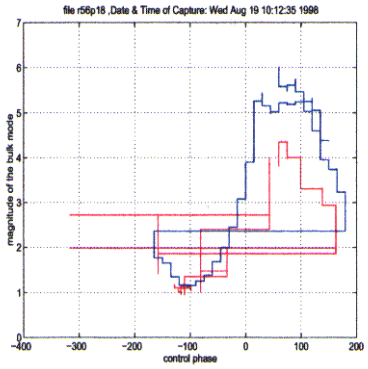


Figure 27: Controller phase tuning using triangular search algorithm. Initialization transient for higher power. $\theta_m(0) = 170$. Pressure magnitude as function of control phase.

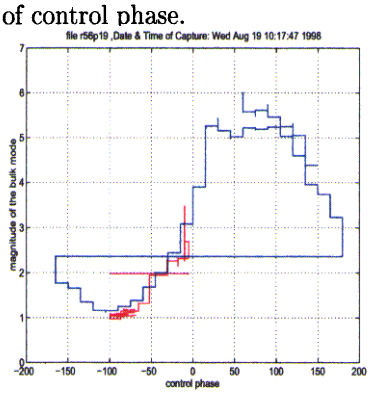


Figure 28: Controller phase tuning using triangular search algorithm. Initialization transient for higher power. $\theta_m(0) = -10$. Pressure magnitude as function of control phase.

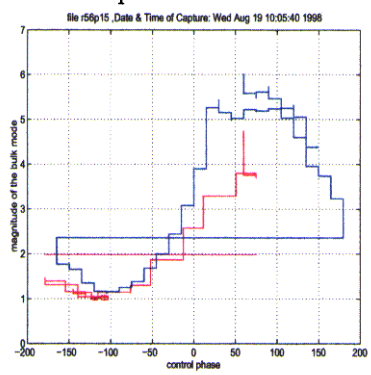


Figure 29: Controller phase tuning using triangular search algorithm. Initialization transient for higher power. $\theta_m(0) = 60$. Pressure magnitude as function of control phase.

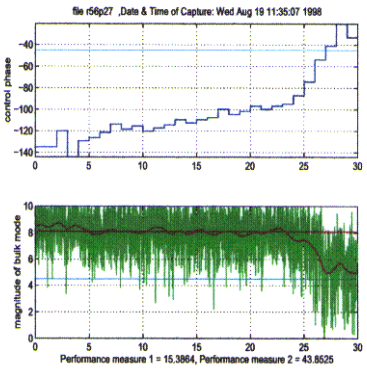


Figure 30: Controller phase tuning using triangular search algorithm. Initialization transient for lower power. $\theta_m(0) = -135$. Control phase and pressure magnitude as functions of time.

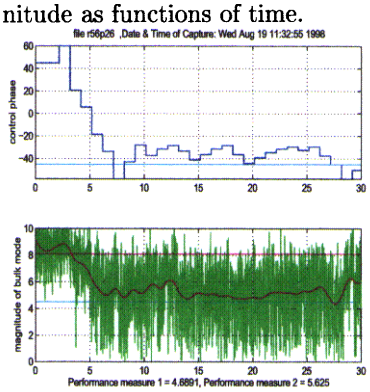


Figure 31: Controller phase tuning using triangular search algorithm. Initialization transient for lower power. $\theta_m(0) = 45$. Control phase and pressure magnitude as functions of time.

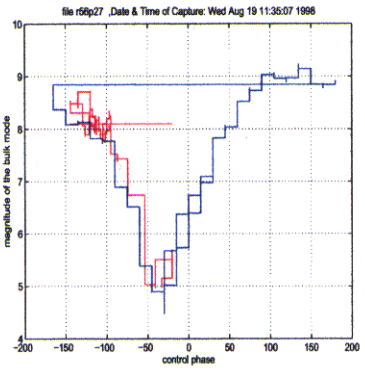


Figure 32: Controller phase tuning using triangular search algorithm. Initialization transient for lower power. . Pressure magnitude as function of control phase.

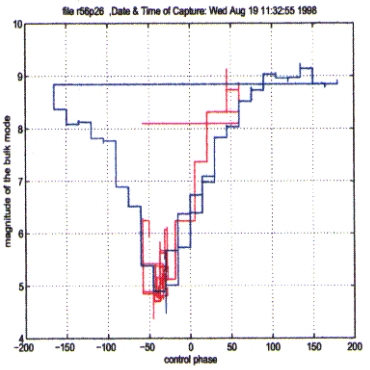


Figure 33: Controller phase tuning using triangular search algorithm. Initialization transient for lower power. $\theta_m(0) = 45$. Pressure magnitude as function of control phase.

PAPER -31, A. Banaszuk

Question (F. E. C. Culick, USA)

Is there (i.e., can you give) a simple reason why your adaptive control algorithm(s) worked better for high power than for lower power conditions?

Reply

It appears that the high power condition was characterized by a linear model and the flat bottomed behavior of the phase-magnitude map was caused by peak-splitting (inability to improve performance beyond a certain point). We speculate that the "notchy" shape of the phase-magnitude function is caused by the system going in and out of a limit cycle. The limit cycling behavior was caused by a subcritical bifurcation. This increases sensitivity of the magnitude to the phase change around the minimum.

This page has been deliberately left blank

Page intentionnellement blanche

Performance Enhancement of Gas-Turbine Combustor by Active Control of Fuel Injection and Mixing Process—Theory and Practice

Christian Oliver Paschereit*
ALSTOM POWER Ltd, AAT-T4 5405 Baden, Switzerland

Ephraim Gutmark†
University of Cincinnati, Aerospace Engineering and Engineering Mechanics Dept.
797 Rhodes Hall, P.O. Box 210070, Cincinnati OH 45221-0070, USA

Bruno Schuermans‡
ALSTOM POWER Ltd, AAT-T4 5405 Baden, Switzerland

Unstable thermoacoustic modes were investigated and controlled in an experimental low-emission swirl stabilized combustor, in which the acoustic boundary conditions were modified to obtain combustion instability. Axisymmetric and helical unstable modes were identified for fully premixed combustion. These unstable modes were associated with flow instabilities related to the recirculation region on the combustor axis and shear layer instabilities at the sudden expansion (dump plane). The combustion structure associated with the different unstable modes was visualized by phase locked images of OH chemiluminescence. The axisymmetric mode showed large variation of the heat release during one cycle, while the helical modes showed circumferential variations in the location of maximal heat release. Two feedback control methods employed to suppress thermoacoustic pressure oscillations and to reduce emissions are reviewed: proportional acoustic control and fuel modulations. Microphone sensors monitored the combustion process and provided input to the control systems. An acoustic actuation modulated the airflow and thus affected the mixing process and the combustion. Suppression levels of up to 25 dB in the pressure oscillations and a concomitant 10% reduction of NO_x emissions were obtained. At the optimal control conditions it was shown that the major effect of the control system was to reduce the coherence of the vortical structures which gave rise to the thermoacoustic instability. The specific design of the investigated experimental burner allowed testing the effect of different modulated fuel injection concepts on the combustion instability modes. Symmetric and antisymmetric fuel injection schemes were tested. Suppression levels of up to 12 dB in the pressure oscillations were observed. In some cases concomitant reductions of NO_x and CO emissions were obtained. Open loop control of low frequency symmetric instability by secondary fuel injection in a pilot flame reduced the pressure oscillations by up to 20 dB.

Introduction

The initial shear layer of a swirling mixed air and fuel jet exiting a burner in a swirl-stabilized combustor undergoes Kelvin-Helmholtz instability. This instability causes the shear layer to roll-up into vortical coherent structures which affects the jet's growth rate by entrainment of ambient fluid and by mixing it with the jet's fluid. Therefore, these vortices play an important role in the combustion and heat release processes by controlling the mixing between the fresh fuel/air mixture and hot combustion products and fresh air in premixed combustors. The initiation and evolution of these structures in nonreacting flows was extensively studied in mixing layers (Oster and Wygnanski 1982,[1] Ho and Huerre 1984[2]), jets (Crow and Champagne 1971,[3] Paschereit et al. 1995[4]) and flows over backward facing steps (Hasan, 1992[5]). However, studies of large structures in swirling flows are scarce. Unlike large scale structures in nonswirling flows which are predominantly axisymmetric, swirl enhances azimuthal unstable modes. Interaction between large scale structures which are related to flow instabilities, acoustic resonant modes in the combustion chamber and the heat release process was shown to cause undesired thermoacoustic instabilities in the combustor (Paschereit et al. 1999,[6] Schuermans et al. 1999[7]). The effect of swirl on the longitudinal and azimuthal instability modes and the way it modifies the combustion process leading to thermoacoustic instabilities requires further investigation.

Realizing the importance of large scale structures as drivers of combustion instabilities, researchers developed passive and active methods to control this instability by modifying the vortical structures in the flow (Schadow and Gutmark 1992,[8] McManus et al. 1993[9] and Annaswamy and Ghoniem 1995[10]). Most of these control methods were applied to bluff-body-

*Email: oliver.paschereit@ch.abb.com
†Email: egutmark@uceng.uc.edu
‡Email: bruno.schuermans@ch.abb.com

Paper presented at the RTO AVT Symposium on "Active Control Technology for Enhanced Performance Operational Capabilities of Military Aircraft, Land Vehicles and Sea Vehicles", held in Braunschweig, Germany, 8-11 May 2000, and published in RTO MP-051.

stabilized combustors and dump combustors in which the flow recirculation is used to stabilize the flame. Passive and active control strategies have been used to suppress thermoacoustic instabilities resulting from coupling between the heat and pressure oscillations in these combustors (Rayleigh Criterion). Passive control strategies utilized non-circular geometries to enhance small scale mixing, reduce the coherence of large-scale vortices and to generate axial vorticity. Active control strategies utilized fuel modulations and phase-shifting to decouple the pressure and heat release cycles. Control strategies have also investigated improving fuel efficiency and reducing pollutants (Gutmark et al. 1990[11]) and extending flammability limits (Schadow et al. 1992[12]).

While many papers describe control of non-swirling gaseous flames, minimal amount of work was reported on control of swirling combustion. Swirl stabilization is utilized in combustion systems such as gas-turbines which also exhibit combustion instabilities. Sivasegaram and Whitelaw (1991[13]) showed that swirl reduces instability for disk-stabilized premixed gaseous flame combustion, but increased the instability for flames stabilized behind sudden expansions. Rational modification of large-scale vortices is important to control swirl induced instability and to increase combustion efficiency. However, flow control has been demonstrated primarily for non-swirling flows, in which the large-scale instabilities are well understood, and the coherence of the vortices can be influenced by flow excitation. Control of swirling flows requires an understanding of the vortical structure in this type of flow and an understanding of the effect of forcing.

Paschereit et al. (1998a, b, c, d, e, f, 1999[14–20]) investigated instability modes in an experimental low-emission swirl stabilized combustor and used acoustical control methods. The two operating modes which were studied included a partially premixed-diffusion flame and premixed combustion. The diffusion flame was tuned to unstable operation with two destabilized modes, axisymmetric and helical. The premixed instability mode, which was obtained by adjusting the acoustic boundary conditions, was predominantly axisymmetric. Pressure fluctuations were detected only for the axisymmetric modes, but heat release fluctuations, which were measured by OH chemiluminescent emission, indicated dual mode behavior. The effect of acoustic excitation on the unstable combustion was investigated using upstream and downstream located loudspeakers. A closed-loop active control system was employed to suppress combustion instabilities and to reduce emissions at various operating conditions. The effect of the control system on the unstable mode structure and combustor performance was reported.

Paschereit et al. (1999[21,22]) extended the thermoacoustic instability control work to include a more practical (compared to acoustic excitation) fuel modulation strategy. Symmetric and antisymmetric fuel pulsations were used to control symmetric and helical instability modes. Open and closed loop control systems that modulated either the premixed or the pilot fuel injection were shown to suppress effectively pressure and heat release oscillations and reduce emissions. The present review summarizes this work.

Experimental Set-up

Combustion Facility

The combustion facility is shown in Fig. 1. The

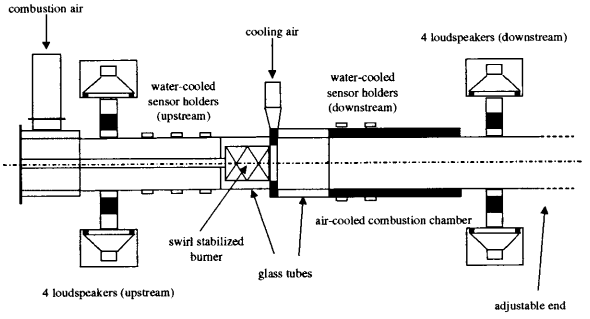


Fig. 1 Experimental facility

atmospheric test rig consists of a plenum chamber upstream of the swirl-inducing burner and a combustion chamber downstream of the burner. The plenum chamber contains perforated plates to reduce the turbulence level of the flow. The circular combustion chamber consists of an air-cooled double wall quartz glass to provide full visual access to the flame. The exhaust system is an air-cooled tube with the same cross-section as the combustion chamber to avoid acoustic reflections at area discontinuities. The acoustic boundary conditions of the exhaust system could be adjusted from almost anechoic (reflection coefficient $|r| < 0.15$) to open end reflection. An experimental swirl stabilized premixed burner was used. The flame was stabilized in a recirculation region near the burner outlet. The burner was operated at atmospheric conditions. Two methods of actuation were investigated: acoustical and fuel modulations. Acoustic controlled excitation of the burner flow was accomplished by a circumferential array of four loudspeakers equally spaced in polar angle.

Premixed fuel injection modulation was obtained by using direct driven valves which have high frequency response of over 200 Hz. The specific design of the experimental burner allowed for symmetric and antisymmetric fuel injection schemes. Pressure fluctuations were measured using Brüel & Kjaer water-cooled

microphones. Time varying heat release was recorded with two filtered fiber optic probes to detect OH radiation.

Control System

Schematic diagrams of the acoustic proportional control and fuel modulations control systems are given in Fig. 2a and b. The signals from the microphone sensors were fed into a signal-processing unit which delayed the input signal by a predetermined time and amplified it. The time-delayed signal was fed-back to drive the loudspeakers through an audio amplifier (Fig. 2a). For fuel modulation control, Fig. 2b, the driving signal had both DC and AC components that could be independently set. The signal from the microphone was amplified and band-pass filtered, then used to trigger a signal generator to produce a phase-shifted signal at the instability frequency which was fed-back to actuate the direct driven valves through an electronic driver.

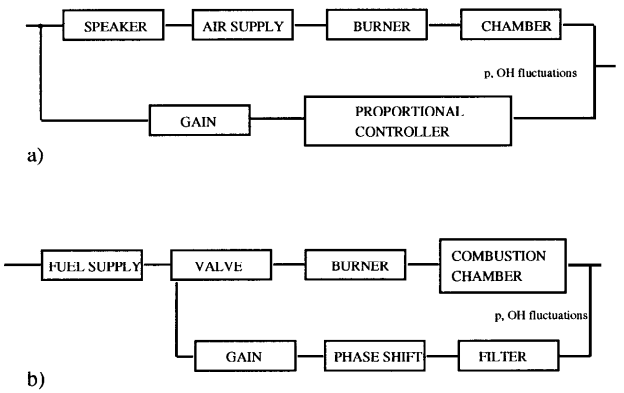


Fig. 2 Schematic diagrams of (a) acoustic proportional and (b) fuel modulation control systems

Visualization and Emissions Measurements

Phase locked images of the flame were obtained using an amplified (micro channel plate) CCD camera with an exposure time of $20\mu s$. The camera was triggered by using either the pressure or OH signals which were band-pass filtered at the instability frequency and phase shifted. The images were filtered using a band-pass filtered with a low and high cutoff wavelength of 290 nm and 390 nm, respectively. The phase locked exposures were then averaged over 64 events. The operating conditions of the burner have been maintained by analyzing the exhaust gas composition using a physical gas analysis system. The nitric oxides NO and NO_2, combined in NO_x have been detected with a chemiluminescence analyzer. The detection of the remaining O_2 in the exhaust gas was based on the paramagnetic properties of oxygen in the analyzing device and was used to determine the equivalence ratio.

Results and Discussion

Structure of the instability

The results of previous investigations showed that several modes of thermoacoustic instability could be excited in the burner when it operates at a premixed mode by proper adjustment of the acoustic boundary conditions (Paschereit et al. 1998[15]). All the instability modes were related to combustion within large-scale structures that were excited in the combustion chamber due to interaction between various flow instabilities and the acoustic resonant modes of the combustor. The instabilities associated with the premixed mode of operation were at a normalized frequency $St = fD/U = 0.58$ and at $St = 1.16$, where f is the instability frequency, D the burner diameter and U the burner exit velocity. The $St = 0.58$ instability was the predominant mode. A typical level of the $St = 0.58$ instability was 29 dB above the background noise level. The instability at $St = 1.16$ was a helical mode while the mode at $St = 0.58$ was axisymmetric. The different instability modes were also visualized using a CCD camera which was triggered at different phase angles relative to the instability pressure signal to obtain a sequence of phase locked images over one sequence of instability. The axisymmetric $St = 0.58$ instability is shown in Fig. 3 a, b, e, f at two phase angles of 0 and 180 degrees, in a premixed operation. The axisymmetric structure is demonstrated as well as the variable heat release during the cycle. The highest heat release, which is related to the OH intensity, was measured at a phase angle of 0 degrees, while the lowest level was measured at 180 degrees. A helical unstable mode was measured in premixed operation (Fig. 3 c, d, g, h). The high OH intensity shifted from the bottom shear layer for a phase-angle of 0 degrees to the upper shear layer at 180 degrees.

Flow Field

The flow exiting the swirl-generating burner was measured in a water tunnel facility. A negative mean velocity region near the burner axis showed the recirculation region, which provides one of the mechanisms for flame stabilization in this burner. The flow pattern near the axis is similar to wake flow behind a bluff-body. The flow instability associated with this region was therefore predominantly helical, resembling wake flow instability. Another region receptive to flow instabilities was the sudden expansion area at the burner exit plane. The flow at this area exhibited features of an annular jet. The jet formed two shear layers, the internal one with the recirculating flow downstream of the stagnation point in the inner backflow region, and the external one with the recirculation zone at the sudden expansion location. Cross-sectional profiles of the mean and turbulent velocity components

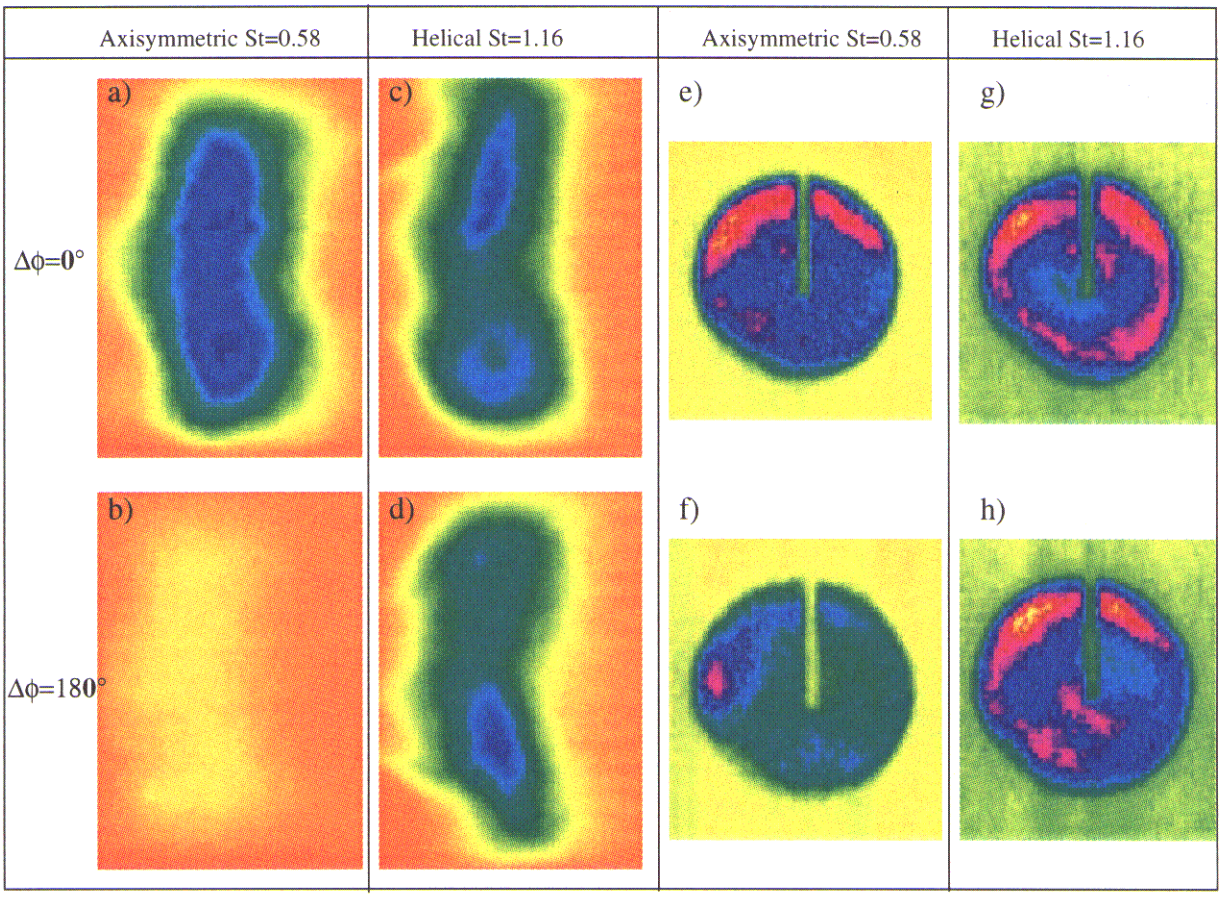


Fig. 3 Visualization of phase averaged OH-images at phase angles of 0 and 180 degrees. (a, b, e, f) Axisymmetric (premixed, $St = 0.58$). (c, d, g, h) Helical (premixed, $St = 1.16$).

are shown in Fig. 4. Only the inner wake region includes significant back flow. The main peak of the turbulent fluctuations was measured at the inflection point of the internal shear layer. The outer shear layer exhibits a small increase in turbulence level. One of the important flow features, which are significant to the thermoacoustic instability, is the dominant unstable mode in the shear layers. The inner shear layer exhibited primarily one fundamental unstable mode at a normalized frequency of $St = 1.2$ (Fig. 5). This mode could be related to the wake like profile of the inner recirculation zone and was of helical type. As shown in the combustion experiments, the outer shear layer was unstable to an axisymmetric mode at a normalized frequency of $St = 0.58$ (Fig. 6).

Combustion Control-Acoustic Actuators

A closed-loop proportional feedback control system was designed to reduce the coherence of the large-scale structures thus to suppress the level of pressure oscillations due to combustion instability. Speakers provided direct excitation of the shear layers in the combustor. The feedback loop consisted of a time delay-amplifier unit that fed the original microphone signal back to the speakers after a predetermined delay and amplification. The time delay or phase between the microphone signal and the speakers driving signal was varied between 0 and 360 degrees. The level of OH fluctuations in the shear layer at an axial distance of $x/D = 0.514$ was simultaneously recorded. The variation of the pressure and OH oscillations as a function of the relative phase between the microphone (sensor) and speakers (actuators) is shown in Fig. 7 for the axisymmetric unstable mode at $St = 0.58$. This controlled behavior is compared with the horizontal line depicting the pressure and OH fluctuations level when the controller is not operating. The amplification (gain setting) of the control signal was varied to study its effect on the reduction of pressure and OH oscillations at the optimal phase of 60 degrees. The results in Fig. 8 show that a minimum gain of 20 dB was necessary to reach maximum suppression of both the pressure and OH fluctuations. The figure also shows the destabilization of a secondary mode at $St = 0.92$ with increased

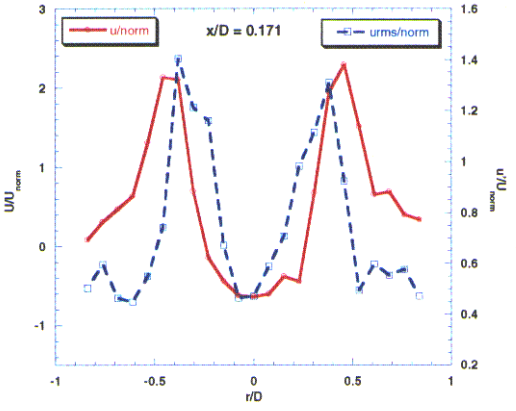


Fig. 4 Radial profiles of the axial mean and RMS velocity at $x/D = 0.171$.

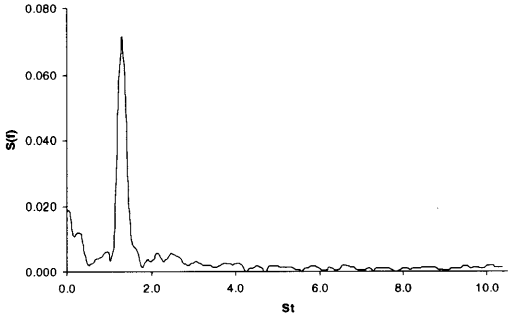


Fig. 5 Spectra of the axial velocity component in the inner shear layer.

gain.

Maximum suppression was obtained at a time delay corresponding to a phase difference of 60 degrees, while maximum destabilization of the combustion was observed at 270 degrees. At the optimal phase angle, the instability was suppressed by nearly 24 dB, while the maximum amplification was 2.9 dB. A phase-lock/phase shift (PLPS) controller achieved a maximum suppression of 5 dB for the same conditions (Paschereit et al. 1998[23]). The maximal suppression of the OH oscillations was obtained at 30-60 degrees. The OH fluctuations were reduced by over 25 dB indicating that the large-scale structures lost their coherence. The structure of the reacting vortices inside the combustor was assessed from radial cross-correlation measurement between two OH chemi-

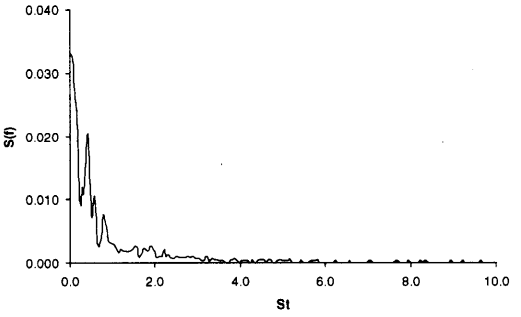


Fig. 6 Spectra of the axial velocity component in the outer shear layer.

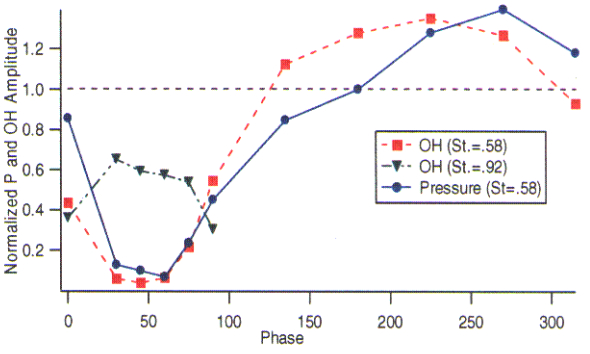


Fig. 7 Controlled pressure and OH oscillations for different phase shift angles.

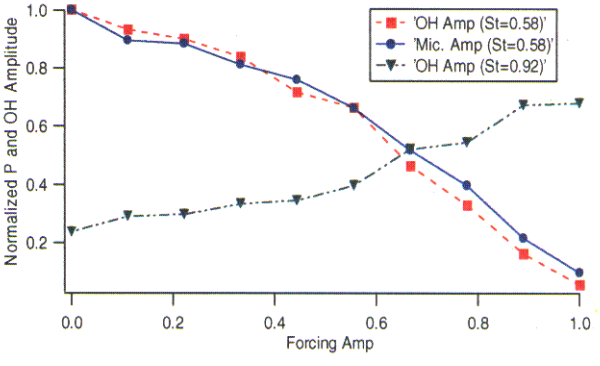


Fig. 8 Controlled pressure and OH oscillations for different forcing amplitudes.

luminescence filtered fiber-optic probes. To measure radial cross-correlation, one of the OH sensors was stationary in the upper shear layer at an axial distance $x/D = 0.514$ from the dump plane, monitoring the shear layer flow, while the other one was traversing the combustion zone radially at the same axial distance. The measurements were performed for two unstable

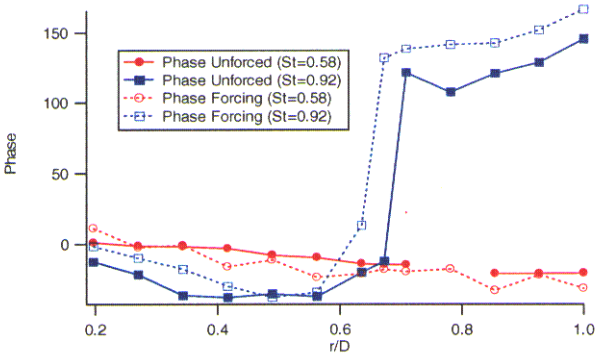


Fig. 9 Phase of radial OH correlations, without and with control.

Strouhal numbers, $St = 0.58$ (axisymmetric instability) and $St = 1.16$ (helical instability). The relative phase angles between the two OH signals are plotted as a function of $\Delta r/D$ in Fig. 9. The instabilities at $St = 1.16$ underwent a phase change of nearly 180 degrees corresponding to helical modes while the mode at $St = 0.58$ remained close to zero phase angle across the combustor, indicative of an axisymmetric mode. NO_x and CO emissions were monitored in the entire range of pressure oscillations control. The results, depicted in Figs. 10 and 11 show a 20% reduction of the NO_x and virtually no effect on CO levels, at the same time delay range that yielded pressure fluctuations stabilization. Nearly 10% increase in NO_x emissions

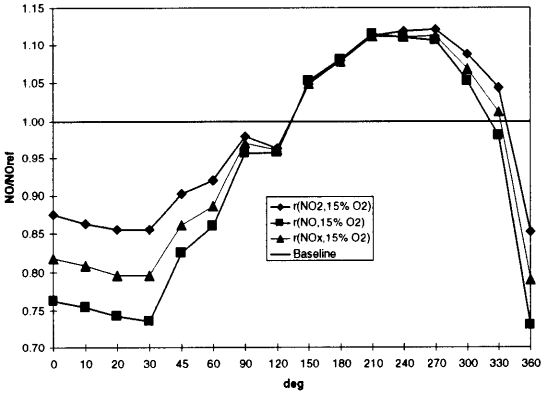


Fig. 10 NO_x emissions for various phase shifts in a closed-loop control system.

was observed at 240 degrees. The concomitant NO_x emissions reduction and pressure oscillations suppression are both related to the reduced coherence of the vortical structures. Acoustic control caused uniform mixing, improved combustion without effect on CO production and evenly distributed temperature yielding low NO_x emission.

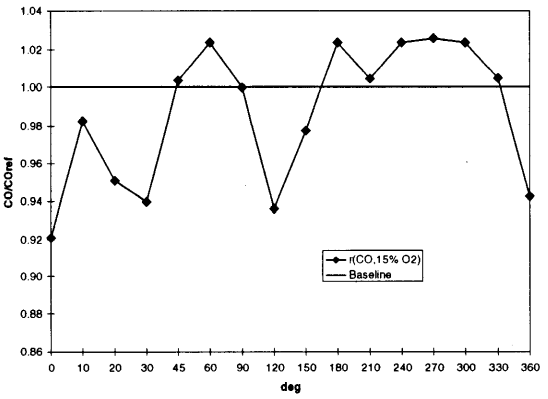


Fig. 11 CO emissions for various phase shifts in a closed-loop control system.

Combustion Control-Fuel Modulation Actuators

Closed-loop active control tests were performed in a premixed combustion mode by modulating the fuel injection through the premixing fuel injection ports. The tests were performed at lean equivalence ratio conditions. The tests were performed when the combustor was destabilized in the axisymmetric mode at a normalized frequency of $St = 0.58$. Two different fuel excitation schemes, symmetric and antisymmetric, were used to control the unstable combustion. The pressure fluctuations were monitored using a microphone near the dump plane. OH radiation was measured at a distance of $x/D = 0.046$ from the burner exit in the shear layer.

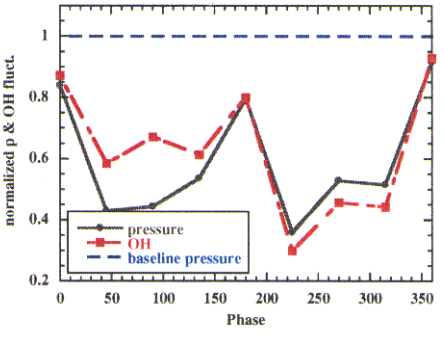


Fig. 12 Pressure and OH fluctuations suppression in a closed loop controller with antisymmetric pulsed fuel injection (amplitude $F/F_{max} = 50\%$).

Symmetric Fuel Pulsations

The closed loop tests were conducted by monitoring the pressure fluctuations in the combustion chamber and using the recorded signal to pulse the fuel out-of phase relative to the pressure oscillations. For

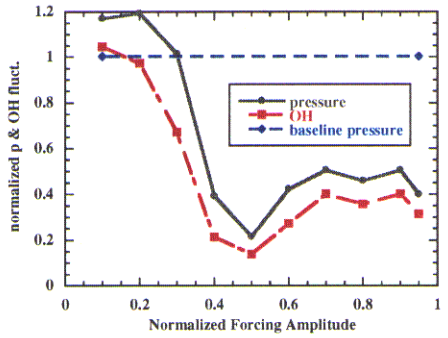


Fig. 13 Effect of amplitude variation on pressure and OH fluctuations suppression, antisymmetric fuel injection (phase=330 deg). Closed loop controller

symmetric fuel injection a level of pressure instability suppression of 12 dB was obtained at a fuel pulsation amplitude $F/F_{max} = 35\%$. The flame was near blow out at a certain range of phase angles.

Antisymmetric Fuel Pulsations

At a forcing amplitude of $F/F_{max} = 50\%$ the flame maintained stability in the entire range of phases (Fig. 12) and yielded suppression of over 8 dB. The optimal normalized forcing level of $F/F_{max} = 50\%$ was determined in amplitude variation tests shown in Fig. 13. At this forcing level, the NO_x emissions were substantially decreased (Fig. 14) as well as the CO emissions (Fig. 15).

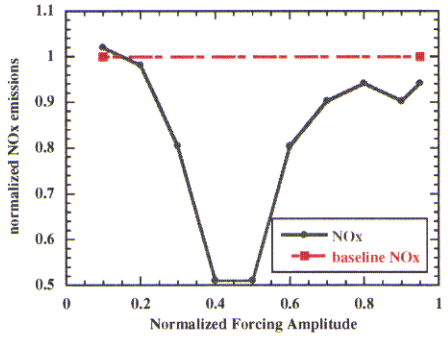


Fig. 14 NO_x emissions as a function of amplitude, antisymmetric pulsed fuel injection (phase=330 deg.). Closed loop controller.

Open Loop Control by Pilot Flame Modulations

The axisymmetric instability mode (St=0.58) was stabilized by injecting secondary fuel to establish a pilot diffusion flame. The level of the pressure and OH fluctuations decreased with increased secondary fuel mass flow rate, until a minimum was reached for

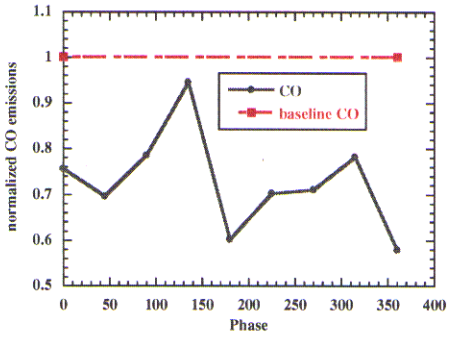


Fig. 15 CO emissions as a function of phase, antisymmetric pulsed fuel injection amplitude $F/F_{max} = 50\%$. Closed loop controller.

4.4% pilot fuel addition (Fig. 16). At this point the axisymmetric instability was reduced by 20 dB.

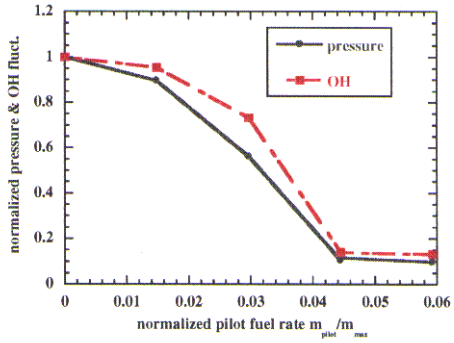


Fig. 16 Suppression of pressure and OH fluctuations by pilot fuel injection. Open loop controller.

It is usually undesirable to add diffusion flame to a premixed combustion due to potential increase in emissions. In the present case, NO_x emissions decreased while the secondary fuel addition was less than 3% and rapidly increased as the amount of secondary fuel exceeded this level (Fig. 17). Concurrently, the amount of CO decreased with increasing the secondary fuel indicating improved combustion efficiency (Fig. 17).

To minimize the amount of fuel injected in the pilot flame, pulsed injection at low frequencies was utilized. The low frequency pulsations were adjusted to be in the range commensurate with the time scales associated with the central recirculation zone. The pulsed injection also enabled modification of the duty-cycle to minimize the total amount of secondary fuel injected while maintaining sufficient heat release at each injection cycle.

The fuel flow rate was set at an intermediate level of 4.4% such that the increase in NO_x will not be excessive, and the duty-cycle was fixed at 20%. The

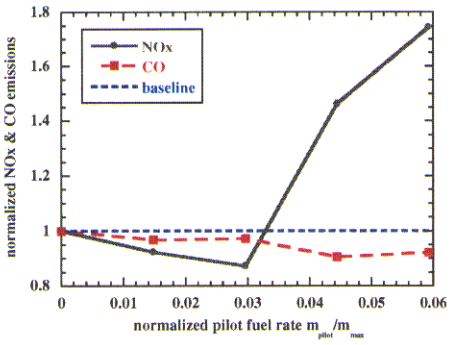


Fig. 17 NO_x and CO emissions as a function of pilot fuel injection. Open loop controller.

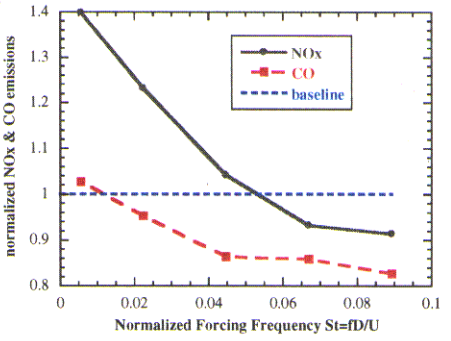


Fig. 19 Variation of NO_x and CO emissions with secondary fuel modulation frequency. Pilot fuel at 20% duty-cycle. Open loop controller.

pressure and OH fluctuation levels decreased monotonically with increasing normalized frequency (Strouhal number), until reaching a flat minimum level at $St = 0.065$, yielding a suppression level of over 20 dB (Fig. 18). The baseline level in this figure is the fluctuations level with continuous secondary fuel injection at the same flow rate. Emissions of NO_x increased at the lowest pulsation frequency, followed by a continuous decrease with increasing frequency until reaching a lower level than the reference conditions with continuous pilot fuel injection at $St > 0.055$ (Fig. 19). CO emissions exhibited similar behavior except that the CO level decreased below the baseline for $St > 0.01$.

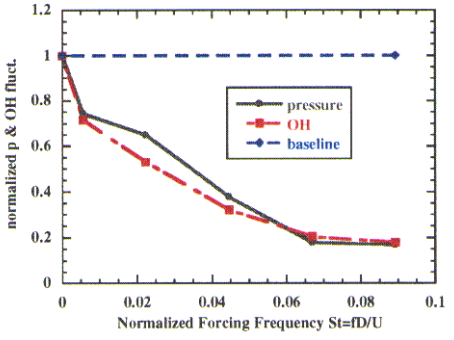


Fig. 18 Response of pressure and OH fluctuations to modulations of pilot flame. Pilot fuel at 20% duty-cycle. Open loop controller.

Conclusions

Active combustion control systems using proportional acoustic actuation and fuel modulations were applied to an experimental low-emission swirl stabilized combustor, in which the acoustic boundary conditions were modified to obtain unstable operation. Two unstable modes were investigated in fully premixed combustion: axisymmetric and helical. The unstable modes were associated with flow instabilities related to the recirculation region on the combustor axis and shear layer instabilities at the sudden expansion. The axisymmetric mode showed large variation of heat release during one period of oscillations, while the helical modes showed azimuthal variations of maximal heat release. Closed loop active control systems were employed to suppress the thermoacoustic pressure oscillations while maintaining low NO_x and CO emissions. Pressure sensors (microphones) monitored the combustion process and provided input to the control system. The signal of the microphone was delayed and amplified before being fed to the actuator. Acoustic actuation was utilized to modulate the airflow entering the swirl-generating burner. The acoustic excitation varied the mixing process between fuel and air and the combustion products. Suppression levels of up to 25 dB in the pressure oscillations and a concomitant 20% reduction of NO_x without affecting CO emissions were obtained using low acoustic power. Fuel or equivalence ratio modulations were used to control symmetric and helical unstable modes. Two methods were tested: symmetric and antisymmetric fuel injection. The tests showed that the antisymmetric modulations were more effective in suppressing the symmetric mode instability than symmetric fuel excitation. Symmetric excitation was quite efficient in abating the symmetric mode as well, however, at a certain range of phase shift the combustion was destabilized to an extent that caused blow out of the flame. Antisymmetric fuel injection was effective in abating the symmetric mode instability providing that the modulation level was not excessive. Concomitant with pressure oscillation control, the emission levels of both NO_x and CO were reduced by up to 50 and 40%, respectively. The major effect of the control system was to reduce the coherence of the vortical structures that gave rise to the axisymmetric thermoacoustic instability. In addition to decoupling the combustion process from the flow instability, the

temperature became uniform and NO_x forming high temperature zones within vortices were eliminated.

An open loop control system utilized by modulations of a secondary pilot flame. Control of low frequency symmetric instability was investigated. Adding a continuous flow of fuel into the pilot flame controlled the instability. However, modulating the fuel injection significantly decreased the amount of necessary fuel. The reduced secondary fuel resulted in a reduced power generation by the pilot flame and therefore yielded lower NO_x emissions. The pulsation frequency was chosen to match the time scales typical to the central flow recirculation zone that is used to stabilize the flame in the burner. Low frequency required longer duty-cycle, while at high frequency modulations a duty cycle of less than 10% was necessary. Suppression of pressure oscillations by up to 20 dB was recorded.

References

[1]Oster, D. and Wygnanski, I., "The forced mixing layer between parallel streams," *Journal of Fluid Mechanics*, Vol. **123**, 1982, pp. 91–130.

[2]Ho, C. and Huerre, P., "Perturbed free shear layers," *Ann. Rev. Fluid Mech.*, Vol. **16**, 1984, pp. 365–424.

[3]Crow, S. and Champagne, F., "Orderly structure in jet turbulence," *Journal of Fluid Mechanics*, Vol. **48**, 1971, pp. 567.

[4]Paschereit, C. O., Wygnanski, I., and Fiedler, H. E., "Experimental investigation of subharmonic resonance in an axisymmetric jet," *Journal of Fluid Mechanics*, Vol. **283**, 1995, pp. 365–407.

[5]Hasan, M. A. Z., "The Flow Over a Backward Facing Step under Controlled Perturbation: Laminar Separation," *Journal of Fluid Mechanics*, Vol. **238**, 1992, pp. 73–96.

[6]Paschereit, C. O., Schuermans, B., Polifke, W., and Mattson, O., "Measurement of transfer matrices and source terms of premixed flames," *ASME Turbo Expo '99*, Indianapolis, Indiana, USA, June 7-10 1999.

[7]Schuermans, B., Paschereit, C. O., and Polifke, W., "Modeling transfer matrices of premixed flames," *ASME Turbo Expo '99*, Indianapolis, Indiana, USA, June 7-10 1999.

[8]Schadow, K. C. and Gutmark, E., "Combustion instability related to vortex shedding in dump combustors and their passive control," *Progress of Energy and Combustion Science*, Vol. **8**, 1992, pp. 117–132.

[9]McManus, K. R., Poinsot, T., and Candel, S. M., "A review of active control of combustion instabilities," *Progress of Energy and Combustion Science*, Vol. **19**, 1993, pp. 1–29.

[10]Annaswamy, A. M. and Ghoniem, A. F., "Active Control in Combustion Systems," *IEEE Control Systems*, December 1995, pp. 49–63.

[11]Gutmark, E., Parr, T. P., Wilson, K. J., Hanson-Parr, D. M., and Schadow, K. C., "Use of Chemiluminescence and Neural Networks in Active Combustion Control," *Twenty third Symp. (Intl.) on Comb.*, The Comb. Inst., 1990, pp. 1101–1106.

[12]Schadow, K. C., Gutmark, E., and Wilson, K. J., "Active combustion control in a coaxial dump combustor," *Combustion, Science and Technology*, Vol. **81**, 1992, pp. 285–300.

[13]Sivasegaram, S. and Whitelaw, J. H., "The Influence of Swirl on Oscillations in Ducted Premixed Flames," *Combustion, Science and Technology*, Vol. **85**, 1991, pp. 195–205.

[14]Paschereit, C. O., Gutmark, E., and Weisenstein, W., "Role of Coherent Structures in Acoustic Combustion Control," *29th AIAA Fluid Dynamics Conference*, No. AIAA Paper 98-2433, Albuquerque, New Mexico, June 15-18 1998.

[15]Paschereit, C. O., Gutmark, E., and Weisenstein, W., "Flow-acoustic interactions as a driving mechanism for thermoacoustic instabilities," *4th AIAA/CEAS Aeroacoustics Conference*, No. AIAA paper 98-2274, Toulouse, France, June 2-4 1998.

[16]Paschereit, C. O., Gutmark, E., and Weisenstein, W., "Control of thermoacoustic instabilities and emissions in an industrial type gas-turbine combustor," *27th International Symposium on Combustion*, The Combustion Institute, August 2-7 1998.

[17]Paschereit, C. O., Gutmark, E., and Weisenstein, W., "Suppression of Combustion Instabilities by Acoustic Control of Shear Layer Properties," *Advances in Turbulence*, edited by U. Frisch, Kluwer Academic Publishers, Dordrecht/Boston/London, 1998, pp. 293–296.

[18]Paschereit, C. O., Gutmark, E., and Weisenstein, W., "Acoustic Control of Combustion Instabilities and Emissions in a Gas-Turbine Combustor," *Proceedings of the 1998 IEEE International Conference on Control Applications*, September 1-4 1998.

[19]Paschereit, C. O., Gutmark, E., and Weisenstein, W., "Suppression of Acoustically Excited Combustion Instability in Gas- Turbines," *5th AIAA/CEAS Aeroacoustics Conference*, Seattle, WA, USA, May 10-12 1999.

[20]Paschereit, C. O., Gutmark, E., and Weisenstein, W., "Coherent structures in swirling flows and their role in acoustic combustion control," *Physics of Fluids*, Vol. **9**, 1999, pp. 2667–2678.

[21]Paschereit, C. O., Gutmark, E., and Weisenstein, W., "Control of Thermoacoustic Instabilities in a Premixed Combustor by Fuel Modulation," *37th AIAA Aerospace Science Meeting and Exhibit*, No. AIAA Paper 99-0711, Reno, Nevada, January 11-14 1999.

[22]Paschereit, C. O., Gutmark, E., and Weisenstein, W., "Control of combustion driven oscillations by equivalence ratio modulations," *ASME Turbo Expo '99*, Indianapolis, Indiana, USA, June 7-10 1999.

[23]Paschereit, C. O., Gutmark, E., and Weisenstein, W., "Structure and Control of thermoacoustic instabilities in a gas-turbine combustor," *Combustion, Science and Technology*, Vol. **138**, 1998, pp. 213–232.

This page has been deliberately left blank

Page intentionnellement blanche

ACTIVE OPTIMISATION OF THE PERFORMANCE OF A GAS TURBINE COMBUSTOR

M. M. Miyasato, V. G. McDonell, and G. S. Samuelsen

UCI Combustion Laboratory, Bldg. 323, Room 221
University of California
Irvine, CA 92697-3550, USA
(949) 824-5950 gss@uci.edu

ABSTRACT

The increasingly stringent regulation of gas turbine exhaust emissions, combined with the need to reduce overall cost of operation, is requiring advancements to be made in the combustion system. In particular, the ability of these systems to attain both low emissions and high efficiency over increasingly longer periods of operation, in order to reduce maintenance costs, is requiring new thinking with respect to the system control strategies. This new thinking is further necessitated by operation of these devices at conditions that are prone to combustion instabilities. As a result, development of a gas turbine that can actively respond to changes in load, system wear, and/or fuel composition, while maintaining efficiency and emissions performance, would be well received. Many technological hurdles must be overcome for this to occur, including the development of sensors, control strategies, and hardware capable of "self-tuning" or "active optimization."

In the present study, a model natural gas-fired industrial gas turbine combustor is utilized to evaluate the performance of different active optimization strategies. Sensors for exhaust species and reaction zone chemiluminescence are utilized in conjunction with an adaptive fuel injection strategy in a closed loop control system. This system has been developed to maintain overall performance in light of environmental changes (e.g., fuel composition changes, injector wear, load changes). The feedback sensor consists of traditional extractive probe based exhaust measurements of major species including carbon monoxide and oxides of nitrogen. This sensor is utilized to provide direct measurement of emissions performance in terms of CO and NO_x emissions. Chemiluminescence is utilized to evaluate the ability of inferential methods to provide very fast, yet accurate indicators of performance. For the current study, a simulated injector perturbation scenario (partial fuel jet blockage) is utilized to examine the robustness of the different optimization strategies. And, as a first step, a direction-set algorithm is utilized to search for the region of optimal performance. The results obtained illustrate (1) the relative correlation of the different sensor strategies with system performance, and (2) the ability of the closed loop control to maintain combustion performance in light of an unexpected hardware perturbation.

INTRODUCTION

Due to increasingly stringent emissions regulations for industrial, stationary combustion sources, low emissions technologies are relying more and more on lean, well-mixed or premixed strategies. These strategies, although proficient at reducing NO_x emissions, suffer from reduced stability or decreased system efficiency under operating conditions which are often desirable for low emissions; as a result, high performance operation can present operational and safety challenges. An attractive technology to address these challenges is the application of *active optimization* of the combustion process using feedback sensors, an optimization algorithm, and computer control of the combustor. Major challenges associated with conducting this type of adaptive optimization on industrial combustion systems are identifying (1) parameters amendable for control, (2) reaction characteristics appropriate for feedback sensing, (3) sensor and control time response requirements, and (4) low maintenance and cost impacts. This study investigates the applicability of adaptive fuel injection to stationary gas turbines in relation to these challenges and over several operational scenarios.

Active control of gas turbines has been studied using dynamic control of the fuel injection to offset combustion instabilities (e.g. Neumeier and Zinn, 1996; Hong, et al., 1998). An alternative strategy is to tailor the fuel and air mixing in order to (1) minimize emissions and (2) avoid instabilities; the amount of mixing has been shown to significantly effect the emissions (Appleton and Heywood, 1973, and Lyons, 1981) as well as stability (Shih et al, 1996). The research addressed in this paper investigates this latter strategy, i.e., to minimize emissions by actively controlling the spatial fuel and air mixedness such that high performance is achieved despite changes in load (equivalence ratio) or hardware degradation. Toward this end, a novel fuel injection strategy is applied to provide sufficient, flexible, and simple control over the entire turndown or duty cycle range of the gas turbine. The active optimization strategy is tested over the stability range of the combustor and then under a simulated hardware degradation or unexpected perturbation mode, where two injector fuel jets are partially blocked.

In order to respond rapidly to unexpected changes, fast feedback sensors are required. Previous work identified the need for such feedback control in order to attain and maintain high performance under changing load conditions (St. John and Samuelsen, 1994; Davis and Samuelsen, 1996; Jackson and Agrawal, 1999). These fast sensors would be situated near the reaction, thereby avoiding the long convection times associated with exhaust sampling, and would therefore provide faster optimization, reduced emissions even during load cycling, and, if possible, stability information. These feedback sensors will most likely be optical in order to provide the fast time response required. As a first step toward this

Paper presented at the RTO AVT Symposium on "Active Control Technology for Enhanced Performance Operational Capabilities of Military Aircraft, Land Vehicles and Sea Vehicles", held in Braunschweig, Germany, 8-11 May 2000, and published in RTO MP-051.

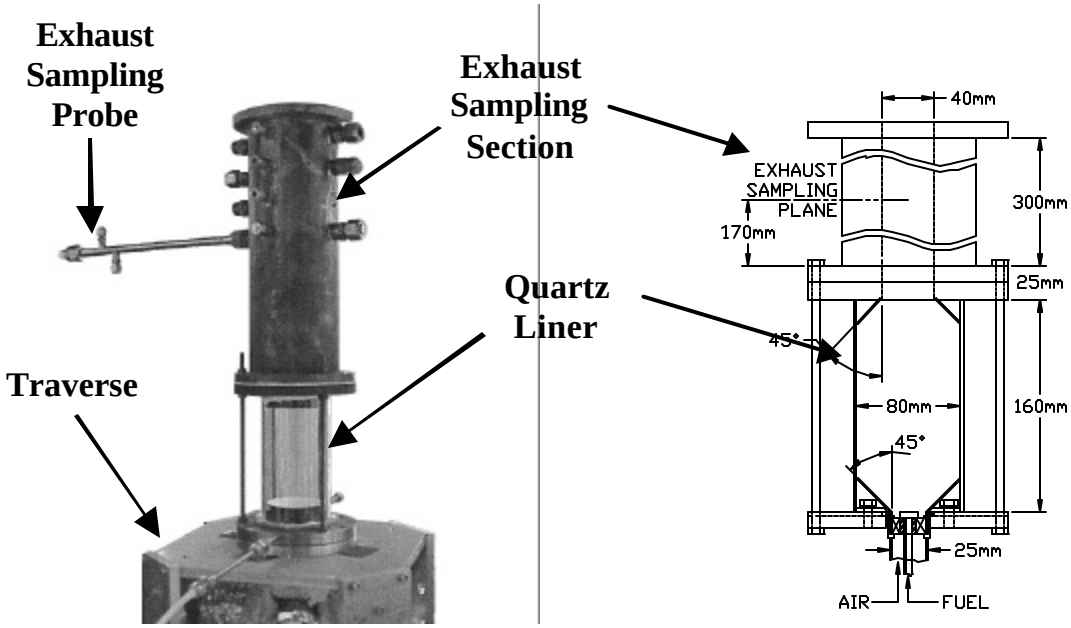


Figure 1: Atmospheric Test Facility

goal, flame chemiluminescence is used to assess its ability to accurately reflect the emissions performance.

OBJECTIVES AND APPROACH

The objectives of the current study are to assess the viability and degree of success of (1) flexible spatial mixing strategy for performance control, (2) the use of flame chemiluminescence as a fast, inferential sensor for faster feedback, and (3) the robustness of the adaptive control strategy over the entire operability range and under a simulated perturbation mode.

A four step approach was utilized in the current study–(1) measure the NO_x, CO, and chemiluminescence emissions over the entire operability range of the model combustor, (2) identify the regions of optimal performance (in terms of low NO_x and CO), (3) apply and compare active control using the chemiluminescence sensor to the conventional emissions analyzers, and (4) simulate a hardware perturbation by blocking two injector jets and apply active control to assess the systems response.

EXPERIMENT

The test facility utilized provides a wide range of operating conditions and flow metering. The test stand is designed to operate at 1 atm with inlet temperatures up to 800 K. The model combustor test rig, shown in Figure 1, has a quartz liner to allow optical access for reaction visualization and chemiluminescence measurements.

Model Combustor

The model combustor utilizes two independent natural gas injection circuits to tailor the fuel distribution. The first fuel circuit injects the fuel radially from the centerbody into the swirling air stream. This centerbody injection circuit, labeled "CB" in Figure 2, consists of six equally spaced fuel holes located circumferentially along the side of the fuel manifold. The fuel manifold is positioned directly above the swirler hub. The second fuel injection circuit allows fuel to be injected radially inward from the surrounding wall. This wall injection circuit, labeled "WJ" in Figure 2, consists of six equally spaced fuel holes in positions that are staggered with respect to the centerbody injection holes. By varying the fuel split between the two fuel circuits, a variety of fuel distributions can be achieved (Flores et al, 2000).

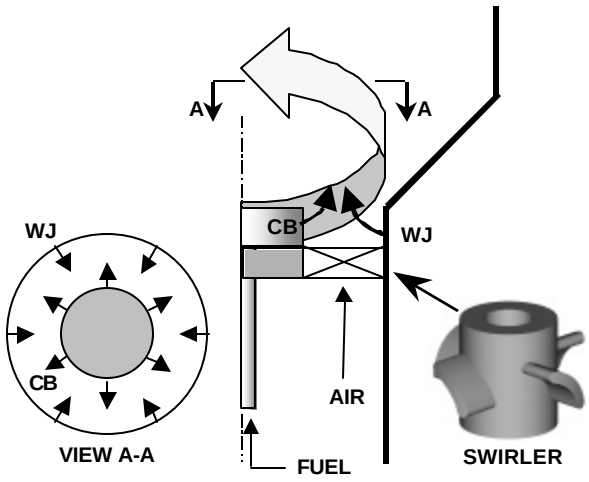


Figure 2: Detail of Fuel Injection Options.

The baseline configuration is a four vane axial swirler. The nominal firing rate for the system is 15 kW of natural gas at 0.0093 kg/sec of air, though the fuel flow rates were varied to assess the system's performance. An air inlet temperature of 700 K was utilized in all cases.

Diagnostics

Since the general objective of the optimisation strategy is to mitigate exhaust gas pollutants, a direct measure of the pollutants is warranted. Exhaust emissions were collected via a 12.7 mm diameter, water-cooled, stainless steel extractive probe. This emissions probe is used to sample the exhaust emissions downstream of the exit plane of the combustor, as shown in Figure 1. This probe is designed to take an integrated average measurement of the emissions over the diameter of the sampling plane. The water in the probe is heated to 325 K to protect the probe and quench the sample while avoiding condensation of water vapor inside the probe. The emissions are pumped through a heated Teflon line to prevent water condensation. The sample stream goes through a converter to reduce any NO_2 to NO prior to the water drop out. After the water drop out, the exhaust gas is delivered to a portable emissions analyzer (Horiba Ltd. model PG250A), which measures carbon monoxide (CO), carbon dioxide (CO_2), oxygen (O_2), and nitrogen oxides (NO_x).

Although the measurement of the combustor exhaust emissions provides a direct indication of the performance, a more convenient strategy with much faster time response is desirable, and likely necessary in order to optimize performance and maintain stable combustion. An optimisation strategy based on an indirect measure must then estimate the associated combustion performance. Two strategies were investigated, acoustics and reaction chemiluminescence. While the acoustic measurements yielded some potentially useful results, they were not very robust and additional work is required to attain the desired performance. As a result, only the results from the chemiluminescence investigations are presented here. For the chemiluminescence, three radial species were considered: OH, CH, and CO_2*. Initial studies were conducted using a polychrometer, and the overall signal levels associated with the CO_2* chemiluminescence were found to be much greater than those were for OH or CH. As a result, the detailed characterizations were conducted using CO_2*.

The basic setup for the chemiluminescence utilized a 200 µm core fiber located approximately 49 cm away from the combustor to allow the 14º expansion of the fiber to encompass the entire reaction volume. The fiber end is attached to a collimating lens, which directs the signal through an appropriate filter and then to a photomultiplier tube (PMT). In the case of CO_2*, a 310-600 nm bandpass filter is utilized to capture the CO_2 continuum. For the system studied , the CO_2* chemiluminescence,

$$CO + O \rightarrow CO_2^*$$

provided an intense and measurable signal over the entire operability range of the combustor. The data values are sampled at a rate of 25000 Hz over 3 seconds. The chemiluminescence has the other obvious advantage in that it could potentially be utilized as an instantaneous reaction monitor, thereby providing an indication of the reaction stability. In this case, additional sampling issues must be addressed.

The basic setup for the direct emissions and chemiluminescence setup is shown schematically in Figure 3. As a result, both direct and estimated performance are determined for the combustor.

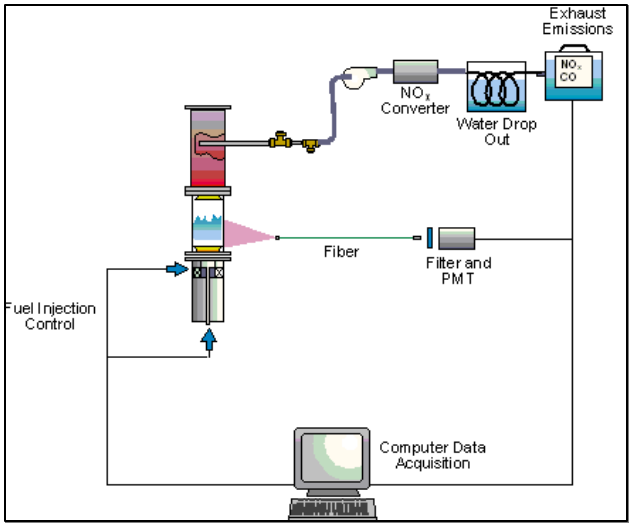


Figure 3: Model Gas Turbine Diagnostics and Control Setup

Active Optimization

The active optimization strategy utilizes a simple hill climbing, or direction-set, methodology for the search algorithm while trying to continually increase or optimize performance in terms of NO_x and CO emissions. In order to quantify performance and deal objectively with the trade-off that often occurs between NO_x and CO, a cost function is defined:

$$J = w_{NOx}{}^{\gamma} f(NO_x) + w_{CO}{}^{\gamma} g(CO)$$

where w_{NOx} and w_{CO} are weighting functions. The definitions and plots of the functions $f(NO_x)$ and $g(CO)$ are shown below:

$$f(NO_x) = \begin{cases} 1 - 0.75 \cdot \left(\dfrac{[NO_x]}{5} \right)^4 & , [NO_x] \le 5\text{ppm} \\ (1 - 0.75) \cdot \dfrac{[NO_x]_{max} - [NO_x]}{[NO_x]_{max} - 5} & , [NO_x] > 5\text{ppm} \end{cases}$$

$$g(CO) = \begin{cases} 1 - 0.90 \cdot \left(\dfrac{[CO]}{8} \right)^4 & , [CO] \le 8\text{ppm} \\ (1 - 0.90) \cdot \dfrac{[CO]_{nax} - [CO]}{[CO]_{max} - 8} & , [CO] > 8\text{ppm} \end{cases}$$

The performance, J, therefore increases with decreasing NO_x and CO, i.e., good performance.

The search algorithm uses the performance index to comparatively seek out conditions of higher performance. The algorithm controls the combustor by varying the two fuel inputs (centerbody and wall jets) to affect the fuel split and equivalence ratio. The feedback sensors provide the information necessary to calculate the performance parameter, *J*, at each condition. The algorithm proceeds along a certain direction until *J* is no longer maximized. The algorithm then simply chooses a new direction at a predetermined angle and step size. If the new condition has a higher performance index then the algorithm proceeds in the new direction; if the performance is not higher, another new angle rotation is selected, and so on. For the present study, the functions of NO_x and CO are equally weighted.

RESULTS

Baseline Configuration

In order to establish the research baseline and know whether the active optimization was successful, exhaust emissions and chemiluminescence measurements were taken over the model combustor's entire operational space. The NO_x and CO emissions were then used to calculate the performance, *J*, as described previously. The resulting performance map is shown in Figure 4 (in all of the subsequent similar figures, the y-axis represents the fuel split as a percentage of fuel injected through the centerbody jets and the x-axis represents the equivalence ratio). The region of peak performance is located in the ridge along 0.42 equivalence ratio and between fuel splits 20-60%. The plot shows that the performance is relatively insensitive to the fuel split, giving rise to the large region of high performance at the 0.42 equivalence ratio.

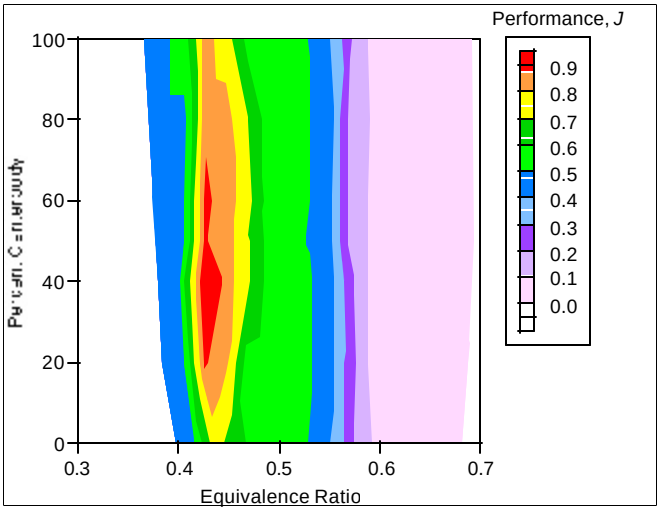


Figure 4: Performance Map for Model Gas Turbine Combustor based on Emissions.

The active optimization control system was applied to the model combustor using the emissions analyzers as the feedback sensors. The resulting search path is shown overlaid on the performance map in Figure 5. The combustor was started at a poor performing condition and allowed to optimize, finishing very near the absolute peak performance condition. The search took 21 iterations and 28 minutes to settle on the optimum ridge.

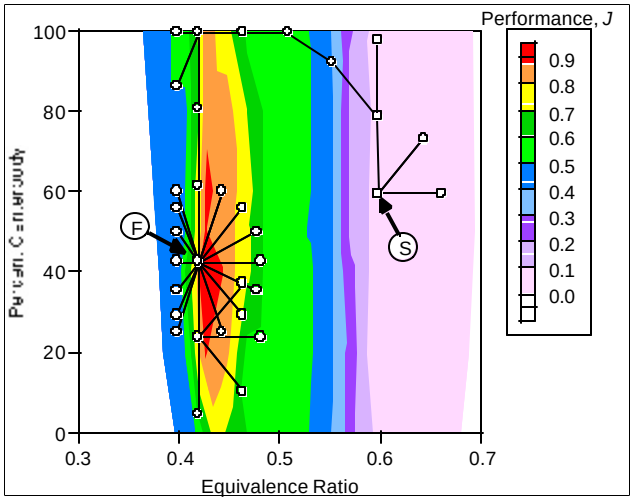
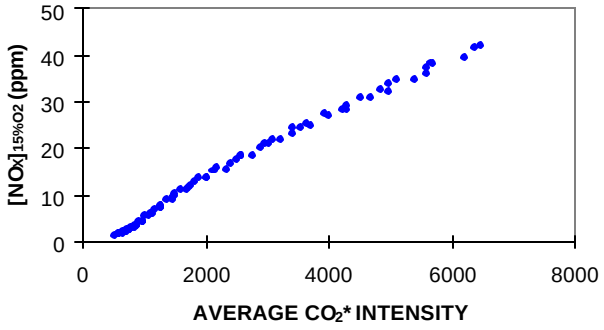


Figure 5: Active Optimization History Using Emissions Analyzers
Ⓢ = starting and Ⓕ = finishing condition

In order to reduce the optimization time, CO_2* chemiluminescence measurements were enlisted. Correlations were developed to relate the average CO_2* signal to the exhaust NO_x concentration and the percent fluctuating CO_2* signal to the exhaust CO emissions (Figure 6).

a) NOx Correlation and Average Chemiluminescence Signal



b) CO Correlation with % Fluctuation of Chemiluminescence

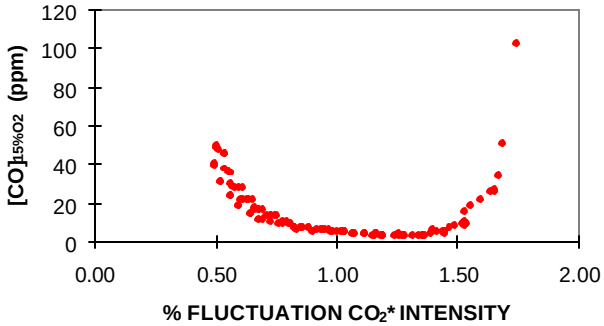


Figure 6. Exhaust Emissions Correlation with Chemiluminescence.

Based on the correlations shown in Figure 6, the optimization process was revisited with the chemiluminescence based feedback (i.e., estimation) for performance incorporated into the active optimization system. The resulting search is shown in Figure 7.

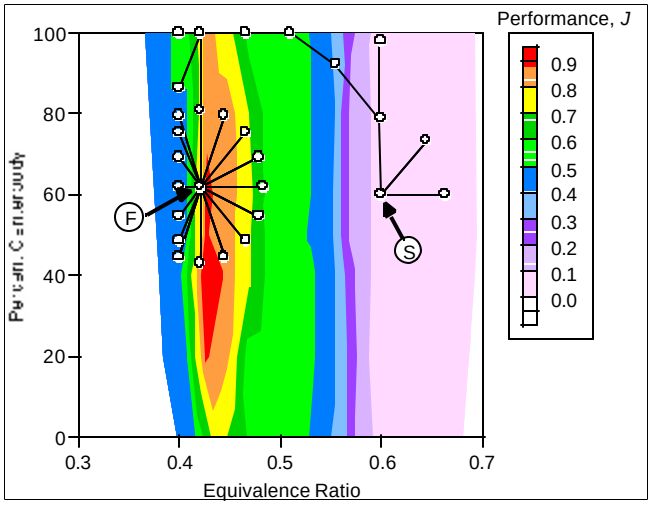


Figure 7: Active Optimization History Using CO_2*

Although the chemiluminescence feedback optimized on a slightly different fuel split than the emissions feedback; the difference in performance index is only about 0.002. Furthermore, the chemiluminescence was able to optimize at a much faster rate, 4 times faster than the emissions feedback case. In fact, the response of the sensor was sufficient to allow even faster optimization, however, the time constant associated with the overall system establishes a reasonable limit. Indeed, this aspect of the system dynamical control for optimization of performance requires careful consideration in the development of actuation and control algorithms. If the controller is too aggressive, damage may result.

As shown in Figure 7, the active optimization strategy employed using flexible fuel injection and two different feedback sensors (emission analyzers and reaction chemiluminescence) was able to successfully identify the regions of highest performance, with the chemiluminescence feedback offering much faster time response. The next test was to determine the robustness of the system by applying a large change to the system hardware.

Partially Block Injector

In order to provide a scenario with which to evaluate the utility of the sensor and optimization strategies, the fuel injector was perturbed by partially blocking two adjacent centerbody fuel injection jets. In practice, such wear and tear may occur gradually, or, in the case of the ingestion of a foreign object, a rather sudden obstruction may occur. Also, scenarios where fuel compositional changes may occur and lead to variation in performance which could then be improved in real time can be envisioned (e.g., Flores, et al., 2000). For the case of the present evaluation, the partially block injector scenario was utilized to provide a significant change in performance as an "extreme" case. Figure 8 illustrates the strategy utilized in the partial blocking. Basically, two adjacent fuel holes on the centerbody were partially blocked.

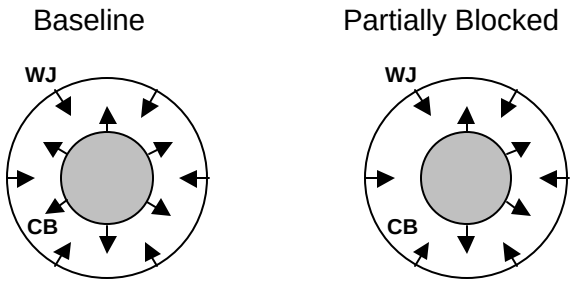


Figure 8. Partially Blocked Centerbody.

This asymmetrical blockage resulted in an altered flame structure compared to the baseline configuration as shown in Figure 9. The difference in centerbody injector pressure drop causes more fuel injection and higher temperatures along the left side of the liner.

a) Baseline Injector



b) Partially Blocked Injector



Figure 9: Reaction Structures at CB=60% ϕ=0.60

To illustrate the impact the partially blocked injector has on the fuel distribution, Figure 10 presents the fuel distributions measured immediately downstream of the centerbody (see Figure 2). Figure 10a reveals that the baseline case exhibits periodic peaks in fuel concentration due to the discrete jets. The apparent asymmetry shown in the baseline case is associated with the location of the fuel jet and the orientation of the axial swirler. The behavior of the fuel jet depends upon the relative wake effect behind the four vanes (Flores, et al., 2000). In the case of the partially blocked injector, shown in Figure 10b, the fuel distribution is clearly skewed to one side of the combustor. In this case, the variation associated with vane wakes appears to be overshadowed by the local increase in

fuel due to the two partially blocked holes. Given the rather significant impact on the fuel distribution, the visible reaction structure changes shown in Figure 9 appear relative minor.

As a result of the partial blockage, some performance changes were expected. The resulting performance map is shown in Figure 11, and does indeed show major changes. Again, the changes in performance are significant given the relatively minor visible differences in reaction structure shown in Figure 9.

The performance contour plot shows a "valley" at high centerbody fuel ratios. This result is due to the asymmetric centerbody fuel injection and the resulting higher NO_x levels. The optimum conditions subsequently occur at higher wall jet ratios but at the same equivalence ratio (0.42) as in the baseline, unblocked case. The maximum performance values, however, are less than for the unblocked condition. Nevertheless, the active optimization strategy was initiated on this hardware configuration, starting at the optimized condition for the baseline case. This scenario represents an unexpected hardware perturbation from sudden hardware failure or the ingestion of a foreign object inside the combustor.

a) Baseline

b) Partially Blocked

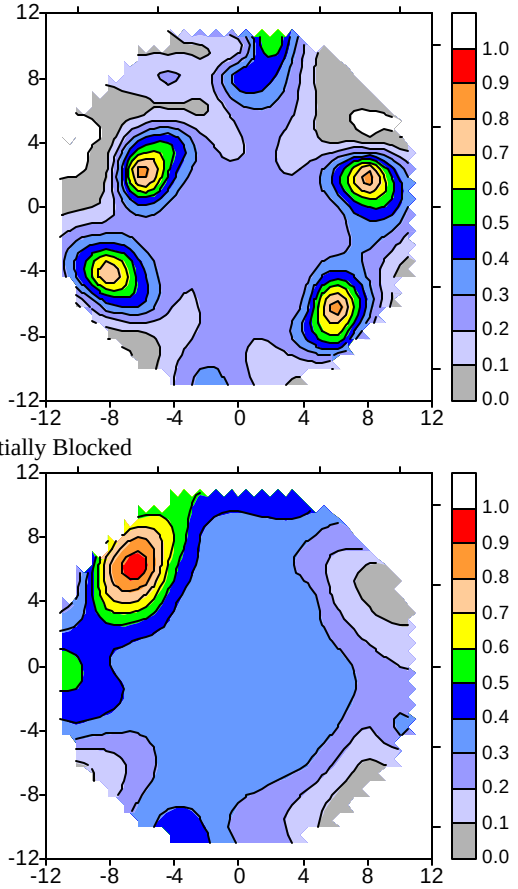


Figure 10. Fuel Distribution 3 mm Downstream of Centerbody.

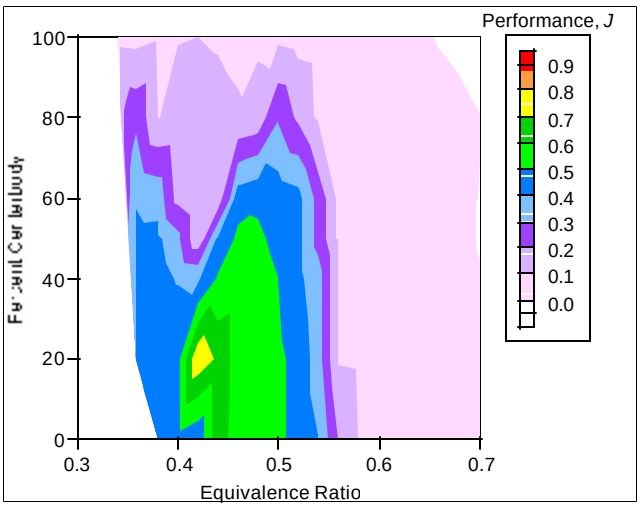


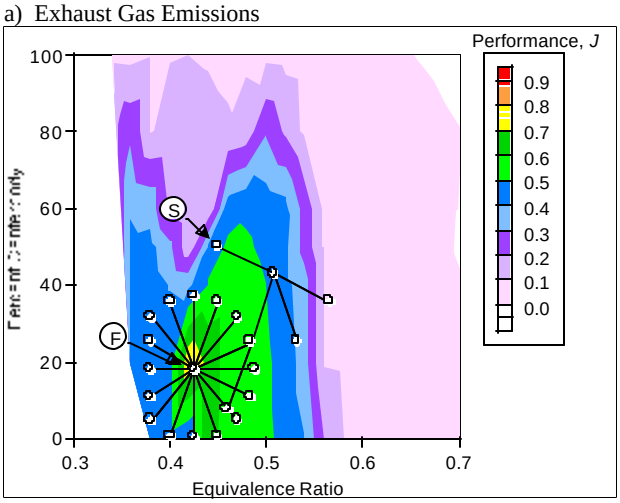
Figure 11: Performance Map for Partially Block Injector based on Exhaust Emissions.

The active optimization histories using the emissions feedback and CO_2* chemiluminescence are shown in Figure 12. The search paths for both optimizations are identical but the chemiluminescence feedback is able to optimize 2.7 times faster than when using emissions feedback.

Thus, the active optimization strategy using the flexible fuel injection and either emissions or chemiluminescence feedback was successful in locating the maximum performance conditions even under degenerated hardware configurations. The chemiluminescence feedback, as in the baseline configuration, provided much faster response and optimization.

It should be noted that the performance contour plot illustrated for the chemiluminescence feedback, Figure 12 (b), represents the *inferred* performance based on the chemiluminescence values. Although careful curve fits were conducted for multiple fuel splits for the range of equivalence ratios, some scatter in the data resulted in differences between the inferred performance [Figure 12(b)] and the emissions-based performance [Figure 12(a)]. These differences and their implications are addressed further in the following section.

a) Exhaust Gas Emissions



b) CO_2* Feedback

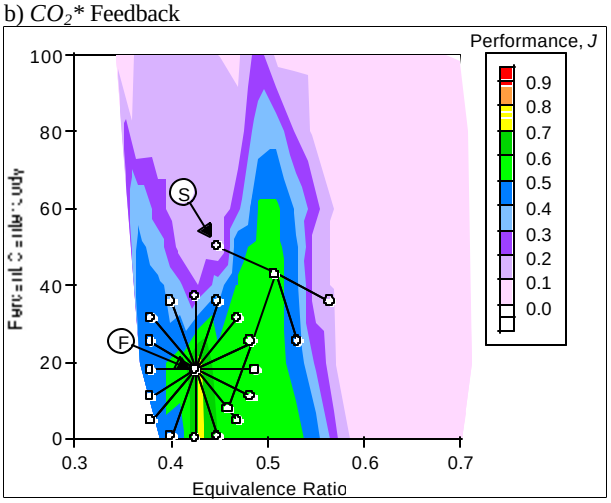


Figure 12: Optimization History for Partially Blocked Injector.

DISCUSSION

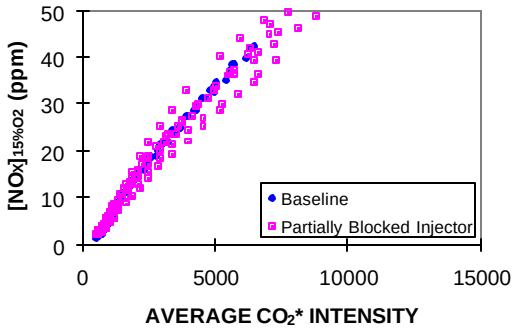
Although not illustrated previously, the differences between the actual performance (NO_x and CO emissions) and the inferred measurement (CO_2* chemiluminescence) can obviously affect the optimization results. The correlations used in the previous optimizations were known *a priori* from detailed measurements. For practical purpose, it would be desirable to have a general sensor which can determine performance in the absense of apriori knowledge. Figure 13 presents the correlations between the chemiluminescence and the gaseous emissions. In contrast to Figure 6, more scatter is observed in Figure 13. This could be due to a variety of factors, including the condition of the quartz, the relative asymmetry associated with the reaction generated by the partially blocked injector. As a result, despite the apparently robust relationship between the emissions and the chemiluminescence shown for the baseline, the relationship does not hold up in general. Note that, the NOx correlation appears to be less sensitive that the CO correlation. It could be argued that chemiluminescence levels should be greater as temperature (and as a result, NOx) increases. Hence the generally well behaved NOx response might be expected. CO, on the other hand has no expected relationship to the chemiluminescence. The fluctuating chemiluminescne intensity may be related to packets of reaction which are quenched as lean blow off approaches. However, other CO formation scenarios can occur on the lean side and a trade off of mechanisms is what gives rise to the scatter shown in Figure 13b. It does bode well for the use of fluctuating chemiluminescence for stability, which has been utilized in studies looking at combustion dynamics. Additional efforts are underway to look again at the optimal location for the sensors as well as other aspects of the chemiluminescence that may allow it to be used in the absence of apriori knowledge of the system behavior in terms of emissions performance.

Even if apriori knowledge is available, the sensitivity of the strategy must be considered. If coarser, i.e., less refined, correlations were used, one wonders if the control scheme would still be able to locate the optimum regions, especially if the search (i.e., operational) space is not well-behaved, as with the hardware perturbation case. Further questions arise regarding the dependency of the optimization scheme to the initial condition and input search parameters (starting angle, increment angle, and step size). In order to begin addressing these questions, the following parameters were changed

- starting location
- starting direction, and
- CO_2* correlations

for the hardware perturbation configuration. The results of these tests are summarized in the Table 1.

a) NOx Correlation and Average Chemiluminescence Signal



b) CO Correlation with % Fluctuation of Chemiluminescence

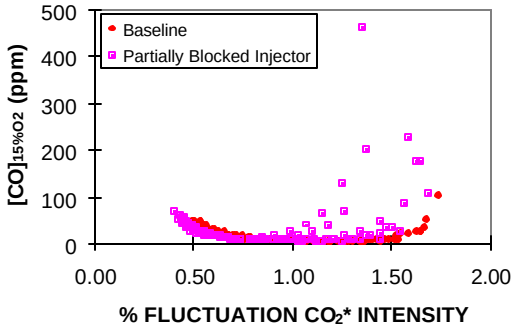


Figure 13. Total Chemiluminescence/Emissions Correlation

CONCLUSIONS

The following conclusions are offered regarding this work:

- The flexible centerbody and wall jet fuel injection strategy is able to provide sufficient mixing scenarios to allow control of the combustor performance over its entire stability range.
- The chemiluminescence sensor provides up to 2.7 times faster feedback and, therefore, allows faster optimization of the system performance.
  - The optimization, however, is dependent on the accuracy of inferential sensor correlations to characterize the actual performance parameters of NO_x and CO.
  - NOx appears to be robustly correlated to chemiluminescence, whereas CO is not.
  - Examples are provided where coarse and fine correlations allow optimization in the correct regions. Care must be taken to accurately reflect the actual parameters of interest, and developing these without *a priori* knowledge will be challenging.
- The active optimization strategy is able to locate the high performance region of the model combustor for both the baseline firing configuration and the hardware perturbation scenario, which simulates extreme degradation or ingestion of a foreign body.
- The direction-set search algorithm employed for these initial tests is subject to many pitfalls depending on the initial search parameters (initial direction, step size, etc) and the contours of the search space (uni-modal, bi-modal, etc.).
- A stability sensor is required to allow fast, confident, and safe optimization.
- More effort is required to establish a robust correlation between inferential sensors and exhaust gas compostion.

ACKNOWLEDGEMENTS

This work was funded in part by the California Energy Commission, California Institute for Energy Efficiency, the DOE Advanced Turbine Systems (ATS) program, and the Southern California Gas Company. The efforts of Mr. Steve Hill are greatly appreciated for his assistance throughout the project.

REFERENCES

J. P. Appleton and J. B. Heywood, “The Effects of Imperfect Fuel-Air Mixing in a Burner on NO Formation from Nitrogen in the Air and the Fuel.” *Fourteenth Symposium (International) on Combustion*/The Combustion Institute, 1976. pp 777-786.

N. T. Davis and G. S. Samuelsen, Optimization of Gas Turbine Combustor Performance Throughout the Duty Cycle.” *Twenty-Sixth Symposium (International) on Combustion*/The Combustion Institute, 1996. pp 2819-2825.

R. M. Flores, M. M. Miyasato, V. G. McDonell, and G. S. Samuelsen, “Reponse of a Model Gas Tubine Combustor to Variation in Gaseous Fuel Composition.” *Journal of Engineering for Gas Turbines and Power*/ASME, 2000.

M. D. Jackson and A. K. Agrawal, “Active Control of Combustion for Optimal Performance.” *Journal of Engineering for Gas Turbines and Power*/ASME, vol. 121, 1999. pp. 437-443.

J. G. Lee, B. S. Hong, K. Kim, V. Yang, D. Santavicca, “Optimization of Active Control Systems for Suppressing Combustion Instability.” *Symposium on Gas Turbine Engine Combustion, Emission, and Alternative Fuels*/RTO – Applied Vehicle Technology Panel, Lisbon, October 12-16, 1998.

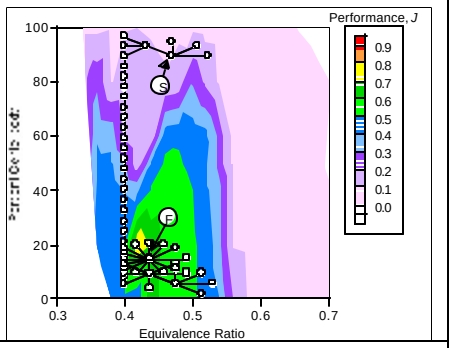
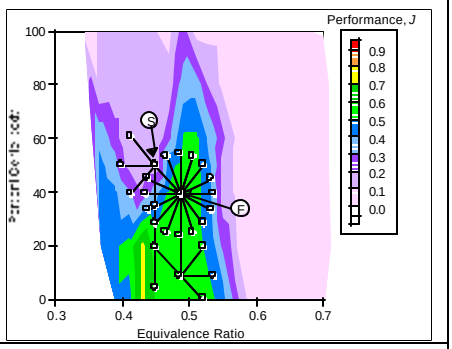
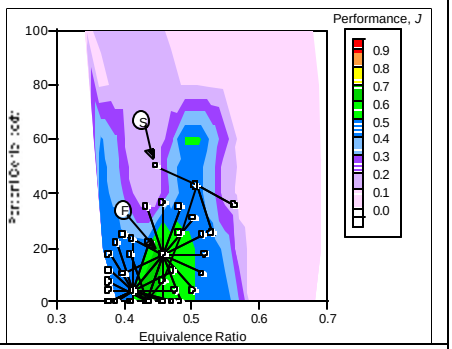
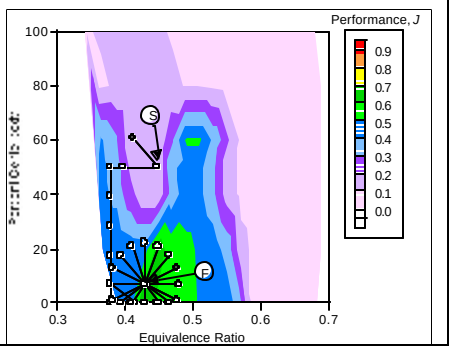
V. Lyons, “Fuel/Air Nonuniformity – Effect on Nitric Oxide Emissions.” *AIAA Journal*, vol. 20, N5, 1981. pp. 660-665.

Y. Neumeier and B. T. Zinn, “Experimental Demonstration of Active Control of Combustion Instabilities Using Real-Time Modes Observation and Secondary Fuel Injection.” *Twenty-Sixth Symposium (International) on Combustion*/The Combustion Institute, 1996. pp 2811-2818.

W. P. Shih, H. G. Lee, and D. A. Santivicca, “Stability and Emissions Characteristics of a Lean Premixed Gas Turbine Combustor.” *Twenty-Sixth Symposium (International) on Combustion*/The Combustion Institute, 1996. pp 2771-2778.

D. St. John and G. S. Samuelsen, “Active, Optimal Control of a Model, Natural Gas–Fired Industrial Burner.” *Twenty-fifth Symposium (International) on Combustion*/The Combustion Institute, 1994. pp. 307–316.

Table 1: Sensitivity Assessment.

Parameter Change	Findings	Implications	Search History
Starting Condition: Placed in region far from optimum in poorly performing "valley"	Emissions feedback, located optimum region	Success dependent on algorithm and initial parameters; also emissions feedback is lengthy process	
Initial Direction: Initial angle pointed in worsening direction	Emissions feedback (not shown) located optimum region CO_2* feedback (shown) optimized on a local peak and "missed" higher performance region	Common detriment to direction-set algorithm Altering step size would increase chances of "hitting" on peak region Inaccurate CO_2* correlation contributed to local peak optimization	
Correlation Accuracy: Coarser correlations used to derive NO_x and CO from CO_2* chemiluminescence	CO_2* feedback the located optimum region in twelve iterations, but took a greater number of iterations to arrive at a peak	Inferential methods may not need high accuracy but must accurately reflect the performance trends	
Correlation Accuracy and Initial Direction Coarser correlations and initial angle pointing in worsening direction	CO_2* feedback located optimum region	No stability parameter was included which may have altered search path away from lean limit	

This page has been deliberately left blank

Page intentionnellement blanche

ACTIVE CONTROL OF OSCILLATIONS IN SIMULATIONS OF GAS-TURBINE COMBUSTORS

S. R. N. De Zilwa, J. H. Uhm and J. H. Whitelaw

Thermofluids Section
Mechanical Engineering Department
Imperial College of Science Technology & Medicine
Exhibition Road
London SW7 2BX, UK

Abstract

The approach to extinction of a premixed methane-air flame stabilised behind a plane sudden-expansion gave rise to cyclic movement of the position of flame stabilisation with a period of the order of 100 ms. These oscillations have been quantified in terms of simultaneous measurements of pressure and light emission, and the pressure maximum corresponded to the flame position closest to the step and the minima to that furthest away. The active control strategy of imposing out-of-phase oscillations was unsuccessful since the period of the near-limit cycles varied over a substantial range and a new approach will be required to track the signal and to implement online actuation that will counteract the tendency for flame movement.

1. Introduction

Combustion oscillations have been studied extensively in laboratory-scale combustors, with emphasis on the large-amplitude acoustic oscillations that occur with near-stoichiometric mixtures of fuel and air by, for example, Sivasegaram and Whitelaw (1987) and Paschereit *et al.* (1998). These oscillations have been controlled with a variety of strategies, the most successful of which has been the feedback-driven imposition of out-of-phase oscillations on either the pressure field or the heat-release by, for example, Poinsot *et al.* (1989) and Lee *et al.* (1999).

Oscillations close to the flammability limits in small-scale combustors have received less attention but De Zilwa *et al.* (1999a) showed that the approach to these limits led to a cyclic longitudinal movement of the location of flame stabilisation with frequencies lower than those associated with acoustic modes and increasing with flow velocity. The pressure fluctuations associated with these oscillations were smaller than those with mixtures close to stoichiometric, but increased with the rate of heat release and, in the presence of an exit nozzle, due to amplification by the bulk-mode resonance of the combustor cavity.

This paper extends the knowledge of the nature of the oscillations close to the lean limit with emphasis on its implications for active control. The flow configuration was that of Khezzar *et al.* (1999) and active control was attempted with the controller of Hendricks *et al.* (1992).

The following section describes the flow configurations, measurement methods and control apparatus. The nature of the near-limit oscillations is then described and is followed by consideration of the implications of these results for control. The paper ends with a summary of the more important conclusions and their implications.

2. Flow configurations, instrumentation and control apparatus

The experiments were conducted in the plane sudden-expansion of figure 1, which comprised acoustically-open upstream and downstream boundaries. A 100 mm long, 3 mm thick quartz window mounted immediately downstream of the expansion plane provided optical access to the flame.

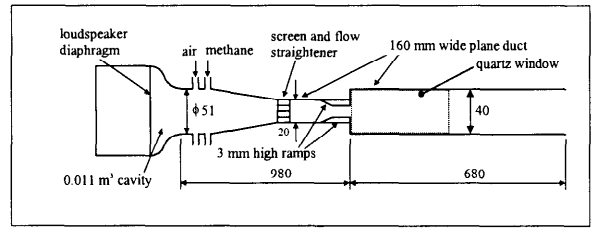


Figure 1: Plane sudden-expansion arrangement. Not to scale. All dimensions in mm except where indicated otherwise.

The pressure fluctuations in the combustor were measured by a water-cooled piezo-electric pressure transducer (Kistler 6121 with charge amplifier 5007) mounted on the wall of the duct 50 mm upstream of the expansion plane. The transducer signal was digitised (National Instruments PC-1200) and the near-limit oscillations characterised by the records of the pressure fluctuations. These oscillations were also examined in terms of a photomultiplier signal which was acquired at the same time as that from the pressure transducer. The photomultiplier gathered light emission along a line across the width of the combustor with a spatial resolution of 2 mm.

Active control by imposing oscillations with the loudspeaker at the frequency of, but out-of-phase with, the combustion oscillations was attempted with the controller of Hendricks *et al.* (1992) with a feedback signal from the pressure transducer.

Paper presented at the RTO AVT Symposium on "Active Control Technology for Enhanced Performance Operational Capabilities of Military Aircraft, Land Vehicles and Sea Vehicles", held in Braunschweig, Germany, 8-11 May 2000, and published in RTO MP-051.

3. The nature of the near-limit oscillations

Isothermal plane sudden-expansion flow at all but very low Reynolds numbers was asymmetric with unequal regions of separation behind the two steps. Though combustion eliminated most of this asymmetry, the branches of flame behind the two steps extinguished independently. Immediately prior to the extinction of the first branch, both branches gave rise to a transverse flapping motion which has been characterised with a CCD camera by De Zilwa *et al.* (1999a), with frequencies less than 10 Hz and the pressure signals showed peak-to-peak variations that increased with flow rate up to around 0.2 kPa at a Reynolds number, based on velocity and equivalent duct diameter just upstream of the expansion, of 81,000. These small amplitudes made it difficult to distinguish the pressure fluctuations associated with the flapping motion from the background noise, and the signals were also complicated by the presence of pressure fluctuations associated with the out-of-phase movements of the two branches of flame which are shown in figure 2.

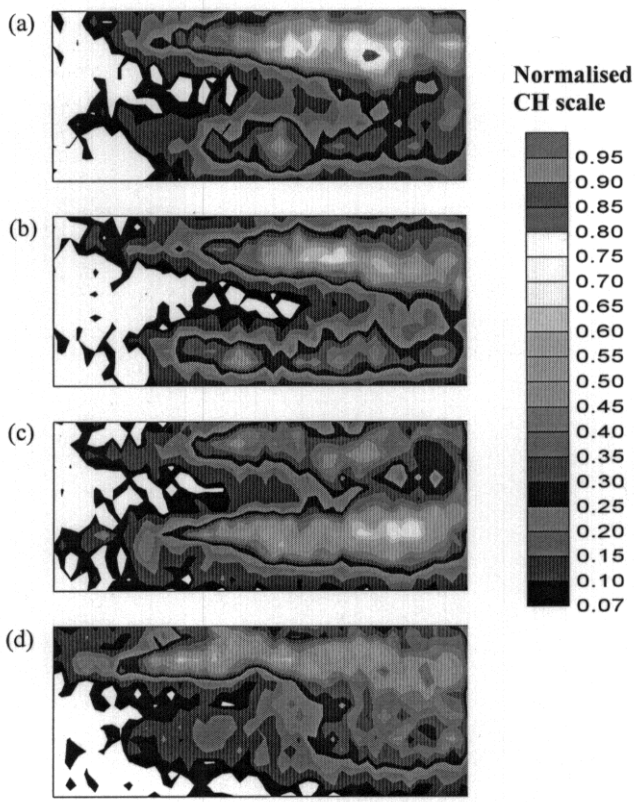


Figure 2: CH emission intensity distributions of the flame prior to the extinction of the first branch of flame. Reynolds number = 42,000, $\phi = 0.68$. Sequence of images obtained at 60 ms intervals with an exposure time of 1 ms. Observation window height and length are 40 and 100 mm, respectively. CH values normalised by maximum.

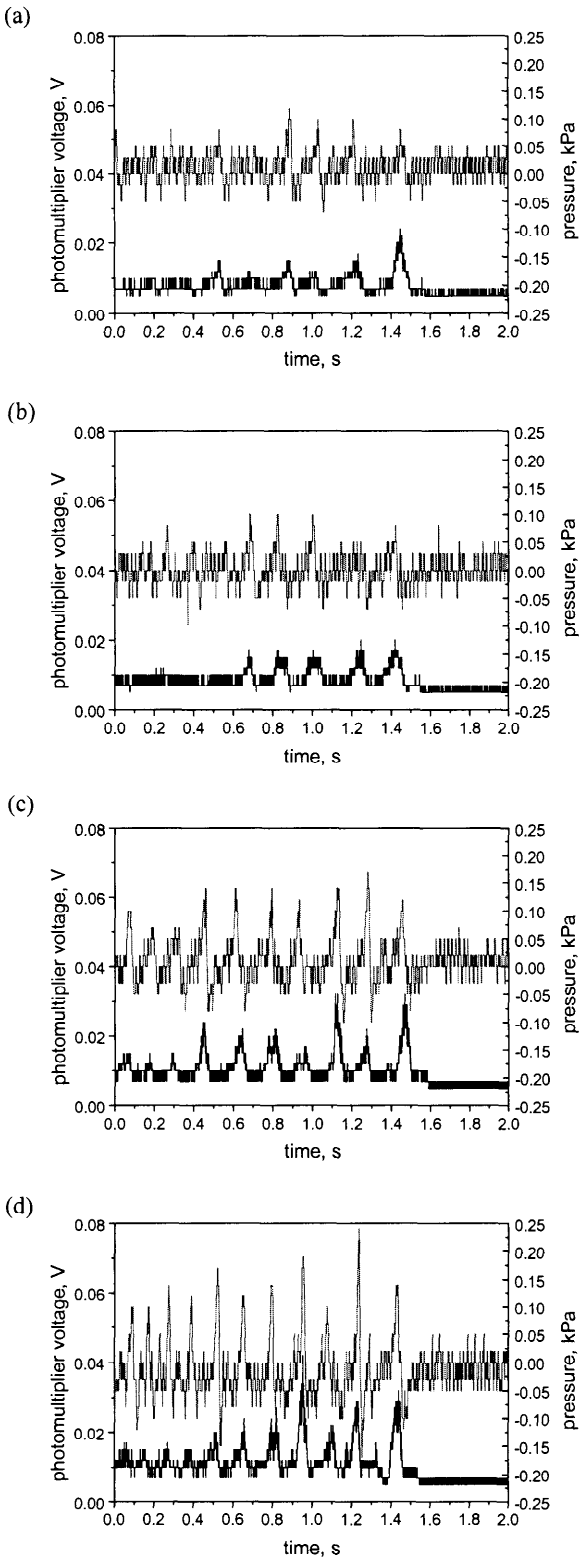


Figure 3: Simultaneous pressure transducer and photomultiplier signals at the lean extinction limit.
——— pressure signal low-pass filtered at 100 Hz,
——— light emission from photomultiplier focussed 10 mm above the bottom wall of the duct and 30 mm downstream of expansion.
Reynolds number: (a) 48,000, (b) 57,000, (c) 68,000 and (d) 81,000.

After the extinction of the first branch of flame, the remaining flame was comparatively stable behind one of the steps until the equivalence ratio was lowered further and extinction was preceded by a lateral and longitudinal oscillation which was also visualised by De Zilwa *et al.* (1999a). Traces of the pressure fluctuations at higher flow rates, at which the low-frequency oscillations can be readily distinguished from the background noise with the aid of low-pass filtering at 100 Hz, are shown in figure 3 for the period of around 1.5 s preceding and 0.5 s following extinction. The periodic nature of the signal prior to extinction is clear and the average frequency increased with flow rate from around 5.4 Hz at a Reynolds number of 48,000 to 7.5 Hz at 81,000. The amplitude of the pressure fluctuations also increased with flow rate, and hence with heat release, from a peak-to-peak value of around 0.15 kPa at a Reynolds number of 48,000 to 0.4 kPa at 81,000.

Though the average frequency of the oscillations increased with flow rate, the range encountered at each flow rate implied variations in the time taken to complete each low-frequency cycle. For example, figure 3c shows variations in the period of oscillation of between 0.1 s and 0.16 s. This variation in period was caused by the variation in the length of the region of separation, as expected in turbulent flows, and consequently in the distance travelled by the flame.

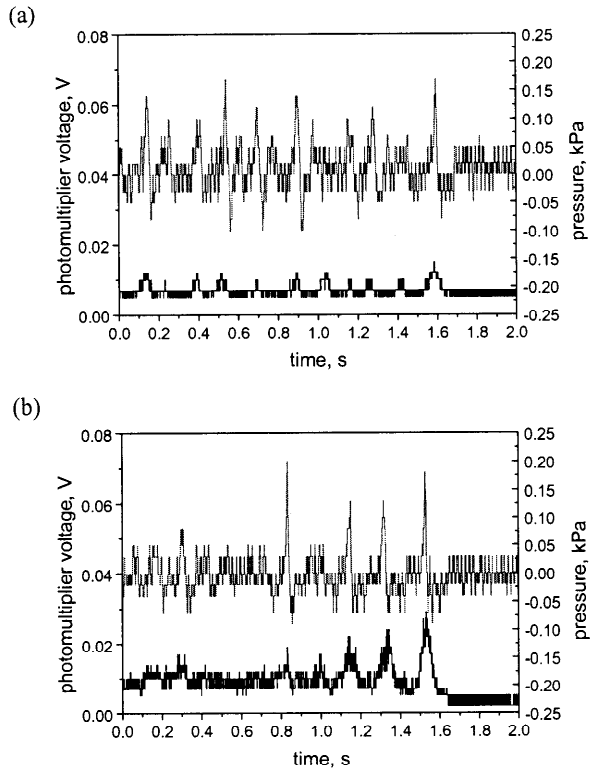


Figure 4: Simultaneous pressure transducer and photomultiplier signals at the lean extinction limit. Reynolds number: 68,000.
——— pressure signal low-pass filtered at 100 Hz,
——— light emission from photomultiplier focussed 10 mm above the bottom wall of the duct and (a) 15 and (b) 40 mm downstream of expansion.

All the pressure signals shown were obtained with the single flame stabilised on the bottom step. The signals obtained simultaneously from the photomultiplier which was focussed along a line 10 mm above from the bottom wall of the duct and 30 mm downstream of the step are also shown and the correlation between the two signals is clear with coincident maxima. Light was collected across the width of the combustor so that the influence of the lateral oscillation was minimised and this was confirmed by the correlation between the two signals being independent of the side of the duct on which the pressure transducer was mounted

Thus, the effect of the longitudinal oscillation was isolated and the correlation between the signals suggests that the strongest light was emitted at the pressure maxima. The light signals obtained from different downstream locations, figure 4, showed that, as expected, the maxima of the signals were smallest close to the step. They also showed that the spikes were wider when obtained further downstream, indicating increased residence time of the flame at locations further away from the step, and confirming the longitudinal motion of the location of flame stabilisation. The coincidence of the maxima of the two signals was independent of downstream position of photomultiplier, which suggested that the longitudinal movements of the flame gave rise to a strengthening and weakening of the entire flame, with the flame strongest when it was closest to the step, consistent with the CCD images of figure 2.

The pressure signals show gradual increases and more rapid declines which suggests different rates of travel of the flame before and after the pressure maximum. This is consistent with the mechanism of oscillation suggested by De Zilwa *et al.* (1999a) that extinction occurred due to strain rates and travelled downstream at the velocity in the shear layer, of the order of a few metres per second, and that the flame returned towards the step at the flame speed of the mixture in the recirculation zone, of the order of tens of centimeters per second. This again implies that the pressure maxima corresponded to the flame positions close to the step, with the sharp decrease when the flame moved downstream, followed by the more gradual increase as the flame moved more slowly back toward the step.

4. Feedback-driven control of the near-limit oscillations

The pressure signals obtained involved oscillations with frequencies less than 10 Hz as extinction was approached. The feedback controller used by Hendricks *et al.* (1992) and subsequently by, for example, Sivasegaram *et al.* (1995) and Bhidayasiri *et al.* (1998) to control the continuous large-amplitude acoustic oscillations that occur close to stoichiometry could not lock on to these lower-frequency oscillations. Indeed, none of the feed-back systems developed to deal with acoustic oscillations, including those of Langhorne *et al.* (1990) and Gutmark *et al.* (1992), which rely on determining a single dominant frequency and imposing an out-of-phase oscillation at that frequency are likely to control this near-limit oscillation. This is partly because the oscillation is transient and allows the controller very few cycles, usually less than twenty, within which to determine the dominant frequency and, more importantly, because the period of the oscillations varied by as much as 60 % from one cycle to another.

The low frequencies imply slow changes and hence, there may be time to track a characteristic of the flame and to take action in response to its magnitude or change in magnitude. The relative time-scales can be estimated for the most straightforward form of control that can be envisaged, which would involve tracking the pressure signal and imposing pressure oscillations that counteract the naturally-occurring fluctuations. The 3 ms delay for a pressure pulse to travel from an actuator located even a metre away from the flame is small compared with the oscillation period of around 100 ms, and suggests that tracking the signal in the time domain together with online actuation may be successful.

The near-limit oscillations were caused by the high strain rates close to the step and the downstream movement of the position of flame stabilisation along the shear layer till the strain rate decreased sufficiently to allow flashback of the flame. Thus it is necessary to counteract the downstream movement of the flame by reducing the strain rate or increasing the robustness of the flame at the instant at which it is most likely to detach by, for example, slowing the flow or by injecting fuel at this instant. A pressure transducer signal is usually the most convenient form of feed-back and, since the pressure maximum corresponded to the flame position closest to the step, actuation should take place just after this maximum to inhibit the downstream movement.

5. Concluding remarks

The pressure and light signals showed oscillations prior to extinction consistent with the cyclic downstream movement of the flame at the flow velocity in the shear layer, followed by a slower return toward the step at the flame speed of the mixture in the recirculation zone. The frequencies and the pressure fluctuations associated with these oscillations increased with flow rate up to around 7.5 Hz and 0.4 kPa at a Reynolds number of 81,000.

De Zilwa *et al.* (1999a) showed that these near-limit oscillations could give rise to much larger pressure fluctuations when there was a resonance frequency in the vicinity and that these increased amplitudes caused the flammability range to narrow. Hence, suppression or control of these oscillations is important. However, the feedback-driven active control strategy of determining the dominant frequency of the combustion oscillations and imposing out-of-phase oscillations was unsuccessful because the period of the near-limit oscillations varied by as much as 60 % from one cycle to another. It may be possible to track the variations in frequency, but it would be preferable to track a flame characteristic and take action at a particular instant in the cycle to counteract the flame movement.

6. Acknowledgements

Financial support from the US Army under Contract N68171-97-C-9009 and useful discussions with Professors H. McDonald and S. Sivasegaram, and with Messrs J. R. Laker and I. Emiris are gratefully acknowledged.

7. References

1. Bhidayasiri, R., Sivasegaram, S. and Whitelaw, J. H. (1998) Control of oscillations in premixed gas turbine combustors. Thermofluids Section report TF/98/08, Mechanical Engineering Department, Imperial College of Science, Technology and Medicine, London. To appear in Advances in Chemical Propulsion, (ed. G. D. Roy).

2. De Zilwa, S. R. N., Uhm, J. H. and Whitelaw, J. H. (1999a) Combustion oscillations close to the lean flammability limit. Submitted to *Combustion, Science and Technology*.

3. De Zilwa, S. R. N., Sivasegaram, S. and Whitelaw, J. H. (1999b) Control of combustion oscillations close to stoichiometry. *Journal of Flow, Turbulence and Combustion*, in press.

4. Gutmark, E., Wilson, K. J., Parr, T. P. and Schadow, K. C. (1992) Feedback control of multi-mode combustion instability. AIAA paper 92-0778.

5. Hendricks, E. W., Sivasegaram, S. and Whitelaw, J. H. (1992) Control of oscillations in ducted premixed flames. ***Aerothermodynamics in Combustors***. Springer, 215-230.

6. Khezzar, L., De Zilwa, S. R. N. and Whitelaw, J. H. (1999) Combustion of premixed fuel and air downstream of a plane sudden-expansion. *Experiments in Fluids*, **27**, 296-309.

7. Langhorne, P. J., Dowling, A. P. and Hooper, N. (1990) Practical active control system for combustion oscillations. *Journal of Propulsion and Power*, **6**, 324-330.

8. Lee, J. G., Hong, B. S., Kim, K., Yang, V. and Santavicca, D. (1999) Optimization of active control systems for suppressing combustion instability. *Proceedings of the RTO AVT symposium on Gas Turbine Engine Combustion, Emissions and Alternative Fuels*, paper 40.

9. Paschereit, C. O., Gutmark, E., Weisenstein, W. (1998) Structure and control of thermoacoustic instabilities in a gas-turbine combustor. *Combustion Science and Technology*, **138**, 213-232.

10. Poinsot, T., Bourienne, S., Candel, S. N. and Esposito, E. (1989) Suppression of combustion instabilities by active control. *Journal of Propulsion and Power*, **5**, 14-20.

11. Sivasegaram, S., Tsai, R-F. and Whitelaw, J. H. (1995) Control of combustion oscillations by forced oscillation of part of the fuel. *Combustion Science and Technology*, **105**, 67-83.

12. Sivasegaram, S. and Whitelaw, J. H. (1987) Oscillations in axisymmetric dump combustors. *Combustion Science and Technology*, **52**, 413-426.

Optimization of Active Control Systems for Suppressing Combustion Dynamics

Kwanwoo Kim
Jongguen Lee
Jacob Stenzler
Domenic A. Santavicca

Department of Mechanical and Nuclear Engineering
132 Research Building East
The Pennsylvania State University
University Park, PA 16802, USA

Abstract

Results from an experimental study of active combustion control using modulated secondary fuel on a laboratory-scale, lean premixed dump combustor are presented. A simple phase-delay, closed-loop controller was used for these tests operating at the 4th sub-harmonic of the dominant frequency of the instability. Tests were conducted using both natural gas and Jet-A as the secondary fuel and the results are compared. Of particular interest are the observed differences in control effectiveness and the causes of those differences.

Introduction

Suppression of combustion dynamics in gas turbine combustors using active combustion control with fuel flow modulation has been successfully demonstrated [1-16] in a number of laboratory-scale combustors and at least one full-scale combustor. Both modulated primary fuel injection and modulated secondary fuel injection have been employed in these demonstrations, as has sub-harmonic injection and both open-loop and closed-loop control. Among these successful demonstrations, however, significant variations in control effectiveness have been observed, not to mention the unreported cases where poor or no control was achieved. An important question is, can the results of these tests be used to make a meaningful assessment of the full potential of active combustion control? The answer to this question is no, and the reason is that in most of these tests the active control system was not optimized for maximum control effectiveness. This in turn raises another question, which is, how does one optimize an active combustion control system. In the case of modulated secondary fuel flow the main technical goal is to achieve (nearly) complete suppression of the pressure oscillations with minimum secondary fuel flow. Minimum secondary fuel is necessary in order to reduce the NO_x penalty that typically results from secondary fuel injection and to minimize the demands on the injector. There are a number of parameters which determine the effectiveness of a control system employing secondary fuel injection, including the phase, duration and frequency of injection, the injection pressure and the number and location of secondary injection sites. What these parameters have in common is that they all provide a means for changing the spatial and temporal fuel distribution in the combustor. Therefore it is reasonable to argue that optimization of an active combustion control system employing modulated secondary fuel injection can be viewed in a more general sense as optimization of the temporal and spatial distribution of the secondary fuel. One of the numerous factors affecting the secondary fuel distribution is whether the secondary fuel is gas or liquid. In this paper preliminary results are presented from a study of active combustion control of a lean premixed combustor employing modulated secondary fuel injection where a comparison is made of the control effectiveness that is achieved using natural gas and Jet-A as the secondary fuel.

Description of Experiment

Combustor

The coaxial dump combustor used in this study is illustrated schematically in Figure 1. The combustor consists of a mixing section and a

Paper presented at the RTO AVT Symposium on "Active Control Technology for Enhanced Performance Operational Capabilities of Military Aircraft, Land Vehicles and Sea Vehicles", held in Braunschweig, Germany, 8-11 May 2000, and published in RTO MP-051.

combustor section, separated by a dump plane. At the inlet of the 36 mm diameter by 330 mm long mixing section the flow is choked. The flame is stabilized on a bluff centerbody which is mounted flush with the dump plane. The 19 mm diameter centerbody is centered in the mixing section using vanes positioned at an angle of 30°, which also serve as an axial swirler. The upstream end of the combustor section is made from a 110 mm diameter fused-silica cylinder and the downstream end is fabricated from a 80 mm diameter stainless steel tube. The overall combustor length is 875 mm, which corresponds to a nominal L/D of 10. In these tests the combustor exit was partially-restricted ($A_{combustor}/A_{exit}$ = 17) but not choked. The primary fuel is natural gas (96% methane), which is introduced well upstream of the choked mixing section inlet, thus giving a uniform, premixed fuel-air distribution at the combustor entrance. In addition, because the fuel and air are mixed upstream of the choked inlet there is no possibility of feed-system coupling .

Measurements

Pressure oscillations are measured using water-cooled piezoelectric pressure transducers located in the dump plane, at various axial locations in the combustor (i.e., 1/2L, 3/4L and L) and in the mixing section. A photomultiplier tube (PMT) is used to monitor temporal variations in the chemiluminescence intensity from the flame. Although there is no general, quantitative correlation between the intensity of flame luminosity and other physical quantities, the chemiluminescence from various flame-radicals such as OH*, C_2*, CH* and CO_2* has been used as an indicator of both global and local heat release in lean premixed hydrocarbon flames [17-20]. In this study, a broad band-pass filter (BG-40) is used to collect the chemi-luminescence from CO_2* which is assumed to provide a qualitative measure of the flame's heat release.

In addition to the PMT chemilumine-scence measurements, an intensified CCD camera is used to record chemiluminescence images of the flame zone with a nominal 100mm by 150mm field of view. The measurements are phase-synchronized with the dump plane pressure measurement, giving a sequence of images which show the temporal and spatial evolution of the heat release distribution during one period of the pressure oscillation. A tomographic deconvolution procedure is used to extract the two-dimension heat release distribution from the original line-of-sight images [21].

And lastly, planar laser induced fluorescence is used to measure the fuel distribution at the annular exit of the mixing section.

Active Control System

An active control strategy based on the use of secondary fuel injection has been implemented using closed-loop control with 4th sub-harmonic injection and a simple phase-delay controller. The pressure transducer mounted in the dump plane is used as the sensor for the control system. The filtered output of the pressure transducer is fed into a custom-built control circuit where the threshold pressure level required to activate the secondary fuel injection valve is selected. The control circuit is also used to set the phase-delay between the pressure signal and the TTL input to the secondary fuel injection valve driver (General Valve Co., Iota One). Actuation, i.e., injection of secondary fuel, is initiated using a fast-acting solenoid valve (General Valve Co., Series 9). Note, that the fuel also flows through a manifold which delivers the fuel from the solenoid valve to the actual injectors.

As shown in Figure 2, secondary fuel is injected transversely into the mixing section through four air-assist injectors equally spaced around the circumference of the mixing tube and located 115mm upstream of the dump plane. Results with secondary injection of both natural gas and Jet-A fuel are presented. In the case of natural gas, no air-assist was used, while in the case of Jet-A the amount of air-assist was varied to investigate the effect of the spray characteristics on control effectiveness.

Results and Discussion

All of the results presented in this paper are for a combustor inlet temperature of 350°C, a combustor mean velocity of 5.25 m/s, and a nominal combustor pressure of 1.2 bar (~17.5 psia). As noted previously, the primary fuel is natural gas which is mixed with the air well upstream of the choked inlet to the mixing section, therefore the fuel distribution at the combustor inlet is uniform and there is no possibility of feed-system coupling. The stability map at this operating condition is shown in Figure 3, where the stability map is a plot of the rms pressure fluctuation in dB (measured by the pressure transducer mounted in the dump plane) versus the overall primary fuel-air equivalence

ratio. As shown in Figure 3, there is a 30 dB increase in the rms pressure fluctuation in going from the stable operating condition at an equivalence ratio of 0.65 to the unstable operating condition at an equivalence ratio of 0.55. For all of the active control results presented in this paper the combustor was operated at an equivalence ratio of 0.55, which is where the strongest instability occurs. The frequency spectrum of the pressure fluctuation at this condition shows that the dominant frequency is 336 Hz which corresponds to the first longitudinal mode of the combustor.

A sequence of twelve phase-synchronized chemiluminescence images, recorded in 30 degree phase angle increments, is shown in Figure 4 for the 0.55 equivalence ratio operating condition. (Each image shown in Figure 4 is an ensemble average of 20 individual images.) These images show clear evidence that flame-vortex interaction plays an important role in the observed instability. Also shown in Figure 4 is the pressure oscillation at this condition, where the numbers on the pressure signal correspond to the numbers on the images. As expected the most intense image (#10) coincides closely with the maximum in the pressure fluctuation.

The first active control tests were run using natural gas as the secondary fuel. As mentioned previously 4th sub-harmonic injection was used in these tests. The results are shown in Figure 5 which is a plot of the reduction in the rms pressure fluctuation in dB versus the phase delay between the negative-going zero-crossing of the pressure oscillation and the leading edge of the trigger signal to the solenoid valve driver. The fuel supply pressure, measured upstream of the solenoid valve, was 150 psig and the time averaged secondary fuel flow rate was measured with a flow meter located upstream of the solenoid valve. The amount of secondary fuel was varied by varying the injection pulse width. Shown are results for three different injection pulse widths, i.e., three different secondary fuel flow rates. At a secondary fuel flow rate equal to 5.7% of the primary fuel flow rate, there is a small reduction in the rms pressure fluctuation, i.e., from 0 dB at a delay of about 1.2 msec to 5 dB at a delay of about 2.6 msec. In the second case, when the secondary fuel flow rate is increased to 6.8% of the primary fuel flow rate, a very pronounced phase dependence is observed for delays between about 2.3 msec and 3 msec, with a maximum reduction of 25 dB at a phase delay of about 2.4 msec. When the secondary fuel flow rate is increased to 7.8% of the primary fuel flow rate, the strong phase dependence is somewhat diminished and effective control, i.e., dB reductions from 20 dB to 30 dB, are observed over the entire range of delay times.

In an attempt to explain these observations, measurements were made of the flame response function. The flame response function is the heat release as a function of time and space due to the injected secondary fuel and it is measured under stable flame conditions. Using the PMT to detect the total CO_2* chemiluminescence as a function of time provides an indication of the temporal variation in the heat release due to the injected secondary fuel. Such measurements are shown in Figure 6 for a range of injection pulse widths. The arrow in this figure shows the leading edge of the trigger signal to the solenoid valve driver, which occurs approximately every 11 msec. There is a delay of about 5 msec. between the solenoid valve trigger signal and the onset of the heat released by the secondary fuel pulse, which is primarily due to the convection time from the point of secondary fuel injection to the flame front. The half-height width of the flame response function shown in Figure 6 is approximately 5 msec, which is about twice the nominal 2.8 msec period of the pressure oscillation. Under these conditions it is somewhat surprising that the control effectiveness depends on the phase of the secondary injection as shown in Figure 5. Apparently the reason for this is the fact that the rise-time of the flame response function is only about 1 msec, which is a fraction of the period of the pressure oscillation.

Next, the results obtained using Jet-A for the secondary fuel are presented. The secondary fuel supply pressure, measured upstream of the solenoid valve, was 60 psig in these tests and the time averaged secondary fuel flow rate was measured with a flow meter located upstream of the solenoid valve. In these tests the time averaged secondary fuel flow rate was held constant at a value which corresponded to 8.6% of the heat release rate of the primary fuel flow. This corresponds to an injection pulse duration of 300 μsec. What was varied was the amount of air assist, which was varied by changing the pressure of the air assist supply line. Shown in Figure 7 is a plot of the reduction in the rms pressure fluctuation in dB versus the phase delay between the pressure oscillation and the trigger signal to the solenoid valve driver. Results are presented for the case with no air assist and for three different air assist pressures, i.e., 10, 15 and 25 psig. The first observation is that there is very

little phase dependence when Jet-A is used for the secondary fuel, although an effect on the magnitude of the rms pressure oscillations is observed. In the case with no air assist, the rms pressure oscillations actually increase by about 2 dB. With the air assist turned on at a pressure of 10 psig there is a 15 to 20 dB reduction in the rms pressure oscillations. However when the air assist pressure is further increased the control effectiveness is substantially diminished such that at an air assist pressure of 25 psig the reduction in the rms of the pressure oscillations is only about 5 dB. The results therefore indicate that there is an optimum air assist pressure in terms of achieving the greatest control.

Again the flame response function was measured in an attempt to explain the Jet-A results presented in Figure 7. In addition, PLIF measurements of the fuel distribution at the entrance to the combustor were also made for each of the air assist cases.

The temporal flame response function for the no air assist, 10 psig air assist and 25 psig air assist cases are shown in Figure 8. Compared to the natural gas case (Figure 6) the delay between the trigger signal and the onset of the secondary heat release has increased from about 5 msec. to about 8 msec. Similarly the rise-time of the heat release pulse has increased from about 1 msec in the natural gas case to about 2 msec in the 25 psig air assist case and about 3 msec in the 10 psig air assist and the no air assist cases. One possible explanation for this behavior is wall wetting due to liquid fuel impinging on the walls of the mixing section. The fact that with Jet-A the rise time has become comparable to the period of the pressure oscillation is possibly the reason why no phase dependence is observed in the Jet-A results. Additional insight into the fuel-air mixing process can be obtained from the fuel distribution measurements which are plotted in Figure 9. Shown are the fluorescence intensity profiles across the 8.5 mm wide annular opening between the outer wall of the centerbody and the inner wall of the mixer tube. Results are shown for all three air assist cases at 9 msec after the trigger signal. Under the conditions of these tests the measured intensities are linearly proportional to the fuel concentration, therefore meaningful comparisons between the results can be made. In the case with no air assist, the fuel concentration is noticeably less than in the other two cases and it increases by about a factor of two from the inner to outer wall of the mixing section. In the case with 25 psig air assist, the fuel concentration is significantly greater than in the no air assist case and increases from the outer to inner wall of the mixing section by about a factor of two. In the case with 10 psig air assist, the fuel concentration is about 50% greater than in the 25 psig air assist case and about 3 times greater than in the no air assist case. The fuel concentration profile is greatest at both the inner and outer walls of the mixing section, with a minimum in between.

The obvious question is can these results explain why the case with 10 psig air assist is so much more effective at controlling the instability. One possible explanation is as follows. In the no air assist case the results in Figures 8 and 9 suggest that the liquid fuel enters the mixing section but then is immediately diverted along the outer wall of the mixing section. Because the liquid fuel wets the outer wall, the rate of fuel-air mixing is limited by the rate of evaporation and as a result the 300 μsec fuel pulse is effective spread out over the entire 11 msec between injections. This significantly diminishes the impact of the injected fuel.

In the 25 psig case, the results suggest that the air assist is effectively transporting the liquid fuel across the annulus towards the inner wall of the mixing section. There is no evidence of significant wall wetting because the flame response function is relatively narrow in this case, but apparently having the secondary fuel along the inner wall of the mixing section is not very effective at controlling the instability.

In the 10 psig air assist case, the resultant fuel distribution seems to be an optimum compromise between the two other cases. The air assist appears to be sufficient to avoid the wall wetting that occurred in the no air assist case, yet not so strong as to transport most of the fuel across the annulus to the inner wall of the mixing section.

This interpretation is supported by a Rayleigh index analysis of the chemiluminescence images of the unstable flame presented in Figure 4. The Rayleigh index is the correlation between the local heat release fluctuations and the pressure fluctuations and identifies locations in the combustor where the instability is being most strongly driven. The Rayleigh index distribution for the instability depicted in Figure 4 is shown in Figure 10. The region of maximum positive Rayleigh index is the white region in the outer portion of the dump plane recirculation zone. If one were to argue that the secondary fuel needs to reach this location, then it seems reasonable that the 10 psig air assist case would be most effective at controlling the instability.

Conclusions

Active combustion control of combustion dynamics in a lean premixed dump combustor using modulated secondary fuel was studied using both natural gas and Jet-A as the secondary fuel. A simple phase delay controller and 4^{th} subharmonic injection was used for all of the tests. The results showed significant differences in control effectiveness when using Jet-A as compared to natural gas. With natural gas a relatively strong dependence on the phase delay between the pressure oscillation and the injection of secondary fuel was observed, whereas with Jet-A the control effectiveness was relatively insensitive to the phase delay. In the Jet-A tests an air assist injector was used which provided the capability of varying the spray characteristics by varying the air assist pressure. In these tests it was found that there was an optimum air assist pressure for which the greatest control was achieved. The differences between gas and liquid injection and the effects of air assist pressure could both be explained in terms of the spatial and temporal fuel distribution of the secondary fuel. In particular it was argued that differences in fuel penetration and the possibility of wall wetting with the liquid fuel were the main controlling factors.

Acknowledgements

This research was supported by the Office of Naval Research, under Grant #ND0014-96-1-0405, and is monitored by Dr. Gabriel D. Roy.

References

1. Candel, S.M., *Twenty-fourth Symposium (International) on Combustion,* The Combustion Institute, 1992, pp. 1277-1296.
2. Schadow, K.C. and Gutmark, E., *Prog. Energy Combust. Sci.*, Vol. 18, 1992, pp. 117-132.
3. McManus, K.R., Poinsot, T. and Candel, S.M., *Prog. Energy Combust. Sci.*,Vol. 19, 1993, pp. 1-29.
4. Poinsot, T., Bourienne, F., Candel, S., Esposito, E. and Lang, W., *J.* Propulsion, Vol. 5, No.1, 1989, pp.14-20.
5. Langhorne, P.J.,Dowling, A.P. and Hooper, N., *J.* Propulsion, Vol. 6, No. 3, 1990, pp.324-333.
6. Gulati, A. and Mani, R., *J. of Propulsion and Power,* Vol. 8, No. 5, 1992, pp. 1109-1115.
7. Billoud, G., Galland, M.A., Huu, C.H. and Candel, S., *Combust. Sci. and Tech.,* Vol. 81, 1992, pp.257-283.
8. Wilson, K.J., Gutmark, E., Schadow, K.C. and Smith, R.A., *J. of Propulsion and Power,* Vol.11, No. 2, 1995, pp. 268-274.
9. Sivasegaram, S., Tsai, R.F. and Whitelaw, J.H, *Combust. Sci. and Tech.,* Vol. 105, 1995, pp.67-83.
10. Richards, G.A., Yip, M.J., Robey, E., Cowell, L. and Rawlins, D., *J. of Engineering for Gas Turbines and Power*, Vol. 119, 1997, pp. 340-343.
11. Neumeier, Y. and Zinn, B.T., *Twenty-sixth Symposium (International) on Combustion,* The Combustion Institute, 1996, pp. 2811-2818.
12. Yu, K.H, Wilson, K.J. and Schadow, K.C., *Twenty-seventh Symposium (International) on Combustion,* The Combustion Institute, 1998, pp. 2039-2046.
13. Paschereit, C.O., Gutmark, E. and Weisenstein, W., *Combust. Sci. and Tech.,* Vol. 138, 1998, pp.213-232.
14. Jones, C.M., Lee, J.G. and Santavicca, D.A., *J. of Propulsion and Power,* Vol.15, No. 4, 1999, pp. 584-590.
15. Seume, J.R., Vortmeyer, N., Krause, W., Hermann, J., Hantschk, C.-C., Zangl, P., Gleis, S., Vortmeyer, D., Orthmann, A., ASME Paper# 97-AA-119, ASME ASIA '97 Congress & Exhibition, Singapore, Sept. 30-Oct.2, 1997.
16. Cohen, J.M., Rey, N.M., Jacobson, C.A. and Anderson, T.J., International Gas Turbine & Aeroengine Congress & Exhibition, Stockholm, Sweden, June 2-5, 1998.
17 Dandy, D.S. and Vosen, S.R., *Combust. Sci. and Tech.,* Vol. 82, 1992, pp.131-150.
18. Samaniego, J.-M, Egolfopoulos, F.N. and Bowman, C.T., *Combust. Sci. and Tech.,* Vol. 109, 1995, pp.183-203.
19. Najm, H.N., Paul P.H., Mueller, C.J. and Wyckoff, P.S., *Combustion and Flame,* Vol. 113, 1998, pp.312-332.
20. Bandaru, R.V., Miller, S., Lee, J.G. and Santavicca, D.A., Proceedings of SPIE- The International Symposium on Industrial and Environmental Monitors and Biosensors, Vol. 3535, pp. 104-114, Boston, MA, Nov. 2-5, 1998.
21. Dasch, C.J., *Applied Optics*, 31(6), 1992.

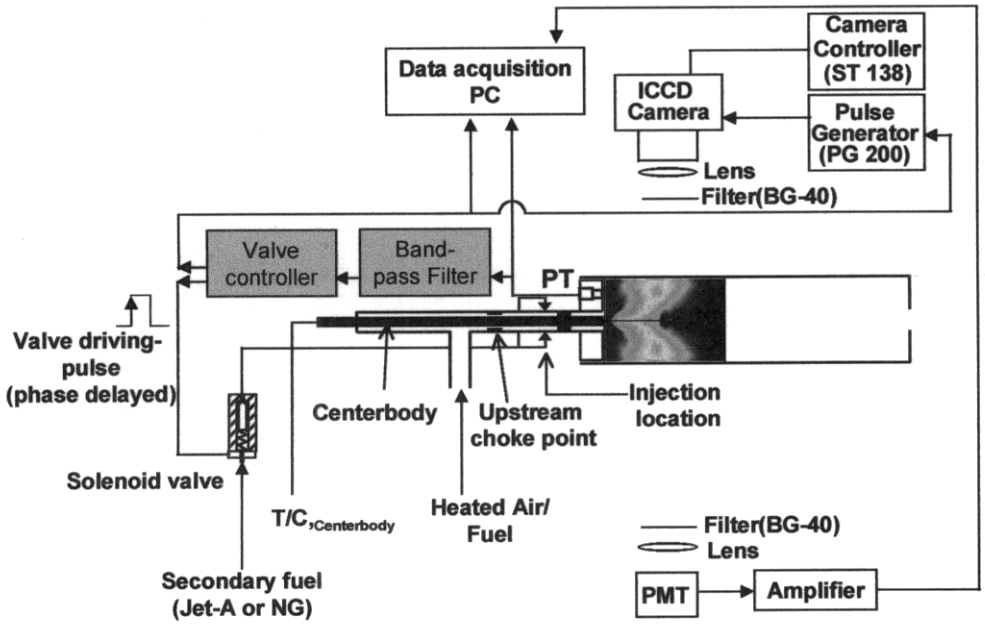


Figure 1. Experimental setup for active control and diagnostics

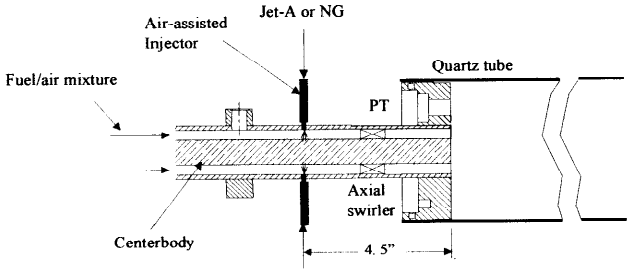


Figure 2. Schematic of mixer section of combustor and secondary fuel injection locations

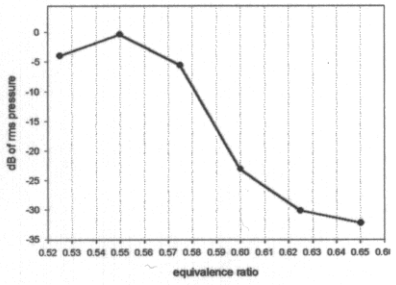


Figure 3. Stability map of the combustor (V=5.25m/sec, T_{in}=350°C)

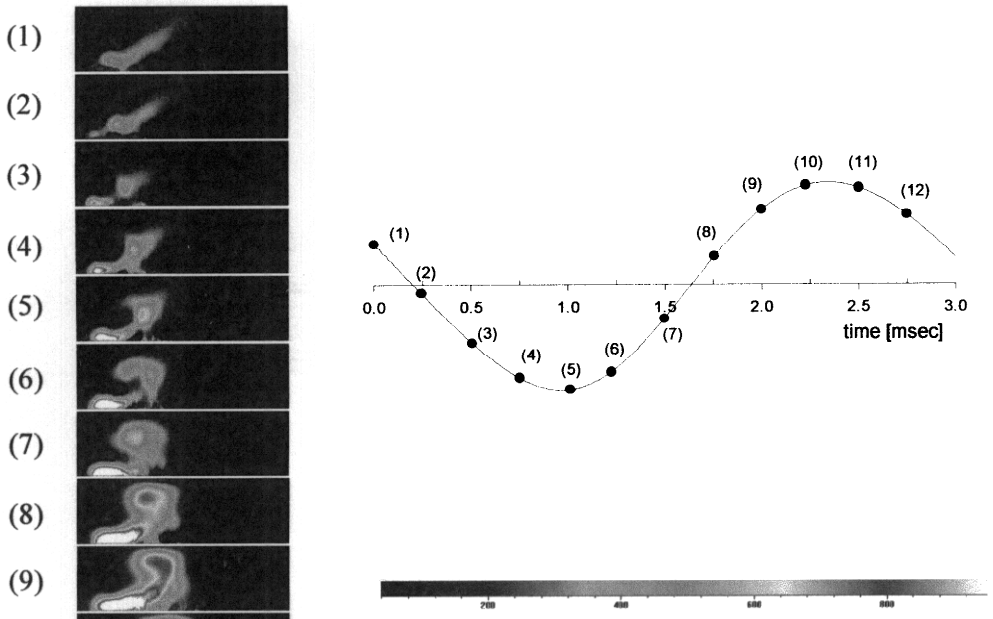


Figure 4. Phase-synchronized unstable flame images of CO_2* chemiluminescence
Φ=0.55, V=5.25m/sec, T_{in}=350°C, 100%PM

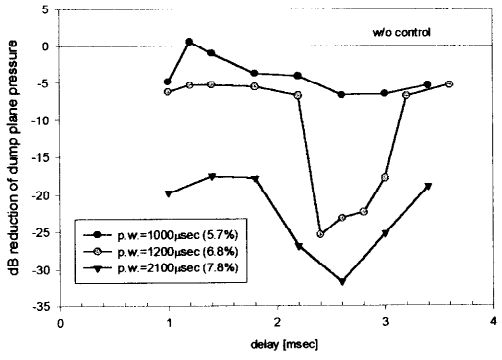


Figure 5. Phase dependence of closed loop control
operating conditions:ϕ=0.55, T_{in}=350°C, V=5.25m/sec, 100%PM, injection through four gaseous injectors(0.061" ID tubing)

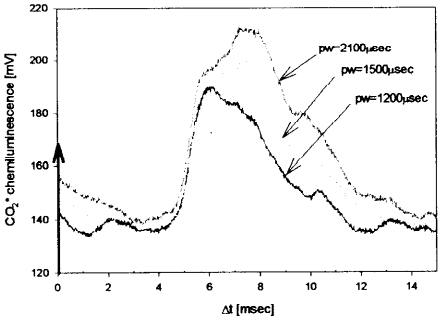


Figure 6. Response of a stable flame to pulse fuel injection
f_{inj}=90Hz, natural gas injection

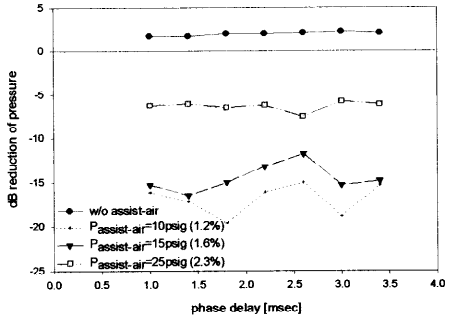


Figure 7. Closed loop control result using jet-A injection (injection frequency: fourth subharmonic, pulse width: 300μsec, addition of 8.6 % heat release by secondary fuel)

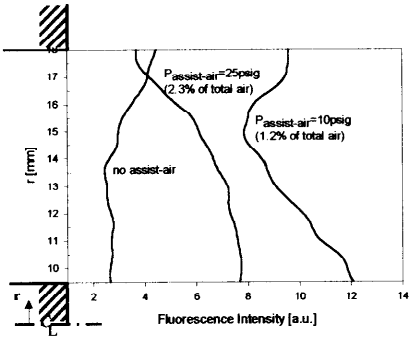


Figure 9. Fuel distribution measurement across annular passage near dump plane using PLIF of jet-A 9 milliseconds after the valve opening trigger (V=5.25m/sec, T_{in}=350°C, excitation by 266nm)

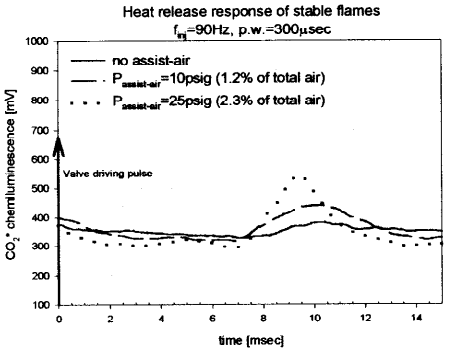


Figure 8. Heat release response of a stable flame to pulsed jet-A injection (injection frequency=90Hz, pulse width=300μsec)

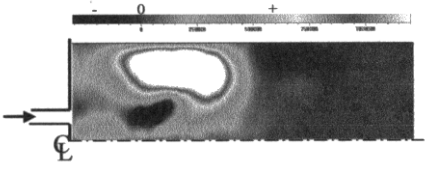


Figure 10. Rayleigh index distribution for unstable flame (100%PM, V=5.25m/sec, ϕ=0.55, T_{in}=350°C)

PAPER -35, D. Santavicca

Question (F. E. C. Culick, USA)

You discussed results for three cases of pulsed fuel injection. Are they three distinct cases or the averaged results of many tests?

Reply

The results presented are averages of many tests.

Question (C. Hassa, Germany)

If the idea of secondary fuel injection is to locally enrich the mixture, why is the position of the fuel injector so far upstream, almost as for a premixing injector?

Reply

We initially attempted to inject the secondary fuel at several locations on the dump plane. Although this was very successful when using natural gas as the secondary fuel, when using Jet-A, significant diffusion flame burning was observed. Therefore the secondary fuel injection location was moved upstream to allow sufficient time for vaporization and some degree of mixing when using liquid fuels. The specific location which was chosen, i.e., approximately 100 mm upstream of the dump lane, was selected based on previous experience with a similar configuration which showed that it was still possible to achieve significant radial stratification of the injected fuel with this injection location.

This page has been deliberately left blank

Page intentionnellement blanche

An Experimental Study on Actively Controlled Dump Combustors

K. Yu
Aerospace Engineering Department
University of Maryland
College Park, MD 20742, USA
email: yu@eng.umd.edu

and

K.J. Wilson, T.P. Parr, and K.C. Schadow
Research Department
Naval Air Warfare Center
China Lake, CA 93555, USA

A closed-loop liquid-fueled active control technique was applied in a dump combustor to enhance its combustion performance. Practical issues involving liquid fuel, scaling effects, and affordable control methods were studied experimentally. The results shed new light on the requirement of critical fuel flux, effects of fuel droplet size on control, and novel controller concepts, that would help the future development work. The critical fuel flux was found to be dependent on the fuel droplet size and initial magnitude of the instabilities. When the fuel droplet size, D_0, was reduced in the controlled injection, the control efficiency for heat flux actuation increased significantly. The analysis yielded an exponential dependency on the droplet size. For a moderate droplet Reynolds number considered in this study, the amplitude of controlled heat release for a given fuel amount was inversely proportional to the droplet size by a factor of $D_0^{-1.4}$. Also, two novel controller concepts, which incorporated practical designs, were tested and were shown to work effectively compared to the baseline case. One of the concepts was based on injecting fuel pulses at sub-harmonic frequencies of the instability, thus addressing the limited actuator frequency response. The other concept utilized both open-loop and closed-loop control schemes to obtain enhanced performance including extension of the stable combustion zone. These results open up the possibility of applying the active combustion control technology to advanced propulsion devices.

1. Introduction

While there has been a renewed interest on active combustion control (ACC) stemming from increasingly restrictive requirements on gas turbine pollution, many of the earlier studies on ACC were motivated by the desire to improve combustion performance in rockets, ramjets, and afterburners. [1] Past studies on active combustion control (ACC) have shown that it is possible to enhance combustion performance through fast-response closed-loop feedback control. [2,3] The scope of earlier investigations, however, often remained relatively basic in nature making it difficult to transition such research results into a practical system. In this paper, we attempt to address some practical issues that will provide the scientific basis for ACC implementation in practical systems. More specifically, various scaling and implementation issues are examined as well as the latest development in our active control study.

Some of the previous studies in this area include instability suppression, [4-13] efficiency improvement, [11-16] flammability limit extension, [11-13,17] and pollutant reduction. [11,15,16,18-19] These studies have opened up the opportunity to study more practical issues related to potential implementation of ACC in real systems. In this paper, we consider applying ACC in a liquid-fueled dump combustor. Such combustors could be used in advanced ramjets, gas turbines, or afterburners. The objectives are to better understand the physical processes and mechanisms involved in liquid-fueled active combustion control and to explore a practical ACC design based on pulsed liquid-fuel injection, that may be suitable for future ramjet combustors. The scope of the present paper is mostly limited to considerations involving instability suppression. However, a result showing flammability limit extension will also be presented at the end.

The result section will include two parts. The first part will describe the general progress on the study of liquid-fueled combustion control. Because of complexity associated with heterogeneous nature of liquid-fueled combustion, it is difficult to use liquid fuel in combustion control. Also, control efficiency needs to be maximized via direct injection into the combustion chamber. The first part will, therefore, include the investigation on the underlying physical processes as well as on some scaling

Paper presented at the RTO AVT Symposium on "Active Control Technology for Enhanced Performance Operational Capabilities of Military Aircraft, Land Vehicles and Sea Vehicles", held in Braunschweig, Germany, 8-11 May 2000, and published in RTO MP-051.

issues. Then, in the second part, we will turn our attention to the latest research results, which involve practical control and actuation strategy. Two novel techniques are introduced that were meant to address potential discrepancy between actuato frequency response and combustor dynamics. Also, more efficient control process involving open- and closed-loop control systems will be described.

2. Active Control System

The experiments were performed in a 102-mm diameter axisymmetric dump combustor with adjustable inlet and nozzle dimensions. The inlet tube was 42 mm in diameter (ID) and the length was between 20 to 60 diameters. Table 1 summarizes the combustor and inlet dimensions for several different cases that have been tested so far. The main fuel, ethylene, was injected through a choked orifice at a 90-degree angle to the oncoming flow. The injection location was 16 inlet diameters upstream of the dump plane causing the inlet flow to be well-mixed entering the combustor. Relatively small amount of liquid fuel was injected directly into the combustor using pulsed fuel actuators. The pulsed fuel injection was closed-loop controlled to affect the dynamics of the reacting flow. Figure 1 shows a picture of the rig with some of the control system components labeled for reference. The controller was operated from inside the control room which is not shown.

Figure 2 shows the control system architecture that was used to control the fuel injection scheduling into the dump combustor. For active instability suppression, the initial approach we had taken was to pulse the liquid fuel at the instability frequency and adjust the timing using a simple closed-loop circuit (Fig. 2a). Because our emphasis was on extending active control to liquid-fueled combustors, a simple phase-delay circuit was utilized instead of a more sophisticated controller, such as those based on an adaptive technique [20] or model-based design approaches [21-23]. Figures 2(b) and 2(c) show the development of more practical controller circuits. First in Fig 2(b), a divider was added to the circuit of Fig 2(a). This allowed periodic injection of fuel at sub-harmonic frequencies of the instability frequency. This would be particularly advantageous if the actuator frequency response was limited in the low frequency range below the characteristic frequencies of the combustor. Also, another novel concept was tested which is based on establishing a controlled amount of oscillations by combining an open-loop injection control with a closed-loop control. The "Output 1" in Fig 2(c) was used to drive one-half of the injectors at the driving frequency f_0, which was one of either harmonic or sub-harmonic frequencies of the instability. Then, a second set of controller was used in a closed-loop fashion to control the amplitude of oscillations. The closed-loop controller in this case was based on time-delayed proportional control concept.

A Kistler™ pressure transducer, mounted at one inlet diameter downstream of the dump plane, was used to detect the oscillations in combustor pressure. Then, with the combustor pressure signal as reference, the phase shift for the injection cycle was digitally controlled using a Wavetek™ Variable Phase Synthesizer. The liquid fuel was injected through the four fuel actuators that were spaced 90 degrees apart along the circumference of the inlet at the dump plane.

The initial injection angle was fixed at 45 degrees with respect to the air flow direction after a parametric study that investigated the most desirable angle for this set of actuators in utilizing flow-droplet interaction. [24] However, in Case 5, another set of actuators that utilized air-assisted atomization mechanism was explored to investigate the effect of droplet size on combustion control ability.

The first set of actuators was a combination of "off-the-shelf" automotive fuel injectors and swirl-based atomizers [25] with 300 μm exit diameter. Such a combination allowed reasonably small fuel droplet size with relatively high frequency response. The second set of actuators consisted of prototype pulsed fuel injectors, that utilized air-assisted atomization mechanism. The latter injectors produced much finer droplets but their frequency response was limited to below 150 Hz. [26] Table 2 summarizes the some of the physical parameters and flow conditions for the actuated experiments.

3. Part I -- Fundamental Results and Progress

With recent advances in actuator technology and enhanced understanding of the involved physical processes, the major emphasis of the present investigation was to concentrate on practical issues involving system integration and components development. The first part of the study was conducted to understand the liquid-fuel related issues and the effect of scale-up, while the second part addressed the development of practical control strategy.

In the first part, the timing of pulsed fuel injection was adjusted using a simple phase delay controller. The injection frequency was matched to that of the oscillation frequency. The fundamental mechanisms associated with liquid-fueled combustion control were investigated.

3.1 Vortex-Droplet Interaction

First, it was necessary to utilize the interaction between fuel droplets and large-scale flow features to disperse the fuel to the desired location. As expected, periodic vortices were shed during the oscillation cycle. [27] Because both the fuel injection and vortex shedding processes were periodic, adjusting the timing between the two resulted in controlled interaction between the transient processes. This mechanism was utilized in the experiments. Figure 3 shows the phase-dependent fuel dispersion behavior over one full cycle of flow oscillation. Depending on the relative timing of pulsed fuel injection, the fuel droplets are distributed in the different parts of the combustor.

The extent of the interaction between fuel droplets and vortices can be expressed in terms of the droplet Stokes number

$$Sto = \frac{\rho_f D^2 F}{18 \mu_g} \qquad (1)$$

where D is the droplet diameter, F the vortex frequency, ρ_f the droplet density, and μ_g the gas viscosity. On one hand, it was desirable that *Sto* be of the order of unity or higher for controlling the dispersion of fuel droplets in space, as larger droplets are less influenced by fluid motion. Recent experiments [28-30] and computations [31,32] suggested that only those droplets with *Sto* on the order of unity are affected by fluid motion and yet have enough momentum to be dispersed further outside the carrier fluid path. On the other hand, for combustion control purpose, finely atomized droplets with very short combustion delay were desirable. Thus, a desired fuel droplet distribution was such that the droplets with *Sto* close to unity constituting the upper end of the size spectrum.

In the experiments, however, the actual distribution of fuel droplet size was determined by the given actuation hardware and was difficult to control in a systematic manner. Thus, two different sets of actuators with substantially different atomization characteristics were employed to study the effect of fuel droplet size on combustion control ability and limit.

3.2 Controlled Heat Release Requirement

It is plausible that a certain minimum amount of acoustic energy is required to obtain control authority in practical flows. Because the combustion-acoustic interaction is a dominant source of acoustic energy generation in the present system, the amplitude of heat release must be considered. Assuming that acoustic energy can be controlled using Rayleigh's criterion, the amount of acoustic energy is directly proportional to the amount of controlled heat release. For instance, the change in local acoustic energy after one period T is given by

$$\Delta\varepsilon \approx \frac{\gamma - 1}{\gamma} \int_{t}^{t+T} \frac{p' \cdot q'}{\bar{p}}\, dt \qquad (2)$$

where p' denotes the time-dependent pressure fluctuation, q' local heat release fluctuation, γ the ratio of specific heats, and p the average pressure. The Rayleigh's criterion illustrates the timing between the pressure fluctuation p' and the controlled heat release q'. The controlled amount of heat release is a function of fuel droplet size as well as fuel amount. For a given amount of fuel, the dependency on droplet size can be modeled [33] and the result is given by

$$|q'|_{\max} \approx \text{Constant} \times \frac{\Delta T}{h_{fg}} D_0^{-1.4} \qquad (3)$$

where • T is the temperature difference between the fuel and the surrounding flow, h_{fg} latent heat of vaporization, and D_0 the initial droplet size. This implies that pulsed fuel sprays with smaller droplet size will be more effective in generating controlled heat flux oscillations.

The amount of acoustic energy needed for control authority, however, will also depend on the initial magnitude of the instabilities. In the next section, the results of the investigation on the critical fuel flux for two different actuator characteristics are presented. Then the results are normalized with respect to the instability magnitude to verify the applicability of Eqn. (3).

3.3 Critical Fuel Flux

In the actuated combustor experiments, the initial distribution of fuel droplet size was determined almost entirely by the actuator characteristics. For each set of actuators, the minimum amount of fuel flux, which is required for obtaining active

instability suppression, was determined. For this purpose, the amount of controller fuel flux was held constant while the overall power output was increased until the instability was no longer controllable. With No. 1 actuators (Cases 1 through 4), which generated about 40 μm Sauter-mean-diameter droplets, this point was reached when the relative amount of controller fuel flux dropped below 8% of the total average fuel flux. At this point, the instability amplitude was no longer suppressed by actively controlled fuel injection.

No. 2 actuators, on the other hand, were more efficient as they produced much finer fuel sprays. Figure 4 shows the comparison between the uncontrolled case in which all the fuel was premixed and the controlled case with the properly phased closed-loop fuel injection. As before, if the relative phase of fuel injection was not properly controlled, however, the oscillation amplitude could become as intense as the uncontrolled case. Figure 4b shows the oscillation amplitude at a few pre-selected electronic phase delay settings. Even at the highest output case tested, the instability was controllable with these actuators. Therefore, the number of actuators was reduced to determine the critical fuel flux. When the controller fuel flux was lowered to an amount below 2% of the total fuel flux, the instability suppression became no longer feasible even with the No. 2 actuators. Figure 5 summarizes these results as a plot of controller fuel flux .vs. the controlled oscillation amplitude.

The results for two actuators were compared by normalizing the results with respect to the initial magnitude of the instability. For this purpose, the theoretical amount of controlled heat release required to suppress the given instability in one cycle was calculated [33] from Eqn. (2).

$$|q'|_{theoretical} \approx \frac{f}{2(\gamma-1)}\left[\frac{\left(\bar{\rho}\, c\, |u'|_{instability}\right)^2}{|p'|_{instability}} + |p'|_{instability}\right] \quad (4)$$

Figure 6 shows the normalized results for these cases. The amount of potential thermal energy, associated with pulsed amount of fuel, was normalized by the reference heat release amount given by Eqn. (4) The comparison of the critical fuel flux for the two actuators shows that the No. 2 actuator is more efficient than the No. 1 actuator by a factor of 6. In other words, the normalized limit data indicate that the No. 2 actuators produced 6 times higher heat release modulation than the No. 1 actuators due to their droplet size difference. The expected value of efficiency improvement, which is based on the droplet size comparison of Eqn. (3), yields a factor of 7 between the two cases. Considering the difference in actuator configurations, the results are in good agreement.

4. Part II -- Practical Control Experiments

The second part of the experiments focused on the practical control issues. Two novel ideas were introduced and tested for validation. The first was based on the use of actively controlled fuel injection at sub-harmonic frequencies. Because the instabilities may occur at frequencies higher than the frequency response of the actuators, a more practical solution was sought. The controller circuit, which was shown in Fig. 2b, was constructed to drive the actuator unit at the first sub-harmonic frequency of the instability.

The second idea addressed the problems associated with multi-mode instability frequencies. It was observed in our earlier study [34] that a simple phase-delay circuit may not be very effective if the instability frequency shifts by more than the predetermined setting of the bandpass filter. To more effectively control the combustor dynamics over a wide range of operating conditions, a combined approach utilizing both open- and closed-loop control methods was tested for the first time. Both tests were conducted at flow conditions corresponding to Case 6, shown in Table 2.

4.1 Sub-harmonic Fuel Injection

It is straightforward applying active control using an actuator with higher frequency response than the combustion dynamics. A problem occurs when the maximum frequency response of available actuators is lower than the combustion process one is trying to control. This is often the case in liquid-fuel actuation as many of the commercially available injectors have relatively low frequency response compared to the instability frequencies. To address this problem, a closed-loop sub-harmonic fuel injection approach was attempted in the experiment.

The results are shown in Fig. 7 which displays the pressure oscillation amplitude as a function of the controlled phase delay settings. The control was attempted either with four fuel injectors or two, but the duty cycle was adjusted so that the average fuel flow through the controller remained almost the same in each case. Figure 7b shows that the closed-loop sub-harmonic control

approach worked just as effectively. The results are encouraging in that there was no significant drop-off in the performance when compared with the baseline case of Fig. 7a, which used the controlled injection at the fundamental frequency. In both cases, there was more than 10 dB suppression when the phase-delay was controlled properly.

Figure 8 shows an illustration of how the suppression would be achieved despite the fact that sinusoidal functions at harmonic frequencies form an orthogonal set. This approach would work in most cases because the pulsed heat release rarely exhibits a perfect sine wave pattern. For instance, in a typical case, the heat release due to pulsed fuel injection exhibits a periodic modulation at the injection frequency but the shape of the signal is such that it contains additional energy in its higher harmonics. Therefore, the integral over a cycle of the resulting product between pressure and heat release oscillations is not zero but a finite value, which in turn becomes either source or sink term for acoustic energy depending on their relative phase difference.

4.2 Pacemaker-Controller

The pacemaker-controller concept uses two outputs. One set of injectors is driven with an open-loop forcing to reinforce the periodic process, while the other set of injectors is used for controlling the combustion process. In general the open-loop forcing frequency was selected either same as the instability frequency or one of the higher harmonics or sub-harmonic frequencies. Another purpose of this open-loop forcing was to sustain controlled oscillations, which would be needed for providing feedback to the control loop, once the dominant oscillations at the instability frequencies were suppressed. Either a simple phase-delay approach or a proportional time-delay controller was used for setting up the closed control loop.

Figure 9 shows the transfer function response of the pacemaker system covering the range of frequencies from 20 to 200 Hz. Except around the resonant frequencies, where the data become meaningless, the transfer function behaves nearly flat across much of the frequencies. Figure 10 shows the effect of adding a closed-loop controller to this system. As before, the instability amplitude was effectively suppressed with the closed-loop control, and the sub-harmonic injection worked just as effectively in this combination controller.

The last controller utilized a proportional time-delay control strategy. The triggering amplitude was set up so that the duration of the closed-loop pulsed injection was dependant on the instability amplitude. As the instability amplitude grew, the duty cycle of fuel injection increased. The pacemaker-controller concept using the proportional time-delay controller was shown in Fig. 2c. Figure11 shows a long time history of the controlled pressure oscillations when this approach was used in a marginally unstable case. The data shows that the closed-loop actuator stopped injecting fuel when the oscillation amplitude was pushed below a certain level at time t near 0.6 sec. Because the stability is at most marginal at the chosen operating condition, pressure oscillations can grow unexpectedly at any instant. The closed-loop controller turns on when the instantaneous pressure oscillation amplitude exceeds a certain limit which is preset. Onset of such unstable oscillations was suppressed effectively using this approach as shown at time t around 2 sec.

4.3 Flammability Limit Extension

When an active combustion control technique is properly applied, it can not only suppress unwanted oscillations but it can also extend the flammability limit. Figure 12 shows the data that were obtained with a pacemaker-controller combination described in the previous section. While this particular controller was not able to suppress fully-blown high-amplitude instabilities in the middle of the unstable zone, it was able to control moderate-amplitude instabilities near the edge of the unstable zone. Consequently, the unstable zone became narrower as the stable zone was expanded. Also, the lean flammability limit was extended much beyond the typical blow-off limit of the premixed flames, which occurs around the equivalence ratio of 0.5.

The data in Fig. 12 were obtained first by reducing the amount of fuel flux while holding the air flux constant. Without the proper active control in place, the combustor was unstable when operated within the shaded zone. The flame blowout was observed when the equivalence ratio was lowered below the dotted line. By actively controlling the fuel injection scheduling, the unstable zone was reduced as shown by the solid gray lines. Furthermore, the lean flame blow-off limit was significantly extended to equivalence ratio just below 0.2 (dark line). The flame was stable in this experiment, even with the minimum amount of controller fuel flux. The air flux had to be increased to finally obtain the flame blowout.

5. Summary and Concluding Remarks

This paper summarized a joint experimental study between the Naval Air Warfare Center and the University of Maryland to better understand the practical issues related to liquid-fueled active combustion control applied to a model ramjet dump combustor. The first part of the study concentrated on understanding the important physical mechanisms involving liquid-fueled instability suppression and scaling laws, while the focus of the second part study was on building the scientific basis for developing a practical controller. It was shown that transient vortex-droplet interaction, which depends on fuel injection scheduling, could be used to effectively control the spatial and temporal distributions of fuel. This mechanism was utilized in a practical manner to apply an active instability suppression technique.

Some of the important findings and observations in the present study are the following:

1) It was shown that there exists a critical fuel flux which is required to obtain active instability suppression. While the critical fuel flux depends on the manner at which the controller fuel is introduced into the combustion zone, it is very sensitive to the initial amplitude of the instability as well as the fuel droplet size.

2) The droplet size dependency was analytically studied and was compared to the experimental data in the present study. For a given fuel type, the critical fuel flux increased with the fuel droplet size by an exponential factor of 1.4. This relation was derived for a moderate droplet Reynolds number considered in the present study.

3) Novel controller concepts were experimentally tested and were shown to work effectively. One concept was based on using a closed-loop fuel injection at sub-harmonic frequencies. The performance was similar to that using the injection at the instability frequency. In the future this fact could be used to relax the requirements on actuators. Another concept used a combination approach bringing an open- and closed-loop controls simultaneously. The latter approach would be useful when there is a significant drift in the natural instability frequency.

The present study has shown that active combustion control can be a practical technology that enables higher performance in dump combustors. Furthermore, it was demonstrated that the present control technique not only suppressed combustion instabilities but it could also be used to extend the lean flammability limit. While the influence of fuel droplet size on controller effectiveness was demonstrated in the present study, other scaling aspects warrants more detailed future investigation. For instance, the present experimental data showed that the instability amplitude increased with the combustor output scale. Thus, a collaborative study is in progress which considers the effects of inlet flow temperature, combustor Damköhler number, as well as the relative intensity of the combustion.

Acknowledgement

This study was sponsored by the Office of Naval Research, with Dr. Gabriel D. Roy as the scientific officer. All of the experiments described in this paper were performed at the Naval Air Warfare Center - Weapons Division.

References

[1] Schadow, K., and Yang, V., "Active Combustion Control for Propulsion Systems," AGARD Workshop Report, Athens, Greece, 1996.

[2] Candel, S.M., “Combustion Instabilities Coupled by Pressure Waves and Their Active Control,” *Twenty-Fourth Sympo. (Inter.) on Comb.*, The Combustion Institute, Pittsburgh, PA, 1992, pp. 1277-1296.

[3] McManus, K.R., Poinsot, T., and Candel, S., “A Review of Active Control of Combustion Instabilities,” *Prog. in Energy & Comb. Sci.*, Vol. 19, 1993, pp. 1-29.

[4] Lang, W., Poinsot, T., and Candel, S., *Comb. & Flame*, 70:281-289 (1987).

[5] Bloxsidge, G.J., Dowling, A.P., Hooper, N., and Langhorne, P.J., *AIAA J.*, 26:783 (1988).

[6] Poinsot, T., Bourienne, F., Candel, S., and Esposito, E., *J. Propul. & Power*, 5:14-20 (1989).

[7] Langhorne, P.J., Dowling, A.P., and Hooper, N., *J. Propul. & Power*, 6:324-333 (1990).

[8] Schadow, K.C., Gutmark, E., and Wilson, K.J., *Comb. Sci. & Tech.*, 81:285-300 (1992).

[9] Gulati, A. and Mani, R., *J. Propul. & Power*, 8(5):1109-1115 (1992).

[10] Sivasegaram, S., Tsai, R-F., and Whitelaw, J.H., *Comb. Sci. and Tech*., 105:67 (1995).

[11] McManus, K.R., Vandsburger, U., and Bowman, C.T., *Comb. & Flame*, 82:75-92 (1990).

[12] Wilson, K.J., Gutmark, E., Schadow, K.C., and Smith, R.A., "Active Control of a Dump Combustor With Fuel Modulation," AIAA Paper 91-0368, 1991.

[13] Gutmark, E., Parr, T.P., Hanson-Parr, D.M., and Schadow, K.C., "Stabilization of Combustion By Controlling The Turbulent Shear Flow Structure," 7th Symposium on Turbulent Shear Flows, Paper No. 23-1, 1989.

[14] Yu, K., Trouve, A., and Candel, S., 29th Aerospace Sciences Meeting, AIAA-91-0367, 1991.

[15] Gutmark, E., Parr, T.P., Hanson-Parr, D.M., and Schadow, K.C., *Twenty-Third Sympo. (Inter.) on Comb.*, The Combustion Institute, Pittsburgh, PA, 1990, pp 1101-1106.

[16] Brouwer, J., Ault, B.A., Bobrow, J.E., and Samuelsen, G.S., *Twenty-Third Symp. (Inter.) on Comb.*, The Combustion Institute, Pittsburgh, PA, 1990, pp 1087-1092.

[17] Gutmark, E., Parr, T.P., Hanson-Parr, D.M., and Schadow, K.C., "Closed-Loop Amplitude Modulation Control of Reacting Premixed Turbulent Jet," AIAA J., 29 (12), 2155-2162, 1991.

[18] Parr, T.P., Gutmark, E.J., Wilson, K.J., Yu, K., Smith, R.A., Hanson-Parr, D.M., and Schadow, K.C., *Twenty-Sixth Sympo. (Inter.) on Combustion*, The Combustion Institute, Pittsburgh, PA, 1996.

[19] Keller, J.O. and Hongo, I., *Comb. & Flame*, 80:219-237 (1990).

[20] Billoud, G., Galland, M.A., Huynh Huu, C., Candel, S., "Adaptive Active Control of Combustion Instabilities," *Combust. Sci. and Tech*. **81**, 257-283, 1992.

[21] Yang, V., Sinha, A., and Fung, Y-T, "State-Feedback Control of Longitudinal Combustion Instabilities," *J. Propulsion & Power*, **8**(1), 66-73, 1992.

[22] Fung, Y-T, and Yang, V., "Active Control of Nonlinear Pressure Oscillations in Combustion Chambers," *J. Propulsion & Power*, **8**(6), 1282-1289, 1992.

[23] Annaswamy, A.M., Fleifil, M., Rumsey, J.W., Hathout, J.P., and Ghoniem, A.F., "An Input-Output Model of Thermoacoustic Instability and Active Control Design," MIT Report No. 9705, Cambridge, MA, 1997.

[24] Yu, K., Wilson, K.J., Parr, T.P., Smith, R.A., and Schadow, K.C., "Characterization of Pulsating Spray Droplets and Their Interaction with Vortical Structures," AIAA 96-0083, 1996.

[25] Parr, T.P., Gutmark, E.J., Hanson-Parr, D.M., and Yu, K., "Control of Sooty High Energy Density Fuel Combustion," *Proc. of 8th ONR Prop. Mtg.*, 215-224, 1995.

[26] Yu, K., and Schadow, K.C.. "Quantitative Data Reduction from Phase-Resolved Spray Images," Proceedings of PSFVIP-2, Honolulu, HW, *PF012*, 1999.

[27] Yu, K.H., Trouve, A., and Daily, J.W. (1991) "Low frequency pressure oscillations in a model ramjet combustor," *J. of Fluid Mechanics* 232, pp. 47-72.

[28] Lazaro, B.J. and Lasheras, J.C., "Paricle dispersion in a turbulent, plane, free shear layer," *Phys. Fluids A* 1: 1035-1044 (1989).

[29] Longmire, E.K. and Eaton, J.K., "Structure and control of a partice-laden round jet," *JFM* 236: 217-257 (1992).

[30] Glawe, D.D. and Samimy, M., “Dispersion of Solid Particles in Compressible Mixing Layers,” *JPP* 9 (1): 83-89 (1993).

[31] Chung, J.N. and Troutt, T.R., “Simulation of particle dispersion in an axisymmetric jet,”*JFM* 186: 199-222 (1988).

[32] Chang, E. and Kaliasanath, K., “Simulations of Particle Dynamics in a Confined Shear Flow,” *AIAA J.* 34(6): 1160-1166 (1996).

[33] Yu, K., Wilson, K.J., and Schadow, K.C., “Liquid-Fueled Combustion Control: Scale-Up Experiments and Effect of Fuel Droplet Size,” AIAA Paper 99-0328, 1999

[34] Yu, K., Wilson, K.J., Parr, T.P., Schadow, K.C., and Gutmark, E. *Twenty-Sixth Sympo. (Inter.) on Combustion*, The Combustion Institute, Pittsburgh, PA, 1996.

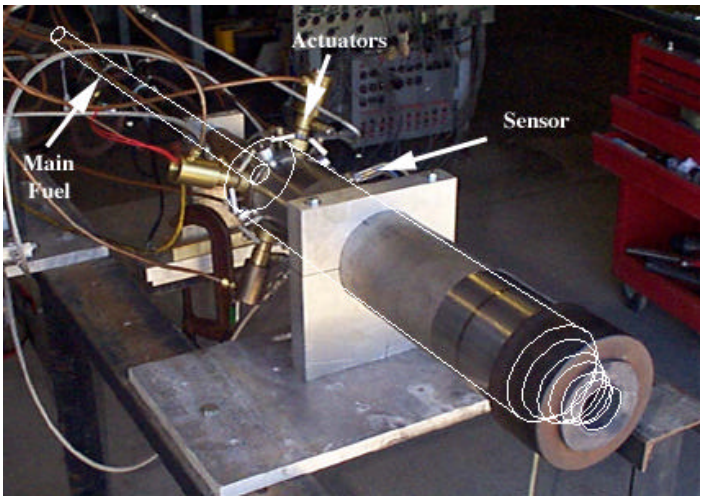


Fig. 1 Actively controlled dump combustor set-up.

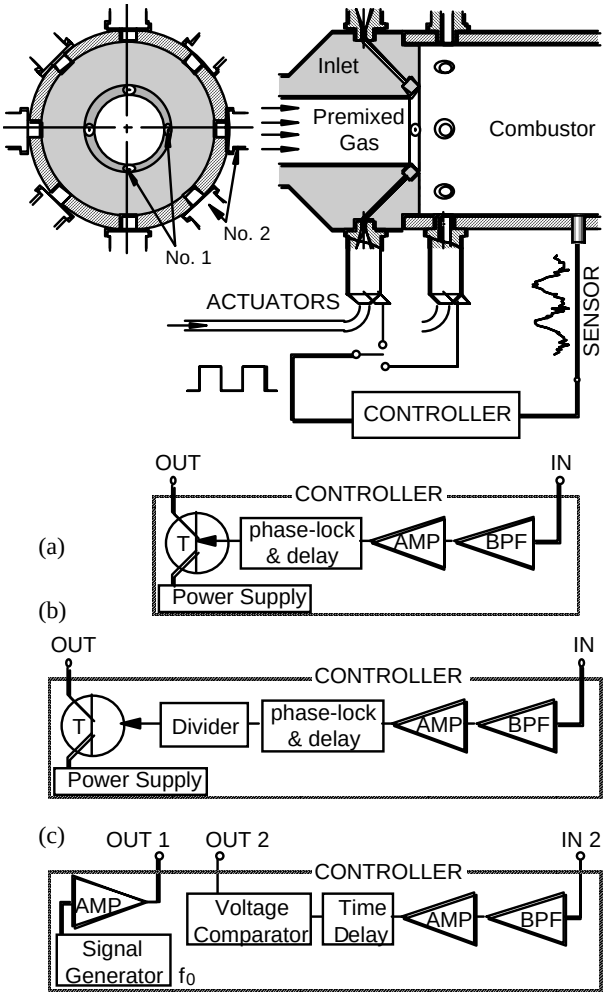
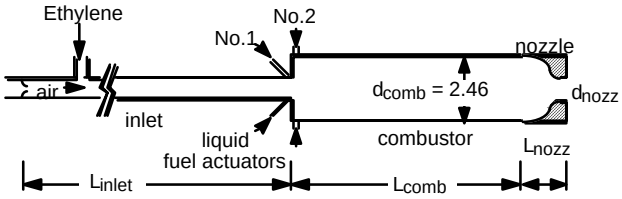


Fig. 2 Active control system. (a) a simple phase-delay circuit, (b) a sub-harmonic fuel injection control circuit, and (c) a pacemaker-controller design.

Table 1 Dump combustor setup for the corresponding cases.



all dimensions are in terms of d_{inlet} = 42 mm

Case	Liquid Fuel	actuator	L_{inlet}	L_{comb}	d_{nozz}	L_{nozz}
1	Ethanol	No. 1	58.5	10.2	1.29	1.85
2	Heptane	No. 1	25.8	12.4	0.615	1.85
3	Heptane	No. 1	25.8	12.9	0.862	1.32
4	Heptane	No. 1	25.8	8.9	0.615	1.85
5	JP-10	No. 2	20.2	15.4	1.36	1.81
6	JP-10	No. 1	20.2	15.4	0.615	1.85

Table 2 Average flow conditions and characteristic parameters for test cases.

Case	Flow Rate (g/sec)					Flow Characteristics			Unstable Conditions			Fuel Droplet			Control Efficiency
	Air	Ethylene	Ethanol	Heptane	JP-10	Power Output (kW)	Re	ϕ	$\frac{\bar{p}_{comb}}{p_{exit}}$	f(Hz)	$\frac{p'_{rms}}{\bar{p}_{comb}}$	D_{32}	Re_f	Stokes	$\frac{(kW)_{pulsed}}{(kW)_{total}}$
1A	45	1.0	0.75	-	-	66	$7.7\ 10^4$	0.47	1.02	34	0.008	50	90	0.21	0.30
1B	45	1.3	0.75	-	-	82	$7.7\ 10^4$	0.58		35	0.005	50	90	0.21	0.25
2	120	3.3	-	0.62	-	180	$2.0\ 10^5$	0.51	2.20	87	0.042	39	180	0.28	0.15
3A	150	5.1	-	0.73	-	270	$2.5\ 10^5$	0.59	1.59	98	0.092	36	210	0.27	0.12
3B	200	7.0	-	0.65	-	360	$3.4\ 10^5$	0.57	2.06	96	0.089	38	300	0.30	0.08
4	120	3.3	-	0.63	-	180	$2.0\ 10^5$	0.51	2.17	95	0.054	39	180	0.31	0.15
5A	270	11	-	-	2.2	630	$4.4\ 10^5$	0.72	1.39	120	0.076	10	100	0.034	0.15
5B	270	11	-	-	1.1	580	$4.4\ 10^5$	0.69	1.38	120	0.11	10	100	0.034	0.079
5C	270	11	-	-	0.55	560	$4.4\ 10^5$	0.66	1.33	122	0.095	10	100	0.034	0.041
5D	610	25	-	-	2.2	1280	$1.0\ 10^6$	0.66	2.67	125	0.13	10	240	0.035	0.072
5E	610	25	-	-	1.1	1230	$1.0\ 10^6$	0.63	2.72	125	0.21	10	240	0.035	0.037
5F	610	25	-	-	0.55	1210	$1.0\ 10^6$	0.62	2.56	125	0.18	10	240	0.035	0.019
6	28	0.48	-	-	0.89	61	$4.7\ 10^4$	0.70	1.07	99	0.019	50	45	0.45	0.62

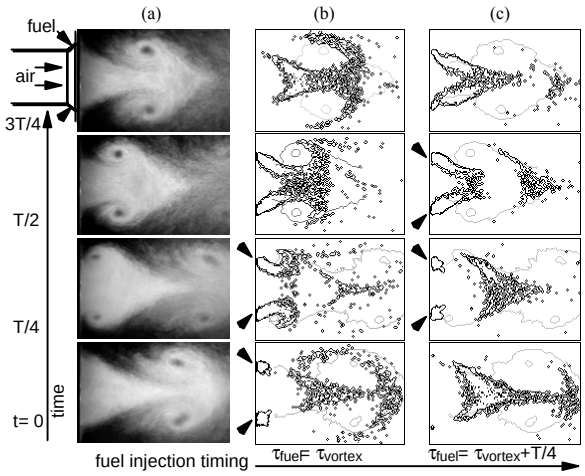


Fig. 3 Fuel dispersion control using timing-dependent vortex-droplet interaction. (a) Underlying flow structure, (b) vortex-synchronized fuel injection, and (c) injection after the vortex shedding

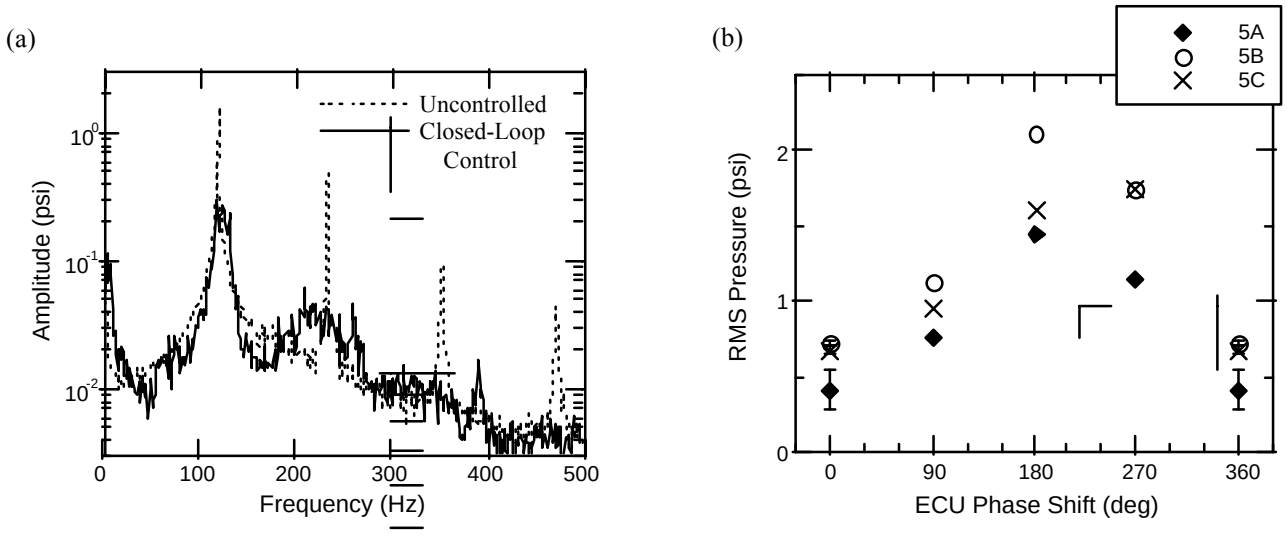


Figure 4. Effect of closed-loop control on pressure oscillation amplitude. (a) Combustor pressure spectra for Case 5A, and (b) pressure oscillation amplitude .vs. relative phase angle.

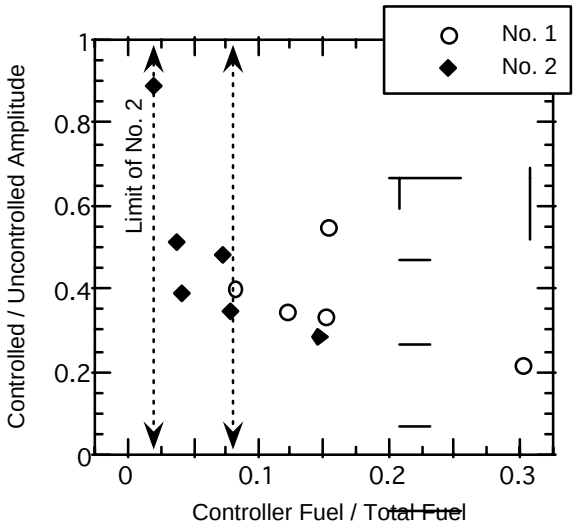


Figure 5. Critical fuel flux for active instability suppression using each actuator system.

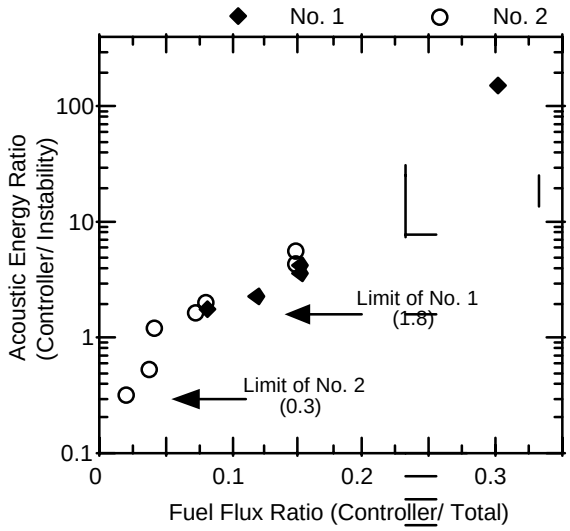


Fig. 6 Comparison of normalized acoustic energy provided by the two actuators.

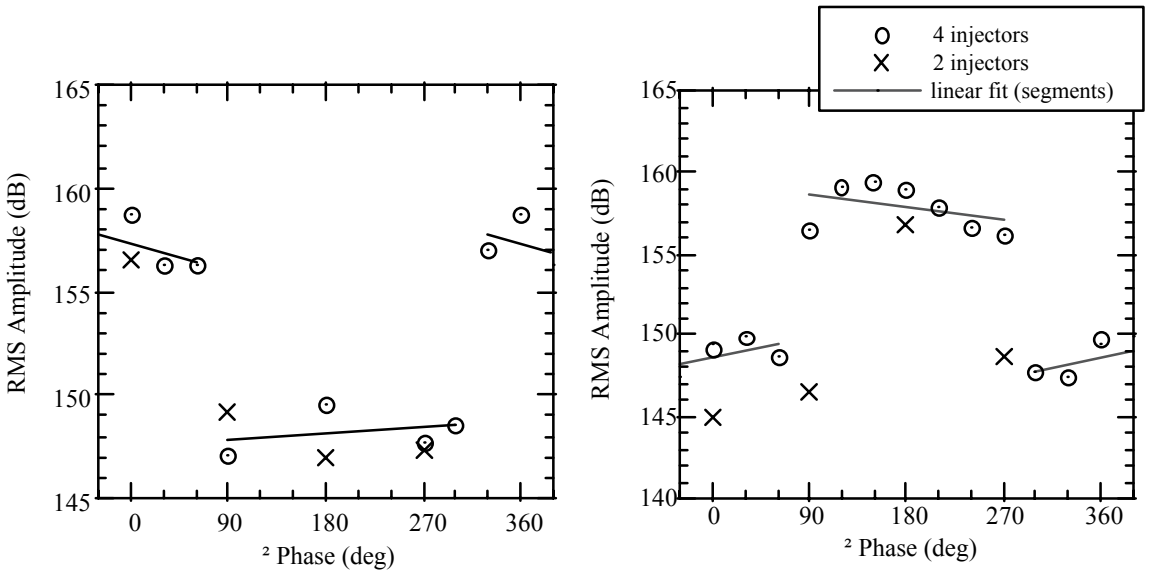


Figure 7. Amplitude of actively suppressed pressure oscillations as a function of controller electronic phase-delay. The plots show the performance of (a) baseline controller using actuation at the instability frequency, and (b) the new controller using actuation at the first sub-harmonic frequency of the instability.

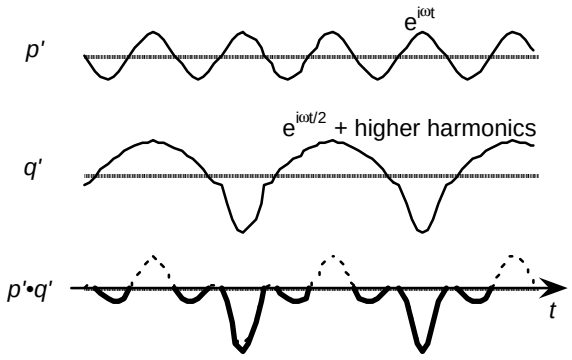


Figure 8. Illustration of acoustic energy reduction even when the actuation frequency is a sub-harmonic of the instability p'.

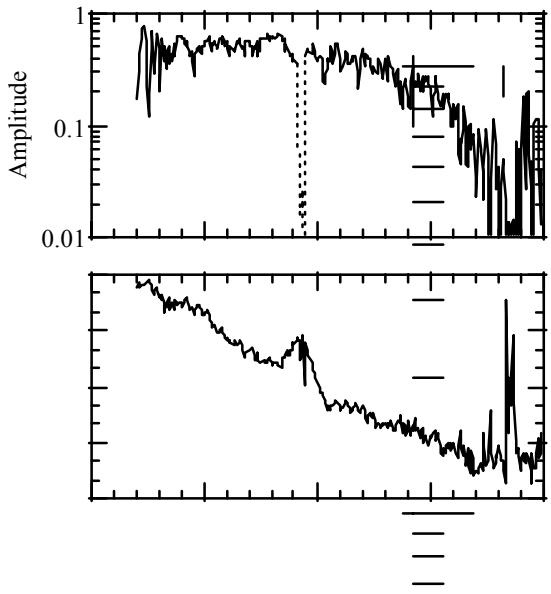


Fig. 9 Transfer function of the pacemaker in the absence of the controller. (a) Amplitude, and (b) phase with respect to the pacemaker frequency.

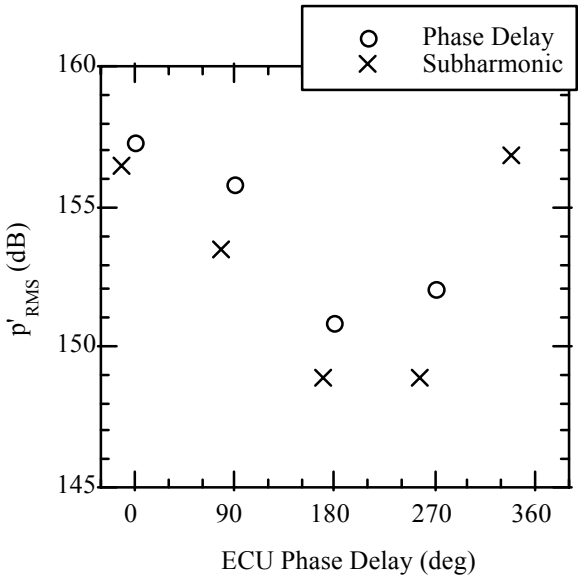


Fig. 10 Demonstration of Pacemaker-Controller in suppressing the instability amplitude.

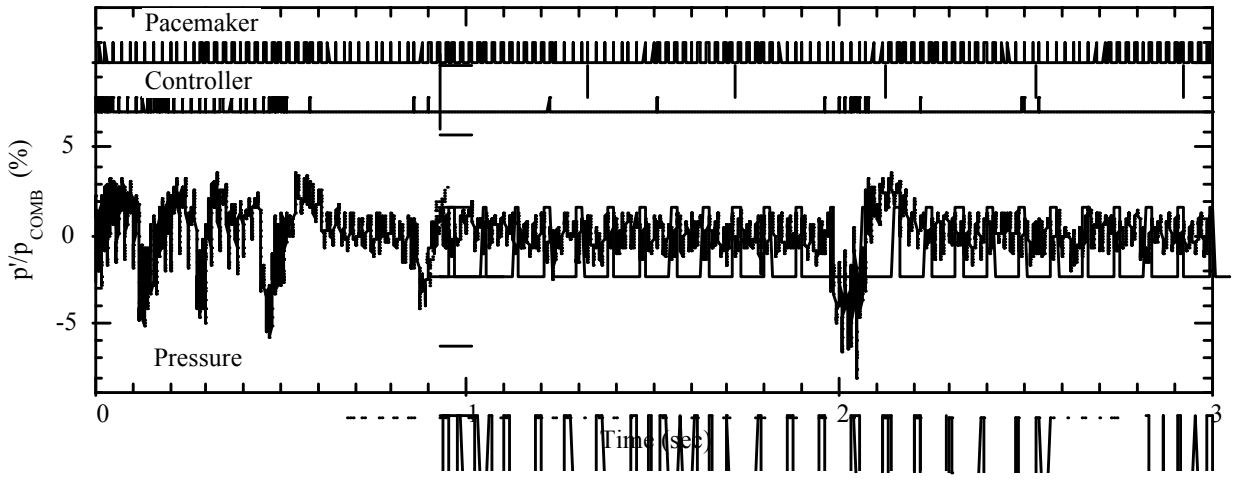


Fig. 11 Instability suppression using a novel Pacemaker-Controller, based on time-delay proportional control design.

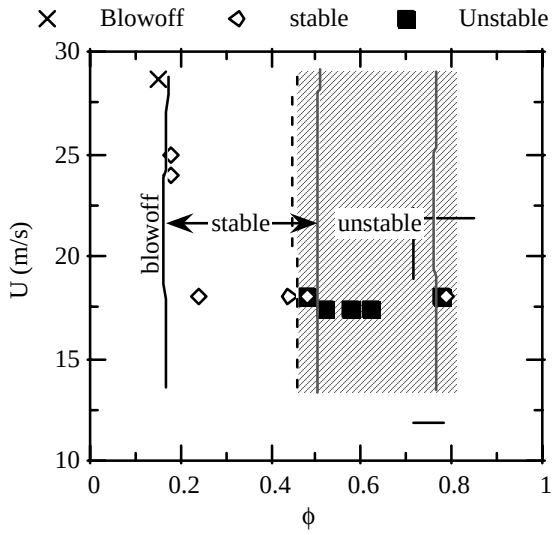


Fig. 12 Flammability map showing the extension of stable combustion limit when a pacemaker-controller was applied.

PAPER -36, K. Yu

Question (F. E. C. Culick, USA)

Towards the end of your paper (Fig 11), you showed that while under control, your system exhibited intermittent instability. Why?

Reply

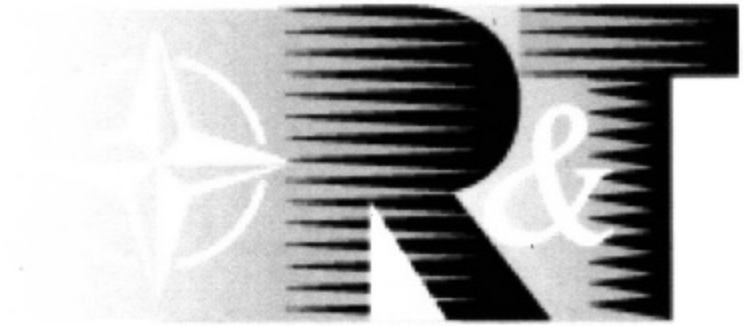
For demonstration of the "Pacemaker-Controller" concept, we chose an operating condition at which the combustor exhibited two states of dynamic behavior – one with low-amplitude oscillations at less than 1% RMS amplitude, and the other with a much greater amplitude. While this condition was similar to the "hysteresis" behavior that Culick described a few years ago, the state of low-amplitude oscillations was only temporary in our case. As a result, the system, if left uncontrolled, would eventually return to high-amplitude oscillations in time. Our approach of control was to intervene with the closed-loop "controller" only during the onset of instability, quickly brining the oscillations amplitude under control. This approach effectively extend the range of stable operating into the marginally unstable regime.

As a side note, the "Pacemaker", on the other hand, was always on. While its main role was to extend the lean blow-out limit at lower equivalence-ratio conditions, the Pacemaker would also contribute at this operating condition by making the instability behavior more predictable.

This page has been deliberately left blank

Page intentionnellement blanche

North Atlantic Treaty Organisation



SYMPOSIUM

on

ACTIVE CONTROL TECHNOLOGY FOR ENHANCED PERFORMANCE OPERATIONAL CAPABILITIES OF MILITARY AIRCRAFT, LAND VEHICLES AND SEA VEHICLES

8 –11 May 2000

in

Braunschweig

PREDICTION OF COMBUSTION-DRIVEN DYNAMIC INSTABILITIY FOR HIGH PERFORMANCE GAS TURBINE COMBUSTORS: PART I

B. SEKAR
Turbine Engine Division
Air Force Research Laboratory
Wright-Patterson AFB, OH

M. A. MAWID & T. W. PARK
Engineering Research & Analysis Company
Wright-Patterson AFB, OH

S. MENON
Department of Aerospace Engineering
Georgia Institute of Technology

OVERALL OBJECTIVES

- Develop a Clear Understanding of the Combustion Instability Driving Mechanisms and their Interactions
- Develop an Appreciation of the Real Impact of Combustion Instability on Combustor Performance, Operability and Life Under High Pressure and Temperature Conditions
- Develop a Design Tool for Actively Controlled Combustors

BACKGROUND

Potential Sources of Instabilities

- Unsteady Compressor Exit Air Flow
- Unsteady Fuel Flow Which Includes:
  - 1-Variations in Fuel Injection Rate
  - 2- Spray Atomization and Formation
  - 3- Spray Droplet Vaporization
- **Finite Rate Chemistry**
- Multiple Shear Layers/Vortex Shedding

BACKGROUND (Cont.)

Consequences of Combustion Instability

- Flame & Heat Release Oscillations
- Amplified Pressure Fluctuations
- Combustion Could Take Place in Turbine
- Distortion of Combustor Exit Temperature
- Severe Variations in Combustor Liner Thermal & Dynamic Stresses

BACKGROUND (Cont.)

Consequences (Cont.)

- **Reduced** Combustor Liner Lifetime and **Durability**
- **Potential** Early Structural Failure
- **Flame** Blow out
- **Higher** Losses

SPECIFIC OBJECTIVES

- **Identify** Existing Analysis Techniques **That Can be** Used As Predictive Design Tools **To Accurately** Capture Instability and Assess **their** Limitation
- **Identify** Existing Data for Analysis Tools **Validation**
- **Improve** on Existing **Analysis Tools for Better** Quantitative Results

EXISTING INSTABILITY ANALYSIS TOOLS

- **One-Dimensional** Linear Stability Tools
- **One-Dimensional** Non-Linear Stability **Tools**
- **Two** & Three-Dimensional Linear **& Non-**Linear Stability Tools **without Heat Release**
- Two & Three-Dimensional **CFD-Based** Tools
- LES-Based Tools (Still in R&D Phase)

One-Dimensional Linear Stability Tools

- Can not Capture Non-Linear Limit Cycle
- Can not Predict Oscillation Magnitude
- Can Provide a Quick Answer of the Frequency of the Pressure Oscillations
- Parametric Studies Can be Easily Conducted

One-Dimensional Non-Linear Stability Tools

- Requires Coupling with an Unsteady Heat Release Model
- Effective in Capturing Non-Linear Limit Cycle Pressure Oscillations
- Can be Used To Develop Active Control Methodologies

2 & 3 Dimensional CFD-Based Tools

- Based on Reynolds Averaged Navier Stokes (RANS) Formulation
- As a Consequence, Models All Turbulent Scales
- Short Simulation Times
- Not a True Unsteady Flow Simulation
- Computationally Affordable
- Can Provide Acceptable Mean Flow Solution and Unsteady Solution If Properly Coupled With the Time-Dependent Boundary Conditions
- Can be Used To Guide Active Control Schemes Development
- Require Highly Non-Dissipative Numerical Algorithms

LES-BASED TOOLS

- Resolve All Length Scales to Cut-Off Size (Grid)
- Compromise between Direct Numerical Simulations (DNS) and RANS
- Potential Engineering Analysis Tool
- Truly Time Accurate Formulation
- Computations Are Still Expensive
- Still Require High Order Numerical Algorithms
- Chemistry Subgrid Modeling is still in the Research & Development Stage

GENERAL APPROACH

- Use Unsteady RANS or LES to Identify Regions of Intensive Heat Release & Pressure Fluctuations in the Combustor
- Use One-Dimensional Non-Linear Based Analysis Tool to Predict Instabilities in the Regions Identified by LES and Suppress Them by an Active Control Methodology and to Guide Further Better Designs

One-Dimensional Non-Linear Combustion Control CFD Model

- To Develop a Methodology to Predict Axial Mode Combustion Instability
- Lumped Element Parameter Approach for Combustor Inlet Mass Flow
- Heat Release is Simulated by Finite Rate Chemistry
- Time Lag Conditions are Input
- Limit Cycle Oscillations can be Obtained
- Fuel Jet could be Pulsated at Different Frequencies through the Boundary Conditions as Primary and Secondary Fuel Modulation given the Amplitude and Phase
- The Final Goal is to Use This Tool for Parametric Evaluation on Combustion Induced Dynamic Instability for Active Combustion Control by Varying the Secondary Fuel Pulsing Frequency, Amplitude and Phase

ONE-DIMENSIONAL NON-LINEAR CFD MODEL

An Existing One-Dimensional Numerical Model (Paxson, D.E., Ref. 19), was Identified as Most Relevant to Our Work and was Selected as A Baseline One-Dimensional Numerical Model.

- The Numerical Model, We Adopted as a Baseline, is Based on the One-Dimensional Euler Equations for :
- Mass Conservation
- Momentum Conservation
- Energy Conservation
- Equation of State

DETAILS OF ONE-DIMENSIONAL MODEL

To Account for Multi Species and Chemical Reactions:

- Species Mass Conservation Equations Were Augmented with the Baseline Numerical Model Along with the Source Terms

To Account for Viscous and Turbulent Diffusion:

- The Diffusion Terms in the Momentum, Energy and Species Conservation Were Retained in the Source Term for System of Equations
- A Constant Turbulent/Laminar Viscosity Ratio Was Used, Based on Numerical Computations with k-ε Model

DETAILS (CONT.)

COMBUSTION/HEAT RELEASE MODEL

As a First Step Towards Rendering the Instability Problem Tractable, the Following Simplifying Assumptions were Made:

- Chemical Reactions are Modeled by a One-Step Global Forward Reaction for JP-8 Fuel as

  $C_{12}H_{24} + 18\ O_2 \Longrightarrow 12\ CO_2 + 12\ H_2O$

- The Combustor Model Numerically Integrated the Governing Equations Using a Predictor-Corrector MacCormack Scheme
- The Integration was Second Order in Space and Time

ASSUMPTIONS (1D MODEL)

- Pressure Oscillations are always Present in the Combustor
- A Time Delay between the Instant of Fuel-Air Mixture Injection and the Onset of Heat Release Exists and is Proportional to the Chemical Time Scale (Premixed Systems)
- The Oscillations in the Heat Release Rate are Created Uniquely by Perturbations in the Fuel-Air Mixture Injection Rate, But After a Time Delay which is Assumed to be Constant in this Study

Large-Eddy Simulations

- Decompose Navier–Stokes Equations into Supergrid and Subgrid terms with spatial filter;

$$\frac{\partial \overline{\rho}}{\partial t} + \frac{\partial \overline{\rho}\widetilde{u}_i}{\partial x_i} = 0$$

$$\frac{\partial \overline{\rho}\widetilde{u}_i}{\partial t} + \frac{\partial}{\partial x_j}[\overline{\rho}\widetilde{u}_i\widetilde{u}_j + \overline{p}\delta_{ij} - \overline{\tau}_{ij} + \tau_{ij}^{sgs}] = 0$$

$$\frac{\partial \overline{\rho}\widetilde{E}}{\partial t} + \frac{\partial}{\partial x_i}[(\overline{\rho}\widetilde{E} + \overline{p})\widetilde{u}_i + \overline{q}_i - \widetilde{u}_j\overline{\tau}_{ji} + H_i^{sgs} + \sigma_{ij}^{sgs}] = 0$$

$$\frac{\partial \bar{\rho}\tilde{Y}_m}{\partial t} + \frac{\partial}{\partial x_i}[\bar{\rho}\tilde{Y}_m\tilde{u}_i - \bar{\rho}\bar{D}_m\frac{\partial \tilde{Y}_m}{\partial x_i} + \Phi_{i,m}^{sgs} + \theta_{i,m}^{sgs}] = \overline{\dot{w}}_m$$

- ^{sgs} terms must be modeled

LES Subgrid Modeling

Resulting Unclosed Subgrid Terms

- Stress Tensor: $\tau_{ij}^{sgs} = \overline{\rho}[\widetilde{u_i u_j} - \tilde{u}_i \tilde{u}_j]$
- Heat Flux: $H_i^{sgs} = \overline{\rho}[\widetilde{E u_i} - \tilde{E}\tilde{u}_i] + [\overline{p u_i} - \overline{p}\tilde{u}_i]$
- Viscous Work: $\sigma_i^{sgs} = [\overline{u_j \tau_{ij}} - \tilde{u}_j \overline{\tau}_{ij}]$
- Species Mass Flux: $\Phi_{i,m}^{sgs} = \overline{\rho}[\widetilde{u_i Y_m} - \tilde{u}_i \tilde{Y}_m]$
- Diffusive Mass Flux: $\theta_{i,m}^{sgs} = \overline{\rho}[\widetilde{V_{i,m} Y_m} - \tilde{V}_{i,m} \tilde{Y}_m]$
- Reaction Rate: $\overline{\dot{w}}_m$

LES Subgrid Modeling (Cont.)

Momentum and Energy Closure

- Subgrid Stress Tensor (τ_{ij}^{sgs}) modeled using local grid size ($\overline{\Delta}$) and subgrid kinetic energy (k^{sgs})

$$\tau_{ij}^{sgs} = -2\overline{\rho}\,\nu_t(\widetilde{S}_{ij} - \frac{1}{3}\widetilde{S}_{kk}\delta_{ij}) + \frac{2}{3}\overline{\rho}k^{sgs}\delta_{ij}$$

- Subgrid Heat Flux (H_i^{sgs}) modeled using conventional gradient–diffusion closure

$$H_i^{sgs} = -\overline{\rho}\frac{\nu_t}{Pr_t}\frac{\partial\widetilde{h}}{\partial x_i}$$

$$\nu_t = C_\nu\sqrt{k^{sgs}}\,\overline{\Delta}$$

LES Subgrid Modeling (Cont.)

Scalar Transport Closure: $\Phi_{i,m}^{sgs} = \bar{\rho}\,\widetilde{u_i'' Y_m''}$

- Conventional Gradient–Diffusion:

$$\Phi_{i,m}^{sgs} = -\bar{\rho}\frac{\nu_t}{Sc_t}\frac{\partial \tilde{Y}_m}{\partial x_i}$$

- Linear–Eddy Model (LEM) Closure:

$$\Phi_{i,m}^{sgs} = \bar{\rho}\,\widetilde{u_i'' Y_m''}\Big|_{\text{LEM}}$$

LES Subgrid Modeling (Cont.)

Linear–Eddy Model

Originally formulated as a mixing model, shown to be capable of accurately predicting small scale mixing phenomena

LEM Subgrid Closure

- Initialize subgrid LEM velocity and species fields at every LES time step
- Evolve both LEM velocity and species fields
- Compute velocity–species correlation
- Ensemble average correlation over LEM domain, $\widetilde{u''Y''_m}$

RESULTS

(ONE-DIMENSIONAL NON-LINEAR CFD MODEL)

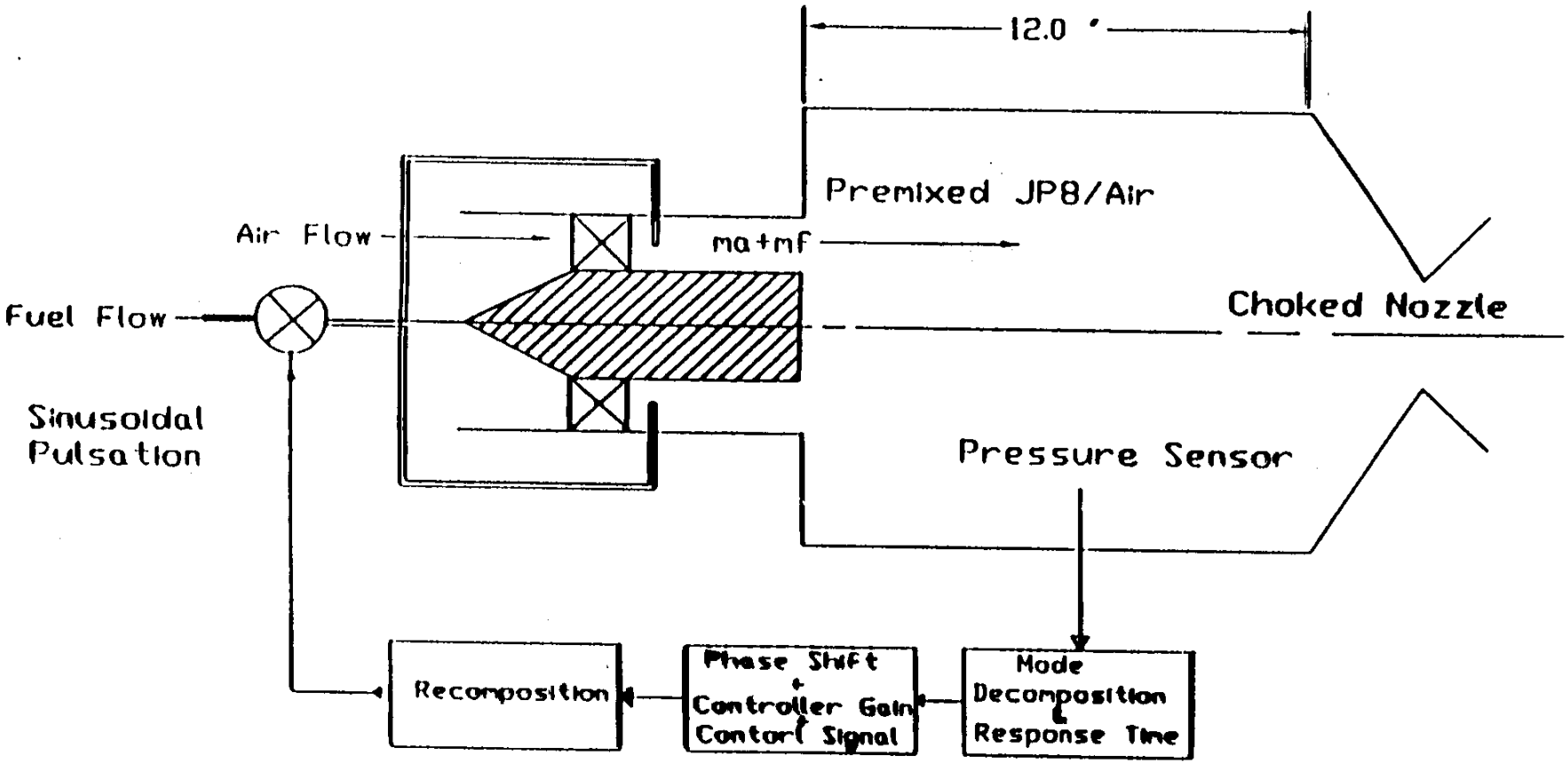
- A Schematic of the Combustor Geometry Along with Boundary & Initial Conditions
- Effect of Time Delay (Lag) Imposed at the Combustor Inlet On the stability of the Combustor
- Combustor's Response to Open-Loop Excitation by Pulsed Fuel Injection for Certain Time Lag Values
- Effect of Fuel Pulsed Frequency on the Combustor Instability
- Effect of the Amount of Fuel Pulsed on the Combustor Instability

RESULTS (CONT.)

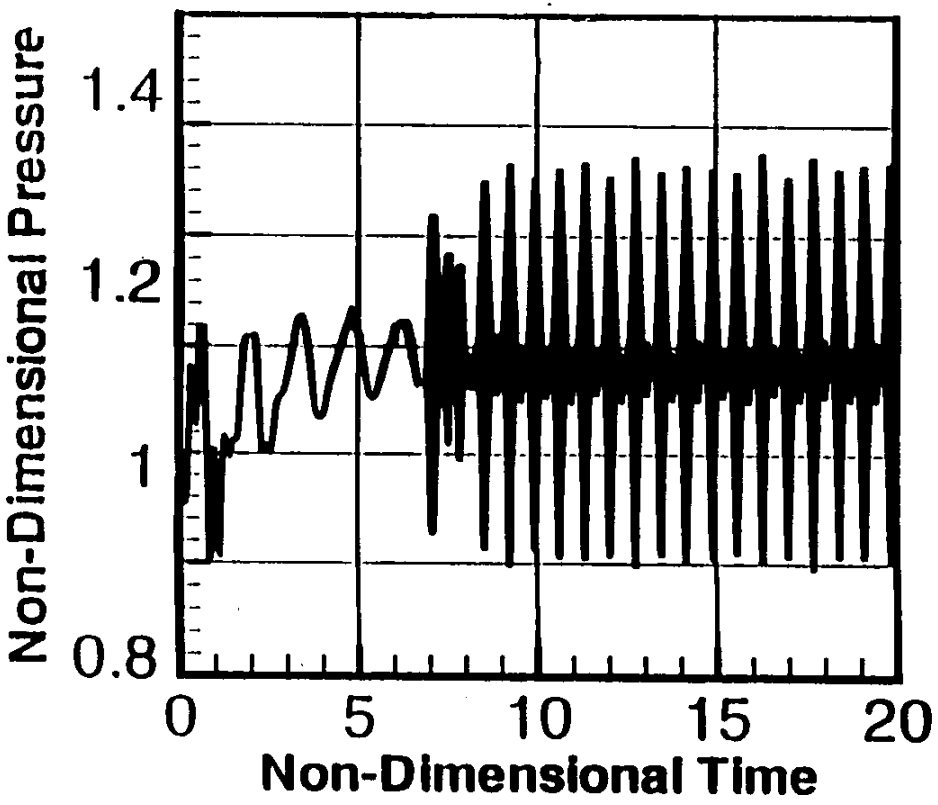
Initial, Boundary Conditions

- Computations were Started from Uniform Initial Fields of Species, Temperature and Velocity and for a Zero Time Lag, $\tau = 0$.
- At the Inlet: Species Mass Fluxes and Temperature were Imposed
- At the Exit: Pressure was Set and Velocity, Species Mass Fractions and Temperature were Extrapolated from Interior

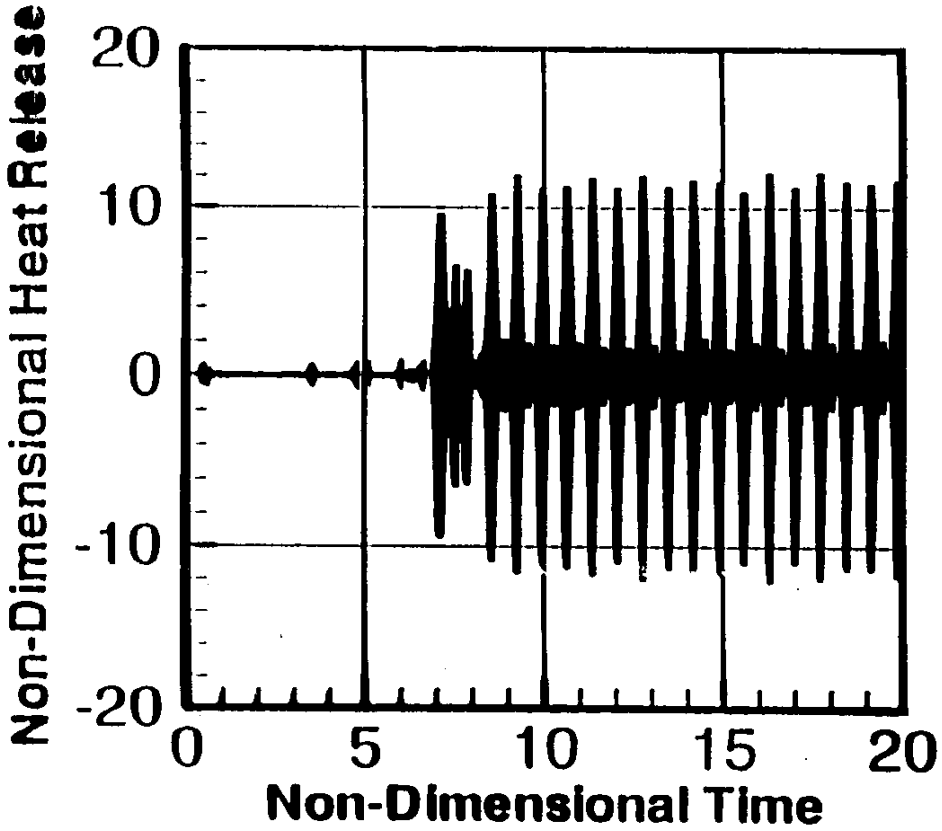
A Schematic of the Combustor and Control System



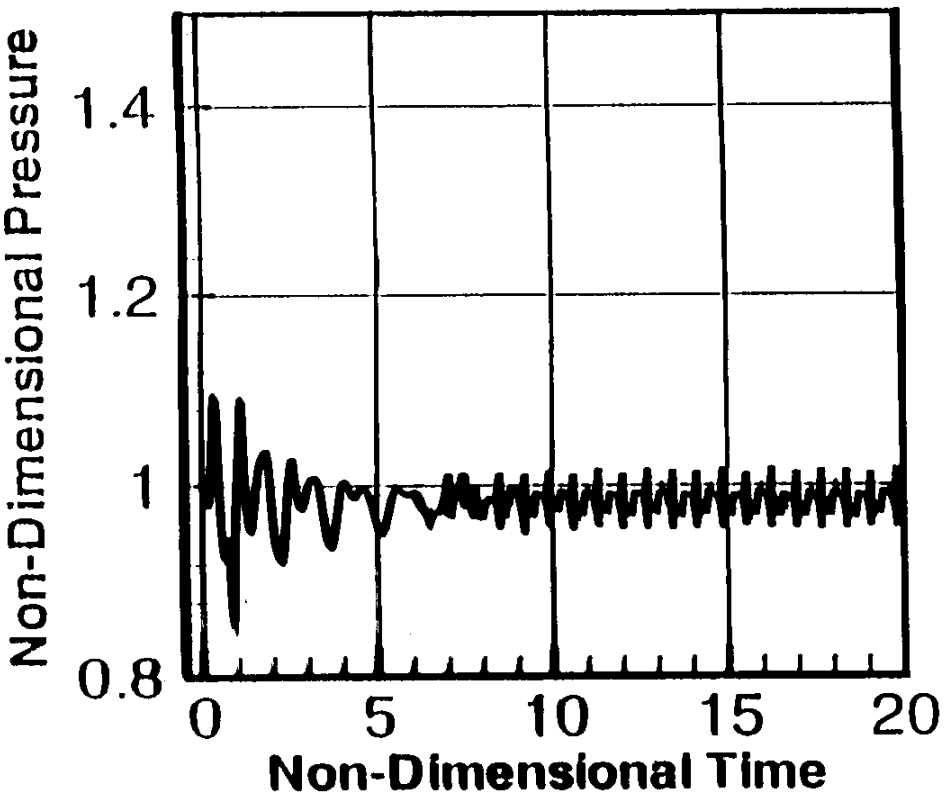
Limit Cycle Pressure Oscillations for a Time Delay $\delta t = 1.97 \times 10^{-3}$ s



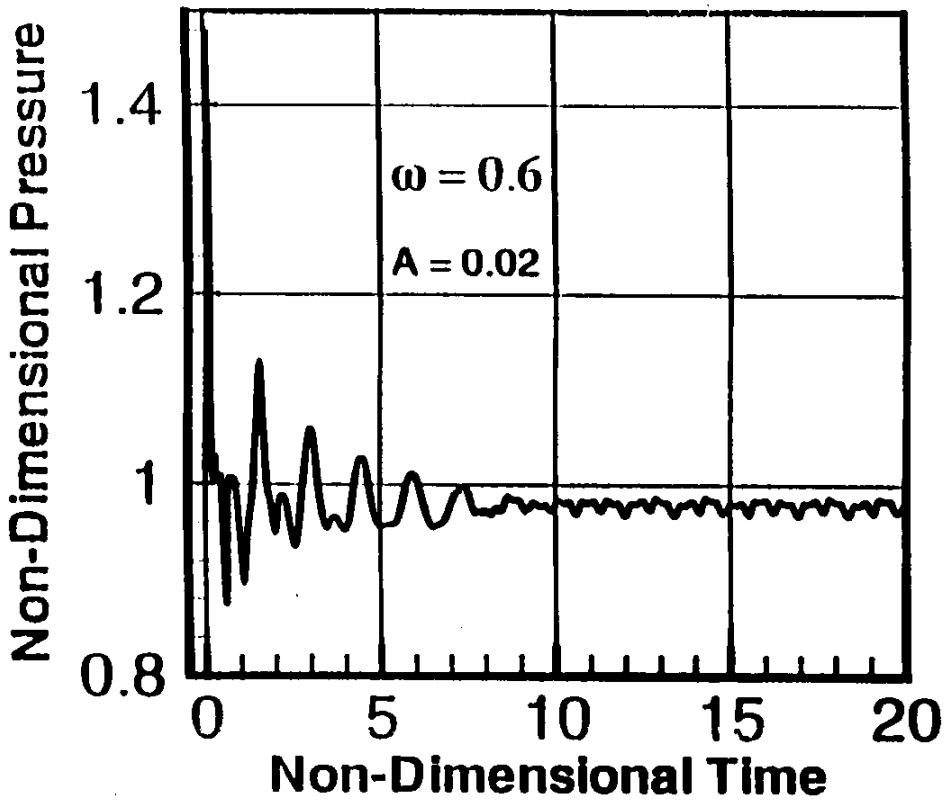
Non-Dimensional Limit Cycle Heat Release Oscillations Corresponding to $\delta t = 1.97 \times 10^{-3}$ s



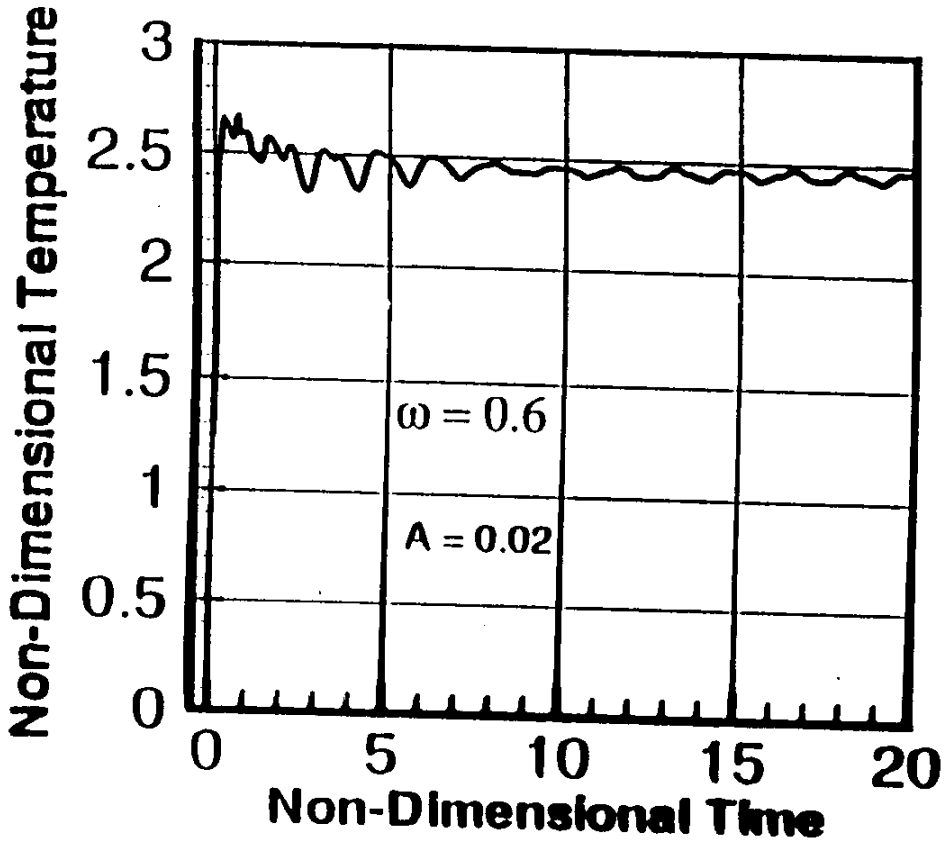
Effect of Time Delay on the Limit Cycle Pressure Oscillations for a Time Delay $\delta t = 1.97x10^{-3} + 1.8x10^{-3}$ s.



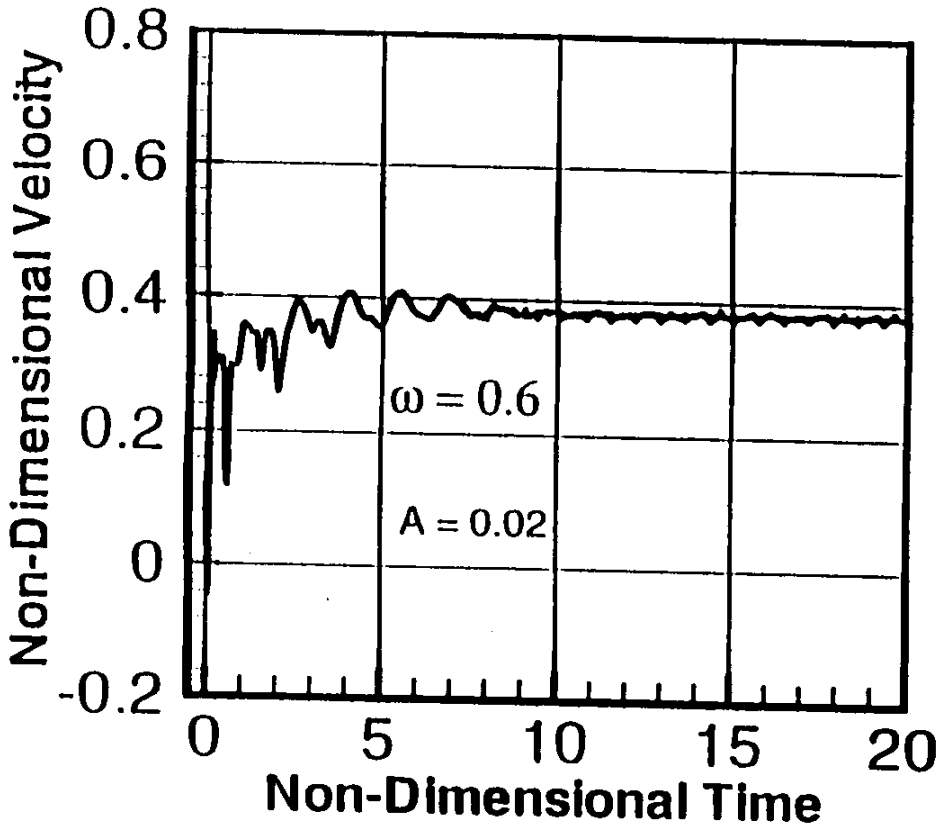
Effect of Fuel Modulation on the Pressure Oscillations for Concurrent Primary and Pulsed Fuel Injection



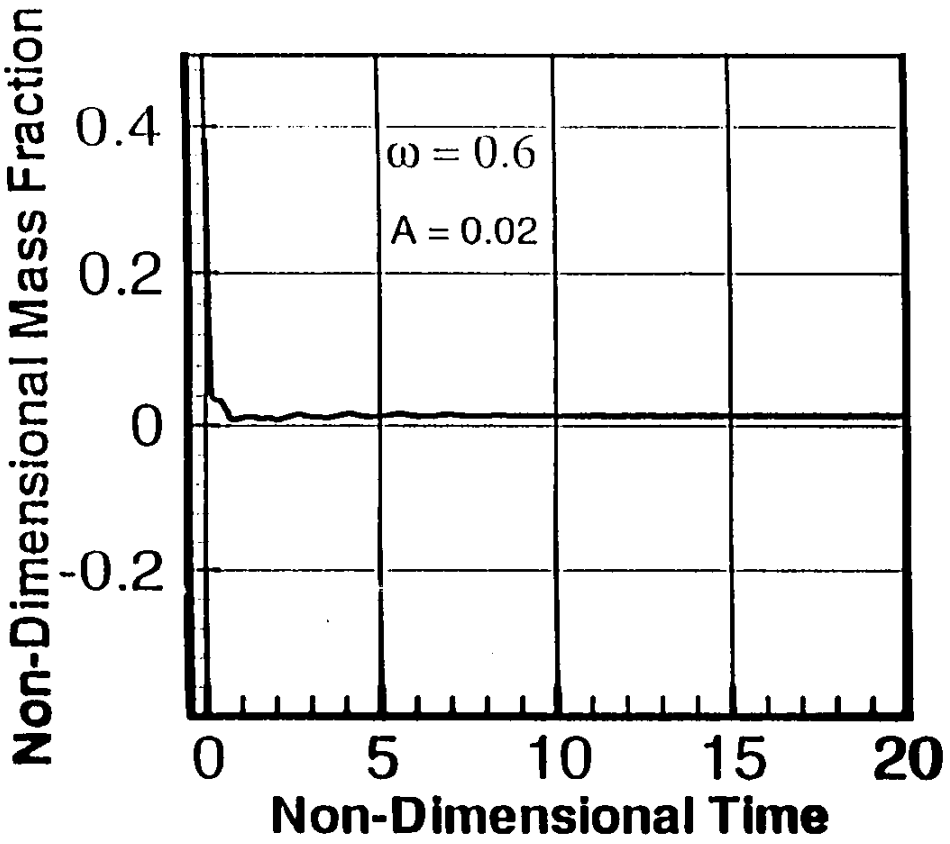
Effect of Fuel Modulation on the Temperature Oscillations for Concurrent Primary and Pulsed Fuel Injection



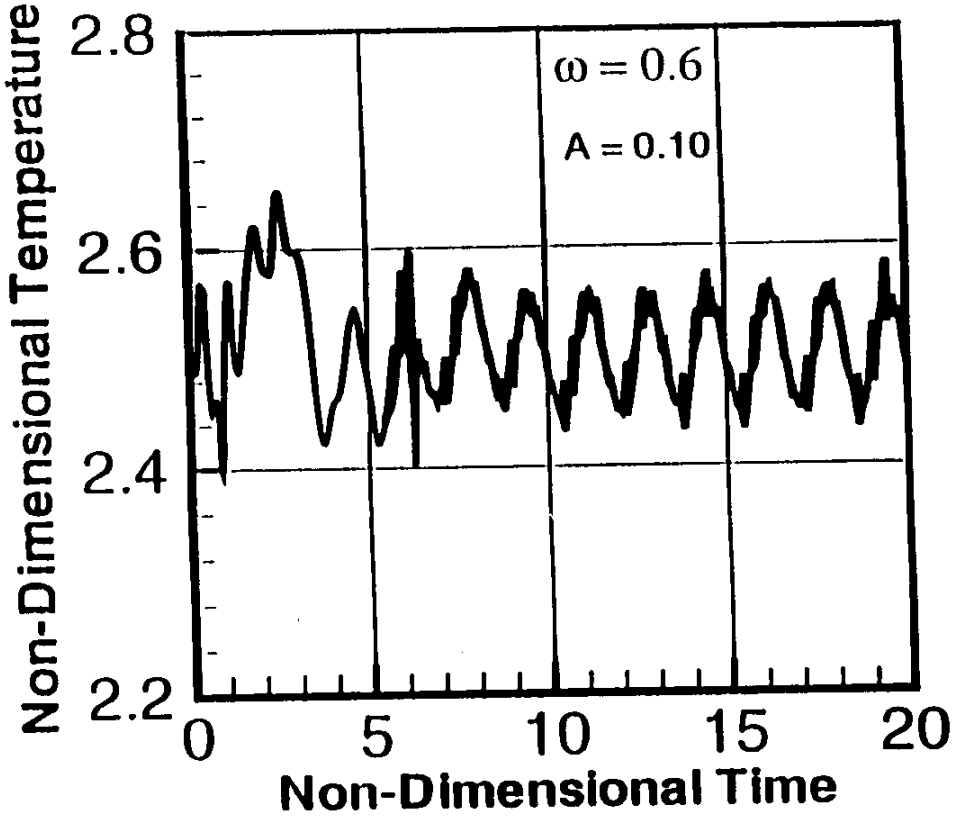
Effect of Fuel Modulation on the Velocity Oscillations for Concurrent Primary and Pulsed Fuel Injection

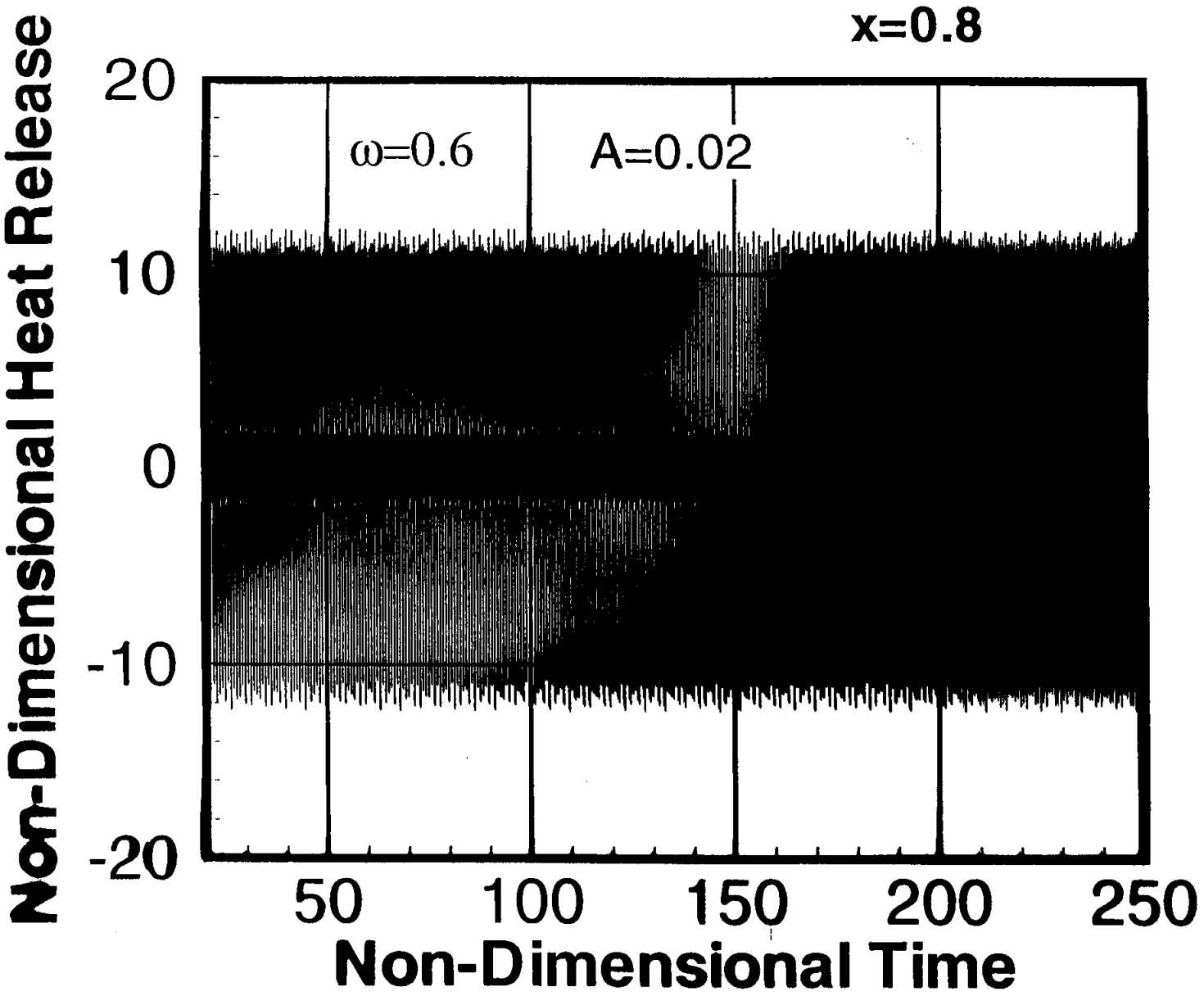


Effect of Fuel Modulation on the Fuel Concentration Oscillations for Concurrent Primary and Pulsed Fuel Injection

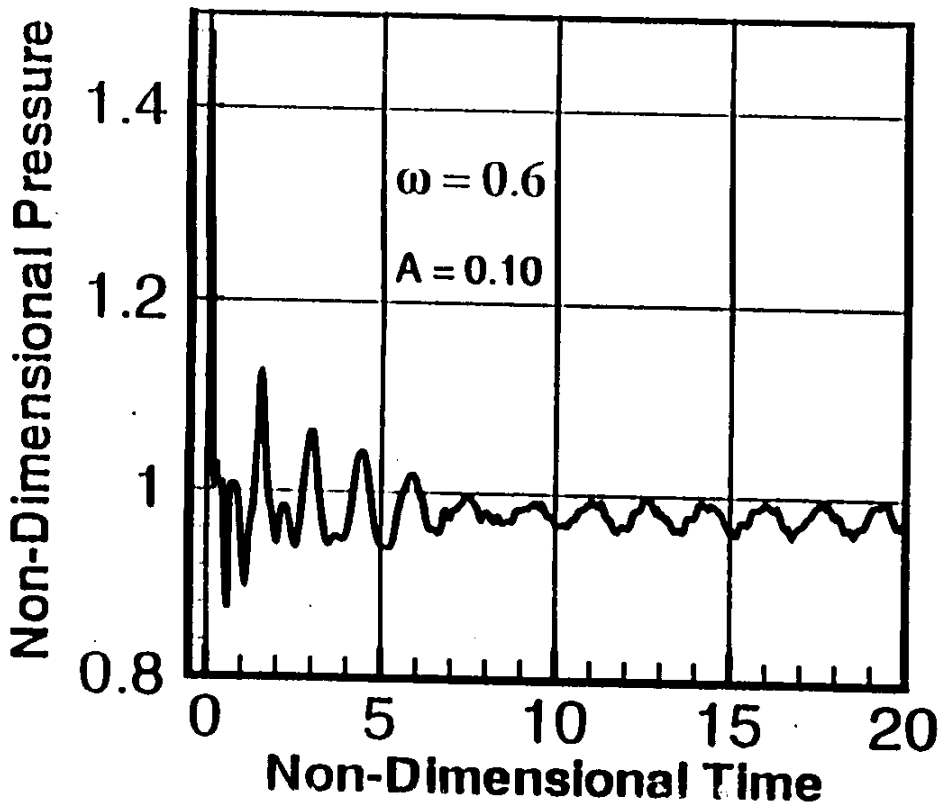


Effect of Fuel Modulation on the Limit Cycle Temperature Oscillations for Non-Concurrent Primary and Pulsed Fuel Injection

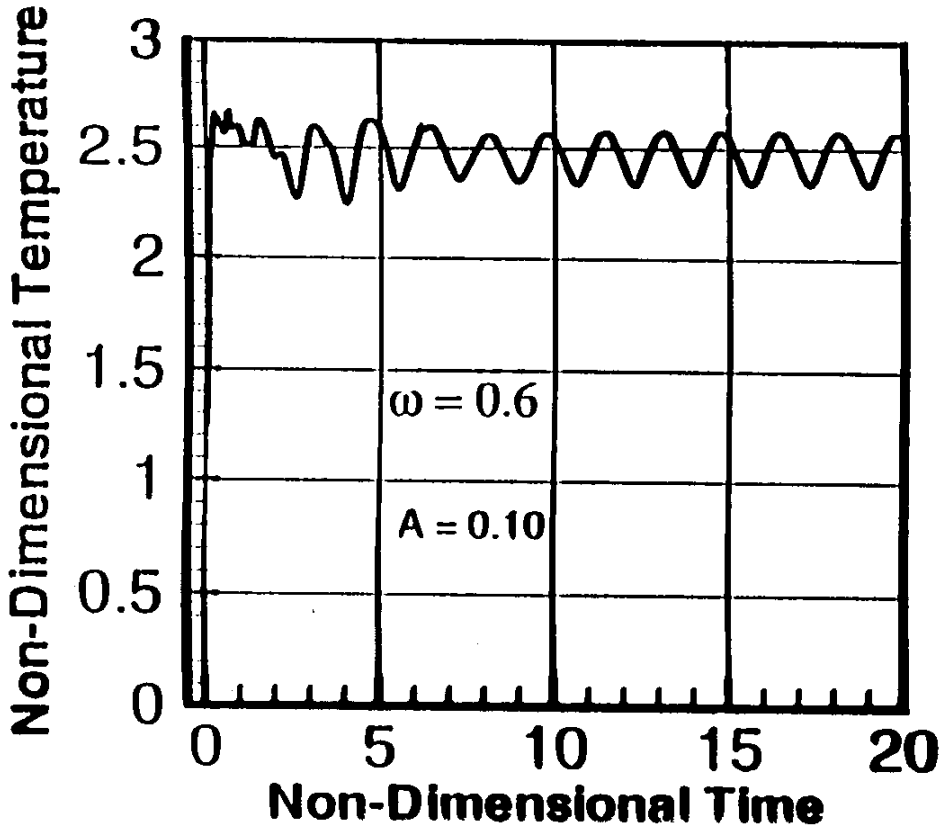



x=0.8
ω=0.6
A=0.02
20
10
0
-10
-20
50
100
150
200
250
Non-Dimensional Heat Release
Non-Dimensional Time

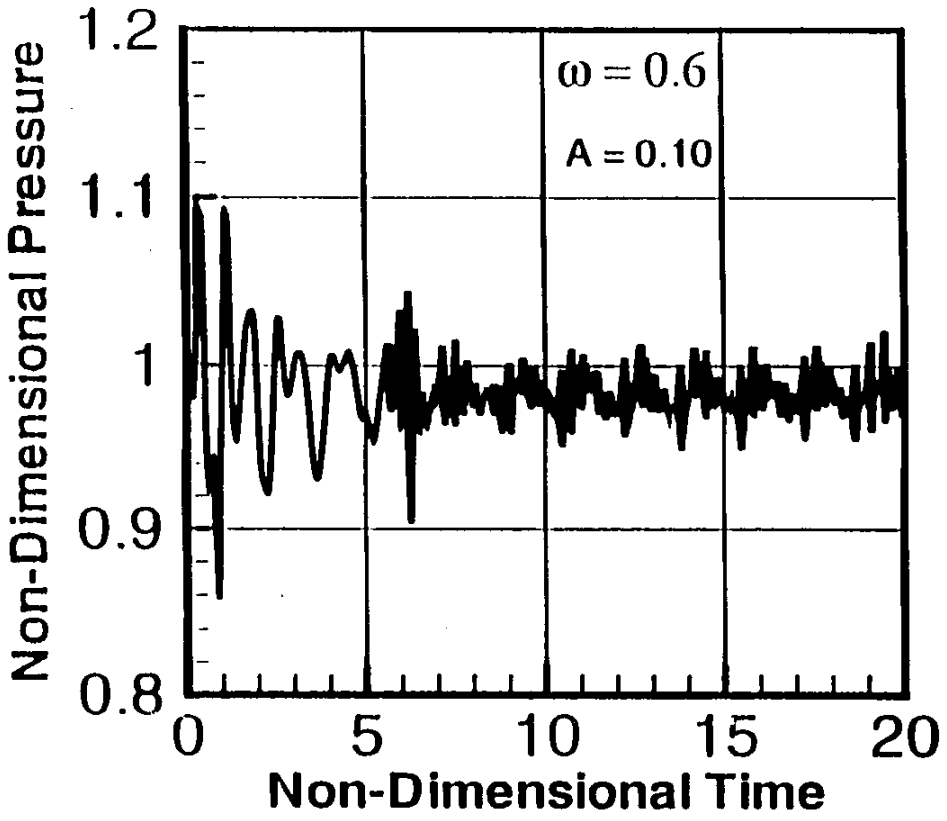
Effect of the Amount of Fuel Modulation on the Pressure Oscillations for Concurrent Primary and Pulsed Fuel Injection



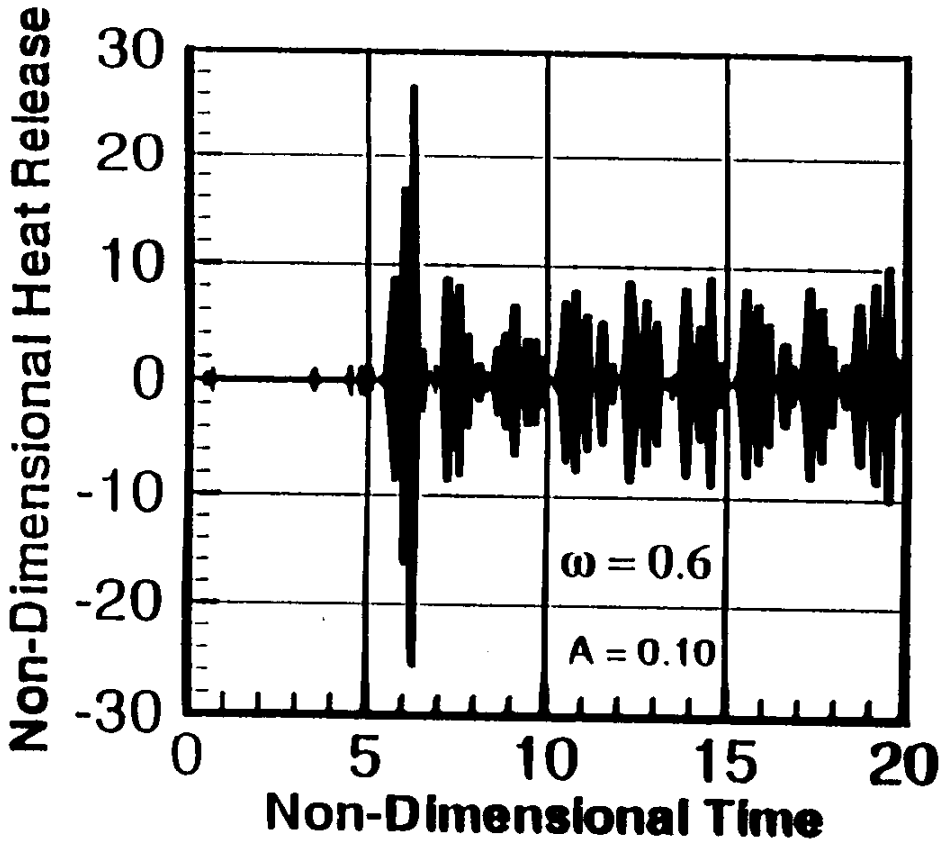
Effect of the Amount of Fuel Modulation on the Temperature Oscillations for Concurrent Primary and Pulsed Fuel Injection



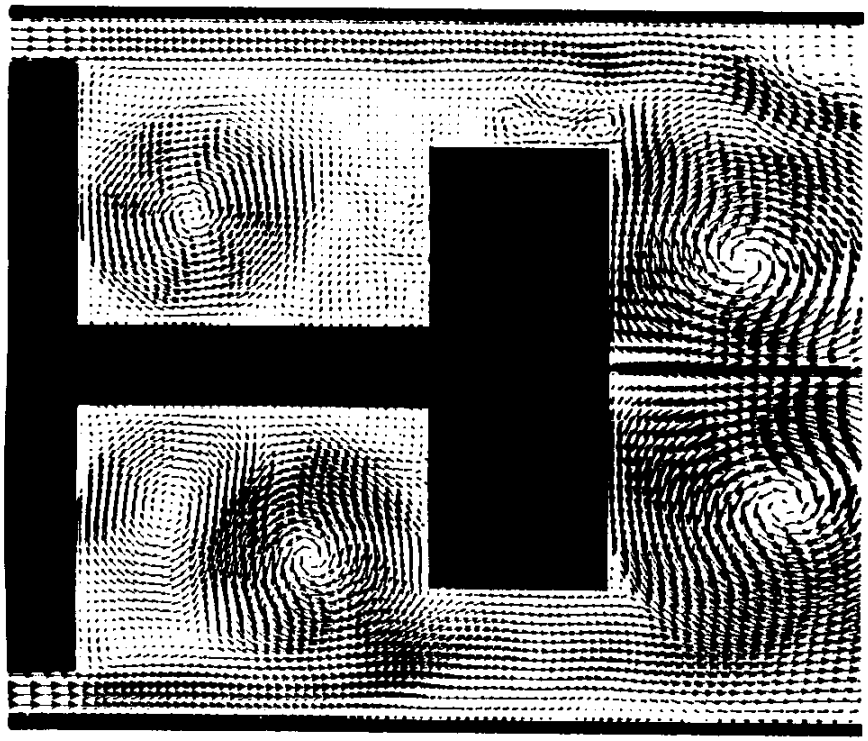
Effect of Fuel Modulation on the Limit Cycle Pressure Oscillations for Non-Concurrent Primary and Pulsed Fuel Injection



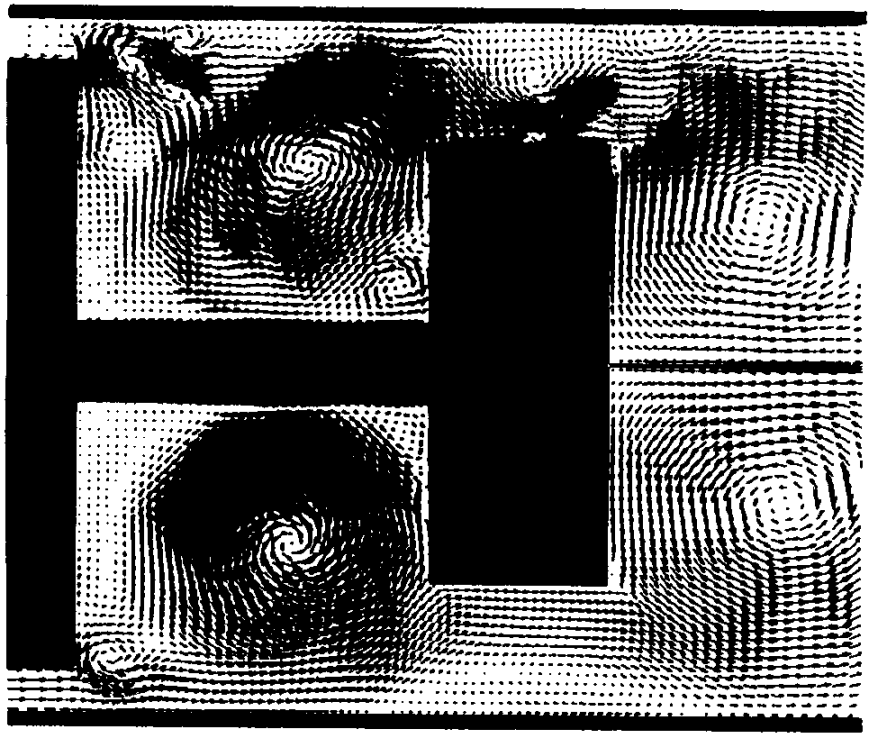
Effect of Fuel Modulation on the Limit Cycle Heat Release Oscillations for Non-Concurrent Primary and Pulsed Fuel Injection



Non–Reacting: Instantaneous and Time Averaged Velocity Vectors



U_O = 20 m/s

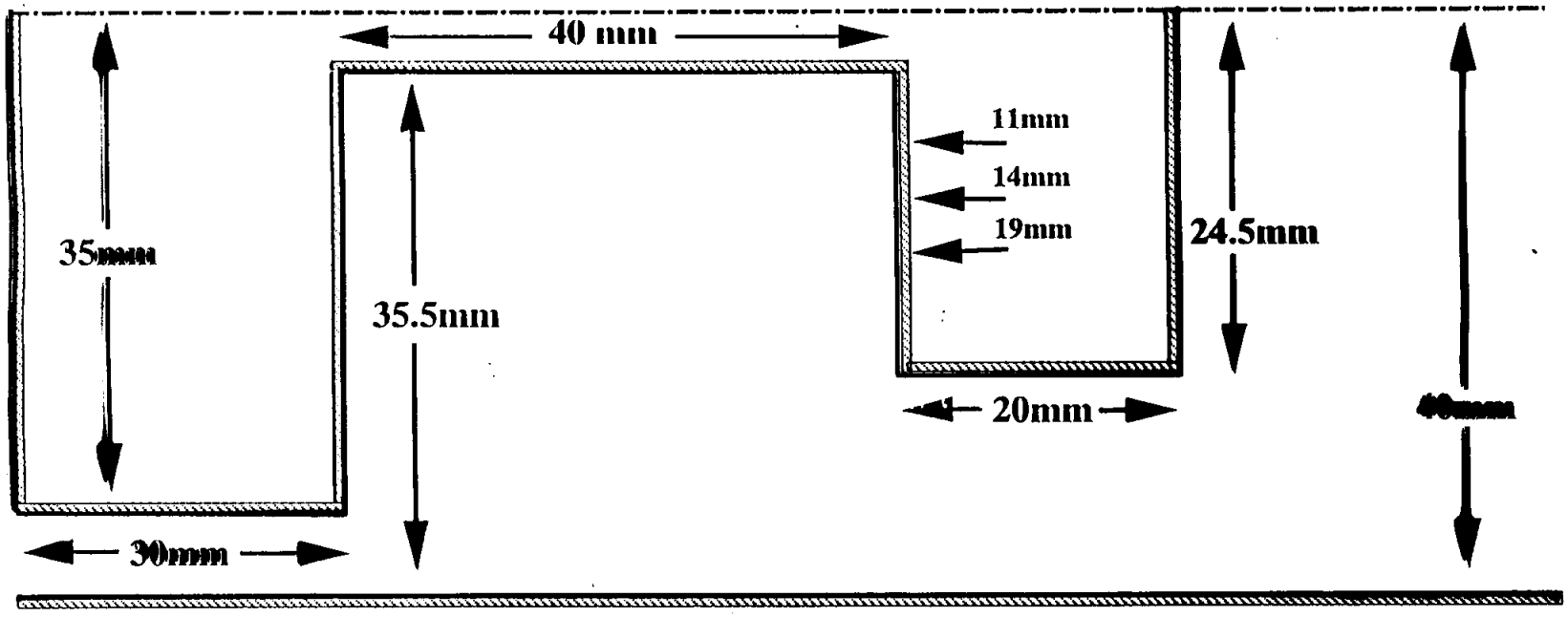


U_O = 40 m/s

- Single, forward rotating vortex completely fills cavity for U_o = 40 m/s
- Vortex strength increases with increased annular velocity

LARGE-EDDY SIMULATION RESULTS

Trapped–Vortex Configuration



— 580 x 138 Grid ($\Delta x \sim 0.25$mm)

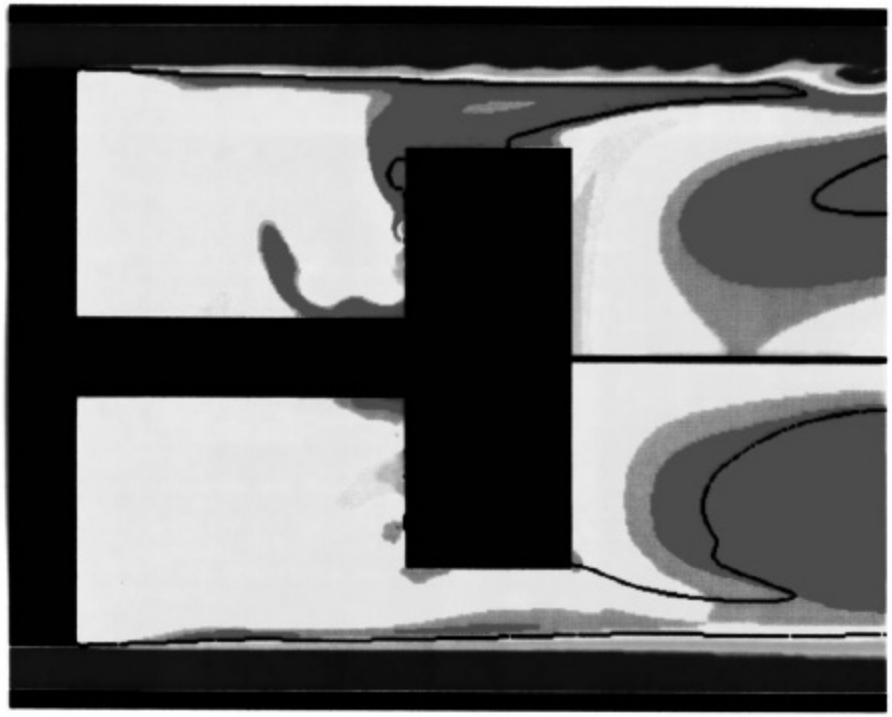
— Inflow Velocity = 20 / 40 m/s

— Total Length = 0.285m

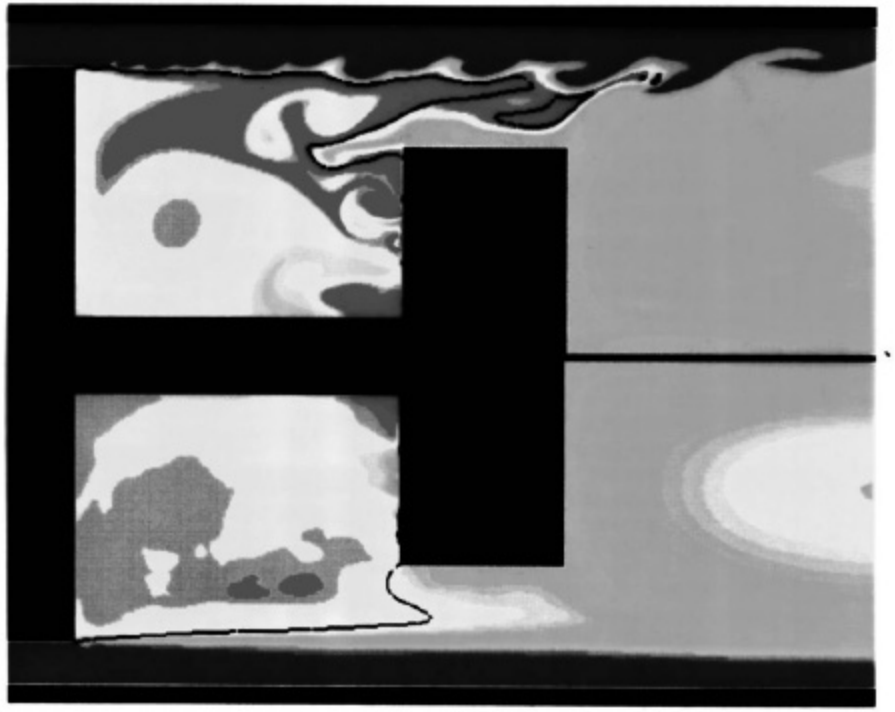
— Inflow Re = 6,250 / 12,500

— Injection Ports Velocities = 12.4 (Air) , 11.5 (Methane) m/s

Reacting: Instantaneous and Time–Averaged Temperature Contours and Stoichiometic Mixture Fraction Surface



U_o = 20 m/s

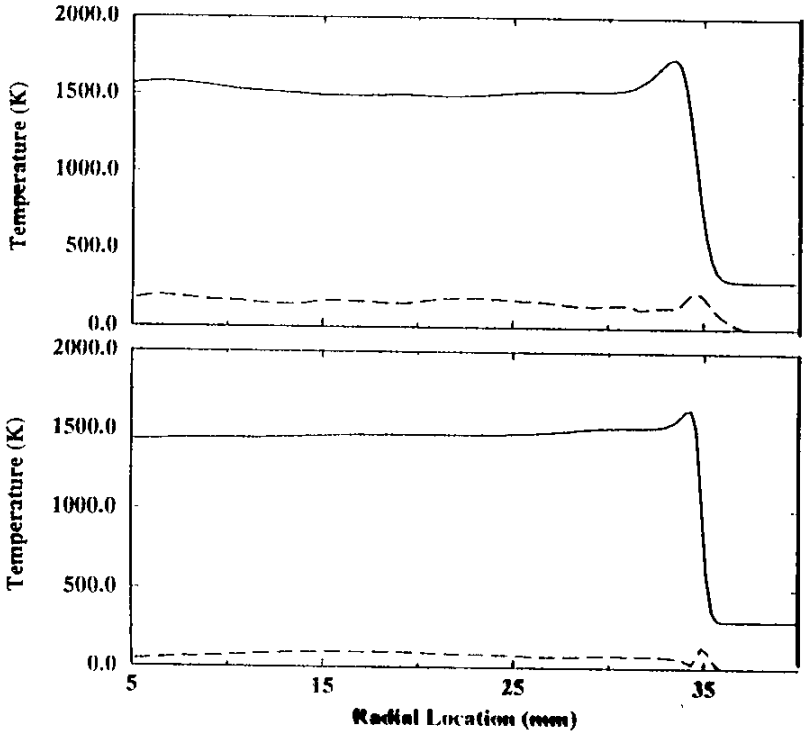


U_o = 40 m/s

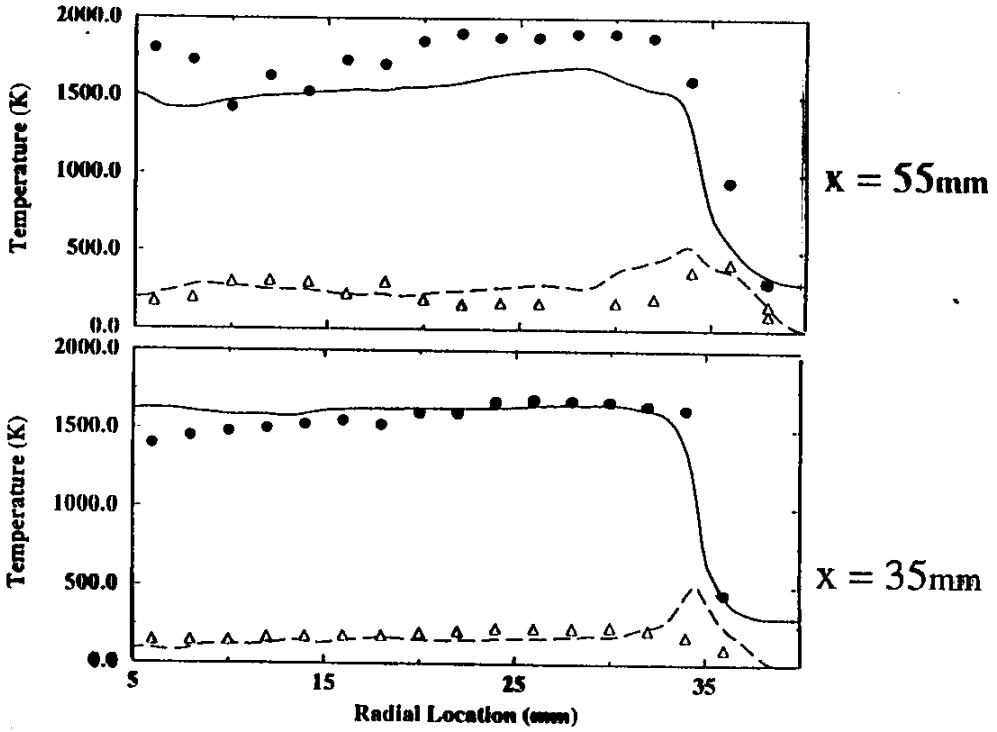
- U_o = 20 m/s: Lower cavity temperature
  Higher downstream temperatures
  Downstream reactions
- U_o = 40 m/s: Reaction contained inside cavity

Reacting: Time–Averaged and RMS Temperature Profiles

——:T ----: T^{rms} ●: T_{exp} Δ: T_{exp}^{rms} (Hsu *et al.*)



U_O = 20 m/s

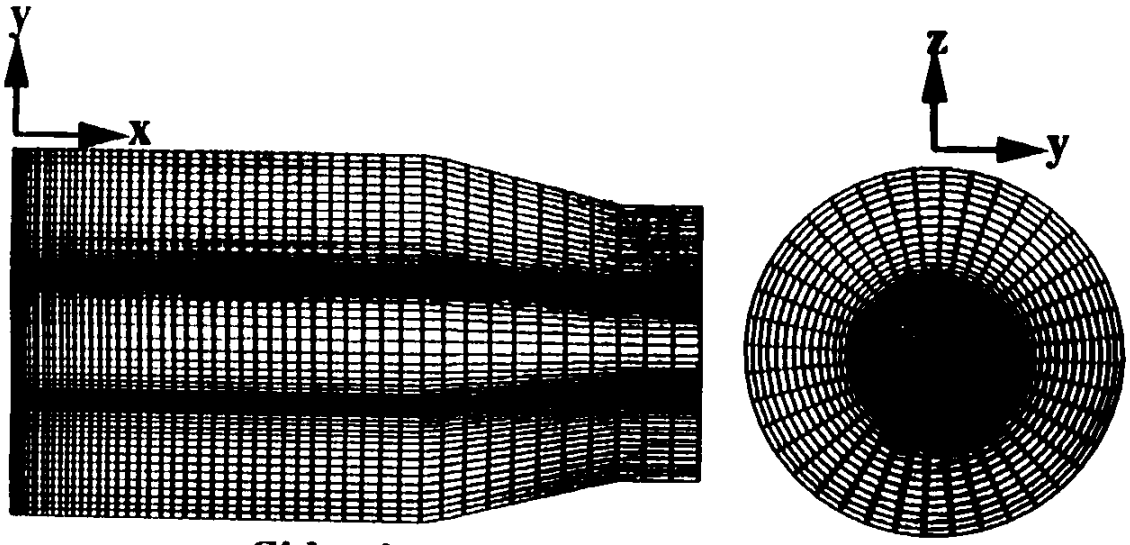


U_O = 40 m/s

- U_o = 20 m/s: Lower cavity temperatures, lower oxygen content
- U_o = 40 m/s:Temperatures under–predicted near injection, reasonable near wall

Numerical Implementation

- Finite–volume code
  (4th in spatial & 2nd in temporal order of accuracy)
- Grid resolution: 101x61x81
- 120 Cray T3E processors used; 2 gigabytes memory
- 700 single processor hours per flow–through time
  (6 hours when 120 processors used)

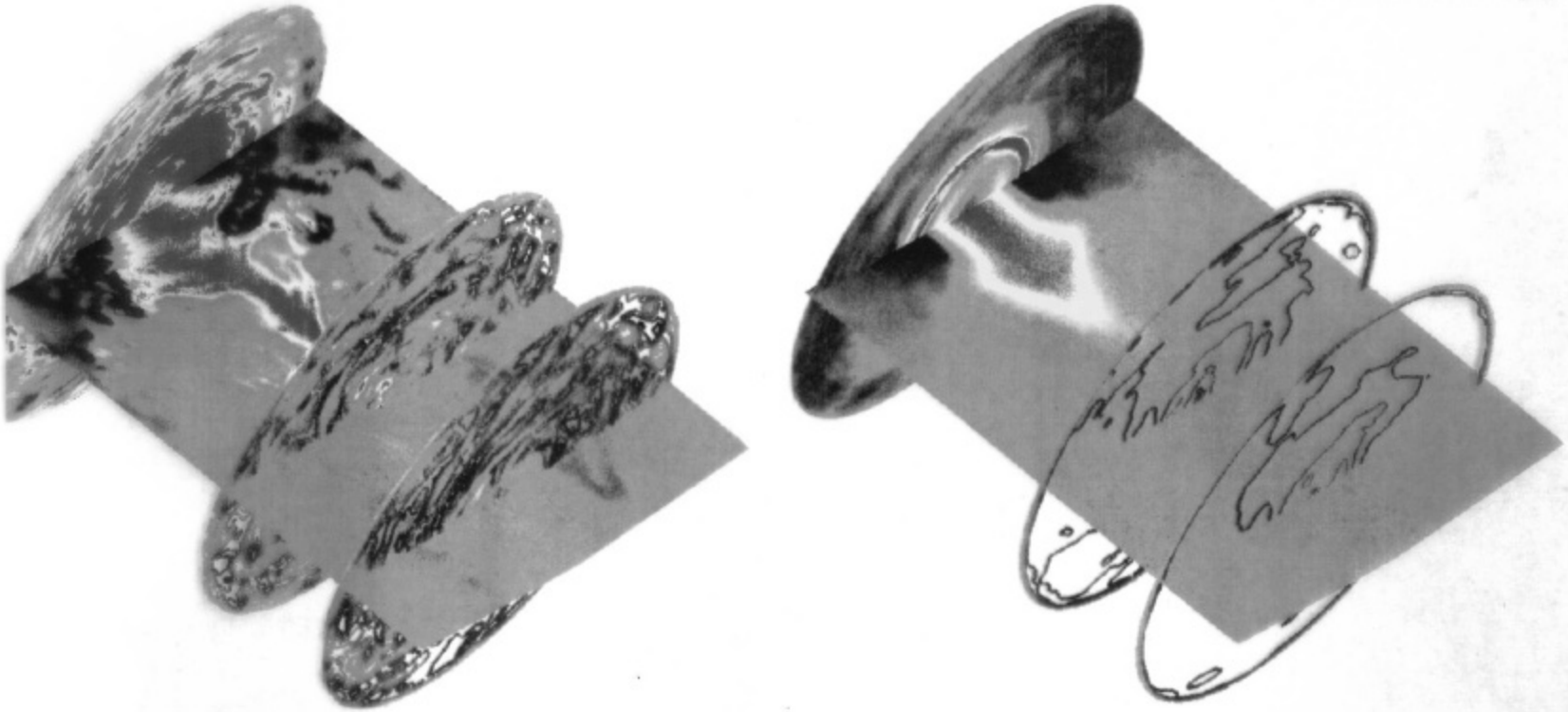


Side view

End view

FUEL-AIR MIXING IN SWIRLING FLOW FULL-SCALE COMBUSTOR

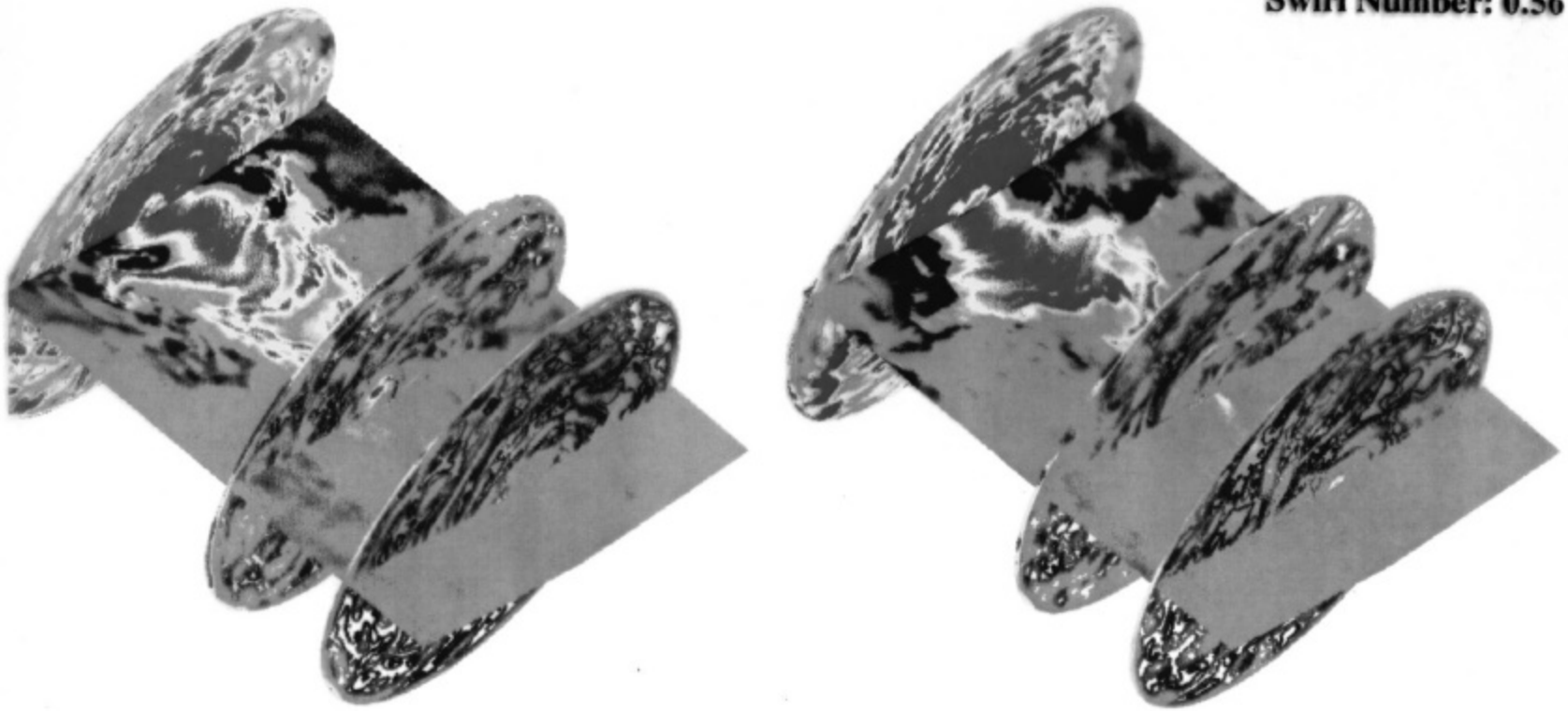
Reynolds Number : 330,000
Swirl Number: 0.56



Instantaneous and Time-averaged views of the vorticity at three axial locations and the fuel species concentration in the spanwise direction. Time averaging results in loss of the finer details of the mixing process

FUEL-AIR MIXING IN SWIRLING FLOW FULL-SCALE COMBUSTOR

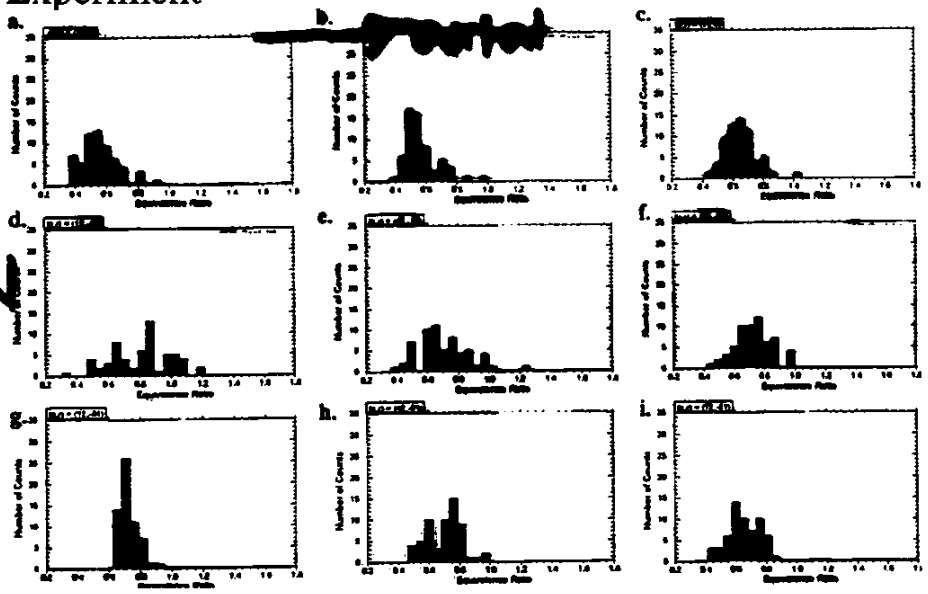
Reynolds Number : 330,000
Swirl Number: 0.56



Instantaneous views of the vorticity at three axial locations and the fuel species concentration in the spanwise direction.

Point Histogram of Local Equivalence Ratio

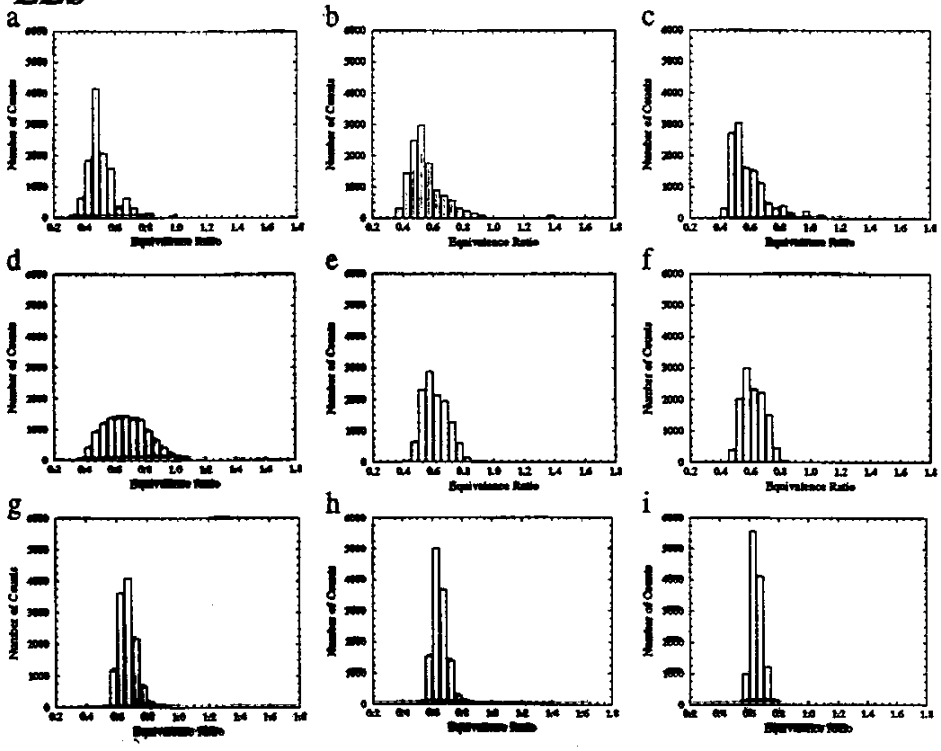
Experiment



radial

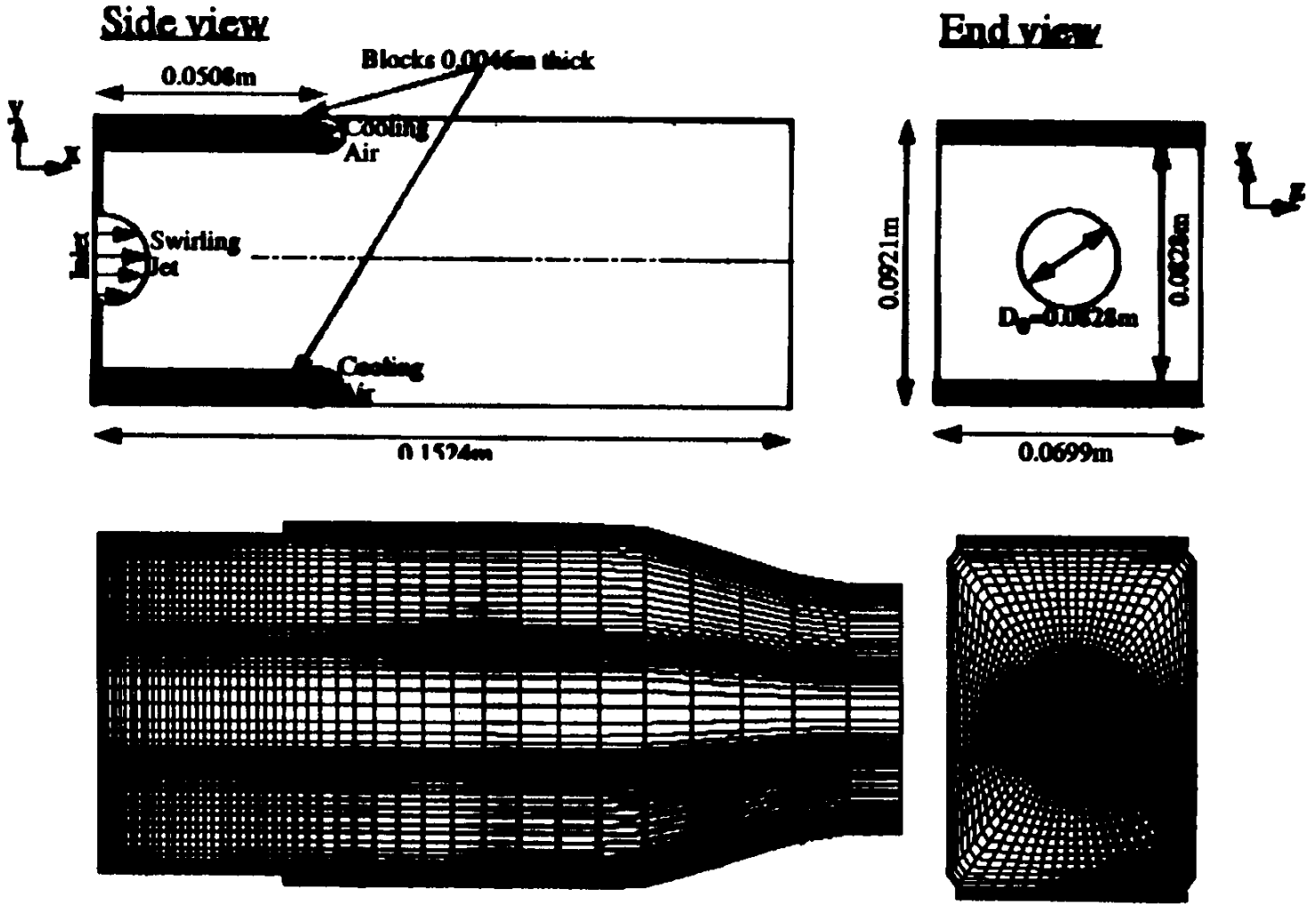
60 samples

LES

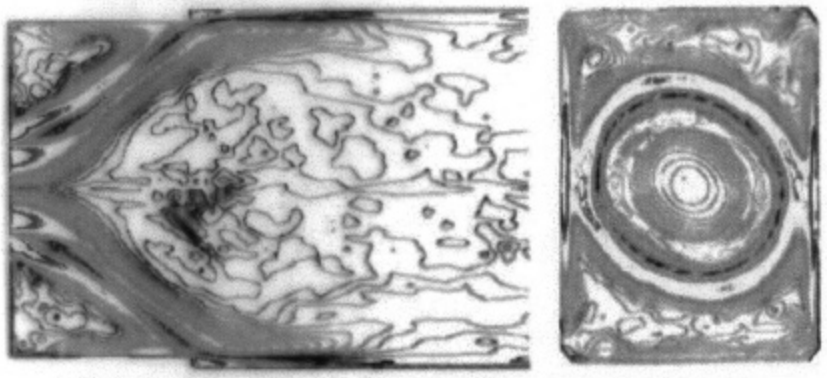


12,000 samples

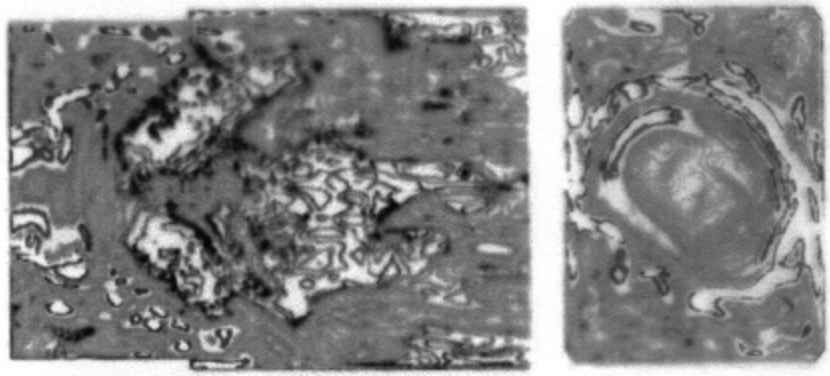
GENERAL ELECTRIC LM6000 (REACTING)
METHANE – AIR



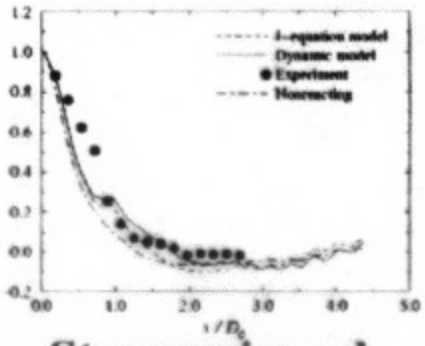
LES of GE LM6000 Gas Turbine Combustor



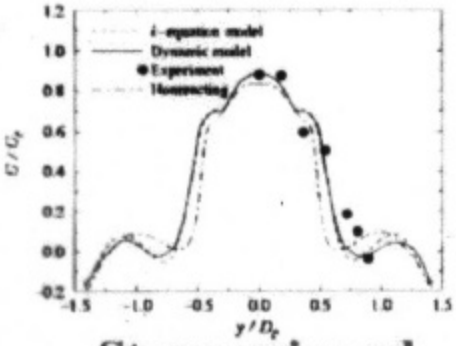
Time-averaged vorticity contours



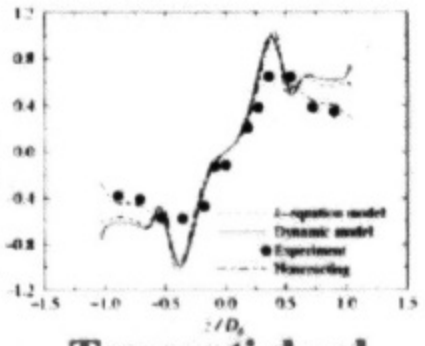
Instantaneous vorticity contours



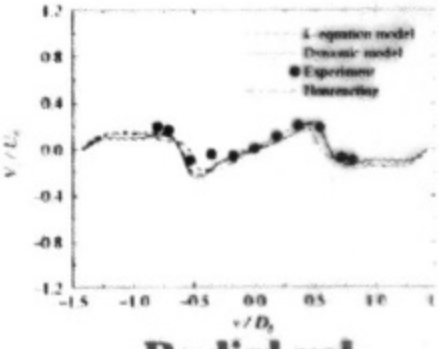
Streamwise vel.



Streamwise vel.

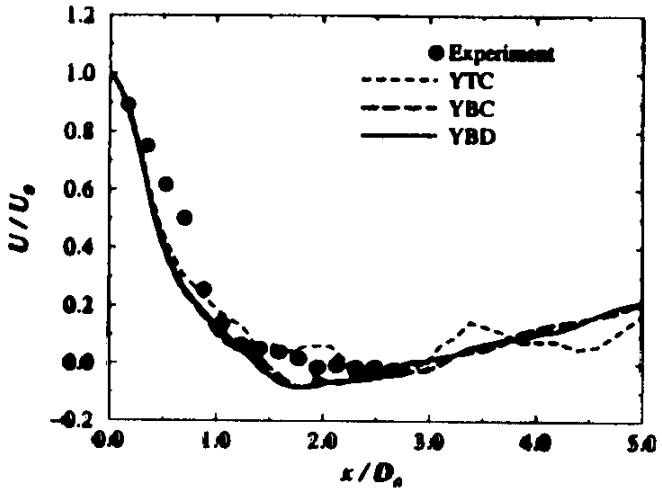


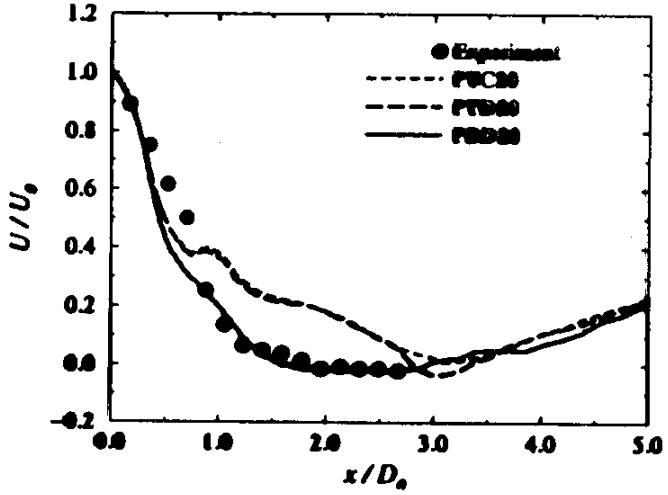
Tangential vel.

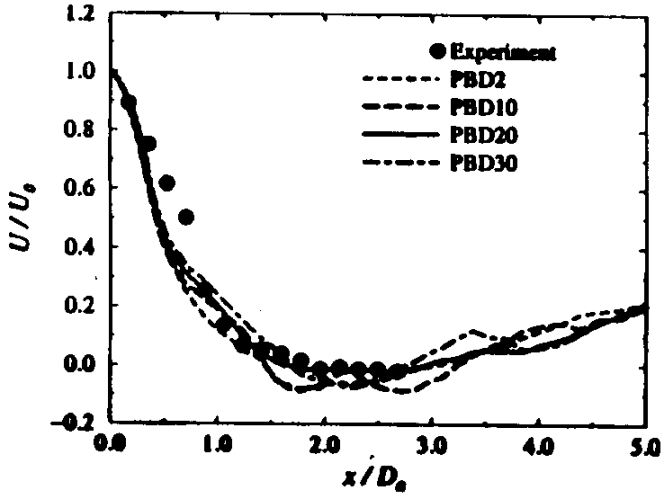


Radial vel.

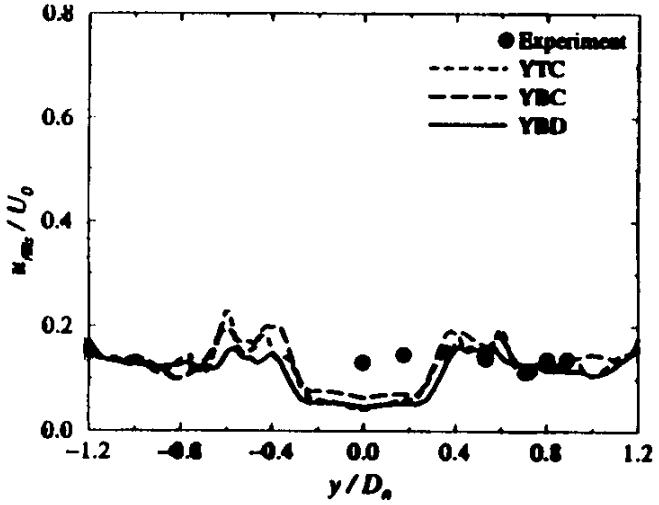
Mean Axial Velocity (along centerline)

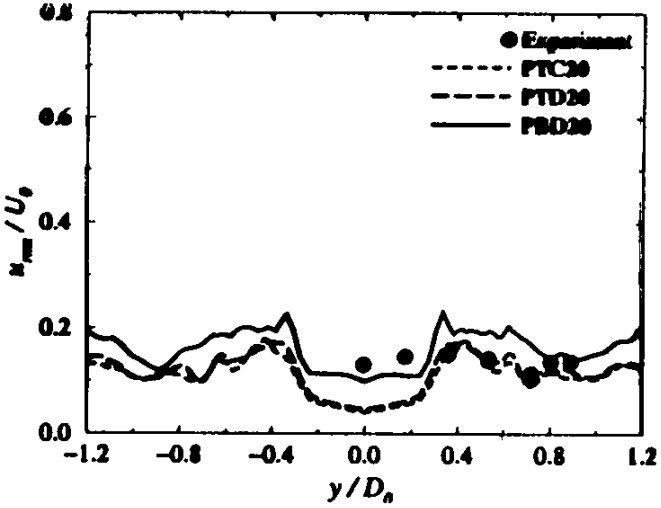


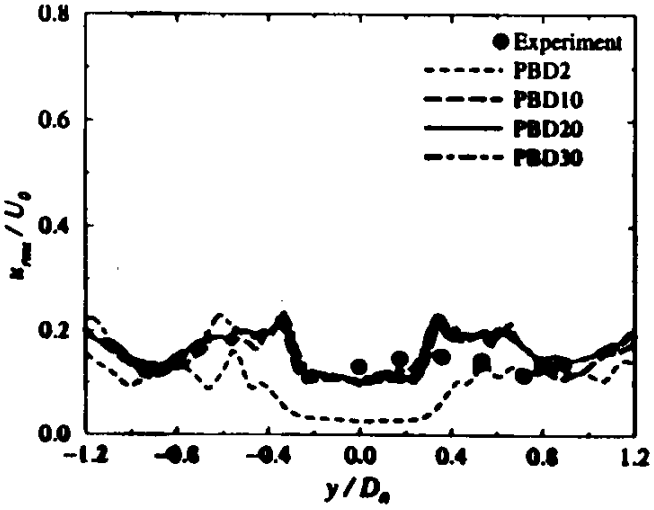




Axial Turbulence Intensity (along y–axis)







@ x/D_0=0.18

CONCLUSION

- A One-Dimensional Unsteady Combustor Model and its Capability was Demonstrated for Studying Fuel Pulsing to Actively Control Gas Turbine Combustors
- Effect of Time Lag of the Fuel-Air Mixture Injection Rate on the Combustor Instability was Predicted and Found to be Qualitatively in Agreement with Time Lag Theory of Crocco
- The Results Indicated that by Increasing or Decreasing the Time Lag Period, the Combustor State of Maximum Oscillations would Shift to Damping

CONCLUSION (CONT.)

- The Results also Demonstrated the Ability of Developed Model to Predict the Combustor's Response to Fuel Flow Modulation
- The Results also Showed that Turning on Fuel Pulsation after the System has Reached its Cycle Limit Oscillations was not as Effective as that of Turning it on at the Start of the Operation
- The Amount of Fuel Pulsed was Found to have very Minimal Effect on the Level of Damping within the range of 2% to 10% of the Primary Fuel Rate

CONCLUSION (CONT.)

- LES Metholodogy Predicts the RMS Fluctuations, Mixing, Local Heat Transfer Values, Pressure Fluctuations and Captures Unsteady Vortex Dynamics and Heat Release to a Greater Accuracy
- With Improvement in Physical Modeling of Subgrid Closure, Machine Hardware, Parallel Processing and Reduced Chemistry Mechanisms, LES Computations could be Used in Analyzing Gas Turbine Combustors to Predict the Unsteady Phenomena

This page has been deliberately left blank

Page intentionnellement blanche

Modeling and Control of Combustion Instability using Fuel Injection

Jean-Pierre Hathout*, Anuradha Annaswamy, and Ahmed Ghoniem

Department of Mechanical Engineering

MIT

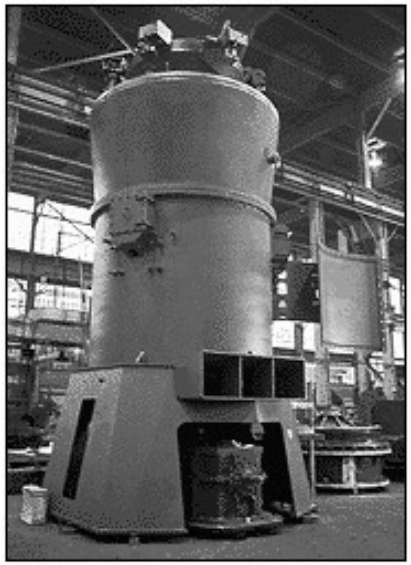


NATO AVT Symposium

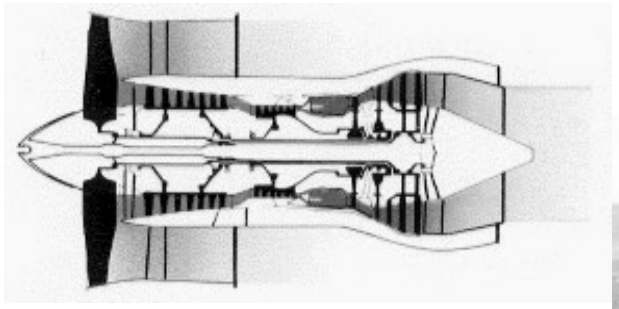
May 8-11, 2000

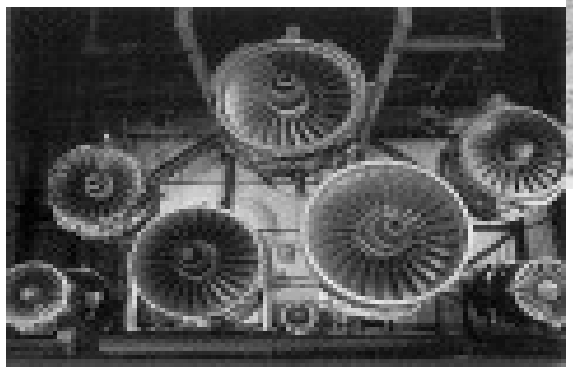
* Dr. Hathout joined the Robert Bosch Corporation Research and Technology Center in Pittsburgh, PA, since July 2000. Email: jean-pierre.hathout@rtc.bosch.com

Continuous Combustion Processes and Thermoacoustic Instability



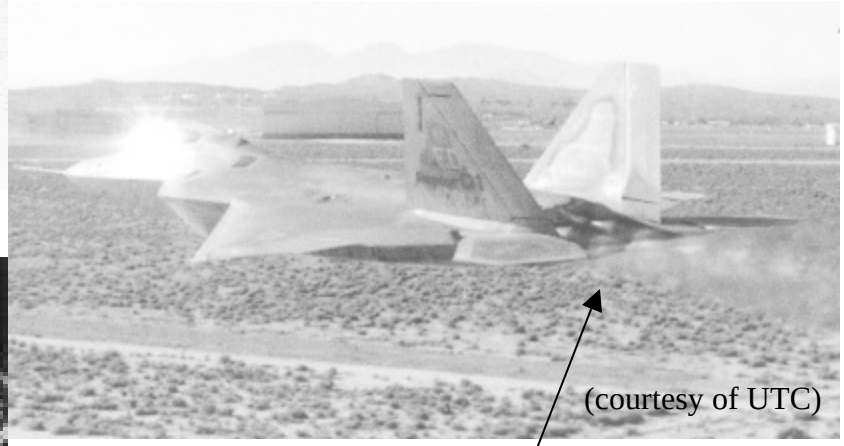
Power Generation
- Boilers
- Burners
- Gas turbines





Propulsion
- Commercial: Environmentally friendly
- Military: high power
- Rockets
- Shuttle main engine

F-22 Raptor



(courtesy of UTC)

Combustion instability in the form of Screech can be seen in the heat-release signature

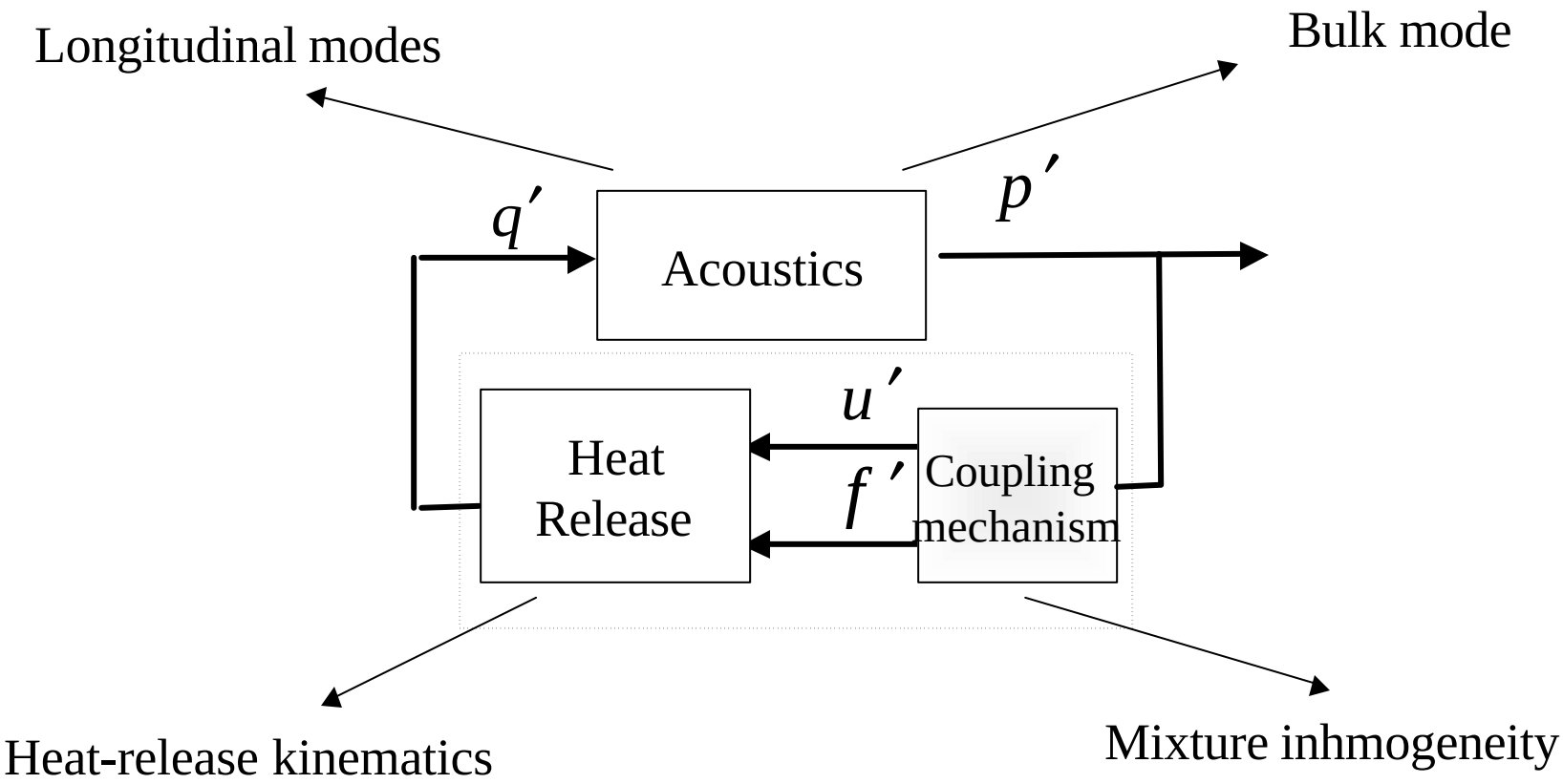
Overview

- Model
  - Heat release
  - Acoustics
  - Coupling dynamics; combustion instability due to
    - Area fluctuations due to velocity fluctuations
    - Mixture inhomogeneity
- Fuel-injector dynamics Model
  - Proportional actuation
  - Two-Position actuation
- Control
  - No delay control: LQG-LTR
  - Time-delay control
  - “Posi-cast” control
- Impact of injector dynamics
  - Bandwidth and authority
  - Nonlinearities

Modeling

1. Organ-pipe combustor (MIT, 1kW)

2. Dump combustor (UTRC, 100kW)



Heat Release Model: Flame Kinematics

Kinematics:

$$\frac{\partial x}{\partial t} = u + v\frac{\partial x}{\partial r} + S_u\sqrt{\left(\frac{\partial x}{\partial r}\right)^2 + 1} \qquad q = K\int_0^R \sqrt{1+\left(\frac{\partial x}{\partial r}\right)^2}\, dr$$

Linearized PDE Model:

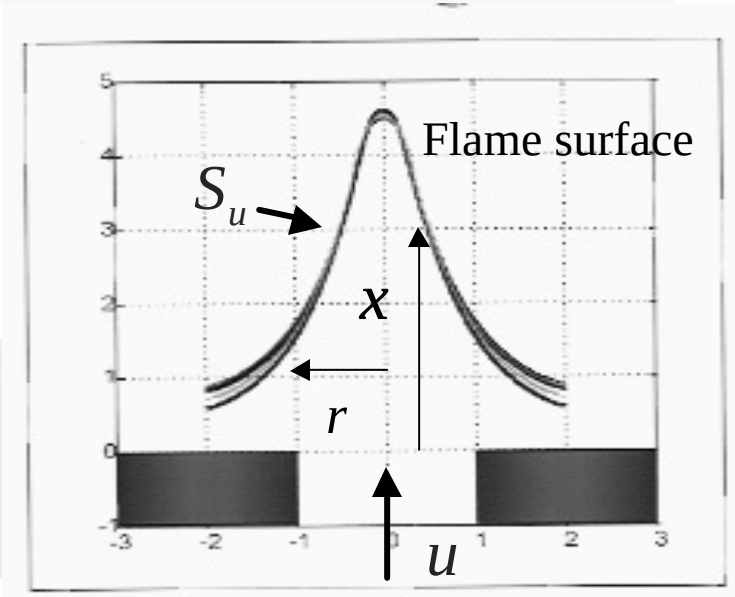
$$\dot{Q}' = d_0 u' + d_1(u_i'(t) - u_i'(t-t_f)) + d_2(f_i'(t) - f_i'(t-t_f)) + d_3 f' + d_4 \dot{f}'$$

$$u_i(t) = \int_0^t u(t)dt\,,\ f_i'(t) = \int_0^t f'(t)dt$$

$t_f = R/S_u$: Propagation delay

- For small t_f, and conical flames reduces to:

$$\dot{Q}_f' + \bar{w}_q Q_f' = A_p \frac{\bar{b}}{\bar{a}}\bar{u}\left(\frac{u'}{\bar{u}} + m\frac{f'}{\bar{f}} + \Lambda_f \frac{\dot{f}'}{\bar{w}_f \bar{f}}\right)$$

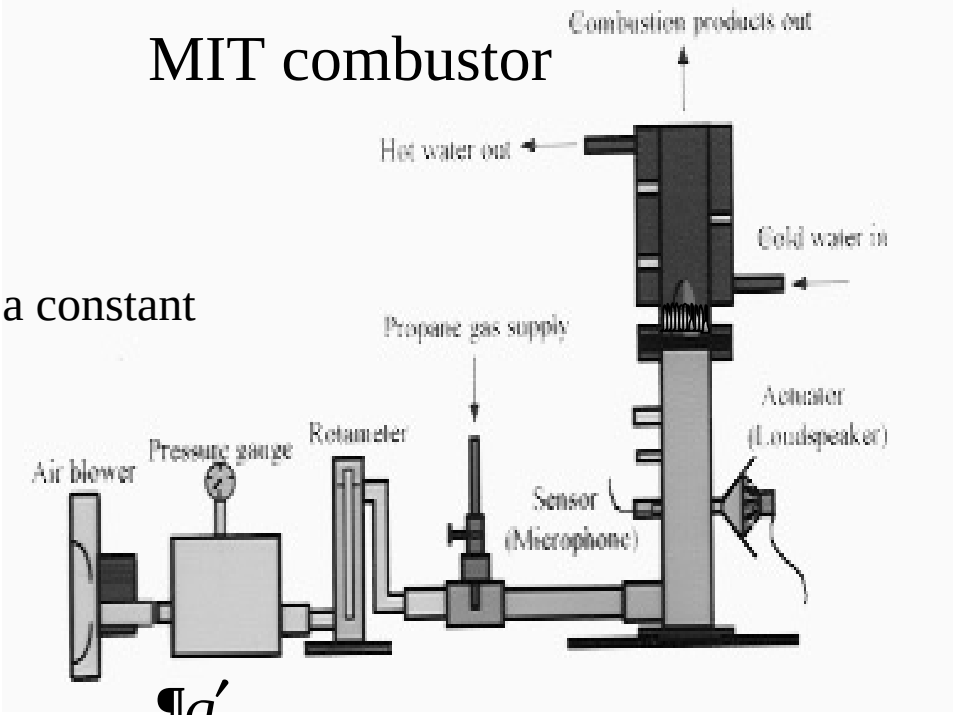


Acoustics: Longitudinal Modes in an Organ-pipe Combustor

Assumptions:

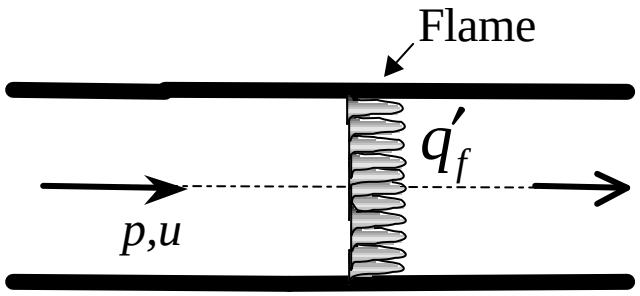
- 1-D flow,
- Inviscid Perfect gas,
- Linear model (perturbations around a constant mean)
- No velocity and heat release.

MIT combustor



- Using Conservation Equations:

PDE Model: $$\frac{\partial^2 p'}{\partial t^2} - \bar{c}^2 \frac{\partial^2 p'}{\partial x^2} = (\gamma - 1)\frac{\partial q'_f}{\partial t}$$



ODE Model: $$\dot{\eta}_i + \omega_i^2 \eta_i = b_i \dot{q}'_f$$

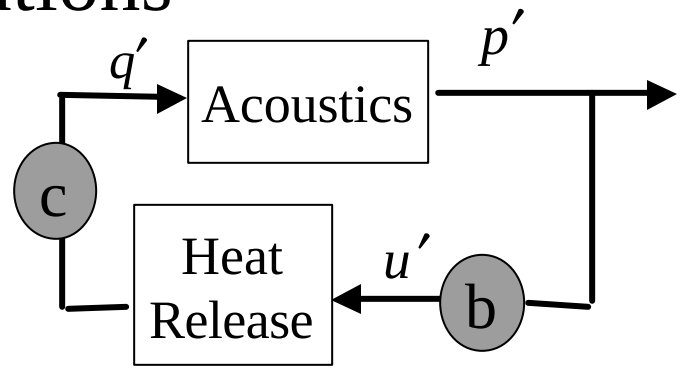
$$p' = \bar{p} \sum_1^n \gamma_i \eta_i$$

Organ-pipe Combustor (MIT): Coupling caused by Velocity Fluctuations

$$\dot{\eta}_i + w_i^2 \eta_i = b_i \dot{q}'_f \qquad p' = \bar{p} \sum_1^n y_i \eta_i$$

$$\dot{q}'_f + b_f q'_f = w_f g_f \bar{f}_f \tilde{u}'_f$$

$$\tilde{u}'_f = \sum c_i \dot{\eta}_i$$

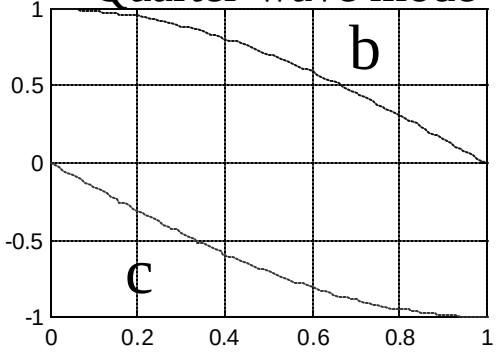


c: *fn* of velocity mode shape

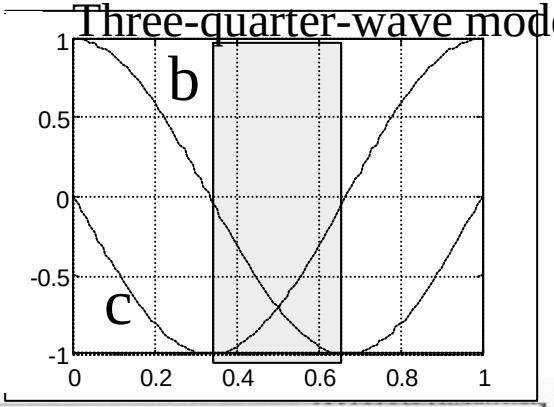
b: *fn* of pressure mode shape

bc>0: system becomes unstable

Quarter-wave mode

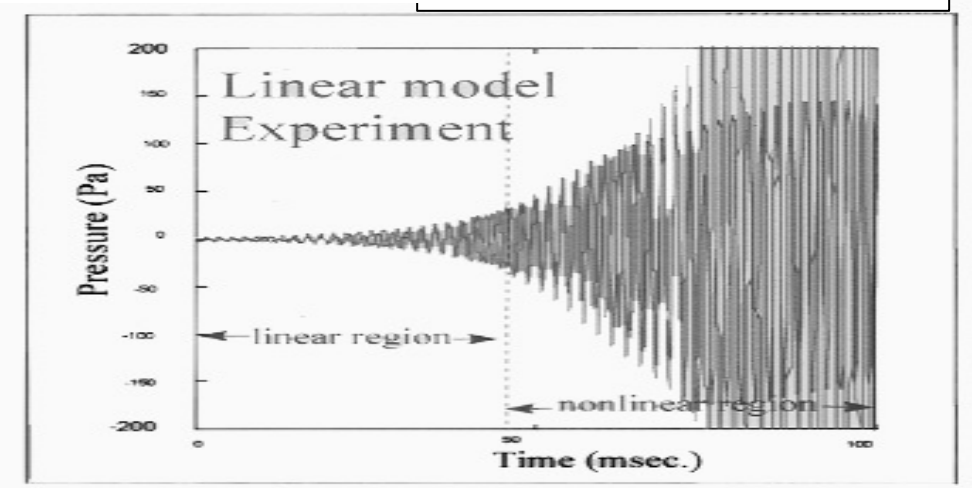


Three-quarter-wave mode



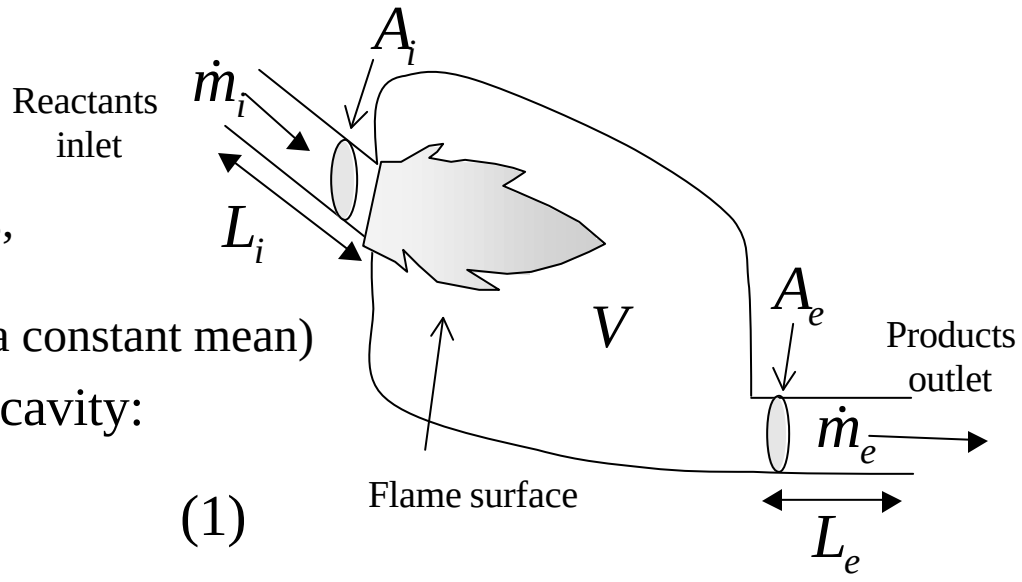
Summary of the model predictions: (2-modes)

	Growth rate(1/s)	Frequency (Hz)
MIT Model prediction:	115.8	620.3
Experimental (Lang et al.'87):	113	630



Acoustics Model: Dump Combustor with a Large Bulk

- Assumptions:
  - 1-D flow,
  - Incompressible in the ducts,
  - Volume of cavity>>Volume of ducts,
  - Inviscid Perfect gas,
  - Linear model (perturbations around a constant mean)



- Mass and energy conservation in the cavity:

$$\frac{dp'}{dt} = \frac{1}{V}\left(c_i^2 \dot{m}_i' - c_e^2 \dot{m}_e' + (g-1)Q_f'\right) \qquad (1)$$

- Mass and momentum conservation in the j[th] duct: (assume ducts open to atmosphere; pressure distribution is negligible)

$$\frac{d\dot{m}_j'}{dt} = -A_j \frac{\partial p'}{\partial x}(L_j, t) = \frac{p'}{L_j} \qquad (2)$$

- Substitute (2) in (1):

$$\frac{d^2 p'}{dt^2} + (2zw\frac{dp'}{dt}) + w^2 p' = \frac{(g-1)}{V}\frac{dQ_f'}{dt}$$

Where the effective Helmholtz frequency is $w = \sqrt{\frac{c_i^2 A_i}{L_i V} + \frac{c_e^2 A_e}{L_e V}}$

UTRC Combustor: Coupling caused by Inhomogeneity Dynamics

• Acoustic velocity perturbation in cavity is small, negligible effect on area perturbation.

⟶ Only perturbations in the equivalence ratio are important

• Instantaneous f at fuel nozzle due to perturbations in the air flow rate:

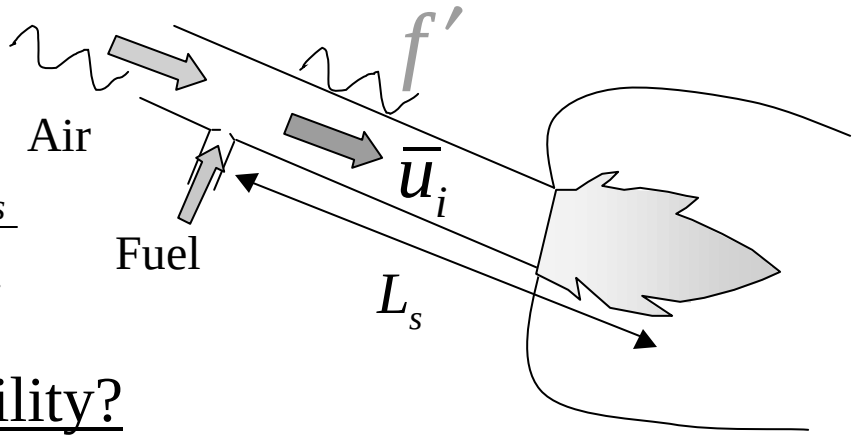
$$f = \frac{\bar{f}}{1 + u'/\bar{u}} \approx \bar{f}\left(1 - u'/\bar{u}\right)$$

• Recall: effect of f' on Q'_f is <u>static</u>, but effect of f' on Q'_f is <u>delayed!</u>

$$\dot{Q}'_f = \Gamma p'(t - t_n), \quad \Gamma = \frac{A_i \bar{b} \Lambda_f}{\bar{r}_i \bar{S}_u L_i}$$

Delay: $t_n = t_s + t_{comb}$

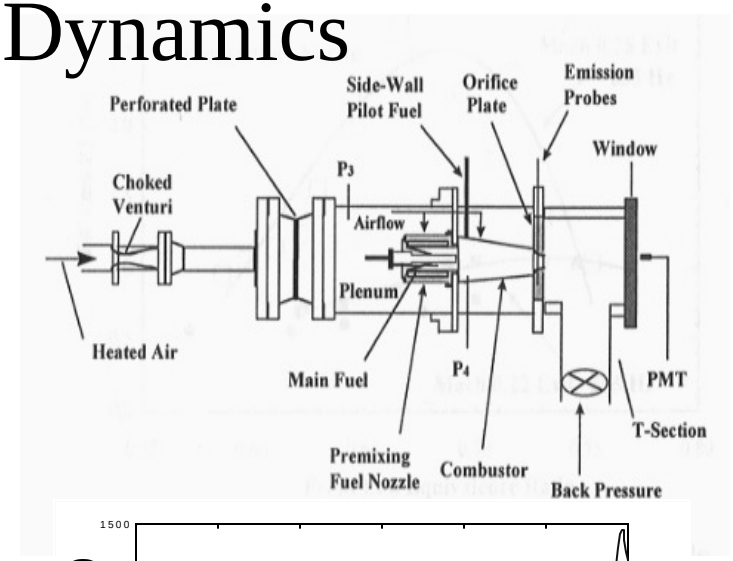
$$t_{comb} << t_s \qquad t_s = \frac{L_s}{\bar{u}_i}$$



•<u>Can a delay trigger the instability?</u>

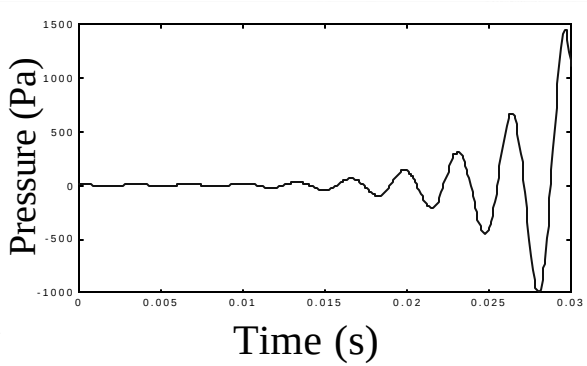
UTRC Combustor: Combustion Instability due to Inhomogeneity Dynamics

- United Technologies combustor:
  - Instability due to f'



- Model prediction:

$$\frac{d^2 p'}{dt^2} - \Gamma p'(t - t_s) + w^2 p' = 0$$

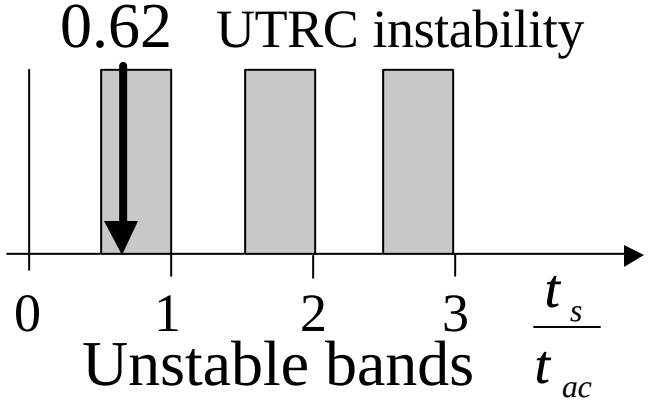


Unstable: $\frac{n+1}{2} < \frac{t_s}{t_{ac}} < \frac{n+2}{2}$ for $n = 0,2,4\ldots$

$t_{ac} = 2p / w$

when $0 < \frac{\Gamma}{w^2} < 1$

$\frac{\Gamma}{w^2} \approx 1 - \frac{T_o}{T_e} < 1$



- Stability bands identified in experiments (Putnam 1971, Richards 1995, Zinn 1998)

Summary of Instability Models

General Model:

$$\frac{d^2h}{dt^2} + 2zw\frac{dh}{dt} + w^2h = d_1u' + d_2\int_{t-t_f}^{t} u'(t)dt + d_3\frac{df'_f}{dt}$$

$$f'_f = f'(t - t_s)$$

When u' fluctuations are dominant

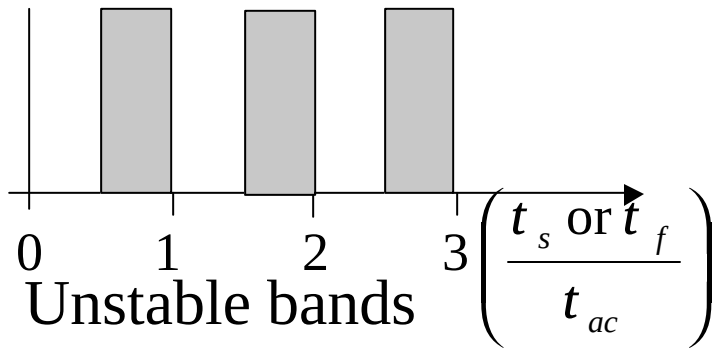
$$\frac{d^2h}{dt^2} + (2zw - d_1)\frac{dh}{dt} + (w^2 + d_2)h - d_2h(t - t_f) = 0$$

Phase-lag instability

Time-delay instability

When f' fluctuations are dominant

$$\frac{d^2h}{dt^2} + 2zw\frac{dh}{dt} + w^2h - d_2h(t - t_s) = 0$$

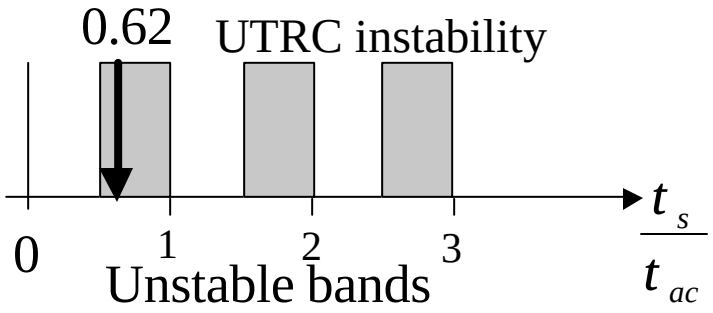


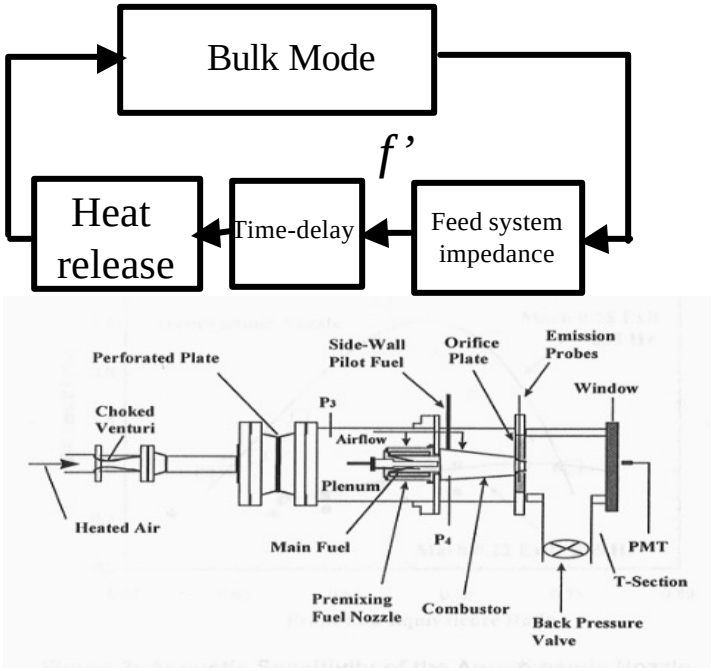
Model Predictions: *f'* oscillations

- UTRC (Cohen et al., 1998)

Unstable: $\frac{n+1}{2} < \frac{t_s}{t_{ac}} < \frac{n+2}{2}$ for $n = 0,2,4...$

when $0 < \frac{\Gamma}{w^2} < 1$, $\left(\frac{\Gamma}{w^2} \approx 1 - \frac{T_o}{T_e} < 1\right)$ and $t_{ac} = 2p / w$



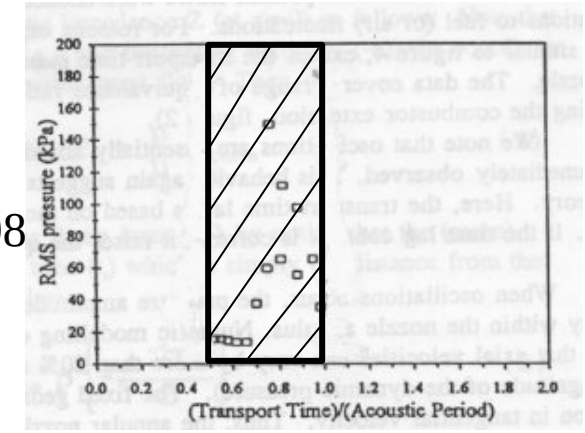


(Cohen et al., 1998)

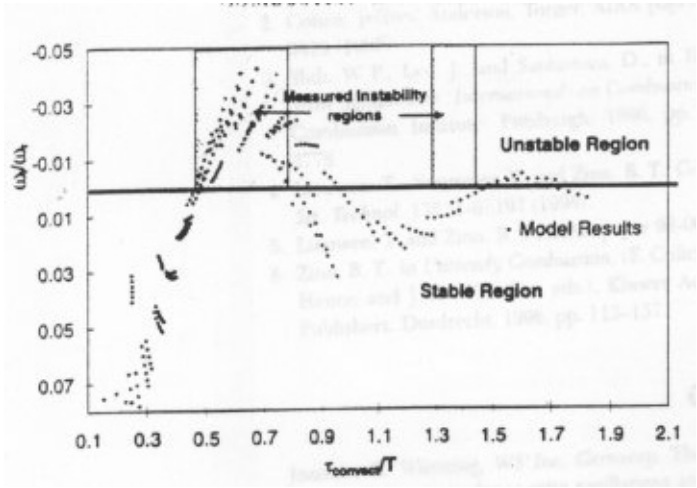
- Experiments:

- Mongia et. al,1997
- Richards and Yip, 1997
- Lieuwen and Zinn et al., 1998

(Similar dynamics also in rockets, Crocco 1960, Tsien 1962)



(Richards and Yip, 1997), "口"

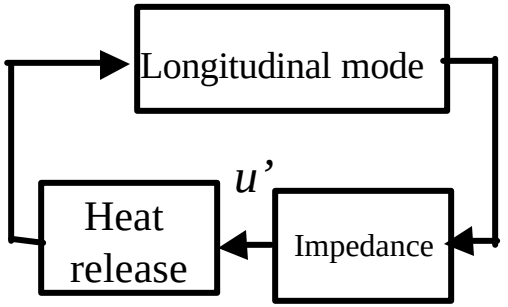


(Lieuwen and Zinn et al., 1998)

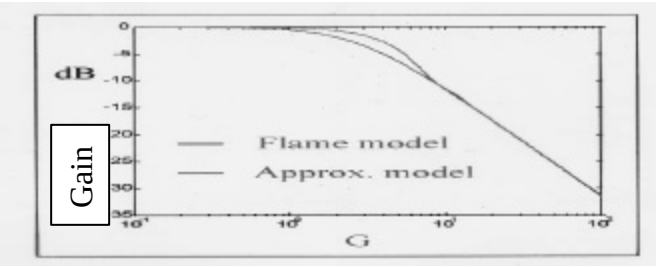
Model Predictions: *u'* oscillations

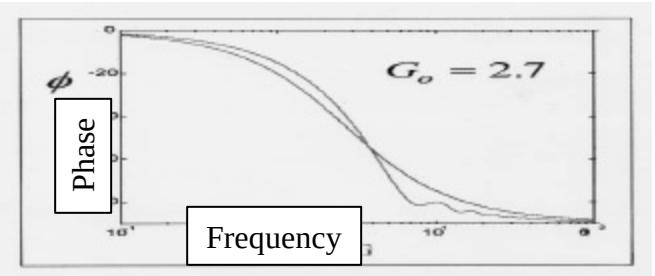
- Phase-lag instability:
  - MIT combustor
  - Poinsot et. al, 1989
  - Gulati and Mani, 1992
  - Sivasegaram and Whitelaw, 1992
  - Seume et. al, (Siemens), 1997

- Time-delay instability:
  - Santavicca et. al, 1998
  - Richards, 1999



Two-modes simulation	Growth rate(1/s)	Frequency (Hz)
MIT Model prediction:	115.8	620.3
Experimental (Poinsot 1989):	113	630





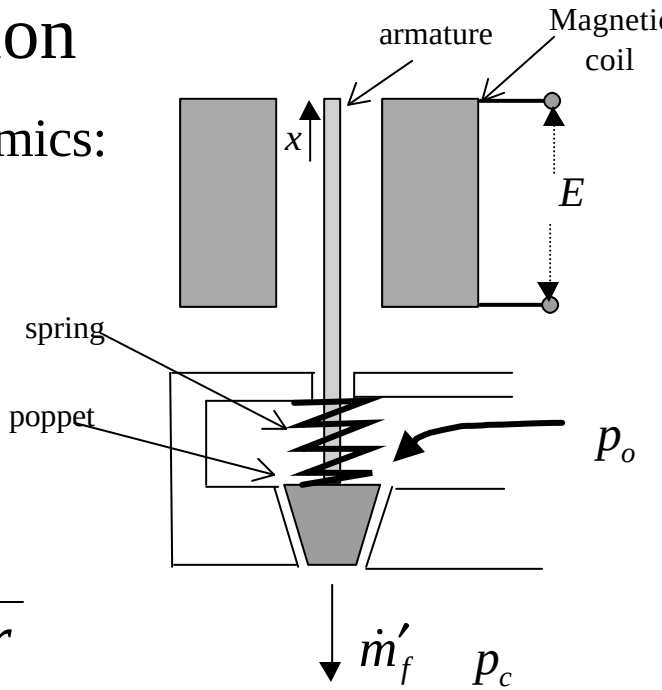
Agrees with Experiments by Bloxsidge et al., 1987

Overview

- Model
  - Heat release
  - Acoustics
  - Coupling dynamics; combustion instability due to
    - Area fluctuations due to velocity fluctuations
    - Mixture inhomogeneity
- Fuel-injector dynamics Model
  - Proportional actuation
  - Two-Position actuation
- Conrol
  - No delay control: LQG-LTR
  - Time-delay control
  - “Posi-cast” control
- Impact of injector dynamics
  - Bandwidth and authority
  - Nonlinearities

Fuel-Injector Dynamics

Proportional Injection



- Electro-magnetic and mechanical components dynamics:

$$E = iR + L\frac{di}{dt} + V, \qquad V = Bl\frac{dx}{dt}$$

$$m\frac{d^2x}{dt^2} + b\frac{dx}{dt} + kx = F_m, \qquad F_m = Bli$$

- Fluid dynamics

$$t_{fluid}\frac{dv'}{dt} + v' \cong \frac{-p'_c}{\sqrt{2\Delta\bar{p}\bar{r}}}, \qquad t_{fluid} = L_i \Big/ \sqrt{2\Delta\bar{p}/r}$$

$$\dot{m}'_f = \bar{r}\bar{A}v' + \bar{r}\bar{v}A', \qquad A' = k_o x$$

- Fuel inlet choked: $v' \approx 0$

- $L_i << 1m, \quad \Delta p = p_o - p_c >> \ , \ r \approx 1kg/m^3$ (for gaseous fuels) $\longrightarrow$ $t_{fluid} <<$

$$\rightarrow \quad \frac{\dot{m}'_f(s)}{E(s)} = \frac{k_v}{(t_e s + 1)(ms^2 + bs + k) + B^2 l^2 s/R} \cong \frac{k_v}{t_m s + 1}$$

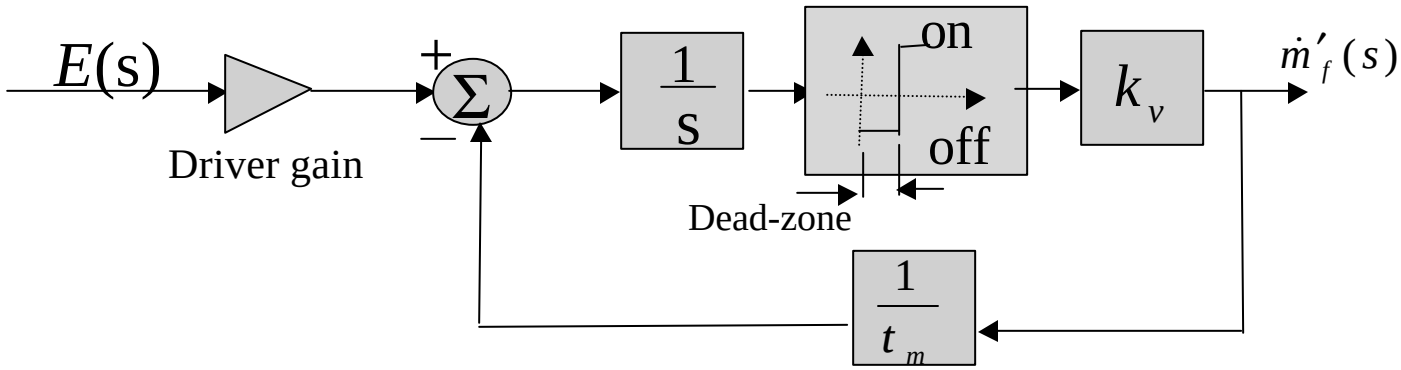
$$t_m = (b + B^2 l^2 / R)/k$$

$$t_e = L/R$$

Fuel-injector Dynamics

Two-position (on-off) injection

- Dynamics: Same as proportional + effect of physical stops (saturation) + Dead-zone



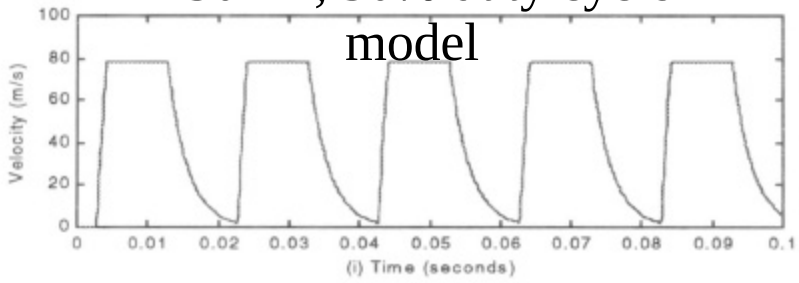
- Hysteresis *On*: $t_m|_{on} = (b + B^2 l^2 / R)/k$

  Off: $t_m|_{off} = b/k$

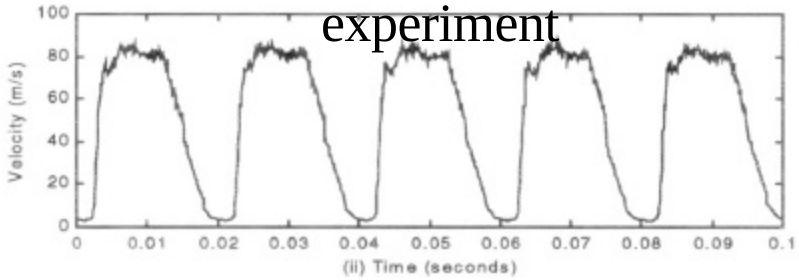
Two-position (on-off) injection: Velocity Response

50 Hz, 50% duty cycle

model

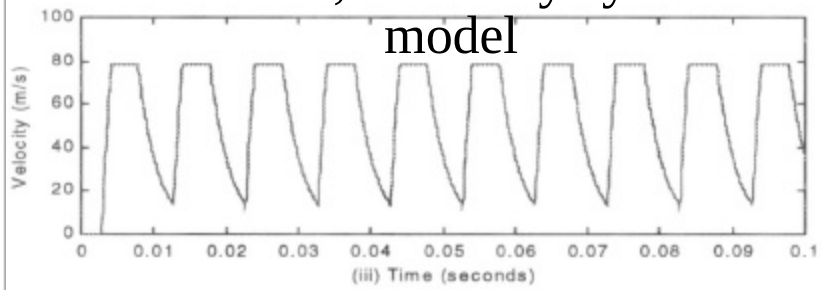


experiment

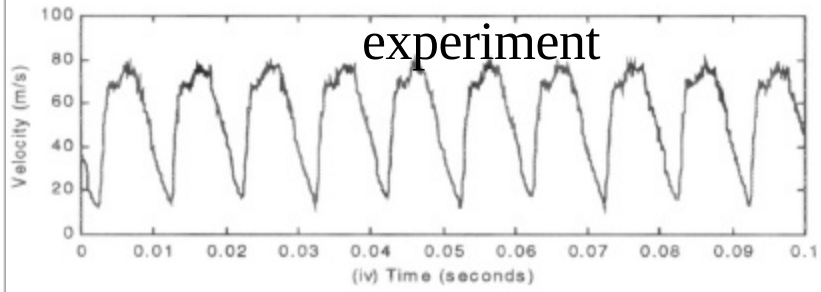


100 Hz, 50% duty cycle

model

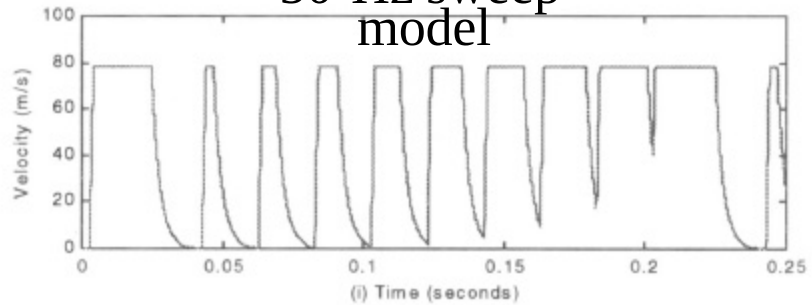


experiment

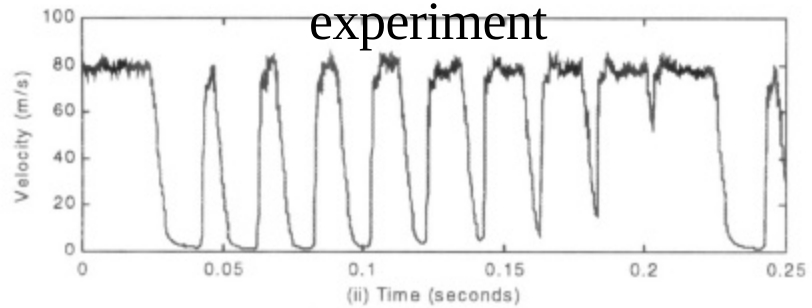


50-Hz sweep

model

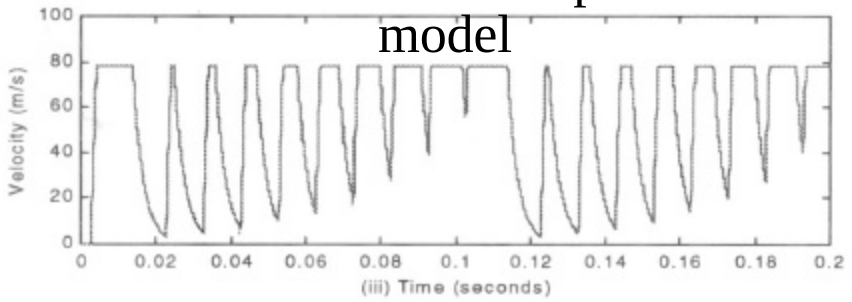


experiment

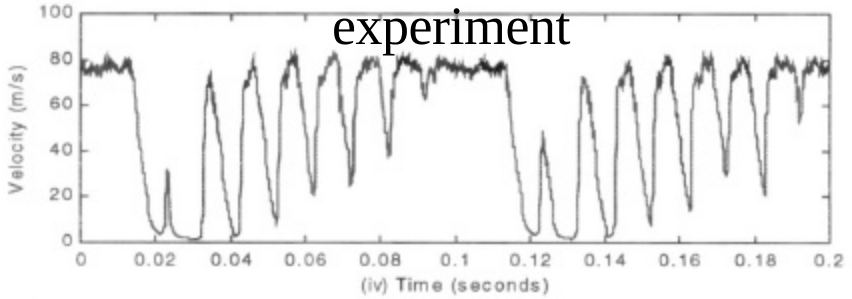


100-Hz sweep

model



experiment



Overview

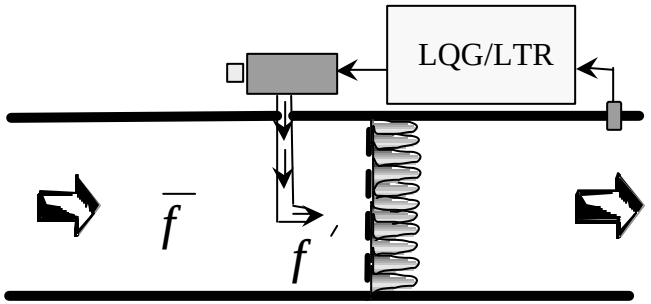
- Model
  - Heat release
  - Acoustics
  - Coupling dynamics; combustion instability due to
    - Area fluctuations due to velocity fluctuations
    - Mixture inhomogeneity
- Fuel-injector dynamics Model
  - Proportional actuation
  - Two-Position actuation
- Conrol
  - No delay control: LQG-LTR
  - Time-delay control
  - “Posi-cast” control
- Impact of injector dynamics
  - Bandwidth and authority
  - Nonlinearities

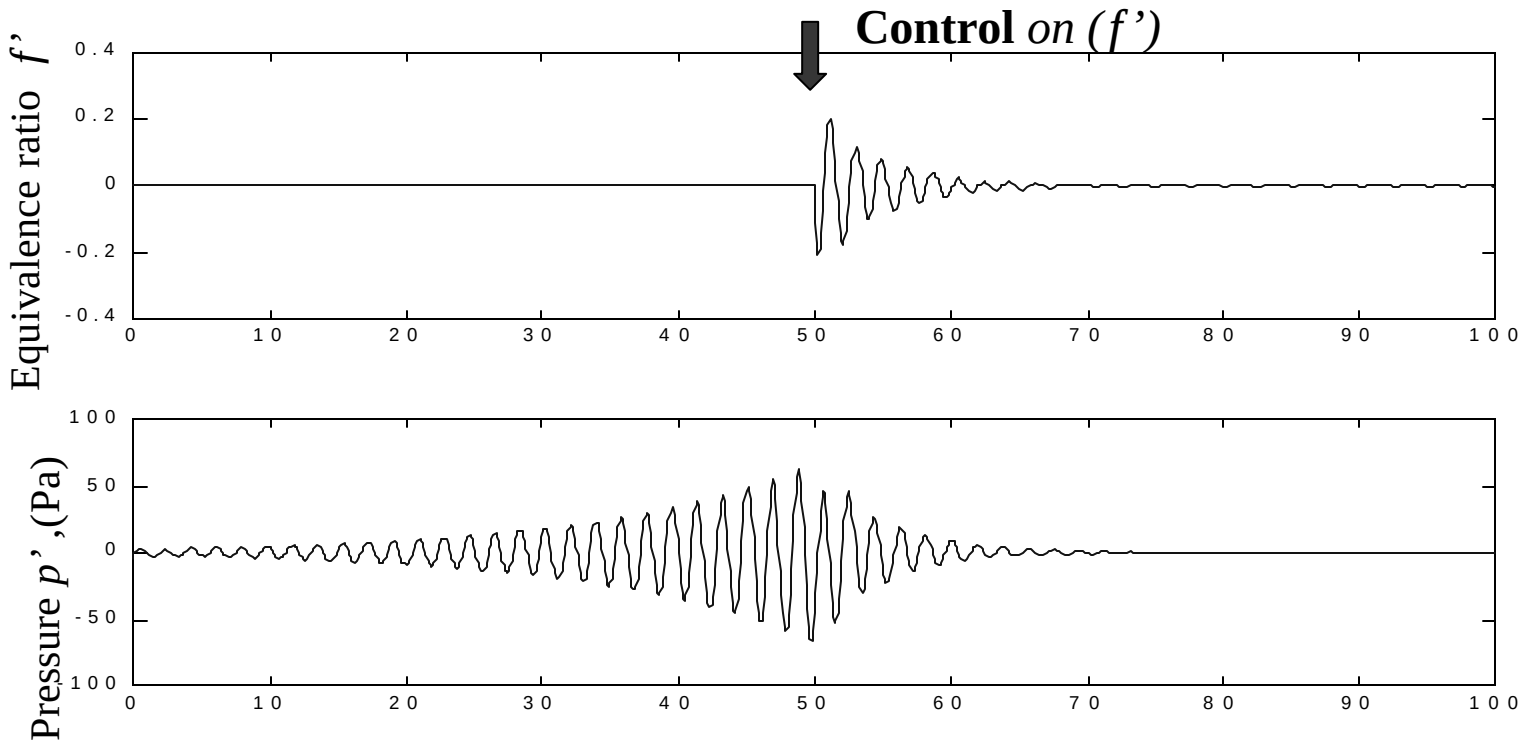
Using Pulsed-fuel Injection (on flame)

Model:

- 2 Acoustics modes, and flame dynamics
- Fuel Injector: - Proportional
  - 200 Hz bandwidth
  - 1st order dynamics
- 5th order model

Controller: LQG/LTR (5th order)



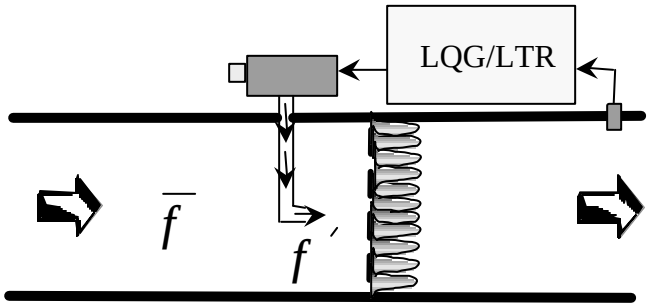


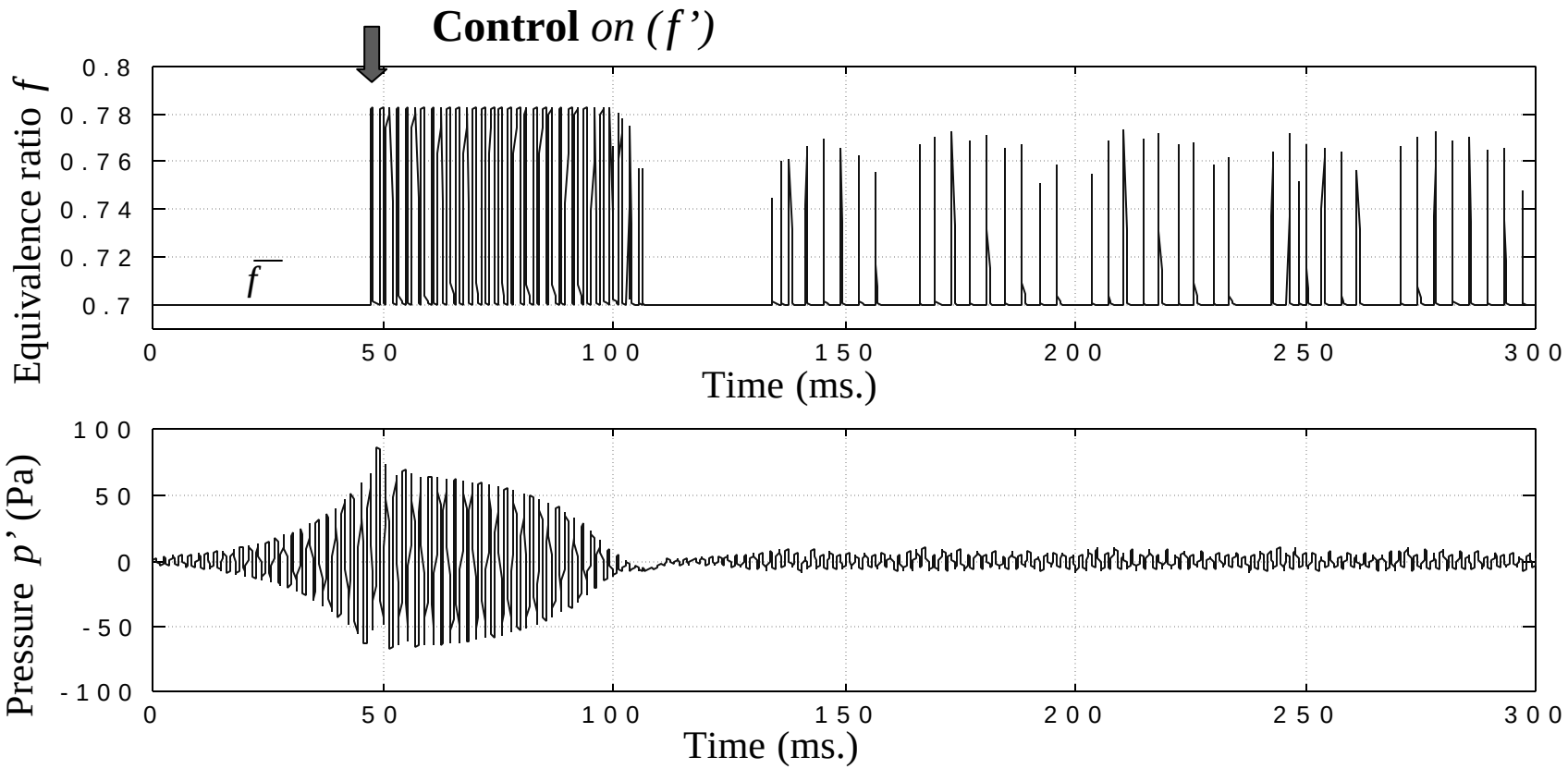
Using Pulsed-fuel Injection (on flame)

Model:

- 2 Acoustics modes, and flame dynamics
- Fuel Injector: - Two-position (on-off)
  - 200 Hz bandwidth
  - 1st order dynamics
- 5th order model

Controller: LQG/LTR (5th order)



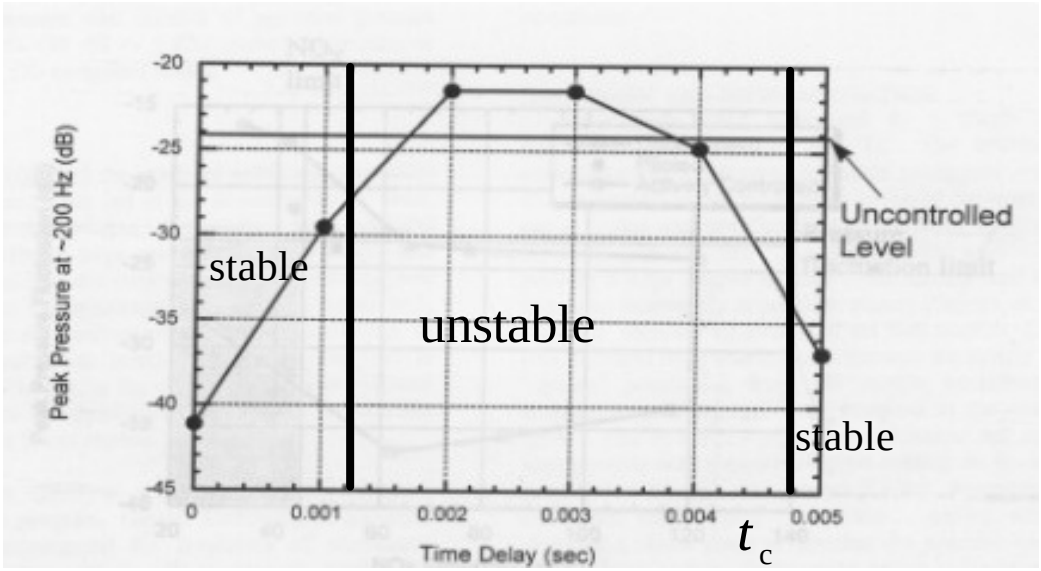


Time-delay Control (injection at main fuel supply)

$$\frac{d^2p'}{dt^2}+2z w\frac{dp'}{dt}-\Gamma p'(t-t_s)+w^2p'=\Gamma_c\frac{df'}{dt}(t-t_s)$$

• Idea: cancel the perturbations in the main fuel causing the instability, stability depends on natural damping in the combustor.

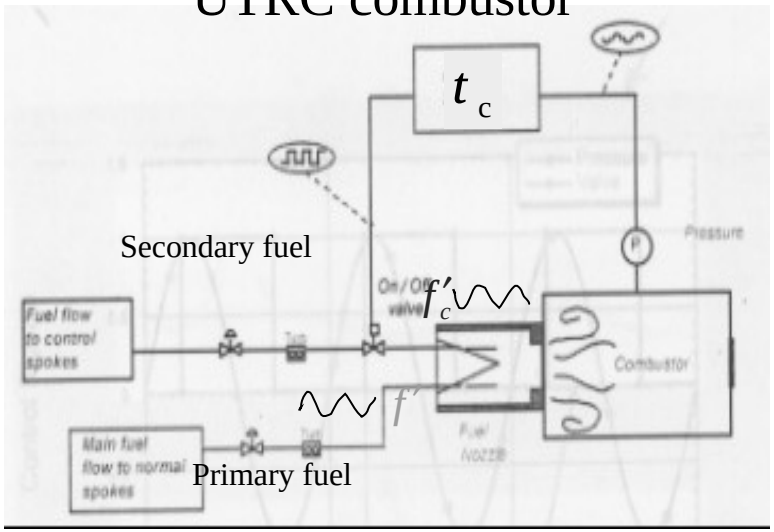
• Choose control: $f'_c=-K_c\int p'(t-t_c)dt$

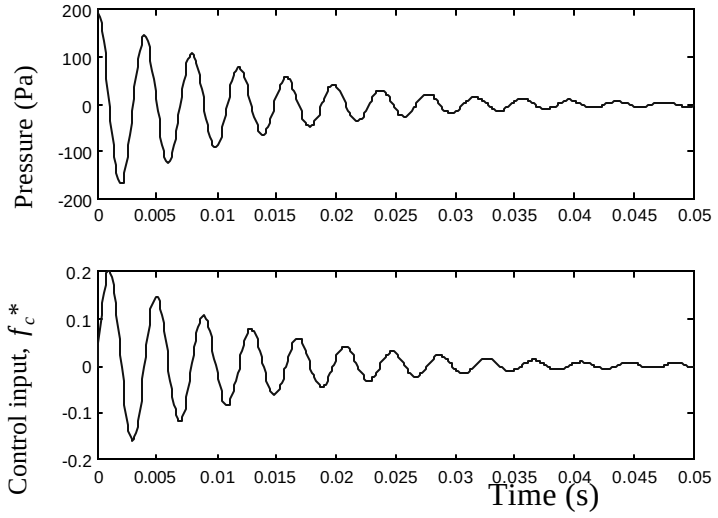


Experimental results (UTRC, Cohen et al.'98): "●"

Stable and unstable zones, model predictions

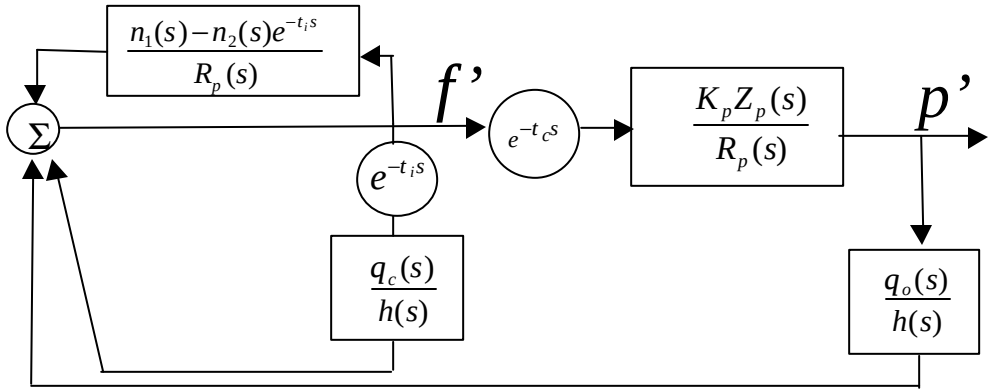
UTRC combustor





Pole-Placement Control for a Combustor with a Delayed Control Input

Controller structure:



Closed-loop:

$$M(s)=\frac{K_p Z_p(s)h(s)e^{-t_i s}}{\underbrace{(R_p(s)-n_1(s))h(s)}_{\text{Stabilize!}}-\underbrace{[q_c(s)R_p(s)-n_2(s)h(s)+q_o(s)K_p Z_p(s)]e^{-t_i s}}_{\text{Cancel!}}}$$

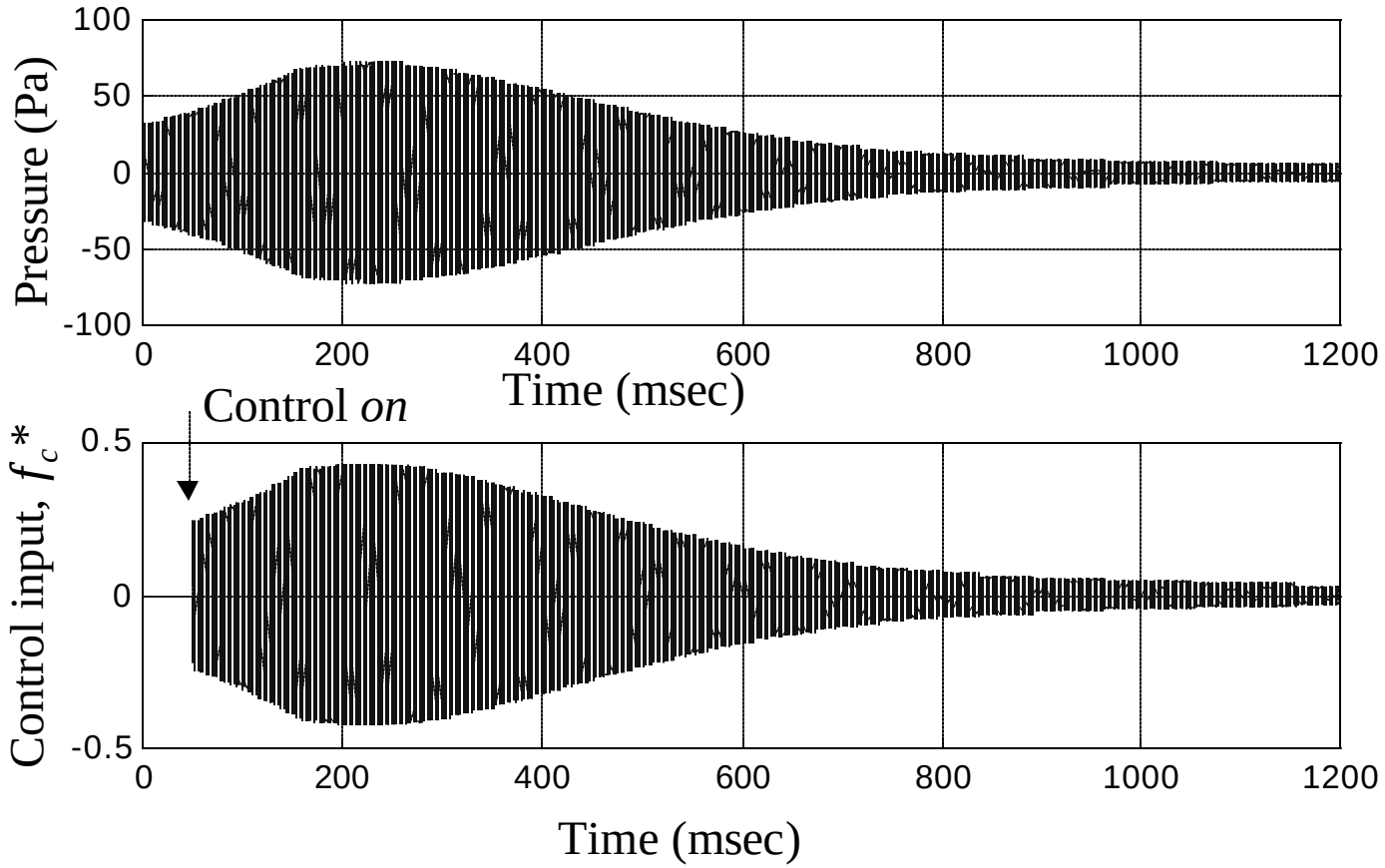
$$\longrightarrow M(s)=\frac{K_p Z_p(s)e^{t_i s}}{R_m(s)}$$

Properties:

- Stable synthesis (Manitius & Olbrot'79, Ichikawa'85)
- Robust (Niculescu & Annaswamy, ACC'99)
- Amenable to adaptation with uncertainties (Niculescu & Annaswamy, ACC'99)
- Validation in turbulent combustors (Evesque, Annaswamy & Dowling, NATO Symposium'00)

Simulation with Time-delay Compensator Control

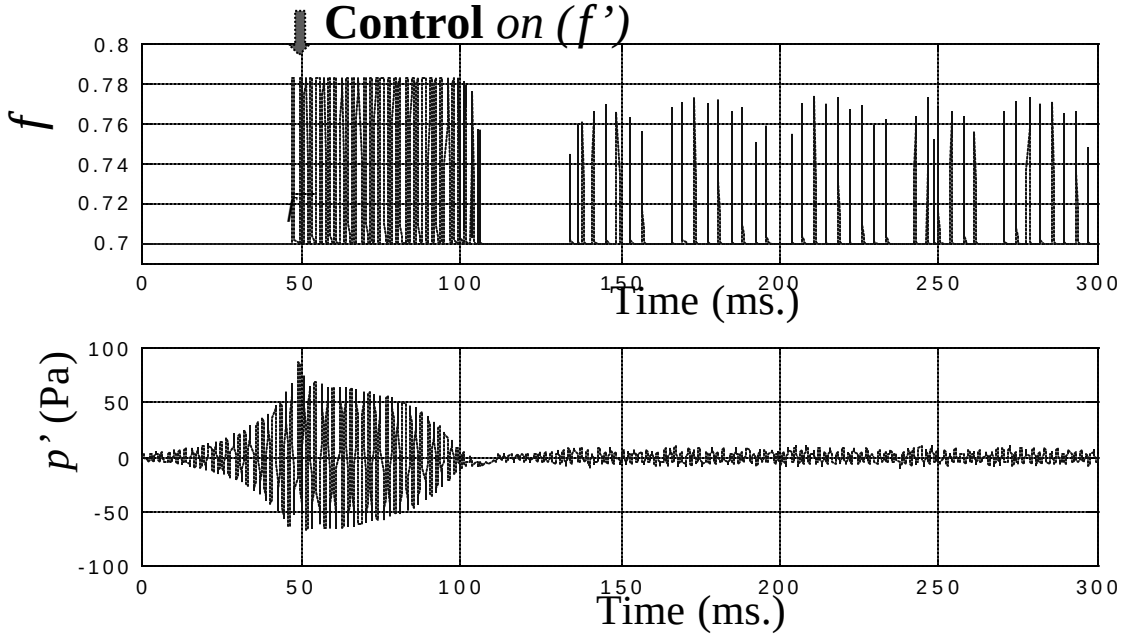
MIT combustor model: $t_i \sim 50\, t_{ac}$. (mean velocity <<)



Overview

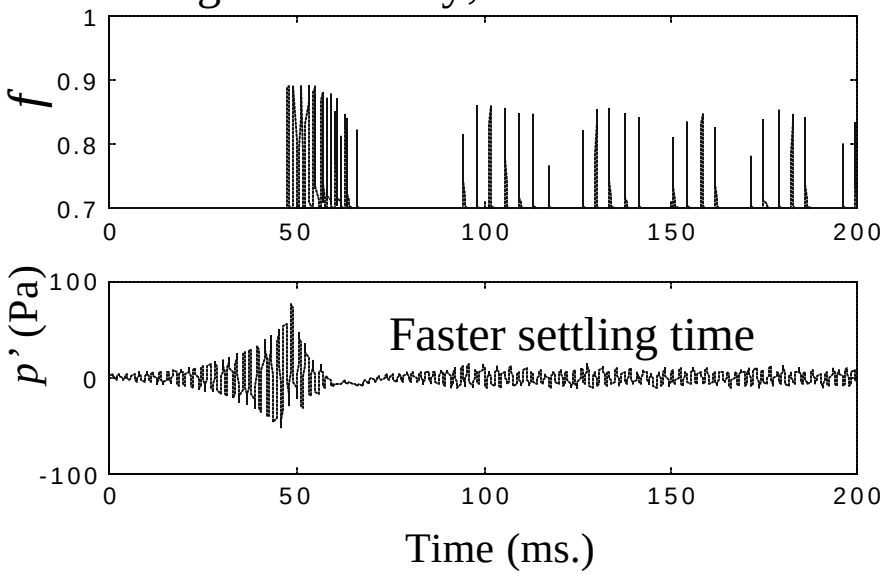
- Model
  - Heat release
  - Acoustics
  - Coupling dynamics; combustion instability due to
    - Area fluctuations due to velocity fluctuations
    - Mixture inhomogeneity
- Fuel-injector dynamics Model
  - Proportional actuation
  - Two-Position actuation
- Conrol
  - No delay control: LQG-LTR
  - Time-delay control
  - “Posi-cast” control
- Impact of injector dynamics
  - Bandwidth and authority
  - Nonlinearities

Actuator Limitations (Sec. Injector)

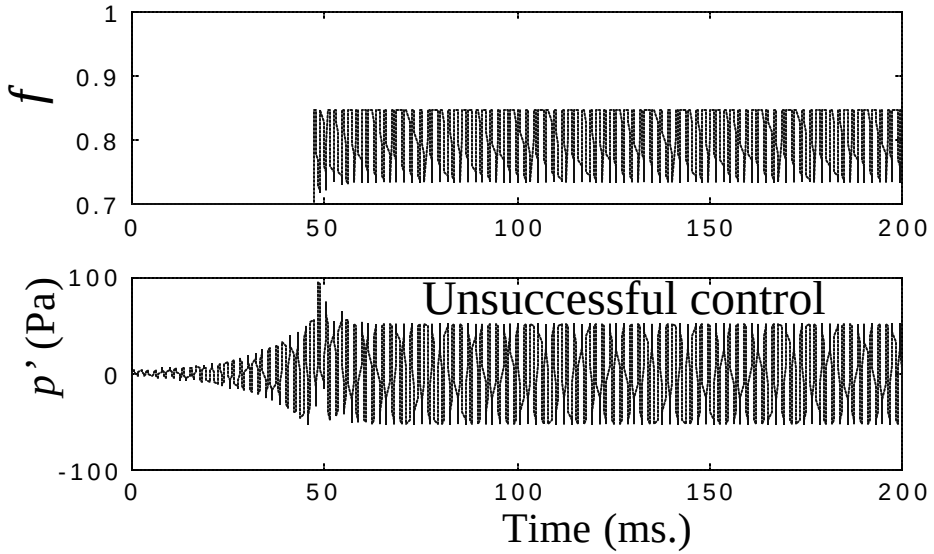


Results similar to observations in Yu (1997)

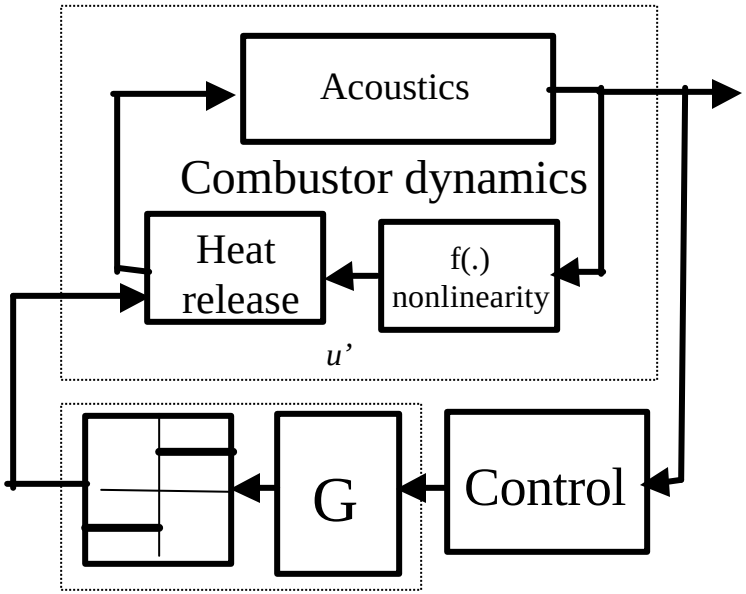
Higher authority, sec. Fuel flow rate

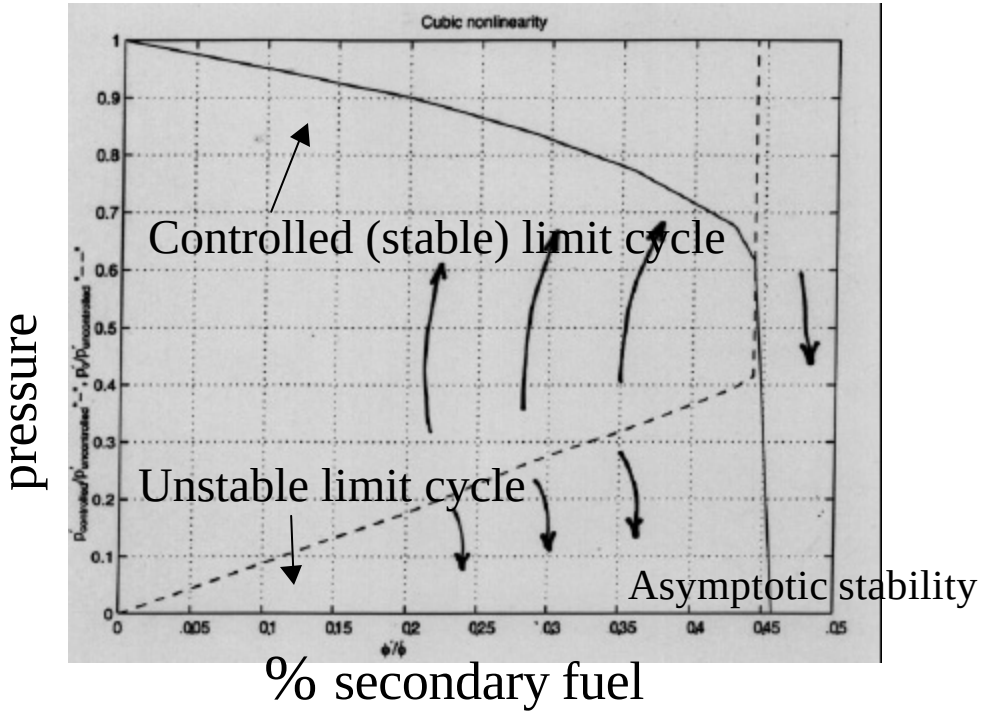


Lower bandwidth

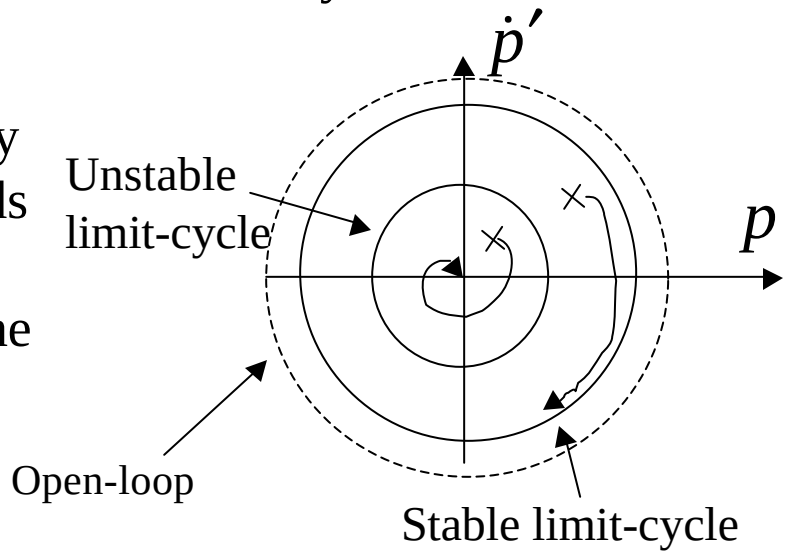


Impact of Nonlinearities in the Actuator





- Saturated/on-off injectors: limited control authority
- Stability (asymptotic, or stable limit-cycle) depends on control authority
- Stable solutions depend on Initial conditions, define an unstable limit-cycle
- In agreement with K. Yu 1997.

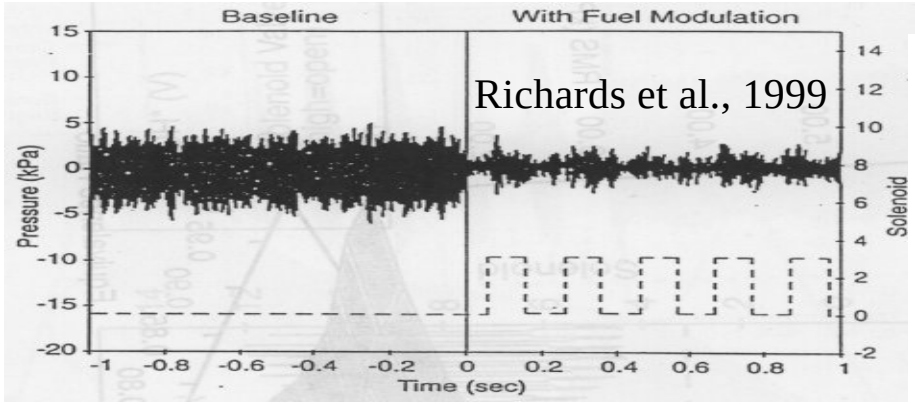


Summary

- Reduced-order models for combustion instability
  - Heat release
  - Acoustics
  - Coupling dynamics; combustion instability due to
    - Area fluctuations due to velocity fluctuations
    - Mixture inhomogeneity
- Model-based control
  - Optimal
  - Accommodates large time-delays
- Injection dynamics
  - Bandwidth and authority limiations
  - Nonlinearities

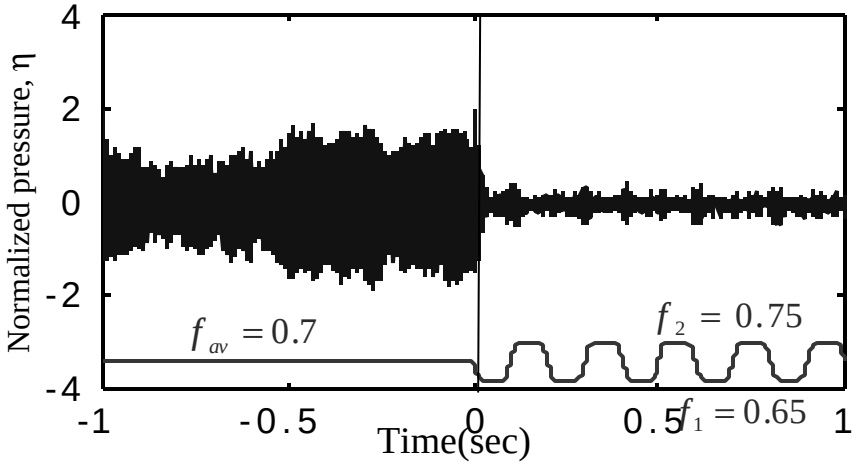
Current Work

- Open-loop subharmonic control using fuel injection



Richards et al., 1999

Prasanth,Annaswamy, Hathout and Ghoniem, 2000



- Extend models to turbulent combustion
- System ID Models

Visit us at
http://centaur.mit.edu/rgd
for further details

NORTH ATLANTIC TREATY ORGANIZATION

RESEARCH AND TECHNOLOGY ORGANIZATION
BP 25 • 7 RUE ANCELLE
F-92201 NEUILLY-SUR-SEINE CEDEX • FRANCE
Télécopie 0(1)55.61.22.99 • E-mail mailbox@rta.nato.int

DIFFUSION DES PUBLICATIONS
RTO NON CLASSIFIEES

L'Organisation pour la recherche et la technologie de l'OTAN (RTO), détient un stock limité de certaines de ses publications récentes, ainsi que de celles de l'ancien AGARD (Groupe consultatif pour la recherche et les réalisations aérospatiales de l'OTAN). Celles-ci pourront éventuellement être obtenues sous forme de copie papier. Pour de plus amples renseignements concernant l'achat de ces ouvrages, adressez-vous par lettre ou par télécopie à l'adresse indiquée ci-dessus. Veuillez ne pas téléphoner.

Des exemplaires supplémentaires peuvent parfois être obtenus auprès des centres nationaux de distribution indiqués ci-dessous. Si vous souhaitez recevoir toutes les publications de la RTO, ou simplement celles qui concernent certains Panels, vous pouvez demander d'être inclus sur la liste d'envoi de l'un de ces centres.

Les publications de la RTO et de l'AGARD sont en vente auprès des agences de vente indiquées ci-dessous, sous forme de photocopie ou de microfiche. Certains originaux peuvent également être obtenus auprès de CASI.

CENTRES DE DIFFUSION NATIONAUX

ALLEMAGNE
Streitkräfteamt / Abteilung III
Fachinformationszentrum der Bundeswehr, (FIZBw)
Friedrich-Ebert-Allee 34
D-53113 Bonn

BELGIQUE
Coordinateur RTO - VSL/RTO
Etat-Major de la Force Aérienne
Quartier Reine Elisabeth
Rue d'Evère, B-1140 Bruxelles

CANADA
Services d'information scientifique pour la défense (SISD)
R et D pour la défense Canada
Ministère de la Défense nationale
Ottawa, Ontario K1A 0K2

DANEMARK
Danish Defence Research Establishment
Ryvangs Allé 1, P.O. Box 2715
DK-2100 Copenhagen Ø

ESPAGNE
INTA (RTO/AGARD Publications)
Carretera de Torrejón a Ajalvir, Pk.4
28850 Torrejón de Ardoz - Madrid

ETATS-UNIS
NASA Center for AeroSpace Information (CASI)
Parkway Center
7121 Standard Drive
Hanover, MD 21076-1320

FRANCE
O.N.E.R.A. (ISP)
29, Avenue de la Division Leclerc
BP 72, 92322 Châtillon Cedex

GRECE (Correspondant)
Hellenic Ministry of National Defence
Defence Industry Research & Technology General Directorate
Technological R&D Directorate
D.Soutsou 40, GR-11521, Athens

HONGRIE
Department for Scientific Analysis
Institute of Military Technology
Ministry of Defence
H-1525 Budapest P O Box 26

ISLANDE
Director of Aviation
c/o Flugrad
Reykjavik

ITALIE
Centro di Documentazione Tecnico-Scientifica della Difesa
Via XX Settembre 123a
00187 Roma

LUXEMBOURG
Voir Belgique

NORVEGE
Norwegian Defence Research Establishment
Attn: Biblioteket
P.O. Box 25, NO-2007 Kjeller

PAYS-BAS
NDRCC
DGM/DWOO
P.O. Box 20701
2500 ES Den Haag

POLOGNE
Chief of International Cooperation Division
Research & Development Department
218 Niepodleglosci Av.
00-911 Warsaw

PORTUGAL
Estado Maior da Força Aérea
SDFA - Centro de Documentação
Alfragide
P-2720 Amadora

REPUBLIQUE TCHEQUE
Distribuční a informační středisko R&T
VTÚL a PVO Praha
Mladoboleslavská ul.
197 06 Praha 9-Kbely AFB

ROYAUME-UNI
Defence Research Information Centre
Kentigern House
65 Brown Street
Glasgow G2 8EX

TURQUIE
Millî Savunma Başkanliği (MSB)
ARGE Dairesi Başkanliği (MSB)
06650 Bakanliklar - Ankara

AGENCES DE VENTE

NASA Center for AeroSpace Information (CASI)
Parkway Center
7121 Standard Drive
Hanover, MD 21076-1320
Etats-Unis

The British Library Document Supply Centre
Boston Spa, Wetherby
West Yorkshire LS23 7BQ
Royaume-Uni

Canada Institute for Scientific and Technical Information (CISTI)
National Research Council
Document Delivery
Montreal Road, Building M-55
Ottawa K1A 0S2, Canada

Les demandes de documents RTO ou AGARD doivent comporter la dénomination "RTO" ou "AGARD" selon le cas, suivie du numéro de série (par exemple AGARD-AG-315). Des informations analogues, telles que le titre et la date de publication sont souhaitables. Des références bibliographiques complètes ainsi que des résumés des publications RTO et AGARD figurent dans les journaux suivants:

Scientific and Technical Aerospace Reports (STAR)
STAR peut être consulté en ligne au localisateur de ressources uniformes (URL) suivant:
http://www.sti.nasa.gov/Pubs/star/Star.html
STAR est édité par CASI dans le cadre du programme NASA d'information scientifique et technique (STI)
STI Program Office, MS 157A
NASA Langley Research Center
Hampton, Virginia 23681-0001
Etats-Unis

Government Reports Announcements & Index (GRA&I)
publié par le National Technical Information Service
Springfield
Virginia 2216
Etats-Unis
(accessible également en mode interactif dans la base de données bibliographiques en ligne du NTIS, et sur CD-ROM)

Imprimé par St-Joseph Ottawa/Hull
(Membre de la Corporation St-Joseph)
45, boul. Sacré-Cœur, Hull (Québec), Canada J8X 1C6

NORTH ATLANTIC TREATY ORGANIZATION

RESEARCH AND TECHNOLOGY ORGANIZATION
BP 25 • 7 RUE ANCELLE
F-92201 NEUILLY-SUR-SEINE CEDEX • FRANCE
Telefax 0(1)55.61.22.99 • E-mail mailbox@rta.nato.int

DISTRIBUTION OF UNCLASSIFIED RTO PUBLICATIONS

NATO's Research and Technology Organization (RTO) holds limited quantities of some of its recent publications and those of the former AGARD (Advisory Group for Aerospace Research & Development of NATO), and these may be available for purchase in hard copy form. For more information, write or send a telefax to the address given above. **Please do not telephone**.

Further copies are sometimes available from the National Distribution Centres listed below. If you wish to receive all RTO publications, or just those relating to one or more specific RTO Panels, they may be willing to include you (or your organisation) in their distribution.

RTO and AGARD publications may be purchased from the Sales Agencies listed below, in photocopy or microfiche form. Original copies of some publications may be available from CASI.

NATIONAL DISTRIBUTION CENTRES

BELGIUM
Coordinateur RTO - VSL/RTO
Etat-Major de la Force Aérienne
Quartier Reine Elisabeth
Rue d'Evère, B-1140 Bruxelles

CANADA
Defence Scientific Information Services (DSIS)
Defence R&D Canada
Department of National Defence
Ottawa, Ontario K1A 0K2

CZECH REPUBLIC
Distribuční a informační středisko R&T
VTÚL a PVO Praha
Mladoboleslavská ul.
197 06 Praha 9-Kbely AFB

DENMARK
Danish Defence Research Establishment
Ryvangs Allé 1, P.O. Box 2715
DK-2100 Copenhagen Ø

FRANCE
O.N.E.R.A. (ISP)
29 Avenue de la Division Leclerc
BP 72, 92322 Châtillon Cedex

GERMANY
Streitkräfteamt / Abteilung III
Fachinformationszentrum der Bundeswehr, (FIZBw)
Friedrich-Ebert-Allee 34
D-53113 Bonn

GREECE (Point of Contact)
Hellenic Ministry of National Defence
Defence Industry Research & Technology General Directorate
Technological R&D Directorate
D.Soutsou 40, GR-11521, Athens

HUNGARY
Department for Scientific Analysis
Institute of Military Technology
Ministry of Defence
H-1525 Budapest P O Box 26

ICELAND
Director of Aviation
c/o Flugrad
Reykjavik

ITALY
Centro di Documentazione Tecnico-Scientifica della Difesa
Via XX Settembre 123a
00187 Roma

LUXEMBOURG
See Belgium

NETHERLANDS
NDRCC
DGM/DWOO
P.O. Box 20701
2500 ES Den Haag

NORWAY
Norwegian Defence Research Establishment
Attn: Biblioteket
P.O. Box 25, NO-2007 Kjeller

POLAND
Chief of International Cooperation Division
Research & Development Department
218 Niepodleglosci Av.
00-911 Warsaw

PORTUGAL
Estado Maior da Força Aérea
SDFA - Centro de Documentação
Alfragide
P-2720 Amadora

SPAIN
INTA (RTO/AGARD Publications)
Carretera de Torrejón a Ajalvir, Pk.4
28850 Torrejón de Ardoz - Madrid

TURKEY
Millî Savunma Başkanliği (MSB)
ARGE Dairesi Başkanliği (MSB)
06650 Bakanliklar - Ankara

UNITED KINGDOM
Defence Research Information Centre
Kentigern House
65 Brown Street
Glasgow G2 8EX

UNITED STATES
NASA Center for AeroSpace Information (CASI)
Parkway Center
7121 Standard Drive
Hanover, MD 21076-1320

SALES AGENCIES

NASA Center for AeroSpace Information (CASI)
Parkway Center
7121 Standard Drive
Hanover, MD 21076-1320
United States

The British Library Document Supply Centre
Boston Spa, Wetherby
West Yorkshire LS23 7BQ
United Kingdom

Canada Institute for Scientific and Technical Information (CISTI)
National Research Council
Document Delivery
Montreal Road, Building M-55
Ottawa K1A 0S2, Canada

Requests for RTO or AGARD documents should include the word 'RTO' or 'AGARD', as appropriate, followed by the serial number (for example AGARD-AG-315). Collateral information such as title and publication date is desirable. Full bibliographical references and abstracts of RTO and AGARD publications are given in the following journals:

Scientific and Technical Aerospace Reports (STAR)
STAR is available on-line at the following uniform resource locator:
http://www.sti.nasa.gov/Pubs/star/Star.html
STAR is published by CASI for the NASA Scientific and Technical Information (STI) Program
STI Program Office, MS 157A
NASA Langley Research Center
Hampton, Virginia 23681-0001
United States

Government Reports Announcements & Index (GRA&I)
published by the National Technical Information Service
Springfield
Virginia 22161
United States
(also available online in the NTIS Bibliographic Database or on CD-ROM)

Printed by St. Joseph Ottawa/Hull
(A St. Joseph Corporation Company)
45 Sacré-Cœur Blvd., Hull (Québec), Canada J8X 1C6

ISBN 92-837-0018-X